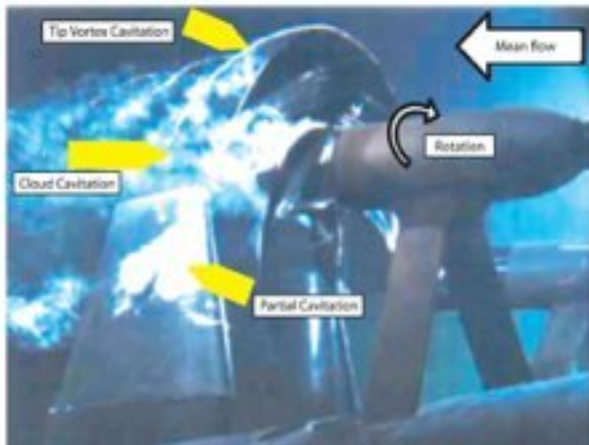


MULTIPHASE FLOW HANDBOOK



EDITED BY
CLAYTON T. CROWE



Taylor & Francis
Taylor & Francis Group

MULTIPHASE FLOW HANDBOOK

EDITED BY

CLAYTON T. CROWE



Taylor & Francis
Taylor & Francis Group
Boca Raton London New York

A CRC title, part of the Taylor & Francis imprint, a member of the
Taylor & Francis Group, the academic division of T&F Informa plc.

CRC Press
Taylor & Francis Group
6000 Broken Sound Parkway NW, Suite 300
Boca Raton, FL 33487-2742

© 2006 by Taylor & Francis Group, LLC
CRC Press is an imprint of Taylor & Francis Group, an Informa business

No claim to original U.S. Government works
Printed in the United States of America on acid-free paper
10 9 8 7 6 5 4 3 2 1

International Standard Book Number-10: 0-8493-1280-9 (Hardcover)
International Standard Book Number-13: 978-0-8493-1280-9 (Hardcover)

This book contains information obtained from authentic and highly regarded sources. Reprinted material is quoted with permission, and sources are indicated. A wide variety of references are listed. Reasonable efforts have been made to publish reliable data and information, but the author and the publisher cannot assume responsibility for the validity of all materials or for the consequences of their use.

No part of this book may be reprinted, reproduced, transmitted, or utilized in any form by any electronic, mechanical, or other means, now known or hereafter invented, including photocopying, microfilming, and recording, or in any information storage or retrieval system, without written permission from the publishers.

For permission to photocopy or use material electronically from this work, please access www.copyright.com (<http://www.copyright.com/>) or contact the Copyright Clearance Center, Inc. (CCC) 222 Rosewood Drive, Danvers, MA 01923, 978-750-8400. CCC is a not-for-profit organization that provides licenses and registration for a variety of users. For organizations that have been granted a photocopy license by the CCC, a separate system of payment has been arranged.

Trademark Notice: Product or corporate names may be trademarks or registered trademarks, and are used only for identification and explanation without intent to infringe.

Library of Congress Cataloging-in-Publication Data

Multiphase flow handbook / edited by Clayton T. Crowe.
p. cm.
Includes bibliographical references and index.
ISBN 0-8493-1280-9
1. Multiphase flow--Handbooks, manuals, etc. I. Crowe, C. T. (Clayton T.)

TA357.5.M84.M85 2005
620.1'064--dc22

2005048623

Visit the Taylor & Francis Web site at
<http://www.taylorandfrancis.com>

and the CRC Press Web site at
<http://www.crcpress.com>

Preface

Multiphase flow is the simultaneous flow of a mixture with two or more phases. They are encountered in many of our day to day activities. Numerous industrial and energy conversion processes rely on the flow of multiphase mixtures.

In 1982, Hemisphere Publishing produced *Handbook of Multiphase Systems* with G. Hetsroni as the editor in chief. This handbook provided information important to the design engineers, researchers, and students involved with multiphase flows. Since then, there have been numerous advances in analysis, modeling, and experimental methods. In particular, there has been such a surge of activity in numerical modeling that computational fluid mechanics is now regarded as a viable tool. The purpose of this handbook is to review the fundamental principles and provide the reader with current information useful in research, industrial design, and education.

I am indebted to the many contributors who spent considerable time and effort in this undertaking. Obviously, this Handbook would not have been possible without their interest in the project. In several instances, the crunch of time put stress on the contributors (and the editor-in-chief, in particular), but, finally, the work was accomplished on time. I particularly want to thank Professor Dyakowski for helping select the contributors for [Chapter 14](#). I also appreciate the efforts of Helena Redshaw, Preethi Cholmondeley and Cindy Carelli for responding to questions and monitoring the schedule. I also express my gratitude to the Production team of Macmillan India Limited for responding to some difficult issues.

I am also indebted to the support of my family, Chad and Brenda, Kevin, Zoe, and Ezra, and my dear friend Jeannette.

The Editor



Clayton T. Crowe is professor emeritus of mechanical and materials engineering at Washington State University. He has had over 30 years of experience in fluid mechanics and multiphase flows, and has been involved in a wide diversity of two-phase flow problems from geothermal power to food and materials processing. He developed the particle-source-in-cell (PSI-Cell) method for the numerical simulation of multiphase flow that has been used extensively in industry and in most commercial software simulations. He has over a hundred publications in the literature and has coauthored an undergraduate textbook, *Engineering Fluid Mechanics*, which is currently in its eighth edition. He has also been the lead author of a book on multiphase flows with droplets and particles published by CRC Press. He is an ASME Fellow and has received numerous awards for his work including the prestigious ASME Fluids Engineering Award. In May 2001, he received the Senior International Prize for Multiphase Flows.

Contributors

Alain Berlemont, Director of Research at National Center for Scientific Research (CNSR), UMR 6614-CORIA, University of Rouen, France.

Steven Ceccio, Associate Vice President for Research, Professor, Department of Mechanical Engineering and Applied Mechanics, University of Michigan, Ann Arbor, MI. Former member of Defense Studies Group, Institute for Defense Analysis.

Yi Cheng, Associate Professor, Department of Chemical Engineering, Tsinghua University, Beijing, China. Formerly Research Associate at Powder technology Research Center, Department of Chemical and Biochemical Engineering, University of Western Ontario, London, Ontario, Canada.

Jacob Chung, Andrew H. Hines Jr./Progress Energy Eminent Scholar Chair, Department of Mechanical and Aerospace Engineering, University of Florida, Gainesville, FL. ASME Fellow. Associate editor of the ASME Journal of Heat Transfer.

Candis Claiborn, Professor, Department of Civil and Environmental Engineering and Associate Dean for Research and Graduate Programs in College of Engineering, Washington State University, Pullman, WA.

James Cullivan, Institute of Particle Science and Engineering, School of Process, Environmental and materials Engineering, University of Leeds, North Yorkshire, UK. Previously with Camborne School of Mines, University of Exeter.

Shrikant Dhadapkar, Research Leader, Solids Processing Laboratory, The Dow Chemical Company, Freeport, TX. Vice-Chair Particle Technology Forum (AIChE), recipient of numerous technology awards at Dow.

Mingzhe Dong, Associate Professor, Petroleum Systems Engineering, University of Regina, Regina, Saskatchewan, Canada.

Yannis Drossinos, Senior Research Scientist, European Commission, Joint Research Centre, Ispra, Italy. Currently Visiting Professor in the School of Mechanical and Systems Engineering at University of Newcastle upon Tyne, United Kingdom.

Francis Dullien, Distinguished Professor Emeritus, Department of Chemical Engineering, University of Waterloo, Waterloo, Ontario, Canada. Fellow of the Royal Society of Canada and Fellow of the Chemical Institute of Canada. Member of Advisory Editorial Advisory Board for Transport in Porous Media and Journal of Porous Media.

Tomasz Dyakowski, Professor, School of Chemical Engineering and Analytical Science, University of Manchester, Manchester, UK. Also Manager of Applied Process Tomography Unit.

John Eaton, Professor and Vice Chairman, Department of Mechanical Engineering, Stanford University, Stanford, CA. ASME Fellow. Tau Beta Pi and Perin Awards for undergraduate teaching.

Said Elghobashi, Professor, Department of Mechanical and Aerospace Engineering, University of California, Irvine, CA. Fellow of the American Physical Society and American Society of Mechanical Engineers.

Thomas Frank, Head of Funded CFX Development Group, ANSYS Germany GmbH, Otterfing, Germany. Formerly Head of the Research Group on Numerical Methods for Multiphase Flows, Chemnitz University of Technology, Chemnitz, Germany.

Udo Fritsching, Director of research group for Multiphase Flow, Heat and Mass Transfer, Foundation Institute for Material Science, University of Bremen, Bremen, Germany.

Kamiel Gabriel, Associate Provost for Research and Graduate Programs, University of Ontario Institute of Technology, Oshawa, Ontario, Canada. Formerly established the Microgravity Research Group at the University of Saskatchewan.

John Grace, Professor of Chemical Engineering, University of British Columbia, Vancouver, British Columbia, Canada. Formerly Department Head and Dean of Graduate Studies. Currently holds Canada Research Chair and is a Fellow of the Canadian Academy of Engineering and of the Royal Society of Canada. Past winner of the R.S. Jane Award of the Canadian Society for Chemical Engineering.

Erling Hammer, Professor, Department of Physics, University of Bergen, Bergen, Norway. Formerly with the Chr. Michelsen Institute. Recipient of the STIMAREC Prize for malfunction analysis of pacemaker systems.

Yassin Hassan, Professor, Department of Nuclear Engineering and the Department of Mechanical Engineering, Texas A&M University, College Station, TX. Fellow of ASME and ANS. Recipient of the ASME George Westinghouse Gold Medal and the ANS Arthur Holly Compton Award.

Christos Housiadis, Senior Research Scientist, Institute of Nuclear Technology and Radiation Protection, "Demokritos" National Centre for Scientific Research, Athens, Greece. Formerly with the European Commission's Joint Research Center, Ispra, Italy and with the French Commissariat à l'Energie Atomique.

Shenggen Hu, Principle Research Engineer/Project Manager, Division of Energy Technology, Commonwealth Scientific and Industrial Research Organisation (CISRO), Brisbane, Australia.

Karl Jacob, Scientist/Technical Leader, Solids Processing Laboratory, The Dow Chemical Company, Midland, MI.

Geir Anton Johansen, Professor, Department of Physics and Technology, University of Bergen, Bergen, Norway. Also Scientific Advisor at Christian Michelsen Research AS.

Chikao Kanaoka, President, Ishikawa National College of Technology, Kitachujo, Isubata, Japan. Formerly Director, Institute of Nature and Environmental Technology, Kanazawa University, Kanazawa, Japan.

Satish Kandlikar, Gleason Professor of Mechanical Engineering at Rochester Institute of Technology, Rochester, NY. ASME Fellow, Associate editor for Heat Transfer Engineering, the ASME Journal of Heat Transfer and the Journal of Nanofluids and Microfluids.

Bo Leckner, Professor, Department of Energy and Environment, Chalmers University of Technology, Göteborg, Sweden. Previously acting Professor of Energy Conversion.

Eric Loth, Professor, Aerospace Engineering, University of Illinois at Urbana-Champaign, Urbana, IL. Professor of Aerospace Engineering, Willet Faculty Scholar, Associate Fellow of American Institute of Aeronautics and Astronautics.

Robert Lyczkowski, Chemical Engineer, Biotechnology and Biodefense Applications Group, Energy Systems Division, Argonne National Laboratory. AIChE Fellow. Editorial advisory board for Advances in Transport Processes.

Hisao Makino, Senior Research Scientist, Energy Engineering Research Laboratory, Staff (Director) Central Research Institute of Electric Power Industry (CRIEPI), Kanagawa, Japan. Formerly Director of CS Promotion Division of CRIEPI, Currently Director of the Combustion Society of Japan and the Society of Particle Technology in Japan. Also Editor of the Journal of the Society of Particle Technology, Japan.

Farzad Mashayek, Professor and Director of Graduate Studies, Department of Mechanical and Industrial Engineering, University of Illinois at Chicago, Chicago, IL. Received CAREER Award from U.S. National Science Foundation, Young Investigator Award from U.S. Office Of Naval Research and is Associate Fellow of AIAA.

Yoichiro Matsumoto, Vice Dean, School of Engineering, University of Tokyo, Tokyo, Japan. JSME Computational Mechanics Award, JSME Fluids Engineering Frontier Award, former editor of JSME International Journal Series B, former associate editor of ASME Journal of Fluids Engineering. JSME Fellow.

Efstathios (E.) Michaelides, Leo S. Weil Professor and Associate Dean for Graduate Studies and Director, Southcentral Regional Center of the National Institute for Global Environmental Change, School of Engineering, Tulane University, New Orleans, LA. Chair of ASME Fluids Engineering Division, ASME Fellow and ASME Freeman Scholar Award.

Paul Mort, Principal Engineer, Procter & Gamble Company, Cincinnati, OH. Chair of Particle Formation area in International Fine Particle Research Institute and the Particle Production area within the Particle Technology Forum.

René Oliemans, Director Multiphase Flow B.V., Part-time Professor Multiphase Flow, Delft University of Technology, Delft, Netherlands. Previously Department Manager for Engineering Physics and Mathematics, Shell Research, Amsterdam.

Yasuo Onishi, Chief Scientist, Environmental Technology Directorate, Pacific Northwest National laboratory, Richland, WA. Graduate Adjunct Faculty, Civil and Environmental Engineering Department, Washington State University.

Ghanem Oweis, Post-Doctoral Research fellow, Mechanical Engineering Department, University of Michigan, Ann Arbor, MI.

Bert Pots, Senior Staff Corrosion Engineer, Shell Global Solutions, Houston, TX. Formerly with Royal Dutch/Shell Laboratories in Amsterdam and Shell International Gas in London, UK.

Michael Reeks, Professor in Multiphase Flow, School of Mechanical and Systems Engineering, University of Newcastle upon Tyne, United Kingdom. Formerly Marie Curie Senior Research Fellow at the European Research Center at Ispra, Italy. Formerly associate editor of the Journal of Fluid Mechanics Research and ASME Journal of Fluids Engineering.

Ted Roberts, Senior Lecturer, School of Chemical Engineering and Analytic Science, University of Manchester, United Kingdom. Current chairman of the Society of Chemical Industry Electrochemical Technology Group.

Ilia Roisman, Chair of Fluid Mechanics and Aerodynamics, Technical University of Darmstadt, Darmstadt, Germany. Formerly Senior Lecturer at the Technion-IIT, Israel.

Akimi Serizawa, Professor, Division of Nuclear Engineering, Kyoto University, Kyoto, Japan. Heat Transfer Society of Japan Academic Award, Societe de Thermique International Award, Fellow of JSME and Atomic Society of Japan.

Olivier Simonin, Professor and Director of the Institute of Mechanics of Fluids of Toulouse, Toulouse, France.

Gabriel Tardos, Professor, Department of Chemical Engineering, The City College of the City University of New York, New York, NY., Formerly department chair.

Cameron Tropea, Chair of Fluid Mechanics and Aerodynamics, Technical University of Darmstadt, Darmstadt, Germany. Editor-in-chief of the journal Experiments in Fluids.

Yutaka Tsuji, Professor, Department of Mechanical Engineering and Graduate School of Engineering, Osaka University, Osaka, Japan. JSME Fluids Engineering Award, Fluid Science Research Award, AIChE Thomas Baron Award, JSME Medal, Jotaki Award from the Society of Powder Technology, JSME Fellow.

Timothy Troutt, Professor, School of Mechanical and Materials Engineering, Washington State University, Pullman, WA.

Gretar Tryggvason, Professor and Head of the Mechanical Engineering Department, Worcester Polytechnic Institute, Worcester, MA. Currently editor-in-chief of the Journal of Computational Physics, associate editor of the International Journal of Multiphase Flows and Fellow of the American Physical Society.

Berend van Wachem, Multiphase Flow Group, Chalmers University of Technology, Göteborg, Sweden.

Richard Williams, Anglo American plc Chair in Mineral and Process Engineering at the University of Leeds, Leeds, UK. Awarded the Ambrose Medal & Premium, the Isambard Kingdom Brunel Award, Beilby Prize and Gold Medal, Noel Webster Award and the Silver Medal of The Royal Academy of Engineering. Fellow of the Royal Academy of Engineering.

Hideto Yoshida, Professor, Department of Chemical Engineering and Graduate School of Engineering, Hiroshima University, Hiroshima, Japan. Editor of Chemical Engineering Journal in Japan.

Jesse Zhu, Director, Powder Technology Research Center, and Professor in the Department of Chemical and Biochemical Engineering, University of Western Ontario, London, Ontario, Canada. Canada Research Chair of Powder Technology Applications, Senior Ontario Research Chair for Ultrafine Powder Technology, Fellow of Canadian Society of Chemical Engineering.

Contents

1	Basic Concepts and Definitions	1-1
	<i>Clayton T. Crowe and Efstatios E. Michaelides</i>	
2	Gas–Liquid Transport in Ducts	2-1
	<i>R.V.A. Oliemans and B.F.M. Pots</i>	
3	Boiling and Condensation.	3-1
	<i>S.G. Kandlikar and J.N. Chung</i>	
4	Fluid–Solid Transport in Ducts	4-1
	<i>Shrikant Dhodapkar, Karl Jacobs, and Shenggen Hu</i>	
5	Fluidized Beds.	5-1
	<i>John R. Grace, Bo Leckner, Jesse Zhu, and Yi Cheng</i>	
6	Aerosol Flows	6-1
	<i>Yannis Drossinos and Christos Housiadas</i>	
7	Particle Separation Systems.	7-1
	<i>Chikao Kanaoka, Hideto Yoshida, and Hisao Makino</i>	
8	Spray Systems	8-1
	<i>Udo Fritsching</i>	
9	Dry Powder Flows	9-1
	<i>Gabriel I. Tardos and Paul R. Mort</i>	
10	Porous Media Flows	10-1
	<i>Mingzhe Dong and Francis A.L. Dullien</i>	
11	Microscale and Microgravity Flows	11-1
	<i>Akimi Serizawa and Kamiel S. Gabriel</i>	

12	Multiphase Interactions	12-1
	<i>G.F. Oweis, S.L. Ceccio, Y. Matsumoto, C. Tropea, I.V. Roisman, Y. Tsuji, R. Lyczkowski, T.R. Troutt, J. K. Eaton, and F. Mashayek</i>	
13	Modeling	13-1
	<i>E. Loth, G. Tryggvason, Y. Tsuji, S.E. Elghobashi, Clayton T. Crowe, A. Berlemont, M. Reeks, O. Simonin, Th. Frank, Y. Onishi, and B. van Wachem</i>	
14	Advanced Experimental Techniques	14-1
	<i>E.A. Hammer, G.A. Johansen, T. Dyakowski, E.P.L. Roberts, J.C. Cullinan, R.A. Williams, Y.A. Hassan, C.S. Claiborn</i>	

Basic Concepts and Definitions

1.1	General Features of Multiphase Flows	1-1
	Dispersed Phase and Separated Flows • Gas–Liquid Flows • Gas–Solid Flows • Liquid–Solid Flows • Three-Phase Flows • Scope of the Handbook	
1.2	Fundamental Definitions.....	1-3
	Volume Fraction and Densities • Superficial and Phase Velocities • Quality, Concentration, and Loading • Response Times • Stokes Number • Disperse Versus Dense Flows • Phase Coupling	
1.3	Size Distribution	1-10
	Size Distributions • Statistical Parameters • Frequently Used Size Distributions	
1.4	Interactions of Fluids with Particles, Drops, and Bubbles	1-17
	Introduction • Mass Transfer • Momentum Transfer • Heat Transfer • Multiple Particle/Droplet/Bubble Effects	

Clayton T. Crowe
Washington State University

Efstathios E. Michaelides
Tulane University

1.1 General Features of Multiphase Flows

Clayton T. Crowe

A phase refers to the solid, liquid, or vapor state of matter. A multiphase flow is the flow of a mixture of phases such as gases (bubbles) in a liquid, or liquid (droplets) in gases, and so on. The purpose of this Handbook is to provide back ground and state-of-the-art information on multiphase flows, including industrial applications, analytic and numerical analyses, and experimental techniques.

1.1.1 Dispersed Phase and Separated Flows

Dispersed phase flows are flows in which one phase consists of discrete elements, such as droplets in a gas or bubbles in a liquid. The discrete elements are not connected. In a separated flow, the two phases are separated by a line of contact. An annular flow is a separated flow in which there is a liquid layer on the pipe wall and a gaseous core. In other words, in a separated flow one can pass from one point to another in the same phase while remaining in the same medium.

1.1.2 Gas–Liquid Flows

Gas–liquid flows occur in many applications. The motion of bubbles in a liquid as well as droplets in a conveying gas stream are examples of gas–liquid flows. Bubble columns are commonly used in several process industries. Atomization to generate small droplets for combustion is important in power

generation systems. Also droplet formation and impaction are important in spray forming for materials processing. Steam-water flows in pipes and heat exchangers are very common in power systems such as fossil fuel plants and nuclear reactors. Gas–liquid flows in pipes can assume several different configurations ranging from bubbly flow to annular flow, in which there is a liquid layer on the wall and a droplet-laden gaseous core flow.

1.1.3 Gas–Solid Flows

Gas–solid flows are usually considered to be a gas with suspended solid particles. This category of flow includes pneumatic transport as well as fluidized beds. Pollution control devices, such as cyclone separators and electrostatic precipitators, are based on the principles of gas–solid flows. The combustion of coal in fossil-fuel power systems depends on the dispersion and burning of coal particles. The micron-size particles in solid-propellant rocket exhausts affect the performance of the rocket. Another example of a gas–solid flow is the motion of particles down a chute or inclined plane. These are known as granular flows where particle–particle and particle–wall interactions are much more important than the forces due to the interstitial gas. If the particles become motionless, the problem reduces to flow through a porous medium in which the viscous force on the particle surfaces is the primary mechanism affecting the gas flow; an example is a pebble-bed heat exchanger. In this case, even though one phase is not “flowing,” it will be included as a type of multiphase flow.

1.1.4 Liquid–Solid Flows

Liquid–solid flows consist of flows in which solid particles are carried by the liquid, and are referred to as slurry flows. Slurry flows cover a wide spectrum of applications that range from the transport of coals and ores to the flow of mud. These flows can also be classified as dispersed phase flows and are the focus of considerable interest in engineering research. The flow of liquid through a solid is another example of porous media flow.

1.1.5 Three-Phase Flows

Three-phase flows are also encountered in engineering problems. For example, bubbles in a slurry flow give rise to three phases flowing together. Not much work has been reported in the literature on three-phase flows.

For many years, the design of multiphase systems has been based primarily on empiricism. However, more sophisticated measurement techniques have led to improved process control and the quantification of fundamental parameters. The increase in computational capability has enabled the development of numerical models that can be used to complement engineering system design. The improvement of numerical models is a rapidly growing field of technology, which have far-reaching benefits in upgrading the operation and efficiency of current processes, and in supporting the development of new and innovative technologies.

1.1.6 Scope of the Handbook

This Handbook is designed to provide a background for engineers and scientists new to the field and to serve as a source of information on current technology for those familiar with the field. Chapter 1 introduces fundamental definitions including size distributions. It also includes the fundamentals of particle–fluid–bubble interaction, which is the kernel of multiphase flows. Chapter 2 addresses gas–liquid flows and provides information on methods of calculating system parameters. Chapter 3 deals with boiling and condensation in multiphase systems. Chapter 4 covers pneumatic transport and slurry transport, which are very important to multiphase systems. Chapter 5 addresses fluidized beds, covering the basic concepts, heat and mass transfer, and applications. The flow of aerosol particles is presented in Chapter 6 with application to respiratory systems. The removal of dust and droplets from gas streams is covered in Chapter 7. The dynamics and features of sprays are covered in Chapter 8, with applications to energy conversion, food processing, and metallurgical processes. Granular and porous media flows are

introduced in [Chapters 9](#) and [10](#). The flow of multiphase systems in microgravity and microscale dimensions are the subjects of [Chapter 11](#). Basic multiphase interactions are addressed in [Chapter 12](#), including cavitation, bubble physics, droplet breakup, particle–particle and particle–wall interactions, erosion, turbulent dispersion, turbulence modulation, and combustion. [Chapter 13](#) introduces numerical modeling, including direct simulation, Lagrangian and two-fluid modeling, the PDF approach and applications to cyclone separators, slurry flow, and fluidized beds. [Chapter 14](#), the final chapter in the Handbook, addresses the current state of the art in instrumentation for measuring multiphase flows.

1.2 Fundamental Definitions

Clayton T. Crowe

This section introduces a few definitions that are fundamental to multiphase flows. For convenience, the term discrete or dispersed phase will be used for the particles, droplets, or bubbles, while carrier or continuous phase will be used for the carrier fluid. The dispersed phase is not materially connected.

1.2.1 Volume Fraction and Densities

The volume fraction of the dispersed phase is defined as

$$\alpha_d = \lim_{\delta V \rightarrow V^o} \frac{\delta V_d}{\delta V} \quad (1.1)$$

where δV_d is the volume of the dispersed phase in volume δV . The volume δV^o is the limiting volume that ensures a stationary average (Crowe et al., 1998). Unlike a continuum, the volume fraction cannot be defined at a point. Equivalently, the volume fraction of the continuous phase is

$$\alpha_c = \lim_{\delta V \rightarrow V^o} \frac{\delta V_c}{\delta V} \quad (1.2)$$

where δV_c is the volume of the continuous phase in the volume. This volume fraction is sometimes referred to as the void fraction and in the chemical engineering literature, the volume fraction of the dispersed phase is often referred to as holdup. By definition, the sum of the volume fractions must be unity, i.e.,

$$\alpha_d + \alpha_c = 1 \quad (1.3)$$

The bulk density (or apparent density) of the dispersed phase is the mass of the dispersed phase per unit volume of mixture or, in terms of a limit, is defined as

$$\bar{\rho}_d = \lim_{\delta V \rightarrow V^o} \frac{\delta M_d}{\delta V} \quad (1.4)$$

where δM_d is the mass of the dispersed phase. The bulk density is related to the material density ρ_d by

$$\bar{\rho}_d = \alpha_d \rho_d \quad (1.5)$$

The sum of the bulk densities for the dispersed and continuous phases is the mixture density

$$\bar{\rho}_d + \bar{\rho}_c = \rho_m \quad (1.6)$$

1.2.2 Superficial and Phase Velocities

For multiphase flow in a pipe, the superficial velocity of each phase is the mass flow rate \dot{M} of that phase divided by the pipe area A and material density. The superficial velocity for the dispersed phase is

$$U_d = \frac{\dot{M}_d}{\rho_d A} \quad (1.7)$$

In other words, it is the velocity of the phase if the phase occupied the whole pipe area. The phase velocity u is the actual velocity of the phase. The superficial velocity and the phase velocity are related by the volume fraction

$$U_d = \alpha_d u_d \quad (1.8)$$

The same relations hold for the carrier phase.

1.2.3 Quality, Concentration, and Loading

Another parameter important to the definition of dispersed-phase flows is the dispersed-phase mass concentration,

$$C = \frac{\bar{\rho}_d}{\bar{\rho}_c} \quad (1.9)$$

which is the ratio of the mass of the dispersed phase to that of the continuous phase in a mixture. This parameter will sometimes be referred to as the particle or droplet mass ratio. Sometimes dispersed-phase volume fraction is designated as concentration.

The quality of a liquid-vapor mixture where the liquid in the dispersed phase is

$$x = \frac{\bar{\rho}_d}{\bar{\rho}_m} \quad (1.10)$$

Another term in common use in multiphase flows is loading, which is the ratio of mass flux of the dispersed phase to that of the continuous phase:

$$z = \frac{\dot{m}_d}{\dot{m}_c} \quad (1.11)$$

However, loading has also been used to denote concentration. The terminology is not uniform, as each author appears to have his/her own choice of symbols for multiphase flow parameters.

1.2.4 Response Times

The response time of a particle or droplet to changes in flow velocity or temperature is important in establishing nondimensional parameters to characterize the flow. The momentum response time relates to the time required for a particle or droplet to respond to a change in velocity. The equation of motion for a spherical particle in a gas is given by

$$m \frac{dv}{dt} = \frac{1}{2} C_D \frac{\pi d^2}{4} \rho_c (u - v) |u - v| \quad (1.12)$$

where v is the particle velocity and u the gas velocity. Defining the dispersed-phase Reynolds number as

$$Re_r = \frac{\rho_c d |u - v|}{\mu_c} \quad (1.13)$$

and dividing through by the particle mass gives

$$\frac{dv}{dt} = \frac{18\mu}{\rho_d d^2} \frac{C_D Re_r}{24} (u - v) \quad (1.14)$$

where μ_c is the viscosity of the gas (continuous phase). For the limits of low Reynolds numbers (Stokes flow), the factor $C_D Re_r / 24$ approaches unity. The other factor has dimensions of reciprocal time and defines the momentum (velocity) response time

$$\tau_v = \frac{\rho_d d^2}{18\mu} \quad (1.15)$$

So the equation can be rewritten as

$$\frac{dv}{dt} = \frac{1}{\tau_v}(u - v) \quad (1.16)$$

The solution to this equation for constant u and an initial particle velocity of zero is

$$v = u[1 - \exp(-t/\tau_v)] \quad (1.17)$$

Thus, the momentum response time is the time required for a particle to be released from rest to achieve 63% ($e-1/e$) of the freestream velocity. This characteristic time has been used extensively in the multiphase flow literature. Often τ_p is used to denote velocity response time.

The thermal response time relates to the responsiveness of a particle or droplet to changes in temperature in the carrier fluid. The equation for particle temperature, assuming that the temperature is uniform throughout the particle, and radiative effects are negligible, is

$$mc_d \frac{dT_d}{dt} = Nu \pi k_c d(T_c - T_d) \quad (1.18)$$

where Nu is the Nusselt number, c_d the specific heat of the particle material and k_c the thermal conductivity of the continuous phase. Dividing through by the particle mass and specific heat gives

$$\frac{dT_d}{dt} = \frac{Nu}{2} \frac{12k_c}{\rho_p c_d D^2} (T_c - T_d) \quad (1.19)$$

For low Reynolds numbers, the ratio $Nu/2$ approaches unity; the other factor is the thermal response time defined as

$$\tau_T = \frac{\rho_d c_d d^2}{12k_c} \quad (1.20)$$

Thus the thermal equation for the particle becomes

$$\frac{dT_d}{dt} = \frac{1}{\tau_T} (T_c - T_d) \quad (1.21)$$

which is the time required for a particle to achieve 63% of a step change in the temperature of the carrier phase.

The momentum and thermal response times are related through the properties of the fluid and the particles, i.e.,

$$\frac{\tau_v}{\tau_T} = \frac{2}{3} \frac{c_c}{c_d} \frac{1}{Pr} \quad (1.22)$$

where Pr is the Prandtl number. For gases, the Prandtl number is of the order of unity; thus response times are of the same order of magnitude. For a liquid, the Prandtl number can be of the order of 10^2 , which means that velocity equilibrium is achieved much more rapidly than thermal equilibrium in a liquid.

Even though the above relations for the ratio of response times have been derived for low Reynolds number (Stokes flow), the ratio changes little for higher Reynolds numbers.

1.2.5 Stokes Number

The Stokes number is a very important parameter in fluid-particle flows. The Stokes number related to the particle velocity is defined as

$$Stk = \frac{\tau_v}{\tau_F} \quad (1.23)$$

where τ_F is the characteristic time of the flow field. If $Stk \ll 1$, the response time of the particles is much less than the characteristic time associated with the flow field. In this case the particles will have ample time to respond to changes in flow velocity and, the particle and fluid velocities will be nearly equal (velocity equilibrium). On the other hand, if $Stk \gg 1$, then the particle will have essentially no time to respond to the fluid velocity changes and the particle velocity will be little affected by fluid velocity change. The symbol St is often used to denote the Stokes number of the particle but symbol Stk has been used here to avoid confusion with the Strouhal number. Also Stk is used more frequently in the aerosol literature.

An approximate relationship for the particle/fluid velocity ratio as a function of the Stokes number can be obtained from the “constant lag” solution. The velocity ratio is expressed as $\phi = v/u$ and is assumed to vary slowly with time. By substituting this value into the particle motion equation, Eq. (1.16), one has

$$\phi \frac{du}{dt} = \frac{u}{\tau_V} (1 - \phi) \quad (1.24)$$

The carrier-phase acceleration can be approximated by

$$\frac{du}{dt} \sim \frac{u}{\tau_F} \quad (1.25)$$

which, when substituted into Eq. (1.24) yields

$$\phi Stk \sim (1 - \phi) \quad (1.26)$$

Finally, solving for ϕ , gives

$$\phi = \frac{u_d}{u_c} \sim \frac{1}{1 + Stk} \quad (1.27)$$

One notes that, as $St_V \rightarrow 0$, the particle velocity approaches the carrier-phase velocity and as $Stk \rightarrow \infty$, the particle velocity approaches zero, i.e., the particle velocity is unaffected by the fluid. The same idea extends to Stokes number based on thermal response time.

1.2.6 Disperse Versus Dense Flows

A disperse flow, is one in which the particle motion is controlled by the fluid forces (drag and lift). A dense flow, on the other hand, is one in which the particle motion is controlled by collisions. A qualitative estimate of the disperse or dense nature of the flow can be made by comparing the ratio of momentum response time of a particle to the time between collisions. Thus, the flow can be considered disperse if

$$\frac{\tau_V}{\tau_C} < 1 \quad (1.28)$$

where τ_C is the average time between particle-particle collisions, because the particles have sufficient time to respond to the local fluid dynamic forces before the next collision. On the other hand, if

$$\frac{\tau_V}{\tau_C} > 1 \quad (1.29)$$

then the particle has no time to respond to the fluid dynamic forces before the next collision and the flow is dense. The time between collisions is generally estimated by using relationships from kinetic theory.

There is a further classification of dense flows: collision- and contact-dominated. In collision-dominated flow the collisions between the particles control the features of the flow, such as in a fluidized bed. In a contact dominated flow, the particle motion is controlled by continuous contact such as in a granular flow.

1.2.7 Phase Coupling

An important concept in the analysis of multiphase flows is coupling. If the flow of one phase affects the other while there is no reverse effect, the flow is said to be one-way-coupled. If there is a mutual effect between the flows of both phases, then the flow is two-way-coupled.

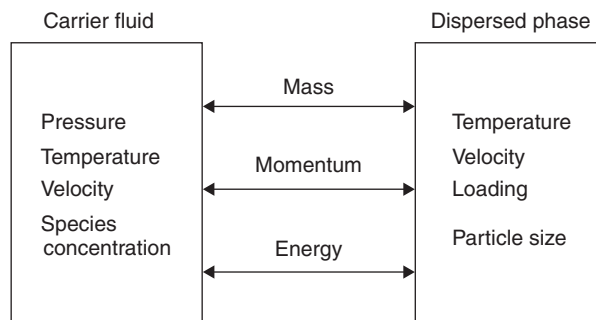


FIGURE 1.1 Schematic diagram of coupling effects.

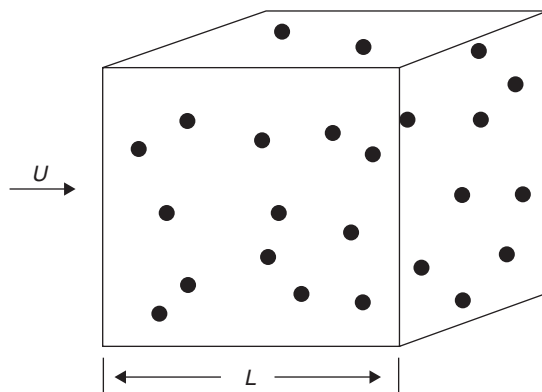


FIGURE 1.2 Dispersed phase elements in a volume.

A schematic diagram of coupling is shown in Figure 1.1. The carrier phase is described by the density, temperature, pressure, and velocity field. However, it may be important to include the concentrations of the gaseous species in a gas phase. The particle or droplet phase is described by concentration, size, temperature, and velocity field. Coupling can take place through mass, momentum, and energy transfer between phases. Mass coupling is the addition of mass through evaporation or the removal of mass from the carrier stream by condensation. Momentum coupling is the result of an interaction force, such as a drag force, between the dispersed and continuous phase. Momentum coupling can also occur with momentum addition or depletion due to mass transfer. Energy coupling occurs through heat transfer between phases. Thermal and kinetic energy can also be transferred between phases owing to mass transfer. Also, the presence of particles and droplets can also affect the carrier phase turbulence. Obviously, analyses based on one-way coupling are straightforward. One must estimate through experience or parameter magnitude if two-way coupling is important.

1.2.7.1 Mass Coupling

Suppose there are n droplets per unit volume in a box with side L as shown in Figure 1.2. Each droplet is evaporating at a rate \dot{m} . Thus, the mass generated by the dispersed phase per unit time due to evaporation is

$$\dot{M}_d = nL^3\dot{m} \quad (1.30)$$

The mass flux of the continuous phase through this volume is

$$\dot{M}_c \sim \bar{\rho}_c u L^2 \quad (1.31)$$

A mass coupling parameter is defined as

$$\Pi_{\text{mass}} = \frac{\dot{M}_d}{\dot{M}_c} \quad (1.32)$$

If $\Pi_{\text{mass}} \ll 1$, then the effect of mass addition to the continuous phase would be insignificant and mass coupling could be treated as one-way coupling. This ratio can be expressed as

$$\frac{\dot{M}_d}{\dot{M}_c} \sim \frac{\bar{\rho}_d}{\bar{\rho}_c} \frac{L\dot{m}}{um} \quad (1.33)$$

The ratio \dot{m}/m scales as the reciprocal of a characteristic evaporation, burning, or condensation time, τ_m ; Thus, the ratio in Eq. (1.32) can be rewritten as

$$\Pi_{\text{mass}} \sim C \frac{L}{u\tau_m} \quad (1.34)$$

By taking L as some characteristic dimension of the system, this ratio can be used to assess the importance of mass coupling on the continuous-phase flow. Note that the ratio $\tau_m u/L$ can be regarded as the ratio of a time associated with mass transfer to a time characteristic of the flow. Thus, the ratio can be thought of as the Stokes number associated with mass transfer

$$Stk_{\text{mass}} = \frac{\tau_m u}{L} \quad (1.35)$$

hence, the mass transfer parameter can be expressed as

$$\Pi_{\text{mass}} = \frac{C}{Stk_{\text{mass}}} \quad (1.36)$$

Thus, if the droplet phase mass concentration and the mass exchange rate of the dispersed phase are low (large τ_m and Stk_{mass}), mass coupling can probably be neglected.

1.2.7.2 Momentum Coupling

The importance of momentum coupling can be assessed by comparing the drag force due to the dispersed phase with the momentum flux of the continuous phase. The momentum coupling parameter can be defined as

$$\Pi_{\text{mom}} = \frac{D_d}{\text{Mom}_c} \quad (1.37)$$

where D_d is the drag force due to the disperse phase in the volume and Mom_c is the momentum flux through the volume. The drag associated with disperse phase in a volume with side L is

$$D_d = nL^3 3\pi \mu d(u - v) \quad (1.38)$$

based on Stokes drag. The momentum flux of the continuous phase is given by

$$\text{Mom}_c = \bar{\rho}_c u^2 L^2 \quad (1.39)$$

The momentum coupling parameter can be expressed as

$$\Pi_{\text{mom}} = \frac{nmL}{\bar{\rho}_c u \tau_V} \left(1 - \frac{v}{u} \right) \quad (1.40)$$

where m is the mass of an individual element of the dispersed phase. The product nm is the bulk phase density of the dispersed phase and the velocity ratio can be related to the Stokes number through Eq. (1.27).

$$\Pi_{\text{mom}} = \frac{C}{1 + Stk_{\text{mom}}} \quad (1.41)$$

which shows the correct limit as the Stokes number approaches zero. Momentum coupling effects become less important for small concentrations (loadings) and large Stokes numbers.

1.2.7.3 Energy Coupling

Energy coupling follows the same model as used for mass and momentum coupling. The significance of energy coupling can be assessed by comparing the heat transfer to (or from) the dispersed phase and the energy flux of the continuous phase. The energy coupling parameter is defined as

$$\Pi_{\text{ener}} = \frac{\dot{Q}_d}{\dot{E}_c} \quad (1.42)$$

Obviously, if $\Pi_{\text{ener}} \ll 1$, then energy coupling is unimportant.

The heat transfer associated with the dispersed-phase elements in volume L^3 is

$$\dot{H}_d = nL^3\pi Nu k_c d(T_d - T_c) \quad (1.43)$$

where Nu is the Nusselt number and k_c is the thermal conductivity of the continuous phase. The energy flux of the continuous phase is

$$\dot{E}_c = \bar{\rho}_c u c_p T_c L^2 \quad (1.44)$$

where c_p is the specific heat of the continuous phase. The thermal coupling parameter can be expressed as

$$\Pi_{\text{ener}} \sim \frac{C}{Stk_T} \left(1 - \frac{T_c}{T_d} \right) \quad (1.45)$$

where St_T is the Stokes number based on the thermal response time ($Stk_T = u\tau_T/L$). As in the case of momentum coupling parameter, there is an indeterminacy as the Stokes number approaches zero. Using the same arguments as before, the energy coupling parameter can be expressed as

$$\Pi_{\text{ener}} = \frac{C}{Stk_T + 1} \quad (1.46)$$

For gaseous flows, the momentum and thermal response times are of the same order; hence,

$$\Pi_{\text{mom}} \sim \Pi_{\text{ener}}$$

and justification of one-way coupling for momentum usually justifies one-way coupling for energy transfer.

If most of the energy transfer in a system is associated with latent heat in the dispersed phase, there is another form of the energy coupling parameter that may be appropriate:

$$\Pi_L \sim C \frac{1}{Stk_{\text{mass}}} \frac{h_L}{c_p T_c} \quad (1.47)$$

which is the mass coupling parameter with an additional factor, $h_L / c_p T_c$. This factor can be large, causing energy transfer due to phase change to be important even though mass transfer itself is unimportant. In many spray problems, the energy coupling due to phase change may be the only two-way coupling that must be included in developing an analysis for a gas-droplet flow.

1.2.7.4 Three- and Four-Way Coupling

Further definitions of coupling include three-way coupling in which wakes and other disturbances in the carrier phase affect the motion of the discrete phase (particles and droplets). Four-way coupling addresses the situation where, in addition to discrete-phase–carrier-phase interaction, particle–particle collisions also affect the multiphase motion. This is the situation in dense flows. Four-way coupling effects become important when particle volume fraction exceeds 10^{-3} . A schematic diagram of coupling is shown in [Figure 1.3](#). Strictly speaking, four-way coupling does not apply to granular flows because the effect of the interstitial fluid is negligible.

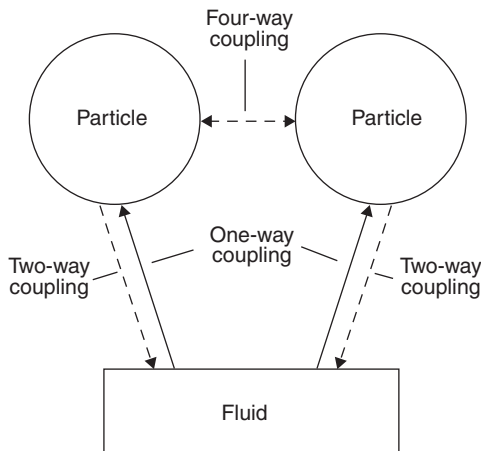


FIGURE 1.3 Schematic diagram of coupling.

However, the definition of three-way coupling could be included in the general category of two-way coupling. If this were the case, three-way coupling would be the case where particle–particle interaction is important.

1.3 Size Distribution

Clayton T. Crowe

Droplets or particle sizes are important parameters that govern the flow of a dispersed two-phase mixture. Hence, it is important to have a basic knowledge of the statistical parameters relating to particle size distributions. For spherical particles or droplets, a measure of the size is the diameter; for nonspherical particles, an equivalent diameter must be selected to quantify the size.

The most general definition of the spread of the particle size distribution is monodisperse or polydisperse. A monodisperse distribution, is one in which the particles are close to a single size, whereas polydisperse distribution suggests a wide range of particle sizes. In monodisperse distribution, the standard deviation is less than 10% of the mean particle diameter.

1.3.1 Size Distributions

Particle or droplet size distributions can be classified as discrete or continuous. The continuous size distribution derives from the discrete distribution as the sampling interval approaches zero.

1.3.1.1 Discrete Size Distribution

Assume that the sizes of many particles in the sample have been measured by a technique, such as photography. One would choose size intervals, Δd that would be large enough to contain many particles, yet small enough to obtain sufficient detail. The representative size for the interval could be the diameter corresponding to the midpoint of the interval. The number of particles in each size interval is counted, recorded, and divided by the total number of particles in the sample. The results are plotted in the form of a histogram (bar chart) shown in Figure 1.4. This is identified as the discrete number frequency distribution for the particle size.* The ordinate corresponding to each size interval is known as the number frequency $\tilde{f}_n(d_i)$. The sum of the number frequency over all the size categories is unity, i.e.,

$$\sum_{i=1}^N \tilde{f}_n(d_i) = 1 \quad (1.48)$$

* This frequency distribution is often referred to as the probability density function or “pdf.”

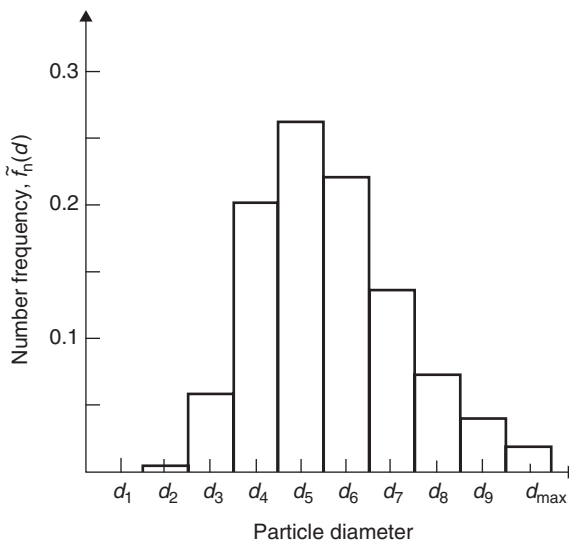


FIGURE 1.4 Discrete number frequency distribution of particle diameter.

where N is the total number of intervals. When the distribution satisfies Eq. (1.48), it is a normalized distribution.

The number-average particle diameter of the distribution is obtained from

$$\bar{d}_n = \sum_{i=1}^N d_i \tilde{f}_n(d_i) \quad (1.49)$$

and the number variance is defined as[†]

$$\sigma_n^2 = \sum_{i=1}^N (d_i - \bar{d}_n)^2 \tilde{f}_n(d_i) \quad (1.50)$$

The variance is a measure of the spread of the distribution; a large variance implies a wide distribution of sizes. An alternative expression for the number variance is

$$\sigma_n^2 = \sum_{i=1}^N d_i^2 \tilde{f}_n(d_i) - \bar{d}_n^2 \quad (1.51)$$

which is sometimes more convenient for calculations. The standard deviation is the square root of the variance.

$$\sigma_n = \sqrt{\sigma_n^2} \quad (1.52)$$

Another approach to describe size distribution is to use the particle or droplet mass (or volume) *in lieu* of the number as the dependent variable. Thus, the mass of each particle would be obtained, or inferred, from measurement and the fraction of mass associated with each size interval would be used to construct the distribution. This is known as the discrete mass frequency distribution and identified as $\tilde{f}_m(d_i)$. With this distribution, one can calculate the mass-average particle diameter and mass variance as

$$\bar{d}_m = \sum_{i=1}^N d_i \tilde{f}_m(d_i) \quad (1.53)$$

$$\sigma_m^2 = \sum_{i=1}^N (d_i - \bar{d})^2 \tilde{f}_m(d_i) = \sum_{i=1}^N d_i^2 \tilde{f}_m(d_i) - \bar{d}_m^2 \quad (1.54)$$

* The sum should be multiplied by the factor $N/(N-1)$ to account for one degree of freedom removed by using the average diameter. However for $N \gg 1$ we have $N/(N-1) \sim 1$.

A very large number of particles or droplets have to be counted to achieve a reasonably smooth frequency distribution function. This is feasible with modern experimental techniques.

Another commonly used method to quantify particle size is the cumulative distribution, which is the sum of the frequency distribution. The cumulative number distribution associated with size d_k is

$$\tilde{F}_n(d_k) = \sum_{i=1}^{d_k} \tilde{f}_n(d_i) \quad (1.55)$$

The cumulative number distribution corresponding to the number frequency distribution shown in Figure 1.4 is illustrated in Figure 1.5. The value of \tilde{F} is the fraction of particles with sizes less than d_k . The value of \tilde{F}_n for the largest particle is equal to unity for normalized distributions. Both cumulative number and mass distributions can be generated from the corresponding frequency distributions.

1.3.1.2 Continuous Size Distributions

If the size intervals were made progressively smaller, then in the limit as Δd approaches zero the continuous frequency function obtained, is

$$f_n(d) = \lim_{\Delta d \rightarrow 0} \frac{\tilde{f}_n(d)}{\Delta d} \quad (1.56)$$

The number fraction of particles with diameters between d and $d + d(d)$ is given by the differential quantity $f_n(d) d(d)$. The variation of the frequency distribution with particle size is a continuous function as shown in Figure 1.6. Similarly, the differential quantity $f_m(d) d(d)$ is the fraction of particle mass associated with sizes between d and $d + d(d)$

If the distribution is normalized, then the area under the frequency distribution curve is unity:

$$\int_0^{d_{\max}} f(d) d(d) = 1 \quad (1.57)$$

where d_{\max} is the maximum particle size.

The continuous cumulative distribution is obtained from the integral of the continuous frequency distribution

$$F_n(d) = \int_0^d f_n(\lambda) d\lambda \quad (1.58)$$

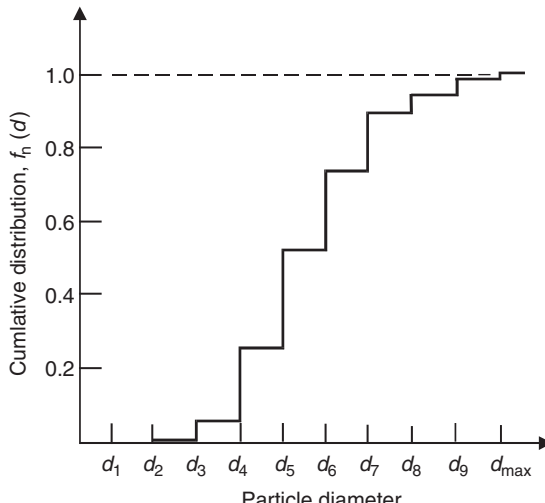


FIGURE 1.5 Discrete cumulative distribution of particle diameter.

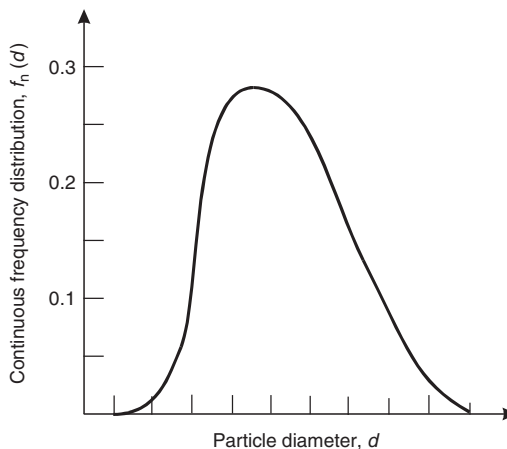


FIGURE 1.6 Continuous number distribution of particle diameter.

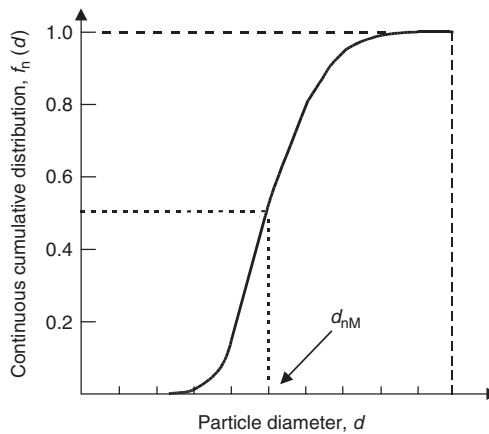


FIGURE 1.7 Continuous cumulative distribution of particle diameter.

and illustrated as the S-shaped curve in Figure 1.7. By definition, the cumulative distribution approaches unity as the particle size approaches the maximum size.

The equivalent continuous frequency and cumulative distributions for mass (or volume) fraction are obvious.

In general, size data are not available as a continuous distribution. It is common practice to consider the data obtained for a discrete distribution as values on a curve for a continuous distribution and to proceed accordingly to evaluate the appropriate statistical parameters.

1.3.2 Statistical Parameters

There are several parameters used to quantify distribution functions. Those used most commonly for dispersed phase flows are presented below.

1.3.2.1 Mode

The mode corresponds to the point where the frequency function is a maximum. The modes of a number and mass frequency distributions for a given sample will not be the same. A distribution that has two local

maxima is referred to as a “bimodal” distribution. The corresponding parameter for a discrete size distribution is the most frequent diameter, i.e., the size that corresponds to the highest value for the frequency curve.

1.3.2.2 Mean

The mean of a continuous distribution is analogous to the average of a discrete distribution. The mean is calculated from the frequency distribution by evaluating the integral:

$$\mu = \int_0^{d_{\max}} df(d) d(d) \quad (1.59)$$

However, there is a number mean μ_n or mass mean μ_m size depending on the frequency function used. This is also called the arithmetic mean, diameter d_{AM} . Other mean diameters include the surface mean

$$d_{SM} = \left[\int_0^{d_{\max}} d^2 f(d) d(d) \right]^{1/2} \quad (1.60)$$

and the volume mean

$$d_{VM} = \left[\int_0^{d_{\max}} d^3 f(d) d(d) \right]^{1/3} \quad (1.61)$$

1.3.2.3 Geometric and Harmonic Mean Diameters

The geometric mean diameter is defined as

$$\ln d_{GM} = \int_0^{d_{\max}} f(d) (\ln d) d(d) \quad (1.62)$$

The geometric mean corresponds to the mode of the log-normal distribution. The harmonic mean is obtained from

$$d_{HM} = \left\{ \int_0^{d_{\max}} [f(d)/d] d(d) \right\}^{-1} \quad (1.63)$$

It is important where surface area is an important characteristic of the particulate product.

1.3.2.4 Sauter Mean Diameter

The Sauter mean diameter (SMD) is encountered frequently in the spray and atomization literature. It is defined as

$$d_{32} = \frac{\int_0^{D_{\max}} d^3 f_n(d) d(d)}{\int_0^{D_{\max}} d^2 f_n(d) d(d)} \quad (1.64)$$

The SMD can be regarded as the ratio of the particle volume to surface area in a distribution that may have physical significance in some applications.

1.3.2.5 Variance

The variance of the distribution is calculated from

$$\sigma^2 = \int_0^{d_{\max}} (d - \mu)^2 f(d) d(d) \quad (1.65)$$

or by the equivalent expression

$$\sigma^2 = \int_0^{d_{\max}} d^2 f(d) d(d) - \mu^2 \quad (1.66)$$

Once again, the variance can be based on the number or mass distribution for particle size. As mentioned, previously, the variance is a measure of the spread of the distribution. The standard deviation is the square root of the variance and has dimensions of diameter.

A distribution can be classified as monodisperse if

$$\frac{\sigma}{\mu} < 0.1.$$

1.3.2.6 Median

The median diameter, d_M , corresponds to the diameter for which the cumulative distribution is 0.5. The number median diameter, d_{nM} , is shown in Figure 1.7. The corresponding mass median diameter, d_{mM} , is determined from the cumulative mass distribution function.

1.3.3 Frequently Used Size Distributions

There are several size distribution functions frequently used to correlate particle or droplet size measurements. The characteristics of these distributions are discussed below.

1.3.3.1 Log-Normal Distribution

The log-normal number frequency distribution (Marshall, 1954) can be expressed as

$$f_n(d) = \frac{1}{\sqrt{2\pi}\sigma_o} \exp\left[-\frac{1}{2}\left(\frac{\ln d - \ln d_{nM}}{\sigma_o}\right)^2\right] \frac{1}{d} \quad (1.67)$$

where d_{nM} is the number median diameter and σ_o is the geometric standard deviation. The corresponding log-normal mass frequency distribution is

$$f_m(d) = \frac{1}{\sqrt{2\pi}\sigma_o} \exp\left[-\frac{1}{2}\left(\frac{\ln d - \ln d_{mM}}{\sigma_o}\right)^2\right] \frac{1}{d} \quad (1.68)$$

where d_{mM} is the mass median diameter. The geometric standard deviation can be found by plotting the cumulative distribution on log-probability coordinates, which yields a straight line with a positive slope. The value for σ_o can be found from

$$\sigma_o = \ln \frac{d_{84\%}}{d_M} \quad (1.69)$$

where $d_{84\%}$ is the diameter corresponding to the 84th percentile on the log-probability plot and d_M is the median diameter (value at the 50% point). The value for σ_o is the same for both the number and mass distributions.

A very useful relationship for manipulation of the log-normal distribution is

$$dk_M \exp(\sigma_o^2 k^2 / 2) = \frac{1}{\sqrt{2\pi}\sigma_o} \int_0^\infty dk \exp\left[-\frac{1}{2}\left(\frac{\ln d - \ln d_M}{\sigma_o}\right)^2\right] \frac{d(d)}{d} \quad (1.70)$$

or

$$d_M^k \exp(\sigma_o^2 k^2 / 2) = \int_0^\infty d^k f(d) d(d) \quad (1.71)$$

which can be used to evaluate the various statistical parameters.

1.3.3.2 Upper-Limit Log-Normal Distribution

An off-shoot of the log-normal distribution is the upper-limit log-normal distribution (Mugele and Evans, 1951), which is designed to set a maximum particle diameter as the upper limit of the distribution. The distribution is represented by

$$f_n(d) = \frac{1}{\sqrt{2\pi}\sigma_o} \exp\left[-\frac{1}{2}\left(\frac{\ln(ad) - \ln(d_{\max} - d)}{\sigma_o}\right)^2\right] \frac{1}{d} \quad (1.72)$$

where d_{\max} is the maximum diameter in the distribution, a is a constant, and σ_o is the geometric standard deviation. As the particle diameter varies from 0 to d_{\max} , the argument of the exponent varies from $-\infty$ to $+\infty$. The value of a is related to the median diameter by

$$a = \frac{d_{\max}}{d_M} - 1$$

The standard deviation can be obtained from the slope of the log-probability plot of the data. This distribution has been used to fit data from spray nozzles.

1.3.3.3 Square-Root Normal Distribution

The square-root normal distribution is given as (Tate and Marshall, 1953)

$$f_n(d) = \frac{1}{2\sqrt{2\pi\sigma^2}} \exp\left[-\frac{(\sqrt{d} - \bar{\sqrt{d}})^2}{2\sigma^2}\right] \quad (1.73)$$

where σ is the variance of the \sqrt{d} distribution. This distribution appears to fit data from vane-type atomizers. Care must be taken when using the distribution because it does not have the tails of a normal distribution, so relationships for normal distributions may not be applicable here.

1.3.3.4 Rosin–Rammler Distribution

The Rosin–Rammler distribution (Mugele and Evans, 1951) is frequently used for representing droplet size distributions in sprays. It is expressed in terms of the cumulative mass distribution in the form

$$F_m(d) = 1 - \exp\left[-\left(\frac{d}{\delta}\right)^n\right] \quad (1.74)$$

where δ and n are two empirical constants. Note that $F_m(0) = 0$ and $F_m(\infty) = 1$.

The empirical constants can be determined by plotting the cumulative distribution on log–log coordinates. By taking the logarithm of the above equation twice gives

$$\ln[-\ln(1 - F_m(d))] = n \ln d - n \ln \delta \quad (1.75)$$

Thus, the slope, n , of the line is obtained by plotting $-\ln[1 - F_m(D)]$ versus the diameter on log–log coordinates. The parameter δ can be obtained by using n and the mass median diameter as

$$\delta = \frac{d_{mM}}{0.693^{1/n}} \quad (1.76)$$

The mass frequency distribution is obtained by taking the derivative of the cumulative distribution:

$$f_m(d) = \frac{dF_m}{dd} = e^{-(D/\delta)^n} \frac{n}{\delta} \left(\frac{d}{\delta}\right)^{n-1} \quad (1.77)$$

A very useful function for evaluating the statistical parameters for the Rosin–Rammler distribution is the gamma function, which is defined as

$$\Gamma(t) = \int_0^\infty e^{-\lambda} \lambda^{t-1} d\lambda \quad (1.78)$$

It can be shown that

$$\int_0^\infty n d^{\alpha} \left(\frac{d}{\delta}\right)^{n-1} \exp\left[-\left(\frac{d}{\delta}\right)^n\right] d\left(\frac{d}{\delta}\right) = \delta^\alpha \Gamma\left(\frac{\alpha}{n} + 1\right) \quad (1.79)$$

to

$$\delta^\alpha \Gamma\left(\frac{\alpha}{n} + 1\right) = \int_0^\infty d^\alpha f_m(d) dd \quad (1.80)$$

can be used to find statistical parameters from the Rosin–Rammler distribution.

1.3.3.5 Nukiyama–Tanasawa Distribution

The Nukiyama–Tanasawa distribution represents a more general distribution for which the Rosin–Rammler distribution is a special case. The Nukiyama distribution is

$$f_n(d) = Bd^2 \exp(-Cd^q) \quad (1.81)$$

where B , C , and q are parameters chosen to fit the distribution. In a spray, q can vary from 1/6 to 2 with higher values corresponding to a narrower distribution.

1.3.3.6 Log-Hyperbolic Distribution

In some studies regarding sprays, it has been shown that neither the log-normal nor the Rosin–Rammler distributions fit the data sufficiently well. Two droplet size distributions fitted with a Rosin–Rammler distribution may have the same parameters but the actual distribution may be quite different.

One of the shortcomings of both the log-normal and Rosin–Rammler distributions is the representation of the tails of the distribution (values of the frequency function for large and small values of the independent variable). Another distribution which is a better fit for the tails of the distributions is the log-hyperbolic distribution proposed by Barndorff-Nielsen (1977). The form of the frequency function is

$$f_n(d) = A \exp[-\alpha \sqrt{\delta^2 + (d - \mu)^2} + \beta(d - \mu)] \quad (1.82)$$

where α , β , δ , and μ are fitting parameters and x is the random variable which, in this case, is the logarithm of the particle diameter. The coefficient A is a normalization factor that is related to the parameters by

$$A = \frac{\sqrt{\alpha^2 - \beta^2}}{2\alpha\delta K_1(\delta\sqrt{\alpha^2 - \beta^2})}$$

where K_1 is the third-order Bessel function of the third kind. The logarithm of the frequency function is

$$\ln f_n(d) = \ln A - \alpha \sqrt{\delta^2 + (d - \mu)^2} + \beta(d - \mu) \quad (1.83)$$

which is the equation of a hyperbola. For $(d - \mu)/\delta < 0$ the slope of the asymptote is $\delta + \beta$, while for $(d - \mu)/\delta > 0$ the slope of the asymptote is $-\alpha + \beta$. Thus, the logarithm of the frequency data can be plotted versus $\ln D$ and the slopes of the asymptotes can be measured to find α and β . The parameter μ is the mode of the distribution. The value for δ must be obtained from some fitting procedure.

1.4 Interactions of Fluids with Particles, Drops, and Bubbles

Efstathios E. Michaelides

1.4.1 Introduction

Because the sphere is the simplest of the three-dimensional shape, heat transfer and fluid dynamics problems pertaining to a sphere have been the subjects of the first applications of most theoretical methods on the solution of the governing equations, as well as of intellectual curiosity among the scientists. These problems belong to the class of the most fundamental problems in fluid dynamics, heat transfer, and mass transfer, and have attracted the attention of many mathematicians, physicists, and engineers. They are also subjects that have numerous practical applications including combustion and propulsion, chemical reactions and catalysis, mixing and separation, boiling and condensation, environmental sedimentation and resuspension as well as biological flows. The transport of momentum, heat, and mass are of primary interest in all of these processes, which are often expressed in terms of *transport coefficients* or in terms of dimensionless parameters of these coefficients. For example, the instantaneous loss or gain of mass of a sphere during any process may be expressed in terms of the mass transfer coefficient, h_M or its dimensionless representation, the

Sherwood number, Sh , and the material properties of the sphere and the carrier fluid:

$$\dot{m} = \frac{dm_s}{dt} = \pi h_M d^2 \rho_f (Y_s - Y_\infty) = \pi (Sh) d \mathcal{D} \rho_f (Y_s - Y_\infty) \quad (1.84)$$

Similarly, the instantaneous temperature change of the sphere, in the case of convective heating (when radiation is negligible) may be expressed in terms of the heat transfer coefficient, h , or its dimensionless representation, the Nusselt number:

$$m_s c_{ps} \frac{dT_s}{dt} = \dot{Q} = \pi h d^2 (T_s - T_\infty) = \pi Nu k_f (T_s - T_\infty) \quad (1.85)$$

Finally, the equation of motion of a sphere may be expressed by Newton's second law in terms of all the instantaneous forces that act on the sphere. These forces are the hydrodynamic drag force on the sphere, F_H (which is composed of two parts, the drag and lift) and the gravity/buoyancy force F_B . The former may be written in terms of two dimensionless factors: the drag coefficient, C_D and the lift coefficient, C_L . The equation of motion becomes:

$$m_s \frac{dv_i}{dt} = F_{Di} + F_{Li} + F_{bi} = \frac{1}{8} \pi d^2 \rho_c C_D (u_i - v_i) |u_i - v_i| + \frac{1}{8} \pi d^2 \rho_c C_L \sqrt{(u_m - v_m)(u_m - v_m)} \frac{e_{ijk} (u_k - v_k) \Omega_j}{\sqrt{\Omega_i \Omega_l}} + \frac{1}{6} (\rho_s - \rho_c) d^3 g_i \quad (1.86)$$

Therefore, for the performance of any calculations on motion of the sphere one would need accurate information on the transport coefficients, i.e., drag coefficient, lift coefficient, heat transfer coefficient, and mass transfer coefficient. The numerical values of these coefficients emanate from analytical or numerical results and from experimental data.

This section intends to be a succinct presentation of the known analytical, experimental, and numerical results that pertain to the transport processes between a carrier fluid and bubbles, drops or particles, and are useful for the performance of engineering calculations. In particular, mass transfer, momentum transfer, and heat transfer from a particle, bubble, or drop with the carrier fluid will be presented. For a historical background and a more extensive description of the development of these subjects one may consult a recent article by Michaelides (2003). Of the other recent studies, the main results on the momentum transfer from a sphere to a fluid as well as the energy and mass transfer at wide ranges of Reynolds and Peclet numbers may be found in several treatises and monographs, such as the ones by Leal (1992), Kim and Karila (1991), Crowe et al. (1998), Sirignano (1999), or the forthcoming one by Michaelides (2005). Also in specific review articles, such as the ones by Leal (1980) on the motion of fine particles at low Reynolds numbers, Brady and Bossis (1988) on the Stokesian formulation of suspensions, Feuillebois (1989) on the asymptotic methods applied to the equation of motion of spheres in viscous liquids, Sirignano (1993) on drops and sprays, Stock (1996) on particulate dispersion, Michaelides and Feng (1996) on the analogies between the heat flux and the motion of particles, Michaelides (1997) on the transient equation of motion of particles, Loth (2000) on the numerical methods for the treatment of the motion of bubbles, drops, and particles, Koch and Hill (2001) on the inertia effects of suspended particles, and Michaelides (2003) on the transient equations of motion and heat transfer. Some older monographs by Levich (1962), Clift et al. (1978), Happel and Brenner (1963), Govier and Aziz (1977), and Soo (1990) contain very useful theoretical and empirical results on the motion and heat/mass transfer processes from spheres as well as irregularly shaped particles.

1.4.2 Mass Transfer

1.4.2.1 Evaporation, Sublimation, and Condensation

Consider a sphere of radius a , inside a carrier gas of density ρ_p in a spherical system of coordinates that follow the center of the sphere. The carrier gas and the sphere have different chemical composition and their species are denoted by c and l , respectively. Mass is allowed to cross the boundary of the sphere due to one of the processes of sublimation, evaporation, or condensation. Because of this, the gaseous phase is

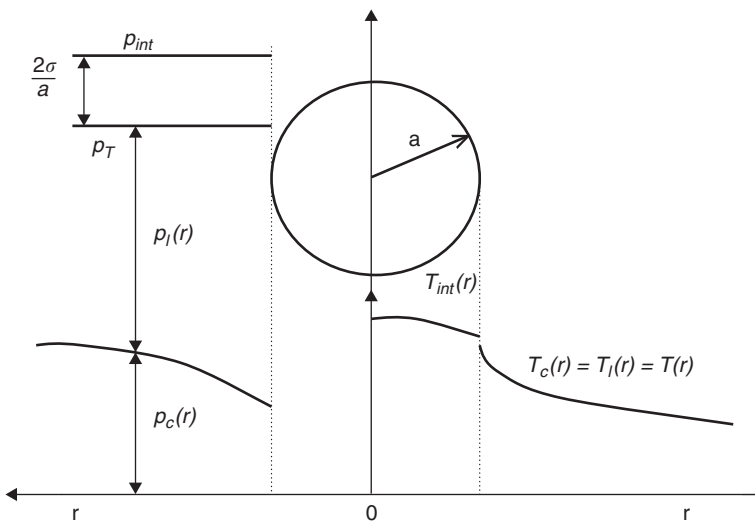


FIGURE 1.8 Pressure and temperature fields developed in the vicinity of a drop carried by a fluid of different composition.

composed of both the species l and c, while the sphere, which may be either solid or liquid, is composed solely of the species l. Figure 1.8 is a schematic diagram of such a process. The directions and numerical signs of the pressure and temperature gradients in this figure are such that they correspond to the case of condensation. The total pressure in the gaseous mixture is constant and equal to p_T ; the total pressure is comprised of two parts: the partial pressure, or vapor pressure, of the species l, p_l , and the partial pressure of the carrier gaseous species c, p_c . In all the transport processes that are pertinent to mass transfer to or from the sphere, both partial pressures are functions of the radial direction, r :

$$p_T = p_c(r) + p_l(r) \quad (1.87)$$

If the carrier phase is composed of a number of species, c_1, c_2, c_3, \dots , as for example in the case of air, then the total pressure is the sum of all the partial pressures of these species:

$$p_T = \sum_i p_{ci}(r) + p_l(r) \quad (1.88)$$

When the sphere is a liquid drop, the pressure in the interior of the drop would be higher than p_T by the amount contributed by the surface tension:

$$p_{int} = p_T + \frac{2\sigma}{a} \quad (1.89)$$

In most practical applications the radius of the sphere, a , is large enough to satisfy the condition $p_T \gg 2\sigma/a$. Hence, the internal pressure, p_{int} , is approximately equal to the total pressure in the gas phase, p_T . Thermodynamic equilibrium implies that the temperatures of the species l and c anywhere in the gaseous mixture are equal, i.e., $T_c(r) = T_l(r) = T(r)$, where $r > a$. The temperature inside the sphere may be non-uniform and, hence, a function of the radial distance. This temperature will be denoted as $T_{int}(r)$, where $r < a$.

At the surface of the sphere, there is a phase transition, liquid–vapor or solid–vapor that normally occurs within a very short layer of molecular dimensions. The phase of the matter in this film layer is not well defined. Hence, the material and thermodynamic properties within this molecular layer are not well defined. For this reason, they are depicted by the dashed lines in Figure 1.8. It is known that the specific properties of matter exhibit a jump discontinuity within this layer, e.g., from liquid enthalpy to vapor enthalpy. The intensive properties of matter, temperature, and pressure, exhibit a discontinuity of much

smaller magnitude that is connected to the molecular transition. This discontinuity of the intensive properties is not noticeable unless the Knudsen number of the flow is higher than 0.001 (see [Section 1.4.3.5](#) for more details) and the molecular effects play an important role in the behavior of the sphere.

With the exception of very fast combustion processes, in most of the practical applications involving drops and particles that undergo mass, momentum, or heat exchange transfer with a carrier fluid, the thermodynamic relaxation time is much shorter than the characteristic time of the sphere. For this reason, thermodynamic equilibrium is normally established at the interface of the sphere and the carrier fluid. In the case where the interface may be considered sufficiently flat for the surface tension to have a negligible impact, the partial pressure of the vapor and the temperature of the vapor at the interface are related via the Clausius–Clapeyron equation:

$$\frac{dp_l}{dT} \Big|_a = \frac{h_{fg}}{T(a) \left[\frac{1}{\rho_v(a)} - \frac{1}{\rho_s(a)} \right]} \quad (1.90)$$

where the symbols in parentheses denote arguments of functions and the derivative must be evaluated at the conditions of the interface $r = a$. Thus, $T(a)$ is the temperature at the interface, $\rho_v(a)$ is the density of the species l in its vapor phase at the interfacial pressure and temperature, and $\rho_s(a)$ is the density of the material in the sphere, evaluated also at the interfacial pressure and temperature. Therefore, the temperature and vapor pressure at the interface of the sphere are related by the so-called “saturation relation,” $p_l = p_{\text{sat}}(T)$. The function $p_{\text{sat}}(T)$ for any of the commonly used materials may be obtained in tabular form in thermodynamics texts or in tables of properties. It must be emphasized that this thermodynamic relationship between the prevailing pressure and temperature applies only at the surface of the sphere $r = a$. Thus, in general $p_l(r)$ and $T_l(r)$ are two independent functions that are only related at $r = a$.

As in the case of the pressure ([Eq. \[1.89\]](#)), the surface tension may have an influence on the saturation relation. In this case, the value for the partial pressure of the vapor at the interface must be corrected as follows:

$$p_l(a) = p_{\text{sat}}(T(a)) \exp \left[\frac{2\sigma(T(a))}{a\rho_s(a)R_v T(a)} \right] \quad (1.91)$$

where the parentheses denote arguments of functions, ρ_s is the density of the material of the sphere and R_v is the specific gas constant for the material species of the vapor, l, i.e., $R_v = R/M_l$ and $R = 8.314 \text{ kJ/kg K}$. The term in the square brackets is sometimes called the “Kelvin number,” Ke , and in most practical applications it is insignificant ($Ke \ll 1$). Hence, in most practical applications, $p_l(a) \approx p_{\text{sat}}(T(a))$. A glance at [Eq. \(1.91\)](#) proves that the Kelvin number and, hence the effects of surface tension become significant when $a \rightarrow 0$, a condition met at the last stages of combustion, evaporation, or sublimation of a sphere.

Within the gaseous phase that comprises the vapor of the sphere and the carrier fluid, the mole fraction of the vapor and the mole fraction of the components of the carrier fluid at any distance $r > a$ are defined in terms of their partial pressures as follows:

$$X_v(r) = \frac{p_l(r)}{p_T} \quad \text{and} \quad X_{ci}(r) = \frac{p_{ci}(r)}{p_T} \quad (1.92)$$

Obviously, at any point the condition applies that the sum of all the mole fractions in the gaseous mixture is equal to one. At the surface of the sphere, where the interface is, the pressure $p_l(a)$ is equal to the saturation pressure at the prevailing temperature, $T(a)$. Hence, the mole fraction of the vapor at the interface is determined from the knowledge of the total pressure and the temperature of the sphere.

The mole fraction of any species, denoted by letter j , and the mass fraction of this species, Y_j , are related through the molecular weights, \mathfrak{M}_j , of all the species present in the gaseous mixture as follows:

$$Y_j = \frac{X_j \mathfrak{M}_j}{\sum_i X_i \mathfrak{M}_i} \quad \text{and} \quad X_j = \frac{\frac{Y_j}{\mathfrak{M}_j}}{\sum_i \frac{Y_j}{\mathfrak{M}_i}} \quad (1.93)$$

where the sum in the denominator, denoted by i , is over all the species that are present in the gaseous phase, carrier gas, and vapor. As in the case of the mole fractions, at any point outside the sphere, the sum of all the mass fractions is equal to one.

In the cases of sublimation and evaporation, the variation of the intensive vapor properties $T_v(r)$ and $p_v(r)$ would have been in the opposite direction from the one shown in Figure 1.8. In such processes, any mass flow rate from the sphere to the gas results in a radial velocity w from the surface of the sphere to the gas, which is described by the following conservation equation

$$d^2 \frac{d\rho_f}{dt} + \frac{d(\rho_f d^2 w)}{dr} = 0 \quad (1.94)$$

where d , when it is not part of a differential operator such as d/dt or d/dr , is the diameter of the sphere and r is the radial coordinate. In a quasi-steady case, where the density of the carrier fluid may be considered to be constant, the above equation may be integrated on the surface of the sphere to yield the mass flow rate from the sphere to the fluid:

$$\frac{dm}{dt} = -\pi d^2 \rho_f w \Big|_s \quad (1.95)$$

where the velocity w must be evaluated with respect to the surface of the sphere at the gas side. Since the radial velocity w is an outward velocity with respect to the control volume that encloses the sphere, the negative sign signifies that mass is transferred from the sphere to the fluid when w is positive.

Evaporation, condensation, sublimation, or chemical reactions are the basic processes for the mass transfer to or from a sphere. Processes without chemical reactions will be examined in this section, while processes with chemical reactions, such as combustion, are mentioned briefly in the next section and will be examined in more detail in Section 12.7. It must be recalled that, when mass transfer occurs without chemical reactions, the driving force for the process is the concentration difference of the species the sphere is composed of, evaluated at the surface of the sphere and the concentration of the same species in the carrier fluid, evaluated far from the sphere. For example, in the case of an evaporating water droplet in air, the driving force is the difference of the specific humidity at the surface of the sphere and the specific humidity of the carrier fluid, sufficiently far from the sphere. The former is a function of the temperature and pressure at the surface of the sphere, while the latter is a property of the carrier fluid. If the carrier fluid becomes saturated with water vapor, there is no such difference and, hence, no evaporation would take place.

The mass flux at the surface of an evaporating or condensing droplet in a binary mixture is given by Fick's law:

$$\rho_f w = -\rho_f \mathfrak{D} \frac{\partial Y_s}{\partial r} \Big|_s \quad (1.96)$$

where \mathfrak{D} is the diffusion coefficient of the droplet species in the carrier fluid. For a droplet of diameter $d = 2a$, the gradient of mass fraction of any species at the surface is proportional to the difference between the mass fraction at the surface and in the free stream and inversely proportional to the droplet diameter. Therefore:

$$\frac{\partial Y_s}{\partial r} \Big|_s \sim \frac{Y_\infty - Y_s}{d} \quad (1.97)$$

where Y_∞ is the mass fraction of the species in the free stream far from the droplet. A combination of the last two equations yields:

$$\frac{dm}{dt} \sim \pi \rho_f \mathfrak{D} d (Y_\infty - Y_s) \quad (1.98)$$

The parameter that makes this expression an equation is the Sherwood number, Sh . Thus the following expression may be obtained for the rate of mass transfer from a sphere:

$$\frac{dm}{dt} = Sh \pi \rho_f \mathfrak{D} d (Y_\infty - Y_s) \quad (1.99)$$

With no mass advection resulting from forced or free convection processes, pure diffusion dominates the mass transfer process and, hence, $Sh = 2$. The effect of fluid advection and relative velocity between the droplet and the conveying fluid is often represented by the so-called Ranz–Marshall relation:

$$Sh = 2 + 0.6Re_r^{1/2} Sc^{1/3} \quad (1.100)$$

where Re_r is the Reynolds number based on the relative velocity and Sc is the Schmidt number.

Since the mass transfer process from a sphere is closely related to the heat transfer process via the well-known heat/mass transfer analogy, and also since the evaporation, sublimation and condensation processes are driven by temperature differences many of the results for the mass transfer will be combined with the heat transfer results in Section 1.4.3.5.

1.4.2.2 Chemical Reactions

When chemical reactions take place, the mass transfer from the sphere is related to the reaction rate for the fuel, ξ . This is expressed in units of the reaction per unit time. If we assume that the spherical symmetry of the drop is retained during the processes of mass transfer and chemical reaction, the mass conservation equation for the fuel, the oxidant, and an inert component, such as nitrogen, which may be present in the reaction, may be written as follows:

1. For the fuel, whose mass fraction is denoted by the subscript F:

$$\frac{\partial}{\partial t}(\rho d^2 Y_F) + \frac{\partial}{\partial r}(\rho u d^2 Y_F) - \frac{\partial}{\partial r}\left(\rho d^2 \mathfrak{D} \frac{\partial Y_F}{\partial r}\right) = \rho d^2 \xi \quad (1.101)$$

The last term in the above equation is a measure of the mass of the fuel that is consumed by the reaction.

2. For an oxidant, whose mass fraction is denoted by the subscript O,

$$\frac{\partial}{\partial t}(\rho d^2 Y_O) + \frac{\partial}{\partial r}(\rho u d^2 Y_O) - \frac{\partial}{\partial r}\left(\rho d^2 \mathfrak{D} \frac{\partial Y_O}{\partial r}\right) = \rho d^2 F_{OF} \xi \quad (1.102)$$

where F_{OF} is the stoichiometric ratio of oxidant to the fuel (mass of oxidant per unit mass of the fuel) that is consumed by the reaction.

3. For an inert component, such as nitrogen, the total mass is conserved and the right-hand side of the corresponding equation is equal to zero:

$$\frac{\partial}{\partial t}(\rho d^2 Y_N) + \frac{\partial}{\partial r}(\rho u d^2 Y_N) - \frac{\partial}{\partial r}\left(\rho d^2 \mathfrak{D} \frac{\partial Y_N}{\partial r}\right) = 0 \quad (1.103)$$

4. The mass conservation equation for any product, denoted by the subscript P, which appears as a result of the reaction, is

$$\frac{\partial}{\partial t}(\rho d^2 Y_P) + \frac{\partial}{\partial r}(\rho u d^2 Y_P) - \frac{\partial}{\partial r}\left(\rho d^2 \mathfrak{D} \frac{\partial Y_P}{\partial r}\right) = -\rho d^2 (F_{OF} + 1) \xi \quad (1.104)$$

From the definition of the mass fractions for all the components of the reaction, one may also derive the following identity, which is useful as a closure equation:

$$Y_F + Y_O + Y_N + Y_P = 1 \quad (1.105)$$

The mass balance for any species at the surface of an evaporating or reacting droplet may be imposed on all the species that may be present in the droplet and the gas. Because of the loss of liquid mass, there is a radial convection at the surface that is often called *Stefan convection*. The Stefan convection and diffusion on the side of the gas is equal to the rate of convection on the liquid side:

$$\dot{M}_{is} - \rho \pi d^2 \mathfrak{D} \left. \frac{\partial Y_i}{\partial r} \right|_s = \dot{M} \delta_{if} \quad (1.106)$$

where the subscript i extends over the species of fuel, oxidant, inert, and products and δ_{if} is the Kronecker delta.

More details on the combustion processes and methods for calculating the mass transfer from a burning drop are presented in Section 12.7. Since the subject of mass transfer from a sphere is closely connected to the processes of evaporation or sublimation and since the corresponding “blowing effects” influence significantly the momentum transfer and the hydrodynamic forces exerted on the droplet, the relevant correlations and useful information on engineering computations will be presented in Sections 1.4.3.4 and 1.4.4.3 that specifically pertain to the blowing effects.

1.4.3 Momentum Transfer

The functional form and expressions for the hydrodynamic force exerted by a fluid on a sphere will be presented in this section. For this reason, the body forces that may act on the sphere will not be included in the analysis. These forces may be added later to the hydrodynamic force and all the other forces acting on the sphere to yield the Lagrangian equation of motion. We consider the rectilinear flow of a viscous fluid around a sphere of radius a ($d = 2a$). The fluid velocity field is nonuniform and given by the function $u(x_p, t)$ outside the volume occupied by the sphere. If the sphere is solid, its velocity is only a function of the time and is given by the functional relationship $v(t)$. If the sphere is composed of a viscous fluid (as in bubbles and drops) the velocity is given by the functional relationship $v(x_p, t)$, which signifies that there will be fluid circulation inside the fluid sphere. In both cases, the governing equations for the process of mass and momentum exchange are: (1) the continuity, or mass conservation, equation

$$\frac{\partial \rho_f}{\partial t} + \rho_f \nabla \cdot \mathbf{u} = 0 \quad (1.107)$$

and (2) the momentum conservation equation

$$-\nabla p + \mu_f \nabla^2 \mathbf{u} = \rho_f \left(\frac{\partial \mathbf{u}}{\partial t} + \mathbf{u} \cdot \nabla \mathbf{u} \right) \quad (1.108)$$

Equation (1.108) may be rendered dimensionless by using the characteristic time (or timescale) for the sphere $\tau_s = 4a^2 \rho_f / \mu_f$ which pertains to viscous diffusion effects. This yields the following expression:

$$-\nabla^* p^* + \nabla^{*2} \mathbf{u}^* = \frac{\partial \mathbf{u}^*}{\partial t^*} + \text{Re}(\mathbf{u}^* \cdot \nabla^* \mathbf{u}^*) \quad (1.109)$$

Depending on the details of the process, the characteristic velocity for the definition of u^* is either the characteristic velocity of the fluid itself, or the relative velocity of the sphere with respect to the fluid. Therefore, one may define two Reynolds numbers for the flow, Re , and Re_r , which are given as follows:

$$Re = \frac{2a\rho_f U}{\mu_f} \quad \text{and} \quad Re_r = \frac{2a\rho_f |U - V|}{\mu_f} \quad (1.110)$$

Equations (1.108) and (1.109) are sometimes called “the Oseen equations.” They are the full momentum equation and contain the nonlinear advection term of the fluid flow, which is the last term in the two equations. Oseen (1913) first successfully used this term in the development of an expression for the hydrodynamic force on a sphere. In the case of creeping flow in a quiescent fluid ($Re \ll 1$), the nonlinear advection term may be neglected in comparison to the viscous term. Then the momentum equation becomes linear and reads as follows:

$$\rho_f \frac{\partial \mathbf{u}}{\partial t} = -\nabla p + \mu_f \nabla^2 \mathbf{u} \quad (1.111)$$

or in dimensionless form:

$$-\nabla^* p^* + \nabla^{*2} \mathbf{u}^* = \frac{\partial \mathbf{u}^*}{\partial t^*} \quad (1.112)$$

This is the type of equation that was first solved by Stokes (1845, 1851) in its steady state and, for this reason, it is sometimes called the Stokes equation and the flow field that emanates from it is known as the

"Stokes flow," A name that is also used often for this type of flow is "creeping flow." Creeping or Stokes flow basically implies that the relative Reynolds number of the flow, Re_r , is very small and, hence, all the inertia effects that are represented by the nonlinear term of the governing equation may be neglected.

1.4.3.1 Stokes Flow

A characteristic of the Stokes equation is that neither the Reynolds number nor any other dimensionless parameter appears in it. Its steady-state solution yields the Stokes expression for the hydrodynamic force ($F = 6\pi a v \mu_f$), while the full unsteady solution yields the so-called Boussinesq–Basset expression (Michaelides, 2003). Many industrial applications with small particles and drops in viscous fluids occur at $Re_r \ll 1$ and therefore fall into the category of the Stokes flow.

Consider the motion of a viscous, fluid sphere inside a fluid of different viscosity that moves slowly enough for the condition $Re_r \ll 1$ to be satisfied. The fluid velocity is uniform, equal to U , far from the sphere, and the no-slip condition applies on the surface of the sphere. The center of coordinates is coincident with the center of the sphere and the flow domain is much larger than the diameter of the sphere. This is referred to sometimes as an "infinite domain." This problem was solved independently by Hadamard (1911) and Rybczynski (1911), who were able to obtain the following analytical expressions for the stream functions inside and outside the sphere:

$$\Psi_i = \frac{Ur^2(a^2 - r^2) \sin^2 \theta}{4(\lambda + 1)a^2} \quad (1.113.)$$

and

$$\Psi_o = \frac{Ur^2 \sin^2 \theta}{2} \left[1 - \frac{(3\lambda + 2)a}{2(\lambda + 1)r} + \frac{\lambda a^3}{2(\lambda + 1)r^3} \right] \quad (1.114)$$

where λ is the ratio of the dynamic viscosities, μ_s/μ_f . The case of a solid sphere is given at the limit $\lambda \rightarrow \infty$ and the case of an inviscid sphere, which is a good approximation of a gas bubble in a viscous liquid, is given at the limit $\lambda \rightarrow 0$. It is apparent that, even at this very low relative velocity, the presence of the sphere in a flow field creates a disturbance in the velocity field of the fluid. For a small solid sphere under Stokesian conditions, this velocity disturbance may be determined from the above two equations, which yield the following expressions for the radial and transverse velocity components of the carrier fluid:

$$u_r = U \cos \theta \left[1 - \frac{(3\lambda + 2)a}{2(\lambda + 1)r} + \frac{\lambda a^3}{2(\lambda + 1)r^3} \right] \quad (1.115)$$

and

$$u_\theta = -U \sin \theta \left[1 - \frac{(3\lambda + 2)a}{4(\lambda + 1)r} + \frac{\lambda a^3}{4(\lambda + 1)r^3} \right] \quad (1.116)$$

It is evident that the velocity field described by the above two equations yields $\mathbf{u} = 0$ on the surface of the sphere and $\mathbf{u} = U$ far away from the solid sphere.

Integration of the normal and shear stresses on the surface of the fluid sphere that result from Eqs. (1.115) and (1.116) gives the hydrodynamic force exerted by the fluid on the viscous sphere as follows:

$$F_D = 2\pi a v \mu_f \frac{3\lambda + 2}{\lambda + 1} \quad (1.117)$$

The corresponding drag coefficient for the viscous sphere in Stokes flow becomes:

$$C_D = \frac{2F_D}{\pi \rho v^2 a^2} = \frac{8(3\lambda + 2)}{Re_r(\lambda + 1)} \quad (1.118)$$

The last expression yields the so-called "Stokes drag" C_D for a solid sphere = $24/Re_r$ and $C_D = 16/Re_r$ for an inviscid bubble. The two correspond to the drag forces $F = 6\pi a v \mu_f$ for the solid sphere and $F = 4\pi a v \mu_f$ for the inviscid bubble. The latter expression is often referred to as the "form drag," while the difference of the

two expressions, which is equal to $2\pi av\mu_p$, is often referred to as the “friction drag.” While several authors make this distinction between the two parts of the drag force, it must be emphasized that the drag force is a single entity that arises from the interactions between the fluid and the sphere and not two different forces.

Spheres settling or rising under gravity at Stokes flow conditions are subjected to the gravity/buoyancy force and the hydrodynamic/drag force. At steady state, the two opposing forces are equal in magnitude and the spheres move at constant velocity. Depending on the actual application, this velocity is known as the terminal, rising, or settling velocity of the sphere. An expression for this velocity of a viscous sphere in Stokesian flow is as follows:

$$v_t = \frac{2}{3} \frac{ga^2(\rho_f - \rho_s)}{\mu_f} \frac{\lambda + 1}{3\lambda + 2} \quad (1.119)$$

In actual applications, bubbles and drops seldom follow the predictions of the Hadamard–Rybczynski analysis, because of the presence of impurities that act as surfactants in the fluid. The surfactants, in general tend to dampen the internal velocity field, thus increasing the effective viscosity of the internal fluid. In this case the behavior of the viscous spheres is closer to that of a solid sphere. When the bubble or drop is in motion, the surfactants are swept to the aft, leaving the forward surface relatively uncontaminated. This establishes a concentration gradient on the surface of the sphere, which results in a surface tension gradient and, subsequently, in a tangential stress that opposes the motion of the surface. The net result of this phenomenon is an increase of the total drag force, which is manifested in the retardation of the terminal velocity of the viscous sphere (Levitch, 1962). Therefore, in practical cases of bubble and droplet flows, one must consider the drag given by Eq. (1.117) as the lower limit of the force. This limit is reached only under conditions of exceptional purity. Similarly, the terminal velocity given by Eq. (1.119) must be considered as the upper limit of the velocity that can be attained by a bubble or drop under Stokes flow (or creeping flow) conditions. Since the surfactants are any type of impurities that may be present in the carrier fluid and their chemical composition and concentration are almost always unknown, it is very difficult to determine the exact value of the effective λ to be used in the above expressions. The work by Bond and Newton (1928) and similar more recent studies suggest that as long as the flow may be characterized as Stokes flow ($Re_r \ll 1$), the viscous spheres behave as solid spheres in the range $Eo < 4$. The Eötvös number, Eo , is a dimensionless representation of the surface tension, defined by the expression:

$$Eo = \frac{(\rho_f - \rho_s)gd^2}{\sigma} \quad (1.120)$$

At $Eo = 4$, a transition occurs and the spheres follow more closely the Hadamard–Rybczynski analysis and, hence, the last two equations.

It must be pointed out that in the Stokes flow regime ($Re_r \ll 1$) all viscous spheres (bubbles and drops) remain spherical, regardless of the value of the Eötvös number. The shapes of the viscous spheres will be further discussed in Section 1.4.3.8.

1.4.3.2 Reynolds Number Effects

At finite Reynolds numbers, the fore-aft symmetry of the flow around the sphere, which is implied by the Stokes flow conditions, breaks down and the equations of Section 1.4.3.1 do not apply. Experimental observations have shown that, even at low Reynolds numbers, a wake is formed behind the sphere. This is a steady-state wake that becomes stronger as the Reynolds number increases and the inertia of the flow around the sphere overcomes the viscosity effects on the surface of the sphere. Experimental observations (Taneda, 1956; Achenbach, 1974; Seeley et al., 1975) as well as more recent numerical computations give sufficient evidence that the following flow descriptions, related to the presence and behavior of the wake, may be observed around a rigid sphere:

1. *Attached flow.* In the range $0 < Re_r < 20$ the flow is attached to the sphere and there is no visible recirculation behind it. However, there is a “velocity defect” region behind the sphere, which is the characteristic of a weak wake. The fore-aft asymmetry of the flow becomes progressively more pronounced, as Re_r increases, and is evident especially in diagrams of the vorticity and streamlines.

2. *Steady-state wake.* The onset of separation occurs at approximately $Re_r = 20$. A very weak recirculating wake becomes visible at about this value of Re_r . This wake is very small in volume and is attached to the aft of the sphere. As the Re_r increases, the wake becomes wider and longer and its point of attachment on the sphere moves forward. The wake is at steady state up to an approximate value $Re_r = 150$. In this regime, the separation angle is a monotonically decreasing function of Re_r , while the wake length and volume of the wake are monotonically increasing functions of Re_r . An approximate correlation for the length of the wake in this flow regime is:

$$L_w = 2a[0.0203(Re_r - 20) + 0.00012(Re_r - 20)^2] \quad (1.121)$$

3. *Unsteady wake regime in laminar flow.* The onset of instability for the wake occurs in the range $130 < Re_r < 150$ depending on the conditions of the study. At this Reynolds number, a weak long-period oscillation appears at the tip of the wake and its amplitude increases with Re_r . This is a laminar flow oscillation. Pockets of vorticity begin to be shed from the tip of the sphere and influence the flow field away from the sphere. This unsteady wake regime has been observed in experiments in the range $(130 \text{ to } 150) < Re_r < 270$.
4. *High subcritical range.* This regime covers the range $270 < Re_r < 3 \times 10^5$. As the Reynolds number increases, vortices being are shed regularly from alternate sides of the sphere. At the lower end of this regime, the Strouhal number of the vortices is a monotonic function of Re_r and ranges from 0.1 at $Re_r = 400$ to approximately 2 at $Re_r = 6000$. Above this value of Re_r , separation occurs at a point that rotates around the sphere with frequency equal to the shedding frequency. Although this may suggest the presence of a helical or double-helical wake, it has been proved that this is not the case. The result of this separation above $Re_r = 6000$, is the drastic reduction of the Strouhal number to 0.125. In the range $6000 < Re_r < 3 \times 10^4$ St rises from 0.125 to 0.18, while in the range $3 \times 10^4 < Re_r < 2 \times 10^5$, St to only 0.19 (Achenbach, 1974). It must be pointed out that in this flow regime the wake is periodic but not turbulent. Because of unstable conditions and the different experimental methods used in this range, there is a high amount of scatter in the experimental data of the frequencies of the vortices. The following relationship between the Strouhal and Reynolds numbers shows the best fit with the data in the range $400 < Re < 4000$.

$$st = 1.89 \times 10^{-5} Re^{1.43} \quad (1.122)$$

In the range $4000 < Re < 6000$, there is too much scatter in the experimental data, with st appearing to level at the value 0.21. The observations by Seeley et al. (1975) have shown that at values of Re above 1300 small jets and eddies appeared, signifying three-dimensional rotation of the flow. All observations confirm that in this flow regime the separation point moves forward and the angle where separation occurs is approximated well by the expression

$$\theta_s = 83 + 660 Re^{-0.5} \quad (1.123)$$

5. *Supercritical flow.* The onset of the transition to a turbulent wake occurs at approximately $Re_r = 2 \times 10^5$ and the transition is completed at approximately $Re_r = 3.7 \times 10^5$. At this point changes in the flow pattern occur that are referred to as “critical transition.” Above this Re_r , the separation begins to move downstream and fluctuations in the position of the separation point become evident. The detached free shear layer becomes turbulent and attaches to the surface of the sphere. The most evident result of this change is the sharp drop of the drag coefficient from the value of approximately 0.44 to 0.07. It must be pointed out that the transition to turbulent boundary layer is sensitive to the intensity of the free-stream turbulence and it may be accelerated by “tripping” the flow with a thin wire, a devise that has often been used in experimental studies of turbulent boundary layers (Maxworthy, 1969).

Clift et al. (1978) present several schematic diagrams and actual photographs of the wake behind a solid sphere. They clearly show that, at values of $Re_s > 400$, unsteady vortices are shed from the back of

the sphere. It is evident from the above that steady-state and axisymmetric conditions for the wake of the sphere imply a relatively low value of Re_r , in general less than 150, as well as steady flow around the sphere. In the next paragraphs the steady-state results for the hydrodynamic force at higher Reynolds numbers will be presented. An implicit assumption is that the flow around the spheres is steady or the timescale of the response of the sphere is much smaller than the timescales of the flow. Effects of the free turbulence in the flow field and other transient effects will be presented in Sections 1.4.3.3 and 1.4.3.6, respectively.

The first correct solution for the problem of determination of the hydrodynamic force on a sphere at finite Reynolds numbers is attributed to Oseen (1913). He did not solve completely for the velocity field around the sphere, but used a simple perturbation method to calculate a first-order correction for the steady-state drag coefficient. Oseen's asymptotic expression

$$C_D = 24/Re_r(1 + 3/16Re_r) \quad (1.124)$$

is valid for finite but small values of Re_r . Maxworthy (1975) verified experimentally that Oseen's correction is accurate up to $Re_r = 0.45$. This range covers many practical applications in the chemical industry, where particles are very small and the fluids have high viscosity.

At finite values of Re_r , the nonlinear advection term in the governing momentum Eq. (1.108) or (1.109) must be retained in the solution of the equations. This implies that the vorticity and its gradients around the sphere are transported by the advection of the fluid as well as by the molecular diffusion processes. An analysis of the governing equations reveals that the diffusion part of the process is dominant in an inner region surrounding the sphere with radius aRe^{-1} , while the advection process is dominant at distances far from this region. Close to the sphere, defined by the radius aRe^{-1} , the two processes, advection and diffusion, are of the same order of magnitude and their effects must be calculated simultaneously. In this case, the characteristic time of the advection process is a/U , while that of the diffusion process is equal to a^2/v_f . Since these characteristic times are in general of different orders of magnitude, the problems of the transport of momentum and energy at finite Reynolds or Peclet numbers may only be solved asymptotically, usually by a singular perturbation method.

Proudman and Pearson (1956) employed such a method, correct to $O(Re_r)$, in order to calculate the velocity field around a solid sphere and around a cylinder at steady state. Their method used the expansion of the stream function in suitable polynomials, locally valid in the inner and outer regions of the flow. This expansion and the approximation of the velocity field enabled them to extend Oseen's result and to calculate the steady-state drag coefficient to $O(Re_r^2)$. Their contribution to the calculation of the steady-state hydrodynamic force is a term of the order of $Re_r^2 \ln Re_r$ and their expression for the drag coefficient, when written in terms of the relative Reynolds number, is as follows:

$$C_D = \frac{24}{Re_r} \left[1 + \frac{3}{16} Re_r + \frac{9}{160} Re_r^2 \ln \left(\frac{Re_r}{2} \right) + O(Re_r^2) \right] \quad (1.125)$$

Expressions such as the above may be used with accuracy in applications of finite but small relative Reynolds numbers in the range from 0 to 0.7. At higher values of these dimensionless parameters, it is advisable to use one of the empirical or semiempirical expressions for the steady-state drag coefficient that abound in the literature. One of them is the Schiller and Nauman (1933) correlation, which is relatively simple and accurate:

$$C_D = 24(1 + 0.15Re_r^{0.687})/Re_r \quad (1.126)$$

This expression is recommended to be used in the range $1 < Re_r < 800$. The similar and simpler expression

$$C_D = \frac{24}{Re_r} \left(1 + \frac{1}{6} Re_r^{2/3} \right) \quad (1.127)$$

is easier to integrate analytically and is also recommended to be used in the range $1 < Re_r < 800$.

All these empirical equations give rise to the standard steady-state drag coefficient curve, which is depicted in Figure 1.9. It is observed that in the range of interest of many engineering calculations, the

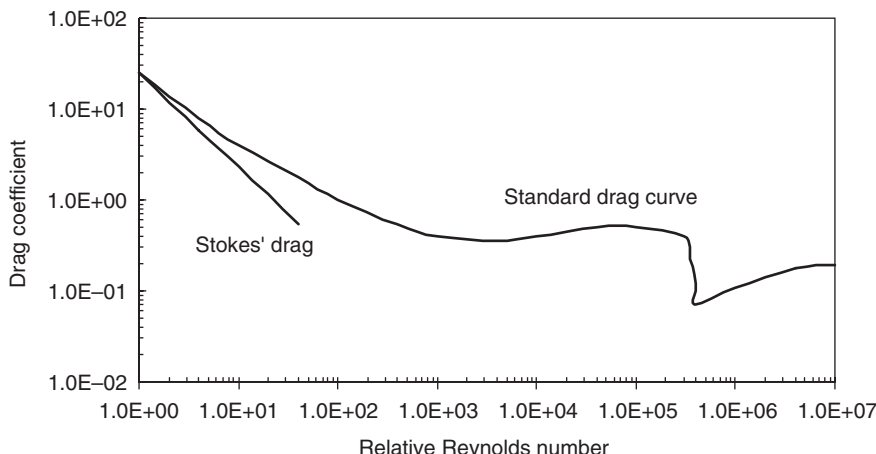


FIGURE 1.9 The standard drag coefficient curve for a solid sphere in steady flow.

drag of a solid sphere behaves according to the Stokesian flow result ($C_D = 24/Re_r$) in the range $0 < Re_r < 0.1$, it follows the Oseen expression in the range $0.1 < Re_r < 0.7$ and thereafter decreases exponentially with the Reynolds number as Eqs. (1.126) and (1.127) imply in the range $0.7 < Re_r < 800$. It is apparent in the figure that the steady-state drag coefficient of a sphere becomes constant and approximately equal to 0.44 in the range $10^3 < Re_r < 3 \times 10^5$. In this range, the friction part of the drag force is insignificant and all the contribution comes from the form drag.

A key determinant of the magnitude of the drag coefficient is the fluid boundary layer that is formed outside the sphere and the separation point of the flow field behind the sphere. As mentioned above, at $Re_r = 3 \times 10^5$, this boundary layer becomes turbulent and the separation point of the flow is moved downstream. The result is a sharp reduction of the form drag and, hence, a drastic reduction of the drag coefficient from 0.42 to 0.07, which is typical of laminar-to-turbulent transitions. At these high values of the relative Reynolds numbers, the flow becomes inherently unsteady because vortices are shed behind the sphere. It must be pointed out that in this case and other transient cases, the steady-state hydrodynamic force on a sphere may be used, instead of the transient expressions that are presented in Section 1.4.3.6, only if the timescale of the sphere ($\tau_s = 4a^2\rho_f/\mu_f$) is much smaller than the timescale of the transients in the carrier fluid, i.e., if $\tau_s \ll \tau_f$. This condition may also be given in terms of the Stokes number as $Stk \ll 1$.

In the case of viscous spheres at higher relative Reynolds numbers, internal circulation creates an internal flow field, which in turn affects the external flow field, and hence, the drag coefficient. Figure 1.10 shows the streamlines (top semicircle) and vorticity (bottom semicircle) of these flow fields for $\lambda = 7$ and for $Re_r = 10, 100$, and 500 . First, it is evident from the streamline figures that there is a fore-aft asymmetry, which is also met in the case of rigid spheres. Even though at $Re_r = 10$ a recirculation region behind the sphere has not been formed, there is an obvious velocity-defect region. At $Re_r = 100$, there is a well-defined recirculation region and at $Re_r = 500$ this region expands considerably and extends to a distance more than one diameter downstream. Secondly, at $Re_r = 500$ there are sharp gradients of the vorticity in the outer field of the sphere that indicate the formation of a boundary layer. This external boundary layer is characteristic of flows with $Re_r > 400$ and its thickness is of the order of $Re_r^{-1/2}$. Thirdly, it is also observed in Figure 1.10 that there are two counterrotating vortices inside the sphere (sometimes referred to as Hill's vortices) and that their strength increases with Re_r . An internal recirculation region at the aft-end of the sphere may also be formed at higher values of Re_r or lower values of λ (Feng and Michaelides, 2001a). The formation of the internal flow in the case of the viscous spheres modifies the whole field and results in lower drag on the sphere.

LeClair and Hamielec (1972), Rivkind et al. (1976), and Oliver and Chung (1987) used analytical and numerical studies to derive expressions for the drag coefficients of viscous spheres (bubbles and drops)

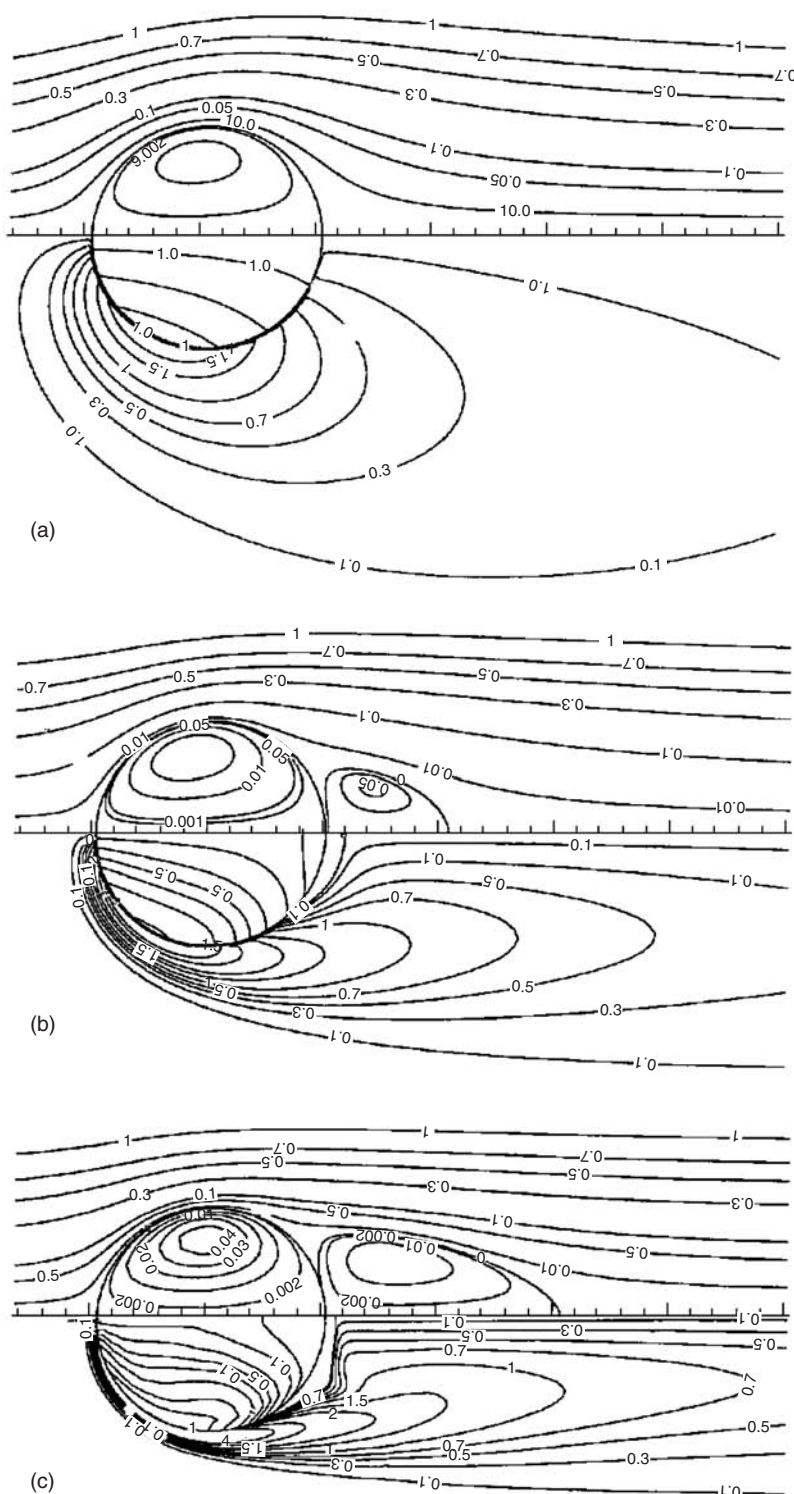


FIGURE 1.10 Streamlines and vorticity around a viscous sphere with viscosity ratio 7, at $Re = 10, 100$ and 500.

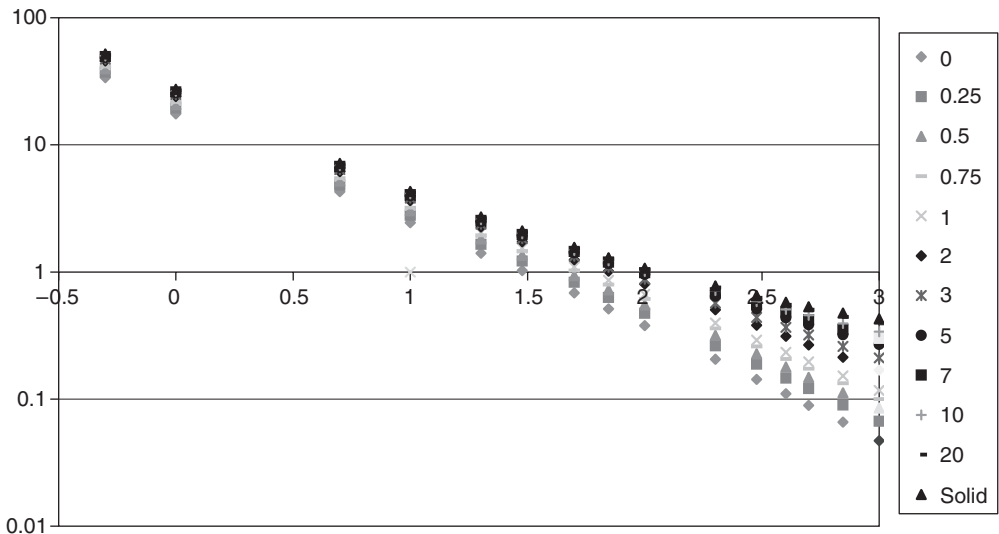


FIGURE 1.11 Drag coefficients for viscous spheres at different values of λ .

at relatively low values of the Reynolds numbers. Feng and Michaelides (2001a) used a two-layer concept for the computational grid and were able to perform more accurate computations that extend to higher Reynolds numbers, where the boundary layer is well formed on the outside surface of the viscous sphere. Feng and Michaelides (2001a) used their computational results to derive simple engineering correlations for the drag coefficients in terms of the viscosity ratio up to $Re_r = 1000$. Figure 1.11 depicts these results for several values of the viscosity ratio, λ . The standard drag coefficient curve for solids spheres in this figure corresponds to the limit $\lambda \rightarrow \infty$.

When expressed in terms of the relative Reynolds numbers, the correlations derived by Feng and Michaelides (2001a) are valid up to $Re_r = 1000$ and may be written as follows:

$$C_D(Re_r, \lambda) = \frac{2 - \lambda}{2} C_D(Re_r, 0) + \frac{4\lambda}{6 + \lambda} C_D(Re_r, 2) \quad \text{for } 0 \leq \lambda \leq 2, \quad 5 < Re_r \leq 1000 \quad (1.128)$$

and

$$C_D(Re_r, \lambda) = \frac{4}{\lambda + 2} C_D(Re_r, 2) + \frac{\lambda - 2}{\lambda + 2} C_D(Re_r, \infty) \quad \text{for } 2 \leq \lambda \leq \infty, \quad 5 < Re_r \leq 1000 \quad (1.129)$$

where the functions $C_D(Re_r, 0)$, $C_D(Re_r, 2)$ and $C_D(Re_r, \infty)$ are the drag coefficients for inviscid bubbles, viscous drops with $\lambda = 2$, and the solid spheres, respectively. The following functions, which represent the drag coefficients of inviscid spheres, spheres in fluids with viscosity ratio $\lambda = 2$, and solid spheres, respectively, are recommended to be used with correlations (1.128) and (1.129):

$$C_D(Re_r, 0) = \frac{48}{Re_r} \left(1 + \frac{2.21}{\sqrt{Re_r}} - \frac{2.14}{Re_r} \right) \quad (1.130)$$

$$C_D(Re_r, 2) = 17.0 Re_r^{-2/3} \quad (1.131)$$

and

$$C_D(Re_r, \infty) = \frac{24}{Re_r} \left(1 + \frac{1}{6} Re_r^{2/3} \right) \quad (1.132)$$

The expressions for $C_D(Re_r, 0)$ and $C_D(Re_r, \infty)$ above are commonly used correlations for the drag coefficients of bubbles and solid particles. The expression for the drag coefficient at $\lambda = 2$ is a simple correlation of the computational results. In the low range of Re_r , which is not covered by the above expressions, the following correlation is recommended:

$$C_D = \frac{8}{Re_r} \frac{3\lambda + 2}{\lambda + 1} \left(1 + 0.05 \frac{3\lambda + 2}{\lambda + 1} Re_r \right) - 0.01 \frac{3\lambda + 2}{\lambda + 1} Re_r \ln(Re_r) \quad 0 \leq Re_r \leq 5 \quad (1.133)$$

This expression has been derived from the results of the computations in a way that it reduces asymptotically to the Hadamard–Rybczynski solution at $Re_r = 0$ and to the Oliver and Chung expression for very small Re_r . The functional form of the last expression has been derived from the natural next order expansion in terms of Re as shown in the study by Proudman and Pierson (1956). Although the last expression was derived from numerical results in the range $1 < Re_r < 5$, calculations have shown that (1.133) accurately represents the numerical results up to $Re_r = 20$ and may be used in this range instead of equations (1.128) and (1.129).

It is apparent in the above correlations that the density ratio ρ_f/ρ_s does not influence the drag coefficient of viscous spheres. This was confirmed by the numerical results of Feng and Michaelides (2001a). They found out that the variation of the density ratio by two orders of magnitude had an effect of less than 2% on the values of the drag coefficients. It must be pointed out that the maximum fractional difference of the correlation functions (1.128), (1.129), and (1.133) from the computational results they are derived from is 4.6%, and the standard deviation of all the fractional differences is 2.1%. At the high range of the Reynolds numbers, the wake behind the spheres is unsteady and a transient expression for the total drag force should be used if one is known. In such cases, the above expressions may be used for the steady-state part of the total hydrodynamic force. The above equations would yield a good approximation for the total hydrodynamic force, only in cases when the steady-state part is much greater than the other parts or when the timescales of the transients are low enough for the flow to be considered quasi-steady.

Regarding viscous spheres, it is well known that at higher Reynolds numbers their shape becomes elongated (see [Section 1.4.3.8](#)). Under these circumstances, the drag coefficient of elongated viscous spheres is a function of the variables that appear in the above correlations as well as of the amount of deformation. The latter may be measured as elongation or eccentricity. Under these circumstances, correction functions must be used with the above correlations, such as the one by Harper (1972) and others that are presented in [Section 1.4.3.7](#). Experimental evidence by Winnikow and Chao (1966) and others on the free fall or rise of drops in liquids shows that a liquid drop will remain spherical when the dimensionless Bond number, Bo , which is equal to the ratio We/Fr , is less than or equal to 0.2, i.e., when

$$Bo = \frac{We}{Fr} = \frac{gd^2|\rho_s - \rho_f|}{\sigma} \leq 0.2 \quad (1.134)$$

According to this criterion, water droplets in air will maintain their spherical shape at values of Re_r up to 470. In the case of substances with high surface tension (liquid metals), the corresponding Re_r would be much larger (up to 1150 for mercury droplets in air).

1.4.3.3 Turbulence Effects

Turbulence in the carrier fluid or free-stream turbulence implies an unsteady flow field and, in turn, unsteady motion of particles, bubbles, or drops. For this reason, the effects of the free-stream turbulence are transient flow effects. Numerous experiments on the drag for solid spheres proved that, in general, the drag coefficients in turbulent flows follow the trends of the standard drag curve and that the effect of the free-stream turbulence is to modify the drag coefficient, sometimes significantly. Typical results of such experiments are reproduced in [Figure 1.12](#) from the experimental projects mentioned in Clift et al. (1978). It is observed in this figure that when the relative Reynolds number is in the range $10 < Re_r < 500$, the drag coefficient of the sphere in a turbulent flow is almost always higher than the values in the standard curve. The influence of the free-stream turbulence on the boundary layer around the sphere and the wake behind the sphere is manifested by the sharp changes observed at approximately $Re_r = 50$ and the leveling

of the drag coefficient curves at values that are 2 to 4 times higher than the corresponding values of the standard curve. In the range $500 < Re_r < 20,000$, the drag coefficient of a sphere is first reduced dramatically in a short range of Reynolds numbers, often reaching a value 50% lower than the value of the standard curve (Clamen and Gauvin, 1969). Then, C_D increases gradually and may reach a maximum, which is 2 to 5 times higher than the values predicted by the standard curve. Thereafter, C_D decreases gradually to the values of the standard curve. The sudden dip of the drag coefficients is often attributed to the formation of a turbulent boundary on the surface of the particle. Therefore, the transition, which in the standard drag curve happens close to the value $Re_r = 3 \times 10^5$, is accelerated and occurs earlier in the presence of free-stream turbulence to values of Re_r , which sometimes is claimed to be less than 1000. Clift and Gauvin (1970) introduced the critical Reynolds number for the gaseous boundary layer. This is the relative Reynolds number at which the turbulent transition happens and is given by the following expressions:

$$Re_{cr} = \begin{cases} 10^{5.477 - 15.81} & \text{for } I_r \leq 0.15 \\ 10^{3.371 - 1.751} & \text{for } I_r > 0.15 \end{cases} \quad (1.135)$$

where I_r is the turbulence intensity based on the relative velocity of the sphere.

As with all the correlations that involve exponential expressions, the results of the above two equations must be strictly used within the range of the experimental conditions (Reynolds numbers and turbulence intensities) at which they were derived.

It must be pointed out that the experimental uncertainty associated with the results of Figure 1.12 and Eq. (1.135) is significant and that there is a considerable discrepancy of the data emanating from the different experimental studies. Part of this uncertainty is inherent to the measurements in unsteady turbulent flows. Another part of the uncertainty stems from the fact that the response of particles in a turbulent flow has been implicitly treated as a static and not as a transient process. It is known that the response of a particle to the turbulent eddies depends strongly on the frequency of these eddies and that the response process is dynamic.

It is apparent from recent results, presented in Section 1.4.3.6, that the transient part of the force exerted by the fluid is significant and that it depends strongly on the Stokes number of the particles, which in this case is defined as the product of the characteristic time of the particle and the characteristic frequency of the eddies. The Stokes number and its inverse, the Strouhal number, are important variables that determine the response of particles to transient flows including turbulent flows. Since these two dimensionless parameters have not been taken into account in the experimental studies of the past, it is expected that

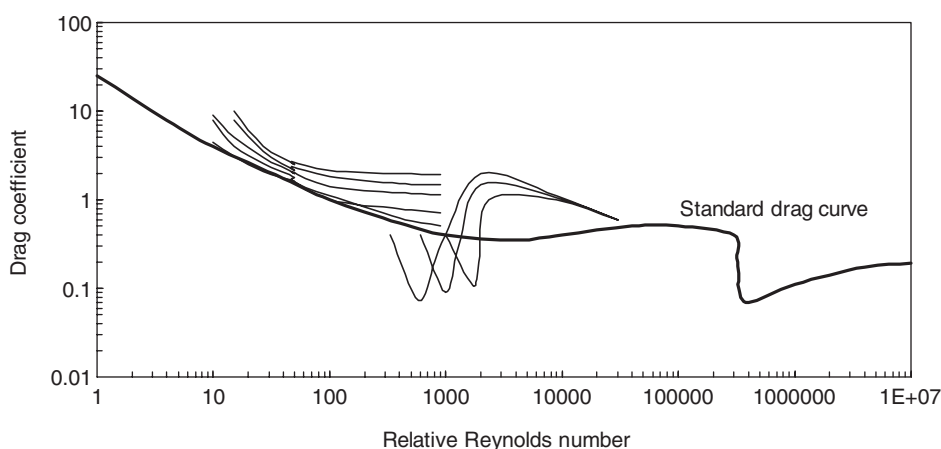


FIGURE 1.12 The effect of the free-stream turbulence on the standard drag coefficient for a solid sphere.

large discrepancies would be observed and that the results obtained would pertain to the specific conditions of the experiments. Hence, the results of different studies might not agree. This is apparent by comparing the results of the two sets of curves in Figure 1.12 in the vicinity of $Re_r = 500$. One set shows that turbulence transition of the boundary layer occurs at this Reynolds number and, hence, there is a significant reduction of the drag coefficient, while the other does not show the consequences of such a transition and indeed shows a significant increase in the value of the drag coefficient. In this context, a recent study by Warnica et al. (1994) concluded that, given the magnitude of the experimental error, in the range $20 < Re_r < 100$ there is no clear evidence to suggest that the drag coefficient is substantially different from the values given by the standard drag coefficient curve. It is clear further research is needed to generate more reliable data and expressions and that all the results of the past, such as those shown in Figure 1.12, should be used only within the range of the experimental conditions from which the results emanate.

The presence of particles, bubbles, and drops in turbulent flows also has an effect on the intensity and characteristics of the carrier fluid turbulence. This was observed in many relatively recent experimental studies and is called “modulation” or “modification” of the turbulence, regardless of any transition in the boundary layer of the particles. A great deal of work was devoted in the last 20 years on this subject, which will be treated extensively in Section 12.6.

1.4.3.4 Blowing Effects

The mass transfer from the surface of a sublimating particle or an evaporating droplet causes an outward radial flow and, hence, a drastic change in the gaseous boundary layer around the sphere. This in turn tends to reduce the drag coefficient from the steady-state value as it is given by the standard curve. The exchange of mass from the particle or droplet to the surrounding fluid causes two significant effects:

1. The change of the viscosity of the surrounding fluid, which occurs because of temperature changes and composition changes, and
2. A regression of the droplet surface, which is associated with the flow of the vapor from the surface to the carrier fluid. This is called “Stefan convection.”

Yuen and Chen (1976) conducted experiments for the drag force on evaporating drops and on the effect of the change of the transport properties of the carrier fluid as a result of the transfer of mass from the surface of the droplet. They concluded that their results are well represented when a reference viscosity for the carrier fluid is used, i.e., film viscosity. This is defined as follows:

$$\mu_r = \mu_s + \frac{1}{3}(\mu_\infty - \mu_s) \quad (1.136)$$

where μ_∞ is the viscosity of the fluid far from the sphere and μ_s is the gaseous viscosity on the surface of the sphere. This is sometimes referred to as the “1/3 rule” for the film properties. The experimental data and analysis on the density and viscosity averages by Lerner et al. (1980) confirmed this relationship. They also suggested that the standard drag curve with the above correction for the viscosity could be applied to slightly ellipsoidal drops if the effective diameter of the ellipsoid, d , is used and the two axes of the ellipsoid are within 10% of each other. In the latter case, Lerner et al. (1980) recommend that the effective diameter for the ellipsoid should be equal to $(a^2b)^{1/3}$, where a and b are the major and minor axes of the ellipsoid, respectively.

Eisenklam et al. (1967) and, later, Renksizbulut and Yuen (1983) examined the effects of the radial flow and of the Stefan convection process away from the surface of an evaporating droplet. They recommended a simple correction for the effect of the Stefan convection on the drag coefficient be used in calculations:

$$C_D = \frac{C_{D,0}}{1 + B_M} \quad (1.137)$$

where $C_{D,0}$ is the value of the drag coefficient obtained in the absence of mass transfer, which may be obtained from the correlations presented in Section 1.4.3.2. The coefficient B_M is called as the “blowing coefficient.” It is based on the mass transfer from the surface of the sphere and is defined in terms of the

mass fraction of the droplet vapor on the surface of the sphere and far away from the sphere:

$$B_M = \frac{Y_s - Y_\infty}{1 - Y_s} \quad (1.138)$$

Chiang et al. (1992) conducted a numerical study of evaporating droplets with variable transport properties and derived a correlation for their drag coefficients, which is valid in the range $30 < Re_r < 200$:

$$C_D = \frac{24.432}{(1 + B_H)^{0.27}(Re_m/2)^{0.721}} \quad (1.139)$$

The relative Reynolds number Re_m is defined in terms of the gas-film viscosity (Eq.[1.136]) and the free-stream gas density, ρ_∞ . In the last equation, B_H is another blowing coefficient or transfer number, which is based on the thermodynamic enthalpy of the evaporating fluid, i.e.,

$$B_H = \frac{h_\infty - h_s}{h_{fg}^{\text{eff}}} \quad (1.140)$$

The effective latent heat of vaporization, h_{fg}^{eff} in the denominator of the last expression, is the sum of the latent heat of the vapor at the drop surface and the sensible heat that is conducted to the interior of the drop.

In the case when the radial velocity of blowing, V_n , is known or may be calculated from the mass flow rate data, Clift and Lever (1985) used a numerical analysis and derived the following relationship for the drag coefficient, which was also verified by the study of Miller and Bellan (1999):

$$C_D = \frac{24}{Re_r} \frac{1 + 0.545Re_r + 0.1Re_r^{0.5}(1 - 0.03Re_r)}{1 + ARe_n^B} \quad (1.141)$$

where Re_n is the blowing Reynolds number, $Re_n = dV_n/\nu$, and the functions A and B are correlated to the relative Reynolds number of the flow as follows:

$$A = 0.09 + 0.077\exp(-0.4Re_r) \text{ and } B = 0.4 + 0.77\exp(-0.04Re_r) \quad (1.142)$$

The last two expressions are valid in the ranges $10 < Re_r < 200$ and $1 < Re_n < 20$. At lower values of the Reynolds numbers, $Re_r < 10$ and $Re_n < 1$, the following modification in the function $A(Re_r)$ has been recommended:

$$A = 0.06 + 0.077 \exp(-0.4Re_r) \quad (1.143)$$

The correlations presented above and the pertinent studies suggest that the drag coefficient of burning and evaporating droplets shows only a small departure from the corresponding values derived without mass transfer. These correlations may be perceived as corrections to the standard drag curve for spheres that are caused by the different composition of the gaseous boundary layer and by the mass convection from the sphere.

1.4.3.5 Compressibility and Rarefaction Effects

When particles and drops are present in rarefied gases, for example under conditions that are prevalent in the upper atmosphere, the length of the molecular free path, l_m , becomes comparable or even greater than the size of the particle/drop. Therefore, the medium surrounding the particle or drop may not be considered to be a continuum and, hence, the hydrodynamic force is not the same as in the case of continuum flows. The Knudsen number,

$$Kn = \frac{l_m}{d} \quad (1.144)$$

is a dimensionless measure of the relative magnitude of the two length scales. Continuum flows imply that $Kn \ll 1$. Since the molecular free path of a gas is proportional to the ratio of the viscosity divided by the product of the speed of sound and the gas density ($l_m \sim \mu/c\rho$), it follows that Kn is also proportional to the

ratio of the Mach number and the Reynolds number ($Kn \sim M/Re$). Schaaf and Chambre (1958) identified four flow regimes to characterize rarefaction flows, and Crowe et al. (1969) showed that in the case of rocket nozzles a burning particle or droplet is usually subjected to all four flow regimes:

1. The *free molecule flow*, where interactions among the molecules are absent and individual molecules collide with the particles, thus exchanging momentum ($Kn > 10$ and $M > 3Re_r$).
2. The *transitional flow*, where the size of the particles is comparable to the size of the mean free path. Since molecules interact by collisions, the collisions between the particles and the molecules create a distinct flow around the particles. The effect of this flow field and the collisions is manifested on the force exerted by the gas on the particles ($0.25 < Kn < 10$, $0.1Re_r^{1/2} < M < 3Re_r$).
3. In the *slip flow* regime, there is a distinct flow field around the particles. The temperature and velocity at the surface of the particle are different from the temperature and velocity on the side of the gas that is close to the surface ($0.001 < Kn < 0.25$ and $0.01Re_r^{1/2} < M < 0.1Re_r^{1/2}$). This gives rise to a slip between the two velocities at the surface. When the Knudsen number is relatively low, $Kn < 0.01$, the flow field around the particles may be obtained by a solution of the Navier–Stokes equations with the stipulation of a suitable closure equation for the slip.
4. The *continuum flow* is characterized by the absence of velocity slip on the surface of the particles ($Kn < 0.001$, $M < 0.1Re_r^{1/2}$). The no-slip condition applies on the surface of the particles and the flow field may always be obtained by analytical or numerical solutions of the Navier–Stokes equations.

It is intuitive that a droplet that completely evaporates or a particle that completely sublimates would pass through all these flow regimes. However, when $Kn > 0.001$, there is so little mass remaining that, under the normal rates of evaporation, sublimation, or burning, the process passes through the first three regimes in a very short amount of time. When treating these processes by a numerical scheme, one has to be cognizant of this fact and to use timescales and time steps that are appropriate to the rapid processes taking place.

At high Reynolds numbers, the effects of the Mach number on the drag coefficient become significant when $M > 0.6$. This is sometimes called the critical Mach number and the flow around the particle is characterized by the formation of a shock wave, which significantly increases the form drag of the particle. Hence, the drag coefficient, which is almost constant in the range $0 < M < 0.6$, increases beyond $M = 0.6$, reaches a maximum, which depends on the value of Re but is always greater than 2, and, thereafter, decreases gradually and asymptotically approaches the theoretically predicted value of 2 for free molecular flows (Schaaf and Chambre, 1958). At low Reynolds numbers, an increased Mach number signifies that the flow is rarefied. There is a shock wave associated with the presence of the particle and the drag coefficient decreases monotonically.

In general, the effect of the Knudsen number and the Mach number on the drag coefficient is given by correction factors $f(M)$ and $f(Kn)$. The classic experiment for free molecular flow by Millikan (1923) yields the following correction factor for drops in rarefied flows, valid in the Stokesian flow regime:

$$f(Kn) = \frac{C_D}{C_{D,0}} = \left[1 + Kn \left[2.49 + 0.84 \exp\left(-\frac{1.74}{Kn}\right) \right] \right]^{-1} \quad (1.145)$$

This factor is known as the Cunningham correction factor. An equation for the drag coefficient, proposed by Crowe et al. (1973) and later simplified by Hermsen (1979), has been applied successfully to the case of burning particles in solid propellant rocket nozzles:

$$C_D = 2 + (C_{D,0} - 2) \exp\left[-\frac{3.07\sqrt{k}g(Re_r)M}{Re_r}\right] + \frac{h(M)}{M\sqrt{k}} \exp\left(-\frac{Re_r}{2M}\right) \quad (1.146)$$

where k is the ratio of the specific heats of the gas and $g(Re)$ and $h(M)$ are two functions defined as follows:

$$g(Re) = \frac{1 + Re_r(12.278 + 0.548Re_r)}{1 + 11.278Re_r}, \quad h(M) = \frac{5.6}{1 + M} + 1.7 \sqrt{\frac{T_p}{T_c}} \quad (1.147)$$

In the last experiments T_c is the mean temperature of the carrier gas far from the particle and T_p is the temperature of the particle.

Alternatively, Carlson and Hoglund (1964) derived the following empirical relationship for the function $f(M)$, which is used in some computations pertaining to particles in shock waves and other compressible flow fields:

$$f(M) = \frac{1 + \exp\left(-\frac{0.427}{M^{4.63}} - \frac{3}{Re_r^{0.88}}\right)}{1 + \frac{M}{Re_r} \left[3.82 + 1.28 \exp\left(-1.25 \frac{Re_r}{M}\right) \right]} \quad (1.148)$$

It must be pointed out that the last three equations are correlations of experimental data and must be used within the range of the independent variables for which the original data have been derived. Also, Crowe (1970) has shown that Eq. (1.148) is not valid in the flow regimes usually encountered by particles in a rocket nozzle.

1.4.3.6 Transient Flow Effects

Most of the practical applications of dispersed multiphase flows involve time-dependent flows. When the characteristic time of the transients in the flow is of the same order of magnitude as the characteristic time of the elements of the dispersed phase (bubbles, drops, or particles), a transient equation should be used for the exchange of momentum between the carrier fluid and the dispersed phase. Exact analytical expressions for transient flows have been derived for creeping flow conditions ($Re_r \ll 1$), and asymptotic expressions have been derived for finite but small Reynolds numbers ($Re_r < 1$). Semiempirical expressions, which emanate from a combination of experimental data and analysis, have also been developed and frequently used at high Re_r .

1.4.3.6.1 Analytical Expressions at Creeping Flow ($Re_r \ll 1$)

The so-called Boussinesq–Basset equation,

$$F_i(t) = -6\pi\alpha\mu_f(V_i - u_i) - \frac{1}{2}m_f \frac{d}{dt}(V_i - u_i) - 6\alpha^2\sqrt{\pi\mu_f\rho_f} \int_0^t \frac{\frac{(d)}{(d\tau)}(V_i - u_i)}{\sqrt{t-\tau}} d\tau \quad (1.149)$$

which was independently derived by Boussinesq (1885) and Basset (1888a), was the first equation developed for the transient hydrodynamic force acting on a solid sphere as a result of the motion of the fluid. This expression was derived for creeping flow conditions ($Re_r \ll 1$) where the inertia terms in the momentum equation of the fluid may be neglected in comparison with the viscous effects. Maxey and Riley (1983) performed a more sophisticated analysis for a rigid sphere in an arbitrary nonuniform flow field, whose velocity is given by the functional relationship $u_i(x_i, t)$. The latter is not an arbitrary function since it must be a solution of the Navier–Stokes equations. Maxey and Riley (1983) obtained the following expression for the equation of motion of such a sphere:

$$\begin{aligned} m_s \frac{dv_i}{dt} = & -\frac{1}{2}m_f \frac{d}{dt} \left(v_i - u_i - \frac{a^2}{10} u_{i,jj} \right) - 6\pi a \mu_f \left(v_i - u_i - \frac{a^2}{6} u_{i,jj} \right) \\ & - \frac{6\pi a^2 \mu_f}{\sqrt{\pi \nu_f}} \int_0^t \frac{\frac{(d)}{(d\tau)} \left(v_i - u_i - \frac{a^2}{6} u_{i,jj} \right)}{\sqrt{t-\tau}} d\tau + (m_s - m_f) g_i + m_f \frac{Du_i}{Dt} \end{aligned} \quad (1.150)$$

In the last equation m_s is the mass of the sphere and m_f is the mass of the fluid that occupies the same volume as that of the sphere. The repeated index (jj) denotes the Laplacian operator and the derivative D/Dt is the total Lagrangian derivative following the particle. All the spatial derivatives are evaluated at the center of the sphere. The left-hand side in the above equation represents the acceleration of the sphere. Of the terms on the right-hand side, one easily recognizes in the first, second and third terms as the added mass, the steady-state drag and the history terms of Eq. (1.147). The other terms in the right-hand side are the gravitational, or body, force and the Lagrangian acceleration term, caused by the acceleration of the fluid. The Laplacian terms in all the parentheses account for the nonuniformity of the fluid velocity field. They are second-order corrections for the curvature of the flow field and are called sometimes “the Faxen terms.” All the spatial derivatives in (1.150) must be evaluated at the center of the sphere. These derivatives become zero when the fluid velocity field is uniform and, in this special case, the corresponding terms of the

hydrodynamic force of the Maxey and Riley equation become the same as those of the Boussinesq–Basset equation. The Faxen terms scale as a^2/L^2 , where L is the macroscopic characteristic length of the fluid velocity field and in most practical applications of dispersed multiphase flows, where $a/L \ll 1$, they are small enough to be neglected in practical computations.

It must be pointed out that the derivation of Eq. (1.150) is based on the following assumptions:

- Spherical shape
- Infinite fluid domain initially undisturbed
- No rotation
- Rigid sphere ($\mu_f/\mu_s \ll 1$)
- Zero initial relative velocity
- Negligible inertia effects ($Re_i \ll 1$)

If the initial relative velocity is different than zero, the following expression/correction must replace the history term of Eq. (1.150):

$$\frac{6\pi a^2 \mu_f}{\sqrt{\pi} v_f} \int_0^t \frac{\frac{(d)}{(d\tau)} \left[v_i - u_i - \frac{a^2}{6} u_{ijj} \right]}{\sqrt{t-\tau}} d\tau + \frac{6\pi a^2 \mu_f [v_i(0) - u_i(0)]}{\sqrt{\pi} v_f t} \quad (1.151)$$

where the quantity $v_i(0) - u_i(0)$ represents the initial relative velocity (at time $t = 0$). Although expression (1.151) has been recommended for use as a correction to the equation of motion, the concept of an “initial” relative velocity or temperature, while mathematically acceptable as an initial condition to a partial differential equation, is physically questionable in the light of the implicit assumption of the original equation of motion, (1.150) that pertains to an initially undisturbed fluid: how does one introduce a sphere with a different velocity in an “initially undisturbed” fluid? Surely the mechanism of the introduction of the sphere would result in some sort of disturbance to the fluid velocity field, which is not accounted for in the initial and boundary conditions used for the derivation of the original equation. Therefore, one has to reconsider the concept of a finite relative velocity as the mathematical representation of a physical initial condition of a problem where the sphere is present in an unbounded fluid that must be initially undisturbed by its presence. An interesting approach to this subject is through the use of irreversible thermodynamics, where the relative velocity may be described as an internal variable (Lhuillier, 2001).

Integrodifferential equations, such as (1.150), do not have an explicit analytical solution for the dependent variable (v_i). Since they are implicit in their dependent variable, they must be solved numerically by an iteration method, which consumes a great deal of computational resources in both memory and CPU time. This becomes especially restrictive when these equations are applied to repetitive calculations, such as the Lagrangian computations of a set of particle trajectories. For this reason, several Lagrangian simulations for the motion of particles and bubbles that were performed in the last 20 years have neglected the history term, often without a sound justification or scientific reasoning. Michaelides (1992) and later Vojir and Michaelides (1994) have devised an analytical method to convert such first-order implicit integrodifferential equations to second-order integrodifferential equations, which are explicit in the dependent variables v_i (or T_s in the case of temperature). The method used for these transformations is a straightforward transformation of Eq. (1.150) into the Laplace domain and a back transformation into the time domain after some algebraic manipulations. The transformed equation, written in dimensionless form in terms of the relative velocity, w_i , is as follows:

$$\begin{aligned} & \frac{4a^4 \rho_s^2}{81\mu_f^2} \frac{d^2 w_i}{dt^2} + \frac{2a^2 \rho_s}{9\mu_f} \gamma \left(2 - \frac{9\beta k}{2} \right) \frac{dw_i}{dt} + \gamma^2 w_i = \left| -\frac{4a^4 \rho_s^2}{81\mu_f^2} \gamma (1 - \beta) \frac{d^2 u_i}{dt^2} \right. \\ & \left. - \frac{2a^2 \rho_s}{9\mu_f} \gamma^2 (1 - \beta) \frac{du_i}{dt} + \frac{2a^2 \rho_s}{9\mu_f} \gamma^2 (1 - \beta) \sqrt{\frac{\beta}{\pi} \frac{a^2 \rho_s}{\mu_f}} \int_0^t \frac{d\sigma^2}{(t - \sigma)^{0.5}} d\sigma \right. \\ & \left. + \gamma \sqrt{\frac{\beta}{\pi} \frac{a^2 \rho_s}{\mu_f}} \left[\gamma (1 - \beta) \frac{du_i}{dt} \Big|_{t=0} - \gamma (1 - \beta) \frac{2g_i a^2 \rho_s}{9\mu_f} \right] + \gamma^2 (1 - \beta) \frac{2g_i a^2 \rho_s}{9\mu_f} \right] \end{aligned} \quad (1.152)$$

with initial conditions:

$$w_i(0) = v_i(0) - u_i(0) = 0 \quad (1.153)$$

and

$$\frac{dw_i}{dt} \Big|_{t=0} = -\gamma[1 - \beta] \frac{du_i}{dt} \Big|_{t=0} + \gamma[1 - \beta]g_i \quad (1.154)$$

The parameter β is the ratio of the fluid to sphere densities, $\beta = \rho_f/\rho_s$, and the parameter γ is equal to $(1 + 0.5\beta)^{-1}$. The solution of the last set of equations instead of the original equation of motion results in significant computational economy, because there is no need for extensive memory usage and numerical iterations. For this reason Eq. (1.152) is recommended in repetitive computations. However, it must be pointed out that Eq. (1.152) as a second-order equation is not unconditionally stable (the stable region is $\beta < 0.6$). Equation (1.150) is unconditionally stable and should be the only one used in computations when $\beta > 0.6$.

In the case of viscous spheres (drops and bubbles) that are present in a carrier fluid, there are two timescales for the motion of the fluid inside the sphere and the motion of the external fluid. For this reason, an analytical expression for the equation of motion, similar to expression (1.150) is impossible to be derived in the time domain. Galindo and Gerbeth (1993) were the first to derive a correct expression for the hydrodynamic force on a viscous sphere under creeping flow conditions in the Laplace domain, which is as follows:

$$F_i = -6\pi a \mu_f [v_i - u_i] \left\{ \frac{\chi_f^2}{9} + (\chi_f + 1) - \frac{(\chi_f + 1)^2 f(\chi_s)}{[\chi_s^3 - \chi_s^2 \tanh(\chi_{ss}) - 2f(\chi_s)]\lambda + (\chi_f + 3)f(\chi_s)} \right\} \quad (1.155)$$

The overbar in the last expression denotes functions in the Laplace domain and χ represents the two dimensionless timescales, also in the Laplace domain,

$$\bar{\chi}_f = \sqrt{\frac{s\alpha^2}{\nu_f}}, \quad \bar{\chi}_s = \sqrt{\frac{s\alpha^2}{\nu_s}} \quad (1.156)$$

and the function $f(\chi)$ is defined as follows:

$$f(\chi) = (\chi^2 + 3)\tanh(\chi) - 3\chi \quad (1.157)$$

While normal slip on the surface of a sphere is not permissible from the kinematic conditions on the surface of spheres, tangential slip, $w_\theta = (v - u)_s$, which results from the action of the tangential shear stress at the interface, τ_θ , cannot be excluded *a priori*. Conditions when tangential slip may be present include very small spheres, e.g., submicron-sized drops, nanoparticles, or colloidal particles as well as larger drops and particles in rarefied carrier fluid environments. Michaelides and Feng (1995) performed a study that included the effect of the viscosity ratio, $\lambda = \mu_s/\mu_f$, and also allowed for the existence of a finite tangential velocity slip at the interface of the sphere and the carrier fluid. The resulting expression for the hydrodynamic force, which is exerted on a viscous sphere in the Laplace domain is as follows:

$$F_i = -6\pi a \mu_f [v_i(s) - u_i(Y(t), s)] \left\{ \frac{\chi_1^2}{9} + \chi_1 + 1 - \frac{(\chi_f + 1)^2 ([\chi_s^3 - \chi_s^2 \tanh(\chi_s) - 2f(\chi_s)]\lambda\sigma + f(\chi_s))}{[1 + \sigma(\chi_f + 3)][\chi_s^3 - \chi_s^2 \tanh(\chi_s) - 2f(\chi_s)]\lambda + (\chi_f + 3)f(\chi_s)} \right\} \quad (1.158)$$

where the variables χ_p and χ_s are defined in Eq. (1.156) and σ is a dimensionless parameter for the tangential slip. It is defined in terms of the tangential velocity difference at the interface, $w_\theta = (v - u)_s$, and the tangential shear stress at the interface, τ_θ , as follows:

$$\sigma = \frac{\mu_f w_\theta}{a \tau_\theta} \quad (1.159)$$

When there is no slip on the surface of the sphere, i.e., $\sigma = 0$, Eq. (1.158) reduces to the Galindo and Gerbeth Eq. (1.155). Remarkably, the case of a sphere with perfect slip, $\sigma = \infty$, and the case of an inviscid sphere, $\lambda = 0$, are equivalent and result in the same equation of motion. Such an equation was first derived for an inviscid bubble by Morrison and Stewart (1976) in an implicit integrodifferential form. This outcome leads one to conclude that if extremely small particles, such as nanoparticles in any kind of carrier fluid, drops in the last stages of vaporization or particles in the last stages of sublimation or burning, are to be modeled by a continuum approach with finite velocity slip allowed at their interface, then the values of the resulting drag coefficients would be between the theoretical values for the drag coefficients of bubbles and the drag coefficients of rigid particles.

Because of the two timescales and its complexity, Eq. (1.158) cannot be transformed analytically to yield the resulting disturbance force in the time domain. However, parts of it may be transformed. In such a transformation, the first term in the braces would yield the typical added mass contribution; the second term, which is proportional to the square root of s , would yield the typical history integral; and the third term, the number 1, will yield the steady-state drag term. Given the complexity of the last term in the equation, it is difficult to speculate the type of its contribution on the resultant force. This term may be considered as a residue of all the other terms, applicable to the case of nonrigid spheres. Thus, it would contribute to parts of the history and the added mass components of the hydrodynamic force, which are not included in the force acting on a rigid sphere. In some special cases, it becomes the new memory integral, of Lawrence and Weinbaum (1986), but in general its contribution is more complex than that of the typical memory/history term.

An asymptotic solution of Eq. (1.158) may be derived in the case of steady state with slip. This solution yields an explicit form of the hydrodynamic force exerted on a small particle, when there is slip in the interface:

$$F_i = 6\pi\mu(u_i - v_i)\frac{1 + 2\sigma}{1 + 3\sigma} \quad (1.160)$$

The same expression was derived also by Basset (1888b). At zero slip ($\sigma = 0$), this expression reduces to the Stokes drag for a solid particle and in the case of infinite slip ($\sigma \rightarrow \infty$) it reduces to the case of an inviscid bubble. An early work by Epstein (1924) noted that the phenomenological assumption, $w_\theta = (v - u)_s = \beta\tau_\theta$, on which expressions (1.158) and (1.160) are based, is consistent with continuum flow under the conditions $Kn \ll 1$. Epstein (1924) also suggested the following expression to be used in the cases of rarefied gases as a correction to the Stokes drag law:

$$F_i = 6\pi\mu(u_i - v_i)(1 - \sigma) \quad (1.161)$$

This is a first-order Taylor expansion of Eq. (1.160). He also derived an expression for the dimensionless slip parameter in terms of the Knudsen number, Kn , which is:

$$\sigma = 1.4008\left(\frac{2}{s} - 1\right)Kn \quad (1.162)$$

with s being the fraction of the gas molecules that undergoes diffuse reflection on the surface of the sphere, a parameter rather difficult to determine.

Equation (1.158) yields the following transient equation of motion for a small solid sphere in creeping motion with slip at its interface:

$$F_i(t) = -\frac{1}{2}m_f\frac{d(V_i - u_i)}{dt} - \frac{1 + 2\sigma}{1 + 3\sigma}6\pi a\mu(V_i - u_i) - \frac{[1 + 2\sigma]^2}{\sigma[1 + 3\sigma]}6\pi a\mu\int_0^t \exp\left(\frac{[1 + 3\sigma]^2 v[t - \tau]}{a^2\sigma^2}\right) \operatorname{Erfc}\left(\frac{1 + 3\sigma}{a\sigma}\sqrt{v[t - \tau]}\right) \frac{d(V_i - u_i)}{d\tau} d\tau \quad (1.163)$$

As expected, Eq. (1.163) yields the Boussinesq–Basset expression for the hydrodynamic force when there is no slip ($\sigma = 0$) and reduces to the transient equation for inviscid spheres when the slip is infinite.

Although the last term may appear to be a history term of a different kind, this is not the case. This term is, rather, a “residual term,” where the history part of the force as well as all the other effects that do not appear in the first two terms and are associated with the slip are present. In this respect, it should be recalled that the hydrodynamic force is a single entity and not three different forces. For this reason, equations such as (1.163) should be viewed as representing the single entity of the transient hydrodynamic force and not parts that have been identified for the partial case of solid spheres without slip.

1.4.3.6.2 Finite but Small Reynolds Numbers

Sano (1981) used an asymptotic analysis and derived an expression for the transient hydrodynamic force acting on a rigid sphere at small but finite values of the Reynolds number, when the sphere undergoes a step change in its velocity from 0 to v_i . Written in terms of a Reynolds number based on the diameter, d , Sano’s expression is:

$$F_i(t) = 3\pi d \mu_f v_i \left[H(t^*) + \frac{1}{3} \delta(t^*) + \frac{1}{2\sqrt{\pi t^*}} + \frac{3}{16} Re_r \left[\left(1 + \frac{16}{Re_r^4 t^{*2}} \right) \operatorname{erf}(0.5 Re_r t^{*1/2}) + \frac{2}{(\pi t^*)^{1/2} Re_r} \left(1 - \frac{2}{Re_r^2 t^*} \right) \exp\left(-\frac{1}{4} Re_r^2 t^*\right) - \frac{8}{3(\pi t^*)^{1/2} Re_r} \right] + \frac{9}{160} Re_r^2 \ln\left(\frac{1}{2} Re_r\right) \right] + O(Re_r^2) \quad (1.164)$$

The time variable in the above equation has been made dimensionless by dividing with a characteristic time based on the properties of the viscous fluid, $\tau_f = a^2 \rho_f / \mu_f$. The expression in the square brackets results from the contribution of the outer velocity field and is a consequence of the advective terms in the Oseen equations. For this reason, it has been referred to as the “Oseen contribution.” It appears that the most important effect of the higher Re_r on the hydrodynamic force is on the history term. The last term of the Oseen contribution cancels the third term in the right-hand side $(\pi t)^{-1/2}$. The remaining transient history terms decay exponentially. This rate of decay is faster than the decay of the transient terms of the creeping flow equation. From the physical point of view, this occurs because the finite velocity difference allows for the faster advection and evolution of the vorticity field around the sphere. While in the creeping flow case the vorticity field around the sphere was transported by viscous diffusion alone, which is a slower molecular process, in the case of advection the finite velocity “carries” the vorticity field far from the sphere with the characteristic velocity of advection. With the faster decay of the transient terms, a spherical particle does not retain any “memory” of its initial velocity, which is characteristic of the $t^{-1/2}$ rate of decay.

With the fast development of the numerical methods during the 1980s, computational studies appeared to complement the analytical results on the transient equation of a sphere. Mei et al. (1991) conducted such a numerical study on the motion of a rigid spherical particle in the range $0 < Re_r < 50$ when the free-stream velocity fluctuates with small amplitude. The numerical results of this study show that, in the low-frequency limit, the history term of the hydrodynamic force decays faster than the conventional $t^{-1/2}$ rate. Subsequently, Mei and Adrian (1992) obtained an analytical solution for the motion of a solid sphere, which is valid at very low frequencies ($St \ll Re_r < 1$). Their results revealed a different history term for the hydrodynamic force acting on the particle, which may be written as follows:

$$\frac{dv_i}{dt} - \frac{du_i}{dt} \int_0^t \frac{1}{\left[\left(\frac{\pi v_f}{a^2} (t-\tau) \right)^{1/4} + \left(\frac{\pi}{2 a v_f} \left(\frac{|u_i(\tau)|}{f_H} \right)^3 (t-\tau)^2 \right)^{1/2} \right]^2} d\tau \quad (1.165)$$

where f_H is a function of the Reynolds number, which has been correlated from the numerical data:

$$f_H = 0.75 + 0.105 Re \quad (1.166)$$

It is evident that at short times this history term matches the behavior of the typical history term at creeping flow, while at long times this term decays asymptotically as t^{-2} . With this functional form of longterm decay the sphere does not retain any memory of its initial velocity.

Lovalenti and Brady (1993a, 1993b) essentially followed Sano's method and derived the hydrodynamic force on a sphere undergoing an arbitrary motion. They used a different scheme for scaling and rendering the governing equations dimensionless and introduced the product of the Reynolds and Strouhal numbers ($St Re_r$) in their solution, which is also valid for finite but small Reynolds numbers. They also concluded that the unsteady terms of the equation of motion decay faster when the advection terms in the governing equations are retained. Some of the other noteworthy results of these studies are that the behavior of the sphere when its motion commences from rest is different than when the sphere starts with a finite velocity. The main physical reason for this is the formation and presence of an unsteady wake behind the sphere, which influences the motion of the sphere. The effects of this wake were explained by Hinch (1993), who presented simple arguments and quick asymptotic methods to explain the physical meaning of the solutions. He reduced the effect of the Oseen contribution, i.e., the advection terms in the governing equation, to the action of sources and sinks associated with the presence of the wake behind the sphere. It is apparent from these physical arguments that, with advection, any memory of a possible initial velocity of the sphere fades at long times. Also, because of differences of the velocity field developed in the surrounding fluid and the advection, the acceleration and deceleration processes of the sphere are not attained with the same force, even though the initial and final velocities of the sphere are the same. Therefore, the acceleration and deceleration processes at finite values of Re_r are not symmetric with respect to time. This is in contrast to the case of the creeping flow, where flow field is symmetric; the resulting Boussinesq–Basset expression is invariant with respect to the direction of time and yields the same magnitude for the forces in the acceleration and deceleration processes. This concept of time invariance should not be confused with thermodynamic reversibility: both the motions at finite and at zero Re_r are irreversible processes from the thermodynamic point of view and result in finite energy dissipation, which is approximately equal to the absolute value of the difference of the kinetic energy at the beginning and the end of the process.

1.4.3.6.3 High Reynolds Numbers — the Semi-Empirical Expressions

While all the known analytical expressions for the hydrodynamic force on particles, bubbles, or drops apply to low Reynolds numbers, many engineering applications of the transport processes occur at higher ranges of this parameter. Slurry transport and practical pneumatic conveying systems operate in the range $10^1 < Re_r < 10^3$; drops in combustion processes may reach Reynolds numbers up to 10^3 , bubble columns in chemical processes operate in a range from 0 to 10^3 ; depending on the properties of the carrier fluid; and particulate flows in the environment may reach relative Reynolds numbers, Re_p , up to 10^4 . Since there is no applicable theory, other than some asymptotic studies that only lead to approximate analytical expressions for the hydrodynamic force at $Re > 1$, experimental data and empirical correlations have been used for the calculation of the steady state as well as for the transient hydrodynamic force and the corresponding drag coefficient.

The steady-state empirical relations for the drag coefficients of a solid or a viscous sphere have been presented in Section 1.4.3.2. Regarding the transient terms of the hydrodynamic force, Odar and Hamilton (1964) were the first to propose modifications and correlation functions that extend to the transient terms, following the practice used for the steady-state term. They essentially treated the three terms of the Boussinesq–Basset expression (Eq. [1.146]) as separate forces and associated each one of them with a correction factor or function that accounts for the higher Reynolds number. Their proposed extension of the Boussinesq–Basset expression is as follows:

$$F_i = C_1 6\pi a \mu_f (\nu_i - u_i) + \Delta_A \frac{1}{2} m_f \frac{d(\nu_i - u_i)}{dt} + \Delta_H a^2 \sqrt{\pi \rho_f \mu_f} \int_0^t \frac{d\tau}{\sqrt{t-\tau}} d\tau \quad (1.167)$$

where the functions C_1 , Δ_A and Δ_H are empirical functions determined by experiments. Odar and Hamilton used Schiller and Nauman's (1933) correlation for the coefficient C_1 (Eq.[1.153]) and reduced their experimental data to derive the following expressions for the added mass and history term coefficients:

$$\Delta_A = 1.05 - \frac{0.066}{0.12 + Ac} \quad \text{and} \quad \Delta_H = 2.88 + \frac{3.12}{(0.12 + Ac)^3} \quad (1.168)$$

where Ac is the dimensionless acceleration number:

$$Ac = \frac{|u_i - v_i|^2}{2a|dv_i/dt|} \quad (1.169)$$

In a subsequent study, Odar (1966) verified the accuracy of these coefficients over the recommended range of Re_r . A few years later, Al-taweel and Carley (1971) performed independently their own experiments for the determination of Δ_A and Δ_H but derived different correlations for the two coefficients. In a related study, they also computed the magnitude of these terms and determined under what conditions the history terms were significant (Al-taweel and Carley, 1972).

The use of the semiempirical expressions became widespread in several applications for the determination of the lateral dispersion of particles and for the transient reaction force exerted on the fluid by particles, bubbles, or drops. Based on these expressions, Schoneborn (1975) explained and verified the experimentally observed retardation of spheres in oscillating fluids at very low frequencies. While there have been several numerical studies that have used Eq. (1.167) as the fundamental form for the expression of the hydrodynamic force, there is no general agreement as to the use of the associated correlation functions in Eqs. (1.168) and (1.169).

Other than the studies by Al-taweel and Carley, the experiments by Karanfilian and Kotas (1978), suggest constant values for Δ_A and Δ_H of 0.5 and 6, respectively, in the range of the lower values of Re_r . The same authors attribute the effect of the acceleration number solely to the coefficient C_1 and, instead, suggest the correlation $C_1 = C_{1s}(1 + 1/Ac)^{1.2}$, where C_{1s} is the value of the steady-state drag coefficient from the standard drag curve. Temkin and Mehta (1982) also suggested that the acceleration number affects only C_1 and recommended a different correlation for it. On the other hand, Tsuji et al. (1991) in an extensive experimental study of gas-solid flows confirmed the expressions by Odar and Hamilton (1964) and concluded that the accuracy of their expressions may be reasonably extended to Reynolds numbers up to 16,000 for gas-solid flows. In addition, Bataille et al. (1990) measured independently the added mass coefficient for bubbles and concluded that, within the experimental error of the measurements, it is consistently equal to $\frac{1}{2}$ in the range $500 < Re_r < 1000$, even when some of the bubbles are not exactly spherical. This implies that the added mass coefficient Δ_A is equal to 1 in this range of Reynolds numbers regardless of the acceleration number. Also Mei et al. (1991), Rivero et al. (1991), and Auton et al. (1988) confirmed analytically that the potential flow solution, which yields the value $\Delta_A = 1$ for the added mass coefficient is correct, and that neither the Reynolds number nor the acceleration number have a significant impact on this term. All these results call for the reinterpretation of the sets of experimental data for the total hydrodynamic force that have resulted in the semiempirical correlations.

The general practice of separating the transient force into three independent components and the use of the empirical values for C_1 , Δ_A , and Δ_H was deemed successful (i.e., it is meant agreement with the experimental data) and became very popular in engineering calculations since the 1970s. The rationale for this accuracy and popularity of the expression are the relative ease of calculations with the aid of computers and the close agreement of the results with experimental data. This agreement is due to the following reasons:

1. The semiempirical equations have a sound experimental basis, i.e., they are essentially correlations of experimental results, and
2. The semiempirical expressions have been derived from measurements of the entire hydrodynamic force and have always been used in calculations to determine the entire hydrodynamic force, and not any of its three parts.

It must be recalled that the pertinent experiments, from which the empirical coefficients emerge, measured the total hydrodynamic force on the sphere under various conditions. Then, by a series of assumptions and deductions, the experimentalist measured the total of the three parts of the hydrodynamic force and by a series of deductions estimated the three parts of Eq. (1.167) and, hence, determined the three coefficients. Similarly, for any verification of the derived expressions that followed, the resulting equation was used as a single entity to always calculate the total hydrodynamic force and not any parts of it separately. Subsequently, the results of such calculations were compared to other experiments, similar to the

ones from which the force was determined in the first place. Because of this coincidence in the determination and verification of the results, it would have been rather surprising if close agreement between experiment and "theory" was not obtained. It appears that this fortuitous agreement, which is based on a circular argument, is the reason why the semiempirical expressions are still considered accurate enough to be used in engineering calculations and are being used rather extensively in transient flows. Therefore, even if the calculations of the three parts individually have a high error, the calculation of their sum, which is equal to the total hydrodynamic force, has very low error. The derived results for the total hydrodynamic force can be trusted within their range of their applicability because they have a sound experimental basis.

Regardless of the perceived accuracy of the semiempirical expressions, it is a fact that they are based on a form of the hydrodynamic force that was derived under conditions where the relative Reynolds numbers approach zero, but the expressions themselves were developed to be used at very high Reynolds numbers. A glance at Eqs. (1.149), (1.150), and (1.162) will prove that the form of the function of the hydrodynamic force changes dramatically, when the relative Reynolds number is finite. Therefore, there is no *a priori* theoretical justification to using the functional form of expressions such as Eq. (1.167) for the total hydrodynamic force at higher values of Re_r . Any agreement of the semiempirical expressions with experimental results is fortuitous and due to the fact that the semiempirical expressions are essentially correlations of sets of experimental data. Therefore, when they are applied under similar conditions, they yield relatively accurate results. While using a semiempirical equation, one has only to ensure that the range of validity of the coefficients in terms of Re_r and Ac covers the range of the application or calculations. However, if the conditions change, for example, if the frequency of variation of the fluid field is significantly different than the frequency used in the derivation of the experimental data, the semiempirical expressions may fail. It is believed that differences in the conditions of the underlying experiments account for the manifest differences of the correlations proposed by Odar and Hamilton (1964), Al-taweel and Carley (1971), and Karanfilian and Kotas (1978).

It must be emphasized that the hydrodynamic force on a sphere is a single entity and not three different forces. For this reason a physical experiment, which would determine independently the values of the three terms of a semiempirical equation, such as Eq. (1.167) was never conducted (and it is not possible to conduct). With the development of numerical techniques, it is now possible to infer the value of these terms by separating the effect of the pressure term and of the steady-state results in the solution of the governing equations. The numerical studies by Chang and Maxey (1994, 1995) have separated the pressure effect and computed the history term for a sphere in the cases of oscillatory and accelerated motion. These studies also cast doubts on the validity and accuracy of the semiempirical Eq. (1.161) when it comes to the behavior of the history term and do not support the decomposition of the total transient hydrodynamic force.

Kim et al. (1998) developed a version of a semiempirical expression, based on numerical results rather than experimental data. They used the same process of decomposition of the hydrodynamic force into several components and concentrated their attention to the history term. They used the standard drag coefficient curve for the steady-state component, a coefficient equal to $\frac{1}{2}$ for the added mass coefficient, a convolution integral for the usual history term and another function to account for any initial difference of the velocity between the fluid and the sphere. Thus, they derived an expression that applies to a stationary or oscillating fluid in the range $0 < Re_r < 150$ and appears as follows:

$$\begin{aligned} m_s \frac{dv_i}{dt} = & -\frac{1}{2} c_{D0} \pi a^2 \rho_f (v_i - u_i) |v_i - u_i| - \frac{1}{2} m_f \left(\frac{dv_i}{dt} - \frac{Du_i}{Dt} \right) \\ & - 6\pi a \mu_f \int_0^t K(t - \tau, \tau) \frac{d}{d\tau} (v_i - u_i) d\tau - 6\pi a \mu_f K_l(t) [v_i(0^+) - u_i(0^+) + v_i(0^-) - u_i(0^-)], \\ & + (m_s - m_f) g_i + m_f \frac{Du_i}{Dt} \end{aligned} \quad (1.170)$$

where the functions K and K_l were determined from a series of numerical results after ensuring that their limits at $Re = 0$ for low and high frequencies agree well with analytical and asymptotic solutions. Kim

et al. (1998) claim good accuracy of their expression in the range $0 < Re_r < 150$ and $0.2 > \rho_f/\rho_s > 0.005$, though this expression has not been widely used by others. However, given the discussion on the physical meaning of an initial relative velocity in subsection 1.4.3.6.1, it is doubtful that the determination of the function K_1 can be verified by a physical experiment or can be physically derived in a meaningful manner.

Bagchi and Balachandar (2001) followed a similar approach and derived a semiempirical equation based on their own computational results. Their expression, however, is more general and allows for the transverse motion of particles and lift effects, which are inherent with some types of high Reynolds number flow. Given that accurate computations of the unsteady motion of a particle in high Reynolds numbers is an area developed only recently, it is almost certain that several other semiempirical expressions similar to the last equation will appear in the near future.

1.4.3.7 Deformable and Irregular Particles

Simple experiments based on the sedimentation of irregular particles have shown that the drag coefficients for nonspherical particles are different than those of spheres. Shape factors have been proposed for the quantification of the effect of nonsphericity of particles, bubbles, and drops. Wadell (1933) suggested that the volume-equivalent diameter of a sphere, d_n , or the area-equivalent diameter be used as the characteristic length of the particles for the determination of the actual drag coefficient. These two diameters may be given in terms of the volume and the projected area of the irregular particle as follows:

$$d_n = \sqrt[3]{6V/\pi} \quad \text{and} \quad d_A = \sqrt{4A_p/\pi} \quad (1.171)$$

where V is the total volume and A_p is the projected area of the particle in the direction of the flow. It follows that for the use of the parameter, d_A , one must have information on the orientation of the particle during the flow process. A shape factor, Ψ , may be defined as a dimensionless measure of the irregularity of the particle. Wadell (1933) used the following expression for the shape factor:

$$\Psi = \frac{A_s}{A} = \frac{d_n^2}{d_A^2} = \frac{\pi^{1/3}(6V)^{2/3}}{A_p} \quad (1.172)$$

Since the drag coefficient is defined in terms of the projected area of the particle, the shape factor may be used to correct for the irregular shape of particles according to the following expression:

$$\Psi C_D A = (C_D A)_s \quad (1.173)$$

In this expression, the quantity in the parenthesis pertains to the characteristics of a sphere, defined in terms of the volume-equivalent diameter d_n .

While Eq. (1.173) may be used as a first approximation for a correction to the steady-state drag coefficient, in the case of close-to spherical particles, other researchers (Pettyjohn and Christiansen, 1948; Haider and Levenspiel, 1989; Hartman and Yates, 1993) found that, in the case where particles are very elongated and the correction factors very large, this equation introduces significant errors in the determination of the actual drag coefficient. For this reason another quantity, the circularity, which is also called sometimes surface sphericity, c , was introduced:

$$c = \pi d_A / P_p \quad (1.174)$$

where P_p is the projected perimeter of the particle in its direction of motion. This is an easier parameter to measure in particles than the projected area, but suffers from the drawback that it yields the same value for some three-dimensional and two-dimensional objects. For example, spheres and disks that fall on their flat sides have the same circularity, while their drag coefficients differ significantly.

Based on these parameters, expressions for the drag coefficients of irregular particles have been derived by several researchers for different types and shapes of particles, including Pettyjohn and Christiansen (1948), Masliyah and Epstein (1970), Lasso and Weidman (1986), Haider and Levenspiel (1989), and Hartman and Yates (1993). Each one of these correlations applies to a specific type of particles (e.g., disks, pyramids,

prisms) or to a group of shapes. Chhabra et al. (1995) conducted an experimental study and determined the drag coefficients of chains of agglomerates of spheres in viscous fluids at relatively low Reynolds numbers ($Re_r < 2.5$). They concluded that in all cases the drag of the irregular agglomerate is higher (up to 50%) than the drag on a sphere with diameter d_n . Also, Madhav and Chhabra (1995) presented experimental data for the terminal velocity and the drag coefficients of spheres, cylinders, needles, and prisms in the range $1 < Re_r < 400$. More recently, Tran Cong et al. (2004) performed an experimental study that included several types of particles: spheroids, prisms, star-shaped, H-shaped, elongated bars/cylinders, X-shaped or cross-shaped. They correlated their data using several functional forms and concluded that the following expression not only correlates the data best, but also agrees very well with the correlations of the others:

$$C_D = \frac{24}{Re_r d_n} \left[1 + \frac{0.15}{\sqrt{c}} \left(\frac{d_A}{d_n} Re_r \right)^{0.687} \right] + \frac{0.42}{\sqrt{c} \left[1 + 4.25 \times 10^4 \left(\frac{d_A}{d_n} Re_r \right)^{-1.16} \right]} \quad (1.175)$$

Equation (1.175) is valid in the ranges $0.15 < Re_r < 1500$, $0.80 < d_A/d_n < 1.50$, and $0.4 < c < 1.0$. These ranges cover most of the irregularly shaped particles in engineering applications.

Regarding the transient equation of motion for slightly non-spherical particles, Lawrence and Weinbaum (1986, 1988) conducted an analytical study on the motion of a rigid spheroid of revolution with small eccentricity, under creeping flow conditions. Their study used essentially the method employed by Maxey and Riley (1983) with the added complexity of domain decomposition to a second-order expansion in terms of the eccentricity of the spheroid, ϵ . The resulting expression for the transient hydrodynamic force exerted on the spheroid is as follows:

$$F_i = -6\pi\mu_f a \left[(v_i - u_i) \left(1 - \frac{\epsilon}{5} + \frac{37\epsilon^2}{175} \right) + \frac{a}{\sqrt{\nu\pi}} \left(1 - \frac{2\epsilon}{5} + \frac{81\epsilon^2}{175} \right) \int_0^t \frac{d\tau}{\sqrt{t-\tau}} \right. \\ \left. + \frac{a^2}{9\nu} \left(1 + \frac{\epsilon}{5} - \frac{26\epsilon^2}{175} \right) \frac{d(v_i - u_i)}{dt} + \frac{8a\epsilon^2}{175\sqrt{\nu\pi}} \int_0^t \frac{d(v_i - u_i)}{d\tau} G(t-\tau) d\tau \right] \quad (1.176)$$

where the function G of the last term is frequency-dependent and is defined as follows:

$$G(t) = \text{Im} \left[\sqrt{\frac{\pi\phi}{3}} e^{\phi t} \text{erfc} \sqrt{\phi t} \right] \quad \text{with} \quad \phi = \frac{3}{2} (1 + i\sqrt{3}) \quad (1.177)$$

A comparison of Eq. (1.176) with Eq. (1.149) or (1.150) reveals that the first three terms of (1.175) are similar to the steady-state drag, the history and the added mass term of the Boussinesq–Basset equation. Their form is the same as the form of the corresponding terms of Eq. (1.149) with the expected correction terms due to the eccentricity of the spheroid. However, the last term of Eq. (1.176) does not have a counterpart in the Boussinesq–Basset expression. It depends on the eccentricity as well as the frequency of variation of the velocity of the fluid and vanishes asymptotically as ϵ^2 . This is a new history integral term, which derives from the elongated shape of the immersed object. The presence of such terms in an equation derived under the creeping flow assumption is another indication that the transient Boussinesq–Basset and Maxey–Riley expressions must be significantly modified when there are departures from the assumptions, these equations were derived from and which are listed in Section 1.4.3.6. Given that the modifications are on the functional form of these expressions, simple empirical corrections of the three terms of the hydrodynamic force would not in general be sufficient for the development of the correct transient expressions.

1.4.3.8 Deformable Bubbles and Drops

The motion of bubbles and drops in viscous fluids creates surface stresses that tend to deform the spherical symmetry of these objects. This has a very important effect on the transport coefficients, because the shape of an object is one of the primary determinants of the hydrodynamic force, the heat, and the mass transfer

coefficients. The physical properties of the bubbles, the drops, and the carrier fluid, such as surface tension and viscosity, play an important role in the deformation of the bubbles and drops as well as the determination of the shape of the flowing object. For bubbles freely rising in a column of water under the action of gravity, Haberman and Morton (1953) concluded that the following variables determine their shape:

1. The terminal velocity, v
2. The characteristic length, defined as the diameter of the volume-equivalent sphere, d_e
3. The density of the carrier fluid, ρ_f
4. The viscosity of the carrier fluid, μ_f
5. The surface tension, σ
6. The gravitational acceleration

Three independent dimensionless groups can be derived from these six variables:

1. The Reynolds number, $Re = \rho_f d_e v / \mu_f$, or, equivalently, the relative Reynolds number, Re_r
2. The Eötvös number, $Eo = g \rho_f d_e^2 / \sigma$
3. The Morton number, $Mo = g \mu_f^4 / \rho_f \sigma^3$

Another dimensionless group, the Weber number, that has also been used in the literature, is a derivative of the above three groups. The Weber number is defined by the relationship $We = \rho_f v^2 d_e / \sigma$ or $We = Re^2 (Mo/Eo)^{-1/2}$.

When experiments are carried in a constant gravitational field, such as laboratories on the Earth's surface, the list of the important variables is reduced to five. This leaves only two dimensional groups that would determine the shape of bubbles. This pair may be one of the combinations: (Re, Eo) , (Re, Mo) , or (Eo, Mo) . It is standard practice to reduce experimental observations on the shape of bubbles and drops in the so-called "shape-maps" with two of the above dimensionless groups as coordinates. Such a shape-map has been constructed from the data by Bhaga and Weber (1981) and is reproduced in Figure 1.13. The various acronyms on the map are as follows:

- s: spherical
- scc: spherical cap with steady, closed wake
- sco: spherical cap with open unsteady wake

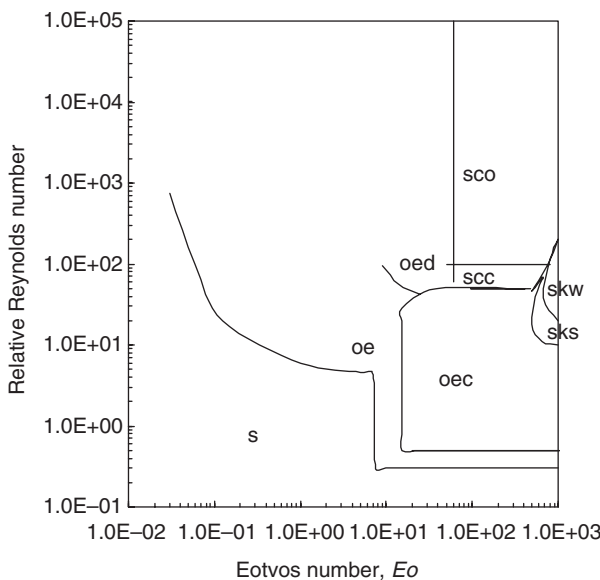


FIGURE 1.13 The shape-map of the deformed bubbles.

- oe: oblate ellipsoidal
- oed: oblate ellipsoidal disk (very elongated and wobbling in motion)
- oec: oblate ellipsoidal with cap in the bottom
- sks: skirted with steady skirt
- skw: skirted with wavy unsteady skirt

It is apparent in the figure that, while there is a complexity with the conditions on the shapes of bubbles, in general bubbles assume the spherical shape at low Reynolds numbers, regardless of the value of the Eötvös number. Also, bubbles are spherical at intermediate values of Re_r , when $Eo < 1$. Bubbles become ellipsoidal at intermediate values of Eötvös numbers and high Reynolds numbers. Finally, bubbles assume the shape of a spherical cap at high Eötvös numbers and at relatively high Re_r .

While a shape-map, such as the above, which represents static or steady-state conditions, is useful in determining the shape of flowing bubbles, recent experimental studies on the subject suggest that the method of the creation and release of the bubble affects its shape, the drag coefficient, and its trajectory. Tomiyama (2001) observed that when bubbles are released with small initial deformation, their shape remains very close to spherical, their drag coefficient is higher than expected, and their motion is rectilinear or zigzag on a plane. However, when the bubbles are released with high initial deformations as ellipsoids, their shape continues to be ellipsoidal with high aspect ratio, their drag coefficient is higher, and their motion is helical or rectilinear. In a similar study, Wu and Gharib (2002) also found that the initial method of the release of bubbles (whether they are released from a narrow or from a wide tube) plays a role in the eventual shape, the rise velocity, and the drag coefficient. Apparently, the shape oscillations that occur after a bubble is detached from the nozzle are strong enough to disperse the contaminants and to render the bubble surface clean, at least in the initial stage of the bubble trajectory. In most practical cases, the surrounded water contains a sufficient concentration of contaminants for the bubble surface to become immediately contaminated. However, in the case of very pure systems such as the ones used in the study by Wu and Gharib (2002), the recontamination process of the surface was very slow, the bubbles surface remained clean for the duration of the experiment and the bubbles remained spherical at significantly higher values of Re_r .

The drag coefficient of inviscid spheres (bubbles) is of particular importance in practical applications, such as boiling, aeration, and water purification. It is generally accepted that the surfactants and contaminants that line up on the interface of the bubble and the carrier fluid play a very important role in the determination of the drag coefficient of bubbles. Among the various studies on the drag coefficients, Tomiyama et al. (1998) studied the rise of bubbles in a wide range of Reynolds and Eötvös numbers and derived the following expression for the drag coefficients of clean, uncontaminated bubbles:

$$C_D = \max \left\{ \min \left(\frac{16}{Re_r} (1 + 0.15 Re_r^{0.687}), \frac{48}{Re_r} \right), \frac{8Eo}{3Eo + 12} \right\} \quad (1.178)$$

This expression is consistent with the correlations of the numerical data that were given in section (1.4.3.3), Eqs. (1.128) and (1.130) for small values of λ . It must be pointed out that when the bubbles become bigger, their shape becomes ellipsoid. Consequently, their drag coefficient depends strongly on the surface tension, which is a determinant of their shape. In the case of elongated bubbles, their drag coefficient is independent of the Reynolds number and is given by the last expression in Eq. (1.178), which is simply a function of the Eötvös number. This expression is valid even for fairly large hemispherical bubbles, up to 3 cm in diameter.

Because the state of the gas–fluid interface plays a major role in the friction part of the drag force and contaminants/surfactants accumulate on this interface, the degree of contamination of the liquid is an important factor in the determination of the drag coefficient of bubbles. The data by Sridhar and Katz (1995) suggest that small bubbles in filtered water, which may be characterized as “contaminated,” behave as solid spheres and their drag coefficients are very well correlated by the Schiller and Nauman (1933) expression (Eq. [1.126]) up to $Re_r = 85$. In the case of “grossly contaminated” conditions, such as those involving tap or industrial water, Loth (2000) recommends the Oseen expression for $Re_r < 1$ and the

following expressions that are based on data from Clift et al. (1978):

$$\begin{aligned} C_D &= \frac{24}{Re_r}(1 + 0.1935Re_r^{0.0305}) \quad \text{and} \quad 1 < Re_r < 78 \\ C_D &= \frac{24}{Re_r}(1 + 0.03875Re_r), \quad 78 < Re_r < 300 \end{aligned} \quad (1.179)$$

Beyond this range of relative Reynolds numbers, it is very likely that the bubbles are not spherical and, hence, their shape is the major factor that influences the drag coefficient.

It must be pointed out that the drag coefficient expressions for “clean” and “grossly contaminated conditions” may be considered as the lower and the upper limits for bubbles. The actual value of the drag coefficient of bubbles in industrial systems should be expected to lie between these two limits.

1.4.3.9 Lift Effects and Transverse Forces

The drag force is always acting in the direction of motion and its magnitude is monotonically increasing with the relative velocity of the sphere. Rotation combined with finite relative velocity, or fluid velocity gradients (shear) even in the absence of particle rotation, will induce a transverse component in the hydrodynamic force on the sphere, which is often called the lift force. When the rigid, spherical particle travels in a fluid with a relative velocity and also rotates with respect to the far field of the flow, transverse pressure differences appear on the surface of the sphere that result in *the Magnus force* (Magnus, 1861). The Magnus force is given by the expression:

$$F_{LMi} = \pi\alpha^3[\rho_f e_{ijk}\Omega_j(u_k - v_k)] \quad (1.180)$$

where Ω_j is the relative rotation of the particle with respect to the fluid and the term $e_{ijk}\Omega_j(u_k - v_k)$ represents the vector (cross) product of the relative rotation and relative velocity vectors. The direction of the Magnus force is perpendicular to the plane of the relative velocity and the axis of rotation and the force itself is the consequence of a sideway pressure difference induced because of streamline asymmetry, which results from the rotation of the sphere. It is apparent that this force is independent of the fluid viscosity and, therefore, it appears in viscous as well as in inviscid flows.

As with the steady-state drag force, the magnitude of the Magnus lift force is often expressed as a function of a dimensionless “lift coefficient,” C_{LM} , which is then correlated by experimental data. While many expressions have appeared in the past, the investigation by Oesterle and Bui-Dihn (1998) appears to be based on accurate data and is recommended to be used for the lift coefficient of a sphere rotating in an infinite fluid:

$$C_{LM} = 0.45 + \left(\frac{Re_R}{Re_r} - 0.45 \right) \exp(-0.05684Re_R^{0.4}Re_r^{0.3}) \quad \text{for } Re_R < 140 \quad (1.181)$$

where Re_R is the Reynolds number based on the relative rotational speed of the sphere:

$$Re_R = \frac{\rho_f d^2 |\boldsymbol{\Omega}|}{\mu_f} \quad (1.182)$$

The lift coefficient is in general a monotonically decreasing function of the relative Reynolds number, Re_r and in general increases with the dimensionless *rotation parameter*, $\frac{|\boldsymbol{\Omega}|d}{|u - v|}$, which is a dimensionless measure of the rotational speed of the particle. Experiments at low values of the rotation parameter suggest that C_{LM} may become negative (Tanaka et al. 1990). This is most likely due to a higher relative velocity on one side of the sphere and the premature transition to turbulence of the boundary layer on that side. As a consequence, the wake behind the sphere deflects in the direction opposite to that, which is expected in rotating flow. Hence, the lift force acts in the opposite direction.

Saffman (1965, 1968) considered the case of a very small sphere in a shear flow at the limit of vanishing Reynolds numbers (creeping flow). Thus, he derived an expression for this force whose magnitude is

$$F_{LS} = 6.46\mu_f a^2 |v - u| \kappa^{1/2} v^{-1/2} \quad (1.183)$$

where κ is the fluid velocity shear evaluated at the center of the sphere. The direction of the force is the perpendicular direction to the plane defined by the relative velocity vector and the shear vector. Sufficient conditions for the validity of the above expression are very low Re_r as well as:

$$|\mathbf{v} - \mathbf{u}| \ll (\kappa v)^{1/2}, \quad \kappa a^2/v \ll 1, \quad a^2 |\boldsymbol{\Omega}|/v \ll 1 \quad (1.184)$$

These conditions imply one of the following two alternatives:

1. Either very low particle velocity, shear, and angular rotation for the particle.
2. Extremely high kinematic viscosity for the fluid if the particle has finite velocity, shear, or angular rotation.

The first alternative is compatible with the assumptions implied in the derivation of the Basset–Boussinesq equation. The second alternative implies very high viscosity in combination with finite shear or rotation and is not strictly compatible with the implied conditions of the Basset–Boussinesq equation. It must be pointed out that although Saffman's result (Eq. [1.183]) is occasionally referred to as *the* Saffman force, it is not a separate force from the Magnus force but a special case of the latter at the limit $Re_r \rightarrow 0$ in shear flow. For this reason, the lift force must be only accounted once in computations of particle dynamics.

The appearance of the lift force is related to the inertia of the particle and is inconsistent with the governing equations from which the creeping flow solutions have been derived. Under the creeping flow conditions and the assumptions underlined in Section 1.4.3.6, a sphere only experiences a symmetric force that opposes its rectilinear motion. Transverse forces do not appear in creeping flow conditions, because the flow domain resulting from the introduction of the sphere is symmetric (Maxey and Riley, 1983; Michaelides and Feng, 1995). At finite Re_r , transverse forces may appear if the velocity field exhibits an asymmetry. However, most of the analytical and numerical derivations of drag coefficients at finite Re_r implicitly assume that the fluid velocity field is symmetric.

The lift force developed on a sphere is in general very much weaker than the longitudinal drag force. However, the transverse lift force plays a dominant role in the lateral migration of bubbles, drops, and particles toward the walls of cylindrical pipes as well as in dispersion processes. This occurs because in most engineering systems particles, bubbles and drops have to travel relatively very short distances in order to approach the walls of a pipe or a channel and, hence, a weak force would be sufficient to induce the lateral motion that covers such short distances. Therefore, these weak transverse forces contribute significantly to radial diffusion and dispersion, wall deposition, and mixing and separation processes.

Among the recent developments on the lift forces exerted by a viscous fluid on a sphere, Tsuji et al. (1985) measured experimentally the shear-induced lift on bubbles and concluded that the expression by Saffman yields satisfactory results on the magnitude of the force. McLaughlin (1991) extended the theoretical analysis by Saffman to higher Re_r and derived a correction to the expression by Saffman, which shows that the magnitude of F_{LS} decreases with the increase of Re_r . McLaughlin's expression for the lift force is as follows:

$$F_{LS} = \frac{9}{\pi} \mu a^2 |\mathbf{v} - \mathbf{u}| \sqrt{\frac{\kappa}{v}} J(\varepsilon) \quad (1.185)$$

where ε is the dimensionless velocity ratio, $\varepsilon = \kappa v / |\mathbf{v} - \mathbf{u}|$, and the function $J(\varepsilon)$ is given in tabular form by McLaughlin (1991). Two approximate asymptotic expressions for this function are $J(\varepsilon) = 2.255 - 0.6463/\varepsilon^2$ for $\varepsilon \gg 1$ and $J(\varepsilon) = 32\pi^2\varepsilon^5 \ln(\varepsilon^{-2})$ for $\varepsilon \ll 1$. This correction improved the accuracy of Saffman's Eq. (1.183) and extended the range of its applicability to higher Reynolds numbers, a fact that was later confirmed experimentally by Cherukat et al. (1994) for a solid sphere near a wall.

The numerical results for the lift force exerted on a sphere by the shear obtained by Dandy and Dwyer (1990) were reduced to a useful correlation by Mei (1992). His proposed correction factor is as follows:

$$C_{LS} = \begin{cases} \frac{F_L}{6.44\rho_f a^2 k^{1/2} v^{-1/2}} = (1 - 0.3314\sqrt{\beta}) \exp\left(-\frac{Re_r}{10}\right) + 0.3314\sqrt{\beta} & \text{for } Re_r \leq 40 \\ 0.0524\sqrt{\beta} Re_r & \text{for } Re_r > 40 \end{cases}$$

$$\text{where } \beta = \frac{d|\nabla \times \mathbf{u}|}{2|\mathbf{u} - \mathbf{v}|} \quad (1.186)$$

The parameter β in the last equation is a dimensionless measure of the shear. The recommended range of the above correlation is $0.005 < \beta < 0.4$ and Mei (1992) showed that this empirical equation fits well McLaughlin's results.

It must be pointed out that there is no widespread agreement on the magnitude of the lift coefficients. The experimental results by Sridhar and Katz (1995) suggest that at least for bubbles, the magnitude of the lift component of the hydrodynamic force is higher than the values predicted by the above two expressions. Another experimental study by Tomiyama et al. (1999) on bubbles in shear flows concluded that the lift coefficient of larger bubbles depends on the surface tension and, hence, the dependence on the Eötvös number should be included in the correlation. Tomiyama et al. (1999) also concluded that rising bubbles tend to accumulate close to the walls if their radii are less than 6 mm, while bigger bubbles with $a > 6$ mm tend to migrate toward the center of the apparatus.

The lift of growing bubbles that are formed close to a wall is very important in the boiling and evaporation processes, because the global rate of the heat transfer greatly depends on the amount of vapor in contact with the wall or in the immediate vicinity of the wall. In boiling convective systems, such as heated pipes, the lift due to shear facilitates the detachment of small spherical bubbles from the wall and subsequently the nucleation and the commencement of the growth process of other bubbles. Thorncroft et al. (2001) studied the growth and detachment of bubbles from a surface and concluded that the growth of a bubble, whose radius, a , is given as a function of time, that is $a(t)$, close to a wall enhances the lift force exerted by the shear. In their analytical and computational study, Thorncroft et al. (2001) derived the following expression for the lift due to the shear:

$$F_{\text{SLi}} = \frac{1}{2} |\mathbf{u} - \mathbf{v}| (u_i - v_i) \pi \rho_f a^2(t) \kappa^{1/2} \left\{ \left[\frac{1.46J}{Re_f^{1/2}} \right]^2 + \left[\frac{3}{4} \kappa^{1/2} \right]^2 \right\}^{1/2} \quad (1.187)$$

where J is a scalar function of the dimensionless shear rate and the Reynolds number. The augmented lift force in this case facilitates the detachment of the bubble from the wall, reduces the amount of vapor close to this wall and, thus, contributes to the enhancement of the heat transfer from the wall to the bulk fluid.

The transverse force on particles is also influenced by the presence of other particles in the flow. The shear-induced lift on solid spheres attached or deposited on a boundary, in the presence of other spheres in the flow field, known as suspension flow, was studied numerically by Feng and Michaelides (2002a). Their results show that the instantaneous hydrodynamic force exerted by the suspension flow on a solid particle attached to a wall is increased by a factor of 2 to 4 by the presence of similar particles in the flow field. This is depicted in [Figure 1.14](#), which shows the instantaneous lift on an embedded sphere, when other spheres in suspension flow pass in its vicinity. This force augmentation includes both the lift and the drag components of the hydrodynamic force. It is caused by the interactions of the suspended spherical particles with the stationary particle when they are in close proximity, within 3 diameters. As a result of this type of hydrodynamic interaction, a particle that lies on a horizontal plane may be lifted and become part of the suspension flow without any physical collisions with other particles in the flow.

Regardless of the method of evaluation of the lift component, the ratio of the transverse component to the longitudinal component of the hydrodynamic force, F_L/F_D , is of the order of $d(\kappa/v)^{1/2}$. This is necessarily a very small number according to all the assumptions used in the derivation of the lift force. Despite of this, the transverse component of the hydrodynamic force is very important because it causes the lateral migration and dispersion of spheres, and plays an important role in several engineering applications, such as bubble detachment from the pipe walls during boiling, particle sedimentation and resuspension in water as well as particulate and aerosol dispersion in the atmosphere. For this reason, the accurate knowledge of the transverse component of the hydrodynamic force is of importance in engineering calculations that pertain to such processes, even though the method of the determination of the drag component is not fully compatible with the assumptions used for the determination of the lift. It is common practice in such calculations to superpose an expression for the transverse or lift component, (such as Eq. [1.180] or [1.183]), with an expression for the transient hydrodynamic force in the longitudinal direction, (such as Eq. [1.138]), and thus to calculate the longitudinal and transverse motion of particles, bubbles, and drops. The result of such a superposition is that the transient hydrodynamic force on a sphere

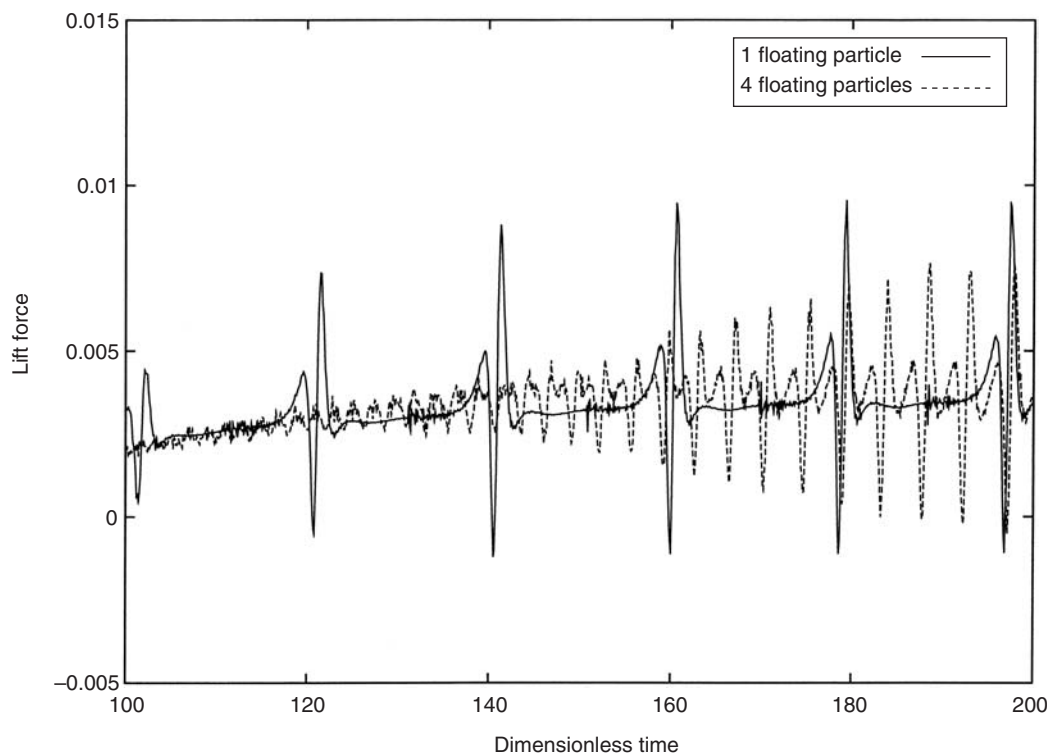


FIGURE 1.14 The effect of the flow of suspended particles on the lift of a stationary particle.

appears to have a lateral, albeit steady-state, component in addition to the longitudinal component. Although this superposition is not justified on analytical grounds, it is very convenient to use and the results obtained appear to be accurate in most cases. When one uses this superposition, it is important to ensure that the necessary conditions for the validity of the expressions used for the several components of the hydrodynamic force are not violated. In most of the cases this means that there is very low relative velocity, and that the local shear is low.

The influence of mass transfer from the sphere (evaporation or sublimation) on the lift is investigated under experimentally and numerically. A recent numerical study by Kurose et al. (2003) determined that in linear shear flow, the outflow from a sphere acts in a way to push the sphere toward the lower flow velocity side. Thus, a negative lift is developed at high Reynolds numbers. This tends to counteract the positive lift on the sphere, which is directed toward the higher velocity side. According to the numerical study by Kurose et al. (2003), the diffusion and reaction rates are strongly affected by the outflow velocity and the fluid shear because of the deformation of the vortices that appear behind the evaporating sphere. This suggests that surface evaporation and reaction is of great importance to the lateral motion of drops and, hence, to the determination of the pertinent scalar concentration fields.

1.4.3.10 Effects of the Walls

The motion of particles, bubbles, and drops in the vicinity of a wall is very important in many practical applications, especially those related to boiling of liquids and transport of particulates and slurries. As was mentioned in the previous section, the lift on small bubbles, which is induced by the shear layer close to any wall, influences the rate of heat transfer from a surface during several practical processes. In particulate transport processes, particle collisions with the walls result in pipeline erosion and particle adhesion to the walls, cause scale buildup and oftentimes pipeline clogging. The effect of a wall in general is to retard the motion of particles in both the parallel and the perpendicular direction to the wall, thus

reducing the rate of mass transport. In addition, the presence of particles and bubbles in boundary layers and mixing layers significantly modifies the stability and transport properties of these layers.

The first to consider the motion of a particle in rectilinear motion parallel to a wall and to derive an expression for the hydrodynamic force on a spherical particle was Faxen (1992). He used the method of reflections for the movement of the sphere under creeping flow conditions and obtained an asymptotic solution for the total force acting on a sphere that settled following the centerline of an orthogonal circular cylinder. In this case, the ratio, Ξ , of the particle diameter, d , to the characteristic dimension of the cylinder, L , ($\Xi = d/L$) is the most important parameter that affects the hydrodynamic force. Faxen's expression for the hydrodynamic force may be given in terms of a wall drag multiplier, K_{wall} , which is the ratio of steady-state hydrodynamic force in the presence of the wall, to the Stokesian force that a sphere experiences in an unbounded flow. By using the same method of reflections, Bohlin (1960) obtained a higher order approximation for the wall drag multiplier, which may be written as follows:

$$K_{\text{wall}} = \frac{1}{1 - 2.01443\Xi + 2.088777\Xi^3 - 6.94813\Xi^5 - 1.372\Xi^6 + 3.87\Xi^8 - 4.19\Xi^{10} + \dots} \quad (1.188)$$

Haberman and Sayre (1958) developed a theoretical method to compute the wall correction factor, K_{wall} , for spheres settling in cylinders up to very high values of the parameter Ξ , and later Paine and Scherr (1975) used this method in order to compute the values for K_{wall} . These results are tabulated and they are valid in the range $0 \leq \Xi \leq 0.9$. A comparison between the expression by Bohlin (Eq. [1.188]) and the exact theory by Haberman and Sayre (1958) shows that the last equation yields accurate results only up to $\Xi = 0.6$. Apart from the analytical/computational studies, there are also several experimental studies pertaining to the settling of a sphere along the centerline of an orthogonal circular cylinder or next to a plane wall. Among them, the experimental studies by Iwaoka and Ishii (1979) and Miyamura et al. (1981) show good agreement with the theoretical predictions by Faxen (1922), Bohlin (1960), and Paine and Scherr (1975).

Happel and Brenner (1986) considered creeping as well as inertia flows for the settling of a sphere in a cylinder, and stipulated that the total effect on the hydrodynamic force acting on the sphere is a simple linear combination of the separate effects of proximity to the outside boundary and inertia. Thus, the total correction factor for the hydrodynamic force acting on a sphere is given by the expression:

$$K = K_{\text{wall}} + K_{\text{inertia}} - 1 \quad (1.189)$$

where K_{wall} is the effect of the wall at creeping flow conditions as calculated by an expression similar to (1.188) and K_{inertia} is the additional correction factor due to the inertia effects of the flow at higher Re . The last equation simply implies that the drag on a sphere is composed of two additive terms: one term is due to the effect of the cylindrical boundary and the other is due to the flow inertia. The latter is usually obtained from one of the empirical correlations for the drag coefficient at high Reynolds numbers, such as the one by Schiller and Nauman (1933). Equation (1.189) is essentially a conjecture, partly based on the experimental data by Fayon and Happel (1960). The data set pertains to a diameter ratio, Ξ , in the range of 0.1250 to 0.3125 and Reynolds numbers in the range 0.1 to 40. Feng and Michaelides (2002b) conducted a more general numerical study in the ranges $0.1 < \Xi < 0.8$ and $0 < Re < 35$ for cylindrical as well as prismatic enclosures. They concluded that the two effects of inertia and of flow confinement are not always additive and may not be linearly combined as Eq. (1.189) implies. Because of this, in calculating the hydrodynamic force on a sphere, it is more accurate to use computational or experimental results, which are not restricted by the conjecture (Eq. [1.189]) and which yield the total correction factor, K , as a function of the pertinent parameters of the flow. One of the results by Feng and Michaelides (2002b) is that at the higher values of the parameter, $\Xi > 0.5$ the effect of inertia is less than 10% of the correction factor. Table 1.1, which is reproduced from Feng and Michaelides (2002b), shows the total correction factor, K , for a sphere of diameter, d , when it falls in a rectangular prismatic enclosure whose cross section has length, L , and width, W . The results shown are for $Re \ll 1$.

It must be pointed out that the effect of the walls on the settling of a sphere is different in the case of prismatic enclosures than in cylinders, because secondary flows are induced in the corners of the prisms. Even though these secondary flows are relatively weak, they affect considerably the hydrodynamic force developed on the sphere.

TABLE 1.1 Wall Correction Factors for Various Orthogonal Rectangular Prisms

$L/W = 1.0$								
$\Xi (= d/W)$	0.2	0.3	0.4	0.5	0.6	0.7	0.8	0.9
K	1.72	2.30	3.18	5.01	8.03	13.98	27.9	61.8
$L/W = 1.5$								
$\Xi (= d/W)$	0.3	0.4	0.5	0.6	0.7	0.8		
K	1.90	2.47	3.32	4.46	6.11	9.24		
$L/W = 2.0$								
$\Xi (= d/W)$	0.3	0.4	0.5	0.6	0.7	0.8		
K	1.73	2.12	2.67	3.33	4.37	5.76		
$L/W = 5.0$								
$\Xi (= d/W)$	0.3	0.4	0.5	0.6	0.7	0.8		
K	1.53	1.75	2.11	2.48	3.06	3.78		

The repulsive effect of the wall on spheres results in a radial migration of particles in pressure-driven flows in pipes and small capillaries. Poiseuille (1841) was the first to perform an experimental study on this subject and, for this reason, such flows now bear his name. Poiseuille's objective was to model the distribution of cells in blood flow. Wang and Skalak (1969) studied analytically the flow of an array of spheres located at the centerline of a cylindrical tube under creeping flow conditions and calculated the pressure drop in the cylinder with the particle size and interparticle distance as parameters. Cox and Brenner (1967) expressed the effect of a vertical wall on a particle by using the concept of a *migration velocity* of a sphere that is falling close to a wall. An analytical expression for the migration velocity is as follows:

$$V_r = \frac{6\pi v_s^2}{\nu} I_h \quad (1.190)$$

where v_s is the sedimentation velocity of the sphere in a stagnant fluid and I_h is an integral of Green's function for the point force representing the sphere. The last expression is valid under the conditions $Re \ll a/l_w \ll 1$, where l_w is the distance of the center of the sphere from the wall. The implications of this condition are that the sphere is relatively far from the wall and the flow field is Stokesian (creeping flow). Later, Cox and Hsu (1977) calculated the integral, I_h , for the case of a sphere and derived the following expression for the migration velocity:

$$V_r = \frac{3}{64} Re_r v_s \quad (1.191)$$

which is also valid under the condition: $Re \ll a/l_w \ll 1$. A close look at the last expression reveals that the migration velocity of the sphere is independent from its distance of the wall. This does not constitute a paradox, because the expression is valid only at distances sufficiently far from the wall as required by the condition $a/l_w \ll 1$.

Vasseur and Cox (1976) derived analytically an expression for the lateral migration velocity of a sphere that falls in a quiescent fluid in the proximity of a plane wall. Their expression for the lateral velocity is as follows:

$$V_r = \frac{3}{8} \frac{\alpha v_z^2}{\nu} \left[\left(\frac{\nu}{l_w v_z} \right)^2 + 2.219 \left(\frac{\nu}{l_w v_z} \right)^{5/2} \right] \quad (1.192)$$

where v_z is the (vertical) sedimentation velocity of the particles. The terms in the two parentheses are obviously the inverse of a Reynolds number, which is based on the distance of the center of the sphere from the wall. The last expression was later confirmed by the experimental data of Cherukat and McLaughlin (1990) to be valid up to $Re = 3.0$.

The repulsive effect of the wall on particles is very important in the distribution of phases in dispersed flows in pipes as well as in sedimentation–resuspension processes with particles. This effect has been demonstrated in a number of experimental and numerical studies, such as the one by Segré and Silberberg (1962) with neutrally buoyant spheres. They concluded that neutrally buoyant particles in a pressure-driven Poiseuille flow (pipe flow) experience a radial force and tend to align at a distance, which is at approximately 0.6 pipe radii away from the centerline. This shows that there exists an equilibrium position where the radial force is zero and, where particles tend to accumulate. Two-dimensional numerical studies have also concluded that there is an equilibrium position for cylinders at a distance of 0.4234 half-channel width away from the centerline. Inamuro et al. (2000) concluded that this distance is the same for both a single cylinder and for a group of naturally buoyant cylinders in a pressure-driven channel flow. Mortazavi and Tryggvason (2000) also studied the lateral migration of two-dimensional drops in a Poiseuille flow and found that drops either move halfway between the pipe centerline and the wall, as Segré and Silberberg (1962) also observed, or they oscillate around an off-center equilibrium position. In a study involving the resuspension of particles in simple shear flow over a flat plate, Feng and Michaelides (2003) concluded that particles that are slightly heavier than the fluid do not settle down on a flat surface, but reach an equilibrium position at a certain height and then drift with the main flow at this position. Their numerical results are shown in Figure 1.15. The dividing line separates the settled particles from the ones that reach an equilibrium position, which is usually at a height less than a single diameter from the flat surface. It appears that the equilibrium position of the particles depends on the relative Reynolds number, the density ratio, and the magnitude of the shear in the flow. This implies that there is a relationship between the dimensionless shear, the shear Reynolds number, and the density ratio for which a particle will either settle on the bottom flat surface or will remain suspended and will drift with the flow. Feng and Michaelides (2003) derived the following expression for this relationship, which is shown by the line in Figure 1.15:

$$Re_{\kappa} = \frac{\rho_f \kappa d^2}{\mu_f} = 58 \left[\frac{\rho_s}{\rho_f} - 1 \right]^{0.59} \quad (1.193)$$

At a given shear Reynolds number heavier particles settle while lighter particles, with density lower than Eq. (1.193) would predict if solved for the density ratio, travel to an equilibrium position and stay suspended in the flow, even though they may be heavier than the fluid. Patankar et al. (2001) also examined the behavior of particles close to the wall in a Poiseuille flow and observed a similar behavior for the particles. They developed a corresponding expression for the shear Reynolds number and the density

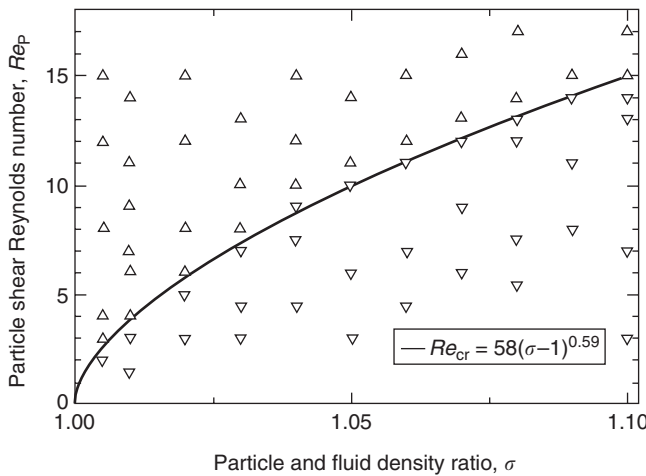


FIGURE 1.15 Settling or suspended particles with σ and Re_p , as parameters. Δ represents suspended particles and ∇ denotes settled particles.

ratio, which may be written as follows:

$$\frac{\rho_s}{\rho_f} - 1 = 2.3648 \frac{\mu_f^2}{d^3 \rho_f^2 g} Re_\kappa^{1.3904} \quad (1.194)$$

Equation (1.193) should be used for shear flows over flat plates, while Eq (1.194) should be used in pipes, where Poiseuille flows are more likely to occur. It must be pointed out that neither of the last two equations takes into account turbulence in the flow nor turbulent bursts that result in the advection of particles and the resuspension of groups of particles.

Regarding the flow of a sphere perpendicular to a wall, Brenner (1961) obtained asymptotically a first-order correction for the drag coefficient of a small rigid sphere moving toward the wall and concluded that the Stokes drag coefficient, f , increased by a factor equal to

$$f = \frac{C_D}{24/Re_r} = 0.625 \frac{d}{l_w} \quad (1.195)$$

where l_w is the distance from the center of the sphere to the wall. Brenner's results indicate that the hydrodynamic force on the particle increases dramatically when the particle approaches very short distances from the wall. This is related to the thin fluid layer that develops between the particle and the wall. Draining such thin layers where viscous effects dominate is a very slow process. The hydrodynamic force exerted opposing the motion of the sphere becomes very large and the velocity of its approach to the wall becomes extremely low. The study by Kalio (1993) also indicates that the influence of the wall on the drag of the particles is important when the particle is within 20 diameters from the wall. Within this distance, the drag of the particle moving perpendicular to the wall is increased significantly from the value obtained from the standard drag curve. The more recent experimental and computational study by Ten Cate et al. (2002) confirmed this rapid and significant increase of the drag coefficient of settling spheres, which are within one diameter from a horizontal wall.

When particles, bubbles, or drops are present in a flow field and also experience a transverse temperature gradient, they are subject to a force, the thermophoretic force, which is due to the molecular velocities of the carrier fluid. Molecules at the high-temperature side of the particle have, on the average, higher kinetic energies and through molecular collisions with the particle impart a higher rate of momentum on the high-temperature side than the low-temperature side. The net effect of all these collisions is a net force in the direction opposite to that of the temperature gradient. Obviously the thermophoretic force depends on the temperature gradient in the carrier fluid. Talbot et al. (1980) recommended the following expression for the thermophoretic force, F_T :

$$F_T = -6\pi\mu_f\nu_a \frac{2C_s}{1+6C_mKn} \frac{k_f/k_s + 2C_iKn}{1+2k_f/k_s + 4C_iKn} \frac{\nabla T}{T} \quad (1.196)$$

where Kn is the Knudsen number in the carrier fluid and C_s , C_i , and C_m are three coefficients whose recommended values are 1.17, 2.18, and 1.146, respectively. It is evident from this expression that the thermophoretic force is very weak for particles in continuum flow where $Kn \gg 1$. However, this force becomes significant with submicron and nanoparticles, and may be used for the control of the motion of such particles and their settling or their collection. In the case of tiny particles, the gravitational force, which is proportional to d^3 , is extremely small. With a sufficiently high temperature gradient, the thermophoretic force becomes significant enough to control the motion of nanoparticles and to affect their deposition on a cold surface. Thus, one may use the thermophoretic force for the collection of nanoparticles in a cold cup or a cold plate (Leung and Crowe, 1993).

Turbophoresis is a phenomenon similar to thermophoresis and results from the gradient of turbulence intensity, which exists in boundary and shear layers. In this case, the particle is subjected to a higher force on the side where turbulence is higher and, thus, the net turbophoretic force acts in the direction opposite to $\nabla u'^2$. Analysis and experiments have shown that, in a wall boundary layer, the process of turbophoresis tends to bring the particles closer to the wall, where the turbulent fluctuations are weaker. However, when the particle concentration at the wall becomes high, the accumulation of particles close

to the wall results in a “drift velocity” toward the center, which is the result of the high particle concentration gradient. The balance of the two driving forces, turbulence and concentration, yields an equilibrium condition. Models that are based on this equilibrium predict fairly well the particle behavior close to the wall in turbulent pipe flow. Portela et al. (2002) concluded that the local equilibrium models predict well the particulate concentration, except very close to the wall ($y^+ < 20$), where the turbulent fluctuations are very weak and turbophoresis cannot even be defined in a physically meaningful way.

It must be pointed out that our knowledge of all transverse components of the hydrodynamic force and on the effect of the walls on the motion of a sphere is not based on the rigorous derivation of the transient equation of motion that originates from the solution of the governing equations, which would include both the longitudinal as well as the transverse motion, but on specific analytical, experimental, and numerical studies, most of which were performed at specific conditions and at steady state. One has to be aware that the rectilinear transient equations of motion mentioned in Section 1.4.3.6 implicitly assume that there is no rotation of the sphere, no significant shear in the flow and that the sphere is in an unbounded fluid, which essentially means far from any wall or other boundary. This far-away condition is usually satisfied at distances, $l_w > 20a$. For this reason, the addition of the lift or any wall effect on a rigorously derived transient equation for the rectilinear motion of a particle must be viewed as an *ad hoc* assumption. Such assumptions are frequently used, because practice has shown that they yield reliable results on the behavior of particles. It must be remembered however, that such assumptions even though justified by validation with experiments or other means, have their own limitations and their own range of applicability.

1.4.4 Heat Transfer

While the development of the equation of motion for a sphere was based predominantly on analytical work followed by corrections derived from experiments, most of the analyses on the subject of heat transfer are based on Fourier's (1822) work. This treatise, which was preceded by seven shorter articles by Fourier, has been subsequently supplemented by numerous experimental studies that have provided semiempirical correlations for the rate of heat transfer or, equivalently, for the Nusselt number. For this reason, the subject of heat transfer from spheres is based primarily on correlations that stem from experiments or, in the recent past, from numerical studies.

At first, it must be pointed out that the governing continuum equations for the heat transfer and for the mass transfer are strictly similar. For this reason, the solution of one equation also yields the solution of the other equation by simple substitution of the corresponding dimensionless numbers. Therefore, all the results, analytical, experimental, or computational, for the heat transfer coefficients are also applicable to the mass transfer coefficients.

An important parameter in the study of convective heat and mass transfer from spheres is the Peclet number, which accounts for the heat or mass advected by the fluid. The Peclet number is analogous to the Reynolds number in the equation of motion and is defined as follows for the cases of heat transfer and mass transfer, respectively:

$$Pe = d\rho_f c_{pf} U / k_f \quad (\text{or } Pe = Re Pr) \quad \text{and} \quad Pe_M = dU / \mathfrak{D} \quad (1.197)$$

where U is the characteristic velocity of the fluid; c_{pf} is the specific heat capacity of the fluid; k_f is the conductivity of the fluid; and \mathfrak{D} is the diffusivity of the fluid. The Prandtl number Pr , is the dimensionless group of the fluid properties $Pr (= \mu_f c_{pf} / k_f)$. When there is relative motion between the sphere and the fluid, which is characteristic of most advection processes, the magnitude of the relative velocity should be used as U in the expressions for the Peclet number in analogy with the use of the relative Reynolds number:

$$Pe_r = d\rho_f c_{cf} |\mathbf{u} - \mathbf{v}| / k_f \quad (\text{or } Pe_r = Re_r Pr) \quad \text{and} \quad Pe_{Mr} = d|\mathbf{u} - \mathbf{v}| / \mathfrak{D} \quad (1.198)$$

Among the other important equivalent dimensionless numbers that represent the dimensionless rates of heat transfer, h , and mass transfer, h_M , are the Nusselt number, Nu and the Sherwood number, Sh . In the general case of a sphere, subjected to a temperature difference and in the presence of reactions as well as

mass transfer, these parameters are defined as follows:

$$Nu = \frac{dh}{k_f} = \frac{d\frac{\partial T}{\partial r}\Big|_s}{T_{\infty} - T_s + \frac{\xi\Delta H}{c_p} F_{AF} Y_{O\infty}}, \quad Sh = \frac{dh_M}{\mathfrak{D}} = \frac{d}{Y_{\infty} - Y_s} \frac{\partial Y}{\partial r}\Big|_s \quad (1.199)$$

where the subscripts s and ∞ represent conditions on the surface of the sphere and far away from the surface, respectively; F_{AF} is the oxygen to fuel mass ratio; ξ is the extent of the reaction; and ΔH is the heat of combustion of the reaction, both evaluated at the conditions on the surface of the sphere. The last term in the denominator of the expression for Nu is only pertinent to the case of chemical reactions with an oxidant and is written in terms of the mass fraction of the oxidant. For combustion in ambient air, the mass fraction of oxygen far from the sphere is: $Y_{O\infty} \approx 0.233$. In most practical cases of nonreacting particles drops and bubbles this term would be equal to zero.

1.4.4.1 Creeping/Stokes Flow

The case of creeping flow or Stokes flow implies $Re_r \ll 1$. Because of the relationship $Pe_r = Re_r \times Pr$, unless Pr for the sphere is very large, as is the case of some organic oils, this condition also implies that $Pe_r \ll 1$ or at least $Pe_r < 1$. Convection is comprised of two parts, conduction and advection and, in this case, the conduction part dominates in the convection process, while the advection part is insignificant. Therefore, studies that implicitly or explicitly assume that $Pe \ll 1$ or $Re_r \ll 1$ essentially neglect the effects of the advection parts of the process and are treating the conduction part of the process alone. The steady-state solution of the conduction equation yields the following expression for the Nusselt number:

$$Nu = 2 \quad (1.200)$$

Acrivos and Taylor (1962) conducted a study on the heat transfer from a sphere, analogous to the study by Proudman and Pierson (1956) for the equation of motion. They implicitly assumed a Stokesian flow around a sphere and derived an asymptotic heat transfer solution, which is valid at higher order of Pe_r . With the corrections in the coefficients (Acrivos, 1980; Leal, 1992) their expression for the steady-state Nusselt number, which is applicable in the ranges of the parameters $Re_r \ll 1$ and $Pe_r < 1$, is as follows:

$$Nu = 2 + \frac{Pe_r}{2} + \frac{1}{4} Pe_r^2 \ln \frac{Pe_r}{2} + 0.2073 Pe_r^2 + \frac{1}{16} Pe_r^3 \ln \frac{Pe_r}{2} \quad (1.201)$$

In the same study, Acrivos and Taylor (1962) proved that the functional relationship $Nu(Pe)$ as obtained in Stokesian flow is less sensitive to an increase of Re than the corresponding functional relation for the drag coefficient, $C_D(Re)$. Therefore, it is generally accepted that Eq. (1.201) is valid not only under creeping flow conditions, but also when Re_r is finite but small. Acrivos and Goddard (1965) also derived an asymptotic solution for high Pe assuming a Stokesian velocity distribution. Their expression, which is valid for $Pe > 5$, may be written as follows:

$$Nu = 1.249 \left(\frac{Pe_r}{2} \right)^{1/3} + 0.922 \quad (1.202)$$

In the case of viscous spheres, with viscosity ratio λ , Levich (1962) provided an asymptotic first-order solution for a liquid sphere at very large Pe_r under the condition of creeping flow ($Re_r \ll 1$):

$$Nu = \sqrt{\frac{4Pe_r}{3\pi(1+\lambda)}} \quad (1.203)$$

More recently, Feng and Michaelides (2000b), under the assumption of a Stokesian velocity profile around a viscous sphere (drop or bubble), solved numerically the energy equation. They derived the following correlation for the heat transfer coefficients from a sphere in terms of Pe_r and λ :

$$Nu = 1.49 Pe_r^{0.322 + 0.113/(0.361\lambda + 1)} \quad (1.204)$$

It must be pointed out that the implicit conditions for the use of the last three expressions (1.202), (1.203), and (1.204) are $Re_r \ll 1$, or at least $Re_r < 1$, and $Pe_r \gg 1$. These conditions are satisfied only for spheres with $Pr \gg 1$. Several organic liquids, including gasoline and engine oil satisfy these conditions.

1.4.4.2 Reynolds Number Effects

Among the correlations of experimental data that have been used for the steady-state heat transfer from a solid sphere without mass transfer on the surface, e.g., in the absence of evaporation, sublimation, or chemical reactions, are the expressions derived by Ranz and Marshal (1952) and Whitacker (1972) which may be written, respectively, as follows:

$$Nu = 2 + 0.6Re_r^{0.5} Pr^{0.33} \quad (1.205)$$

and

$$Nu = 2 + (0.4Re_r^{1/2} + 0.06Re_r^{2/3})Pr^{0.4} \quad (1.206)$$

These correlations are valid in the case of solid spheres only and may be used up to $Re_r = 10^4$.

Feng and Michaelides (2000a, 2001b) conducted two numerical studies on the subject of heat transfer from viscous spheres without mass transfer and derived useful correlations, with Re_r and Pe_r as independent variables. The first study pertains to high Re_r and any Pe_r (Feng and Michaelides, 2000a) and the second to any values of Re_r and Pe_r (Feng and Michaelides, 2001b). Their results in correlation form may be summarized as follows:

1. At small but finite values of Re_r ($0 < Re_r < 1$) and $Pe_r > 10$, the general expression for the Nusselt number is as follows:

$$Nu(\lambda, Pe_r, Re_r) = \left(\frac{0.651}{1+0.95\lambda} Pe_r^{1/2} + \frac{0.991\lambda}{1+\lambda} Pe_r^{1/3} \right) [1 + \alpha(Re_r)] + \left(\frac{1.65(1-\alpha(Re_r))}{1+0.95\lambda} + \frac{\lambda}{1+\lambda} \right) \quad (1.207)$$

where the function $\alpha(Re_r)$ may be written as follows:

$$\alpha(Re_r) = \frac{0.61Re_r}{Re_r+21} + 0.032 \quad (1.208)$$

2. As with the case of the expression of the drag coefficient in Section 1.4.3.2, for higher Re_r , the analysis of the data revealed that the best correlations of the numerical data are obtained when the general expression for the Nusselt number is given in terms of the following three functions, which pertain to specific values of the viscosity ratio λ :

A. The correlation for an inviscid sphere ($\lambda = 0$), which is given by the following expression:

$$Nu(0, Pe_r, Re_r) = 0.651 Pe_r^{1/2} \left(1.032 + \frac{0.61 Re_r}{Re_r+21} \right) + \left(1.60 + \frac{0.61 Re_r}{Re_r+21} \right) \quad (1.209)$$

B. The Nusselt number expression for a solid sphere ($\lambda = \infty$):

$$Nu(\infty, Pe_r, Re_r) = 0.852 Pe_r^{1/3} (1 + 0.233 Re_r^{0.287}) + 1.3 - 0.182 Re_r^{0.355} \quad (1.210)$$

C. The corresponding function for a sphere with viscosity ratio equal to 2, which was derived from the numerical results and may be written as follows:

$$Nu(2, Pe_r, Re_r) = 0.64 Pe_r^{0.43} (1 + 0.233 Re_r^{0.287}) + 1.41 - 0.15 Re_r^{0.287} \quad (1.211)$$

Hence, the final correlations for the heat transfer coefficients are given by the following expressions in the two ranges of the viscosity ratio, $0 \leq \lambda < 2$ and $2 < \lambda \leq \infty$:

$$Nu(Re_r, Pe_r, \lambda) = \frac{2-\lambda}{2} Nu(Re_r, Pe_r, 0) + \frac{4\lambda}{6+\lambda} Nu(Re_r, Pe_r, 2) \quad (1.212)$$

for $0 \leq \lambda \leq 2$, $10 \leq Pe_r \leq 1000$

and

$$Nu(Pe_r, Re_r, \lambda) = \frac{4}{\lambda+2} Nu(Pe_r, Re_r, 2) + \frac{\lambda-2}{\lambda+2} Nu(Pe_r, Re_r, \infty) \quad (1.213)$$

for $2 \leq \lambda \leq \infty, \quad 10 \leq Pe_r \leq 1000$

In the case of smaller values of $Pe_r < 10$, it was not possible to obtain a simple correlation of the numerical results, $Nu(Pe_r, Re_r, \lambda)$, with any satisfactory degree of accuracy. For this reason, for applications in the range $0 < Pe_r < 10$, it is recommended that one uses the numerical results in the original publication (Feng and Michaelides, 2001b). These results are given in tabular form and their accuracy is only limited by the numerical accuracy of the method used.

As in the case of the hydrodynamic force on a viscous sphere, it was found that, for a fixed value of Re_r and viscosity ratio, λ , the variations of the density ratio, ρ_s/ρ_p have only a minimal effect on the external flow field. When one considers the governing equation for the heat or mass transfer processes and the pertinent boundary conditions, one will conclude that the density ratio (or equivalently the internal Reynolds number, Re_i) would not affect the corresponding transport coefficients, h or h_M and, consequently, the Nusselt or Sherwood numbers. This was verified numerically by Feng and Michaelides (2001a, 2001b) in extensive numerical computations for both the hydrodynamic force and for the rate of heat transfer. The results of the computations show conclusively that the influence of the density ratio on the heat transfer coefficient is less than 0.1%, a number that is of the same order of magnitude as the numerical uncertainty of the computations and much lower than the required accuracy for any engineering calculations.

1.4.4.3 Blowing Effects

Blowing effects are important for burning droplets when the timescale of burning (mass transfer from the droplet) is of equal or lesser order of magnitude than the timescale for energy transfer. As in the case of momentum transfer, corrections to the heat transfer coefficient have been developed. These corrections take into account the change of the properties of the gaseous boundary layer and the phase change on the surface of the sphere. The two dimensionless numbers, called *blowing factors* or *transfer numbers*, B_H and B_M , which were defined in Eqs. (1.138) and (1.140), account for any heat and mass transfer effects on the surface of the sphere. These factors are used in corrections for the empirical or analytical correlations on heat and mass transfer from the surface of a constant volume sphere.

Since the origin of the two blowing factors is the radial mass transfer from the surface of the sphere to the carrier fluid, it is evident that the two are not independent. Abramzon and Sirignano (1989) conducted an analytical study on the evaporation of drops and derived expressions for these blowing factors to be used in engineering calculations. In the case of a fuel droplet that burns in air, they derived the following relationship between the two blowing factors:

$$B_H = (1 + B_M)^n - 1 \quad (1.214)$$

where the exponent n is given by the ratio

$$n = \frac{c_{pf}}{c_{pf} Le} \frac{1 + \frac{k \sqrt{Re_r/2}}{2 F(B_M)}}{1 + \frac{k \sqrt{Re_r/2}}{2 F(B_H)}} \quad (1.215)$$

In the last equation, c_{pf} is the specific heat of the fuel vapor, c_{pf} is the specific heat of the carrier gas, Le is the dimensionless Lewis number,

$$Le = k_f / (\rho_f c_{pf} \mathcal{D}_{fp}) = Sc/Pr \quad (1.216)$$

k is an empirical coefficient equal to 0.848, and F is a function of the corresponding blowing factor,

$$F(B) = (1 + B)^{0.7} \frac{\log(1+B)}{B} \quad (1.217)$$

Under the conditions of thermodynamic equilibrium and properties that satisfy the equalities $Pr = Sc = 1$, the two transfer coefficients are equal: $B_H = B_M$ (Sirignano, 1999).

Abramzon and Sirignano (1989) obtained semianalytical expressions for the Nusselt and Sherwood numbers for a drop with mass transfer on its surface. Later, Chiang et al. (1992) improved on that study by relaxing some of the most restrictive assumptions and by conducting numerical computations on the vaporization of drops. They derived more general and, very likely, more accurate correlations for the heat and mass transfer coefficients, which may be written as follows:

$$Nu = 1.275(1 + B_H)^{-0.678}Re_m^{0.438}Pr_m^{0.619} \quad (1.218)$$

and

$$Sh = 1.224(1 + B_M)^{-0.568}Re_m^{0.385}Sc_m^{0.492} \quad (1.219)$$

The Schmidt number, Sc is the dimensionless group of the fluid properties, $Sc (= \mu_f/\rho_f\mathcal{D})$. Both the Reynolds and Schmidt numbers, Re_m and Sc_m , must be calculated using the mean-film transport coefficients, which are defined by Eq. (1.136) and, in the case of Re_m , the free-stream gas density, $\rho_{f\infty}$. A few useful details, on the definition of the film properties and their usage are given in Section 1.4.3.4, and the corresponding correction for the steady-state drag coefficient is given by Eq. (1.138).

One may combine the above correlations and derive the following expressions for the rate of heat and mass transfer of vapor from the surface of a spherical drop:

$$\begin{aligned} \dot{Q} &= 1.275\pi k_f d(T_s - T_\infty)(1 + B_H)^{-0.678}Re_m^{0.438}Pr_m^{0.619} \\ \dot{m} &= 1.224\pi\rho_f d\mathcal{D} (Y_s - Y_\infty)B_M(1 + B_M)^{-0.568}Re_m^{0.385}Sc_m^{0.492} \end{aligned} \quad (1.220)$$

An alternatively way is to use the empirical relationship derived from the experimental results by Renksizbulut and Yuen (1983). They correlated their experimental data on the heat transfer from a sphere with mass transfer at its surface by the following expression:

$$Nu = \frac{2 + 0.584Re_m^{0.5}Pr^{0.33}}{(1 + B_M)^{0.7}} \quad (1.221)$$

Equation (1.221) yields the following expressions for the rates of heat and mass transfer from the surface of the spherical drop:

$$\dot{Q} = \pi k_f d(T_s - T_\infty) \frac{2 + 0.584Re_m^{0.5}Pr^{0.33}}{(1 + B_M)^{0.7}} \quad (1.222)$$

and

$$\dot{m} = \pi d\rho_f \mathcal{D} (Y_s - Y_\infty) \frac{2 + 0.584Pe_m^{0.5}Sc^{0.33}}{(1 + B_M)^{0.7}} \quad (1.223)$$

All the fluid properties in the last four equations that define the Nusselt, Prandtl, and Schmidt numbers, are the film properties defined by Eq. (1.136). The relative Reynolds and Peclet numbers Re_m and Pe_m are defined in terms of the gas-film viscosity as in (1.136) and the free-stream gas density, $\rho_{f\infty}$. It is evident from an inspection of these equations that their functional form and coefficients are very similar. It has been confirmed (Sirignano, 1999) that the results of the two expressions do not differ substantially.

Correlations such as (1.220), (1.222), and (1.223) are frequently used in engineering computations in order to provide the necessary transport coefficients in models for the gas-phase flow and to determine the details of the processes of droplet motion, heating, and vaporization or burning.

1.4.4.4 Transient Effects

Michaelides and Feng (1994) conducted a study on the transient energy equation for spheres. This study is analogous to the one by Maxey and Riley (1983) for the equation of motion, which was presented in

Section 1.4.3.7. The implicit and explicit assumptions for this study are also similar to the assumptions for the derivation of the equation of motion and may be summarized as follows:

1. Spherical shape
2. Infinite fluid domain
3. No rotation
4. Highly conducting ($Bi \ll 1$ or $k_f/k_s \ll 1$)
5. Zero initial relative temperature
6. Negligible advection ($Pe \ll 1$).

For a rigid, isothermal sphere, which is present in a time-variable and nonuniform fluid temperature field $T_f(x_p, t)$, the final form of the transient Lagrangian energy equation is as follows:

$$m_s c_{ps} \frac{dT_s}{dt} = -m_f c_{pf} \frac{DT_f}{Dt} - 4\pi a k_f \left[T_s - T_f - \frac{1}{6} a^2 T_{f, jj} \right] - 4\pi a^2 k_f \int_0^t \frac{d}{d\tau} \left[\frac{T_s - T_f - \frac{1}{6} a^2 T_{f, jj}}{\pi \alpha_f (t - \tau)^{1/2}} \right] d\tau \quad (1.224)$$

where c_{pf} and c_{ps} are the specific heat capacities of the fluid and the sphere, respectively; α_f the denominator of the last term is the thermal diffusivity of the fluid, which is equal to $k_f/\rho_f c_{pf}$; the operator D/Dt represents the Lagrangian derivative with a reference system of coordinates at the center of the sphere; and the temperature T_f is the temperature function of the fluid far from the sphere.

The left-hand side of the above equation denotes the change of the temperature of the sphere due to the heat transfer. The first term in the right-hand side is analogous to the inertia term in the momentum equation and accounts for the (Lagrangian) change of temperature of the equivalent mass of the fluid. The second term is the usual conduction term from the sphere to the fluid and is analogous to the steady-state drag term of the equation of motion. This term represents the rate of heat transfer due to the bulk temperature difference between the fluid and the sphere. It is similar to the well-known conduction term that appears in texts, with the inclusion of the Laplacian derivative, which accounts for any nonuniformities of the temperature field. These Laplacian terms are analogous to the Faxen terms of the equation of motion and scale as a^2/L^2 . In most of the practical applications where the particle radius is significantly smaller than the characteristic dimension of the fluid and $a^2/L^2 \ll 1$, these corrections are insignificant and may be neglected. The last term in the energy equation is a history integral, which results from the diffusion of the temperature gradients in the fluid temperature field and is also corrected for the nonuniformity (curvature) of the temperature field. Again, this correction is represented by the Laplacian derivative term. It is apparent that this history term depends on the temporal as well as the spatial variation of the temperature field and is exactly analogous to the history term of the equation of motion. Previously, this term was unknown and had been absent from all derivations and uses of the energy equation of spheres (particles, bubbles or drops). The history term may account for a significant part of the transient heat transfer to a sphere, as can be seen in [Figure 1.16](#).

It must be pointed out that the added mass term in the equation of motion derives from the pressure gradient term in the governing Eq. (1.108). Since the governing equation for the energy transfer does not have a term equivalent to ∇p , there is no term corresponding to the added mass term in the transient energy equation. This constitutes the main difference in the functional forms of the equations of motion and temperature variation under the creeping flow conditions as well as at finite Reynolds numbers. For this reason, there is not a strict similarity between the transient equations of motion and the energy for particles, drops or bubbles although analogous results and behavior in the momentum and heat exchange processes for viscous and solid spheres abound.

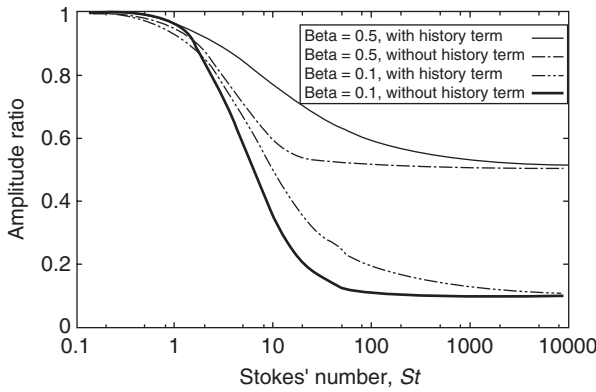


FIGURE 1.16 The effect of the Stokes number on the heat transfer from rigid particles with and without the history term.

As with the equation of motion, the fifth assumption listed in Section 1.4.3.6 may be relaxed. In this case, the history term should be substituted by the following expression:

$$4\pi a^2 k_f \int_0^t \frac{(d/d\tau) \left[T_s - T_f - \frac{1}{6} a^2 T_{f,ij} \right]}{[\pi \alpha_f(t-\tau)]^{1/2}} d\tau + 4\pi a^2 k_f \frac{T_s(0) - T_f(0)}{\sqrt{\pi a_f t}} \quad (1.225)$$

Gay and Michaelides (2003) conducted a thorough numerical study to compute the effect of the history term on the heat transferred to a sphere at creeping flow conditions and considered three types of variation for the carrier fluid temperature: (a) a step variation; (b) a ramp change; and (c) a sinusoidal variation of the fluid temperature. The main parameters for this study are the volumetric heat capacity ratio $\beta' = \rho_f c_{pf}/\rho_s c_{ps}$ and a thermal Stokes number, Stk , which is defined as the ratio of the thermal timescale of the particle, $\tau_s = a^2 \rho_f c_f / k_f$ to the characteristic timescale of the fluid. The conclusion of this study is that the history term is of importance in the computations of the heat flux when the ratio of the volumetric heat capacities, β' , is between 0.002 and 0.5. This is the range of liquid–solid flows and droplet flows in heavier gases. The study found almost no effect of the history term on the heat transfer for bubbles with $\beta' > 10$. Typical result of these computations for a sinusoidal oscillation of the fluid temperature field with frequency ω are depicted in Figure 1.16. In this case, the Stokes number is defined as

$$Stk = \frac{a^2 \rho_f c_f \omega}{k_f} \quad (1.226)$$

Figure 1.16 demonstrates that neglecting the history term in the energy equation may lead to an underestimation of the instantaneous rate of heat transfer by as much as 30%, a significant fraction for most engineering computations.

Feng and Michaelides (1997) performed a study on the transient energy equation for a spheroid of eccentricity ε , which is analogous to the study by Lawrence and Weinbaum (1986) that was presented in Section 1.4.3.7. They derived the following equation for the heat transfer from a spheroid:

$$\begin{aligned} Q(t^*) = & -4\pi \left\{ \left(1 + \frac{2}{3}\varepsilon - \frac{1}{45}\varepsilon^2 \right) (T_s - T_\infty) + \left(1 + \frac{4}{3}\varepsilon - \frac{2}{3}\varepsilon^2 \right) \int_0^{t^*} \frac{(d/d\tau^*)(T_s - T_\infty)}{\sqrt{\pi(t^* - \tau^*)}} d\tau^* \right. \\ & \left. + \frac{1}{3} \left(1 + \frac{2}{9}\varepsilon + \varepsilon^2 \right) \frac{DT_\infty}{Dt^*} + \varepsilon^2 \frac{4}{45} \sqrt{\frac{\pi}{3}} \int_0^{t^*} \left[\frac{d}{dt^*} (T_s - T_\infty) \right] G'(t^* - \tau^*) d\tau^* \right\} \end{aligned} \quad (1.227)$$

where the new function $G'(t)$ depends on the frequency of variation of the temperature field and is defined as follows:

$$G'(t^*) = \text{Im}[\sqrt{\pi\Phi}e^{\Phi t^*}\text{erfc}(\sqrt{\Phi t^*})] \quad \text{and} \quad \Phi = 3e^{i\pi/3} \quad (1.228)$$

The last term in Eq. (1.227) is analogous to the new history term in Eq. (1.176) and depends entirely on the eccentricity and the frequency of variation of the external temperature field. The kernels of these terms do not necessarily follow the $t^{-1/2}$ decay of the typical history term in creeping flows and depend on the frequency of the variation of the velocity or temperature fields. Regarding the practical significance of these new history terms, Feng and Michaelides (1997) showed that, when the frequency of variation of the velocity and temperature fields is not high, the contributions of these terms to the total heat flux and the hydrodynamic force are much smaller than the contributions of the other terms of the corresponding transient equations.

Feng and Michaelides (1998a) also performed a study on the energy equation of a particle with arbitrary motion and in an arbitrary temperature field with finite but small inertia. This study is analogous to the one performed by Lovalenti and Brady (1993a) for the equation of motion. The results have been presented in terms of the pertinent Peclet number, Pe_r , and Strouhal number, St . A transient expression for the heat transfer from a solid particle of arbitrary shape, undergoing arbitrary motion, with a velocity given by the vector \mathbf{u}^s was derived. At short dimensionless times, which are less than $O(St^{-2})$, the advection effects are insignificant and the conduction solution, which is Eq. (1.224), applies to this case as well. At timescales that are higher than $O(St^{-2})$, the advection becomes significant and the total dimensionless heat transfer is given by the following expression:

$$\begin{aligned} Q(t^*) = & \frac{4\pi Pe_r St}{3} \frac{dT_f}{dt^*} - 4\pi(T_s - T_f) - 2\pi\sqrt{Pe_r St} \int_0^{t^*} \frac{T_s - T_f}{\sqrt{t^* - \tau^*}} \frac{\text{erf}|A'|}{|A'|} d\tau^* \\ & - 2Pe_r \sqrt{\pi} \int_0^{t^*} \frac{(T_s - T_f)|\mathbf{u}^s|}{(t^* - \tau^*)|A'|} \left[\frac{\sqrt{\pi}}{2|A'|} \text{erf}|A'| - \exp(-|A'|^2) \right] d\tau^* + O(St^{1+}) \end{aligned} \quad (1.229)$$

where the vector A' is defined as:

$$A' = \frac{Pe_r}{2} \left(\frac{t^* - \tau^*}{Pe_r St} \right)^{1/2} \frac{\int_{\tau^*}^{t^*} \mathbf{u}^s(\xi) d\xi}{t^* - \tau^*} \quad (1.230)$$

Of the terms in Eq. (1.229), the first term represents the contribution of the time-varying undisturbed fluid temperature field, which is far from the particle. The second term is the usual steady-state conduction term. The third and fourth terms are history terms emanating from the temperature gradients, which are simultaneously diffused and advected, since the inception of the heat transfer process. It must be pointed out that this equation is valid at long times after the inception of the process [$t = O(St^{-2})$], when the resulting temperature gradients have been advected to distances far from the characteristic Oseen distance for the energy transport process, which is of the order of a Pe^{-1} .

It is evident that the vector A' scales as $(t - \tau)^{1/2}$. Therefore, in the case where advection is significant, the history terms scale as $(t - \tau)$, $(t - \tau)^{1.5}$ and $(t - \tau)^{1.5} \exp[(t - \tau)^{1/2}]$. Hence, as in the equation of motion, the effect of advection is the faster decay of the history terms. This is a consequence of the fact that advection transports, among other variables, vorticity and temperature gradients far from the sphere.

Pozrikidis (1997) also performed an analytical study to determine the transient heat and mass transfer from a suspended particle of arbitrary shape at low Peclet numbers. He used a method of matched asymptotic expansions and used the Green's function in order to derive analytical expressions for the transport from a sphere in a fluid undergoing a step temperature change and a sphere in a time-periodic flow. His results are expressed in terms of the fractional increase of the rate of heat transfer from the case of pure conduction $[Q(t) - Q_0]/Q_0$, where Q_0 is the result for pure conduction and may be

summarized as follows:

$$[Q(t) - Q_0]/Q_0 = \begin{cases} 1/4Nu_0Pe_r & \text{for uniform flow} \\ 0.1285Nu_0Pe_\gamma^{1/2} & \text{for simple shear flow} \\ 0.68Nu_0Pe_\gamma^{1/2} & \text{for two-dimensional straining flow} \\ 1.0Nu_0Pe_\gamma^{1/2} & \text{for axisymmetric straining flow} \end{cases} \quad (1.231)$$

In Eq. (1.231) Pe_r is the instantaneous Peclet number $Pe_r(t)$ and Pe_γ is the instantaneous Peclet number based on the pertinent strain, γ , and defined as $Pe_\gamma = (d^2\rho_f c_{pf} \gamma/k_f)$. Both these numbers are functions of time. These expressions confirm the fact that the type of the velocity field that is developed around the sphere influences significantly the rate of heat transfer from the sphere.

1.4.4.5 Turbulence Effects

As in the case of the drag coefficient of particles, free-stream turbulence results in an increase of the heat transfer coefficients as well. Early experimental studies by Raithby and Eckert (1968) in grid-generated turbulence show that the Nusselt number increases rapidly with turbulence intensity up to $I_r = 1\%$ when the Reynolds number is of the order of 10^3 . The Nusselt number subsequently increases, but only linearly with I_r . When the Reynolds number is of the order of 10^4 , Nu is proportional to I_r in the whole range of investigations. Based on several sets of available experimental data, Clift et al. (1978) suggest the following correlation for the increase of the heat transfer coefficient:

$$\frac{Nu}{Nu_0} = 1.0 + 4.8 \times 10^{-4} \frac{I_r}{I_{rc}} Re_r^{0.57} \quad (1.232)$$

where, in this case, Nu_0 is the Nusselt number in the absence of free-stream turbulence, I_r is the turbulence intensity, and I_{rc} is the critical turbulence intensity. The critical turbulence intensity is defined in a way that it makes the Reynolds number of the particle, Re_r , equal to the critical Reynolds number. From the expression for the critical Reynolds number in Eq. (1.135), one may derive the following expression for the critical turbulence intensity I_{rc} :

$$I_{rc} = \begin{cases} [5.477 - \log_{10}(Re_r)]/15.8 & \text{for } I_r \leq 0.15 \\ [3.71 - \log_{10}(Re_r)]/1.75 & \text{for } I_r > 0.15 \end{cases} \quad (1.233)$$

A more recent study on the effect of free-stream turbulence by Yearling and Gould (1995) conducted with evaporating droplets of water, ethanol, and methanol yields the following dependence of the Nusselt number on the intensity of turbulence:

$$\frac{Nu}{Nu_0} = 1 + 3.4I_r^{0.843} \quad (1.234)$$

Yearling and Gould (1995) considered evaporating droplets and, hence, Nu_0 is the Nusselt number with the blowing effects, which may be given by Eq. (1.221). The film properties must be used for all the properties of the materials in Eq. (1.234).

1.4.4.6 Radiation Effects

Thermal radiation is the mode of heat transfer through which electromagnetic energy is continuously emitted by a body. This emission applies to the system under observation as well as all the other systems that exist in its surroundings. Thus, for a sphere whose surface temperature is T_s , the emitted radiation energy is equal to

$$\dot{Q}_{rad}^{\text{em}} = \sigma \varepsilon \pi d^2 T_s^4 \quad (1.235)$$

where σ is the Boltzmann constant, which has the value $5.669 \times 10^{-8} \text{ W/m}^2 \text{ K}^4$ and ε is the emissivity of the sphere. The emissivity of a black body is equal to 1.

Similarly, the sphere absorbs heat from all the objects in its surroundings. In the simple case where the sphere is enclosed by a single medium of temperature T_∞ , the sphere absorbs thermal radiation equal to

$$\dot{Q}_{\text{rad}}^{\text{ab}} = \sigma \alpha \pi d^2 T_\infty^4 \quad (1.236)$$

where α is the absorptivity of the sphere. In general, the absorptivity and the emissivity of a material are functions of its temperature and are equal in magnitude; $\alpha(T_s) = \varepsilon(T_s)$.

The net rate of energy that enters the sphere as a result of thermal radiation is equal to the difference of the above two equations and, in analogy with the convection mode of heat transfer, may be given in terms of a thermal radiation coefficient, h_{rad} :

$$\dot{Q}_{\text{rad}}^{\text{ab}} - \dot{Q}_{\text{rad}}^{\text{em}} = \sigma \varepsilon \pi d^2 (T_\infty^4 - T_s^4) = \pi d^2 h_{\text{rad}} (T_\infty - T_s) \quad (1.237)$$

The thermal radiation coefficient is a strong function of temperature. It is obvious that, when the temperature difference of the sphere and its surroundings is sufficiently high, the net radiation energy is significant and may actually surpass the energy exchange due to the other two modes of heat transfer, conduction, and convection. The total rate of heat entering the sphere is the sum of the convection and radiation:

$$\dot{Q}_r = \pi d^2 (h_{\text{rad}} + h) (T_\infty - T_s) \quad (1.238)$$

It must be pointed out that, in the case of radiation, one has to account not only for the carrier gas, but also for all the boundaries and other objects in the vicinity of the sphere. The sphere and in general any body, exchanges radiation with any other object or surface that it "sees." In the general case when this body is surrounded by many objects, including other similar bodies in the same carrier fluid, the determination of the net thermal radiation or the thermal radiation coefficient must be carried out by carefully evaluating the effects of all the surfaces in the surroundings and the shape factors of these surfaces, which may become a challenging task. A more extensive description of the processes and the methods used for the determination of radiative heat transfer may be found in a specialized treatise on the subject, such as the one by Siegel and Howell (1981).

1.4.5 Multiple Particle/Droplet/Bubble Effects

While most of the theories and experiments on spheres have been developed for single spheres, the majority of practical applications involve the flow of groups of interacting particles, bubbles, or drops. Interactions of the spheres and the formation of clusters and groups of spheres with correlated motions play an important role on the value of the hydrodynamic force exerted by the fluid. Hence, the motion of the spheres in a viscous fluid depends on these interactions, which become more pronounced as the concentration of the spheres increases. In general, it is accepted that one may use the results and apply the theory of a single sphere inside a flowing mixture of monodisperse spheres if the average distance between the centers of the spheres is greater than $2d$, i.e., if the outer surfaces of the spheres are separated by a distance, which is greater than one diameter. Such mixtures are known as dilute mixtures. Simple geometric arguments show that the average concentration, C , of the spheres in dilute mixtures is lower than 6%. Intermediate concentrations are in the range 6 to 30%. In this range, particle-particle interactions are as important in the determination of all the transport coefficients as particle-fluid interactions. In applications with dense concentrations, $C > 30\%$, particle interactions are the main determinant of the transport coefficients and particle-fluid interactions are of lesser importance.

Regarding the steady state of the hydrodynamic force, Richardson and Zaki (1954) carried one of the earlier and relatively more accurate series of experiments on the sedimentation of particles in a quiescent fluid and, by correlating the settling velocity of the particles to the concentration of the mixture. They concluded that the drag coefficient of a single sphere must be multiplied by a correction factor equal to

$$(1 - C)^{-K} \quad (1.239)$$

where C is the concentration of solids and K is a weak function of the Reynolds number, given by the following correlations:

$$K = \begin{cases} 4.65 + 19.5d/D, & Re_r < 0.2 \\ (4.35 + 17.5d/D)Re_r^{-0.03}, & 0.2 < Re_r < 1 \\ (4.45 + 18d/D)Re_r^{-0.1}, & 1 < Re_r < 200 \\ 4.45Re_r^{-0.1}, & 200 < Re_r < 500 \\ 2.39, & Re_r > 500 \end{cases} \quad (1.240)$$

Because of the spread of their data, it is apparent that the exponent K may attain any value in the range 2.5 to 5.7. Later experimental data by Rowe (1961) with arrays of solid spheres in water and air are better correlated with the constant value $K = 3$.

Another correlation, which is widely used in fluidization systems, is the one by Wen and Wu (1966). They included the effects of the relative Reynolds number in the expression for the terminal velocity of a single particle and, therefore, derived a correlation for the effect of concentration that is independent of the Reynolds number:

$$C_D = C_{D0}(1 - C)^{-K} \quad \text{with } K = 3.7 \quad (1.241)$$

Wen and Wu (1966) recommend the Schiller and Nauman expression for the drag coefficient at zero concentration, $C_{D0} = 24(1 + 0.15Re_r^{0.687})/Re_r$.

More recently, Di Felice (1994) used several sets of data available in the literature, including those by Richardson and Zaki (1954) and Wen and Wu (1966), to develop a more general and probably more accurate expression for the drag coefficient. He derived the following correlation, which is applicable in the range $10^{-2} < Re_r < 10^4$:

$$C_D = C_{D0}(1 - C)^{-K} \quad \text{with } K = 3.7 - 0.65 \exp\left[-\frac{(1.5 - \log Re_r)^2}{2}\right] \quad (1.242)$$

The subject of interacting particles, bubbles, and drops is rather difficult to investigate experimentally, but ideally suited for computational simulations, where different initial conditions may be examined and statistical results are relatively easy to derive. Modern computational techniques and more powerful computers have allowed the modeling of groups of spheres with the flow properties of solid particles, bubbles, or drops to be studied in numerical experiments. Finite element methods (FEM) and the Lattice Boltzmann method (LBM) have enabled scientists and engineers to perform “thought experiments” of groups of interacting spheres and, thus, to obtain the effect of interactions on the hydrodynamic force exerted on individual spheres under specific and well-defined conditions. In particular, the LBM and its derivative the immersed boundary–lattice Boltzmann method, (IB–LBM), (Feng and Michaelides, 2004b, 2004c) are ideally suited methods for the determination of the interaction of groups of particles with any shape and properties. These two recently developed methods have enabled the simulation of processes involving very large groups of particles, of the order of thousands. There are several current studies employing these methods for the determination of the interaction of particles, bubbles, and drops and it is expected that a great deal of significant results will become available in the near future.

Among the past studies on the effects of interactions of spheres, Kaneda (1986) used an asymptotic method to derive the steady-state component of the hydrodynamic force on an array of solid spheres at small but not vanishing Reynolds number and very low concentration. He developed the following functional relationship for the average drag coefficient, C_D :

$$C_D = 1 + (\sqrt{2}/3)C^{1/2} + (\sqrt{2}/40)C^{-1/2}Re_r^2 \quad (1.243)$$

This expression is valid at distances where the inertia of the sphere is important. In the case of flows with several interacting objects, inertia becomes important at distances far from the *Brinkman screening length*. In the case of an array of spheres, the Brinkman screening length is equal to $C^{1/2}$ and, hence, the range of applicability of this expression is $C^{1/2} \gg Re_r$. Kaneda (1986) also concluded that in the opposite limit ($C^{1/2} \ll Re_r$), the Oseen correction to the Stokes drag ($1 + 3/16Re_r$) is valid for the average drag coefficient of the spheres, even in the case of an array with several interacting particles. Working with arrays of two-dimensional particles in flows at small but finite Reynolds numbers and using the LBM, Koch and Ladd (1997) and Rojas and Koplik (1998) also confirmed that the Oseen relationship for the steady-state component of the hydrodynamic force applies to particles at low but finite Reynolds numbers.

By using the LBM for a packed bed of particles, Koch and Sangani (1999) performed calculations on the rectilinear drag coefficients with fixed arrays of spheres. This is essentially a well-organized porous medium. They found out that the steady-state drag component may be scaled as Re_r^2 in high-concentration suspensions and depends very much on the concentration. Koch and Sangani (1999) obtained a functional relationship for the steady-state part of the hydrodynamic force in dense concentrations, higher than 40%, which applies to finite but small values of Re_r :

$$C_D = C_{D0}(C) + C_{D1}(C)Re_r^2 \quad (1.244)$$

The first function of this expression, which is the equivalent of the dimensionless Stokes drag force, is given by the formula:

$$C_{D0}(C) = \frac{1 + 3(C/2)^{1/2} + 2.11C\ln C + 16.14C}{1 + 0.681C - 8.48C^2 + 8.16C^3} \quad (1.245)$$

The ratio of the functions C_{D1}/C_{D0} diminishes with increasing concentration of the solid particles. Hence, the second term in Eq. (1.244) is very small in comparison to the first term at sufficiently high values of the concentration of particles. Because of this, Koch and Sangani (1999) claimed that the nonlinear behavior of the steady-state part of the average hydrodynamic force for close-packed arrays is difficult to be observed with the currently available experimental means.

Koch and Hill (2001) also performed computational studies using the LBM at higher Reynolds numbers and concluded that the steady-state component of the hydrodynamic force increases linearly with Re_s , according to the following correlation:

$$C_D = C_{D0}(C) + [0.0673 + 0.212C + 0.0232(1 - C)^{-5}]Re_s \quad (1.246)$$

where the function $C_{D0}(C)$ is the same as in Eq. (1.245). Koch and Hill (2001) concluded that this expression agrees very well with experimental results and empirical relations derived in the past for packed beds of particles.

In contrast to solid particles, bubbles have been always modeled as inviscid and weightless spheres moving in a medium, which is occasionally idealized as an inviscid fluid. Because in the case of bubbles the added mass term is by far greater than the other components of the hydrodynamic force, such spheres accelerate as if their masses were equal to the mass of the fluid occupying half of their volume, i.e., fluid of mass $m_s = 2/3\pi\rho_f a^3$. In the case of swarms of bubbles moving in a fluid with concentration C , the added mass coefficient, Δ_A , is a function of the concentration of the bubbles. Zuber (1964) used the simple theory of a bubble in a cell model for the flow of groups of bubbles to obtain analytically the following correction to the added mass coefficient:

$$\Delta_A = \frac{1 + 2C}{1 + C} \quad (1.247)$$

This expression is very simple to use in repetitive computations and according to Sangani et al. (1991) it is fairly accurate and applies to a wide variety of conditions. Van Wijngaarten (1976) performed an asymptotic analytical study in the case of a swarm of bubbles that are impulsively accelerated and

concluded that, with an accuracy of the order of C^2 , the added mass coefficient of a group with concentration C is equal to

$$\Delta_A = 1 + 2.76C + O(C^2) \quad (1.248)$$

A great deal of knowledge on the behavior of interacting bubbles has been recently developed as a result of recent computer simulations. Spelt and Sangani (1998) performed such a simulation to determine the influence of the fluid pseudoturbulence (that is the velocity fluctuations of the fluid, which are due to the motion of particles) and bubble concentration on the hydrodynamic force and the drag coefficient of a swarm of bubbles. They concluded that there is a weak dependence of the added mass coefficient on the fluid velocity fluctuations, but a significant dependence of the added mass on the bubble concentration. Their final expression, which is valid in the range $C < 0.3$, may be given as follows:

$$\Delta_A = \frac{1 + 2C + 0.225CA}{1 - C} \quad (1.249)$$

where A is a dimensionless measure of the temporal velocity fluctuations of the fluid. With a similar analysis, Spelt and Sangani (1998) obtained the following expression for the steady-state viscous drag coefficient for a swarm of bubbles in a viscous fluid:

$$C_D = \frac{1 + 0.15CA}{(1 - C)^2} \quad (1.250)$$

Oftentimes, large groups of interacting spheres in dense flows may be approximated and treated as a porous medium. The permeability and porosity of such a porous medium depends on the concentration of the system of spheres. Similarly, clouds or large groups of smaller spheres may be approximated as larger porous spheres that are transported in a fluid medium. Jones (1973) was among the first to study such porous spheres and obtained an expression for the steady-state hydrodynamic force on a porous sphere at creeping flow conditions:

$$F_i = 3\pi d\mu_f(u_i - v_i) \frac{2\zeta^2(1+2\eta\zeta^{-1})}{2\zeta^2+3+6\eta\zeta+6\eta\zeta^{-1}} \quad (1.251)$$

In (1.253) ζ is the inverse of the dimensionless permeability of the sphere ($\zeta = a/\kappa^{1/2}$, with κ being the permeability of the sphere) and η is a dimensionless constant that depends on the properties of the porous medium.

The permeability, κ , of a group of particles that form a porous medium is related to the porosity of the porous medium and, by extent, to the concentration, C , by the so-called Carman–Kozeny equation:

$$\kappa = \frac{(1-C)^3}{180C^2}d^2 \quad (1.252)$$

Feng and Michaelides (1998b) used an asymptotic expansion and extended this result to finite Reynolds numbers, Re_r , for the porous sphere by developing corrections for Re_r up to the order of Re_r^2 . Their final expression for the drag coefficient of such porous spheres is as follows:

$$F_i = 3\pi d\mu_f(u_i - v_i) \frac{2(1+\frac{\eta}{\zeta})\zeta^2}{4\eta\zeta+2\zeta^2+3\frac{\eta}{\zeta}+1} \\ \left[1 + Re_r \frac{3(1+\frac{\eta}{\zeta})\zeta^2}{4(4\eta\zeta+2\zeta^2+3\frac{\eta}{\zeta}+1)} + Re_r^2 \ln(Re_r) \frac{9(1+\frac{\eta}{\zeta})^2\zeta^4}{10(4\eta\zeta+2\zeta^2+3\frac{\eta}{\zeta}+1)^2} \right] \quad (1.253)$$

where Re_r is the Reynolds number based on the diameter of the whole cloud of small spheres and on the average relative velocity of the cloud. The last equation yields the correct behavior in the extreme cases of zero and infinite permeability: for a solid sphere ($\kappa \rightarrow \infty$) the last expression yields the hydrodynamic force obtained by Proudman and Pearson (1956) (1.125), while at low permeability ($\kappa \rightarrow 0$) it yields the result by Joseph and Tao (1964). At creeping flow, i.e., $Re_r = 0$, it yields the same expression for the drag force that was first predicted by the study of Saffman (1971).

In a recent study, Looker and Carnie (2004) studied the transient hydrodynamic force of an oscillating porous sphere with velocity slip at its interface (a condition that was studied by Saffman, 1971). They derived an asymptotic expression for the transient hydrodynamic force on the porous sphere with slip, valid up to the order of $\kappa^{1/2}$. This expression may be written as follows in terms of the slip factor that was introduced by equation

$$\begin{aligned} F_H = & -3\pi d\mu_f(1-\sigma)(v-u) - 3\pi\mu_f d^2 \left(\frac{1}{2} - \sigma\right) \sqrt{\frac{\pi}{\nu_f}} \int_0^t \frac{d\tau}{\sqrt{(t-\tau)}} d\tau \\ & - \frac{1}{12} \pi d^3 (1-9\sigma) \frac{d(v-u)}{dt} + O(\kappa) \end{aligned} \quad (1.254)$$

It is rather remarkable that Eq. (1.254) as well as most of the other results and conclusions in the study by Looker and Carnie (2004) may be obtained from Eq. (1.158), by applying the following conditions for the ratio of the viscosities and the slip factor σ (Feng and Michaelides, 2004a).

- $\nu_s \rightarrow \infty, \chi_s \rightarrow 0, \tanh(\chi_s) \rightarrow \chi_s$, and $\lambda \rightarrow \infty$ from the condition that the porous sphere is composed of rigid material.
- $\sigma = \varepsilon/\gamma (\varepsilon = \kappa^{1/2}/a)$ from the application of the interfacial slip boundary condition on the surface of the sphere.

Nomenclature

Latin

a	Particle,droplet radius (m)
A	Area (m^2)
B_H	Blowing factor
B_M	Blowing parameter
c	Specific heat
c_p	Specific heat at constant pressure (J/kg-K)
c_v	Specific heat at constant volume (J/kg-K)
C	Concentration, solids fraction
C_D	Drag coefficient
C_L	Lift coefficient
d	Particle, droplet diameter (m)
d_A	Area equivalent diameter (m)
d_n	Volume equivalent diameter (m)
\mathfrak{D}	Diffusion coefficient (m^2/s)
f	Frequency distribution (continuous)
\tilde{f}	Frequency distribution (discrete)
F	Force (N), cumulative distribution

\tilde{F}	Cumulative distribution (discrete)
$\mathbf{F}_D, F_{D,i}$	Drag force vector (N)
$\mathbf{F}_L, F_{L,i}$	Lift force vector (N)
\mathbf{g}, g_i	Gravity vector (m/s^2)
h	Specific enthalpy (J/kg), heat transfer coefficient ($\text{J/m}^2\text{-K}$)
h_{fg}	Latent heat of evaporation (J/kg)
h_M	Mass transfer coefficient
ΔH	Heat of combustion
I	Intensity
k	Thermal conductivity ($\text{J/m}\cdot\text{K}$), ratio specific heats coagulation coefficient
l_m	Molecular mean free path
l_w	Distance to wall
L	Characteristic length, axial position, height (m)
m	Mass (kg)
\dot{m}	Mass flux ($\text{kg/m}^2\cdot\text{s}$)
\mathfrak{M}	Molecular weight (kmol/kg)
\dot{M}	Mass flow rate (kg/s)
n	Number density ($1/\text{m}^3$)
p	pressure (Pa)
\dot{Q}	Heat transfer rate (W)
\mathbf{r}, r_i	Radius vector
R	Gas constant (kJ/kg/K)
R_u	Universal gas constant (kJ/kmol-K)
T	Temperature (K)
t	Time (s)
u_a	Phase velocity of phase "a", (m/s)
U_a	Superficial velocity of phase "a" (m/s)
u	Velocity component in x-direction (m/s), specific internal energy (J/kg)
u_p, \mathbf{u}	Velocity vector, continuous phase (m/s)
U	Characteristic velocity (m/s)
v	Velocity component in y-direction (m/s)
v_p, \mathbf{v}	Velocity vector, dispersed phase (m/s)
V	Volume (m^3), Velocity magnitude
V_r	Migration velocity
V_s	Settling velocity (m/s)
w	Velocity in z-direction (m/s), relative velocity
\mathbf{w}_i	Relative velocity vector
x_i	Coordinate vector (m)
x	Quality, coordinate direction (m)
X	Mole fraction
y	Coordinate direction (m)
Y	Mass fraction
z	Vertical coordinate direction (m), local loading

Greek

α	Absorptivity
α_a	Volume fraction of phase "a"
β	Density ratio

Γ	Gamma function
Δ_A	Added mass coefficient
Δ_H	History term coefficient
Ξ	Particle-cylinder diameter ratio
ε	Emmisivity
κ	Rate of strain (1/s), permeability
λ	Viscosity ratio
μ	Dynamic viscosity (N/m-s), mean value
ν	Kinematic viscosity (m ² /s)
Π	Coupling parameter
θ	Angle, azimuthal angle, (°)
ρ	Density (kg/m ³)
$\bar{\rho}_a$	Bulk density of phase "a" (kg/m ³)
ρ_m	Mixture density (kg/m ³)
σ	Surface tension (N/m), standard deviation, Boltzman constant
τ_V	Velocity response time (s)
τ_T	Thermal response time (s)
τ_c	Collision time (s)
τ_F	Fluid time (s)
φ	Velocity ratio
χ	Dimensionless time scale
Ψ	Shape factor, stream function
Ω	Angular velocity (1/s)

Subscripts

c	Continuous phase, cluster
cr	Critical
d	Dispersed phase
f	Fluid
GM	Geometric mean
HM	Harmonic mean
m	Maximum, mass
M	Magnus, median
n	Number
p	Particle
r	Relative
S	Saffman
SM	Surface mean
VM	Volumetric mean
w	Wall
θ	Circumferential, tangential direction
∞	Free stream

Dimensionless Numbers

Ac	Acceleration number
Bo	Bond number
Eo	Eötvös number
Kn	Knudsen number
Le	Lewis number
Ma	Mach number

Mo	Morton number
Nu	Nusselt number
Pe	Peclét number
Pr	Prandtl number
Re	Reynolds number
Re_i	Internal Reynolds number
Re_M	Film Reynolds number
Re_K	Shear Reynolds number
Re_r	Relative Reynolds number
Re_R	Rotation Reynolds number
Sc	Schmidt number
Sh	Sherwood number
Stk	Stokes number
St	Stanton number, Strouhal number
We	Weber number
We_r	Relative Weber number

References

- Abramzon, B. and Sirignano, W.A., Droplet vaporization for spray combustion calculations, *Int. J. Heat Mass Transfer*, 32, 1605–1618, 1989.
- Achenbach, E., Vortex shedding from spheres, *J. Fluid Mech.*, 62, 209–221, 1974.
- Acrivos, A., A note on the rate of heat or mass transfer from a small particle freely suspended in linear shear field, *J. Fluid Mech.*, 98, 299–304, 1980.
- Acrivos, A. and Goddard, J.D., Asymptotic expansions for laminar convection heat and mass transfer, *J. Fluid. Mech.*, 23, 273–291, 1965.
- Acrivos, A. and Taylor, T.E., Heat and mass transfer from single spheres in Stokes flow, *Phys. Fluids*, 5, 387–394, 1962.
- Al-tawee, A.M. and Carley, J.F., Dynamics of single spheres in pulsated flowing liquids: Part I. Experimental methods and results, *A.I.Ch.E. Symp. Ser.*, 67, 114–123, 1971.
- Al-tawee, A.M. and Carley, J.F., Dynamics of single spheres in pulsated flowing liquids: Part II. Modeling and interpretation of results, *A.I.Ch.E. Symp. Ser.*, 67, 124–131, 1972.
- Auton, T.R., Hunt, J.R.C., and Prud'homme, M., The force exerted on a body in inviscid unsteady non-uniform rotational flow, *J. Fluid Mech.*, 197, 241–257, 1988.
- Bagchi, P. and Balachandar, S., On the effect of nonuniformity and the generalization of the equation of motion of a particle, in the *Proceedings of the 4th International Conference on Multiphase Flow*, Michaelides, E.E., Ed., New Orleans, Louisiana, 2001.
- Barndorff-Nielsen, O., Exponentially decreasing distributions of the logarithm of particle size, *Proc. Roy. Soc. Lond. A.*, 353, 401, 1977.
- Basset, A.B., *Treatise on Hydrodynamics*, Bell, London, 1888a.
- Basset, A.B., On the motion of a sphere in a viscous liquid, *Philos. Trans. Roy. Soc. London*, 179, 43–63, 1888b.
- Bataille, J., Lance, M., and Marie, J.L., Bubbly turbulent shear flows, in *ASME-FED*, 99, Kim, J., Rohatgi, U., and Hashemi, M., Eds., 1990, pp. 1–7.
- Bhaga, D. and Weber, M.E., Bubbles in viscous liquids: shapes, wakes and velocities, *J. Fluid Mech.*, 105, 61–85, 1981.
- Bohlin, T., Terminal Velocities of Solid Spheres in Cylindrical Enclosures, *Transactions of the Royal Institute of Technology*, Stockholm, Report # 155, 1960.
- Bond, W.N. and Newton, D.A., Bubbles, drops and Stokes law, *Philos. Mag.*, 5, 794–800, 1928.
- Boussinesq, V.J., Sur la Resistance qu'Oppose un Liquide Indéfini en Repos..., *Comptes Rendu, Acad. Sci. Paris*, 100, 935–937, 1885.
- Brady, J.F. and Bossis, G., Stokesian dynamics, *Annu. Rev. Fluid Mech.*, 20, 111–157, 1988.

- Brenner, H., The slow motion of a sphere through a viscous fluid toward a plane surface, *Chem. Eng. Sci.*, 16, 242–251, 1961.
- Carlson, D.J. and Hoglund, R.F., Particle drag and heat transfer in rocket nozzles, *AIAA J.*, 2, 1980–1984, 1964.
- Chang, E.J. and Maxey M.R., Unsteady flow about a sphere at low to moderate Reynolds number. Part 1. Oscillatory motion, *J. Fluid Mech.*, 277, 347–79, 1994.
- Chang, E.J. and Maxey M.R., Unsteady flow about a sphere at low to moderate Reynolds number. Part 2. Accelerated motion, *J. Fluid Mech.*, 303, 133–153, 1995.
- Cherukat, P. and McLaughlin, J.B., Wall-induced lift on a sphere, *Int. J. Multiphase Flow*, 16, 899–907, 1990.
- Cherukat, P., McLaughlin, J.B., and Graham, A.L., The inertial lift on a rigid sphere translating in a linear shear flow field, *Int. J. Multiphase Flow*, 20, 339–353, 1994.
- Chhabra, R.P., Singh, T., and Nandrajog, S., Drag on chains and agglomerates of spheres in viscous Newtonian and power law fluids, *Can. J. Chem. Eng.*, 73, 566–571, 1995.
- Chiang, C.H., Raju, M.S., and Sirignano, W.A., Numerical analysis of a convecting, vaporizing fuel droplet with variable properties, *Int. J. Heat Mass Transfer*, 35, 1307–1327, 1992.
- Clamen, A. and Gauvin, W.H., Effects of turbulence on the drag coefficients of spheres in a supercritical flow regime, *A.I.Ch.E. J.*, 15, 184–189, 1969.
- Clift, K.A. and Lever, D.A., Isothermal flow past a blowing sphere, *Int. J. Numer. Methods Fluids*, 5, 709–715, 1985.
- Clift, R. and Gauvin, W.H., The motion of particles in turbulent gas streams, *Proc. Chem. E.C.A.*, 1, 14–24, 1970.
- Clift, R., Grace, J.R., and Weber, M.E., *Bubbles, Drops and Particles*, Academic Press, New York, 1978.
- Cox, R.G. and Brenner, H., The slow motion of a sphere through a viscous fluid towards a plane surface, *Chem. Eng. Sci.*, 22, 1753–1777, 1967.
- Cox, R.G. and Hsu, S.K., The lateral migration of solid spheres in a laminar flow near a plane, *Int. J. Multiphase Flow*, 3, 201–222, 1977.
- Crowe, C.T., Inaccuracy of nozzle performance predictions resulting from the use of an invalid drag law, *J. Spacecraft and Rockets*, 7, 1491–1492, 1970.
- Crowe, C.T., Babcock, W.R., and Willoughby, P.G., Drag coefficient for particles in rarefied low Mach number flows, *Prog. Heat Mass Transfer*, 6, 419–428, 1973.
- Crowe, C.T., Babcock, W.R., Willoughby, P.G., and Carlson, R.L., Measurement of Particle Drag Coefficients in Flow Regimes Encountered by Particles in a Rocket Nozzle, *United Techn. Report*, 2296-FR, 1969.
- Crowe, C.T., Sommerfeld, M., and Tsuji, Y., *Multiphase flows with Droplets and Particles*, CRC Press, Boca Raton, FL, 1998.
- Dandy, D.S. and Dwyer, H.A., A sphere in shear flow at finite Reynolds number: effect of particle lift, drag and heat transfer, *J. Fluid Mech.*, 226, 381–398, 1990.
- Di Felice, R., The voidage function for fluid–particle interaction systems, *Int. J. Multiphase Flow*, 20, 153–162, 1994.
- Eisenklam, P., Arunachalam, S.A., and Weston, J.A., Evaporation rates and drag resistance of burning drops, *Proceedings of the 11th International Symposium on Combustion*, Pittsburgh, PA, 1967, pp. 715–721.
- Epstein, P.S., On the resistance experienced by spheres in their motion through gases, *Phys. Rev.*, 23, 710–733, 1924.
- Faxen, H., Der Widerstand gegen die Bewegung einer starren Kugel in einer zum den Flüssigkeit, die zwischen zwei parallelen Ebenen eingeschlossen ist, *Ann. Phys.*, 68, 89–119, 1922.
- Fayon, A.M. and Happel, J., Effect of a cylindrical boundary on a fixed rigid sphere in a moving viscous fluid, *A.I.Ch.E. J.*, 6, 55–58, 1960.
- Feng, Z.-G. and Michaelides, E.E., Transient heat and mass transfer from a spheroid, *A.I.Ch.E. J.*, 43, 609–616, 1997.
- Feng, Z.-G. and Michaelides, E.E., Transient heat transfer from a particle with arbitrary shape and motion, *J. Heat Transfer*, 120, 674–681, 1998a.

- Feng, Z.-G. and Michaelides, E.E., Motion of a permeable sphere at finite but small Reynolds numbers, *Phys. Fluids*, 10, 1375–1383, 1998b.
- Feng, Z.-G. and Michaelides, E.E., A numerical study on the transient heat transfer from a sphere at high Reynolds and Peclet numbers, *Int. J. Heat Mass Transfer*, 43, 219–229, 2000a.
- Feng, Z.-G. and Michaelides, E.E., Mass and heat transfer from fluid spheres at low Reynolds numbers, *Powder Technol.*, 112, 63–69, 2000b.
- Feng, Z.-G. and Michaelides, E.E., Drag coefficients of viscous spheres at intermediate and high Reynolds numbers, *J. Fluids Eng.*, 123, 841–849, 2001a.
- Feng, Z.-G. and Michaelides, E.E., Heat and mass transfer coefficients of viscous spheres, *Int. J. Heat Mass Transfer*, 44, 4445–4454, 2001b.
- Feng, Z.-G. and Michaelides, E.E., Inter-particle forces and lift on a particle attached to a solid boundary in suspension flow, *Phys. Fluids*, 14, 49–60, 2002a.
- Feng, Z.-G. and Michaelides, E.E., Hydrodynamic force on spheres in cylindrical and prismatic enclosures, *Int. J. Multiphase Flow*, 28, 479–496, 2002b.
- Feng, Z.-G. and Michaelides, E.E., Equilibrium position for a particle in a horizontal shear flow, *Int. J. Multiphase Flow*, 29, 943–957, 2003.
- Feng, Z.-G. and Michaelides, E.E., Comment on “The hydrodynamics of an oscillating porous sphere,” *Phys. Fluids*, 16, 2004a, pp. 4758–4759 (in print).
- Feng, Z.-G. and Michaelides, E.E., An immersed boundary method combined with lattice Boltzmann method for solving fluid and particles interaction problems, *J. Comput. Phys.*, 195, 457–472, 2004b.
- Feng, Z.-G. and Michaelides, E.E., Proteus, a novel computational technique for solving fluid–particle interaction problems, *5th International Conference on Multiphase Flow, ICMF'04*, Yokohama, Japan, 2004c.
- Feuillebois, F., Some theoretical results for the motion of solid spherical particles on a viscous fluid, *Multiphase Sci. Technol.*, 4, 583–794, 1989.
- Fourier, J., *Theorie Analytique de la Chaleur*, Paris, 1822.
- Galindo, V. and Gerbeth, G., A note on the force on an accelerating spherical drop at low Reynolds numbers, *Phys. Fluids*, 5, 3290–3292, 1993.
- Gay, M. and Michaelides, E.E., Effect of the history term on the transient energy equation of a sphere, *Int. J. Heat Mass Transfer*, 46, 1575–1586, 2003.
- Govier, G.W. and Aziz, K., *The Flow of Complex Mixtures in Pipes*, Kruger Publishers, Huntington, 1977 (reprint).
- Haberman, W.L. and Morton, R.K., An Experimental Investigation of the Drag and Shape of Air Bubbles Rising in Various Liquids, D.W. Taylor Model Basin Report, Vol. 802, Department of the Navy, Washington, DC, 1953.
- Haberman, W.L. and Sayre, R.M., Motion of Rigid and Fluid Spheres in Stationary and Moving Liquids Inside Cylindrical Tubes, Report No. 1143, David Taylor Model Basin, U.S. Navy, Washington, DC, 1958.
- Hadamard, J.S., Mouvement Permanent Lent d'une Sphere Liquide et Visqueuse dans un Liquide Visqueux, *Compte-Rendus de l' Acad. des Sci.*, Paris, 152, 1735–1738, 1911.
- Haider, A.M. and Levenspiel, O., Drag coefficient and terminal velocity of spherical and nonspherical particles, *Powder Technol.*, 58, 63–70, 1989.
- Happel, J. and Brenner, H., *Low Reynolds Number Hydrodynamics*, Martinus Nijhoff, Washington (reprint, orig. publ. 1963), 1986.
- Harper, J.F., The motion of bubbles and drops through liquids, *Adv. Appl. Mech.*, 12, 59–129, 1972.
- Hartman, M. and Yates, J.G., Free-fall of solid particles through fluids, *Collect. Czech. Chem. Commun.*, 58, 961–974, 1993.
- Hermsen, R.W., Review of particle drag models, *JANAF Performance Standardization Subcommittee 12th Meeting*, Vol. CPIA 113, 1979.
- Hinch, E.J., The approach to steady state in Oseen flows, *J. Fluid Mech.*, 256, 601–603, 1993.
- Inamuro, T., Maeba, K., and Ogino, F., Flow between parallel walls containing the lines of neutrally buoyant circular cylinders, *Int. J. Multiphase Flow*, 26, 1981–2004, 2000.

- Iwaoka, M. and Ishii, T., Experimental wall correction factors of single solid spheres in circular cylinders, *J. Chem. Eng. Jpn.*, 12, 239–242, 1979.
- Jones, I.P., Low Reynolds number flow past a porous spherical shell, *Proc. Camb. Philos. Soc.*, 73, 231–238, 1973.
- Joseph, D.D. and Tao, L.N., The effect of permeability on the slow motion of a porous sphere in a viscous liquid, *Z. Angew. Math. Mech.*, 44, 361–367, 1964.
- Kalio, G.A., Random walk modeling of particle deposition, in *Gas-Solid Flows –1993*, Stock et al., Ed., ASME FED, 166, New York, 1993, pp. 161–167.
- Kaneda, Y., The drag on a sparse random array of fixed spheres in flow at small but finite Reynolds number, *J. Fluid Mech.*, 167, 1986, pp. 455–463.
- Karanfilian, S.K. and Kotas, T.J., Drag on a sphere in unsteady motion in a liquid at rest, *J. Fluid Mech.*, 87, 85–96, 1978.
- Kim, I., Elghobashi, S., and Sirignano, W.A., On the equation for spherical-particle motion: Effect of Reynolds and acceleration numbers, *J. Fluid Mech.*, 367, 221–253, 1998.
- Kim, S. and Karila, S.J., *Microhydrodynamics: Principles and Selected Applications*, Butterworth-Heinemann, Boston, 1991.
- Koch, D.L. and Hill, R.J., Inertial effects in suspension and porous media flows, *Annu. Rev. Fluid Mech.*, 33, 619–647, 2001.
- Koch, D.L. and Ladd, A.J.C., Moderate Reynolds number flows through periodic and random arrays of aligned cylinders, *J. Fluid Mech.*, 349, 31–66, 1997.
- Koch, D.L. and Sangani, A.S., Particle pressure and marginal stability limits for a homogeneous monodisperse gas fluidized bed: kinetic theory and numerical calculations, *J. Fluid Mech.*, 400, 229–263, 1999.
- Kurose, R., Makino, H., Komori, S., Nakamura, M., Akamatsu, F., and Katsuki, M., Effects of outflow from surface of sphere on drag, shear lift and scalar diffusion, *Phys. Fluids*, 15, 2338–2351, 2003.
- Lasso, I.A. and Weidman, P.D., Stokes drag on hollow cylinders and conglomerates. *Phys. Fluids*, 29, 3921–3934, 1986.
- Lawrence, C.J. and Weinbaum, S., The force on an axisymmetric body in linearized time-dependent motion: a new memory term, *J. Fluid Mech.*, 171, 209–218, 1986.
- Lawrence, C.J. and Weinbaum, S., The unsteady force on a body at low Reynolds number; the axisymmetric motion of a spheroid *J. Fluid Mech.*, 189, 463–498, 1988.
- Le Clair, B.P. and Hamielec, A.E., A theoretical and experimental study of the internal circulation in water drops falling at terminal velocity in air, *J. Atmos. Sci.*, 29, 728–740, 1972.
- Leal, L.G., Particle motions in a viscous fluid, *Annu. Rev. Fluid Mech.*, 12, 435–476, 1980.
- Leal, L.G., *Laminar Flow and Convective Transport Processes*, Butterworth-Heinemann, Boston, 1992.
- Lerner, S.L., Homan, H.S., and Sirignano, W.A., Multicomponent droplet vaporization at high Reynolds numbers-size, composition and trajectory histories, *A.I.Ch.E. Annual Meeting*, Chicago, 1980.
- Leung, A.L. and Crowe, C.T., Collection of nanoclusters by thermophoresis, in *Gas-Solid Flows-1993*, Stock, D.E., et al., Eds., ASME, New York, 1993.
- Levich, V.G., *Physicochemical Hydrodynamics*, Prentice-Hall, Englewood Cliffs, NJ, 1962.
- Lhuillier, D., Internal variables and the non-equilibrium thermodynamics of colloidal suspensions, *J. Non-Newtonian Fluid Mech.*, 96, 19–30, 2001.
- Looker, J.R. and Carnie S.L., The hydrodynamics of an oscillating porous sphere, *Phys. Fluids*, 16, 62–72, 2004.
- Loth, E., Numerical approaches for the motion of dispersed particles, droplets, or bubbles *Prog. Energy Combust. Sci.*, 26, 161–223, 2000.
- Lovalenti, P.M. and Brady, J.F., The hydrodynamic force on a rigid particle undergoing arbitrary time-dependent motion at small Reynolds numbers, *J. Fluid Mech.*, 256, 561–601, 1993a.
- Lovalenti, P.M. and Brady, J.F., The force on a bubble, drop or particle in arbitrary time-dependent motion at small Reynolds numbers, *Phys. Fluids A*, 5, 2104–2116, 1993b.
- Madhav, G.V. and Chhabra, R.P., Drag on non-spherical particles in viscous fluids, *Int. J. Miner. Process.*, 43, 15–29, 1995.

- Magnus, G., A note on the rotary motion of the liquid jet, *Ann. Phys. Chem.*, 63, 363–365, 1861.
- Marshall, W.R., Atomization and spray drying, *Chem. Engr. Prog. Monograph Series*, No. 2, Vol. 50, 1954.
- Masliyah, J.H. and Epstein, N., Numerical study of steady flow past spheroids. *J. Fluid Mech.*, 44, 493–512, 1970.
- Maxey, M.R. and Riley, J.J., Equation of motion of a small rigid sphere in a non-uniform flow, *Phys. Fluids*, 26, 883–889, 1983.
- Maxworthy, T., Experiments on the flow around a sphere at high Reynolds numbers, *J. Appl. Mech.*, 91, 598–607, 1969.
- Maxworthy, T., Accurate measurements of a sphere drag at low Reynolds numbers, *J. Fluid Mech.*, 23, 369–372, 1975.
- McLaughlin, J.B., Inertial migration of a small sphere in linear shear flows, *J. Fluid Mech.*, 224, 261–274, 1991.
- Mei, R., An approximate expression of the shear lift on a spherical particle at finite Reynolds numbers, *Int. J. Multiphase Flow*, 18, 145–160, 1992.
- Mei, R. and Adrian, R.J., Flow past a sphere with an oscillation in the free-stream and unsteady drag at finite Reynolds number, *J. Fluid Mech.*, 237, 323–341, 1992.
- Mei, R., Lawrence, C.J., and Adrian, R.J., Unsteady drag on a sphere at finite Reynolds number with small fluctuations in the free-stream velocity, *J. Fluid Mech.*, 233, 613–631, 1991.
- Michaelides, E.E., A novel way of computing the Basset term in unsteady multiphase flow comput., *Phys. Fluids A*, 4, 1579–1582, 1992.
- Michaelides, E.E., Review — The transient equation of motion for particles, bubbles, and droplets, *J. Fluids Eng.*, 119, 233–247, 1997.
- Michaelides, E.E., Hydrodynamic force and heat/mass transfer from particles, bubbles and drops — The Freeman Scholar Lecture, *J. Fluids Eng.*, 125, 209–238, 2003.
- Michaelides, E.E., *Particles, Bubbles and Drops — Their Motion, Heat and Mass Transfer*, World Scientific Publishers, Singapore, in print, 2006.
- Michaelides, E.E. and Feng, Z.-G., Heat transfer from a rigid sphere in a non-uniform flow and temperature field, *Int. J. Heat Mass Transfer*, 37, 2069–2076, 1994.
- Michaelides, E.E. and Feng, Z.-G., The equation of motion of a small viscous sphere in an unsteady flow with interface slip, *Int. J. Multiphase Flow*, 21, 315–321, 1995.
- Michaelides, E.E. and Feng, Z.-G., Analogies between the transient momentum and energy equations of particles, *Progr. Energy Combust. Sci.*, 22, 147–163, 1996.
- Miller, R.S. and Bellan, R.J., Direct numerical simulation of a confined three-dimensional gas mixing layer with one evaporating hydrocarbon-droplet-laden stream, *J. Fluid Mech.*, 384, 293–307, 1999.
- Millikan, R.A., The general law of fall of a small spherical body through a gas and its bearing upon the nature of molecular reflection from surfaces, *Phys. Rev.*, 22, 1–23, 1923.
- Miyamura, A., Iwasaki, S., and Ishii, T., Experimental wall correction factors of single solid spheres in triangular and square cylinders, and parallel plates, *Int. J. Multiphase Flow*, 7, 41–46, 1981.
- Morrison, F.A. and Stewart, M.B., Small bubble motion in an accelerating fluid, *J. Appl. Mech.*, 97, 399–402, 1976.
- Mortazavi, S. and Tryggvason, G., A numerical study of the motion of drops in Poiseuille flow. Part 1:Lateral migration of one drop, *J. Fluid Mech.*, 411, 325–350, 2000.
- Mugele, R.A. and Evans, H.D., Droplet size distribution in sprays, *Ind. Eng. Chem.*, 43, 1317–1324, 1951.
- Odar, F., Verification of the proposed equation for calculation of the forces on a sphere accelerating in a viscous fluid, *J. Fluid Mech.*, 25, 591–592, 1966.
- Odar, F. and Hamilton, W.S., Forces on a sphere accelerating in a viscous fluid, *J. Fluid Mech.*, 18, 302–303, 1964.
- Oesterle, B. and Bui-Dinh, Experiments on the lift of a spinning sphere in the range of intermediate Reynolds numbers, *Exp. Fluids*, 25, 16–22, 1998.
- Oliver, D.L. and Chung, J.N., Flow about a fluid sphere at low to moderate Reynolds numbers, *J. Fluid Mech.*, 177, 1–18, 1987.

- Oseen, C.W., Über den Geltungsbereich der Stokesschen Widerstandsformel, *Ark. Mat. Astron. Fysik*, 9 (19), 1913.
- Paine, P.L. and Scherr, P., Drag coefficients for the movement of rigid spheres through liquid-filled cylindrical pores, *Biophys. J.*, 15, 1087–1091, 1975.
- Patankar, N., Ko, T., Choi, H.G., and Joseph, D.D., A correlation for the lift-off of many particles in plane Poiseuille flows of Newtonian fluids, *J. Fluid Mech.*, 445, 55–76, 2001.
- Pettyjohn, E.S. and Christiansen, E.R., Effect of particle shape on free-settling rates of isometric particles, *Chem. Eng. Prog.*, 44, 157–172, 1948.
- Poiseuille, J.L.M., Recherches sur le Mouvement du Sang dans les Vein Capillaires, *Mem. de l' Acad. Roy. des Sci.*, 7, 105–175, 1841.
- Portela, L.M., Cota, P., and Oliemans, R.V.A., Numerical study of the near-wall behaviour of particles in turbulent pipe flows, *Powder Technol.*, 125, 149–157, 2002.
- Pozrikidis, C., Unsteady heat or mass transport from a suspended particle at low Peclet numbers, *J. Fluid Mech.*, 289, 652–688, 1997.
- Proudman, I. and Pearson, J.R.A., Expansions at small Reynolds numbers for the flow past a sphere and a circular cylinder, *J. Fluid Mech.*, 2, 237–262, 1956.
- Raithby, G.D. and Eckert, E.R.G., The effect of turbulence parameters and support position on the heat transfer from spheres, *Int. J. Heat Mass Transfer*, 11, 1233–1246, 1968.
- Ranz, W.E. and Marshall, W.R., Evaporation from drops, *Chem. Eng. Prog.*, 48, 141–146, 1952.
- Renksizbulut, M. and Yuen, M.C., Experimental study of droplet evaporation in high temperature air stream, *J. Heat Transfer*, 105, 364–388, 1983.
- Richardson, J.F. and Zaki, W.N., The fall velocities of spheres in viscous fluids, *Trans. Inst. Chem. Eng.*, 32, 35–41, 1954.
- Rivero, M., Magnaudet, J., and Fabre, J., Quelques Resultats Nouveaux Concernants les Forces Exercées sur une Inclusion Sphérique par Ecoulement Accéléré, *Comptes Rendu, Acad. Sci. Paris*, 312, 1499–1506, 1991.
- Rivkind, V.Y., Ryskin, G.M., and Fishbein, G.A., Flow around a spherical drop in a fluid medium at intermediate Reynolds numbers, *Appl. Math. Mech.*, 40, 687–691, 1976.
- Rojas, S. and Koplik, J., Non-linear flow in porous media, *Phys. Rev.*, E58, 4776–4782, 1998.
- Rowe, P.N., The drag coefficient of a sphere, *Trans. Inst. Chem. Eng.*, 39, 175–181, 1961.
- Rybaczynski, W., On the translatory motion of a fluid sphere in a viscous medium, *Bull. Acad. Sci. Krakow, Series A*, 40–46, 1911.
- Saffman, P.G., The lift on a small sphere in a slow shear flow, *J. Fluid Mech.*, 22, 385–398, 1965.
- Saffman, P.G., The lift on a small sphere in a slow shear flow-corrigendum, *J. Fluid Mech.*, 31, 624–625, 1968.
- Saffman, P.G., On the boundary condition at the surface of a porous medium, *Stud. Appl. Math.*, 50, 93–101, 1971.
- Sangani, A.S., Zhang, D.Z., and Prosperetti, A., The added mass, Basset and viscous drag coefficients in nondilute bubbly liquids undergoing small-amplitude oscillatory motion, *Phys. Fluids*, A3, 2955–2970, 1991.
- Sano, T., Unsteady flow past a sphere at low Reynolds number, *J. Fluid Mech.*, 112, 433–441, 1981.
- Schaaf, S.A. and Chambre, P.L., Fundamentals of gas dynamics, in *High Speed Aerodynamics and Jet Propulsion*, Emmons, H.W., Ed., Vol. 3, 1958, pp. 689–793.
- Schiller, L. and Nauman, A., Über die grundlegende Berechnung bei der Schwerkraftaufbereitung, *Ver. Deutch Ing.*, 44, 318–320, 1933.
- Schoneborn, P.R., The interaction between a single sphere and an oscillating fluid, *Int. J. Multiphase Flow*, 2, 307–317, 1975.
- Seeley, L.E., Hummel, R.L., and Smith, J.W., Experimental velocity profiles in laminar flow around spheres at intermediate Reynolds numbers, *J. Fluid Mech.*, 68, 591–608, 1975.
- Segre, G. and Silberberg, A., Behavior of macroscopic rigid spheres in Poiseuille flow, *J. Fluid Mech.*, 14, 115–157, 1962.

- Siegel, R. and Howel, J.R., *Thermal Radiation Heat Transfer*, McGraw-Hill, New York, 1981.
- Sirignano, W.A., Fluid dynamics of sprays, *ASME J. Fluids Eng.*, 115, 345–378, 1993.
- Sirignano, W.A., *Fluid Dynamics and Transport of Droplets and Sprays*, Cambridge University Press, Cambridge, 1999.
- Soo, S.L., *Multiphase Fluid Dynamics*, Science Press, Beijing, 1990.
- Spelt, P.D.M. and Sangani, A.S., Properties and averaged equations for flows of bubbly liquids, In *Fascination of Fluid Dynamics*, Biesheuvel, A. and van Heijst, G.F., Eds., Kluwer Academic, Dordrecht, 1998, pp. 337–386.
- Sridhar, G. and Katz, J., Drag and lift forces on microscopic bubbles entrained by a vortex, *Phys. Fluids*, 7, 389–399, 1995.
- Stock, D.E., Particle dispersion in flowing gases, *J. Fluids Eng.*, 118, 4–17, 1996.
- Stokes, G.G., On the theories of internal friction of the fluids in motion, *Trans. Cambridge Philos. Soc.*, 8, 287–319, 1845.
- Stokes, G.G., On the effect of the internal friction of fluids on the motion of a pendulum, *Trans. Cambridge Philos. Soc.*, 9, 8–106, 1851.
- Talbot, L., Cheng, R.K., Schefer, R.W., and Willis, D.R., Thermophoresis of particles in a heated boundary layer, *J. Fluid Mech.*, 101, 737–758, 1980.
- Tanaka, T., Yamagata, K., and Tsuji, Y., Experiment on fluid forces on a rotating sphere and a spheroid, *Proceedings of the 2nd KSME-JSME Fluids Engineering Conference*, 1, 266–378, 1990.
- Taneda, S., Experimental investigation of the wake behind a sphere at low Reynolds numbers, *J. Phys. Soc. Jpn.*, 11, 1104–1108, 1956.
- Tate, R.W. and Marshall, Jr., W.R., Atomization by centrifugal pressure nozzles (Part II), *Ind. Eng. Prog.*, 49, 226–234, 1953.
- Temkin, S. and Mehta, H.K., Droplet drag in an accelerating and decelerating flow, *J. Fluid Mech.*, 116, 297–313, 1982.
- ten Cate, A., Nieuwstad, C.H., Derkxen, J.J., and Van den Akker, H.E.A., Particle imaging velocimetry experiments and lattice-Boltzmann simulations on a single sphere settling under gravity, *Phys. Fluids*, 14, 4012–4025, 2002.
- Thornicroft, G.E., Klausner, J.F., and Mei, R., Bubble forces and detachment models, *Multiphase Sci. Technol.*, 13, 35–76, 2001.
- Tomiyama, A., Reconsideration of three fundamental problems in modeling bubbly flows, *39th European Two-Phase Flow Group Meeting*, Aveiro, Portugal, 2001.
- Tomiyama, A., Kataoka, I., Zun, I., and Sakaguchi, T., Drag coefficients of single bubbles under normal and micro gravity conditions, *JSME Int. J., Ser. B*, 41, 472–479, 1998.
- Tomiyama, A., Tamai, H., Zun, I., and Hosokawa, S., Transverse migration of single bubbles in simple shear flows, *Proceedings 2nd International Symposium on Two-Phase Flow Modeling and Experimentation*, 2, 941–948, 1999.
- Tran Cong, S., Gay, M., and Michaelides, E.E., Drag coefficients of irregularly shaped particles, *Powder Technol.*, 139, 21–32, 2004.
- Tsuji, Y., Kato, N., and Tanaka, T., Experiments on the unsteady drag and wake of a sphere at high Reynolds numbers, *Int. J. Multiphase Flow*, 17, 343–354, 1991.
- Tsuji, Y., Morikawa, Y., and Mizuno, O., Experimental measurements of the magnus force on a rotating sphere at low Reynolds numbers bubble in an axisymmetric shear flow, *J. Fluids Eng.*, 107, 484–498, 1985.
- van Wijngaarden, L., Hydrodynamic interaction between bubbles in a liquid, *J. Fluid Mech.*, 77, 27–44, 1976.
- Vasseur, P. and Cox, R.G., The lateral migration of spherical particles in two-dimensional shear flow, *J. Fluid Mech.*, 78, 385–413, 1976.
- Vojir, D.J. and Michaelides, E.E., The effect of the history term on the motion of rigid spheres in a viscous fluid, *Int. J. Multiphase Flow*, 20, 547–556, 1994.
- Wadell, H., Sphericity and roundness of rock particles, *J. Geol.*, 41, 310–331, 1933.
- Wang H. and Skalak, R., Viscous flow in a cylindrical tube containing a line of spherical particles, *J. Fluid Mech.*, 38, 75–96, 1969.

- Warnica, W.D., Renksizbulut, M., and Strong, A.B., Drag coefficient of spherical liquid droplets. Part II. Turbulent gaseous fields, *Exp. Fluids*, 18, 265–272, 1994.
- Wen, C.Y. and Wu, Y.H., Mechanics of fluidization, *Chem. Eng. Prog. Symp. Ser.*, 62, 100–125, 1966.
- Whitaker, S., Forced convection heat transfer correlations for flow in pipes past flat plates, single cylinders, single spheres, and for flow in packed beds and tubes bundles, *A.I.Ch.E. J.*, 18, 361–371, 1972.
- Winnikow, S. and Chao, B.T., Droplet motion in purified systems, *Phys. Fluids*, 9, 50–61, 1966.
- Wu, M. and Gharib, M., Experimental studies on the shape and path of small air bubbles rising in clean water, *Phys. Fluids*, 14, L49–L52, 2002.
- Yearling, P.R. and Gould, R.D., Convective heat and mass transfer from a single evaporating water, ethanol and methanol droplet, *Proc. ASME-FED* 233, 33–39, 1995.
- Yuen, M.C. and Chen, L.W., On drag of evaporating droplets, *Combust. Sci. Technol.*, 14, 147–154, 1976.
- Zuber, N., On the dispersed two-phase flow in the laminar flow regime, *Chem. Eng. Sci.*, 19, 897–917, 1964.

2

Gas-Liquid Transport in Ducts

2.1	Two-Phase Pressure Drop	2-1
	Single-Phase Flow • Homogeneous (No-Slip) Model • Lockhart–Martinelli Correlation • The Flow-Pattern-Dependent Method • Application of Flow-Pattern-Dependent Method to High-Pressure Gas–Oil Flow	
2.2	Omni-Angle Flow-Pattern Map	2-24
	Introduction • Stratified to Nonstratified Transition • Stratified Smooth to Stratified Wavy • Annular to Nonannular Transition • Bubble Flow • Intermittent (Slug and Froth–Churn) Flow • Calculation Scheme for Flow Pattern Determination • Application of the Angle-Dependent Flow-Pattern Map	

R.V.A. Oliemans
Delft University of Technology

B.F.M. Pots
Shell Global Solutions

2.1 Two-Phase Pressure Drop

R.V.A. Oliemans

A key aspect of gas–liquid flow in ducts is how to calculate the pressure gradient. A characteristic feature of two-phase flow in ducts is that the liquid holdup being different from the liquid volume fraction due to slip between the phases. The slip effect is different for different flow patterns. It is large for separated flow and small for mixed flow. Figure 2.1 shows the flow patterns that can occur in vertical and horizontal pipes. For vertical upflow we see (from left to right), as the amount of gas is gradually increased, the following flow patterns evolve: bubbly flow, slug flow, churn flow, and annular flow. In the horizontal situation, gravity tends to change the distribution of the phases. In this figure (from bottom to top), we see, as the amount of gas is gradually increased, the following flow patterns evolve: dispersed bubble flow, slug (intermittent) flow, stratified flow, and annular dispersed flow. For annular flow, the liquid film at the wall no longer has a uniform thickness. It is very thin at the top of the pipe and can be thick at the bottom. In the case of dispersed bubble flow, the bubble concentration is far from homogeneous, since the bubbles tend to accumulate at the top of the pipe. Finally, stratified flow is a flow pattern typical for horizontal and near-horizontal flows. Depending on the gas velocity, stratified flow can occur with a smooth liquid–gas interface without any droplets entrained in the turbulent gas layer, or it can occur with a wavy interface with strong entrainment of droplets.

The slip between the phases is highest for stratified smooth flow without drop entrainment. For this configuration, one observes a large difference between the liquid holdup in the pipe under flowing conditions and the liquid volume fraction injected. The slip will be small (but not zero) for the bubbly flow patterns for which the gas bubbles are finely dispersed in the turbulent liquid phase. Phase holdups are important for two-phase pressure gradient calculations, since they affect both its frictional and gravitational parts.

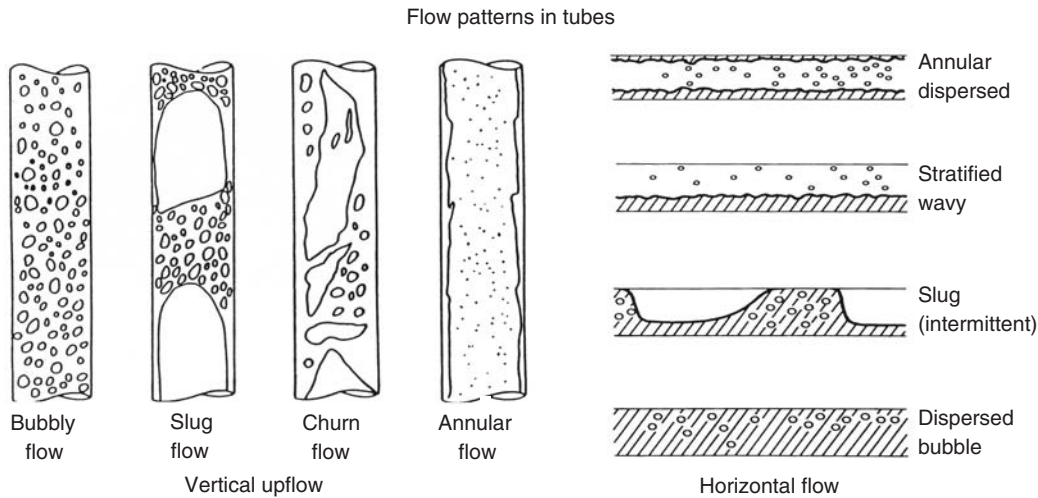


FIGURE 2.1 Flow patterns for two-phase gas–liquid flow in vertical and horizontal pipes.

The purpose of this chapter is to provide insight into the flow-pattern-dependent method to calculate two-phase gas–liquid pressure gradients in pipes. Before discussing this method, we present a survey of the calculation methods for single-phase flow-pressure gradients, the homogeneous (no-slip) model, and the Lockhart–Martinelli correlation for two-phase pressure gradients. In the homogeneous model, one ignores slip between the phases and simply assumes the gas–liquid holdup to be equal to the gas–liquid volume fraction. This simplifies the calculation considerably. Unfortunately, in industrial applications, homogeneous flow rarely occurs. The Lockhart–Martinelli correlation is based on two-phase flow measurements, ignoring any effects of flow patterns. In Section 2.1.4, we discuss the two-phase pressure gradient calculation methods for the flow patterns introduced above. Key elements of the modeling are the choices made for the submodels to close the set of equations for the different flow patterns. Finally, in Section 2.2, the scheme to determine the flow patterns as function of pipe angle, phase velocities, and fluid properties is addressed.

2.1.1 Single-Phase Flow

For steady, isothermal single-phase pipe flow, the momentum equation for a pipe segment provides the following expression for the pressure gradient:

$$-\frac{dp}{dx} = \tau_w \frac{P}{A} + \rho g \sin \theta + \frac{G^2 d(1/\rho)}{dx}$$

total frictional gravitational acceleration (2.1)

where A is the cross-sectional area of the pipe, P the pipe perimeter ($= \pi D$ in this case), τ_w the wall shear stress, g the acceleration due to gravity, θ the angle of the pipe to the horizontal, and G the mass flux in $\text{kg}/(\text{m}^2 \text{ sec})$.

Thus, the total pressure gradient is the sum of three components. The difficulty for the single-phase flow case lies in the determination of the wall shear stress τ_w . It is defined as

$$\tau_w = f \frac{\rho u^2}{2} \quad (2.2)$$

where f is the Fanning friction factor, which, for turbulent flow, is determined via a purely empirical method from the Reynolds number $Re = D \rho u / \mu$ and the relative pipe wall roughness k/D . A widely used correlation is that of Colebrook (1939):

$$1/\sqrt{f} = -4 \log(2k/D + 9.35/Re\sqrt{f}) + 3.48 \quad (2.3)$$

while for laminar flow ($Re < 2300$) the usual expression is employed:

$$f = 16/Re \quad (2.4)$$

Values for the Fanning friction factor can be read from Figure 2.2, where k is the hydraulic roughness, SW the smooth wall, and Re_k the Reynolds number, with the roughness k as length scale.

A convenient relationship, which covers the above two expressions with a laminar-turbulent flow transition at $Re = 2100$, is that of Churchill (1977):

$$f = 2[(8/Re)^{1/2} + 1/(a+b)^{3/2}]^{1/12} \quad (2.5)$$

where

$$a = [2.547 \ln((7/Re)^{0.9} + 0.27k/D)]^{1/6}, b = (37530/Re)^{1/6}$$

2.1.2 Homogeneous (No-Slip) Model

In the case of the two-phase flow, one can also express the pressure gradient as the sum of three components due to friction, gravity, and acceleration:

$$-\frac{dp}{dx} = \tau_{WG} \frac{P_G}{A} + \tau_{WL} \frac{P_L}{A} + (\alpha_G \rho_G + \alpha_L \rho_L) g \sin \theta + \frac{d}{dx} \left[\rho_G \frac{u_{SG}^2}{\alpha_G} + \rho_L \frac{u_{SL}^2}{\alpha_L} \right] \quad (2.6)$$

Here u_{SG} and u_{SL} are the superficial velocities of gas and liquid (the velocities of the phases when flowing alone in the pipe). Several difficulties arise in the calculation of the pressure gradient: the phase holdups, α_G and α_L (which, due to slip, differ from the phase volume fractions $\lambda_G = u_{SG}/u_m$ and $\lambda_L = u_{SL}/u_m$, with $u_m = u_{SG} + u_{SL}$, the mixture velocity) and the pipe perimeters, P_G and P_L , along which the shear stresses act, are unknown. They are expected to depend on the flow pattern. When two phases are flowing simultaneously in a pipe, only a part of the cross-sectional area A is available for the fluids, A_L for the liquid, and

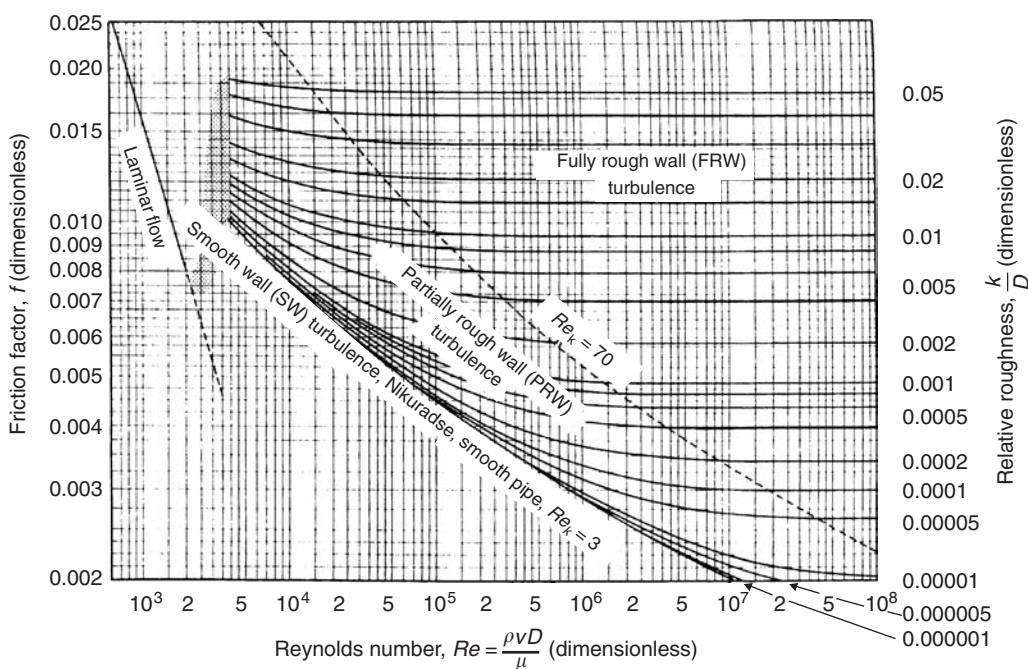


FIGURE 2.2 Fanning friction factor for flow in pipes. (Adapted from Moody, L.F., *Trans. ASME*, 671, 1944.)

A_G for the gas. The liquid holdup present in a pipe segment of length dx under two-phase flow conditions is then defined as $\alpha_L = A_L dx / (A dx) = A_L/A$, and similarly, $\alpha_G = A_G/A$. Note that $\alpha_G + \alpha_L = 1$. As can easily be shown the phase holdups make it possible to compute the actual phase velocities from the superficial velocities: $u_L = u_{SL}/\alpha_L$ and $u_G = u_{SG}/\alpha_G$.

For homogeneous flow, when we can treat the two phases as a single fluid traveling at the mixture velocity $u_m = u_{SG} + u_{SL}$, the problem of calculating the phase holdup is simple. In this case, the phases are well mixed and no slip occurs, i.e., $\alpha_L = \lambda_L$. The frictional shear term becomes equal to $\tau_{Wh} P/A = 4 \tau_{Wh} D$, since $P_G = P_L = P$. For the shear stress, relation (2.2) is used with a friction factor f_h , the mixture velocity u_m , and a homogeneous density calculated from the homogeneous (no-slip) holdup (which is equal to the phase volume fraction, λ):

$$\rho_h = \lambda_G \rho_G + \lambda_L \rho_L \quad (2.7)$$

The equation for the frictional pressure gradient (the first two terms on the right-hand side of Eq. [2.6]) then becomes

$$-\left(\frac{dp}{dx}\right)_F = 2f_h \rho_h u_m^2 / D \quad (2.8)$$

The only uncertainty remaining is the expression for the viscosity of the homogeneous mixture, which has to be known before the Reynolds number $Re_h = D \rho_h u_m / \mu_h$, needed to calculate the friction factor via Eqs. (2.3) and (2.5), can be computed. Various suggestions have been made in the literature; we use here:

$$\mu_h = \lambda_G \mu_G + \lambda_L \mu_L \quad (2.9)$$

It is unfortunate that the homogeneous model works well only in a limited number of applications. Whalley (1987) states that it gives good results if $\rho_L/\rho_G < 10$ or if the total mass flux $G > 2000 \text{ kg}/(\text{m}^2 \text{ sec})$. For oil–gas production and transportation applications, the homogeneous flow model is convenient as a reference case. In particular, at high pressures (with small density ratios) and high throughputs, the more elaborate slip models are expected to approximate the homogeneous results.

2.1.3 Lockhart–Martinelli Correlation

The Lockhart–Martinelli (Lockhart and Martinelli, 1949) correlation is perhaps the oldest available correlation for two-phase friction in horizontal pipes. It was widely used in the process industry. It is very simple to apply, but not very accurate. No liquid holdup information is needed to compute the frictional pressure gradient. It is calculated by multiplying the frictional pressure gradient for single-phase flow (either liquid or gas) by a two-phase flow multiplier Φ_L^2 or Φ_G^2 :

$$-\left(\frac{dp_F}{dx}\right) = \Phi_L^2 \left(-\frac{dp_F}{dx}\right)_{SL} = \Phi_G^2 \left(-\frac{dp_F}{dx}\right)_{SG} \quad (2.10)$$

where

$$-\left(\frac{dp_F}{dx}\right)_{SL} = 2f_{SL} \rho_L u_{SL}^2 / D \quad (2.11)$$

$$-\left(\frac{dp_F}{dx}\right)_{SG} = 2f_{SG} \rho_G u_{SG}^2 / D \quad (2.12)$$

with variables as defined before; f_{SG} and f_{SL} being the friction factors for superficial gas and liquid flow, respectively.

The two-phase flow multipliers are correlated with the parameter X , known as the Lockhart–Martinelli parameter, which is defined as the square root of the ratio of the single-phase frictional pressure gradient of liquid and gas flow:

$$X = \left[\frac{(dp_F/dx)_{SL}}{(dp_F/dx)_{SG}} \right]^{1/2} \quad (2.13)$$

$$\Phi_G^2 = 1 + CX + X^2 \quad (2.14)$$

$$\Phi_L^2 = 1 + \frac{C}{X} + \frac{1}{X^2} \quad (2.15)$$

The correlations for Φ^2 derived on the basis of air–water experiments are shown in Figure 2.3. Different curves are used for liquid and gas in turbulent and laminar flow. Chisholm (1967) introduced a convenient expression for the two-phase multipliers with the following C values for different types of flow:

Liquid	Gas	C
Turbulent	Turbulent	20
Laminar	Turbulent	12
Turbulent	Laminar	10
Laminar	Laminar	5

Note for $X = 1$ (single-phase frictional pressure losses are equal) and both phases in turbulent flow, which is quite common in industrial applications with low-viscosity fluids, that the Lockhart–Martinelli correlation predicts that the two-phase friction loss will be more than 20 times that of single-phase flow!

The liquid holdup needed for the pressure gradient contribution due to gravity and acceleration (see Eq. [2.6]) is also determined by a correlation developed by Lockhart and Martinelli:

$$\alpha_L = \left(\frac{1}{\Phi_L^2} \right)^{1/3} \quad (2.16)$$

2.1.4 The Flow-Pattern-Dependent Method

2.1.4.1 Introduction

One-dimensional flow pattern and angle-dependent modeling is widely used to calculate two-phase pressure gradients and phase holdups for gas–liquid flow in tubes. This type of modeling was already

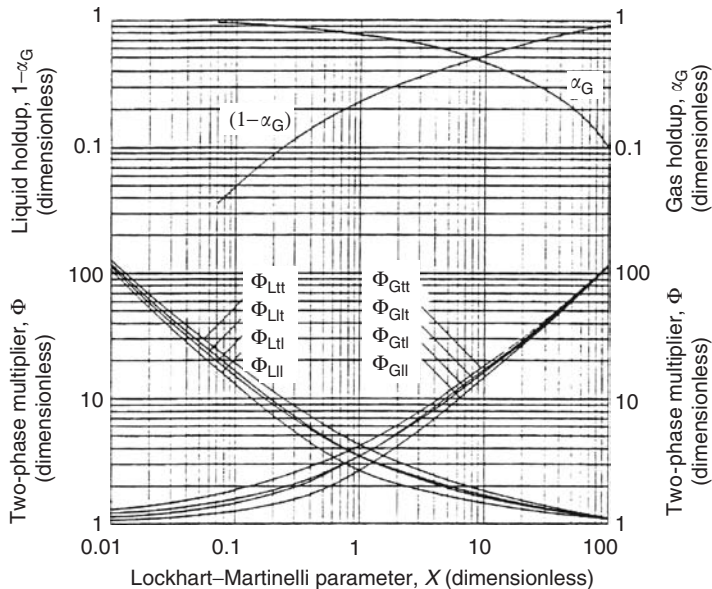


FIGURE 2.3 Lockhart and Martinelli friction correlation.

described by Wallis in 1969. In order to apply these models, the set of transport equations for the fluids has to be extended by submodels or closure relations. The submodels required depend on the flow pattern. Table 2.1 summarizes, for the one-dimensional two-phase flow models that are discussed below, the submodels that are needed to have a closed set of equations for solving gas–liquid tube flow problems. The choice of submodels for the various flow patterns is crucial for scaling up to practice (pipe size, fluid properties, and pressure-temperature conditions), since these submodels are empirically based. There is much ongoing two-phase flow-research activity aimed at improving the description of physical processes that are assumed to be relevant for the submodels for various flow patterns. An impression of the state of the art may be obtained from Hewitt and Lahey (1992).

2.1.4.2 Dispersed Bubble Flow

In the case of dispersed bubble flow, one could think of using the homogeneous model, assuming that there is no slip between the phases. However, it is more common to use a single-fluid two-phase flow model with slip, known as the drift-flux model. Details can be found in Wallis (1969).

In the drift-flux version for dispersed bubble flow, the actual gas velocity is supposed to respond to the centerline velocity in the pipe, which, in the case of turbulent flow, is assumed to be 25% greater than the mixture velocity u_m . Moreover, the gas bubbles experience a bubble rise velocity u_b due to their buoyancy, which is calculated according to

$$u_b = 1.53 \left[\frac{\sigma g \Delta \rho}{\rho_L^2} \right]^{1/4} \sin \theta \quad (2.17)$$

(see also Zuber and Findlay [1965], who use a coefficient of 1.41 and a centerline velocity only 13% larger than the mean velocity).

For vertical flow, the actual gas velocity becomes

$$u_G = C_0 u_m + u_b \quad (2.18)$$

where the parameter C_0 , known as the distribution parameter, reflects the effect of the centerline velocity and has a value of 1.25. by knowing the actual gas velocity it is easy to calculate the gas holdup from the superficial gas velocity:

$$\alpha_G = u_{SG}/u_G \quad (2.19)$$

For the vertical upflow of oil and gas at 150 bar and 50°C in a 0.1 m tube, the phase holdups and the no-slip values (phase volume fractions) of 0.70 and 0.30 for liquid and gas, respectively, are shown in [Figure 2.4](#).

TABLE 2.1 Submodels for Two-Phase Flow Modeling

Flow Pattern	Model and Submodels
Dispersed bubble flow	Drift-Flux Model Distribution parameter Bubble rise velocity
Separated flow (stratified/annular)	Two-Fluid Model Interfacial friction Interfacial velocity Shape of interface Liquid entrainment
Intermittent flow	Drift-Flux + Two-Fluid Model Distribution parameter Bubble rise velocity Holdup in liquid cylinder Slug frequency Slug cylinder or film length Bubble shape

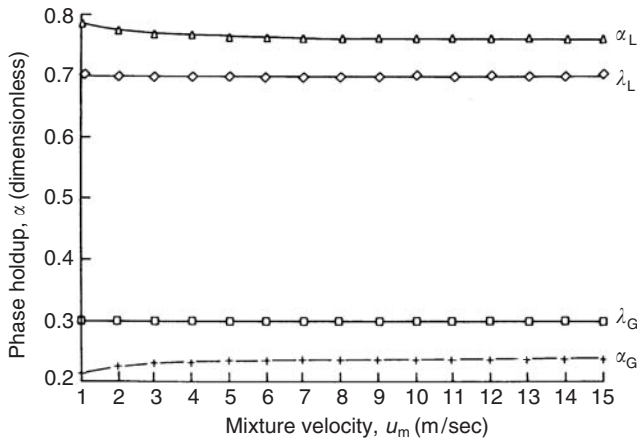


FIGURE 2.4 Dispersed bubble flow: comparison of phase holdups, $C_0 = 1.25$.

In this example, the liquid holdup is about 10% larger than the no-slip holdup, λ_L . The fluid properties used for the calculation are $\rho_L = 800 \text{ kg/m}^3$, $\rho_G = 100 \text{ kg/m}^3$, $\mu_L = 5 \times 10^{-3} \text{ Pa sec}$, $\mu_G = 0.02 \times 10^{-3} \text{ Pa sec}$, and $\sigma = 0.010 \text{ N/m}$, giving a bubble rise velocity of 0.16 m/sec . With the hold up known, it is possible to compute the contributions to the pressure gradient from gravity and acceleration in Eq. (2.6). The frictional pressure gradient is calculated using mixture properties:

$$-\left(\frac{dp}{dx}\right)_F = 2f_m \rho_m u_m^2 / D \quad (2.20)$$

with

$$\rho_m = \alpha_L \rho_L + \alpha_G \rho_G$$

The friction factor f_m is calculated from the mixture Reynolds number,

$$Re_m = D \rho_m u_m / \mu_L$$

and the relative wall roughness k/D ($k = 0.06 \text{ mm}$ for standard pipe material used for well tubing and pipelines).

2.1.4.3 Separated (Stratified and Annular Dispersed) Flow

2.1.4.3.1 Two-Fluid Model Equations

For the description of stratified and annular two-phase flow, the most accurate holdup and pressure-loss predictions are obtained with a two-fluid approach (see Wallis, 1969; Taitel-Dukler, 1976; Oliemans, 1987). In its most general (time-dependent, nonisothermal) form, one starts with six equations for the conservation of mass, momentum, and energy of the two phases. Here, the results are used for the simpler case of steady, isothermal flow without mass transfer between the fluids. The two momentum equations will then lead to two equations of the two unknowns: the phase holdup and the two-phase pressure gradient. In order to solve these equations, however, a number of empirical correlations have to be specified.

The momentum equations for the two fluids can be written as

$$-\alpha_G \frac{dp}{dx} - \tau_{WG} \frac{P_G}{A} - \tau_i \frac{P_i}{A} - \alpha_G \rho_G g \sin\theta + \alpha_G \rho_G g \cos\theta \frac{dh_G}{dx} - \frac{d}{dx} (G_G u_G) = 0 \quad (2.21)$$

$$-\alpha_L \frac{dp}{dx} - \tau_{WL} \frac{P_L}{A} + \tau_i \frac{P_i}{A} - \alpha_L \rho_L g \sin\theta + \alpha_L \rho_L g \cos\theta \frac{dh_L}{dx} - \frac{d}{dx} (G_L u_L) = 0 \quad (2.22)$$

with

$$\alpha_G + \alpha_L = 1 \quad (2.23)$$

It can easily be shown, for a constant liquid level h_L , Eq. (2.6) for the pressure gradient follows when the two momentum equations (2.21) and (2.22) are added. In these equations, P_G , P_L , and P_i are the perimeters for gas against the pipe wall, liquid against the pipe wall, and for the interface, respectively. The shear stresses occurring in the equations are all of the familiar form,

$$\tau = f \frac{\rho u^2}{2} \quad (2.24)$$

where f is the Fanning friction factor. For separated (stratified and annular) flow the expressions for the shear stresses τ_{WG} , τ_{WL} , and τ_i are

$$\tau_{WG} = f_G \frac{\rho_G u_G^2}{2} \quad (2.25)$$

$$\tau_{WL} = f_L \frac{\rho_L u_L^2}{2} \quad (2.26)$$

$$\tau_i = f_i \frac{\rho_G (u_G - u_i)^2}{2} \quad (2.27)$$

where, in the calculation of f_G , f_L , and f_i using Eq. (2.5), the actual average velocities and hydraulic diameters are employed. The actual phase velocities can be calculated from the superficial phase velocities by using the phase holdups: $u_G = u_{SG}/\alpha_G$ and $u_L = u_{SL}/\alpha_L$. For the interfacial shear stress an additional complication that arises is the determination of the interfacial velocity, u_i , and the interfacial roughness, k_i .

In the case of stratified flow, gas flows at a velocity u_G on top of a liquid layer of height h_L and velocity u_L . The gas occupies a cross-sectional area, $A_G = \alpha_G A$, with a pipe wall perimeter, P_G , and a liquid-gas interface perimeter, P_i . The cross-sectional area for the liquid is indicated by $A_L = \alpha_L A$ and the pipe wall perimeter is P_L . All variables mentioned depend on the height of the liquid layer h_L and hence on the liquid holdup α_L (see Figure 2.5).

Eliminating the pressure gradients by combining Eqs. (2.21) and (2.22), and ignoring the acceleration terms, yields a relation F that can be used to calculate the liquid holdup, α_L , by solving for the liquid height, h_L :

$$F = \tau_{WG} \frac{P_G}{A_G} - \tau_{WL} \frac{P_L}{A_L} + \tau_i P_i \left(\frac{1}{A_L} + \frac{1}{A_G} \right) - (\rho_L - \rho_G) g \sin \theta - \Delta \rho g D \cos \theta \frac{\partial h_L / D}{\partial \alpha_L} \frac{\partial \alpha_L}{\partial x} \quad (2.28)$$

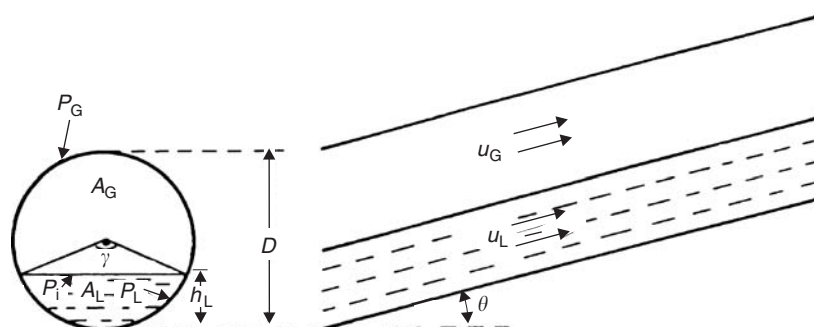


FIGURE 2.5 Inclined stratified flow.

The equilibrium holdup follows from the holdup relation (2.28) by putting $F = 0$ with $\partial\alpha_L/\partial x = 0$. For the calculation of liquid and gas friction factors according to the Churchill equation for turbulent and laminar flow, we use liquid and gas Reynolds numbers:

$$Re_L = \frac{D_L \rho_L u_L}{\mu_L} \quad (2.29)$$

$$Re_G = \frac{D_G \rho_G u_G}{\mu_G} \quad (2.30)$$

where μ_L and μ_G are liquid and gas viscosity, and $D_L = 4 A_L / P_L$ and $D_G = 4 A_G / (P_G + P_i)$ are the hydraulic diameters for liquid and gas. In the case of annular flow, the pipe diameter D is used instead of the hydraulic diameter D_L to calculate the relative wall roughness to avoid unrealistic results. For stratified flow, the liquid holdup α_L and the perimeters are related to the top angle γ , defined in [Figure 2.5](#) by

$$\alpha_L = \frac{\gamma - \sin \gamma}{2\pi} \quad (2.31)$$

$$h_L = 1/2[1 - \cos(\gamma/2)]D \quad (2.32)$$

$$P_L = \gamma D/2 \quad (2.33)$$

$$P_i = \sin(\gamma/2)D \quad (2.34)$$

$$P_G = \pi D - P_L \quad (2.35)$$

If the depth, h_L , is an input parameter rather than the angle γ , the angle γ follows from

$$\gamma = 2 \arccos(1 - 2h_L/D) \quad (2.36)$$

In the case of a uniform film thickness for annular flow, the liquid holdup and perimeters are

$$\alpha_L = 4h_L/D(1 - h_L/D) \quad (2.37)$$

$$P_L = \pi D \quad (2.38)$$

$$P_i = \pi(1 - h_L/D)D \quad (2.39)$$

$$P_G = 0 \quad (2.40)$$

It is convenient to rewrite the equation for the liquid holdup ($F = 0$; F is given by Eq. [2.28]; $\partial\alpha_L/\partial x = 0$) in the dimensionless form, as used by Taitel and Dukler (1976):

$$-X^2 \tilde{f}_L \frac{\tilde{P}_L}{\tilde{A}_L} \tilde{u}_L^2 + \left[\tilde{f}_G \frac{\tilde{P}_G}{\tilde{A}_G} \tilde{u}_G^2 + \tilde{f}_i \left(\frac{\tilde{P}_i}{\tilde{A}_G} + \frac{\tilde{P}_i}{\tilde{A}_L} \right) \tilde{u}_R^2 \right] - 4Y = 0 \quad (2.41)$$

where the friction factors for gas, liquid, and interface with a tilde are defined as

$$\tilde{f}_G = f_G/f_{SG} \quad (2.42)$$

$$\tilde{f}_L = f_L/f_{SL} \quad (2.43)$$

$$\tilde{f}_i = f_i/f_{SG} \quad (2.44)$$

and

$$X^2 = \left| \frac{(dp_F/dx)_{SL}}{(dp_F/dx)_{SG}} \right| = \frac{2f_{SL}(\rho_L u_{SL}^2/D)}{2f_{SG}(\rho_G u_{SG}^2/D)} = \frac{f_{SL}}{f_{SG}} \frac{F_L^2}{F_G^2} \quad (2.45)$$

$$Y = \frac{(\rho_L - \rho_G)g \sin \theta}{|(dp_F/dx)_{SG}|} = \frac{(\rho_L - \rho_G)g \sin \theta}{2f_{SG}(p_G u_{SG}^2/D)} = \frac{\sin \theta}{2f_{SG} F_G^2} \quad (2.46)$$

where $F_G = (\rho_G/\Delta \rho g D)^{0.5}$ u_{SG} and $F_L = (\rho_L/\Delta \rho g D)^{0.5}$ u_{SL} are the densimetric gas and liquid Froude numbers, which are important scaling parameters for gravity-dominated problems.

The other dimensionless variables that depend on h_L/D are as follows:

$$\tilde{A}_{L,G} = A_{L,G}/D^2 \quad (2.47)$$

$$\tilde{P}_{L,G,i} = P_{L,G,i}/D \quad (2.48)$$

$$\tilde{u}_{L,G} = u_{L,G}/u_{SL,SG} = A/A_{L,G} \quad (2.49)$$

$$\tilde{u}_R = u_R/u_{SG} \quad (2.50)$$

Here, u_{SL} and u_{SG} are superficial liquid and gas velocities, while $u_R = u_G - u_i$ is the relative velocity, i.e., the difference between the gas velocity, u_G , and the interfacial velocity, u_i .

The dimensionless liquid height can be determined as a function of the Lockhart–Martinelli parameter X and the gravity parameter Y using Eq. (2.41). The liquid holdup then follows from

$$\alpha_L = \frac{1}{\pi} [\arccos(1 - 2\tilde{h}_L) - (1 - \tilde{h}_L)\tilde{P}_i] \quad (2.51)$$

where

$$\tilde{P}_i = [1 - (1 - 2\tilde{h}_L)^2]^{1/2} \quad (2.52)$$

2.1.4.3.2 Empirical Correlations

In order to solve the set of stratified flow equations for liquid holdup (Eq. [2.41]) and pressure loss (Eq. [2.6]), we require methods for calculating the liquid interface velocity, u_i , and the interfacial friction factor, f_i , which are needed to compute the interfacial shear, τ_i .

Typically, the liquid interface velocity selected corresponds to that of a highly turbulent liquid flow:

$$u_i = u_L \quad (2.53)$$

In the case of laminar liquid flow, a value of twice the average liquid velocity would be appropriate (see Oliemans et al., 1986). In the literature, the liquid interface velocity in Eq. (2.27) is often taken to be zero on the assumption that it is negligible compared to the gas velocity, u_G . However, this assumption is not justified for the situation of gas–oil transport in long, large-diameter pipelines, where actual liquid velocities can reach values of about 20 to 25% of the gas velocity, u_G .

For the interfacial friction factor, f_i , a number of correlations have been published. Taitel and Dukler use

$$f_i = f_{SG} \quad (2.54)$$

in their stratified flow model. (Typically, f_{SG} has a value of 0.005 for highly turbulent flow.) Cheremisinoff and Davis (1979) used

$$f_i = 0.008 + 2 \times 10^{-5} Re_L \quad (2.55)$$

for calculating the interfacial shear, τ_i . This correlation was derived by Miya et al. (1971) from flow between parallel plates up to a Reynolds number of 1700. In their study on stratified turbulent–turbulent

gas-liquid flow in horizontal and inclined pipes, Shoham and Taitel (1984) reject this correlation, since for Reynolds numbers larger than 1700 it seems to give unrealistically large values for f_i . They propose a constant value (corresponding to a fully developed rough interface due to the presence of small waves, as reported by Cohen and Hanratty, 1968):

$$f_i = 0.0142 \quad (2.56)$$

In the KSLA (Koninklijke Shell-Laboratorium, Amsterdam) model, the interfacial friction factor f_i is calculated in the same manner as the friction factor for gas and liquid, i.e., by using the Colebrook formula (Eq. [2.3]) with the gas Reynolds number, Re_G (Eq. [2.30]), and a relative roughness, k_i/D_G . Consequently, determination of the friction factor requires knowledge of the effective roughness of the gas-liquid interface, k_i .

Cohen and Hanratty (1968) have shown that the equivalent sand-grain roughness on the gas-liquid interface, k_i , is related to the root-mean-square wave height, Δh , through

$$k_i = 3\sqrt{2} \times \Delta h \quad (2.57)$$

Wave information to compute the interfacial roughness is derived from laboratory measurements on air-water channel flow. However, when Δh is larger than the height of the liquid layer h_L , k_i is calculated by using h_L instead of Δh in Eq. (2.57), namely,

$$k_i = \begin{cases} 3\sqrt{2}\Delta h & \text{for } \Delta h < h_L \\ 3\sqrt{2}h_L & \text{for } \Delta h \geq h_L \end{cases} \quad (2.58)$$

According to this procedure, the interfacial friction factor f_i increases with the relative velocity. For trunk line applications, the f_i values may vary typically from that of a smooth pipe (0.002) to a value as high as 0.0165.

A check was made on the empiricism for u_i and f_i in the stratified flow model described above using the data of Hoogendoorn (1959) for horizontal air-water and air-gas-oil stratified flow in a 6-in. pipe. Excellent agreement was achieved for both holdup and pressure loss.

For horizontal or downward-sloping segments, when $Y \leq 0$, the solution to the holdup equation (2.41) has a single value (see Figure 2.6a, determined for an interfacial friction factor ratio $f_i/f_{SG} = 1$). For upwardly inclined pipes ($Y > 0$), the solution can be multivalued, with three possible mathematical solutions. The intermediate solution is physically unstable because increasing the liquid flow rate leads to a decrease in holdup, and is therefore not considered practical. This leaves the low and high holdup values as possible solutions. Barnea and Taitel (1992) concluded from their stability analysis that only the solution of the thinnest liquid film is stable, whereas the other two solutions are practically unstable. The common practice in industry is to use the lowest holdup as the relevant solution. Ullmann et al. (2003) warn that multi-holdups can be associated with multivalue pressure drops and other flow characteristics. Under these conditions, the modeling and design should be performed with care to guarantee stable operation.

The liquid holdup is a decreasing function of f_i/f_{SG} . Crowley and Rathe (1988) states that a friction factor ratio f_i/f_{SG} of 10 provides a lower limit for the liquid holdup in stratified flow. Figure 2.6b shows the dimensionless liquid level as a function of X for parameter values of Y for the case $f_i = 10f_{SG}$. For horizontal flow, the effect of a change in interfacial friction factor ratio on liquid holdup is shown in Figure 2.7a (taken from Crowley and Rathe 1988). Figure 2.7b shows the influence on the frictional pressure loss as an effect on the two-phase multiplier, which is the factor by which the single-phase friction pressure loss for gas has to be multiplied to obtain the two-phase pressure loss.

The liquid holdup values are shown in Figure 2.8 for the example of a horizontal gas-oil flow at 150 bar in a 0.1 m pipe. In the calculations, a constant superficial liquid velocity of 0.2 m/sec was selected, while the gas velocity was allowed to vary to obtain a mixture velocity range of 1 to 15 m/sec. As with the previous example for dispersed bubble flow, the liquid volume fraction λ_L (the no-slip holdup) is shown as well to enable one to appreciate the slip effect for stratified flow.

For annular flow, the interfacial roughness is calculated by replacing the factor $3\sqrt{2}$ in Eq. (2.57) by a smaller factor, namely $30/We$, where the Weber number $We = \rho_G(u_G - u_i)^2 h_L / \sigma$ typically varies from 20

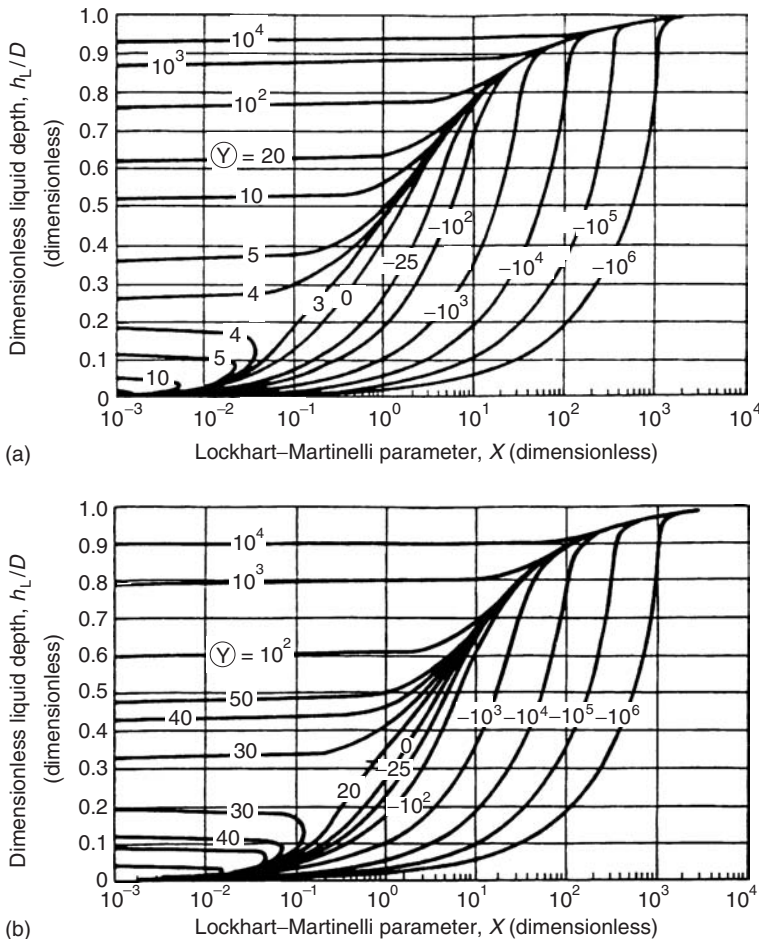


FIGURE 2.6 (a) Liquid level in stratified two-phase flow for $f_i/f_{SG} = 1$; (b) Liquid level in stratified two-phase flow for $f_i = 10f_{SG}$. (Crowley and Rathe [1988].)

to 200 for gas well tubing (σ is the surface tension, which for a 100 bar gas-condensate system is as low as 0.005 N/m). This correlation was found by Oliemans et al. (1986) to best fit the Harwell databank of vertical annular dispersed flow experiments. It also gave good results for annular vertical flow tests performed at Shell Amsterdam in tubes ranging in size from 0.5 to 4 in.

Employing a simplified model in a procedure similar to that for stratified flow (Eq. [2.41] and Figure 2.6a), the liquid holdup can be determined from the parameters X and Y as shown in Figure 2.9, taken from Pots (1985). As shown in Figure 2.10, note that in large horizontal pipelines, used in many industrial applications, the gas velocity is low and the liquid film is highly asymmetric. The resulting flow pattern is intermediate between stratified wavy and annular dispersed flow. The gas velocity is simply not high enough for a liquid film of uniform thickness to form.

2.1.4.3.3 Liquid Entrainment

In order to incorporate the entrainment fraction E in the separated flow model, the gas and the entrained droplets are regarded as one phase, and the remaining liquid layer at the pipe wall as the other phase. It is assumed that there is no slip between the droplets and the gas. The gas and liquid droplets are therefore lumped together, and modified flow parameters are calculated as follows:

$$u'_{SG} = u_{SG} + Eu_{SL} \quad (2.59)$$

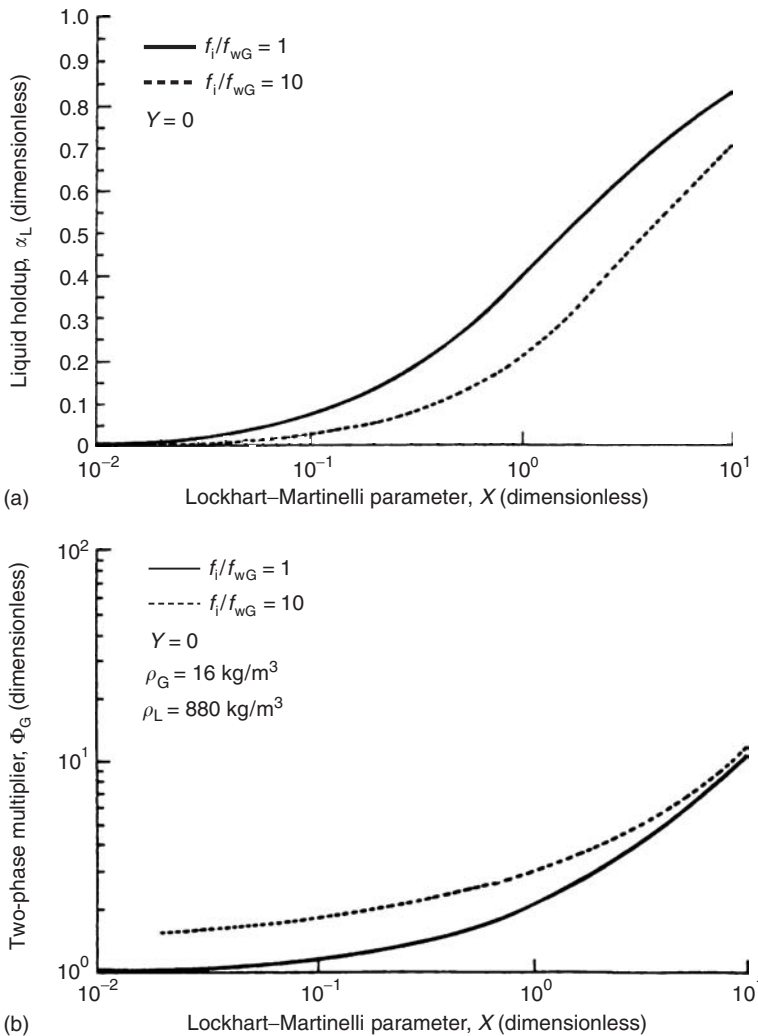


FIGURE 2.7 (a) Liquid hold-up and (b) Multiplier in the stratified flow pattern. (From Crowley and Rathe [1988].)

$$u'_{SL} = (1-E)u_{SL} \quad (2.60)$$

$$\rho'_G = (\rho_G u_{SG} + \rho_L E u_{SL}) / u_{SG} \quad (2.61)$$

$$\mu'_G = (\mu_G u_{SG} + \mu_L E u_{SL}) / u_{SG} \quad (2.62)$$

The total liquid holdup is the sum of the liquid holdup in the film and in the gas phase:

$$\alpha'_L = \alpha_{Lf} + (1 - \alpha_{Lf}) \frac{E u_{SL}}{u_{SG} + E u_{SL}} \quad (2.63)$$

For annular flow in horizontal pipes, Pan and Hanratty (2002) propose the following expression for the entrainment of liquid droplets in the gas phase:

$$\frac{(E/E_M)}{1 - (E/E_M)} = \frac{k'_A D u_G^3 S (\rho_G \rho_L)^{0.5}}{4 < K_D (C_W/C_B) > \sigma} \quad (2.64)$$

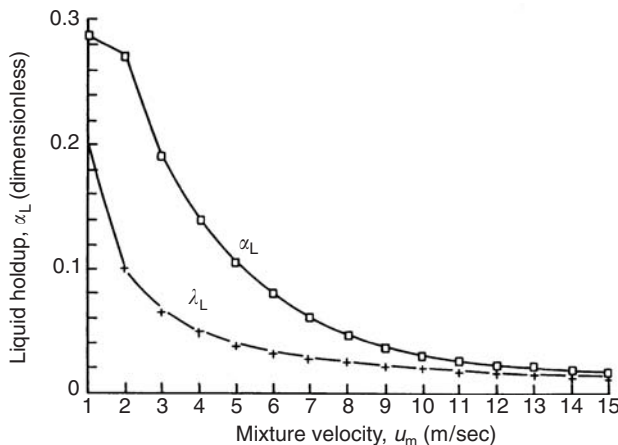


FIGURE 2.8 Results of calculations with the stratified wavy model for horizontal gas–oil flow in a 0.1 m pipe.

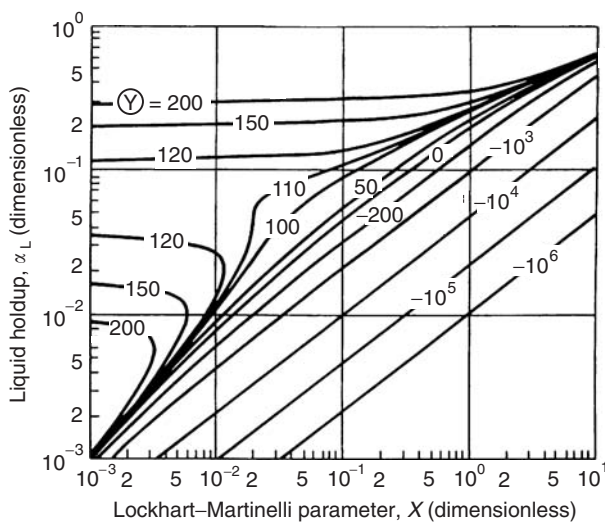


FIGURE 2.9 Liquid holdup in annular two-phase flow. (From Pots [1985].)

Entrainment is considered to result from a balance between the rate of atomization of the liquid layer flowing along the pipe wall and the rate of deposition of drops. The latter is controlled by gravitational settling at low gas velocities and by droplet turbulence at high gas velocities. In order to apply the above expression, one has to define the rate of atomization, k'_A , the rate of deposition, k_D , the drop concentration, C_W/C_B , the ratio of drop to gas velocity, S , and the maximum entrainment, E_M . Pan and Hanratty conclude that the implementation of their theory is handicapped by the sparsity of measurements on drop size and entrainment in horizontal pipes. Scale-up to industrial applications with large pipe sizes and fluids other than air–water under atmospheric conditions remains uncertain.

2.1.4.4 Intermittent (Slug and Froth–Churn) Flow

For slug flow, the model of Dukler and Hubbard (1975) has been used as a basis for development. The model has been generalized such that the gas phase is treated in a similar way to the liquid phase. This is necessary for the model to be valid for high-pressure applications, since neglect of gas density is then no longer justified. Furthermore, inclined pipe situations are properly accounted for (Pots et al., 1988).

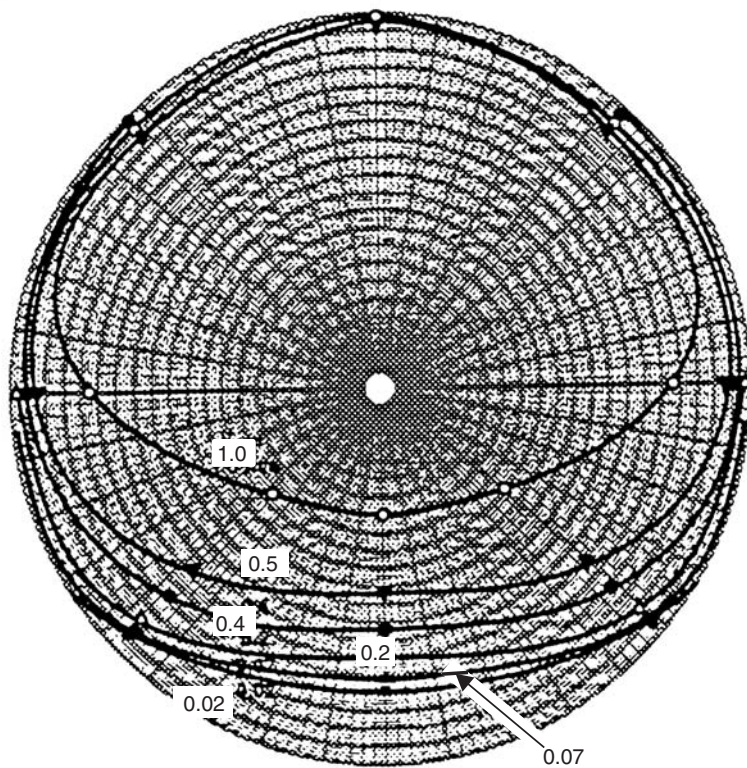


FIGURE 2.10 Measured distribution in the pipe at Bacton. ($u_{SG} = 7 \text{ m/sec}$, $u_{SL} = 0.02, 0.07, 0.2, 0.4, 0.5$, and 1.0 m/sec (From Wu et al., *Proceedings of the 3rd Conference on Multiphase Flow*, The Hague, Netherlands, 1987, pp. 13–21. With permission.).

An important extra feature is that, as the mixture velocity increases, the equations for slug flow gradually converge with those for froth–churn flow, with reduced slip between the phases. In oil wells, such a transition is expected in the upper part of the tubing when, due to a reduction in pressure, more gas is formed and the gas present expands, leading to a low volume fraction of liquid. In that case, less liquid is available to maintain liquid cylinders, which, in turn, tend to become more and more foamy and ultimately fall apart.

Figure 2.11 shows the slug geometry. It consists of two parts. The bubble represents a separated flow configuration, with a liquid film at the bottom of the pipe for near-horizontal flow, and completely surrounding it for near-vertical flow. The liquid cylinder contains gas bubbles in a dispersed bubble flow configuration. Model wise, it is a hybrid system made up of two model types already treated: a two-fluid model for the separated flow component and a drift-flux model for the dispersed flow component.

The slug propagates at the translational velocity u_t , which can be obtained from the mixture velocity u_m :

$$u_t = (1 + C)u_m = u_G = C_0u_m + u_b \quad (2.65)$$

where C is related to the amount of liquid that is shed from the slug into the film and is known as the shedding parameter. It can be derived from Zuber's distribution parameter, C_0 , which is used in the drift-flux model:

$$C = (C_0 - 1) + u_b/u_m \quad (2.66)$$

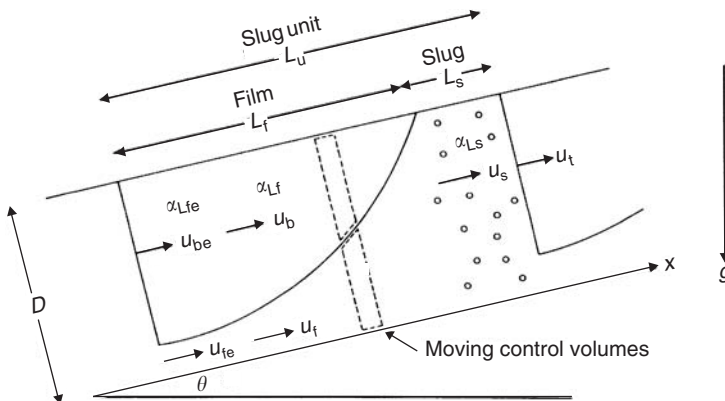


FIGURE 2.11 Slug-flow geometry (ϵ = end of film [bubble] region).

The distribution parameter is calculated according to a procedure introduced by Collins et al. (1978) as

$$C_0 = \begin{cases} 2 & \text{for laminar flow} \\ \frac{\log Re_m + 0.089}{\log Re_m - 0.74} & \text{for turbulent flow} \end{cases} \quad (2.67)$$

where $Re_m = D\rho_L u_m / \mu_L$ is the mixture Reynolds number, defined by the liquid density and viscosity. Note that for $Re_m = 10,000$, a value not unusual for oil transport in flow lines, $C_0 = 1.25$ is obtained, which is equal to the value introduced earlier for dispersed bubble flow. For $Re_m = 100,000$, C_0 decreases to 1.19, a value often used in the literature in the drift-flux approach to slug flow.

The bubble rise velocity is calculated by

$$u_b = C_1 \sqrt{\frac{\Delta \rho}{\rho_L} g D} \quad (2.68)$$

where C_1 is a function of pipe size and surface tension, derived by Oliemans (1976) on the basis of measurements by Zukoski (1966). For vertical upflow, $C_1 = 0.35$. However, it attains a maximum value at an angle of about 45° from the vertical and is zero for horizontal flow.

In the calculation of the liquid holdup and the pressure loss for a slug unit, the complication arises that the contributions from the film component having a length l_f and the liquid cylinder component of length l_s have to be accounted for. When the liquid mass conservation law is applied to the slug unit, and no slip is assumed in the slug cylinder ($u_s = u_m$ in Figure 2.11), it is possible to express the ratio of film and total slug-unit length, l_f/l_u , in terms of velocities and the unknown liquid holdups of the film (α_{Lf}) and slug-cylinder (α_{Ls}) components of the slug unit:

$$\bar{l}_f/l_u = \frac{u_m}{u_t} \frac{\alpha_{Ls} - \lambda_L}{\bar{\alpha}_{Ls} - \bar{\alpha}_{Lf}} \quad (2.69)$$

where the overbar on α_{Lf} denotes the average over the film length. The liquid holdup of the total slug unit then follows immediately:

$$\alpha_L = \frac{\alpha_{Ls} l_s + \bar{\alpha}_{Lf} l_f}{l_u} = \frac{C \alpha_{Ls} + \lambda_L}{1 + C} \quad (2.70)$$

The liquid holdup depends on two correlating parameters: the shedding parameter C (determined from the distribution parameter as indicated above) and the as yet unknown liquid holdup in the slug cylinder, α_{Ls} .

It is interesting to observe here that if one uses a drift-flux approach to model the total slug unit, the relation for the liquid holdup is equal to Eq. (2.70), but with $\alpha_{Ls} = 1.0$. It is known from observations, however, that gas bubbles are present in the liquid cylinder during slug flow, so α_{Ls} should be < 1.0 . The

derivation of a proper method to determine the holdup in the slug cylinder as a function of flow and fluid parameters (turbulence in the liquid phase, physical mechanism of gas entrainment) is currently under active investigation. For the time being, a correlation developed by Andreussi and Bendiksen (1989) on the basis of small-scale laboratory data is being used. In this approach, the slug-cylinder holdup is correlated with the mixture velocity, u_m , the bubble disperse velocity, u_{m1} , which gives the lower limit below which no bubbles are produced, and a velocity u_{m0} that is proportional to the fraction of entrained bubbles reaggregating with the Taylor bubble of the film part of the slug unit. The slug-cylinder holdup expression is

$$C_0 = \begin{cases} \frac{u_{m0} + u_{m1}}{u_{m0} + u_m} & \text{for } u_m \geq u_{m1} \\ 1.0 & \text{for } u_m < u_{m1} \end{cases} \quad (2.71)$$

Although in the original paper the bubble dispersion velocity u_{m1} is shown to increase with pipe size, discussions with one of the authors and comparisons with data available at KSLA have resulted in the use, temporarily, of a fixed value $u_{m1} = 1.0$ m/sec (Andreussi, 1988). The equation for the bubble loss velocity is

$$u_{m0} = \frac{240}{C_0 - 1} Eo^{-1/2} \left(1 - \frac{1}{3} \sin \theta \right) \left[\frac{g\sigma\Delta\rho}{\rho_L^2} \right]^{1/4} + \frac{u_b}{C_0 - 1} \quad (2.72)$$

Here, the parameter Eo , defined as $Eo = g\Delta\rho D^2/4\sigma$, may be recognized as the Eötvös number.

Figure 2.12 shows α_{ls} values calculated with this correlation for vertical upflow in a 0.1 m tube of air and water at 1 bar and of gas and oil at 150 bar.

The calculations have been performed for a constant superficial liquid velocity of 1 m/sec for superficial gas velocities ranging from 0 to 14 m/sec. The holdup in the slug cylinder for the high-pressure hydrocarbon system is considerably lower than that of air and water at 1 bar. The Andreussi-Bendiksen correlation has the advantage of adequately describing the trend expected when the mixture velocity increases and the surface tension of the liquid phase becomes smaller: more and more gas bubbles will be entrained in the liquid cylinder and slug flow will change into churn-froth flow at a value of the slug-cylinder holdup of 0.48. The decrease in α_{ls} with mixture velocity is illustrated clearly in Figure 2.12 for the two test fluids selected. This result strongly contrasts with the result of $\alpha_{ls} = 1.0$ obtained when the drift-flux model is used for the total slug unit, or the constant value of $\alpha_{ls} = 0.75$ that Fernandes (1981) recommends for vertical flow. Note that in this example, a transition to churn/froth flow occurs at a mixture velocity of 6 m/sec for the oil-gas flow at 150 bar, while for the 1-bar air-water flow this transition is predicted at a velocity of almost 15 m/sec.

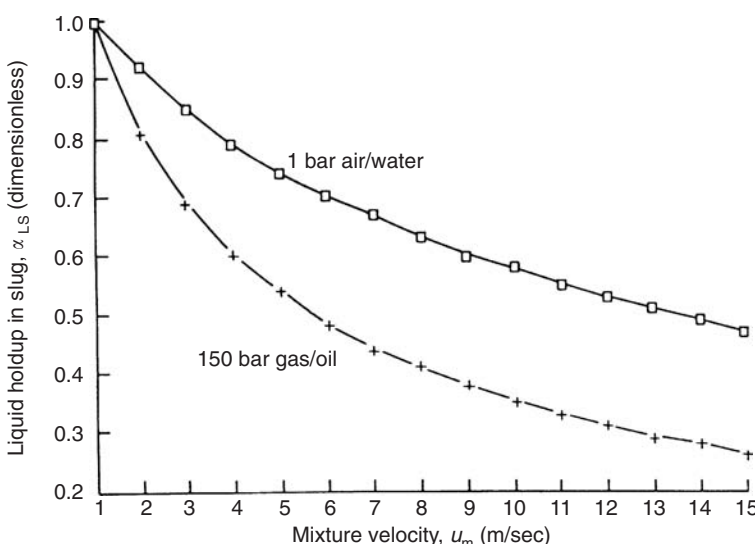


FIGURE 2.12 Slug-cylinder holdup (α_{ls}) values for vertical air-water and gas-oil flow. ($u_{SL} = 1$ m/sec).

For the example shown in [Figure 2.12](#), the distribution parameter, C_0 , decreases with the mixture velocity for air–water from a value of 1.19 to 1.15, while for the 150-bar gas–oil system it ranges from 1.24 to 1.18. For a particular mixture velocity, the translational velocity of the slug will then be larger for gas–oil flow.

The liquid holdup can now be calculated according to Eq. (2.70) with the correlations for the shedding parameter C and the slug–cylinder holdup α_{Ls} . In [Figure 2.13](#), the calculated liquid holdup for the gas–oil example is compared with the liquid volume fraction.

Typically, holdups for intermittent flow in this case are 30 to 50% larger than the no-slip holdups. Comparison with liquid holdups calculated via the drift-flux model ($\alpha_{Ls} = 1$) and the model by Fernandes ($\alpha_{Ls} = 0.75$) is shown in [Figure 2.14](#). In these models, liquid holdups at high mixture velocities are appreciably larger than those calculated via the current model.

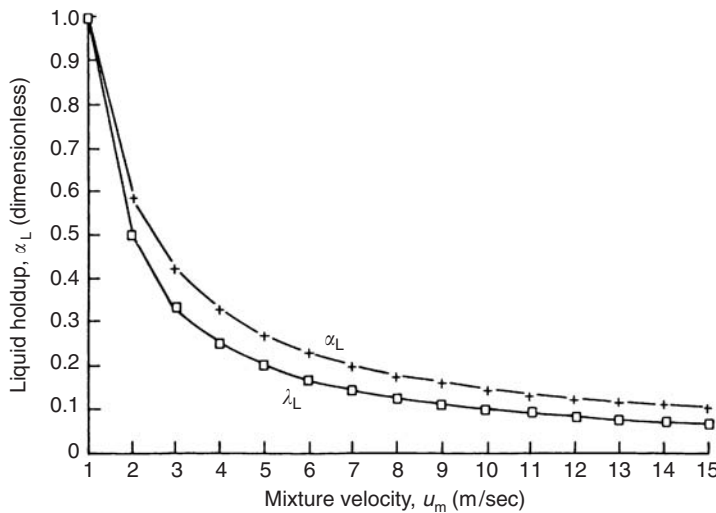


FIGURE 2.13 Holdup of slug unit ($u_{SL} = 1$ m/sec; 150-bar gas–oil).

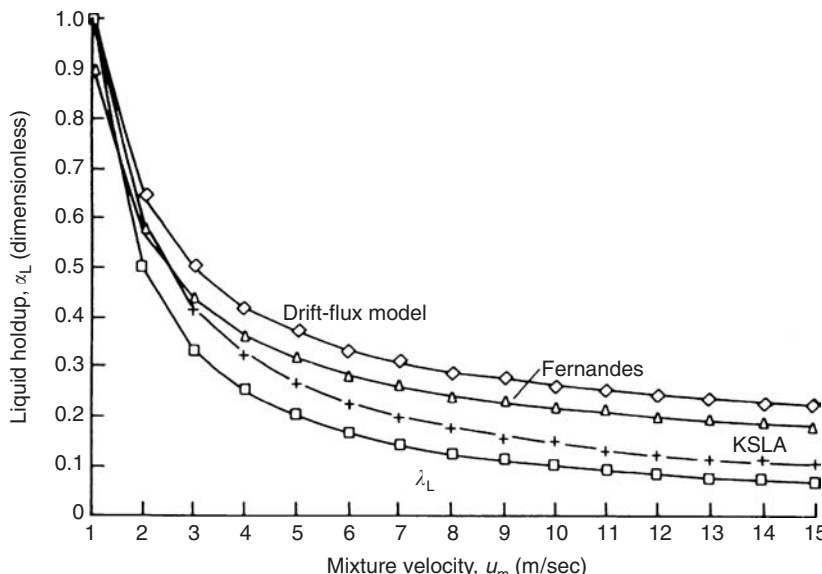


FIGURE 2.14 Holdup of α_L slug unit ($u_{SL} = 1$ m/sec; 150-bar gas–oil).

With the liquid holdup known, it is possible to compute the contributions of gravity and acceleration to the total pressure gradient (Eq. [2.6]). The frictional part of the pressure gradient for intermittent flow can be written as a sum of film and liquid cylinder contributions:

$$-\left(\frac{dp}{dx}\right)_F = \frac{l}{l_u} \left[\int_0^{l_f} \left(\tau_{wf} \frac{P_f}{A} + \tau_{wb} \frac{P_b}{A} \right) dx + \tau_s \frac{P_s}{A} l_s \right] \quad (2.73)$$

The slug-cylinder part is calculated in the usual manner for dispersed bubble flow:

$$-\left(\frac{dp}{dx}\right)_s = 2f_s \rho_s u_m^2 / D \quad (2.74)$$

where the slug density is

$$\rho_s = \alpha_{ls} \rho_L + (1 - \alpha_{ls}) \rho_G \quad (2.75)$$

and the Reynolds number Re_s used to compute the friction factor, is defined as $Re_s = D \rho_s u_m / \mu_L$.

The complication lies in calculating the contribution from the film. In order to determine the perimeters P_f and P_b for the liquid and gas bubbles, the liquid holdup has to be determined in the way described earlier for the two-fluid model applied to separated (stratified or annular) flow. From the momentum equations for the gas and liquid phases (Eqs. [2.21] and [2.22]), Dukler and Hubbard (1975) derived a function $W(\alpha_{lf})$ from which, for a known value of the film length l_f , the film holdup can be determined:

$$\int_{\alpha_{lfe}}^{\alpha_{ls}} W(\alpha_{lf}) d\alpha_{lf} = l_f / D \quad (2.76)$$

At the back of the liquid cylinder $\alpha_{lf} = \alpha_{ls}$; just before pickup by the next slug $\alpha_{lf} = \alpha_{lfe}$.

The function $W(\alpha_{lf})$, derived by Pots et al. (1988), is considerably more complex than that used in the original approach by Dukler-Hubbard, since for the high-pressure oil-gas applications in inclined pipes, the effect of both the gas and the angle of inclination had to be incorporated.

The $W(\alpha_{lf})$ function can be written as a ratio of the balance of momentum flux and gravity-spreading terms to the liquid holdup relation F of Eq. (2.28):

$$w(\alpha_{lf}) = \frac{(M_G + M_L) + (G_G - G_L)}{F} \cdot \frac{1}{D} \quad (2.77)$$

where M is the momentum flux and G the gravity-spreading term of liquid and gas phases, given by

$$M_L = \rho_L \left(\frac{\alpha_{ls}}{\alpha_{lf}} C u_m \right)^2 \frac{1}{\alpha_{lf}} \quad (2.78)$$

$$G_L = \rho_L g D \zeta(\gamma) \frac{1}{\alpha_{lf}} \quad (2.79)$$

Similar expressions exist for M and G for the gas phase, with $\pi - \gamma$ being substituted for γ , and subscript G for L. The function $\zeta = d[\alpha_{lf} \xi(\alpha_{lf})] / d\alpha_{lf}$ in which ξ is the distance from the film interface to the center of pressure in the liquid and is a function of the local film holdup α_{lf} (see original paper by Dukler and Hubbard), is

$$\zeta = \frac{\pi/2 \alpha_{lf} \sin(\gamma/2) + \sin^2(\gamma/2) \cos(\gamma/2)}{1 - \cos \gamma} - 1/2 \cos(\gamma/2) \quad (2.80)$$

The gravity term is only included for stratified flow; for annular flow this term is set to zero.

The denominator F in Eq. (2.77) is the liquid holdup relation (2.28) for inclined flow:

$$F = \tau_{Wb} \frac{P_b}{A_b} - \tau_{Wf} \frac{P_f}{A_f} + \tau_{IPi} \left(\frac{1}{A_b} + \frac{1}{A_f} \right) - \Delta \rho g \sin \theta - \left[\Delta \rho g D \cos \theta \frac{\partial(h_f/D)}{\partial \alpha_{Lf}} \right] \frac{\partial \alpha_{Lf}}{\partial x} \quad (2.81)$$

The integration of Eq. (2.76) must be performed numerically and requires a value of l_f . This film length can be expressed as a function of α_{Lf} provided the length l_u of the total slug unit is known. For this, a correlation is required for the slug frequency, since

$$l_u = u_t / v_s \quad (2.82)$$

For the slug frequency v_s the correlation based on data from Heywood and Richardson (1979) is used:

$$v_s = [F_{\min} + A(F_m^{0.1} - F_{s,\min}^{0.1})^2](g/D)^{0.5} \quad (2.83)$$

where

$$F_{\min} = 0.048 F_{SL}^{0.81} \quad (2.84)$$

$$F_{s,\min} = 4.9 F_{SL}^{0.64} \quad (2.85)$$

$$A = 0.73 F_{SL}^{2.34} \quad (2.86)$$

$$F_{SL} = \lambda_L F_m \quad (2.87)$$

$$F_m = \sqrt{\frac{u_m^2}{gD}} \quad (2.88)$$

Note that according to this correlation, the frequency does not depend on the fluid properties.

With known values for the slug-cylinder holdup α_{Ls} (hence liquid holdup of the slug unit α_L via Eq. [2.70]), the film holdup α_{Lf} and film length l_f , it is possible to determine the pressure gradient according to Eqs. (2.6) and (2.73). In the frictional part (Eq. [2.73]), the shear stresses τ_{Wf} and τ_{Wb} for the film region of the slug unit are calculated using the following expressions for the actual velocities of liquid and gas in that region:

$$u_{Lf} = \left(1 - C \frac{\alpha_{Ls} - \alpha_{Lf}}{\alpha_{Lf}} \right) u_m \quad (2.89)$$

and

$$u_{Gf} = \left(1 + C \frac{\alpha_{Ls} - \alpha_{Lf}}{1 - \alpha_{Lf}} \right) u_m \quad (2.90)$$

These expressions can be derived from continuity requirements in the slug unit (see Eqs. [2.28] and [2.45] in the paper by Dukler and Hubbard [1975]).

An estimate of the pressure gradient for slug flow, avoiding the complexities involved in the calculation of α_{Lf} and l_f according to the set of equations (2.76)–(2.81) can be obtained by adopting the following simplified approach. Determine the ratio of the length of the slug cylinder to the length of the total slug unit, l_s/l_u , by using a correlation introduced by Heywood and Richardson (1979),

$$\frac{l_s}{l_u} = \lambda_L - 0.10 \quad \text{for } \lambda_L > 0.10 \quad (2.91)$$

By substituting this length ratio in Eq. (2.70), a value for the average liquid holdup in the film part of the slug unit is obtained. With this holdup value, the parameters needed to compute the perimeters, hydraulic diameters, and shear stresses for stratified flow can be calculated by Eqs. (2.31)–(2.35), and for annular flow by Eqs. (2.37)–(2.40). The first flow configuration will occur in near-horizontal pipes, and the second

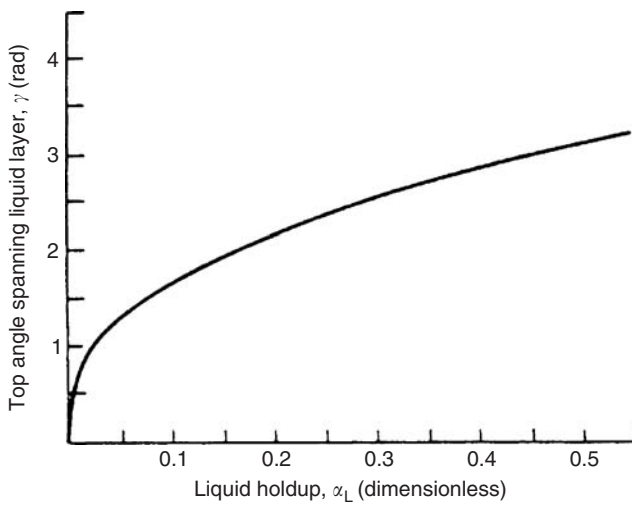


FIGURE 2.15 Relationship between liquid holdup and the top angle γ that spans the liquid layer in stratified flow (Eq. [2.31]).

in near-vertical pipes (see [Section 2.2](#)). For stratified flow, the angle γ has to be calculated from Eq. (2.31), which is presented in graphical form in Figure 2.15.

With this simplified approach, Eq. (2.73) for the frictional pressure gradient of the slug unit, ignoring axial variation of the liquid layer thickness in the film part, becomes

$$-\left(\frac{dp}{dx}\right)_F = \left[\left(\tau_{Wf} \frac{P_f}{A} + \tau_{Wb} \frac{P_b}{A} \right) \frac{l_f}{l_u} + 2f_s \rho_s \frac{u_m^2}{D} \frac{l_s}{l_u} \right] \quad (2.92)$$

This means that, for the calculation of the frictional pressure gradient, the length ratios and not the actual lengths of the film and slug parts of the slug unit are required.

The total pressure gradient for inclined slug flow then becomes

$$-\left(\frac{dp}{dx}\right) = \left[\left(\tau_{Wf} \frac{P_f}{A} + \tau_{Wb} \frac{P_b}{A} \right) \frac{l_f}{l_u} + 2f_s \rho_s \frac{u_m^2}{D} \frac{l_s}{l_u} \right] + (\alpha_G \rho_G + \alpha_L \rho_L) g \sin \theta \quad (2.93)$$

The length of the liquid slugs, important for separator design, can be calculated from Eqs. (2.82) and (2.83) with Eq. (2.91). Since the expressions for the slug frequency and the relative slug length have been derived from atmospheric air–water measurements, applications to industrial pipe flow conditions have to be done with care.

For the example of gas–oil flow at a pressure of 150 bar in the 0.1 m tube, the length of the slug as calculated using Eq. (2.91) decreases with mixture velocity, as shown in [Figure 2.16](#) (the superficial liquid velocity is 1 m/s here). As shown in the figure, the liquid slug reaches its minimum value (8D according to Moissis and Griffith (1962)) at a mixture velocity of 7 m/sec, which is not very different from the slug–churn transition caused by excessive gas content, as discussed above. Consequently, the submodels for liquid slug length and gas content are consistent with respect to the slug–churn transition.

2.1.4.5 Scheme for Flow-Pattern-Dependent Calculation of Pressure Gradient

The following steps summarize the calculation of liquid holdup and pressure gradient for dispersed bubble, stratified, annular, and slug flow in a pipe. As a prerequisite, the following input parameters have to be determined:

- Pipe diameter: D (m)
- Relative wall roughness: k/D (dimensionless)

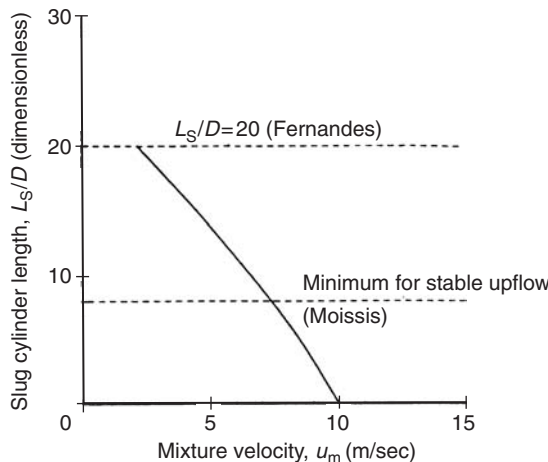


FIGURE 2.16 Dimensionless slug cylinder length for vertical gas–oil flow at 150 bar ($D = 0.1$ m; $-l_s/D$ from Heywood–Richardson).

- Pipe inclination: θ (rad)
- Liquid density: ρ_L (kg/m³)
- Gas density: ρ_G (kg/m³)
- Liquid viscosity: μ_L (Pa s)
- Gas viscosity: μ_G (Pa s)
- Surface tension: σ (N/m)
- Superficial liquid velocity: u_{SL} (m/s)
- Superficial gas velocity: u_{SG} (m/s)
- Liquid volume fraction: λ_L (dimensionless)

For the flow patterns mentioned above, the calculation steps are given below.

2.1.4.5.1 Dispersed Bubble Flow

- Determine the bubble rise velocity u_b (Eq. [2.17])
- Calculate the actual gas velocity u_G (Eq. [2.18])
- Calculate the gas holdup α_G (Eq. [2.19])
- Calculate the frictional pressure gradient (Eq. [2.20])
- Substitute into Eq. (2.6) to obtain total pressure gradient

2.1.4.5.2 Stratified Flow

- Calculate dimensionless parameters X and Y (Eqs. [2.45] and [2.46])
- Determine dimensionless liquid layer using Figure 2.6a and b
- Calculate angle γ that spans liquid layer (Eq. [2.36])
- Calculate liquid holdup α_L (Eq. [2.31])
- Determine perimeters P_L , P_i , and P_G (Eqs. [2.33]–[2.35])
- Determine hydraulic diameters $D_L (= 4A_L/P_L)$ and $D_G (= 4A_L/(P_G + P_i))$
- Calculate actual gas and liquid velocities
- Determine f_G and f_L from Re_G and Re_L , using k/D_G and k/D_L and by using Eqs. (2.3) and (2.4) or the Moody chart (Figure 2.2)
- Calculate shear stresses τ_{WG} and τ_{WL} (Eqs. [2.25] and [2.26])
- Substitute into Eq. (2.6) to obtain the total pressure gradient

2.1.4.5.3 Annular Flow

- Calculate dimensionless parameters X and Y (Eqs. [2.45] and [2.46])
- Determine liquid holdup, α_L , from [Figure 2.9](#)
- Calculate dimensionless film thickness h_l/D (Eq. [2.37])
- Determine perimeter P_L (Eqs. [2.38]–[2.40])
- Calculate the hydraulic diameter D_L ($= 4A_L/P_L$)
- Calculate the actual gas and liquid velocities
- Determine f_L from Re_L , using k/D , and by using Eqs. (2.3) and (2.4) or the Moody chart ([Figure 2.2](#))
- Calculate shear stress τ_{WL} (Eq. [2.26])
- Substitute into Eq. (2.6) to obtain the total pressure gradient

2.1.4.5.4 Slug Flow

- Calculate the distribution parameter C_O (Eq. [2.67])
- Determine bubble rise velocity u_b (Eq. [2.68])
- Calculate shedding parameter C (Eq. [2.66])
- Determine liquid holdup in slug cylinder α_{L_s} (Eqs. [2.71] and [2.72])
- Calculate liquid holdup of slug unit α_L (Eq. [2.70])
- Determine slug cylinder–slug unit length ratio l_s/l_u (Eq. [2.91])
- Calculate average liquid holdup in film (Eq. [2.70])
- Calculate actual gas and liquid velocities u_{Gf} and u_{Lf} in the film region (Eqs. [2.89] and [2.90])
- Calculate perimeters and shear stresses in film region with either stratified or annular flow model; in case of stratified flow, use [Figure 2.15](#) to determine angle γ
- Calculate frictional pressure gradient $(dp/dx)_F$ (Eq. [2.92])
- Calculate total pressure gradient (Eq. [2.93])

2.1.5 Application of Flow-Pattern-Dependent Method to High-Pressure Gas–Oil Flow

In applying the flow-pattern-dependent method for gas–oil pipeline transport, one has to realize that it is limited to stationary flow and ignores any development length needed for transition from one flow pattern to another. Therefore, care should be taken in designing short pipelines with strong undulations, when both assumptions may lead to inaccuracies.

The prediction accuracy of the flow-pattern-dependent methods for pressure gradients and holdups has been tested by comparing the results of calculations with laboratory and field data contained in a number of databases (Oliemans, 1987). For the field data, gas–oil pipelines that are very long and do not show strong undulations have been selected. Of course, the information from tests in existing pipelines is limited. At best, one can obtain data on the two-phase pressure gradient and the average holdup in the pipeline. Local variations in holdup due to changes in flow pattern or in angle could not be detected for these offshore pipelines.

The results of the testing have subsequently been used as a yardstick to check the performance of the submodels for the flow patterns. They have not been used to adapt submodels such that the prediction accuracy for a data bank is improved, but rather to stimulate the search for more reliable closure relations for these submodels, derived on the basis of separate, dedicated experiments.

An example of experiments dedicated to improve closure relations for hydrocarbon fluids are the experiments performed at the Shell gas terminal at Bacton, in the Norfolk area of the United Kingdom. For the horizontal and upward inclined flow of gas and condensate in this industrial scale 0.2-m-diameter pipe, measurements were possible at a pressure of 75 bar. In this facility, tests were performed for a range of superficial gas and liquid velocities ($u_{SG} = 0.5$ to 10 m/s and $u_{SL} = 0$ to 2.5 m/s) such that observations could be made for all four flow patterns. In addition to pressure gradients and holdups, data on flow-pattern transitions, film thickness, interfacial waves, liquid entrainment, and liquid-drop distributions have been collected. Details of the facility and its instrumentation are given in Wu et al. (1987).

2.2 Omni-Angle Flow-Pattern Map

R.V.A. Oliemans and B.F.M. Pots

2.2.1 Introduction

The flow-pattern map discussed here aligns closely with the thinking of the school of Dukler (University of Houston), Taitel (Tel Aviv University), and their co-workers (see papers by Taitel and Dukler, 1976; Taitel et al., 1980; Barnea et al., 1982a, 1982b, 1985; Dukler and Taitel, 1986; Barnea, 1987). Here again, as with the one-dimensional flow-pattern-dependent models, the formulation used had to be scrutinized for its applicability to industrial conditions such as high-pressure gas–oil flow in large-size pipes. This made it necessary, on occasion, to rederive the equations used, since now the gas density could no longer be neglected and pipe size effects had to be taken into account (Pots, 1985).

The pipe angle effect on flow-pattern transitions is another important element. Most developments are either for vertical and near-vertical upward flow or for horizontal and near-horizontal flow. Generalization to all angles of inclination, unfortunately, is still guesswork. Nevertheless, a flow map for all angles is a necessity, since, for instance, oil–gas production via inclined tubes (from near-horizontal to vertical flow) is common practice nowadays. Although the flow-pattern map described here is applicable to all angles of inclination, predictions for angles between 10 and 70° from the horizontal have to be treated with care, since they rest on an ad hoc basis.

The procedure for the determination of the flow-pattern map is as follows. First, stratified flow is assumed. The liquid holdup and other stratified flow characteristics are calculated employing the stratified flow model. Then, it is examined whether, under the given conditions, stratified flow can exist. This is done by evaluating the mechanisms that are responsible for the transition from stratified to nonstratified flow. If stratified flow can exist, this pattern is assumed to occur and a further distinction is made between stratified smooth and stratified wavy flow. If stratified flow cannot exist, the possibility of annular flow occurring is investigated. The liquid holdup is now calculated, employing the annular flow model. Then the mechanisms that lead to nonannular flow are evaluated. Finally, bubble flow is assumed, the liquid holdup is calculated from the dispersed bubble flow model, and the mechanisms that lead to no-bubble flow are evaluated. If bubble flow can exist, this pattern is assumed to occur. If none of the three above-mentioned flow patterns can exist, intermittent (= slug) flow is assumed to prevail. For vertical upward flow, a further distinction can be made between slug and froth flow. [Figure 2.17](#) is a flowchart of the above procedure.

2.2.2 Stratified to Nonstratified Transition

2.2.2.1 Linear Stability Criterion of Wallis

For the transition from stratified to nonstratified flow, a stability criterion that is based on a linear stability analysis of the stratified flow equations is used. The principles can be found in the work of Wallis (1969). In a linear stability analysis, variables u are perturbed around their equilibrium values with a small sinusoidal disturbance as

$$u = \bar{u} + \tilde{u} \exp[i(\omega t - kx)] \quad (2.94)$$

After substitution and linearization of the continuity and momentum equations, a dispersion relation (relation between angular frequency ω and wavevector k) results. It can be established from the dispersion relation whether disturbances will grow or damp, depending on the sign of the imaginary part of ω (assuming k to be real). According to Wallis, the linear stability analysis procedure outlined above leads to the criterion for instability:

$$u_w^2 > c^2 \quad (2.95)$$

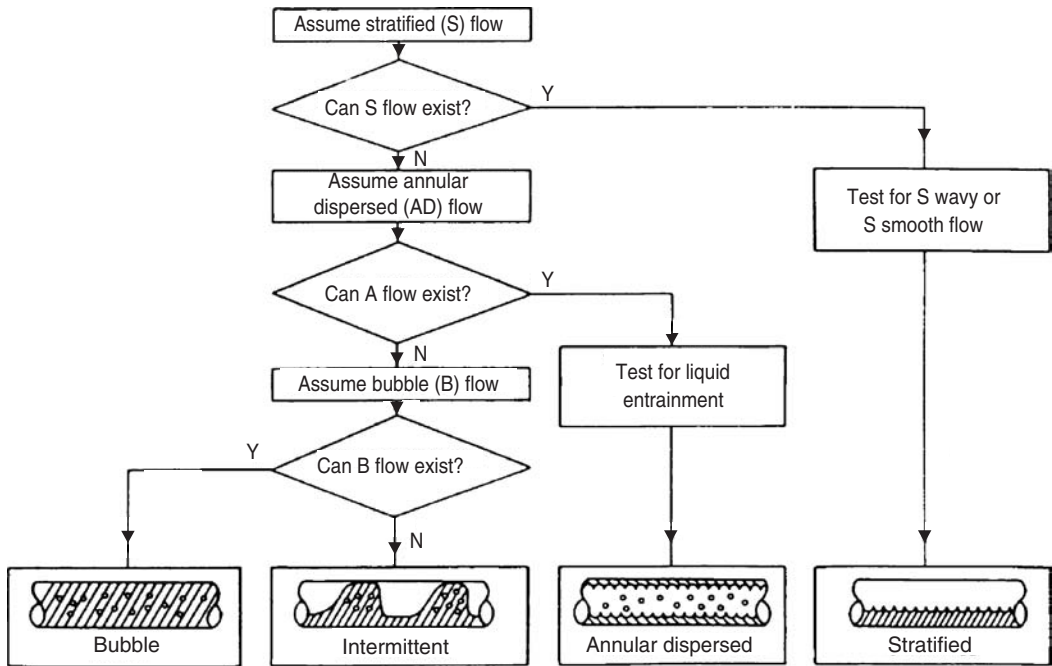


FIGURE 2.17 Two-phase flow-pattern map flowchart.

where u_w is the phase velocity of a continuity or kinematic wave, and c that of a dynamic wave. The phase velocities refer to a frame moving at a weighted mean velocity:

$$u_0 = \frac{\rho_L u_L / \alpha_L + \rho_G u_G / \alpha_G}{\rho_L / \alpha_L + \rho_G / \alpha_G} \quad (2.96)$$

Dynamic waves move at velocity $\pm c$ relative to this weighted mean velocity, while a continuity wave propagates in one direction only. Consequently, Eq. (2.95) implies that an instability results when a continuity wave overtakes one of the dynamic waves.

The phase velocity of a continuity wave in the stationary frame can be derived from the holdup relation, Eq. (2.28), according to

$$u_w = u_w + u_0 = \frac{-\partial F / \partial \alpha_L}{\partial F / \partial u_{SL} - \partial F / \partial u_{SG}} \quad (2.97)$$

considering the holdup relation function F to be a function of α_L , u_{SL} , u_{SG} , and $\partial \alpha_L / \partial x$. The phase velocity of a dynamic wave in the moving frame follows from

$$c^2 = u_0^2 - A' \quad (2.98)$$

where

$$A' = \frac{\rho_L u_L^2 / \alpha_L + \rho_G u_G^2 / \alpha_G - \partial F / \partial (\partial \alpha_L / \partial x)}{\rho_L / \alpha_L + \rho_G / \alpha_G} \quad (2.99)$$

$$c = \pm \sqrt{\frac{(\partial F / \partial (\partial \alpha_L / \partial x)) - ((u_G - u_L)^2 (\alpha_L / \rho_L + \alpha_G / \rho_G))}{\rho_L / \alpha_L + \rho_G / \alpha_G}} \quad (2.100)$$

Hence, if c^2 is negative, then the flow is always unstable. Therefore, the gravity-restoring force in the momentum equations and the corresponding term in the holdup relation, Eq. (2.28), are crucial in order to give a positive term:

$$\frac{\partial F}{\partial(\partial\alpha_L/\partial x)} = \Delta\rho gD \cos\theta \frac{\pi D}{4 P_i} \quad (2.101)$$

where $\Delta\rho = \rho_L - \rho_G$, and, for stratified flow, $\partial(h_L/D)/\partial\alpha_L = \pi D/(4 P_i)$, in Eq. (2.100), even though the above-mentioned force might seem negligible. It has been noted by Ferschneider et al. (1985), who carried out the same analysis as Wallis, that omitting friction in the source terms in the momentum equations leads to a disappearance of the interaction between the continuity and dynamic waves, and instability results for $c^2 < 0$, referred to as Kelvin–Helmholtz instability. Therefore, friction is required for the interaction between continuity and dynamic waves, and it also lowers the threshold for instability. Kelvin–Helmholtz instability leads to a dimensionless critical gas velocity above which the flow is unstable,

$$\left(\frac{\rho_G}{\Delta\rho g D} \right)^{0.5} (u_G - u_L) = \left[\alpha_G \left(1 + \frac{\rho_G \alpha_L}{\rho_L \alpha_G} \right) \cos\theta \frac{\pi D}{4 P_i} \right]^{0.5} \quad (2.102)$$

which is the more generalized result of the type of linear stability analysis of Taitel and Dukler (1976), who assumed $u_G \gg u_L$ and $\rho_G \ll \rho_L$. The former assumption is not generally valid at the transition discussed, while the latter is not valid for high-pressure systems.

Note that the Kelvin–Helmholtz instability relates to two fluid layers flowing at different velocities on top of each other. In a pipe, such a configuration becomes unstable when the flow rate of one of the fluids reaches a certain critical level. At interface disturbances, Bernoulli suction, which leads to wave growth, exceeds the equilibrium-restoring forces caused by gravity.

The well-known criterion of Taitel and Dukler is obtained by multiplying the right-hand side of Eq. (2.102) by a factor smaller than unity:

$$C_2 = 1 - h_L/D \quad (2.103)$$

Taitel and Dukler argued that finite-amplitude waves are responsible for the onset of the instability, because such waves have a lower threshold than infinitesimally small disturbances. Therefore, the C_2 factor in Eq. (2.103) was introduced; however, as stated by the authors themselves, the finite-amplitude effect was included merely on the basis of speculative arguments. In dimensionless form, Taitel and Dukler's rule reads

$$F_G > \left(C_2^2 \alpha_G^3 \frac{\pi D}{4 P_i} \right)^{1/2} \quad (2.104)$$

where

$$F_G = [\rho_G / (\Delta\rho g D)]^{1/2} u_{SG} \quad (2.105)$$

is the densimetric Froude number.

It has been proven (Wu et al., 1987) that the above generalized model, based on the stability criterion of Wallis, gives better agreement than the Taitel and Dukler model for the high-pressure large-diameter data obtained at Bacton. The application of the Taitel–Dukler rule (Eq. [2.104]) to high-pressure and large-diameter systems with gas-condensate shows a transition to intermittent flow at a liquid flow rate that is too low.

To apply the above criterion, a value is needed for the liquid holdup (or liquid layer level in stratified flow, h_L). Note that all the terms on the right-hand side of Eqs. (2.102) and (2.104) depend on the liquid holdup only. Therefore, in the flow-pattern map, the stratified flow model is employed to calculate this quantity. Its use can be illustrated with a simplified version of the model, first introduced by Taitel and

Dukler (1976). In this model, the liquid layer level is a function of only two dimensionless groups, viz. the Lockhart–Martinelli parameter X and an inclination or gravity parameter Y , where

$$X^2 = \frac{(\mathrm{d}\rho_F/\mathrm{d}x)_{\mathrm{SL}}}{(\mathrm{d}\rho_F/\mathrm{d}x)_{\mathrm{SG}}} = \frac{f_{\mathrm{SL}} \rho_L u_{\mathrm{SL}}^2}{f_{\mathrm{SG}} \rho_G u_{\mathrm{SG}}^2} = \frac{f_{\mathrm{SL}} F_L^2}{f_{\mathrm{SG}} F_G^2} \quad (2.106)$$

and

$$Y = \frac{\Delta\rho g \sin\theta}{(\mathrm{d}\rho_F/\mathrm{d}x)_{\mathrm{SG}}} = \frac{\sin\theta}{2f_{\mathrm{SG}} F_G^2} \quad (2.107)$$

Note that

$$\left(\frac{\mathrm{d}\rho_F}{\mathrm{d}x} \right)_{\mathrm{SL}} = 2 f_{\mathrm{SL}} \rho_L u_{\mathrm{SL}}^2 / D$$

$$\left(\frac{\mathrm{d}\rho_F}{\mathrm{d}x} \right)_{\mathrm{SG}} = 2 f_{\mathrm{SG}} \rho_G u_{\mathrm{SG}}^2 / D$$

are the frictional pressure gradients for the individual phases as though they were flowing alone in the pipe. Also note the introduction of the densimetric liquid Froude number $F_L = (\rho_L/\Delta\rho g D)^{1/2} u_{\mathrm{SL}}$ in Eq. (2.106). The friction factors f_{SL} and f_{SG} , for turbulent and laminar flow, can be calculated from the Churchill equation (2.5).

Figure 2.6a and b shows the liquid level h_L/D for a wide range of X and Y (Y positive means upward flow values). The occurrence of nonstratified flow can now be established by first determining the liquid level h_L/D from X and Y . Then the critical gas Froude number from Eq. (2.104) (or [2.102] and [2.103] for high-pressure applications) is compared with the actual gas Froude number present. To calculate the right-hand side of Eq. (2.104) (or [2.102]), it is noted that the gas–liquid perimeter can be calculated from

$$P_i = \left[1 - \left(1 - 2 \frac{h_L}{D} \right)^2 \right]^{1/2} D \quad (2.108)$$

and the liquid holdup follows from ($\alpha_G = 1 - \alpha_L$)

$$\alpha_L = \frac{1}{\pi} \left[\arccos \left(1 - 2 \frac{h_L}{D} \right) \left(1 - 2 \frac{h_L}{D} \right) \tilde{P}_i \right] \quad (2.109)$$

where the tilde on P_i indicates that it has been made dimensionless by dividing by D (see Eq. [2.48]). To facilitate the determination of the critical gas Froude number, Figure 2.18 can be used (see Barnea, 1987). In the limit $h_L/D \ll 1$, the critical gas Froude number approaches $F_G = (\pi/8)^{1/2}/(h_L/D)$.

To indicate the sensitivity of the holdup determination with respect to the interface friction factor, Figure 2.6a and b shows the liquid level in stratified two-phase flow for $f_i = f_{\mathrm{SG}}$ (a smooth interface) and $f_i = 10 f_{\mathrm{SG}}$ (a rough interface), respectively. The latter friction factor could be considered as an upper limit.

2.2.2.2 Trajectory of Drops Torn from Liquid Film

For steeply downward-inclined pipes, the liquid level in stratified flow is small and the liquid velocity is high. Under these conditions, droplets are torn from the (wavy) liquid surface and deposited on the upper wall, causing a transition to nonstratified flow. This transition is modeled by Barnea et al. (1982a,) and Dukler and Taitel (1986) by considering the trajectory of droplets after they leave the interface at an initial velocity that is assumed to be the turbulent fluctuating velocity. If the height of the trajectory exceeds the distance to the upper wall, a transition to nonstratified flow occurs. The transition rule, modified to account for the effect of larger density ratios, ρ_G/ρ_L , is

$$N_L > \frac{(1 - h_L/D)^{1/2} \alpha_L}{(f_L/f_{\mathrm{SL}})^{1/2}} \quad (2.110)$$

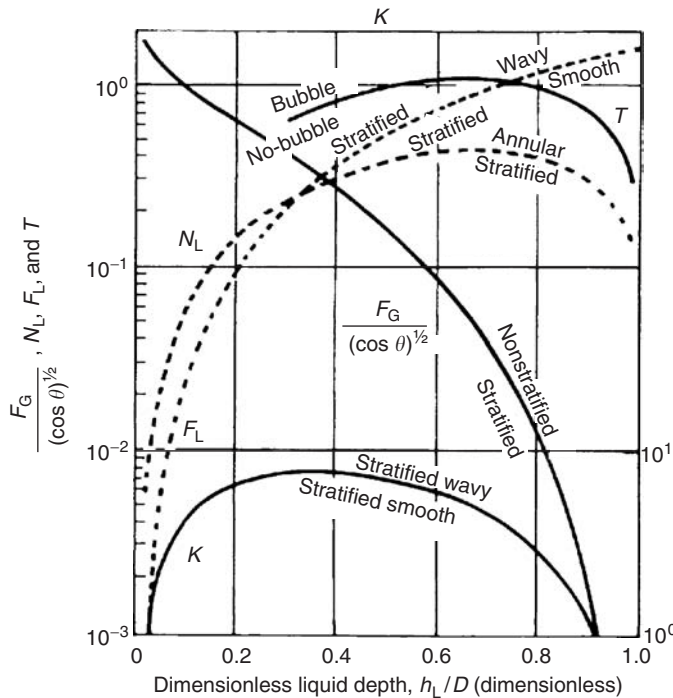


FIGURE 2.18 Flow-pattern transition lines based on liquid level h_L/D of stratified flow (—, horizontal flow; ---, downward flow).

with dimensionless liquid velocity

$$N_L^2 = \frac{f_{SL} F_L^2}{\cos \theta} \quad (2.111)$$

The transition as a function of the liquid level can be read from Figure 2.18.

2.2.3 Stratified Smooth to Stratified Wavy

2.2.3.1 Jeffreys' Wind-Wave Interactions

In stratified flow, when the gas velocity is sufficiently high, but not too high to cause a transition to non-stratified flow, interface waves will form. Waves will be initiated when pressure and shear work on a wave overcome viscous dissipation in the waves. Although the phenomenon of wave generation is not completely understood, Taitel-Dukler (1976) were able to obtain a criterion for the transition from smooth to wavy flow. In dimensionless form, the criterion is

$$K > \frac{2\alpha_L^{1/2}\alpha_G}{s^{1/2}} (\cos \theta)^{1/2} \quad (2.112)$$

with dimensionless gas velocity

$$K = F_G Re_{SL}^{1/2} \quad (2.113)$$

and sheltering coefficient $s = 0.01$. The right-hand side of Eq. (2.112) depends only on the liquid level of stratified flow, h_L/D , so that the critical value for K can be calculated or read from Figure 2.18 for known h_L/D .

2.2.3.2 Gravity Waves

In stratified flow in downward-inclined pipes, surface waves can form under the influence of gravity, even in the absence of gas flow. Barnea et al. (1982a) and Dukler and Taitel (1986) propose a simple criterion

for the condition at which waves appear. Pots (1985) modified this criterion to account for the effect of larger density ratios ρ_G/ρ_L . The transition rule is

$$F_L > 1.5 (h_L/D)^{1/2} \alpha_L \quad (2.114)$$

with the liquid densimetric Froude number given by

$$F_L = [\rho_L/(\Delta\rho gD)^{1/2} u_{SL}] \quad (2.115)$$

2.2.4 Annular to Nonannular Transition

2.2.4.1 Pipe Liquid Bridging Above $\alpha_L = 0.35$

As a result of pipe bridging by the liquid, large liquid holdups cause a transition from annular to nonannular flow. Taitel and Dukler (1976) suggest that nonannular flow will develop above liquid holdup values of 0.5. Their reasoning is based on the following physical point of view (horizontal and near-horizontal pipe): if the interface is considered as a sinusoid, above a holdup value of 0.5, the crest of a wave reaches the top of the pipe before the trough reaches the bottom, blocking the gas passage and resulting in slugging. To account for the effect of voids in the slugs that are formed, a lower critical holdup value is generally used. In the KSLA map, a void fraction of 0.30 is assumed, leading to a critical holdup $\alpha_L = 0.35$. The above concept was developed for horizontal and near-horizontal pipes, but the suggestion is that it can be applied to any inclination (see also Barnea et al. (1982b)).

2.2.4.2 Film Stability

For upward flow, if the value of the gravity group

$$Y = \frac{\Delta\rho g \sin\theta}{(dp_F/dx)_{SG}} = \frac{\sin\theta}{2f_{SG}F_G^2} \quad (2.116)$$

exceeds about 100, three holdup roots may satisfy the holdup relation. Oliemans et al. (1986) have suggested that this situation might be associated with jumping between the low and high holdup values, indicating intermittent flow. For vertical flow, using a friction factor $f_{SG} = 0.005$, the above Y value corresponds to $F_G = 1$, a value close to Wallis' value of $F_G = 0.9$ for flooding. Using the gravity group Y as a basis for the transition from annular to nonannular flow is believed to have a wider applicability than the densimetric gas Froude number F_G .

Vertical upward flow tests conducted by Vassiliadou and Schellekens (1988) in 10-m-long tubes of 0.5, 1, 2, and 4 in. in size, using air-water and air-kerosine as test fluids, revealed that the transition to churn flow for large pipe size and low-surface-tension liquid will occur at gas Froude numbers appreciably lower than 1. The laboratory observations were best described by the Richter (1981) criterion:

$$F_G^2 < \frac{75}{Eo_D^2} \left[\left(1 + \frac{(Eo_D/75)^2}{f_w} \right)^{1/2} - 1 \right] \quad (2.117)$$

where f_w is the wall friction factor (typically 0.005 to 0.008) and

$$Eo_D = D \left(\frac{\Delta\rho g}{\sigma} \right)^{1/2} \quad (2.118)$$

is the Eötvös number with tube diameter as length scale.

The critical gas Froude numbers for the churn flow-transition range from 0.9 to 0.3 as Eo_D varies from 2 to 100. Note that for 4-in. (0.1 m) tubing producing gas and condensate at 100 bar, $Eo_D \sim 90$. The critical gas Froude number then is as low as 0.3. Similar values are obtained for the 150 bar gas-oil example in 0.1 m pipe discussed earlier ($Eo_D = 83$, $F_G \sim 0.4$).

2.2.4.3 Liquid Entrainment

The inception criteria of Ishii and Grolmes (1975) are often applied to establish the occurrence of liquid droplet entrainment. Here, only a simple approximation of these inception criteria will be

considered. For the completely rough turbulent regime ($Re_{SL} > 1635$), liquid entrainment is expected to exist for

$$Ku > 3.2 \quad (2.119)$$

where

$$Ku = \frac{\rho_G^{1/2}}{(\Delta\rho g\sigma)^{1/4}} u_{SG} \quad (2.120)$$

is the Kutateladze number.

For the transition regime ($160 < Re_{SL} < 1635$), the critical Kutateladze number increases with decreasing Reynolds number. At the lower Reynolds side of the regime, the critical Kutateladze number is $Ku \approx 7.5$.

Below $Re_{SL} = 160$, the critical Kutateladze number increases sharply and liquid entrainment is difficult to achieve.

Strictly speaking, the inception criteria of Ishii and Grolmes are applicable to thin films in vertical upward annular two-phase flow.

For the sample case of vertical upflow of air–water at 1 atm and gas–oil at 150 bar, respectively, the inception velocities for liquid entrainment according to the above criterion are widely different: 15 and 0.9 m/sec, respectively.

2.2.5 Bubble Flow

2.2.5.1 Turbulent Fluctuations Versus Buoyancy for Pipes Inclined at an Angle $< 10^\circ$

In horizontal and near-horizontal pipes, a transition to dispersed bubble flow takes place when the turbulent fluctuations are strong enough to overcome the buoyancy forces tending to keep the gas at the top of the pipe, assuming that neither stratified nor annular flow can exist. The expression for the buoyancy force is

$$F_b = \Delta\rho g \cos\theta A_G$$

The dispersion force on the gas at the interface due to turbulence in the liquid layer is

$$F_{turb} = \frac{1}{2} \rho_L \langle u'^2 \rangle P_i = \frac{1}{4} f_L \rho_L u_L^2 P_i$$

The gas phase then disperses into the liquid layer, when

$$u_L \geq \left[\frac{4A_G \Delta\rho g \cos\theta}{\rho_L f_L P_i} \right]$$

A description of the mechanism by Taitel and Dukler (1976) leads to the transition rule

$$T^2 > 2\pi \frac{\alpha_L^2 \alpha_G D}{(f_L/f_{SL}) P_i} \quad (2.121)$$

where

$$T^2 = \frac{(dp_F/dx)_{SL}}{\Delta\rho g \cos\theta} = \frac{2f_{SL} F_L^2}{\cos\theta} \quad (2.122)$$

is the ratio of turbulent to buoyancy forces. Equation (2.121) is evaluated from the stratified flow characteristics (e.g., liquid holdup, α_L , and friction factor, f_L), which are obtained from the first stage of the flow-pattern prediction procedure. To facilitate manual calculations, the occurrence of dispersed bubble flow can be established from Figure. 2.18 after h_L/D has been determined from a stratified flow model.

2.2.5.2 Bubble Flow for Pipes Inclined at an Angle >10°

To establish the occurrence of bubble flow for pipes with $|\Theta| > 10^\circ$, the liquid holdup is calculated from the bubble flow model. Above void fractions of 0.52, no bubble flow can exist, regardless of the turbulence level. The flow pattern will then be intermittent or annular dispersed.

For $0.25 < \alpha_G < 0.52$, dispersed bubble flow prevails if turbulent fluctuations are vigorous enough to break bubbles below a diameter where they remain spherical, and coalescence is suppressed. To check whether dispersed flow is possible, the maximum bubble size in a turbulent flow field, d_{\max} , has to be smaller than critical bubble sizes for deformation, d_{def} , and for bubble migration to the upper part of the pipe, d_{migr} . Hinze (1955) determined that the characteristic size of bubbles results from a balance between surface tension forces and those due to turbulent fluctuations. The expression used for d_{\max} (Dukler and Taitel, 1986; Barnea, 1987) is

$$d_{\max} = \left[0.725 + 4.15 \left(\frac{u_{SG}}{u_m} \right)^{1/2} \right] \left(\frac{\sigma}{\rho_L} \right)^{3/5} (2 f_m u_m^3 / D)^{-2/5} \quad (2.123)$$

while for the critical bubble size at which coalescence may occur the following expressions are used for deformation and for migration, respectively:

$$d_{\text{def}} = 2 \left(\frac{0.4\sigma}{\Delta\rho g} \right)^{1/2} \quad (2.124)$$

$$d_{\text{migr}} = \frac{3}{8} \frac{\rho_L}{\Delta\rho} \frac{f_m u_m^2}{g \cos\theta} \quad (2.125)$$

where f_m is the friction factor based on the mixture velocity u_m .

If the void fraction is < 0.25 , no coalescence of bubbles, which would cause a transition to intermittent flow, can take place, and bubble flow is assumed to exist.

2.2.6 Intermittent (Slug and Froth-Churn) Flow

The intermittent pattern is usually subdivided into elongated bubble, slug and froth/churn flow. A transition from slug to froth-churn flow is assumed to occur when the liquid holdup in the slug cylinder becomes less than 0.48:

$$\alpha_{Ls} < 0.48 \quad (2.126)$$

In vertical flow, a transition from annular flow to churn flow can be determined from the flooding criterion.

2.2.7 Calculation Scheme for Flow Pattern Determination

The following scheme is proposed for the determination of flow patterns for gas-liquid flow in tubes:

- Determine the following input parameters:

- Pipe diameter D (m)
- Pipe wall roughness k (m)
- Pipe inclination θ (rad)
- Superficial liquid velocity u_{SL} (m/sec)
- Superficial gas velocity u_{SG} (m/sec)
- Liquid density ρ_L (kg/m^3)
- Gas density ρ_G (kg/m^3)
- Liquid viscosity μ_L ($\text{N sec}/\text{m}^2$)
- Gas viscosity μ_G ($\text{N sec}/\text{m}^2$)
- Surface tension σ (N/m)

2. Calculate the following dimensionless groups:

- Superficial liquid Reynolds number:

$$Re_{SL} = \frac{\rho_L u_{SL} D}{\mu_L}$$

- Superficial gas Reynolds number

$$Re_{SG} = \frac{\rho_G u_{SG} D}{\mu_G}$$

- Superficial liquid Fanning friction factor $f_{SL} = F(Re_{SL}, k/D)$ (calculated from Eqs. [2.3] and [2.4] or derived from [Figure 2.2](#))
- Superficial gas Fanning friction factor $f_{SG} = F(Re_{SG}, k/D)$ (calculated from Eqs. [2.3] and [2.4] or derived from Figure 2.2)
- Liquid Froude number

$$F_L = \left(\frac{\rho_L}{\Delta \rho g D} \right)^{1/2} u_{SL}$$

$$(\Delta \rho = \rho_L - \rho_G, g = 9.81 \text{ m/s}^2)$$

- Gas Froude number

$$F_G = \left(\frac{\rho_G}{\Delta \rho g D} \right)^{1/2} u_{SG}$$

- Lockhart–Martinelli parameter

$$X = \left(\frac{f_{SL}}{f_{SG}} \right)^{1/2} \frac{F_L}{F_G}$$

- Inclination or gravity parameter

$$Y = \frac{\sin \theta}{2 f_{SG} F_G^2}$$

3. Assume stratified flow and determine h_l/D from X and Y using [Figure 2.6a](#) and b

4. Test Kelvin–Helmholtz instability:

- Calculate $F_G/(\cos \theta)^{1/2}$
- Determine $(F_G/(\cos \theta)^{1/2})_{\text{critical}}$ from [Figure 2.18](#)
- If

$$\frac{F_G}{(\cos \theta)^{1/2}} > \left(\frac{F_G}{(\cos \theta)^{1/2}} \right)_{\text{critical}}$$

then go to step 8

5. Test trajectory of drops torn from liquid film:

- If $\theta \geq 0$ then go to step 6
- Calculate

$$N_L = \left(\frac{f_{SL} F_L^2}{\cos \theta} \right)^{1/2}$$

- Determine $(N_L)_{\text{critical}}$ from Figure 2.18
- If $N_L > (N_L)_{\text{critical}}$ go to step 8
- go to step 7

6. Test Jeffreys' wind-wave interactions for stratified wavy flow:

- Calculate

$$K = \frac{F_G Re_{SL}^{1/2}}{(\cos\theta)^{1/2}}$$

- Determine $(K)_{critical}$ from [Figure 2.18](#)
- If $K > K_{critical}$, then flow pattern is Stratified Wavy, otherwise flow pattern is Stratified Smooth
- Stop

7. Test gravity waves:

- Determine $(F_L)_{critical}$ from [Figure 2.18](#)
- If $(F_L) > (F_L)_{critical}$ and $\Theta < 0$ then flow pattern is Stratified Wavy otherwise flow pattern is Stratified Smooth
- Stop

8. Assume annular flow:

- Determine α_L from X and Y using [Figure 2.9](#)

9. Test pipe liquid bridging above $\alpha_L = 0.35$

- If $\alpha_L > 0.35$ then go to 11
- If $\theta = 90^\circ$ go to 10
- Flow pattern is Annular or Annular Dispersed
- Stop

10. Test film stability:

- Determine the critical gas Froude number from Eq. (2.117)
- If $F_G < F_{G,critical}$ then go to step 11
- Flow pattern is Annular or Annular Dispersed
- Stop

11. Test for bubble or intermittent flow:

- If $|\theta| < 10^\circ$ go to step 12
- Determine α_G for dispersed bubble flow from Eqs. (2.17)–(2.19)
- If $\alpha_G > 0.52$ flow pattern is Intermittent
- If $\alpha_G < 0.25$ flow pattern is Dispersed Bubble
- If $0.25 < \alpha_G < 0.52$ determine bubble sizes from Eqs. (2.123)–(2.125)
- If $d_{max} < d_{def}$ and $d_{max} < d_{migr}$ then the flow pattern is Dispersed Bubble; otherwise flow pattern is Intermittent
- Stop

12. Test turbulent fluctuations vs. buoyancy:

- Calculate

$$T = \left(\frac{2 f_{SL} F_L^2}{\cos\theta} \right)^{1/2}$$

- Determine $T_{critical}$ from [Figure 2.18](#)
- If $T > T_{critical}$, then flow pattern is Bubble; otherwise flow pattern is Intermittent
- Stop

Example of a horizontal gas/condensate pipeline: A gas/condensate line is considered with the following parameters of two-phase flow: $\rho_L = 610 \text{ kg/m}^3$, $\rho_G = 120 \text{ kg/m}^3$, $\mu_L = 0.35 \times 10^{-3} \text{ N s/m}^2$, $\mu_G = 0.015 \times 10^{-3} \text{ N s/m}^2$, $\sigma = 0.008 \text{ N/m}$, $u_{SL} = 0.60 \text{ m/s}$, $u_{SG} = 1.20 \text{ m/s}$, $D = 0.58 \text{ m}$, $\theta = 0^\circ$.

Following the scheme for manual calculation proposed, we find $Re_{SL} = 6.1 \times 10^5$, $Re_{SG} = 5.6 \times 10^6$, $f_{SL} = 3.2 \times 10^{-3}$, $f_{SG} = 2.1 \times 10^{-3}$, $F_L = 0.28$, $F_G = 0.25$, $X = 1.38$, $Y = 0$. From step 3, $h_L/D = 0.45$. From step 4,

$F_G/(\cos\theta)^{1/2} = 0.25$, while $[F_G/(\cos\theta)^{1/2}]_{\text{critical}} = 0.21$, so nonstratified flow occurs. So go to step 8. From step 8, $\alpha_L = 0.22$, so annular or annular dispersed flow is expected.

Example of a gas well: A gas well is considered with the following parameters of two-phase flow: $\rho_L = 560 \text{ kg/m}^3$, $\rho_G = 100 \text{ kg/m}^3$, $\mu_L = 0.25 \times 10^{-3} \text{ N s/m}^2$, $\mu_G = 0.015 \times 10^{-3} \text{ N s/m}^2$, $\sigma = 0.002 \text{ N/m}$, $u_{SL} = 0.30 \text{ m/s}$, $u_{SG} = 10 \text{ m/s}$, $D = 0.10 \text{ m}$, $\theta = 50^\circ$.

Following the calculation scheme, $Re_{SL} = 6.7 \times 10^4$, $Re_{SG} = 6.7 \times 10^6$, $f_{SL} = 5.0 \times 10^{-3}$, $f_{SG} = 2.0 \times 10^{-3}$, $F_L = 0.33$, $F_G = 4.7$, $X = 0.11$, $Y = 11$. From step 3, $h_L/D = 0.55$.

From step 4, $F_G/(\cos\theta)^{1/2} = \infty$, so nonstratified flow occurs. Go to step 8. From step 8, $\alpha_L = 0.032$, so annular or annular dispersed flow is expected.

2.2.8 Application of the Angle-Dependent Flow-Pattern Map

The flow-pattern map in its most generalized form is incorporated in computer codes for the design of two-phase gas-pipelines and well tubing. With such a code, one can generate a map in which, for a fixed

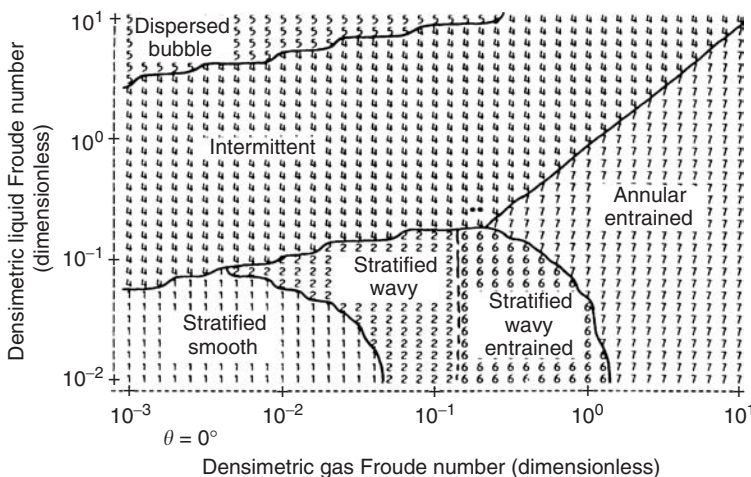


FIGURE 2.19 Flow-pattern map for horizontal flow: $\theta = 0^\circ$.

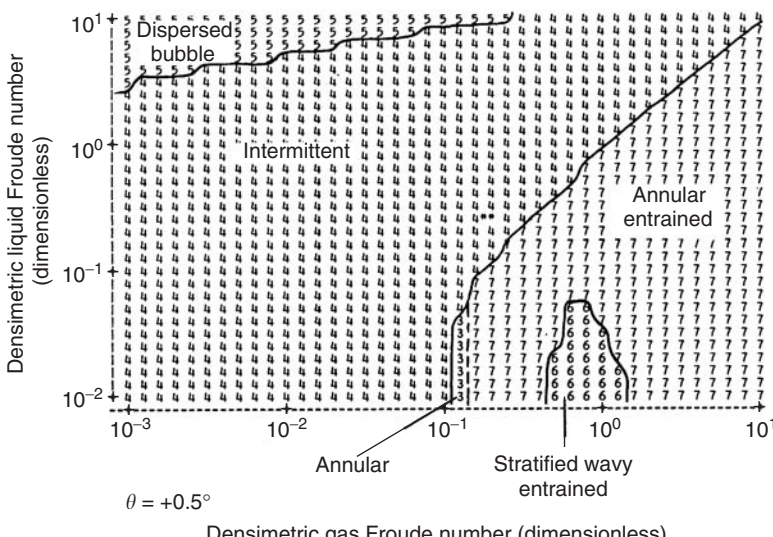


FIGURE 2.20 Flow-pattern map for upward flow: $\theta = +0.5^\circ$.

inclination θ , the occurrence of flow patterns is given in terms of the densimetric Froude numbers for liquid and gas, F_L and F_G , respectively. It should be realized that, strictly speaking, eight groups are involved (for instance: F_L , F_G , ρ_G/ρ_L , Re_{SL} , Re_{SG} , Ku , k/D , and θ). Therefore, using only three groups is not a sound basis for a more general flow-pattern map. Generally speaking, maps obtained in this way should be applied only to those cases for which the detailed computer runs have been carried out. However, for the more important transitions (stratified to nonstratified and annular to nonannular), for liquids that are not too viscous ($Re_{SL} \gg 0$), the pipe inclination and the Froude numbers appear to be among the more important groups in the current flow-pattern map if the Kelvin-Helmholtz instability approach by Dukler and Taitel is chosen. If the more general approach to this instability is selected, the density ratio ρ_G/ρ_L comes into the picture as an important group as well.

Taking as an example a 4-in. pipe with gas-oil flowing at 150 bar, Figures 2.19–2.26 give an overview of the occurrence of two-phase flow patterns at various pipe inclinations from -90° to $+90^\circ$. The most

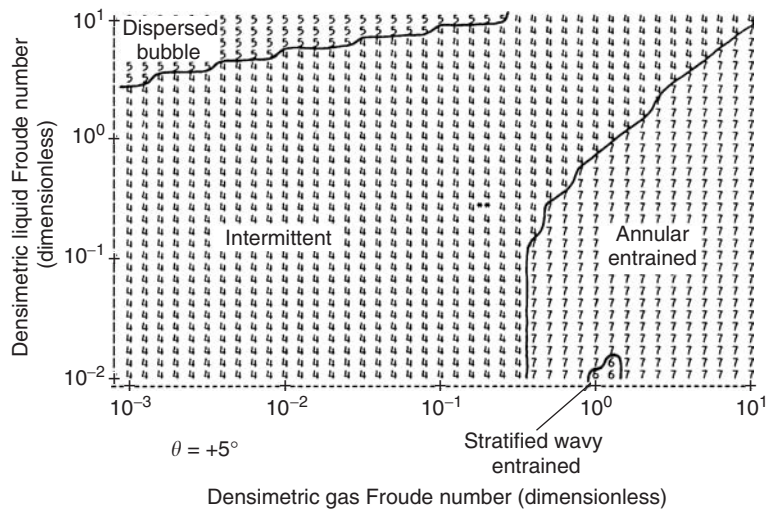


FIGURE 2.21 Flow-pattern map for upward flow: $\theta = +5^\circ$.

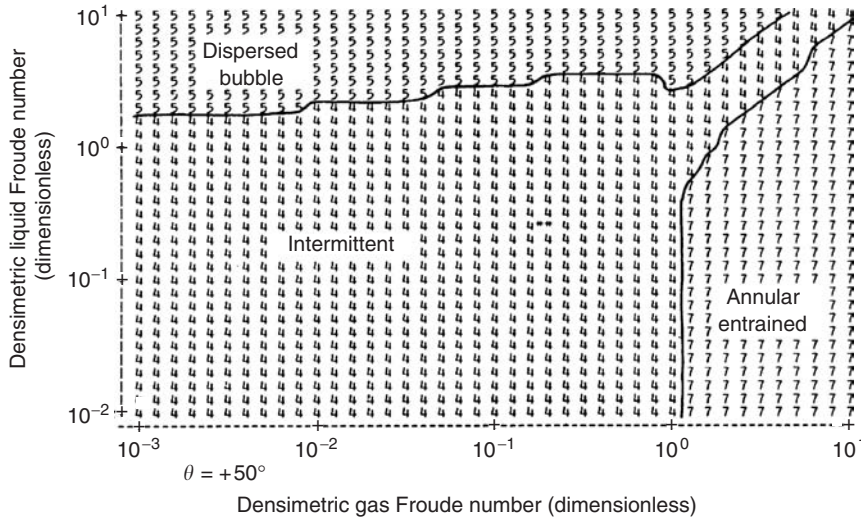
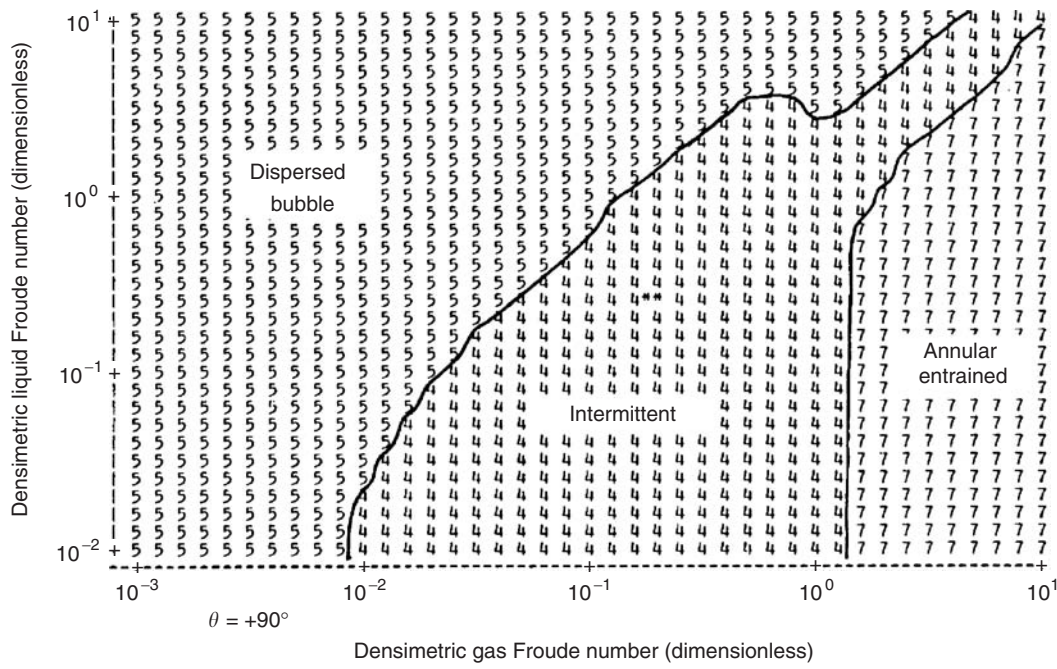
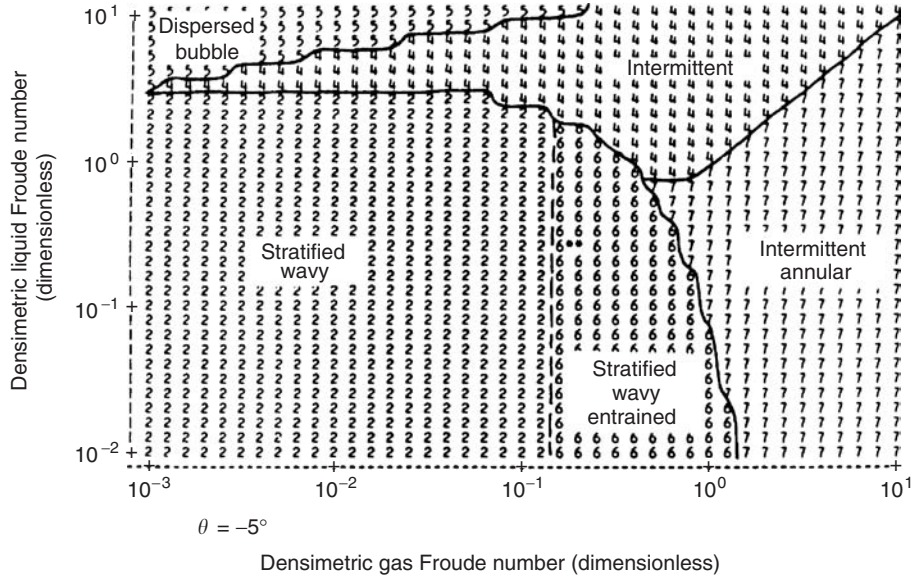
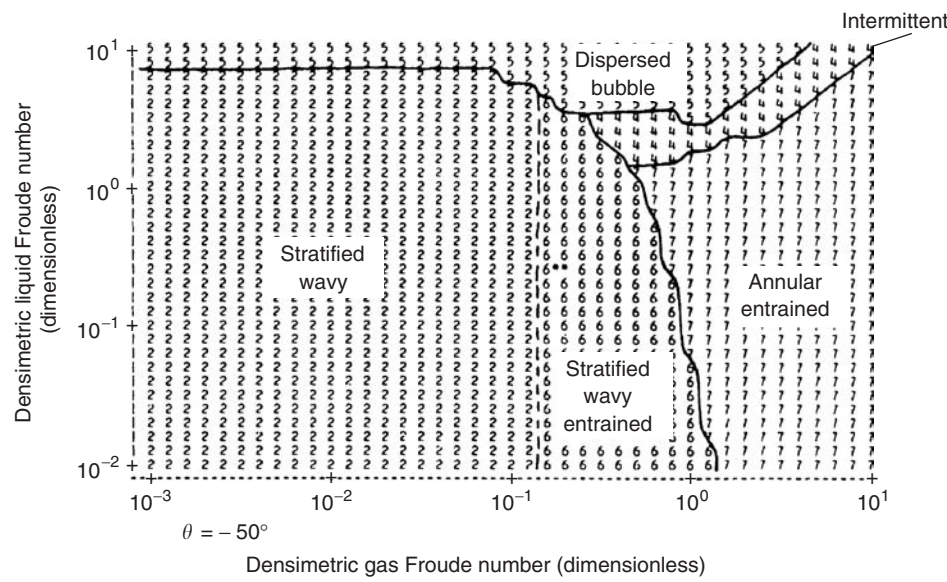
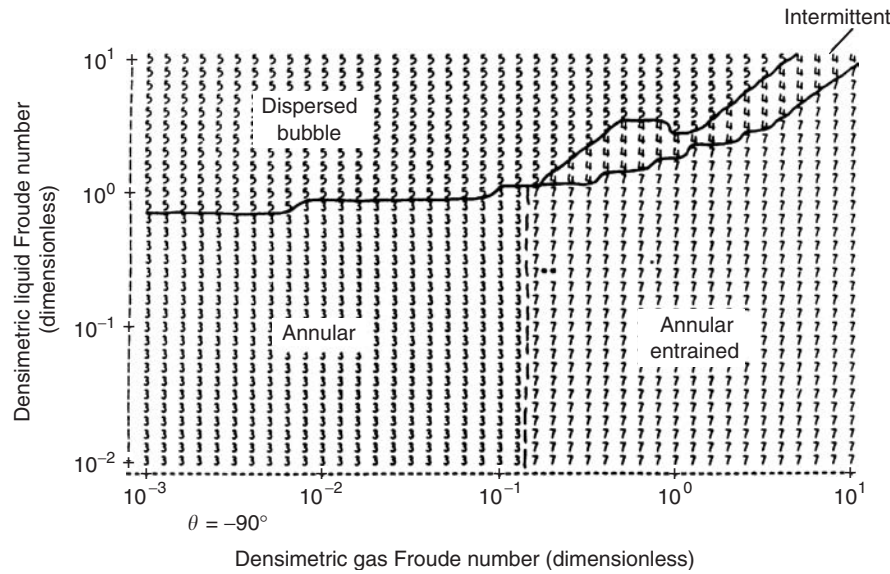


FIGURE 2.22 Flow-pattern map for upward flow: $\theta = +50^\circ$.

FIGURE 2.23 Flow-pattern map for upward flow: $\theta = +90^\circ$.FIGURE 2.24 Flow-pattern map for downward flow: $\theta = -5^\circ$.

significant changes with inclination can be seen for stratified flow. The stratified regime largely disappears at even small upward inclinations, while the regime becomes more extended for downward flow. At vertical downward flow, however, no stratified flow exists.

FIGURE 2.25 Flow-pattern map for downward flow: $\theta = -50^\circ$.FIGURE 2.26 Flow-pattern map for downward flow: $\theta = -90^\circ$.

Nomenclature

A	Area
c	Phase velocity of dynamic wave
C	Shedding parameter
C_o	Distribution parameter
D	Pipe diameter

E	Entrainment fraction
Eo	Eötvös number
f	Fanning friction factor
F_{rm}	Froude number of mixture
F_L	Liquid Froude number
g	Acceleration due to gravity
G	Mass flux per unit area
h	Height
k	Wave vector
Ku	Kutateladze number
l	Length
M	Momentum flux
N_L	Dimensionless liquid velocity
p	Pressure
P	Perimeter
Re	Reynolds number
u_s	Superficial velocity
v_s	Slug frequency
x	Distance
X	Lockhart-Martinelli parameter

Greek Symbols

α	Phase holdup
γ	Top angle
θ	Inclination angle
λ	Volume fraction
μ	Viscosity
ρ	Density
σ	Surface tension
τ	Shear stress
Φ	Two-phase flow multiplier
ω	Frequency

Subscripts

G	Gas
h	Homogeneous
i	Interface
L	Liquid
m	Mixture
w	Wall

References

- Andreussi, P., Private communication, 1988.
- Andreussi, P. and Bendiksen, K., An investigation of void fraction in liquid slugs for horizontal and inclined gas /liquid pipe flow, *Int. J. Multiphase Flow*, 15, 937–946, 1989.
- Barnea, D., A unified model for predicting flow pattern transitions for the whole range of pipe inclinations, *Int. J. Multiphase Flow*, 13, 1–12, 1987.
- Barnea, D., Shoham, O., and Taitel, Y., Flow pattern transition for down ward inclined two-phase flow: horizontal to vertical, *Chem. Eng. Sci.*, 37, 735–740, 1982a.

- Barnea, D., Shoham, O., and Taitel, Y., Flow pattern transition for vertical downward two-phase flow, *Chem. Eng. Sci.*, 37, 741–746, 1982b.
- Barnea, D., Shoham, O., and Taitel, Y., Gas–liquid flow in inclined tubes: flow pattern transitions for upward flow, *Chem. Eng. Sci.*, 40, 131–136, 1985.
- Barnea, D. and Taitel, Y., Structural and interfacial stability of multiple solutions for stratified flow, *Int. J. Multiphase Flow*, 18, 821–830, 1992.
- Cheremisinoff, N.P. and Davis, E.J., Stratified turbulent–turbulent gas/liquid flow, *AIChE J.*, 25, 48–56, 1979.
- Chisholm, D., A theoretical basis for the Lockhart–Martinelli correlation for two-phase flow, *Int. J. Heat Mass Transfer*, 10, 1767–1778, 1967.
- Churchill, S.W., Friction-factor equation spans all fluid-flow regimes, *Chem. Eng.*, 7, 91, 1977.
- Cohen, L.S. and Hanratty, T.J., Effect of waves at a gas/liquid interface on turbulent air flow, *J. Fluid Mech.*, 31, 467–479, 1968.
- Colebrook, C.F., Turbulent flow in pipes with particular reference to the transition region between the smooth and rough pipe laws, *J. Inst. Civil Eng.*, 11, 133, 1939.
- Collins, R., de Moraes, F.F., Davidson, J.F., and Harrison, D., The motion of a large gas bubble rising through liquid flowing in a tube, *J. Fluid Mech.*, 89, 497–514, 1978.
- Crowley, C.J. and Rathe, P.H., Assessment of mechanistic two-phase analysis methods for gas/condensate pipelines, *PSIG Annual Meeting*, Toronto, October, 20–21, 1988.
- Dukler, A.E. and Hubbard, M.G., Model for gas–liquid flow in horizontal and near-horizontal tubes, *Ind. Eng. Chem. Fundam.*, 14, 337–347, 1975.
- Dukler, A.E. and Taitel, Y., Flow pattern transitions in gas–liquid systems. Measurements and modelling, in *Multiphase Science and Technology*, Vol. II, G.F. Hewitt, J.M. Delhaye, and N. Zuber, Eds., Hemisphere, Washington, DC, 1986.
- Fernandes, R.C., Experimental and Theoretical Studies of Isothermal Upward Gas–Liquid Flows in Vertical Tubes, Ph.D. thesis, University of Houston, 1981.
- Ferschneider, G., Lagière, M., Bourgeois, T., and Fitremann, J.M., How to calculate two-phase flow of gas and oil in pipelines, *Pipe Line Industry*, 63, 33–39, 1985.
- Hewitt, G.F. and Lahey, R.T., *Proceedings Third International Workshop on Two-Phase Flow Fundamentals*, June 15–19, London, UK, 1992.
- Heywood, N.I. and Richardson, J.F., Slug flow of air/water mixtures in a horizontal pipe: determination of liquid hold-up by γ -ray absorption, *Chem. Eng. Sci.*, 34, 17–30, 1979.
- Hinze, J.O., Fundamentals of the hydrodynamic mechanism of splitting in dispersion processes, *AIChE J.*, 1, 289–295, 1955.
- Hoogendoorn, C.J., Gas/liquid flow in horizontal pipes, *Chem. Eng. Sci.*, 9, 205–216, 1959.
- Ishii, M. and Grolmes, M.A., Inception criteria for droplet entrainment in two-phase concurrent film flow, *AIChE J.*, 21, 308–318, 1975.
- Lockhart, R.W. and Martinelli, R.C., Proposed correlation of data for isothermal two-phase, two-component flow in pipes, *Chem. Eng. Prog.*, 45, 39–45, 1949.
- Miya, M., Woodmansee, D.E., and Hanratty, T.J., A model for roll waves in gas/liquid flow, *Chem. Eng. Sci.*, 26, 1915–1931, 1971.
- Moody, L.F., Friction factors for pipe flow, *Trans. ASME*, 671, 1944.
- Moysis, R. and Griffith, P., Entrance effects in a two-phase slug flow; *J. Heat Transfer*, 82, 29–39, 1962.
- Oliemans, R.V.A., Liquid Hold-Up during Two-Phase Slug Flow in Inclined Pipes, KSLA Internal Report, 1976.
- Oliemans, R.V.A., Modelling of gas/condensate flow in horizontal and inclined pipes, Paper presented at 1987 ETCE Conference, Dallas, February 15–19, ASME, PD. Vol. 6, pp. 73–81.
- Oliemans, R.V.A., Pots, B.F.M., and Trompé, N., Modelling of annular dispersed two-phase flow in vertical pipes, *Int. J. Multiphase Flow*, 12, 711–732, 1986.
- Pan, P. and Hanratty, T.J., Correlation of entrainment for annular flow in horizontal pipes, *Int. J. Multiphase Flow* 28, 385–408, 2002.

- Pots, B.F.M., An Omni-Angle Flow Pattern Map for Gas/Liquid Two-Phase Flow in Pipes, Internal Shell Report, 1985.
- Pots, B.F.M., Oliemans, R.V.A., and Trompé, N., The KSLA Method for Gas/Liquid Two-Phase Pipe Flow Calculations, KSLA internal report, 1988.
- Richter, H.J., Flooding in tubes and annuli, *Int. J. Multiphase Flow*, 7, 647–658, 1981.
- Shoham, O. and Taitel, Y., Stratified turbulent-turbulent gas/liquid flow in horizontal and inclined pipes, *AIChE J.*, 30, 377–385, 1984.
- Taitel, Y. and Dukler, A.E., A model for predicting flow regime transitions in horizontal and near-horizontal gas-liquid flow, *AIChE J.*, 22, 47–55, 1976.
- Taitel, Y., Barnea, D., and Dukler, A.E., Modelling flow pattern transitions for steady upward gas-liquid flow in vertical tubes, *AIChE J.*, 26, 345–354, 1980.
- Ullmann, A., Zamir, M., Gat, S., and Brauner, N., Multi-holdups in co-current stratified flow in inclined tubes, *Int. J. Multiphase Flow*, 29, 1565–1581, 2003.
- Vassiliadou, E. and Schellekens, C., Liquid Loaded Gas Wells. Physical Mechanisms Related to Unstable Flow, KSLA Internal Report, 1988.
- Wallis, G.B., *One-Dimensional Two-Phase Flow*, McGraw-Hill, New York, 1969.
- Whalley, P.B., *Boiling, Condensation, and Gas/Liquid Flow*, Clarendon Press, Oxford, 1987.
- Wu, H.L., Pots, B.F.M., Hollenberg, J.F., and Meerhoff, R., Flow pattern transitions in two gas/condensate flow at high pressure in an 8-inch horizontal pipe, *Proceedings of the 3rd International Conference on Multiphase Flow*, The Hague, The Netherlands, May, 18–20, 13–21, 1987.
- Zuber, N. and Findlay, J.A., Average volumetric concentration in two-phase flow systems, *J. Heat Transfer*, 87, 453–468, 1965.
- Zukoski, E.E., Influence of viscosity, surface tension, and inclination angle on motion of long bubbles in closed tubes, *J. Fluid Mech.*, 25, 821–837, 1966.

3

Boiling and Condensation

3.1	Boiling	3-1
	Pool Boiling • Flow Boiling	
3.2	Condensation	3-31
	Fundamentals of Condensation • Condensation on Flat Surfaces • Condensation on and in the Tubes • Effects of Noncondensable Gases and Other Secondary Effects • Direct Contact Condensation • Enhanced Condensation • Surface Promoter for Dropwise Condensation • Electric Field Enhanced Condensation	

S.G. Kandlikar
Rochester Institute of Technology

J.N. Chung
University of Florida

3.1 Boiling

S.G. Kandlikar

3.1.1 Pool Boiling

A change of phase from liquid to vapor across a liquid–vapor interface is called evaporation. Boiling refers to heat transfer-induced evaporation associated with vapor bubbles. The nature of the specific liquid–vapor system gives rise to different types of boiling:

1. *Pool boiling* refers to the boiling process in which the liquid is essentially quiescent and vapor bubbles rise as a result of buoyancy forces induced by gravity or other body forces.
2. *Flow boiling* refers to the boiling process in which the liquid and the resulting vapor phase are subjected to a flow field.

In the literature, additional terminology is employed to identify specific configurations; *thin-film evaporation* or *falling-film evaporation* refers to evaporation across the liquid–vapor interface of a thin liquidfilm that is formed on a heater surface. The term *convective flow boiling* refers to a change of phase from liquid to vapor during internal flow, while *external flow boiling* refers to a change of phase from liquid to vapor during external flow such as flow over tube banks.

Pool boiling is also of interest from the perspective of understanding the boiling phenomenon. Some of its applications include kettle reboilers, batch-type vaporizers, liquid immersed electronic component cooling, and quenching of metals in metallurgical processes. Flow boiling is employed in many applications, such as steam generators and refrigeration evaporators, and is being considered for high-flux cooling of electronic components.

3.1.1.1 Introduction to Pool Boiling

Although a number of investigators have observed different regions of pool boiling heat transfer, Nukiyama (1934) conducted a systematic study on pool boiling over electrically heated nichrome and

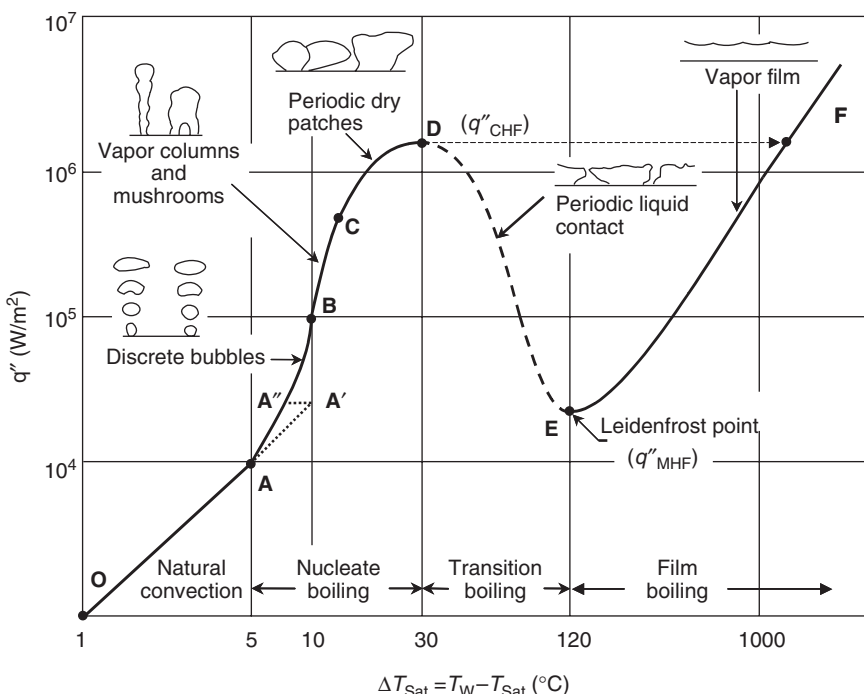


FIGURE 3.1 Boiling curve showing different regions in pool boiling.

platinum wires and presented a boiling curve. Figure 3.1 shows a boiling curve that incorporates a number of additional features that have been identified by later investigators. The heat flux q'' at the heater surface is plotted against the wall superheat ($\Delta T_{\text{Sat}} = T_{\text{Heater}} - T_{\text{Sat}}$). The nature of bubble or vapor film surrounding the heater is also depicted in Figure 3.1. The pool of water is held at its saturation temperature of T_{Sat} corresponding to the system pressure (hence the term saturated pool boiling).

In the region O–A in Figure 3.1 with small ΔT_{Sat} , heat is transferred by *natural convection*. At location A' corresponding to a certain value of $\Delta T_{\text{Sat}} = \Delta T_{\text{Sat,ONB}}$, bubble nucleation is initiated on cavities present on the heater surface. This condition is called *onset of nucleate boiling* (ONB). With the inception of nucleation, the heater surface temperature drops to A'' for a given imposed heat flux. This hysteresis effect shown by the dotted lines AA'A'' disappears during repeated boiling cycles with increasing and decreasing values of heat flux. The slope of the curve beyond the ONB point increases at higher ΔT_{Sat} values as the bubbles grow and depart more rapidly (region A''–B), more nucleation sites become active and *fully developed nucleate boiling* ensues (region B–C). At higher heat fluxes, the heater surface becomes overcrowded with bubbles at various stages of growth. In addition, the intense evaporation near the bubble bases leads to periodic dry patches on the heater surface that are rewetted by the surrounding liquid, resulting in a reduction in the slope of the boiling curve (the heat transfer coefficient begins to decrease). At higher wall superheat, liquid is unable to rewet the heater surface, causing a sudden formation of a dry patch that eventually covers a large region of the heater surface. A thin film of vapor separates the liquid from the heater surface, causing a large temperature excursion of the heater surface (drastic reduction in the heat transfer coefficient). The heat flux corresponding to this condition at location D, q''_{CHF} , which represents the maximum heat flux sustained under the nucleate boiling condition, is called the *critical heat flux* (CHF). As the heat flux is further increased, the heater temperature jumps to point F. The ensuing mode of heat transfer at a higher heat flux in which the heater is blanketed with a thin vapor film is called *film boiling*. Through experimental investigation, Nukiyama (1934) observed that the high temperature following the CHF point leads to physical burnout of the nichrome wires, while platinum wires were able to withstand the higher temperatures.

The dotted region D–E in [Figure 3.1](#) following the CHF represents the *transition boiling* region. This region is not accessible with an electrical heater providing a constant heat flux boundary condition; it can only be traced under stable conditions by employing a constant temperature boundary condition on the heated wall. In the transition region, the formation of dry patches and the rewetting of the dry regions occur very rapidly. Eventually, the rewetting cannot be sustained at the Leidenfrost condition represented by E, and the heater is surrounded by a stable vapor film. The heat flux at E is called the minimum heat flux, q''_{MHF} . The region E–F is the film boiling region in which heat is transferred by combined radiative and convective modes.

In studying boiling phenomena, the nucleation characteristics and bubble behavior are of great importance. Some of the early investigators, including Moissis and Berenson (1963), Gaertner (1965), and Johnston et al. (1966), have employed high-speed photography to reveal the bubble behavior. Gaertner obtained still and video images at 3000 frames/sec identifying various boiling regions, such as the discrete bubble region, first transition region (vapor columns are observed), and second transition region (stems of vapor column become unstable with the formation of local dry patches). Additional regions based on bubble shapes at departure have been proposed by later investigators (e.g., Williamson and El-Genk, 1991). The actual mechanism is still a subject of active research, as the Helmholtz instability in the second transition region is used as the basis of some of the CHF models (Zuber, 1959; Haramura and Katto, 1983), while the interpretation of photographs and the presence of a thin liquid layer (macrolayer) still remain inconclusive (see, e.g., Williamson and El-Genk, 1991).

3.1.1.2 Onset of Nucleate Boiling

Bankoff (1958) showed that the presence of nucleating cavities on a heater surface leads to nucleation at lower superheats (heterogeneous nucleation) compared to the homogeneous nucleation in which vapor embryos are formed in a highly superheated liquid. Cavities trap vapor and gases and act as nucleation sites for bubbles on a heater surface. A certain amount of wall superheat is needed to activate the cavities depending on various factors: (1) cavity size and shape; (2) fluid properties, including surface tension and contact angles; and (3) temperature profile in the liquid immediately surrounding the heater surface.

Consider a vapor bubble of radius R_b in a pool of liquid at a temperature T and pressure p_L as shown in [Figure 3.2](#). The pressure inside the bubble is p_G . Taking a diametric section reveals the forces due to pressure difference and the surface tension along the circumference. At equilibrium, equating these two forces yields

$$p_G - p_L = \frac{2\sigma}{R_b} \quad (3.1)$$

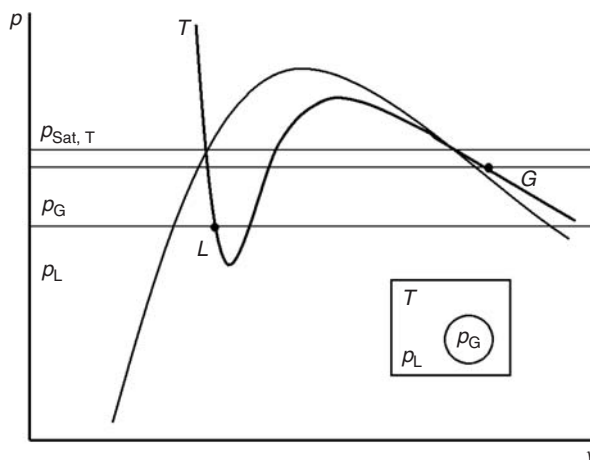


FIGURE 3.2 Metastable liquid and vapor conditions for a bubble growing in a pool of liquid.

The liquid and vapor states corresponding to the above condition are shown as L and G, respectively, in [Figure 3.2](#). The liquid state L lies in a metastable condition corresponding to p_L and T . The metastable equilibrium liquid line in the saturation dome represents the equilibrium over a curved interface. The lowest pressure point on this curve corresponds to the homogeneous nucleation condition.

The vapor state G is in the superheated region corresponding to p_G and T . The saturation pressure $p_{\text{Sat},T}$ over a planar interface corresponding to T can be expressed in terms of pressures p_L and p_G by equating the molar Gibbs free energies for the two phases (Fujita, 1999):

$$p_{\text{Sat},T} - p_G = \left(\frac{\nu_L}{\nu_{G,\text{Sat},T} - \nu_L} \right) \frac{2\sigma}{R_b} \quad (3.2)$$

$$p_{\text{Sat},T} - p_L = \left(\frac{\nu_{G,\text{Sat}}}{\nu_{G,\text{Sat},T} - \nu_L} \right) \frac{2\sigma}{R_b} \quad (3.3)$$

For low reduced pressures, ($P_r \ll 1$), ν_L , $\nu_{G,\text{Sat}}$ and Equations (3.2) and (3.3) simplify as follows:

$$p_G = p_{\text{Sat},T} \quad (3.4)$$

$$p_L = p_{\text{Sat},T} - \frac{2\sigma}{R_b} \quad (3.5)$$

[Figure 3.3](#) shows the growth of a bubble inside and over a cavity. The residual vapor or gas in the cavity activates the cavity. As the wall temperature rises, the liquid–vapor interface moves out toward the mouth of the cavity, assumed to be circular for the purpose of this analysis. Eventually, the bubble becomes anchored on the cavity's mouth as the contact angle adjusts from the inner cavity surface to the heater surface. The minimum radius of the bubble occurs when the bubble assumes a hemispherical shape with a radius R_b equal to the cavity's mouth radius R_C .

Hsu (1962) and Hsu and Graham (1961) postulated that a vapor bubble will grow, thus initiating nucleate boiling, if the temperature in the liquid at the top of the hemispherical bubble cap exceeds the

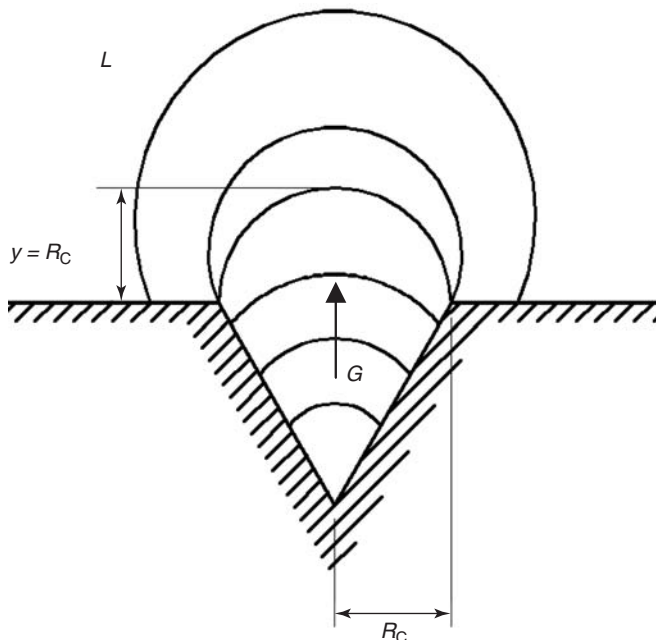


FIGURE 3.3 Growth of a vapor bubble nucleating from a cavity.

saturation temperature corresponding to the pressure p_G inside the bubble. Under this condition, Eq. (3.1) becomes

$$p_G - p_L = \frac{2\sigma}{R_C} \quad (3.6)$$

Applying the Clausius–Clapeyron equation, $dp/dT = h_{fg}/(\nu_{fg} T_{\text{Sat}})$, and assuming $\nu_{fg} \approx \nu_G$, Eq. (3.6) becomes

$$T - T_{L,\text{Sat}} = \frac{2\sigma T_{\text{Sat}} \nu_G}{h_{fg} R_C} \quad (3.7)$$

where T is the temperature of the liquid surrounding the bubble. Since there is a temperature gradient in the liquid normal to the heated wall, the minimum liquid temperature adjacent to the bubble interface occurs at $y = R_C$, where y is the distance normal to the heater surface. Using this temperature T in Eq. (3.7) as T_G , the equilibrium temperature of the vapor in the hemispherical bubble on the bubble mouth, Eq. (3.7) becomes

$$T_G - T_{L,\text{Sat}} = \frac{2\sigma T_{\text{Sat}} \nu_G}{h_{fg} R_C} \quad (3.8)$$

where $T_{L,\text{Sat}}$ ($= T_{\text{Sat}}$) is the saturation temperature (in K) corresponding to the liquid pressure p_L .

The liquid temperature profile in the vicinity of the heater surface can be approximated by applying the heat conduction equation in the liquid. Thus

$$\frac{dT}{dy} = \frac{T_w - T_L}{y} = \frac{q''}{k_L} \quad (3.9)$$

The liquid temperature T_L at $y = R_C$ can be found from Eq. (3.9).

Graphically, Figure 3.4 shows the plots of Eqs. (3.8) and (3.9). The intersection points of these two plots yield the range of the cavity radii, R_{\min} and R_{\max} , for which $T_L > T_G$ at $y = R_C$. Introducing $\Delta T_{\text{Sat}} = T_w - T_{\text{Sat}}$ at system pressure p_L , the following range is obtained by solving Eqs. (3.8) and (3.9):

$$R_{C,\max} R_{C,\min} = \frac{\Delta T_{\text{Sat}} k_L}{q''} \pm \sqrt{\left(\frac{\Delta T_{\text{Sat}} k_L}{q''} \right)^2 - \frac{8\sigma T_{\text{Sat}} \nu_G k_L}{h_{fg} q''}} \quad (3.10)$$

Bubble nucleation further depends on the availability of cavities in the range between $R_{C,\min}$ and $R_{C,\max}$ over the heater surface. On the other hand, if cavities of all sizes are present, the minimum heat flux and the critical radius, defined as the radius of the first cavity to nucleate under a given heat flux q'' , are obtained by drawing a line with a slope given by Eq. (3.9) that is tangent to the curve for T_G , resulting in $T_w = T_{w,\text{crit}}$

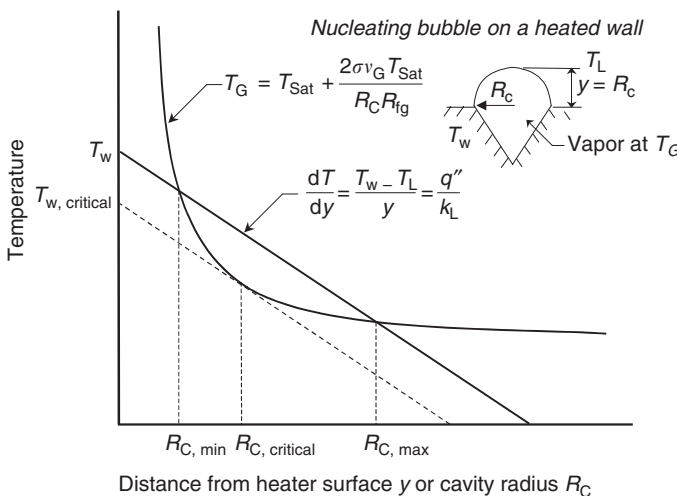


FIGURE 3.4 Nucleation criterion for the activation of a cavity in pool boiling.

as shown in [Figure 3.4](#). Equating the slope dT_G/dR to the slope given by Eq. (3.9), the critical radius R_{crit} at ONB is given by

$$R_{C,\text{crit}} = \left[\frac{2\sigma T_{\text{Sat}} v_G k_L}{h_{fg} q''} \right]^{1/2} \quad (3.11)$$

The wall superheat at the ONB is then obtained by setting the term under the radical in Eq. (3.10) to zero:

$$\Delta T_{\text{Sat,crit}} = \left[\frac{8\sigma T_{\text{Sat}} v_G q''}{h_{fg} k_L} \right]^{1/2} \quad (3.12)$$

The nucleation criterion has been further investigated by researchers to include (i) the effect of cavity shape (Lorentz et al., 1974); (ii) the effect of contact angles, resulting in bubbles that are of different shapes when compared with the hemispherical shape at the critical condition (Hsu and Graham, 1961; Davis and Anderson, 1966); (iii) subcooling; (iv) stagnation temperature at the leading face (Kandlikar et al., 1997); and (v) transient conduction effects due to liquid renewal (Marcus and Dropkin, 1965). Equations (3.10)–(3.12) provide reasonable estimates of ONB conditions and are used extensively in practical applications.

Cavitation is similar to nucleation in boiling, except that the bubbles are generated as a result of lowering the pressure, rather than increasing the temperature. The presence of dissolved gases leads to early nucleation before the local saturation conditions corresponding to a pure liquid are reached. As the liquid temperature increases, the solubility of a dissolved gas decreases and it begins to come out of the liquid at nucleation sites on the heater surface. Murphy and Bergles (1972) used the partial pressure of vapor in a gas–vapor mixture inside a vapor bubble for developing the nucleation criterion under these conditions.

Further effects of dissolved gases, boiling history, surfactants, and cavity shapes, including reentrant cavities, liquid metals, and binary mixtures, on the onset of nucleation are beyond the scope of the present work.

3.1.1.3 Bubble Dynamics in Nucleate Pool Boiling

A bubble on a heater surface goes through an ebullition cycle consisting of the following four stages during nucleate boiling. (i) Bubble nucleation — when the temperatures of the wall and liquid in the vicinity of a cavity reach conditions conducive to nucleation, a bubble forms on the cavity mouth. (ii) Growth period — relaxation of liquid superheat around the liquid–vapor interface due to evaporation causes the bubble to grow. (iii) Bubble departure — as the bubble grows, eventually the forces tending to push the bubble away from the heater surface become greater than the retaining forces, and the bubble leaves the heater surface. (iv) Waiting period — as the cooler liquid from the bulk rushes to take the place of the departed bubble, the temperature of the heater wall and the liquid adjacent to the cavity begin to rise until the nucleation criterion is met. A bubble is then formed, and the ebullition cycle continues.

3.1.1.3.1 Bubble Nucleation

Bubble nucleation is closely related to the size and shape of the cavity holding gases or vapors. For a given wall superheat, a range of nucleation cavities are activated. As the wall superheat increases, the active cavity size range increases as the liquid temperature distribution line moves higher in [Figure 3.2](#). The presence of a vapor phase in the cavity is essential for the activation of a cavity. Reentrant cavities are able to trap the gases or vapor left behind from a previously departed bubble. Bubble nucleation also depends on the availability of cavities, their shape and size ranges, local temperature profile in the liquid near the wall (dependent on the wall superheat and liquid subcooling), presence of dissolved gases, hysteresis effects, liquid properties, and contact angle.

3.1.1.3.2 Growth Period

The bubble continues to grow due to evaporation occurring at expanding the liquid–vapor interface on the bubble and, according to some models, also from the thin film left behind on the heater surface. The growth period is divided into two regions. Inertia-controlled growth occurs in the early stages of bubble

growth. Rayleigh (1917) analyzed the growth process and derived the following equation for the bubble growth rate:

$$R(t) = \left\{ \frac{2}{3} \left[\frac{T_L - T_{\text{Sat}}(p_L)}{T_{\text{Sat}}(p_L)} \right] \frac{h_{fg} \rho_g}{\rho_L} \right\}^{1/2} t \quad (3.13)$$

The growth rate is linear in the early stages as seen from Eq. (3.13). Superheated liquid provides the thermal energy for rapid evaporation at the interface in this region, but the bubble growth is limited by the inertia of the surrounding liquid.

Subsequent to the initial rapid growth, evaporation is limited by conduction heat transfer from the surrounding liquid to the interface. Thus, bubble growth is thermally controlled. Plesset and Zwik (1954) derived the following equation for bubble growth in this region:

$$R(t) = \frac{2\Delta T_{\text{Sat}} k_L}{h_{fg} \rho_G} \left(\frac{3t}{\pi \alpha_L} \right)^{1/2} \quad (3.14)$$

where α_L is the thermal diffusivity of the liquid.

The above equations for bubble growth are derived for the case of uniformly heated liquid over a spherical bubble. Mikic et al. (1970) derived the following equation by incorporating the shape of a bubble growing in the vicinity of a heated surface. The entire growth cycle including the inertia- and thermally controlled regions are covered:

$$R^+ = \frac{2}{3} \left[(t^+ + 1)^{3/2} - (t^+)^{3/2} - 1 \right] \quad (3.15)$$

where

$$R^+ = \frac{R(t)A}{B^2}, \quad t^+ = \frac{t A^2}{B^2}$$

$$A = \left\{ \frac{2[T_L - T_{\text{Sat}}(p_L)]h_{fg}\rho_G}{\rho_L T_{\text{Sat}}(p_L)} \right\}^{1/2}, \quad B = \left(\frac{12\alpha_L}{\pi} \right)^{1/2} \left\{ \frac{2[T_L - T_{\text{Sat}}(p_L)]c_{p,L}\rho_L}{\rho_G h_{fg}} \right\}$$

In the limit, Eq. (3.15) reduces to Eq. (3.13) in the inertia-controlled region for small values of t , and to Eq. (3.14) in the thermally controlled region for large values of t .

3.1.1.3.3 Bubble Departure Diameter

As the bubble grows, it experiences the following forces: (1) surface tension force — holds down the bubble on the heater surface through the contact angle; (2) inertia force — as the bubble grows, the acceleration and deceleration of the interface introduce inertia forces that push the bubble onto the heater surface during the earlier part of the growth period, while the bubble is pulled away during the later part; and (3) buoyancy force — depending on the orientation and geometry, the buoyancy force helps or opposes the bubble removal. Additionally, there are viscous forces as well as forces due to Marangoni convection in the liquid around the bubble. As a result of all these forces, a bubble departs the heater surface after attaining a certain size. The bubble shape also undergoes considerable changes. The departure bubble diameter D_b is of great interest in boiling studies and has been extensively studied. Before applying any correlation, it should be realized that D_b depends on a number of additional variables, such as nucleation site interactions and convection currents that are statistical in nature. A wide variation in D_b , up to 50%, from the predicted value is not uncommon.

The following correlations by Jensen and Memmel (1986) were developed from a data bank of 504 data points for 15 fluids, including water, boiling on mostly horizontal plates and wires over a wide range of pressures. The correlations were compared with 12 other correlations and were found to perform consistently better than other correlations available in the literature.

For the case when wall superheat is available,

$$[g(\rho_L - \rho_G)D_b^2/\sigma]^{1/2} = 0.19(1.8 + 10^5 K_1)^{2/3} \quad (3.16)$$

where

$$K_1 = \left(\frac{Ja}{Pr_L} \right)^2 \left\{ \left[\frac{g(\rho_L - \rho_G)}{\mu_L^2} \right] \left[\frac{\sigma}{g(\rho_L - \rho_G)} \right]^{3/2} \right\}^{-1} \quad (3.17)$$

where Ja ($= \rho_L c_{p,L} \Delta T_{\text{Sat}} / (\rho_G h_{fg})$) is the Jakob number, Pr ($= \mu c_{p,L} / k$) is the Prandtl number, and the wall superheat is given by $\Delta T_{\text{Sat}} = T_w - T_{\text{Sat}}$.

For cases where wall superheat is not available,

$$D_b = 2.97 \times 10^4 \left(\frac{p}{p_{\text{cr}}} \right)^{-1.09} \left(\frac{KT_{\text{cr}}}{p_{\text{cr}} M} \right)^{1/3} \quad (3.18)$$

where K ($= 1.38 \times 10^{-23}$ J/K) is the Boltzman constant, M the molecular weight, and subscript "cr" refers to the critical point for the fluid.

The average deviations for Eqs. (3.16) and (3.18) were 44 and 52%, respectively, when compared with 30 data sources covering 15 different fluids at pressures from about 4.7 to 13,500 kPa.

3.1.1.3.4 Bubble Frequency

The frequency of bubbles being released from cavities depends on a number of factors, including wall superheat, fluid thermal properties, contact angle, cavity size, and interaction with neighboring bubbles. An empirical correlation by Malenkov (1971) takes into account the interaction between the bubble departure diameter and bubble departure frequency and is recommended:

$$fD_b = V_b/\pi \left(1 - \frac{1}{1 + V_b \rho_G h_{fg} / q''} \right) \quad (3.19)$$

where

$$V_b = \left[\frac{D_b g(\rho_L - \rho_G)}{2(\rho_L + \rho_G)} + \frac{2\sigma}{D_b(\rho_L + \rho_G)} \right]^{1/2} \quad (3.20)$$

and D_b is the departure bubble diameter.

3.1.1.4 Heat Transfer Mechanisms During Nucleate Pool Boiling

Heat transfer in nucleate pool boiling is a result of a number of interacting mechanisms:

1. *Transient conduction.* As a bubble departs, bulk liquid rushes over the heater surface surrounding the nucleating cavity. The liquid undergoes a transient heat conduction process. The wall thermal properties also play a role during the transient heat conduction process. The superheated liquid moves away into the bulk during bubble growth and departure. The superheated liquid also contributes to the evaporation at the bubble interface.
2. *Enhanced convection.* The bubble ebullition cycle introduces convective currents that contribute to the heat transfer during nucleate pool boiling.
3. *Microlayer evaporation.* A thin layer of liquid, called a microlayer, is left below an expanding bubble during the bubble growth period. Evaporation of this liquid film is believed to contribute to heat transfer at higher heat fluxes (Judd and Hwang, 1976).

The periodic nature of liquid flow in the bubble ebullition cycle, development of the superheated liquid layer, release of the liquid sensible energy in the form of evaporation at the bubble interface, and evaporation from the microlayer have all been extensively studied in the literature. Hewitt (1998) provides a good overview of the developments in this field. However, in spite of these developments, the contributions from each mechanism are still not conclusively proven and continue to be topics of current research interest.

3.1.1.5 Models and Correlations for Nucleate Pool Boiling

It has been recognized that the heat transfer during nucleate pool boiling is closely related to the bubble activity over a heater surface. In principle, the heat transfer rate can be predicted by knowing the bubble frequency, active nucleating cavity site density (per unit heater surface area), and heat transferred during each bubble ebullition cycle. Although such an approach is being pursued by researchers (e.g., Dhir, 1999), complete analytical treatments have not yet been developed for practical design applications.

A number of empirical and semiempirical correlations are available in the literature. Two of the more successful correlations are given below.

Rohsenow (1952) developed a semiempirical model by using the liquid Reynolds number in the vicinity of a bubble. The influence region was considered to be twice the diameter of the departure bubble diameter. Rohsenow introduced an empirical constant C_{sf} to account for the fluid–surface effect on nucleate boiling and proposed the following correlation:

$$\frac{c_{p,L}\Delta T_{\text{Sat}}}{h_{fg}} = C_{sf} \left\{ \frac{q''}{\mu_L h_{fg}} \sqrt{\frac{\sigma}{g(\rho_L - \rho_G)}} \right\}^{0.33} Pr_L^n \quad (3.21)$$

The values of C_{sf} and n for different heater materials and surface finishes are given in Table 3.1. These values are derived from Rohsenow (1952) and Vachnon et al. (1968).

In case the constant C_{sf} is not available for a given fluid–surface combination, a value of 0.013 is recommended as an initial guess. Liaw and Dhir (1989) established a clear dependence of the constant C_{sf} and the contact angle during pool boiling of water on copper surfaces. By varying the surface finish, they obtained different contact angles and showed that the contact angle and C_{sf} decreased as the surface was made smoother. This trend is also seen in Table 3.1 for different surface treatments.

Among other empirical correlations, the Stephan and Abdelsalam (1980) correlation is recommended. It is based on 5000 data points derived from 72 published sources. Stephan and Abdelsalam conducted a dimensional analysis and arrived at eight nondimensional groups to represent the nucleate pool boiling phenomenon. By carefully carrying out a regression analysis of the data, the following correlations were developed. The ranges of reduced pressures p/p_{cr} and contact angles θ are listed for different fluids.

Water (mean absolute error = 11.3%):

$$Nu = 2.46 \times 10^6 X_1^{0.673} X_4^{-1.58} X_3^{1.26} X_8^{5.22} \quad \text{for } 10^{-4} \leq p/p_{cr} \leq 0.886, \theta = 45^\circ \quad (3.22)$$

Hydrocarbons (mean absolute error = 12.2%):

$$Nu = 0.0546(X_5^{0.5} X_1)^{0.67} X_8^{4.33} X_4^{0.248} \quad \text{for } 5.7 \times 10^{-3} \leq p/p_{cr} \leq 0.9, \theta = 35^\circ \quad (3.23)$$

TABLE 3.1 Values of C_{sf} and n in the Rohsenow Correlation
(Eq. [3.21])

Fluid–Surface Combination	C_{sf}	n
Water–Copper		
Scored	0.0068	1.0
Polished	0.0130	1.0
Lapped	0.0147	1.0
Water–Brass	0.006	1.0
Water–Stainless Steel		
Chemically etched	0.0130	1.0
Mechanically polished	0.0130	1.0
Ground and polished	0.0060	1.0
Teflon-pitted	0.0058	1.0
Water–platinum	0.013	1.0
Water–nickel	0.006	1.0
Benzene–chromium	0.101	1.7
Carbon tetrachloride		
polished copper	0.007	1.7
Ethanol–chromium	0.0027	1.7
Isopropanol–copper	0.0025	1.7
<i>n</i> -Butanol–copper	0.003	1.7
<i>n</i> -Pentane–chromium	0.015	1.7
<i>n</i> -Pentane–copper		
Polished	0.0154	1.7
Emery-rubbed copper	0.0074	1.7
Lapped	0.0049	1.7

Cryogenic liquids (mean absolute error = 14.3%):

$$Nu = 4.82 X_1^{0.624} X_7^{0.117} X_5^{0.257} X_3^{0.374} X_4^{-0.329} \quad \text{for } 4.0 \times 10^{-3} \leq p/p_{cr} \leq 0.97, \theta = 1^\circ \quad (3.24)$$

Refrigerants (mean absolute error = 10.6%):

$$Nu = 207 X_1^{0.745} X_5^{0.581} X_6^{0.533} \quad \text{for } 3.0 \times 10^{-3} \leq p/p_{cr} \leq 0.78, \theta = 35^\circ \quad (3.25)$$

All fluids (general correlation for all of the above fluids; mean absolute error = 22.3%):

$$Nu = 0.23 X_1^{0.674} X_5^{0.297} X_4^{0.371} X_8^{-1.73} X_2^{0.35} \quad \text{for } 10^{-4} \leq p/p_{cr} \leq 0.97 \quad (3.26)$$

The definitions of Nusselt number, d , and nondimensional groups X_1-X_8 are given below:

$$\begin{aligned} Nu &= \frac{q'd}{\Delta T_{\text{Sat}} k_L}, \quad d = 0.145\theta \left[\frac{2\sigma}{g(\rho_L - \rho_G)} \right]^{1/2} \\ X_1 &= \frac{q''d}{k_L T_{\text{Sat}}}, \quad X_5 = \frac{\rho_G}{\rho_L} \\ X_2 &= \frac{\alpha_L^2 \rho_L}{\sigma d}, \quad X_6 = \frac{\mu_L}{\rho_L \alpha_L} \\ X_3 &= \frac{c_{pL} T_{\text{sat}} d^2}{\alpha_L^2}, \quad X_7 = \frac{(\rho c_p k)_S}{(\rho c_p k)_L} \\ X_4 &= \frac{h_{fg} d^2}{\alpha_L^2}, \quad X_8 = \frac{\rho_L - \rho_G}{\rho_L} \end{aligned}$$

where $\alpha (=k/(\rho c_p))$ is the thermal diffusivity, d the equilibrium break-off bubble diameter as defined above, θ the contact angle in degrees (not in rad), and the subscripts S and L refer to the solid surface and liquid, respectively.

3.1.1.6 Effect of Subcooling

Judd et al. (1991) studied the effect of subcooling on pool boiling heat transfer with water on a copper surface. Their results indicate that first, at low subcooling, the wall superheat increases due to changes in the number of active nucleation sites and bubble departure frequency. The subcooling effect is more pronounced at higher heat fluxes. For water with a heat flux of 1.26 MW/m², the wall superheat varied from 24 K at the saturation condition to about 32 K at a subcooling of 60 K. For higher values of subcooling, the wall temperature begins to decrease as the natural convection heat transfer is able to accommodate higher heat fluxes. No single predictive equation is available to predict the comprehensive effect of subcooling on nucleate pool boiling.

3.1.1.7 Enhanced Surfaces

Enhancement in nucleate boiling heat transfer is mainly accomplished by providing more active nucleation sites on the heater surface. A reentrant shape that traps gases or vapors in the cavities is found to be most effective. Figure 3.5 shows a schematic of a reentrant cavity. The reentrant cavities are manufactured by a variety of processes, including rolling of perforated fins protruding from the base, structured surfaces, porous surfaces created through sintering or other techniques, such as machined tunnels with openings of predetermined shapes and sizes, etc. A number of enhanced geometries are commercially available. They are routinely employed in cryogenic, air separation, refrigeration, and chemical industries. A good survey of enhancement mechanisms is given by Bergles (1997).

Other techniques include the application of an electric field and vibrations. The electric field causes enlargement of the bubble base area, thereby exposing more of the thin film underneath a bubble.

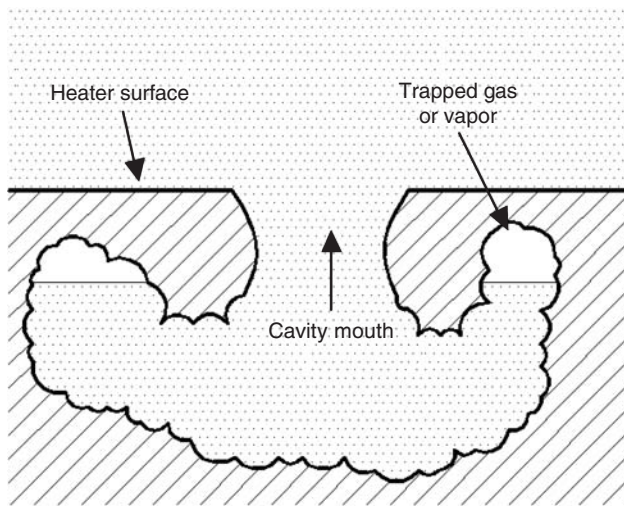


FIGURE 3.5 Schematic representation of a reentrant cavity trapping gas or vapor.

Mechanical vibrations provide pressure fluctuations that are especially effective under subcooled boiling conditions.

Enhancement of pool boiling with forced flow is covered under flow boiling heat transfer.

3.1.1.8 Effect of Orientation

Orientation affects the bubble removal process at low heat fluxes. A horizontal surface provides the most efficient heat transfer geometry. As the orientation angle changes to a vertical surface and then a downward facing surface, heat transfer deteriorates systematically. El-Genk (1996) presents an extensive overview of the effect of orientation on the entire pool boiling curve as shown in Figure 3.6. It is

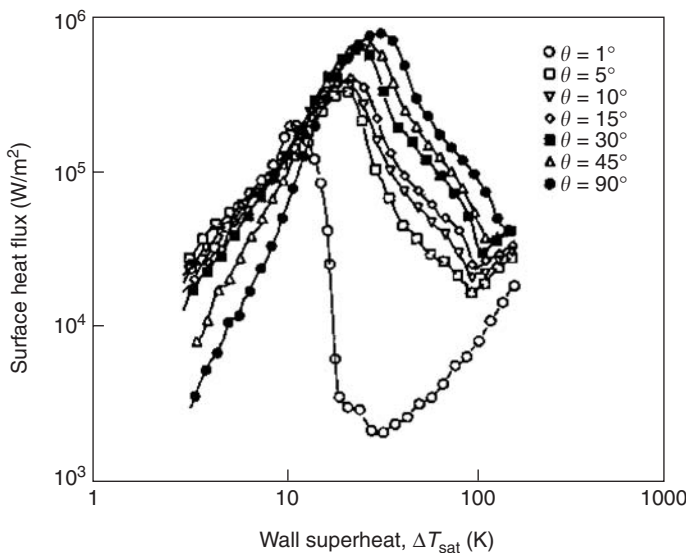


FIGURE 3.6 Effect of orientation on the pool boiling curve. (From El-Genk, M., in 2nd European Thermal-Sciences and 14th UIT National Heat Transfer Conference, Celta, G.P., Di Marco, P., and Mariani, A., Eds., Edizioni ETS, Italy, 1996. Reproduced with permission from Edizioni ETS, Italy.)

important to note that at high heat fluxes all curves tend to merge, but the boiling curve is affected in almost every region.

3.1.1.9 Nucleate Boiling with Mixtures

Nucleate boiling of mixtures of two liquids with different boiling points results in the preferential evaporation of the more volatile component at the evaporating liquid–vapor interface. The more volatile component is depleted at the interface, and the heat transfer is degraded as the more volatile component diffuses through the bulk of the liquid toward the interface. The interface temperature therefore rises and heat transfer is degraded. A number of researchers have studied the phenomena and presented detailed models. Kandlikar (1998a) presented a methodology to predict the interface concentration, which can be used in predicting the interface temperature. An extensive survey of the earlier work can be found in Kandlikar (1999). In general, the heat transfer coefficient for the mixture is below the linear-averaged heat transfer coefficient obtained from the respective pure component values.

Fujita et al. (1996) developed an empirical correlation from their own experimental data on methanol/water, ethanol/water, methanol/ethanol, ethanol/*n*-butanol, methanol/benzene, benzene/*n*-heptane, and water/ethylene glycol systems. It incorporates several key features of previous investigators and

$$h_m = \frac{(\tilde{x}_1/h_1 + \tilde{x}/h_2)^{-1}}{1 + \left\{ 1 - \exp \left[-2.8 \frac{\tilde{x}_1 \Delta T_1 + \tilde{x}_2 \Delta T_2}{T_{\text{Sat},2}|_p - T_{\text{Sat},1}|_p} \right] \right\} \left\{ \frac{T_{\text{dp}} - T_{\text{bp}}}{\tilde{x}_1 \Delta T_1 + \tilde{x}_2 \Delta T_2} \right\}} \quad (3.27)$$

where h_1 , h_2 , and ΔT_1 and ΔT_2 are the heat transfer coefficients and the wall superheat values with the two pure components, respectively, and $T_{\text{Sat},1}|_p$ and $T_{\text{Sat},2}|_p$ refer to the saturation temperatures of the pure components at the total system pressure p . Component 1 is the more volatile component with a lower boiling point. T_{dp} and T_{bp} are the dew point and bubble point temperatures, respectively.

3.1.1.10 Critical Heat Flux in Pool Boiling

Critical Heat Flux (CHF) is defined as the highest heat flux that can be sustained under the nucleate boiling mode. As the heat flux is increased, bubble activity increases dramatically over a heater surface. Both the number of nucleation sites as well as bubble frequency increase. The intense vapor–liquid interaction at the heater surface has prevented researchers from gaining clear visual access to the events occurring just prior to CHF.

Early researchers, e.g., Kutateladze (1948) and Zuber (1959), formulated their models based on the hydrodynamic instability theory. They assumed the presence of either a stable liquid–vapor interface or stable vapor columns, which are then analyzed for stability conditions based on Helmholtz or Taylor's instability criteria. The hydrodynamic model does not represent the events leading to the CHF, and further, it does not address the interaction between the liquid–vapor interface and the solid heated surface during frequent rewetting occurring just prior to CHF. The following equation was proposed by Zuber:

$$\frac{q''_{\text{CHF}}}{h_{\text{fg}} \rho_G^{1/2} [\sigma g (\rho_L - \rho_G)]^{1/4}} = K \quad (3.28)$$

where K is a constant equal to 0.13. Another model, developed by Haramura and Katto (1983), considers the depletion of a liquid macrolayer that exists under vapor mushrooms. Estimation of the initial macrolayer thickness and the role of the rewetting phenomenon and contact angles are not adequately addressed by this model.

Kandlikar (2001a) proposed a model based on the rapid evaporation of the liquid–vapor interface near the base of the liquid–vapor contact line at the heater surface. The rapid evaporation occurring in this region introduces a force due to momentum change that causes the interface to retreat, leaving a thin film of vapor underneath. [Figure 3.7](#) depicts the cutback phenomenon, and [Figure 3.8](#) shows a high-speed photographic sequence showing the vapor cutback under a liquid droplet placed on a flat heater surface (Kandlikar and Steinke, 2002).

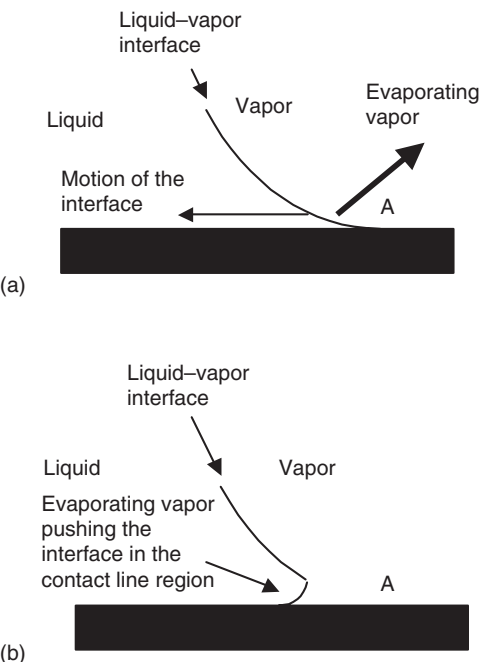


FIGURE 3.7 Schematic representation of vapor cutback under liquid during rapid evaporation in the contact line region. (From Kandlikar, S.G. and Steinke, M.S., *Int. J. Heat Mass Transfer*, 45, 3771–3780, 2002. Reproduced with permission.)

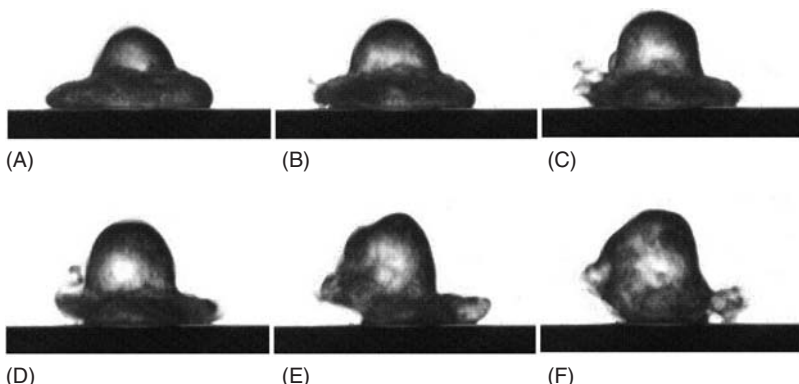


FIGURE 3.8 High-speed image sequence showing interface movement under a liquid droplet during rapid evaporation, 1 msec interval between successive frames, $T_w = 150^\circ\text{C}$, droplet diameter 2.8 mm. (From Kandlikar, S.G. and Steinke, M.S., *Int. J. Heat Mass Transfer*, 45, 3771–3780, 2002. Reproduced with permission from Elsevier.)

The balance between the evaporation momentum force and the retaining surface tension force was used by Kandlikar (2001a) in deriving an expression for CHF. The receding contact angle was introduced in the force balance for the retaining surface tension force. The final expression for CHF is given by

$$q''_{\text{CHF}} = h_{fg} \rho_G^{1/2} \left(\frac{1 + \cos \theta_r}{16} \right) \left[\frac{2}{\pi} + \frac{\pi}{4} (1 + \cos \theta_r) \cos \phi \right]^{1/2} [\sigma g (\rho_L - \rho_G)]^{1/4} \quad (3.29)$$

where θ_r is the receding contact angle and ϕ the angle of orientation of the heater surface with respect to horizontal. This expression accounts for the contact angle and orientation. Equation (3.29) reduces to the

Table 3.2 Variation of Equivalent K Factor (Product of the Two Bracketed Terms in Eq. [3.26])

Receding Contact Angle (deg)	Equivalent K
0	0.186
20	0.178
45	0.150
60	0.126
90	0.0745
120	0.0317
150	0.0072
180	0

Source: Kandlikar, S.G., *J. Heat Transfer*, 123, 1071–1079, 2001a.
With permission.

expression given by Kutateladze (1948) with $K = 0.13$ for a horizontal surface with a receding contact angle of 57.5° . Table 3.2 shows the variation of K with contact angle for a horizontal surface as predicted from Eq. (3.29).

3.1.1.11 Film Boiling

The post-CHF region consists of transition boiling (D–E in Figure 3.1), minimum heat flux (MHF) condition in film boiling (point E), and fully developed film boiling (E–F). Heat transfer in the transition region depends on the rewetting characteristics of the heater surface. Some empirical form of averaging techniques is employed between the CHF and MHF locations. The early work by Bromley (1950) provides an excellent insight into the film boiling phenomenon.

The minimum heat flux q''_{MHF} is predicted by a correlation developed by Zuber (1959):

$$q''_{\text{MHF}} = C \rho_G h_{\text{fg}} \left[\frac{g\sigma(\rho_L - \rho_G)}{(\rho_L + \rho_G)^2} \right]^{1/4} \quad (3.30)$$

The value of constant C was determined to be 0.09 by Berenson (1961) based on his data for MHF for a flat plate.

The film boiling heat transfer coefficient h_F consists of the convective and radiative components.

$$h_F = h_{F,c} + h_{F,r} \quad (3.31)$$

The radiative component is approximated by using appropriate radiation correlations between the heater surface and the surrounding vapor film. The emissivity of the liquid surface is generally taken as 1 and an empirical shape factor value of 0.75 is used.

The following correlation by Hsu and Westwater (1960) is recommended for $h_{F,c}$ for a vertical flat plate of length L :

$$h_{F,c} = 0.943 \left[\frac{g(\rho_L - \rho_G)\rho_G k_G^3 h'_{\text{fg}}}{L \mu_G (T_w - T_{\text{sat}})} \right]^{1/4} \quad (3.32)$$

where $h'_{\text{fg}} = h_{\text{fg}}(1 + 0.34c_{p,G}(T_w - T_{\text{sat}})/h_{\text{fg}})$ is the latent heat corrected for the vapor superheating.

For a horizontal flat plate, the correlation by Berenson (1961) is used extensively:

$$h_{F,c} = 0.425 \left\{ \left[\frac{k_G^3 g \rho_G (\rho_L - \rho_G) h'_{\text{fg}}}{\mu_G (T_w - T_{\text{sat}})} \right] \left[\frac{g(\rho_L - \rho_G)}{\sigma} \right]^{1/2} \right\}^{1/4} \quad (3.33)$$

where $h'_{\text{fg}} = h_{\text{fg}}(1 + 0.50c_{p,G}(T_w - T_{\text{sat}})/h_{\text{fg}})$.

3.1.2 Flow Boiling

3.1.2.1 Introduction to Flow Boiling

The process of flow boiling of a liquid heated in a confined passage is commonly encountered in many applications, such as steam generators in power plants, evaporators in refrigeration and air-conditioning equipment, distillation and other processes in chemical and petrochemical industries, and high flux heat removal systems.

Figure 3.9 shows the flow boiling process in a uniformly heated circular tube. Subcooled liquid enters the tube and is heated by single-phase convection. The heat transfer coefficient in the single phase is almost constant except for the variation due to property changes with increasing liquid temperature along the tube length. As the wall temperature reaches the saturation temperature, nucleation does not occur immediately because a certain amount of wall superheat is needed to nucleate cavities existing on the wall. The first bubbles appear on the wall at a location identified as the ONB. The wall temperature begins to level off, as more nucleation sites are activated beyond ONB. Further downstream, as more sites are activated, the contribution to heat transfer from the nucleate boiling continues to rise, while the single-phase convective contribution diminishes. This region is called the *partial boiling region*. The convective contribution continues to diminish, and eventually *fully developed boiling* (FDB) is established. Subsequently, the wall temperature remains almost constant in the FDB region until some point where the convective effects become important again due to the two-phase flow in the newly defined *significant void flow* region.

The bubbles generated at the wall immediately following ONB cannot grow due to the condensation occurring at the bubble surface exposed to the subcooled liquid flow. A thin layer of bubbles is formed on the wall. As the bulk liquid temperature increases in the flow direction, the layer becomes populated with more bubbles, whose sizes also increase with decreasing subcooling. At some location, identified as the point of *net vapor generation* NVG (also called OSV), the bubbles eventually detach from the wall and flow toward the liquid core. Some bubbles condense along the way. Heat transfer following NVG is in the two-phase region.

The vapor present in the subcooled flow following NVG is at the saturation temperature. This gives rise to a thermodynamic nonequilibrium condition with the liquid temperature falling below the equilibrium subcooled liquid temperature dictated by the local enthalpy. As heat addition continues downstream, the saturation condition ($x = 0$) under thermodynamic equilibrium is reached. Flow beyond the $x = 0$ location falls under the saturated flow boiling region.

The state of the subcooled liquid can be defined in terms of an equilibrium “quality” based on the liquid enthalpy relative to the saturation state:

$$x = (h_L - h_{L,\text{Sat}})/h_{fg} = -c_p \Delta T_{\text{Sub}}/h_{fg} \quad (3.34)$$

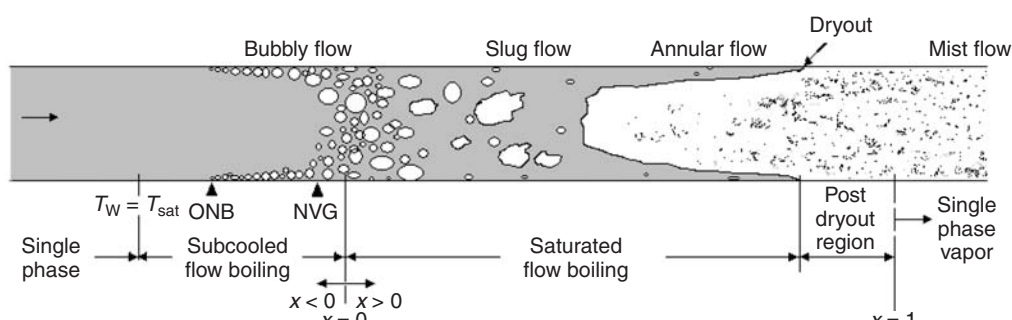


FIGURE 3.9 Flow boiling in a circular tube.

where $\Delta T_{\text{Sub}} (=T_{\text{Sat}} - T_{\text{L}})$ is the liquid subcooling. Equation (3.34) results in a negative quality in the subcooled region. In the single-phase region of the subcooled flow before any boiling is initiated, the heat flux is expressed in terms of the single-phase liquid heat transfer coefficient and the wall-to-liquid temperature difference:

$$\dot{q} = h_{\text{L}}(T_{\text{W}} - T_{\text{L}}) = h_{\text{L}}(\Delta T_{\text{Sat}} + \Delta T_{\text{Sub}}) \quad (3.35)$$

The single-phase heat transfer coefficient h_{L} is given by the appropriate single-phase heat transfer coefficient in the laminar or turbulent region.

Heat transfer to a liquid flowing inside a tube is by the single-phase mode as long as the liquid and wall are both below the saturation temperature of the liquid at the local pressure. As the wall temperature exceeds the local saturation temperature, boiling can occur depending on the tube surface characteristics and the operating conditions. The bulk liquid may still be in the subcooled region. Boiling under these conditions is called subcooled flow boiling. Saturated flow boiling covers the region when the wall temperature exceeds the local saturation temperature of the liquid and the equilibrium thermodynamic quality (mass fraction of vapor) is between 0 and 1.

3.1.2.2 Onset of Nucleate Boiling

The condition for the ONB under flow conditions is obtained as an extension to the pool boiling analysis presented in Section 3.1.1.2. The liquid temperature profile near the heater surface is obtained from the single-phase heat transfer coefficient prior to nucleation. In the absence of hysteresis effects, the nucleation criterion suggested by Hsu and Graham (1961) has been confirmed by many later investigators. Bergles and Rohsenow (1964) described the nucleation criterion graphically in terms of the tangency condition and presented an empirical correlation for the ONB condition. Hsu (1962) and Sato and Matsumura (1964) presented equations for $\Delta T_{\text{Sat,ONB}}$ and q_{ONB} :

$$\Delta T_{\text{Sat,ONB}} = \frac{4\sigma T_{\text{Sat}} v_{\text{fg}} h_{\text{L}}}{k_{\text{L}} h_{\text{fg}}} \left[1 + \sqrt{1 + \frac{k_{\text{L}} h_{\text{fg}} \Delta T_{\text{sub}}}{2\sigma T_{\text{Sat}} v_{\text{fg}} h_{\text{L}}}} \right] \quad (3.36)$$

and

$$q''_{\text{ONB}} = [k_{\text{L}} h_{\text{fg}} / (8\sigma v_{\text{fg}} T_{\text{Sat}})] [\Delta T_{\text{Sat,ONB}}]^2 \quad (3.37)$$

The range of active cavity radii were also presented by Hsu, Sato, and Matsumura. A nondimensionalized form of these equations was presented by Kandlikar and Spiesman (1997) using the following parameters:

$$R_c^* = \frac{R_c}{\delta_t} \quad (3.38)$$

$$\Delta T_{\text{Sat}}^* = \frac{\Delta T_{\text{Sat}} h_{\text{fg}} \delta_t}{8\sigma T_{\text{Sat}} v_{\text{fg}}} \quad (3.39)$$

$$\Delta T_{\text{Sub}}^* = \frac{\Delta T_{\text{Sub}} h_{\text{fg}} \delta_t}{8\sigma T_{\text{Sat}} v_{\text{fg}}} \quad (3.40)$$

where the single-phase thermal boundary layer thickness in the liquid is given by $\delta_t = k_{\text{L}}/h_{\text{L}}$.

The range of the active cavity radii in nondimensional form is then given by the following equation:

$$R_{\text{max}}^* R_{\text{min}}^* = \frac{1}{2} \left[\frac{\Delta T_{\text{Sat}}^*}{\Delta T_{\text{Sat}}^* + \Delta T_{\text{Sub}}^*} \pm \sqrt{\left(\frac{\Delta T_{\text{Sat}}^*}{\Delta T_{\text{Sat}}^* + \Delta T_{\text{Sub}}^*} \right)^2 - \frac{1}{(\Delta T_{\text{Sat}}^* + \Delta T_{\text{Sub}}^*)}} \right] \quad (3.41)$$

The properties in Eqs. (3.36)–(3.41) are evaluated at the saturation temperature and h_{L} is determined from an appropriate single-phase correlation incorporating a wall temperature correction if necessary. Additional factors such as dissolved gases and cavity geometry further affect the nucleation characteristics.

3.1.2.3 Flow Patterns

The distribution of liquid and vapor phases in the tube plays an important role in the pressure drop and heat transfer during flow boiling. Figure 3.9 shows the flow patterns observed in a horizontal tube. The major flow patterns are: (1) bubbly flow – discrete bubbles – exist in the flow field with continuous liquid phase, generally observed at low vapor qualities; (2) slug or plug flow – as vapor quality increases, bubbles start to coalesce and fill the entire tube with liquid and vapor flowing alternately in the channel; (3) annular flow — at higher vapor qualities, the vapor forms a continuous core with liquid flowing around the periphery as a smooth or wavy film; and (4) mist flow — it consists of liquid droplets flowing in a continuous vapor phase, this flow pattern occurs beyond the “Dryout” location (see Figure 3.9). There are additional flow patterns, such as a stratified flow pattern, that occurs at low flow rates. The transitional flow patterns, such as bubbly–slug and annular–mist also appear as the flow patterns change with increasing quality along the evaporator length. All flow patterns, except for the mist flow and single-phase vapor, can be classified under wetted a wall condition, which is desirable from a heat transfer perspective. Heat transfer and pressure drop are closely related to the existing flow patterns.

The flow patterns described in Figure 3.9 refer to flow boiling in a horizontal tube. Figure 3.10 shows the flow patterns in a vertical tube. The major differences are the existence of a churn flow pattern, in which the liquid and vapor flow as an agitated mixture, the distortion of the vapor plugs due to buoyancy forces, and the absence of a stratified flow. Vertical upflow and downflow have some differences, mainly at low flow velocities.

Numerous attempts have been made in the literature to identify flow patterns existing under a given set of operating conditions — liquid- and vapor-phase properties, tube diameter, and mass flux. Flow pattern maps developed for adiabatic flows are generally used for flow boiling, although such an approach introduces significant errors at higher heat fluxes.

The influence of boiling on flow patterns becomes important at higher heat fluxes as the rapidly evaporating liquid–vapor interface of a growing bubble or a vapor plug introduces additional forces. In the studies conducted on the conventional channels (>3 mm hydraulic diameter), the effect of heat flux has been ignored and researchers have used the adiabatic flow pattern maps for flow boiling as well. As the heat flux increases, the rapid expansion at a nucleating bubble causes major changes in the flow patterns, particularly for small hydraulic diameter channels ($D_h < 3$ mm). This aspect has been extensively discussed by Kandlikar (2003) for flow boiling in microchannels.

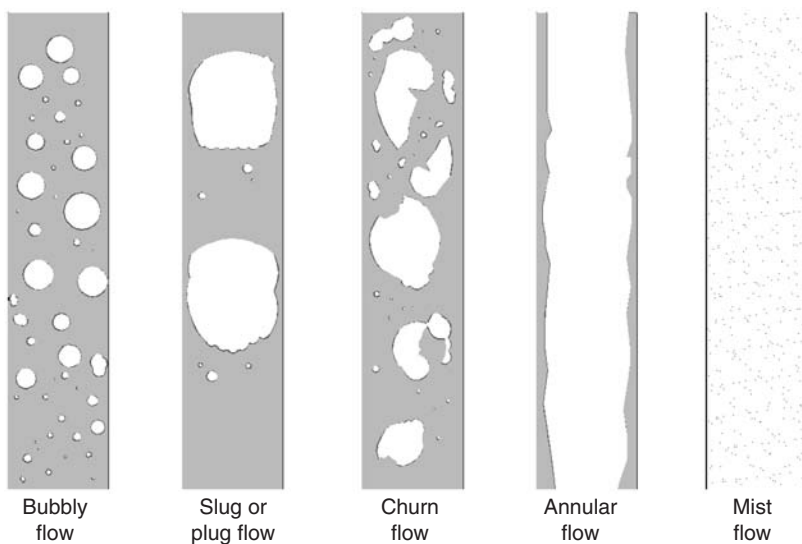


FIGURE 3.10 Flow patterns during flow boiling in a vertical tube.

3.1.2.4 Subcooled Flow Boiling Heat Transfer

Kandlikar (1998a) proposed that the nucleate boiling term in the nucleate boiling region of the saturated flow boiling correlation by Kandlikar (1990) (see Eq. [3.56]) should be able to represent the fully developed boiling in a subcooled flow since the convective contribution is negligible. One of the features of this correlation, as reported by Kandlikar (1991a), is its ability to predict the trends in h vs. x in the low-quality region, explaining the reasons for increasing or decreasing h for different cases. The heat transfer coefficient h^* in the FDB region is thus given by the following equation derived from the nucleate boiling dominant region of the Kandlikar correlation.

$$h^* = 1058.0 Bo^{0.7} F_{\text{Fl}} h_{\text{LO}} \quad (3.42)$$

Note that h^* is based on the wall superheat with $q'' = h^* \Delta T_{\text{Sat}}$. The boiling number is defined as $Bo = q''/(G h_{\text{fg}})$, with G (kg/m² sec) being the total mass flux, F_{fl} the fluid–surface parameter that accounts for the different nucleation characteristics of different surface–fluid combinations, and h_{LO} the single-phase heat transfer coefficient for all flow in the liquid phase at the saturation temperature obtained from appropriate equations for the laminar flow — $Nu = \text{constant}$ for fully developed laminar flow; or for the turbulent flow — Gnielinski (1976) and Petukhov and Popov (1963) correlations along with the following property correction factor recommended by Petukhov (1970):

$$Nu_{\text{LO}} = Nu_{\text{LO, cp}} (\mu_b / \mu_w)^{0.11} \quad (3.43)$$

where $Nu_{\text{LO, cp}}$ is the Nusselt number with constant properties obtained from the following equations, and the subscripts b and w refer to the properties at bulk and wall temperatures, respectively.

Petukhov and Popov (1963), for $0.5 \leq Pr \leq 2000$ and $10^4 \leq Re_{\text{LO}} \leq 5 \times 10^6$, obtained

$$Nu_{\text{LO, cp}} = \frac{Re_{\text{LO}} Pr_L (f/2)}{[1.07 + 12.7(Pr_L^{2/3} - 1)(f/2)^{0.5}]} \quad (3.44)$$

and Gnielinski (1976), for $0.5 \leq Pr \leq 2000$ and $2300 \leq Re_{\text{LO}} < 10^4$, obtained

$$Nu_{\text{LO, cp}} = \frac{(Re_{\text{LO}} - 1000)(f/2)Pr_L}{[1 + 12.7(Pr^{2/3} - 1)(f/2)^{0.5}]} \quad (3.45)$$

where f is the friction factor given by the following equation:

$$f = [1.58 \ln(Re_{\text{LO}}) - 3.28]^{-2} \quad (3.46)$$

The location of where the fully developed boiling begins, corresponding to $q''_{\text{FDB,i}}$ is obtained by first locating the heat flux q''_{int} at the intersection of the extended single-phase line and the fully developed boiling curve given by Eq. (3.42):

$$1058F_{\text{Fl}}(G h_{\text{fg}})^{-0.7} q''_{\text{int}} - q''_{\text{int}}^{0.3} - 1058h_{\text{LO}}F_{\text{Fl}}(G h_{\text{fg}})^{-0.7} \Delta T_{\text{Sub}} = 0 \quad (3.47)$$

A model proposed by Bowring (1962) is then used to obtain the location where FDB begins:

$$q''_{\text{FDB,i}} = 1.4q''_{\text{int}} \quad (3.48)$$

A comparison of the predicted heat flux in the fully developed boiling region using Eq. (3.42) with experimental data of Bergles and Rohsenow (1964) is shown in Figure 3.11. The other three prediction methods by Shah (1977), Thom et al. (1965), and Mikic and Rohsenow (1969) are also shown in Figure 3.11. It is seen that the present model is able to predict the trend as well as actual values in the FDB region accurately.

Heat transfer in the partial boiling region, from $x = 0$ to the beginning of the fully developed region, is obtained by interpolation between the two end locations. Further details of the interpolation method are described by Kandlikar (1998a, 1999).

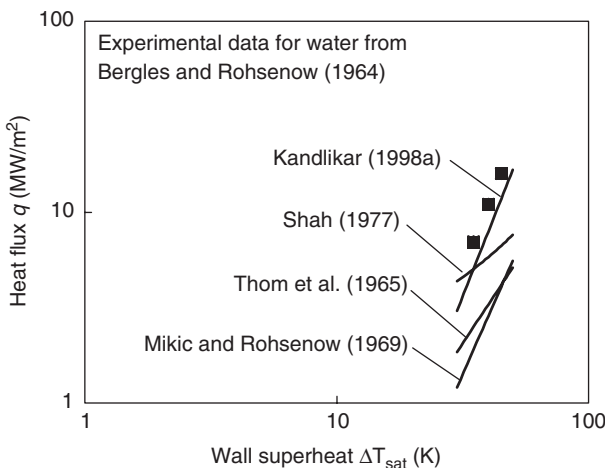


FIGURE 3.11 Comparison of the predictions from Eq. (3.42) in the fully developed boiling with experimental data of Bergles and Rohsenow (1964). (From Kandlikar, S.G., *J. Heat Transfer*, 120, 395–401, 1998a. Reproduced with permission from ASME.)

The *partial boiling* region is identified as the region between the onset of nucleate boiling ONB and the onset of fully developed boiling FDB. Heat transfer in this region is calculated by a procedure outlined by Kandlikar (1998a) as follows.

The heat flux q''_{FDB} at FDB is obtained from Eq. (3.48), and q''_{ONB} at ONB is obtained from Eq. (3.37). For the heat flux q''_{PB} in the partial boiling region, the following equation is employed:

$$q''_{\text{PB}} = a + b(T_w - T_{\text{Sat}})^m \quad (3.49)$$

The constants a and b are obtained from the known heat fluxes at FDB and ONB as follows:

$$b = \frac{q''_{\text{FDB}} - q''_{\text{ONB}}}{(\Delta T_{\text{Sat,FDB}})^m - (\Delta T_{\text{Sat,ONB}})^m} \quad (3.50)$$

and

$$a = q''_{\text{ONB}} - b(\Delta T_{\text{Sat,ONB}})^m \quad (3.51)$$

The exponent m is allowed to vary linearly with heat flux as follows:

$$m = n + pq''_{\text{PB}} \quad (3.52)$$

where the constants n and p are obtained by matching the slopes of $m = 1$ at ONB to $m = 1/0.3$ at FDB:

$$p = (1/0.3 - 1)/(q''_{\text{FDB}} - q''_{\text{ONB}}) \quad (3.53)$$

and

$$n = 1 - pq''_{\text{ONB}} \quad (3.54)$$

The above procedure assures smooth transitions from the single-phase region to the partial boiling region, and then to the FDB region. The gradual increase in the exponent m also reflects the fact that more nucleation sites are activated as the wall superheat increases.

A comparison of the present model with the experimental data of McAdams et al. (1949) is shown in Figure 3.12. Equations (3.47)–(3.54) are used in the predictive model. It is seen from this figure that the agreement is quite good in the partial boiling region.

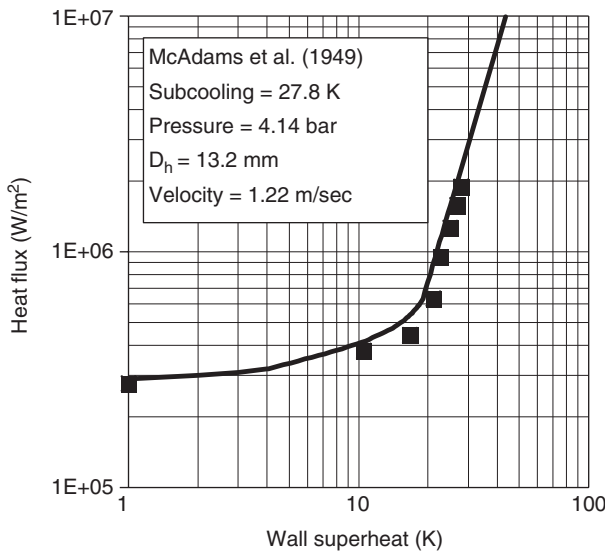


FIGURE 3.12 Comparison of predictions from Eqs. (3.47) – (3.54) in the partial boiling region with experimental data of McAdams et al. (1949). (From Kandlikar, S.G., *J. Heat Transfer*, 120, 395–401, 1998a. Reproduced with permission from ASME.)

3.1.2.5 Saturated Flow Boiling Heat Transfer

As liquid flows inside a heated tube surface, nucleate boiling initiates the process of vapor generation during flow boiling. As the bubbles grow and depart, the vapor quality in the flow increases and two-phase flow ensues. The higher specific volume of the vapor causes the flow velocity to increase. Heat transfer in this mode is thus a combination of the nucleation phenomena and enhanced convection, each being influenced by the other mode. The presence of nucleate boiling and convective boiling modes in flow boiling has long been recognized. Heat transfer in saturated flow boiling is thus a combination of the convective heat transfer from the wall to liquid and subsequent film evaporation at the liquid–vapor interface, and nucleate boiling at the wall.

There are a large number of correlations available in the literature on flow boiling of saturated liquids. The Chen (1966) correlation was developed on an additive model with convective enhancement and nucleate boiling suppression due to two-phase flow. It works reasonably well with low-pressure water data, but yields significantly higher errors with high-pressure water data and refrigerants. Shah (1982) proposed a correlation in a chart form that worked well with many fluids. Gungor and Winterton (1987) combined the Chen model and the Shah model. Other recent correlations, such as those used by Liu and Winterton (1991) and Steiner and Taborek (1992), employ an asymptotic model in which $h_{\text{TP}}^n = h_{\text{conv}}^n + h_{\text{nuc}}^n$ with $n = 2$ and 3 , respectively. The h_{conv} and h_{nuc} are obtained from a combination of earlier models published in the literature. These models work well in some cases; however, because of their highly empirical nature, they do not correctly represent the trends of h_{TP} vs. x . Also, because of their exponentially averaged form, it becomes difficult to identify the role of different mechanisms in studying the parametric effects.

The correlation by Kandlikar (1990, 1991b) is developed from a large data bank consisting of over 10,000 data points and different fluids, including water, refrigerants, and cryogens. It is also able to accurately predict the parametric trends. In particular, it has been shown to predict the variation in h_{TP} well, yielding an increasing trend in h_{TP} with increasing x for fluids with low boiling number ($Bo = q''/(Gh_{fg})$) and high liquid-to-vapor density ratio (ρ_L/ρ_G), representative of the convective-boiling-dominant (CBD) region, for example, with water at low pressure and low Bo . In contrast, a decreasing trend is predicted for high Bo and low-density ratio, representative of the nucleate-boiling-dominant (NBD) region, for example, with some refrigerants with low density ratios and with high heat fluxes. The flow boiling correlation

has been successfully extended to subcooled flow boiling (Kandlikar, 1998a), binary mixtures (Kandlikar, 1998c), and flow boiling in microchannels and minichannels (Kandlikar and Steinke, 2003; Kandlikar and Balasubramanian, 2003). In addition, it accounts for the nucleation characteristics of a given surface through a fluid–surface parameter F_{Fl} . The Kandlikar (1990, 1991b) correlation is given by

$$h_{\text{TP}} = \text{larger of } \begin{cases} h_{\text{TP}}|_{\text{CBD}} \\ h_{\text{TP}}|_{\text{NBD}} \end{cases} \quad (3.55)$$

where h_{TP} in the respective regions are given by the following equations:

$$h_{\text{TP, NBD}} = 0.6683 Co^{-0.2}(1-x)^{0.8} f_2(Fr_{\text{LO}}) h_{\text{LO}} + 1058.0 Bo^{0.7}(1-x)^{0.8} F_{\text{Fl}} h_{\text{LO}} \quad (3.56)$$

and

$$h_{\text{TP, CBD}} = 1.136 Co^{-0.9}(1-x)^{0.8} f_2(Fr_{\text{LO}}) h_{\text{LO}} + 667.2 Bo^{0.7}(1-x)^{0.8} F_{\text{Fl}} h_{\text{LO}} \quad (3.57)$$

where $Co = (\rho_G / \rho_L)^{0.5}((1-x)/x)^{0.8}$ is the convection number, $Bo = q''/(Gh_{fg})$ is the boiling number and $Fr_{\text{LO}} = G^2/(\rho_L g D)$ is the Froude number with all flow as liquid. The Froude number multiplier $f_2(Fr_{\text{LO}})$ is 1 for vertical tubes and for horizontal tubes with $Fr_{\text{LO}} \geq 0.4$.

For $Fr_{\text{LO}} \leq 0.4$, $f_2(Fr_{\text{LO}})$ is given by the following equation:

$$f_2(Fr_{\text{LO}}) = (25 Fr_{\text{LO}})^{0.3} \quad (3.58)$$

The single phase all liquid heat transfer coefficient h_{LO} is obtained from the Gnielinski (1976) correlation in the range $0.5 \leq Pr_L \leq 2000$ and $2300 < Re_{\text{LO}} \leq 10^4$:

$$h_{\text{LO}} = \frac{(Re_{\text{LO}} - 1000)Pr_L(f/2)(k_L/D)}{1 + 12.7(Pr_L^{2/3} - 1)(f/2)^{0.5}} \quad (3.59)$$

The Petukhov and Popov (1963) correlation is employed for $0.5 \leq Pr_L \leq 2000$ and $10^4 < Re_{\text{LO}} \leq 5 \times 10^6$:

$$h_{\text{LO}} = \frac{Re_{\text{LO}} Pr_L(f/2)(k_L/D)}{1.07 + 12.7(Pr_L^{2/3} - 1)(f/2)^{0.5}} \quad (3.60)$$

The friction factor f is given by the following equation:

$$f = [1.58 \ln(Re_{\text{LO}}) - 3.28]^{-2} \quad (3.61)$$

F_{Fl} is a fluid–surface parameter that depends on the fluid and the heater surface characteristics. [Table 3.3](#) lists the F_{Fl} values for several fluids in copper tubes. These values should be considered as representative for commercial tubing. For stainless-steel tubes, F_{Fl} should be taken as 1.0 with all fluids.

Introduction of F_{Fl} in the nucleate boiling term is an important aspect of the Kandlikar correlation. It has been recognized that the nucleation characteristics and associated heat transfer depend on contact angle, surface tension, and available cavity sizes and their distribution on the heater surface. Gaertner (1965) noted that

...analytical treatments of nucleate boiling that do not consider the nature of the surface cannot accurately predict heat transfer relationships...

The flow boiling model is thus able to account for the different nucleation characteristics of different fluid–surface combinations through the incorporation of F_{Fl} . However, this constant needs to be obtained from the experimental data. [Table 3.2](#) provides the values of F_{Fl} obtained from Kandlikar (1990, 1991b, 1999) and Melin (1996) for different fluids.

[Figure 3.13](#) shows a comparison of the Kandlikar (1990) correlation with the experimental data of Schrock and Grossman (1962). The correlation is able to predict correctly the increasing trend in h_{TP} with x for the low-pressure data (large values of ρ_L/ρ_G), and a decreasing trend for the high-pressure data (low values of ρ_L/ρ_G).

Table 3.3 F_{Fl} Values in the Kandlikar Correlation

Fluid	F_{Fl}
Water	1.00
R-11	1.30
R-12	1.50
R-13B1	1.31
R-22	2.20
R-32 ^a	1.88
R-113	1.30
R-114	1.24
R-125 ^a	2.27
R-134a	1.63
R-142b ^a	1.74
R-143a ^a	2.39
R-152a	1.10
R-32/R-132	3.30
60–40% (by wt)	
Butane ^a	1.50
Kerosene	0.488
Propane ^a	2.15

Note: For stainless-steel tubes, use $F_{\text{Fl}} = 1.0$ for all fluids.

^aValues obtained by Melin (1996).

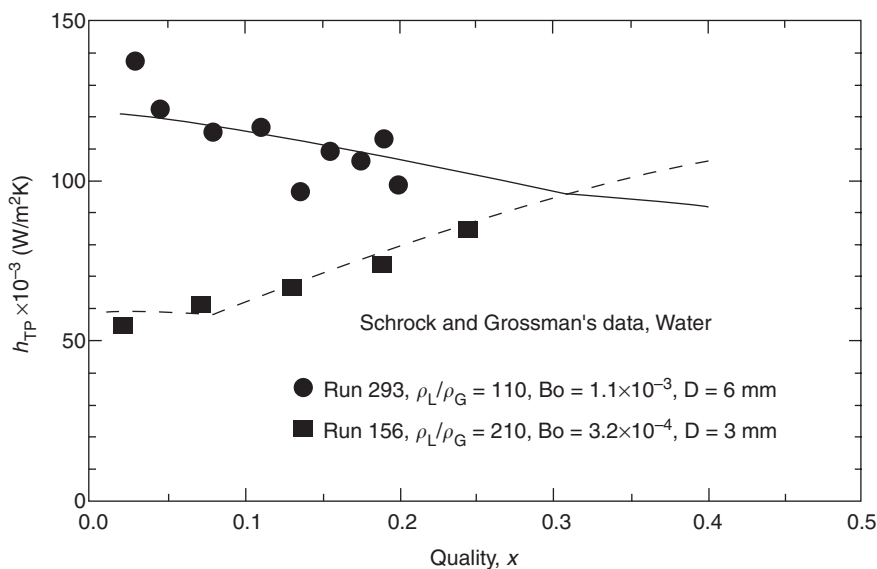


FIGURE 3.13 Comparison of Schrock and Grossman's experimental data with the Kandlikar (1990) correlation. (From Kandlikar, S.G., in *Handbook of Phase Change, Boiling and Condensation*, Kandlikar, S.G., Dhir, V.K., and Celata, G.P., Eds., Taylor & Francis, Philadelphia, PA, 1999. Reprinted with permission from Taylor & Francis.)

The Kandlikar correlation is recommended in the wetted wall region below a quality of about 0.8. At higher qualities, local dryout may occur with a significant reduction in the heat transfer coefficient.

The Kandlikar (1990, 1991b) correlation was extended to microchannels ($10 \mu\text{m} < D_h \leq 200 \mu\text{m}$) and minichannels ($200 \mu\text{m} < D_h \leq 3 \text{ mm}$) by Kandlikar and Steinke (2003) and Kandlikar and Balasubramanian (2003). As the all-liquid flow Reynolds number enters the laminar region, the use of $Nu_{\text{LO}} = \text{constant}$ is recommended for calculating h_{LO} instead of the single-phase turbulent flow correlations. Furthermore, for microchannels, it is found that h_{TP} falls entirely in the NBD region and is given

by Eq. (3.56) without the Froude number correction (use $f_2(Fr_{LO}) = 1$). The flow boiling heat transfer mechanisms in these geometries are discussed in detail by Kandlikar (2003).

3.1.2.6 Flow Boiling Map

The main parameters governing flow boiling heat transfer can be represented in terms of the following four nondimensional groups:

1. Nondimensionalized heat transfer coefficient, h_{TP} / h_{LO}
2. Modified boiling number, $Bo^* = Bo(F_{fl})^{1/0.7} = q''(F_{fl})^{1/0.7}/(Gh_{fg})$
3. Density ratio, ρ_L/ρ_G
4. Vapor quality, x

The parametric trends of h_{TP} with various operating parameters was represented by Kandlikar (1991a) in terms of a flow boiling map, as shown in Figure 3.14. Density ratio is seen as an important factor governing the role of the convective contribution, which gives rise to an increasing trend in an h_{TP}/h_{LO} vs. x plot in the CBD region. The magnitude of Bo^* governs the nucleate boiling contribution, which essentially displays a decreasing trend in an h_{TP}/h_{LO} vs. x plot in the NBD region. These parametric trends have been confirmed for a number of fluids, including water and refrigerants.

3.1.2.7 Flow Boiling of Binary Mixtures

Flow boiling of mixtures is encountered in many practical applications, including chemical, petrochemical, process, and refrigeration industries. The difference in boiling points of the pure components in a mixture causes preferential vaporization of the more volatile component across liquid-vapor interfaces at the nucleating bubbles, near an annular film or around a vapor slug. Depletion of the more volatile component raises the local saturation temperature at the liquid-vapor interface. This also results in the diffusion of the more volatile component in the liquid phase toward the interface. The net result is the lowering of the heat transfer coefficient for the mixture below the average value obtained from the linear mass- or mole-fraction-averaged interpolation between the pure component values.

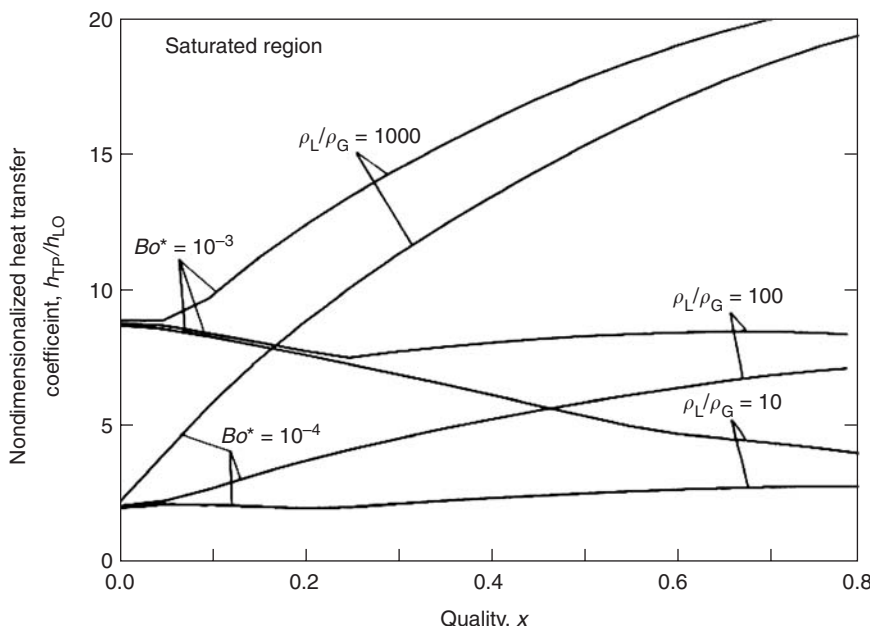


FIGURE 3.14 Flow boiling map for subcooled and saturated flow boiling. (From Kandlikar, S.G., *Trans. ASME, J. Heat Transfer*, 113, 190–200, 1991a. Reproduced with permission from ASME.)

A number of researchers have provided useful correlations to predict the heat transfer coefficients in a binary (two components in both liquid and vapor phases) system. Among the more successful ones are Calus et al. (1973), Bennett and Chen (1980), Jung (1988), and Kandlikar (1998c). One of the main difficulties encountered in modeling binary flow boiling is the uncertainty in predicting the interfacial concentration at the nucleating bubble interface. Kandlikar (1998b) used a control volume approach to obtain the interfacial concentration in pool boiling, and later extended it to flow boiling.

In the Kandlikar (1998c) model, a volatility parameter V_1 is defined as

$$V_1 = \left(\frac{c_{p,L}}{h_{fg}} \right) \left(\frac{\alpha}{D_{12}} \right)^{0.5} \left| \frac{dT}{dx_1} (y_1 - x_1) \right| \quad (3.62)$$

where α is the thermal diffusivity of the liquid, D_{12} the mass diffusivity of component 1 in a mixture of components 1 and 2, and x_1 and y_1 are the liquid and vapor mass fractions of the more volatile component 1.

Three regions in binary flow boiling are identified based on the value of V_1

Region I: Near-azeotropic region, $V_1 < 0.03$:

$$h_{TP} = \text{larger of } \begin{cases} h_{TP}|_{\text{CBD}} \\ h_{TP}|_{\text{NBD}} \end{cases} \quad (3.63)$$

Use pure component correlations, Eqs. (3.56) and (3.57), with mixture properties.

Region II: Moderate diffusion-induced suppression region, $0.03 < V_1 < 0.2$, and $Bo > 1E-4$:

$$h_{TP} = h_{TP}|_{\text{CBD}} \quad (3.64)$$

The heat transfer is entirely in the CBD region. Use the pure component correlation in the NBD region, Eq. (3.57), with mixture properties.

Region III: Severe diffusion-induced suppression region; (a) for $0.03 < V_1 < 0.2$ and $Bo < 1E-4$, and (b) $V_1 > 0.2$,

$$h_{TP, \text{CBD}} = 1.136 Co^{-0.9} (1-x)^{0.8} f_2(Fr_{LO}) h_{LO} + 667.2 Bo^{0.7} (1-x)^{0.8} F_D h_{LO} F_D \quad (3.65)$$

A diffusion-induced suppression factor F_D is introduced in the nucleate boiling term to reflect the reduction in heat transfer coefficient due to the mass diffusion resistance present at the interface. F_D is given by the following equation:

$$F_D = 0.678 \left[1 + \left(\frac{c_{p,L}}{h_{fg}} \right) \left(\frac{\alpha}{D_{12}} \right)^{0.5} \left| \frac{dT}{dx_1} (y_1 - x_1) \right| \right]^{-1} \quad (3.66)$$

The equilibrium phase mass concentrations are calculated at the total system pressure, and dT/dx_1 corresponds to the slope of the bubble point curve at a liquid-phase concentration of x_1 . The diffusivity D_{12} is calculated from the following equation:

$$D_{12} = (D_{12}^0)^{\tilde{x}_1} (D_{21}^0)^{\tilde{x}_2} \quad (3.67)$$

where \tilde{x}_1 and \tilde{x}_2 are respective molar concentrations of components 1 and 2, and D_{12}^0 and D_{21}^0 are individual component diffusivities at very low concentrations given by the following Wilke–Chang correlation:

$$D_{12}^0 = 1.1782 \times 10^{-16} \frac{(\phi M_2)^{1/2} T}{\mu_{L,2} V_{m,1}} \quad (3.68)$$

where ϕ is the association factor for the solvent (2.26 for water, 1.9 for methanol, 1.5 for ethanol, 1.9 for ethylene glycol, and 1.0 for unassociated solvents, including benzene, methane, and refrigerants), M the molecular weight, μ_L the liquid viscosity, V_m the molar volume in $\text{m}^3/\text{kg mol}$, and T the temperature in K.

Table 3.4 shows the mean deviations between the predicated values using the Kandlikar (1998c) correlation described above and the experimental data of Jung et al. (1988), Hihara et al. (1989), Takamatsu

TABLE 3.4 Comparison of the Binary Flow Boiling Correlation of Kandlikar (1998c) with Experimental Data from the Literature

Data Source	Binary System	$Bo \times 10E-5$	Co	V_1	Mean Absolute Deviation (%)
Jung et al. (1988)	R-12/R-152a	6.1–6.3	0.52–1.8	0.025–0.044	8.3
	R-12/R-152a	8.8–71	0.01–1.45	0.013–0.022	10.4
	R-22/R-114	7.1–77	0.04–1.39	0.1–0.72	13.0
	R-500	7.5–77	0.01–1.83	0.0006–0.002	11.4
Hihara et al. (1989)	R-12/R-22	47–61	0.01–1.91	0.015–0.064	13.3
	R-22/R-114	37–60	0.023–1.64	0.07–0.67	9.0
Takamatsu et al. (1993)	R-22/R-114	19–76	0.018–3.2	0.28–0.54	9.2
Celata et al. (1993)	R-12/R-114	9.4–88	0.52–1.83	0.06–0.15	8.9
Murata and Hashizume (1993)	R-134a/R-123	20–185	0.004–0.05	0.28–0.34	12.1

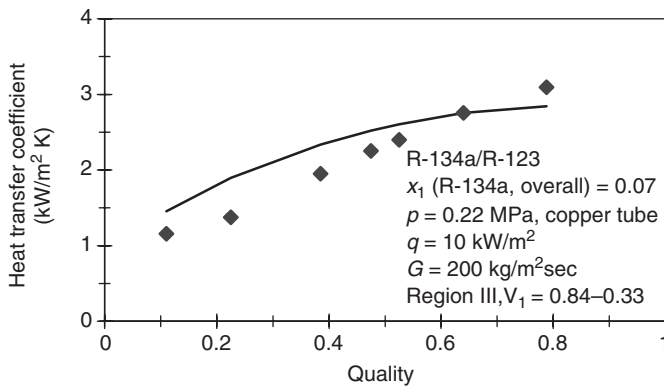


FIGURE 3.15 Comparison of the Kandlikar (1998c) correlation with R-134a/R-123 flow boiling data of Murata and Hashizume (1993) in the severe diffusion-induced suppression region (Region III). (From Kandlikar, S.G., *J. Heat Transfer*, 120, 388–394, 1998c. Reproduced with permission from ASME.)

et al. (1993), Celata et al. (1993), and Murata and Hashizume (1993). The ranges of parameters are also included in Table 3.4. It is seen that the agreement is quite good in all three regions. Figure 3.15 shows a comparison of a data set obtained by Murata and Hashizume (1993) for R-134a/R-123 mixture in the severe suppressed region, i.e., Region III.

Heat transfer coefficients in multicomponent systems are even more difficult to predict. There is no reliable general methodology available to make any recommendation for mixtures of three or more components. It is suggested that the most volatile component be taken as component 1 and the rest of the mixture treated as component 2, and the binary flow boiling correlation scheme applied as a first approximation.

3.1.2.8 Critical Heat Flux in Flow Boiling

The heat transfer coefficient in flow boiling dramatically reduces as the liquid ceases to be in contact with the walls of the flow channel. CHF condition represents the upper limit and subsequent sudden termination of (in heat flux controlled systems) or considerable degradation (in temperature-controlled systems) in nucleate boiling heat transfer (Kandlikar, 2001b). *Dryout* condition represents the upper limit of the convective boiling heat transfer. It follows the gradual depletion of liquid due to evaporation and entrainment of the liquid film. Knowledge of the conditions leading to CHF and the prediction of CHF for a given geometry under a given set of operating conditions are extremely important in the safe operation of flow boiling equipment, such as nuclear reactors, boilers, refrigeration and cryogenic evaporators, and cooling of high heat flux components and devices.

The risks associated with the catastrophic failures following the CHF condition have attracted significant research efforts worldwide for over 40 years. Earlier, Lang (1888) recognized the existence of severe heat transfer degradation through his experiments with high-pressure water. Drew and Mueller (1937) provide an excellent summary of historical developments in this area. Extensive experimental and numerical studies have been conducted since the 1960s on the CHF with water in nuclear reactors under safe operating as well as under accident conditions. A better CHF predictive ability allows the operation of a nuclear reactor with reduced safety margins, thereby increasing the output capacity of the nuclear power plant. Understanding the mechanisms leading to CHF permit the development of techniques or operating procedures to increase the CHF for a given system configuration.

Critical Heat Flux in subcooled and saturated flow boiling has been studied under a number of different conditions: (1) uniform heat flux along a channel length; (2) uniform heat flux along a tube, with a short length of higher heat flux; (3) circumferentially uniform, but axially nonuniform heat flux; and (4) with water and some other fluids.

A brief overview of CHF under subcooled and saturated flow boiling conditions in uniformly heated circular tubes is presented in this section. For more extensive coverage, the reader is referred to the detailed treatise on this topic, see e.g., Tong (1965), Boyd (1983a, 1983b), Tong (1988), Collier and Thome (1994), Hewitt (1998), Celata and Mariani (1999), Kandlikar et al. (1999), and Tong and Tang (1997).

3.1.2.8.1 CHF in Subcooled Flow Boiling

The CHF in subcooled flow boiling is reached in one of the following three ways (Tong and Hewitt, 1972):

1. A dry patch forms on the heater surface after a bubble has departed. The local temperature in some cases rises to a point where the water fails to rewet the surface, leading to the CHF condition.
2. A thin layer of bubbles is formed on the wall at moderate heat and mass fluxes. The neighboring bubbles then cluster together to form a vapor layer between the bulk liquid and restrict the access of liquid to the heater wall.
3. A slug flow is observed under certain conditions at low mass fluxes. The liquid film surrounding the vapor bubble evaporates and dries out. If the vapor bubble is sufficiently long, the heater wall becomes heated during the passage of the bubble and leads to the CHF condition.

Celata and Mariani (1999) summarize the previous models in the following five categories: (1) boundary layer ejection model; (2) critical enthalpy in the bubble layer model; (3) liquid flow blockage model; (4) vapor removal limit and near-wall bubble crowding model; and (5) liquid sublayer dryout model. A brief description of each of the mechanisms is given below (Kandlikar, 2001b).

1. *Boundary layer ejection model:* This model was originally proposed by Kutateladze and Leont'ev (1966). The boiling mechanism is compared with the injection of a gas stream into the liquid flow through a permeable plate. The ejection of bubbles into the mainstream is postulated to be the cause of the boundary layer separation at the heater surface. However, the photographic study conducted by Mattson et al. (1973) does not show any abrupt changes or high-velocity vapor ejection in the macroscopic structure of the flow near the CHF location.
2. *Critical enthalpy in the bubble layer model:* This model was proposed by Tong et al. (1966). They assume that a layer of small bubbles flowing adjacent to the heater surface traps the liquid between the bubble layer and the heated surface. This bubble layer separates the trapped superheated liquid layer from the mainstream. They postulated that the CHF condition is reached when this superheated liquid layer attains a certain limiting enthalpy. This model does not provide a clear explanation of the CHF phenomenon other than stating the existence of a critical liquid enthalpy in the superheated liquid layer.
3. *Liquid flow blockage model:* Bergelson (1980) proposed this model based on the assumption that the flow of liquid toward the heated surface is blocked by the outflow of vapor from the heater surface. This behavior may be feasible under very low mass flux conditions, where the liquid and vapor flow structure is similar to that in the case of pool boiling. However, the vapor flow away from the wall is not seen to be a limiting factor in subcooled flow boiling. Owing to inadequate evidence supporting this mechanism, this model is not being pursued by other researchers.

4. *Vapor removal limit and near-wall bubble crowding model:* This model is based on the limit of turbulent interchange between the bubbly layer and the bulk of the liquid, and the crowding of bubbles preventing liquid access to the heated wall (Hebel et al., 1981).

Weisman and Pei (1983) consider the existence of a bubbly layer adjacent to the wall at subcooled or low-quality conditions. It is postulated that the CHF condition occurs when the volume fraction of vapor in the bubbly layer just exceeds the critical volume fraction at which an array of ellipsoidal bubbles can be maintained without significant contact between the bubbles. Weisman and Pei used the homogeneous flow model in the bubbly layer. The resulting model has three adjustable empirical constants that are evaluated from the experimental data. This model includes the two-phase flow considerations that are readily extendable to the saturated flow conditions as well.

5. *Liquid sublayer dryout model:* Katto and Yokoya (1968) proposed a preliminary model describing the macrolayer dryout as the mechanism leading to CHF in pool boiling. Later, Haramura and Katto (1983) completed the development of the model by introducing the mechanism for macro-layer formation. This model is extended to flow boiling by considering a liquid film trapped between a bubble and the heater wall. Numerous vapor stems emerge on the heater surface through the liquid film. Under flow conditions, both the liquid sublayer and the vapor film move in the flow direction. Liquid is fed into the film from the upstream end, whereas the film thickness decreases along the flow direction due to evaporation. CHF condition is reached when the heat supplied by the heater surface provides the necessary latent heat required to completely evaporate the liquid entering the film. Katto (1990a, 1990b) provided a detailed description of the model based on the macrolayer evaporation. His model uses several empirical constants in determining the thickness, liquid film flow rate, and temperature of the liquid entering into the sublayer.

Lee and Mudawar (1988) considered the effect of velocity in the subcooled flow in terms of stretching the large bubble in the Haramura and Katto (1983) model to a vapor blanket of length equal to the critical Helmholtz wavelength. The sublayer mass velocity, its thickness, and the vapor blanket length were calculated by considering the buoyancy and drag forces acting on the vapor blanket. The modeling resulted in a correlation scheme with three empirical constants that were determined from a large set of experimental data.

Celata et al. (1994) eliminated the empirical constants in the Katto (1990a, 1990b) and Lee and Mudawar (1988) models by using the homogeneous flow model and introducing appropriate correlations from available literature to calculate the sublayer thickness, flow rate, enthalpies, and vapor blanket length. However, the basic features of the model are similar to that proposed by Lee and Mudawar (1988).

The recent models discussed in the preceding section present a considerable improvement over the earlier models by considering CHF as a local phenomenon. However, further improvements are needed to account for the effect of contact angle on CHF. A major question that remains unanswered in the above models is the description of the mechanism that prevents rewetting of the dry patches. The pool boiling model of Kandlikar (2001a) considers the evaporation momentum force experienced by an evaporating interface, and it is postulated that this force is responsible for pushing the liquid front away. Recently, Kandlikar (2003) developed two nondimensional groups that compare the evaporation momentum, surface tension, and inertia forces. The use of these new nondimensional groups in CHF prediction in flow boiling shows promising results.

3.1.2.8.2 CHF in Low-Quality Saturated Flow Boiling

CHF at low qualities in saturated flow boiling is similar to CHF in subcooled flow boiling. Bubble crowding and liquid film dryout under a growing bubble or a slug are the two main mechanisms leading to CHF in low-quality subcooled flow boiling. The mechanisms and correlations are therefore the same under these conditions.

3.1.2.8.3 Correlations for CHF in Subcooled Flow Boiling and Low-Quality Saturated Flow Boiling

Numerous correlations specific to certain geometries and operating conditions are available in the literature and are recommended for use if they match the desired conditions. An extensive review of CHF correlations for different geometries and operating conditions is given by Tong and Tang (1997).

For general usage, Gunther's (1951) correlation should be used to provide a good approximation:

$$q''_{\text{CHF}} = 7198u^{0.5}\Delta T_{\text{Sub,exit}} \quad (3.69)$$

(recommended ranges are: $p = 0.1 - 1.1$ MPa; $u = 1.5 - 12.1$ m/sec; $q''_{\text{CHF}} = 0.4 - 11.4$ MW/m²; and $\Delta T_{\text{Sub,exit}} = 11 - 39$ K).

Note that this correlation is valid for water and cannot be extrapolated beyond the quoted ranges of parameters (it does not approach the pool boiling CHF as $u \rightarrow 0$).

The correlation of Tong et al. (1968) for CHF with water in uniformly heated tubes is widely accepted:

$$\frac{q''_{\text{CHF}}}{Gh_{fg}} = \frac{C}{Re^{0.6}} \quad (3.70)$$

(recommended ranges are $p = 5.5 - 13.6$ MPa; $u = 0.68 - 5.9$ m/sec; void fraction at CHF < 0.35; $D = 3 - 10$ mm; $L/D = 5 - 100$; void fraction evaluated using Thom et al. (1965) model; and Δ and $T_{\text{Sub,exit}} = 11 - 39$ K) where G is the mass flux, Re the Reynolds number and

$$C = 1.76 - 7.433x_{\text{exit}} + 12.222x_{\text{exit}}^2 \quad (3.71)$$

All properties are evaluated at saturation condition. Celata et al. (1994) extended the range of the proposed correlation to lower pressures by replacing C with C' given by the following correlation:

$$C' = (1.76 - 7.433x_{\text{exit}} + 12.222x_{\text{exit}}^2)\psi \quad (3.72)$$

(recommended ranges are; $p \leq 5.5$ MPa; $u = 2.2 - 40$ m/sec; Δ and $T_{\text{Sub,exit}} = 15 - 190$ K; and $D = 0.33 - 15$ mm) with ψ (in MPa) is given by the following equations:

$$\psi = \begin{cases} 1 & \text{for } x_{\text{exit}} < -0.1 \\ 0.825 + 0.986x_{\text{exit}} & \text{for } 0 > x_{\text{exit}} \geq 0.1 \end{cases} \quad (3.73)$$

In evaluating CHF from the above equations, the heat balance method requiring an iterative procedure is recommended (Celata and Mariani, 1999).

3.1.2.8.4 CHF in Annular Flow Due to Liquid Film Dryout in Saturated Flow Boiling

As quality increases, the flow pattern changes to annular flow with its characteristic liquid film around the circumference and a central vapor core. The liquid film dryout depends on the rates of its evaporation, liquid entrainment in the vapor, and deposition of liquid back from the vapor core into the film. The rates of evaporation as well as entrainment to some extent depend on the imposed heat flux. The location of the dryout and the corresponding value of CHF at this location are of interest. It is desirable to extend the dryout location to higher qualities as the heat transfer rate is dramatically reduced following the *Dryout*.

Simple correlations are not available to predict the *Dryout* location. Elaborate methods are available in literature to predict the entrainment and deposition rates (e.g., Collier and Thome, 1994). Another method that is widely followed consists of extensive tabulation of CHF data for a standardized circular tube of 8mm diameter as a function of pressure, mass flux, and quality at CHF. This approach was originally developed by Doroshchuk et al. (1975). The recent updated tables are published by Groeneveld et al. (1996). Using these tables, the CHF value for a different tube diameter under the same pressure, mass flux, and quality conditions is obtained by the following equation:

$$q''_{\text{CHF}} = q''_{\text{CHF}, 8 \text{ mm}} \left(\frac{D}{0.008} \right)^k \quad (3.74)$$

Groeneveld et al. (1996) recommends a value of $k = -1/2$ based on 22,946 data points for water covering the ranges of pressure from 0.1 to 20 MPa, mass flux up to 8000 kg/m² sec, and quality of -0.5 to 1.0 at discrete values covering tube diameters from 3 to 25 mm. Other researchers proposed a value of $k = -1/3$ (Groeneveld et al., 1986; Smith, 1986).

For small-diameter tubes, the experimental data by Vandervort et al. (1994) were fitted by Kandlikar (2003) using two new dimensionless groups K_1 and K_2 . These groups were obtained by considering evaporation momentum forces, inertia forces, and surface tension forces. K_1 represents the ratio of evaporation momentum force to inertia force, whereas K_2 represents the ratio of evaporation momentum and surface tension forces:

$$K_1 = \left(\frac{q}{G h_{fg}} \right)^2 \frac{\rho_L}{\rho_G} \quad (3.75)$$

and

$$K_2 = \left(\frac{q}{h_{fg}} \right)^2 \frac{D}{\rho_G \sigma} \quad (3.76)$$

The pool boiling CHF equation given by Eq. (3.29) can be stated as $K_{2,\text{CHF, Pool Boiling}} = f(\phi, \theta_r)$, where ϕ and θ_r are the orientation of the heated wall and receding contact angle, respectively. Using this parameter, the data of Vandervort et al. (1994) for CHF are plotted as a function of tube diameter for three mass fluxes in Figure 3.16. The three plots fall on three separate lines. As a first attempt, a new parameter $K_{2,\text{CHF}} K_{1,\text{CHF}}^{0.75}$ is plotted against D in Figure 3.17. It is seen that this new parameter is able to account for both the diameter and the mass flux effects reasonably well, taking into consideration the original scatter in the experimental data points. Thus,

$$K_{2,\text{CHF}} K_{1,\text{CHF}}^{0.75} = C \quad (3.77)$$

where C is a constant, which is specific for the data set. Comparing Eq. (3.77) with Eq. (3.74), it is seen that the exponent $k = -1/3.5$ in Eq. (3.77) for tube diameters is in the range 0.5 to 2.15 mm for data sets of Vandervort et al. The absolute value of k is thus seen to decrease somewhat, from $-1/2$ (Groeneveld et al., 1996) or $-1/3$ (Groeneveld et al., 1986; Smith, 1986) to $-1/3.5$ (Eq. [3.77]) for smaller diameter tubes. The actual CHF modeling for smaller diameter tubes needs to consider the additional effects of viscous forces, which may be represented through Reynolds or Weber number, quality, and contact angle.

Heat transfer in the post-CHF region depends on the extent of droplet deposition on the tube wall. Beyond a certain temperature, the heater surface may exceed the Leidenfrost temperature and the heat transfer rate by convection would reduce significantly. Correlations by Groeneveld (1973) and Nishikawa

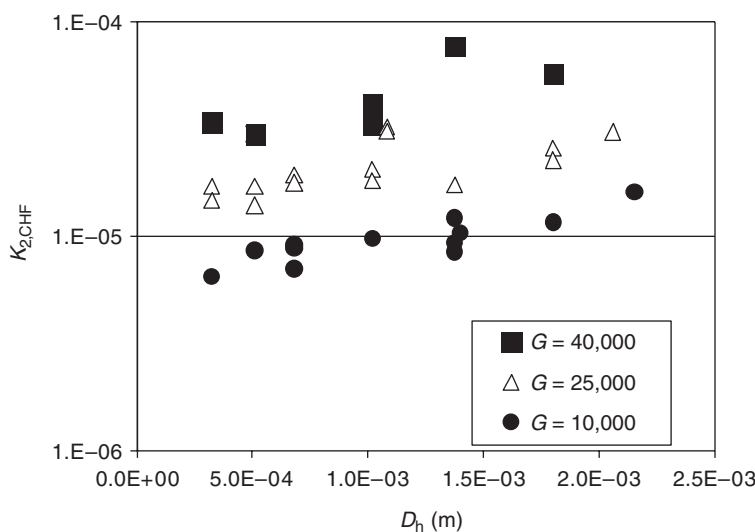


FIGURE 3.16 Variation of $K_{2,\text{CHF}}$ with diameter for flow boiling CHF data of Vandervort et al. (1994) for different values of G in $\text{kg}/\text{m}^2 \text{ sec}$. (From Kandlikar, S.G., *J. Heat Transfer*, 125, 2003. Reproduced with permission from ASME.)

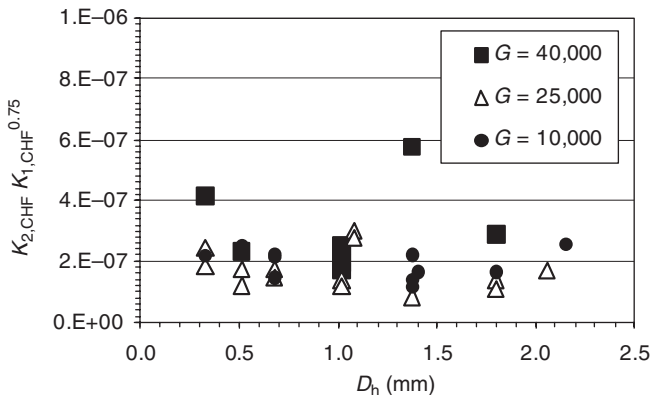


FIGURE 3.17 Effect of diameter on critical heat flux for small-diameter tubes, comparison of experimental data of Vendervort et al. (1994) with the product $K_{2,CHF} \cdot K_{1,CHF}^{0.75}$. (From Kandlikar, S.G., *J. Heat Transfer*, 125, 2003. Reproduced with permission from ASME.)

et al. (1986) are recommended. Since these correlations are developed for specific fluids, geometries, and operating conditions, extreme caution should be exercised while extending their applicability to parameter ranges beyond their parent database.

3.1.2.9 Flow Boiling in Compact Heat Exchangers

Flow boiling in compact heat exchangers is extensively employed in chemical, process, air-liquefaction, and refrigeration applications. The use of plate-fin and plate heat exchangers is common in these applications. A detailed survey of this topic is presented by Kew and Cornwell (1999). They have reviewed a number of available correlations for offset-strip fins, perforated fins, and louvered fins. The correlation schemes presented by Feldman et al. (1996), Kandlikar (1991b), and Wieting (1975) are noteworthy. In general, it is found that, contrary to the common expectation, the role of nucleate boiling becomes more important in narrow channels found in compact heat exchanger passages when compared to conventional channels.

3.1.2.10 Flow Boiling Augmentation

Although the heat transfer coefficients during flow boiling are relatively high compared to the corresponding single-phase liquid flows, further enhancements are desired in a number of applications. Many augmentation techniques have been proposed in the literature; a comprehensive review of various techniques for accommodating high heat fluxes is given by Bergles (1997). Among the methods employed, microfin tubes, also called grooved tubes in Japanese and Korean literature, have proved to be quite attractive in flow boiling applications. Tubes of different microfin geometries have been studied in the literature (e.g., Khanpara et al., 1986, 1987; Koyama et al., 1995), and are now routinely applied in refrigeration evaporators. The flow boiling performance of these tubes can be predicted by a number of correlation schemes proposed in the literature (e.g., Kandlikar, 1991b, Kandlikar and Raykoff, 1997).

Structured and porous surfaces that promote pool boiling heat transfer have been successfully applied for flow boiling enhancement as well. The use of such surfaces is common especially in the air separation and cryogenic industries, where very small temperature differences are often employed in evaporation of air constituents during the separation processes.

3.1.2.11 Enhancement of CHF in Flow Boiling

The techniques to enhance the CHF in subcooled and low-quality saturated boiling regions can be divided into passive and active types. Detailed surveys of various enhancement techniques are presented by Celata and Mariani (1999) and Boyd (1985).

The passive devices consist of twisted tapes and swirl flow devices, helically coiled tubes, surface roughness, and extended surfaces. These devices induce secondary radial and circumferential velocity components

over the tube wall resulting in an increase in CHF. These devices result in significantly higher pressure drop penalties compared with a smooth tube. The CHF enhancement is 1 to 3 times the corresponding smooth tube values under the same operating conditions, whereas the pressure drop increase is higher, depending on the specific enhancement technique. The Nariai et al. (1992) correlation is recommended for the prediction of CHF enhancement with twisted tapes:

$$\frac{q''_{\text{CHF}}}{q''_{\text{CHF, smooth}}} = \{1 + 10^{-2}\vartheta \exp[(-10^{-6}p)^2]\}^{1/6} \quad (3.78)$$

ϑ is the non-dimensional centrifugal acceleration given by

$$\vartheta = \frac{\pi^2 u^2}{2gD \text{TTR}} \quad (3.79)$$

where u is the average flow velocity, D the tube diameter, and TTR the twist ratio.

CHF in the high-quality region resulting from *dryout* can be enhanced by effectively replenishing the heated surface with liquid. Liquid retention in grooves and roughness structures effectively delays the dryout location.

3.2 Condensation

J.N. Chung

3.2.1 Fundamentals of Condensation

3.2.1.1 Homogenous Nucleation

Thermodynamically, condensation is defined as a change of phase from vapor to liquid with the release of latent heat. The driving force for condensation is a subcooling of the vapor phase under a metastable condition. As shown in Figure. 3.18, assume that a droplet embryo is formed with a radius of a that is larger than the mechanical equilibrium radius or the critical radius a^* . The critical radius is defined by the Laplace–Young equation based on the mechanical equilibrium as follows :

$$p_l - p_g = \frac{2\sigma}{a^*} \quad (3.80)$$

where p_l and p_g are liquid and vapor phase pressures, respectively, and σ is the surface tension coefficient.

Under the thermal equilibrium condition $T_l = T_g$; for the vapor phase, Thomson (1871) showed that the actual saturation pressure of the vapor, p_g , surrounding the droplet is increased due to surface tension as given by:

$$p_g = p_o \exp(2\sigma v_l M / a^* R_u T_g) \quad (3.81)$$

$$p_g \approx p_o(1 + 2\sigma v_l / a^* p_o v_g) \quad (3.82)$$

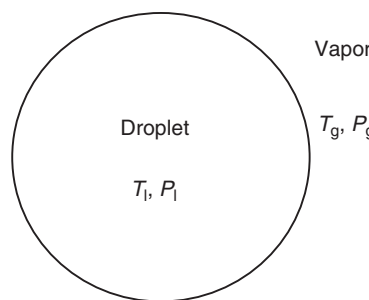


FIGURE 3.18 Schematic of a droplet embryo in a quiescent vapor environment.

where p_o is the saturation pressure corresponding to T_g on a flat surface. The ratio, p_g/p_o , is called the supersaturation ratio. If T_{Sat} is the saturation temperature corresponding to p_g on a flat surface and $p_l > p_g$, as shown in Figure 3.19, it is clear that the vapor phase is supersaturated and subcooled because of $p_l > p_g$ and $T_{\text{Sat}} > T_g$. With the use of the Clausius–Clapeyron equation, it can be shown that

$$T_{\text{Sat}} - T_g \approx \frac{2T_{\text{Sat}}\sigma V_l}{h_{fg}a^*} \quad (3.83)$$

The above equation provides the degree of subcooling and it is also called the Gibbs–Thompson condition. As illustrated in Figure 3.20, the initial growth of a droplet embryo is driven by the subcooling

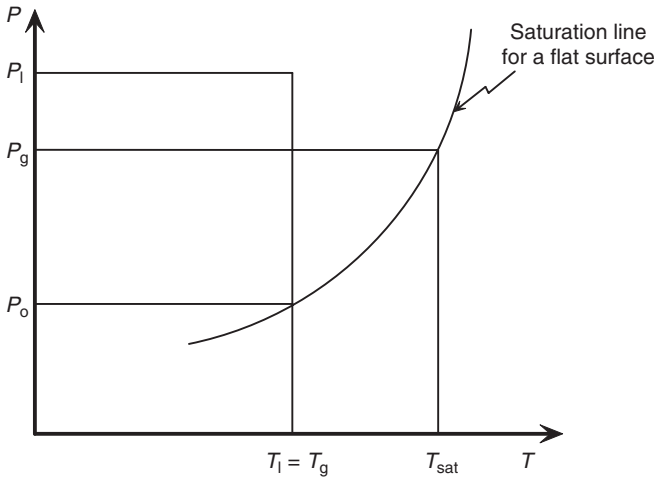


FIGURE 3.19 Pressure–temperature relationships at saturation.

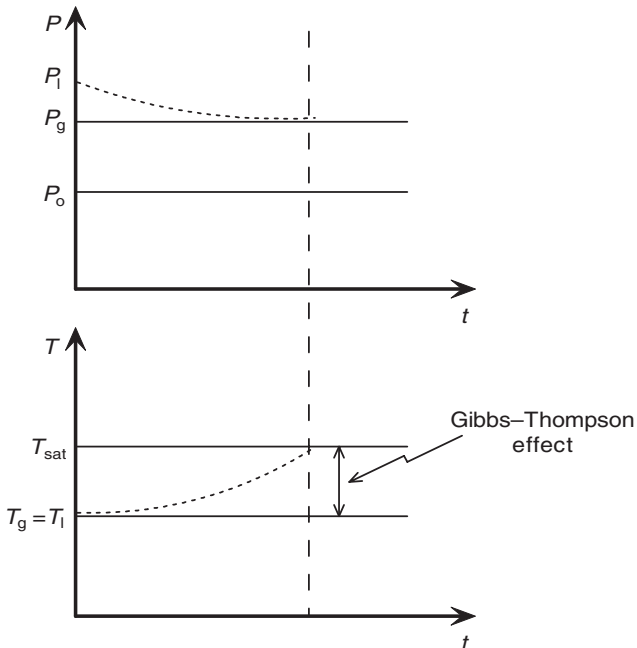


FIGURE 3.20 Thermodynamics of droplet initial growth.

condition indicated by Eq. (3.83). As the growth continues, the droplet gets larger and the degree of subcooling decreases, which causes the growth rate to decrease.

In an analytical study, Lai (1999) found that the droplet growth is associated with three timescales. The first and second timescales, that are generally small, describe, respectively, the transient temperature distributions of the vapor phase and the droplet phase. The largest timescale controls the droplet growth process. For the case of a large Stefan number, $C_{p,v}(T_{\text{Sat}} - T_g)/h_{fg}$, the subcooling effect is dominating, which results in a faster droplet growth. The Gibbs–Thompson effect actually suppresses the droplet growth and its effectiveness is diminished as time progresses. If the density difference between the liquid and the vapor phases becomes larger, the induced convection effect becomes more relevant.

Oswatitsch (1942) suggested a droplet growth equation for the rate of change of droplet radius with time, which is based on the kinetic theory of gases for droplets smaller than 2 μm ,

$$\frac{dR(t)}{dt} = \frac{3p_0}{8h_{fg}\rho_l} \sqrt{\left(\frac{3R_u}{T_g M}\right)(T_{\text{Sat}} - T_g)} \quad (3.84)$$

For larger droplet growth in the continuum regime, Ford and Lekic (1973) derived an equation for the droplet radius growth rate using conduction and convection heat transfer theories,

$$\frac{dR(t)}{dt} = \pi^2 \frac{\alpha\eta}{D_i} \frac{\exp(-\pi^2 Fo)}{[1 - \exp(-\pi^2 Fo)]^{1/2}} \quad (3.85)$$

where

$$\eta = \left[1 + \frac{C_{p,l}(T_{\text{Sat}} - T_i)}{h_{fg}} \right] - 1 \quad (3.86)$$

and $Fo = 4\alpha_l t/D_i^2$ is the Fourier number, α_l is the liquid thermal diffusivity, T_i the droplet initial temperature, and D_i the droplet initial diameter.

3.2.1.2 Heterogeneous Nucleation

When the nucleation takes place on entrained particulate matter in a vapor environment or on a cold solid surface, the process is called heterogeneous nucleation. There are basically two forms of heterogeneous condensation: dropwise and filmwise condensation. Dropwise condensation usually occurs when the condensate does not wet the surface and, therefore, instead of spreading into a thin film, it takes the shape of droplets. Sometimes dropwise condensation is just a precursor to film condensation. Filmwise condensation prevails generally on wettable surfaces where a stable condensate removal mechanism is provided.

3.2.2 Condensation on Flat Surfaces

3.2.2.1 Dropwise Condensation

As stated above, dropwise condensation occurs on surfaces that are hard to wet. Usually, this type of surface is associated with high free energy. Droplet embryos first form as a result of nucleation, then these embryos start to grow, which promotes coalescence among small droplets to form larger ones. Then these larger drops are removed by external forces such as gravity or shear. Therefore, from an individual droplet point of view, the process is highly transient and, in general, a cyclic process from one droplet generation to the next. For example, on a cold beer can, when condensed droplets reach sizes that are large enough, gravity force would overcome the surface tension such that droplets would be removed by sweeping down and leave a freshly wiped path for next generation of droplets to nucleate to start a new cycle.

The transport mechanisms that govern the nucleation, two-phase flow and heat transfer in dropwise condensation are still in the developmental stage. There are many controversial issues that need to be clarified in the future. Up to this point, there are two basic theoretical models: nucleation theory and film-rupture theory.

The nucleation theory was first introduced by Eucken (1937) and later further developed by Umur and Griffith (1965), Graham and Griffith (1973), Tanaka (1975), and Rose (1988). According to the nucleation

theory, the dropwise condensation process starts with very thin liquid film layer and then it breaks up into droplets. These droplets subsequently grow by condensing vapor on their surfaces with the latent heat transported to the surface by conduction. Heat flux is maximum at the vapor–liquid–solid contact line. Following this, droplet–droplet interaction and coalescence produce larger droplets, but the remainder of the surface stays dry.

The film-rupture theory was introduced first by Jakob (1936) and further developed by Welch and Westwater (1961), Silver (1964), and Sugawara and Katsuta (1966). The film-rupture theory claims that vapor condenses on a cold surface and forms microscale thin liquid films. When the film reaches a critical thickness, it would then rupture to form microdroplets.

It is almost impossible to develop a general correlation for the dropwise condensation because of the strong surface property dependence and the condensate removal mechanisms. For the development of a heat transfer correlation, the heat flux is given by

$$q = h\Delta T \quad (3.87)$$

where q is the heat flux in kW/m^2 and ΔT the temperature difference between the vapor and the condenser surface in degrees K. For steam and ethylene glycol, Peterson and Westwater (1966) proposed

$$h = Nu\rho_l h_{fg} k_l (T_{\text{Sat}} - T_w) / 2\sigma T_{\text{Sat}} \quad (3.88)$$

where

$$Nu = 1.46 \times 10^{-6} Re_l^{-1.63} \Pi_k^{1.16} Pr_l^{0.5} \quad (3.89)$$

in which

$$Re_l = \frac{k_l(T_{\text{Sat}} - T_w)}{\mu_l h_{fg}} \quad (3.90)$$

and

$$\Pi_k = -\frac{2\sigma T_{\text{Sat}}}{\mu_l^2 h_{fg}} \left(\frac{\partial \sigma}{\partial T} \right) \quad (3.91)$$

with the following limited range :

$$\begin{aligned} 1.75 &\leq Pr_l \leq 23.6 \\ 2 \times 10^{-4} &\leq Re_l \leq 3 \times 10^{-2} \\ 7.8 \times 10^{-4} &\leq \Pi_k \leq 2.65 \times 10^{-2} \end{aligned}$$

The above correlation was recommended only for the fluids with which it was developed. Rose (1999) indicated that because of improvements in experimental quality, recent results from various countries are found to be in reasonably good agreement. For dropwise condensation of pure steam, Rose (1999) suggested the following general correlation that also takes the system pressure into consideration :

$$\dot{q} = T_v^{0.8} (5\Delta T + 0.3(\Delta T)^2) \quad (3.92)$$

In the above equation, \dot{q} is the heat flux in kW/m^2 , T_v the vapor temperature in Celsius, ΔT the temperature difference between the vapor and the condenser surface in degrees K.

3.2.2.2 Film Condensation

3.2.2.2.1 Laminar Film

For Laminar film condensation on a vertical flat surface, a simplified model was first introduced by Nusselt (1916). The model is based on the following assumptions :

1. The liquid film is laminar and two-dimensional.
2. Thermal properties of the film are constant.
3. Subcooling of the film is negligible.

4. Momentum changes through the film are unimportant.
5. The bulk of the vapor is stagnant, saturated and free of noncondensables.
6. Interfacial shear is negligible.
7. The heat transfer in the liquid film is dominated by conduction.

The local condensation heat transfer coefficient is defined as follows :

$$h_x = \frac{\dot{q}_x}{(T_{\text{Sat}} - T_w)} \quad (3.93)$$

where \dot{q}_x is the local heat flux and $T_{\text{Sat}} - T_w$ the degree of subcooling. The average condensation heat transfer coefficient over a plate of length L is given as

$$\bar{h}_L = \frac{\bar{\dot{q}}_L}{(T_{\text{Sat}} - T_w)} \quad (3.94)$$

where $\bar{\dot{q}}_L$ is the average heat flux over the entire plate. The local and average heat transfer coefficients for a plate of length L are given by Nusselt (1916) as

$$h_x = \left[\frac{k_l^3 h_{fg} \rho_l (\rho_l - \rho_v) g \sin \theta}{4(T_{\text{Sat}} - T_w) \mu_l x} \right]^{1/4} \quad (3.95)$$

$$\bar{h}_L = 0.943 \left[\frac{k_l^3 h_{fg} \rho_l (\rho_l - \rho_v) g \sin \theta}{(T_{\text{Sat}} - T_w) \mu_l L} \right]^{1/4} \quad (3.96)$$

Rohsenow (1956) suggested an effective latent heat of condensation to compensate for the liquid subcooling,

$$h'_{fg} = h_{fg} \left[1 + 0.68 \left(\frac{c_{p,l}(T_{\text{Sat}} - T_w)}{h_{fg}} \right) \right] \quad (3.97)$$

Sadasivan and Lienhard (1987) introduced a different effective latent heat of condensation that is also a function of the Prandtl number,

$$h'_{fg} = h_{fg} \left[1 + (0.683 - 0.228/Pr_l) \left(\frac{c_{p,l}(T_{\text{Sat}} - T_w)}{h_{fg}} \right) \right] \quad (3.98)$$

The above equation is limited for $Pr_l > 0.6$. Many researchers have investigated the validity of the constant thermal property assumption. One acceptable method of including the variation of thermal properties in the liquid film is to use a reference temperature T_r , to evaluate the thermal properties. This reference temperature is defined as

$$T_r = T_w + F(T_{\text{Sat}} - T_w), \quad 0.25 < F < 0.31 \quad (3.99)$$

One of the assumptions in the Nusselt model allows the neglect of the interfacial shear between the liquid film and the ambient vapor; Koh et al. (1961) investigated this assumption further and found that the interfacial shear is indeed very small for most gases and liquids ($Pr \geq 1$). For condensation of liquid metals, they discovered that the inclusion of the interfacial shear does cause a substantial reduction in heat transfer and suggested the following correction equation:

$$\frac{h}{h_{Nu}} = \left(\frac{1 + 0.68A + 0.02AB}{1 + 0.85B - 0.15AB} \right) \quad (3.100)$$

where

$$A = [c_{p,l}(T_{\text{Sat}} - T_w)/h_{fg}]$$

$$B = [k_l(T_{\text{Sat}} - T_w)/\mu_l h_{fg}] \quad (3.101)$$

Also, h_{Nu} is the heat transfer coefficient based on the Nusselt model. For laminar film condensation on geometries other than the vertical flat plate, Dhir and Lienhard (1971) introduced the concept of effective

gravity for an arbitrary axisymmetric body. Using the coordinates defined in Figure 3.21, Dhir and Lienhard (1971) showed that the local film thickness may be determined by

$$\delta(x) = \left(\frac{4\mu_l k_l (T_{\text{Sat}} - T_w)x}{\rho_l(\rho_l - \rho_v)h'_{\text{fg}}g_{\text{eff}}} \right)^{1/4} \quad (3.102)$$

In the above equation, g_{eff} is the effective gravity defined as

$$g_{\text{eff}} = \frac{x(gR)^{4/3}}{\int_0^x g^{1/3} R^{4/3} dx} \quad (3.103)$$

The local Nusselt number is therefore given as

$$Nu = \left(\frac{g_{\text{eff}} \rho_l (\rho_l - \rho_v) h'_{\text{fg}} x^3}{4\mu_l k_l (T_{\text{Sat}} - T_w)} \right)^{1/4} \quad (3.104)$$

For example, the average Nusselt number for condensation on a sphere with diameter, D , is equal to

$$\overline{Nu}_D = 0.785 \left(\frac{gD^3}{A} \right)^{1/4} \quad (3.105)$$

where

$$A = \frac{\mu_l k_l (T_{\text{Sat}} - T_w)}{\rho_l (\rho_l - \rho_v) h'_{\text{fg}}} \quad (3.106)$$

3.2.2.2.2. Turbulent Film

As the film thickness increases, the smooth vapor–liquid interface gradually becomes wavy, but the bulk of the liquid film remains laminar. As the thickness increases further, the liquid film eventually becomes turbulent. In order to gage quantitatively the three different regimes, a Reynolds number must be defined first. The local Reynolds number that characterizes the liquid film flow is based on the mean liquid velocity and the hydrodynamic diameter of the two-dimensional liquid film, which is equal to 4δ , where δ is

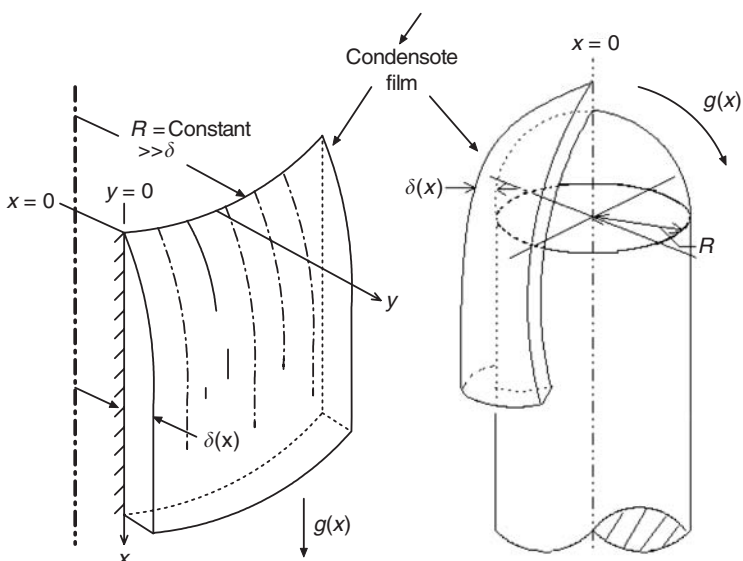


FIGURE 3.21 Coordinate system for effective gravity model.

the film thickness. If the liquid film local mass flow rate is represented by the Nusselt model, then the Reynolds number is in the following form:

$$Re_{D_h} = \frac{4g\rho_l(\rho_l - \rho_v)\delta^3}{3\mu_l^2} \quad (3.107)$$

The three liquid film flow regimes are characterized by:

1. $Re_{D_h} \leq 30$ (laminar film with smooth interface). In this regime, the Nusselt solution mentioned above can be applied.
2. $30 \leq Re_{D_h} \leq 1800$ (laminar film with wavy interface). Kutateladze (1963) proposed the following equation for this regime:

$$\frac{\bar{h}_L(v_l^2/g)^{1/3}}{k_l} = \frac{Re_{D_h}}{1.08 Re_{D_h}^{1.22} - 5.2} \quad (3.108)$$

3. $1800 \leq Re_{D_h}$ (turbulent liquid film). For the turbulent film, Labuntsov (1957) recommended

$$\frac{\bar{h}_L(v_l^2/g)^{1/3}}{k_l} = \frac{Re_{D_h}}{58 Pr_l^{-0.5} (Re_{D_h}^{0.75} - 263) + 8750} \quad (3.109)$$

3.2.3 Condensation on and in the Tubes

3.2.3.1 Condensation in a Tube

Condensation in circular tubes is strongly affected by the vapor inlet velocity and the orientation of the tube. For vertical tubes, the flow pattern is in reverse order as that of boiling. As shown in Figure 3.22 the

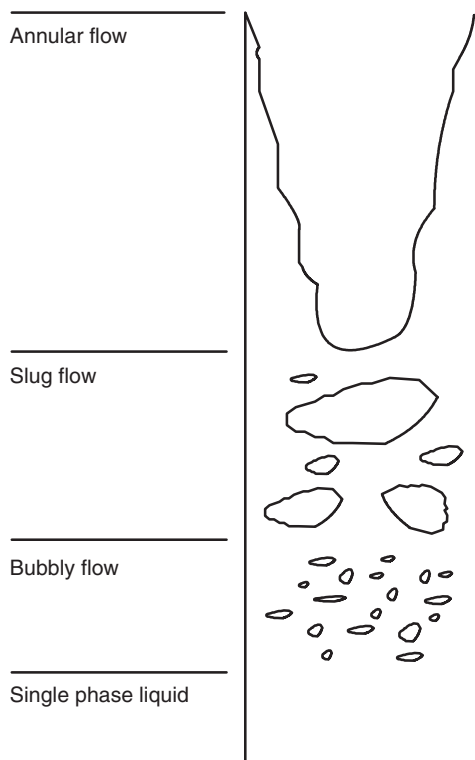


FIGURE 3.22 Schematic of condensing flow regimes in a vertical tube.

annular flow pattern generally prevails, which is followed by slug flow and then bubbly flow. If the vapor flows upward against the gravity (countercurrent flow), annular liquid film flowing downward would experience substantial interfacial shear, whereas for cocurrent flows, the interfacial shear is negligible as a result of the large density difference between the vapor and the liquid phases. For horizontal tubes, the annular flow would be maintained if the inlet vapor velocity is relatively high; otherwise the stratified annular flow would take place because the gravity would tend to drain the liquid condensate in the direction perpendicular to the vapor flow, which would thicken the liquid film along the gravity direction.

Based on experimental results, Jaster and Kosky (1976) proposed the following criteria for the transition from initial annular flow to the stratified flow regime:

$$F > 29 \quad \text{annular flow}$$

$$29 \geq F \geq 5 \quad \text{transition flow}$$

$$F < 5 \quad \text{stratified flow}$$

The stress ratio, F , is defined as $\tau_w / \rho_l g \delta$, where δ is the liquid film thickness. Jaster and Kosky (1976) also recommended the following for the Nusselt number in the transition flow regime:

$$Nu_{tr} = Nu_{an} + \frac{F - 29}{24} (Nu_{an} - Nu_{str}) \quad (3.110)$$

The error associated with the above equation is of the same order of magnitude as those methods established for annular and stratified flows.

3.2.3.1.1 Stratified Annular Flow in Horizontal tubes

For horizontal tubes, when the inlet vapor Reynolds number is $< 35,000$, which corresponds to a mass flow flux of $400 \text{ kg/m}^2 \text{ sec}$ for a 1 cm tube, the liquid film is affected by the gravity and the stratified annular flow pattern would be present. Because of the effects of gravity, Chato (1962) proposed a correlation based on Nusselt's film condensation model,

$$h = 0.728 K_c \left[\frac{g \rho_l (\rho_l - \rho_v) k_l^3 h'_{fg}}{\mu_l (T_{sat} - T_w) D} \right]^{1/4} \quad (3.111)$$

where h'_{fg} is the effective latent heat of condensation to include the subcooling in the liquid film,

$$h'_{fg} = h_{fg} \left[1 + 0.68 \frac{c_{pl}(T_{sat} - T_w)}{h_{fg}} \right] \quad (3.112)$$

It is noted that Eq. (3.111) is identical to the classical Nusselt result for laminar film condensation on a vertical flat plate with height D if K_c is set to 1.295. The physical meaning of K_c is that it is a provision to account for the accumulation of condensate on the bottom of the tube that changes the void fraction. Chato (1962) suggested a value of 0.76 based on the experimental data of R-113.

3.2.3.1.2 Annular Flow in Horizontal Tubes

As mentioned above, when the inlet vapor Reynolds number is $> 30,000$, the annular flow pattern would be maintained along most of the tube length. Near the end of relatively long tubes, the vapor-phase Reynolds number drops substantially such that gravity effects become a factor. Under this situation, the above stratified annular flow model would then describe flow and heat transfer more appropriately.

Heat transfer correlations for condensation in a horizontal tube with an annular flow pattern was first addressed by Ananiev et al. (1961) for single-component pure vapor and smooth tubes. Based on the analogy between momentum and heat transport, they proposed that the heat transfer coefficient for the two-phase condensing flow, h , can be correlated with the liquid single phase forced convection heat transfer coefficient, h_l , as follows:

$$h = h_l \sqrt{\frac{\rho_l}{\rho_m}} \quad (3.113)$$

where the equivalent mixture density, ρ_m , is defined as

$$\frac{1}{\rho_m} = \left(\frac{1}{\rho_l} \right) (1 - x) + \left(\frac{1}{\rho_v} \right) x \quad (3.114)$$

and h_l is evaluated based on a correlation for convective-forced convection of single-phase liquid in a circular tube, for example, the Dittus–Boelter-type correlations. Based on the experiments, Boyko and Kruzhilin (1967) found

$$h_l = C Re_l^{0.8} Pr_f^{0.43} \left(\frac{Pr_f}{Pr_w} \right)^{0.25} \left(\frac{K_l}{D} \right) \quad (3.115)$$

where $C = 0.024$ and 0.032 for steam condensing on carbon steel tubes and copper tubes, respectively, and Pr_f and Pr_w are the Prandtl numbers evaluated at the stream core and wall temperatures, respectively.

Cavallini and Zecchin (1974) offered the following correlation for saturated vapor inside tubes based on the Reynolds analogy concept and a multiple linear regression analysis:

$$Nu = 0.0344 Re_l^{0.83} [1 + x((\rho_l/\rho_v)^{0.5} - 1)]^{0.82} Pr_l^{0.35} \quad (3.116)$$

The above equation is suggested for the dimensionless groups and thermal property ratios in the ranges listed below:

$$\begin{aligned} 10 < \rho_l/\rho_v &< 2000, \quad 0.1 < X < 0.9, \quad 0.01 < \mu_v/\mu_l < 0.1 \\ 15 < Fr = \frac{G \rho_v}{\sqrt{gD}} &< 4000, \quad 5000 < Re_f = \frac{GD}{\mu_l} < 5000,000, \\ 0.8 < Pr_l < 20, \quad 0.01 < Ja &= c_{p,l}(T_v - T_w)/h_{fg} < 0.2 \end{aligned}$$

where G is the total stream mass flux in $\text{kg}/\text{m}^2 \text{ sec}$ and x is the vapor quality.

3.2.3.1.3 Annular Flow in Vertical Tubes

Chen et al. (1987) divided this problem into two categories: zero-shear (cocurrent flow) and high interfacial shear (countercurrent flow) processes. For countercurrent vapor flow, the interfacial shear retards the condensate flow and, therefore, decreases the heat transfer by thickening the liquid film. On the other hand, the cocurrent vapor flow enhances the heat transfer. They suggested the following: for cocurrent flow,

$$Nu_o = [(Nu_{lw})^{n1} + (Nu_l)^{n1}]^{1/n1} \quad (3.117)$$

for countercurrent flow,

$$Nu_x = [(Nu_o)^{n2} + (Nu_{hs})^{n2}]^{1/n2} \quad (3.118)$$

where all the Nusselt numbers are defined as $(h/k_l)/(v_l^2/g)^{1/3}$. Chen et al. (1987) found that $n1 = 6$ and $n2 = 2$ resulted in the best fit to the reported data. For the laminar wavy flow, Nu_{lw} and Chen et al. (1987) recommended the Chun and Seban (1971) correlation,

$$Nu_{lw} = 0.823 Re_x^{-0.22} \quad (3.119)$$

$$Re_x = \frac{G(1-x)D}{\mu_l} \quad (3.120)$$

For the turbulent film flow, Nu_t , Chen et al. (1987) recommended the following correlation:

$$Nu_t = 0.00402 Re_x^{0.4} Pr_l^{0.65} \quad (3.121)$$

Finally, for the Nusselt numbers for high shear flows, Nu_{hs} , Chen et al. (1987) proposed the Soliman et al. (1968) correlation,

$$Nu_{hs} = 0.036 Pr_1^{0.65} \bar{\tau}_i^{1/2} \quad (3.122)$$

$$\bar{\tau}_i = \frac{\tau_i}{\rho_l(gv_i)^{2/3}} \quad (3.123)$$

Chen et al. (1987) proposed the following general equation for the local heat transfer for a vertical cocurrent annular flow:

$$Nu_x = \left[\left(0.31 Re_x^{-1.32} + \frac{Re_x^{2.4} Pr_1^{3.9}}{2.37 \times 10^{14}} \right)^{1/3} + \frac{Pr_1^{1.3} A}{771.6} (Re_T - Re_x)^{1.4} \right]^{1/2} \quad (3.124)$$

For the case of annular flow in a horizontal tube, the above equation simplifies to

$$Nu_x = 0.036 Pr_1^{0.65} A^{0.5} (Re_T - Re_x)^{0.7} Re_x^{0.2} \quad (3.125)$$

$$A = \frac{0.252 \mu_l^{1.177} \mu_v^{0.156}}{D^2 g^{2/3} \rho_l^{0.553} \rho_v^{0.78}} \quad (3.126)$$

where Re_T is the film Reynolds number when a total condensation takes place. For the countercurrent flow, the recommended local Nusselt number is

$$Nu_x = \left[\left(0.31 Re_x^{-1.32} + \frac{Re_x^{2.4} Pr_1^{3.9}}{2.37 \times 10^{14}} \right) - \frac{C Pr_1^{1.3}}{771.6} Re_x^{1.8} \right]^{1/2} \quad (3.127)$$

$$C = \frac{0.023 \mu_l^{1.133} \mu_v^{0.2}}{D^2 g^{2/3} \rho_v \rho_l^{0.333}} \quad (3.128)$$

The general correlations by Chen et al. (1987) can be readily incorporated into a condensation model once the interfacial shear is known.

Shah (1989) proposed an alternative formula based on experimental data reported in the literature that includes working fluids of water, refrigerants (R-11, R-12, R-22, and R-113), and organic compounds (methanol, ethanol, benzene, toluene, and trichloroethylene) for vertical, horizontal, and inclined tubes with diameters ranging from 7 to 40 mm:

$$Nu = 0.023 Re_l^{0.8} Pr_l^{0.4} \left[(1 - x)^{0.8} + \frac{3.8x^{0.76}(1 - x)^{0.04}}{(p_{\text{Sat}}/p_c)^{0.38}} \right] \quad (3.129)$$

The Shah correlation is valid for the following parameter ranges: $0.002 < p_{\text{Sat}}/p_c < 0.44$, $100 < Re_l < 63,000$, $1 < Pr_l < 13$, $21^\circ\text{C} < T_{\text{Sat}} < 310^\circ\text{C}$, $3 \text{ m/sec} < u_v < 300 \text{ m/sec}$, $0 < x < 1$, and $39,000 < \dot{m}(\text{kg/m}^2 \text{ h}) < 758,000$. The mean deviation of Shah's correlation with 474 data points used in the study is 15.4%.

3.2.3.2 Mathematical Modeling of Two-Phase Flow and Heat Transfer in Tubes

3.2.3.2.1 Laminar Film Condensation in a Vertical Tube with Upward Vapor Flow

The goal of the mathematical model is to predict the liquid boundary layer thickness along the tube because it is directly related to the condensation rate. This is accomplished by first addressing the liquid fluid dynamics, then the vapor flow and finally accounting for the interaction between each along the tube. The following analytical model is based on Seban and Hodgson (1982). All of the Nusselt assumptions, for the vertical flat plate, are applied except that the flow here is an axisymmetric two-dimensional flow that results in an annular flow pattern. Seban and Hodgson (1982) further assumed that the tube radius is relatively large, so the curvature effects were neglected. A schematic representation of the coordinates is shown in [Figure 3.23](#).

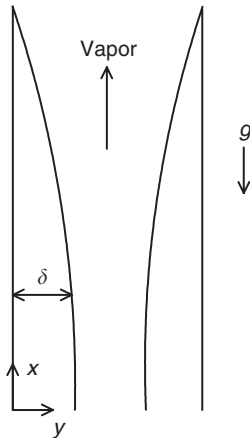


FIGURE 3.23 Coordinate system for condensation with an upward vapor flow.

3.2.3.2.1.1 Liquid Layer. The momentum equation is

$$\mu_l \frac{d^2 u}{dy^2} - \frac{dp}{dx} - \rho_l g = 0 \quad (3.130)$$

After rearrangement,

$$\begin{aligned} \frac{\mu_l}{\rho_l g} \frac{d^2 u}{dy^2} &= \left(1 + \frac{1}{\rho_l g} \frac{dp}{dx} \right) \\ &= G_p \end{aligned} \quad (3.131)$$

It is noted that G_p is a constant. After integration, one obtains the velocity profile as

$$u(y) = \frac{G_p \rho_l g}{\mu_l} \left(\frac{y^2}{2} - \delta(x)y \right) + \frac{\tau_i}{\mu_l} y \quad (3.132)$$

where τ_i is the interfacial shear stress and δ the liquid layer thickness. The above equation is nondimensionalized as

$$\bar{\delta} = \delta \left(\frac{g}{\nu_l^2} \right)^{1/3}, \quad \bar{y} = y \left(\frac{g}{\nu_l^2} \right)^{1/3}, \quad \bar{u} = \frac{u}{(\nu_l g)^{1/3}} \quad (3.133)$$

The dimensionless velocity profile is therefore given as

$$\bar{u} = G_p \left(\frac{\bar{y}^2}{2} - \bar{\delta} \bar{y} \right) + \frac{\tau_i}{\rho_l g} \left(\frac{g}{\nu_l^2} \right)^{1/3} \bar{y} \quad (3.134)$$

The local Reynolds number is defined by neglecting the pressure drop term, which is $G_p = 1$, as follows:

$$\begin{aligned} Re_l &= \frac{1}{\nu_l} \int_0^\delta u \, dy \\ &= N_1 \frac{\bar{\delta}^2}{3} - \frac{\bar{\delta}^3}{3}, \end{aligned} \quad (3.135)$$

$$N_1 = \frac{\tau_i}{\rho_l g} \left(\frac{g}{\nu_l^2} \right)^{1/3} \quad (3.136)$$

The local liquid mass flow rate per unit film width is

$$\Gamma = \rho_l \int_0^\delta u \, dy \quad (3.137)$$

The condensation mass flux at a local downstream position, $\dot{m}_c(x)$, is

$$\dot{m}_c = \frac{d(\Gamma)}{dx} \quad (3.138)$$

which is expressed as

$$\dot{m}_c = \mu_l \frac{d(\Gamma/\mu_l)}{dx} = \mu_l \frac{N_2}{\delta} \quad (3.139)$$

for later use. From an energy balance at the vapor–liquid interface, one has

$$\dot{m}_c h_{fg} = \frac{k_l(T_{\text{Sat}} - T_w)}{\delta} \quad (3.140)$$

Equating Eqs. (3.139) and (3.140) one has

$$N_2 = \frac{c_{p,l}(T_{\text{Sat}} - T_w)}{h_{fg}} \left[\frac{k_l}{\mu_l c_{p,l}} \right] \quad (3.141)$$

3.2.3.2.1.2 Vapor Layer. The detailed velocity profile of the vapor layer is not required to solve the problem if an appropriate friction coefficient is used. First evaluate the friction coefficient of the vapor. If the vapor were occupying the tube completely in a single-phase flow, the friction coefficient for a fully developed flow would be

$$\frac{c_f}{2} = \begin{cases} \frac{8}{Re_V} & \text{for } Re_V < 2000 \\ 0.04 & \text{for } Re_V > 4000 \end{cases} \quad (3.142)$$

and

$$\frac{c_f}{2} = \begin{cases} \frac{(Re_V)0.33}{3050} & \text{for } 2000 \leq Re_V \leq 4000 \\ \frac{0.04}{(Re_V)^{0.25}} & \text{for } Re_V > 4000 \end{cases} \quad (3.143)$$

then, with interpolation, one has

$$\frac{c_f}{2} = \frac{(Re_V)0.33}{3050} \quad \text{for } 2000 \leq Re_V \leq 4000 \quad (3.144)$$

In the above equation, $Re_V (=4\dot{M}_V / \pi D \mu_v)$ is the Reynolds number for the single-phase vapor, where D is the diameter of the tube and \dot{M}_V the total vapor mass flow rate. For condensation two-phase flow, the existence of the liquid layer must be accounted for. The vapor Reynolds number is modified as $Re_V = 4\dot{M}_V / \pi D' \mu_v$, where $D' = D - 2\delta$. For the turbulent vapor flow, the single-phase friction factors specified by the above equations should be multiplied by a quantity which will then produce the effective friction factor $(c_f/2)_E$ to include the liquid layer effects.

$$\left(\frac{c_f}{2} \right)_E = \frac{c_f}{2} (1 + 1400F) \quad (3.145)$$

The value for F is related to F' and is defined as

$$F' = \frac{\sqrt{2}(\Gamma/\mu_l)^{1/2}}{Re_V^{0.9}} (\nu_v/\nu_l)(\rho_l/\rho_v)^{1/2} \quad (3.146)$$

When the liquid flow is laminar, $F = F'$. For low vapor velocities, the factor F must be corrected further since the vapor flow is no longer fully turbulent,

$$\begin{aligned} F &= F' \left[1 - \exp\left(\frac{-\tau_i}{\rho_l g \delta}\right) \right] \\ &= F' \left[1 - \exp\left(\frac{-N_1}{\delta}\right) \right] \end{aligned} \quad (3.147)$$

$$F = 0 \quad \text{for } Re_V < 2000 \quad (3.148)$$

The interfacial shear, τ_i , can now be linked to the vapor friction coefficient. The condensation causes a mass flux into the liquid layer and the interfacial shear stress is affected. The shear stress is

$$\tau_i = \left(\frac{c_f}{2} \right)_E \rho_l (u_v - u_{l,\delta})^2 + \dot{m}_c (u_v - u_{l,\delta}) \quad (3.149)$$

where u_v is the mean vapor velocity based on the total vapor mass flow rate. $u_{l,\delta}$ is the liquid velocity at the edge of the liquid film, which can be obtained from Eq. (3.134). Equation (3.149) can be nondimensionalized using Eqs. (3.133), (3.136), and (3.141):

$$N_1 = \left(\frac{c_f}{2} \right)_E \left(\frac{\rho_v}{\rho_l} \right) (\bar{u}_v - \bar{u}_{l,\delta})^2 + \frac{N_2}{\delta} (\bar{u}_v - \bar{u}_{l,\delta}) \quad (3.150)$$

If the body force on the vapor flow is neglected ($\rho_v = \rho_l$), Seban and Hodgson (1982) used the integral vapor momentum balance equation, in which the momentum flux term is approximated using u_v as the vapor velocity at the interface instead of $u_v - u_{l,\delta}$ and show that

$$\frac{1}{\rho_l g} \frac{dp}{dx} = -\frac{4N_1}{D'} - \left(\frac{\nu_v}{\nu_l} \right)^2 \left(\frac{\rho_v}{\rho_l} \right) \frac{d}{dx} \left(\frac{4\dot{M}_v}{\pi D' \mu_v} \right) \quad (3.151)$$

In general, Seban and Hodgson (1982) concluded that the pressure drop term is negligibly small, which supports the earlier assumption that $G_p = 1$.

For the current case of upward vapor flow in a tube, based on heat and mass transfer coupling and applying Eq. (3.139), the liquid layer has the following relationship:

$$\frac{d(\Gamma/\mu_l)}{dx} = \frac{N_2}{\delta} \quad (3.152)$$

By differentiating Eq. (3.135) with respect to $\bar{\delta}$ and using Eq. (3.137), one has

$$\frac{d(\Gamma/\mu_l)}{d\bar{\delta}} = \left(N_1 + \frac{\bar{\delta}}{2} \frac{dN_1}{d\bar{\delta}} - \bar{\delta} \right) \bar{\delta} \quad (3.153)$$

Combining Eq. (3.152) with Eq. (3.153), one obtains the governing equation for the liquid film thickness:

$$\frac{d\bar{\delta}}{dx} = \frac{N_2}{\left(N_1 + \frac{\bar{\delta}}{2} \frac{dN_1}{d\bar{\delta}} - \bar{\delta} \right) \bar{\delta}^2} \quad (3.154)$$

The solution procedure is outlined as follows:

1. For a given vapor inlet mass flow rate, $\dot{M}_{V,0}$, at the pipe bottom edge indicated as the starting point of the x coordinate in Figure 3.23, the corresponding condensate flow rate per unit film width, Γ_0 , at the same point can be obtained based on an overall mass balance for a steady condition, which means all the vapor is condensed, i.e.,

$$\Gamma_0 = \dot{M}_{V,0}/\pi D \quad (3.155)$$

With $\dot{M}_{V,0}$ and Γ_0 known, Eqs. (3.135) and (3.150) are used to find the corresponding $N_{1,0}$ and $\bar{\delta}_0$ at the bottom edge through an iterative procedure.

2. The next step is to march upward using Eq. (3.152). First choose a small $\Delta\bar{x}$ and then find the condensate flow rate per unit film width, Γ_1 , at this new location by using

$$\Gamma_1 = \mu_l(N_2/\bar{\delta})\Delta\bar{x} + \Gamma_0 \quad (3.156)$$

3. The corresponding vapor mass flow at this new location is then calculated as

$$\dot{M}_{V,1} = \dot{M}_{V,0} - \pi D(\Gamma_0 - \Gamma_1) \quad (3.157)$$

Following the same procedure as given in Step 1, one can find $N_{1,1}$ and $\bar{\delta}_1$ with known $\dot{M}_{V,1}$ and Γ_1 .

4. Repeat Step 2 and march upward to another $\Delta\bar{x}$. Repeating steps 1 to 3 until $\bar{\delta}$ reaches zero.

Seban and Hodgson (1982) made several sample calculations for specific vapor inlet conditions. They investigated both downward and upward liquid film flow cases. Some of these cases were for an inlet pressure of 900 psia and are related to the operating condition of an industrial steam generating unit. It was reported that for these cases, a complete condensation occurs within a very short height up the tube.

3.2.3.2.2 Turbulent Film Theory

For annular film flow to take place, the vapor velocity must be high. Therefore, the film is generally in the turbulent or, at least, nonlaminar state. The following is a summary of the theory. The basic assumptions are:

1. The entrainment of vapor by the liquid film is neglected.
2. The film is thin with a smooth interface.
3. The inertia of the liquid film is small.

The schematic representation of the coordinate system is shown in Figure 3.24. From time-averaged turbulence modeling, the shear stress is defined as

$$\tau(y) = \rho_l(v_l + \varepsilon_m) \frac{du}{dy} \quad (3.158)$$

where ε_m is the eddy diffusivity for momentum transport. The heat flux is governed by the following equation:

$$\dot{q}(y) = -\rho_l c_{p,l} (\alpha_l + \varepsilon_h) \frac{dT}{dy} \quad (3.159)$$

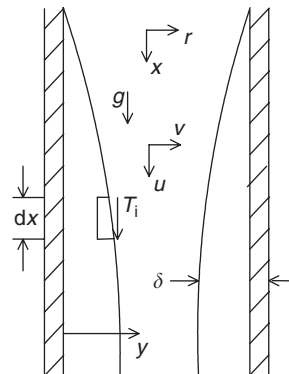


FIGURE 3.24 Schematic and coordinate system for turbulent film condensation in a tube.

where ε_h is the eddy diffusivity for thermal transport. Using the conventional nondimensional scheme, one has

$$\bar{u}^+ = \frac{u}{\sqrt{\tau_w/\rho_l}}, \quad y^+ = \frac{y\sqrt{\tau_w/\rho_l}}{v_l}, \quad \bar{T}^+ = \frac{\rho_l c_{p,l}(T_w - \bar{T})}{\dot{q}_w} \sqrt{\frac{\tau_w}{\rho_l}} \quad (3.160)$$

The dimensionless shear stress and heat flux equations become

$$\left(1 + \frac{\varepsilon_m}{v_l}\right) \frac{d\bar{u}^+}{dy^+} = 1, \quad \frac{\dot{q}}{\dot{q}_w} = \left(\frac{1}{Pr_l} + \frac{\varepsilon_h}{v_l}\right) \frac{d\bar{T}^+}{dy^+} \quad (3.161)$$

For the portion where the film is very thin, it is assumed that $\varepsilon_m/v_l = 1$, with a no-slip condition at the wall. This leads to the velocity profile of $\bar{u}^+ = y^+$ in the liquid film. On the basis of a mass conservation of the liquid film flow, the following dimensionless equation is obtained as

$$\frac{GD(1-x)}{4\mu_l} = \int_0^{\delta^+} \bar{u}^+ dy^+ \quad (3.162)$$

Using the velocity profile, the dimensionless film thickness is found to be

$$\delta^+ = \sqrt{\frac{1}{2} Re_{D,l}^{1/2}} dy^+ = \frac{GD(1-x)}{\mu_l} \quad (3.163)$$

The heat flux is constant across the liquid film so

$$\frac{\partial}{\partial y} \left[\rho_l c_{p,l} (\alpha_l + \varepsilon_h) \frac{\partial T}{\partial y} \right] = 0 \quad (3.164)$$

Based on Eq. (3.160), the heat flux is therefore constant in the liquid film. After integration and using the boundary conditions, one has

$$\frac{T_{Sat} - T_w}{\dot{q}_w / (\rho_l c_{p,l} \alpha_l)} = \int_0^\delta \frac{1}{1 + Pr_l \varepsilon_h / v_l} dy \quad (3.165)$$

Following rearrangement, Eq. (3.161) becomes

$$\frac{k_l \sqrt{\tau_w/\rho_l}}{hv_l} = \int_0^{\delta^+} \frac{1}{1 + (Pr_l/Pr_t)(\varepsilon_m/v_l)} dy^+ \quad (3.166)$$

where $h = \dot{q}_w / (T_{Sat} - T_w)$. Next, the von Karman's mixing length model is adopted for ε_m :

$$\varepsilon_m = l^2 \left| \frac{du}{dy} \right|, \quad l = \kappa y \quad (3.167)$$

$$\varepsilon_m/v_l = \kappa^2 (y^+)^2 \quad (3.168)$$

For the turbulence, the model proposed by Carey (1992) has been used. Carey adopted similar concepts from the general approach for liquid film turbulence:

$$\frac{\varepsilon_m}{v_l Pr_t} = \begin{cases} \kappa^2 (y^+)^2 / Pr_t & \text{for } 0 \leq y^+ \leq \delta^+/2 \\ \kappa^2 (\delta^+ - y^+)^2 / Pr_t & \text{for } \delta^+/2 \leq y^+ \leq \delta^+ \end{cases} \quad (3.169)$$

The equation for the $\delta^+/2 \leq y^+ \leq \delta^+$ region is based on the experimental finding that the eddy diffusivity should approach zero as $(\delta - y)^2$. With the above information, it may be shown that

$$h = \frac{\kappa k_l \sqrt{\tau_w/\rho_l}}{2v_l I} \sqrt{\frac{Pr_l}{Pr_t}} \quad (3.171)$$

where

$$\begin{aligned} I &= \tan^{-1}\left(\sqrt{Pr_l/Pr_t}\kappa\delta^+/2\right) \\ &\approx \pi/2 \quad \text{for large } Pr_l \end{aligned} \quad (3.172)$$

Using commonly accepted values of $\kappa = 0.4$ and $Pr_t = 0.9$, one has

$$h = 0.134k_l\sqrt{Pr_l\tau_w/\rho_l/v_l} \quad (3.173)$$

The wall shear stress, τ_w , is determined from a force balance :

$$\pi D\tau_w = -\left(\frac{dp}{dx}\right)_f \pi D^2/4 \quad (3.174)$$

The pressure drop due to friction at the wall for two-phase pipe flows is (see [Chapter 2](#))

$$-\left(\frac{dp}{dx}\right)_f = \phi_f \frac{2f_l G^2(1-x)^2}{D\rho_l} \quad (3.175)$$

where

$$\begin{aligned} \phi_f &= \left(1 + \frac{20}{\chi_{tt}} + \frac{1}{\chi_{tt}^2}\right)^{1/2}, \quad \chi_{tt} = \left(\frac{\rho_v}{\rho_l}\right)^{1/2} \left(\frac{\mu_l}{\mu_v}\right)^{0.1} \left(\frac{1-x}{x}\right)^{0.9}, \\ f_l &= 0.05 \left(\frac{G(1-x)D}{\mu_l}\right)^{-0.2} \end{aligned} \quad (3.176)$$

With the wall shear stress known, the Nusselt number may be written as

$$\begin{aligned} Nu &= \frac{hD}{k_l} \\ &= 0.134\phi_f\sqrt{f_l} \left[\frac{G(1-x)D}{\mu_l} \right] \sqrt{Pr_l} \end{aligned} \quad (3.177)$$

3.2.3.3 Condensation on a Tube

As discussed above, the laminar condensation on the outside of a horizontal tube can be estimated by the Nusselt theory with the effective gravity modification of Dhir and Lienhard (1971). For a horizontal tube, the average heat transfer coefficient follows Incropera and DeWitt (2002):

$$\bar{h}_D = 0.729 \left[\frac{g\rho_l(\rho_l - \rho_v)k_l^3 h'_{fg}}{\mu_l(T_{\text{Sat}} - T_w)D} \right] \quad (3.178)$$

For a vertical tier of N horizontal tubes, Incropera and DeWitt (2002) suggest that the average condensation heat transfer coefficient for the N tubes is $\bar{h}_{D,N} = \bar{h}_D N^{-1/4}$. The decrease in heat transfer is attributed to the increase in the film thickness for the downstream tubes.

3.2.4 Effects of Noncondensable Gases and Other Secondary Effects

In most of the condensation processes, noncondensables are usually present such as air for those operating in the atmospheric environment. The first comprehensive and detailed study that quantitatively addressed the role of noncondensables was presented by Minkowycz and Sparrow (1966). It is based on the model of Nusselt (1916) except that the environment is a mixture of condensing vapor and noncondensables. Because the vapor–gas phase can no longer be neglected and decoupled from the liquid phase, the coupled boundary layer equations describing continuity, momentum, and energy for both phases were formulated and transformed into similarity variables. The resulting set of coupled nonlinear ordinary equations was solved numerically. To assess exclusively the effects of noncondensable gases, they used the saturated steam–air system with the mixture pressure ranging from 0.5 psia to 14.7 psia. The results that are based

on comparisons with the Nusselt model, where the pure vapor occupies the surroundings, show that the air has a decisive effect in reducing the condensation heat transfer rates. A typical case shows that under 1 atmosphere, when compared with the pure steam condition, a reduction in condensation heat transfer ranging from 35 to 60% for a wall subcooling of 2 to 40° R was found for the air bulk mass fraction as small as 0.5%. In general, when the bulk noncondensable mass fraction increases the condensation heat transfer decreases monotonically. At a given value of noncondensable bulk mass fraction, the heat transfer decreases with increasing wall subcooling except at very small degrees of wall subcooling and large noncondensable bulk mass fractions. The mixture pressure has a strong influence. For a bulk pressure of 0.5 psia, the reduction in heat transfer is from 67 to 83% compared to 35 to 60% for 1 atm.

The physics explains why a small amount of noncondensables have such a detrimental effect on the condensation heat transfer is interesting. The theory is based on the binary convective-diffusive transport in the mixture phase. The net convection flow is moving toward the wall bringing both the vapor and noncondensables to the liquid surface. Since the noncondensables do not condense, a mechanism must be established to remove them at the same rate as that of arrival during the steady state, thus preventing them from accumulating at the interface. This removal mechanism is basically a diffusion process that sends the noncondensable back to the bulk through a very steep concentration gradient because the diffusion process is much less efficient than the convective process. The requirement for a steep concentration gradient of the noncondensables results in a high noncondensable mass fraction at the liquid-gas interface that drastically reduces the partial pressure of vapor at the interface. The reduction in the vapor pressure at the interface correspondingly decreases the liquid surface temperature, which is the saturation temperature of the condensing vapor. The net consequence is that the temperature difference between the liquid surface and the wall, the condensation driving force, is reduced when compared to the pure vapor case.

The effects of noncondensables discussed above are pertinent to a quiescent mixture of vapor and noncondensable gases. Sparrow et al. (1967) investigated the case where a net forced flow field is maintained for the mixture phase, thus resulting in a forced-convection laminar boundary layer. Again, a set of coupled nonlinear ordinary different equations was solved numerically and by an integral method. Their results were presented in terms of heat transfer reduction based on the identical system conditions, except that the ambient is composed of pure vapor only. For mixture pressure of 1 atm, the reduction in condensation heat transfer is only about 2 to 5% for the wall subcooling ranging from 2 to 40° R at a noncondensable gas bulk mass fraction of 0.5%. For the low-pressure mixture of 0.5 psia, the reduction in heat transfer is about 3 to 10% for the same wall subcooling range and noncondensable gas bulk mass fraction. The reduction becomes substantial at about 40 to 55% for the noncondensable gas bulk mass fraction of 10%. The other trends remain similar to those of the quiescent ambient case. Therefore, it is concluded that the forced convection drastically mitigates the noncondensable gas effects on the heat transfer.

Minkowycz and Sparrow (1966) also examined the effects of superheating the mixture phase. In general, for the pure vapor case, the superheating only causes the heat transfer to increase by about 1% at 100° Rankine to 5% at 400° R, whereas for the case of noncondensables, the enhancement in heat transfer due to superheating is more appreciable. For example, with the noncondensable gas bulk mass fraction at 0.5% and a wall subcooling of 10° R, the reductions in heat transfer are 55, 47, 43, and 37% for superheating of 100, 200, 300, and 400° R, respectively. The effect of superheating decreases with decreasing mixture pressure.

Minkowycz and Sparrow (1966) systematically examined the effects of interfacial resistance, diffusion thermo, thermodiffusion, and variable property when noncondensables are present. They concluded that all these effects are of second-order importance.

3.2.5 Direct Contact Condensation

Direct contact condensation usually refers to vapor condensing on liquid heat sinks that are not attached to a solid surface, for example, condensation on drops, liquid jets and sheets. For the drop condenser, cold liquid drops are sprayed into a chamber of saturated or superheated vapor. One such design is associated with the emergency cooling system of the nuclear reactor containment. During a main coolant

pipe rupture accident, cold water droplets are sprayed into the vapor-filled containment to reduce pressure and temperature by condensing steam.

3.2.5.1 Condensation on Drops

Lekic and Ford (1980) published a complete study of vapor condensation on a spray of subcooled droplets. They developed a mathematical model that includes the drop size distribution, motion of drop, and heat transfer rate. The model is capable of predicting the average spray temperature as a function of the given spray length. The experimental investigation was also performed where they used three full cone nozzles with different pressure drops. The main results from the experiment are quantified by thermal utilization defined as

$$\varepsilon = \frac{Q_z}{Q_T} \quad (3.179)$$

where Q_z represents the quantity of heat absorbed per unit time by the spray from nozzle outlet to distance z and Q_T is the maximum amount of heat per unit time that can be absorbed by the spray. The heat transfer Q_z is obtained from

$$Q_z = \frac{\pi}{6} \rho_l h_{fg} \int_0^{D_m} (D^3 - D_i^3) d\dot{n} \quad (3.180)$$

where \dot{n} is the number of drops per unit time generated by the nozzle. The following equation provides a relationship between \dot{n} and D_i :

$$d\dot{n} = \frac{\dot{M}}{\rho_l} \frac{\xi}{\sqrt{\pi}} \frac{D_m}{D_i(D_m - D_i)} \frac{6}{\pi D_i^3} \exp \left[-\xi^2 \left(\ln \frac{\varphi D_i}{D_m - D_i} \right)^2 \right] dD_i \quad (3.181)$$

where D is the drop diameter, D_i and D_m are drop initial diameter and maximum diameter, respectively, \dot{M} is mass flow rate of the spray, and ξ and φ are the spray distribution parameters for uniformity and skewness. Therefore, ε measures the percentage of maximum heat removal capacity. Their experimental results show that the thermal utilization ranges from 0.783 to 0.987 for spray distances of 42 to 356 mm from the nozzle. The model predictions compared well with the experimental results. They concluded that direct condensation is a highly efficient way of condensing pure steam.

Most of the theoretical and analytical investigations were focused on a single droplet. Jacobs and Cook (1978) developed a mathematical model based on pure conduction in the droplet and thin liquid condensate film formed on the droplet surface. The droplet radius history, R_t , is given as

$$\frac{R(t)}{R_i} = \left[1 + \frac{3}{Ja} \int_0^1 \left(\frac{r}{R_i} \right)^2 \frac{(T_{ri} - T_i)}{R_i(T_{sat} - T_i)} dr \right] \quad (3.182)$$

where R_i and T_i are initial radius and temperature of the drop, respectively, and r and T_{ri} are the radial coordinate and temperature at the radial location r , respectively. Chung et al. (1984a, 1984b) used asymptotic analysis and numerical methods to evaluate the condensation on droplets in the small Reynolds number regime. They included the effects of internal circulation and noncondensable gases. For intermediate and high Reynolds number flows, Sundararajan and Ayyaswamy (1984, 1985a, 1985b) and Huang and Ayyaswamy (1987a, 1987b) have published theoretical and numerical results that address the internal flow field and external boundary layer in addition to the effects of noncondensable gases.

3.2.5.2 Condensation on Liquid Jets, Liquid Sheets, and Liquid Films

Condensation on jet and sheets has been used in special type condensers. Hasson et al. (1964a) presented a theoretical analysis for vapor condensing on laminar jets. From the same group, Hasson et al. (1964b) experimentally investigated the condensation of steam on laminar water sheets. Later, Taitel and Tamir (1969) extended the study of direct contact condensation by examining the effects of noncondensable gases. For a more complete analysis, Jacobs and Nadig (1987) included the resistance in the condensate that was not addressed in previous work. They introduced the concept of coolant capacity utilization and produced its relationship with the Graetz number for different noncondensable mass fractions. For example, the percent coolant capacity utilized drops from 100 to 55% for the Graetz number increasing

from 0 to 60 at the noncondensable mass fraction of 0.0005. The percent coolant capacity utilized changed from 100 to 30% for the same Graetz number range at the noncondensable mass fraction of 0.1.

3.2.6 Enhanced Condensation

The enhancement of condensation heat transfer is generally based on the following principles. Because the major heat transfer resistance is associated with the condensate layer, thinning of the condensate film and creating turbulence in the film would accomplish the goal. Increasing the effective condenser surface area such as fluted, finned, corrugated, or wire-wrapped tubes would also enhance the condensation heat transfer. Marto (1988) gave a complete review of the progress made on the enhancement of condensation heat transfer on horizontal integral-fin tubes. It was pointed out that condensate flooding significantly affects the finned tube performance. Heat transfer enhancements are more substantial than the surface area enhancement by adding more fins. Fin spacing has been considered as an important parameter. As the ratio of the surface tension to density of the working fluid is increased, the optimal fin spacing also increases, but the magnitude of the heat transfer enhancement decreases. In cases where the fin shape is important, there is an associated small degree of condensate flooding. When using metals of high thermal conductivities, tall and thin fins are more beneficial. For working fluids of high surface tensions, improvement in the condensate removal may be useful for providing additional heat transfer enhancement. Kedzierski and Webb (1990) proposed a new family of high-performance fin profiles for surface tension-drained condensers that offer improvement over existing commercial fin shapes. They specified each design in terms of the fin tip radius, the fin height and the fin base thickness.

3.2.7 Surface Promoter for Dropwise Condensation

In Section 3.2.2.1, it was mentioned that dropwise condensation relies on a relatively nonwetting condition between the condensate and the condenser surface for the drops to grow to larger sizes without spreading to liquid films. In most engineering applications, polished metal surfaces that are generally wettable by most liquids are usually used for condensers. Promoters are required to induce the nonwetting condition for dropwise condensation. In general, there are two types of promoters. One is called the additive agent that is sprayed onto the condensing surface or into the vapor phase. The other is coating or plating the condenser surface with thin layer of materials with high free energy.

3.2.8 Electric Field Enhanced Condensation

Gerstman and Choi (1962) were the first to perform an experiment to demonstrate the enhancement of condensation on a vertical plate by thinning the liquid film with an electrical stress. The idea of using an electric field to enhance the condensation heat transfer was then attempted by Velkoff and Miller (1965). They used Freon-113 vapor condensing on a vertical copper plate. Various electrode geometries and strengths were investigated. It was found that screen electrodes placed parallel to the cold plate generated the largest heat transfer enhancement. Controllable and reproducible increases of 150% were achieved. On the theoretical side, Melcher (1966) was the first to introduce the electrohydrodynamic (EHD) induction pumping based on the electrostatic shear stress at the two-phase interface. Melcher and Taylor (1969) gave a comprehensive review of the EHD-driven convection by a DC or AC field. They also discussed the effects of interfacial instability waves due to the electric field. Jones (1978) further summarized the progress in EHD-enhanced condensation heat transfer. On the basis of the suggestions by Velkoff and Miller (1965), Jones (1978) generalized the following possible mechanisms of EHD-driven condensation:

1. Nucleation sites provided by ions.
2. Corona wind to drive ions to heat transfer surfaces.
3. Nonuniform electric fields to collect condensate.
4. Condensate film surface wave destabilization.
5. Electrostatic pumping of condensate.
6. Internal mixing of condensate liquid.

Nomenclature

a, b	Constants in Eq. (3.49)
A, B	Constants in Eq. (3.15)
Bo	Boiling number ($=q''/(Gh_{fg})$)
c_p	Specific heat constant, J/kg °C
Co	Convection number ($=(\rho_G/\rho_L)^{0.5} ((1-x)/x)^{0.8}$)
$C_{s,f}$	Fluid-surface effect constant, Eq. (3.21)
D_b	Bubble diameter, m
D_h	Hydraulic diameter, m
D_{12}	Mass diffusion coefficient of species 1 in a mixture of 1 and 2
d	Equilibrium break-off bubble diameter, m, Eq. (3.26)
D	Tube diameter, m
F_{Fl}	Fluid-surface parameter accounting for nucleation characteristics of different fluid surface combinations in Kandlikar (1990) correlation
Fo	Fourier number
Fr	Froude number
Fr_{LO}	Froude number with all flow as liquid ($=G^2/(\rho_L^2 g D)$)
f	Bubble departure frequency, Eq. (3.19)
f	Friction factor, Eqs. (3.44)–(3.46)
$f_2(Fr_{LO})$	Froude number multiplier in Eqs. (3.56) and (3.57)
F_D	Diffusion-induced suppression parameter, defined by Eq. (3.66), F_{Fl}
g	Gravitational acceleration, m/sec ²
G	Mass flux, kg/m ² sec
h	Heat transfer coefficient, W/m ² °C
h_{fg}	Latent heat of vaporization, J/kg
h'_{fg}	Latent heat corrected for vapor superheating, Eqs. (3.32) and (3.33), J/kg
h_L	Heat transfer coefficient for the liquid, W/m ² °C
h_{LO}	Single-phase heat transfer coefficient for all flow in the liquid phase at saturation temperature, W/m ² °C
$h_{L,Sat}$	Heat transfer coefficient for the liquid at the saturation point, W/m ² °C
h_m	Heat transfer coefficient for the mixture, W/m ² °C
h_{TP}	Two-phase heat transfer coefficient, W/m ² °C
$h_{TP,CBD}$	Two-phase heat transfer in the convective boiling dominant region, W/m ² °C
$h_{TP,NBD}$	Two-phase heat transfer in the convective boiling dominant region, W/m ² °C
h^*	Heat transfer coefficient using T_{Sat} as the fluid temperature in the subcooled flow boiling, W/m ² °C
Ja	Jakob number
K	Boltzman constant, $k (= 1.38 \times 10^{-23} \text{ J/K})$
K_1	Parameter in Eq. (3.16)
K_1, K_2	New nondimensional groups defined by Eqs. (3.75) and (3.76)
k_L	Thermal conductivity, W/m °C
l	Mixing length
M	Molecular weight
\dot{m}	Total mass flux, kg/m ² sec
Nu	Nusslet number
Nu_{LO}	Nusslet number with all flow as liquid
$Nu_{LO, cp LO, cp}$	Nusslet number with constant properties and all flow as liquid
\dot{n}	Number of drops per unit time
p	Pressure, N/m ²
p_{cr}	Critical pressure, N/m ²

p_G	Pressure of the gas inside bubble, N/m ²
p_L	Pressure of the liquid, N/m ²
$p_{\text{Sat},T}$	Saturation pressure over a planar interface, N/m ²
Pr	Prandtl number
Pr_L	Prandtl number for liquid
q	Heat transfer rate, W
q''	Heat flux, W/m ²
q''_{CHF}	Critical heat flux, W/m ²
$q''_{\text{FDB,i}}$	Heat flux at initial point of fully developed boiling, W/m ²
q''_{int}	Heat flux at intersection of the extended single-phase line and the fully developed boiling curve, W/m ²
q''_{MHF}	Minimum heat flux, W/m ²
q''_{ONB}	Heat flux at onset of nucleate boiling, W/m ²
q''_{PB}	Heat flux in the partial boiling region, W/m ²
R	Radius
R_b	Radius of a bubble, m
R_c	Cavity mouth radius, m
$R_{c,\text{crit}}$	Cavity radius at the ONB
$R_{c,\text{Max}}, R_{c,\text{Min}}$	Minimum and maximum cavity radii available on a surface, m
Re	Reynolds number
$R(t)$	Bubble growth rate function
R_c^*	Nondimensional cavity radius
R_{\min}^*, R_{\max}^*	Minimum and maximum radii of active cavities
T	Temperature, °C or K
$T_{\text{Sat},1 p}, T_{\text{Sat},2 p}$	Saturation temperatures of the pure components at the total system pressure, p , °C
t	Time, sec
TTR	Tape twist ratio for twisted tapes
u	Velocity, m/sec
v	Specific volume, m ³
V	Volatility parameter, defined by Eq. (3.62)
V_b	Bubble volume, Eq. (3.20)
V_m	Molar volume, m ³ / kg mol
X_{1-8}	Nondimensional groups defined in Eqs. (3.22)–(3.26)
x	Equilibrium quality
x_1, x_2	Mass fractions of 1 and 2, respectively, in the liquid phase of a mixture of species 1 and 2
\tilde{x}	Molar concentration in Eq. (3.27)
y	The distance normal to the heater surface to the center of the bubble, m
y_1, y_2	Mass fractions of 1 and 2, respectively, in the vapor phase of a mixture of species 1 and 2

Greek Letters

α	Thermal diffusivity ($= k/(\rho c_p)$) m ² /sec
Γ	Liquid mass flow rate per unit film width
ΔT_{Sat}	Wall superheat ($T_{\text{Wall}} - T_{\text{Sat}}$), °C
ΔT_{Sat}^*	Nondimensional wall superheat, Eq. (3.39)
$\Delta T_{\text{Sat,ONB}}$	Wall superheat at the ONB, °C
ΔT_{Sub}	Liquid subcooling ($T_{\text{Sat}} - T_L$), °C
ΔT_{Sub}^*	Liquid subcooling ($T_{\text{Sat}} - T_L$), nondimensional
δ_T	Single-phase thermal boundary layer thickness
ε_m	Eddy diffusivity for momentum transport
ε_h	Eddy diffusivity for heat transport

ϕ	Angle of orientation of the heated surface with respect to the horizontal, deg
ϕ	Association factor in Eq. (3.68)
φ	Spray distribution parameter for skewness
κ	Mixing length constant
μ_B	Viscosity of the bulk liquid, N sec/m ²
μ_L	Viscosity of the liquid, N sec/m ²
μ_W	Viscosity of the fluid at the wall temperature, N sec/m ²
ξ	Spray distribution parameter for uniformity
θ	Contact angle, deg
θ_r	Receding contact angle, deg
ϑ	Nondimensional centrifugal acceleration, Eqs. (3.78) and (3.79)
ρ	Density, kg/m ³
σ	Surface tension, N/m ²
ψ	Parameter in Eqs. (3.72) and (3.73)

Subscripts

an	Annular flow
1, 2	Species 1 and 2
b	Bubble
bp	Bubble point
c	Critical state
CHF	Critical heat flux
CBD	Convective boiling dominant region
conv	Convective boiling component
crit, cr	Critical point for the fluid
dp	Dew point
exit	Exit section
f	Stream core
FDB, <i>i</i>	Initial point of fully developed boiling
F,c	Convective component of film boiling
F, r	Radiative component of film boiling
Fl	Fluid-surface-dependent parameter in Kandlikar (1990) correlation
fl	Fluid
fg	Latent quantity (vapor property – liquid property)
i	At the interface or initial state
int	Intersection of the extended single-phase line and the fully developed boiling curve given by Eq. (3.41)
L	Liquid
LO	All flow as liquid
G	Gas
MHF	Minimum heat flux
max	Maximum
min	Minimum
NBD	Nucleate-boiling-dominant region
NVG	Point of net vapor generation
Nu	Nusselt-type solution
nucl	Nucleate boiling component
0	On a flat surface
ONB	Onset of nucleate boiling
PB	Partial boiling region

r	Receding
F,r	Radiative component of film boiling
F,c	Convective component of film boiling
Sat	Saturation point
Smooth	Smooth tube value
str	Stratified flow
Sub	Subcooling
t	Turbulent flow
tr	Transition flow
T	Thermal layer
TP	Two phase
v	Vapor phase
W	Wall
δ	Edge of liquid film

Superscripts

-	Averaged, average over the entire length or dimensionless quantity
+	Dimensionless quantity
m	Exponent in Eq. (3.51)
n	Constant in Eq. (3.52)
p	Constant in Eq. (3.52)
*	Nondimensional form
0	Pure component value at infinite dilution, Eqs. (3.67) and (3.68)

References

- Ananiev, E.P., Boyko, L.D., and Kruzhilin, G.N., Heat transfer in the presence of steam condensation in a horizontal tube, *Proceedings. First Int. Heat Transfer Conf.*, Part II, 290, 1961.
- Bankoff, S.G., Entrapment of gas in the spreading of liquid over a rough surface, *AIChE J.*, 4, 24–26, 1958.
- Bennett, D.L. and Chen, J.C., Forced convective boiling in vertical tubes for saturated pure components and binary mixtures, *AIChE J.*, 26, 454–461, 1980.
- Berenson, P.B., Film Boiling heat transfer from horizontal surfaces, *J. Heat Transfer*, 83, 351–358, 1961.
- Bergel'son, B.R., Burnout under conditions of subcooled boiling and forced convection, *Thermal Eng.*, 27, 48–50, 1980.
- Bergles, A.E. and Rohsenow, W.M., The determination of forced convection surface boiling heat transfer, *Trans. ASME, J. Heat Transfer*, 86, 365–372, 1964.
- Bergles, A.E., Heat transfer enhancement — the encouragement and accommodation of high heat fluxes, *J. Heat Transfer*, 119, 8–19, 1997.
- Bowring, W.R., *Physical Model of Bubble Detachment and Void Volume in Subcooled Boiling*, OECD Halden Reactor Project Report HPR-10, 1962.
- Boyd, R.D., Subcooled flow boiling critical heat flux (CHF) and its application to fusion energy components. Part I. A review of fundamentals of CHF and related data base, *Fusion Technol.*, 7, 7–30, 1983a.
- Boyd, R.D., Subcooled flow boiling critical heat flux (CHF) and its application to fusion energy components. Part II. A review of microconvective, experimental, and correlational aspects, *Fusion Technol.*, 7, 31–51, 1983b.
- Boyd, R.D., Subcooled flow boiling critical heat flux (CHF) and its application to fusion energy components. Part I. A review of fundamentals of CHF and related data base, *Fusion Technol.*, 7, 7–30, 1985.
- Boyko, L.D. and Kruzhilin, G.N., Heat transfer and hydraulic resistance during condensation of steam in a horizontal tube and in a bundle of tubes, *Int. J. Heat Mass Transfer*, 10, 361, 1967.
- Bromley, L.A., Heat transfer in stable film boiling, *Chem. Eng. Prog.*, 46, 221–227, 1950.

- Calus, W.F., di Montegnacco, A., and Kenning, D.B.R., Heat transfer in a natural circulation single tube reboiler, Part II. Binary Liquid Mixtures, *Chem. Eng. J.*, 6, 251–264, 1973.
- Carey, V.P., *Liquid-Vapor Phase-Change Phenomena*, Taylor & Francis, Bristol, PA, 1992.
- Cavallini, A. and Zecchin, R., A dimensionless correlation for heat transfer in forced convection condensation, *Proc. 5th Int. Heat Transfer Conference*, Tokyo, 3, 309–313, 1974.
- Celata, G.P., and Mariani, A., CHF and post-CHF (post-dryout) heat transfer, in *Handbook of Phase Change—Boiling and Condensation*, Kandlikar, S.G., Dhir, V.K., and Shoji, M., Eds., Taylor & Francis, Philadelphia, PA, Chap. 16, 1999.
- Celata, G.P., Cumo, M., and Mariani, A., Assessment of correlations and models for the prediction of CHF in subcooled flow boiling, *Int. J. Heat Mass Transfer*, 37, 237–255, 1994.
- Celata, G.P., Cumo, M., and Setaro, T., Forced convective boiling in binary mixtures, *Int. J. Heat Mass Transfer*, 36, 3299–3309, 1993.
- Chato, J., Laminar condensation inside horizontal and inclined tubes, *ASHRAE J.*, 12, 62, 1962.
- Chen, J.C. A correlation for boiling heat transfer to saturated fluids in convective flow, *Industrial Eng. Chem., Process Des. Dev.*, 5, 322–329, 1966.
- Chen, S.L., Gerner, F.M., and Tien, C.L., General film condensation correlation, *Exp. Heat Transfer*, 1, 93, 1987.
- Chun, K.R. and Seban, R.A., Heat transfer to evaporating liquid film, *ASME J. Heat Transfer*, 93, 391, 1971.
- Chung, J.N., Ayyaswamy, P.S., and Sadhal, S.S., Laminar condensation on a moving drop, Part 1. Singular perturbation technique, *J. Fluid Mech.*, 139, 105, 1984a.
- Chung, J.N., Ayyaswamy, P.S., and Sadhal, S.S., Laminar condensation on a moving drop, Part 2. Numerical solutions, *J. Fluid Mech.*, 139, 131, 1984b.
- Collier, J.G., and Thome, J.R., *Convective Boiling and Condensation*, 3rd ed., McGraw-Oxford University Press, New York, 1994.
- Davis, E.J., and Anderson, G.H., The incipience of nucleate boiling in forced flow, *AIChE J.*, 12, 774–780, 1966.
- Dhir, V. and Lienhard, J.H., Laminar film condensation on plane and axisymmetric bodies in nonuniform gravity, *ASME J. Heat Transfer*, 93, 97, 1971.
- Dhir, V.K., Nucleate boiling, Sections 4.1–4.6, in *Handbook of Phase Change, Boiling and Condensation*, Kandlikar, S.G., Dhir, V.K., and Shoji, M., Eds., Taylor & Francis, Philadelphia, PA, 1999.
- Doroshchuk, V.E., Levitan, L.L., and Lantzman, F.P., Investigation into Burnout in Uniformly Heated Tubes, ASME Publication 75-WA-HT-22, 1975.
- Drew, T.B. and Muller, A.C., Boiling, *Trans. 33*, 449–4715, 1937.
- El-Genk, M., A review of pool boiling from inclined and downward-facing flat surfaces, *2nd European Thermal-Sciences and 14th UIT National Heat Transfer Conference 1996*, Celata, G.P., Di Marco, P., and Mariani, A., Eds., Edizioni ETS, Italy, 1996.
- Eucken, A., Condensation nucleation theory, *Naturwissenschaften*, 25, 209, 1937.
- Fatica, N. and Katz, D.L., Dropwise condensation, *Chem. Engr. Prog.*, 45, 661, 1949.
- Feldman, A., Marvillet, C.H., and Lebouche, M., An experimental study of boiling in plate-fin heat exchangers, *2nd National UK Heat Transfer Conference*, IMechE, 2, 1257–1268, 1996.
- Ford, J.D. and Lekic, A., Rate of growth of drops during condensation, *Int. J. Heat Mass Transfer*, 16, 61, 1973.
- Fujita, Y., Bai, Q., and Tsutsui, M., Heat transfer of binary mixtures in nucleate pool boiling, *2nd European Thermal Science and 14th UIT National Heat Transfer Conference*, Celata, G.P., Di Marco, P., and Mariani, A., Eds., 1639–1646, 1996.
- Fujita, Y., Vapor liquid equilibrium properties, in *Handbook of Phase Change, Boiling and Condensation*, Kandlikar, S.G., Dhir, V.K., and Shoji, M., Eds., Taylor & Francis, Philadelphia, PA, 1999.
- Gaertner, R.F., Photographic study of nucleate pool boiling on a horizontal surface, *J. Heat Transfer, Trans. ASME, Series C*, 87, 17–29, 1965.
- Gerstman, J. and Choi, H.Y., Electrohydrodynamics Effects in Condensation, Report 62-3, Department of Mech. Eng., Tufts University, 1962.
- Gnielinski, V., New equations for heat and mass transfer in turbulent pipe and channel flow, *Int. Chem. Eng.*, 16, 359–368, 1976.

- Graham, C. and Griffith, P., Drop size distribution and heat transfer in dropwise condensation, *Int. J. Heat Mass Transfer*, 16, 337, 1973.
- Groeneveld, D.C., Cheng, S.C., and Doan, S.C., AECL-UO critical heat flux lookup table, *Heat Transfer Eng.*, 7, pp. 46–62, 1986.
- Groeneveld, D.C., Leung, L.K.H., Kirillov, P.L., Bobkov, V.P., Smogalev, I.P., Vinogradov, V.N., Huang, X.C., and Royer, E., The 1995 lookup table for critical heat flux in tubes, *Nucl. Eng. Des.*, 163, 1–23, 1996.
- Groeneveld, D.C., Post-dryout heat transfer at reactor operating conditions, AECL-4513, 1973.
- Gungor, K.E. and Winterton, R.H.S., Simplified general correlation for saturated flow boiling and comparisons of correlations with data, *Can. J. Chem. Eng.*, 65, 148–156, 1987.
- Gunther, F.C., Photographic study of surface-boiling heat transfer to water with forced convection, *Trans. ASME*, 73, 115–123, 1951.
- Haramura, Y. and Katto, Y., A new hydrodynamic model of CHF applicable widely to both pool and forced convection boiling on submerged bodies in saturated liquids, *Int. J. Heat Mass Transfer*, 26, 387–399, 1983.
- Hasson, D., Luss, D., and Navon, V., An experimental study of steam condensing on a laminar water sheet, *Int. J. Heat Mass Transfer*, 7, 983, 1964b.
- Hasson, D., Luss, D., and Peck, R., Theoretical analysis of vapor condensation on laminar jets, *Int. J. Heat Mass Transfer*, 7, 969, 1964a.
- Hebel, W., Detavernier, A., and Decreton, M., A contribution to the hydrodynamics of boiling crisis in a forced flow of water, *Nucl. Eng. Des.*, 64, 433–445, 1981.
- Hewitt, G.F., Boiling, in *Handbook of Heat Transfer*, 3rd ed., Rohsenow, W.M., Hartnett, J.P., and Cho, Y.I., Eds., McGraw-Hill, New York, 1998.
- Hihara, E., Tanida, K., and Saito, T., Forced convective boiling experiments of binary mixtures, *JSME Int. J.*, Ser. II, 32, 98–106, 1989.
- Hsu, Y.Y. and Graham, R.W., An Analytical and Experimental Study of the Thermal Boundary Layer and Ebullition Cycle in Nucleate Boiling, NASA TND-594, NASA Lewis Research Center, Cleveland, OH, 1961.
- Hsu, Y.Y. and Westwater, J.W., Approximate theory for film boiling on vertical surfaces, *AIChE Chem. Eng. Prog. Symp. Ser.*, 30, 15–24, 1960.
- Hsu, Y.Y., On the size range of active nucleation cavities in a heating surface, *Trans. ASME, J. Heat Transfer*, 84, 207–216, 1962.
- Huang, L.J. and Ayyaswamy, P.S., Drag coefficient associated with a moving drop experiencing condensation, *ASME J. Heat Transfer*, 109, 1003, 1987a.
- Huang, L.J. and Ayyaswamy, P.S., Heat and mass transfer associated with a spray drop, a fully transient analysis, *Int. J. Heat Mass Transfer*, 30, 881, 1987b.
- Incropera, F.P. and DeWitt, D.P., *Fundamental of Heat and Mass Transfer*, Wiley, New York, 2002.
- Jacobs, H.R. and Nadig, R., Condensation on coolant jets and sheets including the effects of noncondensable gases, *ASME J. Heat Transfer*, 109, 1013, 1987.
- Jacobs, H.R. and Cook, D.S., Direct contact condensation on a non-circulating drop, *Proceedings of the Sixth International Heat Transfer Conference*, Toronto, Canada, Vol. 3, p. 389, 1978.
- Jakob, M., Film rupture theory of dropwise condensation, *Mech. Eng.*, 58, 729, 1936.
- Jaster, H. and Kosky, P.G., Condensation heat transfer in a mixed flow regime, *Int. J. Heat Mass Transfer*, 19, 95, 1976.
- Jensen, M.K., and Memmel, G.J., Evaluation of bubble departure diameter correlations, *Heat Transfer 1986, Proceedings of the Int. Heat Transfer Conference*, San Francisco, 1907–1912, 1986.
- Johnston, M.A., Jr., Pena, De La Pena, J. and Mesler, R.B., Bubble shapes in nucleate boiling, *AIChE J.*, 12, 334–348, 1966.
- Jones, T.B., Electrohydrodynamically enhanced heat transfer in liquids — a review, *Adv. Heat Transfer*, 14, 107, 1978.
- Judd, R.L. and Hwang, K.S., A comprehensive model for nucleate boiling heat transfer including micro-layer evaporation, *J. Heat Transfer*, 98, 623–629, 1976.

- Judd, R.L., Merte, H., and Ulucakli, M.E., Variation of superheat with subcooling in nucleate pool boiling, *J. Heat Transfer*, 113, 201–208, 1991.
- Jung, D.S., Horizontal Flow Boiling Heat Transfer Using Refrigerant Mixtures, Ph.D. dissertation, University of Maryland, 1988.
- Jung, D.S., McLinden, M., Radermacher, R., and Didion, D., Horizontal flow boiling experiments with a mixture of R-22/R-114, *Int. J. Heat Mass Transfer*, 32, 131–145, 1988.
- Kandlikar, S.G. and Balasubramanian, P., Extending the applicability of the flow boiling correlation to low reynolds number flows in parallel flow microchannels, *First International Conference on Microchannels and Minichannels*, April 24–25, Kandlikar, S.G., Ed., ASME, 2003, 603–608.
- Kandlikar, S.G. and Ikenze, E., Bubble nucleation and growth characteristics in subcooled flow boiling, *HTD-Vol. 342, ASME Proceedings of the 32nd National Heat Transfer Conference*, 4, 11–18, 1997.
- Kandlikar, S.G. and Raykoff, T., Predicting flow boiling heat transfer of refrigerants in microfin tubes, *Enhanced Heat Transfer*, 4, 257–268, 1997.
- Kandlikar, S.G., Mizo, R., Cartwright, M., and Steinke, M.S., Contact angles and interface behavior during rapid evaporation of liquid on a heated surface, *Int. J. Heat Mass Transfer*, 45, 3771–3780, 2002.
- Kandlikar, S.G. and Steinke, M.S., Predicting heat transfer during flow boiling in minichannels and microchannels, *ASHRAE Trans.*, 109, 667–676, 2003.
- Kandlikar, S.G., A general correlation for two-phase flow boiling heat transfer coefficient inside horizontal and vertical tubes, *J. Heat Transfer*, 112, 219–228, 1990.
- Kandlikar, S.G., A model for predicting the two-phase flow boiling heat transfer coefficient in augmented tube and compact heat exchanger geometries, *J. Heat Transfer*, 113, 966–972, 1991b.
- Kandlikar, S.G., A theoretical model to predict pool boiling CHF incorporating effects of contact angle and orientation, *J. Heat Transfer*, 123, 1071–1079, 2001a.
- Kandlikar, S.G. and Spiesman, P.H., Effect of surface characteristics on flow boiling heat transfer, *Engineering Foundation Conference on Convective and Pool Boiling*, Irsee, Germany, May 18–25, 1997.
- Kandlikar, S.G., Boiling heat transfer in binary systems, Part I — Pool boiling, *J. Heat Transfer*, 120, 380–387, 1998b.
- Kandlikar, S.G., Boiling heat transfer with binary mixtures, Part II — Flow boiling, *J. Heat Transfer*, 120, 388–394, 1998c.
- Kandlikar, S.G., Critical heat flux in subcooled flow boiling — an assessment of current understanding and future directions for research, *Multiphase Sci. Technol.*, 13, 207–232, 2001b.
- Kandlikar, S.G., Development of a flow boiling map for subcooled and saturated flow boiling of different fluids in circular tubes, *Trans. ASME, J. Heat Transfer*, 113, 190–200, 1991a.
- Kandlikar, S.G., Dhir, V.K., and Shoji, M., *Handbook of Phase Change—Boiling and Condensation*, Taylor & Francis, Philadelphia, PA, 1999.
- Kandlikar, S.G., Flow boiling in circular tubes, in *Handbook of Phase Change, Boiling and Condensation*, Kandlikar, S.G., Dhir, V.K., and Celata, G.P., Eds., Secs. 15.1–15.3, Taylor Francis, Philadelphia, PA, 1999.
- Kandlikar, S.G., Heat transfer and flow characteristics in partial boiling, fully developed boiling, and significant void flow regions of subcooled flow boiling, *J. Heat Transfer*, Vol. 120, 395–401, 1998a.
- Kandlikar, S.G., Heat transfer mechanisms during flow boiling in microchannels, *J. Heat Transfer*, 125, 8–16, 2004.
- Katto, Y. and Yokoya, S., Principal mechanism of boiling crisis in pool boiling, *Int. J. Heat Mass Transfer*, 11, 993–1002, 1968.
- Katto, Y. Prediction of critical heat flux of subcooled flow boiling in round tubes, *Int. J. Heat Mass Transfer*, 33, 1921–1928, 1990b.
- Katto, Y., A physical approach to critical heat flux of subcooled flow boiling in round tubes, *Int. J. Heat Mass Transfer*, 33, 611–620, 1990a.

- Kedzierski, M.A. and Webb, R.L., Practical fin shapes for surface tension drained condensation, *J. of Heat Transfer*, 112, 479–485, 1990.
- Kew, P. and Cornwell, K., Flow boiling in compact heat exchangers, in *Handbook of Phase Change, Boiling and Condensation*, Sec. 16.2, Taylor & Francis, Philadelphia, PA, 1999.
- Khanpara, A.E., Pate, M.B., and Bergles, A.E., Augmentation of R-113 in-tube evaporation in microfin tubes, *ASHRAE Trans.*, 92, 506–524, 1986.
- Khanpara, J.C., Pate, M.B., and Bergles, A.E., Local Evaporation Heat Transfer in a smooth tube and a microfin tube using refrigerants 22 and 113, *Boiling and Condensation in Heat Transfer Equipment*, ASME HTD, Vol. 68, pp. 35–46, 1987.
- Koh, J.C.Y., Sparrow, E.M., and Hartnet, J.P., The two-phase boundary in laminar film condensation, *Int. J. Heat Mass Transfer*, 2, 69, 1961.
- Koyama, S., Yu, J., Momoki, S., Fuji, T., and Honda, H., Forced convective flow boiling of pure refrigerants inside a horizontal microfin tube, *Engineering Foundation Conference on Convective Flow Boiling*, ASME, April 30-May 5, 1995, Banff, Canada, 1995.
- Kutateladze, S.S. and Leont'ev, A.I., Some applications of the asymptotic theory of the turbulent boundary layer, *Proceedings of the 3rd International Heat Transfer Conference*, Vol. 6, 2373–2378, 1966.
- Kutateladze, S.S., *Fundamental of Heat Transfer*, Academic Press, New York, NY, 1963.
- Kutateladze, S.S., On the transition to film boiling under natural convection, *Kotloturbostroenie*, Vol 3, pp. 10–12, 1948.
- Labuntsov, D.A., Heat transfer in film condensation on vertical surfaces and horizontal tubes, *Teploenergetika*, 4, 72, 1957.
- Lai, C.L., Gibbs-Thomson effect on droplet condensation, *ASME J. Heat Transfer*, 121, 632, 1999.
- Lang, C., *Transactions of Institute of Engineers and Shipbuilders*, Scotland, Vol 32, pp. 279–295, 1888.
- Lee, C.H. and Mudawar, I., A mechanistic critical heat flux model for subcooled flow boiling based on local bulk flow conditions, *Int. J. Multiphase Flow*, 14, 711–728, 1988.
- Lekic, A., and Ford, J.D., Direct contact condensation of vapor on a spray of subcooled liquid droplets, *Int. J. Heat Mass Transfer*, 23, 1531, 1980.
- Liaw, S.P. and Dhir, V.K., Void fraction measurement during saturated pool boiling of water on partially wetted vertical surfaces, *J. Heat Transfer*, 111, 731–738, 1989.
- Liu, Z. and Winterton, R.H.S., A general correlation for saturated and subcooled flow boiling in tubes and annuli based on nucleate pool boiling, *Int. J. Heat Mass Transfer*, 34, 2759–2765, 1991.
- Lorentz, J.J., Mikic, B.B., and Rohsenow, W.M., The effect of surface conditions on boiling characteristics, *Proceedings of 5th International Conference*, Vol. 5, Hemisphere, NY, 1974.
- Malenkov, I.G., Detachment frequency as a function of size of vapor bubbles, *Translated Inzh. Fiz. Zhur.*, 20, 99, 1971.
- Marcus, B.D. and Dropkin, D., Measured temperature profiles within the superheated boundary layer above a horizontal surface in saturated nucleate pool boiling of water, *Trans. ASME, J. Heat Transfer*, 87, 333–341, 1965.
- Marto, P.J., An evaluation of film condensation on horizontal integral-fin tubes, *J. Heat Transfer*, 110, 1287–1305, 1988.
- Mattson, R.J., Hammitt, F.G., and Tong, L.S., A photographic study of the Subcooled Flow Boiling Crisis in Freon-113, Paper No. HT-39, ASME, 1973, 8 pp.
- McAdams, W.H., Minden, C.S., Carl, R., Picornell, D.M., and Dew, J.E., Heat transfer at high rates to water with surface boiling, *Ind. Eng. Chem.*, 41, 1945–1963, 1949.
- Melcher, J.R. and Taylor, G.I., Electrohydrodynamics-a review of role of interfacial shear stress, *Annual Review of Fluid Mechanics*, 1, 111, 1969.
- Melcher, J.R., Traveling wave induced electro-convection, *Phys. Fluids*, 9, 1548, 1966.
- Melin, P., Measurements and Modelling of Convective Vaporization for Refrigerants in a Horizontal Tube, Ph.D. thesis, Department of Heat and Power Technology, Chalmers University of Technology, Göteborg, Sweden, 1996.

- Mikic, B.B. and Rohsenow, W.M., New correlation of pool boiling data including the effect of heating surface characteristics, *J. Heat Transfer*, 91, 241–250, 1969.
- Mikic, B.B., Rohsenow, W.M., and Griffith, D., On bubble growth rates, *Int. J. Heat Mass Transfer*, 13, 657–666, 1970.
- Minkowycz, W.J., and Sparrow, E.M., Condensation heat transfer in the presence of noncondensables, interfacial resistance, superheating, variable properties, and diffusion, *Int. J. Heat Mass Transfer*, 9, 1125, 1966.
- Moissis, R. and Berenson, P.J., On the hydrodynamic transitions in nucleate boiling, *J. Heat Transfer Trans. ASME, Ser. C*, 85, 221–229, 1963.
- Murata, K. and Hashizume, K., Forced convection boiling of nonazeotropic refrigerant mixtures inside tubes, *J. Heat Transfer*, 115, 680–689, 1993.
- Murphy, R.C. and Bergles, A.E., Subcooled flow boiling of fluorocarbons — hysteresis and dissolved gas effects on heat transfer. *Proceedings of Heat Transfer and Fluid Mechanics Inst.*, Stanford University Press, Stanford, CA, 1972, 400–416.
- Nariai, H., Inasaka, F., Fujisaki, W., and Ishiguro, H., Critical heat flux of subcooled flow boiling in tubes with internal twisted tapes, *Proceedings of ANS Winter Meeting (THD)*, San Francisco, November, 1992, 38–46.
- Nishikawa, K., Fujita, Y., Uchida, S., and Ohta, H., Effect of heating surface orientation on nucleate boiling heat transfer, *ASME-JSME Thermal Eng. J. Conf.*, 1, 129–136, 1983.
- Nishikawa, K., Yoshida, S., Mori, H., and Takamatsu, H., Post-dryout heat transfer to Freon in a vertical tube at high subcritical pressures, *Int. J. Heat Mass Transfer*, 29, 1245–1251, 1986.
- Nukiyama, S., Maximum and minimum values of heat transmitted from metal to boiling water under atmospheric pressure, *J. Soc. Mech. Eng. J.*, 37, 367, 1934.
- Nusselt, W., Die Oberflächenkondensation des Wasser dampfes, *Z. Vereins deutscher Ininiuere*, 60, 541, 1916.
- Oswatitsch, K., Rate of droplet growth in condensation, *Z. Angew. Math. U. Mech.*, 22, 1, 1942.
- Peterson, A.C. and Westwater, J.W., Dropwise condensation of ethylene glycol, *Chem. Eng. Prog. Symp. Ser.*, 62, 135–142, 1966.
- Petukhov, B.S. and Popov, V.N., Theoretical calculation of heat exchange in turbulent flow in tubes of an incompressible fluid with variable physical properties, *High Temp.*, 1, 69–83, 1963.
- Petukhov, B.S., Heat transfer and friction in turbulent pipe flow with variable physical properties, in *Advances in Heat Transfer*, 6, 503–564, 1970.
- Plessset, M.S. and Zwik, S.A., The growth of vapor bubbles in superheated liquids, *J. Appl. Phys.*, 25, 493–500, 1954.
- Rayleigh, J.W.S., On the pressure developed in a liquid during the collapse of a spherical cavity, *Philos Mag.*, 34, 94–98, 1917.
- Rohsenow, W.M., A method of correlating heat transfer data for surface boiling of liquids, *Trans. ASME*, 74, 969–976, 1952.
- Rohsenow, W.M., Heat transfer and temperature distribution in laminar film condensation, *Trans. ASME*, 79, 1645, 1956.
- Rose, J.W., Some aspects of dropwise condensation theory, *Int. J. Commun. Heat Mass Transfer*, 15, 449, 1988.
- Rose, J.W., Condensation heat transfer, *Heat Mass Transfer J.*, 35, 479, 1999.
- Sadasivan, P. and Lienhard, J.H., Sensible heat correction in laminar film boiling and condensation, *ASME J. Heat Transfer*, 109, 545, 1987.
- Sato, T. and Matsumura, H., On the conditions of incipient subcooled boiling with forced convection, *Bull. JSME*, 7, 392–398, 1964.
- Schrock, V.E. and Grossman, L.M., Forced convection boiling in tubes, *Nucl. Sci. Eng.*, 12, 474–481, 1962.
- Seban, R.A. and Hodgson, J.A., Laminar film condensation in a tube with upward vapor flow, *Int. J. Heat Mass Transfer*, 25, 1291, 1982.
- Shah, M.M. Chart correlation for saturated boiling heat transfer: equations and further study. *Trans. Am. Soc. Heat., Refrig. Air Conditioning Eng.*, 88, Part I, 185–196, 1982.

- Shah, M.M., A general correlation for heat transfer during subcooled boiling in pipes and annuli, *ASHRAE Trans.*, 83, Part 1, 205–215, 1977.
- Shah, M.M., A general heat transfer correlation during film condensation inside pipes, *Int. J. Heat Mass Transfer*, 22, 547, 1989.
- Silver, R.S., An approach to a general theory of surface condensers, *Proc. Inst. Mech. Eng.*, 179, Part 1, 339, 1964.
- Smith, R.A., Boiling Inside Tubes: Critical Heat Flux for Upward Flow in Uniformly Heated Tubes, ESDU Data Item No. 86032, London: Engineering Science Data Unit International, 1986.
- Soliman, M., Schuster, J.R., and Berenson, P.J., A general heat transfer correlation for annular flow condensation, *ASME J. Heat Transfer*, 90, 267, 1968.
- Sparrow, E.M., Minkowycz, W.J., and Saddy, M., Forced convection condensation in the presence of non-condensables and interfacial resistance, *Int. J. Heat Mass Transfer*, 10, 1829, 1967.
- Steiner, D. and Taborek, J., Flow boiling heat transfer in vertical tubes correlated by an asymptotic model, *Heat Transfer Eng.*, 13, 43–69, 1992.
- Stephan, K. and Abdelsalam, M., Heat transfer correlation for natural convection boiling, *Int. J. Heat Mass Transfer*, 23, 73–87, 1980.
- Sugawara, S. and Katsuta, K., Fundamental study on dropwise condensation, *Proceedings of the Third International Heat Transfer Conference*, Chicago, U.S.A. Vol. 2, p. 354, 1966.
- Sundararajan, T. and Ayyaswamy, P.S., Heat and mass transfer associated with condensation on a moving drop: solution for intermediate Reynolds numbers by a boundary layer formulation, *ASME J. Heat Transfer*, 107, 409, 1985a.
- Sundararajan, T. and Ayyaswamy, P.S., Hydrodynamics and heat transfer associated with condensation on a moving drop: solution for intermediate Reynolds numbers, *J. Fluid Mech.*, 149, 33, 1984.
- Sundararajan, T. and Ayyaswamy, P.S., Numerical evaluation of heat and mass to a moving drop experiencing, *Numer. Heat Transfer*, 8, 689, 1985b.
- Taitel, Y. and Tamir, A., Condensation in the presence of a noncondensable gas in direct contact, *Int. J. Heat Mass Transfer*, 12, 1157, 1969.
- Takamatsu, H., Momoki, S., and Fujii, T., A correlation for forced convection boiling heat transfer of non-azeotropic refrigerant mixture of HCFC22/CFC114 in a horizontal smooth tube, *Int. J. Heat Mass Transfer*, 36, 3555–3563, 1993.
- Tanaka, H., A theoretical study on dropwise condensation, *ASME J. Heat Transfer*, 97, 72, 1975.
- Thom, J.R.S., Walker, W.M., Fallon, T.A., and Reising, G.F.S., Boiling in subcooled water during flow up heated tubes or annuli, paper presented at the *Symposium on Boiling Heat Transfer in Steam Generating Units and Heat Exchangers*, Manchester, Sept. 15–16, Institute of Mech. Eng., London, 1965.
- Thomson, W., *Philos. Mag.*, 42, 448, 1871.
- Tong L.S. *Principles of Design Improvement for Light Water Reactors*, Hemisphere, New York, 1988.
- Tong, L.S. and Hewitt, G.F., Overall Viewpoint of Flow Boiling Mechanisms, ASME Paper 72-HT-54, 1972.
- Tong, L.S. and Tang, Y.S., *Boiling Heat Transfer and Two-Phase Flow*, Taylor & Francis, Washington, DC, 1997.
- Tong, L.S. *Boiling Heat Transfer and Two-Phase Flow*, John Wiley, New York, 1965.
- Tong, L.S., Curin, H.B., and Thorp, A.G., An evaluation of the departure from nucleate boiling in bundles of reactor fuel rods, *Nucl. Sci. Eng.*, 33, 7–15, 1968.
- Tong, L.S., Efferding, L.E., and Bishop, A.A., A Photographic Study of Subcooled Boiling and DNB of Freon-113 in a vertical channel, ASME Paper 66-WA/HT-39, ASME Winter Annual Meeting, ASME, New York, 1966.
- Umur, A. and Griffith, P., Mechanism of dropwise condensation, *ASME J. Heat Transfer*, 87, 275, 1965.
- Vachnon, R.I., Nix, G.H., and Tanger, G.E., Evaluation of constants for the Rohsenow pool-boiling correlation, *J. Heat Transfer*, 90, 239, 1968.
- Vandervort, C.L., Bergles, A.E., and Jensen, M.K., An experimental study of critical heat flux in very high heat flux subcooled boiling, *Int. J. Heat Mass Transfer*, 37 (Suppl. 1), 161–173, 1994.
- Velkoff, H.R. and Miller, J.H., Condensation of vapor on a vertical plate with a transverse electrostatic field, *ASME J. Heat Transfer*, 87, 197, 1965.

- Weisman, J. and Pei, B.S., Prediction of critical heat flux in flow boiling at low qualities, *Int. J. Heat Mass Transfer*, 26, 1463–1477, 1983.
- Welch, J.F. and Westwater, J.W., Microscopic study of dropwise condensation, *ASME Int. Dev. Heat Transfer*, Part II, 1961.
- Wieting, R.A., Empirical correlations for heat transfer and flow friction characteristics of rectangular offset fin plate heat exchangers, *J. Heat Transfer*, 97, 488–490, 1975.
- Williamson, C.R. and El-Genk, M.S., High-Speed Photographic Analysis of Saturated Nucleate Pool Boiling at Low Heat Flux, Paper 91-WA-HT-8, ASME Winter Annual Meeting, Atlanta, ASME, 1991.
- Zuber, N., Hydrodynamic Aspects of Boiling Heat Transfer, Ph.D. thesis, University of California, Los Angeles, CA, 1959.

4

Fluid-Solid Transport in Ducts

4.1	Pneumatic Conveying	4-1
	Background • Classification of Pneumatic Conveying Systems • Components of Conveying System • Calculating Pressure Drop in Dilute Phase Systems • Designing Conveying Systems • Stepping Pneumatic Conveying Lines • Modeling and Designing Dense Phase Conveying • Practical Design Considerations	
4.2	Slurry Flows	4-50
	Introduction • Basic Concepts of Slurry Flows • Homogeneous Flow of Nonsettling Slurries • Heterogeneous Flow of Settling Slurries • Design and Operational Aspects • Measurement Techniques	

Shrikant Dhodapkar

Karl Jacob

Engineering Science and Market Development

The Dow Chemical Company

Shenggen Hu

CSIRO/Queensland Centre for Advanced Technology

4.1 Pneumatic Conveying

Shrikant Dhodapkar and Karl Jacob

4.1.1 Background

One of the earliest pieces of documentation, dating back to 1847, of conveying solids for industrial application was an exhaust system for dust removal from grindstones in a Peugeot plant (Molerus, 1996). Later in 1878, applications of pneumatic conveying of agricultural products (grains and wood chips) emerged. While the basic concept matured quickly, advances in the design of air movers, feeders and dust collectors resulted in a widespread application of this technology. The research in gas particle dynamics has helped create a systematic approach for designing pneumatic conveying systems. Presently, pneumatic conveying is the primary means of moving solid products and intermediates between process stages and the transfer of materials to and from silos. Most of the bulk solid unloading operations rely on some kind of pneumatic transfer.

A pneumatic conveying system consists of a gas mover (fan, centrifugal blower, rotary lobe blower, etc.), a product feeder (rotary feeder, screw feeder, blow tank, etc.), conveying line, and a gas–solid separator (cyclone, baghouse, etc.). With a suitable choice of components, bulk material can be reliably conveyed over considerable distance. The conveying line can be routed to provide maximum flexibility in layout and operation. The material can be picked up from multiple sources and delivered to many destinations easily. Due to the enclosed nature of transfer in pipe, no dust is emitted to the environment. Pneumatic conveying systems are also easy to automate. However, there are some drawbacks to this technology:

1. High specific power consumption
2. Potential particle breakage or degradation

3. High wear rate on components
4. Relatively short distances (typically less than 3000 ft)

It is not uncommon to come across pneumatic conveying systems that are not meeting performance expectations. High particle degradation, capacity limitations and unstable flow are some of the common problems faced by plant personnel. In most cases, these systems have been designed using generalized correlations and procedures that do not reflect the conveying characteristics of the material at hand. This results in a nonoptimal system design. Lack of clear design guidelines and calculation procedures makes it difficult to optimize these operations.

More accurate design calculations can be made by empirically correlating test data on conveying characteristics. These data can be obtained on a pilot-scale test loop or from a properly instrumented conveying system in the plant. Generally, it is easier to vary conveying conditions and measure the air and solid flow rates along with pressure drops in various sections in a test loop than to adapt conveying systems in the plant. The test data can be condensed into material-specific correlations for solids friction factor, saltation velocity correlation, and pressure drop correlation for bends and acceleration region. This information can then be used to design new systems and optimize existing systems.

Pneumatic conveying of materials implies the conveying of material in pipelines using gas as a motive fluid. When the fluid is a liquid, it is known as hydraulic conveying. Gas-particle dynamics is the foundation of pneumatic conveying technology and, hence, discussed briefly here.

4.1.1.1 Flow Patterns in Gas–Solid Systems

Consider co-current flow of gas and solid particles in a horizontal pipe, where the gas velocity is high enough to keep the particles homogeneously suspended as shown in flow pattern 1 in [Figure 4.1](#). This flow pattern represents ideal dilute phase flow. If the gas velocity were increased from this point the flow pattern would visually appear to be the same. However, if it were decreased, at some velocity the solids would no longer be homogeneously suspended as shown in flow pattern 2. A moving strand is often observed at the bottom of the pipe. As the gas flow is further reduced, more of the solids fall out of suspension resulting in a layer of solids on the bottom of the pipe. Further reduction in gas flow results in the formation of dunes (flow patterns 4 and 5) and eventually slugs of solids that completely fill the pipe cross section (flow pattern 7). For most materials, the flow of solids will stop before reaching flow patterns 9 and 10; however, for some materials that aerate easily and have good air-retention characteristics, the material can be moved in the form of a fluidized plug. Dilute phase flow is characterized by predominantly flow patterns 1 and 2, with some occurrence of flow pattern 3 at or near the point where solids are injected into the conveying line. Dense phase conveying includes all other flow patterns, although stable conveying will most likely not be achieved for any given material in all flow patterns shown.

The range of flow patterns observed during pneumatic conveying of bulk materials depends on the material characteristics (particle size, size distribution, shape, hardness, and density). Broadly speaking, fine powders and coarse materials show characteristically different flow patterns. Fine powders, such as PVC powder, HDPE (High Density Polyethylene) powder, fly ash, cement, fine coal, and carbon fines, can be transported in fluidized-or moving-bed mode at low gas velocities. The flow can be turbulent and sometimes appears like a fast moving bed, waves, or dunes (see [Figure 4.2](#)). At higher solids loadings, the entire cross section of the pipe is filled with a dense mixture of gas and solids. The transition from dilute phase to dense phase is smooth and predictable. Some coarse materials with significant fraction of fines (less than 75 μm) will also exhibit similar behavior. On the other hand, coarse particles, such as plastic pellets, grains, and coffee beans, form slugs naturally when conveyed at low velocity in nonsuspension mode. These slugs show periodic and self-regulating behavior. The transition from dilute to dense flow is marked by an unstable region that corresponds to dune flow ([Figure 4.3](#)).

4.1.1.2 Classification of Bulk Solids

Classification or characterization is an essential step in the selection of a suitable conveying mode (dilute or dense) and to optimize the operation of an existing conveying system. Various approaches have been proposed in the literature to predict the expected behavior of a bulk material in a pneumatic conveying

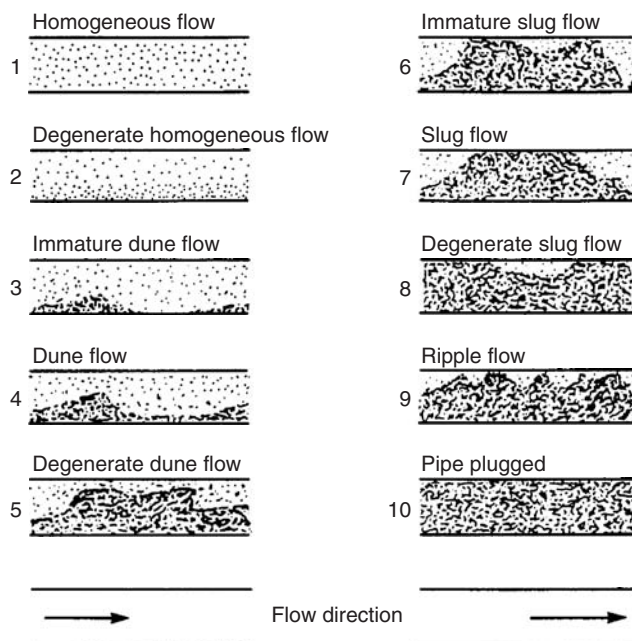


FIGURE 4.1 Flow patterns in horizontal pneumatic conveying lines (From Wen, US Department of Interior, Bureau of Mines, PA, IC 8314, 1959. With permission.)

system. Unfortunately, due to the complexity of interactions, none of them is definitive but they do provide a good basis for evaluation. It is the authors' experience that a combination of approaches coupled with practical experience must be used. Product classification approaches by Geldart (1973), Dixon (1981), Mainwaring and Reed (1987), Jones and Mills (1990), and Pan (1999) are discussed briefly here. This should provide initial guidance to a process engineer. It is recommended that conveying trials be conducted on new materials to understand the conveying characteristics.

The following properties affect the conveying characteristics of bulk solids:

1. Particle size and size distribution
2. Particle shape
3. Bulk density (loose and tapped)
4. Particle density
5. Permeability
6. Daeaeration rate or air-retention characteristics
7. Surface characteristics: sticky, wet, cohesive, and electrostatic charging
8. Temperature sensitivity (hardness, modulus, and surface tackiness)

4.1.1.2.1 Geldart or Dixon Classification

In his classic paper, Geldart (1973) demarcated regions of different fluidization behaviors based on a two-dimensional plot (Figure 4.4). The x -axis is surface volume mean particle size and the y -axis is density difference between particle and fluid. This diagram has stood the test of time and is still used to classify the fluidization behavior of bulk solids. Subsequent work by Dixon (1981) on classification of slugging behavior in vertical pipes produced a similar diagram. Fluidization, permeability and deaeration characteristics are closely related to pneumatic conveyability (see Table 4.1).

Wypych (1989) has shown that the use of surface-volume mean diameter underemphasizes the influence of finer fraction on fluidization behavior. He recommended the use of volume median diameter instead. The boundaries in Geldart classification are ambiguous when the particle size distribution is wide

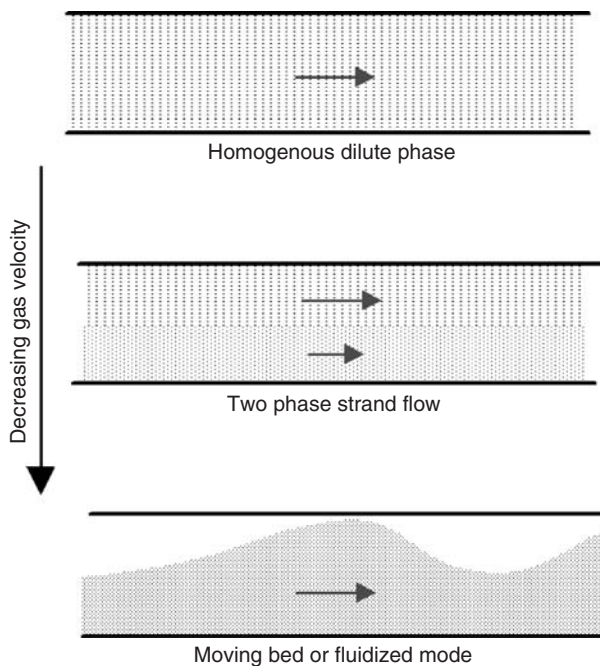


FIGURE 4.2 Flow patterns for fine powders.

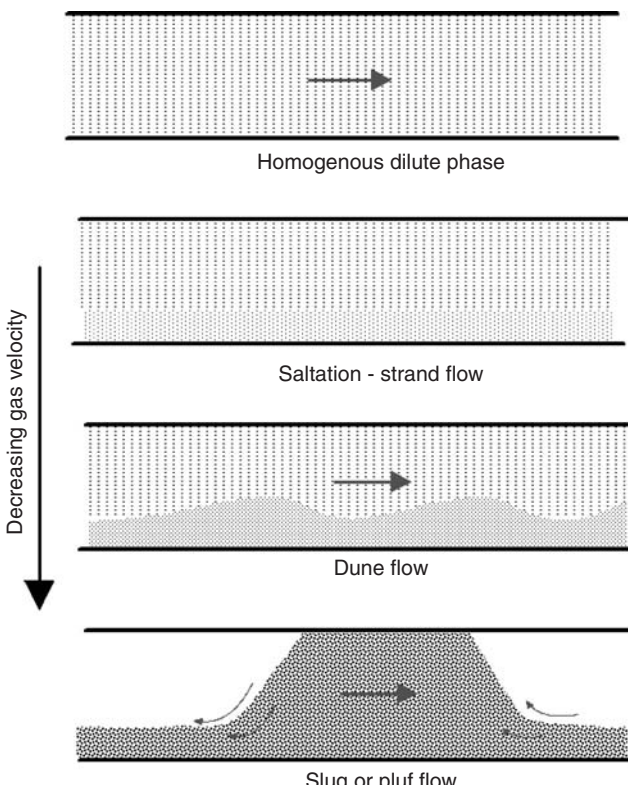


FIGURE 4.3 Flow patterns for coarse granular materials.

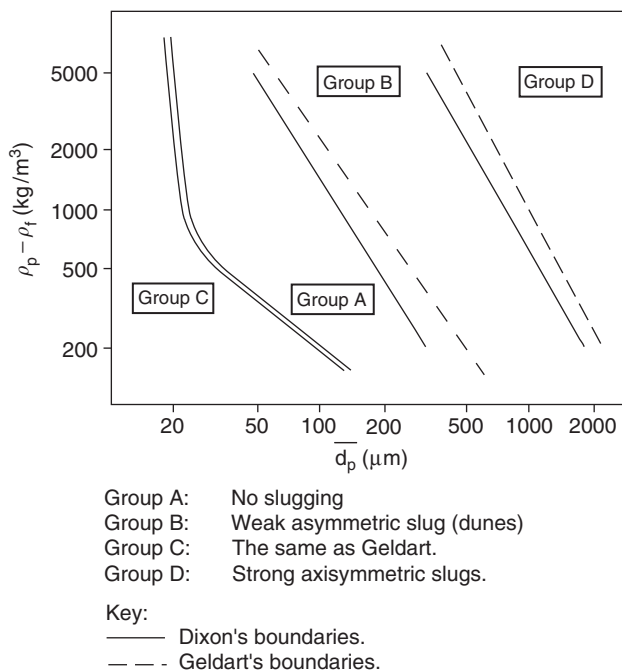


FIGURE 4.4 Comparison of Geldart and Dixon Classification (From Mason, Ph.D. Thesis, Thomes Polytechnic, London, U.K., 1991. With permission.)

TABLE 4.1 Characteristics of Geldart (1973) or Dixon (1981) Classification

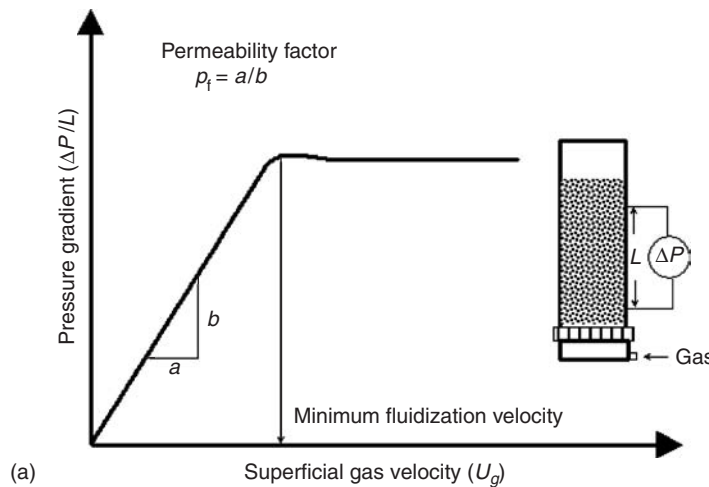
Geldart or Dixon Classification	Fluidization Characteristics	Dense Phase Conveying Characteristics
A	Fine powders, good air retention, small bubble size, considerable bed expansion	Can be conveyed in fluidized mode, easy to convey, do not form slugs naturally
B	Coarse granules, poor air retention, low bed expansion, large bubbles, asymmetric slugging	Difficult to convey in "conventional" dense phase, unsteady and unpredictable plug formation, large pipe vibrations
C	Cohesive, difficult to fluidize, tends to channel, once aerated might retain air for extended periods, adhesion to walls	Very difficult to convey in conventional dense phase, forms impermeable plugs that break up. Special techniques required to convey
D	Highly permeable, negligible bed expansion, high minimum fluidization velocity, large bubbles or slugs can form, axisymmetric slugs	Natural slugging ability and high permeability helps in dense phase conveying. Operationally easiest to convey in dense phase

or the particle shape is nonspherical. Wypych (1989) also pointed out that the ratio of particle size to pipe diameter plays a role in the determination of natural slugging behavior. It is recommended that full-scale tests be conducted to ascertain actual behavior.

4.1.1.2.2 Mainwaring and Reed Classification (1987)

Permeability and deaeration have proven to be the two most important properties of bulk material in establishing the conveying behavior. While Geldart (1973) or Dixon (1981) classification is based on a similar concept, this classification relies on direct measurement of permeability factor and deaeration factor. These measurements are used to determine whether the material can be conveyed in plug type dense phase conveying, moving-bed type dense phase conveying, or only in dilute phase mode.

4.1.1.2.2.1 Permeability Factor. Permeability is a measure of resistance of gas flow through a packed bed of given bulk material under conditions below minimum fluidization. It can be measured by measuring the pressure gradient across a packed bed at various gas velocities (Figure 4.5a). The permeability factor,



(a)

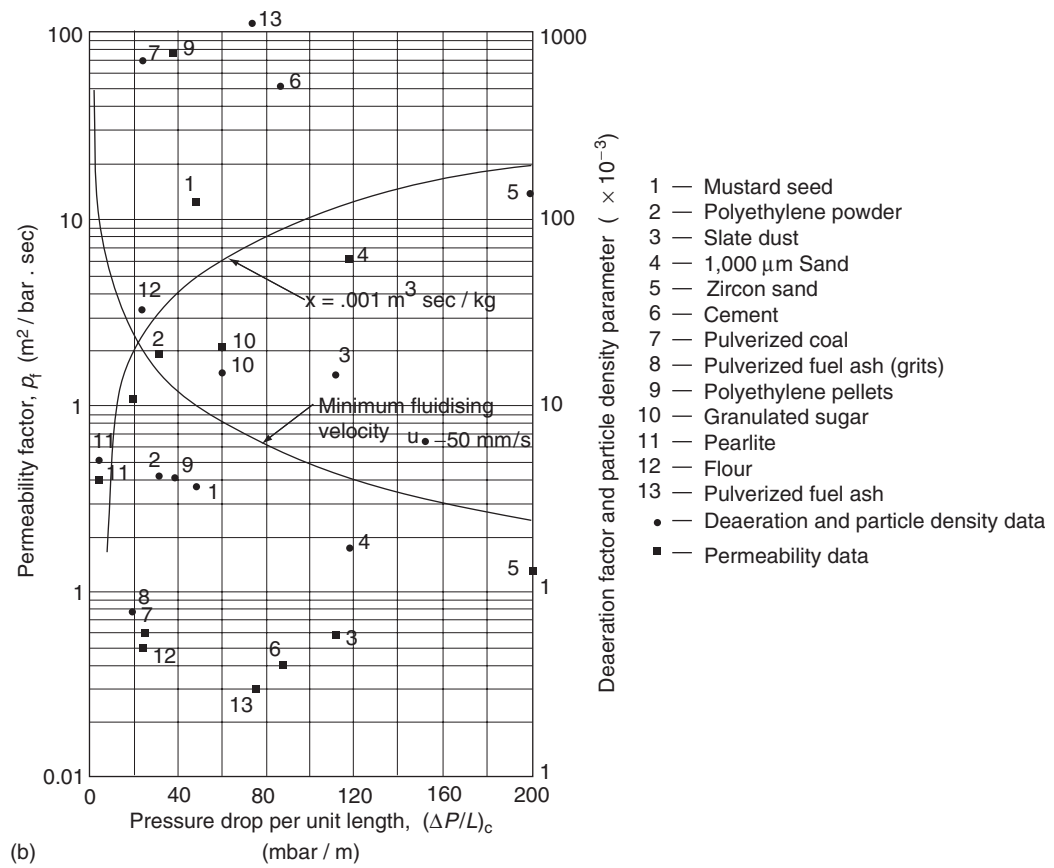


FIGURE 4.5 (a) Measurement of permeability using a fluidized bed set up; (b) Classification based on permeability. (From Mainwaring and Reed, *Bulk Solids Handling*, 7, 415–425, 1987. With permission.)

p_f is the ratio A/B . The higher the permeability factor, lesser is the resistance it offers to gas flow:

$$p_f = \frac{U_g}{(\Delta P/L)_c}$$

The pressure drop curve reaches an asymptotic value at high gas velocities when the drag force on the particles equals the weight of the bed. This critical pressure gradient $(\Delta P/L)_c$ is a property of the bulk material.

The permeability data for various bulk solids were plotted against the critical pressure gradient by Mainwaring and Reed (1987) as shown in [Figure 4.5b](#). A line of constant minimum fluidization can be plotted on the same graph. It has been found from practical experience that a line representing minimum fluidization velocity of 0.05 m/sec (50 mm/sec) classifies materials that can be conveyed in plug or slug type dense phase conveying and those that can be conveyed in moving-bed type dense phase or dilute phase only. All materials with high permeability (data above the line) can be conveyed in plug or slug conveying mode, whereas materials with low permeability can be conveyed either in moving-bed type dense phase flow or in dilute phase only. The basic assumption here is that no special air injection or vibration flow aids are being used.

4.1.1.2.2 Daeaeration Factor. Air retention or deaeration characteristics are measured by bringing the bed to a state of minimum fluidization and rapidly turning off the air supply. The bulk density increases and the level falls as the bed deaerates. It would be ideal to monitor the bed height as a function of time. However, most fine powders tend to coat the wall of the column, thereby making the observations difficult. It is reasonable to measure the pressure decay characteristics instead. Research has shown that the pressure gradient in the bed is inversely proportional to the time, as shown in [Figure 4.6a](#):

$$\frac{\Delta P}{L} t = A_f$$

The product of pressure gradient and time is defined as the deaeration constant, A_f . The shape of deaeration curve is sensitive to many parameters. This test needs to be standardized or it must be used for comparative purposes only.

To account for the effect of particle density, it was further proposed that a new factor X ($\text{m}^3 \text{s/kg}$) be defined as follows:

$$X = \frac{(A_f/\rho)}{(\Delta P/L)}$$

Low values of X imply low air retention and vice versa. As shown in Figure 4.6b, it has been proposed that a curve representing $X = 0.001 \text{ m}^3/\text{s kg}$ classifies materials that can be conveyed in slug or plug type dense phase conveying (below the curve) and those suitable for only moving bed or dilute phase (above the curve).

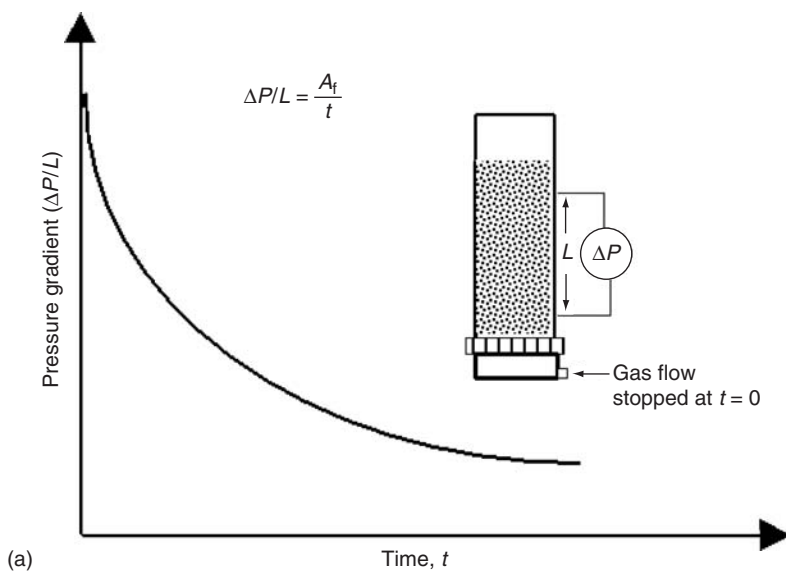
4.1.1.2.3 Jones and Mills (1990)

Jones and Mills (1990) have rightly pointed out the limitations of Geldart and Dixon diagram in their failure to account for particle size distribution and shape. Similar to Mainwaring and Reed, they used permeability and deaeration as the two primary factors to determine flow modes. However, the deaeration characteristics were generated in the presence of vibration to assist deaeration of powders, which can take an inordinate amount of time. The proposed product classification is shown in [Figure 4.7](#).

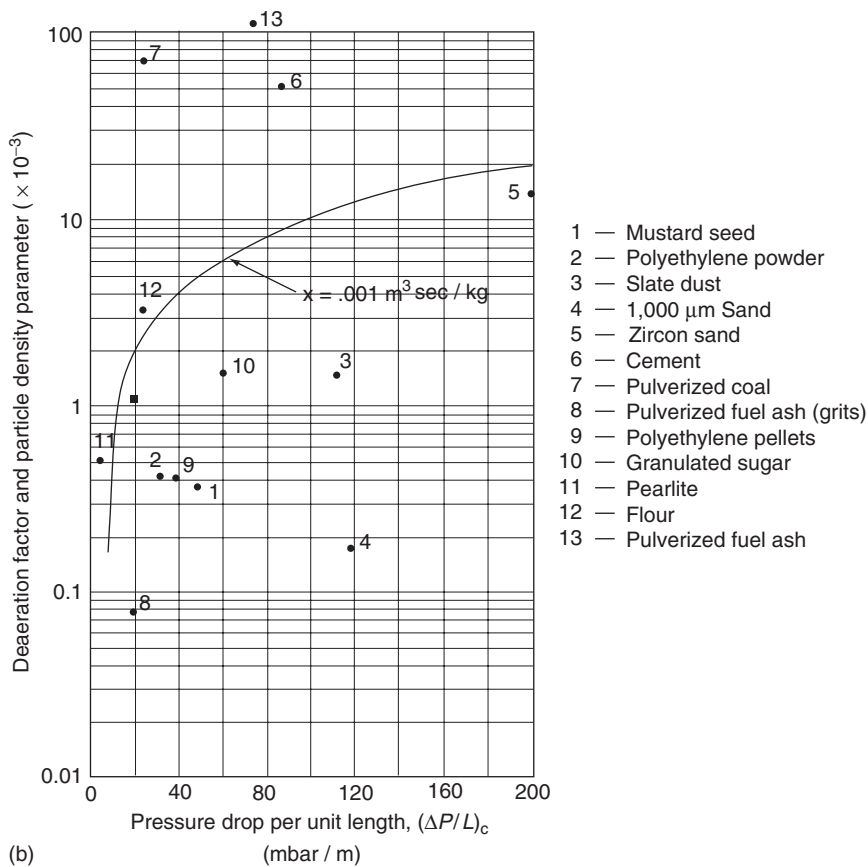
As evident from Jones and Mills classification:

1. Materials with low permeability and high air retention (small deaeration constant) can be conveyed in moving bed or fluidized mode.
2. Materials with high permeability and low air retention can be conveyed in plug type of dense phase flow.
3. The rest of the materials can be conveyed only in dilute phase mode.

The boundaries between dilute phase (Group 2) and dense phase (Groups 1 and 3), however, are tentative.



(a)



(b)

FIGURE 4.6 (a) Interpretation of deaeration data and proposed test setup; (b) classification based on deaeration factor.

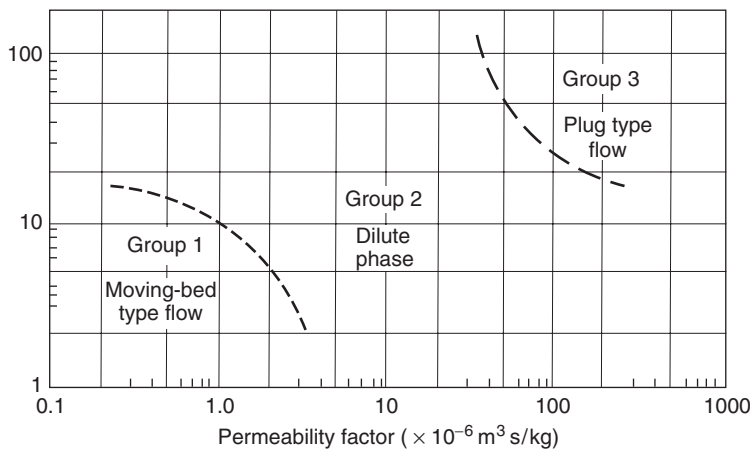


FIGURE 4.7 Jones and Mills classification. (From Jones and Mills, *Powder Handling Processing*, 2, 117–122, 1990. With permission.)

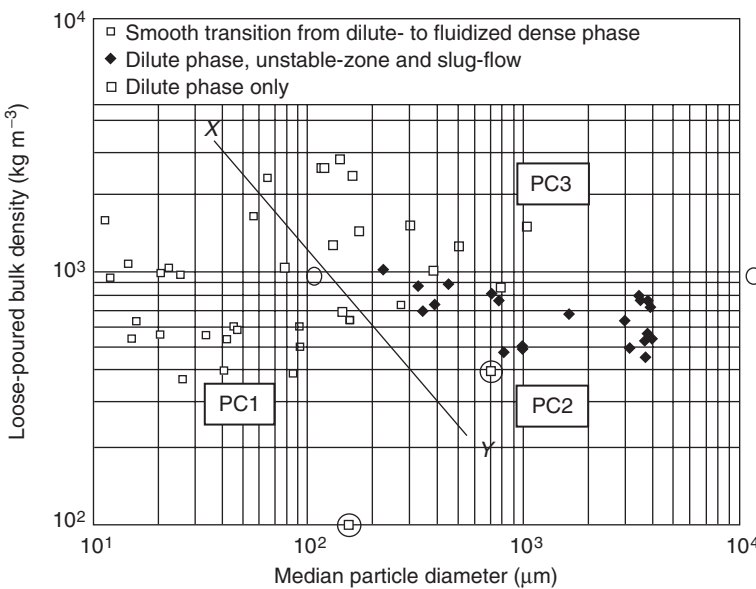


FIGURE 4.8 Pan classification. (Permission from Pan, R., *Powder Technology*, 104, 157–163, 1999.)

4.1.1.2.4 Pan (1999)

Pan (1999) proposed a simplified flow mode diagram based on loose, poured bulk density and median particle size. This diagram (Figure 4.8) is based on a database of over 50 materials. The materials are grouped into three categories:

- Materials in group PC 1 can be transported in dilute phase and dense phase fluidized- or moving-bed mode. Examples are fly ash, pulverized coal, cement, flour, PVC powder, fuel ash, and others.
- Materials in group PC 2 can be transported in dilute phase and slug or plug type dense phase mode. The transition from dilute phase to dense phase is marked by an unstable zone. Examples are plastic pellets, wheat, mustard seeds, granulated sugar, semolina, and others.
- Materials in group PC 3 can be transported only in dilute phase. Examples are silica sand, alumina, zircon sand, fuel ash grit, and others.

4.1.1.2.5 Limitation of Classification Diagrams

Many materials classified as difficult to convey in dense phase can be conveyed by applying special techniques, such as air injection, air bypass, air knife, and pulse piston method. No generalized classification has been developed to predict the effectiveness of these techniques. It is recommended that pilot-scale tests be conducted to determine the feasibility of dense phase conveying for such materials.

4.1.1.3 Phase Diagram

While observing flow patterns is an easy way to differentiate between dilute and dense phase conveying, most conveying systems do not provide this opportunity. Consequently, process measurements such as differential pressure are used in conjunction with the gas and solids flow rates to provide a picture of what occurs within the conveying line. An elegant way to represent the performance characteristics of pneumatic conveying systems is to plot the pressure gradient vs. gas velocity for different solids flow rates. This is often known as the “Zenz plot” (see [Figure 4.9](#)). The pressure gradient is measured across a test section of known length, pipe diameter, and orientation. Each curve represents system characteristics at constant solids flow rate. It should be noted that Zenz used logarithmic scales for the two axes. In a log-log plot, the pressure curve due to single-phase gas flow becomes a straight line; however, the curves for gas–solid flow remain nonlinear. It is now a common practice to plot the data with linear axes. The saltation transition can be visualized better by using a linear plot.

In the absence of solids, the well-known Darcy’s or Fanning’s friction factors can be used to quantify the pressure drop in pipes for single-phase flow. The pressure gradient in the conveying line decreases with the gas flow rate and eventually becomes zero under stationary conditions.

4.1.1.3.1 Dilute Phase Conveying

Dilute phase pneumatic conveying refers to transport of solid particles in gas such that all particles are fully entrained in the gas phase. It is possible to achieve dilute phase conveying or fully suspended mode for all materials. The difference in velocity between gas molecules and solid particles, also known as slip velocity, provides necessary drag force to propel them forward. The addition of particles in the gas stream complicates the dynamics. Due to gas–particle interaction, additional energy lost by the gas manifests itself as additional pressure drop. The energy imparted to the particles is used to move them and to overcome the frictional and impact losses at the pipe wall. Unlike the curve for single-phase airflow, a distinct minimum can be observed for two-phase gas–solid flow.

In horizontal orientation, the suspension becomes progressively nonhomogenous as the gas velocity is reduced ([Figure 4.9](#)). The particles start to fall out of the suspension, as the drag and lift forces are no longer able to keep them suspended. The condition when the particles begin to fall out of suspension is called *saltation*. The superficial gas velocity corresponding to this condition is called the saltation velocity. For coarse particles, saltation velocity and the minima in the pressure drop curve are the same, whereas the pressure minima occurs at a velocity greater than saltation velocity for fine powders. Since the operating condition at saltation corresponds to minimum pressure drop, it also results in lowest power consumption. Generally, a safety factor of 10 to 20% is added to saltation velocity to account for nonidealities in system configuration.

4.1.1.3.2 Dense Phase Conveying

Conveying in nonsuspension flow (slugs, plugs, moving bed, or fluidized bed) is called dense phase conveying. As the gas velocity is reduced below the minimum requirement to maintain the particles in suspension, there are two possibilities:

1. Smooth transition from dilute phase to moving beds or dunes to fluidized mode
2. Transition to dune or degenerate dune flow that eventually transforms into smooth slug flow

The following important observations can be made from this diagram.

1. The pressure gradient curve does not decrease monotonically with gas velocity when conveying solids. This is unlike single-phase gas flow.
2. There is a minimum in the pressure characteristic (at constant solids conveying rate). This point also corresponds to lowest power consumption. In dense phase, the pressure gradient increases as the gas velocity is further decreased.

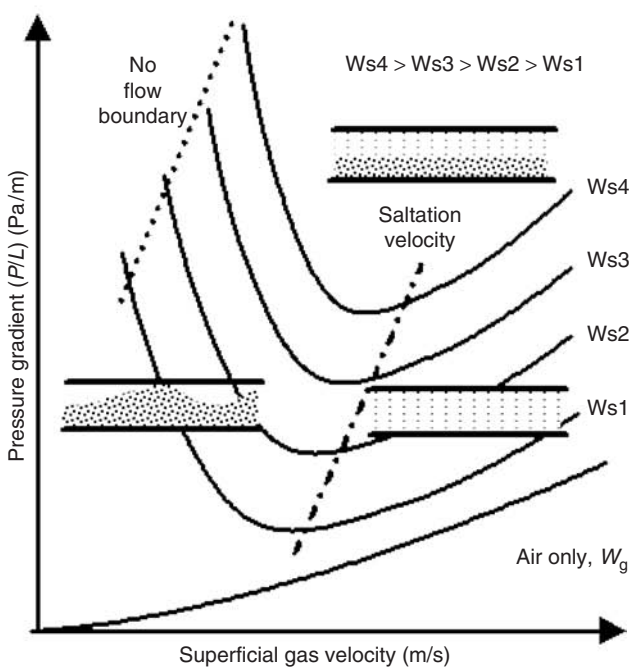
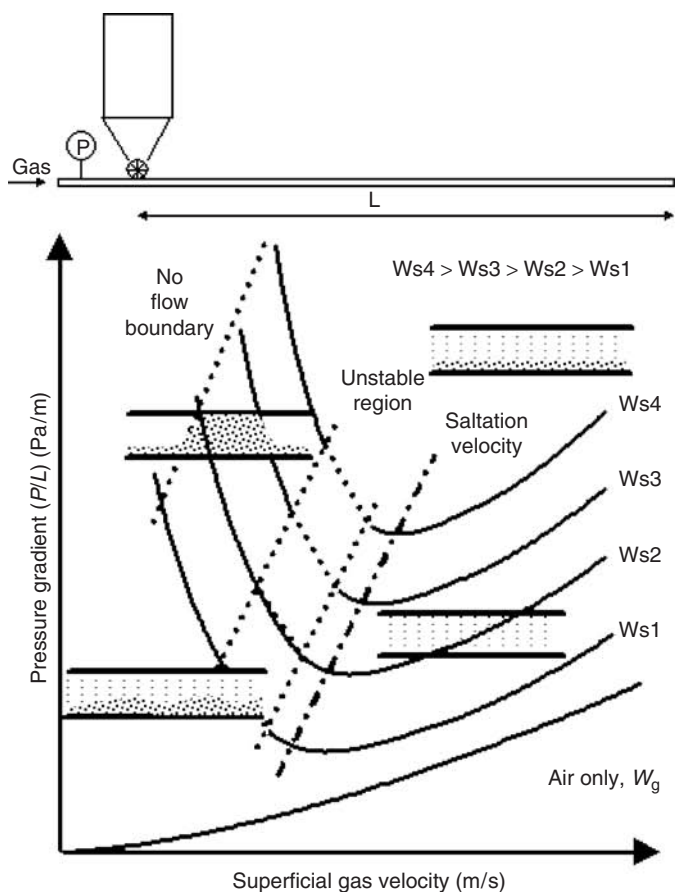


FIGURE 4.9 Zenz plot with superimposed flow patterns for coarse materials (top) and fine materials (bottom).

3. At a given pressure gradient and dilute phase flow condition, the conveying rate (capacity) decreases with increase in gas velocity (gas flow rate), as shown by A → B line in [Figure 4.10](#). This can be explained by the fact that more energy is expended in solids frictional and impact losses at the higher velocity. This observation is extremely important and useful when we are optimizing conveying systems.

In vertical orientation, as the gas velocity reduces at the same solids mass flow rate, solids concentration in the pipe increases and the wall frictional loss decreases. Initially, the decrease in wall frictional loss is significantly higher than the increase in gravitational component, therefore, the overall pressure gradient decreases with reduction in gas velocity. However, at sufficiently low gas velocity, the gravitational component due to solids holdup becomes predominant and the overall pressure gradient starts to increase ([Figure 4.11](#)). The flow conditions at and below this gas velocity are classified as dense phase flow.

The mechanism of choking is not clearly understood: Also, not all systems exhibit this behavior. Whether the system will exhibit slugging or nonslugging behavior with internal recirculation of solids depends on the properties of the material and the pipe size. In general, fine particles in large pipes tend toward nonslugging dense phase flow, while choking with slugging is observed with coarse particles in small diameter pipes. If the transition from dilute or lean phase to dense phase is sharp, then choking corresponds to the pressure minimum. However, if the transition from dilute to dense phase is “fuzzy,” then actual choking can occur at a velocity lower than that corresponding to the pressure minimum.

Comparison of saltation velocity and choking velocity data for different materials suggests that:

1. For fine particles, saltation velocity is about 3 to 5 times larger than the choking velocity.
2. For coarse particles, the saltation and choking velocity are almost identical.

Most of the conveying systems are configured such that the material is fed into a horizontal section of the pipe. Therefore, saltation velocity (with appropriate safety factor) should be used for design calculations; this will result in a conservative design. From a design point of view, it is desirable to choose an operating point that would result in minimum pressure drop, power consumption, erosion, and particle degradation, and yet provide reliable and stable operation. The region immediately to the right (toward higher gas velocity) of the minimum is considered to be the optimal region.

4.1.1.3.3 Saltation Velocity

As discussed earlier, saltation velocity of coarse particles (such as pellets) can be estimated by locating the minimum in the pressure gradient curve in Zenz plot. A nondimensional representation of the saltation velocity data was proposed by Barth (1958) and then successfully extended by Rizk (1976). A straight line relationship is obtained by plotting solids loading vs. Froude number corresponding to each of the pressure minimums (same as saltation) on a log–log scale. This straight line represents a relationship of the form

$$\mu_{\text{saltation}} = \alpha Fr_{\text{saltation}}^{\beta}$$

α and β can be estimated from regression where α and β are dimensionless coefficients.

Barth (1958) suggested that the power law index β is 4.0. Rizk (1976) proposed the following expressions to estimate the indices:

$$\alpha = \frac{1}{10^{(1.4d_p + 1.96)}}$$

$$\beta = (1.1d_p + 2.5)$$

with d_p in millimeters. It should be noted that Rizk's correlation does not include the effect of particle density.

Saltation velocity can be explicitly derived from the above expression as follows.

$$U_{gs} = \left[\frac{W_s(gD)^{\beta}}{A\rho_g \alpha} \right]^{1/(2\beta + 1)}$$

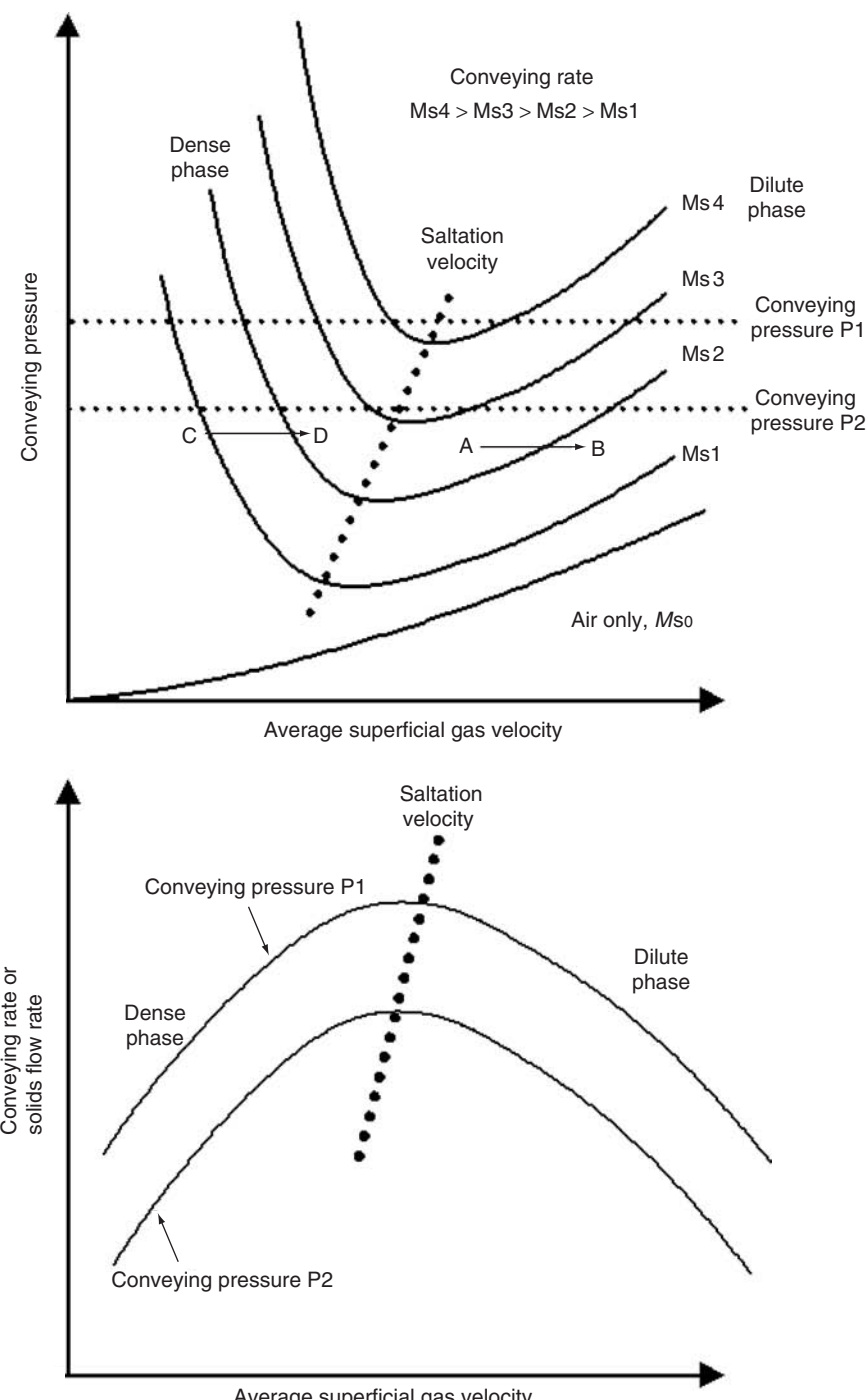


FIGURE 4.10 Influence of gas velocity on conveying capacity.

Based on an extensive experimental database, Matsumoto et al. (1977) proposed the following correlations. He observed that coarse and fine materials behave differently. The saltation velocity of fine powders decreases with particle size until a critical particle diameter, d_p^* , is reached, and then the saltation velocity increases with particle size.

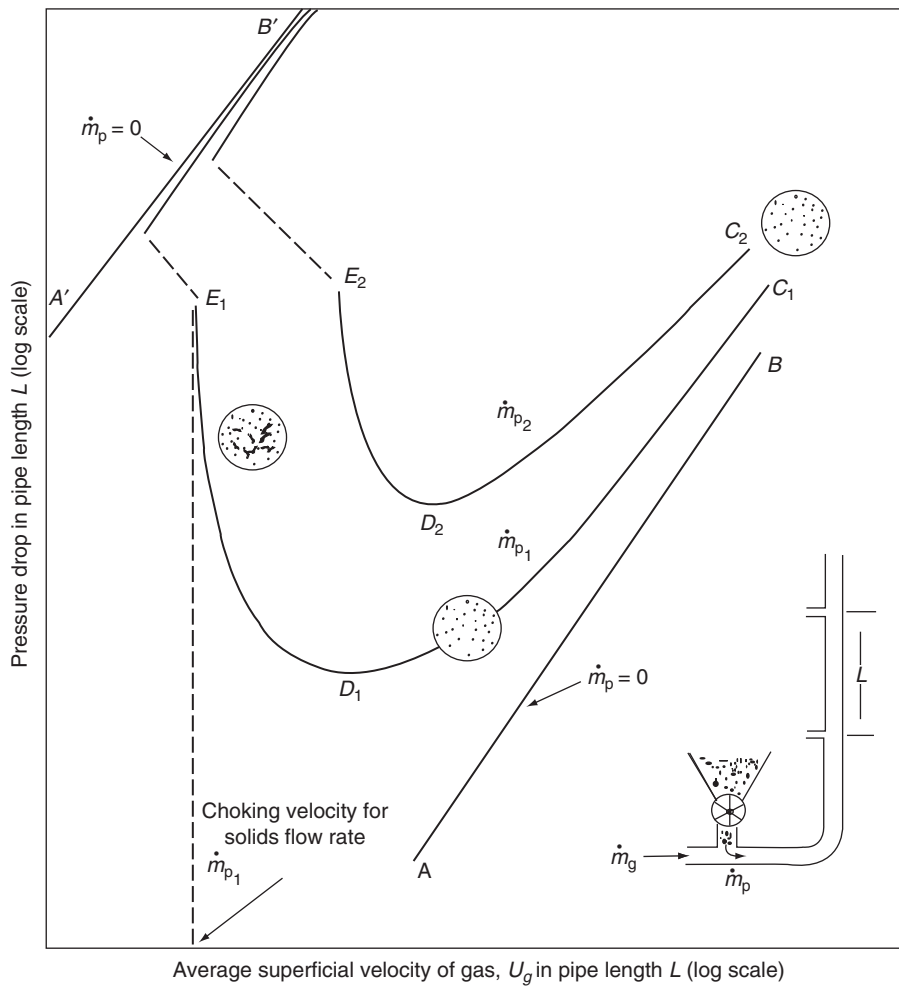


FIGURE 4.11 Conveying characteristics for vertical pneumatic conveying (From Zenz and Othmer, *Fluidization and Fluid Particle Systems*, Reinhold, New York. With permission.)

Critical particle diameter, d_p^* is defined as

$$\frac{d_p^*}{D} = 1.39 \left(\frac{\rho_p}{\rho_f} \right)^{-0.74}$$

For $d_p \geq d_p^*$:

$$\mu_s = 0.373 \left(\frac{\rho_p}{\rho_f} \right)^{1.06} \left(\frac{Fr_p}{10} \right)^{-3.7} \left(\frac{Fr_{ss}}{10} \right)^{3.61}$$

where,

$$Fr_p = \frac{U_t}{\sqrt{g d_p}}$$

$$Fr_{ss} = \frac{U_{gs}}{\sqrt{g D}}$$

$$\mu_s = \frac{W_s}{W_g} \quad (\text{solids loading at saltation condition})$$

For $d_p < d_p^*$

$$\mu_s = 55 \left(\frac{d_p}{D} \right)^{1.43} \left(\frac{Fr_{ss}}{10} \right)^{4.0}$$

Guidelines for Correlation Selection

- For coarse particles ($d_p > 500 \text{ }\mu\text{m}$) and particle specific gravity less than 3, use the Rizk correlation.
- For coarse particles ($d_p > 500 \text{ }\mu\text{m}$) and particle specific gravity greater than 3, use Matsumoto correlation.
- For fine particles ($d_p < 500 \text{ }\mu\text{m}$), use Matsumoto correlation.

Example 4.1. Calculate the saltation velocity using the following data.

- Particle density $\rho_p = 950 \text{ kg/m}^3 = 59.3 \text{ lbm/ft}^3$
- Gas density (ρ_g) = $1.2 \text{ kg/m}^3 = 0.075 \text{ lbm/ft}^3$
- Average particle diameter (d_p) = $0.003 \text{ m} = 3 \text{ mm}$
- Inner diameter of the pipe $D = 0.161 \text{ m} = 6.357 \text{ in.}$
- Conveying rate for solids (W_s) = $3.0 \text{ kg/s} = 23,760 \text{ lbm/h}$

(A) Calculation of Rizk saltation velocity :

$$\mu_s = \frac{1}{10^\delta} Fr_s^x$$

$$\delta = 1.44d_p + 1.96 = 6.28$$

$$\chi = 1.1d_p + 2.5 = 5.8$$

$$Fr_s = \frac{U_{gs}}{\sqrt{gD}}$$

$$\mu_s = \frac{\text{solids flow rate}}{\text{gas flow rate}} = \frac{W_s}{W_g} = \frac{W_s}{A\rho_f U_{gs}}$$

$$\frac{W_s}{A\rho_f U_{gs}} = \frac{1}{10^\delta} \left(\frac{U_{gs}}{\sqrt{gD}} \right)^x$$

$$U_{gs} = \left[\frac{W_s 10^\delta}{A\rho_f} (\sqrt{gD})^x \right]^{1/(x+1)}$$

$$U_{gs} = \left[\frac{3 \times 10^{6.28}}{0.02 \times 1.2} (\sqrt{9.81 \times 0.161})^{5.8} \right]^{1/6.8}$$

$$U_{gs} = (8.938 \times 10^8)^{1/6.8}$$

$$U_{gs} = 20.72 \text{ m/s} = 4077 \text{ ft/min}$$

(B) Calculation of Matsumoto saltation velocity of calculation:

$$\frac{d_p^*}{D} = 1.39 \left(\frac{\rho_p}{\rho_f} \right)^{-0.74} = 1.39 \left(\frac{950}{1.2} \right)^{-0.74} = 0.00995$$

$$\frac{d_p^*}{D} = 0.0016 \text{ m}$$

Since $d_p^* < d_p$

$$\frac{W_s}{W_g} = 0.373 \left(\frac{\rho_p}{\rho_f} \right)^{1.06} \left(\frac{Fr_p}{10} \right)^{-3.7} \left(\frac{Fr_s}{10} \right)^{3.61}$$

$$Fr_p = \frac{U_t}{\sqrt{gd_p}} = \frac{7.93}{\sqrt{9.81 \times 0.003}} = 46.22$$

$$Fr_s = \frac{U_{gs}}{\sqrt{gD}}$$

Rearranging,

$$U_{gs} = \left[\left(\frac{\rho_p}{\rho_f} \right)^{-1.06} \left(\frac{Fr_p}{10} \right)^{3.7} \frac{W_s \times 10^{3.61} (\sqrt{gD})^{3.61}}{(0.373)(A\rho_f)} \right]^{1/4.61}$$

$$U_{gs} = \left[\left(791.66 \right)^{-1.06} \left(4.622 \right)^{3.7} (3115189.4) \right]^{1/4.61}$$

$$U_{gs} = 18.87 \text{ m/s} = 3713 \text{ ft/min}$$

4.1.1.3.4 Choking Velocity (Yousifi and Gau, 1974)

There are numerous correlations available in the literature on choking velocity (Chong and Leung, 1986). The following correlation has been found to be reliable (especially for Geldart A and B class of materials).

$$\frac{U_c}{\sqrt{gd_p}} = 32Re_p^{-0.06}\mu^{0.28}$$

where

$$Re_p = \frac{\rho_f U_t d_p}{\mu_f}$$

$$\mu = \frac{W_s}{W_g}$$

Example 4.2. Calculate the choking velocity using the following data.

- Particle density $\rho_p = 950 \text{ kg/m}^3 = 59.3 \text{ lbm/ft}^3$
- Gas density $\rho_g = 1.2 \text{ kg/m}^3 = 0.075 \text{ lbm/ft}^3$
- Average particle diameter $d_p = 0.003 \text{ m} = 3 \text{ mm}$
- Inner diameter of the pipe (D) = 0.161 m = 6.357 in.
- Conveying rate for solids $W_s = 3 \text{ kg/s} = 23,760 \text{ lbm/h}$
- Gas viscosity $\mu_g = 1.8 \times 10^{-5} \text{ kg/(ms)} = 0.018 \text{ cP}$

$$Re_p = \frac{\rho_f U_t d_p}{\mu_f} = \frac{1.2 \times 7.93 \times 0.003}{1.8 \times 10^{-5}} = 1586$$

$$U_c = \left[\sqrt{gd_p} \times 32Re_p^{-0.06} \left(\frac{W_s}{A\rho_f} \right)^{0.28} \right]^{1/1.28}$$

$$U_c = \left[\sqrt{(9.81 \times 0.003)} \cdot 32(1586)^{-0.06} \left(\frac{3}{0.02 \times 1.2} \right)^{0.28} \right]^{1/1.28}$$

$$U_c = 7.69 \text{ m/s} = 1514 \text{ ft/min}$$

Note that saltation velocity \gg choking velocity.

4.1.2 Classification of Pneumatic Conveying Systems

Pneumatic conveying systems can be configured and operated in a number of different ways for a given application. The common classifications and their basis are summarized in Table 4.2. The most fundamental classification from a design and operation perspective is based on flow pattern, i.e., dilute phase vs. dense phase systems.

Dilute Phase Conveying: The particles are in a fully suspended state along the entire system. All segments of the system operate at velocities greater than the saltation velocity. Dilute phase conveying systems are typically designed to operate at less than 1 bar gauge with a maximum solids loading less (kg of solids/kg of gas) than 10.

Dense Phase Conveying: When the material is conveyed in nonsuspension mode (slugs, strand, moving bed, and fluidized mode) for the entire conveying length, the system is classified as a dense phase conveying system. It should be noted that the flow pattern can change from the feed point to the end of the line due to the continual expansion of gas. It is not uncommon to have a well-defined slug flow at the feed point and fully suspended flow at the end of a long transfer system. Therefore, a definition based solely on solids loading is misleading.

4.1.2.1 Classification of Dilute Phase Conveying Systems

4.1.2.1.1 Pressure Type

Any pneumatic conveying system can be operated either at a positive pressure or under vacuum depending on configuration of its components. Positive pressure or push systems (Figure 4.12) have the air mover positioned upstream of the solids feed point and the cyclone or dust collector operated near atmospheric pressure. The air mover is situated closer to the feed point to provide higher than ambient air pressure, which results in positive pressure in the entire line.

The air mover for a vacuum system or pull system is located downstream of the dust collector and the pressure at the feed point is near atmospheric pressure (Figure 4.13). A combined system (pull-push) uses a single blower to vacuum convey material from one or more sources to a dust collector and then

TABLE 4.2 Classification of Pneumatic Conveying Systems

Basis	Type of System
Flow pattern	Dilute phase, strand flow or medium dense phase, dense phase
Loop configuration	Open loop, closed loop
Pressure (type)	Pressure (push), Vacuum (pull), Combined (pull-push)
Pressure (magnitude)	Low pressure (-0.1 bar to +0.1 bar), Medium pressure (-0.5 bar to 1 bar), High pressure (>1 bar)
Feeder type	Air into solids, Solids into air
Air mover type	Fan, Rotary lobe blower, compressor, other
Solids loading	Very low (<1), Low (0-5), medium (5-15), high (>15), very high (>100)

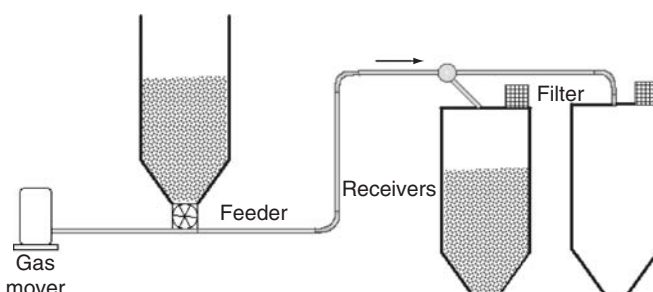


FIGURE 4.12 Typical positive pressure or push system.

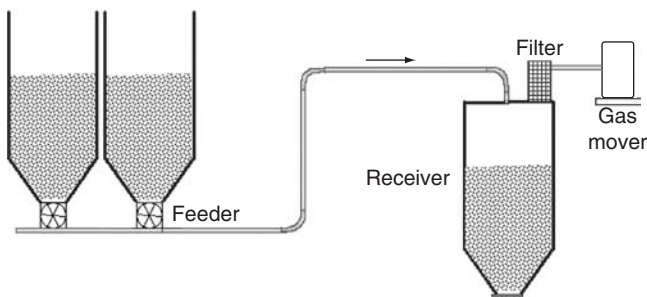


FIGURE 4.13 Typical vacuum or pull system.

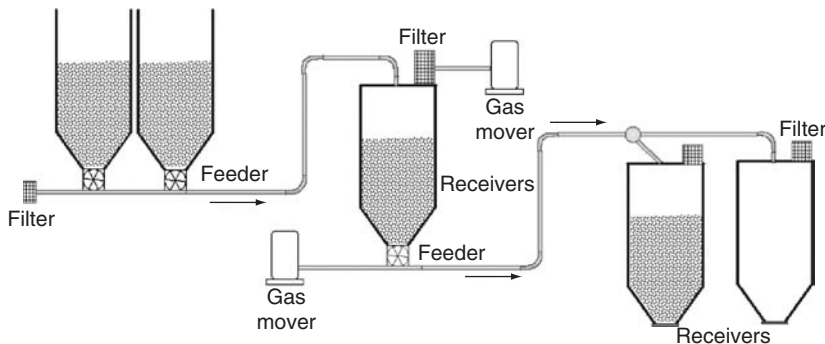


FIGURE 4.14 Typical combined or pull-push system.

TABLE 4.3 Comparison of Pressure, Vacuum, and Combined Conveying Systems

Process Requirement	Vacuum or Pull System	Pressure or Push System	Combined Vacuum Pressure or Pull-Push System
Multiple source, single destination	Preferred	Expensive to implement	Use when single destination is far
Single source, multiple destinations	Expensive to implement	Preferred	Used if high-pressure feeder cannot be used, e.g. railcar unloading system
Handle toxic material (containment)	Preferred	No	No
Explosive material	No	Only with inert gas	No
Long distance conveying (>500 ft)	Limited capacity	Feasible	Feasible but not necessary
Control	Sluggish	Good	Sluggish

pressure convey the material using the same gas to one or more destinations (Figure 4.14). A summary of characteristics based on this classification is given in Table 4.3.

4.1.2.1.2 Loop Configuration

Most pneumatic conveying systems operate as open-loop systems. An open-loop system is one where the conveying gas is vented (or treated and vented) after a single pass through the conveying line. A closed-loop system recycles the gas to the feed point (Figure 4.15).

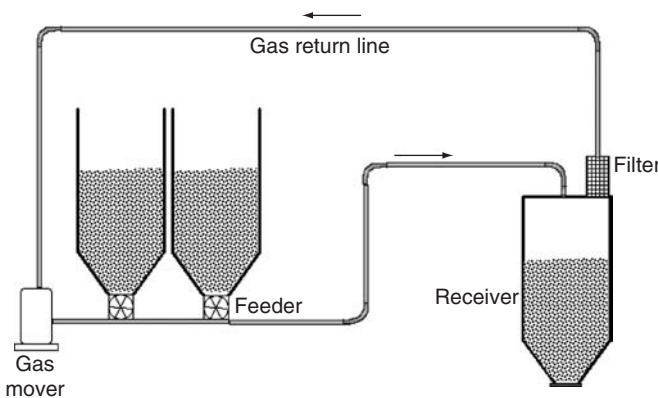


FIGURE 4.15 Typical closed-loop system.

TABLE 4.4 Classification Based on Air Movers

Air-Mover Type	Typical System Characteristics
Fan or centrifugal blower	Short or lightly loaded systems, low-pressure drop, cannot tolerate surging solids feed, low noise, can tolerate material passthrough
Rotary lobe blower	Most common for dilute phase systems, pressure drop up to 1 bar, blower characteristics ideal for varying feed rates
Screw compressors	Common for dense phase system, pressure drop up to 6 bar, blow tanks or high-pressure airlock as feeders

4.1.2.1.3 Feeder Type or Air–Solids Mixing Device

Conveying gas and solids need to be mixed together to create a gas–solid suspension. This can be accomplished in two ways:

1. Air into material: Using pressure vessel (e.g., blow tank)
2. Material into air: Using mechanical feeders (e.g., screw feeder, rotary feeder, and venturi eductor)

Air-into-material systems are generally batch-type systems that can be operated at very high pressures. It is possible to achieve low velocity, high solids loading, and long distance conveying with these systems. Material-into-air systems are continuous systems limited only by pressure rating, leakage rate, wear rate, and feed characteristics of the material.

4.1.2.1.4 Air Mover Type

Air movers provide the motive force or energy for conveying. Energy efficiency, system stability, and conveying capacity limitation is largely dictated by the choice of air mover (Table 4.4). Some applications, such as when the material passes through the air mover, require specific types of air movers (e.g., fans).

4.1.2.2 Classification of Dense Phase Conveying Systems

As mentioned earlier, a dense phase pneumatic conveying system operates in a flow regime to the left of saltation velocity (Figure 4.9). The material moves in a nonsuspended mode within the pipe. Unlike dilute phase conveying, where fluid–particle interactions and particle–wall interactions determine the flow behavior, in dense phase conveying the inter-particle forces and contact mechanics dominate the flow behavior.

Simple examples of dense phase conveying are conveying of cement and plastic pellets. Once aerated, cement retains air for a long time and remains essentially fluidized. It can be transported through a conveying line at very high solids loading with non-specialized hardware over large distances. Similarly, plastic

pellets have a natural tendency to slug when fed into a pipe with motive air. This system is self-adjusting and easy to operate.

However, there is a broad range of materials that do not possess the high aeration or natural slugging ability of plastic pellets. To convey these materials in smooth dense phase mode, various innovations have been implemented in the industry. The objective of these innovations has been to extend the range of applicability of dense phase system and to make them less sensitive to product characteristics.

Dhadapkar (1990) proposed a broad classification for various dense phase conveying concepts (see Figure 4.16).

Two-Phase Flow: Refers to systems operating just below saltation. The material moves in a strand type flow. The hardware requirements are similar to dilute phase conveying systems but these systems can operate at much higher pressures (between 1 and 6 bar).

Extrusion Flow: A typical example would be dense phase conveying of cement, fine coal, or fly ash. The material is highly aerated and the gas is homogeneously dispersed with the solids.

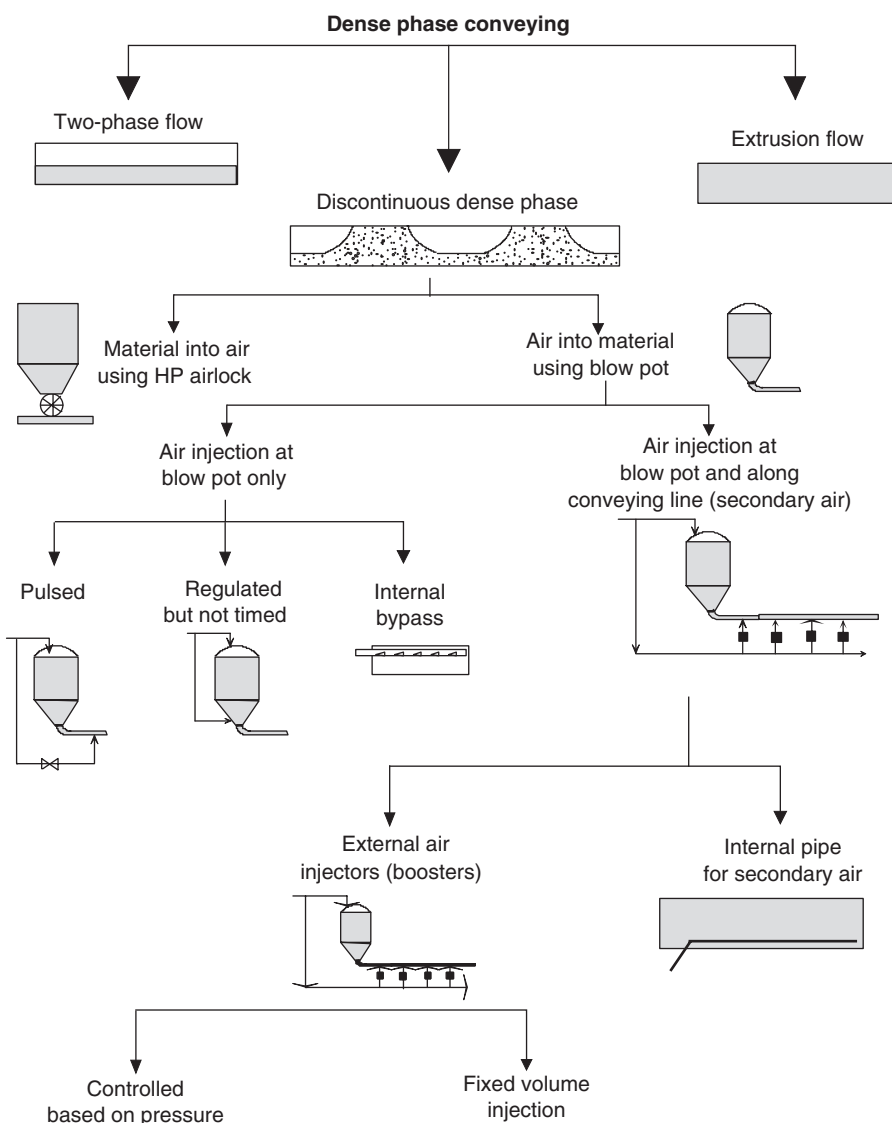


FIGURE 4.16 Classification of dense phase conveying system.

Discontinuous Dense Phase: Refers to plug or slug type of conveying. The conveying gas and material are nonuniformly dispersed to create a variety of flow patterns, from slugs and dunes to waves.

Discontinuous dense phase conveying can be achieved either by feeding material into air stream, commonly using a rotary airlock or feeder, or by injecting air into material such as in a blow-tank system.

Material into Air: Refers to systems using a high-pressure rotary airlock as a feeder. The construction of these feeders is very similar to conventional rotary airlock with the exception of tight clearances, robust shaft design, and design modifications to minimize gas leakage. It is possible to design continuous dense phase system with high-pressure feeders. The limitations due to abrasive wear and particle degradation can be addressed on a case by case basis.

Air into Material: Conventional blow tank type of systems fall into this category. The blow tank acts as a high-pressure feeder. These systems typically run in batch mode unless two tanks are operated in tandem. The discharge characteristic of a blow tank is affected by downstream pressure and the nature of air distribution around the blow tank. The main advantage of a blow tank is the lack of moving parts in constant contact with the material. Loss of conveying air due to wearing of valve seat can be a maintenance problem.

Air distribution at the blow tank and along the conveying line can be used as a tool to create and maintain smooth dense phase conveying mode.

4.1.2.2.1 Air Injection Only at Blow Pot or Tank

Various methods are possible:

- *Pulsed.* Air injection is used at regular intervals (pulsed) to create air gaps between slugs and plugs and limit their length. The ability to change the length of air gaps between plugs is helpful to run the conveying system at low solids rate without causing unstable flow. There are several commercial adaptations of this concept.
- *Regulated, not timed.* The conveying air is split between the top and bottom of the blow tank in a regulated fashion. The top air controls the discharge rate, while the secondary air at the bottom is used to control the solids/air ratio.
- *Internal bypass.* This concept provides a bypass for the conveying air so that it can reach the location of a plug easily. It is assumed that conveying consists of making and breaking of impermeable plugs. No external air is added. The internal bypass line may not be continuous along the conveying length.

4.1.2.2.2 Air Injection at Blow Pot or Tank and Along Conveying Line

External air injection can be accomplished either by providing discrete injection points or a perforated tube along the conveying line for continuous air injection.

- *Discrete Air Injection.* It is commonly known as “*Booster Systems*.” The air injectors or boosters are installed on the conveying line. Each location has a check valve, which prevents the solids from backing into the air supply header. The majority of systems presently in operation today are based on the concept of fixed-volume air injection. Each injector or booster station has a flow control valve that can be set to feed a constant volume of air into the system. The pressure profile or flow conditions in the conveying line generally does not affect the air flow, since these flow control valves act as a critical flow orifice. Some systems are designed with pressure sensors to inject air at locations with high-pressure gradient, which will correspond to a long or stalled plug. The air injection helps to break the plug and maintain smooth conveying conditions.
- *Continuous air injection.* This is accomplished by a pipe, in pipe arrangement. The internal pipe has holes at regular intervals for air injection. Very few of these are commercially available. The clogging of internal pipe is the biggest reason.

4.1.3 Components of Conveying System

A short discussion of the three major components of a conveying system, namely, feeder, air mover, and gas-solid separator, is given here.

4.1.3.1 Feeders

A feeder in a pneumatic conveying system that serves the purpose of an airlock between the conveying line and feed hopper, and regulates the feed rate of solids into the line. In vacuum systems, where the feed point is at ambient pressure, the airlock function is not required. [Table 4.5](#) summarizes the operating range and material suitability of various common feeders.

The design of feeder–hopper interface is critical to assure reliable flow out of the hopper. The mass flow pattern in a hopper can be disrupted by a feeder that extracts material preferentially from one corner of the outlet, which in turn affects the flow into the feeder. Also, the feed shoe or feed box that connects the feeder to the conveying line must be properly designed to provide good mixing and entrainment of solids in gas.

Among these feeders, rotary airlock or feeders and blow tanks are the workhorses of the industry and deserve more attention.

4.1.3.1.1 *Rotary Airlock or Feeder*

This feeder comprises vanes welded on a shaft where the space (pockets) between the vanes fills and empties as the shaft turns ([Figure 4.17](#)). The high and low-pressure sides are isolated by tight clearances between the vanes and the housing. A range of designs are available and careful selection of features and operating range must be made, based on bulk properties. The critical issues are:

- Volumetric capacity of the rotor and its relationship with r/min
- Gas leakage rate at various pressures and r/min
- Particle degradation and wear
- Venting arrangement of gas
- Design of inlet and outlet
- Seal and bearing design

4.1.3.1.2 *Blow Tank*

Blow tanks or blow pots are commonly used as feeders for high-pressure applications. There are two common configurations of blow tanks : bottom discharge and top discharge. The top discharge blow tanks are used for fine powders, whereas bottom discharge blow tanks can be used for powders and coarse materials. The conveying air can be injected at various locations at the blow tank and along the conveying line (as shown in [Figure 4.18](#)). Blow tanks operate in batch mode. A complete cycle consists of filling, valve setting, pressurization, conveying, and depressurization ([Figure 4.18](#)). The average conveying rate is lower than instantaneous conveying rate due to time lost in nonconveying steps.

The advantages of the blow tank as a feeder are

1. No moving parts in contact with solids
2. Can operate or feed against high pressures (>3 bar)
3. Good for abrasive materials
4. Low maintenance

However, the disadvantages are

1. Do not provide good control on discharge rate or solids loading
2. Unsuitable for very cohesive or sticky materials
3. Batch operation, but can be made continuous using two blow tanks

4.1.3.2 Air Movers

Air movers provide the motive energy for pneumatic transfer. Fans, centrifugal blowers, rotary lobe (Roots type) blowers, screw compressors, sliding vane compressors, and reciprocating compressors cover the majority of the applications. The suitability of an air mover must be judged based on the operating conditions and requirements of the application.

4.1.3.2.1 *Fans*

Fans convert kinetic energy of the gas generated by the rotating impeller into pressure and the volume as a result of displacement of the blades. Depending on the direction of flow through the impeller, fan

TABLE 4.5 Summary of Feeders for Pneumatic Conveying Applications

Feeder	Suitable for System Types	Operating Pressure	Suitable Materials	Unsuitable Materials	Conveying Mode	Comments
Suction nozzle	Vacuum	Up to 0.5 bar vacuum	All free flowing	Caking, large chunks, sticky, cohesive	Continuous dilute phase	Feed rate control is difficult
Rotary feeder	Vacuum and pressure	0.5 bar vacuum – 3.5 bar pressure (6 bar maximum)	Wide range of materials	Abrasive, caking, sticky, very cohesive	Continuous dilute and dense phases	Most common feeder. Wide variety of design features
Eductor	Pressure	0.25 bar	Free flowing	Abrasive, friable, highly cohesive	Continuous dilute phase	Special design for abrasive materials, high-pressure motive gas may be required
Blow tank-bottom discharge	Pressure	0 – 10 bars	Wide range of materials, abrasive materials	Very cohesive, sticky or compressible materials	Batch dilute and dense phases	Poorly flowing materials will require air injection in the cone, difficult to control conveying rate
Blow tank-fluidization type, top discharge	Pressure	0 – 10 bar	Fine fluidizable materials (Geldart class A/C, A)	Geldart class B, B/D, D or material with large chunks	Batch dilute and dense phases	
Double flapper valve	Pressure	0 – 0.5 bar	Abrasive and free-flowing material	Cohesive	Continuous dilute phase	Pulsing feed
Screw feeder	Pressure and vacuum	0.5 bar vacuum to 1 bar pressure	Wide range of materials	Sticky, compressible	Continuous dilute phase	Improper design will result in feed rate control (what do we mean by this?). Rate sensitive to material properties.
Fuller-Kinyon Pump	Pressure	2 bar	Fine powders	Coarse materials	Continuous dilute and dense phase	Typically used in cement industry
Slide gate	Vacuum	Up to full vacuum	Coarse materials, preferably free-flowing	Cohesive, sticky materials	Continuous dilute phase	Simple, discharge rate depends on material properties
Other specialized feeders: diaphragm pump	Pressure	0 – 0.5 bar	Materials with high air retention or low deaeration, preferably low bulk density	Sticky, cohesive, low air retention	Continuous dilute and dense phases	

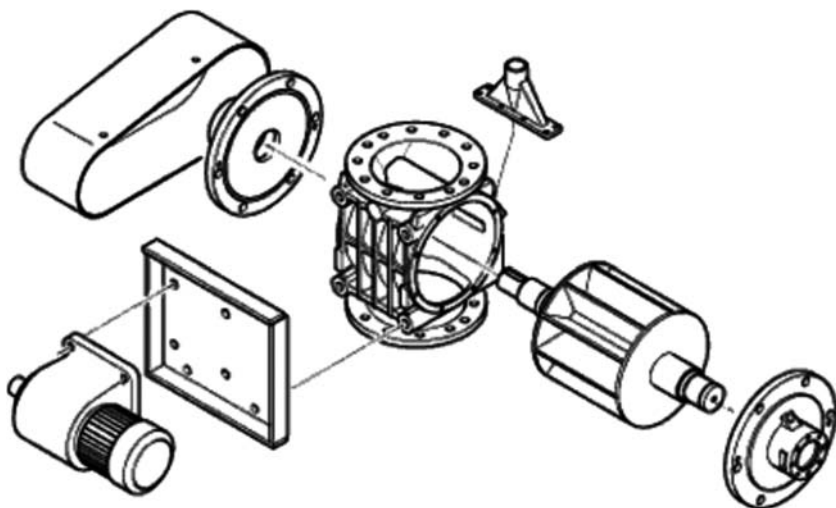


FIGURE 4.17 Exploded view of a rotary airlock/feeder. (Courtesy of Coperion Waeschle.)

designs can be broadly classified into four categories, namely, axial flow, radial flow (centrifugal fans), mixed flow (axial and radial), and cross-flow. In pneumatic conveying applications, radial flow or centrifugal fans are primarily used.

There are three primary impeller designs available for centrifugal fans: radial, backward curving, and forward curving. The forward-curved design provides maximum pressure head for a given rotor size and speed, while the backward curved design provides the least. On the other hand, backward-curved impeller design is more energy efficient with lower operating costs. Radial flow fans offer the best compromise. Radial flow design can also tolerate particulate material in the gas stream and tend to be more robust.

Fans are generally driven directly with a motor that limits the speed of rotation. To change the gas flow rate, inlet or outlet throttling valves can be used. Proper balancing of the fans is necessary to minimize maintenance of the bearings.

The performance of all fans is governed by fan laws which state:

1. Air volume varies directly with fan speed.
2. Static pressure varies with square of the speed.
3. Brake horsepower and air horsepower varies with the cube of the speed.
4. For geometrically similar fans, air volume varies with the cube of size.
5. For geometrically similar fans, static pressures vary with the square of the size.
6. For geometrically similar fans, break horsepower varies with the fifth power of size.

These laws can be used to scaleup or predict the performance of a machine at different operating conditions. In order to convert the performance curve of a fan from one speed to another select a number of points on the curve convert the corresponding data for air volume, static pressure, brake horsepower, and noise using the following equations:

$$\frac{Q_2}{Q_1} = \left(\frac{D_2}{D_1} \right)^3 \frac{\text{rpm}_2}{\text{rpm}_1}$$

$$\frac{P_2}{P_1} = \left(\frac{D_2}{D_1} \right)^2 \left(\frac{\text{rpm}_2}{\text{rpm}_1} \right)^2$$

and

$$\frac{HP_2}{HP_1} = \left(\frac{D_2}{D_1} \right)^5 \left(\frac{\text{rpm}_2}{\text{rpm}_1} \right)^3$$

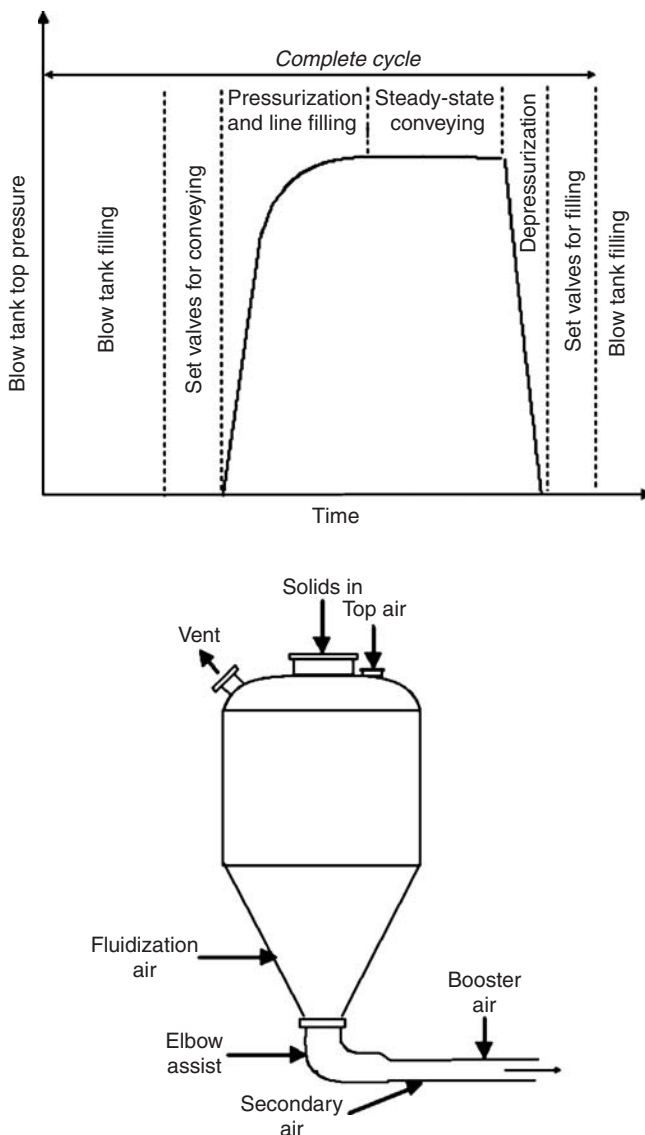


FIGURE 4.18 Typical bottom discharge blow tank configuration and conveying cycle.

where Q is the air flow rate, P the static pressure, D the impeller diameter of fan, and HP the break horsepower. For detail treatment of fan design, operation and performance, see Fan Engineering (2003).

4.1.3.2.1.1 Controlling Air Flow Rate. The most efficient means of reducing air flow rate from a fan is to change the fan speed. While the efficiency remains unchanged, the noise level and power consumption are significantly reduced. Since the fan curves are shifted, there is no risk of operation in the unstable region. The cost of a variable speed motor can be high if the adjustment needs to be made very often.

Another approach is to install adjustable inlet and outlet vanes. Vane control systems are cheaper to implement, but do not provide the same level of power savings as speed control. Inlet vane control is used for large fans since it is cheaper, but the power savings are better than that in outlet vane control.

4.1.3.2.2 *Rotary-Lobe Blowers*

Rotary-lobe blowers (Roots type blowers) are ideally suited for pneumatic conveying applications operating at less than 1 bar guage pressure or 0.5 bar vacuum and require oil-free gas. The air mover operates on positive displacement principle where the gas at the inlet is trapped between two counterrotating lobes. As the two lobes rotate, the gas is expelled at the discharge end (see [Figure 4.19](#)). There is no gas compression within the lobes and all the compression occurs as the gas is expelled against the higher pressure at the outlet. Therefore, the horsepower consumption is proportional to discharge pressure and the inlet air volume remains relatively constant with back pressure. The slight decrease in air delivery volume is due to slippage of gas owing to clearances between the lobes. These blowers can be very noisy during the operation and hence inlet or outlet silencers are highly recommended. The pulsating nature of the gas flow can be reduced by using a trilobe design. The pulsations also result in loss of thermodynamic efficiency.

In specifying blower performance, one may use actual cubic feet per minute (ACFM) and inlet cubic feet per minute (ICFM) alternately. These refer to the flow rate at the inlet of blower based on actual conditions of temperature, pressure and RH% (relative humidity) at the blower inlet. It is essential to distinguish ACFM/ICFM from standard cubic feet per minute (SCFM). SCFM refers to gas flow rate at a standard reference pressure, temperature, and RH%. According to ASME and CAGI standards, the standard reference is 14.7 psia, 68°F and 36% relative humidity. Most blower curves are based on ICFM and not SCFM.

4.1.3.2.3 *Screw Compressors*

Screw compressors are required when conveying pressure exceeds 1 bar. The screw compressor is a positive displacement volume reduction machine. In simplest configuration, it consists of a male rotor (driver) and a female rotor (driven). The gas is trapped in the void space between the counterrotating rotors at the inlet. As the screws turn, the volume is reduced and the compression is achieved. Unlike reciprocating compressors, there are no discharge valves in screw compressors. The end of compression automatically occurs at the discharge port. Since the energy is already spent on compressing the gas through the compressor, any changes in system characteristics (reduced load) will not affect the power consumption. The performance of a screw compressor must be controlled independently either through throttling of the inlet valve or the variable speed drive on the rotor.

A comparison of the characteristics of fan, rotary lobe blower, and screw compressor is shown in [Figure 4.20](#) and [Table 4.6](#).

4.1.3.3 *Gas–Solid Separation Devices*

The three common gas–solid separation devices are

1. Inertial separator
2. Cyclone separator
3. Dust collector or baghouse

Selection and specification of suitable gas–solid separation device will depend on process requirements and material properties, namely,

1. Desired efficiency of separation based on particle size distribution of incoming solids
2. Acceptable pressure drop range
3. Operating pressure and temperature
4. Cleanout and contamination requirement
5. Dust explosion potential
6. Acceptable turn down in gas flow rate
7. Compatibility with material (corrosiveness, abrasion, etc.)

A simplified guideline is presented in [Table 4.7](#).

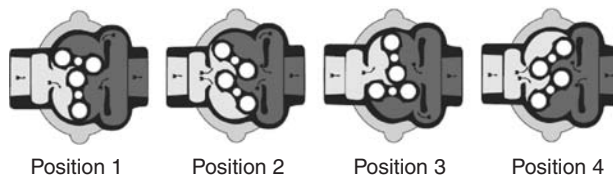


FIGURE 4.19 Roots blower operating principle (Courtesy of Roots Dresser Industries.)

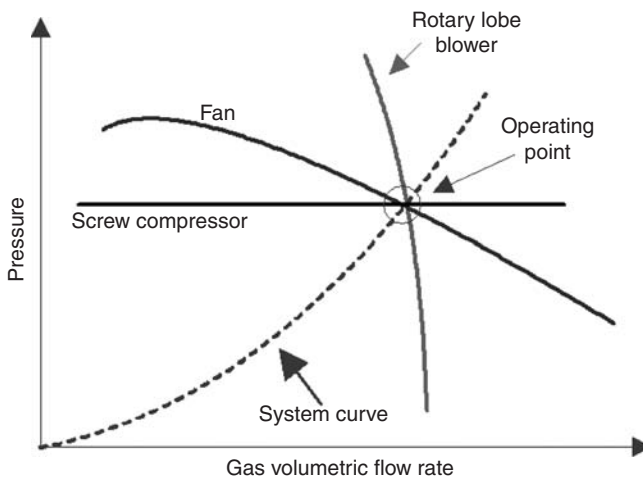


FIGURE 4.20 Comparison of air mover characteristics and relationship with system characteristics.

TABLE 4.6 Comparison of Air Movers (Typical Performance Limits)

Type	Maximum Delivery Pressure or Vacuum (bar)	Maximum Flow Rate (m^3/min)
Fans	± 0.2	1000
Single-stage centrifugal blowers	-0.5 to + 0.5	1000
Rotary lobe blowers	- 0.5 to + 1	1200
Screw compressors	0 to 10	1000
Reciprocating compressor	No limit	200
Sliding-vane compressor	1 to 5	100

TABLE 4.7 Comparison of Major Gas–Solid Separation Devices

Type of Gas–Solid Separation Device	Suitable for	Unsuitable for	Comments
Inertial separator	Separating large nonhazardous particles with minimal fines	Fine powders or hazardous materials	Simple, low-pressure drop, no maintenance
Cyclone separator	Most nonfriable and nonabrasive materials	Very hazardous materials where 99.5% collection efficiency must be guaranteed	Typical pressure drop of 10" WC (25 millibar), proper design and installation is critical, scalability with gas flow rate is limited
Dust collector or baghouse	Efficient solution for most materials	Very few materials	Gives high degree of separation, collection efficiency independent of gas flow rate and particle size, bag replacement is major maintenance issue

4.1.4 Calculating Pressure Drop in Dilute Phase Systems

The total pressure drop across a conveying system can be assumed to be the sum of pressure drops across various components. The total pressure drop in turn must be overcome by the air mover to satisfy the pressure balance:

$$\Delta P_{\text{air-mover}} = \Delta P_{\text{blower-piping}} + \Delta P_{\text{feed-section}} + \Delta P_{\text{acceleration(gas+solids)}} + \Delta P_{\text{straight-sections}} \\ + \Delta P_{\text{bends}} + \Delta P_{\text{filter-receiver}}$$

The equations of pressure drop for the various components are presented below.

4.1.4.1 Blower Piping and Feed Section Pressure Drop

The pressure drop in the piping carrying gas from the blower to feed section of the conveying system can be calculated by using the standard calculations for single-phase gas flow in pipes. Additional pressure drop due to inlet or outlet filters and inlet or outlet silencers must be added.

4.1.4.2 Acceleration (Gas–Solids) Pressure Drop

When solids are fed into a gas stream, additional energy is expended to accelerate the solids to their steady-state velocity. This loss occurs at the feed (pickup) point. Similar loss occurs when accelerating the gas phase; however, it is relatively smaller.

For the solid phase,

$$\Delta P_{\text{ACC-solids}} = \frac{U_p W_s}{A}$$

For the gas phase,

$$\Delta P_{\text{ACC-gas}} = \frac{\rho_g U_g^2}{2}$$

By adding the above components,

$$\Delta P_{\text{ACC}} = \Delta P_{\text{ACC-solids}} + \Delta P_{\text{ACC-gas}} \\ \Delta P_{\text{ACC}} = \frac{U_p W_s}{A} + \frac{\rho_g U_g^2}{2} \\ \Delta P_{\text{ACC}} = \frac{\rho_g U_g^2}{2} \left(1 + 2 \frac{W_s}{A \rho_g U_g} \left(\frac{U_p}{U_g} \right) \right) \\ \Delta P_{\text{ACC}} = \frac{\rho_g U_g^2}{2} \left(1 + 2 \mu \left(\frac{U_p}{U_g} \right) \right)$$

The velocity ratio, U_p/U_g , for horizontal flow can be calculated by the (1953) Hinkle correlation:

$$\frac{U_p}{U_g} = 1 - 0.044 d_p^{0.3} \rho_p^{0.5}$$

or modified Hinkle correlation (IGT correlation):

$$\frac{U_p}{U_g} = 1 - 0.68 d_p^{0.92} D^{-0.54} \rho_p^{0.5} \rho_g^{-0.2}$$

where d_p and D in m and ρ_p and ρ_g in kg/m.³

For vertical flow, one may simply use slip condition based on single-particle terminal velocity.

$$U_p = U_g - U_t$$

4.1.4.3 Steady-State Pressure Drop in Straight Sections

The overall pressure drop for fully accelerated and steady-state dilute phase conveying in straight pipe can be considered as the sum of static and frictional components:

$$\Delta P_{\text{total}} = \Delta P_{\text{static}} + \Delta P_{\text{frictional}}$$

$$\Delta P_{\text{static}} = \rho_p(1 - \varepsilon)\Delta Zg + \varepsilon\rho_g\Delta Zg$$

where the first term on the right-hand side is the contribution due to solids and the second term is due to gas. ΔZ is the change in elevation or height of the vertical section. The static component is zero for horizontal orientation.

The voidage, ε , can be calculated as

$$\varepsilon = 1 - \frac{W_s}{A\rho_p U_p}, \quad U_p = U_g - U_t$$

where the pressure drop term due to gas–solid friction is customarily split into gas and solids contributions.

$$\Delta P_{\text{frictional}} = \Delta P_{\text{air}} + \Delta P_{\text{solids}}$$

The first term represents the contribution due to gas friction and the second term due to solids friction. The pressure drop due to air is calculated by well-established single-phase calculation methods:

$$\Delta P_{\text{air}} = \lambda_f \frac{\rho_g U_g^2 L}{2D}$$

where the friction factor for gas alone can be estimated by the explicit correlation of Swamee and Jain (1976):

$$\lambda_f = \frac{1.325}{[\ln(k_s/3.7D + 5.74/Re^{0.9})]^2}$$

For common pipes, the pipe roughness, k_s/D , is typically 0.001.

The expression for pressure drop due to solids is formulated similar to single-phase gas flow with added solids loading factor:

$$\Delta P_{\text{solids}} = (\mu\lambda_z) \frac{\rho_g U_g^2 L}{2D}$$

4.1.4.3.1 Estimation of Friction Factor λ_z

Several approaches have been proposed in the literature to calculate the solids friction factor based on material properties and system parameters. Unfortunately, none of them are comprehensive and fundamental enough to cover all factors. Weber (1982, 1991), after analyzing a large set of data, proposed the following expression:

$$\lambda_z = K\mu^a Fr^b Fr_s^c \left(\frac{D}{d_p}\right)^d$$

where

$$\mu = \text{solids loading} = \frac{W_s}{W_g}$$

$$Fr = \frac{U_g^2}{gD}, \quad Fr_s = \frac{U_t^2}{gd_p}$$

In pneumatic conveying literature, two forms of Froude number can be found:

$$Fr_1 = \frac{U_g^2}{gD}, \quad Fr_2 = \frac{U_g}{\sqrt{gD}}$$

TABLE 4.8 Summary of Exponents for Friction Factor Correlation

Investigator/Material	K	a	b	c	d
Stegmaier, fine powder ($d_p < 0.5$ mm)	2.1	-0.3	-1	0.25	0.1
Weber(Siegel data), coarse material ($d_p > 0.5$ mm)	0.082	-0.3	-0.86	0.25	0.1

Source: Weber, M., *Bulk Solids Handling*, 2(2), 231-233, 1982. With permission.

The reader is cautioned to verify the definition of Froude number before applying any correlation.

In the absence of any experimental data on a material, the parameters listed in Table 4.8 can be chosen for preliminary calculations. It should be noted that the above correlation does not account for the effect of elastic properties of particles and wall, surface characteristics, particle size distribution, and particle shape. It should be noted that the coefficient of Froude number is always negative; however, the coefficient of solids loading in the correlation need not be negative.

In the authors' experience using a constant value of friction factor will usually suffice for preliminary calculations. This value can be backcalculated if operating data from an installed system is available.

From Experimental Data If conveying data can be generated on a pilot-scale test rig, a more accurate estimation of material-specific friction factor can be made. It is advisable to install a differential pressure transmitter across a straight horizontal section that is away from the bends at each end. A static gage at the test section is necessary to calculate the local gas velocity:

$$\Delta P_{\text{total}} = \Delta P_{\text{frictional}} = \Delta P_{\text{air}} + \Delta P_{\text{solids}}$$

$$\Delta P_{\text{solids}} = \Delta P_{\text{total}} - \Delta P_{\text{air}}$$

where ΔP_{air} can be estimated by regressing pressure drop data for single-phase air flow in the test section. Solids friction factor can be calculated from experimental data at each of the test condition by using the following equation:

$$\lambda_z = \frac{\Delta P_{\text{solids}} 2D}{\rho_g U_g^2 \mu L}$$

These data can be correlated with the generalized format or a simplified expression if the test data is not available for a range of pipe sizes:

$$\lambda_z = K \mu^a F r^b$$

4.1.4.4 Pressure Drop in Vertical Section

The pressure drop in vertical section can be calculated as follows:

$$\Delta P_{\text{total}} = \Delta P_{\text{frictional}} + \Delta P_{\text{static}}$$

$$\Delta P_{\text{static}} = \rho_p (1 - \varepsilon) \Delta Z g + \varepsilon \rho_g \Delta Z g$$

$$\Delta P_{\text{frictional}} = \Delta P_{\text{total}} - \Delta P_{\text{static}}, \quad \Delta P_{\text{frictional}} = \Delta P_{\text{solids}} + \Delta P_{\text{air}}$$

$$\Delta P_{\text{solids}} = \Delta P_{\text{frictional}} - \Delta P_{\text{air}}, \quad \lambda_z = \frac{\Delta P_{\text{solids}} 2D}{\rho_g U_g^2 \mu L}$$

4.1.4.5 Pressure Drop in Bends

In contrast to straight sections, frictional losses have relatively minor contribution to the pressure drop across a bend. The majority of the pressure drop is due to reacceleration of solids that were slowed down during transit through the bend. Since the particles may continue to reaccelerate even after they exit the bend, the

pressure drop due to a bend cannot be measured simply by pressure difference between inlet and outlet of the bend. Also, the pressure drop across a bend depends on its geometry and orientation. No generalized correlation that takes all the factors into account is available in the literature. Bradley (1990), Chambers et al. (1986), Marcus et al. (1990), Morikawa et al. (1978), Park et al. (1980), Schucharl (1970). The following correlations are sufficiently accurate for practical design:

4.1.4.5.1 Chambers–Marcus Correlation (1986)

The Chamber–Marcus correlation is given as follows:

$$\Delta P_B = B(1 + \mu) \frac{\rho_g U_g^2}{2}$$

This expression is very similar to the expression proposed by EEuA (1963). The bend loss coefficient B depends on the ratio of bend radius to pipe diameter. In the absence of experimental data, Chambers and Marcus (1986) recommend the use of the values given in Table 4.9.

4.1.4.5.2 Correlation (1987) of Westman et al.

The correlation of Westman et al. is given as follows

$$\begin{aligned} \frac{\Delta P_{\text{Bend}}}{0.5 \rho_g U_g^2} &= \zeta_{\text{Total}} = \zeta_{\text{air}} + \zeta_{\text{solids}} \\ \zeta_{\text{air}} &= 0.167 \left[1 + 17.062 \left(\frac{D_B}{D} \right)^{-1.219} \right] \text{Re}^{-0.17} \left(\frac{D_B}{D} \right)^{0.84} \\ \zeta_{\text{solids}} &= \frac{5.4 \mu^{1.293}}{Fr^{0.84} (D_B/D)^{0.39}} \end{aligned}$$

4.1.4.6 Pressure Drop in Gas–Solid Separator or Filter Receiver

The pressure drop across gas–solid separators depends on the gas flow rate and solids loading (see the vendor of the unit for pressure drop estimation). Typically, these units are designed for 5 to 10 in. WC in the normal operating range.

4.1.4.7 Calculation of Overall Pressure Drop in Dilute Phase Conveying System

The overall pressure drop in a dilute phase conveying system (pressure or vacuum) can be determined by systematically calculating the pressure gradient across various elements (straight-horizontal, straight-vertical, or bends). It is logical to begin the calculation from a point in the system where the pressure conditions are well defined and then work toward the other end. For pressure systems, the exit conditions are known, whereas feed conditions are known for vacuum systems. The following example outlines the approach for pressure system that can be modified slightly for vacuum system calculations:

Example 4.3. Given

1. Material properties : particle size and particle density
2. Conveying rate
3. Conveying line layout (see Design Tips)

TABLE 4.9 Bend Constant B or Various Bends

R_B/D	B
2	1.5
4	0.75
≥ 6	0.50

Note: RB is the radius of the bend curve. Bends are often specified by the RB/D ratio. RB/D>10 is considered as a long radius bend.

4. Pipe diameter D
5. Pickup or saltation velocity U_{pickup}

find

1. Overall pressure loss
2. Total gas flow rate (SCFM) required

It is assumed that the temperature of the conveying gas is constant along the conveying line. Appropriate corrections to the gas volume must be made if a temperature gradient exists.

Step 1: Draw an isometric layout of the conveying system. Mark all the bends, elbows, and diverter valves.

As mentioned earlier, the gas velocity and gas density continually changes from feed point to destination. The use of an average value leads to inaccurate estimation of the pressure drop. It is recommended that the conveying line has to be broken down into smaller segments of 50 ft (15 m) or less. The calculations are performed on an incremental basis by using local values of gas velocity and gas density.

It is assumed that the flow conditions (pressure, velocity, gas density, temperature, etc.) in a segment are represented by the conditions calculated at the exit of the segment (see Figure 4.21). The last segment is the n th segment.

Step 2: (1) Depending on the total length of the system and material type, select solids to air loading ratio μ from Table 4.10.

(2) Assume the pressure at pickup point (P_{pickup} , psia). Calculate the saltation velocity. As a first approximation, use saltation velocity as pickup velocity:

$$\mu = \frac{W_s}{W_g} = \frac{W_s}{AU_{\text{gsaltation}} \rho_f}$$

$$D = \sqrt{\frac{4W_s}{\pi U_{\text{gsaltation}} \rho_f}}$$

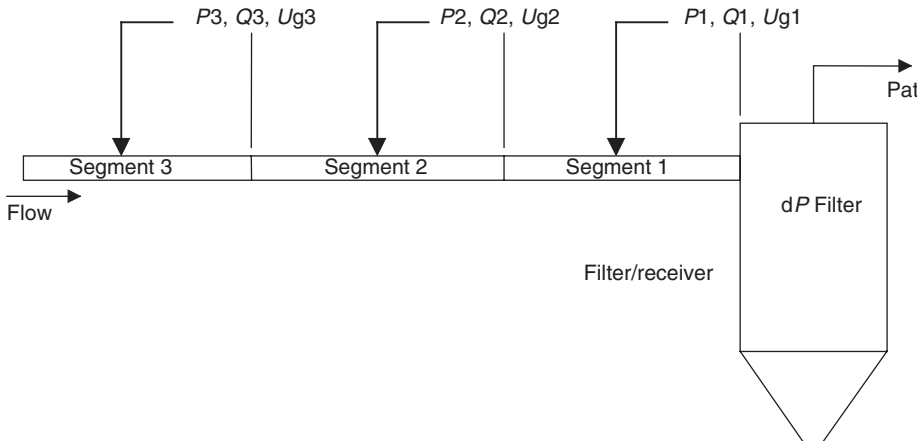


FIGURE 4.21 Segmentation and flow condition representation.

TABLE 4.10 Selection of Approximate Solids Loading

System Length (ft)	Coarse Material $d_p > 0.5 \text{ mm}$	Fine Material $d_p < 0.5 \text{ mm}$
0–500	5	6
500–1000	4	4
1000–1500	2.5	3

where ρ_f is the gas density at P_{pickup} .

(3) Calculate the conveying gas flow rate at standard conditions

$$Q_0(\text{scfm}) = U_{\text{g saltation}} (\pi/4^* D^2)(P_{\text{pickup}})/P_{\text{atm}}$$

Step 3: Estimate the flow conditions at the first segment:

$$P_1 = P_{\text{atm}} = dP_{\text{filter}}$$

$$Q_1 = Q_0(\text{SCFM})P_{\text{atm}}/P_1$$

$$U_{g1} = Q_1/A$$

$$\rho_{f1} = (\rho_{f-\text{atm}}/P_{\text{atm}})P_1$$

Temperature correction for density must be made where temperature gradient exists.

Step 4: Estimate the pressure drop across the segment.

If the segment is a straight section,

$$\Delta P_{\text{segment}} = \Delta P_{\text{static}} + \Delta P_{\text{frictional}}$$

$$\Delta P_{\text{static}} = \rho_p(1 - \varepsilon)\Delta L \frac{g}{g_c} + \varepsilon \rho_g \Delta L \frac{g}{g_c}$$

where

$$\varepsilon = 1 - \frac{W_s}{A\rho_p U_p}$$

Use IGT correlation to calculate U_p :

$$\frac{U_p}{U_g} = 1 - 0.68d_p^{0.92}D^{-0.54}\rho_p^{0.5}\rho_g^{-0.2}$$

where d_p, D are in meters and ρ_p, ρ_g are in kg/m³.

ΔP_{static} , which is the pressure drop due to static head of gas-solid mixture, is zero for horizontal orientation:

$$\Delta P_{\text{frictional}} = (\lambda_f + \mu\lambda_z)\frac{\rho_g U_g^2 \Delta L}{2Dg_c} = \lambda_f \frac{\rho_g U_g^2 \Delta L}{2Dg_c} + (\mu\lambda_z)\frac{\rho_g U_g^2 \Delta L}{2Dg_c}$$

Swamee and Jain (1976) correlation for gas friction factor, λ_f , is recommended:

$$\lambda_f = \frac{1.325}{[\ln(k_s/3.7D + 5.74/Re^{0.9})]^2}$$

Use generalized form of solids friction factor correlation, λ_z :

$$\lambda_z = K\mu^a Fr^b Fr_s^c \left(\frac{D}{d_p}\right)^d$$

$$\mu = \text{solids loading} = \frac{W_s}{W_g}$$

$$Fr = \frac{U_g^2}{gD}$$

$$Fr_s = \frac{U_t^2}{gd_p}$$

TABLE 4.11 Coefficients for Solids Friction Factor Correlation

Investigator/Material	K	a	b	c	d
Stegmaier fine powder ($d_p < 0.5$ mm)	2.1	-0.3	-1	0.25	0.1
Weber (Siegel data) coarse material ($d_p > 0.5$ mm)	0.082	-0.3	-0.86	0.25	0.1

In the absence of material-specific data, use Stegmaier's coefficients for fine powders and Weber's coefficient for coarse materials (Table 4.11) as suggested by Chambers and Marcus (1986). The values of K can be adjusted to fit the available plant data and then used for predictive calculations.

If the segment is a bend or an elbow, use Chambers–Marcus bend pressure drop correlation:

$$\Delta P_{\text{segment}} = \Delta P_B = (1 + \mu) \frac{\rho_g U_g^2}{2g_c}$$

where the bend constant B can be experimentally determined or read from [Table 4.9](#) when no data are available.

The flow conditions in the next (upstream) segment ([Figure 4.21](#)) can then be established as follows:

$$P_2 = P_1 + \Delta P_{\text{segment}}$$

$$Q_2 = Q_0 (\text{SCFM}) P_{\text{atm}} / P_2$$

$$U_{g2} = Q_2 / A_2$$

$$\rho_{f2} = (\rho_{f-\text{std}} / P_{\text{atm}}) P_2$$

Step 5: Repeat Step 4 until the pressure and velocity profile in the entire system is obtained. The last segment corresponds to the feed section.

For remaining segments,

$$P_{i+1} = P_i + \Delta P_{\text{segment}}$$

$$Q_{i+1} = Q_0 \frac{P_{\text{atm}}}{P_{i+1}}$$

assuming isothermal conditions.

Step 6: Estimate the pressure at the inlet of the last n th segment (see [Figure 4.22](#)). Add acceleration zone pressure drop:

$$P_{\text{pickup}} = (P_n + \Delta P_{\text{last segment}}) + \Delta P_{\text{ACC}}$$

where P_{pickup} and P_n are in psia and $\Delta P_{\text{last segment}}$ and ΔP_{Acc} are in psi

$$\Delta P_{\text{ACC}} = \frac{\rho_g U_g^2}{2g_c} \left(1 + 2\mu \left(\frac{U_p}{U_g} \right) \right)$$

and ρ_g and U_g are calculated for conditions at the feed point.

Use IGT correlation to calculate U_p / U_g :

$$\frac{U_p}{U_g} = 1 - 0.68 d_p^{0.92} D^{-0.54} \rho_p^{0.5} \rho_g^{-0.2}$$

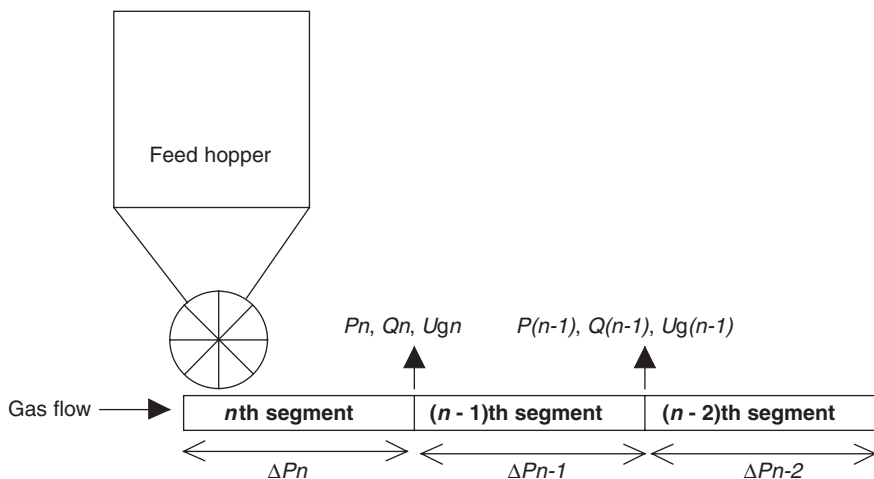


FIGURE 4.22 Flow conditions at feed point.

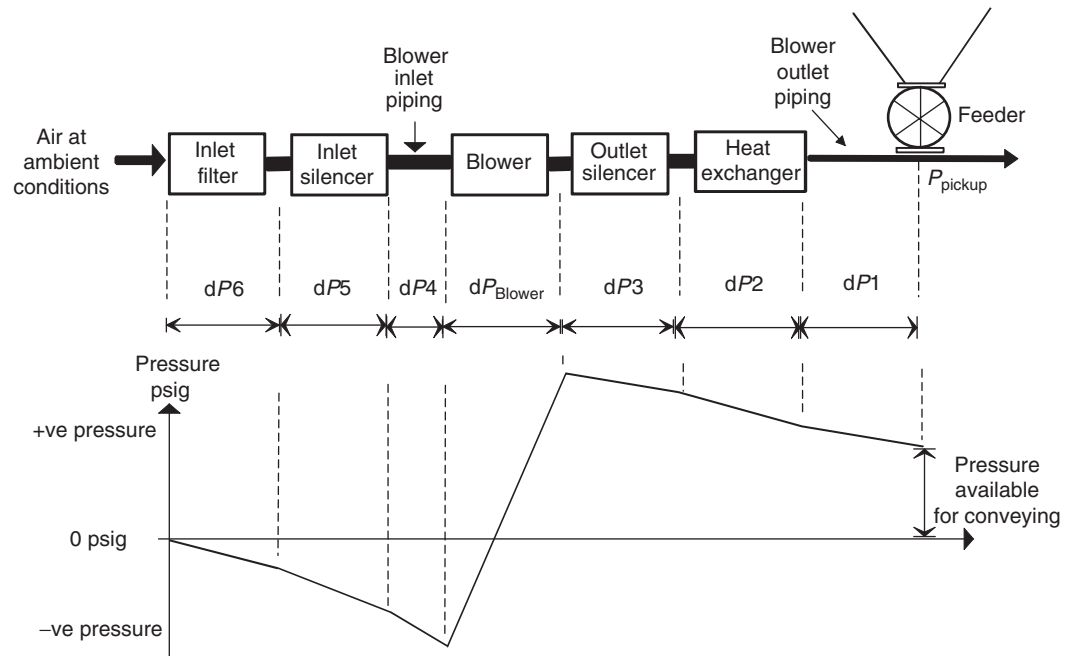


FIGURE 4.23 Pressure profile at the blower.

Step 7: Compare P_{pickup} with the value used in Step 2. Update the estimation of P_{pickup} . Repeat Steps 2 to 6 until convergence is reached.

Step 8: Add the miscellaneous pressure drops due to blower piping and filters or silencer to estimate the blower outlet pressure:

$$\Delta P_{\text{misc}} = dP_1 + dP_2 + dP_3$$

(see Figure 4.23 for more details)

$$P_{\text{blower outlet}} = \Delta P_{\text{misc}} + P_{\text{pickup}}$$

Step 9: Add the leakage loss through the rotary airlock or feeder to estimate the blower gas delivery rate:

$$Q_{\text{blower outlet}} = (Q_0 + Q_{\text{leakage}})P_{\text{atm}}/P_{\text{blower outlet}}$$

Q_{leakage} (scfm) must be estimated from vendor charts and corrected for pressure at the feed point. Blower inlet cfm can be calculated by using the Gas law:

$$Q_{\text{blower inlet}} = Q_{\text{blower outlet}}P_{\text{blower outlet}}/P_{\text{blower inlet}}$$

where

$$P_{\text{blower inlet}} = P_{\text{atm}} - (dP_6 + dP_5 + dP_4)$$

From Figure 4.7,

$$P_{\text{blower inlet}} = P_{\text{atm}} - (dP_6 + dP_5 + dP_4)$$

$P_{\text{blower outlet}}$ and $Q_{\text{blower inlet}}$ define the operating point for the blower.

Example 4.4. Calculate the pressure drop given

- Material: PE Pellets
- Conveying rate $W_s = 30,060 \text{ lb/h} = 8.35 \text{ lbm/s}$
- Particle density $\rho_p = 59 \text{ lbm/ft}^3$
- Particle size $d_p = 4 \text{ mm} = 0.0131 \text{ ft}$
- Pipe roughness $k_s/D = 0.0002$
- Gas density at standard conditions (14.7 psia, 68°F) = 0.075 lbm/ft³
- Gas viscosity $\mu_g = 0.018 \text{ cP} = 1.2 \times 10^{-5} \text{ lbm/(ft s)}$
- Pickup or saltation velocity = 4885 ft/min

Assume:

- Pressure drop across cyclone = 0.1 psi
 - Gas temperature = 68°F is constant across the system
- Conveying line layout is shown in Figure 4.24.

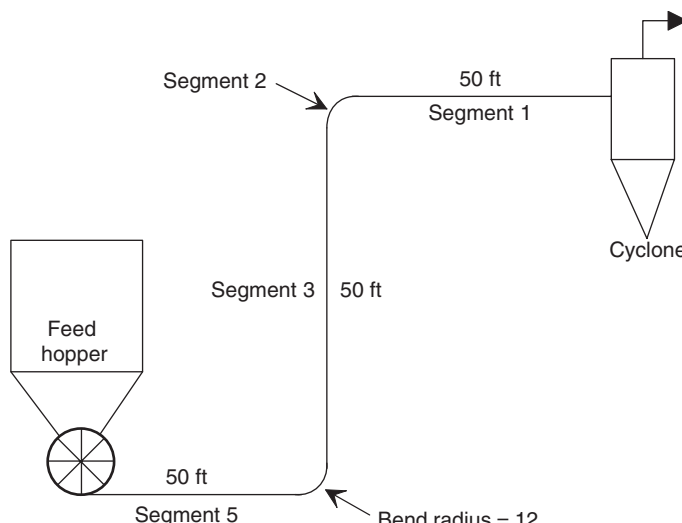


FIGURE 4.24 Conveying line layout for test problem.

Divide the system into segments starting from the filter or receiver end as shown in [Figure 4.21](#). Start the analysis from segment 1.

Segment 1: System pressure at exit = $(14.7 + 0.1)$ psia = 14.8 psia

$$\rho_g = \left(\frac{14.8}{14.7} \right) 0.075 = 0.0755 \text{ lbm/ft}^3$$

$$U_g = \left(\frac{2680}{0.545} \right) \left(\frac{14.7}{14.8} \right) = 4884 \text{ ft/min}$$

$$Re = \frac{DU_g \rho_g}{\mu_g} = \frac{\left(\frac{10}{12} \right) \left(\frac{4884}{60} \right) (0.0755)}{1.2 \times 10^{-5}} = 4.268 \times 10^5$$

$$\lambda_f = \frac{1.325}{[\ln(k_s/3.7D + 5.74/Re^{0.9})]^2} = \frac{1.325}{[\ln(0.000054 + 0.000049)]^2} = 0.0157$$

$$\Delta P_{\text{air}} = \lambda_f \frac{\rho_g U_g^2 L}{2Dg_c} = \frac{0.0157(0.0755)(4884/60)^2 50}{2(10/12)32.2} = 7.31 \text{ lb/ft}^2 = 0.050 \text{ psi}$$

$$\Delta P_{\text{solids}} = \mu \lambda_z \frac{\rho_g U_g^2 L}{2Dg_c}$$

For coarse particles,

$$\lambda_z = 0.082 \mu^{-0.3} Fr^{-0.86} Fr_s^{0.25} \left(\frac{D}{d_p} \right)^{0.1}$$

$$\mu = 2.5$$

$$Fr = \frac{(4884/60)^2}{32.2(10/12)} = 246.9$$

$$Fr_s = \frac{(1840/60)^2}{(32.2)(0.0131)} = 2229$$

$$\frac{D}{d_p} = 63.6$$

$$\lambda_z = 0.082(2.5)^{-0.3}(246.9)^{-0.86}(2229)^{0.25} (63.6)^{0.1} = 0.00568$$

$$\Delta P_{\text{solids}} = 2.5(0.00568) \frac{(0.0755)(4884/60)^2 50}{2(10/12)32.2} = 6.62 \text{ lbf/ft}^2 = 0.046 \text{ psi}$$

$$\Delta P_T = \Delta P_{\text{air}} + \Delta P_{\text{solids}} = 0.050 + 0.046 = 0.096 \text{ psi}$$

Pressure at the outlet of segment 2 = $14.8 + 0.096 = 14.896$ psia.

Segment 2: Segment 2 is a bend:

$$\Delta P_{\text{segment}} = \Delta P_B = B(1 + \mu) \frac{\rho_g U_g^2}{2g_c}$$

Use $B = 0.5$:

$$\rho_g = \frac{14.896}{14.7} - 0.075 = 0.076 \text{ lbm/ft}^3$$

$$U_g = \frac{2680}{0.545} - \frac{14.7}{14.896} = 4852 \text{ ft/min}$$

$$\mu = 2.5$$

$$\Delta P_{\text{segment}} = \Delta P_B = 0.5(1 + 2.5) \frac{0.076(4852/60)^2}{2.32.2} = 13.5 \text{ lbf/ft}^2 = 0.093 \text{ psi}$$

Therefore, pressure at the outlet of segment 3 = $14.896 + 0.093 = 14.989$ psia.

Segment 3: Segment 3 is vertical:

$$\Delta P_{\text{segment}} = \Delta P_{\text{static}} + \Delta P_{\text{frictional}}$$

$$\Delta P_{\text{frictional}} = \Delta P_{\text{air}} + \Delta P_{\text{solids}} = 0.050 \text{ psi} + 0.046 \text{ psi} = 0.096 \text{ psi}$$

$$\Delta P_{\text{static}} = \rho_p(1 - \varepsilon)\Delta L \frac{g}{g_c} + \varepsilon \rho_g \Delta L \frac{g}{g_c}$$

where

$$\varepsilon = 1 - \frac{W_s}{A \rho_p U_p}$$

$$\varepsilon = 1 - \frac{8.35}{0.545(59)(0.74)(4822/60)} = 0.995$$

$$\Delta P_{\text{static}} = 59(1 - 0.995)50 \frac{32.2}{32.2} + 0.995(0.0765)50 \frac{32.2}{32.2} = 18.55 \text{ lbf/ft}^2 = 0.129 \text{ psi}$$

$$\Delta P_v = 0.096 + 0.129 = 0.225 \text{ psi}$$

Pressure at the outlet of segment 4 = $14.989 + 0.225 = 15.214$ psia.

Segment 4: Segment 4 is a bend. Calculating similar to segment 2,

$$\Delta P_B = 0.092 \text{ psi}$$

Pressure at the outlet of segment 5 = $(15.214 + 0.092)$ psia = 15.306 psia.

Segment 5: Segment 5 is a straight horizontal section:

$$\Delta P_{\text{frictional}} = \Delta P_{\text{air}} + \Delta P_{\text{solids}} = 0.049 \text{ psi} + 0.047 \text{ psi} = 0.096 \text{ psi}$$

Pressure at segment 5 inlet = $(15.306 + 0.096)$ psia = 15.402 psia.

Add acceleration dP:

$$\Delta P_{\text{ACC}} = \frac{\rho_g U_g^2}{2g_c} \left(1 + 2\mu \left(\frac{U_p}{U_g} \right) \right)$$

$$\Delta P_{\text{ACC}} = \frac{(0.078)(4893/60)^2}{2(32.2)} (1 + 2(2.5)(0.74)) = 34.83 \text{ lb/ft}^2 = 0.242 \text{ psi}$$

Pressure at feed point = $(15.402 + 0.242)$ psia = 15.644 psia

Assume $\Delta P_{\text{blower piping}} = 0.1$ psi. Pressure at blower outlet = 15.744 psia = 1.044 psig. Then the overall $\Delta P = 1.044$ psi = 28.9 in WC

4.1.5 Designing Conveying Systems

The design of a dilute phase conveying system can be subdivided into eight steps, namely:

1. Acquire material properties
2. Establish conveying requirements and performance criterion
3. Selection of system type or conveying mode
4. Identify suitable line layout
5. Select initial pipe diameter based on expected loading
6. Calculate the overall pressure drop and gas flow rate requirement
7. Recheck selection of pipe diameter, consider stepping
8. Select dust collection system, feeder, and air mover

4.1.5.1 Acquire Material Properties

Characterization of bulk material is the first step in designing conveying system. It is important to acquire a representative sample for analysis and be aware of the variability in properties along with their effect on system performance. Table 4.12 summarizes the relevance of particle properties to selection and specification of a conveying system.

4.1.5.2 Establish Conveying Requirements and Performance Criterion

Many failures in design of dilute phase conveying systems can be traced back to omissions by the designer regarding conveying requirements and performance criteria. Here are some guidelines to avoid costly mistakes.

- Identify the entire range of products (product wheel): It may be impossible to identify a single product as a representative product. For example, the product with least friction factor may be most friable. If one needs to minimize product attrition and maintain conveying rate for all the products, more products need to be tested.
- Establish the correct conveying capacity: If the operation is in batch mode, instantaneous conveying rate will be higher than average conveying rate. Occasionally, even higher rates may be required to catch up after process upsets.
- Identify sources and destinations: All sources and destinations must be identified upfront. Proper thought should be given to future expansions in conveying distance and capacity.
- Identify special requirements for temperature, humidity, inert, containment, toxicity, cross-contamination, and ease of cleanout.

TABLE 4.12 Material Properties for Conveying System Selection and Specification

Material Property	Required for Determination of
Particle size distribution and average particle size	Conveying characteristics, feeder selection, filter design
Particle density	Conveying mode, conveying characteristics
Bulk density	Feeder capacity, storage silo capacity, conveying mode
Permeability	Conveying mode, dense phase design
Aeration and deaeration characteristics	Conveying mode, dense phase design
Moisture content, cohesion, and flowability	Storage silo design, feeder selection, dust collector design
Friability	Conveying mode, feeder selection, dust collector selection
Abrasiveness	Feeder selection, dust collector selection, material of construction
Toxicity	Conveying mode, dust collector filter design
Dust explosion potential	Selection of conveying gas, dust collector design and grounding requirements
Hygroscopic nature	Conditioning of conveying gas, conveying mode
Sensitivity to temperature	Cooling requirement for conveying gas, selection of conveying mode
Corrosiveness	Material of construction
Stickiness or tackiness	Mode of conveying, coating of parts

- Establish limits on acceptable product degradation: Pneumatic conveying system, especially dilute phase system, result in breakage or degradation of the product. It is important to identify acceptable limits, method of measurement, and sensitivity to operating conditions.
- Wear life of components: When dealing with abrasive materials, it is important to outline expectations on the performance and wear life of components, especially feeder and pipeline.
- Identify the need to have a spare air mover online if the conveying system is a critical link in the process.
- Conveying system can be used for a dual purpose, for example, as a dryer or cooler. The operational range can be severely limited by combining the two operations and it is important to establish that upfront.

4.1.5.3 Selection of Conveying System Type and Conveying Mode

A fundamental design decision when configuring a new pneumatic conveying system is whether to convey a dilute phase or dense phase mode. Dilute phase conveying can be generally characterized by high velocities, low pressure drops, and low ratios of solids to gas. Conversely, dense phase conveying systems have lower velocities, higher pressure drops, and higher solid to gas ratios (Table 4.13). Due to gas expansion or secondary gas injection along the conveying line, some systems will convey in the dense phase mode near the feed point, but will transition into dilute phase near the end of the conveying line.

The advantages for selecting dilute phase conveying are as follows:

1. Many more materials can be conveyed successfully in dilute phase mode than in dense phase.
2. Dilute phase conveying systems are generally less susceptible to plugging due to changes in material properties or operational upsets such as temporary loss of conveying gas.
3. Dilute phase conveying systems are easier to design. The window of stable operation for dense phase conveying is much smaller than that of dilute phase conveying.
4. Dilute phase systems require less specialized feeders and air movers.

The greatest advantages of dense phase conveying stem from the fact that the conveying velocities are lower. This can impact the amount of particle attrition and the amount of erosion of pipe bends and other system components that can occur. Both these phenomena tend to vary with velocity raised to the third power, although literature values for this exponent range from 2 to 6. For a specific application particle attrition may or may not be a consideration. The definition of particle attrition includes both the breakage or chipping of brittle particles to produce fine fragments and the smearing of polymeric materials along the pipe walls to create fines, floss, and snake skins. Some reasons why particle attrition could be problematic are:

1. Attrition can create a real or perceived quality issue.
2. It may adversely affect downstream gravity flow characteristics, such as the minimum hopper outlet size.

TABLE 4.13 Comparison of Dilute Phase and Dense Phase Conveying Modes

Characteristic	Dilute Phase Conveying	Dense Phase Conveying
Degradation or particle attrition	Can be high	Usually low
Change in product properties (particle size distribution, etc.)	Conveying characteristics will change but system can continue to perform at reduced capacity	Conveying characteristics are significantly affected. May result in plugging
Turndown of conveying rate	Easy	Limited turndown
Wear	Can be high for abrasive materials	Slow motion conveying results in minimum wear
Line vibration	None	Significant, special design considerations required
Inert gas conveying	Accomplished by closed-loop system	Low amounts can be once through

3. It may increase specific surface area, which may influence product properties or downstream processing.

Dense phase conveying can be a viable option if:

1. Low particle degradation is a requirement.
2. Material is highly abrasive and metal contamination is an issue.
3. Low gas usage (especially inert gases) is desirable.
4. The material does not change significantly from batch to batch.
5. Pressure conveying does not pose problems (toxicity or hygiene).
6. Conveying operation is not from multiple sources to single destination type.
7. The particle size distribution is not very wide.
8. The material tends to coat and plug the conveying line at high velocity.

4.1.5.3.1 Selection of System Type: Open Loop Versus Closed Loop

Unless there is a compelling reason to do otherwise, a conveying system should be operated in an open-loop manner ([Figures 4.12–4.14](#)). The advantages for operating this way are:

1. *Lower capital cost.* This is due to not needing a gas return line to the feed point, a smaller blower or compressor, less instrumentation, and less extensive conveying gas conditioning.
2. *Simpler operations.* The mass of gas in the conveying system changes during startup and shut down. This process is self-regulating in an open-loop system, whereas it needs to be actively managed for a closed-loop process. Also, unless there is an adequate purge on the closed-loop system or a sophisticated gas conditioning system, moisture or other undesirable condensable materials may accumulate in the recycled gas stream to concentrations where condensation can occur. This can result in restrictions in and possible plugging of the conveying line or blinding of filter media in the dust collector. Also, heat due to compression needs to be removed from the closed-loop system.

Despite the advantages of an open-loop system, there are circumstances where closed-loop systems are preferable and will reduce the overall cost of installing and operating the system. The selection of a closed-loop system ([Figure 4.15](#)) should be considered when:

1. The conveying gas is expensive or the supply is limited.
2. Treatment of the gas prior to venting requires more than just gas–solid filtration. If there are either toxic or simply noxious nature of vapors present in the conveying gas stream after the solids have been separated, the gas stream may need to be sent through a carbon bed or incinerated prior to venting to the atmosphere.
3. The solids need to be conveyed in a carefully controlled environment such as very low moisture or oxygen concentrations. The use of a closed-loop system in this case will reduce the size of the gas conditioning equipment required.

4.1.5.3.2 Selection of Pressure Mode: Vacuum, Pressure, or Combined

In most situations, it is mechanically feasible to convey in both pressure or vacuum mode. Therefore, the selection of conveying mode is dictated by process issues. For instance, a pressure system should be used where ambient air leakage into the conveying system cannot be tolerated. This could be due to a quality or product degradation concern by exposure to oxygen or moisture. Another case where a pressure system should be used is if an oxygen lean environment is used as a line of defense for prevention of a dust or vapor explosion. On the other hand, a pressure system should not be used if material spill cannot be tolerated due to safety or industrial hygiene concerns. A vacuum system should be strongly considered if there are significant consequences in the event of a leak of material from the conveying system, such as cases where the solids are extremely toxic to humans, animals, or plants. While all equipment connections can be made “dust tight,” all shaft seals for rotary and diverter valves can be purged, and all high wear areas

such as elbows can be monitored for erosion. Experience has shown that considerable preventative maintenance effort is required to keep a pressure conveying system dust tight in all places and at all times.

The final criteria for determining the conveying pressure mode, if not fully dictated by any of the considerations above, is based on the number of sources and destination and, to a lesser extent, the source or destination layout:

1. *Single source to single destination* ([Figure 4.12](#)): Either pressure or vacuum system will work for this case. Use a pressure system for long distance (greater than 300 ft) and high throughput requirements.
2. *Single source to multiple destinations* ([Figure 4.12](#)): Use a positive pressure (or push) system with diverter valves to direct material to multiple destinations. A vacuum system would require an air mover at each destination and would be expensive to install.
3. *Multiple sources to a single destination* ([Figure 4.13](#)): Use a vacuum (or pull) system. Unless the sources are close together, a blower would be needed for each source if the pressure conveying mode were used. However, if a single conveying line can be routed past the pickup points for each source without significantly altering the number of bends or the overall length of the conveying line, the pressure conveying mode may be a reasonable option as well as vacuum conveying.
4. *Multiple sources to multiple destinations* ([Figure 4.14](#)): Use a combined vacuum-pressure or pull-push system. This recommendation logically follows from the previous two items.

4.1.5.4 Identify Suitable Line Layout

Conveying line layout should never be an afterthought during plant layout. Conveying pipe cannot be routed like other utilities (steam, air and water) without paying significant penalty on performance. Some effective line layout practices are outlined below:

- Layout conveying routes when the plant process equipment is being laid out. This will provide flexibility for optimization of conveying route.
- Consider creative ways to minimize conveying distance.
- For dilute phase systems, provide sufficient horizontal run after the feed point and before any change in direction (bend) occurs. It is recommended to provide at least 50D of horizontal run. There is no such requirement for dense phase systems.
- For dilute phase systems, avoid inclined lines near the feed point.
- Minimize change in directions (bends, elbows, or 45°bends).
- Avoid placing bends within 50D of one another.
- Minimize the use of flexible hoses
- For dense phase systems, proper consideration must be given to design line support to handle pipeline vibrations. Current state of knowledge is insufficient to predict the line forces accurately.
- Do not use process equipment or silos to support dense phase lines.
- Components, such as diverter valves, need maintenance. They should be made accessible.

4.1.5.5 Select Initial Pipe Diameter Based on Expected Loading and Velocity at Feed Point

Initial pipe diameter can be calculated by assuming solids loading based on previous experience or general guidelines:

$$\mu = \frac{W_s}{W_g} = \frac{W_s}{A\rho_g U_g}$$

$$A = \frac{W_s}{\mu\rho_g U_g} = \frac{\pi}{4} D^2$$

$$D = \sqrt{\frac{4W_s}{\pi\mu\rho_g U_g}}$$

where U_g is the gas velocity at feed point, ρ_g the gas density at feed point, and μ the assumed solids loading

4.1.5.6 Calculate Overall Pressure Drop and Gas Flow Rate Requirement

See [Section 4.1.4](#) for details on pressure drop calculations.

4.1.5.7 Recheck Selection of Pipe Diameter

With refined values of conveying pressure at the feed point, the line diameter calculation should be rechecked. The conveying pressure estimation should also be compared with the typical limits of air movers. If the pressure drop is higher than expected, choose a large pipe size. Redo the calculations until convergence is achieved.

4.1.5.8 Select Dust Collection System, Feeder, and Air Mover

4.1.5.8.1 Gas–Solid Separator Selection

Factors affecting the selection of gas–solid separation device are

1. Desired efficiency of separation based on particle size distribution of incoming solids
2. Acceptable pressure drop range
3. Operating pressure and temperature
4. Cleanout and contamination requirement
5. Dust explosion potential
6. Acceptable turndown in gas flow rate
7. Compatibility with material (corrosiveness, abrasion, etc.)

4.1.5.8.2 Feeder Selection

Factors affecting the selection of feeder are

1. Operating pressure/pressure differential
2. Type of conveying system.
3. Material characteristics: bulk density, size, abrasiveness, tackiness, fluidization, etc.

(see [Table 4.5](#) For more details.)

4.1.5.8.3 Air Mover Selection

Factors affecting the selection of air mover are

1. Range of pressure or vacuum during operation
2. Volumetric flow rate
3. Stability of solid feed rate and nature of operation
4. Control requirements: turndown and adjustability
5. Special requirements (e.g., material flow through)

4.1.6 Stepping Pneumatic Conveying Lines

The superficial velocity increases as the pressure decreases from feed point to discharge point. From mass balance on the conveying gas, we obtain,

$$(A\rho_g U_g)_{\text{feed_zone}} = (A\rho_g U_g)_{\text{discharge_zone}}$$

By applying gas laws,

$$\frac{U_{g1}}{U_{g2}} = \frac{P_2}{P_1}$$

where P is the absolute pressure. The superficial gas velocity in a conveying system increases from feed point to destination in all conveying systems. Since higher superficial velocity is related to higher wear and product attrition, it is beneficial to reduce the gas velocity by increasing the line diameter at some point in the system. The same effect is achieved by leaking some gas out of the system.

There are two approaches to stepping (increasing) the line size:

1. To keep the Froude number constant between the feed point and the step location. In other words, maintain a Froude number greater than the minimum required (Fr_{min}) at the stepped location.
2. To keep the superficial velocity at the feed point and at the step location higher than saltation velocity.

Currently, there is no consensus on the best approach for designing stepped lines.

4.1.7 Modeling and Designing Dense Phase Conveying

The mechanisms for dense phase conveying are not as well understood and quantified as dilute phase flow. Significant progress in modeling of noncohesive granular materials has been made in the last 20 years (Konrad and Harrison 1980; Legel and Schwedes, 1984; Konrad, 1986; Mi and Wypych, 1994). The design equations by Mi and Wypych (1994) are discussed in this section. For fluidized-mode conveying, is recommended that scaleup approach be used.

4.1.7.1 Modeling of Plug/Slug Flow

Noncohesive coarse granular material (e.g., plastic pellets) exhibits a natural slugging ability. When conveyed in nonsuspension mode, they form slugs or plugs that move in a wave-like fashion. Each slug is constantly picking up material from the stationary layer in the front and dropping off material from the tail end. The material moves a short distance with the passing of each slug.

A force balance on the plug results in the following equation (Figure 4.25):

$$\frac{\Delta P}{l_s} = \frac{4\mu_w \lambda}{D} \sigma_f + 2\rho_b g \mu_w$$

where λ is the stress transmission coefficient or the ratio of radial stress to axial stress. A theoretical estimation of the stress transmission coefficient can be made by assuming active conditions for failure; however, experimental data indicate that the values are between active and passive estimates:

$$\lambda = \frac{1 - \sin\phi_s \cos(\omega - \phi_w)}{1 + \sin\phi_s \cos(\omega - \phi_w)}$$

$$\sin \omega = \frac{\sin\phi_w}{\sin\phi_s}$$

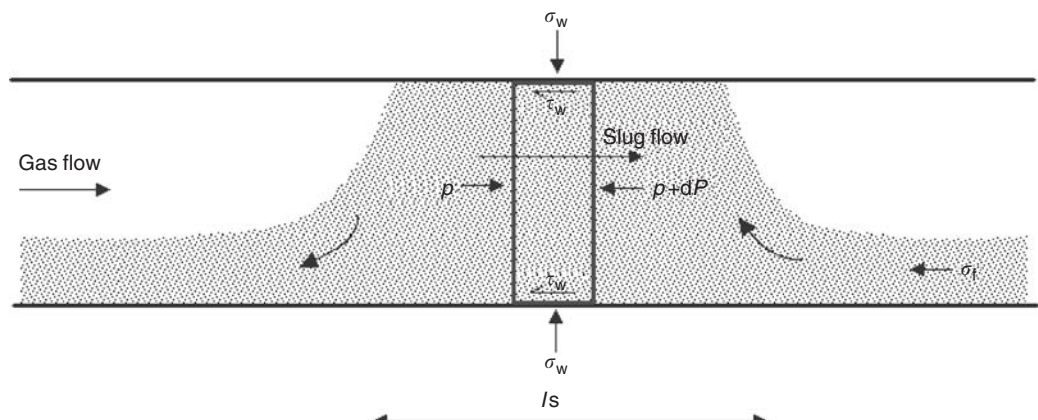


FIGURE 4.25 Force balance on slug or plug in dense phase conveying.

σ_f represents is the frontal stress experienced by the slug due to the stationary layer and uptake of material from the stationary layer. The momentum balance gives the following expression:

$$\sigma_f = \alpha \rho_b U_s^2$$

The existence of stationary layer plays a critical role in formation, stability, and movement of the slug. The average height of a stationary layer in the line depends on the superficial gas velocity at that location. It decreases with an increase in superficial gas velocity.

The cross-sectional area ratio of stationary bed to pipe, α , is calculated by the following expression:

$$\alpha = \frac{1}{(1 + U_s/0.542\sqrt{gD})}$$

In reality, there are multiple slugs in a transfer system that is separated by air pockets. As the pressure drops and gas expands, the superficial gas velocity increases along the conveying length. Consequently, the slug velocity will also increase. For analysis, if we assume that each slug goes through the same velocity profile, then we can characterize the bulk movement of material through the system by an average slug velocity. Further, if the pressure drop across the air pockets is assumed to be negligible, all the slugs in the system of length L_t can be assumed to be of an equivalent length l_s .

$$l_s = \frac{m_s L_t}{A(1 - \alpha)\rho_b U_s}$$

The overall system pressure drop can be calculated by an appropriate substitution.

$$\Delta P_{\text{system}} = \left(1 + 1.084 \lambda \sqrt{Fr} + \frac{0.542}{\sqrt{Fr}} \right) \frac{2g\mu_w m_s L_t}{AU_s}$$

where

$$Fr = \frac{U_s^2}{gD}$$

4.1.7.2 Slug or Plug Velocity Estimation

As evident from the previous section, a reliable estimate of slug velocity is critical for design calculations. The slug velocity for impermeable bulk solids is equal to the superficial gas velocity (Figure 4.26). For permeable materials (e.g., plastic pellets, grains, etc.), a slip between gas and solids has been observed. A minimum gas velocity can also be identified below when the slug velocity is zero, when implies a plugged condition.

Mi and Wypych (1993) have experimentally shown that (see Table 4.14)

$$U_s = K(U_g - U_{g \min})$$

The minimum conveying velocity for plugged condition can also be calculated theoretically:

$$U_{g \min} = \frac{\rho_p g \tan \phi_w \epsilon^3 d_p^2}{180(1 - \epsilon)\eta}$$

The slope of the slug-slip characteristic is empirically calculated as follows:

$$K = C \frac{\epsilon d}{D} \left(\frac{\tan \phi_w}{\tan \phi_s} \right)^{1/3}$$

where C is a dimensionless constant. Use a value of 100 as an initial estimate.

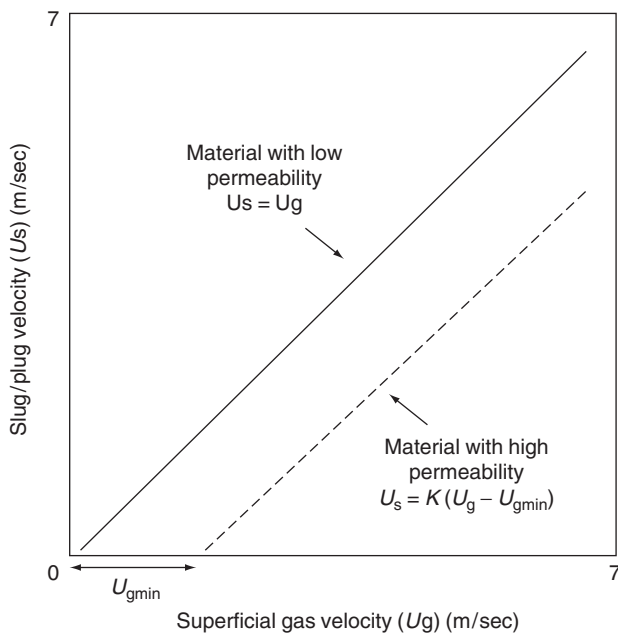


FIGURE 4.26 Relationship between slug velocity and superficial gas velocity.

TABLE 4.14 Examples of K and $U_{g\min}$ values

Test Material	K	$U_{g\min}$ (m/sec)
Plastic pellets		
White	0.873	1.02
Black	1.059	1.566
Wheat	1.013	2.19
Barley	1.359	2.77

Source: Mi, B., and Wypych, P.W., *Powder Handling and Processing*, 5(3), 233, 1993. With permission.

4.1.7.3 Pressure Drop Calculation in Slug-Type Dense Phase System

According to Mi and Wypych (1994), the following steps are involved:

1. Calculate stress transmission coefficient
2. Assume initial value of total pressure drop. Calculate mean air density and superficial velocity
3. Estimate mean slug velocity and Froude number
4. Calculate pressure drop using the proposed analytical equation
5. Compare the estimate with assumption in step 2. Recalculate until convergence is obtained.

4.1.7.4 Control of Dense Phase System

As discussed earlier, a dense phase conveying system must be operated within an operating window of gas velocity and solids flow rates to maintain the line vibrations to its minimal. The operating limits also depend on material properties and system configuration. Therefore, in a multiproduct plant, one must implement an active controller to modulate the gas flow rate to maintain a stable conveying regime. A number of effective control schemes have been developed by various vendors. The reader is referred to vendor literature for more information.

4.1.8 Practical Design Considerations

4.1.8.1 Common Design Errors

Given the simplicity of the task of moving product from one point to another in a plant, it would appear that design of pneumatic conveying systems would be relatively straightforward. However, design errors that compromise the system performance are routinely committed. While it would be impossible to list all of the design errors for pneumatic conveying systems, the following section highlights some common ones.

4.1.8.1.1 Selection of Conveying Velocity

The optimum conveying for dilute phase system is saltation velocity with an additional 10% factor added for safety. Additional safety factor must be added if the first elbow is within 5 m (15 ft) from feed point. Since saltation velocity depends on the conveying rate, the highest instantaneous rate must be used.

Systems are routinely designed where the design conveying velocity is excessive. In dilute phase conveying systems, this will result in high product degradation or attrition and system wear. Also, the conveying capacity is substantially reduced. The effect of conveying velocity on conveying capacity has been explained in [Figure 4.10](#).

Dense phase conveying systems must be operated within two limits of gas velocity, the lower bound corresponds to fixed bed or nonmoving plugs and the upper bound corresponds to the unstable conveying regime (see [Figure 4.9](#)). Excessive gas velocity will result in the system operating in the unstable region and cause severe line vibrations and pressure fluctuations.

4.1.8.1.2 Conveying Line Layout and Use of Elbows and Bends

The layout of conveying systems is usually done after the process equipment is laid out and structural steel is designed. A pipe designer adept at configuring process piping will try to route a conveying line in a similar way, with little regard to the negative influence of bends or elbows. In stark contrast to incompressible single-phase fluid flow where the fluid does not slow through a bend, the particles will slow considerably as they proceed through a bend. This problem is further magnified if bends are placed one after another without sufficient distance to permit the solids to reaccelerate. A good conveying layout will minimize the number of bends or elbows and avoid inclined lines.

4.1.8.1.3 Failure to Account for System Gas Leakage

It is important to account for gas leakage in and out of the system when estimating conveying velocity and air mover size. For positive pressure systems, the air leakage from the rotary feeder can be significant and can result in plugging at the feed point. If the material is a fine powder, the air leakage will impede material feed and cause reduced capacity. Also the air leakage can be a significant fraction of the total air flow for dense phase system, and therefore, it must be correctly estimated.

4.1.8.1.4 Multiple Source and Multiple Destination Systems

For systems where there are either multiple destinations (when product is moved from the production process to storage silos) or multiple sources (when material is moved from the storage silos to a packaging operation), care must be taken to ensure that the conveying capacity is estimated based on the longest pipe run. In many cases, systems are designed for the midpoint of a bank of silos; consequently, those silos that are located further than the midpoint will not deliver the required flow rate. Another extremely important consideration is the potential leakage of conveying gas through multiple rotary, diverter, or flapper valves in multiple source and destination systems. In the vacuum case, gas leakage into the conveying system along its length means that there may be insufficient gas at the pickup point.

4.1.8.1.5 Insufficient Attention to Component Selection

Improper selection of air mover, feeder, and dust collector can result in a problematic system. For instance, fans are commonly selected as air movers for low-pressure applications. As discussed earlier, fans typically have a strong relationship between pressure head and volume of gas delivered. If fans are used for systems where the solids flow is not regulated, it could lead to a plugged condition on account of the fan's inability

to deliver the required volume of air for the increased pressure drop. Similarly, if a rotary feeder is chosen for feeding abrasive solids then excessive gas leakage can result in frequent plugging.

4.1.8.1.6 Understand the Limitations of Dual Purpose Systems

There is a tendency when conveying wet material (from a centrifuge or filter to a dryer, for example) to use the conveying system to both move the material within the plant and dry at the same time. This will work *only* when the solids loading is low (0.05 to 0.25 kg solids/kg of gas).

4.1.8.1.7 Insufficient Support for Dense Phase Conveying Lines

Lines forces in dense phase system are orders of magnitude higher than dilute phase systems. It is essential to design the supports and structure to bear these high dynamic loads. A safety factor of 3 to 5 is often recommended for specifying the structural supports.

4.1.8.2 Performance Measurement in Conveying

Unlike to many pieces of process equipment in plants in which the material is significantly changed either physically or chemically (e.g., composition, particle size, etc.), the conveying system is relatively simple — it is required to move bulk solids from point A to point B. In that sense, the measurement of performance can be distilled into two points: (1) how quickly is material moved from one point in the plant to another (system throughput); and (2) does the material undergo any attrition (and lose important attributes) during the conveying process. It could be argued that power consumption would be a third important metric. With most conveying systems, it is far more important for the system to deliver the product at the desired rate with little or no attrition as opposed to save a few kW-h of power. This is particularly the case for higher value-added products being manufactured today.

System throughput is important because it is undesirable that the conveying system be the plant bottleneck. In many cases, both dilute and dense phase systems are routinely designed to operate near the maximum pressure that the air mover can deliver in order to maximize system throughput. The speed of the feeding device (quite often a rotary valve with electronic variable speed control) is tied to the air mover discharge or suction pressure to maximize solids flow through the conveying system.

Another key metric is attrition or degradation. In many cases, product specifications or customer requirements demand that a product be “fines free.” As indicated earlier, the creation of fines is a strong function of gas velocity in a conveying system. These fines can have a substantial impact on flowability, dustiness, dissolution rate, to name a few.

Another example is the conveying of polyethylene (PE). Many grades of PE will form angel hair or streamers during conveying. These streamers (they vary in size from short, low centimeter, long threads to large ribbons of several meters long) are formed on the inside of the conveying pipe during the conveying process and subsequently are released from the pipe surface. Often streamers will aggregate in a silo to form a low-density ball, which in many cases will clog downstream equipment such an extruder. In this case, the product itself shows little or no degradation as a result of the streamer formation process, but it is the streamers that will compromise system performance due to process blockages.

An ancillary metric to attrition is that of wear. Wear can be an important performance metric, especially in cases where extremely abrasive products are handled, such as sand, glass batch and mineral ores, for example. It is important that the wear situation be addressed such that it is not either a maintenance (and consequently cost) problem or a source of metal contamination in the process.

4.1.8.3 Troubleshooting Basics

Conveying systems will not always perform as designed or the performance may degrade gradually or suddenly. Consequently, there is a need to troubleshoot conveying systems. This should be done in a logical manner with emphasis on finding the root cause of the problem (Dhadapkar and Jacob, 2002), i.e., to clearly identify the nature of the problem. For conveying systems, problems fall in to three broad categories:

1. Lack of system throughput — the inability for the conveying system to deliver the required throughput. This could mean that the system is operating at less than the desired rate or the instantaneous rate is fine but cycle times are slow (similar to dense phase blow-pot systems) or plugging may be occurring.

2. Material degradationon on attrition — on account of the velocities in conveying systems, products may attrite or break as a result of the conveying process.
3. System degradation — with high velocities or particularly abrasive products, both pipe and system components can experience high wear resulting in an inoperable system. Even systems where the product is thought to be relatively benign can experience wear after significant service. For example, aluminum elbows can wear through in conveying service.

Once the nature of the problem is identified, the next logical step in the troubleshooting process is the data gathering phase. A key philosophy in this process is to take the “systems approach” when examining the problem. This means that rather than focusing on the conveying system alone, it is important to look at the process steps both before and after the system as they may be contributing to the problem. For example, if a dryer precedes the conveying system, moisture fluctuations in the product out of the dryer could have a substantial effect on the ability of product to be conveyed.

Initially it is important to examine the process flowsheet, the original design specifications for the system, if available, and the pneumatic conveying control system as implemented. Equally important is a physical examination of the entire conveying system to check if the system was built as designed and if there have been modifications to the system since start-up. At this point, it is useful to note any abnormalities such as misaligned pipe, worn valves (such as squeaky rotary valves and diverter valves not returning to a fully closed or open position), etc.

Key process data must be gathered for effective troubleshooting. Key items would be pressure drop across the conveying system, pressure drop across the dust collection device, pipe size, gas velocity (either measured directly or calculated from blower speed, preferably both), system conveying rate. If data are available from a process control system, it can be very useful in troubleshooting a conveying problem, particularly those that are erratic in nature. During the troubleshooting process, it is not uncommon for conflicts in data to occur. For example, a blower curve and a set of measurements made with a Pitot tube or anemometer may not give the same value for gas flow through the system. In these situations, one must experimentally resolve this conflict in data. In this particular case, one can look at the pressure drop across a specific section of pipe in the system for only conveying gas or measure the pressure drop across a cyclone and infer the gas flow rate from that number.

Depending on the nature of the problem, a number of different fixes are possible. The key is to provide the most robust solution at the most economical cost. In many instances, the speed of the blower can be reduced (see prior discussions on the Zenz curve) to increase the capacity. In other cases, where the blower may be operating at or near maximum pressure, it may be logical to step the pipe (see stepping), in order to increase the throughput.

The key to optimization is an understanding of the operating limits (window) of a system and to make sure that the system operating conditions stay within these limits. A detailed discussion on this can be found in Agarwal and Dhodapkar (2004).

4.1.8.4 Startup of Conveying Systems

Many of the procedures used for the starting up conveying systems are common to that of all process equipment. It makes sense that the plant is built as designed and also ensures that all instrumentation is operating correctly. The following is a list of startup issues specific to both dense and dilute phase conveying systems:

1. Check that rotary valve rotation is correct in order to minimize reentrainment of solids into the emptied pockets.
2. Check the valve sequencing is appropriate for blow-tank operation.
3. Check the piping for both alignment (application of self-aligning flange systems is very useful) and the intrusion of welds into the conveying flow.
4. Check that an appropriately designed pipe cushioning system is in place so as to tolerate the dynamic stresses associated with large plugs moving through the conveying system for dense phase systems (especially those $> 150\text{mm}$ pipe diameter).
5. Check that the blower rotation must be correct.

6. Check the clearances on the rotary valves such that the valves not only rotate freely, but also are sufficiently close so as to minimize leakage.
7. Check that the relief valves and rupture disks are in place so as to minimize damage associated with an accidental over or underpressurization. This is particularly important for systems where a dust collector or baghouse is used and the bags have the possibility of being coated over with bulk solid on account of moisture, etc.

4.1.8.5 Wear

Wear issues are pervasive in pneumatic conveying applications. Many studies have been undertaken to quantify the effect of various parameters to predict the wear life of components. While we now understand the influence of various factors and their relative importance, it is not possible to generalize the conclusions. The solution to one wear problem cannot necessarily be applied to another problem. Further details can be found in Section 12.4.3.

4.2. Slurry Flows

Shenggen Hu

4.2.1 Introduction

Slurry is a suspension of solid particles in a carrier liquid. Transport of slurries through circular pipelines is widespread in the minerals, coal, chemical, food, water, and other industries. Unlike the flow of single-phase liquid, the flow velocity of slurries must be higher than a certain value to maintain solid particles in suspension. The flow of single-phase liquid is homogeneous at all velocities, while slurry flows may behave heterogeneously or exhibit some combination of both. The slurry may also behave rheologically as a Newtonian fluid or may exhibit a variety of non-Newtonian rheological properties.

The large number and range of variables encountered in slurry flows in pipelines cause the flow behavior of these slurry systems to vary over a wide range, and therefore different approaches have been used to describe their behavior in various flow regimes. The variables that influence the behavior of slurry flows include the orientation of the pipeline, the characteristic dimension of the conduit, flow velocity, particle size, particle size distribution, particle density, particle shape, solids concentration, and the properties of the fluid–particle interface, which are determined by the compositions of the fluid and the solids. Due to the wide range of variables and their variations, the literature abounds with numerous studies of special cases that cover a limited range of conditions. Consequently, it is not feasible to provide a thorough or even an adequate survey of the subject of slurry pipeline flows in a single section of this Handbook.

The intent of this section is to summarize what appears to be the most widely accepted and comprehensive studies and results in the context of slurry flow, which may apply to various flow regimes. In particular, we will examine the classification of slurry flow regime, the frictional pressure loss estimation for both homogeneous and heterogeneous slurry flows, the prediction of the critical velocity for horizontal pipe flow, the design and operation aspects, and the measurement techniques.

4.2.2 Basic Concepts of Slurry Flows

4.2.2.1 Basic Definitions

4.2.2.1.1 Slurry Flow Velocity

The mean slurry flow velocity, U_m , is defined by

$$U_m = (\dot{V}_s + \dot{V}_l)/A \quad (4.1)$$

where \dot{V}_s and \dot{V}_l are volumetric flow rates of solid, and liquid, respectively.

4.2.2.1.2 Solids Concentration

The solids concentration can be expressed as volume fraction α_s or mass fraction. The volumetric fraction of solids is given by

$$\alpha_s = \dot{V}_s / (\dot{V}_s + \dot{V}_l) \quad (4.2)$$

and the mass fraction of solids, C_s , is defined as

$$C_s = \rho_s \dot{V}_s / (\rho_s \dot{V}_s + \rho_l \dot{V}_l) \quad (4.3)$$

It can be shown that

$$C_s = \alpha_s \rho_s / (\alpha_s \rho_s + (1 - \alpha_s) \rho_l) \quad (4.4)$$

4.2.2.1.3 Slurry Density

The density of slurry mixture, ρ_m , is given by

$$\rho_m = \alpha_s \rho_s + (1 - \alpha_s) \rho_l \quad (4.5)$$

4.2.2.1.4 Apparent Viscosity

The steady-state rheological behavior of most slurry mixtures can be expressed by the following general form:

$$\tau = \eta \dot{\gamma} \quad (4.6)$$

where τ is the shear stress, $\dot{\gamma}$ the shear rate, and η the apparent viscosity. The plot of shear stress τ vs. the shear rate is $\dot{\gamma}$ called a *rheogram*, which is schematically illustrated in Figure 4.27. If η is a constant and equal to the slope of the straight line from the origin, the slurry rheological behavior is Newtonian. Slurry mixtures that do not behave in this fashion are termed non-Newtonian slurry mixtures, in which η is not a constant and may be expressed as a function of either $\dot{\gamma}$ or τ . In regions where η decreases with increase in shear rate $\dot{\gamma}$ the behavior is termed as *pseudo-plastic* or *shear thinning*; in regions where η increases with increase in shear rate the behavior is termed as *dilatant* or *shear thickening*. The curve intercepts at zero shear rate are called as *yield stresses*.

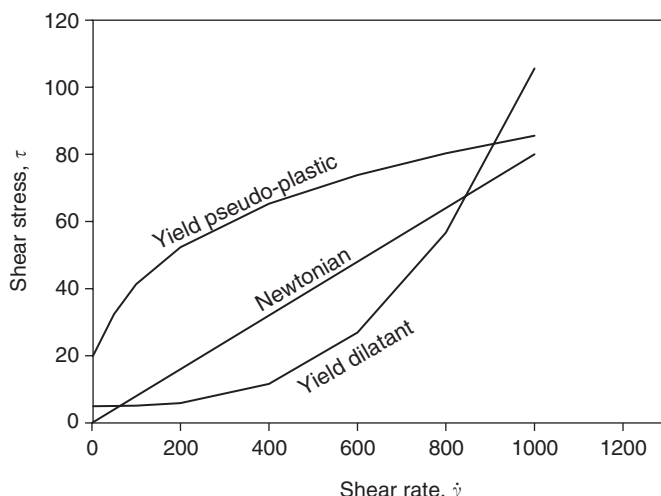


FIGURE 4.27 Illustrative rheograms.

4.2.2.2 Slurry Flow Regimes

The slurry flow regime (also referred to as flow pattern) varies with the properties of the solid particles relative to those of the liquid. The flow regime affects the dependence of the pressure drop on the flow rate as well as the magnitude of the pressure drop and also influences the pipe erosion and other performance characteristics. Owing to the complexity of slurry flows and the gradual transitions between flow regimes, only an imperfect classification of the regimes is possible.

Since Durand and Condolios (1952) proposed the initial classification of slurry flow regimes based on average particle size, a number of refined classifications have been developed over the years (Newitt et al., 1955; Thomas, 1964; Wicks, 1971; Ercolani et al., 1979; Brown, 1991). One of the most common classifications is to broadly categorize slurry flows in pipelines into four regimes: homogeneous, heterogeneous, heterogeneous with a moving bed, and heterogeneous with a stationary bed. The schematic views of particle spatial distributions and solids concentration profiles in a pipe for different slurry flow regimes are shown in Figure 4.28.

Homogeneous slurry flow is characterized by a uniform distribution of solid particles throughout the carrier liquid and across the pipeline cross section. Typically, this type of slurry has a high solids concentration of fine solid particles ($<40\text{ }\mu\text{m}$) with low particle density and exhibits viscous behavior. An example of homogeneous flow is the minerals ore slurry after comminution and thickening, in which the particles are very fine and the solids concentration is high ($>40\%$ by weight). Although no slurry is completely homogeneous because it consists of distinct phases, there are situations in which the slurry can be described satisfactorily by single-phase models. Therefore, the principle of continuum mechanics may be applied to the analysis of homogeneous slurry flow, and the rheological properties of the slurry are most often non-Newtonian.

In heterogeneous slurry flow, solid particles that are sufficiently large and dense, and in a sufficiently dilute state will settle to various degrees such that the particles are no longer uniformly distributed in the flow field, i.e., the slurry is heterogeneous, but the majority of the particles are still fully suspended. The different phases retain their properties and the analysis of this flow behavior needs to consider the forces on the particles, resulting from interaction with the surrounding suspending medium separately. Heterogeneous slurries are encountered in many industrial processes, such as mineral processing. Solids concentration in these slurries is relatively low, typically $>35\%$ (by weight). Heterogeneous slurry flows are much more complicated than the homogeneous slurry flow, and consequently most of the experimental

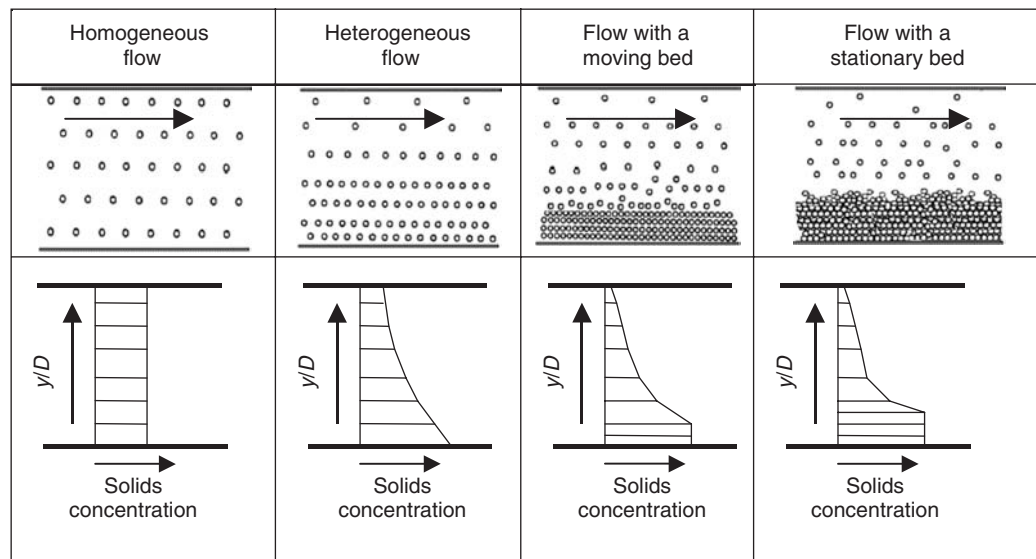


FIGURE 4.28 Illustration of particle distributions and solids concentration profiles in a pipe for different slurry flow regimes.

studies in the literature are concerned with these flows. Both critical deposit velocities and pressure losses are of interest.

The terms nonsettling and settling have often been used synonymously with homogeneous and heterogeneous.

When a large fraction of particles in a slurry are fine but a sufficient fraction of coarse particles remains, intermediate regimes may occur, in which the fine particles are homogeneously distributed and the coarse particles are heterogeneously distributed or may deposit as the flow speed is reduced below a minimum value. Intermediate regime flows include tailings from mineral processing plants and a wide range of industrial slurries. Although many of slurry flow cases are clearly homogeneous or heterogeneous, many more are a combination of both. This is because the particle size is the single most important parameter that governs the flow regime. Most of the practical slurry systems contain solid particles having a rather broad particle size distribution. Such systems are often considered to be in a mixed homogeneous–heterogeneous mode, and their flow behavior must be analyzed accordingly.

Under certain conditions, the flow regime of heterogeneous system with moving bed can be observed. In this flow regime, the larger and/or denser particles will accumulate at the bottom of the conduit and form a bed. The particles in the bed will move or slide along the bottom of the conduit as the shear forces due to the moving fluid are sufficiently high. The concentration of this bed corresponds to maximal packing, or nearly so, and the upper part of the pipe cross section is occupied by a heterogeneous mixture.

In the regime of heterogeneous flow with a stationary bed, the slurry flow velocity is too low to enable motion of all immersed particles, and a stationary deposit bed is formed at the bottom of the pipe. Also the deposited bed particles are transported as a separate moving layer. Although stationary-bed type flows can be encountered in practical situations, they should be avoided whenever possible, since they tend to result in a highly unsteady type of flow behavior at best, and plugging at worst.

The prediction of the flow regime, which would exist in the pipe for any given set of operational conditions, is very important. One would avoid the formation of a stationary deposit, which causes partial blockage of the pipe, thus reducing its efficiency. A moving bed probably enhances pipe wear. Moreover, the pressure drop behavior is different from one flow regime to another. A variety of criteria have been proposed for determining whether a given slurry flow is considered homogeneous or heterogeneous, or flows with deposited solids bed. However, criteria based on a single parameter, such as particle size (Durand and Condolios, 1952), are incomplete, since slurry flow behavior also depends on other parameters. The more reliable approach for the determination of the flow regime is the use of suitable empirical correlations (Turian and Yuan, 1977; Turian et al., 1987) or mechanistic models, such as two- (Wilson, 1970, 1976; Gillies et al., 1991) or three-layer models (Doron and Barnea, 1993, 1996). Some of these correlations and models will be examined in Section 4.2.4.

A typical flow regime plot for slurry flow in a pipe is shown in [Figure 4.29](#). This figure was generated by using Turian and Yuan's correlations (Turian and Yuan, 1977) for the conditions as given in the figure. As seen from Figure 4.29, a slurry containing particles of 300 μm would be in the homogeneous regime, if the slurry velocity is higher than 2.3 m/sec. Such a plot is useful in determining the flow regime that applies under a given set of conditions and the magnitude of the slurry velocity must change before the flow enters another regime.

4.2.3 Homogeneous Flow of Nonsettling Slurries

4.2.3.1 Rheological Models

In homogeneous slurry flows, slurries show no segregation or low but finite tendency to settle when allowed to stand. In this respect, the slurries resemble a single-phase fluid, for which the science of rheology and continuum mechanics are well established. The major technical tasks for assessing homogeneous slurry flows are:

1. To determine an appropriate rheological model from a test program and evaluate the specific coefficients for the slurry at the temperature and solids concentration of interest.
2. To predict the pressure loss for laminar and turbulent flow, and the transition point between them.

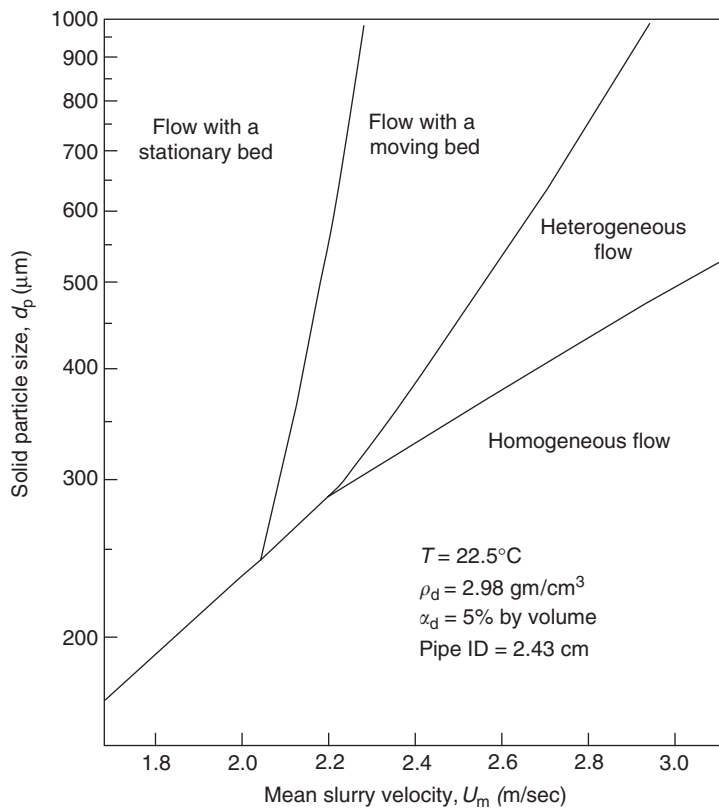


FIGURE 4.29 Flow regime diagram for slurry flow in 25 mm pipe under the conditions given in the figure. (Adapted from Turian, R.M. and Yuan, T.F., *AIChE J.*, 23, 232–243, 1977, reprinted with permission.)

Rheological property is one of the major factors influencing the homogeneous flow behavior and pressure loss. Presently, it is not possible to predict slurry rheological properties or the viscosity–concentration–shear rate relationship for most of industrial slurries, except for Newtonian slurries. Experimental characterization of the rheological property is possible and essential, and measurement techniques will be examined in Section 4.2.6.1.

The rheological data may be utilized directly for predicting flow behavior under certain conditions. However, it is more convenient and useful if the data can be represented by an appropriate model. It is also desirable to have a model that is as simple mathematically as possible, and yet adequately describes the slurry rheological property. A number of models have been proposed for representing the viscosity function of homogeneous slurries. Although there is some degree of logical deduction behind some of the models, they are largely empirical. The more complex models are capable of representing more complex behavior, although they are also more difficult to evaluate and apply and often are insignificant in a practical sense.

4.2.3.1.1 Newtonian Slurries

In homogeneous slurry flows, the nonsettling slurries may behave as a Newtonian fluid under certain conditions, such as sufficiently low solids concentration, low particle densities, and high fluid viscosities. Rheological properties of Newtonian slurries are a function of both liquid and solids characteristics, but independent of the magnitude of the shear stress or the shear rate. The viscosity of the Newtonian slurry is often presented as the relative viscosity μ_r , the viscosity of the mixture μ_m normalized with that of the carrier fluid μ_l :

$$\mu_r = \mu_m / \mu_l \quad (4.7)$$

The viscosity μ_r may vary with the volume fraction of solids, particle size and size distribution, particle shape, particle surface properties, fluid electrolyte concentration and ionic charge, and temperature. Some models that relate the relative viscosity μ_r to the volumetric fraction of solids α_s are listed in Table 4.15.

The Einstein model is only applicable to slurries with the volumetric fraction of solids, i.e., $\alpha_s < 1\%$. The other models listed in the table can be used for slurries with a high volumetric fraction of solids. Although a number of other models have been also proposed, one of those shown in Table 4.15 will probably suffice for fitting experimental data. Since solids concentration is not the only relevant parameter, there is no best model for the relationship between μ_r and α_s . The relative viscosity is also affected by solids particle size distribution (Probstein and Sengun, 1987) and particle shape (Happel and Brenner, 1965).

4.2.3.1.2 Non-Newtonian Slurries

As the solids concentration increases, the rheological properties of nonsettling slurries will deviate from Newtonian behavior. When this deviation occurs, the apparent viscosity η , as defined in Eq. (4.6), is no longer a constant, but is instead dependent on the magnitude of the shear stress τ or the shear rate $\dot{\gamma}$. Such nonsettling slurries are called as non-Newtonian. For the majority of non-Newtonian slurries, η is a decreasing function of shear stress τ or shear rate $\dot{\gamma}$ (pseudo-plastic or shear thinning). However, for some slurries of very fine particles (e.g., starch), η may increase with increase in τ or $\dot{\gamma}$ (dilatant or shear thickening). Certain slurries, such as flocculated slurries encountered in minerals processing plants, may develop an internal structure leading to time-dependent non-Newtonian behavior (i.e., the thixotropic slurry). Since the dilatant type of behavior is relatively rare and time-dependent non-Newtonian slurry flows are difficult to model, the examination of rheological models for non-Newtonian slurries in this sections will be limited to the time-independent pseudo-plastic behavior.

Many models have been proposed for representing the viscosity function of non-Newtonian slurries. The model equation that best represents a given slurry depends not only on the nature of the behavior of that slurry, but also the quality and range of viscosity data available for the slurry. Hence, a relatively simple equation might be adequate to represent viscosity data over only a limited range of shear rate. However, if a wide range of shear rate is covered, a complex equation might be needed to represent the entire range of data.

Typical models that have been found useful for representing rheological properties of non-Newtonian slurries are listed in [Table 4.16](#). Each model is written in three equivalent equations, except the Sisko model. Limitations associated with each model are also indicated in the table.

Both the Bingham plastic and the Casson models contain two parameters: a yield stress (τ_b or τ_c) and a limiting viscosity (η_b or η_c). Both models approach Newtonian behavior with a viscosity of η_b or η_c as the shear stress τ or the shear rate $\dot{\gamma}$ increases. Although these two models are simple, they exhibit proper limiting behavior at both extremes of the shear rate and are consequently useful for representing the viscous properties of slurries that exhibit an apparent yield stress resulting from the interparticle contact resistance in a rest state. The Casson model is a theoretical two-parameter model. Recent work in the prediction of laminar and turbulent pipeline flow of non-Newtonian, nonsettling slurries seems to focus largely on the use of the Casson model rather than the Bingham plastic and the Herschel–Bulkley models for describing shear-thinning slurry behavior. The Casson model has an advantage over the Bingham plastic model, since it can predict curvature of the rheogram curve at low shear rates. The Casson model has been used to describe the non-Newtonian flow behavior of a wide variety of materials, including printing inks, blood, chocolate, and oil-based drilling mud.

TABLE 4.15 Some Common Relative Viscosity Models for Newtonian Slurries

Model Equation	Model Parameters	Reference
$\mu_r = 1 + 2.5\alpha_s$		Einstein(1906)
$\mu_r = \exp(B\alpha_s)/(1 - \alpha_s/\alpha_{max})$	B and α_{max}	Krieger (1972)
$\mu_r = 1 - \alpha_s/\alpha_{max}$	α_{max}	Krieger (1972)
$\mu_r = \exp[(B - n/\alpha_{max})\alpha_s]/(1 - \alpha_s/\alpha_{max})^n$	B , n , and α_{max}	Vocadlo (1976)
$\mu_r = 1 + 2.5\alpha_s + 10.05\alpha_s^2 + 0.00273\exp(16.6\alpha_s)$		Thomas (1965)

TABLE 4.16 Typical Rheological Models for Non-Newtonian Slurries

Model Name	Model Equation	Limitations
Bingham plastic (Bird et al., 1960)	$\tau = \tau_b + \eta_b \dot{\gamma}$ for $\tau > \tau_b$ $\dot{\gamma} = 0$ for $\tau < \tau_b$ $\eta = \eta_b + \tau_b / \dot{\gamma}$ or $\eta = \tau \eta_b / (\tau - \tau_b)$	τ_b and η_b depend on solids concentration α_s and particle size distribution (PSD)
Casson (1959)	$\tau^{1/2} = \tau_c^{1/2} + (\eta_c \dot{\gamma})^{1/2}$ $\eta = [\eta_c^{1/2} + (\tau_c / \dot{\gamma})^{1/2}]^2$ or $\eta = \tau \eta_c / (\tau^{1/2} - \tau_c^{1/2})^2$	τ_c and η_c depend on α_s and PSD
Power-Law (Bird et al., 1960)	$\tau = K_p \dot{\gamma}^n$ $\eta = K_p \dot{\gamma}^{n-1}$ or $\eta = \tau (\tau_h / \dot{\gamma})^{1/n}$	Predict $n \rightarrow \infty$ for $n < 1$ and $\dot{\gamma} \rightarrow 0$; predict $n \rightarrow 0$ for $n < 1$ and $\dot{\gamma} \rightarrow \infty$; K_p and n depend on solids concentration and PSD
Herschel–Bulkley (1926)	$\tau = \tau_h + K_h \dot{\gamma}^p$ $\eta = K_h \dot{\gamma}^{p-1} + \tau_h / \dot{\gamma}$ or $\eta = \tau [K_h / (\tau - \tau_h)]^{1/p}$	Predict $n \rightarrow 0$ for $p < 1$ and $\dot{\gamma} \rightarrow \infty$; τ_h , K_h , and p depend on α_s and PSD
Sisko (1958)	$\tau = \eta_s \dot{\gamma} + K_s \dot{\gamma}^m$ $\eta = \eta_s + K_s \dot{\gamma}^{m-1}$	η_s , K_s , and m depend on α_s and PSD

The power-law model can represent Newtonian (for $n = 1$), shear thinning (for $n < 1$), or shear thickening (for $n > 1$) behavior. Although most non-Newtonian slurries can exhibit a “power-law” region over a certain range of shear rate, the model will fail at very high and low shear rates. For example, the model will predict $\eta \rightarrow \infty$ for $n < 1$ and $\dot{\gamma} \rightarrow 0$, and $\eta \rightarrow 0$ for $n < 1$ and $\dot{\gamma} \rightarrow \infty$, both of which are unrealistic for slurries with no yield stress.

The Herschel–Bulkley model (also referred to as the *yield power-law* or *generalized Bingham* model) is basically the power-law model with an added yield stress parameter. Although this model is more flexible than the Bingham model for fitting rheogram data due to the additional model parameter, it suffers the same limitation as the power-law model with regard to unrealistic limiting behavior at high shear rates (or stresses). The estimation of Herschel–Bulkley model parameters from curve fitting often contains a significant degree of uncertainty (Turian et al., 1997), as it is found that different sets of values of the model parameters in the model can provide equivalent fit of the experimental data. This is a fundamental weakness of the Herschel–Bulkley model.

The Sisko model has been found to be efficient for describing the shear stress–shear rate dependence for many non-Newtonian slurries over the range of shear most appropriate to flow in pipes (Turian et al., 1992, 1998a). Unlike the other three-parameter empirical models, one of the model parameters, η_s can be determined independently, as it is given by the high-shear asymptote of the viscosity–shear rate plot. Consequently, the parameter value of η_s is instrument-geometry indifferent, and depends on the suspension microstructure. The remaining two model parameters, K_s and m , are then determined through the best curve fitting to the data over the whole range of shear. The rheogram curves for most concentrated non-Newtonian slurries usually possess a power-law region covering the lower and the intermediate shear rate ranges, followed by an asymptotic approach to a high-shear Newtonian limit. The Sisko model not only describes such behavior well, but also does so over the entire range of shear rates attainable even in the highest shear rheometer, and with a unique set of unambiguously determined model parameter values.

The model parameters in the equations listed in Table 4.16 can be estimated through linear or nonlinear regression. However, extrapolation outside the experimental shear rate range should be done only with caution. Heywood and Cheng (1984) have used two different methods for the curve fitting. One involves nonlinear least-squares regression on weighted data, while in the other method the data are not weighted. They have shown that while both methods will give best estimates of the three parameters, which will then allow prediction of τ to within $\pm 2\%$ over the original viscometric shear rate range, extrapolation well outside this shear rate range leads to very different τ predictions using the two methods.

Bingham plastic, Casson, and Herschel–Bulkley models include a yield stress parameter, τ_b , τ_c and τ_h , respectively. However, Turian et al. (1998a) indicated that curve-fitting shear stress–shear rate data to

determine these yield stress parameters will not generally ensure that a yield stress, as an intrinsic, instrument-geometry-indifferent slurry property has been determined or exists for that slurry. The yield stress values obtained from curve fitting should not necessarily be considered as an absolute property of the slurry but rather a constant, which arises out of the correlation of shear stress–shear rate data. The true yield stress of a slurry, if exists, may have a value quite different from the value derived from the curve fitting of experimental data for which the lower limit of the viscometric shear rate range is of the order of tens or even hundreds of reciprocal seconds. A knowledge of the true yield stress facilitates the calculation of the startup pressure gradient for stagnant fluid in a pipe according to Section 4.2.5.3 on page 4-86. A detailed discussion of determination of yield stresses for slurries has been given by Turian et al. (1992).

It should be noted that all model parameters for the models listed in Table 4.16 are influenced by solids concentration, particle size distribution, and the properties of the interface between the solids and liquid. Bird et al. (1982) have summarized various equations from the literature that relate the parameters of the Bingham and Casson models to various properties of slurries, including solids concentration. In general, the dependence of parameters in Bingham and power-law models on solids concentration can be modeled using the following equation:

$$\tau_b(\text{or } \eta_b, K_p, n) = E \exp(F \alpha_s) \quad (4.8)$$

where E and F are constants derived from tests measuring particle size distribution, shape, and the nature of their surface. A number of other empirical models for correlating the parameters in non-Newtonian rheological models with various factors have been reported in the literature (Thomas, 1961; Bird et al., 1982; Turain et al., 1997).

4.2.3.2 Pressure Loss through Straight Circular Pipe

4.2.3.2.1 Friction Factor in Pipe Flows

For steady slurry flows in a piping system with straight conduit of uniform cross section, the total pressure change, Δp , is written as

$$\Delta p = p_f + p_{ft} + \rho_m g \Delta z \quad (4.9)$$

where p_f is the frictional pressure loss in the pipe and p_{ft} is the frictional pressure loss arising from flow through fittings. The last term, $\rho_m g \Delta z$, is the pressure loss or gain resulting from elevation changes and is negative for a reduction in static head and positive for an increase in static head, and Δz is the net change in pipeline elevation, assuming that the pipeline is full of slurry.

The frictional pressure loss over a straight pipe with a length L and an internal diameter D is given by

$$P_f = f(4L/D)(\rho_m U_m^2/2) \quad (4.10)$$

where f is the friction factor of pipe flow. This equation shows that the evaluation of f is the major task in the determination of the frictional pressure loss. The friction factor can also be defined in terms of the shear stress at the pipe wall, τ_w :

$$f = \tau_w / (\rho_m U_m^2/2) \quad (4.11)$$

4.2.3.2.2 Laminar Flows

For laminar flow, the pipeline pressure loss can be calculated from first principles for any given rheological data or model fitted to the data. The accuracy of pressure drop prediction is limited only by the accuracy of the data and the closeness with which the slurry flow properties fit any chosen model. The rheological models as presented in Section 4.2.3.1 can be used either to obtain analytical expressions for volumetric flow rate as a function of wall shear stress and other relevant variables in the laminar flow regime or for the friction factor as a function of model-specific modified Reynolds number.

The volume flow rate through a pipe with a local slurry velocity $v(r)$ at the radial position r in the pipe is given by

$$\dot{V}_m = \int_0^{D/2} 2\pi v(r) dr \quad (4.12)$$

The shear stress at a radial position, r , can be related to the frictional pressure loss over the pipe of length, L , by equating the resultant force, $\pi r^2 p_f$, from the pressure drop over a cylinder of radius, r , with the force derived from the shear stress, $2\pi r\tau$

$$\tau = \frac{r}{2} \frac{p_f}{L} \quad (4.13)$$

After integration by parts and by using Eq. (4.13), Eq. (4.12) becomes

$$\dot{V}_m = \frac{\pi}{8} (D/\tau_w)^3 \int_0^{\tau_w} \tau^2 \dot{\gamma} d\tau \quad (4.14)$$

where the shear stress at the pipe wall τ_w is given by

$$\tau_w = \frac{Dp_f}{4L} \quad (4.15)$$

4.2.3.2.2.1 Newtonian Slurries. For steady, fully developed, laminar flow of Newtonian slurries in a circular pipe, the apparent viscosity η ($\eta = \mu_m$) is independent of the shear rate or shear stress. Substitution of the Newtonian model (i.e., $\tau = \mu_m \dot{\gamma}$) into Eq. (4.14) leads to the well-known Hagen–Poiseuille equation

$$\dot{V}_m = \frac{\pi D^4 p_f}{128 \mu_m L} = \frac{\pi D^3 \tau_w}{32 \mu_m} \quad (4.16)$$

by using Eq. (4.16) to eliminate τ_w in Eq. (4.11) and rearranging to solve for f gives

$$f = \frac{16\mu_m}{DU_m \rho_m} \quad (4.17)$$

This equation can be rewritten in dimensionless form as

$$f = 16/Re \quad (4.18)$$

where Re ($= DU_m \rho_m / \mu_m$) is the pipe flow Reynolds number. The upper limit of Newtonian laminar flow regime is defined by the Reynolds number with a value of 2100.

4.2.3.2.2.2 Non-Newtonian Slurries. For non-Newtonian slurries, analytical expressions for the volumetric flow rate and the friction factor can be obtained by substituting a non-Newtonian rheology model into Eq. (4.14) and then evaluating the integral of the equation. For rheology models with a yield stress (e.g., Bingham plastic), the lower limit of the integral in Eq. (4.14) must be replaced by the yield stress. In the evaluation of Eq. (4.14), by using either data or a model, the range of shear stress (or a yield stress) from 0 to $\tau = Dp_f / 4L$ is involved. Experimental data may not cover this entire range, especially at the lower limit. Consequently, some extrapolation is inevitable. In this situation, the reliability of the results depends upon the degree to which the database covers the range of conditions (i.e., shear stress) of interest.

Power-Law Model

For the power-law model, $\tau = K_p \dot{\gamma}^n$, the integration of Eq. (4.14) gives

$$\dot{V}_m = \frac{\pi D^3}{32} \left(\frac{4n}{3n+1} \right) \left(\frac{\tau_w}{K_p} \right)^{1/n} \quad (4.19)$$

which is the power-law-equivalent of the Hagen–Poiseuille equation and reduces to Eq. (4.16) for $n = 1$ and $K_p = \mu_m$. By using Eq. (4.19) to eliminate τ_w in Eq. (4.11) and rearranging to solve for f gives

$$f = 16/Re_p \quad (4.20)$$

where Re_p is the equivalent Reynolds number for power-law non-Newtonian slurries, and is given by

$$Re_p = \frac{\rho_m U_m D}{K_p} \left(\frac{4n}{3n+1} \right)^n \left(\frac{D}{8U_m} \right)^{n-1} \quad (4.21)$$

It should be noted that the definition of Re_p does not have any physical meaning and is defined so that Eqs. (4.20) and (4.18) are of identical form.

Bingham Plastics Model

Due to the yield stress in the Bingham plastic model (i.e., $\tau = \tau_b + \eta_b \dot{\gamma}$), a region extending from the center of the pipe to $r = R\tau_b/\tau_w = r_0$ will move as a “plug.” Therefore, the total volume flow rate will be the sum of flow rate in the “plug” and in the deformed region surrounding the plug and is given by

$$\dot{V}_m = \dot{V}_{\text{plug}} + \int_{r_0}^{D/2} 2\pi v(r) dr \quad (4.22)$$

After integration by parts and substituting the Bingham plastic model equation, the evaluation of Eq. (4.22) yields the Buckingham (1921) equation

$$\dot{V}_m = \frac{\pi D^3 \tau_w}{32 \eta_b} \left[1 - \frac{4}{3} \frac{\tau_b}{\tau_w} + \frac{1}{3} \left(\frac{\tau_b}{\tau_w} \right)^4 \right] \quad (4.23)$$

Substituting $\tau_w = f \rho_m U_m / 2$ into Eq. (4.23) and solving for f give the equivalent dimensionless expression

$$f = \frac{16}{Re_b} \left[1 + \frac{1}{6} \frac{He_b}{Re_b} - \frac{1}{3} \frac{He_b^4}{f^3 Re_b^7} \right] \quad (4.24)$$

where

$$Re_b = DU_m \rho_m / \eta_b \quad \text{and} \quad He_b = D^2 \rho_m \tau_b / \eta_b^2 \quad (4.25)$$

in which He_b is the Hedstrom number defined for Bingham plastics model. Since Eq. (4.24) is implicit in terms of f , an iterative technique is necessary to obtain f . If the last term in the bracket is small compared with the other terms, a brief iteration using the first two terms as the starting value will converge very rapidly.

Herschel–Bulkley or Generalized Bingham Model

A procedure analogous to that given above can be followed using the Herschel-Bulkley model (i.e., $\tau = \tau_h + K_h \dot{\gamma}^p$) with Eq. (4.22) to determine the flow rate and friction factor. The analytical expressions for volume flow rate and the friction factor are

$$\dot{V}_m = \frac{\pi D^3 p}{8(3p+1)} \left(\frac{\tau_w - \tau_h}{K_h} \right)^{1/p} \left[\chi^3 + \frac{2(3p+1)}{2p+1} \frac{\tau_h}{\tau_w} \chi^2 + \frac{(3p+1)}{2p+1} \left(\frac{\tau_h}{\tau_w} \right)^2 \chi^2 \right] \quad (4.26)$$

where $\chi = (1 - \tau_h/\tau_w)$ and

$$f = \frac{2He_h}{Re_h^2} + \frac{16}{Re_h} \left[\chi^3 + \frac{2(3p+1)}{2p+1} \frac{\tau_h}{\tau_w} \chi^2 + \frac{(3p+1)}{2p+1} \left(\frac{\tau_h}{\tau_w} \right)^2 \chi^2 \right]^{-p} \quad (4.27)$$

where

$$Re_h = \frac{\rho_m U_m D}{K_h} \left(\frac{4p}{3p+1} \right)^p \left(\frac{D}{8U_m} \right)^{p-1} \quad (4.28)$$

and

$$He_h = (\tau_h/\rho_m) (Re_h/U_m)^2 \quad (4.29)$$

Since $\tau_w = f\rho_m U_m/2$, Eq. (4.27) requires an iterative procedure to solve for f . Unlike the Bingham model, no simplifying assumption can be made easily to derive an expression from Eq. (4.27) which is explicit in f .

Casson Model

For the Casson model (i.e. $\tau^{1/2} = \tau_c^{1/2} + (\eta_c\dot{\gamma})^{1/2}$), the analytical expressions are

$$\dot{V}_m = \frac{\pi D^3 \tau_w}{32 \eta_c} \left[1 + \frac{4}{3} \frac{\tau_c}{\tau_w} - \frac{16}{7} \left(\frac{\tau_c}{\tau_w} \right)^{1/2} - \frac{1}{21} \left(\frac{\tau_c}{\tau_w} \right)^4 \right] \quad (4.30)$$

and

$$f = \frac{16}{Re_c} \left[1 - \frac{1}{6} \frac{He_c}{Re_c} + \frac{1}{7} (2fHe_c)^{1/2} + \frac{1}{21} \frac{He_c^4}{f^3 Re_c^7} \right] \quad (4.31)$$

where

$$Re_c = DU_m \rho_m / \eta_c \text{ and } He_c = D^2 \rho_m \tau_c / \eta_c^2 \quad (4.32)$$

Numerical Integration Method

Substituting Eq. (4.15) into Eq. (4.14) and solving for P_f gives

$$P_f = \left(\frac{8\pi L^3}{\dot{V}_m} \int_0^{\tau_w} \tau^2 \dot{\gamma} d\tau \right)^{1/3} \quad (4.33)$$

The above relationship suggests a simplified but rigorous approach to estimate the frictional pressure loss for the laminar flow of a slurry having any rheological property. If a rheogram curve (also called flow curve) data for a slurry have been obtained using a smaller (or larger) pipe diameter and there are no wall-slip effects, the integral in the above equation can be readily evaluated by plotting $\tau^2 \dot{\gamma}$ against τ and calculating the area under the curve. The method is useful for complex rheogram curves because simplified rheological models have difficulties in predicting the frictional pressure loss. It should also be noted that the relationship is valid for any pipe diameter as long as the flow remains in the laminar regime. Thus, this master curve may be used to predict the frictional pressure loss for flows in pipes of different sizes.

4.2.3.2.3 Turbulent Flows

4.2.3.2.3.1 Newtonian Slurries. In contrast to laminar flow, in turbulent flow of a Newtonian slurry, the relative pipe wall roughness can be important and correlations for the friction factor f can be classified according to the characteristics of the pipe wall, i.e., whether it is essentially smooth or is sufficiently rough to affect frictional losses. These correlations are obtained with or without theoretical guidance. Different versions of correlations have been developed (e.g., von Karman, 1931; Colebrook, 1939; Moody, 1947; Olujic, 1981). For turbulent flow of a Newtonian fluid in smooth tubes, the classical mixing length theory of Prandtl was applied by von Karman (1931) to derive the well-known expression

$$1/\sqrt{f} = 4.0 \log(Re\sqrt{f}) - 0.4 \quad (4.34)$$

When the pipe wall is not smooth, an estimate for the relative roughness, e/D , is required, as it is an additional variable in equations for the prediction of friction factor (Colebrook, 1939). For rough pipe surfaces, Eq. (4.34) was modified by Colebrook (1939) to include the effect of relative roughness, e/D :

$$\frac{1}{\sqrt{f}} = -4.0 \log \left[\frac{e/D}{3.7} + \frac{1.255}{Re\sqrt{f}} \right] \quad (4.35)$$

This equation is the basis for the well-known Moody diagram for pipe friction factors and applies for $Re > 2100$.

However, the equation by Churchill (1977) is probably the most useful for turbulent flows, as it is explicit in f and valid for either smooth or rough pipe surface in both the laminar and turbulent flow regimes:

$$f = 2[(8/Re)^{12} + (A + B)^{-1.5}]^{1/12} \quad (4.36)$$

where

$$A = [2.457 \ln(1/C)]^{16}, \quad B = \left(\frac{37,530}{Re} \right)^{16}, \quad C = \left(\frac{7}{Re} \right)^{0.9} + 0.27 \frac{e}{D} \quad (4.37)$$

4.2.3.2.3.2 Non-Newtonian Slurries. Turbulence is a natural form of fluid motion that is characterized by random eddy motions both parallel and transverse to the direction of the main flow. Both direction and magnitude of solids and liquid velocities fluctuate on a continuous random basis. The turbulent flow of non-Newtonian slurries is more complex than that of Newtonian slurries, as turbulent behavior of non-Newtonian slurries appears unrelated to their laminar behavior and yet has been found similar to Newtonian turbulent flow behavior, in spite of the obvious difference in rheology. Many theoretical models have therefore been developed to predict turbulent flow behavior of non-Newtonian slurries.

Many empirical, semianalytical, and analytical models for turbulent non-Newtonian flow have been developed. Most equations are based on the power-law or Bingham plastic model, for example, those developed by Dodge and Metzner (1959), Tomita (1959), and Szilas et al. (1981), while others have been derived specifically for use with the Herschel–Bulkley flow model, i.e., Torrance (1963) and Hanks (1978). Govier and Aziz (1972) present a review of these models.

Dodge and Metzner (1959) developed a semitheoretical equation for the smooth wall, fully developed turbulent friction factor for, time-independent, purely viscous, non-Newtonian fluids. This was based upon Prandtl's mixing length theory with different values for the empirical constants obtained from experimental data. Tomita (1959) used a similar method to develop equations specifically for Bingham plastic and power-law fluids. Torrance (1963) extended this work for yield-pseudo-plastics to account for pipe roughness. Wilson and Thomas (1985) developed the work further by including terms for the viscous sublayer due to shear thinning.

Most of the models or methods for turbulent non-Newtonian flow are based on a specific rheological model, while a few of them are generalized models, such as the Wilson and Thomas (1985) model. We will proceed in our discussion from a generalized model to those based on a specific rheological model.

4.2.3.2.3.3 The Wilson and Thomas Model. Non-Newtonian rheological properties can increase the turbulent microeddy size, leading to an increase in the thickness of the viscous sublayer. If other quantities are unaffected, the thickened sublayer will, in turn, produce a higher mean velocity for the same wall shear stress, giving a lower friction factor. Based on this consideration, Wilson and Thomas (1985), and Thomas and Wilson (1987) developed a predictive model for non-Newtonian turbulent flow. The model uses the ratio of the integrals under the non-Newtonian and Newtonian rheograms, denoted by α , to estimate the size increase of the microeddies, and it was found that the thickness of the sub layer should also be multiplied by a factor equal to α . As shown by Wilson and Thomas (1985), the value of the mean velocity, U_m that results from this thickened viscous sublayer is given by

$$\frac{U_m}{u^*} = \frac{U_N}{u^*} + 11.6(\alpha - 1) - 2.5 \ln \alpha - \Omega \quad (4.38)$$

where U_m is the mean slurry velocity, u^* the friction velocity ($u^* = (\tau_w / \rho_m)^{0.5}$), and U_N the mean velocity for equivalent Newtonian flow, i.e., flow with the same wall shear stress τ_w for Newtonian fluid with the same viscosity corresponding to the non-Newtonian value at $\tau = \tau_w$. The term Ω represents the reduction

in mean velocity due to flattening of the central core of the velocity profile when the fluid possesses a yield stress, τ_y

$$\Omega = -2.5 \ln(1 - \xi) - 2.5\xi(1 + 0.5\xi), \quad \xi = \tau_y/\tau_w \quad (4.39)$$

The work by Wilson and Thomas (1985) has some theoretical justification and has been shown to be in fairly good agreement with experimental data. It is generally accepted that this model is the most successful of the Prandtl type models. For the power-law and some other models, expressions for the area ratio α have been derived (Thomas and Wilson, 1987).

For a yield power-law fluid (i.e., Herschel–Bulkley fluid, $\tau = \tau_h + K_h\dot{\gamma}^p$ and $\tau_y = \tau_h$), the area ratio α is

$$\alpha = 2(1 + \xi p)/(1 + p) \quad (4.40)$$

For a power-law fluid ($\tau = K_p\dot{\gamma}^n$ and $\tau_y = 0$), the expression for α is

$$\alpha = 1/(1 + n) \quad (4.41)$$

For a Bingham fluid ($\tau = \tau_b + \eta_b\dot{\gamma}$ and $\tau_y = \tau_b$), the area ratio α is given by

$$\alpha = 1 + \xi \quad (4.42)$$

For a Casson fluid ($\tau^{1/2} = \tau_c^{1/2} + (\eta_c\dot{\gamma})^{1/2}$ and $\tau_y = \tau_c^{1/2}$), the area ratio α is

$$\alpha = 1 + 2\chi^{0.5}/3 + \chi/3 \quad (4.43)$$

Theoretically, the Wilson and Thomas model, i.e., Eq. (4.38) is applicable to a slurry having any rheological property. If a rheogram curve data for a slurry have been obtained, the ratio of the integrals under the non-Newtonian and Newtonian rheograms can be readily evaluated using a numerical technique.

The mean velocity of the equivalent Newtonian flow, U_N , is evaluated using a friction factor determined by using the model-specific Reynolds number $Re_M = DU_N\rho_m/\eta$. The effective viscosity η is evaluated from the slurry rheogram ($\tau, \dot{\gamma}$) or a rheological model at τ_w . The effective viscosity evaluated at τ_w using typical rheological models is listed in Table 4.17.

The Wilson and Thomas model is not explicit in the friction factor f . Equation (4.38) requires the following iterative procedure to solve f for a given slurry mean velocity U_m :

1. Assume a value of wall shear stress, τ_w .
2. Calculate the effective viscosity at τ_w using a suitable rheological model such as those shown in Table 4.17.
3. Evaluate the friction velocity using $u^* = (\tau_w/\rho_m)^{0.5}$.
4. Assume a value of the mean velocity of the equivalent Newtonian flow U_N .
5. Evaluate the friction factor f at the model specific Reynolds number $Re_M = DU_N\rho_m/\eta$. The friction factor f is calculated using Eq. (4.34) for smooth pipe wall or Eq. (4.36) for rough pipe wall.
6. Evaluate U_N using $U_N = (2\tau_w/\rho_m f)^{0.5}$.

TABLE 4.17 Effective Viscosity of Typical Rheological Models at τ_w

Model Name	Model Equation
Bingham plastic	$\eta = \tau_w\eta_b/(\tau_w - \tau_b) = \eta_b/(1 - \chi), \quad \chi = \tau_b/\tau_w$
Casson	$\eta = \tau_w\eta_c/(\tau_w^{1/2} - \tau_c^{1/2})^2 = \eta_c/(1 - \chi^{1/2})^2, \quad \chi = \tau_c/\tau_w$
Power law	$\eta = \tau_w(K_p/\tau_w)^{1/n}$
Herschel–Bulkley	$\eta = \tau_w[K_h/(\tau_w - \tau_h)]^{1/p}$

7. Return to Step 4 if the difference between the U_N from Step 6 and the one assumed at Step 4 is higher than a specified tolerance.
8. Evaluate the U_m using the Wilson and Thomas model.
9. Return to Step 1 if the difference between U_m from Step 8 and the given value is higher than a specified tolerance.

The effect of the pipe wall roughness on turbulent flow of non-Newtonian slurries can be accommodated in the Wilson and Thomas model by using the appropriate roughness in the determination of U_N , as indicated in the above procedures. However, this can only be approximate, since the interaction between the pipe roughness and the laminar sublayer will be different when the thickened laminar sublayer is present.

4.2.3.2.3.4 Models for Power-Law Slurries. The equations for the friction factor f , based on the power-law ($\tau = K_p \dot{\gamma}^n$) Reynolds number Re_p defined in Eq. (4.21), are given by:

- (a) *Dodge and Metzner (1959).* Dodge and Metzner developed a model of turbulent flow of a power-law fluid in a smooth pipe based on the laminar flow model of Metzner and Reed (1955). The model was developed following the form of the von Karman–Nikuradse equation for Newtonian turbulent flow, and the final relationship is of the same format as Newtonian smooth wall turbulent flow, and reverts to the Newtonian form under Newtonian conditions ($K_p = \mu$ and $n = 1$). The model is

$$\frac{1}{\sqrt{f}} = \frac{4.0}{n^{0.75}} \log(Re_p f^{1-n/2}) - \frac{0.4}{n^{1.2}} \quad (4.44)$$

- (b) *Tomita (1959).* For power-law fluids, Tomita extended his laminar flow model to turbulent flows in smooth pipes by applying Prandtl's mixing length concept and developed an implicit equation

$$\frac{1}{\sqrt{f_{T_0}}} = 4.0 \log(Re_{T_0} \sqrt{f_{T_0}}) - 0.4 \quad (4.45)$$

where

$$f_{T_0} = \left(\frac{1 + 2n}{1 + 3n} \right) \frac{4}{3} f \quad (4.46)$$

and

$$Re_{T_0} = Re_p 8^{1-n} \left(\frac{1 + 3n}{4n} \right)^n \frac{6[(1 + 3n)/n]^{1-n}}{2n[(1 + 2n)/n]} \quad (4.47)$$

- (c) *Szilas et al. (1981).* Szilas et al. developed the following equation for power-law oil flow in rough pipes at a high Reynolds number:

$$\frac{1}{\sqrt{f}} = \frac{4.0}{n} \log(Re_p (4f)^{1-n/2}) + 1.51^{1/n} \left(4.24 + \frac{1.414}{n} \right) - \frac{8.03}{n} - 2.114 \quad (4.48)$$

- (d) *Irvine (1988).* Irvine developed the following generalized Blasius equation for power-law fluids in smooth pipes:

$$f = \frac{F'(n)}{Re_p^{1/(3n+1)}} \quad (4.49)$$

where

$$F'(n) = \frac{2}{8^{n-1}} \left[\frac{8n^n}{7^{7n}(1 + 3n)^n} \right]^{1/(3n+1)} \quad (4.50)$$

4.2.3.2.3.5 Models for Herschel-Bulkley or Generalized Bingham Slurries. The turbulent flow of Herschel–Bulkley or generalized Bingham fluids in circular pipes has been studied by a number of people, including

1. *Torrance (1963).* Torrance developed a theoretical equation for Herschel–Bulkley or generalized Bingham fluids ($\tau = \tau_h + K_h \dot{\gamma}^p$) to include a wall shear stress. For fully turbulent flows in smooth pipes, the Torrance equation is

$$\frac{1}{\sqrt{f}} = \frac{1.966}{n} \ln((1 - \xi) Re_n f^{1-n/2}) + \frac{0.682}{n} (5n - 8) + \frac{2.678}{n} - 2.949 \quad (4.51)$$

where $\xi = \tau_h/\tau_w$, and $Re_n = 8^{1-p} D^p U_m^{2-p} \rho_m / K_h$

For flows in rough pipes with a relative roughness, e/D , the Torrance equation is

$$\frac{1}{\sqrt{f}} = 1.767 \log\left(\frac{Re_n}{e}\right) + 6 - \frac{2.65}{n} \quad (4.52)$$

2. *Slatter et al. (1996).* Slatter et al. proposed a new model for describing turbulent pipe flow of Herschel–Bulkley or generalized Bingham fluids. In analogy with the Newtonian approach, they defined the roughness Reynolds number, Re_r , in terms of friction velocity, Herschel–Bulkley model parameters, and the representative particle diameter, d_{85} :

$$Re_r = \frac{8\rho_m (u^*)^2}{\tau_h + K_h [8u^*/d_{85}]^p} \quad (4.53)$$

If $Re_r < 3.32$, the smooth wall turbulent flow exists and the mean velocity is given by

$$\frac{U_m}{u^*} = 2.5 \ln\left(\frac{D}{2d_{85}}\right) + 2.5 \ln(Re_r) + 1.75 \quad (4.54)$$

If $Re_r > 3.32$, the fully developed rough wall turbulent flow exists and the mean velocity is given by

$$\frac{U_m}{u^*} = 2.5 \ln\left(\frac{D}{2d_{85}}\right) + 4.75 \quad (4.55)$$

and the friction factor is a constant.

Prediction of f for turbulent flow in rough pipes can also be based on the relations for smooth wall pipe. Govier and Aziz (1972) suggested that if the pipe is rough, the pressure loss calculated by the methods for smooth pipes should be multiplied by the ratio of the friction factor for a rough pipe to the friction factor for a smooth pipe, as determined from the Moody chart for Newtonian materials at the appropriate Reynolds number consistent with the fluid model used, i.e., Re_b , for the Bingham plastic model or Re_p for the power-law models. For pipe flows where friction factors are independent of Reynolds number but are dependent upon relative roughness, e/D , the Torrance equation, i.e., Eq. (4.52) should be used.

4.2.3.2.3.6 Models for Bingham Plastic Slurries. The equations for the friction factor f based on the Bingham plastic ($\tau = \tau_b + \eta_b \dot{\gamma}$) Reynolds number Re_b defined in Eq. (4.25) are given by:

1. *Thomas (1963):* For slurries whose rheograms may be adequately described by Bingham plastic model, Thomas has developed a Blasius-type equation

$$f = B_T Re_b^{-\beta} \quad (4.56)$$

where the parameters B_T and β are related to fluid properties using data in smooth pipes:

$$\begin{aligned} B_T &= 0.079[(\eta_f/\eta_b)^{0.48} + (\rho_m \tau_b K_{T1}^2 / \eta_f^2)^2] \\ \beta &= 0.25[(\eta_f/\eta_b)^{0.15} + (\rho_m \tau_b K_{T2}^2)^2] \end{aligned} \quad (4.57)$$

in which $K_{T1} = 1.94 \mu\text{m}$, $K_{T2} = 1.73 \mu\text{m}$, and η_f is the Newtonian viscosity of the suspending medium.

2. *Darby and Melson (1981)*: Darby and Melson employed the approach taken by Churchill (1977) to combine the Buckingham equation for f_L in a laminar flow (Eq. [4.24]) with an empirical correlation for f_T in a turbulent flow regime to arrive at a single friction factor expression valid for all flow regimes:

$$f = (f_L^m + f_T^m)^{1/m} \quad (4.58)$$

where the exponent m depends on the Bingham Reynolds number according to

$$m = 1.7 + 40,000/Re_b \quad (4.59)$$

and the empirical correlation for f_T in a turbulent flow regime is

$$\begin{aligned} f_T &= 10^\beta Re_b^{-0.193} \\ \beta &= -1.378[1 + 0.146 \exp(-0.29 \times 10^{-5} Re_b)] \end{aligned} \quad (4.60)$$

Equation (4.60) does not apply when the Hedstrom number, defined by Eq. (4.25), is less than 1000, but this is not a practical constraint for most slurries with a measurable yield stress.

4.2.3.2.4 Laminar–Turbulent Transition

It is important to identify the transition between laminar and turbulent flow for the following reasons:

- The fluid behavior and relevant equations for pressure loss prediction change fundamentally at this point. Once this transition point is defined for a slurry with a particular flow property, it is then possible to decide whether expressions for laminar flow are relevant or whether turbulent flow equations need to be used.
- Overall optimization of slurry pipeline system often suggests that it is most economical to operate the pipeline system in the transition region between the laminar and turbulent regimes.
- It is necessary in some cases to operate into the turbulent flow regime in order to maintain coarse size fraction of the solids in suspension.

For Newtonian slurries the lower critical Reynolds number Re_1 for the initial breakdown of laminar flow is 2100 and the upper value of Re_2 for the commencement of fully turbulent flow is approximately 3000. The flow region between these two critical Reynolds numbers is typically referred to as the transitional flow regime. However, for non-Newtonian slurries, the individual values of Re_1 and Re_2 are much more difficult to predict. Various methods have been developed for Re_1 prediction based on different flow models. Cheng (1970) has also developed an approach for predicting both Re_1 and Re_2 that are valid for both power-law slurries and generalized Bingham slurries. The most economical design often suggests that flow should be in the transitional regime, and some pipelines operate just above Re_2 . However, Re_2 is difficult to define precisely due to the fact that the fluctuations in pressure gradient prevalent in the transitional regime diminish progressively rather than abruptly as flow velocity is increased, when the fully turbulent flow regime is reached.

4.2.3.2.4.1 Intersection Method. A practical and simple approach toward dealing with the transitional region between laminar and turbulent flow is to assume that the transition, as the flow velocity is progressively increased, occurs completely at a single operating point. In this case, only one critical Reynolds

number needs to be predicted and this can be achieved by taking the intersection of the (f, Re) or (f, U_m) relationships for laminar and turbulent flow for the non-Newtonian fluid model under consideration. The degree of success of this method is entirely dependent on the accuracy of the turbulent model used. It should be noted that this approach cannot explain the flow behavior, as done by the Newtonian Reynolds number approach. This approach also does not work with Newtonian behavior, where the critical point is clearly not the intersection of the laminar and turbulent theoretical lines.

4.2.3.2.4.2 Stability Function Method. Ryan and Johnson (1959) defined a stability parameter in terms of the velocity distribution, $v(r)$, in the pipe as follows:

$$Z = -\frac{D}{2\tau_w} \rho_m v(r) \frac{dv}{dr} \quad (4.61)$$

which is the ratio of energy input to energy dissipation within a fluid element. It is clear that Z has the form of a Reynolds number with no reference to a fluid model. It vanishes at both the pipe wall and the centerline, attaining a maximum at some intermediate position. For a Newtonian fluid, the laminar flow solution indicates that Z attains a maximum at the reduced radial position $r/R = 1/\sqrt[3]{3}$, with

$$Z_{\max} = 0.3849 Re \quad (4.62)$$

Taking the transition Reynolds number for laminar flow as $Re_c = 2100$ gives $Z_{\max} = 808$. Since Z is not restricted to any fluid model, Ryan and Johnson (1959) proposed that the laminar–turbulent transition occurs at the same ratio (i.e., $Z_{\max} = 808$) for non-Newtonian fluids as it does for Newtonian fluids. For Newtonian fluids, the stability parameter pertaining to this ratio can be expressed in terms of transition Reynolds number. However, since the definition of Reynolds number for non-Newtonian fluids is model-dependent, laminar–turbulent transition criteria also appears to be the same. By using Eqs. (4.61) and (4.62) together with the velocity distribution $v(r)$ appropriate to the rheological model, laminar–turbulent transition criteria can be derived.

When applied to the power-law model ($\tau = K_p \gamma^n$), Ryan and Johnson (1959) obtained an expression for the lower critical Reynolds number Re_c :

$$Re_c = \frac{6464n(n+2)^{(n+2)/(n+1)}}{(1+3n)^2} \quad (4.63)$$

or, alternatively, the lower critical friction factor f_c is given by

$$f_c = \frac{(1+3n)^2}{404n} \frac{1}{(n+2)^{(n+2)/(n+1)}} \quad (4.64)$$

Such results have also been obtained for Bingham plastic slurries by Hanks (1981) and for the Casson and Herschel–Bulkley slurries by Hanks and Ricks (1974).

4.2.3.2.4.3 Metzner-Reed Method. Metzner and Reed (1955) developed a generalized Reynolds number for the correlation of non-Newtonian pipe flow data. They define two rheological parameters K' and n' :

$$\tau_w = K'(8U_m/D)^{n'} \quad (4.65)$$

which represents the tangent to the logarithmic plot of τ_0 vs. $8U_m/D$. The Reynolds number is then defined as

$$Re_{MR} = \frac{8\rho_m U_m^2}{K'(8U_m/D)^{n'}} \quad (4.66)$$

The transition criterion is $Re_{MR} = 2100$.

4.2.3.3 Pressure Losses from Pipe Fittings

Pressure losses arising from flow through pipe fittings are required before total system head loss estimation can be made. Pipeline fittings may be classified as branching (tees), reducing or expanding (bushes and sudden changes in flow area), or deflecting (elbows and bends).

The literature on Newtonian flow through pipe fittings is extensive, and embodies experimental and theoretical studies as well as extensive tabulations of resistance coefficients and empirical correlations. For the turbulent flow of Newtonian nonsettling slurries, much information exists with pressure loss often expressed in terms of the number of equivalent pipe diameters of straight pipe giving the same pressure loss (Perry and Chilton, 1985).

Friction losses for fittings are expressed in terms of the so-called resistance coefficients K_f defined by

$$K_f = p_f / (\rho U_m^2 / 2) \quad (4.67)$$

Alternatively, the friction loss can be expressed in terms of the equivalent length of straight pipe of the same diameter and having the same friction loss as the fitting. The equivalent length is expressed in terms of pipe diameters :

$$L_e/D = K_f / (4f) \quad (4.68)$$

Edwards et al. (1985) reviewed the flow of non-Newtonian slurries in laminar regimes and they proposed that the model-specific Reynolds numbers (such as Re_b or Re_h) should be used to correlate with the resistance coefficients K_f of Newtonian flows in laminar regimes.

For non-Newtonian flows in transition and turbulent regimes, Govier and Aziz (1972) proposed that the method of equivalent length should be used, i.e., that the equivalent length of pipe fittings for Newtonian liquids should be added to computations of total length for the pressure loss of the non-Newtonian slurry. Both Cheng (1970) and Turian et al. (1983) have concluded that the pressure losses of non-Newtonian flows through pipe fittings do not depend significantly on the non-Newtonian character of the slurry.

Turian et al. (1998b) carried out an experimental investigation on the friction losses of non-Newtonian slurry flows through pipe fittings and concluded that the resistance coefficients for all the fittings tested approached constant asymptotic values that are same as those for the corresponding coefficients for flow of water. This means one can establish the turbulent flow friction loss characteristic for any pipe fitting, using data with water. Then, one only needs to use the density of the suspension to calculate the applicable friction loss.

4.2.4 Heterogeneous Flow of Settling Slurries

4.2.4.1 Transitional Velocities of Horizontal Pipe Flows

Although most of the industrial slurries consist of small size particles (usually up to a few tens of microns), slurries containing coarse and high-density particles are also widely encountered in various industries. These types of slurries cannot be treated as pseudo-fluids with effective rheological properties, since the solid particles are not uniformly mixed in the horizontal plane and tend to settle at the bottom of the pipe due to the effect of gravity. Hence they are considered as settling slurries.

Due to the settling tendency of the solids particles, several flow regimes or patterns may be encountered in a horizontal pipe flow of settling slurries. As illustrated in [Figure 4.28](#), slurry flows of settling slurries can be classified into flow regimes as follows: (1) heterogeneous flow—at high slurry mixture velocities all the solids particles are fully suspended by the carrier liquid as a result of high turbulence; (2) flow with a moving bed—at lower slurry mixture velocities the fluid turbulence is not sufficient to overcome gravity, hence the particles accumulate at the bottom of the pipe, forming a packed bed of moving particles; (3) flow with a stationary bed—when the slurry mixture velocity is too low to move all the immersed particles, and some of them form a stationary deposit bed at the bottom of the pipe.

The flow regimes affect the dependence of the pressure drop on the flow velocity as well as the magnitude of the pressure drop and they also influence pipe erosion and other performance characteristics. Figure 4.30 shows a schematic diagram of pressure gradient dependence on mean slurry mixture velocity for various flow regimes. The straight line in this figure represents the behavior of a carrier fluid, such as water, in a given pipe size. The pressure gradient for the slurry is always higher than that of the carrier fluid at the same velocity, and the difference increases with the increase in the degree of heterogeneity. As the velocity decreases, the pressure gradient for slurry decreases till it reaches a minimum, and then increases with a decrease in the velocity. This was first noticed by Blatch (1906).

There are four transitional velocities (Figure 4.30) between the flow regimes that are usually determined by visual observations. The transitional velocities are defined as:

- U_{m1} : velocity at or above which all solids move as a homogeneous suspension.
- U_{m2} or U_c : velocity at or above which all particles move as a heterogeneous suspension and below which the solids start to settle and form a moving bed.
- U_{m3} : velocity at or above which the mixture flows as a heterogeneous mixture with the coarser particles forming a moving bed.
- U_{m4} : velocity at or above which the bed in the lower half of the pipe is stationary. In the upper half of the pipe, some solids may move by saltation or suspension.

Transitional velocities U_{m3} and U_{m4} are obviously not used for the operation of slurry pipelines, and therefore the prediction of U_{m3} and U_{m4} will not be discussed here. The transitional velocity U_{m2} or U_c marks the transition to a generally undesirable condition, since deposited particles will greatly enhance erosion problems and a bed of solids promotes unstable operation. Approaches for the prediction of U_c will be presented in the next section.

The determination of the transitional velocity U_{m1} from homogeneous to heterogeneous flow is required in some applications. Newitt et al. (1955) expressed the transitional velocity U_{m1} in terms of terminal velocity of particles as

$$U_{m1} = 38.7(gDV_s)^{1/3} \quad (4.69)$$

One of the more accurate approaches for the prediction of U_{m1} is the Tuain–Yuen's correlation, which will be presented in the following section.

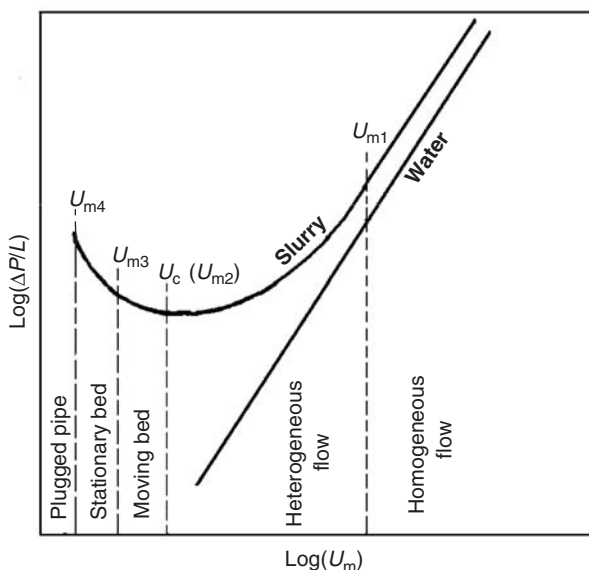


FIGURE 4.30 Schematic diagram of pressure gradient dependence on mean slurry velocity for various flow regimes.

4.2.4.2 Critical Velocity of Horizontal Pipe Flows

The transition velocity demarcating flows in which the solid particles form a bed at the bottom of the pipe is very difficult to determine experimentally, because the flow becomes unstable near the transition velocity. The definition of transition velocities naturally depends on the definitions of the flow regimes. Therefore, various reports assign different names to the same transition velocity, or same name to different transition velocities, between the flow regimes, leading to quite confusing terminology for the transition velocities. Most of the confusion is associated with the transition from the flows with a stationary bed, since it was claimed by some researchers that it is associated with the velocity at minimal pressure gradient. However, Wasp et al. (1970) claimed that the minimum in the pressure loss *vs* velocity curve has nothing to do with the transition velocities.

The term limit deposit velocity has been employed by a number of investigators, for example, Wilson (1970) for highlighting the separation between the deposit and nondeposit regimes. This transition velocity is also called as the *critical deposit velocity* (Kazanskij, 1979). The deposit velocity was used for the same purpose by Parzonka et al. (1981). Shook and Roco (1991) used *deposition velocity*. The term *critical velocity* is defined as the velocity below which there are deposited particles (Oroskar and Turian, 1980; Turian et al., 1987). However, the velocity at minimal pressure gradient was also called as critical velocity by Bain and Bonnington (1970).

In the present contribution, the mean flow velocity required to prevent the accumulation of a layer of stationary or sliding particles on the bottom of a round horizontal pipe is termed as the critical velocity, U_c . The prediction of this velocity for any given set of operational conditions is very important, since it is rarely desirable to operate with a partially blocked pipeline. Head losses would be increased by the reduced cross-sectional area and a bed layer would increase the pipe wear. In fact, once a deposit forms, fluctuating flow conditions may eventually lead to blockage.

A large number of investigations have been devoted to the prediction of the critical velocity, but majority of the more useful results are based primarily on empirical correlations. The approaches used for obtaining empirical correlations or theoretical expressions include the minimum in the pressure loss *vs.* velocity relationship (e.g., Bain and Bonnington, 1970), fluctuating solids velocity (e.g., Ercolani et al., 1979), balancing the energy required to suspend the particles with that derived from dissipation of an appropriate fraction of turbulent eddies (Oroskar and Turian, 1980), the equilibrium of forces on the first particle layer that is formed (Hanks and Sloan, 1981) and the velocity distribution of solids near the bottom of the pipe (Roco and Shook, 1985). Carleton and Cheng (1974) reviewed over 60 correlations and documented clearly the disagreement between them. Since correlations rely on experimental data, the wisest choice is always to use the one with the largest base of reliable data.

4.2.4.2.1 Wilson's Nomogram

The critical velocity increases with the delivered solids concentration, reaches a maximum (denoted U_{cm}), and then decreases with the solids concentration. The effects of pipe diameter, particle diameter, and relative density on the U_{cm} are expressed concisely by means of a nomographic chart as shown in Figure 4.31 (Wilson, 1979). This nomogram provides a useful simple method for estimating the conditions where stationary deposition becomes likely.

The left-hand panel in the nomographic chart deals with materials with the weight of sand (relative density $S = \rho_s/\rho_l = 2.65$). The pipe diameter appears on the left vertical axis, with U_{cm} on the central vertical axis. The particle diameter is plotted on the curved scale. To estimate the critical velocity for particles with a relative density $S = 2.65$ in a given pipe diameter, D , a line is drawn from the pipe diameter D -axis through the appropriate particle diameter on the curved scale. The critical velocity U_{cm} is then obtained by projecting to the central vertical scale. For example, if a slurry flow in a pipe diameter of 0.4 m contains particles with a relative density $S = 2.65$, a particle size d_p of 0.7 mm gives a U_{cm} of about 4.5 m/sec. For particles of other relative density values (i.e., $S \neq 2.65$), a point on the central vertical axis ($S = 2.65$) is first determined from a pipe diameter and a particle density, and then this point is joined by a straight line to an appropriate particle relative density on the inclined axis. The extrapolated line intersects with the right-hand side vertical axis, giving a value of U_{cm} .

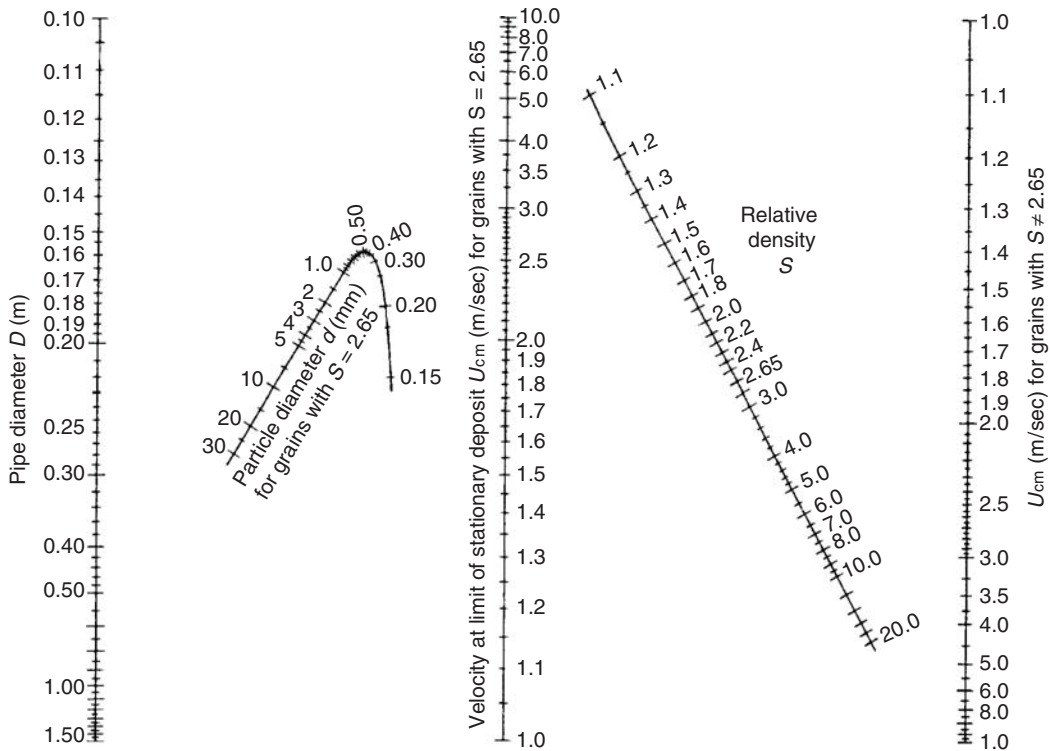


FIGURE 4.31 Nomogram for estimating the critical velocities. (Adapted from Wilson, K.C., *Proceedings of Hydrotransport 6th conference BHRA*, Cranfield, U.K., 1979, pp. 1–12. With permission.)

The nomogram summarized the effects of particle size and pipe diameter. According to the nomogram a maximum critical velocity occurs near a particle diameter of 0.5 mm. However, it has been observed that (Carleton et al., 1978) the decrease in the critical velocity with the particle diameter does not always occur above about 0.5 mm particle diameter. This means that an additional safety allowance is desirable when the nomogram is used for particle sizes greater than 0.5 mm. The nomogram is generated for viscosities near 1 cp and the effect of viscosity is not included in the nomogram so that caution is required when dealing with slurries containing a significant portion of fines.

For applications with limited control of particle size, the conservative estimation of the U_{cm} may be based on the particle size, which gives the largest value of U_{cm} for the pipe under consideration. In this case, it should be noted that the values of U_{cm} obtained from the nomogram tend to be conservatively high, especially for large pipe diameters, and hence can be considered to be directly suitable for use as operating velocities.

4.2.4.2.2 Turian's Correlations

Turian's empirically fitted correlations (Turian et al., 1987) were developed based on a total collection of 864 experimental critical velocity data with pipe diameters up to 0.5 m and particle sizes up to 19 mm, representing a broad variety of solids and pertaining to wide ranges of the important variables involved. The correlations take the following form:

$$\frac{U_c}{[2gD(S-1)]^{0.5}} = \chi_1 \alpha_s^{\chi_2} (1 - \alpha_s)^{\chi_3} \left\{ \frac{D\rho_l [gD(S-1)]^{0.5}}{\mu_l} \right\}^{\chi_4} \left(\frac{d_p}{D} \right)^{\chi_5} \quad (4.70)$$

Five different forms of the above equation were developed and the corresponding values of the adjustable constants in each case are listed in Table 4.18. It should be noted that the above correlations do not take into account the effect of the width of particle size distribution.

TABLE 4.18 Parameter Values of Eq. (4.70) for Five Different Cases

Case	χ_1	χ_2	χ_3	χ_4	χ_5	SD ^a	RMS ^a
1	1.7951	0.1087	0.2501	0.00179	0.06623	20.53	0.3416
2	108471	0.1126	0.03421	-0.03093	0	21.54	0.3447
3	1.8176	0.1086	0.2525	0	0.06486	20.57	0.3412
4	1.3213	0.1182	0.3293	0	0	21.04	0.3552
5	1.1228	0.07367	0	0	0	21.35	0.3559

^aSD is the overall absolute average per cent deviation and RMS is the root mean square deviation.

According to the SD and RMS values in Table 4.18, the correlations corresponding to all the five forms are almost equally effective in predicting the critical velocity. The parameter values also indicate that the dependence of the U_c on the particle diameter is quite weak and on pipe diameter is nearly $D^{0.5}$.

4.2.4.2.3 Gillies and Shook's Correlation

Gillies and Shook (1991) developed a correlation based on data obtained with pipes up to 0.5 m in diameter and aqueous slurries with viscosities between 0.5 and 5 cp. The correlation uses an equivalent fluid density defined as

$$\rho_f = \frac{\rho_s \alpha_f + \rho_l (1 - \alpha_r)}{1 - \alpha_r + \alpha_f} \quad (4.71)$$

where α_r is the mean *in situ* total solids concentration and α_f defined as $\alpha_r \times (\text{volume of less than } 74 \mu\text{m solids} / \text{total volume of solids})$.

The correlation for calculating the critical velocity is given by

$$\frac{U_c}{[gD(\rho_s - \rho_f)/\rho_f]^{0.5}} = \exp(0.51 - 0.0073C_D - 12.5K_2) \quad (4.72)$$

where C_D is the drag coefficient of the median diameter (d_{50}) of the + 74 μm fraction, calculated with the density ρ_f and viscosity μ_f . The viscosity μ_f can be measured or estimated from a correlation in Table 4.15 if data are not available. K_2 is calculated by

$$K_2 = \left[\frac{(\mu_f/\rho_f)^{2/3}}{g^{1/3}d_{50}} - 0.14 \right]^2 \quad (4.73)$$

4.2.4.2.4 Correlations of Wani et al.

Most of the published correlations developed for the critical velocity did not sufficiently account for the breadth of particle size distribution, and hence are not suitable for slurries containing particles with a broad size range. Wani et al. (1982) believed that the particle size distribution and its width are best represented by the weighted mean diameter d_w and the standard deviation σ of the particle size distribution, and they also developed correlations for the critical velocity by including the variables of d_w and σ . Two of the correlations that have been reported to give better predictions are:

$$U_c = \left[2.3 \times 10^{-4} gd_w(S - 1) Re_p^{0.27} \left(\frac{100\sigma}{d_w} \right)^{0.973} \alpha_s^{0.307} \epsilon_f^{1.67} \right]^{0.5} \quad (4.74)$$

for Re_p in Stokes range (i.e., $Re_p \leq 1$) and

$$U_c = \left[7.7 \times 10^{-6} gd_w(S - 1) Re_p^{0.0014} \left(\frac{100\sigma}{d_w} \right)^{-1.25} \alpha_s^{0.272} \epsilon_f^{4.77} \right]^{0.5} \quad (4.75)$$

for Re_p in intermediate range (i.e., $1 \leq Re_p \leq 1000$). The particle Reynolds number is given by $Re_p = d_w V_s \rho_f / \mu_f$, where V_s is the free settling velocity of the particle with a diameter of d_w and ϵ_f is the Hazen-Williams pipe roughness factor.

It has been reported by Wani et al. (1982) that the above correlations give better predictions for slurry mixtures with multisized particles.

4.2.4.2.5 Three-Layer Model of Doron and Barnea's

Doran and Barnea (1993, 1995, 1996) developed a three-layer model for the prediction of hydrodynamic characteristics for pipe flow of slurries containing relatively coarse particles. At low slurry flow velocities, the flow is considered as consisting of three layers: a stationary layer deposit at the bottom of the pipe, a moving bed layer above it, and an upper layer that contains a heterogeneous suspended mixture. The height of the stationary bed is postulated such that the velocity of the moving bed above it is at a certain minimal value. When the moving-bed velocity assumes this value, the particles at the interface between the two bed layers are on the verge of rolling. Within the context of this model, the critical velocity is the slurry velocity for which the stationary bed height approaches zero. The details of this three-layer model will be discussed in Section 4.2.4.3. Doran and Barnea (1995) have claimed that the three-layer model performs better than the other methods in terms of the prediction of the critical velocity.

4.2.4.3 Pressure Loss of Horizontal Pipe Flows

In addition to the prediction of critical velocity, other important technical problems in the pipe flow of heterogeneous slurries are the determination of the pressure loss–throughput relationship and the prediction of the prevailing flow regimes. The literature contains many correlations and a few mechanistic models for prediction of pressure drop, and a number of schemes for delineating slurry flow regimes. Empirical correlations for the determination of the pressure loss include those by Durand and Condolios (1952), Newitt et al. (1955), Zandi and Govatos (1967), Turian and Yuan (1977), and Wasp et al. (1977). Mechanistic models are mainly represented by the two- (Wilson, 1970; Gillies et al., 1991) and three-layer models (Doron and Barnea, 1993, 1995).

Most of the correlations make use of the dimensionless excess pressure loss ϕ , which is defined as

$$\phi = \frac{i_m - i_l}{\alpha_s i_l} \quad \text{or} \quad i_m = i_l(1 + \phi \alpha_s) \quad (4.76)$$

where i_m is the slurry frictional pressure loss in terms of meters of fluid per meter of pipe, i_l the frictional pressure loss for an equivalent volume of carrier fluid, and α_s the volumetric solids concentration in a homogeneous slurry. For a truly homogeneous slurry flow, ϕ approaches $(S-1)$ if the friction factor for a slurry is the same as that for a liquid flowing at the same velocity in the same pipe.

4.2.4.3.1 Durand–Condolios Correlation for Fully Suspended Heterogeneous Flow

The first comprehensive empirical correlation was that of Durand and Condolios (1952). In terms of dimensionless excess pressure loss ϕ and the drag coefficient C_D , the correlation can be written in the form

$$\phi = K\psi^{m'} \quad \text{and} \quad \psi = \frac{U_m C_D^{0.5}}{gD(S-1)} \quad (4.77)$$

where the adjustable parameters K and m' were found to have the values 84.9 and -1.5 based on 310 data points from sand–water slurries. The drag coefficient C_D is that for settling of a particle at its terminal velocity in the quiescent unbounded liquid. For the equivalent spherical particle of diameter d_p , it is given by $C_D = 4gd_p(S-1)/(3V_s^2)$.

For particles with a broad size distribution, the weighted mean drag coefficient C_{DM} for the particle mixture is better than the use of the median particle size (Shook et al., 1986). C_{DM} is computed as

$$\frac{1}{C_{DM}} = \sum \left(\frac{\alpha_i}{C_{Di}} \right) \quad (4.78)$$

where α_i is the volume fraction of i th size fraction with mean diameter d_i with $\sum \alpha_i = 1$, and C_{Di} the drag coefficient of i th size fraction.

Although this correlation does not account sufficiently for the effect of solids concentration, the particle size, and the nonuniform distribution of solids in the flow field, it is still useful for predicting the behavior of slurry flows compatible with these assumptions, i.e., narrow particle size distribution and highly turbulent flows. From the analysis of a large number of data points, Zandi and Govatos (1967) concluded that the Durand–Condolios correlation would apply only if

$$N_1 = \frac{U_m C_D^{0.5}}{\alpha_s g D(S-1)} > 40 \quad (4.79)$$

According to Zandi and Govatos (1967), data corresponding to $N_1 < 40$ do not belong to the fully suspended flow regime.

Equation (4.77) does not approach the $(S-1)$ limit as the flow is near-pseudo-homogeneous, i.e., $\Psi \rightarrow \infty$. Charles (1970) proposed a modified version of the correlation to rectify the deficiency:

$$\phi = (S-1) + 120\Psi^{-1.5} \quad (4.80)$$

For slurries with coarse particles or in which friction is dominated by the coarse fraction of the mixture, the Durand–Condolios correlation or its modified versions are not recommended.

4.2.4.3.2 Zandi–Govatos Correlation for Fully Suspended Heterogeneous Flow

By using 990 data points, Zandi and Govatos (1967) modified the Durand–Condolios correlation to the following improved form for the prediction of slurry pressure loss:

$$\phi = \begin{cases} 280\Psi^{-1.93} & \text{for } \Psi < 10 \\ 6.30\Psi^{-0.354} & \text{for } \Psi > 10 \end{cases} \quad (4.81)$$

This correlation is valid when the conditions obey the inequality $N_1 > 40$.

4.2.4.3.3 Newitt Correlation

In a frequently cited paper, Newitt et al. (1955) developed correlations for a wide range of velocities, solids loading, and particle size in a 1 in. pipe, which covered homogeneous flow, fully suspended heterogeneous flow, and flows with a moving bed. The correlations consist of a set of criteria for defining the flow regime and a regime-specific set of equations.

For homogeneous flow, i.e., $U_m > (1800gDV_s)^{1/3}$, they assumed that the friction factor for the slurry is the same as that for carrier fluid, such that the difference in density is the only factor causing the difference in pressure loss, leading to

$$\phi = 0.6(S-1) \quad (4.82)$$

where the 0.6 is an empirical constant.

For fully suspended heterogeneous flow, i.e., $17V_s < U_m < (1800gDV_s)^{1/3}$, it was assumed that there is no relative velocity between the particles and the fluid, and that the extra energy required to transport the particles is proportional to the energy expended when the particles fall at their terminal velocity V_s . The resulting equation can be written as

$$\phi = 1100 \frac{gDV_s}{U_m^3} (S-1) \quad (4.83)$$

For flow with a moving bed, i.e., $U_m < 17V_s$, they assumed that the work done to overcome sliding friction between the bed and the pipe wall leads to the extra pressure loss due to the solids. The resulting expression is

$$\phi = 66 \frac{gD}{U_m^2} (S-1) \quad (4.84)$$

The transition velocities, $U_H = (1800gDV_s)^{1/3}$ and $U_B = 17V_s$, can be used for delineating the three flow regimes. The boundary between homogeneous and fully suspended heterogeneous flow is obtained by equating Eqs. (4.82) and (4.83), and the boundary between fully suspended heterogeneous flow and flow with a moving bed is obtained by equating Eqs. (4.83) and (4.84).

The Newitt correlation applies only to monodispersed systems. For solids with broad size distribution, Newitt suggested a weighted mean particle diameter as

$$d_{pm} = \sum_{i=1}^n C_{si} d_{pi} \quad \text{and} \quad \sum_{i=1}^n C_{si} = 1 \quad (4.85)$$

where C_{si} is the mass fraction of solids with the particle diameter d_{pi} .

4.2.4.3.4 Model of Wasp et al.

Many practical slurries contain both coarse and fine particles. The fines particles move as a homogeneous mixture, while the coarse particles move as a heterogeneous mixture. For the analysis of this type of compound or heterogeneous-homogeneous mixtures, Wasp et al. (1977) proposed a method based on the assumption that the total pressure loss can be split into two parts: pressure loss due to the vehicle (homogeneously distributed particles) and excess pressure drop due to the bed formation (heterogeneously distributed particles). The method is an iterative procedure that can be summarized as follows:

1. Divide the particles into 4 to 6 size fractions.
2. Assume the slurry mixture to be completely homogeneous and calculate the pressure gradient using the formula

$$i_{\text{vehicle}} = \frac{2fU_m^2}{gD} \quad (4.86)$$

where i_{vehicle} is the pressure gradient due to homogeneously distributed particles (vehicle) and f the friction factor evaluated by Wood's equation:

$$f = a + bRe_m^{-c} \quad (4.87)$$

where $a = 0.026(\epsilon/D)^{0.225} + 0.133(\epsilon/D)$, $b = 22(\epsilon/D)^{0.44}$ and $c = 1.62((\epsilon/D)^{0.134} - 1)$. ϵ/D is the relative pipe roughness, Re_m is the Reynolds number for the slurry and is calculated by $Re_m = \rho_m U_m D / \mu_m$. The slurry viscosity μ_m can be calculated using appropriate correlations such as those listed in Table 4.15. For higher flow velocities, the modified Wood's equation (Mukhtar, 1991) should be used for the calculation of the friction factor:

$$f = a + bRe_m^{-c}(1 - 0.33C_{wf}) \quad (4.88)$$

where C_{wf} is the efflux solids concentration by weight.

3. For each size fraction the percentage of solids in the vehicle is calculated as

$$\log \frac{\alpha_j}{\alpha_A} = -1.8 \frac{V_s}{\beta \kappa u^*} \quad (4.89)$$

where α_j/α_A is the ratio of volumetric concentration of j th particle size fraction at $0.08D$ from top to that at pipe axis, $\kappa (= 0.4)$ the von Karman coefficient, u^* the friction velocity calculated from the pressure loss obtained in Step 2, V_s the settling velocity of j th particle size fraction calculated using standard drag relationships, and β (≈ 1) the dimensionless particle diffusivity.

4. The total percentage of solids in the vehicle is calculated after computing the vehicle portion for each particle size fraction, and then calculate the vehicle pressure loss for slurry with this concentration using Eq. (4.86).

5. Calculate the pressure loss due to the coarse particles in moving bed in each particle size fraction using Durand-type of relationship given as

$$i_{j\text{bed}} = 82i_w C_{v\text{bed}} \left[\frac{gD(S-1)}{U_m^2 C_D^{0.5}} \right]^{1.5} \quad (4.90)$$

where i_w is the pressure gradient due to the flow of carrier liquid, $C_{v\text{bed}}$ the volumetric concentration of bed portion of j th size particles, and S the specific gravity of solids. The total pressure drop due to the bed is the sum of pressure drop due to each particle size fraction in the bed:

$$i_{\text{bed}} = \sum_{j=1}^n i_{j\text{bed}} \quad (4.91)$$

6. Calculate the total pressure loss that is the sum of pressure loss due to the vehicle and the total pressure loss due to the moving bed. If the difference in the pressure drops in two successive iterations is $>5\%$, repeat steps 2 to 6.

The critical factors in this model determine the particle size split between the homogeneous vehicle and the heterogeneous phase and the knowledge of the equivalent homogeneous vehicle properties (i.e., density and viscosity) as a function of particle size fraction and concentration. Experimental data would be required to evaluate these effects. Although Wasp assumed the homogeneous vehicle to behave as a Newtonian fluid, Hanks (1980) has extended this approach to account for non-Newtonian properties of the vehicle.

4.2.4.3.5 Turian-Yan Correlation

Turian and Yuan (1977) developed an extended pressure loss correlation scheme, which takes into account the fact that various flow regimes are observed to prevail in slurry transport depending upon the flow conditions. Their correlation is given by the following relationship:

$$f - f_L = K \alpha_s^{m1} f_L^{m2} C_D^{m3} \left[\frac{U_m^2}{Dg(S-1)} \right]^{m4} \quad (4.92)$$

where K , $m1$, $m2$, $m3$, and $m4$ are regime-specific coefficients listed in Table 4.19. In the above equation, f and f_L are the friction factors for slurry and water, respectively, at the same mean velocity. Both f and f_L are defined in terms of the carrier liquid density ρ_L . Thus,

$$f = \frac{1}{2} \frac{D}{\rho_L U_m^2} \left(- \frac{\Delta p_f}{L} \right) \quad (4.93)$$

Turian and Yuan (1977) proposed a regime delineation scheme based on their pressure loss correlation, given by Eqs. (4.92) and (4.93). In this scheme, maps of the various flow regimes may be drawn using the regime transition number R_{ij} , which pertains to transition between regimes i and j . The flow regime code is defined in Table 4.19. The expression for the regime transition numbers is given by the following equation:

$$R_{ij} = \frac{U_m^2}{K_t \alpha_s^{n1} f_w^{n2} C_D^{n3} g D (S-1)} \quad (4.94)$$

The coefficients in the above equation are given in Table 4.20.

TABLE 4.19 Coefficients in Turian-Yuan Correlation of Eq. (4.92)

Flow Regime	Regime Code	K	$m1$	$m2$	$m3$	$m4$
Homogeneous	3	0.8444	0.5024	1.428	0.1516	-0.3531
Heterogeneous	2	0.5513	0.8687	1.200	-0.1677	-0.6938
With moving bed	1	0.9857	1.018	1.046	-0.4213	-1.354
With stationary bed	0	0.4036	0.7389	0.7717	-0.4054	-1.096

TABLE 4.20 Coefficients for Determining Regime Number (Eq. [4.94])

Regime Number	K_t	$n1$	$n2$	$n3$
R_{01}	31.93	1.083	1.064	-0.0616
R_{02}	0.4608	-0.3225	-1.065	-0.5906
R_{03}	0.3703	0.3183	-0.8837	-0.7496
R_{12}	2.411	0.2263	-0.2334	-0.3840
R_{23}	0.2859	1.075	-0.670	-0.9375
R_{13}	1.167	0.5153	-0.3820	-0.5724

TABLE 4.21 Coefficients for Determining Regime Number (Eq. [4.94])

$R_{01}-1$	$R_{12}-1$	$R_{23}-1$	$R_{02}-1$	$R_{03}-1$	$R_{13}-1$	Regime Code
-	-	-				0
+	-	-				1
+	+	-				2
+	+	+				3
-	-	+	-			0
-	-	+		+		3
-	+	+		-		0
-	+	+		+		3
-	+	-	-			0
-	+	-	+			2
+	-	+			-	1
+	-	+			+	3

Adapted from Turian, R.M. and Yuan, T.-F., *AICHE J.*, 23, 232–243, 1977. With permission.

The transition point between flow regimes i and j is given by $R_{ij}=1$. For a given set of conditions, the corresponding flow regime can be determined by evaluating the signs (i.e., “+” or “−”) of $(R_{ij}-1)$ and then inspect Table 4.21 to find the regime code. An example of flow regime diagram determined by this delineation procedure is given in Figure 4.29.

4.2.4.3.6 Two-Layer Model

It has long been appreciated that the only satisfactory method for predicting pressure loss for heterogeneous slurry flows in horizontal pipelines are those that take into account the flow mechanisms. In the early 1970s, Wilson (1970) developed a mechanistic model approach by introducing the concept of a two-layer model in which particles were in suspended flow in the upper layer and, for at least a proportion of the particles in the lower layer, the solids interaction forces at the pipe wall counterbalanced by were partly buoyant. After undergoing progressive developments (Shook et al., 1986; Wilson, 1988; Gillies et al., 1991), this two-layer model has been discussed in Shook and Roco (1991) in a form that is easy to follow.

In the two-layer model, heterogeneous slurry flows in a horizontal or sloping pipe are considered to consist of two layers separated by a hypothetical horizontal interface, as shown schematically in Figure 4.32. The assumptions made in this model are summarized as follows:

- The slurry flowing in a horizontal pipe comprises two hypothetical layers: an upper layer of particles less than 74 µm and a lower layer containing all particle sizes in the slurry.
- Each layer has its own uniform velocity (U_{m1} , U_{m2}) and uniform volumetric solids concentration (α_{s1} , α_{s2}) and there is no slip between the solids and the liquid within either layer.
- The slurry mixture in the upper layer of volumetric solids concentration α_{s1} behaves essentially as a liquid as far as the wall shear stress is concerned, and the wall shear stress in the upper layer is kinematic, i.e., velocity-dependent.
- The total solids concentration in the lower layer α_{s2} comprises packed bed and is taken as 0.6. The solids are considered as constituting a suspended load of concentration α_{s1} and solids of concentration

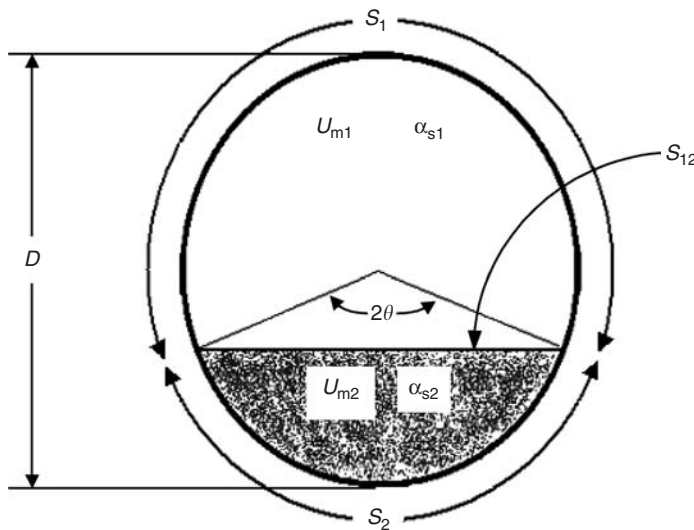


FIGURE 4.32 Basic concept of the two-layer model.

$\alpha_{s2} - \alpha_{s1}$ whose buoyant weight is supported at the walls as a result of interparticle contacts. This concentration, averaged over the total cross-section of the pipe, is defined as the “contact load” α_c , and is given by $\alpha_c = (\alpha_{s2} - \alpha_{s1})A_2/A$.

- The particles in contact with the pipe wall in the lower layer experience a Coulombic friction force.

By referring to Figure 4.32, the total cross-sectional area of flow for the upper layer of fines particles and the lower layer of coarser particles is $A = A_1 + A_2$, and A_1 and A_2 are given by

$$A_1 = 0.25D^2(\pi - \theta - \sin\theta \cos\theta) \quad \text{and} \quad A_2 = 0.25D^2(\theta - \sin\theta \cos\theta) \quad (4.95)$$

The upper and lower perimeters S_1 and S_2 , and the width of interface, S_{12} , in terms of the half-angle θ subtended at the centre of the pipe are given by $S_1 = D(\pi - \theta)$, $S_2 = D\theta$, and $S_{12} = D \sin \theta$.

The model employs both mass and force balances. The mass balances in terms of mean delivered concentration α_s are

$$U_m A = U_{m1} A_1 + U_{m2} A_2 \quad \text{for the mixture} \quad (4.96)$$

$$\alpha_s U_m A = \alpha_{s1} U_{m1} A_1 + \alpha_{s2} U_{m2} A_2 = \alpha_{s1} U_m A + (\alpha_{s2} - \alpha_{s1}) U_{m2} A_2 \quad \text{for solids} \quad (4.97)$$

$$(1 - \alpha_s) U_m A = (1 - \alpha_{s1}) U_{m1} A_1 + (1 - \alpha_{s2}) U_{m2} A_2 \quad \text{for liquid} \quad (4.98)$$

For narrow particle size distribution and $Ar < 3 \times 10^5$ (Ar is the Archimedean number defined by $4gd_p^3/(S-1)\rho_l^2/3\mu_l^2$), the contact load α_c is calculated by using an empirical correlation

$$\frac{\alpha_c}{\alpha_r} = \exp \left[-0.124 Ar^{-0.061} \left(\frac{U_m}{gd_p} \right)^{0.028} \left(\frac{d_p}{D} \right)^{-0.431} (S-1)^{-0.272} \right] \quad (4.99)$$

where $\alpha_r (= \alpha_1 + \alpha_c)$ is the mean *in situ* concentration.

The two-layer model employs momentum equations for each layer. They are written in terms of the boundary and interfacial stresses. The upper layer is considered to contribute only kinetic friction, such that the momentum equation for horizontal flow is

$$i_m = (\tau_1 S_1 + \tau_{12} S_{12}) / (A_1 \rho_l g) \quad (4.100)$$

where i_m is the pressure gradient, τ_1 the wall stress of upper layer, τ_{12} the interfacial stress at hypothetical interface, S_1 the partial perimeter of upper layer, and S_{12} the width of the interface.

The momentum equation for the lower layer is

$$i_m = (\tau_2 S_2 - \tau_{12} S_{12} + F_z) / (A_2 \rho_1 g) \quad (4.101)$$

where τ_2 is the kinetic stress at the partial perimeter of lower layer S_2 and F_z is the total force per unit length exerted normally to the surface of the pipe by the contact load solids. If the interfacial stress terms are eliminated between Eqs. (4.100) and (4.101), we have the force balance for the pipe as a whole:

$$i_m = (\tau_1 S_1 + \tau_2 S_2 + F_z) / (A \rho_1 g) \quad (4.102)$$

The boundary stress τ_1 is evaluated by using the velocity and density of the upper layer:

$$\tau_1 = \frac{1}{2} f_1 U_{m1}^2 \rho_1 \quad (4.103)$$

where the friction factor f_1 is based on the Reynolds number of the liquid flowing at the mean slurry velocity U_m in the pipe, i.e., $D U_m \rho_1 / \mu_1$ and on the relative roughness of the pipe ϵ/D . f_1 is calculated by using the Churchill (1977) equation, which is equivalent to the well-known Moody diagram:

$$f = 2 \left[(8/Re)^{12} + (A + B)^{-1.5} \right]^{1/12} \quad (4.104)$$

where $A = \{-2.45 \ln[(7/Re)^{0.9} + (0.27\epsilon/D)]\}^{1/6}$ and $B = (37,530/Re)^{1/6}$.

At the boundary S_2 of the lower layer, the boundary stress τ_2 is given by

$$\tau_2 = \frac{1}{2} f_1 U_{m2}^2 \rho_2 \quad (4.105)$$

where ρ_2 is the density of (liquid + suspended solids) in the lower layer.

The interface S_{12} is visualized as a boundary with a roughness depending on the diameter of particles. The interfacial stress τ_{12} is calculated from friction factor f_{12} and the difference in velocity between the layers:

$$\tau_{12} = \frac{1}{2} f_{12} (U_{m1} - U_{m2})^2 \rho_1 \quad (4.106)$$

where the interface fraction factor f_{12} is calculated using the following equation suggested by Wilson (1988):

$$f_{12} = (1 + 2Y) / [4 \log(D/d_p) + 3.36]^2 \quad (4.107)$$

where $Y = 4 + 1.42 \log(d_p/D)$ for $d_p/D > 0.0015$ and $Y = 0$ otherwise.

The term F_z in Eq. (4.101) reflects the balance of forces in the vertical direction in the lower layer for the fluid, the suspended solids, and the contact load particles. F_z can be calculated by using the following equation given by Shook and Roco (1991):

$$F_z = 0.5 f_c D^2 g (\rho_s - \rho_l) (\sin \theta - \theta \cos \theta) \left[\frac{(\alpha_{s2} - \alpha_{s1})(1 - \alpha_{s2})}{1 + (\alpha_{s1} - \alpha_{s2})} \right] \quad (4.108)$$

where f_c is the coefficient of Coulombic friction between the particle and the pipe wall. This coefficient depends upon the nature of the two surfaces (the particles and the substrate) and can be experimentally determined using a direct shear cell (Shook and Roco, 1991). The value of f_c is generally between 0.42 and 0.5.

The tentative values of the coefficients in Eq. (4.99) can be improved with the availability of validation data covering a wider range of experimental conditions. For sand slurries with a size range of

$0.15 \text{ mm} < d_{50} < 2.5 \text{ mm}$ and the mean *in situ* concentration $\alpha_r < 0.35$, Shook and Roco (1991) have modified Eq. (4.99) into

$$\frac{\alpha_c}{\alpha_r} = \exp \left[-0.122 A r^{-0.12} \left(\frac{d_p}{D} \right)^{-0.51} (S-1)^{-0.255} \left(\frac{U_m}{U_c} \right)^{0.3} \right] \quad (4.109)$$

The two-layer model was developed from experimental results of fairly narrow particle size distribution. For industrial slurries with broad particle size distributions, the effects of the fine particles ($< 74 \mu\text{m}$) on the viscosity and density of the carrier liquid should be taken into account (Shook and Roco, 1991). An appropriate model from Table 4.15 can be used for calculating the viscosity of slurries with fine particles. However, the slurry in the upper layer needs to be represented as a non-Newtonian fluid if the slurry contains sufficient fine particles. Shook and Roco (1991) also indicated that the two-layer model is not suitable for slurry flows with very low contact load concentration. For cases with low contact load concentrations, a homogeneous slurry flow model or correlation should be used.

It must be stressed that the existence of two distinct layers within the pipeline is a concept used only for modeling purposes and is not of a physical reality; anything more than a boundary layer formed during the flow of a fluid over a surface has a distinct identity.

Some models similar to the two-layer model have been proposed since Wilson (1970) reported the original two-layer model. Khan and Richardson (1996) proposed a simplified model that has the major features of the original two-layer model of Wilson (1970). Doron et al. (1987) developed a model with either a stationary or moving bed at the bottom of the pipe and a heterogeneous suspension in the upper portion. Based on this model, Doron and Barnea (1993) proposed a three-layer model, which will be discussed in the next section.

4.2.4.3.7 Three-Layer Model

Based on observations of the flow in the laboratory and a renewed analysis, a three layer model was developed by Doron and Barnea (1993, 1995, 1996). As shown in Figure 4.33, this model assumes that the slurry flow in a horizontal or inclined pipe comprises three layers, a stationary layer at the bottom, a moving bed layer above it, and a heterogeneous mixture layer at the top. The basic assumption underlying the model is the postulation of a minimal bed velocity that is required to induce the bed motion. If the mean velocity of the moving bed is below this limiting value, part of it would become stationary, forming the third layer, while the other part of the bed would move at this minimal velocity.

The three layer model is described by a set of six equations for the six unknowns: U_h (the mean velocity of the upper layer), U_b (the mean velocity of the moving bed, which in the case of flow with a stationary

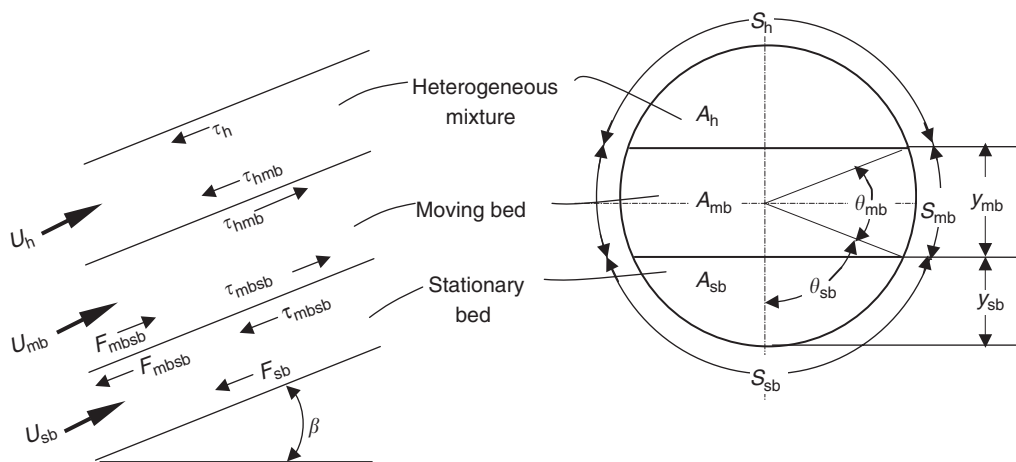


FIGURE 4.33 Basic concept of the three-layer model.

bed is equal to the minimal bed velocity, U_{bc} , C_h (the mean concentration in the upper layer), and y_{mb} , y_{sb} (the heights of the moving bed and of the stationary bed, respectively), and dp/dx (the pressure gradient). The main model equations for these six unknowns and the expressions affected by the pipe inclination will be described here. Additional expressions and constitutive relations required for closure of the equation set can be found in Doron and Barnea (1993). The model can also be used to predict the flow pattern transitions, as described in Doron and Barnea (1996).

The minimal bed velocity is obtained from the balance of driving and opposing torques acting on the solid particles in the lowermost stratum of the moving layer. For a particle at the interface between the moving bed and the stationary bed, the driving torque (that arises from the drag exerted by the moving bed layer on the particle) and the opposing torque (that arises from the submerged weight of the particle and the moving bed particles, which lie on top of it) must balance. For slurry flows in inclined pipes, the minimal bed velocity is given by (Doron et al., 1997)

$$U_{bc} = \frac{\sqrt{1.55(\rho_s - \rho_l)gd_p \left[\sin\left(\frac{\pi}{6} + \beta\right) + \frac{\cos\beta}{2} C_{mb} \left(\frac{y_{mb}}{d_p} - 1 \right) \right]}}{\rho_l C_D}, \quad (4.110)$$

where U_{bc} is the minimal bed velocity in case of three-layer flow (namely, with a stationary layer at the bottom), β the inclination angle of the pipe, C_{mb} is the moving-bed concentration (assumed to be $C_{mb} = 0.52$ for cubic packing), and y_{mb} the height of the moving-bed layer. When the slurry flow rate is increased, the height of the stationary bed diminishes, until it finally vanishes.

Assuming the uniform velocities in each of the three layers and constant layer thickness, the continuity equation for the solid particles can be written as

$$U_h C_h A_h + U_{mb} C_{mb} A_{mb} = U_s C_s A \quad (4.111)$$

and for the liquid phase as

$$U_h (1 - C_h) A_h + U_{mb} (1 - C_{mb}) A_{mb} = U_s (1 - C_s) A \quad (4.112)$$

where U is the mean axial velocity, C the volumetric concentration of solids, A the cross-sectional area of the pipe; the subscripts h and mb denote the heterogeneous upper layer and the moving-bed layer, respectively; U_s the superficial velocity of the mixture, C_s the delivered concentration, and A_h and A_{mb} are the cross-sectional areas occupied by the dispersed layer and by the moving bed, respectively.

Assuming the heterogeneous mixture in the upper dispersed layer to be a pseudo-liquid with effective properties, the force balance for the force components parallel to the mean flow velocity can be written as

$$A_h \frac{dp}{dx} = -\tau_h S_h - \tau_{hmb} S_{hmb} - F_{hG} \quad (4.113)$$

where dp/dx is the pressure drop, τ_h and τ_{hmb} are the upper layer shear stress and the interfacial shear stress acting on the perimeters S_h and S_{hmb} , respectively, and F_{hG} ($F_{hG} = \rho_h g A_h \sin\beta$) the gravitational force acting on the mixture in the upper layer (that is the only component affected by the pipe tilt).

For the moving bed layer, the force balance yields

$$A_{mb} \frac{dp}{dx} = -F_{mbsb} - \tau_{mbsb} S_{mbsb} - F_{mb} - \tau_{mb} S_{mb} + \tau_{hmb} S_{hmb} - F_{mbG} \quad (4.114)$$

where F_{mbsb} is the Coulombic frictional force acting at the interface (S_{mbsb}) between the moving bed and the stationary bed, τ_{mbsb} the hydrodynamic shear stress acting on that interface, F_{mb} is the Coulombic friction force acting at the surface (S_{mb}) of contact of the moving bed with the pipe wall, τ_{mb} the hydrodynamic shear stress acting on that surface, and F_{mbG} the gravitational force acting on the moving bed. Expressions and constitutive relations required for the evaluation of F_{mbsb} , F_{mb} , and F_{mbG} can be found in Doron and Barnea (1993) and Doron et al. (1996).

The dispersion of the solids particles in the upper heterogeneous layer is assumed to be governed by the well-known diffusion equation. Integration over the upper layer cross-section yields the mean concentration in that layer:

$$\frac{C_h}{C_{mb}} = \frac{D^2}{2A_h} \int_{\theta_{sb} + \theta_{mb}}^{\pi/2} \exp\left(-\frac{DV_s \cos \beta}{2\varepsilon} [\sin \gamma - \sin(\theta_{sb} + \theta_{mb})]\right) \cos^2 \gamma d\gamma, \quad (4.115)$$

where ε is the diffusion coefficient and V_s the terminal settling velocity.

The six equations, Eqs. (4.110)–(4.115), define the three-layer model that can be used to obtain state variables for any given set of operational conditions. The critical velocity or limit deposit velocity is obtained when y_{sb} approaches zero, and transition to fully suspended flow is predicted when y_{mb} vanishes (Doron and Barnea, 1995).

4.2.4.4 Combined Homogeneous–Heterogeneous Flows in Horizontal Pipes

In many practical systems, the solids are not of uniform size. The combined heterogeneous–homogeneous slurry system is, therefore, the most important and most common in slurry transportation. It involves coarse and fine particles. The fine particles move as a homogeneous mixture, while the remainder move as a heterogeneous mixture.

Condolios and Chapus (1963) suggested that the particle drag coefficient in correlations, such as Eq. (4.77), is replaced by a weighted mean value (Eq. [4.78]) determined by the relative concentration of each particle size fraction. Newitt et al. (1955) proposed the use of a weighted average particle diameter (Eq. [4.84]), but Hill et al. (1986) proposed that the particles should be divided. The finer particles would move as a heterogeneous flow, while the coarser particles would move as a bed by saltation. The friction loss for each size fraction is calculated by correlations, such as Newitt correlation (Eqs. [4.81]–[4.83]). This approach worked well when applied to pumping water–coal mixtures (Hill et al., 1986; Wasp et al., 1977).

Wasp et al. (1977) employed the concept of a two phase vehicle for the analysis of a combined homogeneous–heterogeneous system. The approach is to consider that portion of the suspension occupying at the top of the conduit, with its corresponding concentration and size distribution, to comprise the homogeneous vehicle uniformly distributed over the entire conduit, with the remainder of the suspension comprising the heterogeneous phase. The total friction loss is considered to be the sum of that due to the homogeneous vehicle alone, and that due to the heterogeneous phase carried by the vehicle. The critical factors in this approach are determining the particle size split between the homogeneous vehicle and the heterogeneous phase, and a knowledge of the equivalent homogeneous vehicle properties (i.e., density and viscosity) as a function of particle size fraction and concentration. Wasp et al. assumed that the vehicle could be described as a Newtonian fluid, although Hanks (1980) has extended this approach to account for non-Newtonian properties of the vehicle, assuming the vehicle behaves as a Bingham plastic. The method proposed by Wasp et al. (1977) has been summarized in Eqs. (4.86)–(4.91).

4.2.4.5 Vertical Pipe Flows of Slurries

In a steady vertical slurry flow operated at a velocity higher than the minimum velocity, it would not be possible to develop dunes, bed, or saltation, although redistribution of the particles can occur within the slugs as the coarse, or more dense, material settles through fine or less dense particles. There is no concentration gradient and the flow may be treated as pseudo-homogeneous for frictional pressure loss calculations, as discussed in Section 4.2.3.2. At low concentrations of solids (in the region of 2 to 5%, by volume) the frictional pressure loss at high flow rates is frequently reported to be almost indistinguishable from that of the clear liquid flow. At higher concentrations, Einstein and Graf (1966) reported that the frictional pressure drop can be approximated by a mixture-density correction to the clear fluid frictional loss.

For preliminary design, it is commonly assumed that the minimum velocity should be twice the settling velocity of the largest particles in the flowing mixture (Govier and Aziz, 1972). This suggestion used the settling velocity to estimate the maximum possible slip and included an allowance for the effect of the variation of solids concentration over the cross-section. If the operating velocity falls below the minimum

value required to fluidize the solids high axial stresses are generated, which result in a plugged line.

Although it is possible to operate at such low velocities for slurries with narrow particle size distributions, Sellgren's (1982) criterion (a factor of 6 or 7 instead of 2) seems to be a useful practical guide. If the pipeline is to have any horizontal sections, to avoid deposition in these, the velocity will be much greater than a limiting value chosen to accommodate the vertical pipe.

4.2.4.6 Inclined Slurry Pipe Flows

Inclined slurry pipe flows are important, but are not the subject of extensive studies since fairly long inclined pipes are necessary to allow the disturbance produced by a bend to decay before representative measurements are made. One important issue in designing a pipeline is the determination of the critical slope of the pipe to avoid areas of blockage once the flow is shut down. Owing to lack of predictive approaches, the critical slope has to be experimentally determined. To avoid blockage of the pipeline due to solids sliding back in the inclined pipeline during shutdown, it is necessary to adopt the design restriction of 10 to 16% slope or 5.7 to 9° inclined angle when there is no knowledge of the critical slope.

Both the two- and three-layer models presented in Section 4.2.4.3 have been applied to inclined slurry pipe flows (Shook and Roco, 1991; Doron and Barnea, 1997).

4.2.5 Design and Operational Aspects

4.2.5.1 Design Procedure

There are four types of practical slurry pipeline design problems : (1) determination of the net driving force required to move a given slurry through a given pipe at a given flow rate; (2) determination of the flow rate that would result in a slurry with the known properties being transported through a given pipe with a specified driving force; (3) determination of the pipe diameter required to transport a slurry with known properties at a specified flow rate with a given driving force; (4) determination of economic optimum pipe diameter at specified flow rate and slurry properties, but free to select both the driving force (e.g., the pumping power), and the pipe diameter. Only the fourth type of design problem will be discussed here since it is probably the most frequently used and most practical.

Similar to the flowchart in [Figure 4.34](#), the design of a slurry transport system begins with an identification of the slurry to be conveyed, and the relevant information to be collected in this step are solids density, particle size distribution, solids concentration, flow rate, and carrier liquid. The next important step is to determine whether the slurry can be considered as settling or non-settling with regard to pipeline transportation. Typically, nonsettling slurry has a high solids concentration of fine solid particles ($< 40 \mu\text{m}$) of low particle density and exhibits viscous behavior. Slurries stabilized with additives and those behaving as non-Newtonian fluids are nonsettling. The remaining steps in the design procedure depend on the settling tendency of slurries because the analysis approach for settling slurries is different from those for nonsettling slurries.

4.2.5.1.1 Settling Slurries

In the specification of design requirements for settling slurries, a route selection has to be carried out to determine the length of pipe sections of different orientation, number of pipe fittings of different types, and slopes of inclined pipe sections. The major difference of route selection between nosettling and settling is the requirement that slopes be kept between 10 and 16% for settling slurries. The initial pipe diameter can be selected using [Figure 4.31](#) based on the flow rate and top particle size. Selection of the final pipe diameter will result from an economic balance weighing factors such as initial pipe cost, pipe wear as a function of slurry velocity, solids abrasivity, slurry corrosiveness, and projected operating costs largely in terms of system horsepower requirements.

After specifying the design requirements, the designer must choose an operating velocity. Pipelines for slurries that settle under conditions of no-flow are usually operated without a deposit. The formation of a moving or stationary deposit bed is associated with unstable operating regime. Under these conditions, a small decrease in flow rate can result in an increase in holdup of solids, which may cause a blockage if

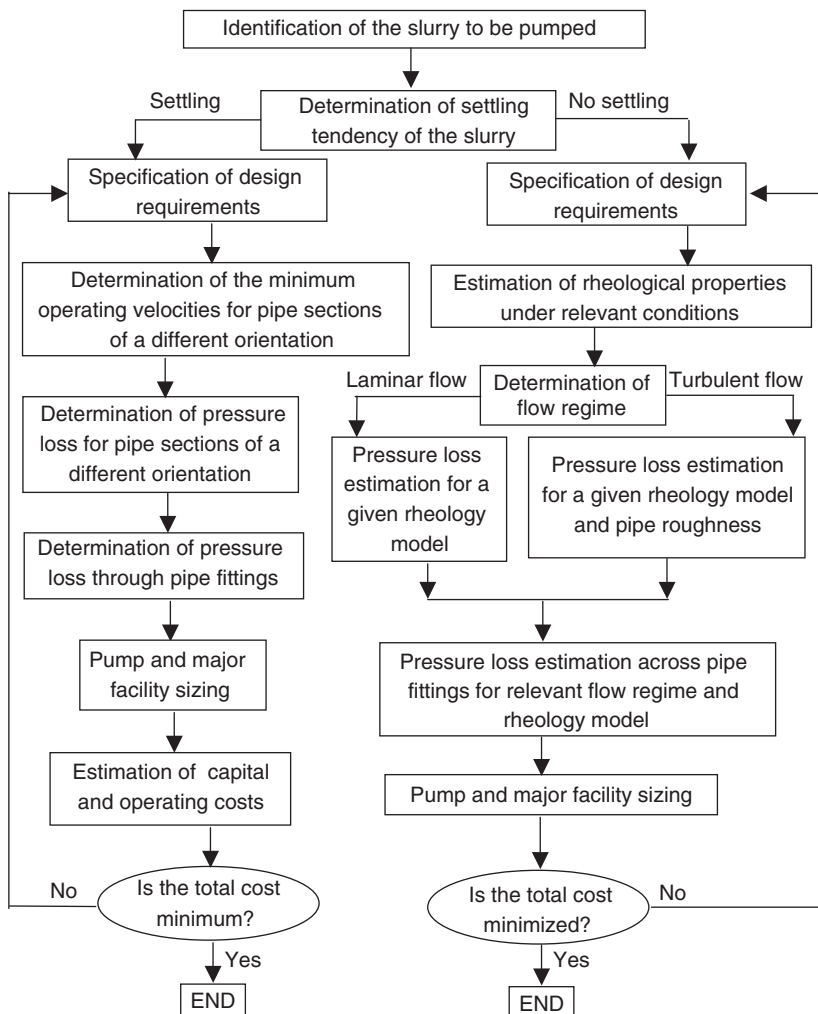


FIGURE 4.34 Flowchart for slurry pipeline design procedure.

sufficient pumping capacity is not available to overcome the increase in pressure head. Prediction of the minimum carrying velocity that will sustain transport is an essential starting point from which an operating velocity can be assigned. The critical velocity discussed in Section 4.2.4.2 is the minimum carrying velocity for horizontal pipe slurry flows. This velocity can be determined by predictive models presented in Section 4.2.4.2 or through small-scale experimental tests. The practical operating velocity should be higher than the minimum carrying velocity of pipe sections with different orientation, and the offset must include an allowance for the effect of the variations of solids concentration and particle size distribution.

The next step is to evaluate the corresponding frictional pressure loss for pipe sections of different orientation as a function of pipe diameter and operating velocity. Estimation of the pressure loss is an essential precursor to pump sizing. For heterogeneous flows of settling slurries, the estimation of the frictional pressure loss of horizontal pipe flows can follow the predictive models described in Section 4.2.4.3. For the vertical pipe flow of settling slurries, approaches presented in Section 4.2.3.2 can be used for estimating the frictional pressure loss since vertical slurry flows can be treated as homogeneous.

Pressure losses arising from flow through pipe fittings are required before a total system head loss estimation can be made. Both the resistance coefficient and the equivalent length methods discussed in

Section 4.2.3.3 are suitable for estimating pressure loss from pipe fittings. The total pressure change is the sum of hydrostatic (or potentially recoverable) pressure, frictional (irrecoverable) pressure loss of straight pipe sections, and pressure loss from pipe fittings.

Pumping requirement and other major facility sizing can then be determined from the design parameters (e.g., pipe diameter, operating flow velocity, total pressure loss, and slurry characteristics). Once proper pump and facility sizing are completed, an economic analysis of the pipeline can be carried out to estimate the capital and operating costs.

To find the design parameters that minimize the total costs of the pipeline system, the design procedure can be repeated for a few times. The optimum values of the design parameters depend on how these parameters affect the capital and running costs for the whole pipeline system and on the effects of likely changes in the operating conditions under normal operation.

4.2.5.1.2 Nonsettling Slurries

In the route selection for nonsettling slurries, there is no restriction on slopes of inclined pipe sections. For nonsettling slurries, the flow can be laminar or turbulent, as the slurry mixture will not segregate under any circumstance, and therefore the selection of operating flow velocity and hence the pipe diameter is mainly based on the minimum total cost.

Nonsettling slurries may behave as a Newtonian or different types of non-Newtonian fluid. One of the major tasks in the pipeline design for nonsettling slurry flows is to determine an appropriate rheological model from experimental tests, including viscometric and small-scale pipe flow tests. Relevant measurement techniques for characterizing slurry properties can be found in Section 4.2.6.1.

After the determination of slurry rheological property, the next step is to determine whether the flow regime is considered as laminar or turbulent flow with regard to pipeline transportation. The identification of the transition between laminar and turbulent flow is of paramount importance because the fluid behavior and flow equations change fundamentally at this point. As described in Section 4.2.3.2.4, an estimate of the laminar–turbulent transition condition can be obtained. Although most practical operating velocities are in turbulent flow regime, laminar flow can be found in practical slurry pipelines due to high viscosity or other considerations.

Using suitable approaches as discussed in Section 4.2.3.2, the pressure loss under given flow regime, rheology model, and pipe roughness can be evaluated and then pumping requirement and other facilities can be selected.

The procedures outlined in this section are suitable for both preliminary and detailed design. They also provide a sensible starting point for the design of full-scale tests that are necessary if accurate design data are required. The designer of a slurry pipeline will generally start with a conceptual or preliminary design to generate sufficient data for a budget estimate of capital investment and operating costs. The difficulty in many cases is that a designer will be required to provide a preliminary design before any tests can be performed. In this case, the designer has very few options. He can try to find operating data of systems using similar materials to arrive at approximate figures for operating flow velocity, pressure drop, and pipe diameter. For a detailed design, it is important to perform laboratory tests to establish the actual slurry characteristics to be used for the pipeline under consideration.

4.2.5.2 Limitations of Predictive Models

Many different empirical correlations based on dimensional analysis have been proposed for predicting the critical velocity and pressure loss in the heterogeneous pipe flows of settling slurries, each reportedly providing an improved description of existing or new data. While many successful pipelines have been designed using empirical correlations, prediction outside the range of variables for which they were developed is unsatisfactory, since correlations do not consider physical processes that occur within the slurry. It is advisable to check the original data. Empirical correlations could be considered as effective tools when correct correlation coefficients are obtained by experimental testing of the slurry system to be pumped.

Considerable success has been achieved in predicting the behavior of settling slurries using mechanistic approaches, such as two- and three-layer models. However, these models contain model parameters that

require careful calibration, which reduces their generality and utility for preliminary design. Therefore, the use of a model validated with similar slurry flows is recommended.

There are a number of assumptions and approximations involved in the development of predictive models for settling slurries, which provide limits to the degree of accuracy of the predictions. One assumption is that the superficial velocity in each layer is uniform in the two- or three-layer model. It should be evident that this assumption is adequate for model development, but would contribute to the limitation. The error contained in data for the development of empirical correlation is another contribution to the limited accuracy of predictions.

Although predictive models proposed for the turbulent friction factor for non-Newtonian fluids or homogeneous slurries cover a wide range of possible combinations of properties, flow rates, pipe sizes, etc., there is insufficient data in the literature to provide experimental confirmation of the predictions over a large portion of the range represented by these models. Therefore, caution has to be taken in applying these models to predict turbulent pipe flow behavior, especially for Bingham plastic slurries with high values of the Hedstrom numbers or power-law slurries with low values of the flow index, where the nature of turbulence is much different from that of Newtonian fluids.

Accuracy of the predictions depends not only on the quality of predictive model, but also on the validity of a particular rheological model. Predictions of the turbulent friction factor for non-Newtonian fluids from models are generally very sensitive to appropriate determination of parameters of rheological models. However, parameter estimates for various rheological models contain a certain degree of uncertainty due to the extrapolation outside the experimental shear rate range. This is because the experimental shear rate ranges employed in viscometric measurement are rarely wide enough to cover most of the relevant shear rate range unless adequate resources are available for such work. Thus, it may be worthwhile sometimes to assess different methods of flow model parameter estimation to determine which method gives the least uncertainty in the predictions of shear stress outside the shear rate range used in viscometric tests. The proper selection of a suitable rheological model can reduce the uncertainty in the model parameter estimation. The Sisko model has been found to be a model for which a unique set of unambiguously determined model parameter values can be obtained (Turian et al., 1992, 1997, and 1998).

In lieu of the limitations of predictive models for slurry flows, the design of large-scale slurry pipeline system still demands pipeline trials to insure success, and is generally justified because of the costs involved. Data for industrial slurries are highly specific to the slurry mixture for which it has been measured and depends on a large number of variables including relative density of the phases, solids concentration and particle shape, and size distribution. In addition, the chemical environment of the particles and surface charge can be particularly important to flocculation in fine particle systems and fluid particle and particle-wall friction in settling slurry systems.

There is no substitute for good quality experimental data. Testing in flow loops generally requires substantial quantities of slurry, and experiments are often costly to execute. Small-scale testing can provide important operating velocities and frictional data. Experimental data are used to validate a predictive model or improve the parameters in the model. The validated model can then be used to scale up the small-scale pipe flow test data.

4.2.5.3 Transient Pipe Flow Behavior

For non-Newtonian slurries with a yield stress, the start up pressure developed by the pumping system must be more than adequate to initiate a wall shear stress along the pipeline which exceeds the yield stress. The start-up pressure, p_{st} , for pumping a Bingham plastic expressed in terms of yield stress, τ_0 , is given by

$$p_{st} = \frac{4\tau_0 L}{D} \quad (4.116)$$

It is particularly important to determine if yield stress progressively increases with time as the structure in a slurry builds up at rest. The proposed pumping system must be able to cope with the highest yield stress levels that the slurry could develop. Calculations should be made to establish the maximum permissible shutdown period beyond which the pumping system would be unable to restart the pipeline flow.

When a velocity change occurs in a flowing slurry, some of the kinetic energy is converted into pressure energy giving an effect called *hydraulic surge*. This can be caused by valve closure or opening, pump start-up or shutdown. The hydraulic surge could create pressures significantly above or below those occurring during steady conditions, leading to the risk of mechanical failure. It is prudent for the designer to include hydraulic surge considerations from the earliest stage of the design to remove the risk of failure by modifying either the design or operating conditions.

The pressure rise, Δp , caused by the velocity change, ΔU , is given by

$$\Delta p = -\rho_m \alpha_0 \Delta U \quad (4.117)$$

where α_0 is the pressure wave speed and ρ_m the density of the slurry. If the fluid velocity increases then there is a pressure decrease. The pressure wave speed, α_0 , in a slurry is given by (Thorley and Hwang, 1979)

$$\alpha_0 = \sqrt{\frac{1/\rho_m}{((1-\alpha_s/K_L) + (\alpha_s/K_s) + (D/Ee))}} \quad (4.118)$$

where E is Young's modulus for the pipe wall, e the pipe wall thickness, K_L the bulk modulus of the liquid phase, and K_s the bulk modulus of solid particles. The K_L for water is 2.06 GPa and for sand is 16.0 GPa (Bechteler and Vogel, 1981).

4.2.6 Measurement Techniques

4.2.6.1 Slurry Viscosity

The experimental determination of slurry viscosity is often required for the analysis of slurry flows. However, many existing standard viscometers for single-phase liquid, such as cone and plate, parallel plate, bob and cup, and capillary tube are not suitable for measuring the viscosity of settling slurries, as they cannot prevent the particles from settling during the measurement. Therefore, there are a number of viscometers that are potentially useful for measuring the viscosity of nonsettling slurries (Dealy, 1984; Heywood, 2000), but only few of the instruments are applicable to settling slurries (Albert et al., 1966; Ferrini et al., 1979; Akroyd and Nguyen, 2003). Basic types of viscometers suitable for measuring slurry viscosity are listed in [Table 4.22](#). Important features of viscometers that are suitable for slurries include:

- Fast response to changes in slurry properties
- Knowing the shear rate at which viscosity is being measured
- Operating at different shear rates
- Maintaining slurry in homogeneous state but not promoting turbulence

Coaxial cylinders are probably the most versatile and hence commonly used viscometers in both laboratory and online applications. The measured quantities are the angular velocity, ω of the inner cylinder with a radius R_1 and the torque per unit height, T . The expression linking the parameters in a rheological model to the measured quantities is given by

$$\omega = \int_{\tau_2}^{\tau_1} \left(\frac{\dot{\gamma}}{2\tau} \right) d\tau \quad (4.119)$$

where τ_1 and τ_2 are equal to $T/2\pi R_1^2$ and $T/2\pi R_2^2$, respectively, and R_2 is the radius of outer cylinder. The relationship between $\dot{\gamma}$ and τ for various rheological models can be found in [Table 4.16](#). For a power-law slurry, the integration of Eq. (4.119) gives

$$\omega = (n/2)(T/2\pi K_p)^{1/n}(1/R_1^{2/n} - 1/R_2^{2/n}) \quad (4.120)$$

By fitting the data (ω, T) to the above equation, parameters (n, K_p) can be determined.

TABLE 4.22 Viscometers for Measuring Slurry Viscosity

Viscometer	Operating Principle	Advantages	Limitations
Coaxial cylinder (Shook and Roco, 1991)	Inner cylinder is rotated inside an outer cylinder at a known speed and the resulting torque on the inner cylinder is measured	Shear rate can be varied, simple procedure for data analysis	Must be mounted vertically, not suitable for settling slurries
Helical flow in co-axial cylinder (Akroyd and Nguyen, 2003)	Rotating inner or outer cylinder with axial slurry flow in the upward or downward direction	Can handle settling slurries, shear rate can be varied	Must be mounted vertically, complex procedure for data analysis
Tube (Shook and Roco, 1991)	Pressure loss required to create the flow is measured across a suitable length of pipe at different flow rate and pipe diameter	Inexpensive, simple procedure for data analysis, shear rate can be varied by changing diameter	Not suitable for settling slurries
Vibrating sphere (Ferry, 1977)	Immersed sphere oscillates with a controlled amplitude. The viscosity is computed from the force needed to maintain the predetermined amplitude of oscillation	Fast response time, simple installation	Requiring independent density measurement, undefined shear rate
Falling cylinder [Dealy, 1984]	A piston falling in a sample contained in a tube with a closed end. The time of fall is proportional to viscosity	A wide operating range	Not suitable for settling

The data analysis procedure for other viscometers can be found in the references indicated in Table 4.22. Flow conditions in viscometers must be laminar as this is one of the assumptions that must be met for the calculation of viscosity. The criteria of laminar flow in coaxial cylinders is

$$R_\omega \leq 45(R_m/\delta)^{0.5} \quad (4.121)$$

where $R_\omega = R_m \omega \delta \rho_m \mu_m$, $R_m = 0.5(R_1 + R_2)$, and $\delta = (R_2 - R_1)$.

4.2.6.2 Solids Concentration

Solids concentration is one of the major process variables in slurry flows. A number of methods have been developed for online measurement of solids concentration in the past. Generally, these methods seek to find a specific property which is significantly different for the solids and liquid phases. The value of this property for the mixture will thus depend on the solids concentration, which can be found by measuring this property. Examples of specific properties are electrical properties (e.g., conductivity), density, and absorption of light or radioactive radiation. Measurement techniques suitable for measuring solids concentration of slurries are listed in Table 4.23.

Nucleonic gauges are commonly used instrumentation for measuring solids concentration of industrial slurries due to their high precision and robustness. The basic principle is that if a narrow collimated beam of photons is passed through a slurry, the attenuation of the beam will strictly obey the relationship

$$I/I_0 = \exp(-B_\mu \rho_m L) \quad (4.122)$$

where I is the beam intensity after distance L , I_0 the initial beam intensity, B_μ the mass attenuation coefficient of the material, and ρ_m is the density of the slurry over distance L . In practice, the predictable logarithmic nature of the gauge response to density means that online calibration can be readily achieved by sampling a minimum of two different densities. Major factors to be considered in their application include the following:

TABLE 4.23 Measurement Techniques for Solids Concentration of Slurries

Measurement Technique	Operating Principle	Advantages	Limitations
Nucleonic gages (Fanger et al., 1978; Brown, 1988)	Gammarays are attenuated as they pass through matter. The attenuation is an exponential function of the path length and the density	Applicable to a wide range of slurries and large diameter pipes, high precision and robustness	Sensitive to slurry chemical composition, radioactive nature of the sources
Conductivity (Nasr-El-in et al., 1987)	The conductivity of slurry is a function of volumetric concentration of solids	Inexpensive, simple procedure for data analysis	Sensitive to the change of carrier liquid conductivity
Electrical impedance spectrum (Hu and Firth, 2002; 2003)	The electrical impedance spectrum (EIS) of slurry is a function of volumetric concentration of solids	Applicable to slurry streams where the conductivity of the liquid phase changes with time	A large number of cases required for calibration
Differential pressure cell (Clift and Clift, 1981; Shook and Roco, 1991)	The differential pressure over a fixed height of slurry is proportional to the slurry density through a vertical pipe with a constant dynamic head	Simple construction and operation	Not suitable to low solids concentrations with large particle sizes and wear of the diaphragm face; requires periodic maintenance
Pipe weighing (Kachel, 1986)	Weighing an isolating section of pipe	Direct measurement	Limited pipe diameter and operating pressure
Ultrasonic reflection (Greenwood and Bamberger, 2002)	The amount of ultrasonic beam reflection at the wedge–slurry interface depends on the slurry density	Compact design	The wedge material has to have a low acoustic impedance, and subject to wear

- Pipes have to be full and free of air, as even a small amount of air bubbles will seriously affect the estimation of solids concentration for low-density solids such as coal.
- Solids need to be uniformly distributed across the pipe section, hence it is recommended that installations only be carried out on vertical pipes with upward flows.

Precise and safe measurement of electrical conductivity requires relatively simple instrumentation. Thus, methods based on conductivity have been widely used in practice for measuring solids concentration. The electrical conductivity of a slurry depends upon the conductivity of the carrier fluid and the volume fraction of solids. For nonconductive solids, the relationship between slurry conductivity and the volume fraction is given by (Maxwell, 1881)

$$\frac{\sigma_m}{\sigma_l} = \frac{2(1-\alpha_s)}{2 + \alpha_s} \quad (4.123)$$

where σ_m and σ_l are conductivities for slurry and the carrier fluid, respectively. MacTaggart et al. (1993) has given a review on other correlations for the relationship between slurry conductivity and the volume fraction.

However, electrical-conductivity-based methods are very sensitive to the variations in the electrical conductivity of the aqueous phase of slurry mixtures. When the conductivity of the liquid phase changes with time, the conductivities of both the slurry mixture and the liquid phase are required in order to calculate the solids content. However the online measurement of the conductivity of the liquid phase in a slurry mixture is generally difficult due to the requirement of separating solids from the liquid phase. Hu and Firth (2002, 2003) developed a new technique for measuring solids concentrations in slurries. In this technique, the electrical impedance spectrum of slurry mixtures is measured at different excitation signal amplitudes and over a wide frequency range. Changes in the frequency response reflect changes in the slurry composition and

the electrical conductivity of the liquid phase. The volumetric fraction of the solids phase can be determined by analyzing the spectra through an artificial neural network. The technique has been successfully tested for various slurries under different conductivities of liquid phase and temperatures. In contrast with previous techniques based on conductivity, this new technique can be used for online measurement of solids concentration in slurry streams even when the conductivity of the liquid phase changes with time.

Another simple technique for measuring solids concentration is based on the differential pressure over a fixed height of vertical slurry flow in a full and air-free pipe. The differential pressure is then given by

$$\Delta p = \rho_m gh + H_d \quad (4.124)$$

where h is the vertical height between the two pressure sensor tappings and H_d the dynamic head, which is the pressure drop along the pipe due to frictional hydraulic loss. Hence, by regulation of the flow of slurry through the pipe (such as feeding from a constant head and restricting the outlet through an orifice plate), the dynamic head should be relatively constant. By suitable calibration procedures, the pressure drop can then be related directly to the average density of the slurry.

If a vertical U-bend as shown schematically in Figure 4.35 is used, the pressure drops for the upward and downward flowing sections can be combined on the assumption that the frictional effects are the same in the two limbs of the U-bend. The analysis given by Clift and Clift (1981) shows that the averaged slurry density can be obtained from

$$\rho_m = \frac{(p_1 - p_2) + (p_4 - p_3)}{2gh} \quad (4.125)$$

4.2.6.3 Flow Rate

The measurement of flow rate is another common requirement in processes involving slurry flows. Numerous flowmeter types based on a variety of measurement principles are available. Each type has its own advantages and limitations. Typical flowmeter types for slurry flows are listed in [Table 4.24](#). Except for the Coriolis flowmeter, these flowmeters are restricted to fully filled vertical pipe flows where the slurry flow is homogenous.

Magnetic flowmeters can be used to measure the flow rate or superficial velocity of slurries with conductive carrier liquids. Although their initial purchase price is relatively high, especially for large diameter pipes, they are highly accurate (typically $\pm 1.0\%$ of full scale) and can be used with confidence without calibration with a wide range of slurries.

There are two types of ultrasonic flow meters: Doppler and transit-time flowmeters that have been extensively used in slurry flows. Ultrasonic flowmeters have gone through many technological advances,

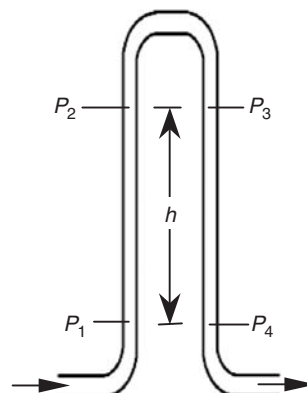


FIGURE 4.35 U-bend used for solids concentration measurement.

TABLE 4.24 Flowsmeters for Slurry Flows

Flowmeter	Operating Principle	Advantages	Limitations
Magnetic flowmeter (Heywood and Melita, 1988)	Creates a magnetic field within a pipe, typically using electrical coils. As electrically conductive fluid moves through the pipe, it generates a voltage. Flow rate is proportional to the amount of voltage, which is detected by electrodes	Independent of fluid rheology, density, temperature, and pressure; high accuracy and no pressure drop	Sensitive to magnetic noise from other equipment, not suitable for slurries containing ferrous particles, high initial cost, electrodes subject to coating
Ultrasonic doppler (Sanderson and Hemp, 1981)	Calculates flow rate based on the shift in frequency observed when ultrasonic waves bounce off particles in the flow stream	Can meter dirty flows, no pressure drop, clamp-on convenience	Sensitive to the velocity profile and air bubble, sensitive to gaps between metal pipe wall and lined materials
Ultrasonic transit time (Sanderson and Hemp, 1981)	The velocity of the acoustic signal is increased when the direction of propagation is with the flow and decreased when it is against. The time difference between the two signals is used to calculate a velocity of the flow	Multiple-path model offers higher accuracy, no pressure loss, clamp-on convenience	Sensitive to variations in concentration and air bubbles, affected by flow profile, some models have high initial cost, attenuation of ultrasound by high solids concentration.
Cross-correlation (various) (Bech and Plaskowski, 1987)	Flow rate measurement based on measuring the transit time of some kinds of disturbance such as electrical resistance between two points	Simple construction and operation	Not suitable to low solids concentrations with fine particles
Differential pressure (Shook and Roco, 1991)	A flow restriction element (e.g., orifice plate, venturi) in the pipeline causes a pressure loss that is proportional to the density of the medium and the square of the volumetric flow rate	Low initial price, ease of installation, well understood	Creating nonrecoverable pressure loss, flow restriction element subject to wear, requires periodic maintenance, wear of the diaphragm face
Coriolis (Young, 1985)	Slurry is passed through a vibrating tube; this causes the tube to twist. Mass flow is proportional to the amount of twisting by the tube	High accuracy, low maintenance, insensitive to flow profile, pipeline pressure and temperature	High initial costs, units for larger sized pipes are restricted in pressure capability, and bent tubes subject to fouling

especially in electronic circuitry, and with the power of computers crunch numbers faster. Both Doppler and transit time flowmeters may use clamp-on sensors with their associated assemblies and detect flow rate from the outside of the pipe without stopping the process or cutting through the pipe. The clamp-on types of applications have considerably eased the job of the flow survey. Now users are able to make sure that the old or new pump is working to its capacity, gather data for flow balancing, check if permanently installed meters are measuring incorrectly or are in need of maintenance, or simply clamp on a flow meter where there is none or where other flowmeter installations are impractical. Doppler ultrasonic flowmeters require the presence of reflectors, such as solids, in the flow stream so the signal can bounce off them. Hence, they are particularly suitable for slurry flows. Transit-time flowmeters send an ultrasonic signal from one side of a pipe to the other. A signal is then sent in the reverse direction. When an ultrasonic signal travels with the flow, it travels faster than when it travels against the flow. The flowmeter measures both transit times. The difference between the two transit times (across the pipe and back again) is proportional to the flow rate. Transit-time flowmeters are mainly used for slurries with low solids concentration.

Cross-correlation flowmeters are based on measuring the transition time of some types of disturbances, such as electrical resistance between two points in a flow system (Beck et al., 1970, 1974). Schematic representation of the cross-correlation flowmeter technique is shown in Figure 4.36. In slurry flows, suspended particles in carrier fluids can lead to fluctuations in the conductivity of slurry flows due to the conductivity difference between solids and water. Two conductance sensors located at X and Y , arranged at an axial distance L in the pipe, detect conductance fluctuations as caused by the random changes of slurry phase composition. $X(t)$ and $Y(t)$ are electrical conductance signals measured at upstream (X) and downstream (Y) sensor locations. The patterns are similar in both signals but time-shifted according to the traveling time of disturbances of slurry composition between the two sensor locations. With the assumption of the pipe slurry flow having the constant (bulk) velocity U_m and the fluctuation patterns "frozen" during the flowing from location X to Y , the signal $X(t)$ detected by the first (upstream) sensor should be equal to the signal $Y(t)$ perceived by the second (downstream) sensor, but delayed by the transit time τ^* :

$$X(t) = Y(t + \tau^*) \quad (4.126)$$

However, turbulent pipe flow causes the fluctuation patterns to be convected with velocities dependent on the radial position and Reynolds number, and to be dispersed due to turbulent diffusion. As a consequence

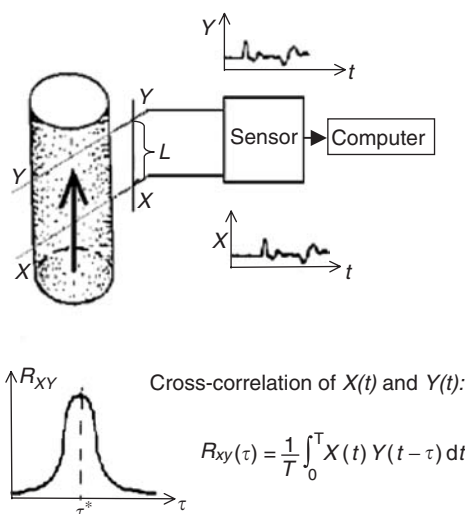


FIGURE 4.36 Schematic representation of cross-correlation flowmeter.

of these unavoidable processes, the traveling time from location X to Y of individual fluctuation event is a distribution with the transit time τ^* as the norm. The distribution of the traveling (or delay) time can be determined from the cross-correlation function of the two signals according to the stochastic process theory (Ross, 1996). The cross-correlation function, $R_{xy}(\tau)$, is given by

$$R_{xy}(\tau) = \frac{1}{T} \int_0^T X(t) Y(t + \tau) dt \quad (4.127)$$

where T is the total sampling time and τ the delay time of similar signal perturbations.

The transition time τ^* is assumed as the delay time τ for which the cross-correlation function has the maximum: $\tau^* = \tau|_{R_{xy}(\tau) = \max(R_{xy}(\tau))}$. The mean velocity is therefore given by $U_m = L/\tau^*$.

Differential pressure (DP) flowmeter is a less expensive, older technology that measures flow rate based on the principle of conservation of energy between the liquid static and velocity head. A flow constriction element (e.g., orifice plate, venturi, nozzle, and pitot) in the pipeline causes a pressure loss that is proportional to the density of the medium and the square of the volumetric flow rate. The two advantages of this technology are its consistency and common usage. However, its disadvantage is the permanent pressure loss due to the pipe constriction, potential for fouling and wear of the constriction element. This type of flowmeter requires regular maintenance to prevent fouling at the constriction point.

Coriolis flowmeters comprise one or more vibrating tubes. Slurry flows passing through a vibrating tube would cause the tube to twist. The amount of twisting motion is directly proportional to mass flow. Position detectors can sense the positions of the vibrating tubes. Temperature is constantly measured because the oscillatory properties of the tube vary with temperature. This makes it possible to make any necessary adjustments in the measurement. Although these meters are highly accurate, they are limited in terms of the pipe sizes that can efficiently be used on. While they can be used in pipes up to 6 in. in diameter, the flowmeters become expensive. The higher cost of Coriolis flowmeters is normally offset by low maintenance costs.

The selection process for a flow measurement device for slurry flows should be based on the following criteria; application (volumetric or mass, pipe size, process temperature and pressure, fluid condition, fluid density and viscosity, flow profile, range, and Reynolds number constraints), performance (accuracy, reliability, range, and repeatability), cost (purchase price, installation cost, cost of ownership, and maintenance cost), and supplier (flowmeter type, service requirements, training, and responsiveness). Reliability and accuracy are the two highest rated performance criteria by flowmeter users. Coriolis meters have the highest accuracy, followed by ultrasonic and magnetic meters. While Coriolis flowmeters typically have a higher purchase price, many users are now deciding between initial cost and cost of ownership. A flowmeter that offers reduced maintenance costs may be of better value than the one with a lower purchase price that requires significant maintenance.

4.2.6.4 Pressure

Pressure needs to be measured in the majority of slurry handling applications. High-quality pressure transducers are readily available from specializing manufacturers, and the selection of the type of transducer and signal transmitter are not usually of prime importance in slurry flows. However, slurry applications frequently require the sensing element contained in the transducer to be isolated from the slurry in order to reduce wear and corrosion and to prevent fouling with solids. Isolation is usually achieved by using elastomeric sleeves or diaphragm seals.

4.2.6.5 Particle Size

A large number of techniques are available for offline determination of particle size (Allen, 1981). For samples containing particles above ~ 1 mm, the choice of techniques is limited to screen analysis. Although wet mechanical screening can be used to analyze samples down to ~ 5 μm , more sophisticated automated techniques are available that can analyze smaller particle size. Particle size analyzers based on laser diffraction (e.g., Malvern laser particle size analyzer) are widely used for the laboratory determination. These laboratory systems operate on highly diluted solutions (< 5 g solids/L).

Present commercial online slurry particle size analyzers have been based on distance measurement (Miettunen et al., 1993), laser scattering (Sparks and Dobbs, 1993), laser diffraction, and ultrasound. The laser scattering technique is based on a scanning laser microscope in which the sample is scanned at a constant speed by a high-intensity laser beam and the reflected light is measured. This analyzer has the advantage that dilution of the stream is not necessary. An online version of the Malvern laser particle size analyzer has been made available. However, this analyzer has the disadvantages of high cost, sample by-lines, high dilution, and sensitivity to window fouling. Particle size analyzers based on ultrasonic techniques (Reibel and Loffler, 1989; McClements, 1991; Pendse and Sharma, 1993; Dukhin and Goetz, 1996) have advantages of operating on undiluted and optically opaque slurries and are rapid, precise, robust, compact, and comparatively inexpensive.

Nomenclature

<i>a</i>	Coefficient in generalized friction factor correlation
<i>A</i>	Cross-sectional area of pipe
<i>A_f</i>	Deaeration constant
<i>b</i>	Coefficient in generalized friction factor correlation
<i>B</i>	Bend constant in Chambers–Marcus correlation
<i>c</i>	Coefficient in generalized friction factor correlation
<i>C_s</i>	Mass fraction of solids
<i>C_D</i>	Drag coefficient
<i>d</i>	Coefficient in generalized friction factor correlation
<i>d_p</i>	Particle diameter
<i>d_p*</i>	Critical particle diameter in Matsumoto correlation
<i>D</i>	Pipe diameter
<i>D_B</i>	Bend diameter (diameter of curvature)
<i>f</i>	Friction factor
<i>Fr</i>	Froude number, gas $\left(\frac{U_g^2}{gD} \right)$
<i>Fr_s</i>	Froude number, solids $\left(\frac{U_t^2}{gd_p} \right)$
<i>Fr_p</i>	Froude number, solids $\left(\frac{U_t}{\sqrt{gd_p}} \right)$
<i>Fr_{ss}</i>	Froude number, solids $\left(\frac{U_{gs}}{\sqrt{gD}} \right)$
<i>Fr_{saltation}</i>	Froude number corresponding to saltation or pressure drop minimum in Zenz plot
<i>g</i>	Acceleration due to gravity
<i>He</i>	Hedstrom number
<i>H_d</i>	Dynamic head
<i>I</i>	Intensity
<i>k_s</i>	Pipe roughness
<i>K</i>	Coefficient in generalized friction factor correlation
<i>K_f</i>	Resistance coefficient
<i>l_s</i>	Length of the slug or plug
<i>L</i>	Length of pipe or height of packed bed
<i>P</i>	Local absolute static pressure, Frictional pressure loss
<i>p_f</i>	Permeability factor

P_{atm}	Atmospheric pressure
ΔP	Pressure drop
ΔP_{ACC}	Additional pressure drop due to acceleration of solids
ΔP_{BEND}	Pressure drop across a bend
ΔP_{sys}	Pressure drop across entire conveying system
Q	Gas flow rate
r	Radius
R	Universal gas law constant
R_B	Radius of curvature of bend
Re	Reynolds number ($DU_g \rho_g / \mu_g$)
S	Relative density
T	Absolute temperature (°K)
u^*	Friction velocity
U_c	Choking velocity
U_g	Superficial gas velocity
U_m	Mean slurry velocity
U_p	Particle velocity
U_s	Slug velocity
U_t	Single particle terminal velocity
U_{gs}	Superficial velocity at saltation conditions
V	Volumetric flow rate
v	Velocity
W_g	Solids flow rate or conveying rate
W_s	Solids flow rate or conveying rate
Z	Energy ratio
ΔZ	Length of a vertical section

Greek Letters

α	Coefficient in saltation correlation
β	Coefficient in saltation correlation
$\dot{\gamma}$	Strain rate
ε	Voidage
ε_c	Voidage at choking
η	Apparent viscosity
θ	Half angle
ϕ_s	Angle of internal friction
ϕ_w	Angle of wall friction
σ	Conductivity
λ_f	Gas friction factor
λ_Z	Solids friction factor
λ_{ZL}	Solids friction factor with loading term included
λ_{GS}	Combined gas–solids friction factor
μ	Solids loading (mass of solids/mass of gas)
μ_g	Gas viscosity
μ_w	Wall friction coefficient
$\mu_{\text{saltation}}$	Solids loading at saltation condition
μ_s	Solids loading at saltation condition
σ_f	Frontal stress in a plug
σ_w	Wall stress in a plug
τ	Shear stress

Subscripts

B	Bulk
f	Fluid
g	Gas
l	Liquid
m	Mixture
N	Equivalent Newtonian flow
P	Particle
s	Solids

References

- Agarwal, A. and Dhodapkar, S.V., De bottleneck Pneumatic Conveying Systems, *Chem. Eng.*, April, 38–44, 2004.
- Akroyd, T.J. and Nguyen, Q.D., Continuous rheometry for industrial slurries, *Exp. Thermal Fluid Sci.*, 27, 507–514, 2003.
- Albert, C., Dierckes, J.R., and Schowalter, W.R., Helical flow of a non-Newtonian polyisobutylene solution, *I & EC Fundam.*, 5, 263–271, 1966.
- Allen, T., *Particle Size Measurement*, 3rd ed., Chapman & Hall, London, U.K., 1981.
- Bain, A.G. and Bonnington, S.T., *The Hydraulic Transport of Solids by Pipeline*, Pergamon Press, Oxford, 1970.
- Barth, W., Transport and Whirling of Solid Dust in an Air Stream, *Chem. Ing. Tech.*, 35, 209–214, (in German), 1958.
- Bech, M.S. and Plaskowski, A., *Cross-Correlation Flowmeters—Their Design and Application*, Adam Hilger, Bristol, U.K., 1987.
- Bechteler, W. and Vogel, G., Theoretical considerations and laboratory investigations about water hammer propagation in slurry pipelines, *Proceeding of the Slurry Transport Association* 6, Las Vegas, NV, 1981.
- Beck, M.S., Gough, J.R., and Mendies, P.J., Flow velocity measurement in a hydraulic conveyor, *Proceedings of the Hydrotransport 1 Conference*, BHRA Fluid Eng., Cranfield, U.K., Paper B3, 1970, pp. 25–53.
- Beck, M.S., Mendies, P.J., Walecki, T., and Gatland, H.B., Measurement and control in hydraulic transport systems using cross-correlation measurement systems and fluidic diverters, *Proceedings of the Hydrotransport 3 Conference*, BHRA Fluid Eng., Cranfield, U.K., Paper F5, 1974, pp. 69–80.
- Bird, R.B., Dai, G.C., and Yarusso, B.L., The rheology and flow of viscoplastic materials, *Rev. Chem. Eng.*, 1, pp 1–70, 1982.
- Bird, R.B., Stewart, W.E., and Lightfoot, E.N., *Transport Phenomena*, Wiley, New York, 1960.
- Blatch, N.S., Water filtration at Washington, DC, discussion trans., *Amer. Soc. Civil. Eng.*, 57, 400–408, 1906.
- Bradley, M.S.A., Pressure Losses Caused by Bends in Pneumatic Conveying Pipelines, *Powder Handling Process.*, 2, 315–321, 1990.
- Brown, N.P., An instrument to measure chord-averaged concentration profiles in two-phase pipeline flows, *J. Pipelines*, 7, 177–189, 1988.
- Brown, N.P., Flow regimes of settling slurries in pipes, *Slurry Handling Design of Solid-Liquid Systems*, Brown, N.P. and Heywood, N.L., Eds., Elsevier, London, 1991, pp. 41–52.
- Buckingham, E., On plastic flow through capillary tubes, *ASTM Proc.*, 21, 1154, 1921.
- Buffalo Forge Company, *Fan Engineering*, 2003.
- Carleton, A.J. and Cheng, D.C., Design velocities for hydraulic conveying of settling suspensions, *Proceedings of the Hydrotransport 3 Conference*, BHRA Fluid Eng., Cranfield, U.K., Paper E5, 1974, pp. 57–74.
- Carleton, A.J., French, R.J., James, J.G., Broad, B.A., and Streat, M., Hydraulic transport of large particles using conventional and high concentration conveying, *Proceedings of the Hydrotransport 5 Conference*, BHRA Fluid Eng., Cranfield, U.K., Paper D2, 1978, pp. 15–28.

- Casson, N., A flow equation for pigment-oil suspension of the printing ink type, in *Rheology of Dispersed Systems*, Pergamon Press, New York, 1959, pp. 84–104.
- Chambers, A.J. and Marcus, R.D., *Proceedings of the Second International Conference on Bulk Materials Storage Handling and Transportation*, Wollongong, Australia, 1986.
- Charles, M.E., Transport of solids by pipelines, *Proceedings of the Hydrotransport 1 Conference*, BHRA Fluid Eng., Cranfield, U.K., Paper A3, 1970, pp. 25–36.
- Cheng, D.C.-H., A design procedure for pipeline flow of non-Newtonian dispersed systems, *Proceedings of the Hydrotransport 1 Conference*, BHRA Fluid Eng., Cranfield, U.K., Paper J5, 1970, pp. 77–96.
- Chong, Y.O and Lueng, L.S., *Comparison of Choking velocity Correlations in Vertical Pneumatic Conveying*, 47, pp. 43–50, 1986.
- Churchill, S.W., Friction factor equation spans all fluid-flow regimes, *Chem. Eng.*, 84, 91–92, 1977.
- Clift, R. and Clift, D.H.M., Continuous measurement of the density of flowing slurries, *Int. J. Multiphase Flow*, 75, 555–561, 1981.
- Coghill, P.J., Millen, M.J., and Sowerby, B.D., On-line measurement of particle size in mineral slurries, *Miner. Eng.*, 15, 83–90, 2002.
- Colebrook, C.F., Turbulent flow in pipes with particular reference to the transition region between smooth and rough pipe laws, *J. Inst. Civil Eng.*, 11, 133–156, 1939.
- Condolios, E. and Chapus, E.E., 1963, Designing solids-handling pipelines, *Chem. Eng.*, 73, 131–138, 1939.
- Darby, R. and Melson, J., How to predict the friction factor for the flow of Bingham plastics, *Chem. Eng.*, 88, 59–61, 1981.
- Deal, J.M., Viscometers for on-line measurement and control, *Chem. Eng.*, 91, 62–70, 1984.
- Dhadapkar, S.V., Personal communication, 1990, as referenced in klizing, G.E., *Powder Handling Process.*, 12(1), 57, 2000.
- Dhadapkar, S.V. and Jacob, K.V., 2002, Smart ways to troubleshoot pneumatic conveyors, *Chem. Eng.*, March, 95–98.
- Dixon, G., Pneumatic Conveying, in *Plastics Pneumatic Conveying and Bulk Storage*, Butters, G., Eds., Applied Science Publishers, London, 1981, pp. 18–144.
- Dodge D.W. and Metzner A.B., Turbulent flow of non-Newtonian systems, *AICHE J.*, 5, 189–204, 1959.
- Doron, P. and Barnea, D., A three-layer model for solid–liquid flow in horizontal pipes, *Int. J. Multiphase Flow*, 19, 1029–1043, 1993.
- Doron, P. and Barnea, D., Pressure drop and limit deposit velocity for solid–liquid flow in pipes, *Chem. Eng. Sci.*, 50, 1595–1604, 1995.
- Doron, P. and Barnea, D., Flow pattern maps for solids–liquid flow in pipes, *Int. J. Multiphase Flow*, 22, 273–283, 1996.
- Doron, P., Granica, D., and Barnea, D., Slurry flow in horizontal pipes — experimental and modelling, *Int. J. Multiphase Flow*, 13, 535–547, 1987.
- Doron, P., Simkhis, M., and Barnea, D., Flow of solid–liquid mixtures in inclined pipes, *Int. J. Multiphase Flow*, 23, 313–323, 1997.
- Dukhin, A.S. and Goetz, P.J., Acoustic and electroacoustic spectroscopy, *Langmuir*, 12, 4336–4344, 1996.
- Durand, R. and Condolios, E., *Experimental investigation of the transport of solids in pipes*, Paper presented at Deuxieme Journée de l'hydraulique, Société Hydrotechnique de France, 1952.
- Edwards, M.F., Jadallah, M.S.M., and Smith, R., Head losses in pipe fittings at low Reynolds numbers, *Chem. Eng. Res. Des.*, 63, 43–50, 1985.
- Einstein, A., Zur Theorie der Brownschen Bewegung, *Annalen der Physik*, 19, pp. 248–258, 1906.
- Einstein, H.A. and Graf, W.H., Loop system for measuring sand-water mixtures, *Proc. ASCE (J. Hydraulics Div.)*, 92, 1–12, 1966.
- Engineering Equipment User's Association (EEUA) Handbook, *Pneumatic Handling of Powdered Materials*, Vol. 15, Constable, London, 1963.
- Ercolani, D., Ferrini, F., and Arrigoni, V., Electric and thermic probes for measuring the limit velocity, *Proceedings of the Hydrotransport 6 Conference*, BHRA Fluid Eng., Cranfield, U.K., Paper A3, 1979, pp. 27–42.

- Fanger, H.-U., Michaelis, W., Pipelnik, R., and The, H.L., Application of gamma ray absorptionmetry in the hydraulic transport of solids, *Proceedings of the Hydrotransport 5 Conference*, BHRA Fluid Eng., Cranfield, U.K., Paper G5, 1978, pp. 43–45.
- Ferrini, F., Ercolani, D., de Cindio, B., Nicodemo, L., Nicolais, L., and Ranaudo, S., Shear viscosity of settling slurries, *Rheol. Acta*, 18, pp. 289–296, 1979.
- Ferry, J.D., Oscillation viscometry — effects of shear rate and frequency, *Meas. Control*, 11, 89–91, 1977.
- Frankel, N.A. and Acrivos, A., On the viscosity of a concentrated suspension of solid spheres, *Chem. Eng. Sci.*, 22, 847–853, 1967.
- Geldart, D., 1973, Types of gas fluidization, *Powder Tech.*, 7, 285–292
- Gillies, R.G., Shook, C.A., and Wilson, K.C., An improved two layer model for horizontal slurry pipeline flow, *Can. J. Chem. Eng.*, 69, 173–178, 1991.
- Gillies, R.G. and Shook, C.A., A Deposition Velocity Correlation for Water Slurries, *Can. J. Chem. Eng.*, 69, 1225–1227, 1991.
- Govier, G.W. and Aziz, K., *The Flow of Complex Mixtures in Pipes*, Van Nostrand Reinhold, New York, 1972.
- Greenwood, M.S. and Bamberger, J.A., Ultrasonic sensor to measure the density of a liquid or slurry during pipeline transport, *Ultrasonics*, 40, 413–417, 2002.
- Hanks, R.W., Laminar-turbulent transition in pipe flow of Casson model fluids, *J. Energy Resour. Tech. Trans. ASME*, 103, 318–321, 1981.
- Hanks, R.W. and Ricks, B.L., Laminar-turbulent transition in flow of pseudoplastic fluids with yield stress, *J. Hydronaut.*, 8, 163–166, 1974.
- Hanks, R.W., The influence of non-Newtonian rheology in mixed homogeneous–heterogeneous slurry flow, *Proceedings of the 5th International Technical Conference on Slurry Transportation*, Lake Tahoe, 1980, p. 251.
- Hanks, R.W., Low Reynolds number turbulent pipeline flow of pseudohomogeneous slurries, *Proceedings of the Hydrotransport 5 Conference*, BHRA Fluid Eng., Cranfield, U.K., Paper C2, 1978, pp. 23–34.
- Hanks, R.W. and Sloan, D.G., A rheology-based correlation for minimum deposition velocity, *Proceedings of the 6th International Conference on Slurry Transportation*, Slurry Transport Association, Washington, DC, 1981, pp. 107–112.
- Happel, J. and Brenner, H., *Low Reynolds Number Hydrodynamics*, Prentice-Hall, Englewood Cliffs, NJ, 1965.
- Herschel, W.H. and Bulkley, R., Measurement of consistency as applied to rubber–benzene solutions, *Proceedings of ASTM*, 26(II), 1926, pp. 621–633.
- Heywood, N.I., Online monitoring of slurry flows in the process industries, *Proceedings of the 10th Conference on the Transport and Sedimentation of Solid Particles*, Wroclaw, Poland, 2000, pp. 59–83.
- Heywood, N.I. and Cheng, D.C-H., Comparison of methods for predicting head loss in turbulent pipeflow of non-Newtonian fluids, *Trans. Inst. Meas. Control*, 6, 33–45, 1984.
- Heywood, N.I. and Melita, K., A survey of non-invasive flowmeters for pipeline flow of high concentration settling slurries, *Proceedings of the Hydrotransport 11 Conference*, BHRA, Cranfield, U.K., 1988, pp. 131–156.
- Hill, R.A., Snock, P.E., and Gandhi, R.L., Hydraulic transport of solids, in *The Pump Handbook*, 2nd ed., Karassik, I.J., Messina, J.P., Cooper, P., Heald, C.C., Eds., McGraw-Hill, New York, 1986.
- Hinkle B.L., *Acceleration of Particles and Pressure Drops Encountered In Horizontal Pneumatic Conveying*, PhD Thesis, Georgia Institute of Technology, June 1953.
- Hu, S. and Firth, B., Smart sensor for on-line monitoring of coal preparation processes, *Proceedings of the 9th Australian Coal Preparation Conference*, Yeppoon, Australia, 2002.
- Hu, S. and Firth, B., Intelligent data analysis of electrical impedance spectra for on-line monitoring of industrial processes, *5th International Congress of Industrial and Applied Mathematics*, Sydney, Australia, 2003.
- Ikemori, K. and Munakata, H., A new method of expressing pressure drop in horizontal pipe bend in pneumatic transport of solids, *Proceedings of the BHRA Fluid Engineering Conference (PNEUMO-TRANSPORT 2)*, Surrey, U.K., Paper A3, 1973.
- Irvine, T.F., A generalised Blasius equation for power-law fluids, *Chem. Eng. Commun.*, 65, 39–47, 1988.

- Jones, M.G. and Mills, D., Product classification for pneumatic conveying, *Powder Handling Process.*, 2, 117–122, 1990.
- Kachel, G.C., The slurry monitor, a new development in the precision determination of the density of slurries flowing in pipelines, Paper presented at Symposium on Slur Flows and Measurement — Instrumentation, Anaheim, CA, U.S.A., 1986.
- Kazanskij, I., Critical velocity of depositions for fine slurries — new results, *Proceedings of the 6th International Conference on the Hydraulic Transport of Solids in Pipes*, Canterbury, England, Paper A4, 1979, pp. 43–56.
- Khan, A.R. and Richardson, J.F., Comparison of coarse slurry pipeline models, *Proceedings of the Hydrotransport 13 Conference*, BHR Group, Cranfield, U.K., 1996, pp. 259–281.
- Klinzing, G.E., "Material Properties and Pneumatic Conveying" *Powder Handling Process.*, vol. 12, No. 1, p. 57, 2000.
- Konrad, K. and Harrison, D., Prediction of pressure drop for horizontal dense phase pneumatic conveying of particles, *Proceedings of Pneumotransport 5*, BHRA Fluid Engineering, London, U.K., 1980, pp. 225–244.
- Konrad, K., Dense-phase pneumatic conveying:a review, *Powder Tech.*, 49, 1–35, 1986.
- Kraus, M., *Pneumatic Conveying Systems for Bulk Materials*, 3rd ed., Prentice-Hall, New Jersey, 1991.
- Krieger, I.M., Rheology of monodisperse lattices, *Adv. Colloid Interface Sci.*, 3, 111–136, 1972.
- Legel, D. and Schwedes, J., *Investigation of Pneumatic Conveying of Plugs of Cohesionless Bulk Solids in Horizontal Pipes*, Bulk Solids Handling, Vol. 4, No. 2, p.399, 1984.
- MacTaggart, R.S., Nasr-El-Din, H.A., and Masliyah, J.H., A conductivity probe for measuring local solids concentration in a slurry mixing tank, *Sep. Technol.*, 3, 151–160, 1993.
- Mainwaring, N.J. and Reed, A.R., Permeability and air retention characteristics of bulk solid materials in relation to modes of dense phase pneumatic conveying, *Bulk Solids Handling*, 7, 415–425, 1987.
- Marcus, R.D., Hilbert, J.D., and Klinzing, G.E., Flow through bends and acceleration zones in pneumatic conveying systems, *Bulk Solids Handling*, 5, 769, 1985.
- Marcus, R.D., Leung, L.S., Klinzing, G.E., and Rizk, F., *Pneumatic Conveying of Solids*, Chapman & Hall, New York, 1990.
- Mason, J.S., A Study of Modes of Gas–Solid Flow in Pipelines, Ph.D. thesis, Thames Polytechnic, London, U.K., 1991.
- Matsumoto, S., Harada, S., Saito, S., and Maeda, S.J., Effect of particle size on minimum transport velocity for horizontal pneumatic conveying of solids, *Chem. Eng. Jap.*, 10, 273–279, 1993.
- Maxwell, J.C., *A Treatise on Electricity and Magnetism*, 2nd ed., Clarendon Press, Oxford, 1881.
- McClements, D.J., Ultrasonic characterization of emulsions and suspensions, *Adv. Colloid Interface Sci.*, 37, 33–72, 1991.
- Metzner, A.B. and Reed, J.C., Flow of non-Newtonian fluids — correlation of laminar, transition and turbulent regions, *AIChE J.*, 1, 434–440, 1955.
- Mi, B. and Wypych, P.W., Particle slug velocities in horizontal slug-flow pneumatic conveying, *Powder Handling and Process.*, 5, 233, 1993.
- Mi, B. and Wypych, P.W., Pressure drop prediction in low-velocity pneumatic conveying, *Powder Tech.*, 81, 125–137, 1994.
- Miettunen, J., Lahteenmaki, S., and Jamsa-Jounela, S.L., New methods for the control of autogenous grinding circuit, *XVIII International Mineral Processing Congress*, Sydney, 1993, pp. 301–317.
- Matsumoto, S., Harada, S., Saito, S., and Maeda, S.J., *Chem. Eng. Japan*, 1997.
- Mills, D., *Pneumatic Conveying Design Guide*, Butterworths, Publishers, London, 1990.
- Mills, D., *Pneumatic Conveying Design Guide*, Butterworths, London, 1996.
- Molerus, O., Overview: pneumatic transport of solids, *Powder Tech.*, 88, 309–321, 1996.
- Moody, L.F., An approximate formula for pipe friction factors, *Trans. ASME*, 69, 1005–1006, 1947.
- Morikawa, Y., Tsuji, Y., Matsui, K., and Jittani, Y., Pressure drops due to pipe bends in air-solids two phase flows; circular and elliptical bends, *Int. J. Multiphase Flow*, 4, 575–583, 1978.
- Mukhtar, A., Investigations of the Flow of Multisized Heterogeneous Slurries in Straight Pipe and Pipe Bends, Ph.D. thesis, IIT, Delhi, India, 1991.

- Nasr-El-Din, H., Shook, C.A., and Colwell, J.A., A conductivity probe for local concentration measurement in slurry flows, *Int. J. Multiphase Flow*, 13, 365–378, 1987.
- Newitt, D.M., Richardson, J.F., Abbott, M., and Turtle, R.B., Hydraulic conveying of solids in horizontal pipes, *Trans. Inst. Chem. Eng.*, 33, 93–113, 1955.
- Newitt, D.M., Richardson, J.F., Abbott, M., and Turtle, R.B., Hydraulic conveying of solids in horizontal pipes, *Trans. Inst. Chem. Eng.* 33, 93–113, 1955.
- Olujic, Z., Compute friction factors fast for flow in pipes, *Chem. Eng.*, 88, 91–93, 1981.
- Oroskar, A.R. and Turian, R.M., The critical velocity in pipeline flow of slurries, *AICHE J.*, 26, 550–558, 1980.
- Pan, R., Material properties and flow modes in pneumatic conveying, *Powder Tech.*, 104, 157–163, 1999.
- Park, Y. and Zenz, F., Pressure loss in horizontal to vertical upflow elbows, *Proceedings of the BHRA Fluid Engineering Conference (PNEUMOTRANSPORT 5)*, London, U.K., Paper D3, 1980.
- Parzonka, W., Kenchington, J.M., and Charles, M.E., Hydrotransport of solids in horizontal pipes: effects of solids concentration and particle size on the deposit velocity, *Can. J. Chem. Eng.*, 59, 291–296, 1981.
- Pendse, H.P. and Sharma, A., Particle size distribution analysis of industrial colloidal slurries using ultrasonic spectroscopy, *Particle Particle Systems Charact.*, 10, 229–233, 1993.
- Perry, R.H. and Chilton, C.H., Eds., *Chemical Engineers' Handbook*, 6th ed., sec. 5, McGraw-Hill, New York, U.S.A., 1985.
- Probstein, R.F. and Sengun, M.Z., Dense slurry rheology with application to coal slurries, *Physico-Chem. Hydron. J.*, 8, 299–313, 1987.
- Reibel, U., Loffler, F., The fundamentals of particle size analysis by means of ultrasonic spectroscopy, *Particle Particle Systems Charact.*, 6, 135–143, 1989.
- Rizk, F., Pneumatic Conveying At Optimal Operating Conditions and a solution of Barth's Equation, *Proceedings of the BHRA Fluid Engineering (PNEUMOTRANSPORT 3)*, Cranfield, U.K., Paper D4, 1976.
- Roco, M.C. and Shook, C.A., Critical deposit velocity in slurry flow, *AICHE J.*, 31, 1401–1404, 1985.
- Ross, S. M., *Stochastic Processes*, Wiley, New York, 1996.
- Ryan, N.W. and Johnson, M.M., Transition from laminar to turbulent flow in pipes, *AICHE J.*, 5, 433–435, 1959.
- Sanderson, M.L. and Hemp, J., Ultrasonic flow meters — A review of the state of the art, *International Conference on Advances in Flow Measurement Techniques*, BHRA, Cranfield, U.K., 1981, pp. 157–178.
- Schlichting, H., *Boundary Layer Theory*, 4th ed., McGraw-Hill, New York, 1960.
- Schuchart, P., Pneumatic conveying, *Chem. Proc. Eng.*, May, 76–80, 1970.
- Shamlou, P.A., *Handling of Bulk Solids*, Butterworths, London, 1990.
- Sellgren, A., The choice of operating velocity in vertical solid-water pipeline systems, *Proceedings of the Hydrotransport 8 Conference*, BHRA, Cranfield, U.K., 1982, pp. 211–226.
- Sengun, M.Z. and Probstein, R.F., High-shear-limit viscosity and the maximum packing fraction in concentrated monomodal suspensions, *Physico-Chem. Hydron. J.*, 11, 229–241, 1989.
- Shook, C.A. and Roco, M.C., *Slurry Flow: Principles and Practice*, Butterworth-Heinemann, 1991.
- Shook, C.A., Geller, L., Gillies, R.G., Husband, W.H.W. and Small, M., Experiments with coarse particles in 250 mm pipeline, *Proceedings of the Hydrotransport 10 Conference*, BHRA Fluid Eng., Cranfield, U.K., 1986, pp. 219–227.
- Sisko, A.W., The flow of lubricating greases, *Ind. Eng. Chem.*, 50, 1789–1792, 1958.
- Slatter, P.T., Thorvaldsen, G.S., and Petersen, F.W., Particle roughness turbulence, *Proceedings of the 13th International Hydrotransport Symposium on Slurry Handling and Pipeline Transport*, Johannesburg, South Africa. BRH Group, Cranfield, U.K., 1996.
- Smith, R.A., Experiments on the flow of sand-water slurries in horizontal pipes, *Trans. Inst. Chem. Eng.*, 33, 85–92, 1955.
- Sparks, R.G., Dobbs, C.L., The use of laser backscatter instrumentation for the on-line measurement of the particle size distribution of emulsions, *Particle Particle Charact.*, 10, 279–289, 1993.
- Stegmaier, W., Zur Berechnung der horizontalen pneumatischen Forderung feinkorniger Stoffe, *Fordern Heben*, 28, 363–366, 1978.

- Swamee, P.K. and Jain, A.K., Explicit Equations for Pipe Flow Problems, *J. Hydraul. Eng.*, ASCE, 102, 657–664, 1976.
- Szilas, A.P., Bobok, E., and Navratil, L., Determination of turbulent pressure loss of non-Newtonian oil flow in rough tubes, *Rheol. Acta*, 20, 487–96, 1981.
- Takaoka, T., Hisamitsu, N., Ise, T. and Takeishi, Y., Blockage of slurry pipeline, *Proceedings of the 7th International Conference on the Hydraulic Transport of Solids in Pipes*, Sendai, Japan, Paper B4, 1980, pp. 71–88.
- Thomas, A.D. and Wilson, K.C., New analysis of non-Newtonian turbulent flow, yield power law fluids, *Can. J. Chem. Eng.*, 65, 335–338, 1987.
- Thomas, D.G., Transport characteristics of suspensions, Part II, *AICHE J.*, 7, 423–430, 1961.
- Thomas, D.G., Non-Newtonian suspensions, Part 2, *Ind. Eng. Chem.*, 55, 27–35, 1963.
- Thomas, D.G., Transport characteristics of suspensions, Part IX, *AICHE J.*, 10, 303–308, 1964.
- Thomas, D.G., Transport characteristics of suspensions: VIII. A note on the viscosity of Newtonian suspensions of uniform spherical particles, *J. Colloid Sci.*, 20, 267–277, 1965.
- Thorley, A.R.D. and Hwang, L.Y., Effects of rapid change in flowrate of solid–liquid mixtures, *Proceedings of the Hydrotransport 6 Conference*, BHRA Fluid Engineering, Cranfield, U.K., 1979, pp. 229–242.
- Tilly, G.P., Sand erosion of metals and plastics: a brief review, *Wear*, 14, 241–248, 1969.
- Tomita, Y., On the fundamental formula of non-Newtonian flow, *Bull. JSME*, 2, 469–474, 1959.
- Torrance, B.M., Friction factors for turbulent fluid flow in circular pipes, *South African Mech. Eng.*, 13, 89–91, 1963.
- Turian, R.M., Hsu, F.L., and Ma, T.W., Estimation of the critical velocity in pipeline flow of slurries, *Powder Technol.*, 51, 35–47, 1987.
- Turian, R.M., Hsu, F.L., and Sami Selim, M., Friction losses for flow of slurries in pipeline bends, fittings and valves, *Part. Sci. Technol.*, 1, 365–92, 1983.
- Turian, R.M., Hsu, F.L., Avramidis, K.S., Sung, D.J., and Allendorfer, R.K., Settling and theology of suspensions of narrow-sized coal particles, *AICHE J.*, 38, 969–987, 1992.
- Turian, R.M., Ma, T.M., Hsu, F.L., and Sung, D.J., Characterization, settling, and rheology of concentrated fine particulate mineral slurries, *Powder Technol.*, 93, 219–233, 1997.
- Turian, R.M., Ma, T.M., Hsu, F.L., and Sung, D.J., Flow of concentrated non-Newtonian slurries: 1. Friction losses in laminar, turbulent and transition flow through straight pipe, *Int. J. Multiphase Flow*, 24, 225–242, 1998a.
- Turian, R.M., Ma, T.M., Hsu, F.L., Sung, D.J., and Plackmann, G.W., Flow of concentrated non-Newtonian slurries: 2. Friction losses in bends, fittings, valves and Venturi meters, *Int. J. Multiphase Flow*, 24, 243–269, 1998b.
- Turian, R.M. and Yuan, T.-F., Flow of slurries in pipelines, *AICHE J.*, 23, 232–243, 1977.
- Vocadlo, J.J., Role of some parameters and effective variables in turbulent slurry flow, *Proceedings of the Hydrotransport 4 Conference*, BHRA, Cranfield, U.K., Paper D4, 1976, pp. 49–62.
- Von Karman, T., Mechanische Ahnlichkeit und Turbulenz, *Proceedings of the III International Congress of Applied Mechanics*, Vol. 85, Stockholm, Sweden, 1931.
- Wani, G.A., Sarkar, M.K., and Mani, B.P., Critical-Velocity in multisized particle transportation through horizontal pipes, *J. Pipelines*, 2, 57–62, 1982.
- Wasp, E.L., Kenny, J.P., and Gandhi, R.L., *Solid Liquid Flow -Slurry Pipeline Transportation*, 1st ed., Trans-Tech Publications, Clausthal, Germany, 1977.
- Wasp, E.J., Aude, T.C., Kenny, J.P., Seiter, R.H., and Jacques, R.B., Deposition velocities, transition velocities and spatial distributions of solids in slurry pipelines, *Proceedings of the Hydrotransport 1 Conference*, BHRA, Cranfield, U.K., Paper H4, 1970, pp. 53–76.
- Weber, M., Correlation analyses in the design of pneumatic transport plant, *Bulk Solids Handling*, 2, 231–233, 1982.
- Weber, M., Friction of the air and the air/solid mixture in pneumatic conveying, *Bulk Solids Handling*, 11, 99, 1991.

- Wen, C.Y., Flow characteristics of solids-gas transportation systems, US Department of Interior, Bureau of Mines, PA, IC 8314, 62-72, 1959.
- Westman, M.A., Michaelides, E.E., and Thomson, F.M., *J. Pipelines*, 7, 1987.
- Wicks, M., Transportation of solids of low concentrations in horizontal pipes, *Advances Solid-Liquid Flow in Pipes and Its Application*, Zandi, I., Ed., Pergamon Press, New York, 1971.
- Wilson K.C. and Thomas A.D., A new analysis of the turbulent flow of non-Newtonian fluids, *Can. J. Chem. Eng.*, 63, 539-547, 1985.
- Wilson, K.C., Slip point of beds in solid-liquid pipeline flow, *Proc. ASCE, J. Hydrol. Div.*, 96, 1-12, 1970.
- Wilson, K.C., A unified physically-based analysis of solid-liquid pipeline flow, *Proceedings of the 4th International Conference on the Hydraulic Transport of Solids in Pipes*, Banff, Alberta, Canada, Paper A1, 1976, pp. 1-16.
- Wilson, K.C., Deposition limit nomograms for particles of various densities in pipeline flow, *Proceedings of the Hydrotransport 6 Conference*, BHRA, Cranfield, U.K., 1979, pp. 1-12.
- Wilson, K.C., Evaluation of interfacial friction for pipeline transport models, *Proceedings of the Hydrotransport 11 Conference*, BHRA Fluid Eng., Cranfield, U.K., 1988, pp. 107-116.
- Woodcock, C.R. and Mason, J.S., Fluidized bed conveying, *PNEUMOTRANSPORT 3*, BHRA Fluid Engineering, Cranfield, Bedford, U.K., Paper E1, 1987.
- Wypych, P.W., Pneumatic Conveying of Bulk Solids, Ph.D. thesis, Department of Mechanical Engineering, University of Wollongong, Australia, 1989.
- Young, A.M., Coriolis-based mass flow measurement, *Sensors*, December 6-10, 1985.
- Yousifi and Gau, *Aerodynamique de l'ecoulement vertical de suspensions concentrees gaz-solides-I. Regimes d'ecoulement et stabilite aerodynamique*, Chemical Engineering Science, Vol. 29, 9, pp. 1939-1946, 1974.
- Zandi, I. and Govatos, G., Heterogeneous flow of solids in pipeline, *Proceedings of the ASCE Journal of Hydrol Division*, 93, 1967, pp. 145-159.
- Zenz, F.A. and Othmer, D.F., *Fluidization and Fluid Particle Systems*, Reinhold, New York, 1960.

5

Fluidized Beds

John R. Grace
University of British Columbia

Bo Leckner
Chalmers University of Technology

Jesse Zhu
University of Western Ontario

Yi Cheng
Tsinghua University

5.1	Hydrodynamics of Fluidization.....	5-1
	Key Properties Affecting Fluidization Hydrodynamics • Flow Regimes and Their Transitions • Particulate and Bubble-Free Fluidization • Bubbling Fluidization • Slugging Fluidization • Turbulent Fluidization • Fast Fluidization and Dense Suspension Upflow • Spouted Beds • Three-Phase Fluidization • Practical Considerations for Gas–Solid Systems	
5.2	Heat and Mass Transfer	5-30
	Bed to Surface Heat Transfer • Gas–Particle Heat and Mass Transfer	
5.3	Fluidized-Bed Reactors and Applications	5-55
	Fluidized-Bed Reactors • Catalytic Gas-Phase Reactions • Noncatalytic Gas-Phase Reactions • Gas–Solid Reactions • Physical Operations • Other Fluidized-Bed Reactors and Applications	

5.1 Hydrodynamics of Fluidization

John R. Grace

5.1.1 Key Properties Affecting Fluidization Hydrodynamics

Fluidization occurs when a gas or liquid is forced to flow vertically through a bed of particles at such a rate that the buoyed weight of the particles is completely supported by the drag force imposed by the fluid. The particles are then able to move relative to one another. When fluidization occurs, the bed of particles gains the appearance and many properties of a true liquid or fluid. The term “fluidization” reflects this conferring of fluid-like properties onto the solid particles, much as the term liquefaction is used to denote the act of making liquid or conferring liquid properties.

Most applications of fluidized beds are for cases where the fluidizing fluid is a gas, rather than a liquid. Hence, except where liquid-fluidized and gas–liquid–solid (three-phase) beds are considered explicitly in the sections below, this chapter is devoted to consideration of fluidized beds where the fluidization is caused by upward flow of a gas.

As detailed in Section 5.3, fluidized beds have many applications. These take advantage of a number of useful features such as a low-pressure drops (relative to packed beds), temperature uniformity, excellent surface-to-bed heat transfer, the ability to accommodate a wide range of particle properties, and the capability of handling limited quantities of liquids (e.g., sprayed reactants). Desirable (in some cases necessary) properties of particles and gas for fluidized beds are delineated in Table 5.1. Observing the guidelines with respect to desirable properties will generally lead to good-quality fluidization. It is sometimes possible to extend the range of particle properties which can be fluidized. For example, the ability

TABLE 5.1 Desirable Properties of Particles and Gases for Gas–Solid Fluidization

Property	Desirable Range	Comments
Particle Properties		
Mean diameter ^a	50 μm to 1.6 mm	
Size distribution ^b	Neither too narrow nor too broad, e.g., 90th to 10th decile ratio 5 to 25	Finer particles are too cohesive; coarser ones give less desirable fluidization properties Too narrow distribution gives less desirable fluidization properties; too broad a distribution results in particle segregation
Density	Wide range of values possible, but uniform from particle to particle	Density differences among particles can cause segregation; very low-density materials (e.g., <500 kg/m ³) may be difficult to retain in the bed
Shape	Rounded and with length-to-thickness ratio no larger than ~3	Avoid extreme shapes like disks and needles which inhibit fluidization; sharp corners and edges can cause excessive wear of surfaces
Surface roughness	Smooth	Some roughness is tolerable
Surface stickiness	Avoid sticky surfaces	Stickiness causes agglomeration and fouling
Attrition resistance	Usually strong as possible	Particles typically spend hours in the bed; they must withstand the stresses of the bed.
Hardness	Avoid resilience, but also excessive hardness	Compressible particles give excessive interparticle forces; very hard ones tend to cause excessive wear of the equipment components
Gas Properties		
Density	No restriction, but higher value improves properties	High pressure results in improved fluidization characteristics
Viscosity	No restriction	
Relative humidity	Typically 10 to 90%	Below ~10% RH, electrostatics may well be excessive; above ~90%, capillary forces tend to be dominant

^a The mean diameter is conventionally defined as $1/\sum (x_i/d_{pi})$, where x_i is the mass fraction of particles of mean size d_{pi} , usually obtained from the arithmetic average sieve opening in a sieve analysis.

^b Note that the size distribution in the bed at any point will, in general, differ from the feed or original size distribution due to such factors as attrition, elutriation, and agglomeration.

to fluidize fine powders can be enhanced by such means as gentle vibration or stirring, high velocity to cause elementary particles to agglomerate into particles of more favorable sizes, using a tapered bed (larger cross section with increasing height), or some combination of these factors (Deiva et al., 2002).

Geldart (1973) proposed a popular classification scheme for particles fluidized in air under atmospheric conditions. Four powder groups were suggested in order to distinguish broad types of behavior. These four groups (A, B, C, and D) are frequently referred to in the literature. Boundaries between adjacent groups for fluidization by air at room temperature and atmospheric pressure are shown in Figure 5.1. Later, this classification was extended (Grace, 1986a) to cover gases other than air as well as operating temperatures and pressures other than atmospheric. The characteristics of the four groups and criteria to distinguish them are summarized in Table 5.2. Group C particles are usually inappropriate for fluidization due to excessive interparticle forces, whereas groups A, B, and D can be fluidized, and used in practical applications. Criteria to distinguish among the powder groups are as follows:

CA Boundary. This boundary can be thought of as dividing systems where interparticle forces are so strong that normal fluidization is impossible from those where unaided fluidization is possible despite significant interparticle forces. It is the most difficult boundary to predict since it depends on a number of nonhydrodynamic factors, such as electrostatic charges and relative humidity, which can affect interparticle forces, primarily caused by van der Waals forces. Hence, there is no generally applicable equation; for a useful discussion, see Visser (1989).

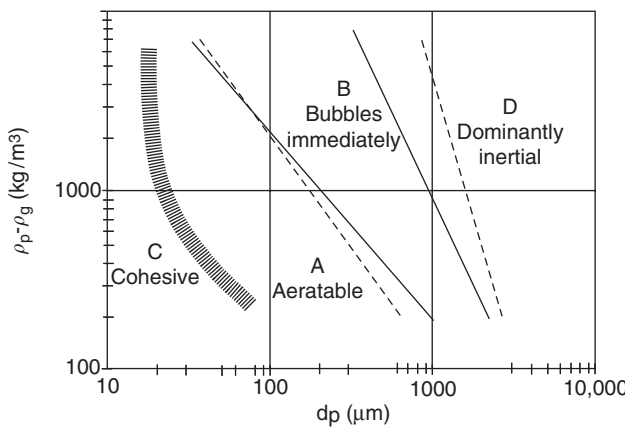


FIGURE 5.1 Geldart powder groups for fluidization by air at room temperature and atmospheric pressure. CA boundary is typical, but varies with properties such as moisture content of the particles. Solid lines give AB and BD boundaries as suggested originally by Geldart (1973). Dashed lines are AB and BD boundaries from Eqs. (5.1) and (5.2), respectively.

TABLE 5.2 Powder Groups and their Key Characteristics

Group	Mnemonic	Example	Key Features	Interparticle Forces Relative to Weight-Buoyancy	Typical Particle Size μm
C	Cohesive	Flour	Fluidize poorly due to strong interparticle forces; show channeling	Dominant	< 30
A	Aeratable	Fluid cracking catalyst	Excellent fluidization; small bubbles; deaerate slowly when gas flow stopped; high bed expansion, rapid particle mixing	Appreciable	~30–100
B	Bubble readily	Normal sand	Deaerate quickly when gas is shut off; large bubbles; intermediate solids mixing	Negligible	~100–800
D	Dominantly inertial	Peas	Deaerate quickly when gas is shut off; large bubbles; relatively poor solids mixing	Negligible	>800

Source: Geldart, D., *Powder Technol.*, 7, 285, 1973; Grace, J.R., *Can. J. Chem. Eng.*, 64, 353, 1986a.

AB Boundary. The AB boundary distinguishes systems where interparticle forces are significant (but not dominant, group A) from those (group B) where interparticle forces do not play a significant role. Data for this boundary for various gases, including air, and for different temperatures and pressures have been correlated (Grace, 1986a) by

$$Ar_{AB} = \left| \frac{g \rho_g (\rho_p - \rho_g) d_p^3}{\mu_g^2} \right|_{AB \text{ boundary}} = 1.0 \times 10^6 \{(\rho_p - \rho_g)/\rho_g\}^{-1.275} \quad (5.1)$$

BD Boundary. This boundary separates systems where the flow through the particles is dominated by viscous forces from those where inertial effects are dominant. The boundary between groups B and D can therefore be based on whether the flow through the particulate phase is laminar or turbulent, leading (Grace, 1986a) to

$$Ar_{BD} = \left| \frac{g \rho_g (\rho_p - \rho_g) d_p^3}{\mu_g^2} \right|_{BD \text{ boundary}} = 1.45 \times 10^5 \quad (5.2)$$

5.1.2 Flow Regimes and Their Transitions

Gas-fluidized beds show a number of distinct flow regimes. The principal ones appear schematically in Figure 5.2 for increasing superficial gas velocity and a column of high height-diameter ratio equipped to return essentially all of the particles entrained from the top. A corresponding flow regime diagram is shown in Figure 5.3 for cases where the column is large enough that the slug flow regime (see Section 5.1.5) is never reached. This form of regime diagram is convenient because the abscissa is simply a dimensionless particle diameter, whereas the ordinate is a dimensionless superficial gas velocity. Approximate boundaries between the powder groups introduced in the previous section are also shown in the figure. Details of the transitions between the flow regimes are considered in the rest of this section.

5.1.2.1 Minimum Fluidization

Consider a bed of solid particles in a cylindrical containing vessel whose bottom is permeable, with gas forced upward through it. The details of the base plate, usually called a “distributor,” “distribution plate” or “grid,” are considered in Section 5.1.10. As noted above, fluidization requires that the pressure drop across the beds match the buoyed weight of the particles, so that

$$\frac{dP}{dz} = -(\rho_p - \rho_g)(1 - \langle \varepsilon \rangle_A)g \quad \text{or} \quad \Delta P_{\text{bed}} = (\rho_p - \rho_g)(1 - \langle \varepsilon \rangle_{\text{av}})gH \quad (5.3)$$

where $\langle \varepsilon \rangle_A$ and $\langle \varepsilon \rangle_{\text{av}}$ are the volume fraction of gas (usually called “voidage”) averaged over the cross-sectional area and the entire bed volume, respectively, while H is the expanded bed depth. If one neglects contributions of wall friction and acceleration to the pressure drop, as it is usually possible to do, this equation should apply no matter what the flow regime. In effect, the time-mean pressure varies as in a

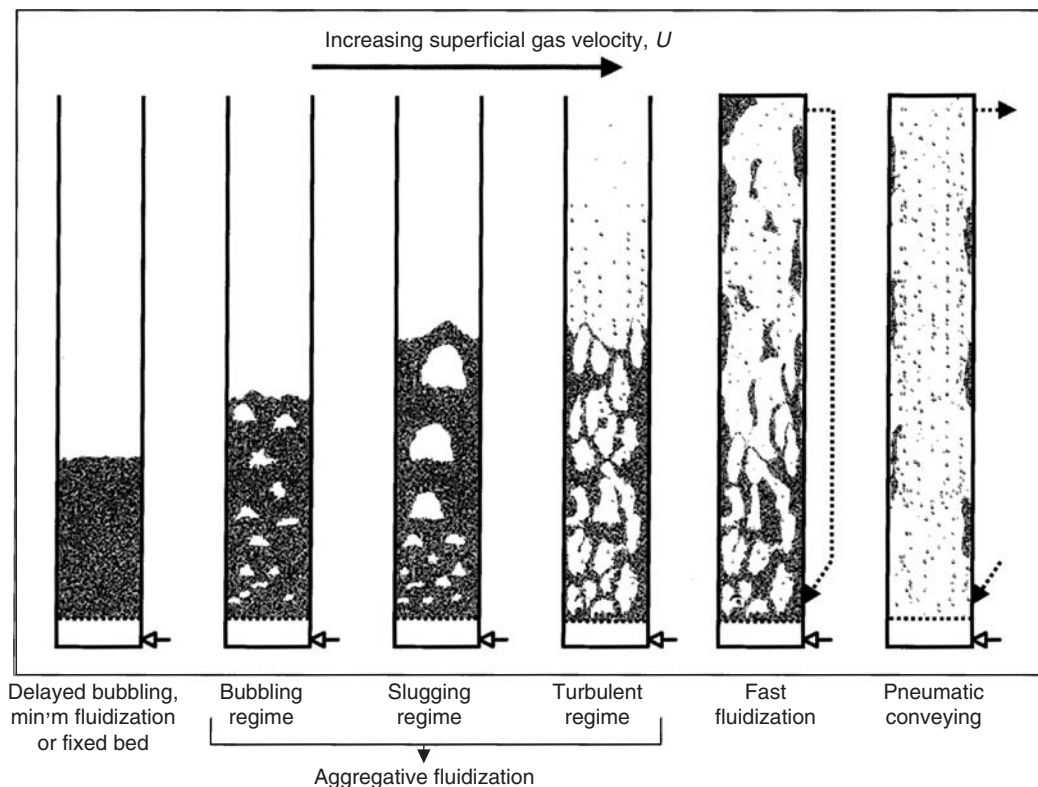


FIGURE 5.2 Schematic representation showing appearance of flow regimes relevant to gas–solid fluidization.

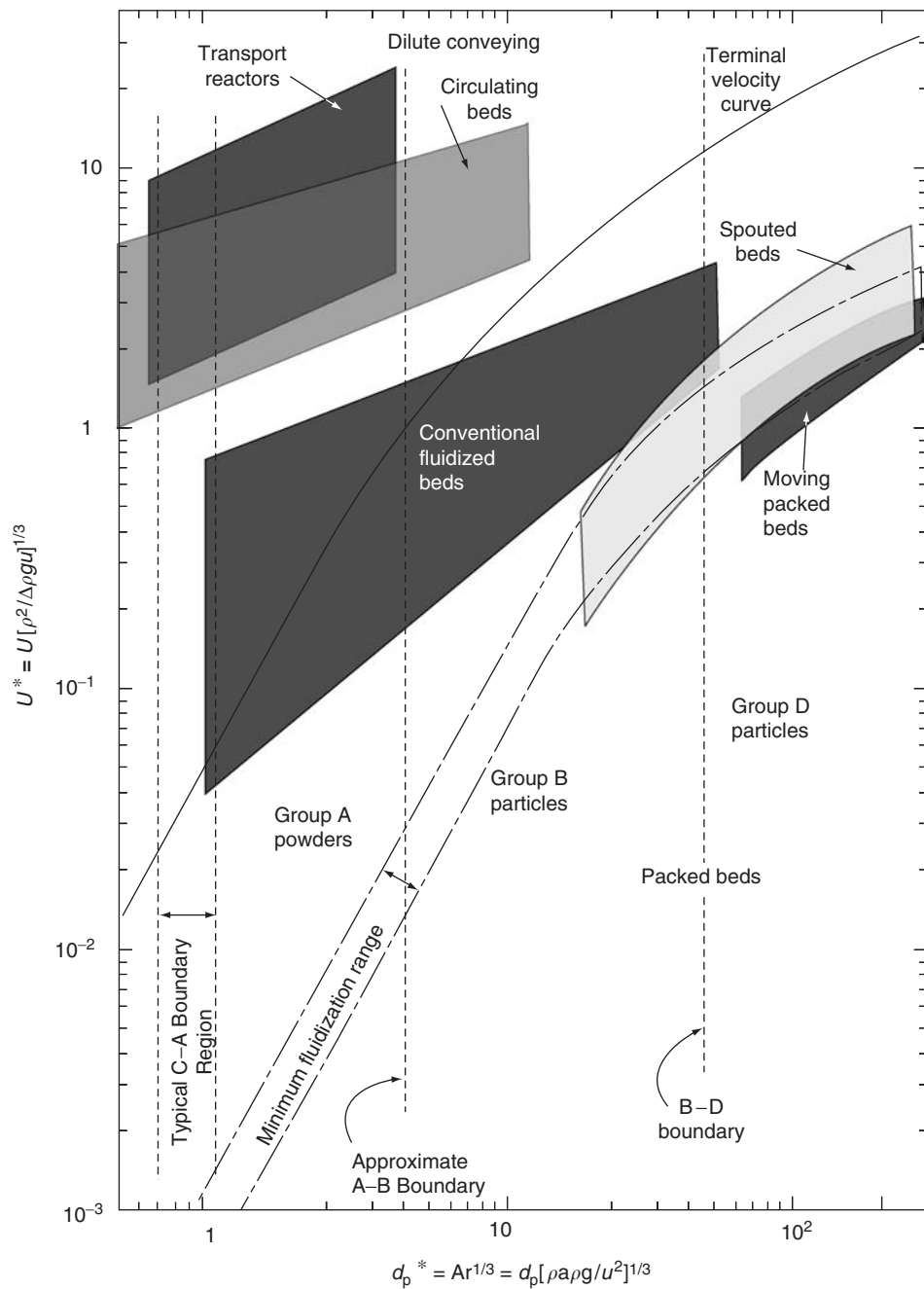


FIGURE 5.3 Dimensionless flow regime map for upward gas flow through solid particles diagram. Column diameter is assumed to be significantly larger than any bubbles formed, so that slug flow regime is excluded in this diagram. (Adapted from Grace, J.R., *Can J. Chem. Eng.*, 64, 353, 1986a.)

static liquid of density $(\rho_p - \rho_g)(1 - \langle e \rangle_A)$. In practice, Eq. (5.3) is generally accurate for well-fluidized materials in cylindrical columns (with vertical walls). Except in high-density circulating fluidized beds (see Section 5.1.7.2), where wall friction and acceleration terms can be appreciable, deviation by more than approximately $\pm 5\%$ from Eq. (5.3) usually indicates “channeling” (i.e., the gas finds fissures or other fixed

passages through stationary particles) or other poor gas distribution in the column. Note that Eq. (5.3) is also valid for liquid-fluidized beds with the gas density, ρ_g , then replaced by the liquid density, ρ_l .

Pressure drops in fixed beds are commonly predicted by the Ergun equation

$$\Delta P_{\text{fixed}} = \frac{150\mu_g U(1 - \langle \varepsilon \rangle_{\text{av}})^2}{\psi^2 d_p^2 \langle \varepsilon \rangle_{\text{av}}^3} + \frac{1.75\rho_g U^2(1 - \langle \varepsilon \rangle_{\text{av}})}{\psi d_p \langle \varepsilon \rangle_{\text{av}}^3} \quad (5.4)$$

where U is the “superficial gas velocity” (total gas volumetric flow rate divided by total column cross-sectional area) and ψ is a particle shape factor called the sphericity, defined as the surface area of a volume-equivalent sphere divided by the true external surface area of the particle. Transition from a fixed bed to a fluidized bed occurs when the pressure drop across a loosely packed fixed bed reaches the value given by Eq. (5.3). Hence, one can estimate the superficial velocity, U_{mf} , at the transition between a fixed and fluidized bed, called the “minimum fluidization velocity,” by solving the quadratic equation obtained when the right-hand sides of (5.3) and (5.4) are equated. The result is then an equation of the form

$$Re_{\text{mf}} = \frac{\rho_g d_p U_{\text{mf}}}{\mu_g} = \sqrt{C_1^2 + C_2 Ar} - C_1 \quad (5.5)$$

where

$$Ar = \frac{g \rho_g (\rho_p - \rho_g) d_p^3}{\mu_g^2} \quad (5.6)$$

Different values of the constants, C_1 and C_2 , are available in the literature, with the most popular being $C_1 = 33.7$ and $C_2 = 0.0408$, as recommended by Wen and Yu (1966). Typically this equation predicts the minimum fluidization velocity no better than within approximately $\pm 25\%$, so it is best to measure it experimentally whenever possible. The most common method of measurement requires that the pressure drop across the bed be recorded as the superficial velocity is increased stepwise through U_{mf} and beyond; U_{mf} is then taken at the intersection of the straight lines corresponding to the fixed-bed and fluidized-bed portions of the graph obtained when ΔP_{bed} is plotted against U on log-log coordinates. At the same time as U_{mf} is being measured, it is important to also determine the bed voidage at minimum fluidization, ε_{mf} , requiring that one find the mass, M_p , of the particles, the bed height, H_{mf} , at minimum fluidization, and the particle density, ρ_p , with

$$\varepsilon_{\text{mf}} = 1 - M_p / (\rho_p A H_{\text{mf}}) \quad (5.7)$$

Figure 5.4 plots minimum fluidization velocities for particles of different mean diameters and densities fluidized by air at room temperature and atmospheric pressure, based on Eqs. (5.5) and (5.6) with the C_1 and C_2 values given above. As expected, U_{mf} increases with increasing particle diameter and increasing particle density.

Equation (5.5) can be simplified when the particles are either small (low Ar) or large (high Ar). With the C_1 and C_2 values specified above, then

$$\text{for } Ar < 10^3: \quad Re_{\text{mf}} = 6.1 \times 10^{-4} Ar \quad \text{or} \quad U_{\text{mf}} = 0.00061 \frac{g(\rho_p - \rho_g)d_p^2}{\mu_g} \quad (5.8)$$

$$\text{for } Ar > 10^7: \quad Re_{\text{mf}} = 0.202 Ar^{0.5} \quad \text{or} \quad U_{\text{mf}} = 0.20 \sqrt{\frac{g(\rho_p - \rho_g)d_p}{\rho_g}} \quad (5.9)$$

In all of these expressions, d_p is the mean particle diameter, as defined in the footnote of **Table 5.1**. Equations (5.5)–(5.9) can also be used for liquid-fluidized beds with ρ_g replaced by ρ_l . Equations (5.8) and (5.9) are important, not only because they are useful in their own right for small and large particles, respectively, but also because they show the influence of key variables on U_{mf} . For example, for small particles fluidized by gases, pressure is seen to have virtually no effect, whereas U_{mf} decreases with increasing temperature, and it is proportional to the square of the mean particle diameter. On the other hand, for large particles, U_{mf} decreases with an increasing pressure for gas fluidization, increases with increasing temperature, and is proportional to the square root of the mean particle diameter. Equations (5.8) and (5.9) are also notable because they are identical, except for the coefficients, to expressions for terminal settling velocities of small

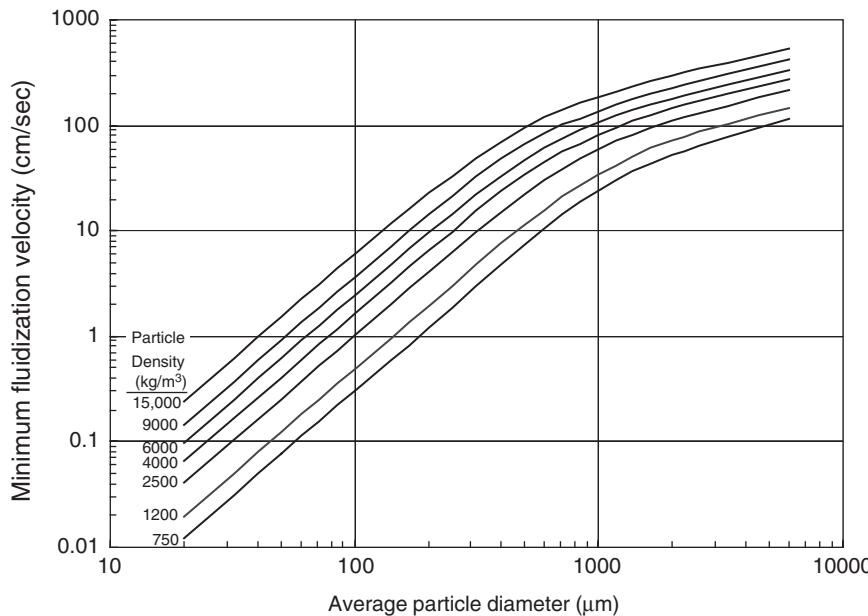


FIGURE 5.4 Minimum fluidization velocity vs. particle diameter for particles of different densities fluidized by air at atmospheric temperature and pressure.

and large spherical particles of diameter d_p in Newtonian fluids. For small spherical particles ($Ar < 10^3$), Stokes law replaces 6.1×10^{-4} in Eq. (5.8) by 1/18, meaning that the terminal settling velocity is approximately 90 times U_{mf} , suggesting a relatively wide range for fluidization before significant entrainment of particles occurs. For large particles ($Ar > 10^7$), where the coefficient in a terminal-velocity equation (Clift et al., 1978) of the form of Eq. (5.9) is 1.73, the corresponding V_s/U_{mf} ratio is only 8.6.

5.1.2.2 Overview of Flow Regimes

As the superficial gas velocity, U , is increased stepwise beyond U_{mf} for a bed of solid particles, one encounters a number of different flow regimes. In the most general case they are, in order of increasing U :

- Bubble-free bed expansion (Section 5.1.3)
- Bubbling fluidization (Section 5.1.4)
- Slug flow (Section 5.1.5)
- Turbulent fluidization (Section 5.1.6)
- Fast fluidization and dense suspension upflow (Section 5.1.7)

These flow regimes are shown diagrammatically in Figure 5.2, together with dilute pneumatic conveying (see Chapter 4), reached at even higher gas velocities. In the rest of this section, we consider the transitions between these flow regimes and the corresponding transitional superficial gas velocities.

5.1.2.3 Minimum Bubbling Velocity

For particles in groups B and D of the Geldart classification (see Section 5.1.1), bubbling begins as soon as U exceeds U_{mf} . The minimum bubbling velocity, U_{mb} , is then equal to U_{mf} . For group A powders, on the other hand, there is an appreciable gap between these two. Since interparticle forces play a role in determining U_{mb} , correlations in terms of purely hydrodynamic quantities are not very successful. A dimensional correlation due to Abrahamsen and Geldart (1980) gives

$$U_{mb} = 2.07 \exp\{0.716\chi\} \frac{d_p \rho_g^{0.06}}{\mu_g^{0.347}} \quad (5.10)$$

where χ is the fraction by mass of particles finer than 45 μm (from a sieve analysis) and d_p is again the mean particle diameter defined as in the footnote of [Table 5.1](#). Note that U_{mb} cannot be less than U_{mf} , so that if the value calculated from Eq. (5.10) < U_{mf} obtained from Section 5.1.2.1, then set $U_{mb} = U_{mf}$ from Eqs. (5.5), (5.8), or (5.9).

5.1.2.4 Minimum Slugging Velocity

Slugs are gas bubbles which are large enough that their volume-equivalent diameters exceed about 50% of the column diameter. In order for slug flow to occur in fluidized beds, several conditions must be satisfied:

- The ratio of expanded bed depth to column inside diameter (H/D) must be sufficient to give the bubbles enough distance in which to coalesce to voids of a size large enough to be considered slugs. This requires (Darton et al., 1977)

$$H/D \geq 3.5(1 - N_{or}^{-0.5}) \quad (5.11)$$

- The maximum stable bubble diameter for the particle/gas system (see [Section 5.1.4.1](#)) must be of the same order as D or greater.

If both these conditions are met, the superficial gas velocity at minimum slugging is (Stewart and Davidson, 1967)

$$U_{ms} = U_{mf} + 0.07\sqrt{gD} \quad (5.12)$$

For columns of noncircular cross section, D is replaced by the hydraulic diameter, $D_h = 4A/P_c$, where P_c is the column perimeter. This substitution works less well than the width-to-thickness ratio falls outside the range of ~0.4 to 2.5.

5.1.2.5 Onset of Turbulent Fluidization

Turbulent fluidization occurs when, as U is increased, a point is reached where the bubbles or slugs, instead of continuing to increase in size, begin to break down. The “critical velocity,” U_c , which demarcates the onset of the turbulent fluidization flow regime, is usually determined experimentally as the superficial gas velocity at which the standard deviation of pressure fluctuations reaches a maximum. Unfortunately, U_c tends to vary also with level in the bed. Moreover, gage pressure readings lead to different values of U_c than differential pressure measurements. Gage signals register fluctuations from distant locations (including those due to bed surface oscillations and bubble formation), as well as local features, whereas differential signals filter out most information arising from outside the interval between the pair of pressure taps across which the pressure readings are being recorded.

Most correlations of U_c are of the form

$$Re_c = \frac{\rho_g d_p U_c}{\mu_g} = B Ar^\eta \quad (5.13)$$

Values of $B = 0.565$ and $\eta = 0.461$ are recommended based on a wide range of data for absolute pressure fluctuations (Bi et al., 2000). However, equations of this form fail to include the influence of H/D ratio, which can be significant for relatively shallow beds. A correlation (Ellis et al., 2004) taking this into account and covering columns up to a diameter of 1.6 m is

$$Re_c = \frac{(H/D)^{0.43} Ar^{0.74}}{\sqrt{4.2(H/D)^{0.86} + 3.1Ar^{0.33}}} \quad (5.14)$$

5.1.2.6 Onset of Fast Fluidization Flow Regime

As the superficial gas velocity is increased further, a superficial velocity, called the transport velocity, U_{tr} , is reached where there ceases to be a “bed,” i.e., there is so much entrainment that there is no distinct upper bed surface. Massive recycling of solids is then required to maintain a large number of particles in suspension. Particles are carried upward in the core of the column and then descend as streamers and

clusters along the outer wall. The transition to fast fluidization corresponds to onset of ‘significant entrainment’ and can be predicted (Bi et al., 1995) from

$$Re_{se} = 1.53Ar^{0.5} \quad \text{or} \quad U_{se} = 1.53 \sqrt{\frac{g(\rho_p - \rho_g)d_p}{\rho_g}} \quad (5.15)$$

This equation is of the same form as Eq. (5.9), which, as noted above, is also identical to the expression for terminal settling velocities of large spheres, except for its different constant coefficient. For cases (which only occur for relatively large particles) where the U_{tr} predicted from Eq. (5.15) is less than the corresponding terminal settling velocity, V_s , of particles of mean size, U_{tr} should be taken to be equal to V_s .

5.1.2.7 Onset of Dense Suspension Upflow

Dense suspension upflow occurs when, in addition to having a large superficial gas velocity, there is also a high net particle circulation flux, G_s , sufficient to cause the time-mean flux of solids to be upward over the entire column cross section and the solids volume fraction is 7% or more (Grace et al., 1999). The transition condition where this occurs is a function of both U and G_s . A recent correlation (Kim et al., 2004a) suggests that the onset occurs at

$$\frac{U_{DSU}}{\langle \epsilon \rangle_A V_s} = 22.8 \left\{ \frac{G_s}{\rho_p(1 - \langle \epsilon \rangle_A)V_s} \right\}^{0.59} Ar^{-0.20} \quad (5.16)$$

Since the cross-sectional average voidage, $\langle \epsilon \rangle_A$, varies with height, as discussed in Section 5.1.7.1, it is possible for regions of fast fluidization and dense suspension upflow to coexist in the same column.

5.1.2.8 Transition from Fast Fluidization to Dilute Pneumatic Conveying

At high gas velocities and solids holdups $\leq 7\%$, particles are conveyed upward throughout the entire cross-section of a riser column, and the dilute pneumatic conveying flow regime is reached. This condition again demarcates termination of fast fluidization. The transition superficial velocity has been correlated (Kim et al., 2004a) by

$$\frac{U_{DPC}}{\langle \epsilon \rangle_A V_s} = 1160 \left\{ \frac{G_s}{\rho_p(1 - \langle \epsilon \rangle_A)V_s} \right\}^{-0.90} Ar^{-0.20} \quad (5.17)$$

As in the previous case, it is seen that this transition is a function of the cross-sectional average voidage, which varies with height in risers, so that transition can again occur within the riser (part way up).

5.1.3 Particulate and Bubble-Free Fluidization

Almost all liquid-fluidized beds expand smoothly without bubbles when the superficial velocity of the fluidizing fluid is increased beyond U_{mf} . This has commonly been called “particulate” or homogeneous fluidization, in contrast to so-called “aggregative fluidization” (involving division into distinct dilute and dense regions or phases), which occurs for almost all gas-fluidized beds, including all those of practical importance. Particulate beds, gently and homogeneously fluidized by liquids in this manner, are also sometimes referred to as “expanded beds.” In practice, the expansion is not perfectly homogeneous, but regions of somewhat increased and decreased voidage propagate slowly enough that beds of practical height can be considered to be homogeneous. An extensive review of liquid fluidization has been published recently (Epstein, 2003). As already noted above, the pressure drop, U_{mf} and ϵ_{mf} can be predicted by the same relationships as for gas-fluidized beds in Section 5.1.2.1, with the gas density ρ_g replaced by the liquid density ρ_l . The bed expansion can be predicted from the relationship

$$H = H_{mf} \frac{1 - \epsilon_{mf}}{1 - \langle \epsilon \rangle_{av}} \quad (5.18)$$

where the volume-average bed voidage (or liquid fraction) is estimated from an empirical equation suggested by Richardson and Zaki (1954):

$$\langle \epsilon \rangle_{av} = \left\{ \frac{U}{kV_s} \right\}^{1/n} \quad (5.19)$$

with the exponent n and the coefficient k obtained from empirical relationships (Khan and Richardson, 1989)

$$\frac{4.8 - n}{n - 2.4} = 0.043Ar^{0.57} \quad \text{and} \quad k = 1 - 1.15 \left\{ \frac{d_p}{D} \right\}^{0.6} \quad (5.20)$$

These equations are derived from experimental data covering a broad range of conditions, $0.01 < \rho_l d_p V_s / \mu_l < 7000$ and d_p/D up to 0.2. Caution should be exercised for voidages greater than about 0.85 where significant deviations can occur (Epstein, 2003).

As we have seen in Section 5.1.2.3, gas-fluidized beds of group A particles experience a range of conditions for which $U_{mf} \leq U < U_{mb}$, where the bed expands without bubbles. Since the interstitial gas travels more slowly than bubbles would rise in the same beds, the expansion is greater for given values of U in this range than would be the case if U were to have exceeded U_{mb} . While this range is also often referred to particulate fluidization, there are significant differences between gas-fluidized beds in this range and liquid-fluidized beds (Martin, 1983). The most notable difference is that interparticle forces play a significant role in gas-fluidization case, whereas they are of little or no importance for liquid-fluidized beds.

Bubble-free gas fluidized beds are of little practical importance because of the low gas velocities. However, it is helpful to be able to predict the bed expansion at the minimum bubbling point. Abrahamsen and Geldart (1980) give

$$H_{mb}/H_{mf} = (U_{mb}/U_{mf})^{0.22} \quad (5.21)$$

with U_{mf} and U_{mb} obtained from the relationships and procedures described above.

5.1.4 Bubbling Fluidization

This section considers the hydrodynamics of the bubbling flow regime, which extends from U_{mb} (Section 5.1.2.3) at the lower limit to either U_{ms} (Section 5.1.2.4) or U_c (Section 5.1.2.5), depending on whether or not slug flow is encountered before reaching the turbulent fluidization flow regime. The bubbles, also often called “voids,” form in gas-fluidized beds because a homogeneous bed is unstable to perturbations once $U \geq U_{mb}$. The bubbles themselves are analogous to spherical-cap bubbles in liquids (Clift et al., 1978). Surrounding the bubbles is a “dense-phase,” composed of particles and interstitial gas, acting (Grace, 1970) like a non-Newtonian liquid of effective viscosity of order 0.1 to 1 Pa·s, 2 to 3 orders of magnitude greater than the viscosity of liquid water. As shown in Figure 5.5, the resulting bubbles are well-rounded, with total included wake angles (Rowe and Partridge, 1965) of ~ 200 to 260° . The wake approximately completes the base of the sphere, and plays a very important role in determining solids mixing as discussed below. Note that the boundaries of bubbles, unlike those of bubbles in liquids, are permeable. Given the lower pressure at the top of the bubble than at the bottom, an observer riding upward with the bubble on its inside would experience an updraught, often referred to as “throughflow.” This plays a vital role in determining mass transfer between the bubbles and surrounding dense phase, while stabilizing the roof of the bubble against collapse. Note that there is no load-bearing arch on the bubble roof (Rowe, 1964). In fact, the voidage around the periphery tends to be a little higher than elsewhere in the dense phase (Lockett and Harrison, 1967).

5.1.4.1 Bubble Properties and Bed Expansion in Freely Bubbling Bed without Tubes

The volumetric flow accounted for by the displacement of bubbles or voids rising in the bed can be written

$$\dot{V}_b = Y(U - U_{mf})A \quad (5.22)$$

Originally it was assumed that $Y = 1$, and this simple equation, implying that all the gas beyond that required to just fluidize the bed travel as bubbles, is often referred to as the “two-phase theory of fluidization.” The literature data obtained by many laboratories using various experimental techniques have indicated, however, that Y is usually < 1 in practice. Typically, one can assume $Y \approx 0.8$ for group A particles, ~ 0.7 for group B solids, and ~ 0.3 for group D particles.

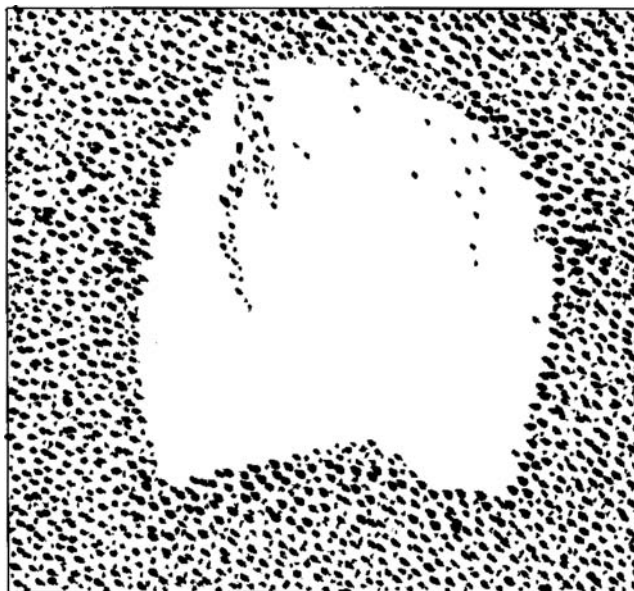


FIGURE 5.5 Shape of a typical isolated bubble in a three-dimensional fluidized bed. Based on x-ray photograph of Rowe, P.N. and Partridge, B.A., *Trans. Instn. Chem. Engrs.*, 43, 157, 1965.

There are a number of empirical and semi-empirical equations for predicting the mean bubble size as a function of height in fluidized beds. The approach due to Darton et al. (1977) usually works well for cylindrical columns without any internal tubes or baffles. This considers chains of bubbles rising from the distributor and coalescing pair-wise up the bed. The mean bubble diameter as a function of height, z , is then given (Darton et al., 1977) by

$$D_b(z) = \frac{0.54(U - U_{mf})^{0.4}(z + 4.0\sqrt{A_c})^{0.8}}{g^{0.2}} \quad (5.23)$$

where A_c is the area of the distributor plate per orifice in the distributor. This equation is intended for cases where bubbles form right at the gas distributor and where the particles are large enough (essentially group B and D solids) that negligible bubble splitting occurs. For group A solids, bubbles commonly reach a “maximum stable diameter,” where there is a dynamic equilibrium between bubble coalescence and splitting. This imposes an upper limit on the bubble diameter. The maximum stable bubble diameter can be estimated (see Grace, 1982) by

$$D_{b\max} = 2.0(V_s^e)^2/g \quad (5.24)$$

where V_s^e is the terminal settling velocity of a particle of diameter $2.7d_p$ in the fluidizing gas at the same pressure and temperature as in the bed. An alternative approach, which accounts for bubble splitting as well as coalescence, was suggested by Horio and Nonaka (1987). As suggested by these authors, the height coordinate, z , should be taken from the termination of gas jets in cases where vertical jets form at the distributor (see [Section 5.1.10](#)).

Once the mean bubble diameter has been estimated as a function of height from Eq. (5.23), subject to the constraint imposed by Eq. (5.24), it is then possible to calculate the corresponding bubble rise velocity from

$$U_b(z) = 0.71\sqrt{gD_b(z)} + (U - U_{mf}) \quad (5.25)$$

The first term accounts for the velocity of rise of a spherical-cap bubble with a typical wake angle, whereas the second term corrects, in an approximate manner, for bubble interaction effects inside the bed (Grace and Harrison, 1969).

With the estimates of bubble volumetric flow, i.e., \dot{V}_b , and rising velocity, i.e., U_b , from above, it is now possible to predict the expansion of the bubbling bed, aided by the common assumption that the dense phase retains the same voidage as at minimum fluidization, i.e., ε_{mf} . In the next two relationships, it is also assumed that a negligible fraction of the particle inventory is displaced into the freeboard, cyclones, and return system. If this is not the case, then one needs to correct the H_{mf} below to use an effective value which accounts only for particles in the dense bed (i.e., below the expanded bed surface.) An iterative procedure is required to estimate the bed expansion: Firstly guess a value of ε_b , the fraction of dense bed volume occupied by bubbles. Then calculate a first estimate of the expanded bed depth as

$$H = H_{mf}/(1 - \varepsilon_b) \quad (5.26)$$

Next calculate the mean bubble diameter at $z = H/2$ using Eq (5.23) or Eq. (5.24), whichever gives the smaller value. Then find the corresponding bubble rise velocity, $U_{b|z = H/2}$, from Eq. (5.25). Hence find a new estimate of ε_b from

$$\varepsilon_b = \dot{V}_b/[AU_{b|z = H/2}] \quad (5.27)$$

If this value is within a chosen tolerance of the original guess, it is accepted; H is then specified as the value calculated previously from Eq. (5.26). Otherwise, calculate a new estimate of H from Eq. (5.26) using the most recently calculated value of ε_b and proceed as above. Generally, three or four iterations should be sufficient to give a good estimate of the bed expansion and other mean bubble properties calculated via this procedure.

Once the bubble properties have been calculated in this manner, it may also be useful to estimate the mean frequency of bubbles passing any level,

$$f_b = \dot{V}_b/V_b \quad \text{with} \quad V_b = \text{bubble volume} = (\pi/6)D_b^3 \quad (5.28)$$

One of the important features, however, of bubbling fluidized beds is that the bubbles are not uniformly distributed across the cross section of the column, even on a time-averaged basis. Instead, as shown both by experimental results and coalescence models, the bubbles tend to become depleted near the outer wall, with the maximum frequency and bubble volumetric flow initially occurring about one mean bubble diameter in from the outer wall, and then this position migrates inward toward the axis of the column as bubbles grow and the slug flow regime is approached (Grace and Harrison, 1969; Werther, 1974).

5.1.4.2 Influence of Tubes and Baffles on Bubbling and Bed Expansion

The procedure described above for estimating bed expansion and bubble properties applies to cases where there are no internal heat-transfer tubes or other fixed surfaces inside the column. In any section of the column containing an array of horizontal tubes, bubbles can be assumed to grow by coalescence according to Eq. (5.23) until they reach either the diameter given by Eq. (5.24) or the minimum center-to-center tube separation distance, whichever is smaller. If the array terminates before the top of the bubbling bed, then growth beyond the latter limit will recommence, but of course with the limit imposed by the maximum stable size, Eq. (5.24), still in place. In such cases, the expansion is predicted by estimating ε_b separately for each section—i.e., below the array of tubes, inside the tube bundles, and above the tubes—and then applying a procedure analogous to that described above to balance the total in-bed inventory of solids with the sum of the solids within all of the individual sections.

For vertical tubes or other baffle geometries and configurations, there are no reliable methods for predicting the evolution of bubble size, and hence of bed expansion. In general, bubbles are smaller when baffles are present, as the internal fixed surfaces limit bubble coalescence (Grace and Harrison, 1971), and baffles may also promote bubble splitting. Hence, bed expansion is usually increased by the presence of fixed internal surfaces, with the degree of increase depending strongly on the extent to which the mean bubble size is reduced.

5.1.4.3 Solids Mixing and Motion in a Bubbling Bed

The dominant mechanism by which solids are dispersed in bubbling fluidized beds involves displacement of particles by bubble wakes and due to the drift caused by the bubbles. These diplacement are illustrated schematically in Figure 5.6. In the case of wake transport, particles are gathered up in the wake at the bottom (back) of rising bubbles and transported upward, with occasional shedding of clumps or fragments of particles along the way (Rowe et al., 1965). In the case of drift, particles undergo net displacement outside the wake due to the passage of bubbles, upwards near the bubble axis and downwards at several bubble radii from the axis, just as for drift net displacement caused by a sphere passing in potential flow through a fluid (Baeyens and Geldart, 1973). Let f_w represent the volume of the wake divided by the volume of the corresponding bubble. Some experimental results for f_w are shown in [Figure 5.4](#) based on X-ray photography of bubbles in fully three-dimensional fluidized beds (Rowe and Partridge, 1965). An effective drift fraction may be defined in a similar manner, with experimental results (Baeyens and Geldart, 1973) suggesting that this is approximately $1.6f_w$. Hence, the upward mass flux of particles due to the rise of bubbles at any level in the bed can be estimated as

$$G_s = 2.6\rho_p(1 - \varepsilon_{mf})f_w\dot{V}_b/A \quad (5.29)$$

where \dot{V}_b is obtained from Eq. (5.22) and f_w can be estimated based on X-ray photographs of bubbles reported by Rowe and Partridge (1965). A characteristic mixing time, sometimes called a “turnover time,”

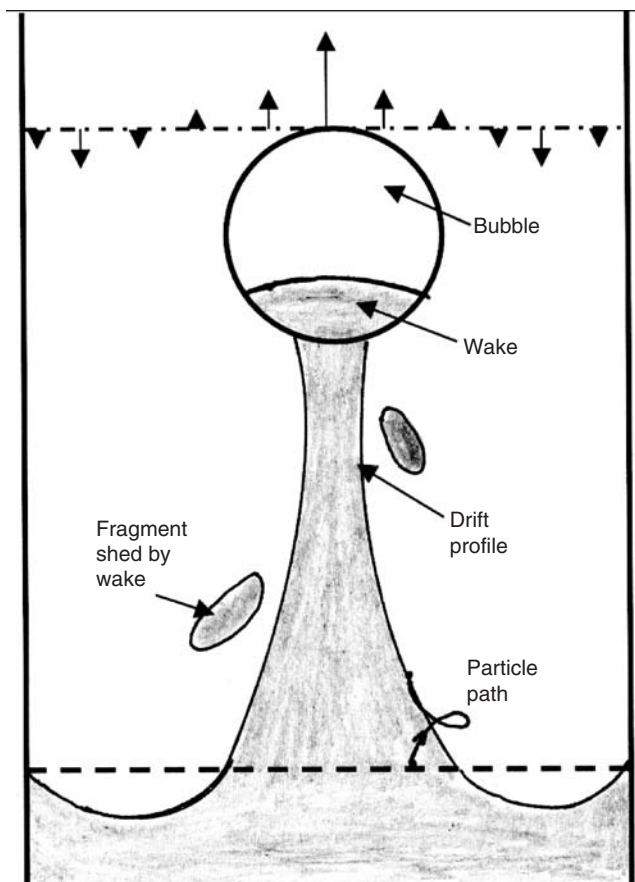


FIGURE 5.6 Schematic showing particle wake transport and drift due to passage of bubble. Arrows at top indicate relative vertical components of particle velocity across the bed just ahead of the approaching bubble.

can then be estimated as the average time for the inventory of particles in the bed to travel through one cycle, from the bottom of the bed to the top and back again to the bottom, leading to

$$t_{\text{mix}} = H_{\text{mf}} / \{2.6 f_w Y(U - U_{\text{mf}})\} \quad (5.30)$$

Experimental results indicate that homogeneity is effectively achieved in two to three mixing times. For most fluidized beds of practical importance, t_{mix} turns out to be of order 10–100 s, whereas particles usually spend much longer times in the bed. Hence, the particles are quickly blended in the vertical direction and perfect axial mixing can commonly be assumed. As long as bubbling is well established, i.e., $(U - U_{\text{mb}}) > \sim 0.1 \text{ m/s}$, and the distributor has been well designed, height-wise classification by size of particles whose diameters are within an order of magnitude of the mean particle diameter is unlikely to be a problem. Nonuniform particle densities are more likely to give rise to vertical segregation (Rowe and Nienow, 1976). However, vigorous bubbling is usually sufficient to prevent segregation of particles whose densities are within ~30% of each other.

The above results refer to vertical mixing (often referred to as axial dispersion). Commonly the literature describes the mixing process in terms of an axial dispersion coefficient, defined by analogy with molecular diffusion, and having the same units (m^2/s) as a molecular diffusivity. However, molecular diffusion involves small random steps, clearly differing from the large bubble-generated (and hence deterministic) displacements that dominate the mixing process in bubbling fluidized beds. As a result, axial dispersion coefficients vary widely and are not very useful in practice, except as a gross means for comparing data and seeing trends, as in the review by van Deemter (1980), which provides data on mixing in industrial-scale fluidized beds.

Particle transport by bubbles also provides the principal mechanism for horizontal (or radial) solids mixing in bubbling beds. When bubbles that are not perfectly aligned vertically interact and coalesce, gas and particles are displaced horizontally. In addition, particles are displaced horizontally when bubbles erupt at the dense bed surface, resulting in splashing and spraying of particles into the freeboard. Typically, the magnitudes of mixing coefficients are about an order of magnitude less in the horizontal direction than in the vertical direction. Although dispersion models are still strictly inappropriate in this case, as for axial mixing, they are often used (van Deemter, 1980), and the objection to their use for radial (or lateral) dispersion is less than for vertical (axial) dispersion coefficients, since the displacement steps are smaller and less ordered.

An issue of considerable importance in bubbling fluidized beds is the establishment of gross overall “gulf streaming” of solid particles. Such overall circulation patterns are associated with the bubble coalescence pattern referred to above, whereby bubbles initially become more concentrated near the outer wall, and then the region of increased bubbling migrates inward toward the axis of the bed with increasing height. Since bubbles carry particles upward in their wakes and propel particles upward by drift, the nonuniform radial distribution of bubbling leads to nonuniform solids movement. On a time-mean basis, the patterns then tend to be as indicated in Figure 5.7. As shown, there is a relatively weak cell near the bottom where particle motion is primarily upwards near the wall and downward near the center. In bubbling beds of height/diameter ratio of about 1 or more, this then gives way to a stronger up-the-center, down-the-outside time-mean circulation pattern. These patterns, often referred to as “gulf-streaming,” are self-reinforcing, as bubbles tend to be pulled into the upflow regions, where the bubbles are already more abundant, as they rise from the distributor. However, it is important to note that the pattern at any instant may differ significantly from the time-mean patterns described above.

5.1.4.4 Gas Mixing and Gas–Solid Contacting in a Bubbling Bed

Gas mixing patterns are strongly influenced by solids motion (May, 1959) and also by the two-phase nature of the bed. Since particles are transported upward by bubbles and the bubbles are nonuniformly distributed, as we have seen above, particles must travel downward in other parts of the column to maintain the bed of solids in place. Wherever particles descend with a vertical component of velocity larger than the interstitial velocity relative to particles, which is given approximately by $U_{\text{mf}}/\varepsilon_{\text{mp}}$ the local absolute velocity of gas elements is directed downward toward the distributor plate. Hence, the regions of net downflow of particles indicated in Figure 5.7 can also be regions where, in a time-mean sense, gas

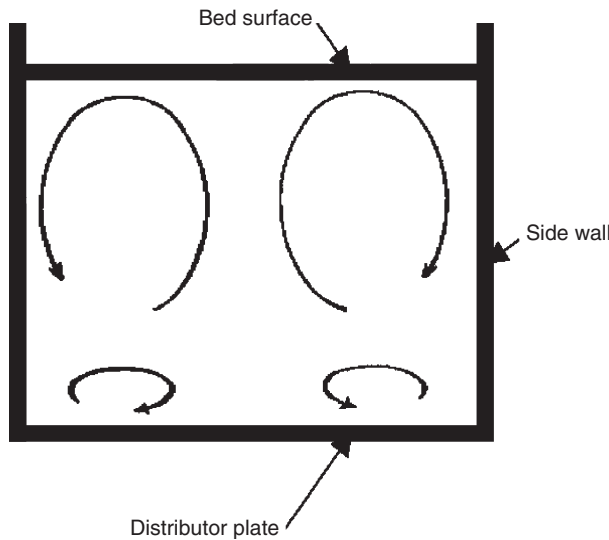


FIGURE 5.7 Typical time-mean solids motion (“gulf-streaming”) in bubbling beds.

elements are carried downward (Latham et al., 1968; Kunii and Levenspiel, 1991). This is one factor contributing to axial dispersion of gas in bubbling fluidized beds, and it can even lead to true “backmixing,” i.e., displacement of gas upstream (downward).

Gas dispersion is also affected by the fact that bubbles travel in general with velocities that differ, usually widely, from the interstitial gas velocity. For example, for group A solids, the bubble velocity is typically of order 0.6 to 1.2 m/sec compared with interstitial gas velocities relative to the particles of order 0.01 m/sec or less. Hence, even if elements of gas in the dense phase are not descending, they are certainly rising much less quickly than gas elements associated with bubbles. Interphase mass transfer diminishes this effect to some extent, but differences in gas velocities between the two phases are a major contributor to substantial deviations from plug flow. While gas mixing deviates considerably from plug flow, the residence time distribution is also far from that corresponding to perfect mixing (Gilliland and Mason, 1952; van Deemter, 1980; Kunii and Levenspiel, 1991). The fact that bubbles are widely distributed in size, and hence in rising velocity (see Eq. [5.25]) further contributes to nonuniform gas residence times of gas elements in the bed. Yet another contributor is that the “throughflow” component of gas velocity, defined above, tends to increase as bubbles elongate while bubbles are interacting and coalescing (Levy and Dorfman, 1995; Grace, 2002). Axial mixing can be significantly reduced by the addition of horizontal baffles (Overcashier et al., 1959).

Reactor models for bubbling beds must take into account the difference in gas–solid contacting, axial dispersion, and gas velocity between the dense phase and bubble phase. A simple two-phase bubbling bed model (Grace, 1986b) that covers the major factors assumes stagnant gas in the dense phase and plug flow in the bubble phase. A small proportion of the bubble phase volume, of order 0.1 to 1%, is assumed to be occupied by particles. Interphase mass transfer is predicted by a semiempirical equation due to Sit and Grace (1981):

$$k_{bd} = \frac{U_{mf}}{3} + \left\{ \frac{4D_{AB}\epsilon_{mf}U_b}{\pi D_b} \right\}^{0.5} \quad (5.31)$$

where D_{AB} is the molecular diffusivity of the reacting component. Mole balances are then written for each phase. For example, for a first-order gas-phase reaction, the mole balance for the bubble and dense phases, respectively, are

$$U \frac{dC_{Ab}}{dz} + k_{bd}a_b\epsilon_b(C_{Ab} - C_{Ad}) + k_r\varphi_b C_{Ab} = 0 \quad (5.32)$$

$$k_{bd}a_b\epsilon_b(C_{Ad} - C_{Ab}) + k_r\varphi_d C_{Ad} \quad (5.33)$$

where C_{Ab} and C_{Ad} are bulk gas concentrations in the bubble and dense phases at height z , k_r is a first-order kinetic rate constant, and $a_b \approx 6/D_b$ is the interphase area per unit volume, whereas ϕ_b (≈ 0.001 to $0.01\epsilon_b$) and ϕ_d ($\approx (1 - \epsilon_b)(1 - \epsilon_{mf})$) are the fractions of the total dense bed volume occupied by solids associated with the bubble and dense phases, respectively.

With the boundary condition $C_A = C_{A0}$ at $z = 0$, these equations can be integrated to estimate the concentration at the top ($z = H$) of a bubbling bed:

$$C_{AH} = C_{A0} \exp \left\{ \frac{-k_r^*[k_{bd}^*(\phi_b + \phi_d) + k_r^*\phi_b\phi_d]}{k_{bd}^* + k_r^*\phi_d} \right\} \quad (5.34)$$

where k_{bd}^* and k_r^* are dimensionless interphase mass transfer and kinetic rate constants defined by

$$k_{bd}^* = \frac{k_{bd}\alpha_b\epsilon_b H}{U} \quad \text{and} \quad k_r^* = \frac{k_r H}{U} \quad (5.35)$$

This simple model illustrates how conversions depend on both interphase mass transfer and chemical kinetics, with the former usually being the rate-determining step. Effectively some of the gas bypasses the bed by short-circuiting through the bubbles, which, because they are much more dilute and usually travel much faster, and are much less effective for reaction than an equal volume of dense phase. Mass transfer resistance within the individual phases is seldom important for gas-phase reactions, but can be important, especially for gas-solid reactions and large (e.g., Geldart group D) particles.

This reactor model can be readily extended to cases where the kinetics are not first order, including multiple reactions; some analytical solutions are available for simple cases (Grace, 1986b). It can also be extended to account for more complex kinetics, axial dispersion in one or both phases, and gas-solid reactions, with numerical solution definitely then being required in such cases.

5.1.4.5 Entrainment

When bubbles burst at the surface of fluidized beds, clumps of bed particles are ejected into the freeboard region (region between bed surface and top of column). The velocities of the ejected particles are of the same order as the bubble rise velocities. When coalescence is in the process of occurring just as two bubbles reach the surface, especially energetic bursts of particles can occur, with the initial vertical component of particle velocity in the freeboard approximately doubled. Most evidence suggests that ejected particles come predominantly from the wake of the bubbles, rather than from the nose. As a result some particles from deep within the bed can find themselves quickly dispersed in the freeboard, where they may escape altogether with the exit gas stream or be disengaged and land at some other horizontal position on the bed surface, thereby contributing to lateral mixing. Because small particles experience more drag relative to their weight than larger ones, the finer material is preferentially lost from the bed. This process of preferentially losing finer material from the mixture is often called "elutriation." The overall particle size distribution in the bed is also, of course, influenced by other factors such as agglomeration, attrition, and growth or shrinkage in particle size as a result of chemical reactions occurring in the reactor.

Two quantities are generally used to characterize the entrainment. The "transport disengaging height", usually abbreviated TDH, is the effective freeboard height (measured from the surface of the dense bed below) beyond which there is negligible change in the entrainment flux. In other words, any ejected particles which, due to gravity, are able to reverse their direction of motion and return to the dense bed, do so within the TDH. In practice, the TDH is the freeboard height usually provided by fluid bed designers, as any greater height results in a negligible decrease in entrainment, whereas a shorter freeboard increases the carryover from the bed. Experimental evidence shows that the TDH is a strong function of both the gas velocity and the column diameter. A graphical correlation by Zenz and Othmer (1960) is commonly used to provide a conservative estimate of the TDH. This correlation is plotted in SI units in [Figure 5.8](#). Several other approaches are also available to predict the TDH, as summarized by Geldart (1986) and by Werther and Hartge (2003).

The other quantity of importance with respect to particle carryover is the entrainment flux as a function of particle size above the TDH. This is needed to estimate the efficiency of cyclones or other gas-solid

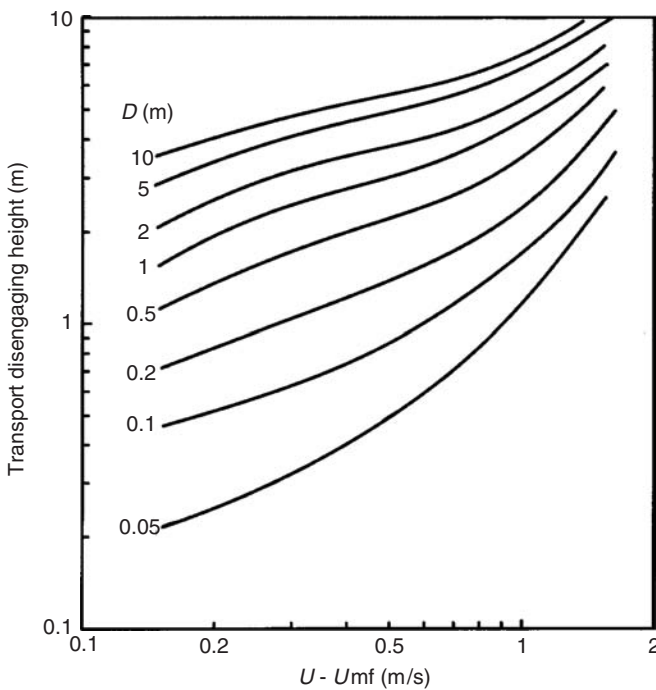


FIGURE 5.8 Transport disengaging height correlation. Adapted from Zenz, F.A. and Othmer, D.F., *Fluidization and Fluid-Particle Systems*, Reinhold, New York, 1960.

separation devices downstream of the bed, and hence to estimate the overall entrainment from the complete system. There are many empirical correlations which can be used to predict the specific rate constant, K_i^* (also called the elutriation constant by some authors). K_i^* is defined in such a way that the flux of particles in a narrow size range of mean diameter d_{pi} is given by

$$G_{si} = m_i K_i^* \quad (5.36)$$

where m_i is the mass fraction of particles in the i th size interval. Available approaches and correlations for K_i^* differ widely, commonly by orders of magnitude, in their predictions. Summaries of these correlations have been published (Geldart, 1986; Werther and Hartge, 2003). It is important to choose an approach which was derived for particles and conditions as similar as possible to those of interest. This makes it very difficult to predict entrainment with any degree of accuracy. A correlation based on an extensive range of materials and operating conditions, including data on units up to 1 m in diameter and data obtained at high temperature and pressure (Choi et al., 1999), gives

$$\frac{K_i^* d_{pi}}{\mu_g} = Ar_i^{0.5} \exp \left\{ 6.92 - 2.11 F_g^{0.303} - \frac{13.1}{F_d^{0.902}} \right\} \quad (5.37)$$

where

$$F_g = g d_{pi} (\rho_p - \rho_g) \quad \text{and} \quad F_d = C_D \rho_g U^2 / 2 \quad (\text{SI units}) \quad (5.38)$$

Entrainment at the bed surface itself can be approximated (Wen and Chen, 1982) by

$$G_{so} = 9.6 A (U - U_{mf})^{2.5} g^{0.5} \rho_g^{3.5} \mu_g^{-2.5} \quad (5.39)$$

Below the TDH, the particle flux decays approximately exponentially with height, with

$$G_{si} = m_i K_i^* + G_{so} \exp\{-\alpha_i z'\} \quad (5.40)$$

where z' is the vertical coordinate measured from the bed surface. The decay constant, α_t , was found (Wen and Chen, 1982) to vary from 3.5 to 6.4 m^{-1} , and can be taken as 4.0 m^{-1} in the absence of specific information.

Solids entrained by the outlet gas usually passes through at least one stage of cyclones and other separators to remove as many particles as possible. Vertical standpipes are employed to return the captured solids to the bottom of the dense bed. To prevent short-circuiting of gas in the wrong direction up the standpipe, trickle valves are commonly installed at the exit of the standpipe.

5.1.5 Slugging Fluidization

The conditions required for slug flow are summarized in Section 5.1.2.4. These conditions are most likely to apply at high H/D ratios in vessels of relatively small diameter. They are satisfied in many laboratory and pilot units, but are unlikely to be applicable in vessels of commercial scale. A useful review of slugging in fluidized beds was provided by Hovmand and Davidson (1971).

Slugs are bullet-shaped voids, rounded at the top and almost flat at the bottom, as shown in Figure 5.9(a). In most cases, they rise nearly symmetrically in the column, though asymmetric slugs clinging to the wall are sometimes observed. Once continuous slugging has become established, the inter-slug spacing, i.e., the separation distance between the bottom of one slug and the nose of the next slug, typically reaches $\sim 2D$. The flow is then fully developed and the length of slugs, ℓ_s , can be estimated from the quadratic equation

$$\ell_s/D = 0.495(\ell_s/D)^{0.5}(1 + \beta) + 0.061 - 1.94\beta = 0 \quad (5.41)$$

where

$$\beta = \frac{U - U_{mf}}{U_{si}} \geq 0.2 \quad \text{and} \quad U_{si} = 0.35\sqrt{gD} \quad (5.42)$$

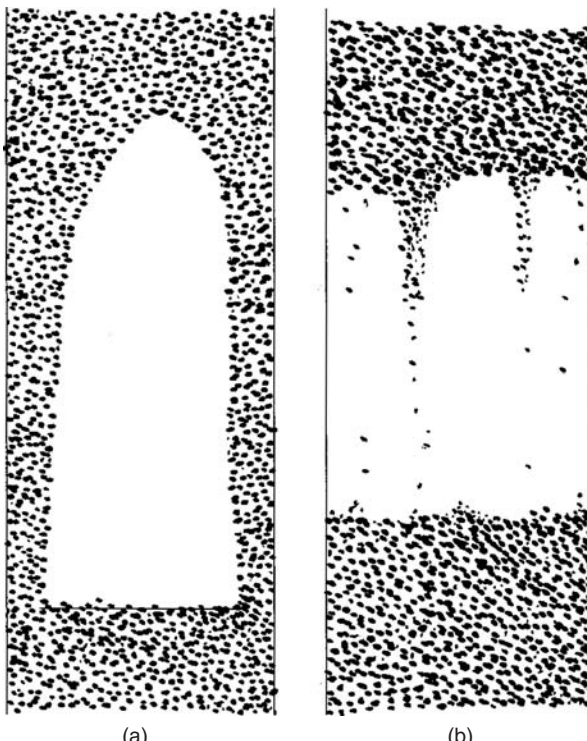


FIGURE 5.9 Shapes of slugs: (a) axisymmetric round-nosed slug; (b) square-nosed slug.

The velocity of each slug is approximately given by

$$U_s = U_{si} + (U - U_{mf}) \quad (5.43)$$

The frequency with which slugs pass a given level and also reach the upper bed surface is then

$$f_s = U_s / (\ell_s + 2D) \quad (5.44)$$

In slugging beds, the upper surface rises smoothly as the top slug approaches and then falls sharply as the slug breaks the upper surface. The maximum expanded bed height for slugging beds, achieved just as each slug breaks the surface, is approximately

$$H_{\max} = H_{mf}(1 + \beta) \quad (5.45)$$

Like bubbles, slugs have wakes at the bottom, but these are stunted relative to wakes of bubbles of similar size. As a result, both solids and gas mixings are less for slugging beds than for comparable bubbling beds.

The equations above provide good estimates of the major hydrodynamic properties of most slugging fluidized beds where $H \gg D$. Results for gas and solids mixing and models for chemical reaction are also available for this flow regime (Hovmand and Davidson, 1971).

Another mode of slug flow, usually called “square-nosed slugging,” is also sometimes encountered in columns of small diameter. In this case, the slugs are relatively flat both at top and bottom, as indicated in [Figure 5.9\(b\)](#). These slugs rise relatively slowly as particles rain from the top surface (roof) of each slug. Square-nosed slugs are usually attributable to relatively large d_p/D ratios or large cohesive particles, coupled with smooth-walled columns. This mode has no useful features, nor can it be scaled up. Therefore, it should be avoided in practice and is not pursued further here.

5.1.6 Turbulent Fluidization

When the superficial gas velocity reaches U_c (see [Section 5.1.2.5](#)), there is a transition to the turbulent fluidization flow regime. The turbulent regime bridges between the bubbling (or slugging) regime, where bubbles (or slugs) are dispersed in a continuous dense phase of particles and interstitial gas, and the fast fluidization regime, where particles streamers and clusters are dispersed in a continuous dilute suspension of particles in gas. While voids appear in the turbulent fluidization flow regime, they are much more transitory in nature, irregular in shape, and generally smaller than the bubbles and slugs encountered in the bubbling or slugging flow regimes. Hence, the distinction between a dense phase and a dilute phase is generally unnecessary for the turbulent flow regime. The turbulent flow regime turns out to be especially favorable for carrying out chemical reactions and certain physical operations. An extensive review of the turbulent flow regime was published by Bi et al., (2000).

5.1.6.1 Hydrodynamics of Turbulent Fluidization Flow Regime

The overall mean (spatial- and time-average) voidage in the turbulent flow regime is generally in the range 0.65 to 0.75, intermediate between that in bubbling and fast fluidization. There is little variation in the axial direction until one approaches the bed surface. Because of surging and eruption of voids, the upper surface is indistinct, and hence the time-mean expanded bed depth is commonly inferred from pressure profiles, ideally involving a series of pressure taps extending from low in the bed to well into the freeboard region. X-rays and γ -rays can also be employed for this purpose. Radial profiles of local time-mean voidage show significantly higher values in the core of the column than near the outer wall. A correlation (Wang and Wei, 1997) which accounts for this variation is

$$\varepsilon = 1 - (1 - \langle \varepsilon \rangle_A) \{0.908 + 0.276(r/R)^4\} \quad (5.46)$$

Data on axial and radial voidage variations are summarized by Bi et al. (2000).

The local flow structure within turbulent fluidized beds is complex, as demonstrated by a number of different characterization techniques including spectral analysis, chaos analysis, and wavelet analysis. Whichever of these techniques is used, the character of the profiles for the turbulent regime tend to be quite distinctive (Bai et al., 1999). For cases where the turbulent regime is preceded by slug flow (usually restricted to group B or D solids), there is local intermittency between periods of slug-flow-like behavior and fast-fluidization-like structures. However, when turbulent fluidization is preceded by bubbling (generally encountered with group A solids), the structure is more homogeneous.

Given the relative homogeneity of turbulent fluidized beds and the transient nature of voids, internal baffles are generally not required. When vertical or horizontal heat transfer tubes are present, they tend to influence the hydrodynamics less than for the bubbling bed flow regime.

5.1.6.2 Gas and Solids Mixing

Since mixing within the turbulent flow regime occurs by much smaller and more random steps than in bubbling fluidized beds, it is more appropriate to apply models based on the analogy with molecular diffusion. The axial dispersion coefficient, $D_{g,ax}$, has been correlated (Bi et al., 2000), based on data from a number of studies, by

$$Pe_{g,ax} = \frac{UH}{D_{g,ax}} = 3.47 Ar^{0.149} Re^{0.0234} Sc^{-0.231} \left(\frac{H}{D} \right)^{0.285} \quad (5.47)$$

There are relatively few data available with respect to radial gas mixing in the turbulent flow regime. The results which are available indicate that radial mixing is again about an order of magnitude smaller than axial mixing. Hence one can take $D_{g,rad} \approx 0.1D_{g,ax}$ as a first approximation.

Solids mixing in turbulent beds has received only limited attention. Recommended correlations are:

- (i) For group A particles (Lee et al., 1991):

$$D_{s,ax} = 0.365 Re_D^{-0.368} [g(U - U_{mf})D^4]^{1/3} \quad (5.48)$$

- (ii) For group B particles (Lee and Kim, 1990):

$$Pe_{s,ax} = \frac{UH}{D_{s,ax}} = 4.22 \times 10^{-3} Ar \quad (5.49)$$

One may again assume that radial or lateral mixing coefficients are an order of magnitude less than for the corresponding axial dispersion. Overall solids mixing is generally large enough that temperature gradients are small within turbulent fluidized beds, as for bubbling beds.

5.1.6.3 Mass Transfer and Chemical Reaction

Given the broad spectrum of local voidages, rapid disintegration and reforming of voids and the lack of a coherent two-phase structure in the turbulent flow regime, inter-phase mass transfer is unlikely to provide a significant resistance when considering chemical reactions in turbulent fluidized beds. Hence single-phase axially dispersed reactor models can be used (e.g. Foka et al., 1996) to predict the conversion and selectivity of gaseous components. The axial dispersion coefficient can then be estimated from Eq. (5.47) above. Reaction in the freeboard region may be significant, requiring that it also be estimated. Note also that it may be important to make allowance for the radial variation of void fraction when modeling turbulent fluidized-bed reactors.

The simple axially dispersed plug flow approach has been extended (Thompson et al., 1999; Abba et al., 2003) to consider gradual transitions between the flow regimes, rather than assuming regime-specific reactor models with step changes at the regime boundaries. In this approach, probabilistic averaging is performed so that, as U increases, the probability of bubbling falls from nearly unity, whereas the probability of turbulent fluidization increases to nearly unity and then falls, and the probability of fast fluidization is initially 0 but ultimately approaches unity.

5.1.6.4 Entrainment

Entrainment above the TDH of particles from turbulent fluidized beds can be predicted by means of the equation (Tasarin and Geldart, 1998)

$$K_i^* = 14.5 \rho_g U^{2.5} \exp\{-5.4 V_{si}/U\} \quad (5.50)$$

The TDH can be predicted using [Figure 5.8](#), or alternatively from correlations in the literature (Wen and Chen, 1982; Baron et al., 1988).

5.1.7 Fast Fluidization and Dense Suspension Upflow

Fast fluidization is usually encountered with group A and B solids at superficial gas velocities > 1.5 m/s. To maintain continuous operation, particles must be continuously fed to the bottom of the vertical shaft to replace those carried over from the top. Whereas lower velocity fluidization flow regimes have a relatively dilute freeboard region to disengage particles ejected at the bed surface, there is no bed surface, and hence no “bed,” nor is there any freeboard region, in the fast fluidization flow regime. Instead particles are conveyed upwards, individually and as loose clusters, through the entire column height. Efficient gas–solids separators (usually cyclones, but occasionally inertial separators) are relied upon to capture entrained particles and return them via a standpipe or “downer” (Li et al., 2004) to near the bottom of the main column or riser. The overall configuration, including the riser (where the main gas–solid contacting and chemical reaction[s] take place), the gas–solid separator(s), standpipe, and any non-mechanical or mechanical valves in the recirculation line, together constitute the CFB system. A typical CFB configuration is shown schematically in [Figure 5.10\(b\)](#). Note that the H/D ratio is usually $\gg 1$, especially for small-scale systems.

5.1.7.1 Hydrodynamics of Fast Fluidization Flow Regime

The riser of a CFB system is usually operated in the fast fluidization flow regime. Since, as indicated in [Figure 5.10\(b\)](#), the exit at the top of the riser is usually at one side, while the return of solids to the bottom of the riser also involves asymmetric re-entry, flow at the top and bottom of a CFB riser is generally not symmetric about the axis. On the other hand, axisymmetric flow (in risers of circular cross-section) or planar symmetry (in risers of rectangular cross-section) can commonly be assumed throughout the middle portion of the riser.

To a first approximation, the acceleration and wall friction terms in the momentum equation for flow in CFB risers can be neglected for fast-fluidized beds relative to the gravity terms. It is then possible to derive an approximate profile of axial density from the axial pressure profile, since, with $\rho_p \gg \rho_g$,

$$1 - \langle \varepsilon \rangle_A \approx - \frac{1}{g\rho_p} \frac{dP}{dz} \quad (5.51)$$

The cross-sectional average voidage within a fast-fluidized bed is generally lowest near the distributor plate, increasing with height, reaching a plateau approximating fully developed conditions at some distance above the bottom, and then varying again toward the top outlet. When the top is constricted (i.e., the area of the exit is less than that of the riser), there tends to be an increase in solids concentration (decrease in voidage) near the exit, whereas a very open or smoothly tapered exit tends to cause an increase in voidage toward the top. The various shapes of axial voidage profile and the influence of various operating variables on them have been summarized nicely by Bai et al. (1992). Some typical axial profiles of solids holdup are plotted in [Figure 5.11](#). The main variables, in addition to the exit geometry, are the net solids circulation flux, G_s , and the superficial gas velocity, U . With increasing G_s , U , ρ_p or d_p , the solids holdup ($= 1 - \langle \varepsilon_A \rangle$) increases, and there is more likely to be an upturn in the axial solids holdup profile near the top exit. This arises because the top of the column acts as a crude inertial gas–solids separator, in which the particles have more difficulty negotiating the turn into the exit duct if they are larger, denser, moving more quickly, or present in greater numbers.

Expressions which can be used to estimate the limiting cross-sectional average voidages, ε_d in the lower dense region and ε^* at the top exit, are given by Bai and Kato (1999).

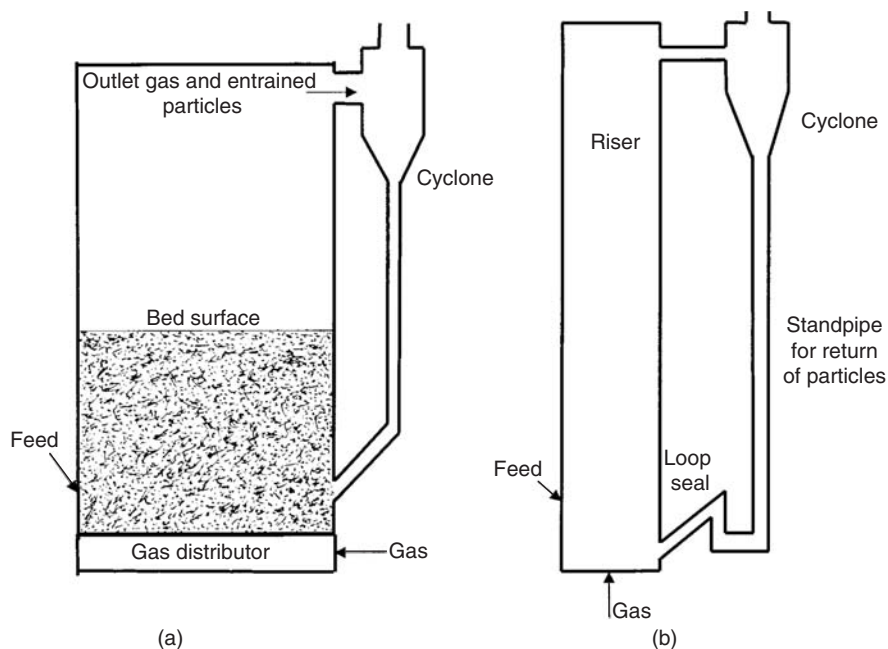


FIGURE 5.10 Typical equipment configurations of (a) dense (bubbling, slugging, or turbulent) fluidized beds and (b) circulating fluidized beds.

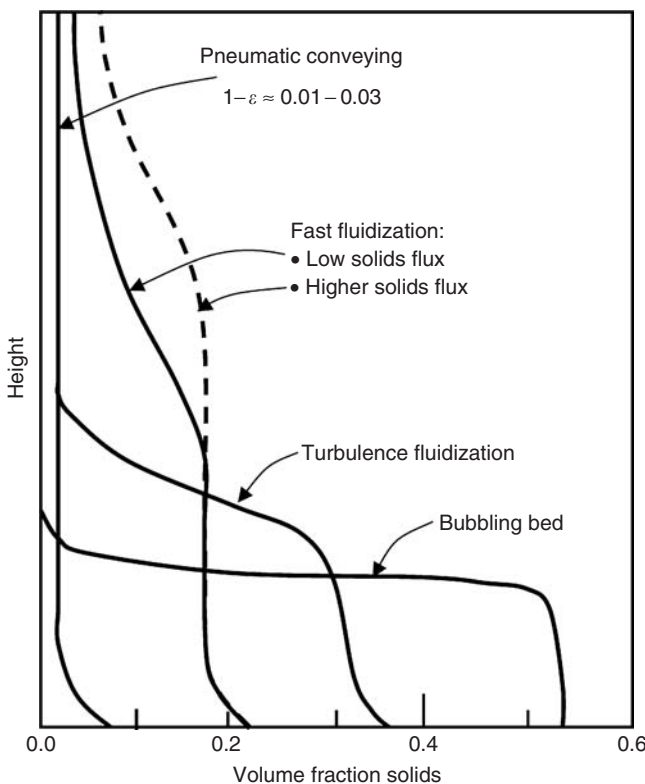


FIGURE 5.11 Typical solids holdup profiles in bubbling, turbulent, fast fluidization, and dilute pneumatic conveying flow regimes.

One first calculates the saturation carrying capacity, G_s^{sat} :

$$\frac{G_s^{\text{sat}} d_p}{\mu_g} = 0.125 \left(\frac{U}{\sqrt{gd_p}} \right)^{1.85} Ar^{0.63} \left(\frac{\rho_p - \rho_g}{\rho_g} \right)^{-0.44} \quad (5.52)$$

and

$$\varepsilon' = 1 - G_s / [\rho_p(U - V_s)] \quad (5.53)$$

For $G_s < G_s^{\text{sat}}$ one then calculates

$$\varepsilon_d = 1 - \varepsilon' \left\{ 1 + 6.14 \times 10^{-3} \left(\frac{G_s}{\rho_p U} \right)^{0.23} \left(\frac{\rho_p - \rho_g}{\rho_g} \right)^{1.21} \left(\frac{U}{\sqrt{gD}} \right)^{-0.383} \right\} \quad (5.54)$$

and

$$\varepsilon^* = 1 - 4.04(1 - \varepsilon')^{1.214} \quad (5.55)$$

On the other hand, when $G_s \geq G_s^{\text{sat}}$,

$$\varepsilon_d = 1 - \varepsilon' \left\{ 1 + 0.103 \left(\frac{\rho_p U}{G_s} \right)^{1.13} \left(\frac{\rho_p - \rho_g}{\rho_g} \right)^{-0.013} \right\} \quad (5.56)$$

and

$$\varepsilon^* = 1 - (1 - \varepsilon') \left\{ 1 + 0.208 \left(\frac{\rho_p U}{G_s} \right)^{0.5} \left(\frac{\rho_p - \rho_g}{\rho_g} \right)^{-0.082} \right\} \quad (5.57)$$

These relationships provide estimates of the voidages in the lower dense region and at the top of the column. Between the bottom region and the top, the voidage varies, asymptotically approaching ε_d as one approaches the lower dense zone and ε^* as the top exit is approached. Hence, these relationships facilitate estimation of the full axial voidage profiles.

The solids holdup in fast fluidization is much higher toward the outer wall, where there are descending streamers, than in the core of the riser, where there is upward motion of gas and widely dispersed particles. Except near the solids entry or re-entry ports and asymmetrically located exit ports, the radial profile of time-mean voidage can then be predicted (Issangya et al., 2001) by

$$\varepsilon = \varepsilon_{\text{mf}} + \{ \langle \varepsilon \rangle_A - \varepsilon_{\text{mf}} \} \langle \varepsilon \rangle_A^{-1.5 + 2.1(r/R)^{3.1} + 5.0(r/R)^{8.8}} \quad (5.58)$$

For columns of rectangular or square cross section, the corners are regions of decreased voidage and more prominent solids downflow.

Solids velocities are upward throughout most of the cross section of the column, but downward velocities are experienced at the wall, with a time-mean value of approximately (Griffith and Louge, 1998)

$$v_{sw} = -36 \sqrt{gd_p} \quad (5.59)$$

The negative sign in this equation indicates that the solids are traveling downward on average at the wall of the riser when the fast fluidization flow regime is present. This downward velocity corresponds to dense streamers or clusters of elongated lens-shapes, descending jerkily along the outer wall of the riser. The thickness of the wall layer subject to net downflow of solids has been correlated (Kim et al., 2004b), covering a broad range of conditions by

For $U_{\text{slip}}^* < 6.5$,

$$\frac{\delta_w}{D^{0.85}(U^2/g)^{0.15}} = 1.73(U_{\text{slip}}^*)^{0.21} \left\{ \frac{U}{\sqrt{gd_p}} \right\}^{-0.97} \left\{ \frac{\rho_p[1 - \langle \varepsilon \rangle_A]}{\rho_g \langle \varepsilon \rangle_A} \right\}^{0.16} \quad (5.60)$$

For $U_{\text{slip}}^* \geq 6.5$,

$$\frac{\delta_w}{D^{0.85}(U^2/g)^{0.15}} = 0.53(U_{\text{slip}}^*)^{-0.32} \left\{ \frac{G_s}{\rho_p[1 - \langle \varepsilon \rangle_A]U} \right\}^{-0.55} \left\{ \frac{\rho_p[1 - \langle \varepsilon \rangle_A]}{\rho_g \langle \varepsilon \rangle_A} \right\}^{-0.70} \quad (5.61)$$

where

$$U_{\text{slip}}^* = \left\{ \frac{\rho_g^2}{g\mu(\rho_p - \rho_g)} \right\}^{1/3} \left[U - \frac{G_s \langle \varepsilon \rangle_A}{\rho_p [1 - \langle \varepsilon \rangle_A]} \right] \quad (5.62)$$

The time-mean particle velocity is upward everywhere, except for this outer wall layer, reaching a maximum at the axis of the column. Radial profiles of solids flux are similar to those of time-mean local particle velocity, positive (upward) and at a maximum at the axis of the column, and negative (downward) at the outer wall. Gas velocity profiles are difficult to measure, but follow similar trends. However, the gas motion is upward relative to the particles.

In some CFB processes such as combustion of solid fuels, gas is fed from the sides of the column through nozzles or orifices at some height well above the principal gas distributor. The resulting gas jets tend to disrupt the downward-moving wall layers. Moreover, the region of lower gas velocity below the secondary nozzles tends to be denser and somewhat isolated from the region above the secondary nozzles. If these secondary jets are introduced tangentially, the resulting swirl tends to cause an increase in solids holdup near the outer wall due to centrifugal forces.

5.1.7.2 Dense Suspension Upflow

The downflow of particles in streamers and clusters at the wall, which is a major feature of the fast fluidization flow regime, no longer occurs when the solids flux is sufficiently high, typically beyond ~ 200 to $300 \text{ kg/m}^2\text{s}$. Instead, the time-mean particle and gas motion is upward throughout the entire cross-section, with ~ 7 to 20% or more of the overall cross-sectional area occupied by particles. This flow regime has been called “dense suspension upflow” (or DSU) (Grace et al., 1999). It is encountered in fluid catalytic cracking (FCC) and other catalytic processes where there are group A solids combined with high solids throughputs. The transition to the DSU flow regime is covered in Section 5.1.2.7 above. As noted there, the DSU and fast fluidization flow regimes can coexist, occupying different portions of the same riser.

While there is no net local downflow in the DSU flow regime and the flow is generally more homogeneous, there are still marked radial gradients, with much higher time-average voidages near the axis of the riser than near the wall (Issangya et al., 2000; Liu et al., 2003). The voidage can approach ε_{mf} at the wall. Equation (5.58) can again be used to predict the radial voidage variation, as it is based on DSU data, in addition to data from the fast fluidization flow regime. Particle velocities also reach a maximum at the axis of the column, approaching, or even exceeding, $2U$. Local solids fluxes are typically 1.5 to 2.5 G_s at the axis of the column, falling to close to 0 at the wall. Local fluctuations in voidage are strongly correlated with local fluctuations of particle velocity (Liu et al., 2003), so that it is not possible to obtain time-mean solids fluxes from time-mean voidages and particle velocities.

5.1.8 Spouted Beds

Spouted beds provide an alternative to fluidized beds for relatively coarse particles (larger than about 1 mm in diameter). The geometry of a typical spouted bed is shown in Figure 5.12. This generally involves a single central orifice at the bottom and a conical section at the base leading to a vessel of cylindrical cross section at the top. However, there are many variants on this geometry, including flat-bottomed vessels, completely cylindrical and completely conical vessels, columns of rectangular cross section equipped with slot orifices, and reactors equipped with nonporous or porous draught tubes, extending over most of the height of the particles. It is also possible to have multiple orifices (leading to multiple spouts) and a hybrid of spouting and fluidization (called a “spout-fluid bed”) as discussed below. For comprehensive reviews of spouted beds, see Mathur and Epstein (1974) and Epstein and Grace (1997).

A spouted bed is composed of three separate regions: a relatively dilute spout (or jet) region above the orifice extending right up to the bed surface, a surrounding moving-packed-bed annulus region, and a fountain region above the bed (annulus) surface, where particles travel upward through a certain distance from the top of the spout and then rain back under gravity onto the surface of the annulus. Systematic solids circulation occurs as particles descend in moving-packed-bed flow through the annulus, are entrained from the spout–annulus interface into the upward jet of gas in the spout where they are

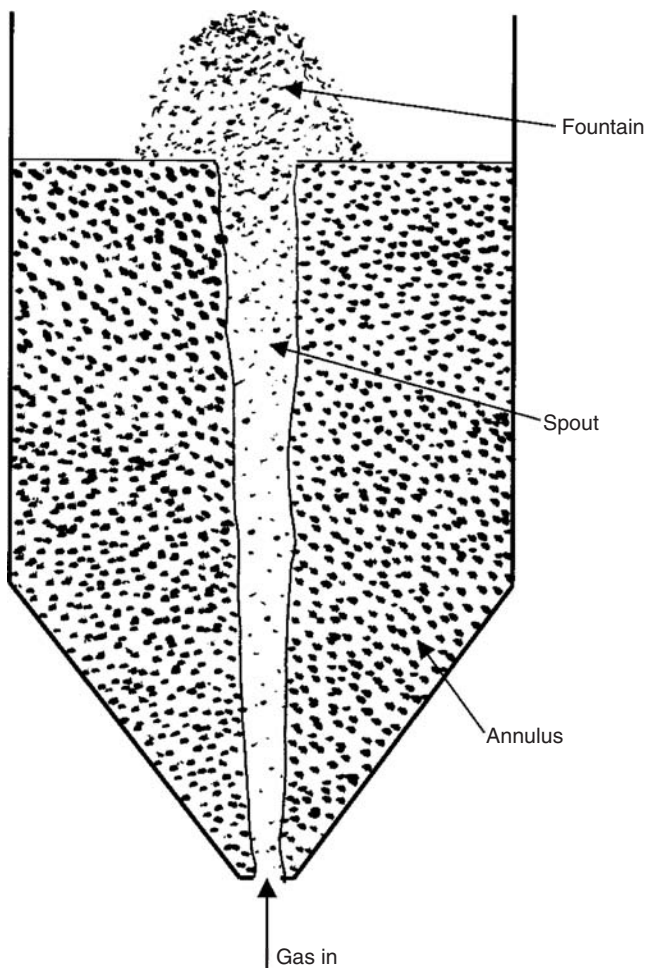


FIGURE 5.12 Schematic of typical spouted bed.

accelerated upwards and carried through the top of the spout, and thence return in the fountain to the top surface of the annulus.

Unlike a fluidized bed where all of the weight-minus-buoyancy is supported by drag from the fluid, in a spouted bed only part is provided by drag, with the rest of the weight of particles in the annulus borne by particles below. Hence the pressure drop across a spouted bed is lower, typically by 25 to 30%, than in a corresponding fluidized bed. This lower pressure drop results in lower energy costs and therefore constitutes one of the advantages of spouted beds. Other advantages are that the gas and particle motion are more systematic and predictable than in fluidized beds. Disadvantages are that narrower particle size distributions tend to be needed, that scaleup is only possible over a much lower range of column diameters, that particle-particle contact is more likely to cause agglomeration, and that the range of gas velocities which can be used is less broad than for fluidized beds.

Typically a spouted bed is constrained by certain limits for good operation. In order for a coherent spout to form, the ratio d_{or}/d_p should not exceed about 25, while the ratio D/d_{or} must be greater than ~ 3 for coarse particles or ~ 10 for relatively fine materials. The included angle of a conical base should generally be at least 40° .

The minimum spouting velocity is usually predicted by an early correlation proposed by Mathur and Gishler (1955):

$$U_{ms} = \left(\frac{d_p}{D} \right) \left(\frac{d_{or}}{D} \right)^{1/3} \sqrt{\frac{2gH(\rho_p - \rho_g)}{\rho_g}} \quad (5.63)$$

Unlike the minimum fluidization velocity U_{mf} (Eq. [5.5] above), U_m depends on the bed depth, H , and on the equipment used (via the orifice diameter, d_{or}). For relatively large columns where $D > 0.5$ m, the right-hand side of Eq. (5.63) should be multiplied by $2D$ (with D in meters) to compensate empirically for systematic underestimation by the original correlation (Epstein and Grace, 1997).

The maximum spoutable bed depth, beyond which it is not possible to obtain spouting, can be predicted from the correlation

$$H_m = \frac{D^2}{d_p} \left(\frac{D}{d_{or}} \right)^{2/3} \frac{568b^2}{Ar} \times \left\{ \sqrt{1 + 35.9 \times 10^{-6} Ar} - 1 \right\}^2 \quad (5.64)$$

where the empirical constant b can be taken as 1.11 for room temperature conditions and 0.9 for elevated temperatures. It can be shown by differentiation that H_m reaches a maximum at $Ar = 223,000$, corresponding typically to $d_p \approx 1\text{--}1.5$ mm.

Once spouting has been achieved, the pressure drop across the bed, ΔP_s , is approximately 65 to 70% of that across a fluidized bed of the same particles of the same depth, and the axial pressure distribution can be approximated (Lefroy and Davidson, 1969) by

$$\frac{dP}{dz} = \frac{-\Delta P_s}{2H} \pi \sin\left(\frac{\pi z}{2H}\right) \quad (5.65)$$

The flow of gas in the annulus at height z can be estimated by a result derived by Mamuro and Hattori (1968):

$$\frac{U_a}{U_{mf}} = 1 - \left(1 - \frac{z}{H_m} \right)^3 \quad (5.66)$$

This relationship works well even when $H < H_m$ and for a wide range of particle sizes. The fraction of the total flow that passes through the annulus at any height, z , is then given by $(U_a/U)[1 - (d_s/D)^2]$, where d_s is the spout diameter, which in turn can be estimated from an empirical dimensional correlation due to McNab (1972):

$$d_s = 2.0(\rho_g U)^{0.49} D^{0.68} \rho_b^{-0.41} \quad (5.67)$$

where ρ_b is the bulk density of the particulate material. In practice, the spout diameter varies with height, with the shape varying, e.g. diverging continuously or necking (Epstein and Grace, 1997). The above equation should therefore be regarded as predicting a longitudinal average spout diameter.

The voidage in the annulus can be approximated as being uniform and equal to the packed-bed value, which for the relatively coarse particles of interest is also nearly equal to ε_{mf} , the voidage at minimum fluidization, with a typical value of 0.41 to 0.43. The voidage in the spout starts out at 1 at $z = 0$ and then decreases approximately linearly with increasing height, z . The depth of the annulus under operating conditions is generally very nearly the same as the depth of the same bed of particles without any flow through it. The fountain height can be estimated (Grace and Mathur, 1978) from the semi-empirical equation

$$H_f = \frac{\rho_p (\varepsilon_{SH}^{0.93} v_{OSH})^2}{2g(\rho_p - \rho_g)} \quad (5.68)$$

where ε_{SH} is the voidage in the spout at the bed surface, i.e., at $z = H$ and v_{OSH} is the particle velocity in the spout on the column axis at the same level. Several models are available for predicting the latter two quantities, and the particle circuit times and trajectories (Mathur and Epstein, 1974; Epstein and Grace, 1997).

When spouted beds are employed as chemical reactors, they have better gas–solid contacting in the annulus than in the spout. Hence, two-region models are required to predict gas conversions, with a molar balance at the bed surface to estimate the overall composition of the gas at that level. This approach is analogous to the two-phase models for fluidized-bed reactors discussed above. Allowance may also be made for additional gas–solid contacting in the fountain region. When the particles are reacting (e.g., in spouted-bed combustion or gasification of solid fuels), mole balances for the gas must be coupled with those for the solid phase. The particles can usually be assumed to be perfectly mixed.

As noted above, spout-fluid beds are intermediate between spouted beds and fluidized beds. In addition to the spouting gas (or liquid) introduced through a central orifice, a fraction of the total fluid is also introduced around the outer periphery at the bottom, for example, distributed over a lower conical surface. This generally helps avoid particle agglomeration, improves the distribution of gas between the annulus and spout regions, increases the solids circulation rate, and reduces temperature gradients in the annulus (Epstein and Grace, 1997). Various flow regimes exist depending on geometry, total flow rate, and whether or not the auxiliary gas injected at the bottom is sufficient to fluidize the particles.

5.1.9 Three-Phase Fluidization

Gas–liquid–solid fluidization is practiced in some biochemical reactors and in certain chemical processes where solid particles need to be contacted with both liquid and gas, for example, in hydrotreating of liquid hydrocarbons by gaseous hydrogen in the presence of solid catalyst particles. A thorough review of three-phase fluidized beds (covering their fundamentals as well as their applications) has been published by Fan (1989). Many contacting modes and geometries are possible. This brief section only deals with cases where the gas and liquid are both introduced at the bottom and travel cocurrently upward in a cylindrical column without any draught tube or other internal surfaces.

There is considerable extra complexity due to having three distinct phases (gas, liquid, and solid) interacting with each other. Some of the simpler results are presented here. First, the sum of the holdups of the individual phases must be unity, i.e.,

$$\varepsilon_s + \varepsilon_l + \varepsilon_g = 1 \quad (5.69)$$

Since wall friction and accelerational effects are usually negligible, the hydrostatic pressure gradient in the bed can be written as

$$\frac{dP}{dz} = -\{\rho_p \varepsilon_s + \rho_l \varepsilon_l + \rho_g \varepsilon_g\}g \quad (5.70)$$

The gas contribution ($\rho_g \varepsilon_g$) term in the brackets can usually be ignored relative to the other terms on the right-hand side. If the pressure gradient is measured experimentally, then a third equation is needed to solve for the three unknown holdups. Frequently, this is obtained as a fair approximation by assuming that all of the particles stay in the bed and that the solids holdup is independent of height, i.e.,

$$M_p = \rho_p \varepsilon_s A H \quad (5.71)$$

where M_p is the mass of particles present and H the expanded bed height.

The minimum fluidization condition depends on the flow of both gas and liquid. If the gas flow is fixed at some low value, the liquid minimum fluidization velocity, U_{lmf} , can be predicted by a gas-perturbed liquid model (Zhang et al., 1995) in which the primary role of the gas is assumed to be the occupation of space, causing an increase in the velocity of liquid due to the smaller area available for liquid flow. The best agreement is provided (Lee et al., 2003) when the buoyancy is based on the gas–liquid mixture (rather than the liquid alone) and when allowance is made for a decrease in voidage, observed experimentally, when gas is added to a bed of particles through which liquid is percolating. The resulting equation, analogous to Eq. (5.5) for two-phase systems, is

$$Re_{lmf} = \frac{\rho_l d_p U_{lmf}}{\mu_l} = \sqrt{C_1^2 + C_2 Ar'(1 - \alpha_{mf})^3} - C_1 \quad (5.72)$$

where

$$Ar' = \frac{\rho_l (\rho_p - [\rho_g \alpha_{mf} + \rho_l (1 - \alpha_{mf})]) g d_p^3}{\mu_l^2} \quad (5.73)$$

and α_{mf} is the gas holdup expressed on a solids-free basis at minimum fluidization, which can be predicted from the empirical correlation of Yang et al. (1993):

$$\alpha_{\text{mf}} = \frac{0.16U_g}{\varepsilon_{\text{mf}}(U_g + U_l)} \quad (5.74)$$

The observed variation in voidage at minimum fluidization due to gas addition is accounted for by the empirical equation

$$\varepsilon_{\text{mf}} = \varepsilon_{\text{mf}|U_g=0} \left\{ 1 - 0.34(1 - U_{\text{lmf}}/U''_{\text{lmf}}) + 0.22(1 - U_{\text{lmf}}/U''_{\text{lmf}})^2 \right\} \quad (5.75)$$

where U_{lmf} and U''_{lmf} are the liquid superficial velocities at minimum fluidization for three-phase (gas–liquid–solid) and two-phase (liquid–solid) fluidization, respectively. Equations (5.72)–(5.75) are solved simultaneously to yield values of the three unknowns: α_{mf} , ε_{mf} , and U_{lmf} . The Wen and Yu (1966) values of the constants, i.e., $C_1 = 33.7$ and $C_2 = 0.0408$, are recommended, as in Section 5.1.2.1. Experimental values of the voidage at minimum fluidization without any gas present are recommended whenever they are available; otherwise one can employ the correlation of Limas-Ballesteros (1980):

$$\varepsilon_{\text{mf}|U_g=0} = 0.42/\psi^{0.376} \quad (5.76)$$

where ψ is the particle sphericity. A similar approach can be used to predict minimum fluidization velocities of inverse fluidization (where the particle density is less than the liquid density) and three-phase systems where the liquid flow is far less than that required to fluidize the solids (Zhang et al., 1998).

When three-phase fluidization has been achieved, it is difficult to obtain accurate predictions of behavior, due to such factors as different flow regimes, the wide range of possible properties and operating conditions, and the role of wettability and surfactants. In practical systems, the liquid phase may be non-Newtonian in nature, further complicating the predictions. Fan (1989) provides a useful summary of the empirical and semi-empirical methods available to predict such properties as solids, gas, and liquid holdups, solids holdup in the freeboard region and bed expansion.

The most successful models for predicting three-phase bed hydrodynamics are heavily based on bubbles and their wakes. Small bubbles are spherical or nearly so. With increasing size, they become ellipsoidal and wobbly, ultimately undergoing a transition to spherical-cap bubbles, whose wakes approximately complete the spheres of which the bubbles form the tops. These wakes (Fan and Tsuchiya, 1990), carried at the back of rising bubbles, are responsible for a number of key behavioral aspects of three-phase systems:

- They transport liquid and solids rapidly in an upward direction, accounting for much of the rapid axial mixing and transport of both liquid and solids.
- The rapid transport of liquid in the wake can explain a surprising feature of some three-phase systems, where the introduction of gas bubbles into a liquid–solid system actually causes a decrease in bed expansion. Several criteria are available (Fan, 1989) for when bed contraction, rather than expansion, occurs upon the addition of gas.
- When the bubbles reach the bed surface, their wakes transport solid particles right into the freeboard region, often leading to significant carry-over.

5.1.10 Practical Considerations for Gas–Solid Systems

Important aspects of particle and gas properties are covered in Table 5.1. This section briefly considers some of the important aspects of equipment design and operation. More design tips and details are provided in major texts and information sources on fluidization (Zenz and Othmer, 1960; Hetsroni, 1982; Geldart, 1986; Pell, 1990; Kunii and Levenspiel, 1991; Grace et al., 1997; Yang, 2003).

The most important design variable for fluidized beds is the gas distributor (see Figure 5.10a). This should provide: (a) a pressure drop across it of approximately 30%, and definitely not less than 10%, of that across the fluidized solids above it; (b) distribute the gas uniformly over the cross section above it, typically

requiring that the gas entry points should not be more than 100 mm apart; (c) damp out pressure fluctuations from the blower or compressor; (d) not cause “sand blasting” (erosion) of surfaces or excessive attrition, typically meaning that entry velocity of the gas should not exceed 30 to 50 m/sec and the jet should not impinge directly on fixed surfaces such as vessel walls or heat transfer tubes; (e) support the dead weight of the bed when the gas is shut off; (f) not cause weeping or dumping of solids into the windbox below (due to pressure fluctuations); and (g) not become blocked by particles or deposits. Many different geometries are used in practice including nozzles, tuyeres, downward-facing orifices and shrouded orifices, etc.

Jet penetration into a zone which does not contain bubbles can be predicted by correlations due to Merry (1971, 1975):

Vertical jets:

$$L_j = 5.2d_{\text{or}} \left(\frac{\rho_g d_{\text{or}}}{\rho_p d_p} \right)^{0.3} \left\{ 1.3 \left(\frac{u_{\text{or}}^2}{gd_{\text{or}}} \right)^{0.2} - 1 \right\} \quad (5.77)$$

Horizontal jets:

$$L_j = d_{\text{or}} \left\{ 5.25 \left[\frac{\rho_g u_{\text{or}}^2}{(1 - \varepsilon_{\text{mf}}) \rho_p g d_p} \right]^{0.4} \left(\frac{\rho_g d_p}{\rho_p d_{\text{or}}} \right)^{0.2} - 4.5 \right\} \quad (5.78)$$

Jet penetration is reduced if the region into which the jet penetrates contains bubbles. In some cases, gas may be introduced in a downward direction, or obliquely downward. Penetration is then considerably reduced, but at the expense of higher particle attrition. It is especially important to assure excellent dispersion and mixing in cases where liquid must be sprayed into the bed or where particles are wet or sticky. In such cases, high gas velocities coupled with uniform gas distributors and a lack of locations where particles can sit without being immediately set into motion are important to maintain the continuity of fluidization and prevent defluidization, hot spots, and fouling.

Attrition of particles in fluidized beds may occur due to impact of particles with fixed surfaces or with other particles (e.g., in jets or in cyclones), due to abrasion wearing away surface roughness, due to rapid heating causing thermal stresses, or some combination of these factors. Standard tests are available to test the friability of particulate materials. Particle growth may occur as a result of elutriation of fines from the vessel, agglomeration (e.g., due to sintering), deposition, or chemical reaction.

Pressure taps and other orifices installed along the walls of the column should be purged, with gas entering at a linear velocity of not less than 0.5 m/s, to prevent particles from entering. Common instrumentation includes pressure transducers (both gauge and differential) and thermocouples. Both mean values and fluctuations can be employed to warn of local defluidization and to provide indications of the flow regime and hydrodynamic behavior of the bed.

When heat transfer surfaces or other fixed surfaces are immersed into fluidized beds, they should be either vertical or horizontal, not inclined, as oblique surfaces cause short-circuiting of gas up the underside. Fixed surfaces should be separated by at least 20 particle diameters (and preferably $50d_p$) to avoid channeling upward in the gap, causing defluidization of the region and local bypassing, reducing gas/solids contacting in the neighborhood. Natural frequencies of bubbles in fluidized beds are usually of order 1 Hz, as it is important to design tubes and other surfaces so that their natural frequencies lie well outside this range. Convective heat transfer coefficients between fixed surfaces and fluidized beds are usually of order 300 to 500 W/m² K for bubbling beds of group A materials, and 200 to 300 W/m² K for group B materials or fast-fluidized beds of group A materials.

Scale up of fluidized beds is often based on experience rather than first principles. Scaling rules summarized by Glicksman et al. (1994) can sometimes be used to provide hydrodynamic scaling based on geometric and dynamic similarity using a scale model, with matching of key dimensionless groups between the model and full-scale unit. Dimensionless quantities to be matched include Ar , a particle Reynolds number, Froude number, density ratio ρ_p/ρ_g , particle sphericity, and dimensionless particle size distribution. For scale up of difficult chemical processes in fluidized beds, a common approach is to build a series of units of different scale, beginning with a unit of minimum diameter 100 to 150 mm and progressing through a substantial pilot plant scale unit to the full-scale unit.

5.2 Heat and Mass Transfer

Bo Leckner

5.2.1 Bed to Surface Heat Transfer

Heat is transferred across various kinds of surfaces:

1. Fluidization gas \leftrightarrow bed material; bed internal heat transfer
2. Fluidization gas and bed material \leftrightarrow heat transfer surfaces in contact with the bed; external heat transfer to surfaces in or above the bed.

In this section, external heat transfer in dense or dilute particle suspensions will be discussed. Internal heat transfer will be treated in Section 5.2.2.

Heat transfer in fluidized beds has been summarized in several reviews, such as those of Zabrodsky (1966), Gelperin and Einstein (1971), Botterill (1975), Kunii and Levenspiel (1991), Baskakov and Filippovsky (1991) and Molerus and Wirth (1997). Heat transfer, especially in circulating fluidized bed (CFB), has been treated in several proceedings of the Conference on CFB. Furthermore, reviews related to CFB have been published by Basu and Nag (1996), Breitholtz and Leckner (1997) and Glicksman (1997).

Definition. The heat transfer coefficient h W/m², deg for heat exchange between the bed and a heat transfer surface, A(m²), in the bed is defined by the heat flow expression

$$Q = hA(T_b - T_w) \quad (5.79)$$

where T_b and T_w (°C or K) are the bulk bed and wall temperatures. As an approximation, the radiative (index r) and convective (index c) constituents of heat transfer from gas (gc) and particles (pc) are often assumed to be additive. The heat transfer coefficient then becomes

$$h = h_r + h_{gc} + h_{pc} \quad (5.80)$$

Sometimes the gas and particle convective constituents are treated together as $h_c = h_{gc} + h_{pc}$. Data on thermal properties are normally taken at the average of surface and bed temperature.

5.2.1.1 Heat Transfer in the Dense, Bubbling Fluidized Bed

5.2.1.1.1 Correlations

The bed is fluidized between the minimum fluidization velocity

$$Re_{mf} = Ar/(1400 + 5.22 Ar^{1/2}) \quad (5.81)$$

and the terminal velocity of a single particle

$$Re_t = Ar/(18 + 0.61 Ar^{1/2}) \quad (5.82)$$

according to empirical correlations (Aerov and Todes, 1968), incorporating Ergun's correlation for minimum fluidization velocity under the assumption that the voidage is $\varepsilon = 0.4$, where Ar is the Archimedes number, a relationship between gravity and drag force representing the particle size, and Re the particle Reynolds number related to superficial velocity.

Figure 5.13 shows heat transfer in beds consisting of monosized particles of various sizes. The beds are fluidized at velocities between minimum fluidization velocity and terminal velocity. The particle convective heat transfer to a surface in the bed increases when the velocity rises from the minimum fluidization velocity and reaches a maximum due to the enhancement of heat transfer following an increase in movement of the bed. Despite further agitation of the bed caused by the increase in velocity towards the

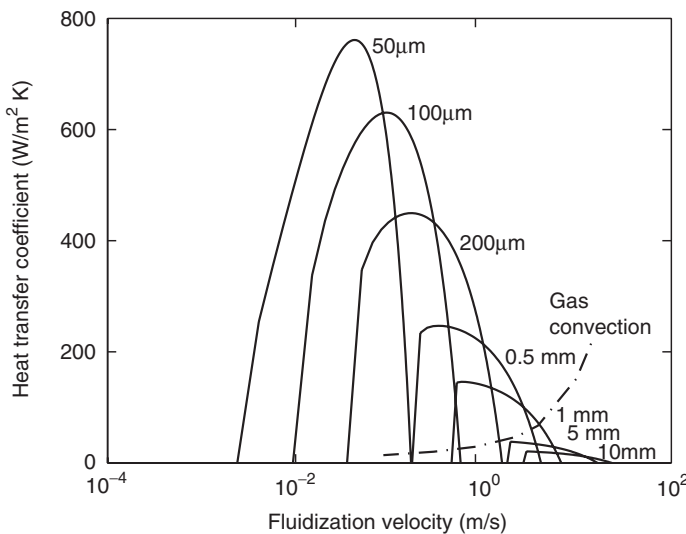


FIGURE 5.13 Schematic representation of the particle (lines) and gas convective (dashed) heat transfer coefficients vs. fluidization velocity (log scale) in dense, bubbling fluidized beds of different particle sizes, each consisting of monosized particles. (Plotted according to a model for fluidization in air, 25°C and $\rho_p = 2500 \text{ kg/m}^3$.)

terminal velocity, the particle convective heat transfer coefficient decreases after the maximum due to a simultaneous increase in voidage. Superimposed on the particle convective heat transfer there is a contribution from the gas flowing through bubbles and particulate phase in the form of a gas convective heat transfer constituent. The gas convection heat transfer is very small at low velocities (small particle sizes), but for large particles the particle convective heat transfer is small and the gas convective heat transfer is high. The gas convection is often disregarded for small particles (less than a millimeter), but must be considered for large particles (larger than a millimeter).

In the surveys on heat transfer in dense, bubbling beds, mentioned above, there are many correlations and modeling efforts describing the detailed behavior of heat transfer. The result of one of these models illustrates the general behavior of the heat transfer coefficient, as shown in Figure 5.13. However, the situation in a fluidized bed is complex and the multitude of efforts has led to a qualitative understanding of the phenomena rather than to a generally valid predictive description. This statement will be illustrated below with an example. Here, a simplified approach is preferred and the presentation will focus on the most reliable data, namely those of the maximum heat transfer coefficient, for which correlations are available. The maximum heat transfer coefficient to a rounded fixed object in the interior part of a dense, bubbling fluidized bed, joining the maximum points shown in Figure 5.13, has been determined empirically and expressed by the Archimedes number. One such correlation (Varygin and Martyushin, 1959) is as follows:

$$Nu_{c,\max} = 0.86 Ar^{0.2} \quad (30 < Ar < 10^5) \quad (5.83)$$

where $Nu_c = h_c d_p / k_g$ and k_g is the thermal conductivity of the gas. The location of the optimum can be described according to Aerov and Todes (1968), Gelperin and Einstein (1971),

$$Re_{\text{opt}} = Ar / (18.0 + 5.22 Ar^{1/2}) \quad (5.84)$$

The optimum fluidization velocity is in the range between the terminal and minimum fluidization velocities, as seen in Figure 5.13 and in a different way in Figure 5.14. The maxima determined empirically are

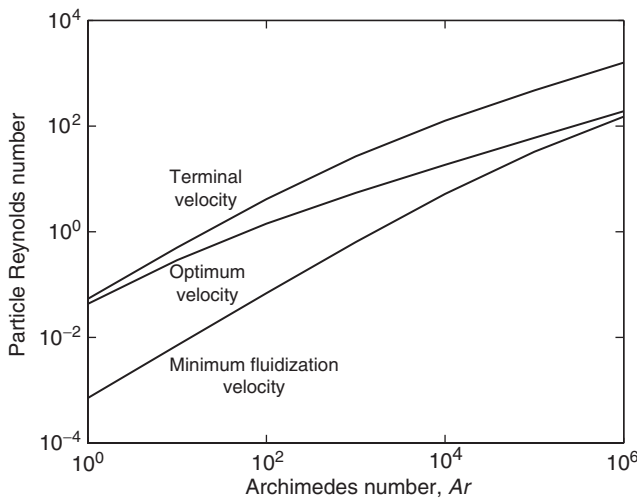


FIGURE 5.14 The minimum, terminal and optimum fluidization velocities for different particle sizes (Ar) according to Eqs. (5.81), (5.82) and (5.84).

quite wide and the optimum velocity is not as exactly described by experimental data as may be the impression from Figure 5.13 and Figure 5.14.

Equation (5.83) can be written as

$$h_{c,\max} \sim d_p^{-0.4} \rho_p^{0.2} k_g \mu g^{-0.4} \rho_g^{0.2} \quad (5.83a)$$

which can be compared with the well-known Zabrodsky's (1966) formula, expressed in SI units, valid for objects of sizes between 10 and 60 mm and bed particles between 0.06 and 1 mm at room temperature:

$$h_{c,\max} = 35.7 d_p^{-0.36} \rho_p^{0.2} k_g^{0.6} \quad (5.85)$$

Both formulae show an approximately equal impact of bed particle size. The thermal conductivity of gas has a different power, which means that the temperature dependence could be different. This is not the case, however, as the gas density term in Eq. (5.83) provides an additional temperature influence. None of the expressions consider the impact of specific heat of the bed material. As seen below from the packet model, Eq. (5.93a), both density and specific heat of the particles are important, since they account for the transport of heat by particles to the wall. However, the properties of materials reveal that specific heat and density are correlated for most conceivable bed materials. Therefore, in empirical formulae, such as Eqs. (5.83) and (5.85), the particle density also represents the specific heat.

In fluidized-bed applications there is a connection between Re and Ar , as seen from Eqs. (5.81), (5.82), and (5.84), and these dimensionless numbers are often interchanged in heat transfer expressions. In fact, Zabrodsky (1974) tentatively expressed his data Eq. (5.85) in the same form as Eq. (5.83) to $0.88Ar^{0.213}$. With Archimedes number, gas density is introduced in Eq. (5.83), and therefore the correlation becomes sensitive to pressure, which was not included in the database used to establish the relationship. Although pressure may have some impact on gas convection and also to some extent on particle convection (Martin, 1984), this impact may be too strong in Eq. (5.83) owing to the gas density term, and relationships of the type of Eq. (5.83) are therefore applicable only at atmospheric pressure unless not directly supported by heat transfer measurements at other pressures. However, within its range of applicability the simpler dimensional relationship, Eq. (5.85), could be applied in pressurized situations also, if gas convection is not dominant.

In the case of larger particles, the impact of the gas flow is relatively important, and a gas convective constituent should be added (Baskakov et al., 1973):

$$Nu_{gc} = 0.009Ar^{0.5} Pr^{0.33} \quad (5.86)$$

This equation has already been plotted in [Figure 5.13](#).

[Figure 5.15](#) summarizes the details given above. The simple relationships, Eqs. (5.83) and (5.85), include gas convection, but are only valid up to a maximum of $Ar < 10^6$. The minor difference in constants in the expressions is insignificant. The importance of the gas convective constituent increases with particle size, and at $Ar > 10^7$ it dominates heat transfer.

The relationships for total maximum heat transfer can be expressed by a simple Archimedes number relationship over a wide range of particle size, such as that proposed by Baskakov (1985) for total maximum heat transfer

$$Nu_{max} = 0.85Ar^{0.19} + 0.006Ar^{0.5} Pr^{0.33} + h_r d_p / k_g \quad (5.87)$$

valid in the temperature range 20 to 1300°C for Ar from 10^2 to 10^9 and at atmospheric pressure. More refined expressions of the same kind, also considering pressure, have been presented by Borodulya et al. (1991).

The definition of the additive radiative component of heat transfer between bed and surrounding wall is straightforward. Assume a heat-exchanging volume of gas and particles, surrounded by a wall of area A . Then, the radiation heat flow Q_r can be written as

$$Q_r = h_r A(T_b - T_w) = \varepsilon A \sigma (T_b^4 - T_w^4) \quad (5.88)$$

where T_b and T_w are the temperatures of the bulk of the bed and the wall expressed in K, σ the Stefan–Boltzmann's constant ($\text{W/m}^2 \text{K}^4$), and ε the resulting emissivity. (ε is used for emissivity but also for voidage. The different meanings are clear from the context). Equation (5.88) yields a definition of the radiative heat transfer coefficient

$$h_r = \varepsilon \sigma (T_b + T_w) (T_b^2 + T_w^2) \quad (5.89)$$

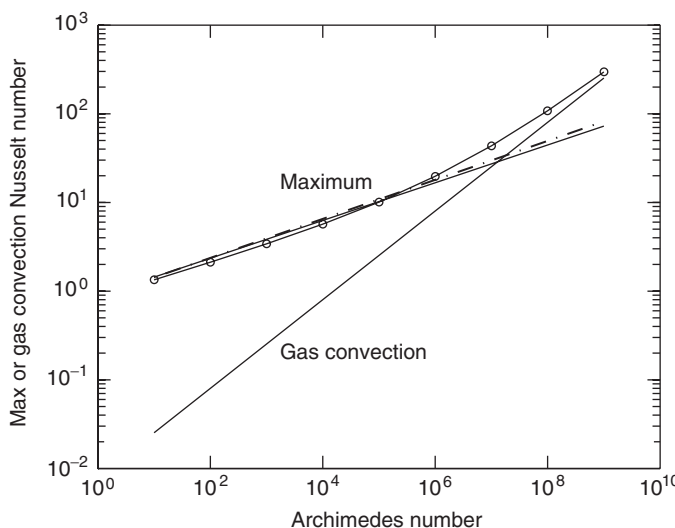


FIGURE 5.15 Total maximum heat transfer compared to gas convective heat transfer. The straight line, representing maximum heat transfer is Eq. (5.83) and the dashed one is Zabrodsky's formula (Eq. [5.85]). Gas convections plotted according to Eq. (5.86). The curve denoted by circles is Baskakov's relationship (Eq. [5.87]) without radiation.

This definition has the consequence that h_r depends on the temperature conditions in each case of application, in the range from one extreme ($h_r = 4\epsilon\sigma T_b^3$ when $T_b = T_w$) to another ($h_r = \epsilon\sigma T_b^3$ when $T_b \gg T_w$). For an enclosure or an infinite plane-parallel layer, the resulting emissivity can be written as

$$\epsilon = 1/(1/\epsilon_b + 1/\epsilon_w - 1) \quad (5.90)$$

where ϵ_b and ϵ_w are the emissivities of bed and wall. The emissivity of the wall can be obtained from handbooks on radiation properties, although it is still an open question if the walls in fluidized beds are more polished by the particles than the materials in general and may have another emissivity for that reason. Owing to the "Hohlraum" effect of the space between the particles, the emissivity of the dense bed, ϵ_b , is higher than that of the surface of the particles ϵ_s . According to Borodulya and Kovensky (1983),

$$\epsilon_b = \epsilon_s^{0.48} \quad (5.91)$$

All data needed for the radiative transfer calculation (T_b, T_w, A, ϵ_b and ϵ_w) are normally available, but still the calculation cannot be carried out, since the temperature of the particle layers adjacent to a heat transfer surface may differ from the bed temperature, more in the case of small particles than in beds of large particles. Therefore Eq. (5.88) represents the maximum radiative transfer and the actual value is normally lower. Various modeling approaches have tried to describe this reduction of the radiative transfer. For simplified estimates, Baskakov (1985) has suggested to maintain Eq. (5.89) as it is, and introduce an empirically defined effective emissivity $\epsilon_{ef} = \epsilon_b$ to take the variations into account; examples are found in the source quoted. For bed temperatures between 1000 and 1500 K and voidages of $0.3 > \epsilon_b > 0.6$, and in the absence of more general expressions, an even more simplified relationship, have been proposed by Baskakov: $h_r = 7.3\sigma \epsilon_b \epsilon_w T_w^3$. The choice of the wall temperature to represent radiative exchange is obviously a considerable approximation and is mostly valid for beds of small particles, where the particles close to the wall approach wall temperature. In Schluender et al. (1987), similar simplifications are found; for instance, it is proposed to use the arithmetic mean between wall and bed temperature as a representative radiation temperature.

5.2.1.1.2 Heat Transfer Mechanisms

The steep rise in heat transfer from the value at minimum fluidization conditions to the maximum value is caused by the increased movement of the bed in the vicinity of the heat transfer surfaces as a consequence of the stirring action of bubbles. Heat transfer to a surface and the fluid dynamic behavior of the bed are strongly linked. The fluid dynamics change with the position within a bed and depend on several conditions, such as fluidizing velocity, bed material, and size of the containing vessel. This has made it difficult to establish generally valid heat transfer relationships, although many correlations and models have been published. The correlations differ from one another and give different results, showing the complexity of the situation. In [Figure 5.16](#), a striking example is given, which illustrates the difficulty involved in the application of heat transfer correlations while it also explains the mechanisms of heat transfer. The left-hand side diagram shows the resulting heat transfer coefficients measured with a heat transfer probe on a vertical water-cooled wall of a fluidized-bed combustor with 10 m^2 cross section, operated with sand as bed material at 850°C bed temperature. The heat transfer coefficient increases from the air distributor plate, that forms the bottom of the bed, to the surface of the bed (which is located above the bed height at rest, given in the figure) during operation at various fluidization velocities. Above the surface of the bed, in the splash zone, the heat transfer coefficient decreases again with height. The right-hand side diagram shows material loss from the heat transfer steel tubes of the wall owing to erosion by the bed material in the same boiler where the heat transfer measurements were made.

The similarity between heat transfer and erosion illustrates the mechanism of heat transfer. At the surface of the bed there is a vigorous movement and the wall is frequently exposed to high temperature particles. The bed material flows downward along the wall and the agitation declines downward, although

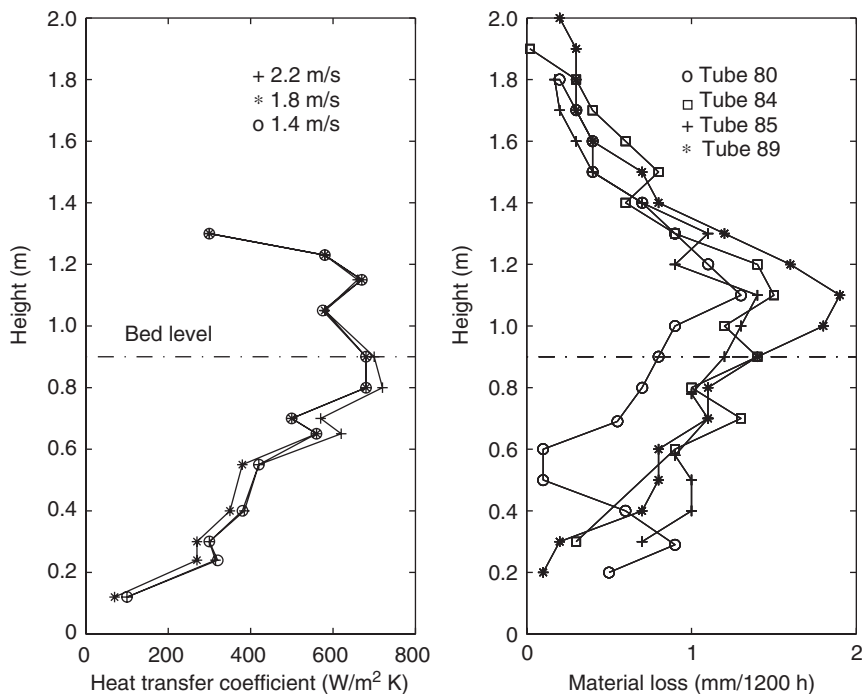


FIGURE 5.16 Heat transfer to a wall of a stationary fluidized-bed boiler (left diagram) compared with erosion on the same membrane tube wall after 1200 h of operation (right-diagram). Conditions: bed temperature 850°C; average particle size 0.55 mm. Bed level is the level at rest. From Andersson, B.-Å. and Leckner, B., *Proceedings of Congreso Europeo de Fluidización*, Macías Machín, A. and Winter, G., Eds., Universidad de las Palmas de Gran Canaria, Vol. 1, 1994, p. 251–260; Leckner, B., Andersson, B.-Å., and Vijil, J., *Proceedings of the 3rd International Fluidised Conference*, The Institute of Energy, London, 1984, Paper Disc/16/134-143.

the bed as a whole was vividly fluidized and the air supply nozzles were active. Changes in the fluidization velocity in the range of 1.4 to 2.2 m/sec did not markedly change the conditions. The particle layers close to the wall transfer their heat to the wall and cool, thereby reducing the heat transfer potential. Heat is transferred by exchange of bed material. If there is only little or almost no exchange of bed material, the material close to a surface attains the temperature of the surface, and eventually heat transfer takes place only due to thermal conduction. The thermal conductivity of a stagnant bed is low, and when the bed serves as an insulating material, heat transfer declines.

5.2.1.1.3 Models

To interpret the variations in heat transfer better, various models have been developed. The most general set of models describes the exchange of bed material at a heat transfer surface as a packet of hot bed material, which is brought to the surface by the movements of the bubbles, remains there for a certain contact time, while its temperature approaches that of the heat transfer wall, and is then replaced by a new packet. A simplified version of the energy equation describes the thermal behavior of the packet, considered as a semiinfinite continuum with effective thermal properties:

$$(\rho c_p)_b \partial T / \partial t' = k_{pb} \partial^2 T / \partial x^2 \quad (5.92)$$

where $\rho_b = \rho_p(1 - \varepsilon)$, ε being the voidage, c_{pb} and k_{pb} are the corresponding specific heat and thermal conductivity of the packet, and x a coordinate oriented normal to the surface. t' and h' denote values at the current time, whereas t is the total residence time of a packet at the surface and h the time-average

heat transfer coefficient. The time-dependent solution for constant wall temperature and with the packet initially at core temperature is

$$h'_{i,c} = \frac{k_{pb}}{x_m} \left(1 + 2 \sum_{n=1}^{\infty} \exp \left[-\frac{n^2 \pi^2 k_{pb} t'}{x_m^2 (\rho c_p)_b} \right] \right)$$

$$\dots = \sqrt{\frac{k_{pb} (\rho c_p)_b}{\pi t'}} \left(1 + 2 \sum_{n=1}^{\infty} \exp \left[-\frac{n^2 x_m^2 (\rho c_p)_b}{k_{pb} t'} \right] \right) \quad (5.93a)$$

Two equivalent solutions are shown: the upper one converges faster for long times and the lower one for short and intermediate times. A truncation gives an approximate expression for short and intermediate times:

$$h'_{i,c} = \frac{\sqrt{k_{pb} (\rho c_p)_b}}{\sqrt{\pi t'}}, \quad \text{i.e.,} \quad Nu_{i,c} = 1/(\pi Fo)^{1/2} \quad (5.93b)$$

whereas for very long times

$$h'_{i,c} = h_c = k_{pb}/x_m, \quad \text{i.e.,} \quad Nu = 1 \quad (5.93c)$$

where $Nu_{i,c} = h'_{i,c} d_p/k_{pb}$ is the Nusselt number of the packet and the Fourier number is $Fo = k_{pb} t' / (c_{pb} \rho_b d_p^2)$. For very short times or large particles this solution leads to unreasonably high heat transfer, and the heat transfer resistance $1/h'_{i,c}$ approaches zero. Therefore, a time-independent contact resistance in the form of a gas layer close to the surface is introduced:

$$1/h_k = \varphi d_p/k_g \quad (5.94)$$

where k_g is the thermal conductivity of the gas adjacent to the surface and φ a coefficient indicating the effective width of the gas layer. Now, the total particle convective heat transfer resistance becomes

$$1/h'_{pc} = 1/h_k + 1/h'_{i,c} \quad (5.95a)$$

Baskakov (1964) integrated Eq. (5.92) considering the gas gap and obtained the heat transfer coefficient

$$h'_{pc} = h_k \exp \left[\frac{h_k^2 t'}{k_{pb} (\rho c_p)_b} \right] \operatorname{erf} \left[\sqrt{\frac{h_k^2 t'}{k_{pb} (\rho c_p)_b}} \right] \quad (5.96)$$

Time averaging for the total residence time t of a packet at the wall yields

$$h_{pc} = \frac{1}{t} \int_{t=0}^t h'_{pc} dt = 2 \sqrt{\frac{k_{pb} (\rho c_p)_b}{\pi t}} - \sqrt{\frac{2k_{pb} (\rho c_p)_b}{\pi t h_k}} \ln \left[1 + \sqrt{\frac{\pi t h_k^2}{k_{pb} (\rho c_p)_b}} \right] \quad (5.97)$$

Similar expressions for various boundary conditions have been given by Gelperin and Einstein (1971). This type of expressions is somewhat inconvenient for engineering calculation and a simpler relationship is preferred:

$$h_{pc} = \frac{1}{1/h_k + 1/h'_{i,c}} \quad (5.95b)$$

where the time-average emulsion heat transfer coefficient during time t is

$$h_{i,c} = 2h'_{i,c} = 2 \frac{\sqrt{k_{pb} (\rho c_p)_b}}{\sqrt{\pi t}}$$

It has been shown (Fang et al., 1995b) that the deviation between Eq. (5.97) and the simplified expression is less than 5%.

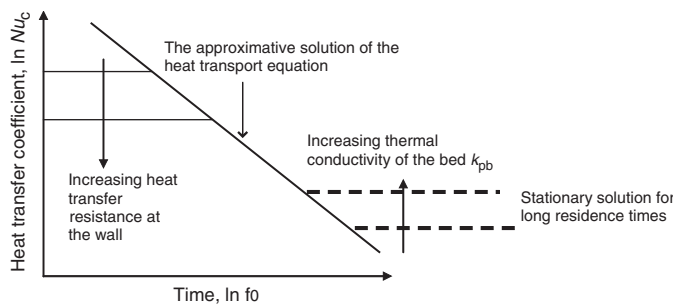


FIGURE 5.17 The particle convective heat transfer coefficient as a function of residence time of a packet at the heat transfer surface.

Figure 5.17 illustrates the limitations of the simplified solution of the heat transfer equation, Eq. (5.93b). At very short times or large particles the heat transfer coefficient is limited by the resistance in the gas layer, Eq. (5.94), and for hypothetically long residence times it approaches the limit of pure conduction through a stagnant particle suspension of thickness x_m and thermal conductivity k_{pb} for hypothetically long residence times, given in Eq. (5.93c). The impact of the particles depends on particle size. In the case of very large particles (larger than 1 mm), the resistance of the gas layer becomes more important than that in the emulsion. For smaller particles, the thermal residence time of the emulsion is important, and the coefficient tends to be represented by the sloping part of the relationship shown in Figure 5.17. The packet model explains the particle convective heat transfer mechanisms at a heat transfer surface, but the resistance coefficient φ in Eq. (5.94), the thermal conductivity of the packet (its density), and its residence time at the surface require further modeling.

If the heat transfer surface is exposed to bubbles during a fraction of time f_0 , the convective heat transfer coefficient can be written as

$$h_c = (h_{gc,bubbles} + h_{r,bubbles})f_0 + (h_{pc} + h_{gc,emulsion} + h_{r,emulsion})(1 - f_0) \quad (5.98a)$$

where the two terms represent the heat transfer coefficients during the passage of a bubble and during the presence of the particle emulsion. In the common case when gas convection is small and radiation is negligible, Eq. (5.98a) can be written as

$$h_c = (1 - f_0)/(1/h_k + 1/h_{i,c}) \quad (5.98b)$$

The significance of the various terms can be understood from the above discussion. Here only two extreme cases will be illustrated: those of small and large particles. In the case of small particles, Eq. (5.98) results in

$$h_c = h_{r,bubbles}f_0 + h_{i,c}(1 - f_0) \quad (5.99)$$

Only radiation through bubbles and heat conduction through the emulsion (the sloping part of the curve in Figure 5.17) play significant roles as constituents of the heat transfer coefficient. In the other extreme case, that of large particles, heat conduction through the emulsion is less important than the thermal resistance of the gas gap. Moreover, in this case the particles at the wall are not essentially cooled and radiation from both emulsion phase and bubbles is important at high temperatures. If radiation and gas convection are expressed for the total time, the result for large particles becomes

$$h_c = h_k(1 - f_0) + h_{gc} + h_r \quad (5.100)$$

The packet model has been the starting point for most of the fluidized-bed heat transfer modeling. However, other ways of modeling have also been followed, where the heat exchange between the row of

particles adjacent to a wall and the wall is regarded as most important for the heat transfer (Zabrodsky, 1966). An example of such an approach is the model developed by Martin (1984), who regarded the transport of heat by particles moving at an average velocity toward a heat transfer surface. As in the case of the packet model, particles exchange their heat while remaining for some time period at a heat exchange surface, but thermal conduction in the particle emulsion is disregarded. The principal mechanism of heat transfer is through the gas film between a particle and a wall, and to some extent heat transport within a particle. The unknown parameters are related to the voidage of the bed, and for practical application of the model, a description of bed expansion is needed. A simplified version of this model has been used to illustrate the heat transfer behavior in [Figure 5.13](#). In the design of the figure, the bed voidage was supposed to vary linearly with the fluidization velocity

$$\varepsilon = \varepsilon_{mf} + (1 - \varepsilon_{mf})(u - u_{mf})/(u_t - u_{mf}) \quad (5.101)$$

where $\varepsilon_{mf} \approx 0.4$. The velocity at minimum fluidization u_{mf} and terminal velocity u_t were obtained from Eqs. (5.81) and (5.82), respectively. The coarse simplification of the description of bed voidage makes the curves more rounded at velocities exceeding the optimum velocity than seen from the measurements. In reality, the curves are flatter, and a heat transfer coefficient of $0.8h_{max}$ is often recommended for rough calculations over a wide range of velocities. The absence of particles at terminal velocity and, as a result, zero particle convective heat transfer (seen in Figure 5.13) is a consequence of the simplification; the bed disappears at this velocity as no particle recirculation was included. These assumptions were introduced for the present purpose and are not necessary limitations in the model. A more realistic modeling of bed expansion in the high velocity range will improve the result. However, the model assumes that the particles remain in contact with the wall, and it is not intended for the high-velocity modes of fluidization occurring when the bed is being converted into a circulating system.

5.2.1.2 Heat Transfer in the Disperse Suspension of the Circulating Fluidized Bed

5.2.1.2.1 General Conditions

The CFB extending in a furnace, or in general terms, in a riser, consists of a dense bottom bed, a splash zone, and a transport zone. In the CFB, the suspension densities are lower and the gas velocities are higher than in a noncirculating bubbling bed. Owing to the high velocity, erosion on a heat transfer surface is potentially severe, and there are restrictions on the allocation of heat transfer surfaces.

The orientation of the surface should be parallel to the principal direction of the particle flow, and the surface should be located where the particle density is low in the transport zone, although, in this zone the rate of particle-related convective heat transfer is also low. The conditions for heat transfer in the transport zone are explained below. In the dense bed, often found in the bottom zone of the CFB riser, the conditions are analogous to what was presented above, but this region is probably not of interest owing to the high rate of erosion on heat transfer surfaces. If heat transfer is to be considered anyway, then in the absence of any information, extrapolation outside of the ranges of validity of the various correlations has to be done. Most work with respect to heat transfer in CFB has been focused on the transport zone, and it has been directed toward combustors.

The heat transfer surfaces of combustors normally consist of membrane tubes ([Figure 5.18](#)). The bottom part of the furnace walls is refractory lined to protect the tube walls from erosion. The heat transfer surface starts from where the refractory ends and extends to the top of the riser. In some cases there are also internal heat transfer surfaces inside the upper part of the riser, again, allocated parallel to the main flow of particles. The area of the heat transfer surface is the entire area exposed to the particle suspension, but for tube walls it may be expressed as projected surface area if the radiation from a distant suspension of gas and particles or from a flame is important. At a given heat transfer rate, the coefficient h depends on whether it is related to the projected or to the total surface. The ratio of total and projected area is always less than $\pi/2$ for tube walls, as can be realized from geometrical reasons.

The heat transfer between suspension and wall is affected both by the density of the suspension and by the temperature. Close to the heat transfer walls, there is a falling film of particles forming particle as well

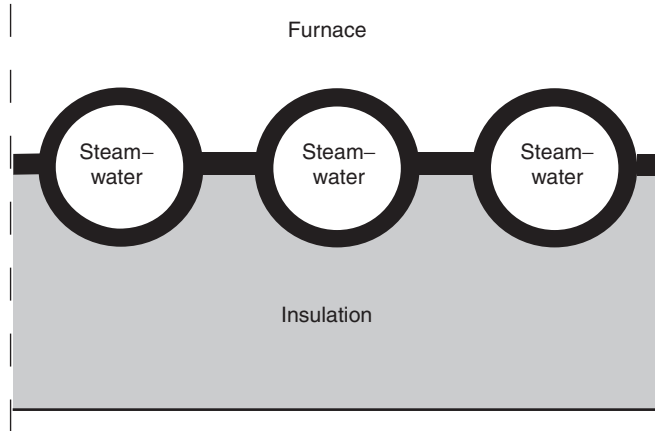


FIGURE 5.18 Cross-section of three tubes of a membrane tube wall.

as thermal boundary layers, having higher suspension density and lower temperature than the core of a riser. The boundary layer not only transfers heat by convection, but also participates in the radiative transfer of heat between the bed and the wall. Much of the radiative transfer originates in the hot core of the riser, but this radiation from the core is partly absorbed by the particles in the wall layer and reaches the wall only after attenuation (Werdermann and Werther, 1994). The wall layer is colder than the core and its own emission is limited. Heat transfer correlations are normally related to the average particle density ρ_{av} of the cross section, since this quantity is relatively easy to evaluate from measured pressure drops dP/dz along the riser's height z . Formally, the average density over the cross-section is expressed by integration of the local suspension density ρ_b over the cross section A_c of the riser as

$$\rho_{av} = A_c^{-1} \int \rho_b \, dA_c = -1/g \, dP/dz \quad (5.102)$$

where the suspension density is

$$\rho_b = (1 - \varepsilon)\rho_p + \varepsilon\rho_g \quad (5.103)$$

with ρ_p and ρ_g being the densities of particles and gas, respectively. With the exception of the thermal boundary layers, the time-average temperature of the suspension, T_b , is usually constant in the riser. Only in large risers there may be a small variation of T_b with height and in the corners. An example of a thermal boundary layer is seen in Figure 5.19, where the temperature starts to fall at about 0.1 m from the wall. The measurements were made in a 14 m high CFB furnace with a cross section of about 2.2 m^2 . Similar results have been obtained in other CFB furnaces. The shape of the temperature curves is similar at all heights, which reveals that heat is supplied to the boundary layer at the same rate as it is removed to the wall. In Figure 5.19, the wall temperature is 200°C , and very close to the wall there is obviously a temperature decrease from about 500 to 200°C with a rather steep temperature gradient that can only be explained by the existence of a gas gap close to the wall. The temperature gradient reveals that more than half of the resistance to heat transfer may be found in this gas gap and that the remaining resistance is in the particle suspension of the boundary layer.

The vertical heat transfer surfaces in a CFB are polished but not severely eroded. Therefore, it can be assumed that the particles touch the walls occasionally and that the gas gap has at least an average size of the order of a particle diameter (in contrast to the dense bubbling bed where the particles are in closer contact with the walls). The thinnest conceivable dimensionless thickness is that of a gas lens between a particle resting on the wall and the wall $\varphi = 1/6$, where the thickness is $\delta_g = \varphi d_p$ (cf. Eq. [5.94]). Another

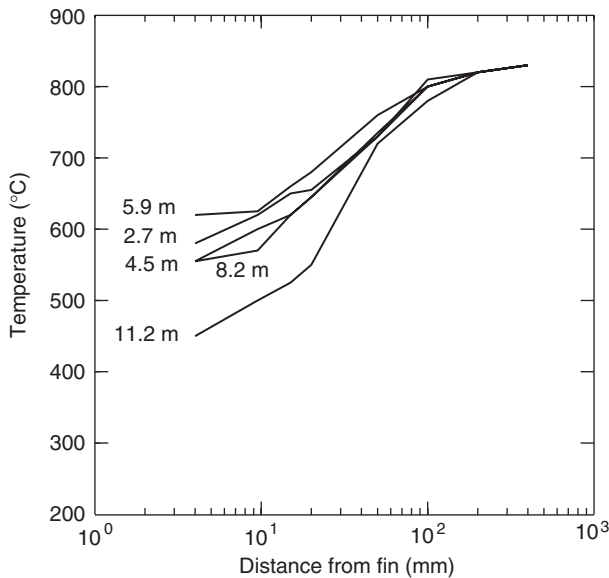


FIGURE 5.19 Thermal boundary layer measured in a 12 MW CFB boiler at various distances from bottom of the furnace. Conditions: particle size, 260 μm ; fluidization velocity, 4 m/sec; bed temperature, 850°C. From Leckner, B., Golriz, M.R., Zhang, W., Andersson, B.-Å., and Johnson, F., *Proceedings of the 11th International Conference on Fluidized Bed Combustion*, Anthony, E. J., Ed., ASME, New York, 1991, pp. 771–776.

geometrically defined limit is that formed by a cubic, expanded, arrangement of particles, assuming that the particle volume fraction at the wall is three times the cross sectional average volume fraction,

$$\varphi = (\pi / (18(1 - \varepsilon_{av})))^{1/3} \quad (5.104)$$

These geometric relationships are compared with various measurements or fits in [Figure 5.20](#).

The temperature in the boundary layer varies with time, as illustrated in [Figure 5.21](#). The figure shows simultaneous variations in the boundary layer temperature measured by six thermocouples inserted at various distances from the fin of the membrane tube surface of a CFB furnace. The variations in temperature are obviously due to high-temperature, extended streamers of particles, occasionally brought to the wall region from the hot core of the riser. They cause corresponding fluctuations in heat transfer. The temperature in the core (at 0.28 m and further into the suspension) is even, without thermal disturbances. It can be assumed that the temperature variations are accompanied by density variations, as observed visually. The density variations are complex and also contain higher frequencies than the temperature fluctuations shown in Figure 5.21 which are filtered by the thermal inertia of the thermocouples used. Wu et al. (1991) have shown that the fast density variations correspond to variations in the heat transfer to a wall. An intermittency index γ has been defined (Brereton and Grace, 1993) to characterize the density fluctuations at a given point, represented by the standard deviation of the density fluctuation σ for two cases with identical time-mean densities

$$\gamma = \sigma \text{ under the actual conditions} / \sigma \text{ for a fully segregated flow} \quad (5.105)$$

This index is zero for a homogeneous flow and unity for a flow consisting of particle swarms of the same volume fraction as a bed at minimum fluidization velocity. [In model representations, the particle suspension is often regarded as having a high intermittency index, in the extreme case consisting of a discrete probability of presence of particles, f_c , the coverage factor, indicating how much the wall is covered by particles, whereas $(1 - f_c)$ then means uncovered wall]. In terms of probability distribution, such a

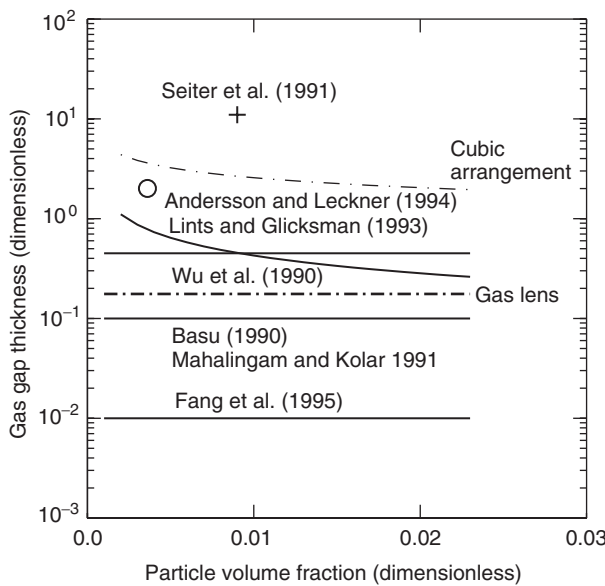


FIGURE 5.20 Measured and fitted dimensionless gas-gap thickness $\varphi = \delta_g / d_p$ vs. cross-section average solid volume fraction. Theoretical limits set by a gas lens and a cubic packing are marked with dashed lines. From Breitholtz, C. and Leckner, B., *Trends Heat Mass Momentum Transf.*, 3, 85–104, 1997. With permission.

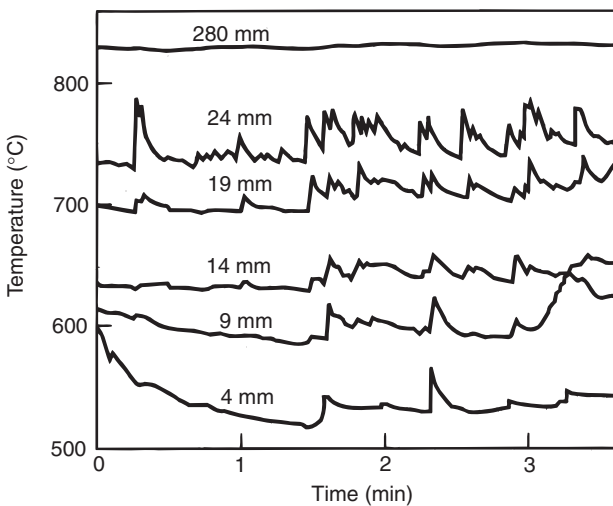


FIGURE 5.21 Example of simultaneous temperature variations in the boundary layer at various distances from the fin of a membrane tube wall 11.2 m above the bottom in the same case as Figure 5.19. From Leckner, B., Golriz, M.R., Zhang, W., Andersson, B.-Å., and Johnson, F., *Proceedings of the 11th International Conference on Fluidized Bed Combustion*, Anthony, E.J., Ed., ASME, New York, 1991, pp. 771–776.

fully segregated flow would have a bimodal distribution of particle density and an intermittency index of one, but measured distributions are continuous around a maximum and are far from bimodal (Breitholtz and Leckner, 1997; Johnsson et al., 1997), and the intermittency index is below 0.5 (Brereton and Grace, 1993; Johnsson et al., 1997). Hence, although there are density fluctuations in the medium, they are not as distinct as assumed in some models; they should be considered as gradual variations against a background of particles of a finite concentration.

The description of heat transfer can be roughly separated into four, sometimes combined, approaches:

1. Gas and particle convection are evaluated separately as average values and added to radiation according to Eq. (5.80).
2. Particle convection is assumed to take place when a dense streamer is present and gas convection (if not neglected) and radiation will be considered during the remaining time.
3. Comprehensive (more or less) modeling, in some cases allowing the mechanisms to be interrelated.
4. Correlations.

5.2.1.2.2 Addition of Radiative and Convective Heat Transfer (Approaches 1 and 2)

It is often assumed that the wall is covered by particles in the form of streamers during a fraction of time f_c , and hence uncovered during the rest of the time $(1 - f_c)$. The resulting heat transfer coefficient h is composed of a contribution from convection h_c (or h_{pc}) and radiation h_{rw} from the boundary layer during coverage f_c , and of radiation from the core of the bed h_r during the particle-free time $(1 - f_c)$. Gas convection may have some minor effect when the wall is uncovered. The heat transfer coefficient can then be written as

$$hA = f_c(h_{pc} + h_{rw})A + (1 - f_c)(h_r A_{proj} + h_{gc}A) \quad (5.106)$$

where radiation from distance is received by the projected surface A_{proj} and convective heat and radiative transfer from the streamers, seen from the wall, is received by A , the total surface area. However, the wall coverage f_c is not known. Normally, the terms h_{rw} and h_{gc} are small and can be neglected. The particle convective coefficient h_c (h_{pc}) consists of two resistances in series

$$1/h_c = 1/h_k + 1/h_l \quad (5.107)$$

where the resistance in the particle boundary layer is $1/h_l$ and the resistance in the gas film at the wall, $1/h_k$.

$$h_k = k_g/\delta_g \quad (5.108)$$

represents the influence of a gas gap between the wall and the suspension (cf. Eq. [5.94]). Here k_g is the thermal conductivity of gas and $\delta_g = \varphi d_p$ the thickness of the gas gap. The heat transport through the remaining part of the particle wall layer can be expressed as

$$h_l = k_s/\delta_s \quad (5.109)$$

implying that the transfer mechanism is conduction, across a particle suspension with the thickness δ_s mostly promoted by the irregular movement in the bed material that results in an effective suspension conductivity k_s . Alternatively, heat is transferred by the movements of the particle suspension, the heat transfer mechanism is assumed to consist of displacement of streamers of particles transferring heat from the core to the wall, similar to the packets of the noncirculating dense bubbling bed (Eq. [5.93]). Glicksman (1997), Basu and Nag (1996) have conducted surveys on various approaches of this type. The streamers are parts of the suspension approaching the wall. They are characterized by having higher density than that of the surrounding suspension and are treated like the packets of particles formed by the agitation of bubbles in the dense bed.

In the above formulation some factors are known: k_g (thermal conductivity of gas), δ_g (Figure 5.20), the contribution of radiation $(f_c h_{rw} A + (1 - f_c) h_r A_{proj})/A \approx 50$ (W/m² deg), (mentioned below) and δ_s (thermal boundary layer thickness), but the essential parameters f_c , τ , and k_{pb} require additional modeling. Glicksman (1997) has reviewed available information about the various parameters involved.

The radiation in CFB is described by the same expressions as for the noncirculating bed, but at the lower particle concentration of the CFB radiation attains longer path lengths. For the calculation of the effective emissivity of the suspension ε_b , two cases can be considered:

1. Combustion gases with low suspension density, for example, in a CFB during low-load operation or in the freeboard of a noncirculating FBC. In this situation the influence of boundary layers can be disregarded.

2. Combustion gases with, relatively seen, high suspension density, for example, CFB during normal load conditions. The boundary layers are important.

Case 1: When the particle concentration is small, scattering of radiation from particles can be neglected, but both combustion gases and suspended particles contribute to the effective bed emissivity

$$\varepsilon_b = 1 - (1 - \varepsilon_g)(1 - \varepsilon_p) = \varepsilon_g + \varepsilon_p - \varepsilon_g \varepsilon_p \quad (5.110)$$

where ε_g is the emissivity of the combustion gases H₂O and CO₂, which can be evaluated for a path length L according to standard radiation correlations (Modest, 2003), ε_p is the emissivity of a particle suspension calculated for the same effective path length L as for the gases, knowing the surface concentration of particles C_p ,

$$C_p = \varepsilon_s n \pi d_p^2 / 4 \quad (5.111)$$

and the number of particles

$$n = \frac{\rho_{av}}{\rho_p \pi d_p^3 / 6} \quad (5.112)$$

where d_p is the particle diameter, ρ_p the particle density, and ρ_{av} the bulk bed density along the path considered. ε_s is the emissivity of the surface of the particles. By these relationships, the resulting effective emissivity of the particle suspension becomes

$$\varepsilon_p = 1 - \exp(-C_p L) \quad (5.113)$$

For an enclosure with surface A and volume V , the mean path length L is calculated according to Hottel and Sarofim (1967) as

$$L = 3.5V/A \quad (5.114)$$

Contributions to the radiative flux from the surface of the bed and from other surfaces also have to be included, according to standard procedures (Modest, 2003).

Case 2: When the particle concentration is high, the gas contribution can be neglected but scattering in the particle suspension should be considered. One obtains $\varepsilon_b = \varepsilon_p$ and this emissivity can be calculated by considering scattering (Brewster, 1986):

$$\varepsilon_p = \left[\frac{\varepsilon_s}{(1 - \varepsilon_s)B} \left(\frac{\varepsilon_s}{(1 - \varepsilon_s)B} + 2 \right) \right]^{1/2} - \frac{\varepsilon_s}{(1 - \varepsilon_s)B} \quad (5.115)$$

For isotropic scattering ($B = 0.5$) or for diffusely reflecting particles ($B = 0.667$) and a particle surface emissivity ε_s , this formula can be represented as in [Figure 5.22](#). Baskakov and Leckner (1997) have shown that several independent derivations of effective emissivity give similar results.

At a high particle concentration, when substantial wall layers are present, radiation and convection are not simply additive. Radiation from the core of the suspended bed ($\varepsilon_b \sigma T_b^4$) is reduced by the colder, relatively dense, wall layer. One approach has been (Breitholtz and Leckner, 1997) to express radiation from an isothermal medium at bed temperature compared with that affected by a boundary layer, employing the radiation heat transport equation. The result of this operation yields a correction to the maximum radiative heat transfer coefficient by an empirical coefficient "the radiation efficiency", η , defined in analogy with Steward et al. (1995) according to

$$h_r = \eta \varepsilon \sigma (T_b + T_w) (T_b^2 + T_w^2) \quad (5.116)$$

where ε is given by Eq. (5.90). The radiation efficiency accounts for absorption of radiation by the wall layer and reduction in emission due to the fall in temperature close to the wall. [Figure 5.23](#) shows the radiation efficiency determined by means of various data sets obtained from the literature. Although there might have been inconsistencies in some of the data, it is seen that, at low suspension density, the impact

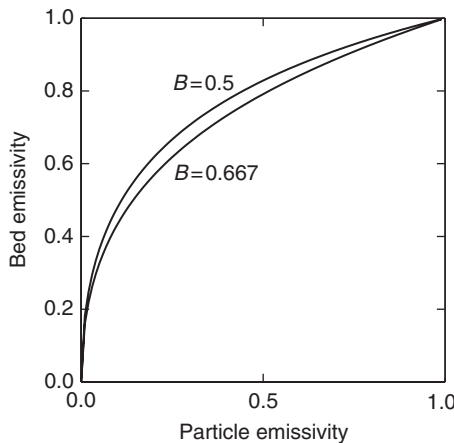


FIGURE 5.22 Effective bed emissivity vs. particle surface emissivity considering scattering (Eq. [5.115]).

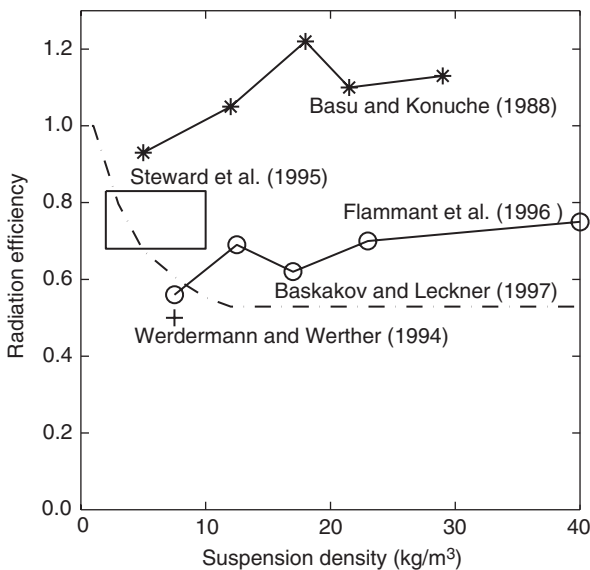


FIGURE 5.23 Radiation efficiency evaluated for a few experimental results. From Breitholtz, C. and Leckner, B., *Trends Heat Mass Momentum Transf.*, 3, 85–104, 1997. With permission.

of the wall layer is small (similar to Case 1) and the radiation efficiency is almost equal to unity, but with an increase in suspension density the wall layers become more important and reduce the contribution of radiation to about half its value in a suspension without wall layers.

The radiation efficiency is presented as a function of suspension density only. Implicitly this relates to density and thickness of the wall layer. The influence of bed and wall temperatures remains to be investigated.

5.2.1.2.3 Modeling

Comprehensive modeling should start with the energy equation, using the flow field from the momentum equation and considering mass and species balances related to chemical reactions. Although the developments in computer technology opens up new possibilities, most approaches related to heat transfer in fluidized bed have been simplified, and are often similar to the models previously developed for

bubbling fluidized beds. A summary of some of the assumptions commonly found in the literature is as follows:

1. Heat transfer between gas and particles is high. This allows the assumption of equal particle and gas-phase temperatures, and an emulsion phase energy equation using lumped thermal properties can be formulated rather than a particle and a gas-phase equation.
2. The main direction of the particle flow is along the wall, and the convective flows in other directions are relatively small and can be neglected.
3. The temperature gradient is large in the horizontal direction and negligible along the wall, ([Figure 5.19](#)). Therefore, the conductive and radiative heat flows in the directions along the wall can be omitted from the equations.
4. Despite the obvious coupling of conduction and radiation toward the wall, in many models, these phenomena are treated separately.
5. Because of the low temperature in the wall layer, combustion is slow and heat release from chemical reactions is neglected.
6. The density of the gas phase is much lower than that of the particle phase and gas convection can be neglected.
7. If dispersion in the direction of the flow is small and the same particles are followed, the particle convective term can be eliminated.
8. An effective thermal conductivity k_{pb} can be defined for the particle suspension.

As a result of these approximations the energy equation becomes equal to Eq. (5.92), and the same solution, Eq. (5.93), is obtained, now with strands instead of packets transporting heat to the surface. The problem with high heat transfer rates at short contact times requires the same solution as for the bubbling bed, and a particle convective heat transfer coefficient is defined according to Eq. (5.95). The fraction of time that the surface is not covered by bubbles ($1-f_0$) is now replaced by the wall coverage f_c of strands. To use these relationships, the thickness of the gas gap, the density of the strands, the descending velocity of the particles, or the residence time and length, have to be known. This requires further modeling or empirical information. Several efforts have been made according to the approach described, (for instance by Wu et al., 1990; Basu, 1990; Lints and Glicksman, 1993; Fang et al., 1995a; Wang et al., 1996).

There is a striking resemblance between the modeling of the streamers falling along a surface in a CFB and the packets of particles induced by bubbles in a dense, bubbling bed bringing heat to a wall. In both the cases, thermal conduction of the particle suspension has an influence. On the other hand, it was mentioned that Martin's model of heat transfer in a bubbling bed focused attention on the gas gap and on the particles close to the wall, neglecting the transfer in the suspension itself. There are a number of CFB heat transfer models that follow the same idea and treat single particle behavior at the wall and the influence of the gas gap (e.g., Goedcke and Reh, 1993; Farag and Tsai, 1993; Wirth, 1995).

Breitholtz and Leckner (1997) compared a number of available models of both kinds with two cases represented by average measurement data using similar physical properties: one under ambient conditions and the other one was a hot case. The results from the various models showed a scatter of $\pm 75\%$. In some comparisons agreement between models was found, but for quite different reasons. Hence, judging from these works as a group, modeling of CFB is not yet a well-established technique and the heat transfer coefficient can only be reliably modeled in special cases when the importance of the particle boundary layer is small, i.e., in the upper part of a CFB and in the freeboard of a noncirculating fluidized bed, where the particle suspension is not dense and absorption of radiation is small; otherwise at present, empirical correlations have to be used.

5.2.1.2.4 Correlations

The collection of experimental results from various literature sources, presented by Basu and Nag (1996), shows a set of highly scattered data, which gives an impression of experimental difficulties in determining heat transfer in CFB. The variation between data sets is greater than the variation of the parameters studied. In contrast to a noncirculating bed, the CFB is a system, which, in addition to bed material and gas parameters, is affected by the size of the fluidized-bed vessel and also by the operation of the circulating loop.

Narrow, hot units have to be heated through the walls (because the wall surface to volume ratio makes heat losses important in small devices) and then the thermal wall layers differ from those of larger units, where the walls are cooled; the conditions for thermal radiation heat transfer are different in small and large equipment. Moreover, it has been pointed out (Wu et al., 1989; Nag and Moral, 1990) that the length of the heat transfer surface is important in research rigs where heat transfer probes and inserts of limited size are used to measure heat transfer. Above a length of a meter or two this effect is negligible. Hence, it is not a concern in industrial equipment, but it has influenced early measurements in research installations.

For this reason given, Breitholtz and Leckner (1997) classified the available results into two groups: results from boilers and results from cold (laboratory scale) units. In both cases long heat transfer surfaces were used for measurements. This reduced the differences in results but the scatter was still considerable. There are only a few results available from measurements of total heat transfer coefficients in boilers. These (related to total wall surface area) have been represented in Figure 5.24. (The results from Wu were from a laboratory unit. They were included for comparison.)

In the upper part of a CFB furnace, the suspension density is low and radiation dominates. Baskakov and Leckner (1997) argued that in such a case the total heat transfer coefficient should approach the radiative one, which should be around $125 \text{ W/m}^2 \text{ deg}$ at $T_w = 340^\circ\text{C}$ and $T_b = 850^\circ\text{C}$ (Eq. [5.89]), and about $100 \text{ W/m}^2 \text{ deg}$ for conditions similar to those of Andersson shown in Figure 5.24 ($T_w = 200^\circ\text{C}$). However, it was also found that, due to the shielding effect of the colder boundary layer, at suspension densities of above 25 kg/m^3 the radiation contribution was only $h_r \approx 50 \text{ W/m}^2 \text{ deg}$.

Neglecting the differentiation between convection and radiation altogether and considering only total heat transfer, a rough estimate was made based on the available data from boilers (see Figure 5.24) and, on an average calculated for the entire heat transfer region in CFB furnaces under normal operation conditions:

$$h = 110 \rho^{0.21} \quad (\text{W/m}^2 \text{ deg}) \quad (5.117a)$$

This expression is related to the projected heat transfer surface in a combustor. In the above equation $\rho (\text{kg/m}^3)$ is the average particle density in the part of the furnace, which is surrounded by the heat transfer surface (Breitholtz et al., 2001). An implicit conclusion from Eq. (5.117a) is that within the scatter of

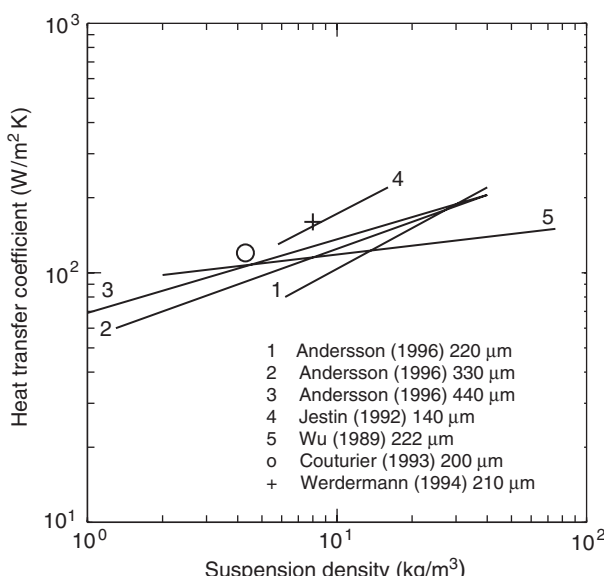


FIGURE 5.24 Heat transfer coefficients measured under hot condition, averaged over the entire heat-receiving wall vs. cross-sectional average suspension density averaged over the corresponding furnace height. From Breitholtz, C. and Leckner, B., *Trends Heat Mass Momentum Transf.*, 3, 85–104, 1997. With permission.

available data only suspension density was found to be important for CFB heat transfer. This must be interpreted in the context of the evaluation, namely for the heat transfer situation in combustors, i.e., a bed of sand, limestone or ashes, operated at a temperature around 850°C and a heat receiving surface consisting of boiler tubes at a temperature of 200 to 500°C in the various cases investigated.

There is a general agreement that the suspension density is a predominant influencing parameter, but often (Basu and Nag, 1996) a power of 0.5 is mentioned instead of 0.2, which was found for the boilers. There are three important aspects in relation to this issue: (1) the value given in Eq. (5.117a) is a furnace-averaged value and therefore the slope is low; (2) there is a considerable scatter between various observations (as seen in Figure 5.24, for example); and (3) radiation is included, which will reduce the power, because radiation is most influential at low suspension densities and its impact is reduced as particle concentration increases.

In fact, subtraction of the estimated radiative contribution from the measured total heat transfer coefficients, Eq. (5.117a), leads to a similar correlation for the convective heat transfer constituent:

$$h_c = 25\rho^{0.58} \quad (\text{W/m}^2 \text{ deg}) \quad (5.117b)$$

valid for $2 < \rho < 40 \text{ kg/m}^3$). The data points decrease from the trend for $\rho < 10$ and approach a convective heat transfer coefficient of $h_c \approx 10$ at very low densities, a value that is in the same order as the heat transfer coefficient of gas in an entrance region of a duct (Breitholtz et al., 2001).

5.2.1.3 Concluding Remarks

Much work on heat transfer in fluidized beds, and in CFB in particular, was motivated by application in combustors. However, it was found during the 1980s that erosion on heat transfer surfaces prevented the use of surfaces which were in contact with a dense bed of a combustor. There are still possibilities to apply heat transfer surfaces in fluidized beds: at low velocities when erosion is minimized and in less exposed positions, such as wall heat transfer tubes surrounding a dense, fluidized bed or vertical surfaces in the upper part of a CFB. The essential difference between the dense bed and the transport zone of a CFB, in addition to erosion and the much higher heat transfer coefficient in the dense bed, is that there is a clear influence of particle size in the dense bed, whereas in the riser of the CFB the contact between wall and suspension is less intensive and consequently the influence of the particle size is small. In fact, there is no marked influence of particle size observed within the scatter of the experiments (Figure 5.24); only in refined laboratory-scale experiments some influence has been noted (Sundaresan and Kolar, 2002). However, the particle diameter affects the heat transfer indirectly through the particle density ρ_{av} . For similar conditions, smaller particles yield higher ρ_{av} than the larger particles, since the latter remain to a larger extent in the bottom region below the heat transfer surface, whereas smaller particles are found in the upper parts of the furnace (at a given total pressure drop over the furnace). Thus, heat transfer depends on particle size through fluid dynamics.

5.2.2 Gas–Particle Heat and Mass Transfer

5.2.2.1 General

The transport of heat and matter may take place inside the particles or at the surface of the particles in a fluidized bed. This section deals with heat and mass transfer across the external surface of the particles. As seen from the point of view of the fluidized bed, it is internal and therefore called internal heat and mass transfer. Accounts for gas–particle heat and mass transfer have been given by Gelperin and Einstein (1971), Kunii and Levenspiel (1991), Agarwal and La Nauze (1989), Tsukada and Horio (1992), Prins (1987) and Palchonok (1998). The structure of the presentation given below is to a large extent based on the work of Palchonok (1998), who in turn supported himself using his own work and experimental data from literature.

Owing to the analogy between heat and mass transfer, these processes are expressed in a similar form:

$$Nu = f(Re,Pr) \quad \text{for heat transfer} \quad (5.118)$$

$$Sh = f(Re,Sc) \quad \text{for mass transfer} \quad (5.119)$$

The Sherwood number $Sh = k_m x_0 / \mathcal{D}$, for mass transfer, is defined similar to the Nusselt number with the mass transfer coefficient k_m and diffusivity \mathcal{D} used instead of heat transfer coefficient h and thermal conductivity k_g . The fields of temperature and concentration coincide if the Lewis number $Le = \alpha/\mathcal{D} = Sc/Pr$ is equal to 1, where $\alpha = k_g/(\rho_g c_{pg})$ is the thermal diffusivity. The dimensionless numbers are usually related to the gas-phase properties and the characteristic dimension x_0 is, except in some cases, that of the bed particles. Most work presented in the literature concerns spherical particles and this form is also treated below, if not otherwise stated. As will be pointed out below, the analogy between heat and mass transfer is not complete. For instance, radiation may affect heat transfer but not mass transfer. Also, in a fluidized bed the neighboring particles interact in different ways for heat and mass transfer.

In addition to Eqs. (5.118) and (5.119) there are boundary conditions. In dimensional form for convective heat transfer at a surface (index w; n is a direction perpendicular to the surface)

$$k_g (\partial(T - T_o)/\partial n)_w = h(T_w - T_o) \quad (5.120)$$

or in dimensionless form

$$(\partial\Theta/\partial N)_w = Nu \quad (5.121)$$

where $N = (n/x_0)$ is the dimensionless coordinate, $\Theta = (T - T_o)/(T_w - T_o)$ the dimensionless temperature, and the Nusselt number is

$$Nu = hx_0/k_g \quad (5.122)$$

Similar boundary conditions can be formulated for mass transfer. Below, only empirical relationships will be treated, but the presentation is based on the analogy of heat and mass transfer.

5.2.2.2 Single Spherical Particle in One-Phase Flow

The conduction heat transfer across a spherical surface of radius R under steady-state conditions in a stagnant medium can be written as illustrated in Figure 5.25:

$$Q = 4\pi r^2 k_g dT/dr \quad (5.123)$$

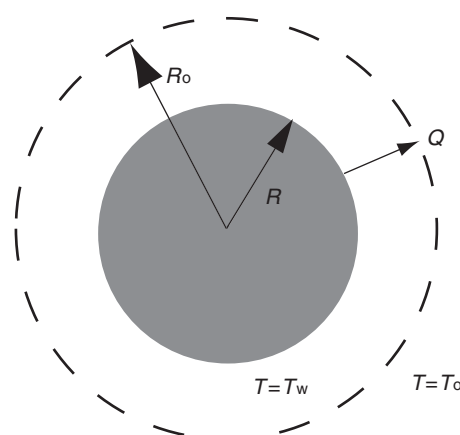


FIGURE 5.25 The heat flow Q leaving a sphere of radius R and a boundary layer of radius R_o .

Integrated between the temperature $T = T_w$ at $r = R$ (the surface of the sphere) and $T = T_o$ at $r = R_o$, a fictitious surface outside the sphere, and combined with the definition of the heat transfer coefficient h (Eq. [5.79]), this becomes

$$Q = \frac{4\pi R k_g}{(1 - R/R_o)} (T_w - T_o) = 4\pi R^2 h (T_w - T_o) \quad (5.124)$$

When R_o tends to infinity, $hR/k_g = 1$ or $Nu = 2$ if Nu is based on the diameter of the sphere. If the sphere is also exposed to convective heat transfer, the following relationship is obtained:

$$Nu = 2 + f(Re, Pr) \quad (5.125)$$

A similar derivation yields $Sh = 2$ for mass transfer, and

$$Sh = 2 + f(Re, Sc) \quad (5.126)$$

These relationships are generally valid for heat and mass transfer to or from single particles and will be applied here to the special case of particles in fluidized beds. The Frössling–Ranz–Marshall equations are well-known relationships for heat and mass transfer to spheres in single-phase flow

$$Nu = 2 + 0.6 Re^{0.5} Pr^{0.33} \quad (5.127)$$

$$Sh = 2 + 0.6 Re^{0.5} Sc^{0.33} \quad (5.128)$$

Two classes of problems to be considered are: (1) transfer between an entire bed and the gas flowing through the bed and (2) transfer between the gas and certain, active, particles mixed with a bed of passive, inert particles. An example of the latter class is a bed of sand or ash for conversion (pyrolysis, gasification, or combustion) of fuel particles. These active fuel particles usually constitute only 1 to 10% of the total bed.

5.2.2.3 Heat and Mass Transfer to a Bed of Particles

In a fluidized particle bed, one would expect more or less the same relationships for heat and mass transfer as for single particles, but this is apparently not the case as shown by Figure 5.26, where the shaded area (4) is the region of published, measured heat and mass transfer data related to particle beds and (3) represents Eqs. (5.127) and (5.128) for a single particle in an one-phase flow. (The other curves in the figure will be further treated below.) Only at higher velocities the coefficients are on the same level. For small particles and low velocities, the overall coefficients of an active bed appear to be much lower than those of single particles.

This discrepancy is explained by the resistance to mass transfer in fine particle beds, where most of the gas passes the bed through the bubble phase, while the flow through the emulsion phase, where the particles are contained, is much smaller. Thus, the overall resistance at the surface of a particle includes the additional resistance caused by the transfer from the bubble phase to the particulate phase. Furthermore, due to the extremely large specific area of beds of small particles, the gas in the particulate phase reaches saturation (or the state of the particles) already close to the gas distributor, making the transfer potential in the upper part of the bed very small. These two factors result in great deviations of the actual gas concentration profiles from the log-mean concentration assumed in the evaluation of most measurements. Consequently, low, measured, overall heat and mass transfer coefficients for an entire fluidized bed are obtained (the shaded region) at the same time, as the actual coefficients of single small particles in the bed are much higher.

For larger particles the gas flow through the particulate phase is larger and the flow through the entire bed is closer to plug flow (the high Re region in Figure 5.26). Therefore, the particles are exposed to the representative gas properties to a greater extent. Furthermore, the flow reaches farther into the bed before saturation is attained. The latter reason is the same for gas–particle heat transfer and explains the similar

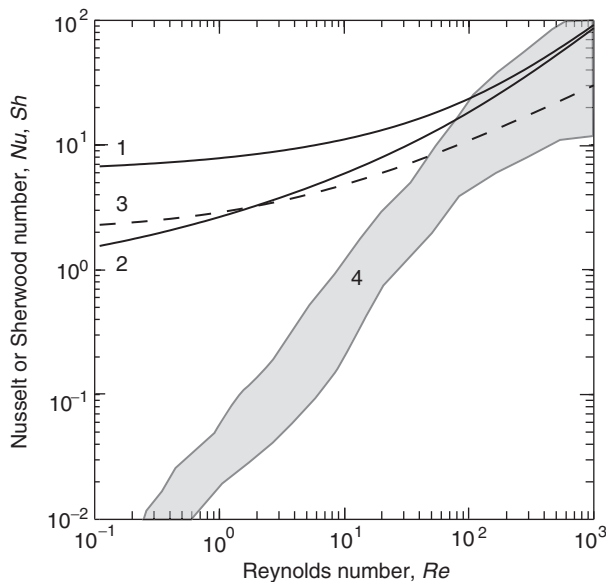


FIGURE 5.26 Heat and mass transfer coefficients as a function of velocity or particle size: (1) Eq. (5.131) for heat transfer and (2) Eq. (5.132) for mass transfer are compared with (3) the sphere in one-phase flow [Eqs. (5.127) and (5.128)]. The shaded region (4) represents various sets of published data from entire beds. Ar in Eqs. (5.131) and (5.132) has been calculated from Re_{mf} (Eq. [5.81]), assuming $\varepsilon = 0.4$ and $Pr = Sc = 0.7$. (Adapted from Palchonok, G.I., Breitholtz, C., Borodulya, V.A., and Leckner, B., in *Fluidization IX*, Engineering Foundation, New York, 1998, pp. 413–420.)

behavior of heat and mass transfer in this case. A detailed account of these phenomena is found in Kunii and Levenspiel (1991).

The large surface area encountered by a gas is one explanation for difficulties in interpretation of experimental data. A further explanation related to fixed beds, where the same phenomenon has been observed, was given by Wakao and Kaguei (1982) to be due to the neglect of the axial dispersion in the evaluation of experimental results, a transport constituent that becomes increasingly important at low velocities (small particles).

As a consequence of the fast transfer, in most practical applications the description of heat and mass transfer to the particles in a bed is not important. The problem of design of a bed is converted to what Gelperin and Einstein (1971) called the “thermal balance problem”. This means that a heat or mass balance across the bed is sufficient in most design tasks. Only in special cases, for instance very thin beds, where gas and particle conditions may not have reached equilibrium, the heat and mass transfer in the bed need to be considered.

5.2.2.4 Heat and Mass Transfer to Active Particles in a Fluidized Bed of Inert Particles

Fuel converted in a fluidized bed forms active fuel particles surrounded by inert bed particles. Usually, the amount of fuel particles in the bed is such that every fuel particle is completely surrounded by inert particles and by a gas at the given concentration and temperature, as illustrated in Figure 5.27. The temperature of the inert particles is practically the same as that of the gas, whereas the temperature of the active particles may differ from that of the surrounding inert bed particles due to release or consumption of heat by some activity such as chemical reaction in the particle or on its surface. The particles are assumed to remain in the particulate phase, where according to traditional thinking, the superficial velocity is of the order of minimum fluidization velocity u_{mf} , and hence there is a direct relation between the Reynolds number (velocity) and the particle size via the Archimedes number according to Eq. (5.81).

Depending on the size of the active particle d_a relative to that of the inert particles d_p , two extreme and one intermediate case can be distinguished: $d_a/d_p \gg 1$, $d_a/d_p \approx 1$, and $d_a/d_p \ll 1$.

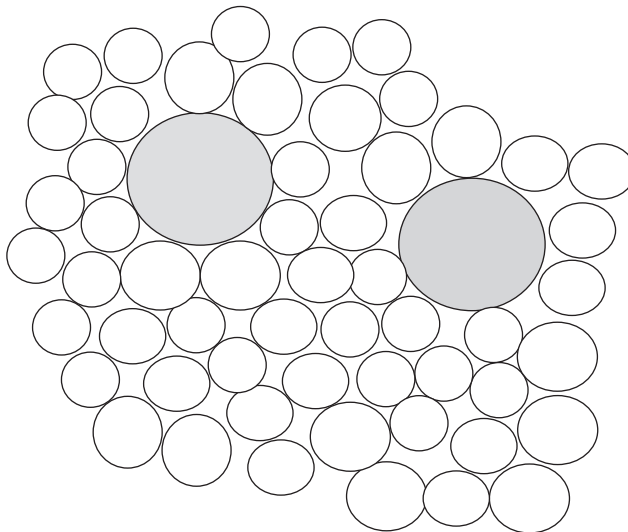


FIGURE 5.27 Two large, active particles surrounded by smaller inert particles.

Large active particles surrounded by smaller inert particles ($d_a/d_i \gg 1$) can be represented by correlations valid for maximum heat and mass transfer from gas and particle convection to large objects fixed in a fluidized bed (see Eqs. [5.83], [5.86] and [5.87]):

$$Nu_{i,\text{large}} = 0.85Ar_i^{0.19} + 0.006Ar_i^{0.5}Pr^{0.33} \quad (5.129)$$

$$Sh_{i,\text{large}} = 0.009Ar_i^{0.5}Sc^{0.33} \quad (5.130)$$

where i indicates that the size included in the dimensionless numbers is that of the inert particles. $Nu_{i,\text{large}}$ is the maximum Nusselt number obtained at optimum fluidization velocity according to Eq. (5.84), which is assumed to be valid also for higher velocities. Naturally, there is no analogy to particle convection that contributes to mass transfer, and the first term of Eq. (5.129) is not included in Eq. (5.130). (The small, insignificant difference in coefficients arises due to slightly different fits to data at different times of publication.) The information regarding the gas convective term is originally gained from mass transfer experiments (Baskakov et al., 1973).

For active particles, which are nearly equal in size to the surrounding inert particles ($d_a/d_i \approx 1$), the heat and mass transfer can be represented by (Palchonok et al., 1992)

$$Nu_1 = 6 + 0.117Ar_i^{0.39}Pr^{0.33} \quad (5.131)$$

$$Sh_1 = 2\varepsilon_{\text{mf}} + 0.117Ar_i^{0.39}Sc^{0.33} \quad (5.132)$$

Index 1 is used to indicate that the dimensionless numbers are related to the inert or active particles of about the same size. The gas convection term (the second term on the right-hand side) is based on numerous sets of measured data and the analogy between heat and mass transfer (Palchonok and Tamarin, 1983, 1985). The high interstitial velocities prevailing in this large particle case can be compared to heat transfer in turbulent flow in a tube, where $Nu \sim Re^{0.8}$. The transformation of the Archimedes number to Reynolds number by means of Eq. (5.81) yields the same power (~ 0.8) in the second term of Eqs. (5.131) and (5.132), which emphasizes the similarity of the phenomena treated to turbulent flow in ducts. The first term represents the limiting case at low velocities, where heat and mass transfer are different. The mass transfer is similar to the one-phase case, approximately corrected for the occlusion caused by the surrounding particles.

through the term ε_{mf} , the voidage at minimum fluidization velocity (Avedesian and Davidson, 1973). In heat transfer there is no similar occlusion. On the contrary, the surrounding inert particles exchange heat both with the active particle and the gas. In this case, the integration of the heat conduction equation, Eq. (5.124), is not carried out from the particle surface to infinity as for one-phase flow, but only to a limit represented by a spherical space containing the nearby gas. The space is $\varepsilon_{mf}d_p^3$ and part of the gas lens between the active particle and the six neighboring particles $6(\pi d_p^3/24)$ in a cubic arrangement (Palchonok et al., 1992). This yields the number 6, seen in Eq. (5.131), a number that agrees with several sets of measurement data. A similar expression for heat transfer has been presented by Baskakov et al. (1987):

$$Nu_1 = 10 + 0.23Ar_1^{0.33}Pr^{0.33} \quad (5.133)$$

where the integration has been carried out for a spherical gas shell in a cubic packing of particles, as explained by Zabrodsky (1966) and Gelperin and Einstein (1971). The difference between Eqs. (5.131) and (5.133) is small in practical applications, which are usually far from the limiting values at low velocities (the first term of Eqs. 5.131 and 5.133), but the expressions are theoretically different. The derivation of Eq. (5.133) concerns a similar gas film for all bed particles implying heat exchange between gas and a particle surrounded by similar bed particles, whereas Eq. (5.131) also accounts for the exchange between an active particle and surrounding inert particles.

The thickness of the surrounding gas film increases if the emulsion phase expands, i.e., $\varepsilon > \varepsilon_{mf}$, and the first term on the right-hand side in Eqs. 5.131 to 5.133, approaches the limiting value of 2 in an expanded bed with a small interaction between particles. Equations (5.131) and (5.132) are compared with the correlation for single phase heat and mass transfer to a sphere in [Figure 5.26](#).

Small active particles (index a) tend to be carried by the gas through the space between the larger inert particles, constituting the bed. They are assumed to behave like particles in a single-phase flow (cf. Eqs. [5.127] and [5.128]):

$$Nu_a = 2 + 0.6Re_{at}^{0.5}Pr^{0.33} \quad (5.134)$$

$$Sh_a = 2 + 0.6Re_{at}^{0.5}Sc^{0.33} \quad (5.135)$$

The small particles follow the interstitial gas when their terminal velocity is equal to or greater than the gas velocity $u_{mf}/\varepsilon \leq u_{at}$. This gives the Reynolds number in the convective terms of Eqs. (5.134) and (5.135) according to $Re_{at} = Ar_a/(18 + 0.61Ar_a^{1/2})$ from Eq. (5.82). Normally these terms are very small, the limiting Nusselt or Sherwood numbers become equal 2, and the value for a single particle in an infinite space can be used as long as the small particles do not severely interact with the bed particles. The correlations for small particles are related to their dimension d_a .

Simple interpolation formulae are recommended (Palchonok, 1998) to represent heat and mass transfer coefficients Nu_i and Sh_i for $d_a/d_i \geq 1$, which in the case of spherical particles look like

$$(Nu_i - Nu_{i,large})/(Nu_1 - Nu_{i,large}) = (d_i/d_a)^{2/3} \quad (5.136)$$

$$(Sh_i - Sh_{i,large})/(Sh_1 - Sh_{i,large}) = (d_i/d_a)^{2/3} \quad (5.137)$$

where $Nu_{i,large}$ and $Sh_{i,large}$ are defined by Eqs. (5.129) and (5.130) and Nu_1 and Sh_1 by Eqs. (5.131) and (5.132). These two limiting expressions and the interpolation range between them are shown in [Figure 5.28](#).

Palchonok (1998) has shown, that the interpolation procedure describes most of the available experimental data from literature within a range of $\pm 30\%$. However there are several data sets that show greater deviation. The reasons for deviation have not yet been explained, and there are matters of discussion, such as the fact that Eqs. (5.129) and (5.130) describe the conditions at optimum velocity and beyond, whereas some tests were carried out at lower velocities. Further work on refinements and validation of the interpolation procedure is necessary, but the representation describes the important published data sets reasonably well and has

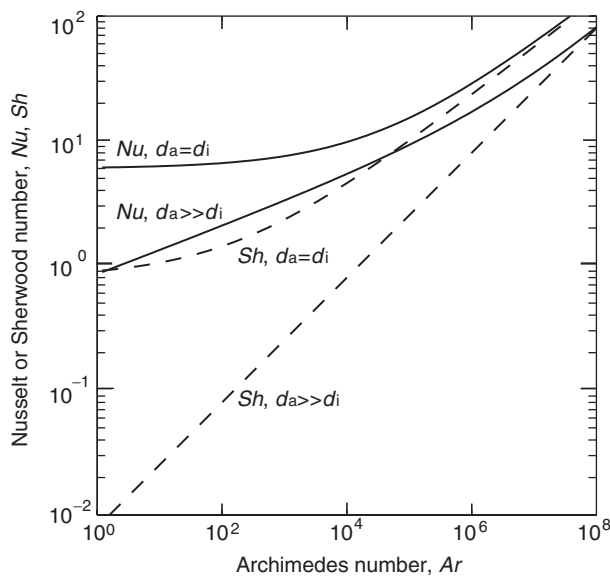


FIGURE 5.28 Limiting Nusselt and Sherwood numbers for active particles of size d_a in a bed of particles d_i . Interpolation between these limits is made by Eq. (5.136) or (5.137).

the advantage of covering the entire range of interest for heat and mass transfer calculations. In addition, radiation has to be estimated along the lines described above for external heat transfer.

5.2.2.5 Active Particles Above a Dense Bed

The above concerns particles in a dense, bubbling fluidized bed. Less information is available about particles in the freeboard or in the disperse phase of a circulating fluidized bed. There are some ways to solve this problem. First, it should be mentioned that in a CFB converter most particles remain in the bottom bed and can be handled by the relationships mentioned in the previous section for a dense, bubbling bed. The particles carried away are small; and the surrounding particle loading of inert particles is small; the voidage ε is almost equal to unity. Hence, the correlations for single-phase flow can be employed. These particles are exposed to a velocity that can be represented by the terminal velocity of a single particle. Refinements, such as accounting for clustering, are not likely to play a key role due to the low particle concentration and the low relative velocity between gas and particles.

A large, fixed object (a cylinder or a sphere), on the other hand, is subjected to the flow of particles and gas from the bed and particles returning from the space above the dense part of the bed down to the bed. There are some experiences from a CFB and the splash zone of bubbling noncirculating beds related to heat transfer in this situation, as illustrated in Figure 5.29. The measured heat transfer is higher than the heat transfer to an object in an undisturbed single-phase flow, represented by the solid lines in the figure, and can be written as

$$Nu = Nu_{\min} + 0.89 Re^{0.5} Pr^{0.33} \quad (5.138)$$

for a sphere ($Nu_{\min} = 2$) or for a cylinder ($Nu_{\min} = 0$).

In this section, radiation is not included. The additional contribution of radiation can be treated with the relationships presented in the section on heat transfer.

Spherical particles were treated above. In general, particles employed in experiments were perfectly spherical or reasonably spherical, such as many types of particles employed in fluidized beds. The correlations can be used for "reasonably" spherical particles, but for highly nonspherical particles corrections

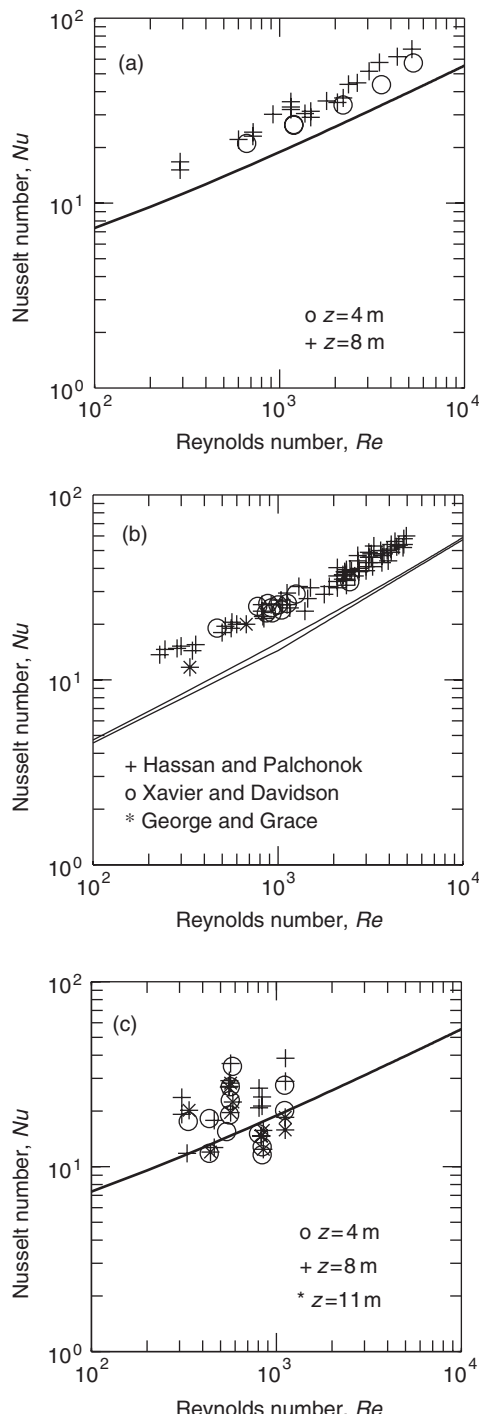


FIGURE 5.29 Convective heat transfer to a fixed sphere located at various distances z above the dense, bottom bed (a) in a cold experimental CFB rig, (b) in the splash zone of a bubbling bed, and (c) in a CFB boiler with radiation subtracted. The measurements are compared with the correlations for spheres in a single-phase flow (Eq. [5.127] in [a] and [c]). The data in (b) are compared with the correlations of Douglas and Churchill (1956) and of Zhukauskas (1990) for a cylinder. (Palchonok, G.I., Breitholtz, C., Borodulya, V.A., and Leckner, B., in *Fluidization IX*, Engineering Foundation, New York, 1998, pp. 413–420.)

have to be considered. Such corrections are not included here, since they relate to a particular feature that has to be modeled. Besides, the experimental support for strongly nonspherical particles is insufficient.

5.3 Fluidized-Bed Reactors and Applications

Jesse Zhu and Yi Cheng

5.3.1 Fluidized-Bed Reactors

Fluidized beds as chemical reactors offer many unique advantages such as large interfacial surface area between fluid (gas or liquid) and the particles, high fluid–particle contact efficiency, excellent heat transfer, uniform temperature, and the ability to handle a wide range of particle properties and a large quantity of particulate materials (Davidson et al., 1985; Geldart, 1986; Kunii and Levenspiel, 1991; Kwauk, 1992). The added benefits for the high-velocity circulating fluidized beds include higher gas and solids throughput, more uniform residence time distributions for both gas and solids phases, higher turndown ratio, and the possibility to realize two different reactions in the riser and the solids downflow return system (Grace et al., 1997). See also to [Sections 5.1](#) and [5.2](#) for more details.

Fluidized-bed reactors include gas–solid, liquid–solid and gas–liquid–solid fluidized-bed reactors in terms of the fluid–particulate systems. In terms of reactor scheme and operation, there are the so-called stationary fluidized beds (SFB) or fixed fluidized beds (FFB), where the particles essentially stay in the fluidized bed and the so-called circulating fluidized beds (CFB), where particles are mostly entrained out of the fluidized beds but at the same time recirculated back to or fresh particles added to the same fluidized beds. SFB are often called conventional fluidized beds since they were the first to be realized and used in various industrial applications. In gas–solid systems, SFB include particulate fluidized beds, bubbling fluidized beds, slugging fluidized beds, and turbulent fluidized beds, which are also called fluidization regimes, as detailed in Section 5.1. In liquid–solid systems, the SFB primarily have one operating regime, the particulate fluidization regime, where the particles are uniformly suspended in the upflowing liquid. In the stationary gas–liquid–solid three–phase fluidized beds, there are three main operating regimes: the dispersed bubble regime, the coalesced bubble regime, and the slug regime (Fan, 1989). Since all SFB have a dense phase of particulate materials in the bed, they are also referred to as dense-phase fluidized beds, in contrast to dilute-phase fluidized beds referring to CFB.

In CFB, the fluidizing gas or liquid (or the two combined) velocity is high enough to entrain all particles out of the bed; and to retain enough particles in the bed so as to keep a fluidized bed, particles (either recycled or fresh) need to be fed into the bottom of the fluidized beds. In CFB, there are also different regimes: the fast fluidization regime, the pneumatic transport regime, and the so-called dense suspension upflow or dense-phase transport regime for higher suspension density and high particle flux operations (Grace et al., 1999). There is also the cocurrent gas–solid downflow operation where both gas and particles are flowing downwards in a downer column (Zhu et al., 1995).

There are also special types of fluidized-bed reactors, such as the spouted-bed reactor (Mathur and Epstein, 1974), which has been broadly included in the fluidized-bed literature by tradition, although it can also be considered as another multiphase reactor. In a spouted bed, gas (or liquid) is injected from the bottom through a central nozzle into the bottom of a normally cylindrical vessel to form a high-velocity upflow stream of gas (or liquid) and particles in the central region (the spout) and a slow downward moving layer of particles between the central spout and the wall (the annulus). In this pattern, a gross internal particle circulation is created, which gives special features such as the ability to handle larger or sticky particles, making the spouted bed very useful in certain physical operations such as drying and particle coating. Another example is pneumatic transportation, which originated earlier than the concept of fluidized beds. With the development of CFB reactors, however, the distinctions between a CFB reactor and a transport reactor has become less clear (Bi et al., 1995). Associated with pneumatic transportation are particle spray and elutriation which are normally not separately considered in the fluidized-bed literature.

In a broad sense, the application of fluidization technology dates back to the ancient times when peasants winnowed their grains. After the grain particles were swung up, a relative upflow of gas stream was created when the particles fall down. In such a fluidized state, the upflow gas preferentially segregates the lighter shells from the heavier seeds, so as to achieve separation. The first record on application of fluidization technology was perhaps found in an ancient Chinese book entitled *Applying the Principles Learned from the Nature* printed in 1637. In this book Song (1959) described a process to separate sands out of grain through vibrating winnowing pans in a certain fashion.

The first modern application of a fluidized-bed reactor was a stationary, dense-phase gas–solid fluidized-bed reactor (Winkler, 1922) operated for coal gasification in Germany to produce synthesis fuel from coal. Over the last 80 years, the concept of such low-velocity “conventional” fluidized-bed reactors has been significantly expanded with the development of new types of fluidized-bed reactors, including high-velocity circulating or riser fluidized-bed reactors by increasing the fluid velocity (Grace et al., 1997), to liquid–solid and gas–liquid–solid three–phase fluidized reactors by changing the fluidizing agent (Fan, 1989; Epstein, 2003a; 2003b), and cocurrent downflow downer fluidized-bed reactors by changing the direction of the fluid–particle flow (Zhu et al., 1995). Experimentally tested but not yet in application is the inverse fluidized-bed reactors, where lighter particles are fluidized inversely by heavier fluid (Karamanov and Nikolov, 1992). The various types of fluidized-bed reactors are listed in Table 5.3.

The numerous applications of fluidized-bed technology can be classified at least into two types. The first is the reaction type. For gas–solid systems, they can be divided into four categories:

1. Gas catalytic reaction, where both reactants and products are in gas phase, but the reaction takes place on the surface of a solid catalyst. This is the most frequently encountered application, counting for majority of all fluidized-bed applications. Examples of such reactions are the fluid catalytic cracking process, and many catalytic synthesis reactions.
2. Gas-phase reaction with solids as heat carriers, where both the reactants and products are in gas phase, but the solids are required as heat carriers to either provide the heat for the reaction or to carry out the heat produced by the reactions. This is very useful for highly exothermic and endothermic reactions, since solid particles have very high heat capacity.
3. Gas–solid reaction, where both gas and solids are the reactants and the products contain either only gas phase or a combination of both gas and solids. Examples are coal combustion and gasification.
4. Physical process, where no chemical reaction occurs. A typical example is fluidized-bed drying.

A similar classification to the gas–solid systems can also be used for liquid–solid and gas–liquid–solid fluidized beds, but it may not be necessary at this stage given the limited number of applications. Applications of liquid–solid fluidized beds and three–phase fluidized beds can often be found in hydrocarbon process and the mineral process industry, and more recently in the biochemical, pharmaceutical and food industry, and the environmental area.

TABLE 5.3 Types of Fluidized-Bed Reactors

Type of Fluidized-Bed Reactors	Fluidizing Medium	Typical Particle Size	Typical Gas/Liquid Velocity
Bubbling bed	Gas	Medium-large	Low
Slugging bed	Gas	Medium-large	Low
Turbulent bed	Gas	Small-medium	Medium
Circulating riser	Gas	Small	High
Circulating downer	Gas	Small	Medium-high
Spouted bed	Gas	Very large	Low
Liquid–solid bed	Liquid	Medium-large	Low
Gas–liquid–solid bed	Gas and liquid	Medium-large	Low
Liquid–solid circulating bed	Liquid	Small-medium	High
Gas–liquid–solid circulating bed	Gas and liquid	Small-medium	High
Inverse bed	Liquid	Small-medium	Low

The second method of classification is to group by the areas of applications in different industrial processes, including:

1. Hydrocarbon processes
2. Catalytic synthesis
3. Roasting and calcination
4. Metallurgical processes
5. Combustion, gasification, and incineration
6. Biochemical and environmental processes
7. Pharmaceutical and food processes
8. Physical processes

This section is primarily structured based on the first method of classification but the type of application for each example in terms of the second type of classification is clearly referred to in the description. For brevity, only the most commonly encountered processes and those of special features are included in this section. There are also many potential applications of fluidized beds. A selected few important potential applications, especially those in the late stage of development, are also described.

5.3.2 Catalytic Gas-Phase Reactions

5.3.2.1 Fluid Catalytic Cracking

Fluid Catalytic Cracking (FCC) was the second major application of fluidized-bed technology after coal gasification by Winkler in the 1920s and is still by far the largest application of fluidized-bed technology, with over 350 units worldwide. The FCC process uses a solid catalyst to crack down the long chain of vaporized heavy oil or residues from the crude and other sources and convert them into light products such as gasoline, kerosene, diesel, and light olefins. Since crude oil, on average, contains less than 10% gasoline with poor octane value, FCC becomes the critical process in meeting the demands for a higher gasoline fraction (over 50%) plus a higher octane value. FCC is therefore often called the heart of a refinery. Some numbers provided in a 1997 review (Avidan, 1997) show the enormous economic impact of FCC on petroleum refining and hence on worldwide economy:

1. There are about 350 FCC units operating worldwide. The total worldwide capacity of FCC units is over 2.4 million tons/day (16 million barrels/day).
2. The uplift across the FCC unit (difference between the value of products and feed) can be as high as US\$10/barrel.
3. The total inventory of FCC catalyst in the average FCC unit is 300 tons. The daily catalyst make-up rate to the typical vacuum gas oil feed FCC unit is 4 tons, whereas the daily make-up rate to a resid processing FCC unit can be as high as 30 tons.
4. Over 450,000 tons of FCC catalyst are manufactured every year, representing a US\$600 million business worldwide. The total catalyst manufactured worldwide is approximately 1200 tons/day corresponding to a surface area of 380,000 km² if laid as single layer particles, the size of Egypt, each year.

Cracking of crude oil to lighter hydrocarbons dates back to the early 20th century (Royal Dutch Shell Group of Companies, 1983). In 1916, the first catalytic cracking process was carried out in a commercial scale with aluminum chloride as the catalyst. Since the catalyst was too expensive, this process did not continue for long. In the 1930s, Houdry obtained an effective catalyst from natural clay and invented the Houdry process. Both were fixed-bed processes, which had a long residence time and required cyclic operations for catalyst regeneration. Such processes also required salt bath heat exchangers that are costly and only partially effective for temperature control. In 1941, the Thermofer Catalytic Cracking (TCC) moving-bed process went on operation where the cracking reaction and catalyst regeneration were for the first time realized in two separate vessels with the catalyst particles circulated between the two vessels initially by bucket elevators and later by pneumatic transport.

Because the fixed-or moving-bed operation had many limitations in terms of solids handling and transportation, heat addition or removal, gas–solid contact, and process capacity, etc., the Standard Oil of New Jersey (now Exxon) began to develop a new FCC process in the late 1930s, with their first commercial unit on line in 1942 (Jahnig et al., 1980). Figure 5.30 sketches the typical early FCC design, the EXXON Model IV, which has two dense-phase fluidized beds, one as cracking reactor and the other as catalyst regenerator. The reactor runs in the temperature range 480 to 550°C and the regenerator in the range 550 to 600°C. The catalyst used was the synthetic amorphous silica–alumina catalyst and the average particle size of FCC is in the range 55 to 80 µm. A much smaller particle size than that in the fixed-bed operation gives much more surface area for the cracking reaction. Figure 5.31 shows an alternative design of the dense-phase FCC, the Universal Oil Products Company (UOP) stacked unit.

During the operation, the regenerated hot catalyst particles flow into the bottom of the reactor with the feed (crude oil or other heavy residue) injected into the transport line at a position near the bottom entrance to the reactor. The feed vaporizes upon contacting the hot catalyst and the catalytic cracking reaction takes place inside the reactor. Cracking yields lighter products that leave the reactor in a gas phase from the top of the reactor. During the cracking process, rejected carbon deposits onto the catalyst, causing it to deactivate. The deactivated catalyst particles are then circulated to the regenerator, after passing through a steam-stripping section below the reactor. The stripping section is either a moving bed or a gently fluidized bed with a very low steam rate and its main function is to displace the products adsorbed on the catalyst. The deactivated catalyst is regenerated in the regenerator by burning off the carbon accumulation, before being circulated back to the reactor. During the regeneration, the temperature of catalyst is also increased by this exothermic combustion process, accumulating substantial heat in the catalyst. The hot catalyst then carries the heat to the reactor, supplying the energy necessary for the endothermic catalytic reaction. Because of fluidization, catalyst particles can be transported easily in the loop between the two units. Both the reactor and the regenerator were reported to operate in the bubbling regimes in the early times. However, it is probable that most of them were operated in the turbulent fluidization regime given the relatively high gas flow rate, although not reported since the concept of the turbulent fluidized bed was not proposed until the early 1970s (Kehoe and Davidson, 1971).

The advantages of the FCC process are the excellent gas–solids contact, the much improved heat transfer, the large interfacial area with the reduction of particle size, and the large and controllable solids circulation between the two units. There are also at least two additional key advantages that distinguish the FCC from other fluidized-bed processes. The first key advantage is that the reaction and regeneration is completed in one cycle with catalyst particles freely circulated between the two units. This solves the problem of quick catalyst deactivation and allows the process to continue. FCC is classified as a gas-phase catalytic

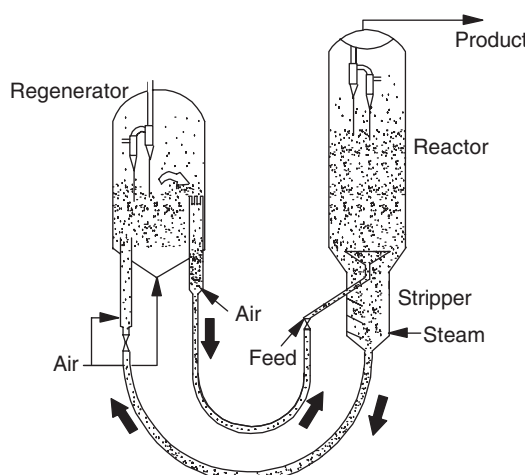


FIGURE 5.30 Exxon dense-phase fluidized-bed FCC, Model IV.

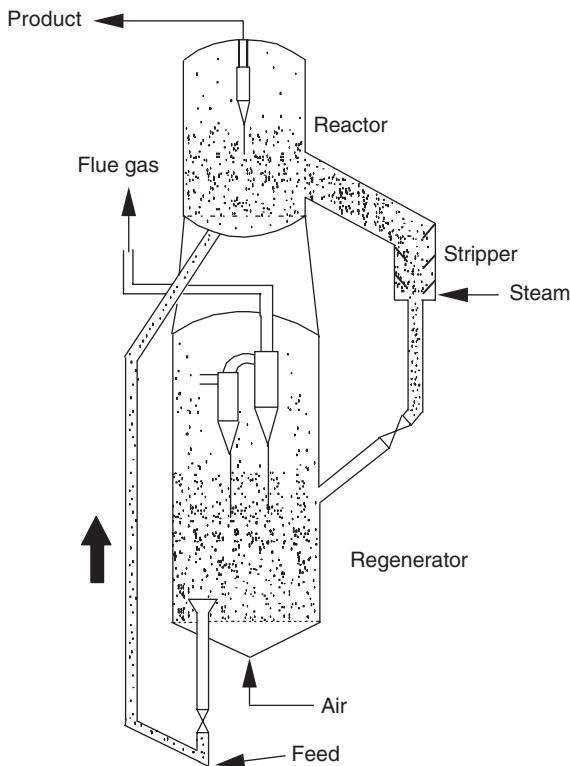


FIGURE 5.31 UOP stacked dense-phase fluidized-bed FCC.

reaction because the solid particles are the catalyst, which does not change its form during the process. The second key advantage is the realization of self-heat sufficiency, by using the heat of carbon combustion in the regenerator to supply the heat required for the endothermic cracking reaction. This also gives the feature of a “gas-phase reaction with solids as the heat carrier” as in the first classification. With the second classification based on the areas of application, FCC clearly belongs to hydrocarbon processing.

While having many advantages, the dense-phase FCC process has at least two distinct disadvantages: (1) the residence time of the gas phase in the reactor cannot be controlled precisely, leading to overcracking of the product, and (2) the residence time of the catalyst is also not uniform in the reactor, and the presence of deactivated catalyst severely affects the selectivity. With the development of more active zeolite catalyst by Mobil, the new “riser-cracker” was commercialized in the early 1960s. This new FCC replaced the dense-phase fluidized-bed reactor with a transport riser reactor, within which the gas velocity was sufficiently high to entrain the particles upward while the cracking reaction takes place. A typical riser FCC unit, the Shell FCC unit, is shown in Figure 5.32a. The riser reactor significantly narrows the residence time distributions for both gas and solid phases so that overcracking is reduced and selectivity is increased. The high-velocity operation, in combination with the more active zeolite catalyst, also shortens the reaction time, further enhancing the formation of liquid products and reducing coke formation. The new zeolite catalyst also allows the increase in the regeneration temperature to about 700°C or higher, enhancing the combustion efficiency with more CO burning and providing a better heat balance. The zeolite catalyst has an average particle size of 50 to 75 µm and the particles usually have a wide size distribution from 1 to 130 µm (Avidan and Shinnar, 1990), with sufficient fines under 45 µm to ensure excellent fluidity.

Typical yields from a modern FCC (Avidan et al., 1990) are (all by wt%):

Fuel gas	4
Dry gases (C_3 's + C_4 's)	13

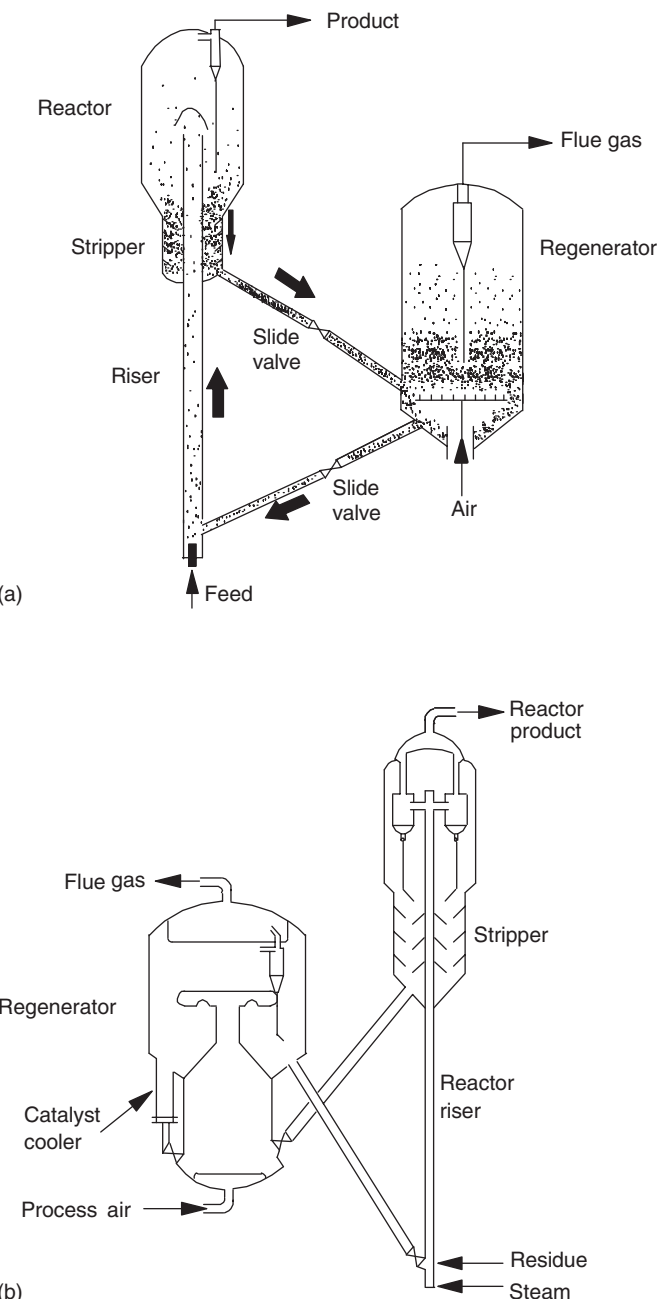


FIGURE 5.32 (a) Shell riser FCC; (b) SINOPEC riser RFCC.

Gasoline	50
Light cycle oil	20
Heavy cycle oil	7
Coke	6

The highly endothermic cracking reaction significantly reduces the molecular weight of the feed to yield much more valuable products. The moderate temperature (500 to 550°C) ensures the preference of a more selective catalytic cracking over the less selective thermal cracking. By changing the temperature

and other operating conditions, the relative fractions of the different product components can be adjusted to reflect the market requirements.

In the recent years, the demand for more light products has led to the cracking of heavier feed. This is sometimes referred to as residue fluid catalytic cracking (RFCC). RFCC requires “deeper” cracking under a higher catalyst/oil ratio. In addition, the heavier feed produces more carbon on the deactivated catalyst, increasing the load of the regenerator. Many new regenerators have been designed, featuring two-stage combustion, larger unit, additional catalyst cooler, etc. The catalyst cooler is another external fluidized-bed heat exchanger connected to the regenerator, where excess heat from the regenerator can be optionally removed out of the system. This becomes an essential feature for RFCC, since the heat from carbon combustion is normally more than that required for the cracking reaction. It is also used to control the regenerator and the reactor temperatures. The RFCC unit by SINOPEC is shown in [Figure 5.32b](#) as an example.

Although the modern FCC coupled by CFB riser reactor and the turbulent-bed regenerator is dominating the FCC technology worldwide, they are not free from some inherent problems. In a typical riser, there is significant radial segregation with higher solids concentration and lower gas and particle velocities near the wall, and lower solids concentration and higher gas and particle velocities in the center. This reduces the gas–solids contact efficiency, and also causes axial dispersion of the two phases and therefore nonuniform residence time distributions for the gas and solids. The gas dispersion causes overcracking and solids dispersion causes a reduction of selectivity. Solids acceleration at the riser bottom and gas–solids separation at the riser top lead to the requirement of longer reaction time.

To overcome this problem, the concept of a cocurrent gas–solid downer was proposed as a quick-contact reactor. In the downer, the radial gas and solids segregation existing in the riser is minimized due to the along-gravity flow directions of both gas and particles. The patents by Texaco appears to be the first to publish this downer concept (Avidan et al., 1983; Gross and Ramage, 1983). Later, Murphy (1992) reviewed the evolutionary design changes of FCC processes and pointed out that the future FCC will involve high-temperature, short residence time cracking, and dispersed-phase regeneration. He then proposed the use of a downer for cracking reaction and a riser for catalyst regeneration, as shown in [Figure 5.33](#). The Quick Contact (QC) reactor tested by Stone and Webster (Gardside, 1989) and the short contact-time fluidized reactor tested by Bassi et al. (1994), although mainly developed for thermal cracking, are both downer reactors that can also be used for FCC. More recently, bench-scale pilot studies by Deng et al. (2002a) show the excellent properties of the downer reactor that have led to a significant improvement in selectivity, but similar pilot studies by Talman et al. (1999) reveal that the actual conversion in their downer reactor is less than that expected from a pseudo-homogeneous reactor. Associated with hot model studies are many hydrodynamic studies as reviewed by Zhu et al. (1995), most of them showing favorable characteristics of the downer reactor. In the longer run, it is evident that the downer is superior to the riser for the FCC process. Results from a recent 0.2 b/d demonstration downer unit in Saudi Arabia operated at a high reaction temperature (above 550°C), short contact time and with a high C/O ratio, report enhanced gasoline and light olefins production, reduced backmixing and suppressed thermal-cracking reactions (Maadhah et al., 2000). Based on the above results, a 30 b/d demonstration unit is being built near a Saudi refinery.

5.3.2.2 Catalytic Synthesis — Fischer–Tropsch Process

Fischer–Tropsch (F–T) process is the collective name for a group of synthetic reactions that synthesize CO and H₂ to form hydrocarbons of longer chains under high temperature and pressure. This is a strong exothermic reaction. The application of fluidized beds in the F–T process has been an on-going competition between the SFB and the CFB, and important lessons can be learned from the evolution of this process.

The application of fluidized bed in the F–T process started with the failure of the first such attempt in the United States in the 1950s (Kunii and Levenspiel, 1991). It was the Hydrocol process that aimed at the production of high-grade gasoline from cheap natural gas. It was a dense-phase (bubbling) fluidized bed (SFB) of iron catalyst with cooling tube banks immersed in the bed to remove the heat (Zenz and Othmer, 1960). Although laboratory experiments were very promising (90% conversion), the 5 m ID commercial

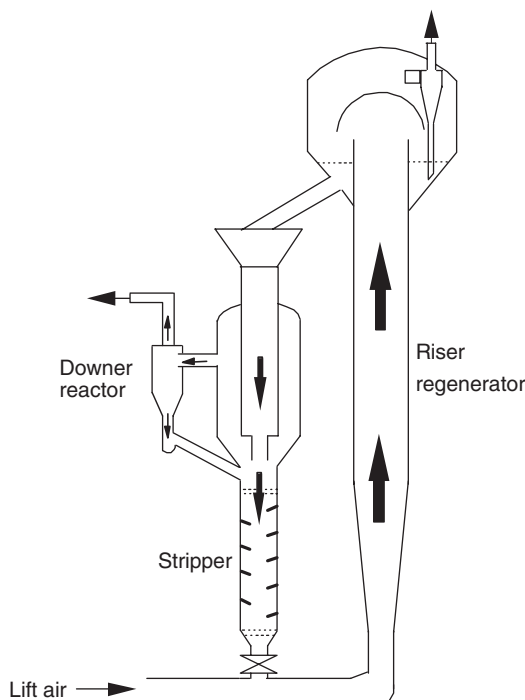


FIGURE 5.33 Future FCC unit as proposed by Murphy, with downer reactor and riser regenerator.

unit had much lower conversion. One key reason was attributed to the group C iron catalyst particles, which result in poor fluidization quality including channeling, poor gas–solid contact, and poor mixing. The operation was abandoned later, with the added consideration of the rising natural gas price.

At the same time, the South African Synthetic Oil Limited (Sasol) approached Kellogg to develop a new reactor for the same process. At that time Kellogg was deeply involved in a consortium of companies to develop the FCC reactors, the first generation of which was a CFB (Shingles and McDonald, 1988). In essence, Kellogg decided to try the CFB approach since they already had the detailed design for FCC, which was then shelved because of the low activity of the amorphous silica–alumina catalyst. The pilot study was a success and CFB was chosen as the Sasol Synthol reactor. The first commercial Sasol reactor, Sasol I, was in production in 1955 and was also the first industrial application of CFB, although it turned out later that there was no need to have a CFB, but a more carefully designed SFB would suffice.

The Sasol Synthol reactor is schematically shown in Figure 5.34. It is more like a loop reactor, but has most of the essential features of CFB. The feed is pushed into the bottom of the riser where the F-T reaction takes place. Heat exchangers are located in the middle portion of the riser to remove the heat produced by the reaction. The product is then separated from the recirculating catalyst and the catalyst is returned to the bottom of the standpipe to restart the cycle. The reaction temperature is above 320°C and the pressure is 10 to 17 bar. The reactor side gas velocity needs to be above a critical velocity of 1.2 m/sec, below which the operation becomes unstable. The voidage on the reactor side is around 0.90 at the bottom and 0.97 at the top (Shingles and McDonald, 1988). A series of scaleups after the first commercial unit has increased the single unit capacity by several times. Shingles and McDonald (1988) provide a detailed account of the initial startup experience of the first Sasol reactor and the subsequent scaleups to Sasol II and III reactors.

The main reason for using a fluidized bed for the F-T process is the high heat transfer rate that ensures a nearly uniform reaction temperature. However, because catalyst deactivation is not an issue and there is no need to remove and return the catalyst continuously, the particles are in a complete mixed mode in the Sasol reactors. In this case, a turbulent fluidized-bed reactor, an SFB, should suffice and actually is better

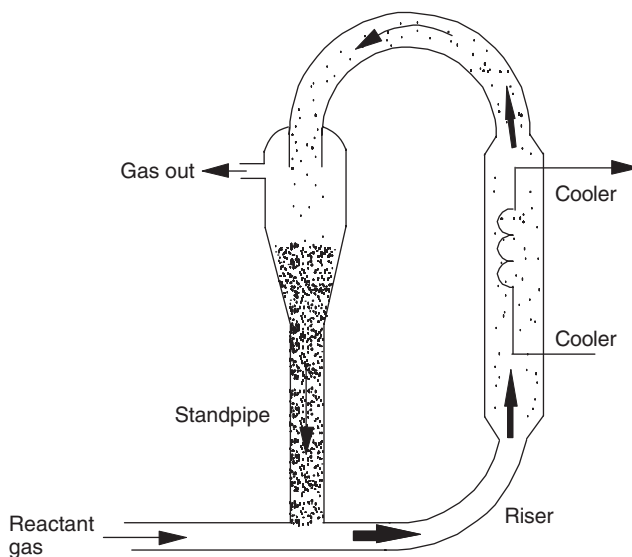


FIGURE 5.34 Sasol Synthol CFB Fischer-Tropsch reactor.

given the lower cost. While Sasol did make a quick comparison between a CFB and an SFB back in the 1950s, Shingles and McDonald (1988) suggested that the comparison was not made properly since different particle sizes were used for the two types of reactors. At that time, little was known about the turbulent fluidized bed, so that its benefits on the F-T process were left to be discovered 30 years later (Silverman et al., 1986).

The competition between the SFB and the CFB on the application of F-T process now finally has a “verdict” with the turbulent bed winning the race. An important lesson is that there is no need to “over kill” and CFB is not necessarily better if not needed. The latter is often wrongly portrayed to students and young engineers as always being superior when they read the vast literature that gives the benefits of CFB.

5.3.2.3 Other Catalytic Reactions

Besides the F-T process, there are also a number of catalytic gas-phase processes that have been realized in fluidized-bed reactors. In most of these cases, the catalyst does not deactivate quickly, i.e., there is no need to change the catalyst frequently, so that these catalytic reactions take place in SFBs. One key feature of gas-phase catalytic reactions is the large thermal effect of the reactions, and in this regard fluidized beds are superior to fixed beds because a uniform temperature can be easily maintained in the fluidized beds. Another key feature for catalytic gas-phase reactions is that the reaction rate is usually very high. As a result, almost all such catalytic reactions employ the turbulent fluidized bed, given the advantages of a smaller particle size that gives a higher gas-solid contact area, the reduction of bubble size, the high gas throughput, and reduced gas backmixing in the turbulent fluidized beds. Some of the reactions may have been reported to operate in the bubbling fluidized beds, due to the fact that the turbulent fluidization regime was not separately defined until the earlier 1970s (Kehoe and Davidson, 1971). Even if some of the earlier catalytic reactors did operate in the lower gas velocity bubbling regime, the operators have learned quickly through on-line experience that increasing the gas velocity most likely benefits both the yield and productivity, as the bed transfers from the bubbling to the turbulent regime.

Such catalytic gas-phase reactions include the production of phthalic anhydride, acrylonitrile, aniline, ethylene dichloride, polyethylene, and polypropylene. Some of these processes are illustrated in Figure 5.35. Since Kunii and Levenspiel (1991) and Yerushalmi (1982) have given a good review for several of these processes with detailed reaction conditions, an extensive review is not repeated here. Some common key features required for these fluidized-bed reactors include good feed nozzle design for liquid feed, uniform

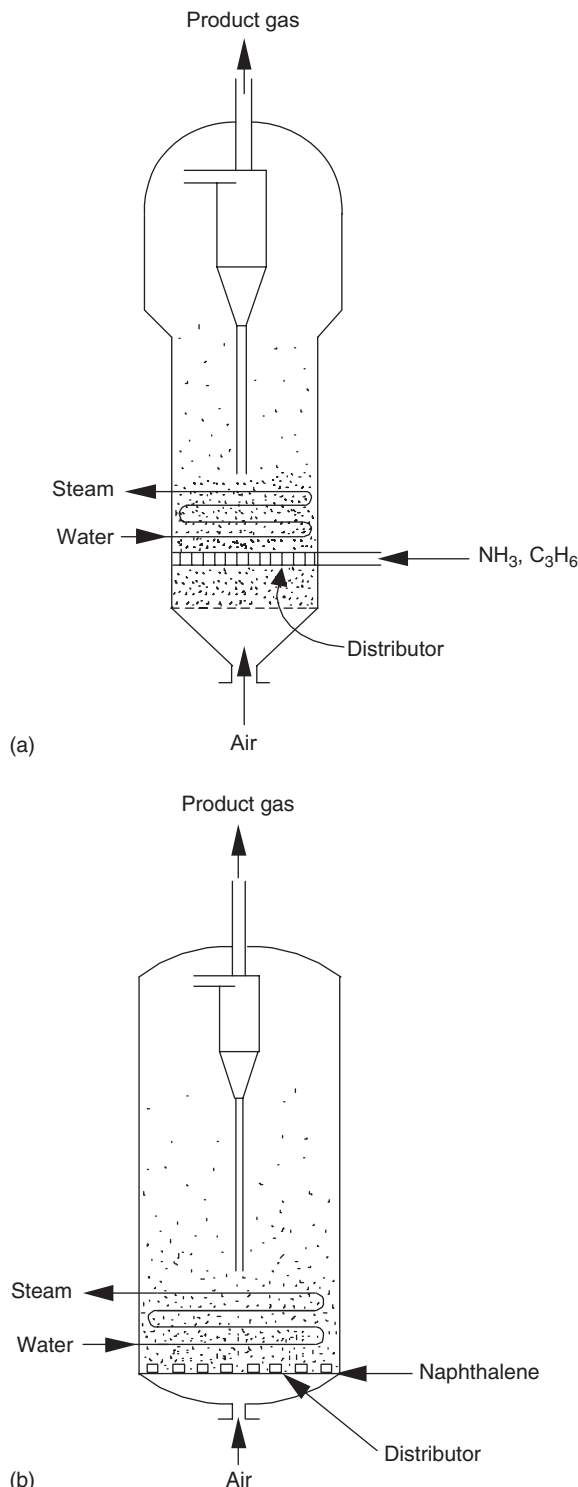


FIGURE 5.35 Fluidized-bed reactor for the production of: (a) acrylonitrile; (b) phthalic anhydride.

gas distribution, efficient heat exchangers, and excellent gas–solid separation. Makeup of the catalyst may also be needed during the process due to catalyst attrition and carryovers.

A point worth mentioning is that the addition of proper internal baffles can enhance these catalytic reactions. Horizontal baffles lead to more staging for the gas flow and can normally increase the conversion and yield. Some more exotic baffles have also been used, which may provide more benefits to certain reactions. For example, the installation of pagoda baffles leads to a significant increase of both conversion and yield for the production of pathalic anhydride from the oxidation of naphthalene (Yu, 1994). The reason for this success is that the pagoda baffles lead to an earlier transition to the turbulent fluidization regime at lower gas velocities, providing a better fluidization quality (Jin et al., 1986).

5.3.3 Noncatalytic Gas-Phase Reactions

5.3.3.1 Thermal Cracking

The purpose of thermal cracking is to produce light olefins. This is often achieved in a tubular furnace reactor, where the feed is cracked in tubes going through a high-temperature furnace. Currently, most of the world's ethylene is produced in this manner. However, the coke produced in the cracking process deposits on the inner wall of the tube and blocks up the reactor, so that the feeds to the tubular reactors are limited to light hydrocarbons such as ethane, naphtha, and kerosene, which are much more expensive than the heavier feed such as crude.

A fluidized-bed reactor can be used to achieve the same process to crack light hydrocarbons into olefins, with the required heat for the reaction provided by burning additional fuel oil, or burning partially either the feed or product. Kunii and Levenspiel (1991) described two such processes developed by Luigi and Fujinagata in the 1950s. In these earlier processes, sand particles are used as the heat carrier, and the reaction and heating take place in two different fluidized beds, with the sand circulating in between to transfer the heat generated from a combustion process to the endothermic cracking reactor. The entire concept is similar to the FCC process, but there are no catalyst particles and the reaction temperature is much higher, in the range of 700–750°C.

The real benefits of using a fluidized bed is for the direct cracking of crude oil or heavy oil to lower olefins. This will alleviate the pressure on the use of light hydrocarbons for the ever-increasing demands for light olefins. Such a process, like the FCC process, produces rejected carbon. The carbon deposition, while bad for the tubular reactors, can be beneficial in a fluidized-bed process, as burning the deposited carbon on the heat carrier particles in a separate fluidized bed can produce the required heat for the endothermic thermal cracking. A similar setup as that of an FCC unit can be envisaged, either with two turbulent fluidized beds or two CFB or a combination of both, for the thermal cracking. In comparison with FCC, this would represent a “deeper” cracking of crude to lighter olefins than the mainly gasoline–kerosene product stream from FCC.

While there have been several encouraging developments on pilot studies for such a deep cracker, there appears to be no commercial application yet. Kunii and Levenspiel (1991) reported two earlier efforts by BASF (Badische Anilin und Soda-Fabrik) and by MITI (Ministry of International Trade and Industry) in Japan, at 36 and 120 tons/day capacity to produce light olefins directly from crude. Both are pilot studies with two dense-phase fluidized beds (SFB) with coke particles circulated between the reactor and the combustor. About 25% (by wt) ethylene and 11% (by wt) propylene are produced in both cases at a reaction temperature of 750°C. The lower conversion appears to be the reason that hinders the further development of these fluidized units.

The relatively low conversion may be caused by the backmixing of gas and the long residence time, therefore overcracking results in the two pilot reactors mentioned above. In response to this problem, Stone and Webster developed a QC reactor, starting from the 1970s. This is a downer reactor with a very short contact time (as low as 200 msec) and uniform residence time distributions for both gas and solids, permitting “the quick controlled contacting and separation of the fluidizable solids with a feedstock.” The process is completed with an entrained bed combustion system to provide the heat required for thermal cracking; alumina is used as inert particles. A semicommercial demonstration unit was operated in the

early 1980s, with flow capabilities of 34 tons/day hydrocarbon feed and 1200 tons/day of solids operated at temperatures ranging from 650 to 1000°C, to show the feasibility of the downer concept. The system comprises a short downer reactor, a rapid mixer, and a quarter turn quick gas–solids separator. The reported reaction residence time from the point of oil–catalyst initial contact to the point of product quench, including solids separation can be as low as 200 msec. No conversion rate is given but it is believed to be higher than that of the SFB units.

Fluidized-bed reactors also permit the possibility of adding catalyst into the unit to further promote the cracking reaction, as initially suggested by Gartside (1989). This route combines the thermal and catalytic cracking and can increase the cracking efficiency. Deng et al. (2002b) have used this concept in a so-called downer catalytic pyrolysis process in a pilot downer reactor, for light olefins production from heavy feeds. Their results show that high olefin yields can be obtained at the temperature of 659°C and a residence time of 0.75 sec, with the total yields of ethylene, propylene, and butylenes just above 50% (by wt). The added benefit to the combined catalytic–thermal cracking is the flexibility to adjust the relative ratio of ethylene, propylene, and butylenes, by switching catalysts that favor either ethylene or propylene–butylenes production. Increasing the temperature boosts the production of ethylene and decreasing the temperature promotes the production of propylene and butylenes. Such flexibility is extremely useful to respond to the changing demands of industry.

5.3.3.2 Coking

Coking is a process that converts heavy residual petroleum stocks into lighter and more valuable products. It is essentially a thermal cracking process at high temperature, but occurs at the “higher end” in terms of molecular weight, compared to the thermal cracking discussed in the previous section. This is an extremely important process in the petroleum industry, to convert very heavy stocks into lighter fractions. One situation is the need to crack heavy bitumen from oil sand to yield synthetic crude and the other is to crack the heavy residue matters left over from the atmospheric or vacuum distillation of crude or other feedstocks. When such cracking occurs, long-chain hydrocarbons break down into smaller molecules by rupture of carbon-to-carbon bond. Because the number of hydrogen atoms present in the parent molecules are insufficient to provide the full complement for each carbon atom, some carbon is rejected to form coke, hence the name “coking.”

There are two such coking processes using fluidized beds. The fluid coking process and the flexi coking process. The world’s two largest fluid cokers are in Alberta, Canada, operated by Syncrude, where hot atmospheric-topped bitumen (ATB), vacuum-topped bitumen (VTB), and residue are cracked or broken down into lighter products (Syncrude, 2004). High temperatures in the coking reactors cause the long-chain molecules to thermally crack in a bubbling fluidized bed of coke. The high temperature comes from the recirculating coke that has been heated in the accompanying coker burner. The lighter liquid products, primarily naphtha and gas oils, are sent to hydrotreaters for sulfur and nitrogen removal. The coking reaction also produces sour fuel gas, which is sent to amine treaters for removing hydrogen sulfide. The resulting sweet fuel gas (much like natural gas) is used as an energy source throughout the upgrading and utility operations. The coking reaction also produces coke, some of which is burned to produce heat for the high temperatures in the reactor. Excess coke is mixed with water and transported to coke cells in the mine area to be stored for potential future use. These two fluid cokers are designed to process 72,900 barrels of bitumen per day, but currently are able to process over 110,000 barrels of bitumen per day, as a result of continuous improvement efforts (Syncrude, 2004).

A typical fluid coker, similar to that operating at Syncrude, is shown in [Figure 5.36](#). The reactor (480 to 550°C) operates in the bubbling fluidization regime with large bubbles produced mainly as a result of the formation of lighter products. The residue is fed into the reactor through nozzles from the side and a small amount of steam is injected from the bottom to maintain the fluidization at the bottom and also to displace any product desorbed on the coke particles as they travel down through the stripper at the bottom of the coker, before being transported to the coke burner. A part of the coke particles are combusted in the burner (590 to 690°C) to heat up the coke particles, which are then returned to the reactor to supply the heat required for the coking reaction. The remaining coke is discharged as a byproduct. The coke particles are of Geldart type B particles with an average size close to 200 µm, which is maintained by a

balance between the growth of particle size due to coke deposition and the reduction of particle size by attrition. Operation with Geldart type B particles leads to a bubbling bed with large bubbles. Cracked products vaporize inside the reactor and escape quickly in the form of large bubbles. Large bubbles are not favorable in most fluidized-bed reactors because they cause bypass of reactants. In fluid coking, however, large bubbles become desirable since they can quickly carry the products out of the reactor to minimize the residence time of the vapor products, which in turn avoids overcracking. The large bubbles also ensure vigorous mixing between the wet coke particles covered by the injected liquid and dry coke particles, to ensure uniformity in the reaction and also to avoid the wet particles from sticking to each other. All fluid cokers also have a reversed cone shape to accommodate the vapor product formed during the process. Since only a very small amount of steam is supplied from the bottom of the reactor to fluidize the coke particles, the cross section of the reactor needs to be small in the bottom but gradually increases to maintain a relatively constant fluidization velocity as the products vaporize.

Flexi coking, an Exxon technology as shown in Figure 5.37, is similar to fluid coking but with the addition of a coke gasifier at the end of the line to produce boiler fuel, after removing sulfur (Yerushalmi, 1982). In this case, hot coke for the cracking reaction is usually provided by the particles from the gasifier rather than the combustor.

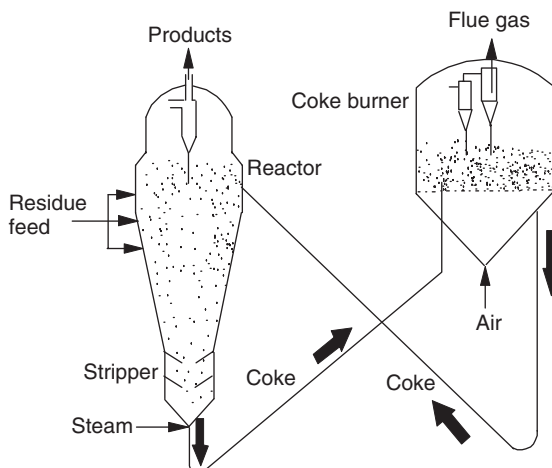


FIGURE 5.36 A typical fluid coking unit.

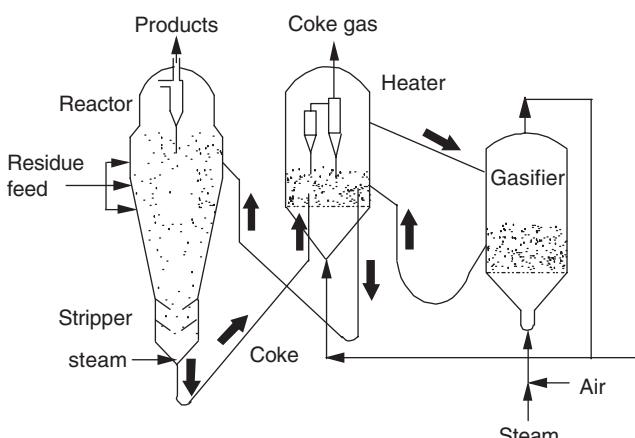


FIGURE 5.37 Flexi coking unit by Exxon.

5.3.4 Gas–Solid Reactions

Fluidized-bed gas–solid reactions have many applications. Such reactions take place in either a dense phase SFB or dilute phase CFB, making use of the special characteristics of fluidized beds, such as excellent heat and mass transfer, the uniform temperature distribution, and the ability to handle a large quantity of solids and a wide range of solid materials. Coal utilization is a major part of such fluidized-bed gas–solid reactions. The fact that the world's reserves of coal are significantly larger than those of oils and natural gas renders them of primary importance both as fuel and a feedstock for chemicals and steel-making. Fluidized coal combustion and gasification have been shown to have many advantages. In the more recent years, sustainable development and environmental concerns have also led to a significantly increased utilization and consumption of biomass materials, in incineration and gasification.

5.3.4.1 Coal Combustion

In an FBC, coal particles are suspended in an upflowing gas stream (normally air or oxygen-enriched air) with a large amount of inert particles, which help in stabilizing the combustor temperature and facilitating excellent heat transfer. In an FBC, a coal particle experiences the following process: after a coal particle is fed into the FBC, its temperature rises as the inert particles at higher temperature transfer heat to this colder coal particle. For a short period of time, volatile matters are released and are burned at or beyond the coal particle. Then the remaining solid combustible matter, mainly chars, starts to be oxidized (burned) with the generation of heat, leaving behind noncombustible matter such as ash. The oxidation step of char takes by far the longest time during the combustion.

The FBC has many advantages, including:

- efficient and large-scale operation
- very easy to maintain a uniform temperature
- low-temperature operation, 750 to 900°C
- very high heat transfer rate
- suitable for burning a wide variety of fuels, including low-grade coals and other low-end combustible materials
- no moving parts inside the combustor
- *in-situ* capture of sulfur pollutants
- lower emission of nitrogen oxides, especially in CFB combustors

Coal particles contain mainly volatiles, char, and ash, with their relative quantities varying with the type of coal. Anthracite contains the least amount (a few percent) of volatiles and lignite can contain as high as over 50% volatiles. The ash in the coal is a mixture of adventitious ash and inherent ash, which is in the form of very small particles (typically 2 μm size), bound within the coal pieces (Howard, 1983). Most of the adventitious ash is removed in the coal cleaning plant, so that the treated coals have lower sulfur and ash contents and higher calorific values than the untreated coal. In most of the developed countries, only treated coal is combusted given the tight environmental control.

The following details are given for the volatiles and their combustion properties (Howard, 1983):

1. The volatilization process is not a simple physical vaporization, but the consequence of chemical reactions.
2. The volatiles released are hydrocarbon gases arising from irreversible chemical reactions, i.e., thermal decomposition, which occur when the coal is heated. Condensation and further cooling of these gases will not reconstitute their original chemical and physical form.
3. Volatiles are emitted from the interior of the coal particle from which they seep out to the exposed surface.
4. The chemical reactions may be exothermic.
5. There is no clearly defined temperature at which the volatiles are released, but the higher the surface heat flux into the coal particles, the shorter the time taken for all the volatiles to be released.

6. The volatiles burn in the same way as liquid fuel vapors, with the flame located at a short distance away from the solid surface. The flame provides heat to the particle surface to assist further volatilization until all the volatiles have been evolved.
7. The evolved hydrocarbon gases may not burn completely in the region around the coal particle, but often appear as a smoky yellow flame and deposit soot on the surfaces downstream.
8. Partially burnt volatiles can be burned completely only if they are passed through a high-temperature zone containing excess oxygen.

One key advantage of the fluidized-bed coal combustion is that it operates at low temperature (750 to 900°C), minimizing the volatilization of alkali metals in the fuel and avoiding any sintering of the coal ash and sand materials. This partially results from the uniform temperature in a fluidized bed, which is facilitated by the presence of inert particles, mostly sand or ash from coal combustion, and sorbent particles. The inert particles form the majority of the fluidized-bed materials, as the coal particles only constitute not more than 10% of the bed materials. The large quantity of inert particles act as a huge heat sink that quickly takes away the heat produced by combustion, transfers a large amount of heat to the heat exchangers, and maintains an excellent temperature uniformity. They also act as a heat source to rapidly heat up the cold coal particles fed into the system. Sand particles are usually used as the initial inert materials, which are then gradually replaced by ash from the combustion. Depending on the ash content and the size range of the ash produced, addition of makeup bed materials may be required from time to time. Finer ash leaves the combustor through the cyclone as fly ash and larger-sized ash is collected from the bottom drain of the combustor.

Another important advantage of fluidized-bed combustion is the ability to capture sulfur within the combustor using low-cost sorbent. Sulphur exists in almost all types of coals, varying from less than 1% up to 10%, in the form of pyrites (FeS_2) and organic sulfur compounds. When coal is burned, sulfur is released as sulfur dioxide and, to a smaller extent, as sulfur trioxide; both are air pollutants that form acid rain. The most common method to remove sulfur oxides is to add lime, either in the form of limestone (calcium carbonate) or in the form of dolomite (combined calcium and magnesium carbonate) into the FBC, where they react with the released sulfur to form calcium sulfate (CaSO_4). With this method, sulfur is “fixed” in calcium sulfate, which is then removed with ash. The retention of sulfur by lime in FBC has the advantage of not requiring a separate gas-scrubbing plant, easier handling and disposal of spent sorbent, and greater overall thermal efficiency. Lime sorbent can be fed into the combustor either with the coal (premixed) or separately.

Another major pollutant of fluidized-bed combustion is nitrogen oxides, including nitrogen monoxide and nitrogen dioxide, also collectively called NO_x , and nitrous oxide. Nitrogen monoxide and dioxide are sources of acid rain and nitrous oxide induces ozone decomposition in the stratospheric layer. Nitrogen oxides in fluidized bed combustors comes from the nitrogen in the fuel, typically 0.5 to 2% (by wt). The formation of NO_x is a complex process, but it is clearly known that increases in temperature or excess air both favor the formation of NO_x due to the increased oxidation rate. Therefore, the low temperature of FBC helps to limit NO_x formation. However, low temperature and limited excess air ratio alone are currently not enough for the stationary (bubbling) fluidized-bed combustors (SFBC) to meet the more stringent NO_x emission standard. In this regard, the circulating fluidized-bed combustor (CFBC) is much more advantageous given its ability to create separate reducing and oxidizing zones inside the combustor.

CFBC emerged as a better alternative to bubbling bed combustors in the late 1970s and early 1980s. A typical CFBC is shown in [Figure 5.38](#). CFBC has a large diameter riser where most combustion occurs. Flue gas and entrained particles are separated in the cyclone on top of the solids return pipe. Collected solids, including inert particles, sorbent, and unburnt char, are gathered in the return pipe, and then further recirculated to the bottom of the riser combustor. Air is divided into two streams, the primary stream is fed into the riser through the bottom air distributor to fluidize the particles in the bottom region and the secondary air is fed mid-way in the riser to further entrain the particles upward and to bring the combustion to completion. Coal and limestone as well as the returned solids from the

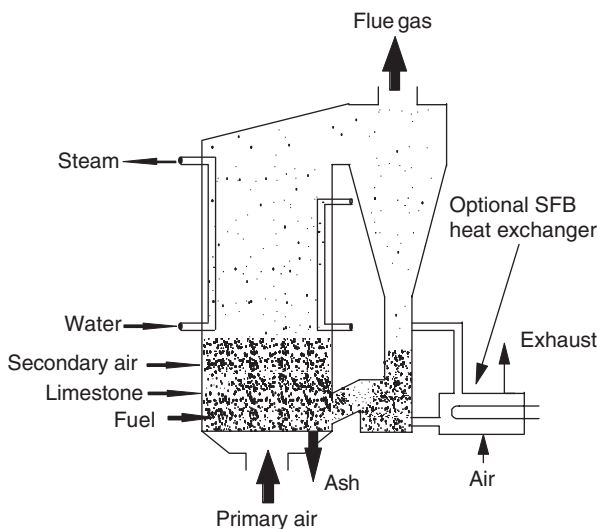


FIGURE 5.38 A typical circulating fluidized-bed combustor.

return pipe are fed into the bottom region of the riser. The splitting of air flow results in a lower gas velocity in the bottom region of the riser. This creates a bubbling fluidized bed in the bottom, which significantly enhances lateral solids mixing to quickly mix the coal, sorbent, and the returned solids. The bubbling bed also ensures excellent heat transfer to heat up the newly fed coal and sorbent particles. The temperature in the riser is normally 750 to 900°C and that in the return pipe is 100 to 200°C lower. Major heat transfer is through the membrane wall of the riser and also through the fluidized-bed heat exchangers in the return pipe, and possible additional fluidized-bed heat exchangers. The size of the bed materials is in the range of 100–300 µm but the coal and sorbent are usually fed in much larger sizes, in the range of several millimeters. The larger size permits the newly fed and cold coal and sorbent to remain in the bottom bubbling bed region, so that there is sufficient time for them to heat up and react. As the reactions continue and their temperature rises, the larger particles are broken down into smaller fractions and then entrained into the upper region for continued and higher temperature combustion.

The partial feeding of the total amount of air required for combustion into the bottom region creates a reducing zone, which favors the formation of N₂ over the formation of NO_x from the released nitrogen from the fuel. The temperature in the bottom region is also lower, again favoring the reduction of NO_x formation. In addition, the low gas velocity and the larger coal particle size increase the residence time of the newly fed coal in the bottom bubbling region, to ensure that all volatiles, including most of the fuel nitrogen, are released in the bottom reducing region. All of these factors favor the reduction of NO_x emission, making CFBC more preferable than SFBC. Above the point of the secondary air injection, the temperature rises and an oxidizing region forms to promote fast combustion. However, NO_x emission is not affected since most fuel nitrogen has been consumed at this time.

Such staging effect also increases the combustion efficiency, by maintaining a higher temperature in the upper region of the riser. Excellent heat transfer is ensured by operating the riser combustor at lower gas velocity to promote particle reflux near the wall, creating a dense particle annulus for better bed-to-wall heat transfer. CFBC also provides better gas–solids contact efficiency for the combustion.

Overall, CFBC has several advantages over SFBC:

- High combustion efficiency
- Adjustable primary-to-secondary air flow ratio
- Significantly reduced NO_x emission

- Separate control of air and particle feeds
- Higher turndown ratio

As a result, CFBC is now quickly replacing SFBC as the industry standard for fluidized-bed combustion. However SFBC is still used for many small-scale combustors, given its low construction cost, and some special-purpose combustors.

Prior to the 1980s, many SFBCs of different designs have been commercialized all over the world. For example, China had over 2000 small SFBC in operation in the 1980s. An excellent comprehensive review on the application of SFBC has been provided by Highley and Kaye (1983). Given the rapid replacement of SFBC by CFBC, these design features are not detailed here.

Circulating fluidized-bed combustion is the fastest growing application of CFB technology and is projected to overtake FCC in this decade, to become the largest application of CFB technology. Both capacity and the number of CFB boilers in use have increased drastically in the past 20 years. More than 500 CFB boilers are either in operation or under construction (Basu, 1999). In recent years, CFBC has surpassed the bubbling bed firing system not only by total unit capacity, but also by the number of plants. Now, atmospheric CFB plants represent about two thirds of the total installed capacity worldwide. The demand also triggered a fast increase in unit size (Jacobs, 1999). Reh (1999) reported that boiler companies such as ABB Combustion Engineering, and Lurgi and Foster Wheeler Power Systems are now pursuing several projects in the 250 to 400 MWe capacity range, while Electricité de France (EdF) is planning to scale up its atmospheric CFBC into the 600 MWe capacity range.

A pressurized fluidized-bed combustor (PFBC) has the added benefit of also employing high pressure flue gas to drive a gas turbine to form a combined cycle power generation, giving higher thermal efficiency. However, operating at a higher pressure causes many problems so that PFBC has not been widely used. In connection with the recent development of CFBC, pressurized CFBC (PCFBC) will represent the future direction of fluidized-bed combustion, although the current economy does not make PCFBC profitable.

5.3.4.2 Coal Gasification

Coal gasification is the first industrial application of fluidization technology in modern history. The concept was first envisaged by Fritz Winkler in his German patent in 1922. In 1926, the first Winkler commercial unit began its operation with four additional units added by 1929 (Squires, 1983). In the gasifier, a fluidized bed of coal particles were suspended by a gas mixture of air and steam, or a gas mixture of oxygen and steam after the 1930s, to produce raw gas for the chemical industry, such as ammonia synthesis. The temperature was about 800 to 900°C and the thermal power was up to 100 MW (Squires, 1983).

As shown in Figure 5.39, the Winkler gasifier is a relatively simple unit, with gas entering from the bottom and product leaving from the top. The coal crushed to about 10 mm and dried of surface moisture, is fed by a screw feeder into the dense phase. The products are mainly carbon monoxide and hydrogen, sometimes with a small quantity of methane. When air is used, the products are diluted by nitrogen. The energy required for gasification is supplied by the partial oxidation of coal. There is usually an expanded section above the particle bed to allow the return of ejected particles through bubble eruption and a cyclone is usually there as well to catch and recycle fine carbon particles. In the later models, some additional air or oxygen was injected into the freeboard region to increase the carbon efficiency by burning off the fine carbon particles there. The resulting temperature rise in the freeboard furthers the decomposition of produced methane to the desired CO and H₂. Both primary and secondary gases are injected through nozzles to increase the contact efficiency. Compared to modern technology, the Winkler gas producer is inefficient because of its high oxygen consumption and its large (> 20%) carbon loss through dust carryover. Given the abundance of cheap petroleum and natural gas in the 1950s, most Winkler gasifiers went out of service due to poor economy. Kunii and Levenspiel (1991) reported that all Winkler units had been shut down in the 1950s, while Yerushalmi (1982) seemed to suggest that a few Winkler units were still in operation in the 1980s.

From the 1970s, the oil crises raised the importance of coal so that a number of companies started to develop new coal gasifiers. There are a number of benefits of coal gasification over straight combustion,

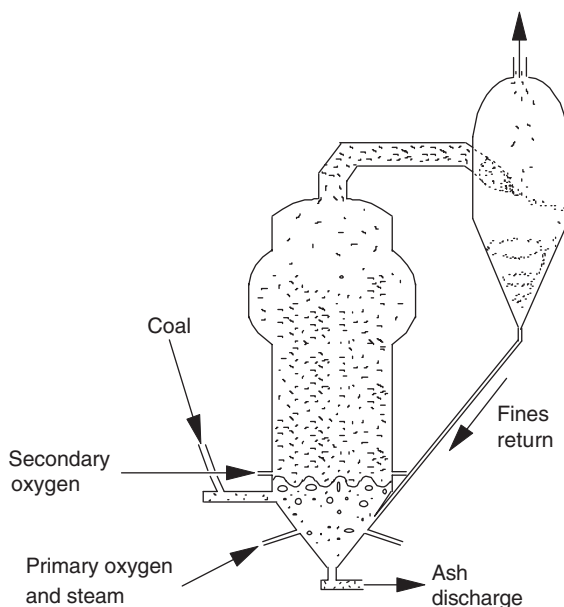


FIGURE 5.39 A typical Winkler gasifier.

including a higher electricity efficiency through the gas–turbine–steam–turbine binary cycle via gasification than the conventional steam–turbine system via combustion. Gasification also provides clean gaseous fuels and raw chemicals for synthesis. For example, in the Sasol Synthol process described in Section 5.3.2, the syn-gas for the F–T process was supplied by coal gasification.

However, there are a number of inherent limitations for fluidized-bed gasification of coal (Yerushalmi, 1982):

1. The operating temperature is limited, with the highest limited by the sintering temperature and the lowest by the reactivity of coal.
2. Carbon fines are produced within the fluidized bed, giving rise to problems such as loss of carbon through entrainment.
3. Loss of carbon through purging of ash.

The above limitations imply that complete gasification cannot be achieved in a single-stage fluidized-bed operating below the sintering temperature. Therefore, the development of new fluidized-bed gasifiers needs to overcome these problems. Many designs include multiple stages to increase the efficiency of carbon use. Unfortunately, there appears to be no commercialization of the fluidized-bed gasifier to date (after Winkler), although numerous studies including many pilot studies have been carried out. Kunii and Levenspiel (1991) summarized the various routes and concepts of fluidized-bed gasifiers, and pointed out, although the development has been much slower than expected, the fluidized-bed route is still beneficial for large-scale production of fuel gas for binary cycle power plants.

5.3.4.3 Incineration of Solids Wastes

Fluidized-bed incinerators are mainly used for the elimination of harmful materials and for the utilization of heat value in the wastes. Examples of the subject materials are solids municipal and industrial wastes, saw dust, plastic wastes, dried sewage sludge, and special wastes such as hospital wastes. Electricity generation may be a good use of the energy produced. Fluidized-bed incineration is similar to fluidized-bed combustion in their structure and in that both fluidized beds are composed of mainly inert particles

with the combustible wastes fed into the fluidized bed in the dense phase. However, there are special issues that must be considered for the incineration of wastes:

1. *Pretreatment.* Some solids waste may contain large objects that need to be crushed or removed, some have high moisture content that need to be at least partially removed, some contain too many noncombustibles such as glass and metal that need to be screened out.
2. *Combustibility, flame stability, auxiliary fuel, and cofiring.* Not all waste materials have enough heating value, good combustibility, and flame stability, so that auxiliary fuel(s) may be needed to cofire the incinerator (Sondreal et al., 2001). Most common cofiring fuels are coal and natural gas. In most cases, a cofiring facility is normally required although not necessarily always used, because it is needed when switching waste materials and during startup and the period when the waste supplies are short if a continuous energy supply is required.
3. *Variations in waste compositions.* Certain solids wastes such as municipal wastes can have their compositions fluctuating. The incinerator must be designed to handle such variations in the change of heating values, ash content, moisture, etc. In this regard, the standby of cofiring is essential to maintain good operation of a fluidized-bed incinerator.
4. *Feeding.* Special attention is needed to feed the different solids wastes. If multiple wastes are to be burned in the same unit, the feeding device must be versatile enough to handle all situations.
5. *Secondary air injection.* As in coal combustion, secondary air injection may be beneficial for certain cases. This, however, changes with the type of solids wastes and the type of fluidized beds adopted (SFB or CFB).
6. *Temperature.* Temperature is another key factor. In addition to those issues discussed in Section 5.3.4.1 related to coal combustion, there may be additional factors coming into play. For example, the temperature needs to be high enough to decompose certain harmful constituents.
7. *Emission control.* Other than the acid rain cursors of SO_2 and NO_x encountered in coal combustion, other harmful gases such as chlorine and bromine might be released during the combustion of, for example, plastic wastes. Dioxins are an even worse issue. Special measures need to be taken to eliminate these harmful gases or trap them in the flue gas.
8. *Heavy metals and other toxic solid contents, residue solids disposal.* Some wastes contain much higher fractions of heavy metals such as vanadium, lead, and mercury and can cause long-term damages. The containment of these heavy metals must be solved before the incineration of those materials. A related issue is the residue solids disposal, the presence of heavy metals making it much harder.

5.3.4.4 Gasification and Pyrolysis of Biomass

Sustainable development requires the use of renewable energy and biomass provides the main renewable energy resource (Bridgwater, 2003; Bridgwater and Peacocke, 2000). Biomass includes grain husk and stalk, saw dust, grass, and wood, especially wood from short rotation forestry. There are three methods that can utilize the energy contained in the biomass; combustion, gasification, and pyrolysis. Direct combustion provides heat for use in heating, for steam production and electricity generation; gasification provides fuel gas for combustion for heat or for electricity generation in an engine or turbine or raw materials for the chemical industry; pyrolysis provides a liquid fuel that can substitute for fuel oil and that can produce a range of specialty and commodity chemicals. Combustion of biomass using a fluidized bed is currently not competitive, unless the feeds are the wastes, such as those from pulp and paper, and agricultural and forestry industries (Bridgwater, 2003). The nature of biomass combustion is similar to those discussed in the previous sections.

Gasification is the (thermochemical) conversion of biomass into a gaseous fuel by heating in a gasification medium such as air, oxygen, or steam. It is advantageous over combustion because the gaseous fuel is easier and more versatile to use and can also be standardized in its quality. The main reactions are partial or complete combustion and water gas shift reaction to convert the carbon into CO , CO_2 , and H_2 ,

with some methane. Gasification starts from driving out the moisture, followed by a pyrolysis process to yield gas, vaporized tars or oils and char residue, and then the much slower process to gasify the solid char, pyrolysis tars, and pyrolysis gases. Alkali metals present in wood ash can act as a catalyst to accelerate the reactions.

Bubbling and circulating fluidized beds can be used for biomass gasification. Both have good temperature control and high reaction rates, but high particulate content in the product gas and high carbon loss with the ash. CFB has the additional advantage of increased process efficiency, more operational flexibility, and better emission control.

The financial assessment of biomass gasification, however, is not always favorable and is very sensitive to many factors. Biomass is of low energy density and is not produced centrally. In developed countries, the high cost of collecting and transporting the biomass may make the gasification process cost-inhibitive, but the potential of being paid to process biomass wastes should help greatly enhance the economics of power generation. However, biomass gasification can be economically viable in developing countries, where the cost of biomass at feed is not very expensive. Wu et al. (2004) concludes that their 1 MW unit is still profitable if the cost of biomass is less than US\$25 per metric ton.

In China, biomass is abundant but electricity is in short supply, especially in the rural areas. In the past few years, the Guangzhou Institute of Energy Conversion has been demonstrating the BGPG (Biomass Gasification and Power Generation) concept using one 1 MW CFB unit in Fujian Province to gasify rice husk and another 1.2 MW CFB unit in Sanya to gasify saw dust (Wu et al., 2002). Taking the 1.2 MW CFB as an example, the unit is a simple CFB gasifier as shown in Figure 5.40, with saw dust fed into the bottom region of the riser through a screw feeder. The solids recirculation rate is not very high so the riser diameter is significantly larger than the diameter of the return column under the primary cyclone. The product gas passes through a simple scrubber to remove ash and tar, before being burnt in four parallel gas engines (Wu, C.Z., personal communications, 2004). Wu et al. (2002), Yin et al. (2002) and Wu (personal communications, 2004) reached a conclusion that BGPG can reach reasonable efficiency at certain scale and provide a high-quality power supply to the users. It is especially suitable for rural areas in developing countries where such simple and robust technology can assist the development of rural economies by providing electricity produced from local sources of biomass. Larger units are planned for full commercialization.

The use of a catalyst can further increase the efficiency and therefore the economy of biomass gasification (Sutton et al., 2001). It can also lower the reaction temperature. Asadullah et al. (2002a, 2002b)

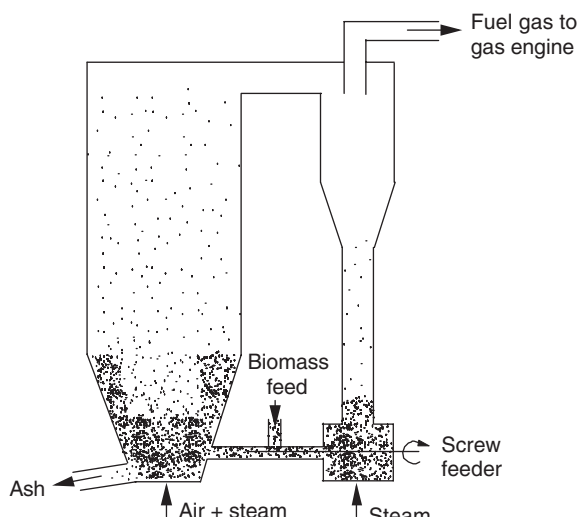


FIGURE 5.40 CFB biomass gasifier developed by GIEC, for the BGPG process.

reported a catalytic gasification process developed for the gasification of wood powder to proceed completely at lower temperature, in the presence of a Rh/CeO₂/SiO₂ catalyst.

Pyrolysis is a thermal decomposition process in the absence of oxygen. When the reaction is controlled within a short period of time, of the order of milliseconds, more valuable liquid products can be obtained. The liquid products continue to decompose to lighter hydrocarbons of less value, if the reaction continues. Thus, it is very important to control the short reaction time and such a pyrolysis process is therefore called fast pyrolysis. In this process, the critical issues are to bring the reacting biomass particles quickly to the optimum process temperature and minimize its exposure to the intermediate temperatures that favor formation of charcoal, and to stop quickly the reaction at the desired time.

Bassi et al. (1994) proposed a short contact-time fluidized reactor developed for the ultra-pyrolysis of biomass and heavy oil. The design is very similar to the QC concept developed by Stone and Webster (Gartside, 1989), where the process is realized in a downer reactor. Preheated hot inert solids (sands) and the biomass are injected separately into the top of the downer, where vigorous heat transfers quickly bring the biomass to the reaction temperature. While flowing cocurrently downward, pyrolysis proceeds quickly, within about 500 msec. At the bottom of the downer reactor, the products are quickly separated from the sands and quenched.

Based on the above concept, Ensyn developed a new rapid thermal pyrolysis (RTP) process for fast pyrolysis to produce gaseous and liquid fuels and chemicals of high value. Instead of a downer, an upflowing riser reactor is used to facilitate rapid and uniform contacts between the biomass and the hot recirculated sand at the riser entrance. Before feeding to the reactor, biomass is comminuted to approximately 6 mm and dried to no more than 10% moisture. At the riser top, the products pass through two cyclones to separate solids and the vapor after the cyclones are rapidly quenched to stop further decomposition of the thermally unstable liquid intermediates of the pyrolysis. The above process was commercialized in 1989 to produce food flavorings and additives (Graham and Huffman, 1995). There are currently eight such plants in operation. A variety of feeds including cellulose, wood, lignin, agricultural residues, heavy oils, heavy distillates, asphalt and bitumen can be processed (Bridgwater, 2000). It may be possible to burn the produced "bio-oil" in an internal combustion engine.

Another technology developed at the University of Waterloo in Canada uses an SFB for fast pyrolysis instead of a CFB, and bench-scale experiments seem to indicate that they can achieve the same performance as in CFB (Scott et al., 1985, 1999).

The liquid "bio-oil" contains valuable chemicals and can be easily stored and transported. It can be used as an alternative liquid fuel or as chemical feedstock because it contains a significant fraction of useful organic chemicals. However, there are still many challenges, such as higher cost, incompatibility with conventional fuels, high viscosity, chemical instability, lack of standards for use and distributions, and the variations in its quality (Bridgwater, 2003).

5.3.4.5 Mineral and Metallurgical Processes — Roasting and Calcination

Another area of application of fluidized-bed reactors is in the mineral and metallurgical process. The use of fluidized bed for roasting started in the late 1940s in Ontario, Canada, for roasting arsenopyrite and to obtain a cinder suitable for gold production by cyanidation (Kunii and Levenspiel, 1991). The roaster is a simple one-stage SFB operated most likely in the bubbling fluidization regime. Air is usually the fluidizing medium that also supplies the oxygen, and the roaster is usually operated at a high temperature. The advantages of using fluidized beds for roasting are the excellent mass transfer, uniform temperature, and the ability of continuously adding and withdrawing the particles. Many roasting processes have been realized in fluidized beds, such as the roasting of pyrites, pyrrhotite, zinc sulfide, copper, and cobalt concentrates, and other various sulfides and sulfates. Readers are referred to Yerushalmi (1982) for a more comprehensive review on the application of fluidized-bed roaster, given the limited space here.

Calcination is another important gas–solid reaction. For example, calcination of aluminum hydroxide is an essential step for the production of aluminum, since only completely dehydrated alumina can be fed into the electrolytic cells. Calcination of calcium carbonate is another example. Again, calcination in

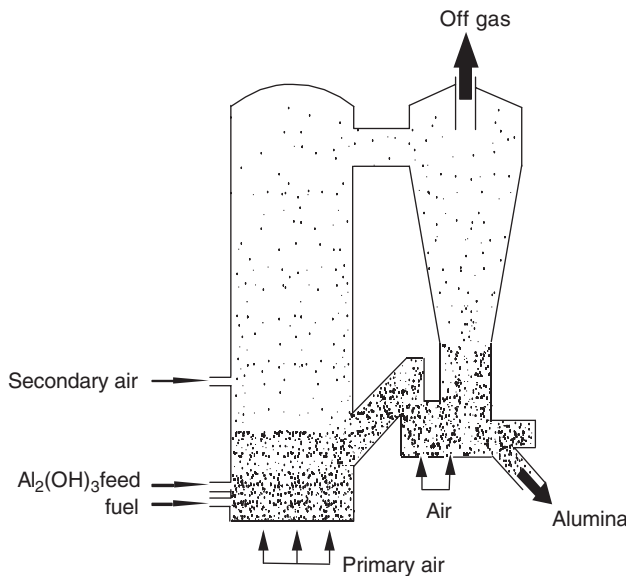


FIGURE 5.41 Lurgi's CFB calciner.

fluidized bed is to make better use of the special features of the fluidized bed. The added advantages of CFB can also be utilized. In the late 1960s, Lurgi commercialized the world's CFB calciner, the so-called fast fluidized-bed alumina calciner (Reh, 1971, 1986). As shown in Figure 5.41, the CFB calciner has a very similar structure as a CFB combustor. Aluminum hydroxide is fed into the bottom dense region of the riser. Natural gas or fuel oil is fed into the riser to provide the high temperature for calcination. The air is also split into primary and secondary streams, with the purpose of creating a dense phase at the bottom to accelerate the heat transfer from the hot bed materials to the newly fed cold $\text{Al}_2(\text{OH})_3$ particles and to promote lateral mixing.

5.3.5 Physical Operations

There are many examples of using fluidized beds for physical operations, where no chemical reaction occurs. These processes use one or more of the special features of the fluidized beds:

- The large interfacial surface area between fluid and the particles for excellent gas–solid contact, due to the small particle size.
- The excellent heat transfer between the gas and particles given the vigorous relative movement between the fluid and the particles.
- The excellent heat transfer between the gas–solids suspension and the heat exchanger surfaces.
- The uniform temperature from the excellent heat transfer and gross movement of particles.
- The ability to handle a large quantity of particulate materials.
- The flexibility to fluidize a wide range of particle properties.

5.3.5.1 Drying

Fluidized-bed dryers have been applied in many industries, such as the food and agriculture industry, pharmaceutical industry, and chemical process industry. During a drying process, a significant amount of heat needs to be transferred from air (as in most cases) to the particles and a significant amount of mass (steam) needs to be transferred from the particles back to the air stream. Fluidized beds are very efficient dryers because they have the ability to provide rapidly a large amount of heat and to take away quickly a large amount of vapour. These essential features ensure the excellent use of energy, which is the

biggest concern in all nonspecialty drying processes. Aside from the excellent heat and mass transfers, fluidized beds also contain the following special features, which make them especially suitable for most drying processes:

1. Fluidized beds have a very uniform and well-controlled temperature. This allows the drying temperature to be raised very close to the maximum allowed temperature for most efficient drying, without worrying about localized overheating. This is particularly useful for drying heat-sensitive particles, such as grains and pharmaceutical products where overheating will permanently damage the materials.
2. Fluidized-bed dryers can handle a very large quantity of particulate materials, with easy feeding and product withdrawal. This helps to ensure a continuous and large-scale operation.
3. The vigorous movements of particles inside the fluidized bed promote the uniform drying of all particles and over all surfaces of each particle. This is in favor of more uniform drying products.

The drying process usually has two stages: The first is the constant rate stage when the moisture on the particle surface is being taken away. During this stage, the driving force, the difference between the moisture content in the air stream and that on the particle surface, remains the same so that the drying rate remains the same. The second drying stage is the reducing rate stage that removes the hard-to-dry moisture contained inside the particles. The first stage is fast and requires a large amount of air flow to provide the heat for evaporation and to remove the steam, while the second stage is slower and requires a longer drying time. Obviously, it is best that the drying process can be designed to suit the needs of both stages.

Figure 5.42 sketches a basic fluidized-bed dryer design where hot air passes through the fluidized bed and leaves from the top, and wet particles enter from one side of the fluidized bed and the dry particles leave from the other side. When this is run in a continuous mode, it will not be the most efficient since the particles are well mixed in such a dense-phase fluidized bed. Some wet particles can quickly bypass the dryer, while others may stay in the bed for too long, causing under and overdried particles. In order to ensure that the drying is complete, the residence time of the particles has to be significantly increased, leading to a much larger unit and the waste of energy through increased air flow. A significant portion of the hot air also tends to pass through the bed as bubbles, bypassing the dryer, leading to a less efficient use of energy.

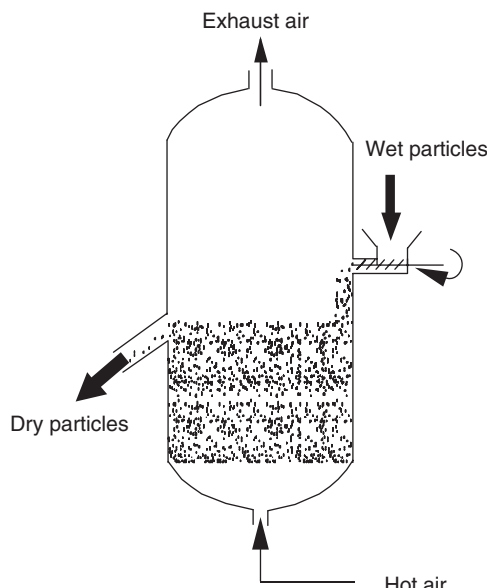


FIGURE 5.42 A typical fluidized-bed drier.

To increase the uniformity of the solids products in a continuous drying process, it is useful to create some staging effect to prevent the drier particles from remixing (backmixing) with fresh wet particles. Figure 5.43 illustrates several alternative designs of fluidized-bed dryers. Figures 5.43a and b show two examples of staged drying operations, one with vertical staging and one with horizontal staging. Such staging reduces solids bypassing and therefore increases drying efficiency. The vertical one with countercurrent flow is more efficient than the horizontal one with cross-current flow for energy use. Figures 5.43c and d are two special designs that accommodate closely the features of the two drying stages. In Figure 5.43c, the two fluidized beds are operated at different hot air velocities: the one on the right at a higher air flow rate to quickly take away the moisture on the particle surface in a relatively short time, and the one on the left at much lower air flow rate but with much longer residences of both air and solids, plus horizontal baffles to create extra staging, to remove the moisture inside the particles. A similar method (Figure 5.43d) is to realize the first stage in a riser where the air-particle mass transfer is very high, and a very high air velocity

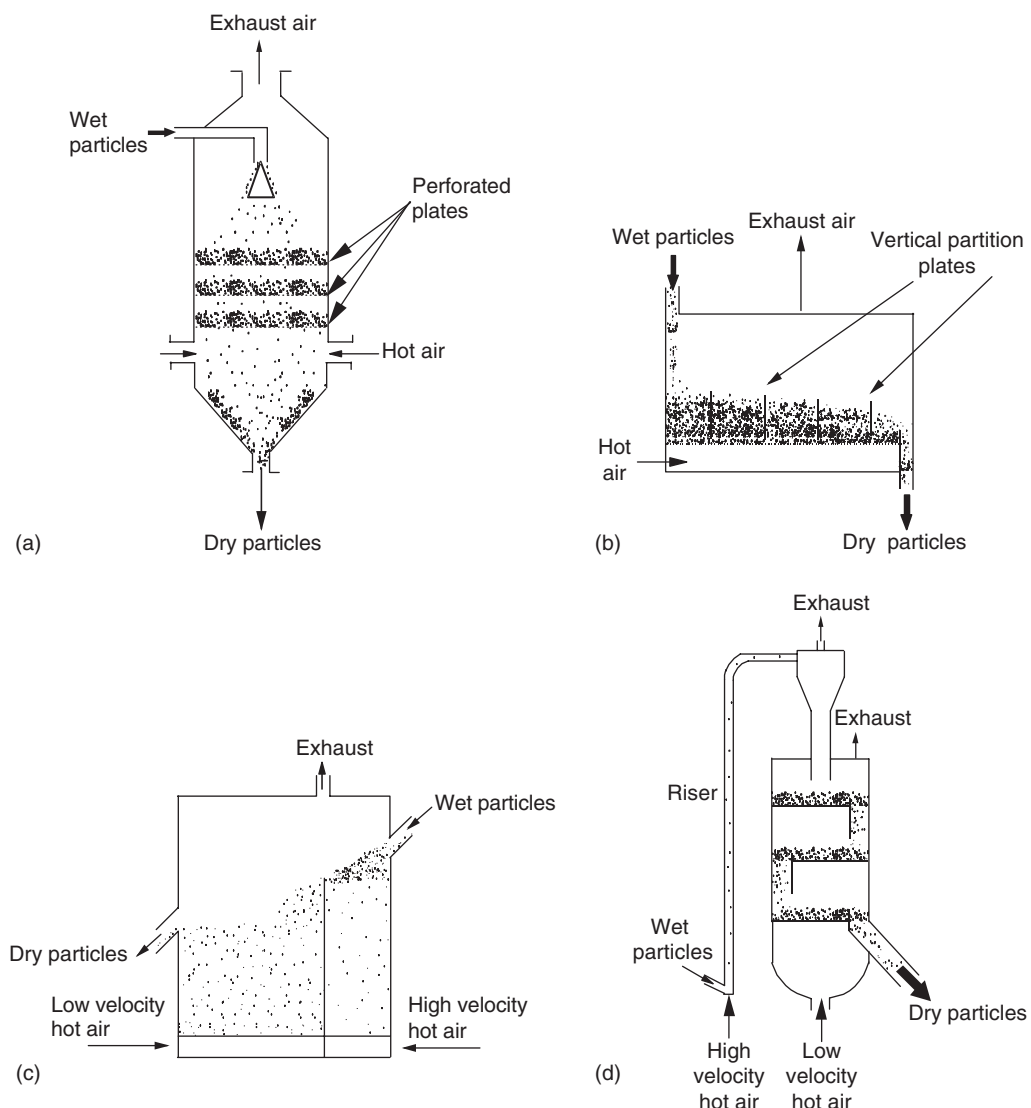


FIGURE 5.43 (a) Vertically staged fluidized-bed drier; (b) horizontally staged fluidized-bed drier; (c) two-stage SFB fluidized-bed drier; (d) two-stage CFB-SFB fluidized-bed drier.

can be used to quickly remove the moisture on the particle surface and then to realize the second stage in a vertically staged fluidized bed at air velocity not much above the minimum fluidization with horizontal baffles to ensure uniform and longer residence time distribution of the particles.

5.3.5.2 Heat Exchangers

Fluidized beds are excellent heat exchangers, given the high heat transfer rate and the huge heat capacity of solid particles. Such a process is usually realized in a setup similar to a shell-tube heat exchanger, where the fluidized particles are usually in the shell side of the exchanger. For example, fluidized-bed heat exchangers have been used to dissipate the large amount of heat generated from chemical reactions. Because of the high heat transfer rate and large heat capacity, such fluidized-bed heat exchangers are highly efficient, and because of higher solids concentration, most fluidized-bed heat exchangers are dense-phase SFB rather than the CFB, given the much higher heat capacity of the solids.

Fluidized beds with inert particulate materials can also be used to maintain a constant temperature for some operations. For instance, it can act as a temperature bath that encases a chemical reactor. It can also be used as a heat sink to provide a well-controlled and uniform temperature source with high heat capacity. Kunii and Levenspiel (1991) mentioned the use of such a fluidized bed to quench rapidly and temper hot metalware to a definite temperature to obtain the desired properties of an alloy.

There are also the direct contact heat exchanges inside a fluidized bed. For example, hot flue gas can be used to warm up sand particles that are to be added into the combustor as makeup materials in fluidized-bed combustion. This also happens during the start-up of fluidized-bed coal combustion when hot air, obtained from burning of natural gas, for example, is first passed through the fluidized-bed combustor to heat up the bed materials to a certain temperature, before coal particles can start to burn on themselves. Similarly, air or other gas can be used to fluidize hot particulate materials in product line to recover the residue heat.

Fluidized-bed heat exchangers can also be used as a heat exchanger within a chemical process that already utilizes the fluidized bed. For example, as discussed in Section 5.3.2.1, a catalyst cooler is an essential component of modern RFCC, to dissipate the extra heat from the combustion in order to maintain the heat balance. In combustors, besides the heat exchanger installed inside the fluidized-bed combustion chamber, additional dense phase fluidized bed(s) can also be installed in the solids return loop to dissipate extra heat if required.

There are some additional distinct advantages of fluidized-bed heat exchangers and two examples are given below:

1. They can be kept at a relatively high temperature, which is difficult to maintain by gas or liquid. For example, to maintain a highly endothermic chemical reaction inside a reactor at 350°C, it is required to have an efficient heat exchanger that can maintain a constant temperature just slightly higher. This is usually realized using molten salt, since the evaporation temperatures of the most commonly used gases and liquids are not in this range. However, molten salt causes many problems such as corrosion. Fluidized beds, with sand for example, are now being used to replace such molten salt heat exchangers.
2. The heat transfer rate can be easily adjusted in most fluidized-bed heat exchangers. Their heat transfer capacity can be “turned up” or “turned down” almost instantaneously by increasing or decreasing the fluidization gas. As the fluidizing gas velocity increases in a dense-phase fluidized bed, there are more gross movements of solids and therefore higher heat transfer rates. Such fluidized-bed heat exchangers can also be easily “turned off” and “turned on” by shutting off and restarting the fluidization gas, without having to stop any other operations.

5.3.5.3 Fluidized-Bed Coating

Coating of particles with a thin layer of film can be realized in a fluidized bed. In such a process, the particles to be coated are first fluidized with air or inert gas, if needed, and the coating materials, usually in solution, are sprayed into the fluidized bed. Owing to the vigorous movement of the particles and the gross flow pattern in the fluidized bed, particles are uniformly coated; very often, spouted beds are preferentially used for coating. Given the gross particle circulation, particles that get sticky after being

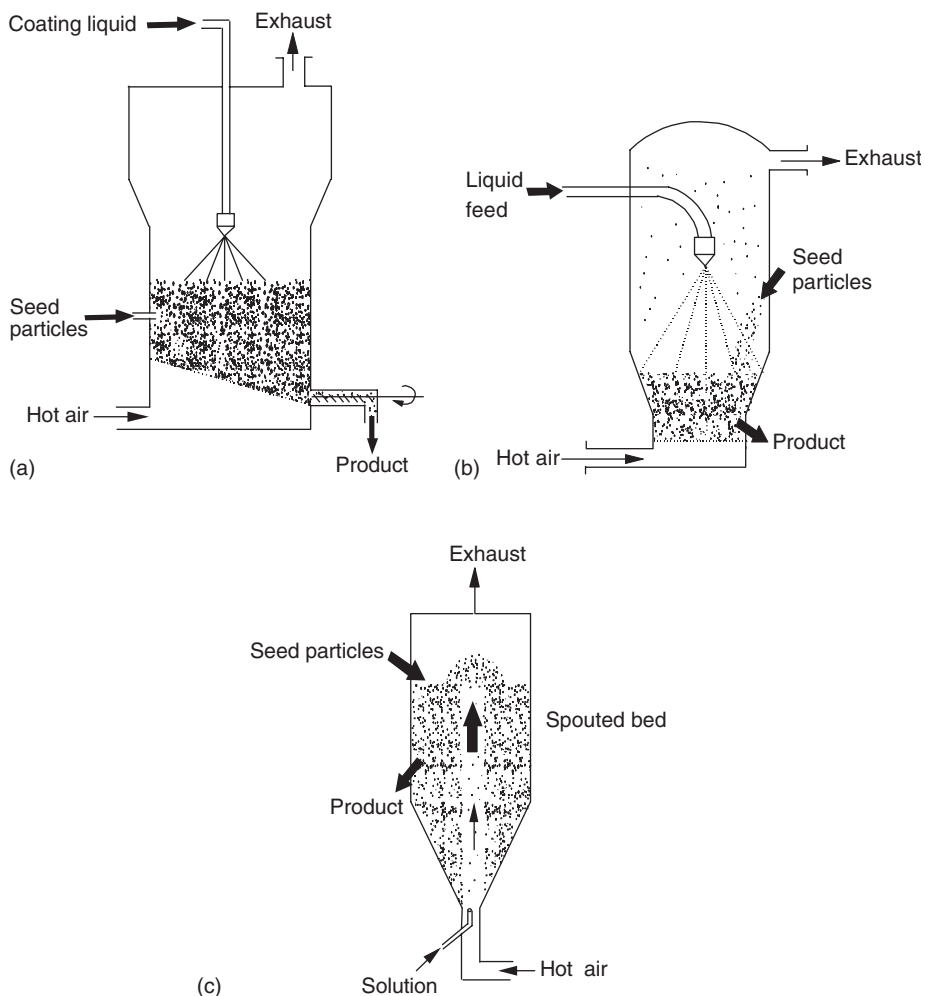


FIGURE 5.44 Fluidized-bed coaters.

sprayed by the coating solution can still be nicely circulated in the spouted bed. The spouted bed is also a better choice when handling large particles. Figure 5.44 shows three examples of fluidized-and spouted-bed coaters.

5.3.5.4 Powder Coating

Powder coating is a process where the materials initially in powder form are coated onto larger objects such as dishwasher racks, filing cabinets, and automotive parts. The powder materials can be thermoplastic or thermosetting. Thermoplastic materials are usually used for simple indoor parts with less stringent requirement. When applying thermoplastic coating, the thermoplastic powder is fluidized with cold or warm air and the heated metal part such as a dishwasher rack is dipped into the bed for a short period of time, normally a few seconds, and then quickly removed. A uniform thermoplastic coating is thus formed onto the dishwasher rack, making it a fine final product.

Thermosetting powder coating is used much more widely and also much more durable than thermoplastic powder coatings. In the thermosetting powder coating process, pigment, resin, and other materials are first dry-mixed together and then put through an extrusion process to homogenize the materials. The solid paint chips from the extrusion are then grinded down to about 30 to 60 μm to be used as the paint powder.

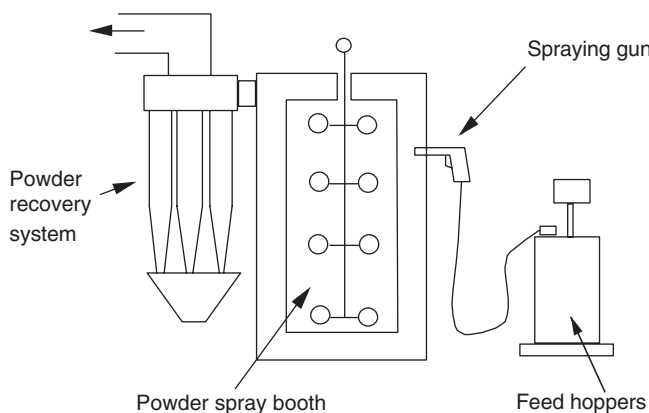


FIGURE 5.45 The powder-coating process.

There are two methods to apply the paint powder onto workpieces, both using electrostatics. The first method is fluidized-bed coating, where the air is electrically charged when flowing through the plenum with a high-voltage electrode. The parts are then dipped into the fluidized bed of paint powder and the powder forms a thin layer on the surface of the parts caused by electrostatic adhesion. The parts are then transported to an oven for curing. This procedure is simple but is limited to only continuous coating of simple parts of similar size and shape.

The mostly widely used powder coating process, over 90%, is the electrostatic spraying method. A typical powder spray booth with accessories is given in Figure 5.45. Paint powder is first fed into the fluidized feed hopper from which the powder is “picked up” by the Venturi effect using a high velocity air flow in the transport line. At the end of the air transport line is the spray gun that produces an air and particle flow mixture, flowing toward the parts that are conveyed in the direction perpendicular to the powder flow. The powder, now charged by the high-voltage electrode at the tip of the powder spray gun, preferentially flows onto the earthed metal parts and cling onto them. The coated parts are then conveyed by the continuous conveyor to the oven for solidification (curing). Particles not adhered to the parts are sucked into the solids separation system, typically with cyclones and bag house filters, and the paint particles collected are recycled back to the feeder.

There are many significant advantages of electrostatic spraying powder coating over regular solvent-based coating. First, it eliminates the use of a solvent, which not only eliminates the associated emission problem but also realizes cost savings. The second key advantage is that any unused paint can be recycled and reused. Therefore, dry powder coating has developed very quickly and is replacing solvent coating at an unprecedented rate. However, due to the use of Geldart A powders, the surface quality of powder coating is not very smooth so that powder coating has not been used for high end products such as automobile bodies. While the use of much finer Geldart C paint powder should lead to a much better surface quality, the problem of powder agglomeration makes the results even worse, preventing the use of powder coating from being used for high-end products. A new technology has been invented at the authors’ university that can essentially eliminate the interparticle forces (Zhu and Zhang, 2004). Using this new technology, Geldart C particles are made to flow freely, just like Geldart Group A particles. This new technology has now been commercialized in a local company to produce high-end powder coating products.

5.3.6 Other Fluidized-Bed Reactors and Applications

Besides the various gas–solids fluidized-bed reactors discussed earlier in this section, there are also other types of fluidized-bed reactors, namely, the spouted bed and spout–fluid bed reactors, the liquid–solid fluidized-bed reactors and the gas–liquid–solid three-phase reactors. Given the space constraints of this handbook, only the special features are highlighted here while the readers are directed to key references for more details.

5.3.6.1 Spouted Beds

The spouted bed is essentially a fluidized bed with maldistribution of gas. The fluidizing gas enters in a central nozzle from the bottom of the bed, which has reversed cone shape and all the special features of the spouted bed trace back to the central nozzle. As outlined in Section 5.3.1, particles in the spouted bed flow rapidly upward in the spout, reach the top fountain and then move down slowly in the annulus. Most gas passes through the bed in the central spout and there may be a gas downflow in the annulus as gas is dragged downward by the particles. The gross internal particle circulation inside the spouted bed gives rise to several additional features, which lead to the application of spouted beds.

First of all, the gross solids circulation and the more vigorous particle movement allow the spouted bed to handle larger and sticky particles. This makes the spouted bed very useful in certain physical operations such as drying and particle coating. As a matter of fact, the invention of spouted bed was directly associated with the drying of Canadian wheat (Mathur and Gishler, 1955). Mathur and Epstein (1974) reviewed most of the early applications of spouted beds, including drying and particle coating. During the 1980s and early 1990s spouted beds were studied for coal combustion and gasification, which, however, appears to have not led to commercialization. There were also studies on pyrolysis in spouted beds with and without draft tubes (Huff and Vasalos, 1998; Aguago et al., 2002), and the spouted bed with a more “complete” draft tube is also referred to as an “internal circulating fluidized bed”.

Spouted beds are also finding applications in new areas such as the food industry (Dewettinck and Huyghebaert, 1999; Gibbs et al., 1999) and pharmaceutical industry (Jono et al., 2000). In the food industry, encapsulation with thin film of polymers provides specific properties that the natural product does not offer. For example, encapsulation can separate the reactive components within a mixture, mask undesirable flavors, protect unstable ingredients from degradation (due to heat, moisture, air and light), provide controlled or delayed release and reduce hygroscopicity, and change the characteristic of the original material (such as flowability, compressibility, dust reduction, and density) (Teunou and Poncelet, 2002).

5.3.6.2 Liquid–Solid Fluidized Beds

Liquid–solid fluidized beds (LSFB) have very uniform liquid–solid suspension. Unlike a gas–solid fluidized bed where excess fluidizing gas beyond minimum fluidization forms bubbles, which lead to bypassing of reactant and many other problems, “excess” liquid in LSFB merely leads to higher bed expansion. Such phenomena are referred to as particulate fluidization (Kwauk, 1992) and provide many benefits: very uniform contact between the two phases throughout the entire fluidized bed and the ability to adjust the liquid–solids ratio inside the bed by changing the liquid fluidization velocity.

The modern applications of LSFB appear to date back to the 1960s. The more traditional applications of LSFB include classification of particles by size and density, backwashing of granular filters, crystal growth, adsorption, ion exchange, and electrolysis with both inert and electrically conducting fluidized particles (Epstein, 2003a). Another area of applications is leaching and washing (Kwauk, 1992). More recent applications of the LSFB are in the bio industry and wastewater treatment industry. A very recent review paper by Epstein (2003a) provides an excellent collection of applications of LSFB.

It is worth mentioning that the emergence of the liquid–solid circulating fluidized beds (LSCFB) as a new liquid–solid reactor, gives added benefits over the traditional LSFB (Zhu et al., 2000). The added features include more uniform residence time distribution, better mass transfer, the independent control of solids concentration, the higher turndown ratio, and the possibility of accommodating two reactions or processes in the same LSCFB unit. LSCFB has found potential applications in the chemical industry (Liang and Zhu, 1997), the biotech industry (Lan et al., 2002), and the wastewater treatment industry (Nakhla et al., 2004).

5.3.6.3 Gas–Liquid–Solid Three-Phase Fluidized Beds

Gas–liquid–solid fluidized beds (GLSFB) or three-phase fluidized beds may be considered as LSFB with the additional injection of gas. The GLSFB is generally divided into two phases: the gas or bubble phase and the fluidized dense phase where there are only liquids and solids. In a GLSFB, bubbles form as soon

as the gas is injected, since, unlike in the gas–solid fluidized bed, the gas is not present in the dense phase. Interaction between the gas phase and particles are mostly indirect through the liquid phase. Generally speaking, a GLSBF is more uniform than a gas–solid fluidized bed, but less uniform than a LSFB. In the stationary GLSBF, there are three main operating regimes: the dispersed bubble regime, the coalesced bubble regime, and the slug regime. The dispersed bubble regime under higher liquid velocity is more uniform than the coalesced bubble regime under higher gas velocity. This also reflects the point that a “gas-driven” fluidized system is less uniform than a “liquid-driven” fluidized system.

GLSBF also has many applications. The more traditional applications are in the petrochemical industry for upgrading heavy stocks such as hydrocracking and hydrotreating. Applications in fermentation and pharmaceutical industry also have a long history. More recent applications in the last 20 to 30 years are seen mostly in the biotech industry and wastewater treatment industry. A very thorough review has been provided by Fan (1989).

Nomenclature

a_b	Bubble interfacial area per unit volume of bubbles, m^{-1}
A	Cross-sectional area of column, m^2
A_c	Area of distributor per orifice, m^2
Ar	Archimedes number defined by Eq. (5.6), dimensionless
Ar'	Modified Archimedes number defined by Eq. (5.73), dimensionless
b	Empirical constant in Eq. (5.64), dimensionless
B	Empirical constant in Eq. (5.13), dimensionless
C_1, C_2	Empirical constants in Eq. (5.5) and (5.72), dimensionless
C_{Ab}	Concentration of reactant A in bubble phase, mol/m^3
C_{Ad}	Concentration of reactant A in dense phase, mol/m^3
C_D	Drag coefficient, dimensionless
d_{or}	Orifice diameter, m
d_p	Mean particle diameter, m
d_{pi}	Diameter of i th particle size fraction, m
d_s	Spout diameter, m
D	Column diameter, m
D_{AB}	Molecular diffusivity of reacting or tracer gas, m^2/s
D_b	Bubble diameter, m
$D_{g,ax}$	Gas axial dispersion coefficient, m^2/s
D_h	Hydraulic diameter of column, m
$D_{s,ax}$	Solids axial dispersion coefficient, m^2/s
f_b	Bubble frequency, s^{-1}
f_w	Bubble wake fraction ($=$ volume of wake/volume of bubble), dimensionless
F_d	Drag force per unit area defined by Eq. (5.37), $\text{kg}/\text{m s}^2$
F_g	Gravity force per unit area defined by Eq. (5.37), $\text{kg}/\text{m s}^2$
g	Acceleration due to gravity, m/s^2
G_s	Net solids flux through column, $\text{kg}/\text{m s}^2$
G_{so}	Upwards flux of solids at dense bed surface, $\text{kg}/\text{m s}^2$
G_{si}	Entrainment flux of solids of fraction I above the TDH, $\text{kg}/\text{m s}^2$
H	Expanded bed depth, m
H_f	Fountain height above spouted bed, m
H_m	Maximum spoutable bed depth, m
H_{mf}	Bed depth at minimum fluidization, m
k	Empirical constant given by Eq. (5.19), dimensionless
k_{bd}	Bubble-to-dense-phase interphase mass transfer coefficient, m / s
k_{bd}^*	Dimensionless interphase mass transfer coefficient defined by Eq. (5.34), dimensionless

k_r	First-order gas-phase reaction rate constant, s^{-1}
k_r^*	Dimensionless first-order rate constant defined by Eq. (5.34), dimensionless
L_j	Jet penetration distance into the fluidized bed, m
l_s	Slug vertical length, m
m_i	Mass fraction of particles belonging to the i th size fraction, dimensionless
M_p	Total mass of particles in the bed, kg
n	Empirical constant index, dimensionless
N_{or}	Number of orifices in the gas distributor, dimensionless
Nu	Nusselt number, dimensionless
P	Local pressure, Pa
P_c	Inner perimeter of fluidization column, m
$Pe_{g,ax}$	Peclet number for axial gas dispersion defined by Eq. (5.47), dimensionless
$Pe_{s,ax}$	Peclet number for axial solids dispersion, dimensionless
Pr	Prandtl number, dimensionless
r	Radial coordinate, m
R	Radius of column, m
Re	Reynolds number based on particle diameter ($= \rho_g d_p U / \mu_g$), dimensionless
Re_c	Reynolds number corresponding to onset of turbulent regime, Eq. (5.13), dimensionless
Re_D	Reynolds number based on column diameter ($= \rho_g D U / \mu_g$), dimensionless
Re_{lmf}	Reynolds number defined in Eq. (5.72), dimensionless
Re_{mf}	Reynolds number defined in Eq. (5.5), dimensionless
Re_{se}	Reynolds number corresponding to $U_{se} (-\rho_g d_p U_{se} / \mu_g)$, dimensionless
Sc	Schmidt number for gas, dimensionless
Sh	Sherwood number, dimensionless
t_{mix}	Characteristic solids mixing or turnover time, sec
u_{or}	Gas velocity through orifice into fluidized bed, m/sec
U, U_g	Superficial gas velocity, m/sec
U_a	Superficial velocity in annulus of spouted bed, m/sec
U_b	Bubble rise velocity, m/sec
U_c	Superficial gas velocity at onset of turbulent fluidization, m/sec
U_{DSU}	Superficial gas velocity at onset of dense suspension upflow, m/sec
U_l	Superficial liquid velocity, m/sec
U_{lmf}	Superficial liquid velocity at minimum fluidization, m/sec
U''_{lmf}	Superficial liquid velocity at minimum liquid-solid fluidization, m/sec
U_{mf}	Superficial gas velocity at minimum fluidization, m/sec
U_{ms}	Superficial gas velocity at minimum slugging, m/sec
U_{mS}	Superficial gas velocity at minimum spouting, m/sec
U_{se}	Superficial gas velocity at significant entrainment, m/sec
U_{si}	Velocity of rise of a single isolated slug, Eq. (5.42), m/sec
U_{slip}^*	Dimensionless slip velocity defined in Eq. (5.62), dimensionless
v_{oSH}	Velocity of particles on axis of spouted bed at $z = H$, m/sec
v_{sw}	Time-mean particle velocity at wall of riser, m/sec
V_b	Bubble volume, m^3
V_b	Volumetric flow accounted for by displacement of bubbles, m/sec
V_s	Settling velocity of particles, m/sec
V_s^e	Settling velocity of particles of diameter d_p in the fluid in question, m/sec
V_{si}	Settling velocity of particles in the i th size fraction, m/sec
Y	Coefficient modifying two-phase theory of fluidization, Eq. (5.22), dimensionless
z	Vertical height coordinate measured from gas distributor, m
$'z$	Vertical height coordinate measured from surface of dense bed, m

Greek Letters

α_i	Decay constant in Eq. (5.40) for entrainment in TDH, m^{-1}
α_{mf}	Gas holdup/(gas + liquid holdup) at minimum fluidization, dimensionless
β	Dimensionless gas velocity for slug flow defined by Eq. (5.42), dimensionless
ΔP	Pressure drop, Pa
ΔP_{bed}	Pressure drop across dense fluidized bed, Pa
ΔP_{fixbd}	Pressure drop across fixed bed, Pa
ΔP_{mf}	Pressure drop across fluidized bed at minimum fluidization, Pa
ΔP_S	Pressure drop across spouted bed, Pa
ε	Local time-mean voidage
ε'	Voidage defined by Eq. (5.53), dimensionless
ε^*	Voidage at top exit of riser, Eq. (5.55) and (5.57), dimensionless
$\langle \varepsilon \rangle_A$	Voidage averaged over cross-sectional area, dimensionless
$\langle \varepsilon \rangle_{av}$	Voidage averaged over entire bed
ε_b	Fraction of bed volume occupied by bubbles, dimensionless
ε_d	Voidage in dense phase region at bottom of riser, dimensionless
ε_g	Gas hold-up = fraction of bed volume occupied by gas, dimensionless
ε_l	Liquid hold-up = fraction of bed volume occupied by liquid, dimensionless
ε_{mf}	Bed voidage at minimum fluidization, dimensionless
ε_s	Solid hold-up = fraction of bed volume occupied by partial dimentionless
ε_{SH}	Spout voidage at top of spout (i.e., at $z = H$), dimensionless
η	Constant index in Eq. (5.13),dimensionless
μ_g	Gas viscosity, kg/m sec
μ_l	Liquid viscosity, kg/m sec
ρ_b	Bulk density of particulate material, kg/m^3
ρ_g	Gas density, kg/m^3
ρ_l	Liquid density, kg/m^3
ρ_p	Particle density, kg/m^3
φ_b	Fraction of bed volume occupied by particles associated with bubble phase, dimensionless
φ_d	Fraction of bed volume occupied by particles associated with dense phase, dimensionless
χ	Mass fraction of particles which are finer than $45 \mu m$, dimensionless
ψ	Particle sphericity, dimensionless

Abbreviations

ATP	Atmospheric-topped bitumen
BGPG	Biomass gasification and power generation
CFB	Circulating fluidized bed
CFBC	Circulating fluidized bed combustor
DSU	Dense suspension upflow
FCC	Fluid catalytic cracking or fluid cracking catalyst
FFB	Fixed fluidized bed
GIEC	Guangzhou Institute of Energy Conversion
GLSFB	Gas-liquid-solid fluidized beds
GLSCFB	Gas-liquid-solid circulating fluidized beds
LSCFB	Liquid-solid circulating fluidized beds
LSFB	Liquid-solid fluidized beds
PCFBC	Pressurized circulating fluidized-bed combustor
PFBC	Pressurized fluidized-bed combustor
QC	Quick contact

RFCC	Residue fluid catalytic cracking
RTD	Residence time distribution
SFB	Stationary fluidized-bed
SFB	Stationary fluidized bed combustor
SINOPEC	Chinese National (Sino) Petroleum Enterprises Corporation
TDH	Transport disengagement height
TCC	Thermofer Catalytic Cracking
UOP	Universal Oil Products Company
VTP	Vacuum-topped bitumen

Subscripts

AB	Boundary between group A and B solids
BD	Boundary between group B and D solids
b	Bubble
d	Dense phase
g	Gas
l	Liquid
p	Particle
s	Solid particles, slug
S	Spout, spouted bed

References

- Abba, I.A., Grace, J.R., Bi, H.T., and Thompson, M.L., Spanning the flow regimes: generic fluidized-bed reactor model, *AICHE Journal*, 49, 1838, 2003.
- Abrahamsen, A.R. and Geldart, D., Behaviour of gas fluidized beds of fine powders, *Powder Technol.*, 26, 35, 1980.
- Aerov, M.E. and Todes, O.M., *Hydraulic and Thermal Fundamentals on the Operation of Apparatus with Static and Fluidised Particle Bed*, Chimia, Leningrad, (in Russian) 1968.
- Agarwal, P.K. and La Nauze, R.D., Transfer processes local to the coal particle: A review of drying, devolatilization and mass transfer in fluidized bed combustion, *Chem. Eng. Res. Des.*, 67, 457–480, 1989.
- Aguado, R., Olazar, M., San José, M.J., Gaisán, B., and Bilbao, J., Kinetic study of polyolefin pyrolysis in a conical spouted bed reactor, *Ind. Eng. Chem. Res.*, 41, 4559, 2002.
- Andersson, B.-Å. and Leckner, B., Bed-to-wall heat transfer in a 10 m² bubbling fluidized bed, in *Fluidisación, Proceedings of Congreso Europeo de Fluidisación*, Macías Machín, A., and Winter, G., Eds., Universidad de Las Palmas de Gran Canaria, Vol. 1, 1994, pp. 251–260.
- Asadullah, M., Ito, S., Kunimori, K., and Tomishige, K., Role of catalyst and its fluidization in the catalytic gasification of biomass to syngas at low temperature, *Ind. Eng. Chem. Res.*, 41, 4567, 2002a.
- Asadullah, M., Ito, S.I., Kunimori, K., Yamada, M., and Tomishige, K., Energy efficient production of hydrogen and syngas from biomass: Development of low-temperature catalytic process for cellulose gasification, *Environ. Sci. Technol.*, 36, 4476, 2002b.
- Avedesian, M.M. and Davidson, J.F., Combustion of carbon particles in a fluidized bed, *Trans. Inst. Chem. Eng.*, 51, 121–131, 1973.
- Avidan, A.A. Fluid catalytic cracking, in *Circulating Fluidized Beds*, Grace, J.R., Avidan, A.A., and Knowlton, T.M., Eds., Blackie Academic & Professional, New York, 1997, p. 466, chap. 13.
- Avidan, A.A., and Shinnar, R., Development of catalytic cracking technology. A lesson in chemical reactor design. *Ind. Eng. Chem. Res.*, 29, 931, 1990.
- Avidan, A.A., Edwards, M., and Owen, H., Fluid catalytic cracking. Past and future challenges, *Rev. Chem. Eng.*, 6, 1, 1990.
- Baeyens, J. and Geldart, D., Particle mixing in a gas fluidized bed, in *Fluidization and Its Applications*, Society Chim. Ind., Toulouse, 1973, p. 182.

- Bai, D., Issangya, A.S., and Grace, J.R., Characteristics of gas fluidized beds in different flow regimes, *Ind. Eng. Chem. Res.*, 38, 260, 1999.
- Bai, D., Jin, Y., Yu, Z-Q., and Zhu, J.X., The axial distribution of the cross-sectionally averaged voidage in fast fluidized beds, *Powder Technol.*, 71, 51, 1992.
- Bai, D. and Kato, K., Quantitative estimation of solids holdups at dense and dilute regions of the circulating fluidized bed, *Powder Technol.*, 101, 183, 1999.
- Baron, T., Briens, C.L., and Bergougnou, M.A., Study of the transport disengaging height, *Can. J. Chem. Eng.*, 66, 749, 1988.
- Baskakov, A.P., The mechanism of heat transfer between a fluidized bed and a surface, *Int. Chem. Eng.*, 4, 320–324, 1964.
- Baskakov, A.P. and Leckner, B., Radiative transfer in CFB furnaces, *Powder Technol.* 90, 213–218, 1997.
- Baskakov, A.P. and Filippovsky, N.F., Transfer of heat in fluidized bed, in *Fluidization*, Einstein, V.G., and Baskakov, A.P., Eds., Chimia, Moscow, 1991, chap. 6 (in Russian).
- Baskakov, A.P., Filippovsky, N.F., Munts, V.A., and Ashikhmin, A.A., Temperature of particles heated in a fluidized bed of inert material, *J. Engrn. Phys.*, 52, 574–578, 1987.
- Baskakov, A.P., Radiative heat transfer in fluidized beds, in *Fluidization*, Davidson, J.F., Ed., Academic Press, London, 1985, chap. 13B.
- Baskakov, A.P., Berg, B.V., Vitt, O.K., Filippovsky, N.F., Kirakosyan, V.A., Goldobin, J.M., and Maskaev, V.K., Heat transfer to objects immersed in fluidized beds, *Powder Technol.* 8, 273–282, 1973.
- Bassi, A.S., Briens, C.L., and Bergougnou, M.A., Short contact time fluidized reactors (SCTFRs), in *Circulating Fluidized Bed Technology IV*, Avidan, A.A., Ed., AIChE, New York, 1994, p. 15.
- Basu, P., Heat transfer in fast fluidized beds, *Chem. Eng. Sci.*, 45, 3123–3136, 1990.
- Basu, P., Combustion of coal in circulating fluidized-bed boilers: a review, *Chem. Eng. Sci.*, 54, 5547, 1999.
- Basu, P. and Nag, P.K., Heat transfer to walls of a circulating fluidized-bed furnace, *Chem. Eng. Sci.*, 51, 1–26, 1996.
- Bi, H.T., Grace, J.R., and Zhu, J., Regime transitions affecting gas–solids suspensions and fluidized beds, *Trans. Inst. Chem. Eng.*, 73, 154, 1995.
- Bi, H.T., Ellis, N., Abba, I.A., and Grace, J.R., A state-of-the-art review of gas–solid turbulent fluidization, *Chem. Eng. Sci.*, 55, 4789, 2000.
- Borodulya, V.A. and Kovensky, V.I., Radiative heat transfer between a fluidized-bed and a surface, *Int. J. Heat Mass Transf.*, 26, 277–289, 1983.
- Borodulya, V.A., Teplitsky, Yu.S., Markevich, I.I., Hassan, A.F., and Yeryomenko, T.P., Heat transfer between a surface and a fluidized bed: consideration of pressure and temperature effects, *Int. J. Heat Mass Transf.*, 34, 47–53, 1991.
- Botterill, J.S.M., *Fluid-Bed Heat Transfer*, Academic Press, London, 1975.
- Breitholtz, C. and Leckner, B., Heat transfer in CFB boilers — do we know sufficiently, *Trends Heat Mass Momentum Transf.*, 3, 85–104, 1997.
- Breitholtz, C., Leckner, B., and Baskakov, A.P., Wall heat transfer in CFB boilers, *Powder Technol.*, 120, 14–48, 2001.
- Brereton, C.M.H. and Grace, J.R., Microstructural aspects of the behaviour of circulating fluidized bed, *Chem. Eng. Sci.*, 48, 2565–2572, 1993.
- Brewster, M.Q., Effective absorbtivity and emissivity of particulate media with application to a fluidized bed, *J. Heat Transf.*, 108, 710–713, 1986.
- Bridgwater, A.V., Renewable fuels and chemicals by thermal processing of biomass, *Chem. Eng. J.*, 91, 87, 2003.
- Bridgwater, A.V. and Peacocke, G.V.C., Fast pyrolysis processes for biomass, *Renewable and Sustainable Energy Reviews*, 4, 1, 2000.
- Choi, J-H., Chang, I-Y., Shun, D-W., Yi, C-K., Son, J-E., and Kim, S-D., Correlation on the particle entrainment rate in gas fluidized beds, *Ind. Eng. Chem. Res.*, 38, 2491, 1999.
- Clift, R., Grace, J.R., and Weber, M.E., *Bubbles, Drops and Particles*, Academic Press, New York, 1978.
- Darton, R.C., LaNauze, R.D., Davidson, J.F., and Harrison, D., Bubble growth due to coalescence in fluidized beds, *Trans. Inst. Chem. Eng.*, 55, 274, 1977.

- Davidson, J. F., Clift, R., and Harrison D., *Fluidization*, 2nd ed., Academic Press, London, Toronto, 1985.
- Deiva V., Grmela, R., and Chaouki, J., Improvement of fluidizability of fine powders, Proceedings of the World Congress on Particle Technology, Sydney, Australia, Paper 671, 2002.
- Deng, R.S., Wei, F., Jin, Y., Zhang, Q., and Jin, Y., Experimental study of the deep catalytic cracking process in a downer reactor, *Ind. Eng. Chem. Res.*, 41, 6015, 2002a.
- Deng, R.S., Wei, F., Jin, Y., Zhang, Q., and Jin, Y., Downer catalytic pyrolysis (DCP): a novel process for light olefins production, *Chem. Eng. Technol.*, 25, 711, 2002b.
- Dewettinck, K. and Huyghebaert, A., Fluidized bed coating in food technology, *Trends Food Sci. Technol.*, 10, 163, 1999.
- Douglas, W.J.M. and Churchill, S.W., Recorrelation of data for convective heat transfer between gases and single cylinders with large temperature differences, *Chem. Eng. Progr. Symp. Ser.*, 52 (18), 23–28, 1956.
- Ellis, N., Bi, H.T., Lim, C.J., and Grace, J.R., Hydrodynamics of turbulent fluidized beds of different diameters, *Powder Technol.*, 141, 124, 2004.
- Epsstein, N., Applications of liquid–solid fluidization, *Int. J. Chem. Reactor Eng.*, 1, 1, 2003a.
- Epsstein, N., Liquid-solids fluidization, in *Handbook of Fluidization and Fluid-Particle Systems*, Yang, W.C., Ed., Marcel Dekker, New York, 2003b, chap. 26.
- Epsstein, N. and Grace, J.R., Spouting of particulate solids, in *Handbook of Powder Science and Technology*, 2nd ed., Fayed, M.E. and Otten, N., Eds., Chapman & Hall, New York, 1997, chap. 10.
- Fan, L-S., *Gas-Liquid-Solid Fluidization Engineering*, Butterworths, Boston, 1989.
- Fan, L-S., and Tsuchiya, K., *Bubble Wake Dynamics in Liquids and Liquid-Solid Suspensions*, Butterworth-Heinemann, Boston, 1990.
- Fang, Z.H., Grace, J.R., and Lim, C.J., Radiative heat transfer in circulating fluidized beds, *J. Heat Transf.*, 117, 963–968, 1995a.
- Fang, Z.H., Grace, J.R., and Lim, C.J., Local particle convective heat transfer along surfaces in circulating fluidized beds, *Int. J. Heat and Mass Transf.*, 38, 1217–1224, 1995b.
- Farag, I.H. and Tsai, K.Y., Surface-to-suspension heat transfer model in lean gas–solid freeboard flow, *Can. J. Chem. Eng.*, 71, 514–524, 1993.
- Foka, M., Chaouki, J., Guy, C., and Klvana, D., Gas phase hydrodynamics of a gas–solid turbulent fluidized bed reactor, *Chem. Eng. Sci.*, 51, 713, 1996.
- Gartside, R.J., QC — A new reaction system, in *Fluidization VI*, Grace, J.R., Shemilt, L.W., and Bergougnou, M.A., Eds., Engineering Foundation, New York, 1989, p. 25.
- Geldart, D., Types of gas fluidization, *Powder Technol.*, 7, 285, 1973.
- Geldart, D., Ed., *Gas Fluidization Technology*, Wiley & Sons, Chichester, 1986.
- Gelperin, N.I. and Einstein, V.G., Heat transfer in fluidized beds, in *Fluidization*, Davidson J.F., and Harrison, D., Eds., Academic Press, London, 1971, chap. 10.
- Gibbs, B.F., Kermasha, S., Alli, I., and Mulligan, C.N., Encapsulation in the food industry: a review, *Int. J. Food Sci. Nutri.*, 50, 213, 1999.
- Gilliland, E.R. and Mason, E.A., Gas mixing in beds of fluidized solids, *Ind. Eng. Chem.*, 44, 218, 1952.
- Glicksman, L.R., Hyre, M., and Farrell, P., Dynamic similarity in fluidization, *Intern. J. Multiphase Flow*, 20S, 331, 1994.
- Glicksman, L.R., Heat transfer in circulating fluidized beds, in *Circulating Fluidized Beds*, Grace, J.R., Avidan, A.A., and Knowlton, T.M., Eds., Blackie, London, 1997, pp. 261–311.
- Goedelke, F. and Reh, L., Particle induced heat transfer between walls and gas solid fluidized beds, *AICHE Symp. Ser.* 89, 123–136, 1993.
- Grace, J.R., The viscosity of fluidized beds, *Can. J. Chem. Eng.*, 48, 30, 1970.
- Grace, J.R., Fluidized bed hydrodynamics, in *Handbook of Multiphase Systems*, Hetsroni, G., Ed., Hemisphere Press, Washington, 1982, Sect. 8.1.
- Grace, J.R., Contacting modes and behaviour classification of gas–solid and other two-phase suspensions, *Can. J. Chem. Eng.*, 64, 353, 1986a.
- Grace, J.R., Fluid beds as chemical reactors, in *Gas Fluidization Technology*, Geldart, D., Ed., Wiley & Sons, Chichester, 1986b, Sect 8.1.

- Grace, J.R., Interphase mass and heat transfer in gas-fluidized beds, in *Transport Processes in Bubbles, Drops and Particles*, 2nd ed., deKee, D., and Chhabra, R.P., Eds., Taylor & Francis, New York, 2002, chap. 7.
- Grace, J.R., Avidan, A.A., and Knowlton, T.M., Eds., *Circulating Fluidized Beds*, Blackie Academic & Professional, New York, 1997.
- Grace, J.R. and Harrison, D., The distribution of bubbles within a gas-fluidized bed, *Inst. Chem. Eng. Symp. Ser.*, 30, 105, 1968.
- Grace, J.R. and Harrison, D., The behaviour of freely bubbling fluidized beds, *Chem. Eng. Sci.*, 24, 497, 1969.
- Grace, J.R. and Harrison, D., Fluidized beds with internal baffles, in *Fluidization*, Davidson, J.F., and Harrison, D., Ed., Academic Press, London, 1971, chap. 13.
- Grace, J.R., Issangya, A.S., Bai, D., Bi, H.T., and Zhu, J.Z., Situating the high-density circulating fluidized bed, *AICHE J.*, 45, 2108, 1999.
- Grace, J.R. and Mathur, K.B., Height and structure of the fountain region above spouted beds, *Can. J. Chem. Eng.*, 56, 533, 1978.
- Graham, R.G. and Huffman, D.R., Commercial aspects of rapid thermal processing (RTP), in *Proceedings of the Power Production from Biomass II Conference*, Espoo, Finland, April 1995.
- Griffith, A.E. and Louge, M.Y., The scaling of cluster velocity at the wall of circulating fluidized bed risers, *Chem. Eng. Sci.*, 53, 2475, 1998.
- Gross, B. and Ramage, M.P., FCC Reactor with a Downflow Reactor Riser, U.S., Patent 4385985, 1983.
- Hetsroni, G., Ed., *Handbook of Multiphase Systems*, Hemisphere, Washington, 1982.
- Highley, J. and Kaye, W.G., Fluidized bed industrial boilers and furnaces, in *Fluidized beds Combustion and Applications*, Howard, J. R., Ed., Applied Science Publishers, London, 1983.
- Horio, M. and Nonaka, A., A generalized bubble diameter correlation for gas-solid fluidized beds, *AICHE J.*, 33, 1865, 1987.
- Hottel, H.C. and Sarofim, A.F., *Radiative Transfer*, McGraw-Hill, New York, 1967.
- Howard, J.R., Ed., *Fluidized beds Combustion and Applications*, Applied Science Publishers, London. 1983.
- Hovmand, S. and Davidson, J.F., Pilot plant and laboratory scale fluidized reactors at high gas velocities; the relevance of slug flow, in *Fluidization*, Davidson, J.F., and Harrison, D., Eds., Academic, London, 1971, chap. 5.
- Huff, G.A. and Vasalos, I.A., Oxidative pyrolysis of natural gas in a spouted bed reactor: Reaction stoichiometry and experimental reactor design, *Catalysis Today*, 46, 39, 1998.
- Issangya, A.S., Grace, J.R., Bai, D., and Zhu, J., Further measurements of flow dynamics in a high-density circulating fluidized bed riser, *Powder Technol.*, 111, 104, 2000.
- Issangya, A.S., Grace, J.R., Bai, D., and Zhu, J., Radial voidage variation in CFB risers, *Can.J.Chem.Eng.*, 79, 279, 2001.
- Jacobs, J.P., The future of fluidized-bed combustion, *Chem. Eng. Sci.*, 54, 5559, 1999.
- Jahnig, C.E., Campbell, D.L., and Martin, H.A., History of fluidized solids development at EXXON, in *Fluidization*, Grace J.R., and Matsen J.M., Eds., Plenum Press, New York, 1980, p. 3.
- Jin, Y., Yu, Z., and Cai, P., A criterion for transition from bubbling to turbulent fluidization, in *Fluidization V*, Ostergaard, K., and Sorensen, A., Eds., Engineering Foundation, New York, 1986, p. 289.
- Johnsson, F., Zhang, W., Johnsson, H., and Leckner, B., Optical and momentum probe measurements in a CFB furnace, in *Circulating Fluidized Bed Technology V*, Kwauk, M., and Li, J., Eds., Science Press, Beijing, 1997, pp. 652–657.
- Jono, K., Ichikawa, H., Miyamoto, M., and Fukumori, Y., A review of particulate design for pharmaceutical powders and their production by spouted bed coating, *Powder Technol.*, 113, 269, 2000.
- Karamanev, D. and Nikolov, L., Bed expansion of liquid–solid inverse fluidization, *AICHE J.*, 38, 1916, 1992.
- Kehoe, P.W.K. and Davidson, J.F., Continuously slugging fluidized beds, *Chemeca'70, Inst. Chem. Eng. Symp. Ser.*, 33, 97, 1971.
- Khan, A.R. and Richardson, J.F., Fluid-particle interactions and flow characteristics of fluidised beds and settling suspensions of spherical particles, *Chem. Eng. Comm.*, 78, 111, 1989.
- Kim, S.W., Kirbas, G., Bi, H.T., Lim, C.J., and Grace, J.R., Flow behaviour and regime transition in a high-density circulating fluidized bed riser, *Chem. Eng. Sci.*, 59, 3955, 2004a.

- Kim, S.W., Kirbas, G., Bi, H.T., Lim, C.J., and Grace, J.R., Flow structure and thickness of annular down-flow layer in a circulating fluidized bed riser, *Powder Technol.*, 142, 48, 2004b.
- Kunii, D. and Levenspiel, O., *Fluidization Engineering*, 2nd ed., Butterworth-Heinemann, Boston, 1991.
- Kwauk, M., *Fluidization: Idealized and Bubbleless, with Applications*, Science Press, Beijing; Ellis Horwood, New York, Toronto, 1992.
- Lan, Q., Bassi, A.S., Zhu, J.-X., and Margaritis, A., Continuous protein recovery from whey using liquid-solid circulating fluidized bed ion-exchange extraction, *Biotech. Bioeng.*, 78, 157, 2002.
- Latham, R., Hamilton, C., and Potter, O.E., Back-mixing and chemical reaction in fluidized beds, *Br. Chem. Eng.*, 13, 666, 1968.
- Leckner, B., Andersson, B.-Å., and Vijil, J., Operational results from the 16 MW FBB at Chalmers University, *3rd International Fluidised Conference*, The Institute of Energy, London, 1984, Paper Disc/16/134–143.
- Leckner, B., Golriz, M.R., Zhang, W., Andersson, B.-Å., and Johnsson, F., Boundary layers—first measurements in the 12 MW CFB research plant at Chalmers University, *Proceedings of the 11th International Conference on Fluidized Bed Combustion*, Anthony, E.J., Ed., ASME, New York, 1991, pp. 771–776.
- Lee, D.H., Epstein, N., and Grace, J.R., The variable-voidage effect on modeling the minimum liquid fluidization velocity of gas-liquid fluidized beds, *J. Chem. Eng. Jpn.*, 36, 1111, 2003.
- Lee, G.S. and Kim, S.D., Axial mixing of solids in turbulent fluidized beds, *Chem. Eng. J.*, 44, 1, 1990.
- Lee, G.S., Kim, S.D., and Baird, M.H.I., Axial mixing of fine particles in fluidized bed, *Chem. Eng. J.*, 47, 47, 1991.
- Lefroy, G.A. and Davidson, J.F., The mechanics of spouted beds, *Trans. Inst. Chem. Eng.*, 47, 120, 1969.
- Levy, Y. and Dorfman, Y., Two-phase flow in the vicinity of elongated bubbles in a fluidized bed, *AICHE J.*, 41, 1113, 1995.
- Li, Z.Q., Wu, C.N., Wei, F., and Jin, Y., Experimental study of high-density gas-solids flow in a new coupled circulating fluidized bed, *Powder Technol.*, 139, 214, 2004.
- Liang, W.-G. and Zhu, J.-X., Effect of radial flow nonuniformity on the alkylation reaction in a liquid-solid circulating fluidized bed (LSCFB) reactor, *Ind. Eng. Chem. Res.*, 36, 4651, 1997.
- Limas-Ballesteros, R., Thèse de doctorat, Institut National Polytechnique, Toulouse, France, 1980.
- Lints, M.C. and Glicksman, L.R., Parameters governing particle-to-wall heat transfer in circulating fluidized beds, in *Circulating Fluidized Bed Technology*, Avidan, A.A., Ed., AICHE, New York, 1993, pp. 297–304.
- Liu, J., Grace, J.R., and Bi, H.T., A novel multi-functional optical fiber probe: II. High-density CFB measurements, *AICHE J.*, 49, 1421, 2003.
- Lockett, M.J. and Harrison, D., The distribution of voidage fraction near bubbles rising in gas-fluidized beds, *Proc. Int. Symp. Fluidization*, Drinkenburg, A.A.H., Ed., Netherlands University Press, Amsterdam, 1967, p. 257.
- Maadhah, A.G., Abul-Hamayel, M., Aitani, A.M., Ino, T., and Okuhara, T., Down-flow FCC reactor, *Oil Gas J.*, 98, 66, 2000.
- Mamuro, T. and Hattori, H., Flow pattern of fluid in spouted beds, *J. Chem. Eng. Jpn.*, 1, 1, 1968.
- Martin, P.D., On the particulate and delayed bubbling regimes of fluidization, *Trans. Inst. Chem. Eng.*, 61, 318, 1983.
- Martin, H., Heat transfer between gas fluidized beds of solid particles and the surfaces of immersed heat exchanger elements, Part I and Part II, *Chem. Eng. Process.*, 18, 157–169 and 199–223, 1984.
- Mathur, K.B. and Epstein N., *Spouted Beds*, Academic Press, New York, 1974.
- Mathur, K.B. and Gishler, P.E., A technique for contacting gases with coarse solid particles, *AICHE J.*, 1, 157, 1955.
- May, W.G., Fluidized-bed reactor studies, *Chem. Eng. Progr.*, 55, No. 12, 49, 1959.
- McNab, G.S., Predictions of spout diameter, *Br. Chem. Eng. Proc. Tech.*, 17, 532, 1972.
- Merry, J.M.D., Penetration of a horizontal gas jet into a fluidized bed, *Trans. Inst. Chem. Eng.*, 49, 189, 1971.
- Merry, J.M.D., Penetration of vertical jets into fluidized beds, *AICHE J.*, 21, 507, 1975.

- Milne, B.J., Berruti, F., Behie, L.A., and de Brujin, T.J.W., The hydrodynamics of the internally circulating fluidized bed at high temperature, in *Circulating Fluidized Bed Technology VI*, Avidan, A.A., Ed., AIChE, New York, 1994, p. 28.
- Modest, M. F., *Radiative Heat Transfer*, 2nd ed., Academic Press, Amsterdam, 2003.
- Molerus, O. and Wirth, K.-E., *Heat Transfer in Fluidized Beds*, Chapman & Hall, London, 1997.
- Murphy, J.R., Evolutionary design changes mark FCC process, *Oil Gas J.*, 90, 49, 1992.
- Nag, P.K. and Moral, M.N.A., Effect of probe size on heat-transfer in circulating fluidized beds, *Int. J. Energy Res.*, 14, 965–974, 1990.
- Nakhla, G., Zhu, J., and Cui, Y., Liquid-Solid Circulating Fluidized Bed Waste Water Treatment System for Simultaneous Carbon, Nitrogen and Phosphorus Removal, *U.S. Patent*, applied, February, 2004.
- Overcashier, R.H., Todd, D.B., and Olney, R.B., Some effects of baffles in a fluidized system, *AIChE J.*, 5, 54, 1959.
- Palchonok, G., Heat and Mass Transfer in a Fluidized Bed, Ph.D. thesis, Chalmers University of Technology, 1998.
- Palchonok, G.I., Dolidovich, A.F., Andersson, S., and Leckner, B., Calculation of true heat and mass transfer coefficients between particles and a fluidized bed, *7th International Conference on Fluidization*, Engineering Foundation, New York, 1992, pp. 913–920.
- Palchonok, G.I. and Tamarin, A.I., Study of heat exchange between a model particle and a fluidized bed, *J. Eng. Phys.*, 45, 427–433, 1983.
- Palchonok, G.I., and Tamarin, A.I., Mass transfer to a moving particle in a fluidized bed of coarse material, *J. Eng. Phys.*, 47, 916–923, 1983.
- Palchonok, G.I., Breitholtz, C., Borodulya, V.A. and Leckner, B., Effect of turbulence on heat and mass transfer in the freeboard region of stationary and circulating fluidized beds, in *Fluidization IX*, Fan, L.-S., and Knowlton, T.M., Eds., Engineering Foundation, New York, 1998, pp. 413–420.
- Pell, M., *Gas Fluidization*, Elsevier, Amsterdam, 1990.
- Prins, W., Fluidized Bed Combustion of a Single Particle, Ph.D. thesis, Twente University, The Netherlands, 1987.
- Reh, L., Fluidized bed processing, *Chem. Engng. Prog.*, 67, 58, 1971.
- Reh, L., The circulating fluid bed reactor — a key to efficient gas/solid processing, in *Circulating Fluidized Bed Technology I*, P. Basu, Ed., Pergamon, Toronto, 1986, 105.
- Reh, L., Challenges of circulating fluid-bed reactors in energy and raw materials industries, *Chem. Eng. Sci.*, 54, 5359, 1999.
- Richardson, J.F., and Zaki, Sedimentation and fluidization, Part I, *Trans. I. Chem. Eng.*, 32, 35, 1954.
- Rowe, P.N., A note on the motion of a bubble rising through a fluidized bed, *Chem. Eng. Sci.*, 19, 75, 1964.
- Rowe, P.N. and Nienow, A.W., Particle mixing and segregation in gas-fluidized beds, a review, *Powder Technol.*, 15, 141, 1976.
- Rowe, P.N. and Partridge, B.A., An X-ray study of bubbles in fluidised beds, *Trans. Inst. Chem. Eng.*, 43, 157, 1965.
- Rowe, P.N., Partridge, B.A., Cheney, A.G., Henwood, G.A., and Lyall, E., The mechanism of solids mixing in fluidized beds, *Trans. Inst. Chem. Eng.*, 43, 271, 1965.
- Royal Dutch Shell Group of Companies, *The Petroleum Handbook*, 6th ed., Elsevier, Amsterdam, Oxford, New York, Tokyo, 1983.
- Schlunder, E.-U., et al., *Heat Exchanger Design Handbook*, VDI-Verlag, Duesseldorf, and Heishere Publishing Corporation, Washington, 1987, Part 2, chapter 2.8.4.
- Scott, D.S., Plskor, J. and Radlien, D., Liquid products from the continuous flash pyrolysis of biomass, *Ind. Eng. Chem. Process Des. Dev.*, 24, 581, 1985.
- Scott, D.S., Majerski, P., Piskor, J. and Radlein, D., Second look at fast pyrolysis of biomass – the RTI process, *J. Anal. App. Pyrolysis*, 51, 23, 1999.
- Shingles, T. and McDonald, A.F. Commercial experience with synthol CFB reactors, in *Circulating Fluidized Bed Technology II*, Basu, P. and Large, J. F., Eds., Pergamon Press, Toronto, 1988, p. 43.

- Silverman, A., Thompson, A.H., Sterynberg, A., Yukawa, Y., and Shingles T., Development of a dense phase fluidized bed Fischer-Tropsch Reactor, in *Fluidization V*, Ostergaard, K., and Sorensen, A., Eds., Engineering Foundation, New York, 1986, p. 441.
- Sit, S.P. and Grace, J.R., Effect of bubble interaction on interphase mass transfer in gas fluidized beds, *Chem. Eng. Sci.*, 36, 327, 1981.
- Sondreal, E.A., Benson, S.A., Hurley, J.P., Mann, M.D., Pavlish, J.H., Swanson, M.L., Weber, G.F., and Zygarlicke, C.J., Review of advances in combustion technology and biomass cofiring, *Fuel Process. Technol.*, 71, 7, 2001.
- Song, Y.-X., *Applying the Principles Learned from the Nature (Tian-Gong-Kai-Wu)*, Shanghai Chinese Book Bureau, Shanghai, 1959.
- Squires, A.M., Three bold exploiters of coal gasification: winkler, godel and porta, in *Fluidized beds Combustion and Applications*, Howard, J.R., Ed., Applied Science Publishers, London, 1983.
- Stewart, P.S.B. and Davidson, J.F., Slug flow in fluidized beds, *Powder Technol.*, 1, 61, 1967.
- Steward, F.R., Couturier, M.F., and Poolpol, S., Analysis for radiative heat transfer in a circulating fluidized bed, *Proceedings of the 13th International Conference on Fluid Bed Combustion*, Heinschel, K.J., Ed., ASME, New York, 1995, pp. 507–513.
- Sundaresan, R. and Kolar, A.K., Core heat transfer studies in circulating fluidized bed, *Powder Technol.*, 124, 138–151, 2002.
- Sutton, D., Kelleher, B., and Ross, J.R.H., Review of literature on catalysts for biomass gasification, *Fuel Process. Technol.*, 72, 155, 2001.
- Syncrude, Website of Syncrude, www.syncrude.ca, July 2004.
- Talman, J.A., Geier, R., and Reh, L., Development of a downer reactor for fluid catalytic cracking, *Chem. Eng. Sci.*, 54, 2123, 1999.
- Tasirin, S.M. and Geldart, D., Entrainment of FCC from fluidized beds, *Powder Technol.*, 95, 240, 1998.
- Teunou, E. and Poncelet, D., Batch and continuous fluid bed coating – review and state of the art, *J. Food Eng.*, 53, 325, 2002.
- Thompson, M.L., Bi, H.T., and Grace, J.R., A generalized bubbling/turbulent fluidized-bed reactor model, *Chem. Eng. Sci.*, 54, 2175, 1999.
- Tsukada, M. and Horio, M., Maximum heat transfer coefficient for an immersed body in a fluidized bed, *Ind. Eng. Chem. Res.*, 31, 1147–1156, 1992.
- van Deemter, J.J., Mixing patterns in large-scale fluidized beds, in *Fluidization*, Grace, J.R., and Matsen, J.M., Eds., Plenum, New York, 1980, p. 69.
- Varygin, N.N. and Martyushin, I.G., Calculation of the heat transfer surface in fluidized bed equipment, *Khim. Mashinostr.*, 5, 6–9, 1959 (in Russian).
- Visser, J., Van der Waals and other cohesive forces affecting powder fluidization, *Powder Technol.*, 58, 1, 1989.
- Wakao, N. and Kaguei, S., *Heat and Mass Transfer in Packed Beds*, Gordon and Breach Science Publishers, New York, 1982.
- Wang, X.S., Gibbs, B.M., Rhodes, M.J., and Geldart, D., Convection wall-to-suspension heat transfer in circulating fluidized bed risers, *AIChE J.*, 42, 2112–2117, 1996.
- Wang, Z. and Wei, F., Similarity of the particle concentration distribution between bubbling and turbulent fluidized beds, *Proceedings of the Symposium of the Chinese Society, of Particle Technology*, Beijing, 1997, p. 396.
- Wen, C.Y. and Chen, L.H., Fluidized bed freeboard phenomena: entrainment and elutriation, *AIChE J.*, 28, 117, 1982.
- Wen, C.Y. and Yu, Y.H., Generalized method for predicting the minimum fluidization velocity, *AIChE J.*, 12, 610, 1966.
- Werdermann, C.C. and Werther, J., Heat transfer in large-scale circulating fluidized bed combustors of different sizes, in *Circulating Fluidized Bed Technology*, Avidan, A.A., Ed., AIChE New York, 1994, pp. 428–435.
- Werther, J. The influence of the bed diameter on the hydrodynamics of fluidized beds, *AIChE Symp. Ser.*, 70, No. 141, 53, 1974.

- Werther, J. and Hartge, E-U., Elutriation and entrainment, in *Handbook of Fluidization and Fluid Particle Systems*, Yang, W-C., Ed., Marcel Dekker, New York, 2003, chap. 4.
- Wirth, K.-E., Heat transfer in circulating fluidized beds, *Chem. Eng. Sci.*, 50, 2137–2151, 1995.
- Winkler F., German Patent, 437, 970, 1922.
- Wu, R.L., Grace, J.R., and Lim, C.J., A model for heat transfer in circulating fluidized bed, *Chem. Eng. Sci.*, 45, 3389–3398, 1990.
- Wu, R.L., Grace, J.R., Lim, C.J., and Brereton, C.H.M., Suspension-to-surface heat-transfer in a circulating fluidized bed combustor, *AIChE J.*, 35, 1685–1691, 1991.
- Wu, R.L., Lim, C.J., Grace J.R., and Brereton, C.H.M., Instantaneous local heat transfer and hydrodynamics in a circulating fluidized bed, *Int. J. Heat Mass Transf.*, 34, 2019–2027, 1991.
- Wu, C.Z., Huang, H., Zheng, S.P., and Yin, X.L., An economic analysis of biomass gasification and power generation in China, *Bioresour. Technol.* 83, 65, 2002.
- Yang, W.-C., *Handbook of Fluidization and Fluid-Particle Systems*, Marcel Dekker, New York, 2003.
- Yang, X.L., Wild, G., and Euzen, J.P., Study of liquid retention in fixed-bed reactors with upward flow of gas and liquid, *Int. Chem. Eng.*, 33, 72, 1993.
- Yerushalmi, J., Applications of fluidized bed, in *Handbook of Multiphase Systems*, Hetson, G., Ed., Hemisphere Publishing Co., Washington, 1982, chap. 8.3.
- Yin, X. L., Wu, C.Z., Zheng, S.P., and Chen, Y., Design and operation of a CFB gasification and power generation system for rice husk, *Biomass Bioenergy*, 23, 181, 2002.
- Yu, Z-Q., Application collocation, *Adv. Chem. Eng.*, 20, 39, 1994.
- Zabrodsky, S.S., *Hydrodynamics and Heat Transfer in Fluidized Beds*, MIT Press, Cambridge, Massachusetts, 1966.
- Zabrodsky, S.S., Choice of design correlations for the estimation of the heat transfer coefficient in a high-temperature fluidized bed to an immersed body, *BSSR Ser. Fiz. Eng. Nauk.*, 4, pp. 193–107, 1974 (in Russian).
- Zenz, F.A. and Othmer, D.F., *Fluidization and Fluid-Particle Systems*, Reinhold Publishing Corp., New York, 1960.
- Zhang, J-P., Epstein, N., and Grace, J.R., Minimum fluidization velocities for gas–liquid–solid three-phase systems, *Powder Technol.*, 100, 113, 1998.
- Zhang, J-P., Epstein, N., Grace, J.R., and Zhu, J-X., Minimum liquid fluidization velocity of gas–liquid fluidized beds, *Trans. Inst. Chem. Eng.*, 73, 347, 1995.
- Zhukauskas, A.A., *Convective Heat Transfer in Heat Exchangers*, Nauka Publishing House, Moscow, 1990 (in Russian).
- Zhu J.-X., Yu, Z.-Q., Jin Y., Grace J.R., and Issangya, A., Cocurrent downflow circulating fluidized bed (downer) reactors – a state of the art review, *Can. J. Chem. Eng.*, 73, 662, 1995.
- Zhu, J.-X., Zheng, Y., Karamanov, D.G., and Bassi, A.S., (Gas-)liquid-solid circulating fluidized beds and their potential applications to bioreactor engineering, *Can. J. Chem. Eng.*, 78, 82, 2000.

6

Aerosol Flows

6.1	Introduction	6-1
6.2	General Dynamic Equation	6-2
	Internal Processes • External Processes • Moment Equations • Numerical Methods	
6.3	Coagulation and Agglomeration	6-9
	Coagulation • Agglomeration	
6.4	Gas-to-Particle Conversion	6-14
	Nucleation • Growth	
6.5	Single-Particle Motion – Deposition Mechanisms	6-29
	Gravitational Settling • Diffusion • Inertial Effects — Impaction • Motion in an Electric Field • Phoretic Effects	
6.6	Convective Transport-Deposition	6-37
	Convective Diffusion from Laminar Flow in Ducts • External Flows • Turbulent Flow • Convective-Gravitational Deposition in Ducts • Deposition in Filters • Respiratory Deposition	

Yannis Drossinos
European Commission
Joint Research Centre

Christos Housidas
Demokritos"National Centre
for Scientific Research

6.1 Introduction

An aerosol is a dispersion of small solid or liquid particles suspended in a gas, usually air. The term aerosol refers to both the particles and the suspending gas. Aerosol particle sizes range from $0.001 \mu\text{m}$ ($0.001 \mu\text{m} = 10^{-9} \text{ m} = 1 \text{ nm} = 10 \text{ \AA}$) to $100 \mu\text{m}$ (10^{-4} m), hence, the particle sizes of interest span over several orders of magnitude, ranging from almost macroscopic dimensions down to near molecular sizes. An aerosol is a two-phase system with a gas phase and a dispersed phase, called particulate phase, which may be solid or liquid. In aerosols, the particulate phase is diluted. Particles represent a very small fraction, $<0.0001\%$, of the total aerosol mass or volume. In most cases the two phases are one-way coupled: the hydrodynamics of the gas phase influences the behavior of the particulate phase, while the particulate phase exerts negligible influence on the hydrodynamics of the gas phase.

The technical term aerosol, has a much broader meaning than the popular term aerosol which refers to the spray of droplets released from a spray can. The technical term applies to a large variety of systems such as clouds, dust, fog, fume, haze, smog, smoke, sprays, and it may even include airborne biological material such as viruses, pollen, bacteria, fungi, etc. Particle size is the most important parameter characterizing an aerosol. In modern aerosol literature, particle size is specified by the particle diameter, d_p , most commonly expressed in micrometers and occasionally in nanometers. Based on their size, aerosol particles can be classified into a number of categories that, however, are not rigorously defined and are usually application-specific. In ambient aerosols, for instance, the classification of Whitby (1978) is often used: particles are divided into two main fractions, the *coarse* fraction ($d_p > 2 \mu\text{m}$) and the *fine* fraction ($d_p < 2 \mu\text{m}$).

The fine fraction is further subdivided into the *nucleation* mode ($d_p < 0.1 \mu\text{m}$) and the *accumulation* mode ($0.1 < d_p < 2 \mu\text{m}$). Yet, the above classification is not standard. Several aerosol scientists consider the diameter of $1 \mu\text{m}$ as the division line between the coarse and fine fractions. To characterize a generic aerosol particle with $d_p < 0.1 \mu\text{m}$, the term *ultrafine particle* is frequently employed. Nowadays, there is an increasing interest in *nanoparticle* applications. Pui and Chen (1997) recommended the convention $d_p < 50 \text{ nm}$ to define nanometer particles, but occasionally particles smaller than 100 nm ($0.1 \mu\text{m}$) are also considered as nanoparticles.

In this chapter, elements of aerosol dynamics and physics will be summarized and critically reviewed. Space limitations do not allow us to cover a number of important topics in aerosol physics, including experimental techniques (which, however, are covered in Section 14.6), aerosol optical properties, nanoparticle formation and synthesis (for a review see, e.g., Kruis et al., 1998), particle resuspension and bouncing (for a review see, e.g., Ziskind et al., 1995), whereas our treatment of electrochemical properties is limited.

6.2 General Dynamic Equation

The primary quantity of interest in aerosol flows is the particle size distribution and its variation in space and time. The size distribution is in general a multivariate distribution function that depends on position \mathbf{r} , time t , and on variables that describe particle morphology and chemical composition. If particle morphology is neglected and particles are assumed to be spherical, then a single-species particle is solely specified by its volume $v = \pi d_p^3/6$. Here, the choice of particle volume as an independent variable is preferred to the use of particle diameter (radius) because particle volume is conserved during coagulation. The single-component, continuous particle-size distribution for spherical particles is denoted by $n(v; \mathbf{r}, t)$, where $n(v; \mathbf{r}, t) dv$ is the number of particles per unit volume (number density) for particles with particle volume within the range v and $v+dv$ at location \mathbf{r} and time t . Its discrete version $n_k(\mathbf{r}, t)$ gives the number of particles per unit volume for particles with k subunits (also referred to as k -molecules or k -mers) at time t and location \mathbf{r} . It should be noted that with these definitions the continuous size distribution has dimensions of number of particles per volume squared, whereas the discrete size distribution has dimensions of number of particles per volume.

Particle morphology, and in general the description of nonspherical particles, requires the introduction of additional variables (shape descriptors) to account for particle shape. For example, Koch and Friedlander (1990) introduced surface area as a second independent variable to account for aggregate sintering, whereas Kostoglou and Konstandopoulos (2001) used the fractal dimension of colliding particles as additional variables in their analysis of agglomerate structure and coagulation. If the chemical composition of the aerosol particles is important, then an extended multispecies (multicomponent) size distribution function is required. In this chapter, we will concentrate on aerosol flows of spherical, single-species particles, although a few remarks about particle shape, chemical composition, and agglomerate structure will be made in the appropriate sections. The generalized l -species distribution function is discussed in, for example, Williams and Loyalka (1991).

The size distribution of an aerosol within a volume element may change due to processes that occur within it, referred to as *internal* processes, and due to processes that transport particles across the volume boundaries, *external* processes. Figure 6.1 presents a schematic diagram of aerosol processes that occur within an elemental volume. Internal processes include coagulation, agglomeration, fragmentation, and gas-to-particle conversion, a term that refers collectively to particle condensation or evaporation and nucleation, homogeneous or heterogeneous. Coagulation and agglomeration modify the size distribution without changing the mass concentration, whereas gas-to-particle conversion modifies the aerosol mass concentration. External processes include transport across the boundaries due to gas flow, diffusion, particle motion induced by temperature, concentration or other gradients in the gas, gravitational and other external forces. All the processes that modify the size distribution are described by a population balance equation that is known as the *General Dynamic Equation* (GDE). The solution of this nonlinear, integrodifferential equation for different initial and boundary conditions provides a complete description of the size distribution for arbitrary geometries and gas flows.

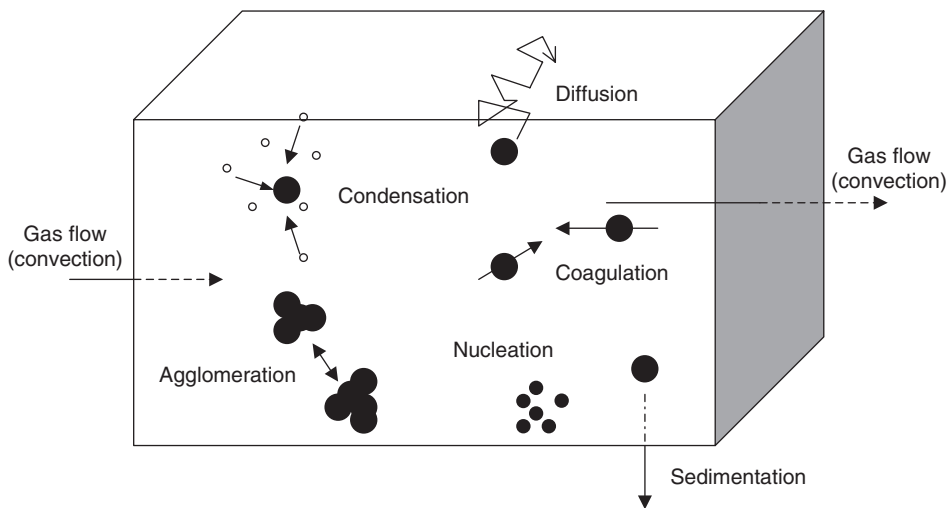


FIGURE 6.1 Schematic representation of aerosol processes (internal and external) within an elemental volume.

6.2.1 Internal Processes

Smoluchowski (1916) presented the first treatment of the effect of particle coagulation on the discrete particle size distribution. Although his derivation referred to hydrosols (a liquid colloidal suspension), the derivation and the final equation are equally applicable to aerosols. He considered a physical situation without spatial dependencies and particle gains or losses, but where particle coagulation occurred due to Brownian motion and motion induced by a laminar shear. Under the assumption that all particles are spherical, he showed that the dynamic equation for the discrete size spectrum $n_k(t)$ is

$$\frac{dn_k}{dt} = \frac{1}{2} \sum_{i+j=k} K(v_i, v_j) n_i n_j - n_k \sum_{i=1}^{\infty} K(v_i, v_k) n_i \quad (6.1)$$

where $K(v_i, v_j)$, expressed in dimensions of volume per unit time, is the collision frequency function between particles of volume v_i (i -mers) and v_j (j -mers). The first term on the right-hand side (RHS) of Eq. (6.1) is the rate (per unit volume) at which k -mers are formed from the collision of i -mers with $(k-i)$ -mers; the factor 1/2 avoids overcounting. The second term is the rate at which k -mers are removed by collisions with other particles that convert them into different-size particles. If the collision frequency function is independent of particle size and equal to K , and the aerosol is initially monodisperse of initial particle volume v_0 , the equation for the discrete-size distribution may be solved analytically to give

$$n_k(t) = \frac{N_{\infty}(0)}{(1 + t/\tau)^{k+1}} \left(\frac{t}{\tau} \right)^{k-1} \quad (6.2)$$

where $N_{\infty}(0)$ is the total number of particles per unit volume at $t = 0$ and $\tau = 2/[KN_{\infty}(0)]$ is the characteristic time scale. The total number concentration, $N_{\infty} = \sum_{i=1}^{\infty} n_i$, and the monomer concentration n_1 are found to decrease monotonically in time, whereas the average volume $v_{\text{ave}} = N_{\infty}(0) v_0 / N_{\infty}(t)$ increases linearly with time.

The inclusion of the other internal process, gas-to-particle conversion, by the addition of evaporative fluxes generalizes the Smoluchowski equation. Accordingly, the time-dependent equation for the discrete size distribution within an elemental volume fixed in space and in the absence of sources or sinks (Seinfeld and Pandis, 1998; Friedlander, 2000) becomes

$$\frac{dn_k}{dt} = \frac{1}{2} \sum_{i+j=k} K(v_i, v_j) n_i n_j - n_k \sum_{i=1}^{\infty} K(v_i, v_k) n_i + \alpha_{k+1} s_{k+1} n_{k+1} - \alpha_k s_k n_k \quad (6.3)$$

As before, the first two terms on the RHS are coagulation terms. The last two are the evaporative rates (per unit volume) under the assumption that evaporation occurs via single-molecule events. The evaporative flux from a k -mer is α_k , and the effective area for evaporation is the k -mer surface area s_k . Equation (6.3) includes condensation and evaporation terms that appear in a kinetic treatment of homogeneous nucleation. This is seen by rewriting the coagulation terms as a group of terms that describe collisions between larger particles ($i, j \neq 1$) and terms that describe single-molecule collisions with other particles, for example, terms such as $K(v_1, v_{k-1})n_1 n_{k-1}$. These single-molecule collision terms added to the evaporative fluxes give the particle current associated with homogeneous nucleation.

For particle volumes much larger than the molecular volume, it is convenient to replace the discrete distribution $n_k(t)$ by the continuous distribution $n(v; t)$. Then the population balance equation, expressed in a compact form, becomes

$$\frac{\partial n(v; t)}{\partial t} = \left. \frac{\partial n}{\partial t} \right|_{g-p} + \left. \frac{\partial n}{\partial t} \right|_{coag} \quad (6.4)$$

The gas-to-particle conversion term, denoted as g–p term, is occasionally rewritten in terms of the gradient of a particle current in a form suggestive of motion in particle-volume space. This formulation, according to which the current consists of two terms, renders the incorporation of condensation or evaporation and nucleation in the GDE easier (Friedlander, 2000). One term is proportional to a concentration gradient, and thus it is interpreted as cluster diffusion with a spatially dependent diffusion coefficient. This diffusion term, which is proportional to $\partial n / \partial v$ and which leads to a spread in particle space of an initially monodisperse distribution, is important for homogeneous nucleation. The other term represents cluster transport, or migration, under the influence of an external force. For the growth of large particles the diffusion term is not significant, since the concentration gradient is small, and migration dominates. Thus, it is customary to consider (see, also, Seinfeld and Pandis, 1998)

$$\left. \frac{\partial n}{\partial t} \right|_{g-p} = J_{nuc} \delta(v - v^*) - \frac{\partial}{\partial v} \left(n \frac{dv}{dt} \right) \quad (6.5)$$

where the first term J_{nuc} is the particle current due to homogeneously nucleated particles of critical size v^* [J_{nuc} is the nucleation rate per unit volume, see Eq. (6.51)] and the second term ndv/dt is the condensation current with the growth law dv/dt [see Eq. (6.77)]. The delta function in Eq. (6.5) is the Dirac delta function.

The second term on the RHS of Eq. (6.4) is the coagulation term, here written for a continuous size distribution

$$\left. \frac{\partial n}{\partial t} \right|_{coag} = \frac{1}{2} \int_0^v d\tilde{v} K(\tilde{v}, v - \tilde{v}) n(\tilde{v}) n(v - \tilde{v}) - n(v) \int_0^\infty d\tilde{v} K(v, \tilde{v}) n(\tilde{v}) \quad (6.6)$$

As mentioned earlier, the first term on the RHS of Eq. (6.6) denotes the formation of particles of size v from the collision of particles $v - \tilde{v}$ and \tilde{v} and second the loss of particles of size v through collisions with other particles. Note that the lower limit in the coagulation integrals has been set to 0 instead of the size of the smallest stable (critical) cluster v^* . This approximation renders the evaluation of the integrals easier. It does not cause any significant problems since the initial distribution may be taken to be zero up to the critical size and particles smaller than the critical size are not generated in time. Equation (6.6) is reminiscent of the gain–loss master equation of stochastic theory since $n(v; r, t)$ is a probability distribution function. However, its nonlinearity, which arises from particle collisions, gives it remarkable properties that are absent from the linear master equation. In fact, the nonlinearity and gain–loss nature of GDE render Eq. (6.6) similar to the molecular Boltzmann equation.

6.2.2 External Processes

In the presence of a gas flow, the GDE for a continuous size distribution becomes (Friedlander, 2000)

$$\frac{\partial n}{\partial t} + \nabla \cdot (n \mathbf{v}_p) = \frac{\partial n}{\partial t} \Big|_{g-p} + \frac{\partial n}{\partial t} \Big|_{coag} \quad (6.7)$$

where \mathbf{v}_p is the average particle velocity and $n(v; \mathbf{r}, t)dv$ the number density of particles with particle volume in the range v to $v + dv$. The particle flux density $J_p = n\mathbf{v}_p$ depends on the gas flow velocity and external body forces. The LHS of Eq. (6.7) describes changes of the particle size distribution due to external processes and the RHS changes due to internal processes.

In the aerosol physics literature, it is frequently assumed that transport mechanisms act independently of each other, an assumption that usually leads to fairly good results. The average particle velocity, as obtained from the sum of the various fluxes, becomes

$$\mathbf{v}_p = \mathbf{u} - \mathfrak{D} \nabla \ln n + \mathbf{v}^{\text{ext}} \quad (6.8)$$

where \mathbf{u} is the carrier gas velocity, \mathfrak{D} the Brownian diffusion coefficient [see Eq. (6.103)], and \mathbf{v}^{ext} the sum of all other transport velocities, for example, thermophoretic, diffusiophoretic, photophoretic, or other velocities induced by external forces (gravitational and electrostatic). Each of these terms will be discussed in the appropriate sections. The relation of \mathbf{v}^{ext} to the associated external force is given by Eq. (6.105). The GDE, then, takes the form

$$\frac{\partial n(v; \mathbf{r}, t)}{\partial t} + \nabla \cdot (n \mathbf{u}) = \nabla \cdot \mathfrak{D} \nabla n + \frac{\partial n}{\partial t} \Big|_{g-p} + \frac{\partial n}{\partial t} \Big|_{coag} - \nabla \cdot (n \mathbf{v}^{\text{ext}}) \quad (6.9)$$

If the coagulation and g-p terms are neglected, and in the absence of external forces, Eq. (6.9) becomes the usual convective diffusion equation

$$\frac{\partial n}{\partial t} + \nabla \cdot (n \mathbf{u}) = \nabla \cdot \mathfrak{D} \nabla n \quad (6.10)$$

whose solutions for different geometries in laminar flow are discussed in Section 6.6.1. Inspection of Eq. (6.8) shows that the effect of particle inertia has been neglected. Thus, an assumption inherent in the usual convective diffusion equation is neglect of inertial particle transport (and, of course, of all internal processes) and the absence of external forces.

Inertial transport is best described in terms of a Lagrangian description, where the particle equations of motions are solved, and not in terms of the Eulerian description implicit in the usual formulation of the population balance equation where processes in a fixed elemental volume are analyzed. The proper incorporation of inertial transport in the Eulerian description of Eq. (6.7) requires an approach similar to that presented in the two-fluid modeling chapters of this Handbook (see, e.g., [Chapter 13](#)) and the solution of the coupled two-fluid equations for mass, momentum, and energy conservation (Reeks, 1991). The simultaneous description of inertial and diffusional transport is an active area of current research; only a brief summary will be presented in this chapter. In particular, developments to decouple the mass conservation equation from the momentum equation by performing a low Stokes number expansion of the (average) particle velocity will be summarized.

In a two-fluid approach to aerosol transport the average particle velocity \mathbf{v}_p is obtained from the average particle momentum equation, as is common in multi-fluid modeling approaches to multiphase flows and is described elsewhere in the Handbook. If the aerosol particles are considered as a dispersed phase within a continuous phase, the average momentum equation for the dispersed (particulate) phase may be formally written as (Fernández de la Mora and Rosner, 1982; Konstandopoulos, 1990)

$$\frac{\partial \mathbf{v}_p}{\partial t} + (\mathbf{v}_p \cdot \nabla) \mathbf{v}_p = \beta_V (\mathbf{u} - \mathbf{v}_p) + \frac{1}{n} \nabla \cdot \overleftrightarrow{\Pi}_p + \beta_V \sum_i \mathbf{v}_i^{\text{ext}} \quad (6.11)$$

where the Stokes drag has been used, $\vec{\Pi}_p$ is the particle stress tensor, and the external forces per unit particle mass are expressed in terms of β_V , the inverse particle relaxation time, as specified in Eq. (6.105) [$\beta_V = 1/\tau_V$, where τ_V is the particle relaxation time, see Eq. (6.104)]. In the limit of small particle relaxation times ($\beta_V \rightarrow \infty$), a diffusive description of the particle flux becomes appropriate (as discussed in other chapters in the Handbook). Different approximations for the particle stress tensor and the inertial acceleration term [LHS of Eq. (6.11)] lead to different forms of the GDE and the corresponding convective diffusion equation.

Ramshaw (1979) proposed a phenomenological theory of the motion of Brownian particles in a flowing, nonisothermal, incompressible fluid that leads to a modification of the particle velocity given in Eq. (6.8). The derivation clarifies the assumptions and approximations inherent in the usual convective diffusion equation, or, equivalently those related to the linear addition of the various particle currents, as in Eq. (6.8). The theory relies on neglecting the particle viscous stresses and assuming that the dispersed (particulate) phase behaves as an ideal gas. The approximation is summarized by $\vec{\Pi}_p = -\vec{I}p_p$, where \vec{I} is the identity tensor and p_p the particle phase partial pressure (this approximation was examined in Ramshaw, 1981). The approximate expression for the particle stress tensor, coupled to the assumption that the particle phase behaves as an ideal gas

$$p_p(\mathbf{r}, t) = k_B n(\mathbf{r}, t) T(\mathbf{r}, t) \quad (6.12)$$

with k_B Boltzmann's constant, leads to the following expression for the particle flux:

$$\mathbf{J}_p = n \mathbf{u} - \mathfrak{D} \nabla n - \mathfrak{D}_{th} \nabla \ln T \quad (6.13)$$

The corresponding transport coefficients are the Brownian diffusion coefficient \mathfrak{D} [see Eq. (6.103)] and the thermal diffusion coefficient \mathfrak{D}_{th} , which expressed in terms of the Schmidt number Sc_p [see Eq. (6.102)] and the thermophoretic coefficient K_{th} [see Eqs. (6.111) and (6.114)] becomes

$$\mathfrak{D}_{th} = n \mathfrak{D} (1 + K_{th} Sc_p) \quad (6.14)$$

As discussed in Section 6.5.2, and shown in Table 6.1, the particle Schmidt number is much greater than unity. Therefore, for typical aerosol particles (limit of large Sc_p), the thermophoretic term dominates the expression

TABLE 6.1 Aerosol Particle Parameters: Spherical Particles of Standard Density (1000 kg/m³) in Air at 101 kPa (1atm) and 293 K (20°C)

Particle Diameter d_p (μm)	Slip Correction C_c	Settling Velocity V_s (m/sec)	Diffusion Coefficient \mathfrak{D} (m ² /sec)	Schmidt Number Sc_p	Relaxation Time τ_V (sec)
0.001	224.3	6.75×10^{-9}	5.32×10^{-6}	2.83	6.89×10^{-10}
0.002	112.5	1.35×10^{-8}	1.33×10^{-6}	1.13×10^1	1.38×10^{-9}
0.005	45.34	3.41×10^{-8}	2.15×10^{-7}	7.00×10^1	3.48×10^{-9}
0.01	22.98	6.92×10^{-8}	5.45×10^{-8}	2.76×10^2	7.05×10^{-9}
0.02	11.80	1.42×10^{-7}	1.40×10^{-8}	1.07×10^3	1.45×10^{-8}
0.05	5.120	3.85×10^{-7}	2.43×10^{-9}	6.19×10^3	3.93×10^{-8}
0.1	2.928	8.82×10^{-7}	6.94×10^{-10}	2.17×10^4	8.99×10^{-8}
0.2	1.878	2.26×10^{-6}	2.23×10^{-10}	6.74×10^4	2.31×10^{-7}
0.5	1.316	9.91×10^{-6}	6.24×10^{-11}	2.41×10^5	1.01×10^{-6}
1.0	1.155	3.48×10^{-5}	2.74×10^{-11}	5.49×10^5	3.54×10^{-6}
2.0	1.077	1.30×10^{-4}	1.28×10^{-11}	1.18×10^6	1.32×10^{-5}
5.0	1.031	7.76×10^{-4}	4.89×10^{-12}	3.08×10^6	7.91×10^{-5}
10.0	1.015	3.06×10^{-3}	2.41×10^{-12}	6.24×10^6	3.12×10^{-4}
20.0	1.008	1.21×10^{-2}	1.19×10^{-12}	1.26×10^7	1.24×10^{-3}
50.0	1.003	7.55×10^{-2}	4.76×10^{-13}	3.16×10^7	7.70×10^{-3}
100.0	1.002	2.49×10^{-1}	2.37×10^{-13}	6.35×10^7	3.07×10^{-2}

for the thermal diffusion coefficient. Hence, in the limit of large particle Schmidt numbers, the last term of Eq. (6.13) becomes $-nK_{\text{th}}v_g \nabla \ln T$, the usual flux associated with thermophoresis [see Eq. (6.11)].

Forced and pressure diffusions are absent in Eq. (6.13) since external forces (e.g., gravitational or electromagnetic) and imposed pressure gradients (e.g., centrifugation) were not considered. Their contribution to the total mass flux is discussed by Ramshaw (1979). Thus, if these contributions are neglected, the total flux relative to the carrier fluid becomes the sum of concentration and thermal diffusion.

A comparison of Eq. (6.13), which was derived in the small-particle limit, with Eq. (6.11) shows that the inertial acceleration term has been neglected in the small-particle limit. Fernández de la Mora and Rosner (1982) considered explicitly the effect of inertia on Brownian diffusional transport in isothermal aerosol flows under steady-state conditions. Following arguments similar to those summarized earlier, in particular the approximate expression for the particle stress tensor, they obtained a first-order correction to the particle velocity field due to particle inertia. They performed a low Stokes number expansion, see Eq. (6.107), (a low τ_v expansion) of the average momentum equation to obtain

$$\mathbf{v}_p = \mathbf{u} - \mathfrak{D} \nabla \ln n - \tau_v (\mathbf{u} \cdot \nabla) \mathbf{u} + O(\tau_v^2) \quad (6.15)$$

This relation shows that the particle velocity field of inertial particles is compressible, even for an incompressible carrier gas flow and in the absence of diffusion. Equation (6.15) leads to a generalized form of Eq. (6.9) (in the absence of external forces),

$$\frac{\partial n}{\partial t} + \nabla \cdot (n \mathbf{u}) - \tau_v \nabla \cdot [n(\mathbf{u} \cdot \nabla) \mathbf{u}] = \nabla \cdot \mathfrak{D} \nabla n + \left. \frac{\partial n}{\partial t} \right|_{g-p} + \left. \frac{\partial n}{\partial t} \right|_{coag} \quad (6.16)$$

that incorporates in an Eulerian description effects due to particle inertia to first order in the particle relaxation time. The coupled calculation of diffusion and inertia in an Eulerian description is important because these two mechanisms act parallel in many aerosol processes, for example, in filtration and sampling. A Lagrangian description is much more computationally intensive due to the stochastic nature of particulate diffusion.

The GDE in turbulent flow has not received the attention it deserves, although in many cases encountered in practice, for example in atmospheric dispersion, the underlying flow is turbulent. It will not be discussed here, but the interested reader is referred to Friedlander (2000), where the full GDE for turbulent flow is presented. It suffices to mention that the starting point of the derivation is the Reynolds assumption. Specifically, if nucleation is neglected, the fluid velocity, the size distribution, and the growth law are each written as the sum of a mean and a fluctuating component. As a result of time averaging several new terms appear in the GDE, including a fluctuating growth term and contributions to coagulation from the fluctuating concentrations.

6.2.3 Moment Equations

The GDE may be appropriately integrated to obtain differential equations for moments of the particle size distribution. The moments of the size distribution are defined as

$$M_j(\mathbf{r}, t) = \int_0^\infty dv v^j n(v; \mathbf{r}, t) \quad (6.17)$$

where we have extended the lower limit to zero, an approximation valid for very small molecular or detection volumes. The zeroth moment of the distribution is of particular interest, since it gives the total number concentration $N(\mathbf{r}, t)$,

$$N(\mathbf{r}, t) = \int_0^\infty dv n(v; \mathbf{r}, t) \quad (6.18)$$

Moment equations may be obtained by performing moment averages of the GDE, for example, of Eqs. (6.7) or (6.9). For spherical particles the moments may also be defined in terms of particle diameters:

$$M_j(\mathbf{r}, t) = \int_0^\infty d(d_p) d_p^j n(d_p; \mathbf{r}, t) \quad (6.19)$$

The most important moments are the total number concentration, $N(\mathbf{r}, t) = M_0$, the average particle diameter, $\bar{d}_p = M_1(\mathbf{r}, t)/M_0(\mathbf{r}, t)$, the average surface area per particle, $\bar{S} = \pi M_2(\mathbf{r}, t)/M_0(\mathbf{r}, t)$, and the average volume per particle, $\bar{V} = \pi M_3(\mathbf{r}, t)/[6M_0(\mathbf{r}, t)]$. If particle density is independent of size, the third moment is proportional to the mass concentration of the particulate phase.

6.2.4 Numerical Methods

Most numerical techniques developed to solve the GDE neglect spatial inhomogeneities by assuming that the aerosol is well mixed. Hence, the numerical methods concentrate on the numerical solution of Eq. (6.3) or, more often, its continuous version, Eq. (6.4) coupled to Eqs. (6.5) and (6.6). Since the evaluation of the particle size distribution is at the core of aerosol physics calculations, the numerical methods are usually categorized in terms of the functional representation of the size distribution. They may be divided into discrete methods, modal methods, and sectional (group) methods (Seigneur et al., 1986). These methods may be combined: for example, sectional methods have been combined with discrete methods to optimize the description of the distribution at small particle sizes (Wu and Flagan, 1988).

Whitby and McMurray (1997) presented a brief summary of the available numerical aerosol modeling techniques, and a review of modal methods. The modal methods, which lead to the numerical solution of the moment equations and thus are also called moment methods, are appropriate when the characteristic shape of the size distribution remains unaltered during the simulation period. The GDE is appropriately integrated to obtain integrodifferential equations for the moments of the particle size distribution. These coupled, due to the coagulation kernel and the growth law, equations are usually decoupled by postulating a functional form for the unknown distribution function. The usual choices for the distribution function are lognormal (see, e.g., Pratsinis, 1998), gamma, or multimodal lognormal (see, e.g., Wilck and Stratmann, 1997). In the case of a lognormal distribution, the independent variables reduce to the total particle number, the geometric standard deviation, and the geometric mean. The modal methods, thus, convert the solution of the GDE into the numerical solution of differential equations for these moments.

A recent development in modal methods that avoids the specification of a distribution function was made by McGraw and coworkers (McGraw, 1997; McGraw and Wright, 2003). The fundamental problem with moment methods is the closure of the evolution equations. McGraw (1997) addressed this issue by introducing a quadrature-based closure technique, a technique that is applicable to arbitrary growth laws and coagulation kernels. In essence, this method replaces the exact closure by an approximate but less restrictive closure condition.

According to the sectional method, the particle spectrum is discretized and divided into a number of sections (particle-size bins), thereby approximating the size distribution by a histogram. The GDE is then solved for each section. This method does not require *a priori* choices of the functional form of the size distribution, it handles coagulation easily, but it simulates condensation with difficulty. In the stationary grid method (Sutugin and Fuchs, 1970; Gelbard et al., 1980; Raes and Janssens, 1986; Jokiniemi et al., 1994), where the particle bins remain fixed, condensation is modeled by transferring particle concentration from one size bin to the other. In the moving-grid method (Gelbard, 1990), the bins are allowed to move along the particle size axis to allow for condensation. Whereas numerical diffusion is an inherent problem of the stationary grid method (Zhang et al., 1999), the moving-grid method eliminates discretization errors associated with condensation or evaporation. However, in the moving-grid method, the implementation of nucleation and coagulation is not as transparent as in the stationary grid method since situations may occur where there are no sections in the particle size of interest, for example at the size of nucleating particles. Furthermore, the moving-grid method may become problematic in spatially multidimensional problems.

The Monte Carlo method, a powerful numerical technique for the evaluation of multidimensional integrals, has been used to solve population balance equations. For example, Kostoglou and Konstandopoulos (2001) used it to study the evolution of fractal aggregates. Coagulation of nonspherical particles has also been studied with a sectional method (Jeong and Choi, 2001).

6.3 Coagulation and Agglomeration

Aerosol particles suspended in a fluid collide due to their relative motion induced by Brownian motion, by fluid inhomogeneities (as those generated by turbulence or shear), or by motion caused by external forces (gravitational, electrostatic, van der Waals, etc.). Concentration or temperature gradients in the gas induce relative motion but these effects are considered secondary. When the particles collide they may agglomerate, namely, the colliding primary particles retain their identity and shape, or coagulate, i.e., the colliding particles fuse together and lose their identity.

6.3.1 Coagulation

For a discrete particle spectrum, the collision frequency function, or coagulation kernel, $K(v_i, v_j)$, which has dimensions of volume per unit time, is defined as follows:

$$N_{ij} = K(v_i, v_j) n_i n_j \quad (6.20)$$

where N_{ij} is the number of particle collision occurring per unit time per unit volume between particles with volumes v_i and v_j and concentrations n_i, n_j . The collision frequency function depends on particle and fluid properties, with a dependence that is a function of the mechanisms that force the particles to collide. The particle concentrations in Eq. (6.20) are the local, instantaneous values: in the aerosol literature, these local values are frequently approximated by average values (well-mixed aerosol assumption), thereby introducing an error that is difficult to quantify. The effect of spatial inhomogeneities on Brownian coagulation kinetics has been addressed by Kasper (1984).

The kernels presented here refer to aerosol particles that are perfect, rigid spheres undergoing instantaneous collisions that yield spheres. The kernels do not include the effect of the modification of the local fluid flow as the particles approach each other. Since these local flows are expected to decrease the collision efficiency, due to an increased resistance as the particles move closer, the kernels provide an upper bound to the collision efficiency. Alam (1987) proposed an analytical expression for the effect of the fluid, based on the concept that the fluid resists being squeezed out from the region between the approaching particles.

We describe only the most commonly used coagulation kernels, neglecting less frequently encountered kernels, as, for example, the acoustic (or ultrasonic) coagulation kernel.

6.3.1.1 Brownian

The most extensively studied, both experimentally and theoretically, coagulation process is the one due to Brownian motion. This process, initially studied by Smoluchowski (1916) and occasionally referred to as thermal coagulation, is important for particles smaller than 1 μm . The collision frequency function in the continuum regime (particle diameter much larger than the gas mean free path) is

$$K_B(v_i, v_j) = 2\pi(d_i + d_j)(\mathcal{D}_i + \mathcal{D}_j) = \frac{2k_B T}{3\mu_g} \left[\frac{C_c(v_i)}{v_i^{1/3}} + \frac{C_c(v_j)}{v_j^{1/3}} \right] (v_i^{1/3} + v_j^{1/3}) \quad (6.21)$$

where d_i and d_j are the diameters of the colliding particles. The second equality arises from the expression for the Brownian diffusion coefficient [Eq. (6.103)] that incorporates the slip correction factor C_c [Eq. (6.91)]. The derivation of the Brownian kernel is based on the calculation of the diffusional flux toward a sphere assuming that the particle diffusion coefficients do not change as the particles approach each other. In the free molecular regime (particles smaller than the mean free path of the gas), the collision frequency function is obtained from the kinetic theory of gases, assuming that particle collisions are collisions of rigid elastic spheres (Friedlander, 2000):

$$K_B(v_i, v_j) = \left(\frac{3}{4\pi} \right)^{1/6} \left(\frac{6k_B T}{\rho_p} \right)^{1/2} (v_i^{-1} + v_j^{-1})^{1/2} (v_i^{1/3} + v_j^{1/3})^2 \quad (6.22)$$

where ρ_p is the particle mass density. Fuchs (1964) proposed an interpolation formula for the collision frequency function of spherical particles valid over the entire particle spectrum

$$K_B(d_i, d_j) = 2\pi(d_i + d_j)(\mathfrak{D}_i + \mathfrak{D}_j) \left[\frac{d_i + d_j}{d_i + d_j + 2(g_i^2 + g_j^2)^{1/2}} + \frac{8(\mathfrak{D}_i + \mathfrak{D}_j)}{(d_i + d_j)(\bar{c}_i^2 + \bar{c}_j^2)^{1/2}} \right]^{-1} \quad (6.23)$$

where the mean particle velocity is $\bar{c}_i = (8k_B T / \pi m_i)^{1/2}$ with $m_i = \rho_p v_i$ the particle mass, and g_i is the so-called Fuch's length

$$g_i = \frac{1}{3d_i l_i} \left[(d_i + l_i)^3 - (d_i^2 + l_i^2)^{3/2} \right] - d_i \quad (6.24)$$

with $l_i = 8\mathfrak{D}_i / (\pi \bar{c}_i)$ being the mean free path of the aerosol particle. The particle diffusion coefficients in Eq. (6.23) are obtained from the Stokes–Einstein expression, but they often include the Cunningham factor to provide an additional correction for the transition from the slip to the continuum regime [see Eq. (6.103) and subsequent discussion]. The interpolation formula was derived under the assumption that every collision results in coagulation. Fuchs (1964) also discusses the effects of relaxing this assumption in terms of the collision efficiency α (fraction of collisions that result in coagulation).

6.3.1.2 Brownian in an External Force Field

The collision kernel is modified when the colliding particles exert a force on each other. For spherical particles interacting via a conservative force field, $\mathbf{F} = -\nabla\Phi$, where Φ is the interaction potential, the steady-state coagulation flow of particles (number of collisions per unit time per unit volume) is modified by a correction factor W as follows:

$$N_{ij} = \frac{1}{W} K_B(v_i, v_j) n_i n_j \quad (6.25)$$

The correction factor is related to the interaction potential. Analysis of the diffusional flux toward a spherical particle leads to the following expression:

$$W = \frac{1}{2} (d_i + d_j) \int_{0.5(d_i + d_j)}^{\infty} \frac{dx}{x^2} \exp \left[\frac{\Phi(x)}{k_B T} \right] \quad (6.26)$$

Thus, for an attractive interaction potential (Φ negative) the collision frequency increases, whereas for a repulsive potential the collision frequency decreases.

We consider specific applications of Eq. (6.26) in two cases: van der Waals forces, which are always present, and Coulomb forces between charged particles. The van der Waals interaction potential between two spheres of different radii is a complicated function of the separation distance and particle radii, and depends on Hamaker's constant A (see, e.g., Israelachvili, 1992). For two spheres of equal radius a_p separated by a distance R (distance between centers of the spheres), the interaction potential simplifies to

$$\Phi = -\frac{A}{6} \left[2 \left(\frac{a_p}{R} \right)^2 + \frac{2a_p^2}{R^2 - 4a_p^2} + \ln \left(1 - \frac{4a_p^2}{R^2} \right) \right] \quad (6.27)$$

For electrically charged particles, neglecting induction forces, the Coulomb potential between two particles of radii a_i and a_j leads to a correction factor that may be analytically calculated to give

$$W = \frac{1}{y} (e^y - 1) \quad (6.28)$$

where the dimensionless parameter y is

$$y = \frac{z_i z_j e^2}{\epsilon k_B T (a_i + a_j)} \quad (6.29)$$

with ϵ the dielectric constant of the medium and z_i the number of charges on particle i . Thus, for uncharged particles the correction factor vanishes, whereas for unipolar particles the correction factor is positive and greater than unity, resulting in collision rates lower than those for uncharged particles. The reverse is true for bipolar particles.

6.3.1.3 Laminar Shear

Particles in a laminar shear collide due to their relative motion induced by the gas flow spatial inhomogeneity, and thus they may coagulate. Smoluchoski (1916) showed that in a uniform shear flow with a velocity gradient $\gamma = du/dy$, in the absence of Brownian motion, the collision frequency function becomes

$$K_{LS}(d_i, d_j) = \frac{\gamma}{6} (d_i + d_j)^3 \quad (6.30)$$

As remarked earlier, this expression is approximate in that the approaching, interacting particles influence the fluid flow and the fluid streamlines around the particles are not rectilinear, but they curve around it. This effect has not been taken into account in Eq. (6.30): it can be considered by integrating the associated equations of motion in the presence of the shear (or other inhomogeneities or external forces).

6.3.1.4 Gravitational Settling

In a polydisperse aerosol in a gravitational field heavier particles move faster than the lighter ones, catching up with them and eventually colliding. This process is significant in the atmosphere where falling raindrops may scavenge aerosol particles. The coagulation kernel becomes the product of the effective target area times the relative particle velocity to give

$$K_G(d_i, d_j) = \frac{\pi}{4} (d_i + d_j)^2 |V_{s,i} - V_{s,j}| \quad (6.31)$$

where the settling velocities are denoted by $V_{s,i}$ [see Eq. (6.95)]. For spherical particles of the same material density ρ_p , the coagulation kernel may be expressed in terms of particle volume to become

$$K_G(v_i, v_j) = \frac{\rho_p g}{6\mu_g} \left(\frac{3}{4\pi} \right)^{1/3} (v_i^{2/3} + v_j^{2/3}) |v_i^{2/3} C_c(v_i) - v_j^{2/3} C_c(v_j)| \quad (6.32)$$

where $C_c(v_i)$, the Cunningham factor, accounts for corrections in the slip regime [see Eq. (6.91) and Section 1.4]. The standard derivation (see, e.g., Williams and Loyalka, 1991) neglects interparticle forces, which may lead to particles not colliding even though they would have done so in a purely geometrical calculation. Gravitational coagulation may be neglected for submicrometer particles, but it becomes significant for particle diameters larger than a few micrometers.

6.3.1.5 Turbulent Coagulation

Particles in a turbulent flow may collide due to inertial effects (described in Section 6.6.3) and instantaneous fluid-flow inhomogeneities, i.e., local velocity gradients. The first mechanism is due to the large (material) density differences between the fluid and the particle, whereas the second is always present. Saffman and Turner (1956) analyzed both mechanisms. Particles distributed uniformly in a turbulent fluid collide as a result of small-scale shear flows over distances smaller than the Kolmogorov microscale. Thus, the analysis also requires the particle concentrations to be relatively high so that the distance between colliding particles is less than the Kolmogorov microscale. In general, turbulent shear coagulation is similar to coagulation induced by laminar shear. Dimensional analysis arguments lead to the following result for the coagulation kernel due to turbulent shear

$$K_{TS}(d_i, d_j) = \frac{1.3}{8} \left(\frac{\epsilon_d}{\nu_g} \right)^{1/2} (d_i + d_j)^3 \quad (6.33)$$

where ε_d is the energy dissipation rate per unit mass of the fluid. Note the similar functional dependence of the turbulent coagulation kernel and the laminar shear kernel [Eq. (6.30)] on particle diameter and on the local shear rate (which in isotropic turbulent flow has been related to the energy dissipation rate and the fluid kinematic viscosity).

Levich (1962) presented an alternative derivation of the turbulent coagulation kernel using concepts of classical diffusion. In the limit of dominant Brownian motion over turbulent motion, the expression he derived reproduces the classical Brownian coagulation kernel [Eq. (6.21)], whereas in the other limit it reproduces the Saffman and Turner result except that the numerical prefactor 1.3 [actually the prefactor in Eq. (6.33) is $(8\pi/16)^{1/2}$] becomes 5.65.

Saffman and Turner (1956) also considered coagulation due to inertial effects. They used the particle equations of motion to describe relative particle motion and statistical arguments for isotropic turbulent flow in the high Reynolds number limit to obtain the collision frequency kernel

$$K_{TI}(d_i, d_j) = \frac{5.7}{4} (d_i + d_j)^2 \left| \frac{1}{\beta_{V,i}} - \frac{1}{\beta_{V,j}} \right| \frac{\varepsilon_d^{3/4}}{v_g^{1/4}} \quad (6.34)$$

where $\pi(d_i + d_j)^2/4$ is the collision cross-section. Williams and Loyalka (1991) summarized results for the coagulation kernels in the turbulent flow. They also presented a generalized theory of turbulent coagulation that incorporates in a single formula the combined effects of Brownian diffusion, turbulent diffusion, and turbulent inertial motion. Their generalized result reproduces the formulae summarized in this section [also with slightly different numerical prefactors, for example, the numerical prefactor 5.7 in Eq. (6.34) becomes 6.2] and provides an approximate expression for the combined effects of Brownian diffusion and gravitational settling. Such derivations are important to estimate inaccuracies inherent in linear (or quadratic) additions of coagulation kernels (see Section 6.3.1.6).

Recent theoretical developments (Reeks, 2001) suggest that the turbulent agglomeration kernels summarized in Eqs. (6.33) and (6.34) neglect the effect of coherent turbulent structures. Since these effects were shown to have a nonnegligible effect on single-particle motion in such flows, it was argued that they might influence significantly coagulation in turbulent flows.

6.3.1.6 Kernel Addition

Some of the mechanisms responsible for coagulation may act simultaneously, for example, Brownian and gravitational coagulation, or gravitational and turbulent. A linear addition of Brownian with turbulent or gravitational kernels is frequently made, since particle coagulation may occur in regimes where one of them is significant and the others are not. This is not the case for the gravitational and turbulent kernels that have similar functional forms, and may be of the same order of magnitude. An alternative, and more frequently used, approximation based on the work of Saffman and Turner (1956) is to add them quadratically as follows:

$$K_{\text{total}}(v_i, v_j) = K_B(v_i, v_j) + [K_G^2(v_i, v_j) + K_{TS}^2(v_i, v_j) + K_{TI}^2(v_i, v_j)]^{1/2} \quad (6.35)$$

The precise nature of this approximation, or the magnitude of the error introduced in Eq. (6.35), is not quantitative at the moment. Williams and Loyalka (1991) discuss a number of cases where two coagulation mechanisms act simultaneously (e.g., Brownian and shear coagulation) and provide analytical expressions for the combined kernels.

6.3.2 Agglomeration

The previous analysis of colliding particles considered that two colliding spherical particles would coagulate to form larger particles. However, experiments and numerical simulations show that in some cases (e.g., combustion aerosols) the colliding particles tend to form agglomerates composed of smaller, primary particles (Colbeck, 1998). The size of the primary particles ranges from nanometers

to approximately $0.1 \mu\text{m}$, and the resulting agglomerate structures vary from $0.1 \mu\text{m}$ to several micrometers. For simplicity, and lack of theoretical tools, it is frequently assumed that the primary particles are monodisperse, although it is known that primary combustion particles are almost always polydisperse.

The most compact measure of an agglomerate structure is its fractal (Hausdorff) dimension d_f that relates the number of primary particles N_p to R_g , the radius of gyration of the cluster:

$$N_p \sim R_g^{d_f} \quad (6.36)$$

This relation holds in a statistical sense, i.e., after averaging over many aggregates, and it requires self-similarity, a property satisfied approximately over a limited size range by most experimentally studied agglomerates. The fractal dimension is a measure of the degree to which a structure fills physical space: for example, a compact three-dimensional structure has $d_f = 3$ and a line has $d_f = 1$. The value of the experimentally observed fractal dimension depends on the agglomeration process. Note, however, that shapes of particles may not be always self-similar and may not be well characterized by a single-fractal dimension (Xie et al., 1994).

The formation of agglomerate structures has been the subject of extensive numerical and theoretical work. Numerical simulations predict different fractal exponents depending on the nature of the colliding objects (e.g., particles or clusters colliding with clusters), the agglomeration model used (ballistic, diffusion-limited and reaction-limited), or the spatial dimension (two or three dimensions). Three-dimensional simulations of cluster-cluster growth by diffusion-limited aggregation give $d_f \sim 1.80$, ballistic-limited cluster-cluster growth gives $d_f \sim 2.50$, and particle-cluster growth gives $d_f \sim 2.50$ (cf. Table 1.6 in Colbeck, 1998). Alternative measures of aggregate morphology include the fractal structure of the boundary of the agglomerate, obtained from a two-dimensional projection of the particle, and mass- or density-based fractal dimensions.

Experimental techniques developed to measure fractal dimensions of agglomerates are usually based on electron or optical microscopy, or on scattering of visible or ultraviolet radiation (Colbeck, 1998). An alternative technique was proposed by Colbeck et al. (1989), who determined the fractal dimension of smoke aggregates by measuring particle terminal velocities and the electric field strengths required to balance the gravitational force. They obtained $d_f = 1.9$, a value at the high limit of the range 1.7 to 1.9 predicted by model simulations of cluster-cluster, diffusion-limited aggregation.

Most theoretical work on the dynamics of agglomerate size distributions concerns the effect of Brownian motion on agglomeration. In fact, the Smoluchowski derivation has been extended to describe the collision kernel for power-law aggregates, i.e., aggregates that have fractal-like structure. There is an important difference between the approach based on the Smoluchowski equation and numerical simulations: in the latter the fractal dimension of the aggregate is directly obtained from the simulation whereas in the former the fractal dimension is an input. Arguments similar to those that led to the Brownian coagulation kernel give the following kernel for aggregates obeying a power-law relationship (and $d_f \geq 2$) in the free molecular regime:

$$K_{\text{agg}}(v_i, v_j) = \left(\frac{6k_B T}{\rho_p} \right)^{1/2} \left(\frac{3}{4\pi} \right)^\lambda a_{p0}^{2 - 6/d_f} (v_i^{-1} + v_j^{-1})^{1/2} (v_i^{1/d_f} + v_j^{1/d_f})^2 \quad (6.37)$$

where

$$\lambda = \frac{2}{d_f} - \frac{1}{2} \quad (6.38)$$

and a_{p0} is the radius of a primary particle. For coalescing spheres ($d_f = 3$), Eq. (6.37) reduces to the kernel for Brownian coagulation in the free molecular regime, [Eq. (6.22)]. The derivation of Eq. (6.37) assumes that the collision diameter is only a function of the fractal dimension, whereas studies have

shown that the collision rate between primary particles and aggregates also depends on the primary particle Knudsen number. In the continuum regime and for agglomerates with large number of primary particles, so that the agglomerate diffusion coefficient approaches the Stokes–Einstein value [Eq. (6.103)], the kernel becomes

$$K_{\text{agg}}(\nu_i, \nu_j) = \frac{2k_B T}{3\mu_g} (\nu_i^{-1/d_f} + \nu_j^{-1/d_f})(\nu_i^{1/d_f} + \nu_j^{1/d_f}) \quad (6.39)$$

For $d_f = 3$, the previous equation reduces to the Brownian coagulation kernel in the continuum regime, Eq. (6.21) without the slip correction. Brownian agglomeration is discussed extensively in Williams and Loyalka (1991) and Friedlander (2000).

6.4 Gas-to-Particle Conversion

Gas-phase physical or chemical processes may generate a supersaturated [$p_{\text{vap}}(T) > p_{\text{sat}}(T)$, and hence, metastable] vapor state that relaxes to equilibrium either via the generation of new particles (homogeneous nucleation) or via growth of existing particles (condensation or heterogeneous nucleation). Physical processes that lead to a supersaturated state include cooling at a surface, adiabatic expansion or mixing, and turbulent mixing, whereas condensable vapor species may be generated by gas-phase chemical reactions.

6.4.1 Nucleation

A metastable vapor-phase state relaxes to equilibrium via homogeneous nucleation in the absence of aerosol particles. Homogeneous nucleation is important in numerous fields: in the atmosphere, for example, ice nucleation in supercooled water droplets is the main mechanism for the formation of cirrus clouds in the upper troposphere, whereas nanoparticle formation in engine emissions occurs via homogeneous nucleation. Here, we concentrate on the transition from the gas phase (supercooled vapor) to a condensed phase by the formation of liquid droplets: the opposite process, bubble nucleation in superheated liquids is discussed in Section 3.1.1.1. Similarities and differences between these two processes will be briefly mentioned.

Nucleation is a physical process that refers to the appearance of a new phase during a first-order phase transition. It is a thermally activated process that occurs via large amplitude, localized fluctuations, which may be viewed as “droplets” of the new, stable phase. Being an activated process new particle formation requires the surmounting of a nucleation barrier. At the given thermodynamic conditions (e.g., constant temperature and pressure) the new condensed phase is stable with respect to the vapor phase (its chemical potential is lower), but there is a free energy cost associated with the creation of the interface between the two phases. The competition between the free energy gain due to the creation of the stable phase, and the free energy loss due to the creation of an interface generates the nucleation barrier. Whereas a metastable state decays via nucleation, an unstable state decays via a process that does not involve barrier crossing and which is called spinodal decomposition. Spinodal decomposition, not addressed herein, occurs via the growth of small-amplitude, long-wavelength fluctuations.

Owing to space limitations some important nucleation topics including experimental measurements of nucleation rates [see, e.g., the review by Heist and He (1994)], computer simulations, rigorous definitions of physically consistent clusters, ion-induced nucleation, and Ostwald ripening are not included.

6.4.1.1 Classical Nucleation Theory

The original work of Becker and Döring (1935) on isothermal nucleation and, subsequently refined by Zeldovich (1942), forms what is now referred to as classical nucleation theory (CNT). These authors argued that nucleation is an activated process and that the rate should depend exponentially on the reversible work of cluster formation. For an early review of homogeneous nucleation, cf. Feder et al.

(1966), whereas for more recent presentations and reviews of CNT, cf. Laaksonen et al. (1995) and Debenedetti, (1996).

A complete theory of nucleation considers the dynamics of growth of stable clusters (also referred to as embryos, droplets, or nuclei) of the new phase. For nonassociated vapors and low cluster concentrations, clusters grow or shrink by the addition or removal of a single molecule. Thus, the rate per unit volume (expressed in number of clusters per unit volume and unit time) at which the number concentration of i -molecule clusters changes is

$$J(i) = f_{i-1}s_{i-1}\beta_{i-1} - f_is_i\alpha_i \quad (6.40)$$

where f_i is the nonequilibrium number concentration of i -molecule clusters, s_i the respective surface area, β_i the forward (condensation) flux per unit time and area at which an i -cluster gains a molecule, and α_i the backward (evaporation) flux at which the cluster loses a molecule. The following assumptions are usually made:

- The forward and backward fluxes are independent of cluster size and they do not depend on whether the system is in equilibrium.
- An equilibrium concentration of clusters is established in the bulk metastable state. This assumption converts a kinetic problem into a thermodynamic one by defining an equilibrium cluster distribution that obeys usual Boltzmann statistics. Microscopic reversibility, then, relates n_i , the equilibrium i -cluster concentration, to n_{i-1} :

$$\beta s_{i-1}n_{i-1} = \alpha s_in_i \quad (6.41)$$

- Thus, the assumption of an equilibrium distribution allows the determination of the evaporation flux α , a quantity that is difficult to evaluate, in terms of the condensation flux β , a quantity that may be easily calculated from, for example, the kinetic theory of gases. The difficulty to calculate α is thus transformed to the calculation of the equilibrium droplet concentration or equivalently, to the study of the energetics of embryo formation. For the equilibrium, unsaturated system the evaporation flux may be calculated from the Kelvin relation [see Eq. (6.45)].
- A steady-state, i -independent, current (nucleation rate per unit volume) J is established.

Frenkel (1955) argued that the equilibrium cluster distribution takes the form

$$n_i = n_1 \exp\left(-\frac{\Delta G_i}{k_B T}\right) \quad (6.42)$$

where the free energy of an i -cluster is ΔG_i . The proportionality constant is taken to be the total number density of the bulk metastable state n_1 (i.e., the monomer number density, which is frequently denoted as the vapor number density n_{vap}), since it is assumed that there is no free energy change associated with the formation of a single molecule cluster. The free energy of formation of an i -cluster is calculated by invoking the capillarity approximation, which is the fundamental assumption of CNT. Accordingly, the cluster free energy is determined by treating the cluster as an incompressible macroscopic spherical droplet with macroscopic (bulk and surface) properties. A perfectly sharp interface is assumed to obtain a droplet free energy that depends on a volume and a surface term

$$\Delta G_i = -\frac{4}{3}\pi a_p^3 n_{\text{liq}} k_B T \ln S + 4\pi a_p^2 \sigma = -ik_B T \ln S + (36\pi)^{1/3} v_{\text{liq}}^{2/3} \sigma i^{2/3} \quad (6.43)$$

where $i (= 4\pi a_p^3 n_{\text{liq}} / 3)$ is the number of molecules in the droplet, n_{liq} the bulk liquid number density, $S (= p_{\text{vap}} / p_{\text{sat}})$ the saturation ratio with p_{vap} the vapor pressure and p_{sat} the saturation pressure (over a flat surface), v_{liq} ($= 1 / n_{\text{liq}}$) the molecular volume in the liquid phase, and σ the macroscopic surface tension. The liquid number density is related to the liquid material density via $n_{\text{liq}} = \rho_{\text{liq}} N_A / \mathfrak{M}$; a similar expression holds for the vapor number density. For a stable vapor phase (saturation ratio less than unity),

the droplet free energy is a monotonically increasing function of the droplet radius. For $S > 1$ (metastable vapor phase) the volume term becomes negative. The competition between the negative volume contribution and the positive surface energy term generates a free energy maximum at the critical radius a_p^* :

$$a_p^* = \frac{2\sigma v_{\text{liq}}}{k_B T \ln S} \quad (6.44)$$

Equation (6.44) determines the equilibrium radius of a droplet as a function of the saturation ratio. If rearranged and the saturation ratio is interpreted as the ratio of the vapor pressure at the surface of a spherical droplet p_{drop} to the saturation pressure far from the droplet p_{sat} then

$$p_{\text{drop}}(a_p) = p_{\text{sat}} \exp\left(\frac{2\sigma v_{\text{liq}}}{k_B T a_p}\right) \quad (6.45)$$

Equation (6.45), known as the Kelvin equation, is a fundamental equation in the thermodynamics of aerosols as it relates the vapor pressure of a droplet to the (saturation) vapor pressure above a planar interface of the bulk material p_{sat} . It shows that the vapor pressure above a droplet is higher than the vapor pressure above a flat surface, an effect that becomes significant for $d_p < 0.1 \mu\text{m}$.

The nucleation current is obtained from Eq. (6.40) by approximating it according to the previously summarized CNT assumptions. The equilibrium cluster distribution (6.42) is used. The current, then, is related to the sum of cluster equilibrium distributions times their respective surface areas, summed up to an arbitrarily large cluster size (see, e.g., Debenedetti, 1996). The discrete sum may be replaced by an integral, and the clusters free energy of formation is expanded to second order (an excellent approximation as the integrand is sharply peaked about the critical cluster) to give

$$J = j_{i^*} Z n_{i^*} \quad (6.46)$$

where j_{i^*} is the rate of arrival of single molecules to the critical droplet, Z the so-called Zeldovich non-equilibrium factor, and n_{i^*} the equilibrium number concentration of critical nuclei. The rate of arrival of monomers is the product of the forward flux constant β (also known as the impingement rate per unit area), which is the single-molecule growth rate calculated from the kinetic theory of gases (with a unity accommodation coefficient), times the critical droplet surface area:

$$j_{i^*} = 4\pi(a_p^*)^2 \beta = 4\pi(a_p^*)^2 \frac{p_{\text{vap}}}{(2\pi m_{\text{mol}} k_B T)^{1/2}} \quad (6.47)$$

where $m_{\text{mol}} = \mathfrak{M}/N_A$ is the molecular mass of an impinging molecule. The Zeldovich nonequilibrium factor arises from number fluctuations in the critical cluster

$$Z = \frac{\nu_{\text{liq}} \sigma^{1/2}}{2\pi(a_p^*)^2 (k_B T)^{1/2}} \quad (6.48)$$

The equilibrium number concentration of critical nuclei n_{i^*} is obtained from Eq. (6.42) evaluated at the critical cluster. For completeness, note that the critical droplet free energy expressed in terms of the critical radius is

$$\Delta G^* = \frac{4\pi}{3} (a_p^*)^2 \sigma \quad (6.49)$$

whereas the number of molecules in the critical cluster is

$$i^* = \frac{32\pi \nu_{\text{liq}}^2 \sigma^3}{3(k_B T \ln S)^3} \quad (6.50)$$

Hence, the CNT expression for the nucleation rate per unit volume becomes

$$J_{\text{CNT}} = J_0^{\text{CNT}} \exp\left(-\frac{\Delta G^*}{k_B T}\right) = n_{\text{liq}} n_{\text{vap}}^2 \left(\frac{2\sigma}{\pi m_{\text{mol}}}\right)^{1/2} \exp\left[-\frac{16\pi}{3} \frac{\sigma^3 v_{\text{liq}}^2}{(k_B T)^3 (\ln S)^2}\right] \quad (6.51)$$

where the number density in the vapor phase has been used, $n_{\text{vap}} = p_{\text{vap}}/(k_B T)$. The classical prefactor is often expressed in terms of n_{liq} , the bulk liquid number density:

$$J_0^{\text{CNT}} = \frac{n_{\text{vap}}^2}{n_{\text{liq}}} \left(\frac{2\sigma}{\pi m_{\text{mol}}}\right)^{1/2} \quad (6.52)$$

Note that the CNT expression is occasionally divided by the saturation ratio (Seinfeld and Pandis 1998), a correction that arises from a different treatment of nucleation kinetics (see below the discussion on consistency issues of CNT).

CNT is one of the most frequently used nucleation theories due to its simplicity and the availability of required molecular data. Even though its predictions are not very accurate (usually they are accurate to 5–10 orders of magnitude) it provides a qualitative understanding of nucleation. It gives, however, reasonable results for the critical saturation ratio $S_c(T)$, the saturation ratio at which the nucleation rate is $J_{\text{nuc}}[S_c(T)] = 1 \text{ cm}^{-3} \text{ sec}^{-1}$. Two important conclusions can be drawn from comparisons of CNT predictions with experimental data (see Figure 6.2):

1. The isothermal dependence of the nucleation rate on the saturation ratio is well predicted. Theoretical predictions and experimental measurements of the slopes of $\ln J_{\text{nuc}}$ vs. $\ln S$ are in reasonable agreement.
2. The temperature dependence of the rate is in considerable disagreement with experimental values: CNT consistently underpredicts experimental rates at low temperature, whereas it may overpredict at high temperatures.

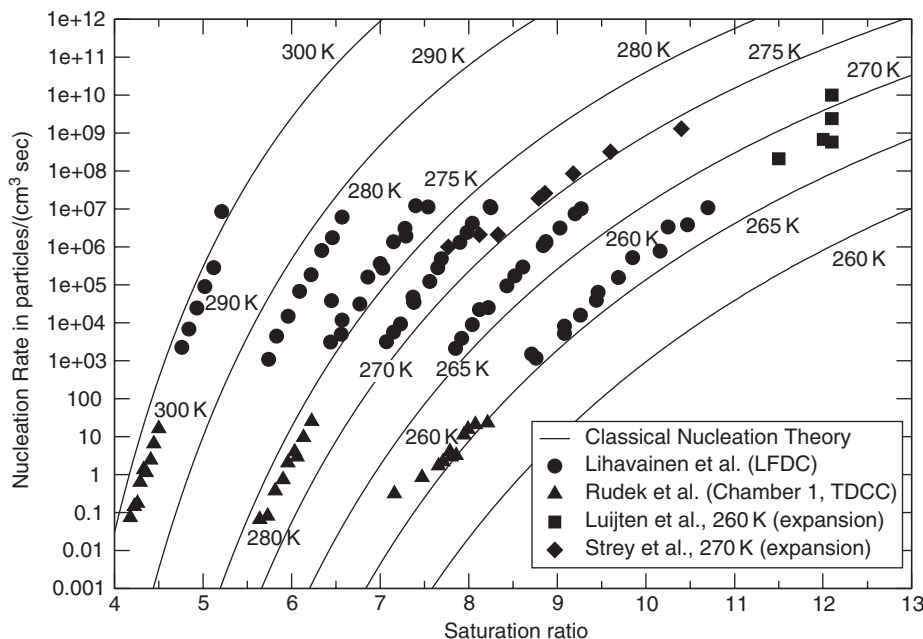


FIGURE 6.2 Experimental measurements of *n*-pentanol nucleation rates and classical nucleation theory predictions. LFDC refers to laminar flow diffusion chamber (*n*-pentanol in helium), TDCC to thermal diffusion cloud chamber (*n*-pentanol in helium), and expansion either to pulse-expansion wave tube (Luijten et al., 1997; *n*-pentanol in helium) or to two-piston expansion chamber (Strey et al., 1985; *n*-pentanol in argon).

The CNT gas-to-liquid nucleation rate differs from the rate frequently used in bubble nucleation, as derived by Blander and Katz (1975), in the preexponential kinetic factor by a factor of $(n_{\text{liq}} / n_{\text{vap}})^2$. This difference stems from the calculation of the concentration of elementary vacancies in the liquid; for the gas-to-liquid transition this concentration is identified to the monomer concentration, the concentration of the metastable vapor [see Eq. (6.42)]. For bubble nucleation, the calculation of the concentration of elementary vacancies is not as straightforward. Nevertheless, both droplet and bubble nucleation rates are predicted to have an Arrhenius dependence on the critical cluster free energy, a dependence that dominates the rate calculation.

The main limitation of CNT is the use of macroscopic (bulk and surface) thermodynamic properties to describe the critical droplet. It assumes a sharp interface, thereby neglecting the curvature dependence of the surface tension. The capillarity approximation, moreover, does not distinguish between metastability and instability, i.e., it does not predict the existence of a spinodal curve, along which the free energy barrier vanishes and the decay process changes from nucleation to spinodal decomposition. Another important limitation of the classical derivation is the requirement that an equilibrium cluster distribution be established in the metastable state allowing the use of microscopic reversibility to calculate the evaporative flux α , and thus leading to an equilibrium cluster distribution of the form shown in Eq. (6.42).

The preexponential factor in Eq. (6.42) is established by requiring that there is no free energy cost for the formation of a single-molecule cluster, $\Delta G_i = 0$. However, the free energy change in the capillarity approximation does not vanish for $i = 1$, rendering CNT internally inconsistent (limiting inconsistency). The internally consistent classical nucleation theory (ICCT) (Girschick and Chiu, 1990) removes this inconsistency by requiring that $\Delta G_i = 0$ for monomers. As a result, the classical rate is multiplied by c/S , where c is a constant. It should be noted, however, that the physical basis of this correction is questionable as is the requirement that the capillarity approximation be valid for monomers.

In addition, the CNT cluster distribution (6.42) violates the law of mass action. Courtney (1961) suggested an equilibrium cluster distribution that satisfies the law of mass action, a modification that leads to the previously mentioned division of the CNT rate by the saturation ratio. Numerous attempts have been made to make the classical theory internally consistent and to satisfy mass action (for a critical review see Wilemski, 1995). However, all these attempts require consistency in CNT, instead of a critical reevaluation of the underlying assumptions of the theory.

CNT calculates the free energy of formation for a stationary droplet, thereby neglecting the effect of translational fluctuations on the cluster free energy and the nucleation rate. Equivalently, CNT does not take into account the effect of translational invariance on the rate (i.e., that the droplet may appear anywhere within the system volume). Lothe and Pound (1962) proposed one of the most intriguing corrections to CNT. They argued that the translational and rotational degrees of freedom of a nucleating droplet are not properly accounted for in CNT. The additional terms they suggested increased theoretical predictions by 10^{18} . The so-called “translation–rotation” paradox resulted in a long-standing controversy.

Reiss and coworkers (see, e.g., Reiss and Kegel, 1996) emphasized the important relation between a proper counting of translational degrees of freedom and the mixing entropy in mesoscopic, continuum descriptions of nucleation phenomena. Recently, Reiss et al. (1997) suggested that the volume scale required to enumerate states for the calculation of the mixing entropy is the variance of volume fluctuations: a nucleating droplet may be identified as a physical object up to its volume fluctuations. Ford (1997), who used a detailed analysis of the statistical mechanics of molecular clusters, and Barrett (1997) suggested that the scaling volume in the classical expression should be the molecular volume in the liquid phase. Instead, CNT implicitly assumes that the scaling volume is the molecular volume in the metastable vapor phase. Even though these attempts to resolve the paradox stem from different considerations and are theoretically sound, they have not managed to improve significantly comparison with experiments; nevertheless in some cases improved temperature dependence was noted.

Drossinos and Kevrekidis (2003) presented a field-theoretic derivation of a correction to the nucleation rate that arises from the contribution of the translational degrees of freedom of a nucleating droplet (viewed as the translational eigenfunctions of the droplet) to the rate. They argued that the proposed correction is consistent with CNT. Their derivation provides a heuristic justification of the capillarity

approximation starting from microscopic, molecular considerations. They concluded that the droplet free energy is modified by an additive mixing-entropy term. The additional contribution, which contains a logarithmic correction to the surface energy term, defines a scaling volume that depends on the range of the coarse-grained, attractive intermolecular interaction potential.

A number of phenomenological modifications of CNT are based on removing the assumption of a sharp interface. Dillmann and Meier (1991) extended the work of Tolman on the dependence of the surface tension on the droplet radius, through the so-called Tolman length, and proposed

$$\sigma = \sigma_\infty(1 + c_1 i^{-1/3} + c_2 i^{-2/3}) \quad (6.53)$$

where σ_∞ is the planar surface tension, i the number of molecules in the i -cluster, and c_1, c_2 constants. Initial predictions greatly improved comparison with experiments, but Laaksonen et al. (1994) pointed out an inconsistency in the Dillmann and Meier theory, which when corrected rendered theoretical predictions worse.

Gránásy in a series of papers (see, e.g., Gránásy, 1997) developed the so-called diffuse interface theory where the finite interface thickness is taken into consideration. A new length scale is introduced to characterize the interface thickness, which can be calculated in terms of measurable quantities, as opposed to the determination of Tolman's length. The resulting model predicts reasonably well nucleation rates for nonane and toluene, but fails for more polar substances.

Ruckenstein and co-workers (see, e.g., Nowakowski and Ruckenstein, 1991) took a different approach by developing a kinetic theory of nucleation, thereby avoiding the equilibrium assumption of CNT. The theory is based on the calculation of the evaporation rate α_i at which a single molecule leaves an i -cluster. Their approach is based on a diffusion equation in energy space. The theory predicts nucleation rates higher than CNT, with more pronounced effects at high supersaturation ratios.

CNT refers to isothermal nucleation where latent heat release is neglected. Barrett (1994) considered nonisothermal nucleation by incorporating energy fluctuations of the critical cluster, but his results did not significantly improve agreement with experiments. Lazaridis and Drossinos (1997) reached a similar conclusion for binary nucleation.

6.4.1.2 Density Functional Theory

Density functional theory (DFT) is an alternative approach to phenomenological corrections to CNT. It is intermediate between the capillarity approximation and a purely microscopic theory, as the more rigorous attempts by Reiss and coworkers (Reiss et al., 1990; Senger et al., 1999) or modern computer simulations (Weakliem and Reiss, 1994; ten Wolde et al., 1996). The main idea of DFT as used in nucleation theory is to treat a nucleating droplet within a metastable vapor phase as an inhomogeneous fluid. Then, as is usually done in density functional theories, a free energy functional that depends on the nonuniform average density profile is postulated. The spatially inhomogeneous average density profile $\rho(\mathbf{r})$ is obtained by extremizing the free energy functional. In the grand canonical ensemble, where the number of molecules fluctuates, the critical nucleus is unstable with respect to growth or shrinkage. Equivalently, the matrix of second-order derivatives of the free energy functional with respect to the density has one negative eigenvalue corresponding to droplet growth or decay; the other nonzero eigenvalues are positive. The critical nucleus, thus, is a saddle point of the free energy functional that separates the metastable and stable phases. By introducing a spatially nonuniform density profile, DFT incorporates curvature effects on the surface tension. It can also be shown that it predicts the existence of a spinodal curve.

Cahn and Hilliard (1958, 1959) in their study of spinodal decomposition of a binary fluid presented the first use of DFT in descriptions of phase transitions. They used a square-gradient approximation of the free energy functional since during spinodal decomposition average density changes are small in comparison to atomic dimensions. Oxtoby and coworkers pioneered the use of DFT in vapor-to-liquid nucleation. They extended the van der Waals theory of interfaces, also used by Cahn and Hilliard, by applying liquid-state perturbation theory to obtain the Helmholtz free energy of the inhomogenous fluid.

Oxtoby and Evans (1988) decomposed the Helmholtz free energy into a local, hard-sphere repulsive part and a nonlocal part that depends on the nonlocal attractive part of the interaction potential. The

decomposition is based on liquid-state perturbation theory, according to which equilibrium fluid properties may be related to a hard-sphere reference fluid with known equilibrium properties; the attractive intermolecular forces are then treated as a perturbation. The highly accurate Carnahan–Starling equation of state was used to determine the properties of the hard-sphere fluid. The grand canonical potential $\Omega[\rho]$ of the inhomogeneous system was accordingly written as

$$\Omega[\rho(\mathbf{r})] = \int d\mathbf{r} f_h[\rho(\mathbf{r})] - \mu \int d\mathbf{r} \rho(\mathbf{r}) + \frac{1}{2} \int \int d\mathbf{r} d\mathbf{r}' \rho(\mathbf{r})\rho(\mathbf{r}')V_{\text{att}}(|\mathbf{r} - \mathbf{r}'|) \quad (6.54)$$

where $f_h(\rho)$ is the Helmholtz free energy density of a uniform, hard sphere fluid of density ρ , μ the chemical potential of the metastable vapor, and $V_{\text{att}}(\mathbf{r})$ the long-range attractive part of the intermolecular interaction potential. The attractive part has been modeled by, for example, the attractive Yukawa potential or the Lennard–Jones potential decomposed according to the Weeks–Chandler–Andersen perturbation theory. The critical nucleus profile is obtained by extremizing Eq. (6.54) with respect to density variations. This procedure amounts to setting the functional derivative of the grand canonical potential to zero, $\delta\Omega(\rho)/\delta\rho(\mathbf{r}) = 0$. The resulting equation, known as the Euler–Lagrange equation, is

$$\mu_h[\rho(\mathbf{r})] = \mu - \int d\mathbf{r}' \rho(\mathbf{r}')V_{\text{att}}(|\mathbf{r} - \mathbf{r}'|) \quad (6.55)$$

with μ_h the chemical potential of the hard-sphere reference fluid:

$$\mu_h = \left. \frac{\partial f_h(\rho)}{\partial \rho} \right|_T \quad (6.56)$$

Equation (6.55) has to be solved iteratively with the boundary condition that the density far away from the droplet becomes the metastable vapor density. As mentioned earlier, the nonuniform density profile is not a minimum but a saddle point of $\Omega[\rho]$, rendering the iteration process unstable. Oxtoby and Evans (1988), and Zeng and Oxtoby (1991a), suggested an iterative numerical procedure to calculate the saddle-point configuration. It consists of an initial guess for the density profile that is substituted on the RHS of Eq. (6.55) to obtain the hard-sphere chemical potential at each point, which in turn yields a new density profile and the iterative procedure continues. For a judicious initial guess the iteration initially converges, allowing the determination of the critical nucleus density profile, but eventually it diverges away from the saddle point. Once the density profile has been calculated, the nucleation barrier associated with the creation of the critical nucleus is obtained, $\Delta\Omega_{\text{DFT}}^* = \Omega(\rho_{\text{drop}}) - \Omega(\rho_{\text{vap}})$. Most DFT calculations proceed by determining the nucleation rate using $\Delta\Omega^*$ as calculated from DFT and retaining the classical pre-exponential factor, $J_{\text{DFT}} = J_0^{\text{CNT}} \exp(-\Delta\Omega_{\text{DFT}}^*/k_B T)$.

Oxtoby and Evans (1988) noted significant nonclassical effects in that the DFT-calculated liquid density at the center of the droplet was found to differ significantly from either the liquid-state density or the coexistence density at the same chemical potential. Moreover, the nucleation barrier was found to be smaller than the barrier predicted by CNT, and it was found to vanish at the spinodal. A sensitive dependence of the nucleation barrier height (and, thus, of the nucleation rate) on the range of the attractive potential was observed.

Density functional theory is a powerful technique for rigorous calculations of the free energy barrier to nucleation. It has been used extensively in bubble nucleation in superheated liquids, liquid nucleation in dipolar fluids, binary nucleation of liquids and bubbles, phase transitions in micropores, crystallization, and many other systems (see Oxtoby, 2002, for a recent review of the multiple uses of DFT). The studies of bubble nucleation (keeping as previously mentioned the CNT kinetic prefactor) showed that deviations from CNT are more dramatic than those calculated for droplet nucleation. Recently a time-dependent DFT theory of fluids (Marini Bettolo Marconi and Tarazona, 1999) was developed.

The calculation of the kinetic prefactor J_0 has received much less attention. Langer and Turski (1973) calculated it for a system close to the critical point using a hydrodynamic model, but their numerical results were not significantly different from those of CNT. Talanquer and Oxtoby (1994) using a

dynamical density functional theory of gas–liquid nucleation concluded that the correction to the preexponential factor due to cluster translation is relatively small. Barrett (1997) used mean-field DFT to calculate the effect of cluster translation on the kinetic prefactor. He showed that the compensation for translational motion leads to a significant increase in the rate, an amount approximately equal to the ratio of liquid to vapor densities. Drossinos et al. (2001) combined DFT with field-theoretic methods to calculate the effect of the translational eigenfunctions of the droplet on the nucleation-rate prefactor by deriving an expression for their functional form [see, also, the discussion following Eq. (6.62)].

6.4.1.3 Nucleation Theorems

The derivation of nucleation theorems constitutes a significant recent development in nucleation theory. The first nucleation theorem was proposed by Kashchiev (1982) and later extended by Oxtoby and Kashchiev (1994), Ford (1997), and Bowles et al. (2001). It relates the derivative of the work of formation of the critical droplet with respect to the chemical potential in the metastable phase to the number of molecules in the droplet

$$\left. \frac{\partial \Delta G^*}{\partial \mu} \right|_{V,T} = - (i^* - \bar{i}) \quad (6.57)$$

where i^* is the total number of molecules within the volume occupied by the critical droplet, and \bar{i} the number of molecules that would have occupied the same volume in the uniform metastable phase. Their difference gives the excess number of molecules in the critical droplet over those present in the same volume in the metastable vapor. For most cases of interest, the metastable vapor is dilute and hence the term \bar{i} is neglected. The initial derivation required that the cluster surface energy be independent of the chemical potential. Oxtoby and Kashchiev (1994) generalized it to multicomponent nucleation showing that it is a much more general result. Bowles et al. (2001) extended further the nucleation theorem and confirmed the conclusion that it is more valid than the initial derivation had suggested.

The importance of the nucleation theorem becomes apparent when it is rewritten in a form that relates experimental quantities. The Arrhenius form of the nucleation rate

$$J_{\text{nuc}} = J_0 \exp\left(-\frac{\Delta G^*}{k_B T}\right) \quad (6.58)$$

combined with the nucleation theorem yields

$$i^* = \left. \frac{\partial k_B T \ln J_{\text{nuc}}}{\partial \mu} \right|_{V,T} - \left. \frac{\partial k_B T \ln J_0}{\partial \mu} \right|_{V,T} \quad (6.59)$$

Since the kinetic prefactor J_0 is weakly dependent on the chemical potential of the metastable phase the correction to i^* is expected to be in the range 0 to 1. Ford (1997) using a combination of statistical mechanics and population cluster dynamics showed that Eq. (6.59) becomes

$$\left. \frac{\partial \ln J_{\text{nuc}}}{\partial \ln S} \right|_{V,T} = 1 + i^* \quad (6.60)$$

Typical values for i^* are 30 to 50 molecules. Thus, $i^* + 1 \approx i^*$, allowing the replacement of the RHS of Eq. (6.60) by i^* , a form that is occasionally reported in the literature. Note that since the chemical potential derivative is taken at constant temperature, it has been replaced by a derivative with respect to $k_B T \ln S$. The nucleation theorem in the form of Eq. (6.60) is extremely useful in the analysis of experimental results and computer simulations, because the number of molecules in a critical cluster may be determined from the slopes of the logarithm of isothermal nucleation rates vs. $\ln S$.

It is worth noting that CNT does not satisfy the first nucleation theorem, a violation that according to Ford (1997) stems from the neglect of translational corrections. As mentioned earlier, Section 6.4.1.1, in the capillarity approximation the droplet free energy is calculated for a droplet fixed within the system

volume, thereby neglecting the mixing entropy associated with translational fluctuations of the cluster. Oxtoby and Kashchiev (1994), as well as Ford (1997), note that the internally consistent classical theory (ICCT) satisfies the nucleation theorem, but the agreement is considered fortuitous since ICCT does not satisfy the second nucleation theorem.

Ford (1997) presented a second nucleation theorem that concerns the temperature dependence of the nucleation rate at constant supersaturation; in a sense, the second theorem is conjugate to the first. It is usually written as

$$\frac{\partial \ln J_{\text{nuc}}}{\partial T} \Big|_{\ln S} = \frac{1}{k_B T^2} [L_p - k_B T + E_x(i^*)] \quad (6.61)$$

where L_p is the latent heat per molecule and $E_x(i^*)$ is the excess internal energy of the critical nucleus.

Another recent development parallel to the use of nucleation theorems in the study of nucleation phenomena is the use of scaling relations for molecular properties of the critical cluster and the nucleation rate. McGraw and Laaksonen (1996) derived scaling relations for the number of molecules in the critical cluster and the nucleation barrier height. They argued that these scaling relationships constrain functional dependencies of departures from CNT. Thus, they may help in the construction of consistent phenomenological models. These scaling relations were later extended to bubble nucleation (Shen and Debenedetti, 2001).

6.4.1.4 Multicomponent Nucleation

Multicomponent nucleation is an important mechanism for new particle formation since it occurs even in mixtures of unsaturated vapors, as opposed to the unary (single-component) nucleation discussed earlier where supersaturation is required. Multicomponent nucleation is important in the atmosphere where various condensable species, for example sulfuric acid and water, occur at relatively low concentrations. Langer (1969) proposed a general expression for the decay rate of a metastable state that can be used to calculate multicomponent nucleation rates. Under some general conditions, he showed that the nucleation rate I_{nuc} (not its density J_{nuc}) may be written as

$$I_{\text{nuc}} = \frac{k}{2\pi} V J_{\text{tran}} \Omega' \exp\left(-\frac{\Delta\Omega^*}{k_B T}\right) \quad (6.62)$$

where, as before, $\Delta\Omega^*$ is the nucleation barrier (in the grand canonical ensemble) and k , the so-called dynamical prefactor, is related to the initial growth rate of a droplet slightly greater than the critical size. The other terms constitute the so-called the statistical prefactor: V is the system volume, and Ω' a generalization of the Zeldovich factor that contains contributions of Gaussian fluctuations about the uniform metastable and the spatially nonuniform droplet density profiles [see Eq. (6.48) for the Zeldovich factor in unary nucleation, a correction that arises from number fluctuations in the critical cluster]. The generalized Zeldovich factor may be viewed as a leading-order fluctuations correction to the droplet free energy. The prime in Ω' denotes that fluctuations corresponding to the translational eigenmodes of the droplet have been excluded. These fluctuations are treated separately to obtain the term $V J_{\text{tran}}$, where J_{tran} is the Jacobian for the change of variables to the collective coordinates associated with the translational eigenfunctions of the droplet. The complete expression is reported in Langer and Turski (1973), whereas an alternative formal expression that relates the nucleation rate to the imaginary part of the true system free energy is reported in Langer (1967, 1974). One of the main difficulties in using Eq. (6.62) is the evaluation of the statistical prefactor.

The formal procedure introduced by Langer (1969) to solve multidimensional Fokker–Planck equations that arise in nucleation problems, also used to obtain the nucleation rate Eq. (6.62), has proven to be useful and versatile. It has been used to calculate the effect of energy fluctuations on the nucleation rate (Barrett, 1994; Lazaridis and Drossinos, 1997), to calculate the contribution of translational fluctuations to the rate (Drossinos et al., 2001), and to calculate nucleation rates in ternary systems (Lazaridis, 2001).

Trinkhaus (1983) presented a slightly different expression for the nucleation rate in multicomponent systems. His result, which does not consider the contribution of the droplet translational eigenmodes, is

$$J_{\text{nuc}} = \frac{|\kappa|/\pi}{\sqrt{-\det(\overset{\leftrightarrow}{D}/\pi)}} n_{\text{tot}} \exp\left(-\frac{\Delta G^*}{k_B T}\right) \quad (6.63)$$

where $n_{\text{tot}} \exp(-\Delta G^* / k_B T)$ is the number density of critical clusters, $\overset{\leftrightarrow}{D}$ the matrix of second-order derivatives of the droplet free energy with respect to the number of molecules n_j of each species evaluated at the saddle point,

$$D_{ij} = \frac{1}{2k_B T} \left. \frac{\partial^2 \Delta G}{\partial n_i \partial n_j} \right|_* , \quad i, j = 1, \dots, m \quad (6.64)$$

m being the number of species. The factor κ is the negative eigenvalue of the product of a growth tensor, a multicomponent generalization of Eq. (6.47), times $\overset{\leftrightarrow}{D}$. Note that the determinant of $\overset{\leftrightarrow}{D}$ is negative since the critical nucleus corresponds to a saddle point in number composition space (see the discussion on DFT in [Section 6.4.1.2](#)). This expression has been used to calculate binary nucleation rates in the sulfuric acid–water system (Noppel et al., 2002), and in ternary nucleation of sulfuric acid–ammonia–water (Napari et al., 2002).

For the specific case of two-component nucleation, Reiss (1950) presented the first rigorous binary nucleation theory. He argued that the nucleation rate should be calculated at the saddle point in droplet-composition space by following a steepest-descent path. Stauffer (1976) noted that the steepest-descent path resulted in an inconsistent evaluation of the steady-state nucleation rate; instead he proposed a self-consistent method. Stauffer's result is the most frequently used expression to calculate binary nucleation rates. More recently, Kevrekidis et al. (1999) used the method introduced by Langer (1969) to obtain the rate. Their result is formally identical to Stauffer's result, but much easier to evaluate. Accordingly, the binary nucleation rate for nonassociated vapors is

$$J_{\text{nuc}} = -\frac{n_{\text{vap}} \exp(-\Delta G^* / k_B T)}{2(D_{12}^2 - D_{11}D_{22})^{1/2}} \left[D_{11}R_{11} + D_{22}R_{22} - \sqrt{(D_{11}R_{11} - D_{22}R_{22})^2 + 4D_{12}^2 R_{11}R_{22}} \right] \quad (6.65)$$

where $n_{\text{vap}} = n_{\text{vap},1} + n_{\text{vap},2}$ is the total number density of condensable vapors and R the droplet growth tensor. As in unary nucleation, the growth matrix (which is diagonal for nonassociated vapors) is expressed as the product of the droplet surface area times the impingement rate of a molecule of species i , $R_{ij} = \delta_{ij} \beta_i 4\pi (a_p^*)^2$, with δ_{ij} the Kronecker symbol [see Eq. (6.47) for the corresponding expression for unary nucleation]. The impingement rate (per unit area) β_i may be calculated as summarized in the CNT analysis of the condensation flux, Eq. (6.47), to give $\beta_i = p_i / (2\pi m_{\text{mol},i} k_B T)^{1/2}$ with p_i the partial vapor pressure of species i .

Similar to unary nucleation, the free energy barrier in the capillarity approximation, cf. Eq. (6.49), is expressed as

$$\Delta G^* = \frac{4}{3} \pi (a_p^*)^2 \sigma \quad (6.66)$$

where a_p^* , the radius of the (spherical) critical droplet, and σ , the droplet surface tension, are functions of the composition of the droplet. According to the revised classical theory, which distinguishes between surface and interior droplet compositions as if the droplet were macroscopic (Wilemski, 1984; 1987), the Gibbs–Thomson equation can be solved for the critical radius and composition. Accordingly, the bulk composition x of the critical cluster, in particular the mole fraction of component 2 in the bulk of the droplet [$x = n_2 / (n_1 + n_2)$ with n_i the number of moles of species i in the bulk interior] is found by solving

$$\nu_{\text{sol},1} \Delta \mu_2 = \nu_{\text{sol},2} \Delta \mu_1 \quad (6.67)$$

where $\nu_{\text{sol},i}$ is the partial molecular volume in the solution droplet of species i ($i = 1, 2$), and $\Delta\mu_i = \mu_i^{\text{liq}} - \mu_i^{\text{vap}} = -k_B T \ln S_i$ the chemical potential difference. The critical radius is

$$a_p^* = \frac{-2\sigma\bar{\nu}_{\text{sol}}}{(1-x)\Delta\mu_1 + x\Delta\mu_2} \quad (6.68)$$

where the molecular volume of the solution $\bar{\nu}_{\text{sol}} = (1-x)\nu_{\text{sol},1} + x\nu_{\text{sol},2}$ is expressed in terms of the partial molecular volumes in the liquid-solution droplet.

An alternative approach to binary nucleation was taken by Zeng and Oxtoby (1991b) who developed a density functional theory for gas–liquid nucleation in binary fluids.

6.4.1.5 Heterogeneous Nucleation

In the presence of a solid substrate, for example, an aerosol particle, the surface provides an interface upon which the new phase may nucleate. The surface limits the extent of penetration in the metastable region, thus heterogeneous nucleation upon insoluble particles takes place at lower saturation ratios than homogeneous nucleation. In the atmosphere, where saturation ratios are low, most nucleation is heterogeneous on already existing particles, for example, on cloud condensation nuclei.

According to the classical theory, the free energy of formation of the critical cluster on a flat surface is modified as follows (Seinfeld and Pandis, 1998):

$$\Delta G_{\text{het}}^* = \Delta G_{\text{hom}}^* f(\cos\vartheta) \quad (6.69)$$

where the angle ϑ , which can vary from 0 to 180° , is the contact angle between the nucleus and the solid substrate. For water nucleation the solid is considered hydrophobic or hydrophilic, according to whether the contact angle is greater or less than 90° . At (mechanical) equilibrium the contact angle is given by Young's equation

$$m \equiv \cos\vartheta = \frac{\sigma_{\text{vl}} - \sigma_{\text{sl}}}{\sigma_{\text{lv}}} \quad (6.70)$$

where σ_{ij} are the surface tensions between the various phases: vapor (v), liquid (l), and solid (s). The function $f(m)$, which assumes values between 0 and 1, is a measure of the lowering of the activation energy required for nucleation due to the surface, and is given by

$$f(m) = \frac{1}{4}(2+m)(1-m)^2 \quad (6.71)$$

In the limit $\vartheta \rightarrow 0$, which corresponds to complete wetting, the nucleation barrier disappears [$f(m = 1) = 0$], and nucleation begins at saturation. At the other limit $\vartheta \rightarrow 180^\circ$, $f(m = -1) = 1$; thus, in that limit, heterogeneous nucleation is not favored over homogeneous nucleation, and homogeneous nucleation occurs.

6.4.1.6 Thermodynamics of Aqueous Droplets

According to the Kelvin relation, Eq. (6.45), a pure solvent droplet is in unstable equilibrium: a small perturbation in the form of an infinitesimal droplet radius change would cause the droplet to shrink or grow. However, a solution droplet may be stabilized due to solute vapor-pressure lowering.

For the specific case of an ideal, dilute water solution containing a fixed amount of solute, the vapor pressure of the solution droplet is (Rogers and Yau, 1989)

$$\ln \left[\frac{p_1(d_p)}{p_{\text{sat},1}} \right] = \frac{4\sigma_1\bar{\nu}_1}{R_u T d_p} - \frac{6n_2\bar{\nu}_1}{\pi d_p^3} \quad (6.72)$$

where subscript 1 refers to water (the solvent) and 2 to the solute, and $p_{\text{sat},1}$ is the pure water vapor pressure above a planar, water surface (i.e., a pure-solvent surface). The number of moles of solute is denoted

by n_2 , and \bar{v}_1 is the molar volume of water in the solution. For a dilute solution the molar volume of water may be taken to be the molar volume of pure water, $\bar{v}_1 \approx \mathfrak{M}_1/\rho_1$. Similarly, to a good approximation, the solution surface tension may be taken to be independent of concentration and equal to the surface tension of water.

Equation (6.72), referred to as the Koehler equation or curve, is the fundamental equation of the thermodynamics of aqueous droplets. It combines the two primary effects that determine the vapor pressure above a liquid droplet: the Kelvin effect that increases the pressure and the solute effect that decreases it. Since the two effects have different dependencies on the droplet diameter (and different signs), the curvature (Kelvin) effect behaves as d_p^{-1} and the solute effect as d_p^{-3} , a critical droplet diameter exists. For small droplets the solute effect dominates, whereas for large droplets the dominant effect is the Kelvin effect. Stability arguments show that droplets in the ascending part of the Koehler curve (d_p less than the critical droplet diameter) are in stable equilibrium with their environment, whereas those in the descending part (d_p greater than the critical droplet) are in unstable equilibrium. Hence, the Koehler equation gives the wet droplet diameter as a function of saturation ratio. It is frequently used to determine the stability of atmospheric particles.

The saturation ratio S_c of a particle at the critical diameter, obtained by evaluating Eq. (6.72) at the critical droplet diameter, is an important particle property. If the ambient saturation ratio S is lower than S_c , droplets of diameter less than the critical droplet diameter are in stable equilibrium, whereas larger droplets are in unstable equilibrium (since the Kelvin effect dominates). If $S > S_c$, no stable equilibrium particle size exists: droplets will grow indefinitely as long as the inequality $S > S_c$ holds. Atmospheric particles for which $S_c < S$ are said to be activated, and they start growing rapidly becoming cloud or fog droplets (Seinfeld and Pandis, 1998).

6.4.2 Growth

In the presence of supersaturation ($p_{\text{vap}} > p_{\text{sat}}$), preexisting aerosol particles or newly generated particles (via homogeneous nucleation) grow. Condensation or evaporation is driven by the pressure difference between the ambient vapor pressure and the vapor pressure at the surface of the particle: the direction of net vapor flux (evaporation or condensation) depends on their relative magnitude. Since latent heat is released or absorbed at the particle surface during these processes, the treatment of particle growth or shrinkage requires considerations of heat and mass transfer between the particle and the ambient gas mixture. Isothermal conditions prevail when the heat of vaporization may be neglected, otherwise heat and mass transfer should be considered simultaneously.

Clement (1985) presented a general treatment of heat and mass transfer and their coupling in vapor–gas mixtures. He argued that in addition to the Lewis number, the ratio of the rate of heat transport by conduction to the rate of mass transport by diffusion, another dimensionless number, the surface condensation number, is useful in heat and mass transfer processes. The condensation number is defined as the ratio of the conductive heat current to the latent heat carried by the mass current at the surface. The importance of the Lewis number in nucleation experiments has been discussed by, among others, Housiadas et al. (2002).

Chemical reactions may also lead to particle growth. Growth laws, i.e., laws that express the rate of change in particle size as function of particle size and chemico-physical properties of the aerosol system, may be transport- or reaction-limited. If growth is limited by gas-phase transport, the growth law is transport limited; otherwise, it may be surface-reaction- or volume-reaction-controlled. Moreover, if growth depends on surface reactions and the reaction rate is fast with respect to transport, the growth law is still determined by gas-phase transport. Surface reactions will lead to growth if the reaction products accumulate at the surface. When the surface reaction is slow, it is frequently assumed that the gas-phase concentration of the reacting species near the surface is the same as the bulk concentration far away from the particle. Volume-reaction-controlled growth refers to growth that depends on the conversion of a dissolved species into a condensed phase species. Reaction-controlled growth will be only briefly mentioned herein.

For simplicity, only diffusional growth, primarily in the continuum regime, will be considered in this section: other smaller additional fluxes due to Stefan flow, thermal diffusion, and the Dufour effect are discussed in Kulmala and Vesala (1991).

6.4.2.1 Single-Particle Growth

Isothermal, steady-state growth rates of a single spherical particle in a stagnant gas are presented. Diffusional processes toward a moving particle are discussed in Hindy and Brock (1970). In the continuum regime, the vapor condensation rate (expressed in molecules per second) toward a spherical particle of the same composition is calculated from the steady-state diffusion equation ($\nabla^2 n = 0$ around a sphere) to be

$$J = \frac{2\pi d_p \mathfrak{D}}{k_B T} (p_\infty - p_{\text{sur}}) \quad (6.73)$$

where $p_\infty = p(T_\infty)$ is the ambient vapor pressure and p_{sur} the vapor pressure at the surface of the particle. For $p_\infty > p_{\text{sur}}$ the droplet grows, whereas for $p_\infty < p_{\text{sur}}$ the droplet shrinks. The diffusional flow toward a spherical particle and the associated temperature change were first derived by Maxwell (1890) in a paper in *Encyclopaedia Britannica* on the theory of the wet-bulb thermometer. The theory of steady-state growth of a spherical particle in the continuum regime is known as Maxwell theory.

In the molecular regime, the net condensation rate (molecules per second) is obtained from kinetic theory to be

$$J = \frac{\alpha \pi d_p^2}{(2\pi m_{\text{mol}} k_B T)^{1/2}} (p_\infty - p_{\text{sur}}) \quad (6.74)$$

where α is the accommodation coefficient or sticking probability ($0 \leq \alpha \leq 1$). It gives the fraction of incident molecules that are adsorbed. A value of unity means that once a vapor molecule hits the surface the probability of sticking is unity. The accommodation coefficient may depend on whether evaporation or condensation is considered and its value is determined experimentally.

The calculation of the steady-state flow of vapor molecules toward a spherical droplet in the transition regime requires the solution of the Boltzmann equation. In the absence of a general solution a number of approximations based on the so-called flux-matching techniques (introduced by Fuchs, 1964) have been proposed. These techniques require matching of the continuum expression with the kinetic at a given distance from the particle surface. For an extensive presentation of the various interpolation formulae see, for example, Seinfeld and Pandis (1998). The most frequently used interpolation formula was proposed by Fuchs and Sutugin (1971):

$$f_{\text{FS}}(\lambda, d_p) = \frac{1 + 2\lambda/d_p}{1 + 3.42\lambda/d_p + 5.33(\lambda/d_p)^2} \quad (6.75)$$

where λ is the mean free path of the vapor species, see Eq. (6.92). Thus, the vapor condensation rate becomes

$$J = \frac{2\pi d_p \mathfrak{D}}{k_B T} f_{\text{FS}}(\lambda, d_p) (p_\infty - p_{\text{sur}}) \quad (6.76)$$

Equation (6.76) is approximate, i.e., it reproduces the continuum expression, but in the free molecular regime it gives the kinetic expression multiplied by approximately 1.2 (for $\alpha = 1$).

The previous expressions may be converted into transport-limited growth laws by performing a mass balance on the growing or evaporating particle. Since the rate of change of the number of molecules in a particle equals the total rate of condensing or evaporating molecules,

$$\frac{dv}{dt} = \frac{2\pi \mathfrak{D} d_p \nu_{\text{liq}}}{k_B T} f_{\text{FS}}(\lambda, d_p) (p_\infty - p_{\text{sur}}) \quad (6.77)$$

where ν_{liq} is the molecular volume of the condensing species ($\nu_{\text{liq}} = 1/n_{\text{liq}}$ when expressed in terms of the condensed-phase number density). In Eq. (6.77) the accommodation coefficient has been set to unity. Growth laws are frequently used for the rate of change of particle radii,

$$\dot{a}_{\text{p}} = \frac{\mathfrak{D}\nu_{\text{liq}}}{a_{\text{p}}k_{\text{B}}T} f_{\text{FS}}(\lambda, d_{\text{p}})(p_{\infty} - p_{\text{sur}}) \quad (6.78)$$

For surface reaction growth, if the surface reaction rate is slow compared to transport, the concentration of the reacting species at the particle surface is taken approximately equal to the concentration far away from the particle. The growth law becomes

$$\frac{d\nu}{dt} = \frac{\alpha\pi d_{\text{p}}^2 \nu_{\text{liq}}}{(2\pi m_{\text{mol}} k_{\text{B}} T)^{1/2}} p_{\infty} \quad (6.79)$$

where α , the fraction of effective collisions, is usually much less than unity. A summary of limiting growth laws for gas-to-particle conversion is presented in Friedlander (2000).

Equation (6.77) or (6.78) may be used to calculate the change of mass of a particle if the appropriate expression for the vapor pressure at the particle surface is used. As argued in Section 6.4.1.6 [cf. Eq. (6.72)], the vapor pressure above a droplet depends on the curvature and, for a solution droplet, on the amount of solute present. For small liquid droplets the exponential terms are usually expanded to obtain [the notation is explained in the discussion following Eq. (6.72)]

$$\frac{p_{\text{sur}}(T)}{p_{\text{sat}}(T)} = 1 + \frac{4\sigma_1 \bar{v}_1}{R_u T d_{\text{p}}} - \frac{6n_2 \bar{v}_1}{\pi d_{\text{p}}^3} \quad (6.80)$$

As mass transfer continues the particle temperature changes due to latent heat release or absorption. The growth rate is then obtained by solving the coupled equations for heat and mass transfer. In the continuum regime, the particle temperature is determined from the steady-state heat conduction equation. Mason (1971) introduced an analytical approximation to the two coupled equations for the rate of growth of a droplet by condensation (see, also, Rogers and Yau, 1989). He proposed

$$\dot{a}_{\text{p}} = \frac{1}{a_{\text{p}}} \left(\frac{S - 1}{f_{\text{mass}} + f_{\text{heat}}} \right) \quad (6.81)$$

where $S = p_{\infty} / p_{\text{sat}}(T_{\infty})$ is the ambient saturation ratio. The term f_{mass} represents the contribution associated with vapor diffusion, and thus it is related to the continuum growth law presented in Eq. (6.78):

$$f_{\text{mass}} = \frac{k_{\text{B}} T_{\infty}}{\nu_{\text{liq}} \mathfrak{D} p_{\text{sat}}(T_{\infty})} \quad (6.82)$$

The term f_{heat} is the contribution to the growth rate due to heat conduction

$$f_{\text{heat}} = \left(\frac{L_{\text{mol}}}{k_{\text{B}} T_{\infty}} - 1 \right) \frac{L_{\text{mol}}}{\nu_{\text{liq}} T_{\infty} k_g} \quad (6.83)$$

where L_{mol} is the latent heat per molecule ($= L \mathfrak{M}/N_A$ if expressed in terms of the latent heat per unit mass) and k_g the thermal conductivity of the gas (e.g., air). The temperature T_{∞} is the temperature far away from the droplet surface. Equation (6.81) is known as Mason's equation. As before, solution and curvature effects may be incorporated in Mason's equation by modifying the droplet's equilibrium surface pressure according to Eq. (6.72), namely, by replacing the term $S - 1$ in the numerator of Eq. (6.81) by

$$S - 1 - \frac{4\sigma_1 \bar{v}_1}{R_u T_{\infty} d_{\text{p}}} + \frac{6n_2 \bar{v}_1}{\pi d_{\text{p}}^3} \quad (6.84)$$

Pruppacher and Klett (1997) present modifications of Mason's equation that account for noncontinuum effects in the transition regime. Their results are expressed in terms of a modified diffusion coefficient \mathfrak{D}' and thermal conductivity k'_g that should be used in Eqs. (6.82) and (6.83). Seinfeld and Pandis (1998) proposed simplified expressions for \mathfrak{D}' and k'_g for the case of air–water vapor system. The modified diffusion coefficient is

$$\mathfrak{D}' = \frac{\mathfrak{D}}{1 + \frac{2\mathfrak{D}}{\alpha_c d_p} \left(\frac{2\pi \mathfrak{M}_1}{R_u T} \right)^{1/2}} \quad (6.85)$$

where α_c is the condensation coefficient (mass accommodation coefficient). The modified form of the thermal conductivity is

$$k'_g = \frac{k_g}{1 + \frac{2k_g}{\alpha_T d_p \rho_a \hat{c}_p} \left(\frac{2\pi \mathfrak{M}_1}{R_u T} \right)^{1/2}} \quad (6.86)$$

where α_T is the thermal accommodation coefficient (frequently assumed to be equal to the mass accommodation coefficient), and ρ_a and \hat{c}_p the density and specific heat of humid air, respectively.

Barrett and Clement (1988) used the generalized equations for heat and mass transfer in vapor–gas mixtures (Clement, 1985) to study growth rates for liquid droplets. They obtained, in addition to expressions for growth in the molecular regime and the transition regime, an expression for the droplet growth rate in the continuum regime that generalizes Mason's equation. They argued that for water droplets the most important uncertainty is the choice of the molecular sticking probability.

6.4.2.2 Population of Droplets

As discussed earlier, a polydisperse aerosol is characterized by its size distribution, whose change in time and space is described by the GDE. Since condensation and evaporation are aerosol processes that occur much faster than coagulation, changes induced by them may be calculated separately without solving the full dynamic equation. In general, the GDE must be solved numerically: inclusion of a growth term in sectional methods leads to numerical diffusion, a problem that has stimulated the development of a number of different numerical schemes (summarized in Section 6.2.3). Alternatively, approximate analytical techniques have been developed. The GDE in the absence of coagulation, homogeneous nucleation, and external processes takes the form (expressed here in terms of the particle radius)

$$\frac{\partial n(a_p; t)}{\partial t} + \frac{\partial}{\partial a_p} [n(a_p; t) \dot{a}_p] = 0 \quad (6.87)$$

In Eq. (6.87) the particle current, introduced in Section 6.2.1, see Eq. (6.5), has been approximated by the migration term only, $n\dot{a}_p$, because homogeneous nucleation has been neglected. Inclusion of the homogeneous nucleation term would replace the zero on the RHS of Eq. (6.87) by the nucleation rate $J_{\text{nuc}} \delta(a_p - a_p^*)$, $\delta(a)$ being the Dirac delta function. Equation (6.87) is occasionally referred to as the condensation equation.

The condensation equation can be solved analytically for constant gas-phase supersaturation, unity accommodation coefficient, and in the continuum regime. Under these approximations, the growth law is inversely proportional to the particle radius, $\dot{a}_p = A/a_p$, with A a constant easily determined from Eq. (6.78). After a suitable transformation Eq. (6.87) may be solved via the method of characteristics. Along the characteristic the solution is

$$d_p^2(t) = d_{p0}^2 + 2At \quad (6.88)$$

where d_{p0} is the initial ($t = 0$) diameter. Initially, $2At \ll d_{p0}^2$ and thus particles do not grow perceptively. In fact, smaller particles grow much faster than larger particles. In the long-time limit the growth term $2At$ dominates so that condensation tends to shrink the size distribution, and the distribution tends to become more and more monodisperse.

The total condensation rate, defined as the change of aerosol mass due to condensation or evaporation, is related to a single droplet growth rate by considering the third moment of the GDE to obtain (Clement, 1985)

$$\frac{dm}{dt} = 4\pi\rho_1 \int da_p n(a_p; t) a_p^2 \dot{a}_p \quad (6.89)$$

The previous equation is obtained by differentiating the third moment of the number distribution (see Section 6.2.3) and substituting Eq. (6.87).

6.5 Single-Particle Motion – Deposition Mechanisms

In this section, we focus on the mechanisms determining the motion of a single aerosol particle suspended in a fluid. The fluid itself may be stagnant or in motion. In the latter case, in particular in accelerating fluid motion, the effects associated with the particle's own inertia become manifest. The mechanisms driving particle motion can be synonymously called deposition mechanisms because their result is to make particles migrate from the suspending fluid to a surface and deposit there. Clearly, the same mechanisms are also responsible for transferring particles across boundaries within the flow. Therefore, the mechanisms discussed in this section correspond to the external processes in the GDE discussed in Section 6.2.2, with the exception of convection. Convective transport of particles will be addressed separately in Section 6.6.

In most cases, the flow around a moving aerosol particle is in the Stokes regime, $Re_p \ll 1$, where $Re_p (=d_p V_p / v_g)$ is the particle Reynolds number. The fundamentals of the mechanics of a single particle are presented in earlier sections of this Handbook (see Section 1.4). The only point that merits further discussion here is related to noncontinuum flow effects in aerosol systems. In the aerosol literature, the Knudsen number (defined in Section 1.4.3.5) is defined in terms of particle radius, $Kn = 2\lambda/d_p$, rather than particle diameter. However, the use of Knudsen number is generally limited because it has the particular characteristic of becoming larger as particle size gets smaller. For small particles there is a departure from the continuum flow regime and a corresponding decrease in the Stokes drag force. This effect is taken into account by introducing a correction factor, in an equivalent way as in Eq. (1.143), as follows:

$$F_D = \frac{3\pi\mu_g V_p d_p}{C_c} \quad (6.90)$$

The correction factor C_c , known as Cunningham correction factor or slip correction factor, is given by

$$C_c = 1 + \frac{\lambda}{d_p} \left[2.34 + 1.05 \exp\left(-0.39 \frac{d_p}{\lambda}\right) \right] \quad (6.91)$$

This correction factor is presented and discussed in Section 1.4. To evaluate Eq. (6.91) the mean free path λ must be known. The mean free path according to the kinetic theory of gases is

$$\lambda = \frac{1}{\sqrt{2}n_g \pi d_M^2} \quad (6.92)$$

where n_g is the number concentration of gas molecules and d_M the collision diameter of a molecule. For air at 101 kPa (1 atm) and 293 K (20°C), the mean free path is $\lambda_{ref} = 0.0664 \text{ } \mu\text{m}$, while for air at other conditions the following formula can be used (Willeke, 1976):

$$\lambda = \lambda_{ref} \left(\frac{101}{p} \right) \left(\frac{T}{293} \right) \left(\frac{1 + 110/293}{1 + 110/T} \right) \quad (6.93)$$

where p is in kPa and T in K. For other gases accurate determination of the mean free path from kinetic theory, Eq. (6.92), is difficult. One may resort to the theory that relates the mean free path to gas macroscopic properties, such as viscosity. A good approximate formula is

$$\lambda = \frac{\mu_g}{p} \left(\frac{\pi R_u T}{2 M} \right)^{1/2} \quad (6.94)$$

Table 6.1 gives values for the slip correction factor at different particle diameters. For a 1 μm particle at standard conditions in air, the slip correction is of the order of 15% and it increases rapidly as size decreases. On the other hand, slip effects can be considered negligible for particles with $d_p > 10 \text{ } \mu\text{m}$.

6.5.1 Gravitational Settling

The terminal velocity of a spherical particle due to gravitational settling can be obtained from Eq. (1.119) as follows

$$V_s = \frac{\rho_p d_p^2 g C_c}{18 \mu_g} \quad \text{for } Re_p < 0.1 \quad (6.95)$$

Since slip correction has been taken into account, the above expression can be used for any particle size. Equation (6.95) is valid only for Stokes flow, which is the usual case for most aerosols. The Stokes regime strictly holds for $Re_p < 0.1$; however, Eq. (6.95) is a good approximation over the extended range $0.1 < Re_p < 1$ (Vincent, 1995; Hinds, 1999). Methods to calculate V_s at higher particle Reynolds numbers are given in Hinds (1999). Note that buoyancy effects have been neglected in Eq. (6.95), which is a largely legitimate assumption because in most practical cases $\rho_p \gg \rho_g$.

A quantity related to the terminal settling velocity (not necessarily restricted to gravitational settling) and frequently used in aerosols is the particle mechanical mobility, B , in m/N/sec. It is defined as the ratio of the terminal velocity to the steady-state force that produces it. In the Stokes regime

$$B = \frac{C_c}{3\pi\mu_g d_p} \quad (6.96)$$

Thus, the terminal velocity a particle acquires is the applied force times its mechanical mobility.

For nonspherical particles a correction is introduced in Eq. (6.95), called the dynamic shape factor χ . Also, diameter d_p must be replaced by the equivalent volume diameter, d_e , which is the diameter of a sphere having the volume of the particle. With these conventions, Eq. (6.95) becomes

$$V_s = \frac{\rho_p d_e^2 g C_c}{18 \mu_g \chi} \quad \text{for } Re_p < 0.1 \quad (6.97)$$

The slip correction factor for an irregularly shaped particle is difficult to determine with accuracy. However, it can be approximated through $d_p = d_e$ in Eq. (6.91). **Table 6.2** gives values for the dynamic shape factor for various particle shapes.

A characteristic diameter used to characterize nonspherical particles is the Stokes diameter d_s . This is the diameter of a sphere of the same density and same settling velocity as the particle. Usually, the Stokes diameter is defined in terms of the bulk material density of the particle, ρ_b , to avoid the problem of

TABLE 6.2 Dynamic Shape Factors

Shape	Dynamic Shape Factor χ
Sphere	1.00
Cube	1.08
Cylinder (orientation averaged motion)	1.09 (for $L/d=2$) 1.23 (for $L/d=5$) 1.43 (for $L/d=10$)
Chain of spheres	1.12 (2-sphere chain) 1.27 (3-sphere chain) 1.32 (4-sphere chain)
Compact cluster of spheres	1.15 (3 spheres) 1.17 (4 spheres)
Dusts	
Bituminous coal	1.05–1.11
Quartz	1.36–1.82
Sand	1.57
UO_2	1.28
Talc (plate-like particle)	1.88
Agglomerates	
Carbonaceous smoke	3.26–6.77
Pb fume	1.5–3.5
$(PuU)O_2$	1.96–2.85

Source: Adapted from Colbeck, I., *Physical and Chemical Properties of Aerosols*, Chapman & Hall, London, 1998; Hinds, W. C., *Aerosol Technology: Properties, Behaviour, and Measurement of Airborne particles*, 2nd ed., Wiley, New York, 1999.

defining the true density that may be affected by porosity or agglomerated structure. From Eq. (6.97) it follows

$$d_s = d_e \left(\frac{\rho_p}{\rho_b \chi} \right)^{1/2} \left(\frac{C_c(d_e)}{C_c(d_s)} \right)^{1/2} \quad (6.98)$$

Obviously, for a spherical particle of uniform density, $d_s = d_p$. Since the Cunningham slip correction factor depends on diameter, an iterative procedure is required in Eq. (6.98) to achieve consistency between the Stokes diameter and the respective slip correction factor. For particles with $d_e > 1 \mu\text{m}$ the slip correction is, however, small, and the ratio $C_c(d_e)/C_c(d_s)$ becomes approximately 1. On the other hand, for particles with $d_e < 1 \mu\text{m}$ and shape factor close to unity, the difference between d_e and d_s is such that the influence of the ratio $C_c(d_e)/C_c(d_s)$ is not very large. Therefore, very often, Eq. (6.98) can be simplified to

$$d_s = d_e \left(\frac{\rho_p}{\rho_b \chi} \right)^{1/2} \quad (6.99)$$

Another characteristic diameter, extensively used in aerosol science and technology, is the aerodynamic diameter d_a . This is the diameter of a spherical particle of density $\rho_0 = 1000 \text{ kg/m}^3$ that settles with the same terminal velocity as the particle. The aerodynamic diameter is given by

$$d_a = d_e \left(\frac{\rho_p}{\rho_0 \chi} \right)^{1/2} \left(\frac{C_c(d_e)}{C_c(d_a)} \right)^{1/2} = d_s \left(\frac{\rho_b}{\rho_0} \right)^{1/2} \left(\frac{C_c(d_s)}{C_c(d_a)} \right)^{1/2} \quad (6.100)$$

and, as in Eq. (6.98), the calculation requires an iterative procedure. As before, there are many practical cases in which the effect of ratios of slip factors is not very large (namely, for large particles with $d_e > 1 \mu\text{m}$, or small particles of smooth shape and density close to ρ_0), and Eq. (6.100) is approximately written as

$$d_a = d_e \left(\frac{\rho_p}{\rho_0 \chi} \right)^{1/2} = d_s \left(\frac{\rho_b}{\rho_0} \right)^{1/2} \quad (6.101)$$

The aerodynamic diameter and, to a lesser extent, the Stokes diameter, are essential parameters, both used to characterize aerosol behavior irrespective of particle geometry and material. For example, the aerodynamic diameter is used to characterize filtration or respiratory deposition. Several instruments, such as impactors and elutriators, measure aerodynamic diameter.

6.5.2 Diffusion

As a result of their continuous bombardment by the molecules of the surrounding gas, aerosol particles exhibit a random motion called Brownian motion. The macroscopic effect of Brownian motion is the net transfer of particles from regions of high to low concentration, a process known as diffusion. Diffusion of aerosol particles due to Brownian motion is described by the well-known Fick's law in terms of number of particles diffused, namely, $J_p = -\mathfrak{D}\nabla n_p$, where J_p is the number flux vector (particles/m²/sec), n_p the number particle concentration (particles/m³), and \mathfrak{D} a diffusion coefficient (m²/sec).

The diffusion coefficient depends strongly on particle size, with smaller particles diffusing much more efficiently than larger particles. Table 6.1 gives values of the diffusion coefficient in air for particles of various sizes. The effect of particle size is strong: under the same concentration gradient the diffusive mass flux of a 0.01 μm particle is about 20,000 times larger than that of a 10 μm particle. A related dimensionless number is the particle Schmidt number defined as in molecular mass transfer,

$$Sc_p = \frac{\nu_g}{\mathfrak{D}} \quad (6.102)$$

where ν_g is the kinematic viscosity of the suspending gas. Table 6.1 lists values of the particle Schmidt number. Generally, the diffusion coefficient of aerosol particles is orders of magnitude smaller than the diffusion coefficient of molecular diffusion in gases, and comparable in magnitude to diffusion coefficients observed in molecular diffusion in liquids. Accordingly, the particle Schmidt number is generally very large, $Sc_p \gg 1$. Hence, as a rule, the concentration boundary layer of aerosol particles is much thinner than the viscous or thermal boundary layers over a surface.

The diffusion coefficient of particles can be determined from

$$\mathfrak{D} = \frac{k_B T_g C_c}{3\pi\mu_g d_p} \quad (6.103)$$

which, without the slip correction factor C_c , is known as the Stokes–Einstein equation. In this equation, $k_B = 1.381 \times 10^{-23}$ J/K is Boltzmann's constant, and the correction factor C_c can be inferred from Eq. (6.91). Note that the diffusion coefficient depends on particle diameter and gas properties (temperature and viscosity), but not on particle physical properties (e.g., density).

A quantity used to characterize the strength of Brownian diffusion is $x_{rms}^2 = \langle [x(t + \Delta t) - x(t)]^2 \rangle$, the root mean square (rms) net displacement of a diffusing particle over a time interval Δt . This displacement is related to the diffusion coefficient through the expression $x_{rms} = \sqrt{2\mathfrak{D}\Delta t}$. The ratio $x_{rms}/V_s \Delta t$, where $V_s \Delta t$ represents the displacement due to gravitational settling, is an indicator of the importance of diffusion. For spherical particles of standard density in air this ratio is of order 1 for $d_p \approx 1$ μm, whereas it is of order 10^3 for $d_p \approx 0.01$ μm and of order 10^{-3} for $d_p \approx 10$ μm. It follows that Brownian diffusion is an important transport mechanism only for small particles of the submicrometer range. Instead, for particles greater than 1 μm in diameter, gravitational settling and inertial effects outweigh diffusional transport.

In turbulent flows particles diffuse due to eddies, an important mechanism that is extensively discussed in the other sections of this Handbook (see, e.g., [Section 12.5](#)).

6.5.3 Inertial Effects — Impaction

In an accelerating flow field, particles are not able to follow perfectly the fluid motion due to their own mass. For instance, in straight-line accelerating (decelerating) motion, aerosol particles lag behind (ahead) the Lagrangian “fluid particles.” In curvilinear motion, for example, in a flow around a body

surface, the particle trajectories deviate from the fluid streamlines and may impinge on the surface. This mechanism, known as *impaction*, is a major deposition mechanism, of great practical importance in inertial size classifiers (e.g., cascade impactors), aerosol sampling, filtering, gas-cleaning equipment, respiratory deposition, and generally, in all processes involving particle collection. Such inertial effects become increasingly important with increasing particle size. As a rule of thumb, inertial effects become important for particles with diameter $\geq 1 \mu\text{m}$.

The extent to which the motion of an aerosol particle adjusts to or deviates from the motion of the fluid is described by three interrelated characteristic parameters: the relaxation time τ_v , the stop distance S_L , and the Stokes number Stk . These parameters are defined below for the case of Stokesian particles (strictly for $Re_p < 0.1$, but to a good approximation also for $0.1 < Re_p < 1$).

The particle relaxation time, or velocity response time, is a time scale characterizing the adjustment of particle velocity to a changing fluid velocity. It is calculated by considering the time required by the particle to reach its terminal settling velocity when released with zero initial velocity in a quiescent fluid. The relaxation time is given by

$$\tau_v = \frac{\rho_p d_e^2 C_c}{18 \mu_g \chi} \quad (6.104)$$

Therefore, by Eq. (6.97), it can be regarded as the settling velocity of a particle on which a unit gravitational acceleration acts, namely, $V_s = \tau_v g$. This permits to derive the following useful expression for the calculation of the terminal velocity V_p of an aerosol particle subjected to a constant force F ,

$$V_p = \tau_v \frac{F}{m_p} \quad (6.105)$$

where m_p is the mass of the particle. The values of particle relaxation times as a function of particle size for particles in air at standard conditions are listed in [Table 6.1](#). It is important to realize that particle relaxation time, and generally inertial effects and impaction, depend not only on the properties of the particle, but also on the properties of the combined particle–fluid system. The dependence on fluid properties is clearly attested by Eq. (6.104), which involves the viscosity of the gas as well as the mean-free path of the gas through the slip correction.

Stop distance is a length scale that characterizes the persistence of a particle to continue its original motion in a changing flow field before it equilibrates again with the fluid motion. The stop distance is simply the initial velocity times the relaxation time:

$$S_L = V_0 \tau_v \quad (6.106)$$

The above result is obtained by considering the distance a particle will travel in still fluid before it comes to rest, following injection with initial velocity V_0 and in the absence of external forces.

The Stokes number, introduced in Section 1.2, is a dimensionless number defined as the ratio of the stop distance to a characteristic length of the flow or, equivalently, the product of a characteristic velocity and the relaxation time divided by a characteristic length:

$$Stk = \frac{S_L}{L} = \frac{V_0 \tau_v}{L} = \frac{\rho_p d_e^2 C_c V_0}{18 \mu_g \chi L} \quad (6.107)$$

The Stokes number is an important similarity parameter used to scale particle trajectories, and hence impaction deposition, in particle-flow systems that are geometrically and hydrodynamically similar. Also, it is a widely used practical criterion to determine the responsiveness of aerosol particles to changes of fluid velocity, thereby predicting if impaction will take place. For $Stk \ll 1$, particles follow closely the fluid motion and do not impact on surfaces, whereas for $Stk \gg 1$ they escape the flow and may deposit by impaction.

It should be noted that all the above definitions assume the validity of Stokes law for the drag force throughout the entire period of motion of the particle. Occasionally, for large particles and high initial

velocities particle motion may be found outside the Stokes regime. Some results on impaction deposition of non-Stokesian particles are given in Section 6.6.2.2.

An important case of inertial transport arises in turbulent flow, stemming from the inability of particles with significant inertia to follow the fluid turbulent eddies. Inertial deposition due to turbulence is commonly referred to as turbulent impaction, eddy impaction or, also, turbophoresis (Reeks, 1983); it is presented in Section 6.6.3.

6.5.4 Motion in an Electric Field

A charged particle placed in an electric field of strength E is subjected to an electrostatic force $F_E = neE$, where n is the number of elementary units of charge on the particle and e the charge of an electron ($e = 1.609 \times 10^{-19}$ C). Large particles frequently acquire multiple charges ($n > 1$), but the probability of charging decreases with decreasing particle size. For small particles usually $n = 1$. Aerosol particles can readily acquire charge through a variety of processes, such as thermionic emission (e.g., in a flame), diffusion charging (attachment of diffusing ions to particles), field charging (collision of particles with ions in a strong electric field, e.g. a corona discharge), or static electrification (e.g., spray electrification). Radioactive aerosols become self-charged by emitting α or β particles, and they may acquire very high charge during radioactive decay.

Electrostatic forces may give rise to appreciable particle drifts due to the high mobility of aerosol particles. The terminal velocity, referred to as electrical drift velocity, can be obtained for the case of a Stokesian spherical particle with the help of Eq. (6.105) as follows:

$$V_E = \frac{neEC_c}{3\pi\mu_g d_p} = neEB \quad (6.108)$$

The above expression is the basic formula used to analyze electrical migration of aerosol particles. It is also customary to use the so-called electrical mobility of the particle, Z , which is the particle velocity in a field of unit intensity, namely,

$$Z = \frac{neC_c}{3\pi\mu_g d_p} \quad (6.109)$$

The electrical mobility is related to the mechanical mobility by

$$Z = neB = qB \quad (6.110)$$

where q is the charge of the particle. In terms of the electrical mobility, the particle velocity in an electrical field is simply written as $V_E = ZE$.

The electrical properties of aerosols find wide application in air cleaning equipment (electrostatic precipitators), electrodynamic levitation techniques (electrodynamic balances), and measurements of particle size distribution (or, generally, in size classification) with electrical mobility analyzers. For information on electrical measurement techniques the reader is referred to the reviews by Flagan (1998, 2001) and Davis (2001).

6.5.5 Phoretic Effects

Besides gravitational and electrostatic forces, aerosol particles may be subjected to a variety of forces arising from other external fields. Such forces, negligible for macroscopic objects, may influence significantly the motion of small aerosol particles because of their high mobility. The induced motion is generally coined after the name of the causal agent and the conjunctive "phoresis," which in Greek means "being carried by." Accordingly, a particle may move by thermophoresis (motion induced by a temperature gradient in the carrier gas), diffusiophoresis (induced by the concentration gradient of a vapor diffusing through the carrier gas), photophoresis (induced by a light beam), radiation pressure (induced by an incident

electromagnetic radiation), sonophoresis or acoustic pressure (induced by acoustic waves). The description below is limited to the two most common phoretic effects: thermophoresis and diffusiophoresis.

6.5.5.1 Thermophoresis

It has been known for long (since the 19th century) that a hot body placed in a dusty gas creates a dust-free zone around it. Indeed, aerosol particles suspended in a nonisothermal gas tend to migrate from the hotter to the colder regions. This movement is called *thermophoresis*: it arises from the asymmetric bombardment exerted on a particle by the gas molecules in the presence of a temperature gradient in the gas. The momentum received on the “hotter side” of the particle is more than that on the “colder side,” and the macroscopic result is the net transport in the direction of decreasing temperature.

The thermophoretic velocity can, thus, be expressed as a function of the local temperature gradient as follows:

$$v_{\text{th}} = -K_{\text{th}} \frac{V_g}{T} \nabla T \quad (6.111)$$

and, by Eq. (6.105), the thermophoretic force is written as $F_{\text{th}} = v_{\text{th}} m_p / \tau_v$. In Eq. (6.111) K_{th} is a dimensionless parameter, the thermophoretic coefficient, that depends on properties of both the gas and the particle. Theoretical expressions for K_{th} have been rigorously derived only in the limits of continuum flow ($d_p \gg \lambda$), the so-called Epstein expression (Fuchs, 1964),

$$K_{\text{th}}^{\text{Epstein}} = \frac{3}{2} \frac{k_g/k_p}{(1 + 2k_g/k_p)} \quad \text{for } Kn \rightarrow 0 \quad (6.112)$$

or in the limit of free molecular flow ($d_p \ll \lambda$), the so-called Waldmann expression (Fuchs, 1964),

$$K_{\text{th}}^{\text{Waldmann}} = \frac{3}{4(1 + \pi/8)} \quad \text{for } Kn \rightarrow \infty \quad (6.113)$$

Talbot and coworkers (Talbot et al., 1980) proposed a fitting formula over the entire range $0 \leq Kn = 2\lambda/d_p \leq \infty$, which agrees to within 20% or better with most of the available experimental data. The fitting formula was obtained by introducing an improved value for the numerical factor in the theoretical expression of Brock (1962), who had suggested an expression for the thermophoretic force valid in the slip-flow regime. The Brock–Talbot expression is

$$K_{\text{th}} = 2C_s \frac{C_c(k_g/k_p + 2C_t\lambda/d_p)}{(1 + 6C_m\lambda/d_p)(1 + 2k_g/k_p + 4C_t\lambda/d_p)} \quad (6.114)$$

In the above equation, k_g/k_p is the ratio of gas-to-particle thermal conductivity and C_c the Cunningham correction factor [cf. Eq. (6.91)]. The order-unity constants C_s , C_t , and C_m arise from noncontinuum effects at the particle interface: they are associated with the temperature and velocity boundary conditions (jump conditions) at the particle–gas interface. The recommended values are $C_s = 1.17$ (thermal creep coefficient), $C_t = 2.18$ (temperature jump coefficient), and $C_m = 1.14$ (velocity jump coefficient).

Figure 6.3 shows the thermophoretic coefficient K_{th} as a function of the Knudsen number $Kn = 2\lambda/d_p$ and parametrized by k_g/k_p . As can be seen, K_{th} has values around 0.5 and becomes a constant for very small particles (free molecular regime). For large particles it depends both on particle size and on the gas-to-particle thermal conductivity ratio. This dependence is due to the nonnegligible temperature gradient established within a particle of appreciable size, which affects locally the temperature gradient of the gas.

6.5.5.2 Diffusiophoresis and Entrainment by Stefan Flow

Particles suspended in a nonequilibrium binary gas mixture, where the two gases interdiffuse, experience unequal momentum transfers by collisions with the molecules of the gas diffusing in one direction and the molecules of the other, oppositely diffusing, gas. A net force is exerted on the particle in the direction of diffusion of the heavier gas molecule. The resulting motion, which is driven by the prevailing concentration

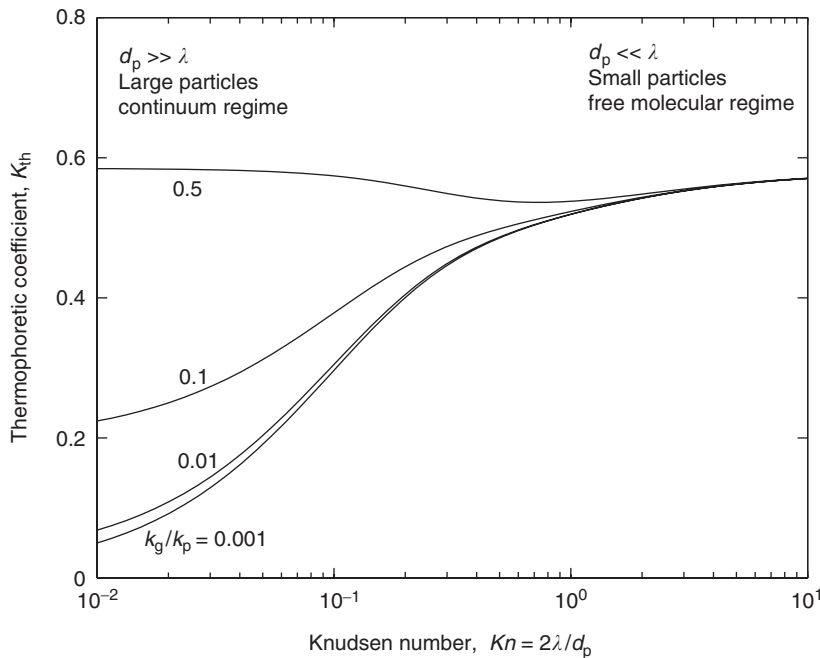


FIGURE 6.3 Thermophoretic coefficient K_{th} as a function of Knudsen number, $Kn = 2\lambda/d_p$, for various gas-to-particle thermal conductivity ratios k_g/k_p .

gradient, is called *diffusiophoresis*. The diffusiophoretic motion of particles should not be confused with the diffusion of particles: the former is driven by the concentration gradient of a diffusing gas, whereas the latter is driven by the concentration gradient of the particles themselves.

The above mentioned fact, i.e., diffusion of two noncondensable gases into each other, is not very usual in aerosol flows. Instead, most practical cases are concerned with diffusion of a condensable vapor through a background gas (e.g., evaporation or condensation of water drops in air, or wall condensation of steam in nitrogen–steam or air–steam mixtures in nuclear safety experiments). Under such circumstances, a secondary convective flow is established within the gas, known as *Stefan flow*, which arises from a subtle mass balance between the diffusive flows of the gas and the vapor. The direction of Stefan flow is always away from an evaporating surface or toward a condensing surface. Therefore, the motion of the particle is determined by the combined action of Stefan flow and diffusiophoresis. The latter still takes place due, as described earlier, to diffusion of vapor and counterdiffusion of gas. For the combined motion due to diffusiophoresis and Stefan flow, Waldmann and Schmitt (1966) provided the following theoretical expression for the particle drift velocity:

$$V_p = - \frac{\sqrt{\mathfrak{M}_1}}{\psi_1\sqrt{\mathfrak{M}_1} + \psi_2\sqrt{\mathfrak{M}_2}} \frac{\mathfrak{D}_{12}}{\psi_2} \nabla \psi_1 \quad (6.115)$$

where $\mathfrak{M}_1, \mathfrak{M}_2$ are the molecular weights of the condensable vapor and the background gas, ψ_1, ψ_2 the molar fraction of the vapor and the gas, and \mathfrak{D}_{12} the binary gas diffusion coefficient. Note that the velocities obtained from Eq. (6.115) are independent of particle size. The predictions of Eq. (6.115) are in very good agreement with the experimental data of Goldsmith and May (1966) that were obtained with small nichrome particles ($0.02 \leq d_p \leq 0.2 \mu\text{m}$) in diffusing water vapor in air and helium. The use of Eq. (6.115) for larger particles requires caution. The measurements of Goldsmith and May (1966) for the case of water vapor in air can be correlated within $\pm 5\%$ as

$$V_p = -1.9 \times 10^{-4} (\text{cm}^2/\text{sec}/\text{mb}) \frac{dp_1}{dx} \quad (6.116)$$

where dp_1/dx is the gradient of the partial pressure of the condensable vapor. If Eq. (6.115) is evaluated for water vapor diffusing in air at standard conditions a numerical expression identical to Eq. (6.116) is recovered [note that $(1/\psi_2)d\psi_1/dx$ can be written as $(1/p_2) dp_1/dx$ where p_2 is the partial pressure of the gas]. Therefore, Eq. (6.116) has the appealing property of being both an empirical and a theoretical formula suitable for the calculation of the particle drift velocity due to combined diffusiophoresis and Stefan flow in water vapor-air systems.

6.6 Convective Transport-Deposition

The behavior of aerosol particles as they are transported in a flowing fluid is of fundamental importance in predicting rates of deposition onto surfaces in a great variety of applications, including gas-cleaning equipment, aerosol filtration, aerosol instrumentation and measurements, nuclear safety relevant experiments, respiratory deposition, etc. For submicrometer particles, and in the absence of external force fields, Brownian or turbulent diffusion are the basic mechanisms that drive deposition. For particles larger than about 1 μm , deposition is primarily due to inertial impaction and gravitational settling.

A basic quantity characterizing convective transport of an aerosol is the *penetration ratio*, or *penetration fraction*, defined as the fraction of the inflowing particles that exit the flow system. It can be written as

$$f_p = \frac{C_{\text{out}}}{C_0} \quad (6.117)$$

where C_{out} and C_0 are the particle concentrations (either mass or number) at the outlet and inlet, respectively. Alternatively, a *removal efficiency*, or *collection efficiency*, can be defined as the fraction of the inflowing particles that is lost by deposition. The removal efficiency is simply related to penetration fraction by

$$n_R = 1 - f_p \quad (6.118)$$

Another quantity widely employed to characterize deposition in convective aerosol flows is *deposition velocity*, defined as

$$V_d = \frac{G_p}{C_{\text{av}}} \quad (6.119)$$

where G_p is the particle mass flux to the wall and C_{av} the average particle concentration above the surface. The latter is taken equal to the average concentration over the cross-section of the conduit, or, in external flow systems, equal to the concentration in the undisturbed stream. The usual boundary condition employed at the wall is that deposited particles are totally absorbed there, thus a zero particle concentration is imposed, $C_w = 0$. Then, Eq. (6.119) can be rewritten as $G_p = V_d(C_{\text{av}} - C_w)$. As seen, deposition velocity should be interpreted as the mass transfer coefficient of the process, and not as the velocity with which particles arrive at the surface (as its name implies).

In closed ducts, flow can be generally considered hydrodynamically fully developed. The particle Schmidt number is large and as a result, velocity profiles develop much more rapidly than particle concentration profiles. Chen and Comparin (1976) demonstrated that the effects of a developing velocity become negligible when $Sc_p \geq 10$, a condition usually satisfied for particles with $d_p > 0.002 \mu\text{m}$.

The most usual cases of convective transport deposition are addressed below. First, cases of convection combined with a single additional transport mechanism (e.g., diffusion, inertial transport, and gravitational settling) are reviewed. The section concludes by addressing two important cases in which all deposition mechanisms act in combination, in particular, filtration and respiratory deposition.

6.6.1 Convective Diffusion from Laminar Flow in Ducts

6.6.1.1 Circular Tube

The analytical solution for the fundamental case of convective diffusion of small particles suspended in laminar flow inside a circular tube, cf. Eq. (6.10) was derived by Gormley and Kennedy (1949). The Gormley and Kennedy solution is a classical result in the aerosol literature and, as such, reproduced here:

$$\begin{aligned} f_p &= 1 - 6.46\Delta^{2/3} + 4.8\Delta + 1.124\Delta^{4/3} + \dots \quad \text{for } \Delta < 0.0312 \\ f_p &= 0.8191 \exp(-14.628\Delta) + 0.0975 \exp(-89.2\Delta) \\ &\quad + 0.0325 \exp(-228\Delta) + \dots \quad \text{for } \Delta > 0.0312 \end{aligned} \quad (6.120)$$

where Δ is the dimensionless parameter,

$$\Delta = \frac{\mathcal{D}L}{D^2U} = \frac{\pi}{4} \frac{\mathcal{D}L}{\dot{V}} \quad (6.121)$$

with L the length of the tube and U the mean velocity through the tube. The parameter Δ corresponds to the standard dimensionless length $L/(D Re Sc_p)$ commonly used in the mass transfer literature. However, in the aerosol literature, it has become customary to use expression (6.121) that manifestly shows that deposition depends (for a given aerosol) on the flow rate and the length of the tube and not on the tube diameter. Hence, the same deposition result is obtained by passing the same flow through a single long tube or by cutting it into a large number of parallel short tubes. This principle has found wide application in the design of diffusion batteries, apparatuses relying on convective diffusional losses in laminar flow to determine the diffusion coefficient and thus particle size. It can also be used to analyze convective diffusion inside a tube bundle (Housiadas et al., 1998).

Ingham (1975) derived a single asymptotic expression for the penetration fraction that is valid for both large and small values of Δ :

$$\begin{aligned} f_p &= 0.819 \exp(-14.63\Delta) + 0.0976 \exp(-89.2\Delta) + 0.0325 \exp(-228\Delta) \\ &\quad + 0.0509 \exp(-125.9\Delta^{2/3}) \end{aligned} \quad (6.122)$$

Equation (6.122) is accurate to better than 0.5% for all values of Δ as compared with other accurate solutions. Furthermore, a working expression for the case of plug flow (uniform velocity) is (Ingham, 1975)

$$\begin{aligned} f_p &= \frac{4}{\alpha_1^2} \exp(-4\alpha_1^2\Delta) + \frac{4}{\alpha_2^2} \exp(-4\alpha_2^2\Delta) + \frac{4}{\alpha_3^2} \exp(-4\alpha_3^2\Delta) \\ &\quad + \left\{ 1 - 4 \left(\frac{1}{\alpha_1^2} + \frac{1}{\alpha_2^2} + \frac{1}{\alpha_3^2} \right) \right\} \exp \left[- \frac{8\Delta^{1/2}}{\sqrt{\pi} [1 - 4(1/\alpha_1^2 + 1/\alpha_2^2 + 1/\alpha_3^2)]} \right] \end{aligned} \quad (6.123)$$

where α_1 , α_2 , and α_3 are the first three zeros of the Bessel function J_0 , which, to an accuracy of four decimal points, are $\alpha_1=2.4048$, $\alpha_2=5.5201$, and $\alpha_3=8.6537$. As mentioned before, Eq. (6.123) is valid for all dimensionless lengths Δ to an accuracy of better than 0.5%. Expression (6.123), in combination with Eq. (6.122), permits the calculation of the envelop values of f_p for the case of a hydrodynamically developing flow at the entrance of a tube.

6.6.1.2 Nonuniform Inlet Concentration

In practical situations, the distribution of aerosol mass at the inlet of the tube may deviate from uniformity. Consider, for example, the case of an aerosol flow through a circular tube with nonuniform inlet concentration, whose profile is described as a function of the dimensionless radial coordinate $r^*=r/R$ by a polynomial of degree K :

$$C_0 \sim a_0 + a_1 r^* + a_2(r^*)^2 + a_3(r^*)^3 \dots a_K(r^*)^K \quad (6.124)$$

The penetration ratio can be calculated with the help of the series solution of the convective diffusion equation and methods proposed by Housiadis et al. (1999, 2000),

$$f_p = -8 \sum_{n=1}^{\infty} \frac{I_n \exp(-2\lambda_n^2 \Delta)}{\lambda_n \Lambda_n} \quad (6.125)$$

In the expression above the constants I_n are determined by

$$I_n = a_0(E_1^n - E_3^n) + a_1(E_2^n - E_4^n) + \dots + a_K(E_{K+1}^n - E_{K+3}^n) \quad (6.126)$$

whereas the coefficients E_j^n are calculated from the recurrence relation

$$E_j^n = \frac{R_n}{\lambda_n^2} + \frac{(j-3)^2}{\lambda_n^2} E_{j-4}^n + E_{j-2}^n, \quad j = 4, 5, \dots, K+3 \quad (6.127)$$

Table 6.3 gives the eigenvalues λ_n and constants Λ_n , R_n , E_0^n , E_1^n , and E_3^n required in the numerical evaluation of the solution up to order $n = 5$. By using five terms, the series solution (6.125) converges to the correct result with an accuracy of better than 1% for all dimensionless lengths $\Delta > 4 \times 10^{-4}$ (better than 2% for all dimensionless lengths $\Delta > 5 \times 10^{-5}$, i.e., for all practical values of Δ).

6.6.1.3 Ducts of Other Geometry

Flat rectangular geometry is generally considered the most efficient geometry for the collection of submicrometer particles. Accurate solutions have been derived for particle penetration through a rectangular channel of long-side W and short-side H with $W \gg H$ (Tan and Thomas, 1972; Bowen et al., 1976):

$$f_p = 1 - 1.526\Delta^{2/3} + 0.15\Delta + 0.0342\Delta^{4/3} \quad \text{for } \Delta \leq 0.05 \quad (6.128)$$

$$\begin{aligned} f_p = & 0.9104 \exp(-2.8278\Delta) + 0.0531 \exp(-32.147\Delta) \\ & + 0.01528 \exp(-93.475\Delta) + 0.00681 \exp(-186.805\Delta) \quad \text{for } \Delta > 0.05 \end{aligned} \quad (6.129)$$

The dimensionless parameter Δ is defined as $\Delta = 8\mathfrak{D}L/3UH^2 = 8\mathfrak{D}LW/3VH$. Hinds (1999) suggests a simplified form of the above expressions by neglecting the last term of Eq. (6.128) and the two last terms of Eq. (6.129). With these simplifications, the calculated penetration fractions agree within 1% with more accurate predictions over the whole range of values of Δ .

The case of a circular-tube annular cross-section has been treated by Kerouanton et al. (1996), who presented the solution as an infinite series

$$f_p = \sum_{n=1}^{\infty} K_n \exp(-2\lambda_n^2 \Delta) \quad (6.130)$$

TABLE 6.3 Eigenvalues and Related Constants for the Numerical Evaluation of the Series Solution, Eq. (6.125).

	λ_n	R_n	Λ_n	E_0^n	E_1^n	E_2^n	E_3^n
1	2.7044	-1.0143	-0.5009	0.5782	0.1968	0.0979	0.0581
2	6.6790	1.3492	0.3715	0.0512	-0.0830	-0.0707	-0.0527
3	10.6734	-1.5723	-0.3183	0.1518	0.0526	0.0449	0.0388
4	14.6711	1.7460	0.2865	0.0256	-0.0385	-0.0347	-0.0304
5	18.6699	-1.8909	-0.2645	0.0864	0.0303	0.0275	0.0249

Source: Adapted from Housiadis, C. et al., *Int. J. Heat Mass Transfer*, 42, 3013, 1999; *J. Aerosol Sci.*, 31, 959, 2000.

with

$$\Delta = \frac{\mathfrak{D}L}{4U(R_2 - R_1)^2} = \frac{\pi}{4} \frac{\mathfrak{D}L}{\dot{V}}$$

where R_2 and R_1 are the outer and inner radii of the annulus, respectively. Table 6.4 provides the first three eigenvalues λ_n and coefficients for different R_1/R_2 ratios, as reported in Kerouanton et al. (1996). The use of the three terms in the series enables an accurate evaluation of the solution for $\Delta > 0.005$.

6.6.2 External Flows

Here the collection of particles by objects placed in an unconfined aerosol flow is considered. There is a great variety of practical cases involving external aerosol flow as, for example, particle capture by fibers in a filter, buildup of deposits on the outer surfaces of heat exchanger tube bundles, icing of airplane wings, particle scavenging by falling raindrops, and deposition from the atmosphere on rough elements of the surface.

In flows around bodies, the particle removal (collection) efficiency n_R is defined as the ratio of the particles collected by the body to the particles geometrically incident on the body, as shown in the schematic diagram of Figure 6.4.

6.6.2.1 Deposition at Low Stokes Number ($Stk \ll 1$)

This generally refers to particles with $d_p < 1 \mu\text{m}$ for which the basic deposition mechanism is diffusion and, occasionally, direct interception. The latter arises from the finite physical size of the particle, which results in capture when the particle trajectory, although not directed to the surface, passes by within a distance of one particle radius. Interception is characterized by the dimensionless parameter

$$R = \frac{a_p}{L} \quad (6.131)$$

where a_p is the particle radius and L a characteristic dimension of the body. For macroscopic bodies $R \ll 1$ and interception can be ignored or, equivalently, particles can be taken as point particles.

TABLE 6.4 First Eigenvalues and Coefficients for Different R_1/R_2 Ratios of a Circular-tube Annulus

R_1/R_2	0.05	0.1	0.25	0.5	0.75	0.9	0.95
λ_1	3.493	3.6102	3.7641	3.8507	3.8776	3.8828	3.8833
λ_2	7.906	8.0870	8.3141	8.4356	8.4728	8.4798	8.4805
λ_3	12.31	12.557	12.866	13.033	13.083	13.093	13.094
K_1	0.879	0.889	0.9004	0.9076	0.9098	0.9103	0.91034
K_2	0.036	0.026	0.0118	0.0033	0.0006	0.00007	0.00002
K_3	0.044	0.046	0.050	0.052	0.053	0.05312	0.05314

Source: Adapted from Kerouanton et al., *J. Aerosol Sci.*, 27, 345, 1996.

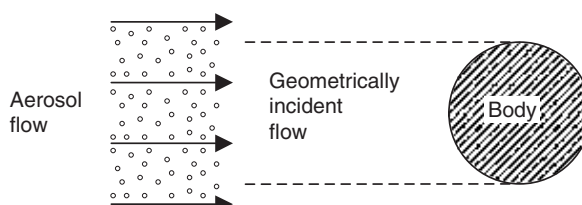


FIGURE 6.4 Schematic representation for particle collection efficiency in an external aerosol flow around a body.

However, interception may be important in deposition onto very fine objects like filter fibers or for particles small in terms of Stokes diameter, but of elongated form like asbestos or mineral fibers.

If interception can be ignored, the problem of aerosol deposition becomes formally identical to the problem of convective heat transfer in an external flow, for which extensive amount of information is available in standard books. For combined diffusion and interception, Friedlander (2000) gives a detailed analysis for an aerosol flow around a cylinder placed with its axis normal to the flow.

For $Re < 1$ (e.g., around a filter fiber), the analysis leads to the functional relationship

$$n_R R \text{Re} S_{\text{C}_p} = \frac{\pi V_{\text{d,mean}} d_p}{\mathfrak{D}} = f(\Pi) \quad \text{for } Re < 1 \quad (6.132)$$

where $V_{\text{d,mean}}$ is the mean deposition velocity (taken over the whole circumference of the cylinder). In Eq. (6.132), Π is a dimensionless group dependent on the interception parameter, the Reynolds number, and the particle Schmidt number,

$$\Pi = R(A \text{Re} S_{\text{C}_p})^{1/3} \quad (6.133)$$

where $A = (4 - 2 \ln Re)^{-1}$. The function f in Eq. (6.132) cannot be analytically determined, but the dependence of n_R on particle size can be shown to exhibit a characteristic U-shape variation, i.e., it passes through a minimum. First, n_R decreases with increasing particle size, because diffusion decreases with increasing particle size, until a size is reached where the interception parameter R becomes nonnegligible, and interception becomes effective by reversing the decreasing trend. An analytical solution can be obtained for the deposition velocity at the forward stagnation point, $V_{\text{d},0}$, which reads

$$V_{\text{d},0} = \frac{(2\mathfrak{D}/d_p) \exp(-AR^3 \text{Re} S_{\text{C}_p}/3)}{\int_1^\infty \exp(-AR^3 \text{Re} S_{\text{C}_p} z/3) dz} \quad (6.134)$$

Although the above result applies only at the region of the forward stagnation point, the deposition is greatest there and it reflects the dependence on Re and S_{C_p} over the entire cylinder.

The case $Re \gg 1$ (e.g., around macroscopic objects) was analyzed in Fernández de la Mora and Friedlander (1982). Based on this analysis, approximate expressions were provided by Parnas and Friedlander (1984) for cylinders and spheres. For cylinders

$$n_R = 1.88 \text{Re}^{-1/2} S_{\text{C}_p}^{-2/3} + 0.8R^2 \text{Re}^{1/2} \quad \text{for } 10^2 < Re < 10^4 \quad (6.135)$$

and for spheres

$$n_R = 2.40 \text{Re}^{-1/2} S_{\text{C}_p}^{-2/3} + 1.10R^2 \text{Re}^{1/2} \quad \text{for } 10^2 < Re < 10^4 \quad (6.136)$$

6.6.2.2 Deposition at High Stokes Number ($Stk \gg 1$)

This case is mainly concerned with particles greater than 1 μm in diameter. Such particles are primarily deposited by inertial impaction. In this case the removal efficiency n_R is usually called impaction efficiency. Figure 6.5 shows the removal efficiency by impaction on a single sphere, a single cylinder placed normal to the flow, and an airfoil placed with zero angle of attack. The data are taken from Golovin and Putnam (1962) who surveyed experimental and theoretical results on inertial impaction on single elements for bodies of various shapes. They are presented in terms of removal (impaction) efficiency as a function of Stokes number. In Figure 6.5 the Stokes number does not include the Cunningham correction factor, cf. Eq. (6.107), because as such it was used in the original data. This exclusion is not a serious limitation, as for supermicrometer particles slip correction is close to unity (see Table 6.1). The parameter Φ_p shown in Figure 6.5 is $\Phi_p = Re_p^2/Stk$ and accounts for deviations from the Stokes regime. For $\Phi_p = 0$ particle motion obeys the Stokes law. The results with $\Phi_p = 2000$ correspond to non-Stokesian particle behavior.

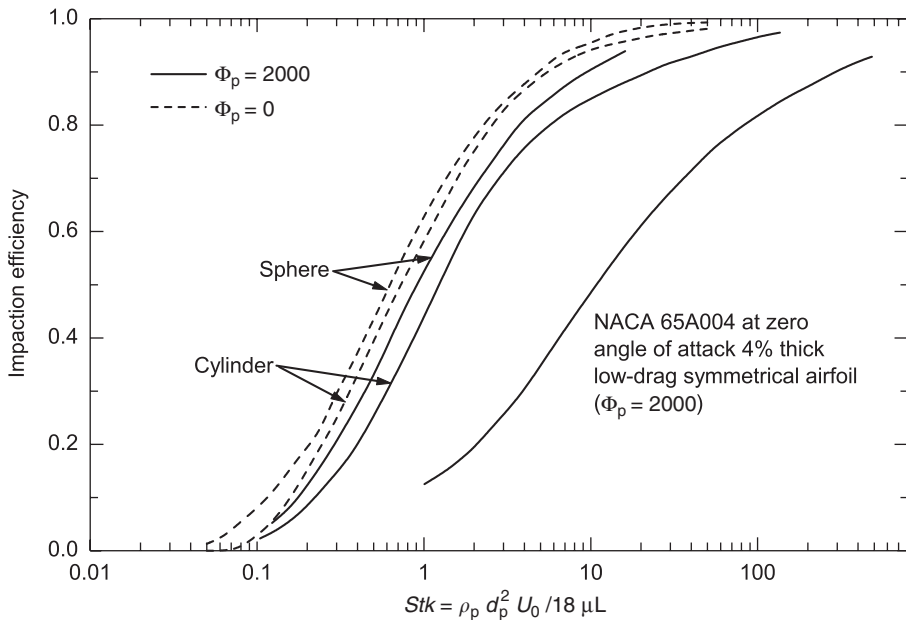


FIGURE 6.5 Impaction efficiency as a function of Stokes number for a number of different target shapes: for cylinder and sphere, L = diameter; for airfoil, L = thickness (maximum distance between upper and lower surfaces of the cross-section).

6.6.3 Turbulent Flow

Under turbulent flow conditions, small particles of the submicrometer range migrate from the flow to the wall, primarily by the action of Brownian and turbulent diffusion. For larger particles, inertial deposition becomes the dominant mechanism, largely overwhelming diffusional deposition. The underlying phenomenology of inertial deposition has been discussed before (Section 6.5.3). Statistically, more particles are inertially transported (injected) from regions of high turbulence intensity to regions of lower intensity. The net result is a significant enhancement of deposition, as well as a preferential accumulation of particles close to the wall. The situation is illustrated in Figure 6.6, which shows results from many experiments on deposition in turbulent pipe flow in terms of the (dimensionless) deposition velocity as a function of (dimensionless) particle relaxation time. The dimensionless particle relaxation time is defined by $\tau_v^* \equiv \tau_v(u^*)^2/v_g$ where u^* is the friction velocity, and the dimensionless deposition velocity is $V_d^* \equiv V_d/u^*$, with V_d the deposition velocity [see also Eq. (6.119)]. For $\tau_v^* < 0.3$ deposition is almost exclusively due to gradient diffusion, whereas for $\tau_v^* > 0.3$ inertial effects become important, resulting in a spectacular increase in deposition velocity with particle size. The theoretical investigation of particle interactions with turbulence is a vast area of intensive research. The subject is thoroughly discussed in other parts of this Handbook (see Section 13.4). Below, the discussion is limited to providing practical means for the calculation of particulate deposition in turbulent flow.

For fully developed turbulent flow in a circular pipe of length L , the deposition velocity V_d may be considered as nonvarying along the tube, and the penetration fraction can be expressed as

$$f_p = \exp\left(-\frac{4V_d L}{UD}\right) \quad (6.137)$$

The above expression results from a simple mass balance along the tube and enables the calculation of penetration through knowledge of the deposition velocity.

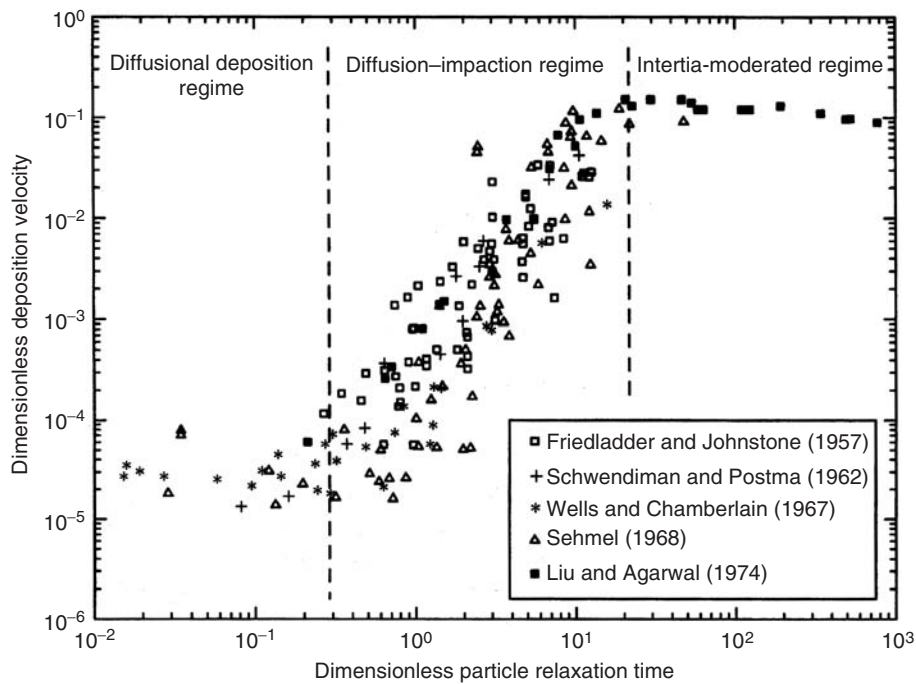


FIGURE 6.6 Particle deposition from fully developed turbulent pipe flow: a summary of experimental data. (From Young, J. and Leeming, A., *J. Fluid Mech.*, 340, 129, 1997. With permission from Cambridge University Press.)

For deposition in the diffusional regime, the expression for deposition velocity proposed by Wells and Chamberlain (1967) can be used:

$$V_d/u^* = 0.2Sc_p^{-2/3}Re^{-1/8} \quad (6.138)$$

The above correlation applies for particles with $\tau_v^* < 0.3$. In most of the cases, this condition is satisfied for particles with diameter $d_p < 1 \mu\text{m}$. For deposition in the impaction regime ($\tau_v^* > 0.3$, or roughly, for sizes $d_p > 1 \mu\text{m}$), the theory of Friedlander and Johnstone (1957) is frequently used. This theory, known as the "free-flight" or "stop-distance" model, assumes that particles diffuse with an eddy diffusion coefficient equal to that of the fluid up to one stop distance of the wall, where the particles dispose sufficient inertia to escape the flow and reach the wall by flying freely through the quiescent viscous sublayer. The model presents the shortcoming of requiring injection "free-flight" velocities too high in comparison to the fluid radial rms velocities encountered close to the surface. Nevertheless, the model finds wide application because it is based on correct physical arguments and has proved very successful in reproducing experimental results. The deposition velocity is calculated as follows:

$$\frac{V_d}{U} = \begin{cases} \frac{f/2}{1 + \sqrt{f/2}(1525/(S_L^*)^2 - 50.6)} & \text{for } S_L^* < 5 \\ \frac{f/2}{1 + \sqrt{f/2}\{5\ln[5.04/(S_L^*/5 - 0.959)] - 13.73\}} & \text{for } 5 \leq S_L^* \leq 30 \\ \frac{f}{2} & \text{for } 30 < S_L^* \end{cases} \quad (6.139)$$

where S_L^* , the dimensionless stop distance, is calculated from Eq. (6.106) using $0.9u^*$ as injection velocity (which approximates the experimentally determined mean square radial fluctuating velocity) to obtain

$$S_L^* = \frac{\rho_g d_p^2 \rho_p U^2 f / 2}{18 \mu_g^2} \quad (6.140)$$

It is also useful to express the deposition velocity as a function of particle relaxation time. In the region $\tau_v^* > 0.3$, the experimental results of Figure 6.6 can be described by

$$V_d/u^* = \min[6 \times 10^{-4}(\tau_v^*)^2, 0.1] \quad (6.141)$$

The above correlation follows very closely the data of Liu and Agarwal (1974) that are the most frequently quoted experimental results among those summarized in Figure 6.6.

6.6.4 Convective-Gravitational Deposition in Ducts

The case of gravitational deposition from laminar flow in a circular tube is analyzed in Fuchs (1964), Pich (1972), and Heyder and Gebhart (1977). The penetration fraction is

$$f_p = 1 - \frac{2}{\pi} [2\Phi\sqrt{1-\Phi^{2/3}} - \Phi^{1/3}\sqrt{1-\Phi^{2/3}} + \arcsin(\Phi^{1/3})] \quad (6.142)$$

$$\Phi = \frac{3LV_s}{4UD} \cos\theta \quad (6.143)$$

for

$$\frac{V_s \sin\theta}{U} \ll 1 \quad (6.144)$$

with θ the inclination angle to the horizontal. The criterion expressed by Eq. (6.144) requires the streamwise component of the particle settling velocity to be small in comparison to the fluid velocity.

For gravitational deposition from turbulent flow inside a circular tube, Fuchs (1964) provides the following approximation:

$$f_p = \exp\left(-\frac{16\Phi}{3\pi}\right) \quad (6.145)$$

with parameter Φ defined as in Eq. (6.143). In general, for the same value of Φ , Eq. (6.145) yields higher penetration fractions than Eq. (6.142). However, the difference is significant only for $\Phi > 0.3$. Instead, for $\Phi < 0.3$ the penetration through the tube is essentially the same for both laminar and turbulent flow conditions.

6.6.5 Deposition in Filters

Filters are the most commonly used means to collect aerosol particles for sampling or air cleaning purposes. There are several types of filters, but the two most important types are fibrous filters and porous membrane filters. Fibrous filters consist of mats of individual fibers (e.g., cellulose fibers or glass fibers) that are arranged normal to the flow. Porous membrane filters consist of films (usually a polymeric material) of a porous structure that allows the air to flow through under pressure. The structure of a fibrous filter is characterized by a high void fraction, or porosity, i.e., the space between fibers is large relative to their diameter. Typically, porosities in fibrous filters range from 70 to greater than 99%, with fibers having diameters between less than 1 μm and 100 μm . Porosities in porous membrane filters are typically

between 50 and 90%, and the pore sizes are 0.01 to 10 μm . Despite the differences in structure, both fibrous filtering and porous membrane filtering rely on the same collection mechanisms. The filtering characteristics of a porous membrane filter are equivalent to those of a fibrous filter having fibers with a diameter that is slightly less than the actual pore size. The choice of a given type is mostly based on post-sampling criteria, rather than collection characteristics.

It is important to realize that an aerosol filter does not work like a sieve, where particles smaller than the holes pass and larger particles are collected, but rather as a trap that collects all sizes. The "holes" in fibrous filters are much larger than particles but the latter are very efficiently collected by the fibers as they flow through the holes by the combined action of various deposition mechanisms, namely, diffusion, interception, inertial impaction, gravitational settling, and, occasionally, electrostatic deposition.

Single fiber efficiency can be analyzed using the same principles discussed in Section 6.6.2. The overall collection efficiency of a filter can be shown to depend on the collection efficiency of a single fiber and the volume fraction of fibers. The collection efficiency of a filter as function of particle size is shown in Figure 6.7. The trend is characteristic in aerosol filtering: large particles deposit very efficiently due to impaction and, eventually, gravitational sedimentation; small particles deposit efficiently as well, as they undergo significant Brownian diffusion due to their high diffusion coefficient. In between, there is a size range where retention drops, because particles are too large to diffuse effectively and too small to exhibit significant inertial effects. In this size range, the transition from diffusion to interception takes place and the characteristic U-shaped variation with size is obtained, as discussed in Section 6.6.2.1. As Figure 6.7 shows aerosol filtration exhibits a rather counterintuitive behavior: the difficulty is not in collecting ultra-fine particles from a flow, but particles of intermediate sizes. The particle size corresponding to the minimum efficiency point is called the most penetrating particle size. As shown in Figure 6.7, this size also depends on the velocity at the face of the filter. Depending on the filter and velocity, the minimum

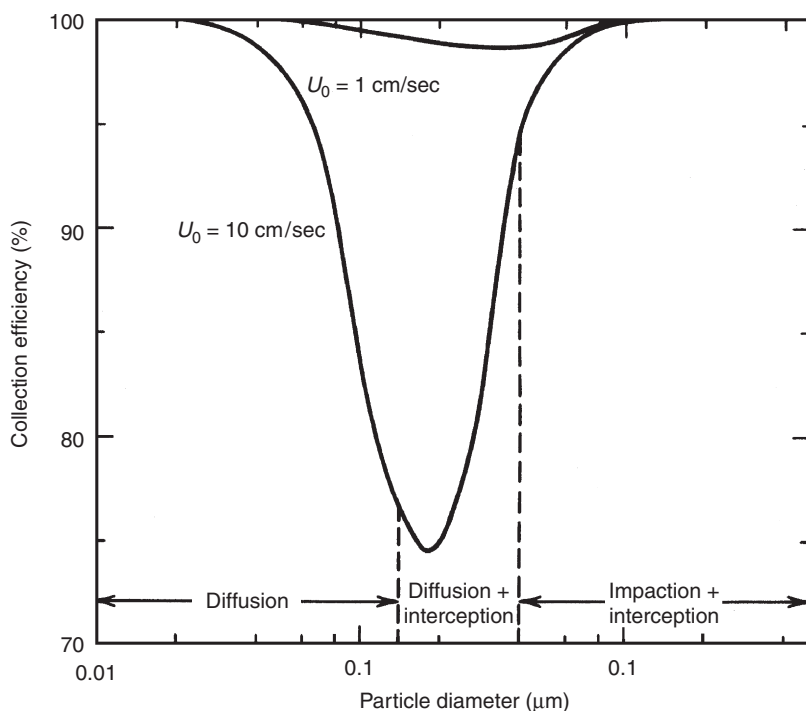


FIGURE 6.7 Filter collection efficiency vs. particle size for face velocities of 0.01 and 0.1 m/sec; the filter thickness is 1 mm and the fiber diameter 2 μm . (From Hinds W.C., *Aerosol Technology: Properties, Behavior, and Measurement of Airborne Particles*, 2nd ed., Wiley, New York, 1999. This material is used by permission of John Wiley & Sons, Inc.)

efficiency is usually in the range 0.05 to 0.5 μm , but is generally taken to be approximately at $d_p = 0.3 \mu\text{m}$. This is the basis for the standard DOP (dioctyl phthalate) test method, where DOP particles of 0.3 μm in diameter are used to characterize the collection efficiency of high-efficiency particulate air (HEPA) filters.

Aerosol filtration is a vast domain. Other important issues in aerosol filtration are pressure drop, loading and clogging, selection criteria, etc. For detailed information the reader may refer to Davies (1973) and Brown (1993).

6.6.6 Respiratory Deposition

Respiratory deposition refers to the convective transport processes that determine the quantity of airborne material in the inspired air that remains in the respiratory system, and in which part of the system. Such analyses originated for radiological protection purposes, in relation with the assessment of doses incurred to the lungs of workers in nuclear industry. In recent times, they embrace a much broader application range, and are of importance in inhalation toxicology, drug delivery (pharmaceutical aerosols), occupational hygiene, industrial hygiene, or environmental health.

The respiratory system consists of organs of complicated anatomy, morphology and physiology. An accurate description of the convective transport requires very complicated modeling of geometry and flow. There are many analyses based on computational fluid dynamics (CFD) which enable a detailed description of particulate deposition in selected elements of the respiratory system in isolation from the rest of the system (e.g., in the nasopharyngeal region, in an alveolated duct, etc.). However, a sophisticated CFD-based methodology cannot be implemented in a practical (i.e., routinely operational) model owing to its complexity and computing resource requirements. To treat the respiratory system as a whole, modeling is necessarily based on approximations and some empiricism. The recommended model for practical calculations is the model proposed by the International Commission on Radiological Protection (ICRP) (ICRP, 1994).

According to the ICRP model the human respiratory tract (RT) is divided into five regions: (1) the anterior nose (code-named ET1); (2) the posterior nasal passage together with larynx, pharynx, and mouth (ET2); (3) the bronchial region comprising the trachea and bronchi (BB); (4) the bronchiolar region comprising the bronchioles and terminal bronchioles (bb); and (5) the alveolar-interstitial region comprising the respiratory bronchioles, the alveolar ducts, and the alveoli (AI). Regions ET1 and ET2 make up the *extrathoracic* part of the RT, also known as *head airways region* or *nasopharyngeal region*. Regions BB, bb and AI make up the *thoracic* part of the system. Often, the two regions BB and bb are taken together as a single region, called *tracheobronchial region*. The alveolar-interstitial region, AI, is also termed *alveolar region*, *pulmonary region*, or *acinar region*. The flow path can be regarded as a series of bifurcating tubes that become smaller in diameter, shorter, and more numerous as they penetrate deeper into the lung (like a tree). According to the classical morphometric model of Weibel (1963), there is a sequence of 24 airway generations (23 levels of bifurcations), which branch symmetrically (dichotomously), with trachea being generation zero and alveoli generation 23. The geometrical characteristics differ significantly among generations: generation 0 consists of 1 airway with $D = 1.8 \text{ cm}$ and $L = 12 \text{ cm}$; generation 23 consists of 2^{23} airways with $D = 0.041 \text{ cm}$ and $L = 0.050 \text{ cm}$ each.

During normal breathing, the inhaled air is approximately 500 cm^3 per breath. This volume is called *tidal volume*. The tidal volume is mixed with the volume of air reserved deep in the lungs, called functional residual capacity. The volumetric flow rate of inspired air, equal to the product (tidal volume) \times (respiratory frequency), is called *ventilation rate* or *breathing rate*, and corresponds to the flow rate that is convected in and out during the breathing cycle. [Table 6.5](#) lists reference values of ventilation rates to be employed in respiratory deposition calculations.

Not all particles present in the inspired air enter through the nose or mouth during inhalation. The situation is similar to what is normally encountered in aerosol sampling, where losses exist at the inlet of the sampler due to distortion of the streamlines and particle inertia. *Inhalable Fraction* (IF), or *inhalability*, is called the ratio between particle concentration in the inhaled air and particle concentration in the

ambient air. The ICRP standard gives the following expression for inhalability, as a function of particle aerodynamic diameter d_a (expressed in μm) and wind speed U (in m/sec):

$$IF = 1 - 0.5 \left(1 - \frac{1}{7.6 \times 10^{-4} d_a^2 + 1} \right) + 10^{-5} U^{2.75} \exp(0.055 d_a) \quad (6.146)$$

Figure 6.8 shows the inhalable fraction calculated with the above expression for various wind speeds. It is seen that particles with $d_a < 2 \mu\text{m}$ are predicted to be 100% inhalable. For particles with $d_a > 2 \mu\text{m}$ inhalability is less than 1. With light wind only 50% of the very large particles effectively enter the human body. However, under conditions of strong wind and for very large particles, inhalability may become even greater than 1.

In respiratory deposition, most of the convective transport mechanisms and processes are present. The relative importance of each mechanism depends on particle size and flow characteristics in each region of the RT. In the head airways, impaction is important because the flow is turbulent and abrupt changes in flow direction take place. In the tracheobronchial region the flow is mainly laminar and impaction becomes less important, except at the branching points (called carina) of the first generations. Deeper in

TABLE 6.5 Reference Ventilation Rates According to the ICRP Standard (ICRP, 1994) for a General Caucasian Population at Different levels of Activity

Age	Ventilation Rate (m^3/h)			
	Sleep	Rest, sitting	Light exercise	Heavy exercise
Adult male	0.45	0.54	1.5	3.0
Adult female	0.32	0.39	1.25	2.7
Child (10 year boy)	0.31	0.38	1.12	2.22
Child (10 year girl)	0.31	0.38	1.12	1.84
Child (5 year)	0.24	0.32	0.57	N/A

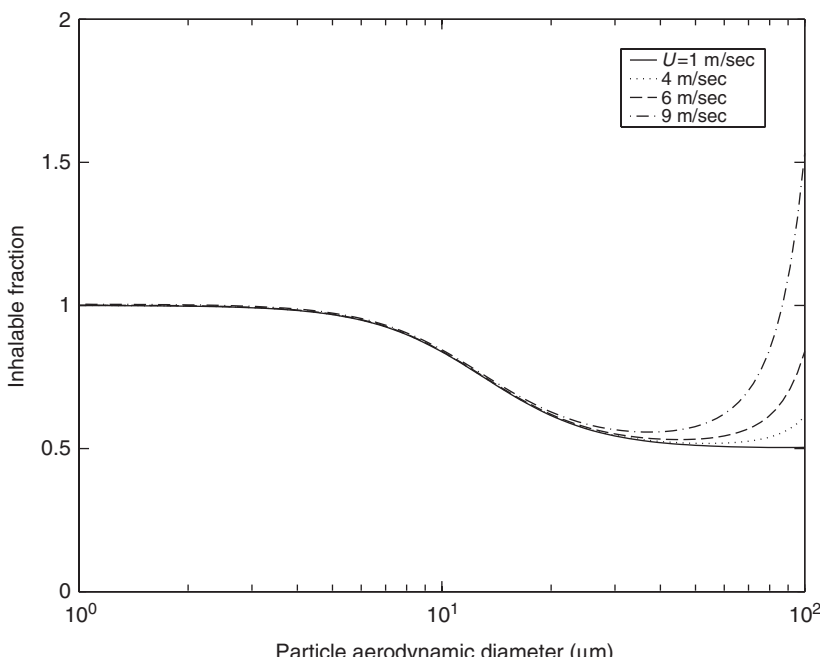


FIGURE 6.8 Inhalability fraction as a function of particle aerodynamic diameter and wind speed.

TABLE 6.6 Regional Deposition Data Calculated with the ICRP Model (ICRP, 1994)

d_a (μm)	Adult					Child (5 year)					Child (10 year)				
	ET1	ET2	BB	bb	AI	ET1	ET2	BB	bb	AI	ET1	ET2	BB	bb	AI
0.001	19.85	45.88	9.99	20.12	2.12	—	—	—	—	—	20.00	46.32	10.67	18.69	1.90
	39.76	40.31	8.02	10.11	0.35	40.70	41.05	9.44	6.99	0.11	39.78	40.32	8.19	9.73	0.39
	42.23	42.25	9.77	3.96	0.01	42.33	42.33	10.47	3.26	0.00	42.25	42.26	9.99	3.74	0.01
0.002	14.79	32.68	8.10	28.89	11.66	—	—	—	—	—	14.96	33.09	8.80	27.67	10.83
	29.67	31.78	8.58	22.22	4.32	30.75	32.75	11.01	18.87	2.27	29.68	31.79	8.80	21.32	4.59
	32.62	34.40	13.05	14.80	0.44	32.73	34.51	14.48	13.45	0.39	32.63	34.42	13.45	14.36	0.48
0.005	2.67	16.38	3.98	23.81	40.98	—	—	—	—	—	7.80	16.68	4.39	23.45	38.88
	15.39	17.36	5.23	26.46	27.66	16.16	18.21	7.21	27.01	20.51	15.41	17.38	5.39	25.09	27.91
	17.54	19.69	9.55	30.56	10.67	17.63	19.79	10.89	29.33	10.28	17.55	19.71	9.89	29.57	11.15
0.01	4.35	9.14	2.05	15.26	57.30	—	—	—	—	—	4.54	9.62	2.36	15.80	51.53
	8.58	9.68	2.83	18.77	48.14	9.27	10.55	4.14	21.53	36.33	8.74	9.91	3.00	18.29	45.52
	9.80	11.07	5.42	26.55	28.87	9.95	11.27	6.32	26.46	26.65	9.85	11.14	5.65	25.74	28.87
0.02	2.72	5.64	1.19	9.81	51.29	—	—	—	—	—	2.92	6.10	1.40	10.42	42.27
	5.17	5.75	1.64	12.43	50.00	5.86	6.58	2.53	15.40	34.16	5.47	6.12	1.80	12.52	42.74
	5.62	6.27	3.03	18.67	38.92	5.99	6.73	3.75	19.86	31.56	5.81	6.50	3.27	18.63	35.96
0.05	1.51	3.02	0.63	5.02	27.40	—	—	—	—	—	1.59	3.19	0.73	5.19	21.01
	2.91	3.07	0.91	6.71	29.62	3.24	3.45	1.37	8.13	18.31	3.04	3.22	0.97	6.58	23.19
	3.15	3.36	1.71	10.84	27.61	3.38	3.62	2.11	11.33	19.58	3.28	3.50	1.84	10.71	23.52
0.1	0.92	1.78	0.40	2.79	14.65	—	—	—	—	—	0.96	1.85	0.45	2.83	10.97
	1.81	1.81	0.58	3.84	16.38	1.98	1.99	0.85	4.53	9.78	1.87	1.86	0.61	3.68	12.44
	2.00	2.04	1.12	6.47	16.20	2.10	2.14	1.35	6.55	10.95	2.05	2.09	1.19	6.27	13.40

	0.74	1.14	0.26	1.56	7.93	—	—	—	—	—	0.85	1.23	0.29	1.56	5.87
0.2	1.44	1.23	0.37	2.17	9.01	1.77	1.48	0.53	2.52	5.27	1.76	1.45	0.38	2.04	6.72
	1.28	1.22	0.72	3.76	9.19	1.39	1.30	0.86	3.73	6.06	1.32	1.25	0.76	3.59	7.49
	2.88	3.02	0.62	0.76	5.88	—	—	—	—	—	3.57	3.86	0.70	0.75	4.24
0.5	5.51	5.18	0.32	1.05	6.62	7.50	7.54	0.38	1.18	3.70	7.73	7.83	0.38	0.95	4.73
	1.75	1.35	0.40	2.00	7.20	3.45	2.94	0.47	1.86	4.56	2.44	1.96	0.42	1.83	5.75
	8.18	10.99	2.64	0.78	10.01	—	—	—	—	—	10.01	13.61	2.91	0.74	7.08
1.0	15.86	19.79	1.00	0.87	10.32	19.91	26.77	0.97	0.81	5.44	20.21	27.34	1.19	0.71	6.85
	5.65	5.41	0.35	2.25	12.80	10.99	12.28	0.50	1.48	7.75	7.98	8.24	0.41	1.66	10.09
	14.56	25.18	8.89	2.74	15.20	—	—	—	—	—	15.81	28.49	9.47	2.78	10.53
2.0	28.82	42.53	2.42	1.60	11.43	32.55	48.95	2.06	1.26	5.39	32.70	48.61	2.46	1.25	6.50
	14.83	18.43	0.94	4.41	20.91	23.80	34.05	1.29	2.48	10.96	19.29	25.85	1.13	3.12	15.63
	21.04	43.68	19.54	4.40	5.74	—	—	—	—	—	21.63	47.53	18.00	4.17	3.32
5.0	41.89	48.10	2.42	1.07	2.60	43.56	48.84	1.77	0.80	1.18	43.72	48.66	1.99	0.77	1.19
	31.29	40.26	2.20	4.57	11.73	38.46	47.20	1.88	1.99	4.40	35.19	44.54	2.09	2.94	7.54
	20.19	55.48	7.81	0.08	0.01	—	—	—	—	—	20.35	57.19	6.01	0.05	0.00
10.0	40.32	42.17	1.07	0.12	0.06	40.76	42.16	0.72	0.07	0.02	40.80	42.15	0.74	0.05	0.01
	36.71	41.34	1.85	1.55	1.31	39.29	42.10	1.18	0.49	0.37	38.20	41.87	1.50	0.87	0.74

the bronchial region and in the alveolar region, residence times are longer and duct diameters smaller, so gravitational settling and diffusion become the dominant deposition mechanisms. Also, interception may be an effective mechanism in all regions of the RT for fibrous long in one dimension (e.g., asbestos) particles.

The ICRP model permits to determine the so-called *regional deposition*, i.e., deposition in regions ET1, ET2, BB, bb, and AI. The model considers the RT as a filtering system of five filters in series, each corresponding to one region, followed by the same filters in reverse order to simulate the expiration phase. The filtering efficiencies are semiempirical algebraic expressions derived from experiments, theory, and fittings to numerical results from more advanced models. To implement the model only algebraic calculations are required, however, quite intensive to be performed by hand. The interested reader may find all necessary details to set up a program for the calculation of regional deposition in Chapter 5 of ICRP, (1994). Moreover, relatively inexpensive software suitable for lung deposition calculations are commercially available. Table 6.6 provides detailed regional deposition data for an adult, a 5- and a 10-year child, as obtained with the recommended ICRP model. The data provided are deposited fractions (%) of the inhaled particulate matter (effect of inhalability included), and refer to an average for male and female results. In each row (particle diameter), the upper, middle, and lower values correspond to the “heavy exercise,” “light exercise,” and “sleep” activity levels, respectively. Total deposition is obtained by adding the five regions. Detailed data are given for particles with $d_a < 10 \mu\text{m}$. Larger particles, if they enter into the nose or mouth, are all collected by the head airways of the extrathoracic regions (regions ET1+ET2). Hence, for $d_a > 10 \mu\text{m}$, the total deposited fraction in the respiratory tract is practically equal to the inhalable fraction, Eq. (6.146).

Figure 6.9 shows graphically the total deposition and the depositions in the extrathoracic region (regions ET1 + ET2), the tracheobronchial region (BB + bb), and the alveolar region (AI) as a function of particle size, as inferred from the ICRP model. Monodisperse spheres of standard density (1000 kg/m^{-3}) are considered. The data refer to an average for males and females at the “light exercise” level. The trend is similar to what is typically observed in filtering (see Figure 6.7): large particles, as well as small particles, deposit very efficiently, and in between there is a size range of decreased retention. Roughly, particles with

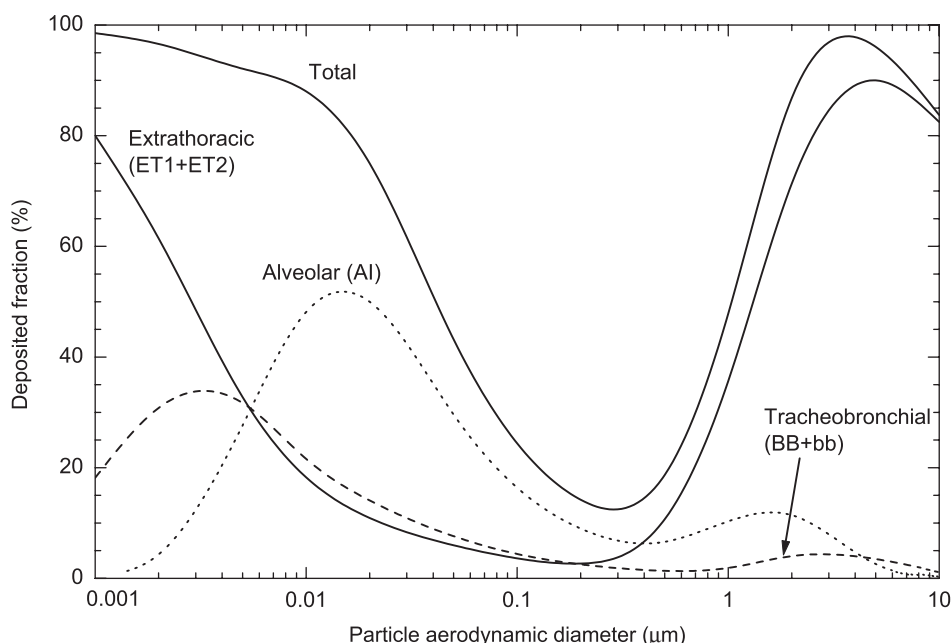


FIGURE 6.9 Deposition fractions in different regions of the respiratory tract for an adult at the “light exercise” activity level as calculated with the ICRP model (ICRP, 1994).

$d_a = 0.3 \text{ } \mu\text{m}$ deposit in the respiratory tract by less than, say, 15% (i.e., more than 85% of the inhaled particulate matter is exhaled). Particles greater than $1 \text{ } \mu\text{m}$ and ultrafine particles smaller than $0.003 \text{ } \mu\text{m}$ deposit practically in the extrathoracic region. The particles that deposit preferentially in the alveolar region, which is the most sensitive with respect to health effects, are in the range $0.007 < d_a < 0.3 \text{ } \mu\text{m}$.

Nomenclature

Latin

a_p	Particle radius
\dot{a}_p	Growth rate
a_p^*	Critical droplet radius
B	Mechanical mobility
C	Concentration (number or mass)
C_c	Cunningham slip correction factor
d_a	Aerodynamic diameter
d_e	Equivalent volume diameter
d_f	Fractal (Hausdorff) dimension
d_s	Stokes diameter
d_p	Particle diameter
D	Tube diameter
\mathfrak{D}	Brownian diffusion coefficient
\mathfrak{D}_{th}	Thermal diffusion coefficient
e	Electronic charge
E	Electric field strength
f	Nonequilibrium number concentration, Helmholtz free energy, Friction factor
f_p	Penetration ratio
F	Force
g	Gravitational acceleration
ΔG	Free energy of formation of a droplet
G	Mass flux
i	Number of molecules in a cluster (i -mer)
i^*	Number of molecules in the critical cluster
I_{nuc}	Nucleation rate
J_{nuc}	Nucleation rate per unit volume
J_o	Nucleation-rate prefactor
\mathbf{J}_p	Particle flux vector
k_B	Boltzmann's constant
K_{th}	Thermophoretic coefficient
K	Collision frequency function
l	Mean free path
L	Length, Latent heat
m	Mass
\mathfrak{M}	Molecular weight
M_j	j-th Moment of the particle size distribution
n	Continuous particle size distribution (number density), number concentration, number of moles
n_{liq}	Bulk liquid number density
n_R	Removal efficiency
n_{vap}	Vapor density
N	Total number concentration, number of particle collisions per unit time, per unit volume
N_A	Avogadro's number

p	Pressure
q	Particle charge
r	Radial vector
R	Radius, Interception parameter (diamensionless)
R_g	Radius of gyration
R_u	Universal gas constant (kJ/k mole-k)
Re	Reynolds number
s	Surface area
S	Saturation ratio ($p_{\text{vap}}/p_{\text{sat}}$)
Sc	Schmidt number
S_L	Stopping distance
Stk	Stokes number
t	Time
T	Temperature
u^*	Friction velocity
u	Carrier gas velocity vector
U	Carrier gas velocity
v	Particle volume
v_p	Particle velocity vector
v_{liq}	Molecular volume in liquid phase
V	System volume
V_d	Particle deposition velocity
V_E	Electrical drift velocity
V_p	Particle velocity
V_s	Settling velocity
Z	Zeldovich nonequilibrium factor, Electrical mobility

Greek Symbols

α	Accommodation coefficient, Monomer evaporative flux
β	Monomer condensation flux
β_v	Inverse particle relaxation time
δ	Dirac delta function
Δ	Dimensionless length
ϵ_d	Energy dissipation rate per unit mass
θ	Inclination angle
ϑ	Contact angle
κ	Thermal conductivity
λ	Mean free path, Eigenvalue
μ	Chemical potential, viscosity
ν	Kinetic viscosity
$\vec{\Pi}_p$	Particle-phase stress tensor
ρ	Density
ρ_p	Particle mass density
σ	Surface tension
σ_∞	Planar surface tension
τ_V	Particle relaxation (response) time
τ_v^*	Dimensionless particle relaxation time
Φ	Interaction potential
χ	Dynamic shape factor
ψ	Mole fraction
Ω	Grand canonical thermodynamic potential

Subscripts

agg	Agglomeration
av	Average
b	Bulk
coag	Coagulation
CNT	Classical Nucleation Theory
drop	Droplet
DFT	Density Functional Theory
g	Gas
g-p	Gas-to-particle conversion
h	Hard-sphere reference fluid
i	Number of molecules in an i-cluster
lig	Liquid
mol	Molecule
nuc	Nucleation
o	Inlet, Initial
out	Outlet
p	Pressure
sat	Saturation ratio
sol	Solution
sur	Surface
th	Thermophoretic
vap	Vapor
w	Wall
∞	Undisturbed flow, Total

Superscripts

*	Dimensionless, Critical droplet
---	---------------------------------

References

- Alam, M.K., The effect of van der Waals and viscous forces on aerosol coagulation, *Aerosol Sci. Technol.*, 6, 41, 1987.
- Barrett, J., Equilibrium and steady-state distributions of vapour clusters in nucleation theory, *J. Phys. A: Math. Gen.*, 27, 5053, 1994.
- Barrett, J., Cluster translation and growth in density functional theories of homogeneous nucleation, *J. Chem. Phys.*, 107, 7989, 1997.
- Barrett, J.C. and Clement, C.F., Growth rates for liquid drops, *J. Aerosol Sci.*, 19, 223, 1988.
- Becker, R. and Döring, W., Kinetische Behandlung der Keimbildung Übersättigten Dampfen, *Ann. Phys.*, (Leipzig) 24, 719, 1935
- Blander, M. and Katz, J.L., Bubble nucleation in liquids, *AIChE*, 21, 833, 1975.
- Bowen, B.D., Levine, S., and Epstein, N., Fine particle deposition in laminar flow through parallel-plate and cylindrical channels, *J. Colloid Interface Sci.*, 54, 375, 1976.
- Bowles, R.K., Reguera, D., Djikaev, Y., and Reiss, H., A theorem for inhomogeneous systems: The generalization of the nucleation theorem, *J. Chem. Phys.*, 115, 1853, 2001.
- Brock, J.R., On the theory of thermal forces acting on aerosol particles, *J. Colloid Sci.*, 17, 768, 1962.
- Brown, R.C., *Air Filtration, An Integrated Approach to the Theory and Applications of Fibrous Filters*, Pergamon Press, Oxford, 1993.
- Cahn, J.W. and Hilliard, J.E., Free energy of a nonuniform system. I. Interfacial free energy, *J. Chem. Phys.*, 28, 258, 1958.

- Cahn, J.W. and Hilliard, J.E., Free energy of a nonuniform system. III. Nucleation in a two-component incompressible fluid, *J. Chem. Phys.*, 31, 688, 1959.
- Chen, R.Y. and Comparin, R.A., Deposition of aerosols in the entrance of a tube, *J. Aerosol Sci.*, 7, 335, 1976.
- Clement, C.F., Aerosol formation from heat and mass transfer in vapour-gas mixtures, *Proc. R. Soc. Lond.*, A 398, 307, 1985.
- Colbeck, I., Introduction to aerosol science, in *Physical and Chemical Properties of Aerosols*, Colbeck, I., Ed., Blackie Academic & Professional (Chapman & Hall), London, 1998.
- Colbeck, I., Eleftheriadis, K., and Simons, S., The dynamics and structure of smoke aerosols, *J. Aerosol Sci.*, 20, 875, 1989.
- Courtney, W.G., Remarks on homogeneous nucleation, *J. Chem. Phys.*, 35, 2249, 1961.
- Davies, C.N., *Air Filtration*, Academic Press, London, 1973.
- Davis, E.J., Electrodynamic levitation of particles, in *Aerosol Measurement: Principles, Techniques, and Applications*, Baron, P.A. and Willeke, K., Eds., Wiley, New York, 2001.
- Debenedetti, P.G., *Metastable liquids: Concepts and principles*, Princeton University Press, Princeton, 1996.
- Dillmann, A. and Meier, G.E.A., A refined droplet approach to the problem of homogeneous nucleation from the vapor phase, *J. Chem. Phys.*, 94, 3872, 1991.
- Drossinos, Y., Kevrekidis, P.G., and Georgopoulos, P.G., Translational invariance in nucleation theories: Theoretical formulation, *Phys. Rev. E*, 63, 036123, 2001.
- Drossinos, Y. and Kevrekidis, P.G., Classical nucleation theory revisited, *Phys. Rev. E*, 67, 026127, 2003.
- Feder, J., Russell, K.C., Lothe, J., and Pound, G.M., Homogeneous nucleation and growth of droplets in vapours, *Adv. Phys.*, 15, 111, 1966.
- Fernández de la Mora, J. and Friedlander, S.K., Aerosol and gas deposition to fully rough surfaces: Filtration model for blade-shaped elements, *Int. J. Heat Mass Transfer*, 25, 1725, 1982.
- Fernández de la Mora, J. and Rosner, D.E., Effects of inertia on the diffusional deposition of small particles to spheres and cylinders at low Reynolds numbers, *J. Fluid Mech.*, 125, 379, 1982.
- Flagan, R.C., History of electrical aerosol measurements, *Aerosol Sci. Technol.*, 28, 301, 1998.
- Flagan, R.C., Electrical techniques, in *Aerosol Measurement: Principles, Techniques, and Applications*, Baron, P.A. and Willeke, K., Eds., Wiley, New York, 2001.
- Ford, I.J., Nucleation theorems, the statistical mechanics of molecular clusters, and a revision of classical nucleation theory, *Phys. Rev. E*, 56, 5615, 1997.
- Frenkel, J., *Kinetic Theory of Liquids*, Dover, New York, 1955 chap. 7.
- Friedlander, S.K. and Johnstone, H.F., Deposition of suspended particles from turbulent gas streams, *Indus. Eng. Chem.*, 49, 1151, 1957.
- Friedlander, S.K., *Smoke, Dust, and Haze: Fundamentals of Aerosol Dynamics*, 2nd ed., Oxford University Press, New York, 2000.
- Fuchs, N.A., *The Mechanics of Aerosols*, Dover Publication Inc., New York, 1964.
- Fuchs, N.A. and Sutugin, A.G., High dispersed aerosols, in *Topics in Current Aerosol Research*, Vol II, Hindy, G.M. and Brock, J.R., Eds., Pergamon, Oxford, 1971.
- Gelbard, F., Modeling multicomponent aerosol particle growth by vapor condensation, *Aerosol Sci. Technol.*, 12, 399, 1990.
- Gelbard, F., Tambour, Y., and Seinfeld, J., Sectional representations for simulating aerosol dynamics, *J. Colloid Interface Sci.*, 76, 541, 1980.
- Girshick, S.L. and Chiu, C.-P., Kinetic nucleation theory: a new expression for the rate of homogeneous nucleation from an ideal supersaturated vapor, *J. Chem. Phys.*, 93, 1273, 1990.
- Goldsmith, P. and May, F.G., Diffusiophoresis and thermophoresis in water vapour systems, in *Aerosol Science*, Davies, C.N., Ed., Academic Press, London and New York, 1966.
- Golovin, M.N. and Putnam, A.A., Inertial impaction on single elements, *Ind. Eng. Chem. Fund.*, 1, 264, 1962.
- Gormley, P.G. and Kennedy, M., Diffusion from a stream flowing through a cylindrical tube, *Proc. Royal Irish Acad.*, 52, 163, 1949.

- Gránásy, L., Nucleation and spinodal decomposition, *Solid State Phenom.*, 56, 67, 1997.
- Heyder, J. and Gebhart, J., Gravitational deposition of particles from laminar aerosol flow through inclined circular tubes, *J. Aerosol Sci.*, 8, 289, 1977.
- Heist, R.H. and He, H., Review of vapor to liquid homogeneous nucleation experiments from 1968 to 1992, *J. Phys. Chem. Ref. Data*, 23, 781, 1994.
- Hind, G.M. and Brock, J.R., *The Dynamics of Aerocolloidal Systems*, Pergamon Press, Oxford, 1970.
- Hinds, W.C., *Aerosol Technology: Properties, Behavior, and Measurement of Airborne Particles*, 2nd ed., Wiley, New York, 1999.
- Housiadas, C., Ezquerro Larrodé, F., and Drossinos, Y., Numerical evaluation of the Graetz series, *Int. J. Heat Mass Transfer*, 42, 3013, 1999.
- Housiadas, C., Ezquerro Larrodé, F., and Drossinos, Y., Convective diffusion in a tube with non-uniform inlet conditions, *J. Aerosol Sci.*, 31, 959, 2000.
- Housiadas, C., Papanicolaou, E., and Drossinos, Y., Combined heat and mass transfer in laminar-flow diffusion nucleation chambers, *J. Aerosol Sci.*, 33, 797, 2002.
- Housiadas, C., Schrader, K.H., and Drossinos, Y., Dehumidification of air flow through cooling at sub-freezing temperatures, *Int. J. Heat Mass Transfer*, 41, 1821, 1998.
- ICRP Publication 66, Human respiratory tract model for radiological protection, Technical Report, Pergamon, 1994.
- Ingham, D.B., Diffusion of aerosols from a stream flowing through a cylindrical tube, *J. Aerosol Sci.*, 6, 125, 1975.
- Israelachvili, J., *Intermolecular and Surface Forces*, 2nd ed., Academic Press, London, 1992.
- Jeong, J.I. and Choi, M., A sectional method for the analysis of growth of polydisperse non-spherical particle undergoing coagulation and coalescence, *J. Aerosol Sci.*, 32, 565, 2001.
- Jokiniemi, J., Lazaridis, M., Lehtinen, K., and Kauppinen, E., Numerical simulation of vapour-aerosol dynamics in combustion processes, *J. Aerosol Sci.*, 25, 429, 1994.
- Kashchiev, D., On the relation between nucleation work, nucleus size, and nucleation rate, *J. Chem. Phys.*, 76, 5098, 1982.
- Kasper, G., On the coagulation rate of aerosols with spatially inhomogeneous particle concentrations, *J. Colloid Interface Sci.*, 102, 560, 1984.
- Kerouanton, D., Tymen, G., and Boulaud, D., Small particle diffusion penetration of an annular duct compared to other geometries, *J. Aerosol Sci.*, 27, 345, 1996.
- Kevrekidis, P.G., Lazaridis, M., Drossinos, Y., and Georgopoulos, P.G., A unified kinetic approach to binary nucleation, *J. Chem. Phys.*, 111, 8010, 1999.
- Koch, W. and Friedlander, S.K., The effect of particle coalescence on the surface area of coagulating aerosols, *J. Colloid Interface Sci.*, 140, 419, 1990.
- Konstandopoulos, A.G., Deposition of inhaled aerosol particles in a generation of the tracheobronchial tree, *J. Aerosol Sci.*, 21, 983, 1990.
- Kostoglou, M. and Konstandopoulos, A.G., Evolution of aggregate size and fractal dimension during Brownian coagulation, *J. Aerosol Sci.*, 32, 1399, 2001.
- Kruis, F.E., Fissan, H., and Peled, A., Synthesis of nanoparticles in the gas phase for electronic, optical and magnetic applications—a review, *J. Aerosol Sci.*, 29, 511, 1998.
- Kulmala, M. and Vesala, T., Condensation in the continuum regime, *J. Aerosol Sci.*, 22, 337, 1991.
- Laaksonen, A., Talanquer, V., and Oxtoby, D.W., Nucleation: measurements, theory, and atmospheric applications, *Annu. Rev. Phys. Chem.*, 46, 489, 1995.
- Laaksonen, A., Ford, I.J., and Kulmala, M., Revised parametrization of the Dillmann-Meier theory of homogeneous nucleation, *Phys. Rev. E*, 49, 5517, 1994.
- Langer, J.S., Theory of the condensation point, *Ann. Phys. (NY)*, 41, 108, 1967.
- Langer, J.S., Statistical theory of the decay of metastable states, *Ann. Phys. (NY)*, 54, 258, 1969.
- Langer, J.S., Metastable states, *Physica*, 73, 61, 1974.
- Langer, J.S. and Turski, L.A., Hydrodynamic model of the condensation of a vapor near its critical point, *Phys. Rev. A*, 8, 3230, 1973.

- Lazaridis, M. New particle formation of ternary droplets in the atmosphere-a steady-state nucleation kinetics approach, *Atmos. Environ.*, 35, 599, 2001.
- Lazaridis, M. and Drossinos, Y., Energy fluctuations in steady-state binary nucleation, *J. Phys. A: Math. Gen.*, 30, 3847 1997.
- Levich, V.G., *Physicochemical Hydrodynamics*, Prentice Hall, Englewood Cliffs, NJ, 1962.
- Lihavainen, H., Viisanen, Y., and Kulmala, M., Homogeneous nucleation of n-pentanol in a laminar flow diffusion chamber, *J. Chem. Phys.*, 114, 10031, 2001.
- Liu, B.Y.H. and Agarwal, J.K., Experimental observation of aerosol deposition in turbulent flow, *J. Aerosol Sci.*, 5, 145, 1974.
- Lothe, J. and Pound, G.M., Reconsiderations of nucleation theory, *J. Chem. Phys.*, 36, 2080, 1962.
- Luijten, C.C.M., Baas, O.D.E., and van Dongen, M.E.H., Homogeneous nucleation rates for *n*-pentanol from expansion wave tube experiments, *J. Chem. Phys.*, 106, 4152, 1997.
- Marini Bettolo Marconi, U. and Tarazona, P., Dynamic density functional theory of fluids, *J. Chem. Phys.*, 110, 8032, 1999.
- Mason, B.J., *The physics of clouds*, Clarendon Press, Oxford, 1971.
- Maxwell, J.C., *The Scientific Papers of James Clerk Maxwell*, Vol. II, Niven, W.D., Ed., Cambridge University Press, Cambridge, 1890, p. 636.
- McGraw, R., Description of aerosol dynamics by the quadrature method of moments, *Aerosol Sci. Technol.*, 27, 255, 1997.
- McGraw, R. and Laaksonen, A., Scaling properties of the critical nucleus in classical and molecular-based theories of vapor-liquid nucleation, *Phys. Rev. Lett.*, 76, 2754, 1996.
- McGraw, R. and Wright, D.L., Chemically resolved aerosol dynamics for internal mixtures by the quadrature method of moments, *J. Aerosol Sci.*, 34, 189, 2003.
- Napari, I., Noppel, M., Vehkämäki, H., and Kulmala, M., An improved model for ternary nucleation of sulfuric acid–ammonia–water, *J. Chem. Phys.*, 116, 4221, 2002.
- Noppel, M., Vehkämäki, H., and Kulmala, M., An improved model for hydrate formation in sulfuric acid–water nucleation, *J. Chem. Phys.*, 116, 218, 2002.
- Nowakowski, B. and Ruckenstein E., A kinetic approach to the theory of nucleation in gases, *J. Chem. Phys.*, 94, 1397, 1991.
- Oxtoby, D. Density functional methods in the statistical mechanics of materials, *Ann. Rev. Mater. Res.*, 32, 39, 2002.
- Oxtoby, D. and Evans, R., Nonclassical nucleation theory for the gas-liquid transition, *J. Chem. Phys.*, 89, 7521, 1988.
- Oxtoby, D.W. and Kashchiev, D., A general relation between the nucleation work and the size of the nucleus in multicomponent nucleation, *J. Chem. Phys.*, 100, 7665, 1994.
- Parnas, R. and Friedlander, S.K., Particle deposition by diffusion and interception from boundary-layer flows, *Aerosol Sci. Technol.* 3, 3, 1984.
- Pich, J., Theory of gravitational deposition of particles from laminar flows in channels, *J. Aerosol Sci.*, 3, 351, 1972.
- Pratsinis, S.E., Simultaneous nucleation, condensation, and coagulation in aerosol reactors, *J. Colloid Interface Sci.*, 124, 416, 1998.
- Pruppacher, H.R. and Klett, J.D., *Microphysics of Clouds and Precipitation*, 2nd ed., Kluwer Academic Publishers, Dordrecht, 1997.
- Pui, D.Y.H. and Chen, D.-R., Nanometer particles: a new frontier for multidisciplinary research, *J. Aerosol Sci.*, 28, 539, 1997.
- Ramshaw, J.D., Brownian motion in a flowing fluid, *Phys. Fluids*, 22, 1595, 1979.
- Ramshaw, J.D., Brownian motion in a flowing fluid revisited, *Phys. Fluids*, 24, 1210, 1981.
- Raes, F. and Janssens, A., Ion-induced aerosol formation in a H₂O-H₂SO₄ system-II. Numerical calculations and conclusions, *J. Aerosol Sci.*, 17, 715, 1986.
- Reeks, M.W., The transport of discrete particles in inhomogeneous turbulence, *J. Aerosol Sci.*, 14, 729, 1983.

- Reeks, M.W., On a kinetic equation for the transport of particles in turbulent flows, *Phys. Fluids, A*, 3, 446, 1991.
- Reeks, M.W., Particle drift in turbulent flows: the influence of local structure and inhomogeneity, *4th Int. Conference Multiphase Flow*, New Orleans, 2001.
- Reiss, H., The kinetics of phase transitions in binary systems, *J. Chem. Phys.*, 18, 840, 1950.
- Reiss, H. and Kegel, W.K., Replacement free energy and the 1/S factor in nucleation theory as a consequence of mixing entropy, *J. Phys. Chem.*, 100, 10428, 1996.
- Reiss, H., Kegel, W.K., and Katz, J.L., Resolution of the problems of replacement free energy, 1/S, and internal consistency in nucleation theory by consideration of the length scale for mixing entropy, *Phys. Rev. Lett.*, 78, 4506, 1997.
- Reiss, H., Tabazadeh, A., and Talbot, J., Molecular theory of vapor phase nucleation: the physically consistent cluster, *J. Chem. Phys.*, 92, 1266, 1990.
- Rogers, R.R. and Yau, M.K., *A Short Course in Cloud Physics*, 3rd ed., Pergamon Press, Oxford, 1989.
- Rudek, M.M., Katz, J.L., Vidensky, I.V., Zdímal, V., and Smolík, J., Homogeneous nucleation rates of *n*-pentanol measured in an upward thermal diffusion cloud chamber, *J. Chem. Phys.*, 111, 3623, 1999.
- Saffman, P. and Turner, J., On the collision of drops in turbulent clouds, *J. Fluid Mech.*, 1, 16, 1956.
- Schwendiman, L.C. and Postma, A.K., Turbulent deposition in sampling tubes, *Tech. Inf. Div. Rep.*, TID-7628, Book 1 (USAEC), 1962.
- Sehmel, G.A., Aerosol deposition from turbulent airstreams in vertical conduits, *Batelle Northwest Lab.*, Richland, Washington, USA, Rep. BNWL-578, 1968.
- Seigneur, C., Hudishevskyj, A.B., Seinfeld, J.H., Whitby, K.T., Whitby, E.R., Brock, J.R., and Barnes, H.M., Simulation of aerosol dynamics – A comparative review of mathematical models, *Aerosol Sci. Technol.*, 5, 205, 1986.
- Seinfeld, J.H. and Pandis, S.N., *Atmospheric Chemistry and Physics: From Air Pollution to Climate Change*, Wiley, New York, 1998.
- Senger, B., Schaaf, P., Corti, D.S., Bowles, R., Voegel, J.-C., and Reiss, H., A molecular theory of the homogeneous nucleation rate. I. Formulation and fundamental issues, *J. Chem. Phys.*, 110, 6421, 1999.
- Shen, V.K. and Debenedetti, P.G., Density-functional study of homogeneous bubble nucleation in the stretched Lennard-Jones fluid, *J. Chem. Phys.*, 114, 4149, 2001.
- Smoluchowski, M., Drei Vortrage über Diffusion, Brownsche Molekularbewegung und Koagulation von Kolloidteilchen, *Physik Zeits.*, 17, 557, 1916.
- Stauffer, D., Kinetic theory of two-component (“hetero-molecular”) nucleation and condensation, *J. Aerosol Sci.*, 7, 319, 1976.
- Strey, R., Wagner, P.E., and Schmeling, T., Homogeneous nucleation rates for n-alcohol vapors measured in a two-piston expansion chamber, *J. Chem. Phys.*, 84, 2325, 1986.
- Sugutin, A. and Fuchs, N., Formation of condensation aerosols under rapidly changing environmental conditions, *J. Aerosol Sci.*, 1, 287, 1970.
- Talanquer, V. and Oxtoby, D.W., Dynamical density functional theory of gas-liquid nucleation, *J. Chem. Phys.*, 100, 5190, 1994.
- Talbot, L., Cheng, R.K., Schefer, R.W., and Willis, D.R., Thermophoresis of particles in a heated boundary layer, *J. Fluid Mech.*, 101, 737, 1980.
- Tan, C.W. and Thomas, J.W., Aerosol penetration through a parallel-plate diffusion battery, *J. Aerosol Sci.*, 3, 39, 1972.
- Trinkaus, H., Theory of the nucleation of multicomponent precipitates, *Phys. Rev. B*, 27, 7372, 1983.
- Vincent, J.H., *Aerosol Science for Industrial Hygienists*, 1st ed., Elsevier Science Inc., New York, 1995.
- Waldmann, L. and Schmitt, K.H., Thermophoresis and diffusiophoresis of aerosols, in *Aerosol Science*, Davies, C.N., Ed., Academic Press, London and New York, 1966.
- Weakliem, C.L. and Reiss, H., Toward a molecular theory of vapor phase nucleation. IV. Rate theory using the modified liquid drop model, *J. Chem. Phys.*, 101, 2398, 1994.
- Weibel, E.R., *Morphometry of the Human Lung*, Academic Press, New York, 1963.

- Wells, A.C. and Chamberlain, A.C., Transport of small particles to vertical surfaces, *Brit. J. Appl. Phys.*, 18, 1793, 1967.
- Wilemski, G., Composition of the critical nucleus in multicomponent vapor nucleation, *J. Chem. Phys.*, 80, 1370, 1984.
- Wilemski, G., Revised classical binary nucleation theory for aqueous alcohol and acetone vapors, *J. Phys. Chem.*, 91, 2492, 1987.
- Wilemski, G., The Kelvin equation and self-consistent nucleation theory, *J. Chem. Phys.*, 103, 1119, 1995.
- Willeke, K., Temperature dependence of particle slip in a gaseous medium, *J. Aerosol Sci.*, 7, 381, 1976.
- Whitby, K.T., The physical characteristics of sulfur aerosols, *Atmos. Environ.*, 12, 135, 1978.
- Whitby, E.R. and McMurry, P.H., Modal aerosol dynamics modeling, *Aerosol Sci. Technol.*, 27, 673, 1997.
- Wilck, M. and Stratmann, F., A 2-D multicomponent modal aerosol model and its application to laminar flow reactors, *J. Aerosol Sci.*, 28, 959, 1997.
- Williams, M.M.R. and Loyalka, S.K., *Aerosol Science: Theory and Practice*, Pergamon Press, Oxford, 1991.
- ten Wolde, P.R., Ruiz-Montero, M.J., and Frenkel, D., Numerical calculation of the rate of crystal nucleation in a Lennard-Jones system at moderate undercooling, *J. Chem. Phys.*, 104, 9932, 1996.
- Wu, J.J. and Flagan, R.C., A discrete-sectional solution to the aerosol dynamic equation, *J. Colloid Interface Sci.*, 123, 339, 1988.
- Xie, Y., Hopke, P.K., Casuccio, G., and Henderson, B., Use of multiple fractal dimensions to quantify airborne particle shape, *Aerosol Sci. Technol.*, 20, 161, 1994.
- Young, J. and Leeming, A., A theory of particle deposition in turbulent pipe flow, *J. Fluid Mech.*, 340, 129, 1997.
- Zeldovich, Ya.B., On the theory of new phase formation: Cavitation, *J. Exp. Theor. Phys.*, 12, 525. 1942
Translated in *Selected works of Yakov Borisovich Zeldovich. Volume 1. Chemical physics and hydrodynamics*, Ostriker, J.P., Barenblatt, G.I., and Sunayev, R.A., Eds., Princeton University Press, Princeton, 1992, p.120.
- Zeng, X.C. and Oxtoby, D.W., Gas-liquid nucleation in Lennard-Jones fluids, *J. Chem. Phys.*, 94, 4472, 1991a.
- Zeng, X.C. and Oxtoby, D.W., Binary homogeneous nucleation theory for the gas-liquid transition: a nonclassical approach, *J. Chem. Phys.*, 95, 5940, 1991b.
- Zhang, Y., Seigneur, C., Seinfeld, J.H., Jacobson, M.Z., and Binkowski, F.S., Simulation of aerosol dynamics: a comparative review of algorithms used in air quality models, *Aerosol Sci. Technol.*, 31, 487, 1999.
- Ziskind, G., Fichman, M., and Gutfinger, C., Resuspension of particulates from surfaces to turbulent flows-Review and analysis, *J. Aerosol Sci.*, 26, 613, 1995.

7

Particle Separation Systems

7.1	Separation Efficiency and Grade Efficiency	7-1
7.2	Classification of Particle Separation Systems	7-4
7.3	Flow-Through Type Separator	7-6
	Separation Efficiency	
7.4	Gravitational Collectors.....	7-8
7.5	Centrifugal Separation.....	7-9
	Gas-Solid Separation, Dry Cyclone • Liquid-Solid Separation, Hydrocyclones	
7.6	Electrostatic Precipitation	7-24
	Principle of Electrostatic Precipitator • Characteristics of ESP	
7.7	Obstacle Type Separator	7-33
7.8	Inertial Dust Collector	7-38
7.9	Air Filter	7-38
7.10	Scrubber	7-44
7.11	Barrier Type Separator	7-48
7.12	Bag Filter	7-48
	Collection Mechanism • Pressure Drop • Method of Dislodging Dust	

Chikao Kanaoka
*Ishikawa National College of
Technology*

Hideto Yoshida
Hiroshima University

Hisao Makino
*Central Research Institute
Electric Power Industry*

The operation to separate dust from a fluid stream is referred to as particle collection and has been utilized to recover valuable materials from many chemical processes and to remove air pollutants consisting of particulate matter from exhaust streams before exiting to the atmosphere.

In this operation, it is essential to produce a sufficiently large relative velocity between the particles and the fluid. Hence, many types of collectors have been developed and used to accomplish the tasks mentioned above. In this chapter, the principles and features of particle separation and typical particle collectors are described.

7.1 Separation Efficiency and Grade Efficiency

Chikao Kanaoka

Separation (overall) efficiency is the ratio of the amount of dust collected to the total amount of dust entering the collector in a given period of time. However, it is difficult, practically, to determine separation efficiency of an actual dust collector. The efficiency is calculated by one of following three

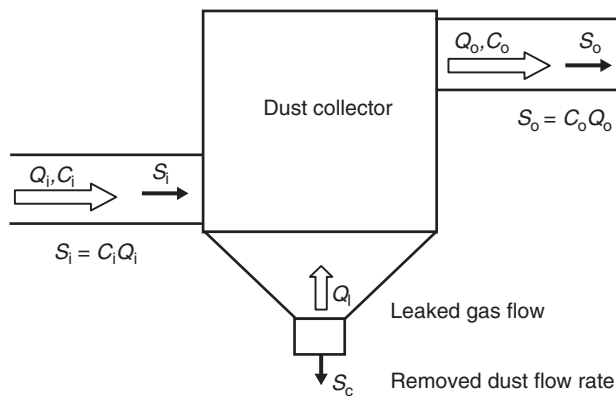


FIGURE 7.1 Symbols relating the performance of dust collector.

methods using inlet and outlet dust flow rates, dust concentration, and gas flow rate as shown in Figure 7.1.

1. Efficiency evaluation using the dust flow rate at the inlet and outlet ducts.

$$E = \begin{cases} \frac{S_i - S_o}{S_i} = 1 - \frac{S_o}{S_i} \\ = \frac{C_i Q_i - C_o Q_o}{C_i Q_i} = 1 - \frac{C_o Q_o}{C_i Q_i} \\ = \frac{C_{iN} Q_{iN} - C_{oN} Q_{oN}}{C_{iN} Q_{iN}} = 1 - \frac{C_{oN} Q_{oN}}{C_{iN} Q_{iN}} \end{cases} \quad (7.1)$$

where S is the mass flow rate of dust (kg/sec), C the dust concentration (kg/m^3), and Q the volume flow rate of the gas. The subscripts i and o refer to the inlet and outlet, respectively, and N refers to the standard conditions (dry basis, 20°C , 1 atm)

Without gas leakage and temperature change, the efficiency is

$$E = 1 - \frac{C_o}{C_{oN}} = 1 - \frac{C_{oN}}{C_{iN}} \quad (7.2)$$

2. Efficiency evaluation using the dust flow rate in the inlet duct and the amount of dust removed per unit time in the collector, S_c :

$$E = \frac{S_c}{S_i} \quad (7.3)$$

3. Efficiency evaluation using the dust flow rate at the outlet and the amount of dust removed per unit time in the collector:

$$E = \frac{S_c}{S_c + S_o} \quad (7.4)$$

Although separation efficiency can be determined by any of the above methods, Eqs. (7.1) and (7.2) are the only methods viable in practice.

Dust particles accumulating in the collector are polydisperse and their size distribution depends on the source. The separation efficiency of each individual particle depends on its size because the particle

is separated by some separation mechanism that depends on its physical property and operational conditions. Hence, separation efficiency for a given particle size is called "grade efficiency" or "partial separation efficiency." The separation efficiency for a whole particle size range is a sum of the individual grade efficiencies accounting for the particle size distribution. This is called "overall separation efficiency."

Hence, overall separation efficiency E is expressed schematically by the hatched area in Figure 7.2 and in terms of grade efficiency $\eta(d_p)$ and particle size distribution $f(d_p)$ as

$$E = \int_0^{\infty} \eta(d_p) f(d_p) d(d_p) \quad (7.5)$$

Since $\eta(d_p)$ can be acquired for a given dust collector as a function of particle properties and operational conditions. The overall separation efficiency of the dust collector can be estimated without any measurement by knowing the particle size distribution.

The total separation efficiency of dust collectors in series is expressed by

$$E_T = 1 - (1 - E_1)(1 - E_2)\cdots(1 - E_n) \quad (7.6)$$

where E_T is the separation efficiency of the overall system, E_1, E_2, \dots, E_n are the separation efficiencies of the elemental collectors, and n is the number of dust collectors.

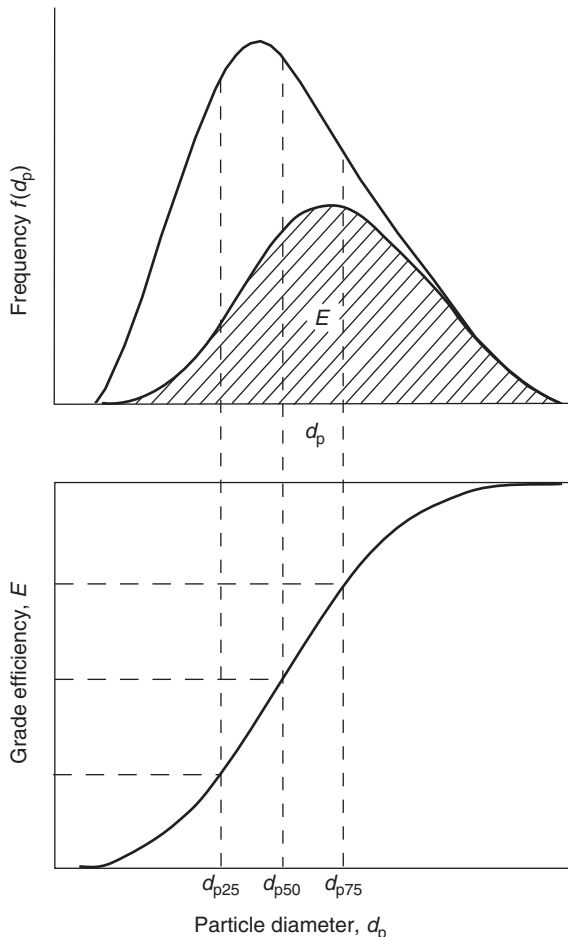


FIGURE 7.2 Relation between overall separation efficiency and grade efficiency.

Hence, when the separation efficiency of each elemental collector is the same, E_T is expressed as

$$E_T = 1 - (1 - E)^n \quad (7.7)$$

7.2 Classification of Particle Separation Systems

Chikao Kanaoka

Dust removal equipment can be classified as dry or wet collectors depending on whether collection medium is liquid or solid. They are also classified according to industrial dust collectors or air filters, depending on inlet dust concentration, which for industrial collectors is usually several orders of magnitude higher than air filters. When they are classified according to the gas flow and dust collection mechanism, every dust collector belongs to one of the categories shown in Figure 7.3 (Kanaoka, 1997):

1. Flow-through type dust collector: This type of collector utilizes the external force perpendicular to the mean gas flow to remove particles from the flow. Hence the flow does not change with time and removal performance and pressure drop of the system are always the same. The gravitational dust collector, cyclone, and electrostatic precipitator all belong to this collector type.
2. Obstacle type dust collector: This type of collector captures dust on obstacles inside the equipment. When particles are captured by a solid obstacle, the collected particles remain on the obstacle, which results in an increase in both collection performance and flow resistance with time. This also makes the release of captured particles from the obstacles difficult. Therefore this type of dust collector is normally used as a disposable type of collector. The air filter, granular bed filter, louver type dust collector, and venturi scrubber belong to this collector type.
3. Barrier type dust collector: This type of collector uses a permeable media for the gas but not for the dust, so that the dust is captured and accumulated on the surface. To maintain a continuous operation of this type of dust collector, the accumulated dust has to be removed when pressure drop becomes too high. The bag and ceramic filters are the typical dust collectors of this type.

Table 7.1 summarizes general features of dust collectors. Compared with the other collectors, the bag filter shows the highest collection performance, but the collector size has to be large, as its lowest filtration velocity is of the order of 1 m/min. Furthermore, its highest operating temperature is limited to 250°C owing to the poor thermal durability of the filter material.

On the other hand, the electrostatic precipitator can treat gases as high as 1 m/sec with a very low pressure drop. However, its collection performance depends on the electrical properties of dust particles. Figure 7.4 and Figure 7.5 show the collection efficiency of dust collectors in relation to gas velocity and

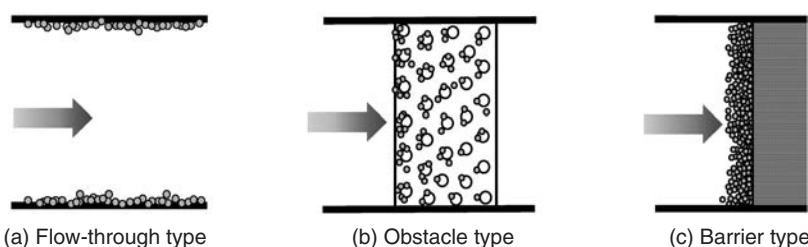


FIGURE 7.3 Classification of dust collector according to gas flow and collection mechanism.

TABLE 7.1 General Features of Dust Collectors

Type	Removable Practical Size (μm)	Pressure Drop (Pa)	Maximum Temperature (°C)	Inlet Concentration (g/m^3)	Initial Capital Cost	Remarks
Flow-Through Type						
Gravitational collector	> 20	50–150	1,000	50 >	Low	Predust collector
Cyclone	> 1	2,000 >	1,000	500 >	Middle	Convenient
Electrostatic precipitator	> 0.02	300 >	400	20 >	Highest	Not for explosive material
Obstacle Type						
Scrubber	> 0.2	10,000 >	1,000	100 >	Middle	Require waste water treatment
Air Filter	> 0.01	500 >	100	0.01 >	Low	For building and house
Air cleaner	> 1	1,000 >	50	1 >	Low	Engine and compressor
Granular bed	> 1	10,000 >	1,000	50 >	High	Good for hot gas cleaning
Barrier Type						
Bag filter	> 0.01	2,000 >	250	20 >	High	Not good for condensable material
Ceramic filter	> 0.01	50,000 >	1,000	50 >	Highest	Good for hot gas cleaning

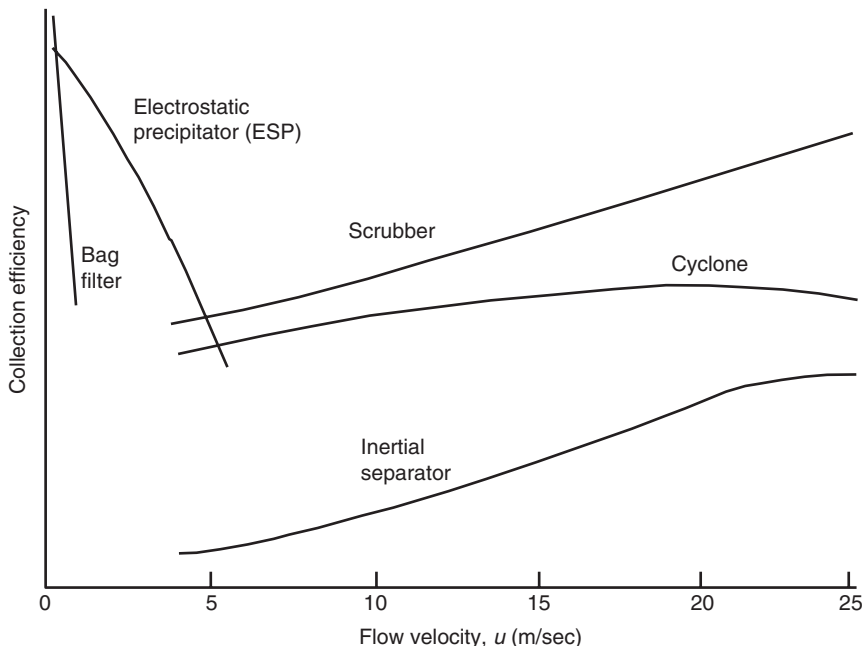


FIGURE 7.4 Rough sketch of separation performance for various dust collectors.

the initial capital cost of the equipment as a function of the handling gas flow rate. The total annual cost to operate a dust collector is usually the lowest at a gas velocity that differs from the velocity for best performance. Hence, one has to have criteria for the selection of dust collectors.

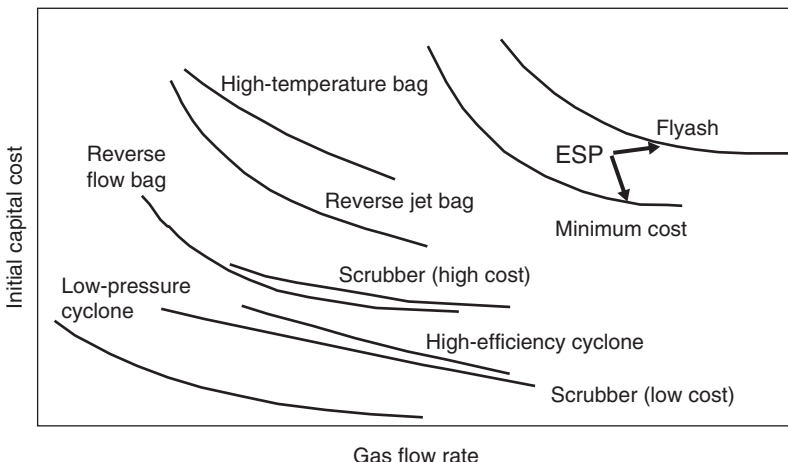


FIGURE 7.5 Relationship between initial capital cost and dust collector type.

7.3 Flow-Through Type Separator

Chikao Kanaoka

This type of collector utilizes the external force perpendicular to the mean gas flow to remove particles from the flow. The flow does not vary with time, hence the collection performance and pressure drop of the system are also essentially constant with time.

7.3.1 Separation Efficiency

7.3.1.1 Laminar Flow

When dust particles collect into a rectangular-shaped dust collector with height H , width B , and length L , as shown in Figure 7.6, the separation efficiency of the collector can be obtained as follows. For simplicity, the gas flow is assumed as laminar and the only force acting on particles is in the direction perpendicular to the gas flow. Then the particle motion in the collector can be expressed by

$$\nu_x = \frac{dx}{dt} = u(y) \quad (7.8)$$

$$\nu_y = \frac{dy}{dt} = -\nu_{EF} \quad (7.9)$$

where ν_x and ν_y are the particle component velocities in the x and y directions, $u(y)$ the gas velocity in the flow direction, and ν_{EF} the migration velocity of the particle determined from the force balance between the applied external force and fluid drag force. The migration velocities due to different external forces are summarized in Table 7.2

The particle trajectory can be obtained by integrating

$$\nu_{EF} dx = -u(y) dy \quad (7.10)$$

with the initial condition $y|_{x=0} = h$. Three typical trajectories are illustrated in Figure 7.6. The shapes of these trajectories are the same but each trajectory shifts horizontally depending on the inlet height. The lowest trajectory that intersects the bottom plate and the intermediate one reaches at the exit of the collector, while the highest trajectory passes through the collector. In other words, those particles that impact the collector plate and lie below the intermediate trajectory are collected, but those particles higher than the intermediate trajectory are not collected. Hence, the intermediate trajectory is regarded as the “limiting particle trajectory” and

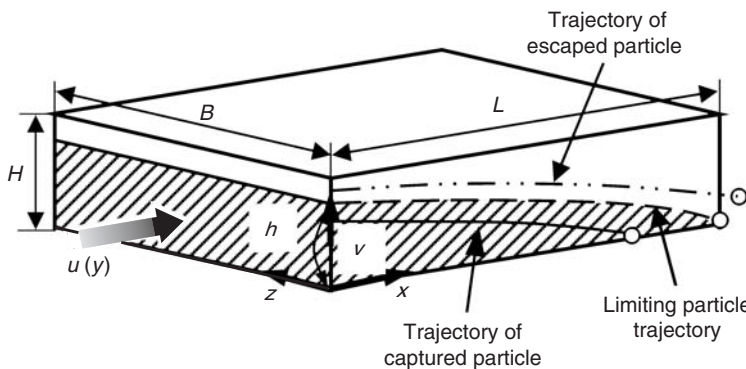


FIGURE 7.6 Concept of flow-through type dust collector.

TABLE 7.2 Migration Velocity by External Force

External Force	Migration Velocity v	Symbols
Gravitational $\frac{\pi}{6} \rho_p d_p^3 g$	$\frac{C_c \rho_p d_p^2 g}{18\mu}$	C_c , Cunningham's correction factor d_p particle size E , electric field strength e , electrostatic charge unit g , acceleration due to gravity n , number of charges R , radius of rotation u_θ , circumferential velocity
Centrifugal $\frac{\pi}{6} \rho_p d_p^3 \frac{u_\theta^2}{R}$	$\frac{C_c \rho_p d_p^2 g}{18\mu} \frac{u_\theta^2}{R}$	
Electrostatics neE	$\frac{neEC_c}{3\pi\mu d_p}$	
μ , gas viscosity		ρ_p , particle density

the separation efficiency of this dust collector is defined as the ratio of particle flow rate below the limiting particle trajectory (hatched area in the Figure 7.6) to the total particle flow rate entering the collector.

$$E = \frac{CB \int_h^0 u(y) dy}{CB \int_h^0 u(y) dy} = \frac{B \int_0^L v_{EF} dx}{Q} = \frac{BLv_{EF}}{Q} = \frac{Sv_{EF}}{Q} \quad (7.11)$$

where Q is the flow rate of treated gas and $S = BL$ is the area where particles deposit, namely the total collection area of the collector.

Equation (7.11) has been derived based on assumption that the flow is laminar (without turbulent mixing). Therefore, it is applicable for any flow through the dust collector so long as the flow is laminar.

7.3.1.2 Turbulent Flow

The situation becomes different when flow inside the collector is turbulent and it is very difficult to obtain an analytical expression except for the following two extreme cases: (1) complete mixing across the cross-section of the collector, i.e., uniform concentration throughout the cross-section and (2) complete mixing in the whole collector, i.e., uniform concentration everywhere.

For the first case, the concentration change along the mean flow direction can be obtained from the mass balance as

$$CuBH - (C + dC)uBH = Cv_{EF} B dx \quad (7.12)$$

$$E = 1 - \frac{C_o}{C_i} = 1 - \exp(-Sv_{EF}/Q) \quad (7.13)$$

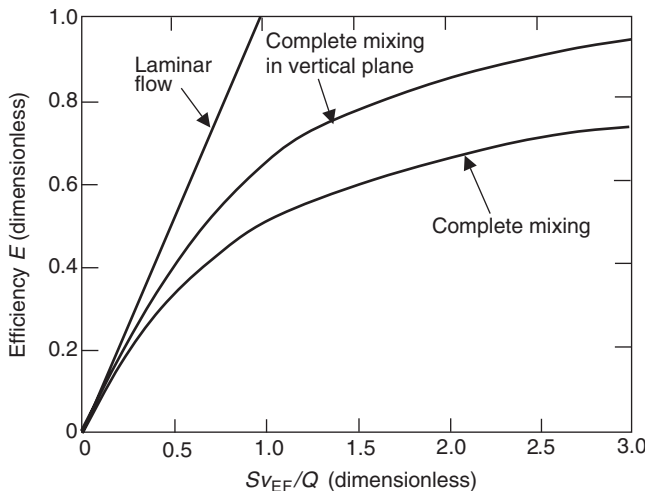


FIGURE 7.7 Separation efficiency of a flow-through type dust collector at different flow velocities.

For the second case, the particle concentration in the equipment and outlet are the same, such that separation efficiency becomes

$$E = 1 - \frac{1}{1 + Sv_{EF}/Q} = \frac{Sv_{EF}/Q}{1 + Sv_{EF}/Q} \quad (7.14)$$

The calculated separation efficiency for each case is shown in Figure 7.7. As seen from the figure, the separation efficiency increases with Sv_{EF}/Q for any flow condition but it is the highest for laminar flow. In other words, the presence of turbulence decreases the collection efficiency. Any actual flow is between these two extreme cases and thus separation efficiency of each dust collector can be approximated by knowing the turbulent intensity and Sv_{EF}/Q .

From Figure 7.7, the separation efficiency E becomes higher when v_{EF} and S become larger and Q smaller. In practice, the flow rate is usually given so in order to enhance the separation efficiency; either v_{EF} has to be increased or S made larger, i.e., increasing the size of the dust collector.

Furthermore, it is remarkable that Eqs. (7.11), (7.13), and (7.14) were derived without any restrictions, other than types of gas flow, i.e., laminar and turbulent. This suggests that they are applicable for all flow-through type dust collectors such as gravity, centrifugal force, electrostatic force, and so on. Equation (7.13) is called the “Deutsch equation” for electrostatic precipitators.

7.4 Gravitational Collectors

Chikao Kanaoka

The gravitational dust collector is the most typical flow-through type dust collector and separates particles by the difference in gravitational settling velocity between particles. Figure 7.8 shows some typical dust collectors. Type (a) is the box-type settling chamber and (b) is multiplate type collector. As indicated above, separation efficiency increases as Sv_{EF}/Q becomes large. In the multiplate type collector, several horizontal trays are installed to shorten the vertical migration distance to separate the particles and thus increase the separation area in keeping with increasing Sv_{EF}/Q . In both the cases, to improve the gravitational effect, the cross-sectional area of the collector is enlarged to operate at a low gas velocity. Gas velocity in this type of collector is usually 1 m/sec and thus the pressure drop is low (of the order of 100 to 1000 Pa). However, discharging the separated particles and cleaning the equipment are difficult.

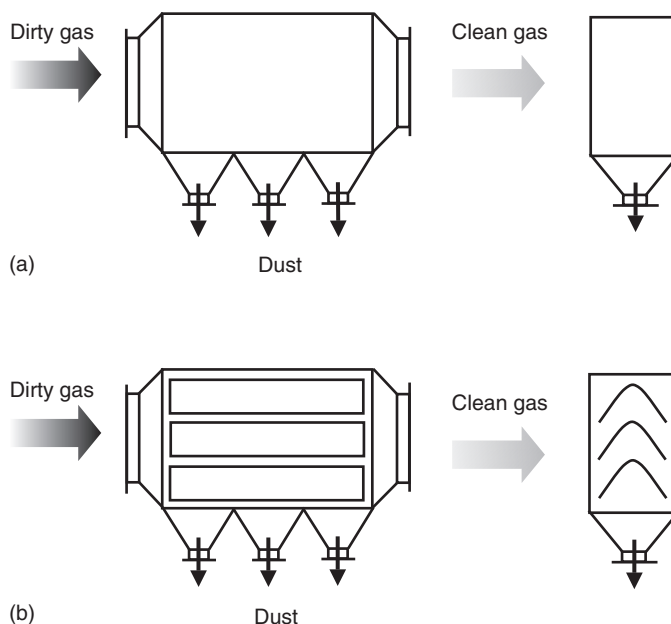


FIGURE 7.8 Typical gravity dust collector: (a) Gravity settling chamber; (b) Multistage settling chamber.

7.5 Centrifugal Separation

Hideto Yoshida

7.5.1 Gas–Solid Separation, Dry Cyclone

Cyclones are widely used for separating powders. Recently, excellent performance with cut size $< 0.5 \mu\text{m}$ has been obtained by Iinoya et al. (1990, 1992, 1993). The optimization of cyclone dimensions in each part is, however, mainly determined by experiment, because the analyses of fluid flow and particle motions are very complicated. Numerical calculations of fluid flow and particle motions in the cyclone have been conducted by Ayers et al. (1985), Zhou et al. (1990), and Yamamoto et al. (1993, 1994) but their calculations are conducted by assuming axisymmetrical flow. In order to model the complicated flow field in the cyclone, it is necessary to perform the numerical calculation in three dimensions. Yoshida et al. (1991) have reported such calculations. An example of the use of computational fluid mechanics applied to a cyclone separator is provided in Section 13.5.

Centrifugal acceleration is created either by airflow in cyclone-type classifiers or by mechanical revolution in air separators. Two types of centrifugal separators are in practical use, the forced vortex type and the free vortex type. For the forced vortex type, a variety of centrifugal classifiers are available. Changing rotational speed in the separator controls the cut size. On the other hand, the conventional cyclone belongs the free vortex type. Changing inlet velocity can control the cut size. Compared with the forced vortex type, the range of cut size variation in the conventional free-vortex-type cyclone is small. However, Yoshida et al. (1993) have shown that it is possible to change the cut size over a wide range by using special designs of the conventional cyclone separator.

In this section, recent results using a three-dimensional simulation for the performance of a dry cyclone are presented. The predicted fluid flow pattern and particle trajectories in the cyclone are compared with experimental results. The effects of using blow-down and an apex cone on particle collection efficiency are also shown. Recent results for submicron classification using an improved-type cyclone are also presented.

7.5.1.1 Classification Theory of Cyclone

Cyclones are widely used in industrial applications. If N is the number of revolutions required for the particle to reach the wall, the particle residence time is

$$t_r = \frac{2\pi RN}{u_0} \quad (7.15)$$

In Figure 7.9, R is the cyclone radius and u_0 the inlet fluid velocity. The radial velocity of the particle toward the wall is represented by

$$V_r = \tau_v \frac{u_0^2}{R} \quad (7.16)$$

where τ_v is the particle velocity response time defined by

$$\tau_v = \frac{(\rho_p - \rho_f)d_p^2}{18\mu} \quad (7.17)$$

Assuming that those particles initially at a distance of x from the wall are collected, the time it takes for the particle to reach the wall is

$$t_x = \frac{x}{V_r} = \frac{xR}{\tau_v u_0^2} \quad (7.18)$$

By using Eqs. (7.15) and (7.18), one has

$$\frac{xR}{\tau_v u_0^2} = \frac{2\pi RN}{u_0} \quad (7.19)$$

$$x = 2\pi N u_0 \tau_v \quad (7.20)$$

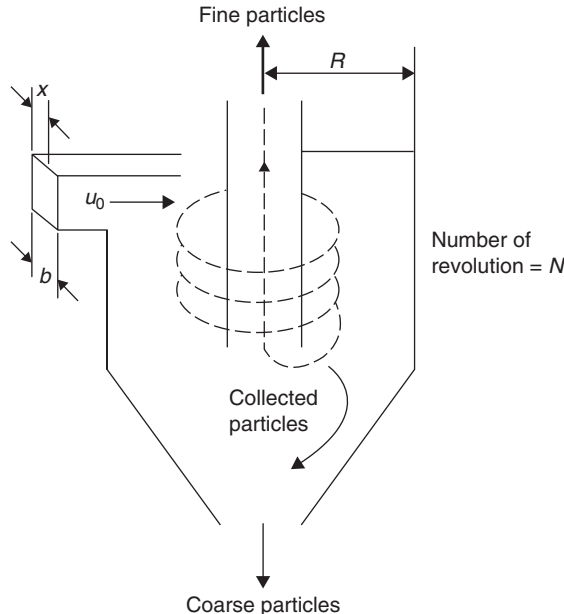


FIGURE 7.9 Simplified model in cyclone classifier.

If the inlet width of cyclone is b , the fractional collection efficiency is given by

$$\eta = \frac{x}{b} = \frac{2\pi u_0 (\rho_p - \rho_f) N d_p^2}{18\mu} \quad (7.21)$$

Then, the cut size, which is the particle size corresponding to $\eta = 0.5$, is

$$d_{pc} = \sqrt{\frac{9\mu b}{2\pi N u_0 (\rho_p - \rho_f)}} \quad (7.22)$$

The value of N can vary from 3 to 8, depending on the cyclone configuration.

Leith and Licht (1972) proposed estimating cut size by using various dimensions of cyclone separator. More detailed information regarding cyclone performance is obtained from recent results of numerical simulation.

7.5.1.2 Numerical Calculation

A three-dimensional numerical simulation of the cyclone separator has been performed by Yoshida et al. (1993,1994). The flow fields were modeled and particle trajectories were calculated according to the methods presented in [Chapter 13](#). Two approaches were used in numerical simulation. In the direct-method approach, a constant (eddy) viscosity was assumed and different values were tried as reflected by using three Reynolds numbers: 3,000, 5,000, and 10,000. The Reynolds numbers are based on the inlet velocity and diameter of the cyclone. The other approach was to use the $k-\epsilon$ turbulence model.

The component of the fluid velocity in the $r-z$ plane at different circumferential angles is shown in [Figure 7.10](#). The definition of the circumferential angle θ is defined in Figure 7.10. In this figure, the flow Reynolds number in the cyclone is 5000. It is found that the flow field depends on the circumferential angle and the assumption of axial symmetry of the flow in the cyclone is not always correct. For example, the velocity vectors just below the exit tube point toward the central axis in case of $\theta = 3.8^\circ$, but the velocity points in the opposite direction in case of $\theta = 183.8^\circ$. The downward velocity components near the conical wall (region A) are large and the down-flow (region A) and up-flow (region B) are in close proximity near the entrance of the dust box. It is assumed that a small particle located near the cyclone wall moves downward, but close to the entrance of the dust box, the particle may be entrained in the up-flow velocity and move towards the exit tube. The calculations also show upward velocity components in the upper part of dust box.

The predicted particle trajectories for different particle diameters projected on a plane are shown in [Figure 7.11](#). It was assumed that the particles are collected when they contact the wall surface. The large particles ($d_p = 2.4 \mu\text{m}$) are collected on the conical wall, but some particles ($d_p = 2.0 \mu\text{m}$) enter into the dust box, then move out of the cyclone because of the upward axial velocity component. If the particles are much smaller ($d_p = 0.8 \mu\text{m}$), they do not enter the dust box, but move around the vortex finder and exit the cyclone.

The experimental data for fractional collection efficiency obtained by Iinoya and Nakai (1969) are shown in [Figure 7.12](#).

The inertial parameter Ψ is defined as

$$\Psi = \frac{C_c \rho_p d_p^2 u_0}{18\mu D} \quad (7.23)$$

where C_c is the Cunningham's slip correction factor, D the cyclone diameter, and u_0 the inlet velocity. The inertial parameter is equivalent to the Stokes number. The test particles were Latex, Kanto Loam ($d_p = 1.8 \mu\text{m}$), and stearic acid. The experimental results are compared with the numerical calculations. The solid line indicates calculated results of the direct method and the dotted line is the result when turbulence is included ($k-\epsilon$ model). The experimental flow Reynolds number is greater than 40,000. The experimental data agree well with the predicted results when the turbulence model is used.

7.5.1.3 The Effect of Blow-Down

Numerical and experimental studies of fractional separation efficiency under blow-down conditions were carried out by Yoshida et al. (1995). With the blow-down method, a portion of fluid is discharged from

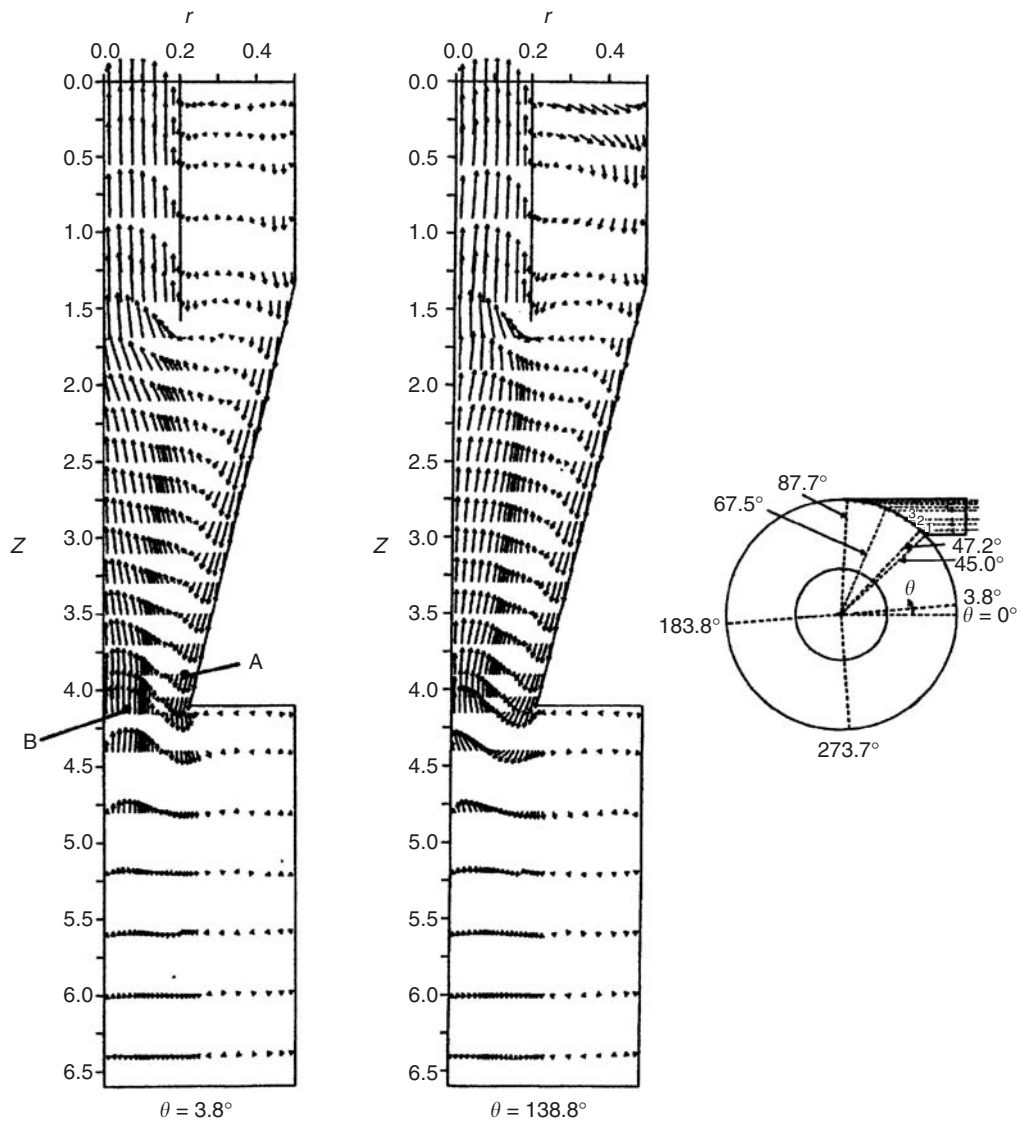


FIGURE 7.10 Fluid velocity distribution in the r - z plane at two circumferential angles ($Re = 5000$).

the dust box. With the blow-up method, particle-free fluid is introduced into the dust box. The blow-down and blow-up ratios are defined as follows:

$$R_d = \frac{Q_b}{Q_0}, \quad R_u = \frac{Q_u}{Q_0} \quad (7.24)$$

where Q_0 the inlet flow rate, Q_b the discharge from the dust box, and Q_u the additional flow rate into the dust box.

Fluid velocity vectors with and without blow-down are shown in Figure 7.13. The k - ε turbulence model was used in numerical calculations. The blow-down flow is located at the upper part of the dust box. In this case, the blow-down ratio is 10%. In the case of blow-down, the downward velocity components near the conical wall are larger than those without blow-down. With blow-down, small particles collected on the cyclone wall move downward near the conical wall and the particles are more likely to enter the dust box.

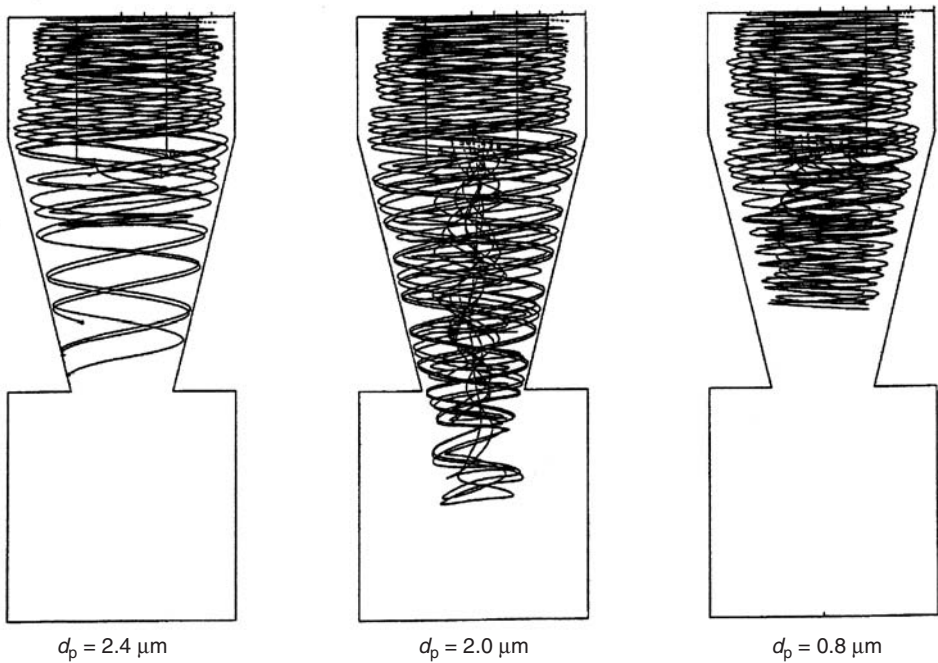


FIGURE 7.11 Particle trajectories in a cyclone.

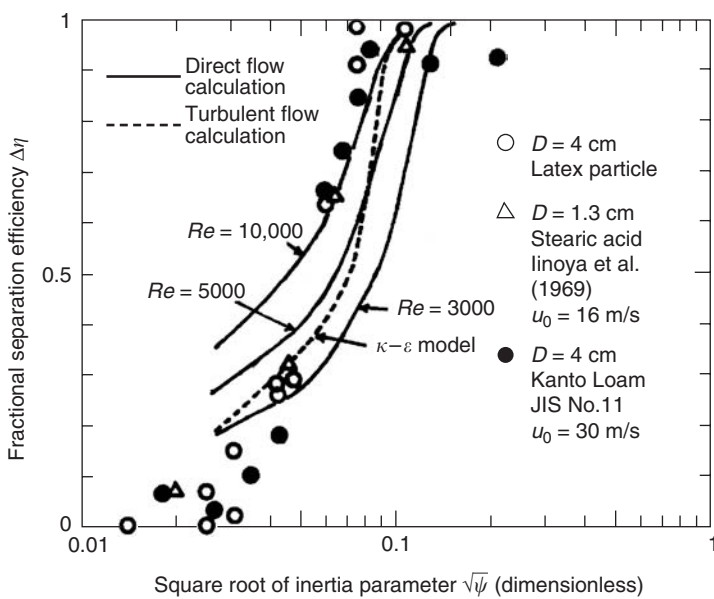


FIGURE 7.12 Fractional separation efficiency data compared with calculated results.

The effects of the circumferential angle of the particle starting position on predicted particle trajectories are shown in [Figure 7.14](#) and [Figure 7.15](#). The particle diameter is $0.8 \mu\text{m}$ and three initial circumferential angles are 47° , 65° , and 88° . These circumferential angles correspond to different starting positions for the particles in the inlet duct as shown in [Figure 7.10](#). The results with and without blow-down are shown in

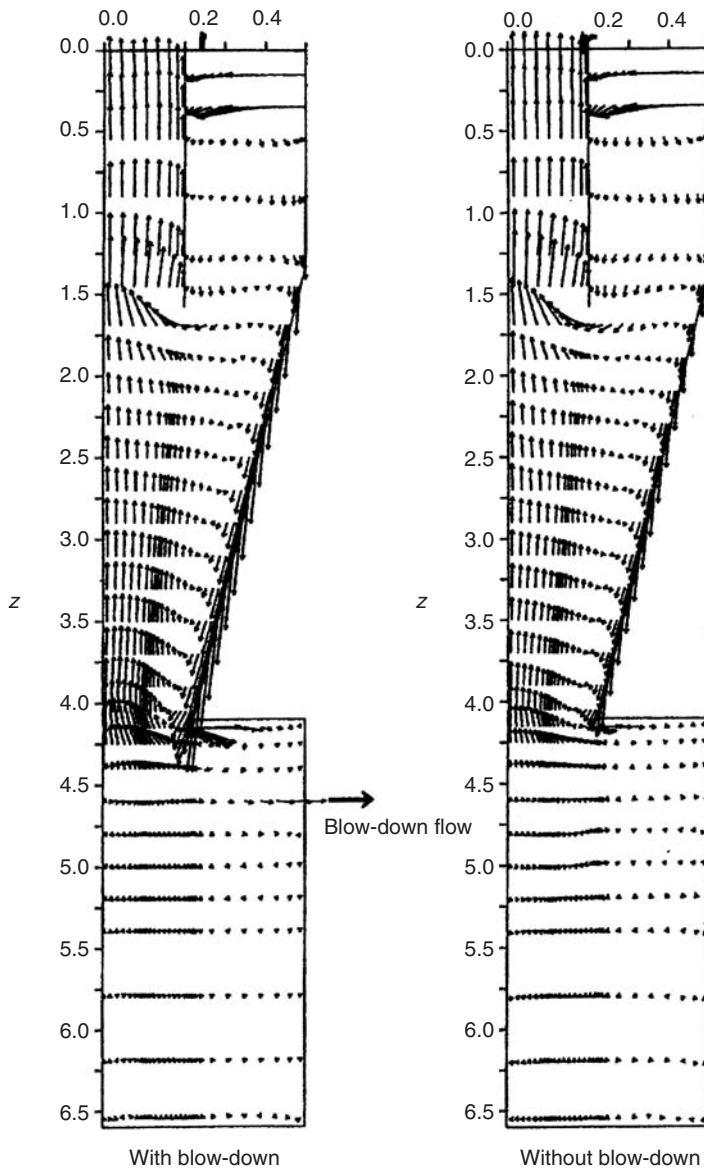


FIGURE 7.13 Fluid velocity distributions with and without blow-down.

[Figure 7.14](#) and [Figure 7.15](#), respectively. With blow-down, some of the particles are collected near the blow-down hole in the dust box. On the other hand, nearly no particles are collected without blow-down.

The correlation between fractional separation efficiency and the inertial parameter with and without blow-down is shown in [Figure 7.16](#). The experimental data agree well with the numerical predictions. It is found that the fractional separation efficiency with blow-down approaches the value of blow-down ratio as the inertial parameter decreases.

Iinoya et al. (1993) found that submicron classification is possible by using a specially designed cyclone.

7.5.1.4 Cut Size Control by Using Free Vortex Type Classifier

The use of a movable slide plate, shown in [Figure 7.17](#), is effective in controlling the cut size in a gas-cyclone. Data for classification performance obtained by Yoshida et al. (1993,1994) are shown in [Figure 7.18](#). Using a movable slide plate and employing the blow-down method changed the cut size. Both methods are

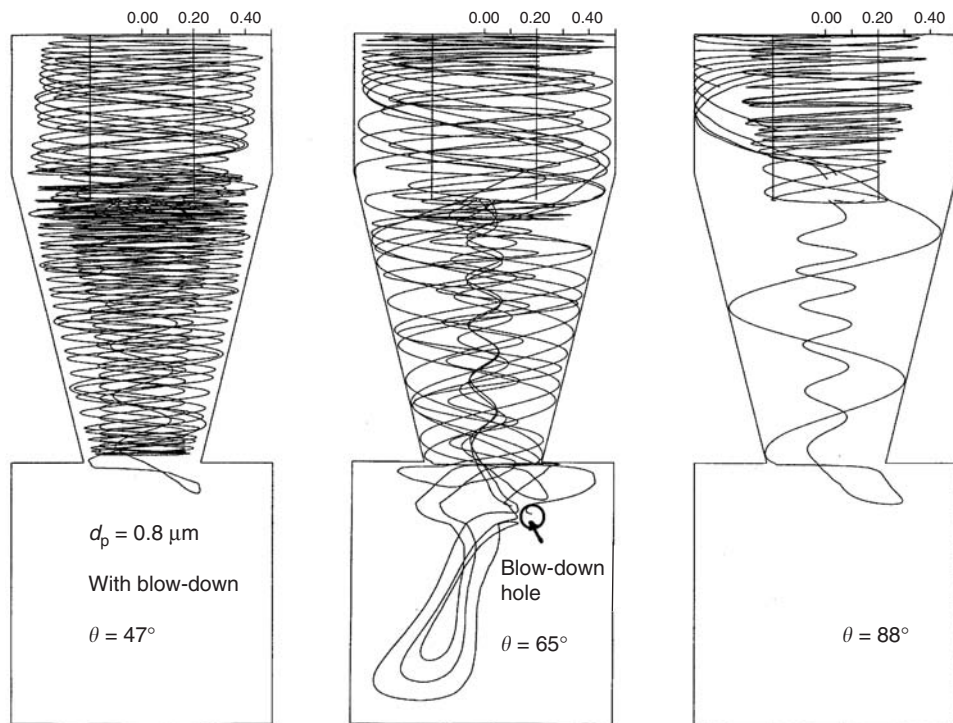


FIGURE 7.14 Particle trajectories for different initial circumferential angle (with blow-down).

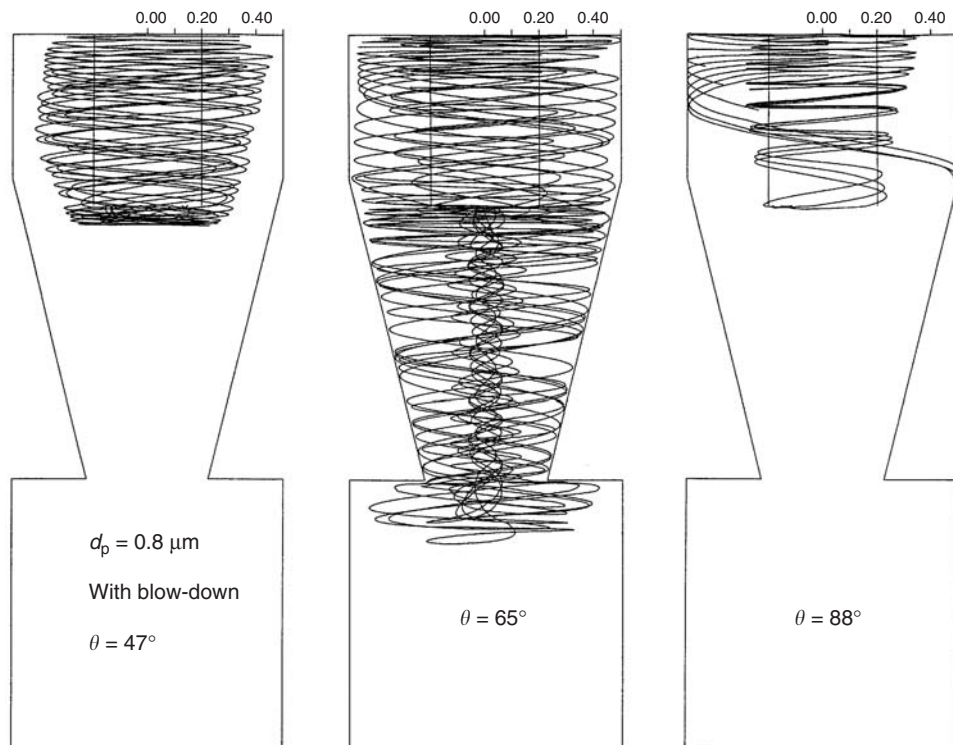


FIGURE 7.15 Particle trajectories for different initial circumferential angle (without blow-down).

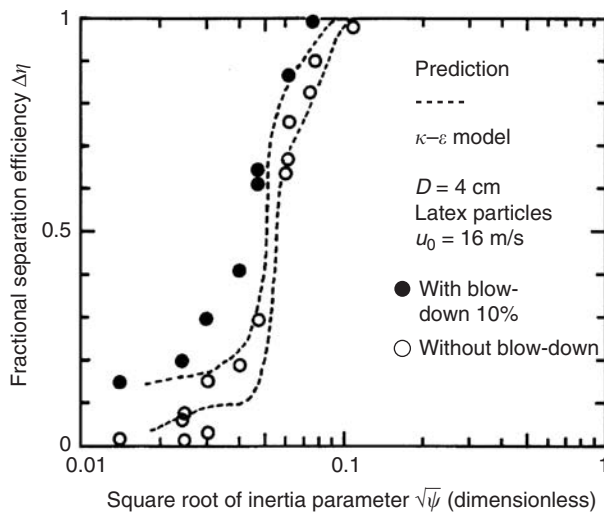


FIGURE 7.16 Fractional separation efficiency with and without blow-down.

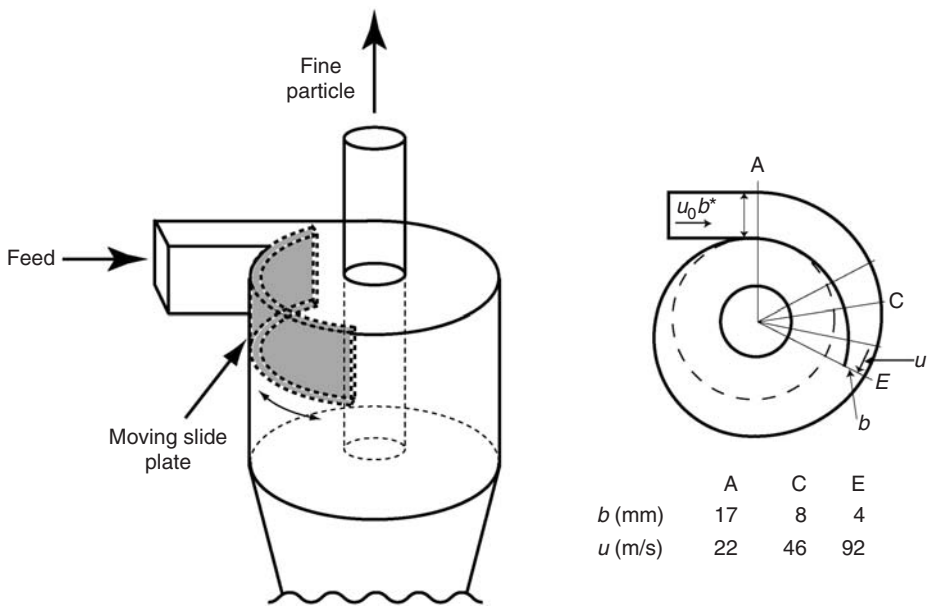


FIGURE 7.17 Cyclone with moving slide plate.

effective in decreasing the cut size. The effect of an apex cone located at the upper part of the dust box is to decrease the cut size and to increase the collection efficiency.

The fluid vectors predicted by Yoshida et al. (2001) are shown in Figure 7.19. The two cases with and without an apex cone are examined. By using the apex cone, it is possible to decrease the magnitude of the fluid velocity component in the dust box. As a result, it is possible to reduce reentrainment of particles from the dust box to the vortex finder.

The predicted particle trajectories with and without the apex cone are shown in Figure 7.20. Particle reentrainment is not observed with the apex cone. The cut size of cyclones with an apex cone is smaller than that without an apex cone as demonstrated in Figure 7.21. By using the apex cone, it is possible to move the cut size into fine particle region.

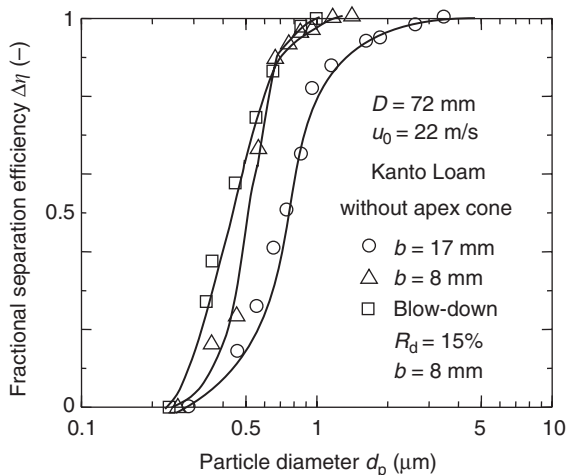


FIGURE 7.18 Effect of slide plate and blow-down on fractional separation efficiency.

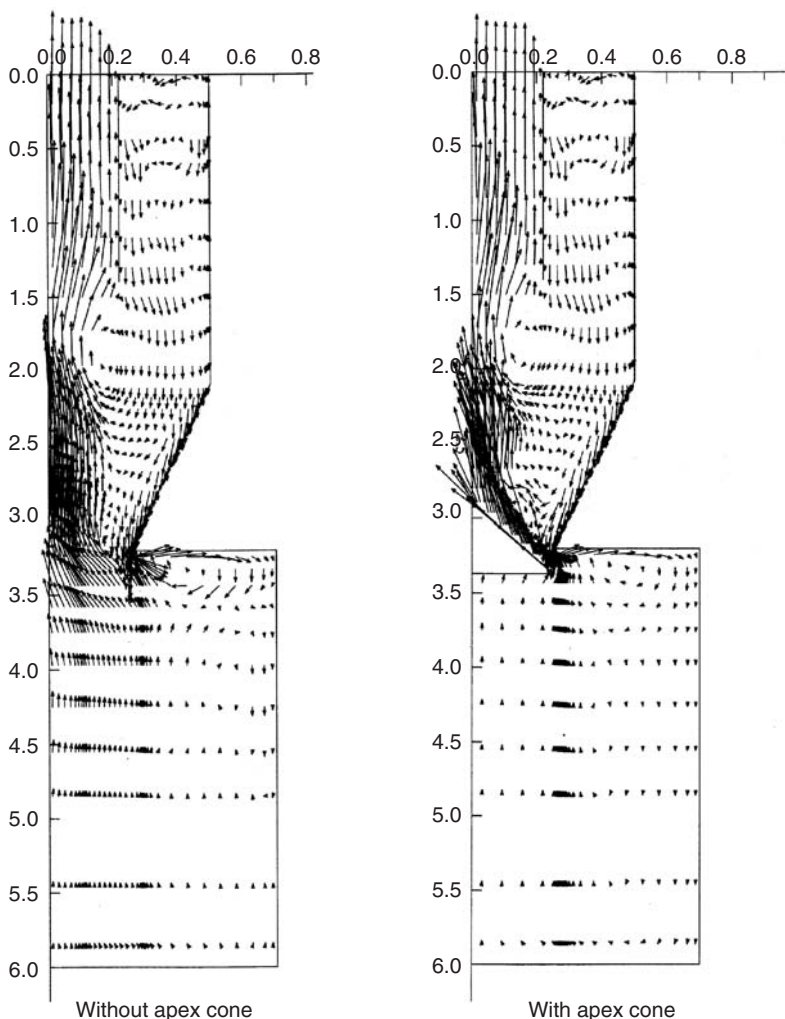


FIGURE 7.19 Calculated fluid velocity vectors with and without apex cone.

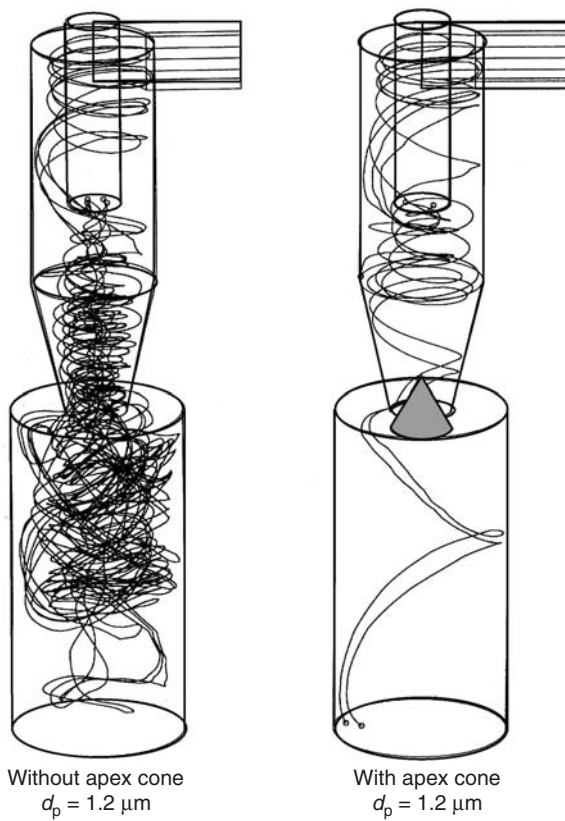


FIGURE 7.20 Particle trajectories for the two cyclones ($d_p = 1.2 \mu\text{m}$).

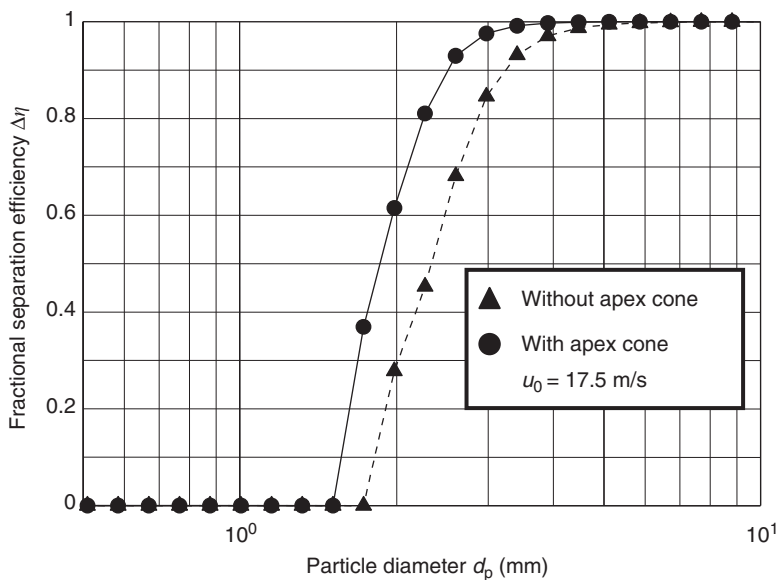


FIGURE 7.21 Fractional separation efficiency with and without apex cone.

7.5.2 Liquid–Solid Separation, Hydrocyclones

The principle of liquid–solid separation is the same as gas–solid separation. Recently, wet separation has been used for producing ceramic particles and in recycling processes. The following facts should be considered in the wet separation:

1. Particle dispersion control is easy compared to gas–solid separation.
2. A drying or dewatering process is necessary to separate particles from liquid.
3. The viscosity of the slurry decreases with increasing temperature, and the particle sedimentation velocity increases as the slurry temperature rises.

7.5.2.1 Hydrocyclone

Hydrocyclones are widely used in many industrial processes. Experimental studies of the separation efficiency and pressure drop of a hydrocyclone have been reported by Bradley (1958) and Yoshioka (1955,1962). Several flow controlling methods at the outlet pipe of a hydrocyclone have been proposed by Yamamoto et al. (1997) and Chu et al. (2002). Also, a prediction of the flow within a hydrocyclone was made by using several turbulence models by Petty and Parks (2001). The performance of axial-flow-type hydrocyclone was studied by Sineath et al. (1959). Performance between conical and cylindrical hydrocyclones was examined by Chine et al. (1997).

The characteristics of hydrocyclones are:

1. The size of hydrocyclone is small compared to other types of wet classifiers.
2. The cut size decreases with an increase in inlet velocity or with a decrease in the cyclone diameter.
3. The pressure drop is about 0.1 to 0.5 MPa, depending on the operating conditions.

The general flow pattern in the standard hydrocyclone is shown in [Figure 7.22](#). The coarse particles are collected in the under-flow exit and the fine particles in the over-flow exit. The ratio of inlet volume flow rate to underflow volume flow rate is referred to as the under-flow ratio, R_d . The normal operating conditions for a hydrocyclone are as follows:

1. Cyclone inlet velocity $u_0 = 2 \sim 10$ m/s
2. Cyclone diameter $D_c = 1 \sim 30$ cm
3. Pressure drop $\Delta P = 0.1 \sim 0.5$ MPa
4. 50% cut size $d_{pc} = 5 \sim 50$ μm
5. Under-flow ratio $R_d = 5 \sim 20\%$

The details of the standard cyclone in Japan (Yoshioka,1962), with each dimension scaled with the cyclone diameter D_c , is also shown in [Figure 7.22](#). The bottom diameter of the conical section is relatively small compared to a gas cyclone. As the under-flow rate increases, a fluctuating air core is occasionally observed near the axis. In order to improve the sharpness of classification, the air core region should be eliminated.

Measurements of the tangential velocity distribution for different axial positions obtained by Ohashi et al. (1958) is shown in [Figure 7.23](#). The tangential velocity profiles are similar to a gas cyclone. Solid body rotation occurs near the axis and a near-free vortex profile, is created in the outer region, represented by the following equation,

$$u_\theta r^n = C \quad (7.25)$$

The maximum tangential velocity occurs at about 60% of the vortex finder diameter, and the index n in the above equation varies from 0.7 to 0.9.

A typical separation efficiency curve obtained by using the standard hydrocyclone is shown in [Figure 7.24](#). The fractional separation efficiency approaches the under-flow ratio R_d as the particle diameter decreases. The experimental data for fractional separation efficiency, $\Delta\eta_c$, shown in the figure, is normalized for different under-flow ratios using

$$\Delta\eta_c = \frac{\Delta\eta - R_d}{1 - R_d} \quad (7.26)$$

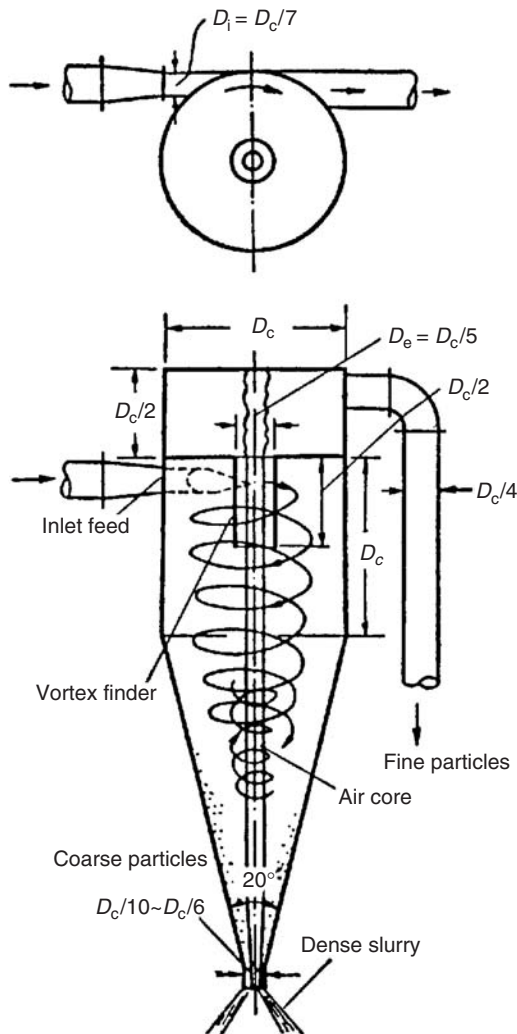


FIGURE 7.22 Standard hydro-cyclone and flow pattern.

where d_{pc} denotes a 50% cut size where R_d is zero. The normalized collection efficiency shown in Figure 7.24 can be represented approximately by the following equation:

$$\Delta\eta_c = 1 - \exp\left(-\left(\frac{d_p}{d_{pc}} - 0.115\right)^3\right), \quad 0.02 \leq \Delta\eta_c \leq 0.98 \quad (7.27)$$

7.5.2.2 Control of Cut Size

To control the cut size easily, the modified hydrocyclone shown in Figure 7.25 has been developed by Yoshida et al. (1997, 2001). The inlet of the hydrocyclone is fitted with a movable guide plate. The apex cone at the inlet of underflow side is also attached. Both blow-down and blow-up methods, similar to the gas cyclone are used to increase classification sharpness at the fine sizes. By using the blow-up method, pure fluid without particles is introduced in the blow-up nozzle shown in Figure 7.25. By using the blow-down method, the under-flow is discharged in the blow-down nozzle. In order to decrease the 50% cut size, a movable guide plate, shown in Figure 7.26, is used. Under constant feed rate conditions, the inlet

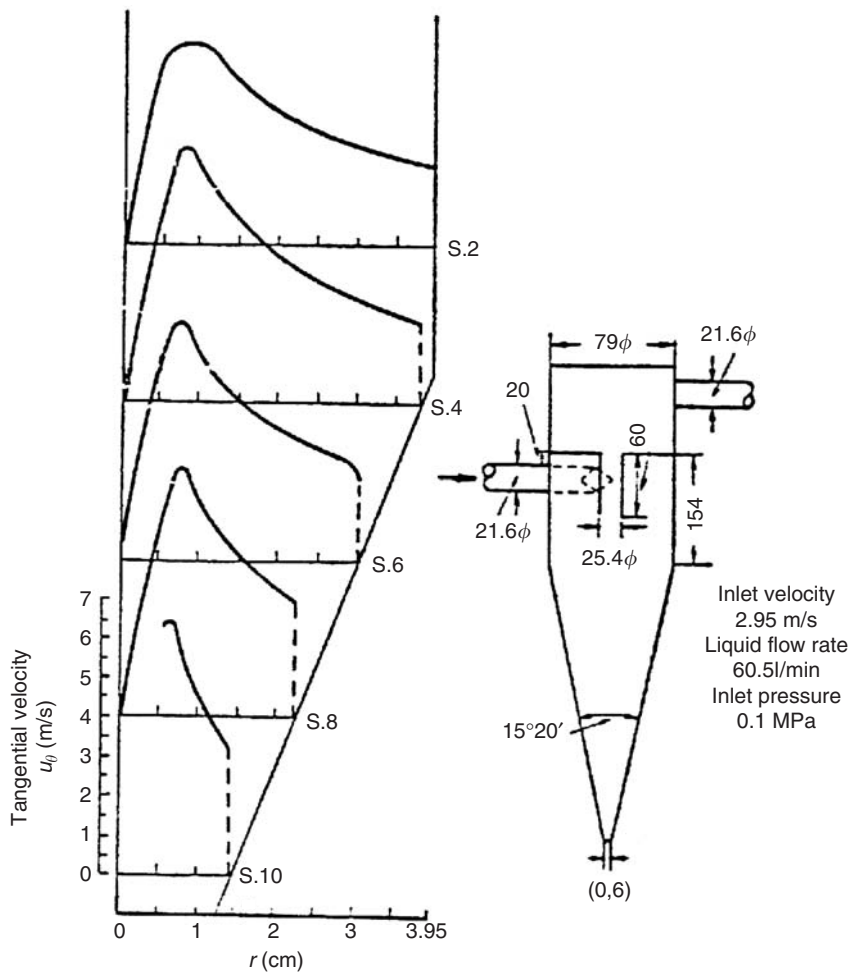


FIGURE 7.23 Tangential liquid velocity distribution.

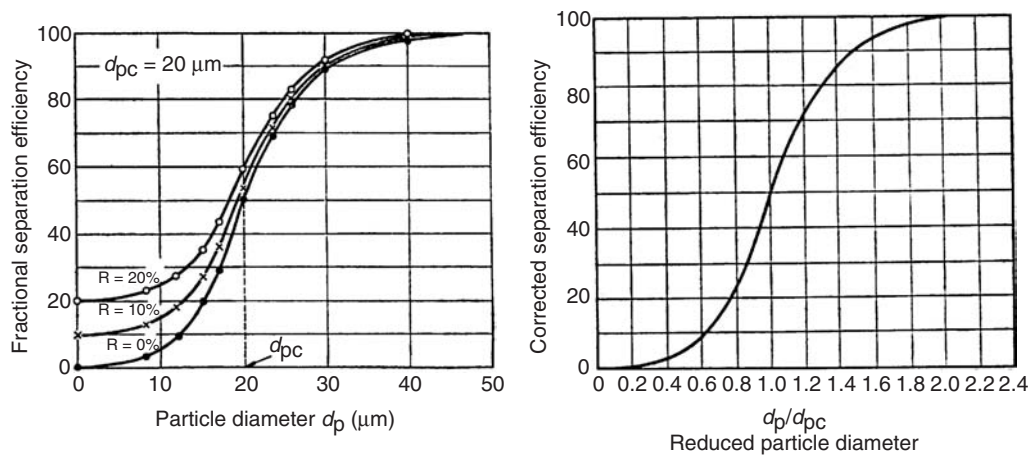


FIGURE 7.24 Fractional separation efficiency and corrected fractional separation efficiency.

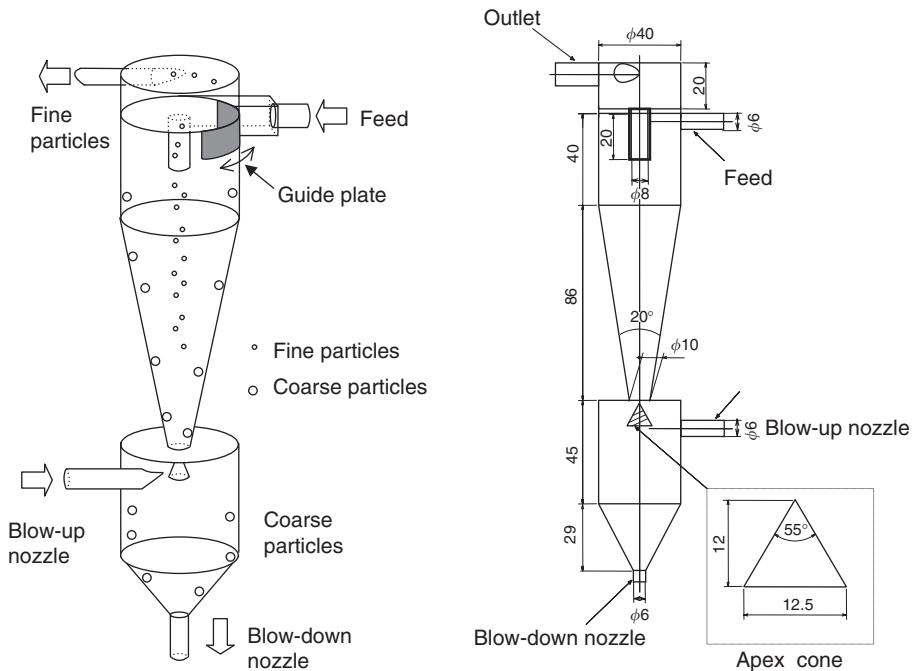


FIGURE 7.25 Experimental apparatus of hydro-cyclone.

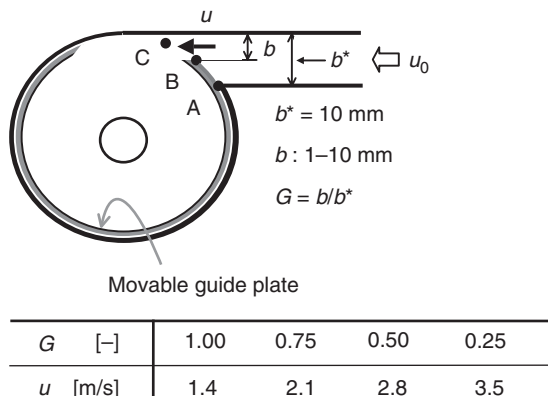


FIGURE 7.26 Cross section of cyclone with a guide plate.

velocity u increases with a decrease in inlet width b . The inlet width ratio G , defined by the following equation, is used as a control parameter:

$$G = \frac{b}{b^*} \quad (7.28)$$

For the standard case, the value of G is unity. Owing to an increased centrifugal force and the smaller radial sedimentation distance, small particles are easily collected for the case of a small inlet width. Typical experimental results using the guide plate are shown in Figure 7.27. The 50% cut size decreases from 10 to 7 μm as the inlet width ratio decreases under a constant inlet flow rate. The fractional separation efficiency approaches 0.1 for a particle diameter less than 5 μm . In order to increase classification sharpness in the small particle diameter region, blow-up and blow-down methods are used simultaneously.

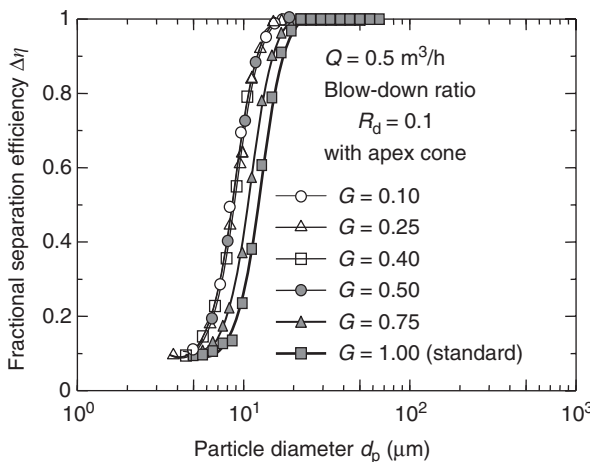


FIGURE 7.27 Classification performance using a guide plate and the blow-down method.

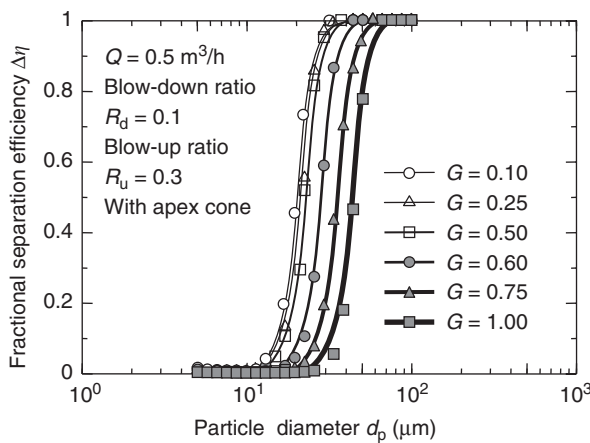


FIGURE 7.28 Classification performance using a guide plate, blow-down and blow-up methods.

Some experimental results for fractional separation efficiency are shown in Figure 7.28. In this case, the blow-up, and blow-down methods and a movable guide plate were used. The blow-up ratio was 30%, the blow-down ratio was 10%, and the inlet width ratio was changed from 1 to 0.1. The 50% cut size changes from 35 to 10 μm as the inlet width ratio decreases from 1 to 0.1. The fractional separation efficiency in this case approaches zero as the particle diameter decreases.

7.5.2.3 Effect of Inlet Slurry Temperature

The viscosity of the slurry decreases with increasing fluid temperature. It is expected that the cut size reduces when the inlet slurry temperature increases. Yoshida et al. (2004) examined the effect of inlet slurry temperature on cut size change of hydrocyclone. A comparison between the calculated and experimental fractional separation efficiency for conditions of high slurry temperature is shown in Figure 7.29. For a given value of the fractional separation efficiency, the particle diameter corresponding to the reference temperature of 20°C changes according to

$$d_{p,t^\circ\text{C}} = \sqrt{\frac{(\mu/(\rho_p - \rho))_{t^\circ\text{C}}}{(\mu/(\rho_p - \rho))_{20^\circ\text{C}}}} d_{p,20^\circ\text{C}} \quad (7.29)$$

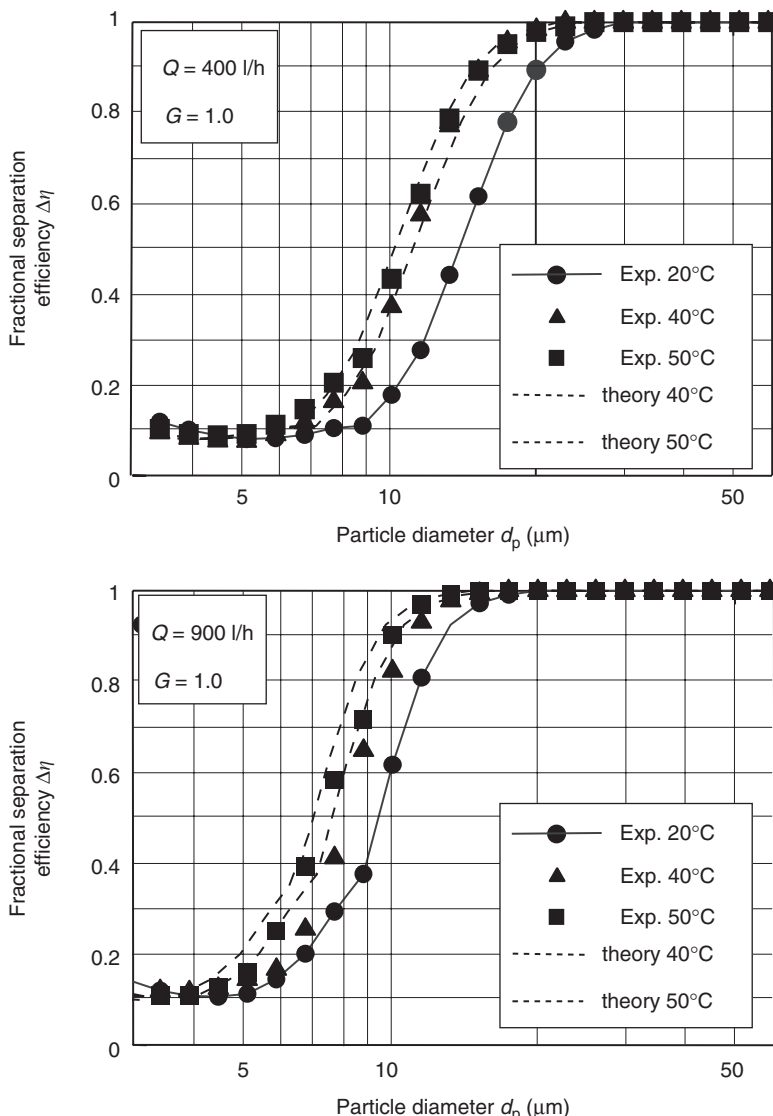


FIGURE 7.29 Comparison between predicted and experimental fractional separation efficiency under various temperature conditions.

Based on the experimental data at 20°C, the fractional separation efficiency for high-temperature conditions can be readily estimated. The experimental data are in good agreement with the results calculated using this equation.

In order to decrease the 50% cut size, the use of the guide plate and an increase in slurry temperature are recommended for practical applications.

7.6 Electrostatic Precipitation

Hisao Makino

7.6.1 Principle of Electrostatic Precipitator

In the electrostatic precipitator (ESP), dust particles in the flue gas are charged by corona current and removed by the electric field. There are two types of ESP: one stage and two stage. In the one stage ESP,

dust charging and separation are performed simultaneously, whereas in the two-stage type, particle charging is performed in the first stage, and collection of the charged particles is performed in the second stage. The one stage ESP, shown in Figure 7.30, is the most common. This type of ESP with flat-plate collection electrodes is easy to scale up. The wire discharge electrodes are centered between two parallel flat collection electrodes. The pressure drop in the ESP is very low compared to the fabric filter or granular bed. The ESP is suitable for dust collection in large-scale facilities.

A negative high voltage is applied to the discharge electrodes and the collection electrodes are grounded. The negative ions generated by the corona at the discharge electrodes collide with the dust particles in flue gas to charge the particles. The particles then move toward the collection electrodes by the electric mobility due to the electric field formed between the discharge and collection electrodes.

The collected dust particles are released to the hopper under the ESP. The particles adhering to the discharge and collection electrodes are dislodged by tapping the electrodes, which then fall into the hopper.

The ESP is utilized as a dust collector in large-scale plants, such as thermal power plants, because it has a high collection efficiency and is capable of handling large flue gas volume flow rates.

7.6.1.1 Particle Charging

In the ESP, the dust particles are charged by the ions in the field generated by corona discharge. The amount of charge is determined by particle size, electric field strength, corona current density, and residence time. The mechanisms responsible for particle charging are field and diffusion charging. The particle charge acquired by each of these two mechanisms is

$$\text{diffusion } q = \frac{d_p kT}{2e^2} \ln \left(1 + \frac{\pi d_p \bar{G}_i n_i e}{2kT} t \right) \quad (7.30)$$

$$\text{field } q = \left[1 + \frac{2(\varepsilon - 1)}{\varepsilon + 2} \right] \frac{Ed_p^2}{4e} \cdot \frac{\pi e B_i n_i t}{1 + \pi e B_i n_i t} \quad (7.31)$$

where \bar{G}_i is the mean thermal mobility of ions (4.5×10^4 cm/s), n_i the concentration of ions, ε the dielectric constant, and B the electric mobility of ions ($1.4 \text{ cm}^2/\text{s/V}$).

The relationship between particle charge and particle size is shown in Figure 7.31. In diffusion charging, the particle charge is not affected by the electric field strength and tends to increase linearly with particle size. In field charging, the particle charge increases with an increase in electric field strength and tends to increase linearly with the square of the particle size. In general, diffusion charging is most effective for fine particles less than 1 μm in diameter, while the field charging is most effective for particles greater than 1 μm .

Since it is necessary to charge particles as much as possible in a short period of time, high electric field strength and high current density are required. The charging methods utilized are DC charging, AC charging, and the pulse charging.

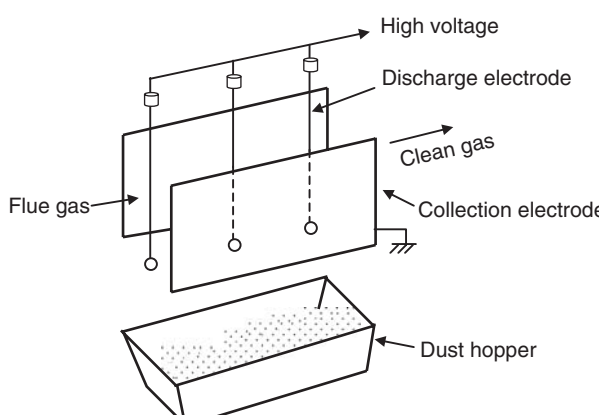


FIGURE 7.30 Electrostatic precipitator.

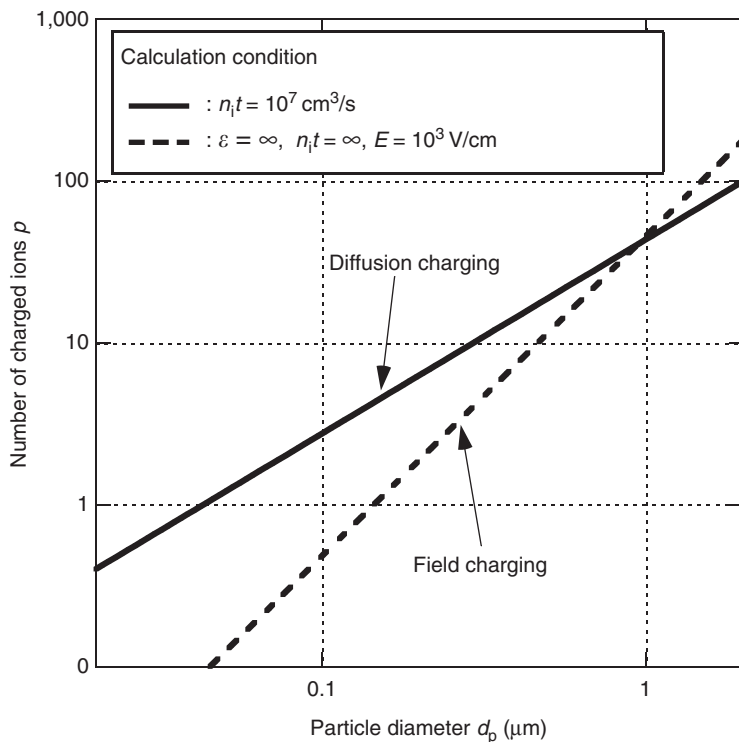


FIGURE 7.31 Number of charged ions and particle diameter. (From Kanaoka et al., 1997.)

1. *DC charging* : The dust particles are charged in a DC electric field. This charging method is the most common. In this method, the ions move in the same direction and the applied voltage is limited to prevent arc discharge, and hence the charging efficiency is reduced for high-resistivity particles.
2. *AC charging* : The dust particles are charged in the AC electric field. The direction of ion movement alternates constantly. In this method, the particles are charged by ion motion from two directions. Thus it is more effective for the high-resistivity particles than the DC charging method.
3. *Pulse charging* : This type of charging adds the high-voltage pulse to the DC charging type. However, in this type, the DC charging voltage is applied at lower voltage than in the usual simple DC charging method in order to control arc discharge. The maximum voltage in the pulse charging can be higher than in the usual DC charging method and the voltage increases with a decrease in the pulse period. Using this method a high and uniform ion density can be achieved with no restriction on the shape of the discharge electrode or dust adhesion to the electrode. It is suitable for high-resistivity particles.

The most effective charging method depends on the resistivity of dust particles. The electric mobility in the DC charging method is higher than that in pulse charging for particles with electric resistivity less than $10^9 \Omega \text{ m}$, while the reverse trend is observed for the high-resistivity dust particles.

7.6.1.2. Electric Mobility of Particles

Under the condition of a uniform electric field in the ESP, the electric mobility (velocity) of charged particles toward the collection electrode is expressed by

$$v_e = \frac{C_c q E}{3\pi \mu d_p} \quad (7.32)$$

where q is the particle charge, E the electric field strength, and C_c the Cunningham correction factor (see [Section 1.3](#)) given by Kanaoka (1997), which is derived from the equation given by Takahashi (1978)

$$C_c = 1 + \left\{ 1.25 + 0.42 \exp\left(-\frac{0.435d_p}{l_m}\right) \right\} \frac{2l_m}{d_p} \quad (7.33)$$

where d_p is the particle diameter and l_m the mean free path of the gas molecules which, in turn, is given by

$$l_m = 0.709 \nu \left(\frac{\pi M}{RT} \right)^{1/2} \quad (7.34)$$

where M is the molecular weight, ν is the kinetic viscosity, T gas temperature, and R the gas constant.

7.6.1.3 Collection Efficiency

The collection efficiency of ESP is generally expressed by the following equation, called the Deutsch equation:

$$E = 1 - \exp\left(-\frac{Av_e}{Q}\right) \quad (7.35)$$

where A is the area of the collection electrodes, which is the product of the length and height of the collection electrode, v_e the mobility of charged particles, and Q the volume rate of flue gas. This equation is developed on the basis of assumptions of uniform electric field, monodisperse particle size and a locally uniform dust concentration. However, in an actual ESP, the situation is quite different and therefore this equation is useful only as an estimate of the collection efficiency.

The overall collection efficiency of an ESP is approximately 99%, and the fractional collection efficiency $\Delta\eta$, which is the collection efficiency for the respective particle size, has a minimum value in the range of particle size of 0.1 to 1.0 μm , as shown in Figure 7.32. In this figure, p represents the penetration efficiency using

$$p = 1 - \Delta\eta \quad (7.36)$$

The reason for the minimum fractional collection efficiency can be explained as follows. According to Eq.(7.33), the Cunningham correction factor increases with a decrease in particle size, but the charge on

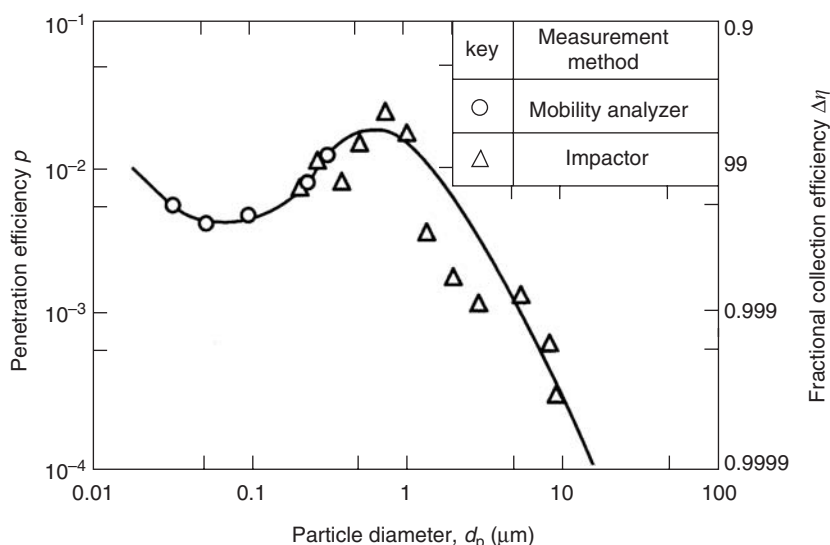


FIGURE 7.32 Fractional collection efficiency of ESP.

the particle q increases with an increase in particle size as shown in Figure 7.31. For particles less than $1 \mu\text{m}$ the particle charge accumulation varies linearly with the particle size, but for particles greater than $1 \mu\text{m}$ the charge increase with the square of the particle size. Therefore, the fractional collection efficiency shows a minimum value at the particle size in the range of 0.1 to $1.0 \mu\text{m}$.

7.6.2 Characteristics of ESP

7.6.2.1 Effect of Collection Conditions

7.6.2.1.1 Influence of Dust Resistivity

As the dust particles accumulate at the collection electrodes, they discharge electrons. The performance parameters of the ESP, such as collection efficiency, applied voltage, and corona current, depend on the dust resistivity, ρ_d , as shown in Figure 7.33. In the regions of $\rho_d < 10^2 \Omega \text{ m}$, and $\rho_d > 5 \times 10^8 \Omega \text{ m}$, the collection efficiency is low. On the other hand, in the region of $10^2 \Omega \text{ m} < \rho_d < 5 \times 10^8 \Omega \text{ m}$, the collection efficiency is high. This tendency is explained as follows.

In the case of $\rho_d < 10^2 \Omega \text{ m}$, when the dust particles accumulate at the collection electrodes, they discharge the electrons immediately and are charged to the same electrostatic potential by the electrostatic conductor. Then the dust particles are reentrained in the direction of the discharge electrode and the collection efficiency is decreased. In the case of $\rho_d > 5 \times 10^8 \Omega \text{ m}$, it is difficult for dust particles to discharge on the collection electrodes and the electrons are stored in the dust layer, hence the applied voltage is decreased by the dust layer. In addition, as the effective electric field strength becomes lower, the collection efficiency decreases. If ρ_d becomes higher than $10^{11} \Omega \text{ m}$ back discharge ensues and the collection efficiency is significantly decreased.

On the other hand, in the case of $10^2 \Omega \text{ m} < \rho_d < 5 \times 10^8 \Omega \text{ m}$, the discharge rate of dust particles is moderate and the collection efficiency remains high.

The resistivity ρ_d is affected by dust properties, temperature, humidity, etc. The relationship between ρ_d of coal ash and the temperature for various humidity conditions is shown in Figure 7.34. The resistivity

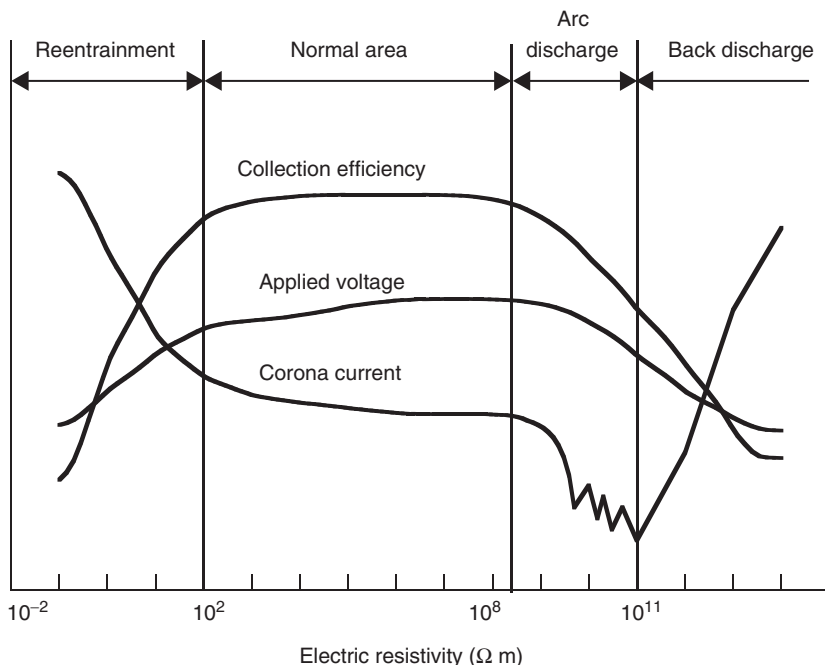


FIGURE 7.33 Collection characteristics and electric resistivity. (From Kanaoka et al., 1997.)

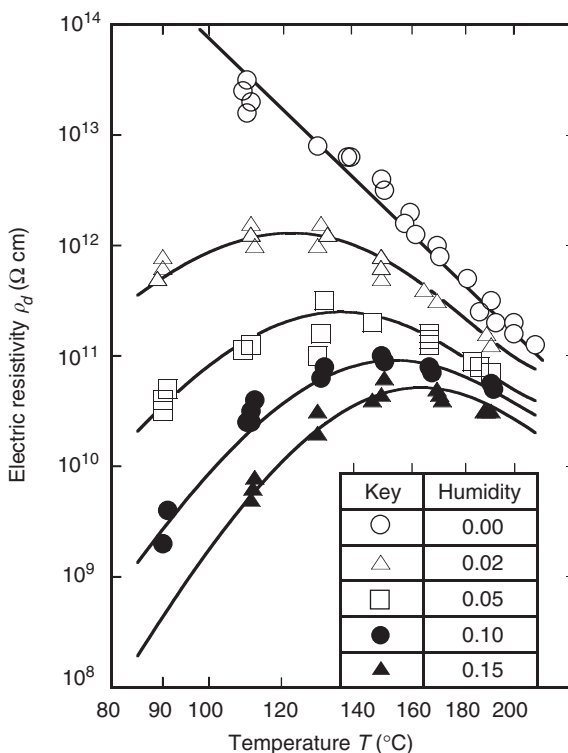


FIGURE 7.34 Electric resistivity of fly ash. (From Kanaoka et al., 1997.)

has a maximum value in the temperature range 100 to 200°C, except under condition of 0% humidity. At the same temperature condition, the resistivity becomes higher with a decrease in humidity. This tendency is explained as follows.

In the low-temperature region, the coal ash particles adsorb moisture from the atmosphere and form a water layer on the particle surfaces. Ions can move easily through this water layer hence resistivity is reduced. This layer becomes thicker with a decrease in temperature and an increase in humidity, therefore the resistivity becomes lower. On the other hand, in the high-temperature region, electrical conduction must take place through the particles, since there is no surface water layer at high temperature conditions. In this case, the electric resistivity decreases with an increase in temperature. Overall, the resistivity is determined by a combination of these mechanisms showing maximum values in the temperature range between 120 and 160°C depending on the humidity.

7.6.2.1.2 Space between Collection Electrodes

The space between collection electrodes is usually set to be 250 to 300 mm. However, if a sufficient corona current can be achieved, a wider space between collection electrodes can help to maintain or improve the collection efficiency. From Deutsch's equation (Eq. (7.35)), one notes that to maintain a high collection efficiency, it is necessary to increase the mobility of particles v_e because with wider spacing the number of electrodes (and collection area) is decreased for space limited systems.

7.6.2.2 Dust Collection of Low Resistivity Particles

An example of a low resistivity dust is the ash from the residual oil combustion . The relationship between applied voltage and collection efficiency for the ash from residual oil combustion is shown in Figure 7.35. The collection efficiency of the ESP increases with an increase in applied voltage, and saturates at 30 ~ 40 kV. The collection efficiency is affected by gas temperature and becomes higher with an increase in gas temperature at the same applied voltage.

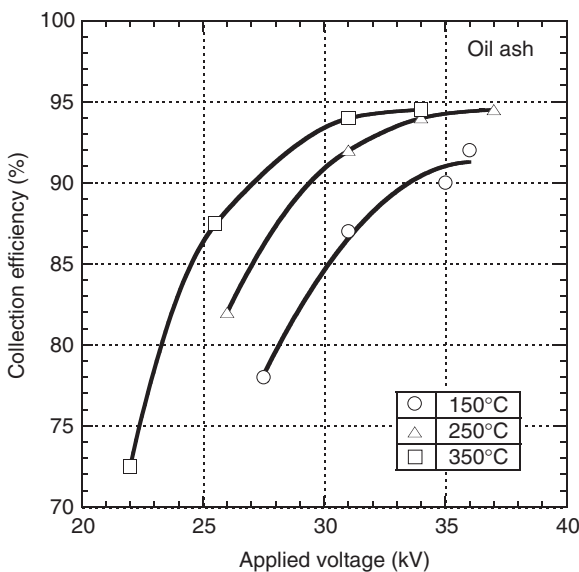


FIGURE 7.35 Applied voltage and collection efficiency. (From Kanaoka et al., 1997.)

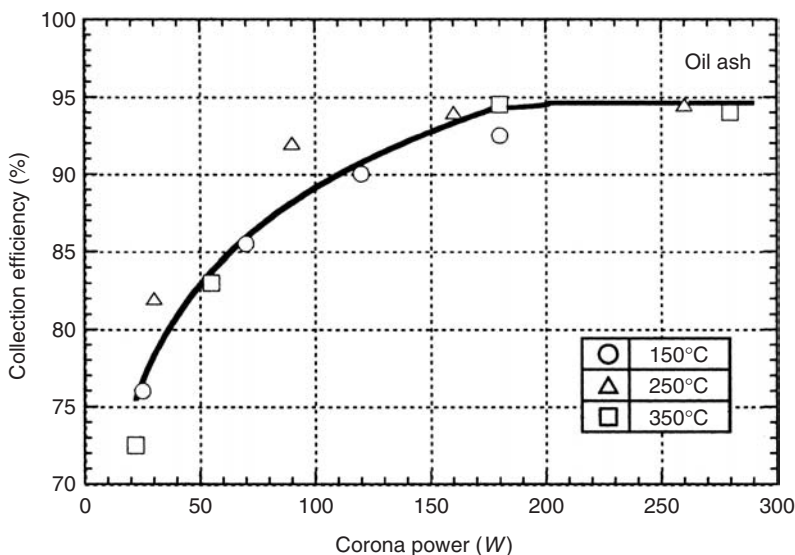


FIGURE 7.36 Influence of corona power on collection efficiency. (From Kanaoka et al., 1997.)

The flue gas density decreases with an increase in gas temperature and the corona current increases with a decrease in gas density. On the other hand, as the applied voltage decreases with an increase in gas temperature, the collection efficiency decreases for the same corona current. By these trends, it is evident that collection efficiency is directly related to corona power, which is the product of the applied voltage and corona current, regardless of the gas temperature, as shown in Figure 7.36. This is due to the fact that the properties of the ash from residual oil combustion remain constant with changes in gas temperature. In other words, if the dust properties are held constant, the collection efficiency of an ESP can be estimated based on corona power.

7.6.2.3 Dust Collection of High Resistivity Particles

Ash produced by the combustion of pulverized coal is an example of high resistivity dust.

The relationship between corona current density and collection efficiency of an ESP for pulverized coal ash is illustrated in Figure 7.37. The collection efficiency increases with an increase in current density and saturates at 0.3 mA/m^2 , which is the typical operational condition at a coal-fired plant. If the gas velocity is increased, the collection efficiency decreases owing to the lower residence time of the flue gas in the precipitators.

The effect of gas temperature on collection efficiency is shown in Figure 7.38. For the same corona current density, the collection efficiency decreases with an increase in gas temperature. The reason for this trend is as follows. When the gas temperature decreases, the corona current becomes higher owing to the decrease in gas density and the resistivity of the fly ash. In other words, for the same corona current density, the applied voltage becomes lower with an increase in gas temperature and the collection efficiency decreases. The relationship between applied voltage and corona current is shown in Figure 7.39, which indicates that at higher gas temperature the corona current becomes higher at the same applied voltage.

The relationship between corona power, which is the product of the applied voltage and the corona current, and collection efficiency is shown in Figure 7.40. For the same corona power, the collection efficiency decreases with an increase in gas temperature, in contrast to the residual oil combustion ash. This is due to the fact that the resistivity of coal ash decreases with an increase in gas temperature and the applied voltage becomes lower, because of the higher corona current.

In a conventional pulverized coal combustion boiler, the ESP is operated at approximately 150°C . At this temperature, the maximum value of the resistivity of the coal ash is achieved. The collection efficiency for various kinds of coal is shown in Figure 7.41. The collection efficiency depends on coal properties, i.e., the collection efficiency for high resistivity ash is lower. Improvements in technology to deal

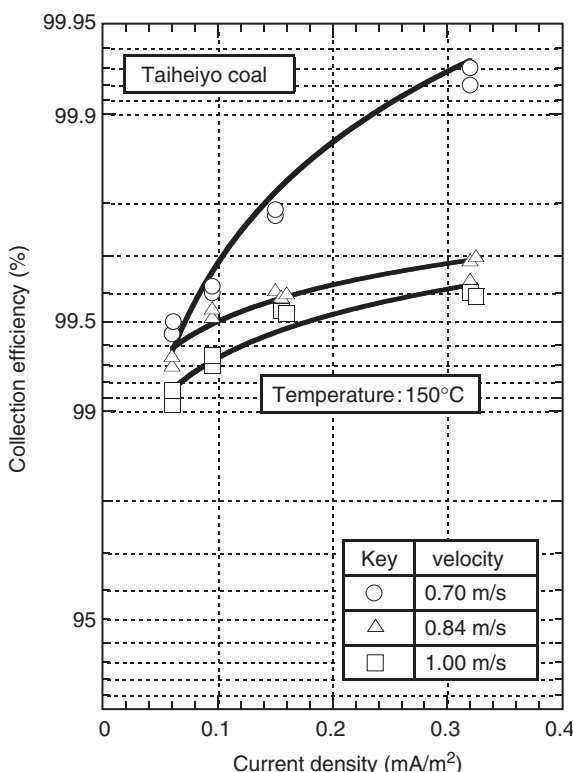


FIGURE 7.37 Influence of corona current density on collection efficiency. (From Kanaoka et al., 1997.)

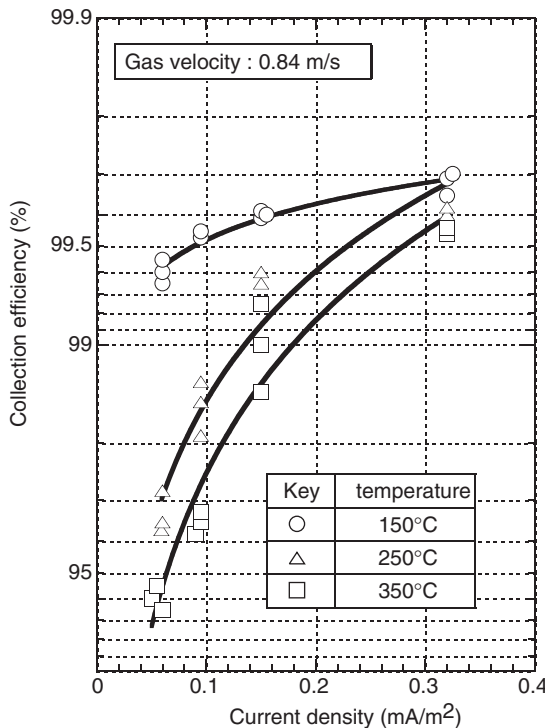


FIGURE 7.38 Influence of temperature on collection efficiency. (From Kanaoka et al., 1997.)

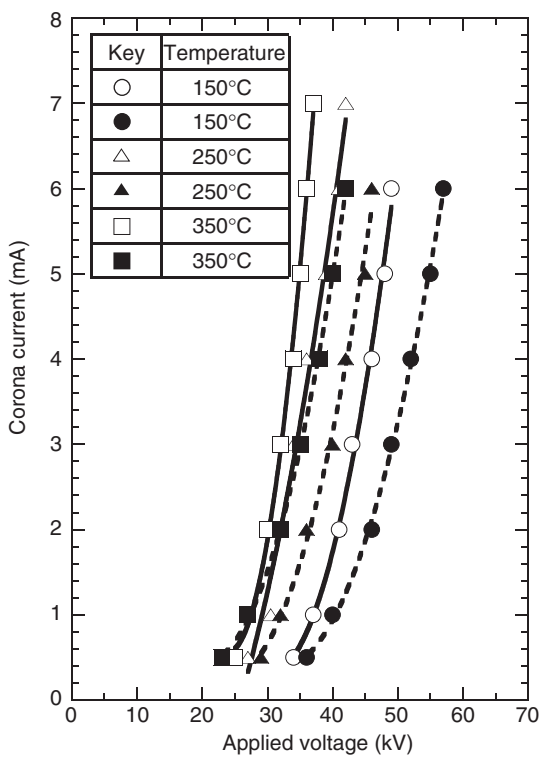


FIGURE 7.39 Applied voltage and corona current. (From Kanaoka et al., 1997.)

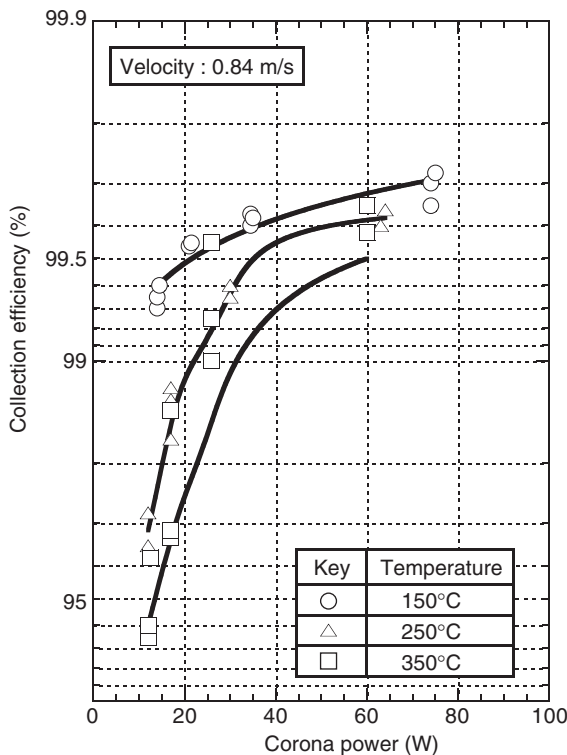


FIGURE 7.40 Corona power and collection efficiency. (From Kanaoka et al., 1997.)

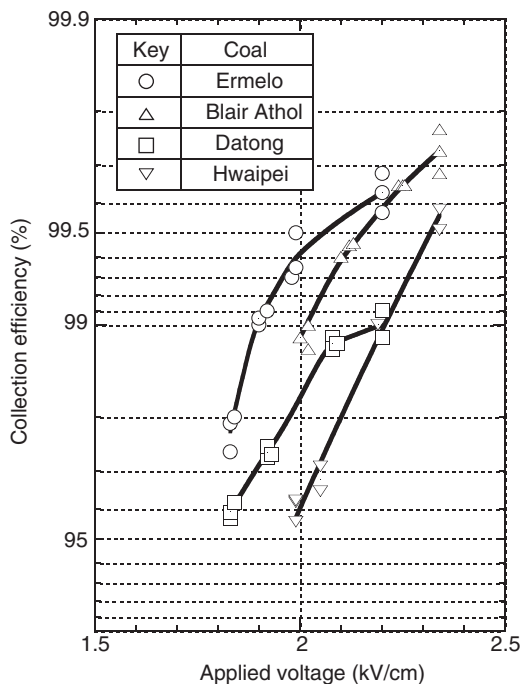


FIGURE 7.41 Collection efficiency of various kinds of coal.

with the decrease in the collection efficiency for high electric resistivity ash are very important to flue gas clean up.

One such approach is the high-temperature ESP operating at 350°C. This ESP utilizes the fact that the resistivity of coal ash is less at high temperature. Although the gas volume increases with an increase in gas temperature and the corona power increases with an increase in corona current, the high-temperature ESP can use the higher corona power for high electric resistivity ash, because arc discharge is suppressed as shown in Figure 7.42.

Another method to reduce dust resistivity is to inject SO₃. When the SO₃ concentration in flue gas is high, a liquid layer is formed on the surface of the ash particles by the condensation of SO₃ and the collection efficiency is improved due to the decreased resistivity of the ash. The effect of SO₃ concentration on the collection efficiency and the dust concentration at the ESP outlet is shown in Figure 7.43. With an increasing SO₃ concentration, the collection efficiency becomes higher and the dust concentration at the ESP outlet decreases.

When the operating temperature of the ESP is reduced, the dust resistivity decreases due to the formation of a liquid layer on the surface of the ash particles. The method that utilizes this trend is a new development in low-temperature ESPs which operate below 100°C. The relationship between gas temperature and the collection efficiency is shown in Figure 7.44. The collection efficiency is remarkably improved below 120°C. In future, this type of ESP will be the choice for high-resistivity ash.

On the other hand, since the reduction in collection efficiency for ESP's operating with high-resistivity ash is due to the dust layer adhered on the collection electrodes, methods to minimize this problem are

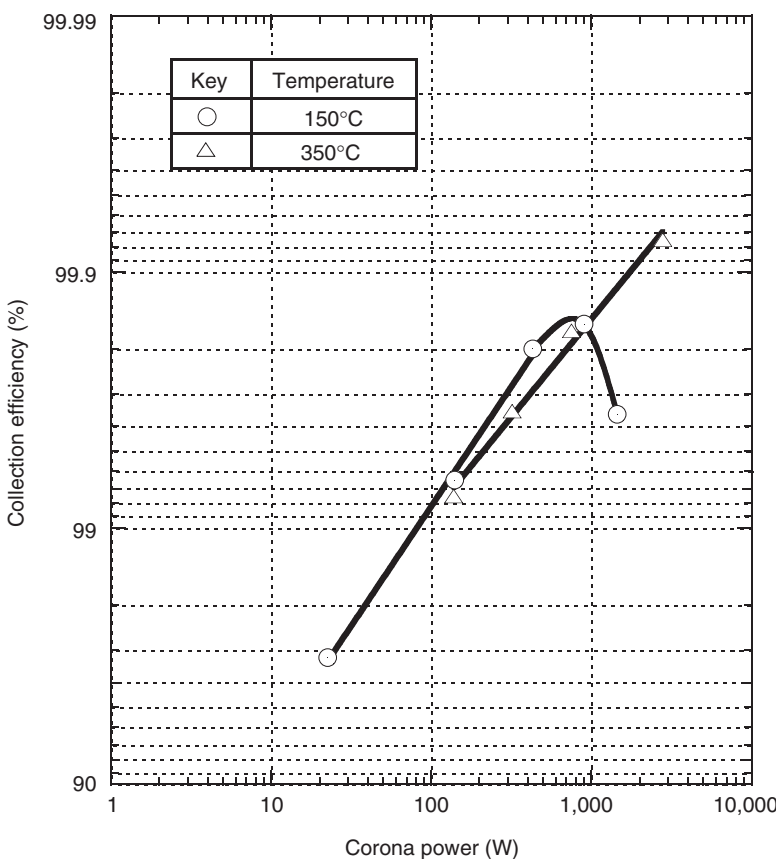


FIGURE 7.42 Influence of gas temperature on collection efficiency.

being developed. One of the techniques is a moving collection electrode in which the dust is removed by a brush. Another is the semi-wet type ESP in which the dust layer is removed by washing with water. These two methods offer potential for performance improvement.

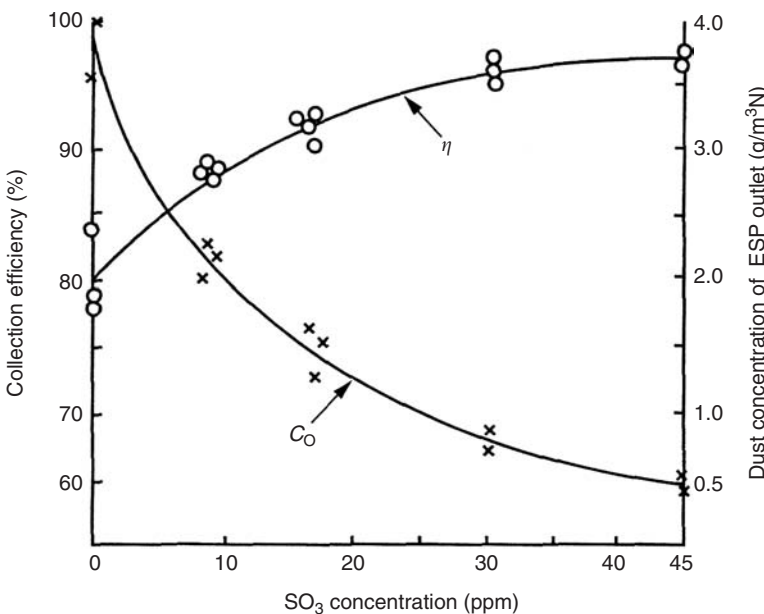


FIGURE 7.43 Improvement of collection efficiency of ESP by SO_3 injection.

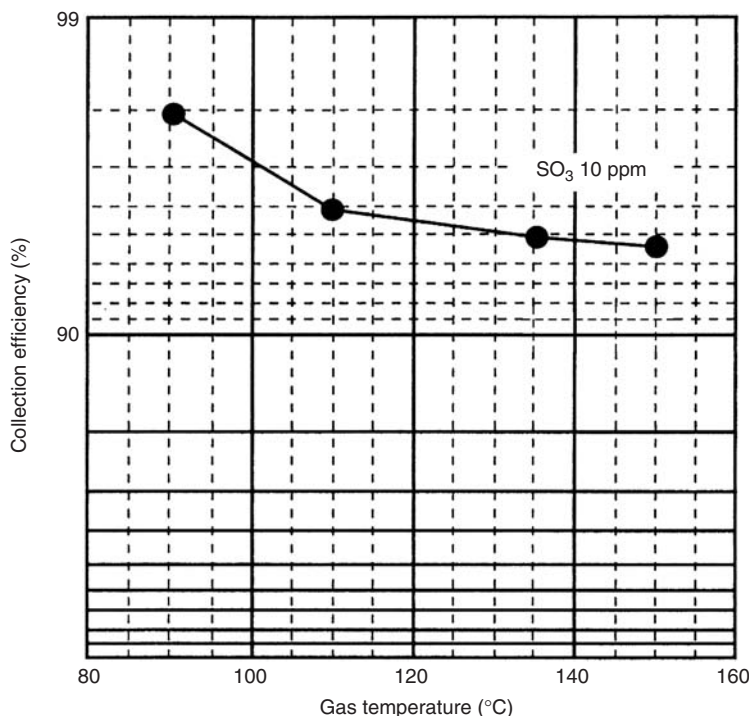


FIGURE 7.44 Influence of collection efficiency of ESP by low temperature operation.

7.7 Obstacle Type Separator

Chikao Kanaoka

As described in the Section 7.2, this type of collector captures dust particles on each individual obstacle in the system, i.e., capturing particles by creating a relative velocity between the gas and particle. Most of the dust collectors belong to this category. Many different shapes and designs to create a relative velocity and enhance particle collection have been developed for this type of equipment.

As shown in Figure 7.45, when a dust-laden gas enters the dust collector with a cross-section A and length L , and obstacles are packed into the collector with a packing density α , the separation efficiency can be derived by considering the mass balance in the differential thickness Δx as:

$$uAC - uA(C + \Delta C) = \eta nA \frac{u}{1 - \alpha} C\Delta x \quad (7.37)$$

where n is the number of obstacles in Δx and u the imposed gas velocity. Furthermore, η is the collection efficiency of a single collection obstacle (body) defined by the following equation:

$$\eta = \frac{\dot{m}_c}{\dot{m}_u} \quad (7.38)$$

where \dot{m}_c is the rate at which particles are collected on the obstacle and \dot{m}_u the flow rate of particles in the area projected by the obstacle.

For the case of cylindrical and spherical collectors, the collection efficiency is

$$\eta = \begin{cases} \frac{Cu2y}{Cud_c} = \frac{2y}{d_c} = \frac{y}{(d_c/2)} & \text{cylinder} \\ \frac{Cu(\pi y^2)}{Cu(\pi d_c^2/4)} = \left(\frac{2y}{d_c}\right)^2 = \left(\frac{2y}{d_c/2}\right)^2 & \text{sphere} \end{cases} \quad (7.39)$$

This is schematically illustrated in Figure 7.46. As seen in the figure, the single body efficiency is defined by the ratio of the upstream area of limiting trajectory to the projected area of the collection body. The limiting trajectory is thus the critical particle trajectory that defines collection efficiency. Particles within the limiting trajectory are collected, but particles beyond the limiting trajectory are not collected.

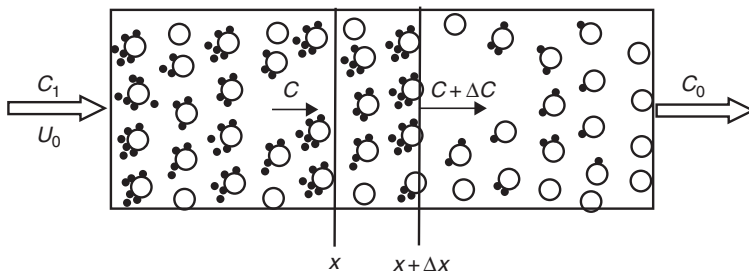


FIGURE 7.45 Schematic representation of dust collection.

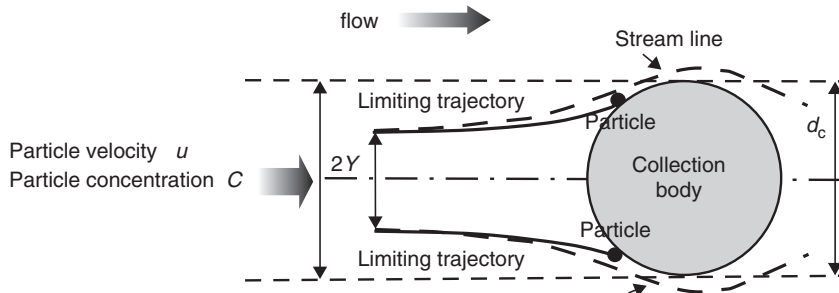


FIGURE 7.46 Definition of single body collection efficiency.

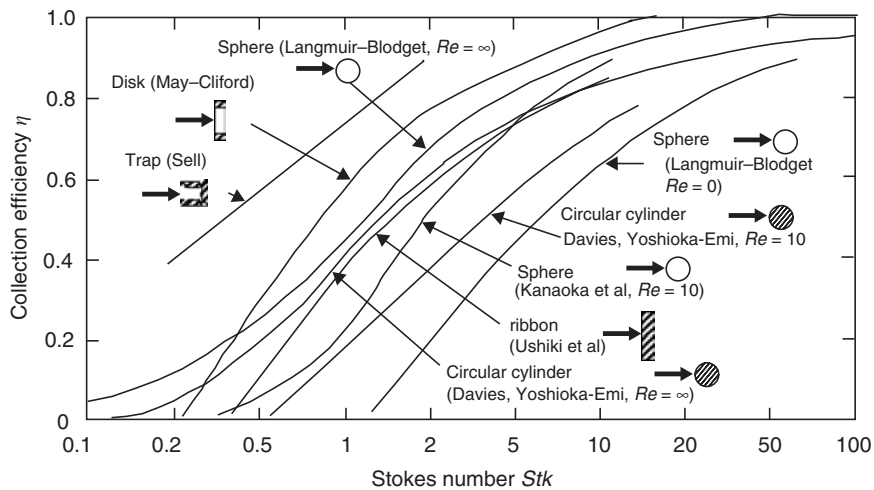


FIGURE 7.47 Calculated collection efficiencies for single collecting obstacles. (From Kanaoka et al., 1997.)

The separation efficiency of the collector is obtained by integrating Eq. (7.37) as

$$E = 1 - \exp\left(-\frac{A}{v_c} \frac{\alpha}{1-\alpha} \eta L\right) \quad (7.40)$$

where v_c is the volume of one collection obstacle, α the packing density of the obstacles, L the packed thickness of obstacles, and A the constant determined by the shape of obstacle, i.e., $A / v_c = 4/(d_c)$ for a cylindrical collector and $3/(2d_c)$ for a sphere. The symbol d_c is the nominal size of the obstacle.

In Eq. (7.37), the constants other than η are determined from the equipment itself, such that E can be estimated if η is specified for a given collector and operational conditions. The collection efficiency for obstacles with different shapes is calculated as shown in Figure 7.47. In this figure, Stk is the Stokes number defined by

$$Stk = \frac{C_c \rho_p d_p^2 u}{9 \mu d_c} \quad (7.41)$$

where C_c is the Cunningham's slip correction factor, ρ_p the particle density, d_p the particle diameter, d_c the representative size of the collecting body, u the gas velocity, and μ the gas viscosity.

7.8 Inertial Dust Collector

Chikao Kanaoka

The inertial dust collector is one of the typical obstacle dust collectors and separates particles by the difference in the particle trajectory and gas streamlines as shown in Figure 7.48. Various obstacles are designed to create a relative velocity between particle and gas flow. Typical obstacles are shown in Figure 7.49. The Louver type dust collector, shown in Figure 7.50, intensifies the inertial effect by a large inclination angle and a small gap between blades.

In practical applications, inertial collectors are used mainly to separate mist rather than solid particles.

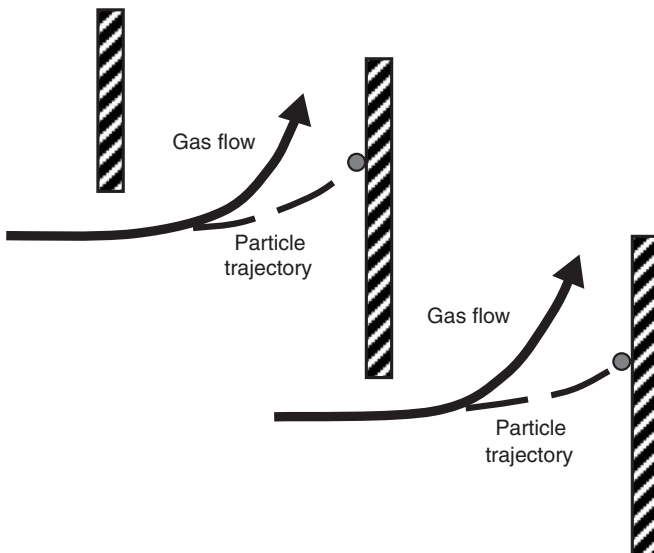


FIGURE 7.48 Collection mechanism of inertial dust collector.

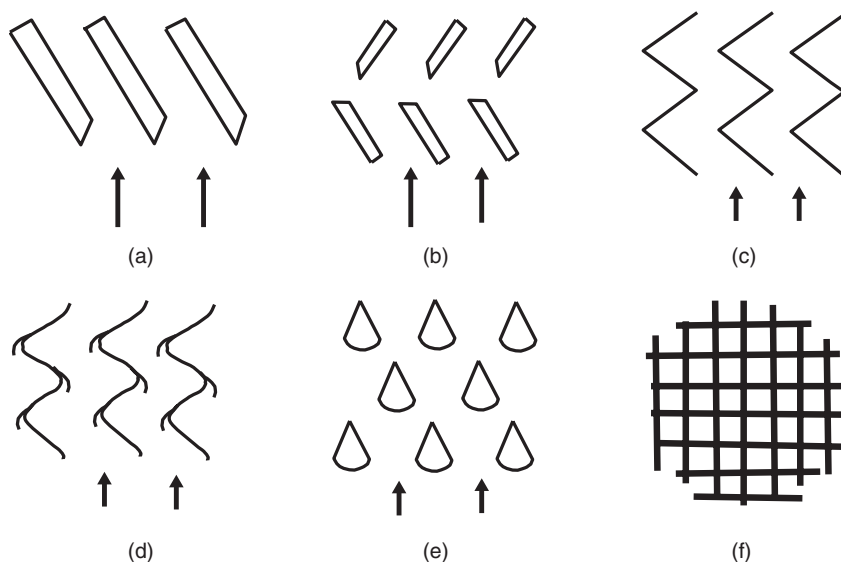


FIGURE 7.49 Typical shape of obstacles.

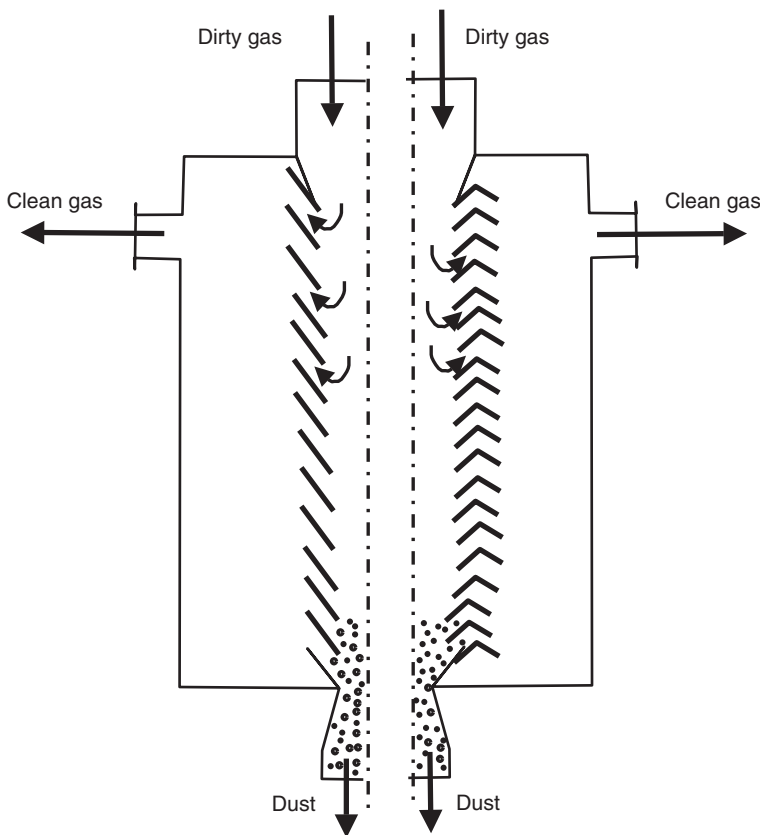


FIGURE 7.50 Louver type dust collector.

7.9 Air Filter

Chikao Kanaoka

The air filter is one of the most reliable and efficient methods for dust collection and mainly used at low dust concentration. Particles are captured inside the filter and hence this type of particle collection system is referred to as depth filtration.

An air filter is mainly used to purify the air in local environments such as hospitals, manufacturing lines, working spaces, and so on. In these environments, the dust concentration is usually lower than 10 mg/m^3 and the particle size is less than several micrometers. Hence, packed filter materials, especially fibrous mats, are used for this purpose. The porosity of a filter mat is generally higher than 85%; hence, particles are captured on individual fibers in the filter.

Therefore, the filter efficiency E can be calculated from the single fiber collection efficiency for a given filtration condition as follows:

$$E = 1 - \exp\left(-\frac{4}{\pi} \frac{\alpha}{1-\alpha} \frac{L}{d_f} \eta\right) \quad (7.42)$$

where d_f , α , and L are the fiber diameter, fiber packing density, and filter thickness, respectively.

Although particles are collected on a fiber through a combination of effects, the mechanisms of inertia, Brownian diffusion, interception, and gravity are predominant in mechanical filtration. Electrostatic force becomes important when either fibers or particles or both are electrically charged or an external electrical field is applied.

Many theoretical and empirical expressions have been proposed for each collection mechanism. Figure 7.51 to Figure 7.53 show typical single fiber collection efficiencies by different mechanisms and Figure 7.54 provides the efficiency chart obtained by taking inertia, Brownian diffusion, interception, and gravity into the account simultaneously. It is clear from the figure that there exists a particle size or

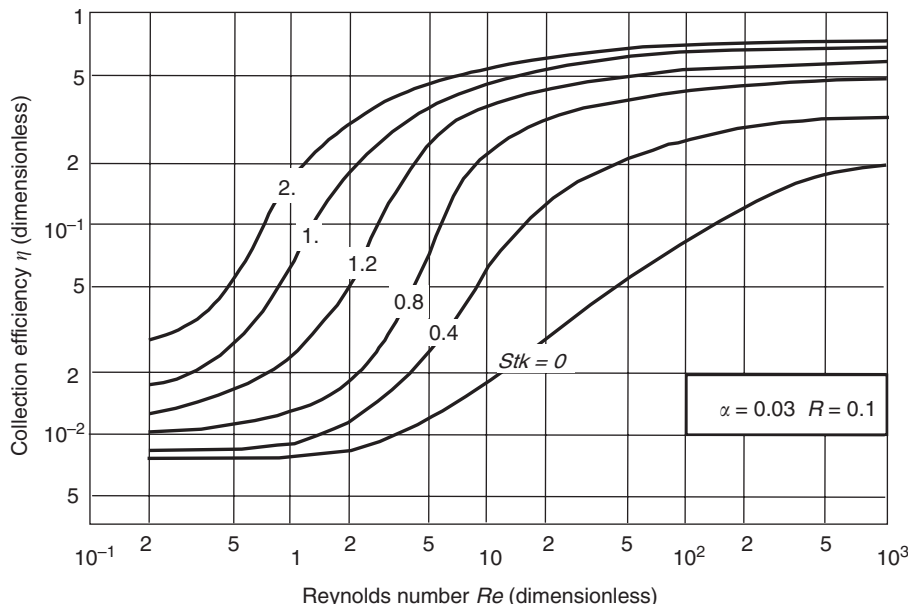


FIGURE 7.51 Calculated single fiber collection efficiency by inertia and interception effect. (Modified from Emi et al., 1977.)

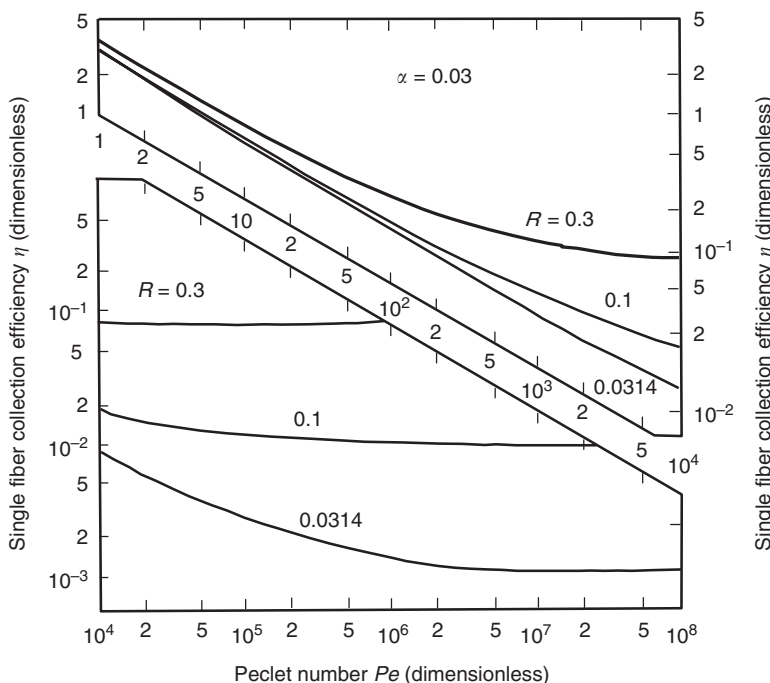


FIGURE 7.52 Calculated single fiber collection efficiency by diffusion and interception. (Modified from Kanaoka et al., 1997.)

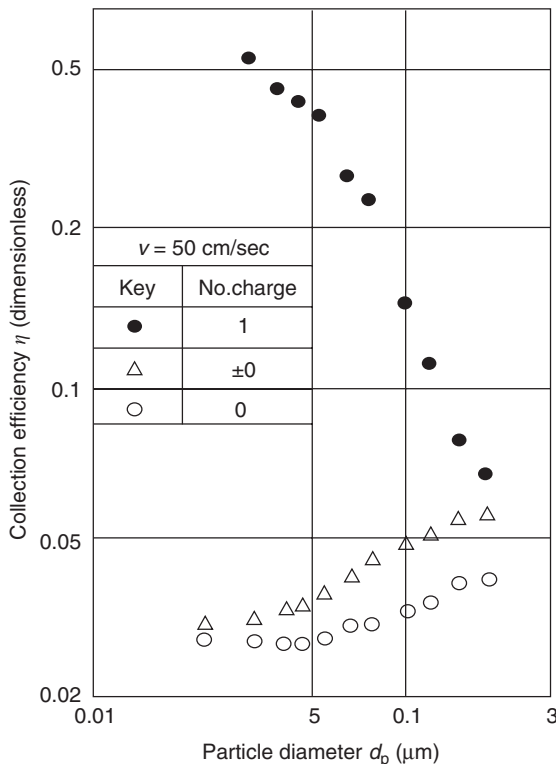


FIGURE 7.53 Experimental collection efficiency of particles at different charging state by an electret fiber. (Modified from Emi et al., 1987.)

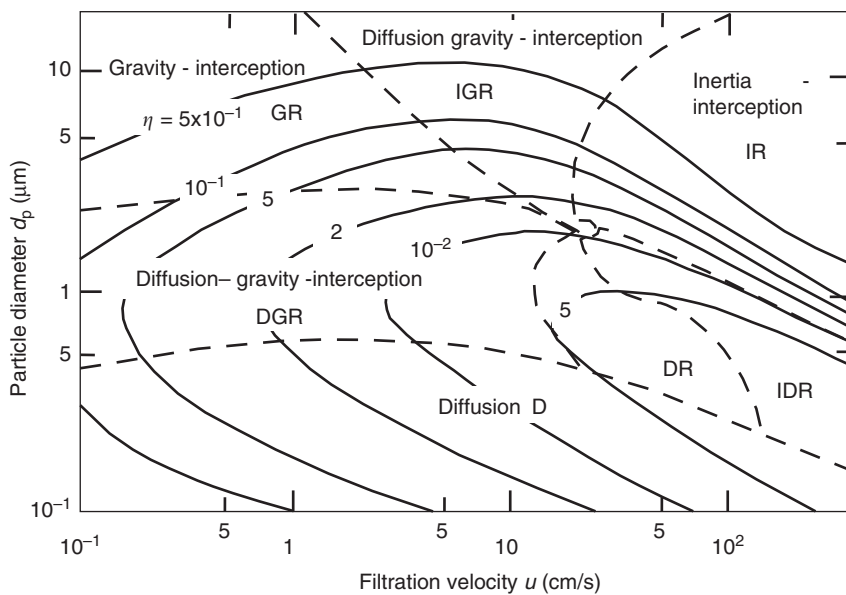


FIGURE 7.54 Total single fiber collection efficiency ($d_f = 10 \mu\text{m}$, $\alpha = 0.03$). (Modified from Emi et al., 1973.)

a filtration velocity, which gives minimum efficiency, corresponding to the transition region for different mechanisms.

Filter performance, such as collection efficiency and pressure drop, change with time and state of particles as shown in Figure 7.55 and Figure 7.56. These changes are caused by the shadowing effect of already captured particles on the collection of incoming particles as shown in [Figure 7.57](#) to [Figure 7.59](#). [Figure 7.60](#) summarizes the general morphologies of captured particles by this collection mechanism.

There are two types of air filters: disposable and renewable. For the former type, fiber materials such as glass, metal, and natural and synthetic fibers, are packed loosely in a frame or are formed into a mat-like structure. Since captured particles accumulate inside the filter, the pressure drop increases with filtration time, such that a zigzag structure is adopted to increase the filtration area to lengthen its service life. It is finally replaced when the pressure drop reaches a certain level to avoid an increase in the operational cost.

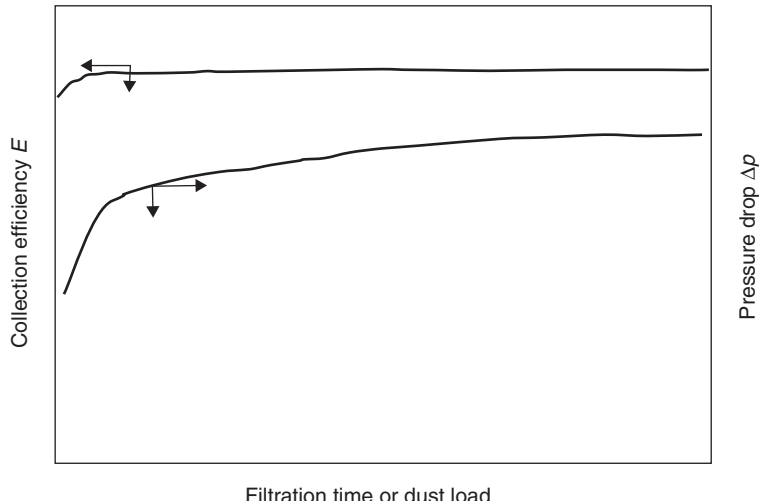


FIGURE 7.55 Experimental time dependency of performance of an air filter with liquid particles.

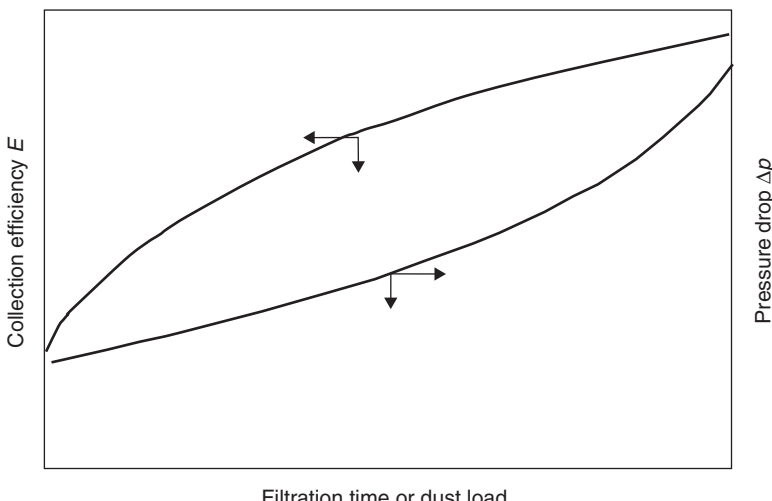


FIGURE 7.56 Experimental time dependency of performance of an air filter with solid particles.

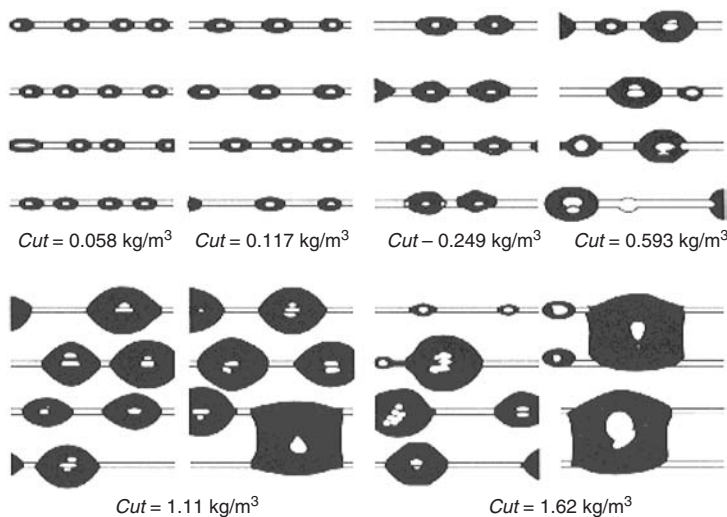


FIGURE 7.57 Time dependency of morphology of captured mist particles on parallel wires. (From Kanaoka et al., 1997.) Fiber diameter $d_f = 60 \mu\text{m}$, fiber interval $h_t = 525 \mu\text{m}$, filtration velocity $u = 4 \text{ m/s}$.

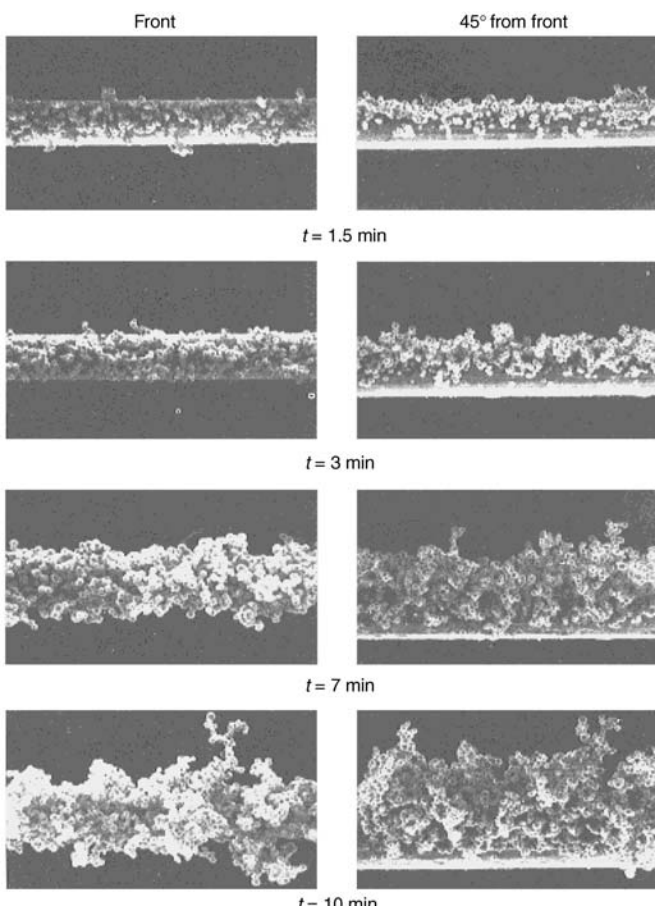


FIGURE 7.58 Time dependency of morphology of captured solid particles on a wire. (From Kanaoka et al., 1997.) $d_f = 10 \mu\text{m}$, $d_p = 1 \mu\text{m}$, $u = 50 \text{ cm/sec}$, $\rho_p = 11.34 \text{ g/cm}^3$, $Stk = 3.5$, $R = 0.1$.

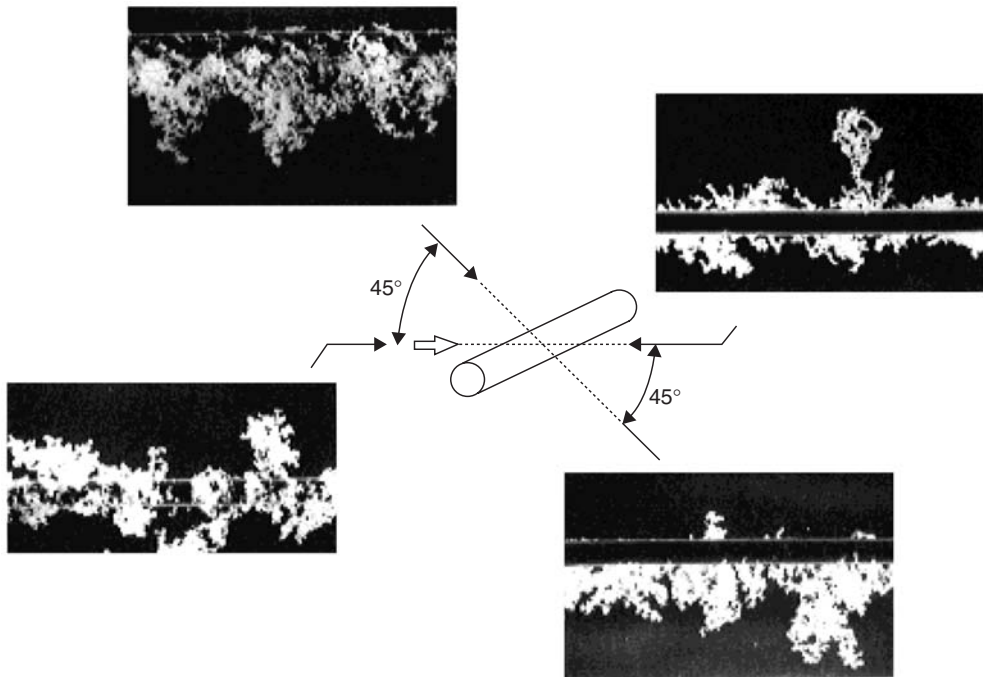


FIGURE 7.59 Morphology of captured particles on a fiber by inertia and interception effect. (From Kanaoka et al., 1997.) Fiber diameter $d_f = 10 \mu\text{m}$, particle diameter $d_p = 0.86 \mu\text{m}$, particle density $\rho = 2.33 \text{ g/cm}^3$, filtration velocity $u = 50 \text{ cm/sec}$, Stokes number $Stk = 0.632$, interception parameter $R = 0.086$, ratio of total particle volume captured in a unit fiber length to that of fiber volume with unit length $V_c = 0.10$, ratio of total income particle volume in projection area with unit fiber length to fiber volume with unit length $V_i = 1.99$.

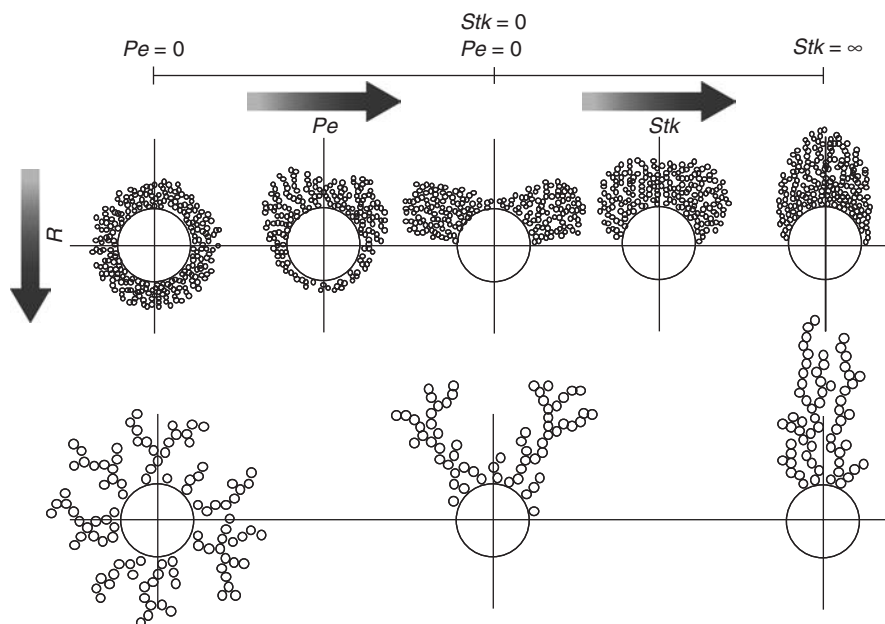


FIGURE 7.60 General morphology of accumulation on a cylindrical fiber by the change of collection mechanism. (From Kanaoka, 1989.)

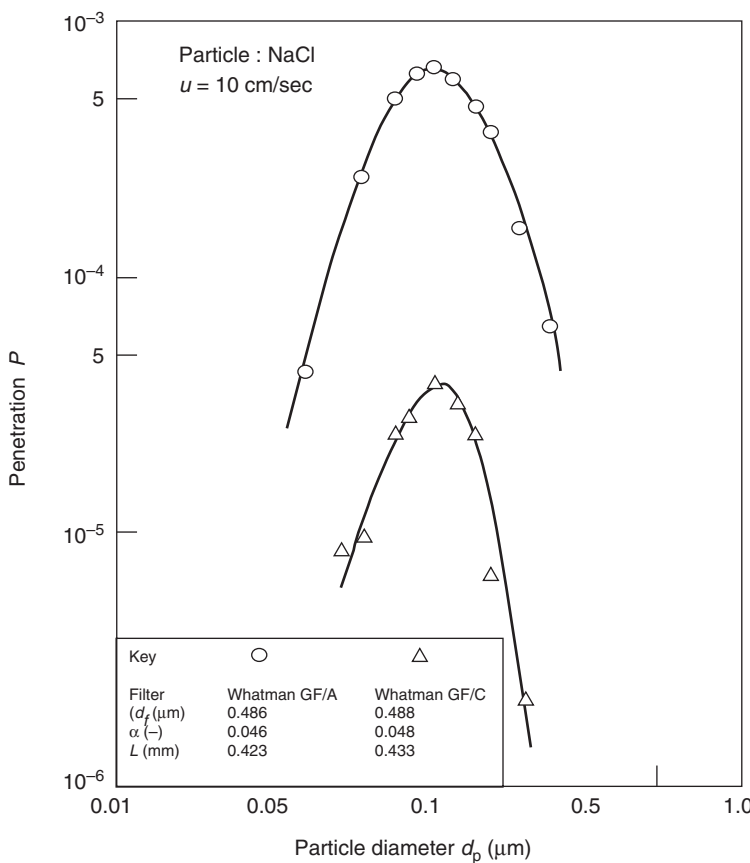


FIGURE 7.61 Experimental penetration of HEPA filter. (From Emi, 1989.)

High-efficiency particulate air (HEPA) and ultralow penetration air (ULPA) filters are types of paper filters composed of very fine fibers, less than 1 μm on average. They are defined as the filters that collect 0.3 μm particles at an efficiency higher than 99.7% and 0.1 μm particles at higher than 99.9997%, with a pressure drop that does not exceed 12.7 mm H_2O at their specified flow rate, usually 2.5 cm/sec. Therefore, HEPA and ULPA filters are used to create highly purified environments, which are necessary in the semiconductor industry, the precision machine industry, and so on. Penetration curves for HEPA and ULPA filters vary parabolically with particle size and the maximum appears around 0.1 μm (i.e., the collection efficiency of the filter is poorest around this particle size at the conventional filtration condition and decreases as the filtration velocity increases) as shown in Figure 7.61. Hence, the filter collection performance can be roughly evaluated by measuring the efficiency around this size range.

An electrostatic fibrous filter is another type of air filter that utilizes electrostatic force to remove particles. An electrostatic attractive force becomes effective when either fiber or particle is charged, but not when both of them are charged with the same polarity. Therefore, several types of electrostatic fibrous filters have been designed, depending on the charging state of fiber and particle. In general, an electrostatic fibrous filter is superior in collection performance to a mechanical fibrous filter but difficult to operate stably. The electret filter is a stable electrostatic fibrous filter because it is composed of fibers with permanent dipoles and is capable of collecting particles at a high efficiency in the initial filtration stage. However, the efficiency decreases with filtration time owing to dust loading. This drawback has to be eliminated in practical use.

7.10 Scrubber

Chikao Kanaoka

The scrubber is the generic name for a group of dust collectors utilizing liquid droplets or film as collecting media. Most of them can be classified into obstacle type dust collectors.

The most important difference between this group and the so-called dry type is that the collection of dust particles is carried out in two operational steps, the capture of the dust by liquid component and then separation from the liquid by some other means. Since a liquid medium is used, this type of collector can be used for the collection of mist particles, even under hot gas conditions. Furthermore, the simultaneous separation of dust and gaseous material are also accomplished. However, the collector consumes a large amount of liquid. Also secondary treatments of the collected liquid, the resulting sludge and so on are required. This type of equipment is used only when a cheap and abundant amount of water is available or when a dry type collector cannot be utilized.

The scrubber can be classified into four types as shown in Figure 7.62: (a) the water reservoir type; (b) the pressurized water type; (c) the packed tower type; and (d) the forced rotary type. Their performance is summarized in the Table 7.3.

As seen from Figure 7.62 and Table 7.3, the scrubber is, in general, relatively simple in structure but shows good performance. Most scrubbers are capable of removing particles several micrometers in diameter with little difficulty. However, it is rather difficult to separate particles finer than $1 \mu\text{m}$, except with a venturi scrubber operating at very high speed.

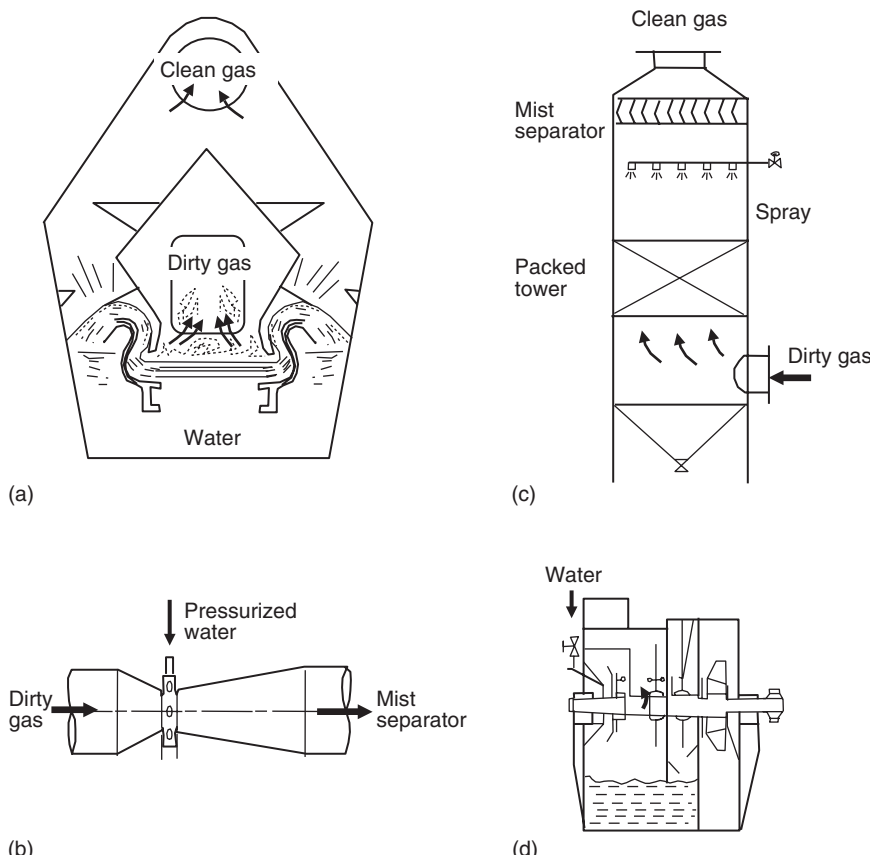


FIGURE 7.62 Typical scrubbers: (a) water reservoir type; (b) pressurized water type; (c) packed tower type; (d) forced rotation type.

As described earlier, droplets are often used in the scrubber and their space density is not very high. Therefore, single sphere collection efficiency, shown in Figure 7.47, is directly applicable to the prediction of the separation efficiency of the scrubber. However, both the dust particle and collecting droplet move in the air and the collection takes place only when there is a relative velocity, which does not last very long. Separation efficiency of the collector is expressed as

$$E = 1 - \exp(-R'L) \quad (7.43)$$

where L is the liquid–gas ratio and R' is the dimensionless parameter for the amount of particles captured by a single collecting body (water droplet) defined by

$$R' = \frac{3 \int_0^X \eta dx}{2d_w} \quad (7.44)$$

where X is effective collection length of the collector is the water droplet diameter.

Figure 7.63 shows the calculated R' vs. collector diameter d_w for a venturi scrubber with a throat velocity of 80 m/sec and $X = 1$ m.

TABLE 7.3 Typical Scrubber

	Gas Velocity (m/s)	Gas Volume Flow Rate (m ³ /min)	Pressure Drop (Pa)	Liquid–Gas Ratio	Separation Diameter (μm)
Water Reservoir Type	20–30	1,000	500–1,500	0.1–0.3	0.5
Rotocclone					
Pressure Water Type	1–2	5,000	500–2000	0.5–5	1
Cyclone scrubber	40–100	10,000	2,000–20,000	0.3–1	0.1
Venturi scrubber					
Packed Tower Type	1–2	1,000	100–500	0.1–1	3
Spray scrubber	1–2	1,000	1,000–3,000	1–10	1
Packed tower					
Forced Rotary Type	1–5	1,000	2,000–1,000	0.5–2	0.2
Theisen washer					

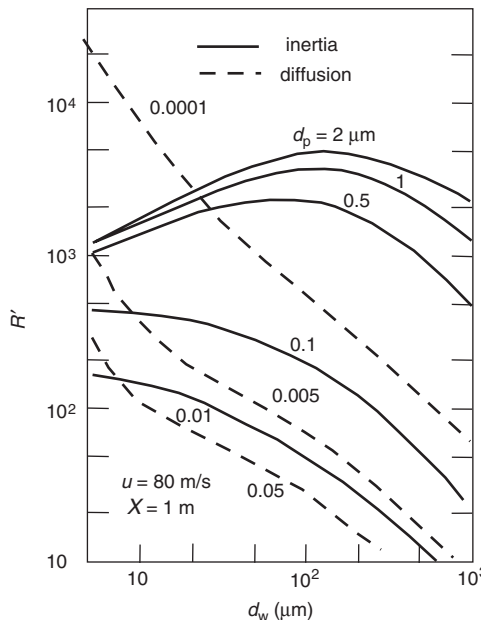


FIGURE 7.63 Dimensionless amount of particles captured by a droplet in a venturi scrubber. (Modified from Morishima's, 1967.)

As seen from the figure, R' decreases with increasing droplet size for diffusion but displays a maximum for droplet sizes greater than 0.5 μm for inertial collection. The maximum R' for inertial collection can be explained by trends in collection efficiency with Stokes number and Reynolds number defined as

$$Stk = \frac{C_c \rho_p d_p^2 \Delta u}{9\mu d_w} \quad Re = \frac{\rho_f d_w \Delta u}{\mu} \quad (7.45)$$

where Δu is the velocity difference between the droplet and the fluid. As the water droplet diameter increases, the velocity difference increases Reynolds number and the Stokes number goes through a maximum value. As seen from Fig. 5.51, the collection efficiency will increase and approach an asymptotic value near unity. The value for R' first increases with collection efficiency, reaches a maximum and decreases as the water droplet diameter becomes larger. The same trend is not observed from the small droplets because they are in the lower Reynolds number range.

7.11 Barrier Type Separator

Chikao Kanaoka

As described earlier, this type of collector uses a permeable medium for the gas, but not for the dust, and is used to separate dust at high concentrations. Hence, the most pronounced feature of dust collectors of this type is almost perfect particle collection, regardless of size, except just after the dislodgement of accumulated particles on the barrier. This occurs because most of the particles are collected due to the particles captured earlier by a sieving effect. This type of collection is usually referred to as surface or cake filtration. The bag filter is the most common barrier-type dust collector. Recently, the ceramic filter has become popular for high temperature dust cleaning.

7.12 Bag Filter

Chikao Kanaoka

7.12.1 Collection Mechanism

The bag filter is commonly made of fabric in a cylindrical “bag” shape. Consequently this type of filter is called a bag filter. The designation “fabric” filter is also popularly used. Figure 7.64 shows the typical shape of the bag filter.

Although any type of fiber with a different weave, such as woven and nonwoven, can be used as a filter material, synthetic fibers such as polyester, polypropylene, nylon, and glass fibers are most often employed owing to their strong resistivity to gas and dust.

The collection of particles by a fabric depends on the weave of the fabric, i.e., woven or nonwoven. For a woven fabric, initially (or after cleaning) the particles are captured on fibrils in the texture by inertia, interception, diffusion, and so on. After the texture is filled with captured particles, the capture area expands to the whole fabric surface and forms a very coarse dust layer of porosity ranging between 80 and 85%. At this stage, particles are mainly captured by the sieving effect because particles have to go through the openings in the layer, the size of which is of the same order as the particles. Hence, the collection performance is not affected by the particle size and is usually very high.

Nonwoven fabric consists of independent fibers and hence the porosity is much higher than that of woven fabric with same weight. Therefore, it can operate at higher flow rates than woven fabric and the particle collection behavior is more or less similar to that of an air filter in the initial stage. In this case, the collection behavior after the formation of dust layer is not much different than that of the woven fabric.

As mentioned earlier, the dust release from the fabric is carried out repeatedly either after some prescribed time interval or when the filter pressure drop reaches a predetermined value, above which con-

tinuous operation cannot be maintained. However, a small amount of dust remains in the fabric after the release action and forms a primary dust layer which plays an important role in dust collection in bag filtration. This can be seen from Figure 7.65 which shows the grade efficiency of a flat nonwoven felt just before and after dust release at different cleaning cycles. As seen from the figure, the grade efficiency before dust cleaning is almost 100%, regardless of particle size but after cleaning is considerably lower but increases with the number of cleanings, suggesting the formation of the primary dust layer. Once the primary layer is formed, the collection efficiency of the filter does not radically decrease even after cleaning.

Figure 7.66 shows the change measured for outlet dust concentration as a function of dust load. The dust load is the product of the particle concentration, filtration velocity, and time and represents the

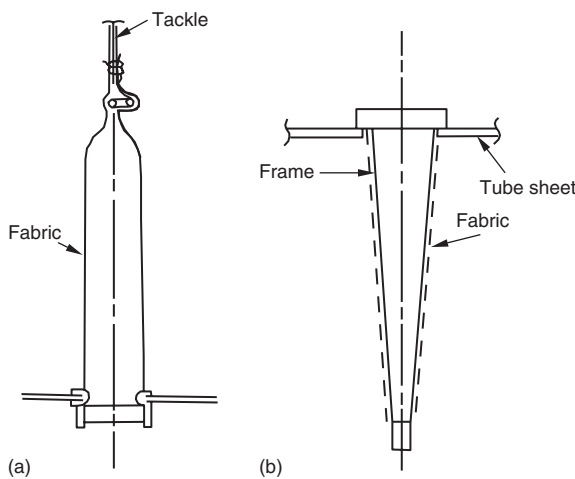


FIGURE 7.64 Typical shape of bag filter element: (a) cylindrical type; (b) envelope type.

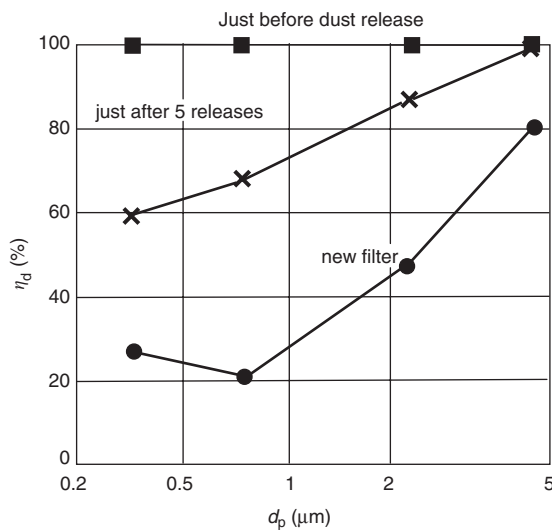


FIGURE 7.65 Grade efficiency of a singed polyester filter element. (From Kanaoka, 2003.) Fabric: singed polyester nonwoven felt, fiber diameter: 14 μm ; weight: 600 g/m^2 ; particle: JIS No. 11 test dust (Kanto loam powder, mean diameter 1.5 μm), filtration velocity, 3 cm/s ; pressure drop of fabric for cleaning, 2 kPa; cleaning air pressure, 100k Pa; duration of air injection, 200 ms.

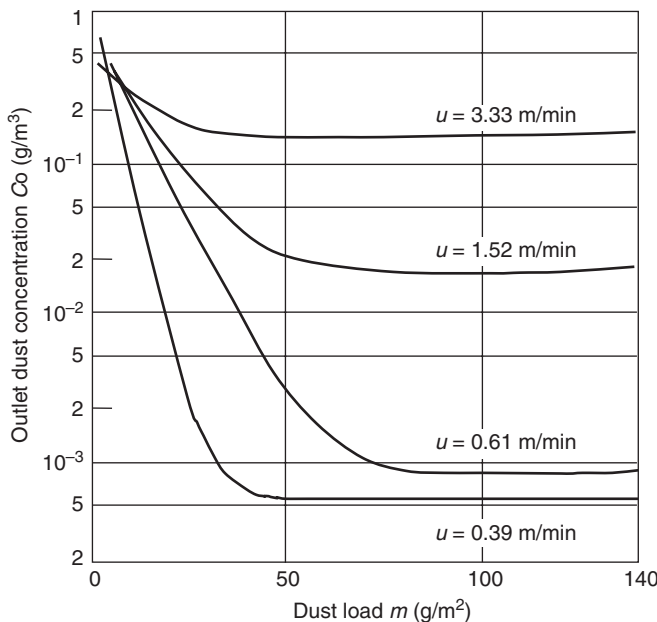


FIGURE 7.66 Time change of outlet dust concentration at different filtration velocity. (Modified from T. Chaing and R.P. Ostrop, 1982.)

total incoming particle mass per unit filter area. As seen from the figure, the outlet concentration decreases with time, but the decrease rate is higher for slow filtration velocity and the final stabilized dust concentration is more than two orders of magnitude different, despite the fact that the filtration velocity varied only one order of magnitude. This suggests the possibility of pinhole formation in the dust layer at the faster filtration velocity and thus fairly large penetration of particles from the holes.

7.12.2 Pressure Drop

Pressure drop of a bag filter Δp is expressed by the sum of the pressure drop in the fabric and the dust accumulated on the fabric as

$$\Delta p = \Delta p_0 + \Delta p_d = (\zeta_0 + \alpha m) \mu u \quad (7.46)$$

where Δp is the pressure drop of a dust loaded fabric (Pa), Δp_0 and Δp_d are the pressure drops through the fabric and covering dust layer, ζ_0 is resistance coefficient of the fabric (1/m), α the specific resistance of dust layer (m/kg^2), m the dust load (kg/m^2), μ the gas viscosity (Pa sec), and u filtration velocity (m/s).

At the initial stage of the filtration, the Δp_0 of a woven fabric is usually very low and thus negligible. However, it may not be negligible for a very thick nonwoven fabric. Under dust-loaded conditions, the porosity of the fabric decreases so that pressure drop increases as $\Delta p \propto u^n$, where n ranges between 1.5 and 2.

Flow through the dust layer is usually laminar, such that the pressure drop Δp_d is proportional to the filtration velocity and is expressed by the following Kozeny–Carman equation:

$$\Delta p_d = \frac{180(1 - \varepsilon)m_d \mu u}{d_{ps}^2 \varepsilon^3 \rho_p} \quad (7.47)$$

where ε is the porosity, d_{ps} the specific surface diameter (m^2/m^3), and ρ_p the particle density(kg/m^3).

TABLE 7.4 Classification of Bag Filter and Feature

Cleaning Mode	Filter			Filtration Side	Filtration Velocity (m/min)	Temperature (°C)	Remarks
	Weave	Shape	Material				
Mechanical shaking		Cylinder		Inside	0.6–1.6	~200	General purpose : Applicable for any gas flow rate and temperature range
	Woven		Synthetic fiber				Reliable cleaning performance. Suited for the collection of fume
		Envelope		Outside	1–2	~100	Small size collector less than several 10 m ³ /min
Pulse jet							Dust cleaning can be carried out without stopping gas flow
	Nonwoven	Cylinder	Synthetic fiber		1–4	~200	Gas flow fluctuation is small. Suited for small gas flow rate
							Applicable for high concentration and abrasive dust
	Woven	Cylinder	Glass fiber	Outside	0.5–1.5	~250	Applicable higher filtration velocity
	Nonwoven	Cartridge	Synthetic fiber or paper Metal fiber or Ceramic		0.3–1	~140	High resistivity for hot gas
Reverse flow							Large filtration area
	Sintered	Cylinder			0.5–1.5	~450 ~1200	Applicable to low dust concentration requiring high separation performance like air purification
	Woven or	Cylinder	Synthetic fiber		0.6–1.2	~200	High-temperature gas cleaning
	nonwoven		Glass fiber	Inside	0.3–1	~250	Widely used in cement and iron refining industeres
	nonwoven	Envelope	Synthetic fiber	Outside	1–2	~140	Suited for high-temperature fume-like carbon black, non-iron refinery and so on
							Compact size
							Suited to large gas flow rate

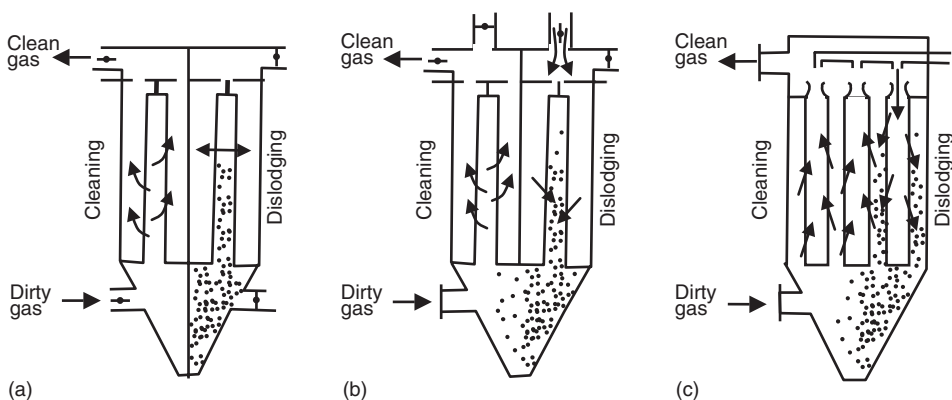


FIGURE 7.67 Schematics of bag filters: (a) mechanical shaking type; (b) reverse flow type; (c) pulse jet type.

7.12.3 Method of Dislodging Dust

The collected dust particles accumulate on a fabric surface and increases the pressure drop. The accumulated dust has to be dislodged to maintain continuous operation. Bag filters are categorized into mechanical shaking, reverse flow, and pulse jet types, depending on the method of dislodging dust as shown in Figure 7.67.

The dislodging method can be further categorized as intermittent or continuous dislodging. The mechanical shaking and reverse flow type filters belong to the intermittent category and pulse jet type to the continuous category. With the intermittent type, the gas flow has to be suspended during dislodging so the bag house is divided into several compartments so that the entire house does not have to be shutdown during cleaning. With the pulse jet type, the cleaning can be performed without ceasing operation, since the injection of intense cleaning air is only needed for a short time. [Table 7.4](#) summarizes the classification of bag filters and their features.

Nomenclature

Latin

<i>A</i>	Area
<i>B</i>	Electric mobility of ions
<i>C</i>	Dust concentration
<i>C_c</i>	Cunningham correction factor
<i>D</i>	Cyclone diameter
<i>d_c</i>	Collector diameter
<i>d_{pc}</i>	Cut size diameter
<i>d_{ps}</i>	Specific surface diameter
<i>d_w</i>	Water droplet diameter
<i>E</i>	Overall collection efficiency, electric field strength
<i>e</i>	Charge on an electron
<i>G</i>	Inlet ratio
$\frac{G}{G_i}$	Mean thermal mobility of ions
<i>g</i>	Acceleration due to gravity
<i>k</i>	Boltzmann's constant
<i>L</i>	Length
<i>l_m</i>	Mean free path

M	Molecular weight
m	Dust load
\dot{m}_a	Particle mass flow rate in projected area of collector
\dot{m}_c	Particle mass collection rate
N	Number of turns
n_i	Ion concentration
p	Penetration
Δp	Pressure drop
Δp_o	Pressure drop through fabric
Δp_d	Pressure drop through dust layer
Q	Volumetric flow rate
q	Charge on particle
R	Cyclone radius, universal gas constant
R_d	Blow-down ratio
R_u	Blow-up ratio
Re	Reynolds number
S	Mass flow rate of dust, surface area
Stk	Stokes number
T	Temperature
t_r	Residence time
t_x	Time to reach wall
u	Velocity in x-direction
u_0	Initial velocity
u_θ	Tangential velocity
v	Velocity in y-direction
V_r	Velocity in radial direction
v_{EF}	Migration velocity
x	Distance, x-coordinate
y	Distance, y-coordinate

Greek Letters

α	Packing density, specific resistance
ε	Dielectric constant, porosity
ζ_o	Fabric resistance coefficient
η	Grade efficiency, fractional collection efficiency
μ	Absolute viscosity
ν	Kinematic viscosity
ρ	Density
τ_v	Particle response time

Subscripts

i	In
f	Fluid
N	Standard conditions
o	Out
p	Particle
x	In x -direction
y	In y -direction

References

- Ayers, W.H., Boysan, F., Swithenback, J., and Ewan, B.C.R., Theoretical modelling of cyclone performance, *Filtration and Separation*, 22, 39–43, 1985.
- Bradley, D., Separation efficiency of hydro-cyclone, *Ind. Chem.*, 473–485, 1958.
- Chaing, T. and Ostop, R.P., EPA-666/9-82-005C, 1982, p. 261.
- Chine, B. and Ferrara, B., Comparison between flow velocity profile in conical and cylindrical hydro-cyclones, *KONA (Powder and Particle)*, 15, 170–179, 1997.
- Chu, L.Y., Chen, W.M., and Lee, X.Z., Enhancement of hydro-cyclone performance by controlling the inside turbulence structure, *Chem. Eng. Sci.*, 57, 207–212, 2002.
- Emi, H., Okuyama, K., and Yoshioka, N., Prediction of collection efficiency of aerosols by high-porosity fibrous filter, *J. Chem. Eng. Jpn.*, 6, 349, 1973.
- Emi, H., Okuyama, K., and Adachi, M., The effect of neighbouring fibers on the single fiber inertia interception efficiency of aerosols, *J. Chem. Eng. Jpn.*, 10, 148, 1977.
- Emi, H., *Aerosol Engineering (in Japanese)*, Yokendo Publisher, 1984, p.186.
- Emi, H., Kanaoka, C., Otani, Y., and Ishiguro, T., Collection mechanisms of electret filter, *Particulate Sci. and Tech.*, 5, 161, 1987.
- Iinoya, K., Hisakuni, H., Sue, E., Fuyuki, T., and Yamada, Y., Air cyclone classifier for sub-micron size, 1990 *Proceedings of the Second World Congress on Particle Technology*, Sept., 19–22, Kyoto, Japan, 120–126, 1990.
- Iinoya, K., Fuyuki, T., Yamada, Y., Hisakuni, H. and Sue, H., Dry sub-micron classification by a small blow-down cyclone, *J. Soc. Powder Tech.*, Japan, 29, 351–355, 1992.
- Iinoya, K., et al., Dry sub-micron classification by a small blow-down cyclone, *KONA (Powder and Particle)*, 11, 223–227, 1993.
- Kanaoka, C. and Emi, H., Collection performance of air filter with dust load, *Kuuki Seijo*, 22, 1, 1985 (Japanese).
- Kanaoka, C., Time dependency of air filter performance, *Earozoru Kenkyu*, 4, 256, 1989.
- Kanaoka, C., Tamori, I., Makino, H. and Yoneda, T., Principle and equipment of dust collectors in (Japanese), *Fundamentals in Aeorsol Science (in Japanese)* Nikkan Kogyo Shinbun, 24–99, 1997.
- Kanaoka, C., *Industrial Pollution Control Technologies and Regulations (in Japanese)* Maruzen, 250, 2003 (Japanese).
- Leith, D. and Licht, W., The Collection Efficiency of Cyclone Type Particle Collectors, New Theoretical Approach, *A.I.Ch.E. Symp. Ser.*, 126, 196–206, 1972.
- Morishima, N., Study on the Venturi Scrubber, Ph.D. thesis, Osaka City University, 1967.
- Ohashi, H. and Maeda, S., Measurement of velocity distribution in hydro-cyclone, *Chemical Eng. Japan*, 22, 4, 200–208, 1958.
- Petty, C.A. and Parks, S.M., Flow prediction within hydro-cyclone, *Filtration and Separation*, 28, 28–34, 2001.
- Sineath, H.H. and Della Valle, J.M., Performance of axial-flow type hydro-cyclone, *Chem. Eng. Prog.*, 55, 59–69, 1959.
- Takahashi, K., Yokendo, 1978
- Yamamoto, K. and Jiao, X., Hydro-cyclone with a Perforated Inner Cylinder”, *Trans. Jpn. Soc. Mech. Eng., Ser. B*, 63, 133–138, 1997.
- Yamamoto, M., Kitamura, O., and Arakawa, C., Computation of Turbulent Flow in a Cyclone Chamber with a Reynolds Stress Turbulence Model, *Trans. Jpn. Soc. Mech. Eng.*, 59, 1959–1964, 1993.
- Yamamoto, M. and Kitamura. O., Computation of Turbulent Flow in a Cyclone Chamber with a Reynolds Stress Model, *Trans. Jpn. Soc. Mech. Eng.*, 60, 4002–4009, 1994.
- Yoshida, H., Akiyama, S., and Taniguchi, S., Fine Control of Cut Size with Dry Cyclone, *Kagaku Kogaku Ronbunshu*, 27, 574–580, 2001.
- Yoshida, H., Akiyama, S., Fukui, K., and Kumagaya, A., Particle classification with improved hydro-cyclone separator, *J. Soc. Powder Tech. Jpn.*, 38, 626–632, 2001.

- Yoshida, H. et al., The control of particle size separation by use of hydro-cyclone, *J. Soc. Powder Tech. Jpn.*, 34, 690–696, 1997.
- Yoshida, H., Fujioka, T., Hashimoto, K., and Nagahashi, K., Effect of blow-down on fluid flow and Particle movement in cyclone classifier, *Kagaku Kogaku Ronbunshu*, 21, 594–602, 1995.
- Yoshida, H., Fukui, K., and Iwanaga, T., 2004, Effect of inlet shape and slurry temperature on the classification performance of hydro-cyclone, *Powder Tech.*, 140, 1–9, 2004.
- Yoshida, H., Saeki, T., Fujioka, T., and Fuyuki, T., Fine particle separation by revised type air-cyclone classifier, *KONA (Powder and Particle)*, No. 12, 178–185, 1994.
- Yoshida, H., Saeki, T., Fujioka, T., and Fuyuki, T., Fine particle separation by revised type air-cyclone classifier, *Kagaku Kogaku Ronbunshu*, 19, 476–482, 1993.
- Yoshida, H., Saeki, T., Hashimoto, K., and Fujioka, T., Size classification of submicron powder by air cyclone and three-dimensional analysis, *J. Chem. Eng. Jpn.*, 24, 640–647, 1991.
- Yoshioka, N. and Hotta, Y., Performance of hydro-cyclone, *Chem. Eng. Japan*, 19, 632–642, 1955.
- Yoshioka, N., Ekitai-cyclone, *Nikkan Kogyo*, 38–41, 1962.
- Zhou, L.X. and Soo, S.L., Gas–solid Flow and Collection of Solids in a Cyclone Separator, *Powder Technol.*, 3, 45–53, 1990.

8

Spray Systems

8.1	Atomization	8-1
	Introduction • Atomization Principles • Atomizer Types	
	• Some Global Atomization and Spray Definitions and Characteristics • Internal Flow in Atomizers • Primary Atomization • Secondary Atomization • Special Liquids • Drop Size Correlations in Sprays	
8.2	Spray Behaviour	8-44
	Dense Spray • Dilute Spray • Heat and Mass Transfer	
8.3	Spray Impact.....	8-58
	Drop Impingement • Heat Transfer in Impinging Sprays/Spray Quenching	
8.4	Spray Applications	8-60
	Energy Conversion–Spray Combustion • Metallurgical Processes • Spray Drying • Spray Painting and Coating	

Udo Fritsching
University of Bremen

8.1 Atomization

8.1.1 Introduction

Atomization of liquids (e.g., pure liquids, solutions, suspensions and emulsions, or melts) is a classic process engineering unit operation. The process of liquid atomization has applications in numerous industrial branches, for example, in chemical, mechanical, aerospace, and civil engineering as well as in material science and technology and metallurgy, food processing, pharmaceuticals, agriculture and forestry, environmental protection, medicine, and others.

Within atomization, the bulk fluid (continuous liquid phase) is transformed into a spray system (dispersed phase: droplets). The disintegration process itself is caused either by intrinsic (e.g., potential) or extrinsic (e.g., kinetic) energy, where the liquid, which is typically fed into the process in the form of a liquid jet or sheet, is atomized either due to the kinetic energy contained in the liquid itself, by the interaction of the liquid sheet or jet with a (high-velocity) gas, or by means of mechanical energy delivered externally, e.g., by rotating devices.

The main purpose of technical atomization processes is the generation of a significantly increased gas–liquid interface in the dispersed multiphase system. All transfer processes across the gas–liquid phase boundary directly depend on the driving potential difference of the exchange property (heat, mass, or momentum) and the size of the exchange surface. This gas–liquid contact area in a dispersed spray system is correlated with the integral sum of the surfaces of all individual droplets within the spray. An increase in the relative interphase area in a dispersed system intensifies momentum, heat, and mass-transfer processes between the gas and liquid. Total flux of exchange within spray systems is thereby increased by several orders of magnitude.

Applications of atomization techniques in process technology or chemical engineering processes can be divided into:

- Impact related spray processes
- Spray structure related processes

In impact related spray processes, the spray typically impinges onto a solid surface or a liquid or semi-liquid material deposited by the spray. The spray may be used for coating, preform buildup, or hot surface cooling applications. In spray structure related processes, the main aim of the spray process is to produce dispersed spray droplets of a defined size, for example, for powder production or in spray combustion.

Some examples for spray process applications in engineering following this subdivision can be given as follows:

- For impact related spray applications within the continuous fine spatial distribution of a liquid continuum, for example, in the field of coating applications:
 - Corrosion protection of (metal) surfaces by spray coating applications
 - Coating applications for technical specimen and parts for use in private or industrial applications including surface protection and colour (paint) applications
 - Crop and plant protection by applying agricultural chemicals
 - Protection coatings by thermal spray applications (e.g., plasma or flame spraying of particles) for ceramic or metallic coatings in the metal industry
 - Spray granulation or coating of particles (for e.g., in pelletizers or in fluidized beds) for pharmaceutical or food industry applications
 - Spray cooling in steel manufacturing or heat treatment of metallic specimen
- For changing the structure or properties of liquids or particulate solids by gas-dispersed phase exchange processes (spray structure related spray process) within:
 - Thermal exchange processes, for example, within rapid cooling and solidification purposes of fluid (metal) melts in powder generation
 - Coupled mass and thermal transfer processes, for example, within spray drying (or spray crystallization) in food or dairy industry or chemical mass products production
 - Solid particle separation or chemical gas cleaning (e.g., desulfurization) from exhaust gases, for example, in conventional power plants (wet scrubbers, see Chapter 7.1.5)
 - Gas conditioning processes, for example, for room air-conditioning (moisture control)
 - Reaction processes within fuel applications for energy conversion in furnaces, automotive, airplane or aerospace turbine, or fuel jet applications
- In the combination of the aforementioned impact and spray structure related spray process applications within:
 - Droplet-based manufacturing technologies, for example, for rapid prototyping
 - The generation of specimen and preforms by spray forming of metals

Each technical process couples several subprocesses in a complex way. Therefore, the complete process (in a first analysis approach) is subdivided into individual process steps for further analysis. In this context, a common subdivision of a technical atomization and spray process into modular subprocesses is performed. From the viewpoint of multiphase flow analysis, a typical subdivision for the atomization and spray process is illustrated in [Figure 8.1](#). The sketch shows a (relatively rough) subdivision of a general atomization and spray process into four main subprocesses as:

1. Media Delivery. The internal liquid flow in the atomizer and delivery (and possible mixing) of atomization media and energy, typically liquid and gas.
2. Atomization. The process of fluid disintegration or fragmentation, from the continuous delivery of the fluid or melt and the necessary supporting materials (e.g., gases or additives), to the primary resulting spray structure and droplet-ligament spectrum from the atomization process.
3. Spray. The establishment and spread of the spray, described as a dispersed multiphase flow process with momentum, heat, and mass transfer, and possible chemical reactions in all phases. The

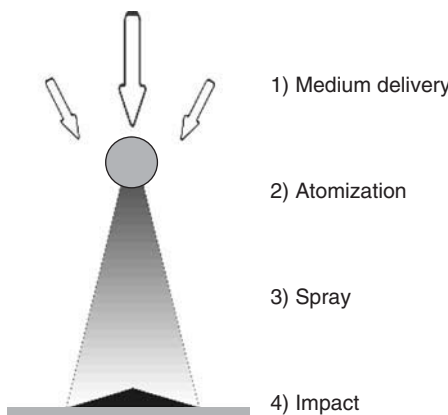


FIGURE 8.1 Subdivision of atomization and spray process into subprocesses.

TABLE 8.1 Material Properties for Atomization Liquids

Liquid	Density ρ (kg/m ³)	Surface Tension σ (kg/s ²)	Dynamic Viscosity μ (kg/ms) $\times 10^3$
Fuel (benzene)	660	0.017	0.27
Water	1,000	0.073	1.0
Melt (copper)	7,800	1.31	3.12
Melt (iron)	8,000	1.83	5.0
Fuel (oil)	830	0.026	20.1
Melt (ceramic)	5,000	0.5	1,000
High-viscosity liquid	1,000	0.035	20,000

exchange between the phases as well as a possible secondary disintegration process of fluid ligaments or coalescence of droplets.

4. Impact. The impact of the spray droplets onto a solid or liquid surface and compaction and possible film formation of the impacting fluid or melt mass as well as the buildup of a remaining layer or preform.

A common viewpoint for analysis of all atomization and spray processes is seen from multiphase flow analysis with integral heat and mass transfer. Spray processes typically involve two-phase flows of liquid and gas or even three-phase flow of solid, liquid and gas (e.g., within atomization of slurries and suspensions or within (solidifying) melt atomization).

8.1.2 Atomization Principles

The type of atomization principle or atomizer used for a specific application depends on the operational parameters that have to be tackled. Here the material properties of the liquid that has to be atomized play an important role. The significant properties of liquid material are (in the order of significance): viscosity, surface tension, and density. These parameters may typically differ by several orders of magnitude. Some typical examples of spray liquid properties are given in Table 8.1. Compared with the other atomized liquids, fuel and water (or water mixtures) are the most commonly used. Metal and ceramic melts are used for powder production and highly viscous liquids are, for example, found in chemical process technology (e.g., paints). The viscosity of these liquids varies up to six orders of magnitude. In addition, material properties typically are not constant within an atomization process, especially for viscosity, liquids may show nonNewtonian (e.g., shear-dependent) viscosity behaviour (e.g., for slurries,), or

temperature-dependent behavior (melts). Therefore, the type of atomizer used for a specific application depends on:

- The liquid material properties
- The liquid material throughput
- The spray characteristics to be achieved (e.g., droplet sizes or spray shape or spray angle)

8.1.3 Atomizer Types

The most common characterization of atomization principles is a subdivision based on the energy used for the disintegration of the liquid. Here, energy from the liquid itself may be used (pressure) or energy from external media like gas energy (pneumatic), mechanical energy (rotation), or electrical or acoustic energies are used.

8.1.3.1 Pressure Atomizer

The pressure atomizer (single-fluid atomizer) is the most common type of atomizer used in all (by number) technical applications. The main characteristic of this atomizer type is the ejection of a (pressurized) fluid through a small opening at high speeds into a (almost quiescent) gas atmosphere. The energy for atomization is carried by the liquid itself, and the potential energy is transferred into kinetic energy of the liquid. The liquid discharge geometry is either of straight simple type (circular round or flat stream) or swirling type (annular sheet). Pressure atomization is typically used for low-viscosity fluids. A principal sketch of a pressure atomizer is illustrated in [Figure 8.2a](#), and a pressure swirl atomizer is shown in [Figure 8.2b](#). For the latter, the swirl is generated either by tangential inlet ports and fluid delivery into the atomizer (right panel in [Figure 8.2b](#)) or, for example, insertion of a vaned swirl generator on top of the atomizer (left panel). Owing to the swirling liquid flow and the resulting pressure distribution, a hollow air core is produced in the center of the atomizer chamber by suction and the liquid discharges as a swirling annular film from the atomizer. The simplex pressure nozzle produces a full cone or flat sheet spray and the swirl pressure atomizer typically produces a hollow cone spray. The drawbacks of the application of pressure atomizer are (1) the need for pressurizing the liquid (which may be difficult in some cases) (2) the relatively coarse spray droplet sizes and (3) low mass flow rates ([Table 8.2](#))

8.1.3.2 Pneumatic Atomizer

Pneumatic atomizers (twin-fluid atomizers) typically use the kinetic energy of a pressurized gas that interacts with the liquid surface to disintegrate the liquid. Here, the atomizers with external and internal mixture of gas and liquid are distinguished. Both principles are shown in [Figure 8.2c](#) and [Figure 8.2d](#). Within internal mixing atomizers, gas and liquid are mixed in a premixing chamber and the gas–liquid mixture is ejected from the atomizer orifice directly. In twin-fluid atomizers with external mixing, the gas interacts with the liquid outside of the atomizer. Twin-fluid atomizers typically produce a full cylindrical spray cone with relatively small droplets at high liquid mass flow rates.

8.1.3.3 Rotary Atomizer

Within rotary atomization the liquid is fed onto a rotating surface, where it spreads under the action of centrifugal forces. From the rim of the rotating device, for example, a liquid film is ejected at fairly high speed and disintegrates into droplets. The rotating device as illustrated in [Figure 8.3a](#) may be in the form of flat disk, cup, or slotted (vaned) wheel. Since the liquid in a rotary atomizer is not flowing through any tiny passages, this kind of atomizer is typically used in process industries where possible nozzle blockage by the fluid (or slurry) may cause major problems. The main drawback of this simple rotary atomizer is the possible slip between liquid and solid surface, thereby limiting the use of this device. This problem is solved in a practical way by using rotating wheels with vanes or channels.

8.1.3.4 Ultrasonic Atomizer

Ultrasonic atomizers either use directly the acoustic energy in a gaseous atmosphere or indirectly the vibrational energy of an ultrasonic excited surface. Within ultrasonic-standing wave atomization,

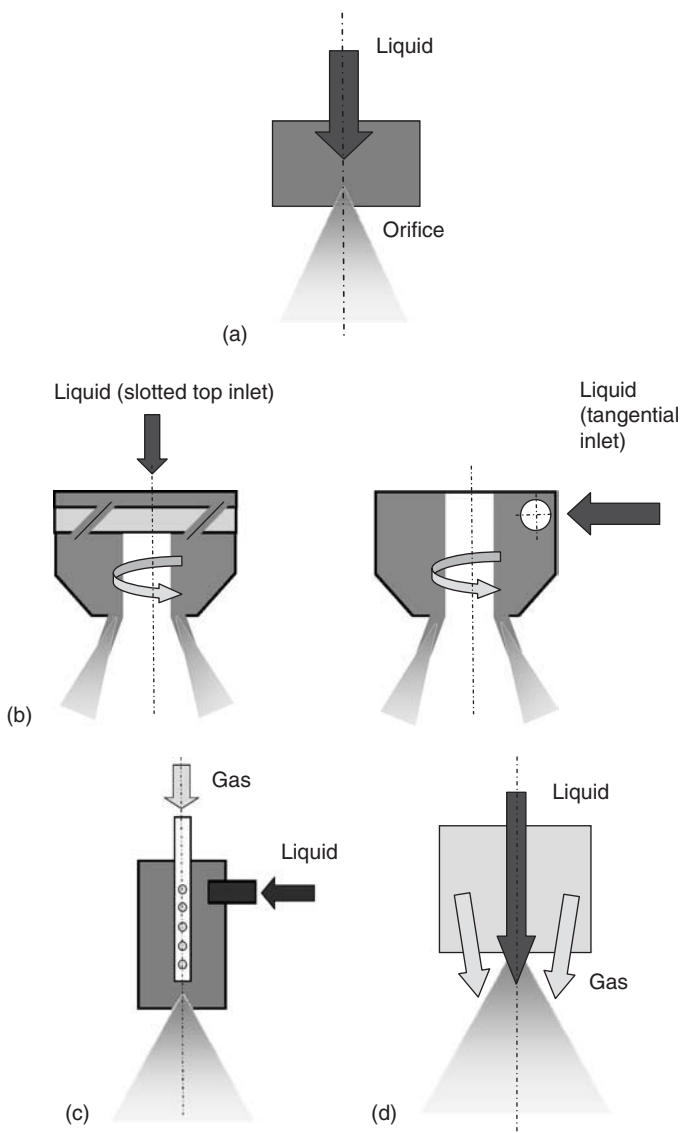


FIGURE 8.2 (a) Pressure atomizer (full cone or flat sheet spray); (b) pressure swirl atomizer (hollow-cone spray), internal swirl generator (left panel), tangential inflow (right panel); (c) twin-fluid (pneumatic) atomizer with internal mixing; (d) twin-fluid (pneumatic) atomizer with external mixing.

(USWA) a resonant standing acoustic wave is produced by a system of two opposing ultrasound transducers (or a single transducer and an opposing reflector) that are separated by a distance of a multiple of the half wavelength (typically 1.5 to 5λ , i.e., 25 to 85 mm at a typical frequency of 20 kHz). The acoustic energy in the resulting resonant wave is used to disintegrate the liquid stream that is poured into the center of the standing wave. This principle is illustrated in Figure 8.3b. The main advantage of this atomizer type is the possibility of disintegrating highly viscous liquids due to its specific disintegration mechanism, (see below). Its disadvantage is the limitation to relatively small mass flow rates.

In another type of ultrasonic atomization, vibrating surfaces are used to quickly form oscillating capillary waves on the surface of the liquid covering the vibrating solid (see Figure 8.3c). The oscillating liquid ejects droplets from the wave tips. This device produces significantly narrow droplet size distributions at small overall droplet sizes, but is limited to small liquid throughputs.

TABLE 8.2 Power Demand of Various Liquid Atomization Principles Per Mass of Liquid

Type of Atomizer	Power Demand (W/kg)
Simple pressure	2–4
Pressure swirl	2–4
Pneumatic twin-fluid	50–60
Rotary	15

Source: Adapted from: Bayvel, L. and Orzechowski, Z., *Liquid Atomization*, Taylor & Francis Publ., Washington, DC, 1993.

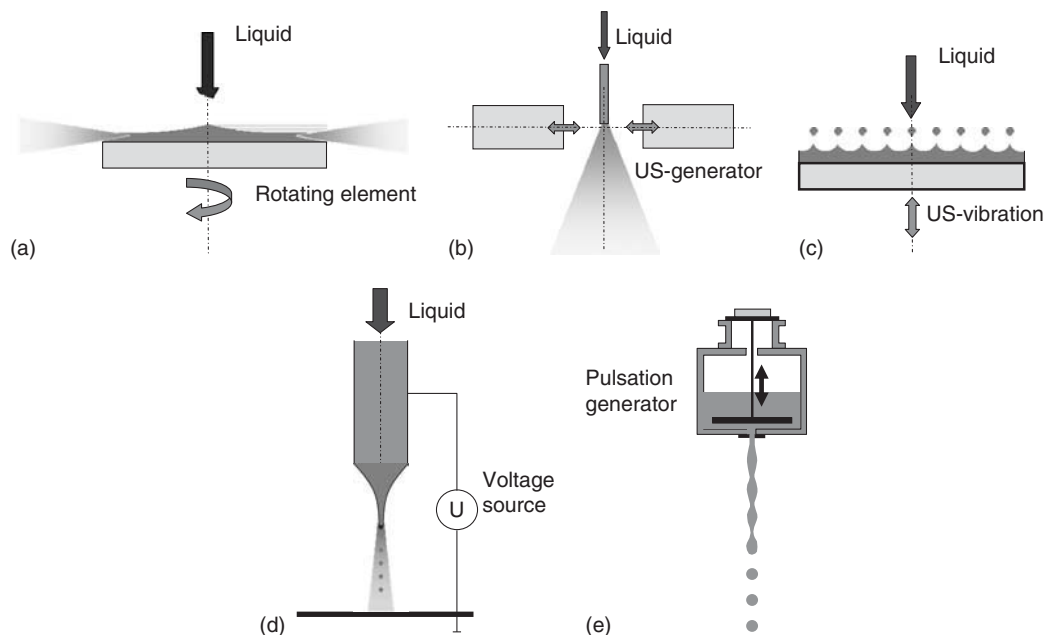


FIGURE 8.3 (a) Rotary (spinning disc) atomizer; (b) ultrasonic atomizer USWA; (c) ultrasonic capillary wave atomization; (d) electrostatic atomization; (e) monosized droplet generation (jet excitation is by vibrating plunger).

Ultrasonic gas atomization is a twin-fluid atomization process that uses a resonance cavity in the gas delivery path to generate fluctuating gas flow behavior at the nozzle exit (velocity and pressure fluctuations). The gas fluctuations support the atomization process, especially when their main fluctuating frequency corresponds to the frequency of the fastest growing instability wave of the liquid stream or jet (see, Hartmann nozzles in Yule and Dunkley, 1994). A direct excitation of the liquid flow may be performed to enhance the natural instability of the liquid jet (see, Chavez and Obermeier, 2002).

8.1.3.5 Electrostatic Atomizer

Within electrostatic atomization, an electrically charged liquid is accelerated in an electric field, thereby forming an accelerating tiny liquid jet (e.g., Taylorcone) that finally breaks down into fine droplets at the tip, as shown in Figure 8.3d. The yield achieved is relatively low ($\sim 1 \text{ kg/h}$). Typical electric potentials are of the order less than 100 kV. Narrow-sized droplets at sizes smaller than the submicron scale may be produced by electrostatic atomization at very small quantities (Michelson, 1990; Lohmann, 2000).

In the coating applications the charging of the droplets in an electric field is used to additionally accelerate the droplets toward a (grounded) target and to spray-coat shadow areas. Thus, the overspray amount

of the process (particles that are deflected around the target e.g. by aerodynamic effects) is minimized and a sufficient yield of the spray process is achieved. The atomization itself in this case may be performed, for example, by a rotary atomizer.

8.1.3.6 Monosized Droplet Generation

In several applications droplets or particles of almost identical size are needed (Armster et al., 2002). Here, the droplet generators that control the disintegration behavior and the instability mode of the liquid jets or sheets obtain a proper solution. The principal characteristic of a monosize droplet generator is illustrated in [Figure 8.3e](#). An emerging liquid jet is excited (e.g., by mechanical vibration or acoustic excitation) at its most unstable wavelength. The disturbance generates waves of uniform size that leads to continuous breakup of the liquid jet into identical droplets. For an increase in the overall mass yield, several individual jets may be combined within a single generator. Another possibility for (almost) monosized drop generation is the controlled breakup of a liquid within rotary atomizer in the ligament formation mode (see below). Here also perforated cylindrical elements are used.

8.1.4 Some Global Atomization and Spray Definitions and Characteristics

An initial division of atomization principles has to be done on account of the specific energy input for atomization. The energy supplied to the atomizer is given by

$$E = E_A + E_K + E_L \quad (8.1)$$

where, E_A is the surface energy of the liquid, i.e., the energy used to overcome the resistance or surface tension forces during disintegration of the liquid into droplets, E_k and the kinetic energy, i.e., the energy used to accelerate the liquid and droplets in the spray, and E_L the energy loss, due to friction in the atomizer. The efficiency of atomization is given by

$$\eta = \frac{E_A}{E} \quad (8.2)$$

The efficiency of atomization depends mainly on the type of atomizer, the droplet size distribution in the resulting spray, and the physical properties of the liquid. For all conventional atomizers, this efficiency is very small, namely of the order of less than 0.1%. Pressure atomizers have the relatively best efficiency (e.g., 5% for generation of droplets of 100 μm size, but even much smaller when the mean droplet size in the spray is lower).

Another measure for characterization of an atomization process is the approximate energy demand for atomization of a specific liquid amount, as listed in [Table 8.2](#). Here, pressure atomization is also most efficient.

Atomization and spray process analysis is done by means of theoretical, numerical, and experimental approaches. From these results, characterization of atomization and spray processes is most successfully done in terms of nondimensional analysis based on characteristic numbers. For atomization and spray processes, the most important characteristic numbers are:

$$M = \frac{\rho_g}{\rho_l} \quad (\text{density ratio}) \quad (8.3)$$

$$N = \frac{\mu_g}{\mu_l} \quad (\text{viscosity ratio}) \quad (8.4)$$

$$Re_l = \frac{\rho_l u_l d_l}{\mu} \quad (\text{liquid Reynolds number}) \quad (8.5)$$

$$We_l = \frac{\rho_l u_l^2 d_l}{\sigma} \quad (\text{liquid Weber number}) \quad (8.6)$$

$$We_g = \frac{\rho_g u_{rel}^2 d_l}{\sigma} \quad (\text{aerodynamic [gas] Weber number}) \quad (8.7)$$

$$Oh = \frac{\sqrt{We_l}}{Re_l} = \frac{\mu_l}{\sqrt{\rho_l \sigma d_l}} = \frac{1}{\sqrt{Lp}} \quad (\text{Ohnesorge number Oh [or Laplace number Lp]}) \quad (8.8)$$

$$L = \frac{\rho_g u_g^2}{\rho_l u_l^2} \quad (\text{momentum ratio}) \quad (8.9)$$

$$ALR = \frac{\dot{m}_g}{\dot{m}_l} \quad (\text{gas [air] to liquid mass flow ratio}) \quad (8.10)$$

Atomization processes yield a spray containing a certain range of droplet sizes. These droplet size spectrum is identified by suitable size distribution functions. General description of particle size distribution functions has been discussed in Chapter 1.3. Here, in addition, only the most spray relevant size parameters will be given. A spray is typically characterized by:

- (a) A suitable droplet size distribution function
- (b) The (mean) size parameter
- (c) The relative width of the distribution (distribution parameter)

For description of the drop size distribution in sprays, either the probability density function (pdf) $q(d)$ or the cumulative distribution function $Q_l(d)$ is used. The most common description is a fit of the drop size distribution by means of (1) the log-normal distribution function, (2) the Rosin–Rammler distribution function, or (3) the Nukiyama–Tanasawa distribution function. A discussion of statistical parameters for classifying size and various size distribution functions is presented in Section 1.3. The arithmetic number mean diameter d_{10} or the arithmetic volume mean diameter d_{30} is used as typical mean droplet size for these functions. An important spray characteristic parameter to describe drop size distributions in sprays is the volume to surface area mean diameter d_{32} (Sauter mean diameter, [SMD]), i.e., the drop diameter with the same total volume to surface area than the entire spray (important for all spray related atomization processes). In addition, characteristic spray droplet sizes may be identified as the modal diameter d_m (corresponding to the most probable drop size in the spray or peak value of the pdf), and the mass median diameter (or MMD) $d_{0.5}$ that divides the drop size distribution in two identical halves by mass. The width of the drop size distribution may be characterized by the standard deviation (geometric or logarithmic) or the span value of the distribution:

$$\text{span} = \frac{d_{0.9} - d_{0.1}}{d_{0.5}} \quad (8.11)$$

8.1.5 Internal Flow in Atomizers

From the viewpoint of multiphase flows in atomization and spray processes, the various kinds of atomization principles that have been illustrated before vary in type, shape, and form of the gas–liquid interface prior to atomization. The liquid disintegration process is caused by the forces acting in or on the liquid. Disintegration is more easily achieved if the liquid is fed in the form of a thin jet or sheet into the atomization area, because here the liquid jet already has its highest surface energy and thus the greatest instability potential.

8.1.5.1 Liquid Flow

8.1.5.1.1 Pressure Atomizer

For simplex pressure atomizers, the overall characteristic of the single-phase (liquid) flow in the atomizer is described by the pressure drop and the state of the liquid at the nozzle exit. The former is described by the discharge coefficient C_D as

$$m_l = C_D A_0 \sqrt{(2\rho_l \Delta p_l)} \quad (8.12)$$

The discharge coefficient depends on the geometry of the atomizer outlet as well as on fluid material properties (Schneider et al., 2001; Roach et al., 2001; Le et al., 1999) and liquid Reynolds number (Lefebvre, 1989). For Reynolds numbers below 10,000, and for a length to diameter ratio l/d_0 between 2 and 120 for the nozzle orifice, the discharge coefficient may be linearly correlated by (Lichtarowicz et al., 1965):

$$C_D = 0.827 - 0.0085 \frac{l}{d_0} \quad (8.13)$$

The flow state of the liquid (jet) at the exit of the atomizer depends on the flow field in the atomizer and the orifice. Typically, spray nozzles are of compact size, with short orifices (l/d_0) to minimize the pressure loss. The degree of turbulence in the fluid is determined by the flow state upstream of the orifice and the disturbances generated the converging region and in the orifice itself. A laminar to turbulent transition within the orifice is unlikely, though the Reynolds number may exceed the typical transition value in tubes ($Re = 2300$). Although in typical atomizer configurations, maximum Reynolds numbers of up to $Re = 10,000$ may be achieved, these high values occur only on a very small length scale where the laminar–turbulent transition of the flow is not realistic. During the investigation of the influence of nozzle geometry on the critical intake length of fluid jets within pressure atomization, van de Sande and Smith, (1976) derived a critical Reynolds number Re_{crit} for transition of the flow configuration from the laminar to the turbulent state as

$$Re_{crit} = 12,000 \left(\frac{l}{d_0} \right)^{-0.3} \quad (8.14)$$

This critical Reynolds number is not reached in atomizer configurations. However, the local distribution and degree of turbulence may strongly influence the atomization process. Based on the description of Giffen and Muraszew (1953), the state of the jet at the atomizer exit may be described as illustrated in [Figure 8.4](#). The jet profile may be either a fully developed laminar profile (Figure 8.4a1), a developing boundary layer profile (Figure 8.4a2), or turbulent (Figure 8.4b). Also, the liquid jet may include a turbulent core (Figure 8.4c) or vice versa, the jet may exhibit a turbulent or disturbed outer shell (e.g., vortex shedding from edges or cavitation at the wall inside the nozzle (Figure 8.4d)). Especially, a turbulent outer liquid surface structure of the jet will influence the development of surface instabilities and waves at the liquid–gas interface when the surface wavelength is of the order of the natural instability wavelength. In this case, turbulence may inhibit or promote the disintegration process.

For a pressure film atomizer, Heukelbach and Tropea (2001) have shown that turbulence may have a stabilizing effect on the disintegration of the free film. As long as the velocity fluctuations remain below a certain value (i.e., below 50% in the near-wall region and below 5% in the central flow region) turbulence stabilizes the disintegration process. This result has been explained by the increased vorticity of the turbulent flow, which produces additional shear stresses. These may be interpreted as increased turbulent viscosity, stabilizing the flow. Only if the disturbance level is beyond a certain threshold value, do the disruptive forces of the fluctuations seem to overcome the stabilizing effects, even exceeding the effect of aerodynamic forces. For a cylindrical jet, Mansour and Chigier (1994) found that in the absence of aerodynamic effects, turbulent jets are as stable as laminar jets. Marked differences, however, were found in the breakup behavior and droplet formation patterns of both laminar and turbulent jets.

8.1.5.1.2 Pneumatic Atomizer

Typical atomizer configurations spray vertically downward in the direction of gravity. Here, the geometrical shape of the liquid jet in the gravity field and liquid velocity change prior to disintegration is of importance. By neglecting surface tension and frictional effects within and on the liquid jet behavior, the velocity distribution of a cylindrical falling jet is

$$u_l = \sqrt{u_0^2 + 2gx} \quad (8.15)$$

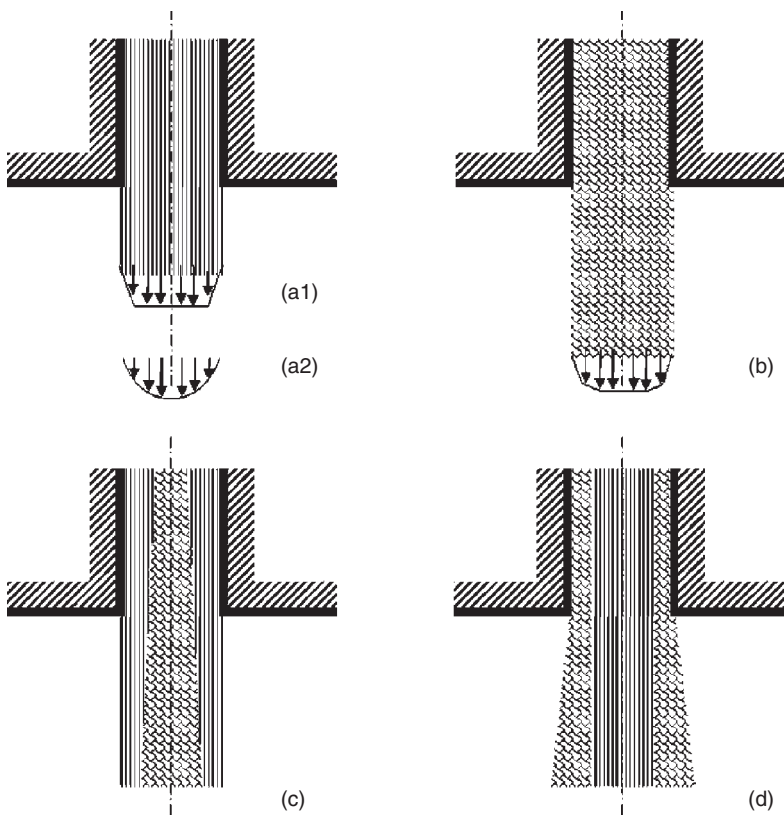


FIGURE 8.4 Liquid jet condition at the exit of an atomizer: (a) laminar; (b) turbulent; (c) turbulent core; (d) turbulent shell.

and, therefore, the jet diameter can be calculated as

$$\frac{d}{d_0} = \left(1 + \frac{2gx}{u_0^2} \right)^{-0.25} \quad (8.16)$$

which is independent of the liquid density. By adding surface tension effects to this one-dimensional analysis (see Anno, 1997; Schneider and Walzel, 1998; Schröder, 1997), a nonlinear relation is achieved, which describes the fluid jet contour behavior in a gravity field as a function of the nozzle distance:

$$\frac{d}{d_0} = \left[1 + \frac{2gx}{u_0^2} + \frac{4\sigma(d - d_0)}{\rho u_0^2 dd_0} \right]^{-0.25} \quad (8.17)$$

The numerical evaluation of this correlation is shown in [Figure 8.5](#) for the jet contour of a liquid jet for different values of the surface tension, including $\sigma = 0$ N/m (without surface tension effects), $\sigma = 0.0725$ N/m (surface tension of water), and $\sigma = 1.83$ N/m (surface tension of a molten steel). Two different Reynolds numbers of the jet are plotted. From this analysis, it is apparent that the effect of surface tension is aimed to slow down the decrease in the liquid jet diameter for low Reynolds numbers. The jet diameter as a function of distance from the nozzle increases with a increase in surface tension.

In case of a fully developed parabolic (laminar) velocity profile of the liquid jet at the nozzle exit, Middleman, (1999) derived an approximate solution for a decreasing jet diameter (neglecting surface tension effects) as

$$\frac{d}{d_0} = \left(\frac{4}{3} + \frac{2gx}{u_0^2} \right)^{-0.25} \quad (8.18)$$

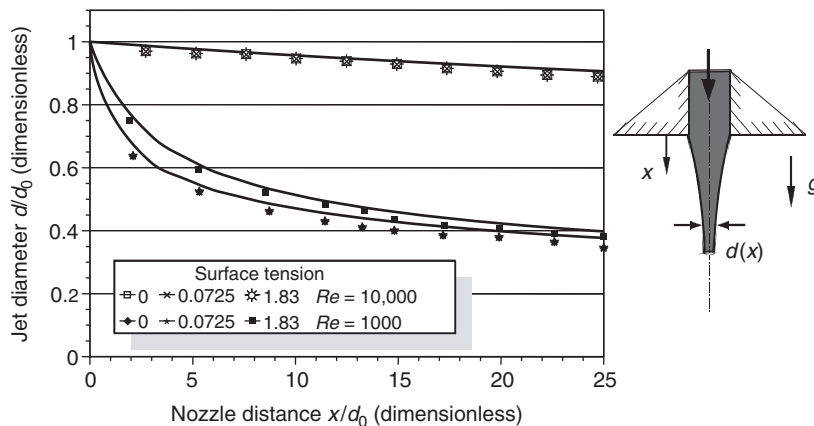


FIGURE 8.5 Dimensionless jet diameter of a free-falling circular liquid jet in gravity field, the effect of density and surface tension.

A numerical calculation of an exiting fluid jet having a velocity profile, taking into account friction, gravity, and surface tension, has been performed by Duda and Vrentas (1967) for Reynolds numbers $Re > 200$. Their results indicate that flattening of the developed velocity profile in the jet due to the low tangential stresses on the jet surface is very slow. As shown in Fritsching (2001), a two-dimensional numerical simulation of the liquid jet behavior (taking into account additional frictional effects and velocity profiles in the liquid jet due to the interaction with surrounding gas) produces only small deviations from the analytical solution.

8.1.5.1.3 Pressure Swirl Atomizer

For a pressure swirl atomizer, the discharge coefficient and the film thickness at the nozzle exit (or the corresponding air core diameter) have been calculated with inviscid assumptions by Taylor (1948, 1949), Giffen and Muraszew (1953), Horvay (1985), and Löffler-Mang (1992). A relationship between the atomizer dimensions, the size of the air core, and the discharge coefficient of the nozzle is given as

$$C_D = \left[\frac{1}{K_1^2 X} + \frac{1}{(1 - X^2)} \right]^{-0.5} \quad (8.19)$$

where

$$X = \frac{A_{\text{core}}}{A_0} = \frac{\pi r_{\text{core}}^2}{\pi r_0^2} = \frac{r_{\text{core}}^2}{(r_{\text{core}} + b)^2} \quad (8.20)$$

is the ratio of the air core to the exit area in the outlet and

$$K_1 = \frac{A_p}{\pi r_0 R_s} \quad (8.21)$$

describes the inlet port of the swirl chamber. The film thickness in the nozzle exit is b . For derivation of either the discharge coefficient or the air core size, it has been stated that the air core will always be such that it gives a maximum flow rate, thus the discharge coefficient C_D as a function of X tends to a maximum. Hence, the discharge coefficient is

$$C_D = \left[\frac{(1 - X)^3}{1 + X} \right]^{0.5} \quad (8.22)$$

To fit with experimental data, Giffen and Muraszew (1953) have multiplied Eq. (8.22) by a constant value of 1.17

A dimensionless swirl parameter, S , is defined as the ratio of swirl momentum flux to axial momentum flux as

$$S = \frac{i_\phi}{i_{ax}} = \frac{\int_r u_\phi r \, dm}{r \int_r u_z \, dm} \quad (8.23)$$

For a vaned swirl generator at the nozzle inlet, the geometrical swirl parameter is calculated from

$$i_\phi = \frac{\dot{Q}}{A_e} r_e \quad (8.24)$$

and, therefore, the film thickness b at the nozzle exit may be deduced from Eq. (8.20) and

$$S_0 = \frac{1}{K} = \left[\frac{2X^2}{(1-X)^3} \right]^{0.5} \quad (8.25)$$

From tangential velocity measurements at the nozzle inlet, Horvay (1985) derived a factor of 1.3 that has to be multiplied with Eq. (8.25). This is a pure geometrical dependency, and no fluid properties are taken into account. The behavior of the dimensionless film thickness vs. the geometrical swirl parameter (in this inviscid case) approaches zero as the swirl is increased to infinity. The effective swirl parameter, taking into account the effective area of the film at the nozzle exit, may be calculated from the equation derived by Horvay (1985):

$$S_a = S_0(1 - X) \quad (8.26)$$

8.1.5.1.4 Rotary Atomizer

The film thickness at the rim of a rotating disc has been analyzed in several approaches by solving the equations of motion for the liquid film. Based on the local velocity difference between the angular film and the solid disc velocity, Nikolaev et al. (1967) derived the resulting film thickness. Bruin (1969) analyzed the simplified Navier–Stokes equation using complex functions and Matsumoto et al. (1973) obtained a numerical solution from the Navier–Stokes equations. Their results as well as the experimental results (see Lefebvre, 1989) agree in principle and may be empirically correlated in terms of the dimensionless film thickness vs. the dimensionless liquid flow rate by

$$\frac{t}{[\mu_l/\rho_l\omega]} = -14.5 \left(\frac{\dot{Q}}{2\pi R^2 [\mu_l\omega/\rho_l]^{0.5}} \right)^2 + 6.72 \frac{\dot{Q}}{2\pi R^2 [\mu_l\omega/\rho_l]^{0.5}} + 0.2 \quad (8.27)$$

8.1.5.1.5 Internal Mixing (Effervescent) Twin-Fluid Atomizer

In the narrowest cross-section (typically in the exit) of an internal mixing, effervescent atomizer for the gas–liquid mixture critical mass flow is observed (Chawla, 1969; and Chawla and Böckh, 1971; Lund et al., 1993; Buckner and Sojka, 1991; Whitlow and Lefebvre, 1993). Leaving the nozzle, the gas flow expands and the liquid is dispersed into ligaments and droplets. The atomizer efficiency and temporal and spatial distribution of the diameter and velocity of the droplet depend on the total pressure in front of the nozzle, the volumetric flow rate of liquid and gas as well as the spatial and temporal distribution of gas and liquid at the nozzle exit. These distributions are affected by the two-phase flow inside the mixing chamber and the nozzle. Chin and Lefebvre (1993) as well as Lörcher (2003), Lörcher et al. (2003) and Kim and Lee (2001) analysed experimentally the flow regimes inside of an internal mixing atomizer and in its exit, where bubbly, plug or annular flow regimes are found. Their findings for the different flow regimes have been incorporated in the general flow map of Oshinowo and Charles (1974). As this general flow map has been derived for fully developed two-phase flow (in terms of a two-phase Froude number), the flow regimes inside the internal mixing atomizer do not fit well into this general scheme. Here, the atomizer and mixing chamber lengths are too small to achieve fully developed flow conditions. Model developments for the different flow regimes in an effervescent atomizer are found in Lörcher (2003) and Lörcher et al. (2003) and the transition between the modes has been characterized in Kim and Lee (2001).

The spray from an effervescent atomizer has been investigated by Whitlow and Lefebvre (1993), Jicha et al. (2002), and Luong and Sojka (1999).

The critical pressure $p_{c,c}$ in the nozzle exit was correlated by (Churchill and Usagi, 1972)

$$\left(\frac{p_c}{p_0}\right)_c = \left[\left(\frac{\kappa + 1}{2} \right)^{4\kappa/3(\kappa - 1)} + \left(\frac{\kappa}{2} \frac{1 - \alpha_0}{\alpha_0} \right)^{4\kappa/3(\kappa + 1)} \right]^{-3/4} \quad (8.28)$$

The discharge coefficient and the critical mass flow rate at the exit have been empirically correlated by Chen and Lefebvre (1994), Landwehr et al. (1999), and Kim and Lee (2001). Lörcher (2003) found to be in best agreement with the simulation results of Richter (1983) and the analytical expression of Leung and Epstein (1990). From the corresponding critical pressure and mass flow rate at the nozzle exit, the void fraction and mean velocities at the exit can be derived.

8.1.5.1.6 Ultrasonic Standing Wave Atomizer (USWA)

Within a typical application of the USWA technique, a cylindrical liquid jet is poured into a node of the standing acoustic wave (Lierke et al., 1988). Here, the liquid surface interacts with the acoustic field, resulting in a force on the liquid surface, regarded as sound radiation pressure. The sound radiation pressure is a result of the temporal-averaged difference of surface pressure and ambient pressure and therefore the local temporal-averaged density increases (Langevin sound radiation pressure). Its distribution on a spherical surface was first calculated by King (1934). The sound radiation pressure leads to a deformation of the cylindrical jet into a disc-shaped film (see Figure 8.6). In addition, suction forces act at the rim of the disc. This suction makes the USWA process ideal for disintegration of viscous liquids. The liquid velocity in the disc increases when the liquid moves from the center toward the rim of the disc, thereby resulting in a decrease in the sheet thickness. The liquid velocity distribution inside the disc has been derived theoretically by Hansmann (1996) and compared with experimental results as illustrated in Figure 8.6. The liquid disintegrates at the rim of the disc when the film becomes thin and instability occurs.

8.1.5.2 Gas Flow

Analysis of the gas flow field in the atomizer configurations is done in external mixing twinfluid atomizers, especially to identify the disintegration potential in terms of the operation conditions (gas pressure, nozzle arrangement, etc.). The geometric configuration and arrangement of the gas jet system as well as the geometry or contour of the individual gas nozzles may be adapted for suitable application of the atomization gas (Dielewicz et al., 1999; Espina and Piomelli, 1998a, 1989b; Espina, 1999; Czisch et al., 2003; Heck, 1998).

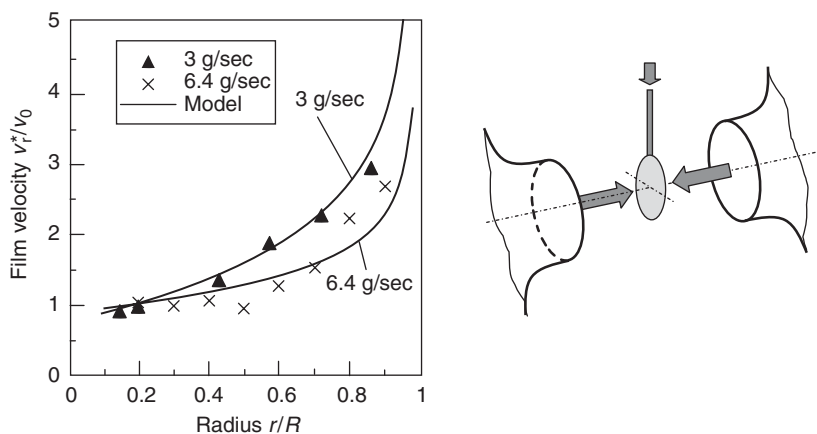


FIGURE 8.6 Film formation and radial film velocity in ultrasonic standing-wave field. (Adapted from Hansmann, S., Dissertation, Universität Bremen, 1996.)

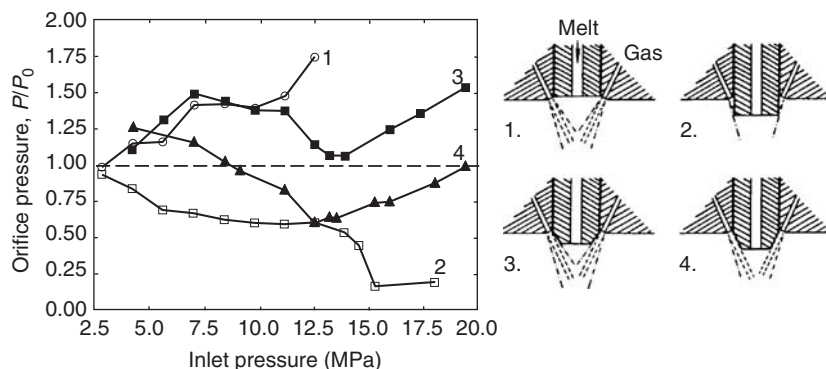


FIGURE 8.7 Aspiration pressure for different nozzle tip arrangements in close-coupled atomizer. (Adapted from Anderson, I.E. and Figliola, R.S., *Modern Developments in Powder Metallurgy*, Gummesson, P.U. and Gustafson, D.A., Eds., Vol.20, 1998, pp. 205–223.)

The gas flow behavior in front of an external mixing twin-fluid atomizer may have an influence on fundamental atomization parameters like the liquid mass flow rate (yield) or the resulting drop size distribution in the spray. The typical concentric gas flow configuration in an atomizer results in a pressure change in the central liquid feed area that causes variations in the pressure ratio between the liquid feed (or reservoir) and the pressure level in front of the liquid exit. Some possible arrangements of the nozzle tip in an external mixing twin-fluid atomizer are illustrated in Figure 8.7 (Anderson and Figliola, 1988), together with the corresponding measurements of the orifice pressure (also called aspiration pressure) in the gas only flow field (without liquid atomization). Typically technical atomizers are constructed to give a suction pressure (lower pressure than ambient) at the liquid delivery port rather than overpressure. Also the arrangement and number of discrete jets or the configuration of the gas nozzle as an annular slit nozzle result in different aspiration pressure behavior (see Lohner et al., 2003). If the spacing between the individual jets is large enough and the interaction between the jets is small, pressure equalization takes place and in between the discrete jets the aspiration pressure effect is decreased. For a slit nozzle, the aspiration pressure effect tends to a maximum.

Depending on the individual gas jet nozzle contour, underexpansion, overexpansion, or ideal expansion (within a Laval nozzle contour) may be achieved. The gas jet exit condition has a major influence on the jet behavior. In the gas nozzle exit, overexpanded jets in principle contain the highest exit momentum at a constant mass flow rate. This jet configuration is of special interest to achieve a maximum gas kinetic energy in the atomization area (in order to achieve the maximum slip velocity between gas and fluid). The results of a comparison of simulation data for overexpanded, underexpanded, and ideally expanded circular gas jets are illustrated in Figure 8.8. The velocities on the jet center lines are plotted vs. the nozzle distance for constant gas prepressure ($p_0 = 5.5$ bar abs.) and mass flow rate. For the latter, the gas nozzle exit areas of the three jets are different, calculated from isentropic flow conditions. Therefore, the exit area is highest for the overexpanded jet under identical conditions. Since the overexpanded jet also delivers the highest exit gas velocity, the resulting exit momentum in this case is highest (at constant mass flow rates), but downstream of the nozzle exit, the underexpanded jet has the highest velocity values after the first shock cell in the transonic region, especially immediately behind the shock fronts. For analysis of the atomization potential of the three different gas flow configurations, the behavior further downstream in the far field is important. In the subsonic free jet region the ideally expanded jet shows the highest velocity values on the center line. For ideally expanded jet behavior without any shock structures, the highest potential for atomization purposes is achieved in the far field.

Figure 8.9 shows on the left the simulated gas flow field (velocity contours) in an external mixing atomizer configuration for different gas exit boundary conditions. The gas exit geometry is an annular slit configuration where the gas emerges from a concentric ring slit nozzle. The left hand side of Figure 8.9a

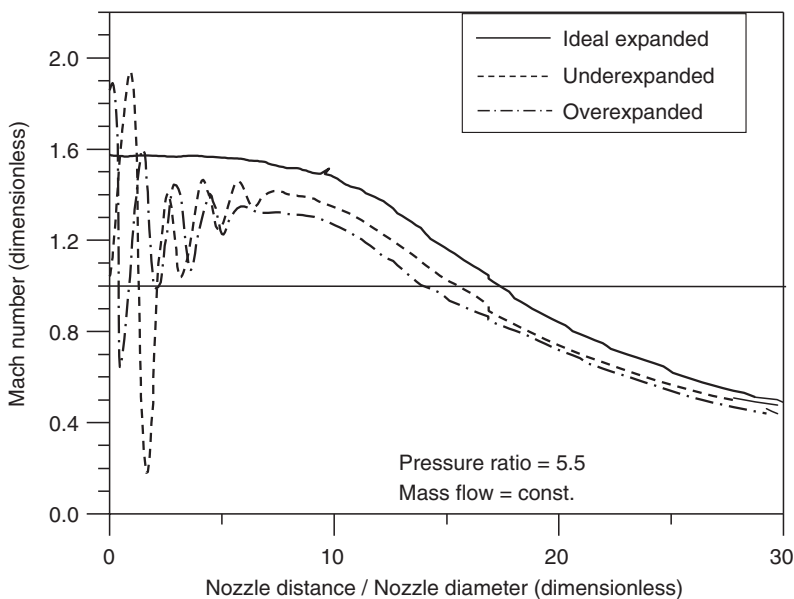


FIGURE 8.8 Gas jet velocities on the center line of under-, over- and ideally expanded jets. (From Heck, U., Ph.D. thesis, Universität Bremen, 1998. With permission.)

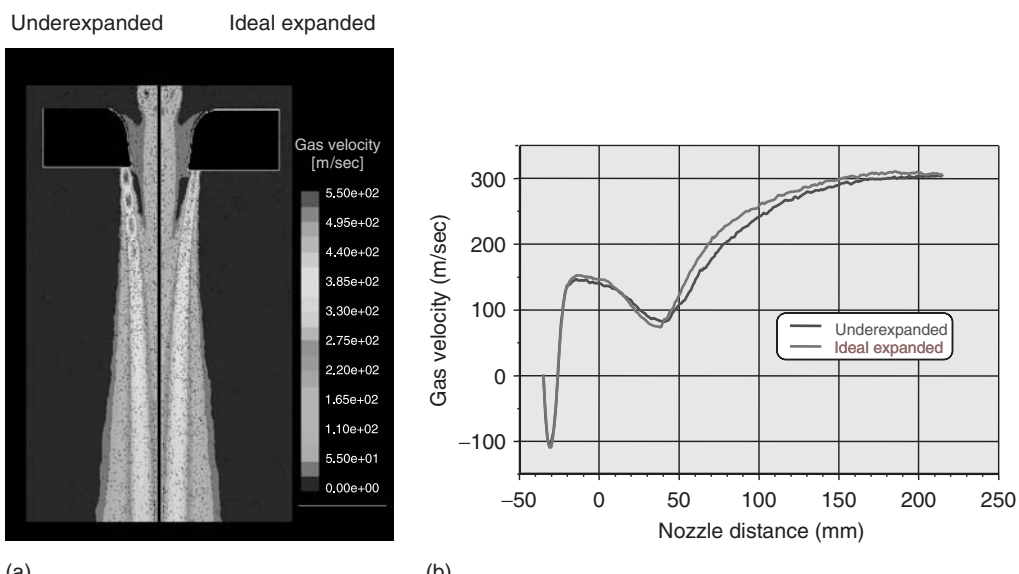


FIGURE 8.9 (Color insert follows page 13-40) Gas flow field simulation for an external mixing (free-fall) atomizer: (a) gas velocity contours: underexpanded exit condition (left panel), and ideal expanded exit condition (right), (b) gas velocity on center line, comparison of under- and ideally expanded exit conditions. (From Heck, U., Ph.D. thesis, Universität Bremen, 1998. With permission.)

shows an underexpanded gas flow and the right-hand side shows the result for the ideal expanded case, both cases have been calculated for identical mass flow rates. In the underexpanded case, a shock cell structure in the gas jet is in front of the nozzle. The use of ideally expanded gas in atomizer jets increases the velocity potential as seen in Figure 8.9b (right-hand side). Comparison of the gas velocities on the atomizer center line illustrates that approximately 50 to 100 in mm below the nozzle, where the primary

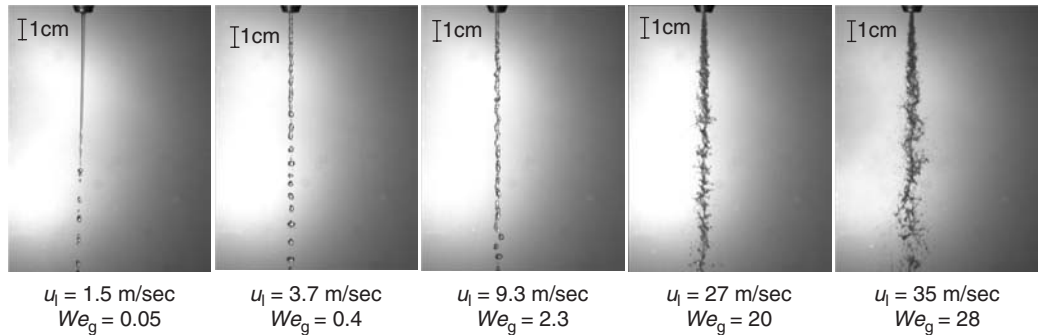


FIGURE 8.10 Disintegration of a liquid jet in pressure atomization, water ($d_i = 1.5$ mm).

disintegration of the liquid takes place, an increase in the gas velocity by approximately 10 to 20% is achieved.

8.1.6 Primary Atomization

8.1.6.1 Flow Regimes and Flow Maps

For a first classification of liquid fragmentation in various configurations, the disintegration behavior of a liquid jet or sheet is subdivided into different atomization modes depending on the boundary conditions. As a result of several investigations, the disintegration behavior of a liquid has been globally classified, regimes have been identified, and interfaces between the different regimes have been correlated.

8.1.6.1.1 Single Fluid (Pressure) Atomization

This case holds for a liquid jet emerging into a quiescent gaseous atmosphere. Some examples for water atomization in a pressure nozzle are illustrated in Figure 8.10. Ohnesorge (1936), in an early investigation, divided the breakup regimes of a circular liquid jet into three areas, depending on the liquid Reynolds number and a dimensionless number that contained only liquid properties, later referred to as the Ohnesorge number Oh (Figure 8.11). These regimes have been further detailed, for example, by Haenlein (1932) and Reitz (1978).

- (1) At low Reynolds numbers, the jet disintegrates due to surface tension effects (*Rayleigh regime* [1], symmetric, or varicose instability) into fairly identical droplet sizes.
- (2) At intermediate Reynolds numbers, drop formation is influenced by aerodynamic forces (nonaxisymmetric Rayleigh breakup). These forces cause symmetric (*first wind-induced mode* [2]) and asymmetric (*second-wind induced mode* [3], asymmetric or sinusoidal instability) wave growth of the gas–liquid interface that finally leads to jet disintegration. This is the aerodynamic regime.
- (3) At higher Reynolds number, the jet disintegrates almost spontaneously at the nozzle exit. This mode is called the *atomization regime* [4].

The transition line from the Rayleigh regime to the aerodynamic mode is identified by

$$We_l = \frac{1.74 \times 10^4}{Re^{0.5}} \quad (8.29)$$

and the transition line between aerodynamic disintegration and the atomization regime is characterized as

$$We_l = \frac{9.4 \times 10^5}{Re^{0.5}} \quad (8.30)$$

8.1.6.1.2 Twin-Fluid Atomizer

The first map of breakup regimes for a liquid jet in a coaxial gas flow was introduced by Farago and Chigier (1992). Hopfinger (1998) introduced the momentum ratio between gas and liquid as an additional

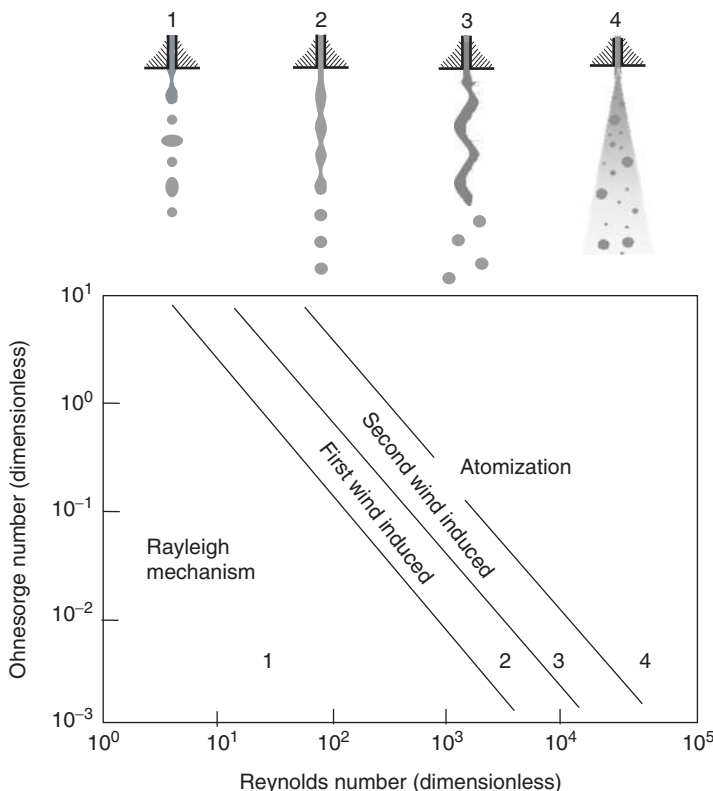


FIGURE 8.11 Primary fragmentation modes of a liquid jet in pressure atomization. (Adapted from Reitz, R.D., Ph.D. thesis, Princeton University, 1978.)

parameter (see also Lasheras and Hopfinger, 2000). The main disintegration modes are characterized in Figure 8.12 and some examples are illustrated in Figure 8.13.

- (1) At small aerodynamic Weber numbers the jet mainly breaks up due to Rayleigh instabilities (*axisymmetric and nonaxisymmetric Rayleigh mode*).
- (2) If the Weber number is increased, ligaments are formed. The surface tension acts now at smaller scales. Owing to its smaller radius of curvature, the tip of the ligament recedes and a bulge is formed that may be blownup by the gas to form a membrane. This breakup regime is called the *membrane mode*.
- (3) With a further increase in Weber numbers, the size of the ligaments decreases and the breakup occurs in the form of fibers (*fiber mode*).

At present, sufficient data are not available to identify the interfaces between the different regimes in general.

8.1.6.1.3 Rotary Atomizer

The flow configuration and liquid condition (and therefore the effective atomization mode) at the rim of a rotating disc, where the fluid is continuously fed to the disc center, depends on the liquid flow rate, the disc rotational speed and size, and the liquid physical properties. A general division may be done based on the liquid feed rate as has been done by Hinze and Milborn (1950). For rotary atomization, the liquid Weber number is expressed as

$$We_l = \frac{\rho_l \omega^2 d^3}{\sigma} \quad (8.31)$$

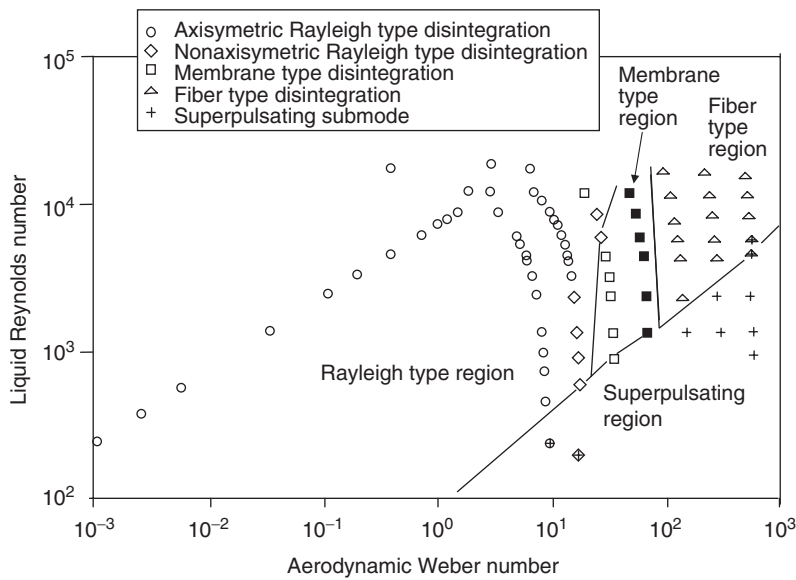


FIGURE 8.12 Disintegration modes in twin-fluid atomization. (Adapted from Farago, Z. and Chigier, N., *Atomization and Sprays*, 2, 137–153, 1992.)

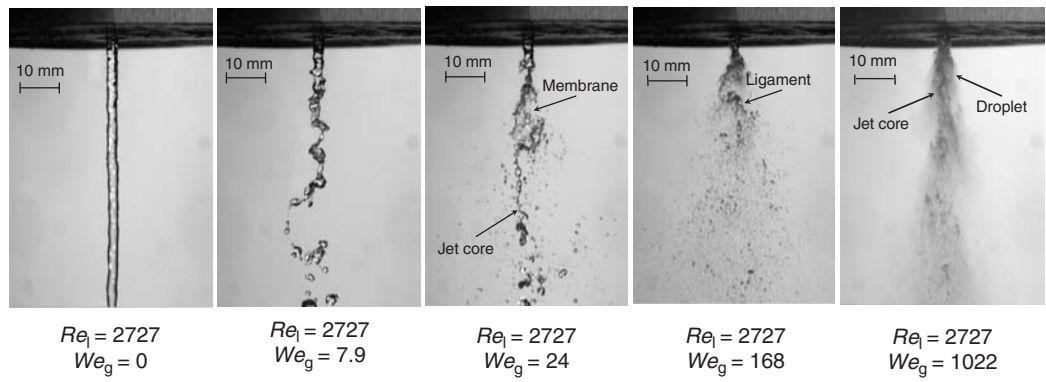


FIGURE 8.13 Atomization of a liquid jet in twin-fluid atomization with external mixing: main disintegration modes, $d_i=3$ mm.

The main fragmentation modes in rotary atomization are illustrated in [Figure 8.14](#) and may be analyzed as follows:

- (1) At low liquid flow rates the liquid spreads out across the disc surface and is centrifuged off in the form of droplets with a narrow size spectrum. This mode is called the direct *drop formation mode* (a).
- (2) If the flow rate is increased, ligaments are formed along the periphery, which later disintegrate into droplets. This mode is termed the *ligament or fiber formation mode* (b). The number of ligaments increases with an increase in flow rate up to a maximum value; beyond this maximum it remains constant, regardless of the flow rate. The thickness of the ligaments increases with the flow rate.
- (3) With continuing increase in the flow rate, a condition is finally reached, where the ligaments have attained their maximum number and size and can no longer accommodate the flow of liquid. A thick film is produced that extends outward to some distance beyond the cup rim. When this film disintegrates into ligaments, it does so in an irregular manner, which results in a wider droplet size distribution. This disintegration mode is termed the *film formation mode* (c).

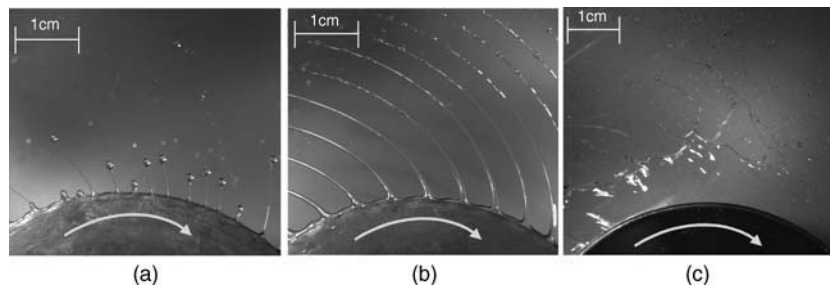
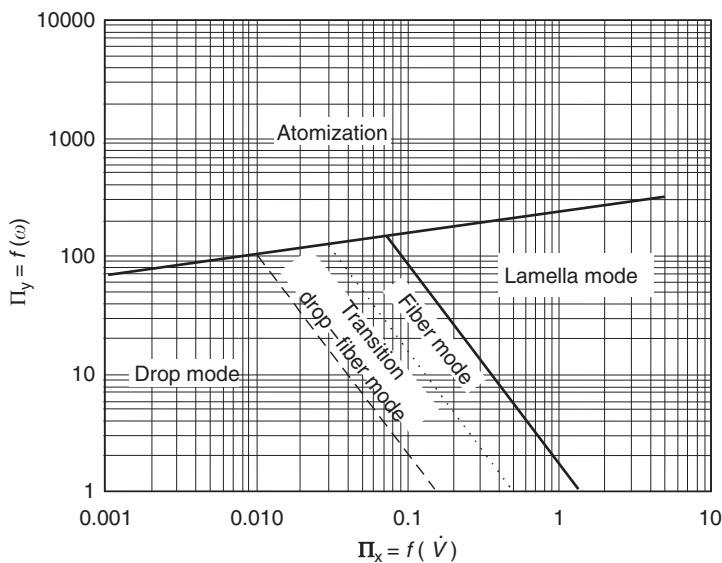


FIGURE 8.14 Main liquid disintegration modes in rotary atomization.

FIGURE 8.15 Disintegration mode map in rotary atomization. (Adapted from Brauer, H., *Grundlagen der Einphasen- und Mehrphasenströmungen*, Sauerländer Verlag, Frankfurt, 1971.)

Based on an analysis of a wide range of liquid properties within rotary atomization, Brauer (1971) introduced the fluid number K_F as an additional parameter:

$$K_F = \frac{\rho_l \sigma^3}{\mu_l^4 g} \quad (8.32)$$

and the volume flow rate number

$$\dot{Q}^* = \frac{\dot{Q}_l^2 \rho_l}{d^3 \sigma} \quad (8.33)$$

The breakup map for rotary atomization on a spinning disc is illustrated in Figure 8.15. The dimensionless ordinate and abscissa are labeled as

$$\Pi_y = We^{0.5} Oh^{0.922} K_F^{0.491}, \quad \Pi_x = \frac{\dot{Q}^{*0.5}}{Oh^{0.47} K_F^{0.295}} \quad (8.34)$$

Transition between the individual breakup regimes is characterized in terms of the volume flow rate number, the liquid Weber number, and the Ohnesorge number by

$$\dot{Q}^* We_l^{0.25} Oh^{0.835} < 2.08 \times 10^{-5} \quad (8.35)$$

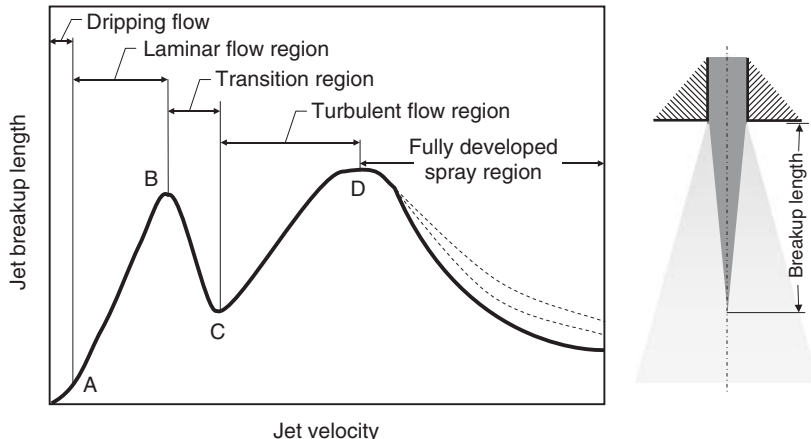


FIGURE 8.16 Breakup length in different modes.

for the transition from the drop formation mode to the ligament formation mode and

$$\dot{Q}^* We_l^{0.6} Oh^{0.835} > 1.77 \quad (8.36)$$

for the transition from fiber formation to film formation mode.

8.1.6.2 Continuous Jet Length

The continuous jet breakup length is an important parameter characterizing the atomization process that determines the region of the liquid jet, where the liquid (at least in the center of the jet) remains as a continuous medium. The breakup length is taken as the distance from the nozzle exit to the breakup point. The general behavior of the breakup length vs. the liquid jet velocity is illustrated in Figure 8.16. The initial part of the curve is described as the dripping region of the jet. The laminar flow region is located from point A to point B, where symmetric Rayleigh instabilities prevail. Here, the breakup length increases linearly with jet velocity and has been empirically determined as, (Grant and Middleman, 1966)

$$\frac{L}{d_0} = 19.5 We_l^{0.5} (1 + 3 Oh)^{0.85} \quad (8.37)$$

The upper point B indicates the transition from varicose to sinuousoidal breakup mode. It has been correlated from experiments by Grant and Middleman, (1966) for a laminar (fully developed) velocity exit profile of the jet as:

$$Re_{crit} = 3.25 Oh^{-0.28} \quad (8.38)$$

The breakup length decreases in the transition region B to C. When the fluid at the nozzle exit is already in a turbulent flow stage, and aerodynamic interaction between the liquid jet and the gas dominates the breakup, the jet breakup length increases with increasing velocity (from point C to D) (see Walzel, 1980). Here, Grant and Middleman (1966) proposed the empirical relationship:

$$\frac{L}{d_0} = 8.51 We^{0.32} \quad (8.39)$$

The behavior of the liquid jet breakup length at jet velocities beyond point D is not uniquely defined yet, but, in general, tends to decrease.

8.1.6.3 Stability Analysis

A cylindrical fluid element in a quiescent gaseous atmosphere is inherently unstable. Small perturbations of the surface (at wavelengths $\lambda > \pi d_l$) will always tend to grow. The first stage of the liquid jet disintegration

process in atomization is described by an initial perturbation of the liquid–gas interface and then by the growth of surface waves of the liquid. The instability itself, for example, is promoted due to the establishment of the surface tension, leading to a local pressure distribution on the phase boundary dependent on the local liquid surface curvature. A first quantitative analytical description of this process has been successfully given by Rayleigh (1878). In his contribution, the fundamental system of describing energy conservation equations (by neglecting viscous contributions) and solution of the resulting equation system is defined. Rayleigh's analysis is limited to the case of sinusoidal initial perturbations of small amplitude. The liquid jet that is affected by surface tension forces will become unstable only to any axisymmetric disturbance whose wavelength satisfies

$$\lambda_\delta < \pi d \quad (8.40)$$

For asymmetrical disturbances, the system is always stable. Rayleigh showed that the exponential growth of the fastest growing disturbance is given by

$$q_{\max} = 0.97 \left(\frac{\sigma}{\rho_l d^3} \right)^{0.5} \quad (8.41)$$

and the corresponding wavelength of the fastest growing wave is

$$\lambda_{\text{opt}} = 4.51d \quad (8.42)$$

A spherical drop forms from the separate ligament (cylinder of length 4.51d) due to surface tension force at equal volumes and finally the resulting drop size becomes

$$d_p = 1.89d \quad (8.43)$$

This relation is used, for example, in droplet generators to produce monosized droplets by excitation of the liquid jet at the frequency corresponding to its most unstable (see Figure 8.10).

Weber (1931) extended Rayleigh's work to include viscous effects. He neglected inertial effects and this solution is only valid for small initial perturbations. He also found an exponential growth of small perturbations at unstable wavelengths. Process and liquid properties of real atomization processes afford the inclusion of viscous effects (boundary layer) of the gas flow field. The upper limit for which the inviscid assumption in the instability process can be made with tolerable error for the case of a planar liquid sheet has been derived by Cousin and Dumouchel (1996). The result is summarized in terms of a limiting dimensionless number. The influence of viscous forces on the jet disintegration can be neglected if the dimensionless number M_c is

$$M_c = \frac{\mu_l \rho_g^2 u_{\text{rel}}^3 h_f}{\rho_l \sigma^2} < 10^{-3} \quad (8.44)$$

where the properties of the gas (g) and of the liquid (l), the relative velocity between gas and liquid u_{rel} , and the liquid film thickness h_f are used.

Based on the pioneering works of Rayleigh and Weber, the following analytical stability analyses are all generally limited by one or more basic simplifying assumptions, such as neglecting the viscous effects of either gas/or liquid, the partial neglect of inertial effects, or the limitation of small initial perturbation amplitudes.

Investigations of jet instability processes in the area of small perturbation wavelengths (aerodynamic interaction and liquid disintegration), based on the linearized conservation equations and partially neglecting inertial effects and gas viscosity (neglecting the gas boundary layer), was performed for the first time by Taylor (1949, 1959). If, in addition, the liquid viscosity is neglected, this result leads to the classical case of the aerodynamic fluid disintegration based on Kelvin–Helmholtz instability.

A stability analysis that is independent of the ratio of wavelength to jet diameter λ_d/d has been performed by Mayer (1993), based on the contributions of Taylor (1949) and Reitz (1978). The reference system in this

analysis moves with the fluid velocity u_l and the results are related to the relative velocity between the gas and liquid $u_{\text{rel}} = u_g - u_l$. The complex formulation is based on perturbation of the basic flow in the form of a surface wave with the amplitude

$$\eta_s = \text{Re}(\eta_0 e^{ikx + im\theta + \omega t}) \quad (8.45)$$

where $k = 2\pi/\lambda_d$ is the wave number, m the mode of the perturbation, and the parameter $\omega = \omega_r + i\omega_i$ is the complex growth rate of the perturbation. The real part of the complex growth rate $\text{Re}(\omega) = \omega_r$ describes the reaction function of the liquid jet by external excitation and the behavior of the perturbation. For negative growth rates, ($\omega_r < 0$) the perturbation will be damped out, and positive growth rates ($\omega_r > 0$) will lead to an exponential growth of the initial wave. In this derivation, the linearized flow conservation equations for gas and liquid are solved, based on the introduction of the stream function ψ and the velocity potential ϕ and the related perturbation formulations. Here the velocity distribution of the gas is neglected resulting in a velocity jump at the phase boundary between liquid and gas. The solution of the equation system is

$$\begin{aligned} \omega^2 - \frac{2\mu_l}{\rho_l} k^2 \omega \frac{I_1(kr_0)}{I_0(kr_0)} \left[1 - \frac{1kI}{k^2 + I^2} \frac{I_1(kr_0)}{I_0(kr_0)} \right] \\ = \frac{I^2 - k^2}{I^2 + k^2} \frac{I_1(kr_0)}{I_0(kr_0)} \left\{ \frac{\sigma k}{\rho_l r_0^2} [1 - (kr_0)^2] + \frac{\rho_g}{\rho_l} \left(U_{\text{rel}} - \frac{i\omega}{k} \right) \frac{K_0(kr_0)}{K_1(kr_0)} \right\} \end{aligned} \quad (8.46)$$

containing the modified Bessel functions I_n and K_n of the nth order and their derivatives I' , as well as $I^2 = k^2 + \omega/v_l$. From the general solution in Eq. (8.46) some specific cases can be derived, which are discussed in the following section

8.1.6.3.1 Large-Wavelength Area

When aerodynamic effects as well as the fluid viscosity, the gas density, and the relative velocity between fluid jet and gas flow field are neglected, the classical solution of Rayleigh (1978) is obtained:

$$\omega^2 - \frac{\sigma}{\rho_l r_0^2} k [1 - (kr_0)^2] \frac{I_1(kr_0)}{I_0(kr_0)} = 0 \quad (8.47)$$

In this equation I_0 and I_1 are the Bessel functions of zero and first order. As mentioned, earlier perturbations with wavelengths $\lambda > \pi d_l$ are unstable, resulting always in positive growth rates. If in the total unstable wave spectrum only the particular wavelength with maximum growth rate is considered (the fastest growing wave of all unstable waves, and maximum of the instability function), the analysis ultimately leads to the classical case of the Rayleigh disintegration of a liquid jet.

8.1.6.3.2 Small-Wavelength Area

The excitation of the primary disintegration process in the region of small wavelengths within coaxial atomization of liquids, assuming inviscid flow, is the classic Kelvin–Helmholtz instability theory as derived by Bradey (1973).

In the limiting case of very small wavelengths ($\lambda \ll d_l$), the solution of the instability problem leads to

$$(\omega + 2v_l k^2)^2 + \frac{\sigma}{\rho_l} k^3 - 4v_l^2 k^2 \sqrt{k^2 \frac{\omega}{v_l}} + \xi_g (\omega + iu_{\text{rel}} k)^2 \frac{\rho_g}{\rho_l} = 0 \quad (8.48)$$

An assumption for the viscosity influence of the gas flow on jet stability, which has been derived by Sterling and Schleicher (1975) is introduced in this solution. These authors found that accounting for boundary layer effects of the gas flow field stabilizes the wave growth. This can be taken into account as a damping effect on the perturbation pressure at the liquid jet surface. The factor ξ is related to this influence where (1) $\xi_g = 1$ corresponds to inviscid gas flow and (2) $\xi_g = 0.8$ accounts for a turbulent boundary layer profile of the gas flow field at the phase boundary between liquid and gas.

In a similar way, Miles (1957, 1958, 1960, 1961) had earlier taken into account the turbulent boundary layer character of the gas flow field at the phase boundary. By neglecting the gas viscosity, the turbulent logarithmic velocity profile in the fully turbulent region is expressed in terms of a suitable pressure distribution on the wavy liquid surface (see also Bürger et al., 1989, 1992).

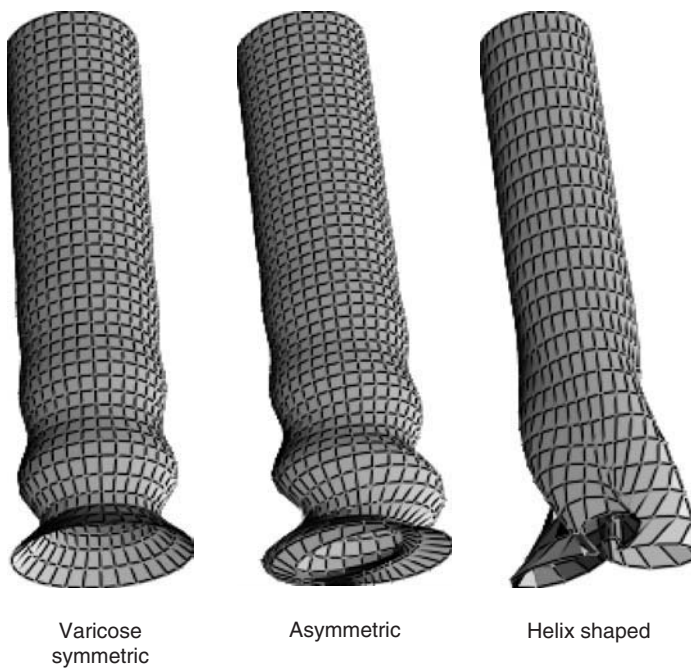


FIGURE 8.17 Instability modes of a circular liquid jet.

Generally from analyses of aerodynamic disintegration behaviors, the influence of surface tension is found as having a stabilizing effect (shifting of the maximum unstable wavelength toward lower values) and the influence of fluid viscosity is characterized as having a damping effect (lowering of the amplitude of the growth rate while keeping the value of the wavelength with maximum growth rate constant). An increase in the relative velocity between gas and liquid phase always has a destabilizing effect.

The instability of a liquid–gas-phase boundary of a jet or sheet is divided into several modes, which are described by their specific spatial growth function. Besides the symmetric mode ($m = 0$) of wave growth of phase boundaries, the liquid jet may tend toward a long wave oscillatory movement (asymmetric jet oscillations, see Figure 8.17). By neglecting the gas and liquid viscosities and the region of high relative velocities between the gas and liquid, a stability analysis of the first asymmetric mode ($m = 1$) of a liquid jet has been given by Levich (1962) as

$$\omega^2 + \rho_g k^4 r_0^2 u_{\text{rel}}^2 \frac{(\ln kr_0/2)}{2\rho_l} - \frac{\sigma k^2}{2\rho_l r_0} (1 - m^2 - k^2 r_0^2) = 0 \quad (8.49)$$

In the case of a planar liquid sheet, Hagerty and Shea (1955) have shown that an inviscid fluid shows higher values of the growth rate in the asymmetric mode than in the symmetric mode. Here the asymmetric mode is always dominant.

A comparison of the initial stability for laminar and turbulent liquid jet conditions has been made by Mansour and Chigier (1994). The growth rates of initial disturbances have been found as essentially the same for both laminar and turbulent conditions in agreement with the analysis of Weber (1931). For laminar flow conditions, the optimum wavelength corresponding to the fastest-growing disturbance is $\lambda_{\text{opt}} = 4.45d_0$, which is in agreement with the theoretical value from Weber's solution of the stability problem. For turbulent flow conditions, $\lambda_{\text{opt}} = 9.2d_0$ has been found, which is approximately twice the optimum wavelength as calculated by theory.

Despite the relatively crude assumptions and simplifications that have to be made to apply linear stability analyzes, the use of linear theory has a number of advantages when used as the first step in a general analysis of the fluid atomization process. First, the linear stability analysis is based on simple assumptions and second, the mathematical efforts for the solution are quite small. This makes the handling of this

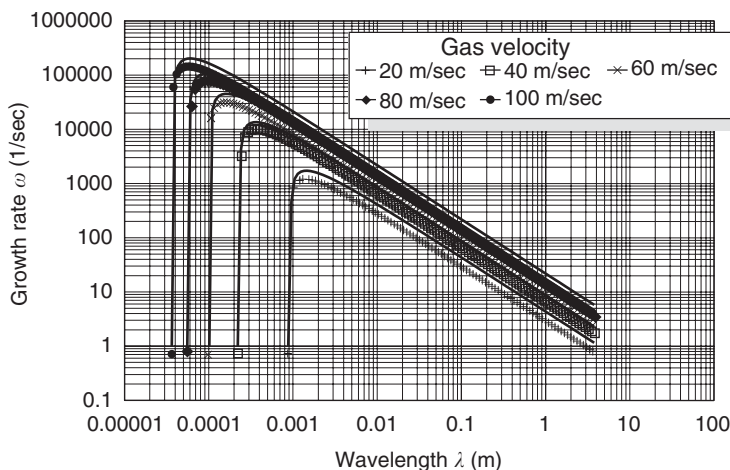


FIGURE 8.18 Instability growth rates of varicode mode in twin-fluid atomization of circular water jet ($d_l = 2$ mm, $m = 0$).

method easy. Linear stability analyses deliver general stability criteria and trends for the liquid–gas system under investigation and allow calculation of wavelengths and growth rates that mainly cover the disintegration process. An overview of classic solutions for the system of linear ordinary differential equations in the frame of linear stability analyses has been given by Markus et al. (2000). But, as will be described below, in comparison to experimental results in technical applications, the linear stability analysis typically over-predicts the wavelength by up to one order of magnitude (Markus et al., 2000; Klein, 2002).

Non-linear stability analyses, taking into account some of the simplifications necessary to carry out linear theories, have been reported in the literature for some actual cases and geometrical boundary conditions. The resulting system of conservation equations is solved in the sense of stability analysis using a perturbations approach or by numerical analysis with discrete perturbations (see, e.g., Rangel and Sirignano, 1991; Shokohi and Elrod, 1987; Dumouchel, 1989; Panchagnula et al., 1998).

For illustration, the results of a linear stability analysis based on the above-mentioned assumptions for a coaxial twin-fluid atomizer with external mixing and the water–air reference system with a liquid jet diameter of $d_l = 2$ mm will be discussed. The results in terms of growth rates for the symmetric mode ($m = 0$, short-wavelength perturbations) and the asymmetric case ($m = 1$, long-wavelength perturbations) are shown in Figures 8.18 and 8.19, respectively, for a variation of the relative velocity between coaxial atomizer gas and central liquid. The principal influence of process parameters on the phase boundary excitation can be shown. The relative maximum of each growth rate curve corresponds to the fastest growing wavelength. Comparing the symmetric mode and the asymmetric mode in this example shows that here, the symmetric perturbations always yield higher growth rates than the asymmetric ones. Therefore, in this case, the symmetric jet behavior should finally lead to disintegration of the jet. This result cannot be confirmed by experimental studies for these boundary conditions (Farago and Chigier, 1992; Hardalupas et al., 1997). When analyzing experimentally the spray from a similar type of nozzle, Hardalupas et al. (1997) found only a small number of droplets that were immediately sheared from the phase boundary at small wavelengths. These droplets make only a small contribution to the resulting spray, therefore the results of the stability analysis need to be scrutinized or extended to more realistic boundary conditions. In addition, the linear evaluation from Figure 8.19 also indicates that the wavelengths having the maximum growth rate show only a small dependence on the relative velocity between fluid and gas. This result is confirmed by the experimental atomization investigations by Hardalupas et al. (1997).

The behavior of the jet changes with different liquid properties. Particularly liquid metals show remarkable differences as these have high surface tension at comparably low viscosity. Comparison of different modes of stability for a jet of molten metal in a coaxial gas flow has been discussed by Markus et al. (2000)

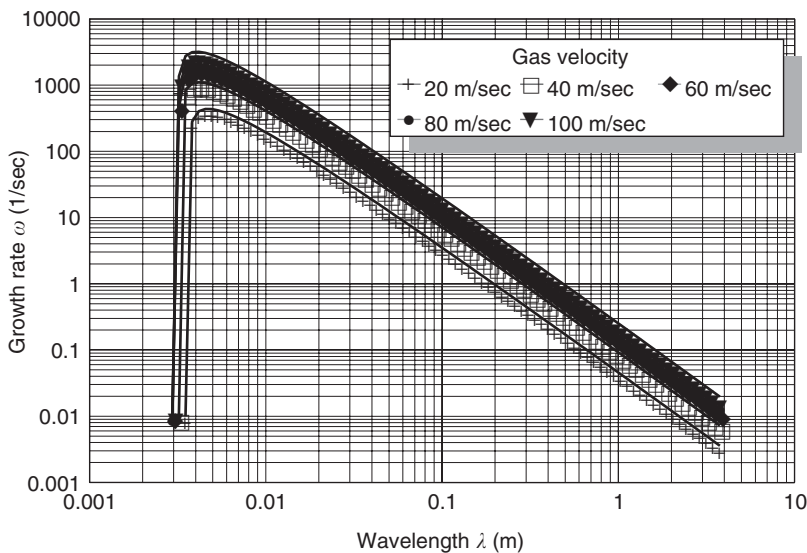


FIGURE 8.19 Instability growth rates of asymmetric mode in twin-fluid atomization of circular water jet ($d_l = 2$ mm, $m = 1$).

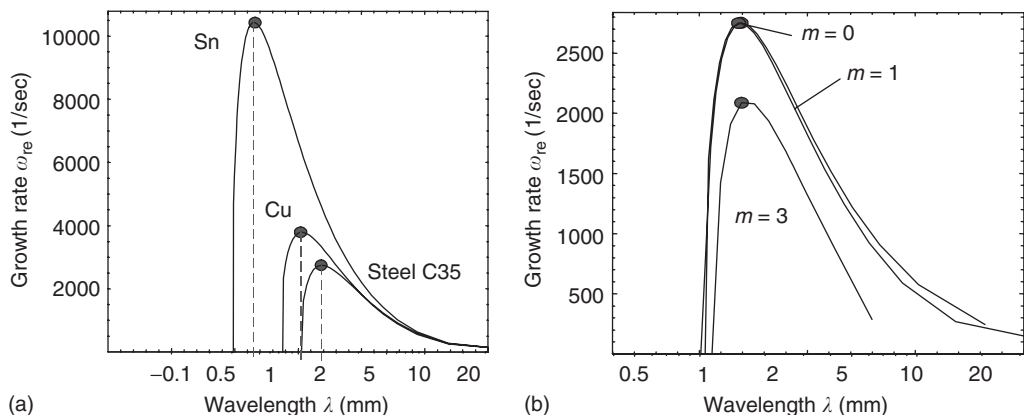


FIGURE 8.20 Stability curves for liquid metal jets: (a) different metal melts; (b) basic instability modes. (From Markus and Fritsching, 2003b, Proc. ICLASS 2003. With permission.)

based on the solution of the stability problem provided by Li (1995). Results for growth rates of different metal melts are shown in Figure 8.20a and results for the three basic modes of instability ($m = 0, 1, 3$) for a molten steel jet are illustrated in Figure 8.20b. The results are calculated for a jet diameter of $d_l = 4$ mm moving at a velocity of $u_l = 2$ m/sec in a coaxial gas flow at a constant velocity of $u_g = 100$ m/sec. The influence of material properties on melt jet stability is observed on the left. Here, mainly the effect of the surface tension, which increases from tin ($\sigma = 0.544$ N/m) via copper ($\sigma = 1.31$ N/m) to steel ($\sigma = 1.83$ N/m), can be observed. An increase in values for surface tension result in a decrease in Weber numbers, which also finally result in smaller amplitudes of the growth rate. In the same way, the dominant wavelength of jet disintegration increases. In comparison to water jets, the growth rates for molten metal jets are much lower, where comparatively higher energies (relative gas velocities) are needed to achieve atomization characteristics similar to water atomization. At higher relative velocities, the higher instability modes become more significant. Maximum growth rates in this case are observed for the symmetric mode $m = 0$. The asymmetric

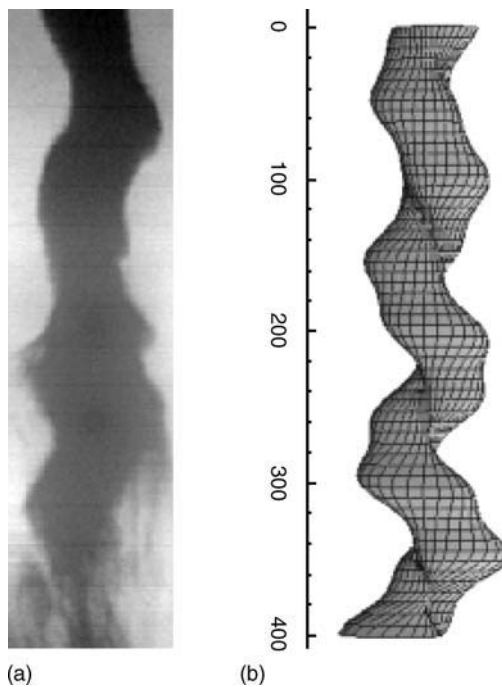


FIGURE 8.21 Superposition of instability modes, (a) experiment and (b) model comparison. (From Markus and Fritsching, 2003b, Proc. ICLASS 2003. With permission.)

growth mode $m = 1$ has almost identical growth rates, while higher modes show maximum growth rates at much smaller values (see [Figure 8.20b](#)).

A comparison of calculated growth rates and wavelengths with high-speed video pictures for primary perturbation of tin and steel melt jets (Markus et al., 2000) has shown that the theoretically calculated wavelengths are smaller than those observed in the experiments by one order of magnitude. This same trend has also been found by comparing experiments and direct numerical simulations and the results from linear theory for atomization of liquid sheets, for example, by Klein et al. (2002). However, a superposition of different modes with adapted growth rates (which do not match those in [Figure 8.20](#)) result in quite a good representation of the relevant processes of the primary perturbations of the liquid tin melt jet just in front of the atomizer nozzle exit. In [Figure 8.21a](#), a picture of a primary excitation of a tin melt jet within a twin-fluid atomizer is compared to a simulated picture of the superposed three main instability modes in [Figure 8.21b](#).

In the above-introduced initial models for gas–liquid interface instability, the focus is on the excitation and initial growth of surface perturbations of the liquid jet. In a further step of fragmentation analysis it needs to be specified when (or where) a growing liquid element is separated from the excited liquid jet (primary droplet or ligament formation). An initial analysis for derivation of the jet disintegration model and a correlation equation for the resulting droplet size distribution have been performed by Dombrowski and Johns (1963). These authors discuss the aerodynamic disintegration behaviour as illustrated in [Figure 8.22](#) for the plane liquid jet emerging from a planar slit nozzle. Starting from the growth of an instability on the interface, the liquid elements or ligaments in longitudinal direction plane first separate from the jet and deform into cylindrical elements further downstream. In the next step, these cylindrical ligaments disintegrate due to capillary instabilities (Rayleigh) in the fragments that form the resulting droplet structure in the initial spray by the action of surface tension.

Additional refinements of such fundamental models for primary disintegration within twin-fluid atomization are based on a more detailed analysis of the liquid stripping mechanism from the liquid surface and the description of the most relevant wavelengths at highest growth rates. Here the work of Berg

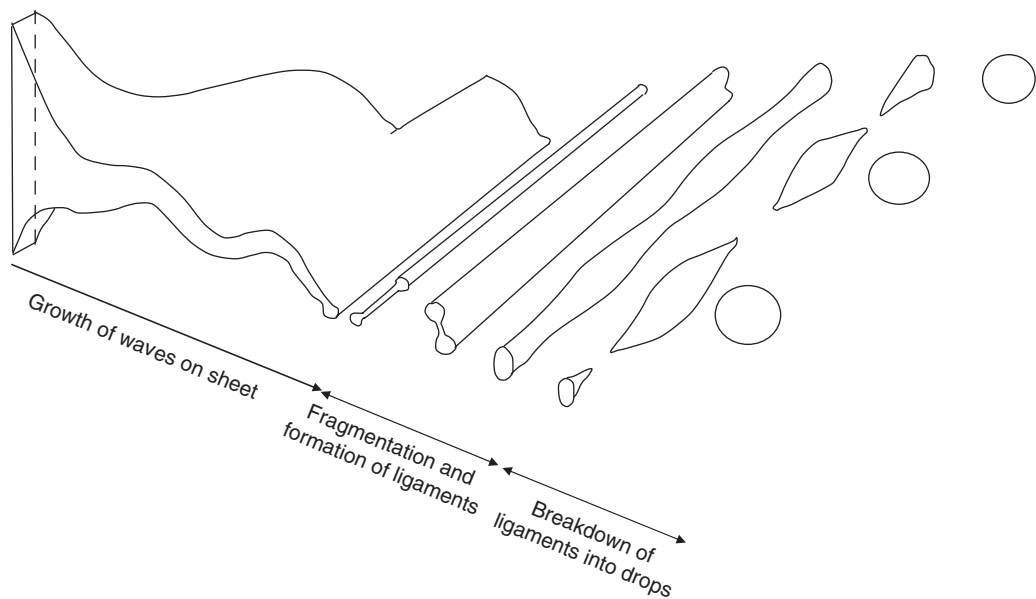


FIGURE 8.22 Principle of aerodynamic disintegration of a planar liquid jet. (Adapted from Dombrowski, N. and Johns, W.R., *Chem. Eng. Sci.*, 18, 203–214, 1963.)

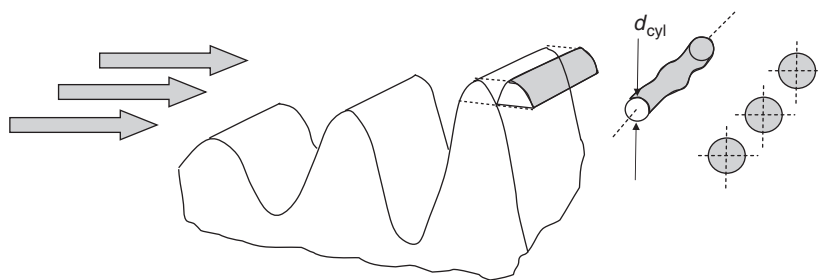


FIGURE 8.23 Stripping of a liquid fragment from the wave crest of a liquid sheet. (Adapted from Bürger et al., *Powder Metall. Int.*, 21, 10–15, 1989.)

et al. (1995) and Bürger et al. (1989 and 1992) provide useful and detailed correlations. These authors observed, in agreement with Jeffrey (1924), that the gas flow field interacting with the wave in its critical condition results in a stripping mechanism only on the wave crest and not on the whole wave volume, while the mean height of the wave in its temporal average remains practically unchanged. A principal sketch of this model is shown in Figure 8.23. The turbulent boundary layer character of the gas flow is taken into account using a linear stability analysis of the liquid jet as in the model of Miles (1957). Starting from an energy balance at the wave crest, where the work done by the gas flow on the wave crest is related to the free surface energy that is created by the newly generated liquid surface, the critical wave height for stripping $\Delta h = \eta_{ab} - \eta_B$ is calculated as.

$$\Delta h = \frac{4\sigma}{C_d \rho_g u_{rel}^2} \quad (8.50)$$

In this model, a resistance coefficient C_d is introduced for the gas flow at the wave crest. This coefficient takes either a constant value (Bürger et al., 1984) or, alternatively, is derived from the local pressure distribution at the wave geometry (Bürger et al., 1992). In the latter case, the resistance coefficient depends on the local height of the wave. The basic height of the wave η_B is taken as constant with a value of half

of the wavelength (length to height ratio of the wave is $l/d = 2$). From this value the variable diameter of the stripped liquid elements (in the case of a cylindrical element) d_{cyl} is derived.

A two-stage liquid fragmentation model based on stability theory has been introduced by Fritsching (2001) for coaxial twin-fluid atomization (round liquid jet) and a similar model for ring film disintegration by Lund et al. (1993). These models combine a stability analysis in the first stage resulting in primary fragmentation of the liquid stream with a Rayleigh breakup model to yield the final drop size distribution in the spray. Input parameters for the models have been obtained by experimental and numerical flow field studies.

As a refinement of the modeling approach for liquid disintegration, the primary liquid fragmentation process has been coupled directly into a two-phase flow simulation in the disintegration area. Here, the behavior of both phases is analysed simultaneously based on full conservation equations. In the first step, a stepwise stripping of fluid elements from the central jet is calculated. From this, the resulting decrease of liquid mass within the remaining liquid jet is obtained. The contribution of the stripped fluid ligament to the successive fragmentation process and the resulting drop size distribution are calculated. In the next step, the development of the reduced liquid jet diameter is directly related to the local gas flow field at that particular location. The stripped fluid drops and ligaments are introduced as source terms for mass and momentum in the calculation of the multiphase flow field. The continuation of the fragmentation process leads to successive stripping and smaller jet diameter. The coupling and interaction between the phases is treated in this way. The calculated local drop size contributions of the discrete stripping events are combined to yield the final droplet size distribution in the spray. The initial configuration of the spray after atomization is derived in this way. An ongoing further fragmentation of these droplets due to secondary atomization processes is not taken into account and, therefore, the finest droplets in the calculated droplet size distribution are underrepresented (see [Section 8.1.7](#)).

Recent investigations describe the complex behavior of the liquid jet and the gas–liquid interface, including the primary fragmentation process in atomization, using direct numerical simulation (DNS) of the multiphase flow system (see, e.g., Klein et al., 2001, 2002; Lafaurie et al., 1998; Lozano et al., 1994; Mayer, 1993; Zaleski et al., 1995, 1997, 2003; Scardovelli and Zaleski, 1999). Such complete three-dimensional, transient, direct numerical analyses, from initial liquid jet deformation to the primary fragmentation of the liquid jet are based on modeling approaches such as the volume of fluid (VOF) method (Nichols et al., 1980), in combination with continuum and surface reconstruction methods (Brackbill et al., 1992) such as the piecewise linear interface calculation (PLIC) method (Zaleski et al., 1995). The primary liquid fragmentation and also the simultaneous coalescence of fluid elements are described in this way. Typically, the excited fragmentation of a planar liquid sheet in a parallel gas flow field is observed in a three-dimensional calculation as will be described next.

In [Figure 8.24](#) a sequence of the result from the fragmentation simulation by Zaleski et al. (1997) is shown. The calculation has been performed for a liquid Reynolds number $Re_l = 200$ and a liquid Weber number of $We_l = 300$ at an artificially low density ratio of $\rho_l/\rho_g = 10$ between liquid and gas (at higher density ratios no stable solutions are achieved). From the tip of the evolving wave a finger-type ligament is formed, which is stripped off in a later stage from the main liquid jet and is deformed and stretched into the main flow direction to form a cylindrical fluid element. This unstable fluid element is fragmented later on as a result of capillary instabilities. This disintegration results in smaller fragments of different sizes. It is interesting to note that one of the results of this simulation is that a primary fluid ligament is created from the initial fragmentation that is oriented in the direction of the main flow (fingering in flow direction). In contrast to this result, the former classic aerodynamic fragmentation models, such as those developed by Dombrowski and Johns (1963) (see [Figure 8.22](#)), used a stripped-off fluid ligament oriented perpendicular to the main flow direction.

A direct numerical calculation (only in two dimensions) of the dynamics of phase boundaries of a planar liquid sheet has also been performed by Lafaurie et al. (1998) and Klein et al. (2002). In their contributions some major effects of liquid parameters like density ratio, viscosity ratio, and capillary effects on the primary fragmentation mechanism are discussed based on simulation results and comparisons to experimental results.

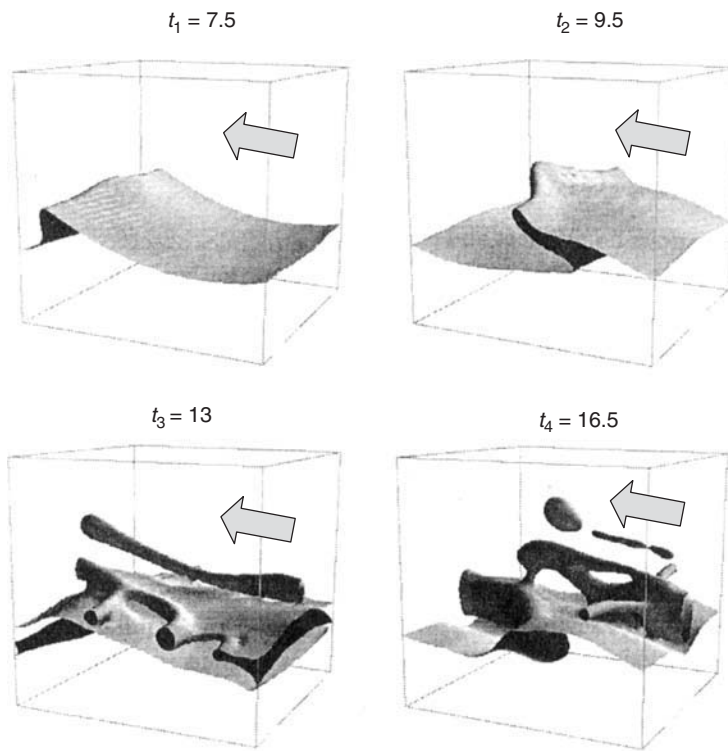


FIGURE 8.24 Direct numerical simulation of liquid jet fragmentation, $Re_l = 200$, $We_l = 300$, and $\rho_l/\rho_g = 10$; t = dimensionless time. (Adapted from Zaleski, S. and Li, J., *Proceedings of ICLASS-’97*, Seoul, Korea, August 1997, pp. 812–819.)

8.1.7 Secondary Atomization

Secondary breakup in sprays is defined as the disintegration of larger droplets and ligaments into smaller droplets. The breakup of a single droplet in a gas is caused by either relative velocity, turbulence, or shock structure interaction, acting separately. The main features of binary droplet collisions are presented in Section 12.3.

In sprays, the instabilities that occur for high relative velocities between the deformable liquid droplet and the surrounding fluid mainly cause secondary fragmentation. For very low relative velocities the droplet remains stable. If the aerodynamic forces overcome the forces due to surface tension, the droplet will deform (Triebnigg, 1929; Low and List, 1982). For higher relative velocities the deformed droplet will breakup. The gas or aerodynamic Weber number We_g (Eq. 8.7) gives the main criterion for breakup. If Weber numbers exceed a critical Weber number We_{crit} , the droplet breaks up. As surface tension has a stabilizing effect, an increase in viscosity damps unstable perturbations. The effect of viscosity on the breakup is included in the Ohnesorge number, Oh (see Eq. 8.8). For Ohnesorge numbers $Oh < 0.1$, the effect of viscosity is negligible. According to the review of Faeth (2002), based on a number of contributions of droplet breakup studies relevant in sprays (see Berthomieu et al., 1998; Chou et al., 1997, 1998; Dai and Faeth, 2001; Hsiang and Faeth, 1992, 1993, 1995; Tseng et al., 1992), it has been shown that

$$We_{crit} = \begin{cases} \text{constant for } Oh < 0.1 \text{ and} \\ \sim Oh^2 \text{ for } Oh > 0.1 \end{cases} \quad (8.51)$$

The critical Weber number found for low-viscosity liquids ranges from 6 to 13, but usually is assumed as

$$We_{crit} = 12 \quad (8.52)$$

The behavior of highly viscous liquids was first approximated by Brodkey (1967) in the range of $5 < We_g < 60$, and has been extended by Gelfand et al. (1973); Pilch and Erdman (1981, 1987) and Hsiang and Faeth (1992) for higher Weber numbers up to $We_g < 200$

$$We_{\text{crit}} = 12(1 + 1.077 Oh^a) \quad (8.53)$$

where the exponential factor a has been given in the range 1.6 to 1.64. For highly viscous liquids, the breakup behavior is different from that of low-viscosity liquids. Also, if the droplet size becomes smaller, the effect of viscosity increases.

For Weber numbers above We_{crit} , different types of droplet breakup regimes are obeyed (see [Section 12.3](#)). The classification of breakup regimes of Pilch and Erdmann (1987), Krzeczkowski (1980), and Faeth (2002) includes a description of breakup mechanisms for high Weber numbers $We_g > 350$. In general, there are two main types of breakup mechanisms in sprays: the bag breakup for low Weber numbers and the shear breakup for high Weber numbers as illustrated in Figure 8.25. While the bag breakup is associated with the Kelvin–Helmholtz instability (parallel shear flow), the shear breakup, particularly for very high Weber numbers, is associated with the Rayleigh–Taylor instability (cross-flow) (see Anderson and Wolfe, 1965).

The dynamics of the secondary fragmentation process depends on aerodynamic and viscous forces. For spray analysis, in a simplified model of the dynamic breakup process, the droplet for impulsive aerodynamic loading initially deforms to a disc and then breaks up into new droplets (Figure 8.26). The characteristic time scale needed for breakup is given as

$$t^* = \frac{d_0}{u_{\text{rel}}} \sqrt{\frac{\rho_l}{\rho_g}} \quad (8.54)$$

The deformation time before breakup according to Hsiang and Faeth (1992) is given as $t_{\text{def}} = 1.6t^*$. During deformation, the droplets drag coefficient changes (see Wiegand (1987) for $We_g < 10$ and $0.4 < C_d < 1$,

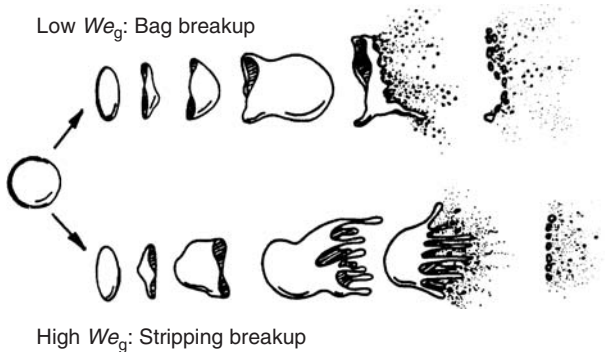


FIGURE 8.25 Secondary fragmentation of a liquid drop: breakup modes. (Adapted from Yule, A.J. and Dunkley, J.J., *Atomization of Melts*, Clarendon Press, Oxford, 1994.)

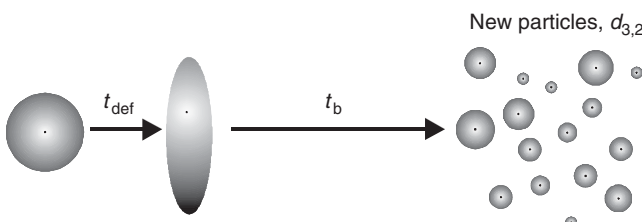


FIGURE 8.26 Secondary breakup model: deformation, breakup, spheroidization.

and at higher Weber numbers, see: Schmehl et al. [2000], Dai and Faeth (2001). The temporal evolution of droplet deformation and breakup has been investigated by Pilch and Erdmann (1981), and Samenfink et al., (1994) (see also Simpkins and Bales, 1972; Chou et al., 1997; Chou and Faeth, 1998; Dai and Faeth, 2001; Kolev, 2002; Schmehl, 2003). The total breakup time has been summarized as:

$$\frac{t_{\text{breakup}}}{t^*} = K_{\text{breakup}}; \quad 2.0 < K_{\text{breakup}} < 6.0 \quad (8.55)$$

For the viscous case, the temporal evolution of droplet deformation and breakup has been summarized by Gelfand et al. (1996) and Nigmatulin (1990) as $t_{\text{breakup}}/t^* = f(\text{We}, \text{Oh})$.

For computations of the droplet breakup process, models used include the following properties:

- Criteria to determine if the droplet breaks up or not
- An estimation of the breakup time t_{breakup} ,
- The resulting droplet size distribution (e.g., in terms of d_{32}),
- The spatial distribution of the resulting droplets and their velocities after breakup.

Typical spray secondary breakup models have been implemented in simulation codes. The so-called Taylor Analogy Breakup (TAB) Model introduced by O'Rourke und Amsden (1987) uses the analogy of a damped oscillation of a mass and the early droplet deformation motion, first mentioned by Taylor (1949) as

$$\ddot{y} + C_d \frac{\mu_l}{\rho_l r^2} \dot{y} + C_k \frac{\sigma}{\rho_l r^3} y = \frac{C_F}{C_b} \frac{\rho_g u_{\text{rel}}^2}{\rho_l r^2} \quad (8.56)$$

where $y = x/C_b r$ is the dimensionless droplet deformation and r the droplet radius. The constants are given as $C_k = 8$, $C_d = 5$ and $C_b = \frac{1}{2}$ (Lamb, 1986), and $C_F = \frac{1}{3}$. The condition for breakup is $y > 1$ and for the low-viscosity liquids is simplified to $y_{\text{undamped}} > 1$. By balancing the deformation energy and surface energy before and after breakup, the resulting droplet diameter and the number of new droplets are obtained. For

$$t_{\text{breakup}} \geq \frac{\pi}{\sqrt{8}} \sqrt{\frac{\rho_l d_0}{\sigma}} \quad \text{for } \text{We} \rightarrow \text{We}_{\text{crit}} \quad (8.57)$$

$$t_{\text{breakup}} < \sqrt{3} \sqrt{\frac{\rho_l}{\rho_g} \frac{d_0}{u_{\text{rel}}^2}} \quad \text{for } \text{We} \rightarrow \infty \quad (8.58)$$

and

$$d_{32} = \begin{cases} \frac{3}{7} d_0 & \text{for } \text{We} \rightarrow \text{We}_{\text{crit}} \\ 12 \frac{d_0}{\rho_g u_{\text{rel}}^2} & \text{for } \text{We} \rightarrow \infty \end{cases} \quad (8.59)$$

$$(8.60)$$

Based on the TAB model, Tanner (1997) proposed the enhanced TAB model (ETAB) using an energy balance under the assumption that the droplet production rate is proportional to the number of the produced droplets. Schmehl (2003) proposed a nonlinear model (NLTAB) to describe the behavior for strong deformations. Patterson (1997) and Patterson and Reitz (1998) described an approach based on the Rayleigh–Taylor instability, the so-called Ryleigh–Taylor (RT) wave model which also includes an arbitrary constant for the spray characteristics. Results from different model approaches have been compared by Liu et al. (1993), von Künsberg Sarre and Tatschl (1998), and Bauman (2001).

The result of a discrete secondary spray breakup model (Markus and Fritsching, 2003) is illustrated in Figure 8.27. Here, atomization in a twin-fluid gas atomizer configuration is studied. In this direct numerical approach, each particle has been tracked throughout the flowfield and droplet deformation and breakup are considered. If a ligament–droplet breaks up, all daughter droplets created are further tracked. The gas velocity distribution is based on measurements. Figure 8.27 shows a typical cumulative droplet size distribution at increasing distances from the atomizer. Most droplets are created in a short distance behind the region of the primary breakup. Then the droplets are accelerated and spread out due to turbulence.

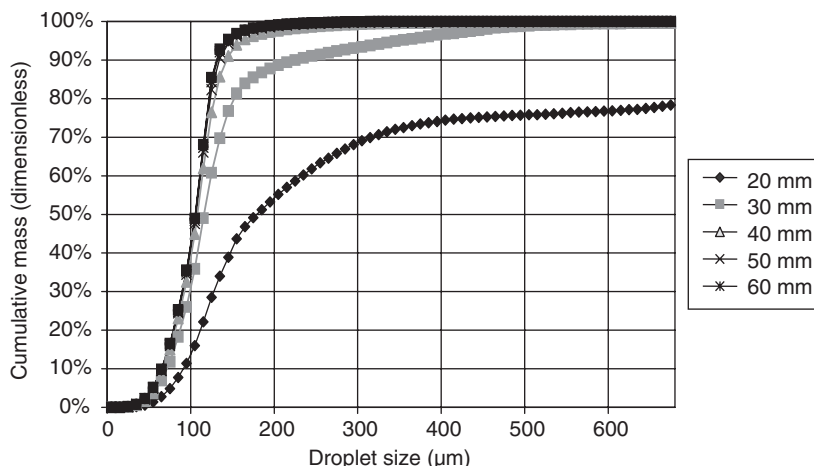


FIGURE 8.27 Secondary drop fragmentation in liquid spray: evolution of the drop size distribution vs. the distance to the atomizer nozzle. (From Markus and Fritsching, 2003b, Proc. ICLASS 2003. With permission.)

8.1.8 Special Liquids

8.1.8.1 Highly Viscous Liquids

Atomization of very viscous liquids (i.e., at dynamic viscosities above 1 Pa · s) is a difficult task as these liquids exhibit a certain resistance to the primary deformation process. In this context, prefilming of the liquid stream is a possibility to enhance the size of the gas–liquid interface area prior to the atomization process and, therefore, contribute to the efficiency of the primary fragmentation mechanism. Pofilming of the liquid stream may be achieved by:

- Geometrical arrangement of the liquid feed (in twin-fluid atomization)
- Centrifugal forces (in rotary or pressure-swirl atomization)
- Pressure forces (in ultrasonic standing-wave atomization)

In a variant of the effervescent atomizer (internal mixing), Campanile and Azzopardi (2003) used a mixing chamber that was designed to create annular liquid flow in the nozzle to enhance interaction between gas and liquid (see Figure 8.29). Newtonian liquids at viscosities up to 50 Pa · s have been atomized with air. The liquid mass flow rate was approximately 50 kg/h. In Figure 8.28 spray patterns in the fragmentation area are seen. For higher viscosities, the liquid is more pronounced to form fibers within primary fragmentation. In Figure 8.29, the achieved MMD at liquid viscosities of 5 and 50 Pa · s are illustrated. Typical droplet sizes achieved are in the range of several millimetres. From a model based on the observation that ligaments are formed from the annular film rim acting against surface tension, which tends to form a new liquid surface, the optimum wavelength for lateral instability is

$$\lambda_{\text{opt}} = 2\pi \sqrt{\frac{3\sigma}{\rho_l A_c}}, \quad A_c = \frac{1}{\rho_l} \frac{dp}{dx} + g \quad (8.61)$$

By taking into account the effects of viscosity and compressibility, especially for very viscous liquids at higher air velocities, the model is in good agreement with measured particle sizes.

The application of the atomizing media (gas) from the inside of an annular liquid sheet results in a radial droplet size variation in the spray that shows an increase in drop size values with an increase in radius (Lohner et al., 2003). On the other hand, typical twin-fluid atomizers with external mixing show a decrease in droplet sizes at the outer side of the spray with an increase in radius. The fluctuations in both cases are due to the specific gas velocity distribution and the fact that the kinetic energy of the gas is partially absorbed by the dispersed phase. Based on these results, a prefilming atomizer with inner and

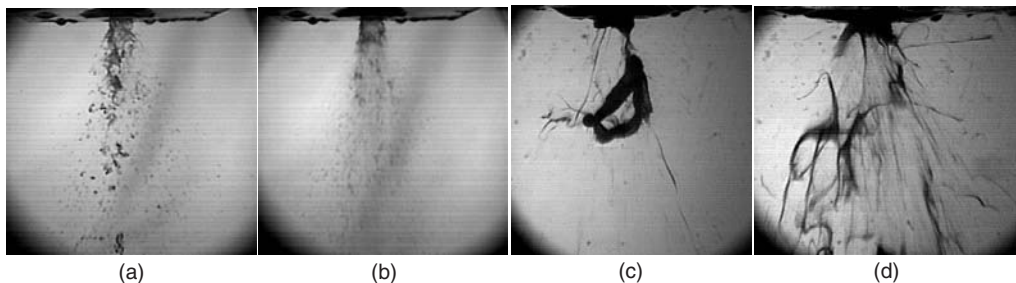


FIGURE 8.28 Fragmentation process and spray pattern in viscous liquid atomization. (From Campanile, F. and Azzopardi, B.J., *Proceedings of the International Conference on Liquid Atomization and Spray System ICLASS 2003*, Sorrento, Italy, 2003. With permission.)

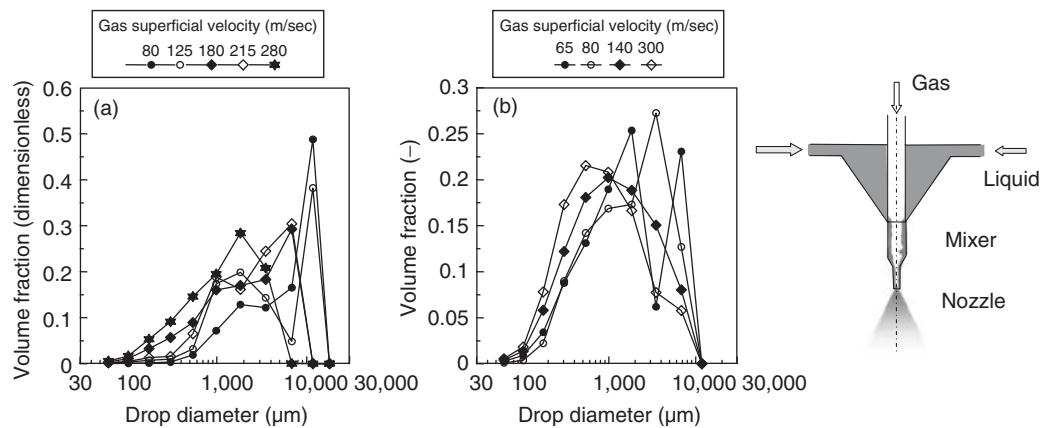


FIGURE 8.29 Mass median diameter for internal mixing twin-fluid atomization of highly viscous liquid: (a) $u_g = 0.15 \text{ m/sec}$, $\mu = 50 \text{ Pa}\cdot\text{s}$, (b) $u_g = 0.07 \text{ m/sec}$, $\mu = 5 \text{ Pa}\cdot\text{s}$. (From Campanile, F. and Azzopardi, B.J., *Proceedings of the International Conference on Liquid Atomization and Spray System ICLASS 2003*, Sorrento, Italy, 2003. With permission.)

outer atomization has been proposed for highly viscous liquids as shown in Figure 8.30. This atomizer is essentially a combination of an external mixing atomizer and the internal atomizer. The aim is that by this design the gas–liquid contact area is increased for fragmentation of viscous liquids and that a more homogeneous particle size distribution across the spray cross section can be achieved compared with the other two individual atomizers described earlier. In Figure 8.30 the principal behavior for the radial distribution of the mean droplet sizes in the spray is shown. The mass median particle size is nearly constant when the pressure ratio between the inside and the outside nozzles is unity, as has been verified in experiments by Lohner et al. (2003).

As described in Section 8.1.3, the ultrasonic standing-wave atomization USWA process is the most suitable method for atomization of highly viscous liquids. The sound radiation pressure within the resonant ultrasound field between two opposing sonotrodes leads to a deformation of the cylindrical feed liquid jet into a disc-shaped film (see Figure 8.6), thereby accelerating the liquid radially outward. With additional suction forces act at the rim of the disc, the sheet becomes unstable and disintegrates into droplets or ligaments. The tensile forces in the sheet support the disintegration process at the rim of the disc, especially for viscous liquids. In Figure 8.31, a comparison of a liquid atomization photo and a direct simulation of the primary fragmentation process within the USWA process is illustrated (Reipschläger, 2002a, 2002b). The MMD achieved with USWA atomization of a Newtonian viscous liquid (up to $10 \text{ Pa}\cdot\text{s}$) as measured by Hansmann (1996) is shown in Figure 8.32 as a function of the liquid throughput.

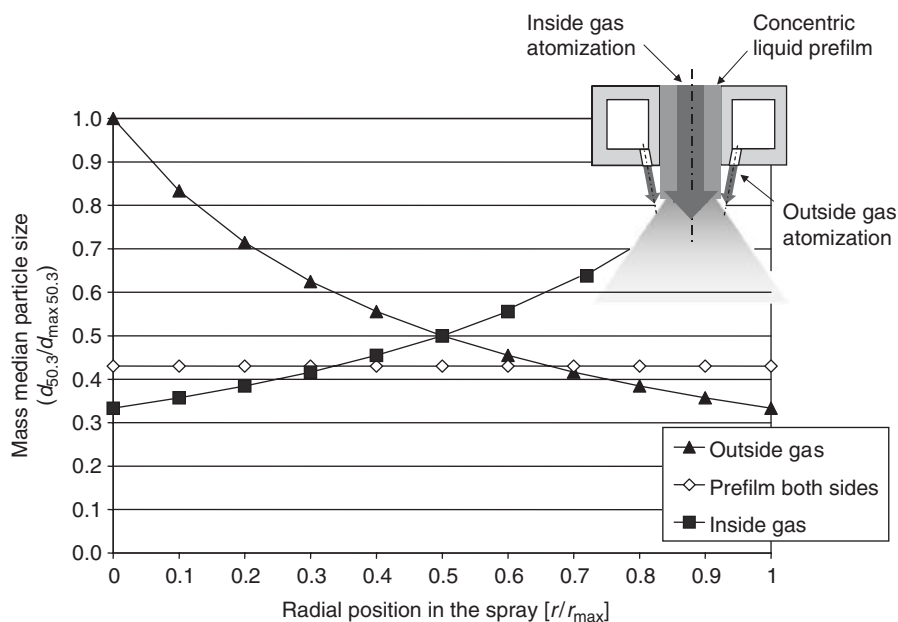


FIGURE 8.30 Atomizer configuration for viscous liquids and high throughputs, radial droplet size distribution in spray. (From Lohner et al., *Proceedings of the International Conference on Liquid Atomization and Spray System ICLASS 2003*, Sorrento, Italy, 2003. With permission.)

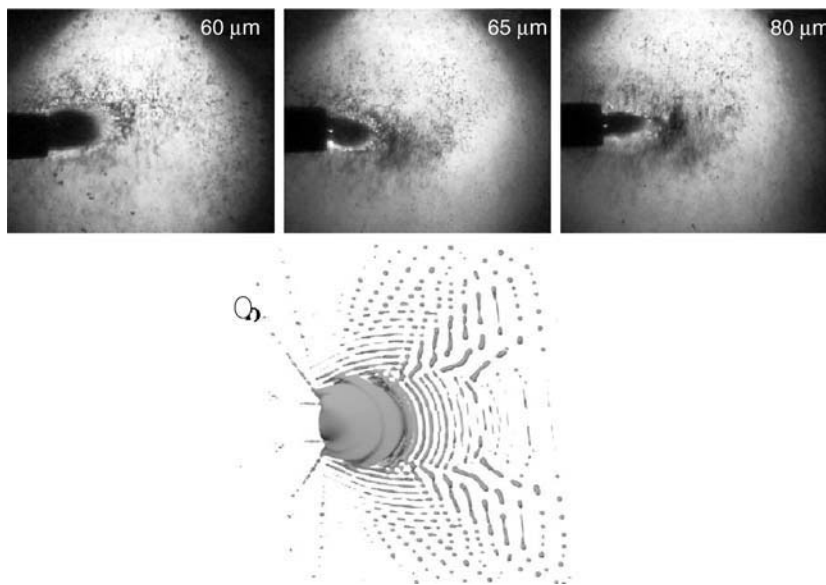


FIGURE 8.31 Atomization process in USWA , comparison of experiment and simulation. (From Reipschläger et al., *Proceedings of the 18th Annual Conference on Liquid Atomization and Spray System ICLASS Europe*, Zaragoza, Spain, 2002. With permission.)

8.1.8.2 Melts (Polymers, Minerals, or Metals)

Melts of polymers, metals, and glass or ceramic materials are atomized for powder production or coating and preforming applications. The atomization process of molten materials, in addition to their typically

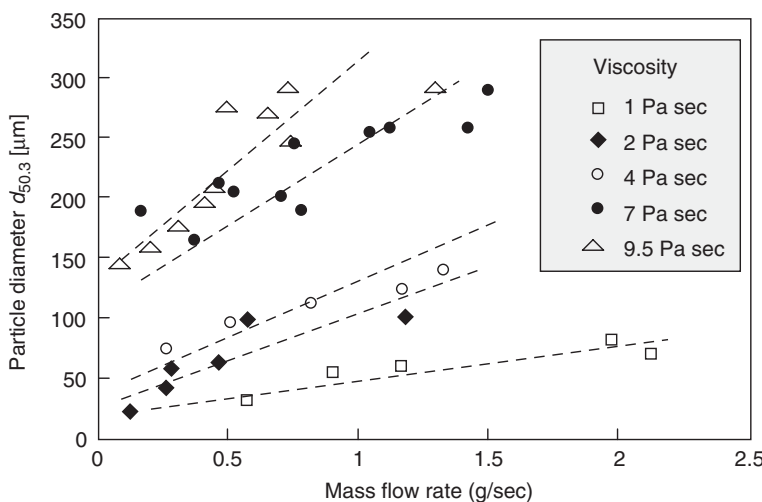


FIGURE 8.32 Mass median diameter within viscous fluid disintegration by USWA. (Adapted from Hansmann, S., Dissertation, Universität Bremen, 1996.)

difficult material properties*, must also ensure that sufficient thermal energy is available in the area close to the atomizer in order to prevent liquid fragments that may get in contact with the atomizer from sticking and freezing. Here, typical process problems in melt atomization arise (Bauckhage et al., 2001). Also, for achieving almost spherical particles, the cooling and solidification of the liquid fragments after atomization needs to be completed after a sufficiently high residence time in the molten stage for the liquid droplets (solidification time < spheroidization time). In addition to the thermal related freezing problem within the melt nozzle, chemical or metallurgical related-problems in melt delivery systems are also found frequently in applications. Problems may arise from melt-tundish reactions or melt segregational effects from diffusion.

Polymer melts may be sufficiently atomized by using the USWA technique (Reipschläger, 2002a, 2002b) or gas atomization (Watkinson et al., 2001). The energy requirement to overcome the effect of viscosity and surface tension in atomization may be expressed by the ratio of liquid Weber and Reynolds numbers as

$$\frac{E_\mu}{E_\sigma} = \frac{\mu_l u_{\text{rel}}}{\omega} = \frac{We_l}{Re_l} \quad (8.62)$$

Typically, this ratio is < 1 for a steel melt and above 1000 for polymers.

Mineral melts like glass or slags (e.g., from blast furnace process) have a high viscosity and a low surface tension compared with other melts. When these melt types are conventionally atomized under cold conditions, the material characteristics lead to a fiber product or at least to a product with a high fibre content instead of a particle product because the viscosity steadily and significantly increases with a decrease in temperature within the atomization process. Thus it is possible to disintegrate the melt stream into ligaments, owing to the high temperature and the low viscosity at the beginning of the atomization process. However, as the temperature of the ligaments decreases and the viscosity increases rapidly, the ligaments cannot be disintegrated further into smaller particles in the secondary atomization step. Therefore, the ligaments remain in a fiber state. To prevent the early termination of the atomization after the first fragmentation step and to allow further disintegration of the ligaments; one possibility is to increase the atomizing gas temperature. The lower temperature difference between the hot atomizer gas and the melt results in a

*Polymer melts typically are highly viscous and show non-Newtonian flow behavior, metal melts have high surface tensions, and ceramic melts have high viscosities that markedly change with melt temperature.

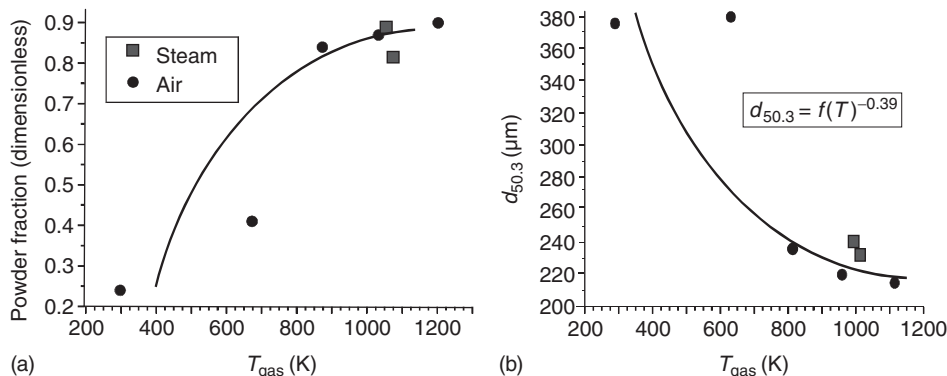


FIGURE 8.33 Powder fraction and mass median particle size for mineral melt atomization at increased gas temperatures. (From Lohner, H., Dissertation Univ. Bremen, 2003. With permission.)

lower heat transfer. Thus, the melt stays longer in a liquid state at low viscosity and the atomization process can be completed and finally the fragments spheroidize into globular particles. Figure 8.33a shows as an experimental result of the continuous decrease of the fiber content of a gas-atomized ceramic melt with an increase in gas temperature (Lohner, 2003). An external mixing twin-fluid atomizer was used, where a maximum gas temperature of 1000°C could be achieved. In Figure 8.33b it is evident that in addition to the decrease in the particle size, the efficiency of the atomization process increases with an increase in gas temperature (the gas mass flow rate at constant gas pressure decreases with an increase in gas temperature, see also Strauss, 1997). Here, the MMD of the powder fraction decreases with increase in gas temperature. From an energetic point of view, Strauss and Dunkley (2000) showed that the particle diameter at constant gas pressure should vary with gas temperature as:

$$d = KT^{-0.25} \quad (8.63)$$

This correlation has been validated in (molten metal) atomization trials (Strauss and Dunkley, 2000). Experiments for a ceramic melt have shown an exponent that is approximately -0.4 (Czisch et al., 2003).

It has been shown in Lohner (2003) that in the case of hot gas atomization of a viscous ceramic melt, the velocity difference between melt and gas has the primary effect on the atomization process. The kinetic energy of the gas (ρu^2) is constant (for constant gas pressure) with an increase in gas temperature. Therefore, assuming a constant surface tension, the aerodynamic Weber number We_g is constant and not a function of the gas temperature:

$$We_g = \frac{\rho_g \Delta u^2 D_l}{\sigma} = \text{const} \quad (8.64)$$

The influence of the increase in shearing action between the melt jet and the gas flow with an increase in gas temperature and constant gas pressure is formulated in the gas Reynolds number Re_g based on the relative velocity Δu between gas flow and melt jet. By rearrangement, the gas Reynolds number may be written as

$$Re_g = \frac{\rho_g \Delta u D_l}{\mu} = \frac{\rho_g \Delta u^2}{\mu \Delta u / D_l} \quad (8.65)$$

Several atomization mechanisms and devices are used for disintegration of *molten metals*; an overview has been given in by Lawley (1992), Bauckhage (1992), Yule and Dunkley (1994), Liu (2000), and Nasr et al. (2002). Especially twin-fluid atomization by means of (inert) gases or liquids (water) is used, owing to:

- The possibility of high throughputs and disintegration at high mass flow rates
- The high heat transfer rates for rapid cooling of the melt droplets

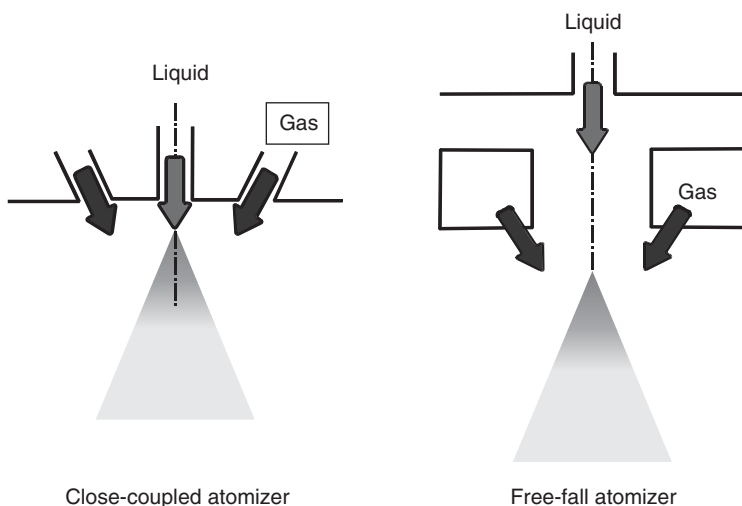


FIGURE 8.34 Twin-fluid atomizer: close-coupled and free-fall atomizer principles.

- The direct delivery of kinetic energy to accelerate the droplets (for compaction purposes)
- The minimization of oxidation by use of inert gases.

In most gas atomization cases with external mixing, the central melt jet stream is surrounded by a gas flow from a single (slit) jet configuration or a set of discrete gas jets, which flow parallel or incline toward the melt stream. The coaxial atomizer gas usually exits the atomizer at high pressures with high kinetic energy. Two main configurations and types of external mixing twin-fluid atomizers need to be distinguished as they result in different fragmentation characteristics. The first one is the confined or close-coupled atomizer and the second is the free-fall atomizer (Figure 8.34). The gas flow in the close-coupled atomizer immediately covers the flowing melt jet. Within the confined atomizer the distance between gas exit and melt stream is smaller than in the free-fall arrangement, where the melt jet moves a certain distance in the direction of gravity before the gas flow impinges onto the central melt jet; therefore the close-coupled configuration generally results in higher atomization efficiencies (in terms of smaller particles at identical energy consumption). But the confined atomizer type is more susceptible for freezing problems of the melt at the nozzle tip. This effect can be due to the extensive cooling of the melt by the expanding gas flow, which exits in the close-coupled type near the melt stream and contributes to rapid cooling of the melt at the tip of the melt nozzle. The thermal-related freezing problem is most important directly in the initial phase of the spray process when the melt stream is initiated and exits the nozzle for the first time. At this point, the nozzle tip is still cool and needs to be heated first either externally or by the hot melt flow.

In a close-coupled atomizer, the liquid–melt typically is prefilmed at the nozzle face due to the action of the gas recirculation from the concentric arrangement (see Figure 8.35). Modeling the fragmentation process of metal melts within a close-coupled atomizer arrangement has been derived by Antipas et al. (1993) and Liu (1997). Based on experimental observations of fragmentation processes within atomization in close-coupled atomizers (Ünal, 1987; Anderson and Figliola, 1988; Ting et al., 2000; Anderson and Terpstra, 2002), it is assumed that (at least under general conditions) the emerging fluid from the atomizer is moving from the tundish exit as a radial film at the lower side of the nozzle tip toward the gas jets delivery area. The local liquid film thickness τ_f is derived from a Couette flow analogy as

$$\tau_f = \left[\frac{\mu_l}{\mu_g} \frac{\dot{m}_l}{\pi \rho_l r} \left(\frac{du_g}{dz} \right)^{-1} \right]^{0.5} \quad (8.66)$$

At the outer edge of the wetted nozzle tip the liquid film is influenced by the gas flow field and is reflected into the main gas flow direction. From this point onward the liquid moves as a free concentric ring

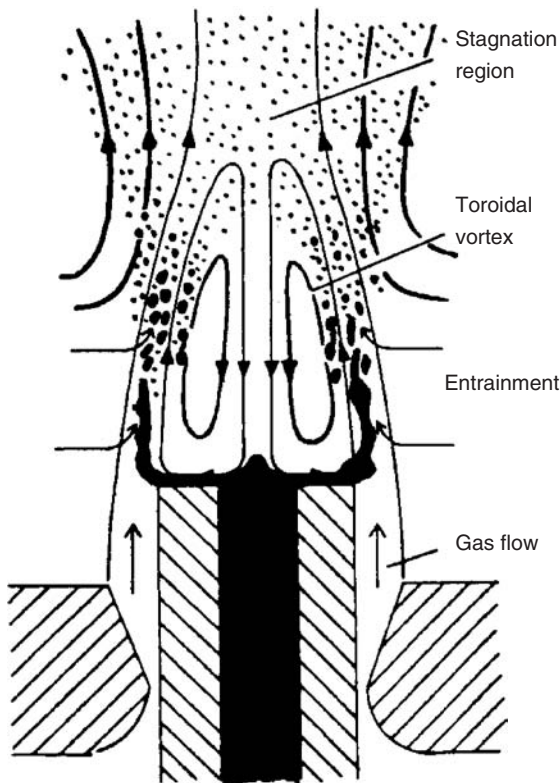


FIGURE 8.35 Flow field configuration in atomization area of close-coupled atomizer. (Adapted from Ünal, A., *Metall. Trans.*, 20B, 613–622, 1989.)

configuration in the direction of the gas streamlines. In this area the liquid film is fragmented after a certain distance in a primary fragmentation process into droplets. The characteristic distance from the atomizer to the fragmentation point is derived from empirical data as

$$L_f = 1.23 \tau_f^{0.5} We_f^{-0.5} Re_f^{0.6} \quad (8.67)$$

Here, the film Weber number We_f and the film Reynolds number Re_f are based on the local film thickness τ_f and the relative velocity between gas and liquid u_{rel} (resp. the film velocity u_f) as

$$We = \frac{\tau_f \rho_g u_{\text{rel}}}{2\sigma}, \quad Re = \frac{\tau_f \rho_l u_g}{\mu_l} \quad (8.68)$$

Developments for understanding fragmentation of a metal melt in a close-coupled atomizer during atomization have been introduced in Ting et al. (2000). These authors discuss especially the effect of the aspiration pressure on the flow of gas and liquid at gas pressures up to 5.5 MPa. The atomization gas flow field results in a fluctuating pressure distribution at the melt outlet. Based on gas dynamic assumptions for the gas flow field in the nozzle vicinity for increasing gas pressures, these authors finally conclude that for increased gas pressures an oscillating flow field of the gas may occur. This effect will result in the temporal occurrence of central orthogonal shock structures in front of the nozzle. Based on this observation a fragmentation process model is developed, which predicts, for gas pressures exceeding a configuration dependent threshold value, a pulsating flow field configuration of the melt flow at the nozzle tip (see Figure 8.36) and therefore highly transient atomization behavior.

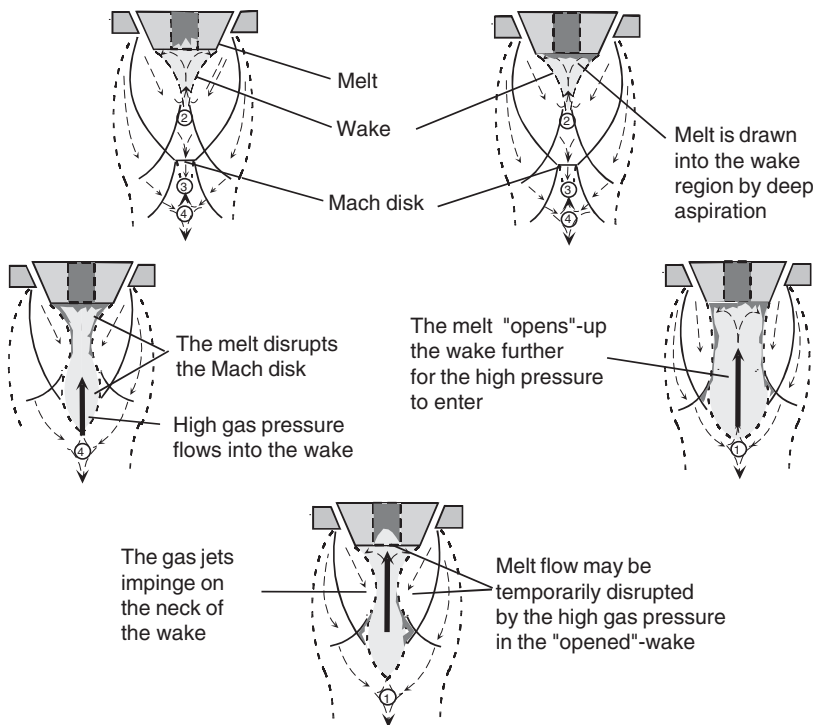


FIGURE 8.36 Pulsating melt flow in close-coupled atomization. (From Ting et al., *Mater. Sci. Eng. A*, 326, 110–121, 2002. With permission.)

8.1.8.3 Solid-Liquid Suspensions

The atomization of solid-liquid suspensions is important in chemical, food, and pharmaceutical industrial applications (e.g., for paints, paper coatings, printing inks, ceramics, and cosmetics, detergents) and in energy conversion (coal water slurries). In typical technical suspensions, the solid particle size may range from 1 nm to 1 mm, while the solid concentration may be up to 70% (weight/volume %) depending on the specific application. The presence of solid particles in the carrier liquid, that may lead to plugging or wear out of the atomizer material, introduces an additional criterion for the selection of a specific atomizer type (pressure, twin-fluid, or rotary) for suspension atomization.

Interactions between the three different phases (solid particles, liquid, and gas) as well as the non-Newtonian rheological properties of the suspension, which strongly depend on the solid particles, play an important role in the disintegration process of suspensions. These parameters make an extension of basic fragmentation theories of pure liquids for analysis of suspension atomization processes difficult. Theoretical work on this subject has been presented by Parthasarathy (1999), who studied the breakup of two-dimensional slurry sheets subjected to gas flow using linear spatial stability analysis for the case of a dilute slurry and a dense slurry. Schütz et al. (2003) used the semi empirical Carreau-Yasuda model to describe the flow behavior of a suspension in a mathematical-physical model to calculate the resulting mean droplet diameter in a suspension spray produced by a hollow-cone nozzle. In the case of suspension disintegration, experimental research dominates the research effort (see e.g., [Shirley et al., 1987; Shimizu et al., 2002; Dombrowski and Fraser, 1954; Glaser, 1989; Mulhem et al., 2002, 2003; Kurt et al., 2002]).

The most important parameters controlling the formation process of the droplet in a suspension spray are the atomization energy, the capillary pressure, the cohesion forces between the solid particles, and the suspension viscosity. While the atomization energy depends on the type of the atomizer, the other parameters are strongly influenced by the size and concentration of solid particles. The adhesion forces and

suspension viscosity increase with a decrease in solid particle size and an increase in solid particle concentration in the suspension. Therefore, the droplet formation process becomes difficult in the case of a suspension containing small solid particles /or high solid concentrations.

The influence of the solid particle characteristics and the carrier liquid properties on suspension atomization in film formation atomization processes (e.g., by means of hollow-cone nozzles or rotary atomization) is reported in Schütz et al. (2003), Glaser (1989), and Kurt et al. (2002). In the film formation process, the breakup length of the suspension sheet is shorter than the breakup length of the comparable pure carrier liquid sheet due to the disturbance of the liquid surface by the particles.

8.1.9 Drop Size Correlations in Sprays

8.1.9.1 Theoretical Analysis

Approaches for general theoretical descriptions of drop size distributions resulting from atomization processes can be based on statistical approaches and tools that derive a pdf in relation to the process to be analyzed. The maximum entropy formalism (MEF) is an example for a statistical tool that delivers partial information for a specific process (based on a number of compulsory conditions) by transformation into a suitable distribution function. It does not contribute any physical aspects to the analysis of fragmentation processes. The development of fundamental models in the areas of applying MEF to the analysis of fragmentation processes of liquids and the derivation of the resulting droplet size distributions in sprays have been performed by Sellens (1989), Sellens and Brzustowski (1985), and Li and Tankin (1987). Their approaches have been further developed by Ahmadi and Sellens (1993) and Cousin and Dumouchel (1997). The fundamental idea of this modeling is the description of a pdf of the particle size distribution $q_r(d)$ from the Shannon entropy (uncertainty) Sha :

$$Sha = -k_s \int_0^{\infty} q_r(d) \ln(q_r(d)) d(d) \quad (8.69)$$

where k_s is a constant, which has to be determined by the dimensionality of the specific process under investigation.

The MEF allows the prediction of the droplet size pdf depending on a number of mathematical constraints. These constraints are described based on a number of known conservation properties of the process and their distribution and are equivalent to the moments of different orders of the distribution. Without further limitations, a number of different pdf fulfil a given set of constraints. The MEF describes the best-fit solution for which entropy reaches a maximum value. Cousin et al. (1996) describe the resulting number density based particle size distribution of a pressure-swirl atomizer from this formalism as

$$q_0(d) = \frac{p^{(p-1)/p}}{\Gamma_s(1/p)d_{p0}} e^{(-d_p/pd_{p0})} \quad (8.70)$$

containing the Gamma function Γ_s . The determination of input parameters such as p and d_{p0} in the above derivation is done based either on specific singular measurements (Ahmadi and Sellens, 1993) of moments of a measured spray particle size distribution or a primary analysis of the fragmentation process based on linear stability analysis (Cousin and Dumouchel, 1997). For an atomization process where the principal mode of the disintegration process is constant (constant fragmentation mode), the resulting particle size distribution in terms of a mean or characteristic particle size and the particle size distribution width can be similarly determined. Applications are described by Malot and Dumouchel (1999), Prud'homme, and Ordoneau (1999). (For application within ultrasonic liquid atomization see Dobre and Bolle (1998)).

Another model is the approach of Platzer and Sommerfeld (2003). It originates from a structural effects theory based on the work of Naue and Bärwolf (1992) as detailed by Hartmann (1993), and provides functions for drop size and volume distribution. In contrast to conventional MEF models, no mean drop diameter needs to be provided as input parameter. The SMD and the drop size distribution are calculated iteratively using only known geometrical information and operating conditions. This is done by assuming a structure formation process that is a function of the critical Weber number. Some varying

functions are derived, differing in the number of drops in each class and in the function of the critical Weber number describing the number of classes formed. The complete spray model from internal and primary fragmentation flow to the spray structure simulation is described. The two-fluid model including the prediction of the drop size distribution is used for the first part, and the Euler–Lagrange method for the second part.

A two-stage modeling approach of atomization may also be based on primary fragmentation from stability analyses in the first step and ligament fragmentation, described as a Rayleigh breakup process (see 8.1.6.3.2) in the second step for round liquid jets in coaxial twin fluid atomization (Fritsching, 2001) and for annular ring films (Lund et al., 1993). The description of the gas and liquid state prior to atomization within these models has been derived by means of experimental and numerical flow field studies. Mean drop size correlations in the initial spray are derived.

8.1.9.2 Empirical Drop Size Correlations

A large number of empirical correlations for drop size distributions in sprays have been derived (Lefebvre, 1989; Liu, 2000; Bayvel and Orzechowski, 1993). These drop size correlations typically fit only a specific atomizer type (respectively, atomization principle) and a certain (narrow) range of boundary conditions or disintegration modes. The boundary conditions include the geometric constraints of the atomizer design and operational parameters such as liquid properties, flow rates, pressures, and others. The characteristic droplet size in the spray spectrum (typically given as mean, median, or Sauter diameter) is either correlated in terms of dimensionless numbers or in terms of direct material and operational properties. A few of those correlations discussed earlier with respect to some different atomizer types are listed in Table 8.3. The analysis of the drop size distribution width and correlation in a spray is given in few cases only.

TABLE 8.3 Examples of Empirical Droplet Size Distributions for Various Atomizer Types

Application	Drop size	Source
Pressure atomizer	$d_{32} = 47 \frac{d_0}{u_0} \left(\frac{\sigma}{\rho_g} \right)^{0.25} \left[1 + 331 \left(\frac{\mu_l}{\rho_l \sigma d_0} \right)^{0.5} \right]$	Tanasawa and Toyoda (1955)
Pressure swirl atomizer	$d_{32} = 2.25 \sigma^{2.25} \mu_l^{0.25} \dot{m}_l^{0.25} \Delta P_l^{-0.25} \rho_g^{-0.25}$	Lefebvre (1983)
Twin-fluid atomizer (external)	$d_{32} = 0.585 \left(\frac{\sigma}{\rho_l u_{rel}^2} \right)^{0.5} + 53 \left(\frac{\mu_l^2}{\sigma \rho_l} \right)^{0.225} \left(\frac{\dot{Q}_l}{\dot{Q}_g} \right)$	Nukiyama and Tanasawa (1939)
Twin-fluid atomizer (internal, bubbly flow regime)	$d_{32} = \left[0.023 \text{ALR} \frac{\rho_l R T_a}{\sigma(\kappa - 1)} \left(1 - \left(\frac{P_a}{P_c} \right)^{\kappa - 1/\kappa} \right) + \frac{2.35}{d_0} \right]^{-1}$ Kim and Lee (2001)	Kim and Lee (2001)
Twin-fluid atomizer (internal, annular flow regime)	$d_{32} = 0.14 d_0 f \left(\alpha, \frac{\rho_g}{\rho_l} \right) \left(\frac{\rho_g j^2 d_0}{\sigma} \right)^{-0.5}$ $f \left(\alpha, \frac{\rho_g}{\rho_l} \right) = \frac{\alpha \sqrt{1 - \alpha}}{\sqrt{1 - \rho_g / \rho_l [1 + 75(1 - \alpha) / \sqrt{\alpha}]^{0.5}}}$	Kim and Lee (2001)
Rotary atomizer (drop mode)	$d_{32} = \frac{27}{n_z} \left[\frac{\sigma}{2\rho_l r} \left(1 + 0.003 \frac{\dot{Q}\rho_l}{2r\mu_l} \right) \right]^{0.5}$	Tanasawa et al. (1978)
Rotary atomizer (fiber mode)	$d_{32} = 0.119 \frac{\dot{Q}^{0.1} \sigma^{0.5}}{n_z (2r)^{0.5} \sigma_l^{0.4} \mu_l^{0.1}}$	Tanasawa et al. (1978)
Rotary atomizer (film mode)	$d_{32} = 15.6 \frac{\dot{Q}^{0.5}}{n_z} \left[\frac{\sigma}{(2r)^2 \rho_l} \right]^{0.4}$	Tanasawa et al. (1978)
Ultrasonic standing-wave atomization	$d_{50,3} = 0.53 \dot{Q}^{0.27} d_0^{-0.24} \mu_l^{0.69} \rho_l^{-0.21} P_{max}^{-0.97} \rho_0^{0.48} C_0^{0.97}$	Hansmann (1996)

8.1.9.3 Suspension Atomization

Some correlations for suspension droplet sizes in sprays generated by using different atomizer types are summarized in Table 8.4.

The experimental results of Son and Kihm (1998), using laser diffraction particle analysis and assuming a Rosin–Rammller type droplet size distribution (RRSB) in the spray showed that the SMD (d_{32}) of coal–water–slurry (CWS) containing smaller coal particles is larger than the SMDs of CWS containing larger coal particles. The separation of the solid particles from each other in the suspension spray has to be controlled by the solid particle characteristics. Mulhem et al. (2003b) confirm this assertion experimentally in the case of twin-fluid suspension atomization. Figure 8.37 shows a bimodal droplet size distribution of suspension spray containing large solid particles $d_{50,3} = 94 \mu\text{m}$ (right hand) and a monomodal droplet size distribution of suspension spray containing small solid particles $d_{50,3} = 6 \mu\text{m}$ (left hand).

The influence of the solid particle characteristics and the carrier liquid properties on suspension atomization in the case of a twin-fluid suspension atomization process may be summarized as follows. In the case of suspension containing large solid particles the solid particles tend to separate from the carrier liquid (Glaser, 1989; Mulhem et al., 2003b). Dry solid particles are seen in the spray, their characteristic diameter is independent of the atomization energy, and pure carrier liquid drops, which disintegrate further with an increase in atomization energy, as shown in Figure 8.38. The solid particle size in the suspension influences the resulting diameter of the pure carrier liquid drops, which is explained as a result of a reduction in the volume of the liquid bridge between the solid particles by a decrease in the solid size in the suspension. Investigation of the influence of solid particle concentration on the atomization of suspension containing large solid particles showed only a small influence on the resulting pure liquid diameter. The diameter of the carrier liquid drops in the spray increases with an increase in the viscosity of the carrier liquid.

TABLE 8.4 Drop Size Correlations for Suspension Atomization

Application	Drop Size	Source
Internal mixing twin-fluid atomizer	$\frac{d_{50,3}}{d} = [(A(We_g)^{-x} + B(Oh)^{2x})] \left[1 + \frac{1}{ALR} \right]^y$ $We_g = \frac{\rho_g u_g^2 d_L}{\sigma}, Oh = \frac{\mu_l}{\sqrt{\rho_l \sigma d}}, ALR = \frac{\dot{m}_g}{\dot{m}_l}$	Shirley et al. (1987)
External mixing twin-fluid atomizer	$d_{32,susp} = 0.21 d_L (Oh)^{0.0622} (We_{aero} \times ALR)^{-0.4}$ $We = \frac{\rho_g u_{rel}^2 d_{susp}}{\sigma}, Oh = \frac{\eta_c}{\sqrt{\rho_{susp} \sigma d_{susp}}}, ALR = \frac{\dot{m}_g}{\dot{m}_{susp}}$ <p>for: $70 \leq u_{rel}(\text{m/sec}) \leq 220$ solid particles: $d_{50,3} \leq 26 \mu\text{m}$, $C_p \leq 50 \text{ wt\%}$</p>	Mulhem et al. (2003)
High-pressure injection	$d_{32,susp} = 0.279 \Delta p^{-0.702} \rho_g^{0.285} x^{1.521}$ $28 \leq \Delta p(\text{MPa}) \leq 110; 1.2 \leq \rho_g (\text{kgm}^{-3}) \leq 25,$ $60 \leq x(\text{mm}) \leq 120$ <p>coal particles: $d_{50,3} \leq 5 \mu\text{m}$, $C_p \leq 50 \text{ wt\%}$</p>	Son and Kihm (1998)
Hollow-cone nozzle	$\frac{d_{32,susp}}{D_E} = 7.8 \Delta p^{*-0.651} \left[\left(Oh^{0.129} \left(\frac{D_k}{D_E} \right)^{0.027} \left(\frac{D_A}{D_E} \right)^{0.05} \rho^{*-0.268} \right) + \left[38.5 (1 - C_p)^{-5.862} \left(\frac{\rho_p}{\rho_c} \right)^{-0.295} \left(\frac{d_{32,p}}{D_E} \right)^{0.86} \right] \right]$ $0.4 \leq (1 - C_p) \leq 1; 0 \leq \frac{\rho_p}{\rho_c} \leq 2.43; 0 \leq d_{32,p}(\text{mm}) \leq 0.082$ <p>Subscripts: P; solid particle; C; carrier liquid; E; inlet; K; chamber; A; outlet</p>	Glaser (1989)

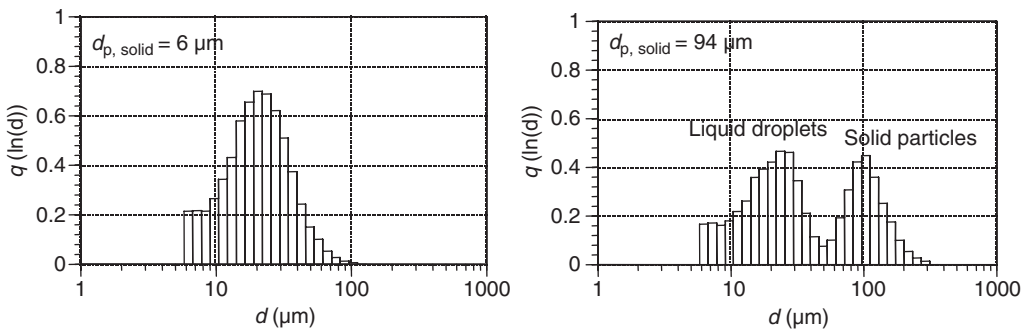


FIGURE 8.37 Drop size distribution in suspension atomization, monomodal and bimodal distribution. (From Mulhem et al., *Atomization and Sprays*, 13, 321–343, 2003b. With permission.)

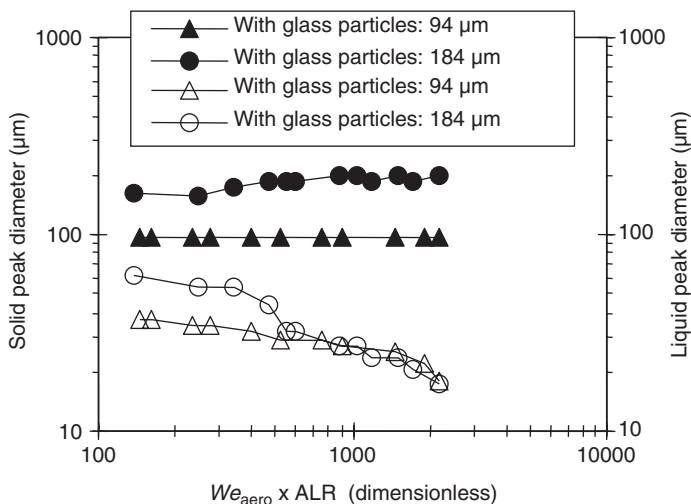


FIGURE 8.38 Peak of the logarithmic particle size distribution for suspension atomization containing large solid particles. (From Mulhem et al., *Atomization and Sprays*, 13, 321–343, 2003b. With permission.)

In the case of suspension spray containing relatively small solid particles the large cohesion forces between the particles prevent the liquid–solid separation process. The majority of the droplets in the spray are suspension droplets, which behave like pure liquid droplets that take into account the change in material properties due to the particles. In essence the suspension droplets may disintegrate into smaller ones with increasing atomization energy. The diameter of the suspension drops in the spray is comparable with the diameter of carrier liquid drops (Isenschmid, 1992). The droplet diameter in the suspension spray increases with an increase in solid concentration.

8.1.9.4 Melts

In Table 8.5, some empirical correlations for particle sizes within molten metal atomization in free-fall and close-coupled atomization are listed. In Lubanska's correlation, a liquid Weber number $We_l = \rho_l u_{\text{max}}^2 d_l / \sigma_l$ and the inverse of the mass flow rate ratio (1/GMR; where GMR is gas to metal mass flow ratio) are used. The empirical constant K_{lub} reflects different atomizer geometries. Lubanska has given its value to be between 40 and 80, but other investigators have found much larger values. A sample evaluation of particle sizes in molten metal sprays for various metals vs. the atomizer gas pressure based on Lubanska's correlation is illustrated in Figure 8.39. Several investigations were directed toward the verification of Lubanska's formula for particle size distributions from melt atomization. Rao and Mehrotra (1980)

TABLE 8.5 Drop Size Correlations for Molten Metal Atomization

Application	Drop Size	Source
Free-fall atomizer	$d_{50,3} = d_0 K_{\text{lub}} \left[\frac{v_l}{v_g} \frac{1}{W \tilde{\epsilon}_l} \left(1 + \frac{\dot{m}_l}{\dot{m}_g} \right) \right]^{0.5}$	Lubanska (1970)
Close-coupled atomizer	$d_{3,2} = \frac{12\sigma}{\rho_l u_{\text{rel}}^2 / 1 + 1 / (\varepsilon \dot{m}_g / \dot{m}_l) + 4\sigma/\tau_f};$ $\varepsilon = \frac{1.62}{u_g^{1.3} / (\dot{m}_g / \dot{m}_l)^{0.63} \mu_l^{0.03}}$	Liu (1997)

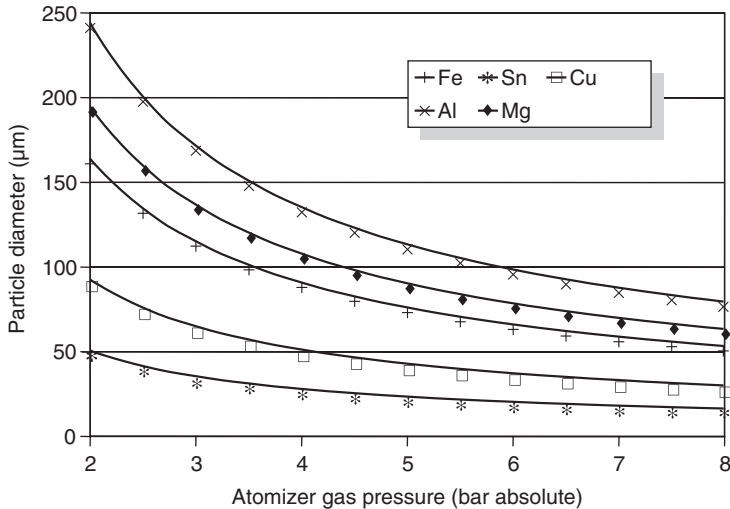


Figure 8.39 Mean particle sizes in molten metal atomization, evaluation of Lubanska (1970) correlation. (From Lubanska, H., J. Metals, 2, 45–49, 1970. With permission.)

investigated the influence of nozzle diameter and atomization angle on particle sizes, and found that the mean droplet size decreases with a decrease in nozzle diameter and an increase in atomization angle. They found a different value of the exponential factor as well as the atomizer constant in Lubanska's correlation. Another modification has been proposed by Rai et al. (1985). These authors studied melt atomization within ultrasonic gas atomizers and also proposed a modification of Lubanska's formula.

A discussion and evaluation of the relevance of Lubanska's formula for the atomization of metal melts in twin-fluid atomization is found in the work of Bauckhage and Fritsching (2000). A general overview for a number of empirical correlations for mean and median droplet sizes dependent on operational conditions and nozzle types and geometries for melt atomization within different atomizer configurations can be found in Liu (2000), Yule and Dunkley (1994).

8.2 Spray Behavior

In terms of a multiphase flow approach to spray analysis, the main features of the dispersed spray described are

- the overall spray geometry (e.g., spray angle)
- the local fluxes of droplet mass, momentum, and enthalpy (where appropriate)

- the equivalent droplet concentrations by number or volume
- the local droplet size and droplet state, including velocity and temperature distribution

The analysis of the spray behavior is divided into two regions, depending on the relevance of droplet–droplet interactions and the possibility and frequency of droplet–droplet collisions. A rough estimate for the relevance of collisional effects for the overall spray behavior can be performed based on the ratio of particle relaxation time τ_p to the timescale between individual particle collisions τ_c . The particle relaxation time is the time that a droplet takes to accelerate from velocity u_1 to u_2 . This is (in the Stokes flow regime) expressed as (see [Section 1.2.6](#))

$$\tau_p = \frac{\rho_l d_p^2}{18\mu_g} \quad (8.71)$$

The time constant between collisions for particles is derived from the collision frequency as

$$\tau_c = \frac{1}{f_c} \quad (8.72)$$

At low droplet concentrations (dilute flow) particulate transport is mainly determined by fluid dynamic interactions of the individual particles or droplets with the continuous carrier phase (e.g., drag, lift, etc.). At high particle concentrations (dense flow), the influence of particle collisions affects the movement of the droplets and the droplet size distribution. These two regions may be separated in terms of the ratio of the characteristic time scales as (see also [Section 1.2.7](#))

$$\text{dilute } \frac{\tau_p}{\tau_c} < 1; \text{ dense } \frac{\tau_p}{\tau_c} > 1 \quad (8.73)$$

In a dense spray the time between droplet collisions is smaller than the droplet relaxation time. Before reaching another steady slip velocity from the droplet–gas interaction another collision may occur. Therefore, the droplet movement is determined mainly by collisions, and fluid dynamic effects are of less importance. In sprays, the area close to the atomizer is typically a dense spray region, as here the number concentration of droplets is high, while with an increase in distance to the atomizer due to the spreading of the spray cone, droplet collisional effects decrease and transition to dilute flow is achieved.

8.2.1 Dense Spray

8.2.1.1 Collisions and Coalescence

When two liquid droplets are interacting during flight, several events may occur. The colliding droplets may (1) bounce, (2) stably coalesce, (3) temporarily coalesce followed by disruption, or (4) temporarily coalesce followed by fragmentation. Details on binary droplet collision phenomena are discussed in [Section 12.1](#).

Experimental works on water–water and hydrocarbon–hydrocarbon droplet collisions have been studied extensively for relevance in spray processes. Orme (1997) reviewed the experimental studies of water and hydrocarbon droplet binary collisions. The basic phenomena of coalescence and separation of droplets during binary collision have been experimentally addressed by, for example, Ashgriz and Poo (1990), Qian and Law (1997) for water and fuel droplets, and Menchaca-Rocha et al. (1997) for mercury droplets. Direct numerical simulation of the behavior of two droplets during collision has been reported by Nobari and Tryggvason (1996a, 1996b), Frohn and Roth (2000). Some principal physical details of drop collisions can be explained by this numerical approach. The outcome of a binary collision can be visualized from these droplet collision studies, (see [Section 12.1](#)). Typically droplet collision models are implemented into numerical spray codes such as Sommerfeld (1996), Georjon and Reitz (1999), Aamir and Watkins (1999), and Rüger et al. (2000).

8.2.1.2 Numerical Models of Droplet Collisions in Sprays

The most commonly used water–water collision model is based on the work of O'Rourke (1981). This model considers only grazing collisions (bounce) and permanent coalescence. The decision criteria, whether grazing or coalescence collisions occur, is the critical collision angle

$$\sin^2 \phi_{\text{crit}} = \min \left[2.4 \frac{f(\gamma = d_{p,1}/d_{p,2})}{We}; 1 \right] \quad (8.74)$$

In case of a collision angle less than ϕ_{crit} , the droplets coalesce, otherwise a grazing collision occurs. The function f has been fitted by Amsden et al. (1989) using experimental results as

$$f(\gamma) = \gamma^3 - 2.4\gamma^2 + 2.7\gamma \quad (8.75)$$

Podvysodski and Shraiber (1994) proposed an empirical formula for liquid droplet collisions in a wide range of material properties. The mathematical expectation $\phi_{1,2}$ of the ratio between a mass change of target droplet and total mass of “projectile” droplets impacting on the target is

$$\begin{aligned} E\left[\frac{dm_2/dt}{m_1}\right] &= \phi_{1,2} = 1 - 0.246 Re_{1,2}^{0.407} Lp_2^{-0.096} \left(\frac{d_2}{d_1}\right)^{-0.278}, \\ Re_{1,2} &= \frac{u_{1,2} d_1 \rho_1}{\mu_1}, \quad Lp_2 = \frac{d_2 \rho_2 \sigma_2}{\mu_2^2} \end{aligned} \quad (8.76)$$

The mass of the droplet after the collision is predicted from

$$m_{2,\text{ac}} = m_{2,\text{bc}} + \phi_{1,2} m_{1,\text{bc}} \quad (8.77)$$

where ac and bc stand for after and before collision, respectively. This empirical formula was obtained within the parameter range $30 \leq Re_{1,2} \leq 6000$, $5 \leq Lp_2 \leq 300,000$, and $1.9 \leq d_2/d_1 \leq 12$. The parameter $\phi_{1,2}$ should be in the range $-1 \leq \phi_{1,2} \leq 1$.

Dubrovski et al. (1992) studied collisions between liquid drops and solid particles. According to their experimental results, collision outcome between a fast moving small drop and a large solid particle was always accompanied by liquid breakup and a certain number of fragments. For a small solid particle colliding with a large liquid drop target, they reported four modes of collision outcome; (i) projectile capture by target, (ii) shooting through, (iii) gas bubble formation, and (iv) target destruction.

Lagrangian – Eulerian simulation models are the most widely used tools to calculate droplet spray behavior. The gas flow is treated as a continuum (Eulerian) and discrete parcels of particles (Lagrangian) are injected into the flow field. Each parcel contains many identical droplets. The Lagrangian step may be performed by simultaneously tracking all parcels in an integral time step as developed by Amsden et al. (1989), or tracking each complete trajectory of the parcel in a serial manner as performed by Crowe (1977). Collision models are incorporated in the main gas-spray flow model. Spray collision models reflect the two approaches: (1) simultaneous tracking of all droplet parcels and search for collision partners, as performed by Amsden (1989), (2) serial tracking of parcel and sampling individual collision partners from statistical information, as performed by Sommerfeld (1992, 1993, 1995) and Oesterle and Petijean, (1993). The second approach significantly reduces the calculation task. However, as the collision partner is sampled from a statistical value, the postcollision properties have to be treated carefully if the information of both partners is required.

In both the models, the collision partners are the uniform particle cloud contained in each parcel. All parcels presented in a control volume are taken into account for determining the collision probability (all real droplets for O’Rourke model and statistical droplets for Sommerfeld model). Therefore, stochastic collision is treated and kinetic theory of gases is applied. Particle collision is assumed to take place within the collision cylinder as shown in Figure 8.40. The collision cylinder has a cross-sectional diameter of $d_{p,1} + d_{p,2}$ and length of $U_{\text{rel}} \Delta t$, where Δt is the time step considered.

The model presented by O’Rourke (1981) and implemented in the KIVA computer program (Amsden et al., 1989) tracks all parcels simultaneously and the possibility of collision between each pair of parcels is evaluated by searching all collisional partners that are present in the computational cell. The criterion whether collision takes place is determined by the probability of no collision:

$$P_{\text{no_collision}} = e^{-f \Delta t} \quad (8.78)$$

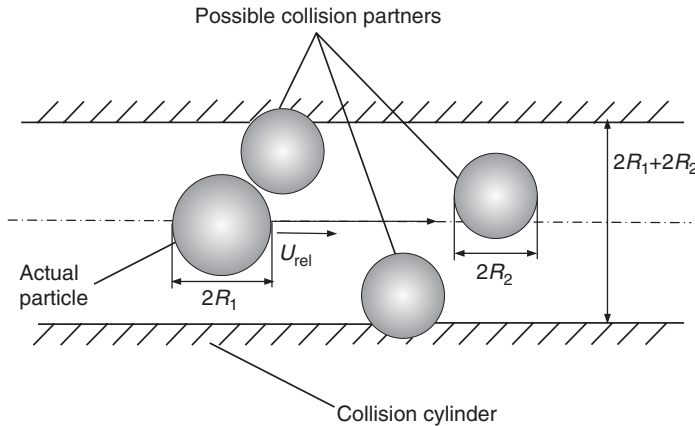


FIGURE 8.40 Drop collision cylinder from kinetic gas theory.

where f is the collision frequency in a collision cylinder:

$$f = \frac{N_{r,s}}{V} \pi (r_l + r_s)^2 | \bar{V}_{r,l} + \bar{V}_{r,s} | \quad (8.79)$$

$N_{r,s}$ the number of smaller radius droplets, V the volume of the computational cell, and r_l and r_s describe the properties of the larger and smaller droplets respectively. To decide whether a collision takes place, a random number RN is generated from a uniform distribution and compared with $P_{\text{no_collision}}$, if a collision event is valid, $\text{RN} > P_{\text{no_collision}}$. The position of contact point during collision is directly calculated since the collisional partners are both “real” and their trajectories are known. Since the model considers the collision of particles within the same computational cell only, “artifacts” concerning neighboring particles located in an adjacent cell may arise.

Schmidt and Rutland (2000) developed the no-time counter (NTC) collision model that predicts how many collisions should occur in a given cell and then randomly samples collision pairs within the cell. In the NTC model, the collision computation is performed on a special collision mesh that is optimized for both sample size and spatial resolution. The mesh is different every time step to further suppress the artifacts.

The proximity collision model has been developed in Bauman (2001) and is designed to improve the previous discrepancy in the KIVA code collision model. To counter the artifacts problem, possible collision pairs are chosen based on the proximity of the two particles from each other, irrespective of their placement relative to the computational grid. A user-defined collision radius is introduced to define the maximum distance between the two particles, which are to be considered for collision. The equations for determining whether collision occurs and the outcome of the collision, are nearly identical to the KIVA collision model.

Within the models proposed by Oesterle and Petitjean (1993) and Sommerfeld et al. (1992, 1993), each parcel is tracked in a serial manner and statistical values of particle number density, average and rms velocity-size relationship, and other variables are calculated and stored in each computational cell. The collision probability assumes a moving droplet, while the other droplet (fictitious) is fixed, and is calculated within the collision cylinder

$$P_{\text{collision}} = 0.25 \frac{N_2}{V} \pi (D_l + D_s) | U_r | \Delta t \quad (8.80)$$

where N_2 is the total particle number density in the computational cell (from the stored particle number in the last Lagrangian step). The particle size of the collision partner (fictitious droplet) is sampled from the local particle size distribution. Rüger et al. (2000) validated this collision model in a spray with experimental results. A comparison of measurements and predictions showed very good agreement with the profiles of mean properties of both phases and the local droplet size distributions as well as size-velocity

correlations. According to the calculation results, an increase in the integral droplet SMD along the spray distance is mainly due to coalescence, while the impact of droplet evaporation on mean diameter decrease is of minor importance.

In a further extension, Sommerfeld (2001) developed an interparticle collision model taking into account the correlation of the fictitious particle with the velocity of the real particle as a consequence of gas turbulence. The model has been validated with results from large eddy simulations (LES) in the literature. For all test cases considered, good agreement between model calculations with the results obtained by LES has been found.

8.2.1.3 Clustering of Droplets

Due to the dynamics of the primary liquid fragmentation process, especially in the dense spray region, a clustering of droplets may occur. Experimental characterizations of sprays in most cases are focussed on single point statistics of the spray in time or space. Such a description yields a measure of the mean number density or flux rate of the spray. Progress in measurement techniques such as the Phase doppler anemometry (PDA) and particle image velocimetry has also made temporal correlated droplet measurements and the space correlations information available for sprays. Marx et al. (1994) and Edwards and Marx (1995a, 1995b) developed a multipoint statistical description of a spray. Based on this theoretical approach it is possible to distinguish between steady and unsteady sprays by using the interparticle arrival time τ at a certain position. Steady sprays are defined as those whose interparticle arrival time distribution obeys inhomogeneous Poisson statistics. Unsteady sprays are defined as those whose interparticle arrival time distribution do not obey inhomogeneous Poisson statistics. An example of unsteady spray behavior with droplet clustering is illustrated in Figure 8.41 with a high-speed-video sequence of a disintegrating liquid jet. Areas at higher and lower droplet concentrations in the initial spray are seen, which are attributed to the asymmetric instability and primary fragmentation of the liquid jet.

The experimental interparticle time distribution h_{exp} can be determined from a single realization (SR) or multiple short realizations that are ensemble-averaged (ER). Edwards and Marx (1995a, 1995b) showed that

$$h_{\text{exp}}(\tau_j) = \frac{H(\tau_j)}{N\Delta\tau_j} \quad (8.81)$$

where τ is the interparticle time gap, $H(\tau_j)$ the number of events that fall within the j th interparticle time gap, N the total number of interparticle events, and $\Delta\tau_j$ the width of the j th interparticle time gap. To

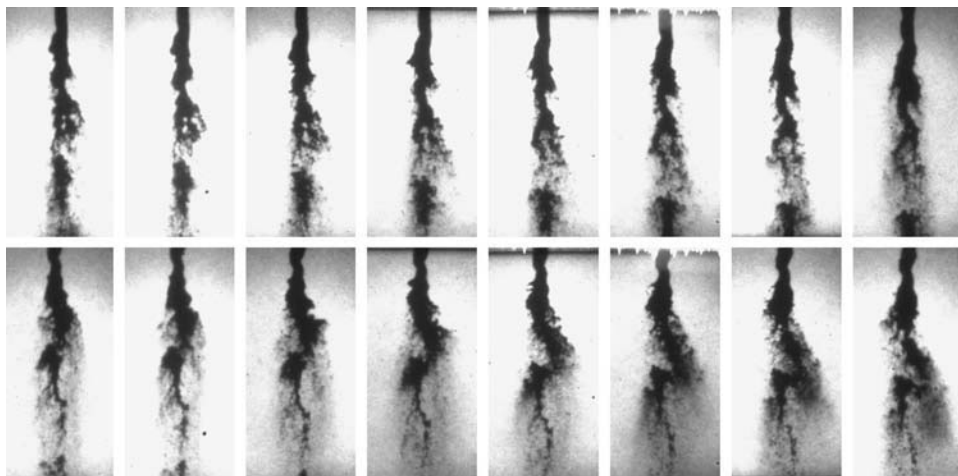


FIGURE 8.41 Drop clustering in sprays: high-speed photo series of liquid fragmentation process, liquid jet diameter 4 mm, time increment: 0.2 msec.

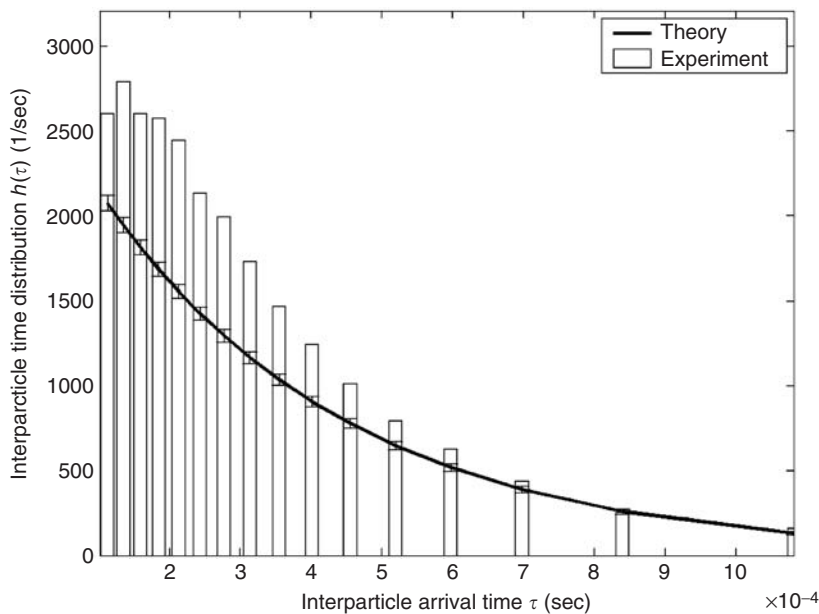


FIGURE 8.42 Drop clustering: experimental vs. theoretical data.

determine the theoretical interparticle time distribution, the spray is modeled as a marked inhomogeneous Poisson process. The Poisson process is described by the intensity function λ that represents the expected number of particles to be sampled per unit time. The theoretical finite interparticle time distribution is

$$h_{\text{th}}(\tau_j) = \frac{\lambda^2(T - \tau_j)\exp(-\lambda\tau_j)}{\lambda T - 1 + \exp(-\lambda T)} \quad (8.82)$$

The theoretical interparticle function is compared with the experimental interparticle distribution function and a decision on spray steadiness or unsteadiness is made based on the statistical analysis using the χ^2 tests to get the significance level (Luong and Sojka, 1999).

Figure 8.42 illustrates a sample comparison between experimental data and theoretical steady interparticle time distributions. The data were taken 100 mm downstream of a pressure atomizer (flat sheet cone) on the spray center line for a liquid mass flow rate of 0.05 kg/min. The bars represent the experimental data in discrete time bins. The solid curve represents the theoretical value, where the error bars show the expected scattering of the theoretical results due to the random nature of a theoretical spray. The experimental interparticle time distribution differs for the first bins from that of the steady theoretical case (e.g., by more than 12 deviations for the first bin). The χ^2 value = 307 shows the significance and that the two distribution functions are not different due to random fluctuations. For this case a high probability for having droplets at shorter interparticle arrival times is found, i.e., droplet clustering occurs in this spray (unsteady spray). Droplet clustering in spray will lead to significant changes in the main interphase transport mechanisms (momentum, heat, and mass, see Section 1.4.5), because here, the local bulk properties vary in between and outside of a droplet cluster.

8.2.2 Dilute Spray

The majority of spray investigations deals with the dilute spray region, where mainly gas–droplet interaction determine the spray behavior. A variety of sophisticated measurement instruments and experimental

and numerical techniques are used to investigate gas and droplet behavior details in this spray region. These include:

- nonintrusive laser diagnostic instruments for dispersed multiphase flows, such as PDA, diffraction particle sizer, particle – image and particle – tracking velocimetry, holography, laser-Induced-fluorescence, and others (see [Chapter 14](#) for measurement techniques)
- Numerical models, based on Euler–Lagrange techniques, Euler–Euler techniques (two-fluid models), Direct – Numerical - or LES (Bellan, 2000), (Bergström et al., 1999), pdfs among others (see [Chapter 13](#) on modeling)

These numerical and experimental techniques have contributed to the understanding of multiphase transport processes in sprays. Parameters describing the dilute spray structure identify the behavior of the droplets in the spray, the interaction with the gas phase, and the macrostructure of the spray development. These results typically are specific for the spray application under investigation (medium, atomizer type, operational parameters etc.)

8.2.2.1 Individual Droplet Behavior

The behavior of (individual) droplets in the gaseous atmosphere, such as in a spray, is substantially based on aerodynamic and gravitational forces acting on the particles, balanced by the inertia of the droplets (see [Chapter 1.4](#)). Based on a one-dimensional numerical analysis using the droplet trajectory equation (without coupling effects)

$$m_p \frac{du_p}{dt} = m_p g - \frac{1}{2} \rho_g (u_p - u_g) |u_p - u_g| A_p C_d \quad (8.83)$$

a principal investigation for the droplet behavior in a spray such as the identification of different atomizer nozzle characteristics is possible. Fritsching and Bauckhage (1987) analyzed the interaction of droplets and the surrounding gas phase in a water spray as a function of the distance from the nozzle for single-fluid (pressure) and twin-fluid (gas) atomizers. Measurement results of droplet velocities and sizes on the spray center line measured by PDA have been used for comparison with the one-dimensional model. The two nozzle types and their respective dimensions have been chosen by the criterion of comparable droplet size and velocity spectra in the spray.

For the uncoupled solution of the droplet trajectory an assumption for a velocity distribution of the gas phase is necessary. This boundary condition has been determined from PDA measurements of droplet velocities of the smallest detected droplets in the spray based on an assumption that these droplets act as tracer particles and the local gas velocity equals the measured droplet velocity (zero-slip velocity). The initial droplet (starting) velocity value has to be prescribed. For the twin-fluid nozzle it has been assumed that the initial velocity of the droplets equals the liquid feed velocity from the nozzle. For the pressure atomizer, a constant initial velocity for all droplet size classes has also been assumed. Its value has been obtained by extrapolating the droplet velocities measured for the largest droplet size class detected from the first measurement location in front of the nozzle backward to a common starting location for the droplets in the vicinity of the nozzle.

In [Figure 8.43](#) a comparison between the model results and measurement results (these have been averaged over a certain drop size class) for the pressure atomizer is illustrated. The dash-dotted line in front of the figure indicates the derived distribution of gas velocity as a function of nozzle distance $v_l(z)$. The figure shows that smaller droplets in the spray, immediately after fragmentation, lose their initial momentum carried from the liquid delivery. This initial momentum is directly transferred to the slow moving (entrained) gas. Further downstream these smaller droplets move at almost the same velocity as that of the gas (The relative velocity between droplet and gas is the constant droplet settling velocity). The bigger droplets are decelerated comparatively more slowly. Therefore, a continuous momentum transfer from the droplets to the slower moving gas occurs. The velocity distribution exhibits strong gradients dependent on droplet size in the nozzle vicinity, while at increased nozzle distances the velocity distribution for all droplet sizes becomes uniform.

In the twin-fluid atomizer spray a change in the direction of momentum transfer occurs. This is to be seen in [Figure 8.44](#). Close to the atomizer the faster moving atomizer gas accelerates all droplets comparatively

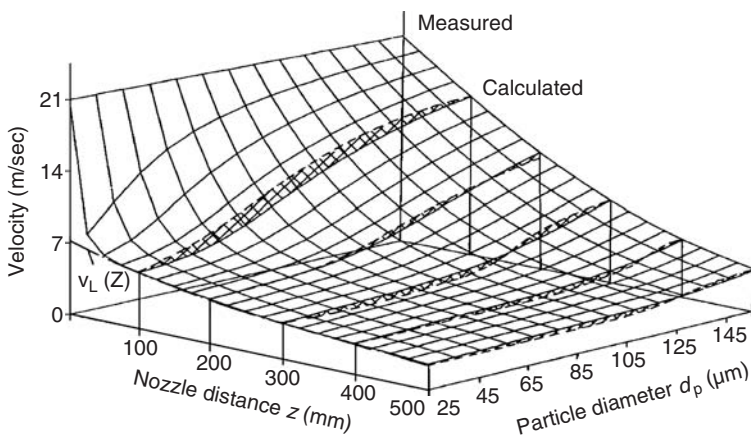


FIGURE 8.43 Drop velocity on spray center line: pressure atomization. (From Fritsching, U. and Bauckhage, K., *Chem.-Ing.-Tech.*, 59, 744–745, 1987. With permission.)

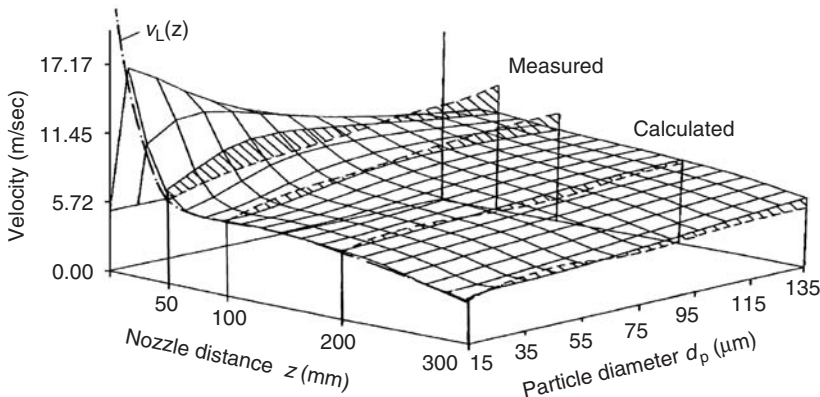


FIGURE 8.44 Drop velocity on spray center line: twin-fluid atomization. (From Fritsching, U. and Bauckhage, K., *Chem.-Ing.-Tech.*, 59, 744–745, 1987. With permission.)

depending on the size. The direction of the momentum transfer is always from the gas to the slower particles. Therefore, the gas loses a significant amount of kinetic energy within a small distance from the atomizer. At a certain distance from the atomizer the direction of momentum transfer is reversed. At larger nozzle distances, all droplets are moving faster than the gas and the direction of momentum transfer is from the droplets to the gas. The droplets in this area accelerate the gas. The point where the momentum transfer changes direction depends on the droplet size. While the smaller droplets already exhibit this change of momentum transfer closer to the atomizer due to their smaller inertia, the bigger particles change the momentum transfer direction at a larger nozzle distance.

By comparing the characteristics of these nozzle types, a common characteristic for technical spray processes can be seen. When the aim of the atomizer application is the achievement of almost identical droplet velocities at a specific distance from the atomizer (e.g., for coating application), this behavior is achieved much closer to the atomizer for the twin-fluid atomizer. In addition, the reversal of the momentum transfer direction has to be recognized as an important feature of twin-fluid atomizers.

An important property of a droplet spray is the correlation of drop sizes and velocities. This leads to a two-dimensional distribution of drop properties in sprays. Typical behavior of a drop size–velocity

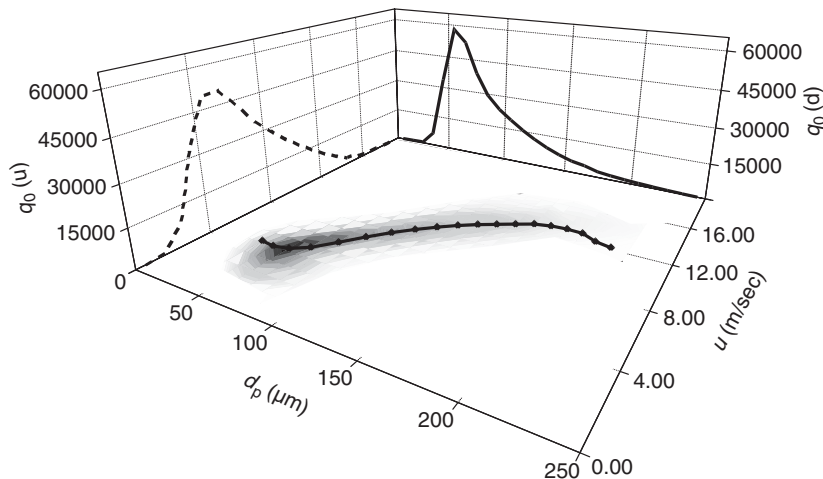


FIGURE 8.45 Drop size vs. velocity correlation in spray. (From Schulte, 1994. With permission.)

correlation at a single point in the spray of a pressure atomizer is illustrated (from a simultaneous measurement of drop size and velocity by PDA) in Figure 8.45 (Schulte, 1995). In the ground plane of the plot, the measurement result of several thousands of individual particles is shown (individual droplet size and velocity), while at the two sides of the plot, the integration in terms of number frequencies of drop sizes and velocities is illustrated.

8.2.2.2 Spray Cone Spreading

The spray cone angle describes the macro geometry of a spray. Different atomizers yield different spray characteristics, for example, flat, round, or hollow cone. The spray cone angle initially is determined by the liquid exit condition, the main disintegration mode within primary fragmentation (and here the growth rate of asymmetrical disturbances), later on by gas turbulence effects (particle dispersion), interaction with the ambient air (gas entrainment), and finally gravity.

Within pressure swirl atomization, as discussed earlier in Section 8.1.5.1, by assuming an inviscid liquid, the spray cone angle is expressed as a function of the nozzle dimensions only. The half cone angle is (Giffen and Muraszew, 1953)

$$\sin \Theta = \frac{(\pi/2)C_D}{K_1(1 + \sqrt{X})} \quad (8.84)$$

For a simplex pressure atomizer with a full spray, the work of Reitz and Bracco (1979, 1982) concluded that the spray angle can be determined by combining the radial velocity of the fastest growing unstable waves in the primary fragmentation process with the axial injection velocity. This hypothesis results in an expression for the spray angle that was later simplified by Bracco et al. (1985) in the form

$$\tan \Theta = \frac{2\pi}{\sqrt{3}A} \left(\frac{\rho_g}{\rho_l} \right)^{0.5} \quad (8.85)$$

where A is a function of the orifice length to diameter ratio that must be experimentally determined (Lefebvre, 1989).

The distribution of the sprayed liquid mass in the spray cone is described by the mass flux distribution. Adopting the concept of self-similarity from a single-phase jet, the droplet mass flux distribution in a spray may be described. In full cone sprays, this can be expressed in terms of a general empirical formula as (Uhlenwinkel, 1992):

$$\frac{\dot{m}}{\dot{m}_{cl}} = e^{-k_1(r/r_{0.5})k_2} \quad (8.86)$$

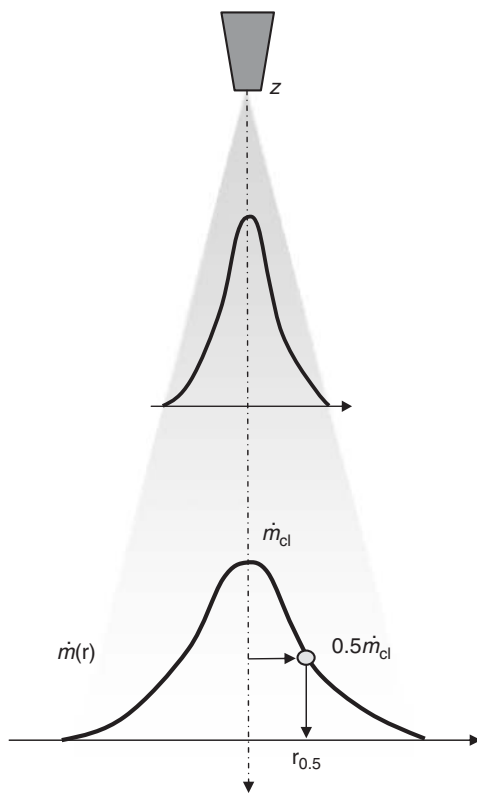


FIGURE 8.46 Mass flux distribution in sprays.

where \dot{m}_{cl} is the maximum value of the mass flux distribution function on the spray center line and $r_{0.5}$ is the half-width of the mass flux distribution (see Figure 8.46). The proposed empirical constants have been given as $k_1 = \ln(2.0)$ and $1.2 < k_2 < 2.0$. The constant k_2 depends on operational process conditions and liquid properties. The spreading behavior of the spray cone may be described either by a function of the mass flux on the center line or by the distribution of the half-width of the mass flux distribution versus nozzle distance, which for a Gaussian type distribution is

$$r_{0.5} = \sqrt{k_2 \frac{\dot{M}_l}{\dot{m}_{cl}}} \quad (8.87)$$

The behavior of the center line mass flux has been empirically correlated by Uhlenwinkel (1992), and Kramer (1997)

$$\dot{m}_{cl} \approx z^{-k_3} \quad (8.88)$$

For water sprays, Uhlenwinkel (1992) has found $k_3 \approx 2$ while for metal melt atomization Kramer (1997) found $k_3 < 2$. Spray cone spreading (namely the coefficient k_3) depends on atomization parameters. For water atomization, the spreading of the spray increases with higher gas flow rates while for metal melt the reverse trend is observed. In this case, the spray cone width narrows when the gas mass flow rate increases with higher pressure (Uhlenwinkel, 1992).

8.2.2.3 Spray–Environment Interaction, Entrainment

The spray system interacts with the environmental gas. Similar to a single-phase jet, it accelerates the ambient gas due to friction (entrainment). Thereby, the plume of the dispersed phase (the droplet spray) maintains a narrower width than the complete flowing gas jet (see Section 8.4.2.1).

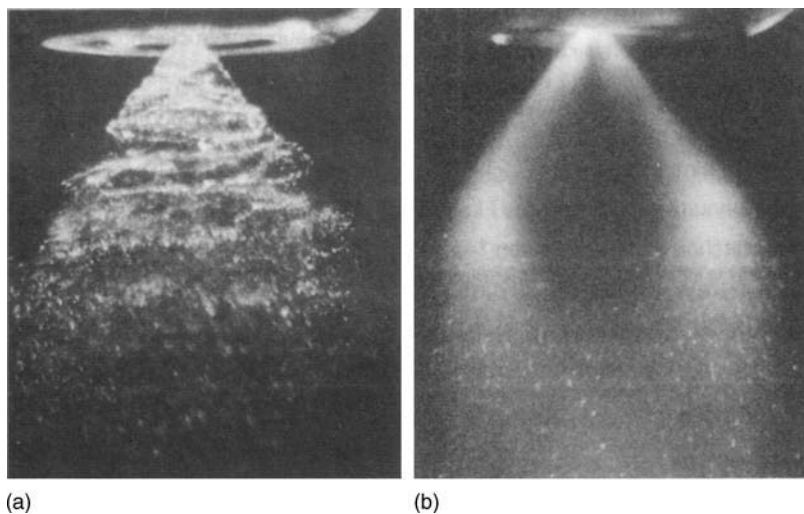


FIGURE 8.47 Spray from pressure swirl atomizer: (a) short; (b) long time exposure, droplet entrainment in hollow cone spray. (From Lampe, K., Dissertation, Universität Bremen, 1994. With permission.)

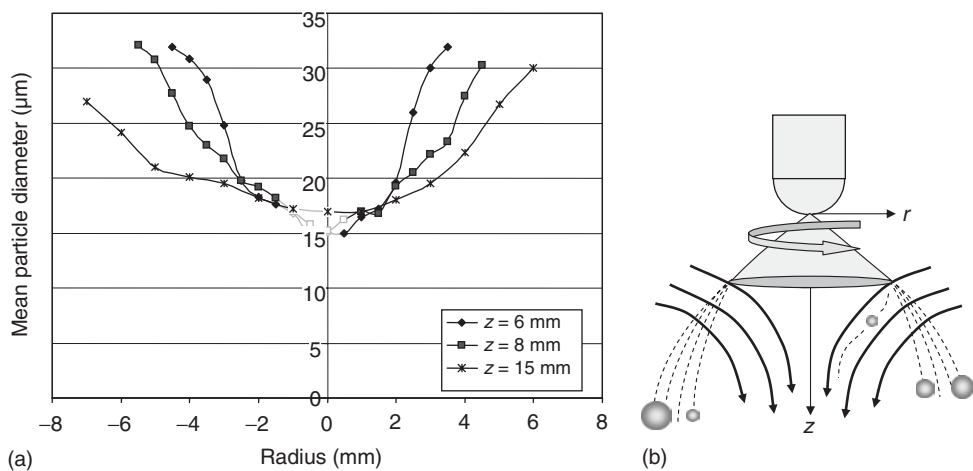


FIGURE 8.48 Gas and droplet entrainment in hollow cone spray: (a) drop size distribution, (b) spray sketch. (From Lampe, K., Dissertation, Universität Bremen, 1994. With permission.)

The spray–gas interaction and gas entrainment may lead in some cases to a change in the spray structure with an increase in distance from the atomizer, namely a drop size segregation. Generally, this effect is pronounced in pressure atomizers; as in this case the entrainment effect is strongest, and is typically found in pressure swirl atomization. Here, due to the entrainment of ambient gas into the initially hollow-cone spray, droplets are accelerated and transported into the core region of the spray (see Figure 8.48). The primary hollow-cone structure changes to a solid cone with an increase in spray distance. Figure 8.47a illustrates the change as a short exposure view onto the spray (instantaneous structure) from outside in comparison with a light-sheet illumination of the central plane of the spray in Figure 8.47b. Owing to lesser inertia, smaller droplets are more easily transported into the spray core than bigger drops. Here, a size segregation effect follows, where the droplet size distribution in the spray is changed, typically as shown in Figure 8.48b. As an example, in Figure 8.48a, PDA data are presented as radial distributions of the arithmetic number mean of the measured droplet size distribution at several planes below

the atomizer. With an increase in spray distance, the edge of the spray shows an increase in drop sizes, while in the spray core the smaller droplets are more prevalent.

The total spray–gas entrainment rate depends on the atomizer type. With twin-fluid atomization, entrainment can be estimated based on the overall gas flow rate in circular, turbulent jet, and the distance from the nozzle. The ratio of the total gas flow rate to the initial jet flow rate is a linear function:

$$\frac{\dot{Q}_{\text{total}}}{\dot{Q}_0} = \text{constant} \frac{x}{d_0} \quad (8.89)$$

The constant is 0.4565 calculated from the analytical solution for a turbulent jet and varies from 0.30 to 0.45 in experimental and simulation studies of single- and two-phase jets and spray flows.

8.2.3 Heat and Mass Transfer

Fundamentals of heat and mass transfer from droplets in gases have been derived in Section 1.4.2 and 1.4.4. Heat transfer mechanisms are important in melt atomization and spray processes (see [Section 8.4.2](#)). Simultaneous heat and mass transfer is important in coating applications (e.g., paint sprays) or spray drying processes (see [Section 8.4.3](#)).

As a liquid droplet spray comes in contact with hot atomization gas, three transfer mechanisms (mass, momentum and energy) become operative simultaneously. By applying spray drying processes, Crowe (1980) and Crowe et al. (1998) described these transfer mechanisms. At the droplet–hot air interface, heat is transmitted into and moisture is transmitted out of the droplet surface. The external transfer of mass or heat can be obtained from

$$\Phi = kA\Delta X \quad (8.90)$$

where k is the transfer coefficient, A the particle surface area, and ΔX the driving potential. The transfer is described by the Nusselt number, Nu , for heat transfer and Sherwood number, Sh , for mass transfer, and can be obtained from the following correlations (Ranz and Marshall, 1952)

$$Nu = 2 + 0.6Re^{0.5}Pr^{0.33} \quad (8.91)$$

and

$$Sh = 2 + 0.6Re^{0.5}Sc^{0.33} \quad (8.92)$$

This correlation has been extended for turbulent effects by Yearling and Gould (1995) (see also Clift et al., 1978). The driving potential ΔX for heat transfer is the temperature difference between droplet and surrounding air, and for mass transfer the vapor concentration difference between the surrounding air and the vapor film on the droplet surface (Delplanque and Sirignano, 1994).

8.2.3.1 Drop Evaporation and Solidification

8.2.3.1.1 Drying Mechanism of a Dispersed Droplet

Most feed materials in a spray-drying application are dispersed liquids (colloidal or suspension). Drying of a dispersed liquid droplet may yield a porous-solid shell (or crust) on the droplet skin that significantly changes heat and mass transfer rates compared with those of a pure liquid droplet. When the crust formation begins, the internal mass transfer rate through the porous-solid shell becomes the controlling factor for evaporation.

Dolinski (2001) described the drying mechanism of a dispersed material in high-temperature gas streams ($T_{\text{air}} > T_{\text{boil}}$). From the analysis of experimental data, five successive drying periods have been identified (see [Figure 8.49](#)).

1. The period of droplet heating from its initial temperature T_0 up to the temperature of equilibrium evaporation T_{eq} .
2. The period of equilibrium evaporation during which intense removal of moisture from the liquid droplet surface occurs. The period of equilibrium evaporation (t_{cr1}) ends when the solid content

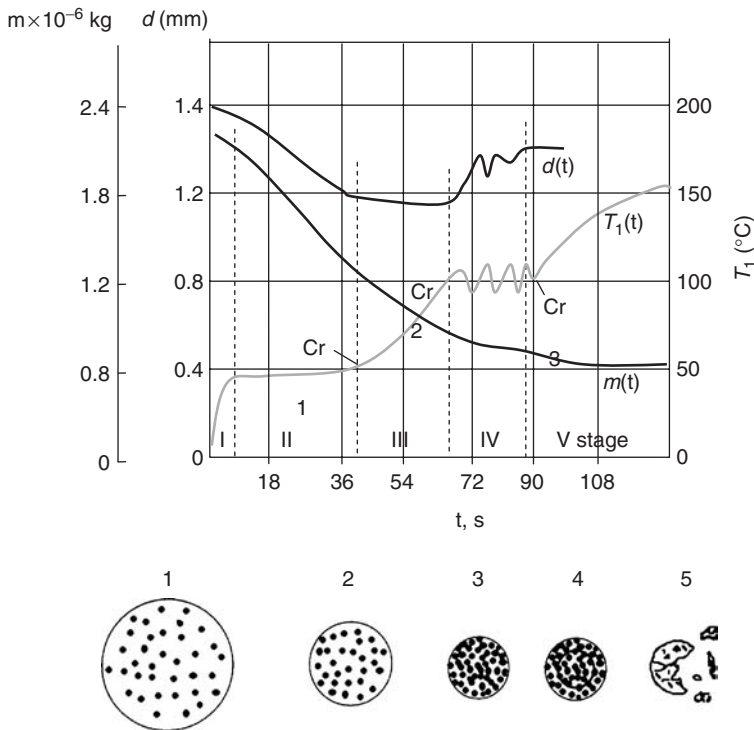


FIGURE 8.49 Successive drying periods of a suspension droplet, variation of diameter, temperature and mass in a hydration process. (Adapted from Dolinski, A.A., *Drying Technol.*, 19, 785–806, 2001.)

on the drop surface is increased to the point that a shell is formed on the surface of the evaporating droplet.

3. The period of crust formation when the droplet temperature increases sharply due to the formation of the dense shell made from dispersed substance.
4. Boiling period: the temperature inside the particle reaches the boiling point and steam is generated.
5. Drying period: The particle temperature sharply increases almost to the temperature of the hot gas. During this period removal of the bound moisture occurs. Fragmentation may also occur in this period.

Mathematical models permit analysis of the evaporation process at the different stages of a drying droplet. Typically in these models a plug flow of air, no droplet deformation, and no droplet–droplet and droplet–wall collision are assumed. The concentration of average volume at the moment of crust formation, when the equilibrium drying stage ends is given by

$$C_s = \frac{C_{\text{sat}}[C_0 + 3Ki(C_{\text{sat}} - C_0)]}{C_{\text{sat}} + 3Ki(C_{\text{sat}} - C_0)} \quad (8.93)$$

where Ki is Kirpichev number

$$Ki = \frac{D_1 \rho_1}{D_2(\gamma_s - \gamma_c)} \quad (8.94)$$

The coefficients C_0 and C_{sat} are the initial and saturation concentration of the solution in an average volume, respectively. D_1 and D_2 are the diffusion coefficients for water in solution and in gas, respectively. This crust-formation concentration is used as a criterion to distinguish constant drying rate period (stage 2) and falling rate period (stage 3). Mass transfer rate during crust formation has to be obtained experimentally.

Elperin and Krasovitov (1995) developed a model that takes into account effects of compressibility and filtration of the gas–vapour mixture within the porous shell. They used the critical volume ratio as crust formation criteria, which could be calculated from a minimum void fraction (ϵ) attained in packing of spherical particles:

$$\delta_c = V_s N_l = \frac{1 - \epsilon}{\epsilon} \quad (8.95)$$

The mathematical model, that takes into account porosity, permeability, surface tension of solid–gas, solid–liquid, and liquid–gas interface, effective thermal conductivity, and diffusion coefficient, is developed and solved numerically. A pressure balance equation at the liquid interface inside the particle is also included and investigated in this work. Numerical results showed that, at the ambient gas temperature above the liquid boiling point, the pressure at the liquid interface increased significantly and resulted in the fragmentation of the porous shell.

Straatma et al. (1991 and 1999) developed numerical drying models for food products, where crust formations are generally found. The drying models take into account both external and internal phenomena. The driving force for mass transfer (from Eq. [8.90] is expressed as

$$\Delta X = C_a^* - C_a \quad (8.96)$$

where C_a^* is the water vapor concentration, which is in equilibrium with the wet surface of droplet. In this work, the GAB equation (Guggenheim, Anderson and de Boer) was used to calculate C_a^* :

The unstationary diffusion process inside the spherical particles is described by the one-dimensional differential equation

$$\frac{\delta c}{\delta t} = \frac{1}{r^2} \frac{\delta}{\delta r} \left(r^2 D \frac{\delta c}{\delta r} \right) \quad (8.97)$$

The diffusion coefficient D depends on the moisture content and the temperature (Ferrari et al., 1989). The differential equation (8.97) is solved numerically in conjunction with external heat and mass transport equations (8.90–8.92) using the gas–liquid interface boundary condition and zero gradient boundary condition at the center ($r = 0$). The moisture content at various positions inside the droplet can be determined.

8.2.3.1.2 Solidification of a Melt Droplet

Solidification of a melt is described by the processes of nucleation and crystal growth. A droplet solidification process model typically is based on equilibrium phase diagrams for slow solidification and time-transfer phase change diagrams and experimental solidification investigations for some more realistic (higher) cooling rates. In fact, in spray processes, the cooling rate of droplets, especially immediately after atomization, might be very high (e.g., maximum 10^7 K/sec). Therefore, the possibility of undercooling prior to nucleation has to be considered. In [Figure 8.50b](#) a typical qualitative temperature–time distribution for a single melt droplet for an equilibrium phase diagram is shown. Here a low carbon steel droplet ($C = 0.3$ w%, shown in [Figure 8.50a](#)) is considered as an example. Starting with the initial melt temperature (superheat) T_m , the droplet cools down to liquidus temperature T_l . Depending on the actual cooling rate, the droplet may undercool until it reaches the nucleation temperature T_n before solidification starts. Due to the rapid release of latent heat of fusion during recalescence, the droplet temperature increases until it reaches a local maximum in the cooling curve at T_r . During the following segregated solidification, droplet temperature decreases continuously. At the temperature T_{per} in this specific case, a peritectic transformation takes place at a constant droplet temperature. After termination of the peritectic transformation, again segregated solidification occurs until the droplet is completely solidified at T_s . From here on, droplet cooling is in the solid state of the fully solidified particle. The droplet cooling behavior in the various stages of solidification is described based on thermal balances (internal and external). For metal droplets, typically no internal temperature gradient is assumed, as the Biot number Bi is small for most metal droplets ($Bi \ll 1$).

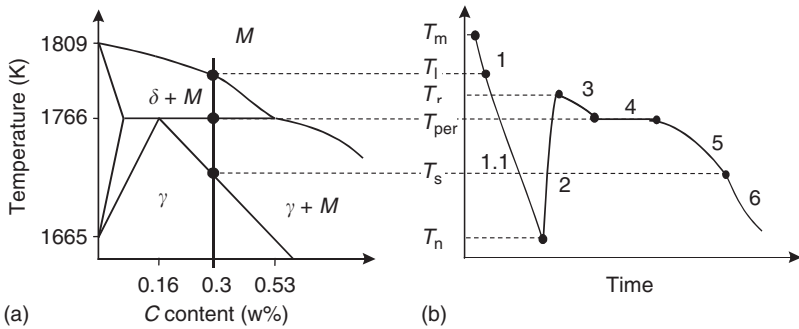


FIGURE 8.50 Solidification model for melt droplets (here low-carbon steel).

Depending on cooling rate and droplet size, the temperature T_n where nucleation occurs can be much lower than the liquidus temperature T_l . The nucleation temperature for continuous cooling is defined as the certain temperature, where the number of nuclei N_n in the droplet volume V_d is equal to 1

$$N_n = V_d \int_{T_l}^{T_n} \frac{J(T)}{\dot{T}} dT = 1 \approx \frac{0,01 J(T_n) V_d \Delta T_{hom}}{\dot{T}} \quad (8.98)$$

Here, $J(T)$ is the nucleation rate and \dot{T} the cooling rate (Lavernia, 1996); (Lavernia and Wu, 1996); (Pryds et al., 1999). Hirth (1978) has introduced the simplification in the above equation. ΔT_{hom} is the undercooling temperature difference for homogeneous nucleation. The nucleation rate may be expressed as (Libera et al., 1991)

$$J(T_n) = K \exp\left(-\frac{16\pi\sigma_{sl}^2 V_m^2 T_l^2}{3kT_n \Delta h_{fm}^2 \Delta T_{hom}^2}\right) \quad (8.99)$$

In the work of Turnbull (1950) and Woodruff (1973), a correlation has been given between the solid–liquid interfacial energy σ_{sl} , the latent heat of fusion per atom Δh_{fa} , and the atomic volume V_a . In technical processes, heterogeneous nucleation, rather than homogeneous nucleation mechanisms, limit the degree of undercooling (Libera et al., 1991). Homogeneous nucleation plays an important role during solidification only in very small droplets. Based on experimental results for different alloys, Mathur et al. (1989a, 1989b) derived a correlation between the actual undercooling and the amount of undercooling necessary for homogeneous nucleation (Libera et al., 1991; Levi and Mehrabian, 1982). Simulation of molten metal droplet sprays including solidification submodelling has been done by Lee and Ahn (1994), Bergmann (2000), Bergmann et al. (2000 and 2001), and Pedersen (2000) (see also Su and Tsao, 1997; Wang and Matthys, 1992; Voller et al., 1991).

8.3 Spray Impact

8.3.1 Drop Impingement

Drop impingement is an important process, for example, in coating and surface cooling applications. The different mechanisms for individual drop behavior during wall impact (e.g., deposition, rebound, or splashing) are introduced in Section 12.3.3. A main criterion for the different impact regimes is the impact liquid drop Weber number.

8.3.1.1 Spray Deposition

In impact related spray processes, the deposition rate (or the compaction efficiency) and the deposition mass flux distribution are important. An approach for deposition efficiency is given in Section 8.4.2.2.

8.3.2 Heat Transfer in Impinging Sprays/Spray Quenching

Spray quenching is used extensively in metal casting and welding processes as well as in heat treatment of metals such as aluminum, steel, and other metallic alloys. The combination of large droplet numbers (at small droplet sizes) and large droplet impact momentum are the key attributes of spray cooling, resulting in a significant increase in cooling efficiency per flow rate over other cooling techniques. Gas-assisted twin-fluid atomization typically is employed in the cooling of steel, while pressure atomizers are used in aluminum industry (Stewart et al., 1995).

During quenching or cooling of a metallic part, the surface experiences successively four different heat transfer regimes (from temperatures above the Leidenfrost temperature to room temperature): film boiling, transition boiling, nucleate boiling, and single-phase liquid cooling. The different heat transfer regimes are identified by the aid of the cooling curve (Nukiyama curve, see [Section 3.1](#)). Owing to the relatively high initial temperature, quenching of most metallic surfaces commences in the film boiling regime. Despite the possibility of a momentary contact of the liquid with the surface at the point of drop impact (see [Section 12.3.3](#)), a thermally insulating vapor layer quickly develops on the surface, resulting in a relatively slow cooling process. Better liquid-surface contact is maintained once the surface temperature reaches values below the Leidenfrost temperature (minimum heat flux point). In the transition regime, liquid maintains partial contact with the surface in region undergoing intense boiling while other regions remain insulated with vapor. The transition from film to boiling does not occur homogeneously across the metal surface, but strongly depends on local surface properties (e.g., geometry, and roughness). This significant variation and change in the local heat transfer rate across the specimen causes large stresses in the metallic part that may lead to undesired damage or distortion of the specimen. The intermittent contact in the transition boiling regime accelerates the cooling to a large extent. In the nucleate boiling regime, the surface becomes available for liquid-surface contact that accelerates the cooling due to vigorous bubble production and convection. Quenching is concluded in the slow, singlephase liquid cooling regime, where the wall superheat becomes too weak to sustain bubble nucleation (Mudawar and Deiters, 1994).

Several investigations have derived correlations for the heat transfer coefficient in the different boiling regimes, depending on atomizer type, spray conditions, and surface conditions. Among them, for example, Brimacombe et al. (1980), Bolle and Moureau (1982), Mudawar and Valentine (1989), Choi and Yao (1987), Viskanta and Incropera (1992), and Choi and Kang (1993) summarized the results of previous studies for steady-state and transient conditions in liquid and spray jets. Typically, correlations are presented for the heat flux or heat transfer coefficient in the spray center at different boiling regimes.

In the stable film boiling regime, the heat transfer coefficient, of an impinging (dense) spray is independent of the surface temperature. Here, the impinging liquid mass flux (in this context, occasionally referred as impingement density or spray density) has an effect only on heat transfer. Other spray parameters such as drop velocities and sizes as well as spray distance and nozzle type have a very small effect. Due to the continuous liquid film above the stable vapor film, individual droplets do not impinge directly onto the hot wall. In this region, Müller and Jeschar (1983) derived an equation for the heat transfer coefficient:

$$\alpha = 200 + 109.2\dot{m}_l \quad (8.100)$$

In the transition boiling regime as well as in the single-phase regime, the mean spray droplet size also influences the heat transfer process. In the nucleate boiling regime, the heat transfer coefficient has been found as a function of surface temperature alone, unaffected by variations in any of the spray parameters (Mudawar and Valentine, 1989). As in this contribution, it has been found that the spray boiling curve is insensitive to the type of metallic surface. Müller and Jeschar (1983) found a distinct influence of the metal type on heat transfer at temperatures below the Leidenfrost temperature. This effect has been attributed directly to the coefficient of heat penetration, which is influenced by the possible oxide layer formations.

With twin-fluid atomization of water for cooling purposes, when the liquid mass flow rate is decreased by about one order of magnitude to the aforementioned regime, a dilute spray situation results and individual droplets impinge onto the hot liquid surface. Rather than coalescing to a liquid film (with the

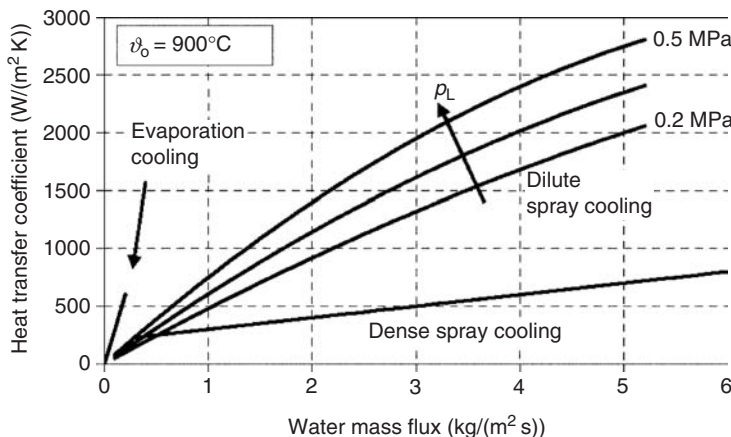


FIGURE 8.51 Heat transfer coefficient in spray cooling. (From Puschmann, F., Dissertaion, Universität Magdeburg, 2003.)

associated vapor film between liquid and hot solid), the individual droplets either evaporate directly in the liquid–solid contact phase or are blown away by the gas flow field after rebouncing. Therefore, the heat transfer is increased in a range between the conventional spray cooling and a pure evaporative cooling (Choi and Yao, 1987; Puschmann et al., 2001; Puschmann, 2003). The total heat transfer rate in dilute spray cooling is a combined effect of heat transfer during drop contact and heat transfer due to the gas flow field. Also, in this dilute spray quenching, the heat transfer is controlled mainly by the liquid mass flux. Drop size and velocity distribution in the spray play only a minor role. Puschmann (2003) correlated his experimental results based on an investigation of liquid–solid contact time for evaporating single droplet impact (Wruck, 1999) by:

$$\alpha = \dot{m}_l u^{0.12} d^{-0.29} \quad (8.101)$$

For twin-fluid atomization in this dilute spray regime, the heat transfer is also influenced by the atomizer gas flow rate. In Figure 8.51, the result of dilute spray quenching (Puschmann, 2003) is shown. The heat transfer coefficient of dilute spray quenching, is higher than that for spray quenching, but lower than that for evaporation quenching. The dependency of heat transfer on atomizer gas pressure is explained by changing the spray characteristics with respect to drop size and drop velocity (Puschmann, 2003); hence, the impact Weber number.

8.4 Spray Applications

8.4.1 Energy Conversion–Spray Combustion

Spray combustion is a process found in stationary power generation, gas turbines, and internal combustion engines. The combustion of a liquid (or liquid–solid slurry) fuel spray is either a simultaneous or sequential complex process involving fluid dynamics of liquid and gas, heat and mass transfer, and chemical reactions (Williams, 1990; Warnatz et al., 1996). The combustion of individual droplets and groups of droplets is presented in Section 12.7. From atomization, the fuel is present in the form of discrete liquid droplets, which have a range of sizes, velocities, and trajectories. This lack of uniformity in the unburnt mixture results in irregularities in the ignition and propagation of the flame through the spray and thus the combustion zone is poorly defined geometrically.

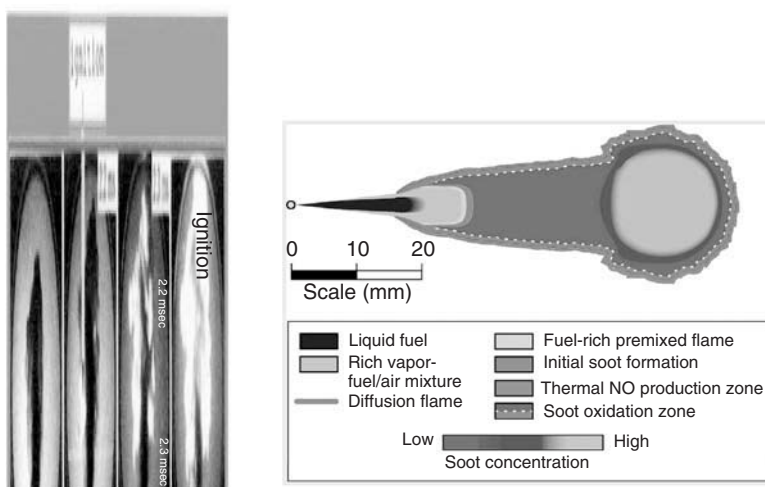


FIGURE 8.52 (Color insert follows page 13-40) Diesel spray flame: photo of injection and ignition, principal stationary flame structure. (From Tao, F., Ph.D. thesis, Chalmers University of Technology, Sweden, 2003.)

8.4.1.1 Fuel Injection

Direct fuel injection (DI) is applied in diesel and autocombustion engines (Heywood, 1998). From a first spray analysis, this process is defined as transient high-pressure injection and atomization of a liquid jet. The resulting spray is externally (spark) or self-ignited (diesel). The principal structure of a “developed” DI diesel flame is depicted in Figure 8.52 as derived in Dec (1997). The sketch shows conceptually how DI diesel combustion develops prior to the end of fuel injection. After the liquid fuel leaves the injector and travels downstream, it atomizes into the droplet spray, entrains hot ambient air, and vaporizes rapidly forming a sheath-like fuel-air mixture along the sides of the jet. Due to the penetrating nature of the injected liquid jet, macroscopically a mushroom-like spray structure occurs. The liquid spray penetrates a short distance, at which the vaporized fuel and entrained air form a relatively uniform, rich mixture. The flame fed by the mixture stabilizes at a certain distance from the nozzle as long as the fuel injection continues. Several zones of chemical reaction product formation are found in the spray flame. Soot particles are formed and distributed throughout the cross-section of the flame zone and then oxidized in the diffusion flame layer due to the attack of OH and O radicals. NO is formed around the jet periphery on the lean side of the diffusion flame (Tao and Chomiak, 2002). DI diesel combustion is a complex phenomenon in which relevant subprocesses of spray, flow, heat transfer, mass transfer, and chemistry take place over a wide span of timescales. For example, within the sheath near the nozzle at relatively low temperature, the chemical time scale is of the order of 10^0 sec, while in the high-temperature zone chemical reaction timescales span over several orders of magnitude, from about 10^{-6} to 10^0 sec.

8.4.1.1.1 DI Diesel Injection

Typical operating parameters of a DI diesel injection spray in a cylinder are fuel injection pressure up to 200 MPa, injection fuel mass ~ 5 to 50 mg, injection duration of the order of 1 msec, liquid jet diameter (hole size) about 100 μm , resulting in SMD droplet sizes of around 10 μm (Tschöke and Leyh, 2003; Spicher, 2001). Two different systems for pressure generation are used; the in line pump system (called unitinjectionssystem [UIS]), where each cylinder is connected to and fed by an individual pump and the common rail system (CRS), where pressure generation and liquid injection are separated as the pressurized fuel is kept at high pressure. An advantage of the CRS is that the injection pressure value as well as the injection time characteristics (initial time, preinjection, maininjection, and postinjection) may be managed electronically, depending on the actual engine load. Multihole nozzles are applied at the tip of an injector as illustrated in Figure 8.53. Two main nozzle configurations are used, namely, valve covered orifice (VCO) and mini-sac

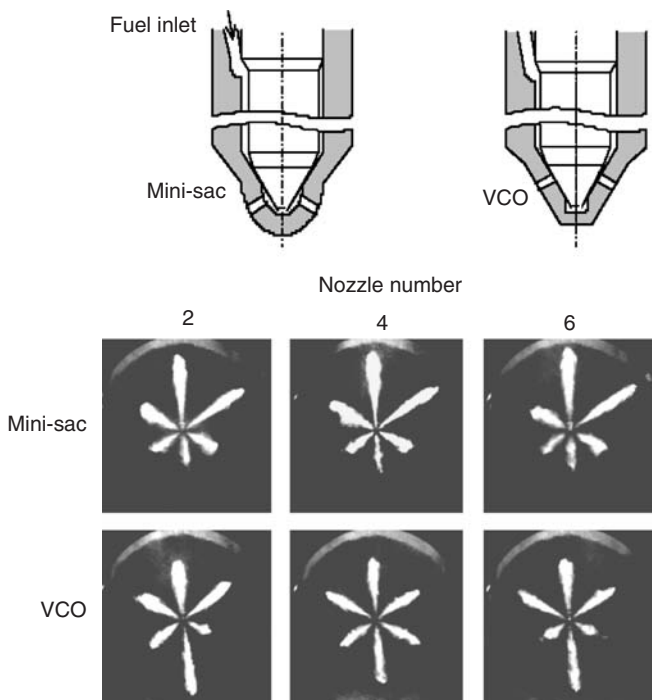


FIGURE 8.53 Nozzle configurations in high-pressure diesel injection systems: valve-covered orifice and mini-sac nozzle; samples of sprays from high-pressure injection. (Adapted from Tsunemoto et al., *Proceedings of the 5th International Symposium on Diagnostics and Modeling Internal Combustion Engines*, Nagoja, Japan, 2001.)

nozzles. Samples of the injection sprays from these configurations are illustrated in Figure 8.53 (Tsunemoto et al., 2001). These authors deduced that the spray configuration deviations in the VCO nozzle sprays are larger than in the mini-sac nozzle sprays. Eccentricity of the needle valve as well as slight deviations in hole production deviations may cause asymmetrical spray behavior (from hole to hole and from cylinder to cylinder). The deviation between individual nozzles decreases when the injection pressure increases. These have been identified as sources of emission.

The detailed flame zone structure of a DI diesel spray during combustion may be studied by numerical simulation, which is based on the analysis of transient spray development and drop evaporation (see, e.g., Hohmann, 1999). One of the key modeling issues in spray combustion is the complex turbulence–chemistry interaction and the formulation of equation closure for mean reaction rates. Typical numerical engine spray combustion studies (Ramos, 1989) use simplified models such as the eddy breakup model (EBU) (Spalding, 1971), the eddy dissipation concept (EDC) (Magnussen and Hjertager, 1989), models such as flamelet models (Kong et al., 1995; Wan et al., 1997) or the “subgrid” partial stirred reactor (PaSR) model (Karlsson, 1995; Tao, 2003). The latter has been used to calculate a diesel flame as reported in Tao (2003) and Tao and Chomiak (2002). The KIVA-3 code (Amsden et al., 1989) has been modified to include the complex chemical mechanisms based on *n*-heptane kinetics, where 65 species and 273 elementary chemical reactions are taken into account. Autoignition and lift-off of the flame are calculated in the simulation. The calculated transient diesel spray formation, autoignition, and flame development processes are illustrated in Figure 8.54 as temperature contours in the spray flame between 1 and to 4 ms after injection has started. The fuel jet penetrates deeply into the hot, highly compressed (5 MPa) air before autoignition. The ignition occurs in a fuel-lean premixed region at the side of the jet, downstream from the exit of the nozzle at about 2 msec after injection has started. Following that rapid development of the ignited hot spot leads to a flame propagation toward the axis of the fuel jet, modifying the pattern of the jet penetration. Then, the flame propagates upstream and downstream

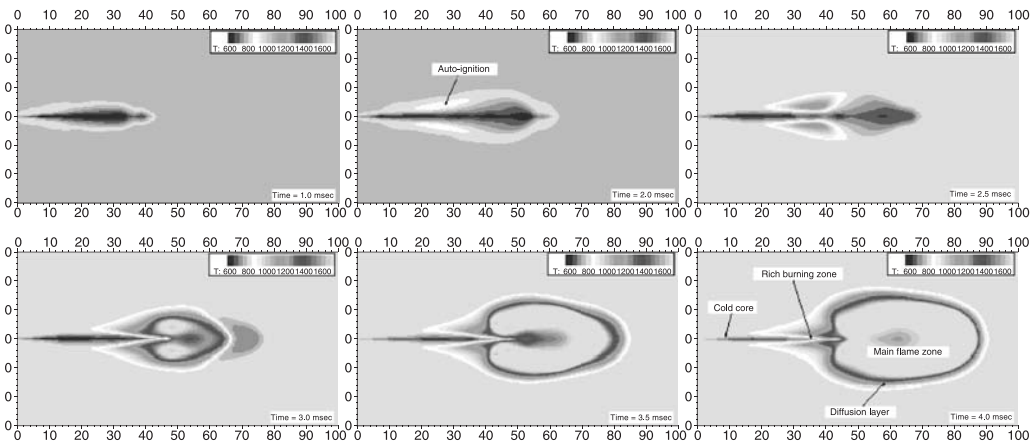


FIGURE 8.54 (Color insert follows page 13-40) Simulation of a DI-diesel spray flame and temperature contours. (From Tao, F., Ph.D. thesis, Chalmers University of Technology, Sweden, 2003. With permission.)

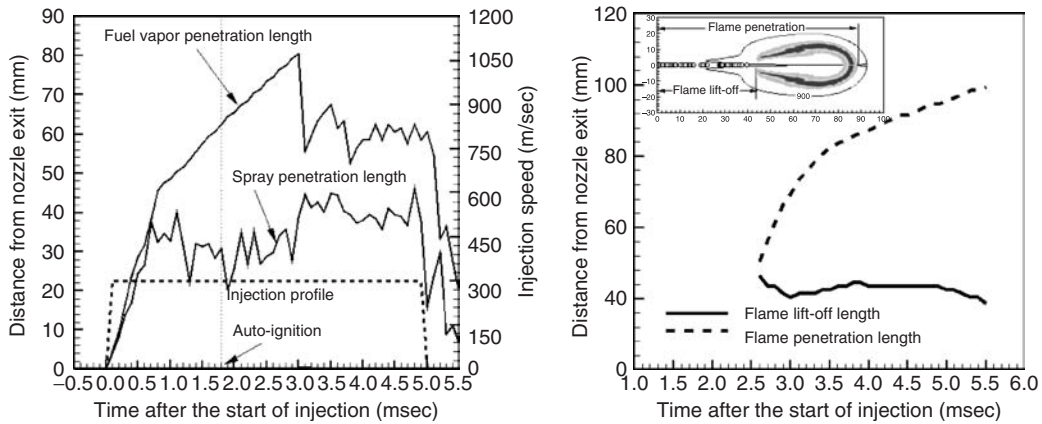


FIGURE 8.55 Flame structure in DI-diesel spray flame and spray and fuel vapor penetrations. (From Tao, F., Ph.D. thesis, Chalmers University of Technology, Sweden, 2003. With permission.)

and finally its development becomes “quasi-steady”, stabilizing on the top of the jet. This flame feature is retained until the end of the injection. The spray and fuel vapor penetrations are plotted in Figure 8.55a and b. The plot shows that, even after autoignition, the spray penetration does not vary much and its length remains constant until the end of the fuel injection process. The quasi-steady flame zone structure may be subdivided into (1) a cold core zone, (2) a fuelrich burning zone, (3) a main flame zone, and (4) a lean, thin oxygen diffusion layer. In the cold core region, the combined effect of high-velocity gradients and evaporation cooling prevents the flame from propagating upstream to the nozzle exit. The leading edge of the flame, located on the lean side of the stoichiometric surface, stabilizes at a considerable distance downstream from the nozzle. This distance is referred to as the lift-off length of the diesel flame, distinguishing the cold zone from the fuel-rich burning and main combustion zone. From the transient reaction analysis in these zones, emission formations as soot and NO_x in the flame are deduced.

In addition to the model combustion flame configuration discussed earlier, in car engine applications, the three-dimensional interaction of the injected spray with the cylinder-piston geometry and the interaction of fuel droplets with the hot walls during impingement play an important role (Lee and Ryan, 2001).

8.4.2 Metallurgical Processes

8.4.2.1 Metal Powder Production

Powders of different metals and alloys are produced by melt atomization. The amount produced in industries vary from a few kilograms to a million ton per year (for a single facility), from the production of dental amalgams to steel or iron shot (Yule and Dunkley, 1994). Particle sizes vary from micrometer (e.g., for corrosion protection paints) to millimeter (e.g., for shot blasting). Depending on the application, the desired particle shape may also vary from spheres and aggregates to fibers and flakes. These shapes can be achieved by variation in atomizer type, cooling conditions, and atomization liquid. Samples of metal particles produced by atomization are illustrated in Figure 8.56. The width of the particle size distribution ranges from single size particles to large values. The rapidly quenched metal powders (at high cooling rates of 10^4 to 10^7 K/sec) from spray processes may exhibit specific material compositions and properties, due to fine grain sizes or even amorphous metallographic structures.

A major use of metal powders is in manufacturing of complex-shaped mechanical components such as by sintering or (hot or cold) isostatic pressing. In metal injection moulding, fine metal powders are blended with a resin or binder to be pressure-injected into a mould, where the resin is removed later. Thermal spraying is a coating technique that uses ceramic or metal powders as feed materials.

Twin-fluid atomization is by far the most common atomization technique for metal powder production, as it achieves a high yield. When using oil or water as atomization media, the particle shape is non-spherical, while gas atomized powders show spherical shape. With water atomization generally higher mass flow rates can be achieved. Gas atomization is typically performed by inert gases prevent oxidation (or also vice versa, by partial or full oxygen content for controlled oxidation of the material). Twin-fluid atomized powders are in the size range from 10 to 500 μm at a distribution width (standard variation) of about 2.

For specific applications, metal powder production via atomization is also achieved by rotary or centrifugal atomizers (Halada et al., 1990), metal atomization by means of ultrasound (Andersen et al., 1995; Bauckhage and Fritsching, 1995) in laminar supersonic flows (Gerking, 1993), or by controlled pulses (Henein, 2002) to produce a narrower width of the size distribution. A general overview on atomization

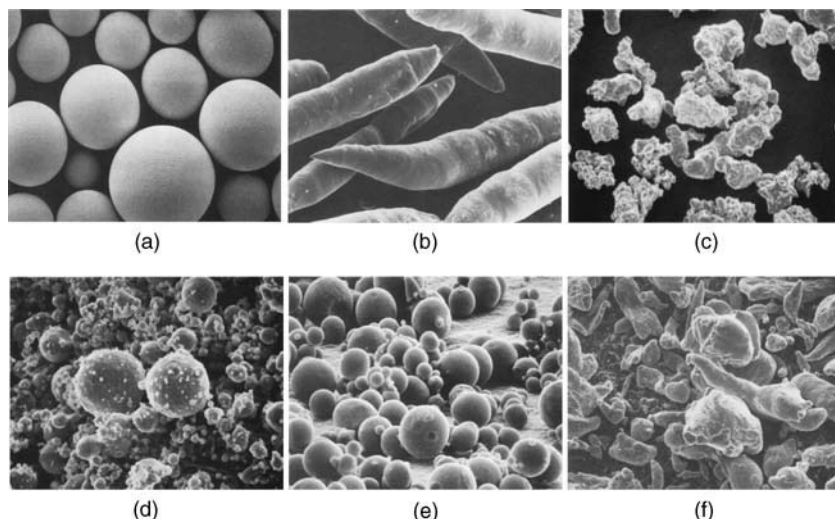


FIGURE 8.56 Particle shapes in molten metal atomization processes. Upper panel: (a) René 95 superalloy powder, produced by the plasma rotating electrode process; (b) aluminum needles produced by rotary atomization with perforated cup; (c) copper particles, produced by twin-fluid atomization with water, Lower panel: (d) aluminum powder, gas atomized with helium; (e) IN-1000 superalloy powder, pressure-atomized; (f) aluminum powder, gas-atomized with air. (Adapted from Huppmann, W.J. and Dalal, K., *Metallographic Atlas of Powder Metallurgy*, Schmid, Freiburg, 1986.)

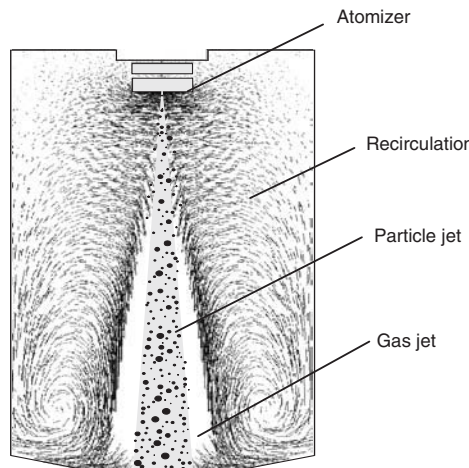


FIGURE 8.57 Flow field in a spray chamber for powder production, simulation result.

techniques for metal powder production is found in Klar and Fesko (1984), Yule and Dunkley (1994), Lawley (1992), Bauckhage (1992), Dunkley (1998), Nunez et al. (1999), and Liu (2000).

In molten metal atomization, the specific atomizer design is typically more complex than that for conventional liquids. Molten metals need to be superheated above liquidus for feeding into the atomizer. Here, these materials become chemically active, and chemical reactions and erosions with the containing material in the crucible or tundish may occur. Thermal losses, especially in combination with cold atomization media such as gas, can lower the melt temperature locally below its specific liquidus temperature, which may cause solidification and thermal freezing problems of melt atomizer nozzles, influencing the whole process. In this case, local isolation and heat sources in combination with suitable materials have to be applied. Molten metals typically have a high density, high surface tension, and low viscosity, also affording specific measures to achieve a proper disintegration process. The spray structure in metal atomization is governed by the gas–drop interaction, in combination with the high heat transfer between the hot melt and (usually) cold environment.

The principal two-phase flow field in a typical powder production chamber employing gas atomization obtained by numerical simulation is illustrated in Figure 8.57. The flow is subdivided into three regions (Connelly et al., 1986): (a) the droplet spray in the core, surrounded by the gas jet (b) and a recirculation zone (c) in the outer area of the spray chamber. Typically, within the recirculation zone, a large amount of fine particles swirl around in the spray chamber (dust formation). Here, preferably, the fine particles are to be found due to their low inertia. These particles cool down and solidify in their upward movement and possibly are reentrained into the spray as fine solid particles. As there are a large number of these fine solid particles, collisions with spray droplets are probable and result in the so-called satellite formation in melt-sprayed particles. These satellite formations lower the quality of sprayed powders, such as a reduction in free-flow ability. A possibility for satellite formation prevention has been proposed by Dunkley and Telford (2002). Here a part of the exhaust gas (after particle separation) is reinjected from the top into the spray chamber (as illustrated in Figure 8.58). The recirculation gas flow rate is controlled for replacing the natural jet entrainment flow (conventionally achieved by recirculating gas inside the chamber) into the spray (see Section 8.2.2.3). As a result, dust recirculation and satellite droplet formation is reduced. In Figure 8.59, sprayed particles with and without an antisatellite device are shown, where the number of nonspherical particles is dramatically reduced.

8.4.2.2 Spray Forming

The spray-forming process is a metallurgical manufacturing process that combines the main advantages of the classical processes:

- Metal casting: high-volume production, near-net shape forming.
- Powder metallurgy: near-net shape forming (at small volumes) with homogeneous, finegrained microstructure.

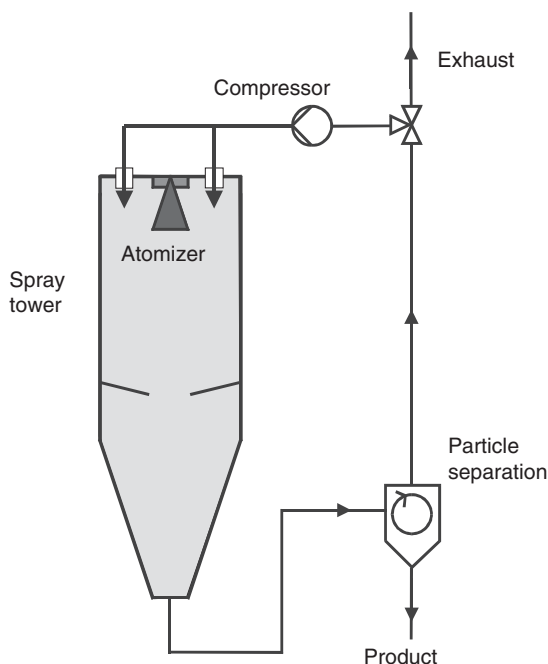


FIGURE 8.58 Concept for flow configuration in powder production spray process for decrease in satellite drop formation.

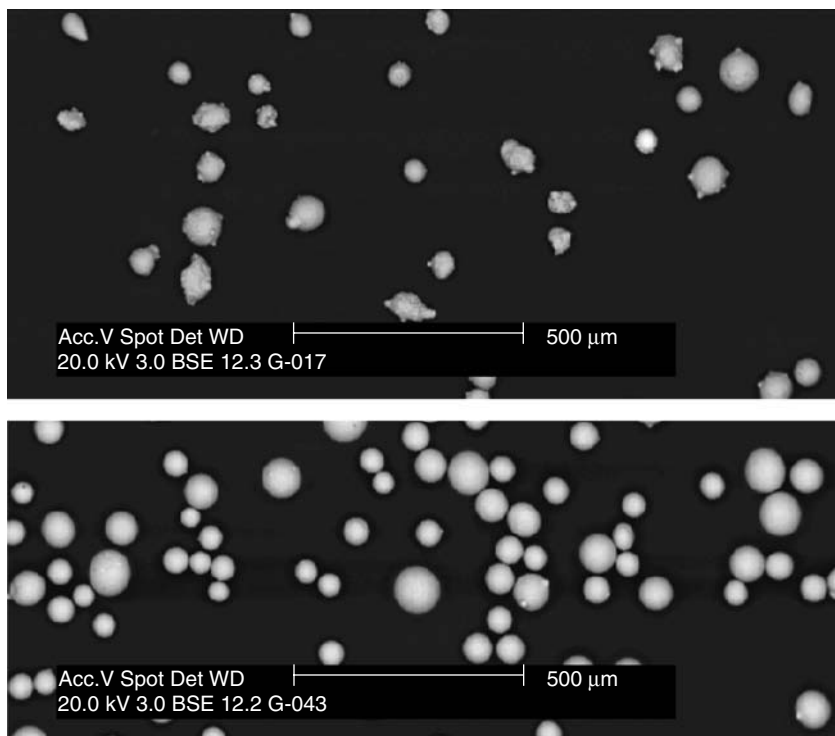


FIGURE 8.59 Satellite drop formation in melt sprays. (From Dunkley, J.J. and Telford, B., *Proceedings of the World Congress on Powder Metallurgy and Particulate Materials PM²TEC 2002*, Orlando, FL, USA, 2002.)

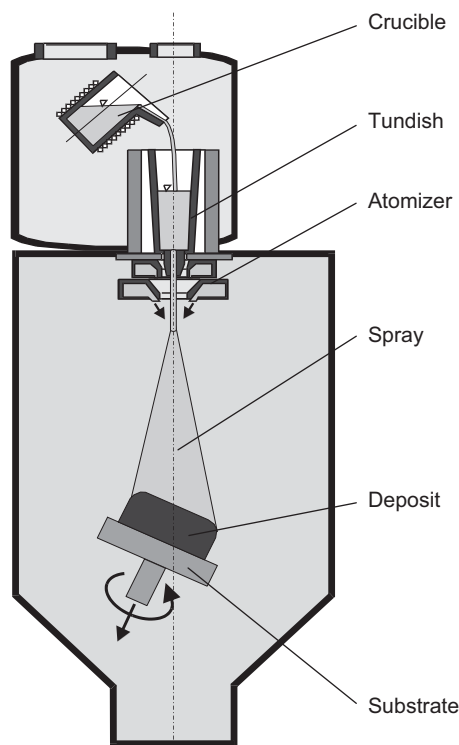


FIGURE 8.60 Principle of the spray-forming process.

The spray-forming process combines the atomization and spraying of a metal melt with the consolidation and compaction of the sprayed mass on a substrate. A typical scheme of the spray forming process is illustrated in Figure 8.60. The metallurgically prepared metal melt is distributed from the melting crucible via a tundish into the atomization area. Typically, by means of a twin-fluid atomizer with external mixing, inert gas jets with high kinetic energy impinge onto the metal stream and cause the melt disintegration. In the resulting spray, the droplets are accelerated toward the substrate and thereby cool down and partly solidify by intensive heat transfer to the cold atomization gas. The mixture of liquid droplets and semisolid or solidified particles in the spray impinge onto the substrate consolidating to the desired deposited product. This mixture of droplets in different solidification stages of impingement is an essential feature of the spray-forming process. The overall amount of the superheat (above the liquidus temperature) and latent heat (solidification) is extracted from the sprayed mass in the spray at high cooling rates ($\sim 10^5$ K/sec). The solidification of the remaining melt in the deposit (typically 10 to 40% of the remaining liquid) starts at a high (finely distributed) solid content (Annavarapu and Doherty, 1995; Doherty et al., 1997), thereby resulting in extremely fine and equiaxed grain structures. After consolidation, the remaining metal finally solidifies and cools down further, at cooling rates that are just comparable to casting processes.

An overview on industrial applications and the objectives of spray forming has been given by Lawley et al. (1990), Grant (1995), Lavernia and Wu (1996), Leatham and Lawley (1993), Bauckhage (1997 and 2003), and Fritsching and Bauckhage (1999). The potential applications of spray forming have been reviewed by Lawley (2000). Several materials and alloys are produced with specific advantages via spray forming such as:

- Conventional metallic materials and alloys
- Materials and alloys in which alloying components tend to segregate within conventional casting processes, for example, alloys on aluminium, copper, and iron bases, and super alloys (e.g., on nickel base) for applications in the aircraft and aerospace industries

- Intermetallic composite materials (IMCs)
- Metal matrix composite materials (MMCs), for example, ceramic particle inclusions into a metal matrix
- Lightweight materials (e.g., magnesium)

Typical geometries of spray-formed preforms in industrial applications are: flat products, tubes or rings, and cylindrical billets.

The main advantage of spray-formed materials, compared to conventionally produced materials, is related to their outstanding material properties. These are due to the specific cooling and solidification history in the spray process and finally result in:

- Absence of macro segregations
- Homogeneous, globular microstructure
- Increased yield strength
- Decreased oxygen contamination
- Good hot workability and deformability.

8.4.2.2.1 Atomization of the Liquid Melt

In spray forming, typically twin-fluid atomization with inert gas is used in a free-fall atomizer configuration because:

- High mass flow rates of melt can be atomized
- High heat transfer rates from the droplets can be realized in the spray
- High momentum transfer rates are achieved to accelerate the droplets
- Low oxidation rates of the material in the spray process are obtained

The analysis of the atomization process requires primary knowledge of the gas flow field of the atomizer gas in the nozzle vicinity. The primary gas flow emerging at low pressure close to the melt exit is responsible for guiding the melt flow into the atomization region below the atomizer, while a secondary gas flow field emerges from the lower gas ring and impinges onto the central melt stream, well below the atomizer, and is applied for disintegration of the melt (Uhlenwinkel et al., 1990; Heck et al., 2000).

In [Figure 8.61](#), the results of a numerical simulation of the (subsonic) gas flow in the nozzle vicinity are shown as vector diagrams, in comparison with the pictures of the atomization of a model fluid (water) in a free-fall atomizer (Fritsching and Bauckhage, 1992). The atomization gas pressure in this case is $p_2 = 1.89$ bar absolute, therefore, the gas exit condition is just critical with an exit velocity equal to the velocity of sound ($M = 1$). In the first example (upper panels), no primary gas flow is applied ($p_1 = 0$). The secondary atomizer gas flow exits from the gas ring at inclination angle of 10° , but contracts even more than this angle indicates, and hits the center line of the atomizer well above the theoretical atomization point, which is the intersection point of the atomizer center line with the gas jet exit line. By gas entrainment effects, ambient gas is accelerated into the inner flow field. This gas stream flows through the gap between the main body of the nozzle and the lower atomizer gas ring into the inner area of the flow field. In the middle of the inner area, a recirculating vortex flow can be seen (indicated by a solid line in the figure). Gas velocities of up to 50 m/sec pointing vertically upward are achieved in this area. Individual particles entering this area of upward flowing gas are accelerated toward the main body of the nozzle and the melt exit. This result can also be observed in some experimental observations of the atomization process, where individual droplets that are transported vertically upward can be seen above the atomization region. For melt droplets, this effect may cause sticking and even possible blocking of the nozzle. The calculated gas flow field in an optimized free-fall nozzle configuration is shown in the second example (lower panels) in [Figure 8.61](#) for an atomization gas pressure of $p_2 = 1.89$ bar absolute and a primary gas pressure of $p_1 = 1.4$ bar absolute (Fritsching and Bauckhage, 1992). Here, a gas flow field without recirculation is seen in the nozzle vicinity. The observation of the atomization model shows the successful prevention of droplet recirculation and illustrates the importance of the primary gas flow for this nozzle.

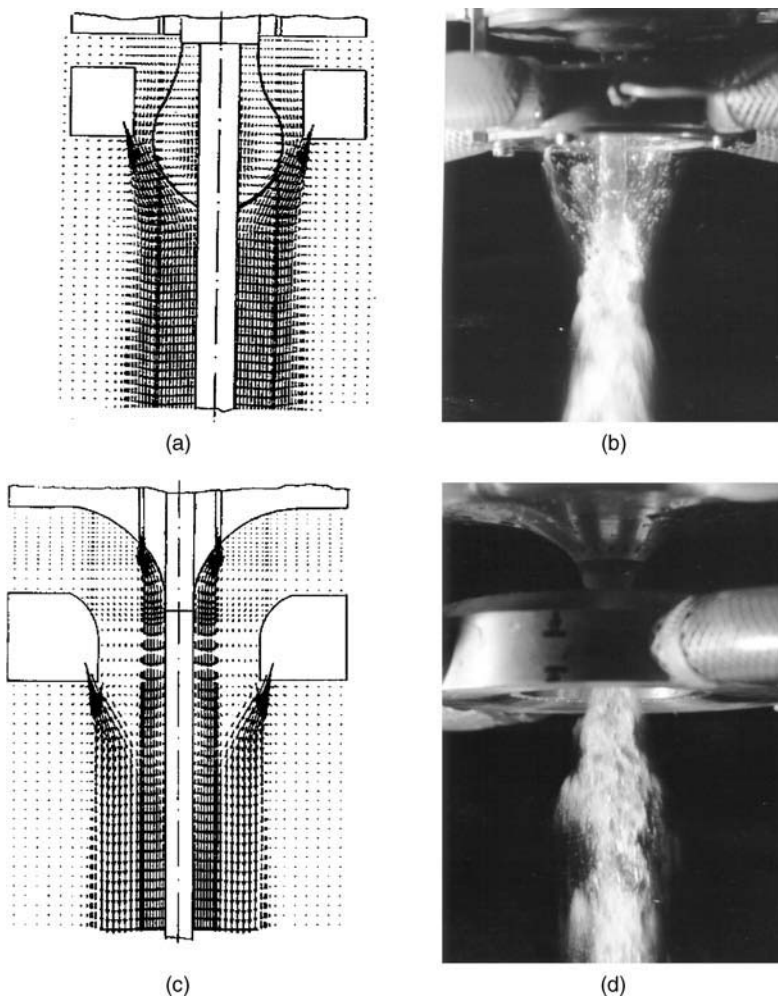


FIGURE 8.61 Fragmentation process in free-fall atomizer for spray-forming application, comparison of gas flow simulation and water atomization. Upper panel: droplet recirculation; $p_2 = 0.189$ MPa, $p_1 = 0$; Lower panel: optimized process condition; $p_2 = 0.189$ MPa, $p_1 = 0.14$ MPa. (From Fritsching, U. and Bauckhage, K., *PHOENICS J. Comp. Fluid Dyn.*, 5, 81–98, 1992. With permission.)

The interaction of the gas flow and the melt stream has been investigated in Antipas et al. (1993), Markus and Fritsching (2003b), and Liu (1997). Here, the primary jet fragmentation and the secondary droplet disintegration have been calculated in a direct way. The principal parameter describing the spray is the droplet size distribution, which in spray forming is typically based on the correlation by Lubanska (1970) (see Table 8.5). In this correlation, a specific liquid Weber number is used :

$$We_l = \frac{\rho_l u_{g,max}^2 d_0}{\sigma} \quad (8.102)$$

which needs to be calculated by using the melt properties and the maximum gas velocity of the atomizer gas flow field. The maximum gas velocity in the atomization region has been calculated based on simulations (Fritsching and Bauckhage, 1992) and also measured and correlated for a typical free-fall arrangement (Heck, 1998) as

$$u_{g,max} = 645.25 \dot{m}_g^{0.585} \quad (8.103)$$

where the gas mass flow rate is correlated to the absolute atomization gas pressure in the choked flow regime (for nitrogen at pressures above 0.189 MPa) by

$$\dot{m}_g = 0.685 C_D A_g \frac{p_0}{\sqrt{RT_0}} \quad (8.104)$$

The total gas exit area is A_0 and a typical value for the friction coefficient C_D is 0.84. The result of a sample calculation of the resulting mean droplet sizes for different atomized metals (i.e., aluminum, magnesium, iron, copper, and tin) is shown in Figure 8.39. The main parameter describing the atomization efficiency (achieving smaller droplets) is the inverse product of dynamic viscosity and surface tension ($\mu\sigma$)⁻¹.

8.4.2.2.2 Particle Transport in a Spray

In a spray, a complex two-phase flow situation involving gas and particles/droplets occurs. The high-speed gas loses its momentum by accelerating the droplets. Due to the heat transfer from the droplets, the gas undergoes intensive heating in the zone close to the atomizer. The droplets are accelerated and partly solidified during their flight. Complete dispersed two-phase flow modeling, including momentum and heat coupling is used to describe and analyze the spray behavior (Grant et al, 1993a, 1993b; Fritsching, 1995; Bergmann, 2000; Pedersen, 2003). As an example of modeling, Figure 8.62 and Figure 8.63 show the behavior of different droplet size classes on the center line and on the edge of a steel melt spray, atomized with nitrogen (Bergmann et al., 1995). The boundary conditions include an atomizer prepressure of $p_2 = 3$ bar abs., a gas to metal flow rate (GMR) of 1.25, and a log-normal droplet size distribution with a MMD of 133 μm . The axial velocity distributions on the spray center line of the gas and particles with different diameters are illustrated in Figure 8.62. The gas velocity upstream of the

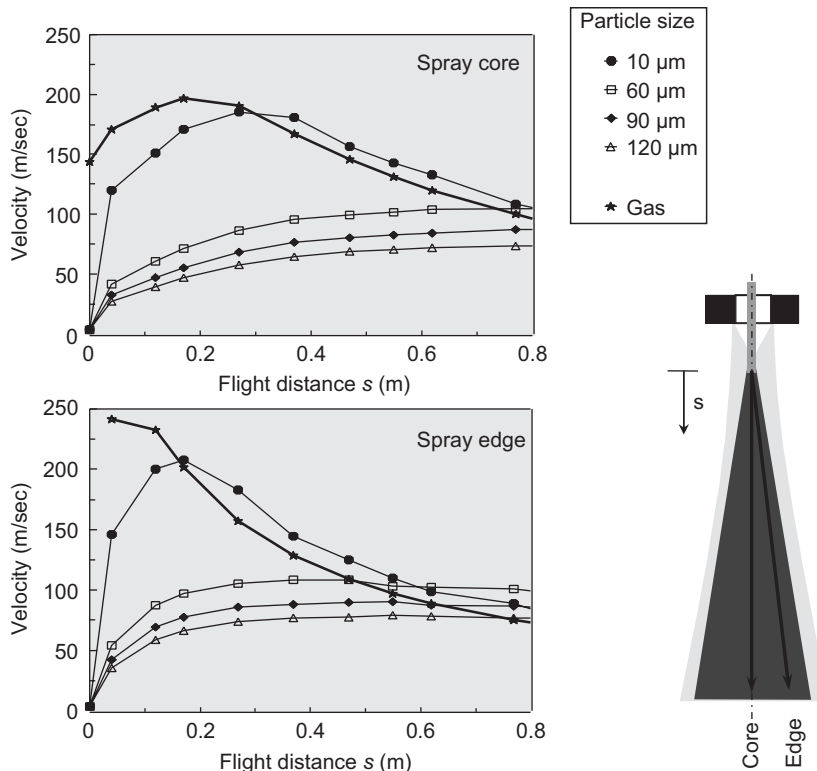


FIGURE 8.62 Modeling result for gas and particle velocity behavior on spray center line and edge within spray forming of steel. (From Bergmann et al., *Proceedings of the 2nd International Conference on Multiphase Flow*, Kyoto, Japan, April 3–7, 1995, Vol.1, pp. SP1–SP8. With permission.)

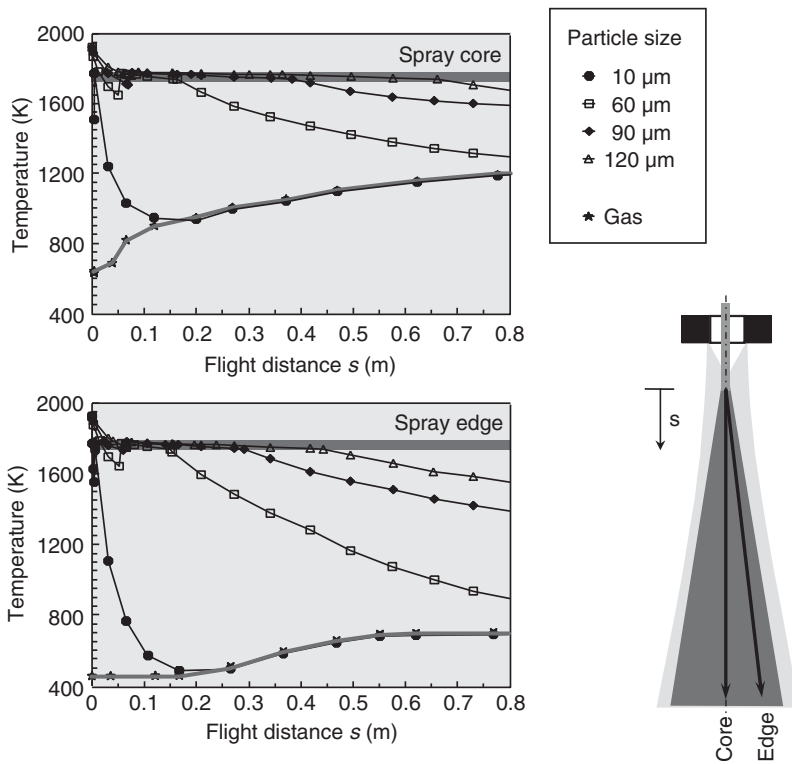


FIGURE 8.63 (Color insert follows page 13-40) Modeling result for gas and particle temperature behavior on spray center line and edge in spray forming of steel. (From Bergmann et al., *Proceedings of the 2nd International Conference on Multiphase Flow*, Kyoto, Japan, April 3–7, 1995, Vol. 1, pp. SP1–SP8. With permission.)

atomization area is unaffected by the particles. Close to and in the atomization region, the gas velocity decreases due to the momentum transfer associated with acceleration of the droplets. Then, the gas velocity further increases owing to the heating of the gas and thermal expansion and, also, the entrainment of momentum from the edge of the spray cone. The maximum gas velocity is reached at a nozzle distance of ~ 330 mm. Then, the gas velocity decreases due to the spreading of the spray cone. Particles are accelerated in the atomization region and further downstream. In the main region of the spray cone, particle velocities for the bigger particles remain approximately constant.

The gas reaches high temperatures in the atomization region up to 1200 K, as can be seen from Figure 8.63. Further downstream, the local gas temperature on the center line decreases, but heat transfer from the particles continues, due to the spreading of the spray and mixing with the colder ambient gas. After cooling down to solidification temperature, the phase change occurs inside the particles and the latent heat of the particles is released, whereby the particle temperature remains constant. When the latent heat content of the droplets is removed, the particles cool down further. From these calculations, it can be seen that particles above 210 μm are still in the state of phase change when impacting the substrate or deposit.

Experimental investigations have verified these simulation results. Online measurement techniques have been used to monitor the spray conditions in spray forming. With a modified phase doppler anemometer (Ziesenis, 2003), local droplet sizes and velocities are measured and used for process control (Bauckhage, 1998). Measurements of individual droplet temperatures (and droplet sizes and velocities) in metal sprays have been performed by means of a high-speed pyrometer instrument (Krauss et al., 2002).

To determine the overall heat and mass fluxes from the spray to the deposit, the droplet data have to be averaged in a suitable manner. Thermal averaging may be performed in two different ways, describing two extreme situations that occur in a molten metal spray (Bergmann et al., 1999). The first averaging method

(the enthalpy method) describes the thermal status of the particle mass in thermal equilibrium. In this way, the thermal state of a certain particle mass is described after adiabatic equilibration. This means the particle mass has a specific enthalpy that is directly related to its thermal state (temperature and solid fraction).

In an impinging molten metal spray for forming or coating processes, situations may occur where the particle mass should already be fully solidified according to its average properties (when calculated by the enthalpy method), although it still contains some liquid. This may occur when the main spray consists of a large proportion of cold, of solidified particles and only a small number of large, fluid, and hot melted particles. These liquid droplets still deliver a certain amount of liquid melt to the mushy layer on the deposit surface, which is not accounted for by the enthalpy method. However, if the second method (separation averaging method) is used, this difficulty can be overcome. Here, the amount of solidified mass or fluid melt mass that remains in the spray is calculated separately.

The enthalpy averaging approach yields the thermal equilibrium condition of the total droplet mass (in terms of a discrete number of droplet size classes) as:

$$\bar{h}_p = \frac{1}{\sum_i m_{p,i}} \sum_i \{m_{p,i}[(C_{pl}(T_{p,i} - T_s) + \Delta h_f)(1 - f_{s,i}) + C_{ps}((T_{p,i} - T_s)f_{s,i} + T_s)]\} \quad (8.105)$$

Based on the calculated average specific enthalpy \bar{h}_p , the mean spray solid fraction $f_{s,h}$ and the mean temperature T_h can be calculated depending on the solidification state of the droplet mass. In the separation averaging approach, the nonequilibrium situation in the spray process is taken into account. The energy exchange within the total particle mass is due only to the specific heat content and not due to the remaining latent heat content of the particles:

$$f_{s,m} = \frac{1}{\sum_i m_{p,i}} \sum_i (m_{p,i} f_{s,i}) \quad (8.106)$$

$$T_m = \frac{1}{(C_{ps}f_{s,m} + C_{pl}(1 - f_{s,m})) \sum_i m_{p,i}} \sum_i (m_{p,i} T_{p,i} (C_{ps}f_{s,m} + C_{pl}(1 - f_{s,m}))) \quad (8.107)$$

Differences in the results obtained using the two averaging methods are shown in Figure 8.64, for the averaged temperatures and solid fractions of the spray along the center line as a function of the particle flight distance. The results of the enthalpy method represent the thermal equilibrium with respect to the particle mass, considering all particles from a specific location (point of impingement) together and leaving this

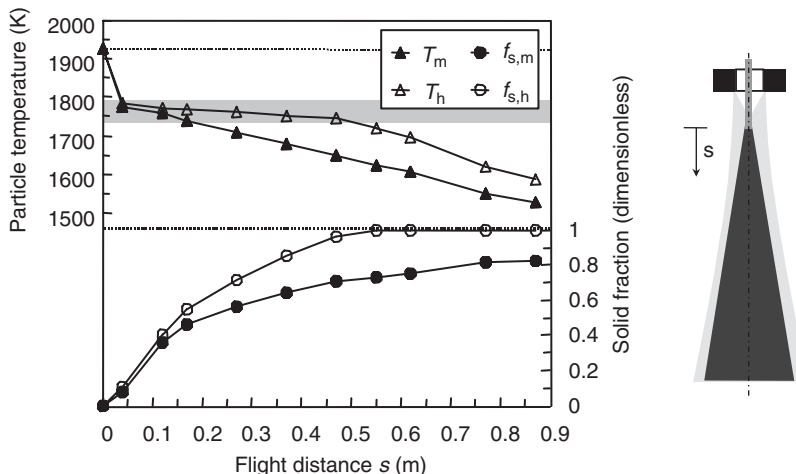


FIGURE 8.64 Integral temperature and remaining solid fraction in steel melt spray vs. the spray distance, two different averaging methods. (From Bergmann, D., Dissertation, Universität Bremen, 2000. With permission.)

mass under adiabatic conditions for an inner compensation process (heat conduction and solidification). This compensation process in spray forming immediately occurs when the sprayed particle mass impinges onto the deposit. In the semisolidified mixing layer on top of the deposit, an equilibration process will take place. Therefore, the enthalpy method well describes the thermal state of the particle mass in the top mushy layer after deposition. In contrast, the separation method describes the instantaneous local thermal state (temperature and solid content) of the particle mass in the spray. As seen in [Figure 8.64](#), the instantaneous mean particle temperatures and mean solidification fractions calculated for the whole particle flight distance by the separation model are lower than the values derived by the equilibrium state (enthalpy) method. With respect to the solidification process after the deposition, this difference means that the overall particle mass is undercooled and may be reheated after the deposition (in the mixing layer) by the latent heat released during solidification.

The mass flux distribution in the spray cone is directly connected to the resulting shape of the sprayed deposit. For varying deposit shapes, either the atomizer or the substrate can be moved. For a stationary atomizer, the radial profile of the mass flux distribution in the spray cone can be described as an exponential function by Eq. (8.108). The maximum mass flux is always found on the spray cone center line and $r_{0.5}$ is the half-width of the mass flux profile (see [Figure 8.46](#)). The exponential factor has been correlated as $k_1=1.3$ (Uhlenwinkel, 1992) and $k_1=1.124$ (Kramer, 1997) for steel atomization. The half-width of the mass flux profile is proportional to the maximum mass flux value as:

$$\dot{m}(r) = \dot{m}_{\max} \exp\left(\ln(0.5) \left| \frac{r}{r_{0.5}} \right|^{k_2} \right) \quad (8.108)$$

For calculating the mass flux distribution at each position within the spray cone, a single calibrating measurement on the spray center line in combination with the mass flux correlations is sufficient.

8.4.2.2.3 Deposition and Consolidation of Droplets

The impinging droplets transport mass, momentum, and thermal energy to the top layer of the deposit (Kramer, 1997; Bauckhage et al., 1999; Djuric et al., 1999; Djuric and Grant, 2001). The compacted mass is not identical to the mass flux in the spray because:

- Particles may have a spray trajectory that does not impinge onto the deposition surface
- Smaller droplets of low inertia will follow the gas streamlines and will be deflected, (aerodynamic overspray)
- Droplets may bounce-off or splash (Trapaga et al., 1992; Berg and Ulrich, 1997; Berg, 1999; Bussmann et al., 2000) and secondary droplets may not be incorporated in the deposit
- Particles with high momentum may tear off parts of the already compacted (soft) mushy top layer

This particle mass contributes to the overspray. The difference between the mass flux value in the spray cone and the compacted mass is described by the deposition efficiency

$$k(\vec{x}, t) = \frac{\dot{m}_{\text{compac}}(\vec{x}, t)}{\dot{m}_{\text{spray}}(\vec{x})} \leq 1 \quad (8.109)$$

This depends on (1) the thermal state of the impingement surface and (2) the momentum, temperature, and state of solidification of the impinging droplets

The deposition efficiency for spray forming of Gaussian-shaped deposits (produced with a stationary atomizer spraying on a stationary cylindrical substrate) from steel is correlated by (Kramer, 1997), as

$$k(T_p, f_p, I_p) = C_4 \left[C_1 + C_2 \left(\frac{T_p}{T_{\text{surf}}} \right)^{C_3} \right] f_p^{C_5} I_p^{C_6} \quad (8.110)$$

where the coefficients are $C_1 = 0.422$, $C_2 = 0.80$, $C_3 = 30.48$, $C_4 = 0.489$; $C_5 = 0.249$, and $C_6 = -0.062$. The main parameter influencing the deposition efficiency is the temperature of the droplets at impact (here normalized by the liquidus temperature).

During spraying time, the deposit grows continuously and releases its thermal energy by (1) conduction to the substrate, and (2) convection and radiation to the surrounding gas. To calculate the temperature

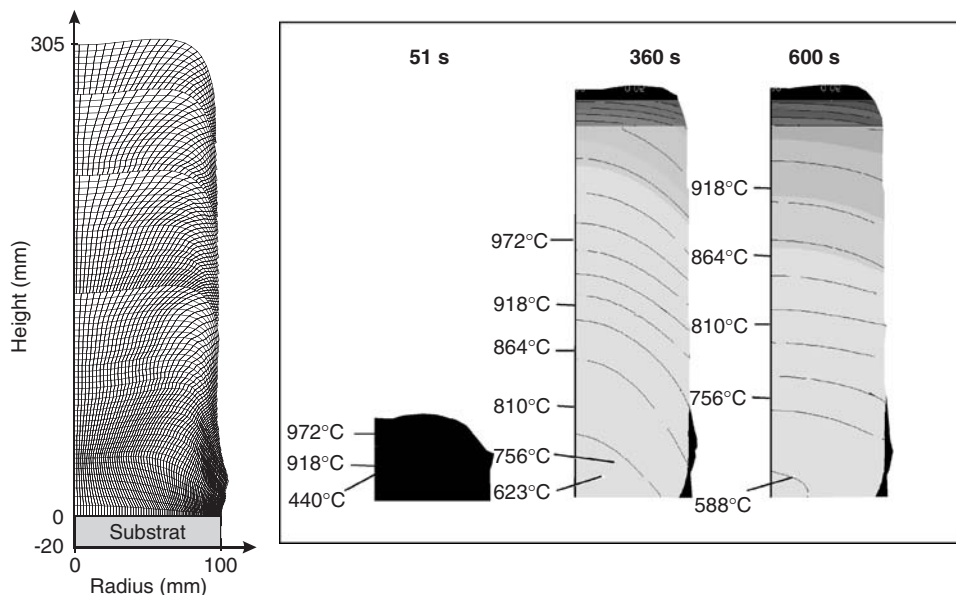


FIGURE 8.65 (Color insert follows page 13-40) Temperature and solid content distribution during spray forming of a copper billet. (From Meyer et al., *Int. J. Thermal Sci.*, 42, 2003. With permission.)

distribution and history in the deposit and substrate, numerical methods and measurements have been used (Mathur et al., 1989a, 1989b; Fritsching et al., 1993, 1994a, 1994b; Gutierrez-Miravete et al., 1988). The result of a simulation for production of a copper billet is shown in Figure 8.65 (Meyer et al., 2003a, 2003b).

By numerical modeling, a description of the complete material cooling process of metals in the different stages of spray forming, i.e., during flight, deposition, and further cooling periods (which are of major importance for the understanding, control, and optimization of the process) can be obtained and analyzed. Integral models of the spray-forming process can be found in Lavernia et al. (1988), Mathur et al. (1991), Payne et al. (1993, 1996), Ottosen (1993), Pedersen (2003), Pedersen et al. (2000), Bergmann (2000), and Fritsching (2000). The quality of spray-formed products in terms of homogeneity and improved material properties is directly controlled by the cooling rate of particles in the spray cone and the further cooling behavior of the resulting preform. The solidification and cooling behavior of the material directly depends on operational parameters. Such temperature simulations based on heat balance in the deposit and substrate show possibilities for thermal homogenization and avoidance of hot spots (Meyer et al., 2003).

8.4.3 Spray Drying

In the spray-drying process, the liquid feed material (in the form of solution or slurry) is atomized into a hot air environment, where the moisture is evaporated from the suspended droplets until the dried particles are obtained and collected as a final product. Typical examples can be found in spray drying of food stuff (e.g., milk or coffee powders) or chemical industry (e.g., detergents drying). This process is ideally suited to dry heat-sensitive feed materials, since the droplet–hot air contact time (residence time in the process) is reasonably short. Another advantage of spray drying is its ability to handle high sticky or corrosive materials (Mujumdar, 1997; Masters, 1991, 2002).

The spray drying process is subdivided into the following three steps (Crowe, 1980):

1. *Atomization:* Here either a rotary, pressure swirl nozzle, or twin-fluid nozzle is used to atomize the liquid and discharge into the spray chamber.
2. *Droplets–hot air contact:* the droplet spray is dried by the interaction with hot gases in the spray chamber. The spray–air flow pattern can be further categorized into three types: cocurrent flow (Figures 8.66a and b), countercurrent flow (Figure 8.66c), and mixed co-countercurrent flow

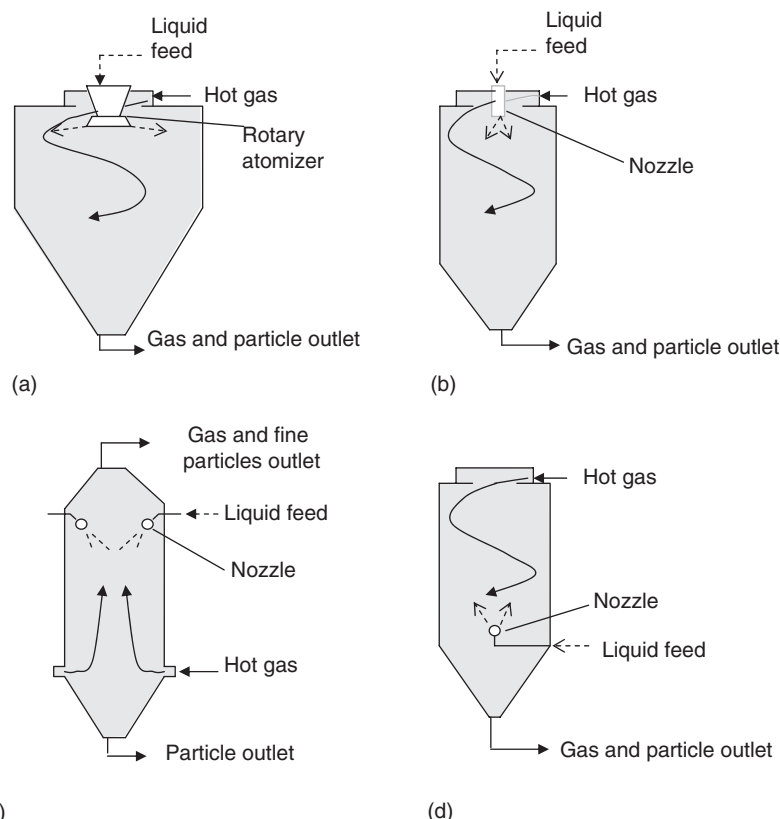


FIGURE 8.66 Spray dryer configurations: (a) cocurrent with rotary atomizer; (b) cocurrent with pressure nozzle; (c) countercurrent with pressure nozzle; (d) mixed flow with pressure nozzle.

(Figure 8.66d). The spray chamber geometry depends on the atomizer used. If a rotary atomizer is used, a “wide-form” (Figure 8.66a) chamber is required; If a pressure nozzle or twin-fluid nozzle is used a “tall-form” dryer (Figures 8.66b–d) is required. The cocurrent flow arrangement is more suitable for heat-sensitive material, since the air–spray contact time is shorter and the spray is protected from the high inlet air temperature due to evaporative cooling and the dried particles contact with cooler air at the lower section of dryer. The counter-current flow arrangement is suitable for materials that are not heat-sensitive, since the dried particles come in contact with high inlet air temperatures. Although comparatively less common than the cocurrent arrangement, the counter-current arrangement is suitable in some particular applications. For example, in spray drying of detergent powder, multiple pressure nozzles are used with the counter-current arrangement to attain a high bulk density agglomerate form. Typical temperature and vapor pressure profiles (as indicator of moisture content) of co- and counter-current spray dryers are illustrated in [Figure 8.67](#).

3. Removal of the powder from the drying medium, by means of gravity settling or cyclone separation.

A typical spray-drying process configuration is illustrated in [Figure 8.68](#).

8.4.3.1 Particle–Gas Interaction

In the droplet spray contact with the drying gas, all three interface transfer mechanisms (mass, momentum, and energy) become operative. Crowe (1980) and Crowe et al. (1998) described these transfer mechanisms applied to spray drying. Momentum transfer consists mainly of the drag force and gravity force. Nikas et al. (2001) reported the importance of buoyancy force acting on the particles according to their numerical simulation of flow in a spray dryer. At the droplet–hot air interface, heat is transferred into the

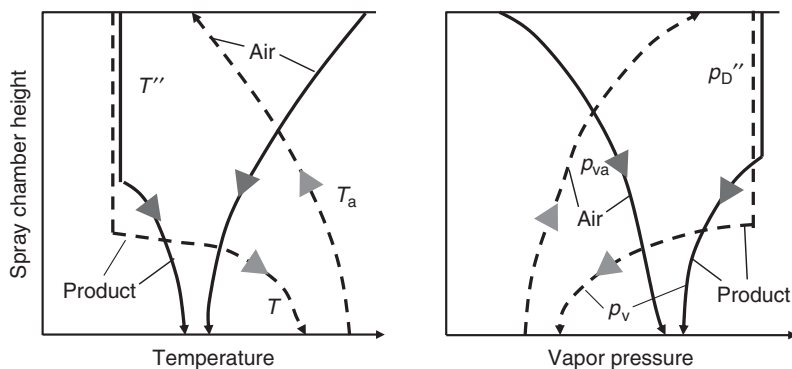


FIGURE 8.67 Temperature and vapor pressure distribution in co- and countercurrent spray drying process. (Adapted from Mujumdar, 1987.)

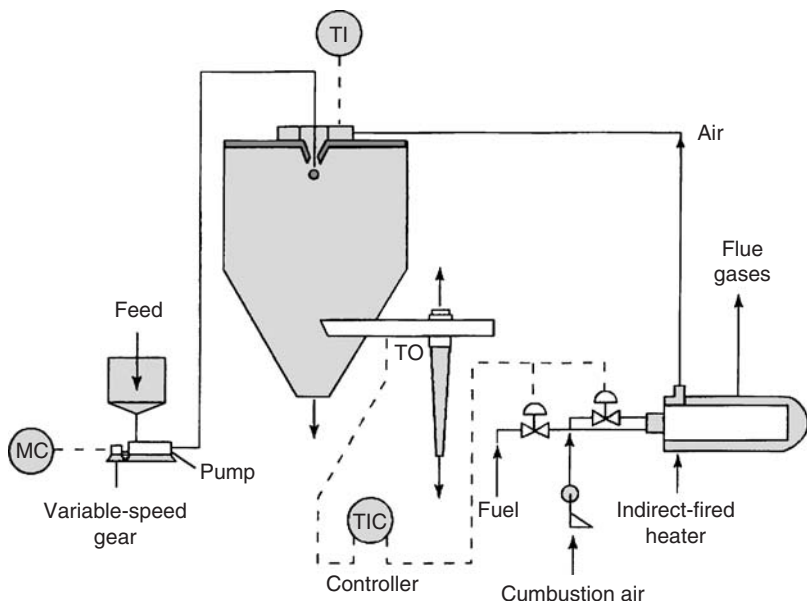


FIGURE 8.68 Configuration of a spray drying plant. (Adapted from Oakley, D.E., *Chem. Eng. Prog.*, 12, 48–54, 1997.)

droplet surface, and thereby moisture is removed. According to the heat and mass transfer analogy, the external transfer of mass or heat is obtained from the transfer relation Eq. (8.90), expressed in terms of the Nusselt number (Nu) for heat transfer and the Sherwood number (Sh) for mass transfer (see [Section 1.4](#)) together with a suitable droplet drying model (see [Section 8.2.3](#)).

8.4.3.2 Air-Spray Flow Pattern

The transient behavior and complex structure of the two-phase flow within a spray dryer has been investigated for many systems. If a swirl vane is mounted at the air inlet, the swirl vane angle affects the air-spray flow pattern as reported by Oakley (1997), Oakley et al. (1988), Stafford et al. (1997), Kieviet and Kerkhof (1995), and Southwell and Langrish (2000, 2001). The common pattern of air flows during spray operation with no swirl induced (or 0° swirl vane angle) exhibits a fast flowing, central core surrounded by a large recirculation zone (Kröger, 2001). As the inlet swirl increases, the large recirculation zone near the wall becomes less stable. From approximately 25° swirl vane angle and higher, a precessing vortex core (PVC) begins to form in the core region and at swirl vane angle above 30° , the near-wall recirculation zone

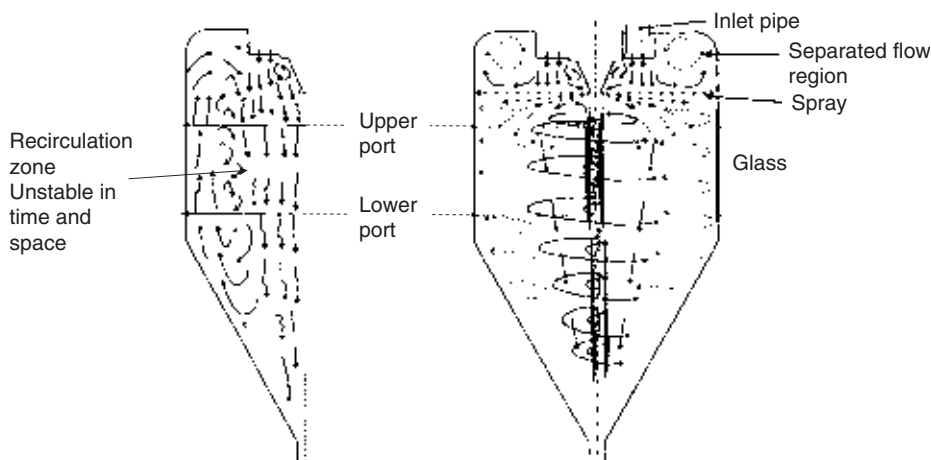


FIGURE 8.69 Spray dryer flow field. (Adapted from Southwell, D.B. and Langrish, T.A.G., *Drying Technol.*, 18, 661–685, 2000.)

is less visible and finally disappears. At a higher swirl vane angle and with the atomizer turned off, a central recirculation zone forms, but disappears when the atomizer is turned on. The central recirculation zone is undesirable as the dried particles are pushed back to heat-intensive region, which may cause thermal degradation of products. Southwell and Langrish (2000, 2001) reported the formation of PVC, disappearance of the near-wall large recirculation zone, and the tendency that central recirculation might form at the axial distance further than the measurement point at 45° swirl vane angle. Figure 8.69 illustrates the effect on the air flow pattern of swirl by using vane-wheel atomizer.

Southwell and Langrish (2001) reported the spray patterns at various swirl vane angles. The spray cone region could be clearly identified and only a small spray fluctuation could be observed at 0° swirl vane angle. As the swirl vane angle increased, the spray cone region was less visible and more transient. The width of the spray cone also increased when the swirl vane angle increased. At 45° the spray was torn apart and dispersed toward the wall within 0.2 m of the atomizer. The value of 25° has been found as the optimum swirl vane angle; fine spray-air mixing without excessive spreading of spray cloud and wall deposition is achieved. At this swirl angle, the spray cone did not spread widely or interact with the inlet air as violently as at higher swirl vane angles, but adequate mixing was observed in the main body of dryer. Straatma et al. (1999) reported a computational fluid dynamics (CFD) study of two different cases. In the first case, simulation of an existing spray dryer with a rotary-wheel atomizer was performed. At the actual rotary speeds, reversal of the main air flow circulation occurred and a shortcut of hot air from inlet to outlet could be predicted from calculation (also observed in experiments). In the second case study, an industrial spray dryer equipped with one central and several noncentral air inlet channels with nozzle atomizers is simulated. The powder deposition in the conical section was high since the particle hit the cone when it was still wet and sticky. Larger, noncentral air inlets at a greater distance from the center solved this problem. This illustrates the importance of the air flow pattern in a spray dryer on the drying process.

8.4.3.3 Effect of Turbulence Level at Air Inlet on Evaporation Rate

Zbicinski et al. (1996) investigated the effect of turbulence level on heat and mass transfer during atomization in an experimental air tunnel. Turbulence promoters increased the turbulence level of the air flow in the tunnel to 17%. A comparative analysis of results obtained for heat and mass transfer for natural turbulence and enhanced turbulence showed that an increase in the turbulence of a drying agent can cause 20 to 25% increase in drying efficiency. Southwell and Langrish (1999) studied the experimental results of Zbicinski et al. (1996) using CFD. The simulations consistently predicted an increase in the amount of evaporation resulting from enhanced inlet turbulence. The simulation predicted improvements of between 5 and 11%, which were significantly less than the measured value. Enhancing inlet turbulence appeared to

increase evaporation by improving both spray dispersion and the exchange of air between the spray envelope and the surrounding hot and relatively dry air.

8.4.3.4 Particle Residence Time Distribution

For some heat-sensitive materials, particle residence time distribution in a spray dryer is an important parameter. The effect of the air flow pattern (at different swirl vane angles) on particle residence time was discussed by Southwell and Langrish (2001). Kieviet and Kerchof (1995) measured particle residence time distributions by means of pulse tracer analysis. They showed that the distribution plot contains a very long tail. Wide ranges of residence time have been reported and which suggested that the particle residence time distribution depends not only on the time the particle was airborne, but largely on the time it took for a particle may slide down the cylindrical and conical section of the dryer wall.

8.4.3.5 Particle Collision and Agglomeration

Particle-particle collision is a significant phenomenon in spray processes. In the spray-drying process, especially for hygroscopic materials, droplet collision and agglomeration is desirable (e.g., milk, coffee, and detergent) to attain attractive product features (e.g., reduction of fine particles). Droplets collision effects depend on the droplet surface condition, which, in spray drying, is not a homogeneous liquid, and on the droplet drying stage as (i) surface tension dominated, std (liquid surface), (ii) viscous-dominated, vd (solid-liquid mixture surface), and (iii) dry particle, dp (solid surface).

8.4.3.6 Agglomeration Model

Details on droplet-droplet collision modeling have been given in Section 8.2.1. Within spray drying, Ho and Sommerfeld (2002) developed a stochastic Lagrangian agglomeration model for dry-dry particles (dp), by applying the inter-particle collision model of Sommerfeld (2001). In addition, the collision efficiency due to the geometrical size difference (i.e., small particle hit the larger collector particle), as a function of Stokes number, and the agglomeration efficiency of dry-dry particles determined by the sticking potential due to the van der Waals force, is taken into account. A critical velocity u_{cr} is calculated from the energy balance according to Hiller (1981). The formation of agglomerate takes place when

$$u_{rel} \cos \Psi \leq u_{cr} \quad (8.111)$$

In the case of particles of solid-liquid dispersion, Blei and Sommerfeld (2003) introduced a stochastic Lagrangian agglomeration model for the spray-drying process by applying the simulation model according to Sommerfeld (1995, 2001). Collision of particles with different material properties such as moisture content, density, and surface property (std, vd, or dp) were taken into account. The mathematical analysis is based on the assumptions of a fully plastic collision and nondeforming spherical droplets during collision and Newtonian fluid. The derivation of the model allows a droplet of higher viscosity to penetrate into a droplet of lower viscosity. Criteria and postscollision properties for different modes of collision pair were derived.

8.4.3.7 Industrial Practice of Agglomeration Processes in Spray Dryer

The processes and unit operations for agglomeration in spray dryer are described in Louey and Refstrup (2001). According to their classification, the collision-agglomeration process is a forced-primary agglomeration, which is currently operated by using multiple pressure nozzles and a fine-return particle atomizer (fine particle fractions after separation from the product are mixed into the atomization zone). The relationship between the fine-return-liquid collision distance from atomizer and the agglomerate structure has been discussed. If the collision between fine-return particles and atomized liquid occurs close to the liquid atomizer, the fine-return particles may penetrate into the liquid droplet producing an “onion” structure of agglomeration, which has a high bulk density and low dispersibility. At an optimum distance of collision, the fine-return particles stick onto the liquid droplet producing a “compact grape” structure with good dispersibility and sufficient mechanical strength.

A numerical simulation tool of spray dryer flow conditions and process design including agglomeration has been developed as described by Verduren et al. (2003, 2004). Here, a computer simulation-based design tool, taking into account the relevance of agglomeration processes in industrial-scale food spray dryer, is outlined.

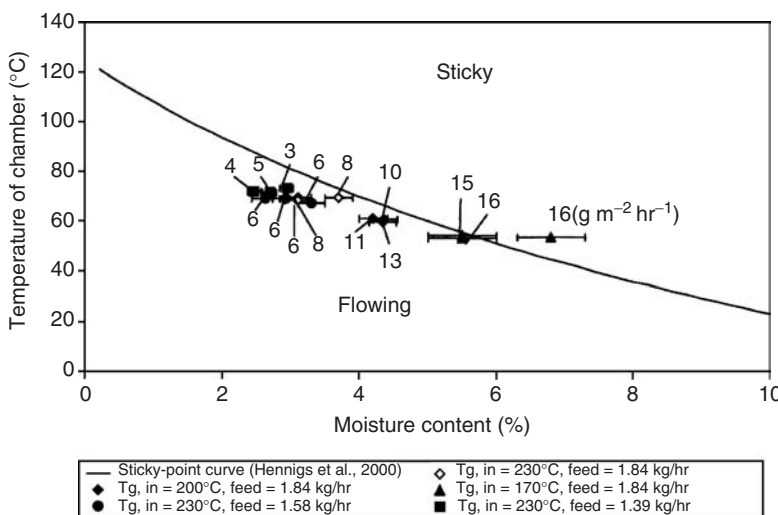


FIGURE 8.70 Operating condition and corresponding wall deposition fluxes on the sticky point diagram for skim milk powder. (Adapted from Ozmen, L. and Langrish, T.A.G., *Proceedings of the 9th APCCHE Congress and CHEMeca*, Christchurch, 2002.)

8.4.3.8 Particle-Wall Deposition

Particle-wall deposition can lead to downtime cleaning, spoiled products, and potential fire hazards. The rate of deposition on the wall is thus the interesting parameter. Chen et al. (1993) investigated particle-wall deposition in an industrial spray dryer. Although the effects of operating parameters on wall deposition were not reported quantitatively, they suggested the modification of the near-wall air flow and inlet air-temperature distribution could reduce wall deposition significantly. They also suggested that wall insulation could reduce wall deposition. It has been concluded that the effect of insulation was to increase the temperature close to the wall, thus preventing both vapor condensation and moisture in the particles. On the other hand, Brennen et al. (1971) found that when the wall was too hot, more deposition was observed. Thus, low inlet air temperatures ($<180^{\circ}\text{C}$) have been used for spray drying of sticky materials to keep the wall cool (Bhandari et al., 1992, 1993).

Ozmen and Langrish (2002) investigated the wall deposition of milk powder in a spray dryer. They measured the wall deposition in terms of wall deposition flux. The effect of inlet air swirl angle, air and chamber temperature, particle moisture content, wall material, and spray duration time on wall deposition flux were investigated. An increase in the angle of swirl from 0 to 30° increases the wall deposition flux by 30%, although this increase air-spray mixing and evaporation rate. In the case of temperature effects, if the temperature and moisture plot of a particle is above the sticky-point curve in a sticky point diagram (Hennigs et al., 2001), the wall deposition flux significantly increases (Figure 8.70). They concluded that the sticky point curve appeared to be a better indicator of tendency for wall deposition flux. With respect to wall insulation, they reported significantly higher deposition flux with insulation relative to noninsulation. The investigation of the adhesion-cohesion process on the measuring plates showed that particle-particle cohesion (which led to agglomerate form) was the controlling process of wall deposition so the near-wall particle dispersion is important. In this work, particle-wall adhesion had negligible effects on the wall deposition. The measuring surfaces were either nonstick food-grade material, adhesive tape, or stainless steel.

8.4.4 Spray Painting and Coating

Application of paints by spray processes provides protection to the surfaces and cosmetic effects to surfaces. Also, controlling of surface properties such as roughness, friction control, fire protection,

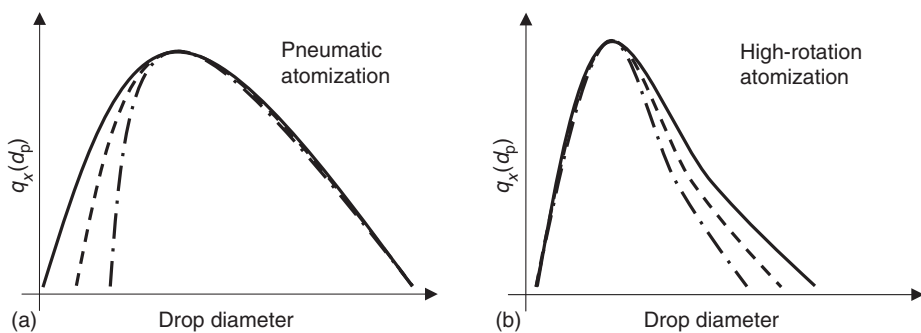


FIGURE 8.71 Overspray characteristic in coating process by means of (a) pneumatic (b) rotary atomizer. (Adapted from Goldschmidt, A. and Streitberger, H.J., *BASF-Handbuch Lackiertechnik*, Vincentz Verlag, Hannover, 2002.)

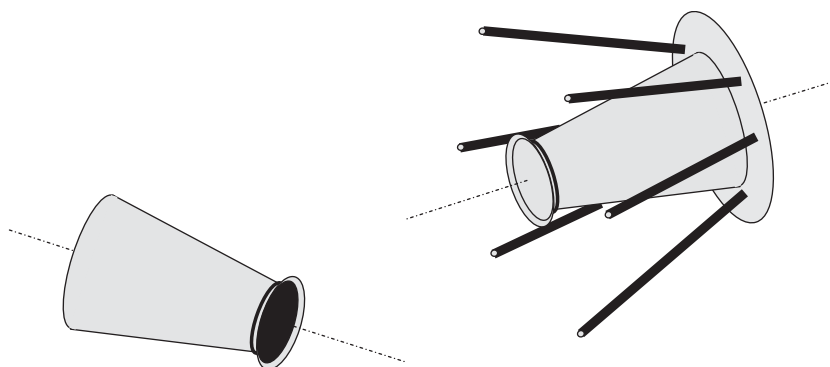


FIGURE 8.72 Droplet charging in electrostatic-assisted coating applications.

biological barriers, isolation, etc., are typically achieved by (spray) coating applications. Achieving specific surface quality and process yield (minimization of overspray) are the main aims of spray painting and coating processes. Typical yield of industrial spray painting processes occasionally is only about 70%.

In spray painting and coating applications, either pressure atomizers (here often called airless atomizer), twin-fluid atomizers (pneumatic atomizer), or rotary atomizers are used. Owing to flexibility and the case of application, pneumatic atomizers are the most common in spray painting. Their disadvantage is the high overspray loss. Airless atomization is typically operated at 100 to 200 bar pressure and is used when higher throughput is to be achieved. Typical coating qualities are lower than those of pneumatic atomizers. For painting large surface areas in combination with high-quality demand on optical coating properties (e.g., in automotive industry), the so-called high-rotation (HR) atomizer is used. Electrocharging of the droplets is used to decrease the overspray thereby increasing the yield in paint applications. Electrostatic fields in spray painting are also used to assist coating of the back and hidden sides of the substrates (Svejda, 2003). The different atomization principles result in different spray characteristics. Drop sizes and drop size–velocity correlations vary. Differences in overspray characteristics of a pneumatic atomizer and a HR atomizer are illustrated in Figure 8.71 (Goldschmidt and Streitberger, 2002). The drop size spectrum in pneumatic atomization typically is broader than in rotary atomization, since, in a pneumatic atomizer (at high gas velocities), the smaller particles are especially deflected by aerodynamic effects around the specimen to be coated. Here, in the spectrum of deposited particles, the smaller drop size fractions are missing (Figure 8.71a). By application of electrostatic forces, the overspray amount is reduced and the yield is increased. In rotary atomization, the larger particles preferably will not be deposited on the surface (even when assisted by an additional air flow). Therefore, in this case, the deposited drop size spectrum shows some missing larger droplets. When the charge of the particles is increased (higher voltage), the overspray amount is decreased (Figure 8.71b).

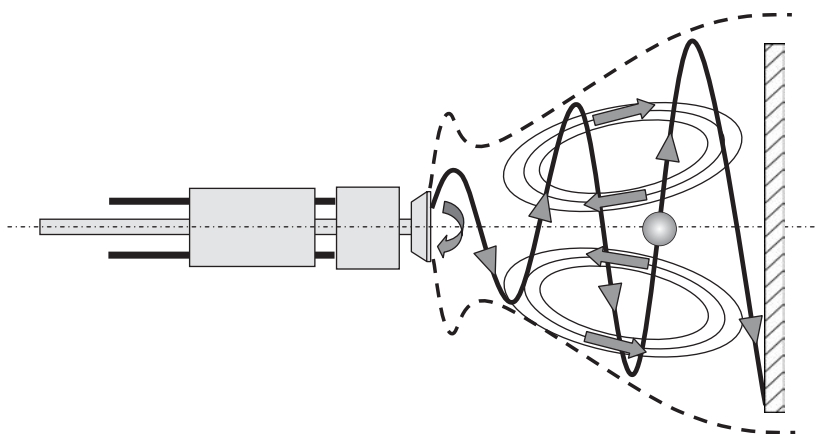


FIGURE 8.73 Droplet trajectories in ESTA-HR spray painting process. (From Scholz, T., Dissertation, Universität Bremen, VDI-Verlag, Düsseldorf, 1998. With permission.)

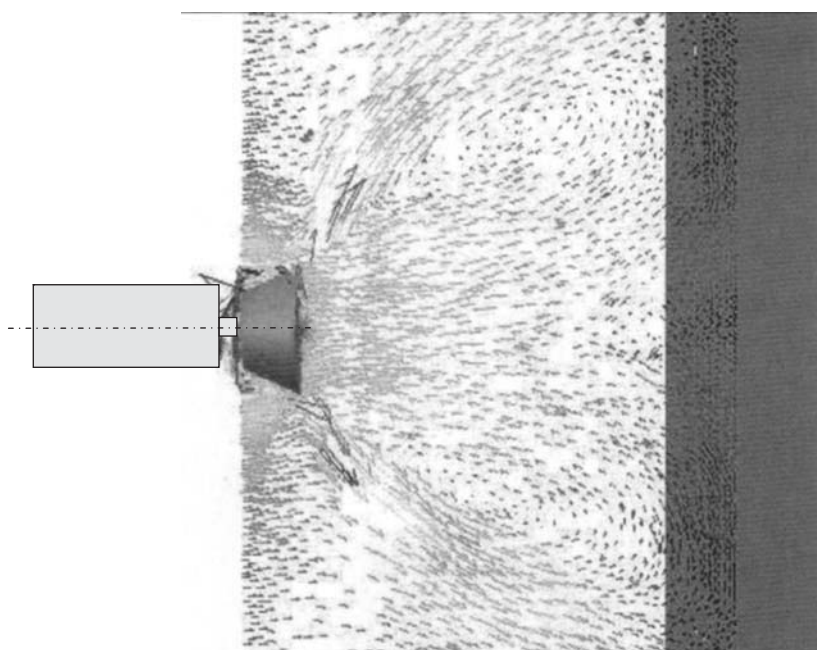


FIGURE 8.74 Simulated gas flow field in ESTA-HR spray painting process. (Adapted from Domnick et al., *Proc. ICLASS 2003*, Sorrento, Italy, 2003.)

8.4.4.1 High-Rotation Atomization

For rotary atomization of paints, either disc-or-cone shaped atomizer geometries are used. Typically, the disintegration mode of rotary atomization for paint applications is the lamella mode (Goldschmidt and Streitberger, 2002). For increasing the yield, in HR atomization, additional gas flow (called steering air flow) and electrostatic charging of the droplets are used (electrostatic-assisted high-rotation atomization [ESTA-HR]). An HR atomizer consists of a bell and a drive (air drive). Depending on the paint material and mass flow rate, HR-atomizers are operated at 15,000 to 60,000 r/min. The bell diameter is typically about 50 mm with variations in geometry and bell-edge surfaces. Charging of the paint material is achieved either by contact charging where the atomizer bell is connected to a high voltage (typically 50 to 120 kV) or by ionization charging, where air ions are deposited on the droplet surface that result from outer free electrodes (see

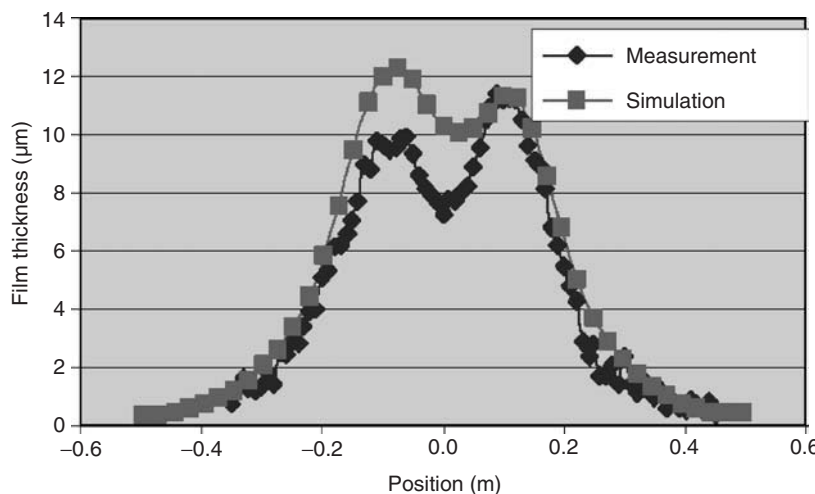


FIGURE 8.75 Derived dynamic coating thickness within electrostatic spray painting process with high-speed rotary atomizer. (Adapted from Domnick et al., *Proceedings of the International Conference on Liquid Atomization Spraying Systems ICCLASS 2003*, Sorrento, Italy, 2003.)

(Figure 8.72). Contact charging is used for electrically nonconduction paints (e.g., paints based on organic solvents), while ionization charging is used for electrically conducting materials (e.g., in powder paint applications). The overall yields of ESTA-HR processes are of the order of 85 to 90% (Svejda, 2003).

The spray geometry during ESTA-HR process is characterized by the interaction of aerodynamic, inertia and electrostatic forces on the droplets (Böttner et al., 1998; Böttner, 2002), resulting in deflection of the droplets toward the substrate in combination with the fragmentation process of the atomizer. After fragmentation, the droplets are first centrifuged radially outward from the rotary atomizer. By directing air perpendicular to the substrate and by the electrostatic forces on the droplets, the droplets are deflected in the direction toward the surface. A model of the resulting droplet trajectories and air flow pattern is shown in Figure 8.73 (Scholz, 1998). A hollow-cone spray geometry results, leading to a paint deposition characteristic that has a local minimum in the spray center and an off-center maximum (Svejda, 2003). The complex flow structure in the spray has been investigated experimentally (Scholz, 1998) and by numerical simulation (Domnick et al., 1998, 2003; Olivas and Marty, 2002). The gas flow field as a vector plot of the steering air flow of a rotating bell (40,000 r/min) obtained by simulation is illustrated in Figure 8.74. The inner recirculating gas vortex flow is observed where gas velocities of 2 to 4 m/s are found directed away from the deposit in the direction toward the atomizer center.

The resulting dynamic deposition film thickness on a stationary flat target in this painting process comparing simulation and experiment is shown in Figure 8.75 (Domnick et al., 2003). The hollow-cone structure of the spray is reflected in the compaction pattern as a maximum in the radial distribution.

Nomenclature

Latin Symbols

A	Area
ALR	Gas-to-liquid mass flow ratio
c	Concentration
C_d	Drag coefficient
C_D	Discharge coefficient

C_p	Specific heat at constant pressure
C_s	Concentration at crust formation
d	Diameter
D	Diffusion coefficient
E	Energy
f_c	Collision frequency
g	Acceleration due to gravity
h	Specific enthalpy
Δh	Critical wave height
i_ϕ	Geometrical swirl parameter
I	Momentum ratio
k	Wave number
Ki	Kirpichev number
l	Length
L	Break-up length
L_f	Fragmentation point
\dot{m}	mass flow rate
M	Density ratio
N	Viscosity ratio
N_n	Number of nuclei
Nu	Nusselt number
Oh	Ohnesorge number
p	Pressure
\dot{Q}	Volumetric flow rate
r	Radius
Re	Reynolds number
S	Swirl parameter
Sha	Shannon number
Sh	Sherwood number
t	Thickness
T	Temperature
u	Velocity
V	Volume
We	Weber number
X	Core/orifice area ratio
ΔX	Driving potential

Greek Symbols

ε	Void fraction
η	Amplitude
θ	Cone half angle
κ	Ratio of specific heats
λ_δ	Wave length
μ	Viscosity
ρ	Density
σ	Surface tension
τ_f	Local film thickness
τ_p	Relaxation time
ω	Swirl ratio, frequency

Subscripts

<i>ac</i>	After collision
<i>bc</i>	Before collision
<i>c</i>	Critical, core
<i>crit</i>	Critical
<i>e</i>	Exit
<i>g</i>	Gas, gravity
<i>hom</i>	Homogeneous
<i>l</i>	Liquid
<i>o</i>	Orifice
<i>rel</i>	Relative
ϕ	Circumferential

References

- Aamir, M.A. and Watkins, A.P., Dense propane spray analysis with a modified collision model, CD-Rom, *Proceedings of the ILASS—Europe'99*, Toulouse, France, July 5–7, 1999.
- Ahmadi, M. and Sellens, R.W., A simplified maximum-entropy-based drop size distribution, *Atomizations and Sprays*, 3, 292–310, 1993.
- Amsden, A.A., O'Rourke, P.J. and Butler, T.D., KIVA-II: A Computer Program for Chemically Reactive Flows with Sprays, Los Alamos National Laboratory, Report, LA-11560-MS, 1989.
- Andersen, O., Bauckhage, K. and Schreckenberg, P., Production of Fine Metal Powders by Ultrasonic Standing Wave Atomization, *The International Journal of Powder Metallurgy*, 31(4), 341–349, 1995.
- Anderson, I.E. and Figliola, R.S., Observations of gas atomization process Dynamics, in *Modern Developments in Powder Metallurgy*, Gummesson, P.U. and Gustafson, D.A. Eds., Metal Powder Industries Federation, Princeton, N.J., vol. 20, 1998, pp. 205–223.
- Anderson, I.E. and Terpstra, R.L., Progress toward gas atomization processing with increased uniformity and control, *Mater. Sci. Eng. A*, 326(1), 101–109, 2002.
- Anderson, W.H. and Wolfe, H.E. Aerodynamic breakup of liquid drops-I. Theoretical, *Proceedings of the International Shock Tube Symposium*, Naval Ordnance Laboratory, White Oak, Maryland, USA, 1965, 1445–1152.
- Annavarapu, S. and Doherty, R.D., Inhibited coarsening of solid–liquid microstructures in spray casting at high volume fractions of solid, *Acta Metall. Mater.*, 43(8), 3207–3230, 1995.
- Anno, J.N., *The Mechanics of Liquid Jets*, Lexington Books, Lexington, MA, 1977.
- Antipas, G., Lekakou, C. and Tsakiroopoulos, P., The break-up of melt streams by high pressure gases in spray forming, *Proceedings of the ICSF-2 Swansea*, Sept. 13–15, 1993, pp. 15–24.
- Armster, S.Q., Delplanque, J.P., Rein, M., and Lavernia, E.J., Thermo-fluid mechanisms controlling droplet based materials processes, *Int. Mater. Rev.*, 47(6), 265–301, 2002.
- Ashgriz, N. and Poo, J.Y., Coalescence and separation in binary collision of liquid drops, *J. Fluid Mech.*, 221, 183–204, 1990.
- Bauckhage, K., Das Zerstäuben metallischer Schmelzen, *Chem.-Ing.-Tech.*, 64(4), 322–332, 1992.
- Bauckhage, K., Stand der Technik beim Sprühkomptieren von Bolzen, *Härterei-Techn.-Mitteil.*, 52(5), 319–331, 1997.
- Bauckhage, K., Use of the phase-doppler-Anemometry for the analysis and the control of the spray forming process, *Proceedings of the PM²TEC'98*, Las Vegas, May– June 4, 1998.
- Bauckhage, K., Fundamentals of melt atomization, spray forming and deposition, *Proceedings of the International Conference on Liquid Atomization and Spray Systems ICCLASS 2003*, Sorrento, Italy, 2003.
- Bauckhage, K., Bergmann, D., Fritsching, U., Lohner, H., Schreckenberg, P., and Uhlenwinkel, V., Das Scaling-Down-Problem bei der Zweistoffzerstäubung von Metallschmelzen, *Chem.-Ing.-Tech.*, 73(4), 304–313, 2001.

- Bauckhage, K., Bergmann, D., and Tillwick, J., Die Massen- und Enthalpiebilanzierung des Sprühkegels als Kopplung für die Modellvorstellung des Materialaufbaus in der Mix-Schicht, *Koll. SFB 372*, Universität Bremen, 1999, Vol. 4, pp. 139–170.
- Bauckhage, K. and Fritsching, U., Powder production from melts by ultrasonic standing wave atomization, *2nd Int. Conf. Multiphase Flow*, Kyoto, Japan, 1995.
- Bauckhage, K. and Fritsching, U., Production of metal powders by gas atomization, in *Liquid Metal Atomization: Fundamentals and Practice*, Cooper, K.P., Anderson, I.E., Ridder, S.D., and Biancanello F.S., Eds., TMS, Warrendale, USA, 2000, pp. 23–36.
- Bauman, S. D., A Spray Model for an Adaptive Mesh Refinement Code, Ph.D. thesis, Madison University, Wisconsin, 2001.
- Bayvel, L. and Orzechowski, Z., *Liquid Atomization*, Taylor & Francis, Washington, DC, 1993.
- Bellan, J., Perspectives on large eddy simulations for sprays: Issues and solutions, *Atomizations and Sprays*, 10, 409–425, 2000.
- Berg, M., Zum Aufprall, zur Ausbreitung und Zerteilung von Schmelztröpfchen aus reinen Metallen, Dissertation, Universität Bremen, 1999.
- Berg, M. and Ulrich, J., Experimental based detection of the splash limits for the normal and oblique impact of molten metal particles on different substrates, *J. Mat. Synth. Proc.*, 5(1), 45–49, 1997.
- Bergmann, D., Fritsching, U., and Crowe, C.T., Multiphase flows in the spray forming process, *Proceedings of the second International Conference on Multiphase Flow*, Kyoto, Japan, April 3–7, 1995, Vol. 1, pp. SP1–SP8.
- Bergmann, D., Modellierung des Sprühkompaktierprozesses für Kupfer- und Stahlwerkstoffe, Dissertation, Universität Bremen, 2000.
- Bergmann, D., Fritsching, U., and Bauckhage, K., Averaging thermal conditions in molten metal sprays, in *Proceedings of the TMS—Annual Meeting*, Mishra, B., Ed., EPD Congress, San Diego USA, Feb. 28–Mar. 4, 1999.
- Bergmann, D., Fritsching, U., and Bauckhage, K., A mathematical model for cooling and rapid solidification of molten metal droplets, *Int. J. Therm. Sci.*, 39, 53–62, 2000.
- Bergmann, D., Fritsching, U., and Bauckhage, K., Simulation of molten metal droplet sprays, *Comp. Fluid Dyn.-J.*, 9, 203–211, 2001a.
- Bergmann, D., Fritsching, U., and Bauckhage, K., Thermische Simulation des Sprühkompaktierprozesses, *Härterei-Techn.-Mitteil.*, 56(2), 110–119, 2001b.
- von Berg, E., Bürger, M., Cho, S.H., and Schatz, A., Analysis of atomization of a liquid jet taking into account effects of the near surface boundary layer, *Proceedings of the 11th ILASS—Europe Conference*, Nürnberg, 21–23. March 1995.
- Bergström, C., Fuchs, L., and Holmborn, J., Large Eddy Simulation of Spray Injected in a Strong Turbulent Cross Flow, CD-Rom, *Proceedings of the ILASS—Europe' 99*, Toulouse, France, July 5–7, 1999.
- Berthomieu, P., Carntz, H., Villedieu, P., and Lavergne, G., Characterization of droplet breakup regimes, in *Proceedings of the ILASS—Europe' 98*, Yule, A. J., Ed., Manchester, UK, July 6–8, 1998, pp. 72–77.
- Bhandari, B.R., Dumoulin, E. D., Richard, H. M. J., Noleau, I., and Lebert, A. M., Flavor encapsulation by spray drying: application to citral and linalyl acetate, *J. Food Science*, 57(1), 217–221, 1992.
- Bhandari, B.R., Senoussi, A., Dumoulin, E. D., and Lebert, A., Spray drying of concentrated fruit juices, *Dry. Technol.*, 11(5), 1081–1092, 1993.
- Blei, S. and Sommerfeld, M., Lagrangian modelling of agglomeration during spray drying process, Ninth International Conference on Liquid Atomization and Spray Systems ICLASS 2003, Sorrento, Italy, 2003.
- Böttner, C.U., Über den Einfluss der elektrostatischen Feldkraft auf turbulente Zweiphasenströmungen, Dissertation Universität Halle, Wittenberg, 2002.
- Böttner, C.U., Kohnen, G., and Sommerfeld, M., Numerical calculations of the interaction between fluid dynamics and electrostatics applied to the powder Painting Process, *Proceedings of the ILASS—Europe' 98*, Manchester, UK, 1998.

- Bolle, L. and Moureau, J.C., Spray cooling of hot surfaces, *Multiphase Sci. Technol.*, 1, 1–97, 1982.
- Bracco, F.V., Chehroudi, B., Chen, S.H., and Onuma, Y., On the Intact Core of Full Cone Sprays, *SAE Trans.*, Vol. 94, Paper 850126, 1985.
- Brackbill, J.U., Kothe, D.B., and Zemach, C., A continuum method for modelling surface tension, *J. Comp. Phys.*, 100, 335–354, 1992.
- Bradley, D., On the atomization of liquids by high-velocity gases, Part 1, *J. Phys. D: Appl. Phys.*, 6, 1724–1736, 1973a.
- Bradley, D., On the atomization of liquids by high-velocity gases, Part 2, *J. Phys. D: Appl. Phys.*, 6, 2267–2272, 1973b.
- Brauer, H., *Grundlagen der Einphasen- und Mehrphasenströmungen*, Sauerländer Verlag, Frankfurt, 1971.
- Brennen, J.G., Herrera, J., and Jowitt, R., A study of some other factors affecting the spray drying of concentrated orange juice on a laboratory scale, *J. Food Technol.*, 6, 295–307, 1971.
- Brimacombe, J.K., Agarwal, P.K., Baptista, L.A., Hibbins, S., and Prabhakar, B., Spray cooling in the continuous casting of steel, *Proceedings of the 63rd National Open Hearth and Basic Oxygen Steel Conference*, Washington, DC, 1980, pp. 235–252.
- Brodkey, R.S., *The Phenomena of Fluid Motions*, Addison-Wesley, Reading, MA, 1967.
- Bruin, S., Velocity distributions in a liquid film flowing over a rotating conical surface, *Chem. Eng. Sci.*, 24, 1647–1654, 1969.
- Buchholz, M., Uhlenwinkel, V., v. Freyberg, A., and Bauckhage, K., Specific enthalpy measurement in molten metal spray, *Mater. Sci. Eng. A*, 326, 165–175, 2002.
- Buckner, H.N. and Sojka, P.E., Effervescent atomization of high-viscosity fluids, Part I: Newtonian liquids, *Atomizations and Sprays*, 1, 239–252, 1991.
- Bürger, M., Schwalbe, W., Kim, D.S., Unger, H., Hohmann, H., and Schins, H., Two-phase description of hydrodynamic fragmentation processes within thermal detonation waves, *J. Heat Transf.*, 106, 728–734, 1984.
- Bürger, M., v. Berg, E., Cho, S.H., and Schatz, A., Fragmentation processes in gas and water atomization plants for process optimization purposes, Part 1: discussion of the main fragmentation processes, *Powder Metall. Int.*, 21, 10–15, 1989.
- Bürger, M., v. Berg, E., Cho, S.H., and Schatz, A., Analysis of fragmentation processes in gas and water atomization plants for process optimization purposes, Part 2: modelling of growth and stripping of capillary waves in parallel shear flow—the Basic fragmentation mechanism, *Powder Metall. Int.*, 24(6), 32–38, 1992.
- Bussmann, M., Aziz, S.D., and Chandra, S., Photographs and simulations of molten metal droplets landing on a solid surface, *J. Heat Transf.*, 122, 422, 2000.
- Campanile, F. and Azzopardi, B.J., Atomisation of very viscous liquids, *Proceedings of the International Conference on Liquid Atomization and Spray Systems ICCLASS 2003*, Sorrento, Italy, 2003.
- Chavez, H. and Obermeier, F., Modelling the effect of modulations of the injection velocity on the structure of liquid jets, *Proceedings of SPRAY 2002*, Freiburg, 2002.
- Chawla, J.M., Flüssigkeitsinhalt in Rohren für Flüssigkeits/Gas-Gemische bei der Zweiphasenströmung, *Chem.-Ing.-Tech.*, 5+6, 328–330, 1969.
- Chawla, M. and v. Böckh, P., Kritische Massenstromdichte von Flüssigkeits/Gas-Gemischen, *Chem.-Ing.-Tech.*, 43, 1106–1108, 1971.
- Chen, S.K. and Lefebvre, A.H., Discharge coefficients for plain-orifice effervescent atomizers, *Atomizations and Sprays*, 4, 275–290, 1994.
- Chen, X.D., Lake, R., and Jebson, S., Study of milk powder deposition on a large industrial dryer, *Food Bioprod. Process. Trans. Inst. Chem. Eng.*, Part C, 71, 180–186, 1993.
- Chin, J.S. and Lefebvre, A.H., Flow patterns in internal-mixing, twin-fluid atomizers, *Atomizations and Sprays.*, 3, 463–475, 1993.
- Choi, K.J. and Kang, B.S., *Fluid Mechanics and Heat Transfer in Sprays*, ASME FED, 78, HTD, Vol. 270, pp. 161–165, 1993.

- Choi, K.J. and Yao, S.C., Mechanisms of film boiling heat transfer of normally impacting spray, *Int. J. Heat Mass Transfer*, 30, 311–318, 1987.
- Chou, W.-H., Hsiang, L.-P., and Faeth, G. M., Temporal properties of drop breakup in the shear breakup regime, *Int. J. Multiphase Flow*, 23, 651–670, 1997.
- Chou, W.-H. and Faeth, G.M., Temporal properties of secondary drop breakup in the bag breakup regime, *Int. J. Multiphase Flow*, 24, 889–912, 1998.
- Churchill, S.W. and Usagi, R., A General Expression for the Correlation of Rates of Transfer and Other Phenomena, *AIChe Journal*, 18, 1121–1128, 1972.
- Clift, R., Grace, J.R., and Weber, M.E., *Bubbles, Drops and Particles*, Academic Press, San Diego, 1978.
- Connelly, S., Coombs, J.S., and Medwell, J.O., Flow characteristics of metal particles in atomised sprays, *Met. Powder Rep.*, 41, 9, 1986.
- Cousin, J. and Dumouchel, C., Effect of viscosity on the linear instability of a liquid sheet, *Atomizations and Sprays*, 6, 563–576, 1996.
- Cousin, J. and Dumouchel, C., Theoretical determination of spray drop size distribution, *Proceedings of ICCLASS—'97*, Seoul, Korea, August 1997, pp. 788–803.
- Cousin, J., Yoon, S.J., and Dumouchel, C., Coupling of the classical linear theory and the maximum entropy formalism for the prediction of drop size distributions in sprays, application to pressure swirl atomizers, *Atomizations and Sprays*, 6, 601–613, 1996.
- Crowe, C.T., Modelling spray-air contact in spray drying systems, *Adv. Dry.*, 1, 63–99, 1980.
- Crowe, C.T., Sharma, M.P., and Stock, D.E., The particle-source-in-cell method for gas droplet flow, *J. Fluid. Eng.*, 99, 325–332, 1977.
- Crowe, C.T., Sommerfeld, M., and Tsuji, Y., *Multiphase Flows with Drops and Particles*, CRC Press, Boca Raton, FL, 1998.
- Czisch, C., Lohner, H., Fritsching, U., and Bauckhage, K., Atomization of highly viscous melts, *Proceedings on Spray Deposition and Melt Atomization SDMA 2003*, Bremen, Germany, 2003.
- Dai, Z. and Faeth, G. M., Temporal properties of secondary drop breakup in the multimode breakup regime, *Int. J. Multiphase Flow*, 27, 217–236, 2001.
- Dec, J.E., A Conceptual Model of DI Diesel Combustion Based on Laser-Sheet Imaging, SAE Paper 970873, 1997.
- Delplanque, J.P. and Sirignano, W.A., Boundary-layer stripping effects on droplet transcritical convective vaporization, *Atomizations and Sprays*, 4, 325–349, 1994.
- Djuric, Z., Newberry, P., and Grant, P.S., Two dimensional simulation of liquid metal spray deposition onto a complex surface, *Modelling Simul. Mater. Sci. Eng.*, 7, 553–571, 1999.
- Dielewicz, L.G., v. Berg, E., and Lampe, M., Computation of transsonic two-phase flow in liquid metal jet atomizers, CD-Rom, *Proceedings of the ILASS—Europe' 99*, Toulouse, France, July 5–7, 1999.
- Djuric, Z. and Grant, P.S., Two dimensional simulation of liquid metal spray deposition onto a complex surface II: Splashing and redeposition, *Model. Simul. Mater. Sci.*, 9, 111–127, 2001.
- Dobre, M. and Bolle, L., Theoretical prediction of ultrasonic spray characteristics using the maximum entropy formalism, in *Proceedings of ILASS—Europe' 98*, Yule, A.J., Ed., Manchester, UK, July 6–8, 1998, pp. 7–12.
- Doherty, R., Cai, C., and Warner Kohler, L.K., Modeling and microstructure development in spray forming, *Int. J. Powder Metall.*, 33, 50–60, 1997.
- Dolinsky, A.A., High temperature spray drying, *Drying Technol.*, 19, 785–806, 2001.
- Dombrowski, N. and Fraser, R.P., A photographic investigation into the disintergration of liquid sheets, *Philos. T. Roy. Soc. A*, 247, 1954.
- Dombrowski, N. and Johns, W.R., The aerodynamic instability and disintegration of viscous liquid sheets, *Chem. Eng. Sci.*, 18, 203–214, 1963.
- Domnick, J., Raimann, J., Wolf, G., Berlemon, A., and Cabot, M.-S., On-line process control in melt spraying using phase-Doppler anemometry, *Proceedings of the ICCLASS—'97*, Seoul, Korea, Aug. 18–22, 1997.
- Domnick, J., Scheibe, A., and Ye, Q., The electrostatic spray painting process with High-Speed rotary bell atomizers: Influences of operating conditions and target geometries, *Proceedings of the International Conference on Liquid Atomization Spraying Systems ICCLASS 2003*, Sorrento, Italy, 2003.

- Dubrovsky, V.V., Podvysotsky, A.M., and Shraiber, A.A., Particle interaction in three-phase polydispersed flows, *Int. J. Multiphase Flow*, 18, 337–352, 1992.
- Duda, J.L. and Vrentas, J.S., Fluid mechanics of laminar liquid jets, *Chem. Eng. Sci.*, 22, 855–873, 1967.
- Dumouchel, C., Problemes lies a la d'un pulverisateur mecanique-hydrodynamique de chambre et instabilité de nappe, Ph. D. thesis, Universität Rouen, 1989.
- Dunkley, J.J., Liquid metal atomization—a suitable case for investigation, in *Proceedings of ILASS—Europe '98*, Yule, A.J., Ed., Manchester, UK, July 6–8, 1998, pp. P1–P6.
- Dunkley, J.J. and Telford, B., Control of satellite particles in gas atomization, *Proceedings of the World Congress on Powder Metallurgy and Particulate Materials PM²TEC 2002*, Orlando, FL, 2002.
- Dykhuijzen, R.C. and Smith, M.F., Gas dynamic principles of spray, *J. Therm. Spray Techn.*, 7, 205–212, 1998.
- Edwards, C.F. and Marx, K.D., Multipoint statistical structure of the ideal spray, Part I: Fundamental concepts and the realization density, *Atomizations and Sprays*, 5, 435–455, 1995.
- Edwards, C.F. and Marx, K.D., Multipoint statistical structure of the ideal spray, Part II: Evaluating steadiness using the interparticle time distribution, *Atomizations and Sprays*, 5, 57–505, 1995.
- Elperin, T. and Krasovitov, B., Evaporation of liquid droplets containing small solid particles, *Int. J. Heat Mass Transfer*, 38, 2259–2267, 1995.
- Espina, P.I., Numerical Simulation of Atomization Gas Flow, *Koll. SFB 372*, Vol. 4, University of Bremen, 1999, pp. 127–138.
- Espina, P.I. and Piomelli, U., Study of the Gas Jet in a Close-Coupled Gas Metal Atomizer, AIAA Paper 98-0959, 1998a.
- Espina, P.I. and Piomelli, U., Numerical simulation of the gas flow in gas metal atomizers, *Proceedings of the 1998 ASME-FED*, Washington, 1998b, FEDSM98-4901.
- Faeth, G.M., Structure and atomization properties of dense turbulent sprays, *23rd Symposium on Combustion*, The Combustion Institute, Pittsburgh, 1990, pp. 1345–1352.
- Faeth, G.M., Dynamics of secondary drop breakup—a rate controlling process in dense sprays, *Proceedings of the ILASS—Europe 2002*, Zaragoza, Sept. 9–11, 2002.
- Ferrari, G., Meerdink, G., and Walstra, P., Drying kinetics for a single droplet of skimmed milk., *J. Food Eng.*, 10, 215–230, 1989.
- Faragó, Z. and Chigier, N., Morphological classification of disintegration of round liquid jets in a coaxial air stream, *Atomizations and Sprays*, 2, 137–153, 1992.
- Fritsching, U., Modelling the spray cone behaviour in the metal spray forming process: momentum and thermal coupling in two-phase flow, *PHOENICS J. Comp. Fluid Dyn.*, 8, 68–90, 1995.
- Fritsching, U., *Spraysimulation — Modellierung und numerische Simulation von verfahrenstechnischen Prozessen am Beispiel des Sprühkompaktierens von Metallen*, Shaker Verlag, Aachen, Germany, 2001.
- Fritsching, U. and Bauckhage, K., Die Bewegung von Tropfen im Sprühkegel einer Ein- und einer Zweistoffdüse, *Chem.-Ing.-Tech.*, 59, 744–745, 1987.
- Fritsching, U. and Bauckhage, K., Investigations on the atomization of molten metals: the coaxial jet and the gas flow in the nozzle near field, *PHOENICS J. Comp. Fluid Dyn.*, 5, 81–98, 1992.
- Fritsching, U. and Bauckhage, K., Lagrangian modelling of thermal and kinetic droplet/particle behaviour in the metal spray compaction process, *Proceedings ILASS-93 / CHISA-93*, Prag, CR, Aug. 29–Sept. 3, 1993.
- Fritsching, U. and Bauckhage, K., Zum Impuls- und Wärmetransport bei der Zerstäubung und anschließenden Kompaktierung von Schmelzen, *Chem.-Ing.-Tech.*, 66, 380–382, 1994.
- Fritsching, U. and Bauckhage, K., Sprayforming of metals, *Ullmann's Encyclopedia of Industrial Chemistry*, 6th ed., 1999 Electronic Release, Wiley VCH, Weinheim, 1999.
- Fritsching, U., Zhang, H., and Bauckhage, K., Thermal histories of atomized and compacted metals, *Proceedings of the Powder Metallurgy World Congress PM-93*, Kyoto, Japan, July 12–15, 1993.
- Fritsching, U., Zhang, H., and Bauckhage, K., Numerical simulation of temperature distribution and solidification behaviour during spray forming, *Steel Res.*, 65, 273–278, 1994a.
- Fritsching, U., Zhang, H., and Bauckhage, K., Numerical results of temperature distribution and solidification behaviour during spray Forming, *Steel Res.*, 65, 322–325, 1994b.

- Frohn, A. and Roth, N., *Dynamics of Droplets*, Springer Verlag, Berlin, 2000.
- Gelfand, B.E., Droplet breakup phenomena in flows with velocity lag, *Prog. Energ. Combust.*, 22, 201–265, 1996.
- Gelfand, B.E., Gubin, S.A., Kogarko, S.M., and Kormar, S.P., Viscous drop destruction peculiarities in shock waves, *J. Eng. Phys.*, 25(3), 467–471, 1973.
- Georjon, T.L. and Reitz, R.D., A drop-shattering collision model for multidimensional spray computations, *Atomizations and Sprays*, 9, 231–254, 1999.
- Gerking, L., Powder from metal and ceramic melts by laminar streams at supersonic speed, *Powder Metall. Int.*, 25, 59–65, 1993.
- Giffen, E. and Muraszew, A., *The Atomization of Liquid Fuels*, Wiley, New York, 1953.
- Glaser, H.W., *Die Zerstäubung von Suspensionen mit Ein- und Zweistoffdüsen*, VDI-Verlag, Düsseldorf, 1989.
- Goldschmidt, A. and Streitberger, H.J., *BASF—Handbuch Lackiertechnik*, Vincentz Verlag, Hannover, 2002.
- Grant, P.S., Spray forming, *Prog. Mater. Sci.*, 39, 497–545, 1995.
- Grant, P.S., Cantor, B., and Katgerman, L., Modelling of droplet dynamic and thermal histories during spray forming-I: Individual droplet behaviour, *Acta Metall. Mater.*, 41, 3097–3108, 1993a.
- Grant, P.S., Cantor, B., and Katgerman, L., Modelling of droplet dynamic and thermal histories during spray forming-II: Effect of process parameters, *Acta Metall. Mater.*, 41, 3109–3118, 1993b.
- Grant, R.P. and Middleman, S., Newtonian jet stability, *AIChE J.*, 12, 669–678, 1966.
- Gutierrez-Miravete, M., Lavernia, E.J., Trapaga, G.M., and Szekely, J., A mathematical model of the liquid dynamic compaction process, Part 2: formation of the deposit, *Int. J. Rapid Solidif.*, 4, 125–150, 1988.
- Haenlein, A., Disintegration of a liquid jet, NACA TN 659, 1932.
- Hagerty, W.W. and Shea, J.F., A study of the stability of plane fluid sheets, *J. Appl. Mech.*, 22(509), 509–514, 1955.
- Halada, K., Suga, H., and Muramatsu, Y., Atomizing parameters for centrifugal atomization of metal Proc. PM'90 World Conference on Powder Metallurgy Vol. 1, The Institute of Metals, London, 1990, p.193.
- Hansmann, S., Einfluss von Stoff- und Betriebsparametern auf die Zerstäubung hochviskoser Flüssigkeiten im Ultraschall-Stehwellenfeld, Dissertation, Universität Bremen, 1996.
- Hardalupas, Y., Tsai, R.-E., and Whitelaw, J.H., Unsteady breakup of liquid jets in coaxial airblast atomizers, *Proceedings of ICLASS—'97*, Seoul, Korea, Aug. 18–22, 1997, pp. 326–333.
- Hartmann, D., Theoretische Untersuchungen zur Tropfenbildung bei Dispergierprozessen, Dissertation, Martin-Luther-Universität Halle, Germany, 1993.
- Hattel, J.H., Pryds, N.H., Pedersen, T.B., and Pedersen, A.S., Numerical modelling of the spray forming process: The effect of process parameters on the deposited material, *Proceedings of SDMA 2000*, Bremen, 2000, pp. 803–812.
- Hattel, J.H., Pryds, N., Thorborg, J., and Ottosen, P., A quasi-stationary numerical model of atomized metal droplets, Part I: Model formulation, *Model. Simul. Mater. Sci.*, 7, 413–430, 1999.
- Heck, U., Zur Zerstäubung in Freifalldüsen, Ph. D. thesis, Universität Bremen, 1998.
- Heck, U., Fritsching, U., and Bauckhage, K., Gas-flow effects on twin-fluid atomization of liquid metals, *Atomizations and Sprays*, 10, 25–46, 2000.
- Henein, H., Single fluid atomization through the application of impulses to a melt, *Mater. Sci. Eng. A*, 326, 92–100, 2002.
- Hennigs, C., Kockel, T.K., and Langrish, T.A.G., New measurements of the sticky behavior of skim milk powder, *Dry. Technol.*, 19, 471–484, 2001.
- Heukelbach, K. and Tropea, C., Influence of the inner flowfield of flat fan pressure atomizers on the disintegration of the liquid sheet, *Proceedings of Institute Liquid Atomization and Spray System ILASS—Europe AGM 2001*, Zurich, Switzerland, 2001.
- Heywood, J.B., *Internal Combustion Engine Fundamentals*, McGraw-Hill, New York, 1998.

- Hiller, R.B., Der Einfluß von Partikelstoß und Partikelhaftung auf die Abscheidung in Faserfiltern, Dissertation, Universität Karlsruhe, VDI-Verlag GMBH, Düsseldorf, 1981.
- Hinze, J.O. and Milborn, H., Atomization of liquids by means of a rotating cup, *J. Appl. Mech.*, 17, 145–153, 1950.
- Hirth, J.P., Nucleation, undercooling and homogeneous structures in rapidly solidified powders, *Metall. Trans. A*, 9A, 401–404, 1978.
- Ho, C.A. and Sommerfeld, M., Modelling of micro-particle agglomeration in turbulent flows, *Chem. Eng. Sci.*, 57, 3073–3084, 2002.
- Hohmann, S., Strahlausbreitung und Tropfenverdunstung bei der dieselmotorischen Direkteinspritzung, Dissertation, RWTH Aachen, Shaker Verlag Aachen, 1999.
- Hopfinger, E.J., Liquid jet instability and the breakup process in liquid–liquid agitated atomization in a coaxial gas stream, *J. Therm. Eng. Jpn.*, 16, 3–319, 1998.
- Horvay, M., Theoretische und experimentelle Untersuchung über den Einfluß des inneren Strömungsfeldes auf die Zerstäubungseigenschaften von Drall-Druckzerstäubungsdüsen, Dissertation, Universität Karlsruhe, 1985.
- Hsiang, L.P. and Faeth, G.M., Near-limit drop deformation and secondary breakup, *Int. J. Multiphase Flow*, 18, 35–652, 1992.
- Hsiang, L.P. and Faeth, G.M., Drop properties after secondary breakup, *Int. J. Multiphase Flow*, 19, 721–735, 1993.
- Hsiang, L.P. and Faeth, G.M., Drop deformation and breakup due to shock wave and steady disturbances, *Int. J. Multiphase Flow*, 21, 545–560, 1995.
- Huppmann, W.J. and Dalal, K., *Metallographic Atlas of Powder Metallurgy*, Schmid, Freiburg, 1986.
- Isenschmid, T., Charaktersisierung von Mehrstoffdüsen für Suspensionen, Dissertation, ETH-Zürich, 1992.
- Jeffrey, H., On the formation of water waves by wind, *Proc. Roy. Soc. A*, 189, 1924.
- Jeschar, R., Specht, E., and Köhler, C., Heat transfer during cooling of heated metallic objects with evaporating liquids, in *Theory and Technology of Quenching*, Tensi, H. et al., Eds., Springer Verlag, Berlin, 1992, pp. 73–92.
- Jicha, M., Jedelsky, J., Otahal, J., and Slama, J., Influence of some geometric parameters on the characteristics of effervescent atomization, *Proceedings of ILASS—Europe*, Zaragoza, Spain, 2002.
- Joseph, D.D., Belanger, J., and Beavers, G.S., Breakup of a liquid drop suddenly exposed to a high-speed airstream, *Int. J. Multiphase Flow*, 25, 1263–1304, 1999.
- Jordan, N., Auswirkungen der Prozeßparameter und der Prozeßführung auf die Eigenschaften sprühkompakter Kupferbasis-Werkstoffe, Dissertation, Universität Bremen, Shaker Verlag, Aachen, 2003.
- Karlsson, J.A.J., Modeling auto-ignition, flame propagation and combustion in non-stationary turbulent sprays, Ph.D. thesis, Chalmers University, Sweden, 1995.
- Kim, J.Y. and Lee, S.Y., Dependence of spraying performance on the internal flow pattern in effervescent atomizers, *Atomizations and Sprays*, 11, 735–756, 2001.
- King, L., On the acoustic radiation pressure on spheres, *Proc. Roy. Soc. London*, 147A, 212–239, 1934.
- Kieviet, F. and Kerkhof, P. J., Measurement of particle residence time distributions in spray dryer, *Drying Technol.*, 13, 1241–1248, 1995.
- Klar, E. and Fesko, J.W., *Powder Metallurgy Metals Handbook*, Vol. 7, American Society for Metals, Materials Park, Ohio, 1984.
- Klein, M., Sadiki, A., and Janicka, J., Influence of the inflow conditions on the direct numerical simulation of primary breakup of liquid jets, *ILASS—Europe 2001*, Zürich, 2001, pp. 475–480.
- Klein, M., Sadiki, A., and Janicka, J., Untersuchung des Primärzerfalls eines Flüssigkeitsfilms: Vergleich direkte numerische Simulation, Experiment und lineare Theorie, *Spray 2002*, Freiberger Forschungshefte A 870 Verfahrenstechnik, TU-Bergakademie Freiberg 2002, pp. 63–72.
- Kolev, N.I., *Thermal and Mechanical Interactions of Multiphase Dynamics*, Vol. 2, Springer, Berlin, 2002.
- Kong, S.C., Han, Z., and Reitz, R.D., The Development and Application of a Diesel Ignition and Combustion Model, SAE Paper, 950278, 1995.

- Kramer, C., Die Kompaktierungsrate beim Sprühkompaktieren von Gauß-förmigen Deposits, Dissertation, Universität Bremen, 1997.
- Krauss, M., Bergmann, D., and Fritsching, U., In-situ particle temperature, velocity and size measurements in the spray forming process, *Mater. Sci. Eng. A*, 326, 154–164, 2002.
- Krzczkowski, S.A., Measurement of liquid droplet disintegration mechanisms, *Int. J. Multiphase Flow*, 6, 227–239, 1980.
- Kröger, B., Einfluß der Luftverteilerströmung auf die Ausbreitung der dispersen Phase in einem Sprühtrocknerturm, Dissertation, Universität Bremen, 2001.
- von Künsberg Sarre, C. and Tatschl, R., Spray modelling/atomisation — current status of break-up models, *Turbulent Combustion of Gases and Liquids, Leading Edge Technologies, ImechE Seminar*, London, UK, 1998.
- Kurt, O., Mulhem, B., Fritsching, U., and Schulte, G., Zerstäubung von Suspensionen mittels eines Rotationszerstäubers, *Spray 2002*, Freiberg, Nov. 21–22, 2002.
- Lafaurie, B., Mantel, T., and Zaleski, S., Direct navier-stokes simulations of the near-nozzle region, in *Proceedings of ILASS—Europe '98*, Yule, A.J., Ed., Manchester, UK, July 6–8, 1998, pp. 54–59.
- Lamb, H., *Hydrodynamics*, 6th ed., Dover, New York, 1986.
- Lampe, K., Experimentelle Untersuchung und Modellierung der Mehrphasenströmung im düsennahen Bereich einer Öl-Brenner-Düse, Dissertation, Universität Bremen, 1994.
- Lane, W.R., Shatter of drops in streams of air, *Ind. Eng. Chem.*, 43, 1312–1317, 1951.
- Landwehr, F., Schmidt, D., and Walzel, P., Messung und Berechnung des kritischen Druckverhältnisses an Zweistoff-Düsen, *Proceedings of Spray '99*, Bremen, Germany, Oct. 5–6, 1999.
- Lasheras, J.C. and Hopfinger, E.J., Liquid jet instability and atomization in a coaxial gas stream, *Annu. Rev. Fluid. Mech.*, 32, 275–308, 2000.
- Lavernia, E.J., Spray Atomization and Deposition of Metal Matrix Composites, *Koll. SFB 372*, Vol. 1, Universität Bremen, 1996 pp. 63–122.
- Lavernia, E.J., Gutierrez, E.M., Szekely, J., and Grant, N.J., A mathematical model of the liquid dynamic compaction process, Part 1: heat flow in gas atomization, *Int. J. Rapid Solidif.*, 4, 89–124, 1988.
- Lavernia, E.J. and Wu, Y., *Spray Atomization and Deposition*, Wiley Chichester, 1996.
- Lawley, A., *Atomization—The Production of Metal Powders*, Metal Powder Industries Federation, Princeton, USA, 1992.
- Lawley, A., Melt atomization and spray deposition-quo vadis, *Proceedings of SDMA 2000*, Bremen, 2000, pp. 3–16.
- Lawley, A., Mathur, P., Apelian, D., and Meystel, A., Sprayforming: process fundamentals and control, *Powder Metall.*, 33, 109–111, 1990.
- Le, T., Stefaniuk, H., Henein, H., and Huaot, J.Y., Measurement and analysis of melt flowrate in gas atomization, *Int. J. Powder Metall.*, 35(1), 51–60, 1999.
- Lee, E. and Ahn, S., Solidification progress and heat transfer analysis of gas atomized alloy droplets during spray forming, *Acta Metall. Mater.*, 42, 3231–3243, 1994.
- Lee, S.H. and Ryan, H.S., Development of a new model and heat transfer analysis of impinging diesel sprays on a wall, *Atomizations and Sprays*, 11, 85–106, 2001.
- Leatham, A.G. and Lawley, A., The Osprey process: principles and applications, *Int. J. Powder Metall.*, 29, 321–329, 1993.
- Lefebvre, A.H., *Gas Turbine Combustion*, Hemisphere, Washington, 1983.
- Lefebvre, A.H., *Atomizations and Sprays*, Hemisphere, New York, 1989.
- Leung, J.C. and Epstein, M., A generalized correlation for two-phase nonflashing homogeneous choked flow, *J. Heat Transf.*, 112, 528–530, 1990.
- Levi, C.G. and Mehrabian, R., Heat flow during rapid solidification of undercooled metal droplets, *Metall. Trans. A: Phys. Metall. Mater. Sci.*, 13A, 221–234, 1982.
- Levich, V.G., *Physicochemical Hydrodynamics*, Prentice Hall, NJ, 1962.
- Li, X., Mechanism of atomization of a liquid jet, *Atomization and Sprays*, 5, 89–105, 1995.
- Li, X. and Tankin, R.S., Droplet size distribution: a derivation of Nukyama-Tanasawa type distribution function, *Combustion. Sci. Tech.*, 56, 65, 1987.

- Libera, M., Olsen, G.B., and van der Sande, J.B., Heterogeneous nucleation of solidification in atomized liquid metal droplets, *Mater. Sci. Eng. A*, 132, 107–118, 1991.
- Lichtarowicz, A., Duggins, R.K., and Markland, E., Discharge coefficients for incompressible non-vanishing flow through long orifices, *J. Mech. Eng. Sci.*, 7, 210–219, 1965.
- Lierke, E.G., Leung, E.W., and Luhmann, D., Atomization by ultrasound, *Third International Coll.*, AIP Conference Proceedings, Vol. 197, Monterey, 1988, p. 71.
- Liu, A.B., Mather, D., and Reitz, R.D., Modeling the Effects of Drop Drag and Breakup on Fuel Sprays, SAE Paper, 930072, 1993.
- Liu, H., Numerical modelling of gas atomization in spray forming process, *Proceedings of 1997 TMS Annual Meeting*, Orlando, Florida, Feb. 9–13, 1997.
- Liu, H., Spray forming, in *Modelling and Simulation for Casting and Solidification: Theory and Applications*, Yu, K.O., Ed., Marcel Dekker Inc., New York, USA, 2000a.
- Liu, H., *Science and Engineering of Droplets: Fundamentals and Applications*, William Andrew Publ., Norwich, USA, 2000b.
- Liu, H., Lavernia, E.J., and Rangel, R.H., Numerical investigation of micropore formation during substrate impact of molten droplets in plasma spray processes, *Atomizations and Sprays*, 4, 369–384, 1994.
- Löffler-Mang, M., Düsenströmung, Tropfenentstehung und Tropfenausbreitung bei rücklaufgeregelten Drall-Druckzerstäubern, Dissertation, Universität Karlsruhe, 1992.
- Lohmann, M., Herstellung von Partikeln durch elektrostatische Zerstäubung von Flüssigmetallen in gasförmiger Umgebung, Dissertation, Universität Duisburg, Germany, 2000.
- Lohner, H., Zerstäuben von Mineralschmelzen mit Heißgas, Dissertation, Universität Bremen, VDI-Verlag, Düsseldorf, Germany, 2003.
- Lohner, H., Czisch, C., and Fritsching, U., Impact of gas nozzle arrangement on the flow field of a twin fluid atomizer with external mixing, *Proceedings of the International Conference on Liquid Atomization and Spray Systems ICCLASS 2003*, Sorrento, Italy, 2003.
- Lörcher, M., Zerstäuben von zweiphasigen Gemischen aus Flüssigkeiten und Gasen, VDI Fortschritt Ber., Reihe 3, 764, VDI Verlag Düsseldorf, Germany, 2003.
- Lörcher, M., Schmidt, F., and Mewes, D., Flow field and phase distribution inside effervescent atomizers, CD-ROM, *Proceedings of the 9th International Conference on Liquid Atomization and Spray System ICCLASS 2003*, Sorrento, Italy, 2003.
- Louey, A.F. and Refstrup, E., Recent advances in agglomeration during Spray drying, *Sixth World Congress of Chemical Engineering*, Melbourne, 2001.
- Low, T.B. and List, R., Collision, coalescence and breakup of raindrops, *J. Atmos. Sci.*, 39, 1591–1618, 1982.
- Lozano, A., Call, C.J., and Dopazo, C., An experimental and numerical study of the atomization of a planar liquid sheet, *Proceedings of ICCLASS-94*, Rouen, France, 1994.
- Lubanska, H., Correlation of spray ring data for gas atomization of liquid droplets, *J. Met.*, 2, 45–49, 1970.
- Lund, M.T., Sojka, P.E., Lefebvre, A.H., and Gosselin, P.G., Effervescent atomization at low mass flow rates, Part 1: the influence of surface tension *Atomization Spray.*, 3, 77–89, 1993.
- Luong, J.T.K. and Sojka, P.E., Unsteadiness in effervescent sprays, *Atomization Spray.*, 9, 87–109, 1999.
- Magnussen, B.F. and Hjertager, B.H., On mathematical modeling of turbulent combustion with special emphasis on soot formation and combustion, *16th International Symposium on Combustion*, The Combustion Institute, Pittsburgh, PA, 1989, pp. 719–729.
- Malot, H. and Dumouchel, C., Volume-based spray drop size distribution: derivation of a generalized gamma distribution from the application of the maximum entropy formalism, CD-Rom, *Proceedings of ILASS—Europe 99*, Toulouse, France, July 5–7, 1999.
- Mansour, A. and Chigier, N., Effect of turbulence on the stability of liquid jets and the resulting droplet size distributions, *Atomization Spray.*, 4, 583–604, 1994.
- Markus, S. and Fritsching, U., Spray forming with multiple atomization, *Proceedings of SDMA 2003*, Bremen, Germany, 2003a.

- Markus, S. and Fritsching, U., Modelling secondary break-up of melts in sprays, *Proceedings of the International Conference on Liquid Atomization and Spray Systems, ICLASS 2003*, Sorrento, Italy, 2003b.
- Markus, S., Fritsching, U., and Bauckhage, K., Jet break up of liquid metals, *Mater. Sci. Eng. A*, 326, 122–133, 2000.
- Marx, K.D., Edwards, C.F., and Chin, W.K., Limitations of the ideal phase-Doppler system: extension to spatially and temporally inhomogeneous particle flows, *Atomization Spray*, 4, 1–40, 1994.
- Masters, K., *Spray Drying Handbook*, 5th ed., Longman Scientific & Technical, England, 1991.
- Masters, K., *Spray Drying in Practice*, Spray DryConsult Int. ApS, Charlottenlund, Denmark, 2002.
- Mathur, P., Annavarapu, S., Apelian, D., and Lawley, A., Spray casting: an integral model for process understanding and control, *Mater. Sci. Eng. A*, 170, 1991.
- Mathur, P., Annavarapu, S., Apelian, D., and Lawley, A., Process control, modeling and applications of spray casting, *J. Met.*, 10, 23–28, 1989.
- Mathur, P., Apelian, D., and Lawley, A., Analysis of the spray deposition process, *Acta Metall.*, 37, 429–443, 1989.
- Matsumoto, S., Belcher, D.W., and Crosby, E.J., Rotary atomizers: performance understanding and prediction, *Proceedings of the Third International Conference on Liquid Atomization and Spray Systems ICLASS*, London, IA/1/1-21, 1985.
- Matsumoto, S., Saito, K., and Takashima, Y., *Bull. Tokyo Inst. Technol.*, 116, 85, 1973.
- Mayer, W., Zur koaxialen Flüssigkeitszerstäubung im Hinblick auf die Treibstoffaufbereitung in Raketentreibwerken, Dissertation, Universität Erlangen, 1993.
- Menchaca-Rocha, A., Huidobro, F., Martinez-Davalos, A., Michaelian, K., Perez, A., Rodriguez, V., and Carjan, N., Coalescence and fragmentation of colliding mercury drops, *J. Fluid Mech.*, 346, 291–318, 1997.
- Meyer, O., Fritsching, U., and Bauckhage, K., Numerical investigation of alternative process conditions for influencing the thermal history of spray deposited billets, *Int. J. Therm. Sci.*, 42, 153–168, 2003.
- Meyer, O., Schneider, A., Uhlenwinkel, V., and Fritsching, U., Convective heat transfer from a billet due to an oblique impinging circular jet within the spray forming process, *Int. J. Therm. Sci.*, 42, 561–569, 2003.
- Michelson, D., *Electrostatic Atomization*, Adam Hilger, Bristol, New York, 1990.
- Middleman, S., *Modeling Axisymmetric Flows, Dynamics of Films, Jets, and Drops*, Academic Press, San Diego, USA, 1999.
- Miles, J.W., On the generation of surface waves by shear flows, Part 1, *J. Fluid Mech.*, 3, 185–204, 1957.
- Miles, J.W., On the generation of surface waves by shear flows, Part 2, *J. Fluid Mech.*, 6, 568–582, 1958.
- Miles, J.W., On the generation of surface waves by shear flows, Part 3, *J. Fluid Mech.*, 7, 469–478, 1960.
- Miles, J.W., On the generation of surface waves by shear flows, Part 4, *J. Fluid Mech.*, 13, 433–448, 1961.
- Mudawar, I. and Valentine, W.S., Determination of the local quench curve for spray-cooled metallic surfaces, *ASME J. Heat Treatment*, 7, 107–112, 1989.
- Mudawar, I. and Deiters, T.A., A universal approach to predicting temperature response of metallic parts to spray quenching, *Int. J. Heat Mass Transfer*, 37(3), 347–362, 1994.
- Müller, H.R. and Jeschar, R., Wärmeübergang bei der Spritzwasserkühlung von Nichteisenmetallen, *Metallkunde*, 74, 257–264, 1983.
- Mujumdar, A.S., *Handbook of Industrial Drying*, Marcel Dekker, New York, 1997.
- Mulhem, B., Bauckhage, K., Fritsching, U., and Schulte, G., Beugungsspektrometrie in Sprays von Suspensionen: Modellexperimente und differenzierte Interpretation der Ergebnisse, GALA, Rostock, Sept. 10–12, 2002.
- Mulhem, B., Fritsching, U., Schulte, G., and Bauckhage, K., Characterisation of twin-fluid atomization for suspensions, *International Conference on Liquid Atomization and Spray Systems ICLASS*, Sorrento, Italy, July 12–18, 2003a.
- Mulhem, B., Fritsching, U., Schulte, G., and Bauckhage, K., Effect of solid particle characteristics on suspension atomization, *Atomization and Sprays*, 13, 321–343, 2003b.

- Muoio, N.G., Crowe, C.T., Fritsching, U., and Bergmann, D., Modelling metal droplet sprays in spray forming, *ASME FED*, 223, 111–115, 1995.
- Nasr, G.G., Yule, A.J., and Bendig, L., *Industrial Sprays and Atomization: Design, Analysis and Applications*, Springer, Heidelberg, 2002.
- Naue, G. and Bärwolf, G., *Transportprozesse in Fluiden*, Deutscher Verlag für Grundstoffindustrie, Leipzig, Germany, 1992.
- Nichols, B.D., Hirt, C.W., and Hotchkiss, R.S., SOLA-VOF: A Solution Algorithm for Transient Fluid Flow with Multiple Free Boundaries, Los Alamos Report, LA-8355, 1980.
- Nigmatulin, R.I., *Dynamics of Multiphase Media*, English Ed., Vols. 1+2, 1990.
- Nikas, K., Bouris D., Gehrmann, D., Steinbeck, M., and Bergeles, G., Optimisation of Spray Dryer via CFD, *SPRAY DRYING'01*, Dortmund, Oct. 8–10, 2001.
- Nikolaev, V.S., Vachagin, K.D., and Barychev, Y.N., *Int. Chem. Eng.*, 7, 595, 1967.
- Nobari, M.R.H., Jan, Y.-J., and Tryggvason, G., Head-on collision of drops—a numerical investigation, *Phys. Fluids*, 8, 29–42, 1996.
- Nobari, M.R.H. and Tryggvason, G., Numerical simulations of three-dimensional drop collisions, *AIAA J.*, 34, 750–755, 1996.
- Nonnenmacher, S. and Piesche, M., Design of hollow cone pressure swirl nozzle to atomize Newtonian fluids, *Chem. Eng. Sci.*, 55, 4339–4348, 2000.
- Nukiyama, S. and Tanasawa, Y., Experiments on the atomization of liquids in an airstream, *Trans. Soc. Mech. Eng. Jpn.*, 5, 68–75, 1939.
- Nunez, L.A., Lobel, T., and Palma, R., Atomizers for molten metals: macroscopic phenomena and engineering aspects, *Atomization and Sprays*, 9, 581–600, 1999.
- Oakley, D.E., Produce uniform particles by spray drying, *Chem. Eng. Prog.*, 12, 48–54, 1997.
- Oakley, D.E., Bahu, R.E., and Reay, D., The aerodynamics of co-current spray dryers, *Proceedings of IDS'88*, Versailles, 1988.
- Oesterle, B. and Petijean, A., Simulation of particle-to-particle interaction in gas-solid flows, *Int. J. Multiphase Flow*, 9, 199–211, 1993.
- Ohnesorge, W., Formation of drops by nozzles and the breakup of liquid jets, *Z. Angew. Math. Mech.*, 16, 355–358, 1936.
- Olivas, P. and Marty, P., Numerical study of the Coanda effect in a rotating spray paint atomizer, *Atomization Spray*, 12, 5–6, 2002.
- Orme, M., Experiments on droplet collision, bounce coalescence and disruption, *Prog. Energ. Combust. Sci.*, 23, 65–79, 1997.
- Oshinowo, T. and Charles, M.E., Vertical two-phase flow, Part 1: flow pattern correlations, *Can. J. Chem. Eng.*, 52, 25–35, 1974.
- O'Rourke, P.J., Collective Drop Effects on Vaporizing Liquid Sprays, Ph.D. thesis, Los Alamos National Laboratory, New Mexico, 1981.
- O'Rourke, P.J. and Amsden, A.A., The TAB Method for Numerical Calculation of Spray Droplet Breakup, Los Alamos National Laboratory Report, LA-UR-87-2105, 1987.
- Ottosen, P., Numerical Simulation of Spray Forming, Ph. D. thesis, Technical University of Denmark, 1993.
- Ozmen, L. and Langrish, T.A.G., Experiment investigation of the wall deposition of milk powder in spray dryer, *Proceedings of the Ninth APCChE Congress and CHEMeca*, Christchurch, Paper 363, 2002.
- Panchagnula, M.V., Sojky, P.E., and Bajaj, A.K., The non-linear breakup of annular liquid sheets, in *Proceedings of ILASS—Europe'98*, Yule, A.J., Ed., Manchester, UK, July 6–8, 1998, pp. 36–41.
- Parthasarathy, R.N., Linear spatial stability analysis of slurry sheets subjected to gas flow, *Atomization Spray*, 9, 519, 1999.
- Patterson, M.A., Modeling the Effects of Fuel Injection Characteristics on Diesel Combustion and Emissions, Ph.D. thesis, University of Wisconsin, Madison, 1997.
- Patterson, M.A. and Reitz, R.D., Modeling the Effects of Fuel Spray Characteristics on Diesel Engine Combustion and Emissions, SAE Paper, 980131, 1998.

- Payne, R.D., Matteson, M.A., and Moran, A.L., Application of neural networks in spray forming technology, *Int. J. Powder Metall.*, 29, 345–351, 1993.
- Payne, R.D., Rebis, A.L., and Moran, A.L., Spray forming quality predictions via neural networks, *J. Mater. Eng. Perform.*, 2, 693–702, 1996.
- Pedersen, T.P., Hattel, J.H., Pryds, N.H., Pedersen, A.S., Buchholz, M., and Uhlenwinkel, V., A new integrated numerical model for spray atomization and deposition: comparison between numerical results and experiments, *Proceedings of SDMA 2000*, Bremen, 2000, pp. 813–824.
- Pedersen, T.B., Spray Forming—A New Integrated Numerical Model, Ph. D. thesis Technical University of Denmark, 2003.
- Pilch, M. and Erdman, C., Acceleration Induced Fragmentation of Liquid Drops, Department of Nuclear Engineering, University of Virginia, Charlottesville, VA, NUREG/CR-2247, 1981.
- Pilch, M. and Erdmann, C.A., Use of breakup time data and velocity history data to predict the maximum size of stable fragments for acceleration-induced breakup of a liquid drop, *Int. J. Multiphase Flow*, 13, 741–757, 1987.
- Platzer, E. and Sommerfeld, M., Modelling of turbulent atomisation with an Euler/Euler approach including the drop size prediction, *Proceedings of the International Conference on Liquid Atomization Spray Systems ICCLASS 2003*, Sorrento, Italy, 2003.
- Podvysotsky, A.M. and Shraiber, A.A., Coalescence and breakup of drops in two-phase flows, *Int. J. Multiphase Flow*, 10, 195–209, 1994.
- Prud'homme, R. and Ordoneau, G., The maximum entropy method applied to liquid jet atomization, CD-Rom, *Proceedings of ILASS—Europe 99*, Toulouse, France, July 5–7, 1999.
- Pryds, N., Hattel, J.H., and Thorborg, J., A quasi-stationary numerical model of atomized metal droplets, II: prediction and assessment, *Model. Simul. Mater. Sci. Eng.*, 7, 431–446, 1999.
- Puschmann, F., Experimentelle Untersuchung der Spraykühlung zur Qualitätsverbesserung durch definierte Einstellung des Wärmeübergangs, Dissertation, Universität Magdeburg, 2003.
- Puschmann, F., Specht, E., and Schmidt, J., Measurement of spray cooling heat transfer using an infrared-technique in combination with the Phase-Doppler technique and a patternator, *Int. J. Heat Technol.*, 19, 51–56, 2001.
- Qian, J. and Law, C.K., Regimes of coalescence and separation in droplet collision, *J. Fluid Mech.*, 331, 59–80, 1997.
- Rai, G., Lavernia, E.J., and Grant, N.J., Factors influencing the powder size and distribution in ultrasonic gas atomization, *J. Met.*, 37, 22–26, 1985.
- Rangel, R.H. and Sirignano, W.A., The linear and nonlinear shear stability of a fluid sheet, *Phys. Fluids A3*, 10, 2392–2400, 1991.
- Ramos, J.I., *Internal Combustion Engine Modeling*, Hemisphere, Washington, DC, 1989.
- Ranz, W.E. and Marshall, W.R., Evaporation from drops — I and II, *Chem. Eng. Prog.*, 48, 141–173, 1952.
- Rao, K.P. and Mehrotra, S.P., *Modern Developments in Powder Metallurgy*, Vol.12, Hausner, H. et al., Eds., Metal Powder Industries Federation, Princeton, NJ, 1980, pp. 113–130.
- Rayleigh, L., On the stability of jets, *Proc. Lond. Math. Soc.*, 10, 4–13, 1878.
- Reichelt, L., Meingast, U., and Renz, U., Aerodynamischer Tropfenzersfall bei hohen Gasdrücken, *Proceedings of Spray 2001*, TU Hamburg-Harburg, 2001, V.3-1–V.3-6.
- Reichelt, L., Pawłowski, A., and Renz, U., Numerische Untersuchungen zum aerodynamischen Tropfenzersfall mit der Volume-of-Fluid (VOF)-Methode, *Proceedings of Spray 2002*, Freiberger Forschungshefte A 870 Verfahrenstechnik, TU-Bergakademie Freiberg, 2002, pp. 133–142.
- Rein, M., The transitional regime between coalescing and splashing drops, *J. Fluid Mech.*, 306, 145–165, 1996.
- Reipschläger, O., Desintegrationsprozesse im Ultraschallfeld: Modellbildung, Simulation, Experiment, Ph.D. dissertation, Universität Paderborn, 2002.
- Reipschläger, O., Bothe, D., Monien, B., Prüss, J., Wiegand, B., and Warnecke, H.-J., Modelling and simulation of the disintegration process in ultrasonic standing wave atomizers, *Proceedings of the 18th Annual Conference on Liquid Atomization and Spray Systems ILASS Europe*, Zaragoza, Spain, 2002.

- Reitz, R.D., Mechanisms of Breakup of Round Liquid Jets, Ph. D. thesis, Princeton University, 1978.
- Reitz, R.D. and Bracco, F.V., On the Dependence of Spray Angle and Other Spray Parameters on Nozzle Design and Operating Conditions, SAE Paper , 790494, 1979.
- Reitz, R.D. and Bracco, F.V., Mechanism of atomization of a liquid jet, *Phys. Fluids*, 25, 1730–1742, 1982.
- Reitz, R.D., Effect of Drop Breakup on Fuel Sprays, SAE Paper, 860469, 1986.
- Reitz, R.D., Modeling atomization processes in high-pressure vaporizing sprays, *Atomisations Spray Technol.*, 3, 309–337, 1987.
- Reitz, R.D. and Diwarkar, R., Structure of High Pressure Fuel Sprays, SAE Paper, 870598, 1987.
- Richter, H.J., Separated two-phase flow model, application to critical two-phase flow, *Int. J. Multiphase Flow*, 9, 511–530, 1983.
- Rieber, M. and Frohn, A., Numerical simulation of splashing drops, *Proceedings of ILASS '98*, Manchester, July 6–8, 1998.
- Roach, S.J., Henein, H., and Owens, D.C., A new technique to measure dynamically the surface tension, viscosity and density of molten metals, *Light Met.*, 4, 1285–1291, 2001.
- Robert B. GmbH, *Dieselmotor-Management*, Vieweg, Braunschweig, 1998.
- Roesler, T.C. and Lefebvre A.H., Studies on aerated-liquid atomization, *Int. J. Turbo Jet Eng.*, 6, 221–230, 1989.
- Rüger, M., Hohmann, S., Sommerfeld, M., and Kohnen, G., Euler/Lagrange calculations of turbulent spray: the effect of droplet collisions and coalescence, *Atomization and Sprays*, 10, 47–82, 2000.
- Ruff, G.A., Wu, P.K., Bernal, L.P., and Faeth, G.M., Continuous- and dispersed-phase strucutre of dense non-evaporating pressure-atomized sprays, *J. Prop. Power*, 8, 280–289, 1992.
- Rumberg, O. and Rogg, B., Spray modelling via a joint-PDF formulation for two-phase flow, CD-Rom, *Proceedings of ILASS—Europe 99*, Toulouse, France, July 5–7, 1999.
- Sadhal, S.S., Ayyaswamy, P.S., and Chung, J.N., *Transport Phenomena with Drops and Bubbles*, Mech. Eng. Series, Springer , New York, 1997.
- Samenfink, W., Hallmann, M., Elsäßer, A., and Wittig, S., Secondary breakup of liquid droplets: experimental investigation for a numerical description, *Proceedings of ICCLASS—94*, Rouen, France, 1994, pp. 156–163.
- Scardovelli, R. and Zaleski, S., Direct numerical simulation of free-surface and interfacial flow, *Annu. Rev. Fluid Mech.*, 31, 567–603, 1999.
- Schelkle, M., Rieber, M., and Frohn, A., Comparison of lattice Boltzmann and Navier-stokes simulations of three-dimensional free surface flows, *ASME-Fluids Eng. Div. Conf.*, 236, 207–212, 1996.
- Schmaltz, K. and Amon, C., Experimental verification of an impinging molten metal droplet numerical simulation, *Proc. ASME Heat Transf. Div.*, 317, 219–226, 1995.
- Schmehl, R., CFD analysis of fuel atomization, secondary droplet breakup and spray dispersion in the premix duct of a LPP combustor, *Proceedings of the 8th International Conference on Liquid Atomization and Spray Systems ICCLASS*, Pasadena, CA, July 2000 .
- Schmehl, R., Modeling droplet breakup in complex two-phase flows, *Proceedings of the Ninth International Conference on Liquid Atomization and Spray Systems ICCLASS 2003*, Sorrento, Italy, Jul. 13–17, 2003.
- Schmehl, R., Klose, G., Maier, G., and Wittig, S., Efficient numerical calculation of evaporating sprays in combustion chamber flows, *AGARD/RTO 92nd Symposium on Gas Turbine Combustion, Emissions and Alternative Fuels*, Lisbon, Portugal, Oct. 12–16, 1998.
- Schmelz, F. and Walzel, P., Breakup of liquid droplets in accelerated gas flows, *Atomizations and Sprays*, 13(6), 357–372, 2003.
- Schmidt, D.P. and Rutland, C.J., A new droplet collision algorithm, *J. Comput. Phys.*, 164, 62–80, 2000.
- Schneider, S. and Walzel, P., Zerfall von Flüssigkeiten bei Dehnung im Schwerefeld, in *Proceedings of SPRAY 98*, Walzel, P. und Schmidt, D., Eds., Essen, Oct. 13–14, 1998.
- Schneider, A., Uhlenwinkel, V., and Bauckhage, K., Zum Ausfließen von Metallschmelzen, *Koll. SFB 372*, Vol. 5, Bremen, pp. 69–96, 2001.

- Scholz, T., Experimentelle Untersuchungen zur Mehrphasenströmung im Sprühkegel eines elktrostatisch unterstützten Hochrotationszerstäubers, Dissertation Universität, Bremen, VDI-Verlag, Düsseldorf, 1998.
- Schröder, T., Tropfenbildung an Gerinneströmungen im Schwere- und Zentrifugalfeld, Fortschr. Ber. VDI Reihe 3: Verfahrenstechnik, Nr. 503, VDI-Verlag Düsseldorf, 1997.
- Schütz, S., Breitling, M., and Piesche, M., Lamellenzerstäubung von Suspension mit strukturviskosen Stoffeigenschaften, *Chem.-Ing.-Tech.*, 75, 559–564, 2003.
- Schulte, G., *Zweidimensionale Verteilungen von Partikeleigenschaften*, Shaker Verlag, Aachen, 1995.
- Sellens, R.W., Prediction of the drop size and velocity distribution in a spray based on the maximum entropy formalism, *Part. Part. Syst. Char.*, 6, 17–23, 1989.
- Sellens, R.W. and Brzustowski, T.A., 1985, A prediction of the drop size distribution in a spray from first principles, *Atomization and Spray Technol.*, 1, 85, 1985.
- Seok, H.K., Yeo, D.H., Oh, K.H., Ra, H.Y., and Shin, D.S., 3-Dimensional forming model of rod in spray forming method, in *Proceedings of the Third International Conference on Spray Forming*, Wood, J.V., Ed., Osprey Metals, Cardiff, UK, 1996, 1997.
- Shimizu, S., Hiroaoka, Y., and Nishiyaman, T., Instantaneous photographic observation of abrasive water suspension jets, influence of abrasive particle on jet structure, *JSME Int. J.*, 45, 4, 2002.
- Shirley, C., Tsai, and Truc, Vu., Atomization of coal-water slurry using twin-fluid jet atomizer, *FUEL*, 66, 1987.
- Shokoohi, F. and Elrod, H.G., Numerical investigation of the disintegration of liquid jets, *J. Comput. Phys.*, 71, 324–342, 1987.
- Simpkins, P.G. and Bales, E.L., Water-drop response to sudden accelerations, *J. Fluid Mech.*, 55, 629–639, 1972.
- Sirignano, W.A., *Fluid Dynamics and Transport of Droplets and Sprays*, Cambridge University Press, New York, 1999.
- Sizov, A.M., *Dispersion of Melts by Supersonic Gas Jets*, Metallurgija Verlag, Moskau, 1991.
- Sommerfeld, M., The importance of inter-particle collisions in horizontal gas-solid channel flows, in *ASME Fluids Eng. Conf.* Stock, D.E., Reeks, M.W., Tsuji, Y., Michaelides, E.E., and Gautams, M. Eds., Hilton Head, SC, FED- 288, 333–345, 1995.
- Sommerfeld, M., *Modellierung und numerische Berechnung von partikelbeladenen turbulenten Strömungen mit Hilfe des Euler/Lagrange Verfahrens*, Verlag Shaker, Aachen, 1996.
- Sommerfeld, M., Validation of a stochastic Lagrangian modelling approach for inter-particle collisions in homogeneous isotropic turbulence, *Int. J. Multiphase Flow*, 27, 1829–1858, 2001.
- Sommerfeld, M., Kohnen, G., and Rüger, M., Some open question and inconsistencies of Lagrangian particle dispersion models, *Proceedings of the Ninth Symposium on Turbulent Shear Flows*, Kyoto, Japan, 1993, pp. 15–1.
- Sommerfeld, M. and Zivkovic, G., Recent advances in the numerical simulation of pneumatic conveying through pipe systems, in *Computational Methods in Applied Science First European Computational Fluid Dynamics*, Hirch, et al., Eds., Brussels, 1992, pp. 201–212.
- Son, S.Y. and Kihm, K.D., Effect of coal particle size on coal-water slurry (CWS) atomization, *Atomizations and Sprays*, 8, 503–519, 1998.
- Southwell, D.B. and Langrish, T.A.G., Observation of flow pattern in a spray dryer, *Dry. Technol.*, 18, 661–685, 2000.
- Southwell, D.B. and Langrish, T.A.G., The effect of swirl on flow stability in spray dryers, *Trans. IChemE*, 79, Part A, 2001.
- Southwell, D.B., Langrish, T.A.G., and Fletcher, D.F., Process intensification in spray dryers by turbulence enhancement, *Trans. IChemE*, 77, Part A, 1999.
- Spalding, D.B., Mixing and chemical reaction in steady confined turbulent flames, *13th International Symposium on Combustion*, The Combustion Institute, Pittsburgh, PA, 1971, pp. 649–657.
- Spicher, U. (Ed.), *Direkteinspritzung im Ottomotor III*, Expert Verlag, Renningen, 2001.
- Stafford, R.A., Fauroux, O., and Glass, D.H., Flow visualization and instantaneous velocity measurements of spraydryer gas and spray flows using particle image velocimetry, *Dry. Technol.*, 15, 1661–1671, 1997.
- Sterling, A.M. and Schleicher, C.A., The instability of capillary jets, *J. Fluid Mech.*, 68, 477–495, 1975.

- Stewart, I., Massingham, J.D., and Hagers, J.J., Heat transfer coefficient effects on spray cooling, *AISE Annual Convention and Iron & Steel Exposition*, Pittsburgh, PA, 1995.
- Sraatma, J., van Houwelingen, G., van Meulman , A.P., and Steenburgen, A.E., DRYSPEC2: a computer model of a two-stage dryer, *J. Soc. Dairy Technol.*, 44, 107–111, 1991.
- Sraatma, J., van Houwelingen, G., Steenburgen, A.E., and de Jong, P., Spray drying of food products: 1. simulation model, *J. Food Eng.*, 42, 67–72, 1999.
- Strauss, J.T., Hotter gas increases atomization efficiency, *Met. Powder Rep.*, 11, 24–28, 1997.
- Strauss, J.T. and Dunkley, J.J., An experimental and empirical study of close-coupled gas atomization, *Proceedings of the PM-World Congress 2000*, Kyoto, Japan, 2000.
- Su, Y.H. and Tsao, C.Y.A., Modeling of solidification of molten metal droplet during atomization, *Met. Mat. Trans. B*, 28B, 1249–1255, 1997.
- Svejda, P., *Prozesse und Applikationsverfahren in der industriellen Lackiertechnik*, Vincentz Verlag, Hannover, 2003.
- Tanasawa, Y. and Toyoda, S., On the atomization of a liquid jet issuing from a cylindrical nozzle, *Tech. Rep. Tohoku Univ., Jpn.*, 19, 135, 1955.
- Tanasawa, Y., Miyasaka, Y., and Umehara, M., Effect of shape of rotating discs and cups on liquid atomization, *International Conference on Liquid Atomization Spray Systems ICLASS*, Tokyo, Japan, 1978.
- Tanner, F.X., Liquid Jet Atomization and Droplet Breakup Modeling of Non-Evaporating Diesel Fuel Sprays, SAE Paper, 970050, 1997.
- Tao, F., *Numerical Modeling of Soot and NO_x Formation in Non-Stationary Diesel Sprays with Complex Chemistry*, Ph.D. thesis, Clamers University of Technology, Sweden, 2003.
- Tao, F. and Chomiak, J., Numerical Investigation of Reaction Zone Structure and Flame Liftoff of DI Diesel Sprays with Complex Chemistry, SAE Paper, 2002-01-1114, 2002.
- Taylor, G.I., The mechanics of swirl atomizers, *Proceedings of the Seventh International Congress on Applied Mechanics*, Part I, 1948, p. 280.
- Taylor, G.I., Generation of ripples by wind blowing over a viscous liquid, *Collected Works of G.I. Taylor*, Vol. 3, 1949.
- Taylor, G.I., The dynamics of thin sheets of fluid, *Proc. Roy. Soc., A* 253, 289, 1959.
- Taylor, G.I., The shape and acceleration of a drop in a high speed air stream, technical report, in *Scientific Papers of G.I. Taylor*, Batchelor, G.K., Ed., 1963.
- Thomas, G.O., The aerodynamic breakup of ligaments, *Atomizations and Sprays*, 13, 117–129, 2003.
- Ting, J., Peretti, M.W., and Eisen, W.B., 2002, The effect of deep aspiration on gas-atomized powder yield, *Mater. Sci. Eng. A*, 326, 110–121, 2002.
- Trapaga, G., Matthys, E.F., Valencia, J.J., and Szekely, J., Fluid flow, heat transfer and solidification of molten metal droplets impinging on substrates—comparison of numerical and experimental results, *Metall. Trans. B: Proc. Metall.*, 23 B, 701–718, 1992.
- Triebnigg, H., *Der Einblase- und Einspritzvorgang bei Dieselmotoren*, Vienna, 1929.
- Tsao, C.Y.A. and Grant, N.J., Modeling of the liquid dynamic compaction spray process, *Int. J. Powder Metall.*, 30, 323–333, 1994.
- Tschöke, H., and Leyh, B., *Diesel- und Benzindirekteinspritzung II*, Eds., Expert Verlag, Renningen, 2003.
- Tseng, L.K., Wu, P.K., and Faeth, G.M., Dispersed-phase structure of pressurized-atomized sprays at various gas densities, *J. Prop. Power*, 8, 1157–1166, 1992.
- Tsunemoto, H., Ishitani, H., Montajir, R.M.D., Hayashi, T., and Kitayama, N., Cylinder to cylinder deviations in fuel spray and exhaust emissions at idling in high pressure DI diesel engines, *Proceedings of the 5th International Symposium on Diagnostics and Modeling Internal Combustion Engines*, Nagoya, Japan, 2001.
- Turnbull, D., Formation of crystal nuclei in liquid metals, *J. Appl. Phys.*, 21, 1022–1028, 1950.
- Uhlenwinkel, V., Zum Ausbreitungsverhalten der Partikeln bei der Sprühkompaktierung von Metallen, Dissertation, Universität Bremen, 1992.
- Uhlenwinkel, V., Fritsching, U., Bauckhage K., and Urlau, U., Strömungsuntersuchungen im Düsenbereich einer Zweistoffdüse-Modelluntersuchungen für die Zerstäubung von Metallschmelzen, *Chem.-Ing. Tech.*, 62, 228–229, 1990.

- Ünal, A., Effect of processing variables on particle size in gas atomization of rapidly solidified aluminium powders, *Mater. Sci. Technol.*, 3, 1029–1039, 1987.
- Ünal, A., Flow separation and liquid rundown in a gas-atomization process, *Metall. Trans.*, 20 B, 613–622, 1989.
- van der Sande, E. and Smith, J.M., Jet breakup and air entrainment by low-velocity turbulent jets, *Chem. Eng. Sci.*, 31, 219–224, 1976.
- Verdurmen, R.E.M., Verschueren, M., Straatma, J., and Gunsing, M., Simulation of agglomeration in spray drying: the EDECAD project, *Ninth International Conference on Liquid Atomization and Spray Systems ICLASS 2003*, Sorrento, Italy, 2003.
- Verdurmen, R.E.M., Menn, P., Ritzert, J., Blei, S., Nhumaio, G.C.S., Sonne Sørensen, T., Gunsing, M., Straatsma, J., Verschueren, M., Sibeijn, M., Schulte, G., Fritsching, U., Bauckhage, K., Tropea, C., Sommerfeld, M., Watkins, A.P., Yule, A.J. and Schönenfeldt, H., Simulation of Agglomeration in Spray Drying Installations: The EDECAD Project, *Drying Technology*, 22(6), 1403–1461, 2004.
- Viskanta, R. and Incropera, F.P., Quenching with liquid jet impingement, *Heat Mass Transf. Mater. Process.*, 455–476, 1992.
- Voller, V.R., Swaminathan, C.R., and Thomas, B.G., General source-based methods for solidification phase change, *Num. Heat Trans.*, B, 19, 175–189, 1991.
- Walzel, P., Zerteilgrenze beim Tropfenaufprall, *Chem.-Ing.-Tech.*, 52, 338–339, 1980a.
- Walzel, P., Turbulenter Zerfall von Flüssigkeitsstrahlen aus der Sicht der Ähnlichkeitstheorie, *Chem.-Ing.-Tech.*, 52, 525–526, 1980b.
- Walzel, P., Zerstäuben von Flüssigkeiten, *Chem.-Ing.-Tech.*, 62, 983–994, 1990.
- Walzel, P., Spraying and atomizing of liquids, *Ullmann's Encyclopedia of Industrial Chemistry*, 6th ed., 1999 Electronic Release, Wiley VCH, Weinheim, 1999.
- Walzel, P., Schmelz, F., and Schneider, S., Herstellen monodisperser Tropfen mit pneumatischen Ziehdüsen, *Chem.-Ing.-Tech.*, 73(12), 1599–1602, 2001.
- Wan, Y.P., Pitsch, H., and Peters, N., Simulation of Autoignition Delay and Location of Fuel Sprays under Diesel-Engine relevant conditions, SAE Paper, 971590, 1997.
- Wang, G.X. and Matthys, E.F., Modelling of heat transfer and solidification during splat cooling: effect of splat thickness and splat/substrate thermal contact, *Int. J. Rapid Solidif.*, 6, 141–174, 1991.
- Wang, G.X. and Matthys, E.F., Numerical modelling of phase change and heat transfer during rapid solidification processes: use of control volume integral with element subdivision, *Int. J. Heat Mass Transfer*, 35, 141–153, 1992.
- Watkinson, D., Hughes, R., Sims, G., Yule, A., and Zhou, C., Gas atomization of polymeric materials, *Proceedings on Liquid Atomization and Spray Systems ICLASS—Europe*, Zurich, Switzerland, 2001.
- Warnatz, J., Mass, U., and Dibble, R.W., *Combustion, Physical and Chemical Fundamentals, Modeling and Simulation, Experiments, Pollutant Formation*, Springer-Verlag, Berlin, 1996.
- Weber, C., Zum Zerfall eines Flüssigkeitsstrahles, *Z. Angew. Math. Mech.*, 11, 138–145, 1931.
- Whitlow, J.D. and Lefebvre, A.H., Effervescent atomizer operation and spray characteristics, *Atomizations and Sprays*, 3, 137–155, 1993.
- Williams, A.W., *Combustion of Liquid Fuel Sprays*, Butterworths & Co. Publ., London, 1990.
- Woodruff, D.P., *The Solid–Liquid Interface*, Cambridge University Press, Cambridge, 1973.
- Wruck, N., *Transientes Sieden von Tropfen beim Wandprall*, Shaker Verlag, Aachen, 1999.
- Yearling, P.R. and Gould, R.D., Convective heat and mass transfer from single evaporating water, methanol and ethanol droplets, *ASME FED*, 223, 33–38, 1995.
- Yule, A.J. and Dunkley, J.J., *Atomization of Melts*, Clarendon Press, Oxford, 1994.
- Zaleski, S. and Boeck, T., Direct numerical simulation of high speed jet atomization, *Proceedings of ICLASS—2003*, Sorrento, Italy, 2003.
- Zaleski, S. and Li, J., Direct simulation of spray formation, *Proceedings of ICLASS—'97*, Seoul, Korea, August 1997, pp. 812–819.
- Zaleski, S., Li, J., Succi, S., Scardovelli, R., and Zanetti, G., Direct numerical simulation of flows with interfaces, *Proceedings of the Second International Conference Multiphase Flow*, Kyoto April 1995.

- Zbicinski, I., Grad, J., and Strumillo, C., Effect of turbulence on heat and mass transfer in the atomization zone, *Dry. Technol.*, 14, 231–244, 1996.
- Zhao, Y.Y., Dowson, A.L., and Jacobs, M.H., Modelling of liquid flow after a hydraulic jump on a rotating disc prior to centrifugal atomization, *Modell. Simul. Mat. Sci. Eng.*, 8, 55–65, 2000.
- Zhao, Y.Y., Dowson, A.L., Johnson, T.P., Young, J.M., and Jacobs, M.H., Prediction of liquid metal velocities on a rotating disk in spray forming by centrifugal spray deposition, *Adv. Powder Metall. Part. Materials* — 1996, Metal Powder Industries Federation, Princeton, 9-79-9-89, 1996.
- Zhou, Z.-W. and Tang, X.-D., The effect of the pulsation in gas flow on the stability of molten metal jet, *Proceedings of the Fourth ICSF*, Baltimore, USA, 1999.
- Ziesenis, J., Weiterentwicklung der PDA-Meßtechnik zur on-line Prozeßkontrolle beim Sprühkompaktieren, Dissertation, Universität Bremen, 2003.

9

Dry Powder Flows

9.1	Introduction	9-1
9.2	Flow in Hoppers and Bins	9-3
	Arching in Hoppers • Jenike's Method of Hopper Design • Concluding Remarks	
9.3	Slow, Frictional Powder Flows.....	9-9
	General Equations of Motion for Incompressible Powders • Incompressible Powder Flow in a Plane Wedge Hopper • Equations of Motion for Compressible Powders • Compressible Powder Flow in a Plane Wedge Hopper • Concluding Remarks	
9.4	Characterization of Bulk Powders.....	9-19
	Brief Survey of Methods • Shear Cell Methods and Analyses • Concluding Remarks on Characterization	

Gabriel I. Tardos

*The City College of the City
University of New York.*

Paul R. Mort

The Procter and Gamble Co.,

9.1 Introduction

The behavior of *flowing powders* is very different from that of fluids. Flowing powders do not exhibit fluid viscosity; rather, energy dissipation in flowing powders is due to frictional and collisional interactions between particles. In contrast to the increasing amount of work in the physics literature on the collisional flow of large grains, the focus of the present work is on smaller-sized bulk powders that are industrially more relevant and where a continuum approach may be more advantageous. Further, the focus of this chapter is on the incipient and relatively slow frictional-flow regimes, in which frictional effects are dominant. The details of the chapter include flow in hoppers (Section 9.2), slow-frictional flows (Section 9.3) and characterization of bulk powders (Section 9.4).

Figure 9.1 depicts a tentative, schematic representation of the different regimes of powder flow as a function of a dimensionless shear rate (Tardos et al., 2003). The dimensionless shear rate in Eq. (9.1) contains a gravitational term, g , and the powder particle size, d_p . For the relatively slow shearing velocities and fine powder particle sizes considered here, the primary consideration is on relatively low dimensionless shear rates covering the slow-frictional regime and transitions from the static to slow flow conditions:

$$\dot{\gamma}^* = \dot{\gamma}\sqrt{d_p/g} \quad (9.1)$$

At zero shear rate, the powder is in a static state and the stresses in the system can be computed using the equations of static equilibrium together with a yield condition. The yield condition defines the point where the bulk powder starts to deform. There are a large number of analytical and numerical solutions to this case and several books have been dedicated to this regime (Drescher, 1991; Nedderman, 1992; Rumpf, 1990; Shamlou, 1990). Since the powder is in equilibrium and the equations do not have velocity terms, only stresses and the condition of onset of flow can be computed by using this approach.

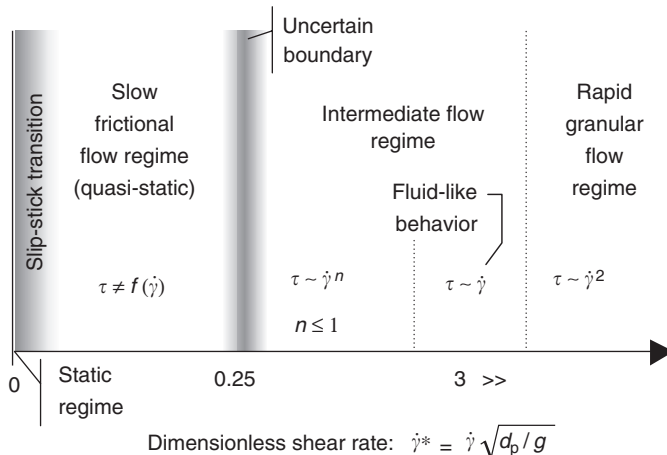


FIGURE 9.1 Schematic representation of different regimes in powder flows.

At low dimensionless shear rates, of the order of 0.2 or less, the so-called *slow, frictional regime* can be identified. In this regime, frictional forces between particles predominate. The main assumptions underlying this regime are the uninterrupted character of the flow and the existence of a continuous shear field. This flow regime is called the *quasi-static regime* in the soil mechanics literature (Schofield and Wroth, 1968). This name is somewhat inappropriate since inertial effects can be included in the study of this regime. A flow rule and an equation of continuity are usually added to the equilibrium equations and the yield condition of the static regime. Schaeffer (1987) has combined these equations to yield a set of differential equations that characterize this regime completely (Tardos, 1997).

A narrow range of very low shear in which the flow exhibits a stick-slip character separates the frictional and the static regimes. This regime is characterized by large swings in stresses as the material flows and stops repeatedly. Another characteristic of this flow regime is the formation of “stress chains” in the case of larger particles. Only very recently has this regime been studied in more depth (Miller et al., 1996; Albert et al., 1999).

At the other end of the spectrum, at very high shear rates, the so-called *rapid granular flow regime* can be identified. Here the particles move so fast that the friction between them can be neglected and only short collisions between particles determine the character of the flow. This regime has been studied extensively and many theoretical and experimental results are available (Campbell and Brennen, 1985; Campbell, 1990; Jenkins and Askari, 1991; Hopkins and Louge, 1990; Nott and Jackson, 1992).

In between the “slow” (quasi-static) and the “rapid” (granular) flow, is the *intermediate regime* where both collisional and frictional interactions between particles must be considered (Savage, 1998; Tardos et al., 2003). This regime is characterized by stress (and strain rate) fluctuations that decrease as the flow slows. The boundaries between the slow-and-intermediate and the intermediate-and-rapid flow regimes are not as clear as shown in the figure, and more work is needed before these boundaries are well defined.

This chapter presents several elements of the static regime and a summary of the slow-frictional regime since they are important from an industrial point of view. We start with a section on arching in hoppers and bins and present Jenike’s method of bin design and continue with the description of powder flows in the slow regime. We present general equations of motion and several analytical solutions to illustrate the main features. We also discuss several experimental procedures relevant to characterize powder flows. Treatment of the intermediate-and-fast flow regimes is beyond the scope of this section and information on these regimes can be found elsewhere (Lun et al., 1984; Rajagopal et al., 1992; Tardos et al., 2003; Srivastava and Sundaresan, 2003).

9.2 Flow in Hoppers and Bins

A silo for powder storage is usually a tall structure that consists of a rectangular or cylindrical body of constant cross-section called a *bin* connected at the lower end to a prismatic or conical section called the *hopper*. The hopper terminates at its lower end in a relatively small outlet that is further connected to a vertical pipe usually called as a *standpipe* or to a powder-feeding device. Silos come in different shapes and sizes, but the most important are the two dimensional (2D) or “plane” silo, where one dimension is large compared with its width $2b$, the 3D square silo and the 3D circular silo that have the characteristic dimension $2b$ (see Figure 9.2 and Figure 9.3). The hopper has two additional geometric characteristics namely the *half-angle*, (α), measured from the vertical and the outlet dimension or *span*, B .

The powder is characterized by its bulk density, $\rho = \rho_s(1 - \varepsilon) = v\rho_s$, where ρ_s is the solid material density of the powder and ε and v are the porosity and solid fraction, respectively. These powder properties are supplemented by an *internal friction angle*, ϕ , an *effective friction angle*, ϕ_{eff} , and a powder-wall characteristic called the *wall-powder friction angle*, ϕ_w . These properties of the bulk material and the wall of the storing vessel have to be measured experimentally as described in detail in Section 9.4.

The method to determine stresses in the bin was originally developed by Janssen (1895) to calculate wall stresses but can also be used to find average stresses in the bulk material. The method was generalized later

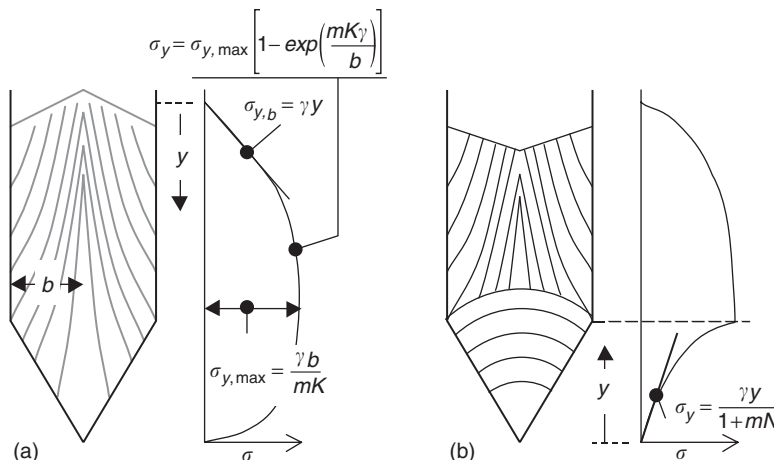


FIGURE 9.2 Average vertical stresses in a bin/hopper geometry: (a) after filling; (b) after partial discharge.

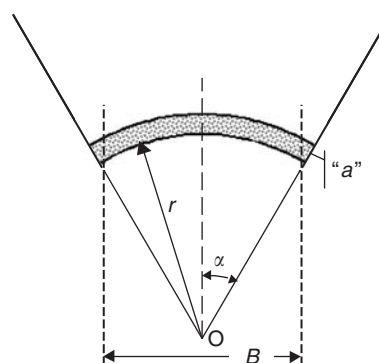


FIGURE 9.3 Schematic representation of a plane 2D arch in a wedge-shaped hopper.

and applied to calculate stresses in converging hoppers. A complete description of these methods can be found in Drescher (1991), where several different methods to calculate stresses in powders are given in detail.

A typical stress distribution in a silo filled with a bulk powder is as shown in Figure 9.2 and, as seen, the material in the bin is subjected to increasing compression as it moves down from the top of the fill. In the converging hopper, the material is under decreasing stress and becomes fully uncompressed at the apex. If a sufficiently small hole is cut out of the lower part of the hopper, it is possible that the material will not flow out since the stresses around the apex are quite small. This is in marked difference with the behavior of fluids where the pressure increases continuously (following the hydrostatic stress distribution $\sigma_{y,h}$ in Figure 2) and reaches a maximum at the bottom.

9.2.1 Arching in Hoppers

To discharge powder from the silo, it is necessary to provide a large enough opening at the bottom of the hopper. Jenike's method of hopper design is based on this observation and on the fact that the material forms arches that bridge the opening and that have to be broken continuously to achieve flow. Hopper design is reduced in this context to the calculation of the minimum outlet dimension B (see Figure 9.2 and Figure 9.3) for which arches of material bridging the exit break under their own weight. This dimension depends on the powder properties that determine the stress in the hopper and the hopper half-angle, α .

Figure 9.3 shows a plane 2D arch formed in a hopper. The maximum stress in the arch (due to its weight) is seen to be proportional to its span B and to the material bulk density. The location of this maximum stress is at the abutment of the arch at point "a" and can be approximated as

$$\sigma_{1,a} \approx \rho g B = \gamma B = 2r\gamma \sin \alpha, \quad \sigma_{1,a} = 2r\gamma \sin \alpha/m \quad (9.2)$$

where the generalized form uses the parameter m to distinguish between plane or 3D conical arches: $m = 1$ for the 2D and $m = 2$ for the conical hopper (Shamloo, 1990).

9.2.2 Jenike's Method of Hopper Design

In order to find the condition of collapse of the arch in the hopper, an additional important powder bulk property has to be measured experimentally. This is the so-called unconfined yield strength, which is the maximum normal stress under which a powder with a free, unstressed surface will yield or deform indefinitely. Figure 9.4 shows the simplest procedure to measure this powder property. The specimen is contained in a cylindrical vessel and precompressed or consolidated by the normal stress, σ_1 , as shown. In a subsequent step, the stress and the walls of the container are removed exposing the free powder surface. The specimen is compressed again until it gives way under the normal stress denoted in Figure 9.4 as f_c .

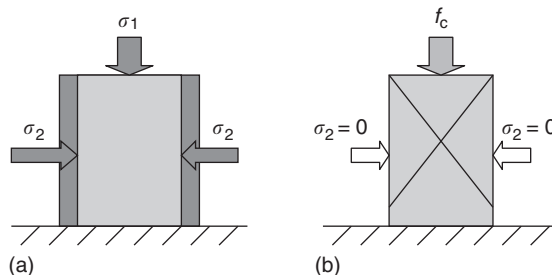


FIGURE 9.4 Measurement of the unconfined yield strength: (a) application of normal consolidation stress σ_1 with confining side wall stress σ_2 ; (b) removal of side wall and measurement of the unconfined yield stress required to break the cake (f_c).

The experiment is repeated several times at increasing consolidations, σ_1 , and the values of the unconfined yield strength are measured. Pairs of stresses are correlated in the form

$$f_c = \text{FF}(\sigma_1) \quad (9.3)$$

This experimentally obtained relationship is an intrinsic characteristic of the powder as is its bulk density, ρ , and its angle of internal friction, ϕ , and was denoted by Jenike as the flow function. In industrial practice, the above powder properties and the angle of wall friction, ϕ_w , are measured in a special device invented by Jenike called a split cell. More modern devices are also available and these are described in Section 9.4. The above correlation (flow function) is characteristic of a compressible powder for which its unconfined yield strength is dependent on consolidation, σ_1 , in that larger strength is associated with higher consolidation. This result has a major implication in silo design in view of the variation of consolidation stresses in the silo as shown in Figure 9.2. The material strengthens as it moves downward in the bin, but subsequently becomes weaker inside the hopper as it approaches the apex.

The majority of fine powders exhibit unconfined yield strength, f_c , when subjected to consolidation; these are usually called cohesive materials. There is, however, a class of larger size powders for which the value of f_c is practically zero for even large consolidations. These are the so-called non-cohesive or free-flowing materials, a few examples are given in Table 9.1. The most commonly known free-flowing material is fine, dry sand. Table 9.2 shows flow functions FF, for several cohesive materials as well as values of the angle of internal and wall friction, as measured by Drescher et al. (1995).

The design criteria for hoppers can now be stated qualitatively by using the maximum stress at the abutment of the arch, $\sigma_{1,a}$, and the unconfined yield strength, f_c , as the so-called flow-no-flow criteria. For the arch to break and hence for the powder to flow, the maximum stress has to overcome the yield strength

$$\sigma_{1,a} \geq f_c \quad (9.4)$$

The critical condition occurs when the equality holds and where the *critical span*, B_{crit} , is obtained. The solution to the above problem is finding the position, r (see Figure 9.3) or equivalently the span, B , where Eq. (9.4) holds with $\sigma_{1,a}$ and f_c given by

$$\sigma_{1,a} = 2r\gamma \sin \alpha/m = B\gamma/m, \quad f_c = \text{FF}(\sigma_1) \quad (9.5)$$

in which σ_1 is the consolidating stress in the hopper. It is possible to express the principal stress, σ_1 , as a function of the radial stress, σ_r (see, e.g., Tardos, 1999) as

$$|\sigma_1| = \sigma_r \left[\frac{1 + \sin \phi}{1 - \sin \phi \cos (\phi_w + \omega)} \right], \quad \sigma_r = \frac{\gamma Mr}{1 + mN} \quad (9.6)$$

TABLE 9.1 Interaction Properties of Several Free-Flowing Materials

Material	Mean Particle Diameter (mm)	Particle Density, ρ_s (g/cm ³)	Bulk Density, ρ (g/cm ³)	Internal Friction, ϕ (deg)	Wall Friction on Lucite, ϕ_w (deg)	Wall Friction on Aluminum, ϕ_w (deg)
Glass beads						
P-0140	0.272	2.47	1.5	18.2	15.7	—
P-0170	0.325	2.47	1.46	24.6	15.3	17.7
P-0280	0.592	2.47	1.48	24.3	14.4	15.1
V-070	1.326	2.92	1.71	26.8	14.2	15.1
V-160	3.23	2.92	1.66	31.7	12.9	—
Mustard seed	2.07	1.22	0.71	38.2	12.0	—
Fine sand	0.224	2.67	1.56	24.1	20.2	—
Medium sand	0.317	2.67	1.53	30.7	17.9	—
Coarse sand	0.681	2.67	1.53	30.6	14.4	24.3

TABLE 9.2 Physical Properties for Several Cohesive Materials

Material	Specific gravity (kN/m ³)	Wall friction on Aluminum, ϕ_W (deg)	Internal Friction, ϕ (deg)	E_{ws}	F_{ws}	q_{ws}	K_{ff}	L_{ff}
Limestone ($w = 5\%$)	15.44	34.0 37.5	57.8 56.0	0.33 0.40	0.04 0.04	1.80 1.95	0.35	3.06
Limestone ($w = 3.2\%$)	12.92	34.0 30.5	45.5 45.5	0.41 0.41	0.1 0.1	1.89 1.89	0.13	3.29
Gypsum	12.85	38.2	54.1 54.6	0.38 0.41	0.1 0.08	1.6 1.72	0.37	3.05
Coal	6.0	26.5 27.7	48.7 48.9	0.25 0.20	0.04 0.04	1.93 1.88	0.11	3.82
Cement	14.45	35.0 35.5	51.8 51.9	0.5 0.41	0.10 0.05	1.90 2.06	0.18	3.72

Adapted from Drescher et al., *Powder technol.*, 84, 165–183, 1995.

where M , N , K and ω are substitution variables, defined in the Nomenclature, and m indicates the hopper geometry: $m = 1$ for plane hopper geometry and $m = 2$ for the conical hopper geometry.

Equations (9.5) and (9.6) form a system of equations that is quite straightforward to solve for the radius r (or span B). The difficulty arises in the nonexplicit form of the flow function, FF, which is usually given graphically. To overcome this difficulty, Jenike used the special dependence of the stresses given in Eqs. (9.2) and (9.6) on the first power of the radius, r , to calculate the dimensionless ratio denoted by Jenike as the *flow factor*, ff (Eq. 9.7):

$$ff = \frac{|\sigma_1|}{\sigma_{1,a}} = \frac{mM(1 + \sin \phi)}{2(1 + mN)\sin \alpha[1 - \sin \phi \cos(\phi_W + \omega)]} \quad (9.7)$$

It is seen that this ratio depends only on material properties and not on position. In view of this, the relations in Eq. (9.5) become

$$f_c = FF(\sigma_1), \quad \sigma_{1,a} = (1/ff)\sigma_1 \quad (9.8)$$

and can be solved graphically by intersecting the curve of the FF with a line through the origin with the slope, $\tan(\eta) = 1/ff$, in a coordinate system with σ_1 as the ordinate as depicted in Figure 9.5. Below the line, continuous collapse of the arch ensures flow while above it arching occurs. At the intersection, the condition in Eq. (9.4) is satisfied and the critical span is obtained from Eq. (9.5) as

$$B_{crit} = m \sigma_{1,a,crit}/\gamma = m f_{c,crit}/\gamma \quad (9.9)$$

where the critical values are taken as shown in the figure. Since the FF is a measured quantity, the only challenge in the design procedure is the calculation of the flow factor, ff.

Two flow functions are given in Figure 9.5 one for material consolidated for a short time called the *instantaneous flow function* and another the *time-flow function*, obtained by consolidating the material for a longer time. In the example given above, the instantaneous values were used to yield a critical span given by Eq. (9.9). The time flow function gives a somewhat larger critical value for the yield strength, f_c , and therefore a larger value for the span, B_{crit} . The smaller span is used for a silo that is in continuous use and where material is loaded and unloaded continuously. The Higher value is employed for silos where material is stored for long times. The time flow function has to be obtained experimentally for consolidation times equal to or longer than the typical storage time.

In the case of free-flowing materials such as those presented in Table 9.1, the unconfined yield strength $f_c = 0$ and all points fall below the line as shown in Figure 9.5. This ensures that such a material will, at least in principle, flow out through any opening with a span B larger than the grain size; hence the name

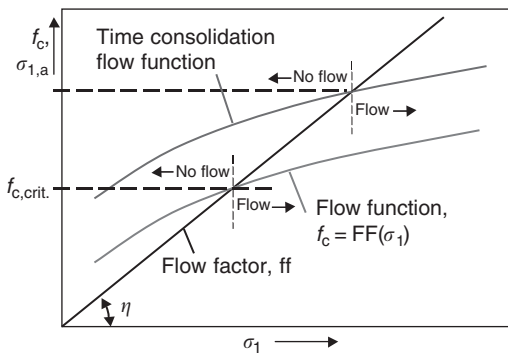


FIGURE 9.5 Graphic solution of the design equations.

for these powders. In practice, it is found that a minimum opening of several particle diameters is necessary (i.e., 6 or more). A theoretical treatment considering the effect of particle size offers an explanation of this in terms of an “intrinsic cohesion” for a discrete-grained powder (Wier, 1999).

In the case of cohesive materials, $f_c = FF(\sigma_1)$, may be computed from a Warren–Spring equation as

$$f_c = E_{WS} \left[\left(\frac{\sigma_1}{F_{WS} + 1} \right)^{1/q_{WS}} - 1 \right] \quad (9.10)$$

where E_{WS} , F_{WS} , and q_{WS} are material constants given in [Table 9.2](#). An alternative way of expressing the flow function is by the use of a linear fit:

$$f_c = K_{FF} \sigma_1 + L_{FF} \quad (9.11)$$

where values for constants K_{FF} and L_{FF} are also given in [Table 9.2](#).

A more general method for plotting continuous-flow functions for various kinds of cohesive and free-flowing materials is presented in [Section 9.4.2](#). The flow functions are defined in terms of common parameters that are used to fit a series of curved yield loci evaluated over a range of consolidation pressures.

The expressions in [Eq. \(9.7\)](#) can be used directly to calculate the flow factor ff . These are however only some of many equations and charts dedicated to the prediction of this variable. Detailed calculations for the flow factor were made by Jenike (1961, 1964), who solved numerically the differential equations of equilibrium of a bulk material in the hopper and gave the results in the now famous charts that bear his name. Analytical expressions, for example, given in [Eq. \(9.7\)](#), are used only if they agree with the more precise values calculated by Jenike. An example of a Jenike chart is given in [Figure 9.6](#) for a plane and a conical hopper for a material with an internal angle of friction of $\phi = 40^\circ$. Similar charts for different angles of friction from 30 to 70° and various geometries can be found in the above-mentioned work. There is a slight difference in the design [Eq. \(9.9\)](#) when using Jenike’s charts in which the geometric constant, m , is replaced by a more complex function, $H(\alpha)$, given in [Figure 9.7](#). As seen, $H(\alpha) \approx m$ for very small values of the hopper half-angle, α , but deviates from it, at larger values.

9.2.3 Concluding Remarks

The design of a hopper is reduced in the above to the determination of the hopper opening B that will prevent the formation of arches and thereby allow the powder to flow out through the opening. The method requires choosing a hopper angle α , and to measure all powder and powder–wall characteristics including the flow function FF .

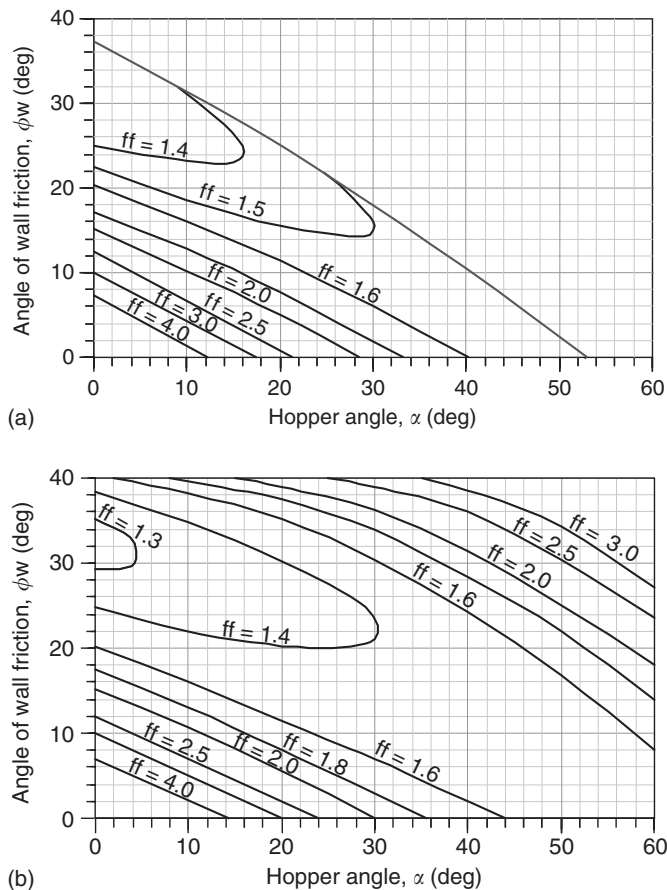


FIGURE 9.6 Values of the flow factor, ff , for (a) a conical hopper; (b) a 2D plane hopper. Material effective angle of internal friction: 40° .

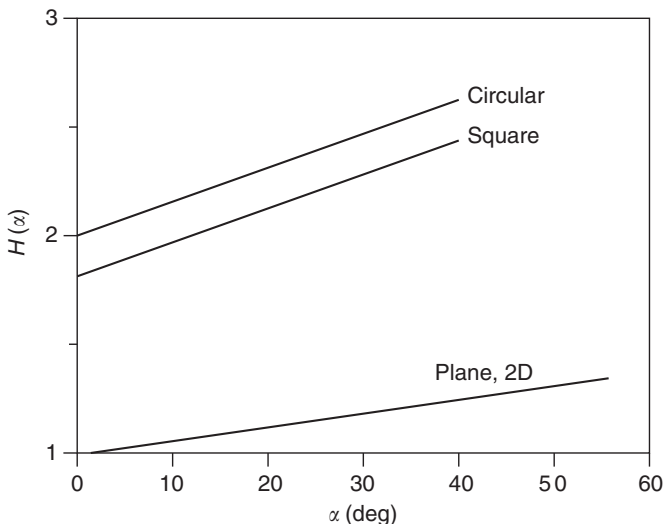


FIGURE 9.7 The function H for 2D and 3D hoppers.

9.3 Slow, Frictional Powder Flows

Slow, frictional powder flows are characterized by frictional forces between particles that overwhelmingly control the behavior of the system. General equations of flow result from:

- Adding inertial effects to the static equations of stress equilibrium
- Considering continuity
- Invoking a “flow rule”

While the first two points are self-evident, the consideration of the flow rule is a concept unique to powders. It is a postulate that specifies the behavior of the powder after the yield condition is satisfied and the powder starts to move. Several of these rules have been proposed and in the present work we use the simplest one named *Levy's flow rule*. According to this rule, the stress in the powder remains proportional to the rate of strain. While this is not always true in a deforming powder, it yields a simple correlation between the two and, in fact, it is quite general for an incompressible powder. Discussion of other flow rules is beyond the scope of the present work.

9.3.1 General Equations of Motion for Incompressible Powders

Conservation of mass or the “continuum” equation can be written in vector notation as

$$\frac{D\rho}{Dt} = \frac{\partial \rho}{\partial t} + \nabla \cdot (\rho \mathbf{u}) = 0 \quad (9.12)$$

where D^*/Dt is the material derivative and \mathbf{u} is the velocity vector. In Cartesian coordinates, the velocity vector reads as

$$\mathbf{u} = u_x \hat{i} + u_y \hat{j} + u_z \hat{k} \quad (9.13)$$

For an incompressible material, the bulk density is constant, $\rho = \rho_s(1-\varepsilon) = \nu\rho_s = \text{constant}$ and thus

$$\nabla \cdot \mathbf{u} = 0 \quad (9.14)$$

Equations of motion in the slow (frictional) regime are similar to the equation of fluid mechanics in that it is possible to combine the yield condition with the “flow rule” to obtain a constitutive equation. The equation of motion or “momentum” equation reads as

$$\rho \frac{Du}{Dt} = -\nabla \cdot \mathbf{S} + \rho g \quad (9.15)$$

which is a vector equation and supplies three equations in three spatial directions. The acceleration due to gravity, g , is also considered here to be a vector (in the direction of the gravitational field). This equation contains the equation of powder statics on the right hand side (RHS) and an inertial term on the LHS. The stress field, \mathbf{S} , is usually decomposed into a *deviatoric part*, \mathbf{D} , and a pressure field, p :

$$S_{ij} = D_{ij} + p\delta_{ij} \quad (9.16)$$

where i and j are indexes denoting, for example the x , y and z directions by 1, 2 and 3, δ_{ij} is the Kronecker delta: $\delta_{ij} = 1$ when $i = j$; $\delta_{ij} = 0$ when $i \neq j$; or the unit tensor

$$\delta = \begin{vmatrix} 1 & 0 \\ 0 & 1 \end{vmatrix} \quad (9.17)$$

The deviatoric tensor takes the form (in, for example, 2D x - y coordinates)

$$D = \begin{vmatrix} \sigma_{xx} - p & \tau_{xy} \\ \tau_{yx} & \sigma_{yy} - p \end{vmatrix} \quad (9.18)$$

where $p = (\sigma_{xx} + \sigma_{yy})/2$. With this, the momentum equations become

$$\rho \frac{D\mathbf{u}}{Dt} = -\nabla p - \nabla \cdot \mathbf{D} + \rho g \quad (9.19)$$

The total derivative on the left hand side (LHS) represents inertial effects.

The above system of four equations given in (9.14) and (9.19) has ten unknowns in 3D (three velocity components, the pressure and six components of the deviatoric stress) and six unknowns in 2D (two velocity components, the pressure and three components of the deviatoric stress) and is therefore unsolvable. Additional information in the form of a correlation between the deviatoric stress, \mathbf{D} , and the velocity is required. This is the so-called *constitutive equation that assures closure*. This equation usually correlates the deviatoric stress, \mathbf{D} , with the rate of deformation defined as

$$e_{ij} = -\frac{1}{2} \left(\frac{\partial u_i}{\partial x_j} + \frac{\partial u_j}{\partial x_i} \right) \quad (9.20)$$

where u_i and x_i are the velocity components and coordinates, respectively.

The constitutive equation for a Newton liquid assumes the simplest possible correlation:

$$D_{ij} = 2\mu e_{ij} \quad (9.21)$$

where, μ , is the viscosity of the fluid and is a material property. Introducing this into the general equation of motion (9.19) and using the definition of the rate of deformation (9.20), one obtains the well-known Navier–Stokes equations that describe incompressible fluid flow:

$$\rho \frac{D\mathbf{u}}{Dt} = -\nabla p - \mu \nabla^2 \cdot \mathbf{u} + \rho g \quad (9.22)$$

where $\nabla^2 \mathbf{u}$ is the Laplacian of the velocity. A simple correlation as given in Eq. (9.21) does not exist for powders since they do not exhibit viscosity and instead a more complex correlation is derived below that takes friction into account.

An analytical expression of a constitutive equation for powders was first proposed by Schaeffer (1987). Such an equation has to obey a yield condition. In this context, we use the more general (3D) von Mises condition that, with the definition of the deviatoric stress, \mathbf{D} (Eq. 9.16), can be written as:

$$\sqrt{\sum_{ij} (D_{ij})^2} = |D| = \sqrt{2}p \sin \phi \quad (9.23)$$

where $|D|$ is simply the magnitude of the (deviatoric) stress as used in simple algebra. This condition, however, only specifies the point of yield (onset of plastic deformation), but does not give any information on the movement of the material once deformation (or flow) starts.

An additional condition is required in the form of a *flow rule* as mentioned above. According to this rule, the deviatoric stress is proportional to the rate of strain that, for an incompressible powder where $\nabla \cdot \mathbf{u} = 0$, reads as

$$\mathbf{D} = \mathbf{S} - p\boldsymbol{\delta} = \lambda \mathbf{e} \quad (9.24)$$

where, λ , is an undetermined constant. Combination of Eqs. (9.23) and (9.24) gives

$$\lambda = \frac{\sqrt{2}p \sin \phi}{\sqrt{\sum_{ij} (e_{ij})^2}} = \frac{\sqrt{2}p \sin \phi}{|e|} \quad (9.25)$$

We use this correlation to obtain the constitutive equation from (24) as

$$D_{ij} = \sqrt{2}p \sin \phi \frac{e_{ij}}{|e|} \quad (9.26)$$

In the above equations, the magnitude of the rate of deformation tensor is given by (in, for example, 2D Cartesian coordinates):

$$|e| = \sqrt{e_{xx}^2 + e_{yy}^2 + 2e_{xy}^2} \quad (9.27)$$

Using Eq. (9.26) in the equation of motion gives, for an incompressible powder obeying the von Mises yield condition and Levy's flow rule

$$\rho \frac{Du}{Dt} = -\nabla p - \sqrt{2} \sin \phi \nabla \cdot \left(p \frac{\mathbf{e}}{|e|} \right) + \rho g \quad (9.28)$$

This equation takes the place of the Navier–Stokes equations of incompressible fluid mechanics and is applicable for powders. It yields three equations that, with the continuity equation $\nabla \cdot \mathbf{u} = 0$, can, in principle, be solved in three velocity components and pressure.

The momentum equation together with the yield condition and the flow rule can also be solved as a complete system without developing the constitutive equation (9.25), for details see Nedderman, 1992. The advantages of the above formulation are that the equations are given in concise form and are easy to analyze and to use in a numerical scheme. They include all parameters of the flow and are familiar to engineers and fluid mechanists. These equations require boundary conditions as do the NS equations and need to be specified *a priori*. The disadvantages of the formulation are that the equations must be solved in velocities first and stresses can only be obtained indirectly from the velocity distributions using Eq. (9.25). The equations are also more difficult to solve than the stress equations. The angle of internal friction, ϕ , is the material constant relevant in this case. In addition, the pressure term is the average normal stress as defined above.

One has to note that neither the von Mises yield condition nor Levy's flow rule is unique and that several forms are available. Furthermore, the above considerations are only valid for an isotropic material and for the condition that the powder is in continuous flow. This observation is essential since for nonflowing materials, $|e| = 0$ and infinitely large stresses are predicted. Moreover, the theory cannot be used for incipient flows where both the stress and strain rates fluctuate enormously and are characteristic of the “stick–slip” regime (see also [Figure 9.1](#)).

Detailed expressions for the equations of motion (9.28) in Cartesian, cylindrical and spherical coordinates for the 2D and axi-symmetric cases, respectively, are provided in [Table 9.3](#). Special cases in each coordinate system that are greatly simplified and satisfy the equations of continuity automatically are given in the last row of Table 9.3.

9.3.2 Incompressible Powder Flow in a Plane Wedge Hopper

This analytical solution was first obtained by Savage (1965) using the simple formulation of the static stress equations and is reproduced in Brennen and Pearce (1978) and Jackson (1982). We give here a solution using the general equations of motion (9.28) as detailed in Table 9.3 (Tardos, 1997) and predict simultaneously both the stresses and the velocity distributions in the powder. A similar solution in spherical coordinates is also possible for the conical hopper (a static solution is given in Nguyen et al., 1979).

The geometry of the system is depicted in [Figure 9.8](#) while the expressions of the differential equations, the rate of deformation tensor, and the corresponding stress are given in the second column of Table 9.3. The main additional simplifying assumption is that the half angle of the hopper, α , is small enough so that the gravitational term can be taken to have only a radial component, $-g$ and all variations in the θ direction can be neglected. Under these conditions, the radial (denoted by “r” in the table) component of the momentum equation becomes

$$\rho u_r \frac{\partial u_r}{\partial r} = -\frac{\partial p}{\partial r} + \sqrt{2} \sin \phi \left[\frac{\partial}{\partial r} \left(\frac{p}{\sqrt{2}} \right) + \sqrt{2} \frac{p}{r} \right] - \rho g \quad (9.29)$$

TABLE 9.3 General Equations of Motion for an Incompressible Material (in 2D) at Steady State

Equation	Cartesian Coordinates	Cylindrical Coordinates	Spherical Coordinates
Continuity	$\frac{\partial u_x}{\partial x} + \frac{\partial u_y}{\partial y} = 0$	$\left(\frac{1}{r}\right)\frac{\partial}{\partial r}(r \cdot u_r) + \left(\frac{1}{r}\right)\frac{\partial}{\partial \theta}(u_\theta) = 0$	$\left(\frac{1}{r^2}\right)\frac{\partial}{\partial r}(r^2 u_r) + \left(\frac{1}{r \sin \theta}\right)\frac{\partial}{\partial \theta}(u_\theta \sin \theta) = 0$
Momentum direction x or r	$\rho_B \left(u_x \frac{\partial u_x}{\partial x} + u_y \frac{\partial u_x}{\partial y} \right) = \rho_B g_x - \frac{\partial p}{\partial x}$	$\rho_B \left[u_r \frac{\partial u_r}{\partial r} + \frac{u_\theta}{r} \frac{\partial u_r}{\partial \theta} - \frac{u_\theta^2}{r} \right] = \rho_B g_r - \frac{\partial p}{\partial r}$	$\rho_B \left[u_r \frac{\partial u_r}{\partial r} + \frac{u_\theta}{r} \frac{\partial u_r}{\partial \theta} - \frac{u_\theta^2}{r} \right] = \rho_B g_r - \frac{\partial p}{\partial r} - (\sqrt{2} \sin \phi)$
Momentum direction y or θ	$\rho_B \left(u_x \frac{\partial u_y}{\partial x} + u_y \frac{\partial u_y}{\partial y} \right) = \rho_B g_y - \frac{\partial p}{\partial y}$	$\rho_B \left[u_r \frac{\partial u_\theta}{\partial r} + \frac{u_\theta}{r} \frac{\partial u_\theta}{\partial \theta} - \frac{u_\theta u_r}{r} \right] = \rho_B g_\theta - \frac{1}{r} \frac{\partial p}{\partial \theta}$	$\rho_B \left[u_r \frac{\partial u_\theta}{\partial r} + \frac{u_\theta}{r} \frac{\partial u_\theta}{\partial \theta} - \frac{u_\theta u_r}{r} \right] = \rho_B g_\theta - \frac{1}{r} \frac{\partial p}{\partial \theta}$
Rate of deformation	$e_{xx} = -\frac{\partial u_x}{\partial x}; e_{yy} = -\frac{\partial u_y}{\partial y}; e_{xy} = e_{yx} = -\frac{1}{2} \left(\frac{\partial u_x}{\partial y} + \frac{\partial u_y}{\partial x} \right)$	$e_{rr} = -\frac{\partial u_r}{\partial r}; e_{\theta\theta} = -\left[\frac{1}{r} \frac{\partial u_\theta}{\partial \theta} + \frac{u_r}{r} \right]; e_{r\theta} = e_{\theta r} = -\frac{1}{2} \left[r \frac{\partial}{\partial r} \left(\frac{u_\theta}{r} \right) + \frac{1}{r} \frac{\partial u_r}{\partial \theta} \right]$	$e_{rr} = -\frac{\partial u_r}{\partial r}; e_{\theta\theta} = -\left[\frac{1}{r} \frac{\partial u_\theta}{\partial \theta} + \frac{u_r}{r} \right]; e_{r\theta} = -\frac{1}{2} \left[r \frac{\partial}{\partial r} \left(\frac{u_\theta}{r} \right) + \frac{1}{r} \frac{\partial u_r}{\partial \theta} \right]; e_{\phi\phi} = -\left(\frac{u_r}{r} + \frac{u_\theta \cot \theta}{r} \right)$
Magnitude	$ e = \sqrt{e_{xx}^2 + e_{yy}^2 + 2e_{xy}^2}$	$ e = \sqrt{e_{rr}^2 + e_{\theta\theta}^2 + 2e_{r\theta}^2}$	$ e = \sqrt{e_{rr}^2 + e_{\theta\theta}^2 + 2e_{r\theta}^2 + e_{\phi\phi}^2}$
Stress tensor	$S_{ij} = p \left[\delta_{ij} + \sqrt{2} \sin \phi \frac{e_{ij}}{ e } \right]$	$S_{ij} = p \left[\delta_{ij} + \sqrt{2} \sin \phi \frac{e_{ij}}{ e } \right]$	$S_{ij} = p \left[\delta_{ij} + \sqrt{2} \sin \phi \frac{e_{ij}}{ e } \right]$
Special cases	$e_{xx} = e_{yy} = 0; e_{xy} = e_{yx} = -\frac{1}{2} \frac{\partial u_x}{\partial y}$ $ e = \frac{1}{\sqrt{2}} \frac{\partial u}{\partial y}; \text{ with } v = 0; u = u(y)$ $S_{xx} = S_{yy} = p; S_{xy} = S_{yx} = -p \sin \phi;$	$e_{rr} = \frac{-A}{r^2}; e_{\theta\theta} = \frac{A}{r^2}; e_{r\theta} = e_{\theta r} = 0; e = \sqrt{2} \frac{A}{r^2}$ $S_{rr} = \sigma_2 = p(1 - \sin \phi); S_{\theta\theta} = \sigma_1 = p(1 + \sin \phi)$ $S_{r\theta} = S_{\theta r} = 0; \text{ with } u_\theta = 0; u_r = -A/r$	$e_{rr} = -\frac{2A}{r^3}; e_{\theta\theta} = e_{\phi\phi} = \frac{A}{r^3}; e_{r\theta} = e_{\theta r} = 0; e = \sqrt{6} \frac{A}{r^3}$ $S_{rr} = p \left(1 - \frac{2}{\sqrt{3}} \sin \phi \right); S_{\theta\theta} = S_{\phi\phi} = p \left(1 + \frac{1}{\sqrt{3}} \sin \phi \right)$ $S_{r\theta} = S_{\theta r} = 0; \text{ with } u_\theta = 0; u_r = -A/r^2$

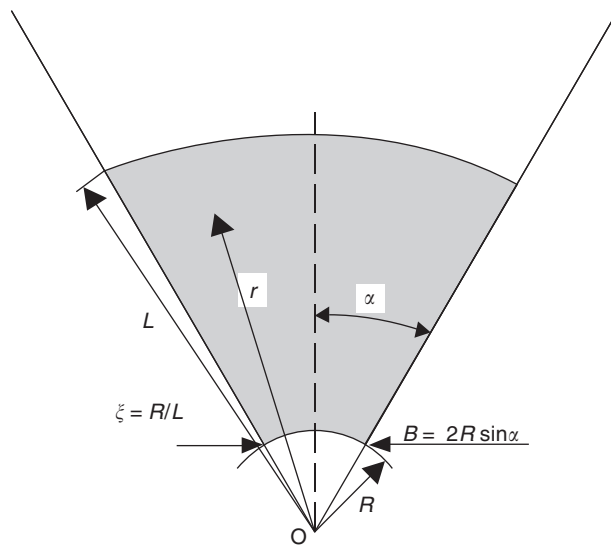


FIGURE 9.8 Schematic representation of the plane wedge hopper.

Using the dimensionless stress (pressure), $p^* = p/\rho g L$ and radius $r^* = r/L$ and replacing the radial velocity component by $u_r = -A/r$ to satisfy the continuity equation identically, the above equation becomes

$$\left(\frac{\partial p^*}{\partial r^*} \right) - \chi \sin \phi \left(\frac{p^*}{r^*} \right) = \frac{\chi}{2} \left[\frac{(A^*)^2}{(r^*)^3} - 1 \right] \quad (9.30)$$

where $\chi = 2/(1 - \sin \phi)$, $A^* = A/L(Lg)^2$ and A is a constant of integration (see also the last row of the third column in Table 9.3). The solution of this equation with no traction boundary conditions $p^* = 0$ at $r^* = 1$ and $r^* = R/L = \xi$ is (for $3\sin \phi \neq 1$):

$$p^* = \frac{1}{3\sin \phi - 1} \left[r^* - \left(1 - \frac{1 - \xi^3}{1 - \xi \chi} \right) (r^*)^{-2} - \frac{1 - \xi^3}{1 - \xi \chi} (r^*)^{\chi \sin \phi} \right] \quad (9.31)$$

while the velocity becomes

$$u_r^* = \frac{u_r}{\sqrt{Rg}} = -\frac{1}{r^*} \sqrt{\frac{2}{\xi(3\sin \phi - 1)}} \left(1 - \frac{1 - \xi^3}{1 - \xi \chi} \right) \quad (9.32)$$

The practically important cases occur for $\sin \phi > 1/3$ since real powders exhibit friction angles larger than about 20° ; on the other extreme, when $\sin \phi < 1/3$, the material becomes more and more fluid-like and for $\phi = 0^\circ$ it becomes a frictionless fluid.

An important result for the average stress, p^* , the so-called quasi-static solution, is obtained by assuming that the material is stationary, i.e., $u_r = 0$ (by taking the term in the square brackets of the above equation equal to zero and by neglecting ξ as compared to unity) and using this in Eq. (9.31):

$$p^* = \frac{r^*}{3\sin \phi - 1} \left[1 - (r^*)^{(\chi(3\sin \phi - 1)/2)} \right] \quad (9.33)$$

The first term in Eqs. (9.31) and (9.33) is the so-called “radial solution”, which predicts a linear dependence of the average stress on the distance from the virtual apex of the hopper. The last term ensures that the stress satisfies the boundary condition on the powder surface and becomes prevalent only at higher values of the radius (provided that $\sin \phi > 1/3$). The middle term in Eq. (9.31) is due to the acceleration of the material and is negligibly small everywhere except close to the hopper outlet where it becomes dominant.

One can easily show that the Navier–Stokes equations for an incompressible fluid (Pnueli and Gutfinger, 1992) reduce to Eq. (9.30) with the coefficient of internal friction taken as $\phi = 0$. The pressure and radial velocity for the fluid are then given by

$$p^* = 1 - r^* - \frac{\xi^2}{1 + \xi} [(r^*)^{-2} - 1], \quad v_r^* = -\sqrt{\frac{2\xi}{1 + \xi}} (r^*)^{-1} \quad (9.34)$$

If the wedge has a very small opening at $r^* = \xi \approx 0$, the pressure distribution in Eq. (9.34) becomes approximately hydrostatic, $p^* = 1 - r^*$, and the fluid velocity at the outlet reduces to $u_r = (2gL)^{1/2}$ as expected.

The stress distribution in both an incompressible Coulomb powder and a Newtonian fluid is depicted in Figure 9.9 for several values of the angle of internal friction, ϕ , for the coefficient $\xi = 0.05$. As seen, the pressure in the fluid is hydrostatic, i.e., is linear and has a maximum towards the bottom of the container (except close to the outlet where it becomes zero due to fluid acceleration). The average stress in the powder, p^* , is quite different from the pressure distribution in the fluid; for values of the angle of internal friction higher than about 30° , the radial stress approximates this distribution fairly well as seen in Figure 9.9 (for $\phi = 45^\circ$ and $\phi = 30^\circ$). For relatively small values of the angle of internal friction, less than about 20° , the stress distribution in the powder cannot be approximated by the radial stress, as seen in Figure 9.9 (for $\phi = 20^\circ$), and approaches in the limit of small angles the pressure distribution in the fluid (for $\phi = 6^\circ$ and lower).

The radial stress is obtained from Eq. (9.33) while the *maximum radial stress* becomes

$$\sigma_1^* = p^*(1 + \sin \phi) = \frac{1 + \sin \phi}{3 \sin \phi - 1} r^* \quad (9.35)$$

The slope of the above stress distribution divided by the coefficient $2\sin \alpha$ was named the “flow factor” by Jenike (1964) and can be written as

$$ff = \frac{1 + \sin \phi}{2(3 \sin \phi - 1) \sin \alpha} \quad (9.36)$$

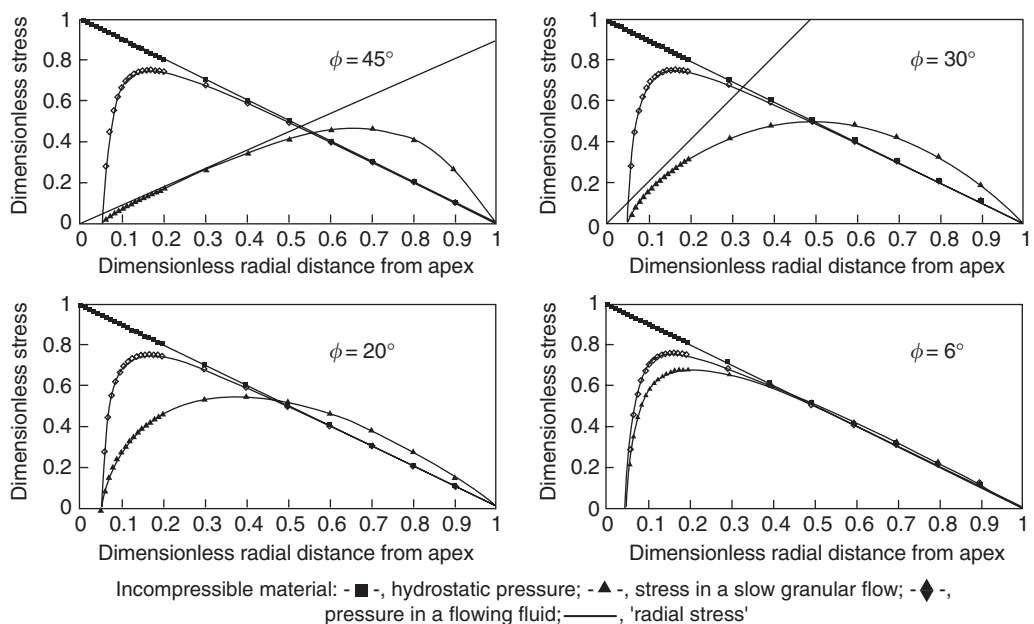


FIGURE 9.9 Stress distribution in a two-dimensional wedge hopper for an incompressible material.(From Tardos, G. I., *Powder Technol.*, 92, 61–74, 1997.)

This factor can be obtained from solutions of the static stress equilibrium equations (Shamlou, 1990 and Drescher et al., 1995) or by using the method of “slices” (Nedderman, 1992) as shown in the previous section. Here we compare, in Table 9.4, values given by Eq. (9.36) to computed values of Jenike (1964) obtained from his numerical quasi-static solution for the symmetrical wedge hopper. One has to note that the values given by the above equation only cover the simple case when the angle of wall friction is $\phi_w = 0$ since it was assumed that the stress and velocity exhibit only radial dependence and therefore no angular boundary conditions could be satisfied. As seen in Table 9.4, the fit of analytical and numerical solutions is quite good despite the large number of assumptions made in the analytical solution; this seems to indicate that the constitutive Eq. (9.26) adequately represents the stress distribution or that the solution is not very sensitive to the choice of the constitutive postulate (it turns out that the second conclusion is correct as seen from the comparison of predicted flow rates, below). Several improvements of the above solution were attempted in an effort to include the boundary conditions on the hopper wall (Brennen and Pearce, 1978; Savage, 1965) but all reduce to the above solution for zero wall friction. A more general solution with more complex boundary conditions is presented for the plane as well as for the conical hopper by Drescher (1991) while a solution that does not assume radial gravity was given by Savage (1967).

The advantage of the above solution is that, in addition to the stress distribution, it also provides an expression for the velocity field and hence the overall flow rate from the hopper at $r = R(r^* = \xi)$ can also be calculated directly. Assuming that the wedge hopper has a width, H (dimension perpendicular to the plane of Figure 9.8) and using the result of Eq. (9.32), the mass flow rate can be expressed as (Davidson and Nedderman, 1973; Cleaver and Nedderman, 1993)

$$W = \rho BH(v_r^*|_{r=\xi})\sqrt{Rg} = [(3\sin \phi - 1)\sin \alpha]^{-1/2}\rho \sqrt{g} HB^{1.5} \quad (9.37)$$

where we used $R = B/2 \sin \alpha$ and neglected ξ with respect to unity.

A correlation used extensively in the powder industry to calculate mass flow rates from hoppers is the so-called Beverloo equation (Shamlou, 1990), which in a simplified form reads

$$W = 0.56\rho \sqrt{g} HB^{1.5} \quad (9.38)$$

The analytical solution (9.37) overpredicts the experimental coefficient of 0.56 and, for values of the internal angle of friction $\phi = 30^\circ$ and a hopper half-angle of $\alpha = 30^\circ$, yields a coefficient of approximately 2.0. This discrepancy is quite large and can be only partly explained by the fact that in the analytical solution wall effects are neglected (Nedderman et al., 1982). In addition, it was shown by Brennen and Pearce (1978) that the no-traction boundary condition at $r = R$ is not quite correct at the outlet of the hopper and that there are many other reasons for this misfit (see also detailed discussion in Jackson, 1982; Shamlou, 1990).

It is interesting to note that the mass flow rate of a fluid discharging from the hopper, obtained by using Eq. (9.34), is

$$W = \sqrt{2} \rho \sqrt{Lg} HB \quad (9.39)$$

which is proportional to the square root of the height of the fluid column above the exit, L , while the flow rate of the Coulomb powder (Eq. [9.37]) only depends on the size of the outlet, B and H . This is mainly

TABLE 9.4 Comparison of Flow Factor Values (ff) from Eq. (36) and Jenike’s Charts (Figure 9.6). Angle of Internal Friction, 40° and Angle of Wall Friction, 0°

Hopper Half Angle α (deg)	14	20	30	44
ff after Jenike (1964)	4.0	3.0	2.0	1.6
ff from Eq. (9.36)	3.65	2.6	1.77	1.27

due to the fact that part of the weight of the powder column rests by friction on the lateral walls while all the weight of the fluid rests on the bottom.

9.3.3 Equations of Motion for Compressible Powders

The general equations of motion for compressible powders can be treated in an analogous way as incompressible powders, only the constitutive equation is rather more complex and the expression ($p \sin \phi = q$) in Eq. (9.26) is replaced by a more general expression, which is density-dependent, $q(p, \rho)$, as given in Table 9.5:

$$S_{ij} = p \delta_{ij} + \sqrt{2} q(p, \rho) \frac{\frac{e_{ij}}{2} \nabla \cdot \mathbf{u} \delta_{ij}}{\left| \frac{e_{ij}}{2} \nabla \cdot \mathbf{u} \delta_{ij} \right|} \quad (9.40)$$

Equation (9.40) is general and reduces to the constitutive equation for an incompressible powder when $\nabla \cdot \mathbf{u} = 0$. One has to note that the elliptic and parabolic yield conditions (and the last expression with $C = \sin \phi$ in Table 9.5) reduce to the simple correlation $q = p \sin \phi$ for $p = a$, which is the model of Roscoe (Schofield and Wroth, 1968), commonly referred to as the Cam–Clay model. For each bulk density, or value of a in the present case, the yield curve is given by a second-order curve while all the maxima lay on the so-called *critical state line* where

$$\frac{\partial q}{\partial p} = 0, \quad \frac{q}{\sin \phi} = p = a = (\rho)^{1/\beta} \quad (9.41)$$

One has to note that the yield function $q(p, \rho)$ as given in Table 9.5 for the case of the compressible powder is incompatible with the characterization by Jenike using the flow function FF as presented earlier in this chapter. This is due to the fact that in order to obtain FF, the curved yield locus given by $q(p, \rho)$ is approximated by a line at low consolidations and a circle at the endpoint of the locus at the highest compression (to determine the value of the uniaxial consolidation) and hence is only piecewise continuous.

Combining the above constitutive equation (9.40) with the momentum equation, one obtains

$$\rho \frac{Du}{Dt} = -\nabla p - \sqrt{2} \sin \phi \nabla \cdot \left[q(p, \rho) \frac{e_{ij} - (\nabla \cdot \mathbf{u} \delta_{ij})/2}{\left| e_{ij} - (\nabla \cdot \mathbf{u} \delta_{ij})/2 \right|} \right] + \rho g \quad (9.42)$$

This equation, together with the continuity equation

$$\frac{\partial \rho}{\partial t} + \nabla \cdot (\rho \mathbf{u}) = 0 \quad (9.43)$$

form a system of four equations with five unknowns, namely the three components of the velocity vector, the average stress p and the density ρ . In order to complete the system, a fifth equation is required in

TABLE 9.5 Values of the Yield Condition $q = q(p, \rho)$ for Incompressible and Compressible Powders

Constitutive Equation: ($n = 2$ in 2D; $n = 3$ in 3D)	$S_{ij} = p \delta_{ij} + D_{ij} = p \delta_{ij} + \sqrt{2} q(p, \rho) \frac{e_{ij} - (\nabla \cdot \mathbf{u} \delta_{ij})/n}{\left e_{ij} - (\nabla \cdot \mathbf{u} \delta_{ij})/n \right }$	Parameters	Remarks
Powder properties	Yield condition, $q(p, \rho)$		
Incompressible and non-cohesive	$p \sin \phi$	—	Critical-state condition
Compressible and noncohesive	$p \sin \phi \sqrt{2 - p/a}$	$a = \rho^{1/\beta}$ $0.001 < \beta < 0.01$	Parabolic condition
Compressible and noncohesive	$p \sin \phi \sqrt{2a/p - 1}$	$a = a_0 \log \frac{\rho_\infty - \rho_0}{\rho_\infty - \rho}$	Elliptic condition
Compressible and cohesive	$a \sin \phi - C \frac{(p - a)^2}{a}$	$a = \rho^{1/\beta}$ $0.001 < \beta < 0.01$	Cam–Clay model with $C = \sin \phi$

the form of the “normality” condition (Jackson, 1982; Pitman and Schaeffer, 1987). This condition relates the rate of deformation of the medium to the geometry of the yield curve and reflects the experimentally observed phenomenon (also contained in the Cam–Clay model) that, in a shearing mass, the powder expands at low and contracts at high compression. The mathematical form of this condition is

$$\nabla \cdot \mathbf{u} = \frac{\partial q(p, \rho)}{\partial p} \times |e_{ij} - (\nabla \cdot \mathbf{u} \delta_{ij})/2| \quad (9.44)$$

and, as seen, specifies the value of the derivative $\partial q/\partial p$ as the material deforms. The derivative is zero on the critical state line, negative to the right at large and positive to the left at low values of compression.

The above system of equations forms a complete set for the solution of compressible powder flows (Jackson, 1982; Pitman and Schaeffer, 1987; Tardos, 1997). A simplified approximate solution by decoupling the bulk density variation from the stress is given in Drescher (1991), who also mentions a semianalytical solution by Savage and Sayed (1979) where a more complex dependence of the density on the stress is used. A more complete analytical solution is given in Tardos (1997) and this is reproduced below.

9.3.4 Compressible Powder Flow in a Plane Wedge Hopper

The solution given in this section is a more general version of the incompressible radial flow in cylindrical coordinates and is presented as an illustration to show the effect of compressibility on the stress distribution and the flow rate from the hopper. The geometry of the system is given in Figure 9.8; the main difference compared to the previous example is the assumption that the powder bulk density is not constant and uniform but rather varies with position according to the relation

$$\rho = \rho_0 \left(\frac{r}{L} \right)^n \quad \text{for } 0 < n < 1 \quad (9.45)$$

In addition, we take the radial velocity as

$$v_r = \frac{A}{r^{(1+n)}} \quad \text{for } 0 < n < 1 \quad (9.46)$$

where n is a small positive number. The continuity equation for compressible materials (Eq. [9.43]), in cylindrical coordinates with only the radial velocity nonzero can be written as

$$v_r \frac{\partial \rho}{\partial r} + \rho \left[\frac{\partial v_r}{\partial r} + \frac{v_r}{r} \right] = 0 \quad (9.47)$$

and is seen to be satisfied identically by the expressions chosen for the bulk density and the radial velocity. There is no physical justification to the density variation in Eq. (9.45), except that it satisfies the continuity equation (Drescher, 1991) and is compatible with the assumed yield condition, i.e., the Cam–Clay model (see below). The expression in square brackets in the above equation is the divergence of the velocity, which is needed to calculate the stress tensor in Eq. (9.40) and is given by

$$\nabla \cdot \mathbf{u} = -\frac{1}{\rho} v_r \frac{\partial \rho}{\partial r} = \frac{nA}{r^{(2+n)}} \approx \frac{nA}{r^2} \quad (9.48)$$

where we used the condition that the compression index, n , is small compared to unity, $n \ll 1$, and is neglected in the exponent of the radial coordinate. This assumption is required in order to obtain an analytical solution for the stress. Introducing the above into the normality condition (9.44), gives $\partial q/\partial p \approx n$; since n is a small parameter, one can assume that the flow in the hopper takes place under conditions very close to the critical state.

The remainder of the solution is similar to the procedure used to obtain the result for the incompressible material. The yield criteria from Table 9.5 and the divergence of the velocity from Eq. (9.48) are introduced into the radial component of the general equation of motion (9.42) which takes the form

$$\frac{\partial p^*}{\partial r^*} - \frac{2\sin \phi}{1 - (1 + n/2)\sin \phi} \left(\frac{p^*}{r^*} \right) = \frac{r^n}{1 - (1 + n/2)\sin \phi} \left[\frac{(n+1)(A^*)^2}{(r^*)^{(3+2n)}} - 1 \right] \quad (9.49)$$

The solution with no-traction boundary conditions at the top and the outlet of the hopper is given by

$$p^* = X \left[(r^*)^{n+1} - (1 - Z)(r^*)^{(-2-n)} - Z(r^*)^{(2\sin\phi/(1-(1+n/2)\sin\phi))} \right] \quad (9.50)$$

while the velocity becomes

$$v_r^* = \frac{v_r}{\sqrt{Rg}} = -\sqrt{\frac{1}{\xi} \frac{X}{Y} [1 - Z]} \cdot (r^*)^{(-1-n)} \quad (9.51)$$

The constants X , Y , and Z are given by

$$X = \frac{1}{(3 + 1.5n)\sin\phi - n - 1}; Y = \frac{n + 1}{2(1 - n\sin\phi) + n}; Z = \frac{1 - \xi^{(2n+3)}}{1 - \xi^{(2(1-n\sin\phi)+n/(1-(1+n/2)\sin\phi))}} \quad (9.52)$$

It is instructive to look at the correlation of the average stress and the powder bulk density from Eqs. (9.45) and (9.50). It is immediately apparent that their ratio is position-dependent and, for the simple case of the radial stress, the correlation becomes

$$p^* \approx X(r^*)^{n+1} = X(\rho/\rho_0)(r^*) = X(\rho^*)(r^*) \quad (9.53)$$

Taking the logarithm and differentiating the above equation, we can easily show that

$$\frac{d(\ln(p^*))}{d(\ln(\rho^*))} = 1 + \left[\frac{1}{d(\ln(\rho^*))/d(\ln(r^*))} \right] = 1 + \frac{1}{n} \approx \frac{1}{n} \quad (9.54)$$

This kind of dependence is equivalent to an equation of state of the form, $p/\rho^{1/n} = \text{constant}$, which is also implied in the result that the powder flows under condition very close to the critical state, i.e., $\partial q/\partial p \approx n$, as seen in Eq. (9.41) and hence one can take $n \approx \beta$ (by assuming that the constant in the equation of state is unity). Jenike (1987) showed that compressible powders may obey such an equation provided that the coefficient n is small and is of the order 0.05 to 0.1. This is quite encouraging as it gives physical meaning to the coefficient n and also yields some legitimacy to the chosen form of the density dependence on radial distance as in Eq. (9.45).

The stress distribution in the compressible powders is shown in Figure 9.10 for values of the compression index, $n = 0$ (incompressible material), and 0.25, and 0.5 and, as seen, the stress is diminished in the compressible powder as the value of the index increases. In the same figure, the variation of the bulk density with distance is also shown. Since, large variations in density such as those depicted for an index of $n = 0.5$ are not very common in powders (but possible, see van Zuilichem et al., 1974), the value of this coefficient should be in the average somewhat smaller. The reduction of the stress is, as compared to the incompressible case, not extremely significant demonstrating again the insensitivity of the stress distribution to the chosen constitutive postulate and the powder's compressibility. The above results are instructive and show, for example, that the linear dependence of the stress on the radial distance is not preserved in compressible powders and also that the stress is diminished in the hopper as intuitively expected. In view of this, the straightforward use of the flow factor, f_f , in the design of hoppers for highly compressible powders (for which the n index is not very small) is not immediately obvious and much more work is required before the simple concepts of arching powders can be applied.

The advantage of the above solution is that the mass flow rate from the hopper can again be estimated directly and this becomes

$$W|_{r=\xi} = \rho_0 \xi^n \left[\frac{(1 - n \sin\phi) + n/2}{(n + 1)[(3 + 1.5n)\sin\phi - n - 1]} \right]^{1/2} \sqrt{\frac{g}{\sin\alpha}} HB^{1.5} \quad (9.55)$$

This equation gives for the same values of the angle of internal friction and hopper half-angle as in Eqs. (9.37) and (9.38), a constant coefficient of 0.42 for $n = 0.5$ and 0.90 for $n = 0.25$ as compared to approximately 2.0 predicted for the incompressible material; this is a major improvement toward the experimental value of 0.56 in Eq. (9.38).

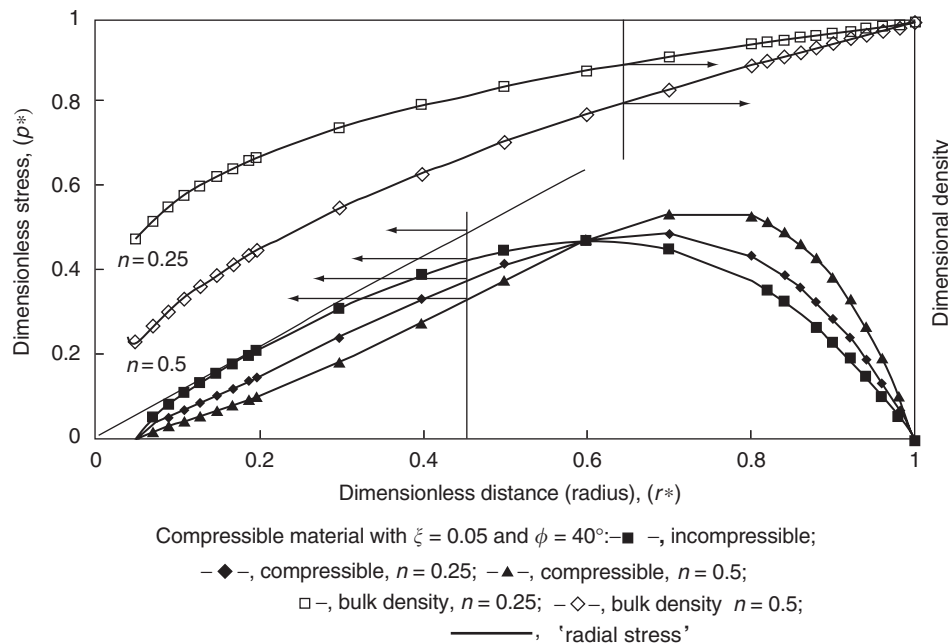


FIGURE 9.10 Stress and density distribution in a two-dimensional hopper for a compressible material. (From Tardos, G. I., *Powder Technol.*, 92, 61–74, 1997.)

9.3.5 Concluding Remarks

A constitutive equation for slow-frictional bulk powder flows is presented, that, together with the continuity and momentum equations, yield a general equation of motion, which is homogeneous in velocity components. Explicit forms of this general equation in all the three coordinate systems are given in Table 9.3. A comprehensive method of solution following general procedures of fluid mechanics was presented for the 2D wedge hopper. Jenike's flow factor, ff , and the kinematic flow rate are both obtained from the same solution. Constitutive equations are also presented for compressible powders while an illustrative example is given for a powder with radial density variation. It is shown that flow rates predicted by this model more closely reflect measured values. Finally, it was shown that the constitutive equations for powders bear some resemblance to similar equations proposed for non-Newtonian fluids. This is significant since many numerical schemes and programs are available for fluid flows that may also be applied to powder flows in more complex geometries by slight modifications of the numerical code.

9.4 Characterization of Bulk Powders

This section discusses characterization methods that can be useful in measuring powder properties. The main focus is on the measurement of bulk properties such as friction, cohesion, and compressibility.

Detailed characterization of particles (size, shape, roughness, etc.) and their material properties (complex modulus, yield strength, dielectric permittivity, etc.) can be considered as fundamental microscopic bases for bulk powder behavior. While there has been considerable progress toward the linkage of particle-scale characteristics with bulk powder behavior, it is clear that much work needs to be done to elucidate the functional relationships better between particles and the bulk, especially for particles with distributed characteristics. Further, the effects of particle size, size distribution, and preconsolidation on bulk flow are not apparent from single-particle characterization; rather these bulk effects depend on ensemble particle packing and may require an intermediate scale of scrutiny (i.e., a mesoscale) combined with statistical mechanics to enable useful linkages between microscale characteristics and bulk-flow behavior. For a more

detailed discussion of the linkage between microscale particle properties and bulk-powder flow, the reader is referred to the recent work of Jones et al. (2003, 2004), which offers parallels between micro-scale analyses of inter-particle friction and bulk flow yield loci.

Bulk flow of powders is routinely characterized using shear cells to measure incipient yield and steady-state slow frictional flows as a function of the consolidation state of the powder. Mohr–Coulomb analyses of shear cell data are used to generate flow functions that are applicable to the design of hoppers as discussed in Section 9.2, specifically for the determination of hopper angles and bottom openings that are required to assure reliable gravity flow from a static storage vessel. Other tests such as packing density, compressibility, angle of repose, funnel flow rates, and avalanching flow statistics can be used to generate indices describing various aspects of powder storage and flow. In an attempt to suggest connections between these routine empirical tests and more mechanistic approaches, discussions of research methods are interspersed in the following survey of routine bulk methods. Other advanced characterization techniques including tomography, particle flow tracking, etc., are discussed in [Chapter 14](#) of this Handbook.

9.4.1 Brief Survey of Methods

A variety of flow indexes have been developed to address the various states of powder in different industrial processes, such as loading and unloading from bins and hoppers, feeders, chute flows, filling dies for tabletting, filling packages, mixing and agglomeration, pneumatic conveying, etc. In addition, there are often multiple methods that can be used to measure similar attributes, but with different degrees of complexity and cost. Many of these index methods are used for specific industrial applications (de Jong et al., 1999; Lee et al., 2000; Bell, 2001). Relatively simple index methods are also employed in academic studies, for example, to provide a basis for comparison between experimental observations and flow simulations (Nase et al., 2001).

The angle of repose formed by discharging a controlled flow of powder into a heap is often used as an indication of bulk powder friction. For relatively free-flowing powders discharged slowly from a relatively narrow orifice, the angle of repose is similar to the steady-state friction angle measured using shear cells. Qualitative observations of the heap flow can show subtle differences in free-flowing powders that are not easily apparent from the flow functions derived by shear cell measurements. For example, the angle of repose measurement is capable of discerning the fluidization properties of relatively free-flowing powders (Wong, 2002).

An alternative method for measuring angle of repose is the so-called dynamic angle of repose. For relatively free-flowing powder, a steady-state repose angle can be observed in a slowly rotating horizontal axis drum as the powder gently rolls down the free surface (Nase et al., 2001). With more cohesive powders, the flow in the rotating drum develops a chaotic avalanching pattern (Kaye, 1996). The analysis of these chaotic flow patterns is performed using a statistical approach to characterize the frequency of avalanche flows (Iacocca and German, 1999).

The relative bulk density of the powder can be used, in some cases, as an indicator of flow properties. A powder that packs naturally to a high packing fraction is generally free flowing (i.e., it is easy for the individual particles to rearrange relative to one another and find a denser packing state). On the other hand, a low relative bulk density often indicates a more cohesive powder where the particles are not easily rearranged because the interparticle cohesive forces are in excess of the consolidation force, for example, the weight of the powder. Several bulk density indices are proposed in the literature, based on variations of dense and loose-packed bulk density ratios. In all cases, methods of packing the powder in its loose state as well as densification by tapping or vibrating are critical.

Measurement of a sample's bulk density in a container under various methods of filling provides indirect evidence on the effect of powder flow on particle packing (Santomaso, 2003; Mohammadi and Harnby, 1997). A commonly used flow index based on bulk density is the Hausner ratio, which is the tapped bulk density or the loose bulk density. The loose bulk density depends on the packing arrangement of the particles in the bulk powder, along with frictional interactions between the powder and the walls of the container. The packing arrangement depends on the nature of the powder flow on filling a cylindrical

container. When a powder is poured into a bulk density cup or other measurement cell, the resulting packed bed will typically exhibit local gradients in packing and bulk density. To avoid packing gradients, a sifting method can be used to distribute particles in the cell, i.e., to allow individual particles to “rain down” into the sample container. In the first case (bulk pouring flow), bulk flow and packing rearrangement occur simultaneously. In the latter case (sifting method), the surface rearrangement of single grains or small clusters of particles results in a more uniform radial packing distribution.

Further insight into the effects of powder flow on bulk packing can be obtained by investigating the permeability of the packed bed. For example, the pressure drop across the bed can be measured by using an instrumented cylinder with an air distributor plate (Abdullah and Geldart, 1999; Jaraiz et al., 1992). The pressure drop is directly related to the interparticle porosity in the bed, which is related to the nature of particle packing obtained when filling or fluidizing the particles in the bed. Similar techniques have been used to investigate bulk powder tensile properties (Watson et al., 2001; Seville and Cliff, 1984). Mercury porosimetry is also used as a diagnostic of powder flow, especially with respect to die-filling flows (Guerin et al., 1999).

Compressibility of the powder under uniaxial compression is another common measurement, for example, as illustrated in Figure 9.4. Essentially, this is a measure of the change in particle packing and increase in cake strength with compression. For compressible powders, an approximate flow function can be obtained by plotting the strength of the unconfined cake (f_c in Figure 9.4b) as a function of the pre-compression stress (σ_i in Figure 9.4a). In addition, simple uniaxial tests are conveniently used to measure time-consolidation effects, i.e., where a compression load is applied for extended periods of time that are representative of storage conditions. The increase in the unconfined strength with consolidation time is an indication of susceptibility to time consolidation. Some of the causes of time consolidation include caking by moisture redistribution, plasticity, recrystallization and hydrate formation (Tomas, 2000).

Funnel flow tests are often used to measure dynamic flow properties of a powder. The flow rate through an orifice is empirically described by the Beverloo equation, discussed in Section 9.3. The comparative mass flow rate through a fixed orifice can be used as an index of flowability between a powder sample and a known standard. The method is often used to assess the effectiveness of flow aids. Typically, a series of funnels with various opening sizes is used to measure the onset of bulk flow as a function of the orifice size. Variations include comparing the flow rate through a single standard funnel as a function of the type of powder or powder blend.

More recently, direct characterization of powder flow during die filling is done using high-speed imaging of the bulk flow (Wu et al., 2003). While direct observation can be difficult in many industrial applications, it is extremely useful in understanding rate effects in filling operations where multiple regimes of flow may occur, i.e., cascading free-surface flow vs. a volume-confined bulk flow. As rate changes, the dominant mechanism of flow may also change, causing significant differences in the resultant in-die density distribution. Chute flow is another example where direct imaging is useful in elucidating gradients in flow behavior, for example, quasi-static basal layers with an intermediate dense flow layer which may, in some cases, approach a free collisional layer at the free surface (Louge and Keast, 2001).

Various devices have been developed to measure powder response to mechanical stirring, typically via a torsion measurement (Orband, 1997; Freeman, 2000). These measurements are typically used as a point of comparison between a powder sample and other known materials or standards. Since such measurements are strictly empirical, they can provide some insight into flow behavior at intermediate shear rates that are representative of many industrial operations.

From a research perspective, particle tracking methods and local stress measurements provide far more detailed descriptions of flow structure. Tracking methods include optical measurements (Ferrari and Polleto, 2002), nuclear magnetic resonance (NMR) (Caprihan and Seymour, 2000) and positron emission particle tracking (PEPT) (Laurent et al., 2000; Laurent and Bridgwater, 2002). The PEPT method has been used to investigate positional or velocity fluctuations of discrete particles in a cascading or agitated mixer flow (Kuo et al., 2003; Stewart, et al., 2001). Direct tracking of flow patterns in a stirred mixer has been correlated to mixer torque (Laurent and Bridgwater, 2001). Stress sensors have been used to measure particle collision stress and fluctuations thereof in transitional and intermediate flows (Tardos et al., 2003;

Mort and Tardos, 2003). The amplitude of stress fluctuations at intermediate shear rates appears to be a useful characteristic of granular flows in the intermediate regime where both friction and collisional effects are important.

9.4.2 Shear Cell Methods and Analyses

Shear cells are used to measure shear stresses in powders that have been consolidated to a series of consolidation states. In addition, many shear cell designs can be used to measure wall friction between a consolidated powder and a wall material. The original analysis developed by Jenike (1961) is focused on the design of bulk storage bins and hoppers, with the objective of using a lab-scale test to predict bin geometry required for reliable flow of a given powder. The procedure involves the construction of a flow function based on a family of incipient yield loci measured over a range of relevant consolidation pressures. The flow function requires determination of the principal consolidation stress, σ_1 and the unconfined yield stress, f_c . While the principal stress calculation is fairly straightforward, the unconfined yield stress is based on the extrapolation of the yield locus to zero normal stress (i.e., the unconfined state of stress). The flow function analysis is of use in designing hoppers for reliable powder flow as discussed in Section 9.3, and is especially relevant for cohesive bulk powders.

The extrapolation of the yield locus to the shear and tensile intercepts can be a source of considerable uncertainty in the analysis. This is especially the case for weakly cohesive granular materials where small differences in the extrapolated curve can have a substantial effect on the calculation of the unconfined yield stress and the flow function. On the one hand, the conventional flow-function analysis for discharge of hoppers may be moot for free flowing and weakly cohesive materials that do not pose significant problems for hopper discharge. On the other hand, some applications require precision dosing of free-flowing powders, often through smaller orifices, where the subtleties of even weak cohesion can be significant. While there has been recent progress in this area (Schulze and Wittmaier, 2003), there is a continuing need to develop better methods of analyzing cohesive and tensile properties in bulk powder flow near the cohesive and tensile intercepts.

A number of shear cell designs are available for analysis of slow frictional flows. It has been demonstrated that such flows are generally anisotropic and are dependent on the specific consolidation pathway in addition to consolidation endpoint (Feise, 1998; Schwedes, 2000; Zetzener and Schwedes, 2001); thus, the results may depend on the pathway of consolidation that is applied by the test device. For a more detailed investigation of anisotropy, it may be necessary to employ a research instrument such as a biaxial tester, which can be used to test the effects of specific loading histories and stress pathways. In routine applications, it is more common to use translational or rotational shear testers. Standard procedures are available for several shear cells including the Jenike translational tester (ASTM D6128), the Peschl rotational split cell (ASTM D6682) and the Schulze rotational ring (ASTM D6773) tester. The rotational testers offer more automated features and are convenient for collecting multiple data points from a single sample (Schulze et al., 2001), whereas translational testers can be used to provide some more detailed information on the effect of the consolidation pathway (i.e., anisotropy), time consolidation (Jenike, 1967), and vibration (Kollmann and Tomas, 2001).

In this section, we present examples using experimental data from a rotational shear cell (Peschl Automatic RO-200, Industrial Powder Technology, Vaduz, Liechtenstein). Samples are prepared by sifting the powder into the split-cell assembly and then consolidating it to its critical state at a target consolidation normal stress, σ_n , over a series of consolidation shear steps as shown in [Figure 9.11](#). The consolidation shear step is repeated until a consistent shear profile is obtained. The consolidated sample is said to be in a critical state when the volume of the sample remains constant during slow-frictional flow.

Subsequent to the critical state consolidation, a series of shear steps with progressively lower normal loads are applied with interspersed consolidation steps to recondition the sample to the critical state. The consolidation normal load is typically adjusted to include the approximate weight of the powder in the cell above the shear zone defined by the split-cell geometry. The peak shear stress is measured for each shear step, and is used to construct the incipient yield locus (IYL) for the consolidation state. The whole

procedure is repeated at progressively higher consolidation states in order to construct a family of yield loci. The steady-state shear stresses, plotted as a function of normal stresses, typically form a single linear trend line for the full family of consolidation states. The slope of the steady-state flow line represents the coefficient of dynamic friction for slow flow.

The consolidation normal load is applied perpendicular to the shear direction and the shear steps are carried out by shearing in the same direction as the consolidation shear step. This convention of shearing in the same direction, as the consolidation shear, is adopted because it emulates the direction of stress in a hopper during unloading. The sample is reconditioned at the critical state before each shear step and the consolidation steps are always done at higher normal stress compared to the shear steps. Hence, shear steps are always overconsolidated and a maximum (peak) stress occurs at the onset of flow (Figure 9.11). The flow onset may be associated with dilation of the sample, after which the sample relaxes toward a steady-state flow with a steady-state shear stress. The plot of the maximum (i.e., incipient) shear stress as a function of the normal load constitutes the IYL, also known as a failure locus.

For simple powders, IYL is often approximated using a linear function (Eq. [9.56]) where the shear stress intercept, ϕ the angle of internal friction; and $\tan\phi$ is the slope. From the linear fit, the principal consolidation stress, σ_1 , and the unconfined yield stress, f_c , can be calculated directly (Eqs. [9.57], and [9.58]). A graphical example is given in Figure 9.12. In the case of noncohesive powders, $f_c \rightarrow 0$ and $\tan\phi$ is the coefficient of static friction:

$$\tau = \sigma \tan \phi + C \quad (9.56)$$

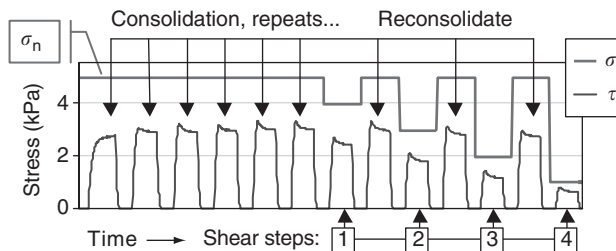


FIGURE 9.11 Consolidation and shear step sequence in a rotational shear cell measurement. Shear steps (1–4) were performed at 80, 60, 40 and 20% of the consolidation normal stress (σ_n), respectively. The incipient yield locus is constructed using the peak shear stress (τ) of each shear step.

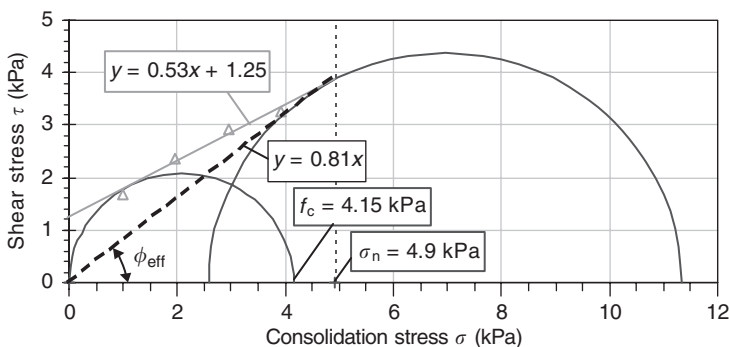


FIGURE 9.12 Linear fit of shear cell data for zeolite powder consolidated at 4.9 kPa; fit parameters according to Eq. (9.56): $C = 1.25$ kPa, $\tan \phi_i = 0.53$ and $\phi_i = 28^\circ$. The principal stress σ_1 is determined by the Mohr's circle drawn tangent to the yield locus at the consolidation stress σ_n . The unconfined yield stress f_c is determined by the Mohr's circle drawn through the origin and tangent to the yield locus. The effective angle of internal friction ϕ_{eff} is defined by the dashed line drawn through the origin and tangent to the principal Mohr's circle: $\tan \phi_{eff} = 0.81$ and $\phi_{eff} = 39^\circ$.

$$\sigma_i = \sigma_c(1 + \tan^2 \phi) + C \tan \phi + (\sigma_c \tan \phi + C)\sqrt{1 + \tan^2 \phi} \quad (9.57)$$

$$f_c = 2C(\tan \phi + \sqrt{1 + \tan^2 \phi}) \quad (9.58)$$

In the more general case including cohesive powders, IYL may be curved, typically with increasing curvature at lower normal stress. However, given that the experimental procedure can be tedious with substantial scatter in the results, there is generally not a great deal of confidence in fitting curved locus functions. One method of fitting curved loci uses the Warren–Spring model (Eq. [9.59]), where C is the cohesion (τ -axis intercept), T the tensile stress (σ -axis intercept), and n the curvature. The exponent, n , has been used as flowability index, where the powder flowability decreases as n increases from 1 to 2.

$$\left(\frac{\tau}{C}\right)^n = \frac{\sigma}{T} + 1 \quad (9.59)$$

More recently, the current authors have shown that a power-law curve is useful in scaling multiple loci for a given material under a series of consolidation states. This scaling approach is described in Eq. (9.60), where σ is the normal force during the shear step, σ_n the normal consolidation force at the critical state (i.e., the consolidation step), σ_0 the isostatic tensile strength (Tomas, 2000) (here we use the convention of positive compressive and negative tensile stresses), k the slope from the tensile intercept to the yield stress at the critical consolidation state, and m is the curvature exponent. The scaling is done using a compound locus (Birks et al., 2001), where each locus is scaled relative to combined applied normal consolidation stress, σ_n , and the isostatic tensile strength of the material, σ_0 . Fitting this common form to multiple loci measured over a range of consolidation stress gives a curve fit that is constrained through the origin with common values of k , m and σ_0 for all loci (Figure 9.13):

$$\frac{\tau}{(\sigma_n - \sigma_0)} = k \left[\frac{(\sigma - \sigma_0)}{(\sigma_n - \sigma_0)} \right]^m \quad (9.60)$$

When performing a scaling analysis, data are collected over a series of consolidation stresses σ_n . While solutions for k and m are obtained by standard linear regression methods (Eq. [9.61]), it is first necessary to find a solution for the tensile intercept, σ_0 . Two approaches are as follows: (1) linear regression of the incipient shear stress at the critical state (i.e., where $\sigma = \sigma_n$), in which case Eq. (9.60) reduces to Eq. (9.62); and (2) linear regression of the steady-state shear stress data collected at each consolidation step (Eq. [9.63]),

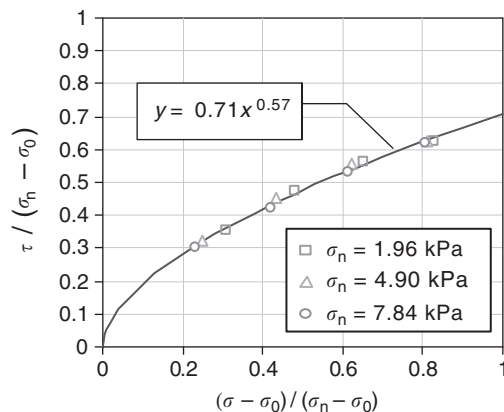


FIGURE 9.13 Common fit of shear cell data for fine zeolite powder consolidated at three stress levels σ_n . In each case, the compound normal and shear stresses are scaled to the compound consolidation stress, $\sigma_n - \sigma_0$. Shear steps were performed at 20, 40, 60 and 80% of each consolidation stress. The common fit parameters according to Eq. (9.60) are: $\sigma_0 = -0.31$ kPa; $k = 0.71$; $m = 0.57$.

where τ_s is the steady-state shear stress and k_s is the dynamic friction ratio on a compound stress basis. In either case, an estimate for σ_0 can be obtained using a standard linear regression

$$\ln\left(\frac{\tau}{(\sigma_n - \sigma_0)}\right) = \ln(k) + m \ln\left(\frac{(\sigma - \sigma_0)}{(\sigma_n - \sigma_0)}\right) \quad (9.61)$$

$$\tau = k(\sigma_n - \sigma_0), \quad \sigma_n = \frac{\tau}{k} + \sigma_0 \quad (9.62)$$

$$\tau_s = k_s(\sigma - \sigma_0), \quad \sigma = \frac{\tau_s}{k_s} + \sigma_0 \quad (9.63)$$

Further, numerical iteration of σ_0 is done to optimize the fit of the scaled locus. The individual IYL can then be plotted by using the common fit parameters (Figure 9.14). This is achieved by inverting the scaling formula for the curved loci according to Eq. (9.64). The steady-state line for slow-frictional flow is also shown in Figure 9.8; the difference in shear stress between the IYL and the steady-state line is related to the difference in static and dynamic friction between particles in the powder:

$$\tau = k(\sigma - \sigma_0)^m(\sigma_n - \sigma_0)^{(1-m)} \quad (9.64)$$

The scaled solution for the Mohr's principal consolidation stress circle is straightforward once the parameters are known in Eq. (9.60). For scaling the loci using a compound basis, all the scaled loci share the same principal stress circle (Figure 9.15). The slope of the curved locus (τ') is defined as the derivative of τ with respect to σ (Eq. [9.65]). At the critical consolidation state (i.e., where $\sigma = \sigma_n$), the slope reduces to km (Eq. [9.66]), the scaled shear stress is k and the scaled normal stress is unity. Simple geometry is used to find the center of the principal circle (Eq. [9.67]) and the principal stress, σ_1 (Eq. [9.68]):

$$\tau' = km(\sigma - \sigma_0)^{(m-1)} \cdot (\sigma_n - \sigma_0)^{(1-m)} \quad (9.65)$$

$$\tau'|_{\sigma = \sigma_n} = km \quad (9.66)$$

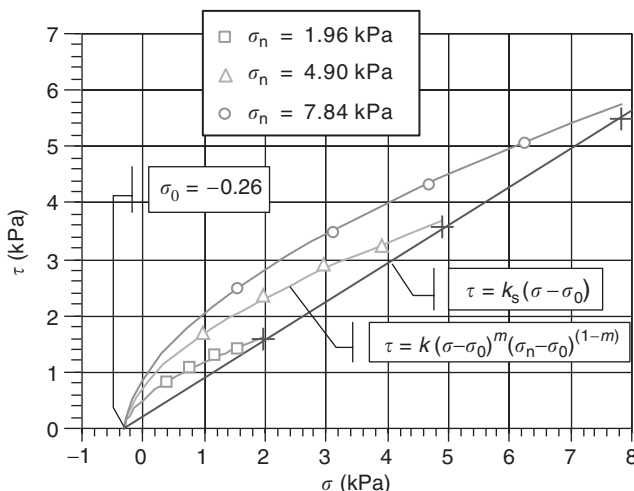


FIGURE 9.14 Curved incipient yield loci for fine zeolite powders consolidated at three consolidation states, drawn on an absolute scale using the common-locus fit parameters given in Figure 9.13. The linear trend of the average of the steady-state data (+) and the tensile intercept describe the steady-state slow-frictional flow behavior (Eq. [9.63]), the steady-state parameters are $k_s = 0.68$, $\sigma_0 = -0.26$ kPa.

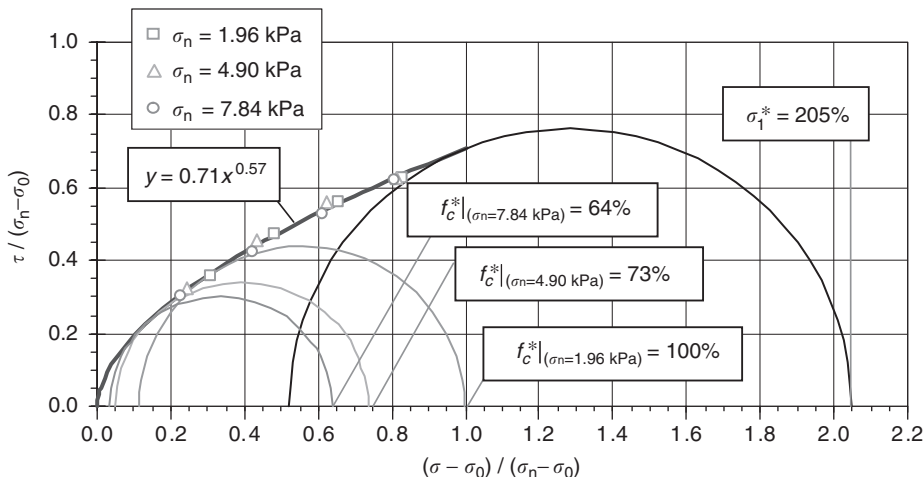


FIGURE 9.15 Common locus plot for zeolite powder showing Mohr's circles for principal and unconfined yield stresses, where f_c^* and σ_1^* are the scaled values of unconfined yield stress and principal stress, respectively. On the scaled plot, all three loci share the same principal Mohr's circle, σ_1^* .

$$\frac{(\sigma_1 + \sigma_2)}{2} = 1 + k^2 m \quad (9.67)$$

$$\sigma_1 = 1 + k^2 m + k \sqrt{1 + (km)^2} \quad (9.68)$$

Each locus in the scaled set has a unique Mohr's circle for its unconfined yield stress. Since scaling is done using the compound basis, each unconfined yield stress circle must pass through the scaled value of the negative tensile stress at its given consolidation state, i.e., $-\sigma_0/(\sigma_n - \sigma_0)$. The unconfined yield stress is the maximum normal force on each circle. Solving for the unconfined yield stress with a curved locus requires an iterative approach, but once this is achieved one can obtain solutions for the principal stress σ_1 and unconfined yield stress f_c as a continuous function of the consolidation normal pressures σ_n .

By using this method, flow functions for several other materials were calculated and are as shown in Figure 9.16. The flow functions for the granular powders (glass beads, sand) are almost horizontal, while the more finely grained cohesive materials (calcium carbonate, zeolite powders) show increasing unconfined yield stress as they are compacted to higher consolidation loads. The difference in slope between these two types of materials is due to compressibility. The fine powders are compressible and increase their bulk strength as they are consolidated. On the other hand, the granular materials are relatively non-compressible and do not significantly increase their bulk strength over the range of consolidation loads. When small amount of liquids are added to the sand (in the examples shown, the moist sand contains about 5% water and the oiled sand contains about 0.5 wt% of thin oil), the unconfined yield strength shifts upward due to liquid bridge cohesion; however, the slope of the flow function remains horizontal because the material remains relatively incompressible.

In addition to the flow function, the effective angle of friction is required to determine the flow factor in a hopper design. The effective friction angle, ϕ_{eff} is plotted from the origin of the absolute stress plot (i.e., zero applied stress) to the tangent of the principal stress circle, as illustrated in Figure 9.12. The friction angle is plotted as function of the principal consolidation stress for the same set of samples (Figure 9.17). Note that the irregular sand particles have a higher friction angle compared to the sphere-like glass beads, although they are essentially with the same chemical composition. The fit parameters used to construct Figures 9.16 and 9.17 are summarized in Table 9.6.

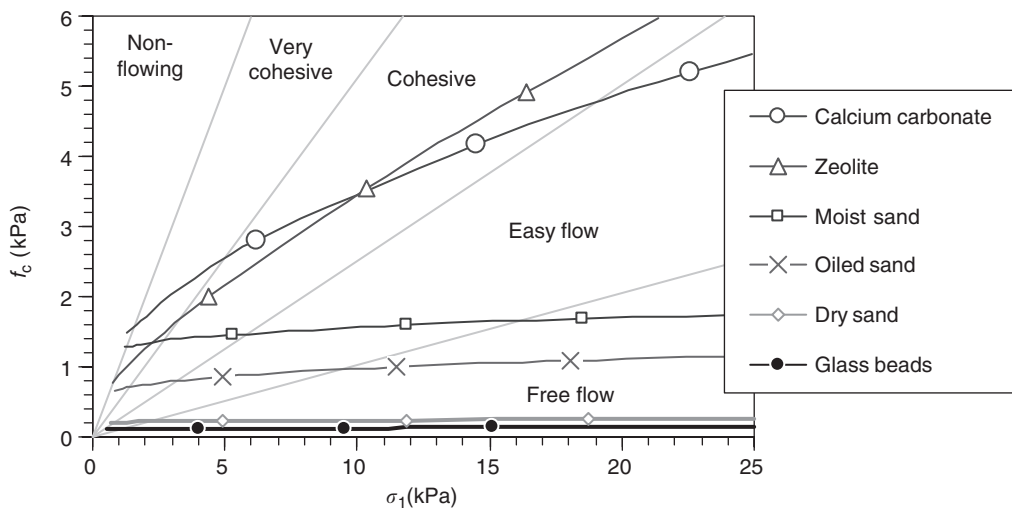


FIGURE 9.16 Flow function plot, where continuous flow functions (lines) are plotted using the common fit parameters from the common locus plot for each material. The discrete data points are the data for the three experimental consolidation states used in this study, $\sigma_n = 1.96, 4.90$ and 7.84 kPa. The calcium carbonate and zeolite samples are compressible fine powders, while the sand and glass beads are granular and relatively incompressible.

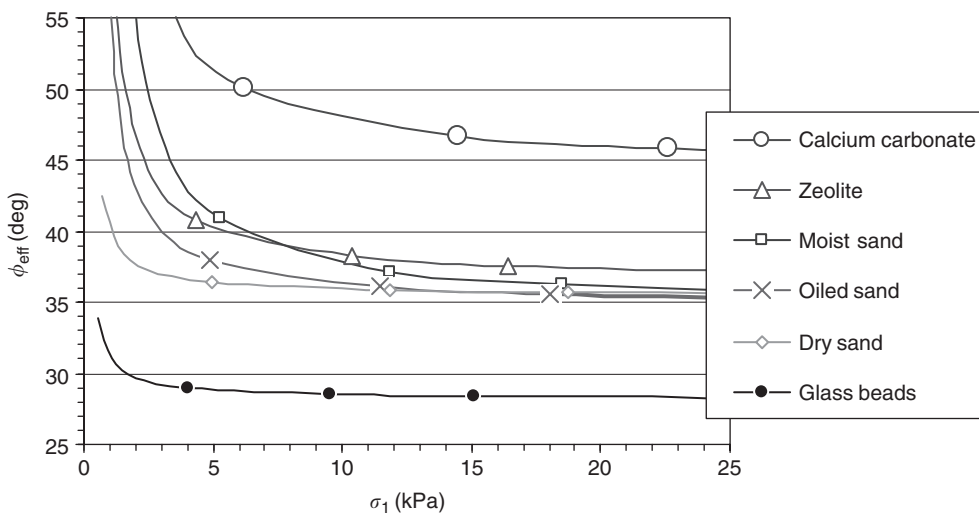


FIGURE 9.17 Effective angle of friction, ϕ_{eff} plotted as a function of the consolidation stress invariant, for the same materials shown in Figure 9.16. The continuous flow functions (lines) are plotted using the common fit parameters from the common locus plot for each material. The discrete data points are the data for the three experimental consolidation states, $\sigma_n = 1.96, 4.90$ and 7.84 kPa.

9.4.3 Concluding Remarks on Characterization

There are multiple methods to characterize powder flow. Typically, no one single method will provide a complete set of characteristics necessary to engineer a powders' handling system. In most cases, a combination of techniques will be useful.

For technical characterization of the static to slow-frictional transition, the shear cell method offers the most detailed information. Several examples are given in this section including granular free flowing,

TABLE 9.6 Common Incipient Yield Locus Fit parameters (σ_0 , k , m) and Experimental Fit Correlation Coefficient (r^2) for Sample Materials Shown in Figures 9.16 and 9.17. The steady-state slow-frictional flow line is described by k_s .

Sample	σ_0 (kPa)	k	m	r^2	k_s
Calcium carbonate	-0.34	0.96	0.71	0.985	0.97
Zeolite	-0.26	0.71	0.57	0.994	0.68
Dry sand	-0.07	0.71	0.96	0.998	0.62
Sand + 5% water	-0.49	0.69	0.93	0.996	0.62
Sand + 1% oil	-0.24	0.69	0.89	0.996	0.62
Glass beads	-0.06	0.54	0.98	0.998	0.45

Note: k , m and k_s are dimensionless.

moist granular and cohesive fine powders. The flow functions for these materials illustrate the differences between these classes of materials with respect to cohesion and compressibility. The effective friction is an additional property that has a functional relationship with applied load.

The power-law scaling approach using the compound stress basis introduces some additional curve-fitting constraints to the well-known procedure developed by Jenike, and is useful for improved extrapolation of flow functions. Since flow functions derived by the more common method of linear fitting are reasonably similar to the flow functions defined by the scaling method, the latter method provides additional constraints that help to elucidate subtle differences in cohesion and frictional properties of materials.

Nomenclature

a	Density parameter in Table 9.5, ($a = \rho^{1/\beta}$)
a_0	Reference value for the coefficient, a
A	Constant of integration
b	Half-width of channel
B	Hopper outlet dimension
C	Cohesive intercept in the Warren–Spring equation
C	Cohesive parameter in the Cam–Clay model
D, D_{ij}	Deviatoric stress
D/Dt	Material derivative
e, e_{ij}	Rate of strain
E_{WS}	Material-dependent constant in Warren–Spring equation (10)
F_{WS}	Material-dependent constant in Warren–Spring equation (10)
ff	Flow factor
FF	Flow function
f_c	Unconfined yield strength
g	Acceleration due to gravity
H	Width of 2D hopper outlet
$H(\alpha)$	Function of α in Figure 9.14
i,j	Indexes
k	Slope or pre-exponential of scaled yield locus
K	Janssen constant, ($= (1 + \sin \phi) / (1 - \sin \phi)$)
K_{FF}	Material-dependent constant in Eq. (11)
L	Height of fill in hopper
L_{FF}	Material-dependent constant in Eq. (11)
m	Geometry coefficient, plane vs. conical hoppers
m	Exponent in scaled yield locus
M	Material constant, ($= [(2 - m)\alpha / \sin \alpha] - [2(1 - m) / (1 + \cos \alpha)]$), α in radians

n	Compression index
n	Exponent in the Warren–Spring curved locus equation
n	Dimensional parameter in constitutive equation, 2D vs. 3D.
N	Material-dependent constant, ($= 1 - K[\cot \alpha + \cot(\phi_W)]$)
$q(p,\rho)$	Yield condition; for incompressible powders, $q = p \sin \phi$
q_{ws}	Material-dependent constant in the Warren–Spring equation
p	Pressure; average principal stress
r	Radial coordinate
R	Radius of hopper outlet
S, S_{ij}	Stress tensor
t	Time
T	Tensile intercept in the Warren–Spring equation
\mathbf{u}, u_i	Velocity vector
W	Mass flow rate
x,y,z	Cartesian coordinates
X,Y,Z	Constants

Greek Letters

α	Half angle of the hopper
β	Compression index in Table 9.5
χ	Variable in equation 9.30 ($= 2 / (1 - \sin \phi)$)
τ	Shear stress
σ	Normal stress
$\sigma_1, \sigma_2, \sigma_3$	Principal stresses
$\sigma_{1,a}$	Principal stress where arch meets wall
σ_0	Isostatic tensile stress
σ_n	Consolidation normal stress
σ_t	Tangential stress
σ_y	Vertical stress at y from the top of powder bed
$\sigma_{y,h}$	Hydrostatic stress
ϕ	Angle of internal friction
ϕ_W	Angle of wall friction
ϕ_{eff}	Effective angle of friction
γ	Specific gravity($= \rho g$)
$\dot{\gamma}$	Strain rate
η	Angle of flow factor ($= \arctan(1/f_f)$)
κ	Coefficient indicating active or passive state
δ, δ_{ij}	Unit tensor
∇	Nabla operator
μ	Shear viscosity
λ	Flow rule correlation coefficient
ρ	Fluid or powder bulk density
ρ_s	Powder solid density
ρ_0	Reference powder bulk density
ε	Porosity
v	Solid fraction ($= 1 - \varepsilon$)
ω	Variable substitution ($= \arcsin[\sin(\phi_W) / \sin \phi]$)
ξ	Dimensionless radius
θ, φ	Angular coordinates

Subscripts and Superscripts

*	Dimensionless quantity
a	At the abutment of the arch
crit	Critical
eff	Effective
max	Maximum value
r	Radial
s	Steady state
W	At the wall of the channel
WS	Warren-Spring
i,j	Indexes (1,2,3)
x,y,z	Spatial coordinates in the Cartesian system
r,θ,z	Spatial coordinates in the cylindrical system
r,θ,φ	Spatial coordinates in the spherical system
0	Reference value

References

- Abdullah, E.C. and Geldart, D., The use of bulk density measurements as flowability indicators, *Powder Technol.*, 102, pp. 151–165, 1999.
- Albert, R., Pfeifer, M.A., Barabasi, A.L. and Schiffer, P., Slow drag in a granular medium, *Phys. Rev. Lett.*, 82, 205–208, 1999.
- ASTM D6128-00, Standard Test Method for Shear Testing of Bulk Solids Using the Jenike Shear Cell, ASTM International, 2003.
- ASTM D6682-01, Standard Test Method for Measuring the Shear Stresses of Powders Using the Peschl Rotational Split Level Shear Tester, ASTM International, 2003.
- ASTM D6773-02, Standard Shear Test Method for Bulk Solids Using the Schulze Ring Shear Tester, ASTM International, 2003.
- Bell, T., Solids flowability measurement and interpretation in industry, in *Handbook of Conveying and Handling of Particulate Solids*, Levy, A. and Kalman, H. Eds., Elsevier Amsterdam, pp. 3–13, 2001.
- Birks, A. H., Bradley, M.S.A. and Rarnish, R., The conversion of the analytical simple shear model for the Jenike failure locus into principle stress space and implication of the model for hopper design, in *Handbook of Conveying and Handling of Particulate Solids*, Levy, A. and Kalman, H., Eds., Elsevier Amsterdam, 2001, pp. 95–105.
- Brennen, C. and Pearce, J.C., Granular material flow in two-dimensional hoppers, *J. Appl. Mech.*, 45, 43–50, 1978.
- Campbell, C.S., Rapid granular flows, *Ann. Rev. Fluid Mech.*, 22, 57–92, 1990.
- Campbell, C.S., and Brennen, C.E., Computer simulation of granular shear flows, *J. Fluid Mech.*, 151, 167–188, 1985.
- Caprihan, A. and Seymour, J., Correlation time and diffusion coefficient imaging: application to a granular flow system, *J. Magn. Resonance*, 144, 96–107, 2000.
- Cleaver, J.A.S. and Nedderman, R.M., Theoretical prediction of stress and velocity profiles in conical hoppers, *Chem. Eng. Sci.*, 48, 3693–3702, 1993.
- Davidson, J.F. and Nedderman, R.M., *Trans. Instn. Chem. Engrs.* 51, 29–35, 1973.
- de Jong, J.A.H., Hoffmann, A.C. and Finkers, H.J., Properly determine powder flowability to maximize plant output, *Chem. Eng. Prog.*, 95, 25–34, 1999.
- Drescher, A., *Analytical Methods in Bin-Load Analysis*, Elsevier, Amsterdam, 1991.
- Drescher, A., Waters, A.J. and Rhoades, C.A., Arching in hoppers: I. Arching theories and bulk material flow properties and II. Arching theories and critical outlet size, *Powder Technol.*, 84, 165–183, 1995.

- Enstad, G., A note on the stresses and dome formation in axially symmetric mass flow hoppers, *Chem. Eng. Sci.*, 32, 339–342, 1977.
- Enstad, G., On the theory of arching in mass-flow hoppers, *Chem. Eng. Sci.*, 30, 1273–1283, 1975.
- Feise, H. J., A review of induced anisotropy and steady-state flow in powders, *Powder Technol.*, 98, 191–200, 1998.
- Ferrari, G. and Poletto, M., The particle velocity field inside a two-dimensional aerated hopper, *Powder Technol.*, 123, 242–253 2002.
- Freeman, R., The Flowability of Powders — an Empirical Approach, presented at *International Conference on Powder and Bulk Solids Handling*, IMechE HQ, London, June 2000.
- Guerin, E., Tchoreloff, P., Leclerc, B., Tangy, D., Deleuil, M. and Couarrazé, G., Rheological characterization of pharmaceutical powders using tap testing, shear cell and mercury porosimeter, *Int. J. Pharm.*, 189, 91–103, 1999.
- Hopkins, M.A. and Louge, M.Y., Inelastic micro-structure in rapid granular flows of smooth disks, *Phys. Fluids A*, 3, 47–57, 1990.
- Iacocca, R. G. and German, R. M., The experimental evaluation of die compaction lubricants using deterministic chaos theory, *Powder Technol.*, 102, 253–265, 1999.
- Jackson, R., Some mathematical and physical aspects of continuum models for the motion of granular materials, in *Theory of Dispersed Multi-Phase Flow*, Meyer, R., Ed., Academic Press, New York, 1982, pp. 291–337.
- Janssen, H.A., Versuche über Getreidedruck in Silozellen, *Zeit. Ver. Deutsch. Ing.*, 39, 1045–1049, 1895.
- Jaraiz, E., Kimura, S. and Levenspiel, O., Vibrating beds of fine particles: estimation of interparticle forces from expansion and pressure drop experiments, *Powder Technol.*, 72, 23–30, 1992.
- Jenike, A.W., Gravity Flow of Bulk Solids, Bulletin No.108, Utah University of Engineering Experiment Station, 1961.
- Jenike, A.W., Storage and Flow of Solids, Bulletin No. 123, Utah Engineering Experiment Station, Vol. 53, No 26, 1964.
- Jenike, A.W., Quantitative design of mass-flow bins, *Powder Technol.*, 237–244, 1967.
- Jenike A.W., A theory of flow of particulate solids in converging and diverging channels based on a conical yield function, *Powder Technol.*, 50, 229–236, 1987.
- Jenkins, J.T. and Askari, E., Boundary conditions for rapid granular flows-phase interfaces, *J. Fluid Mech.*, 223, 497–508, 1991.
- Jones, R., From single particle AFM studies of adhesion and friction to bulk flow: forging the links, *Granular Matter*, 4, 191–204, 2003.
- Jones, R., Pollock, H.M., Geldart, D. and Verlinden, A., Frictional forces between cohesive powder particles studied by AFM, *Probe Microscopy*, 2004, submitted.
- Kaye, B.H., Characterizing the flowability of a powder using concepts of fractal geometry and chaos theory, *Part. Part. Syst. Charact.*, 14, 53–66, 1996.
- Kollmann, T. and Tomas, J., Vibrational flow of cohesive powders, in *Handbook of Conveying and Handing of Particulate Solids*, Levy, A. and Kalman, H., Eds., Elsevier Amsterdam, 2001, pp. 45–56.
- Kuo, H.P., Knight, P.C., Parker, D.J., Burbridge, A.S., Adams, M.J., and Seville, J.P.K., Non-equilibrium particle motion in the vicinity of a single blade, *Powder Technol.*, 132, 1–9, 2003.
- Laurent, B.F.C., and Bridgwater, J., On the relationship between torque and flow structure in powder mixers, *Kona*, 19, 118–130, 2001.
- Laurent, B.F.C. and Bridgwater, J., Influence of agitator design on powder flow, *Chem. Eng. Sci.*, 57, 3781–3793, 2002.
- Laurent, B.F.C., Bridgwater, J. and Parker, D. J., Motion in a particle bed agitated by a single blade, *AIChE J.*, 46, 1723–1734, 2000.
- Lee, Y.S.L., Poynter, R., Podczeck, F. and Newton, J. M., Development of a dual approach to assess powder flow from avalanching behavior, *AAPS Pharm.Sci.Tech.*, 1, 2000.
- Louge, M.Y. and Keast, S.C., On dense granular flows down flat frictional inclines, *Phys. Fluids*, 13, 1215–1233, 2001.

- Lun, C.K.K., Savage, S.B., Jeffrey, D.J. and Chepurniy, N., Kinetic theories for granular flow: inelastic particles in Couette flow and slightly inelastic particles in a general flow field, *J. Fluid Mech.*, 140, 223–256, 1984.
- Miller, B., O’Hern, C. and Behringer, R.P., Stress fluctuations for continuously sheared granular materials, *Phys. Rev. Lett.*, 77, 3110–3113, 1996.
- Mohammadi, M.S. and Harnby, N., Bulk density modeling as a means of typifying the microstructure and flow characteristics of cohesive powders, *Powder Technol.*, 92, 1–8, 1997.
- Mort, P., Shen, R. and Tardos, G.I., Characterization of Weakly Cohesive Granular Flows by Scaling Analysis of Shear Cell Data, *in Proceedings of World Congress on Particle Technology 4*, Sydney, 2002.
- Mort, P. and Tardos, G.I., Characterizing the Transition Between the Quasi-static and Intermediate Regimes in Weakly Cohesive Granular Flows, *in Proceedings of AIChE Annual Meeting*, San Francisco, 2003.
- Nase, S., Vargas, W., Abatan, A. and McCarthy, J., Discrete characterization tools for cohesive granular material, *Powder Technol.*, 116, 214–223, 2001.
- Nedderman, R.M., Tuzun, U., Savage, S.B. and Houlsby, G.T., *Chem. Eng. Sci.*, 37, 1597–1609, 1982.
- Nedderman, R.M., *Statics and Kinematics of Granular Materials*, Cambridge University Press, Cambridge, 1992.
- Nguyen, T.V., Brennen, C. and Sabersky, R.H., Gravity flow of granular materials in conical hoppers, *J. Appl. Mech.*, 46, 529–535, 1979.
- Nott, P. and Jackson, R., Frictional–collisional equations of motion for granular materials and their application to flow in aerated chutes, *J. Fluid Mech.*, 241, 125–144, 1992.
- Orband, J. L. R. and Geldart, D., Direct measurement of powder cohesion using a torsional device. *Powder Technol.*, 92, 25–33, 1997.
- Pierrat, P., Agrawal, D. and Caram, H., Effect of moisture on the yield locus of granular materials: theory of shift, *Powder Technol.*, 99, 220–227, 1998.
- Pierrat, P. and Caram, H., 1997, Tensile strength of wet granular materials. *Powder Technol.*, 91, 83–93, 1997.
- Pitman, E.B. and Schaeffer, D.G., Stability of time dependent compressible granular flow in two dimensions, *Commun. Pure Appl. Math.*, Vol. XL, 421–447, 1987.
- Pnueli, D. and Gutfinger, C., *Fluid Mechanics*, Cambridge University Press, Cambridge 1992.
- Rajagopal, K.R., Troy, W. and Massoudi, M., Existence of solutions to the equations governing the flow of granular materials, *Eur. J. Mech., B/Fluids*, 11, 265–276, 1992.
- Rumpf, H., 1990, *Particle technology*, Chapman & Hall, New York, 1990.
- Santomaso, A., Lazzaro, P. and Canu, P., Powder flowability and density ratios: the impact of granules packing, *Chem. Eng. Sci.*, 58, 2857–2874, 2003.
- Savage, S.B., The mass flow of granular materials derived from coupled velocity-stress fields, *Br. J. Appl. Phys.*, 16, 1885–1888, 1965.
- Savage, S.B., Gravity flow of a cohesion-less bulk solid in a converging conical channel, *Int. J. Mech. Sci.*, 9, 651–659, 1967.
- Savage, S.B., Analyses of slow high-concentration flows of granular materials, *J. Fluid Mech.*, 377, 1–26, 1998.
- Savage, S.B. and Sayed, M., Gravity flow of cohesion-less granular materials in wedge-shaped hoppers, *in Mechanics Applied to the Transport of Bulk Materials*, New York, ASME, Vol. AMD-31, 1979, pp. 1–24.
- Schaeffer, D.G., 1987, Instability in the evolution equations describing incompressible granular flow, *J. Differential Equations*, 66, 19–50, 1987.
- Schofield, A.N. and Wroth, C.P., *Critical State Soil Mechanics*, McGraw-Hill, New York, 1968.
- Schulze, D. and Wittmaier, A., 2003, Flow properties of highly dispersed powders at very small consolidation stresses, *Chem. Eng. Technol.*, 26, 133–137, 2003.
- Schulze, D., Heinrici, H. and Zetzener, H., The ring shear tester as a valuable tool for silo design and powder characterization, *Powder Handling Process.*, 13, 19–24, 2001.
- Schwedes, J., Testers for measuring flow properties of particulate solids, *Powder Handling Process.*, 12, 337–354, 2000.

- Seville, J. P. K. and Clift, R., The effect of thin liquid layers on fluidization characteristics. *Powder Technol.*, 37, 117–129, 1984.
- Shamloo, P.A., *Handling of Bulk Solids—Theory and Practice*, Butterworths, London, 1990.
- Srivastava, A. and Sundaresan, S., Analysis of a frictional-kinetic model for gas-particle flow, *Powder Technol.*, 129, 72–85, 2003.
- Stewart, R.L., Bridgwater, J. and Parker, D.J., Granular flow over a flat-bladed stirrer, *Chem. Eng. Sci.*, 56, 4257–4271, 2001.
- Tardos, G.I., A fluid mechanics approach to slow, frictional powder flows, *Powder Technol.*, 92, 61–74, 1997.
- Tardos, G.I., Stresses in bins and hoppers: use of Jenike's method for hopper design, at <http://www.erpt.org/992Q/tard-00.htm>, Engineering Research Center, University of Florida, 1999.
- Tardos, G.I., McNamara, S., and Talu, I., Slow and intermediate flow of a frictional bulk powder in the Couette geometry, *Powder Technol.*, 131, 23–39, 2003.
- Tomas, J., Particle adhesion fundamentals and bulk powder consolidation, *Kona*, 18, 157–169, 2000.
- van Zuilichem, D.J., van Egmond, N.D. and de Swart, J.G., 1974, Density behavior of flowing granular material, *Powder Technol.*, 10, 161–169, 1974.
- Walker, D.M., An approximate theory for pressures and arching in hoppers, *Chem. Eng. Sci.*, 28, 975–997, 1966.
- Watson, P.K., Valverde, J.M. and Castellanos, A., The tensile strength and free volume of cohesive powders compressed by gas flow, *Powder Technol.*, 115, 45–50, 2001.
- Weir, G.J., The intrinsic cohesion of granular materials, *Powder Technol.*, 104, 29–36, 1999.
- Wong, A.C.-Y., Use of angle of repose and bulk densities for powder characterization and the prediction of minimum fluidization and minimum bubbling velocities, *Chem. Eng. Sci.*, 57, 2635–2640, 2002.
- Wu, C.-Y., Dihoru, L. and Cocks, A.C.F., The flow of powder into simple and stepped dies, *Powder Technol.*, 134, 24–39, 2003.
- Zetxener, H. and Schwedes, J., Influence of the stress history on the time dependent behaviour of bulk solids, in *Handbook of Conveying and Handling of Particulate Solids*, Levy, A. and Kalman, H. Eds., Elsevier Amsterdam, 2001, pp. 57–64.

10

Porous Media Flows

10.1	Flow Through Porous Media.....	10-2
	Porosity • Permeability • Pore Size and Pore Size Distribution •	
	Specific Surface • Resistivity Factor • Hydraulic Conductivity •	
	Hydraulic Radius Theory (Carman–Kozeny Equation) •	
	Friction Factor for Packed Beds	
10.2	Capillarity in Porous Media.....	10-7
	Fundamentals of Capillarity • Imbibition and Drainage	
10.3	Steady Multiphase Flow in Porous Media	10-27
	Introduction • Relative Permeabilities • Fractional and Mixed	
	Wettability • Resistivity Index and Archie's Law	
10.4	Immiscible Displacement	10-34
	Equations of Unsteady State Two-Phase Flow • Cocurrent and	
	Countercurrent Flows of Two Immiscible Fluids • Capillary	
	and Viscous Effects in Two-Phase Flow in Porous Media •	
	Drainage-Type Displacement Front Versus Capillary Number	
	and Viscosity Ratio • Coupling of Two-Phase Flows	

Mingzhe Dong
University of Regina

Francis A.L. Dullien
University of Waterloo

The fluid flow through the porous materials is introduced in this chapter. Porous materials are seen and used everywhere in nature, in science and technology, and everyday life. The definition of a porous material may differ in different studies. In order to study porous media flow, the porous materials have to be solid or semisolid, containing pores or voids and permeable to a variety of fluids.

In Section 10.1, the following macroscopic pore structure parameters, which are solely determined by the pore structure of the medium, are introduced: porosity, permeability, specific surface area, pore-size distribution, and formation resistivity factor. The hydraulic conductivity and the hydraulic radius theory are then presented, followed by a review of friction factor models for packed columns. If two or more fluids are present in a porous medium, capillarity plays an important role in the flow of fluids in the porous medium. In Section 10.2, capillarity in porous media is introduced. The fundamentals of capillary forces in wettability of porous media and two displacement processes, i.e., imbibition and drainage in relation to multiphase flow in porous media, are presented. In Section 10.3, steady two-phase cocurrent flow, for which the experimental techniques and theory have been well developed, is discussed. Steady-state multiphase flow in porous media is characterized by no change in all physical variables with time, i.e., the saturations, flow rates, and pressures of the two phases are independent of time. Finally, in Section 10.4, unsteady two-phase flow in one-dimensional porous media is discussed, where one phase is displacing the other and the saturation is a function of both position and time. Since the saturation is a function of both position and time, the capillary pressure across the two immiscible fluid interfaces changes both with the position in the system and time, and plays an important role in determining the evolution of saturation profiles. In this section, the roles played by both capillary and viscous forces are considered from a purely macroscopic, phenomenological point of view.

10.1 Flow Through Porous Media

10.1.1 Porosity

The porosity ϕ of a porous medium is the volume fraction of its pore space. It is expressed as

$$\phi = \frac{V_p}{V_b} \quad (10.1)$$

where V_b is the bulk volume of the porous medium and V_p the pore volume. The porosity varies between zero and unity, depending on its formation and the type of porous material.

For the purpose of flow in porous media, especially in consolidated media, such as reservoir rocks, it is important to distinguish between two kinds of pores or voids; one is the pore space, called “interconnected” or “effective” pore space; the other is “dead” pore space that consists of “isolated” or “noninterconnected” pores or voids dispersed in the medium. Only the effective or interconnected pore space contributes to the flow of fluids through the porous medium.

Experimental methods commonly used to determine the porosity of a porous sample include:

1. *Imbibition method.* The porous sample is saturated with a preferentially wetting fluid by letting it imbibe into the sample under vacuum. The sample is weighed before and after imbibition. From the two weights, the density of the fluid and the dimensions (bulk volume) of the sample, the porosity can be calculated.
2. *Mercury injection method.* As most materials are not wetted by mercury, it will not penetrate into the pores unless a pressure is applied. After the sample is evacuated, mercury is forced to penetrate into the sample under high pressure.
3. *Gas expansion method.* The porous sample is enclosed in a vessel of a known volume V_1 under a known gas pressure P_1 . When the vessel is connected to an evacuated vessel of known volume V_2 , the gas expands into this vessel and the gas pressure in the first vessel decreases to a lower value P_2 . Applying the ideal gas law to the above process, the effective pore volume V_p of the sample can be calculated by

$$V_p = V_b - V_1 - V_2 \left(\frac{P_2}{P_2 - P_1} \right) \quad (10.2)$$

where V_b is the bulk volume of the sample which is determined in a separate measurement.

4. *Density method.* The bulk density of the sample ρ_b and the density of the solid matrix of the sample ρ_s are determined. The total porosity of the sample is calculated by

$$\phi = 1 - \frac{\rho_b}{\rho_s} \quad (10.3)$$

10.1.2 Permeability

The property of a porous medium, which allows a fluid to flow through it is called permeability. This parameter is determined entirely by the pore structure.

The Darcy permeability k is calculated by applying Darcy's (1856) law to a slow (creeping), one-dimensional, horizontal, steady flow of a Newtonian fluid:

$$Q = \frac{kA}{\mu} \frac{\Delta P}{L} \quad (10.4)$$

where Q is the volumetric flow rate (cm^3/sec), A the cross-sectional area of the sample normal to the flow direction (cm^2), L the length of the sample in the flow direction (cm), ΔP the hydrostatic pressure drop (atm), and μ the viscosity of the fluid (cP). Using these units in Darcy's law results in the practical unit of permeability Darcy (D). [1 Darcy = $0.987 \mu\text{m}^2$ in SI units, 1 darcy is a relatively high permeability, and for tight porous materials the unit millidarcy [mD] is used.]

Measurement of permeability is usually performed with one-dimensional, cylindrically shaped samples. In the measurement, various flow rates of the fluid are recorded as a function of pressure drop. Permeability is obtained by fitting a straight line to the data points. Theoretically, this line should pass through the origin. Departures from this behavior are known and they are discussed by Dullien (1992), among others.

10.1.3 Pore Size and Pore Size Distribution

The distribution of pore size is rather arbitrary. If $\alpha(D)$ is the distribution of pore volume fraction as a function of the pore size, D , then the pore size is selected such that (Dullien, 1992)

$$\int_0^{\infty} \alpha(D) dD = 1 \quad (10.5)$$

In mercury porosimetry, the volume of mercury penetrating the sample is measured as a function of the pressure imposed on the mercury. The pore size is calculated from this pressure by Laplace's equation of capillarity and, using the bundle of capillary tube model of pore structure, the volume of mercury is assigned to this pore size. Mercury porosimetry and adsorption isotherms are widely used for determination of pore size distribution. These and other methods of pore size distribution have been reviewed in depth by Dullien (1992). The principal shortcoming of most methods is the pore model used. The pore structure of porous media does not resemble a bundle of capillary tubes. Rather, the pores resemble irregularly shaped particles (Deddas and Rumpf, 1966). In the case of interconnected pore space, the "body" of each pore is connected to the bodies of adjacent pores via "necks" or "throats." The "sizes" of both the pore bodies and the pore throats play an important role in determining the various macroscopic properties, such as permeability, capillary pressure curves of porous media, etc. Both the body and the throat sizes can be "measured" using computer reconstruction of pore structure from photomicrographs of serial sections of the sample (Kwiecien, 1987).

10.1.4 Specific Surface

The specific surface of a porous medium S is the internal surface area of the voids and pores per unit mass. The specific surface based on the bulk volume of the porous material is designated by S_v and the one based on the solid volume is denoted by S_o .

Specific surface plays an important role in a variety of applications of porous media such as adsorption, catalysis, and ion-exchange processes. For fluid flow in porous media, the specific surface is an important parameter in models of conductivity or permeability of a porous medium. For example, two porous samples with the same porosity may have very different permeabilities owing to different specific surface areas. The sample with a higher specific surface area has a smaller average pore size and lower permeability.

The key methods of determining specific areas include adsorption, optical, and fluid flow methods. For the review of different methods see Collins (1961) and Scheidegger (1974).

10.1.5 Resistivity Factor

The electrical resistivity of a fluid-saturated porous medium is a measure of the ability of the medium to impede the flow of electric current through it. Dry porous samples of zero electrical conductivity exhibit infinite resistivity. The resistivity of porous media containing an aqueous phase is a function of porosity, aqueous-phase saturation, and the salinity of the aqueous phase (Prison, 1963). Measurements using different porous materials show that the resistivity is also dependent on pore structure. A "resistivity factor," often called "formation resistivity factor," is defined as

$$F = \frac{R_o}{R_w} \quad (10.6)$$

where R_o is the electrical resistance of the porous sample saturated with an ionic solution and R_w the bulk resistance of the same ionic solution occupying the same space as the porous sample (same cross-sectional

area and length). It is evident that, in the case of nonconductive solids, R_o is always greater than R_w and, therefore, F is always greater than unity.

Many attempts have been made to correlate the formation resistivity factor with porosity ϕ and a "cementation exponent" m . The first known relationship was suggested by Archie (1942):

$$F = \phi^{-m} \quad (10.7)$$

For random suspensions of spheres, cylinders, and sand in aqueous solution of zinc bromide of approximately the same density as the particles, it was found that the cementation exponent in Eq. (10.7) was equal to 1.5 with a high degree of precision over a range of porosity from 0.25 to 0.55 (De La Rue and Tobias, 1959). For consolidated porous samples, Archie's equation does not generally hold (Tiab and Donaldson, 1999). For example, for chalky rocks, $m=2$; for compact limestones, which are highly cemented rocks, the value of m may be as high as 3. Even for the same or similar formations, m may be different depending on the well where rocks were sampled.

Extensive information on the formation resistivity factors for various reservoir rocks has been presented by Tiab and Donaldson (1999). For detailed discussions of the correlations of F with the "tortuosity factor" of the porous media, readers are referred to the review by Dullien (1992).

10.1.6 Hydraulic Conductivity

For a single fluid flow through a homogeneous porous column, shown in Figure 10.1, Darcy's law is written in the following form:

$$v = \frac{Q}{A} = \frac{k}{\mu} \frac{\Delta p}{L} \quad (10.8)$$

where v is the superficial velocity or flow rate per unit cross-sectional area normal to the flow direction. The pressure p is the modified (or piezometric) pressure (Bird et al., 1960) defined by

$$p = P + \rho g z \quad (10.9)$$

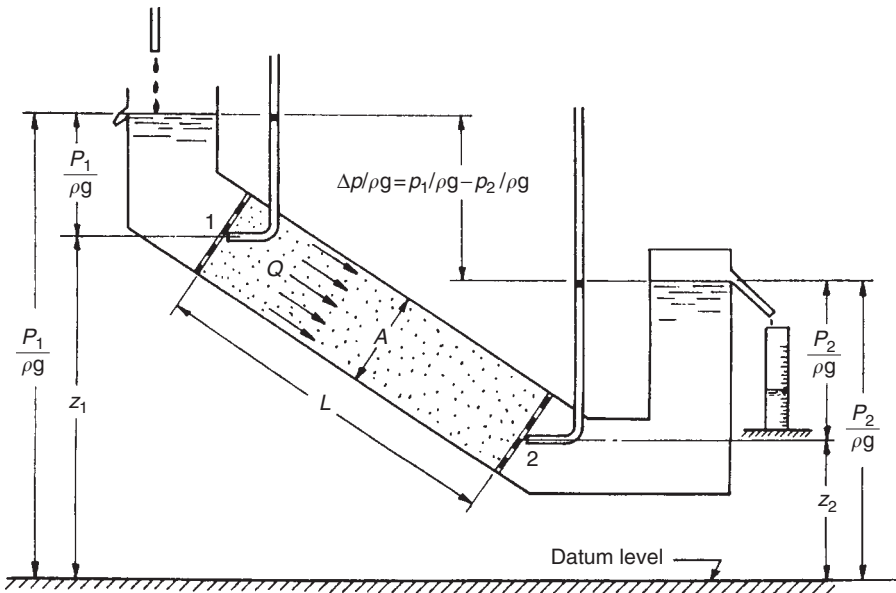


FIGURE 10.1 Illustration of modified pressure in Eq. (10.8). (From Dullien, F.A.L., *Porous Media-Fluid Transport and Pore Structure*, 2nd ed., Academic Press, San Diego, 1992. With permission.)

therefore

$$\Delta p = \Delta P + \rho g \Delta z \quad (10.10)$$

The pressure increment Δp is the pressure drop measured in the fluid flowing through the column, P the hydrostatic pressure, ρ the fluid density, g the gravitational constant, and z the distance upward measured from an arbitrary datum level. Hydrostatic pressure can be measured in terms of head of water by using a pipe, called “piezometer,” as shown in [Figure 10.1](#). The modified pressure p can be expressed as the “piezometer head” ϕ , which is the sum of the “elevation head” z and the “pressure head” $P/\rho g$:

$$\phi = \frac{p}{\rho g} = \frac{P}{\rho g} + z \quad (10.11)$$

Then Darcy's law can be written in another form as

$$v = k_H \frac{\Delta \phi}{L} \quad (10.12)$$

where the coefficient of proportionality, k_H , is called “hydraulic conductivity,” defined as

$$k_H = \frac{k \rho g}{\mu} \quad (10.13)$$

The hydraulic conductivity can be thought as the flow rate per unit cross-section of a porous medium under unit “hydraulic gradient” $\Delta \phi/L$. Therefore, unlike the permeability, which is the property of a porous medium, the hydraulic conductivity depends on both property k of the porous medium and the fluid properties ρ and μ .

10.1.7 Hydraulic Radius Theory (Carman–Kozeny Equation)

Numerous permeability and friction factor models have been used by researchers for different porous media. In this section, the Carman–Kozeny model, the well-known permeability model, is presented. The friction factor models were developed mainly for packed beds and they are discussed in the next section.

The Carman–Kozeny model (Carman 1937, 1938, 1956; Kozeny, 1927), often called the “hydraulic radius theory,” assumes that the sample of the porous medium of length L consists of a bundle of tortuous capillary tubes, each of diameter D_h and length $L_e > L$. The mean hydraulic diameter D_h of the capillaries was assumed to be

$$D_h = \frac{4 \times \text{void volume of medium}}{\text{surface area of channels in medium}} \quad (10.14)$$

By using the definitions of specific surface S_o and porosity ϕ , Eq. (10.14) becomes

$$D_h = \frac{4\phi}{S_o(1 - \phi)} \quad (10.15)$$

The velocity v_p in a capillary of hydraulic diameter D_h and length L_e is calculated by the Hagen–Poiseuille equation

$$v_p = \frac{D_h^2}{16\mu k_o} \frac{\Delta p}{L_e} \quad (10.16)$$

where k_o is a “shape factor.” The following relationship between v , defined by Eq. (10.8), and v_p was assumed:

$$v_p = \frac{v}{\phi} \frac{L_e}{L} \quad (10.17)$$

The physical basis of this relationship is explained by Dullien (1992, [Figure 3.7](#), p. 256). By introducing the expression of Darcy's law (Eq. [10.8]) for v into Eq. (10.17) results in

$$v_p = \frac{k_{CK}}{\mu} \frac{\Delta p}{L} \frac{1}{\rho} \frac{L_e}{L} \quad (10.18)$$

By combining the two expressions for v_p , i.e., Eqs. (10.16) and (10.18), and solving for k_{CK} yields the Carman–Kozeny formula for permeability:

$$k_{CK} = \frac{\phi D_h^2}{16 k_o (L_e/L)^2} \quad (10.19)$$

Substituting Eq. (10.14) into the above equation gives

$$k_{CK} = \frac{\phi^3}{k_o (L_e/L)^2 (1 - \phi)^2 S_o^2} = \frac{\phi^3}{k' (1 - \phi)^2 S_o^2} \quad (10.20)$$

where $(L_e/L)^2$ is called "hydraulic tortuosity factor." The factor $k' = k_o (L_e/L)^2$, called the Kozeny constant, is a function of pore geometry. For packed beds, the best fit to most experimental data gives $k' = 5$.

10.1.8 Friction Factor for Packed Beds

For the flow of a fluid in packed beds or columns, a friction factor f_p has been used to model the resistance of the porous media to fluid flow. The friction factor for packed beds is defined as

$$f_p \equiv \frac{d_p}{L} \frac{\Delta p}{\rho v^2} \quad (10.21)$$

and is a function of the "superficial" of "particle" Reynolds number Re_p :

$$Re_p = \frac{d_p v \rho_f}{\mu} \quad (10.22)$$

where d_p is the surface-average particle diameter, ρ_f the fluid density, and L the length of the bed in the flow direction. The surface-average particle diameter is defined as

$$d_p = \frac{6}{S_o} \quad (10.23)$$

By using Darcy's law, the hydraulic radius model for permeability and Eq. (10.23) leads to the following relation among f_p , ϕ , and Re_p (see Bird et al., 1960):

$$f_p = \frac{(1 - \phi)^2}{\phi^3} \frac{C}{Re_p} = f(\phi) \frac{C}{Re_p} \quad (10.24)$$

where C is a constant and $f(\phi) = (1 - \phi)^2 / \phi^3$ a porosity function.

Much effort has been expended in order to find the best porosity function $f(\phi)$ for low Reynolds number flows. Various forms of $f(\phi)$ have been obtained (see Dullien, 1992). The values of the constant in the various equations relating f_p , ϕ , and Re_p are different, depending on the form of $f(\phi)$ used. However, a linear relationship $f(\phi) = C/Re_p$ generally holds.

For Darcy flow, $Re < 1$, the Blake–Kozeny equation, which gives a good fit to the experimental results for $\phi < 0.5$, is

$$f_p \left[\frac{\phi^3}{(1 - \phi)^2} \right] = \frac{150}{Re_p} \quad (10.25)$$

The Carman–Kozeny equation discussed in the previous section can also be written in the same form as the Blake–Kozeny equation by combining Eqs. (10.14), (10.16), and (10.20), but with a different constant:

$$f_p \left[\frac{\phi^3}{(1 - \phi)^2} \right] = \frac{180}{Re_p} \quad (10.26)$$

At flow rates outside the range of validity of Darcy's law (very low Re_p), the linear relationship between $f(\phi)$ and $1/Re_p$ is no longer valid. The value of Reynolds number for the transition from the linear to non-linear variation lies between 0.1 and 75 (Scheidegger, 1974). An analysis by MacDonald et al. (1979) found that the deviation from $f_p = C/Re_p$ becomes noticeable in the range $Re_p/(1-\phi) \approx 1-10$. For flow in the nonlinear portion, the two well-known equations are (see, e.g., Bird et al., 1960) the Ergun equation:

$$f_p \left[\frac{\phi^3}{(1-\phi)} \right] = \frac{150}{Re_p} (1-\phi) + 1.75 \quad (10.27)$$

for intermediate values of Re_p and the Burke–Plummer equation

$$f_p \left[\frac{\phi^3}{(1-\phi)} \right] = 1.75 \quad (10.28)$$

for high values of Re_p . MacDonald et al. (1979) tested the Ergun equation by fitting much more data, than used by others, and found that the following equation gives the best fit to all the data:

$$f_p \left[\frac{\phi^3}{(1-\phi)} \right] = \frac{180}{Re_p} (1-\phi) + C_r \quad (10.29)$$

The second term C_r varies with the roughness of the particles. For smooth particles, $C_r=1.8$; for the roughest particles, $C_r=4.0$; and for intermediate surface roughness, the value of C_r lies between 1.8 and 4.0.

Equation (10.27) is a special form of the Forchheimer equation (Forchheimer, 1901; Brownell et al., 1950; Greenberg and Weger, 1960), which is the general relationship between the pressure gradient and flow rate:

$$\frac{\Delta p}{L} = \alpha \mu v + \beta \rho v^2 \quad (10.30)$$

where α is the reciprocal permeability and β the so-called inertia parameter. In terms of porosity and mean particle diameter, α and β are expressed as

$$\alpha = A \frac{(1-\phi)^2}{\phi^3 D_p^2} \quad (10.31)$$

and

$$\beta = B \frac{(1-\phi)}{\phi^3 D_p} \quad (10.32)$$

where A and B are constants equal to 180 and C_r given in Eq. (10.29), respectively.

For gas flow, in the absence of slip flow, the Forchheimer equation can be written as (Geertsma, 1974)

$$-\frac{P_2^2 - P_1^2}{2L(RT/M)\mu G_m} = \alpha + \beta \frac{G_m}{\mu} \quad (10.33)$$

where G_m is the mass flow rate per unit cross-section and M the molecular weight of the gas. A detailed review was presented by Scheidegger (1974) on pressure drop–flow rate relations at high flow rates.

10.2 Capillarity in Porous Media

10.2.1 Fundamentals of Capillarity

10.2.1.1 Laplace's Equation

The concept of surface tension at a liquid surface or at the interface between two fluids or a fluid and a solid is discussed in surface chemistry texts (e.g., Adamson, 1990). Examples of a soap film over a wire frame or a soap bubble are commonly used to illustrate the tendency of a surface to decrease spontaneously

its area due to the existence of tension in an interface. The stress causing this spontaneous decrease in surface area is called surface or interfacial tension. Surface tension may be thought of either as a force per unit length in a surface (dyn/cm, or equivalently, mN/m) or a free energy per unit surface area (erg/cm², or equivalently, mJ/m²).

The basic equation of capillarity is Laplace's equation that describes a very important natural phenomenon, i.e., the existence of a pressure difference ΔP at a point p between two sides of a curved fluid surface or interface:

$$\Delta P = \sigma \left(\frac{1}{R_1} + \frac{1}{R_2} \right) \quad (10.34)$$

where σ is the surface tension and R_1 and R_2 the radii of curvature at the point p.

For a surface where both radii are equal, such as a sphere, Laplace's equation becomes

$$\Delta P = \frac{2\sigma}{R} \quad (10.35)$$

For a plane surface, the two radii are infinite and therefore the pressure difference across a plane surface is zero.

10.2.1.2 Wettability and Contact Angle

Immiscible fluids present simultaneously in porous media compete for the occupancy of the pore surface. The configuration of the interface that separates the immiscible fluids is determined by the relative wettability of the pore surface by the two immiscible fluids. The relative wettability of a porous medium by two fluids is characterized by the contact angle θ . It is helpful to consider the situation of a drop of liquid placed on a smooth solid surface as shown in Figure 10.2. The contact angle θ is defined as the angle between the tangent to the liquid–solid boundary constructed at a point on the three-phase line of contact and the tangent to the gas–liquid boundary constructed at the same point. For the situation shown in Figure 10.2, the force balance at the point on the three-phase line of contact along the liquid–solid boundary is expressed by Young's equation:

$$\sigma_{sg} - \sigma_{sl} = \sigma_{lg} \cos \theta \quad (10.36)$$

where σ_{lg} and σ_{sg} are the surface tensions of liquid and solid, respectively, and σ_{sl} the interfacial tension between the liquid and the solid.

The contact angle of a gas–liquid–solid or a liquid–liquid–solid system may have any value between 0 and 180°. It is customary to simply classify fluids into two categories: wetting and nonwetting fluid. For wetting fluids, $0 \leq \theta < 90^\circ$, and for nonwetting fluids, $90^\circ < \theta \leq 180^\circ$. In the pores of porous media, the curved interfaces between two immiscible fluids may take different shapes and directions of the curvature. Figure 10.3 shows two typical menisci that separate water and gas or oil in thin capillaries or pores. In Figure 10.3a, the contact angle measured through the water phase is less than 90°, hence the water is the wetting phase and the gas or the oil is the nonwetting phase, whereas in Figure 10.3b, $\theta > 90^\circ$, and the water is the nonwetting phase and the gas or the oil is the wetting phase. Accordingly, the pore surface in Figure 10.3a is a water-wet surface and the pore surface in Figure 10.3b is as an oil-wet surface.

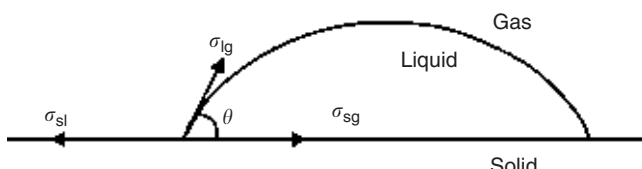


FIGURE 10.2 Contact angle of a liquid on a solid surface.

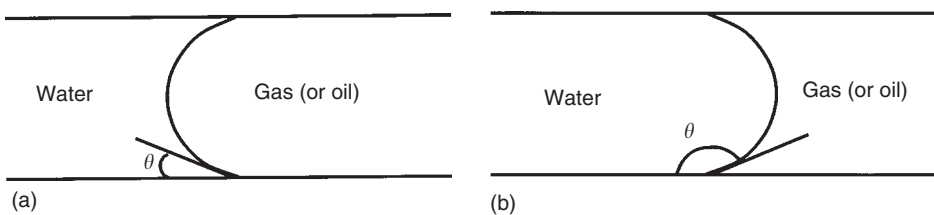


FIGURE 10.3 Menisci in: (a) a water-wet and (b) an oil-wet capillary.

10.2.1.3 Capillary Pressure

Immiscible fluids in porous media are separated from each other by curved interfaces, across which there exists a pressure difference or a step change in pressure. This pressure difference, called capillary pressure P_C , is balanced at equilibrium by a pressure difference ΔP at any points of contact between the two fluids:

$$P_C \equiv \Delta P = P_{nw} - P_w \quad (10.37)$$

where w and nw represent wetting and nonwetting phase, respectively. As, at equilibrium, $P_{nw} > P_w$, the capillary pressure is, by definition, always positive.

Equation (10.37) shows that the capillary pressure always tends to compress the nonwetting phase relative to the wetting phase. Let us consider a fluid pair consisting of water and gas in a capillary, as illustrated in Figure 10.3. If water is used in the wetting phase ($\theta < 90^\circ$), the water surface must be concave in shape as shown in Figure 10.3a. The pressure difference across the interface is calculated by Eq. (10.34) and its direction (or sign) is such that the pressure is less in the water phase than in the gas phase. In contrast, if water is the nonwetting phase as shown in Figure 10.3b, the water surface is convex in shape and the pressure is higher in the water phase than in the gas phase. It is helpful to remember that the pressure in the phase on the concave side of the surface is always greater than the pressure in the phase on the convex side.

Equation (10.34) is a general form for calculating the pressure difference (or capillary pressure) at any point of a curved interface. It is customary to introduce the mean radius of curvature r_m defined by

$$\frac{1}{r_m} = \frac{1}{2} \left(\frac{1}{R_1} + \frac{1}{R_2} \right) \quad (10.38)$$

where Laplace's equation now becomes

$$P_C = \Delta P = \frac{2\sigma}{r_m} \quad (10.39)$$

Typical application of Eq. (10.39) is in a circular capillary of a very small radius. If the contact angle of a liquid on the capillary walls is zero, the meniscus can be approximately thought to be hemispherical. Thus, the mean radius of the curvature is equal to the radius of the capillary. Eq. (10.39) then reduces to

$$P_C = \frac{2\sigma}{r} \quad (10.40)$$

where r is the radius of the capillary.

The general case is when the liquid–gas surface or liquid–liquid interface meets the circular capillary wall through contact angle θ , as illustrated in Figure 10.4. If the meniscus is a spherical cap and both r and R are positive quantities, the following geometric relation holds:

$$R = \frac{r}{|\cos \theta|} \quad (10.41)$$

and Eq. (10.40) becomes

$$P_C = \frac{2\sigma}{r} |\cos \theta| \quad (10.42)$$

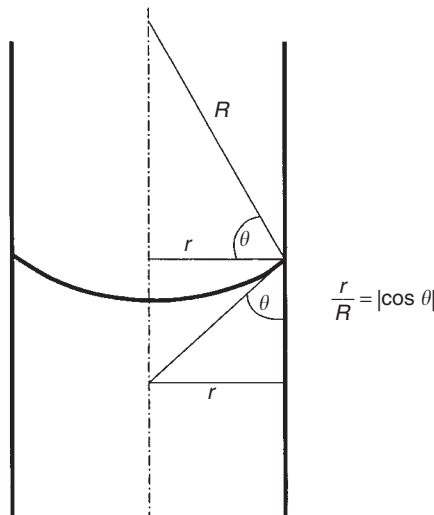


FIGURE 10.4 The relationship between the radius of the curvature of the meniscus and the radius of the capillary tube.

Equation (10.42) is the most widely used form of Laplace's equation in the porous media. Equation (10.42) contains the three most important factors in determining the magnitude of the capillary pressure: interfacial tension, capillary size, and contact angle. The capillary pressure across a meniscus in a conical capillary (see Figure 10.5) is calculated by (Dullien, 1992)

$$P_C = \frac{2\sigma}{r} |\cos \theta + \phi| \quad (10.43)$$

where ϕ is the tilt angle of the solid boundary and $(r/|\cos(\theta+\phi)|)$ the mean radius of curvature of the meniscus.

In a porous medium, which may be a reservoir rock, or soil, or groundwater formation or a packed column, the pores or voids are rarely cylindrical. In the case of capillary pressure in noncylindrical tubes, research has been done only in tubes of rectangular and equilateral triangular cross-sections (Lenormand, 1981; Lenormand et al., 1983; Legait, 1983; Mason and Morrow, 1991). It is not possible, at present, to calculate capillary pressures based on the real pore shapes in porous media. Equation (10.42) has been widely used for determination of pore size distributions with the help of mercury porosimetry and adsorption isotherms. As most materials are not wetted by mercury, i.e., $\theta = 180^\circ$, $|\cos \theta|$ in Eq. (10.42) is equal to unity. At quasi-static injection, hydraulic pressure in mercury is equal to the capillary pressure at each injection stage. By using (Eq. 10.42), the "pore throat sizes" corresponding to different injection pressure can be found. No information is obtained on the "pore body sizes," however. All the volume of mercury injected is assigned to the pore throats, resulting in unrealistic pore size distributions.

10.2.1.4 Capillary Rise

The best illustration of the phenomenon of capillary rise may be the capillary rise method for measuring the surface tension of a liquid, such as water in a clean glass capillary (see Figure 10.6). The contact angle of some fluids on a clean glass surface is near zero; Equation (10.42) can be used directly. At equilibrium, ΔP (or P_C) in Eq. (10.42) must be equal to the hydraulic pressure drop in the liquid column in the capillary, i.e., $\Delta P = \Delta \rho gh$, where $\Delta \rho$ is the difference in density between liquid and gas phase and g the gravitational constant. Equation (10.42) becomes

$$\Delta \rho gh = \frac{2\sigma}{r} \quad (10.44)$$

In soil, where moisture content is sufficiently low, the air is at atmospheric pressure and the water is at a pressure lower than atmospheric pressure. The pressure difference between the air and the water phase is

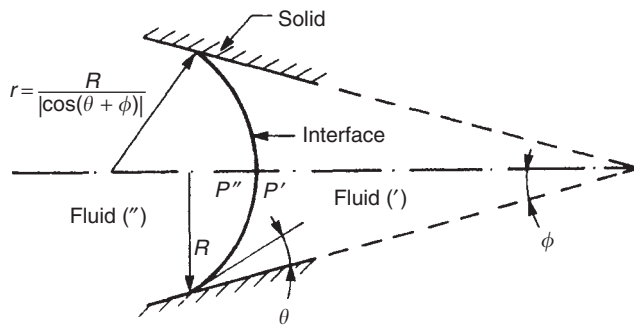


FIGURE 10.5 Meniscus in a conical capillary. (From Dullien, F.A.L., *Porous Media-Fluid Transport and Pore Structure*, 2nd ed., Academic Press, San Diego, 1992. With permission.)

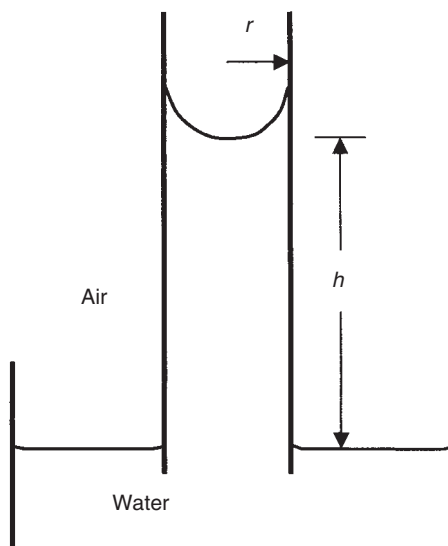


FIGURE 10.6 Capillary rise in a glass tube.

determined experimentally by using a device called porous cup tensiometer at the point of interest as shown in Figure 10.7. The porous cup tensiometer measures the pressure difference between the air at atmospheric pressure and the wetting phase (water), which is under suction. This pressure difference is equal to the capillary pressure across the water–gas menisci in the soil. The reading of the manometer is called the *capillary pressure head*, *moisture tension*, or *suction head*, and is defined as follows:

$$P_c = \frac{P_C}{\rho_w g} = - \frac{P_{wg}}{\rho_w g} \quad (10.45)$$

where P_{wg} is the gauge pressure of water ($P_{wg} = P_w - P_{atm}$) in the soil ($P_{wg} < 0$) and $\Delta\rho$ is approximated by the density of water phase ρ_w . It is customary to define a *piezometric head* or *capillary head* as

$$\phi_c = Z + \frac{P_{wg}}{\rho_w g} = Z - \frac{P_C}{\rho_w g} = Z - h_c \quad (10.46)$$

10.2.2 Imbibition and Drainage

The basic fact of capillarity is that the pressure on the concave side of a curved fluid–fluid interface is greater than that on the convex side. Hence, the pressure in the nonwetting phase at the fluid–fluid interface is

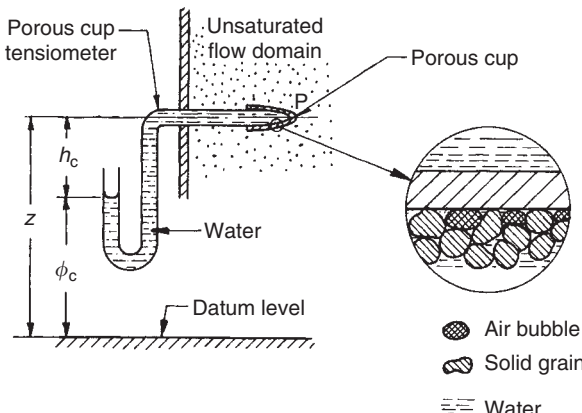


FIGURE 10.7 Porous cup tensiometer. (From Dullien, F.A.L., *Porous Media-Fluid Transport and Pore Structure*, 2nd ed., Academic Press, San Diego, 1992. With permission.)

higher than that in the wetting phase, because the nonwetting phase is always on the concave side and is compressed relative to the wetting phase by a pressure difference (the capillary pressure). In two-phase flow and immiscible displacement in a porous medium, the capillary pressure will affect the process differently, depending on the wettability of the porous material. When the wetting phase displaces the nonwetting phase, the process is called imbibition, infiltration, or wetting. In imbibition, the displacement is driven either partially or entirely by capillary pressure. The process consisting of a nonwetting phase displacing a wetting phase is called drainage or dewetting. In drainage, the capillary pressure opposes the displacement. Owing to capillary forces, the pattern of occupancy of pores by two or more immiscible fluids at the same saturation can be very different, depending on the path along which the saturation was reached, i.e., imbibition or drainage, etc., the wettability and the pore structure of the porous medium.

10.2.2.1 Imbibition and Drainage in Circular Capillaries

The simplest case of imbibition and drainage is in a horizontal, straight circular capillary of uniform diameter with smooth and clean walls. Such a capillary is filled initially with a nonwetting fluid B and is then exposed at one end to the wetting fluid A (Figure 10.8) with the other end staying in contact with fluid B. If there is a zero pressure difference between the two ends of the capillary, then $P_C = 2\sigma|\cos \theta|/r$ (where r is the capillary radius) acting across the A/B meniscus will cause fluid B to be displaced from the capillary by the wetting fluid A in a process called “free spontaneous imbibition.” If, at the end of this displacement, a positive pressure differential $P_B - P_A > P_C$ is imposed between the two ends of the capillary, then the nonwetting fluid will displace the wetting fluid from the capillary in a drainage-type displacement, leaving a very thin film of the latter on the capillary walls. The nonwetting fluid occupying the capillary at the end of drainage is in contact with a solid surface of modified physical properties, owing to the presence of the thin film of the preferentially wetting fluid. This explains why the contact angle in imbibition, in which the solid surface is dry, is greater (advancing contact angle) than in drainage, in which the solid surface is wet (receding contact angle).

In a commentary paper by Rose (2000), seven pressure profiles were summarized for two-phase displacements in a horizontal-oriented capillary tube. P_W and P_N is the pressure in wetting and nonwetting phase, respectively. As shown in Figure 10.9 and summarized in Table 10.1, $P_C = 0$ for cases b and g and $P_C = 0.05$ atmospheres for cases a, c, and d-f. The viscosity ratio for all cases is set as $\mu_W/\mu_N = 1$. When $P_W = P_N$, as in case c, a spontaneous imbibition occurs, i.e., the capillary force is the only driving force for the displacement of the nonwetting phase by the wetting phase. In case a, $P_W - P_N > 0$ and forced imbibition takes place. In case d, where $P_W - P_N = -P_C$, no displacement occurs since the external differential pressure just offsets the capillary pressure. For controlled imbibition (not included in Figure 10.9) $P_W - P_N < 0$, but, for $|P_W - P_N| < P_C$, the wetting phase displaces the nonwetting phase but at a lower rate compared to case c.

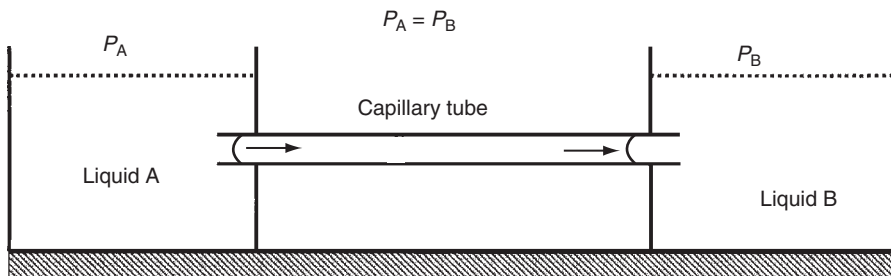


FIGURE 10.8 Schematic of free spontaneous imbibition in a capillary tube.

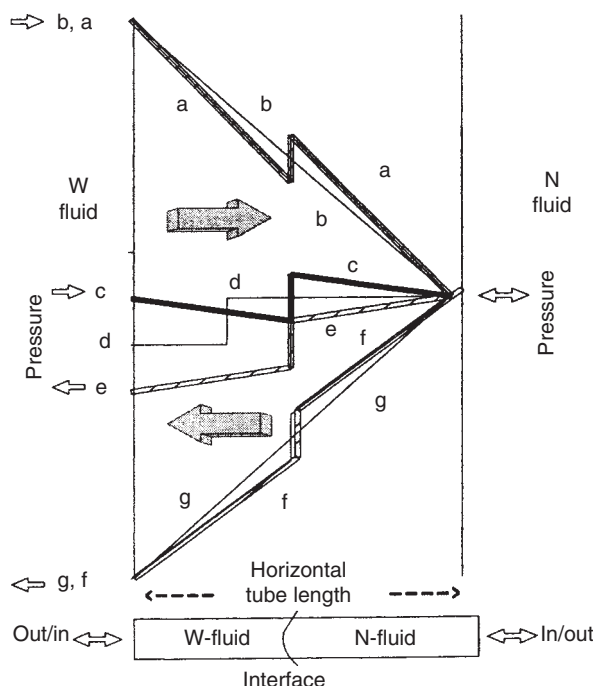


FIGURE 10.9 Pressure profiles in two-phase displacements in a horizontal-Oriented capillary tube. (From Rose, W., *Transport Porous Media*, 36(2), 161–187, 1999, *Transport Porous Media*, 40, 355, 2000. With permission.)

TABLE 10.1 Analysis of Two-Phase Displacement in a Horizontal-Oriented Capillary Tube (see Figure 10.9)

Case	P_C (atm)	$P_W - P_N$	Displacement Process
a	0.05	$P_W - P_N > 0$	Forced imbibition
b	0	$P_W - P_N > 0$	Displacement
c	0.05	$P_W - P_N = 0$	Spontaneous imbibition
d	0.05	$P_W - P_N = -P_C$	No displacement
e	0.05	$P_W - P_N > -P_C$	Drainage
f	0.05	$P_W - P_N \gg -P_C$	Drainage
g	0	$P_W - P_N < 0$	Displacement

In cases e and f, $P_W - P_N > -P_C$, drainage occurs, i.e., the nonwetting phase is displacing the wetting phase through the capillary tube. The displacement rate in case g, where capillary forces are absent, is greater than that in case f, where the forces are present. On the other hand, the displacement rate in case a, where capillary forces are present, is greater than that in case b, where the forces are absent.

10.2.2.2 Imbibition of Wetting Fluid in Films in Angular Capillaries

In porous media, pores have angular cross-sections, rough walls, and nonuniform diameters. In this section, the effects of angular cross-sections and rough walls on imbibition and flow of wetting fluid in porous media are illustrated by presenting expressions for capillary pressure in edges and imbibition of a wetting liquid along the edges of a square capillary.

A cross-section of an edge of an angular tube is shown schematically in Figure 10.10. The capillary pressure across the liquid meniscus in the edge is (Dong et al., 1995)

$$P_C = \frac{\sigma}{R} |\cos(\theta + \phi)| \quad (10.47)$$

where θ is the contact angle of the liquid on the edge walls, ϕ the half angle of the edge, and R one half of the distance between the two liquid–solid contact lines along the two sides of the edge. As long as the effective contact angle ($\theta + \phi$) is in the range $0 \leq (\theta + \phi) < 90^\circ$, spontaneous imbibition of the wetting liquid in the edge will occur under certain conditions. Figure 10.11 illustrates schematically two situations of spontaneous imbibition along edges. One is imbibition of a wetting liquid from high saturation to low saturation along an open edge (a and b). The other is imbibition of a wetting liquid from the central part of a triangular tube into the edges (c and d). This was described as an imbibition process during progressive filling of edges by Mason and Morrow (1991).

If an imbibition experiment is carried out in a square capillary, the wetting fluid will imbibe along the edges ahead of the meniscus in the central part of the capillary (Figure 10.12). It has been shown both theoretically and experimentally that the velocity of the imbibition front of wetting liquid in the edges of a square capillary containing a gas phase is as follows (Dong and Chatzis, 1995):

$$v_f = C \left(\frac{\sigma}{\mu \beta} \right)^{1/2} R^{5/2} t^{1/2} \quad (10.48)$$

where σ is the surface tension, μ the viscosity of the fluid, R the radius of the inscribed circle of the square tube, β a dimensionless resistance factor (Ransohoff and Radke, 1988) defined by the angle of the edge and the contact angle of liquid on the tube walls, t the time, and C a constant. It was also found that at

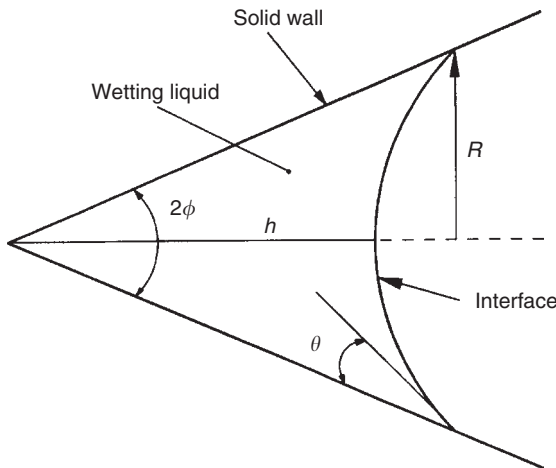


FIGURE 10.10 Imbibition in an edge of an angular capillary. (From Dong et al., *J. Colloid Interface Sci.*, 172, 21, 1995. With permission.)

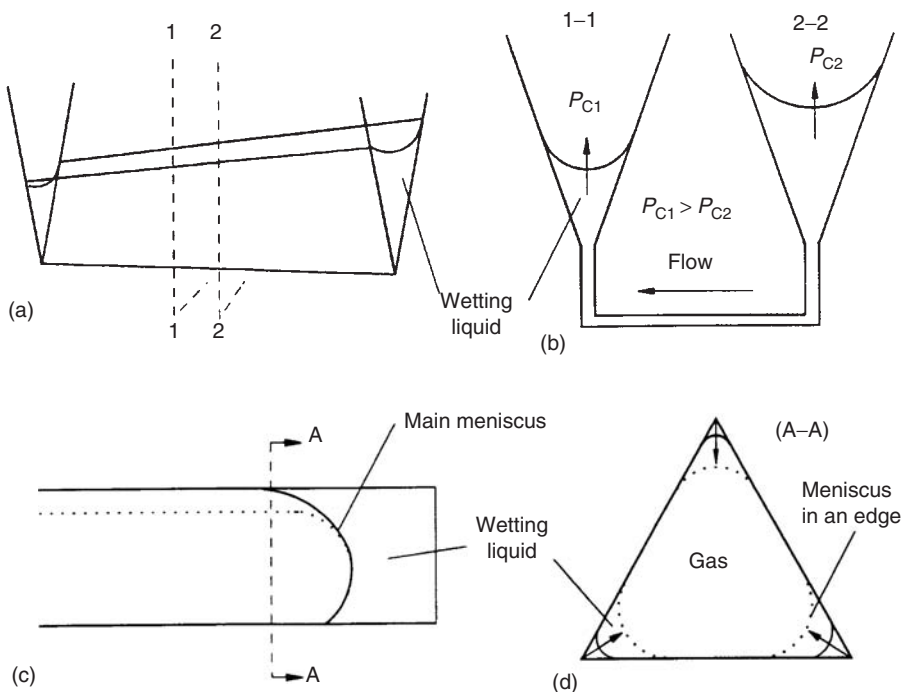


FIGURE 10.11 Imbibition along an open edge and edges of angular capillary: (a) nonuniform saturation in the open edge; (b) analogue of imbibition in (a); (c) imbibition from central part of an angular tube into edges; (d) increase in saturation in edges of (c). (From Dong et al., *J. Colloid Interface Sci.*, 172, 21, 1995. With permission.)

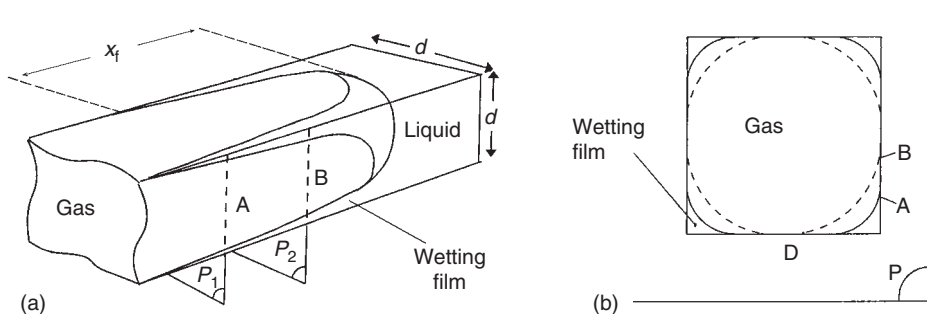


FIGURE 10.12 Imbibition of a wetting liquid in thick films ahead of the main meniscus in a square capillary tube. (From Dong, M. and Chatzis I., *J. Colloid Interface Sci.*, 172, 278, 1995. With permission.)

the same imbibition time, the film length x_f (see Figure 10.11) of the wetting liquid in the edges ahead of the main meniscus in the central part of the tube changes with the tube size d as

$$\frac{x_{f1}}{x_{f2}} = \left(\frac{d_1}{d_2} \right)^{1/2} \quad (10.49)$$

Imbibition of the wetting fluids in edges of pores in a pore network becomes important in the water-flooding method of oil recovery in water-wet media. Equation (10.49) is consistent with the observations in networks of capillaries (Chatzis and Dullien, 1983) and in porous rocks (Chatzis et al., 1983). The mobility of water along the edges of larger pores is very significant and plays an important role in the oil-trapping mechanisms. Further discussion on this is presented in the next section.

At the end of the imbibition process, all the nonwetting fluid is displaced from a square capillary. In a drainage type displacement, following imbibition, however, a “thick film” of the wetting fluid will remain in each edge of the square capillary if $0^\circ \leq (\theta + \phi) < 90^\circ$, as shown in Figure 10.13 (for the square capillary $\phi = 45^\circ$). The equilibrium “displacement pressure” P_d is (Lenormand, 1981; Lenormand et al., 1983; Legait, 1983)

$$P_d = 0.943 \frac{4\sigma}{d} \quad (10.50)$$

for contact angle $\theta=0^\circ$, where d is the edge length of the square. The radius of curvature of the meniscus of the thick film in the corners of the square in Figure 10.12 is approximately $d/4=R/2$, where R is the radius of the inscribed circle. (The other principal radius of curvature is infinite.) The thick films occupy 6% of the cross-section of the square capillary. In an equilateral triangular capillary, the equilibrium films in the edges occupies 12.5% of the cross-section of the tube (Mason and Morrow, 1991).

If, after completion of the drainage displacement, the pressures at the two extremities of the square capillary are made equal, the wetting fluid will displace the nonwetting one in a free spontaneous “secondary imbibition” process. In this imbibition process, the wetting fluid will penetrate both the central part of the square capillary and the thick films present in the edges if these films have a radius of curvature less than approximately $d/4$. Penetration into the thick films makes the thickness of the films increase to a maximum value, which is defined by a radius of curvature of the meniscus of approximately $d/4$.

The important consequence of the presence of both edges and rugosity in the pores is that an interconnected network of grooves may be formed on the pore surface and, therefore, the wetting phase may remain continuous and mobile in porous media even at the lowest wetting phase saturations attainable in practice. A notable exception is presented by packs of smooth glass beads that cannot form an interconnected network of edges.

10.2.2.3 Imbibition of Oil Film over Water along Edges in Angular Capillaries and Pores

In the previous two sections, discussion was limited to conditions involving only two fluid phases. There are situations of considerable practical importance where three phases, water, oil and gas, are present in porous media. One such instance involves the problem of mobilization of oil (petroleum or LNAPL) blobs that are surrounded by water and trapped in the pores by capillary forces. Trapping of oil blobs occurs regularly in water-wet oil reservoirs after water flooding and it can also occur in the soil in the course of attempted clean-up operations. When a gas phase is introduced into pores where water and residual oil are present, spreading or imbibition of oil on the water-gas interface may take place, and oil spreads from blobs into thick films in the pores. Once this occurs in noncylindrical water-wet pores, three phases will coexist as shown in Figure 10.14 (Dong et al., 1995).

It has been observed by numerous researchers (e.g., Chatzis et al., 1988; Kalaydjian et al., 1993) that, if the water is drained from a porous medium containing trapped residual oil blobs, the oil blobs start to spread spontaneously after they have been contacted by the air or other inert gas, such as nitrogen, used to displace the water from the main (central) parts of the pores as shown in Figure 10.15. The

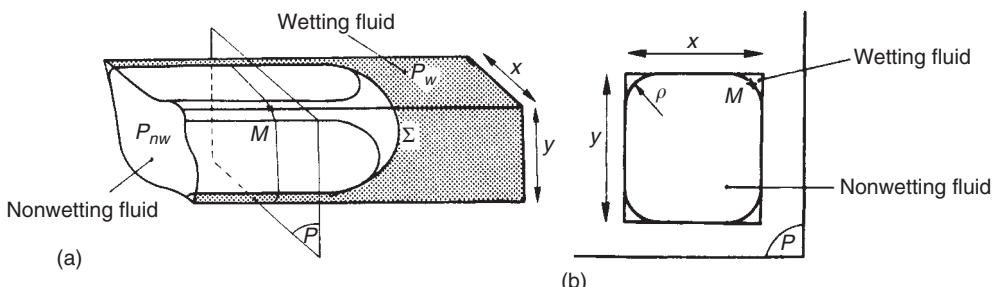


FIGURE 10.13 Capillary equilibrium in a square capillary tube. (From Lenormand et al., *J. Fluid Mech.*, 189, 165, 1988. With permission.)

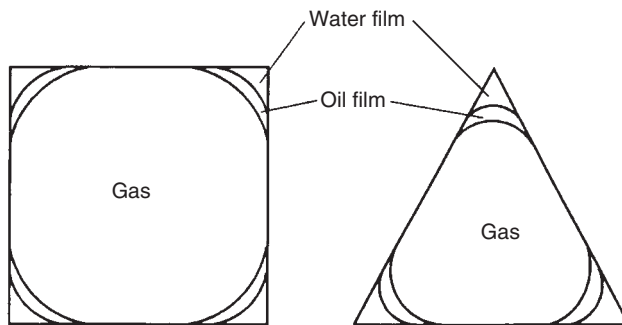


FIGURE 10.14 Three phases in the edges of a square and a triangular capillary. (From Dong et al., *J. Colloid Interface Sci.*, 172, 21, 1995. With permission.)

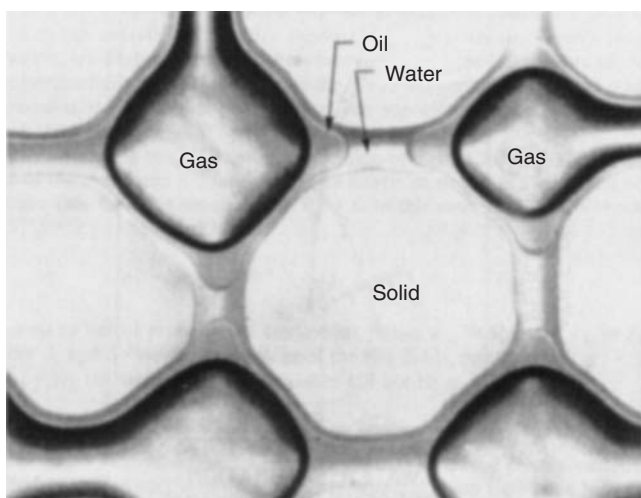


FIGURE 10.15 Spontaneous spreading of oil blobs over the water present in pore edges in a capillary micromodel after being contacted by air. (From Chatzis et al., *Proceedings of the 63rd Annual Technical Conference and Exhibition of the SPE*, Society of Petroleum Engineers, Houston, Texas October 2–5, 1988. With permission.)

explanation of this phenomenon is that oil spreads on the surface of the thick water films remaining on the pore walls after the bulk of the water has drained out, provided that its spreading coefficient S , defined as

$$S = \sigma_{gw} - (\sigma_{go} - \sigma_{ow}) \quad (10.51)$$

has a positive value. The surface tensions σ_{gw} , σ_{go} , and σ_{ow} are the gas–water, gas–oil, and oil–water interfacial tensions, respectively. The phenomenon of spreading oil blobs has resulted in the recovery of a very high percentage of the residual oil, because the oil films thus formed drain under the influence of gravity on the surface of the thick water films, and oil is produced at the bottom of the medium (Catalan et al., 1994).

There have been instances reported in the literature where an unexpectedly high percentage of a “non-spreading” type of oil, that is when the spreading coefficient is negative, was recovered by the spreading of oil and film drainage (e.g., Kalaydjian et al., 1993). In the light of these conflicting and unexplained results obtained with spreading and nonspreading oils, the question of spreading of oil drops on the surface of thick water films present in pores was reexamined by Dong et al. (1995). It was found that the

process of spreading of an oil drop over a thick water film in an edge¹ is different from the spreading of an oil drop on a flat water surface, because solid surfaces, i.e., the walls of the edges as shown in Figure 10.16, are also contacted by the oil. The capillary pressure across the gas–oil interface $P_{C(g-o)}$, namely,

$$P_{C(g-o)} = \frac{\sigma_{go}}{R} \cos(\theta_{gos} + \phi) \quad (10.52)$$

also plays a role in the redistribution of residual oil in the pores. In Eq. (10.52), θ_{gos} is the contact angle of oil at the line of oil–gas–solid contact. As a result, even an oil drop with a negative spreading coefficient may spread over the thick water film under certain conditions and form a film of thickness greater than molecular dimensions. The driving force of this kind of spreading is the capillary pressure and, therefore, it can be regarded as a special case of imbibition.

It has been observed that when a small quantity of nonspreadng ($S < 0$) oil is put in contact with a thick water film in an edge, a small lens of oil is formed. If one adds a little more oil to the lens, the thickness of the center of the lens and the length of the lens along the edge increases. After the addition of a

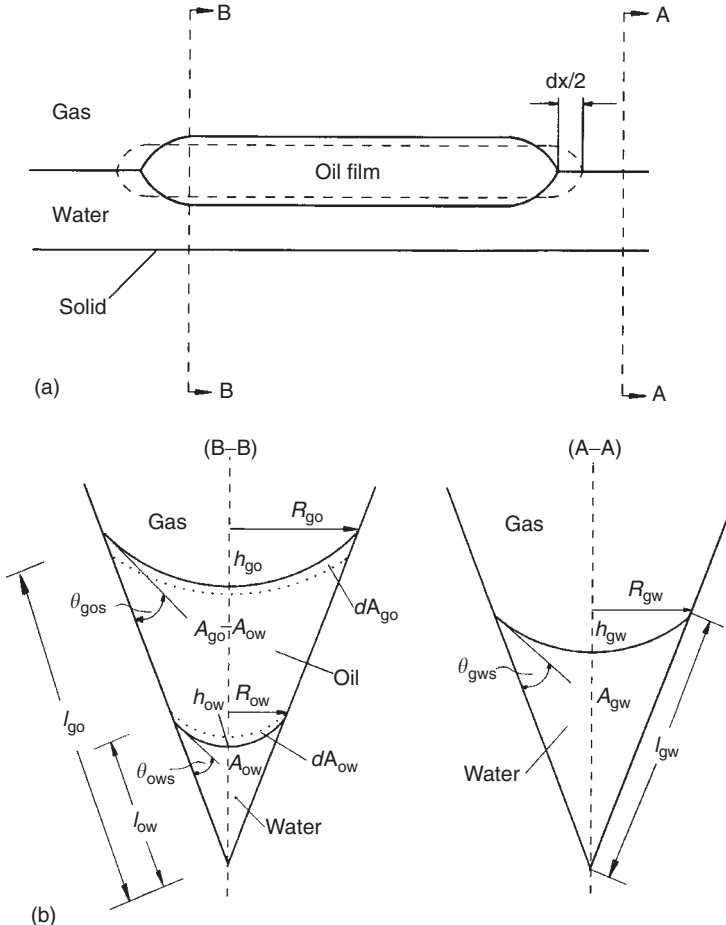


FIGURE 10.16 Equilibrium of three phases in an edge: (a) lengthwise section at mid-point through an edge; (b) cross-sections of three- and two-phase coexist. (From Dong et al., *J. Colloid Interface Sci.*, 172, 21, 1995. With permission.)

¹ The term “edge” is used in the same sense as 12 edges of a cube and it is different from a “corner” of which there are 8 in a cube.

certain amount of oil, the thickness of the lens does not increase any more, but its length constantly increases and the lens grows to a thick film of a constant thickness. This constant thickness of the oil film shown in Figure 10.16 is called the “critical” film thickness for imbibition at an edge. The equations for predicting the critical film thickness have been developed by applying Laplace’s equation of capillary pressure and the minimization of surface free energy to the system shown in Figure 10.16. The film thickness was calculated as a function of the water film thickness at the edge, the half-angle ϕ of the edge, the interfacial tensions and the (negative) spreading coefficient (Dong et al., 1995). The results of these calculations are shown in Figure 10.17.

The results in Figure 10.17 indicate that the critical imbibing oil film thickness over a thick water film along an open edge strongly depends on the water saturation, the geometry of the edge, and the negativity of the spreading coefficient of the oil on water. There is, however, a difference between imbibition into an open edge, where there is no limit to the total thickness (water and oil film thickness), and imbibition into the edges of a capillary of a square or a triangular cross-section, since the edges are closed in the form of a polygon. Consequently, the total film thickness can never exceed the equilibrium value, pointed out in the previous section, which corresponds to 6% of the cross-section of a square capillary and to 12.5% of the cross-section of an equilateral triangular capillary.

The predictions of critical oil film thickness have been confirmed by experiments (Dong et al., 1995) in a 0.05 cm^2 capillary tube with 0.6% water saturation, using benzene (spreading coefficient, equilibrated with water: $S = -1.4 \text{ mN/m}$) and a light paraffin oil ($S = -7.9 \text{ mN/m}$), respectively, as the oil phase. For these conditions, the calculated critical total film thickness is $h_{go} = 4.22 \times 10^{-3} \text{ cm}$ for the

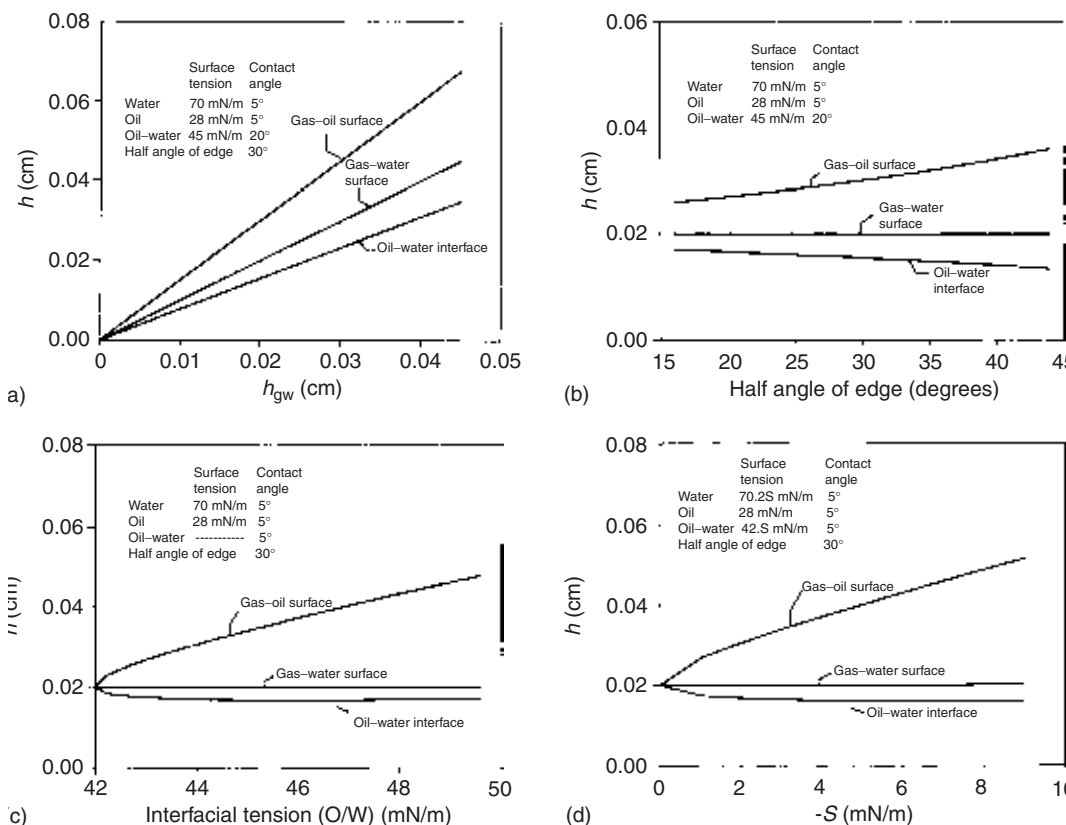


FIGURE 10.17 Critical thickness of oil film as a function of: (a) water film thickness; (b) the half angle of the edge; (c) oil–water interfacial tension; and (d) the spreading coefficient (<0). (From Dong et al., *J. Colloid Interface Sci.*, 172, 21, 1995. With permission.)

benzene–water system and $h_{go} = 6.17 \times 10^{-3}$ cm for the light paraffin oil–water system. Comparing these values with the maximum total equilibrium film thickness $H = 5.47 \times 10^{-3}$ cm, it follows that a slug of benzene can be expected to imbibe into edges over the water whereas a slug of light paraffin oil is not. These predictions were confirmed by experiments in which a slug of benzene did imbibe, whereas a slug of the light paraffin oil did not.

10.2.2.4 Displacement and Trapping in Branched Capillaries of Irregular Cross-Section and Nonuniform Diameters

In porous media, especially in consolidated ones such as reservoir rocks, immiscible displacement of one phase by the other will result in trapping of the displaced phase because of the features of three-dimensional pore-networks, i.e., branching pore paths, pore throats alternating with pore bodies, and angular pore cross-sections.

Trapping of the nonwetting phase occurs in imbibition-type displacements. As pointed out in the previous section, the presence of edges and rugosity of pore surface may result in an interconnected network of surface grooves. In this network, the wetting phase can remain continuous and mobile in the porous medium even at a very low saturation. The continuity of the wetting phase and the trapping of the nonwetting phase have been demonstrated in capillaries of irregular cross-section and nonuniform diameter, containing branches as shown in Figure 10.18 (Chatzis and Dullien, 1983). In such capillaries, much nonwetting fluid (gas) is trapped and bypassed by the imbibing wetting fluid (liquid in black). Trapping takes place either in the bulges, the so-called “pore bodies,” or in ganglia consisting of two or more pore bodies separated by throats. The wetting fluid is never trapped because it can advance from one end of the capillary to the other along edges of past trapped nonwetting fluid, and sometimes by also filling the entire capillary cross-section. The mechanism of trapping in imbibition is “snap-off” of the nonwetting fluid, a result of “choke-off” by the wetting fluid. There is the possibility of completely filling a pore throat with the wetting fluid, whereas in the adjacent pore bodies the wetting fluid may occupy only the edges. The snap-off, or choke-off, of the nonwetting phase is because of (1) the continuity of the wetting phase through the edges and grooves and (2) the equalization of the capillary pressures among menisci on the edges. A detailed explanation is presented below.

At the same fractional filling of an angular capillary by the wetting fluid, there is a smaller radius of curvature of the meniscus in the edges of a throat than in those of a pore body. Consequently, under such conditions, the wetting fluid in a throat is under a lower pressure (i.e., suction) and, therefore, it will flow from the edges of the pore body into the edges of the throat. The concomitant increase in the radius of curvature of the thick films of wetting fluid in the throat edges may lead to the nonwetting fluid in the throat losing contact with the wall as shown in Figure 10.19. At this point, the thread of nonwetting fluid becomes unstable and snap-off occurs. Note that the same radius of curvature of the thick film’s meniscus in the edge of, for example, a larger diameter square capillary, corresponding to a saturation equal to or less than 6%, may result in 21.5% saturation in a smaller diameter square capillary. In this case the menisci in the edges are defined by an inscribed circle in the square, corresponding to the thick film’s stability limit. Once

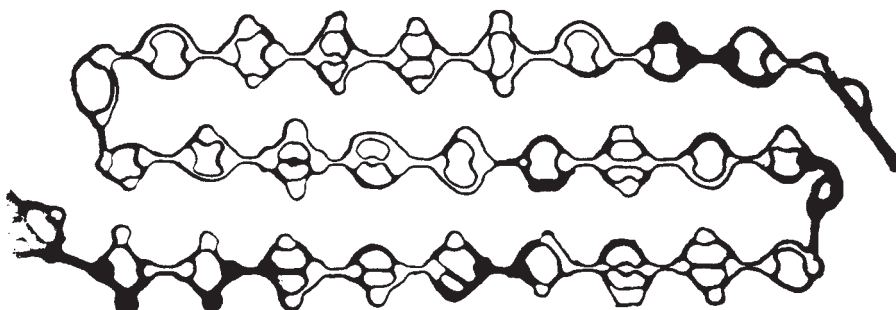


FIGURE 10.18 Trapping of a nonwetting phase during an imbibition displacement in a capillary with rejoining branches. (From Chatzis, I. and Dullien, F.A.L., *J. Colloid Interface Sci.*, 91, 199, 1983. With permission.)

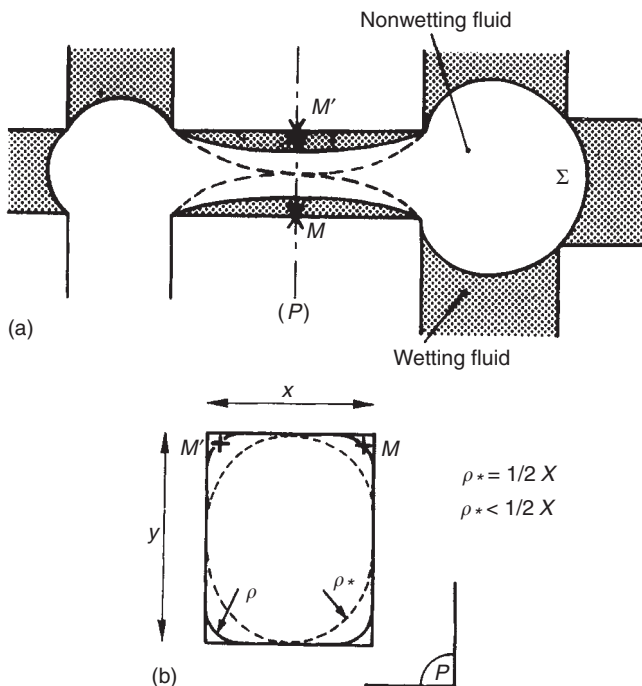


FIGURE 10.19 Capillary instability of a thick wetting film in a square capillary. The dashed curve shows the critical position of instability. (From Lenormand et al., *J. Fluid Mech.*, 189, 165, 1988. With permission.)

the snap-off occurs in a branch with a small diameter, the wetting phase will occupy part of the branch with the full cross-section. The capillary pressure across the menisci in the small branch may still be higher than that in the edges of the larger pores. In this case, the wetting phase will transport under suction to continue to fill the thinner branch until capillary pressure equilibration is reached.

In a drainage-type displacement, the presence of an alternating sequence of pore throats and bodies does not result in trapping. In branching structures (the so-called “pore doublets,” when a capillary splits into two branches that join further down the path to form again a single capillary) there may be trapping of the wetting phase, given the right pore structure and displacement conditions are controlled by capillary rather than viscous forces. Under these conditions, the wetting fluid is trapped in the branch of the smaller diameter as shown in Figure 10.20.

10.2.2.5 Pore Network Models of Imbibition and Drainage

The pore structure of most porous materials consists of an interconnected three-dimensional (3D) network. Numerous research papers have been published using mathematical network models to simulate multiphase flow in physical network models and in real porous media. Pore network modeling has been helpful in understanding two-phase immiscible displacement in two-dimensional (2D) capillary network micromodels and successful in predicting some properties, such as capillary pressure functions, relative permeability curves, and residual saturations (Dullien, 1992; Blunt et al., 2002) of samples of a few porous media. However, there is still a great deal to be learned about the mechanisms of multiphase flow in porous media and it is a great challenge to incorporate these mechanisms into the pore network models. In this section, network models are discussed only from the point of view of predicting capillary pressure curves in both imbibition and drainage.

In typical network modeling, the pore structure is assumed to consist of a 2D or a 3D network of throats (bonds) and pore bodies (nodes). The throats and pore bodies are assumed to have regular, such as circular or square cross-sections. Most importantly, the displacement in both drainage- and imbibition-type

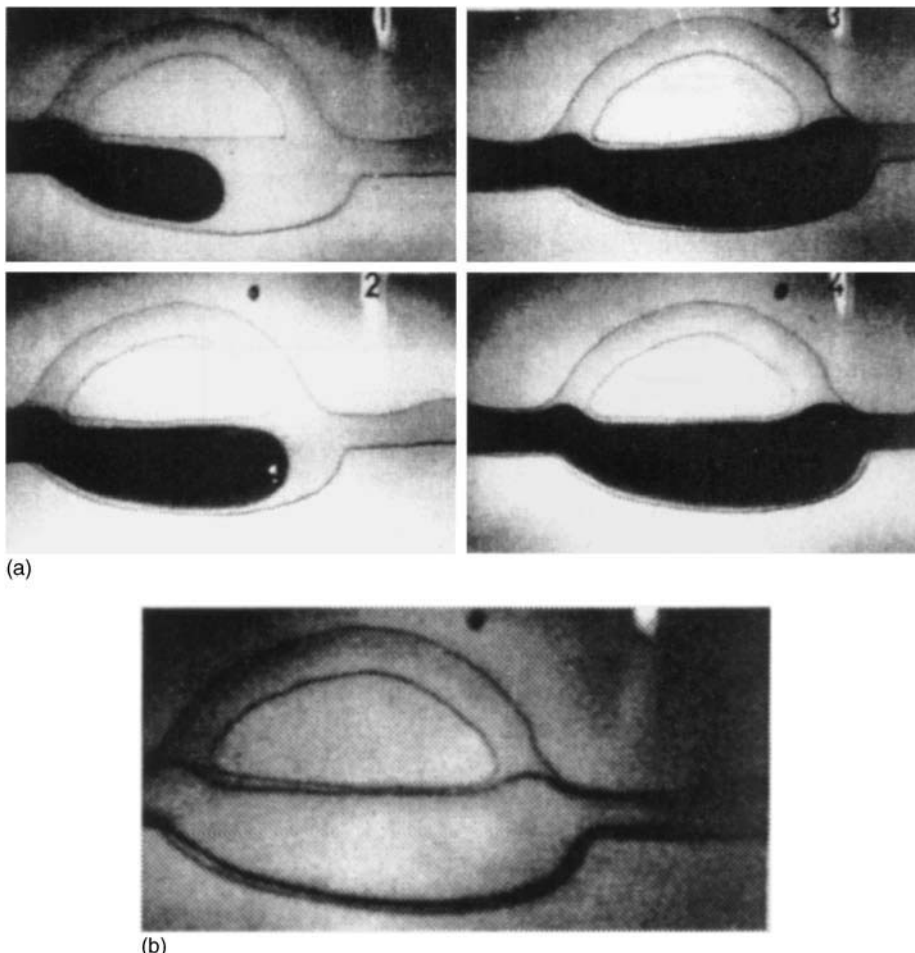


FIGURE 10.20 Trapping of wetting liquids in drainage-type displacement in a pore doublet. (a) *n*-decane (black) displacing water, and (b) air displacing water. (From Chatzis, I. and Dullien, F.A.L., *J. Colloid Interface Sci.*, 91, 199, 1983. With permission.)

displacements is assumed to advance in a piston-like manner in the throats and pore bodies. Different sizes are assigned to both the throats and the pore bodies by using certain rules. One such rule that gave realistic results consists of assigning different diameters, distributed according to some probability density distribution, randomly to the nodes, whereas the bond diameters, distributed according to a different probability density distribution, are subject to the constraint that no bond can have a larger diameter than the smaller one of the two nodes that it connects. The diameter of the bond is correlated with the diameter of the smaller one of the two nodes. This type of percolation is called “bond-correlated site percolation.”

Drainage type of displacement in such networks, generated by the computer, has been studied extensively (e.g., Chatzis and Dullien, 1982, 1985; Diaz et al., 1987), largely by the application of percolation theory. Trapping of the wetting phase was assumed to occur if all of the pores in contact with a cluster of wetting phase were occupied by the nonwetting phase. In the modeling of drainage-type displacements, the nonwetting phase is assumed to advance in a piston-like manner in the pore throats. The penetration is started at one of the faces of the network. The bonds (throats) are penetrated step by step by the invading nonwetting fluid, starting with the largest throat diameter and continuing in the direction of the decreasing throat diameter. Evidently, the bond diameters control the drainage, whereas the volume

invaded is contributed mostly by the nodes. The predictions closely matched the drainage capillary pressure curves of actual porous media samples (mostly sandstones), consisting of plots of equilibrium nonwetting fluid saturation of the sample vs. the capillary pressure as shown in Figure 10.21, where “secondary drainage” is the drainage-type displacement following secondary imbibition.

In the modeling of secondary imbibition-type displacements, the wetting phase is assumed to advance in a piston-like manner in the pore bodies. The penetration is started at one of the network faces. The nodes are penetrated step-by-step by the invading wetting fluid, starting with the smallest diameter and continuing in the direction of the increasing diameter. This displacement process is controlled by the node diameters. As seen in Figure 10.21, the simulation resulted in zero imbibition until a low capillary pressure was reached, at which point there was abrupt displacement. This behavior is in contradiction with the experiment. Subsequently, imbibition was simulated by assuming that the sites anywhere in the network were directly accessible to the wetting phase because of the existence of an interconnected network of thick films of wetting phase on the pore walls. In this simulation, each and every node was invaded by the wetting phase at the capillary pressure corresponding to its size. As seen in Figure 10.21, this simulation gave results in much better agreement with the experiment.

In the course of imbibition, portions of the nonwetting phase become trapped by the choke-off (snap-off) mechanism, while the rest is displaced from the medium. The end of imbibition corresponds to the conditions when all of the nonwetting phase remaining in the medium is trapped, i.e., is discontinuous. The final nonwetting phase saturation is usually called “residual” saturation, but the term “irreducible saturation” would be appropriate as long as the displacement is limited to no-flow conditions. Under static conditions displacement of the trapped nonwetting phase is no longer possible, even if the wetting phase is placed under a higher pressure than the nonwetting phase.

In network simulation of a drainage-type displacement, at low capillary pressures applied in the early stages, displacement is limited to a thin layer of the porous medium. At a critical or threshold

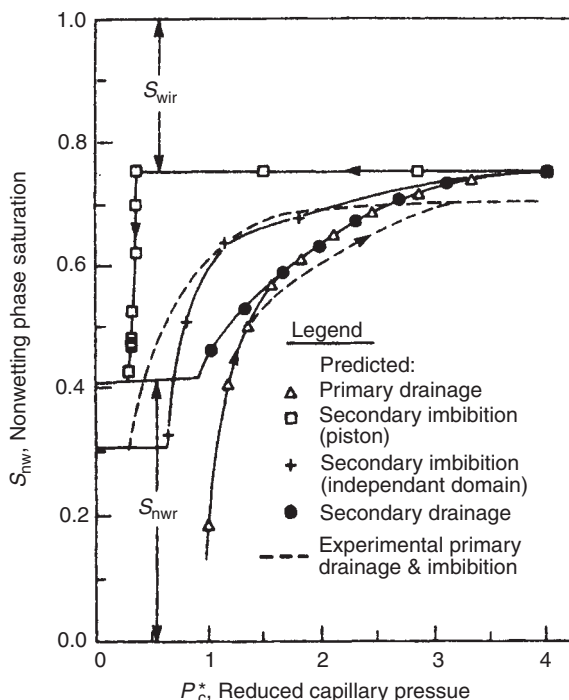


FIGURE 10.21 Measured and network model predicted capillary pressure curves for a sandstone sample. (From Diaz, C.E. et al., *Transport Porous Media*, 2, 15, 1987. With permission.)

value of the capillary pressure, the depth of penetration is without limit and at that point the nonwetting phase breaks through the sample. Therefore, this value is also referred to as "breakthrough." At this point, the nonwetting phase becomes continuous and, therefore, conductive. Breakthrough conditions in a 2D square lattice are shown in Figure 10.22. It is evident that in 2D networks both phases cannot be continuous simultaneously. An important feature is that a portion of the nonwetting phase, although continuous, is not conductive because it forms dead end branches, also called "dendritic structures." In 3D networks, however, the wetting phase remains continuous and conductive at breakthrough. The wetting phase saturation at breakthrough is 70 to 80%. With continued increase in the applied capillary pressure, the nonwetting phase displaces additional wetting phase by invading the smaller throats, while portions of the wetting phase are cut off and become discontinuous. Eventually, a capillary pressure is reached where all of the wetting fluid remaining in the network is discontinuous and is therefore "trapped." The wetting phase saturation corresponding to this point is usually called "irreducible saturation" and is 20 to 50%. It is important to point out, however, that in the network simulation, the role played by the thick films of the wetting phase remaining in the grooves on the pore walls after the pore has been penetrated by the nonwetting fluid has not been considered. As these grooves form an interconnected network, the thick films can be squeezed and made thinner by increasing the applied capillary pressure and allowing enough time for further displacement to take place (Dullien et al., 1989). Therefore, in the presence of surface grooves there is no irreducible wetting phase saturation, but only a residual saturation that decreases at a very slow rate as the capillary pressure is increased.

At intermediate saturations, where both phases are continuous in the network of pore bodies and pore throats, there exist two subnetworks of pores: one subnetwork that is completely filled with the wetting fluid, and the other in which only the main (central) parts of the pores are filled with the nonwetting

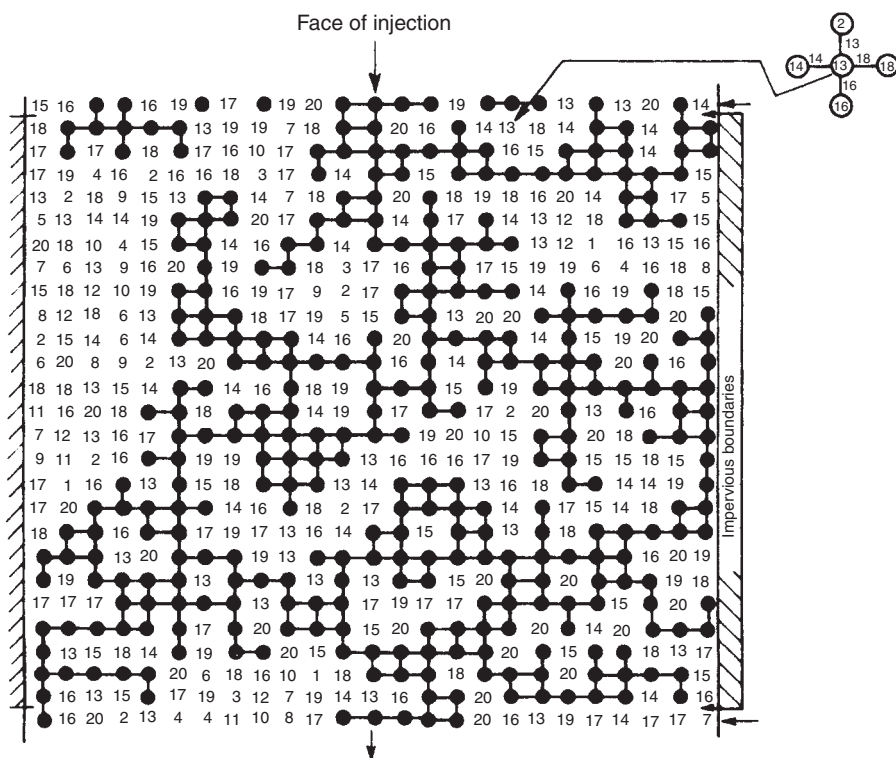


FIGURE 10.22 Breakthrough conditions in a 2D square lattice network (site percolation). (From Chatzis, I. and Dullien, F.A.L., *Int. Chem. Eng.*, 25, 47, 1985. With permission.)

fluid, which is surrounded by the wetting fluid present in the form of thick films on the pore walls. The hydraulic conductivity of the wetting fluid present in the form of thick films is negligibly small compared with that of the wetting fluid present in its own pore subnetwork.

10.2.2.6 Imbibition and Drainage in Porous Media with Neutral or Fractional Wettability

In the previous sections, it has been assumed that one of the fluids is preferentially wetting the pore surface and the pore surface is “uniformly wetted.” In this case, the porous medium does not have portions that are wetted preferentially by one of the two fluids mixed with portions that are preferentially wetted by the other fluid. The dashed curves in Figure 10.21 shows the typical capillary pressure vs. nonwetting-phase saturation functions, i.e., primary drainage and secondary imbibition curves.

However, there are cases in which the porous samples are not uniformly wetted by one fluid relative to the other fluid. These porous samples can be categorized into two types of wettabilities.

1. *Neutral wettability.* When the contact angle is in the vicinity of 90° , neither of the fluids can be called preferentially wetting. The term “intermediate wettability” is also used in such situations.
2. *Fractional wettability.* When portions of the pore surface are wetted preferentially by one of the two fluids, for example, water, while other portions are wetted preferentially by the other fluid, for example, oil. This situation may exist in some porous media, particularly in petroleum-bearing sands or rocks. Such media are best referred to as “fractionally wetted.” Occasionally “mixed wettability” is also used, but this term may have some special connotations (Salathiel, 1973).

The capillary pressure saturation functions for the above two kinds of porous media have been analyzed by Dullien and Fleury (1994). The capillary pressure curves in Figure 10.23 and Figure 10.24 (solid lines) were plotted according to the definition of the capillary pressure, i.e., in a drainage type of

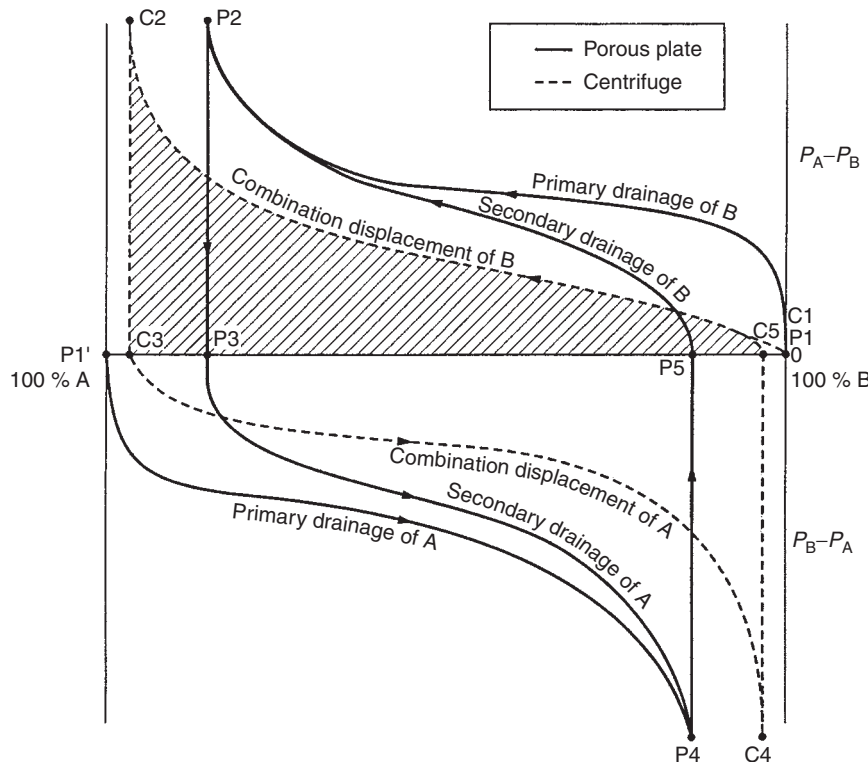


FIGURE 10.23 Schematic of capillary pressure curves for a neutrally wetted porous medium. (From Dullien, F.A.L. and Fleury, M., *Transport Porous Media*, 16, 175, 1994. With permission.)

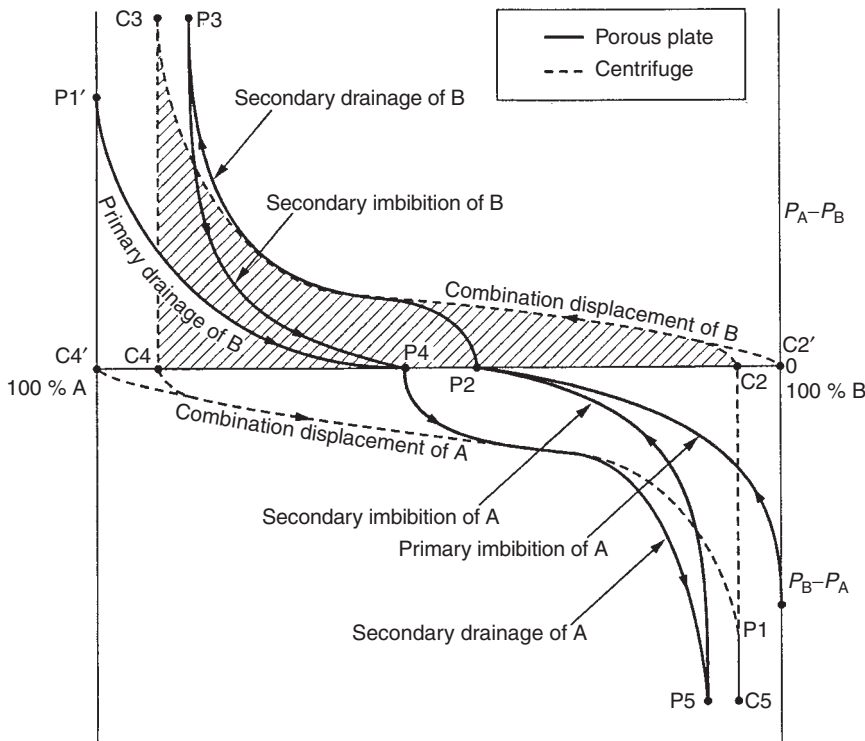


FIGURE 10.24 Schematic of capillary pressure curves for a fractionally wetted porous medium. (From Dullien, F.A.L. and Fleury, M., *Transport Porous Media*, 16, 175, 1994. With permission.)

displacement, the displacing phase is under a higher pressure than the displaced phase (conversely, in imbibition, the displacing phase is under a lower pressure than the displaced phase).

Capillary pressure curves for neutrally wetted conditions are plotted in Figure 10.23. As shown in this figure, there is no spontaneous displacement of either of the fluid by the other because the capillary pressure is zero at certain controlling points in the pore network. The only way either of the fluid can be displaced by the other under conditions of neutral wettability is by imposing an excess pressure on the displacing fluid, i.e., by a drainage mechanism.

It has been observed that in fractionally wetted systems, either of the two fluids (e.g., oil or water) may occasionally imbibe spontaneously and displace the other fluid to a certain extent (Dullien et al., 1990). This behavior can be explained by assuming that both the oil- and the water-wet regions in the pore network are continuous (Dullien and Fleury, 1994). Capillary pressure curves for fractionally wetted conditions are shown in Figure 10.24. If such a medium is initially saturated with fluid A and then brought into contact with fluid B, conditions of capillary equilibrium require that fluid A be at a higher pressure than fluid B; otherwise fluid B would imbibe spontaneously into the sample (Figure 10.24). Lowering the pressure difference $P_A - P_B > 0$ step-by-step results in the displacement of fluid A from pores that are preferentially wetted by fluid B, starting with the smallest pore diameter and continuing in the direction of increasing diameter. No displacement of fluid A from pores preferentially wetted by fluid A takes place as long as $P_A - P_B \geq 0$. The displacement in this range of pressures is of the imbibition type and $P_C = P_A - P_B > 0$. If, after the point $P_A - P_B = 0$ has been reached, fluid B is placed under increasingly higher pressure, i.e., now $P_B - P_A > 0$, then further displacement of fluid A takes place from those pores that are preferentially wetted by fluid A. The displacement mechanism in this range of pressures is drainage and $P_C = P_B - P_A > 0$. There is also trapping of fluid A in the entire displacement process. If, at some point beyond which there is only an incremental additional displacement of A, the pressure difference $P_B - P_A > 0$ is gradually decreased, then fluid B is displaced

by fluid A in secondary imbibition of A from pores preferentially wetted by fluid A in the pressure range $P_B - P_A > 0$. If, after reaching the point $P_B - P_A = 0$, fluid A is placed again under the higher pressure, then fluid B is displaced by A by a secondary drainage mechanism in the pressure range $P_A - P_B > 0$ from those pores preferentially wetted by fluid B.

10.3 Steady Multiphase Flow in Porous Media

10.3.1 Introduction

Multiphase flow in porous media is simultaneous flow of two or more immiscible fluids, or fluids of limited miscibility, e.g., oil and water or air and water, which are in contact with each other over a large number of fluid–fluid interfaces. When two immiscible fluids flow simultaneously through a porous sample under steady conditions, there will be a pattern of occupancies of the two fluids which greatly influence the effective permeabilities of the two fluids in the sample. The distribution of the two fluids depends on a number of factors, including the saturation, the wettability conditions of the pore surface, the interfacial tension, fluid viscosities, and the pore velocity. The case that has been of most interest corresponds to the conditions when one of the two fluids wets the pore surface preferentially, the interfacial tension is large, and the viscosities and the velocities are low.

Four possible occupancy patterns of two fluids in cocurrent steady flow have been depicted by Dullien (1988) as shown in Figure 10.25. In Figure 10.25a both fluids flow in separate channels. Fluid 1 wets the solid surface preferentially and tends to occupy the finer pores in the network. There are thick films of the wetting fluid (not shown in the figure) in the pores, where the non-wetting phase (fluid 2) occupies the central part. The contribution by the thick films to the flow of the wetting fluid is negligible. In Figure 10.25b, both fluids flow in the same pores; the wetting fluid is in the form of thick films (the thickness exaggerated in the figure). Such conditions exist at low wetting fluid saturations, where the wetting fluid is no longer continuous in the central parts of the pores. Distributions of both fluids at various saturations have been presented photomicrographically in sandstone by Yadav et al. (1987).

Figure 10.25c shows the flow pattern in a sample with neutral wettability. There are no thick films of either fluid, and either fluid may fill small as well as large pores. It is even conceivable that the two fluids may flow side-by-side in some pores, as shown in Figure 10.25c. The same situation may exist also in the case of fractional wettability if one “side” of a pore is preferentially wetted by fluid A, whereas the other “side” is preferentially wetted by fluid B. Finally, in Figure 10.25d both fluids flow in the same channel, but one fluid is continuous and the other dispersed. This is the case at low values of the interfacial tension when oil and water form emulsions and it may happen at both low nonwetting phase saturation and high interfacial tensions.

10.3.2 Relative Permeabilities

10.3.2.1 Equations of Relative Permeabilities

Two immiscible fluids, such as water and oil or water and gas, can flow cocurrently through a porous medium. In practice, conditions of steady cocurrent flow are usually established by injecting both fluids at constant rates and allowing time for the discharge rates to become equal to the injection rates. Under these conditions it has been found in experiments that the saturation and the capillary pressure are approximately independent of the position. An extended Darcy's law for two-phase flow in porous media, under steady-state conditions, can be written as (Muskat and Meres, 1936):

$$q_i = \frac{k_i A}{\mu_i} \frac{\Delta P_i}{L} \quad (10.53)$$

where q_i is the volumetric flow rate, ΔP_i the pressure drop, and μ_i the viscosity of phase i. The symbols A and L have the same meaning as in Eq. (10.4) and k_i is referred to as the “effective permeability” of the

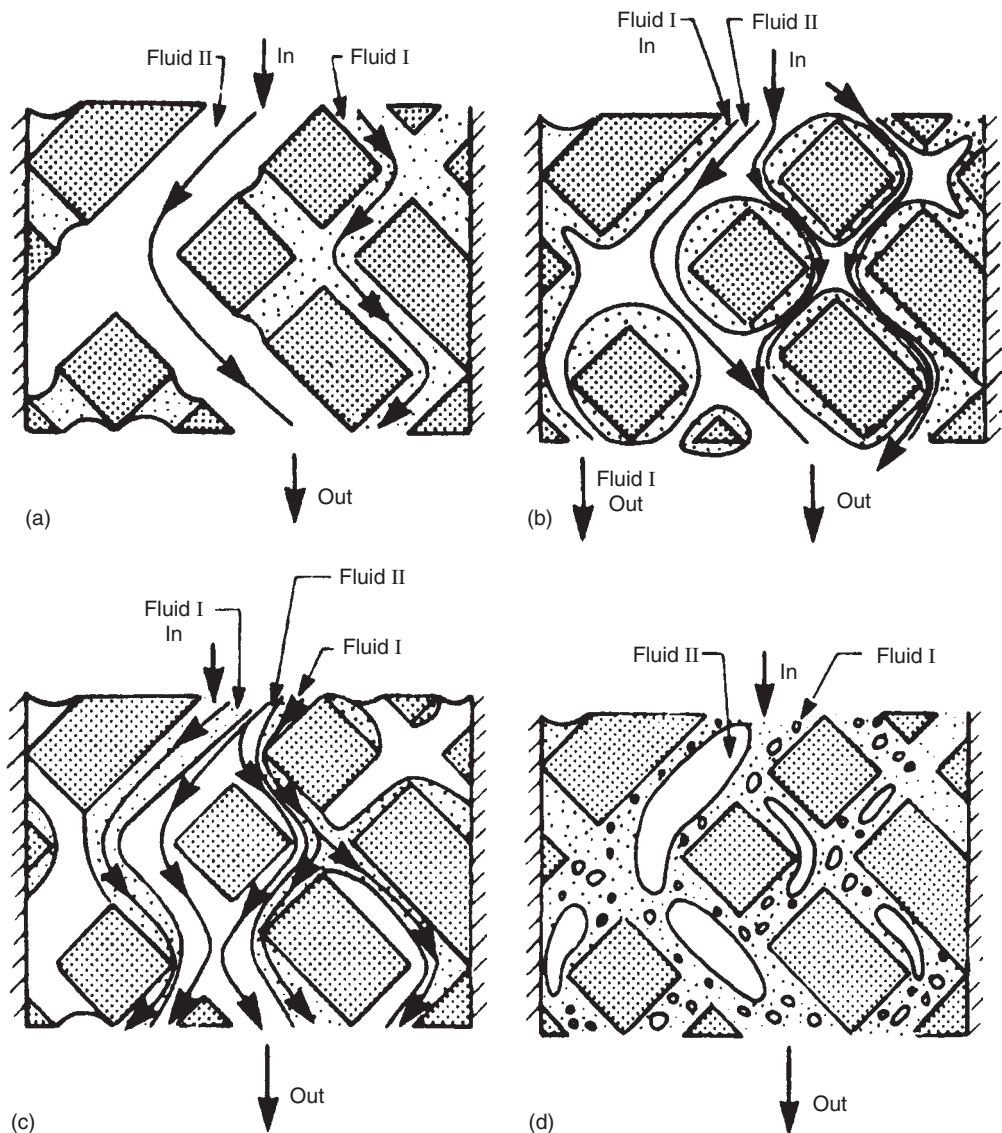


FIGURE 10.25 Two-dimensional representation of cocurrent steady two-phase flow in porous media. (From Dullien, F.A.L., *Chem. Eng. Technol.*, 11, 407, 1988. With permission.)

porous medium to phase i . It is customary to express k_i as relative permeability, i.e., as a fraction of the absolute permeability of the porous medium k :

$$k_{ri} = \frac{k_i}{k}, \quad i = o, w \quad (10.54)$$

and write Eq. 10.53 as

$$q_i = \frac{k_{ri} k A}{\mu_i} \frac{\Delta P_i}{L}, \quad i = o, w \quad (10.55)$$

The relative permeabilities represent the ability of a porous medium to conduct one fluid when more fluids are present. They are usually plotted as a function of wetting phase saturation as shown in Figure 10.26. However, the relative permeabilities for a fluid pair in a porous medium can be affected

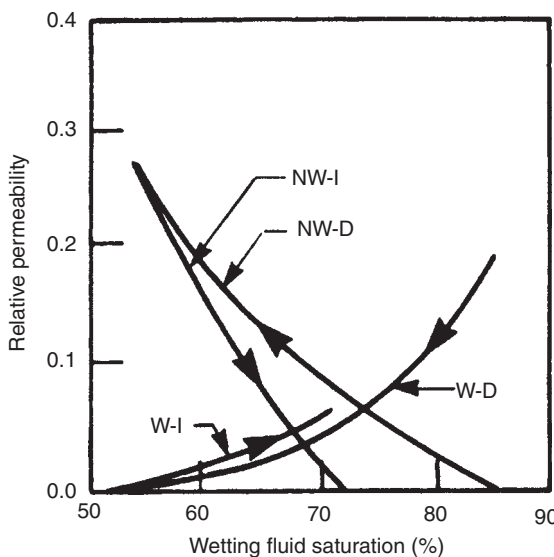


FIGURE 10.26 Schematic representation of relative permeability curves of primary drainage and secondary imbibition. (From Dullien, F.A.L., *Chem. Eng. Technol.*, 11, 407, 1988. With permission.)

by the pore structure, wettability, capillary forces, and saturation history. It has been widely assumed in the literature that the relative permeabilities in a porous medium do not depend on the viscosities, μ_i , of the fluids. It is shown later in this section that the validity of this assumption is limited to certain conditions.

10.3.2.2 Drainage and Imbibition Relative Permeabilities

It has been observed that the capillary pressure function has different values between an upper and lower bound, depending on the path along which the particular saturation is reached (see Figure 10.21). The reason for “capillary pressure hysteresis” is that the saturation history, i.e., the path along which a saturation has been reached, affects the fluid distribution. Whenever capillary forces are controlling, there is also a hysteresis effect of the relative permeability curves, as shown schematically in Figure 10.26 i.e., “imbibition” relative permeability curves are different from “drainage” relative permeability curves. (In imbibition the wetting phase saturation increases, whereas in drainage the wetting phase saturation decreases.)

10.3.2.3 Effect of Wettability

The effect of wettability on relative permeabilities has been investigated in considerable detail (Owens and Archer, 1971; McCaffery and Bennion, 1974). Typical water–oil relative permeability curves for water- and oil-wet reservoir formation samples are presented in Figure 10.27 and Figure 10.28, respectively. The main reason for the difference between the curves in Figure 10.27 and Figure 10.28 lies in the customary procedure used in determining relative permeability curves, i.e., driving the sample down to “irreducible” water saturation and measuring the relative permeabilities at increasing water saturations. Hence, in a water-wet sample imbibition-type relative permeability curves are determined, whereas in an oil-wet sample drainage-type relative permeability curves are determined. The most noticeable difference in relative permeability characteristics of the two types of rocks is the difference in water saturations at which water and oil relative permeabilities are equal: greater than 50% for water-wet and less than 50% for oil-wet. For rocks with neutral wettability, the relative permeabilities are different from the values measured in systems of strongly water-wet or strongly oil-wet. The cause of the above variances is the different topologies of the two immiscible fluids under different wettability conditions.

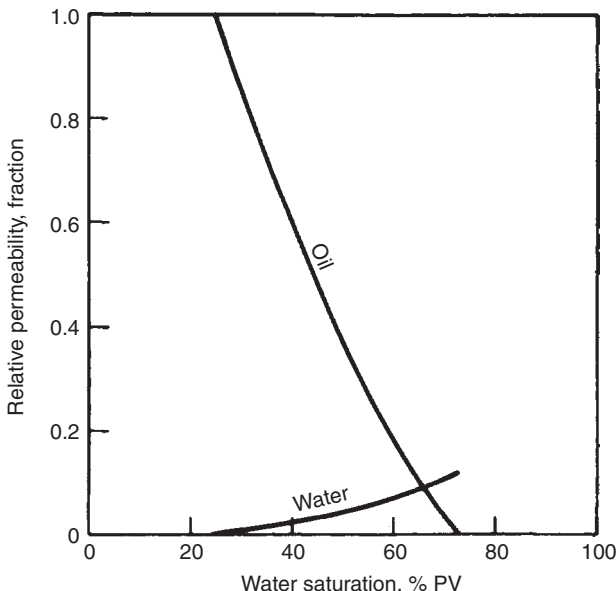


FIGURE 10.27 Schematic representation of typical relative permeability curves for water-wet porous samples (Craig, 1993).

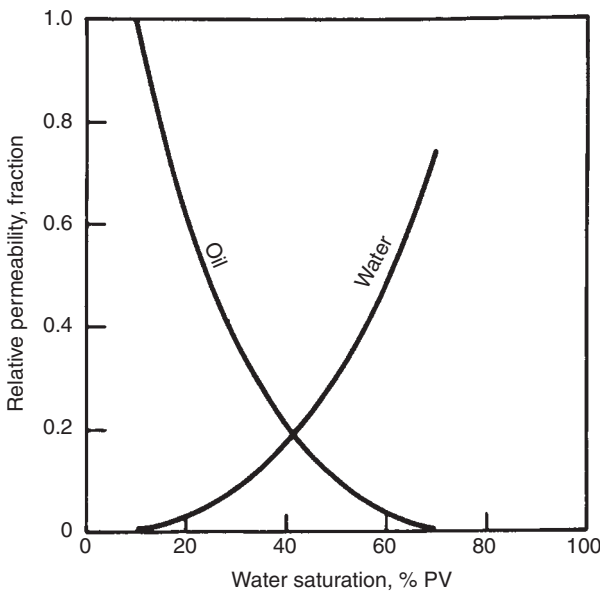


FIGURE 10.28 Schematic representation of typical relative permeability curves for oil-wet porous samples (Craig, 1993).

10.3.2.4 Effect of Interfacial Tension

In the range of interfacial tensions approximately greater than 1 mN/m, the interfacial tension has no effect on the conventional relative permeabilities. For very low interfacial tension systems, however, the networks of the two fluids begin to break up, first in the relatively large pores, and then, at even lower interfacial tensions, and also in the finer pores. Ultimately, an emulsion is formed in the entire pore network (Figure 10.25d) and, at that point, each fluid flows everywhere in proportion to its saturation in the sample. The relative permeability curves become straight diagonal lines for emulsion flows (Figure 10.29) (Bardon and Longeron, 1978).

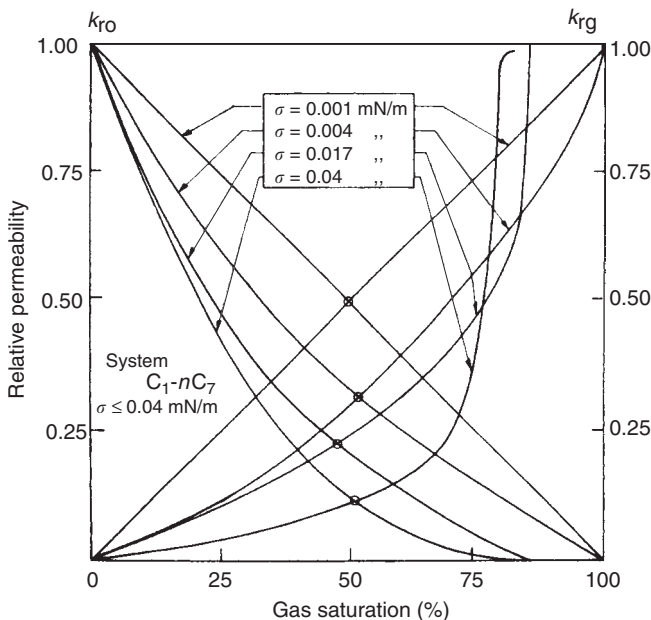


FIGURE 10.29 Gas-oil relative permeability of Fontainebleau sandstone for very low interfacial tensions of a methane-heptane system. (From Bardon, C. and Longeron, D., *Presented at the 53rd Annual Fall Technical Conference and Exhibition*, SPE of AIME, Houston, Texas, SPE 7609, 1978. With permission.)

10.3.2.5 Effect of Viscosity Ratio

The effect of the viscosity ratio of the two immiscible fluids on the relative permeabilities has been investigated extensively since the work by Leverett (1939). There are two different observations for the effect of viscosity ratio on the relative permeabilities.

One observation is that the relative permeability of a porous medium to a given phase in two-phase flow is dependent only on the saturation and independent of the properties of the fluids involved. This conclusion is supported by considerable experimental evidence (see, e.g., Leverett, 1939; Johnson et al., 1959; Donaldson et al., 1966). The explanation is that in cocurrent steady flow under certain conditions each fluid may flow in a separate network of pores and then the two streams do not influence each other (see Figure 10.25a).

The other observation is that in low permeability media at low water saturations, when the wetting phase is no longer continuous in the central part of the pores, the lower viscosity of the water may exert a "lubricating effect" on the oil flow under the conditions of steady-state relative permeability measurements. The essence of the lubricating effect is that, as a result of the presence of the lower viscosity fluid (water) near the pore walls, the oil flows at a higher rate than it would if oil occupied also the regions near the wall, instead of water. In such cases, using the oil viscosity in Eq. (10.53) gives anomalously high oil relative permeabilities. Under these conditions, the oil relative permeability shows an increasing trend with the oil-to-water viscosity ratio, as shown in Figure 10.30 and Figure 10.31 (Odeh, 1959; Danis and Jacquin, 1983). It can be easily understood that the water flowing on the pore walls in the form of thick films provides the oil with a moving boundary, as shown schematically in Figure 10.32b (Dullien, 1993). The probable reason for the strong dependence of this effect on the permeability of the medium is that the pores in low-permeability media are finer than in high-permeability ones, whereas the thickness of the thick films of water is not necessarily less in the low-permeability media. Therefore, in low-permeability media the position of the moving boundary, expressed as a fraction of the pore "radius," is farther away from the pore walls than in high-permeability media, and this results in a greater lubricating effect. This physical picture also explains why the water relative permeability has never been found to vary with

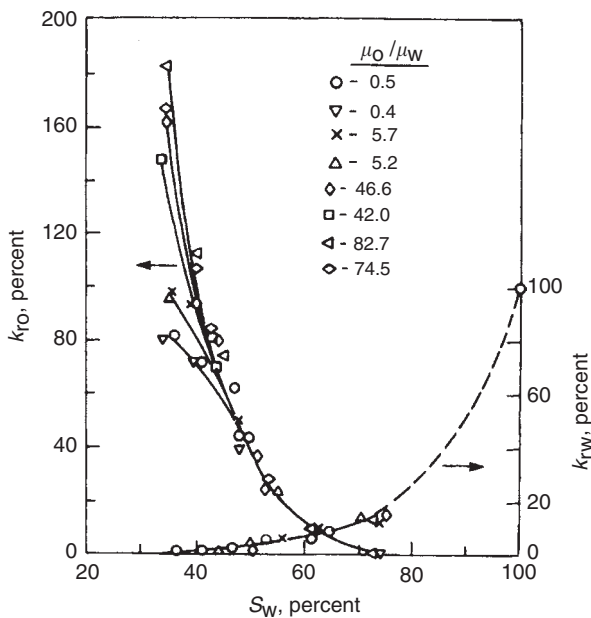


FIGURE 10.30 Measured relative permeability curves in a low permeability sandstone core showing the enhanced oil relative permeabilities at low water saturations at different oil-to-water viscosity ratios. (From Odeh, A.S., *Pet. Trans. AIME*, 216, 346, 1959. With permission.)

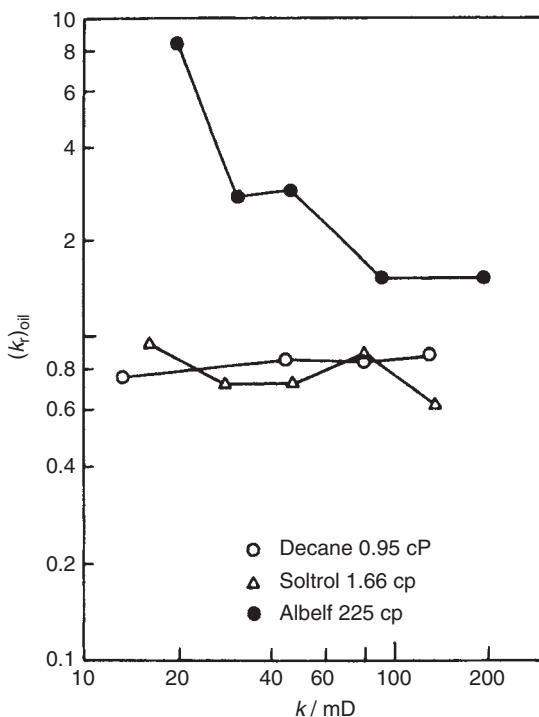


FIGURE 10.31 Relative permeabilities of oil in Rouffach limestone cores at connate water saturation. (From Danis, M. and Jacquin, C., *Rev. d'IFP*, 38, 1983. With permission.)

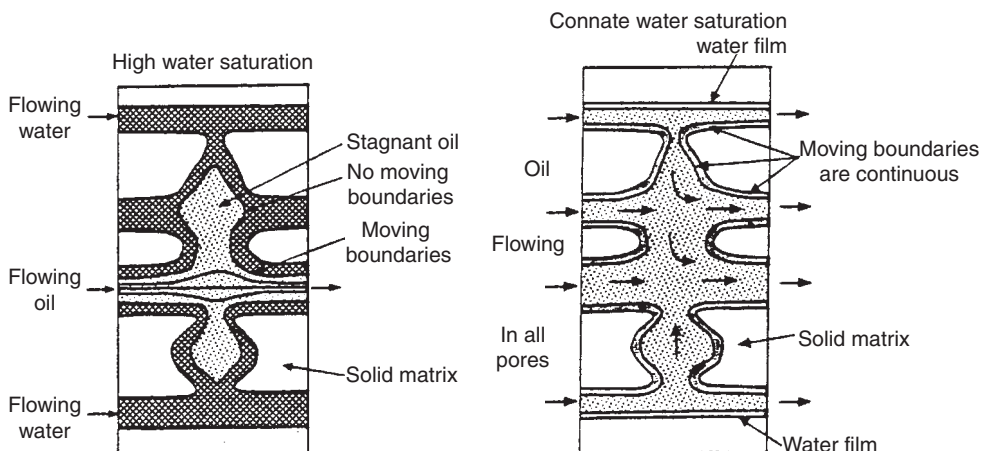


FIGURE 10.32 Schematic of pore level distribution of oil and water in porous media at high and low water (wetting phase) saturations. (From Dullien, F.A.L., *Proceedings of American Geophysical Union 13th Annual Hydrology Days*, Fort Collins, Colorado, Hydrology Days Publication, Atherton, CA, 1993, pp. 363–377. With Permission.)

the viscosity ratio. The probable explanation of the absence of a lubricating effect at higher water saturations, as illustrated in 10.32a, is that the moving boundary of flowing oil is interrupted at frequent intervals at such points in the pore network where there is a nonflow (dendritic) branch of oil.

10.3.3 Fractional and Mixed Wettability

Laboratory investigations have shown that the oil wettability of some natural reservoir porous samples is due to the adsorption of polar compounds present in crude oil (see, e.g., Benner and Bartell, 1941; Leach, 1957). There have also been instances where porous samples were mixed wet, i.e., certain parts of the pore surfaces were oil-wet and the rest were water-wet. If both types of pore surfaces form a continuum, the two fluids may flow side by side in the same pore as depicted in Figure 10.25c. Figure 10.33 shows the measured relative permeability curves in Berea sandstone core artificially aged with crude oil. This mixed-wet core showed unusually high permeabilities to water at low water saturations and the permeability to oil becomes zero at water saturations lower than 50%. It should be pointed out that the distribution of the two types of the pore surface may vary from case-to-case resulting in different relative permeability curves.

10.3.4 Resistivity Index and Archie's Law

If a porous medium contains both an electrically conducting wetting phase (water) and nonconducting fluids (oil and gas), its resistivity is a function of water (brine) saturation S_w . For the same porosity, the effective resistivity R_e of the porous medium is larger than the resistivity R_o of the sample 100% saturated with the same brine because the nonconducting fluids block some pores to the current. The ratio R_e/R_o is called “resistivity index” I at the saturation S_w , i.e.,

$$I = \frac{R_e}{R_o} \quad (10.56)$$

or

$$I = \frac{R_e/R_w}{R_o/R_w} = \frac{F_e}{F} \quad (10.57)$$

where F is the formation factor of a porous medium (see Eq. [10.6]) and F_e is the effective formation factor of the porous medium at partial water saturation.

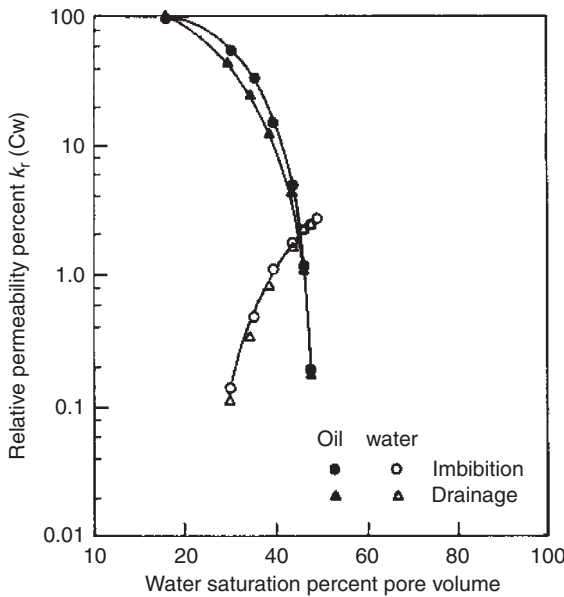


FIGURE 10.33 Relative permeability curves of Berea sandstone core aged with crude oil (From Braun, E.M. and Blackwell, R.J., *Proceedings of the 56th Annual Fall Technical Conference and Exhibition of the Society of the Petroleum Engineers of AIME*, San Antonio, Texas, 5–7, 1981. With permission.)

It has been shown experimentally (see, e.g., Archie, 1942; Wyllie and Spangler, 1952) that for a homogeneous porous medium, the resistivity index varies with S_w as

$$I = S_w^{-n} \quad (10.58)$$

where the exponent n is independent of the saturation S . Equation [10.58] is often referred to as the “Archie’s law.” For a particular porous medium, a plot of resistivity index I vs. the water saturation S_w on logarithmic scales gives a straight line of slope $-n$. However, the values of n are affected by the wettability of the sample, the overburden pressure, the microscopic distribution of the fluids, and the types and amounts of conductive clays (Tiab and Donaldson, 1999). Figure 10.34 shows the $I-S_w$ relationships for a number of both natural and synthetic, consolidated as well as unconsolidated porous media.

10.4 Immiscible Displacement

10.4.1 Equations of Unsteady State Two-Phase Flow

For one-dimensional displacement in a porous sample of constant cross-sectional area A , the equations for incompressible and horizontal flow of a wetting and a nonwetting phase are, respectively,

$$q_w = \frac{k_{rw} kA}{\mu_w} \frac{\partial P_w}{\partial x} \quad (10.59)$$

and

$$q_{nw} = \frac{k_{nrw} kA}{\mu_{nw}} \frac{\partial P_{nw}}{\partial x} \quad (10.60)$$

The total flow q_t is the sum of both flows, i.e.,

$$q_t = q_w + q_{nw} \quad (10.61)$$

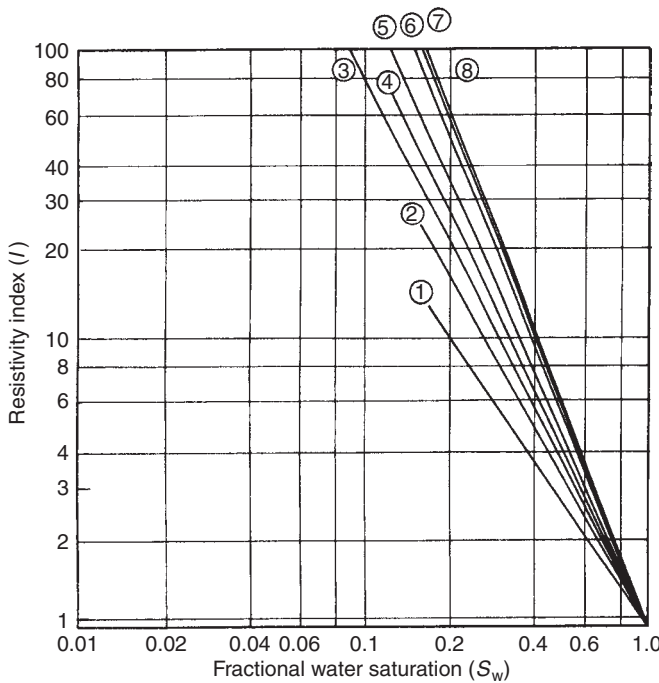


FIGURE 10.34 Measured relationships between resistivity index and saturation : (1) Pennsylvanian sandstone; (2) Berea sandstone; (3, 4) Unconsolidated sand; (5) Tuscaloosa sandstone; (6) Corning Pyrex; (7) Alundum; and (8) Corning Pyrex. From Wyllie, M.R.J. and Spangler, M.B., *Bulletin of the American Association of Petroleum Geologists*, 36, 359, 1952. With permission.)

From the definition of capillary pressure it follows that

$$\frac{\partial P_C}{\partial x} = \frac{\partial P_{nw}}{\partial x} - \frac{\partial P_w}{\partial x} \quad (10.62)$$

The fractional flow of the wetting phase at any point in the sample is (Leverett, 1941)

$$\frac{q_w}{q_t} \equiv f_w = \frac{1 + (k_{rw} kA / q_t \mu_{nw}) (\partial P_C / \partial x)}{1 + k_{rw} \mu_w / k_{tw} \mu_{nw}} \quad (10.63)$$

Material balance over an infinitesimal element of the system in the direction of unidirectional macroscopic flow gives (Buckley and Leverett, 1942)

$$\left(\frac{\partial S_w}{\partial t} \right)_x = - \frac{q_t}{\phi A} \left(\frac{\partial f_w}{\partial x} \right)_t \quad (10.64)$$

Buckley and Leverett transformed Eq. (10.64) to the following equation:

$$\left(\frac{\partial x}{\partial t} \right)_{Sw} = \frac{q_t}{\phi A} \left(\frac{\partial f_w}{\partial S_w} \right)_t \quad (10.65)$$

which states that at a constant displacement rate q_t , the rate of advance of a plane of fixed saturation S_w is proportional to the rate of change in the composition of the flow stream with saturation at that moment.

Displacements of one fluid by another in porous media can be analyzed by solving Eqs. (10.63) and (10.65). To do this, one needs to have the porosity and permeability of the porous medium, the fluid viscosities, the relative permeability curves, and the capillary pressure curve for the fluids–porous medium system.

Buckley and Leverett (1942) gave a simplified solution of Eqs. (10.63) and (10.65) by neglecting the term containing $\partial P_C / \partial x$ in (Eq. 10.63). Their solution gave multiple-valued water saturations for the same value of x , which was realized by them to be physically impossible. In order to make their solution useful, they used the law of conservation of mass to truncate the peak of their S_w vs. x curve, resulting in a saturation discontinuity at the front of the saturation profile. This procedure, known as the Buckley–Leverett (B–L) frontal displacement theory, has gained popularity in the petroleum industry. A large number of papers have been published, attempting to justify the B–L theory on mathematical grounds. This field has been reviewed by Morel–Seytoux (1969).

Dullien and Dong (2002) have reexamined the B–L frontal displacement theory. They have demonstrated by numerical simulations that the physically possible result of the multiple-valued saturation profiles is a direct consequence of neglecting the capillary pressure gradient in Eq. (10.63). For an assumed porous medium of a porosity of 0.35 and an absolute permeability of 1 darcy and an oil–water interfacial tension of 40 mN/m, a capillary pressure function, shown in Figure 10.35, and relative permeability curves, shown in Figure 10.36, were generated by using correlations available in the literature (Dong and Dullien, 1997). In Figure 10.37, saturation profiles calculated for six different times for steady water injection in an $L = 50$ m model are shown, where the water and oil viscosities are 1 and 3 cP, respectively. Selecting a particular saturation profile, the one corresponding to 58 days of water injection, the variation of $\partial S_w / \partial x$ with S_w was calculated and combined with the $\partial P_C / \partial S_w$ values derived from the capillary pressure curve to obtain $\partial P_C / \partial x$ vs. S_w . Then Eq.(10.63) was used to calculate f_w vs. S_w and from this, $\partial f_w / \partial S_w$ vs. S_w . The results are shown in Figure 10.38. If the term containing $\partial P_C / \partial x$ is neglected in Eq. (10.63), which is the common practice in reservoir engineering calculations, f_w and $\partial f_w / \partial S_w$ vs. S_w curves shown in Figure 10.39 are obtained, leading to the triple-valued saturation profile shown in Figure 10.40 instead of the saturation profile at 58 days of water injection shown in Figure 10.37.

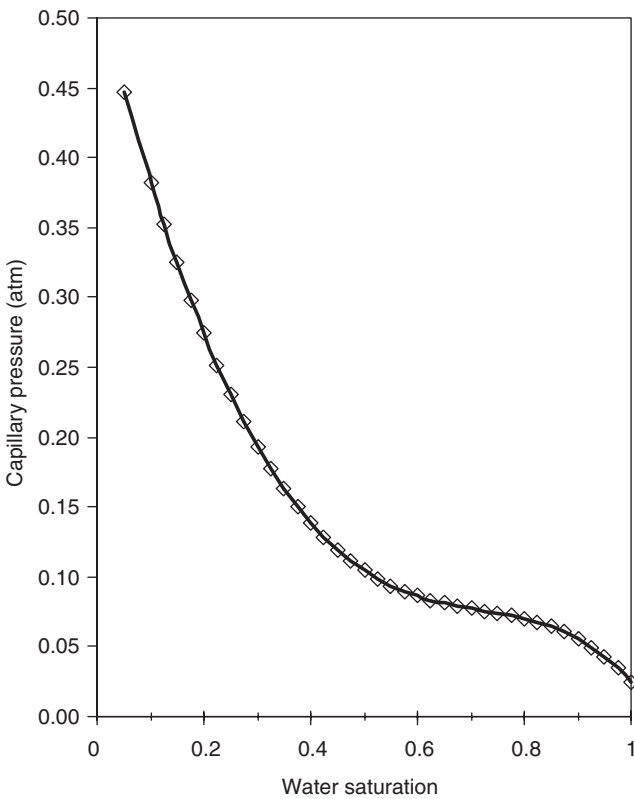


FIGURE 10.35 Capillary pressure–saturation curve used in the reexamination of the Buckley–Leverett frontal displacement theory.

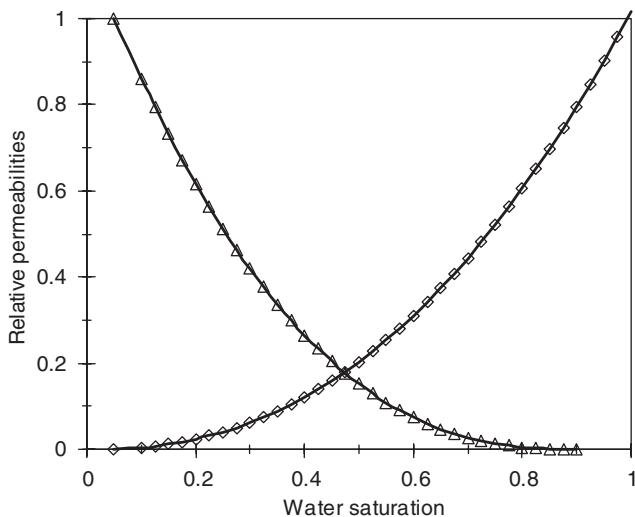


FIGURE 10.36 Relative permeability–saturation curves used in the reexamination of the Buckley–Leverett frontal displacement theory.

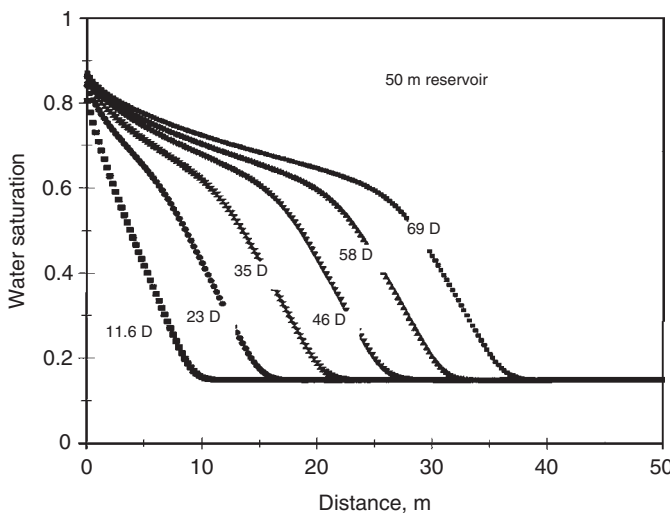


FIGURE 10.37 Simulated saturation profiles in a 50 m porous sample. (From Dullien, F.A.L. and Dong, M., *J. Porous Media*, 5, 1, 2002. With permission.)

The physical reason for obtaining the physically impossible three-valued saturation profiles is the inconsistency inherent in neglecting $\partial P_C / \partial x$ while using relative permeability curves typical of systems with important capillarity.

10.4.2 Cocurrent and Countercurrent Flows of Two Immiscible Fluids

10.4.2.1 Mathematical Model of Cocurrent Imbibition

A simple capillary model has been introduced by Dong et al. (1998), which incorporates with the physical properties of cocurrent imbibition in porous media. This model, illustrated in Figure 10.41a, consists of two parallel capillaries of radii R_1 and R_2 , respectively. It is assumed that there is equilibration of pressures between the two tubes at every distance x measured along the axes of the tubes, but there is no flow from

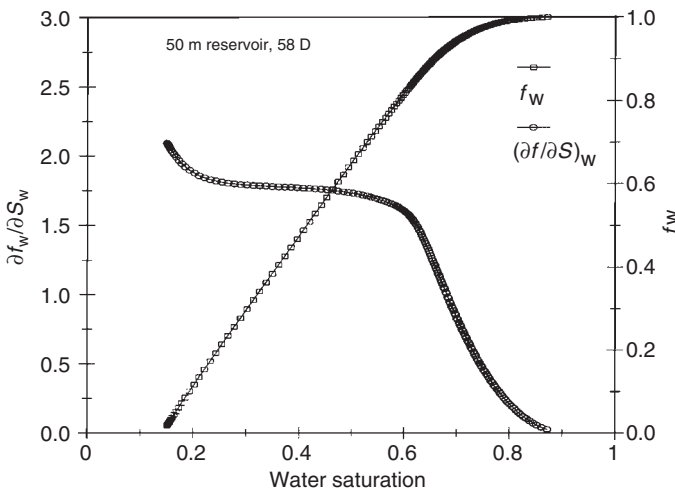


FIGURE 10.38 Complete fractional flow of water and its derivative with respect to water saturation vs. water saturation, calculated from a saturation profile of Figure 10.37. (From Dullien, F.A.L. and Dong, M., *J. Porous Media*, 5, 1, 2002. With permission.)

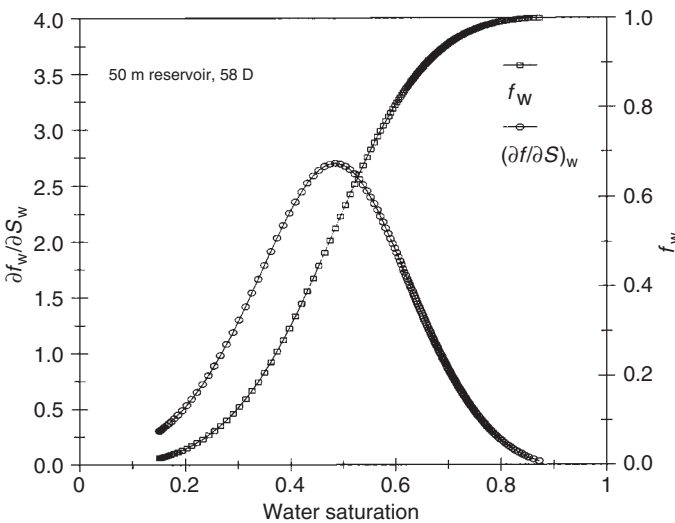


FIGURE 10.39 Fractional flow of water and its derivative with respect to water saturation after the capillary pressure term was neglected in Eq. (10.63) vs. water saturation. (From Dullien, F.A.L. and Dong, M., *J. Porous Media*, 5, 1, 2002. With permission.)

one tube into the other. Equilibration of pressures has the result that, in agreement with experiments using physical capillary models of porous media (Chatzis and Dullien, 1983), the water imbibes first into the narrow tube and also advances at a faster rate there than in the wide capillary. This is the opposite behavior to that predicted by the well-known Washburn equation where the rate of advance is faster in the wide capillary. The reason for this difference is that the Washburn equation applies to individual capillaries and does not consider any interaction between two or more parallel capillaries. In most porous media, however, the pores are interconnected and therefore there is pressure equilibration between adjacent pores.

The pressure profiles in the two capillary tubes of Figure 10.41a, for the case of free spontaneous imbibition of water where $\Delta P = 0$, are shown in Figure 10.41b. Applying the Hagen–Poiseuille equation

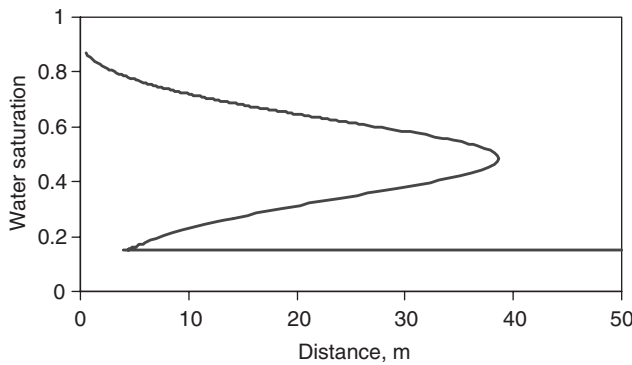


FIGURE 10.40 Calculated triple-valued saturation profile by using the water fractional flow function f_w and its derivative $\partial f_w / \partial S_w$ shown in Figure 10.39.

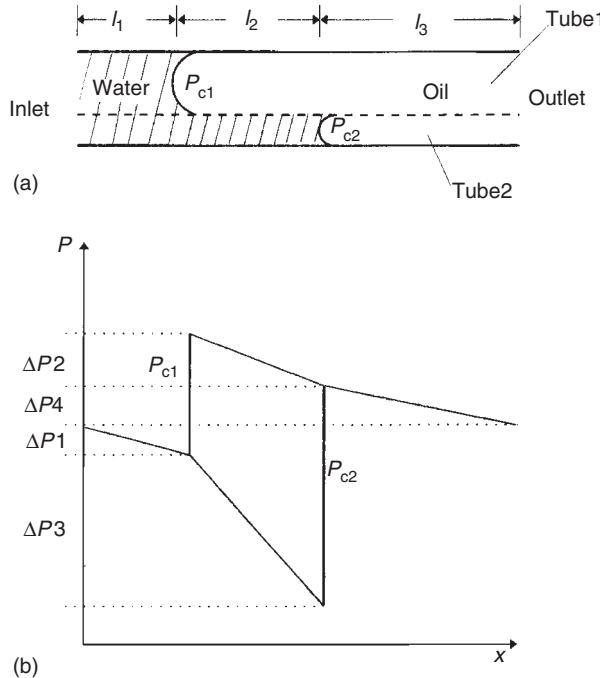


FIGURE 10.41 Free spontaneous imbibition in the capillary model: (a) schematic of the model; (b) pressure profiles in the model. (From Dong, M. et al., *Transport Porous Media*, 31, 213, 1998. With permission.)

to each section of the model yields the following equations for the flows q_1 and q_2 in capillaries 1 and 2, respectively:

$$q_1 = \frac{\lambda_2 q_t - \lambda_2 \lambda_3 (P_{C2} - P_{C1})}{\lambda_2 + \lambda_3} \quad (10.66)$$

and

$$q_2 = \frac{\lambda_3 q_t + \lambda_2 \lambda_3 (P_{C2} - P_{C1})}{\lambda_2 + \lambda_3} \quad (10.67)$$

For $q_t = q_1 + q_2$, it follows

$$q_t = \frac{\lambda_2 P_{C1} + \lambda_3 P_{C2}}{1 + (\lambda_2 + \lambda_3)(\lambda_1 + \lambda_4)/\lambda_1 \lambda_4} \quad (10.68)$$

where q_t is the free spontaneous imbibition rate measured at either end of the model at any point of time before the wetting phase reaches the production end. In Eqs. (10.66)–(10.68), $\lambda_1 = \pi(R_1^4 + R_2^4)/8\mu_w l$, $\lambda_2 = \pi R_1^4/8\mu_o l_2$, $\lambda_3 = \pi R_2^4/8\mu_w l_2$, and $\lambda_4 = \pi(R_1^4 + R_2^4)/8\mu_o l_3$. Substituting the expressions for the λ 's into Eq. (10.67), for the case of $\mu_w = \mu_o = \mu$, gives the following expression for free spontaneous imbibition rate:

$$q_t = \frac{\pi(R_1^4 P_{C1} + R_2^4 P_{C2})}{8\mu L} \quad (10.69)$$

Equation (10.69) shows that at any point of time before the wetting phase reaches the production end of the model, the free spontaneous imbibition rate is constant for the case of $\mu_w/\mu_o = 1$. Experiments with free spontaneous imbibition carried out in sandpacks have confirmed this prediction (see Figure 10.44) and the viability of the capillary model for cocurrent imbibition.

The capillary model of cocurrent imbibition has also been applied by Dong et al. (1998) to forced imbibition, i.e., a waterflood carried out at a constant pumping rate q_t , resulting in a pressure drop ΔP across the model. In this case the pressure profiles of Figure 10.41b become

$$\Delta P_1 + \Delta P_2 + \Delta P_4 = P_{C1} + \Delta P \quad (10.70)$$

and

$$\Delta P_1 + \Delta P_3 + \Delta P_4 = P_{C2} + \Delta P \quad (10.71)$$

Applying the Hagen–Poiseuille equation to q_1 and q_2 and solving Eqs. (10.70) and (10.71) give the following results:

$$q_1 = \frac{\lambda_2 q_t - \lambda_2 \lambda_3 \Delta P_C}{\lambda_2 + \lambda_3} \quad (10.72)$$

and

$$q_2 = \frac{\lambda_3 q_t + \lambda_2 \lambda_3 \Delta P_C}{\lambda_2 + \lambda_3} \quad (10.73)$$

where

$$\Delta P_C = P_{C2} - P_{C1} \quad (10.74)$$

Inspection of the two-phase flow region l_2 of Figure 10.41a shows that in this region $q_1 \equiv q_{nw}$ and $q_2 \equiv q_{ow}$. Introducing the following definitions for the permeability and the relative permeabilities of the simple capillary model,

$$k = \frac{R_1^4 + R_2^4}{8(R_1^2 + R_2^2)} \quad (10.75)$$

$$k_{r1} \equiv k_{nw} = \frac{R_1^4}{R_1^4 + R_2^4} \quad (10.76)$$

and

$$k_{r2} \equiv k_{ow} = \frac{R_2^4}{R_1^4 + R_2^4} \quad (10.77)$$

Equations (10.72) and (10.73), respectively, can be written as follows:

$$q_{nw} = \frac{\lambda_{nw} q_t - \lambda_{nw} \lambda_w \Delta P_C / l_2}{\lambda_w + \lambda_{nw}} \quad (10.78)$$

$$q_{ow} = \frac{\lambda_w q_t + \lambda_{nw} \lambda_w \Delta P_C / l_2}{\lambda_w + \lambda_{nw}} \quad (10.79)$$

where $\lambda_w \equiv kk_{rw}A/\mu_w$, $\lambda_{nw} \equiv kk_{rnw}A/\mu_o$, and $A = A_1 + A_2 = \pi(R_1^2 + R_2^2)$. By replacing $\Delta p_C/l_2$ with $\partial p_C/\partial x$ in Eq. (10.79) it can be readily shown that it is equivalent to Eq. (10.63).

10.4.2.2 Mathematical Model of Countercurrent Imbibition

Dong and Dullien (1997) studied countercurrent imbibition in thin horizontal sandpacks. The experiment was started by injecting water at a high rate at irreducible water saturation to create a step-function saturation profile in the sandpack as shown in Figure 10.42a. Then the system was closed by turning off the inlet and outlet valves. The saturation profile changed with time, as shown schematically in Figure 10.42b, as a result of countercurrent imbibition which was driven only by the gradient of the capillary pressure $\partial p_C/\partial x$.

Figure 10.43 illustrates the capillary model of countercurrent imbibition of Dong and Dullien (1997). The capillary pressure difference $\Delta P_C = \Delta P_{C2} - \Delta P_{C1}$ is equal to the sum of the viscous pressure drops, that is

$$\Delta P_C = \Delta P_w + \Delta P_o \quad (10.80)$$

The flow rates in the two capillaries are

$$q_w = \frac{k_a A_a}{\mu_w} \frac{\Delta P_w}{L} \quad (10.81)$$

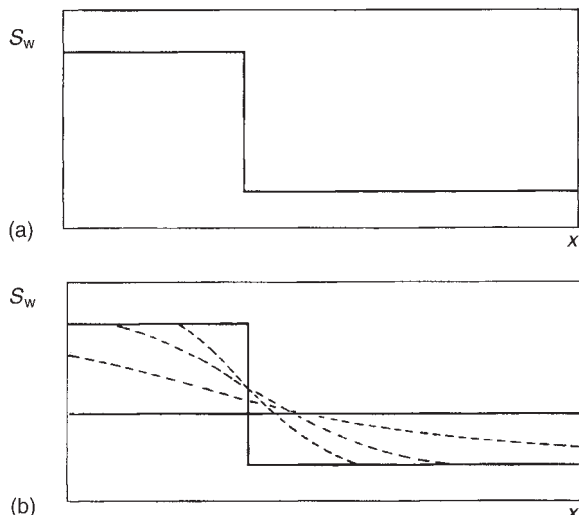


FIGURE 10.42 Schematic of saturation profiles during countercurrent imbibition in a porous medium: (a) step-function of displacement front; (b) change of saturation profile from a step function to uniform saturation. (From Dong, M. and Dullien, F.A.L., *Transport Porous Media*, 27, 185, 1997. With permission.)

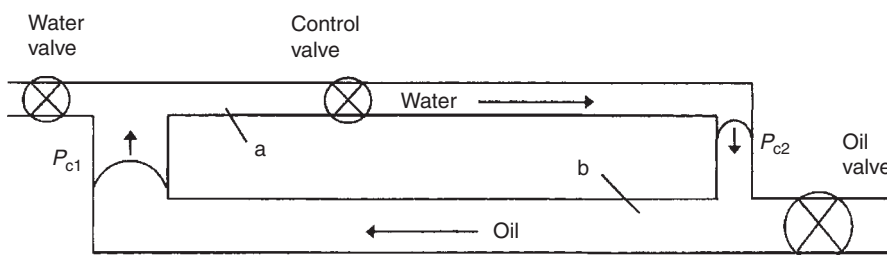


FIGURE 10.43 Capillary model of countercurrent flow. (From Dong, M. and Dullien, F.A.L., *Transport Porous Media*, 27, 185, 1997. With permission.)

and

$$q_o = \frac{k_b A_b}{\mu_o} \frac{\Delta P_o}{L} \quad (10.82)$$

where k_a and k_b are the permeabilities of tube a and tube b, respectively, L is the length of each tube, and A_a and A_b are the cross-sectional areas of tubes a and b, respectively. By combining Eqs. (10.80) to (10.82) one has

$$q_w = -q_o = \frac{\lambda_a \lambda_b}{\lambda_a + \lambda_b} \frac{\Delta P_C}{L} \quad (10.83)$$

where $\lambda_a = k_a A_a / \mu_w$ and $\lambda_b = k_b A_b / \mu_o$. For a porous medium Eq. (10.83) becomes

$$q_w = -q_o = \frac{\lambda_w \lambda_o}{\lambda_w + \lambda_o} \frac{\partial P_C}{\partial x} \quad (10.84)$$

with $\lambda_w = k k_{rw} A / \mu_w$ and $\lambda_o = k k_o A / \mu_o$, where k is the permeability and A the cross-sectional area of the sample, and k_{rw} and k_{ro} are the relative permeabilities of water and oil, respectively.

It has been pointed out by Dong and Dullien (1997) that, in a waterflood, pumping of water makes both the water and the oil flow in the forward direction, whereas the capillary pressure gradient, which is present due to a saturation gradient, produces, on the one hand, additional forward flow of water but, on the other, it also produces oil flow in the direction opposite to the water flow. Hence, the net flows of both water and oil may be regarded as superpositions of the flows due to pumping and the flows due to countercurrent imbibition, i.e.,

$$q_w = -\lambda_w \frac{\partial P}{\partial x} + \frac{\lambda_w \lambda_o}{\lambda_w + \lambda_o} \frac{\partial P_C}{\partial x} \quad (10.85)$$

and

$$q_o = -\lambda_o \frac{\partial P}{\partial x} - \frac{\lambda_w \lambda_o}{\lambda_w + \lambda_o} \frac{\partial P_C}{\partial x} \quad (10.86)$$

where $\partial P / \partial x$ is the pressure gradient associated with the pumping of water and oil, according to Darcy's law, at a rate q_t , which is equal to

$$q_t = q_w + q_o = -(\lambda_w + \lambda_o) \frac{\partial P}{\partial x} \quad (10.87)$$

By combining Eqs. (10.85)–(10.87) the expression of water-phase fractional flow f_w , i.e., Eq. (10.63) can be readily obtained.

The conclusion is that the flows of oil and water in immiscible displacement can be construed either as countercurrent imbibition on which there are superimposed flows of water and oil due to pumping water at a rate q_t , or as "forced" cocurrent imbibition due to a pressure difference ΔP imposed across the medium. The resulting expressions are identical in both cases.

10.4.3 Capillary and Viscous Effects in Two-Phase Flow in Porous Media

10.4.3.1 Complete Capillary Number CA

The distribution of two fluids in a displacement process in a porous medium depends on a number of factors, including the pore structure, the wettability of the porous sample, the interfacial tension σ , the fluid viscosities μ , and the pore velocity v_p . The case that has been of great interest corresponds to the conditions when one of the two fluids wets the pore surface preferentially, the interfacial tension is great, while viscosities and velocities are low. These parameters are often combined in the form of a dimensionless group called the capillary number Ca :

$$Ca = \frac{\mu |v_p|}{\sigma} \quad (10.88)$$

The absolute value of the pore velocity is used in order to make sure that Ca is equally applicable to imbibition and drainage. As the flow direction in drainage is opposite to the flow in imbibition, the

sign of v_p is negative in one of these processes. The capillary number lacks the length scale and the wettability of the system under study (Dullien, 1988, 1992). Imagine a two-phase displacement in a capillary as shown in Figure 10.8. The viscous force is proportional to the length scale L of the capillary. The capillary force is proportional to the radius of the capillary R and to $\cos \theta_A$, where θ_A is the advancing contact angle measured through water. Ca represents the ratio of viscous-to-capillary forces only if $L = R$ and $\cos \theta_A = 1$. As the condition $L = R$ usually does not apply, the numerical values of Ca only permit comparison between experiments or simulations on systems with the same values of L , R and θ_A .

The true value of the ratio of viscous to capillary forces in immiscible displacement in a circular capillary tube is readily obtained as follows (Dullien, 1992). The viscous force F_v is equal to the wall shear stress multiplied by the surface area of the tube (Bird et al., 1960), i.e.,

$$F_v = 8\pi\mu\bar{v}L \quad (10.89)$$

where \bar{v} is the average flow velocity. In Eq. (10.89), it is assumed that oil and water have the same viscosity $\mu_o = \mu_w = \mu$. The capillary force F_c is equal to the capillary pressure P_c times the cross-sectional area of the tube, i.e.,

$$F_c = 2\pi R\sigma \cos \theta \quad (10.90)$$

The ratio of viscous to capillary forces, defined as the complete capillary number CA (Dullien, 1992), is

$$CA \equiv \frac{F_v}{F_c} = \frac{4\mu\bar{v}L}{\sigma \cos \theta R} = \frac{4CaL}{\cos \theta R} \quad (10.91)$$

The following calculations illustrate the difference between the complete capillary number CA and the capillary number Ca . Consider the displacement experiment in Figure 10.8, where the pressure difference $\Delta P = P_A - P_B$ between the two ends of the capillary can be zero, positive or negative (A is the wetting fluid). The net driving force of the displacement is $\Delta P + P_c$ and the velocity of the interface dx/dt is given by the following form of the Poiseuille equation, also called the Washburn equation:

$$v \equiv \frac{dx}{dt} = \frac{R^2}{8} \frac{\Delta P + P_c}{\mu_A x + \mu_B (L - x)} \quad (10.92)$$

The values of CA and Ca presented in Table 10.2 are for $\sigma = 35$ mN/m, $\mu_o = \mu_w = 1.0$ cP, $\theta = 20^\circ$, $R = 0.05$ cm, and $L = 80$ cm. In this case, the capillary pressure is $P_c = 131.5$ Pa. In the domains $\Delta P > 0$ and $-P_c < \Delta P < 0$, there is imbibition. $\Delta P = -P_c$ corresponds to capillary equilibrium and no displacement occurs, and for $\Delta P < -P_c$ there is drainage. The special case $CA = 1$ ($\Delta P = 0$) corresponds to free spontaneous imbibition, driven by the capillary pressure P_c . The region of imbibition is $CA < 1$ ($-P_c < \Delta P < 0$) and the region of forced imbibition is $CA > 1$ ($\Delta P > 0$).

It is evident from these figures that Ca is not equal to the ratio of viscous-to-capillary forces, but for a given system (same fluids, same capillary) it deviates from CA only by a constant factor.

TABLE 10.2 Comparison of Complete Capillary Number CA and Capillary Number Ca for Characterizing Imbibition-Type Displacement Processes

v (cm/sec)	Ca	CA	ΔP (Pa)	Displacement Process	
0	0	0	-131.5	$\Delta P = -P_c$	No displacement
0.001	2.85×10^{-7}	1.94×10^{-3}	-131	$CA < 1$	
0.01	2.85×10^{-6}	1.94×10^{-2}	-129	$-P_c < \Delta P < 0$	Controlled imbibition
0.1	2.85×10^{-5}	1.94×10^{-1}	-106		
0.514	1.47×10^{-4}	1.0	0	$CA = 1, \Delta P = 0$	Free spontaneous imbibition
1	2.85×10^{-4}	1.94×10^0	125	$CA > 1$	
10	2.85×10^{-3}	1.94×10^1	2,429	$\Delta P > 0$	Forced imbibition
100	2.85×10^{-2}	1.94×10^2	25,469		

10.4.3.2 Analysis of Imbibition-Type Displacement in Porous Media in Terms of CA

In a displacement of one fluid by another in porous media, the variation of saturation profiles with time is of particular interest. It has been known for a long time (Rapoport and Leas, 1953) that the saturation profiles are functions of the “scaling coefficient” $Lv\mu_w$, the oil-to-water viscosity ratio, and the preferential wettability, i.e., whether the medium is “water-wet” or “oil-wet.”

It seems probable on physical grounds that, for statistically homogeneous media, a representation of displacement processes in porous media may be possible in terms of the two dimensionless groups, the ratio of viscous to capillary forces and the viscosity ratio. The saturation profile history in imbibition is evidently different from that in drainage. The saturation history data are available for the imbibition case only and for a viscosity ratio equal to 1 (Dong et al., 1998). A fluid pair of the same viscosity was used and the ratio of viscous to capillary forces was varied to ascertain its effect on the evolution of saturation profiles during an imbibition-type displacement. The ratio of viscous to capillary forces is represented by an expression formally identical to the one derived rigorously in the case of a circular capillary tube, i.e.,

$$CA = \frac{4\bar{\mu}v\bar{L}}{R_{eq}\sigma\cos\theta} \quad (10.93)$$

where \bar{v} is the mean pore velocity and R_{eq} is the equivalent pore size of the porous medium. The value of CA in a waterflood conducted at a constant pumping rate q_t of water in a sample of uniform cross-section A and of length L , with an oil–water system of viscosity ratio of 1, is obtained with reference to the initial rate of a free spontaneous imbibition q of water into an identical sample of the same porous medium–water–oil system. In the free spontaneous imbibition $\Delta P = 0$, and since under these conditions the viscous forces in the porous medium are equal to the capillary forces, therefore $CA = 1$. As also $q/q_t = v/v_o$ (v_o is the initial mean pore velocity in free spontaneous imbibition) and $4\mu L/R_{eq}\sigma\cos\theta$ is the same in every waterflood test, the value of CA for a waterflood with a constant injection rate q_t can be calculated by

$$CA = \frac{q_t}{q} \quad (10.94)$$

Imbibition-type displacements were analyzed and interpreted in terms of the complete capillary number CA by Dong et al. (1998).

In a free spontaneous imbibition experiment $CA = 1$ and, therefore, Eq. (10.93) becomes

$$\frac{R_{eq}\sigma\cos\theta}{4\mu} = v_o L = \frac{qL}{A\phi} \quad (10.95)$$

where A is the cross-section and ϕ the porosity of the sample.

In Eq. (10.95) every factor on the left-hand side is a constant for a given fluid pair and a given type of porous medium and, therefore, with A kept at the same value, the product of q and L is expected to be constant. A test of the validity of this relationship was carried out by performing free spontaneous imbibition experiments, using the same pair of fluids and two packs of the same sand (sand A) of $L_1 = 35$ cm and $L_2 = 50$ cm. The fluids used were Soltrol 100 oil and water and both had a viscosity of 1 cP. As apparent from Figure 10.44, the initial rate in the 35 cm model was 1.0 mL/min, whereas it was 0.72 mL/min in the 50 cm model. The product $1.0 \times 35 \approx 0.72 \times 50$ is constant.

Figure 10.45 shows the saturation profiles in three waterfloods with different values of q_t . A wide range values of CA , from $\ll 1$ to $\gg 1$, was covered. It has been found that for $CA \ll 1$, where the capillary forces dominate the process the saturation profile remained practically horizontal and kept rising uniformly throughout the sample. For $CA \gg 1$, where the viscous forces dominate the process, the saturation profile approached a step function. For intermediate values of CA the saturation profiles were S-shaped.

As illustrated in the example of Figure 10.46, the evolutions of saturation profiles in waterfloods carried out with the same type of sand packs (sand A) of lengths L_1 and L_2 were found to be identical, within experimental error, at the same value of CA if plotted against a normalized distance coordinate. Similar to the case of free spontaneous imbibition, the condition of the same saturation profile history, i.e., $CA_1 = CA_2$, can also be expressed as $q_{t1}L_1 = q_{t2}L_2$ provided that the two waterfloods are carried out in samples of the same uniform cross-sectional area.

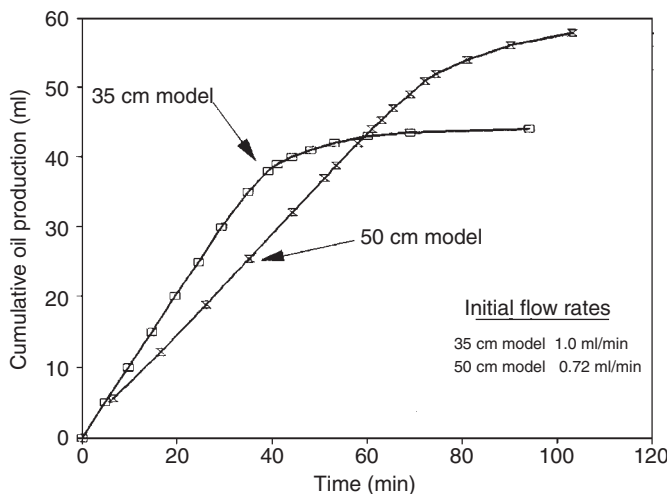


FIGURE 10.44 Free spontaneous imbibition rates in packs of the same sand with different lengths. (From Dong, M. et al., *Transport Porous Media*, 31, 213, 1998. With permission.)

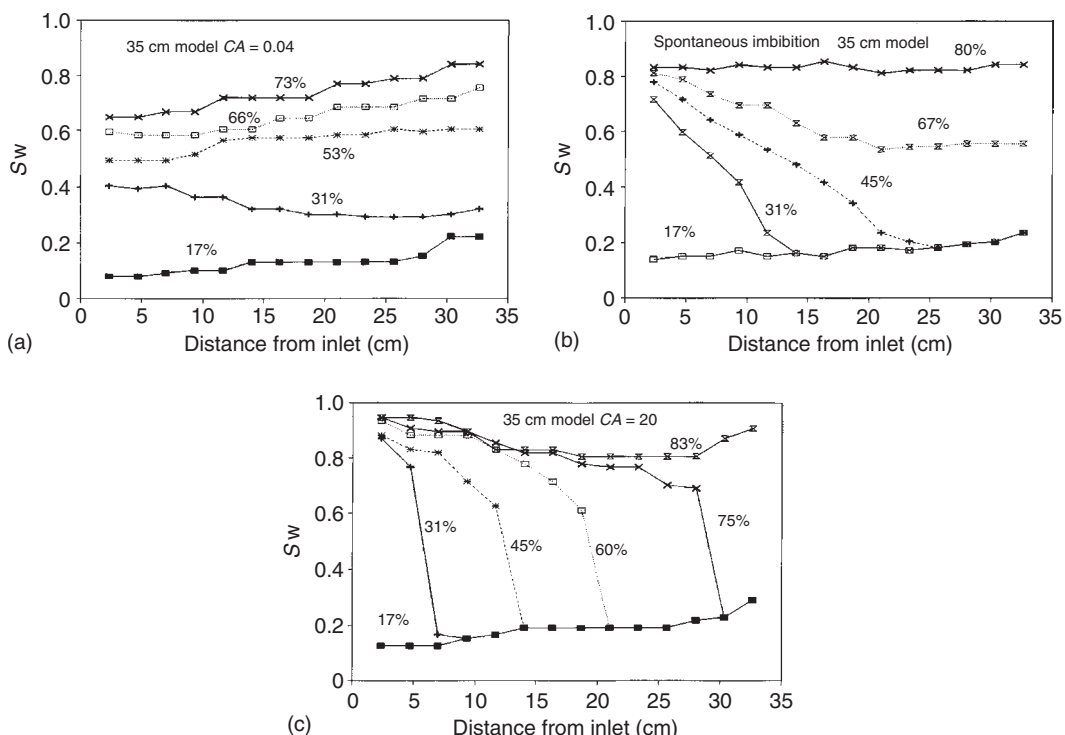


FIGURE 10.45 Saturation profile histories in a sandpack of 35 cm length at: (a) $CA = 0.04$; (b) $CA = 1$; and (c) $CA = 20$. (From Dong, M. et al., *Transport Porous Media*, 31, 213, 1998. With permission.)

It was also found by Dong et al. (1998), that saturation profile histories in waterfloods at 1:1 viscosity ratio in sand B, of about 1/10 of the permeability of sand A, could be matched with the saturation profile histories measured in sand A. The matching occurred not at the same value of CA in the two different sands but for $CA(B) \approx 4CA(A)$, $CA(B)$ and $CA(A)$ being the values of CA for the waterfloods in sand B and sand A, respectively, as illustrated in the example shown in Figure 10.47. This result is a consequence

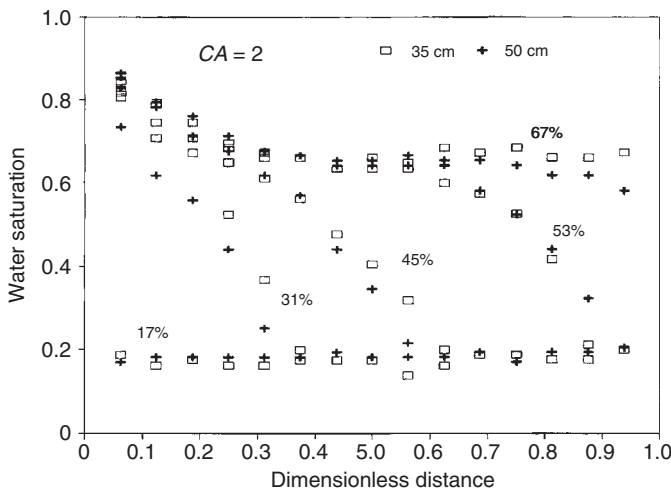


FIGURE 10.46 Normalized saturation profile histories of waterfloods in packs of sand A of two different lengths. (From Dong, M. et al., *Transport Porous Media*, 31, 213, 1998. With permission.)

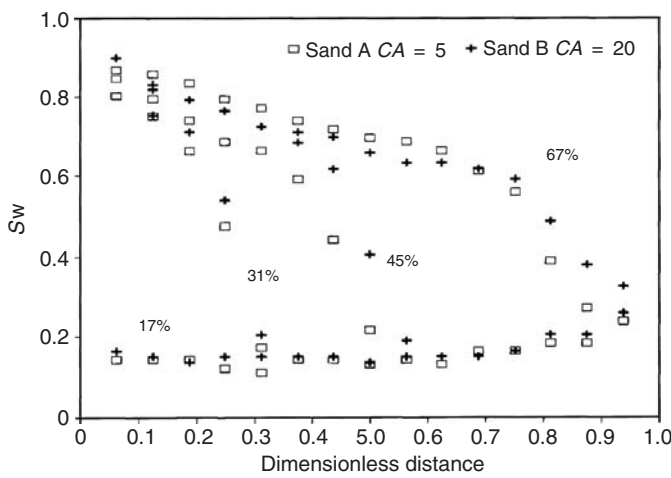


FIGURE 10.47 Matching of saturation profile histories of packs of sand A and B with $CA(A) = 5$ and $CA(B) = 20$. (From Dong, M. et al., *Transport Porous Media*, 31, 213, 1998. With permission.)

of different pore structures of the two sands. It is interesting to note that matching occurred at a ratio of about 4 of the two sets of values of CA which is, for the purpose of such a comparison, approximately same as the square root of the ratio of the two permeabilities, i.e., 3.2.

10.4.4 Drainage-Type Displacement Front Versus Capillary Number and Viscosity Ratio

The evolution of saturation profiles in drainage as a function of CA has not yet been studied. On the other hand, an extensive study of drainage-type displacement in a 2D network model was done by Lenormand et al. (1988). They simulated the displacement patterns as a function of $Ca = \mu v / \sigma$ and the viscosity ratio $\kappa = \mu_2 / \mu_1$ ($2 =$ displacing fluid), also including unfavorable viscosity ratios ($\kappa < 1$). Their simulation results are shown in Figure 10.48. It is evident that for unfavorable viscosity ratios and values of Ca

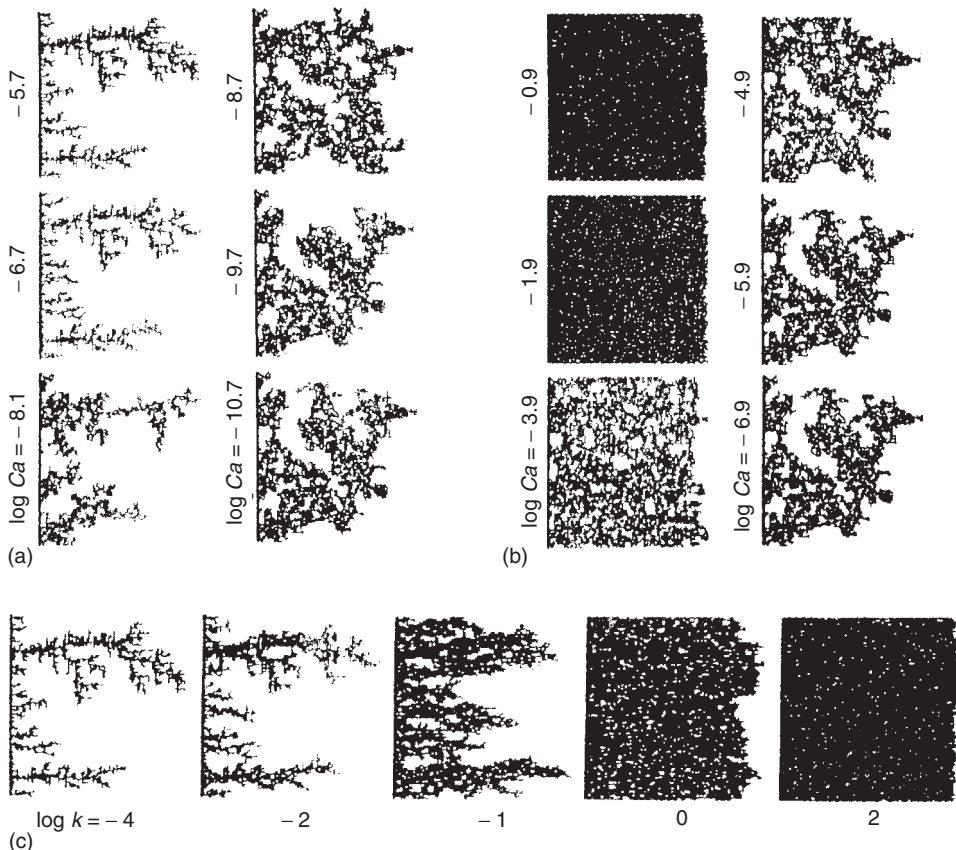


FIGURE 10.48 Network (100×100) simulations of drainage-type displacement at various viscosity ratios κ and capillary numbers Ca : (a) $\log \kappa = -4.7$ (from viscous to capillary fingering); (b) $\log \kappa = 1.0$ (from stable displacement to capillary fingering) and (c) $\log Ca = 0$ (from viscous fingering to stable displacement). (From Lenormand, R. et al., *J. Fluid Mech.*, 189, 165, 1988. With permission.)

corresponding to $CA \gg 1$, i.e., viscous forces controlling, there is viscous fingering, whereas for values of Ca corresponding to $CA \ll 1$, i.e., capillary forces controlling, there is “capillary fingering.” For favorable viscosity ratios, the saturation profile is a step function when viscous forces control, whereas when capillary forces control there is capillary fingering. Displacement experiments, carried out in etched capillary micromodels with the fluid pairs consisting of air–viscous oil, mercury–hexane, mercury–air and glucose solution–oil, yielded results that were in good qualitative agreement with the simulations. Inspection of Figure 10.48 shows that the values of Ca do not represent the true ratio of viscous-to-capillary forces, however, as all the simulations were carried out in the same network model all the values of Ca differ from the corresponding values of CA only by a proportionality factor. Therefore, the values of Ca in Figure 10.48 may be viewed as relative values of the ratio of viscous-to-capillary forces.

10.4.5 Coupling of Two-Phase Flows

In the generalized form of Darcy’s equation for multiphase flow (see Eq. [10.53]), the flows as well as the pressure gradients of the two immiscible fluids present in the porous medium have been assumed to be independent of each other. Many researchers (e.g., Rose, 1972; deGennes, 1983; de la Cruz and Spanos, 1983) have proposed that there exists viscous coupling between the flows of two immiscible fluids, i.e., the flow of either fluid is affected by the pressure gradient and the viscosity of the other

fluid. For the case of one-dimensional flow, one form of the coupled equations that has been proposed is

$$\nu_1 = -\frac{k_{11}}{\mu_1} \frac{dP_1}{dx} - \frac{k_{12}}{\mu_2} \frac{dP_2}{dx} \quad (10.96)$$

$$\nu_2 = -\frac{k_{21}}{\mu_1} \frac{dP_1}{dx} - \frac{k_{22}}{\mu_2} \frac{dP_2}{dx} \quad (10.97)$$

In this formulation of two-phase flow there are four transport coefficients, i.e., k_{11} , k_{12} , k_{21} , and k_{22} . The two diagonal coefficients k_{11} and k_{22} establish the relationship between the flow rate and the pressure gradient in, say, phase 1 that would exist if the other phase 2 were a solid. The two cross-coefficients k_{12} and k_{21} represent the viscous coupling between the two fluids. If two fluids flow side-by-side, the velocity of fluid 1, for example, is assumed to be affected also by the pressure gradient and the viscosity of fluid 2.

In steady cocurrent flow, where both fluids are pumped through the porous sample at constant rates, nearly uniform saturation was found experimentally. As the capillary pressure is approximately the same along the sample, the pressure gradients of the two fluids are approximately uniform and equal. However, in a two-phase immiscible displacement process, a saturation gradient and a capillary pressure gradient exist. The problem at hand is whether or not the flows of the two fluids are predicted correctly by Eq. (10.53) if the appropriately measured (i.e., known) pressure gradients and viscosities of the two fluids are substituted, using effective permeabilities that are assumed to be independent of the pressure gradients and the viscosities.

Experimental determination of the four effective permeability coefficients k_{11} , k_{12} , k_{21} , and k_{22} in Eqs. (10.96) and (10.97) has presented some problems. To determine the effect on the flow of fluid 1, the contribution to the value of ν_1 resulting from dP_2/dx must be measured. As defined in Eq. (10.62), the pressure gradients of the two fluids cannot be either specified or varied independently. In general, according to Eq. (10.62), imposing a pressure gradient dP_2/dx on fluid 2 results in a pressure gradient of dP_1/dx also in fluid 1. Therefore, the value of ν_1 measured in the experiment is influenced from the pressure gradients in both fluids. Unless dP_1/dx is equal to zero, the effect of viscous coupling, presented by the term $(k_{12}/\mu_2)(dP_2/dx)$, cannot be quantified. Inspection of the coupling Eqs. (10.96) and (10.97) shows that if the conditions $dP_1/dx = 0$ and $dP_2/dx \neq 0$ can be imposed experimentally, it follows from Eqs. (10.96) and (10.97) that

$$\nu_1 = -\frac{k_{12}}{\mu_2} \frac{dP_2}{dx} \quad (10.98)$$

and

$$\nu_2 = -\frac{k_{22}}{\mu_2} \frac{dP_2}{dx} \quad (10.99)$$

The coefficients k_{12} and k_{22} can be estimated by measuring ν_1 , ν_2 and dP_2/dx . Similarly, the coefficients k_{11} and k_{21} can be determined experimentally by setting the conditions $dP_2/dx = 0$ and $dP_1/dx \neq 0$ and measuring ν_1 , ν_2 and dP_1/dx . From Eqs. (10.96) and (10.97) it follows that

$$\nu_1 = -\frac{k_{11}}{\mu_1} \frac{dP_1}{dx} \quad (10.100)$$

and

$$\nu_2 = -\frac{k_{21}}{\mu_1} \frac{dP_1}{dx} \quad (10.101)$$

and k_{11} and k_{21} can be calculated.

The above-proposed experimental conditions have been realized in a horizontal sandpack, using Soltrol 100 oil of 1 cP viscosity and water of the same viscosity (Dullien and Dong, 1996). The experimental setup is shown in Figure (10.49). For the tests of $dP_1/dx = 0$, first the conventional steady-state conditions were established, corresponding to some saturation of the pack. Then both the inlet and the outlet of water were shut in; for example in determining k_{12} and k_{22} , oil was pumped at a constant rate until the water pressure gradient became zero in the entire pack. Simultaneously, a saturation and capillary pressure gradient was built up in the sandpack. At this point the water inlet and outlet were opened, and as a result of viscous coupling water was sucked into the pack from a reservoir and produced into another reservoir via a discharge tube, while steps were taken to ensure that the zero pressure gradient in the water in the sandpack was maintained. The pressures in each phase were measured using eight piezometers (not shown in Figure 10.49).

The experiments consisted of two sets. In one set, the pressure gradient of water was zero, while the oil was pumped at a constant rate. This set of experiments was carried out at six different average water saturations. The water flow rate, induced by viscous coupling with oil, was kept constant and was measured. The oil-to-water flow rate ratio varied from 1.7 to 150, depending on the average water saturation in the sandpack. In the other set of experiments, the pressure gradient of oil was kept zero, while the water was pumped at a constant rate. Four experiments were carried out at different water saturations. The oil flow rate, induced by viscous coupling with water, was kept constant and was measured. The water-to-oil flow rate ratio varied from 6.8 to 16, depending on the average water saturation of the sandpack. The typical pressure profiles for tests of $dP_1/dx = 0$ and of $dP_2/dx = 0$ are shown in Figure 10.50. The values of the four effective permeability coefficients are plotted vs. the average saturations in the sandpack in Figure 10.51 along with the Darcy's law effective permeabilities. It is evident that the coupling coefficients measured in this work are significant and also that $\langle k_{12} \rangle \neq \langle k_{21} \rangle$. The latter effect can be explained by different distributions of the two fluids at the same saturation in the two experiments leading to the determination of the two coupling coefficients (Lasseux et al., 1996).

Several researchers combined the steady cocurrent and countercurrent tests (see Figure 10.52) to estimate the coupling coefficients (see, e.g., Kalaydjian, 1990; Bentsen and Manai, 1991, 1993). It was

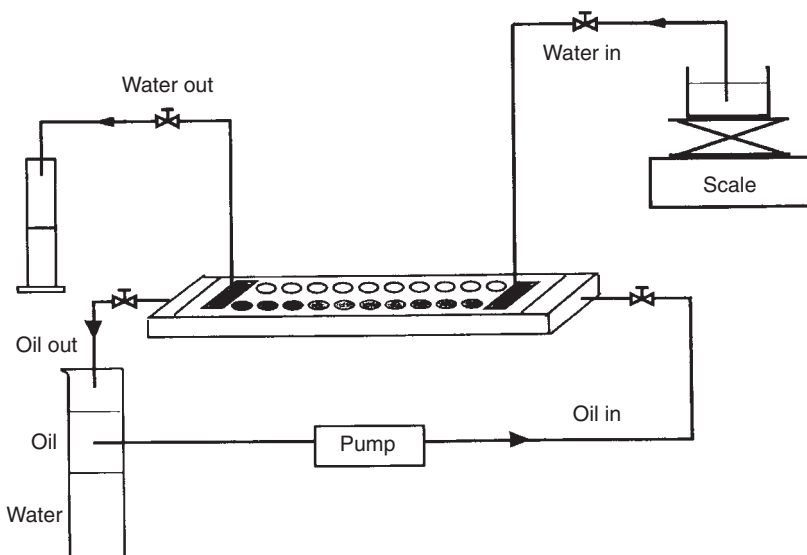


FIGURE 10.49 Experimental setup for measuring viscous coupling. (From Dullien, F.A.L. and Dong, M., *Transport Porous Media*, 25, 97, 1996. With permission.)

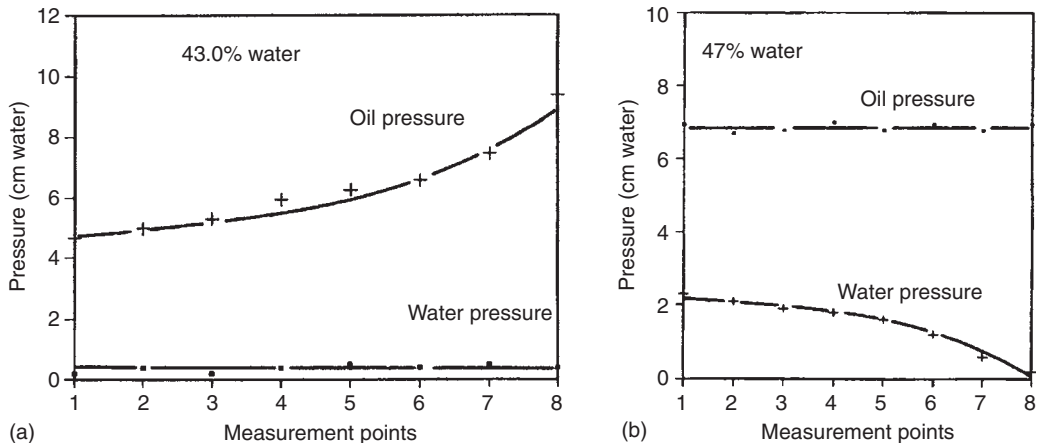


FIGURE 10.50 Steady-state pressure profiles in the viscous coupling measurements; (a) zero pressure gradient in water phase; (b) zero pressure gradient in oil phase.

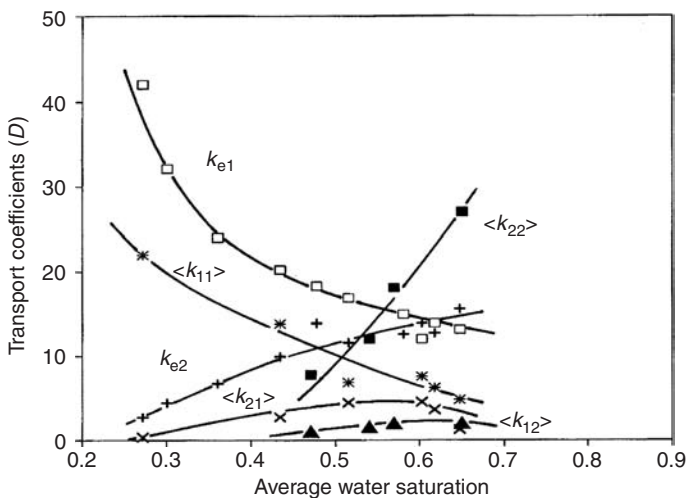


FIGURE 10.51 Measured effective permeability coefficients $\langle k_{11} \rangle$, $\langle k_{12} \rangle$, $\langle k_{21} \rangle$, and $\langle k_{22} \rangle$ vs. average water saturation (From Dullien, F.A.L. and Dong, M., *Transport Porous Media*, 25, 97, 1996. With permission.)

found that the coupling terms are nonnegligible. However, this method needs to couple with complex analysis of the relationships between the standard formulation of two-phase flow and coupling formulation. Zarcone and Lenormand (1994) published the experimental results obtained on viscous coupling between mercury and water in a sandpack, with mercury the driving fluid and water the driven fluid. The induced water flow rate at all the saturations tested was less than 1% of the mercury flow. These authors assumed that the water pressure could be rendered uniform everywhere in their model by connecting the point of water entry into the model with the point of water exit from the model by a tube. A critical discussion of this work and that by Rakotomalala et al. (1995) is presented by Dullien and Dong (1996). Very recently, a review on the viscous coupling has been presented by Ayub and Bentzen (1999).

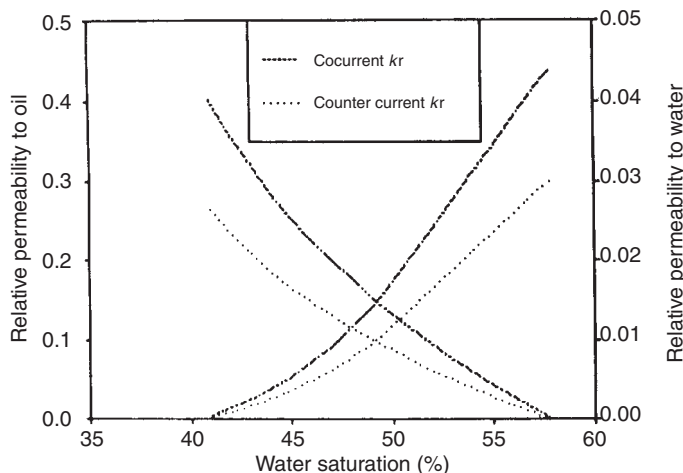


FIGURE 10.52 Measured relative permeability curves in cocurrent and countercurrent flow in natural porous media. (From Kalaydjian, F., *Transport Porous Media*, 5, 215, 1990. With permission.)

Nomenclature

Latin

A	Area
Ca	Capillary number
CA	Complete Capillary number
d_p	Surface area particle diameter
D	Pore size
D_h	Hydraulic diameter
f_p	Friction factor
F	Formation factor
h_c	Capillary pressure head
I	Resistivity index
k'	Kozeny constant
k_H	Hydraulic conductivity
k_i	Relative permeability
k_o	Shape factor
k	Permeability
L	Length
m	Cementation index
M	Molecular weight
p	modified or piezometric pressure
P	Pressure
P_C	Capillary pressure
P_d	Displacement pressure
Q	Volumetric flow rate
q_i	Volumetric flow rate of component "i"
R	Radius, resistance
Re_p	Particle Reynolds number
S	Specific surface, saturation, spreading coefficient

S_v	Specific area based on bulk volume
S_o	Specific area based on solid volume
t	Time
v	Velocity
x	Distance

Greek Letters

κ	Viscosity ratio
θ	Contact angle
μ	Viscosity
ρ	Density
σ	Surface tension
ϕ	Porosity, modified pressure

Subscripts

b	Bulk
e	Effective
f	Fluid
gw	Gas–water
go	Gas–oil
nw	Non-wetting
o	Oil
ow	Oil–water
p	Pore
w	Wetting phase, water

Reference

- Adamson, A.W., *Physical Chemistry of Surfaces*, 5th ed., Wiley, New York, 1990.
- Archie, G.E., The electrical resistivity log as an aid in determining some reservoir characteristics, *Trans. AIME*, 146, 54, 1942.
- Ayub, M. and Bentsen, R.G., Interfacial viscous coupling: a myth or reality? *J. Petroleum Sci. Eng.*, 23, 13, 1999.
- Bardon, C. and Longeran, D., Influence of very low interfacial tensions on relative permeability, presented at the 53rd Annual Fall Technical Conference and Exhibition, SPE of AIME, Houston, Texas, SPE 7609; 1978.
- Benner, F.C. and Bartell, F.E., The effect of polar impurities upon capillary and surface phenomena in petroleum production, *Drill. Prod. Prac.*, API, 1941.
- Bensten, R.G. and Manai, A.A., Measurement of cocurrent and countercurrent relative permeability curves using the steady-state method, *AOSTRA J. Res.*, 7, 169, 1991.
- Bensten, R.G. and Manai, A.A., On the use of conventional cocurrent and countercurrent effective permeabilities to estimate the four generalized permeability coefficients which arise in coupled, two-phase flow, *Transport Porous Media*, 11, 243, 1993.
- Bird, R.B., Stewart, W.E., and Lightfoot, E.N., *Transport Phenomena*, Wiley, New York, 1960.
- Blunt, M.J., Jackson, M.D., Piri, M., and Valvatne, P.H., Detailed physics, predictive capabilities and macroscopic consequences for pore-network models of multiphase flow, *Adv. Water Resour.*, 25, 1069, 2002.
- Braun, E.M. and Blackwell, R.J., A steady-state technique for measuring oil–water relative permeability curves at reservoir conditions, *Proceedings of the 56th Annual Fall Technical Conference and Exhibition of the Society of Petroleum Engineers of AIME*, San Antonio, Texas, October 5–7, 1981.

- Brownell, L.E., Dombrowski, H.S., and Dickey, C.A., Pressure drop through porous media: Part IV — New data and revised correction, *Chem. Eng. Progr.*, 46, 415, 1950.
- Buckley, S.E. and Leverett, M.C., Mechanism of fluid displacement in sands, *Trans. AIME*, 146, 107, 1942.
- Carman, P.C., Fluid flow through a granular bed, *Trans. Inst. Chem. Eng. London*, 15, 150, 1937.
- Carman, P.C., The determination of the specific surface of powders, *J. Soc. Chem. Ind.*, 57, 225, 1938.
- Carman, P.C., *Flow of Gases through Porous Media*, Butterworths, London, 1956.
- Chatzis, I. and Dullien, F.A.L., Mise en oeuvre de la théorie de la percolation pour modéliser le drainage des milieux poreux et la perméabilité relative au liquide non muillant injecté, *Rev. d l'IFP*, 183, 1982.
- Chatzis, I. and Dullien, F.A.L., Dynamic immiscible displacement mechanisms in pore doublets: Theory versus experiment, *J. Colloid Interface Sci.*, 91, 199, 1983.
- Chatzis, I. and Dullien, F.A.L., The modeling of mercury porosimetry and the relative permeability of mercury in sandstones using percolation theory, *Int. Chem. Eng.*, 25, 47, 1985.
- Chatzis, I., Kantzias, A., and Dullien, F.A.L., On the investigation of gravity assisted inert gas injection, using micromodels, long Berea cores and computer assisted tomography, *Proceedings of the 63rd Annual Technical Conference and Exhibition of the SPE*, Society of Petroleum Engineers, Houston, Texas, SPE 18284, October 2–5, 1988.
- Chatzis, I., Morrow, N.R., and Lim, H.T., Magnitude and detailed structure of residual oil saturation, *Soc. Pet. Eng. J.*, 23, 311, 1983.
- Catalan, L., Dullien, F.A.L., and Chatzis, I., The effect of wettability and heterogeneities on the recovery of waterflood residual oil with low pressure inert gas injection assisted by gravity drainage, *Soc. Pet. Eng. Adv. Technol.*, 2, 140, 1994.
- Collins, R.E., *Flow of Fluids through Porous Materials*, Reinhold Publishing Corporation, New York, 1961.
- Craig, Jr., F.F., *The Reservoir Engineering Aspects of Waterflooding*, 4th printing, Society of petroleum Engineers of AIME, New York, 1993.
- Deddas, S. and Rumpf, H., On the randomness of beds packed with spheres or irregular shaped particles, *Chem. Eng. Sci.*, 21, 583, 1966.
- Danis, M. and Jacquin, C., Influence du contraste de viscosité sur les perméabilités relatives lors du drainage: Experimentation et modélisation, *Rev. d l'IFP*, 38, 1983.
- Darcy, H., *Les fontaines publiques de la ville de Dijon*, Victor Dalmint, Paris, 1856.
- de Gennes, P.G., Theory of slow biphasic flows in porous media, *Phys. Chem. Hydr.*, 4, 175, 1983.
- De L Rue, R.E. and Tobias, C.W., The conductivity of dispersions, *J. Electrochem. Soc.*, 106, 827, 1959.
- de la Cruz, V. and Spanos, T.J.T., Mobilization of oil ganglia, *AIChE J.*, 29, 854, 1983.
- Diaz, C.E., Chatzis, I., and Dullien, F.A.L., Simulation of capillary pressure curves using bond correlated site percolation on a simple cubic network, *Transport Porous Media*, 2, 15, 1987.
- Donaldson, E.C., Lorenz, P.B., and Thomas, R.D., The effects of viscosity and wettability on oil and water relative permeabilities, *Soc. Petrol. Eng.*, 1562, 1966.
- Dong, M. and Chatzis, I., The imbibition and flow of a wetting liquid along the corners of a square capillary tube, *J. Colloid Interface Sci.*, 172, 278, 1995.
- Dong, M. and Dullien, F.A.L., A new model for immiscible displacement in porous media, *Transport Porous Media*, 27, 185, 1997.
- Dong, M., Dullien, F.A.L., and Chatzis, I., The imbibition of oil in film form over water present in edges of capillaries with an angular cross section, *J. Colloid Interface Sci.*, 172, 21, 1995.
- Dong, M., Dullien, F.A.L., and Zhou, J., Characterization of waterflood saturation profile histories by the “complete” capillary numbers, *Transport Porous Media*, 31, 213, 1998.
- Dullien, F.A.L., Two-phase flow in porous media, *Chem. Eng. Technol.*, 11, 407, 1988.
- Dullien, F.A.L., *Porous Media-Fluid Transport and Pore Structure*, 2nd ed., Academic Press, San Diego, 1992.
- Dullien, F.A.L., Physical interpretation of hydrodynamic coupling in steady two-phase flow, *Proceedings of American Geophysical Union 13th Annual Hydrology Days, Fort Collins, Colorado*, Atherton, CA, Hydrology Days Publications, 1993, pp. 363–377.
- Dullien, F.A.L. and Dong, M., Experimental determination of the flow transport coefficients in the coupled equations of two-phase flow in porous media, *Transport Porous Media*, 25, 97, 1996.

- Dullien, F.A.L. and Dong, M., The importance of capillary forces in waterflooding: An examination of the Buckley–Leverett frontal displacement theory, *J. Porous Media*, 5, 1, 2002.
- Dullien, F.A.L. and Fleury, M., Analysis of the USBM wettability test, *Transport Porous Media*, 16, 175, 1994.
- Dullien, F.A.L., Zarcone, C., MacDonald, I.F., Collins, A., and Bochard, D.E., The effects of surface roughness on the capillary pressure curves and the heights of capillary rise in glass bead packs, *J. Colloid Interface Sci.*, 127, 362, 1989.
- Dullien, F.A.L., Allsop, H.A., MacDonald, I.F., and Chatzis, I., Wettability and immiscible displacement in Pembina Cardium sandstone, *J. Can. Pet. Technol.*, 29, 63, 1990.
- Forcheimer, P.H., Wasserbewegung durch boden, *Z. Ver. Deutsch. Ing.*, 45, 1781, 1901.
- Geertsma, J., Estimating the coefficient of inertial resistance fluid flow through porous media, *Soc. Pet. Eng. J.*, 14, 445, 1974.
- Greenberg, D.B. and Weger, E., An investigation of the viscous and inertial coefficients for the flow of gases through porous sintered metals with high pressure gradients, *Chem. Eng. Sci.*, 12, 8, 1960.
- Johnson, E.F., Bossler D.P., and Naumann, V.O., Calculation of relative permeability from displacement experiments, *Petrol. Trans. AIME*, 216, 370, 1959.
- Kozeny, J., Über kapillare Leitung des Wassers im Boden, *Royal Acad. Sci, Vienna Proc. Class I*, 136, 271, 1927.
- Kalaydjian, F., Origin and quantification of coupling between relative permeabilities for two-phase flows in porous media, *Transport Porous Media*, 5, 215, 1990.
- Kalaydjian, F., Moulu, J.-C., Vizika, O., and Munkenrud, P.K., Three-phase flow in waterwet porous media: Determination of gas/oil relative permeabilities under various spreading conditions, *Proceedings of the 68th Annual Technical Conference and Exhibition of the SPE*, Society of Petroleum Engineers, Houston, TX, SPE 26671, Oct. 3–6, 1993.
- Kwiecien, M.J., Determination of Pore Size Distributions of Berea Sandstone through Three-Dimensional Reconstruction, M.Sc. Thesis, University of Waterloo, Waterloo, Ontario, 1987.
- Lasseux, D., Quintard, M., and Whitaker, S., Determination of permeability tensors for two-phase flow in homogeneous porous media: Theory, *Transport Porous Media*, 24, 107, 1996.
- Leach, R.O., Surface equilibrium in contact angle measurements, paper presented at *Gordon Research Conference on Chemistry at Interfaces*, Meridan, July 1957.
- Legait, B., Laminar flow of two phases through a capillary tube with variable square cross-section, *J. Colloid Interface Sci.*, 96, 28, 1983.
- Lenormand, R., Ph.D. dissertation, University of Toulouse, France, 1981.
- Lenormand, R., Zarcone, C., and Sarr, A., Mechanisms of the displacement of one fluid by another in a network of capillary ducts, *J. Fluid Mech.*, 135, 337, 1983.
- Lenormand, R., Touboul, E., and Zarcone, C., Numerical models and experiments on immiscible displacements in porous media, *J. Fluid Mech.*, 189, 165, 1988.
- Leverett, M.C., Flow of oil-water mixtures through unconsolidated sands, *Petrol. Trans. AIME*, 132, 149, 1939.
- Leverett, M.C., Capillary behaviour in porous solids, *Trans. AIME*, 142, 152, 1941.
- MacDonald, I.F., El-Sayed, M.S., Mow, K., and Dullien, F.A.L., Flow through porous media—the Ergun equation revisited, *Ind. Eng. Chem. Fundam.*, 18, 199, 1979.
- Mason, G. and Morrow, N.R., Capillary behavior of a perfectly wetting liquid in irregular triangular tubes, *J. Colloid Interface Sci.*, 141, 262, 1991.
- McCaffery, F.G. and Berinion, D.W., The effect of wettability on two-phase relative permeabilities, *J. Can. Pet. Technol.*, 13, 42, 1974.
- Morel-Seytoux, H.J., Introduction to flow of immiscible liquids in porous media, in *Flow through Porous Media*, Dewiest, R. Ed., Academic Press, New York, 1969, Chapter 11.
- Muskat, M. and Meres, M.W., The flow of homogeneous fluids through porous media, *Physics*, 7, 346, 1936.
- Odeh, A.S., Effect of viscosity ratio on relative permeability, *Pet. Trans. AIME*, 216, 346, 1959.

- Owens, W.W. and Archer, D.L., The effect of rock wettability on oil–water relative permeability relationships, *J. Pet. Tech.*, 23, 873, 1971.
- Pirson, S.J., *Handbook of Well Log Analysis*, Prentice-Hall, Englewood Cliffs, NJ, 1963, p. 326.
- Rakotomalala, N., Salin, D., and Yortsos, Y.C., Viscous coupling in a model porous medium geometry: Effect of fluid contact area, *Appl. Sci. Res.*, 55, 155, 1995.
- Ransohoff, T.C. and Radke, C.J., Laminar flow of a wetting liquid along the corners of a predominantly gas-occupied noncircular pore, *J. Colloid Interface Sci.*, 121, 392, 1988.
- Rapoport, L.A. and Leas, W.J., Properties of linear waterfloods, *Trans. Am. Inst. Min. Eng.*, 198, 139, 1953.
- Rose, W., A commentary on the paper titled “Relative permeability analysis of tube bundle model”, by J.T. Bartley and D.W. Ruth, *Transport Porous Media* 36, 161–187, 1999; 40, 355, 2000.
- Rose, W., Petroleum reservoir engineering at the crossroads (ways of thinking), *Iran Pet. Inst. Bull.*, 46, 23, 1972.
- Salathiel, R.A., Oil recovery by surface film drainage in mixed-wettability rocks, *J. Pet. Tech.*, 25, 2216, 1973.
- Scheidegger, A.E., *The Physics of Flow through Porous media*, 3rd ed., University of Toronto Press, Toronto, 1974.
- Tiab, D. and Donaldson, E.C., *Petrophysics: Theory and Practice of Measuring Reservoir Rock and Fluid Transport Properties*, Gulf Publishing Company, Houston, TX, 1999.
- Wyllie, M.R.J. and Spangler, M.B., Application of electrical resistivity measurements to problem of fluid flow in porous media, *Bulletin of the American Association of Petroleum Geologists*, 36, 359, 1952.
- Yadav, G.D., Dullien, F.A.L., Chatzis, I., and MacDonald, I.F., Microscopic distribution of wetting and non-wetting phases in sandstones during immiscible displacements, *SPE Reservoir Eng.*, 2, 137, 1987.
- Zarcone, C. and Lenormand, R., Determination experimentale du couplage visqueux dans les écoulements diphasiques en milieu poreux, *C.R. Acad. Sci. Paris*, Ser. II, 318, 1429, 1994.

11

Microscale and Microgravity Flows

11.1	Gas–Liquid Two-Phase Flow in Microchannels	11-1
	Introduction • Two-Phase Flow Patterns • Void Fraction • Pressure Drop	
11.2	Microgravity Flows.....	11-13
	Applications of Two-Phase Fluid Loops in Thermal Management • Description of a Typical Pumped Flow Loop • Classification of Gas–Liquid Flow Patterns at Reduced Gravity: Flow Patterns at Reduced Gravity Conditions • Gas–Liquid Pressure Drop	

Akimi Serizawa

Kyoto University

Kamiel S. Gabriel

University of Ontario Institute of Technology

11.1 Gas–Liquid Two-Phase Flow in Microchannels

Akimi Serizawa

11.1.1 Introduction

Clarification of microscale effects in transport phenomena in gas–liquid two-phase flow is gradually becoming a challenging topic, especially in the areas of modern science and technology such as biological systems, microstructured heat transfer devices, microfluidics devices, etc. These research areas represent great potential for a wide range of applications in the above areas and also in the area of nuclear reactor thermal-hydraulics and safety analysis. Research on this topic has been rapidly enhanced by the development of MEMS (micro electro-mechanical system) technologies and a growing demand for product miniaturization in many industrial sectors. In fact, extensive discussions have been focused on this topic (Ghiaasiaan and Abdel-Khalik, 2000; Takei and Kimura, 2000; Serizawa, 2001, 2002; Serizawa and Fenz, 2001; Serizawa and Kawara, 2002; Serizawa et al., 2002; Kandlikar, 2003a, 2003b; Kawaji and Chung, 2003).

The performance characteristics of gas–liquid two-phase thermal-hydraulics in practical engineering devices with ordinary or conventional length scales are generally expressed in nondimensional forms, and thus we have, comparatively, well-defined similarity laws based on experiment or theory. However, at present there is severe lack understanding as to the application limits within which the concept of characteristic length scales included in these similarity laws can be successfully applied in the smallest channel. Thus, a question arises as to “what is a microchannel?” Channel classification is often made by using several nondimensional parameters relevant to two-phase flows (Suo and Griffith, 1964; Brauner al., 1992; Ghiaasiaan and Abdel-Khalik, 2000; Kawaji and Chung, 2003). Kawaji and Chung (2003)

proposed a criterion for two-phase microchannel flows in terms of the following six nondimensional variables:

$$\text{Bond number: } Bd = \frac{(\rho_l - \rho_g)g(D/2)^2}{\sigma} \ll 1 \quad (11.1)$$

$$\text{Superficial liquid Weber number: } We_{ls} = \frac{U_l^2 D \rho_l}{\sigma} \ll 1 \quad (11.2)$$

$$\text{Superficial gas Weber number: } We_{gs} = \frac{U_g^2 D \rho_g}{\sigma} \ll 1 \quad (11.3)$$

$$\text{Superficial liquid Reynolds number: } Re_{ls} = \frac{\rho_l U_l D}{\mu_l} < 2000 \quad (11.4)$$

$$\text{Superficial gas Reynolds number: } Re_{ls} = \frac{\rho_g U_g D}{\mu_g} < 2000 \quad (11.5)$$

$$\text{Capillary number: } Ca_l = \frac{\mu_l U_l}{\sigma} \ll 1 \quad (11.6)$$

where D , U_k ($k = l$ or g), and g are the inner diameter or hydraulic equivalent diameter of the channel, phasic volumetric flux (superficial velocity), and acceleration due to gravity, respectively. The variables μ , ρ , and σ are viscosity, density, and liquid surface tension, respectively. The indices k , l , and g denote k th phase, liquid, and gas, respectively. However, it should be noted that these criteria define the flow conditions including the channel diameter range where two-phase flow is dominated by surface tension effects.

Kandlikar and Grand (2002) proposed the following channel classification based on the Knudsen number for gases at near atmospheric pressure by taking into account the mean free path:

Conventional channels: $D_h > 3 \text{ mm}$

Minichannels: $3 \text{ mm} \geq D_h > 200 \text{ }\mu\text{m}$

Microchannels: $200 \text{ }\mu\text{m} \geq D_h > 10 \text{ }\mu\text{m}$

Transitional channels: $10 \text{ }\mu\text{m} \geq D_h > 0.1 \text{ }\mu\text{m}$

Molecular nanochannels: $0.1 \text{ }\mu\text{m} \geq D_h$

In general, the classification for gas–liquid two-phase flow is not as simple as that for single-phase flow, since two-phase flow is a multiscale structured flow with different time- and spatial scales, accompanied by time- and spatially varying interfaces. Nevertheless, they recommended the above classification for two-phase flow as well. The above classification matches fairly well with our observed experimental trends in air–water two-phase flows over the pressure range 1 to 5 atmospheres. However, in view of the experimental evidence that two-phase flow behavior in microchannels drastically changes for channel diameters smaller than 100 μm , the microchannel may well be defined as a channel with diameter smaller than 100 μm . We therefore restrict ourselves here to gas–liquid two-phase flows in channels in this regime.

In microchannel flows, surface forces rather than body force dominate the flow and heat transfer performances, and the interaction between the fluid and the walls becomes therefore very important. In other words, surface tension and viscous forces dominate over gravitational force. The inertia forces are also important. This means that the viscous pressure drop along the flow direction becomes very large and, in a practical sense, significant pumping power is needed to circulate the flow through such small tubes. Flow instability due to compressibility of the gas involved in the entrance section and the supply lines connected to the test tube is another difficult problem to be avoided. Furthermore, submicron channels may change the physical properties of fluids such as viscosity, ice point, etc., due to molecular electrostatic and kinetic forces.

11.1.2 Two-Phase Flow Patterns

11.1.2.1 Mixing Section and Test tubes

The two-phase flow pattern in microchannels generally tends to alternate with time from one flow pattern to another. Optimal design of the mixing section is therefore required to establish stable two-phase flows in microchannels along with the use of a pneumatic pump for liquid circulation to avoid flow pulsation and contamination characteristic of mechanical pumps. High-pressure gas injection at the test section inlet to compensate for the large pressure drop in the microchannel is another problem owing to the effect of gas compression and expansion both in the connecting lines and in the mixing section, which may lead to flow pulsation. We therefore have to pay attention to the design of the mixing section and connecting lines used in microchannel devices, when we interpret the experimental data reported in the literature. Figure 11.1 shows typical examples of the mixing section designs. In order to attain stable two-phase flow, the liquid may naturally form a converging nozzle.

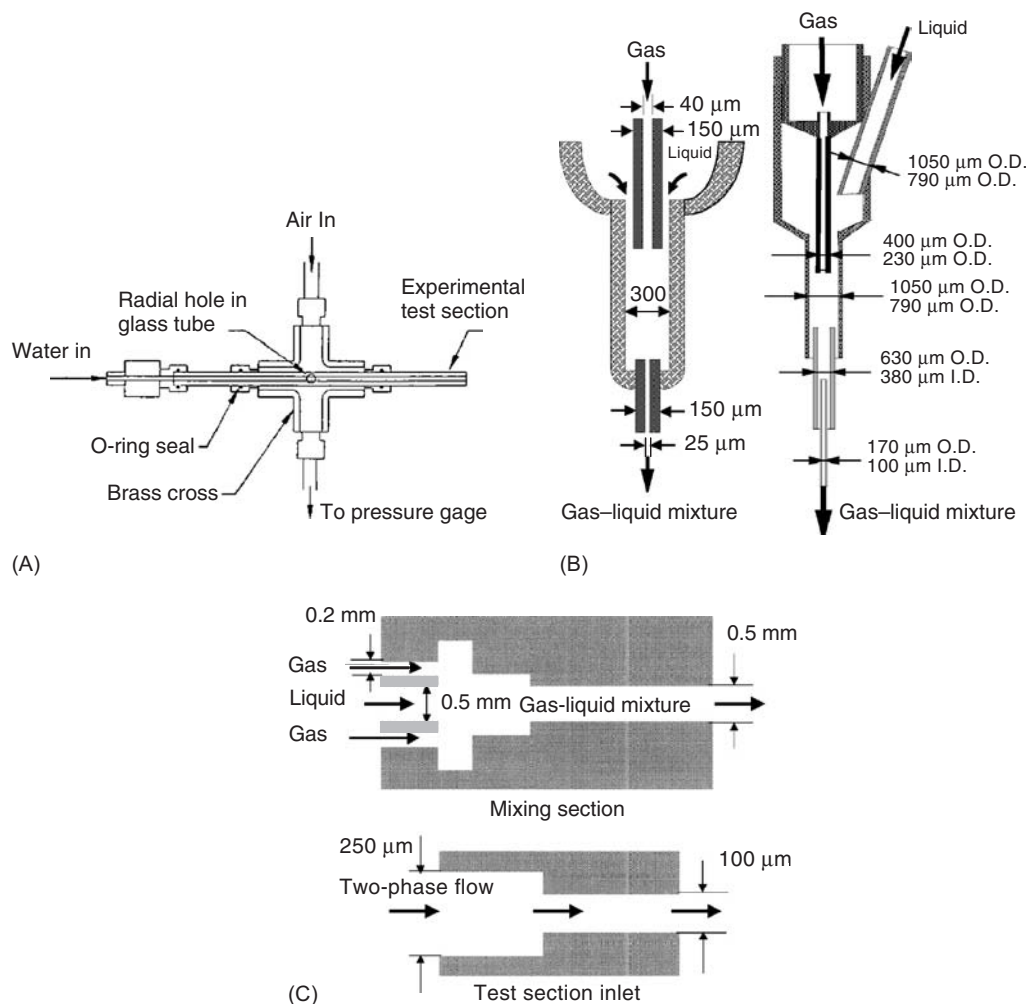


FIGURE 11.1 Example of Mixing Section Design. (A) From Triplett, K.A. et al., *Int. J. Multiphase Flow*, 25, 377–394, 1999a; (B) From Serizawa, A. Report of the Research Committee on Heat Transfer and Fluid Flow in Microchannel, Japan Society for Mechanical Engineers. P-SC295, Editor, 2001; (C) From Kawahara, A. *Int. J. Multiphase Flow*, 28, 141–1435, 2002.

Another important point we should stress is the uniformity of the channel dimensions in the axial and radial directions. An irregular or rough surface may result in a change of two-phase flow patterns and friction loss, while a nonuniform distribution in diameter along the channel axis may cause flow pulsation. The former is the case with metallic tubes and the latter with plastic or glass tubes. Figure 11.2 shows enlarged cross-sectional pictures of typical microchannels reported by Kawahara et al. (2003) and Celata et al. (2002).

11.1.2.2 Minichannels

It is helpful to review the two-phase flow patterns prevailing in conventional and minichannels. Figure 11.3 illustrates typical two-phase flow patterns for air–water flows in a small vertically oriented capillary tube and those in a horizontal minichannel with circular cross-section. It should be noted that, basically, there is no clear distinction between the two cases. One exception is that, in the 1.097 mm I.D. channel experiment, Triplett et al. (1999a, 1999b) observed slug–annular flow, characterized by long sections of the channel displaying an essentially wavy-annular flow, which is interrupted by large-amplitude solitary waves which do not

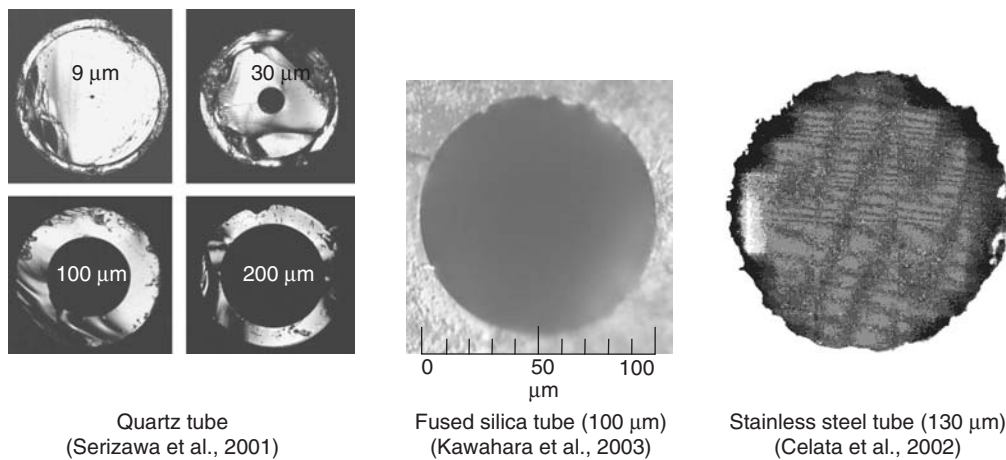


FIGURE 11.2 Uniformity of microchannel dimensions: (A) Fused silica tube (99.7 μm). (From Kawahara, A. et al., *Proceedings of the 1st International Conference on Microchannels and Minichannels*, Rochester, New York, Apr. 24–25, 2003, pp. 479–486. With permission.) (B) Quartz tube (99.7 μm). (From Serizawa, S. et al., *Microscale Thermophy Eng.*, 6, 85–97, 2001. With permission.) (C) Stainless-steel tube (130 μm). (From Celata, G.P. et al., *Microscale Thermophy Eng.*, 6, 85–97, 2002. With permission.)

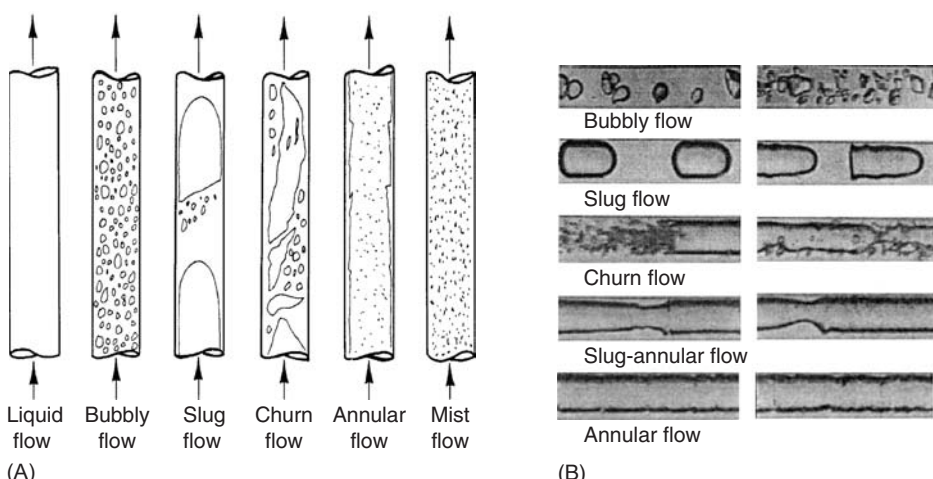


FIGURE 11.3 Typical two-phase flow patterns in conventional and minichannels: (A) Small capillary channel; (B) 1.097 mm I.D. minichannel (From Triplett, K.A. et al., *Int. J. Multiphase Flow*, 25, 395–410, 1999b with permission.)

grow sufficiently to block the flow path. They also reported that, with an increase in U_g , these large-amplitude solitary waves disappear and the flow pattern changes to annular flow. Two-phase flow pattern transition boundaries follow the general trends obtained by Damianides and Westwater (1988) for a 1 mm circular tube.

Based on the experimental database available Akbar et al. (2003) recently proposed two-phase flow regime transition boundaries that fitted all relevant data for air–water flow in circular and near-circular minichannels with $D_h \leq 1.0$ mm. These lines are represented by the following expressions:

$$\text{Surface tension-dominated zone: } We_{gs} \leq 0.11 \quad We_{ls}^{0.315} \quad (\text{for } We_{ls} \leq 3.0)$$

$$We_{gs} \leq 1.0 \quad (\text{for } We_{ls} > 3.0)$$

$$\text{Inertia-dominated zone (annular flow zone): } We_{gs} \geq 11.0 \quad We_{ls}^{0.14}, \quad We_{ls} > 3.0$$

$$\text{Inertia-dominated zone (dispersed flow zone): } We_{ls} > 3.0$$

11.1.2.3 Microchannels

Figure 11.4 and [Figure 11.5](#) show two-phase flow patterns identified in air–water experiments in a 25 μm I.D. silica tube, and in 80 and 100 μm quartz tubes, respectively (Serizawa and Feng, 2001; Serizawa et al., 2002b). The features of the two-phase flow patterns identified are described in [Table 11.1](#).

An interesting observation is the existence of a liquid ring flow. This flow pattern has never been reported before for conventional and minichannels, except under microgravity conditions (Rezkallah, 1998). This flow pattern changes from slug flow when the gas velocity is high. At low gas velocity, the liquid ring first appears in the middle of a long slug bubble. It is likely that this liquid ring originates from a liquid bridge separating two consecutive gas slugs. The liquid ring flow can develop when the gas flow rate increases to such an extent that the liquid slug is too short to support a stable liquid bridge between the two consecutive gas slugs. The force balance between the viscous force from the wall and the drag force from the gas core determines the motion of the liquid ring. When the former is dominant, the liquid

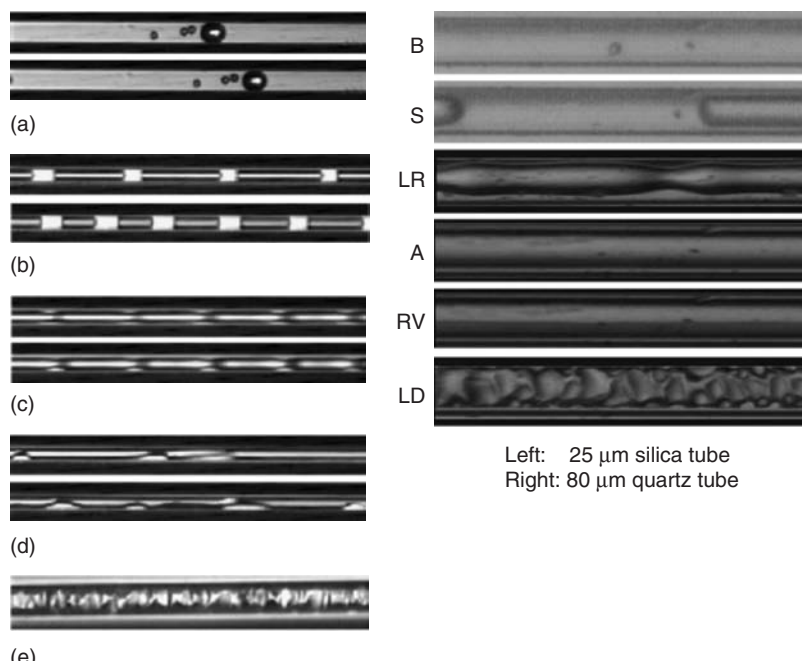


FIGURE 11.4 Two-phase flow patterns in microchannels (air–water): (a) bubbly flow; (b) slug flow; (c) liquid ring flow; (d) liquid lump flow; (e) dispersed annular flow–droplet flow.

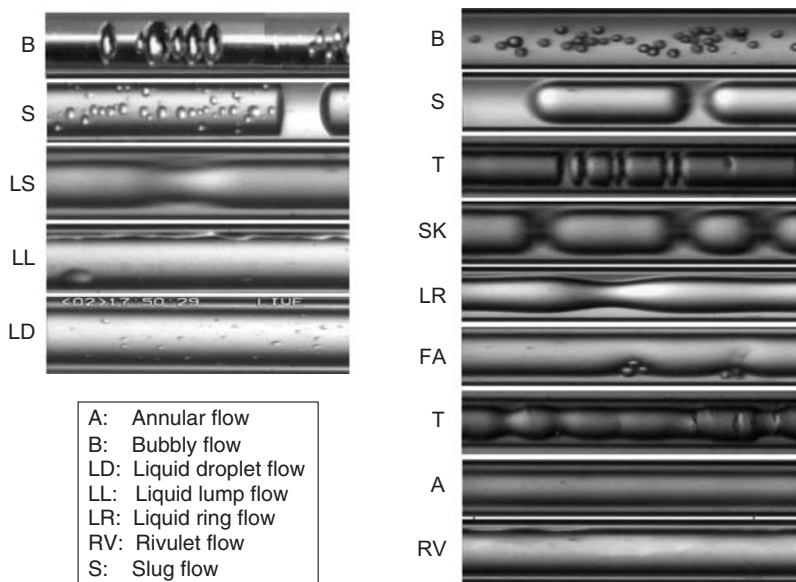


FIGURE 11.5 Two-phase flow patterns in a 100 μm diameter tube. Left Panel: nontreated quartz tube; Right Panel: clean quartz tube.

TABLE 11.1 Observed Two-Phase Flow Patterns and Their Features

Name of Flow Pattern	Features
Bubble flow (B)	Bubbly flow is characterized by discrete bubbles suspended in the liquid flow whose diameter is either roughly equal to or smaller than tube diameter. Small spherical bubbles are formed in very clean tube (Figure 11.5, right panel) and distorted in a slightly cleaned tube (left panel)
Slug flow (S)	Slug flow contains bubbles whose diameter occupy whole tube cross-section with length larger than tube diameter with semi-spherical cap and rather flat tail. At very low liquid velocity conditions, small liquid droplets stick on the tube wall within gas slugs, whereas no distinct liquid films exist between the wall and the gas slug.
Skewered slug flow (SK)	This flow pattern is featured with many slug bubbles with different length being connected in a line by gas stems at tube center.
Liquid ring flow (LR)	The liquid rings are symmetrically distributed on the continuous liquid film at the tube wall with almost an equal interval in flow direction. The gas phase flows in the core of the tube.
Frothy annular flow (FA)	This flow pattern is very similar to annular flow pattern, except that the small bubbles are entrained in the annular liquid film flow.
Annular flow (A)	In this flow pattern, the liquid flows in a film along the tube wall and perhaps also in the liquid droplets entrained in the core gas flow.
Liquid lump flow (LL)	Liquid lumps are sliding from side to side along the tube wall, enhanced by a high-speed core gas flow. The shape of the liquid lumps is similar to a wavy flow in a large horizontal tube, but not limited at the bottom side of the tube.
Rivulet flow (RV)	This flow pattern is characterized by a stream or streams of liquid flows on the tube wall
Liquid droplet flow (LD)	The liquid phase is dispersed as small droplets entrained in the gas flow. These liquid droplets often deposit on to the tube wall to form wavy film flow with irregular surface waves. After a certain time, the wavy liquid film is swept away by the core gas flow, and the liquid droplet flow appears again. This process is repeated periodically.
Transition flow (T)	There is a transition from one flow pattern to another.

ring sticks on the wall and grows. This growth is assumed to be the result of liquid supply from the liquid film in both upstream and downstream regions. When the height of the liquid ring reaches to a certain value, the drag force from the gas core becomes dominant and the liquid ring moves downstream. This flow pattern has been confirmed in microchannels with diameters less than a few hundred microns

by Kawahara et al. (2002, 2003) (nitrogen–water in a 100 μm fused silica tube) and Allen and Son (2003) (gas–silicon oil in a 342 μm capillary tube).

Skewered slug flow is also an interesting flow pattern that has never been reported earlier. Several gas slugs are connected in a line by gas stems located at the tube center similar to food on a skewer stick. This flow pattern is a transition from slug flow to liquid ring flow.

Kawahara et al. (2002) and Kawaji et al. (2003) reported that bubbly flow is very difficult to realize in microchannels, and the two-phase flow exhibits an intermittent character. In their experiments, the two-phase flow pattern changed from time to time from either slug flow to film flows with different thickness and surface wave characteristics or vice versa. They therefore defined time-average two-phase flow patterns taking into consideration the time fraction for individual flow patterns and void fraction. In the recently conducted experiments by the authors, stable bubbly flow was successfully realized, as indicated in [Figure 11.5](#) (right panel), in a 100 μm quartz tube, which was cleaned with ultrasonic vibration in pools of water, ethanol and dilute hydrochloride acid. As mentioned earlier, different designs of the air–water mixing section might be another possible explanation for the difference between the two cases.

The two-phase flow pattern map is a very useful tool for design purposes. For conventional channels, many maps have been proposed so far. However, there are very few maps for minichannels, and the research by Serizawa and Fenz (2001), almost none for microchannels. Serizawa et al. (2002), Kawahara (2002, 2003) and Kawaji et al. (2003) are the only sources of this kind of information for microchannels. [Figure 11.6](#) and [Figure 11.7](#) are presented for a 20 μm silica tube (Serizawa and Kawara, 2001; Serizawa et al., 2002) and a 100 μm channel (Kawahara et al., 2002), respectively.

11.1.2.4 Effect of Surface Contamination

The two-phase flow in microchannels is more or less affected by the surface tension force, and therefore both surface roughness and contamination of the tube inner wall affect the flow pattern evolution. This effect can be seen by comparing a series of pictures in [Figure 11.5](#). The experiments were conducted using

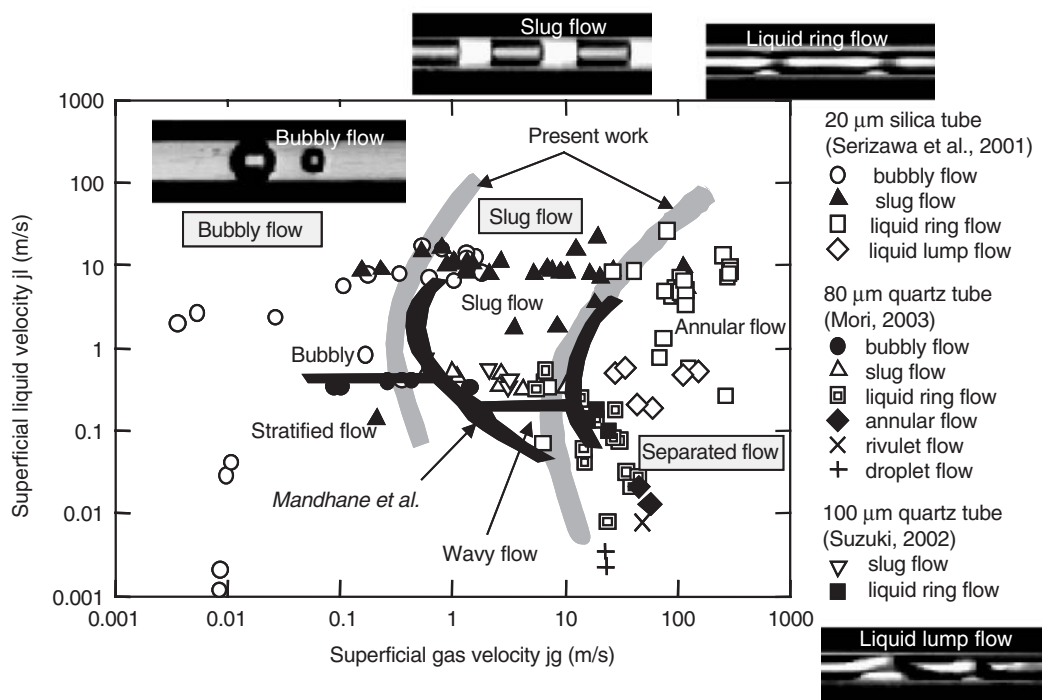


FIGURE 11.6 Flow pattern map for 20 μm tube.

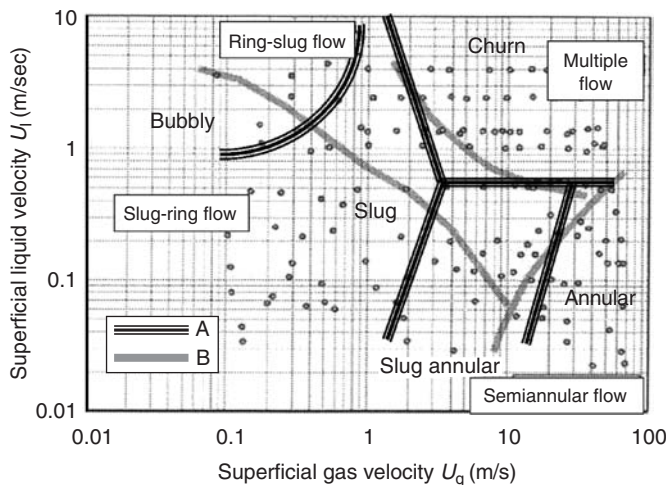


FIGURE 11.7 Flow-pattern map for 100 μm tube. Experimental flow pattern boundary. (A) (From Triplett, K.A. et al., *Int. J. Multiphase flow*, 25, 395–410, 1999b. With permission.) (B) (From Kawahara, A. et al., *Int. J. Multiphase Flow*, 28, 1411–1435, 2002. With permission.)

100 μm I.D. quartz tubes: one being cleaned by blowing ethanol through the tube (Left table) and the other very carefully cleaned by ultrasonic vibration in pools of high-purity distilled water, ethanol and dilute hydrochloride acid–water solution after mechanical cleaning with a soft brush. A variety of two-phase flow patterns were encountered in the clean microchannel, which is much easier to wet under such conditions, and thus a stable annular flow was realized. The water film spreads and the film swallows up small bubbles without being broken due to enhanced wettability (frothy annular flow). However, at low flow rates, formation of a dry area between the gas slug and the tube wall was similarly observed in slightly cleaned tubes (nontreated tube). The two-phase flow structure in microchannels is thus acutely affected by wettability between the tube and the fluids. In other words, the surface contamination and surface roughness are the key parameters that dominate two-phase flow pattern transitions. However, no systematic and quantitative measurements of the contamination effect have been reported so far for microchannels. We may therefore refer to the work of Barajas and Panton (1993) for minichannels.

Barajas and Panton tackled this problem by using water–air systems with four different tube materials of 1.59 mm I.D. i.e., pyrex tube (contact angle $\theta = 34^\circ$), polyethylene tube ($\theta = 61^\circ$), polyurethane tube ($\theta = 74^\circ$), and FEP fluoropolymer tube ($\theta = 106^\circ$). The first three are partially wetting systems, and the last one nonwetting. Their results are provided in Figure 11.8, showing the effect of contact angle in such a way that the biggest change in the transition boundaries occurs for partially the nonwetting FEP fluoropolymer tube ($\theta = 106^\circ$). For this system, the transition boundaries between slug and rivulet flow and between slug and annular flow move to lower gas velocities. Barajas and Panton explained the trend in this way. Owing of partially nonwetted character of the system, shear forces move the liquid much more easily than in the partially wetted systems ($\theta = 34, 61$, and 74°), which require lower gas velocities for the transition to multiple rivulet or annular flow.

11.1.3 Void Fraction

Only a limited number of experimental data are available on void fraction for microchannel two-phase flows. These are the works by Serizawa and Kawara (2001) and Serizawa et al. (2002) (20 μm), Kawahara et al. (2002) (100 μm), Suzuki (2004) (40 μm) and Kawaji et al. (2003) (96 μm) for air–water systems. In all these works, the cross-sectional average void fraction was estimated by analyzing photographs or images recorded by a high-speed video camera frame by frame. Figure 11.9 summarizes all these in the $\varepsilon-\beta$ diagram, where ε and β are cross-sectional average void fraction and volumetric gas flow ratio (homogeneous void fraction), respectively.

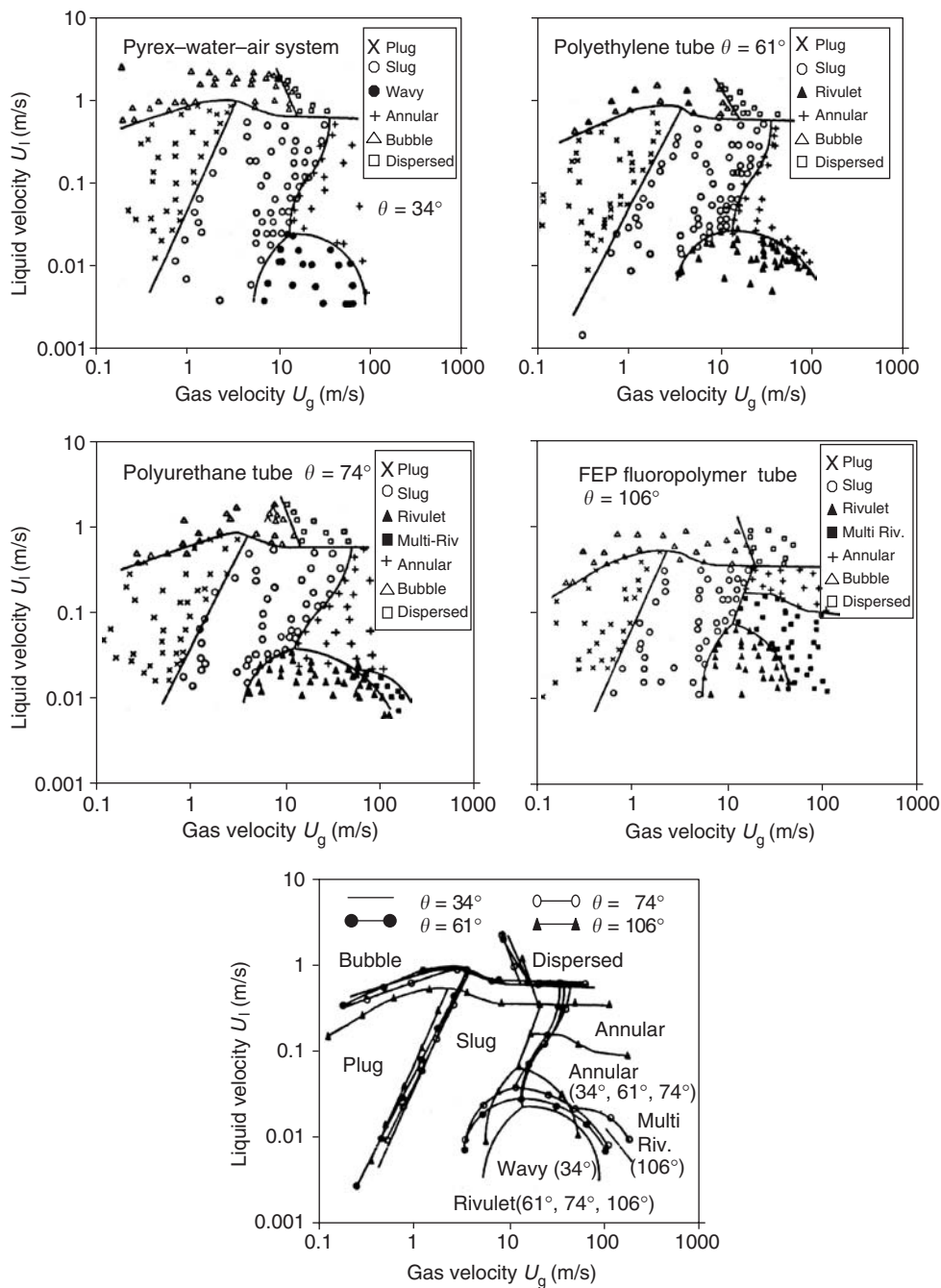


FIGURE 11.8 Effects of contact angle on two-phase flow pattern transitions. (From Barajas, A.M. and Panton, R.L., *Int. J. Multiphase Flow*, 19, 337–346, 1993. With permission.)

For comparison, Figure 11.10 indicates void fraction data obtained by Triplett et al. (1999b) for a 1.1 mm I.D. minichannel.

It is clear from Figure 11.10 that the void fraction for minichannels follows the existing correlations for conventional channels or minichannels, given below.

$$\text{homogeneous flow model: } \varepsilon = \beta \quad (11.7)$$

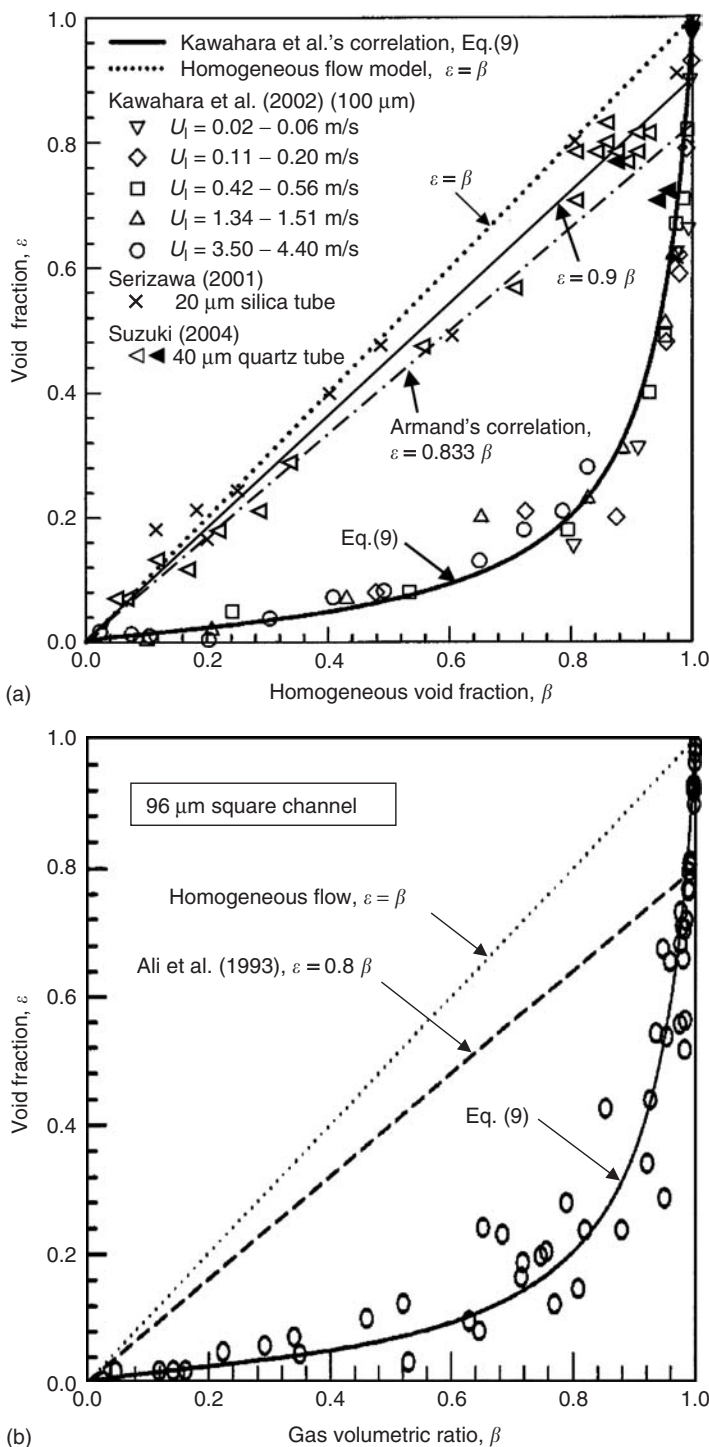


FIGURE 11.9 Comparison of void fraction data with correlations for microchannels: (A) Circular tubes (Serizawa et al. [2001, 2002], Kawahara et al. [2002], Suzuki [2004].)

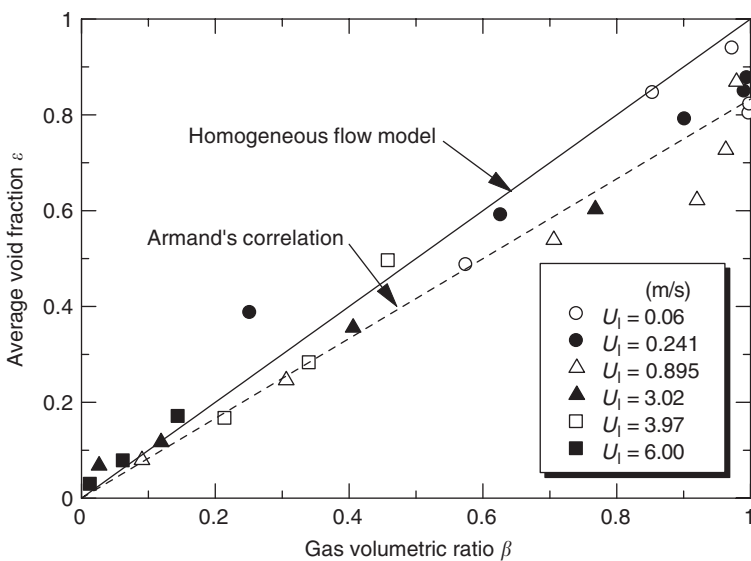


FIGURE 11.10 Void fraction for Mini-channel (From Triplett, K.A. et al., *Int. J. Multiphase flow*, 25, 395–410, 1999b. With permission; 1.1 mm I.D.).

$$\text{Armand correlation: } \varepsilon = 0.833\beta \quad (11.8)$$

However, for microchannel flows, the general trends show a significant bifurcation. The void fraction data of Serizawa et al., clearly follows a homogeneous flow model or the Armand correlation. On the other hand, the void fraction data of Kawahara et al. and those of Kawaji et al., are correlated by the following empirical equation (Kawahara et al., 2002):

$$\varepsilon = \frac{0.03\beta^{0.5}}{1 - 0.97\beta^{0.5}} \quad (11.9)$$

The different behaviors in ε vs. β plots between the data of Serizawa and coworkers (Serizawa and Kawahara, 2001; Suzuki, 2004) and other microchannel data (Kawahara et al., 2003; Kawaji et al., 2003) may be attributed to the different two-phase flow patterns used for comparison. The former covers bubbly flow and slug flow data (symbols x and Δ in Figure 11.9), while the latter is composed of film flow data. As stated in their papers, Kawahara et al. (2002) and Kawaji et al. (2003) observed the simultaneous occurrence of multiple flow patterns for the same flow condition and different flow regimes appeared at the same location at different times. In all the experimental runs, except for liquid alone, they observed (1) gas core with smooth liquid film, (2) gas core with ring-shaped liquid film, and (3) gas core with a deformed liquid film. The first type (1) includes flows with a serpentine-like gas–liquid interface or small ripples on the interface. It is therefore understood that flows with gas cores are inherently flows with very high slip ratio. This means, in turn, much lower void fractions than those predicted by the homogeneous flow model (slip ratio = 1). It is also noted that, in the experiment conducted by Serizawa et al., the void fraction for $\beta \geq 0.8$ shows a trend following Eq. (11.9). This trend shows no contradiction between our experiment and those of Kawahara et al. and Kawaji et al.

11.1.4 Pressure Drop

Several earlier studies on two-phase frictional pressure drop in minichannels reported that the homogeneous flow model predicts the data well, both in boiling systems and in air–water systems (Kureta et al., 1997, 1998) $D = 2$ mm, 6 mm, boiling two-phase flow; Ungar and Cornwell, (1992): $D = 1.46\text{--}3.15$ mm, ammonia–steam flow; Triplett et al., 1999b: $D = 1.1$ mm, 1.45 mm for circular channels, $D_h = 1.09$ mm for

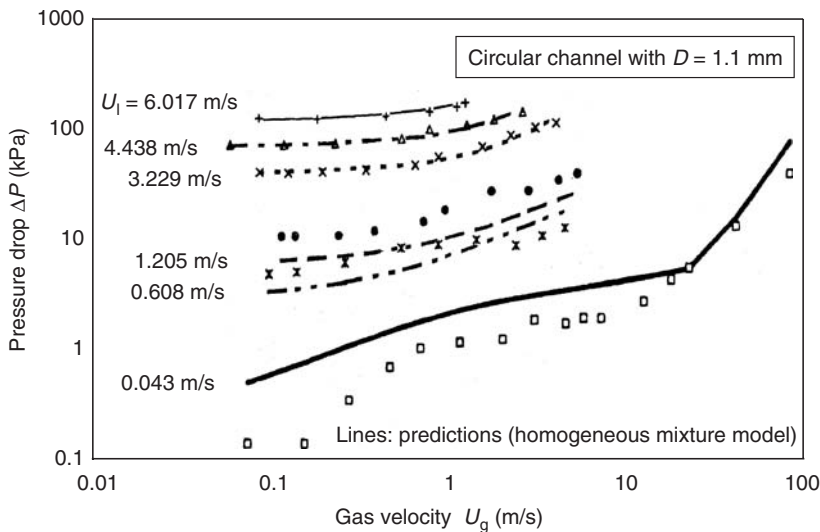


FIGURE 11.11 Comparisons of pressure drop data with predictions. (From Triplett, K.A. et al., *Int. J. Multiphase Flow*, 25, 395–410, 1999b. With permission.)

a semitriangular channel, air–water flow). Figure 11.11 gives a typical example, showing comparisons of experimental data and predictions by the homogeneous mixture model reported by Triplett et al. (1999b).

In the homogeneous mixture model, the two-phase flow pressure drop is calculated from:

$$\left(\frac{\Delta P}{\Delta Z} \right)_m = f_m \frac{1}{D_h} \frac{G^2}{2\rho_m} \quad (11.10)$$

where ρ_m is two-phase mixture density and is given in terms of the quality x by

$$\frac{1}{\rho_m} = \frac{x}{\rho_g} + \frac{1-x}{\rho_l} \quad (11.11)$$

and f_m the two-phase friction factor, which is a function of the homogeneous Reynolds number,

$$Re_H = \frac{GD_h}{\mu_m} \quad (11.12)$$

where μ_m is two-phase mixture viscosity.

Kawahara et al. (2002) tested the homogeneous model with several different two-phase viscosity models against the measured frictional pressure drop obtained in a 100 μm silica tube (microchannel). Their conclusion was that the agreement between the experimental data and homogeneous model is generally poor. A reasonably good prediction within $\mp 20\%$ was only obtained with the model developed by Dukler et al. (1964) for the mixture viscosity given by

$$\mu_m = \beta\mu_g + (1-\beta)\mu_l \quad (11.13)$$

They also carried out very precise measurements of two-phase frictional pressure drop in a 100 μm silica microchannel using nitrogen–water flows (Kawahara et al., 2002, 2003) and nitrogen–ethanol–water solutions (Kawahara et al., 2003). Based on the comparison between their experiments and existing correlations, they concluded that the Lockhart–Martinelli method based on a separated flow assumption can predict their own experimental data well. They proposed a modified Chisholm–Laird correlation (Eq. [11.14]) with value of 24 for the C parameter to fit to their experimental data. This value for the C parameter is very close to the prediction by the Mishima–Hibiki correlation (Eq. [11.16]) for small diameter channels of 1 to 4 mm

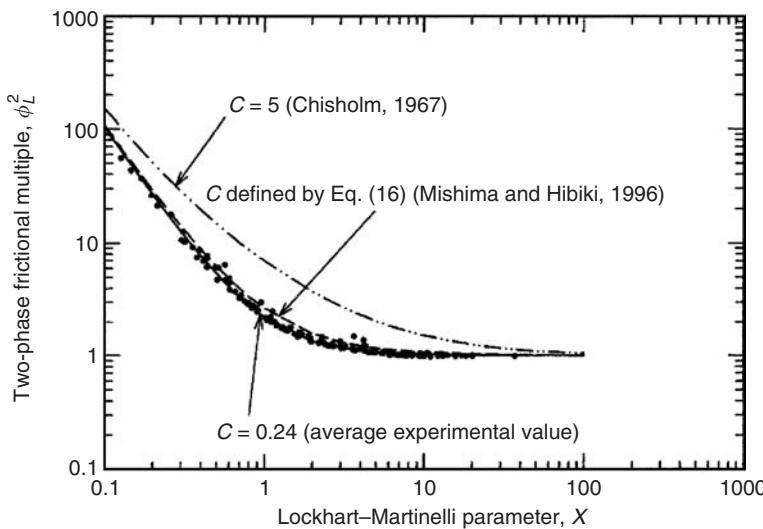


FIGURE 11.12 Two-phase pressure drop in micro channel. (From Kawahara, et al. [2002]. With permission.)

in hydraulic equivalent diameter D_h . This was later confirmed again by Kawaji et al. (2003), using the same test apparatus as used by Kawahara et al. (2002):

$$\phi_L^2 = 1 + \frac{C}{X} + \frac{1}{X^2} \quad (11.14)$$

where X is the Lockhart–Martinelli modulus defined by

$$X^2 = \frac{(\Delta P/\Delta Z)_g}{(\Delta P/\Delta Z)_l} \quad (11.15)$$

The Mishima–Hibiki correlation for the C –parameter is

$$C = 21(1 - e^{-0.319D_h}) \quad (11.16)$$

Figure 11.12 shows the correlation of the two-phase friction multiplier with different C values with the experimental data of Kawahara et al. (2002). As can be seen from this figure, a satisfactory agreement was obtained between prediction and experiment. However, reliable data on microchannel two-phase flows are seriously lacking, so the conclusions reached above are still tentative. Some two-phase frictional pressure drop correlations for mini- and microchannels are listed in [Table 11.2](#).

11.2 Microgravity Flows

Kamiel S. Gabriel

11.2.1 Applications of Two-Phase Fluid Loops in Thermal Management

Most of the earlier research on gas–liquid flows was conducted for terrestrial conditions, where gravity plays a very important role. Mainly, due to the demand for active heat transport systems in future communications and earth observation satellites and space stations, two-phase gas–liquid flows at micro-gravity ($\mu\text{-g}$) conditions have emerged as an active research area in the last decade.

One of the major applications of two-phase flow at microgravity conditions is the design and maintenance of active thermal control systems for future space stations and high power communications satellites. The past thermal management requirements for satellites and orbiting spacecraft have been

TABLE 11.2 Two-Phase Frictional Pressure Correlations for Mini- and Microchannels

Author	Flow Conditions	Correlation
Chisholm and Laird (1958)		$\phi_1^2 = 1 + \frac{C}{X} + \frac{1}{X^2}$ with $C = 5$
Fukano et al. (1990)	Air–water Circular tubes 1.0 mm, 4.9 mm	$Re < 2400$ ($\beta_l = 1 - \beta$) Slug flow: $\phi_1^2 = 0.007\beta_l^{-0.85}Re^{3/4}$ Annular flow: $\phi_1^2 = 0.0011\beta_l^{-1.2}Re^{3/4}$ Plug flow: $\phi_1^2 = 0.0038\beta_l^{-3.5}Re_l^{3/4}$ $Re > 2400$ Bubbly flow: $\phi_1^2 = \beta_l^{-1.75}$ Plug flow: $\phi_1^2 = 1.6\beta_l^{-0.75}$
Lin et al. (1991)	R-12 boiling flow Circular tubes: 0.66 mm, 1.17 mm Pressure: 6.3–13.2 bar	$f = 8 \left[\left(\frac{8}{Re} \right)^{12} + \frac{1}{(A + B)^{1.5}} \right]^{1/12}$ $A = \left\{ 2.457 \ln \left[\frac{1}{(7/Re)^{0.9} + 0.27(\varepsilon/D_h)} \right] \right\}^{16}$ $B = \left(\frac{37530}{Re} \right)^{16}$ $\phi_{10}^2 = \left\{ \frac{\ln[(7/Re_{10})^{0.9} + 0.27(\varepsilon/D_h)]}{\ln[(7/Re_m)^{0.9} + 0.27(\varepsilon/D_h)]} \right\} \left[1 + x \left(\frac{\rho_l}{\rho_g} \right) \right]$
Mishima and Hibiki (1996)	Air–water Circular/rectangular channels: $D_h = 1\text{--}4$ mm	$\phi_1^2 = 1 + \frac{C}{X} + \frac{1}{X^2}$ with $C = 21(1 - e^{-0.319D_h})$
Lee and Lee (2001)	Air–water Rectangular channel: $D_h = 0.78\text{--}6.67$ mm	$\phi_1^2 = 1 + \frac{C}{X} + \frac{1}{X^2}$ with $C = A\lambda^q\psi^\gamma Re_{10}^s$, $\psi = \mu_l j/\sigma$
Kawahara et al. (2002)	Nitrogen–water Circular tube: 100 μm Flow rates: $U_l = 0.02\text{--}4$ m/s $U_g = 0.1\text{--}60$ m/s	$\phi_1^2 = 1 + \frac{C}{X} + \frac{1}{X^2}$ with $C = 24$

characterized by low power (<25 kW) and short life time (<3 years). These modest requirements can usually be satisfied by passive devices, such as heat pipes, or pumped single-phase fluid cooling systems. The performance of passive devices is mostly independent of gravity. Knowledge gained on the performance of such systems on ground can be directly used in the design of the space systems. Two-phase flow systems (capillary or mechanically driven) have been chosen as potential candidates for the design of future thermal subsystems.

11.2.2 Description of a Typical Pumped Flow Loop

A typical thermal transport system for space applications is shown in Figure 11.13. The main components of the system are (1) a pump–separator unit capable of separating the two phases (liquid and vapor) and

pumping the liquid back into the loop, (2) cold plates, where cooling of instruments or utilities occur, (3) a radiator-condenser, where condensation takes place, and (4) a reservoir, where liquid inventory is controlled and vapor is allowed to expand.

In addition, a pressure regulator is used to control the set point and the system operating temperature.

11.2.2.1 Pump-Separator

A conceptual design of a pump (Huckerby and Rezkallah, 1992) is shown in Figure 11.14.

The two-phase flow mixture from the radiator enters a rotating drum through the hot side seal. The liquid is accumulated near the inner wall of the rotating drum due to its rotation, while the vapor phase is directed to the condensing unit. On the other side of the drum, the condensed liquid from the radiator enters through the cold side seal and is directed to the reservoir on the hot side. The liquid is picked up by a pitot-type tube near the wall and is directed back to the main loop for recirculation. A probe immersed directly into the liquid annulus near the wall controls the liquid level.

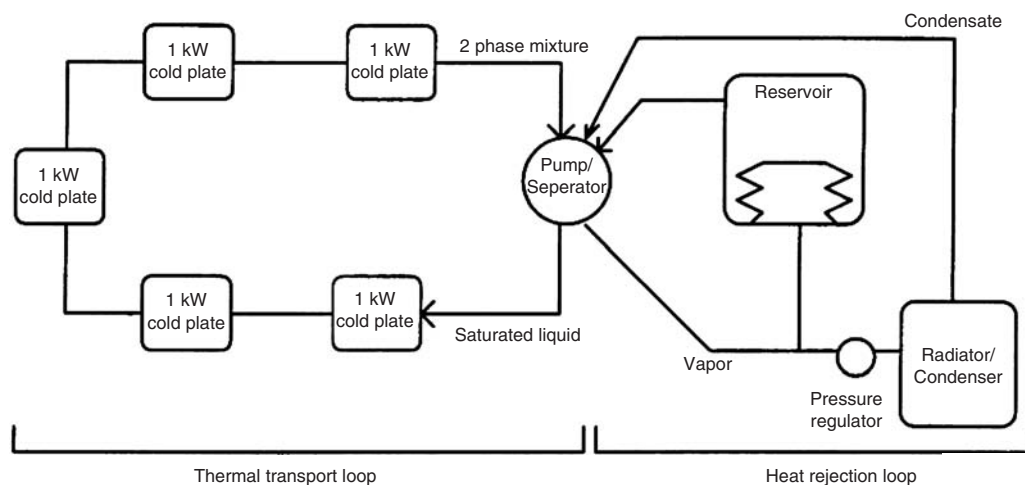


FIGURE 11.13 Schematic of a typical thermal transport system.

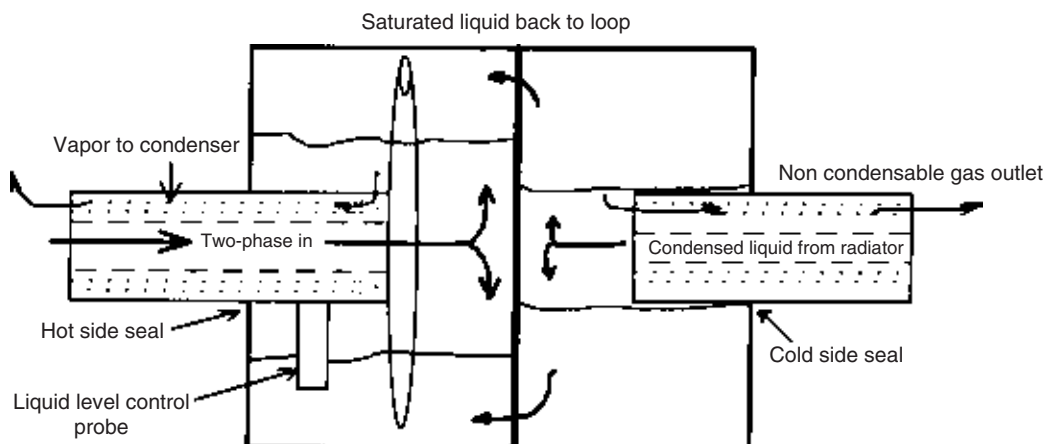


FIGURE 11.14 Two-phase single component pump-separator.

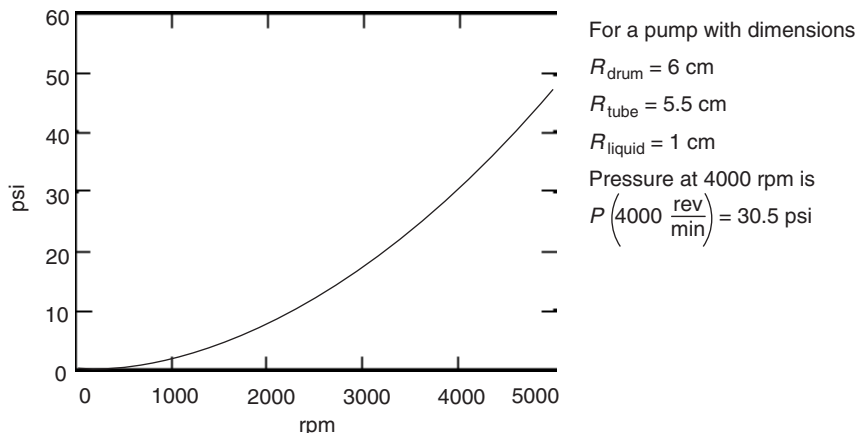


FIGURE 11.15 Pump-separator performance.

The liquid flow rate and the pressure available from the pump are functions of the pump speed. Figure 11.15 shows the relationship between the liquid pressure and the pump speed (rpm) for a small drum size of 12 cm in diameter and a liquid annulus of 1 cm in radius. It is clear that sufficient pressure could be generated using such pumps with speeds ranging from 1000 to 5000 rpm. It should be noted that the flow depends on the downstream conditions of the thermal transport system, and that such dependency is nonlinear. Fortunately, this is not a critical parameter, since the heat carrying capacity of the system is relatively independent of the main flow rate (if the flow rate is sufficient to prevent dryout conditions at the cold plate interface).

11.2.2.2 Cold Plates

There are two categories of cold plates referenced in the literature: forced convection boiling cold plates and those where evaporation of the liquid from a wicking structure occurs. Figure 11.16 presents a novel design for a spiral coil type forced convection cold plate. The layout of a spiral coil and the flow directions on a concentric, reversed-flow cold plate are depicted in the figure.

The cooling fluid passes through the cold plate channels as shown in Figure 11.16b. Shortly after the saturated liquid enters the cold plate, it boils and the heat transfer coefficient dramatically increases. The spiral coil is machined into an aluminum plate, which enhances the conduction process. The design shown helps to prevent hot spots from forming since the channel layout provides almost uniform distribution of gas quality across the plate. In addition, the counterflow arrangement helps to maintain an isothermal surface.

An example of the evaporative type cold plate was examined by Niggemann et al. (1985). They tested a swirl flow evaporative cold plate and found it to be a feasible design for two-phase cooling in a micro-gravity environment.

11.2.2.3 Reservoir

The reservoir balances the vapor pressure (set by the pressure regulator), and the pressure of a spring, with the pressure at a depth of liquid predetermined by the liquid level probe in the pump-separator device (see Figure 11.14). Thus, the liquid inventory is controlled passively. Figure 11.17 shows a conceptual schematic diagram of the reservoir.

11.2.2.4 Pressure Regulator

The regulator is the set-point controller for the system-operating temperature. Increasing the pressure will cause the system pressure to increase leading to a higher boiling temperature.

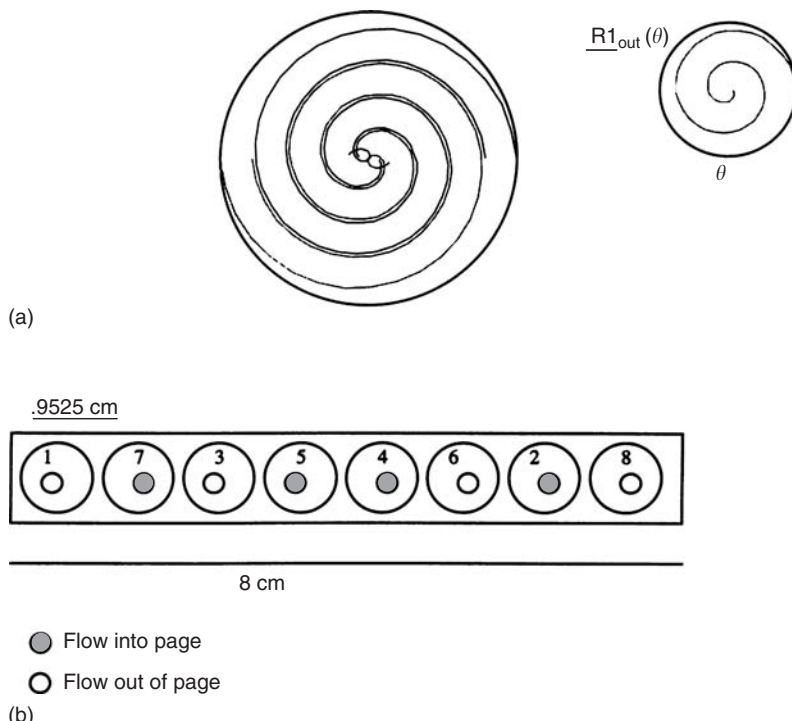


FIGURE 11.16 (a) Novel cold plate design (flow channel layout); (b) cross-section view of cold plate showing flow direction.

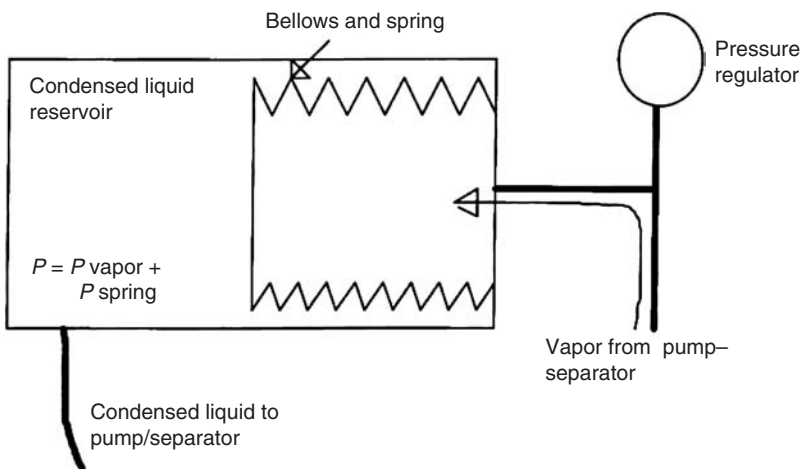


FIGURE 11.17 Reservoir design.

11.2.2.5 Condenser

Many condensers rely on fins to enhance condensation, and gravity is often used as the method to drain the condensate. Another method is necessary for use in microgravity conditions. Valenzuela and Drew (1989) have proposed an alternative condenser in which the condensate drainage network is contained within the condenser walls. In their design, the fins are shaped in a way that creates a capillary pressure

gradient on its surface. The condensate drains into the interior through narrow drainage grooves that separate the fins. This also helps to effectively minimize condensate flooding.

11.2.2.6 Control

The thermal transport system will operate at a predetermined set point. The system will be self-regulating according to the heat load applied to the cold plates. Control of the condenser portion of the system will be passive, responding to the amount of vapor that is required to be condensed from the cold plates.

11.2.3 Classification of Gas–Liquid Flow Patterns at Reduced Gravity: Flow Patterns at Reduced Gravity Conditions

The liquid–gas distribution pattern inside a conduit varies considerably depending on, among other factors, the mass flow rates of both phases, the conduit size, the phase properties, and the gravity vector with respect to the flow direction. Groups with similar phase distribution characteristics are classified into flow patterns (or flow regimes). Tremendous efforts have been made to study the flow patterns and their transitions under normal and microgravity conditions. Since the identification of a particular phase distribution is somewhat subjective, the literature contains a host of flow pattern definitions and descriptions. Recent studies are aimed at minimizing this subjectivity through statistical analysis of void-fraction data (Lowe and Rezkallah, 1999).

Basically, four flow patterns are observed to exist under microgravity conditions; these are bubbly flow, slug flow, transitional flow, and annular flow. Bubbly flow consists of gas bubbles that are less than or equal to the tube diameter, distributed in a liquid continuum. Figure 11.18a shows a group of spherical medium-sized bubbles with some small dispersed bubbles. The bubbles tend to flow at or near the tube center.

Slug flow consists of gas bubbles that are longer than the tube diameter but have diameters close to the tube diameter. Figure 11.18b shows a series of rounded, smooth, uniform bubbles of approximately two to three tube diameters.

Transitional or "frothy slug-annular flow" occurs when the liquid flows in the form of a film at the tube wall and the gas-phase flows in the center of this film. Frothy slugs pass frequently and, although it is difficult to discern the details, they probably consist of densely packed fine gas bubbles in a liquid continuum at relatively low gas flow rates or small liquid droplets at relatively high gas flow rates. Figure 11.18c

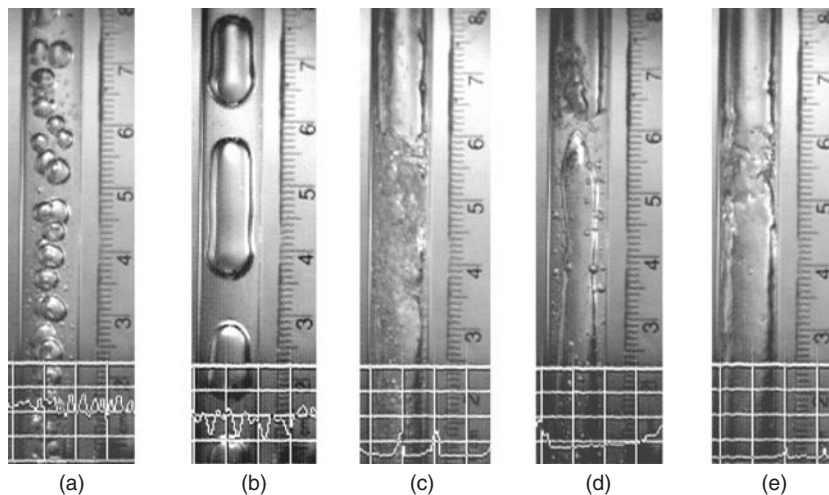


FIGURE 11.18 Four flow regimes: (a) bubbly flow; (b) slug flow; (c) transitional flow I; (d) transitional flow II; (e) annular flow.

shows transitional flow for a liquid flow rate of 0.16 m/sec and a gas flow rate of 5.96 m/sec. The figure shows a smooth film interrupted by a frothy slug region. [Figure 11.18d](#) shows transitional flow for a liquid flow rate of 0.11 m/sec and a gas flow rate of 1.59 m/sec. The figure shows a liquid slug that separates two large bubbles. Small bubbles are disbursed in the thick liquid film.

Annular flow occurs when the liquid-phase flows at the tube wall and the gas-phase flows uninterrupted at the center of the tube. Figure 11.18e shows the passage of a wave at the center of the image.

11.2.3.1 Flow Pattern Transitions

In a two-phase flow system, there are several forces acting on the mixture, each of which has some impact on the overall flow configuration. These forces include those due to inertia, buoyancy, surface tension, and turbulent eddies. The flow pattern is determined by a delicate balance of these forces. The influence of buoyancy force due to gravity can be evaluated by the Froude number

$$Fr = \frac{V_m^2}{gD} = \frac{\text{inertial force}}{\text{buoyancy force}} \quad (11.17)$$

where the velocity, V_m , is the sum of the gas and liquid superficial velocities, $V_m = V_{SG} + V_{SL}$, g the apparent gravity, and D the diameter of the tube. The influence of surface tension is determined by the Weber number

$$We = \frac{\rho V^2 D}{\sigma} = \frac{\text{inertial force}}{\text{surface tension}} \quad (11.18)$$

which represents the balance between inertial force and surface tension. This dimensionless group must be an important correlating parameter at microgravity conditions.

At low gas velocity, and hence for a low We_G , surface tension is dominant. The flow is a bubbly flow, and the bubble shape is determined by surface tension. Owing to the minimum slip in microgravity bubbly flow, the bubble velocity at microgravity can be reasonably represented by:

$$V_G = 1.2(V_{SG} + V_{SL}) \quad (11.19)$$

When the gas velocity is increased, the inertial force becomes large enough to overcome surface tension. The gas phase breaks through the liquid-slug and forms tiny packed gas bubbles. This transition region is called frothy slug-annular due to the continuous appearance of frothy mixtures in the liquid slugs. Based on experimental data, the transition from slug flow to frothy slug-annular flow appears to take place at

$$We_G = \frac{\rho_G V_G^2 D}{\sigma} \approx 1 \quad (11.20)$$

As the gas flow rate further increases, the density of the liquid droplets in the frothy slugs decreases, and the frothy slugs become thinner until eventually annular flow is reached. In this region, the flow pattern is mainly dominated by forces due to inertia. From the experimental data, it was found that annular flow occurs at

$$We_G \approx 20 \quad (11.21)$$

11.2.3.2 Flow Pattern Map

In general, two-phase gas-liquid flow under microgravity conditions can be divided into three main flow regions. These are surface tension-controlled, intermediate, and inertial force-controlled. The first region is where the forces due to surface tension are significantly higher than those due to inertia ($We_G < 1$), which includes bubble and slug flows. The second region is where the two forces are comparable ($1 < We_G < 20$), which is occupied by transitional flows (frothy slug-annular flow). The third region is where the forces due to inertia are dominant ($We_G > 20$), which is occupied by annular flow. A dimensionless flow pattern map based on these criteria is given in [Figure 11.19](#).

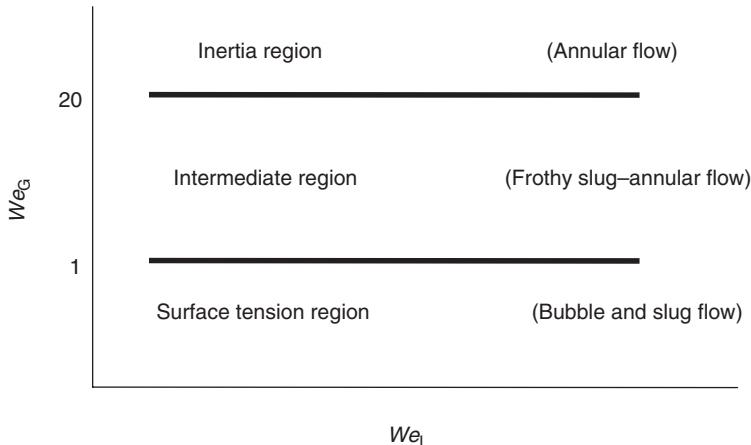


FIGURE 11.19 Two-phase flow regions at microgravity conditions.

11.2.4 Gas–Liquid Pressure Drop

11.2.4.1 Momentum Equations

The determination of pressure losses in two-phase flow systems is essential to the design of a thermal management system. The pressure loss, dp/dz in a two-phase flow system includes pressure losses due to friction, f , gravitational force, g , and momentum change, m . The total pressure loss is estimated from

$$\left(\frac{dp}{dz}\right)_{\text{tot}} = \left(\frac{dp}{dz}\right)_f + \left(\frac{dp}{dz}\right)_g + \left(\frac{dp}{dz}\right)_m \quad (11.22)$$

The calculations of the last two terms, i.e., gravitational and momentum terms, require the knowledge of the void fraction. The gravitational component can be rewritten as

$$\left(\frac{dp}{dz}\right)_g = [\alpha\rho_G + (1 - \alpha)\rho_L]g \quad (11.23)$$

and for the momentum component, the above equation becomes

$$\left(\frac{dp}{dz}\right)_m = G^2 \frac{d}{dz} \left[\frac{x^2}{\alpha\rho_G} + \frac{(1 - x)^2}{(1 - \alpha)\rho_L} \right] \quad (11.24)$$

where G is the total mass flux of both phases. When gravity is changed, the methods to calculate the two terms remain the same, only the void fraction might be different. In this section, only the estimation of the frictional pressure drop component will be discussed in detail.

11.2.4.2 Empirical Methods

Many empirical or semiempirical correlations are available for the prediction of the frictional pressure drop (e.g., Lockhart and Martinelli, 1949; Dukler et al., 1964a, 1964b; Chisom, 1967; Friedel, 1979). For more details see [Chapter 2](#). Such correlations were mostly based on experimental data collected at different orientations on ground, different tube diameters, and a wide range of liquid and gas properties. Some of these models are discussed hereafter.

11.2.4.3 The Homogeneous Model

The basic assumption of this model is that the two phases are well mixed, and that the velocities of the two phases are equal. These assumptions are closer to that which is actually experienced in bubbly and slug flows (short slugs) at microgravity than at 1g. The mixture density is given in terms of the gas quality, x :

$$\frac{1}{\rho_{mi}} = \frac{x}{\rho_G} + \frac{1 - x}{\rho_L} \quad (11.25)$$

The mixture viscosity can be calculated by using one of several methods. One of them is to use the liquid viscosity (let $\mu_{mi} = \mu_L$) in the calculation of the Reynolds number; another is to use a mixture viscosity instead of the liquid viscosity. Several correlations were recommended for μ_{mi} , among which is the one suggested by Dukler et al. (1964b), namely

$$\mu_{mi} = \mu_G \frac{x\rho_{mi}}{\rho_G} + \mu_L \frac{(1-x)\rho_{mi}}{\rho_L} \quad (11.26)$$

The friction factor C_f can be calculated from the Blasius equation, in which the Reynolds number is given by

$$Re_{mi} = \frac{\rho_{mi} V_{mi} D}{\mu_{mi}} \quad (11.27)$$

The pressure drop can then be obtained from

$$\left(\frac{dp}{dz} \right)_F = \frac{2}{D} C_f \rho_{mi} V_{mi}^2 \quad (11.28)$$

where $V_{mi} = V_{SL} + V_{SG}$ is the mixture velocity.

11.2.4.4 The Lockhart–Martinelli Correlation

Another widely used method for the estimation of two-phase flow pressure drop is the Lockhart–Martinelli correlation. The original correlation is given in a graphical form (Lockhart and Martinelli, 1949). The correlation can be written using the following expression (Zhao and Rezkallah, 1993):

$$\left(\frac{dp}{dz} \right)_{TP} = \left(\frac{dp}{dz} \right)_L + C \left(\frac{dp}{dz} \right)_L^{1/2} \left(\frac{dp}{dz} \right)_G^{1/2} + \left(\frac{dp}{dz} \right)_G \quad (11.29)$$

Equation (11.29) implies that the two-phase pressure drop is equal to the sum of the pressure drop for the liquid phase flowing alone, plus the pressure drop for the gas phase flowing alone, plus a two-phase flow effect. The coefficient C represents the importance of the two-phase flow effects. It can be argued that these effects at microgravity conditions are generally high without discriminating between the fluid flow rates. When the velocities of both phases are high, the differences between microgravity and normal gravity conditions are almost negligible. On the other hand, when the flow rates are low, the microgravity pressure drop is higher than that at normal gravity conditions. A constant $C = 20$ fits the experimental data over a wide range of flow rates. In general, the Lockhart–Martinelli correlation underpredicts the pressure drop in microgravity flows.

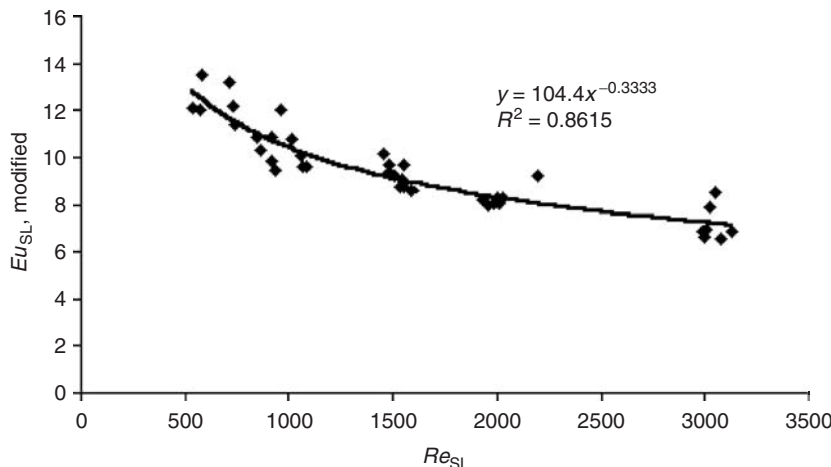


FIGURE 11.20 Euler number based correlation. (From de Jong, P. and Rezkallah, K.S., *Proceedings of Spacebound Conference*, 2000.)

11.2.4.5 Dimensional Analysis Model

The μ -g two-phase pressure drop was correlated (deJong and Rezkallah, 2000) in terms of the Euler number. The correlation was based on a dimensional analysis approach and is given by

$$Eu_{SL} = \left[\frac{(\partial P/\partial z_f)D}{\rho_L V_{SL}^2} \right] = C_L Re_{SL}^{-0.33} \left(\frac{x}{1-x} \right)^{0.80} \left(\frac{\rho_G}{\rho_L} \right)^{0.5} \left(\frac{\mu_G}{\mu_L} \right)^{-0.1} \quad (11.30)$$

The quality ratio term ($x/(1-x)$) has a direct relationship with the superficial liquid Euler number. Modifying Eu_{SL} by dividing it with $(x/(1-x))^{0.8}$ enables us to plot the relationship between Eu_{SL} and Re_{SL} ; this is shown in Figure 11.20. As Re_{SL} increases, the effect is to reduce the Euler number. The relationship is of a power-law type.

Nomenclature

Bd	Bond number
C_f	Friction coefficient
C_L	Constant in Eq. (11.30)
Ca	Capillary number
D	Tube diameter, m
D_h	Hydraulic diameter
dp/dz	Pressure gradient, Pa/m
Eu	Euler number
f	Friction factor
Fr	Froude number
G	Total mass flux, kg/m ² s
g	Gravitational acceleration, m/s ²
P	Pressure, Pa
R	Radius, m
Re	Reynolds number
V	Velocity, m/s
V_m	Sum of gas and liquid superficial velocities, m/sec
We	Weber number
x	Gas mass quality
X	Lockhart-Martinelli parameter
Z	Distance

Greek Symbols

α	Void fraction
β	Volumetric gas flow ratio
ε	Cross-section average void fraction
θ	Contact angle
μ	Dynamic viscosity, N s/m ²
ρ	Density, kg/m ³
σ	Surface tension, N/m

Subscripts

f	Friction
gs	Superficial gas
G,g	Single-phase gas

L,l	Single-phase liquid
ls	Superficial liquid
m	Momentum change
mi,m	Mixture
SG	Superficial gas
SL	Superficial liquid
tot	Total
TP	Two-phase, two-component

References

- Akbar, M.K., Plummer, D.A., and Ghiaasiaan, S.M., On gas–liquid two-phase flow regimes in microchannels, *Int. J. Multiphase Flow*, 29, 855–865, 2003.
- Ali, M.I., Sadatomi, M., and Kawaji, M., Two-phase flow in narrow channels between two flat plates, *Can. J. Chem. Eng.*, 71, 657–666, 1993.
- Allen, J.S. and Son, S.Y., Observation of low Bond number two-phase flow regime transition from slug to annular wavy flow in a microchannel, *Proceedings of the 1st International Conference on Microchannels and Minichannels*, Rochester, NY, 473–477, Apr. 24–25, 2003.
- Armand, A.A. and Treschev, G.G., *Izv. Vses. Teplotek. Inst.*, 16–23, 1946.
- Barajas, A.M. and Panton, R.L., The effects of contact angle on two-phase flow in capillary tubes, *Int. J. Multiphase Flow*, 19(2), 337–346, 1993.
- Brauner, N. and Moalem-Marom, D., Identification of the range of “small diameter” conduits, regarding two-phase flow pattern transition, *Int. Comm. Heat Mass Transfer*, 19, 29–39, 1992.
- Celata G.P., Cumo, M., Guglielmi, M., and Zummo, G., Heat transfer in 0.130 mm capillary tube, *Microscale Thermophy. Eng.*, 6, 85–97, 2002.
- Chisholm, D., A theoretical basis for the Lockhart-Martinelli correlation for two-phase flow, *Int. J. Heat Mass Transfer*, 10, 1767–1778, 1967.
- Chisholm, D. and Laird, A.D.K., Two-phase flow in rough tubes, *Trans. ASME* 80, 276–286, 1958.
- Damianides, C.A. and Westwater, J.W., Two-phase flow patterns in a compact heat exchanger and small tubes, *Proceedings of the 2nd UK National Conference on Heat Transfer*, Glasgow, Sept. 14–16, Mechanical Engineering Publications, London, 1988 pp. 1257–1268.
- deJong, P. and Rezkallah, K.S., A Dimensional Analysis of Microgravity Annular Flow: Pressure Drop and Film characters, *Proceedings of spacebound conference*, 2000.
- Dukler, A.E., Wicks, M., and Cleveland, R.D., Frictional pressure drops in two-phase flow: a comparison of existing correlations for pressure loss and holdup, *AIChE J.*, 10, 38–43, 1964a.
- Dukler, A.E., Wicks, M., and Cleveland, R.D., Frictional pressure drops in two-phase flow: an approach through similarity analysis, *AIChE J.*, 10, 44–51 1964b.
- Dukler, A.E., Wicks, M., III, and Cleveland, R.G., Pressure drop and hold-up in two-phase flow, *AIChE J.*, 10, 1, 38–51, 1964.
- Friedel, L., Improved friction pressure drop correlations for horizontal and vertical two-phase pipe flow, *European Two-phase flow Group meeting*, paper E2, Is Pra, 1979.
- Ghiaasiaan, S.M. and Abdel-Khalik, S.I., Two-phase flow in microchannels, *Adv. Heat Transfer*, 34, 145–254, 2000.
- Huckerby, C.S. and Rezkallah, K.S., flow pattern observations in two-phase gas–liquid flow in a straight tube under normal and microgravity conditions,” *AIChE Proceedings*, 88, *AIChE Conf*, Philadelphia, 332–337, 1992.
- Kandlikar, S.G., and Grande, W.J., Evolution of microchannel flow passages—thermohydraulic performance and fabrication technology, Proc. of the International Mechanical Engineering Conference and Exposition, Nov. 17–21, 2002, New Orleans, LA, Paper No. IMECE2002–32043 (2002).
- Kandlikar, S.G., *Proceedings of the 1st International Conference on Microchannels and Minichannels*, Rochester, NY, Apr. 24–25, 2003a.

- Kandlikar, S.G., Microchannels and minichannels — History, terminology, classification and current research needs, *Proceedings. of the 1st International Conference on Microchannels and Minichannels*, Apr. 24–25, 2003b, Rochester, NY, pp. 1–6.
- Kawahara, A., Chung, P.M.-Y., and Kawaji, M., Investigation of two-phase flow pattern, void fraction and pressure drop in a microchannel, *Int. J. Multiphase Flow*, 28, 1411–1435, 2002.
- Kawahara, A., Sadatomi, M., Okayama, K., and Kawaji, M., Effects of liquid properties on pressure drop of two-phase gas–liquid flows through a microchannel, *Proceedings of the 1st International Conference on Microchannels and Minichannels*, Rochester, NY., Apr. 24–25, 2003, pp. 479–486.
- Kawaji, M. and Chung, M.-Y., Unique characteristics of adiabatic gas–liquid flows in microchannels: diameter and shape effects on flow patterns, void fraction and pressure drop, *Proceedings of the 1st International Conference on Microchannels and Minichannels*, Rochester, NY., Apr. 24–25, 2003, pp. 115–128.
- Kureta, M., Kobayashi, T., Mishima, K., and Nishihara, H., Pressure drop and heat transfer for flow boiling of water in small-diameter tubes, *JSME Int. J., Series B*, 41, 4, 871–879, 1998.
- Lee, H.J. and Lee, S.Y., Pressure drop correlations for two-phase flow within horizontal channels with low aspect ratios, *Int. J. Multiphase Flow*, 27, 783–796, 2001.
- Lockhart, R.W. and Martinelli, R.C., Proposed correlation of data for isothermal two-phase flow, two-component flow in pipes, *Chem. Eng. Prog.*, 45, 39–48, 1949.
- Lowe, D.C. and Rezkallah, K.S., Flow regime identification in microgravity two-phase flows using void fraction signals, *Int. J. Multiphase Flow*, 25, 433–457, 1999.
- Mandhane, J.M., Gregory, G.A., and Aziz, K., A flow pattern map for gas–liquid flow in horizontal pipes, *Int. J. Multiphase Flow*, 1, 4, 537–553, 1974.
- Mishima, K. and Hibiki, T., Some characteristics of air–water two-phase flow in small diameter vertical tubes, *Int. J. Multiphase Flow*, 22, 703–712, 1996.
- Mori, K., *A study of two-phase flow patterns in microchannels*, BE thesis, Kyoto University, 2003.
- Niggemann, R.E., Greenlee, W.J., Hill, D.G., Ellis, W., and Marshall, P., A swirl flow evaporative cold plate, *20th Thermophysics Conference*, Paper AIAA-85-0920, 1985.
- Rezkallah, K.S., Heat transfer and flow characteristics of liquid–gas flows at reduced gravity, *Trends Chem. Eng.*, 4, 161–170, 1998.
- Serizawa, A., *Heat Transfer and Hydraulic in Microchannel Flows*, Report of the Research Committee on Heat Transfer and Fluid Flow in Microchannel, Japan Society for Mechanical Engineers, P-SC295, Editor, Rohester, NY, 2001.
- Serizawa, A., *Proceedings of the 4th Pacific Rim Thermal Science and Energy Engineering Workshop*, May 31–June 2, 2002, Editor Kyoto.
- Serizawa, A. and Feng, Z.P., Two-phase flow in micro-channels, *Proceedings of the 4th International Conference on Multiphase Flow*, New Orleans, Louisianna, USA, Paper No.606 (in CD-ROM), May 27–June 1, 2001.
- Serizawa, A. and Kawara, Z., Two-phase flow in micro-channels, *Proceedings. of the 39th European Two-Phase Flow Group Meeting*, Aveiro, Portugal (in CD-ROM), June, 17–20 2001.
- Serizawa, A., Feng, Z.P., and Kawahara, Z., Two-phase flow in microchannels, *Int. J. of Exp. Heat Transfer, Thermodyn., and Fluid Mech.*, 26, 703–714, 2002.
- Suzuki, *Two-phase flow in microchannels*, BE thesis, Kyoto.
- Suzuki, N., *Two-phase flow characteristics in micro channels*, ME thesis, Kyoto University, 2004.
- Suo, M. and Griffith, P., Two-phase flow in capillary tubes, *J. Basic Eng.*, 86, 576–582, 1964.
- Suzuki, N., *Two-Phase Flow Characteristics in Microchannels*, MS thesis, Department of Nuclear Engineering, Kyoto University (in Japanese), 2004.
- Takei, M. and Kimura, M., *MEMS Workshop “Possibility of MEMS and Multiphase”*, The Japan Society of Multiphase Flow, Sept. 26, 2000, Editors, Tokyo 2000.
- Triplett, K.A., Ghiaasiaan, S.M., Abdel-Khalik, S.I., and Sadowski, D.L., Gas–liquid two-phase flow in microchannels, Part I: two-phase flow patterns, *Int. J. Multiphase Flow*, 25, 377–394, 1999a.
- Triplett, K.A., Ghiaasiaan, S.M., Abdel-Khalik, S.I., Le Mouel, A., and McCord, B.N., Gas–liquid two-phase flow in microchannels, Part II: void fraction and pressure drop, *Int. J. Multiphase Flow*, 25, 395–410, 1999b.

- Ungar, E.K. and Cornwell, J.D., Two-phase pressure drop of ammonia in small diameter horizontal tubes, *AIAA 17th Aerospace Ground Test Conference*. Nashville, Tennessee, July 6–8, 1992.
- Valenzuela, J. and Drew, B., Internally drained condenser for spacecraft thermal management, *24th Thermophysics Conference*, Paper AIAA-89-1725, 1989.
- Zhao, L. and Rezkallah, K.S., Pressure drop in two-phase annular flow at microgravity conditions, *31st Aerospace Sciences Meeting & Exhibit*, Paper AIAA-93-0576, 1993.

12

Multiphase Interactions

G.F. Oweis
S.L. Ceccio
University of Michigan

Y. Matsumoto
University of Tokyo

C. Tropea
I.V. Roisman
*Technical University of
Darmstadt*

Y. Tsuji
Osaka University

R. Lyczkowski
Argonne National Laboratory

T.R. Troutt
Washington State University

J.K. Eaton
Stanford University

F. Mashayek
University of Illinois

12.1	Cavitation	12-1
	Cavitation Nuclei and Bubble Growth • Collapse of Cavitation Bubbles and Erosion • Acoustic Cavitation • Hydrodynamic Bubble Cavitation • Sheet Cavitation • Vortex Cavitation • Cavitation in Hydraulic Machinery • Cavitation in Biomedical Applications • Other Occurrences and Applications of Cavitation	
12.2	Bubble Physics	12-17
	Single Spherical Bubble Dynamics • Bubble Deformation and Fragmentation Due to the Collapse • Bubbles Cloud Dynamics	
12.3	Droplet Breakup, Coalescence, and Wall Impact	12-35
	Droplet Breakup Mechanisms • Binary Drop Collisions • Drop-Wall Impact	
12.4	Particle Interactions	12-51
	Particle–Particle Collision • Particle–Wall Interaction • Erosion	
12.5	Particle and Droplet Dispersion in Turbulent Flows	12-81
	Introduction • Time Scales • Particle Dispersion in Turbulent Shear Flows • Body Force Effects on Particle Dispersion • Two- Way Coupling Effects on Particle Dispersion	
12.6	Turbulence Modulation by Particles	12-86
	Introduction • Mechanisms of Turbulence Modification • Analytical Approaches • Methods for Studying Turbulence Modulation • Observations of Turbulence Modulation • Summary	
12.7	Combustion	12-98
	Introduction • Overview of Single-Phase (Gaseous) Combustion • Isolated Drop • Groups of Drops • Spray Modeling	

12.1 Cavitation

G.F. Oweis and S.L. Ceccio

Cavitation is the physical phenomenon associated with the inception, growth, and implosion of cavities (vapor-filled voids or bubbles) in the body of a flowing or a quiescent liquid due to changes in the fluid pressure. Cavitation may occur entirely in the bulk of the liquid or close to solid boundaries of the flow. Cavitation is similar to boiling in the inception and growth of bubbles, except that in the latter bubble formation is due to a rise in liquid temperature, while in the former bubble formation is driven by a drop

in the liquid static pressure. Pressure variations in the fluid can be achieved hydrodynamically or acoustically. During vaporous (inertial) cavitation, the cavities are filled mostly with fluid vapor. Vaporous cavitation bubbles are often short-lived and produce a high-intensity acoustic pressure upon collapse. Gaseous cavitation bubbles are filled mostly with noncondensable gases, and these gaseous bubbles may persist for longer periods, collapse much less violently, and produce much less noise and damage compared to vaporous bubbles. Pockets of gas and vapor can form and persist on flowing surfaces, and this is referred to as *partial* or *attached* cavitation. Cavitation *inception* occurs when cavitation is first detected in the flow as the mean pressure in the flow is reduced, and *developed* cavitation describes an advanced stage of cavitation, where the size of the cavity is of comparable magnitude to a characteristic flow dimension. *Desinence* occurs when cavitation is eliminated through an increase in the mean pressure. Cavitation is undesirable in liquid handling machinery because it may cause damage to solid surfaces, induce noise and vibrations, and lead to reduction in the mechanical efficiency. Conversely, there are useful scientific and engineering applications that employ cavitation. Comprehensive reviews of this subject can be found in Brennen (1995), Young (1989), and Franc et al. (1995).

12.1.1 Cavitation Nuclei and Bubble Growth

Liquid water can be brought to evaporation at a constant pressure by raising its temperature. This phase change can also be achieved at a constant temperature by reducing the pressure to the corresponding vapor pressure (e.g., water at 1 atm and room temperature, 25°C, can be brought to boiling by heating to 100°C while keeping the pressure fixed, or by reducing the pressure to vapor pressure, 0.03 atm, while keeping the temperature fixed at 25°C). The process of phase change takes place at a phase boundary in the liquid. If such an interface is not present, the bulk of the liquid can sustain pressures below vapor pressure (or remain liquid at temperatures above the saturation temperature) (Carey, 1992). (see [Chapter 3](#) for a discussion on nucleation and boiling.)

Theoretical predictions based on the van der Waals intermolecular forces of attraction indicate that *pure* water (no dissolved gas or impurities) can withstand high levels of tension corresponding to pressures much less than the vapor pressure (several hundred atmospheres of tension). The fracture of the liquid due to the failure of intermolecular forces is called *homogeneous nucleation*. In most practical applications, these high levels of tension are not approached. Instead, voids or bubbles (cavitation) appear in the liquid as the liquid evaporates at the interface of small gas inclusions, or *nuclei*. This process is called *heterogeneous nucleation*, and it is the most common form of cavitation initiation. It is often sufficient to bring the operational pressure to or slightly below the evaporation pressure for these bubbles or voids to appear.

Cavitation nuclei can be present in the body of the liquid, or on the surfaces of suspended particles or boundaries that come in contact with it as described in Section 3.1. Cavitation nuclei often exist as small bubbles of gas (a few microns to a few hundred microns) that are in equilibrium with the liquid, or as gas-filled miniature pockets on the surfaces of solid particles or solid flow boundaries. Nuclei can also form when dissolved gas in the liquid comes out of solution. The amount and properties of nuclei in the fluid can strongly influence the pressure at which inception occurs. The growth of nuclei can often be approximated by the growth of small spherical bubbles in an unbounded liquid.

The Rayleigh–Plesset equation (Brennen, 1995) describes the dynamics of growth and collapse of a spherical bubble nucleus in an otherwise quiescent, infinite fluid medium. It couples the forces acting on the bubble with the motion of the surrounding fluid:

$$\rho_l \left[a_b \frac{d^2 a_b}{dt^2} + \frac{3}{2} \left(\frac{da_b}{dt} \right)^2 \right] + \frac{4\mu}{a_b} \frac{da_b}{dt} = \left(p_{\infty,0} - p_v + \frac{2\sigma}{a_{b,0}} \right) \left(\frac{a_{b,0}}{a_b} \right)^{3k} - p_\infty + p_v - \frac{2\sigma}{a_b} \quad (12.1)$$

where the subscript 0 refers to the initial conditions of the bubble. The liquid pressure far away from the bubble is p_∞ . The bubble contains both vapor and noncondensable gas of partial pressures, p_v and p_g , respectively. The gas obeys the polytropic gas law. The exponent k is the polytropic gas constant, and $k = 1$ for isothermal processes and $k = c_p/c_v$ for adiabatic processes. p_g is equal to the first term on the right-hand side

(RHS) of the equation. In this formulation the liquid compressibility is neglected (see [Section 12.2](#) for further discussion of bubble physics.)

With the left-hand side (LHS) set to zero, Eq. (12.1) describes the quasi-static equilibrium of a bubble (temporal dependence of the bubble radius is negligible). Consider a small bubble (cavitation nucleus) that exists in a quasi-static equilibrium in the body of a liquid. The pressure inside the bubble, p_b , is counteracted by the liquid pressure on the bubble surface, p_l , and by the surface tension forces, or

$$p_g + p_v = \frac{2\sigma}{a_b} + p_l \quad (12.2)$$

where $p_b = p_g + p_v$. When this nucleus experiences a drop in the liquid pressure, such as when it passes through a venturi throat, it may grow quasi-statically from its initial equilibrium radius, $a_{b,0}$, to a larger equilibrium radius, provided that the bubble radius does not exceed the *Blake critical radius*. A bubble exposed to tension will grow unboundedly when its radius is above this critical value given by

$$a_{b,c} = \left[\frac{9km_G T_b K_G}{8\pi\sigma} \right]^{1/2} = \left[\frac{3}{2} \frac{k a_{b,e}^3 p_{g,e}}{\sigma} \right]^{1/2} \quad (12.3)$$

The subscript e refers to the equilibrium state of the bubble. Here, m_G and K_G are the gas mass and gas constant, respectively, and T_b the bubble temperature. An equivalent critical liquid pressure is given by

$$p_{l,c} = p_v - \frac{4}{3}\sigma \left[\frac{8\pi\sigma}{9km_G T_b K_G} \right]^{1/2} = p_v - \frac{4}{3}\sigma a_{b,c} \quad (12.4)$$

In the venturi example, if the liquid pressure drops to or below the critical pressure, the bubble radius will grow explosively to a maximum radius that can be of the order of hundred times its initial size, and the nucleus would then be considered to have cavitated. Figures 12.1a and b show the response of a nucleus,

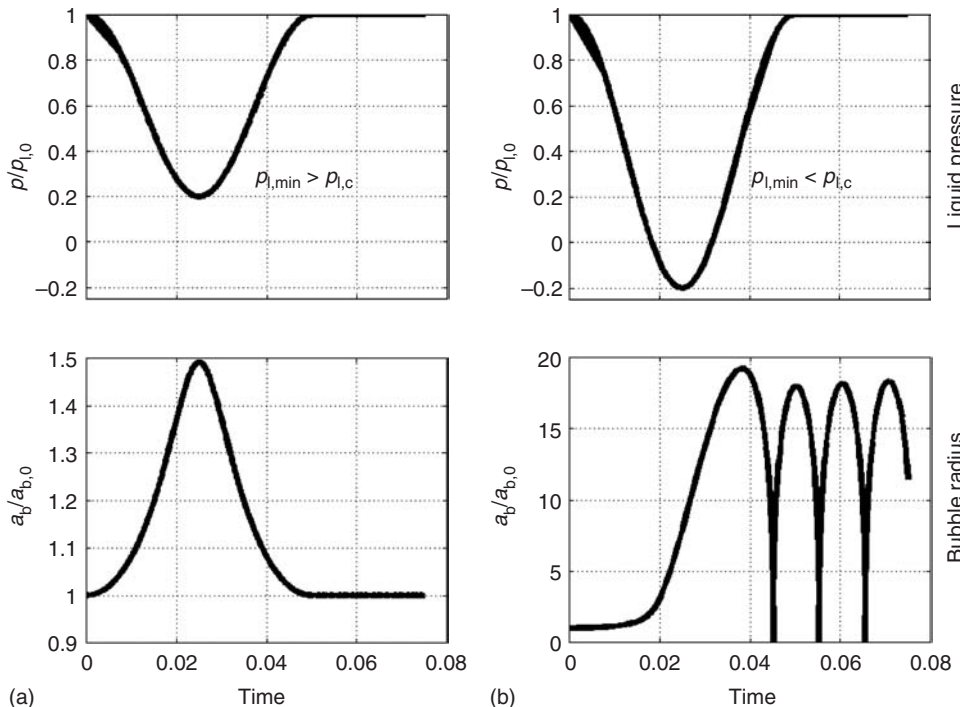


FIGURE 12.1 Changes in the radius of a bubble as it is exposed to a sinusoidal variation in the surrounding pressure: the minimum pressure is above the critical pressure (a) and below the critical pressure (b).

initially in equilibrium, to a sinusoidal variation in the liquid pressure. Figure 12.1a shows the change in bubble radius when the minimum liquid pressure is above the critical pressure: the bubble radius responds quasi-statically. Next, Figure 12.1(b), the tension exceeds the critical pressure. Notice the growth rate of the cavitating nucleus, its violent collapse, and the multiple rebounds. Not all nuclei will lead to cavitation (explosive bubble growth). Only the nuclei that reach the critical radius will cavitate, and these are considered the *active nuclei*.

When a bubble cavitates, its radius will grow asymptotically. Thus, the maximum bubble radius, $a_{b,m}$, is related to the total time that the bubble remains in the region of tension, Δt :

$$a_{b,m} \approx \frac{2}{3} \left(\frac{-p_\infty + p_v}{\rho_1} \right)^{1/2} \Delta t \quad (12.5)$$

The nuclei distribution in a flow can be quite variable, depending on the source of the liquid and the upstream flow conditions. Consequently, the characterization of cavitation inception must be accompanied by a measurement of the nuclei content.

Measurement methods for cavitation nuclei can be hydrodynamic, acoustic, or optical (Gindroz and Billet, 1993). Holography and light scattering have been used to detect the presence of cavitation nuclei (Ran and Katz, 1993). In these methods, the optically measured size of detected bubbles is used to infer the critical pressure. The absorption and scattering of acoustic signals is also used to detect and count nuclei (Chahine and Kalumuk, 2003). A direct measurement of the presence of nuclei is achieved when a liquid sample is passed through a region of known low pressure. Nuclei with radii that exceed the critical radius will cavitate. The Blake critical radius is computed from this pressure and presented as the nuclei radius. The event rate of these cavitating bubbles can then be counted by visual observation. Moreover, when a cavitating bubble is convected to a region of higher pressure downstream, it will collapse producing an acoustic emission. The noise pulses can be detected and counted, giving another independent measurement of the nuclei. Devices that measure nuclei through inducing cavitation events are called *cavitation susceptibility meters* (d'Agostino and Acosta, 1991; Ceccio et al., 1991). The amount of dissolved gas in the liquid will also influence the number of free nuclei and the inception process. Measurements of the total dissolved gas (or of one gas component, such as oxygen) are often reported, but this quantity only indirectly relates to the free gas content.

12.1.2 Collapse of Cavitation Bubbles and Erosion

The collapse of cavitation bubbles is of practical importance, because of the associated high potential for damage and noise production. Once a cavitating bubble has reached its maximum radius and encountered a region of higher pressure (either through convection to a high-pressure region or via a change in the mean pressure field), the bubble will start its collapse. During the final stages of bubble implosion, the bubble wall velocity can reach or exceed the liquid speed of sound, and shock waves are produced in the liquid. Liquid compressibility in the vicinity of the bubble cannot be neglected in this instance, and the Rayleigh–Plesset equation (Eq. [12.1]) should be modified to include this effect. One of the existing modifications is the Gilmore equation (Franc et al., 1995; Leighton, 1994) and is given by

$$a_b U \frac{dU}{da_b} \left(1 - \frac{U}{c_l} \right) + \frac{3}{2} U^2 \left(1 - \frac{U}{3c_l} \right) = h \left(1 - \frac{U}{c_l} \right) + \frac{a_b U}{c_l} \left(1 - \frac{U}{c_l} \right) \frac{dh}{da_b} \quad (12.6)$$

where $U = da_b/dt$, c_l is the liquid speed of sound, and h the enthalpy of the liquid at the bubble wall, with $h = 0$ for the liquid very far away. Whether the bubble wall speed will reach the liquid speed of sound depends on the noncondensable gas mass inside the bubble, which determines the amount of damping of the bubble mechanical energy.

Higher noncondensable gas contents lead to increased damping, and result in less violent collapse and reduced possibility for shock pressure production. Experimentally measured values of the pressure levels in the immediate vicinity of spherically collapsing bubbles in water are of the order of hundreds of atmospheres. The intense pressure waves created in the liquid can cause damage to nearby solid surfaces.

A time scale for the bubble collapse is the Rayleigh collapse time, which depicts the time it takes for a vapor-filled spherical bubble to implode from its maximum to its minimum radius, and is given by

$$t_c = 0.915 a_{b,m} \left(\frac{\rho_l}{\Delta p} \right)^{1/2} \quad (12.7)$$

where $a_{b,m}$ is the maximum bubble radius, Δp the difference between the liquid static pressure and the vapor pressure. The acoustic emission produced by the collapse of a cavitation bubble is proportional to the mechanical potential energy of the bubble:

$$E_M = \frac{4}{3} \pi a_{b,m}^3 \Delta p \quad (12.8)$$

The collapsing bubble is largely a monopole sound source, with the largest emissions taking place during the rapid volume deceleration and acceleration at the point of minimum bubble volume. The amount of this energy converted into acoustic energy during bubble collapse is strongly related to the amount of deformation that the bubble undergoes during collapse.

The collapse of the bubble can be influenced by gravity and the presence of free and solid surfaces (Blake and Gibson, 1987). The quantity

$$\gamma = \left(\frac{\rho_l g a_{b,m}}{\Delta p} \right)^{1/2} \quad (12.9)$$

scales the buoyancy force with the force due to the pressure difference across the bubble interface. When $\gamma > 1$, the bubble collapse becomes nonspherical and is characterized by the formation of a jet, where the lower side of the bubble caves inward and upward, and penetrates the upper wall of the bubble. A similar jet formation occurs when the bubble collapses near a solid boundary as shown in Figure 12.2 reproduced from Tomita and Shima (1990). Note that the jet is directed toward the solid surface. Measurements of jet speeds of upto 150 m/sec have been observed (Philipp and Lauterborn, 1998; Brujan et al., 2002). The water hammer effect of this jet can induce instantaneous pressures on the surface given by $p_{jet} = \rho_l c_l u_{jet}$, where c_l is the liquid speed of sound and u_{jet} the jet velocity. Jet impact on a nearby solid boundary can lead to very high surface stresses and produce instantaneous pressures on the solid surface exceeding hundreds of bars. These high pressures are capable of inducing surface damage.

Cavitation erosion is caused by the repetitive impingement of cavitation-induced pressure pulses on a solid flow boundary and often results from material fatigue. Erosion predictions on metal surfaces have

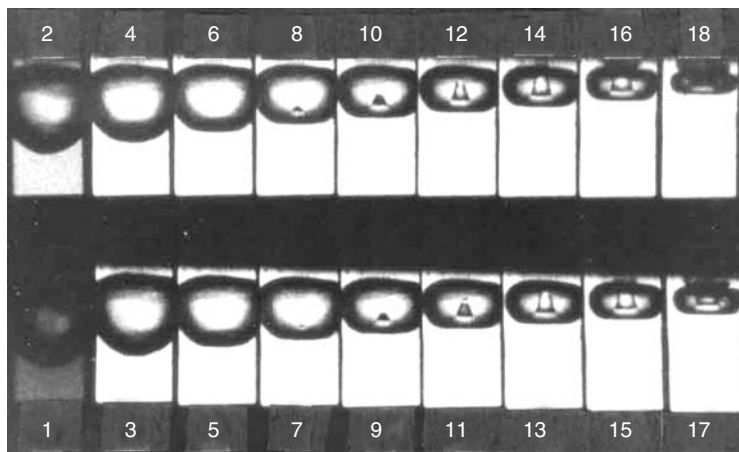


FIGURE 12.2 A series of images that shows the collapse of a cavitation bubble near a solid boundary. The images are with 2 μ sec time intervals, and each is 1.4 mm wide. Note the formation of the reentrant jet directed toward the wall. (Reproduced from Tomita, Y. and Shima, A., *Acustica*, 71, 161, 1990.)

been mostly based on combining the concept of cavitation intensity (frequency of occurrence and levels of peak pressures from collapsing cavities) with one or more representative material properties. Such properties can be the hardness, elastic modulus, tensile strength, or their combinations. An example of such combination is the ultimate resilience, defined as

$$UR = \frac{(\text{tensile strength})^2}{2(\text{Young's modulus})} \quad (12.10)$$

(Hammitt, 1980). Cavitation intensity depends on the flow conditions, and the form of cavitation. Studies on cavitation erosion in metals and alloys often produce scattered results. Erosion measures include mass loss measurements and mean depth of penetration rate (MDPR):

$$MDPR \sim \rho_1 \frac{\eta}{\varepsilon} u^n \quad (12.11)$$

where η is an energy-transfer efficiency term, ε related to the material properties, u the impact speed, and n an exponent. Care should be taken to determine how specific MDPR formulations are derived.

Despite the scatter in cavitation erosion data, a general trend in erosion behavior can be described as depicted in [Figure 12.3](#) for a ductile metal. There is an *incubation period* (I) before a damage to the surface can be noticed, followed by an *acceleration* of the rate of erosion (II). As the specimen is exposed further to cavitation, the erosion rate will *plateau* (III) for quite some time before it drops, in what is known as the *attenuation phase* (IV). The rate of erosion and the damage properties depend also on the microscopic material structure. For ductile materials that have the potential to store elastically and respond to the cavitation hammering energy, damage is often due to fragmentation and is in the form of craters. In fragile alloys, erosion often causes cracks and occurs along crystal lines, and thus causes more material loss than in ductile metals.

12.1.3 Acoustic Cavitation

Sometimes referred to as vibratory cavitation (low driving frequencies) or ultrasonic cavitation (high driving frequencies), acoustic cavitation describes the growth and collapse of cavitation nuclei due to their exposure to acoustic pressure waves in a liquid (Leighton, 1994). As in many forms of cavitation, the presence of cavitation nuclei is usually required to initiate and sustain the cavitation process. Once the cavitation process is initiated, the collapse of the bubbles and their fragmentation can act as nuclei for new cavitation bubbles. Consider an underwater acoustic horn emitting a sinusoidal pressure signal fluctuating about a mean amplitude. The water will experience compression (high pressure) and rarefaction (low-pressure) patterns due to the passage of the wave. If the rarefaction amplitude of the wave drops below the vapor pressure, cavitation can occur. The principle behind the control of acoustic cavitation is the ability to synchronize the acoustic forcing with the dynamics of the bubble in order to achieve the desired effect such as timely bubble growth or collapse. Production of acoustic waves in the liquid can be achieved by magnetostriction type devices, or by the more widely used piezoelectric crystal transducers. The electrical input to a piezoelectric element is transformed into displacement of the piezoelectric crystal surface that is then transferred to the liquid in the form of acoustic waves. To achieve acoustic signals of sufficient amplitude for cavitation, acoustic mirrors or acoustic lenses can be used to focus the acoustic energy into a miniature volume. Focusing can also be achieved by using curved emission transducers. The focusing volume is proportional to the emitted acoustic wavelength and inversely proportional to the transducer size.

Pulsed ultrasound refers to the emission of a train of wave packets of fundamental frequency (f_o), and pulse repetition frequency (f). The pulse duration divided by the pulse repetition period ($1/f$) gives the portion of the time that the transducer is actually emitting or the *duty cycle*. Passive acoustic cavitation describes cavitation events induced by the acoustic emissions from other cavitation bubbles.

It can be shown from the Rayleigh–Plesset equation that a bubble acts as spring–damper system. Consider a cavitation nucleus of initial radius (a_o) that is at the focal point of an ultrasonic transducer emitting at a single frequency (f_o) and with peak amplitude P_o . The bubble wall will oscillate under the

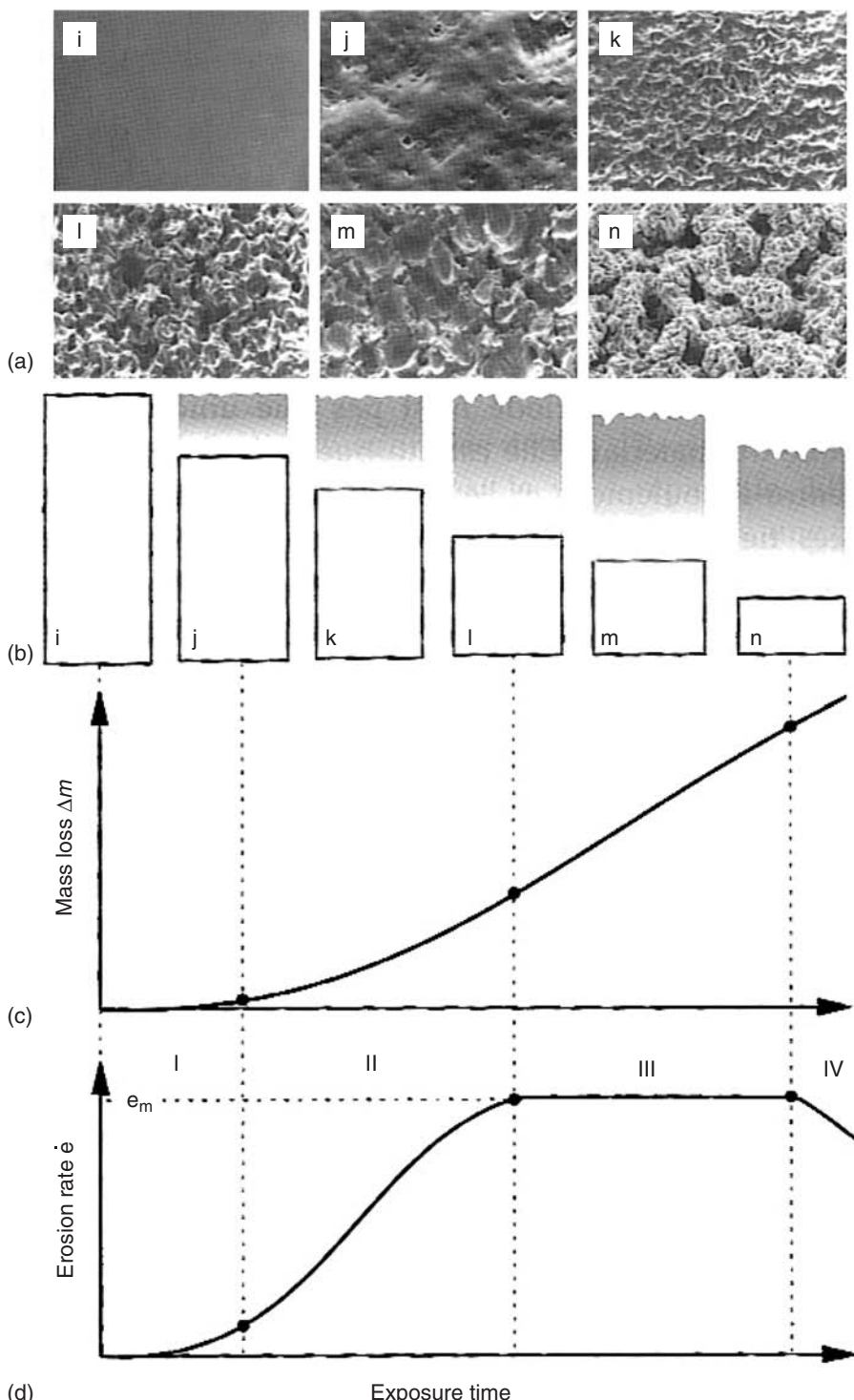


FIGURE 12.3 Erosion behavior of a ductile alloy with cavitation exposure time: (a) scanning electron microscope images showing the surface appearance; (b) cross-sectional schematics of the pitting behavior; (c) accumulative mass loss; (d) erosion rate showing the four stages of erosion. (From Franc et al., *La Cavitation Mécanismes Physiques et Aspects Industriels*, Presses Universitaires de Grenoble, Grenoble, 1995. Copyright EDP Sciences, with permission.)

effect of the forcing acoustic wave, similar to a forced damped oscillator, for *small* bubble oscillation amplitudes. The undamped natural frequency of bubble oscillation in (rad/sec) is given by

$$\omega_n = \left[\frac{1}{\rho_l a_{b,e}^2} \left\{ 3k(p_\infty - p_v + 2(3k-1) \frac{\sigma}{a_{b,e}} \right\} \right]^{1/2} \quad (12.12)$$

The bubble wall motion will be in phase with the forcing pressure if the forcing frequency is less than the bubble natural frequency (resonance). Increasing the forcing frequency above resonance will cause the bubble oscillations to be out of phase with the forcing pressure by 180°. Increasing the driving pressure amplitudes causes the bubble wall motion amplitude to become nonlinear, and undergo large volume oscillations, i.e., cavitation. The oscillations can be stable (*stable cavitation*) or unstable (*transient cavitation*).

During the growth part of bubble oscillation, the increasing bubble size translates into a drop in the non-condensable gas concentration in the bubble interior below the gas concentration in the liquid. This leads to mass diffusion of the gas from the liquid into the bubble. During the contraction phase of the bubble, the opposite occurs, and gas is diffused from the bubble into the liquid. Due to the larger surface area and thinner concentration boundary layer during the growth phase compared with the contraction phase, there would be a net mass diffusion into the bubble. The overall increase in the gas mass in the bubble interior is called '*rectified diffusion*' (Blake, 1949; Hsieh and Plesset, 1961). Since the diffusion time scales are usually much larger than the bubble characteristic time scale (Rayleigh time for instance), diffusion can often be neglected. In transient or unstable cavitation, the driving pressure is increased beyond the linear oscillation until the bubble growth becomes unbounded, followed by violent implosion. The bubble may rebound after collapse or it may fragment into multiple fragments. Brennen (2002) suggests that the bubble fission may be due to an instability forming on the bubble wall or due to jet formation. A number of conditions are required for unstable cavitation to occur; one of them satisfies the Blake critical pressure (or radius) threshold.

When the bubble reaches its minimum radius during implosion, the interior pressure and temperature can momentarily reach extremely high levels. Emission of shock waves in the liquid that travel at liquid Mach numbers greater than 1 has been observed (Pech and Gompf, 2000). Light emission has also been observed from cavitation bubbles collapsing under an ultrasonic pressure field (Holzfuss et al., 1998; Matula et al., 1998; Hilgenfeldt et al., 1999). This phenomena is known as *sonoluminescence*. Puterman and Weninger (2000) discuss how the high pressures and small minimum bubble volumes during the last stages of collapse result in dramatic increases in the bubble energy density, which is essential for the production of light. The detailed physics of sonoluminescence is still a subject of investigation.

The collapse of cavitation bubbles may cause jet formation and pressure shock waves that have useful noninvasive surgical and lithotriptic effects (Vakil and Everbach, 1993; Coleman et al., 1995; Tran et al., 2003). Ultrasonic cavitation is now commonly used in industrial and electronic component cleaning operations (Niemczewski, 1999; Ferrel and Crum, 2002).

12.1.4 Hydrodynamic Bubble Cavitation

Hydrodynamic cavitation occurs when the flow of a liquid leads to reduction in pressure and cavitation. In these flows the cavitation number, which is a measure of the level of pressure in the flow, is defined as

$$\sigma = \frac{p_\infty - p_v}{1/2 \rho U^2} \quad (12.13)$$

Hydrodynamic bubble cavitation (traveling bubble cavitation) and sheet cavitation (Section 12.1.5) are the two major forms of cavitation that take place on the surface of a hydrofoil or the face of a propeller blade. The operational parameters that give rise to one type or the other can be difficult to predict, and subtle changes in flow conditions (e.g., nuclei content, incident flow angle, boundary layer tripping, or Reynolds number) can lead to the inception or desinence of one or both forms. This underlines the complexity involved in predicting and scaling hydrodynamic cavitation behavior on full size prototypes from small models tests. The formation of traveling bubble cavitation can lead to significant noise, vibration, and damage if the bubbles collapse on the blade surface.

In traveling bubble cavitation, singly identifiable bubbles can be seen to move in the flow direction while attached to the surface of the blade or hydrofoil. They often have the form of hemispherical caps during the growth phase (Figure 12.4). A closeup examination of traveling bubbles indicates that there is a thin film of liquid separating a bubble from the surface. The dynamics of the boundary layer and its interaction with the bubble have significant impact on cavitation inception, bubble growth, and the consequent cavity collapse (Kuhn de Chizelle et al., 1995).

The growth and collapse of traveling bubbles can be scaled with spherical bubble dynamics for many applications (Ceccio and Brennen, 1991). However, if the bubbles interact with the boundary layer flow, they can be deformed, which reduces the level of noise they emit upon collapse. If many bubbles are present, interaction between the bubbles can become important. These interactions are discussed in Brennen (1995).

12.1.5 Sheet Cavitation

Sheet cavitation occurs when a pocket of gas or vapor forms on a solid surface due to the flow of the liquid (Figure 12.5). Sheet cavitation is often formed when there is wall-flow reversal or boundary layer separation due to an adverse pressure gradient (rising pressure in the flow direction) on the surface. If the

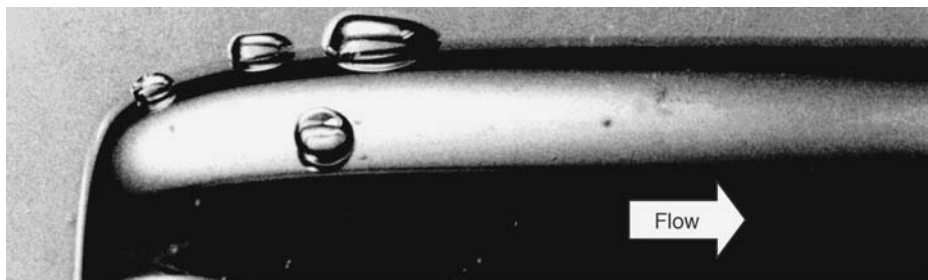


FIGURE 12.4 Traveling cavitation bubbles over an axisymmetric body of revolution.

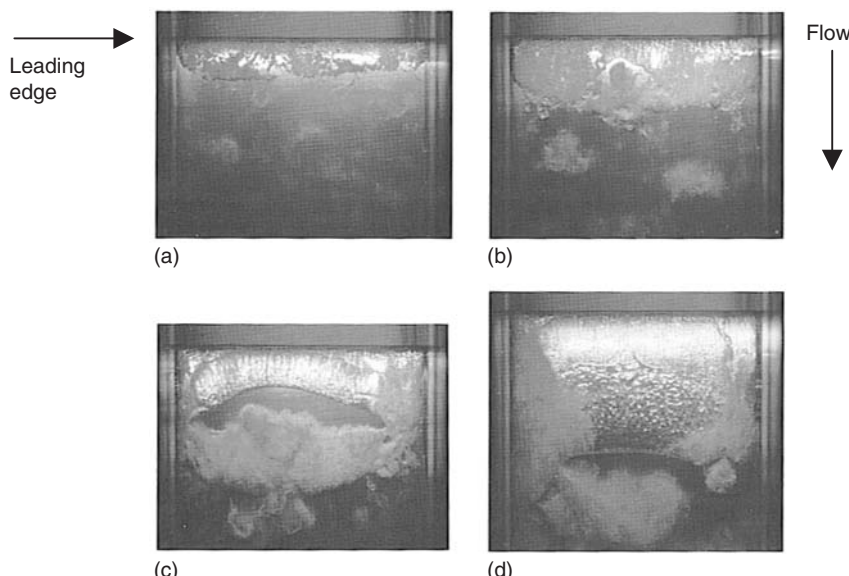


FIGURE 12.5 Sheet cavitation on a two-dimensional NACA009 hydrofoil: (a) incipient cavitation; (b) developing cavitation; (c) cloud shedding; and (d) cavity refilling.

cavity terminates on the cavitating surface, it is called a *partial cavity*. If the cavity extends beyond the cavitating object into the wake of the flow, it is called a *supercavity*. The shape of the cavity in the detachment region is affected by the type of surface material depending on whether it is hydrophilic or hydrophobic (Leger and Ceccio, 1998). For hydrophilic surfaces, the cavity interface curves downstream forming a forward facing step, with a recirculation region just upstream. The forward-facing step and the recirculation region are not present on hydrophobic surfaces, and the cavity detachment is close to the boundary layer separation point. Prediction of the cavity detachment point over a given surface can be performed with very good accuracy by invoking the potential flow theory to provide the pressure distribution in the liquid flow. This can then be combined with boundary layer calculations to predict the separation point. Laberteaux and Ceccio (2001a) present such an example.

When a laminar boundary layer separates from the surface, it can become turbulent and reattach to the surface just downstream of the separation point. In this case, the detachment of the sheet cavity is expected to occur in the narrow region between the laminar separation and turbulent reattachment of the boundary layer, or the ‘separation bubble.’ Turbulent boundary layers are more resistant to adverse pressure gradients and separation and can resist the formation of partial cavities. Increased background flow turbulence levels, surface roughness, and surface trips can induce laminar to turbulent boundary layer transition. By artificially tripping the laminar boundary layer on a hydrofoil into turbulence, Arakeri and Acosta (1973) showed that the occurrence of attached cavities could be delayed. Also, if the underlying boundary layer is transitional or turbulent, complex bubble–boundary layer interactions can occur, as shown in Figure 12.6 (Li and Ceccio, 1996).

Franc et al. (1995) map the σ – α space of a NACA 16-012 hydrofoil at $Re = 1 \times 10^6$ with relation to the shapes of sheet cavitation occurring on the foil, where α is the angle of attack. For low angles of attack, the laminar boundary layer separation is toward the rear end of the foil, and an attached cavity is formed

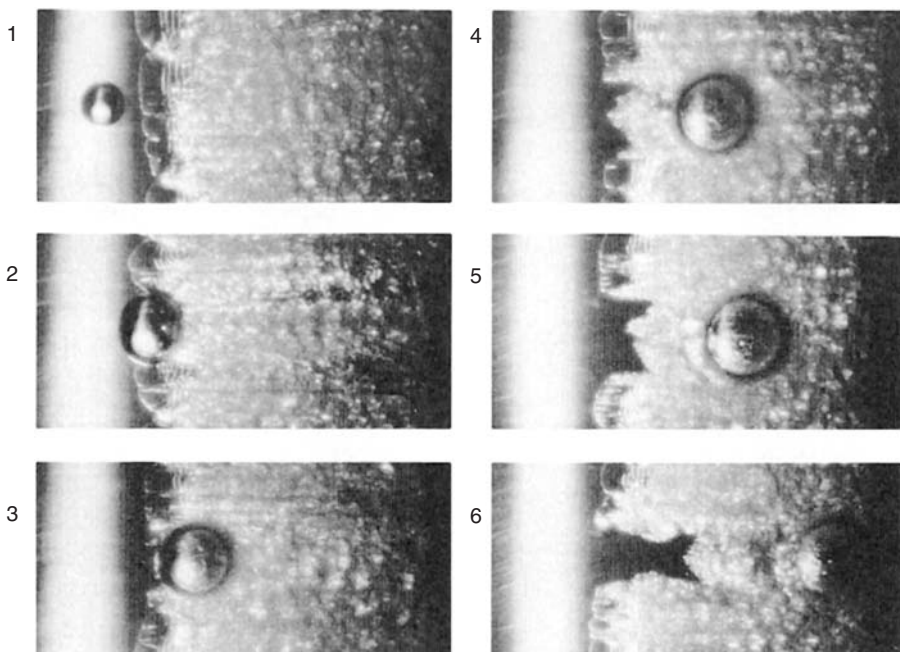


FIGURE 12.6 Images of several bubbles over a two-dimensional NACA 63,A012 hydrofoil. The process of sheet cavity sweeping by the traveling bubble is shown. The bubble does not disturb the cavity, until it has passed downstream, when the sweeping action takes place.

near the separation point and it extends into the blade wake. Increasing α to a moderate angle of attack leads to the formation of a band of a single hemispherical bubbles on the blade surface, which transform with reduction of the cavitation number, σ , into an attached partial cavity terminating on the blade surface. A further reduction in σ forms a supercavity. The interior of partial and super-cavities is single-phase vapor (or single-phase gas–vapor mixture). Further increase in the angle of attack α combined with an increase in the cavitation number can cause the attached cavity to become “frothy” or filled with a liquid–vapor mixture, also known as *open* partial cavity. At extreme angles of attack corresponding to stall, the open cavity is not attached to the blade surface anymore except for the leading edge, and cavitation can be noticed in the wake vortices shed in the liquid.

Under certain conditions of Re , σ , and free-stream turbulence levels, a partial cavity can undergo stable or an unstable pulsation. Wade and Acosta (1966) predict that cavities of length, l_c , on a hydrofoil of cord length, c , become unsteady and pulsatile when $\frac{3}{4}c < l_c < \frac{4}{3}c$. In this pulsatile phenomena, part of the liquid flow that reattaches to the blade surface in the cavity closure region will form a jet that reenters underneath the cavity (jet directed upstream toward the cavity detachment point). When the partial cavity is at its maximum size, the reentrant jet can cause a large portion of the cavity to pinch off and be swept downstream. The bubble cloud will collapse downstream, producing substantial acoustic noise, and possible material damage. The small remaining portion of the cavity left attached to the surface will grow smoothly through evaporation and gas diffusion from the liquid to a maximum size, and the cycle repeats. Thick cavities are often unstable and associated with unsteady pulsation. The pulsation phenomena is associated with periodic, strong structural loading, which is undesirable. In stable quasi-steady pulsatile cavities, a Strouhal number (St) can be defined to describe the pulsation:

$$St = \frac{f_p l_c}{U_\infty} \quad (12.14)$$

where f_p is the pulsation frequency and l_c a characteristic length.

The Strouhal number for strongly shedding partial cavities is often between 0.2 and 0.4 when l_c is the mean cavity length (George et al., 2000). Laberteaux and Ceccio (2001a, 2001b) studied open partial cavities in detail. They showed that the liquid flow behind the cavity resembled the flow aft of a backward facing step. The cavities terminated near the point of maximum cavity thickness, and cavitating vortices were shed in the turbulent cavity wake. The collapse of these cavitating vortices is believed to contribute to cavitation damage. The formation of reentrant flow is strongly related to the shape of the cavitating object. Figure 12.7 shows the difference between two cavitating hydrofoils. The first has no spanwise variation and the second has a swept profile. In the unswept case, the reentrant flow leads to an unstable partial cavity. But, the reentrant flow in the swept geometry is deflected in the spanwise direction, producing a stable, closed cavity.

12.1.6 Vortex Cavitation

The swirling motion of a vortex requires the presence of a pressure gradient directed away from the center of rotation to counterbalance the centrifugal force. Thus, the pressure in the center of the vortex is lower than the surrounding fluid, and it is possible for the pressure in the core of a liquid vortex to drop below vapor pressure. If nuclei are present in this low-pressure region, they may explosively grow, resulting in *vortex cavitation*. The axial flow inside the vortex core can be slower or faster than the fluid outside the core, which may cause an additional pressure difference. Line vortices often occur near the termination of lifting surfaces, and Figure 12.8 shows developed cavitation occurring in a tip vortex.

The Gaussian vortex, which is a widely used model for concentrated line vortices, is characterized by a zero radial velocity profile and a tangential (azimuthal) velocity profile as a function of radial distance from the vortex center, r , given by

$$u_\theta(r) = \frac{\Gamma_o}{2\pi r} (1 - e^{-\eta_i(r/R)^2}) \quad (12.15)$$

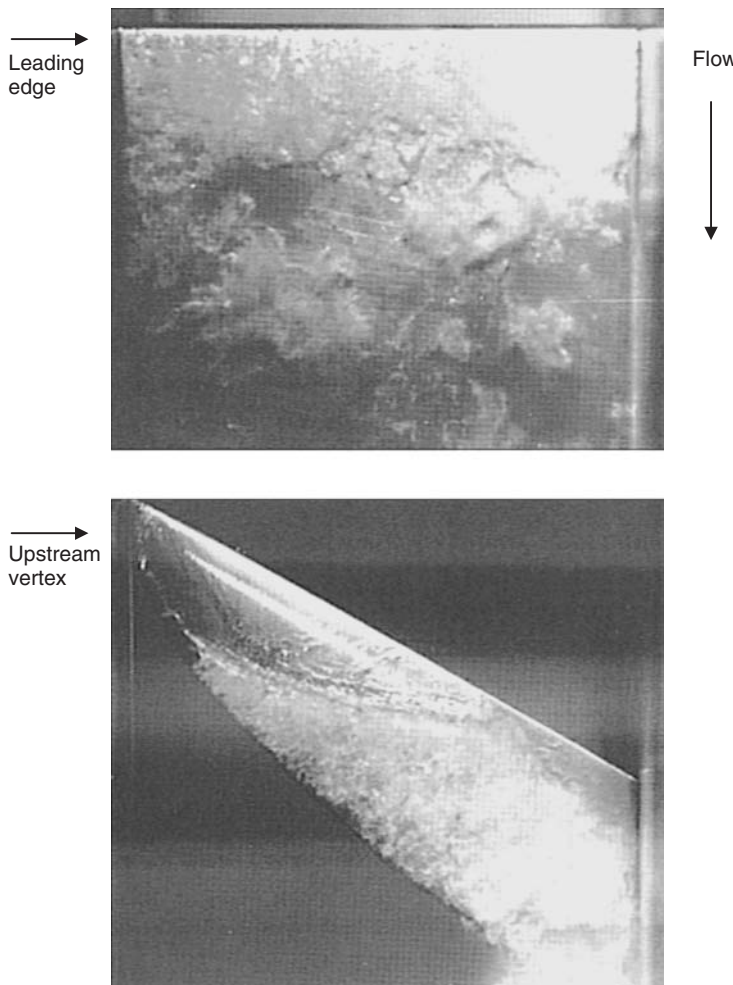


FIGURE 12.7 Partial cavities on a two-dimensional hydrofoil and on a three-dimensional hydrofoil (swept at 30°). Both hydrofoils have the same section shape.

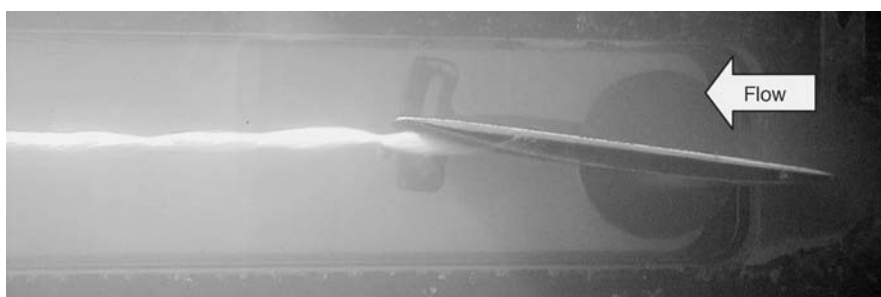


FIGURE 12.8 Developed tip vortex cavitation from a stationary hydrofoil.

Two parameters are needed to characterize the vortex: its core radius, R , which gives the location of maximum tangential velocity, and its total circulation, Γ_o . The circulation distribution is given by

$$\Gamma(r) = \Gamma_o(1 - e^{-\eta_i(r/R)^2}) \quad (12.16)$$

where $\eta_l = 1.257$ is a constant. The pressure drop at the vortex center is given by

$$p_c = p_\infty - 0.870 \rho_l \left(\frac{\Gamma_o}{2\pi R} \right)^2 \quad (12.17)$$

Vortex cavitation is often the first type to appear in hydrodynamic applications. When inception occurs, individual nuclei are captured by the vortex and cavitate. With a further reduction in pressure, the core is filled with a vapor and gas mixture. Based on momentum conservation argument in a Rankine vortex (which has a uniform ‘top hat’ vorticity distribution), Arndt and Keller (1992) predicted the diameter of the vapor-filled region to be 71% of the original liquid vortex core diameter. The inception number is usually *not* equal to the desinence number. This hysteresis pattern is due to the nonlinear bubble dynamics. Vortex cavitation predictions are sensitive to the flow nuclei and dissolved gas content.

The formation of tip vortices results from the pressure difference between the suction side and pressure side near the tip of a finite-span lifting surface. Prediction of tip vortex cavitation follows the viscous scaling of McCormick (1962). He showed that the tip vortex core radius is scaled with the boundary layer thickness on the blade pressure surface, and this is Reynolds number-dependent. In addition, the circulation strength of the tip vortex is related to the lift generated on the lifting surface, or the lift coefficient, C_L . Then, the inception cavitation number has the form

$$\sigma_i = KC_L^2 Re^m \quad (12.18)$$

where K is a scale factor and m a constant depending on the boundary layer regime ($m = 2/5$ for a turbulent boundary layer). In axial pumps and ducted propellers, there is an additional effect due to the confinement gap between the blade tip and the shroud. Other forms of cavitation in concentrated vortices include hub vortex cavitation, which forms on the hub of a propeller or a hydraulic turbine.

Regions of free turbulent shear flow can contain many regions of concentrated vorticity (coherent structures). Shear flow cavitation can form in the high-speed regions of jets, wakes, and separated shear layers. Figure 12.9 shows the cavitating turbulent shear flow associated with a free shear layer. The inception of these flows is often difficult to predict, as it is strongly related to the details of the turbulent flow and nuclei distribution. A recent review of this type of cavitation is found in Arndt (2002).

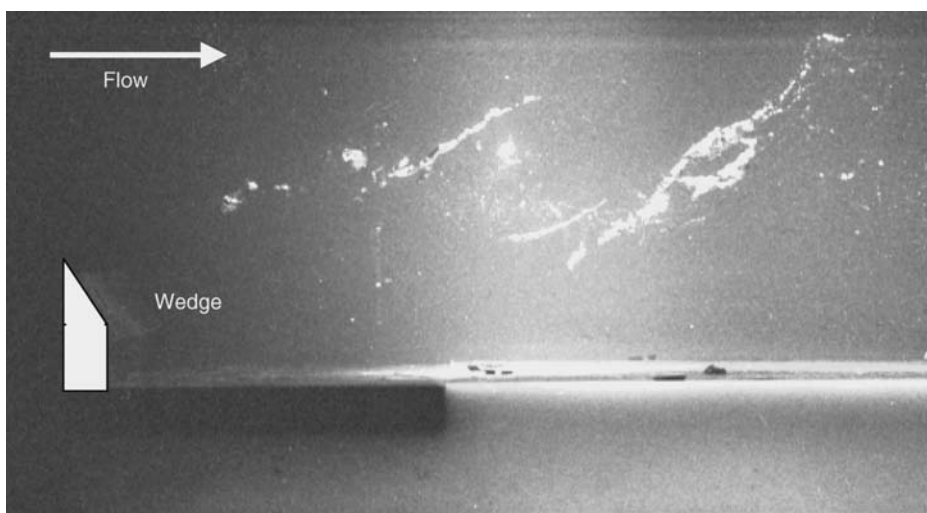


FIGURE 12.9 Cavitation inception in a turbulent shear flow formed downstream of a wedge.

12.1.7 Cavitation in Hydraulic Machinery

Cavitation can occur in both pumps and turbines. Bubble, sheet, and vortex cavitation have all been observed within these devices, and persistent cavitation can lead to reduction in efficiency, vibration, and erosion damage. The cavitation parameter in hydraulic machinery is usually referred to as the *Sigma Thoma number* and is given by

$$\sigma_T = \frac{H_{sv}}{H} \quad (12.19)$$

where H_{sv} is the net positive suction head (NPSH) and is given by

$$H_{sv} = \frac{1}{g} [P_0 - P_v + \frac{1}{2} \rho V_0^2] \quad (12.20)$$

with H being the *total head* under which the turbomachinery is operating. If the nondimensional flow rate $Q/2\pi\Omega D^3$ is held constant (analogous to the angle of attack in stationary hydrofoils), then one can write the Thoma number as

$$\sigma_T = \left(\frac{n_s}{S} \right)^{4/3} \quad (12.21)$$

where

$$n_s = \frac{\Omega Q^{1/2}}{(gH)^{3/4}} \quad (12.22)$$

and

$$S = \frac{\Omega Q^{1/2}}{(gH_{sv})^{3/4}} \quad (12.23)$$

Here n_s is the specific speed, while S is the suction specific speed; D is the impeller eye diameter (in m), Ω the rotational speed (in rad/sec), Q the flow rate (in m³/sec), and H and H_{sv} are (in m). The inlet of a pump or the exit of a turbine are regions of reduced pressure and increased potential for cavitation. Radial flow machines have relatively low specific speeds (high heads and low throughput) and axial machines usually possess high specific speeds (low heads and high throughputs). Knapp et al. (1970) suggest that the flow in radial machines be treated as flow in passages for cavitation studies, while axial flow machines can be geometrically developed, such that the flow is treated as that over cascade of hydrofoils. They also point out common factors and regions of increased cavitation potential in turbomachinery such as surface discontinuities, junctions between surfaces, gaps, unsteady flows and recirculating regions, and surface roughness effects.

The cavitation performance of turbomachinery is often presented as a plot of specific performance (e.g., specific head rise or specific power output) vs. Thoma number. As the Thoma number is decreased to the *inception Thoma number*, cavitation appears, but the performance of the turbomachinery may be only slightly affected. With decreasing Thoma number, cavitation becomes more developed, and the performance of the device will degrade. The *critical Thoma number* is reached when the performance is reduced by a defined fraction from the noncavitating case (e.g., 3%). Further reductions will lead to significant degradation of performance as the *breakdown Thoma number* is reached. Figure 12.10 shows the trends of typical pump performance curves vs. the Thoma number.

For marine propellers, the related cavitation number, σ , depends on the advance coefficient $J = U_\infty/(2\pi\Omega D)$ (analogous to the angle of attack in stationary hydrofoils), the thrust coefficient $K_T = T/\rho_0(2\pi\Omega)^2 D^4$, and the torque coefficient $K_T = Q/\rho_0(2\pi\Omega)^2 D^5$, where T is the thrust and Q the torque.

The degree to which cavitation is developed in turbomachinery can affect various parameters of the device. Incipient cavitation has the possibility of intermittent noise production. In partially developed cavitation, noise, structural vibrations, and damage to surfaces can occur. For fully developed cavitation, where

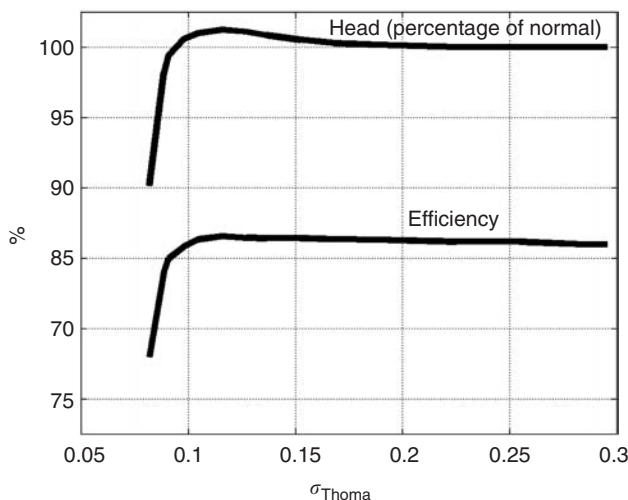


FIGURE 12.10 Typical pump performance curves at a constant flow rate as a function of the Thoma cavitation number.

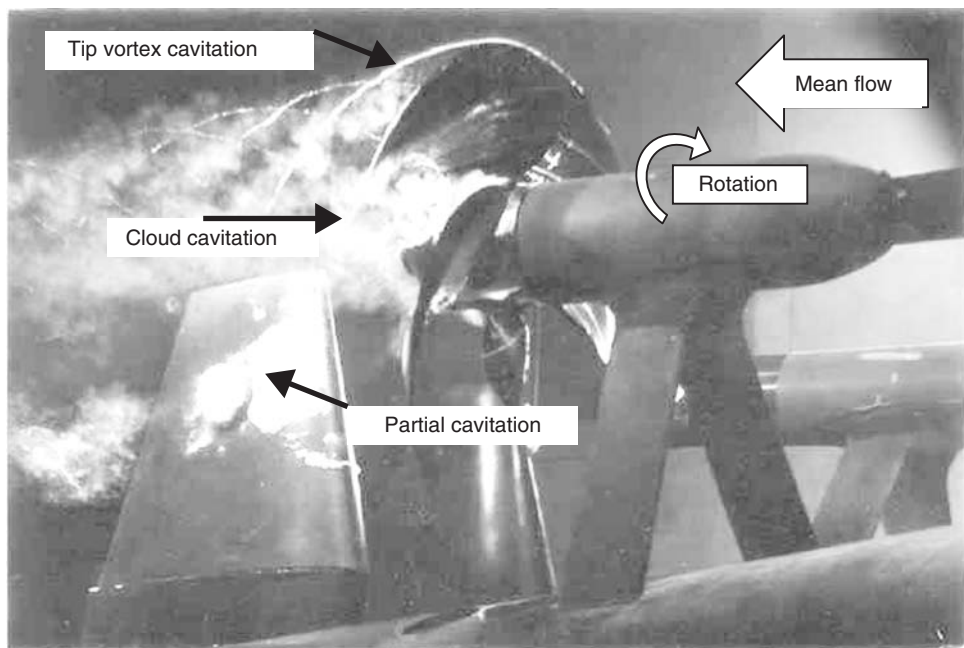


FIGURE 12.11 (Color insert follows page 13-40) Tip vortex cavitation, cloud cavitation, and partial attached cavitation on a model of a marine propeller. (Courtesy of Dr. Y.T. Shen, Naval Surface Warfare Center-Carderock Division.)

the volume of the cavities becomes significant, mechanical efficiency degradation, head loss, and damage are expected. Figure 12.11 shows vortex, sheet, and cloud cavitation on a model of a marine propeller.

Cavitation is a serious problem in hydraulic systems such as valves because of the potential for damage and vibration (Johnston et al., 1991; Jozsa et al., 1994; Porteiro et al., 1997; Carlson, 2001). Cavitation damage (pitting) has been observed in the liners of diesel engines, due to vibratory excitation of nuclei in the liquid (Zhou et al., 1982).

Cavitation can also occur in injector nozzles and fuel pumps in automotive applications. In fuel injection systems, as in diesel engines where the fuel speed is in excess of a 100 m/sec, cavitation can occur and cause flow disturbances that can improve atomization of the injected fuel (Badock et al., 1999; Eisfeld, 2002; Yuan and Schnerr, 2003).

12.1.8 Cavitation in Biomedical Applications

In contrast with industrial and naval applications where cavitation is most often undesirable because of its erosion potential, the same damaging effects of collapsing bubbles have been implemented as a tool in biomedical applications, namely, surgery and lithotripsy. For example, pulsed ultrasound can be focused with precision on kidney or gall stones. An initial high-intensity pulse is often applied to generate cavitation nuclei, and then followed by less intense pulses to drive the bubble nuclei into transient cavitation, i.e., explosive bubble growth and violent implosion that lead to stone damage. The *in vivo* bubble dynamics are often quite complex. Clouds of bubbles are often created, and the bubble dynamics in these clouds are harder to predict than single bubble dynamics. For instance, the speed of sound in the cloud can be lower than the speed of sound in the liquid alone, and thus shock wave formation is more likely to occur. The shock can focus in the center of the cloud, leading to an improved lithotriptic effect over single bubble collapse (Brennen, 2003). Ultrasonic focusing can be also used in noninvasive surgery for pulverizing cancer tumors (*necrosis*). Bubble clouds often occur at the focal point. The cloud can backscatter the incoming acoustic pulses, causing increased absorption in the region upstream of the focal point, thus leading to the growth of the lesion (incised tissue) in a direction opposite to the incoming ultrasonic wave. This unintended effect and the resulting pulverization of blood and tissue into a paste have been observed to arrest bleeding in internal organs (*hemostasis*). Jet formation due to cavitation collapse is believed to puncture cell walls and improve drug delivery or allow targeted drug delivery to certain areas such as tumors. Bailey et al. (2003) provide a review of ultrasound in therapy.

Analogous to ultrasound focusing, very short pulses (pico- to nanoseconds) of infrared laser beams from Q-switched YAG (*Yttrium Aluminum Garnet*) or Ruby lasers are focused in laser-eye-surgery procedures into the intended area of the cornea to induce noninvasive, precise surgical effect. A vaporous cavitation bubble grows explosively at the laser focal volume, collapses violently, and generates a shock wave in what is known as optical cavitation, thus producing the surgical effect (Vogel et al., 1986). Additionally, microbubbles are used as contrast agents in ultrasonic imaging. Microbubbles existing in the area under investigation are excited by ultrasonic emissions from an emitting transducer. In response, the bubble volume will oscillate, and the acoustic emissions from the oscillatory motion of the bubble can then be picked by a receiving transducer.

12.1.9 Other Occurrences and Applications of Cavitation

The high pressures and temperatures associated with the collapse of cavitation bubbles have been used to initiate chemical reactions in a process known as *sonochemistry* (Riesz et al., 1990; Suslick, 1997; Beckett and Hua, 2001). These same extreme pressures and temperatures have also been exploited for environmental water purification (*aquasonolysis*) (Madge and Jensen, 2002; Lifka et al., 2003). The formation of radicals upon bubble collapse accelerates the degradation of contaminants through oxidization. Additionally, the shearing effect due to bubble oscillations can break up long-chain molecules. The production of cavitation bubbles near a metal surface can be used to mechanically work the surface in a process known as 'shot-less peening.' Cavitating jets can be used for this purpose (Soyma and Asahara, 1999).

Lastly, cavitation can occur in natural processes, for example, when the knuckles are cracked with a popping sound. Head trauma has been associated with cavitation when there is a sudden impact of the cranium (Goldsmith, 2001). *Alpheus heterochaelis* (the "snapping shrimp") uses sound produced by a cavitating jet to stun nearby prey (Versluis et al., 2000). Also, the maximum height of trees may be limited by cavitation during the transpiration of water (Koch et al., 2004).

12.2 Bubble Physics

Y. Matsumoto

12.2.1 Single Spherical Bubble Dynamics

Bubble motion from a surrounding pressure variation is one of the most fundamental gas–liquid two-phase flow problems and is closely related to the macroscale behavior of two-phase flows, the performance of cavitating fluid machinery, and medical ultrasound applications. Of great significance to the analysis of such problems is the prediction of the radial motion of a bubble, namely, its growth and collapse. The bubble motion can be solved exactly by the integration of the conservation equations for mass, momentum, and energy for the gas phase inside the bubble and the liquid phase outside the bubble. Since it is not easy to solve the complete equations in many cases, a polytropic change (isothermal or adiabatic) is assumed for the gas inside the bubble. However, it is well known that the thermal phenomena inside the bubble can have a significant influence on the bubble motion (Chapman and Plesset, 1971; Nigmatulin, 1981; Prosperetti et al., 1988; Kamath and Prosperetti, 1989; Prosperetti, 1991; Takemura and Matsumoto, 1994; Kameda and Matsumoto, 1999). To account for thermal effects, a reduced-order model has been introduced using ordinary differential equations (ODEs), instead of the full conservation equations for mass, momentum, and energy.

12.2.1.1 Direct Numerical Simulation (DNS) of a Single Bubble

In a single-phase flow, the conservation equations of mass, momentum, and energy are described by partial differential equations (PDEs) if the flow is treated as a continuum. In multiphase flow, these conservation equations are not described by the same set of PDEs, because there are discontinuities between the phases. However, it is possible to describe the governing equations by PDEs in each phase and connect the two phases at the interfaces. The governing equations and boundary conditions at a bubble interface were described by Hsieh (1965). Matsumoto and Takemura (1994) simulated the collapsing bubble motion numerically by using the full equations for mass, momentum, and energy in the gas and liquid phases. Takemura and Matsumoto (1994) calculated the bubble growth caused by an external pressure reduction by taking into account internal phenomena such as thermal and mass diffusion with mist formation due to homogeneous condensation.

12.2.1.1.1 Governing Equations

12.2.1.1.1 Gas Phase

1. The mass conservation equations:

- For the gas mixture inside the bubble,

$$\frac{\partial \rho_m}{\partial t} + \frac{1}{r^2} \frac{\partial}{\partial r} (r^2 \rho_m u_{mg}) = 0 \quad (12.24)$$

where $\rho_m = \rho_n + \rho_v + \rho_{lg} \rho_m u_{mg} = \rho_n u_n + \rho_v u_v + \rho_{lg} u_{mg}$, (subscript g denotes the gas phase, l the liquid phase, n the noncondensable gas, v the vapor in the gas phase, and m the mixture condition; also, the subscript lg denotes the mist inside the bubble and gl the noncondensable gas in the liquid phase), ρ is the density, r the coordinate in the radial direction and u the radial velocity.

- For the vapor

$$\frac{\partial \rho_v}{\partial t} + \frac{1}{r^2} \frac{\partial}{\partial r} \left\{ r^2 \left(\rho_v u_{mg} - \rho_{mg} D_{mg} \frac{\partial c_v}{\partial r} \right) \right\} = -\Gamma \quad (12.25)$$

where $\rho_{mg} = \rho_n + \rho_v$, $c_v = \rho_v / \rho_{mg}$. D is the diffusion coefficient, c the concentration, and Γ the mass of vapor which changes to mist per unit volume per unit time.

- For the number density distribution function of droplets (Frenkel, 1946),

$$\frac{\partial n(a)}{\partial t} + \frac{1}{r^2} \frac{\partial}{\partial r} (r^2 n(a) u_{mg}) + \frac{\partial (n(a) I_a)}{\partial a} = 0 \quad (12.26)$$

where $n(a)$ is number density distribution function vs. radius of the droplet. I_a is the growth rate of the droplet radius and is given by

$$I_a = \alpha(p_v - p_s)/(\rho_l \sqrt{2\pi \mathfrak{R}_v T}) \quad (12.27)$$

where α is the accommodation factor whose value is estimated to be 0.4 (Hatamiya and Tanaka, 1986), p the pressure, subscript s denotes the saturated condition, \mathfrak{R} the gas constant and T the temperature. Critical radius r^* and the nucleation rate J are given as

$$r^* = 2\sigma/\rho_l \mathfrak{R}_v T \ln(p_v/p_s) \quad (12.28)$$

$$J = \left(\frac{2\sigma m}{\pi} \right)^{1/2} \frac{1}{\rho_l} \left(\frac{p_v}{kT} \right)^2 \exp\left(-\frac{4\pi r^{*2}\sigma}{3kT} \right) \quad (12.29)$$

where σ is the surface tension, m the molecular unit mass, and k the Boltzmann constant. The parameter Γ in Eq. (12.25) is defined as

$$\Gamma = \frac{d}{dt} \int \frac{4}{3} \pi \rho_l a^3 n(a) da \quad (12.30)$$

2. The momentum conservation equation for the mass inside of the bubble is

$$\frac{\partial}{\partial t} (\rho_m u_{mg}) + \frac{1}{r^2} \frac{\partial}{\partial r} (r^2 \rho_m u_{mg} u_{mg}) \quad (12.31)$$

$$= - \frac{\partial p_{mg}}{\partial r} + \frac{4}{3} \frac{\mu_{mg}}{r} \left(\frac{\partial u_{mg}}{\partial r} - \frac{u_{mg}}{r} \right) + \frac{4}{3} \frac{1}{r^2} \frac{\partial}{\partial r} \left\{ r^2 \mu_{mg} \left(\frac{\partial u_{mg}}{\partial r} - \frac{u_{mg}}{r} \right) \right\}$$

where μ is the viscosity.

3. The energy conservation equation for the mass inside of the bubble is

$$\frac{\partial}{\partial t} (\rho_n e_n + \rho_v e_v + \rho_{lg} e_{lg}) + \frac{1}{r^2} \frac{\partial}{\partial r} \{ r^2 (\rho_n e_n u_n + \rho_v e_v u_v + \rho_{lg} e_{lg} u_{mg}) \} \quad (12.32)$$

$$= - \frac{P_{mg}}{r^2} \frac{\partial}{\partial r} (r^2 u_{mg}) + \frac{1}{r^2} \frac{\partial}{\partial r} \left(r^2 \lambda_{mg} \frac{\partial T}{\partial r} \right) + \frac{4}{3} \mu_{mg} \left(\frac{\partial u_{mg}}{\partial r} - \frac{u_{mg}}{r} \right)^2$$

where e is the specific internal energy and λ is the thermal conductivity.

4. The equation of state is

$$p_n = \rho_n \mathfrak{R}_n T \quad (12.33)$$

and

$$p_v = \rho_v \mathfrak{R}_v T \quad (12.34)$$

12.2.1.1.1.2 Liquid Phase

1. The mass conservation equations:

- For mixture of the liquid,

$$\frac{\partial \rho_{ml}}{\partial t} + \frac{1}{r^2} \frac{\partial}{\partial r} (r^2 \rho_{ml} u_{ml}) = 0 \quad (12.35)$$

where $\rho_{ml} = \rho_l + \rho_{gl}$, $\rho_{ml} u_{ml} = \rho_l u_l + \rho_{gl} u_{gl}$.

- For the noncondensable gas in the liquid,

$$\frac{\partial \rho_{gl}}{\partial t} + \frac{1}{r^2} \frac{\partial}{\partial r} \left\{ r^2 \left(\rho_{gl} u_{ml} - \rho_{ml} D_{gl} \frac{\partial c_{gl}}{\partial r} \right) \right\} = 0 \quad (12.36)$$

where $c_{gl} = \rho_{gl}/\rho_{ml}$

- The momentum conservation equation for the liquid phase is

$$\begin{aligned} & \frac{\partial}{\partial t} (\rho_{ml} u_{ml}) + \frac{1}{r^2} \frac{\partial}{\partial r} (r^2 \rho_{ml} u_{ml} u_{ml}) \\ &= -\frac{\partial p_1}{\partial r} + \frac{4}{3} \frac{\mu_{ml}}{r} \left(\frac{\partial u_{ml}}{\partial r} - \frac{u_{ml}}{r} \right) + \frac{4}{3} \frac{1}{r^2} \frac{\partial}{\partial r} \left\{ r^2 \mu_{ml} \left(\frac{\partial u_{ml}}{\partial r} - \frac{u_{ml}}{r} \right) \right\} \end{aligned} \quad (12.37)$$

- The conservation equation of energy for the liquid is

$$\begin{aligned} & \frac{\partial}{\partial t} (\rho_l e_l) + \frac{1}{r^2} \frac{\partial}{\partial r} \{ r^2 \rho_l e_l u_l \} \\ &= -\frac{p_1}{r^2} \frac{\partial}{\partial r} (r^2 u_l) + \frac{1}{r^2} \frac{\partial}{\partial r} \left(r^2 \lambda_l \frac{\partial T}{\partial r} \right) + \frac{4}{3} \mu_l \left(\frac{\partial u_l}{\partial r} - \frac{u_l}{r} \right)^2 \end{aligned} \quad (12.38)$$

- The Tait equation is applied for the equations of state in the following form:

$$\frac{p + B}{p_\infty + B} = \left(\frac{\rho}{\rho_\infty} \right)^n \quad (12.39)$$

where $B = 304.9$ MPa and $n = 7.15$ in the case where the liquid is water.

12.2.1.1.2 Boundary Conditions at the Gas–Liquid Interface

- The boundary conditions for mass conservation follow

The mass flux due to phase change \dot{M}_v is expressed by the following equation:

$$\dot{M}_v = \alpha (p_s - p_v) / (\sqrt{2\pi \mathfrak{R}_v T_w}) \quad (12.40)$$

where the subscript w denotes the bubble wall. The concentrations and gradients of vapor and non-condensable gas in the liquid at the interface are related to \dot{M}_v and \dot{M}_n by the following equations:

$$\dot{M}_v = \frac{D_{mg} \rho_{mgw} (\partial c_v / \partial r)_w}{1 - c_{vw}} + \frac{c_{vw}}{1 - c_{vw}} \dot{M}_n \quad (12.41)$$

$$\dot{M}_n = \frac{D_{gl} \rho_{mlw} (\partial c_{gl} / \partial r)_w}{1 - c_{glw}} + \frac{c_{glw}}{1 - c_{glw}} (\dot{M}_v + \dot{M}_{lg}) \quad (12.42)$$

\dot{M}_{lg} is

$$\dot{M}_{lg} = \begin{cases} 0, & \dot{R} - u_{mg} \geq 0 \\ \rho_{lg} (\dot{R} - u_{mg}), & \dot{R} - u_{mg} < 0 \end{cases} \quad (12.43)$$

where R is the bubble radius and the dot denotes the derivative with respect to time.

- The boundary condition for momentum conservation is

$$\begin{aligned} & -p_{lw} + \frac{4}{3} \mu_l \left(\frac{\partial u_l}{\partial r} - \frac{u_l}{r} \right)_w + \{ \rho_{mg} (u_{mg} - \dot{R}) (u_{mg} - u_l) \}_w \\ &= -p_{mgw} + \frac{2\sigma}{R} + \frac{4}{3} \mu_{mg} \left(\frac{\partial u_{mg}}{\partial r} - \frac{u_{mg}}{r} \right)_w \end{aligned} \quad (12.44)$$

3. The boundary condition for energy conservation is

$$\begin{aligned} \lambda_{ml} \left(\frac{\partial T}{\partial r} \right)_w - \lambda_{mg} \left(\frac{\partial T}{\partial r} \right)_w + \frac{5}{2} (\mathfrak{R}_v - \mathfrak{R}_n) T_w \{(1 - c_{vw}) \dot{M}_v - c_{vw} \dot{M}_n\} \\ = \dot{M}_v \left\{ L + \frac{4}{3} \frac{\mu_l}{\rho_{lw}} \left(\frac{\partial u_l}{\partial r} - \frac{u_l}{r} \right)_w - \frac{4}{3} \frac{\mu_{mg}}{\rho_{mg}} \left(\frac{\partial u_{mg}}{\partial r} - \frac{u_{mg}}{r} \right)_w \right\} \\ + \frac{1}{2} \dot{M}_v \{(\dot{R} - u_{lw})^2 - (\dot{R} - u_{mgw})^2\} \end{aligned} \quad (12.45)$$

where L is the latent heat.

The temperature and concentration at the wall of the noncondensable gas in the liquid are

$$T_{lw} = T_{gw} \quad (12.46)$$

$$c_{glw} = H_n p_{nw} \quad (12.47)$$

where H_n is Henry's constant.

12.2.1.3 Pressure and Temperature Distribution Inside and Outside a Bubble

Figure 12.12 and Figure 12.13 show the time histories of the pressure and temperature distribution inside and outside a bubble and Table 12.1 lists the computational conditions. The pressure surrounding the bubble increases from 10 to 100 kPa in a stepwise manner. When the bubble motion starts, the expansion wave propagates outside and the pressure distribution is formed in the liquid phase according to the motion of the bubble interface. At the rebound of the bubble, the pressure peak appears at some distance from the interface and the pressure propagates outward. The pressure inside the bubble is uniform because the speed of sound is much higher than the velocity of the interface. In Figure 12.13, the temperature distribution is uniform in the liquid phase because of the large heat capacity of the liquid. On the other hand, a nonuniform distribution appears in the gas phase, because the temperature rises during the collapse phase as the heat transfers to the liquid at the interface. After rebounding, the temperature inside the bubble decreases to a value less than its initial value. The internal energy of the gas is reduced by thermal diffusion the heat is deposited and diffuses around the bubble when the gradient of the temperature is negative.

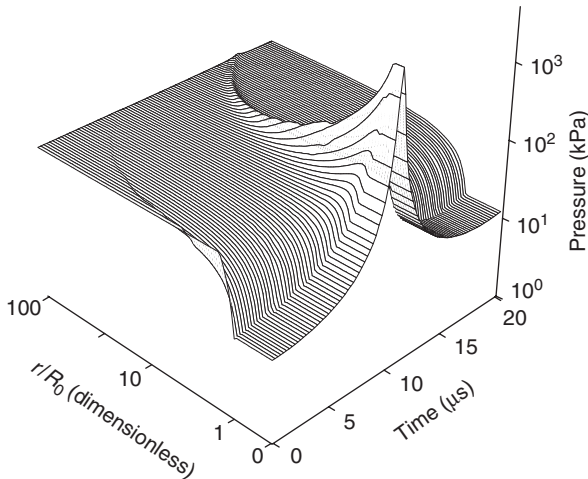


FIGURE 12.12 Time history of the pressure distribution inside and outside a nitrogen bubble.

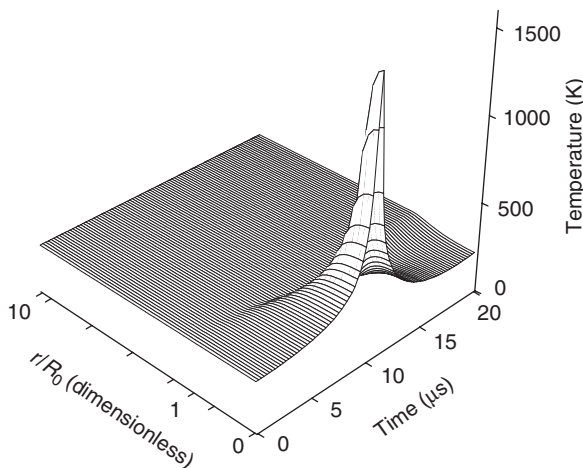


FIGURE 12.13 Time history of the temperature distribution inside and outside a nitrogen bubble.

TABLE 12.1 Computational Conditions

Gas Phase	Nitrogen
Liquid phase	Water
Initial bubble radius, R_{b0}	100 μm
Initial ambient pressure, p_0	10 kPa
Step increase of ambient pressure	10–100 kPa
Initial temperature	293 K

12.2.1.4 Effect of Thermal Diffusion on the Bubble Motion

Figure 12.14 shows the behavior of the bubbles with different gases inside them under the same conditions as Table 12.1, except for the gas species. Table 12.2 shows the properties of the internal gas. The Peclet number Pe is defined as $Pe = \rho_0 c_{p0} R_0^2 \omega_N / \lambda$, where c_{p0} is the isobaric specific heat and ω_N denotes the natural angular frequency of a bubble, assuming adiabatic changes. Nondimensional scales R^* and t^* are defined as $R^* = R/R_0$ and $t^* = t/R_0 \sqrt{\rho_{l0}/\rho_{l0}}$, respectively. When the bubble radius reaches a maximum or minimum value, the pressure has a minimum or maximum value, respectively. The mean temperature (defined as $T_{\text{mean}} = \int_0^R r^2 \rho_g T_g dr / \int_0^R r^2 \rho_g dr$) has a maximum at almost the same time as the bubble radius reaches a minimum. However, it does not have a minimum when the bubble radius reaches a maximum. This is because the heat input has positive or negative values despite the work received from the liquid phase, and has a time lag. Therefore, the sum of the work that the bubble receives per unit time from the liquid phase and the heat input becomes zero before the radius takes the minimum or the maximum value. This is the minimum or the maximum point of the temperature. Upon collapse, the work received from the liquid per unit time decreases so rapidly that the temperature takes the maximum at almost the same time as the radius reaches the minimum value. On the other hand, upon expansion, the bubble supplies work to the liquid phase and the heat flows outward from the gas phase due to the temperature distribution developed during the collapse phase. Therefore, the temperature decreases rapidly and the gradient of the temperature at the gas–liquid interface becomes positive. Subsequently, the heat flows inward from the liquid phase and the mean temperature takes the minimum value when the sum of the work received from the liquid per unit time and the heat input becomes equal to zero.

In the case of a helium bubble (when Pe is relatively small), the heat transfers outward through the bubble wall quickly and the bubble shrinks to a smaller size during the collapse period. The temperature inside the bubble does not become so high. In the case of xenon (where Pe is large), the heat input and

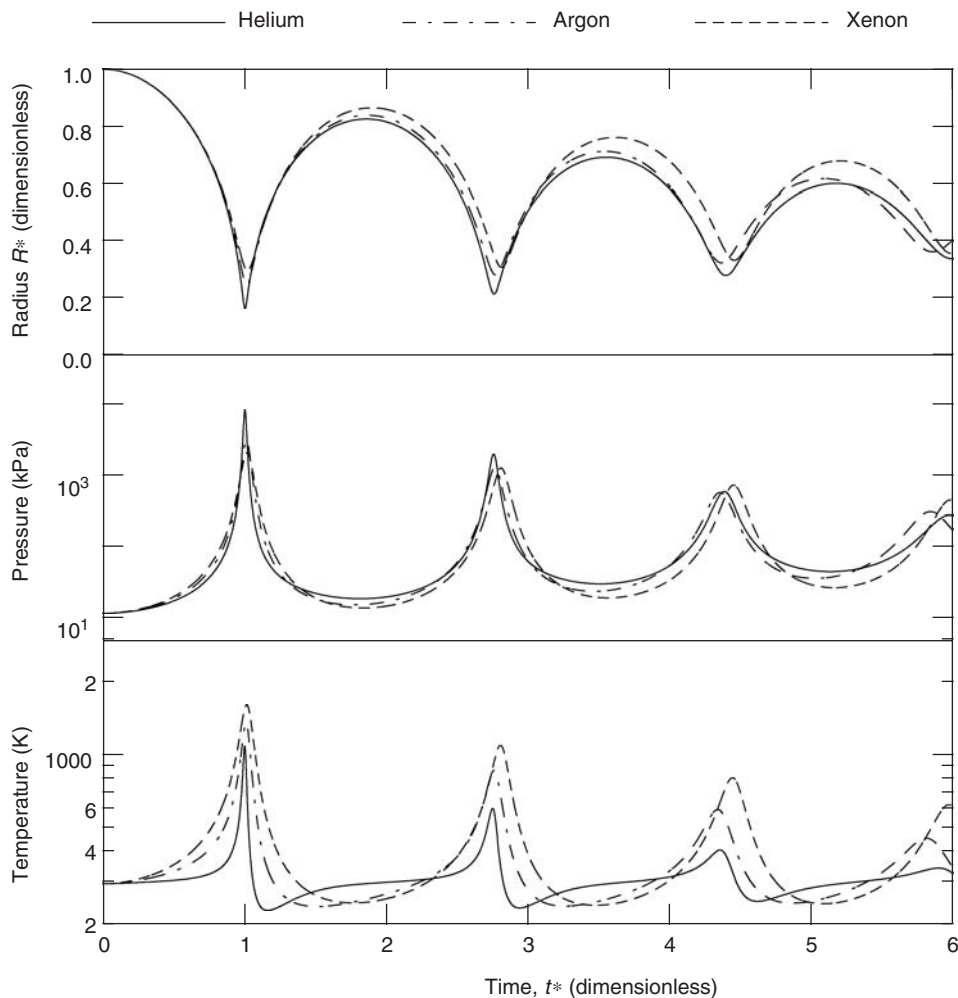


FIGURE 12.14 Time histories of the bubble radius, pressure at the bubble center and mean temperature inside the bubble with different gases.

TABLE 12.2 Properties of the Internal Gas (100 kPa, 293 K)

Gas	Helium	Argon	Xenon
Thermal conductivity (mW/m/K)	153.5	17.4	5.4
Peclet number, Pe	12.3	109.1	347.7

output are not large, so the bubble cannot shrink as much and the temperature inside the bubble reaches higher values.

12.2.1.5 Bubble Motion and Mist Formation Inside a Bubble

Figure 12.15 shows the time histories of the radius, mean temperature, and mean density of mist (upper panel) and the distributions of the temperature, concentration of vapor, and density of mist inside the bubble at several points (lower panel) in the case when the surrounding pressure has a stepwise decrease from 100 to 5 kPa. The other computational conditions are the same as listed in Table 12.1. The lower panel shows the distributions at the times from A to H indicated in the upper panel. In the figure, A to E show the growth period and those from F to H show the collapse period. The abscissa is the

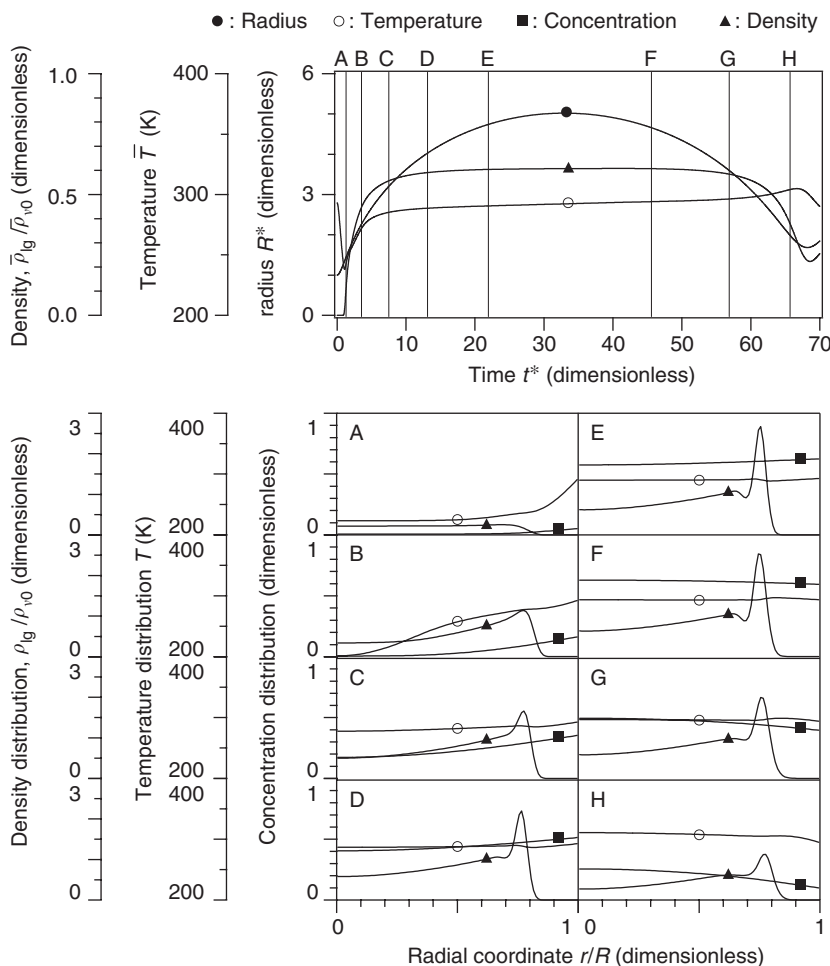


FIGURE 12.15 Time histories of the bubble radius, mean temperature and mean density of the mist inside the bubble (upper panel), and the distributions of the temperature, concentration of the vapor and density of the mist inside the bubble at several points (lower panel) in the case of a nitrogen bubble.

nondimensional distance, in which 0 identifies the bubble center and 1 corresponds to the bubble wall. As the bubble expands, the temperature inside the bubble decreases at the initial stage and then recovers to the surrounding temperature due to the latent heat released by the formation and growth of mist and the heat penetration from the bubble wall. After that, the temperature remains almost constant except during the rebounds. The mean density of the mist increases at the beginning of the expansion, and the formation and growth of the mist exerts an effect on the bubble motion at that time. After the temperature inside the bubble has become almost constant, the mean density of the mist is also nearly constant and the total mass of the mist increases in proportion to the volume of the bubble. The temperature inside the bubble does not become so high at the end of the collapse, because energy from the outside is consumed by the evaporation of the mist. It is evident that distributions of temperature, vapor concentration and density of the mist do occur and the spatial distribution of the mist density is rather complicated due to the slow diffusion process.

12.2.1.2 Reduced-Order Modeling of a Single Bubble

The single bubble motion can be simulated in detail, solving the full equations for the mass, momentum, and energy as outlined in the previous section. However, it is computationally expensive to calculate all

equations when many bubbles are treated, such as in bubbly flows. Many researchers have developed reduced-order models for the liquid and gas phase phenomena.

12.2.1.2.1 Effect of Compressibility in the Liquid Phase

If the liquid is assumed to be incompressible, the momentum conservation equation can be easily integrated from the bubble wall to infinity and the boundary condition for the pressure can be taken into account. Rayleigh (1917) first considered bubble collapse in a liquid, assuming a vacuum cavity. The effect of the surface tension and viscosity in the liquid was taken into account later, and the Rayleigh–Plesset equation (1949) was defined as:

$$R\ddot{R} + \frac{3}{2}\dot{R}^2 = \frac{1}{\rho_l} \left\{ p_b - p_\infty - 4\mu_l \frac{\dot{R}}{R} - \frac{2\sigma}{R} \right\} \quad (12.48)$$

where p_b is the pressure inside the bubble, p_∞ the ambient pressure, and σ the surface tension of the liquid. When the velocity of the bubble wall becomes comparable to the speed of sound of the liquid, the compressibility of the liquid has to be considered (Keller and Kolodner, 1956). The model with a first-order correction for compressibility is often used

$$\left(1 - \frac{\dot{R}}{c}\right)R\ddot{R} + \frac{3}{2} \left(1 - \frac{\dot{R}}{3c}\right)\dot{R}^2 = \left(1 + \frac{\dot{R}}{c}\right) \frac{1}{\rho_l} \{p_b - p_\infty - p_c(t + R/c)\} + \frac{R}{\rho_l c} \dot{p}_b \quad (12.49)$$

where c is the speed of sound and $p_c(t)$ the variable part of the pressure in the liquid at the location of the bubble center in the absence of the bubble.

A nonequilibrium phase change, such as evaporation and condensation during the collapse phase, is discussed next (Tomita and Shima, 1979; Fujikawa and Akamatsu, 1980). Fujikawa and Akamatsu (1980) derived the equations, which take into account the effects of nonequilibrium behavior at the bubble wall on the bubble motion:

$$\begin{aligned} R\ddot{R} &\left(1 - 2\frac{\dot{R}}{c} + \frac{\dot{m}}{\rho_l c}\right) + \frac{3}{2}\dot{R}^2 \left(1 + \frac{4}{3}\frac{\dot{m}}{\rho_l c} - \frac{4}{3}\frac{\dot{R}}{c}\right) - \frac{\dot{m}R}{\rho_l} \left(1 - 2\frac{\dot{R}}{c} + \frac{\dot{m}}{\rho_l c}\right) \\ &- \frac{\dot{m}}{\rho_l} \left(\dot{R} + \frac{\dot{m}}{2\rho_l}\right) + \frac{p_\infty - p_{l,r=R}}{\rho_l} - \frac{R\dot{p}_{l,r=R}}{\rho_l c} = 0 \end{aligned} \quad (12.50)$$

and

$$p_{l,r=R_b} = p_v + p_g - \frac{\dot{m}^2(\rho_{vi} + \rho_{gi} - \rho_l)}{\rho_l(\rho_{vi} + \rho_{gi})} - 2\frac{\sigma}{R} - 4\frac{\mu_l}{R} \left(\dot{R} - \frac{\dot{m}}{\rho_l}\right) \quad (12.51)$$

where \dot{m} is the mass flux caused by the phase change, and ρ_{vi} and ρ_{gi} the density of the vapor and non-condensable gas at the bubble interface, respectively. The nonequilibrium behavior may result in additional cushioning of the bubble collapse.

12.2.1.2.2 Effect of Thermal Phenomena on the Gas Phase

The temperature gradient at the bubble wall is used by some researchers instead of calculating the entire temperature distribution inside a bubble. Prosperetti (1991) investigated the thermal diffusive effects and Storey and Szeri (2001) suggested a model in which the bubble interior is assumed to be isothermal when the bubble radius is larger than the equilibrium value, and to be adiabatic when the radius is smaller. Shimada et al. (2000) investigated the model which assumes a homogeneous heat distribution inside a bubble. Toegel et al. (2000) estimated the penetration depth of mass and heat diffusion, and calculated an approximate energy flux at the bubble wall. Preston et al. (2003) considered a temperature gradient based on a linear analysis (Prosperetti et al., 1988).

Figure 12.16 shows a comparison of the time history of bubble radii between the isothermal model, the adiabatic model, the model, and DNS (Direct Numerical Simulation). In this case, the model of Matsumoto and Beylich (1985) is applied to the governing equations and boundary conditions for the bubble motion, and that developed by Preston et al. (2003) is employed for the temperature gradient at the bubble wall. The gas inside the bubble is air and the initial bubble radius is 10 μm. The other calculation conditions are the

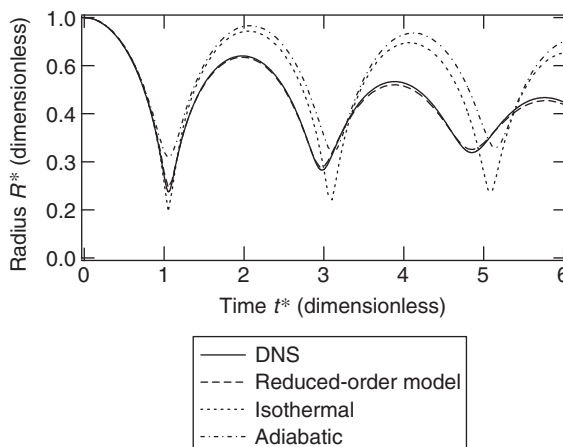


FIGURE 12.16 Comparison of time histories of radii between DNS and reduced-order model.

same as in Table 12.1. Compared with the DNS, the amplitudes of the bubble motions in the case of isothermal and adiabatic model are too large. In the collapse phase, the bubble radius in the case of the isothermal model is too small because the temperature inside the bubble is assumed to be isothermal and the internal energy of the gas phase does not become high. The bubble in the case of the adiabatic model cannot shrink as much as that of DNS, because the heat inside the bubble does not transfer to the liquid phase. On the other hand, the reduced-order model can capture the DNS-predicted bubble motion well. It is reasonable and efficient to apply such a reduced-order model for the computation of a multiple bubble system.

12.2.1.3 Nonlinear Behavior and Acoustic Turbulence

12.2.1.3.1 Nonlinear Oscillation of a Microbubble

To model the dynamics of the bubble in an oscillating field, it is important to take into account the nonlinear phenomena. Many researchers have investigated this topic. Recently, the nonlinear behavior of a microbubble in an ultrasound field has been used for medical ultrasound imaging with microbubble contrast agents. The nonlinear effect was investigated by many researchers (Esche, 1952; Noltingk and Neppiras, 1950; Neppiras and Noltingk, 1951; Flynn, 1964; Borotnikova and Soloukin, 1964; Neppiras, 1969). Lauterborn (1976) simulated the frequency response curve of a bubble (Figure 12.17). This curve shows the amplitudes of the radial oscillation of a bubble of radius $1.0 \mu\text{m}$ in water at a mean ambient pressure of 1 bar (100 kPa) plotted as a function of f/f_N for various amplitudes of oscillation where f is a driving frequency, f_N is the natural frequency of the bubble, R_n is the radius at rest, and R_{\max} is the maximum radius. The numbers above the peaks indicate the order of the resonance, n/m , and the case $m = 1$ with $n = 2, 3, 4$ denoting the higher harmonics and the case $m = 2$ with $n = 1$ denoting the subharmonics. The equations that account for the compressibility of the liquid were employed in this calculation. As the amplitude of the ambient pressure grows larger, the superharmonic and subharmonic peak responses become greater. As the pressure amplitude increases, these peaks shift to lower frequencies. The influence of the internal phenomena on this nonlinear behavior has also been investigated (Matsumoto and Watanabe, 1989).

12.2.1.3.2 Acoustic Turbulence from a Microbubble

The bubble motion in an ultrasound field shows chaotic behavior due to the nonlinearity of the oscillation when the sound amplitude is increased. This phenomenon is called “acoustic turbulence” (Lauterborn, 1989). The bifurcation and chaotic behaviors of bubble oscillation have been calculated by assuming that the interior gas obeys a polytropic relationship, which neglects the thermal dissipation (Lauterborn, 1987).

Figure 12.18 shows the time history of the power spectrum of acoustic pressure from an air microbubble. The bubble motion is simulated when the ambient ultrasound pressure increases linearly from 0 to 1 MPa in 5000 cycles. The initial bubble radius is $2.0 \mu\text{m}$ and the ultrasound frequency is 1 MHz. When the ultrasound

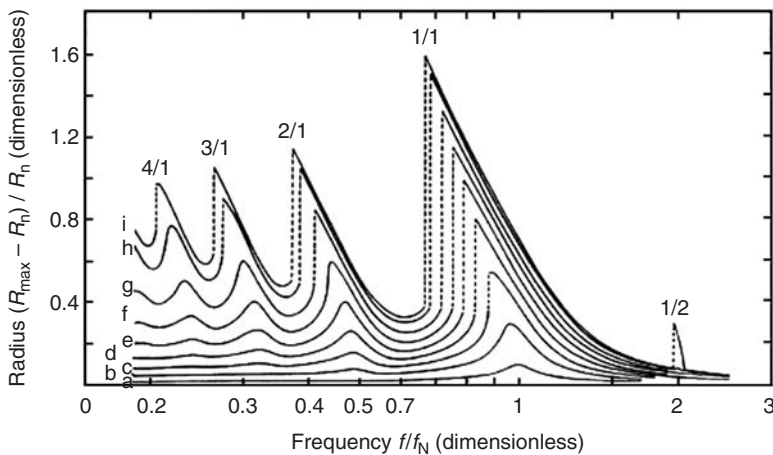


FIGURE 12.17 Numerically computed amplitudes of radial oscillation of a bubble (a) 0.1 (b) 0.3 (c) 0.5 (d) 0.7 (e) 0.9 (f) 1.1 (g) 1.3 (h) 1.5 (i) 1.6 bar. (Adapted from Lauterborn, W., *J. Acoust. Soc. Am.*, 59, 283–293, 1976. With permission.)

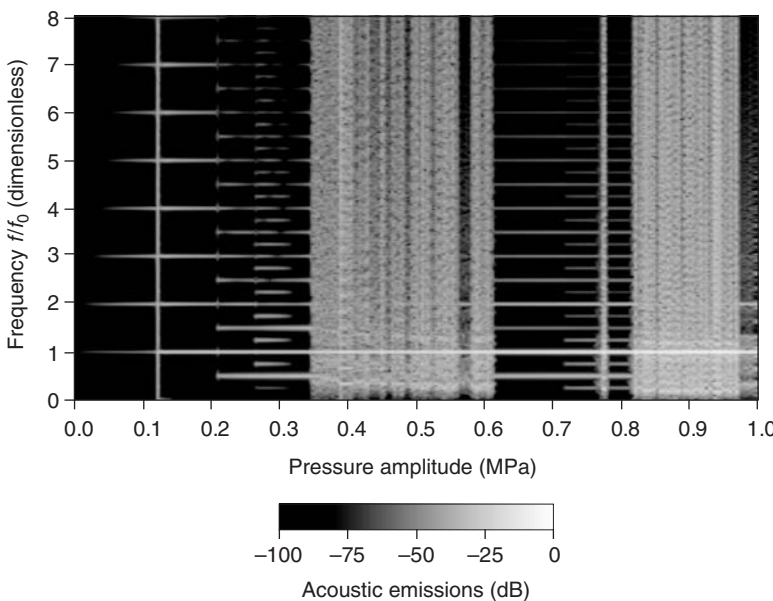


FIGURE 12.18 Power spectrum of the acoustic pressure from an air microbubble.

driving starts, the bubble begins to oscillate in the fundamental mode. As ultrasound amplitude increases, the emitted acoustic pressure increases and it gradually involves the nonlinearity associated with the higher harmonic modes. Bifurcation occurs and the 1/2 harmonic modes begin to appear in each higher harmonic mode, when the pressure amplitude approaches 200 kPa. A further bifurcation appears and the 1/4 harmonic modes emerge at 250 kPa. Thereafter the bubble oscillation becomes chaotic. When the ambient ultrasound pressure reaches about 600 kPa, nonchaotic oscillations occur for a short time, and then the bubble motion returns to chaotic behavior. In this case, the subharmonic modes are barely visible at this relatively low forcing amplitude.

12.2.2 Bubble Deformation and Fragmentation Due to the Collapse

It is well known that the spherical shape of a collapsing bubble is unstable and the shape assume the form of a microjet, which may induce bubble fission. The spherical shape of the bubble is maintained by the surface tension and the viscous force acting on the bubble surface. Deformation will occur when the characteristic anisotropy in the fluid forces overcomes the surface tension and the viscous force. The stability with regard to nonspherical disturbances has been investigated from a hydrodynamic point of view by Birkhoff (1954), Plesset and Mitchell (1956), Brennen (1995, 2002), and Hao and Prosperetti (1999), among others. These analyses essentially examine the spherical equivalent of the Rayleigh–Taylor instability. If the inertia of the gas in the bubble is assumed to be negligible and the viscosity is small enough, then the amplitude, $a_n(t)$, of a spherical harmonic distortion of order n ($n > 1$) will be governed by the equation

$$\ddot{a}_n + \left[3\frac{\dot{R}}{R} + 2(n+2)(2n+1)\frac{\nu}{R^2} \right] \dot{a}_n + (n-1) \left[-\frac{\ddot{R}}{R} + (n+1)(n+2)\frac{\sigma}{\rho R^3} + 2(n+2)\frac{\nu\dot{R}}{R^3} \right] a_n = 0 \quad (12.52)$$

where ν is the kinetic viscosity. The coefficients are determined by the dynamic behavior of the bubble radius, $R(t)$. It can be seen from this equation that the most unstable conditions occur when $\dot{R} < 0$ and $\ddot{R} \geq 0$. These conditions will be reached just before the rebound of a collapsing bubble. The most stable conditions take place when $\dot{R} > 0$ and $\ddot{R} < 0$, which is the case for growing bubbles as they approach their maximum size.

The fact that the coefficients in Eq. (12.52) are not constant in time results in differences from the Rayleigh–Taylor instability for a plane boundary. The coefficient of a is not very different from the case of the plane boundary in the sense that instability is promoted when $\ddot{R} > 0$, while surface tension and viscosity have stabilizing effects. The primary difference is caused by the \dot{a} term. As the bubble grows, the wavelength on the surface increases, and hence the growth of the wave amplitude is lessened. The reverse occurs during collapse. It is easily found from Eq. (12.52) that the initial acceleration phase of bubble growth, in which $\ddot{R} \geq 0$ is unstable with respect to spherical harmonic perturbations of fairly high order, n . However, the remainder of the growth phase during which $\dot{R} > 0$, $\ddot{R} < 0$ is stable with regard to all spherical harmonic perturbations. So, the bubble in the acceleration phase is usually considered to be stable in cavitation experiments. This could be caused either by the brief acceleration phase or the greater stabilizing effect of surface tension in smaller bubbles. On the other hand, it is clear from the theory that the bubble may become highly unstable with respect to nonspherical disturbances during the rebound phase because \ddot{R} reaches very large positive values. The instability appears in several different ways depending on the violence of the collapse and the presence of other boundaries. The instability of the collapsing bubble has been investigated by many researchers (Blake and Gibson, 1987; Tomita and Shima, 1990; Lindau and Lauterborn, 2003). Cavitation bubbles that collapse to a size an order of magnitude smaller than their maximum size inevitably emerge from that collapse as a cloud of smaller bubbles rather than as a single vapor bubble. This fragmentation could be caused by a single micro jet as shown in Figure 12.19, or it could be due to a spherical harmonic disturbance of higher order. The behavior of collapsing bubbles that are filled with a noncondensable gas corresponding with the lower values of \ddot{R} and the instability could be weaker resulting in spherical stability. Thus, acoustically excited cavitation bubbles that contain a substantial amount of gas often remain spherical during their rebound phase. In other instances, the instability is sufficient to cause fragmentation. Several examples of fragmented and highly distorted bubbles emerging from the rebound phase are shown in Figure 12.20. It shows the dynamic behavior of bubble growth and collapse with the sequential decrease and increase of the surrounding pressure. The first pressure reduction creates cavitation bubbles from a heated thin wire at 2.44 msec, and the bubbles grow under the ambient pressure whose value is almost the same as that of the saturated vapor pressure of the bulk temperature. At 4.27 msec the pressure increases and the bubbles begin to shrink. Large fluctuations of the pressure are observed due to

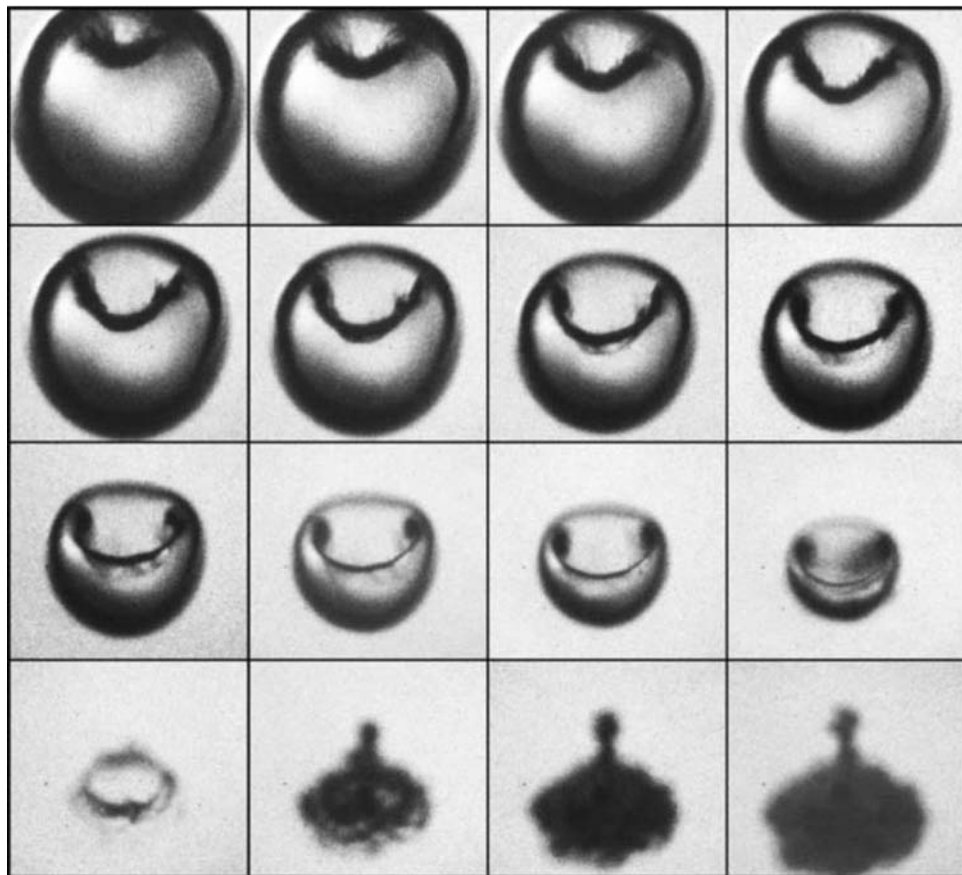


FIGURE 12.19 Jet and counterjet development at an angle of 45° from above the wall; $\gamma = 2.6$ ($\gamma = d/R_{\max}$, the distance of the bubble center from the wall at the moment of formation d and the maximum bubble radius R_{\max}). Interframe time 1 s, exposure time 200 nsec, $R_{\max} = 1.5$ mm, frame size 1.2 mm \times 1.1 mm. (From Lindau O. and Lauterborn W., *J. Fluid Mech.*, 479, 327–348, 2003. With permission.)

the interference with the reflected pressure waves from the bubbles and the bottom. Because of non-spherical instability, the bubbles collapse in an irregular fashion into tiny fragments. This creates many small bubbles, and they grow to cavitation bubbles when the ambient pressure decreases at 9.26 msec. With the next intense expansion wave at 10.50 msec, many cavitation bubbles grow from the remaining bubble nuclei, and at 11.11 msec, they are unified into a single bubble with an irregular shape.

12.2.3 Bubbles Cloud Dynamics

The cavitating collapse of a bubble cloud generates very high pressures and temperatures. The pressure can reach 100 MPa to 1 GPa in a very short period, which causes severe erosion, noise, and vibration in hydraulic machines. However, this high concentration of energy has been utilized recently for biomedical, environmental, and other industrial applications.

Many researchers have investigated the dynamics of a bubble cloud. Omta (1987) investigated the oscillation and sound emission of a bubble cloud analytically and numerically. In his study, the averaged equations derived by Bisheuvel and van Wijngaarden (1984) were used. d'Agostino and Brennen (1989) linearized the governing equations for a bubbly mixture together with the Rayleigh-Plesset equation to

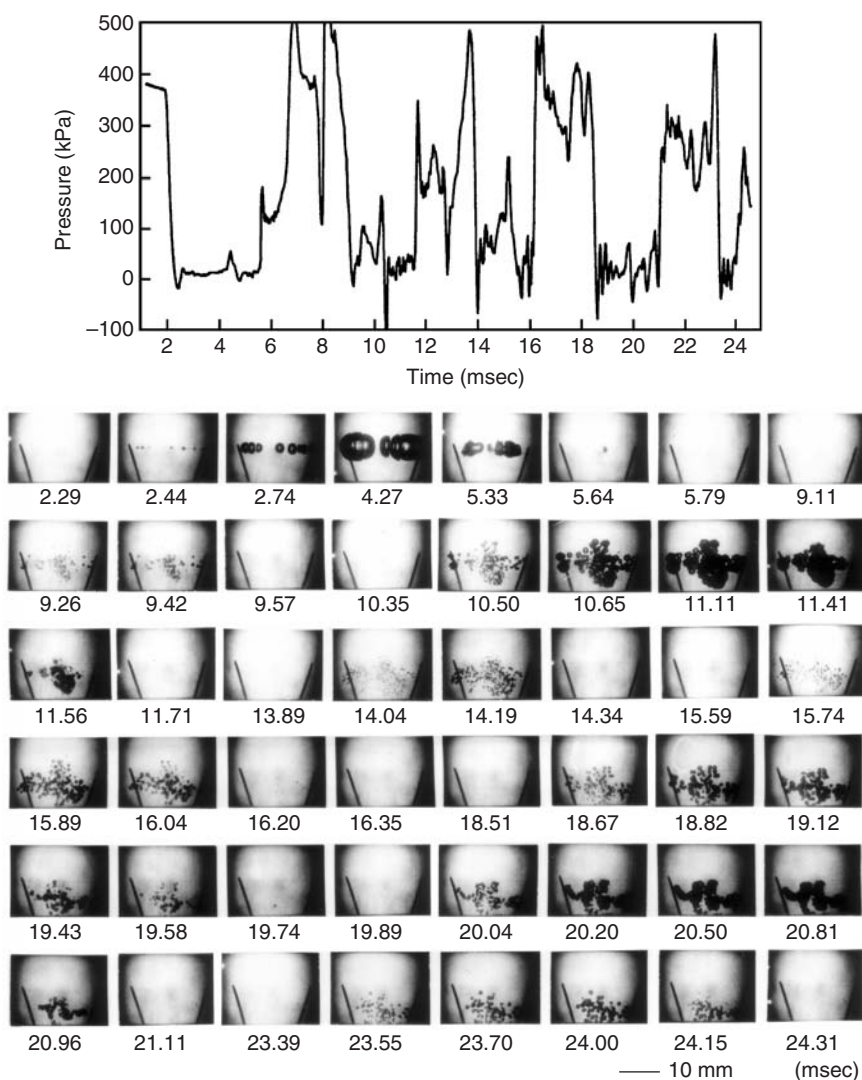


FIGURE 12.20 Growth and collapse of cavitation bubbles due to decrease and increase in the ambient pressure. The gas content is 2.7 ppm. (From Matsumoto, Y. and Aoki, M., *Bull. JSME* 27, 1352–1357, 1984. With permission.)

investigate the analytical solutions for a spherically symmetric bubble cloud. Chahine and Duraiswami (1992) numerically investigated the dynamics of a multibubble cloud consisting of several bubbles and compared their results with analytical results obtained by asymptotic expansions. Shimada et al. (2000) investigated the behavior of cloud cavitation in connection with the cavitation damage using the set of governing equations for the spherical bubble cloud, where the internal phenomena of each bubble and the compressibility of the liquid are taken into account. They concluded that when the bubble cloud collapses, a very high pressure with a high frequency is emitted from each of the bubbles near the center of the cloud.

12.2.3.1 Spherical Bubble Cloud

In this section, the analytical solutions for a spherical bubble cloud are introduced (d'Agostino and Brennen, 1989). The geometry of the spherical cloud is depicted in [Figure 12.21](#).

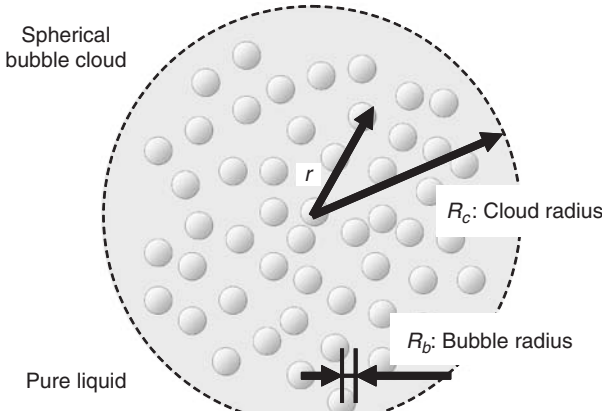


FIGURE 12.21 Spherical bubble cloud.

The relative motion of the two phases, the mass of the dispersed phase and all the damping mechanisms for the bubble dynamics are neglected, and the liquid is assumed to be inviscid and incompressible. The mass and momentum conservation equations are

$$\nabla \cdot \mathbf{u} = \frac{\beta}{1 + \beta\tau} \frac{D\tau}{Dt} \quad (12.53)$$

$$\rho \frac{D\mathbf{u}}{Dt} = -(1 + \beta\tau) \nabla p \quad (12.54)$$

where β is the number density of bubbles per unit liquid volume, τ the individual bubble volume, and D/Dt indicates the Lagrangian derivative. The bubble radius, R_b , is determined by the Rayleigh–Plesset equation.

$$R_b \frac{D^2 R_b}{Dt^2} + \frac{3}{2} \left(\frac{DR_b}{Dt} \right)^2 = \frac{1}{\rho} \left(p_g + p_v - p - \frac{2\sigma}{R_b} \right) \quad (12.55)$$

where p_g is the partial pressure of noncondensable gas, p_v the partial pressure of the vapor, and σ the surface tension.

For simplicity, the following assumptions are employed: (1) The bubble cloud is spherical. (2) The mean-flow velocity is purely radial and small. (3) The void fraction is uniform and relatively low inside the cloud. (4) All the bubbles have the same equilibrium radius, R_{b0} (the subscript 0 indicates the unperturbed value). (5) The vapor pressure inside the bubble is constant. (6) The pressure of the noncondensable gas in the bubbles changes isothermally. Let the perturbation of the far-field pressure be defined in the complex plane by the equation $p_\infty = p_0[1 + \epsilon \exp(i\omega t)]$ with $\epsilon \ll 1$. After applying the assumptions and linearizing eqs. (12.53) – (12.55) with the equation $R_b(r,t) = R_{b0}[1 + \varphi(r,t)]$ with $[\varphi(r,t)] \ll 1$, the normalized variation of the bubble radius φ and the natural frequencies ω_n are

$$\varphi(r, t) = -\epsilon \frac{p_0(1 - \alpha_0)/\rho R_{b0}^2}{\omega_b^2 - \omega^2} \left(\frac{1}{\cos kR_{c0} - \alpha_0 \sin(kR_{c0})/kR_{c0}} \right) \frac{\sin kr}{kr} e^{i\omega t} \quad (12.56)$$

$$\omega_n^2 = \omega_b^2 / \left(1 + \frac{3\alpha_0(1 - \alpha_0)R_{c0}^2}{(n - 1/2)^2 \pi^2 R_{b0}^2} \right) \quad (12.57)$$

$$\omega_b^2 = \frac{3p_{g0}}{\rho R_{b0}^2} - \frac{2\sigma}{\rho R_{b0}^3} \quad (12.58)$$

Here, ω is the frequency of the far-field pressure, ω_b the natural frequency of a single bubble at isothermal conditions, α the void fraction, R_c the cloud radius, and k the wave number in the bubbly flow.

The natural frequencies of the spherical bubble cloud will extend to much lower frequencies than that of a single bubble if the initial void fraction, α_0 , is much larger than the square of the ratio of bubble size to cloud size ($\alpha_0 \gg R_{b0}^2/R_{c0}^2$). Figure 12.22 shows the natural mode shapes of the normalized bubble radius, the pressure and the bubble concentration per unit liquid volume in the cloud ($n = 1 - 4$). The first mode consists of the same phase. Higher modes have n antinodes and $n - 1$ node(s) within the cloud. The envelope is proportional to $1/r$, and the amplitudes at the bubble cloud interface become much smaller at the higher modes.

When the damping effects are included, the attenuation is much greater at the higher frequencies, so that the dominant feature of the response is the first mode natural frequency of the cloud. On the other hand, the response at the bubble natural frequency ($n = \infty$) becomes much less significant.

12.2.3.2 Spherical Bubble Cloud Model

In the previous section, a theoretical analysis for a spherical bubble cloud was introduced; however, the results are limited to the case in which the volumetric change of the bubbles is very small. In this section, the volumetric change of a spherical bubble cloud is simulated by using the model proposed by Shimada et al. (2000), to illustrate nonlinear response.

12.2.3.2.1 Concept and Assumptions of a Spherical Bubble Cloud

Shock waves propagate inside a bubble cloud. Kameda et al. (1996, 1998) clarified that internal phenomena can have a significant influence on shock wave propagation and in certain cases the compressibility of the liquid cannot be ignored, depending on the amount of bubble motion. It has been determined that a very high pressure of $O(10^8)$ – $O(10^9)$ Pa emerges near the center of the cloud cavitation when it collapses violently. In such a case, the compressibility of the liquid should be taken into account. Therefore, to analyze collapsing phenomena of a bubble cloud rigorously, internal phenomena of the individual bubbles and liquid compressibility should be included. Bubbles in the cloud shrink violently, so that gases in a bubble cannot be treated as ideal. For simplicity, the ambient temperature rise of the liquid and the mass transformation of noncondensable gases through the bubble wall are not considered. In the numerical simulation, the following assumptions are employed: (1) The bubble cloud and each bubble maintain spherical symmetry as they oscillate. (2) The bubbly liquid inside the cloud is treated as a continuum fluid,

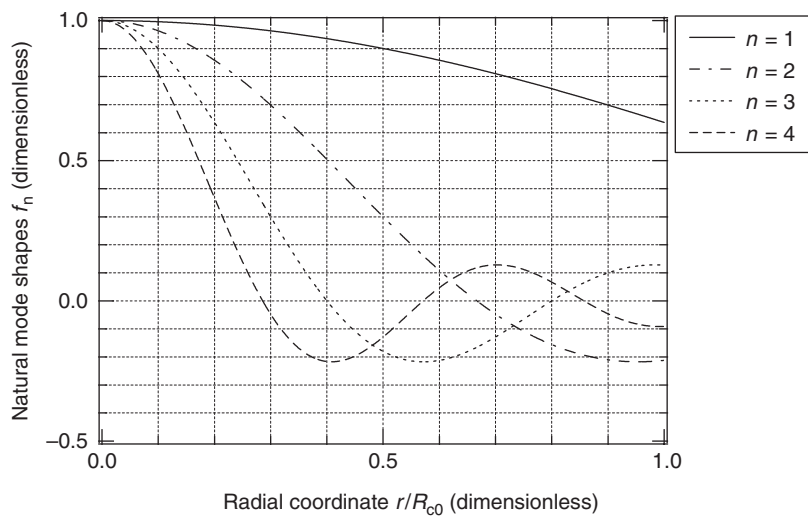


FIGURE 12.22 Natural mode shapes of the normalized bubble radius, the pressure and the bubble concentration per unit liquid volume in the cloud ($n = 1 - 4$).

whose mass and momentum are assumed to be equal to those of the liquid phase, because the mass in a unit volume of the gas phase is much smaller than that of the liquid phase. (3) Bubbles move with the surrounding liquid, and are small enough to ignore the slippage between the bubble and the liquid. (4) Coalescence and fragmentation of bubbles in the cloud are ignored. (5) Viscosity of the bubbly mixture is ignored in the cloud because it has little influence on the wave phenomena. (6) The temperature of the liquid in the cloud is constant. (7) The pressure and temperature inside each bubble are uniform except for the thin boundary layer near the bubble wall, compared with the bubble radius. (8) Temperature at the bubble wall is equal to that of the liquid. (9) Mass of the noncondensable gas inside a bubble is constant. (10) Gases inside a bubble obey the van der Waals gas law. (11) Coalescence and fragmentation of mist inside a bubble are ignored. The thermal behavior inside the bubble and the pressure wave phenomena in the bubble cloud, namely, the evaporation and condensation of liquid at the bubble wall, heat transfer through the bubble wall and the compressibility of the liquid are included.

The geometry of a spherical bubble cloud is the same as in [Figure 12.21](#). A bubble is located at the center of the cloud to avoid a singularity.

12.2.3.2.2 Governing Equations

The Keller equation (Keller and Kolodner, 1956) is applied to the equation of motion of the spherical bubble cloud interface (Eq. [12.59]) to take the compressibility of the surrounding liquid into account.

$$R_c(1 - \frac{\dot{R}_c}{c})\ddot{R}_c + \frac{3}{2}\left(1 - \frac{\dot{R}_c}{3c}\right)\dot{R}_c^2 = \frac{1}{\rho_l}\left(1 + \frac{\dot{R}_c}{c} + \frac{R_c}{c}\frac{d}{dt}\right)\left(p_w - p_\infty - 4\frac{\mu_l}{R_c}\dot{R}_c\right) \quad (12.59)$$

where R_c is the radius of the bubble cloud, c the speed of sound in the surrounding liquid, ρ_l the density of the liquid, p_w the pressure at the surface of the cloud, p_∞ the ambient pressure, and μ_l the viscosity of the liquid. In a bubble cloud, the mass and momentum conservation equations for bubbly flow (Eqs. [12.60] and [12.61]) and the conservation equation for the number density of bubbles (Eq. [12.62]) are also solved. The Tait equation (12.63) is employed as the equation in liquid phase.

$$\frac{\partial(1 - \alpha)\rho_l}{\partial t} + \frac{1}{r^2}\frac{\partial}{\partial r}\{r^2(1 - \alpha)\rho_l u_l\} = 0 \quad (12.60)$$

$$\frac{\partial(1 - \alpha)\rho_l u_l}{\partial t} + \frac{1}{r^2}\frac{\partial}{\partial r}\{r^2(1 - \alpha)\rho_l u_l^2\} + \frac{\partial\rho}{\partial r} = 0 \quad (12.61)$$

$$\frac{\partial n_b}{\partial t} + \frac{1}{r^2}\frac{\partial}{\partial r}\{r^2 n_b u_b\} = 0 \quad (12.62)$$

$$\frac{p + B}{p_\infty + B} = \left(\frac{\rho_l}{\rho_{l\infty}}\right)^n \quad (12.63)$$

where α is the void fraction, u_l the velocity of the liquid, and n_b the number density of the bubbles. The velocity of a bubble, u_b , is assumed to be equal to u_l (assumption [3] above). In the Tait equation, $B = 304.9$ MPa and $n = 7.15$ for water.

For each bubble motion, the following phenomena are taken into consideration: the compressibility of the surrounding liquid, the mass and heat transfer through the bubble wall, the evaporation and condensation of the vapor, and the mist generation from the vapor inside the bubble (Matsumoto and Beylich, 1985). Equations (12.50) and (12.51) are applied as the dynamic equations for the bubble radius. The energy conservation equation in the gas phase with mist and the nucleation rate equation of mist are also solved.

12.2.3.3 Computational Conditions

In this simulation, the behavior of a spherical bubble cloud, which consists of many microbubbles is investigated. Such a microbubble cluster may be generated in high (HIFU) applications, which have attracted much attention recently, because they are less invasive than conventional medical treatments. [Table 12.3](#) lists the computational conditions. Acoustic cavitation induced by ultrasound is highly

TABLE 12.3 Computational Conditions

Gas Phase	Air
Liquid phase	Water
Initial cloud radius, R_{c0}	0.5 mm
Initial bubble radius, R_{b0}	1 μm
Initial ambient pressure, p_0	101.3 kPa
Initial temperature	293 K
Initial void fraction	0.1%
Amplitude of ambient pressure	10–100 kPa
Frequency of ambient pressure	10 kHz–4 MHz

dependent on the ultrasound frequency. In medical applications, a typical frequency of ultrasound is around 0.5 to 5 MHz. When the ultrasound frequency is 4 MHz, the wavelength is about 0.4 mm in water or tissue. The focal region is considered to be around 2 to 4 times the wavelength. In this simulation, it is assumed that the region of the bubble cloud is 0.5 mm in radius and each bubble radius is 1 μm (the natural frequency is about 4 MHz). The ambient pressure fluctuation is assumed to be a pulse wave and the frequency of the wave extends from 10 kHz to 4 MHz for amplitudes of 10, 25, 50, 75, and 100 kPa.

12.2.3.4 Frequency Response of a Spherical Bubble Cloud

The bubbles which are located near the center of the bubble cloud violently collapse when the bubble cloud oscillates at its resonance frequency. The maximum pressures inside the bubbles and maximum cloud radii are calculated for various conditions. [Figure 12.23](#) shows the results. The horizontal axis corresponds to the frequency of the ultrasound. The vertical axis corresponds to the maximum pressure inside the bubbles normalized by the amplitude, and the maximum cloud radius normalized by the initial radius.

When the frequency is sufficiently low, around 10 kHz, the normalized maximum pressure is nearly equal to 1. This means that the ultrasound does not focus in the cloud and the attenuation of the bubbly liquid is negligible corresponding to the long wavelength of the ultrasound. The reason for the normalized maximum pressure inside the bubbles to exceed unity is the effect of the surface tension. In fact, the normalized maximum pressure in the liquid phase converges to unity for the same computational conditions. On the other hand, the normalized maximum pressure converges to 0 due to the large attenuation of the bubbly liquid when the frequency is near the natural frequency of a single bubble, which is about 4 MHz. When the frequency range is from approximately 180 to 200 kHz, the bubble cloud resonates and the normalized maximum pressure becomes very high. Furthermore, the normalized pressure becomes higher as the pressure amplitude of the ultrasound becomes greater. The normalized pressure exceeds 2000, which corresponds to 200 MPa, in the case of 100 kPa pressure amplitude at a frequency of 180 kHz. Additionally, in the case of 100 kPa pressure amplitudes, the high pressures appear even for a lower frequency. The cloud radius hardly changes in each case. This is because the changes of the cloud radius are mainly caused by the volumetric changes of the bubbles in the cloud and the initial void fraction is only 0.1% as shown in Table 12.3.

12.2.3.4.1 Low-Pressure-Amplitude Cases ($\Delta p = 10 \text{ kPa}, 25 \text{ kPa}$)

The response curves of the maximum pressure in the case of 10 and 25 kPa pressure amplitude are almost the same as those shown in [Figure 12.23](#). The ultrasound propagation in these cases are shown since the cloud, at first, shows nearly linear oscillation for these conditions. Two different peaks are observed in the response curves of the maximum pressure: one at 200 kHz and the other at 600 kHz. [Figure 12.24](#) shows the pressure distributions of the liquid phase over about 0.5 T (T is the cycle of the ultrasound), at each 0.01 T. The amplitude of the ambient pressure is 10 kPa at a frequency of 200 kHz (left panel) and 600 kHz (right panel). The pressure inside the cloud changes at almost the same phase as the cloud in the 200 kHz case. This is the first resonance mode of a spherical bubble cloud (see [Figure 12.22](#)). The first mode frequency is slightly lower than the natural frequency calculated by Eq. (12.57) since the damping effects are not considered in that formula. In fact, d'Agostino and Brennen (1989) showed

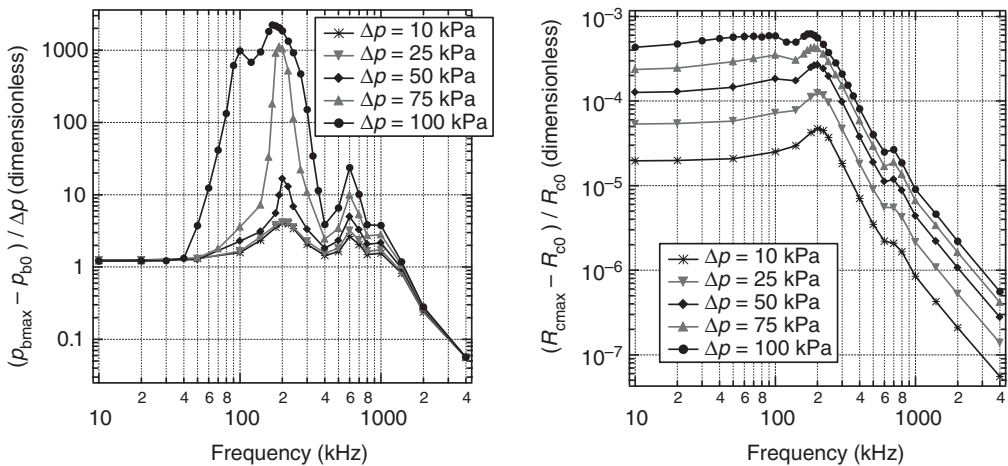


FIGURE 12.23 Frequency response curves at various amplitudes of the ambient pressure. Left panel: maximum pressure inside the bubbles; right panel: maximum bubble cloud radius.

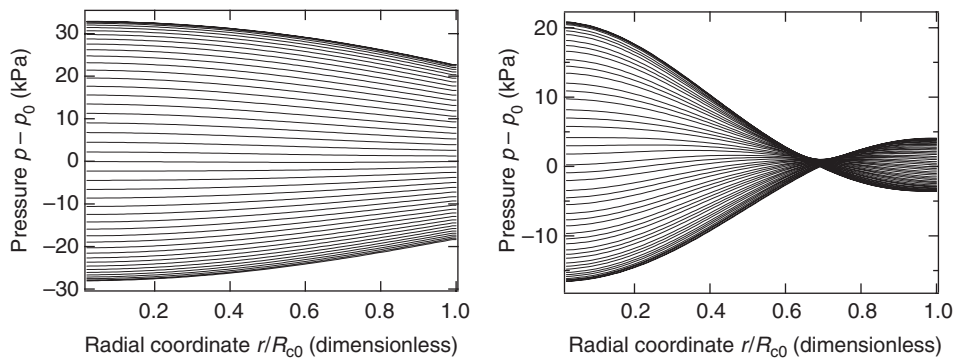


FIGURE 12.24 Pressure distributions of the liquid phase inside a bubble cloud. Left panel: $\Delta p = 10$ kPa, $f = 200$ kHz; right panel: $\Delta p = 10$ kPa, $f = 600$ kHz.

that the natural frequencies become lower when the damping effects are taken into account. In the 600 kHz case, there is one pressure node and the pressure at the center of the cloud is shifted almost π radians backward from that at the boundary of the cloud. This is the second resonance mode of a spherical bubble cloud (see Figure 12.22). As in the case of the first resonance mode, the frequency is almost the same as the second mode natural frequency (d'Agostino and Brennen, 1989).

12.2.3.4.2 High-Pressure-Amplitude Cases ($\Delta p = 75$ kPa, 100 kPa)

When the pressure amplitude becomes higher, the oscillations of the cloud show strong nonlinearity. Figure 12.25 shows the water pressure in the cloud under the same conditions as the surface plot. The range of the normalized time is from $4.05T$ to $4.30T$. In this case, the shock wave is generated inside the cloud by the process of wave focusing. The speed of sound in the bubbly flow strongly depends on the void fraction and is directly dependent on the pressure fluctuations. The harmonic pressure wave easily generates the shock wave inside the bubbly liquid. The shock wave in the bubbly liquid causes the collapse of the bubbles, so that high energy is concentrated near the center of the cloud. As a result, the normalized pressure becomes much higher when the pressure amplitude becomes significant to generate the shock wave. For example, in the case of 100 kPa pressure amplitudes, even when the frequency is much

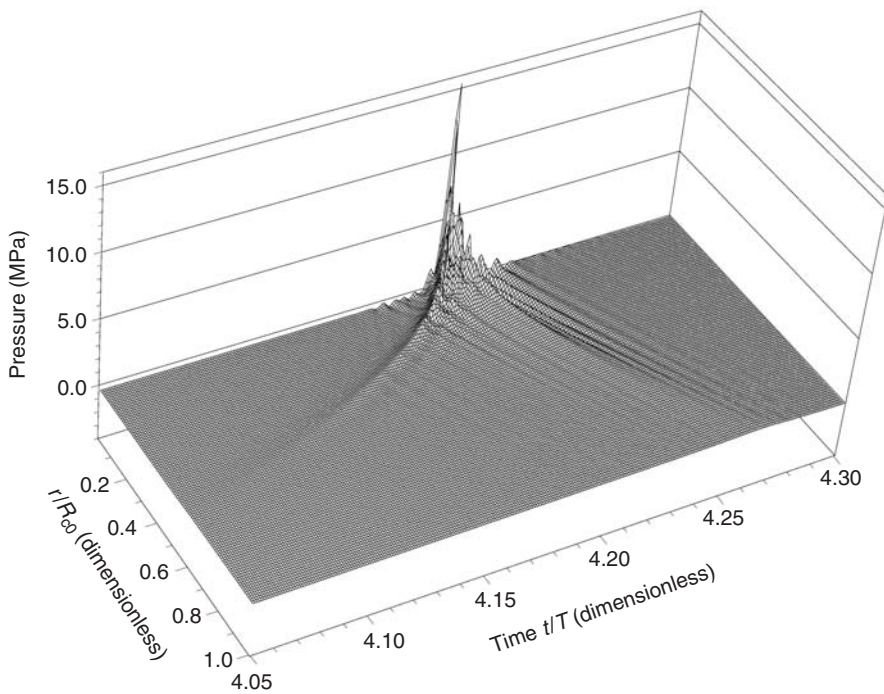


FIGURE 12.25 Surface plot of the liquid pressure inside a bubble cloud ($\Delta p = 100$ kPa, $f = 180$ kHz).

lower, the pressure wave can generate a shock and high pressures as observed for the 180 kHz case. Additionally, since a high pressure wave with a high frequency is generated when the bubbles near the center of the cloud collapse, precursors appear in front of the shock wave before the focusing.

The results indicate that the bubbles inside a bubble cloud violently collapse when the frequency of the irradiated ultrasound is the same or lower than the natural frequency of the cloud for a sufficiently large ultrasound pressure amplitude.

12.3 Droplet Breakup, Coalescence, and Wall Impact

C. Tropea and I.V. Roisman

The usual description of the spray transport involves the solution of the mass and the momentum balance equations for the liquid phase (droplets) and of the ambient gas flow as well as the forces associated with the droplet–gas interactions (drag forces). The details and various approaches to such modeling can be found in Chapter 13. The phenomena considered in the present chapter include the droplet breakup due to the interaction with the air-flow, collisions with another drop or with a wall. In Figure 12.26, the spray atomization, transport, and wall impact are shown schematically, involving these phenomena. They lead to alterations in the distributions of the drop diameters and velocity in the spray. Accounting for such alterations significantly complicates the modeling of spray transport, considerably extends the numerical simulations and thus, in many numerical simulations the effect of the drop break-up and coalescence is assumed negligibly small and neglected. However, the drop fragmentation in the near-atomizer region determines the average drop diameter of the spray obtained and therefore cannot be neglected. The secondary breakup of drops can be caused by the interaction of a spray with a high-speed gas jet or by a shock wave. The effect of binary collisions becomes significant in the region of the interaction of two (or more) sprays, and the case of the propagation of very dense spray, the near-wall region (where the impacting spray interacts with the spray of the secondary droplets produced by spray–wall impact).

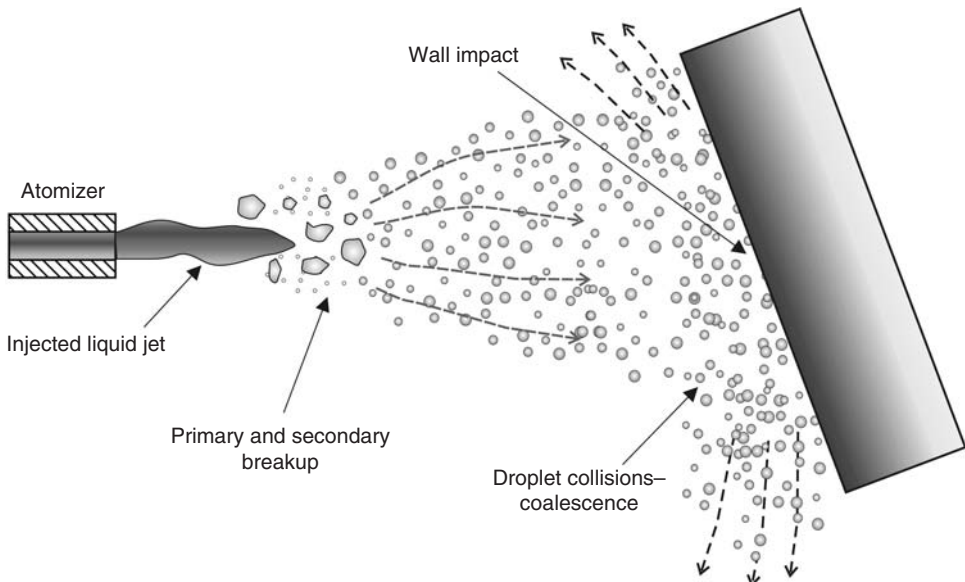


FIGURE 12.26 Sketch of spray atomization, transport and wall impact.

When a spray impacts onto a substrate, a part of the droplet volume deposits on it and forms a thin fluctuating liquid film. Another part of the spray volume rebounds and creates a flow of secondary droplets. One of the key elements in the creation of such secondary spray is the drop impact onto a wall, also described in the present chapter.

The common feature of the phenomena described here is the significant change of the drop shape due to the impact with another drop (binary drop collisions), its deformation and breakup by ambient air flow, or due to the impact onto a dry or wet substrate, as illustrated in Figure 12.27.

The main parameters determining the drop deformation and breakup are the Reynolds number $Re = DU/v$ and the Weber number $We = DU^2/\sigma$, where D is the drop diameter, U the characteristic velocity, v the kinematic viscosity, and σ the surface tension. If both these numbers are large ($Re \gg 1$, $We \gg 1$), the droplet deformation is inertia-dominated. The drop deformation often leads to the creation of an expanded relatively thin free liquid sheet (lamella) bounded by a rim, formed due to capillary forces (see Figure 12.28a). In other cases, the drop deformation leads to the appearance of the finger-like jets ending with a droplet, as shown schematically in Figure 12.28b.

These forms appear due to capillary forces. The rim velocity differs from the velocity of the liquid in the lamella. The motion of the rim is determined by the capillary forces, the internal viscous stresses, the inertia of the liquid entering the rim from the lamella, and the aerodynamic drag force. The simplest case of the motion of the rim bounding a steady uniform liquid sheet was analyzed by Taylor (1959). In this case, the capillary force per unit length, 2σ , is balanced by the inertia of the liquid entering the rim, $\rho w_{\text{rim}}^2 \delta$. The relative rim velocity w_{rim} is expressed in the form:

$$w_{\text{rim}} = \sqrt{\frac{2\sigma}{\rho\delta}} \quad (12.64)$$

The analysis of the droplet appearing at the end of a free liquid jet (Figure 12.28b) is very similar. The momentum equation of this droplet appearing at the end of a steady jet of the diameter D_j expresses the balance of the inertia of the liquid entering the droplet from the jet, the capillary forces, and the pressure in the jet due to surface tension. The relative droplet velocity is

$$w_{\text{droplet}} = \sqrt{\frac{2\sigma}{\rho D_j}} \quad (12.65)$$

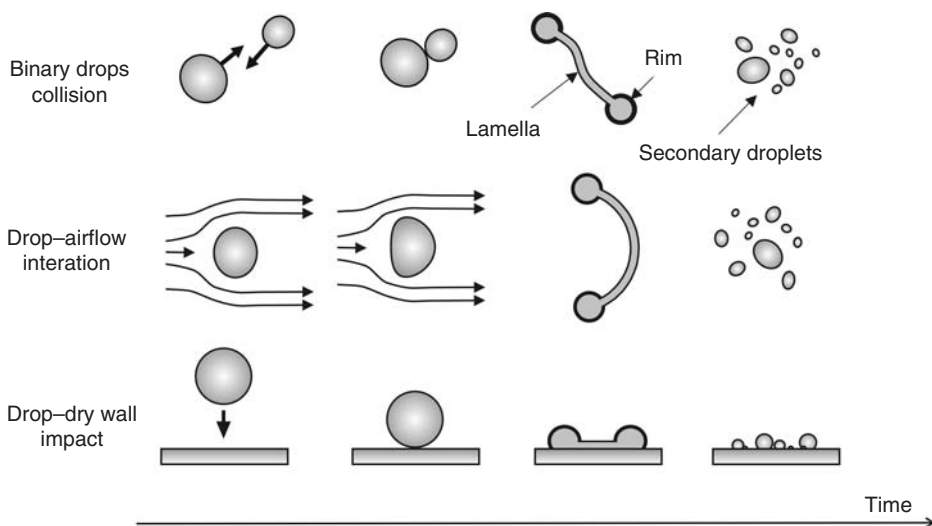


FIGURE 12.27 Successive stages of drop deformation and break up due to the binary drop collision, drop/airflow interaction and drop/wall impact.

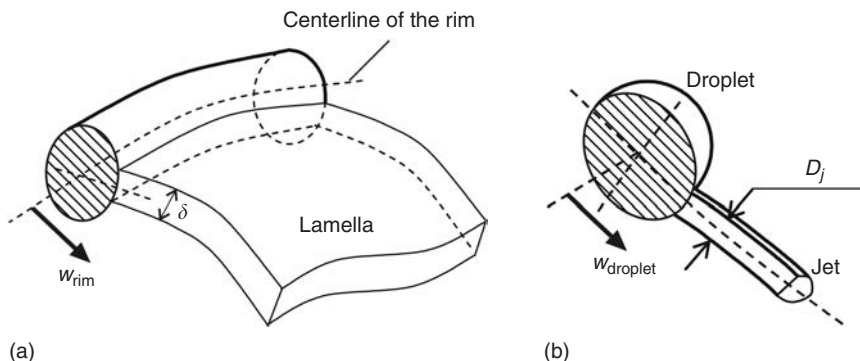


FIGURE 12.28 Capillary effects at the free boundary: (a) element of rim bounding a liquid sheet; (b) droplet appearing at the end of a liquid jet.

12.3.1 Droplet Breakup Mechanisms

The main subjects in the study of the drop breakup are usually the regimes of the breakup, the time of breakup, and the outcome: size, number and velocities of the secondary droplets. We distinguish here two main directions of the breakup study:

- aerodynamic breakup, important for the description of sprays, associated with the drop suddenly exposed to a high-speed gas flow or break-up by a shock wave propagating in the ambient gas. The velocity of the drop relative to the velocity of the ambient gas flow and corresponding pressure gradients at the drop surface are the main reasons for the breakup.
- the breakup in a viscous flow, with the application to the rheology of emulsions, when the drop deforms and breaks up mainly due to the shear stresses appearing in the ambient viscous liquid.

In addition, there are many specific cases of drop impact which will not be described in detail here, for example, the deformation and breakup involving non-Newtonian drops or flows (Ha and Leal, 2001) in an electric field (Ha and Yang, 1998), a turbulent fluid flow (Sevink and Park, 1973), and an acoustic field (Yarin et al., 2002).

12.3.1.1 Regimes of the Aerodynamic Drop Breakup

The typical dimensionless parameters used in the description of the aerodynamic breakup are the Reynolds number $Re_g = \rho_g w D / \mu_g$ and Weber number $We_g = \rho_g w^2 D / \sigma$ based on the properties of the ambient gas, as well as Ohnesorge number $Oh = \mu_l / \sqrt{\rho_l D \sigma}$, where w is the relative droplet–gas velocity. These parameters determine the degree of the drop deformation and the mode of the drop breakup.

The first attempt to classify the various regimes of drop break-up using the Weber number, We_g , and Ohnesorge number, Oh , was made by Hinze, (1955). A more detailed map of these regimes at various Ohnesorge numbers has since been created on the basis of extensive experimental studies on a drop breakup (Hinze, 1955; Hsiang and Faeth, 1992, 1995). Most of the observations show that the critical We_g numbers, corresponding to the regime thresholds, are almost independent of the Ohnesorge number if it is small ($Oh < 0.1$). An increase in the Weber number leads to an increase in drop deformation. At some critical Weber number the drop breaks up. Several main regimes of breakup shown schematically in Figure 12.29 can be observed:

Bag break-up, shown in Figure 12.29a, takes place in the range $12 < We_g < 15$ at $Oh < 0.1$. In this regime the lamella deforms and takes an expanding bag-like shape. At some time instant the lamella disintegrates. The rim then breaks up due to the Rayleigh capillary instability.

At higher relative velocities, $80 < We_g < 350$ at $Oh < 0.1$, the main drop deformation takes place in the thin boundary layer of the frontal surface of the drop. The flow in the liquid layer yields the *boundary layer stripping* (Hinze, 1955; Ranger and Nicholls, 1969; Delplanque and Siringano, 1994). The resulting thin liquid film then disintegrates in the airflow (Figure 12.29b). This mechanism is also called *shear breakup*. An alternative description of the drop breakup mechanism in this range of relative velocities, called *stretching/thinning breakup*, is given in Liu and Reitz (1997) and Lee and Reitz (2000). In these studies the main source of drop deformation is associated with the low-pressure region near the drop equator. The pressure gradient along the drop surface leads to the drop stretching in the plane normal to the direction of the airflow. The edges of the obtained lamella are thin because the inertial forces in the film significantly exceed capillary forces. Such a film is then deflected in the direction of the gas flow (Figure 12.29c)

If the relative velocity is so high such that the gas Weber number exceeds 350 ($We_g > 350$), the droplet deforms very quickly and takes the form of a wavy thin sheet. This sheet then breaks up into ligaments and secondary droplets: *catastrophic breakup* shown in Figure 12.29d (Hwang et al., 1996).

Note that the phenomenon of drop breakup cannot always be classified by the above mentioned regimes. Some studies are devoted to the investigation of *multimode regimes*, mainly in the range between the bag breakup and shear breakup. In Pilch and Erdman (1987) and Joseph et al. (1999) the bag-and-stamen breakup at $50 < We_g < 100$ were mentioned. The description and temporal parameters of bag–plume and plume–shear breakup regimes can be found in Dai and Faeth (2001).

The best fit for the threshold of breakup regimes and the degree of drop deformation by a shock wave based on the experimental data from Hsiang and Faeth (1995) for $Oh < 2 \times 10^{-4}$ is obtained in Schmehl (2003) in the form

$$We < 0.6(1 + 0.8Oh^{0.8} + 9 \times 10^{-5}Oh^{2.4}) \quad \text{deformation} < 5\%, \text{ no breakup}, \quad Oh < 6 \times 10^2$$

$$We = 1.1(1 + 0.7Oh^{0.85} + 1.5 \times 10^{-4}Oh^{2.4}) \quad \text{deformation} 10\%, \text{ no breakup}, \quad Oh < 6 \times 10^2$$

$$We = 2.3(1 + 0.75Oh^{0.8} + 2.5 \times 10^{-4}Oh^{2.4}) \quad \text{deformation} 20\%, \text{ no breakup}, \quad Oh < 6 \times 10^2$$

$$3(1 + 15Oh^{1.2}) < We < 13(1 + 1.7Oh^{1.4}) \quad \text{drop oscillations, no breakup}, \quad Oh < 3 \times 10^{-1}$$

$$13(1 + 1.7Oh^{1.4}) < We < 35(1 + 0.65Oh^{1.4}) \quad \text{bag breakup}, \quad Oh < 4$$

$$35(1 + 0.65Oh^{1.4}) < We < 80(1 + 0.6Oh^{1.5}) \quad \text{multimode breakup}, \quad Oh < 15$$

$$80(1 + 0.6Oh^{1.5}) < We \quad \text{shear breakup}, \quad Oh < 6$$

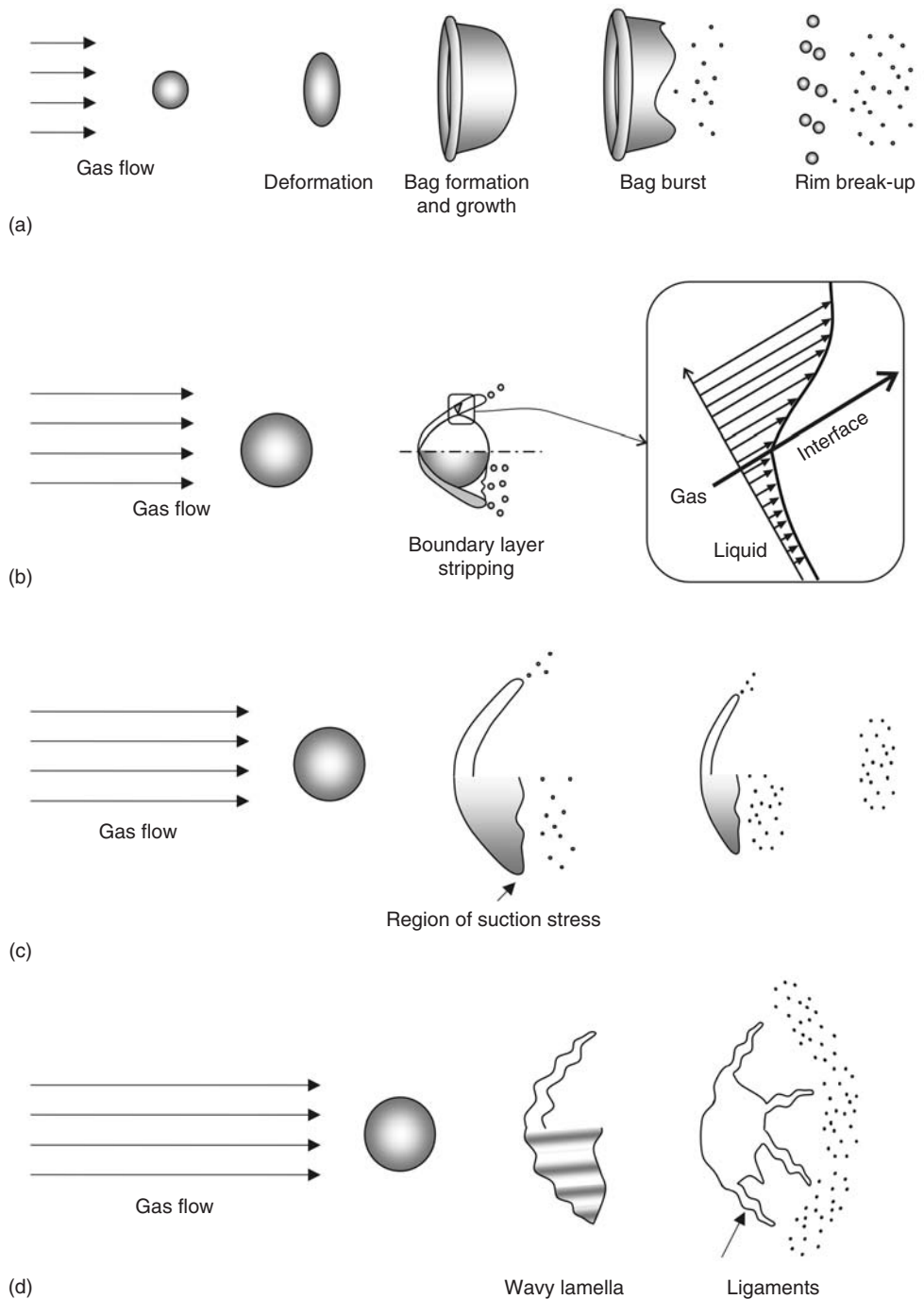


FIGURE 12.29 Mechanisms of aerodynamic breakup.

The increasing drop viscosity slows the rate of drop deformation; however, the maximum drop deformation is virtually not affected by the Ohnesorge number.

The axisymmetric shape of the drop deformed by a shock wave can be approximately described by two dimensions: its length L in the axial direction and its diameter D . The empirical expression for the degree

of the maximum drop deformation by a shock wave is obtained in Hsiang and Faeth (1995):

$$\left(\frac{D}{L}\right)_{\max} = (1 + 0.007 We^{1/2})^3 \quad (12.66)$$

The temporal behavior of the drop during the breakup process is illustrated in Figure 12.30 using the characteristic shear breakup time defined in Ranger and Nicholls (1969):

$$t^* = \frac{D_0}{w_0} \sqrt{\frac{\rho_1}{\rho_g}} \quad (12.67)$$

where D_0 and w_0 are the initial drop diameter and the initial relative velocity to the gas. The gray area corresponds to the time intervals at which a drop breaks up and generates secondary droplets.

12.3.1.2 Aerodynamic Breakup Outcomes

The secondary droplets obtained by drop breakup are usually in a relatively wide range of diameters and velocities. The Sauter mean diameter, D_{32} , is one of the most convenient integral parameters characterizing the drop size. This parameter is modeled in Hsiang and Faeth (1992) as a function of the size of the viscous boundary layer appearing on the front surface of the drop. The resulting expression for small Ohnesorge number ($Oh < 0.1$) is

$$D_{32} = 6.2 D_0 Oh^{1/2} We_g^{-1/4} \quad (12.68)$$

In Schmehl (2003a) an alternative empirical correlation for the Sauter mean diameter (SMD) is proposed, fitting the collected experimental data more precisely:

$$D_{32} = 1.5 D_0 Oh^{0.2} \left(\frac{1 + 1.7 Oh^{1.4}}{We_g} \right)^{0.25} \quad (12.69)$$

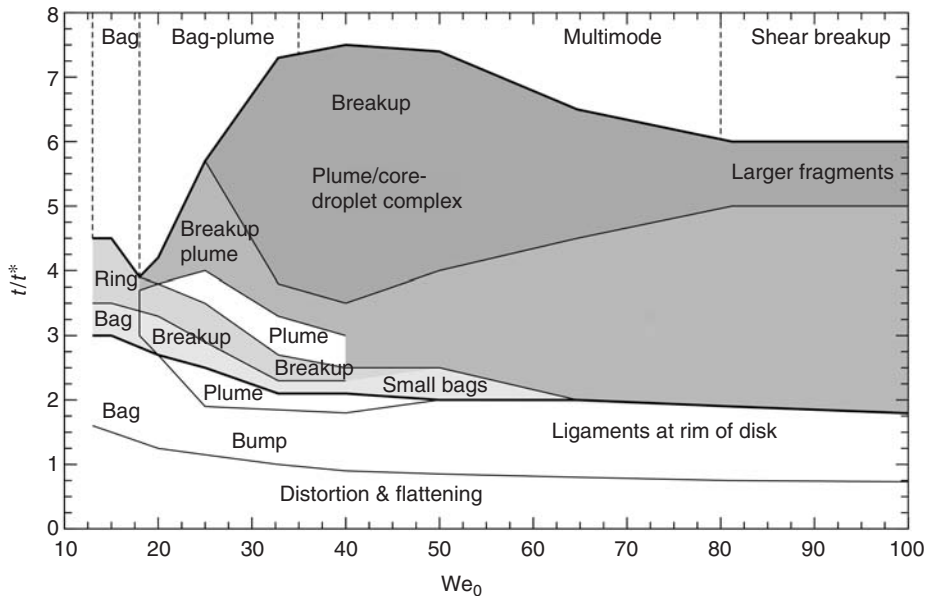


FIGURE 12.30 Stages of droplet deformation and break-up for various regimes of aerodynamic breakup ($Oh < 0.1$). (Adapted from Schmehl, R., *Proceedings of the International Conference on Liquid Atomization and Spray Systems ICLASS-2003*, July 13–18, 2003, Sorrento, Italy, 2003b. The experimental data are from Dai, Z., and Faeth, G.M., *Int. J. Multiphase Flow*, 27, 217, 2001; Krzczkowski, S.A., *Int. J. Multiphase Flow*, 6, 227, 1980; Wiegba, A., *Exp. Fluids*, 9, 1329, 1990.)

Hsiang and Faeth (1992) have found that the diameters of the droplets (excluding the size of the parent drop) can be described well using the universal root normal distribution function with the $D_{0.5}/D_{32} = 1.2$, where $D_{0.5}$ is the mass median diameter (MMD). The definitions of various mean diameters can be found in Lefebvre (1989).

The next parameter characterizing the breakup outcome is the velocity of the fragments. Their velocity changes during the breakup period due to the drag force applied from the ambient gas flow. The deceleration associated with this drag depends on the fragment's size, yielding a velocity-dependent distribution. The velocity distribution of fragments at the instant when the breakup process is completed is obtained in Hsiang and Faeth (1993) in the following form:

$$w_0/w = 1 + 2.7 \left(\sqrt{\frac{\rho_g}{\rho_l}} \frac{D_0}{D} \right)^{2/4} \quad (12.70)$$

In this empirical correlation, w and D are the relative velocity and the diameter of the fragments, and w_0 is the initial relative velocity of the drop.

12.3.1.3 Breakup in a Viscous Flow

The interest in the phenomenon of drop breakup in a viscous flow is derived from the problems of mixing, blending, dispersion, and the studies of rheology and formation of emulsions. A drop located in the viscous flow deforms, stretches, and then, if the velocity gradient reaches some critical value, breaks up. For a description of the dynamics of drop deformation and breakup in viscous flows see the reviews by Stone (1994) and Eggers (1997).

The governing parameters determining the deformation and breakup of drops in a viscous flow are the viscosity ratio $\lambda = \mu_l/\mu_g$, the density ratio $\beta = \rho_l/\rho_g$, the capillary and Reynolds numbers $Ca = G\mu_g D_0/\sigma$ and $Re = P_g G^2 D_0/\mu_g$, where G is the magnitude of the velocity-gradient tensor. However, the drop breakup depends not only on the instantaneous flow conditions, but also on their history (Bently and Leal, 1986; Grace, 1982). Quick changes in flow conditions enhance drop breakup.

Four mechanisms of drop breakup in a viscous flow are shown schematically in Figure 12.31, (Stone, 1994).

Capillary break-up (Tomotika, 1935; Mikami et al., 1975; Tjahjadi et al., 1992) takes place when the diameter of the thread-like drop is so small that it is broken by a growing capillary wave. The drop can also break near the middle of the thread (Barthes-Biesel and Acrivos, 1973). Such *necking breakup* leads to the formation of two similar droplets. *End pinching* (Grace, 1982; Taylor, 1934; Stone and Leal, 1989a,b; Stone et al., 1989) is the breakup of the thread-like (or finger-like) drop near the droplet at its end (see also Figure 12.31). The addition of surfactants to the fluid of a deforming, low-viscosity ratio drop ($\lambda < 0.1$) can lead to *tip streaming* (Ha and Yang, 1998; de Brujin, 1993). Tip streaming was also observed in the experiments with the deformation of viscoelastic drops (Milliken and Leal, 1991).

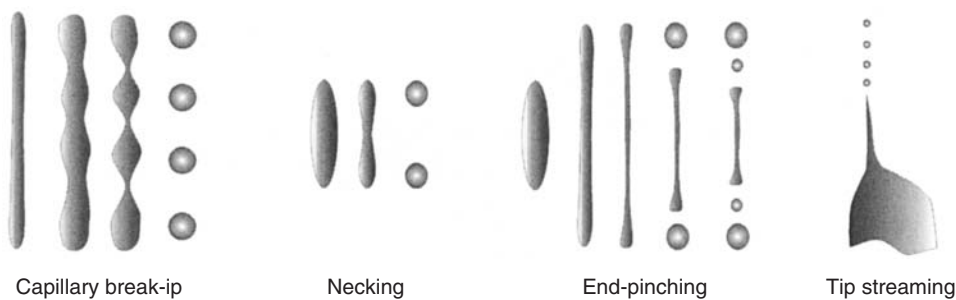


FIGURE 12.31 Modes of drop breakup in a viscous flow.

The shape of the drop deforms under the action of stresses generated by the outer flow. This deformation increases as the capillary number grows. The stable solution for the shape of the deformed drop in an extensional flow is obtained by Acrivos and Lo (1978) for inviscid drops

$$h(z) = \frac{D_0}{8Ca} \left[1 - \left(\frac{z}{10D_0 Ca^2} \right) \right] \quad (12.71)$$

and the asymptotic value for the critical capillary number for the viscous drop is

$$Ca_{\text{cr}} \lambda^{1/6} = 0.148 \quad (12.72)$$

which is valid for the small viscosity ratio ($\lambda \ll 1$).

12.3.2 Binary Drop Collisions

A collision of two drops is shown schematically in Figure 12.32, where the main geometrical parameters of the collision are illustrated: the separation distance between the droplet centers χ and the collision angle $\psi = \arcsin[\chi/(R_1 + R_2)]$. The relative velocity is denoted as w . The main dimensionless parameters governing the binary drop collision phenomenon include the Weber number, $We = \rho_i w^2 (R_1 + R_2)/\sigma_i$, the impact parameter $B = \chi/(R_1 + R_2)$ (see studies of Ashgriz and Poo [1990]; Jiang et al., [1992] and Qian and Law [1997]), the drop diameter ratio, $\Delta = R_1/R_2 < 1$, and the Reynolds number.

The influence of the viscosity of the fluid on the binary collision in vacuum, particularly on the temporal evolution of the drop size, was investigated in Willis and Orme (2003). They found that a higher Reynolds number corresponded to higher characteristic times of drop deformation.

A detailed study of the collision of drops of the same diameter can be found in Qian and Law (1997). Several regimes of collision are observed in this work: coalescence, bouncing, stretching separation, and reflexive separation. These regimes are shown schematically in Figure 12.33.

At relatively high Weber numbers, when the phenomenon is inertia-dominated, the near head-on collision (regimes (c) and (d)) can be subdivided into several main stages, similar to the stages of the impact of a drop on a dry wall (see Section 12.3.3): initial drop deformation leading to the formation of a relatively thin expanding liquid film, bounded by a rim. This rim expands and then recedes. The kinetic energy of the drop accumulates in the rim at the instant when it merges. This kinetic energy leads to the creation of a nearly cylindrical jet bounded by two droplets. The liquid from the jet enters these two droplets. If the time of the jet breakup is smaller than the time of the merging of the droplets, the collision leads to separation; otherwise, it ends with coalescence.

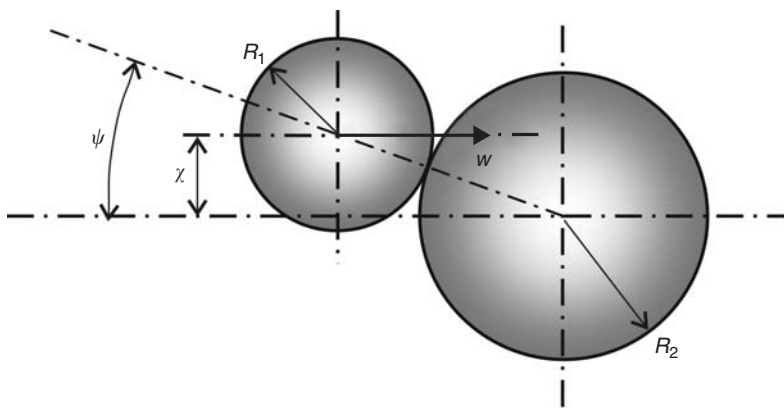


FIGURE 12.32 Sketch of a binary drop collision.

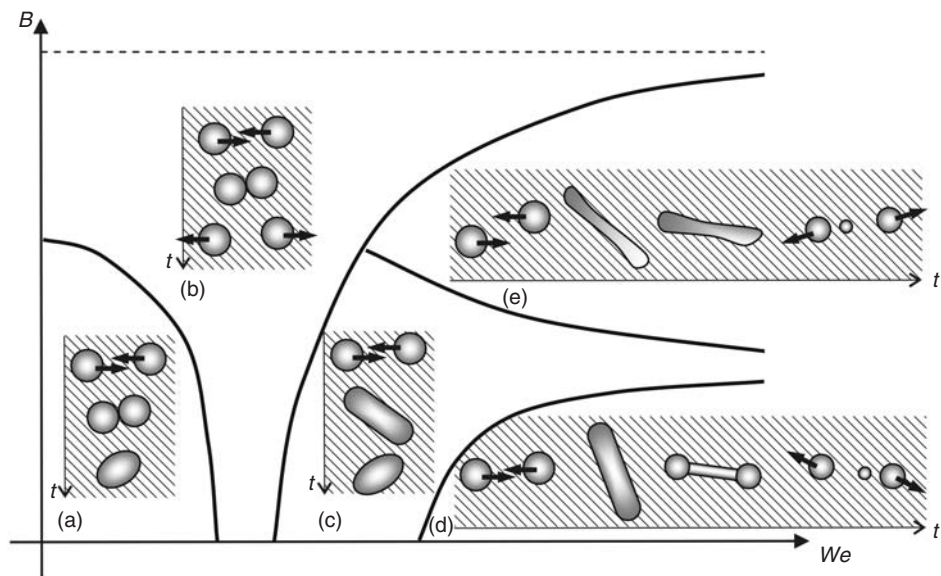


FIGURE 12.33 Regimes of hydrocarbon drops collisions: (a) coalescence; (b) bouncing; (c) coalescence; (d) reflexive separation; (e) stretching separation. (Adapted from Qian, J., and Law, C.K., *J. Fluid Mech.*, 331, 59, 1997.), $\Delta = 1$.

At relatively low values of the Weber number, the phenomenon is governed by the behavior of the film of the ambient liquid–gas in the gap between the approaching drops. It is known that the expression for the pressure in this film is singular if its thickness approaches zero. The drops will coalesce if the film drains to a thickness comparable with the characteristic distance associated with the van der Waals force (Chesters, 1991).

The stretching separation regime corresponds to the nonsymmetric collision of two drops at a high Weber number. Such an impact produces a stretching filament, which breaks up by “end pinching” (Brenn et al., 2001), (Eggers, 1993).

The regimes shown in Figure 12.33 do not reflect all the variations of the considered phenomena. For example, the collision of two drops of $\Delta = 1/4$ observed in Podvysotsky and Shraiber (1984) yields the penetration of the smaller drop into the larger, followed by the creation of a relatively long jet behind the bigger drop. This jet then breaks up into several secondary droplets.

Among the models describing the critical parameters that correspond to the separation–coalescence threshold are the models of Park (1970), based on the balance of the surface forces in the neighborhood of the contact of two drops and the forces associated with the angular momentum. In Brazier-Smith et al. (1972) the kinetic energy of rotation of the drop obtained by coalescence is accounted for. The energy balance of the colliding drops leads to the following expression for the critical impact factor:

$$B_{cr} = \left[\frac{24[1 + \Delta^2 - (1 + \Delta^3)^{2/3}](1 + \Delta^3)^{11/3}}{5We\Delta^5(1 + \Delta)^2} \right]^{1/2} \quad (12.73)$$

The criterion for the reflexive separation based on the energy balance of the system is obtained in Ashgriz and Poo (1990) in the form

$$We > 3 \frac{\Delta(1 + \Delta^3)^2}{\Delta^6 C_1 + C_2} [7(1 + \Delta^3)^{2/3} - 4(1 + \Delta^2)] \quad (12.74)$$

where the parameters $C_1 = 2(1 - C_3)^2(1 - C_3^2)^{1/2} - 1$ and $C_2 = 2(\Delta - C_3)^2(\Delta^2 - C_3^2)^{1/2} - \Delta^3$, with the parameter C_3 being $C_3 = B(1 + \Delta)/2$ and $\Delta < 1$. The above expression is obtained by a simplified approximation of the shape of the deformed drop by a disc.

The model for the critical Weber number of the stretching separation is

$$We = \frac{4(1 + \Delta^3)^2[3(1 + \Delta)(1 - B)(\Delta^3 C_4 + C_5)]^{1/2}}{\Delta^2[(1 + \Delta^3) - (1 - B^2)(C_4 + \Delta^3 C_5)]} \quad (12.75)$$

where

$$C_4 = \begin{cases} 1 - \frac{1}{4\Delta^3}(2\Delta - \tau)^2(\Delta + \tau) & \text{for } \tau > \Delta \\ \frac{\tau^2}{4\Delta^3(3\Delta - \tau)} & \text{for } \tau < \Delta \end{cases}, \quad C_5 = \begin{cases} 1 - \frac{1}{4}(2 - \tau)^2(1 + \tau) & \text{for } \tau > 1 \\ \frac{\tau^2}{4(3 - \tau)} & \text{for } \tau < 1 \end{cases}$$

with the parameter τ being $\tau = (1-B)(1 + \Delta)$.

Qian and Law (1997) have also considered the energy balance of two colliding drops of the same diameter. They have accounted for the energy loss during collision due to viscous dissipation. Their result yields the linear dependence of the critical Weber number that corresponds to the separation-coalescence threshold on the Ohnesorge number. Their result, best fitting the existing experimental data, is given in the form

$$We_{cr} = 30Oh + 15 \quad (12.76)$$

with the Ohnesorge number being defined as $Oh = 16\mu_l/\sqrt{\rho_l R \sigma_l}$.

12.3.3 Drop-Wall Impact

Many processes involving drop and sprays also involve their impact onto a surface. Universal relations describing the outcome of drop-wall impact do not exist simply because of the large number of influencing parameters:

- Reynolds number and Weber number of incident drop
- Surface orientation (normal-inclined)
- Surface structure (rough-smooth) and chemical composition (hydrophobic-hydrophilic)
- Dry or wet surface, including the hydrodynamics of the liquid film in the case of a wet surface
- Surface temperature

Obviously, additional properties of the impinging drop may also be of importance, such as boiling point, heat of vaporization, or contact angle with the surface.

Understanding drop-wall impact represents a key technology for some processes, for example, ink jet printing or near net-shape manufacturing, where solidification must also be accounted for (Madejski, 1983; Poulikakos and Waldvogel, 1996; Liu and Orme, 2001). Very high-speed drop impacts can even lead to damage or erosion of the solid surfaces, like turbine blades or airplane surfaces. In such ultra-high-speed drop impacts, compressibility is one important factor, leading to the propagation of shock waves in the drop and in the target material (Lesser and Field, 1983; Korobkin, 1997). However, drop-wall impact is also an elemental part of spray-wall impact, which itself is an essential process in many technologies: spray cooling, spray painting, fuel injection, drop separators, etc. Whether spray impact can be treated as the superposition of many individual drop impacts depends on the spray density and on the hydrodynamics of the liquid film on the surface. This topic will not be addressed in the present article, but is discussed in Section 8.3.

In the following discussion, the phenomenon of drop impact has been divided into impact onto dry surfaces and onto liquid films. In the former case, the wettability of the surface may become important whereas in the latter case, the hydrodynamics of the liquid film must be considered. A good collection of papers dealing with various specific aspects influencing drop impact phenomena can be found in Rein, (2002).

12.3.3.1 Wetting of a Dry Surface: Static and Dynamic Contact Angles

The stationary shape of a drop on a dry solid surface depends on its volume, density and on the surface wettability property, described by a static (or equilibrium) contact angle θ_e , defined in Figure 12.34. In the case of a smooth, homogeneous, rigid surface, this angle depends on the surface (or interface) free energy of the solid–gas interface, σ_{sv} , the solid–liquid interface, σ_{sl} and the liquid–gas interface, σ (surface tension). The equilibrium condition at the contact line leads to *Young's relation*

$$\cos \theta_e = \frac{\sigma_{sv} - \sigma_{sl}}{\sigma} \quad (12.77)$$

The wetting of the substrate is total, $\theta_e = 0$, if the RHS of (12.77) is > 1 . The surface is partially wettable if the absolute value of the RHS of (12.77) is < 1 , yielding a value of the equilibrium contact angle in the range $0 < \theta_e < \pi$. Within this range, hydrophobic ($\theta_e > \pi/2$) and hydrophilic ($\theta_e < \pi/2$) surfaces can also be distinguished.

When the liquid spreads on the substrate under the action of gravity and capillary forces (spontaneous spreading) or due to inertial forces (forced wetting), the position of the contact line moves and the apparent dynamic contact angle θ_d differs from the static one. The dynamic contact angle depends on the contact line velocity U_c if the capillary number $Ca = U_c \mu / \sigma$ is relatively small. This dependence is shown schematically in Figure 12.35. The sign of U_c is positive if the contact line moves toward the gas phase. Two distinct branches of the curve $\theta_d = \theta_d(U_c)$ are considered in relation to the direction of motion of the contact line: the advancing dynamic contact angle for $U_c > 0$ and receding contact angle for $U_c < 0$.

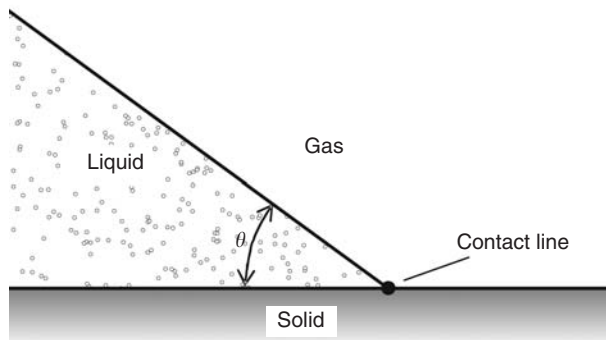


FIGURE 12.34 Sketch defining the contact angle and the contact (or triple) line.

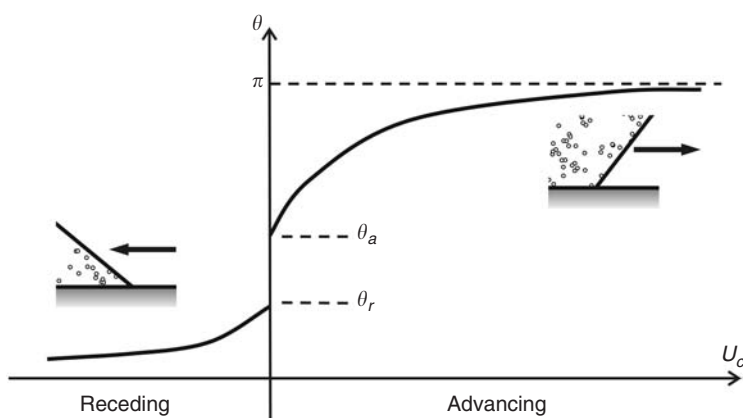


FIGURE 12.35 Hysteresis of the dynamic contact angle.

Next, the static advancing, θ_a , and static receding, θ_r , contact angles can be defined as two different limits of the dynamic contact angle as the velocity U_c approaches zero:

$$\theta_a = \lim_{U_c \rightarrow +0} \theta_d(U_c), \quad \theta_r = \lim_{U_c \rightarrow -0} \theta_d(U_c)$$

The hysteresis in the values of θ_a and θ_r is related to the microstructure of the surface (roughness, chemical nonhomogeneity) and the presence of impurities in the liquid and on the substrate. The contact angle of the liquid in the equilibrium state can thus vary in the range $\theta_r < \theta < \theta_a$.

The dynamic contact angle at $\theta_c \approx 0$ and $Ca \ll 1$ depends on the capillary number Ca only (Hoffman, 1975). An empirical correlation for the dynamic contact angle for such cases is obtained in Voinov (1976) and Tanner (1979) in the form

$$\theta_d \sim Ca^{1/3} \quad (12.78)$$

which is known as the *Hoffman–Voinov–Tanner law* (Kistler, 1993).

Generally, the dynamic contact angle may also depend on the hydrodynamics of the liquid behind the contact line. Two main approaches to the problem of dynamic contact angle are considered to date: the hydrodynamic approach (with the most general analysis in Cox (1986)) and the molecular-kinetic approach (initiated in Blake, 1968; Blake and Haynes, 1969). See the detailed reviews of the wettability phenomena and modelling in Kistler (1993) and Blake (1993). More recent work can be found in Blake et al. (1999).

Some biological or micro- and nanostructured surfaces are extremely hydrophobic. Barthlott and Neinhuis (1997) studied the morphology of lotus plant leaves, revealing a self-cleaning property through rain, fog or dew (Lotus effect). Considerable effort is presently being directed toward producing synthetic water-repellent surfaces with prescribed surface morphologies. Onda et al. (1996) produced a fractal alkylketene dimer (AKD), reaching an apparent contact angle in their experiments of 174°C, Bico et al. (1999) and Richard and Quéré (2000) have investigated a single drop impact onto such highly hydrophobic surfaces, observing that the drop can fully bounce after impact on such surfaces.

Spontaneous drop spreading is analysed in the theoretical works of Hocking and Rivers (1982), Dussan and Chow (1983), Pozdikidis (1990), and Reznik and Yarin (2002). The inertial effects in such low-speed drop impacts are small in comparison with the capillary forces and viscous drag. At higher impact speeds, inertia and viscous forces can no longer be neglected, and this situation is considered in the following section.

12.3.3.2 Drop Impact onto a Dry Substrate

The phenomenon of drop impact onto a dry substrate can be subdivided into several main phases, shown in [Figure 12.36](#). The first phase is the initial drop deformation during which the drop shape transforms from a nearly spherical shape into a thin liquid film (lamella) expanding on the wall. The duration of this first phase is approximately $t_{\text{init}} \sim D_0/U_n$, where D_0 is the initial drop diameter and U_n is the normal component of the impact velocity. During the second phase of the drop impact, the spreading lamella is bounded by a rim, formed by capillary forces. The formation of this rim leads to the typical pizza-like shape of a spreading drop. The position of the rim determines the size and the shape of the wetted spot on the substrate. At some time instant $t = t_{\text{max}}$, the size of the wetted spot reaches a maximum. Then, if the substrate is partially hydrophobic, the drop begins to recede, leading to the third phase of drop impact. At some further time instant $t = t_{\text{merg}}$, the rim merges. If the kinetic energy of the rim at the time instant $t = t_{\text{merg}}$ is high enough, the rim-merging process can lead to the appearance of a finger-like central jet ejected from the surface.

If the Reynolds and the Weber numbers are high, the first phase of the initial deformation and the spreading of the drop are dominated by inertia. The evolution of the drop diameter during these two phases and the value of the maximum spread diameter are almost independent of the static contact angle (Rioboo et al., 2002). The receding of the drop is, in contrast, caused by the forces associated with the wettability.

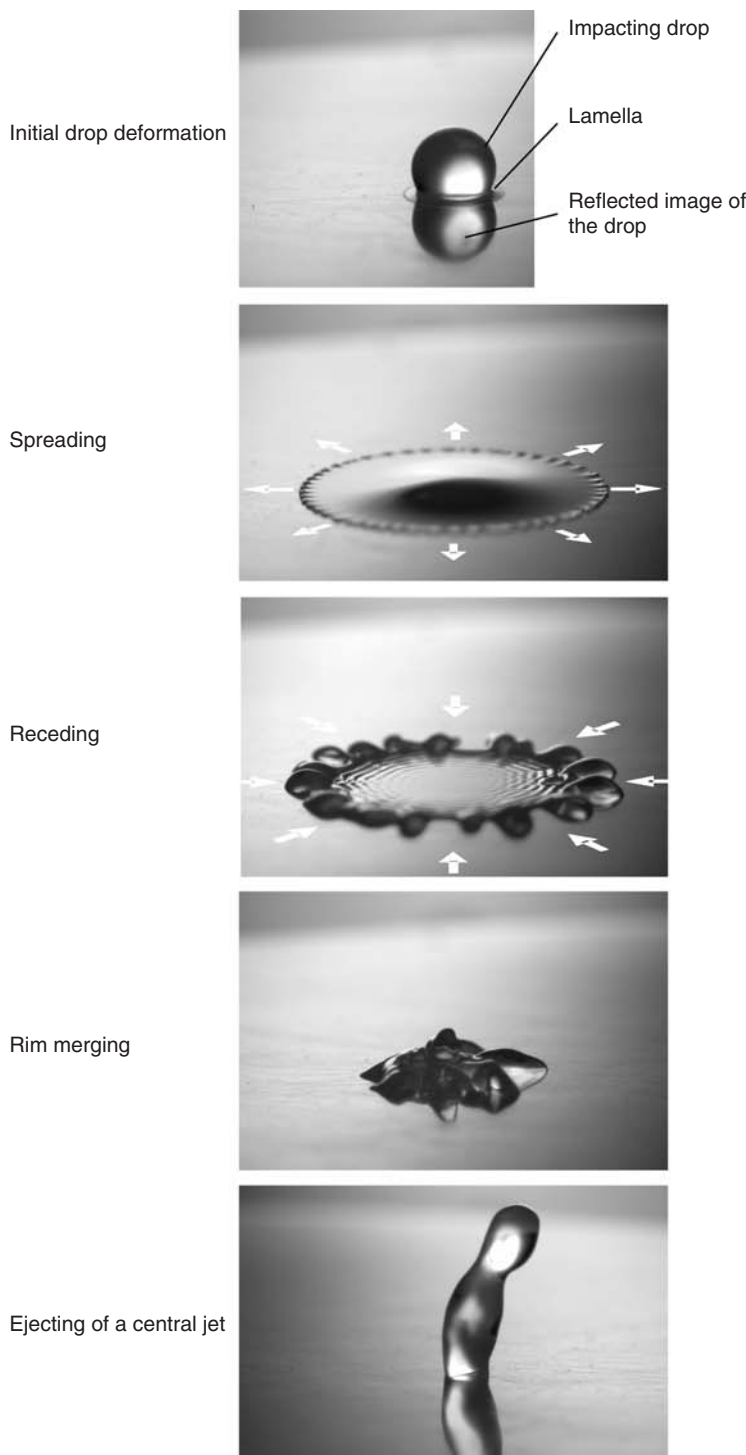


FIGURE 12.36 Stages of single drop impact onto a dry, partially wettable substrate. (Adapted from Rioboo, R., Marengo, M. and Tropea, C., *Exp. Fluids*, 33, 112, 2002.)

In each stage of impact, the drop can lose its stability and break up. The experimental studies of drop impact focus mainly on the determination of the various outcomes of the impact event (see Hartley and Brunskill, 1958; Levin and Hobbs, 1971; Stow and Stainer, 1977; Stow and Hadfield, 1981; Mao *et al.*, 1997; Range and Feuillebois, 1998). The influence of the surfactants added to the liquid on the evolution of the diameter of the spreading drop is studied in Mourougou-Candoni *et al.* (1999).

A number of different outcomes of drop impact are classified in Rioboo *et al.* (2001) (see [Figure 12.37](#)). A *prompt splash* occurs at high impact velocities on a rough surface during the first stage of initial drop deformation. A number of jets are formed in the region of the contact line as a result of its perturbation by the wall's roughness. These jets then break up into secondary droplets. The mechanism of *corona splash* after a drop impact onto a dry wall is not yet completely clear. It can be caused either by air entrainment into the contact line region or by the bending instability of a lamella spreading radially on the substrate. This type of splash is more typical for the high-speed drop impact onto a wetted wall. At some time instant this lamella (initially planar) begins to deform and to eject a nearly cylindrical, uprising crown-like sheet. A number of small jets then appear at the edge of this sheet, subsequently breaking up into secondary droplets. The drop can also break up during its receding phase. This *receding breakup* is caused by a disjoining of the contact line due to the local wall microstructure or chemical inhomogeneity. The *partial rebound* occurs when the duration of the central jet stretching is longer than the time required for its capillary breakup. Drop impact onto a highly hydrophobic surface can lead to a complete *rebound*. If the parameters of drop impact are below the splashing threshold it *deposits* on the surface without breakup.

An empirical relation for the splashing threshold is obtained in Mundo *et al.* (1998). The drop will not splash if

$$K = WeOh^{-0.4} < 657 \quad (12.79)$$

A recent study of drop impact onto inclined surfaces (Šikalo, 2003) indicates that this relation is also applicable if only the wall-normal component of velocity is used. Alternative but very similar relations for the splash limit on dry surfaces have been suggested by Marengo (1999) and Samenfink (1997).

The evolution of drop diameter can also be influenced by the addition of additives to the liquid, for example, surfactants.

12.3.3.3 Drop Impact onto a Wetted Wall

Numerous studies of drop impact onto a liquid film have led to similar data concerning the splash threshold, drop shape, crown propagation, fingering of the rim, etc. (Levin and Hobbs, 1971; Macklin and Metaxas, 1976; Cossali *et al.*, 1997; Cossali *et al.*, 2004).

Depending on the impact parameters and the film thickness, several impingement regimes have been determined. The collision can result in *sticking*, *rebound*, *deposition*, and *splash* (Stanton and Rutland, 1996) as shown in [Figure 12.38](#). In Cossali *et al.* (1997) two types of splash were observed: *corona splash* (when the impact results in the creation of a crown-like sheet, which then breaks up) and *prompt splash* (when small secondary droplets are ejected from the region where the drop contacts the free surface of the film). Also the formation of a central finger-like jet was observed in the case of high-velocity impact into a deep pool or onto a relatively thick film (Oguz and Prosperetti, 1990).

The stick regime occurs when the nearly spherical drop adheres to the film. The condition for the stick regime, $We < 5$ in Stanton and Rutland (1996), is based on the experimental results of Rodrigues and Mesler (1985), Walzel (1980), Jayaratne and Mason (1964).

The rebound regime occurs in the Weber number range $5 < We < 10$ (Rodrigues and Mesler, 1985). For a Weber number > 10 , the deposition of the impinging drop takes place when the parameters of the impact are below the splash threshold.

The splash threshold represents the conditions at which secondary droplets are first observed and takes a form similar to Eq. (12.79), with empirical modifications for the liquid film. (Samenfink, 1997; Mundo *et al.*, 1998; Cossali *et al.*, 1997; Wang and Chen, 2000).

Cossali *et al.* (1997) have obtained images of a splashing drop, showing the details of crown formation and jetting. The following empirical relation for the critical K number, depending on the dimensionless

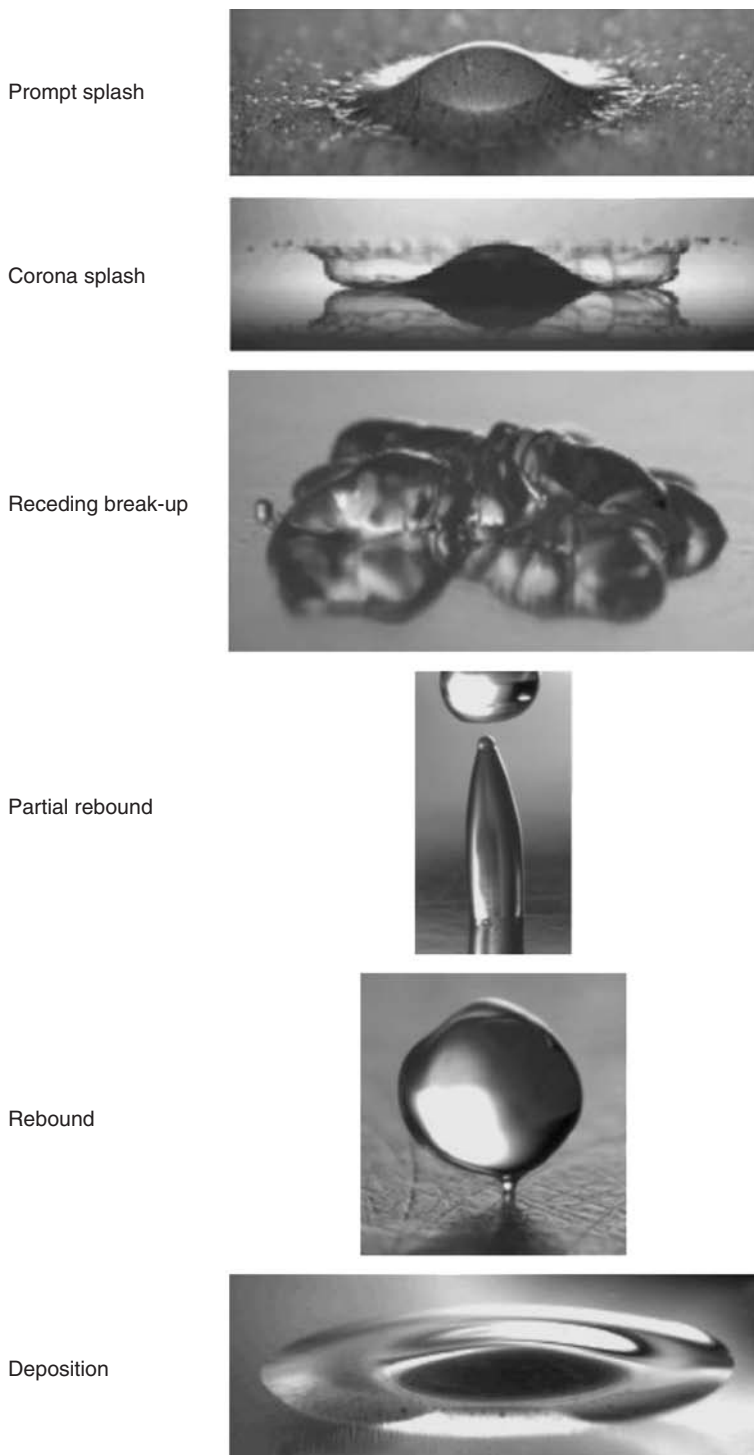


FIGURE 12.37 Classification of different outcomes of drop impact onto a dry substrate. The images are from Rioboo, R. et al., *Atomization Sprays*, 11, 155, 2001.

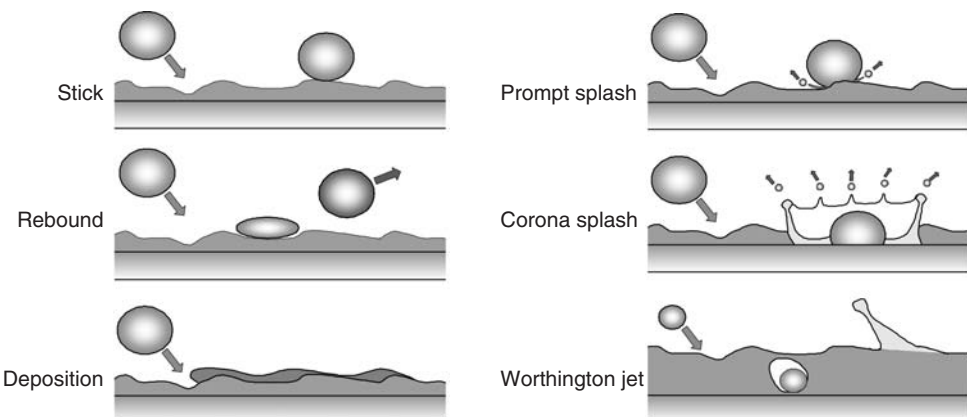


FIGURE 12.38 Single drop impact onto a wetted surface.

film thickness δ (scaled to the drop diameter), has been proposed:

$$K = 2100 + 5800\delta^{1.44} \quad \text{for } 0.1 < \delta < 1 \quad \text{and} \quad Oh > 7 \times 10^{-3} \quad (12.80)$$

Note that in spite of the fact that the K number is a parameter having “round” powers of We and Oh , it is completely empirical.

Oğuz and Prosperetti (1990) have studied the impact of a single drop in a deep pool or relatively thick liquid film. The main subjects of this experimental, theoretical, and numerical study were the crater expansion in the liquid pool, bubble entrainment, and the creation of the central jet. The dominant factors influencing the phenomenon are the inertia of the liquid, capillary forces, and gravity. Bubble entrainment takes place in the range of parameters

$$41.3 Fr^{0.179} < We < 48.3 Fr^{0.247} \quad (12.81)$$

where $Fr = U^2/(gD_0)$ is the Froude number; and g the acceleration due to gravity. These upper and lower bounds are obtained by fitting the experimental data.

12.3.3.4 Theoretical Modeling of Drop Impact

The modeling of drop impact phenomena involves the description of an unsteady flow governed by inertia, capillary forces, and viscous drag. In the case of drop impact onto a dry wall, the forces associated with surface wettability are also important.

One parameter characterizing drop impact onto a dry wall is the maximum spread diameter. Most of the models are based on the energy balance of the drop (Collins et al., 1990; Chandra and Avedisian, 1991; Pasandideh-Fard et al., 1996; Fukai et al., 1995; Mao et al., 1997). In all of these approaches, the drop shape is assumed to be a disc at the instant when the drop diameter reaches its maximum value. Moreover, the total kinetic energy of the drop at this instant is assumed to vanish.

Another feature of drop impact is the instability of the lamella, leading to its breakup, which has been studied by Kim et al. (2000), and Fedorchenko and Chernov (1999).

In the study of the normal impact of a drop onto a dry, partially wettable wall (Roisman et al., 2002), the temporal evolution of the drop diameter — its spreading and receding — is determined by the motion of a torus-like rim, bounding a thin radially expanding film (lamella). The equations of motion of the film are obtained from its mass and momentum balance.

One important result of the studies of drop impact onto a stationary uniform liquid film is the temporal expansion of the radius R_{cr} of the crown. The dependence $R_{cr} \sim \sqrt{t}$ is obtained by Yarin and Weiss (1995), who describe the base of the crown as a kinematic discontinuity in the liquid film. In recent work (Trujillo and Lee, 2001), this theory is modified by taking into account the effect of the viscous forces.

In Roisman and Tropea (2002), the theory of the formation of the uprising sheet and its shape, valid for the general, nonaxisymmetric case, is developed. All of these models have been developed for the case of drop impact onto relatively thin films ($\delta < 0.5$).

12.4 Particle Interactions

Y. Tsuji and R.W. Lyczkowski

With respect to the particle–particle interactions in multiphase flow dynamics, two phenomena are identified. One is collision and the other is contact. From the viewpoint of physics, collision and contact do not differ much. Collision is merely contact with a short time duration. However, the approach of modeling is different for each. For collision or contact, two models are normally used: the hard particle model and the soft-particle model.

The hard particle model is easy to use but applicable only to the binary collision. The relation between the pre- and postcollision velocities is given explicitly using the coefficient of restitution and friction coefficient. When the particulate phase is dispersed, it is sufficient to consider only simple binary collisions and not multiple collisions.

In the soft particle model, the whole process of collision or contact is solved by the numerical integration of the equations of motion. The computation time is much longer using the soft particle model than in the hard particle model, but the applicability is wider for the soft particle model than the hard particle model.

Another important issue is the erosion associated with particle-wall contact. Particles impacting a wall can remove material, the amount depending on the impact velocity, the approach angle and the properties of the material.

12.4.1 Particle–Particle Collision

Y. Tsuji

In general, particle–particle collision is negligible in dilute gas–particle flows. While this is true in most cases, whether particle–particle collision should be considered or not depends not only on particle concentration, but also on the velocity fluctuation or relative velocity between individual particles. If all the particles move at the same velocity, particles do not collide no matter how high the concentration is. On the other hand, recent studies (Yamamoto et al., 2001) have shown that particle–particle collision should not be neglected at volume fractions greater than 10^{-4} . Dense and dilute flows are discussed in Section 1.2.6.

When particles collide, they lose kinetic energy due to the inelastic property of the particle material. The case of the two spheres shown in Figure 12.39 is considered here. Section 12.4.1.1 describes the hard sphere model and Section 12.4.1.2 describes the soft sphere model.

12.4.1.1 Hard Sphere Model

The hard sphere model is based on the impulsive force which is defined by the integral of the force acting on a particle versus time. If the particles are assumed to be rigid spheres, the impulsive equations are given as follows.

$$m_1(\mathbf{v}_1 - \mathbf{v}_1^{(0)}) = \mathbf{J} \quad (12.82)$$

$$m_2(\mathbf{v}_2 - \mathbf{v}_2^{(0)}) = -\mathbf{J} \quad (12.83)$$

$$I_1(\boldsymbol{\Omega}_1 - \boldsymbol{\Omega}_1^{(0)}) = \mathbf{a}_1 \mathbf{n} \times \mathbf{J} \quad (12.84)$$

$$I_2(\boldsymbol{\Omega}_2 - \boldsymbol{\Omega}_2^{(0)}) = \mathbf{a}_2 \mathbf{n} \times \mathbf{J} \quad (12.85)$$

where \mathbf{n} is the normal unit vector directed from particle 1 to particle 2 at the moment of contact and \mathbf{J} is the impulsive force exerted on particle 1, which acts on particle 2 as the reaction; subscripts 1 and 2 refer to the two particles. The superscript (0) signifies values before collision and I is the moment of inertia given by $I = (2/5)m a^2$. In the above equations, the particle mass m , size (radius = a), velocities before collision

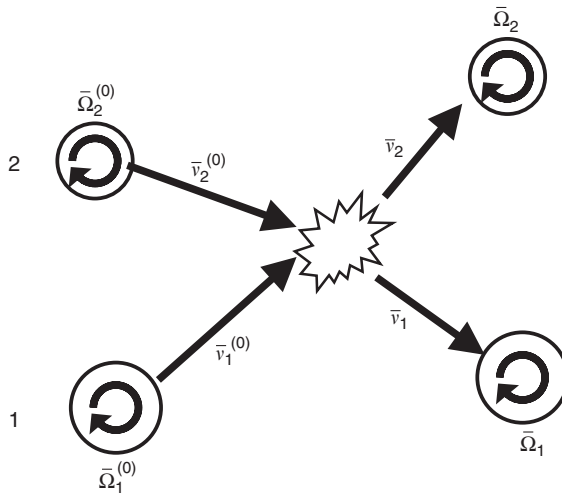


FIGURE 12.39 Particles colliding.

TABLE 12.4 Relation between Particle Velocities Before and After Collision

Condition	$\frac{\mathbf{n} \cdot \mathbf{G}^{(0)}}{ \mathbf{G}_{ct}^{(0)} } < \left(\frac{2}{7}\right) \frac{1}{f(1+e)}$	$\frac{\mathbf{n} \cdot \mathbf{G}^{(0)}}{ \mathbf{G}_{ct}^{(0)} } > \left(\frac{2}{7}\right) \frac{1}{f(1+e)}$
Translation velocity	$V_1 = V_1^{(0)} - (\mathbf{n} - f\mathbf{t})(\mathbf{n} \cdot \mathbf{G}^{(0)})(1+e) \frac{m_2}{m_1 + m_2}$ $V_2 = V_2^{(0)} + (\mathbf{n} - f\mathbf{t})(\mathbf{n} \cdot \mathbf{G}^{(0)})(1+e) \frac{m_1}{m_1 + m_2}$	$V_1 = V_1^{(0)} - \left\{ (1+e)(\mathbf{n} \cdot \mathbf{G}^{(0)})\mathbf{n} + \frac{2}{7} \mathbf{G}_{ct}^{(0)} \mathbf{t} \right\} \frac{m_2}{m_1 + m_2}$ $V_2 = V_2^{(0)} + \left\{ (1+e)(\mathbf{n} \cdot \mathbf{G}^{(0)})\mathbf{n} + \frac{2}{7} \mathbf{G}_{ct}^{(0)} \mathbf{t} \right\} \frac{m_1}{m_1 + m_2}$
Angular velocity	$\Omega_1 = \Omega_1^{(0)} + \left(\frac{5}{2a_1} \right) (\mathbf{n} \cdot \mathbf{G}^{(0)}) (\mathbf{n} \times \mathbf{t}) f(1+e) \frac{m_2}{m_1 + m_2}$ $\Omega_2 = \Omega_2^{(0)} + \left(\frac{5}{2a_2} \right) (\mathbf{n} \cdot \mathbf{G}^{(0)}) (\mathbf{n} \times \mathbf{t}) f(1+e) \frac{m_1}{m_1 + m_2}$	$\Omega_1 = \Omega_1^{(0)} - \frac{5}{7a_1} \mathbf{G}_{ct}^{(0)} (\mathbf{n} \times \mathbf{t}) \frac{m_2}{m_1 + m_2}$ $\Omega_2 = \Omega_2^{(0)} - \frac{5}{7a_2} \mathbf{G}_{ct}^{(0)} (\mathbf{n} \times \mathbf{t}) \frac{m_1}{m_1 + m_2}$

Note: e , coefficient of restitution; f , Coulomb's friction coefficient; $\mathbf{G}^{(0)} = \mathbf{v}_1^{(0)} - \mathbf{v}_2^{(0)}$ is the relative velocity of particle centers before collision; $\mathbf{G}_{ct}^{(0)} = \mathbf{G}^{(0)} + \alpha_1 \Omega_1^{(0)} \times \mathbf{n} + \alpha_2 \Omega_2^{(0)} \times \mathbf{n}$ is the relative velocity of the contact point before collision; $\mathbf{t} = \mathbf{G}_{ct}^{(0)} / |\mathbf{G}_{ct}^{(0)}|$ is the unit vector of the tangential direction.

$\mathbf{v}^{(0)}$, and positions before collision are given. The unknown variables are the impulsive force J and the post-collision velocities \mathbf{v} . The above equations can be solved analytically with some assumptions. The results are shown in Table 12.4. The derivation of the solutions is described in Crowe et al. (1997a).

12.4.1.2 Soft Sphere Model

12.4.1.2.1 Modeling

The basic concept of the soft sphere model is the same as the damping vibration shown in Figure 12.40. The motion of the body with mass m is given by the following differential equation:

$$m\ddot{x} + \eta\dot{x} + kx = 0 \quad (12.86)$$

where x is the distance from the equilibrium position of the mass, η the damping coefficient of the dash-pot, and k is the stiffness of the spring. In the above equation, the relationship between the force and

displacement is assumed to be linear. The kinetic energy is lost in the dashpot. The work by the dashpot is proportional to the velocity of the mass. There are three modes of motion depending on the parameters: underdamping, overdamping, and critical damping modes.

In the soft sphere model, the same mechanism is assumed for the particle-particle interaction. Figure 12.41 shows that particle i approaches particle j under the influence of inertia and external forces. Particle i at the moment of contact is shown by the dotted line, and the two particles contact at the point C. In the next moment, contact forces occur between the two particles. Actually, the particles should deform and the contact forces could be functions of deformation. In the soft sphere model, the two particles approaching with a relative velocity are made to overlap without changing their shapes. The overlap distance δ is made to correspond to the deformation of the particles. The larger the overlap distance, the larger is the contact force.

A model based on the damping vibration is convenient to express the contact force. Thus, a spring, a dash-pot, and other mechanical components are set between particle i and particle j as shown in Figure 12.42, where the figure (a) corresponds to the case of the normal force and (b) to the case of the tangential force. The coupler shown in Figure 12.42 connects the two particles when they are in contact but allows the particles to separate under the influence of repulsive forces. The tangential force is modeled by a spring and dash-pot in the same way as the normal force as shown in Figure 12.42b. If the tangential force exceeds the yield stress, the two particles slide under the application of a normal force and a friction force results. To express this friction force, a friction slider is set in Figure 12.42b. This model for contact forces was proposed by Cundall and Stack (1979). With the soft sphere model, not only can the relationship between pre- and post-collision velocities be obtained but also the forces acting on the spheres during contact.

With the hard sphere model, the post-collision velocities are given as functions of precollision velocities and other parameters such as the coefficient of restitution and the friction coefficient. The soft sphere model starts with the differential equations. Therefore, variations of momentum and displacement are obtained for arbitrary times as solutions of the differential equations.

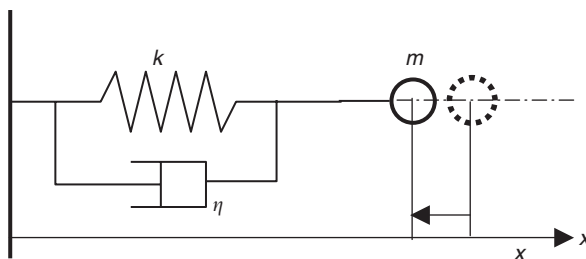


FIGURE 12.40 Damping vibration.

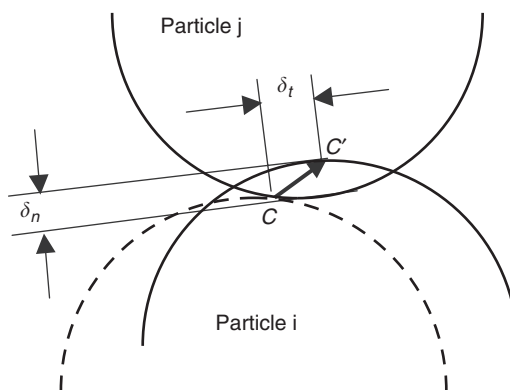


FIGURE 12.41 Two particles contacting.

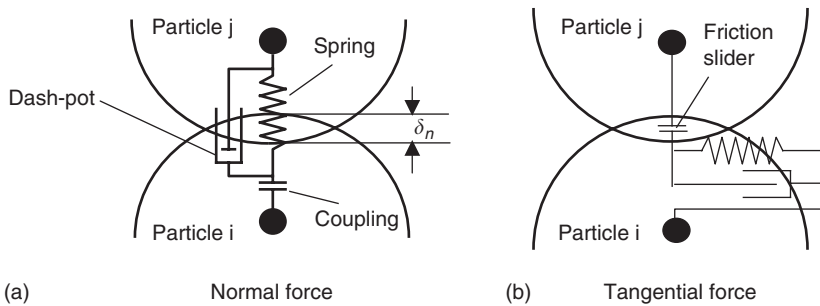


FIGURE 12.42 Soft sphere model.

The effects of these mechanical components on particle motion appear through the following parameters: stiffness K ; damping coefficient η ; and friction coefficient f .

The normal component of the contact force, F_{nij} , acting on particle i is given by the sum of the forces due to the spring and the dash-pot. If the particles are assumed to be two-dimensional disks, the effect of the spring is linear against the overlap distance, and the force F_{nij} is expressed by

$$F_{nij} = (-k_n \delta_n - \eta_{nj} G \cdot n)n \quad (12.87)$$

where δ_n is the overlap distance (displacement of particle caused by the normal force), G is the velocity vector of particle i relative to particle j , and ($G = v_i - v_j$), and n is the unit vector drawn from the center of particle i to that of particle j . According to Hertzian contact theory, the normal force varies to the $3/2$ power of the displacement in the case of three-dimensional spheres and, therefore, the force F_{nij} acting on particle i regarded as a sphere is expressed by

$$F_{nij} = (-k_n \delta_n^{3/2} - \eta_{nj} G \cdot n)n \quad (12.88)$$

The tangential component of the contact force, F_{tij} is given by

$$F_{nij} = -k_t \delta_t - \eta_{tj} G_{ct} \quad (12.89)$$

where k_t and η_{tj} are, respectively, the stiffness and damping coefficient in the tangential direction, and G_{ct} is the slip velocity of the contact point, given by

$$G_{ct} = G - (G \cdot n)n + a_i \Omega_i \times n + a_j \Omega_j \times n \quad (12.90)$$

where a_i and a_j are the radii of particle i and particle j , respectively.

Note that the tangential displacement δ_t is a vector and its direction is not equal to the slip velocity vector G_{ct} in three-dimensional motion in general. If the following relation

$$|F_{tij}| > f |F_{nij}| \quad (12.91)$$

is satisfied, particle i slides and the tangential force is given by

$$F_{tij} = -f |F_{nij}| t \quad (12.92)$$

instead of Eq. (12.89). Equation (12.92) is the Coulomb-type friction law. The friction coefficient f is measurable and regarded as a parameter, that can be given empirically. The vector t in Eq. (12.92) is the unit vector defined by

$$t = \frac{G_{ct}}{|G_{ct}|} \quad (12.93)$$

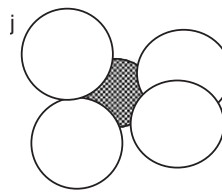


FIGURE 12.43 Particle with several contact forces.

In general, several particles are in contact with particle i at the same time as shown in Figure 12.43. Therefore, the total force and torque acting on particle i is obtained by taking the sum of the above forces with respect to j .

$$\mathbf{F}_i = \sum_j (\mathbf{F}_{nij} + \mathbf{F}_{tij}) \quad (12.94)$$

$$\mathbf{T}_i = \sum_j (\mathbf{a}\mathbf{n} \times \mathbf{F}_{tij}) \quad (12.95)$$

12.4.1.2.2 Determination of Stiffness k , Damping Coefficient η , and Friction Coefficient f

The stiffness k_n can be given using the Hertzian contact theory when physical properties such as the Young's modulus and Poisson ratio are known. The stiffness of a sphere is expressed as

$$k_n = \frac{4}{3} \left(\frac{1 - \sigma_i^2}{E_i} + \frac{1 - \sigma_j^2}{E_j} \right)^{-1} \left(\frac{a_i + a_j}{a_i a_j} \right)^{1/2} \quad (12.96)$$

where E and σ are Young's modulus and Poisson ratio, respectively, and a is the particle radius; subscripts i and j denote particle i and particle j , respectively.

If particle i and j have the same radii and the same physical properties, the stiffness k_n simplifies to

$$k_n = \frac{\sqrt{2r}E}{3(1 - \sigma^2)} \quad (12.97)$$

The tangential stiffness k_t can be given using Mindlin's theory as

$$k_n = 8 \left(\frac{1 - \sigma_i^2}{H_i} + \frac{1 - \sigma_j^2}{H_j} \right)^{-1} \left(\frac{a_i + a_j}{a_i a_j} \right)^{1/2} \delta_n^{1/2} \quad (12.98)$$

where H_i and H_j are the shear modulii of particle i and particle j , respectively. If both particles have the same properties, the tangential stiffness k_t also simplifies to

$$k_t = \frac{2\sqrt{2r}H}{(2 - \sigma^2)} \delta_n^{1/2} \quad (12.99)$$

where H is related to the Young's modulus E and Poisson ratio σ , as follows:

$$H = \frac{E}{2(1 + \sigma)} \quad (12.100)$$

As shown above, the stiffness can be determined by material properties. This is the advantage of this model. Unfortunately, it is often difficult in practice to use the stiffness calculated by the Hertzian theory, because the time step Δt for numerical integration is so small that an excessive amount of computational time is needed. It is empirically known that the time step Δt should be $< 1/10$ of the natural oscillation period $2\pi\sqrt{m/k}$ of a mass-spring system. Therefore, in many cases, a small value of stiffness is assumed for the convenience of the calculation. In some cases, the results based on a stiffness much smaller than an actual value are

not so different from those based on the precise stiffness value. Fortunately, this is the case for fluid–particle multiphase flows, where fluid forces acting on particles make the difference in stiffness a minor effect.

12.4.1.2.3 Damping Coefficient

Cundall and Strack (1979) proposed the following expressions for the damping coefficients:

$$\eta_n = 2\sqrt{mk_n} \quad (12.101)$$

$$\eta_t = 2\sqrt{mk_t} \quad (12.102)$$

which were derived for the critical damping condition of a single degree-of-freedom system consisting of a mass, spring, and dash-pot. The reason for choosing the critical damping condition, as shown in Eqs. (12.101) and (12.102), is the requirement that bouncing motion after collision should be damped as soon as possible.

Another method for determining the damping coefficient is based on the idea that the damping coefficient should be related to the coefficient of restitution, which is regarded as a physical property of the particle material. Fortunately, the coefficient of restitution can be measured in a simple experiment.

If the relationship between spring force and displacement is linear, the solution of Eq. (12.86) can be used to relate the damping coefficient to the coefficient of restitution (Tsuji et al., 1993). Let us assume that x denotes the distance of the particle center from the wall and the particle collides with the wall at time $t = 0$ with the initial velocity $v = v_0$ and initial position of particle center $x = x_0$. The initial velocity is negative. The underdamping solutions are given as

$$\text{Position } x = \frac{v_0}{q} \sin(qt) \exp(-\gamma\omega t) + x_0 \quad (12.103)$$

$$\text{Velocity } \dot{x} = \frac{v_0}{q} \exp(-\gamma\omega t) q \cos(qt) - \gamma\omega \sin(qt) \quad (12.104)$$

where $\omega = \sqrt{k/m}$, $\gamma = \eta/(2\sqrt{mk})$, and $q = \omega\sqrt{1 - \gamma^2}$.

The particle position decreases, reaches the minimum value, and recovers to the initial position at $x = x_0$ at $t = \pi/q$ which is equal to half of the oscillation period. The particle velocity at $t = \pi/q$ is expressed as

$$v_1 = [\dot{x}]_{t=\pi/q} = -v_0 \exp\left(-\frac{\gamma\omega\pi}{q}\right) \quad (12.105)$$

The ratio of v_1 to v_0 corresponds to the coefficient of restitution e :

$$e = \exp\left(-\frac{\gamma\omega\pi}{q}\right) \quad (12.106)$$

From the above equations,

$$\eta = -\frac{2\ln e}{\sqrt{\pi^2 + \ln e}} \sqrt{mk} \quad (12.107)$$

Tsuji et al. (1992) showed that the damping coefficient η_n for a nonlinear spring is numerically related to the restitution coefficient. According to Tsuji et al. (1992) the damping coefficient η_n is expressed by

$$\eta_n = \alpha \sqrt{mk_n} \delta_n^{1/4} \quad (12.108)$$

where α is a constant related to the coefficient of restitution. The relationship between α and coefficient of restitution e is shown in Figure 12.44. With respect to the damping coefficient η_t in the tangential direction, the same value as used for η_n is often used for η_t , but with no firm justification.

12.4.1.3 Cohesive Force

Interparticle forces due to the wetness of particle surfaces, electrostatic charges, and the van der Waals forces are known to cause the adhesion of a particle to a wall or to another particle.

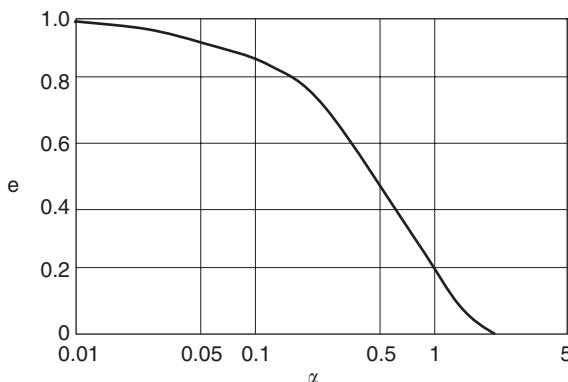


FIGURE 12.44 Relationship between α and coefficient of restitution e .

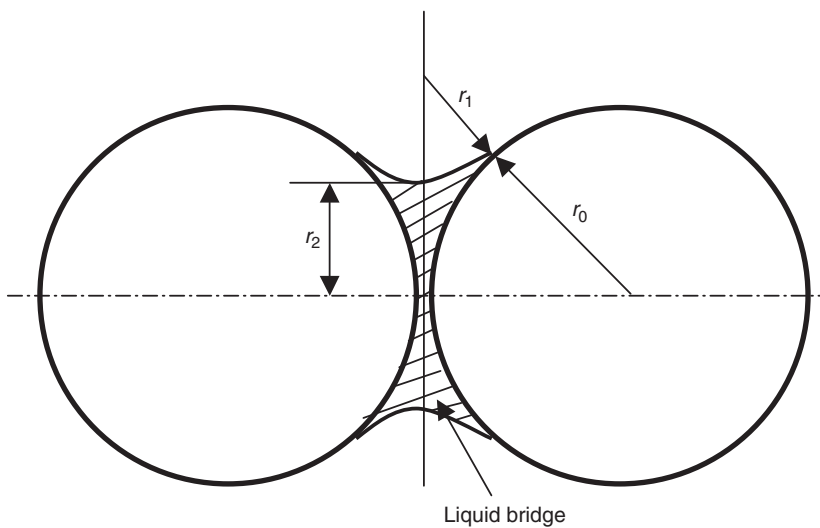


FIGURE 12.45 Liquid bridge between two spheres.

12.4.1.3.1 Force Due to a Liquid Bridge

As shown in Figure 12.45, a liquid bridge is formed between particles due to condensation under an environment of high humidity. The liquid surface is concave due to surface tension and the pressure is negative inside the bridge. The force acting on the particle is the sum of the force due to the negative pressure and the cohesive force due to capillarity.

The force due to the liquid bridge F_l is given as

$$F_l = \pi a_2^2 \sigma \left(\frac{1}{a_1} - \frac{1}{a_2} \right) + 2\pi a_2 \sigma \cos \theta \quad (12.109)$$

where σ is the surface tension (N/m) and θ the contact angle between the liquid and the particle surface. The contact angle θ can be assumed to be zero in the case of water. This equation is called the Laplace–Young equation.

12.4.1.3.2 Electrostatic Force

Particles in the gas are usually charged and an electrostatic force acts on the particles. Electrostatic force F_e between charged particles is given by the Coulomb formula

$$F_e = \frac{1}{4\pi\epsilon_0} \frac{q_1 q_2}{a^2} \quad (12.110)$$

where q_1 and q_2 are charges on the particles, ϵ_0 dielectric constant (F/m) in vacuum, and a is the distance between particle centers. If the signs of q_1 and q_2 are different, an attractive force acts on the two particles, and if not, the force is repulsive.

The cohesive force acting on the spherical particles in contact with each another is given by

$$F_E = \frac{\pi\sigma_1\sigma_2}{\epsilon_0} d^2 \quad (12.111)$$

where σ_1 and σ_2 are charge density (C/m^2) of the two particles. The above equation is derived under the assumptions that the particles are charged uniformly and that charging can be regarded as concentrated at the particle centers. The effect of the particle size on the force is larger for the Coulomb cohesive force than for the van der Waals force.

12.4.1.3.3 van der Waals Forces

The van der Waals forces arise from molecular interaction between solid surfaces. This force becomes apparent when very smooth surfaces are brought into contact. To estimate the magnitude of van der Waals forces acting on solid bodies, the contribution of many molecules comprising the surfaces must be considered. Hamaker (1937) carried out calculations for various geometries. The force F between two infinite flat plates with separation z is expressed by

$$F = \frac{A}{6\pi z^3} \quad (12.112)$$

where F is the force per unit area and A is called the Hamaker constant. The force between the two spheres shown in Figure 12.46 is expressed by

$$F = \frac{Ad}{12z^2} \quad (12.113)$$

where z is the separation distance at the point of contact which is dependant on the roughness of the spheres and d is

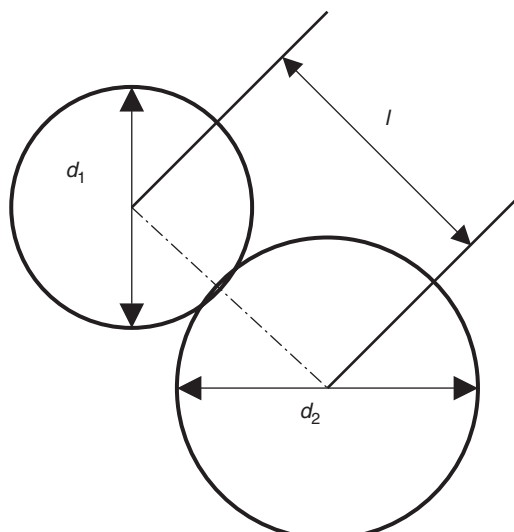


FIGURE 12.46 Two particles in contact.

TABLE 12.5 Hamaker Constant

Hamaker Constant Material	Hamaker Constant ($J \times 10^{20}$)
Water	4.38
Polystyrene	6.15 – 6.6
Al_2O_3	15.5
Cu	28.4
Au	45.5

$$d = \frac{D_{p1}D_{p2}}{D_{p1} + D_{p2}} \quad (12.114)$$

The force between a sphere and a flat plate can be obtained by letting the diameter of one sphere be infinite, i.e., $d = D_p$ in Eq. (12.114). Table 12.5 shows examples of the Hamaker constant of various materials.

The Hamaker constant between different materials is given by

$$A_{12} = \sqrt{A_{11}A_{22}} \quad (12.115)$$

where A_{11} and A_{22} are the Hamaker constants of each material, respectively. The above relation is used for “dry” solids. If two solids are separated by a third material between them, the Hamaker constant is expressed by

$$A_{132} = (\sqrt{A_{11}} - \sqrt{A_{33}})(\sqrt{A_{22}} - \sqrt{A_{33}}) \quad (12.116)$$

where A_{33} is the Hamaker constant of the third material. The Hamaker constant A_{33} of air is very small and thus Eq. (12.116) is reduced to Eq. (12.115) in this case. Comparing Eqs. (12.115) and (12.116), it is found that the attractive force between two solids becomes smaller in water than in air. The above equation means that the sign of the van der Waals force between two solids can be negative, i.e., a repulsion force arises if A_{33} takes a value between A_{11} and A_{22} .

12.4.2 Particle–Wall Interaction

Y. Tsuji

The problem of particle–wall interaction is encountered when analyzing gas–particle flows contained within walls such as pipe flows, channel flows, and fluidized beds. The particle–wall interaction falls into two categories: hydrodynamic forces due to proximity of a wall and the purely mechanical interaction in the absence of a fluid. The Saffman lift force due to the velocity gradient near the wall is one example of hydrodynamic interaction. Another example is the fluid force acting on a particle approaching the wall in the normal direction. This interaction is observed when the case of two approaching particles is addressed. Assuming the diameter of one particle to be infinitely large, the particle–particle interaction is reduced to the particle–wall interaction. A hydrodynamic interaction of this type can prevent a particle from making contact with the wall. The postcollisional velocity of the particle is also affected by this interaction. This hydrodynamic interaction can be neglected if the particle inertia force is so large that collision takes place in a time that is small compared to the hydrodynamic relaxation time of the particle.

The treatment of the mechanical behavior associated with the particle–wall mechanical interaction depends on the inertia of the particle. When a massive particle collides with a wall, it rebounds but loses kinetic energy due to friction and inelasticity. For a very small particle approaching a wall, molecular forces become dominant compared with the inertia force. As a result, the particle is captured by the wall due to cohesion forces (Section 12.4.1.2), and neither rebounds from nor slides along the wall. Energy loss due to wall collision is considered in Section 12.4.2.1, where the analysis is based on a single spherical particle and a smooth wall. The energy loss at walls is readdressed in Section 12.4.2.2 where the case of a nonspherical particle impacting a rough wall is considered.

12.4.2.1 Momentum and Energy Exchange at Walls

Two models are used to deal with particle–wall and particle–particle collisions: the hard sphere model and the soft sphere model. The soft sphere model is based on the integrated forms of the equations of motion, namely, the impulsive equations. The particle velocities change continuously during the entire periods of pre-collision and post-collision, but the hard sphere model considers the momentum difference between periods. The difference in momentum between two instants of time is equal to the impulsive force acting on the particle during that time period:

$$m(v^{(2)} - v^{(1)}) = J \quad (12.117)$$

where $v^{(1)}$ and $v^{(2)}$ are velocities at time 1 and time 2, respectively, and J is the impulsive force acting on the particle during the period between the two times. The difference in angular momentum is expressed by

$$I(\Omega^{(2)} - \Omega^{(1)}) = -\mathbf{r} \times \mathbf{J} \quad (12.118)$$

where $\Omega^{(1)}$ and $\Omega^{(2)}$ are angular velocities at time 1 and time 2, respectively, and I is the moment of inertia of the particle. The impulsive force is defined by the integral of the force versus time when the force acts on the body. In general, Eqs. (12.117) and (12.118) are not sufficient to determine the relationship between the pre and postcollisional velocities. Auxiliary equations are necessary to close a set of equations. The auxiliary equations come from the concept of the coefficient of restitution and the friction coefficient.

In the soft sphere model, not only is the relationship between the pre and postcollisional velocities obtained, but the instantaneous motion during the whole collision process is obtained as well. In this section, the hard sphere model is explained while the soft sphere model is dealt with in Section 12.4.1.2.

Before proceeding to the analysis, it is necessary to define the coefficient of restitution e used in this section because the definition of e is somewhat arbitrary and there are few definitions available in the literature. Consider a particle colliding with a wall as shown in Figure 12.47. The symbol v denotes the translation velocity. The velocity vector has two components: longitudinal component (x component) and the component normal to the wall (y component). The suffixes (0) and (2) denote the precollision velocity and postcollision velocity, respectively. The following definitions have been used in general:

$$e = \frac{|v^{(2)}|}{|v^{(0)}|} \quad (12.119)$$

$$e = \frac{v_y^{(2)}}{v_y^{(0)}} \quad (12.120)$$

$$e_x = v \frac{v_x^{(2)}}{v_x^{(0)}}, \quad e_y = v \frac{v_y^{(2)}}{v_y^{(0)}} \quad (12.121)$$

$$e = \frac{J'_y}{J_y} \quad (12.122)$$

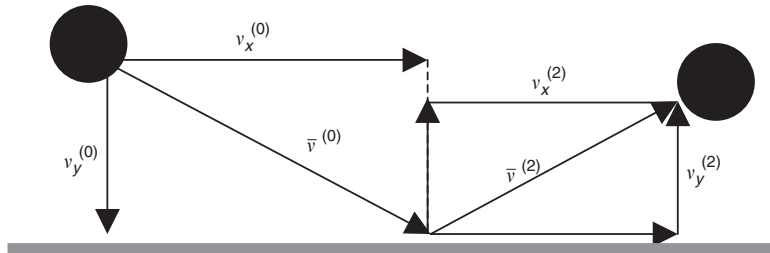


FIGURE 12.47 Particle colliding a wall.

where J_y and J'_y are the normal components of impulses acting on the particle during the collision period. The impulses J_y and J'_y are explained as shown in Figure 12.48. The process of collision is divided into two periods, one in which the material is compressed and the other in which the compression is released. J_y and J'_y are the y components of the impulsive force during the compression and recovery periods, respectively. Among the above four definitions, the second definition is used most widely. However, if this definition is adopted, the value of the coefficient for nonspherical particles depends on the location of the contact point between the particle and the wall. If the restitution coefficient is regarded as a property of the material, its value should not depend on the location of the contact point. From this point of view, a reasonable definition for the coefficient of restitution is given by Eq. (12.122). If the particle is a sphere, it is found that the impulse ratio J'_y/J_y is equal to the velocity ratio $v_y^{(2)}/v_x^{(0)}$.

Consider a three-dimensional collision of a spherical particle with a smooth flat wall, as shown in Figure 12.49. The velocities $v^{(0)}$ and $\Omega^{(0)}$ are the precollision translation and angular velocities, respectively. The corresponding post-collision velocities are expressed by $v^{(2)}$ and $\Omega^{(2)}$. The y -axis is normal to the wall and the x - and z -axis are in the plane of the wall. The subscripts x , y and z signify component directions. If the coefficient of restitution e and kinetic (sliding) friction f are known, the postcollision translation and angular velocities can be obtained by solving the impulsive equations. The results are shown in Table 12.6. In this table ϵ_x and ϵ_y are factors indicating the proportion of the velocity in each component direction, i.e., the direction cosines of the approaching velocity in the x - and z -plane. The factors ϵ_x and ϵ_y satisfy the relation

$$\epsilon_x^2 + \epsilon_z^2 = 1 \quad (12.123)$$

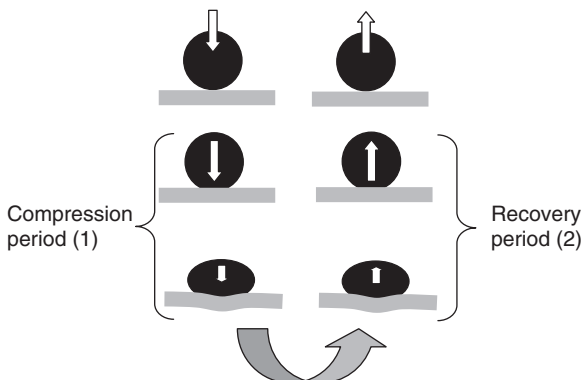


FIGURE 12.48 Compression and recovery periods in collision process.

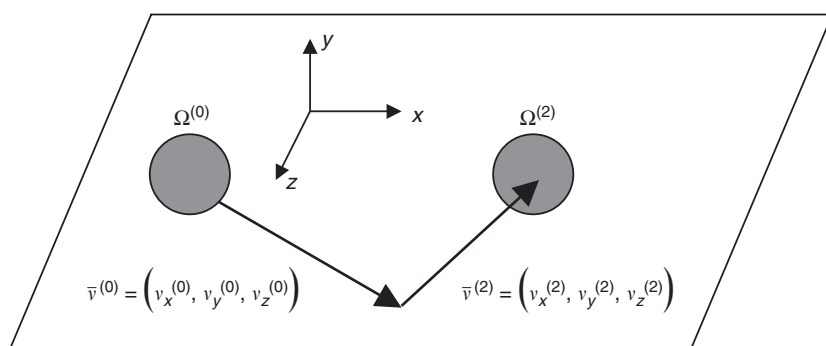


FIGURE 12.49 Three dimensional particle–wall collision.

TABLE 12.6 Relation Between Pre- and Post-Collisional Velocities

Condition	$\frac{v_y^{(0)}}{ \vec{v} } < -\frac{2}{7f(e+1)}$	$-\frac{2}{7f(e+1)} < \frac{v_y^{(0)}}{ \vec{v} } < 0$
Translation velocity	$v_x = \left(\frac{5}{7}\right) \left(v_x^{(0)} - \frac{2a}{5} \Omega_z^{(0)}\right)$ $v_y = -ev_y^{(0)}$ $v_z = \left(\frac{5}{7}\right) \left(v_z^{(0)} + \frac{2a}{5} \Omega_x^{(0)}\right)$	$v_x = v_x^{(0)} + \epsilon_x f(e+1) v_y^{(0)}$ $v_y = -ev_y^{(0)}$ $v_z = v_z^{(0)} + \epsilon_z f(e+1) v_y^{(0)}$
Angular velocity	$\Omega_x = \frac{v_z}{a}$ $\Omega_y = \Omega_y^{(0)}$ $\Omega_x = -\frac{v_x}{a}$	$\Omega_x = \Omega_x^{(0)} - \frac{5}{2a} \epsilon_z f(e+1) v_y^{(0)}$ $\Omega_y = \Omega_y^{(0)}$ $\Omega_z = \Omega_z^{(0)} + \frac{5}{2a} \epsilon_x f(e+1) v_y^{(0)}$

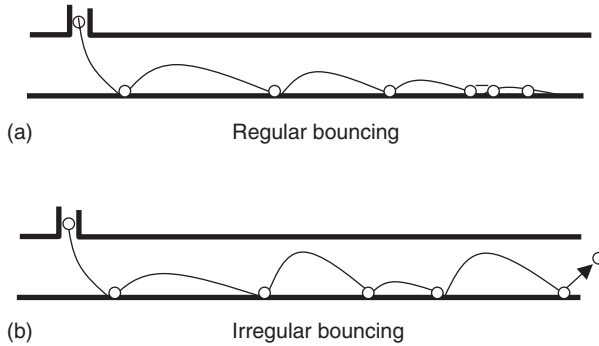


FIGURE 12.50 Regular and irregular bouncing.

In this analysis, Coulomb's friction law is assumed for kinetic (sliding) friction

$$J_\tau = -f \cdot J_n \quad (12.124)$$

where J_τ and J_n are the tangential and normal components of the impulsive forces, respectively, and f is the friction coefficient. The derivation of the results is described in Crowe et al. (1997b).

12.4.2.2 Non-Spherical Particles: Rough Walls

When the coefficients of restitution e and dynamic friction f are given as physical properties of the particles, the postcollisional velocities can be expressed in terms of the precollisional velocities. The relation between these velocities for the case of a spherical particle and smooth wall is shown in Table 12.6. This relationship is useful for calculating particle trajectories in a field enclosed by walls. However, in some cases, the trajectory calculation in multiphase flows is not as straightforward as it might be. The coefficient of restitution e defined by Eq. (12.122) must be less than unity. If trajectory calculations were made for a long horizontal pipe or duct, particles repeatedly colliding with the wall would ultimately lose their vertical velocity component and slide along the wall as shown in Figure 12.50a. To avoid such an unrealistic result, the irregularity of collisions must be considered. If this irregularity is neglected, large particles cannot be suspended in the carrier fluid. Fluid dynamic forces, such as Magnus or shear lift forces, and fluid turbulence acting on the particles are sufficient to suspend small particles. However, the

mechanism responsible for suspending large particles in horizontal pipes is the irregular bouncing of the particles against the wall. In general, the irregularity is caused by particle shape (nonspherical particles) and/ roughness of the wall. In practice, both mechanisms are operative. Several models in regard to the irregular bouncing have been proposed. Those models are classified into two types: one in which the irregularity is attributed to the nonsphericity of the particle (Matsumoto and Saito, 1970a; Tsuji et al., 1989; 1991) and the other to wall roughness (Matsumoto and Saito, 1970b; Tsuji et al., 1987; Sommerfeld, and Zivkovis, 1992; Frank et al., 1993; Sommerfeld and Huber, 1999).

In the following paragraphs, first the nonspherical model and then the rough wall model are described. If the problem is two-dimensional, the treatment is relatively easy, because the cross-sectional shape of the particle is limited to a circle, ellipse, or an arbitrary shape. As shown in Figure 12.51, the distance between the particle center of gravity O and the contact point C depends on the incident attitude of the particle, which does not change in the case of a spherical particle. A set of values for r and θ shown in Figures 12.15b and c describe any particle shape. Impulsive equations are formed for a set of values for r and θ . In the numerical simulation, a pair of values for r and θ is chosen by random numbers. The post-collisional velocities are obtained from solutions of the impulsive equations.

It is difficult to deal, in a rigorous way, with the collision of an arbitrary three-dimensional, nonspherical particle having three components of translational and angular velocity. The complexity of the problem is reduced by using some assumptions. Examples of such assumptions are explained in Tsuji et al. (1991) and Crowe et al. (1997b).

The wall roughness model for irregular bouncing is shown in Figure 12.52. The choice of wall roughness is arbitrary. Several configurations could be considered, such as a wavy pattern, a combination of inclined planes, and so on. The calculation for a spherical particle bouncing on the rough wall is simpler than that for nonspherical particle on a flat wall if the pattern of roughness is specified, because the results shown in Table 12.6 can be used with some modifications. In the rough wall model, the point at which the particle collides with the wall is assumed to be on an inclined plane. Each inclined plane has its own coordinate system. The relationship between the coordinates, with and without an inclination angle, is easily described by using a matrix. Once particle velocities are transformed by the usual linear transformation technique into the coordinates corresponding to the inclined plane, the results shown in Table 12.6 can be used to obtain the post-collisional velocities. After this, the post-collisional velocities based on the coordinates on the

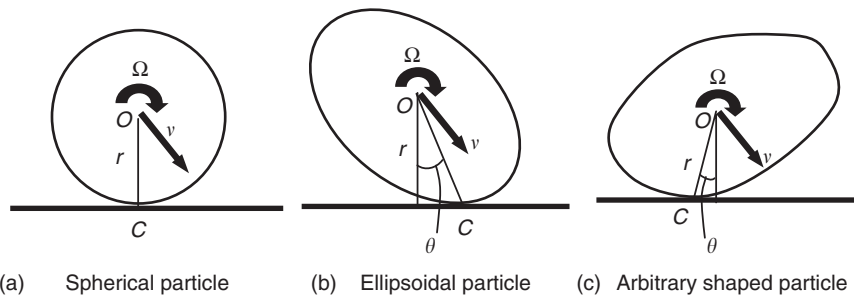


FIGURE 12.51 Contact point between particle and wall.

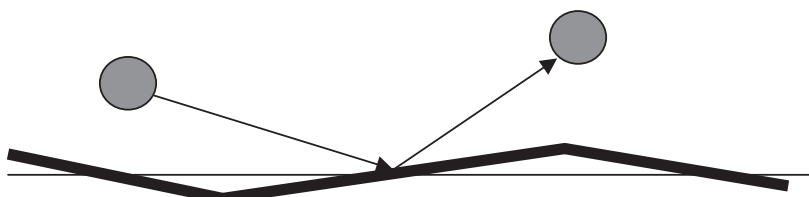


FIGURE 12.52 Particle collision with a rough wall.

inclined plane are retransformed into the original coordinate system. As with the nonspherical particle model, the rough wall models make it possible for the particles to move along with a bouncing motion in long, horizontal pipes or ducts.

Predicting the impact–rebound relations for particles with sharp edges, such as quartz particles, would be very difficult. Experiments (Tabakoff, 1982) with Quarta particles impacting on an aluminum surface show that for a given impact angle, there is a distribution of rebound angles. In this case, it is more pragmatic to use a Monte Carlo method with the measured distribution of rebound angles to model particle–surface impact.

12.4.3 Erosion*

R.W. Lyczkowski

A comprehensive literature review of erosion models is not attempted here. Engel (1978) has provided a good literature review up to 1978 and Sarkar (1980) has provided one up to 1980. The exhaustive review by Meng and Ludema (1995) found 182 equations for wear, and selected 28 for special study. A review done at the Morgantown Energy Technology Center (METC), now the National Energy Technology Laboratory (NETL), deals specifically with erosion in fluidized-bed combustors (FBCs), (Padyhe, 1985). Humphrey (1990) has reviewed the importance of various fundamental considerations relating to the motion of dilute suspensions of solids affected by the carrier fluid and a constraining surface. The summary of the models selected from the literature explains the criteria for their selection and points out their various shortcomings. The reasons leading to the more fundamental energy dissipation approach to modeling erosion are explained.

12.4.3.1 Single-particle Models

Single-particle erosion models treat the erosion process in terms of the interaction of a single particle with the eroding surface. Such models may be more appropriate for the case of erosion due to dilute solid suspensions, as in pneumatic conveying pipelines and elbows or in turbine blade cascades. In these cases, the particle–particle interactions are negligible, and the erosion process may be thought of as removal of surface material by the cumulative action of the individual particles. In this sense, these models are noncontinuum models.

12.4.3.1.1 Finnie's Ductile Erosion Model

According to Engel (1978), Finnie (1958) was the first to derive a single-particle erosive cutting model. Finnie (1960) discussed the assumptions of the model, quoted the results, and compared the results with experimental data. This model set the basic pattern and tone for all single-particle models, so it is discussed here in some detail. The major assumption is that a particle, approaching the eroding surface (or target) at angle α as measured from the surface (called the impingement angle), will remove material in much the same way as a machine tool would. The particle is assumed to be much harder than the surface and does not break up. The surface material is assumed to deform plastically during the cutting process; hence, the material is ductile. Ductile materials, such as aluminum or structural steel, can develop a relatively large tensile strength before they rupture.

The final expression for the volume of target material, W , removed and obtained by Finnie (1960) is as follows:

$$W = \begin{cases} c \frac{MV^2}{\Psi p K} \left[\sin(2\alpha) - \frac{6}{K} \sin^2(\alpha) \right], & \tan(\alpha) \leq \frac{K}{6} \\ c \frac{MV^2}{\Psi p K} \left[\frac{K \cos^2(\alpha)}{6} \right], & \tan(\alpha) > \frac{K}{6} \end{cases} \quad (12.125a)$$

$$W = \begin{cases} c \frac{MV^2}{\Psi p K} \left[\sin(2\alpha) - \frac{6}{K} \sin^2(\alpha) \right], & \tan(\alpha) \leq \frac{K}{6} \\ c \frac{MV^2}{\Psi p K} \left[\frac{K \cos^2(\alpha)}{6} \right], & \tan(\alpha) > \frac{K}{6} \end{cases} \quad (12.125b)$$

*Sections of this book chapter are corrected and condensed sections reprinted from *Progress in Energy and Combustion Science*, 28, Lyczkowski, R. W., and J. X. Bouillard, "State-of-the-Art Review of Erosion Modeling in Fluid/Solids Systems", 543-602, copyright 2002 with permission from Elsevier.

where M is the total mass of abrasive particles, V is the speed of the abrasive particles and, p is the eroding surface "flow stress."

Finnie (1960) took $K = 2$, where K is the ratio of vertical to horizontal (frictional) force, and $\Psi = 1$, where Ψ is the ratio of the depth of contact to the depth of the cut. The constant c allows for the fact that many particles will not be as effective as the idealized model particle; Finnie arbitrarily took $c = 1/2$. To obtain the mass of eroded material removed, W is multiplied by ρ_t , the target density.

The erosion rate (or erosion velocity because it has dimensions of length/time), \dot{E} , is usually given as

$$\dot{E} = \dot{W}/A_t \quad (12.126a)$$

where \dot{W} is the volumetric rate of target material removal, and A_t is the average area of the target material. The erosion rate (or erosion velocity) of the target itself, \dot{E}_t , is given by

$$\dot{E}_t = -\dot{E} = -\dot{W}/A_t \quad (12.126b)$$

because the volumetric rate of change of the target itself is negative.

In order to apply the single-particle Finnie erosion model (or for that matter, any other single particle erosion model) to compute erosion rates for a continuum of solids, Eqs. (12.125a) and (12.125b) must be generalized. One way to do this is described below. Another way to do this is to use the kinetic theory of granular flow as described in Section 12.4.3.4.

First, the total particle mass, M , is replaced by the mass flux of solids, $\dot{m}_s = (1 - \varepsilon)\rho_s v_s$, where $(1 - \varepsilon) = \varepsilon_s$ is the solids volume fraction, ρ_s is the particle density, and v_s is the magnitude of the velocity of the solids phase. The mass flux, \dot{m}_s , is assumed to be positive toward the eroding surface. The particle velocity, V , is replaced by v_s to obtain

$$\dot{E} = \begin{cases} C \frac{(1 - \varepsilon)\rho_s v_s^3}{p} f(\alpha), & \dot{m}_s > 0 \\ 0, & \dot{m}_s < 0 \end{cases} \quad (12.127a)$$

where \dot{E} is the erosion rate (in m/sec) and $C = c/\Psi K$. The erosion rate is positive if the solids velocity vector points toward the eroding surface; otherwise, it is zero.

With $K = 2$, the angular dependency function $f(\alpha)$ is given by

$$f(\alpha) = \begin{cases} \sin(2\alpha) - 3\sin^2(\alpha), & \alpha \leq 18.43^\circ \\ \cos^2(\alpha)/3, & \alpha > 18.43^\circ \end{cases} \quad (12.127b)$$

(12.127c)

Below 18.43° , the surface is cut until the particle leaves the surface; above 18.43° , cutting ceases before the particle leaves the surface. The transition angle 18.43° is close to the angle of maximum erosion, α_{\max} , given by Engel (1978) as

$$\alpha_{\max} = \frac{1}{2} \tan^{-1}(K/3) \quad (12.127d)$$

With $K = 2$, $\alpha_{\max} = 16.85^\circ$. Equation (12.127a) is in the same form as that used by Pourahmadi and Humphrey (1983) in their erosion modeling studies. They defined C as the fraction of particles cutting in an idealized manner, consistent with Finnie's 1972 modification of his model. If one uses Finnie's values of c , Ψ , and K , then $C = 1/8$.

Pourahmadi and Humphrey (1983) used the following expression for $f(\alpha)$:

$$f(\alpha) = \begin{cases} \sin(2\alpha) - 4\sin^2(\alpha), & \alpha \leq 14.04^\circ \\ \cos^2(\alpha)/4, & \alpha > 14.04^\circ \end{cases} \quad (12.128a)$$

$$(12.128b)$$

It may be that they used the original Finnie model with $K = 1.5$, in which case a value of $C = 1/6$ is obtained. Alternatively, they may have used Finnie's (1972) modified model, which accounted for particle inertia, with $K = 2$; in this case, $C = 1/8$. The value of C used by Pourahmadi and Humphrey (1983) is never mentioned, so either case is possible.

At 18.43° , Finnie's model ($K = 2$, $C = 1/8$) yields an erosion rate for ductile target materials given by

$$\dot{E}_{\text{FM}} = 0.075 \frac{\dot{m}_s v_s^2}{2p} \quad (12.129)$$

which is, in effect, the maximum value, \dot{E}_{FM} . Equation (12.129) predicts that only 7.5% of the particle's kinetic energy goes into erosion for a given hardness (or flow stress), p . The corresponding percentage for the Pourahmadi and Humphreys' expression ($C = 1/6$) is 7.8%. Using Eq. (12.129), Finnie (1960) analyzed some data taken for silicon carbide eroding SAE 1020 low carbon steel and found that the value of p exceeded the "true stress at fracture in a tension test" by a factor of almost 3. However, if Finnie's (1972) modification of his model (which accounts for particle inertia) is used together with his recommended values of c , Ψ , and K , then 5.9% of the particle's kinetic energy would go into erosion, instead of 7.5%.

Single-particle erosion models in general, and Finnie's erosion model in particular, cannot be used to calculate absolute erosion rates *a priori*. Finnie's erosion model can be used, together with estimates of target material flow stress (or hardness), to back out a value for parameter C to match the data. On the other hand, if a value for C is assumed, then the value of the flow stress or hardness appropriate for erosion is calculated from the data.

The angular dependence of the erosion rate predicted by using the original Finnie model and its first modifications is quite good up to 45° . Above 45° , the Finnie model underpredicts the erosion rate. At 90° , it predicts no erosion rate at all, whereas the analyzed data clearly indicate that this prediction is not correct. Further reworking of Finnie's theory did not resolve this problem (Finnie and McFadden, 1978). The Finnie model also predicts no erosion at 0° (scouring erosion). Shewmon and Sundararajan (1983) concluded from scanning electron microscope (SEM) examinations of erosion surfaces that the cutting tool analogy is not valid. They regarded the Finnie model to be of historical interest only and suggested other mechanisms for measuring the erosion rate, such as shear localization leading to lip formation and fracture.

12.4.3.1.2 Bitter's Combined Ductile and Brittle Erosion Model

The basic assumptions in Bitter's analysis are that deformation and cutting erosion occur simultaneously and that the two effects can be linearly superimposed (Bitter, 1963, 1963a). Thus, Bitter's work extends Finnie's model and corrects it by bringing in the concepts of a threshold erosion rate and energy dissipation. Physically, the impinging particle cannot erode the target material if its impacting velocity is smaller than a threshold velocity, V_{el} .

12.4.3.1.2.1 Brittle Erosion Model. In Bitter's model the brittle erosion rate is postulated to be equal to the energy dissipation of an elastic sphere deforming the planar target material surface elastically and plastically, divided by an energy (itself dependent on material properties) needed to remove material. This brittle erosion model is given by

$$W_b = \begin{cases} \frac{M[V \sin(\alpha) - V_{\text{el}}]^2}{2\varepsilon_b}, & V \sin(\alpha) > V_{\text{el}} \\ 0, & V \sin(\alpha) < V_{\text{el}} \end{cases} \quad (12.130a)$$

$$(12.130b)$$

where ε_b is the material-dependent deformation wear factor. The threshold velocity, V_{el} , is the velocity of collision at which the elastic limit of the eroding surface is just reached, given theoretically from the Hertz contact theory (Engel, 1978), by

$$V_{\text{el}} = 15.4\sigma_y^{5/2}/(\rho_p^{1/2}E_r^2) \quad (12.131a)$$

where σ_y is the plastic load limit, ρ_p is the particle density, and E_r is the reduced Young's modulus of elasticity. The value of E_r is given by

$$E_r = \frac{1}{[(1 - \gamma_p^2)/(\pi E_p)] + [(1 - \gamma_t^2)/(\pi E_t)]} \equiv \frac{1}{(k_p + k_t)} \quad (12.131b)$$

where γ_p and γ_t are the Poisson's ratios, and E_p and E_t are the Young's moduli of elasticity, of the particle and target, respectively. The threshold velocity, V_{el} , which can be computed from Eq. (12.131a), can be determined from particle rebound data using the following relation (Bitter, 1963):

$$V_2 = (2V_1 V_{el}^2)^{1/2} \quad (12.132)$$

where V_1 and V_2 are the velocities at the beginning (approach) and end (rebound) of collision, respectively.

12.4.3.1.2.2 Ductile Erosion Model. The portion of Bitter's model devoted to ductile erosion consists of the following:

$$W_d = \begin{cases} \frac{2MC'[V \sin(\alpha) - V_{el}]^2 V \cos(\alpha)}{[V \sin(\alpha)]^{1/2}} - \frac{C'[V \sin(\alpha) - V_{el}]^2}{[V \sin(\alpha)]^{1/2}} \phi, & \alpha \leq \alpha_0 \\ \frac{M\{[V^2 \cos^2(\alpha)] - K_1[V \sin(\alpha) - V_{el}]^{3/2}\}}{2\phi} & \alpha > \alpha_0 \end{cases} \quad (12.133a)$$

$$\alpha > \alpha_0 \quad (12.133b)$$

where ϕ is the material-dependent cutting wear factor. The constants C' and K_1 are given by Neilson and Gilchrist (1968) as

$$C' = 0.288(\rho_p/\sigma_y)^{1/4}/\sigma_y \quad (12.134a)$$

and

$$K_1 = 8.036\sigma_y^2 E_r^{-2} (\sigma_y/\rho_p)^{1/4} \quad (12.134b)$$

The angle α_0 may be estimated from Finnie's model (Eq. [12.125]), or by equating Eqs. (12.133a) and (12.133b) and solving for α (Engel, 1978). The total erosion rate, W , is then given by the sum of W_b and W_d . The effect of K_1 is negligible in Eq. (12.133b) (where $\alpha > \alpha_0$) and can safely be dropped (Bitter, 1963a). If ϕ is associated with $3\Psi_p$ then (except for the factor c) Eq. (12.126b) ($\tan \alpha > K/6$) of Finnie's erosion model and Eq. (12.133b) ($\alpha > \alpha_0$) of Bitter's ductile erosion model are the same.

The interesting features of Bitter's model are that (1) for soft ductile materials, it produces wear curves similar to Finnie's, but with nonzero wear at 90° ; and (2) for hard brittle materials, it produces wear curves that reach a maximum at 90° . The shapes of these curves are shown schematically in Figure 12.53.

Bitter's erosion model involves more material properties than Finnie's erosion model and includes those of the particle. However, Bitter's model still predicts zero wear at a zero impingement angle. In fact, the erosion rate is zero when $\alpha < \sin^{-1}(V_{el}/V)$, which is greater than zero. Bitter's model, like Finnie's, also assumes that the particles do not erode. The application of Bitter's model to the calculation of wear for a continuum of solids would be essentially the same as that for Finnie's model.

12.4.3.1.3 Neilson and Gilchrist's Combined Ductile and Brittle Erosion Model

Neilson and Gilchrist (1968) simplified Bitter's combined model by postulating a simplified ductile erosion model while retaining Bitter's brittle erosion model (Eqs. ([12.130]) and [12.131]). The result is

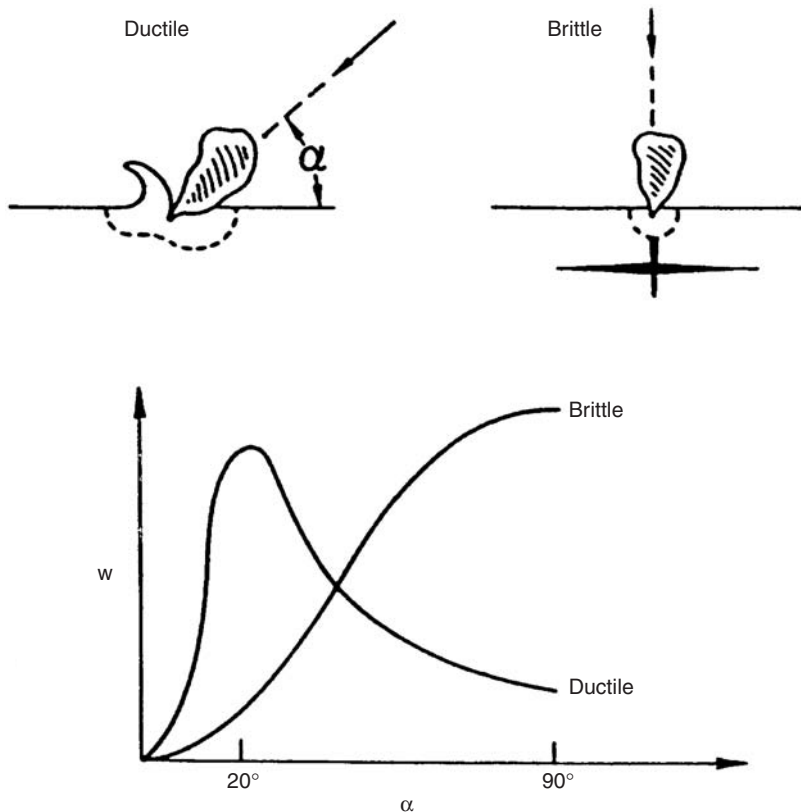


FIGURE 12.53 Erosion mechanisms show wear, W , tends as a function of impingement angle α .

given by

$$W = W_d + W_b = \begin{cases} \frac{M[V^2 \cos^2(\alpha) - V_p]^2}{2\phi} + \frac{M[V \sin(\alpha) - V_{el}]^2}{2\varepsilon_b}, & \alpha \leq \alpha_0 \\ \frac{M[V^2 \cos^2(\alpha)]}{2\phi} + \frac{M[V \sin(\alpha) - V_{el}]^2}{2\varepsilon_b}, & \alpha > \alpha_0 \end{cases} \quad (12.135a)$$

$$(12.135b)$$

with the proviso that $W_b = 0$ when $V \sin(\alpha) < V_{el}$.

In addition to a threshold velocity normal to the eroding surface, $V_n = V_{el}$, there is a threshold velocity parallel to the eroding surface, V_p , given by

$$V_p^2 = V^2 \cos^2(\alpha)[1 - \sin(\alpha)] \quad (12.136)$$

where n is an empirical constant and $\alpha_0 = \pi/2n$. Substitution of Eq. (12.136) into Eq. (12.135) results in

$$W = W_d + W_b = \frac{M[V^2 \cos^2(\alpha) \sin(n\alpha)]}{2\phi} + \frac{M[V \sin(\alpha) - V_{el}]^2}{2\varepsilon_b}, \quad \alpha \leq \alpha_0 \quad (12.137)$$

Comparison of the first terms of Eqs. (12.137) and (12.135b) with Bitter's ductile erosion model (Eq. [12.133]) reveals the extent of Nielson and Gilchrist's simplifications. The first term of Eq. (12.135b) is the same as Bitter's ductile erosion model (Eq. [12.133b]) with $K_1 = 0$. The second terms of Eqs. (12.137) and (12.135b) are the same as Bitter's brittle erosion model, (Eq. [12.130a]).

12.4.3.1.4 Sheldon and Finnie's 90° Brittle Erosion Model

Brittle materials, such as ceramics or glass, cannot deform plastically; instead, they crack and fracture when subjected to tensile stress. The angle of maximum erosion for brittle materials is near 90°. Sheldon and Finnie (1966) analyzed brittle erosion occurring at 90°. Their final result for spherical particles is given by

$$W = C_e R_p^\xi V^\eta \quad (12.138)$$

where

$$\xi = 3f/(f - 2), \quad (12.139a)$$

$$\eta = 2.4f/(f - 2), \quad (12.139b)$$

$$C_e = E_t^{0.8} \sigma_b^2 \quad (12.139c)$$

In the above relations, R_p is the particle radius, f is the coefficient of friction, and σ_b is the flexural strength. This model gives velocity exponents of 3.2, 2.72, and 2.66 for $f = 8, 16.9$, and 20 (glass, graphite, and hardened steel), respectively.

12.4.3.2 Fluidized-Bed Models

Single-particle erosion models have been the subject of much more research than fluidized-bed erosion models. Only two fluidized-bed erosion models have been found in the literature; they are summarized in this section.

12.4.3.2.1 Soo's Ductile and Brittle Erosion Models

Soo (1977) extended his treatment of heat transfer and charge transfer by impact to the treatment of material removal in the case of small deviations from elastic impact. Conceptually, Soo's models resemble Bitter's models in that the energy expended to remove material must exceed the yield stress in order for ductile or brittle failure to produce wear. Soo's erosion models treat ductile wear and brittle wear separately.

12.4.3.2.1.1 Ductile Wear. Soo's ductile wear model is expressed in terms of

$$\dot{E}_d = \cos(\alpha)[1 - K_d^* \sin(\alpha)^{-1/5}] \rho_p V^3 C_d f (1 + r^*) (2.94)(5/16) \eta_d \epsilon_d \quad (12.140)$$

where V is the particle velocity, C_d a correction factor for nonsphericity (≈ 1), r^* the ratio of particle rebound to approach velocities, V_2/V_1 , ϵ_d the energy required to remove a unit volume of ductile material; and η_d the mechanical efficiency of impact ($\sim 10^{-4}$). (The ϵ_d obtained by Soo plays the same role as that of ϕ in Bitter's ductile erosion model.) The dimensionless resistance parameter, K_d , is given by

$$K_d^* = 6\pi^2 \sigma_d (k_p k_t)^{1/2} / [2^{2/5} f C_d (1 + r^*)^{1/5} N_{IM}^{1/5}] \quad (12.141a)$$

where N_{IM} is the impact number given by

$$N_{IM} = (5\pi^2/2) \rho_p V^2 (k_p k_t)^{1/2} [(k_p k_t)^{1/2} + (k_t k_p)^{1/2}]^4 \quad (12.141b)$$

On the assumption that particle motion in a fluidized bed is random, Soo averages Eq. (12.140) over all directions and magnitudes to obtain

$$\dot{E}_{dFB} = (1 - 0.9586 \bar{K}_d^*) \rho_p \bar{V}^3 C_d \bar{f} (1 + \bar{r}^*) (2.94)(5/16) [2/(3\sqrt{\pi})] \eta_d \epsilon_d \quad (12.142)$$

where the overbar denotes averaging. This erosion rate given by Eq. (12.142) is no longer a function of impingement angle, α , and \bar{V}^2 (the intensity of random motion) replaces V^2 in the impaction number

(Eq. [12.141b]). Since particle motion in a fluidized bed is not completely random due to the presence of dead zones and jetting regions, for example, Eq. (12.140) may be preferred over Eq. (12.142).

12.4.3.2.1.2 Brittle Wear.

Soo's brittle wear model is expressed in terms of

$$E_b = \sin(\alpha)[1 - K_b^* \sin(\alpha)^{-1/5}] \rho_p V^3 C_b (1 + r^*) (2.94) (5/16) \eta_b / \varepsilon_b \quad (12.143)$$

where C_b , ε_b , and η_b are the analogous terms for C_d , ε_d , and η_d in the ductile erosion model and K_b^* is given by

$$K_b^* = 6\pi^2 \sigma_b (k_p k_t)^{1/2} / [2^{2/5} C_b (1 + r^*)^{1/5} N_{IM}^{1/5}] \quad (12.144)$$

By averaging over all directions and magnitudes, as in the ductile erosion model, Soo obtains the following fluidized-bed brittle erosion model:

$$\dot{E}_{bFB} = (1 - 0.8981 \bar{K}_b^*) \rho_p \bar{V}^3 C_b (1 + \bar{r}^*) (2.94) (5/16) [2/(3\sqrt{\pi})] \eta_b \varepsilon_b \quad (12.145)$$

Clearly, Soo's erosion models resemble those that have been discussed previously. However, there are differences in the details of the exact angular dependence and the way in which the material properties enter.

Results from Soo's erosion models have not been compared with experimental data. Soo estimates that in the case of 700 μm dolomite particles eroding 316 stainless steel, $1 - K_d^* \approx 10^2$, $f \approx 0.1$, and $\eta_d C_d \approx 10^{-4}$. Assuming that $1 + \bar{r}^* \approx 1$, the ductile erosion estimated using Soo's model (Eq. [12.142]) is as follows:

$$E_{dFB} = 0.69 \times 10^{-7} \frac{\rho_p \bar{V}^3}{2\varepsilon_d} \quad (12.146)$$

This result is five orders of magnitude lower than \dot{E}_{FM} , the maximum erosion rate given by Finnie's model (Eq. [12.129]). Models of ductile erosion of tubes in FBCs are probably more appropriate than brittle erosion models. Soo's model can be used for a continuum of solids by replacing ρ_p with $(1-\varepsilon)\rho_s$ and V^3 with v_s^3 .

The major shortcoming of all the models discussed thus far is that they incorporate the macroscopic or nominal fluid mechanical properties of particle velocity and impact angle, rather than local (or differential) properties. They also fail to account directly for particle fragmentation or attrition and concentration of particles in the fluid stream. An exception is the model developed by Gansley and O'Brien (1990) which uses Davidson's bubble model (1961) in conjunction with the Finnie erosion model (1960). Finnie (1972) stated that no satisfactory explanation of concentration dependence existed, and that very little had been published concerning the effect of the carrier fluid itself. Humphrey (1990) addressed some of these problems in his review article where he also reviewed his group's research on coupling fluid mechanics and single-particle erosion models for dilute flows.

12.4.3.3 Power and Energy Dissipation Models

The origins and derivation of the power dissipation and energy dissipation erosion models are described in this section. We show that the conceptual bases for this approach can be traced back to empirical laws of size reduction, grinding, and comminution. We attempt to unify the concepts of ductile, brittle, abrasive, and impaction erosion. In effect we extend, in a rational manner, single-particle erosion models to continuum erosion models. The power dissipation model is shown to be a special case of what we call the energy dissipation model. The monolayer energy dissipation (MED) erosion model is described below.

12.4.3.3.1 Power Dissipation Erosion Model

Bitter (1963) postulated the concept that energy dissipation of the particles impinging on a surface gives rise to deformation wear. It was, however, the slurry erosion model of Ushimaru, Crowe, and Bernstein (1984), that provided us with the beginning point of the mechanistic monolayer energy dissipation (MED) and simplified closed-form MED (SCFMED) erosion models. Since the angle of approach of the particles eroding a slurry pipeline is essentially zero, none of the models described thus

far appeared to be useful. Therefore, a new model, termed the power dissipation model, was postulated by Ushimaru et al. (1984). No derivation was provided.

We trace the motivation and origins of this power dissipation erosion model in this section. The particle grinding (communition) and abrasive erosion models provide the genesis of the so-called power energy dissipation erosion model. As early as 1885, Kick (1885) postulated that the energy, U , required to fracture particles in ball mills is directly proportional to the particle volume and independent of the number and size of the particles. This postulate, known as Kick's law, can be expressed as

$$U = K_1 V_p \quad (12.147)$$

where V_p is the volume of particles being ground in the ball mill and K_1 is a constant of proportionality having units of pressure (Walker and Shaw, 1954).

Rabinowicz's (1965) much later expression for two-body abrasive (sandpaper or scouring) erosion of a surface by particles is given as

$$\frac{V_t}{L} = kF/(3H) \quad (12.148)$$

where V_t is the volume of target removed, L is the distance traveled by the particle, F is the applied load (force), H is the hardness of the surface, and k is a dimensionless adjustable constant (sometimes called the abrasive wear coefficient) (Fiore et al., 1982) related to the average angularity of the abrasive particles. The equivalence of Eqs. (12.147) and (12.148) is easily seen by rewriting them in terms of V_p and V_t as

$$V_p = U/K_1 \quad (12.149a)$$

and

$$V_t = kFL/(3H). \quad (12.149b)$$

The factor of 3 in Eq. (12.149b) relates the yield strength, σ_y , to hardness, H , by $\sigma_y = 3H$. FL is an energy (force times distance). Comparison of Eqs. (12.149a) and (12.149b) reveals that FL is equivalent to U , K_1 is equivalent to $(3/k)H$, and V_t is equivalent to V_p . Thus, the two seemingly dissimilar processes of grinding of particles in ball mills and abrasive wear of a surface by particles are describable by the same relationship.

In their high-speed-photography slurry studies, Shook et al. (1983) observed that the particle motion was parallel to the pipe wall in the region of high concentration where the erosion rates were high. Hence, the simple Rabinowicz abrasion relationship holds. A heuristic generalization of this relationship is made in order to compute the volumetric loss-per-unit-time-per-unit area, \dot{E} caused by the flow of a slurry. Using Eq. (12.149b), \dot{E} is given by the following for a *constant* applied force, F :

$$\dot{E} = \dot{V}_t/A_t = kFL/(3A_t H) \quad (12.150a)$$

where \dot{V}_t plays the same role as \dot{W} in Eqs. (12.126a) and (12.126b) in the Finnie ductile erosion model described in Section 12.4.3.1. We replace the time rate of change of length, \dot{L} , by the velocity of the solids, v_s , and the applied load, F , by the force of the solids on the material surface, F_s , in Eq. (12.150a) to obtain

$$\dot{E} = \dot{V}_t/A_t = CF_s \cdot v_s/(A_t H) \quad (12.150b)$$

where C is a factor that includes $k/3$, to account for the fact that not all the volume, V_p , is removed (Fiore, et al., 1982). The force of the solids on the surface can be computed from

$$F_s = -(1 - \varepsilon)\rho_s \frac{dv_s}{dt} V_f = -(1 - \varepsilon)\rho_s \left[\frac{\partial v_s}{\partial t} + v_s \cdot \nabla v_s \right] V_f \quad (12.151)$$

where V_f is the volume of the fluid and d/dt^s is the total derivative following the solids velocity, \mathbf{v}_s . Combining Eqs. (12.150b) and (12.151), we obtain

$$\dot{E} = -C(1 - \varepsilon)\rho_s \frac{d\mathbf{v}_s}{dt^s} \cdot \mathbf{v}_s \left(\frac{V_f}{A_t} \right) / H \quad (12.152)$$

Equation (12.152) is the basic form of the “power dissipation” erosion model proposed in 1984 by Ushimaru et al. (1984). The factor C was not explicitly noted but was used, as will be discussed shortly. They used a “layer thickness” Δ , which can be associated with V_f/A_t . Defining the solids mass flux to be $\mathbf{q}_s = (1 - \varepsilon)\rho_s \mathbf{v}_s \Delta$, the power dissipation, P , was defined as

$$P = \frac{d\mathbf{v}_s}{dt^s} \cdot \mathbf{q}_s \quad (12.153)$$

Replacing the hardness, H , by a “specific energy,” E_{sp} , the erosion rate for the power dissipation model, \dot{E}_{PD} , becomes

$$\dot{E}_{PD} = -CP/E_{sp} = -C \frac{d\mathbf{v}_s}{dt^s} \cdot \mathbf{q}_s / E_{sp} \quad (12.154)$$

\dot{E}_{PD} is positive, because the particles must decelerate in order for the force of the solids on the surface, F_s , to be positive according to Eq. (12.151). The sign differs from that of Ushimaru et al. (1984) because they obviously considered their symbol, e , for the erosion rate to stand for $\dot{E}_t = -\dot{E}$, the erosion rate of the target itself (see Eq. [12.126b]).

Equation (12.152) states that the erosion rate is given by the total differential of the particle kinetic energy, multiplied by the mass flow of particles and divided by some material property resembling or related to hardness. Hence, we will write Eq. (12.152) symbolically as follows:

$$\dot{E}_{PD} = -\frac{C}{E_{sp}} \left(\frac{dKE_{spD}}{dt} \right) \left(\frac{V_f}{A_t} \right) \quad (12.155)$$

where the rate of kinetic energy dissipation per unit volume of the solids (which for the sake of brevity we will call the energy dissipation rate) is defined as

$$\frac{dKE_{spD}}{dt} = (1 - \varepsilon)\rho_s \mathbf{v}_s \left[\frac{\partial \mathbf{v}_s}{\partial t} + (\mathbf{v}_s \cdot \nabla \mathbf{v}_s) \right] = E_{PD} \quad (12.156)$$

The power dissipation erosion model has been derived heuristically in this section by generalizing the empirical abrasive erosion relationships. The more general energy dissipation model will be derived by more fundamental means in the next section, where the power dissipation model will be shown to be a special case.

Ushimaru et al. (1984) implemented the apparently fundamental power dissipation erosion model to analyze steady-state scouring erosion in a slurry jet pump and obtained reasonable comparisons with the data. They used a hydrodynamic code similar to that used by Sheldon et al. (1977).

Ushimaru et al. (1984) applied an empiricism that indicates that when the metal is removed with sandpaper, less than 10% of the grains in contact with the surface actually remove metal (Mulhearn and Samuels, 1962). The remaining particles cause only elastic deformation, which does not result in material wear. Hence, the factor C was taken to be 0.1. As discussed above, such factors are influenced by the hardness of the erodent relative to the eroding surface and the erosion mechanism, cutting tool (impaction), or sandpaper (abrasion).

We consider the results of Ushimaru et al. (1984) computations to be fortuitous since the kinetic energy dissipation *increased* through the slurry jet pump as the solids were accelerated. Had the solids decelerated, the kinetic energy dissipation would have *decreased*, and the erosion rate would have the wrong sign. Erosion can occur for both accelerating and decelerating solids flows and, therefore, the power dissipation model derived in this section and used by Ushimaru et al. (1984) cannot be considered to be sufficiently general irrespective of any possible confusion in sign convention. Humphrey (1990) discusses additional particle–surface interactions and related phenomena, which could enter into the factor C .

12.4.3.3.2 Energy Dissipation Models

It is necessary to extend the power dissipation erosion model to a two-phase continuum, consisting of both solids and fluid phases. The power dissipation model will be shown to be a special case of the more general energy dissipation model derived in this section.

The solids-phase momentum equation may be written in nonconservation law form as Bouillard et al. (1989)

$$\begin{aligned} \rho_s(1-\varepsilon)\frac{\partial v_s}{\partial t} + \rho_s(1-\varepsilon)v_s \nabla v_s \\ = -(1-\varepsilon)\nabla P + \beta(v_g - v_s) + G(\nabla \varepsilon) + \rho_s(1-\varepsilon)g + \nabla[(1-\varepsilon)\tau_{sv}] \end{aligned} \quad (12.157)$$

where τ_{sv} is the solids-phase shear stress tensor.

Following Bird et al. (1960) the equation of mechanical energy, extended to two-phase flow, is obtained by taking the scalar product of the solids velocity, v_s , with Eq. (12.157) to obtain

$$\begin{aligned} \rho_s(1-\varepsilon)v_s \cdot \frac{\partial v_s}{\partial t} + \rho_s(1-\varepsilon)v_s \cdot (v_s \cdot \nabla v_s) \\ = -(1-\varepsilon)v_s \cdot \nabla P + v_s \cdot \beta \cdot (v_g - v_s) + v_s \cdot G(\nabla \varepsilon) + \rho_s(1-\varepsilon)v_s \cdot g + v_s \cdot \nabla[(1-\varepsilon)\tau_{sv}] \end{aligned} \quad (12.158)$$

Note that the sign convention of the viscous terms used is opposite to that of Bird, et al Lightfoot (1960).

The last term in Eq. (12.158) may be split into two terms as:

$$v_s \cdot [\nabla \cdot (\varepsilon_s \tau_{sv})] = \nabla \cdot [(\varepsilon_s \tau_{sv}) \cdot v_s] - (\varepsilon_s \tau_{sv}) : \nabla v_s \quad (12.159)$$

The first term on the RHS of Eq. (12.159) represents the rate of reversible work done by the solids viscous forces, while the second term represents the rate of irreversible conversion to internal energy and is shown to be always positive by (Bird et al., 1960). Substitution of Eq. (12.159) into Eq. (12.158) and solving for the rate of irreversible conversion to internal energy, E_{ED} , results in

$$\begin{aligned} E_{ED} &= -\frac{dKE_{ED}}{dt} = (\varepsilon_s \tau_{sv}) : \nabla v_s \\ &= -\left\{ \varepsilon_s \rho_s v_s \cdot \frac{\partial v_s}{\partial t} + \varepsilon_s \rho_s v_s \cdot v_s \cdot \nabla v_s + (\varepsilon_s v_s) \cdot \nabla P + v_s \cdot \beta \cdot (v_s - v_g) \right. \\ &\quad \left. - G(\varepsilon_s) v_s \cdot \nabla \varepsilon - \varepsilon_s \rho_s v_s \cdot g - \nabla \cdot [(\varepsilon_s \tau_{sv}) \cdot v_s] \right\} \end{aligned} \quad (12.160)$$

where ε_s is $(1-\varepsilon)$.

Equation (12.160) is simply the portion of the solids-phase mechanical energy equation resulting in the rate of irreversible conversion to internal energy, a portion of which is available for energy transfer to the solid surface (i.e., the rate of kinetic energy dissipation per unit volume) to produce erosion. It is a direct extension of the well-accepted single-phase expression found in Bird et al. (1960).

Clearly, each term must be present, because each has a physical interpretation contributing to the energy dissipation. Equation (12.160) constitutes the rational extension of the kinetic energy dissipation rate for the power dissipation erosion model.

To see this, Eq. (12.160) is rewritten as

$$-E_{ED} = E_{PD} + \varepsilon_s v_s \cdot \nabla P + v_s \cdot \beta(v_s - v_g) - v_s \cdot G(\varepsilon) \nabla \varepsilon - \varepsilon_s \rho_s v_s \cdot g - \nabla \cdot [(\varepsilon_s \tau_{sv}) \cdot v_s] \quad (12.161)$$

where E_{PD} is the rate of kinetic energy dissipation per unit volume for the power dissipation erosion model given by Eq. (12.156). Equation (12.161) also shows that the sign for the power dissipation rate used by Ushimaru et al. (1984) appears to be incorrect.

From Eq. (12.160), it is clear that the terms representing the irreversible rate of internal energy conversion, $(\varepsilon \tau_{sv}) : \nabla v_s$, are equivalent to all of the seven terms in the braces. The MED model was therefore refined by Bouillard et al. (1989). These energy dissipation rate models, which are programmed into the EROSION/MOD1 computer program (Lyczkowski et al., 1994), are given by

$$U_{ED} = (\text{the terms in braces}) \text{ in Eq. (12.160)} = E_{ED} d_p \quad (12.162a)$$

$$U_{EDv} = [(\varepsilon_s \vec{\tau}_{sv}) : \nabla v_s] d_p = E_{EDv} d_p \quad (12.162b)$$

$$U_{EDvCF} = [(\varepsilon_s \vec{\tau}_{sv}) : \nabla v_s + \vec{\beta}_B v_s^2 / 2] d_p = E_{EDvCF} d_p \quad (12.162c)$$

and

$$U_{EDvREL} = [(\varepsilon_s \vec{\tau}_{sv}) : \nabla v_s + \varepsilon_s \vec{\beta}_B (v_f - v_s)^2] d_p = E_{EDvREL} d_p \quad (12.162d)$$

The particle diameter, d_p , was argued by Bouillard et al. (1989) to arise from the observation that most of the energy dissipation occurs in a monolayer of particles in the vicinity of the eroding surface as shown in Figure 12.54. Hence the ratio V_f/A_t , which arises in the power dissipation model, becomes $V_f/A_t = d_p$.

The erosion rates for the MED erosion model are given by:

$$\dot{E}_{ED} = C U_{ED} / E_{sp} \quad (12.163a)$$

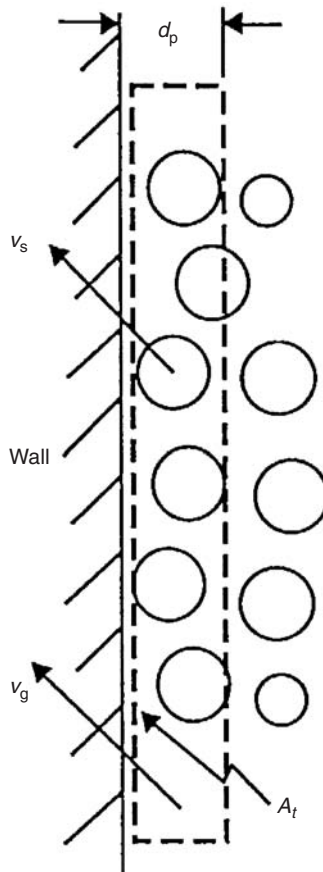


FIGURE 12.54 Conceptual picture of the MED erosion model.

$$\dot{E}_{EDv} = CU_{EDv}/E_{sp} \quad (12.163b)$$

$$\dot{E}_{EDvCF} = CU_{EDvCF}/E_{sp} \quad (12.163c)$$

and

$$\dot{E}_{EDvREL} = CU_{EDvREL}/E_{sp} \quad (12.163d)$$

Equations (12.163a–12.163d) may be written succinctly as

$$\dot{E}_{ED\alpha} = CU_{ED\alpha}/E_{sp} = CE_{ED\alpha}d_p/E_{sp} \quad (12.164)$$

where $U_{ED\alpha}$ and $\dot{E}_{ED\alpha}$ are given by Eqs. (12.162a)–(12.162d) and Eqs. (12.163a)–(12.163d) respectively with $\alpha = 1, v, vCF$, and $vREL$, respectively. Details of the derivation of Eqs. (12.163b)–(12.163d) are given by Bouillard and Lyczkowski (1991). E_{sp} is the specific energy, which is a material property related to hardness or flow stress, p . Some typical values of hardnesses are given by Wood and Woodford (1980) and Ushimaru et al. (1984), who claim that $E_{sp} \approx 2 \times p$.

The MED erosion models given by Eqs. (12.163a)–(12.163d) can be interpreted as an extension of the power dissipation erosion model given by Eq. (12.155) with $V_f/A_t = d_p$. We chose $E_{sp} = p$. Bouillard and Lyczkowski (1991) showed that the factor C is in fact related to the target-particle coefficient of restitution, e , given by

$$V_{s1}^2 - V_{s2}^2 = (1 - e^2)V_{s1}^2 \quad (12.165)$$

where V_{s1} and V_{s2} are the approach and rebound solids velocities, respectively, by

$$C = 1 - e^2. \quad (12.166)$$

Typically, $e^2 \approx 0.9$ (Savage, 1982), which fortuitously agrees with the value used in the power dissipation erosion model by Ushimaru et al. (1984), which was based on the data of Mulhern and Samuels (1962). This is the default value used in the EROSION/MOD1 computer code (Lyczkowski et al., 1994b). Therefore, the definitive form of the MED erosion model becomes

$$\boxed{\dot{E}_{ED\alpha} = (1 - e^2)U_{ED\alpha}/p = (1 - e^2)E_{ED\alpha}d_p/p} \quad (12.167)$$

These MED erosion models are based on the premise that the mechanical energy of the solids is irreversibly dissipated in the neighborhood of stationary surfaces by three competitive mechanisms: (1) heat transfer between the fluid-and-solids phase, between the fluid phase and stationary surfaces, and between the solids phase and stationary surfaces; (2) erosion of stationary surfaces; and (3) attrition of solids. Thus, the rate of energy dissipated during erosion represents only a fraction of the total energy dissipation (which is related to the total entropy production).

The presently recommended MED erosion model, which is essentially the one derived by Bouillard et al. (1989), as refined by Bouillard and Lyczkowski (1991), is Eq. (12.167) with $U_{ED\alpha}$ given by Eq. (12.163c) and is written as

$$\boxed{\dot{E}_{MED} = (1 - e^2)[(\epsilon_s \tau_{sv}) : \nabla v_s + \beta_B v_s \cdot v_s / 2]d_p/p = \dot{E}_{EDvCF}} \quad (12.168)$$

In their cold fluidized-bed erosion experiments, Wood and Woodford (1979) found that the erosion rate increased with increasing particle diameter. For example, they obtained erosion rates of 0.036, 0.48, and 1.16 mm/1000 h for aluminum tubes for 100, 930, and 1900 μm silica sand; these values suggest a very nearly linear dependence. Basically, linear dependence was found for all the other materials tested. Therefore, the choice of the particle size dependence in the MED erosion models given by Eqs. (12.167) and (12.168) appears justified.

12.4.3.3.3 Simplified Closed-Form MED (SCFMED) Erosion Model

Bouillard and Lyczkowski (1991) developed a simplified mechanistic monolayer energy dissipation (MED) erosion model using a variational principle that placed the closed-form MED erosion model derived by Bouillard et al. (1989) on a firm foundation. A modification of that model is presented here to assist the practicing engineer to quickly estimate erosion rates (see [Section 12.4.3.6](#)).

The erosion rate from the simplified quasi one-dimensional MED erosion model, \dot{E}_{EDCF} , may be written in the form, modified for Hydrodynamic Model B (Bouillard et al., 1989; Bouillard and Lyczkowski, 1991) as

$$\dot{E}_{\text{EDCF}} = \dot{E}_o \frac{(1 - \varepsilon)(\varepsilon - \varepsilon_{\text{gd}})}{\varepsilon^2} + K \frac{(\varepsilon - \varepsilon_{\text{gd}})}{\varepsilon^2} (U - \varepsilon V_s) \quad (12.169)$$

where U is the superficial gas velocity, V_s is the solids-phase velocity, and ε is the void fraction. The erosion rate group, \dot{E}_o , is given by

$$\dot{E}_o = (1 - e^2) \frac{75 \mu_g g x_d}{(\varphi_s d_p E_{\text{sp}})} \quad (12.170)$$

and

$$K = (1 - e^2) \frac{0.875 g x_d \rho_g}{E_{\text{sp}}} \quad (12.171)$$

The units of \dot{E}_o are in terms of velocity, commonly expressed in mm/1000 h or $\mu\text{m}/100 \text{ h}$. K is dimensionless, e is the particle-surface restitution coefficient, which is the ratio of particle rebound velocity, V_{p2} to particle approach velocity V_{p1} and x_d is a characteristic acceleration distance of the order of the heat exchanger tube spacing in FBCs. The rest of the symbols are defined in Nomenclature.

Experimental evidence presented by Zhu (1988) strongly supports the additional approximation that the solids velocity V_s in the vicinity of tubes is close to the superficial gas velocity, U . With the approximation $V_s = U$, Eq. (12.169) may be written in the strikingly simple dimensionless form as

$$\dot{E}_{\text{EDCF}}/\dot{E}_0 = f(\varepsilon)(1 + 0.01167 Re) \quad (12.172)$$

where the fluidization Reynolds number $Re = (\varphi_s d_p) \rho_g U / \mu_g$ and

$$f(\varepsilon) = \frac{(1 - \varepsilon)(\varepsilon - \varepsilon_{\text{gd}})}{\varepsilon^2} \quad (12.173)$$

12.4.3.4 Kinetic Theory Models

The kinetic theory of granular flow erosion model developed by Ding and Lyczkowski (1992) offers an alternative approach to extending single particle erosion models. A summary of the approach applied to the Finnie erosion model is given in this section.

The Finnie erosion model given by Eqs. (12.125a) and (12.125b) is written as a function of the particle's instantaneous speed in the vicinity of an eroding surface, c_w , angle of attack, α , and mass $M = \pi d_p^3 \rho_p / 3$ as

$$W = B_F M c_w^2 f(\alpha), \quad (12.174)$$

where

$$B_F = \frac{1}{8 P_H} \quad (12.175)$$

where P_H is the Vickers hardness or flow stress, and $f(\alpha)$ is given by Eqs. (12.127b) and (12.127c).

Finnie's single-particle erosion model is combined with the kinetic theory of granular flow (Ding and Gidaspow, 1990), to obtain an expression for erosion due to repeated impacts on the eroding surfaces. The erosion rate, \dot{E} , of a solid surface caused by repeated impacts with the surface can be obtained by calculating the number of particles within a range c to $c + dc$ per unit volume and unit time times the erosion

caused by a single particle impact. Thus, the erosion rate caused by repeated impacts given by Eq. (12.174) is integrated over all impact velocities in the range of $(-\infty, +\infty)$ to obtain

$$\dot{E} = \int_{c_w n > 0} (c_w \cdot n) B_F M c_w^2 f(\alpha) f_w(r, c, t) dc_w, \quad (12.176)$$

where the single-particle velocity distribution function in the vicinity of the eroding surface, f_w , is assumed to be Maxwellian, (Gidaspow, 1994).

Carrying out the integration of Eq. (12.176), the result is

$$\dot{E} = 2\varepsilon_s \rho_p B_F \left[\frac{(2T)^{3/2}}{\sqrt{\pi}} F_1(\theta_c) + \frac{v_w^2}{2} \sqrt{\frac{2T}{\pi}} F_1(\theta_c) + \frac{3}{2} v_w T F_2(\theta_c) \right], \quad (12.177a)$$

where

$$F_1(\theta_c) = \frac{\pi}{8} - \frac{\theta_c}{4} + \frac{1}{12} \sin^4(\theta_c) + \frac{1}{16} \sin^4(\theta_c) - \frac{3}{4} \cos^4(\theta_c) - 0.1 \quad (12.177b)$$

and

$$\begin{aligned} F_2(\theta_c) = & -\frac{2}{5} + \frac{1}{15} \sin^5(\theta_c) - \frac{2}{5} \cos(\theta_c) \sin^4(\theta_c) + \frac{2}{15} (\cos(\theta_c) \sin^2(\theta_c) + 2 \cos(\theta_c)) \\ & + \frac{3}{5} \cos^2(\theta_c) \sin^3(\theta_c) + \frac{2}{5} \sin^3(\theta_c) = 0.06 \end{aligned} \quad (12.177c)$$

Details of the integration process are given in Ding and Lyczkowski (1992). This approach is similar to that used by Soo (1977) to obtain the fluidized-bed erosion models described in Section 12.4.3.2.

Rogers (1995) developed a similar model using Finnie's (1958) single-particle erosion model and the kinetic theory of granular flow. That model is more involved and requires a certain amount of iteration between the erosion calculations and the experimental data to determine adjustable parameters that minimize the difference. The kinetic theory model given by Eq. (12.177a) requires only the knowledge of the granular temperature and some measure of target hardness.

The input to the kinetic theory erosion model given by Eq. (12.177a) may be the computed granular temperature (Ding and Lyczkowski, 1990) or experimental data, such as the one obtained by Cody et al. (1996) using a nonintrusive vibration probe. They obtained the granular temperature data as a function of fluidizing velocity for glass spheres ranging in diameter from 595 to 63 μm encompassing Geldart type-B (and nearly D) and the transition to Geldart type-A particles. Such data can be used as a check on the consistency between erosion measurements and granular temperature measurements.

The number of particles, P_w , colliding with a wall having an area A in a time interval dt can be estimated as

$$P_w = (c_w \cdot n) f_w(r_w, C_w, t) dc_w dA dt \quad (12.178)$$

Then the number of collisions per unit area per unit time is obtained from

$$N_{pw} = \int_{c_w n > 0} \frac{P_w}{dA dt} = \int_{c_w n > 0} (c_w \cdot n) f_w(r, c, t) dc_w = \frac{6\varepsilon_s}{\pi d_p^3} \sqrt{\frac{T}{2\pi}} \quad (12.179)$$

12.4.3.5 Lagrangian Particle and Discrete Element Models

12.4.3.5.1 Lagrangian Models

Tabakoff (1982, 1991) and co-workers at the University of Cincinnati, Hussain and Tabakoff (1974), and Grant and Tabakoff (1975) have been engaged in turbine blade erosion and particulate flow research since 1971. It is their hope that the incorporation of erosion into the engine design as a parameter could lead to the production of an erosion-tolerant engine. They have developed a steady-state computer program capable of describing three-dimensional particle trajectories through turboaxial or radially rotating turbomachinery. Tabakoff (1991) has reviewed this work up to 1990; the same year Humphrey (1990) reviewed the subject of erosion in turbomachinery and related phenomena.

The experimental data on the coefficient of restitution (the ratio of rebound to approach velocities) and the ratio of rebound to impingement angle are obtained experimentally by the group using high-speed photography or laser doppler anemometry and are expressed in terms of impingement angle. In the computer model first developed by Hussain and Tabakoff (1974), these ratios are used to account for momentum loss of the particles caused by collision with the turbine blades or channel walls in the Lagrangian trajectory calculations.

The major force on the particles is given by a drag expression similar to the one used in the FLU-FIX/MOD2 computer code (Lyczkowski, et.al., 1994a). The added mass, Basset, and Bagnold forces on the particles are neglected. The compressible, nonviscous, steady-state gas-phase momentum equations are assumed to be unaffected by the particles. This implies low particle loadings, an assumption that allows the use of existing single-phase computer codes for turbomachinery. The three-dimensional Eulerian gas flow and Lagrangian particle trajectory equations are solved on a square grid with the coordinates fixed on the rotating blade (one row of blades is solved at a time).

This same group has also simulated erosion with a Monte Carlo technique (Grant and Tabakoff, 1975). The erosion model, used to compute the erosion rates, also incorporates the particle rebound data; it is given by a semiempirical equation that relates the mass of material removed (in mg) to the mass of particles (g), as follows:

$$S = K_1 f(\alpha) V^2 \cos^2(\alpha) (1 - R_T^2) + K_3 (V \sin^4(\alpha)) \quad (12.180)$$

where

$$R_T = 1 - 0.0016 V \sin(\alpha) \quad (12.181a)$$

and

$$f(\alpha) = \begin{cases} 1 + K_{12} \sin [(90/\alpha_0)\alpha], & 0 < \alpha < 2\alpha_0 \\ 1, & 0 > 2\alpha_0 \end{cases} \quad (12.181b)$$

$$(12.181c)$$

in which α_0 is the angle corresponding to maximum erosion. The parameters α_0 , K_1 , K_{12} , and K_3 are material-dependent empirical constants. Comparison of Eq. (12.180) with Eqs. (12.135a) and (12.135b) shows that this model is a variant of the Neilson and Gilchrist combined ductile and brittle erosion model. The approach speed V and impact angle α are computed from the particle trajectory computer program.

Sheldon et al. (1977) developed a numerical method to predict erosion on a horizontal, round tube wall. It is known as particle-source-in-cell (PSI-Cell), (Crowe et al., 1977), in which the particles are treated as sources of mass, momentum, and energy in the gas phase. The momentum equations for the incompressible, two-dimensional viscous Eulerian gas phase include a momentum sink term due to particle drag and, thus, would appear to be an improvement over Tabakoff's equation; however, the model does not contain the void fraction as a variable. Hence, the assumption of low particle loadings is again implicit, and the approach is similar to the "dusty gas" model of Rudinger and Chang (1964). The Eulerian gas flow equations and Lagrangian particle trajectory equations are solved iteratively, using an extension of the TEACH program developed at Imperial College, London (Gosman and Pun, 1974). A two-parameter turbulence model and heat transfer, are included in the PSI-Cell technique but it appears that they were not used in this erosion prediction.

The particle trajectory calculations use empirical rebound angle and coefficient of restitution data in a manner similar to that of Hussain and Tabakoff (1974). The erosion model is very simple and is given by

$$\left(\frac{\text{mass removed}}{\text{mass abrasive}} \right) \simeq f(\alpha) V^{2.35} \quad (12.182)$$

where $f(\alpha)$ is given by an experimental curve. The exponent on the particle velocity is taken from the Sheldon and Finnie 90° brittle erosion model (Sheldon and Finnie, 1966). The erosion curve for $f(\alpha)$ was determined for impingement angles as low as 4° by using hardened steel shot (Ro45) of 270 μm average diameter striking 6061-T6 aluminum alloy, a ductile material. The rebound data were obtained from

multiple flash exposures of 3.175 mm ball bearings striking the same aluminum alloy. Erosion data taken by blasting the steel shot through a horizontal tube 4.95 mm in diameter and 30.5 cm long, made of the same aluminum alloy, were in reasonable agreement, considering that the majority of particles were incident at less than 5° (probably deduced from the trajectory computations), which corresponds to almost pure abrasion (scouring). Whether a coefficient of proportionality was introduced into Eq. (12.182) is uncertain.

12.4.3.5.2 Discrete Element Models

An alternative to extending single-particle erosion models using the hydrodynamic models contained in the FLUFIX/MOD2 computer code (Lyczkowski et al., 1994a) and kinetic theory of granular flow models contained in the IFAP computer code (Ding and Gidaspow, 1990; Ding and Lyczkowski, 1992) is to use the instantaneous time-dependent particle velocities computed by the discrete element method (DEM) (Rong et al., 1999; Rong and Horio 2001). Tsuji et al. (1993) refer to this method as the discrete particle simulation. Tsuji (2000) summarized Japanese activities on discrete particle simulation. Rong et al. (1999) reviewed the DEM literature and applied the technique to describe particle motion and erosion in fluidized beds containing an immersed single tube as well as tube arrays. However, they failed to refer to the work of Walton and collaborators (see e.g., Walton and Braun, 1994), who use basically the same approach as DEM and refer to the technique as particle dynamics. The DEM calculations were performed in two dimensions using a staircase approximation to the round tubes and treated the particles as circles. Walton and Braun generally use spherical particles in three dimensions. Their application is to test the assumptions made in the kinetic theory of granular flow.

The numerical results from the DEM for particle and bubble patterns computed by Rong et al. (1999) agreed qualitatively, and more quantitative computations such as bubble frequency (2 to 3 Hz), bed expansion, bubble velocity (~ 0.7 m/sec), and particle impact velocity bracketed data were taken at atmospheric conditions pressure. The effect of moderate pressure (1.2 MPa) increased the computed bubble frequency from 4 to 8 Hz as well as the particle impact velocity; however, no comparisons were made with these data.

The energy calculated by the DEM was used with the Finnie erosion model; however, no comparisons were made with data. Using a hardness of 6×10^8 kgf/m² (600 kgf/mm² or $\sim 6,000$ MPa) that corresponds roughly to hardened steel (see Wood and Woodford, 1980; Ushimaru et al., 1984), Rong and Horio (2001) computed erosion rates of the order of $10 \mu\text{m}/1000 \text{ h}$ ($0.01 \text{ mm}/100 \text{ h}$), which are in rough agreement with rates predicted by Lyczkowski and Bouillard (2002).

The shortcoming of the DEM is that it uses a system of dashpots and springs, which may render it unsuitable for truly predictive calculations. An alternative is DNS of fluidized particles pioneered by Joseph (2001). This method requires no adjustable parameters and appears to be truly predictive if the number of particles can be made sufficiently large. Videos of their simulations are available at http://www.aem.umn.edu/Solid-Liquid_Flows/

12.4.3.6 Sample Calculations and Data Comparisons

The SCFMED erosion model given by Eq. (12.172) was used to predict erosion rates quickly by using data that are easily obtained experimentally, such as bed expansion. In lieu of actual data, the time-averaged bed expansion was obtained from the detailed hydrodynamic computations performed by Bouillard and Lyczkowski (1991) for a few (three-) tube approximation of the International Energy Agency (IEA) Grimethorpe tube bank “C1” configuration (Parkinson et al., 1986), over the U/U_{mf} range from 1.0 to 2.7 for 500 μm diameter glass beads having a density $\rho_s = 2.44 \times 10^3 \text{ kg/m}^3$. The reader is referred to Bouillard and Lyczkowski (1991) for further details of the calculations.

The fluidized-bed void fraction is obtained as a function of the time-averaged fluidized-bed height, H , from the following solids overall mass conservation equation:

$$\varepsilon = 1 - (H_{\text{mf}} \varepsilon_{\text{smf}} / H) \quad (12.183)$$

where $\varepsilon_{\text{smf}} = (1 - \varepsilon_{\text{mf}})$ is the solids volume fraction at minimum fluidization and $H_{\text{mf}} = 44.2$ cm is the bed height at minimum fluidization. The rest of the parameters used to evaluate Eq. (12.172) at 25°C and 1.01 kPa are given by $\mu_g = 1.82 \times 10^{-5}$ Pa sec, $\rho_g = 1.83 \text{ kg/m}^3$, $E_{\text{sp}} = 294 \text{ MPa}$, $d_p = 0.05 \text{ cm}$, $x_d = 55 \text{ mm}$, $e^2 = 0.9$, $\phi_s = 1.0$, and $\varepsilon_{\text{gd}} = 0.4$.

E_{sp} corresponds to the hardness of pure aluminum (30 kgf/mm^2 , 294 MPa) and x_d is the minimum horizontal spacing between tubes ($89 - 33.7 \text{ mm} = 55.3 \text{ mm}$) for Grimethorpe tube bank "C1" Parkinson et al. (1986). The results of the calculations are listed in Table 12.7 and are plotted in Figure 12.55, where they are compared with the full MED erosion model results. As can be seen, the agreement is excellent. The results of the full MED and SCFMED erosion calculations are compared in Figure 12.55 with the data of Wood and Woodford (1980), Parkinson et al. (1985, 1986), Zhu et al. (1990), and Foster Wheeler (Podolski et al., 1991) taken under similar operating conditions. As can be seen, the agreement is excellent. Also shown is the sensitivity of the results to a threefold increase in the apparent hardness of aluminum due to surface oxidation. (90 kgf/mm^2 , 882 MPa). In spite of the diverse sources of the data, such agreement with the simplified MED erosion model is remarkable. The simplified MED erosion model, Eqs. (12.169)–(12.173) takes a few minutes to compute on a pocket calculator vs. a month on a mainframe computer using the FLUFIX/MOD2 (Lyczkowski et al., 1994a) and EROSION/MOD1 (Lyczkowski et al., 1994b) computer programs.

If the physical input parameters of the SCFMED erosion model are missing, they must be estimated by (1) reviewing available databases for each parameter; (2) estimating the range of uncertainties, e.g., tube hardness; and (3) identifying contradictions from different estimation procedures. Lyczkowski and Bouillard (1986) used the SCFMED erosion model to develop a mechanistic erosion scaling procedure.

TABLE 12.7 Metal Wastage Predictions from SCFMED Erosion Model

U/U_{mf}	$U, (\text{cm/sec})$	$H, (\text{cm})$	ε	$f(\varepsilon)$	Re	\dot{E}_{EDCF}/\dot{E}_o
1.0	0.209	44.2	0.40	0	10.5	0
1.12	0.234	46	0.42	0.066	11.7	0.075
1.7	0.355	50	0.47	0.168	17.8	0.203
2.3	0.481	55	0.52	0.213	24.2	0.273
2.7	0.564	59	0.55	0.223	28.4	0.296

$$\dot{E}_o = 1.8 \text{ mm/1000 h.}$$

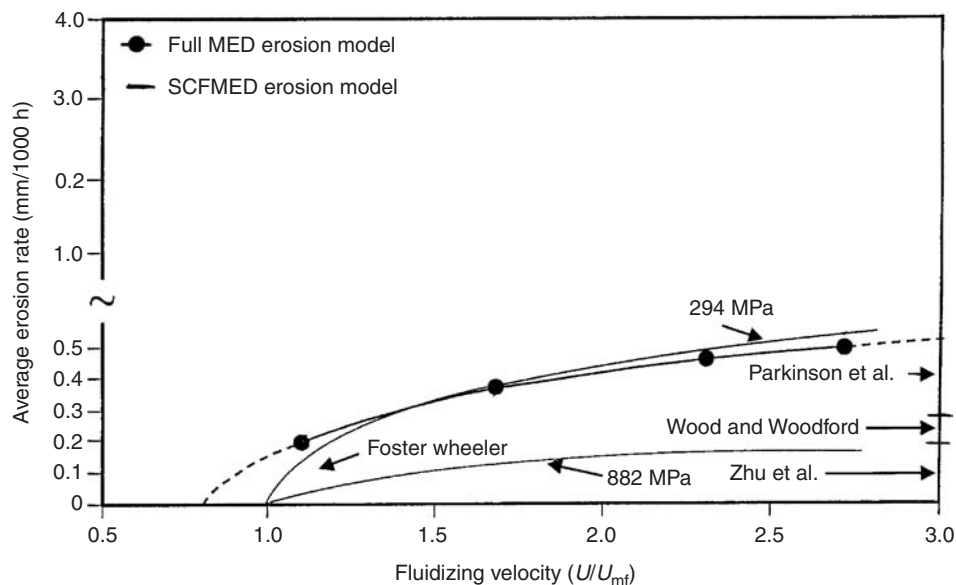


FIGURE 12.55 Comparison of closed-form MED and SCFMED erosion models with available data for aluminum tubes. Data source key: Parkinson et al. (1985, 1986); Wood and Woodford (1980); Zhu et al. (1990); and Foster Wheeler From Podoloski et al. (1991).

A more complete description of the material in this section may be found in Lyczkowski and Bouillard (2002a, 2003), which also includes a review of the work of Chalmers University which extended the MED erosion model.

12.5 Particle and Droplet Dispersion in Turbulent Flows

T.R. Troutt

12.5.1 Introduction

Droplet and particle dispersion in turbulence is important in many engineering applications. The mixing of droplets in liquid-fueled combustion systems is dependent on turbulent dispersion. The degree of mixing establishes the local fuel-to-air ratio, which affects the combustion efficiency and pollution generation. One important parameter which influences the dispersion is the droplet-fluid time ratio or the Stokes number. The objective of this section is to review the current state of understanding of particles and droplets in turbulent structures. This review will primarily involve dilute two-phase turbulent flows.

Dilute models for particle–fluid turbulence interaction with heavy particles may be based on one or two-way coupling. With one-way coupled models it is assumed that the particle phase has a negligible effect on the fluid-phase turbulence, whereas two-way coupled models include particulate effects on the fluid-phase turbulence. A map proposed for coupling interactions projected onto volume fraction–particle Reynolds number space is shown in Figure 12.56. For low particle volume fractions and particle Reynolds numbers, it is expected that one-way coupling dominates. However, as the particle Reynolds number is increased and the particles begin to generate wakes, fluid-phase turbulence will be produced requiring two-way coupled models. An increase in the particle volume fraction will also lead to two-way coupling, since the bulk

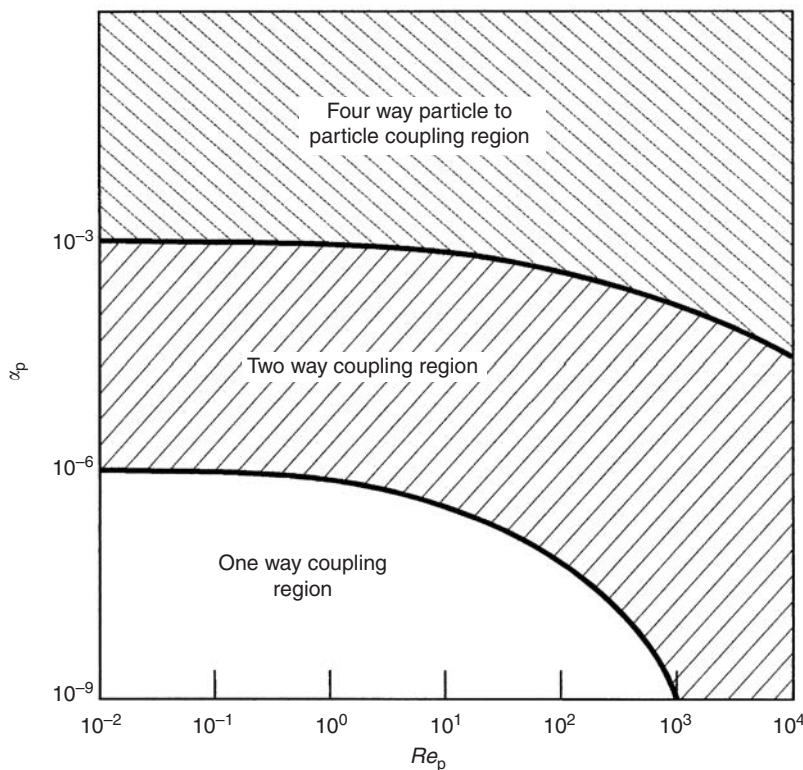


FIGURE 12.56 Two-phase coupling regions for particle-fluid turbulence interaction.

density of the particles will become significant. When particle volume fractions exceed 10^{-3} , the possibility of four-way coupling occurs in which particle–particle interactions are significant (Crowe et al., 1996). This region is associated with dense-phase flows.

12.5.2 Time Scales

To implement the Lagrangian approach on particulate dispersion in a two-phase flow, a particle motion equation is required. For dilute two-phase flow environments with low particle Reynolds numbers, Maxey and Riley (1983) derived a complex integral-differential equation involving six different forces. However, if the material density of the particulate phase is much greater than the density of the fluid phase (heavy particle situation) and body forces are neglected, then the well-known Stokes drag force term is assumed to become the dominate force on the particles. (Crowe et al., 1998)

The Stokes drag term can be associated with a time scale of the particle motion called the particle response time, τ_v , introduced in Section 1.2. If the particle motion equation is nondimensionalized with a characteristic fluid velocity, U , and length scale, ℓ , then the motion equation for heavy particles becomes

$$\frac{dv}{dt} = \frac{f}{Stk} (v - u)$$

where v is the particle velocity, u the fluid velocity, and Stk the Stokes number defined as $Stk = (\tau_v/\tau_f)$, with τ_f being the fluid time scale. The factor f is the ratio of drag to Stokes drag.

For particle dispersion in turbulent flows, the choice of the appropriate fluid time scale to use in the Stokes number ratio introduces some ambiguity into the formulation. Since turbulent flows exhibit a range of time scales from the integral τ_l to the Kolmogorov τ_k and since the ratio of the two time scales, τ_k/τ_l , varies with the turbulence Reynolds number as $Re_t^{-1/2}$, a wide variation of possible Stokes number exist. In addition, the integral time scale may be associated with either Lagrangian or Eulerian viewpoints. Detailed descriptions of various turbulent time scales can be found in Tennekes and Lumley (1972).

12.5.3 Particle Dispersion in Turbulent Shear Flows

During the past 15 years, considerable experimental and numerical research has been conducted concerning particle dispersion in turbulent shear flows. This research has been spurred on by the development of new physical models for the particle dispersion process and the application of new experimental techniques and more powerful computational tools.

The physical model development has emphasized the role that organized vortex structures produced in turbulent flows might have in the particle dispersion process. Organized vortex structures have been recognized for several decades as a significant component of free turbulent shear flows (Ho and Huerre, 1984).

The role that organized vortex structures might play in the particle dispersion process has been investigated both experimentally and numerically by several research groups. Most of the early efforts in this area have concentrated on free shear flows with low particle concentrations and small particle Reynolds numbers (i.e., one-way coupling situations).

The experimental efforts in these two-phase flows have involved flow visualization techniques, laser anemometry techniques and more recently particle image velocimetry (PIV) techniques. A review on standard PIV techniques is available in Liu and Adrian (1993). Information concerning advanced scanning PIV techniques for obtaining three-dimensional flow information can be found in Kiger (1998). Several informative reviews concerning the results of these experimental investigations are available in Crowe et al. (1993, 1995) and Eaton and Fessler (1994). In essence, several important findings obtained from these free shear flow investigations have been reported:

1. Large-scale vortex structures are important controlling mechanisms for the particle dispersion process.
2. Particle dispersion levels tend to maximize at intermediate, 0(1)–0(10), values of Stokes numbers.
3. Intermediate value Stokes number particles tend to concentrate preferentially near the outer boundaries of large-scale vortex structures.

The tendency of intermediate value Stokes number particles to accumulate around the outer boundaries of the organized vortex structures is most apparent in turbulent plane wake experiments. Figure 12.57 from Yang et al. (2000) shows instantaneous particle concentration maps for two nominal Stokes numbers obtained using PIV techniques from a plane wake experiment. The flow time scale for computing the Stokes number is based on the initial wake width and the free-stream velocity. These experimental results clearly illustrate the striking differences that changes in Stokes number can have on the turbulent particle dispersion process.

Extensive numerical studies have been made to examine the particle dispersion process in free shear flows. These numerical studies have employed various approaches including discrete vortex models, direct numerical simulations, and large eddy simulations. Initially, most of these numerical studies concentrated on one-way particle coupling situations with two-dimensional flow fields in order to clarify and simplify the interpretation of the results. The results of these initial numerical efforts strongly supported and extended the experimental efforts.

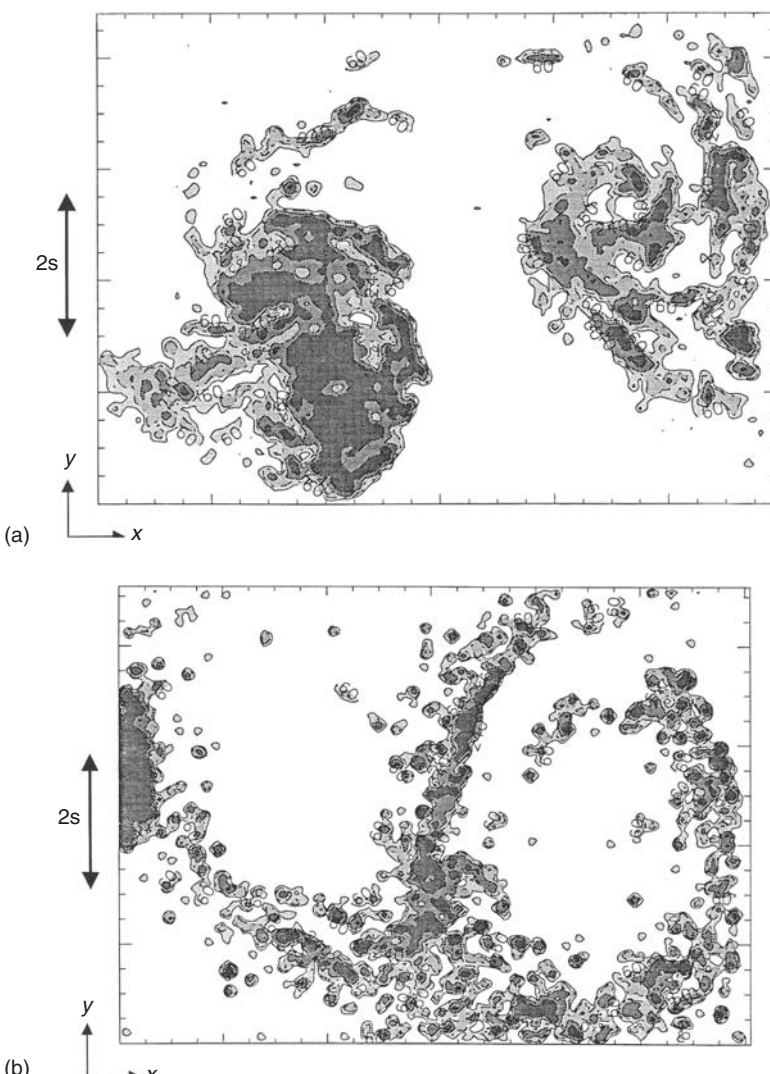


FIGURE 12.57 (a) Instantaneous number density map of $10 \mu\text{m}$ particles, $Stk = 0.15$; (b) Instantaneous number density map of $30 \mu\text{m}$ particles, $Stk = 1.4$. The initial wake width is $2s$.

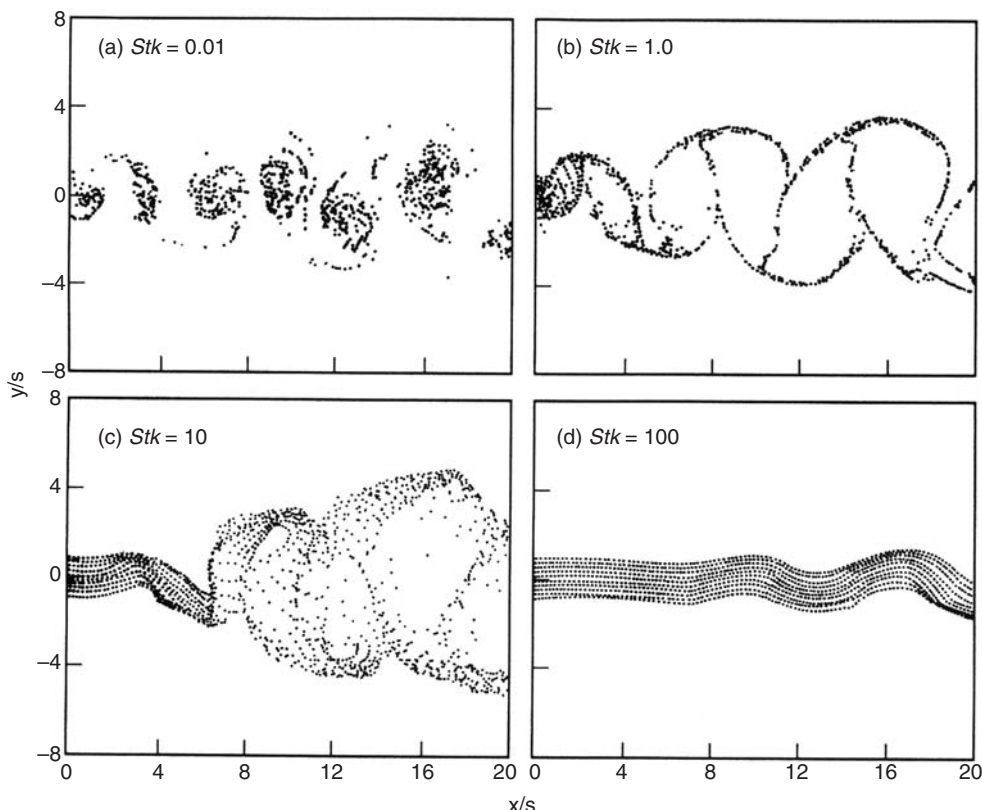


FIGURE 12.58 Instantaneous particle dispersion patterns from numerical simulation of the plane wake: (a) $Stk = 0.01$; (b) $Stk = 1.10$; (c) $Stk = 10$; (d) $Stk = 100$. (Tang et al., 1992)

Figure 12.58 shows an example result from a plane flow simulation over a wide range of particle Stokes numbers. The high degree of order exhibited by the Stokes number unity result indicates that turbulent flows may actually be antimixing agents under specific flow situations. An extensive review discussing the application and results from two-phase numerical studies involving primarily one-way coupling can be found in Crowe et al. (1996).

Although direct experimental confirmation of numerical predictions is difficult to obtain, recently, Yang et al. (2000) have reported some quantitative experimental results of one-way coupling predictions in a plane wake that agree closely with previous numerical studies.

In recent years, the two-phase free shear flow numerical efforts have begun to focus on three-dimensional simulations of particle dispersion in free shear flows (Ling et al., 1998) and on the development of models and simulation techniques involving two-way coupling environments (Crowe 2000; Ling et al., 2000, 2001).

Some relatively recent experimental and numerical two-phase flow studies have also been carried out in confined shear flows. The earliest direct numerical simulation work on wall-bounded two-phase flow involved studies of aerosol deposition in a turbulent channel by McLaughlin et al. (1989) and Brooke et al. (1992). Their results indicated that particles tended to accumulate in streak flow patterns within the viscous sublayer.

Experimental work by Fessler et al. (1994) on particles in turbulent channel flow indicated that preferentially concentrated particle distributions were observed on the centerline for particles with Stokes numbers of order unity based on the Kolmogorov time scale. Later, numerical studies by Rouson and Eaton (2001) concerning a particle laden turbulent channel flow, although at a lower Reynolds number, indicated that the observed particle distributions near the centerline were probably initially produced by

the streak-like particle patterns found in the viscous sublayer and propelled to the centerline by large-scale turbulent mixing.

12.5.4 Body Force Effects on Particle Dispersion

The turbulent dispersion of heavy particles under the influence of body forces was initially investigated during the mid-20th century by researchers interested in atmospheric pollution problems. The equation of motion to be applied in this situation for small Reynolds number particles can be given as

$$\frac{dv}{dt} = \frac{f}{Stk}(u - v) + \frac{\hat{g}}{Fr}$$

where \hat{g} is a unit vector in the direction of the body force or gravitational acceleration and $Fr = U^2/gL$ with g being the magnitude of the body force or gravitational acceleration. The nondimensional gravity term is here related to a reciprocal Froude number. Therefore, small particle dispersion in dilute two-phase turbulent flows involving a gravitational body force can be viewed as a function of particle Stokes number, particle Reynolds number, Froude number, and flow Reynolds number.

An additional quantity for evaluating the significance of gravity or body force in this type of particle dispersion process is the terminal velocity, $V_t = g\tau_v/f$. If this velocity is high, compared with typical turbulent or mean flow velocities, then gravitational or body force effects may dominate the dispersion process. If the terminal velocity is of comparable magnitude to flow velocities then time-scale ratios involving particle residence times in turbulent vortices and Lagrangian vortex time scales become essential for developing qualitative understanding of the gravitational or body force affected dispersion process.

Owing to of the complexity of this problem and the rather limited understanding of the nature of the atmospheric flow, time-averaged isotropic turbulent flow models were initially used for analyzing the dispersion process. A review covering earlier work on this type of problem can be found in Stock (1996).

In more recent times, direct numerical simulation studies involving isotropic and shear flow turbulent particle dispersion with body forces have been carried out by Squires and Eaton (1991a–1991c), Wang and Maxey (1993), and by Raju and Mieberg (1995). These studies have more explicitly illustrated the combination of effects in these situations.

A large eddy simulation (LES) of suspended particles in a homogeneous two-phase turbulent flow was initially carried out by Deutsch and Simonin (1991). Recent examples involving the use of LES for two-phase flow analysis can be found in Wang and Squires (1996), Armenio et al. (1999), and Yuu et al. (2001).

The initial applied problem of pollutant dispersion in environmental flows with complex terrain or complicated weather patterns is still at an incomplete level of understanding. Sophisticated numerical simulation tools such as two-phase LES combined with powerful computational hardware will be needed to develop this area further.

12.5.5 Two-Way Coupling Effects on Particle Dispersion

During the past 10 years, considerable attention has been turned to the effects of coupling, between the particle phase and the fluid carrier phase. In the case of dilute two-phase flows, these effects are typically referred to as two-way coupling. Since the turn of the millennium, these efforts have intensified to a point where this area has become one of the centers of activity within the two-phase community. This activity mostly focuses on modeling and simulation areas; however, a few interesting experimental studies have also been reported. A recent review of the two-way coupled model developed by Crowe (2000) highlights some potential pitfalls and inaccuracies that can arise if temporal and spatial-averaging procedures are not carried out in a consistent manner.

A consistent averaging approach for two-phase flow modeling has been developed by Crowe and Gilliland (1998). This approach produces a two-phase turbulent energy equation with specific new terms for the generation of turbulence by particles and a term for the transfer of kinetic energy from the particles to the carrier phase. Physical models for evaluating the importance of these terms are presently being developed.

At present, there is no general consensus regarding the effect of particles on the turbulent flow. The particle effect on the turbulence level will probably be a function of particle diameter, particle Reynolds number, particle concentration level and the characteristic scales of the turbulent flow. Several on-going studies have been involved with numerical and experimental investigations of two-way coupling effects.

A compilation of previous experimental results by Gore and Crowe (1989) indicated that relatively large particles tend to increase the turbulence intensity levels while relatively small particles tend to have little effect on the turbulence levels or slightly decrease the levels of turbulence. This finding is obviously consistent with the fact that large particles tend to move at high particle Reynolds numbers thereby producing turbulent wakes that consequently increase overall turbulence levels. Whereas small particles at high loading levels may tend to increase effective viscosity levels through an Einstein-Batchelor type mechanism (Batchelor, 1967).

Although the reported Gore and Crowe trend seemed to be consistent with generally accepted physical understanding of particle flow modification effects, one of its basic tenets, namely that small particles tend to attenuate turbulence, was brought into question by Elghobashi and Truesdell (1993). In that study, involving a numerical simulation of homogeneous turbulence and dispersed solid particles, results were produced that showed that turbulence intensity levels might actually increase for small particles at low Reynolds numbers thus contradicting the Gore and Crowe proposal. More recent numerical studies of small particles carried out using similar techniques involving higher resolution and more particles by Ferrante and Elghobashi (2003), however appear to contradict the initial reported contradiction thus bringing the simulation results into general agreement with the original proposal by Gore and Crowe.

A perspective on this issue of turbulence modification by particles can be obtained from a recently presented energy equation derivation by Crowe (2001) and applied to a one-dimensional wall constrained two-phase flow situation. The resulting turbulence energy equation is given as

$$\frac{d}{dt} (mk) = NC_D(U - V)^2 + \tau_w UL - m\epsilon$$

where the first term on the RHS gives the particle drag effect on the flow, the second term involves the shear stress at the constraining wall boundary and the third term represents the dissipation in two-phase flow. If the dissipation term is moved to the LHS of the equation, then the effect of particle drag on the turbulent flow can be clearly delineated.

$$\frac{d}{dt} (mk) + m\epsilon = NC_D(U - V)^2 + \tau UL$$

This result shows that particle drag effects will increase the level of turbulence energy, or increase the dissipation rate, or increase both, or increase one more than it decreases the other.

This finding is consistent with both the previous experimental results and numerical simulations. At high Reynolds number, the primary effect of the particles is probably to increase the turbulence energy levels. At low Reynolds number, the primary effect of the particles is probably to increase the dissipation rate and therefore to slightly decrease turbulence energy levels. At intermediate Reynolds number, both effects are increased creating an approximately nullifying effect on the resulting turbulence energy levels. Obviously, a better understanding of the detailed flow fields generated by the particles is a necessary requirement for progress in this area.

12.6 Turbulence Modulation by Particles

J.K. Eaton

12.6.1 Introduction

This section addresses modification of the carrier-phase turbulence in dispersed multiphase flows. Specifically, high Reynolds number flows with relatively dilute loadings of small particles or droplets in a

turbulent gas or liquid flow are considered. In such cases, there is an equivalent single-phase flow in which the turbulence is produced by mean shear or other mechanisms unrelated to the presence of a second phase. To first order, we may think of the dispersed multiphase flow as a turbulent single-phase flow (the carrier phase) contaminated by a set of widely spaced, small particles. For the present discussion, we use the generic term “particles” to refer to any second phase distributed in small discrete masses.

For very light loadings of particles or very light responsive particles, the turbulence is unchanged by the contaminant phase. The motions of particles may be computed assuming that they do not have any global effect on the turbulence, and the turbulence may be represented by any model that works for an equivalent single-phase flow. This is the case of one-way coupling. However, in many disperse flows, the presence of the particles changes the carrier-phase turbulence significantly. In order to compute the particle motions, heat, and mass transfer, chemical reaction rates, particle-agglomeration, etc., we must first understand and model how the carrier-phase turbulence is modified. This is the case of two-way coupling.

The turbulence properties of the carrier phase can be characterized in terms of various statistical quantities such as turbulent kinetic energy, Reynolds stresses, spectra, or two-point correlations. The term turbulence modulation means that one or more of the statistical properties of the carrier phase turbulence is changed by the presence of particles. Most frequently, one refers to changes in the carrier-phase turbulent kinetic energy, which may be either attenuated or augmented. Turbulence attenuation commonly occurs in gas flows laden with solid particles or liquid droplets, while augmentation is fairly common in liquid flows carrying either particles or bubbles. However, the turbulent kinetic energy changes do not fully describe the changes to the turbulence. For example, in some cases, particles may distort the turbulence energy spectrum substantially, while causing only small changes to the turbulent kinetic energy. In other cases, particles may locally distort turbulent eddies.

An important question is: Why is turbulence modulation an important phenomenon that we need to understand? The most obvious answer is that turbulence modulation is sometimes so large that it completely changes the character of the turbulence and the behavior of engineering devices. [Figure 12.59](#) shows turbulent kinetic energy data from the centerplane of a fully developed turbulent channel flow laden with either 150 μm glass or 70 μm copper particles. At the heaviest mass loading ratio of 0.4, the copper particles reduce the turbulence kinetic energy by a factor of more than 7. Note that this loading corresponds to a volume fraction of only 5.5×10^{-5} and a mean particle separation distance of >20 particle diameters. This is clearly a very dilute flow, but the particles have a dominant effect on the turbulence behavior. Such reductions in the turbulence levels can have major effects on the overall multiphase flow behavior. One effect is that particle dispersion by turbulence is likely to be much lower than a simple one-way coupling model would predict. One would expect that mixing and chemical reaction rates also would be affected when turbulence levels are reduced to such a degree. An example in which this could be very important is fast fluidized beds, where chemical reaction and the turbulence transport properties are critical.

Turbulence augmentation may also have substantial effects, especially in low turbulence flows. The addition of small-scale turbulence induced by turbulent particle wakes can cause large increases in energy and species transport in nominally laminar flows. Even small-scale turbulence is much more effective than molecular diffusion, so again turbulence modulation may lead to substantial changes in the performance of multiphase systems.

The degree of turbulence modulation can vary from very small to quite large. Gore and Crowe (1991) reviewed experimental data for the restricted case of particle-laden pipe and jet flows. The percentage change in the streamwise turbulence intensity varied from -90 to $+350\%$ over the range of particle and flow parameters examined. While many cases showed substantial modulation, a large fraction of the experiments showed only small changes. The only consistent trend that emerged from the data review was that small particles attenuate turbulence, while large particles augment turbulence. They found that the critical particle diameter separating attenuation from augmentation was approximately one tenth of the scale of the most energetic eddies.

The qualitative rule of thumb developed by Gore and Crowe generally holds, but it does not allow prediction of the degree by which the turbulence will be changed. No general theory or data correlation has emerged that allows reliable prediction of the level or character of turbulence modulation for an

arbitrary dispersed multiphase flow. There are several reasons for the lack of progress in this area. First is the difficulty in measuring the carrier-phase turbulence in the presence of a substantial number of particles. Second is the fact that several different mechanisms may produce turbulence modulation as discussed in the next section. In some flows, two or more of these mechanisms may be active and counteract each other. If the counteracting mechanisms are not recognized, the results may be confusing. Finally, there is the huge parameter space involved. An incompressible, single-phase flow is typically defined by only the geometry and the Reynolds number. The addition of a second phase adds many more parameters, even if the second phase consists of monodisperse round spheres. In such a case, additional dimensionless parameters that arise are the particle Stokes number $Stk = \tau_p / \tau_f$, where τ_p is the particle aerodynamic time constant and τ_f is a time scale of the turbulence, the particle diameter normalized by a turbulence length scale d/l_f , and the particle Reynolds number $U_{rel}d/v$. Of course, even more parameters are important if the particles are polydisperse, nonspherical, or if they themselves are fluid (droplets or bubbles).

The following subsections provide a general discussion of the mechanisms by which particles can change the carrier-phase turbulence and give a brief overview of methods used to explore turbulence modulation. This is followed by a survey of experimental and computational observations of turbulence modulation for several types of dispersed flows. These observations provide some general guidance for estimating the likely level of turbulence modulation in a given flow. However, the survey also points out the wide variability in the degree of modulation among seemingly very similar flows.

12.6.2 Mechanisms of Turbulence Modification

The exact mechanisms of turbulence modulation are not very well understood, and the available theories often cannot predict the level or even sign of the change in turbulent kinetic energy. Nevertheless, there are some basic mechanisms of particle-turbulence interaction that we know play a role in turbulence modulation. All the known mechanisms require that the particles be large enough that they cannot follow the flow, so that there is a substantial instantaneous relative velocity between a particle and the carrier fluid.

One route to turbulence modulation by particles is through the carrier-phase mean velocity. If the mean carrier-phase velocity field is changed by the addition of particles, then the mean strain field and the turbulence production rate will also be changed. For example, if a concentrated stream of high-velocity particles is introduced into a gas flow, a local jet will be formed in the carrier flow due to the drag of the particles applied to the gas. The turbulence production in the jet shear layers is likely to increase the turbulent kinetic energy. This mechanism of turbulence modulation will not be considered in detail here. Presumably, the effects of carrier mean flow distortions on the carrier turbulence can be predicted by single-phase turbulence models, and calculation of carrier-phase mean flow distortions by inhomogeneous particle flows is straightforward. However, when considering turbulence modulation experiments, we must be aware that this mechanism may be affecting the results. This is frequently the case in liquid–solid flows.

A mechanism for turbulence augmentation when particles are relatively large is unsteady particle wakes. In a uniform stream, the wake of a sphere is asymmetric for Reynolds number > 210 and unsteady for Reynolds numbers > 270 (Bagchi and Balachandar, 2002). When there is a mean velocity difference between the particles and the carrier fluid due to gravity or acceleration of the carrier phase, energy is transferred from the particles to small-scale, carrier-phase velocity fluctuations. In most dispersed gas–solid flows, the particle volume fraction is very small and the particle wakes occupy only a small fraction of the flow volume, so the unsteady wake effect creates only minor changes in the turbulence. However, the unsteady wakes are a significant source of turbulence augmentation in some liquid–solid flows, where the particle volume fraction is not small and the particle Reynolds number is in the vortex-shedding regime.

A related mechanism is the superposition of many randomly positioned laminar or “laminar-like” wakes as investigated by Parthasarathy and Faeth (1990) and Chen and Faeth (2001). They investigated turbulence modulation in the absence of shear production, so all the observed turbulence was produced

by particle wakes. Chen and Faeth (2001) developed a dimensional correlation that relates the turbulence level to the mean dissipation of energy due to the relative motion of the particles and fluid. For typical multiphase flows, carrier-phase shear production of turbulence dominates, and laminar wakes are relatively unimportant in setting the level of turbulent kinetic energy. However, the superposed effect of the wakes is apparent in several experiments where turbulence spectra are measured. It is common to see a turnup in the spectra at a large wave number, which is apparently related to the particle wakes (cf., Rogers and Eaton, 1991).

The mechanism, believed by most to cause turbulence attenuation is the so-called extra dissipation of turbulence by particles. A particle that cannot respond to the turbulent velocity fluctuations exerts a force on the fluid that opposes the relative motion. When the particles are heavy (i.e., have large Stokes numbers), the relative motion is produced mostly by the carrier-phase fluctuations. The cloud of dispersed particles produces a nonuniform force field that instantaneously opposes the carrier-phase velocity fluctuations, thereby extracting energy from the turbulence. Some of the energy taken from the carrier-phase turbulence is transferred to fluctuating kinetic energy of the particles. However, most goes into producing local flow distortions around each particle. For small particles, the length scales of the flow distortions are small and the corresponding velocity gradients are large, so the local flow distortions are dissipated rapidly by viscosity. Therefore, we see that the particles act as a short circuit of the regular turbulence energy cascade. Energy can be absorbed from the carrier-phase turbulence at any frequency that is too high for the particles to follow. That energy is passed directly to scales comparable to the particle diameter, and is dissipated.

Preferential concentration of particles into specific turbulence structures and preferential sweeping of particles into downflow zones offer two other possible mechanisms of turbulence modulation. Preferential concentration occurs when particles with particle time constants comparable to eddy time scales are swept out of vortex cores and concentrated in convergence zones (Squires and Eaton, 1991). A simplified analysis by Eaton and Fessler (1994) showed that particles apply an angular impulse opposing the vortex rotation as they are spun out of a simple vortex. For Stokes numbers near unity, the ratio of the angular impulse to the initial angular momentum of the vortex is $1.3\phi/Stk$, where ϕ is the mass loading ratio. This would act to suppress vortices with time scales near the particle time constant.

Preferential concentration in a gravitational field results in preferential sweeping of particles into downflow zones, and a higher than expected average settling velocity (Maxey, 1987). Numerical simulations by Ferrante and Elghobashi (2003) indicate that preferential sweeping at moderate mass loading creates substantial anisotropy in the turbulence and slows the decay of isotropic turbulence. It is important to note that at high Reynolds numbers, the turbulence has a wide range of time and length scales. Preferential concentration may occur in a narrow range of scales depending on the particle size range. Therefore, it is likely that eddies in a certain size range would be effected most by the particle forces.

The mechanisms discussed in the previous two paragraphs treat the particles as a cloud that produces a nonuniform but continuous force-field applied to the carrier-phase flow. However, in most cases where turbulence modulation is significant, the particles are too large and too widely spaced to be considered as applying a continuous force field onto the turbulence. An examination of the channel flow case illustrated in [Figure 12.59](#) is instructive. The experiments were performed in air, with a channel half-width of 20 mm and a Reynolds number of 13,800 based on the half-height and the bulk velocity. The particles had a typical Reynolds number based on the relative velocity of about 20. The Kolmogorov length scale and the Taylor microscale at the channel centerplane were approximately 170 and 3000 μm , respectively, and the viscous length scale was 31 μm . The particle diameter of 150 μm was comparable to the smaller scales of the turbulence, and the average particle spacing of 2100 μm (at 40% mass loading) means that each eddy in the energy-containing range would only contain a few particles at the most. Although these values are specific to a single experiment, they are quite characteristic of experiments where strong attenuation is observed.

At the typical particle Reynolds number, the region of significant flow distortion extends several particle diameters from the particle surface, especially in the particle wake. We expect that the particles produce significant local distortion of the small-scale motions. Moreover, the fact that the average particle spacing is so large means that the force applied is not continuous. This is likely to produce a significant

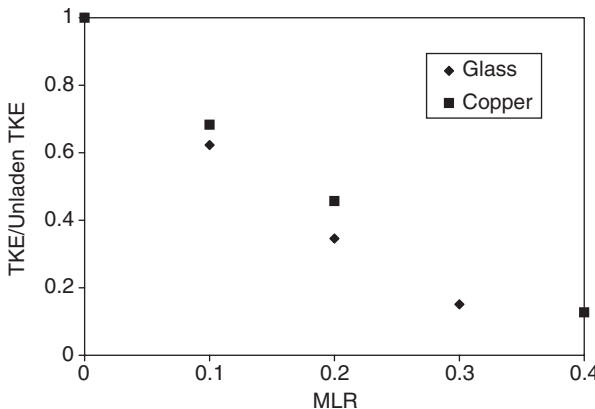


FIGURE 12.59 Attenuation of turbulent kinetic energy as a function of mass loading ratio on the centerplane of fully developed channel flow for 150 μm diameter glass and 70 μm diameter copper beads. (From Paris, T. and Eaton , J.K., Report TSD-137, Department of Mechanical Engineering, Stanford University, 2001. With permission.)

distortion of the energy-containing eddies and could lead to a higher turbulent dissipation rate. Furthermore, the fact that the particle diameter is comparable to the Kolmogorov scale indicates that the particles experience significant velocity gradients rather than the locally uniform flow assumed in most models. This means that the particles experience forces transverse to the relative velocity (cf. Bagchi and Balachandar, 2002). We group these effects of relatively large particle diameter and spacing under the heading “eddy distortion.” It will be shown in the following two sections that these effects are not accounted for in existing two-way coupling models.

12.6.3 Analytical Approaches

A common approach to modeling the effects of particles on turbulence is to treat the particles as applying a continuous force field onto the fluid phase where the force is the reaction force to the particle drag (cf. Chen and Wood, 1985; Berlemont et al., 1990; Rogers and Eaton, 1991). Following the development of Rogers and Eaton, the modified Navier–Stokes equations are

$$u_{i,t} + u_j u_{ij} = - \frac{1}{\rho_f} p_{,i} + \nu u_{i,jj} - \frac{1}{\rho_f} F_i$$

where indicial notation is used and commas imply derivatives. F_i is the force per unit volume applied by the particles onto the fluid. Assuming a linear drag law and neglecting forces other than drag, we get

$$F_i = \frac{c}{\tau_p} (u_i - v_i)$$

where c is the local particle mass concentration, u_i the fluid velocity, and v_i the particle velocity. Next, the Reynolds decomposition is applied, the mean flow component is subtracted, and the fluctuating component is squared and averaged to obtain the turbulent kinetic energy transport equation. Rogers and Eaton assumed homogeneous flow so that transport and diffusion terms could be neglected. Further, assuming constant fluid density and constant particle time constant yields

$$\frac{D}{Dt} \frac{q^2}{2} = P - \varepsilon - \frac{1}{\rho_f \tau_p} [C(\overline{u'_i u'_i} - \overline{u'_i v'_i}) + (U_i + V_i) \overline{c' u'_i} + (\overline{c' u'_i u'_i} - \overline{c' u'_i v'_i})]$$

Here the production term P and the dissipation term ε are identical to the single-phase terms. It is commonly assumed that the second and third terms in the brackets are negligible further simplifying the equation. The term $(C/\rho_f \tau_p)(\overline{u'_i u'_i} - \overline{u'_i v'_i})$ is commonly called the extra dissipation due to particles.

There are several deficiencies in the proceeding analysis. One obvious problem is the assumption that the force applied onto the fluid is linearly proportional to the fluid/particle velocity difference. Most cases in which turbulence attenuation is significant involve particle Reynolds numbers greater than unity. Furthermore, the instantaneous force on a particle is affected by the local straining field. When the particle diameter is comparable to or larger than the Kolmogorov scale, the flow around the particle is highly nonuniform. The force applied by the particle on the fluid is almost never aligned with the instantaneous velocity difference, and the root mean square force magnitude is probably larger than would be estimated by assuming locally uniform flow around the particles.

A second major deficiency is that the analysis assumes that energy transferred to the particle is eliminated from consideration. However, when a force is applied to a particle, that particle accelerates and creates local flow distortion. The assumption is that these fluid motions are at very small scale and are quickly dissipated by viscosity. However, we again note that the particles are often larger than the smallest scales of turbulence. In this case, it is more appropriate to assume the particle–turbulence interaction as transferring energy between different scales of velocity fluctuation.

Crowe et al. (1997) pointed out that the interphase forces do not occur at a point and that the analysis must be carried out over small control volumes possibly incorporating multiple particles. Crowe (2000) developed a model for turbulence modulation applying the volume averaging approach to the mechanical energy equation. The problem with this approach is again that in practical situations, the particles usually have scales comparable with some turbulence scales. If an averaging volume is chosen such that it incorporates at least one interparticle spacing, then we must also consider that some of the turbulence is averaged. A model must account for the effects of this turbulence, which is not resolved by the averaged equation set.

Of course, all analytical models of turbulence have aspects, which cannot be strictly justified on theoretical grounds. The appropriate question is, do these models offer predictive capability over some useful range of turbulence and particle parameters? Unfortunately, the answer in the present case is no. The extra dissipation due to particles terms above and the model presented in Crowe (2000) both show increasing attenuation of turbulence with decreasing particle time constant. Many of the experiments discussed below show the opposite trend. Particles with time constants comparable to the Kolmogorov time scale have not been observed to cause significant attenuation, while larger particles at similar loading cause strong attenuation. Crowe's model captures the fact that very large particles cause turbulence augmentation.

12.6.4 Methods for Studying Turbulence Modulation

Scientific study of turbulence modulation is a relatively recent endeavor because it requires the use of advanced optically based instrumentation or powerful supercomputers to make significant advances. Here we give a very brief overview of the methods used to provide the data on carrier-phase turbulence modulation.

The challenge for laboratory experiments is to measure the turbulence properties of the carrier phase in the presence of a large number of particles. Almost all measurements are made with laser-based instrumentation due to problems of probe interference and probe damage when hot wire or other invasive measurement techniques are used. Laser Doppler anemometry (LDA) has been used extensively since the work of Lee and Durst (1982). The challenge in LDA is to discriminate between signals coming from carrier-phase tracer particles and the generally stronger signals coming from the dispersed particles comprising the second phase. When the dispersed-phase particles are relatively large and monodisperse, the discrimination can be done based on the signal pedestal amplitude (cf. Kulick et al., 1994). Since the mean velocity and turbulence levels may differ significantly between the two phases, crosstalk in which particle-phase signals are interpreted as arising from tracer particles must be carefully monitored to insure reliable turbulence measurements. A more robust but more difficult and expensive technique is phase Doppler anemometry (PDA) in which the particle size and velocity are measured simultaneously (Bachalo and Houser, 1984). This technique can give poor results for nonspherical particles, but generally works well for phase separation if there is a significant difference between the tracer size and the smallest dispersed particles.

Particle image velocimetry (PIV) has been used extensively for multiphase flow research in recent years. As with LDA, the challenge is to measure the fluid phase using tracer particles that are generally significantly smaller than the larger particles comprising the second phase. Imaging the small particles in the presence of strong light scattering from the particulate phase is difficult, and image artifacts caused by out-of-focus particles can result in interphase crosstalk. Khalitov and Longmire (2002) provide a review of different techniques for two-phase PIV measurements. For gas–solid flows, the tracer particles generally are much smaller than the particulate phase. Imaging parameters are chosen so the tracers appear dim and cover only 1 or 2 pixels, while the large particle images are saturated and cover multiple pixels (Sakakibara et al., 1996). Various multistep image processing techniques (cf. Khalitov and Longmire, 2002; Kiger and Pan, 2000; Paris and Eaton, 1999) are used to reduce the noise and crosstalk. Generally, these techniques are effective for volume fractions below about 0.01%. In liquid–solid flows or bubbly flows, the tracer particles can contain fluorescent dye allowing separation of the phase images using color. Measurements at high solids concentration are possible in liquid using refractive index matching (Cui and Adrian, 1997).

There are also considerable difficulties in using numerical solutions of the Navier–Stokes equations to explore turbulence modulation effects. A typical turbulent particle-laden flow contains an extremely large range of length scales ranging from the boundary layer on individual particles to the largest eddies having scales comparable to the flow geometry. For high Reynolds number flow containing a large number of particles, direct solution of the Navier–Stokes equations including a correct specification of the boundary conditions on each particle and resolution of all scales of the flow would require more computer resources than will be available for some time. Therefore, approximate models are required to represent either the particle-scale motions or the energy containing turbulent scales. Squires and Eaton (1990) and Elghobashi and Truesdell (1993) adapted single-phase direct numerical simulation codes for isotropic flows by using simple drag laws to compute the force applied onto each particle by the flow, and applying the reaction force back onto the fluid as a variable body force. The method which has come to be called the “point-force coupling scheme” applies the force only to the grid points immediately surrounding the particles resulting in an intermittent body force field. The method is not valid unless the particles are significantly smaller than both the turbulence Kolmogorov scale and the grid spacing. However, as discussed above, most flows in which there is substantial turbulence modulation violate these conditions. While the point-force coupling scheme has been applied widely, it has not been tested rigorously against experimental data. Simonin and Squires (2003) assert that the point-force coupling method accounts for the direct modification of large scales, but not for turbulence production by particle wakes. Maxey and co-workers (cf. Lonholt et al., 2002) developed an approximate force-coupling scheme that distributes the force applied by a particle with a Gaussian distribution and includes both monopole and dipole contributions. This scheme has been validated for low Reynolds number flows with a small number of particles, but it has not been tested for turbulence modulation cases.

Recently, researchers have begun to address particle-turbulence interaction using simulations that fully resolve the flow around a single particle in a small region of turbulent flow. Bagchi and Balachandar (2003) used a large spherical coordinates grid to examine the forces on a particle in turbulent flow for particle Reynolds numbers of the order of 100 and particle diameters of 1.5 to 10 times the Kolmogorov scale. These simulations used frozen turbulence advected past the particle, so they could not assess the effects of the particle on the turbulence. Burton and Eaton (2002, 2003) used an overset grid code to compute the evolution of decaying homogeneous turbulence with a single embedded particle. These two studies are the beginning of a new approach to provide detailed information that can be used to develop advanced force coupling models.

12.6.5 Observations of Turbulence Modulation

Experiments on turbulence modulation in gas-particle flows show a consistent trend that small particles attenuate turbulence, while large particles augment it. Gore and Crowe (1991) and Crowe (2000) collected data from several experiments in pipe and channel flows and showed that turbulence is attenuated when

the particle diameter is less than about 1/10 of a characteristic turbulence length scale and is augmented for larger particles. Unfortunately, this finding is not sufficient, since the degree of turbulence modulation varies widely between experiments depending on the flow parameters. In this section, we examine the turbulence modulation results from a cross-section of experiments and numerical simulations in an effort to discern other trends that could help to predict turbulence modulation in previously unexplored flows. No effort is made to provide a comprehensive review. Rather, a few specific flow types were chosen based on the existence of multiple experiments or simulations over a similar parameter range.

12.6.5.1 Homogeneous Gas–Solid Flows

The flow regime most commonly explored using numerical simulations is homogeneous gas-phase turbulence with dilute loadings of solid particles. The reader is reminded that these simulations require assumptions that are not strictly valid, and the codes may yield incorrect results. All of the numerical studies have been confined to the small particle regime in which turbulence attenuation is expected, and the Taylor microscale Reynolds number is quite small, ranging from 20 to 94 in the cases discussed below.

Stationary (forced) isotropic turbulence was examined by Squires and Eaton (1990) and Boivin et al. (1998) for particle mass loading ratios ranging from 0.1 to 1.0 and Stokes numbers based on the Kolmogorov scale (Stk_k) ranging from 1.3 to 11.4. Both the studies indicated substantial turbulence attenuation, with the degree of attenuation increasing with increasing mass loading. The maximum reduction in the turbulent kinetic energy (TKE) was 56%. Squires and Eaton found essentially no effect of varying Stk_k from about 1.4 to 4.7, while Boivin et al. found that the attenuation increased monotonically as the Stk_k increased from 1.3 to 11.4 at a mass loading ratio of 0.2. The opposite trend was observed when the mass loading ratio was increased to 1.0. One consistent finding of these studies and several others discussed below is that the turbulence spectra are distorted, showing attenuation at low frequency and augmentation at higher frequency.

Decaying isotropic turbulence analogous to grid turbulence was simulated by Elghobashi and Truesdell (1993), Druzhinin and Elghobashi (1999), Ferrante and Elghobashi (2003), and Sundaram and Collins (1999). It is difficult to discern any consistent trends from these results. Sundaram and Collins varied the particle diameter and the Stokes number maintaining a constant mass loading ratio of 0.14. They found that the attenuation increased as the Stokes number increased from 1.6 to 6.4. Ferrante and Elghobashi observed a similar trend for Stk_k ranging from 0.1 to 5. The overall attenuation levels in the latter case were quite small with a maximum reduction in kinetic energy of 30% at a mass loading ratio of 1.0.

Most of the computations discussed above focused on cases without gravity. However, Druzhinin and Elghobashi, and Ferrante and Elghobashi each ran a case including a body force in the particle equation of motion. In both cases, very substantial turbulence augmentation was observed, even though the particles were quite small ($d_p/l_e < 0.01$). This contradicts the great body of experimental evidence (cf. Gore and Crowe, 1991).

An attempt was made to determine trends in the degree of turbulence modification as a function of various parameters. Turbulence modification was found to increase with increasing mass loading. Figure 12.60 shows a plot of the turbulent kinetic energy (TKE) normalized by the unladen TKE for cases which had Stk_k near 5. Turbulence attenuation was always small (< 22%) for mass loadings less than or equal to 20%. Substantial changes to the turbulence were only found for relatively large loadings.

Figure 12.61 shows the turbulence attenuation plotted against Stk_k for cases in which the mass loading ratio is approximately unity. For the cases of decaying isotropic turbulence, the Stokes number changes with time. A representative value midway through the decay was chosen for the purposes of this plot. There is an evidence of a trend of increasing turbulence attenuation with increasing Stk_k . However, the Squires and Eaton and Boivin et al. cases for Stk_k near 1 break with the trend. The differences between these cases and the case of Ferrante and Elghobashi are quite large, even though the flow and particle parameters are quite similar. This may be due to differences in the implementation of force coupling scheme in the simulation or in the initial conditions for the velocity field. A similar trend of increasing attenuation with increasing Stokes number was seen for cases which had mass loading near 0.2. However, at such a relatively light loading, the attenuation was always small at all Stokes numbers.

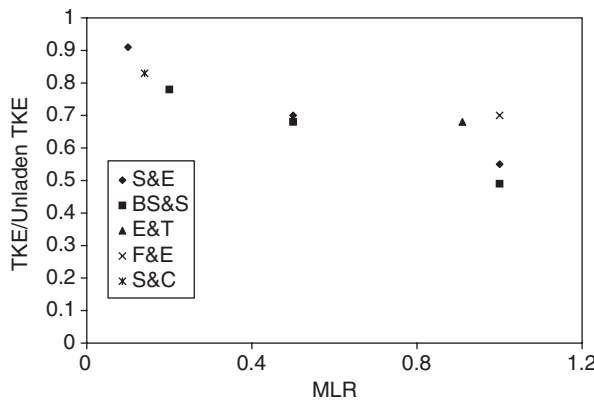


FIGURE 12.60 Attenuation of turbulent kinetic energy in simulated isotropic turbulence for cases with Stk_k near 5. (From Squires, K.D. and Eaton, J.K., *Phys. Fluids A*, 2, 1191–1203, 1990; Boivin, M. et al., *J. Fluid. Mech.*, 375, 235–263, 1998; Elghobashi, S. and Truesdell, G.C., *Phys. Fluids A*, 5, 1790–1801, 1993; Ferrante, A. and Elghobashi, S., *Phys. Fluids*, 15, 315–329, 2003; Sundaram, S. and Collins, L.R., *J. Fluid. Mech.*, 379, 105–143, 1999. With permission.)

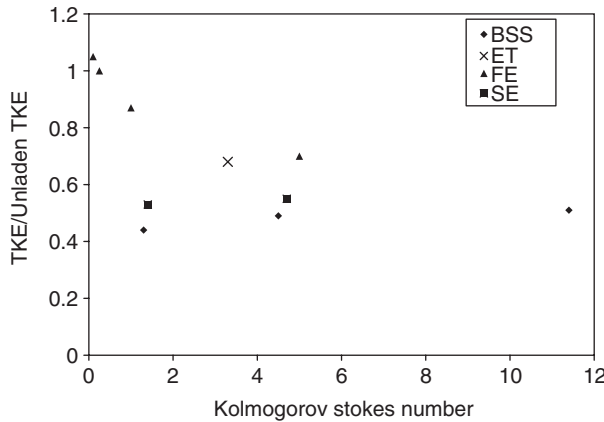


FIGURE 12.61 Attenuation of turbulent kinetic energy in isotropic turbulence for MLR near 1 as a function of Stk_k . (From Boivin, M. et al., *J. Fluid. Mech.*, 375, 235–263, 1998; Elghobashi, S. and Truesdell, G.C., *Phys. Fluids A*, 5, 1790–1801, 1993; Ferrante, A. and Elghobashi, S., *Phys. Fluids*, 15, 315–329, 2003; Squires, K.D. and Eaton, J.K., *Phys. Fluids A*, 2, 1191–1203, 1990. With permission.)

Only a few experiments have been reported on the behavior of particle-laden homogeneous turbulence. Schreck and Kleis (1993) examined grid turbulence in a downflow water channel laden with relatively large solid particles ($d_p/l_k = 5$). Volume concentrations were as large as 1.5%. Reductions in the TKE of 20% were observed for the heaviest particles at the largest concentration. Geiss et al. (2001) examined grid turbulence in a downflow wind tunnel. The flow carried a 35% (by wt) loading of 110- μm -diameter glass particles. This short paper gives few details on the experiment, but kinetic energy reductions of up to 44% were observed at the most downstream station. Note that this reduction is comparable with the reductions observed in some of the simulations at substantially higher mass loading. Based on this experiment and some of the wall-bounded flow measurements reported below, there is an indication that the simulation techniques under-predict turbulence attenuation.

12.6.5.2 Wall-Bounded Gas–Solid Flows

The strongest effects of turbulence modification have been observed in wall-bounded flows including pipe flows, channel flows, and boundary layers. Much of the original experimental work on turbulence

modulation was done in pipe flows with notable contributions from Lee and Durst (1982), Tsuji and Morikawa (1982), and Tsuji et al. (1984). More recently, considerable effort has been focused on fully developed turbulent channel flows and flat plate boundary layers. Kulick et al. (1994), Paris and Eaton (2001), and Kussin and Sommerfeld (2002) all examined fully developed air channel flows at similar Reynolds numbers. Each experiment covered a reasonably broad range of particle parameters lending new insight into turbulence modulation.

Kulick et al. (1994) conducted experiments in a long vertical downflow air channel flow at a Reynolds number of 13,800 based on the channel half-width and the bulk velocity. Special care was taken to insure very uniform particle loading, and as a result, the mean gas-phase velocity profile was the same at all particle mass loading ratios. Experiments were conducted with 50-and 90- μm -diameter glass beads and 70 μm copper beads. The Stokes numbers based on the centerline Kolmogorov time scale were 9, 23, and 50 for the three particle classes. Gas-phase measurements were made using LDA with submicron tracer particles that were easily discriminated from the larger dispersed particles. Turbulence modification was small ($< 10\%$) for particles with $Stk = 9$, substantial for $Stk = 23$, and very large for $Stk = 50$. Figure 12.62 reproduced from Kulick and Eaton shows the streamwise turbulence intensity profiles for copper beads at various mass loading ratios. The turbulence is attenuated across the entire profile, with the largest attenuation near the centerline.

Paris and Eaton (2001) conducted experiments in the same channel flow facility using phase-discriminated PIV to verify the earlier LDA results for copper beads. They also conducted separate experiments by using 150 μm glass beads, which had almost the same aerodynamic time constant as the copper. By virtue of their larger diameter, the particle Reynolds numbers were over two times greater for the glass ($Re_p = 19$ vs. 8). The centerline results, shown in Figure 12.59, showed similar attenuation levels as observed by Kulick for the copper, and also showed consistently that the higher Reynolds number glass particles produced larger attenuation. Note that the data plotted in Figure 12.59 incorporate fluctuating velocity measurements in the streamwise and spanwise directions.

Kussin and Sommerfeld (2002) and Lain et al. (2002) made measurements in a horizontal channel flow for a variety of particle sizes. The half-height Reynolds number was 21,000 and smooth- and rough-wall cases were examined. Measurements were made by using a phase-Doppler anemometer. Unfortunately, the particle size distribution was wide and the flow tracers were large (nominally 4 μm in diameter), so

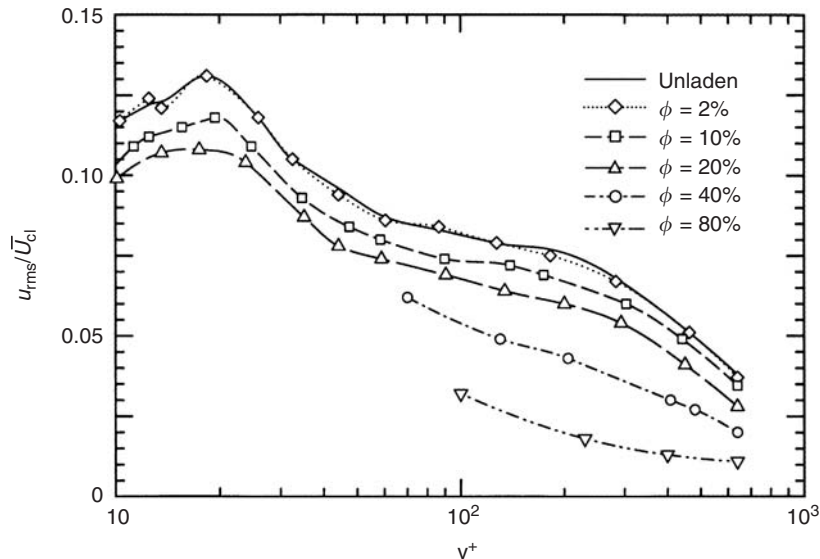


FIGURE 12.62 Streamwise turbulence intensity in fully developed channel flow laden with 70 μm copper beads. (From Kulick et al., *J. Fluid. Mech.*, 277, 285–309, 1994. With permission.)

the gas-phase turbulence measurements were contaminated by particle-phase measurements. As a result, the turbulence measurements are quite noisy. Nevertheless, because both the particle size and mass loading ratio were varied over wide ranges, trends were easily observed. Figure 12.63 shows the streamwise turbulence intensity data for the Kussin and Sommerfeld's rough-wall cases. The data have been averaged across the channel to reduce noise, normalized by the average value from all cases at zero loading, and squared for comparison with the TKE data presented in other plots. The data are presented for 60, 100, and 195 μm glass beads, which have Stokes numbers of 35, 120, and 350 and Reynolds numbers of 7, 23, and 72, respectively. Here the Stokes number is based on the estimated centerline Kolmogorov time scale to allow comparison to the homogeneous turbulence cases discussed above. All three particle sizes produce substantial attenuation with the degree of attenuation decreasing with increasing particle size. Also shown in Figure 12.63, for comparison, are the Paris and Eaton data for the channel centerplane. The copper and glass beads used by Paris and Eaton had Stokes numbers of 47 and 49, respectively. The attenuation was larger for these cases, but note that the largest attenuation in channel flows normally occurs at the centerplane. It is interesting to note that the 60 μm particles, which produced the largest attenuation in the Kussin and Sommerfelds' experiments, have Stokes numbers similar to the 150 μm glass beads that produced the strongest attenuation in the Paris and Eaton experiments.

Kussin and Sommerfeld also presented measurements with 0.6- and 1-mm-diameter glass beads with mass loadings ratios up to 2.0. These cases showed significant turbulence augmentation near the channel centerplane and moderate attenuation near the walls. They concluded that this was a particle Reynolds number effect since the relative velocity between the gas and particles was smaller near the walls than in the channel center region. The particle Reynolds numbers at the centerplane were approximately 350 and 500 for the 0.6 and 1 mm beads, respectively. This indicates that unsteady particle wakes probably played a role in the turbulence augmentation.

The channel flow experiments discussed here along with several other wall-bounded flow experiments give a fairly consistent picture. Very small particles with $Stk \leq 10$ do not cause significant changes to the turbulence. As the particle size increases, the particles cannot follow the turbulent fluctuations and turbulence attenuation increases rapidly. Attenuation reaches a maximum around $Stk = 50$. The attenuation can be very large for particles in this size range. As particle size increases further, the effects of superimposed laminar wakes or unsteady wakes begin to have an effect, decreasing the overall level of turbulence attenuation, and eventually causing substantial augmentation.

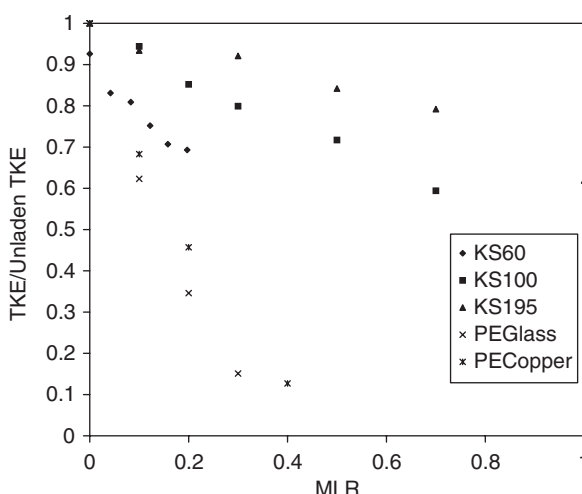


FIGURE 12.63 Streamwise normal stress (from Kussin, J. and Sommerfeld, M., *Exp. Fluids*, 33, 143–159, 2002; with permission) averaged across the channel and centerplane TKE (from Paris, T. and Eaton, J.K., Report TSD-137, Department of Mechanical Engineering, Standford University, 2001. With permission).

12.6.5.3 Free Shear Flows

Particle and droplet-laden jets, mixing layers, and separated flows have a wide range of applications, so the fluid-phase turbulence behavior has been studied in a number of such flows. The flow geometries and particle parameters vary widely from experiment to experiment, so it has not been possible to extract trends as was done in the previous two sections. Here we just discuss a few of the important experimental results to show the types of behaviors that have been observed.

A number of studies, including Shuen et al. (1985), Mostafa et al. (1989) and Longmire and Eaton (1990), have examined round jets discharging downward into quiescent air. Shuen et al. examined the far field of a jet discharging from a pipe for a range of particle sizes and mass loading ratios up to 66%. They observed changes in the turbulent stresses of less than 10%. Mostafa et al. examined the near field of a similar jet at mass loading ratios of 0.2 and 1.0. Detailed comparisons to the unladen turbulence measurements were not presented, but the authors noted a reduction of 40% in the TKE on the jet centerline for a mass loading of 1.0. It is important to note that the jet was supplied from a turbulent pipe flow. Although the jet exit plane was not documented, it is likely that the turbulence level in the plane was substantially lower for the particle-laden case than for the single-phase flow.

Free shear flows are subject to the Kelvin–Helmholtz instability that produces large roller vortices. An important issue to understand is how the particles might affect these vortices. A simplified analysis by Yang et al. (1990) showed that particles slow the development of roller vortices. On the other hand, Longmire and Eaton (1990) found little effect of particles on the near-field development of roller vortices for mass loading ratios up to 0.8. This finding is corroborated by research in backward-facing step flows, which have been studied by Maeda et al. (1982), Hishida and Maeda (1991), Hardalupus et al. (1992), and Fessler and Eaton (1999). All these experiments were conducted in the small particle regime. Some experiments observed almost no change to the turbulence while the others showed either small attenuation or augmentation of the turbulence. Overall, the particle effects on the turbulence are much smaller than in wall-bounded flows probably because the extra dissipation due to particles is overwhelmed by the strong shear production in free shear flows.

12.6.5.4 Liquid–Solid Flows

Another important class of multiphase flows is liquid–solid flows in which solid particles are dispersed in a turbulent liquid flow. We consider here only flows with relatively low volume fraction analogous to the gas–solid flows discussed above. At high particle volume fraction, the interaction among the particles is more important than the particle-turbulence interaction. The liquid–solid material density ratio is usually between 1 and 5, so the mass loading ratio is very small for dilute volume fractions. Another consequence of the near-unity density ratio is that the particle Stokes number is small, unless the particles are quite large. The only cases for which turbulence modulation is observed are thus flows in which the particles are large relative to the turbulence scales.

There are several recent experiments on particle-laden water channel flows, where detailed measurements have been acquired by using laser-based techniques. Kiger and Pan (2002) studied a 40 mm-wide water channel operated at a Reynolds number of 12,000 and laden with 195- μm -diameter glass beads at a mass loading ratio of 0.0006. Relatively small (8 to 10%) increases in the turbulence intensity were observed across the channel.

Suzuki et al. used a 40 mm wide, vertical water channel at a very low Reynolds number ($Re_h = 2900$). The flow was laden with 400 μm ceramic particles at a mass loading ratio of 0.0012. The particle diameter in this case was about two times the Kolmogorov scale near the wall and the particle Reynolds number was of the order of 30. The turbulence was almost unchanged near the wall. However, u'^2 , increased by more than a factor of 4 near the channel center region.

Sato et al. (2000) examined a similar channel at the same Reynolds number using 190 μm ($Re_p = 10$) or 400 μm ($Re_p = 50$) glass beads. The 190 μm particles were smaller than the centerline Kolmogorov scale, while the 400 μm particles were larger. The mass loading ratio was about 0.0004 for the 190 μm particles, and 0.00033 and 0.00086 for the 400 μm particles. Using to the relatively large volume fraction, measurements were only possible near the channel centerline. The smaller particles produced relatively

small increases in the kinetic energy, while the large particles increased the TKE by roughly a factor of 4. Doubling the mass loading for the 400 μm particles had a relatively small effect.

The indication from these liquid–solid experiments is that particles cause very large turbulence augmentation in this regime. It should be noted, however, that in the vertical channels, the particles changed the mean velocity profile significantly, which may have led to increases in the TKE. Overall, based on the recent channel experiments and older pipe flow data, it seems safe to conclude for liquid–solid cases that particles significantly smaller than the Kolmogorov scale produce relatively small changes in the turbulence while larger particles can produce very substantial augmentation. The lack of any effect by the smaller particles is probably due to the fact that small particles have very small Stokes numbers in liquid–solid flows.

12.6.6 Summary

We have seen that dispersed particles in the dilute regime can cause very large changes in the turbulence levels in typical shear flows. In gas flows, very small particles do not affect the flow, but particles with sizes of the order of the Kolmogorov scale can cause very significant attenuation. The attenuation appears to reach a maximum for Stk_k near 50 and particle Reynolds number of the order of 10. As particle size increases, the effect of particle wakes plays an increasing role first decreasing the turbulence attenuation and eventually causing large turbulence augmentation. Turbulence modulation is much weaker in flows such as free shear flows where strong shear production dominates.

In liquid flows laden with solid particles, turbulence attenuation is rarely observed. Because of the small solid–liquid material density ratio, small particles have very low Stokes numbers and thus have little effect on the flow. Particles that are large enough to have significant slip velocity relative to the flow are large relative to relevant turbulent length scales. In this case, the superposed wakes of the particles act to increase the turbulence substantially.

While numerous models for turbulence modulation have been proposed, none of them are capable of accurately predicting the degree of turbulence modulation for arbitrary flow and particle parameters. Further research is needed to understand proper modeling of the particle-fluid interaction in order to fully capture the competing effects of several turbulence modulation mechanisms.

The author received invaluable assistance from graduate students Wontae Hwang, Ryan Rogers, Tomohiko Tanaka, and Ern Soo Lee in preparing this chapter.

12.7 Combustion

F. Mashayek

12.7.1 Introduction

Two-phase flows involving a carrier gas laden with a dispersed phase composed of a large number of solid particles or liquid drops occur in many natural and technological applications. One of the most important applications involves the endothermic chemical reaction of the dispersed phase, as a fuel, with the carrier gas, as an oxidizer. For example, the engines that propel missiles, jets, and many other devices must rely heavily on combustion in a two-phase environment. Within the combustion chamber the liquid fuel, which is first atomized into small drops, undergoes evaporation and reaction with the oxidizer gas. To enhance the rate of mixing and reaction, these systems are designed to operate in the presence of turbulence. Furthermore, chemical reaction triggers the formation of high-gradient regions in the flow and thus serves as a source for generation and amplification of instabilities which lead to turbulence. As a result, turbulence cannot be ignored in majority of the situations involving chemically reacting flows. The presence of turbulence significantly adds to the complexity of such flows and to the challenges encountered in their physical understanding, theoretical description, and practical prediction. These challenges are primarily a consequence of the numerous degrees of freedom associated with a turbulent flow, which

itself has remained as one of the main unsolved problems in science and engineering. The addition of fuel drops, with the associated phenomena of evaporation and chemical reaction, further introduces new sets of variables, often accompanied by large variations in scales.

The topic of combustion, let alone in the presence of a second phase, is too broad to be covered in one section. Furthermore, if the solid phase is carbonaceous, both heterogeneous and homogeneous oxidation occurs. A thorough description of heterogeneous or homogeneous combustion requires basic knowledge in thermodynamics, fluid mechanics, heat transfer, chemical reaction, two-phase transport, etc. Owing to space limitation, in this section, we deal only with drop evaporation and combustion and refer to the review articles by Annamalai and Ryan (1993), Annamalai et al. (1994), and references therein for a detailed discussion of solid-particle combustion. We also restrict our discussion to subcritical conditions and refer to a recent review by Bellan (2000) for supercritical fluid behavior and modeling. As argued above, the presence of turbulence cannot be overlooked in a majority of practical situations. Turbulence effects will be discussed very briefly here and the reader is referred to several other chapters, in this handbook, which are entirely devoted to interactions of the dispersed-phase with turbulence. Nevertheless, regardless of the role of turbulence, the dispersed-phase processes could become "interactive" when the distance between the drops is comparable to a few times the drop radius. In this situation, evaporation and combustion of one drop may significantly be affected by the presence of other drops.

The next section provides a brief overview of single-phase or gaseous combustion. This overview assists the reader, with no or little knowledge of combustion to follow the main discussions on two-phase combustion. The discussion of drop evaporation and combustion is presented first for an isolated drop. Although in an actual spray, isolated drop burning is somewhat unlikely, the study of isolated drops serves as an important first step toward understanding the physical phenomena and the underlying mechanisms for evaporation and combustion. It should be emphasized that the theoretical study of isolated drops involves several simplifying assumptions, the validity of which may be arguable in real sprays, in particular near the injector where the spray is dense. For example, the isolated drop combustion model results predict increasing temperature as the size is reduced, which is contrary to the industrial experience. Therefore, the interactions among the drops must be considered. This is the subject of the second part of this discussion, where a group of drops is considered. From a modeling and theoretical point of view, it is noted that the models for group combustion often use the isolated drop results as their starting point, hence another reason for discussing isolated drops. Finally, we conclude with a general discussion of practical spray modeling. This discussion is of a general nature and addresses various available modeling strategies very briefly. Appropriate references are provided for the interested readers and a combination of models that may be most viable with the existing computational resources is recommended.

12.7.2 Overview of Single-Phase (Gaseous) Combustion

Liquid-fuel combustion systems lead to a chemical reaction between the fuel vapor and the oxidizer gas, thus forming a single-phase, or homogeneous (typically gaseous), combustion process. Therefore, as a necessary prelude to two-phase combustion, in this section we provide a brief overview of the gaseous combustion. Gaseous combustion can be described through continuum transport equations for mass fractions of various species that are participating in the chemical reaction. For a system of n chemically reacting species, the mass balance for the mass fraction Y_i of species i yields

$$\rho \frac{\partial Y_i}{\partial t} + \rho \mathbf{u} \cdot \nabla Y_i = -\nabla \cdot \mathbf{j}_i + \omega_p, \quad i = 1, 2, \dots, n \quad (12.184)$$

where \mathbf{j}_i and ω_p denote the diffusive flux and the chemical source term, respectively. The molecular transport processes that cause the diffusive flux can be quite complicated (Willams, 1985). For turbulent flows, which occur in many practical applications, this term can be simplified by considering a binary flux approximation, $\mathbf{j}_i = -\rho D_i \nabla Y_p$, where D_i is the binary diffusion coefficient, or mass diffusivity, of species i with respect to an abundant species. While this approximation provides a convenient form for describing the governing transport equations in turbulent flows, it should not be used in laminar flame calculations (Peters, 2000).

For a total number of r reactions

$$\sum_{i=1}^n v'_{ik} X_i \Leftrightarrow \sum_{i=1}^n v''_{ik} X_i, \quad k = 1, 2, \dots, r \quad (12.185)$$

that may be considered in the calculation, the chemical source term ω_i in Eq. (12.184) is described as

$$\omega_i = W_i \sum_{k=1}^r (v''_{ik} - v'_{ik}) w_k \quad (12.186)$$

where $\sum_{i=1}^n \omega_i = 0$, and for inert, nonreacting species $\omega_i = 0$. In Eq. (12.185), v'_{ik} and v''_{ik} are the stoichiometric coefficients on the reactants and products sides, respectively, for the i th species in the k th reaction, and X_i represents the chemical formula for species i . In Eq. (12.186), W_i is the molecular weight of species i and w_k is the rate of reaction k in a mechanism containing r chemical reactions

$$\omega_k = k_{fk} \prod_{i=1}^n \left(\frac{\rho Y_i}{W_i} \right)^{v'_{ik}} - k_{bk} \prod_{i=1}^n \left(\frac{\rho Y_i}{W_i} \right)^{v''_{ik}} \quad (12.187)$$

Here k_{fk} and k_{bk} are the rate coefficients of the forward and backward reactions, respectively, and are in general temperature-dependent. They may also depend on pressure in some cases.

To simplify the analysis, a “global” reaction mechanism may be considered. For overall reaction of the fuel F and oxygen O₂, yielding the products P, the global reaction mechanism can be described as



For this single-step reaction, the reaction rate is written as

$$\omega = A \left(\frac{\rho Y_F}{W_F} \right)^{n_f} \left(\frac{\rho Y_{O_2}}{W_{O_2}} \right)^{n_{O_2}} \exp\left(-\frac{E}{RT}\right) \quad (12.189)$$

where A is the preexponential factor and E the activation energy. The exponential expression $A \exp(-E / RT)$ is known as the Arrhenius form and is widely used to describe the temperature dependency of the reaction rate. The exponents n_f and n_{O_2} relate to “reaction order.” According to Eq. (12.189), overall the reaction is of the order $n_f + n_{O_2}$. For global reactions, n_f and n_{O_2} are not necessarily integers and are found by curve-fitting experimental data. In general, a particular global expression in the form of Eq. (12.189) holds only over a limited range of temperatures and pressures, and may depend on the details of the apparatus used to define the rate parameters (Turns, 1996).

In addition to species transport equation (12.184), the overall continuity, momentum, and energy equations of the mixture are needed to describe the gaseous combustion system fully. The continuity and momentum equations are similar to those in nonreacting flows; the energy equation is modified to account for combustion effects. The latter can be derived from the first law of thermodynamics as (Peters, 2000),

$$\rho \frac{\partial h}{\partial t} + \rho \mathbf{u} \cdot \nabla h = \frac{\partial p}{\partial t} + \mathbf{u} \cdot \nabla p - \nabla \cdot \mathbf{j}_q + q_R \quad (12.190)$$

where the frictional heating has been neglected as it has a small contribution for low-speed flows. The last term, q_R , is due to radiation and must be retained in furnace combustion. Here, the enthalpy h of the mixture is defined in terms of the enthalpies h_i of species i

$$h = \sum_{i=1}^n Y_i h_i \quad (12.191)$$

Assuming ideal gas, h_i only depends on temperature T

$$h_i = h_{ref,i} + \int_{T_{ref}}^T c_{pg,i}(T) dT \quad (12.192)$$

where $c_{pg,i}$ is the constant-pressure specific heat of species i and T is in Kelvin. Reference enthalpy $h_{ref,i}$ includes the chemical bond energy and is generally taken to be zero for H₂, O₂, N₂, and solid carbon. The reference enthalpy of combustion products such as CO₂ and H₂O are negative and are tabulated (Burcat, 1984). The specific heat of the mixture is also defined in terms of specific heats of various species

$$c_{pg} = \sum_{i=1}^n Y_i c_{pg,i} \quad (12.193)$$

The heat flux j_q in Eq. (12.190) includes the effect of enthalpy transport by the diffusive fluxes j_i

$$\mathbf{j}_q = -k\nabla T + \sum_{i=1}^n h_i \mathbf{j}_i \quad (12.194)$$

To conclude, the system of continuity, momentum, energy, and species conservation equations is augmented by the equation of state for ideal gas.

12.7.3 Isolated Drop

Evaporation and combustion of a single drop are among the fundamental processes in liquid-fuel combustion and have been studied extensively, since the pioneering works of Spalding (1953) and Godsav (1953). The analysis for a general case involving all important processes such as internal circulation, drop deformation, (Haywood et al., 1994a, 1994b; Mashayek, 2001), turbulence (Sorok et al., 2000; Wu et al., 2001), and gravity (Gogos et al., 2003) effects is quite complicated. Under special circumstances, simplifying assumptions can be made to derive an analytical solution. This solution is very useful in providing insights into the physics of drop evaporation and combustion, and has produced reasonable predictions in real applications. In this section, we briefly review the derivation of the analytical solution and its underlying physical assumptions.

12.7.3.1 Evaporation

Consider an isolated drop evaporating in a quiescent and infinitely large medium and assume that the evaporation is quasi-steady, i.e., at any instant of time, the process can be described as if it were in steady state. The drop temperature is uniform, typically at the saturation temperature $T_s < T_b$, where T_b is the boiling point of the fuel at the given pressure. Without the loss of generality, in the following we assume that the drop is at its boiling temperature. The drop preheat period does not significantly contribute to the overall combustion process and can be neglected. Also, in order to find an analytical solution, all thermophysical properties are assumed constant (Turns, 1996).

With these assumptions, the gas-phase mass conservation for a spherically symmetric drop at quasi-steady state reads

$$\dot{m} = \rho v 4\pi r^2 = \text{constant} \quad (12.195)$$

A relationship for the temperature variation in the gas can be found by considering the gas-phase energy conservation, which states a balance between the conduction and convection heat transfer

$$4\pi k_g \frac{d}{dr} \left(r^2 \frac{dT}{dr} \right) = \dot{m} c_{pg} \frac{dT}{dr} \quad (12.196)$$

Here T is the gas temperature and g refers to the gas properties. For a unitary Lewis number ($Le = k_g/\rho c_{pg} D$), by defining $\xi = c_{pg}/4\pi k_g = 1/4\pi\rho D$, the following problem can be stated for the gas-phase temperature:

$$\frac{d}{dr} \left(r^2 \frac{dT}{dr} \right) = \xi \dot{m} \frac{dT}{dr} \quad (12.197)$$

with boundary conditions $T(r = a) = T_b$ and $T(r \rightarrow \infty) = T_\infty$, where a is the drop radius. The solution of this equation for constant \dot{m} yields

$$T(r) = \frac{(T_\infty - T_b)\exp(-\xi\dot{m}/r) - T_\infty\exp(-\xi\dot{m}/a) + T_b}{1 - \exp(-\xi\dot{m}/a)} \quad (12.198)$$

which indicates a steep temperature gradient near the surface of the drop. This temperature gradient determines the heat conducted into the drop, which will be consumed entirely for evaporation since the drop is at its boiling point. Therefore, writing the energy balance at the drop–gas interface gives

$$4\pi k_g a^2 \frac{dT}{dr} \Big|_a = \dot{m} h_{fg} \quad (12.199)$$

Differentiating Eq. (12.198) and substituting into Eq. (12.199) the mass flow rate of the vapor

$$\dot{m} = \frac{4\pi k_g a}{c_{pg}} \ln(1 + B_e) \quad (12.200)$$

is obtained, where

$$B_e = \frac{c_{pg}(T_\infty - T_b)}{h_{fg}} \quad (12.201)$$

is the transfer number, also known as the Spalding number. With the relation for mass in terms of drop diameter and density, a more common form of Eq. (12.200) is the so-called d^2 law written as

$$d^2(t) = d_0^2 - Kt, \quad K = \frac{8k_g}{\rho_1 c_{pg}} \ln(1 + B_e) \quad (12.202)$$

where d is the drop diameter with an initial value of d_0 and subscript l refers to liquid properties.

To account for the temperature dependency of thermophysical properties, following the approach of Law and Williams (1972) for burning drops, c_{pg} and k_g are evaluated at the temperature $\bar{T} = (T_b + T_\infty)/2$

$$c_{pg} = c_{pF}(\bar{T}), \quad k_g = 0.4k_F(\bar{T}) + 0.6k_\infty(\bar{T}) \quad (12.203)$$

where F refers to fuel vapor. Other approximations are suggested in Hubbard et al. (1975).

Adopting a similar set of assumptions as in the above analysis, Mashayek (2001) investigated the effect of a deformation in the surface of a drop on its rate of evaporation by conducting finite element simulations of the gas surrounding the drop. The drop was assumed to be at its boiling temperature and the gas properties were considered constant for a quasi-steady analysis. The surface of the drop was deformed using spherical harmonics

$$h(\phi) = R_n[1 + \varepsilon_n P_n(\cos \phi)] \quad (12.204)$$

where $P_n(\cos \phi)$ is the Legendre polynomial of degree n , ε_n the amplitude of disturbance (with respect to the spherical shape), and R_n a correction factor introduced to keep the volume of the drop the same as the amplitude is changed. All lengths were normalized with the radius of the unperturbed (spherical) drop. Figure 12.64 shows the computational domain and the coordinate system used. The angle ϕ is measured from the axis of symmetry toward the equator of the drop.

Figure 12.65 shows the deviation parameter ψ as a function of ϕ for $n = 2$ at various amplitudes. Here, ψ indicates the difference between the evaporation rates of the deformed drop and the spherical drop as normalized by the evaporation rate of the spherical drop. The results indicate that the evaporation rate is larger near the axis of symmetry and lower near the equator, and the deviation from the evaporation rate

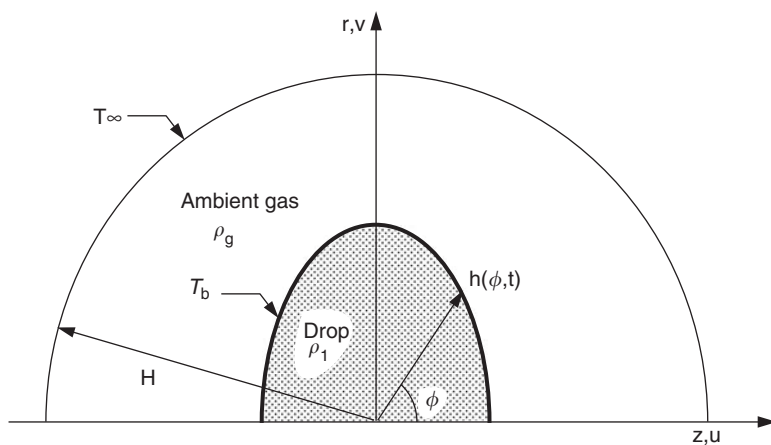


FIGURE 12.64 Coordinate system and solution domain used in computations of a deformed drop (Mashayek, 2001).

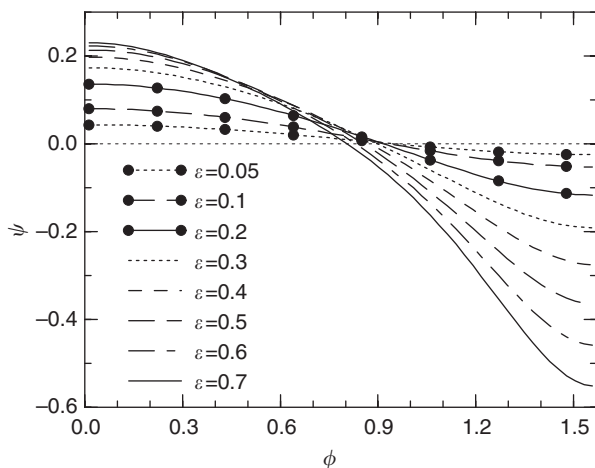


FIGURE 12.65 Variations of the normalized mass flux with angle ϕ at various amplitudes for a drop deformed with second spherical mode $n = 2$ (Mashayek, 2001).

of a spherical drop increases with the increase in the amplitude. Based on the results of the simulations, the following model was presented for calculating the evaporation rate of a deformed drop:

$$\chi = \left[F_n \left(K - \frac{2}{\varrho} \right) + \frac{2}{\varrho} \right] \beta \quad (12.205)$$

where K and ϱ are the surface curvature and the nondimensional radius of the equivalent spherical drop, respectively. Also,

$$\chi = \left[\frac{\rho_1 \sigma}{r_0} \right]^{(-1/2)} \dot{m} \quad (12.206)$$

is the normalized evaporation rate and

$$\beta = \frac{1}{2} (\rho_1 r_0 \sigma)^{(-1/2)} \left(\frac{k_g}{C_{pg}} \right) \ln(1 + B_e) \quad (12.207)$$

where r_0 and σ are the initial radius of the unperturbed drop and the surface tension coefficient, respectively. The function F_n depends on the mode of the surface disturbance and is defined as

$$F_n = \frac{3n + 2}{2[n(n + 1) + 2]} \quad (12.208)$$

Equation (12.205) is valid for surface amplitudes up to 10% of the initial drop radius and has been tested for $0.1 \leq B_e \leq 2$ and for surface deformation up to $n = 8$. It is noted that Eq. (12.205) reduces to Eq. (12.200) for a spherical drop for which the surface curvature $K = 2/\rho$.

12.7.3.2 Combustion

The analysis of a burning drop is understandably more complicated, but an analytical solution can be found for a simplified case. The diffusion flame requires that fuel and oxidizer react in stoichiometric proportions at the spherical flame that forms around the drop at a radius r_f . The reaction is assumed to be infinitely fast and the flame is represented by an infinitesimally thin sheet. A single-component fuel is considered with zero solubility for gases and there is phase equilibrium at the drop surface.

The analysis is also based on a unitary Lewis number, which represents the relative importance of the thermal conductive transfer and transport by mass diffusion. For $Le > 1$, the mass diffusion transports thermal energy in the direction of increasing concentration. The role of the nonunitary Lewis number has been examined quantitatively in Chiu (2000) by using a canonical theory of drop.

Figure 12.66 illustrates the two main regions formed inside and outside the flame. In the first region, between the drop surface and the flame, the fuel vapor concentration decreases monotonically with the radius, whereas the products concentration shows the opposite variation. Since the products do not dissolve in the liquid, they do not move and remain stagnant in this region. At the flame, the products concentration reaches the maximum (unity) and the fuel concentration is zero. In the region outside the flame, the products concentration decreases monotonically with an increase in radius. The oxidizer concentration decreases from its free-stream value of $Y_{Ox,\infty}$ at distances far away from the flame to zero at the flame.

Based on the physical model illustrated in Figure 12.66, the analysis is conducted to determine five parameters: fuel mass flow rate \dot{m}_F , fuel mass fraction at the drop surface Y_{Es} , drop surface temperature T_s , flame temperature T_f and flame radius r_f . The final results can be summarized as follows (Turns, 1996):

$$T_f = \frac{q_{i-l} + h_{fg}}{c_{pg}(Y_{Ox,\infty} + \nu)} [\nu B_c - Y_{Ox,\infty}] + T_s \quad (12.209)$$

$$r_f = a \frac{\ln(1 + B_c)}{\ln[(\nu + Y_{Ox,\infty})/\nu]} \quad (12.210)$$

$$Y_{Es} = \frac{B_c - Y_{Ox,\infty}/\nu}{1 + B_c} \quad (12.211)$$

$$\dot{m}_F = \frac{4\pi k_g a}{c_{pg}} \ln(1 + B_c) \quad (12.212)$$

where

$$B_c = \frac{Y_{Ox,\infty}\Delta h_c/\nu + c_{pg}(T_\infty - T_s)}{q_{i-l} + h_{fg}} \quad (12.213)$$

with Δh_c denoting the lower heating value. One may rewrite Eq. (12.212) as

$$\dot{m}_F = \frac{2Sh\pi k_g a}{c_{pg}} \ln(1 + B_c) \quad (12.214)$$

using the Sherwood number $Sh = h_m d/\rho D$ with h_m denoting the mass transfer coefficient.

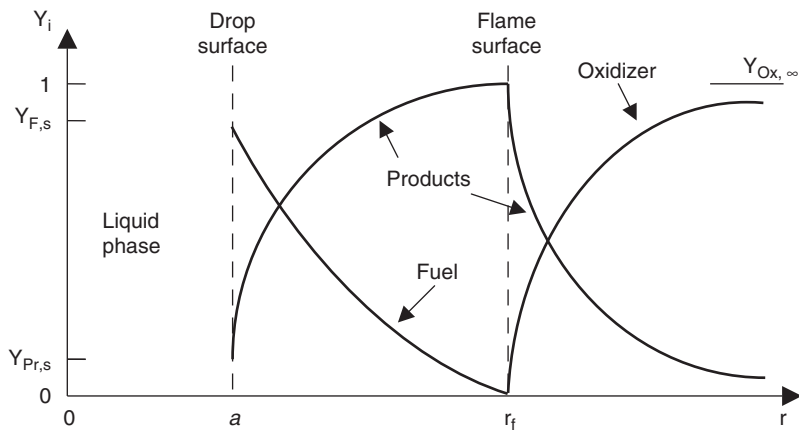


FIGURE 12.66 Species profiles in spherical drop burning without convection effects.

In this form, convective effects can also be included by empirically modifying Sh . For a spherical drop in a quiescent atmosphere, $Sh = 2$ and empirical correlations are found in literature for cases with convective effects. It is also noted that Eq. (12.212) can be expressed in form of the d^2 law in Eq. (12.202) with B_c replacing B_e .

In Eqs. (12.209) and (12.213), q_{i-l} is the rate of heat conducted into the interior of the drop per unit mass flow rate of vapor. The expression for q_{i-l} depends on the model used for drop heatup. If the drop rapidly heats up then one can assume negligible thermal inertia and $q_{i-l} = 0$. The other easily tractable model is the so-called “onion-skin” model for which $q_{i-l} = c_p(T_s - T_0)$, where T_0 is the drop initial temperature.

Equations (12.209)–(12.213) can be evaluated for assumed T_s value. For a saturated drop surface, one may alternately use the Clausius–Clapeyron relation to derive an expression for T_s in terms of the gas pressure P

$$T_s = \frac{-B_c}{\ln \left[\frac{-Y_{F,s} P W_{Pr}}{A(Y_{F,s} W_F - Y_{F,s} W_{Pr} - W_F)} \right]} \quad (12.215)$$

where subscript Pr refers to products. Equation (12.215) can be used in conjunction with an iterative approach to determine T_s along with the other unknowns. The effects of temperature dependency of the properties can be approximated by following the suggestions in Law and Williams (1972):

$$c_{pg} = c_{pF}(\bar{T}), \quad k_g = 0.4k_F(\bar{T}) + 0.6k_{Ox}(\bar{T}), \quad \rho_l = \rho_l(T_s) \quad (12.216)$$

where $\bar{T} = (T_s + T_f)/2$.

The assumption of quasi-steadiness is convenient for arriving at a closed analytical solution. However, this assumption could break down as a consequence of unsteady diffusion, drop heating, fuel vapor accumulation, compositional change of multicomponent drops, natural and forced convection, and finite-rate chemical kinetics (Chiu, 2000). The effect of this assumption was investigated by Law et al. (1980) for both evaporating and burning drops. The quasi-steadiness assumption implies that the total mass of vapor between the flame and the drop surface remains constant. However, when a drop is suddenly placed in an environment for which the vapor mass fraction is less than the saturation vapor mass fraction, the drop starts to evaporate and the mass of the vapor gradually increases. During these initial times, there is not much fuel vapor available for burning. For a lower flow rate of fuel into the flame, a lower supply of O_2 is required, thus the flame stands closer to the drop surface. As more fuel vapor is produced compared to fuel consumption, fuel vapor accumulates, the flame is pushed away from surface,

and the burning rate gradually increases due to larger flame surface area for consumption. At larger times, the drop radius is small, vapor production is low, and hence consumption exceeds supply and as such flame is pushed back toward the surface. This behavior was captured by the analysis in Law et al. (1980) as demonstrated in Figure 12.67, for three different values of $Y_{O_2,\infty}/v$. It is observed that for small $Y_{O_2,\infty}/v$, the flame may not reach a steady location and instead continue to expand outward. The results in Law et al., (1980) also provided the rate of variation of d^2/d_0^2 and indicated that the d^2 law is adequate in predicting the evaporation rate and the instantaneous drop size. This suggests that, despite the variations in flame surface location, the quasi-steady analysis may provide reasonable predictions for the drop burning rate, which is of primary concern in theoretical description of combustion systems.

In the presence of a convective flow, the flame surface could significantly deviate from a spherical shape. Chiu and Huang (1996) formalized the concept of the multistate for a drop, which refers to the existence of more than a single state under a given relative Reynolds number (see below) and ambient temperature. Three distinctive flame shapes were recognized, namely, *envelope* flame, *wake* flame, and *boundary layer* flame. The last flame is stabilized in the boundary layer of the liquid sphere. According to Chiu and Huang, there are five distinct regions of Reynolds number bands in which the following multistates are possible: (1) one-state envelope flame; (2) two-state envelope flame vaporization; (3) three-state envelope flame-wake flame vaporization; (4) two-state wake flame vaporization; and (5) one-state vaporization. This multistate behavior also depends on temperature that affects the transfer number and the Damköhler number Da . The Damköhler number is a measure of the relative importance of the flow time scale and combustion time scale. For an infinitely fast reaction $Da \rightarrow \infty$.

The effects of convection can be considered in the calculations by introducing a Nusselt number, Nu , into Eq. (12.212) as

$$\dot{m}_F = \frac{2\pi k_g a Nu}{c_{pg}} \ln(1 + B_c) \quad (12.217)$$

The following empirical relations have been suggested for Nu as a function of relative Reynolds number, $Re_r = v_r d \rho_g / \mu_g$, where v_r represents the relative velocity between the drop and the surrounding gas:

Ranz and Marshall (1952):

$$Nu = 2 + 0.572 Re_r^{1/2} Pr^{1/3}, \quad 1 < Re_r < 2000 \quad (12.218)$$

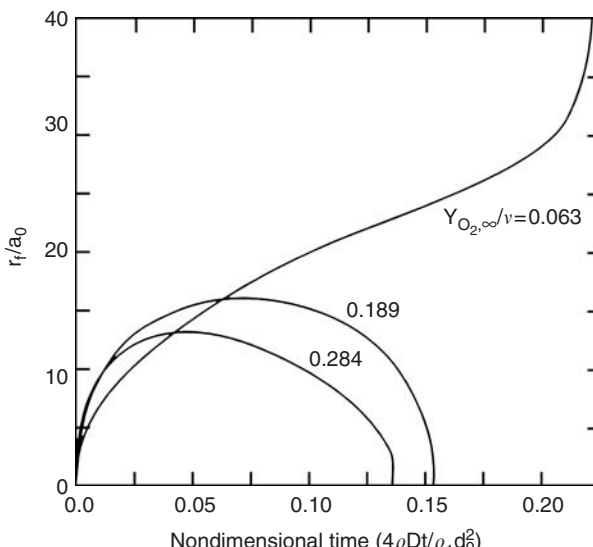


FIGURE 12.67 Temporal variations of the normalized flame radius for a heptane drop burning in the standard atmosphere (Law et al., 1980).

Clift et al. (1978):

$$Nu = \begin{cases} 1 + (1 + Re_r)^{1/3}, & Re_r < 1 \\ 1 + (1 + Re_r)^{1/3} Re_r^{0.077}, & Re_r \geq 1 \end{cases} \quad (12.219)$$

Faeth (1977):

$$Nu = 2 + \frac{0.555 Re_r^{1/2} Pr^{1/3}}{[1 + 1.23/(Re_r Pr^{4/3})]^{1/2}} \quad (12.220)$$

where Pr is the Prandtl number. It is noted that for all these relations $Nu = 2$ in the absence of convection and Eq. (12.217) reduces to Eq. (12.212).

12.7.4 Groups of Drops

The analysis of a single drop is instructive for a basic understanding of evaporation and combustion processes; however, in real applications of liquid fuel sprays, large number of drops are present. In these situations, the interactions between neighboring drops become important for high drop number density (Umemura, 1994). These interactions are discussed in this section.

12.7.4.1 Interactive Evaporation

As the distance between two evaporating drops decreases, the drops compete for heat. Furthermore, the vapor concentration increases, while the temperature decreases. This combination results in a saturation condition in the spacing between the drops. A criterion for interactive evaporation of two drops is given in Annamalai and Ryan (1992) by considering the temperature profiles (Eq. [12.198]) around each drop. Based on this criterion, interaction between two drops becomes significant at a distance where the difference between the drop wet bulb temperature (taken as the drop surface temperature boundary condition) and the local temperature is 90% of the difference between the drop wet bulb temperature and the ambient temperature. This situation occurs at $r = 10a$; therefore, two evaporating drops begin to interact when the interdrop spacing l is such that $l < 20a$.

Theoretical studies often consider a group of drops confined in a spherical region with radius R_c . The analysis is conducted by considering different time scales, including the individual drop heating time and the time for penetration of heat from outside to the core of the group of drops (Annamalai and Ryan, 1992). Another important phenomena is the Stefan flow, which is due to the blowing of vapor from the drops and may drag the drops outwardly in dense sprays (Umemura, 1994). Nevertheless, most studies have neglected the effect of the Stefan flow and, as a result, predict higher evaporation rates. This is also true for an isolated drop, *i.e.*, a higher evaporation rate is predicted for an isolated drop when Stefan effects are neglected. However, the ratio of the evaporation rates, termed as the “correction factor” η remains the same with or without Stefan effects. The correction factor is defined as the ratio of the vapor mass flow rate \dot{m}_s of a single drop in the group to the vapor mass flow rate \dot{m}_{iso} of an isolated drop

$$\eta = \dot{m}_s / \dot{m}_{iso} \quad (12.221)$$

The group evaporation usually results in $\eta < 1$.

In situations like spray combustion, the group of drops is suddenly exposed to a hot ambient gas. In these situations, the drops at the center of the group evaporate rather quickly and create a saturation condition in the spacing between the drops. This case can be analyzed as a confined volume problem with adiabatic condition with respect to the outside gas. A detailed discussion of various studies on group evaporation is presented in Annamalai and Ryan (1992); here we provide a brief summary of the final results from some of these studies.

Zung (1967) presented a ‘cellular model’ in which the inner drops evaporated in an adiabatic impermeable cell. For the drops in the outer cell, it was assumed that only one half of the drop (shaded area in Figure 12.68) participated in evaporation and the other half did not evaporate. When the outside layer evaporated, the next layer was considered. Zung’s analysis did not consider the energy balance equation and predicted that, for a fixed cloud radius, the cloud evaporation time reduces proportional to the drop radius regardless of the heat transfer from the ambient gas. Improved results were later presented by Tishkoff (1979) by considering a ‘bubble model’ as shown in the inset of Figure 12.68. The spherical shell with radius b , considered around the drop with radius a , was permeable and elastic. Mass, energy, and species conservation equations were solved and unsteady drop heating was allowed with a quasi-steady analysis for the gas phase. Saturation was reached for small b/a , whereas for large b/a the drop fully evaporated. The transition from partial to full evaporation was dependent on temperature and pressure of the gas. The ratio b/a increased with the decrease in the initial gas temperature and pressure. Similar studies were also conducted by Bellan and Cuffel (1983), Bellan and Harstad (1987), and Bellan and Harstad (1988), who also included turbulence effects.

The above studies were conducted by concentrating on the details of flow around individual drops within a cell, bubble, etc. A different class of studies has been reported in the literature that provides solutions for the global behavior of a cloud of drops by considering continuum transport equations for the entire cloud. These macroscopic equations are derived by averaging over a volume containing the drops of interest and are similar to equations for the gas, but with source terms due to drop evaporation (and combustion in case of a reacting system). For example, for quasi-steady evaporation of a cloud of monosized

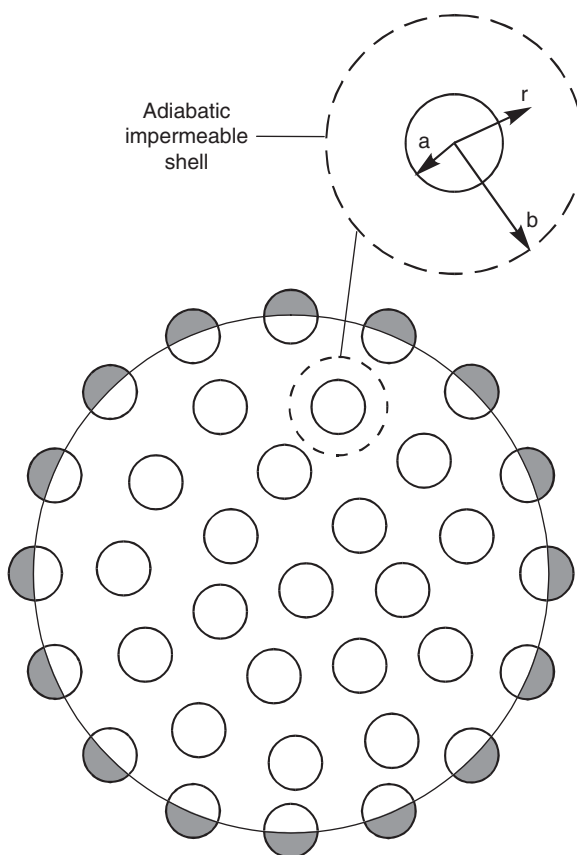


FIGURE 12.68 Illustration of cell model for group combustion (Annamalai and Ryan, 1992).

drops, when the Stefan flow is neglected the continuum equation for the average vapor mass fraction, $Y(r)$, in a spherical coordinate is described as (Annamalai and Ryan, 1992)

$$\frac{1}{r^2} \frac{d}{dr} \left(\rho D r^2 \frac{dY}{dr} \right) = \begin{cases} -\dot{m}''' & \text{for } r < R_c \\ 0 & \text{for } r > R_c \end{cases} \quad (12.222)$$

The volumetric source term \dot{m}''' is due to evaporation of drops and is obtained by averaging over all the drops present in the volume of interest. The appropriate boundary conditions for this problem are

$$Y(r) = Y_\infty, \quad r \rightarrow \infty \quad (12.223)$$

$$dY/dr = 0, \quad r = 0 \quad (12.224)$$

The solution of Eq. (12.222) with boundary conditions Eqs. (12.223) and (12.224) for a monosized and uniform cloud yields the average correction factor as

$$\eta = \frac{3}{G} \left[1 - \frac{\tanh\{G^{(1/2)}\}}{G^{(1/2)}} \right] \quad (12.225)$$

Here G is the group evaporation number:

$$G = 2Sh\pi n a R_c^2 \quad (12.226)$$

where n is the number density of the drops. It should be noted that the definition of G depends on the geometry and spray distribution parameters in the cloud. Various forms used by researchers are summarized in Table 3 of Annamalai and Ryan (1992).

Annamalai (1985) considered Stefan flow in the quasi-steady analysis of a cloud of drops and showed that

$$\dot{m}_c = \dot{m}_{c,SE} \left[1 - \frac{\tanh\{G^{(1/2)}\}}{G^{(1/2)}} \right] \quad (12.227)$$

where \dot{m}_c is the cloud evaporation rate for a monosized and uniform ($n = \text{constant}$) cloud and

$$\dot{m}_{c,SE} = \begin{cases} 4\pi\rho D \ln(1 + B_e) n R_c & \text{(Stefan flow included)} \\ 4\pi\rho D B_e n R_c & \text{(Stefan flow neglected)} \end{cases}$$

The average evaporation rate per drop is

$$\dot{m}_{s,c} = \frac{\dot{m}_c}{\frac{4}{3}\pi n R_c^3} \quad (12.228)$$

which yields

$$\eta = \frac{\dot{m}_{s,c}}{\dot{m}_{iso}} = \frac{3}{G} \left[1 - \frac{\tanh\{G^{(1/2)}\}}{G^{(1/2)}} \right] \quad (12.229)$$

for a monosized and uniform cloud. It is interesting to note that Eq. (12.229) with Stefan flow included is the same as Eq. (12.225), which was obtained by neglecting Stefan flow.

The G number can be used as an indicator for the denseness of a spray. Evaluation of Eq. (12.229) shows $\eta \approx 0.9$ and 0.1 for $G = 0.1$ and 100, respectively. Therefore, for practical purposes, clouds having $G < 0.1$ may be considered dilute enough such that drops can be treated as isolated. Clouds with $G > 100$ should be considered as dense. For very small G values, approaching zero, every drop in the cloud is surrounded

by the gas at T_∞ , whereas for very large values of G , approaching infinity, every drop in the interior of the cloud is at the same temperature. In the latter case, the vapor mass fraction in the spacing between the drops corresponds to the saturated condition and only drops near the outer region of the cloud evaporate. In this case, the cloud is said to evaporate in the “sheath” evaporation mode. It should also be noted that, in a real spray situation, drops move around with the flow and drop–drop collisions are likely for dense clouds. In this situation, the analysis here may not be applicable.

The effects of size distribution was also considered in Annamalai (1985) by assuming a monotonic distribution for the number density n and drop radius a in the form

$$\frac{na}{(na)_{R_c}} = \left[\frac{r}{R_c} \right]^{-q} \quad (12.230)$$

where $(na)_{R_c}$ is the reference quantity at $r = R_c$. For $q = 0$, Eq. (12.230) yields the uniform distribution considered above. The correction factor for this case is given as

$$\eta = \left[1 + \frac{G_1}{3-q} + \frac{G_1^{(1/2)}}{3-q} \frac{l_{(5-2q)/(2-q)} [2G_1^{(1/2)}/(2-q)]}{l_{(3-q)/(2-q)} [2G_1^{(1/2)}/(2-q)]} \right]^{-1} \quad (12.231)$$

with G_1 defined as

$$G_1 = (1-q)^{(1/3)} G \quad (12.232)$$

for fixed size, varying number density, and

$$G_1 = (1-q/3) G \quad (12.233)$$

for fixed number density, varying size. In Eq. (12.231), $l_{(5-2q)/(2-q)}$ represents the modified Bessel function of the order $(5-2q)/(2-q)$.

12.7.4.2 Interactive Combustion

The analysis in previous sections for an isolated drop assumes that a spherical flame is formed at a radius r_f around the drop. This assumption may be valid as long as there is no other drop in the vicinity of the first drop. When the distance l between two drops is decreased there is an opportunity for two flames to interact. This interaction is intensified by the fact that the two drops must also compete for oxygen in order to continue their combustion. This intuitive conclusion can also be drawn from Eq. (12.210), for the flame radius, in which $Y_{\text{O}_x,\infty}$ appears in the denominator. With the decrease in $Y_{\text{O}_x,\infty}$ the denominator becomes smaller and the flame radius increases. As the distance between the two drops is further decreased, their flames merge and a common flame is formed around the two drops. According to Williams (1985), a simple criterion for the interaction of two burning drops can be stated as $l < 2r_f$.

Similar interactions occur for a system consisting of a large number of drops, forming a group of drops. In this case, several different “modes” of group combustion can be identified. A large body of literature is devoted to group combustion studies; however, it appears that the studies by Chiu and co-workers (Suzuki and Chiu, 1971; Chiu and Liu, 1977; Chiu et al., 1982) have been more widely recognized. In order to characterize various combustion modes, Suzuki and Chiu (1971) and Chiu et al. (1982) used the group-combustion number:

$$G = 3[1 + 0.276 Re_r^{(1/2)} Sc^{(1/3)}] Le N^{(2/3)} (d/l) \quad (12.234)$$

where Sc is the Schmidt number and N the total number of drops in the group. This nondimensional number represents the ratio of the heat transfer in the gas phase and the heat transfer between two phases accounting for the convective effect.

The G number has been used to differentiate between weak and strong drop interactions. According to Chiu et al. (1982), four modes of group combustion are identified as shown in Figure 12.69. For low values

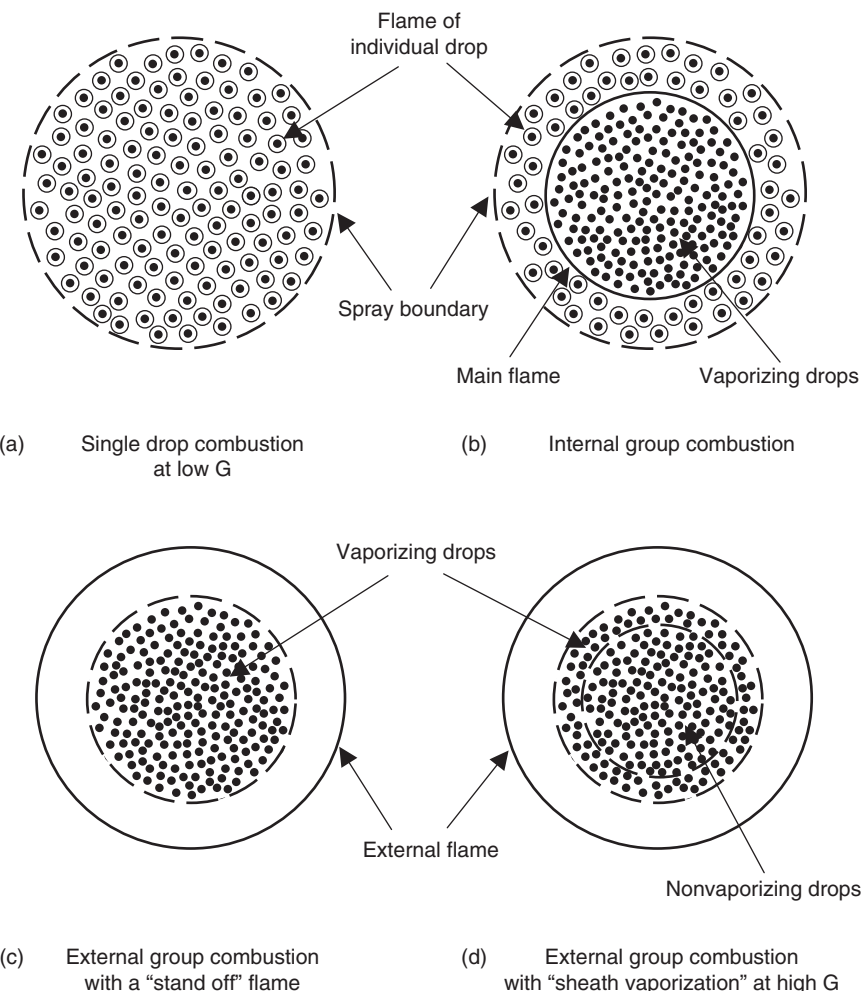


FIGURE 12.69 Four group combustion modes of a drop cloud according to Chiu et al. (1982).

of G , the drops are widely separated and individual drop combustion is dominant (Figure 12.69(a)). As G is increased, the spacing between the drops decreases and the flames from various drops combine. For moderate increases in G , the main flame is located somewhere within the cloud of drops (Figure 12.69(b)). Between this main flame and the external boundary of the cloud, single drop burning is observed. Further increase in G pushes the flame outside the cloud boundary and forms a “stand off” flame (Figure 12.69(c)). In this case, all the drops are vaporizing as combustion takes place at the flame. Finally, for very large values of G , while the standoff flame forms outside the cloud, the drops in the core of the flame are saturated and do not evaporate. In this sheath evaporation case, evaporation occurs only for the drops located near the edge of the cloud (Figure 12.69(d)). As these boundary drops fully evaporate, the evaporation front shrinks toward the center of the cloud and the drops in the core begin to evaporate.

The above group combustion modes can be applied to spray combustion as shown in Figure 12.70 (Chiu and Croke, 1981). Due to cold temperatures and high drop number density in the spray near the nozzle, the ignition of the spray takes place at a distance from the nozzle exit. Once the spray is ignited, an external flame forms, while the core of the spray consists of evaporating drops. Further downstream, the spacing between the drops increases and the flame penetrates into the spray, thus forming multiple group combustion. At the end, combustion continues by consuming the unburnt gaseous fuel.

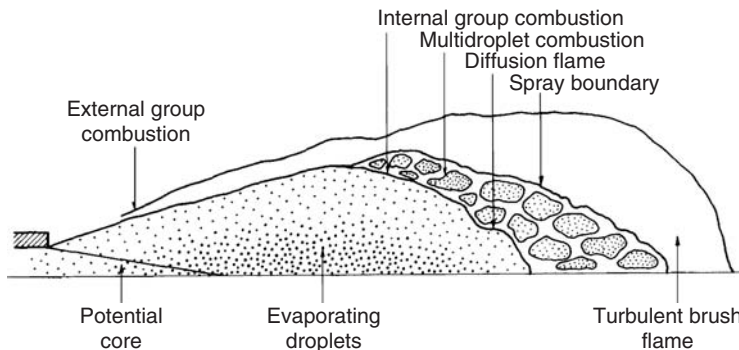


FIGURE 12.70 Schematic of liquid-fuel spray group combustion (Chiu and Croke, 1981).

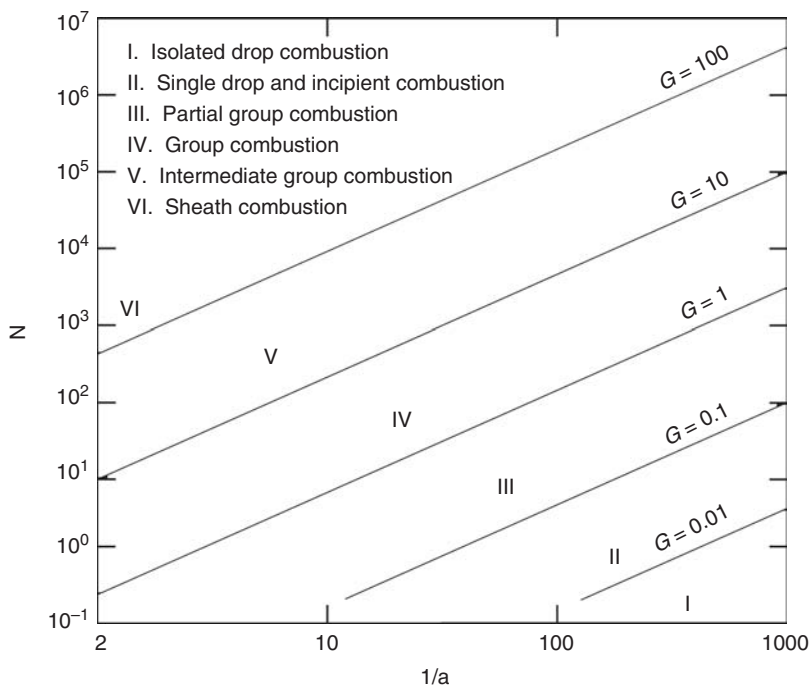


FIGURE 12.71 Group combustion number as a function of nondimensional spacing l/a and the total number of drops (Annamalai and Ryan, 1992).

Annamalai and Ryan (1992) presented a modified form of the spray classification of Chiu and co-workers by considering six modes of combustion as seen in Figure 12.71. This figure maps these various modes on a plot of the total number of drops in the cloud vs. the ratio of the drop spacing to drop diameter l/a for various values of G in Eq. (12.226). Region (I) corresponds to isolated drop combustion for $G < 0.01$, whereas region (II) involves isolated to incipient group combustion for $0.01 < G < 0.1$. The incipient combustion is when the flame radii of the center drops in the cloud just touch each other. Regions (III), (IV), and (V) for $0.1 < G < 1$, $1 < G < 10$, and $10 < G < 100$ are termed as partial group combustion, group combustion, and intermediate group combustion, respectively. In partial group combustion, while there is a group flame for the inner drops, the outer drops burn with individual flames, but still allow O_2 to penetrate into the flame located within the cloud. Finally, for $G > 100$, combustion is in

the sheath mode, where the temperature at the cloud surface is at the wet bulb temperature of the drops and the cloud behaves as an equivalent single drop of radius R_c . Any convective effects will move the lines in Figure 12.71 downward, and this movement will be greater at smaller interdrop spacing.

The model of Chiu and co-workers and their G parameter have been extensively assessed by experimentalists in spray combustion (Chen and Gomez, 1997; Wark et al., 2000). Wark et al. (2000) examined the variation of G in their experiment of an acoustically forced jet. The forcing resulted in the formation of organized structures consisting of core and wings as seen in Figure 12.72. A phase Doppler interferometry was used to obtain drop statistics for calculation of the group-combustion number. It was not possible to generate experimentally the exact conditions to evaluate G using Eq. (12.234). Therefore, several assumptions were made, including the neglect of the convective effects and unity Lewis number. The expression of G used by Wark et al. (2000), after applying the simplified assumptions, was

$$G = 2\pi n d(R_c)^2 \quad (12.235)$$

which is the same as Eq. (12.226) when $Sh = 2$ is used in the absence of convective effects. The drop number density n was obtained directly from the measurements. The mean drop diameter from the measurements was used as a representative diameter for use in Eq. (12.235), although the drop size distribution was not uniform. The assessment of G was very sensitive to the choice of R_c as witnessed from Eq. (12.235). An appropriate value was chosen for R_c , depending on whether the core or the wing region was considered. In the core region, the radius of the drop-laden portion of the jet was considered as a reasonable choice.

Wark et al. (2000) calculated the axial variation of G as shown in Figure 12.73. The results suggested that close to the nozzle, the jet was burning in external sheath mode and then changed to internal group burning after $z/D \approx 2$, where D and z represent the jet diameter and the axial distance, respectively. After the third structure, the value of G dropped significantly, corresponding to individual drop burning. From the comparison of Figure 12.72 and Figure 12.73, it was not unreasonable to expect external sheath burning

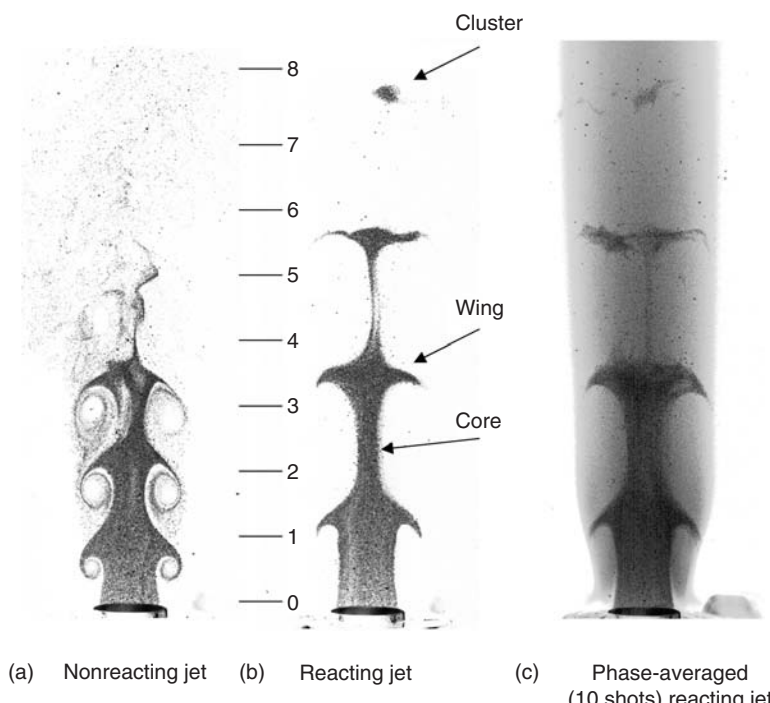


FIGURE 12.72 Phase-locked images of the drop-laden jet considered in the study of Wark et al. (2000).

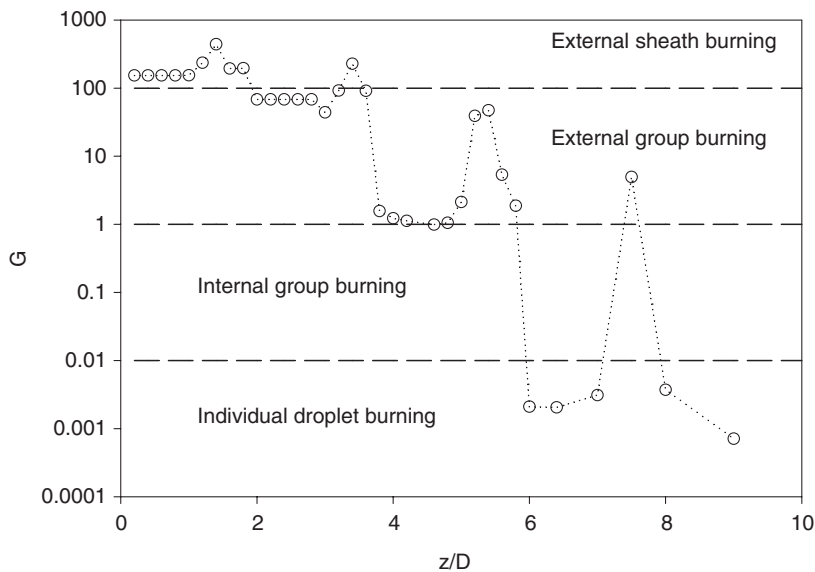


FIGURE 12.73 Phase-locked (0°) axial development of the group combustion behaviour of drops (Wark et al., 2000).

early in the flame. However, Wark et al. (2000) questioned whether individual drop burning occurred between the third and fourth structures, as predicted by the calculation of G . This was in agreement with previous experiments (e.g., McCreath and Chigier, 1973), which did not show any signs of single drop burning in the spray.

Annamalai (1985) provided similar relations to those in Eqs. (12.227), (12.229), and (12.231) for quasi-steady combustion of a cloud of drops. These relations were provided for both monosized uniform cloud and a cloud with the product of size and number density of the drops given as Eq. (12.230). These results gave correction factors, which can be used for the calculation of the cloud burning rate in terms of the burning rate of an isolated drop.

12.7.5 Spray Modeling

The theoretical approaches discussed in previous sections are very useful for developing a fundamental understanding of the physical processes involved in two-phase combustion. However, as emphasized in the introduction, the practical situations encountered in spray combustion often involve turbulence whose effect cannot be fully described by these theories. See Li (1997) for a review of spray combustion in laminar stagnation flows. A thorough description of spray combustion requires modeling of turbulence interactions with drops and its effect on chemical reaction. More specifically, modeling is required for three interactive processes, namely, turbulence, combustion, and drop dispersion.

The modeling of turbulence effects on drop dispersion is extensively discussed in various chapters of this handbook. The different modeling approaches for particle/drop-laden turbulent flows were recently reviewed by Mashayek and Pandya (2003) and were categorized into two main groups as Eulerian–Lagrangian and Eulerian–Eulerian. In both approaches, the carrier gas is considered as a continuum phase and is solved in the Eulerian frame. In the first approach, the drops are treated in the Lagrangian frame, which is more natural. In the second approach, Eulerian (macroscopic) equations are derived for drops using a variety of methods. (Drew, 1983; Jackson, 1997; Zhang and Prosperetti, 1994; Pandya and Mashayek, 2003). This Eulerian–Eulerian approach has received some success, particularly as a theoretical basis for revealing different physical phenomena (Elperin et al., 1996; Pandya and Mashayek, 2002). Nevertheless, it appears that most of the practical treatments of sprays have been

based on the Elerian–Lagrangian approach. Therefore, in this section, we focus our attention exclusively on the Lagrangian approach.

The level of modeling for turbulence varies depending on the nature of the problem and the computational resources available. To this end, the most common Lagrangian approaches may be divided into three groups: direct numerical simulation (DNS), large-eddy simulation (LES), and stochastic simulation. In all these methods, the flow is seeded or injected by a large number of drops, which are followed individually in the Lagrangian frame using the equations described in Section 1.4 of this handbook. In DNS, no modeling is performed for turbulence and all the various time and length scales are resolved exactly by considering small time step and grid sizes. However, for situations involving a large number of drops, it is not possible to resolve the details of the flow in and around each drop. Therefore, physical models are introduced for describing heat, mass, and momentum transfer between the two phases, as elaborated in this section and also reviewed in Section 1.4 of this handbook. DNS requires significant computational resources and its application has been limited to simple geometries and low Reynolds numbers. (Mashayek, 2000; Reveillon and Vervisch, 2000). A remedy to the limitations of DNS would be via LES, where the small scales of the flow are filtered and simulations are conducted for the large scales only. This, however, requires modeling at the so-called subgrid level and has produced some challenges in the past (Lesieur and Métais, 1996; Meneveau and Katz, 2000). The trade-off is a relaxation in the required computational time as compared to DNS. The application of LES to particle-laden flows is still at its early stages and there are several remaining issues that need to be addressed. These include the effect of the (filtered) subgrid-scale fluctuations on the particles and vice versa (Sankaran and Menon, 2002).

The most practical method of choice for simulation of spray combustion has been via stochastic modeling. These models are derived by using various methods, including those based on time-series analysis (Box and Jenkins, 1976; Gao and Mashayek 2004) and the Langevin equation (Pozorski and Minier, 1998). In stochastic simulation, the carrier gas is simulated using various single-point turbulence models, primarily based on Reynolds average Navier–Stokes (RANS) modeling approach. The RANS models provide mean values along with second-order moment statistics of the carrier gas properties such as velocity, temperature, and species concentration. The role of the stochastic model is to provide fluctuating values for carrier-gas properties for each drop in the system. These fluctuating quantities are required in order to capture the effects of turbulence on the drops. Stochastic models can be derived systematically to include important turbulence properties such as spatial and temporal correlations either implicitly or explicitly. From the implementation point of view, the eddy interaction (EI) models offer many simplifications and have been extensively used for modeling of spray combustion (Gosman and Ioannides, 1981). In EI models, a drop is allowed to interact with the same eddy until it crosses the eddy or for the lifetime of the eddy, whichever is shorter. The turbulence intensity of the eddy is sampled randomly based on the second-order moments calculated by RANS.

The other important aspect in theoretical description of spray combustion is the interaction between turbulence and chemical reaction. Turbulence significantly affects chemical reaction by a substantial increase in the rate of mixing of various species, while chemical reaction and its heat release tend to generate high-gradient regions of temperature and density, thus enhancing the flow instability and turbulence. Turbulence modeling for combustion has been the subject of an overwhelming number of studies within the past four decades and is not reviewed in this section in detail. A number of different methods have emerged from these studies with varying levels of success (Peter, 2000; Pope, 1985; Givi, 1989). Nevertheless, the issue of turbulence modeling for combustion still appears far from being fully resolved and is even more complicated by the fact that chemistry mechanisms are not yet well understood. These mechanisms could involve hundreds of steps and are not tractable in the presence of turbulence with the existing computational resources. Many efforts are being devoted to reduce the number of steps, which can be simulated for turbulent flows. Turbulence modeling for combustion has been recently reviewed by Peters (2000). Among the more popular models are the laminar flamelet models, (Williams, 1975; Bray and Peters, 1994), the probability density function (pdf)-based models (Pope, 1985; Givi, 2003), the eddy-breakup models (Spalding; 1971), and the eddy dissipation models (Magnussen and Hjertager, 1977), which provide different levels of accuracy and complexity. The pdf models are based either on an

assumed pdf shape or a modeled transport equation for the pdf of velocity, temperature, and species concentration in time and space. The solution of the full pdf transport equation is computationally intensive and is mostly done via Monte Carlo methods.

The mass loading of the dispersed phase in a spray is usually high, such that the presence of the drops can significantly affect the properties of the carrier gas via exchange of mass, momentum, and energy. This phenomena, referred to as “two-way coupling,” must be considered in describing various transport equations for the carrier phase. Since the drops are followed in a Lagrangian frame, and the carrier gas is simulated in the Eulerian frame, a numerical model is devised to express Eulerian source-sink terms in the carrier-phase equations in terms of the individual drop effects. In most of the practical applications, the drops are treated as point sources within a given computational cell. The effects of each drop are distributed over the nodes of the cell, with some weights inversely proportional to the distance of the drop from various nodes. This approach is known as particle-source in cell (PSI-Cell) method (Crowe et al., 1977). The approximations involved in this approach, has prompted some researchers to seek more accurate methods (see e.g. Maxey et al., 1997); however, due to its simplicity of implementation, PSI-cell has remained as a method of choice for simulation of turbulent sprays. If the number of drops within a cell is large, interaction among the drops must also be considered.

The task of combining various combustion models with two-phase models and turbulence models is understandably much more challenging and many different combinations can be offered. A reasonably accurate and yet computationally feasible combination would be via stochastic modeling for the dispersed phase along with the flamelet approach for combustion. The simulation of turbulence, once dominated by RANS models, is now also being conducted via LES models. By offering advantages in highly transient flows, LES is growing as a viable replacement for RANS in the future. Nevertheless, with the current computational resources, RANS still remains as the primary method of choice for large-scale, high-velocity combustors and boilers.

Nomenclature

Latin

<i>a</i>	Radius
<i>A</i>	Hamaker constant
<i>B</i>	Impact factor
<i>B_e</i>	Transfer number
<i>c_l</i>	Speed of sound in liquid
<i>c_p</i>	Specific heat at constant pressure
<i>Ca</i>	Capillary number
<i>C_D</i>	Drag coefficient
<i>C_L</i>	Lift coefficient
<i>D</i>	Diffusion coefficient
<i>D_j</i>	Jet diameter
<i>e</i>	Specific energy, coefficient of restitution
<i>E</i>	Young's modulus, activation energy
\dot{E}	Erosion rate
<i>E_M</i>	Mechanical potential energy
<i>f_p</i>	Pulsation frequency
<i>Fr</i>	Froude number
<i>F</i>	Force vector
<i>g</i>	Acceleration due to gravity
<i>G</i>	Relative velocity vector
<i>h</i>	Enthalpy

h_{fg}	Latent heat of evaporation
H	Total head, hardness
H_{sv}	Net positive suction head
I	Moment of inertia
j_i	Diffusive flux
J	Impulsive force
k	Ratio of specific heats, Boltzmann's constant, spring constant, turbulence energy
k_g	Conductive heat transfer coefficient
K_G	Gas constant
L	Latent heat
m	Molecular unit mass, mass
m_G	Gas mass
M	Mass of abrasive particles
\dot{M}_v	Mass flux due to phase change
n	Number density
\mathbf{n}	Normal unit vector
N_s	Specific speed
Nu	Nusselt number
Oh	Ohnesorge number
p	Pressure, erosion surface flow stress
q	Charge
q_R	Radiation heat transfer
Q	Volumetric flow rate
r	Radius
\mathfrak{R}	Gas constant
R_b	Rayleigh-Plesset bubble radius
R_c	Bubble cloud initial radius
Re	Reynolds number
St	Strouhal number
t	Time
t_c	Collapse time
T	Temperature
u	Impact speed
\mathbf{u}, \mathbf{v}	Velocity vector
v_s	Solids velocity
W	Volume of target material
W_i	Molecular weight of species "i"
We	Weber number
Y_i	Mass fraction of species "i"

Greek Symbols

α	Accommodation coefficient, angle of impingement
β	Bubble number density
Γ	Circulation
δ_n	Overlap distance
ε	Volume fraction, dissipation rate
ε_o	Dielectric constant
λ	Viscosity ratio
μ	Viscosity
ρ	Density

σ	Surface tension, cavitation number, Poisson ratio, charge density
σ_b	Flexural strength
σ_y	Plastic load limit
σ_T	Thoma number
τ	Individual bubble volume
ω_i	Chemical source term for species "i"
ω_n	Natural frequency
Ω	Rotational speed
Ω	Rotational velocity vector

Subscripts

b	Bubble
cr	Critical
g	Gas
e	Equilibrium state
i	Species "i"
iso	Isolated
l	liquid
m	maximum, mixture
n	noncondensable gas
r	Reduced
s	Solids
w	Wall
∞	Ambient conditions

References

- Acrivos, A. and Lo, T.S., Deformation and breakup of a single slender drop in an extensional flow, *J. Fluid Mech.*, 86, 641, 1978.
- Annamalai, K. and Ryan, W., Interactive processes in gasification and combustion. Part I: Liquid drop arrays and clouds, *Prog. Energy Combust. Sci.*, 18, 221–295, 1992.
- Annamalai, K. and Ryan, W., Interactive processes in gasification and combustion Part II: Isolated carbon, coal and porous char particles, *Prog. Energy Combust. Sci.*, 19, 383–446, 1993.
- Annamalai, K., *Evaporation and Combustion of a Cloud of Drops*, ASME, HTD Vol. 45, 1985, pp. 27–35.
- Annamalai, K., Ryan, W., and Dhanapalan, S., Interactive processes in gasification and combustion. Part III: Coal/char particle arrays, streams and clouds, *Prog. Energy Combust. Sci.*, 20, 487–618, 1994.
- Arakeri, V.H. and Acosta, A.J., Viscous effects in the inception of cavitation on axisymmetric bodies, *ASME J. Fluids Eng.*, 95, 519, 1973.
- Armenio, V., Piomelli, U., and Fiorotto, V., Effect of the subgrid scales on particle motion, *Phys. Fluids*, 11, 3030–3042, 1999.
- Arndt, R.E.A. and Keller, A.P., Water quality effects on cavitation inception in a trailing vortex, *ASME J. Fluids Eng.*, 114, 430, 1992.
- Arndt, R.E.A., Cavitation in vortical flows, *Annu. Rev. Fluid Mech.*, 34, 143, 2002.
- Ashgriz, N. and Poo, J.Y., Coalescence and separation in binary collision of liquid drops, *J. Fluid Mech.*, 221, 183, 1990.
- Bachalo, W.D. and Houser, M.J., Phase Doppler Spray Analyzer for Simultaneous Measurements of Drop Size and Velocity Distributions, *Optical Eng.*, 23, 583–590, 1984.
- Badock, C., Wirth, R., Fath, A., and Leipertz, A., Investigation of cavitation in real size diesel injection nozzles, *Int. J. Heat Fluid Flow*, 20(5), 538, 1999.

- Bagchi, P. and Balachandar, S., Effect of turbulence on the drag and lift of a particle, *Phys. Fluids*, 15, 3496–3513, 2003.
- Bagchi, P. and Balachandar, S., Shear vs. vortex-induced lift on a rigid sphere at moderate Re., *J. Fluid Mech.*, 473, 379–388, 2002.
- Bailey, M.R., Khokhlova, V.A., Sapozhnikov, O.A., Kargl, S.G., and Crum, L.A., Physical mechanisms of the therapeutic effects of ultrasound (Review), *Acoust. Phys.*, 49, 369, 2003.
- Barthes-Biesel, D. and Acrivos, A., Deformation and burst of a liquid drop freely suspended in a shear field, *J. Fluid Mech.*, 61, 1, 1973.
- Barthlot, W. and Neinhuis, C., Purity of the sacred lotus, or escape from contamination in biological surfaces, *Planta*, 202, 1, 1997.
- Batchelor, G.K., *An Introduction to Fluid Dynamics*, Cambridge University Press, Cambridge, 1967, pp. 250–253.
- Beckett, M.A. and Hua, I., Impact of ultrasonic frequency on aqueous sonoluminescence and sonochemistry, *J. Phys. Chem. A*, 105, 3796, 2001.
- Bellan, J. and Cuffel, R., A theory of non-dilute spray evaporation based upon multiple drop interactions, *Combust. Flame*, 51, 55–67, 1983.
- Bellan, J. and Harstad, K., Analysis of the convective evaporation of nonlinear cluster of drops, *Int. J. Heat Mass Transfer*, 30, 125–136, 1987.
- Bellan, J. and Harstad, K., Turbulence effects during evaporation of drops in clusters, *Int. J. Heat Mass Transfer*, 31, 1655–1668, 1988.
- Bellan, J., Supercritical (and subcritical) fluid behavior and modelling: Drops, streams, shear and mixing layers, jets and sprays, *Prog. Energy Combust. Sci.*, 26, 329–366, 2000.
- Bently, B.J. and Leal, L.G., An experimental investigation of drop deformation and breakup in steady, two-dimensional linear flows, *J. Fluid Mech.*, 167, 241, 1986.
- Berlemont, A., Desjonquieres, P., and Gousset, G., Particle Lagrangian simulation in turbulent flows, *Int. J. Multiphase Flow*, 16, 19–34, 1990.
- Bico, J., Marzolin, C., and Quéré, D., Pearl drops, *Europhys. Lett.*, 47, 220, 1999.
- Biesheuvel, A. and van Wijngaarden, L., Two phase flow equations for a dilute dispersion of gas bubbles in liquid, *J. Fluid Mech.*, 148, 301–318, 1984.
- Bird, R.B., Stewart, W.E., and Lightfoot, E.N., *Transport Phenomena*, 3rd ed., Wiley, New York, 1960.
- Birkhoff, G., Note on Taylor instability, *Q. Appl. Math.*, 12, 306–309, 1954.
- Bitter, J.G.A., A study of erosion phenomena, Part I, *Wear*, 6, 5, 1963.
- Bitter, J.G.A., A study of erosion phenomena, Part II, *Wear*, 8, 161, 1963a.
- Blake, F.G., The Onset of Cavitation in Liquids, Tech. Memo, No. 12, Acoustics Res. Lab., Harvard Univ., 1949.
- Blake, J.R. and Gibson, D.C., Cavitation bubbles near boundaries, *Annu. Rev. Fluid Mech.*, 19, 99, 1987.
- Blake, T.D. and Haynes, J.M., Kinetics of liquid-liquid displacement, *J. Coll. Interface Sci.*, 30, 421, 1969.
- Blake, T.D., Bracke, M., and Shikmurzaev, Y.D., Experimental evidence of nonlocal hydrodynamic influence on the dynamic contact angle, *Phys. Fluids*, 11, 1995, 1999.
- Blake, T.D., Dynamic contact angles and wetting kinetics, in *Wettability*, Berg, J.C., Ed. Surfactant Science Series, Marcel Dekker, New York, 1993.
- Blake, T.D., The contact angle and two-phase flow, Ph.D. thesis, University of Bristol, U.K., 1968.
- Boivin, M., Simonin, O., and Squires, K.D., Direct numerical simulation of turbulence modulation by particles in isotropic turbulence, *J. Fluid Mech.*, 375, 235–263, 1998.
- Borotnikova, M.I. and Soloukin, R.I., A calculation of the pulsations of gas bubbles in an incompressible liquid subject to a periodically varying pressure, *Sov. Phys. Acoust.*, 10, 28–32, 1964.
- Bouillard, J.X., and Lyczkowski, R.W., On the Erosion of Heat Exchanger Tube Banks in Fluidized Beds, *Powder Technol.*, 68, 37, 1991.
- Bouillard, J.X., Lyczkowski, R.W., Folga, S., Gidaspow, D., and Berry, G.F., Hydrodynamics of Erosion of Heat Exchanger Tubes in Fluidized-Bed Combustors, *Canadian J. Chem. Eng.*, 67, 218, April 1989.

- Box, G.E.P. and Jenkins, G.M., *Time Series Analysis*, Holden-Day, Oakland, CA, 1976.
- Bray, K.N.C. and Peters, N., Laminar flamelets in turbulent flames, in *Turbulent Reacting Flows*, Libby, P.A. and Williams, F.A., Eds., Academic Press, London, 1994, pp. 63–113.
- Brazier-Smith, P.R., Jennings, S.G., and Latham, J., The interaction of falling water drops: coalescence, *Proc. Roy. Soc. Lond. A*, 326, 393, 1972.
- Brenn, G., Valkovska, D., and Danov, K.D., The formation of satellite droplets by unstable binary drop collisions, *Phys. Fluids*, 13, 2463, 2001.
- Brennen, C.E., Fission of collapsing cavitation bubbles, *J. Fluid Mech.*, 472, 153–166, 2002.
- Brennen, C.E., *Cavitation and Bubble Dynamics*, Oxford University Press, Oxford, 1995.
- Brennen, C.E., Cavitation in biological and engineering contexts, *Proceedings of the 5th International Symposium on Cavitation*, Osaka, Japan, 2003.
- Brooke, J.W., Kontomaris, K., Hanratty, T.J., and McLaughlin, J.B., Turbulent deposition and trapping of aerosols at a wall, *Phys. Fluids A*, 4, 825–834, 1992.
- Brujan, E.A., Keen, G.S., Vogel, A., and Blake, J.R., The final stage of the collapse of a cavitation bubble close to a rigid boundary, *Phys. Fluids*, 14, 85, 2002.
- Burcat, A., Thermophysical data for combustion calculations, in Gardiner, W.C., Ed., *Combustion Chemistry*, Springer-Verlag, New York, NY, 1994, pp. 455–504.
- Burton, T.M. and Eaton, J.K., Fully Resolved Simulations of Particle-Turbulence Interaction, Report TSD-151, Department of Mechanical Engineering, Stanford University, 2003.
- Burton, T.M. and Eaton, J.K., Analysis of a fractional-step method on overset grids, *J. Computat. Phys.*, 177, 336–364, 2002.
- Carey, V.P., *Liquid-Vapor Phase-Change Phenomena: An Introduction to the Thermophysics of Vaporization and Condensation Processes in Heat Transfer Equipment*, Hemisphere, Washington, DC, 1992.
- Carlson, B., Avoiding cavitation in control valves, *ASHRAE J.*, 43, 58, 2001.
- Ceccio, S.L. and Brennen, C.E., Observations of the dynamics and acoustics of travelling bubble cavitation, *J. Fluid Mech.*, 233, 633, 1991.
- Ceccio, S.L., Gowing, S., and Gindroz, B., Comparison of CSM bubble detection methods, *ASME Fluids Eng. Div. FED-226*, 43, 1991.
- Chahine, G.L. and Duraiswami, R., Dynamical interactions in a multi-bubble cloud, *ASME J. Fluids Eng.*, 114, 680–686, 1992.
- Chahine, G.L. and Kalumuck, K.M., Development of a near real-time instrument for nuclei measurement: the ABS Acoustic Bubble Spectrometer®, *Proceedings of the 4th ASME-JSME Joint Fluids Engineering Conference*, Honolulu, Hawaii, 2003.
- Chandra, S. and Avedisian, C.T., On the collision of a droplet with a solid surface, *Proc. R. Soc. London A*, 432, 13, 1991.
- Chapman, R.B. and Plesset, M.S., Thermal effects in the free oscillation of gas bubbles, *ASME J. Basic Eng.*, 93, 373–376, 1971.
- Chen, C.P. and Wood, P.E., A turbulence closure model for dilute gas-particle flows, *Canadian J. Chem. Eng.*, 63, 349–360, 1985.
- Chen, G. and Gomez, A., Dilute laminar spray diffusion flames near the transition from group combustion to individual droplet burning, *Combust. and Flame*, 110, 392–404, 1997.
- Chen, J.-H. and Faeth, G.M., Continuous-phase properties of homogeneous particle-laden turbulent flows, *AIAA J.*, 39, 180–183, 2001.
- Chesters, A.K., The modeling of coalescence processes in fluid liquid dispersions – A review of current understanding, *Trans. Inst. Chem. Eng.*, 69, 259, 1991.
- Chiu, H.H. and Croke, E.J., Group Combustion of Liquid Fuel Sprays, Technical Report 81–2, University of Illinois at Chicago, Energy Technology Lab, 1981.
- Chiu, H.H. and Huang, J.S., Multiple-state phenomena and hysteresis of a combusting isolated droplet, *Atomiz. Sprays*, 6, 1–26, 1996.
- Chiu, H.H., Advances and challenges in droplet and spray combustion. I. toward a unified theory of droplet aerothermochemistry, *Prog. Energy Combust. Sci.*, 26, 381–416, 2000.

- Chiu, H.H. and Liu, T.M., Group combustion of liquid droplets, *Combust. Sci. and Tech.*, 17, 127–142, 1977.
- Chiu, H.H., Kim, H.Y., and Croke, E.J., Internal group combustion of liquid droplets, in *Proceedings of 19th Symposium (International) on Combustion*, The Combustion Institute, Pittsburgh, PA, 1982, pp. 971–980.
- Clift, R., Grace, J.R., and Weber, M.E., *Bubbles, Drops, and Particles*, Academic Press, New York, NY, 1978.
- Cody, G. D., Goldfarb, D.J., Storch, G.V., Jr., and Norris, A.N., Particle Granular Temperature in Gas Fluidized Beds, *Powder Technol.*, 87, 211, 1996.
- Coleman, A.J., Kodama, T., Choi, M.J., Adams, T., and Saunders, J.E., Cavitation threshold of human tissue exposed to 0.2-MHz pulsed ultrasound: preliminary measurements based on a study of clinical lithotripsy, *Ultrasound Med. Biol.*, 21, 405, 1995.
- Collings, E.W., Markworth, J.K., McCoy, J.K., and Saunders, J.H., Splat-quench solidification of freely falling liquid-metal drops by impact on a planar substrate, *J. Mater. Sci.*, 25, 3677, 1990.
- Cossali, G.E., Coghe, A., and Marengo, M., The impact of a single drop on a wetted surface, *Exp. Fluids*, 22, 463, 1997.
- Cossali, G.E., Marengo, M., Coghe, A., and Zhdanov, S., The role of time in single splash on thin film, *Exp. Fluids*, 36, 888, 2004.
- Cox, R.G., The dynamics of the spreading of liquids on a solid surface. Part 1. Viscous flow, *J. Fluid Mech.*, 168, 169, 1986.
- Crowe, C.T., On models for turbulence modulation in fluid-particle flows, *Int. J. Multiphase Flow*, 26, 719–727, 2000.
- Crowe, C.T., Carrier phase turbulence in dispersed phase flows, Key note Address *International Conference on Multiphase Flows*, New Orleans, 2001.
- Crowe, C.T. and Gilliland, I., Turbulence modulation of fluid-particle flows, A basic approach, *3rd International Conference on Multiphase Flows*, Lyon France, June 8–12, 1998.
- Crowe, C.T., Chung, J.N., and Troutt, T.R., Particle dispersion by organized turbulent structures, *Particulate Two-Phase Flow*, Roco, M.C., Ed., Chap. 18, 1993, pp. 626–669.
- Crowe, C.T., Sharma, M.P., and Stock, D.E., The particle-source-in cell (PSI-cell) model for gas-droplet flows, *J. Fluids Eng.*, 99, 325–332, 1977.
- Crowe, C.T., On models for turbulence modulation in fluid-particle flows, *Int. J. Multiphase Flow*, 20S, 169–209, 2000.
- Crowe, C.T., Sharma, M.P., and Stock, D.E., The Particle-Source in cell (PSI-Cell) model for Gas-Droplet flows, *J. Fluids Eng.*, 6, 325–332, 1977.
- Crowe, C.T., Summerfeld, M., and Tsuji, Y., *Multiphase Flows with Droplets and Particles*, CRC Press, Boca Raton, FL, 1998, pp. 12–22.
- Crowe, C.T., Troutt, T.R., and Chung, J.N., Numerical models for two-phase turbulent flows, *Ann. Rev. Fluid Mech.*, 28, 11–43, 1996.
- Crowe, C.T., Troutt, T.R., and Chung, J.N., Particle Interactions with Vortices, Green, S.I., Ed., Chap. XIX, 1995, pp. 829–858.
- Cui, M.M. and Adrian, R.J., Refractive index matching and marking methods for highly concentrated solid–liquid flows, *Exp. Fluids*, 22, 261–264, 1997.
- Cundall, P. A. and Strack, O.D., A discrete numerical model for granular assemblies, *Geotechnique*, 291, 47, 1979.
- d'Agostino, L. and Brennen, C., Linearized dynamics of spherical bubble clouds, *J. Fluid Mech.*, 199, 155–176, 1989.
- d'Agostino, L. and Acosta, A.J., Cavitation susceptibility meter with optical cavitation monitoring. Part Two. Experimental apparatus and results, *ASME J. Fluids Eng.*, 113, 270, 1991.
- Dai, Z. and Faeth, G.M., Temporal properties of secondary drop breakup in the multimode breakup regime, *Int. J. Multiphase Flow*, 27, 217, 2001.
- Davidson, J.F., Symposium on fluidization – discussion, *Trans. Inst. Chem. Engineers*, 39, 230, 1961.
- de Brujin, R.A., Tip streaming of drops in simple shear flows., *Chem. Eng. Sci.*, 48, 277, 1993.

- Delplanque, J.-P. and Siringano, W.A., Boundary layer stripping effects on droplet transcritical convecting vaporization, *Atomization Sprays*, 4, 325, 1994.
- Deutsch, E. and Simonin, O., Large eddy simulation applied to the modeling of particulate transport in turbulent two-phase flows, 8th *Symposium on Turbulence Shear Flows*, Technical University Munich, 1991, pp.10.1.1–10.1.6.
- Ding, J. and D. Gidaspow, A Bubbling Model Using Kinetic Theory of Granular Flow, *AICHE J.*, 36 (4), 523, 1990.
- Ding, J. and R.W. Lyczkowski, Three-Dimensional Kinetic Theory Modeling of Hydrodynamics and Erosion in Fluidized Beds, *Powder Technology*, 73, 127, 1992.
- Drew, D.A., Mathematical modeling of two-phase flow, *Annu. Rev. Fluid Mech.*, 15, 261–291, 1983.
- Druzhinin, O.A. and Elghobashi, S., On the decay rate of isotropic turbulence laden with microparticles, *Phys. Fluids* 11, 602–610, 1999.
- Druzhinin, O.A., The influence of particle inertia on the two-way coupling and modification of isotropic turbulence by microparticles, *Phys. Fluids*, 13, 3738–3755, 2001.
- Dussan, E.B.V. and Chow, R.T., On the ability of drops or bubbles to stick to nonhorizontal surfaces or solids, *J. Fluid Mech.*, 137, 1, 1983.
- Eaton, J.K. and Fessler J.R., Preferential concentration of particles by turbulence, *Int. J. Multiphase Flow*, 26, 719–727, 1994.
- Eaton, J.K. and Fessler, J.R., Preferential concentration of particles by turbulence, *Int. J. Multiphase Flow*, 20, 169–209, 1994.
- Eggers, J., Nonlinear dynamics and breakup of free-surface flows, *Rev. Mod. Phys.*, 69, 865, 1997.
- Eggers, J., Universal pinching of three dimensional axisymmetric free-surface flow, *Phys. Rev. Lett.*, 71, 3458, 1993.
- Eisfeld, F., Investigation of the Penetration, the Spreading, and the Atomization of a Diesel Injection Jet using High Speed Cinematography, *Proc. SPIE Int. Soc. Opt. Eng.*, 4948, 182, 2002.
- Elghobashi, S.E. and Truesdell, G.C., On the two-way interaction between homogeneous turbulence and dispersed solid particles I: turbulence modification, *Phys. Fluids A*, 5, 1790–1796, 1993.
- Elperin, T., Kleeorin, N., and Rogachevskii, I., Turbulent thermal diffusion of small inertial particles, *Phys. Rev. Lett.*, 76, 224–227, 1996.
- Engel, P.A., *Impact Wear of Materials*, Elsevier Scientific Publishing Co., Amsterdam, 1978.
- Esche, R., Untersuchung der schwingungskavitation in Flüssigkeiten, *Acustica*, 2, AB208–AB218, 1952.
- Faeth, G.M., Current status of droplet and liquid combustion, *Prog. Energy Combust. Sci.*, 3, 191–224, 1977.
- Fedorchenko, A.I. and Chernov, A.A., Formation of fingers at the front of an axially symmetric film of liquid upon the impact of a drop with a solid surface, *Dokl. Phys.*, 44, 570, 1999.
- Ferrante, A. and Elghobashi, S., On the physical mechanism of two-way coupling in particle-laden isotropic turbulence, *Phys. Fluids*, 15, 315–329, 2003.
- Ferrel, G.W. and Crum, L.A., A novel cavitation probe design and some preliminary measurements of its application to megasonic cleaning, *J. Acoust. Soc. Am.*, 112, 1196, 2002.
- Fessler, J.R. and Eaton, J.K., Turbulence modification by particles in a backward-facing step flow, *J. Fluid Mech.*, 394, 97–117, 1999.
- Fessler, J.R., Kulick, J.D., and Eaton, J.K., Preferential concentration of heavy particles in a turbulent channel flow, *Phys. Fluids*, 6, 3742–3749, 1994.
- Finnie, I. and McFadden, D.H., On the velocity dependence of ductile metals by solid particles at low angles of incidence, *Wear*, 48, 181, 1978.
- Finnie, I., Erosion of Surfaces by Solid Particles, *Wear*, 3, 87, 1960.
- Finnie, I., Some Observations on the Erosion of Ductile Metals, *Wear*, 19, 81, 1972.
- Finnie, I., The Mechanism of Erosion of Ductile Metals, in *Proceeding of the Third National Congress on Applied Mechanics*, American Society of Mechanical Engineers, 1958, p. 527.
- Fiore, N.F., Anthony, N.C., and Kosel, T.H., Abrasion in Multi phase Alloys, in *Proceedings of the Corrosion-Erosion-Wear of Materials in Emerging Fossil Energy Systems*, Berkeley, CA, Jan. 17–19, 1982, Levy, A.V., Ed., National Association of Corrosion Engineers, Houston, 1982, p. 266.

- Flynn, H.G., *Physics of Acoustic Cavitation in Liquids*, Physical Acoustics, 1B. Academic Press, New York, 1964.
- Franc, J.P., Avellan, F., Belhadji, B., Billard, J.Y., Briançon-Marjollet, L., Fréchou, D., Fruman, D.H., Karimi, A., Kueny, J.L., and Michel, J.M., *La Cavitation. Mécanismes Physiques et Aspects Industriels*, Presses Universitaires de Grenoble, Grenoble, 1995.
- Frank, Th., Schade, K.P., and Petrak, D., Numerical simulation and experimental investigation of a gas-solid two-phase flow in a horizontal channel, *Int. J. Multiphase Flow*, 19, 187, 1993.
- Frenkel, J., *Kinetic Theory of Liquids*. Oxford University Press, New York, 1946.
- Fujikawa, S. and Akamatsu, T., Effect of the non-equilibrium condensation of vapour on the pressure wave produced by the collapse of a bubble in a liquid, *J. Fluid Mech.*, 97, 481–512, 1980.
- Fukai, J., Shiiba, Y., Yamamoto, T., Miyatake, O., Poulikakos, D., Megaridis, C.M., and Zhao, Z., Wetting effects on the spreading of a liquid droplet colliding with a flat surface: Experiment and modelling, *Phys. Fluids*, 7, 236, 1995.
- Gansley, R.R. and O'Brien, T.J., A Model for Bubble-Induced Erosion in Fluidized-Bed Combustors and Comparison with Experiment, *Wear*, 137 107, 1990.
- Gao, Z. and Mashayek, F., Stochastic model for non-isothermal droplet-laden turbulent flows, *AIAA J.*, 42, 255–260, 2004.
- Geiss, S., Sadika, A., Maltsev, A., Dreizler, A., and Janicka, J., Investigations of turbulence modulation in turbulent particle laden flows, *Z. Agnew Math. Mech.*, 81, S527–S528, 2001.
- George, D.L., Iyer, C.O., and Ceccio, S.L., Measurement of the bubbly flow beneath partial attached cavities using electrical impedance probes, *ASME J. Fluids Eng.*, 122, 151, 2000.
- Gidaspow, D., *Multiphase Flow and Fluidization, Continuum and Kinetic Theory Descriptions*, Academic Press, San Diego, CA, 1994.
- Gindroz, B. and Billet, M.L., Influence of the nuclei on the cavitation inception for different types of cavitation on ship propellers, *ASME Fluids Eng. Div. FED-177*, 1, 1993.
- Givi, P., Model free simulations of turbulent reactive flows, *Prog. Energy Combust. Sci.*, 15, 1–107, 1989.
- Givi, P., Subgrid scale modeling in turbulent combustion: A review, *AIAA Paper 2003-5081*, 2003.
- Godsave, G.A.E., Studies of the combustion of drops in a fuel spray, In *Proceedings of 4th Symposium (International) on Combustion*, The Combustion Institute, Baltimore, MD, 1953, pp. 818–830.
- Gogos, G., Soh, S., and Pope, D.N., Effects of gravity and ambient pressure on liquid fuel droplet evaporation, *Int. J. Heat Mass Transfer*, 46, 283–296, 2003.
- Goldsmith, W., The state of head injury biomechanics: past, present and future: Part 1, *Crit. Rev. Biomed. Eng.*, 29, 441, 2001.
- Gore, R.A. and Crowe, C.T., Effect of particle size on modulating turbulence intensity, *Int. J. Multiphase Flow*, 15, 279–285, 1989.
- Gore, R.A. and Crowe, C.T., Modulation of turbulence by a dispersed phase, *ASME J. Fluids Eng.*, 113, 304–307, 1991.
- Gosman, A.D. and Ioannides, E., Aspects of computer simulation of liquid-fueled combustors, *AIAA Paper 81-0323*, 1981.
- Gosman, A.D. and Pun, W.M., Calculation of Recirculating Flows (lecture notes), Report HTS/74/2, Imperial College, London, 1974.
- Grace, H.P., Dispersion phenomena in high viscosity immiscible fluid systems and application of static mixers as dispersion devices in such systems, *Chem. Eng. Commun.*, 14, 225, 1982.
- Grant, G. and Tabakoff, W., Erosion Predictions in Turbomachinery Resulting from Environmental Solid Particles, *J. Aircraft*, 12, 642, May 1975.
- Ha, J.-W. and Leal, L.G., An experimental study of drop deformation and breakup in extensional flow at high capillary number, *Phys. Fluids*, 13, 1568, 2001.
- Ha, J.-W. and Yang, S.-M., Effect of nonionic surfactant on the deformation and breakup of a drop in an electric field, *J. Colloid Interface Sci.*, 206, 195, 1998.
- Hamaker, H. C., The London–Van der Waals' attraction between spheroid particles, *Physica*, 4, 1058, 1937.
- Hammitt, F.G., *Cavitation and Multiphase Flow Phenomena*, McGraw-Hill, New York, 1980.

- Hao, Y. and Prosperetti, A., The effect of viscosity on the spherical stability of oscillating gas bubbles, *Phys. Fluids*, 11, 1309–1317, 1999.
- Hardalupus, Y., Taylor, A.M.K.P., and Whitelaw, J.H., Particle dispersion in a vertical round sudden expansion flow, *Proc. Royal Soc. London A* 341, 411–442, 1992.
- Hartley, G.S. and Brunskill, R.T., Reflection of water drop from surfaces, in *Surface phenomena in chemistry and biology*, Vol. 57, Pergamon Press, Oxford, 1958, pp. 214–223.
- Hatamiya, S. and Tanaka, H., A study on the mechanism of dropwise condensation, *Trans. Jpn. Soc. Mech. Eng.* (in Japanese), B-52, 2214, 1986.
- Haywood, R.J., Renksizbulut, M., and Raithby, G.D., Numerical solution of deforming evaporating droplets at intermediate Reynolds numbers, *Num. Heat Transfer*, 26, 253–272, 1994a.
- Haywood, R.J., Renksizbulut, M., and Raithby, G.D., Transient deformation and evaporation of droplets at intermediate reynolds numbers, *Int. J. Heat Mass Transfer*, 37, 1401–1409, 1994b.
- Hilgenfeldt, S., Grossmann, S., and Lohse, D., A simple explanation of light emission in sonoluminescence, *Nature*, 398, 402, 1999.
- Hinze, J.O., Fundamentals of the hydrodynamic mechanism of splitting in dispersion processes, *AICHE J.*, 1, 289, 1955.
- Hishida, K. and Maeda, M., *Turbulence Characteristics of Particle-laden Flow Behind a Rearward Facing Step*, ASME FED Vol. 121, 207–212, 1991.
- Ho, C.M. and Huerre, P., Perturbed free shear layers, *Ann. Rev. Fluid Mech.*, 16, 365–424, 1984.
- Hocking, L.M. and Rivers, A.D., The spreading of a drop by capillary action, *J. Fluid Mech.*, 121, 425, 1982.
- Hoffman, R.L., A study of the advancing interface. 1. Interface shape in liquid–gas systems, *J. Coll. Interface Sci.*, 50, 228, 1975.
- Holzfuss, J., Ruggeberg, M., and Billo, A., Shock wave emissions of a sonoluminescing bubble, *Phys. Rev. Lett.*, 81, 5434, 1998.
- Hsiang, L.-P. and Faeth, G.M., Drop deformation and breakup due to shock wave and steady disturbances, *Int. J. Multiphase Flow*, 21, 545, 1995.
- Hsiang, L.-P. and Faeth, G.M., Drop properties after secondary breakup, *Int. J. Multiphase Flow*, 19, 721, 1993.
- Hsiang, L.-P. and Faeth, G.M., Near-limit drop deformation and secondary breakup, *Int. J. Multiphase Flow*, 18, 635, 1992.
- Hsieh, D.-Y. and Plesset, M.S., Theory of rectified diffusion of mass into gas bubbles, *J. Acoust. Soc. Am.*, 33, 206, 1961.
- Hsieh, D.-Y., Some analytical aspects of bubble dynamics, *J. Basic Eng.*, 87, 991–1005, 1965.
- Hubbard, G.L., Denny, V.E., and Mills, A.F., Droplet evaporation: Effects of transients and variable properties, *Int. J. Heat Mass Transfer*, 18, 1003–1008, 1975.
- Humphrey, J.A.C., Fundamentals of Fluid Motion in Erosion by Solid Particle Impact, *Int. J. Heat Fluid Flow*, 11, 170, 1990.
- Hussain, M.F. and Tabakoff, W., Computation and Plotting of Solid Particulate Flow in Rotating Cascades, *Comput. Fluids*, 2, 1974.
- Hwang, S., Liu, S., and Reitz, R. D., Breakup mechanisms and drag coefficients of high speed vaporizing drops, *Atomization Sprays*, 6, 353, 1996.
- Jackson, R., Locally averaged equations of motion for a mixture of identical spherical particles and a Newtonian fluid, *Chem. Eng. Sci.*, 52, 2457–2469, 1997.
- Jayaratne, O.W. and Mason, B.J., The coalescence and bouncing of water drops at an air/water interface, *Proc. Roy. Soc. London A*, 280, 545, 1964.
- Jiang, Y.J., Umemura, A., and Law, C.K., An experimental investigation on the collision behaviour of hydrocarbon droplets, *J. Fluid Mech.*, 234, 171, 1992.
- Johnston, D.N., Edge, K.A., and Vaughan, N.D., Experimental Investigation of Flow and Force Characteristics of Hydraulic Poppet and Disc Valves, *Proc. Inst. Mech. Eng., A: Power Process Eng.*, 205, 161, 1991.

- Joseph, D.D., Lift Correlations From Direct Numerical Simulation of Solid–Liquid Flow, Paper 385 presented at *ICMF-2001, 4th International Conference on Multiphase Flow*, May 27–June 1, 2001.
- Joseph, D.D., Belanger, J., and Beavers, G.S., Breakup of a liquid drop suddenly exposed to a high-speed airstream, *Int. J. Multiphase Flow*, 25, 1263, 1999.
- Jozsa, I., Sebestyen, G., and Kiss, J., 1994, Regulating valve cavitation in the power station, *ASME, Fluids Eng. Div. FED*, 194, 89.
- Kamath, V. and Prosperetti, A., Numerical investigation methods in gas-bubble dynamics, *J. Acoust. Soc. Am.*, 85, 1538–1548, 1989.
- Kameda, M. and Matsumoto, Y., Nonlinear oscillation of a spherical gas bubble in acoustic fields, *J. Acoust. Soc. Am.*, 106, 3156–3166, 1999.
- Kameda, M. and Matsumoto, Y., Shock waves in a liquid containing small gas bubbles, *Phys. Fluids*, 8, 322–335, 1996.
- Kameda, M., Shimaura, N., Higashino, F., and Matsumoto, Y., Shock waves in a uniform bubbly flow, *Phys. Fluids*, 10, 2661–2668, 1998.
- Keller, J.B. and Kolodner, I.I., Damping of underwater explosion bubble oscillation, *J. Appl. Phys.*, 27, 1152–1161, 1956.
- Khalitov, D.A. and Longmire, E.K., Simultaneous two-phase PIV by two-parameter phase discrimination, *Exp. Fluids*, 32, 252–268, 2002.
- Kick, F., *Dar Gesetz der proportionalen Widerstände und seine Anwendung*, Leipzig, Germany, 1885.
- Kiger, K.T. and Pan, C., PIV technique for the simultaneous measurement of dilute two-phase flows, *J. Fluids Eng.*, 122, 811–818, 2000.
- Kiger, K.T. and Pan, C., Suspension and turbulence modification effects of solid particulates on a horizontal turbulent channel flow, *J. Turbulence*, 3, 2002.
- Kiger, K.T., Scanning PIV technique to resolve dispersed two-phase flow, *Third International Conference on Multiphase Flow*, ICMF 1-98 Lyon France, June 8–12, 1998.
- Kim, H.-Y., Feng, Z.C., and Chun, J.-H., Instability of a liquid jet emerging from a droplet upon collision with a solid surface, *Phys. Fluids*, 12, 531, 2000.
- Kistler, S.F., Hydrodynamics of wetting, in *Wettability*, Berg, J.C., Ed., *Surfactant Science Series*, Marcel Dekker, New York, 1993.
- Knapp, R. T., Daily, J. W., and Hammitt, F. G., *Cavitation*, McGraw-Hill, New York, 1970.
- Koch, G.W., Silliett, S.C., Jennings, G.M., and Davis, S.D., The limits to tree height, *Lett. Nat.*, 428, 851, 2004.
- Korobkin, A., Analytic theory of liquid-solid impact, *Phil. Trans. R. Soc. Lond. A*, 355, 507, 1997.
- Krzeczkowski, S.A., Measurements of liquid droplet disintegration mechanisms, *Int. J. Multiphase Flow*, 6, 227, 1980.
- Kuhn de Chizelle, Y., Ceccio, S.L., and Brennen, C.E., Observations and scaling of travelling bubble cavitation, *J. Fluid Mech.*, 293, 99, 1995.
- Kulick, J.D., Fessler, J.R., and Eaton, J.K., Particle response and turbulence modification in fully developed channel flow, *J. Fluid Mech.*, 277, 285–309, 1994.
- Kussin, J. and Sommerfeld, M., Experimental studies on particle behavior and turbulence modification in horizontal channel flow with different wall roughness, *Exp. Fluids*, 33, 143–159, 2002.
- Laberteaux, K.R. and Ceccio, S.L., Partial cavity flows. Part 1. Cavities forming on models without spanwise variation, *J. Fluid Mech.*, 431, 1, 2001a.
- Laberteaux, K.R. and Ceccio, S.L., Partial cavity flows. Part 2. Cavities forming on test objects with spanwise variation, *J. Fluid Mech.*, 431, 43, 2001b.
- Lain, S., Sommerfeld, M., and Kussin, J., Experimental studies and modeling of four-way coupling in particle-laden channel flow, *Int. J. Heat Fluid Flow*, 23, 647–656, 2002.
- Lauterborn, W., Acoustic Turbulence, *Front. Phys. Acoust.*, S.I.F.-XC III, 124–144, 1989.
- Lauterborn, W., Numerical investigation of nonlinear oscillations of gas bubbles in liquids, *J. Acoust. Soc. Am.*, 59, 283–293, 1976.
- Lauterborn, W., On the bifurcation structure of bubble oscillators, 11th ISNA, 71–80, 1987.

- Law, C.K. and Williams, F.A., Kinetics and convection in the combustion of alkane droplets, *Combust. Flame*, 19, 393–406, 1972.
- Law, C.K., Chung, S.H., and Srinivasan, N., Gas phase quasi-steadiness and fuel vapor accumulation effects on droplet burning, *Combust. Flame*, 38, 173–198, 1980.
- Lee, C.H. and Reitz, R.D., An experimental study of the effect of gas density on the distortion and breakup mechanism of drops in high speed gas stream, *Int. J. Multiphase Flow*, 26, 229, 2000.
- Lee, S.L. and Durst, F., On the motion of particles in turbulent duct flows, *Int. J. Multiphase Flow*, 8, 125–146, 1982.
- Lefebvre, H., *Atomization and Sprays*, Hemisphere Publishing Corporation, Washington, DC, 1989.
- Leger, A.T. and Ceccio, S.L., Examination of the flow near the leading edge of attached cavitation. Part 1. Detachment of two-dimensional and axisymmetric cavities, *J. Fluid Mech.*, 376, 61, 1998.
- Leighton, T.G., *The Acoustic Bubble*, Academic Press, London, 1994.
- Lesieur, M. and Métais, O., New trends in large-eddy simulations of turbulence, *Annu. Rev. Fluid Mech.*, 28, 45–82, 1996.
- Lesser, M. and Field, J., The impact of compressible liquids, *Annu. Rev. Fluid Mech.*, 15, 97, 1983.
- Levin, Z. and Hobbs, P.V., Splashing of water drops on solid and wetted surfaces: hydrodynamics and charge separation, *Phil. Trans. R. Soc. London A*, 269, 555, 1971.
- Li, C.-Y. and Ceccio, S.L., Interaction of single traveling bubbles with the boundary layer and attached cavitation, *J. Fluid Mech.*, 322, 329, 1996.
- Li, S.C., Spray stagnation flames, *Prog. Energy Combust. Sci.*, 23, 303–347, 1997.
- Lifka, J., Ondruschka, B., and Hofmann, J., The use of ultrasound for the degradation of pollutants in water: a quasonalysis — a review, *Eng. Life Sci.*, 3, 2003.
- Lindau, O. and Lauterborn, W., Cinematographic observation of the collapse and rebound of a laser-produced cavitation bubble near a wall, *J. Fluid Mech.*, 479, 327–348, 2003.
- Ling, W., Chung, J.N., and Crowe, C.T., Direct numerical simulation of the two-way coupled interaction between particles and mixing layer, *Proc. R. Soc. London A*, 456, 2931–2955, 2000.
- Ling, W., Chung, J.N., and Crowe, C.T., Direct numerical simulation of a two-way thermally coupled droplet-laden mixing layer, *J. Fluid Mech.*, 437, 45–68, 2001.
- Ling, W., Chung, J.N., Troutt, T.R., and Crowe, C.T., Direct numerical simulation of a three-dimensional mixing layer with particle dispersion, *J. Fluid Mech.*, 358, 61–85, 1998.
- Liu, Q. and Orme, M., On precision droplet-based net-form manufacturing technology, *Proc.-Inst. Mech. Eng. B, J. Eng. Manufacture*, 215, 1333, 2001.
- Liu, Z. and Reitz, R.D., An analysis of the distortion and breakup mechanisms of high speed liquid drops, *Int. J. Multiphase Flow*, 4, 631, 1997.
- Liu, Z.C. and Adrian, R., Simultaneous imaging of the velocity fields of two phases, in *Particulate Two-Phase Flow*, Roco, M.C., Ed., Butterworth-Heinemann, London, pp. 33–57, 1993.
- Longmire, E.K. and Eaton, J.K., Structure of a particle-laden round jet, *J. Fluid Mech.*, 236, 217–257, 1992.
- Lonholt, S., Stenum, B., and Maxey, M.R., Experimental verification of the force coupling method for particulate flows, *Int. J. Multiphase Flow*, 28, 225–246, 2002.
- Lyczkowski, R.W. and Bouillard, J.X., Scaling and Guidelines for Erosion in Fluidized Beds, *Powder Technol.*, 125, 217, 2002.
- Lyczkowski, R.W. and Bouillard, J.X., Corrigendum to “State-of-the-Art Review of Erosion Modeling in Fluid/Solids Systems” [Prog. Energy Combust. Sci. 28 (2002) 543–602], *Prog. Energy Combust. Sci.* 29(1), 85, 2003.
- Lyczkowski, R.W. and Bouillard, J.X., State-of-the-Art Review of Erosion Modeling in Fluid/Solids Systems, *Prog. Energy Combust. Sci.*, 28, 543, 2002a.
- Lyczkowski, R.W., Bouillard, J.X., and Folga, S.M., Users Manual for FLUFIX/MOD2: A Computer Program for Fluid-Solids Hydrodynamics, Argonne National Laboratory Sponsor Report, Argonne, IL, April 1992. Reprinted by USDOE METC as DOE/MC/24193-3491/NTIS No. DE94000033), available from NTIS, Springfield, VA, 1994a.

- Lyczkowski, R.W., Bouillard, J.X., Chang, S.L., and Folga, S.M., User's Manual for EROSION/MOD1: A Computer Program for Fluid Solids Erosion, Argonne National Laboratory Sponsor Report, Argonne, IL, April 1992. Reprinted by USDOE METC as DOE/MC/24193-3500/NTIS No. 94000032), available from NTIS, Springfield, VA, 1994b.
- Macklin, W.C. and Metaxas, G.J., Splashing of drops on liquid layers, *J. Appl. Phys.*, 47, 3963, 1976.
- Madejski, J., Droplets on impact with a solid surface, *Int. J. Heat Mass Transfer*, 26, 1095, 1983.
- Madge, B.A. and Jensen, J.N., Disinfection of wastewater using a 20-kHz ultrasound unit, *Water Environ. Res.*, 74, 159, 2002.
- Maeda, M., Hishida, K., & Furutani, T., Optical measurements of local gas and particle velocity in an upward flowing dilute gas-solids suspension, *Proceedings of the Polyphase Flow and Transport Technology*, Century 2-ETC, San Francisco, 1980, pp. 211-216.
- Magnussen, B.F. and Hjertager, B.H., On mathematical models of turbulent combustion with special emphasis on soot formation and combustion. In *Proceedings of 16th Symposium (International) on Combustion*, The Combustion Institute, Pittsburgh, PA, 1977, pp. 719-729.
- Mao, T., Kuhn, D.C.S., and Tran, H., Spread and rebound of liquid droplets upon impact on flat surfaces, *AICHE J.*, 43, 2169, 1997.
- Marengo, M., Tropea, C., Aufprall von Tropfen auf Flüssigkeitsfilme, Final report for project Tr 194/10, Deutsche Forschungsgemeinschaft, Technische Universität Darmstadt, Darmstadt, 1999.
- Mashayek, F. and Pandya, R.V.R., Analytical description of particle/droplet-laden turbulent flows, *Progress Energy Combust. Sci.*, 29, 329-378, 2003.
- Mashayek, F., Dynamics of evaporating drops. Part I: Formulation and evaporation model, *Int. J. Heat Mass Transfer*, 44, 1517-1526, 2001.
- Mashayek, F., Numerical investigation of reacting droplets in homogeneous shear turbulence, *J. Fluid Mech.*, 405, 1-36, 2000.
- Matsumoto, S. and Saito, S., Monte Carlo simulation of horizontal pneumatic conveying based on the rough wall model, *J. Chem. Eng. Japan*, 3, 223, 1970b.
- Matsumoto, S. and Saito, S., On the mechanism of suspensions in horizontal pneumatic conveying: Monte Carlo simulation based on the irregular bouncing model, *J. Chem. Eng. Japan*, 3, 83, 1970a.
- Matsumoto, Y. and Aoki, M., Growth and collapse of cavitation bubbles, *Bull. JSME* 27, 1352-1357, 1984.
- Matsumoto, Y. and Beylich, A.E., Influence of homogeneous condensation inside a small gas bubble on its pressure response, *J. Fluids Eng. Eng. ASME*, 107-2, 281-286, 1985.
- Matsumoto, Y. and Takemura, F., Influence of internal phenomena on gas bubble motion (Effects of thermal diffusion, phase change on the gas-liquid interface and mass diffusion between vapor and non-condensable gas in the collapsing phase), *JSME Int. J., B-37*, 288-296, 1994.
- Matsumoto, Y. and Watanabe, M., Nonlinear oscillation of gas bubble with internal phenomena, *JSME Int. J. II-32*, 157-162, 1989.
- Matula, T.J., Hallaj, I., Cleveland, R.O., Crum, L.A., Moss, W.C., and Roy, R.A., The acoustic emissions from single-bubble sonoluminescence, *J. Acoust. Soc. Am.*, 103, 1377, 1998.
- Maxey, M.R. and Riley, J.J., Equation of motion for a small rigid sphere, *Phys. Fluids*, 26, 883-889, 1983.
- Maxey, M.R., Patel, B.K., Chang, E.J., and Wang, L.P., Simulations of dispersed turbulent multiphase flow, *Fluid Dyn. Res.*, 20, 143-156, 1997.
- Maxey, M.R., The gravitational settling of aerosol particles in homogeneous turbulence and random flow fields, *J. Fluid Mech.*, 174, 441-465, 1987.
- McCormick, B.W., On cavitation produced by a vortex trailing from a lifting surface, *J. Basic Eng.*, 84, 369, 1962.
- McCreath, C.G. and Chigier, N.A., Liquid spray burning in the wake of a stabilizer disk. In *Proceedings of 14th Symposium (International) on Combustion*, The Combustion Institute, 1973, pp. 1355-1363.
- McLaughlin, J.B., Aerosol particle deposition in numerically simulated channel flow, *Phys. Fluids A*, 1, 1211-1224, 1989.
- Meneveau, C. and Katz, J., Scale-invariance and turbulence models for large-eddy simulation, *Annu. Rev. Fluid Mech.*, 32, pp. 1-32, 2000.

- Meng, H. C. and Ludema, K.C., Wear Models and Predictive Equations: Their Form and Content, *Wear*, 181–183, 443, 1995.
- Mikami, T., Cox, R.G., and Mason, S.G., Breakup of extending liquid threads, *Int. J. Multiphase Flow*, 2, 113, 1975.
- Milliken, W.J. and Leal, L.G., Deformation and breakup of viscoelastic drops in planar extensional flows, *J. Non-Newtonian Fluid Mech.*, 40, 355, 1991.
- Mostafa, A.A., Mongia, H.C., McDonell, V.G., and Samuelsen, G.S., Evolution of particle-laden jet flows: a theoretical and experimental study, *AIAA J.* 27, 167–183, 1989.
- Mourougou-Candoni, N., Prunet-Foch, B., Legay, F., and Vignes-Adler, M., Retraction phenomena of surfactant solution drops upon impact on a solid substrate of low surface energy, *Langmuir*, 15, 6563, 1999.
- Mulhearn, T.O. and Samuels, L.E., The Abrasion of Metals: A Model of the Process, *Wear*, 5, 478, 1962.
- Mundo, C., Sommerfeld, M., and Tropea, C., On the modelling of liquid sprays impinging on surfaces, *Atomiz. Sprays*, 8, 625–652, 1998.
- Neilson, J.H. and Gilchrist, A., Erosion by a Stream of Solid Particles, *Wear*, 11, 111, 1968.
- Neppiras, E.A. and Noltingk, B.E., Cavitation produced by ultrasonics: theoretical conditions for the onset of cavitation, *Proc. Phys. Soc. London*, 64B, 1032–1038, 1951.
- Neppiras, E.A., Subharmonic and other low-frequency emission from bubbles in sound-irradiated liquids, *J. Acoust. Soc. Am.*, 46, 587–601, 1969.
- Niemczewski, B., Estimation of the suitability of selected organic solvents for ultrasonic cleaning, *Ultrasonics Sonochem.*, 6, 149, 1999.
- Nigumatalin, R.I., Khabeev, N.S., and Nagiev, F.B., Heat and mass transfer of vapours–gas bubbles in a liquid, *Int. J. Heat Mass Transfer*, 24, 1033–1044, 1981.
- Noltingk, B.E. and Neppiras, E.A., Cavitation produced by ultrasonics, *Proc. Phys. Soc., London*, 63B, 674–685, 1950.
- Oğuz, H.N. and Prosperetti, A., Bubble entrainment by the impact of drops on liquid surfaces, *J. Fluid Mech.*, 219, 143, 1990.
- Omta, R., Oscillation of a cloud of bubbles of small and not so small amplitude, *J. Acoust. Soc. Am.*, 82, 1018–1033, 1987.
- Onda, T., Shibuichi, S., Satoh, N., and Tsujii, K., Super-water-repellent fractal surfaces, *Langmuir*, 12, 2125, 1996.
- Padhye, A.R., Literature Review of Fundamental Erosion/Abrasion Models as Applicable to Wear of Fluidized Bed Internals, Topical Report, EG&G WASC, Inc., Morgantown, W.V., December 1985.
- Pandya, R.V.R. and Mashayek, F., Turbulent thermal diffusion and barodiffusion of passive scalar and dispersed phase of particles in turbulent flows, *Phys. Rev. Lett.*, 88, 044501–1–044501–4, 2002.
- Pandya, R.V.R. and Mashayek, F., Non-isothermal dispersed phase of particles in turbulent flow, *J. Fluid Mech.*, 475, 205–245, 2003.
- Paris, A.D. and Eaton, J.K., Measuring velocity gradients in a particle-laden channel flow, *Proceedings of the Third International Workshop on Particle Image Velocimetry, PIV99*, Santa Barbara, 1999, pp. 513–518.
- Paris, T. and Eaton, J.K., *Turbulence Attenuation in a Particle-Laden Channel Flow*, Report TSD-137, Department of Mechanical Engineering, Stanford University, 2001.
- Park, R.W., *Behaviour of Water Drops Colliding in Humid Nitrogen*, Ph.D. thesis, University of Wisconsin, WI, U.S.A., 1970.
- Parkinson, M.J., Jury, A.W., Napier, B.A., Kempton, T.J., and Holder, J.C., Cold Model Erosion Studies in Support of Pressurized Fluidized Bed Combustion, Electric Power Research Institute Final Report for Project 1337-2 , April 1986.
- Parkinson, M.J., Napier, B.A., Jury, A.W., and Kempton, T.J., Cold Model Studies of PFBC Tube Erosion, in *Proceedings of the 8th International Conference on Fluidized-Bed Combustion*, Vol. II, National Technical Information Service, DOE/METC-85/6021, Springfield, VA ,1985, p. 730.
- Parthasarathy, R.N. and Faeth, G.M., Turbulence modulation in homogeneous dilute particle-laden flows, *J. Fluid Mech.*, 220, 485–514, 1990.

- Pasandideh-Fard, M., Qiao, Y.M., Chandra, S., and Mostaghimi, J., Capillary effects during droplet impact on a solid surface, *Phys. Fluids*, 8, 650, 1996.
- Pecher, R. and Gompf, B., Microimplosions: cavitation collapse and shock wave emission on a nanosecond time scale, *Phys. Rev. Lett.*, 84, 1328, 2000.
- Peters, N., *Turbulent Combustion*, Cambridge University Press, Cambridge, UK, 2000.
- Philipp, A. and Lauterborn, W., Cavitation erosion by single laser-produced bubbles, *J. Fluid Mech.*, 361, 75, 1998.
- Pilch, M. and Erdman, C., Use of break-up time data and velocity history data to predict the maximum size of stable fragments for acceleration induced break-up of a liquid drop, *Int. J. Multiphase Flow*, 13, 741, 1987.
- Plesset, M.S. and Mitchell, T.P., On the stability of the spherical shape of a vapor cavity in a liquid, *Q. Appl. Math.*, 13, 419–430, 1956.
- Plesset, M.S., The dynamics of cavitation bubbles, *ASME J. Appl. Mech.*, 16, 228–231, 1949.
- Podolski, W.F., Lyczkowski, R.W., Montrone, E., Drennen, J., Ai, Y.H. and Chao, B.T., A Study of Parameters Influencing Metal Wastage in Fluidized Bed Combustors, in *Proceedings of the 11th (1991) International Conference on Fluidized Bed Combustion*, Vol.2, Anthony, E.J., Ed., American Society of Mechanical Engineers, 1991, p. 609.
- Podvysotsky, A.M. and Shraiber, A.A., Coalescence and break-up of drops in two-phase flows, *Int. J. Multiphase Flow*, 10, 195, 1984.
- Pope, S.B., PDF methods for turbulent reactive flows, *Prog. Energy Combust. Sci.*, 11, 119–192, 1985.
- Porteiro, J.L.F., Weber, S.T., and Rahman, M.M., Experimental study of flow induced noise in counterbalance valves, *ASME Aerospace Division (AD)*, 53, 2, *Proceedings of the 4th International Symposium on Fluid-Structure Interactions, Aeroelasticity, Flow-Induced Vibration and Noise*, 1997, p. 557.
- Poulikakos, D. and Waldvogel, J., Heat transfer and Fluid dynamics in the process of spray deposition, *Adv. Heat Transfer*, 28, 1, 1996.
- Pourahmadi, F. and Humphrey, J.A.C., Modeling Solid-Fluid Turbulent Flows with Application to Predicting Erosion Wear, *Physico Chem. Hydromodyn.*, 4, 191, 1983.
- Pozdikidis, C., The deformation of a liquid drop moving normal to a plane wall, *J. Fluid Mech.*, 215, 331, 1990.
- Pozorski, J. and Minier, J., On the Lagrangian turbulent dispersion models based on the Langevin equation, *Int. J. Multiphase Flow*, 24, 913–945, 1998.
- Preston, A., Colonius, T., and Brennen C. E., Reduced-order modeling of diffusive effects on the dynamics of bubbles, *Proceedings of 5th International Symposium on Cavitation*, GS-2-013, 2003.
- Prosperetti, A., Crum, L.A., and Commander, K.W., Nonlinear bubble dynamics, *J. Acoust. Soc. Am.*, 83, 502–514, 1988.
- Prosperetti, A., The thermal behaviour of oscillating gas bubbles, *J. Fluid Mech.*, 222, 587–616, 1991.
- Puterman, S.J. and Weninger, K.R., Sonoluminescence: How bubbles turn sound into light, *Annu. Rev. Fluid Mech.*, 32, 445, 2000.
- Qian, J. and Law, C.K., Regimes of coalescence and separation in droplet collision, *J. Fluid Mech.*, 331, 59, 1997.
- Rabinowicz, E., *Friction and Wear of Materials*, Wiley, New York, 1965.
- Raja, N. and Meiburg, E., The accumulation and dispersion of heavy particles in forced two-dimensional mixing layers. Part2: The effect of gravity, *Phys. Fluids*, 7, 1241–1264, 1995.
- Ran, B. and Katz, J., Pressure fluctuations and their effect on cavitation inception within water jets, *ASME Fluids Eng. Div. FED*, 177, 31, 1993.
- Range, K. and Feuillebois, F., Influence of surface roughness on liquid drop impact, *J. Colloid Interface Sci.*, 203, 16, 1998.
- Ranger, A.A. and Nicholls, J.A., The aerodynamic shattering of liquid drops, *AIAA J.*, 7, 285, 1969.
- Ranz, W.E. and Marshall, W.R., Evaporation from drops, *Chem. Eng. Prog.*, 48, 141–173, 1952.
- Rayleigh, Lord, On the pressure developed in a liquid during the collapse of a spherical cavity, *Phil. Mag.*, 34, 94–98, 1917.

- Rein, M. Ed., *Drop-Surface Interactions*, Springer, Wien, 2002.
- Reveillon, J. and Vervisch, L., Spray vaporization in nonpremixed turbulent combustion modeling: A single droplet model, *Combust. Flame*, 121, 75–90, 2000.
- Reznik, S.N. and Yarin, A.L., Spreading of a viscous drop due to gravity and capillarity on a horizontal or an inclined dry wall, *Phys. Fluids*, 14, 118, 2002.
- Richard, D. and Quéré, D., Bouncing water drops, *Europhys. Lett.* 50, 769, 2000.
- Riesz, P., Kondo, T., and Krishna, C.M., Sonochemistry of volatile and nonvolatile solutes in aqueous solutions. E.p.r. and spin trapping studies, *Ultrasonics*, 28, 295, 1990.
- Rioboo, R., Marengo, M., and Tropea, C., Time evolution of liquid drop impact onto solid, dry surfaces, *Exp. Fluids*, 33, 112, 2002.
- Rioboo, R., Marengo, M., and Tropea, C., Outcomes from a drop impact on solid surfaces, *Atomization Sprays*, 11, 155, 2001.
- Rodrigues, F. and Mesler, R., Some drops don't splash, *J. Colloid Interface Sci.* 106, 347, 1985.
- Rogers, C.B. and Eaton, J.K., The effect of small particles on fluid turbulence in a flat-plate, turbulent boundary layer in air, *Phys. Fluids*, A 3, 928–937, 1991.
- Rogers, W.A., The Prediction of Wear in Fluidized Beds, *Trans. ASME J. Pressure Vessel Technol.*, 117, 142, 1995.
- Roisman, I.V. and Tropea, C., Impact of a drop onto a wetted wall: description of crown formation and propagation, *J. Fluid Mech.*, 472, 373, 2002.
- Roisman, I.V., Rioboo, R., and Tropea, C., Normal impact of a liquid drop on a dry surface: model for spreading and receding, *Proc. Royal. Soc. London A*, 458, 1411, 2002.
- Rong, D. and Horio, M., Behavior of Particles and Bubbles Around Immersed Tubes In a Fluidized Bed at High Temperature and Pressure: A DEM Simulation, *Int. J. Multiphase Flow*, 27, 89, 2001.
- Rong, D., Mikami, T., and Horio, M., Particle and Bubble Movements Around Tubes Immersed in Fluidized Beds-A Numerical Study, *Chem. Eng. Sci.*, 54, 5737, 1999.
- Rouson, D.W.I. and Eaton, J.K., On the preferential concentration of particles in turbulent channel flow, *J. Fluid Mech.*, 428, 149–169, 2001.
- Rudinger, G. and Chang, A., Analysis of Non-steady Two-Phase Flow, *Phys. Fluids*, 7, 1747, 1964.
- Sakakibara, J., Wicker, R.B., and Eaton, J.K., Measurements of the particle-fluid velocity correlation and the extra dissipation in a round jet, *Int. J. Multiphase Flow*, 22, 863–881, 1996.
- Samenfink, W., *Grundlegende Untersuchung zur Tropfeninteraktion mit schubspannungsgetriebenen Wandfilmen*, Ph.D. thesis, Universität Karlsruhe, Karlsruhe, Germany, 1997.
- Sankaran, V. and Menon, S., LES of spray combustion in swirling flows, *J. Turbulence*, 3, 011, 2002.
- Sarkar, A.D., *Friction Wear*, Academic Press, New York, 1980.
- Sato, Y., Fukuichi, U., and Hishida, K., Effect of inter-particle spacing on turbulence modulation by Lagrangian PIV, *Int. J. Heat and Fluid Flow*, 21, 554–561, 2000.
- Savage, S.B., *Granular Flow at High Shear Rates*, Academic Press, New York, 1982, pp. 339–357.
- Schmehl, R., Modeling droplet breakup in complex two-phase flows, *Proceedings of the International Conference on Liquid Atomization and Spray Systems ICCLASS-2003*, July 13–18, 2003, Sorrento, Italy, 2003b.
- Schmehl, R., *Tropfendeformation und Nachzerfall bei der technischen Gemischaufbereitung*, Dissertation, University of Karlsruhe, Karlsruhe, Germany, 2003a.
- Schreck, S. and Kleis, S.J., Modification of grid-generated turbulence by solid particles, *J. Fluid Mech.* 249, 665–688, 1993.
- Sevik, M. and Park, S.H., The splitting of drops and bubbles by turbulent fluid flow, *J. Fluid Eng.*, 53, 1973.
- Sheldon, G.L. and Finnie, I., The Mechanism of Material Removal in the Erosive Cutting of Brittle Materials, *Trans. ASME, Series 13, J. Eng. Ind.*, 88, 393, 1966.
- Sheldon, G.L., Maji, J., and Crowe, C.T., Erosion of a Tube by Gas Particle Flow, *Trans. ASME, Ser. H, J. Eng. Mater. Technol.*, 99, 138, 1977.
- Shewmon, P. and Sundararajan, G., The Erosion of Metals, *Annu. Rev. Mater. Sci.*, 13, 303, 1983.
- Shimada, M., Matsumoto, Y., and Kobayashi, T., Influence of the nuclei size distribution on the collapsing behavior of the cloud cavitation. *JSME Int., Ser. B*, 43, 380–385, 2000.

- Shook, C.A., Ghosh, S.R., and Pilling, F.E., Wall Erosion in Slurry Couette Flow, in *Liquid-Solid Flows and Erosion Wear in Industrial Equipment*, Roco, M.C., Ed., American Society of Mechanical Engineers, New York, 63, 1983, p. 63.
- Shuen, J.-S., Solomon, A.S.P., Zhang, Q.-F., and Faeth, G.M., Structure of particle-laden jets: measurements and predictions, *AIAA J.* 23, 396–404, 1985.
- Šikalo, Š., *Analysis of droplet impact onto horizontal and inclined surfaces*, Ph.D. thesis, Technische Universität Darmstadt, Darmstadt, Germany, 2003.
- Simonin, O. and Squires, K.D., On two way coupling in gas–solid turbulent flows, *Proceedings of ASME FEDSM03*, Honolulu, 2003.
- Sommerfeld, M. and Huber, N., Experimental analysis and modelling of particle-wall collisions, *Int. J. Multiphase Flow*, 25, 1457, 1999.
- Sommerfeld, M. and Zivkovis, G., Recent advances in the numerical simulation of pneumatic conveying through pipe systems, *Comput. Methods Appl. Sci.*, 1992, 201.
- Soo, S.L., A Note on Moving Dust Particles, *Powder Technol.*, 17, 259, 1977.
- Sorneck, R. J., Dobashi, R., and Hirano, T., Effect of turbulence on vaporization, mixing, and combustion of liquid-fuel sprays, *Combust. Flame*, 120, 479–491, 2000.
- Soyama, H. and Asahara, M., Improvement of the corrosion resistance of carbon steel surface by a cavitating jet, *J. Mater. Sci. Lett.*, 18, 1953, 1999.
- Spalding, D.B., Mixing and chemical reaction in steady confined turbulent flames. In *Proceedings of 13th Symposium (International) on Combustion*, The Combustion Institute, Pittsburgh, PA, 1971, pp. 649–657.
- Spalding, D.B., The combustion of liquid fuels. In *Proceedings of 4th Symposium (International) on Combustion*, The Combustion Institute, Baltimore, MD, 1953, pp. 847–864.
- Squires, K.D. and Eaton J.K., Preferential concentration of particles by turbulence, *Phys. Fluids A*, 3, 1169–1178, 1991.
- Squires, K.D. and Eaton J.K., Particle response and turbulence modulation in isotropic turbulence, *Phys. Fluids A*, 2, 1191–1203, 1990.
- Squires, K.D. and Eaton, J.K., Lagrangian and Eulerian statistics obtained from direct numerical simulation of homogeneous turbulence, *Phys. Fluids A*, 3, 130–143, 1991a.
- Squires, K.D. and Eaton, J.K., Measurements of particle dispersion obtained from direct numerical simulation of isotropic turbulence, *J. Fluid Mech.*, 226, 1–35, 1991c.
- Squires, K.D. and Eaton, J.K., Preferential concentration of particles by turbulence. *Phys. Fluids A*, 3, 1169–1178, 1991b.
- Stanton, D.W. and Rutland, C.J., *Modeling Fuel Film Formation and Wall Interaction in Diesel Engines*, SAE Technical Papers Series 960628, 1996.
- Stock, D.E., Freeman scholar lecture: Particle dispersion in gases, *J. Fluids Eng.*, 118, 4–17, 1996.
- Stone, H.A. and Leal, L.G., Relaxation and breakup of an initially extended drop in an otherwise quiescent fluid, *J. Fluid Mech.*, 198, 399, 1989a.
- Stone, H.A. and Leal, L.G., The influence of initial deformation on drop breakup in subcritical time-dependent flows at low Reynolds numbers, *J. Fluid Mech.*, 206, 223, 1989b.
- Stone, H.A., Bentley, B.J., and Leal, L.G., An experimental study of transient effects in the breakup of viscous drops, *J. Fluid Mech.*, 173, 131, 1989.
- Stone, H.A., Dynamics of drop deformation and breakup in viscous fluids, *Annu. Rev. Fluid Mech.*, 26, 65, 1994.
- Storey, B.D. and Szeri, A.J., A reduced model of cavitation physics for use in sonochemistry, *Proc. R. Soc. Lond. A*, 457, 1685–1700, 2001.
- Stow, C.D. and Hadfield, M.G., An experimental investigation of fluid flow resulting from the impact of a water drop with an unyielding dry surface. *Proc. R. Soc. London A*, 373, 419, 1981.
- Stow, C.D. and Stainer, R.D., The physical products of a splashing water drop, *J. Met. Soc. Japan*, 55, 518, 1977.

- Sundaram, S. and Collins, L.R., A numerical study of the modulation of isotropic turbulence by suspended particles, *J. Fluid Mech.*, 379, 105–143, 1999.
- Suslick, K.S., Sonoluminescence and Sonochemistry, *Proceedings of the IEEE Ultrasonics Symposium*, 1, 523, 1997.
- Suzuki, T. and Chiu, H.H., Multi-droplet combustion of liquid propellants, in *Proceedings of 9th Symposium (International) on Combustion*, The Combustion Institute, Pittsburgh, PA, 1971, pp. 145–154.
- Suzuki, Y., Ikenoya, M., and Kasagi, N., Simultaneous measurement of fluid and dispersed phases in a particle-laden turbulent channel flow with the aid of 3-D PTV, *Exp. Fluids*, 29S, S185–S193, 2002.
- Tabakoff, W., Effect of Environmental Particles on a Radial Compressor, in *Proceedings of the Corrosion-Erosion-Wear of Materials at Elevated Temperatures*, Berkeley, CA, January 31–February 2, 1990, Levy, A.V., Ed., National Association of Corrosion Engineers, Houston, TX, June, 1991, pp. 26–1.
- Tabakoff, W., Erosion Behavior of Materials in Multiphase Flow, in *Proceedings of the Corrosion-Erosion-Wear of Materials in Emerging Fossil Energy Systems*, Berkeley, CA, Jan. 17–19, 1982, Levy, A. V., Ed., National Association Of Corrosion Engineers, Houston, 1982, p. 642.
- Tabakoff, W., Performance deterioration on turbomachinery with the presence of particles, Particulate Laden Flows in Turbomachinery, *AIAA/ASME Joint Fluids, Plasma, Thermodynamics and Heat Transfer Conference*, 3, 1982, p.3.
- Takemura, F. and Matsumoto, Y., Influence of internal phenomena on gas bubble motion (Effects of transport phenomena and mist formation inside bubble in the expanding phase). *JSME Int. J.*, B-37, 736–745, 1994.
- Tang, L., Wen, F., Crowe, C.T., Chung, J.N., and Troutt, T.R., Self-organizing particle dispersion mechanism in a plane wake, *Phy. Fluids*, 4, 10, 1992, 2244–2251.
- Tanner, L.H., The spreading of silicone oil drops on solid surfaces, *J. Phys. D: Appl. Phys.*, 12, 1473, 1979.
- Taylor, G.I., The dynamics of thin sheets of fluid II. Waves on fluid sheets, *Proc. R. Soc. Lond. A*, 263, 296, 1959.
- Taylor, G.I., The formation of emulsions in definable fields of flow, *Proc. R. Soc. London A*, 146, 501, 1934.
- Tennekes, H. and Lumley, J.L., *A First Course in Turbulence*, MIT Press, Cambridge, MA, 1972.
- Tishkoff, J., A model for the effect of droplet interaction on vaporization, *Int. J. Heat Mass Transfer*, 22, 1407–1415, 1979.
- Tjahjadi, M., Stone, H.A., and Ottino, J.M., Satellite and subsatellite formation in capillary breakup, *J. Fluid Mech.*, 243, 297, 1992.
- Toegel, R. and Gompf, B., Does water vapor prevent upscaling sonoluminescence? *Phys. Rev. Lett.*, 85, 3165–3168, 2000.
- Tomita, Y. and Shima, A., High-speed photographic observations of laser-induced cavitation bubbles in water, *Acustica*, 71, 161, 1990
- Tomita, Y. and Shima, A., The effects of heat transfer on the behavior of a bubble and the impulse pressure in a viscous compressible liquid, *Z. Angew. Math. Mech.*, 59, 297, 1979.
- Tomita, Y. and Shima, A., High-speed photographic observations of laser-induced cavitation bubbles in water, *Acustica*, 71, 161–171, 1990.
- Tomotika, S., On the stability of a cylindrical thread of a viscous liquid surrounded by another viscous fluid, *Proc. R. Soc. London A*, 150, 322, 1935.
- Tran, B., Seo, J., Hall, T.L., Fowlkes, J.B., and Cain, C.A., Microbubble-enhanced cavitation for noninvasive ultrasound surgery, *IEEE Transactions Ultrasonics, Ferroelectrics, Frequency Control*, 50, 1296, 2003.
- Trujillo, M.F. and Lee, C.F., Modeling crown formation due to the splashing of a droplet, *Phys. Fluids*, 13, 2503, 2001.
- Tsuji, Y., Kawaguchi, T., and Tanaka, T., Discrete particle simulation of two-dimensional fluidized bed, *Powder Technol.*, 77, 79, 1993.
- Tsuji, Y. and Morikawa, Y., LDV measurements of an air-solid two-phase flow in a horizontal pipe, *J. Fluid Mech.*, 120, 385–409, 1982.
- Tsuji, Y., Activities in Discrete Particle Simulation in Japan, *Powder Technol.*, 113, 278, 2000.

- Tsuji, Y., Morikawa, Y., and Shiomi, H., LDV measurements of an air-solid two-phase flow in a vertical pipe, *J. Fluid Mech.*, 139, 417–434, 1984.
- Tsuji, Y., Morikawa, Y., Tanaka, T., Nakatsukasa, N., and Nakatani, M., Numerical simulation of gas–solid two-phase flow in a two-dimensional horizontal channel, *Int. J. Multiphase Flow*, 13, 671, 1987.
- Tsuji, Y., Shen, N.-Y., and Morikawa, Y., Lagrangian simulation of dilute gas-solid flows in a horizontal pipe, *Adv. Powder Technol.*, 2, 63, 1991.
- Tsuji, Y., Shen, N.-Y., and Morikawa, Y., Numerical Simulation of Gas-Solid Flows. I (Particle-to-Wall Collision), *Technological Reports of Osaka University*, 39, 1989, p. 233.
- Tsuji, Y., Tanaka, T., and Ishida, T., Lagrangian Numerical Simulation of Plug Flow of Cohesionless Particles in a Horizontal Pipe, *Powder Technol.*, 71, 239, 1992.
- Turns, S.R., *An Introduction to Combustion: Concepts and Applications*, McGraw-Hill, New York, Inc, 1996.
- Umemura, A., Interactive droplet vaporization and combustion: Approach from asymptotics, *Prog. Energy Combust. Sci.*, 20, 325–372, 1994.
- Ushimaru, K., Crowe, C.T., and Bernstein, S., *Design and Applications of the Novel Slurry Jet Pump*, Report EI84-108, Energy International, Inc., October 1984.
- Vakil, N. and Everbach, E.C., Transient acoustic cavitation in gallstone fragmentation: a study of gallstones fragmented *in vivo*, *Ultrasound Med. Biol.*, 19, 331, 1993.
- Versluis, M., Schmitz, B., von der Heydt, A., and Lohse, D., How snapping shrimp snap: through cavitating bubbles, *Science*, 289, 2114, 2000.
- Vogel, A., Hentschel, W., Holzfuss, J., and Luterborn, W., Cavitation bubble dynamics and acoustic transient generation in ocular surgery with pulsed Neodymium:YAG lasers, *Ophthalmology*, 93, 1259, 1986.
- Voinov, O.V., Hydrodynamics of wetting, (English translation), *Fluid Dyn.*, 11, 714, 1976.
- Wade, R.B. and Acosta, A.J., Experimental observation on the flow past a plano-convex hydrofoil, *ASME J. Basic Eng.*, 88, 273, 1966.
- Walker, D.R. and Shaw, M.C., A Physical Explanation of the Empirical Laws of Comminution, *AIME Mining Eng. Trans.*, 6, 313, 1954.
- Walton, O. and Braun, R.L., Simulation of Rotary-Drum and Repose Tests for Frictional Spheres and Rigid Sphere Clusters, in *DOE/NSF Workshop on Flow of Particulates on Fluids*, Sept. 29-Oct. 1, 1993, *Proceedings*, available from NTIS, U.S. Dept. Commerce, Springfield, VA, 1994, 131–148.
- Walzel, P., Zetelgrenze beim Tropfenprall, *Chem. Ing. Tech.*, 5, 338, 1980.
- Wang, A.B. and Chen, C.C., Splashing impact of a single drop onto very thin liquid films, *Phys. Fluids*, 12, 2155, 2000.
- Wang, L.P. and Maxey, M.R., Settling velocity and concentration distribution of heavy particles in homogeneous turbulence, *J. Fluid Mech.*, 256, 27–68, 1993.
- Wang, W. and Squires, K.D., Large eddy simulation of particle deposition in a vertical turbulent channel flow, *Int. J. Multiphase Flow*, 22, 667–683, 1996.
- Wark, C., Eickmann, K., and Richards, C., The structure of an acoustically forced, reacting two-phase jet, *Combust. Flame*, 120, 539–548, 2000.
- Wiezba, A., Deformation and breakup of liquid drops in a gas stream at nearly critical Weber number, *Exp. Fluids*, 9, 1329, 1990.
- Williams, F.A., *Combustion Theory*, 2nd ed., The Benjamin/Cummings Publishing Company, Menlo Park, CA, 1985.
- Williams, F.A., Recent advances in theoretical description of turbulent diffusion flames, In Murthy, S. N.B., Ed., *Turbulence in Mixing Operations*, Plenum Press, New York, NY, 1975, pp 189–208.
- Willis, K. and Orme, M., Binary droplet collisions in a vacuum environment: an experimental investigation of the role of viscosity, *Exp. Fluids*, 34, 28, 2003.
- Wood, R.T. and Woodford, D.A., Tube Erosion in Fluidized Beds, Paper No. 42, *Proceedings of the 5th International Conference on Erosion by Liquid and Solid Impact*, Cambridge, England, September 1979.
- Wood, R.T., and Woodford, D.A., *Tube Erosion in Fluidized Beds*, General Electric Co. Report 11/ET-FUC79, U.S. Energy Research and Development Administration Report 81-12, December 1980.

- Wu, J.-S., Liu, Y.-J., and Sheen, H.-J., Effects of ambient turbulence and fuel properties on the evaporation rate of single droplets, *Int. J. Heat Mass Transfer*, 44, 4593–4603, 2001.
- Yamamoto, Y., Potthoff, M., Tanaka, T., Kajishima, T., and Tsuji, Y., Large-eddy simulation of turbulent gas-particle flow in a vertical channel: effect of considering inter-particle collisions, *J. Fluid Mech.*, 442, 303, 2001.
- Yang, Y., Crowe, C.T., Chung, J.N., and Troutt, T.R., Experiments on particle dispersion in a plane wake flow, *Int. J. Multiphase Flow*, 26, 1583–1607, 2000.
- Yarin, A.L. and Weiss, D.A., Impact of drops on solid surfaces: self-similar capillary waves, and splashing as a new type of kinematic discontinuity, *J. Fluid Mech.*, 283, 141, 1995.
- Yarin, A.L., Weiss, D.A., Brenn, G., and Rensink, D., Acoustically levitated drops: drop oscillation and break-up driven by ultrasound modulation, *Int. J. Multiphase Flow*, 28, 887, 2002.
- Young, F.R., *Cavitation*, McGraw-Hill, London, 1989.
- Yuan, W. and Schnerr, G.H., Numerical simulation of two-phase flow in injection nozzles: Interaction of cavitation and external jet formation, *ASME J. Fluids Eng.*, 125, 963, 2003.
- Yuu, S., Ueno, T., and Umekage T., Numerical simulation of the high Reynolds number slit nozzle gas-particle jet using subgrid-scale coupling large eddy simulation, *Chem. Eng. Sci.*, 56, 4293, 2001.
- Zhang, D.Z. and Prosperetti, A., Averaged equations for inviscid disperse two-phase flow, *J. Fluid Mech.*, 267, 185–219, 1994.
- Zhou, Y.-K., He, J.-G., and Hammitt, F.G., Cavitation erosion of diesel engine wet cylinder liners, *Wear*, 76, 321, 1982.
- Zhu, J., Tube Erosion In Fluidized Beds, PhD. Thesis, Department of Chemical Engineering, The University of British Columbia, May 1988.
- Zhu, J., Grace, R., and Lim, C.J., Tube Wear in Gas Fluidized Beds-I. Experimental Findings, *Chem. Eng. Sci.*, 45(4), 1003, 1990.
- Zung, J.T., Evaporation rate and lifetime of clouds and sprays in air — the cellular model, *J. Chem. Phys.*, 46, 2064–2070, 1967.

13

Modeling

E. Loth
University of Illinois

G. Tryggvason
Worcester Polytechnic Institute

Y. Tsuji
Osaka University

S.E. Elghobashi
University of California

Clayton T. Crowe
Washington State University

A. Berlemont
National Centre for Scientific Research

M. Reeks
University of Newcastle upon Tyne

O. Simonin
Institute of Mechanics of Fluids of Toulouse

Th. Frank
ANSYS Germany GmbH

Y. Onishi
Pacific Northwest National Laboratory

B. van Wachem
Chalmers University of Technology

13.1	Overview of Multiphase Modeling	13-1
	Classification of Multiphase Flows • Classification of Methodologies • Overview of Continuous-Phase Flow Methodologies • Overview of Particle-Phase Flow Methodologies	
13.2	Direct Numerical Simulations.....	13-20
	Bubble and Droplet Motion and Deformation • Discrete Element Approach • Direct Simulation of Turbulent Flows Laden with Dispersed Particles • The physical Mechanisms of Two-Way Coupling in Particle-Laden Isotropic Turbulence • DNS of Bubble-Laden Isotropic Turbulence Using the Two-Fluid Approach • DNS of Turbulent Shear Flows Laden by Dispersed Solid Particles or Bubbles	
13.3	Continuous-Phase Equations	13-60
	Averaging Procedures • Mass Conservation • Momentum Conservation • Energy Equation • Turbulence Equations	
13.4	Dispersed Phase Equations	13-70
	Lagrangian Approach • Eulerian Approach • PDF Models	
13.5	Applications	13-113
	Lagrangian Prediction of Performance Parameters in Cyclone Separators • Slurry Flows • Fluidized Bed	

13.1 Overview of Multiphase Modeling

E. Loth

13.1.1 Classification of Multiphase Flows

To numerically model a multiphase flow, it is often important to use separate formulations for the different phases. Let us define the *particle phase* as the phase that consists of bubbles, particles, or drops, and the *continuous phase* as the fluid in which these particles are generally immersed. The particles can be composed of solid, liquid, or gas, whereas the continuous fluid can be a liquid or a gas.

The coupling between the particle motion and its surroundings can be used to classify the character of the multiphase flow, and thus help determine appropriate numerical techniques. The broadest division is between dispersed and dense flows, and refers to which coupling mechanism primarily determines the particle motion. As shown in Figure 13.1, a multiphase flow can be considered dispersed if the effect of particle–fluid interactions dominates the overall transport of the particles. Particle–fluid interaction generally

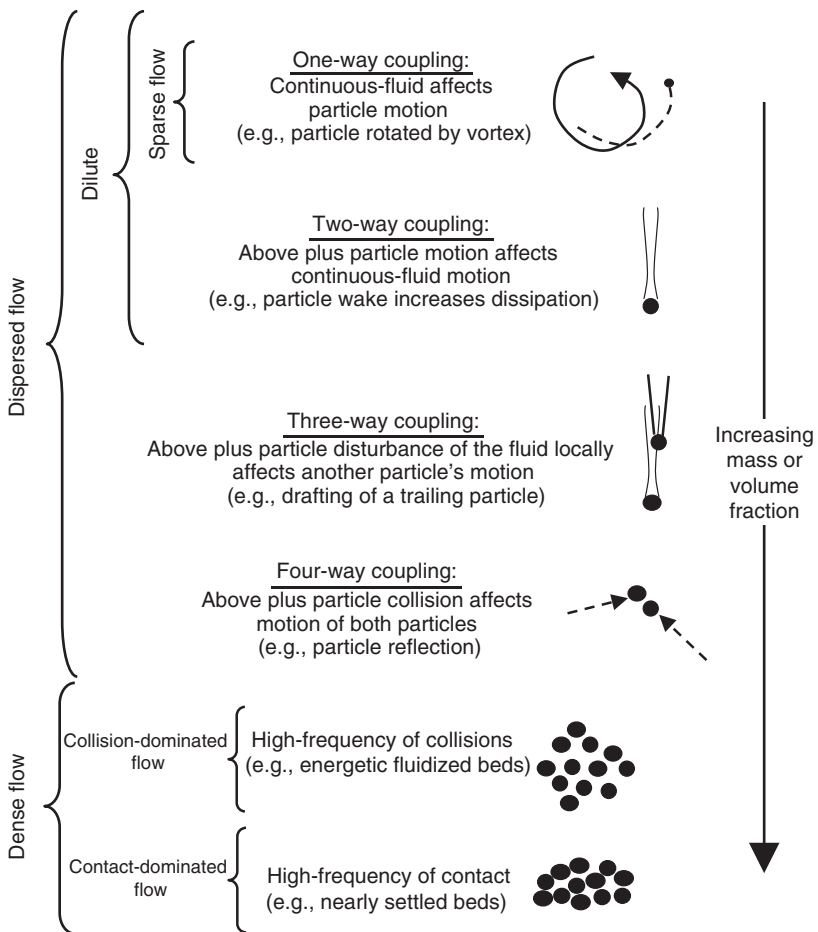


FIGURE 13.1 Dilute, dispersed, and dense flow conditions based on various interphase and intraphase coupling.

includes a drag force, which hinders the relative velocity of the particle, and thus causes particle trajectories to tend toward continuous-fluid trajectories. If the particle–particle motion dominates, the flow can be considered to be dense. Particle–particle interactions can refer to two separate mechanisms: particle–particle collisions (where the particles can rebound, shatter, or coalesce by impinging on each other) and particle–particle fluid dynamic interactions (where the proximity of the particle affects their fluid dynamic forces). Dispersed flow will generally include one-way coupling (where the dispersed-phase motion is affected by the continuous phase, but not vice versa), two-way coupling (where the dispersed phase also affects the continuous phase through the interphase coupling, e.g., drag force), three-way coupling (where particle wakes and other continuous-phase disturbances affect the motion of other particle interactions), and four-way coupling (where collisions and other particle–particle interactions influence, but do not dominate, the overall particle motion). Dense flows will be generally defined as having four-way coupling, although in some cases (e.g., granular flows), the effects of the particles on the continuous fluid are weak and often neglected.

13.1.2 Classification of Methodologies

In addition to the above classification for multiphase flow phenomenon, we can also classify the various numerical formulations. For one-way coupling conditions, the continuous phase can be computed independent of the particle phase. The optimum numerical formulation of the continuous flow is often strongly dependent on the flow Reynolds number, and is discussed in the following section, but is typically described with an Eulerian reference-frame methodology. Typically, a spatial grid resolution (Δx) is specified for which

the continuous-flow equations are discretized in the Eulerian domain and solved. For two-way coupling, these equations need to be modified to include the interphase mass, force, and heat transfer.

Several variations and combinations of these numerical treatments have been put forth, but relevant fluid-particle physics and the available computational resources are the primary determinants for which a set of treatments is more appropriate for a particular flow field. The following two sections separately overview various techniques for simulating the continuous-phase flow and that of the particles, respectively.

13.1.3 Overview of Continuous-Phase Flow Methodologies

In the numerical treatment of the continuous-phase flow, the solution domain and reference frame must be considered. Continuous-flow simulations are typically carried out in an Eulerian reference frame, since it is usually the most computationally efficient description for solution, particularly for steady flows. In the Eulerian reference frame, a domain of fluid is typically considered where the domain motion and boundaries are selected based on convenience, e.g., moving at the speed of a reference frame and with boundaries parallel to solid surfaces. Different spatial discretizations for the fluid characteristics (velocity, temperature, and pressure) are possible, e.g., constant, linear, quadratic, etc. These discretizations can be used with finite-difference, finite-volume, and finite-element treatments. In addition, discretization can be by wavelength, such that spectral and pseudo-spectral representations can be used to describe the flow quantities throughout the domain. Although less common than the Eulerian treatment, the continuous fluid is sometimes treated in a Lagrangian manner, e.g., the discrete eddy tracking techniques termed vortex dynamical models. In addition, there are some hybrid methods such as the Arbitrary-Lagrangian–Eulerian (ALE) technique. In general, the treatments of the continuous-phase flow are subject to standard resolution convergence issues (spatial and temporal) to satisfy the governing differential equations.

In determining the proper equations of motion, it should be noted that various mathematical representations of the continuous-phase fields are possible, depending on the controlling physics. A key issue regarding formulation of the flow surrounding the particles is whether the flow can be considered as a continuum, or whether the effects of random molecular collisions must be considered. In particular, two classes of non-continuum effects can arise in multiphase flow: first, the entire domain can have features that depend on the discrete molecular interactions (regardless of the particle interactions), in which the assumption of a continuous phase is no longer appropriate. In this case, some critical length scale of the domain is on the order of the molecular mean free-path for the surrounding fluid. In the second case, we can assume that all the fluid domain length scales (including particle diameter) are much greater than the molecular mean free-path (as is generally assumed here), and the flow that a particle "sees" can be considered a continuum.

Assuming a continuum, generally, the most important characterization of the continuous-phase flow is whether it is assumed to be inviscid or viscous, since this determines the relevant partial differential equations (PDEs) to be numerically solved. For inviscid flow formulations, the quantitative effects of friction over surfaces and dissipation of vorticity are not of primary relevance to the desired flow properties and are thereby neglected. Note that an inviscid continuous-phase solution does not preclude the effects of viscosity with respect to particle motion, e.g., simulations of a dusty-shock flow can neglect viscosity with respect to interactions with solid surfaces, but can still consider the viscous drag effects on the particles. Inviscid flow formulations primarily fall into three categories with an increase in physical complexity:(1) potential flow (incompressible and irrotational), (2) incompressible rotational flow, and (3) compressible rotational flow (Euler equations); which require a transport equation for energy.

Viscous flows require inclusion of shear stresses in the PDE formulation and thus in the numerical solution. These flows can be subdivided by effects of compressibility, unsteadiness, etc., but they are primarily classified as laminar, transitional, or turbulent. In general, the Reynolds number largely determines the type of numerical treatment. In the following sections the formulations and numerical approaches are considered for various flow Reynolds number regimes.

13.1.3.1 Reynolds Number Effects on Continuous-Phase Flow

The Reynolds number of the flow is often the most important characteristic that determines the flow physics. The flow Reynolds number represents the ratio of convective forces to viscous forces. On a macroscopic scale,

it can be generally defined as $Re_L = \rho_f L u_L / \mu_f$, where L and u_L are a length and a velocity scale associated with the continuous-phase flow domain (e.g., pipe diameter and the mean streamwise flow speed) and ρ_f and ν_f are the density and kinematic viscosity of the continuous phase. Another important characteristic is the flow Mach number, which represents the ratio of convection speed to the speed of isentropic pressure fluctuations (the speed of sound). The macroscopic Mach number can be defined as $M_L = u/a_f$, where a_f is the speed of sound of the continuous phase. It is helpful to consider the limit of $M_L \ll 1$ and negligible thermal variations or stratification, so that one may generally assume constant density of the continuous fluid. In addition, let us ignore the effects of two-way coupling at this point (for simplicity), so that there is no influence of the particle phase on the continuous-phase motion. Written in tensor notation, the continuity and momentum equations in the i direction for the single-phase fluid momentum (White, 1991) become

$$\begin{aligned}\partial u_{fj} / \partial x_j &= 0 \\ \rho_f u_i / t + \rho_f u_j \partial u_i / \partial x_j &= \rho_f g_i - \partial p / \partial x_i + \partial \tau_{ij} / \partial x_j\end{aligned}$$

where p is pressure, u_i the velocity in the i direction, g_i the magnitude of the gravity vector in the i direction, and $\tau_{ij} = \mu_f (\partial u_i / \partial x_j + \partial u_j / \partial x_i)$ which the viscous stress tensor. In the limit of no flow (quiescent conditions), this equation yields $\rho_f g_i = \partial p / \partial x_i$, which is the hydrostatic pressure gradient equation.

If we further assume constant viscosity, the Navier–Stokes PDE becomes (in either tensor or vector form)

$$\begin{aligned}u_i / t + u_j \partial u_i / \partial x_j &= g_i - (1/\rho_f) \partial p / \partial x_i + \nu_f \partial^2 u_i / \partial x_j^2 \\ \partial u / \partial t + \mathbf{u} \cdot \nabla \mathbf{u} &= \mathbf{g} - \nabla p / \rho_f + \nu_f \nabla^2 \mathbf{u}\end{aligned}$$

where $\nu_f = \mu_f / \rho_f$, \mathbf{u} the continuous fluid velocity, \mathbf{g} the gravity vector, and the divergence of the fluid velocity is zero ($\nabla \cdot \mathbf{u} = 0$). As the convective terms become stronger than the viscous terms (corresponding to an increase in the flow Reynolds number), the flow will proceed from laminar conditions to transitional and then to turbulent flow conditions. In the following section (and in Table 13.1), various Reynolds number flow regimes are considered under the assumption that the presence of the dispersed phase does not alter the numerical approach significantly (e.g., as in one-way coupled systems).

13.1.3.1.1 Laminar Flow

For $Re_L \ll 1$, the flow is highly laminar and is typically termed creeping flow. This condition arises in many low-speed flows and microfluidic systems. In this case, the viscous effects dominate and convection

TABLE 13.1 Forms of the Continuous-Flow Incompressible Navier–Stokes Momentum Equations, Assuming No Coupling from the Particles (i.e., Assuming One-Way Coupling)

Flow Condition	Flow Reynolds No.	Tensor Form of Fluid Momentum Equation
Steady creeping flow	$Re_L \ll 1$	$0 = \rho_f g_i - \partial p / \partial x_i + \mu_f \partial^2 u_i / \partial x_j \partial x_j$
Steady laminar flow	$Re_L < Re_{crit}$	$\rho_f u_j \partial u_i / \partial x_j = \rho_f g_i - \partial p / \partial x_i + \mu_f \partial^2 u_i / \partial x_j \partial x_j$
Transitional flow	$Re_{crit} < Re_L < Re_{turb}$	$\rho_f \partial u_i / \partial t + \rho_f u_j \partial u_i / \partial x_j = \rho_f g_i - \partial p / \partial x_i + \mu_f \partial^2 u_i / \partial x_j \partial x_j$
Turbulent flow (DNS)	$Re_L > Re_{turb}$	Same as for transitional flow
Turbulent flow (LES)	$Re_L > Re_{turb}$	$\rho_f \partial \bar{u}_i / \partial t + \rho_f \bar{u}_j \partial \bar{u}_i / \partial x_j + \rho_f \partial (\bar{u}_i' \bar{u}_j') / \partial x_j = \rho_f g_i - \partial \bar{p} / \partial x_i + \mu_f \partial^2 \bar{u}_i / \partial x_j \partial x_j$ where (\cdot) is a spatially filtered quantity
Turbulent flow (RANS)	$Re_L > Re_{turb}$	$\rho_f \bar{u}_j \partial \bar{u}_i / \partial x_j + \rho_f \partial (\bar{u}_i' \bar{u}_j') / \partial x_j = \rho_f g_i - \partial \bar{p} / \partial x_i + \mu_f \partial^2 \bar{u}_i / \partial x_j \partial x_j$ where (\cdot) is a time-averaged quantity

Note: Re_{crit} corresponds to the Reynolds number at which the flow begins to become transitional and Re_{turb} corresponds to the Reynolds number at which the flow becomes fully turbulent.

(second terms on the LHS) is of secondary importance or can be neglected all together. Owing to the Laplacian nature of the viscous term (third term on the RHS), the effects of viscosity are felt throughout the flow and yield a strong elliptic character to the PDE, i.e., the flow features are highly coupled throughout the domain in all directions. To ensure this, elliptic coupling is properly treated; numerical methods typically employ an implicit solution technique, which is converged for a steady-state condition or given as a physically consistent time increment for an unsteady condition. As Re_L becomes an order of unity, the convective terms become important and nonlinear, but the elliptic character of the PDE remains strong, hence direct or iterative numerical approaches are required. As always, the domain discretization in space and time is carefully considered, such that it does not play a significant role in the flow solution.

For $1 \ll Re_L < Re_{crit}$ the flow may retain its laminar character and stability, but typically a boundary layer approximation may be applied to certain regions of the flow. The boundary layer approximation allows certain components of the viscous stress tensor to be ignored, since velocity gradients tend to much larger, normal and perpendicular to the convection direction (e.g., for attached wall-bounded flows the streamwise viscous gradients can be ignored). In this case, a parabolic approach may be employed in the direction for which the viscous diffusion may be neglected. Such an approach allows a space-marching scheme that needs to be coupled (i.e., solved directly or iteratively) along perpendicular planes. However, complex features and flow separation can cause the gradients to be significant in all directions, in which case the full Navier–Stokes equations of momentum are needed. The numerical approaches often include implicit schemes to properly capture the elliptic character of the viscous terms and the pressure coupling (since pressure fluctuations may travel in all directions for $M_L \ll 1$). However, since the convective terms begin to dominate at higher Reynolds numbers and are essentially parabolic locally, explicit schemes are sometimes used to treat these particular terms more efficiently. Often, the overall numerical approach becomes a hybrid of implicit and explicit schemes for incompressible laminar flow. At larger Mach numbers, PDE may become parabolic or hyperbolic such that purely explicit schemes are often appropriate.

13.1.3.1.2 Transitional Flow

For $Re_L > Re_{crit}$ (the critical Reynolds number where transition begins), the flow instabilities become profound and unsteadiness and multidimensionality become important. This can occur in wall-bounded flows where Tollmien–Schlichting instabilities arise, pipe flows where the Taylor–Gortler mechanism arises, free-shear flows where Kelvin–Helmholtz instabilities arise, etc. While transitional flow may be initially two dimensional, the instabilities typically lead to significant three-dimensional characteristics. Transitional is a difficult flow field to simulate, since the higher Reynolds numbers coupled with the small-scale features arising from the flow instabilities place severe restrictions on the space and time discretization employed in these simulations for full Navier–Stokes resolutions. Moreover, unlike fully developed turbulent flow, it is difficult to robustly recast the flow in a time-averaged description.

While most of the numerical approaches for these continuous-phase flows are Eulerian-based, noticeable exceptions are the Lagrangian treatments of vortex points or blobs or filaments (where the latter is used in three dimensions). These techniques can be very useful in predicting the initial instability features for free-shear flows and the Reynolds number effects can be included through viscous diffusion of the vortices. These techniques have the significant advantage of avoiding discretization of the entire computational domain and thus can be efficient in terms of reduced degrees of freedom for similar accuracy as compared with Eulerian methods. However, in highly three-dimensional flows (as the instabilities become highly nonlinear), the technique is highly complicated by the Lagrangian tangling, merging, and rupture of the vortex filaments and blobs. Thus, they can become impractical for complex vortex dynamics.

13.1.3.1.3 Turbulent Flow

For $Re_L > Re_{turb}$ (the minimum Reynolds number for fully developed turbulence), the flow instabilities have become sufficiently profound to have caused a flow field, with vortices and flow structures that occur over a large range of length and time scales. These features are three dimensional, unsteady, and effectively

stochastic at the smallest scales. The flow is sufficiently nonlinear to prevent a unique solution for a given set of initial flow conditions, such that comparisons often require comparison of statistical quantities rather than instantaneous realizations. The range of wavelengths, which must be described to fully resolve such flows, is considerable. To illustrate this aspect, consider a turbulent flow with a relatively low Re_L of the order of 10^5 , for example, a water flow moving at 1 m/sec within a 10 cm pipe. The range of spatial resolution required is based on the domain length scale and the Kolmogorov length scale, the ratio of which increases with Reynolds number, e.g., $L/\lambda_K \sim Re_L^{3/4}$. Thus, the range of length scales can be of the order of 10,000 in each direction in this simple flow example.

13.1.3.2 Numerical Methods for Continuous-Phase Turbulent Flows

Based on the above wavelength range, the total number of points required for the fluid resolution in all the three directions of turbulence approximately scales with $8Re_L^{9/4}$ (assuming two grid points to describe the smallest wavelength). Thus a Reynolds number of 10^5 ; this simulation would require an excess of 10^{12} computational nodes. Thus, turbulent flow predictions at large Reynolds numbers require some time averaging of the PDEs to be simulated (of at least the small-scale structures) in order to allow practical computational resources. Such averaging formulations unfortunately involve some empiricism, and thus it is best to avoid (or minimize) this averaging whenever possible. The degree of averaging can vary, depending on the physics of interest. An important distinction is whether none, some, or all of the eddy structures can be resolved. However, the turbulent flow techniques can be broken up into two categories: (1) time-averaged simulations (no structures resolved) and (2) eddy-resolved simulations (some or all of the structures resolved).

Time-averaged simulations employ a time average with respect to the turbulence, such that only mean statistics are predicted. Moreover, only an average turbulence length scale and time scale can be identified, but no eddy structures or dynamics are produced. The most common example is the Reynolds-averaged technique, where all flow variables are individually time-averaged and the resulting equations are generally called the Reynolds-averaged Navier–Stokes (RANS) equations. Another time-averaged example is the Favre-averaged equations, where the fluid properties are weighted with the instantaneous density before being time-averaged.

Eddy-resolved simulations predict at least some of the individual spatiotemporal features of the turbulent eddy structures (e.g., at least some of the turbulent eddies are resolved within the computational grid). This category includes direct numerical simulations (DNS) where the turbulence is described for all eddy-containing wave numbers (spatial frequency), i.e., up to the wave number constrained by viscosity $1/\lambda_k$. The eddy-resolved category also includes large-eddy simulations (LES) where the turbulence is only resolved up to some cutoff wave number ($1/\Delta$), beyond which a subgrid scale is employed. In addition, hybrid RANS–LES techniques have been used, wherein only the separated flow regions are treated with an LES approach while attached flow regions are treated with a RANS approach. Other eddy-resolved techniques, that predict only some of the spatiotemporal features include detached eddy simulations (DES) and proper orthogonal decomposition (POD), which will be discussed.

The difference between the flow predicted by a time-averaged and an eddy-resolved technique is substantial. [Figure 13.2](#) shows the difference for a turbulent boundary layer, where the RANS description is two-dimensional and steady while the DNS description is three-dimensional and unsteady. Because eddy-resolved techniques can capture the energy-containing eddy structures associated with the turbulence, they have been shown to provide much higher accuracy than the time-averaged techniques in terms of turbulent diffusion and other statistical flow features.

The choice of the continuous-phase eddy-resolving description has a considerable impact on the dispersed-phase predictions. The time-averaged descriptions of the continuous flow allow only approximate prediction of particle mean diffusion, whereas the eddy-resolved techniques can more accurately predict such diffusion, while additionally providing aspects of particle preferential concentration (see [Figure 13.3](#)). In the above, *diffusion* refers to mean-spread of the particle cloud and thus indicates a time-averaged description of the particle concentration, whereas preferential concentration refers to particle motion associated with an individual turbulent flow features (spatio-temporal turbulent structure).

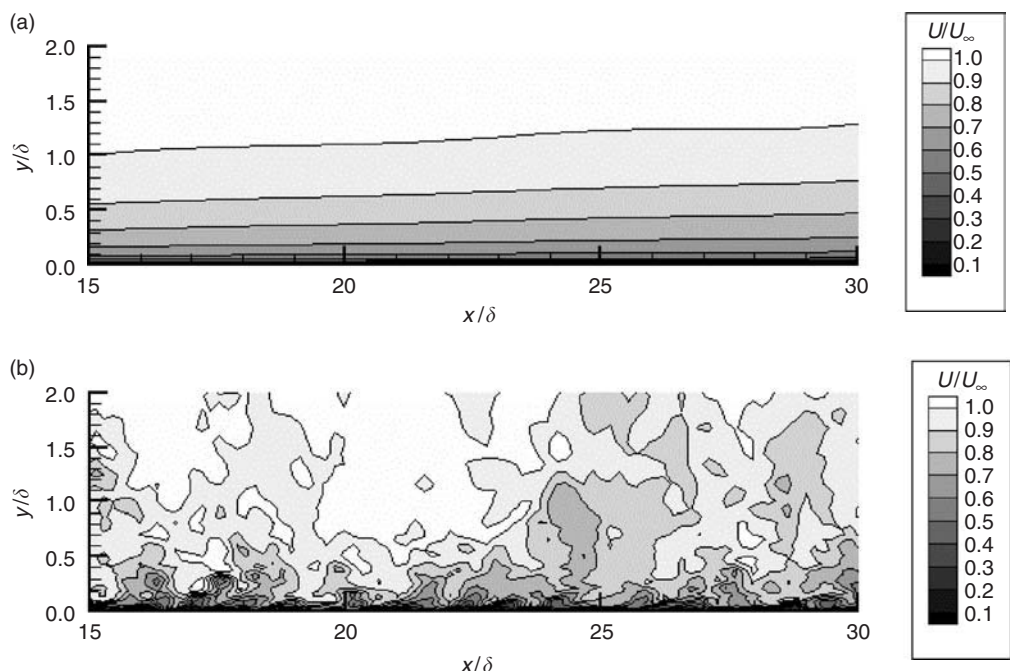


FIGURE 13.2 Different representations for a turbulent boundary layer, where δ is the mean boundary layer thickness, x the streamwise direction, and y normal to the wall showing: (a) a time-averaged (RANS) description and (b) an eddy-resolved (DNS) description for one span wise plane at a single instant in time.

In the latter case, this can include phenomena such as the collection of light particles (with density less than the continuous-fluid density) in low-pressure vortex cores or the centrifugal expulsion of heavy particles (with density greater than the continuous-fluid density). Capturing such structural dispersion physics can be extremely important in predicting instantaneous local regions, which are either depleted or excessive in particle concentration levels as compared to the time-averaged values (Crowe et al., 1998). This “preferential concentration” can result in substantial changes in the relative velocity of the particle measured in an Eulerian framework (Maxey et al., 1997). In addition, structural dispersion can have great importance, when two-, three-, or four-way coupling effects are to be included, since interphase force transfer, particle collision, and particle wake interaction can be locally and nonlinearly enhanced in regions of high local concentration.

The variety of wavenumbers directly simulated by these different techniques ranging from RANS (no dynamics i.e., just an integral length-scale), LES (dynamics of the most energetic eddies) to DNS (the dynamics of all the eddies) is schematically represented in Figure 13.4. However, eddy-resolved formulations come at a price of higher computational resources (in terms of both CPU memory and time). Figure 13.5 shows the approximate computational resources required for attached boundary layers over a distance of L (free shear flows are even more demanding in terms of computational resources). It can be seen that even modest boundary Reynolds numbers of 10^6 require a substantial number of grid points for DNS and LES approaches, as compared with RANS approaches (especially if the time-averaged flow can be considered two-dimensional). In the following section, additional description is given with regard to both time-averaged and eddy-resolved formulations.

13.1.3.2.1 Time-Averaged Formulations

For the category of RANS simulations, all the velocity components are separated into their steady and fluctuating components, $u_i = \bar{u}_i + u'_i$, where \bar{u}_i represents a time-averaged quantity over a time period much greater than τ_A . Application of this averaging quantity to the incompressible constant viscosity

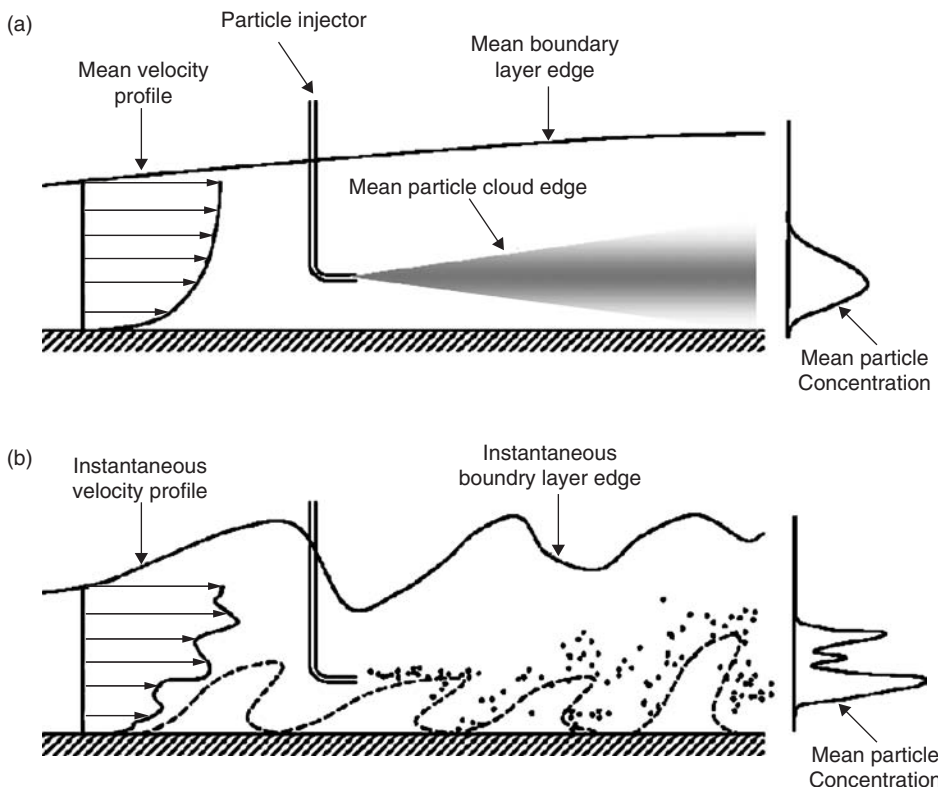


FIGURE 13.3 Schematic of particles injected near the wall of the turbulent boundary layer comparing (a) particle mean (time-averaged) diffusion where a steady particle concentration distribution is obtained and (b) preferential concentration where an unsteady particle distribution is obtained.

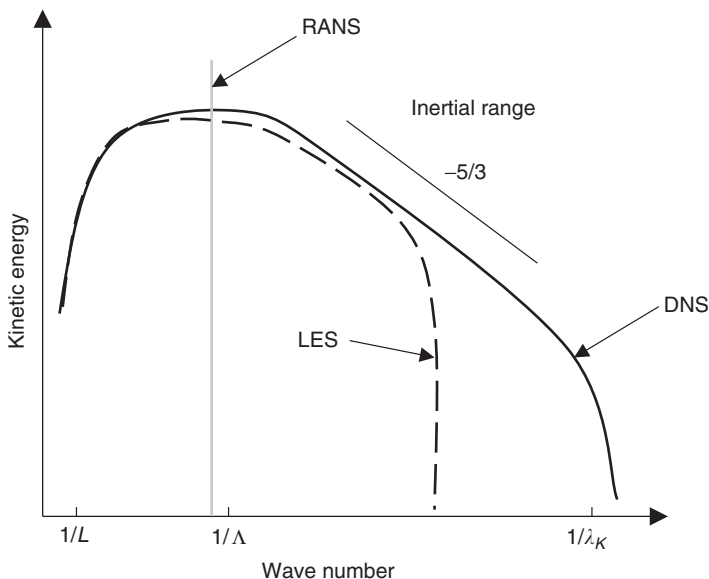


FIGURE 13.4 Schematic of turbulence spectrum described by RANS, LES, and DNS approaches.

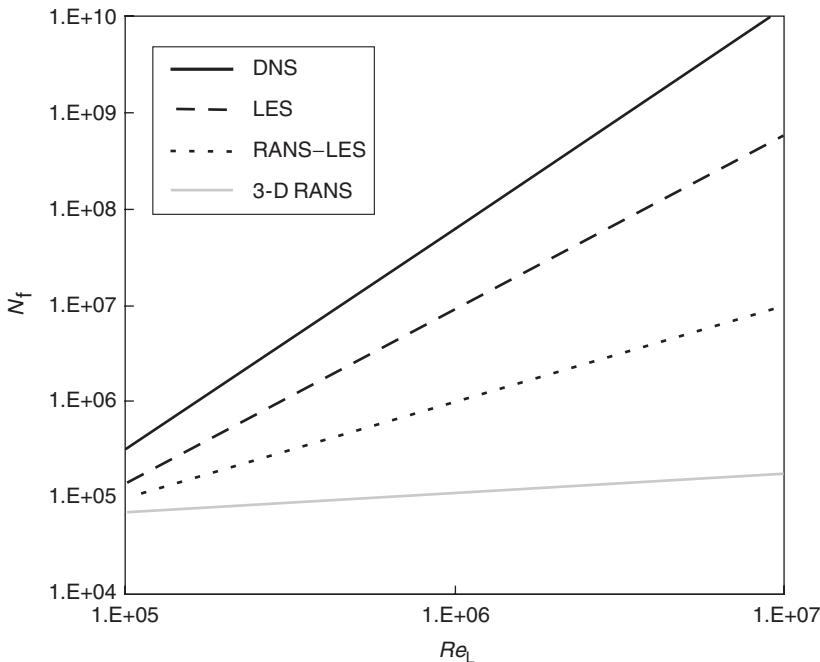


FIGURE 13.5 Approximation of computational node requirements for RANS, LES, and DNS and hybrid RANS–DNS approaches.

Navier–Stokes equation is shown in [Table 13.1](#), where the $\overline{u'_i u'_j}$ term represents the transport of momentum due to turbulent mixing. The primary aim of RANS models is to represent empirically the Reynolds-stress terms (appearing in the source term of the momentum transport equations) using some of the mean flow velocity features. Several of the recent developments in this field for both incompressible and compressible flow are discussed by Vandromme (1997) and briefly overviewed below. The turbulence models are generally classified into the traditional eddy viscosity models and the more advanced Reynolds-stress closure models.

For the eddy viscosity models, $\overline{u'_i u'_j}$ is related to the mean velocity gradients and a mean turbulent viscosity, the latter of which requires modeling and is typically several orders of magnitude higher than the fluid viscosity. The eddy-viscosity models are generally classified according to the number of partial differential transport equations, which must be solved (in addition to those for mean mass, momentum, and energy conservation) to compute $v_{f,i}$. These generally range from zero-equation (algebraic) models where the turbulence is essentially assumed to be in a state of local equilibrium, to two-equation models, to three-equation models where finite-rate production, diffusion, and dissipation processes are individually modeled. In all the cases, empirical coefficients (often several) are used to close the equations, and these are obtained by “tuning” the model to some basic turbulent flow results. Therefore, the robustness of turbulence models will always be limited to conditions for which it has been validated and empirically calibrated, and there is no single “ideal” turbulence model.

For turbulent multiphase simulations, two-equation models (including $k-\varepsilon$, $k-\omega$, and $q-\omega$) have a distinct advantage, since they describe two independently varying properties of the turbulence; for example, the turbulent kinetic energy (TKE) k and the turbulent dissipation ε . Modeling two independent turbulence properties allows specification of a mean eddy integral length λ and eddy time-scale τ_A throughout the flow. These two scales can be used to characterize particle diffusion using random walk approaches.

The Reynolds-stress closure models are inherently anisotropic and seek to avoid a gradient transport approach to the turbulent stress tensor terms by employing individual equations for the individual

turbulent stresses (and potentially the turbulent fluxes as well). The zeroth-order version of this model is Rodi's algebraic stress model, which supplements the $k-\varepsilon$ transport equations with an anisotropic algebraic relationship (White, 1991). As such, it does not allow significant advantages over two-equation eddy viscosity models in terms of sophistication. However, modern Reynolds-stress closure models employ separate transport equations for each tensor component (six equations due to symmetry). This has the obvious advantage of more directly obtaining the anisotropy of the Reynolds-stress tensor by allowing varying states of nonequilibrium for each term. Since Reynolds-stress closure models are well suited to the framework of particle diffusion computation in anisotropic turbulence, they may become increasingly important as they mature in fidelity and convenience. Unfortunately, the large number of transport equations results in a much more computationally intensive and complex CFD (Computational Fluid Dynamics) solution with additional terms to be modeled. Of particular concern are the several third-order (and fourth-order) stress terms, which require modeling not easily gleaned from experiments. While some closure models have shown success for simple flows using heuristic arguments for these terms, e.g., Speziale et al. (1991), a robust set of closure terms tested for several engineering flows has yet to be developed (although the DNS techniques described below are expected to provide improved closure models for such terms at lower Reynolds numbers). Because of these issues and the inability to incorporate preferential concentration, eddy-resolved formulations are becoming much more common for multiphase flow.

13.1.3.2.2 Eddy-Resolved Formulations

For the eddy-resolved simulations, there are quite a number of descriptions of the eddy structures. These can be roughly arranged in order of increasing complexity, physical representation, and required computational resources as follows (see also [Figure 13.5](#)).

Proper Orthogonal Decomposition (POD) models. These simulations employ a low-order construction of the turbulent flow field, typically using spectral or pseudo-spectral functions (Joia et al., 1997), which are tracked in time as 3D dynamical features. As such, they employ only a modest number of degrees of freedom (as compared to full Navier–Stokes resolution) while simulating the large-scale nonlinear flow physics. Unfortunately, POD models typically require a detailed realization (experiment or simulation) in order to solve for the “best fit” of their lower-order dynamical system. Thus, they are sometimes empirical, i.e., they cannot quantitatively self-determine the continuous-flow vortex structures for a general set of boundary and initial conditions. However, once a POD is constructed for a particular flow, it can be reasonably rendered many times to test the transport of a variety of particle conditions.

Hybrid RANS–LES models. Several numerical treatments have emerged which attempt to treat a part of the computational domain using a RANS formulation and on the other part with a LES formulation. Among the first of such models was the DES methodology developed by Spalart (2000). The basic concept was to allow for a one-equation RANS treatment in the attached boundary layer regions (where the approach is known to be robust) and LES treatment in the separated and free-shear flow regions (where the approach is known to be robust). This is achieved by using a wall distance to spatially separate the RANS and LES regions. Several other models have been developed recently based on similar formulations.

Large Eddy Simulations (LES). The governing equations are obtained by a low-pass spatial filtering of the Navier–Stokes equations such that all the velocity components are separated into their resolved (unfiltered) and unresolved (filtered) components. Using a notation similar to that used for the RANS approach, the velocity components for the spatial filtering process are given as $u_i = \bar{u}_i + u'_i$, where some modeling is required for the fluctuations that are at the subgrid level; for example, $u'_i u'_j$, which is the velocity tensor of the unresolved fluctuations. Ideally, this spatial filtering is applied at sufficiently small scales so that the filtered turbulence is at or below the inertial range and thus nearly homogeneous and isotropic, such that Smagorinsky-type models can be reasonably employed. However, the inertial range develops for only very high Reynolds number conditions (Tennekes and Lumley, 1972), such that spatial filtering can be a complex phenomenon sometimes making it difficult to provide accurate and robust predictions of the subgrid turbulence. This problem can be effectively overcome in some flows by allowing

high enough grid resolution, such that the subgrid component is not substantial, but this is not straightforward in wall-bounded flows where small-scale stresses are critical. The LES technique is perhaps the most promising for low to moderate Reynolds number engineering flows, since, with proper care, it can simulate complex separated flow in both the mean and rms statistics. For particle dispersion, the key advantage of LES is the detailed spatio-temporal evolution of the unfiltered large-scale turbulent motions. It should be noted that other variations of LES include very large eddy simulations (VLES), for which the subgrid model is determined by the numerical grid diffusion and RANS-type turbulent viscosity. While the representation of the subgrid scale turbulent stresses of VLES is not formulated based on a rigorous evaluation from the filtered fluid equations of motion, these models can reproduce many features of turbulent flow, since the subgrid turbulence is often not critical to the overall flow development (especially for free-shear flows).

Direct Numerical Simulations (DNS). The governing equations in this case are the full time-dependent Navier–Stokes equations. Typically, the high resolution required for grid-independent solutions results in low Reynolds numbers, simple geometries, and use of spectral methods if flow discontinuities (shock waves, concentration fronts, etc.) are not critical to the flow physics. The primary advantage of DNS is that all the eddy structures are duly resolved and no (empirical) turbulence modeling is necessary. However, for most engineering flows, DNS computations are simply too computationally intensive.

13.1.4 Overview of Particle-Phase Flow Methodologies

Various treatments of the particle field (composed of solid particles, droplets, or bubbles) can be employed. As mentioned earlier, these can include an Eulerian or a Lagrangian reference frame. The Eulerian approach can be further classified into mixed or point-force approaches, while the Lagrangian approach can be further classified into point-force or resolved-surface approaches. Table 13.2 shows the various treatments of the particle and continuous-phase velocity fields without any averaging or mass transfer. In this table, the Eulerian treatments describe the particle concentration through a volume fraction α_p , which is the fraction of the computational volume composed of particles, and where the volume fraction taken up by the continuous phase is α_f , such that $\alpha_p + \alpha_f = 1$. When a Lagrangian treatment is used for the particles, the two-way coupling effect on the continuous phase is usually related to the particle number density n_p , which is the number of particles per unit volume. These particle concentration variables can be related to the average particle volume V_p , such that $\alpha_p = n_p V_p$.

The particle phase has two sets of key classifications. The first is based on the reference frame for the particle properties and is classified as either a Lagrangian or an Eulerian treatment. The second is based

TABLE 13.2 Forms of the Incompressible Unsteady Navier–Stokes Momentum Equations

Dispersed-Phase Approach	Dispersed-Phase Momentum	Continuous-Phase Momentum
Eulerian with mixed-fluid treatment	$\partial(\rho_m u_{mi})/\partial t + \partial(\rho_m u_{mi} u_{mj})/\partial x_j = \rho_m g_i - \partial p/\partial x_i + \mu_m \partial^2 u_{mi}/\partial x_j \partial x_j$ where $\rho_m = \alpha_p \rho_p + \alpha_f \rho_f$ applied throughout the domain	
Eulerian with point-force treatment	$\begin{aligned} \rho_p \partial(\alpha_p v_i)/\partial t + \rho_p \partial(\alpha_p v_i v_j)/\partial x_j &= \rho_f \partial(\alpha_f u_i)/\partial t + \rho_f \partial(\alpha_f u_i u_j)/\partial x_j \\ \alpha_p \rho_p g_i - \alpha_p \partial(p + p_{coll})/\partial x_i + &\quad \alpha_f \rho_f g_i - \alpha_f \partial p/\partial x_i + \\ \alpha_p \mu_f \partial^2 v_i/\partial x_j \partial x_j + \alpha_p F_{int,i}/V_p &\quad \alpha_f \mu_f \partial^2 u_i/\partial x_j^2 - \alpha_p F_{int,i}/V_p \end{aligned}$ applied throughout the domain	
Lagrangian with point-force treatment	$m_p \partial v_i/\partial t = F_{body,i} + F_{surf,i} + F_{coll,i}$ where $F_{surf,i} = F_{Di} + L_i + A_i + S_i + H_i$ applied along particle trajectories	$\begin{aligned} \rho_f \partial(\alpha_f u_i)/\partial t + \rho_f \partial(\alpha_f u_i u_j)/\partial x_j &= \alpha_f \rho_f g_i - \alpha_f \partial p/\partial x_i + \\ \alpha_f \mu_f \partial^2 u_i/\partial x_j^2 - n_p F_{int,i} &\quad \alpha_f \mu_f \partial^2 u_i/\partial x_j^2 - n_p F_{int,i} \end{aligned}$ applied throughout the domain
Lagrangian with resolved-surface treatment	$m_p \partial v_i/\partial t = F_{body,i} + F_{surf,i} + F_{coll,i}$ where $F_{surf,i} = \int[-p n_j + \tau_{ij}] n_j dA_p$ applied along particle trajectories	$\begin{aligned} \rho_f \partial u_i/\partial t + \rho_f u_i \partial u_j/\partial x_j &= \rho_f g_i - \partial p/\partial x_i + \mu_f \partial^2 u_i/\partial x_j^2 \\ \rho_f g_i - \partial p/\partial x_i + \mu_f \partial^2 u_i/\partial x_j^2 &\quad \text{applied outside of particle volume} \end{aligned}$

Note: In the above, n_p is the number density of particles per unit volume of mixed fluid, $F_{int,i}$ is the interphase hydrodynamic force acting on the particles, and p_{coll} is the particle collisional pressure.

on the treatment of the surface forces on the particle and is classified as either a point-force or a resolved-surface treatment. These two sets of classifications will be discussed in more detail.

For the reference frame, the Lagrangian method is sometimes referred to as the discrete method, since it assumes that each particle (or a group of particles) is represented as an individual identity (as opposed to the continuum description for the Eulerian method). For Lagrangian particles, the properties (such as velocity and temperature) are updated along the path of an individual (or cloud of) particles, while in the Eulerian method, the particle properties are averaged in a computational volume, which is generally on a convenient stationary (Eulerian) grid, as demonstrated in Figure 13.6.

For the treatment of the surface forces, the point-force treatment represents the flow over the particle with empirical and theoretical treatments (e.g., specifying a drag coefficient) to obtain the force on the particle. For the resolved-surface treatment, the fluid dynamics (e.g., pressure and shear stress distributions) are fully resolved over the entire particle's surface and then integrated to obtain the overall hydrodynamic forces. Hence, for the resolved-surface treatment, high spatial resolution of the continuous phase is thus required over the particle surface. Therefore, this method is sometimes called "direct simulation." On the other hand, the continuous-flow grid scale can be coarse with respect to particle size for the point-force approach (see Figure 13.7), such that it is much less demanding in terms of computational resources.

13.1.4.1 Lagrangian Approaches: Point-Force Versus Resolved-Surface Treatment

The classification of point-force vs. resolved surface is considered in terms of the Lagrangian equation of motion for the particle momentum (although the same differences are found for an Eulerian approach to the particle equations of motion).

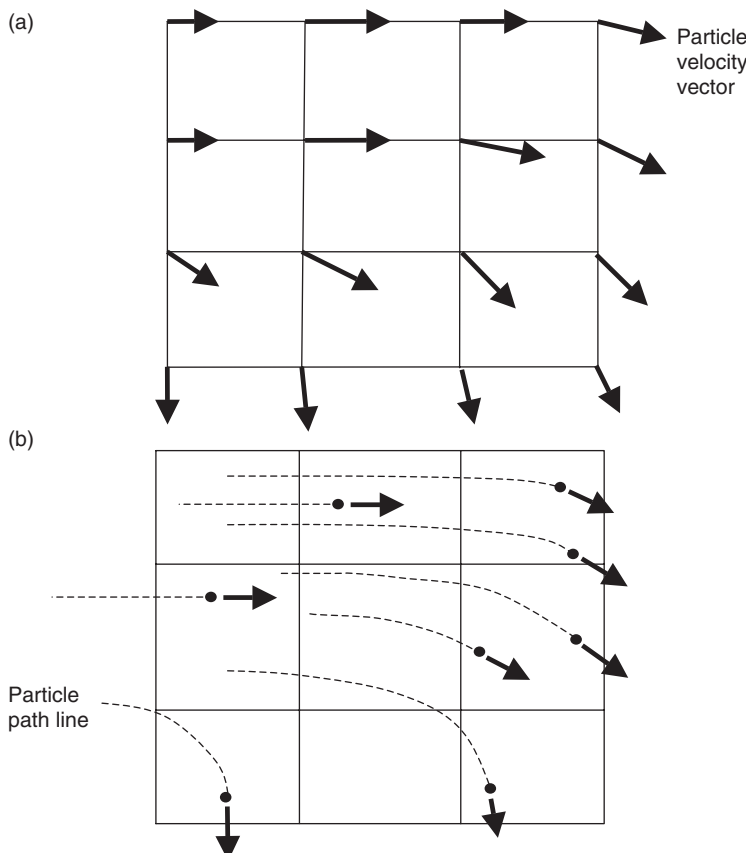
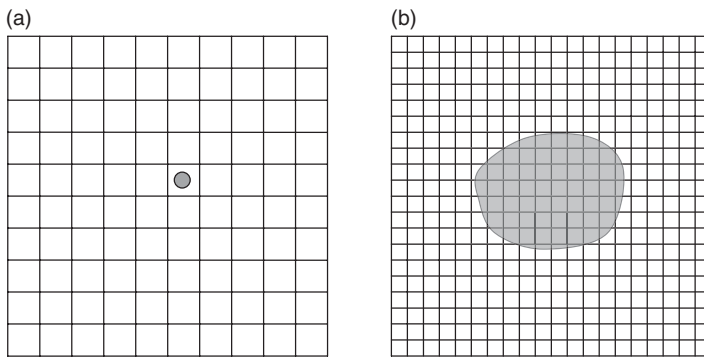


FIGURE 13.6 Comparison of Eulerian and Lagrangian particle velocity fields.



- Neglects particle surface effect on the continuous-fluid grid and flow.
 - Ideal for many particles.
 - Requires models for drag, lift, etc.
- Describes particle volume–interface as part of continuous-fluid solution.
 - Ideal for complex particle shapes.
 - Requires high CPU per particle.

FIGURE 13.7 Different representations for particle treatment where shaded area represents the particle (where d is the effective diameter) and the grid represents the computational resolution for the continuous phase solution (where Δx is the effective cell resolution): (a) point-force representation ($d < \Delta x$) and (b) resolved-surface representation ($\Delta x \ll d$).

For the point-force approach coupled with the Lagrangian reference frame, the fluid or particle is commonly described at a single point that moves at its own (independent) velocity; hence, this approach is often called a discrete element approach, i.e., each particle is treated individually, but with a pointwise representation. If a point-force approximation is used, individual particle trajectories are computed in a Lagrangian sense (i.e., with ordinary differential equations [ODEs] based on the moving particle location), while the continuous-phase flow is typically treated throughout in an Eulerian sense (i.e., with PDEs based on a fixed computational grid). For a large number of particles, computational “parcels” can be used where each parcel represents a cloud of many particles with the same characteristics. The size of the parcel cloud should be less than the continuous-phase local grid resolution (Δx).

For dense flows with the Lagrangian point-force technique, every particle is ideally considered and the possible particle–particle reflections are numerically monitored and then modeled using various collision models. A collision model for smooth solid elastic spheres is reasonably straightforward using conservation of momentum and energy, but finite energy losses are usually important to be considered, using coefficients of restitution and friction. Incorporation of a large number of particles or particles with nonspherical shapes substantially complicates particle collision detection and momentum interaction, hence empirical probabilistic models are needed (Crowe et al., 1998).

If a resolved-surface approach is used, the detailed flow around each particle must be solved to a high resolution. Then, the flow solution can be numerically integrated over the surface to obtain the net momentum interaction of the fluid on the particle. Thus the Lagrangian method updates the particle position based on this integrated interaction. If the particle rotation is allowed, a torque equation can be used to determine the particle angular velocity. The primary drawback of the resolved-surface technique is that the computational requirements of many continuous-fluid grid points around each particle, such that simulation of many (e.g., hundreds or thousands of) particles will generally be impractical on even the most advanced computers.

To highlight the differences between the point-force and the resolved volume approaches, consider the following dynamic equation for a particle, for which v is the velocity at the particle centroid (x_p) and m_p the particle mass:

$$m_p dv/dt = F_{\text{body}} + F_{\text{surf}} + F_{\text{coll}}$$

In this formulation, the description of the particle equation of motion can be given as an ODE along the particle path. The LHS represents the particle mass times the acceleration of the particle along the particle path. The first term on the RHS (F_{body}) represents the forces directly proportional to the particle mass, for example, gravitational forces, while the second term (F_{surf}) represents the fluid dynamic surface forces on the particle, which are proportional to the surface area, and the third term (F_{coll}) represents the forces due to particle–particle or particle–wall collisions.

The body force expression is typically the simplest (if electromagnetic and other body forces are neglected) as it is based on gravitational forces. The resulting expression for the body force of a particle sphere is

$$F_{\text{body}} = \mathbf{g}m_p = \mathbf{g}\rho_p V_p$$

where V_p is the particle volume and ρ_p the volume-averaged density of the particle. The particle volume for spherical shapes can be written as $V_p = \pi d^3/6$, but this equation still remains valid for nonspherical objects as long as d is interpreted as the equivalent diameter based on the particle volume.

As mentioned above, the surface force (F_{surf}) can be treated with two fundamentally different approaches: the resolved-surface approach and the point-force approach. The choice is often based on computational convenience for a given multiphase flow system.

In the resolved-surface (direct simulation) approach, the surface force is determined by integrating the pressure and fluid dynamic shear stress and is shown below in tensor notation as

$$F_{\text{surf},i} = \int [-p + \mu_f(\partial u_i/\partial x_j + \partial u_j/\partial x_i)] n_j dA_p$$

where A_p is the particle surface area and n_j the j projection of the normal unit vector outward from the surface. No specific decomposition of lift, drag, or other surface force effects are needed in this formulation, since all these effects are directly incorporated by the above integration, and thus no limiting assumptions of particle shape, particle Reynolds number, particle or flow acceleration, flow gradients, etc., are required for this formulation. Note that buoyancy effects, which are based on the hydrostatic pressure gradients, are naturally included in this formulation if the gravity force is part of the continuous-phase solution for u_i and p (as discussed in the previous section). The resolved-surface approach allows for the details of the fluid pressure and shear stress to be integrated over the particle surface and avoids empiricism associated with the prescription of fluid dynamic forces.

In the case of a fluid particle, such as a droplet, the interior fluid dynamics may also be resolved. This may be done with a Lagrangian approach (e.g., internal particle domain is given body-fitted coordinates that translate with the particle movement) or an Eulerian approach (e.g., volume-of-fluid method or level set method). The former is better for nondeforming particles where high accuracy of the interface discontinuity is desired, which the latter is more efficient in terms of particle breakup or coalescence. In either of resolved-surface methods, the spatial grid resolution for u_i in the region of the particles must be fine enough to allow description of the detailed stresses around the particle, e.g., the grid scale must be small compared with the particle diameter ($\Delta x \ll d$) as shown in Figure 13.3a. The resolved-surface approach is the most desirable in terms of accuracy as it allows the most physically realistic surface force methodology; however, it is also the most computationally intensive per unit particle. Hence, the resolved-surface technique is only reasonable when there is a single or modest number of particles in the computational domain.

If the number of particles in the simulation is too high for the given computational resources, then the point-force technique can be used as a single equation can be used to describe the force on the particle without actually resolving the flow around the particle surface (such that one may employ $\Delta x > d$, see Figure 13.3b).

For a point-force treatment, the force interaction between the fluid and particles is not computationally integrated over the particle directly, and instead, a surface-averaged force is employed, which is based on

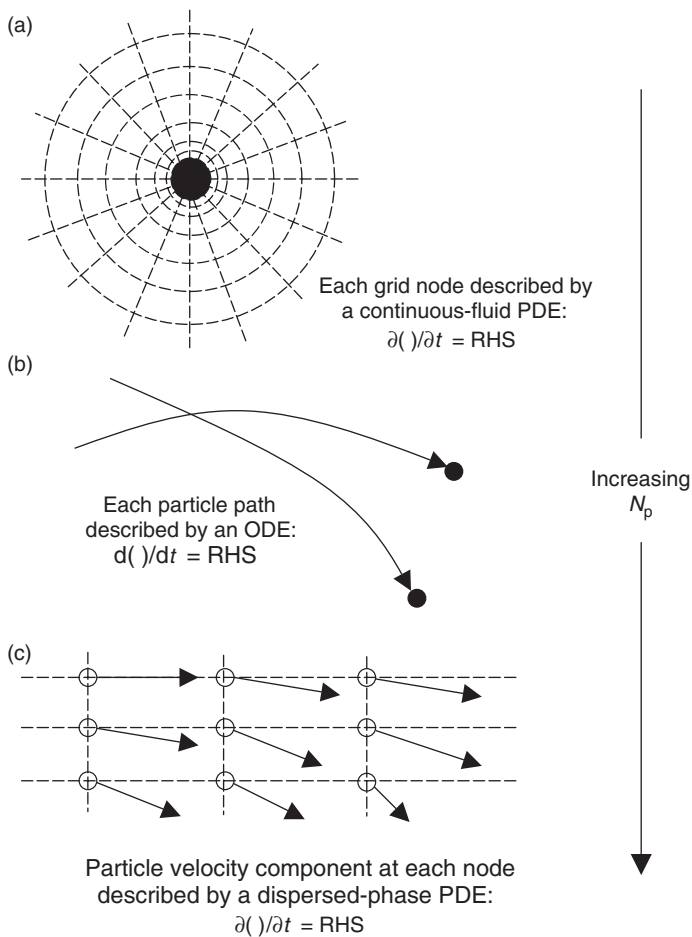


FIGURE 13.8 Comparison of particle treatments for: (a) the resolved surface approach employing body-fitted computational nodes (with a Lagrangian description of particle motion if moving); (b) the Lagrangian approach defined on particle centroids (paths can cross); and (c) the Eulerian approach defined on Eulerian computational nodes.

analytical or empirical force expressions. In general, a surface-averaged force is a linear combination of specific forces, such as drag F_D , lift L , added mass A , stress gradient S , history H , etc.

$$\mathbf{F}_{\text{surf}} = \sum_{k=1}^K \mathbf{F}_{\text{surf},k} = \mathbf{F}_D + \mathbf{L} + \mathbf{A} + \mathbf{S} + \mathbf{H} + \dots$$

where coupling between these K number of components is generally neglected. The particle hydrodynamic surface forces are generally related to the continuous-fluid properties extrapolated to the particle centroid, (X_p) while neglecting the local influence of the particle. The continuous-fluid velocity and vorticity at the particle centroid defined in this way can be denoted as $\mathbf{u}_{@p}$ and $\boldsymbol{\omega}_{@p}$.

The definition of hypothetical continuous-fluid properties at the particle centroid is a key assumption for the point-force treatment and allows significant computational convenience. Thus, this condition assumes that the continuous-fluid velocity is defined everywhere, i.e., $\mathbf{u}_{@p}$ corresponds to $\mathbf{u}(x_p)$. If the continuous-flow characteristics are spatially uniform in instances where the particle presence is not considered (i.e., \mathbf{u} without particles would be everywhere \mathbf{u}_∞), then $\mathbf{u}_{@p} = \mathbf{u}_\infty$ is consistent with the proper limiting value. It should be noted that if there is a nonlinear flow in the region of the particle,

then employing a velocity from a single point may not be sufficient to characterize the surrounding conditions and that some averaging in the vicinity of the particle may be more appropriate. Thus the variations of $\mathbf{u}_{@p}$ in the local vicinity of the particle (neglecting the velocity variations caused by the presence of the particle) are assumed to be weak. Based on the above, a relative particle velocity can be then defined as

$$\mathbf{w} = \mathbf{v} - \mathbf{u}_{@p}$$

This relative velocity can be used to define the direction of the hydrodynamic surface forces, for example, the drag force is defined as a value opposing \mathbf{w} . Similarly, the lift force \mathbf{L} is defined perpendicular to \mathbf{w} and $\boldsymbol{\Omega}_{\text{rel}}$ (the relative rotation of the particle with respect to the fluid):

$$\boldsymbol{\Omega}_{\text{rel}} = \boldsymbol{\Omega}_p - \frac{1}{2} \boldsymbol{\omega}_{@p}$$

where $\boldsymbol{\omega}_{@p}$ is the continuous-fluid vorticity extrapolated to the particle centroid, while neglecting the influence of the particle. This rotation can also be used to track the angular momentum of the particles (Crowe et al., 1998).

A well-known example of the point-force description for linear momentum particle dynamics is the Maxey–Riley (1983) equation, which is derived analytically for the case of incompressible creeping flow (i.e., viscous terms, dominate convective terms, such that the latter can be linearized) around a single solid spherical particle far from any boundaries or other particles. The creeping flow assumption is defined as $Re_p \ll 1$, where $Re_p = \rho_f d w_l / \mu_f$. If the free-stream velocity gradients are assumed to be weak when considered on the scale of the particle diameter (e.g., particle diameter smaller than the Kolmogorov length scale), the Faxen forces (which are proportional to $\nabla^2 \mathbf{u}_{@p}$) and the lift forces (which can arise from fluid shear and particle rotation) can be neglected. If one also neglects mass and heat transfer as well as any temporal discontinuities in \mathbf{u} , the resulting creeping-flow point-force terms are as follows (see [Section 13.1.4](#)):

$$\begin{aligned} \mathbf{F}_D &= -3\pi d \mu_f \mathbf{w} \\ \mathbf{A} &= -\frac{1}{2} \rho_f V_p (\mathbf{d}\mathbf{v}/dt - D\mathbf{u}_{@p}/Dt) \\ \mathbf{S} &= \rho_f V_p D\mathbf{u}_{@p}/Dt - g\rho_f V_p \end{aligned}$$

and

$$H = -\frac{3}{2} d^2 (\pi \rho_f \mu_f)^{1/2} \int_0^t \left[\frac{dw/d\tau}{\sqrt{t-\tau}} \right] d\tau$$

The drag force (\mathbf{F}_D) assumes a no-slip condition at the particle surface. While this condition is satisfied for a solid particle (as long as the flow field can be considered as a continuum), it may also be reasonable for a small droplet or a bubble, if there is a substantial contamination on the surface rendering it nearly immobile. The fluid stress force \mathbf{S} results from the stress arising from the undisturbed fluid stress, and this gives two components: the first term is proportional to the Lagrangian fluid acceleration ($D\mathbf{u}_{@p}/Dt$), which can be nonzero even in steady flow, and the second term is proportional to the hydrostatic pressure gradient, which in turn can be written as proportional to the displaced mass ($\rho_f V_p$) and hence is often called the buoyancy force. The added mass term (\mathbf{A}) is slightly modified from the original Maxey–Riley equation as suggested by Maxey et al. (1997). The last term is the history force and assumes negligible relative velocity acceleration at $t = 0$, although Kim et al. (1998) give a proposed correction if this is not the case. Mei et al. (1991) noted that the above history force expression (H) is not valid for long times or noncreeping flow conditions. Thus, this equation invokes several assumptions.

Under certain conditions, some of the terms become secondary or tertiary and thus can be neglected in the particle dynamic equations. For example, the history force terms are often neglected since these corrections are typically small, numerically cumbersome, and not well posed, except for creeping-flow conditions of simple particle shapes. Furthermore, the case of very light particles (e.g., gas bubbles in a liquid where $\rho_p \ll \rho_f$) indicates that terms associated with ρ_p (e.g., F_{body} and dV/dt) can be reasonably neglected under several (but not all) circumstances. By neglecting lift, yields the following Stokesian point-force expression for very light particles.

$$\begin{aligned} \rho_f V_p dV/dt = & -6\pi d\mu_f w + 3\rho_f V_p D\mathbf{u}_{@p}/Dt - 2g\rho_f V_p \\ & - 3d^2(\pi\mu_f\rho_f)^{1/2} \int_0^\infty \left[\frac{dw/d\tau}{\sqrt{t-\tau}} \right] d\tau + F_{\text{coll}} \quad \rho_p \ll \rho_f \text{ and } Re_p \ll 1 \end{aligned}$$

For very heavy particles compared with the continuous-flow (e.g., drops or solid particles in a gas where $\rho_p \gg \rho_f$), many of the terms associated with ρ_f (e.g., L, A, S, and H) can be reasonably neglected under several (but not all) circumstances. Neglecting these terms, the Stokesian point-force expression for very heavy particles becomes

$$\rho_p V_p dV/dt = -3\pi d\mu_f w + g\rho_p V_p + F_{\text{coll}}, \quad \rho_p \gg \rho_f \text{ and } Re_p \ll 1$$

There are a wide variety of other point-force equations (with both analytical and empirically derived force terms) that have been reported by researchers in order to take into account the particle aspects (such as interface conditions, nonspherical shapes, rotation, deformability, interior fluid motion, and mass transport) and the flow aspects (such as compressibility, turbulence, shear, and strain) as well as the presence of other particles or surfaces. In particular, empirical and semiempirical expressions are often used for conditions, that do not correspond to creeping flow past a simple shape. These empirical expressions are generally limited to specific regimes and may be subject to experimental uncertainties and bias. The various particle dynamic equations that are employed in the multiphase community are thus tailored to specific situations (based on the physics of interest, test conditions, and computational resources) and as such the particle equations appearing in the literature are extremely numerous. This nonuniqueness of multiphase flow equations indicates that there is no single standard equation that should be applied to all the conditions, and thus one must choose the appropriate equations as carefully as one chooses the appropriate numerical solution techniques.

13.1.4.2 Eulerian Approaches: Mixed-Fluid Versus Separated-Fluid Formulations

The Eulerian description applied to the dispersed phase generally assumes the characteristics of the particles (e.g., velocity or temperature) can be described as a continuum. This assumption allows the dispersed phase to be treated with the same discretization and similar numerical techniques as those used for the continuous phase. This is especially important when two-way coupling effects are present and can reduce the overall computational costs. The Eulerian treatment combined with a point-force assumption assumes that there are several particles per control volume, which can be described by a local number density (n_p) in the proper limit. To handle a variety of particle properties within a control volume, the particle characteristics can also be discretized using the multigroup approach, where the number density becomes a vector (n_{pi}), such that each group is identified by a particular characteristic range. For example, polydisperse particles can be separated into various bins, each with a specific particle diameter range (Crowe et al., 1998). In this case, transport equations are needed and computed for each Eulerian particle group.

The Eulerian techniques can be further subdivided into mixed- and separated-fluid approaches. The mixed-fluid approach assumes that the particles and the continuous phase are in local kinetic and thermal equilibrium, i.e., the relative velocities, and temperatures between the two phases are small in comparison to variations in the overall flowfield that are predicted. This approximation is the mixed-fluid method and distinguishes only the mass fractions of the particle and fluid phases in a mixed volume.

It has also been termed the locally homogeneous flow (LHF) by Faeth (1987). Thus, in this approach, the relative velocity (between the particle motion and the continuous-phase motion) is assumed to be negligible, so that one has

$$\mathbf{u}_m = \mathbf{u} = \mathbf{v} \quad (w = 0) \quad \text{for mixed-fluid treatment}$$

Similarly, the temperature difference between the two phases is assumed to be negligible.

The use of the mixed-fluid approximation results in a single set of momentum conservation equations for the flow mixture (as opposed to one set for the continuous phase and one set of the dispersed phase). For example, the resulting equations of motion for a fluid mixture with a single velocity and temperature are shown in [Table 13.2](#), where the particle volume fraction, α_p , is the ratio of volume occupied by the particle to the volume of the mixture of particles and the continuous phase, and where the continuous-phase void fraction is similarly defined, such that $\alpha_p + \alpha_f = 1$. This approximation allows strong numerical simplicity and can generally handle both dispersed and dense conditions. In addition, since it is based on volume averaging of both phases, the exact size and shape of the discontinuous phase is not needed for the flow simulation.

The separated-fluid approach for Eulerian description of the particle phase with the point-force assumption assumes that both the carrier fluid and the particles comprise two separate, but intermixed, continua. Therefore, two sets of momentum equations are required for a two-phase flow: one for the continuous phase and the other for the dispersed phase. The separated fluid method is also often called the two-fluid method, since two sets of PDEs and two sets of velocity fields are required (one for each phase):

$$w \neq 0 \quad \text{for two-fluid treatment}$$

These equations will in general be coupled (e.g., one-way coupled means that the particle equations will depend on solution of the continuous-phase equations, and two-way coupled means that both sets of equations must be solved in companion).

In the coupling of these equations, the separated-fluid approach accounts for (and thus must formulate) the relative interphase mass, velocity, and temperature differences.

The interphase expressions that relate the mass, momentum, and energy of the different phases are then based on a point-force description. For example, the Eulerian separated-fluid PDEs with a point-force approach for the two phases assuming constant density, and viscosity for the continuous fluid may be represented as listed in [Table 13.2](#). Alternatively, a probability distribution function (PDF) approach can be applied to the Eulerian equations to give the evolution of the ensemble-averaged properties. The resulting transport equations can take into account many of the effects incorporated into conventional Eulerian approaches, including near-wall behavior, particle evaporation, etc.

A key assumption regarding Eulerian treatments described above is that the particle concentration (e.g., α_p) is a variable, which is continuously differentiable, such that the PDE description is appropriate as given in [Table 13.2](#). This is termed the particle-phase continuum assumption by Drew and Prassman (1998). From a deterministic point of view, this assumption is physically reasonable only considering control volume lengths that are much larger than the average particle spacing ($\Delta x \gg \Lambda_{p-p}$), i.e., the dispersed phase equations can be considered as a continuum when there are many particles within a single computational cell-volume so that the concentration variations do not induce significant discontinuities (as shown in [Figure 13.9](#)). In contrast, if only two particles are present in a computational cell and have different velocities, then refinement or particle convection which eliminates one of the particles from the cell, can cause a physically discontinuous change in the cell-averaged particle velocity v . Therefore, Eulerian approaches are only deterministically reasonable when large amounts of particles are contained within each cell, and are not well posed for successive grid refinements.

This requirement of many particles per cell can be removed when a probabilistic point of view is considered based on some averaging. As such, a computational cell with 0.1 computational particles in its volume is equivalent to a 10% probability of a particle occurring in the volume at a given time, such that the Eulerian particle properties (α_p, v , etc.) can be considered as the average of all possible realizations (Drew and Prassman, 1998).

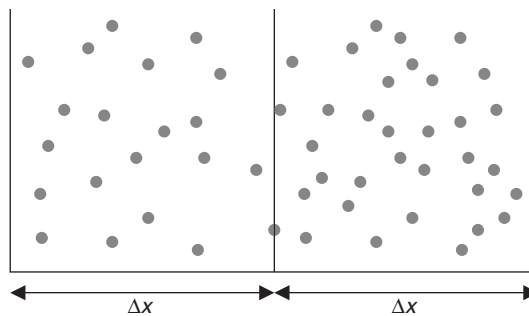


FIGURE 13.9 A two-dimensional description of discrete particles in two adjoining computational cells of an Eulerian grid where ($\Delta x \gg L_{p-p}$) and the continuum approximation can be employed.

However, the computational volume, it must still be much greater than the particle diameter ($\Delta x \gg d$) for the Eulerian continuum approach to be reasonable, if one includes a point-force approximation.

13.1.4.3 Lagrangian Versus Eulerian Point-Force Approaches

Since a variety of descriptions and treatments have been used for multiphase flows, the choice of which numerical approach to employ depends on the particle and fluid physics that are relevant and of interest (Loth, 2000). As discussed above, one of the key distinctions between the various multiphase numerical methods is that of Lagrangian vs. Eulerian representation of the particle characteristics (which include velocity, concentration, diameter, etc.).

Let us now compare the pros and cons of Lagrangian vs. Eulerian approaches for the point-force treatment of the particle fields. Lagrangian approaches are typically more physically robust if the following flow properties are of interest and importance: particle reflection from surfaces, particle breakup, particle–particle interactions (collisions and coalescence), counterflowing particles, and turbulent diffusion. In addition, non-physical numerical diffusion of Eulerian particle density in regions of high gradients can be eliminated by employing Lagrangian particles due to their pointwise spatial accuracy. The Lagrangian method also allows particles to cross over the wake of other particles (as shown in Figure 13.8b), whereas steady-state Eulerian treatments do not allow this phenomenon. In addition, if the particles within the computational domain are not all of the same size or shape, the Lagrangian technique can employ statistical representations of the particle distributions to incorporate these effects. As the number of physical particles increases, such that individual tracking is prohibitive and collisions occur, the particles can be treated in groups for which probability of collisions are modeled and incorporated. Such techniques can use PDFs in simple homogeneous flows with simple geometries or Monte–Carlo methods, which employ random-number generators for more complex flows and domains. The latter is often called a random-walk approach and has been very successful for mean diffusion in homogenous turbulence, and has also shown some success in anisotropic nonhomogeneous turbulence (Bockslé and Loth, 2001).

In contrast, the Eulerian particle-phase approach describes particle properties as part of a continuum throughout the computational domain and has several distinct advantages. For particles distributed throughout the computational domain (instead of locally concentrated), the Eulerian description typically requires fewer degrees of freedom, i.e., less Eulerian nodes than Lagrangian nodes, especially if a stochastic diffusion model is employed for the Lagrangian case. Lagrangian methods can also be problematic if the parcel volume (Ω_p) is larger than the fluid averaging volume, whereas Eulerian methods have no equivalent restriction. In addition, an Eulerian approach allows both phases to be handled with a consistent numerical scheme and a consistent numerical grid. This discretization coincidence for an Eulerian treatment of the particles becomes a distinct accuracy advantage when one attempts to compute the effects of the particles on the continuous fluid for two-way coupling (Shrayber, 1979). For example, Sivier et al. (1996) examined Lagrangian and Eulerian representations of the particle field with respect to the prediction of shock attenuation of the continuous phase, and found that the Eulerian particle treatment

proved significantly more efficient (for the given accuracy levels) in terms of both computational memory and time.

13.1.4.4 Interphase Coupling

For either Lagrangian or Eulerian treatments, it should be noted that the two-way coupling requires description of the particle interphase coupling. This interaction occurs through the interface stresses between the two phases on the surface of the particle. In particular, the interphase coupling force ($F_{int,i}$) is the force acting on a single particle due to pressure and viscous stresses caused by the disturbed surrounding flow, owing to the boundary conditions at the bubble surface (Druzhinin and Elghobashi, 1998). It is equal in magnitude and opposite in direction to the hydrodynamic particle force acting on the continuous phase ($-F_{int,i}$). The interphase coupling force is effectively the hydrodynamic surface forces minus the contributions from the undisturbed flow stresses (i.e., minus the stress gradient forces, which occur independent of the presence of the particle):

$$F_{int} = F_{surf} - S = F_D + L + A + H$$

For two-way coupling, the hydrodynamic force acting on a continuous-fluid computational volume is then $-n_p F_{int}$.

For very heavy particles ($\rho_p \gg \rho_f$), the interphase force is often simplified to include only the particle drag (neglecting lift, added mass, and history effects, since they are proportional to ρ_f), i.e., $F_{int} = F_D$. For very light particles ($\rho_p \ll \rho_f$) with negligible collisions, the particle acceleration and body force can be neglected (as discussed in Section 13.1.4) θ , such that the interphase force can be conveniently written as $F_{int} = -S$ (Druzhinin and Elghobashi, 1998; Xu et al., 2002). In these two limits, the interaction force description is comparatively simple, which is particularly helpful for the Eulerian point-force treatment (see Table 13.2).

As the number of particles increase collisions become more important, leading to dense flows (Gidaspow, 1994). The key aspect for these flows is the proper incorporation of the particle-particle effects on the particle-phase fluid dynamics. In particular, the particle collision result in an effective stresses, which should be incorporated into the particle transport equation. These can be modeled with particle-phase viscosity, particle-pressure, granular temperature, etc., via a kinetic theory. For example, the Eulerian dense particle treatment will typically employ a gradient of the collisional pressure (p_{coll}) to capture this effect (see Table 13.2), while particle-particle momentum interactions are described via F_{coll} for an equivalent Lagrangian particle treatment. Eulerian formulations for the particle-phase generally model the integrated effect, and thus tend to be more empirical. However, such Eulerian formulation are independent of the number of particles, whereas the Lagrangian techniques become increasingly computationally intensive as the number of particles increases. Therefore, Eulerian formulation are most practical for collision-dominated conditions. (Crowe et al., 1998).

13.2 Direct Numerical Simulations

G. Tryggvason, Y. Tsuji, and S.E. Elghobashi

Direct simulation refers to the direct solution of the flow equations describing the two-phase mixture. Bubble and droplet motion are addressed first in which the deformation of the bubbles and/or droplets is included. The second section introduces the discrete element approach in which the details of particle-particle contact is addressed. The third section shows the application of the direct simulation of turbulence in fluid-particle flows.

13.2.1 Bubble and Droplet Motion and Deformation

G. Tryggvason

Understanding the dynamics of multiphase flows is of critical engineering and scientific importance and the literature is extensive. Much of what we know has, however, been obtained by experimentation and

scaling analysis. From a mathematical point of view, multiphase flow problems are notoriously difficult. In addition to the nonlinearity of the governing equations, the location of the phase boundary must generally be found as a part of the solution. Exact analytical solutions therefore exist only for the simplest of problems such as the steady state motion of bubbles and drops in Stokes flow, linear inviscid waves, and small oscillations of bubbles and drops. Experimental studies of multiphase flows are, however, not easy. For many flows of practical interests the length scales are small, the time scales are short, and optical access to much of the flow is limited. The need for numerical solutions of the governing equations has therefore been felt by the multiphase research community since the origin of computational fluid dynamics in the late 1950s and early 1960s. Although much has been accomplished, simulations of multiphase flows have remained far behind homogeneous flows where direct simulations have become a standard tool in turbulence research. Considerable progress has, however, been made in the last few years and it is clear that DNS will play a leading role in multiphase flow research in the next decade. Below we will first review briefly the various numerical techniques developed for computations of multiphase flows and then discuss results for disperse flows.

13.2.1.1 Simple Flows ($Re = 0$ and ∞)

In the limit of high and low Reynolds numbers, it is sometimes possible to simplify the flow description considerably by either ignoring inertia completely (Stokes flow) or by ignoring viscous effects completely (inviscid, potential flow). Most success has been achieved when the particles are undefor mable spheres where in both these limits, it is possible to reduce the governing equations to a system of coupled ODES for the particle positions. For Stokes flow, the main contributor is Brady and collaborators (see Brady and Bossis (1988) for a review of early work), who have investigated extensively the properties of suspensions of particles in shear flows, and other problems. For inviscid flows, see Sangani and Didwania (1993) and Smereka (1993) for simulations of the motion of many bubbles in periodic domains.

For both Stokes flows as well as potential flows, deformable bubbles and drops can be simulated with boundary integral techniques. One of the earliest attempts was due to Birkhoff (1954), where the evolution of the interface between a heavy fluid initially on top of a lighter one (the Rayleigh–Taylor instability) was followed by a method where both fluids were assumed to be inviscid and irrotational, apart from baroclinic generation of vorticity at the interface. This allowed the evolution to be reformulated as an integral equation along the boundary between the fluids. Both the method as well as the problem later became a stable of multiphase flow simulations. A boundary integral method for water waves was presented by Longuet-Higgins and Cokelet (1976) and used to examine breaking waves. This paper was enormously influential and was followed by a large number of very successful extensions and applications, particularly for water waves (Baker et al., 1982; Vinje and Brevig, 1981; Schultz et al., 1994; and others). Other applications include the evolution of the Reyleigh–Taylor instability (Baker et al., 1980), the growth and collapse of cavitation bubbles (Blake and Gibson, 1981; Robinson et al., 2001), the generation of bubbles and drops due to the coalescence of bubbles with a free surface (Oguz and Prosperetti 1990; Boulton-Stone and Blake, 1993), the formation of bubbles and drops from an orifice (Oguz and Prosperetti, 1993), and the interactions of vortical flows with a free surface (Yu and Tryggvason, 1990), just to name a few. All boundary integral (or boundary element, when the integration is element based) methods for inviscid flows are based on following the evolution of the strength of surface singularities in time by integrating a Bernoulli-type equation. The surface singularities give one velocity component and Green's second theorem yields the other, thus allowing the position of the surface to be advanced in time. Different surface singularities allow for a large number of different methods (some that can only deal with a free surface and others that are suited for two-fluid problems) and different implementations multiply the possibilities even further. For an extensive discussion and recent progress see Hou, et al. (2001). Although continuous improvements are being made and new applications continue to appear, two-dimensional boundary integral techniques for inviscid flows are by now – a quarter century after the publication of the paper by Longuet-Higgins and Cokelet – a fairly mature technology. Fully three-dimensional computations are, however, still rare. Chahine and Duraiswami (1992) have computed the interactions of a few inviscid cavitation bubbles and Xue et al. (2001) have simulated a three-dimensional breaking wave.

The key to the reformulation of inviscid interface problems in terms of a boundary integral is the linearity of the field equations. In the opposite limit, where inertia effects can be ignored and the flow is dominated by viscous dissipation, the Navier–Stokes equations become linear (Stokes flow) and it is also possible to recast the governing equations into an integral equation on a moving surface. Boundary integral simulations of unsteady two-fluid Stokes problems appear to have originated with the work of Youngren and Acrivos (1976) and Rallison and Acrivos (1978) who simulated the deformation of a bubble and a drop, respectively, in an extensional flow. Subsequently, several authors have examined a number of problems. Pozrikidis and collaborators have examined several aspects of the suspension of drops, starting with a study by Zhou and Pozrikidis (1993) of the suspension of a few two-dimensional drops in a channel. Simulations of fully three-dimensional suspensions have been done by Loewenberg and Hinch (1996) and Zinchenko and Davis (2000). The method has been described in detail in the book by Pozrikidis (1992) and Pozrikidis (2001), gives a very complete summary of the various applications.

13.2.1.2 Finite Reynolds Number Flows

For intermediate Reynolds numbers, it is necessary to solve the full Navier–Stokes equations. Nearly 10 years after Birkhoff's effort to simulate the Rayleigh–Taylor problem by a boundary integral technique, the Marker-And-Cell (MAC) method was developed at Los Alamos by Harlow and collaborators. In Harlow and Welch (1965) the method was introduced and two sample computations of the so called dam breaking problem shown. Several papers quickly followed: Harlow and Welch (1966) examined the Rayleigh–Taylor problem and Harlow and Shannon (1967) studied the splash when a drop hits a liquid surface. As originally implemented, the MAC method assumed a free surface so there was only one fluid involved. This required boundary conditions to be applied at this surface and the fluid in the rest of the domain to be completely passive. The Los Alamos group quickly realized, however, that the same methodology could be applied to two-fluid problems. Daly (1969) computed the evolution of the Rayleigh–Taylor instability for finite density ratios and Daly and Pracht (1968) examined the initial motion of density currents. Surface tension was then added by Daly (1969) and the method again used to examine the Rayleigh–Taylor instability. The MAC method quickly attracted a small group of followers that used it to study several problems: Chan and Street (1970) applied it to free surface waves, Foote (1973, 1975) simulated the oscillations of an axisymmetric drop and the collision of a drop with a rigid wall, and Chapman and Plesset (1972) and Mitchell and Hammit (1973) simulated the collapse of a cavitation bubble. Although the MAC method was designed specifically for multifluid problems (hence the M for Markers!) it was also the first method to successfully solve the Navier–Stokes equation using the primitive variables (velocity and pressure). The staggered grid used was a novelty and today it is a common practice to refer to any method using a projection based time integration on a staggered grid as a MAC methods.

The next generation of methods for multifluid flow evolved gradually from the MAC method. It was already clear in the Harlow and Welch (1965) paper that the marker particles could cause inaccuracies, and among the number of algorithmic ideas explored by the Los Alamos group, the replacement of the particles by a marker function soon became the most popular alternative. Thus the volume-of-fluid (VOF) method was born. VOF was first discussed in a refereed journal article by Hirt and Nichols (1981), but the method apparently originated a few years earlier (DeBar, 1974; Noh and Woodward, 1976). The VOF method has been extended in various ways by a number of authors. It has also been distributed widely as the NASA SOLA-VOF code and as FLOW3D from Fluid Sciences Inc. In addition, many commercial computational fluid dynamics codes now include the option of simulating free surface or multiphase flows using the VOF method. For a review of VOF methods, see Scardovelli and Zaleski (1999). Other methods, based on similar ideas but advecting the marker function in a different way include the level set method (reviewed by Osher and Fedkiw, 2001; Sethian, 2001) and the CIP method of Yabe and collaborators (see Yabe et al., 2001, for a review).

While the MAC methodology and its successors were being developed, other techniques were also being explored. Hirt et al. (1970) describe one of the earliest use of structured boundary fitted Lagrangian grids. This approach is particularly well-suited when the interface topology is relatively simple and no

unexpected interface configurations develop. In a related approach, a grid line is aligned with the fluid interface, but the grid away from the interface is generated using standard grid generation techniques such as conformal mapping or other more advanced elliptic grid generation schemes. The method was used by Ryskin and Leal (1984), to compute the steady rise of buoyant, deformable, axisymmetric bubbles. Ryskin and Leal assumed that the fluid inside the bubble could be neglected, but Dandy and Leal (1989) and Kang and Leal (1987) extended the method to two-fluid problems and unsteady flows. Several authors have used this approach to examine relatively simple problems such as the steady state motion of single particles or moderate deformation of free surfaces. Fully three-dimensional simulations are relatively rare and it is probably fair to say that it is unlikely that this approach will be the method of choice for very complex problems, such as the three-dimensional unsteady motion of several particles.

A much more general approach to continuously represent a fluid interface by a grid line is to use unstructured grids to resolve the fluid motion. This allows grid points to be inserted and deleted as needed and distorted grid cells to be reshaped. While the grid was moved with the fluid velocity in some of the early applications of this method, the more modern approach is to either move only the interface points or to move the interior nodes with a velocity different from the fluid velocity in such a way that the grid distortion is reduced but adequate resolution is still maintained. A large number of methods have been developed that fall into this general category, but we mention only a few examples. Oran and Boris (1987) simulated the breakup of a two-dimensional drop; Shopov et al. (1990) examined the initial deformation of a buoyant bubble; and Fukai et al. (1995) did axisymmetric computations of the collision of a single drop with a wall.

Several hybrid methods combine the ideas discussed above in a variety of ways. Front-tracking methods where the interface is marked by connected marker points, but a fixed grid is used for the fluid within each phase have been particularly successful. In the method of Tryggvason and collaborators (Unverdi and Tryggvason, 1992; Tryggvason et al., 2001) the tracked front is used to advect a smoothed marker function and to compute the surface tension. The method is therefore very similar to methods that work directly with a grid-marker function, but the advection of the interface is greatly improved. Other methods have been designed to capture the interface more accurately. These include the method of Glimm and collaborators (Glimm and McBryan, 1985), where the fixed grid is modified near the front to make a grid line follow the interface, as well as more recent sharp-interface methods (such as Fedkiw et al., 1999; Ye et al., 1999; and Lee and LeVeque, 2003). The increased accuracy does, however, come at the cost of a considerably increased complexity and it is not clear at the time of this writing what the impact of these new methods will be on DNS of finite Reynolds numbers flows.

The most recent addition to the collection of methods capable of simulating finite Reynolds number multiphase flows is the Lattice-Boltzmann method (LBM). Although there have been some doubts about the accuracy and correctness of the LBM, it seems now clear that they can be used to produce accurate results of accuracy comparable to more conventional methods. It is still not clear whether the LBM is significantly faster or simpler than other methods (as sometimes claimed), but most likely these methods are here to stay. For a discussion see, e.g., Shan and Chen (1993) and Sankaranarayanan et al. (2002).

Many reviews are available that discuss computational methods for multiphase flows. Early reviews include Hyman (1984) and Floyryan and Rasmussen (1989), and more recent reviews are given by Scardovelli and Zaleski (1999), who discuss volume of fluid methods, and Anderson et al. (1998), who review phase field methods. Several up-to-date articles about various aspects of computations of multiphase systems and related problems can be found in a special issue of the *Journal of Computational Physics* (Vol. 169, 2001). The book by Shyy et al. (1996) also discusses several aspects of computations of multiphase flows. For discussions of the role of numerical predictions for industrial problems, see Crowe et al. (1998), for example.

13.2.1.3 Disperse Flows

In many industrial and natural processes, multiphase flows consists of one phase in the form of well defined bubbles, drops, or solid particles dispersed in another continuous phase. Bubbly flows occur in boiling heat transfer, cloud cavitation, aeration, and stirring of reactors in water purification and waste

water treatment plants, bubble columns and centrifuges in the chemical industry, cooling circuits of nuclear reactors, the exchange of gases and heat between the oceans and the atmosphere, and explosive volcanic eruptions, just to name a few examples. Similarly, drops are found in sprays used in the atomization of liquid fuels, painting and coating, emulsions, and rain. Understanding the evolution and properties of *dispersed* flows is therefore of major technological as well as scientific interest.

For engineering applications with a large number of bubbles and drops, computational modeling relies on equations that describe the average flow field. The two-fluid model, where separate equations are solved for the dispersed and the continuous phase, is the most common approach. Since no attempt is made to resolve the unsteady motion of individual particles, closure relations are necessary for the unresolved motion and the forces between the particles and the continuous phase. Closure relations are usually determined through a combination of dimensional arguments and correlation of experimental data. The situation is analogous to computations of turbulent flows using the Reynolds averaged Navier–Stokes equations, where momentum transfer due to unsteady small-scale motion must be modeled. For details of two-fluid modeling, see Drew (1983), Ishii (1987) Drew and Lahey (1992), and Zhang and Prosperetti (1994). For the turbulent motion of single phase flows, direct numerical simulations, where the unsteady Navier–Stokes equations are solved on fine enough grids to fully resolve all flow scales, have had a major impact on closure modeling. The goal of direct numerical simulations of multiphase flows is similar. In addition to information about how the drift Reynolds number, velocity fluctuations, and bubble dispersion change with the properties of the system, the computations should yield insight into how bubbles and drops interact, both with each other and with the continuous phase. The simulations should show whether there is a predominant microstructure or interaction mode, and if the flow forms structures that are much larger than the size of the dispersed particles. Information about the microstructure is essential for the construction of models of multiphase flows and can also help to identify what approximations can be made.

Although the need for direct numerical simulations to help with the construction of reliable closure models has been recognized for a long time, it is only recently that major progress has been made. In the limit of high and low Reynolds numbers major simplifications are possible and the Stokesian dynamics method of Brady and collaborators (for a recent contribution, see Sierou and Brady (2002) for example) has been used to examine many aspects of solid suspensions. For inviscid bubbles, Sangani and Didwania (1993) and Smereka (1993) simulated the motion of spherical bubbles in a periodic box and observed that the bubbles tended to form horizontal “rafts,” particularly when the variance of the bubble velocities was small. As this rafting is generally not observed experimentally, the results cast considerable doubt on the utility of the potential flow approximation for the interactions of many bubbles. This is somewhat unexpected since for a single bubble this approximation is excellent (see, however Harper (1997) for a discussion of bubbles rising in-line). In both Stokes flows and potential flows, deformable bubbles and drops can be simulated using boundary integral techniques. For recent papers on Stokes flow see, for example, the study by Li and Pozrikidis (2000) of the dynamics of two-dimensional drops in a channel and the simulation of a few three-dimensional drops in a channel by Zinchenko and Davis (2000). While transient interactions of a few bubbles have been examined using boundary integral methods, no simulations of the long-time evolution of many deformable bubbles have been done, and given the failure of the potential flow approximation for rigid bubbles at high Reynolds numbers, it seems unlikely that such studies would be applicable to a large range of realistic situations.

For nondilute flows at intermediate Reynolds numbers it is necessary to solve the full unsteady Navier–Stokes equations. Such simulations for the unsteady motion of many bubbles or particles are relatively recent. Unverdi and Tryggvason (1992a, 1992b) computed the interactions of two, two- and three-dimensional bubbles and Esmaeeli and Tryggvason (1996) followed the evolution of a few hundred two-dimensional bubbles. Esmaeeli and Tryggvason (1998, 1999) simulated the unsteady motion of several two- and three-dimensional bubbles and Mortazavi and Tryggvason (2000) examined the motion of a periodic row of drops in a channel. More recently, Bunner and Tryggvason (1999, 2002a, 2002b, 2003) used a fully parallelized version of the method to examine three-dimensional systems with a much larger number of bubbles. Other studies of the motion and interactions of many bubbles have been done by several Japanese authors. Early work, using the VOF method to compute the motion of a single two-dimensional bubble can be found in Tomiyama et al. (1993) and more recent work on bubble interactions, using both VOF and the Lattice-Boltzmann Method, is presented in Takada et al. (2000, 2001).

The numerical simulations of Tryggvason and collaborators have focused on homogeneous bubbly flows, modeled by fully periodic domains. The average bubble Reynolds number has generally been relatively modest, 20 to 30, so that each bubble is fully resolved by 20 to 30 grid points per diameter. Relatively low-order statistics, such as the average rise velocity of the bubbles and the pair probability distribution, converge rapidly with increasing size of the simulated domain and Bunner and Tryggvason (2002) found essentially no difference between the rise velocity of 12 and 216 nearly spherical bubbles. Other quantities, like the self-diffusion coefficient, converge much more slowly. For nearly spherical buoyant bubbles at modest Reynolds numbers, the simulations show that the dominant interaction mode is the “drafting, kissing, and tumbling” mechanism described by Fortes et al. (1987). Thus, a bubble behind another bubble is drawn into the wake of the bubble in front, once in the wake it catches up and collides with the one in front and the two bubbles then “tumble” and move apart. This collision mode is inherently a finite Reynolds number effect, since two buoyant bubbles in Stokes flow do not change their orientation unless acted on by the third bubble and bubbles in potential flow repeal each other if they are rising in an in-line configuration. The simulations have also shown that freely interacting bubbles rise considerably slower than bubbles constrained to remain in a fixed array. At very low Reynolds numbers the opposite is true as predicted theoretically for Stokes flow. While spherical bubbles remained nearly uniformly distributed, Bunner and Tryggvason (2003) found that deformable bubbles could gather into streams or chimneys and rise much faster than when they were uniformly distributed. Figure 13.10 shows the close-up of a few bubbles and the velocity field in a plane cutting through some of the bubbles, taken from a simulation of 27 freely rising bubbles at a void fraction of 6%, before they stream. The simulations are done using a cubic, fully periodic domain resolved by 192^3 grid points and for the particular set of parameters used here, the average rise Reynolds number of the bubbles is about 23.

Major progress has also been made in the simulation of finite Reynolds number suspension of rigid particles. Feng et al. (1994, 1995) simulated the two-dimensional, unsteady motion of one and two rigid particles, Hu (1996) computed the motion of a few hundred two-dimensional particles and fully three-dimensional simulations of 100 particles were presented by Johnson and Tezduyar (1997). Recent papers include simulations of over 1000 spheres by Pan et al. (2002) and a study of the fluidization of 300 circular particles in in plane Poiseuille flow by Choi and Joseph (2001). While there is, of course, some differences between the behavior of deformable bubbles and drops, development of direct numerical simulations for such systems have paralleled the capability for bubbly flows and lessons learned for one system often find applications in the other.

As computer power increases, it is possible to examine both larger and more complex systems. In [Figure 13.11](#), one example of a relatively large-scale simulation of bubbles in a turbulent channel flow is shown. The bubbles and the streamwise velocity in two planes, one parallel to the lower wall and another

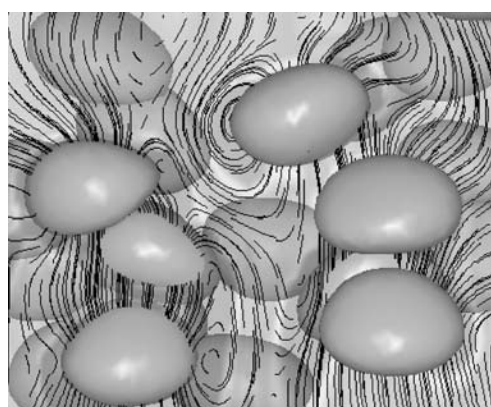


FIGURE 13.10 A closeup of the velocity field around a few interacting bubbles from a simulation of 27 buoyant bubbles in a fully periodic domain. The bubbles and the velocity in a plane cutting through the middle of the domain is shown. (Courtesy of Dr. Bernard Bunner.)

perpendicular to the walls, cutting through the middle of the channel, are plotted at a relatively early time. The domain is $2\pi \times \pi \times 2$ in the streamwise, spanwise, and wall-normal direction, respectively, resolved by a regular structured grid, stretched in the wall-normal direction to provide a finer resolution near the walls. The total number of grid points is $512 \times 256 \times 256$. The initial velocity field was taken from spectral simulations of turbulent channel flows to avoid having to simulate the transition, and the volume flux is kept constant by adjusting the pressure gradient. The turbulent flow was first evolved without bubbles to ensure that the finite-difference method used here correctly simulated the single-phase flow. Initially, 120 bubbles of diameter 0.3 are placed in the flow, next to the walls. The channel Reynolds number is 3000, giving a shear Reynolds number of 135 based on the shear velocity and the wall unit. The domain dimension are $848 \times 424 \times 270$ wall units, and in wall units the bubble diameter is 27.5. As the bubbles interact with the turbulent flow, they are dispersed and slowly migrate away from the walls. The goal of these simulations is to cast some light on how microbubble injection into turbulent boundary layers reduces drag. For the parameters used here, the effect of the bubbles on the wall drag is very small. For other work on this problem, see Kanai and Miyata (2001) and Kawamura and Kodama (2002).

13.2.1.4 Current Status

Direct numerical simulations of multiphase flows have come a long way during the last decade. It is now possible to follow the motion of hundreds of bubbles, drops, and particles at finite Reynolds numbers in simple geometries for sufficiently long time so that meaningful averages can be computed. Much remains to be done, however. At higher Reynolds numbers the number of grid points required to resolve each bubble and the flow around them increases and the cost of doing simulations with many bubbles increases. With larger computers such simulations will become increasingly more feasible. The formation of bubbles and drops as well as coalescence must also be addressed and except for a few simulations of the breakup of drops in well-defined flows, little has been done. These problems are, nevertheless, well within reach.

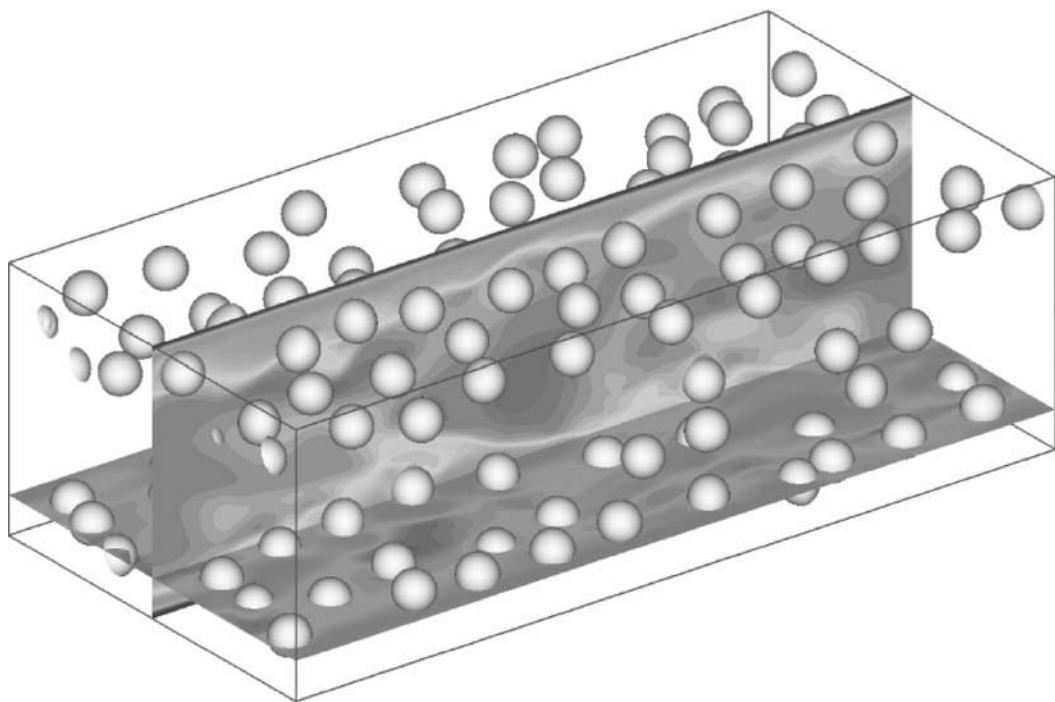


FIGURE 13.11 An example of a direct numerical simulation of bubbles in a turbulent channel flow. The bubbles and the streamwise velocity in a plane near the bottom wall and another one cutting through the middle of the domain is shown. (Courtesy of Dr. Jiaci Lu.)

As direct numerical simulations of multiphase flows become more common, the need for advances in the development of the theoretical framework for modeling such flows is also becoming more urgent. Current models have mostly been developed in an environment where relatively little has been known about the details of the flow, and for the most part these models are far behind what is available for single phase turbulent flows. While our abilities to simulate directly more and more complex multiphase systems will certainly increase dramatically in the next few years, it is important to realize that our desire to compute will always be ahead of what we can do by direct numerical simulations. Even if we could fully compute the behavior of a particular system, we can easily imagine, for example, that we might want to incorporate simulations into a real-time control algorithm that dynamically explored the consequences of several possible control actions. Thus, the condensation of knowledge obtained by direct numerical simulations into reduced or averaged models that allow faster predictions will remain at the core of multiphase flow research for a long time to come.

Although the opportunities for studies of two-fluid disperse systems are enormous, it is the longer-term development of the ability to compute the coupled motion of complex systems that will bring about the full impact of direct numerical simulations. Most engineering fluid systems include a large number of physical phenomena such as fluid flow, evaporation, solidification, and chemical reactions, and while the ability to examine each aspect in detail is important, simulations of the full system will allow unprecedented insight. Here, progress is just starting. A few investigators have simulated boiling flows (Son and Dhir, 1998; Juric and Tryggvason, 1998; Welch and Wilson, 2000; Shin and Juric, 2002; Esmaeeli and Tryggvason, 2003; Yoon et al., 2001), dendritic solidification in the presence of flow (Tonhardt and Amberg, 1988; Boettigner et al., 2002; Jeong et al., 2001; Al-Rawhai and Tryggvason, 2004), and a few other problems. The potential for complexity is virtually unlimited and even relatively simple systems will put considerable demand on computational resources and the solution methodology. Thus, for example, the effect of electric fields on the boiling of binary mixture requires the solution of the fluid flow, species conservation, the energy equation and phase change, as well as an equation for the electric field. It is also likely, as more and more complex problems are dealt with, that the difference between direct numerical simulations — where everything is resolved fully — and simulations where the smallest scales are modeled, will become blurred. Simulations of atomization where the evolution of thin films is computed by subgrid models and very small drops are included as point particles are a relatively obvious example of such hybrids. Other examples include possible couplings with microscopic simulations of moving contact lines, kinematic effects at a solidification interface, and thin flames. Simulations of non-Newtonian fluids, where the microstructure has to be modeled in such a way that the molecular structure is accounted for in some way also falls under this category.

13.2.2 Discrete Element Approach

Y. Tsuji

13.2.2.1 Introduction

The discrete element approach is known by various names, such as particle tracking approach, Lagrangian approach, single-particle approach, and so on. In the field of granular flows, the distinct element method (DEM) is a popular terminology used for expressing simulations employing the soft sphere model. In this approach, trajectories of all individual particles or sample particles of limited number are calculated by making use of the Newtonian equations of motion for a solid body. Equations of fluid motion are the same as those for single-phase flows in one-way coupling. In the two-way coupling the fluid–particle interaction term is added to the equation of fluid motion as external forces. In general, the calculation should be done based on the two-way coupling when the particle concentration is high. Under the condition of such high particle concentrations, not only the two-way coupling, but also the particle–particle interaction should be taken into account. The two-way coupling with the particle–particle interaction is the case in many industrial particle–fluid systems. If the particle concentration is sufficiently low, both fluid–particle and particle–particle interactions are neglected. Such a case corresponds to dilute-phase flow and is not described in this section.

The phenomena associated with particle–particle interaction are different depending on the degree of concentration. When the concentration is moderate, particles are dispersed in the fluid. In such a case,

the particle-particle interaction is different depending on the nature of fluid. If the fluid is a liquid, particles hardly touch due to the lubrication effect. If the fluid is a gas, the particle inertia force is dominant and the particles collide. When the concentration is extremely high, particles are not dispersed and they keep in contact with other particles. The case in which the lubrication effect is important is not described here. Therefore, this section deals with collision- and contact-dominated flow of gas-particle flows.

13.2.2.2 Equation of Motion

Concerning the particle motion, we use the well-known Newtonian equations of motion considering the effects of external forces such as gravitational force and fluid force. Individual particles have two types of motion: translation and rotation. The equations of translational and rotational motion are expressed as

$$\ddot{\mathbf{x}} = \frac{f_c + f_F}{m} + \mathbf{g} \quad (13.1)$$

$$\boldsymbol{\Omega} = \frac{\mathbf{M}}{I} \quad (13.2)$$

where \mathbf{x} is the position vector of the particle gravity center, m the particle mass, f_c the summation of contact forces, f_F the summation of fluid force, \mathbf{g} the gravity acceleration vector, $\boldsymbol{\Omega}$ the particle angular velocity vector, M the summation of torque, I the moment of inertia of the particle, and the (\cdot) time derivative.

Needless to say, the contact force f_c is taken into account only when particles are in contact. The new velocity and position are calculated step by step by using an appropriate time step Δt :

$$\mathbf{v} = \mathbf{v}_0 + \dot{\mathbf{x}}_0 \cdot \Delta t \quad (13.3)$$

$$\mathbf{x} = \mathbf{x}_0 + \mathbf{v} \cdot \Delta t \quad (13.4)$$

and

$$\boldsymbol{\Omega} = \boldsymbol{\Omega}_0 + \dot{\boldsymbol{\Omega}}_0 \cdot \Delta t \quad (13.5)$$

where \mathbf{v} is the particle velocity vector and the subscript (0) the value at the previous time.

The calculation method for the fluid motion can be classified into the following cases: (1) calculation of individual particle base and (2) calculation of local cell base.

In the first method, the instantaneous flow around each particle is found using the Navier-Stokes equation (Hu, 1996; Pan and Banerjee, 1997; Kajishima and Takiguchi, 2002; Pan et al., 2002) or the Lattice-Boltzman method (Qi, 2000) as shown in Figure 13.12. The fluid forces f_F acting on particles are obtained by integrating stresses on the surface of the particles, which are solutions of the basic equations. Thus, such coefficients as drag and lift are not needed. This method is most rigorous but it takes much computational time and large memory capability.

In the second method, a flow field is divided into cells as shown in Figure 13.13; the size of the cells should be larger than the particle size and smaller than the system size of flow. The effects of the presence of particles on fluid are taken into account by the volume fraction of each phase and momentum exchange through the drag force. This approach can be called “local averaging approach,” proposed by Anderson and Jackson (1967).

The equations for fluid motion are given as follows:

$$\frac{\partial \varepsilon}{\partial t} + \frac{\partial(\varepsilon u_j)}{\partial x_j} = 0 \quad (13.6)$$

and

$$\frac{\partial(\rho \varepsilon u_i)}{\partial t} + \frac{\partial(\rho \varepsilon u_i u_j)}{\partial x_j} = -\varepsilon \frac{\partial p}{\partial x_i} + f_{si} + \varepsilon \frac{\partial \tau_{ij}}{\partial x_j} + \rho \varepsilon g \quad (13.7)$$

where u is the velocity, p the pressure, ρ the fluid density, ε the void fraction, f_{si} the force on fluid due to drag, and τ_{ij} the stress tensor.

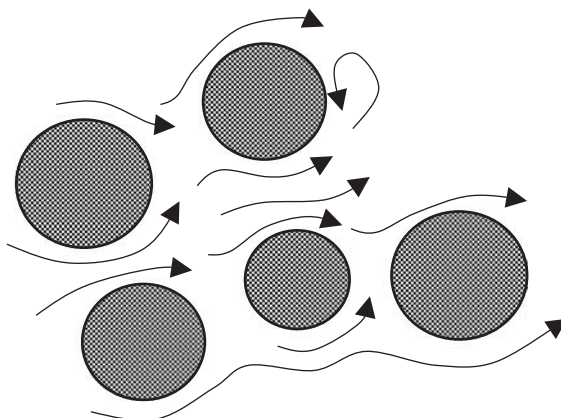
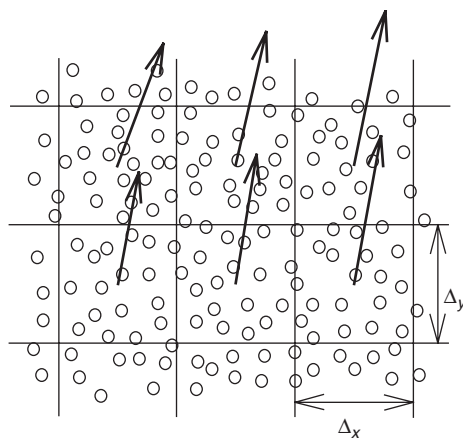


FIGURE 13.12 Treatment of individual particle base.



+FIGURE 13.13 Treatment of local cell base.

Equations (13.6) and (13.7) are the continuity equation and the momentum equations, respectively. Mass transfer is neglected in the above equations. Concerning the drag force, two different expressions are used depending on if the particle motion is collision or contact-dominated. The formula for the drag force acting on a single particle with modification of void fraction (Wen and Yu, 1966) is used for collision-dominated flows and an expression developed for particle beds, such as the Ergun equation (Ergun, 1952), is used for the contact-dominated flow. If the particles are coarse and the fluid is a gas, the particle inertia term is larger than the stress and gravitational terms which can be neglected. Tsuji et al. (1993) showed that calculation based on such simplifications leads to realistic results.

13.2.2.3 Collision-Dominated Flows

Once the external forces are given in Eqs. (13.1) and (13.2), the trajectory calculation is relatively simple during the period when the particle-particle collision does not occur. When a particle collides with another particle, values of particle velocities are reset. The postcollisional velocity can be obtained by the hard sphere model described in Section 12.4.1.1. These calculations are straightforward. The difficulty in the calculation of collision-dominated flows lies in finding collision pairs from a large number of particles in the flow field. There are two methods available for finding collision partners: (1) deterministic method and (2) stochastic method.

In the first method, the collision pairs are found deterministically from trajectories of individual particles. This method takes more computation time as the particle number is increased. The second method

is based on the probability of collision which has been developed in molecular flows. Oesterle and Petitjean (1993) proposed a method assuming the Maxwell distribution for particle fluctuating velocity. Kitron et al. (1990), Yonemura et al. (1993), and Tanaka et al. (1996) used the direct simulation Monte Carlo (DSMC) method. In the DSMC method, trajectory calculations are made only for sample particles; their number is much smaller than the actual number of particles.

The DSMC method is briefly explained below. Imagine that a very large number of particles exist in an actual flow field as shown in [Figure 13.14a](#) and all the particles have different velocity vectors. This actual field of particles is replaced with a simple field that consists of sample particles of a limited number with fixed velocity vectors. Figure 13.14b shows three such sample particles: white, black, and dotted. (In the figure, the number of sample particles shown is only 3; for simplicity of explanation, but in practical calculations, the number of sample particles should be much larger.) Each sample particle represents a group of particles with the same velocity vector, but it is invisible in Figure 13.14b. The invisible particles are assumed to be distributed at random. The actual field shown in Figure 13.14a is replaced with the field shown in Figure 13.14c, where particles that are invisible in Figure 13.14b are shown. The total number of particles in Figures 13.14a and 13.14c are set to be the same. Figures 13.14a and 13.14c appear similar but in Figure 13.14c, all the particles belong to a limited number of groups (here group 3). It can be proven mathematically that if the number of sample particles is sufficiently large, the statistical properties in Figures 13.14a and 13.14c are the same. Instead of the field shown in Figure 13.14a, we treat the field in Figure 13.14c. In this field it is easy to derive the collision probability, i.e., the collision probability can be expressed as a function of the relative velocity between both particle and number density. Once the collision probability is given, trajectory calculations are made in the field of Figure 13.14b, where only sample particles exist.

The next problem is to obtain the collision probability. If the relative velocity between two groups of particles distributed at random is known, the collision frequency P_{ij} at which a particle of the particle group i collides with particles of the particle group j within time Δt is given by

$$P_{ij} = n_j \cdot \pi d^2 \cdot G_{ij} \Delta t \quad (13.8)$$

where n_j is the number density of particle j , G_{ij} the relative velocity $v_i - v_j$, and d the particle diameter.

The next question is how to use this in the trajectory calculation. There are a few methods that have been proposed. Bird(1976) who developed the DSMC method proposed the time count method. Illner and Neunzert(1987) proposed the modified Nanbu (1980) method. The calculation process of the modified Nanbu is as follows.

As described earlier, trajectory calculations are made for sample particles with the time step Δt . Let us consider the motion of sample particle i . At every time step, a random number is produced to find the number of another sample particle, which is the candidate for the collision partner with the sample particle i . The number j chosen by the random number generator corresponds to many particles represented by the sample particle j . The possibility of collision between the sample particle i and one of particles represented by sample particle j depends on the collision probability given by Eq. (13.8). In the modified Nanbu method (Illner and Neunzert, 1987), one random number is used for finding a candidate of collision partner and for deciding if collision occurs. For details, refer to Tanaka et al. (1996).

13.2.2.4 Contact-Dominated Flows

The key idea for the discrete element approach of the contact-dominated flows is the model of the contact force. The soft sphere model described in Section 12. 4.1.2 is used for this purpose. Once the contact forces are given, trajectories of individual particles are obtained by Eqs. (13.1) to (13.3). To provide the readers with an image of how the discrete element approach for contact-dominated flows works, [Figure 13.15](#) shows how particle motion is calculated by using the soft sphere model. Figure 13.15 also shows the case where particle i approaches particle j with a relative velocity $v_i - v_j$. Particle j is made stationary. Instead of considering deformation, the two particles are made to overlap. As the overlap distance increases, the contact force becomes larger and the particle velocity decreases. In the course of time, particle velocity changes direction and the overlap distance decreases. Finally the two particles separate. This process is calculated step-by-step by Eqs. (13.4)–(13.7). The time step Δt is much smaller than that for collision-dominated flows.

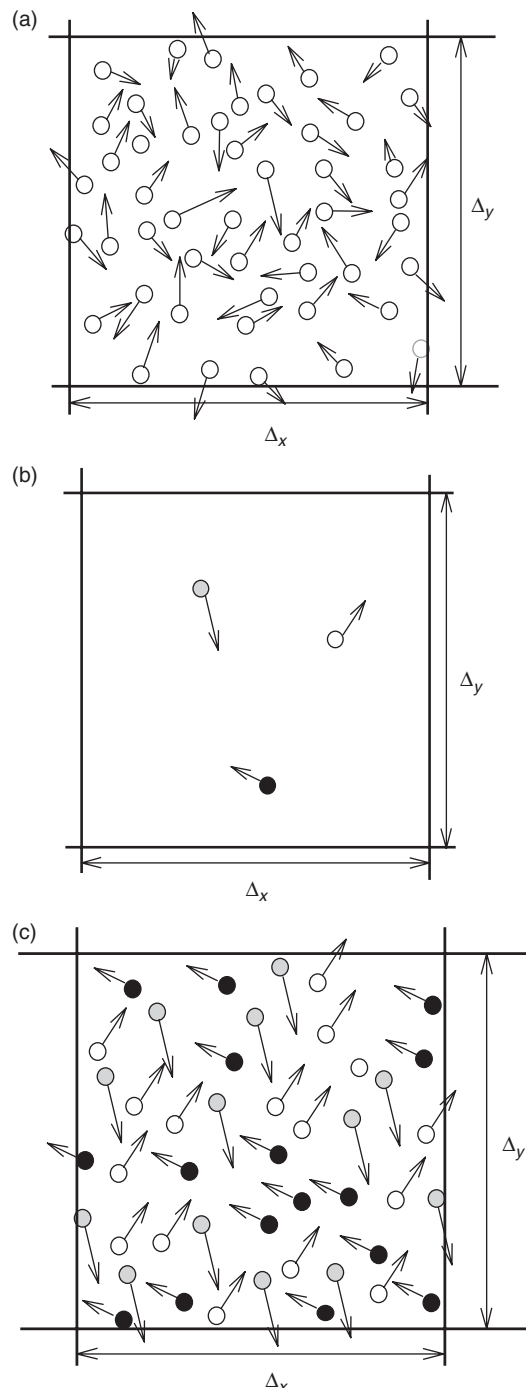


FIGURE 13.14 (a) Field of real particles; (b) sample particles; (c) field replacing.

13.2.2.5 Simulation Example

Figure 13.16 shows a snap shot of particle concentration and velocity vectors of particles and gas calculated by Yonemura et al. (1993), who used DSMC method. An interesting finding is that the in-elastic

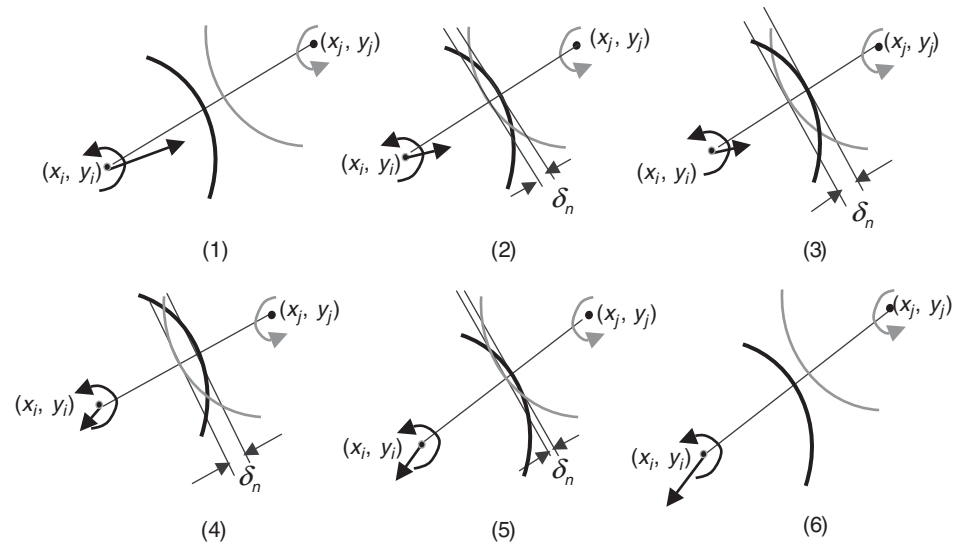


FIGURE 13.15 Calculation of particle motion based on soft sphere model.

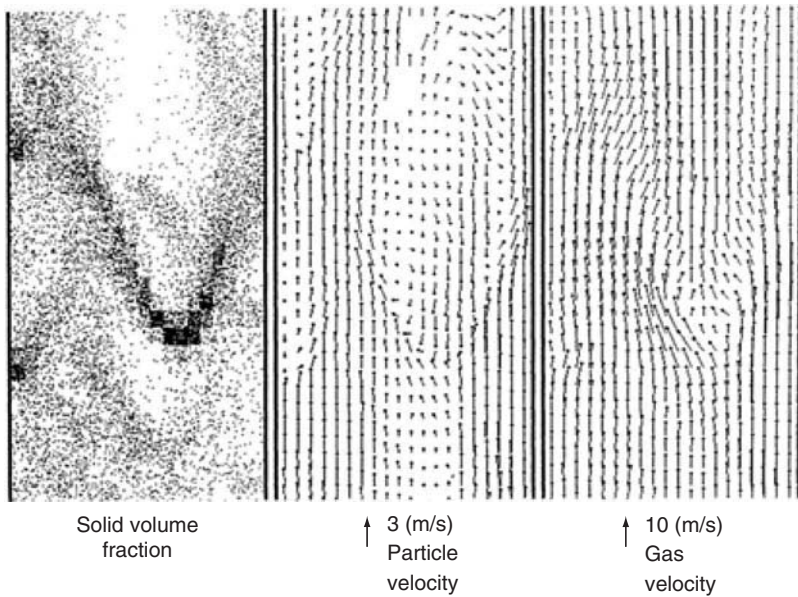


FIGURE 13.16 Collision-dominated flow. (From Yonemura et al., ASME/FED Gas–Solid Flows, 166, 303, 1993. With Permission)

particle-particle collision leads to the formation of clusters. The flow field of the clusters shows large-scale fluctuations. The structure of cluster has been investigated more in details by Tanaka et al. (2002)

The discrete element simulation using the soft sphere model DEM has very wide applicability in particle technology even if the fluid is neglected. The following examples are those to which the discrete element simulation has been applied to contact-dominated flows; gravity flows in hoppers and chutes,

rotary kiln, screw feeder, mixers (drum mixer and V-shape mixer), granulator, sieve, vibrating bed, shear flow, etc. Many scientists are engaged in the research of these particle flows; the research tends to deal with complicated cases. Some researchers take into account the effects of cohesion forces caused by a liquid bridge, some others nonsphericity, while few other include heat transfer.

If the effects of the fluid are included in the discrete particle simulation, the range of applications becomes larger. The first work of Tsuji et al. (1992) is a dense-phase pneumatic conveying example and the calculated results are shown in Figure 13.17. Tsuji et al. (1993) extended their work to the fluidized bed. The results for a bubble rising in the fluidized bed are shown in Figure 13.18. The velocity of the rising bubble agrees with experiments not only qualitatively but also quantitatively. A spouted bed (Figure 13.19) is another example to which the discrete element simulation has been applied. Recently, various complicated factors such as heat transfer (Rong et al., 2001; Liu et al., 2002) and cohesion forces (Mikami et al., 1998; Rhodes et al., 2001; Kuwagi and Horio, 2002) have been added by several workers for a more practical applications.

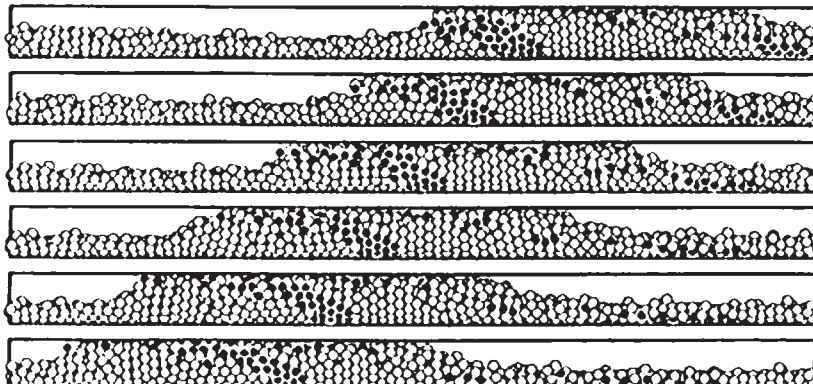


FIGURE 13.17 Plug conveying in horizontal pipe. (From Tsuji et al., *Powder Technol.*, 77, 79, 1993. With permission.)

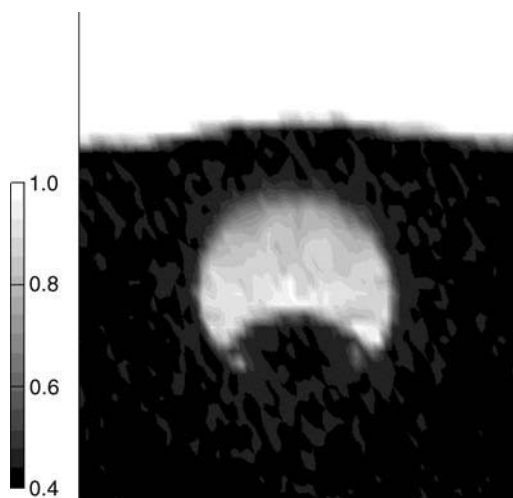


FIGURE 13.18 Single rising bubble in fluidized bed.

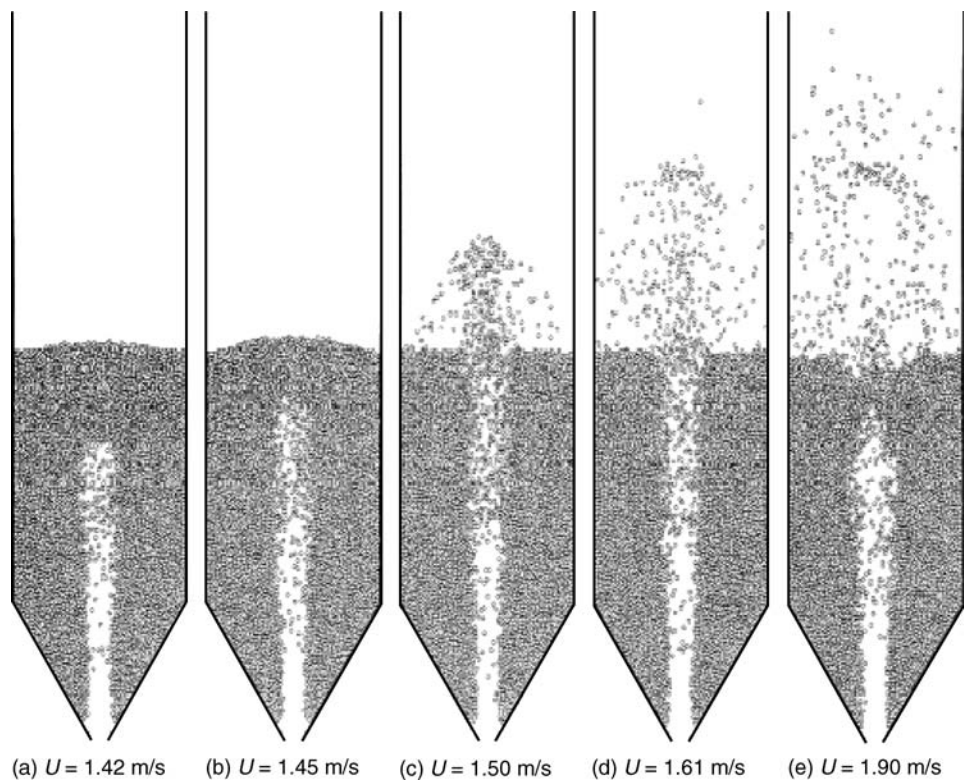


FIGURE 13.19 Spouted bed in cylinder. (From Kawaguchi et al., *Powder Technol.*, 109, 3, 2000. With permission.)

13.2.3 Direct Simulation of Turbulent Flows Laden with Dispersed Particles

S.E. Elghobashi

13.2.3.1 Introduction

DNS of turbulent flows laden with a large number ($\sim 10^8$) of dispersed spherical (solid, liquid, or gas) particles requires the spatial and temporal resolution of all the relevant scales of the carrier fluid motion down to the Kolmogorov scales (η, τ_k), and ideally, the simultaneous resolution of the flow around the surfaces of the individual particles. However, the resolution of the flow around each particle is infeasible at present and in the near future (i.e., the next 15 years; Jimenez, 2003). This infeasibility is only due to computer (memory and speed) limitations as demonstrated next. For example, consider a typical turbulent boundary layer flow of 0.01 m thickness over a flat plate of 1 m length and 0.5 m width (i.e., the fluid volume = $5 \times 10^{-3} \text{ m}^3$ or 5 L), which contains dispersed particles of 50 μm diameter occupying a volume fraction (or concentration) of 10^{-3} . The number of these particles is thus more than 76×10^6 . Now, in order to resolve the motion around each of these 76 million particles, we have to solve the unsteady, three-dimensional Navier–Stokes and continuity equations in a small domain surrounding each particle, at each time step of computing the carrier flow. If we assume that computing the flow around each particle requires only 10^3 CPU S (i.e., many orders of magnitude smaller than the currently required CPU time; Bagchi and Balachandar, 2003) on the fastest computer available, then we would need 76×10^9 sec/time step or 2443 CPU years/time step for a single processor. However, if we use 1024 parallel processors, this time can be reduced to 2.4 CPU years/time step; if we use 10,000 processors, we can reduce this time further to 3 CPU months/time step, and at least 10^4 time steps are needed for a typical DNS run. Thus, it is evident that at present it is not possible to perform DNS of a turbulent flow laden with a large number of dispersed small particles while simultaneously resolving the flow around each

particle. This fact necessitates treating the dispersed particles in DNS as “*points*” whose motion and trajectories are governed by the appropriate differential equations. There are currently two approaches (namely, the Lagrangian–Eulerian or trajectory and the Eulerian–Eulerian or two-fluid) employed in DNS of particle-laden turbulent flows. These two approaches will be described in the two examples that are presented later in this chapter.

13.2.3.2 Classification Map of Particle-Laden Turbulent Flows

The classification map in Figure 13.20 is a slightly modified version of the original map proposed by Elghobashi (1994). The quantities appearing on the dimensionless coordinates are defined below:

α	volume fraction of particles ($= NV_p/V$)
N	total number of particles in the flow
V_p	volume of a single particle
V	total volume occupied by particles and fluid
d	diameter of particle
τ_p	particle response time ($= \rho_p d^2 / (18 \rho_f \nu)$ for Stokes flow)
τ_k	Kolmogorov time scale ($= (\nu/\varepsilon)^{1/2}$)

In the above definitions, ρ is the material density, ν the kinematic viscosity of the fluid, and ε the dissipation rate of turbulence kinetic energy and the subscripts p and f denote, respectively, the particle and carrier fluid. For very low values of α ($\leq 10^{-6}$), the particles have negligible effect on turbulence, and the interaction between the particles and turbulence is termed as *one-way coupling*. This means that particle dispersion, in this regime, depends on the state of turbulence but owing to the negligible concentration of the particles, the momentum exchange between the particles and the turbulence has an insignificant effect on the flow. In the second regime, $10^{-6} < \alpha \leq 10^{-3}$, the momentum exchange between the particles and turbulence is large enough to alter the turbulence structure. This interaction is called *two-way coupling*. Now, in this regime and for a given value of α , there are two zones (A and B), depending on the ratio τ_p/τ_k where the transition from A to B occurs at about $\tau_p/\tau_k = 10$. In zone A, the particle Reynolds number, R_p is ≤ 1 , but within the range $0.01 \leq (\tau_p/\tau_k) \leq 10$ and for a fixed α , the effects of the particles

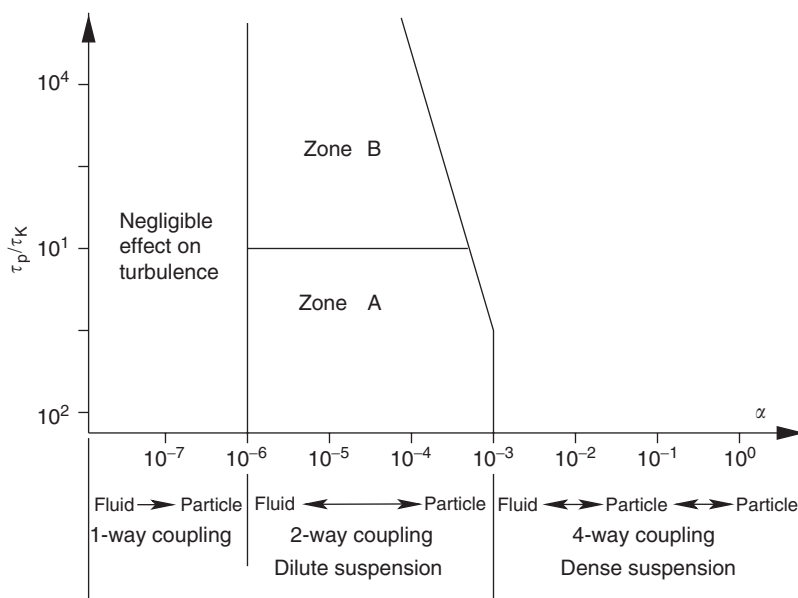


FIGURE 13.20 Classification map of dispersed two-phase flows.

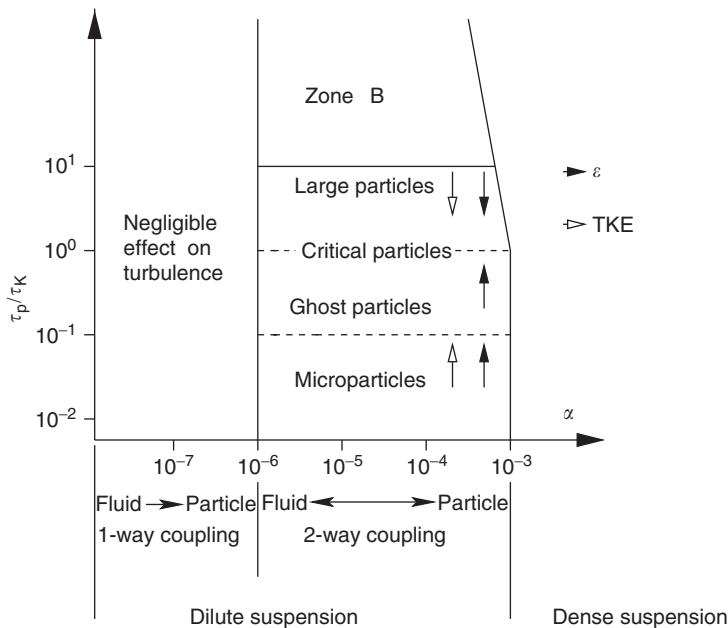


FIGURE 13.21 Classification map of dispersed two-phase flows details of Zone A.

on the turbulence vary significantly as function of (τ_p/τ_k) as shown in Figure 13.21 and will be discussed later. In zone B, as τ_p increases (e.g., with an increase in the particle diameter) for the same α , the particle Reynolds number increases, and at values of $R_p \geq 400$, vortex shedding takes place resulting in an enhanced production of turbulence energy. In the third regime, due to an increase in particle loading, $\alpha > 10^{-3}$, flows are referred to as dense suspensions. Here, in addition to the two-way coupling between the particles and turbulence, particle-particle collision takes place, hence the term *four-way coupling*. As α approaches 1, we obtain a granular flow in which there is no fluid, and, therefore, the granular flow is beyond the scope of this chapter.

The line separating the two- and four-way coupling regimes is inclined to indicate the tendency of particle-particle collision to take place at higher values of τ_p/τ_k , thus transforming the two- to four-way coupling regime even for $\alpha < 10^{-3}$.

The dispersion of particles (and their preferential accumulation) in turbulent flows with one-way coupling is reasonably understood, at least in unconfined homogeneous flows (Elghobashi and Truesdell, 1992, 1993; Ahmed and Elghobashi, 2001; Ferrante and Elghobashi, 2003). On the other hand, flows in the two- or four-way coupling regimes are still a challenge and require more studies to improve their understanding.

We restrict the present discussion to isothermal incompressible fluids without phase changes (e.g., vaporization) or chemical reaction. Also, the effects of particle-particle or particle-wall collisions are not considered here.

In the following subsections we will present two examples of DNS of particle- and bubble-laden turbulent flows and discuss the physical mechanisms of two-way coupling. These flows are: (1) isotropic turbulence laden with solid particles and (2) isotropic turbulence laden with bubbles.

13.2.4 The Physical Mechanisms of Two-Way Coupling in Particle-Laden Isotropic Turbulence

Since isotropic turbulence is the simplest homogeneous turbulent flow it has been the subject of a number of earlier DNS studies on the effects of particles on isotropic turbulence (Elghobashi and Truesdell,

1993; Squires and Eaton, 1990; Boivin et al., 1998; Sundaram and Collins, 1999; Druzhinin and Elghobashi, 1999b; Ferrante and Elghobashi, 2003).

The discussion in the following subsections is a condensed version of our paper (Ferrante and Elghobashi, 2003), whose objective was to analyze our DNS results for a detailed explanation of the main physical mechanisms responsible for the modification of isotropic turbulence by dispersed solid particles. The present study, in comparison with the previous DNS studies, has been performed with higher resolution ($Re_\lambda = 75$) and considerably larger number (80 million) of particles. One of the interesting results to be discussed is that in zero gravity, dispersed particles with $\tau_p/\tau_k = 0.25$ (denoted here as ‘*Ghost particles*’) modify the spectra of the turbulence kinetic energy and its dissipation rate in such a way that the decay rate of the turbulence energy is nearly identical to that of particle-free turbulence, and, thus, the two-way coupling effects of these ghost particles would not be detected, for example, in microgravity environment, by examining only the temporal behavior of the turbulence energy of the carrier flow either numerically or experimentally.

13.2.4.1 Mathematical Description

In this study we use the Eulerian–Lagrangian (or trajectory) approach, where the instantaneous, three-dimensional velocity and pressure fields of the fluid motion are computed on a fixed (Eulerian) mesh; whereas, the instantaneous trajectories of the dispersed particles are obtained by computing the instantaneous positions of the particles.

13.2.4.2 Governing Equations

The governing dimensionless equations for a particle-laden incompressible isotropic turbulent flow are the Navier–Stokes equations,

$$\frac{\partial u_j}{\partial t} + \frac{\partial(u_j u_k)}{\partial x_k} = -\frac{\partial p}{\partial x_j} + \nu \frac{\partial^2 u_j}{\partial x_k \partial x_k} - f_j \quad (13.9)$$

and the continuity equation,

$$\frac{\partial u_j}{\partial x_j} = 0 \quad (13.10)$$

where $j = 1, 2, 3$ for the three coordinate directions x_1 , x_2 , and x_3 , respectively, and ν the dimensionless kinematic viscosity. In Eqs. (13.9) and (13.10) we neglect the volume occupied by the individual particles (in comparison with the volume of the carrier fluid) and thus they are treated as points moving in the flow according to Eq. (13.12). $-f_j$ is the net force per unit mass of fluid exerted in the x_j direction by M particles within the integration control volume and is computed from

$$f_j = \frac{1}{M_f} \sum_{p=1}^M f_{jp} \quad (13.11)$$

where f_{jp} is the drag force acting on particle p in the x_j direction and M_f the mass of fluid within the integration control volume.

The particle equation of motion (Maxey and Riley, 1983) can be written for large ratio (ρ_p/ρ) of the particle density to fluid density as

$$m_p \frac{dv_j}{dt_p} = m_p \frac{(u_j - v_j)}{\tau_p} + (m_p - m_f)g_j \quad (13.12)$$

where m_p is the mass of the particle, m_f the mass of fluid displaced by the particle volume, d/dt_p the time derivative following the moving particle, v_j the particle instantaneous velocity, u_j the instantaneous fluid velocity at the particle location, and g_j is the gravitational acceleration. The numerical solution method is described in detail in Ferrante and Elghobashi (2003) and, thus, will not be discussed here.

13.2.4.3 Results

13.2.4.3.1 Turbulence and Particles Parameters

We studied six cases to understand how particles with different inertia, τ_p , modify the decay rate of isotropic turbulence in both zero- and finite-gravity conditions. The flow parameters are listed in Table 13.3 and the particle properties in Table 13.4. Case A represents the particle-free flow, whereas cases B–E represent particle-laden flows with different inertia particles in zero gravity, and case F represents the particle-laden flow in finite gravity. It is important to note that all the five cases (B–F) of particle-laden turbulence have the same volume fraction of particles, $\alpha = 10^{-3}$, and the same mass loading ratio $\alpha_m = 1.0$ (for $\rho_p/\rho = 1000$) and, thus, the differences between the resulting modifications of turbulence in these cases are only due to the different values of τ_p/τ_k . We changed the particle diameter for each case to obtain a different ratio τ_p/τ_k of the particle response time to the Kolmogorov time-scale at the injection time, for example., $\tau_p/\tau_k = 0.1$ in case B and $\tau_p/\tau_k = 5.0$ in case E. The effects of gravity are studied in case F where $\tau_p/\tau_k = 0.25$ (as in case C) and $v_t/u_0^* = 0.25$, where v_t is the terminal velocity ($v_t = g\tau_p$) of the particle and u_0^* is the rms velocity of the surrounding fluid at the injection time, and gravity is in the negative x_3 direction.

13.2.4.3.2 Turbulence Modification by Particles

In the following two subsections we describe briefly the temporal evolution of the turbulence kinetic energy (TKE) and its spectra, $E(k)$, for all the six cases (A–F). Then we discuss in detail the physical mechanisms of the two-way interaction in four of these cases. The details of the other cases are given by Ferrante and Elghobashi (2003).

13.2.4.3.2.1 Time evolution of turbulence kinetic energy. Figure 13.22 shows the temporal evolution of TKE normalized by its initial value, $E(t)/E_0$, for the zero gravity cases (A–E). The microparticles (case B) with $\tau_p/\tau_k < 0.25$ initially ($1 < t \leq 2.1$) reduce the decay rate of TKE, resulting in TKE being larger than that of case A at all times, whereas particles with higher inertia (critical particles, case D, and large particles, case E), $\tau_p/\tau_k > 0.25$, initially enhance the TKE decay rate considerably, resulting in TKE being smaller than that of case A at all times. Figure 13.22 also shows that particles with $\tau_p/\tau_k = 0.25$ (case C) keep TKE nearly identical to that of case A at all times, with a percentage difference smaller than 0.6%. Thus we denote the particles in case C as ghost particles, since their effects on the turbulence cannot be detected by the temporal behavior of TKE, $E(t)$. However, as we will discuss later (Figure 13.23) these ghost particles do modify the spectrum of $E(k)$ TKE. Figure 13.22 shows that at time $t = 5$, in comparison with TKE in case A, TKE in case B is larger by more than 5%; in case C is nearly identical; in case D is smaller by about 13%; in case E is smaller by about 30%.

TABLE 13.3 Flow Parameters (Dimensionless) at Initial Time ($t = 0$), Injection Time ($t = 1$), and for Case A at Time $t = 5$

t	u_o	ϵ	l	λ	η	Re_l	Re_λ	l/η	τ_k	τ_t
0.0	0.0503	7.4×10^{-4}	0.0684	0.0345	0.00202	150	75	33.8	0.177	1.36
1.0	0.0436	9.8×10^{-4}	0.0685	0.0259	0.00188	129	49	36.4	0.154	1.57
5.0	0.0233	2.0×10^{-4}	0.0891	0.0305	0.00280	90	31	31.9	0.338	3.83

TABLE 13.4 Particle Properties (Dimensionless) at Injection Time ($t = 1$) with $\alpha = 10^{-3}$ and $\alpha_m = 1.0$ (for $\rho_p/\rho = 1000$)

Case	τ_p	τ_p/τ_l	τ_p/τ_k	d	d/l	d/η	d (μm)	M_c	M_r/M_c	$Re_{p,\max}$	v_t/u_0^*
A	—	—	—	—	—	—	—	—	0	—	—
B	0.0154	0.0098	0.1	0.80×10^{-4}	0.00117	0.043	30	80×10^6	46.7	0.11	0.0
C	0.0385	0.0245	0.25	1.26×10^{-4}	0.00185	0.067	47	80×10^6	11.8	0.31	0.0
D	0.1540	0.0979	1.0	2.53×10^{-4}	0.00369	0.134	94	80×10^6	1.5	1.34	0.0
E	0.7700	0.4895	5.0	5.66×10^{-4}	0.00825	0.300	211	10.6×10^6	1.0	5.33	0.0
F	0.0385	0.0245	0.25	1.26×10^{-4}	0.00185	0.067	47	80×10^6	11.8	0.32	0.25

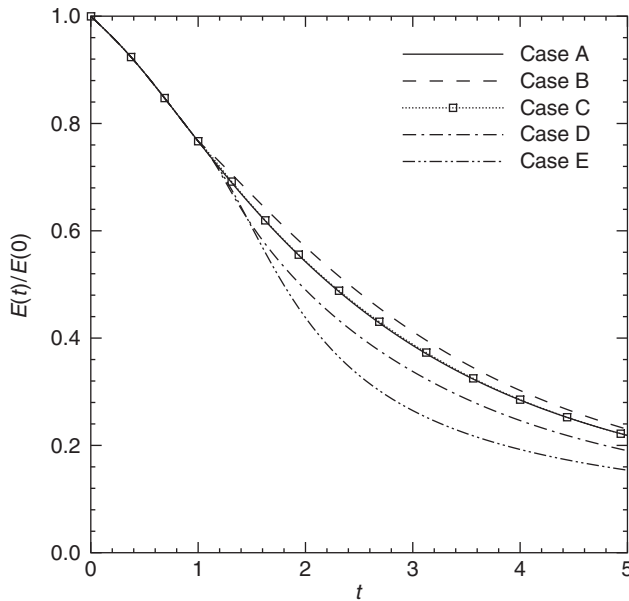


FIGURE 13.22 Time development of the turbulence kinetic energy.

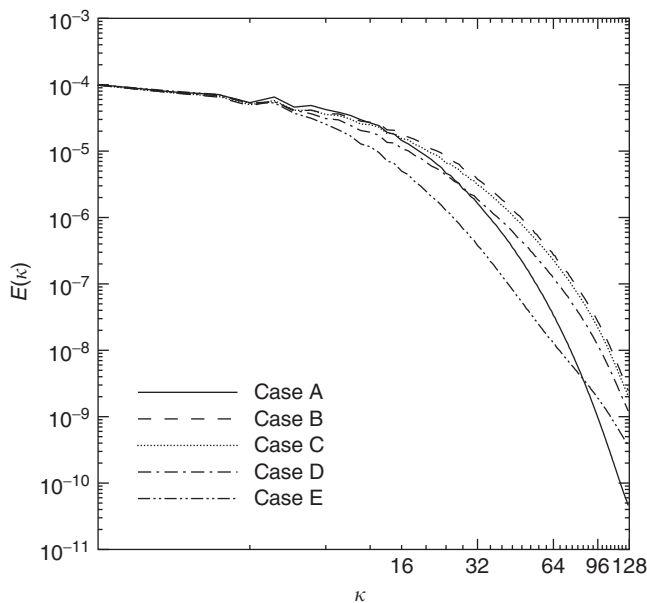


FIGURE 13.23 Three-dimensional spatial spectrum of energy $E(\kappa)$ at $t = 5.0$.

Figure 13.24 displays the effects of gravity on the time evolution of TKE by comparing cases C and F. The figure shows that in the presence of gravity (case F), particles reduce the decay rate of TKE as compared with both case C, the flow laden with ghost particles, and case A, the particle-free flow. The basic physical mechanisms that are responsible for the above-described modifications of $E(t)$ by the dispersed particles for cases B–F are discussed later in this section.

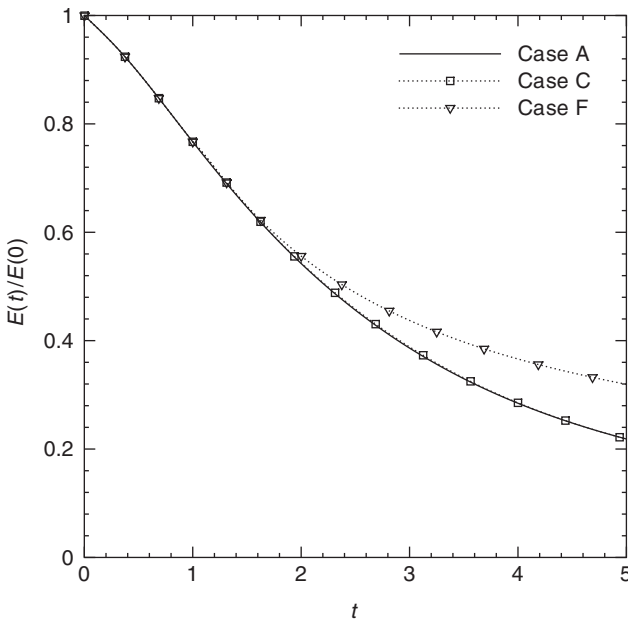


FIGURE 13.24 Time development of the turbulence kinetic energy normalized by its initial value showing the effect of gravity in case F.

13.2.4.3.2.2 Energy spectrum. Figure 13.23 shows the three-dimensional energy spectra $E(\kappa)$ for the five cases A-E at time $t = 5$. Microparticles (case B) increase $E(\kappa)$ relative to case A at wavenumbers $\kappa \geq 12$, and reduce $E(\kappa)$ relative to case A for $\kappa < 12$, such that $\int E(\kappa) d\kappa \equiv \text{TKE}$ in case B is larger than that in case A, as shown in Figure 13.22. For ghost particles (case C), although $E(t)$ is nearly identical to that of case A at all times (Figure 13.22) it is clear in Figure 13.23, that the energy spectrum in case C differs from that in case A, but in such a unique way that its integral, TKE, is nearly identical to that in case A. Figure 13.23 shows that ghost particles reduce $E(\kappa)$ relative to that of case A for $\kappa < 15$, and increase it above that of case A for $\kappa \geq 15$. Critical particles (case D) increase $E(\kappa)$ above that of case A for $\kappa \geq 27$, and reduce it for smaller wavenumbers. In this case (case D) the modulation of $E(\kappa)$ is such that its integral, TKE, is smaller than that in case A (Figure 13.22). Large particles (case E) contribute to a faster decay of TKE by reducing the energy content at almost all wavenumbers, except for $\kappa > 87$, where a slight increase of $E(\kappa)$ occurs.

In order to understand how the particles, $E(\kappa)$, modify we write the evolution equation of the three-dimensional energy spectrum:

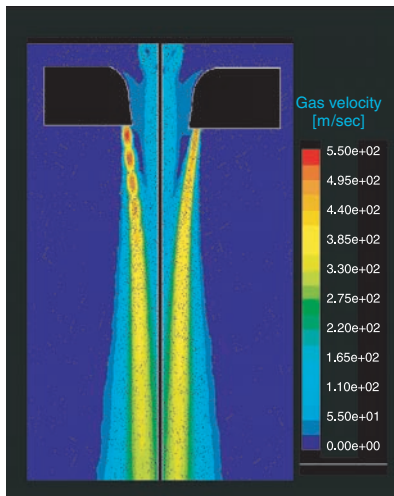
$$\frac{\partial E(\kappa)}{\partial t} = T(\kappa) - \varepsilon(\kappa) + \Psi_p(\kappa) \quad (13.13)$$

Equation (13.13) states that in particle-laden isotropic turbulent flows, the rate of change of spectral turbulence kinetic energy at wavenumber κ is the net result of the spectral energy-transfer rate $T(\kappa)$, the spectral viscous dissipation rate $\varepsilon(\kappa)$, and the spectral two-way coupling (fluid-particle drag interaction) energy rate $\Psi_p(\kappa)$. A discussion on the behavior of $T(\kappa)$, $\varepsilon(\kappa)$, and $\Psi_p(\kappa)$ and their effects on $E(\kappa)$ is provided in the following section.

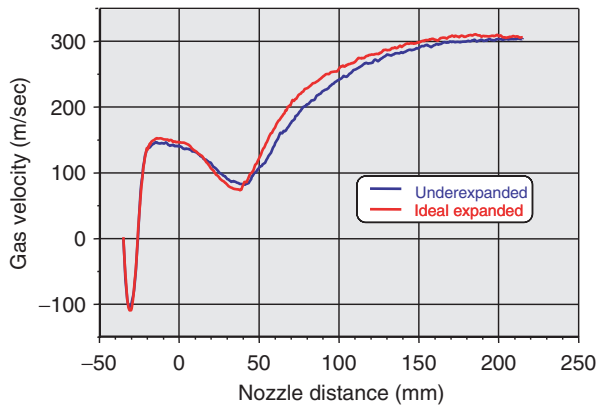
13.2.4.3.3 Mechanisms of Modification of Isotropic Turbulence by the Particles

In this section, we discuss the mechanisms responsible for the modification of decaying isotropic turbulence by the particles for four of the cases listed in Table 13.4: microparticles ($\tau_p/\tau_\kappa \ll 1$ in zero gravity; case B), critical particles with $\tau_p/\tau_\kappa \approx 1$ (case D), and ghost particles with $\tau_p/\tau_\kappa \approx 0.25$ (case C).

Underexpanded Ideal expanded



(a)



(b)

FIGURE 8.9 Gas flow field simulation for an external mixing (free-fall) atomizer: (a) gas velocity contours: underexpanded exit condition (left panel), and ideal expanded exit condition (right), (b) gas velocity on center line, comparison of under- and ideally expanded exit conditions. (From Heck, U., Ph.D. thesis, Universität Bremen, 1998. With permission.)

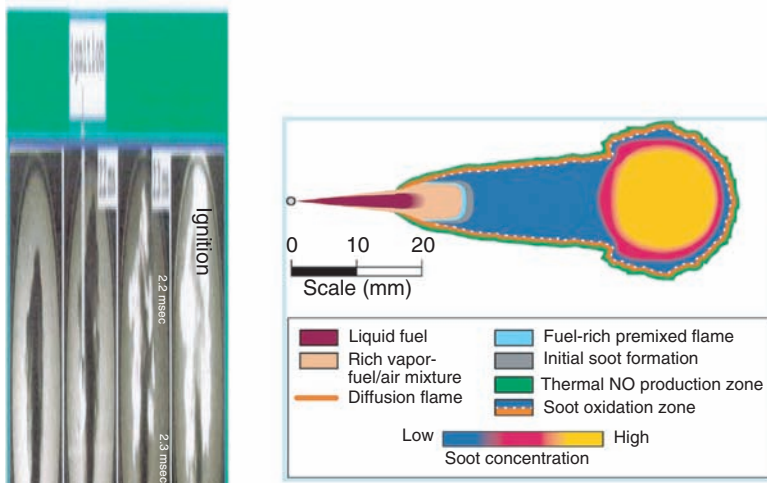


FIGURE 8.52 Diesel spray flame: photo of injection and ignition, principal stationary flame structure. (From Tao, F., Ph.D. thesis, Chalmers University of Technology, Sweden, 2003.)

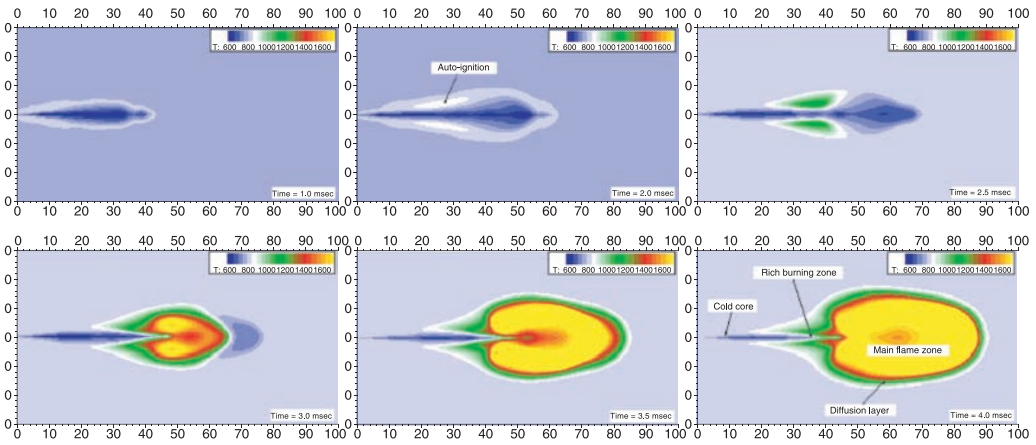


FIGURE 8.54 Simulation of a DI-diesel spray flame and temperature contours. (From Tao, F., Ph.D. thesis, Chalmers University of Technology, Sweden, 2003. With permission.)

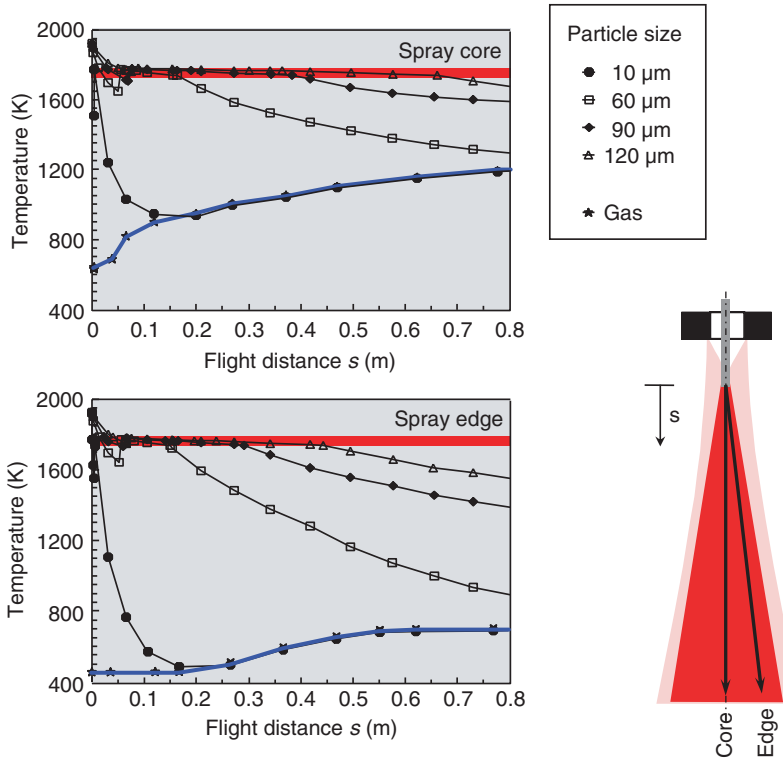


FIGURE 8.63 Modeling result for gas and particle temperature behavior on spray center line and edge in spray forming of steel. (From Bergmann et al., *Proceedings of the 2nd International Conference on Multiphase Flow*, Kyoto, Japan, April 3–7, 1995, Vol.1, pp. SP1–SP8. With permission.)

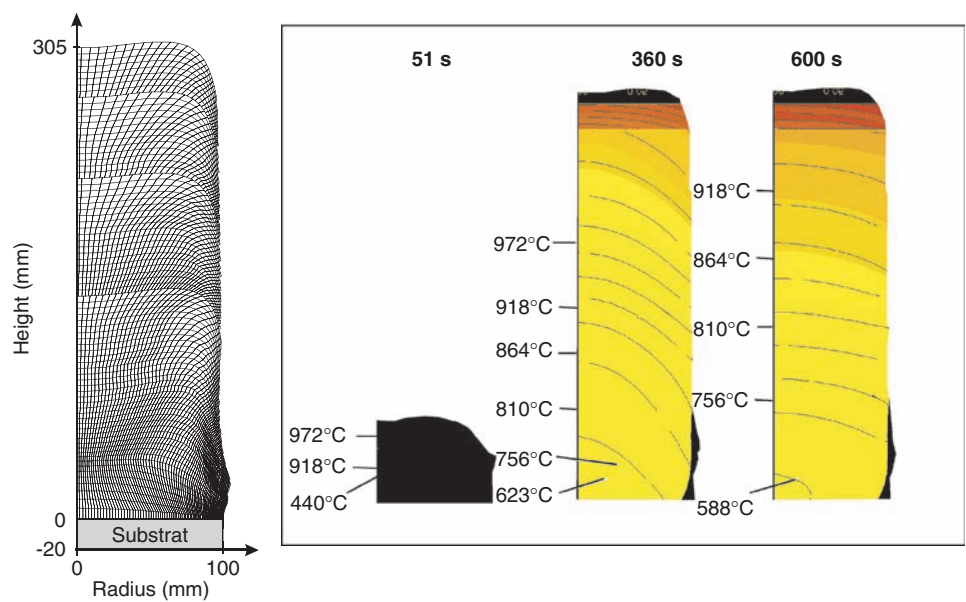


FIGURE 8.65 Temperature and solid content distribution during spray forming of a copper billet. (From Meyer et al., *Int. J. Thermal Sci.*, 42, 2003. With permission.)

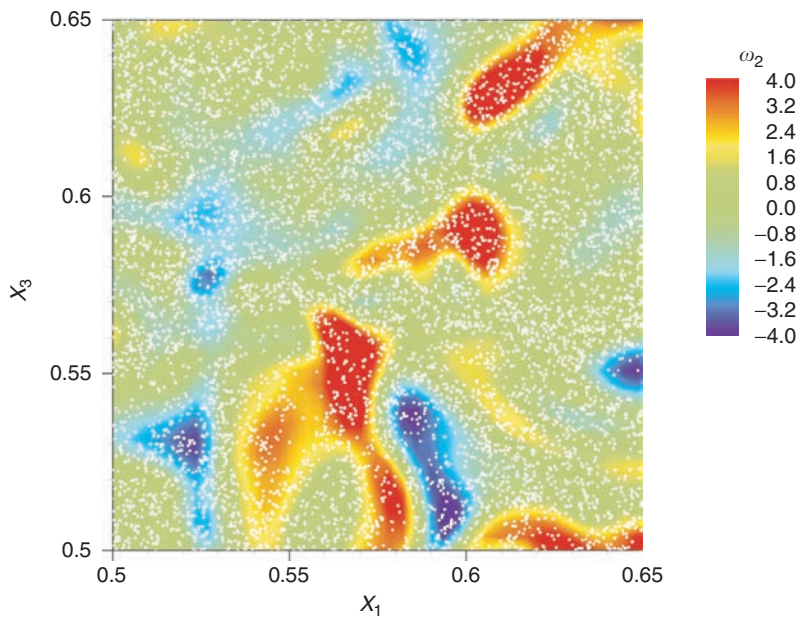


FIGURE 13.25 Case B: microparticles (white dots) superimposed on ω_2 (color contour) at $x_2 = 0.5$ and $t = 5.0$.

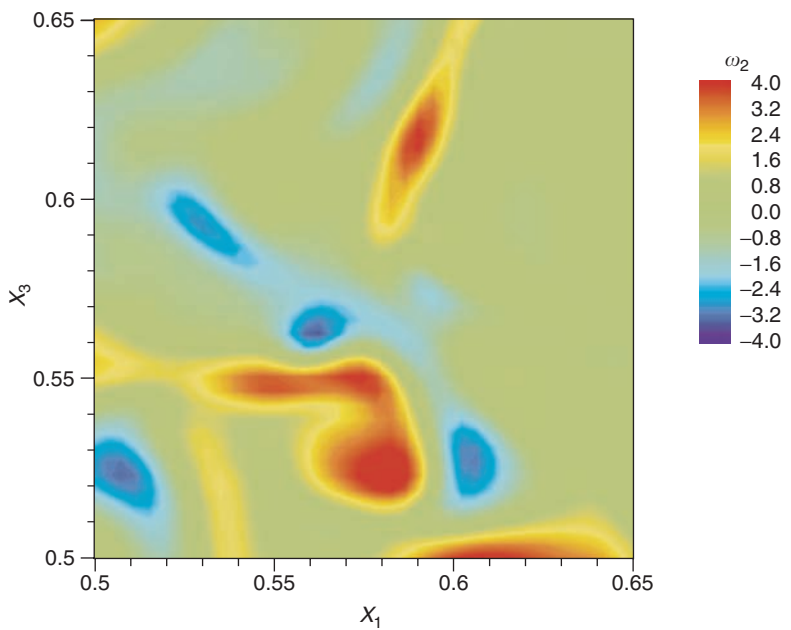


FIGURE 13.26 Case A: ω_2 (color contour) at $x_2 = 0.5$ and $t = 5.0$.

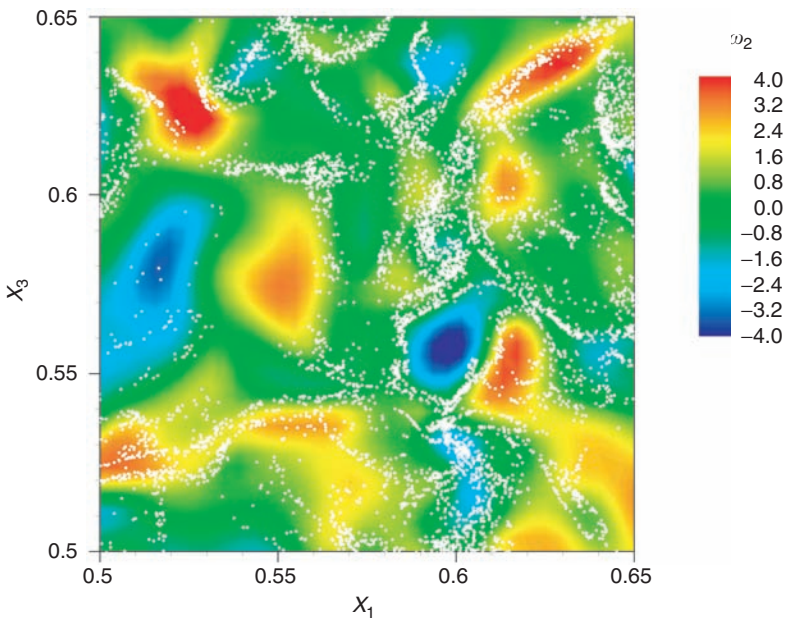


FIGURE 13.36 Case D: critical particles (white dots) superimposed on ω_2 (color contour) at $x_2 = 0.5$ and $t = 5.0$.

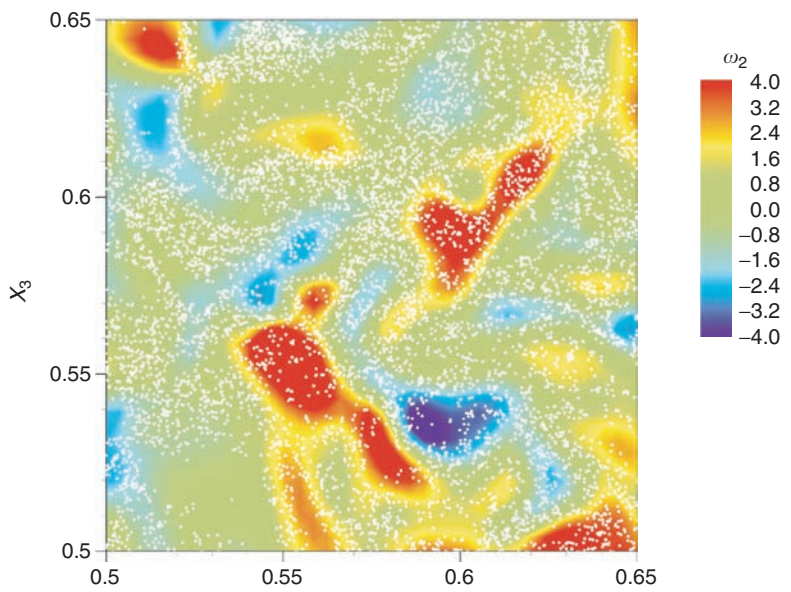


FIGURE 13.37 Case C: “ghost” particles in zero gravity (white dots) superimposed on ω_2 (color contour) at $x_2 = 0.5$ and $t = 5.0$.

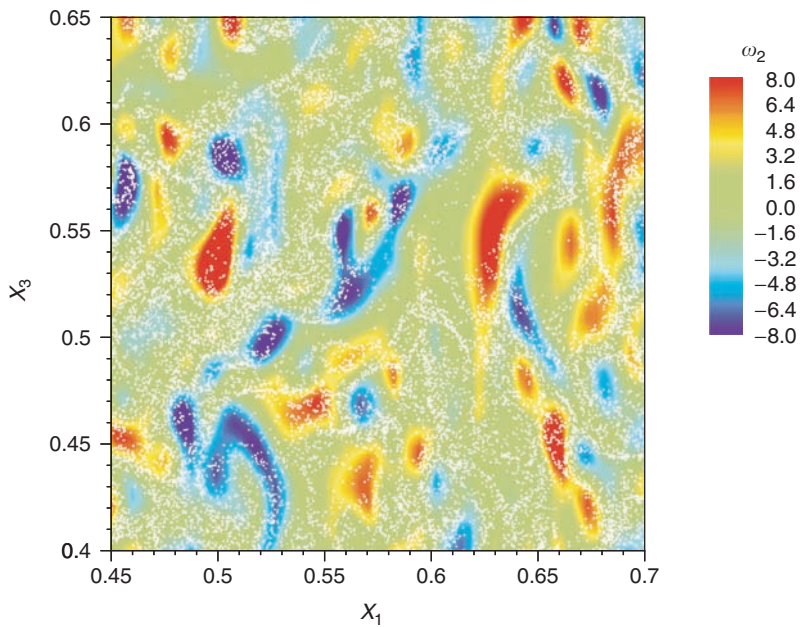
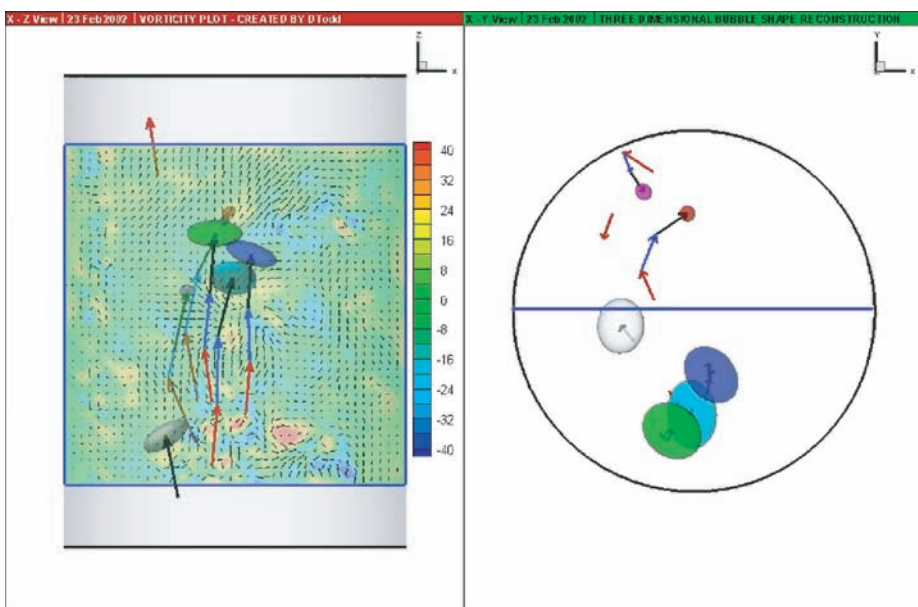
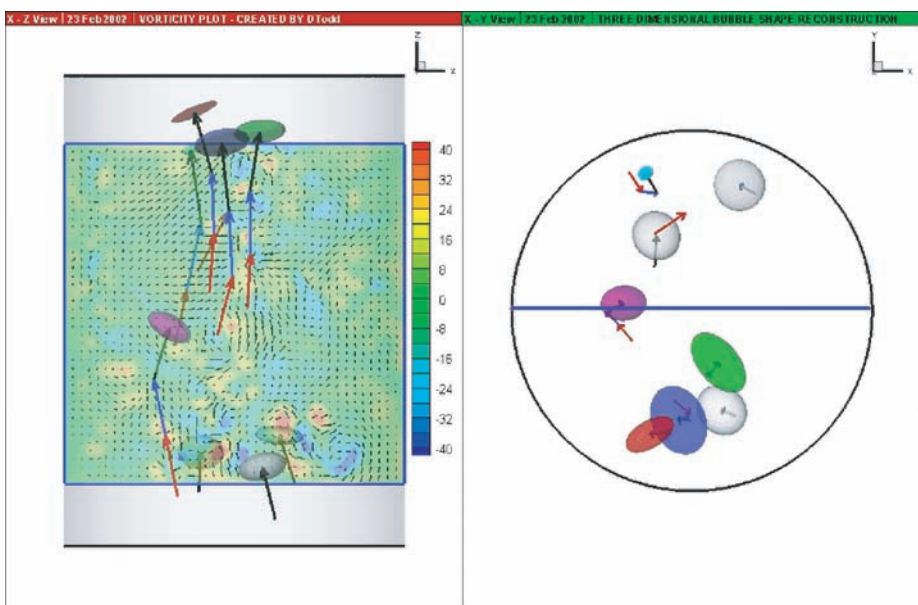


FIGURE 13.39 Case F: “ghost” particles in finite gravity (white dots) superimposed on ω_2 (color contour) at $x_2 = 0.5$ and $t = 5.0$.



(a) time = t_1



(b) time = $t_1 + 33.33 \text{ ms}$

FIGURE 14.85 Snapshots of interactions of the bubbles with the flow at two instants.

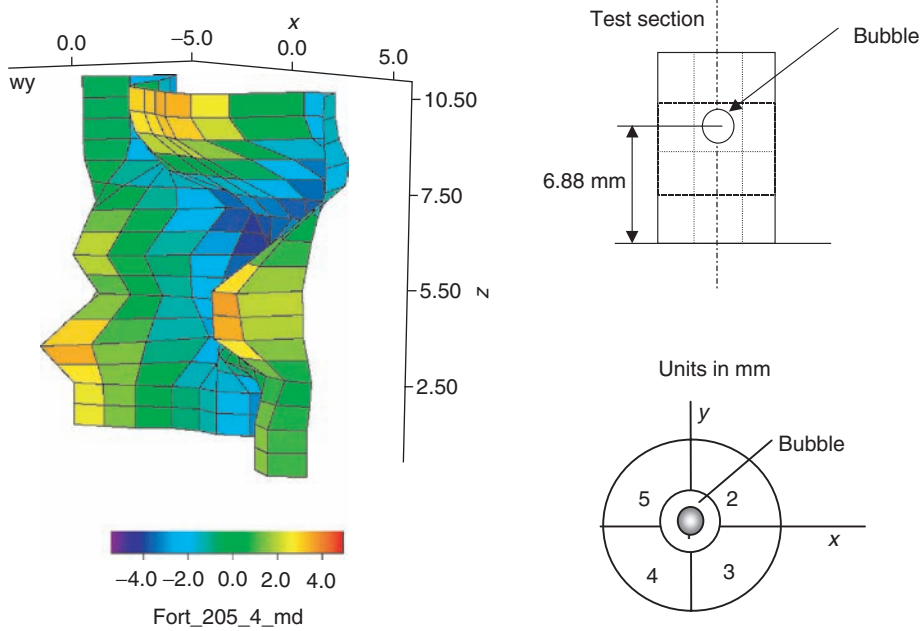


FIGURE 14.88 Surface plot of fluid vorticity component ω_y on X - Z plane, position $y = 0$, at $t = 33.3$ msec after the bubble has entered the viewing volume.

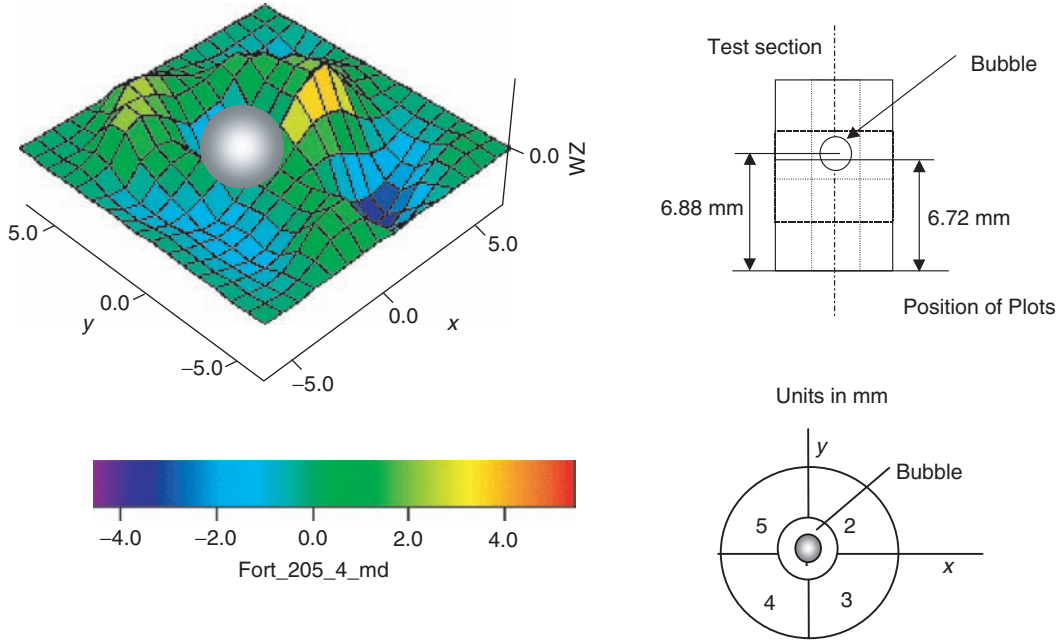


FIGURE 14.89 Surface plot of liquid vorticity component ω_z on X - Y plane, position $z = 6.72$, at $t = 33.3$ msec after the bubble has entered the viewing volume.

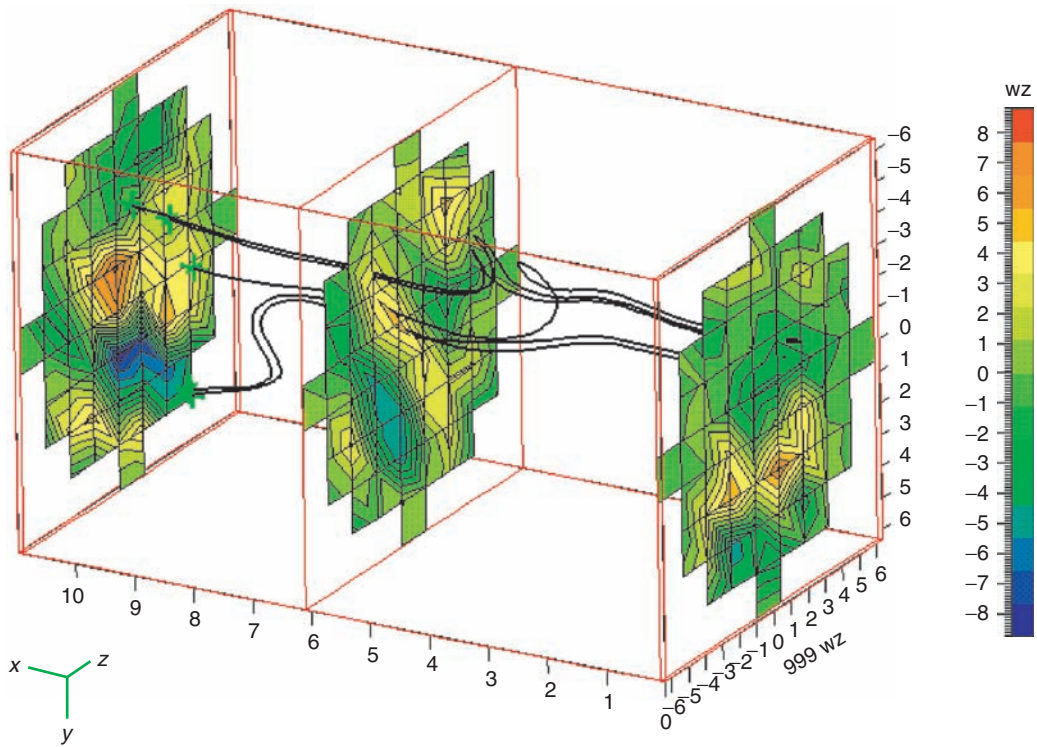


FIGURE 14.90 ω_z vorticity contours on Z-plane slices 16.6 msec after the bubble has departed from the viewing volume.

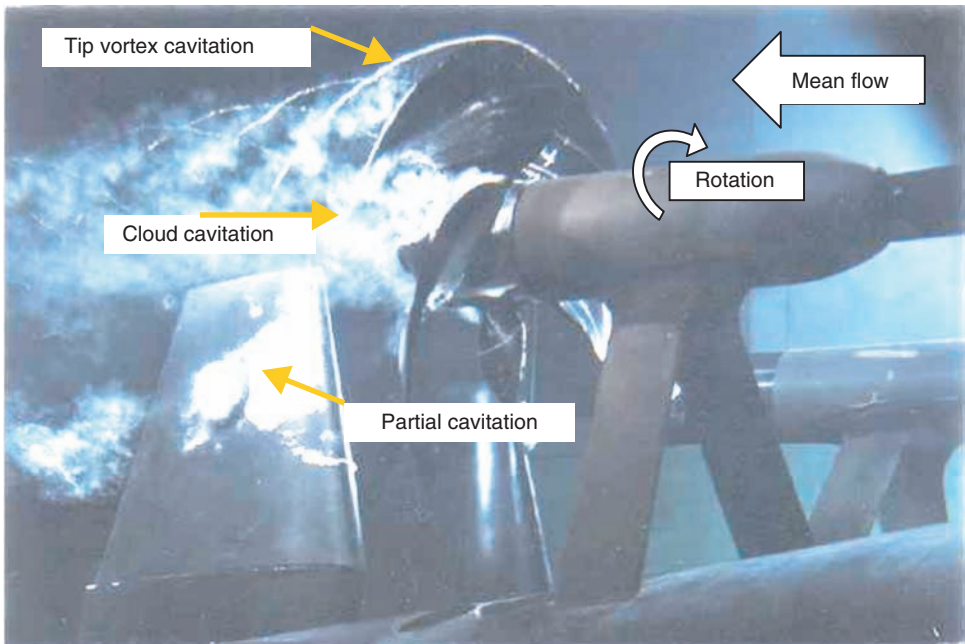


FIGURE 12.11 Tip vortex cavitation, cloud cavitation, and partial attached cavitation on a model of a marine propeller. (Courtesy of Dr. Y.T. Shen, Naval Surface Warfare Center-Carderock Division.)

13.2.4.3.3.1 *Microparticles ($\tau_p/\tau_k \ll 1$).* Microparticles (case B) behave almost like flow tracers because their response time, τ_p , is much lesser than the Kolmogorov time scale, τ_k , but since their material density, ρ_p , is much higher than that of the carrier fluid, ρ , they cause the fluid to behave like a 'heavy gas' (Saffman, 1962).

In order to explain the physical mechanism of the two-way coupling, we write the time evolution equation of TKE, which is obtained by multiplying Eq. (13.1) by u_j and ensemble averaging,

$$\frac{dE(t)}{dt} = -\varepsilon(t) + \Psi_p(t) \quad (13.14)$$

where $\varepsilon(t)$ is the viscous dissipation rate of $E(t)$ and $\Psi_p(t)$ the energy rate of change due to the particles drag force (Ahmed and Elghobashi, 2000):

$$\Psi_p(t) = \alpha_m \langle u_j(v_j - u_j)/\tau_p \rangle \quad (13.15)$$

and α_m is the mass loading ratio ($\alpha_m = \alpha\rho_p/\rho$).

Now we show how the microparticles contribute to both $\Psi_p(t)$ and $\varepsilon(t)$. Because of their fast response to the turbulent velocity fluctuations of the carrier flow, the microparticles are not ejected from the vortical structures of their initial surrounding fluid. Figure 13.25 shows contours of the instantaneous vorticity component ω_2 (in a small zone whose area is 2.25×10^{-2} of the vertical midplane, x_1x_3 , of our computational domain) and particles locations at $t = 5$ for case B. It is seen that the solid particles are not ejected from the vortex cores, and that the contours of maximum positive and negative values of vorticity occupy a larger fraction (~ 18%) of that zone than in case A (~ 9%) in Figure 13.26. Furthermore, the inertia of the microparticles causes their velocity autocorrelation to be larger than that of their surrounding fluid $\langle v_j v_j \rangle > \langle u_j u_j \rangle$, Figure 13.27), indicating, as expected, that the microparticles retain their kinetic energy longer than the surrounding fluid. Since the microparticles trajectories are almost aligned with fluid points trajectories, and their kinetic energy is larger than that of their surrounding fluid, then the correlation $\langle u_j v_j \rangle$ remains higher than the fluid velocity autocorrelation $\langle u_j u_j \rangle$, (Figure 13.27). Consequently, Ψ_p provides a positive contribution to $dE(t)/dt$ in Eq. (13.14) as shown in Figure 13.28, and hence Ψ_p is responsible for the reduction of the decay rate of TKE relative to case A. On the other hand,

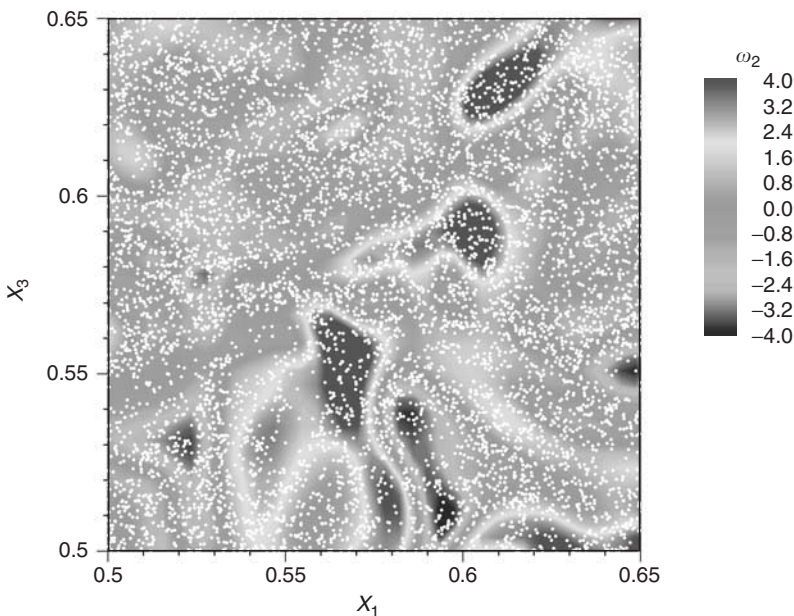


FIGURE 13.25 (Color insert follows page 13-40) Case B: microparticles (white dots) superimposed on ω_2 (color contour) at $x_2 = 0.5$ and $t = 5.0$.

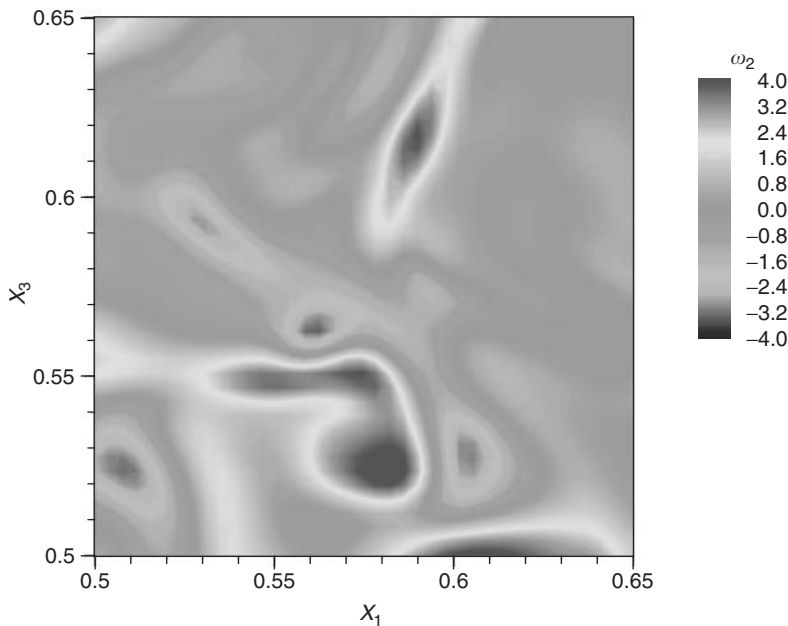


FIGURE 13.26 (Color insert follows page 13-40) Case A: ω_2 (color contour) at $x_2 = 0.5$ and $t = 5.0$.

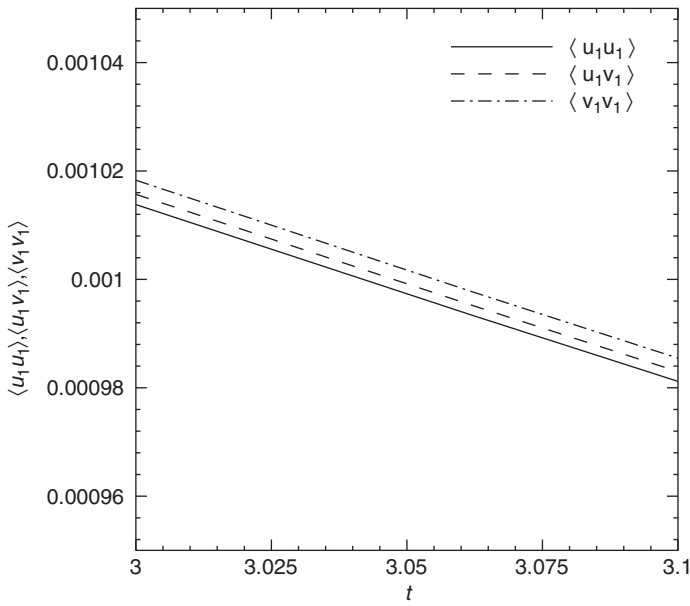


FIGURE 13.27 Case B: time development of fluid velocity autocorrelation $\langle u_1 u_1 \rangle$, correlation $\langle u_1 v_1 \rangle$ between the fluid velocity and particles velocity, and particle velocity autocorrelation $\langle v_1 v_1 \rangle$.

the microparticles increase the viscous dissipation rate, $\varepsilon(t)$, relative to that of case A (Figure 13.28). The reason is that microparticles remain in their initially surrounding vortices (Figure 13.25), and the correlation $\langle u_j v_i \rangle$ remains larger than $\langle u_j u_i \rangle$, as discussed above, thus causing the vortical structures to retain their initial vorticity and strain rates longer than the particle-free flow (case A). Table 13.5 shows that at time $t = 5$, the enstrophy in case B is about 86% larger than that in case A. Table 13.5 also shows that the

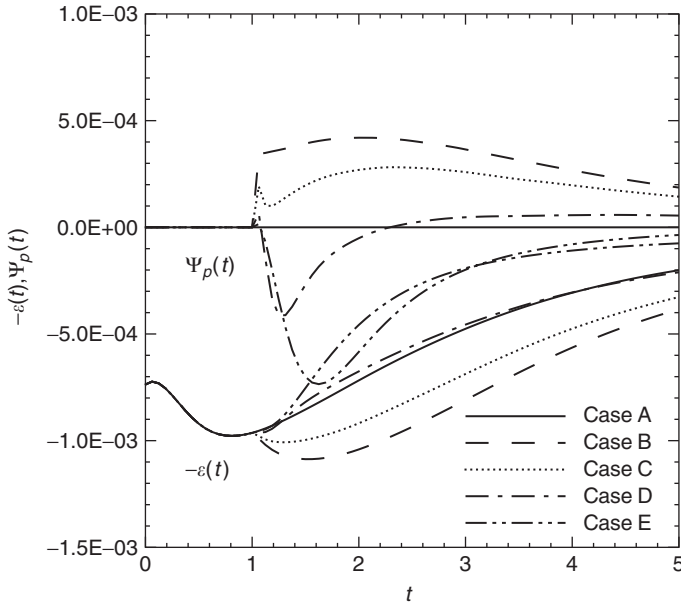


FIGURE 13.28 Time development of the negative of the energy dissipation rate $-\varepsilon(t)$ and the fluid-particle drag interaction energy rate $\Psi_p(t)$.

TABLE 13.5 Mean Values of Enstrophy and Strain Rate at Time $t = 5$

CASE	$\langle \omega^2 \rangle$	$\langle s_{ij} s_{ij} \rangle$
A–no particles	8.37	4.05
B–microparticles	15.6	7.26
C–ghost particles in zero gravity	13.1	6.20
D–critical particles	8.61	4.05
E–Large particles	3.13	1.52
F–ghost particles in finite gravity	33.6	15.6

mean square of the strain rate

$$S_{ij} = (\partial u_i / \partial x_j + \partial u_j / \partial x_i) / 2 \quad (13.16)$$

for case B is nearly 80% higher than that in case A at $t = 5$. The square of the strain rate tensor is related to the three eigenvalues of S_{ij} : the extensional (α), intermediate (β), and compressive (γ) strain rates ($\alpha \geq \beta \geq \gamma$ and $\alpha + \beta + \gamma = 0$ due to incompressibility), through the relation

$$s_{ij} s_{ij} = \alpha^2 + \beta^2 + \gamma^2 \quad (13.17)$$

At time $t = 5$, Figures 13.29–13.31 confirm that the values of α , β , and γ in case B are larger than those in case A (i.e., the probability of finding a large value of α is higher in case B than in case A). The viscous dissipation rate is related to the strain rates via

$$\varepsilon(t) = 2\nu \langle s_{ij} s_{ij} \rangle = 2\nu \langle \alpha^2 + \beta^2 + \gamma^2 \rangle, \quad (13.18)$$

and thus the viscous dissipation rate in case B is larger than that in case A at all times as shown in Figure 13.28. This increase in $\varepsilon(t)$ is manifested in the reduction of the growth rate of the Kolmogorov time-scale

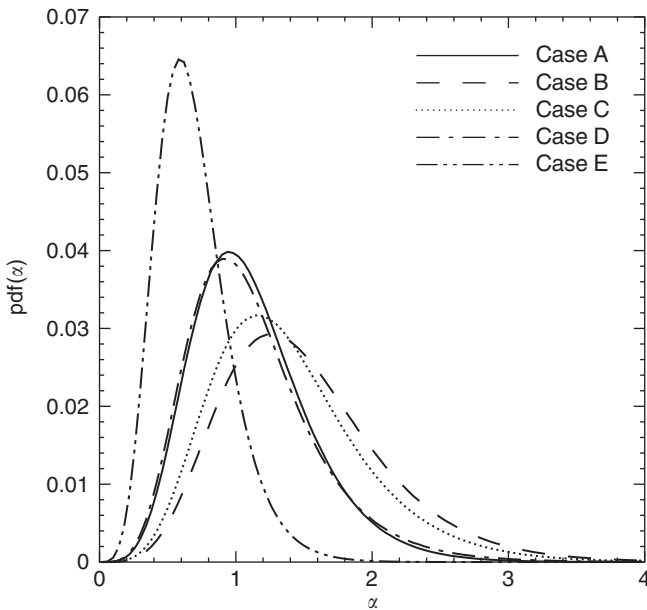


FIGURE 13.29 Probability distribution of the principal extensional strain rate α at $t = 5$.

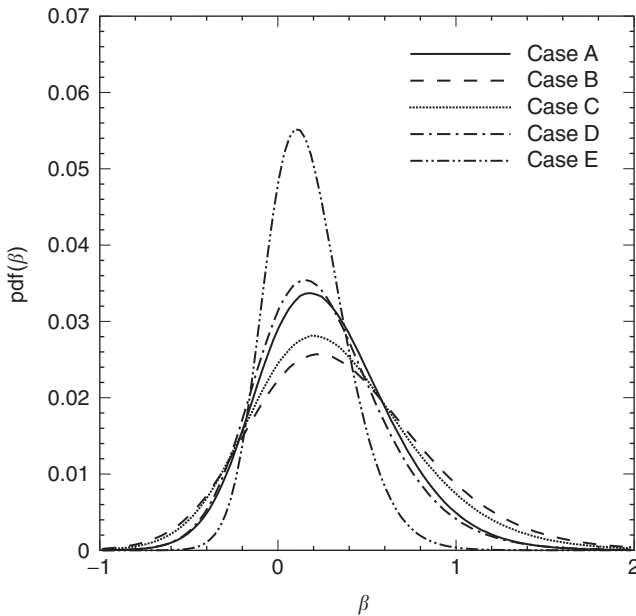


FIGURE 13.30 Probability distribution of the principal intermediate strain rate β at $t = 5$.

$\tau_\kappa(t)$ (not shown here). Figure 13.28 also shows that the magnitude of the increase in $\varepsilon(t)$ in case B relative to case A is less than the magnitude of increase in $\Psi_p(t)$ in the former with the net result of a reduction in the decay rate of $E(t)$ in case B according to Eq. (13.14) and is shown in Figure 13.22. Now we discuss the effects of the microparticles on the energy spectrum $E(\kappa)$ (Figure 13.23) of the carrier fluid. The time evolution of is governed by Eq. (13.13). Microparticles contribute to all the terms on the RHS

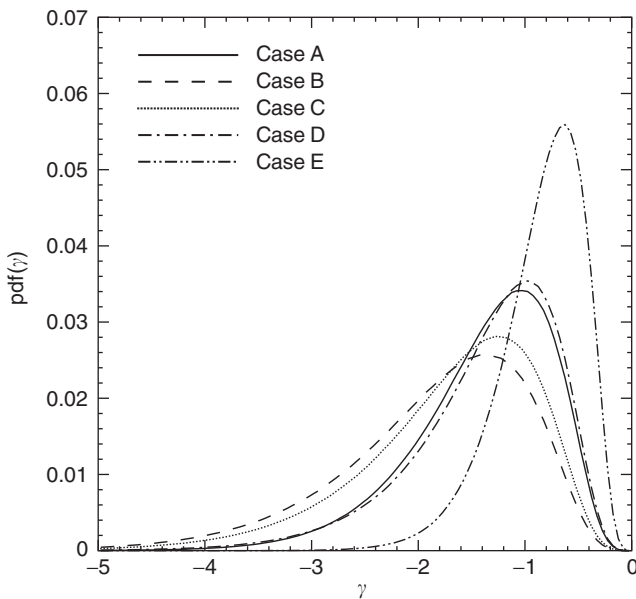


FIGURE 13.31 Probability distribution of the principal compressive strain rate γ at $t = 5$.

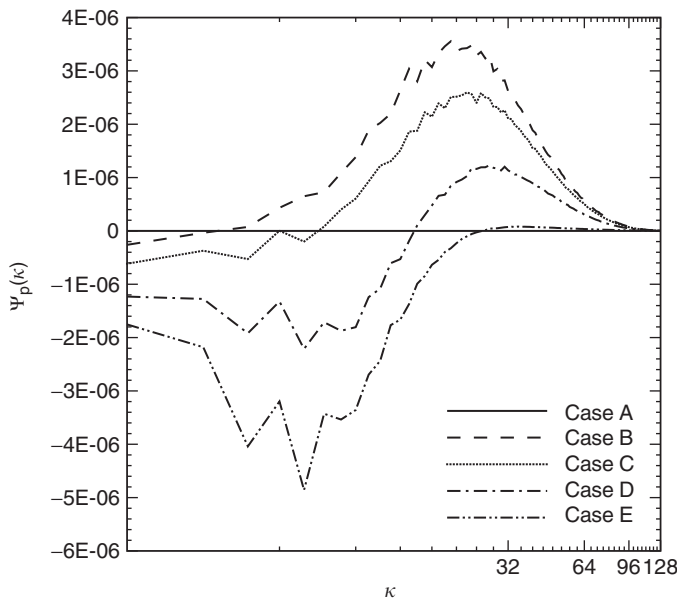


FIGURE 13.32 Three-dimensional spatial spectrum of two-way coupling fluid-particle drag interaction energy rate $\Psi_p(\kappa)$ at $t = 5.0$.

of Eq. (13.13) (Figures 13.32–13.34). The time evolution of $E(\kappa)$, not shown here, indicates that the microparticles first modify the high wave number portion of the spectrum, before the smaller wave numbers are affected as time increases. Because of their properties, microparticles ($d \ll \eta$ and $\tau_p \ll \tau_\kappa$) directly interact with the small scales of motion, augmenting their energy content. The triadic interaction of wave numbers then alters the energy content of the other scales of motion, such that after few integral

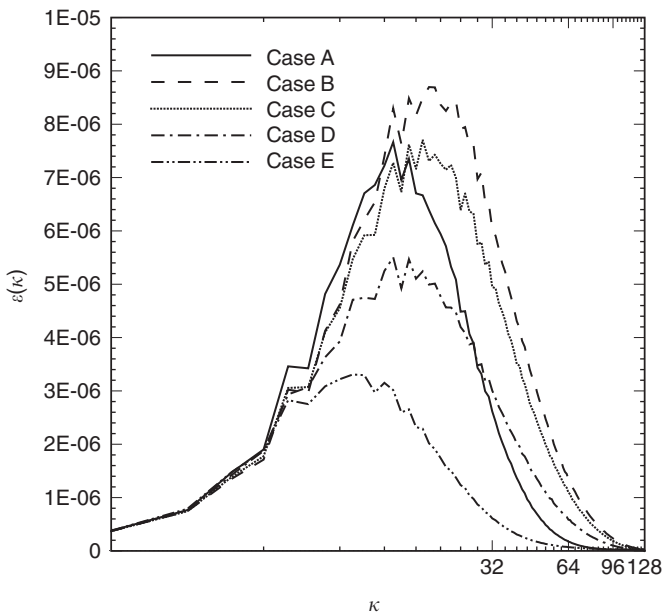


FIGURE 13.33 Three-dimensional spatial spectrum of energy dissipation rate $\varepsilon(\kappa)$ at $t = 5.0$.

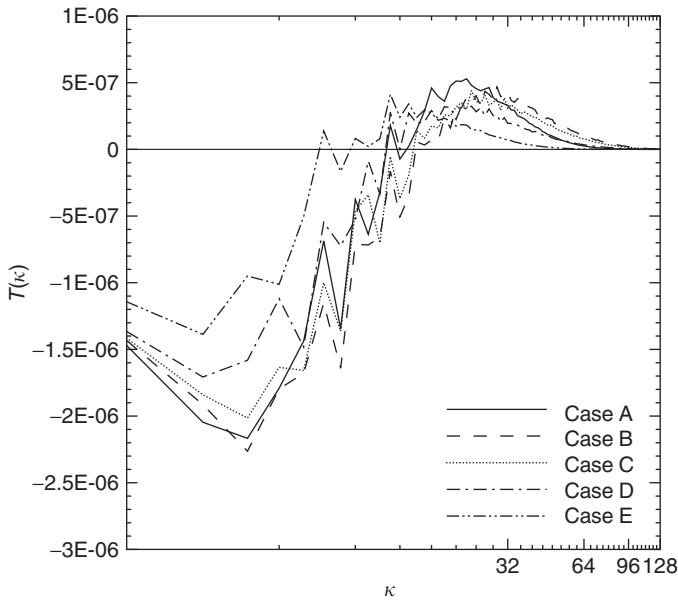


FIGURE 13.34 Three-dimensional spatial spectrum of nonlinear energy transfer rate $T(\kappa)$ at $t = 5.0$.

time scales, $\tau_p, E(\kappa)$ modified at all the wave numbers as compared to the particle-free case (Figure 13.23). We have explained earlier in this section how microparticles produce a positive $\Psi_p(t)$ (Figure 13.28). Since $\Psi_p(t) = \int \Psi_p(\kappa) d\kappa$ at time t , in case B this integral should be positive. Figure 13.32 shows that $\Psi_p(\kappa)$ in case B is positive at almost all the wave numbers, and thus microparticles provide a positive two-way coupling contribution to $\partial E(\kappa)/\partial t$ (Eq. [13.13]).

On the other hand, we have explained how the microparticles increase the dissipation rate, $\varepsilon(t)$, in case B, as compared with the particle-free flow (Figure 13.28). Since $\varepsilon(t) = \int \varepsilon(\kappa) d\kappa$ at time t , $\int \varepsilon(\kappa) d\kappa$ in case B should be greater than that in case A (Figure 13.33). Also $\varepsilon(\kappa) = 2\kappa^2 E(\kappa)$; thus, in accordance with $E(\kappa)$ in Figure 13.23, Figure 13.33 shows that $\varepsilon(\kappa)$ in case B is greater than that in case A at medium-high wave numbers. The increase in dissipation at high wave numbers causes a larger transfer rate of energy to the large κ value from the small κ value. The energy transfer rate $T(\kappa)$ is, thus, modified by shifting κ , at which $T(\kappa) = 0$ toward higher wave numbers for case B as compared with case A (Figure 13.34). Due to the increased transfer of energy from the small κ , the decay rate of $E(\kappa)$ at small κ is increased, and thus $E(\kappa)$ in case B is smaller than in case A at small κ (Figure 13.23).

13.2.4.3.3.2 Critical Particles ($\tau_p/\tau_\kappa \approx 1$). We label the particles in case D ($\tau_p/\tau_\kappa = 1$) as “critical” particles because of their property of maximum preferential accumulation in comparison to other particles as will be discussed later in this section. We will show that these particles are ejected from the large-vorticity cores of the eddies soon after injection, remain in certain orbits (Figure 13.36), and do not move from one eddy into another as larger particles do (case E).

Now we examine how these critical particles affect $\Psi_p(t)$ and $\varepsilon(t)$ to increase the decay rate of TKE with respect to case A (Figure 13.22). For critical particles, $\Psi_p(t)$ is negative after injection (Figure 13.28) and becomes positive at later times, $t > 2.3 \approx t_{\text{inj}} + \tau_l = 1 + \tau_l$, where τ_l is the turnover time of the large-scale motion (Table 13.3). At early times ($1 < t < 1 + \tau_l$) critical particles, similar to large particles, are centrifuged from their initial surrounding fluid and thus $\langle u_j v_j \rangle < \langle u_j u_j \rangle$. Consequently, according to Eq. (13.15), $\Psi_p(t)$ becomes negative (Figure 13.28) and thus contributes to the faster decay of TKE as compared to case A.

At later times ($t > 1 + \tau_l$), after they have been ejected from the cores of vortices, the critical particles do not have sufficient inertia to cross the convergence regions (of high-speed fluid between the counter-rotating vortices) and enter new eddies, similar to large particles, but rather, they accumulate in these regions of low vorticity and high strain (Maxey, 1987; Wang and Maxey, 1993b). The occurrence of preferential accumulation can be indicated by the time development of the D_c factor (Wang and Maxey, 1993b), which measures the sum of the squared differences between the actual probability of concentration, $P_c(C)$, and the probability of random distribution, $p_c^\mu(C)$,

$$D_c = \sum_{C=0}^{N_p} (P_c(C) - P_c^\mu(C))^2 \quad (13.19)$$

where N_p is the total number of computational particles (denoted by M_c in Table 13.4). Figure 13.35 shows the time development of D_c for the four cases (B–E). It is clear that in case D (critical particles), the preferential accumulation is much larger than in the other three cases. Figure 13.36 clearly shows the preferential accumulation of the critical particles in orbits outside the regions of large ω_2 .

The higher inertia of the critical particles relative to the carrier fluid causes their velocity autocorrelation to be higher than that of the surrounding fluid, $\langle v_j v_j \rangle > \langle u_j u_j \rangle$, indicating that critical particles retain their kinetic energy longer than their surrounding fluid. Once these particles are in the high-velocity convergence regions, characterized by pathlines of small curvature, their trajectories become more aligned with those of the fluid points. Consequently, the correlation $\langle u_j v_j \rangle$ becomes larger than $\langle u_j u_j \rangle$ for $t > 1 + \tau_l$. Thus, $\Psi_p(t)$ becomes positive (Eq. [13.15]) for $t > 1 + \tau_l$ (Figure 13.28). Since the high vorticity cores are nearly free of particles, the two-way coupling force $f_\kappa \approx 0$ inside these cores, and thus the evolution equation of vorticity reduces to that of particle-free flow. Table 13.5 confirms that the value of mean enstrophy at time $t = 5$ in case D is nearly equal to that of case A, with a difference smaller than 3%.

Since the vortical structures in case D evolve nearly as that in case A, the growth rates of the turbulence scales are nearly identical in both cases ($\tau_{k_d}(t) \approx \tau_{k_A}(t)$) (not shown here). Consequently, the decay rate of the local velocity gradients will be the same in both the cases, resulting in a similar decay of the magnitude of the local strain rate. Table 13.5 shows that the strain rate for case D is identical to that of case A at $t = 5$. At time $t = 5$, Figures 13.29–13.31 confirm that the values of, α , β , γ and in case D are almost identical to those in case A. Accordingly, the viscous dissipation rates in these two cases are nearly the

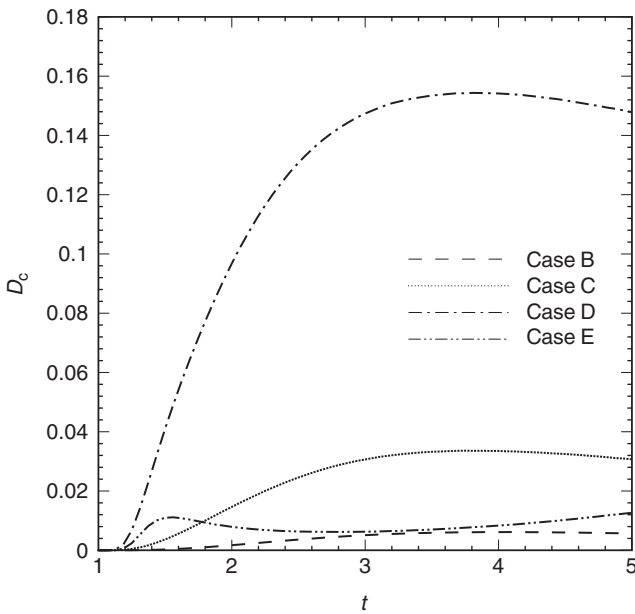


FIGURE 13.35 Time development of the D_c factor.

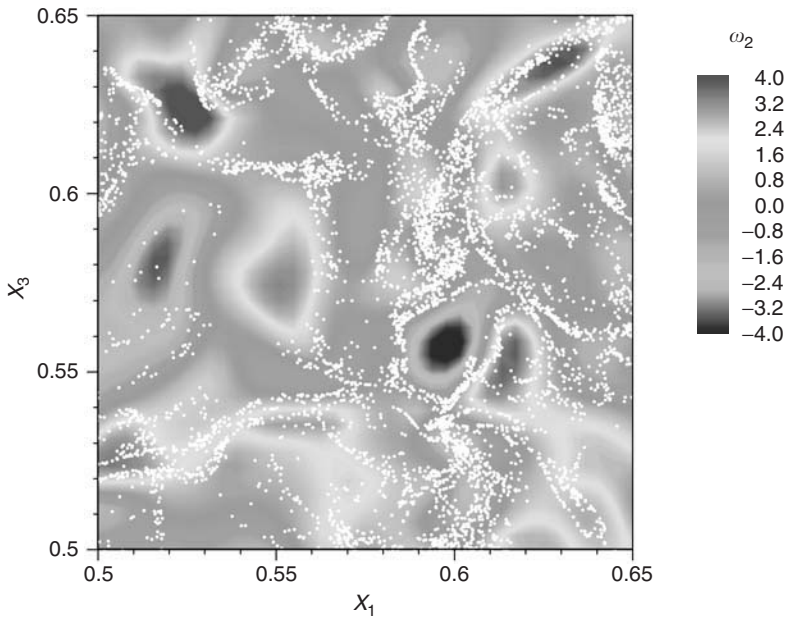


FIGURE 13.36 (Color insert follows page 13-40) Case D: critical particles (white dots) superimposed on ω_2 (color contour) at $x_2 = 0.5$ and $t = 5.0$.

same (see Figure 13.28). Thus, the net effect of the modifications of $\Psi_p(t)$ and $\varepsilon(t)$ in case D (Figure 13.28) is the reduction of $E(t)$ relative to case A. The modification of the energy spectrum $E(\kappa)$ of the carrier flow by the critical particles (case D) is displayed in Figure 13.23. It is seen that $E(\kappa)$ for case D lies between those of case B (microparticles) and case E (large particles). Accordingly, the magnitudes of

$\Psi_p(\kappa)$, $\varepsilon(\kappa)$, and $T(\kappa)$ of case D are intermediate between those of cases B and E (Figures 13.32–13.34). $\Psi_p(\kappa)$ is positive at large κ as for microparticles, and negative at small κ as for large particles. $\varepsilon(\kappa)$ is such that $\varepsilon(t) = \int \varepsilon(\kappa) d\kappa$ is nearly identical to that of case A (See Figure 13.28), as discussed above. The net result of these modifications is that, in case D, the crossover wave number of $E(\kappa)$ with that of the particle-free flow (case A) lies in between the crossover wave numbers of cases B and E.

13.2.4.3.3 Ghost particles in zero gravity. It is clear from Figure 13.22 and the discussion in the previous subsections that in comparison with the particle-free flow (case A), microparticles (case B, $\tau_p/\tau_\kappa = 0.1$) reduce the decay rate of TKE, and critical particles (case D, $\tau_p/\tau_\kappa = 1.0$) enhance this rate. These two opposing effects in cases B and D lead us to search for particles that have a neutral effect on that decay rate. More specifically, we searched for particles whose τ_p is in the range $0.1 < \tau_p/\tau_\kappa < 1.0$ and which maintain the decay rate of TKE as that of the particle-free flow (case A). Our DNS results show that particles with $\tau_p/\tau_\kappa = 0.25$ (case C) satisfy this condition at all times, as shown in Figure 13.22. Thus we denote these particles as ghost particles because their presence in the flow cannot be detected by examining only the temporal development of TKE. It is important to emphasize that the value of $\tau_p/\tau_\kappa = 0.25$ is not universal, but depends on $Re_{\lambda 0}$, α_m , and the magnitude of the gravitational acceleration (zero in our case). However, the significance of this finding is that dispersed particles are capable of modifying the turbulence energy spectrum (Figure 13.23) in such a unique way that the amount of energy gained by the turbulence at high wave numbers balances exactly the amount of energy lost at low wave numbers, with the net result of retaining the integral of the spectrum equal to that of the particle-free flow at all times (Figure 13.22).

Similar to microparticles, ghost particles are not ejected from the vortex cores (Figure 13.37), and thus they enhance the lifetime of the vortical structures, such that, at time $t = 5$, the enstrophy and the strain rate in case C are larger than those in case A by about 56 and 53%, respectively (Table 13.5). Since ghost particles have larger inertia than microparticles, their trajectories tend to deviate from those of their surrounding fluid points more than the trajectories of microparticles. Thus the magnitudes of $\Psi_p(t)$ and $\varepsilon(t)$ for the ghost particles (see Figure 13.28) are smaller than those for the microparticles. However, the magnitudes of $\Psi_p(t)$ and $\varepsilon(t)$ for the ghost particles are in a unique proportion, such that the positive $\Psi_p(t)$ is only equal to the increase ($\Delta\varepsilon(t)$) in the magnitude of $\varepsilon(t)$ with respect to case A, resulting in the net

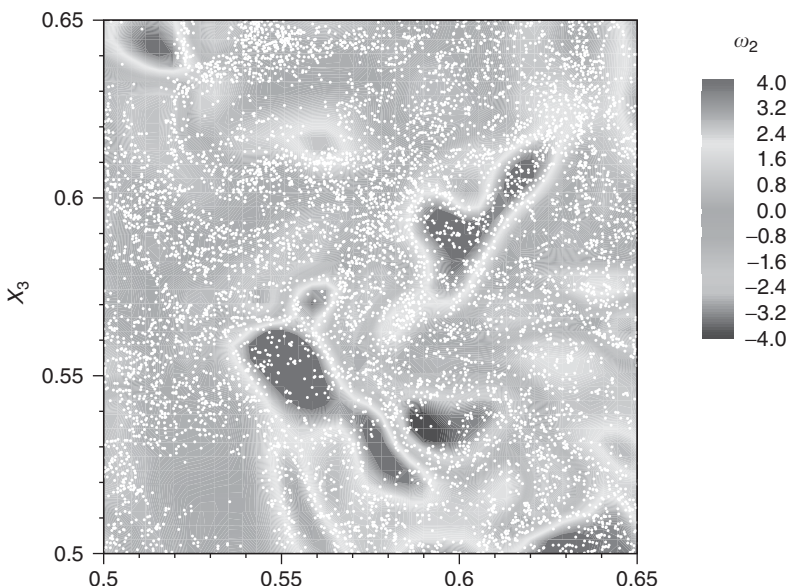


FIGURE 13.37 (Color insert follows page 13-40) Case C: “ghost” particles in zero gravity (white dots) superimposed on ω_2 (color contour) at $x_2 = 0.5$ and $t = 5.0$.

sum ($\Psi_p(t) - \Delta\varepsilon(t)$) being equal to $\varepsilon(t)$ of case A. Consequently, the decay rate of TKE in case C is the same as in case A.

13.2.4.3.3.4 Ghost particles in finite gravity. In case F, we study the effect of gravity on the two-way coupling between the ghost particles of case C ($\tau_p/\tau_k = 0.25$) and decaying isotropic turbulence. A gravitational acceleration is imposed in the negative x_3 direction, and its magnitude is prescribed, such that $(v_t/u_0) = 0.25$ (Table 13.4).

Figure 13.24 shows that due to gravity, the particles in case F reduce the decay rate of TKE relative to cases A and C at all times. Figure 13.38 compares the temporal developments of the three rms velocity components, $u_{i,\text{rms}}(t)$ of the fluid in both cases A and F. It is seen that only the decay rate of the velocity component in the x_3 direction, $u_{3,\text{rms}}$, has been considerably reduced relative to the other components, i.e., the two-way coupling in the presence of gravity in the x_3 direction resulted in augmenting $u_{3,\text{rms}}$. The mechanisms responsible for this modulation will be discussed below by comparing the vorticity fields in cases C (zero gravity) and F (finite gravity).

Figure 13.37 and Figure 13.39 display the contours of the instantaneous vorticity component ω_2 (in a small zone of the vertical midplane x_1x_3 of our computational domain) and particles locations at $t = 5$ for cases C and F, respectively. We see that most of the vortical structures in case F are stretched in the x_3 direction in a banana-like shape, and the values of maximum (positive and negative) vorticity are larger than in case C.

We also see that the particles in case F tend to accumulate in patches according to the mechanism of preferential sweeping described by Wang and Maxey (1993b). The solid particles, settling under the effect of gravity, tend to follow a path where the local fluid instantaneous velocity is in the direction of gravitational acceleration (negative x_3 direction). Figure 13.39 shows that the particles accumulate on the RHS of a vortical structure with positive (clockwise) vorticity (red color) or on the LHS of a structure with negative vorticity (blue color). This preferential accumulation or sweeping, as expected, creates zones that are nearly devoid of particles. Thus only the side of the vortical structure swept by the trajectories of the particles will be subjected to a drag force, $-f_3$, which is directed downward. As a consequence of this asymmetry of the force acting on the fluid, local gradients $\partial f_3/\partial x_1$ and $\partial f_3/\partial x_2$ are generated in the horizontal plane, increasing the magnitudes of the source terms, b_i , the horizontal components of vorticity, and ω_1 and ω_2 , in addition to stretching the structures in the x_3 direction.

The results discussed above provided new information about the behavior of the TKE and its dissipation rate in Zone A of the classification map in Figure 13.20 as shown in Figure 13.21. Zone A includes

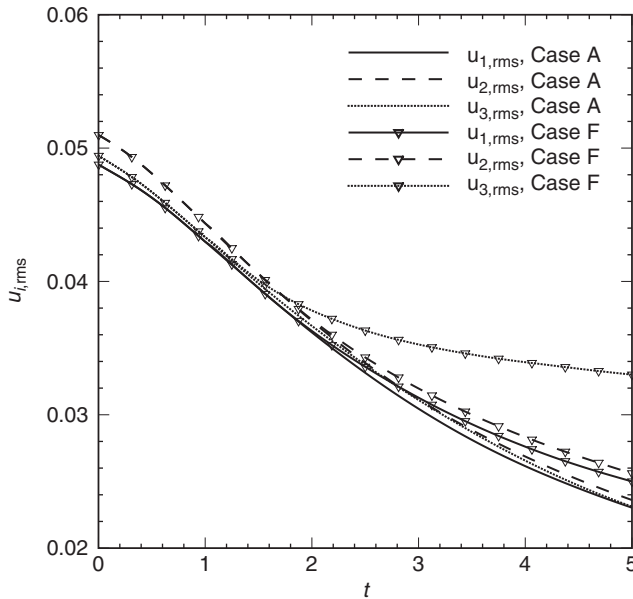


FIGURE 13.38 Time development of rms fluid velocity components.

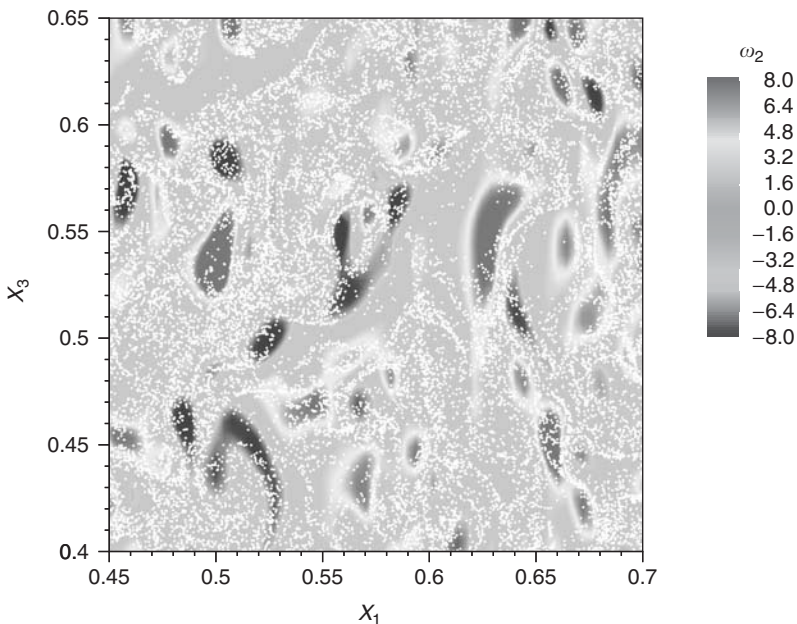


FIGURE 13.39 (Color insert follows page 13-40) Case F: “ghost” particles in finite gravity (white dots) superimposed on ω_2 (color contour) at $x_2 = 0.5$ and $t = 5.0$.

three regions:

- Microparticles ($\tau_p/\tau_\kappa \leq 0.1$) that cause both TKE and its dissipation rate, ε , to be larger than in the single-phase flow.
- Ghost particles ($0.1 < \tau_p/\tau_\kappa < 0.5$) that modify the energy spectrum $E(\kappa)$ in a manner such that TKE is unchanged but ε is larger than that of the single-phase flow.
- Large particles ($\tau_p/\tau_\kappa > 1$) that reduce both TKE and ε relative to their values in the single-phase flow.

13.2.5 DNS of Bubble-Laden Isotropic Turbulence Using the Two-Fluid Approach

In the preceding section we employed the Lagrangian–Eulerian approach to study the two-way coupling interactions between solid particles and isotropic turbulence. In the present section we use the alternative approach, known as the two-fluid or Eulerian–Eulerian approach (Elghobashi, 1994), which has been applied frequently with the Reynolds-averaged equations of motion (Elghobashi and Abou Arab, 1983). Recently Druzhinin and Elghobashi, 1998) employed the two-fluid approach in DNS of bubble-laden isotropic turbulence. This section provides a condensed version of this paper (Druzhinin and Elghobashi, 1998). In this approach, the governing equations are obtained by volume averaging the equations of motion of both the phases, (the carrier flow and bubbles) based on the assumption that the dispersed phase behaves as a continuum under certain conditions.

The objective of this section is to describe how DNS is performed using the two-fluid approach for bubble-laden homogeneous isotropic turbulence without applying force (i.e., decaying turbulence). It is important to point out that in employing the two-fluid approach a difficulty may arise due to the phenomenon of preferential accumulation of the dispersed particles. It is well known (Eaton and Fessler, 1994) that solid particles, due to their inertia, tend to accumulate in the low-enstrophy regions of the flow, whereas gaseous bubbles in a liquid flow tend to accumulate in a high-enstrophy regions (Druzhinin

and Elghobashi, 1998, 2001), generally associated with the centers of vortices. Preferential accumulation in homogeneous turbulence is most pronounced for particles with response times of the order of the Kolmogorov time scale τ_κ (Wang and Maxey, 1993b). This segregation creates regions devoid of particles neighboring regions of high particle concentration. Therefore, performing DNS using the two-fluid approach may generate high concentration gradients causing numerical resolution and stability problems, thus restricting the implementation of that approach. Druzhinin and Elghobashi (1999a) recently developed a numerical scheme that resolves the large gradients of particle velocity and concentration fields created by preferential accumulation.

In this section we show that the two-fluid approach is applicable to bubbles with diameter smaller than the Kolmogorov length scale, and accordingly their response time is much smaller than the Kolmogorov time scale. Thus, the effects of preferential accumulation of bubbles in the high-ensrophy regions of the carrier flow become less pronounced, so that DNS with the two-fluid approach can be successfully used.

13.2.5.1 Equations of Motion for the Bubble-Laden Flow

We consider spherical bubbles with diameter d_b to be much smaller than the characteristic length scale of the flow, L_f , and average the equations of motion of the fluid and bubble over a length scale λ , which is much smaller than L_f but much larger than the bubble diameter, $d_b \ll \lambda \ll L_f$. Thus the bubble phase can be treated as a continuum characterized by the velocity $V_i(r,t)$ and concentration (or volume fraction) $\alpha(r,t) = \pi d_b^3 N_b(r,t)/6$, where $N_b(r,t)$ is the bubble number density.

We assume that the density of the gas and, consequently, the mass of the bubble are negligible compared with those of the surrounding fluid, $\rho_f \gg \rho_b = 0$. By taking into account the effect of the bubbles on the fluid flow in a unit volume of the mixture and neglecting the interactions between the bubbles, we write derive the following equations for the bubble-laden flow (Drew, 1983; Zhang and Prosperetti, 1997).

Fluid momentum equation:

$$(1 - \alpha)\rho_f \frac{DU_i}{Dt} = -(1 - \alpha)\partial_i P + \partial_j(1 - \alpha)\sigma_{ij} - \alpha F_i^d - (1 - \alpha)\rho_f g\delta_{iz} \quad (13.20)$$

Fluid continuity equation:

$$-\partial_i\alpha + \partial_j(1 - \alpha)U_j = 0 \quad (13.21)$$

Bubble-phase momentum equation:

$$0 = -\alpha\partial_i p + \partial_j\alpha\sigma_{ij} + \alpha F_i^d \quad (13.22)$$

Bubble-phase continuity equation:

$$\partial_i\alpha + \partial_j\alpha V_j = 0 \quad (13.23)$$

In the above equations, U_i is the fluid velocity, V_i the velocity of the bubble phase, σ_{ij} the viscous stress tensor, $\sigma_{ij} = \mu(\partial_j U_i + \partial_i U_j)$, the Lagrangian derivatives $D/Dt = \partial/\partial t + U_i \partial_i$ and $d/dt = \partial/\partial t + V_i \partial_i$ are taken along the trajectories of the fluid point and bubble, respectively, and g the projection of the gravity acceleration on the z -axis, $g_i = -g\delta_{iz}$. F_i^d denotes the force acting on the bubble due to the pressure and viscous stresses caused by the disturbance flow U^d owing to the boundary conditions at the bubble surface. The details of the derivation of Eqs. (13.22)–(13.23) are given by Druzhinin and Elghobashi (1998).

Since we assume that the bubble mass is negligible, the sum of the forces acting on the bubble must vanish and thus the equation of the bubble motion becomes

$$F_i^0 + F_i^d = 0 \quad (13.24)$$

where F_i^0 , the force exerted on the bubble by the undisturbed fluid flow U^0 , is obtained by integrating both the pressure and viscous stresses of the undisturbed flow over the bubble surface. For small spherical bubbles with diameter much smaller than the flow length scale,

$$d_b \ll L_f \quad (13.25)$$

and with Weber number less than unity, F_i^0 is given by

$$F_i^0 = \rho_f \left(\frac{DU_i^0}{Dt} + g\delta_{iz} \right) = -\partial_i P^0 + \partial_j \sigma_{ij}^0 \quad (13.26)$$

where P^0 and σ_{ij}^0 are the undisturbed pressure and viscous stresses fields, respectively. The boundary condition at the bubble surface is effectively equivalent to that for a solid sphere, rather than the stress free-condition needed for the Hadamard–Rybaczynski formula (Batchelor, 1967). Thus, for bubbles with Reynolds number less than unity,

$$Re_b = \frac{d_b |U^0 - V|}{\nu} < 1 \quad (13.27)$$

the force due to the disturbance flow, F_i^d , can be calculated from the solution of the corresponding unsteady Stokes problem in the form

$$F_i^d = \frac{18\mu}{d^2} (U_i^0 - V_i) + \frac{\rho_f}{2} \left(\frac{DU_i^0}{Dt} - \frac{dV_i}{dt} \right) \quad (13.28)$$

The first and second terms in Eq. (13.28) correspond to the Stokes drag and added-mass forces, respectively. From Eq. (13.24) we obtain an equivalent expression for the disturbance force:

$$F_i^d = -F_i^0 \quad (13.29)$$

where F_i^0 is given by Eq. (13.26).

Therefore, the equation of the bubble motion Eq. (13.24) can be rewritten in the form

$$\frac{dV_i}{dt} = 3 \frac{DU_i}{Dt} + \frac{1}{\tau_b} (U_i - V_i + W\delta_{iz}) \quad (13.30)$$

where the bubble response time τ_b and terminal velocity w are defined as

$$\tau_b = \frac{d^2}{36\nu} \quad (13.31)$$

and

$$W = 2\tau_b g \quad (13.32)$$

In Eqs. (13.20)–(13.23), (13.30) and the following discussion, we omit the superscript “0” in the notation for the undisturbed fole U^0 .

We assume that the bubble volume fraction, α , is small enough (i.e., $\alpha \leq 10^{-3}$), and therefore, neglect its contribution to the fluid inertia and continuity, i.e., we retain α only in the buoyancy term in the momentum equation of the carrier flow Eq. (13.20). This is analogous to the Boussinesq approximation in a stratified fluid with effective density $(1-\alpha)\rho_f$.

By substituting the expression for the disturbance force obtained from Eqs. (13.29) and (13.26) into the equation for the fluid momentum Eq. (13.20), and using Eq. (13.20), we write equations of the conservation of the fluid- and bubble-phase momentum and mass in the form (Ruetsch and Meiburg, 1994):

$$\frac{DU_i}{Dt} = -\frac{1}{\rho_f} \partial_i \tilde{P} + \nu \Delta U_i + (\alpha - \langle \alpha \rangle) g \delta_{iz} \quad (13.33)$$

$$\partial_j U_j = 0 \quad (13.34)$$

$$\frac{dV_i}{dt} = 3 \frac{DU_i}{Dt} + \frac{1}{\tau_b} (U_i - V_i + W\delta_{iz}) \quad (13.35)$$

$$\frac{\partial \alpha}{\partial t} + \partial_j \alpha V_j = 0 \quad (13.36)$$

By using the analogy between the bubbly flow and a stratified flow with density $(1-\alpha)\rho_f$, we remove the modified hydrostatic part in the pressure field in Eq. (13.33):

$$\tilde{P} = P + \rho_f g \int_0^z (1 - \langle \alpha \rangle) dz \quad (13.37)$$

where $\langle \alpha \rangle$ is the ensemble-averaged bubble volume fraction. In the following discussion, we evaluate $\langle \alpha \rangle$ as an average over a horizontal (z) plane.

13.2.5.2 Numerical Method

The momentum conservation and continuity equations (13.33)–(13.36) for both phases are solved in a cubical domain with periodic boundary conditions. The equations are discretized in an Eulerian framework using a second-order finite-difference technique on a staggered grid containing 96^3 points equispaced within unit length in each of the three coordinate directions (x, y, z). The Adams–Bashforth scheme is used to integrate the equations in time. Pressure is obtained by solving the Poisson equation using fast Fourier transform. More details about the numerical method and its accuracy are discussed by Elghobashi and Truesdell (1993), Gerz et al. (1989), Schumann (1977) and Ferrante and Elghobashi (2003).

13.2.5.3 Results

In this section, we present the DNS results for bubble dispersion in isotropic decaying turbulence with one-way coupling.

13.2.5.3.1 Dispersion of Bubbles in Isotropic Decaying Turbulence (with One-Way Coupling)

DNS of bubble dispersion in isotropic decaying turbulence is performed with the initial conditions: $Re_{\lambda_0} = 25$, $U_0 = 0.05$, and $k_p/k_{\min} = 5$, which correspond to the initial dissipation $\varepsilon(0) = 0.002584$, Taylor microscale $\lambda_0 = 0.027877$, Kolmogorov length scale $\eta_0 = 0.002861$, integral length scale $L_0 = 0.057815$, and viscosity $\nu = 5.57 \times 10^{-5}$. The dimensionless gravity constant g is assumed to equal unity. The reference length and time scales used in normalizing the above dimensionless quantities are $L_{\text{ref}} = 0.098$ m and $T_{\text{ref}} = 0.1$ s, respectively.

The initial bubble velocity and volume fraction (concentration) are prescribed as

$$V_i = \delta_{iz} W, \quad \alpha_0 = C_0 = 5 \times 10^{-4} \quad (13.38)$$

where the bubble terminal velocity W is given by Eq. (13.32).

The ability of the simulation to resolve the motion at the smallest turbulence scales is assured by the criterion $\eta k_{\max} > 1$, where $k_{\max} = N_g \pi$ is the highest resolved wave number for the given number of grid points in each coordinate direction N_g ($= 96$ in the present case). Our simulations show that $1 \leq \eta k_{\max} \leq 2.65$ for $0.75 < t < 10$.

The choice of the bubble response time is restricted by the conditions Eqs. (13.25) and (13.27), which can be rewritten in the form

$$d_b < \eta \quad (13.39)$$

and

$$Re_b = \frac{W d_b}{\nu} < 1 \quad (13.40)$$

The first condition ensures that the bubble size is smaller than the characteristic flow scale, i.e., the Kolmogorov length scale $\eta = (\nu^3/\varepsilon)^{1/4}$ in the case of decaying isotropic turbulence. The second condition restricts the bubble Reynolds number, based on the bubble terminal velocity, to be less than one. Substituting the terminal velocity (13.32) and the bubble diameter ($d_b = (36\nu\tau_b)^{1/2}$) in Eq. (13.39) and Eq. (13.40), and using the equality $\eta^2 = \nu\tau_k$, we rewrite conditions (13.39) and (13.40) as

$$\frac{\tau_b}{\tau_k} < \frac{1}{36} \simeq 0.028 \quad (13.41)$$

and

$$\tau_b < \left(\frac{\nu}{144g^2} \right)^{1/3} = \tau_* \quad (13.42)$$

It should be emphasized that conditions (13.41) and (13.42) are essential for the derivation of the bubble motion equation (13.30). Thus, violating either of these conditions renders the equation of motion (13.30) invalid. Note that Wang and Maxey (1993a) and Maxey et al. (1994) performed DNS of isotropic turbulence laden with bubbles with $\tau_b = \tau_k$ using the Eulerian–Lagrangian approach and Eq. (13.30), i.e., violating the condition (13.41).

Also note that in the case of solid particles, the condition $d_p < \eta$ (which is also required for the derivation of the particle motion equation) is equivalent to $(\tau_p/\tau_k) < (\rho_p/18\rho_f)$, which allows (τ_p/τ_k) to be ≥ 1 for $\rho_p > 18\rho_f$.

In DNS of bubble-laden decaying turbulence we prescribe $\tau_b = 0.04\tau_{k0}$, where the initial dimensionless Kolmogorov time scale is $\tau_{k0} = 0.15$. The bubbles are added to the flow at time $t = 1$, when the magnitude of the skewness of the fluid velocity derivative reaches about 0.47, indicating an established rate of energy transfer across the energy spectrum. At that time, τ_k increases to 0.22, hence ratio $\tau_b/\tau_k = 0.027$ and the time $\tau_* = 0.0073$ (see Eq. [13.42]). Since τ_k increases monotonically in decaying turbulence, condition (13.41) is satisfied throughout the simulation. Thus both conditions Eqs. (13.41) and (13.42) are met for the prescribed value of τ_b . The corresponding bubble Reynolds number (13.40) equals 0.74 (i.e., of the order of unity) and the dimensional bubble diameter is $d_b \simeq 350 \mu\text{m}$ (for the bubble to remain spherical in liquid water, i.e., $d_b < 1 \text{ mm}$). Therefore, the prescribed value of τ_b is close to the maximum limit for the validity of the equation set (13.33)–(13.36).

Figure 13.40 shows the time development of TKE $E(t)$, and its dissipation rate $\varepsilon(t)$, and the concentration variance $\langle \alpha'^2 \rangle = \langle (\alpha - \langle \alpha \rangle)^2 \rangle$ calculated from the corresponding spectra $E(k, t)$ and $E_\alpha(k, t)$ as

$$E(t) = \sum_{k=1}^{N_k/2} E(k, t) \quad (13.43)$$

$$\varepsilon(t) = 2\nu \sum_{k=1}^{N_k/2} k^2 E(k, t) \quad (13.44)$$

and

$$\langle \alpha'^2 \rangle(t) = \sum_{k=1}^{N_k/2} E_\alpha(k, t) \quad (13.45)$$

normalized by the spective initial values $E(0)$, $\varepsilon(0)$ and $\alpha_0'^2$. Both $E(t)$ and $\varepsilon(t)$ decay in time due to the viscous dissipation. On the other hand, the bubbles concentration variance first increases from zero to $\langle \alpha'^2 \rangle \simeq 5.1 \times 10^{-3} \alpha_0'^2$ (for time $1 < t < 5$, where $t = 1$ is the time of injecting the bubbles into the flow), and then decays. The growth of the concentration variance is caused by the preferential accumulation of bubbles in the high-enstrophy regions of the flow. The effects of the bubble accumulation as well as the decay of the concentration variance for $t > 5$ are discussed below.

Figure 13.41 shows the spectra of the fluid kinetic energy, $E(k)$, the dissipation, $\varepsilon(k) = 2\nu k^2 E(k)$, and the bubble concentration fluctuations, $E_\alpha(k)$, at time $t = 3$ (here and below, for convenience, we omit the explicit reference to the time dependence of $E(k, t)$, $\varepsilon(k, t)$ and $E_\alpha(k, t)$). At this time, the energy spectrum

$$Re_{\lambda,0}=25, \tau_b=0.04\tau_{k0} (1\text{-way}), C_0=\alpha_0$$

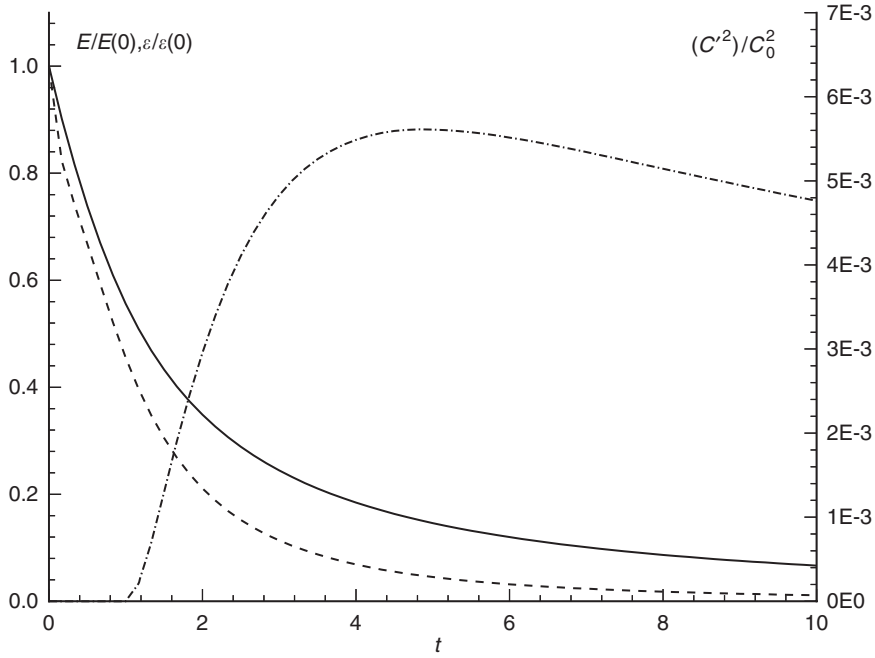


FIGURE 13.40 Time dependence of the normalized turbulence kinetic energy $E(t)/E(0)$ (solid curve), its dissipation rate $\epsilon(t)/\epsilon(0)$ (dashed curve) and variance of bubble volume fraction (concentration) $\langle \alpha'^2 \rangle / \alpha_0^2 \equiv \langle C'^2 \rangle / C_0^2$ (dash-dotted curve).

peaks at $k = 3$. Note that since the transport equation of bubble concentration is of the advection (Lagrangian) type, there is no molecular dissipation of the bubble concentration fluctuations. Thus there is no decay in the spectrum $E_\alpha(k)$ at high wave numbers, rather, the fluctuations intensity piles up at larger wave numbers (cf. Figure 13.41). Note however, that the concentration variance Eq. (13.45) remains finite and small, relative to the average concentration α_0^2 , throughout the computations (cf. Figure 13.40). Figure 13.42 shows the DNS results obtained at $t = 3$ for the bubble concentration (gray scale) and flow enstrophy field (contour lines) in the (x,y) plane at $z = 0.5$. Although the bubble response time is much smaller than the Kolmogorov time scale, we still observe the accumulation of bubbles in the zones of maximum enstrophy (corresponding to the centers of intense vortices). This means that even for such small τ_b , the bubble inertia, owing to the added mass, influences the bubble motion and causes the preferential accumulation of bubbles in the high-enstrophy regions of the flow and the initial growth of the concentration variance. Note that the time interval $\Delta t = 2$ corresponds approximately to six characteristic vortex time scales, $(\omega^2)^{-1/2}$, estimated as an average Kolmogorov $\bar{\tau}_k$ time for $1 < t < 3$, $(\omega^2)^{-1/2} \bar{\tau}_k \approx 0.3$.

In order to quantify the accumulation effects we calculated the enstrophy-conditioned average bubble concentration, $\langle \alpha \rangle_\omega$, and its variance, $\langle \alpha'^2 \rangle_\omega$ defined as

$$\langle \alpha \rangle_\omega = \frac{1}{N(\omega^2)} \sum_{j=1}^{N(\omega^2)} \alpha_j / \alpha_0 \quad (13.46)$$

$$\langle \alpha'^2 \rangle_\omega = \frac{1}{N(\omega^2)} \sum_{j=1}^{N(\omega^2)} (\alpha_j / \alpha_0 - \langle \alpha \rangle_\omega)^2 \quad (13.47)$$

where $N(\omega^2)$ is the number of grid points where the enstrophy value lies within the range $[\omega^2, \omega^2 + \Delta\omega^2]$, and using the data shown in Figure 13.42 with the enstrophy increment $\Delta\omega^2 = 0.5$. Figure 13.43 shows the

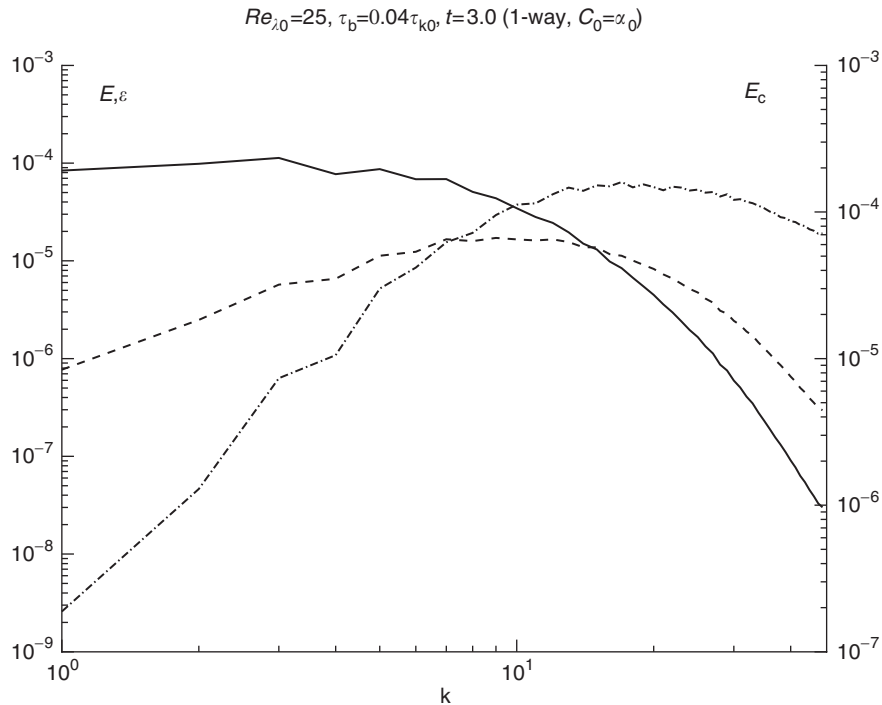


FIGURE 13.41 Spectra of the turbulence kinetic energy $E(k)$ (solid curve), dissipation $\epsilon(k)$ (dashed curve) and bubble volume fraction (concentration) fluctuations $E_\alpha(k) \equiv E_c(k)$ (dash-dotted curve).

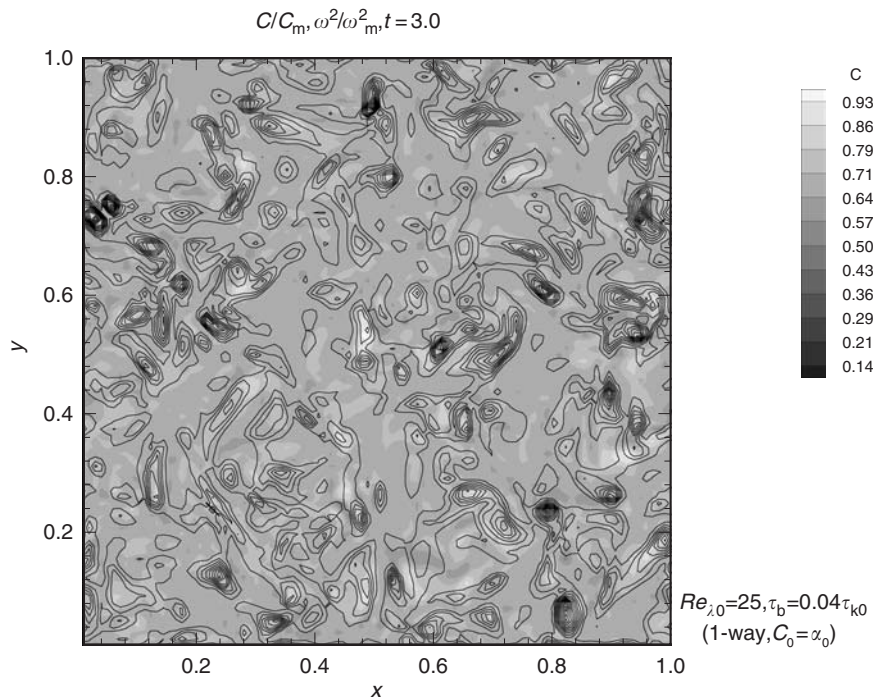


FIGURE 13.42 Turbulence enstrophy and bubble volume fraction (concentration), $\alpha \equiv C$, normalized by the maximum values.

dependence of $\langle \alpha \rangle_\omega$ and $\langle \alpha'^2 \rangle_\omega$ on ω^2 . As in the case of bubble dispersion in the Taylor–Green (TG) vortex discussed in Druzhinin and Elghobashi (1998), both $\langle \alpha \rangle_\omega$ and $\langle \alpha'^2 \rangle_\omega$ increase in the high-ensrophy regions of the flow. However, since the bubble response time is much smaller than the Kolmogorov time scale, the bubble preferential accumulation is significantly reduced compared with the TG-vortex case (Druzhinin and Elghobashi, 1998), where $\tau_b \approx \tau_k$. Also note also that fluctuations of both $\langle \alpha \rangle_\omega$ and $\langle \alpha'^2 \rangle_\omega$ grow as the enstrophy increases, which shows the intermittent nature of the high-ensrophy regions in turbulence.

Now, we introduce a mathematical model to explain how the ratio τ_b/τ_k governs the preferential accumulation process and the growth of the local concentration gradients in isotropic turbulence.

Let us consider a single vortex with a radius of the order of the Kolmogorov length scale η and core vorticity $\omega_0 = 1/\tau_k$. Assume that the bubble response time is much smaller than the Kolmogorov time scale, $\tau_b/\tau_k \ll 1$. Then, the local accumulation rate can be estimated from the solution for the bubbles concentration in the TG vortex (Druzhinin and Elghobashi, 1998) as

$$\frac{\partial \alpha / \partial t}{\alpha_0} \simeq \tau_b \omega_0^2 \simeq \frac{\tau_b}{\tau_k^2} \quad (13.48)$$

Thus the difference in bubble concentration between the inside and the outside of the vortex, $\Delta\alpha = \alpha_i - \alpha_o$, related to (τ_b/τ_k) via

$$\frac{\Delta\alpha}{\alpha_o} \simeq \frac{\tau_b}{\tau_k} \quad (13.49)$$

and the corresponding concentration gradient is

$$\frac{|\nabla\alpha|}{\alpha_o} \sim \frac{\Delta\alpha}{\alpha_o \eta} \sim \frac{\tau_b}{\eta \tau_k} \quad (13.50)$$

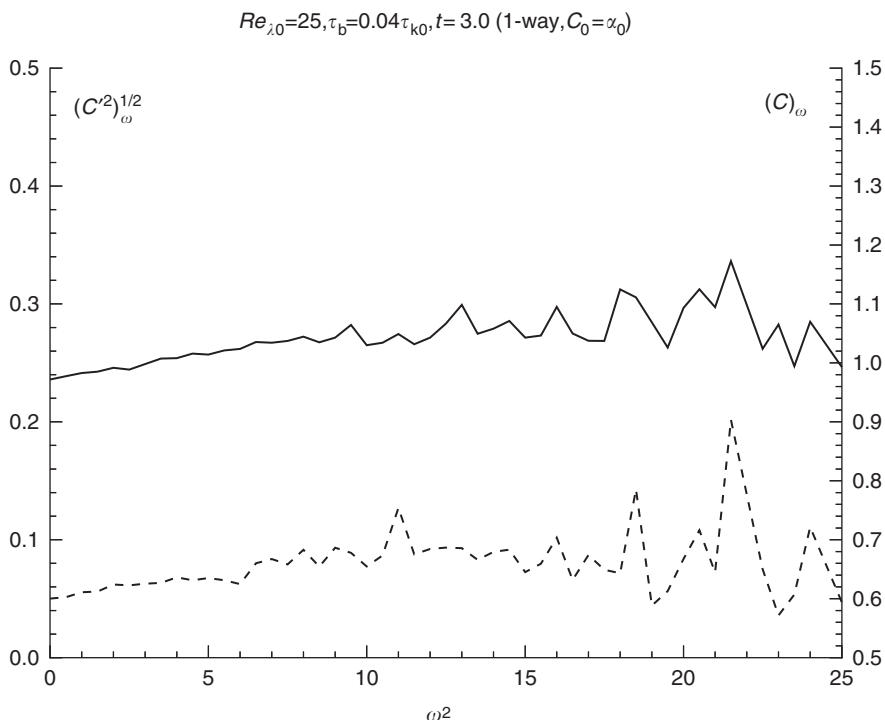


FIGURE 13.43 Dependence of the enstrophy-conditioned average bubble volume fraction (concentration), $\langle \alpha \rangle_\omega \equiv \langle C \rangle_\omega$ (solid curve) and its variance $\langle \alpha'^2 \rangle_\omega \equiv \langle C'^2 \rangle_\omega$ (dashed curve) on the enstrophy.

Note that according to Eq. (13.49), the variance of the concentration fluctuations is proportional to the ratio $(\tau_b/\tau_k)^2$, which decreases with time in decaying turbulence, since the Kolmogorov time scale increases monotonically. This prediction agrees with our DNS results for $\langle \alpha'^2 \rangle$ given in Figure 13.40, which shows that the concentration variance decays with time after the initial transient ($1 < t < 5$).

It should be noted that both the accumulation of bubbles and the absence of the diffusivity in the transport equation for the bubble concentration Eq. (13.36) may lead to instabilities in the numerical solution due to the development of steep gradients in the concentration field. The occurrence of this numerical instability depends on the initial distribution of the bubble concentration, the flow Reynolds number, and the bubble response time. In the DNS, we chose the initial microscale Reynolds number $Re_{\lambda_0} = 25$, so that at the time of the injection of bubbles ($t = 1$), the small-scale motions are resolved, i.e., $k_{\max}\eta \geq 1$, where $k_{\max} = N_g\pi$ is the maximum wave number for the given grid resolution $N_g = 96$. The numerical instability may occur for higher-inertia bubbles, i.e., for τ_b of the order of the Kolmogorov time scale τ_k . However, prescribing $\tau_b \approx \tau_k$ would violate the condition $d_b < \eta$, which is necessary for deriving Eq. (13.35) of bubble motion.

In our DNS we prescribe $\tau_b = 0.04\tau_{k0} = 0.006$, for which the bubble diameter ($d_b \approx 3.47 \times 10^{-3}$) is smaller than the Kolmogorov length scale at the time of bubble injection ($\eta \approx 3.5 \times 10^{-3}$ at $t = 1$) (both d_b and η are dimensionless here), to remain within the validity limit of Eq. (13.35). No instability occurs in our DNS under these conditions, for both the cases of the initially uniform and the initially linear bubble concentration fields. This is evident in Figure 13.44 which shows the instantaneous concentration variance spectra, obtained from our DNS for the initially uniform bubble distribution, at four different times. The time evolution of the concentration spectrum in Figure 13.44 and the corresponding concentration variance $\langle \alpha'^2 \rangle$ (dash-dotted curve in Figure 13.40) show that no numerical instability occurs. The spectrum $E_c(k)$ at high wave numbers approaches an asymptotic form at $t = 10$ (Figure 13.44). The high wave-number range in the spectrum (i.e., $k \geq 40$) would detect any numerical instability if it existed. Furthermore, Figure 13.40 shows that the concentration variance $\langle \alpha'^2 \rangle$, decays with time for $t > 5$.

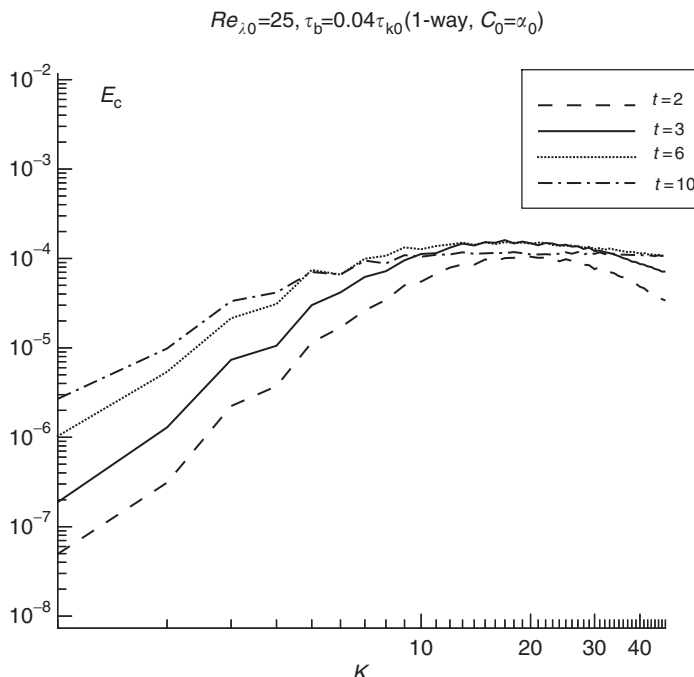


FIGURE 13.44 Instantaneous spectra of the bubble volume fraction (concentration) fluctuations $E_\alpha(k) \equiv E_c(k)$ at four different times (with one-way coupling).

The reason for the absence of the instability is that the fluctuations of the bubble concentration, caused by the preferential accumulation, are proportional to the ratio τ_b/τ_k , which decreases with time ($\sim 1/t$) in decaying turbulence, as discussed above.

13.2.6 DNS of Turbulent Shear Flows Laden by Dispersed Solid Particles or Bubbles

In the above subsections we described our DNS studies for nonsheared turbulent flows. Here we describe briefly two recent DNS studies on turbulent shear flows, one homogeneous shear and the other inhomogeneous, laden with particles or bubbles.

13.2.6.1 The Mechanisms of Modifying the Structure of Turbulent Homogeneous Shear Flows by Dispersed Solid Particles

This study (Ahmed and Elghobashi, 2000) is concerned with answering the question: what are the physical mechanisms responsible for the modification of the turbulence structure by solid particles dispersed in a homogeneous shear flow? We employ DNS to examine the effects of the two-way interaction between the two phases on the turbulence structure. Our results indicate that particles affect the rate of production of turbulence energy via modifying the vorticity dynamics. It is known that regions of large production rate of turbulence energy are sandwiched between counterrotating vortices whose vorticity, ω_s , is aligned with the axes of the longitudinal vortex tubes. These longitudinal vortex tubes are strongly inclined toward the streamwise direction due to the imposed mean shear. The stronger ω_s is the longer the production rate. The dispersed solid particles modify the alignment of the local vorticity vector, ω , with the axis of the longitudinal vortex tube. Increasing this alignment, increases the ω_s , which in turn augments the turbulence production rate, and vice versa. In addition, due to the enhanced strain rate of the carrier fluid by the particles, the dissipation rate of turbulence energy is always increased. The particles also reduce the alignment of the vorticity vector with the intermediate eigenvector (β) of the strain rate tensor. This reduction in alignment is due to an increase in the rotational term and particle-source term in the governing equation of the cosine of the angle between the vorticity vector and the intermediate strain eigenvector.

13.2.6.2 DNS of a Microbubble-Laden, Spatially Developing Turbulent Boundary Layer over a Flat Plate

The objective of the present section (Ferrante and Elghobashi, 2004) is to explain in as much detail as possible, the physical mechanisms responsible for the reduction of skin friction in a microbubble-laden, spatially developing turbulent boundary layer over a flat plate, for $Re_\theta = 1430$. Our DNS results with microbubbles volume fraction ranging from $\alpha = 0.001$ to 0.02 show that the presence of bubbles results in a *local* positive divergence of the fluid velocity, $\nabla \cdot \mathbf{U} > 0$, creating a positive mean velocity normal to (and away from) the wall, which in turn reduces the mean streamwise velocity and displaces the quasi-streamwise longitudinal vortical structures away from the wall.

This displacement has two main effects:

- (1) it increases the spanwise gaps between the wall streaks associated with the sweep events and reduces the streamwise velocity in these streaks thus reducing the skin friction by up to 20.2% for $\alpha = 0.02$;
- (2) it moves the location of peak Reynolds stress production away from the wall to a zone of a smaller transverse gradient of the mean streamwise velocity (i.e., smaller mean shear), thus reducing the production rate of TKE and enstrophy.

13.3 Continuous-Phase Equations

Clayton T. Crowe

Unlike the flow of a single-phase liquid or gas, the carrier phase of a dispersed-phase flow contains dispersed particles or droplets. For analysis, the ideal situation would be to solve the governing conservation

(continuity, momentum, and energy) equations for the carrier phase by accounting for the boundary conditions imposed by each and every particle or droplet in the field. This would provide a complete description of the carrier phase throughout the mixture.

Computationally, this would require a grid dimension at least as small as the smallest particle in the field. Such a solution is beyond current computer capability. Solutions have been obtained in limited cases with a finite number of particles in a low Reynolds number (Stokes) flow (Brady, 1993). Also numerical solutions have been obtained for flows in which the particles occupy no volume but produce a drag force on the flow (Elghobashi and Truesdell, 1992; Squires and Eaton, 1991). These solutions are also limited to low Reynolds numbers. In general, however, one must resort to the use of equations based on the average properties in a flow.

The purpose of this section is to introduce the averaging procedures and to present the equations in volume average form suitable for numerical model development. The equations for kinetic energy of turbulence are presented and discussed at the end of this section.

13.3.1 Averaging Procedures

In essence, there are three approaches to averaging the continuous phase equations: time, volume, and ensemble averaging.

13.3.1.1 Time Averaging

The time average is the result of averaging the flow properties over time at a point in the flow as shown in [Figure 13.45](#). This type of measurement corresponds to a hot-wire or laser-Doppler anemometry, which has been used extensively to obtain average and fluctuation properties in single-phase flows. The time average of property B of the fluid is defined as

$$\hat{B} = \frac{1}{T} \int_0^T B \, dt \quad (13.51)$$

where T is the averaging time.

Assume that the velocity of each phase is measured as particles and fluid pass the measuring point. The signal may appear as shown in [Figure 13.46](#). Obviously, the averaging time must be large compared with the local fluctuation time, t' , in order to define an average value. Yet, the averaging time must be smaller than the time associated with the system change, T' .

$$t' \ll T \ll T'$$

In many transient flow systems, this condition may not be realizable. A true time average can only be obtained in a steady flow system and is given by

$$\hat{u} = \lim_{T \rightarrow \infty} \frac{1}{T} \int_0^T u \, dt \quad (13.52)$$

A more detailed discussion on temporal averaging is provided by Ishii (1975).

13.3.1.2 Volume Averaging

Volume averaging is carried out by averaging properties at an instant in time over a volume and ascribing the average value to a point in the flow. For example, the volume-averaged property B would be defined as

$$\bar{B} = \frac{1}{V} \int_V B \, dV \quad (13.53)$$

where V is the averaging volume. Assume that the distribution of the dispersed-phase mixture appears as shown in [Figure 13.47](#), where ℓ is the nominal distance between the particles and L is a distance that

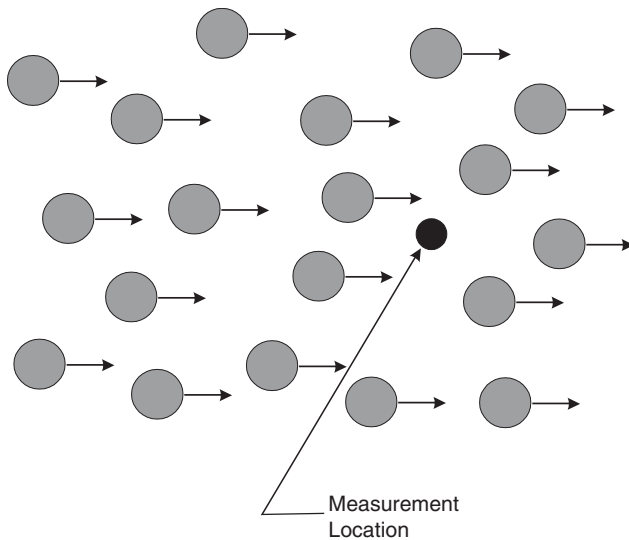


FIGURE 13.45 Measurement location in a multiphase flow field.

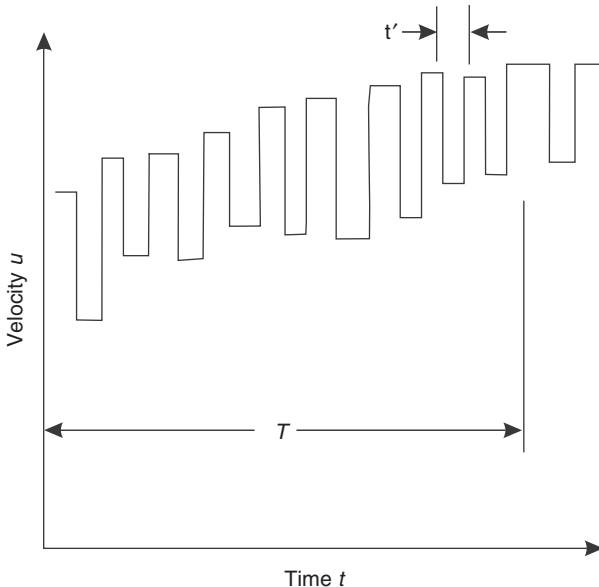


FIGURE 13.46 Velocity variation with time at measurement point.

characterizes the spatial change in mixture properties. Obviously, in order to obtain a near stationary average (an average which does not change with a change in the size of the averaging volume), the averaging volume must be much larger than ℓ^3 . However, in order that the average provide a local value for B in the field, the averaging volume must be much less than L^3 . Thus the constraints on the averaging volume are

$$\ell^3 \ll V \ll L^3 \quad (13.54)$$

This constraint is essential to approximate spatial derivatives of \bar{B} in the flow field. An accurate volume average is only possible for a homogeneous mixture.

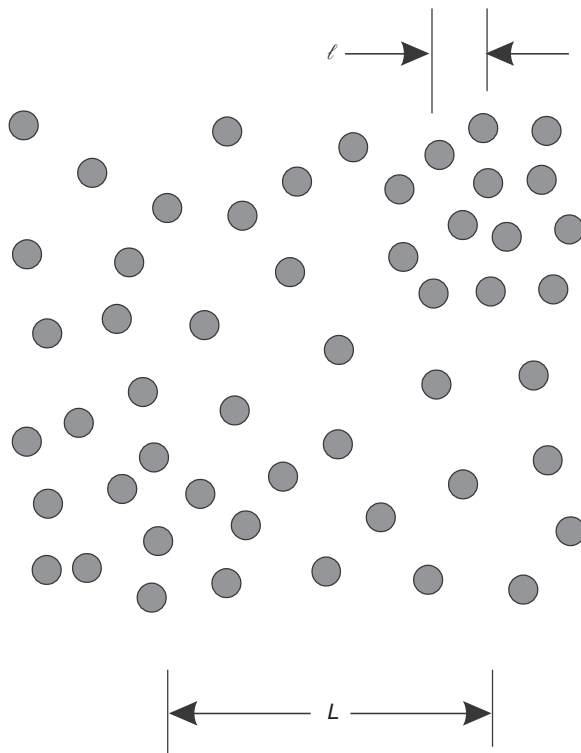


FIGURE 13.47 Spatial distribution of particles in spatial averaging field

Besides the volume average defined by Eq. (13.53), there is also a phase average, which is the average over the volume occupied by the phase:

$$\{B\} = \frac{1}{V_c} \int_{V_c} B dV \quad (13.55)$$

where V_c is the volume associated with the continuous phase. This defines the phase average for the continuous phase. If B is the density of the continuous phase, then $\{\rho_c\}$ is the average material density of the continuous phase. If the density is constant, then $\{\rho_c\} = \rho_c$. The relationship between the volume-averaged property and the phase average for the continuous phase is $\{B\} = \alpha_c \bar{B}$.

Several authors have used the volume averaging approach to derive the equations for the continuous phase in a mixture. Drew (1983) introduced a phase function

$$X_k(x_i, t) = \begin{cases} 1 & \text{if } x_i \text{ is in phase } k \text{ and time } t \\ 0 & \text{otherwise} \end{cases} \quad (13.56)$$

The basic equations are then multiplied by $X_k(x_i, t)$ and averaged including the discontinuity at the surfaces between the dispersed and continuous phases.

Crowe (1998) used the formulation, introduced by Slattery (1972), to relate the volume average of the derivative to the derivative of the volume average

$$\overline{\frac{\partial B}{\partial x_i}} = \frac{\partial}{\partial x_i} \{B\} - \frac{1}{V} \int_{S_d} B n_i dS \quad (13.57)$$

where the integral is taken over the interface, S_d , between the continuous and dispersed phase. The property B can be a scalar or a vector. Another relation used in the analysis is for the volume average of the time derivative

$$\frac{\overline{\partial B}}{\partial t} = \frac{\partial}{\partial t}\{B\} - \frac{1}{V} \int_{S_d} B \dot{r} dS \quad (13.58)$$

where \dot{r} is the local regression rate of the surface with respect to coordinates moving with a dispersed-phase element. The equations presented in this section are based on this approach. Special attention is given to the disperse-phase elements that are severed by the control surface. These are referred to as boundary elements.

Another approach to volume and temporal averaging has been developed by Roco and Shook (1985) and has been applied to liquid–solid flows.

13.3.1.3 Ensemble Averaging

Ensemble averaging avoids the shortcomings of time and volume averaging, but is much more difficult to implement. Ensemble averaging is based on the probability of the flow field being in a particular configuration at a given time. For example, assume that the distribution of the fluid density over a region is measured many times. It is found that there are N different configurations and that the distribution in each configuration (realization) at a given time t is

$$\rho \varepsilon_c = f_\eta(x_p, t) \quad (13.59)$$

where η is one realization of the N configurations (ensemble). Assume that $n(\eta)$ is the number of times that configuration $f_\eta(x_p, t)$ occurred. The ensemble average is then defined as

$$\langle \rho_c \rangle = \frac{\sum_N f_\eta(x_p, t) n(\eta)}{\sum_N n(\eta)} \quad (13.60)$$

In the limit of an infinite number of realizations, the above equation becomes

$$\langle \rho_c \rangle = \int_0^1 f(x_p, t, \mu) d\mu \quad (13.61)$$

where μ is the probability that the realization $f(x_p, t)$ will occur. Obviously, ensemble averaging is not limited by volume or time constraints.

Joseph et al. (1990) applied ensemble averaging techniques to develop the equations for an incompressible fluid–particle suspension. They used an indicator function for both the solid and the fluid. The ensemble average of the indicator functions give volume fractions. The resulting equations differed from those postulated from mixture theory, particularly the form of the stress terms.

Hinch (1977) utilized ensemble averaging to find the relationship between bulk stress and bulk strain rate for force-free particles.

Zhang and Prosperetti (1994) addressed ensemble averaging of a mixture of identical particles in an inviscid, incompressible fluid. They defined a function ζ^N representing a specific configuration of a system with position vectors and velocities. They also defined an indicator function χ_C which is unity for the continuous phase and zero otherwise. Relationships were developed for the ensemble averages of the time and spatial derivatives in terms of the time and spatial derivatives of the ensemble averages. These relationships were then used to develop the ensemble-averaged form of the conservation equations. In 1997, Zhang and Prosperetti extended the model to viscous Newtonian flows. The authors continued their work (Machioro et al., 1999) to address the mixture pressure and shear stress.

The conservation equations presented in this section are based on volume averaging. The detailed derivations for the continuity and momentum equations can be found in Crowe et al. (1998). The majority of numerical models for multiphase flows are based on volume discretization. Also, the volume-averaging approach is amenable to Large Eddy Simulation (LES).

13.3.2 Mass Conservation

The general statement for mass conservation is that the net efflux of mass from a control volume plus the rate of accumulation of mass flow in the volume is zero. Starting with the continuity equation for the continuous phase,

$$\frac{\partial \rho_c}{\partial t} + \frac{\partial}{\partial x_i} (\rho_c u_i) = 0 \quad (13.62)$$

Taking the volume average yields

$$\overline{\frac{\partial \rho_c}{\partial t}} + \overline{\frac{\partial}{\partial x_i} (\rho_c u_i)} = 0 \quad (13.63)$$

Applying Eqs. (13.57) and (13.58) yields (Crowe et al., 1998)

$$\frac{\partial}{\partial t} (\alpha_c \{ \rho_c \}) + \frac{\partial}{\partial x_i} (\alpha_c \{ \rho_c u_i \}) = -\frac{1}{V} \sum_k \dot{m}_k \quad (13.64)$$

where \dot{m}_k is the rate of change of mass of the dispersed-phase element (droplet) k and the summation is carried out over every element in the averaging volume. This is the mass source term or the mass coupling term.

$$S_{\text{mass}} = -\frac{1}{V} \sum_k \dot{m}_k \quad (13.65)$$

For evaporating droplets, $\dot{m}_k < 0$, hence mass coupling term would be positive. If all the droplets evaporate at the same rate, the mass source term simplifies to $S_{\text{mass}} = -n\dot{m}$.

For convenience, the mass-averaged velocity, defined by

$$\tilde{u}_i = \frac{\{ \rho_c u_i \}}{\{ \rho_c \}} \quad (13.66)$$

will be used. If the density of the continuous phase is constant, the volume average and mass average velocities are the same. If, however, the continuous-phase density is nearly constant over the averaging volume, then $\tilde{u}_i \approx \{ u_i \}$. Thus the continuity equation is written as

$$\frac{\partial}{\partial t} (\alpha_c \{ \rho_c \}) + \frac{\partial}{\partial x_i} (\alpha_c \{ \rho_c \} \tilde{u}_i) = S_{\text{mass}} \quad (13.67)$$

All averaging techniques yield the same form of the continuity equation. Some derivations do not include the mass coupling term. For numerical models that treat the dispersed phase as point (no volume) elements, the volume fraction of the continuous phase, α_c , is set equal to unity and the continuity equation simplifies to

$$\frac{\partial}{\partial t} \{ \rho_c \} + \frac{\partial}{\partial x_i} (\{ \rho_c \} \tilde{u}_i) = S_{\text{mass}} \quad (13.68)$$

which is the same as the continuity equation for single-phase flow, except for the mass coupling term.

If the continuous phase is a gas, which consists of component chemical species, then the continuity equation for species A would be

$$\frac{\partial}{\partial t} (\alpha_c \{ \rho_c \} \omega_A) + \frac{\partial}{\partial x_i} (\omega_A \{ \rho_c \} \alpha_c \tilde{u}_i) = \omega_{A,S} S_{\text{mass}} + \frac{\partial}{\partial x_i} \left(\alpha_c \{ \rho_c \} \mathcal{D}_A \frac{\partial \omega_A}{\partial x_i} \right) + \dot{R}_A \quad (13.69)$$

where ω_A is the mass fraction of species A, $\omega_{A,S}$ is the mass fraction of species A at the droplet surface, \mathcal{D}_A the diffusion coefficient, and \dot{R}_A the mass generation rate of species A per unit volume due to a chemical reaction. In this equation, \tilde{u}_i is the mass-averaged velocity for the mixture.

13.3.3 Momentum Conservation

The momentum equation for the continuous phase is

$$\frac{\partial}{\partial t}(\rho_c u_i) + \frac{\partial}{\partial x_j}(\rho_c u_i u_j) = -\frac{\partial p}{\partial x_i} + \frac{\partial \tau_{ij}}{\partial x_j} + \rho_c g_i \quad (13.70)$$

where τ_{ij} is the shear stress tensor and g_i the acceleration due to gravity. Taking the volume average of each term and accounting for the boundary elements yields

$$\begin{aligned} \frac{\partial}{\partial t}(\alpha_c \{\rho_c\} \tilde{u}_i) + \frac{\partial}{\partial x_j}(\alpha_c \{\rho_c\} \tilde{u}_j \tilde{u}_i) &= -\frac{\partial \{p\}}{\partial x_i} - \frac{1}{V} \sum_k v_{k,i} \dot{m}_k \\ &+ \frac{\partial}{\partial x_j} \{\tau_{ij}\} - \frac{\partial}{\partial x_j}(\alpha_c \{\rho_c u'_i u'_j\}) - \frac{1}{V} \sum_k F_{i,k} + \alpha_c \{\rho_c\} g_i \end{aligned} \quad (13.71)$$

where $v_{k,i}$ is velocity of the dispersed phase element k and $F_{i,k}$ is the hydrodynamic force produced by the continuous phase on particle k . The velocity u'_i is

$$u'_i = u_i - \tilde{u}_i$$

or the deviation of the local velocity in the averaging volume from the mass-averaged value.

The term $-1/V \sum_k v_{k,i} \dot{m}_k$ is the momentum coupling term due to addition of mass (and momentum) to the continuous phase and will be identified by

$$S_{\text{mom},\dot{m}} = -\frac{1}{V} \sum_k v_{k,i} \dot{m}_k \quad (13.72)$$

If all the dispersed-phase elements are moving at the same velocity, v_i , then

$$S_{\text{mom},\dot{m}} = v_i S_{\text{mass}} \quad (13.73)$$

If all the dispersed-phase elements are losing mass at the same rate, \dot{m} , then

$$S_{\text{mom},\dot{m}} = -\dot{m} \{v_i\} n \quad (13.74)$$

The term $-(\partial/\partial x_i)(\alpha_c \{\rho_c u'_i u'_j\})$ is analogous to the Reynolds stress in a single-phase flow. The flow does not have to be turbulent to create this stress, because velocity deviations can occur by the flow around individual particles. In order to evaluate the shear stress terms, constitutive models are necessary to relate the shear stress to the properties of the conveying phase. One approach is to define an effective stress

$$\{\tau_{ij}\}^e = -\{\rho_c u'_i u'_j\} \quad (13.75)$$

and to assume that the effective shear stress can be represented by

$$\{\tau_{ij}\}^e = \mu_e \left(\frac{\partial \tilde{u}_i}{\partial x_j} + \frac{\partial \tilde{u}_j}{\partial x_i} \right) \quad (13.76)$$

where μ_e becomes the effective viscosity. This is referred to as the Boussinesq approximation. The effective shear stress is related to the turbulence parameters of the flow. It is a common practice to use the $k-\epsilon$ methodology, common to single-phase flows, to estimate the effective shear stress. It is unlikely that this approach is useful since the gradients in the average velocity do not capture the local gradients imposed by the presence of the particles.

The hydrodynamic force on dispersed-phase element k is the integral of the pressure forces and shear stress acting on the particle surface, S_k .

$$F_{k,i} = \int_{S_k} (-p n_i + \tau_{ij} n_j) dS \quad (13.77)$$

expressing the pressure as $p = \{p\} + \delta p$ and $\tau_{ij} = \{\tau_{ij}\} + \delta \tau_{ij}$, the force becomes

$$\begin{aligned} F_{ij} &= -V_a \frac{\partial \{p\}}{\partial x_i} + V_d \frac{\partial \{\tau_{ij}\}}{\partial x_j} + \int_{S_k} (-\delta p n_i + \delta \tau_d n_j) dS \\ &= -V_d \frac{\partial \{p\}}{\partial x_i} + V_d \frac{\partial \{\tau_{ij}\}}{\partial x_j} + L_{k,i} \end{aligned} \quad (13.78)$$

The last term, $L_{k,i}$, represents the sum of all the other forces: the lift force, the steady-state drag, the virtual mass, and Basset term. Substituting this equation into Eq. (13.69) for the force yields

$$\begin{aligned} \frac{\partial}{\partial t} (\alpha_c \{\rho_c\} \tilde{u}_i) + \frac{\partial}{\partial x_j} (\alpha_c \{\rho_c\} \tilde{u}_j \tilde{u}_i) &= -\alpha_c \frac{\partial \{p\}}{\partial x_i} + S_{mom, \dot{m}} \\ + \alpha_c \frac{\partial}{\partial x_j} \{\tau_{ij}\} - \frac{\partial}{\partial x_j} (\alpha_c \{\rho_c u'_i u'_i\}) - \frac{1}{V} \sum_k L_{i,k} + \alpha_c \{\rho_c\} g_i \end{aligned} \quad (13.79)$$

This is nearly the same form as obtained using ensemble averaging (Zhang and Prosperetti, 1997). With ensemble averaging, there is one additional term relating to the momentum transfer associated with the flow around individual particles. This effect is in the Reynolds stress term, which is not singled out by volume averaging.

If the $L_{k,i}$ force consists only of steady-state drag, the momentum equation becomes

$$\begin{aligned} \frac{\partial}{\partial t} (\alpha_c \{\rho_c\} \tilde{u}_i) + \frac{\partial}{\partial x_j} (\alpha_c \{\rho_c\} \tilde{u}_j \tilde{u}_i) &= -\alpha_c \frac{\partial \{p\}}{\partial x_i} + S_{mom, \dot{m}} \\ + \alpha_c \frac{\partial}{\partial x_j} \{\tau_{ij}\} - \frac{\partial}{\partial x_j} (\alpha_c \{\rho_c u'_i u'_i\}) - \frac{1}{V} \sum_k 3\pi \mu_c d_k f_k (u_i - v_{i,k}) + \alpha_c \{\rho_c\} g_i \end{aligned} \quad (13.80)$$

where f_k is the ratio of the drag to Stokes drag for particle k. If all the dispersed-phase elements have the same size and move at the same speed, v_p , then the momentum equation simplifies to

$$\begin{aligned} \frac{\partial}{\partial t} (\alpha_c \{\rho_c\} \tilde{u}_i) + \frac{\partial}{\partial x_j} (\alpha_c \{\rho_c\} \tilde{u}_j \tilde{u}_i) &= -\alpha_c \frac{\partial \{p\}}{\partial x_i} - n \dot{m} v_i \\ + \alpha_c \frac{\partial}{\partial x_j} \{\tau_{ij}\} - \frac{\partial}{\partial x_j} (\alpha_c \{\rho_c u'_i u'_i\}) - \alpha_d \rho_d \frac{f}{\tau_v} (u_i - v_i) + \alpha_c \{\rho_c\} g_i \end{aligned} \quad (13.81)$$

In the case of bubbles, the steady-state drag is not the most important force and other forces, such as virtual mass, must be included.

If the dispersed-phase elements occupy no volume (point particles), then

$$\begin{aligned} \frac{\partial}{\partial t} (\{\rho_c\} \tilde{u}_i) + \frac{\partial}{\partial x_j} (\{\rho_c\} \tilde{u}_j \tilde{u}_i) &= -\frac{\partial \{p\}}{\partial x_i} - n \dot{m} v_i \\ + \frac{\partial}{\partial x_j} \{\tau_{ij}\} - \frac{\partial}{\partial x_j} (\{\rho_c u'_i u'_i\}) - \bar{\rho}_d \frac{f}{\tau_v} (u_i - v_i) + \{\rho_c\} g_i \end{aligned} \quad (13.82)$$

where $\bar{\rho}_d$ is the bulk density of the dispersed phase.

In DNS of multiphase flows, averaging is not used. In the case of point particles, the equation of motion for the continuous phase is

$$\frac{\partial}{\partial t} (\rho_c u_i) + \frac{\partial}{\partial x_j} (\rho_c u_i u_j) = -\frac{\partial p}{\partial x_i} + \frac{\partial \tau_{ij}}{\partial x_j} + \rho_c g_i + f_{p,i} \quad (13.83)$$

where $f_{p,i}$ is the force acting at the point due to the neighboring dispersed-phase elements. Some of the examples of DNS are provided in Section 13.2.3. Further, examples using DNS and LES with point particles can be found in Boivin et al. (2000)

13.3.4 Energy Equation

There are two forms for the energy equation: the total energy equation that includes the kinetic energies, and the thermal energy equation, which addresses the change of thermal properties of the fluid. The thermal energy equation is obtained by subtracting the dot product of the local velocity and the momentum equation from the total energy equation. The result is

$$\frac{\partial}{\partial t}(\rho_c i_c) + \frac{\partial}{\partial x_i}(\rho_c u_i i_c) = -p \frac{\partial u_i}{\partial x_i} + \tau_{ij} \frac{\partial u_i}{\partial x_j} - \frac{\partial \dot{q}_i}{\partial x_i} \quad (13.84)$$

where i_c is the internal energy of the continuous phase and \dot{q}_i is the heat transfer rate to the continuous phase. If the fluid is incompressible, then $\partial u_i / \partial x_i = 0$ and the first term on the RHS disappears. The second term is the dissipation term, which is always positive, and represents the irreversible conversion of mechanical into thermal energy. This term will be represented by ϕ . The equation reduces to

$$\frac{\partial}{\partial t}(\rho_c i_c) + \frac{\partial}{\partial x_i}(\rho_c u_i i_c) = \phi - \frac{\partial \dot{q}_i}{\partial x_i} \quad (13.85)$$

Performing the volume-averaging operation on this equation yields

$$\begin{aligned} & \frac{\partial}{\partial t}(\alpha_c \{\rho_c\} \tilde{i}_c) + \frac{\partial}{\partial x_i}(\alpha_c \{\rho_c u_i i_c\}) \\ &= -\frac{1}{V} \sum_k \dot{m}_k \dot{i}_{s,k} + \alpha_c \{\phi\} + \frac{\partial}{\partial x_i} \left(k_{\text{eff}} \frac{\partial \langle T_c \rangle}{\partial x_i} \right) + \sum_k \dot{q}_k \end{aligned} \quad (13.86)$$

where the first term on the RHS is the energy input due to mass transfer from the dispersed phase carried out over all elements in the control volume. This term will be designated as $S_{\text{ener,m}}$.

The third term is the conductive heat transfer through the mixture where k_{eff} is the thermal conductivity for the mixture. A first-order model for k_{eff} would be

$$k_{\text{eff}} = \alpha_c k_c + \alpha_d k_d \quad (13.87)$$

where k_c and k_d are the thermal conductivities of the continuous and dispersed phases, respectively. The last term is the conductive heat transfer from the dispersed-phase elements to the continuous phase. It would be evaluated by

$$\sum_k \dot{q}_k = \pi k_c \sum_k N u_k d_k (T_{d,k} - \langle T_c \rangle) \quad (13.88)$$

where $N u_k$ is the Nusselt number and the summation is carried out over all elements in the control volume.

The convection term on the LHS of the Eq. (13.85) can be rewritten as

$$\frac{\partial}{\partial x_i}(\alpha_c \{\rho_c u_i i_c\}) = \frac{\partial}{\partial x_i}(\alpha_c \{\rho_c\} \{u_i\} \tilde{i}_c) + \frac{\partial}{\partial x_i}(\alpha_c \{\rho_c\} \{u'_i i'_c\}) \quad (13.89)$$

where u'_i and i'_c are the deviation in velocity and internal energy from the averaged values. The additional term can be regarded as the heat transfer due to turbulent fluctuations, analogous to Reynolds stress, and possibly may be modeled as

$$\{\rho_c\}\{u'_i u'_c\} \simeq k_t \frac{\partial \{T_c\}}{\partial x_i} \quad (13.90)$$

where k_t is the heat transfer coefficient due to turbulence, which may be determined from the experiment or, possibly, PDF methodologies. By Reynolds analogy, one can make an estimate for k_t using $k_t \simeq \mu_e c_m$, where c_m is the specific heat of the mixture and μ_e is defined by Eq. (13.76).

Taking the internal energy as the product of the temperature and specific heat allows one to write the energy equation as

$$\begin{aligned} & \frac{\partial}{\partial t}(\alpha_c \{\rho_c\} c_m \{T_c\}) + \frac{\partial}{\partial x_i}(\alpha_c \{\rho_c\} \bar{u}_i c_m \{T_c\}) \\ &= S_{\text{ener,m}} + \alpha_c \{\phi\} - \frac{\partial}{\partial x_i} \left[(\alpha_c c_m \mu_e + k_{\text{eff}}) \frac{\partial \{T_c\}}{\partial x_i} \right] \\ & \quad + \pi k_c \sum_k N u_k d_k (T_{d,k} - \{T_c\}) \end{aligned} \quad (13.91)$$

In actual applications of this equation, order or magnitude analyses would be useful to eliminate terms, that can be neglected. The form of the equation is similar to that reported in Zhang and Prosperetti (1997).

13.3.5 Turbulence Equations

Several derivations of the equations for the turbulent energy of the continuous phase have appeared in the literature. Most of the derivations (e.g., Elghobashi and Abou-Arab, 1973; Chen and Wood, 1975), begin with the momentum equation in the form

$$\frac{\partial}{\partial t}(\alpha_c \rho_c u_i) + \frac{\partial}{\partial x_j}(\alpha_c \rho_c u_j u_i) = -\alpha_c \frac{\partial p}{\partial x_i} + \alpha_c \frac{\partial}{\partial x_i} \tau_{ij} - f_i + \alpha_c \rho_c g_i \quad (13.92)$$

where f_i is the force of the disperse phase on the continuous phase per unit volume of mixture. The derivations proceed using a Reynolds decomposition to develop the equations for turbulence energy in the same manner as for single-phase flows. The above equation implies that the velocities are defined at a point, which is not the case for averaged equations. This equation can only be regarded as a short-hand notation for the actual momentum equation (13.79) where the velocities are volume-averaged. Reynolds decomposition using volume (or ensemble)-averaged velocities does not yield the fluctuation velocity

$$\{u_i\} - \widehat{\{u_i\}} \neq u'_i \quad (13.93)$$

Unfortunately, there is a whole body of literature based on this misconception (Crowe, 2000).

Another approach (Crowe, 1998) is to start with the mechanical energy equation for the continuous phase obtained, by taking the dot product of the momentum equation and the velocity. The resulting equation is

$$\frac{\partial}{\partial t} \left(\rho_c \frac{u_i u_i}{2} \right) + \frac{\partial}{\partial x_j} \left(\rho_c u_j \frac{u_i u_i}{2} \right) = -u_i \frac{\partial p}{\partial x_i} + u_i \frac{\partial \tau_{ij}}{\partial x_j} + \rho_c u_i g_i \quad (13.94)$$

By taking the volume average of this equation and subtracting the dot product of Eq. (13.79) and $\{u_i\}$, one obtains an equation for the turbulence kinetic energy

$$k_c = \left\{ \frac{u'_i u'_i}{2} \right\} \quad (13.95)$$

in the form

$$\frac{\partial}{\partial t}(\alpha_c \rho_c k_c) + \frac{\partial}{\partial x_i}(\alpha_c \rho_c \{u_i\} k_c) \quad (13.96)$$

$$\begin{aligned}
&= \frac{\partial}{\partial x_i} \left(\sigma_c \frac{\partial k_c}{\partial x_i} \right) - \alpha_c \rho_c \{u'_i u'_j\} \frac{\partial \{u_i\}}{\partial x_j} \\
&+ \alpha_d \rho_d \frac{f}{\tau_v} \{u_i\} - \{v_i\}^2 + \alpha_d \rho_d \frac{f}{\tau_v} (\{v'_i v'_i\} - \{u'_i v'_i\}) \\
&- \alpha_c \varepsilon
\end{aligned}$$

where the unsteady forces on the disperse phase have been neglected and all dispersed-phase elements are assumed to have the same size. This equation has the same terms as for single-phase flow. The first two terms on the RHS are the diffusion and generation of turbulence and the last term on the RHS is the dissipation. The dissipation is given by

$$\varepsilon = \left\{ \frac{\partial u'_i}{\partial x_j} \frac{\partial u'_i}{\partial x_j} \right\} \quad (13.97)$$

There are two additional terms that account for the presence of the dispersed phase. The third term on the RHS is the turbulence generation due to particle drag. The fourth term relates to the kinetic energy transfer between phases and is generally much smaller than the third term. Similar forms of the turbulence energy equation have been reported by Liljegegren and Fosslein (1994), Hwang and Shen (1993), Kataoka and Serizawa (1989), and Kashiwa and VanderHeyden (2000).

Equations for the dissipation of turbulence are generally adhoc extensions of the dissipation equations used for single-phase flow. More developments with the dissipation equation can be found in Kashiwa and VanderHeyden (2000).

More information on multiphase turbulence is provided in Section 12.6.

13.4 Dispersed Phase Equations

A. Berlemon, Clayton T. Crowe, M. Reeks, and O. Simonin

There are essentially three approaches to modeling the particle flow field. One approach to follow individual particles or sample particles. This is the Lagrangian approach. Another technique is to treat the particles as a cloud with continuum-like equations. This is the Eulerian approach. Another approach is to use particle ditribution functions (PDF approach) to describe the particle flow properties.

13.4.1 Lagrangian Approach

A. Berlemon and Clayton T. Crowe

The Lagrangian approach is applicable to both dilute and dense flows. In dilute flows, the time between particle-particle collisions is larger than the response time of the particles (or droplets), so the motion of the particles is controlled by the particle fluid interaction, body forces, and particle-wall collisions. In a dense-phase flow, the response time of the particles is longer than the time between collisions; thus particle-particle interaction not only controls the dynamics of the particles, but is also influenced by the hydrodynamic and body forces as well as particle-wall interaction. If the flow is steady and dilute, a form of the Lagrangian approach known as the *trajectory method* (Crowe et al., 1977) is easy to implement. If the flow is unsteady and dense, a more general *discrete element approach* is necessary.

13.4.1.1 Trajectory Method

The trajectory approach can be explained best with reference to an example. Consider a nozzle spraying a liquid at a steady rate into the chamber shown in [Figure 13.48](#). Assume, that the flow is steady, so the spatial distribution of the carrier flow properties is invariant with time. The flow field is subdivided into a series of computational cells as shown. The inlet stream is discretized into a series of starting

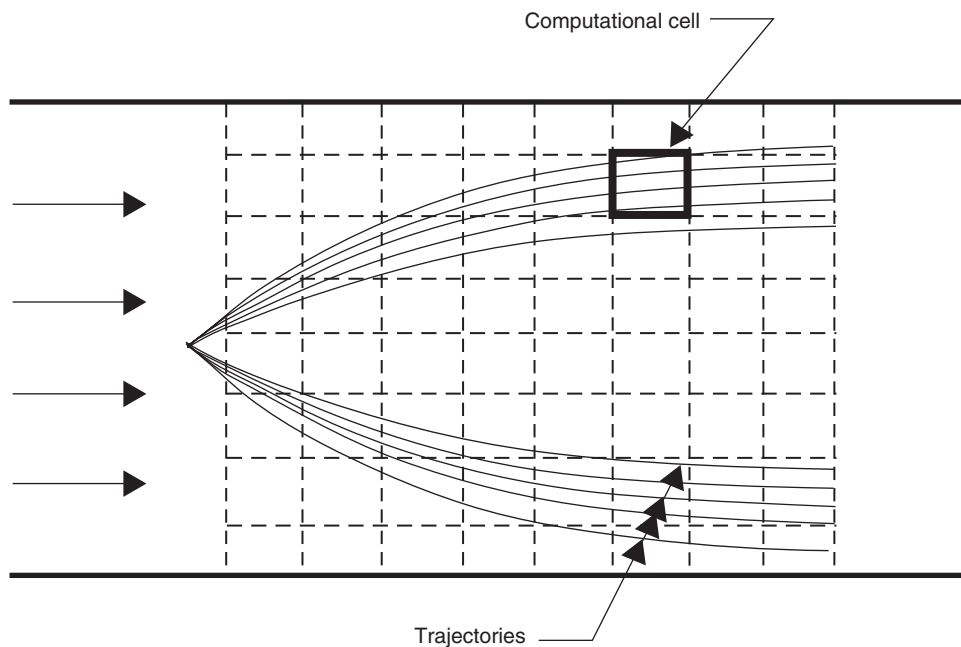


FIGURE 13.48 Droplet trajectories in a spray.

trajectories. If the initial droplet velocity and mass are known, the droplet velocity can be calculated by solving the droplet motion equation (Section 1.4) in the flow field, namely,

$$\frac{dv}{dt} = \frac{F_f}{m} + g \quad (13.98)$$

where F_f is the fluid forces (form and friction forces) acting on the droplet of mass m and g , the gravity vector. The trajectory is obtained from

$$\frac{dx_p}{dt} = v \quad (13.99)$$

where x_p is the droplet position. The integration scheme to be used depends on the desired accuracy and computational efficiency.

Concurrently, the droplet temperature history can be calculated using

$$\frac{dT_d}{dt} = \frac{1}{mc_d}(\dot{Q}_d + \dot{m}h_L) \quad (13.100)$$

where \dot{Q}_d is the sum of both the convective and radiative heat transfer to the particle or droplet. If the Biot number of the droplet is large, this equation must be modified to account for the fact that the surface temperature is not the average temperature in the droplet.

The droplet mass transfer must also be calculated along the trajectory according to the relations given in Section 1.4. Evidently, the droplet diameter must be adjusted to conform with the droplet mass unless the application is the drying of a porous particle.

Assume that the mass flow entering from the atomizer is discretized into j trajectories and the mass flow associated with each trajectory is $\dot{M}(j)$. Then the number flow rate along trajectory j would be

$$\dot{n}(j) = \frac{\dot{M}(j)}{(\pi/6)\rho_d d_0^3} \quad (13.101)$$

where ρ_d is the material density of the droplet and d_0 the initial droplet diameter. If no droplet breakup or coalescence occurs, the flow rate number will be invariant along each trajectory. Of course, more detail is possible obtained by discretizing the starting conditions according to a size distribution as well. For example, if $\tilde{f}_m(D_s)$ is the fraction of particle mass associated with size D_s (see Chapter 3), then the number flow rate associated with size D_s on trajectory j would be

$$\dot{n}(j, D_s) = \frac{\tilde{f}_m(D_s) \dot{M}(j)}{(\pi/6) \rho_d D_s^3} \quad (13.102)$$

Obviously more detail requires more trajectories and increased computational time. In an axisymmetric flow, if the starting locations are discretized to a series of concentric rings, the mass flow rate on each ring must be weighted with the ring radius.

Once all the trajectories are calculated, the properties of the particle cloud in each computational cell can be determined. The particle number density is found using

$$n = \frac{\sum_{\text{traj}} \dot{n} \Delta t_j}{V} \quad (13.103)$$

where Δt_j is the time required for the particle to traverse the cell on trajectory j and V the volume of the computational cell. The summation is carried out over all trajectories which traverse the cell. The particle volume fraction in each computational cell can be determined from

$$\alpha_d = \frac{\sum_{\text{traj}} \dot{n}_j \bar{V}_d \Delta t_j}{V} \quad (13.104)$$

where \bar{V}_d is the average droplet volume along trajectory j in the cell. Other properties such as bulk density, particle velocity, and temperature can be determined in the same way. Thus, the properties of the cloud can be determined once all the trajectories have been calculated.

Particle or droplet wall collisions are included in the calculation by continuing the trajectory after wall collision, according to the models presented in Section 12.4.2. New velocities are established depending on the nature of the collision. In the case of a droplet impact, the droplet may splatter on the surface and the trajectory is terminated or the trajectory is restarted with smaller droplets. In the case of annular mist flows, one would model reentrainment by initializing trajectories of droplets from the liquid layer on the wall. The specific conditions depend on the model selected for the problem.

The Lagrangian method has been the basis of many numerical simulations of gas-particle and gas-droplet flows.

13.4.1.2 Discrete Element Method

If the flow is unsteady and dense (particle-particle collisions are important), the more general discrete element method is required. In this approach, the motion and position (as well as other properties) of individual particles, or representative particles, are tracked with time. Ideally, one would like to track each and every particle, but this may not be computationally feasible. For a gas laden with $100 \mu\text{m}$ particles at a mass concentration of unity, there would be an order of 10^9 particles/ m^3 . If the flow field of interest were one tenth of a cubic meter, then 10^8 particles would have to be tracked through the field. This is impractical, so a smaller number of computational particles are chosen to represent the actual particles. For example, if 10^4 computational particles were chosen, then each computational particle would represent 10^4 physical particles. This computational particle is regarded as a parcel of particles. It is assumed then that the parcel of particles moves through the field with the same velocity and temperature, as a single particle (physical particle). Of course, size distribution effects can be included by specifying parcels with a specific particle size. The parcel is identified as a discrete element. In some simulations, such as fluidized beds, it may not be possible to use parcels of particles without forgoing the details necessary to simulate the system, so the dynamics of each individual particle must be considered.

The equation for particle motion now assumes the form

$$\frac{dv}{dt} = \frac{F_f + F_c}{m} + g \quad (13.105)$$

where F_c is the force due to particle-particle (and particle-wall) contact.

Establishing the initial conditions for the discrete elements, depends on the problem. For the example shown in Figure 13.49, a parcel could be the droplets emerging along a starting trajectory j in time interval Δt_p . Thus, the number of droplets in the parcel would be $N_p = \dot{n}(j, d_s) \Delta t_p$, and the initial velocity would be determined from other information. For modeling a fluidized bed, the initial state may be all the particles at rest as a packed bed, and the interstitial gas flow initiates the motion.

The motion of each parcel over one time interval is obtained by integrating the particle motion equation. At the same time, the particle temperature, spin, and other properties can be calculated. A field with a distribution of sample particle parcels is shown in Figure 13.49. During the time step, there may be particle-particle collisions that alter the trajectories and change the distribution of the parcels in each computational cell.

At every time step, the properties of the droplet cloud can be determined by summing over all the particles in a computational volume. For example, the number density would be

$$n = \frac{\sum_p N_p}{V} \quad (13.106)$$

where the summation is carried out over all the parcels in the computational cell. Also the particle volume fraction would be

$$\alpha_d = \frac{\sum_p N_p V_{d,p}}{V} \quad (13.107)$$

where $V_{d,p}$ is the volume associated with an individual particle and N_p the number of particles in parcel p . The calculation of other properties such as bulk density and particle velocity is obvious. The distribution of

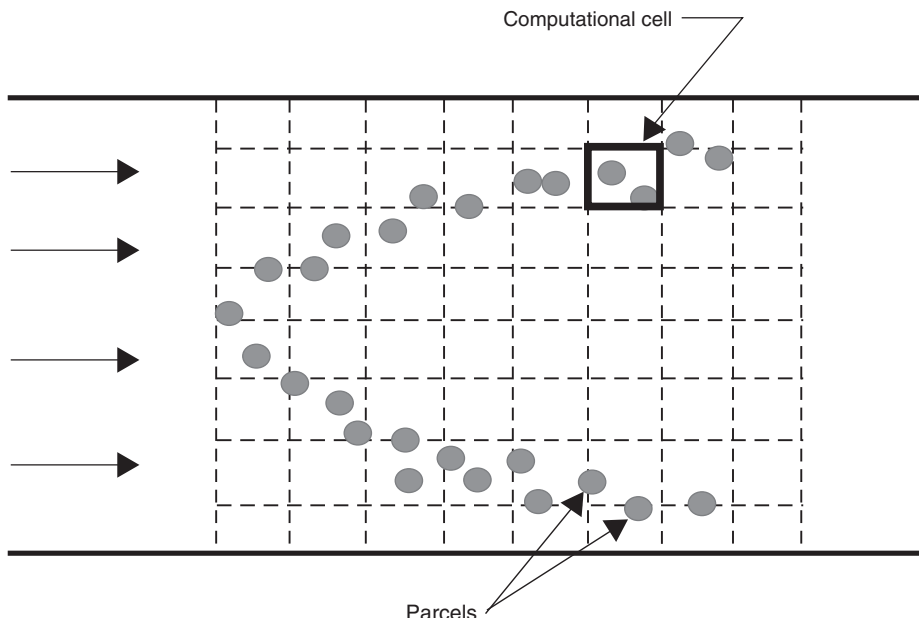


FIGURE 13.49 Distribution of droplet parcels in a spray field.

the volume fraction of the solid phase is important in calculating the interstitial flow field. If each discrete element is an individual particle, then N_p in the above equations is unity.

13.4.1.3 Source Term Evaluation

The mass source term for a computational cell is simply the sum of the mass added by every droplet in the cell:

$$S_{\text{mass}} = - \sum_k \dot{m}_k \quad (13.108)$$

where \dot{m}_k is the rate of change of mass of droplet k and the summation is carried out over every droplet in the cell. The minus sign indicates that a droplet losing mass is adding mass to the carrier phase. The mass source term using the trajectory approach is evaluated by

$$S_{\text{mass}} = - \sum_{\text{traj}} \dot{n}_j \bar{\dot{m}} \Delta t_j \quad (13.109)$$

where $\bar{\dot{m}}$ is the average mass evaporation rate of the droplet during its traverse through the cell. The mass source term is evaluated using the discrete element approach by

$$S_{\text{mass}} = - \sum_p N_p \dot{m}_p \quad (13.110)$$

where summation is carried out over all parcels, which occupy the cell at the given time and \dot{m}_p is the mass evaporation (or condensation) rate of the individual droplets in the parcel. The mass source term per unit volume is

$$S_{\text{mass}} = \frac{S_{\text{mass}}}{V} \quad (13.111)$$

where V is the volume of the computational cell.

The momentum source term in the i direction is given by

$$S_{\text{mom}} = - \sum_k (\mathbf{F}_{f,k} + \mathbf{v}_k \dot{m}_k) \quad (13.112)$$

where $F_{f,k}$ is the fluid forces acting on the droplet and v_k the velocity of droplet k . The force would include both a lift and drag force, but would not include the forces due to pressure gradient, shear stress gradient, and body forces. For the case in which the transient drag forces and lift forces are unimportant, the momentum source term for the trajectory approach becomes

$$S_{\text{mom}} = - \sum_{\text{traj}} \dot{n}_j \Delta t_j \left[m_j \frac{f_j}{\tau_{v,j}} (v_j - u) - \dot{m}_j v_j \right] \quad (13.113)$$

where v_j is the average velocity of droplets, f_j the drag factor and $\tau_{v,j}$ is the velocity response time for the particles on trajectory j . The corresponding momentum source term for the discrete element approach is calculated by

$$S_{\text{mom}} = \sum_p N_p \left[m_p \frac{f_p}{\tau_{v,p}} (v_p - u) - \dot{m}_p v_p \right] \quad (13.114)$$

where the subscript p refers to particles or droplets in the packet. Note that the body force due to gravity is not included in this expression.

The source term for the total energy equation using the trajectory approach is

$$S_{\text{ener}} = - \sum_{\text{traj}} \dot{n}_j \Delta t_j \left[\dot{Q}_j + \dot{m}_j \left(h_{s,j} + \frac{|\mathbf{v}|_j^2}{2} \right) + \mathbf{F}_{f,j} \mathbf{v}_j \right] \quad (13.115)$$

where $h_{s,j}$ is the enthalpy of the carrier phase at the surface of the droplet on trajectory j and \dot{Q}_j the convective heat transfer to the droplet (radiative heat transfer is not included). The corresponding source

term for the discrete element method is

$$S_{\text{ener}} = - \sum_p N_p \left[\dot{Q}_p + \dot{m}_p \left(h_{s,p} + \frac{|v|_p^2}{2} \right) + \mathbf{F}_{f,p} \cdot \mathbf{v}_p \right] \quad (13.116)$$

If the transient drag forces and lift forces are unimportant, the energy source term due to the dispersed phase is

$$S_{\text{ener}} = \sum_p N_p \left[\frac{Nu_p}{2} \frac{m_p c_d}{\tau_{T,p}} (T_{d,p} - T_c) - \dot{m}_p \left(h_{s,p} + \frac{|v|_p^2}{2} \right) + m_p \frac{f_p}{\tau_{v,p}} (\mathbf{v} - \mathbf{u})_p \cdot \mathbf{v}_p \right] \quad (13.117)$$

The source terms for the thermal energy equation can be evaluated in the same fashion.

Source terms can also be evaluated for the turbulence energy and dissipation depending on the models used.

13.4.1.4 Calculation of Particle–Droplet Trajectories in Dilute Turbulent Flows

In dilute two-phase flows the particle motion is controlled by the fluid–particle interaction. The relationships for calculating the trajectories is given by Eqs. (13.98) and (13.99). The force on the particle involves the lift and drag which depends on the fluid velocity at the particle position, $\mathbf{u}_p = f(\mathbf{x}_p, t)$. In turbulent flow, the fluid velocity is the instantaneous velocity, the accurate prediction of which is the primary difficulty in Lagrangian tracking. The instantaneous velocity is decomposed into a mean value (interpolated on particle position) and a fluctuating part, \mathbf{u}'_p . Developing techniques to generate the fluctuating part is the primary problem.

Methods based on DNS provide an accurate simulation of turbulence in simple flows (Yeung and Pope, 1989; Elghobashi and Truesdell, 1993; Wang and Maxey, 1993; Eaton and Fessler, 1994) but are limited to small Reynolds numbers and are not useful for practical applications. LES can handle more complex flows (Squires and Eaton, 1990; Wang and Squires, 1996; Boivin et al., 2000) but the majority of models for engineering problems are based on complete stochastic modeling. This section will address RANS modeling, such as the $k-\epsilon$ model, supplemented with algebraic models to account for anisotropy or Reynolds stress models for more accurate prediction of Reynolds stress.

A significant problem in evaluating the fluid velocity at the particle location derives from the fact that the particle does not follow the fluid path. There are three aspects to this problem.

When no body force is included, particle motion is controlled by the particle mass and drag force. The key parameter is the particle relaxation time, τ_v , that describes the particle response to any fluctuation of the surrounding fluid. For turbulent flow, the relevant scale for fluctuating velocities is the Lagrangian integral time scale, τ_L , and the time scale ratio τ_L/τ_v quantifies the influence of turbulence on the particle motion.

In the presence of a body force such as gravity, a relative mean velocity is generated between the discrete particle and the carrier fluid. In this case, it is obvious that the discrete particle no longer follows the same fluid element or eddy, but is continuously crossing several eddies on its trajectory. This behavior is called crossing trajectory effects as first described by Yudine (1959) and Csanady (1963) and experimentally studied by Wells and Stock (1983). It has been observed that the fluid velocity correlation along the particle trajectory is overestimated by the time scale τ_L , and particle dispersion is correspondingly reduced.

The third effect that can also modify the particle behavior is due to the continuity of the fluid turbulence. The fluid mass conservation equation implies that an eddy that is crossing a plane parallel to the mean flow direction must be replaced by an eddy crossing the same plane in the opposite direction. The net result of this effect is the occurrence of positive and negative fluid velocity correlations in the corresponding direction along the particle trajectory, and thus a decrease in particle dispersion. The continuity effect is a consequence of the difference on the Eulerian fluid velocity correlation with respect to the average velocity. It is known from turbulence theory that if there are no negative loops in the longitudinal correlation, then negative loops will be involved in the transverse correlation.

From the work of Csanady (1963) on stationary homogeneous turbulence with gravity, an integral time scale along the discrete particle trajectory that takes into account crossing trajectory effects and continuity effects can be derived in the form

$$\tau_L^P = \frac{\tau_L}{\sqrt{1 + \beta^2 \xi^2}} \quad (13.118)$$

in the direction parallel to the gravitational force and

$$\tau_L^P = \frac{\tau_L}{\sqrt{1 + 4\beta^2 \xi^2}} \quad (13.119)$$

in the direction normal to the gravitational force. β is the ratio between the Lagrangian integral time scale and the Eulerian time scales and ξ the ratio between the discrete particle mean velocity (here the free fall velocity) and the fluid velocity rms. It will be shown further that these scales can be used in a one-step approach.

13.4.1.4.1 Eddy Lifetime Model

Historically, the first approach to the stochastic modeling of turbulence was developed by Gosman and Ioannides (1981) and has been used widely in engineering calculations. It is referred to as the eddy lifetime model. In this scheme, the particle is assumed to interact with a succession of eddies. Each eddy is characterized by a velocity (fluctuating), a time scale (lifetime), and length scale (size). The fluctuation velocity is randomly sampled from a Gaussian PDF with variance determined from the turbulence kinetic energy, k . The eddy lifetime is related to the integral time scale, τ_L , and the length scale is defined by

$$l_e = b \frac{k^{3/2}}{\varepsilon} \quad (13.120)$$

where ε is the dissipation rate and b is an empirical constant ranging from 0.16 to 0.46. The time for a particle to traverse an eddy is calculated from the particle velocity (at the beginning of the time step) and length scale

$$\tau_e = -\tau_v \ln \left(1 - \frac{l_e}{\tau_v |v - u_p|} \right) \quad (13.121)$$

The particle is assumed to interact with the eddy for a time that is the minimum of the eddy lifetime and the eddy transit time, τ_e . During the interaction time, the fluctuating fluid velocity is assumed constant. Following the interaction time, a new fluctuating velocity is sampled and the process is repeated. Note that in the limit of very small particles that identify fluid particles, the process generates a linear decrease for the fluid Lagrangian correlation function from 1 to 0 in a time delay equal to $2\tau_L$.

The original scheme has been extended in order to include inertia, continuity, and crossing trajectory effects. An analysis of the performance of variants of the eddy lifetime model has been investigated by Graham (1998).

13.4.1.4.2 Coupled Fluid and Particle Trajectories

This method is based on the simultaneous realization of a fluid trajectory and a particle trajectory. Originally developed by Ormancey (1984), the method has been adapted by Zhou and Leschziner (1991), Burry and Bergeles (1993), and Pascal and Oesterlé (2000), among others.

Figure 13.50 presents an overview of the method. Initially the fluid particle and discrete particle are at the same location. Then the fluid particle F is moved to location $x_F(t + \delta t)$ using a one-step stochastic procedure with respect to the fluid Lagrangian integral time scale. In the particular case of fluid particles, the stochastic scheme implies an exponential decrease in the fluid Lagrangian correlation. The discrete particle trajectory P is calculated using the particle equation of motion. The fluid velocity is then transferred from the fluid position to the particle position $x_p(t + \delta t)$ according to the Eulerian correlation. The process is then repeated.

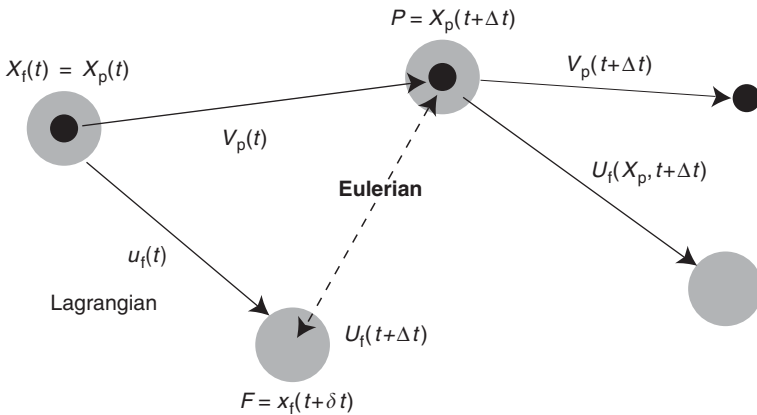


FIGURE 13.50 Coupled fluid and particle trajectories in one-time step.

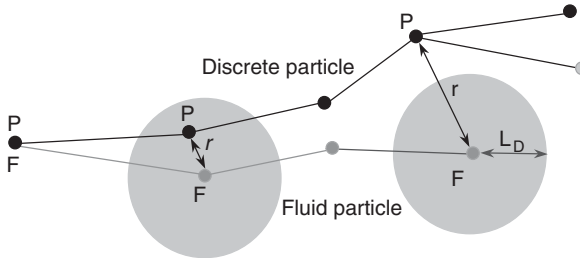


FIGURE 13.51 Coupled fluid and particle trajectories and correlation domain.

This approach has been extended by Berlemon et al. (1990) and includes the correlation matrix method for fluid trajectories in order to handle any kind of correlation. The method is depicted on Figure 13.51. The locations of the fluid particle and discrete particle are calculated simultaneously for several time steps. The fluid velocity at the particle location is determined by the use of Eulerian correlations. This process is carried out until the discrete particle leaves a correlation domain corresponding to the fluid particle. When the distance r between the two particles is greater than the correlation length scale L_D , a new fluid particle is sampled on the discrete particle location and the process is repeated. This scheme accounts for the crossing trajectory effects in a very physical way. It also allows one to incorporate the continuity effect through the Eulerian correlation. It is apparent that whatever method is chosen, the essential problem is the determination of the fluid velocity at the position of the discrete particle.

Using the same ideas with a spatial correlation of a random process for the temporal correlation, it is assumed that the fluid velocity at point P can be expressed as (in one dimension)

$$u'_p = \gamma u'_F + \eta \gamma \quad (13.122)$$

where

$$\gamma = \frac{\langle u'_p u'_F \rangle}{\sqrt{\langle (u'_p)^2 \rangle \langle (u'_F)^2 \rangle}}$$

and

$$\eta = \langle (u'_F)^2 \rangle^{1/2} \sqrt{1 - \gamma^2}$$

When anisotropy of the flow is involved, a change of coordinate system is first carried out, where the first unit vector direction is the direction from x_F to x_p . The above relation is extended to 3D case through the equivalent expression:

$$\mathbf{u}'_p = \{\gamma\}\mathbf{u}'_F + \{\eta\}\mathbf{y}_s \quad (13.123a)$$

$$\{\gamma\} = \langle \mathbf{u}'_p \mathbf{u}'_F^T \rangle \langle \mathbf{u}'_F \mathbf{u}'_F^T \rangle^{-1} \quad (13.123b)$$

$$\{\eta\}\{\eta\}^T = \langle \mathbf{u}'_F \mathbf{u}'_p^T \rangle - \{\gamma\} \langle \mathbf{u}'_F \mathbf{u}'_F^T \rangle \{\gamma\}^T \quad (13.123c)$$

Any kind of relation can be used for the correlation coefficients. For example, the Frenkel function may be used where the loop parameters n_i and n_{ij} can be specified:

$$\langle u'_{i,F} u'_{i,p} \rangle = \sqrt{\langle u'^2_{i,F} \rangle} \sqrt{\langle u'^2_{i,p} \rangle} \exp \left[\frac{-r}{(n_i^2 + 1)L_{E_i}} \right] \cos \left[\frac{n_i r}{(n_i^2 + 1)L_{E_i}} \right] \quad (13.124a)$$

and

$$\langle u'_{i,F} u'_{j,p} \rangle = \langle u'_{i,F} u'_{j,F} \rangle \exp \left[\frac{-r}{(n_{ij}^2 + 1)L_{E_{ij}}} \right] \cos \left[\frac{n_{ij} r}{(n_{ij}^2 + 1)L_{E_{ij}}} \right] \quad (13.124b)$$

The loop parameter n_i can help to introduce the continuity effect in the Eulerian correlation, namely, by choosing $n_i = 0$ in the main flow direction and $n_i = 1$ in the transverse directions. When no information is available on the length scales, the following relations can be used:

$$L_{E_{ii}} = \sqrt{\langle u'^2_i \rangle} \tau_{L_i} \quad (13.125)$$

where

$$\tau_{L_i} = \text{Cste} \frac{\langle u'^2_i \rangle}{\varepsilon}$$

and Cste ranges between 0.2 and 0.6. Also

$$L_{E_{ij}} = C_{ij} \tau_{L_{ij}} \sqrt{\langle u'_i u'_j \rangle} \quad (13.126)$$

where

$$\tau_{L_{ij}} = C_{L_{ij}} \frac{|\langle u'_i(t) u'_j(t) \rangle|}{\varepsilon}$$

and $C_{ij} = C_{L_{ij}} = 1$.

13.4.1.4.3 One-Step Scheme

Another approach, based on a one-step stochastic process, is to approximate the fluid velocity at the particle location with respect to the time scale viewed by the fluid along the particle path. It means that the Lagrangian step and the Eulerian step of the previous method are mixed to give a simpler stochastic scheme. The key issue is then the approximation of the time and length scales T^* , which characterize the fluid viewed by the particles. A Langevin equation is used:

$$u'_{pi}(t + \delta t) = a u'_{pi}(t) + b y_i \quad (13.127)$$

where

$$a = \exp \left(-\frac{\delta t}{T_i^*} \right)$$

and

$$b = \langle u'_{pi}^2(t) \rangle^{1/2} \sqrt{1 - a^2}$$

Different expressions can be found in the literature for scales and for the fluid velocity correlation along discrete particle trajectory. By assuming gravity is in the third dimension, Wang and Stock (1992) proposed

$$R_{33}(\tau) = \exp \left\{ -\frac{\tau}{T_f^p} \sqrt{1 + \left(\frac{v_d T_f^p}{L_f} \right)^2} \right\} \quad (13.128a)$$

$$T_3^* = \frac{T_f^p}{\sqrt{1 + \left(\frac{v_d T_f^p}{L_f} \right)^2}} \quad (13.128b)$$

$$R_{11}(\tau) = R_{22}(\tau) = \left(1 - \frac{v_d \tau}{2 L_f} \right) R_{33}(\tau) \quad (13.128c)$$

and

$$T_1^* = T_2^* = \frac{T_f^p}{1 + (v_d T_f^p / L_f)^2} \left[\sqrt{1 + \left(\frac{v_d T_f^p}{L_f} \right)^2} - \frac{v_d T_f^p}{2 L_f} \right] \quad (13.128d)$$

where the fluid integral time scale along the particle path depends on Stokes number:

$$T_f^p(Stk) = T_{mE} \left[1 - \frac{1 - T_L/T_{mE}}{(1 + Stk)^{0.4/(1 + 0.01 Stk)}} \right] \quad (13.129)$$

where v_d is the drift velocity, T_{mE} is the Eulerian time scale, Stk the Stokes number, and $L_f = \sigma_f T_{mE}$.

Applying the same philosophy, Pozorski and Minier (1998) proposed in a Langevin model:

$$T_3^* = \frac{T_L^*}{1 + (v_d T_L^* / \sigma_f T_E)} \quad (13.130)$$

and

$$T_1^* = T_2^* = \frac{T_L^*}{1 + 2(v_d T_L^* / \sigma_f T_E)} \quad (13.131)$$

where T_L^* is given by

$$\frac{1}{T_L^*} = \frac{x}{\tau_L} + \frac{1-x}{T_E} \quad (13.132)$$

with

$$x = \frac{\sigma_p}{\sigma_f}$$

The problem is the evaluation of x . One possible approach is to assume that Tchen's theory is valid (stationary isotropic turbulence) and x satisfies

$$x = \sqrt{\frac{1}{1 + \tau_v/\tau_L}} \quad (13.133)$$

Another version of the one-step method is that introduced by Sommerfeld et al. (2001). In this model, the component of fluid velocity fluctuation in the i direction, at the new particle position, u'_{in+1} , is correlated with the old position through a correlation function by

$$u'_{in+1} = u'_{i,n} R_{p,i}(\Delta t, \Delta r) + \sigma \sqrt{1 - R_{p,i}^2(\Delta t, \Delta r)} \xi_i \quad (13.134)$$

where $R_{p,i}(\Delta t, \Delta r)$ is the correlation function, σ the mean fluctuation velocity of the fluid at the particle position, and ξ_i a Gaussian random number selected for the i direction with zero mean and standard deviation of unity. The mean fluid fluctuation velocity is obtained from the kinetic energy k by

$$\sigma^2 = 2k/3 \quad (13.135)$$

The correlation function in the i direction is decomposed into a Lagrangian and Eulerian part according to

$$R_{p,i}(\Delta t, \Delta r) = R_L(\Delta t) \times R_{E,i}(\Delta r) \quad (13.136)$$

where the exponential form

$$R_L(\Delta t) = \exp\left(-\frac{\Delta t}{T_L}\right) \quad (13.137)$$

is selected for the Lagrangian part. The Lagrangian time scale is determined from

$$T_L = c_T \frac{\sigma^2}{\varepsilon} \quad (13.138)$$

where ε is the dissipation rate.

The spatial correlation function can be obtained from Eulerian correlation tensor (Von Karman and Horwarth, 1938)

$$R_{E,ij}(\Delta r) = \{f(\Delta r) - g(\Delta r)\} \frac{r_i r_j}{r^2} + g(\Delta r) \delta_{ij} \quad (13.139)$$

where $f(\Delta r)$ and $g(\Delta r)$ are exponential functions of the separation distance and the integral length scales. Generally, only the three main components of the tensor are used and the integral length scales are related to the T_L and σ .

These different schemes have been compared extensively with theoretical and experimental results. But it is important to keep in mind that all these schemes are very sensitive to scale approximation and particle dispersion is roughly proportional to the turbulence time and length scales.

13.4.1.5 Calculation of Particle Motion in Dense Flows

In dense flows, the particle motion is controlled by particle-particle collisions. Different approaches can be developed to study and to understand the underlying physical processes. Simulations on the basis of tracking several particles simultaneously (Tanaka and Tsuji, 1991; Chang, 1998; Berlemont et al., 1998) have been developed. Also Lagrangian simulations have been proposed based on single-particle tracking with stochastic process for collisions (Oesterlé and Petitjean, 1993; Sommerfeld, 1995, 2001; Berlemont and Achim, 1999; 2001; Berlemont et al., 2001).

In the multiple-particle method, several particles are tracked simultaneously and particle pairs are examined on each time step in order to determine if any collision is taking place. Since the number of simultaneous trajectories is limited by computational constraints, the simulation is carried using several starting points for a given number of particles. They are initially randomly distributed in a box, the size of which is established by the mean distance between particle centers derived from the initial concentration and geometry for the case under study. The multiple-particle method is obviously quite expensive in CPU time. Moreover, the multiple-particle method is unrealistic for industrial purposes. In addition, it was found that the overall particle-particle velocity correlation (referring to the two colliding particles) induced by the surrounding fluid is an important parameter requiring particular attention.

In the stochastic approach for particle collisions, a collision probability is defined and a random process is used to first decide if a collision occurs. Several successive random processes are then involved in order to characterize the collision partner in terms of velocity, concentration, impact location, and diameter when polydispersed particles are considered.

13.4.1.5.1 The Stochastic Collision Model

Using the classical one-particle Lagrangian approach, a stochastic particle–particle collision model is needed, as described by Sommerfeld (2001) and Berlemon et al. (2001). The model first requires information on the collision frequency. It is assumed that the fluctuating motion of the discrete phase is similar to the thermal motion of molecules in a gas. A collision frequency can then be estimated by analogy with the kinetic theory.

Consider two particle classes, which are identified through the diameters d_1 and d_2 (radius r_1 and r_2), the instantaneous velocities v_1 and v_2 , and the number of particles per unit of volume, n_{p1} and n_{p2} . The collision frequency with which particle 1 collides with particle 2 is

$$f_{\text{coll}} = \frac{\pi}{4} (d_1 + d_2)^2 n_{p2} \int_{-\infty}^{+\infty} |v_{\text{rel}}| f_p^{(2)} dv_1 dv_2 \quad (13.140)$$

where $|v_{\text{rel}}| = |v_2 - v_1|$,

The most important term in the above equation is the particle–particle pair distribution function $f_p^{(2)}$. If it is assumed that the colliding particle velocities are independent (molecular chaos assumption), then the particle velocity distribution is Gaussian:

$$f_p^{(1)} = \frac{1}{(2\pi\langle v'^2 \rangle)^{3/2}} \exp\left(-\frac{v^2}{2\langle v'^2 \rangle}\right) \quad (13.141)$$

and the particle–particle pair distribution function is the product of the two distribution functions. The collision frequency then reduces to (Abrahamson, 1975; Gourdel et al., 1999)

$$f_{\text{coll}} = \frac{\pi}{4} (d_1 + d_2)^2 n_{p2} \|v_{\text{rel}}\| H(z) \quad (13.142)$$

with

$$H(z) = \frac{\exp(-z)}{\sqrt{\pi z}} + \operatorname{erf}\sqrt{z}\left(1 + \frac{1}{2z}\right)$$

and

$$z = \frac{1}{2} \frac{\|v_{\text{rel}}\|^2}{\langle v_1^2 \rangle + \langle v_2^2 \rangle}$$

The variable z represents the ratio between the mean particle relative velocity and the particle turbulent fluctuation velocity. For large values of z (high drift velocity), $H(z)$ tends to unity, hence:

$$f_{\text{coll}} = \frac{\pi}{4} (d_1 + d_2)^2 n_{p2} \|\langle v_1 \rangle - \langle v_2 \rangle\| \quad (13.143)$$

and the collision frequency depends essentially on mean particle relative velocity. Using a Taylor expansion for $H(z)$ for small values of z (low drift velocity) leads to

$$f_{\text{coll}} = \frac{2^{3/2}\pi^{1/2}}{4} (d_1 + d_2)^2 n_{p2} \|\langle v_1^2 \rangle + \langle v_2^2 \rangle\| \quad (13.144)$$

which means that the collision frequency depends primarily on the particle agitation.

The collision probability p_{12} of particle 1 to collide with particle 2 then reads:

$$p_{12} = f_{\text{coll}} \Delta t \quad (13.145)$$

where the time step Δt is assumed to be small enough (of the order of $\tau_c/10$ where $\tau_c = 1/f_{\text{coll}}$). To decide whether there is a collision or not, a uniform random number (between 0 and 1) is sampled and the collision occurs when it is smaller than the collision probability. Velocities of a fictitious collision partner are then sampled from the local properties.

When two particles collide, the first problem is to determine the point of contact on the particle surfaces. A coordinate system ($Ox'y'z'$) is moved such that the main axis (Ox') is in the v_{rel} direction and O is the center of the tracked particle (Figure 13.52a). A uniformly distributed random number β between 0 and 1 is used to obtain the normalized impact parameter b ($b = B/(r_1 + r_2) = \sqrt{\beta}$) and another uniform random number is then chosen to get the α angle, with $0 \leq \alpha \leq 2\pi$ (Figure 13.52b). The new coordinate system ($Ox''y''z''$) is now used with Ox'' at the particle center direction (Figure 13.52c), and Ψ and Φ angles are defined by

$$\Psi = \arctan\left(\frac{b \sin \alpha}{\sqrt{1 - b^2 \sin^2 \alpha}}\right) \quad \text{and} \quad \Phi = \arctan\left(\frac{-b \cos \alpha}{\sqrt{1 - b^2}}\right) \quad (13.146)$$

When the point of impact is located, the change in particle velocity has to be calculated. These relationships for doing so are provided in Section 12.4.1. Returning to the initial coordinate system completes the process.

When comparing the stochastic approach with LES results, it is found that the molecular chaos assumption was not satisfied. The scheme has to account for the correlation between the fluctuating motion of the colliding particles caused by the surrounding fluid. In order to overcome this problem, Sommerfeld (2001) has recently proposed correlating the fictitious particle velocities with velocities of the real particle through the following relation:

$$v_{2,i} = R(Stk)v_{1,i} + \sigma_i \sqrt{1 - R(Stk)^2}\xi \quad (13.147)$$

where σ_i is the rms value of the velocity component i , ξ a Gaussian random number, and $R(Stk)$ given (comparing model calculations to LES results) by

$$R(Stk) = \exp(-0.55Stk^{0.4}) \quad (13.148)$$

This relation improves the results but is still based on empiricism.

Another approach utilizes an exact relation for the particle-particle pair distribution function $f_p^{(2)}$ which is not the product of two independent distributions $f_p^{(1)}$ for correlated velocities. The correlation between the colliding particle velocities in the turbulent eddy through which they are moving has to be introduced in the distribution function. This important consideration was first stated and solved by Lavieille et al. (1995) for two identical particles. Pigeonneau (1998) proposed an extension for particles with different diameters with no empiricism required. Berlemont et al. (2001) recently proposed to use that approach for particle Lagrangian tracking with particle collisions. The results are limited to nondeformable spherical particles. When the interface between the two phases is not rigid, interface tracking

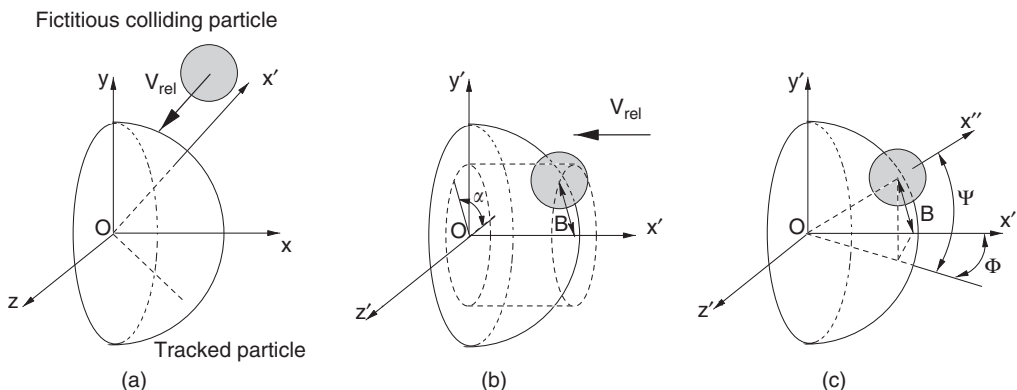


FIGURE 13.52 Sampling point of contact in particle collision.

methods are then used, namely, the volume of fluid method, or the front tracking method, or the Level set method. The examples of calculations with dense-phase flows are provided in Section 13.2.2.

13.4.2 Eulerian Approach

Clayton T. Crowe

In the Eulerian approach, the particle or droplet cloud is treated as a continuous medium with properties analogous to those of a fluid. For example, the bulk density, or mass of particles per unit volume of mixture, is regarded as a continuous property. The particle velocity is the average velocity over an averaging volume. The purpose of this section is to develop and present the governing equations for the Eulerian approach. In that the continuous phase is a fluid, the use of the Eulerian approach for the dispersed phase is commonly referred to as the two-fluid or Eulerian–Eulerian approach. The terms will be used interchangeably here.

A significant advantage of the Eulerian approach is that the equations for both phases have the same form so the same solution techniques can be used for each phase.

There are several levels of description for the Eulerian approach. If the Stokes number is sufficiently small, the particles and carrier fluid will have the same velocity (velocity equilibrium). If the characteristic time used in the definition of the Stokes number is a time representative of the carrier-phase turbulence, a small Stokes number implies that the particles will move with and disperse at the same rate as the carrier flow. In this case, the two-phase mixture can be regarded as a single phase with modified properties (density, thermal capacity, etc.). If the Stokes number is based on some characteristic time of the flow field, a small Stokes number implies that the particles will move with the mean motion of the carrier flow but may not disperse at the same rate due to turbulence.

Of more practical interest is the situation where the velocities of the carrier fluid and particles are not the same. This could be the result of velocity gradients in the mean flow field, turbulent fluctuations, and body forces acting on the particles. The local particle velocity is regarded as the average velocity of particles in an averaging volume

$$\{\mathbf{v}\} = \frac{\sum_k \mathbf{v}_k}{N} \quad (13.149)$$

where N is the number of particles in the volume and $\{\}$ is used to denote volume averaging. Another possibility would be the mass-averaged velocity defined by

$$\tilde{\mathbf{v}} = \frac{\sum_k m_k \mathbf{v}_k}{\sum_k m_k} \quad (13.150)$$

where m_k is the mass of particle k in the averaging volume. This type of averaging is referred to as Favre averaging.

The Eulerian dispersed-phase equations are obtained by summing the conservation equations for individual particles (or droplets) over all particles in the control volume to obtain equations for a particle cloud. A cloud of particles or droplets in a Cartesian control volume is shown in [Figure 13.53](#). The fundamental finite-difference equations are derived by taking into account the flux of properties over all faces. The finite-difference equations are then divided by the control volume and the limit is taken as the volume approaches the limiting value. More details are available in [Crowe et al. \(1998\)](#). Index notation is used throughout.

13.4.2.1 Continuity Equation

The basic continuity equation for each dispersed-phase element is $dm/dt = \dot{m}$. Summing the rate of mass change of all the elements in the computational cell and equating it to the net efflux of droplet mass through the control surfaces plus the rate of change of mass in the cell yields

$$\frac{\partial}{\partial t} (\alpha_d \rho_d) + \frac{\partial}{\partial x_i} (\alpha_d \rho_d \tilde{v}_i) = \sum_k \dot{m}_k / V \quad (13.151)$$

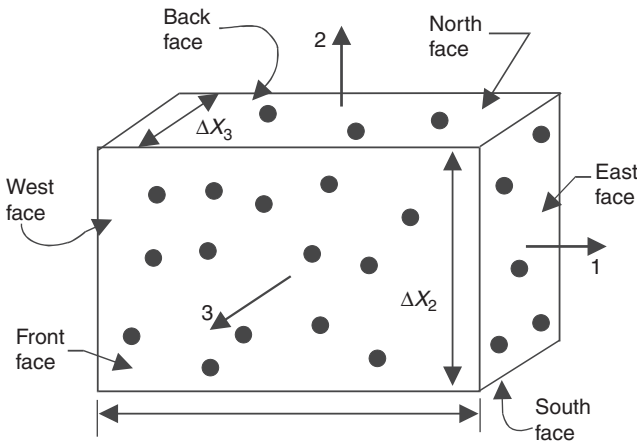


FIGURE 13.53 Three-dimensional control volume for dispersed-phase elements.

where \bar{v}_i is the mass-averaged velocity of the dispersed phase, α_d the volume fraction of the dispersed phase, and ρ_d the material density of the dispersed phase. The summation is carried out over all droplets in the control volume V . The last term in the equation is the mass source term for the dispersed phase, which can be written as $-S_{\text{mass}}$. The minus sign comes from the fact that S_{mass} is the mass source term for continuous phase that is negative for the dispersed phase.

If the simple average velocity is used *in lieu* of the mass-averaged velocity, the continuity equation has to be formulated differently. In this case, the velocity in the averaging volume is expressed as

$$v_i = \{\bar{v}_i\} + v'_i \quad (13.152)$$

where v'_i is the deviation of the velocity from the averaged value. Similarly, the bulk density, ρ_d , is written as

$$\bar{\rho}_d = \bar{\rho}_{d,0} + \bar{\rho}'_d \quad (13.153)$$

where $\bar{\rho}_{d,0}$ is the bulk density at the central point and $\bar{\rho}'_d$ the deviation in bulk density at adjacent points, so the average mass flux is

$$\langle \bar{\rho}_d v_i \rangle = \langle \bar{\rho}_d \rangle \langle v_i \rangle + \langle \bar{\rho}'_d v'_i \rangle \quad (13.154)$$

The additional term can be regarded as a mass diffusion term. In a flow with homogeneous bulk density or uniform particle velocities, this term would be zero. Turbulence, however, will produce a distribution of particle velocities, which will give rise to a net mass flux in nonhomogenous particle density fields.

The gradient transport model is used in the two-fluid formulation to simulate dispersion of particles in turbulent flows. With reference to Fick's law it is assumed that

$$\langle \bar{\rho}_d v'_i \rangle = -D_d \frac{\partial \bar{\rho}_d}{\partial x_i} \quad (13.155)$$

where D_d is the dispersion coefficient for the dispersed phase. The value for the dispersion coefficient has to be determined from experiment or through some auxiliary analysis. Picard et al. (1986) predicted a dispersion coefficient based on an early analysis of particle motion in turbulence reported by Tchen (1949). Adjustments are necessary to account for crossing trajectory effects. Rizk and Elghobashi (1989) employed a semiempirical correlation suggested by Picard et al. Unfortunately, there are no simple analyses or models, which will provide D_d as a function of particle properties and flow turbulence, so the choice of an appropriate value depends on finding or reducing a value from an experiment which is

considered representative of the flow field to be simulated. Reeks has shown through the PDF approach (Section 13.4.3) that the gradient diffusion model is not universally applicable.

A further problem exists with boundary conditions. If the particles bounce specularly from a wall, it is probably appropriate to set the gradient of the bulk density normal to the wall equal to zero. If the bouncing is not specular, another approximation must be made. If droplets impact the wall and there is no reentrainment, setting bulk density equal to zero at the wall does not represent a realistic boundary condition for the bulk density field. The choice of suitable boundary conditions is addressed in Section 13.4.3 for reflecting and perfectly absorbing walls.

The final form for the two-fluid continuity equation using the volume-averaged velocity is

$$\frac{\partial}{\partial t}(\alpha_d \rho_d) + \frac{\partial}{\partial x_i}(\alpha_d \rho_d \{v_i\}) = \frac{\partial}{\partial x_i}\left(D_d \frac{\partial \bar{\rho}_d}{\partial x_i}\right) - S_{\text{mass}} \quad (13.156)$$

If F_{avre} (mass averaging) is used, the diffusion term is eliminated.

13.4.2.2 Momentum Equation

The momentum equation for an individual dispersed-phase element of mass m is:

$$m \frac{dv_i}{dt} = F_i + mg_i \quad (13.157)$$

This equation is valid for an reacting droplet, provided the mass is leaves the surface uniformly. That is, it does not contribute to the momentum of the droplet. Adding $\dot{m}v_i$ to each side gives

$$\frac{dmv_i}{dt} = \dot{m}v_i + F_i + mg_i \quad (13.158)$$

The forces acting on the element are

$$F_i = -V_d \frac{\partial \{p_c\}}{\partial x_i} + V_d \frac{\partial \{\tau_{c,ij}\}}{\partial x_j} + L_i \quad (13.159)$$

where $\{p_c\}$ and $\{\tau_{c,ij}\}$ are the average pressure and shear stress in the continuous phase, respectively. The force L_i includes all the other forces including the lift force, the steady-state drag, the virtual mass force, and the Basset force. In flows with heavy particles, only the steady-state drag may be important.

The momentum equation can also be developed by summing over every dispersed-phase element in the computational cell. The resulting differential equation is

$$\begin{aligned} \frac{\partial}{\partial t}(\alpha_d \rho_d \tilde{v}_i) + \frac{\partial}{\partial x_j}(\alpha_d \rho_d \tilde{v}_i \tilde{v}_j) &= \sum_k \dot{m}_k v_{i,k} / V - \alpha_d \frac{\partial p}{\partial x_j} \\ \alpha_d \frac{\partial}{\partial x_i} \tau_{ij} + \sum_k L_{i,k} + \alpha_d \rho_d g_i - \alpha_d \frac{\partial}{\partial x_j} \left(\sum_k \bar{\rho}_{d,k} v'_i v'_{k,j} \right) \end{aligned} \quad (13.160)$$

where \tilde{v}_i is the mass-averaged velocity and the fluctuation velocity $v'_{i,k}$ is the deviation of the velocity of the k th particle from the mass average velocity.

The first term on the RHS of Eq. (13.158) is the momentum source due to mass exchange between phases. This term is expressed as $-S_{\text{mom},i}$ namely,

$$-\sum_k \dot{m}_k v_{i,k} / V = -S_{\text{mom},i} \quad (13.161)$$

This term represents the momentum associated with the mass issued from the surface of the droplets moving at velocity $V_{i,k}$. The negative sign is chosen so that momentum addition to the carrier phase is defined as positive.

The last term is analogous to a Reynolds stress

$$\tau_{d,ij}^R = -\sum_k \bar{\rho}_{d,k} v'_{i,k} v'_{k,j} \quad (13.162)$$

and is identified as the dispersed-phase Reynolds stress. This term arises because the mass-averaged velocity is not a momentum-averaged velocity. Traditionally, the dispersed-phase Reynolds stress has been modeled using the Boussinesq approximation (stress proportional to the rate of strain):

$$\tau_{ij}^R = \mu_s \left(\frac{\partial v_i}{\partial x_j} + \frac{\partial v_j}{\partial x_i} \right) - \frac{2}{3} \mu_s \frac{\partial v_k}{\partial x_k} \delta_{ij} \quad (13.163)$$

where μ_s is an *solids viscosity*. It is very difficult to select a solids viscosity, since the particle velocity fluctuations depend not only on local turbulence but also on the particle properties and particle history. Chung et al. (1986) related the solids viscosity to the eddy viscosity of the carrier fluid through a function, which depends on the Stokes number based on the integral time scale of the carrier-phase turbulence. Rizk and Elghobashi (1989) simply used a constant ratio between the solids viscosity and the fluid eddy viscosity. The problem with the Boussinesq approximation is that one can visualize a Reynolds stress without a gradient in the mean velocity field (no rate of strain), because the turbulent fluctuations of particles will give rise to a nonzero value for the dispersed-phase Reynolds stress.

The momentum equation, Eq. (13.158), is also valid for a field of bubbles. In the same way, the Reynolds stress term relates to the fluctuations in bubble velocity. A similar form of the dispersed-phase momentum equation is presented in Zhang and Prosperetti (1997).

If the forces acting on the particles or droplets are only the drag forces and the unsteady terms can be neglected, then the momentum equation becomes

$$\begin{aligned} \frac{\partial}{\partial t} (\alpha_d \rho_d \tilde{v}_i) + \frac{\partial}{\partial x_j} (\alpha_d \rho_d \tilde{v}_i \tilde{v}_j) &= - \alpha_d \frac{\partial p}{\partial x_i} - S_{mom,i} + \alpha_d \frac{\partial}{\partial x_j} (\tau_{ij}) \\ &+ \frac{3\pi\mu_c}{V} \sum_k d_k f_k (u_i - v_i)_k + \alpha_d \rho_d g_i + \alpha_d \frac{\partial}{\partial x_j} \tau_{d,ij}^R \end{aligned} \quad (13.164)$$

where m_k is the mass of particle k , λ_k the ratio of the drag to Stokes drag, and τ_v the velocity response time. If all the droplets have the same mass and evaporate at the same rate, the momentum equation reduces to

$$\begin{aligned} \frac{\partial}{\partial t} (\alpha_d \rho_d v_i) + \frac{\partial}{\partial x_j} (\alpha_d \rho_d v_i v_j) &= - \alpha_d \frac{\partial p}{\partial x_i} + nmiv_i \\ &+ \alpha_d \frac{\partial}{\partial x_j} (\tau_{ij} + \tau_{d,ij}^R) + n3\pi\mu_c df (u_i - v_i) + \alpha_d \rho_d g_i \end{aligned} \quad (13.165)$$

The dispersed-phase Reynolds stress can arise from several sources, particle velocity fluctuations due to the carrier-phase turbulence, and particle-particle collisions. Even with no carrier-phase turbulence or collisions, the Reynolds stress term would appear due to particle velocity variations arising from a distribution in particle size. Such a situation would occur for a particle-laden flow at the throat of a venturi, where the smaller particles would tend to move at a velocity near the local fluid velocity, while the larger particles would exhibit a larger velocity lag. In this special case, the Reynolds stress due to velocity variation could be circumvented by introducing a momentum equation for each particle size category.

Kinetic theory models have been used to derive relationships for the solids viscosity and other parameters for dense phase flows. An additional equation is included for the kinetic energy of the fluctuating motion of the particulate phase. Because of the similarities between particle-particle interactions and molecular interactions in a gas, the concepts from kinetic theory can be used to develop the governing equations for dense-phase flows. This approach is nominally credited to Bagnold (1954), who derived an equation for repulsive pressure in uniform shear flow. Many others, particularly Savage (1983), have further contributed to this approach. Complete details of the derivations and applications to dense-phase flows can be found in Gidaspow (1994). The basic concept is that particle-particle collisions are responsible for momentum and energy transfer in the dense-phase flow in the same way as the molecular interactions are responsible for pressure wave propagation and viscosity in a single-phase fluid.

The kinetic energy associated with the particle velocity fluctuations is called the granular temperature and defined as

$$\Theta = \frac{1}{3} \langle C^2 \rangle \quad (13.166)$$

where C is the fluctuational velocity of the particle motion. Granular temperature can be produced by a shearing action in the granular flow and by hydrodynamic forces. Dissipation can occur through inelastic particle-particle and particle-wall collisions and dissipation in the fluid. Granular temperature can also be diffused in the same manner as heat. The stress term in the momentum equation based on kinetic theory becomes (Gidaspow, 1994)

$$\tau_{d,ij} = \left[-p_s + \xi_s \frac{\partial v_k}{\partial x_k} \right] \delta_{ij} + \mu_s \left(\frac{\partial v_j}{\partial x_i} + \frac{\partial v_i}{\partial x_j} \right) - \frac{2}{3} \frac{\partial v_k}{\partial x_k} \delta_{ij} \quad (13.167)$$

where p_s is the solids pressure, ξ_s the solids phase bulk viscosity, and μ_s the solids shear viscosity. These three parameters are functions of the granular temperature as well as the particle restitution coefficient, particle diameter, material density, and volume fraction. The solids pressure is

$$p_s = \rho_d \alpha_d \Theta [1 + 2(1 + e)g_o \alpha_d] \quad (13.168)$$

where g_o is referred to as a radial distribution function

$$g_o = \frac{3}{5} \left[1 - \left(\frac{\alpha_d}{\alpha_{d,max}} \right)^{1/3} \right]^{-1}$$

The solids-phase bulk viscosity assumes the form

$$\xi_s = \frac{4}{3} \alpha_d^2 \rho_s d g_o (1 + e) \left(\frac{\Theta}{\pi} \right)^{1/2} \quad (13.169)$$

and the shear viscosity is

$$\mu_s = \frac{2\mu_{s,dil}}{(1 + e)g_o} \left[1 + \frac{4}{5}(1 + e)g_o \alpha_d \right]^2 + \frac{4}{5} \alpha_d^2 \rho_s d g_o (1 + e) \left(\frac{\Theta}{\pi} \right)^{1/2} \quad (13.170)$$

where $\mu_{s,dil}$ is the solids-phase dilute viscosity given by

$$\mu_{s,dil} = \frac{5\sqrt{\pi}}{96} \rho_d d \Theta^{1/2} \quad (13.171)$$

An additional equation is needed for Θ which relates the change in Θ to the generation by velocity gradients, the dissipation with collisions and the diffusion due to gradients in Θ . The details are available in Gidaspow (1994).

Several numerical models have been implemented for dense-phase flows using the two-fluid models based on granular temperatures. These include flow in chutes, fluidized beds, and sedimentation. Sinclair and Jackson (1989) have used the two-fluid model for modeling dense flows in vertical tubes. Section 13.5.3 provides an application of two-fluid modeling for predicting flow in a fluidized bed using kinetic theory for the constitutive equations. There are several advantages in using the two-fluid model for dense-phase flows. The most significant advantage is that there is no need to consider the dynamics of individual particles, so large systems can be modeled. Also, the numerical formulations used for single-phase flows can be applied to the two-fluid equations for the solid phase. However, there is a level of empiricism that must be introduced in establishing the constitutive equations. Also, features such as particle-particle sliding, particle rotation, and particle size distribution are not included.

The granular temperature model should also extend to dilute flows. In this case, the hydrodynamic effects on particle oscillation in turbulence would have to be more accurately modeled. Extensions of the two-fluid model to dilute flows have been reported by Bolio and Sinclair (1996). In dense flows, the particle-particle contribution to particle fluctuation energy is more significant than that due to local turbulence in the continuous phase.

The PDF approach introduced in Section 13.5.3 provides a more rational approach to evaluating the particle-phase Reynolds stress due to carrier-phase turbulence and particle-particle collisions. This approach, still in development, will yield more reliable models for the Reynolds stress with minimal empiricism.

13.4.2.3 Thermal Energy Equation

The energy equation for an individual dispersed-phase element is

$$\frac{d}{dt}(m_i_d) = -\dot{m} \frac{p_s}{\rho_d} - \frac{d}{dt}(S_d \sigma) + \dot{m} h_s + \dot{Q}_d \quad (13.172)$$

where p_s is the pressure at the surface, S_d the surface area of the element, σ the surface tension, h_s the enthalpy of the matter leaving the surface, and \dot{Q}_d the heat transfer rate to the dispersed-phase element, including both conductive and radiative heat transfer. The first term on the RHS is usually small and neglected.

The Eulerian thermal energy equation for the droplet cloud can be derived in the same way as the continuity and momentum equations by summing up the droplets in a control volume. By following the development in Crowe et al. (1998), the multidimensional thermal energy equation is

$$\frac{\partial}{\partial t}(\alpha_d \rho_d \tilde{t}_d) + \frac{\partial}{\partial x_i}(\alpha_d \rho_d \tilde{v}_{in} \tilde{t}_d) = -\frac{\partial}{\partial x_j} \left(\sum_k \tilde{\rho}_{d,k} v'_{j,k} i'_{d,k} \right) \quad (13.173)$$

$$-\sum_k \dot{E}_{\sigma,k}/V + \sum_k \dot{m}_k h_{s,k}/V + \frac{2\pi k_c}{V} \sum \lambda_k d_k (T_c - T_d)_k + \sum_k \dot{Q}_{r,k}/V$$

where \tilde{t}_d is the mass-averaged droplet internal energy. The first term on the RHS, $\sum_k \tilde{\rho}_{d,k} v'_{j,k} i'_{d,k}$ is analogous to the Reynolds stress term and has to be modeled based on, for example, a gradient diffusion term.

$$-\frac{\partial}{\partial x_j} \left(\sum_k \tilde{\rho}_{d,k} v'_{j,k} i'_{d,k} \right) = \frac{\partial}{\partial x_j} \left(k_{s,eff} \frac{\partial T_d}{\partial x_j} \right) \quad (13.174)$$

where T_d is the dispersed-phase temperature and $k_{s,eff}$ the effective thermal conductivity, which, currently, must be chosen empirically or through kinetic theory for dense flows. In future, PDF modeling will provide more accurate models for this term. The second term is the energy change associated with the surface tension; the third term is the energy (enthalpy) flux from the droplet surface, where $h_{s,k}$ is the enthalpy of the matter emerging at the surface of droplet k and is equal to $-S_{mass} h_s$; the fourth term is the convective heat transfer between the droplets and the carrier fluid, where

$$\lambda_k = Nu_k/Nu_o \quad (13.175)$$

is the ratio of the Nusselt number to the Nusselt number at zero Reynolds number ($v_o = 2$ with no free convection effects) and $\tau_{T,k}$ the thermal response time of particle k ; the last term is the radiative heat transfer. In specific applications, many of these terms can be neglected. Particularly, the first and third terms on the RHS are zero for solid particles. These terms would generally be small compared with

convective heat transfer for droplet flows. For nonreactive particles, the source term associated with mass flux from the dispersed-phase surface would also be zero. Also, for many applications, radiative heat transfer may not be significant.

The internal energy is the product of both temperature and specific heat, so the energy equation written in terms of dispersed-phase temperature is

$$\frac{\partial}{\partial t}(\alpha_d \rho_d c_d T_d) + \frac{\partial}{\partial x_i}(\alpha_d \rho_d \tilde{v}_i c_d T_d) = \frac{\partial}{\partial x_j} \left(k_{s,\text{eff}} \frac{\partial T_d}{\partial x_j} \right) - S_{\text{mass}} h_s \quad (13.176)$$

$$- \sum_k \dot{E}_{\sigma,k} / V + \frac{2\pi k_c}{V} \sum_k \lambda_k d_k (T_c - T_d)_k + \sum_k \dot{Q}_{r,k} / V$$

where c_d is the specific heat of the dispersed-phase. If all the elements have the same size, same specific internal energy, and evaporation rate, and if the first and third terms are neglected, the thermal energy equation becomes

$$\begin{aligned} \frac{\partial}{\partial t}(\alpha_d \rho_d c_d T_d) + \frac{\partial}{\partial x_i}(\alpha_d \rho_d v_i c_d T_d) &= -S_{\text{mass}} h_s + 2\pi n k_c \lambda d (T_c - T_d) \\ &+ \frac{\partial}{\partial x_j} \left(k_{s,\text{eff}} \frac{\partial T_d}{\partial x_j} \right) + n \dot{Q}_r \end{aligned} \quad (13.177)$$

where n is the number density. In dense flows there is also a heat transfer due to particle-particle contact, which is not included here.

13.4.2.4 Advantages and Disadvantages of the Two-Fluid Model

In general, the advantages are:

1. The numerical scheme used for the carrier phase can be used for the dispersed phase, so the two-fluid model may be more computationally efficient.
2. The model is limited by modeling large numbers of particles or droplets.

The disadvantages are:

1. The constitutive equations, which include the effects of carrier-phase turbulence, particle-particle collisions, and size distribution, are not well established.
2. The boundary conditions for mass, momentum, and energy are not straightforward.
3. The equations are not applicable as the flow becomes increasingly dilute.

As PDF methods and similar analyses are forthcoming, the disadvantages will be minimized.

13.4.3 PDF Models

M. Reeks and O. Simonin

13.4.3.1 Introduction

The PDF approach has proved very useful in studying the behavior of stochastic systems. Examples of its usage occur in the study of Brownian motion (Chandrasekhar, 1943) and in the kinetic theory of gases (Chapman and Cowling, 1952). In more recent times, it has been used extensively by Pope and others to model both turbulence (Pope, 1985) and turbulent-related phenomena such as combustion (Pope, 1991) and atmospheric dispersion (MacInnes and Bracco, 1992). In this section, the use of PDF approaches to

model the behavior of a particle-laden turbulent gas is described, where like kinetic theory for modeling gas flows, it may be regarded as a rational approach. This means : first there exists an underlying equation (a master equation) containing terms that can be traced back in a rational manner to the underlying equations of motion of the individual particles themselves. Second, this master equation, in a strictly formal way, can be used to derive both the continuum equations and constitutive relations of a gas or dispersed phase of particles while at the same time handle the natural boundary conditions at the wall (the so-called near-wall behavior). In kinetic theory, the master equation is the well-known Maxwell–Boltzmann equation, while in dispersed flows, it is known as the PDF equation.

There are currently two forms of the PDF equation in use. In the first form, the PDF, as in kinetic theory, refers to the probability density that a particle has a certain velocity and position at a given time. This PDF approach is referred to as the kinetic method (KM). Originated by Buyevich (1971, 1972a, 1972b), and has been developed since by a number of workers, most notably Reeks (1980, 1991, 1993), Hyland et al. (1999a, 1999b), Swailes and Darbyshire (1997), Derevich and Zaichik (1988), Zaichik (1991), Pozorski and Minier (1998) as well as Zhou and Li (1996) . In all these developments the PDF approach was restricted to inert, nonreactive particles. More recently, this approach has been extended to reactive condensing or evaporating particles in a turbulent gas (Pandya and Mashayek, 2001, 2003) and in polydisperse combusting sprays (Laurent and Massot, 2001).

In contrast, the second form of the PDF equation, first proposed by Simonin et al. (1993), is a more general PDF which includes the velocity of the carrier flow local to the particle as a phase-space variable as well as the particle position and velocity. It is a development of the PDF approach used by Haworth and Pope (1986) based on a generalized Langevin model (GLM) for the equation of motion of the carrier flow encountered by a particle. It is referred here as the GLM approach.

As far as two-fluid modeling is concerned, the application of the PDF approach is different from what has been discussed earlier. In the past, for instance, it has been traditional to assume that the particle phase behaves as a simple Newtonian fluid (Elghobashi and Abou Arab, 1983), i.e., the particle Reynolds stresses are assumed to be proportional to the mean symmetric rate of strain of the particle flow via some particle eddy viscosity that is related to that of the carrier flow in some empirical way. Now, using the PDF approach, one can examine the validity of these assumptions within the context of a more reliable and complete framework using techniques that are well tested and understood and ultimately replace them with more legitimate relationships that do not rely on intuition and empiricism. Perhaps, more importantly, an approach that is crucial to the formulation of particle–wall interactions is now available. The particle–wall interactions are referred to here as the natural boundary conditions of a gas–particle flow.

In this section, it is shown how the PDF approach deals with both aspects of a two-fluid model with and without interparticle collisions; namely, how it generates the equations for mass, momentum and energy (the so-called continuum equations) and constitutive relations for the dispersed phase (that would be appropriate for the far-wall solution of a gas–particle flow) and how it generates near-wall solutions that take into account the inhomogeneity of the flow and the natural boundary conditions.

The section has been divided into two parts. The first part deals with a dilute suspension of particles in a turbulent gas and the second part with a dense suspension where interparticle collisions play an equally important part as the underlying turbulence of the gas. In the first part, a basic introduction to PDFs and PDF equations is provided and how they are derived in principle from the underlying particle equations of motion. This introduces the problem of closure of PDF equations, which is the essential problem of all stochastic systems involving turbulence. As an example, it is shown how this has been tackled for the particular case of nonreactive particles in a turbulent gas, examining how it has been dealt with as a closure approximation in the KM approach or through a model for the carrier flow velocity fluctuations encountered by a particle in the case of the GLM approach. This important aspect constitutes the subject of Section 13.4.3.2.

Section 13.4.3.3 deals with the continuum equations and constitutive relations derived from the PDF equations, where the focus is on transport equations for the particle velocity covariance (kinetic stresses)

and the particle fluid covariances. In either case, there is a need for closure approximations for the particle turbulent kinetic energy flux and that of the particle-fluid covariance flux which are tackled using the Chapman–Enskog approach. Predictions are compared with measurements of the particle dispersion of particles in nonuniform unbounded flows, where the local strain rate of the continuous phase introduces a strong anisotropy in the particle kinetic stresses.

Section 13.4.3.4 is concerned with the application of the PDF approach to the prediction of near-wall behavior; in particular, natural boundary conditions involving partial absorption and both specular and diffuse reflection are considered. Finally, the solutions for the well-known problem of particle deposition in a turbulent boundary layer with perfectly absorbing walls are addressed (this is a much studied system both theoretically and experimentally) which highlights the break down of so-called gradient transport due to both strong inhomogeneity of the flow near the wall and the strong departure of the velocity distribution at the wall compared with that in the far wall (bulk flow).

The remaining part of the section is devoted to the treatment of interparticle collisions using the PDF approach and follows largely the approach adopted by Lavieille et al. (1995).

13.4.3.2 PDFs and PDF Equations

As an example of how PDFs and their equations are obtained, consider the motion of evaporating or condensing particles in a dilute suspension in which there are no inter-particle collisions. Let $\mathbf{X}(t)$ be the phase-space vector at time t of a single particle as it moves through phase space. So in this case,

$$\mathbf{X} = [m, \Theta, \mathbf{v}, \mathbf{x}] \quad (13.178)$$

where m is the mass of the particle, Θ the temperature, and \mathbf{v} , \mathbf{x} are the velocity and position of the particle center of mass at time t . The number n of independent variables that defines the phase-space dimension is thus $n = 8$. For a single realization of the underlying carrier flow velocity field $\mathbf{u}(\mathbf{x}, t)$ and temperature field $T(\mathbf{x}, t)$, the number of particles in an elemental volume $d^n \mathbf{X}$ of phase space located at \mathbf{X} will be given by $W(\mathbf{X}, t) d^n \mathbf{X}$, where $W(\mathbf{X}, t)$ is the phase-space density, i.e., the number of particles per unit volume in phase space. So for conservation of particle number within that elemental volume at \mathbf{X} with respect to W , one has

$$\frac{\partial W}{\partial t} + \frac{\partial}{\partial \mathbf{X}} [W \dot{\mathbf{X}}] = 0 \quad (13.179)$$

So, for the case of the evaporating droplet one would have explicitly

$$\dot{\mathbf{X}} = [\dot{m}, \dot{\Theta}, \dot{\mathbf{v}}, \dot{\mathbf{x}}] \quad (13.180)$$

where the components of $\dot{\mathbf{X}}$ represents the *particle equations of motion* in the most general sense and are derived from the mass, momentum and energy conservation equations for an individual particle-droplet. However, because the underlying carrier flow field is turbulent, $\dot{\mathbf{X}}$ has a random component, so one can only usefully refer to the PDF corresponding to a set of values \mathbf{X} at any given time. This is represented by the ensemble average of W over all realizations of the system, symbolically as $\langle W \rangle$. The equation for $\langle W \rangle$ (the PDF equation) can be found by ensemble averaging the conservation equation for W (Liouville equation). For convenience, the instantaneous components of $\dot{\mathbf{X}}$ are separated into their mean $\langle \dot{\mathbf{X}} \rangle$ and fluctuating components $\dot{\mathbf{X}}'$, noting that $\dot{\mathbf{X}} = \mathbf{v}$, so the explicit PDF equation for the evaporating-condensing particle is

$$\begin{aligned} \frac{\partial \langle W \rangle}{\partial t} + \left(\frac{\partial}{\partial m} \langle \dot{m} \rangle + \frac{\partial}{\partial \Theta} \langle \dot{\Theta} \rangle + \frac{\partial}{\partial \mathbf{x}} \cdot \mathbf{v} + \frac{\partial}{\partial \mathbf{v}} \cdot \langle \dot{\mathbf{v}} \rangle \right) \langle W \rangle \\ = - \frac{\partial}{\partial m} \langle \dot{m}' W \rangle - \frac{\partial}{\partial \Theta} \langle \dot{\Theta}' W \rangle - \frac{\partial}{\partial \mathbf{v}} \cdot \langle \dot{\mathbf{v}}' W \rangle \end{aligned} \quad (13.181)$$

where on the LHS one has the convective part (the transport in the absence of the turbulence) and on the RHS, the dispersive part involving the gradients of the net fluxes due to the turbulence. To close the equation, one needs to relate the turbulent fluxes in some way, directly or indirectly, to $\langle W \rangle$ and its derivatives. Thus, there is a closure problem to resolve, which is the most important element of the PDF approach.

To illustrate the way in which the values of \dot{X} depend upon the properties of the particle and the underlying carrier flow, consider the case of the evaporating droplet in more detail. From mass conservation of a spherical droplet of diameter d_p evaporating in a gas of mass density ρ_g , the general relationship is (see [Section 1.4](#))

$$\dot{m} = \pi \rho_g d_p D_v Sh(Re_p, Sc) \ln \left[\frac{1 - \alpha_v}{1 - \alpha_{vs}} \right] \quad (13.182)$$

where α_v is the mass fraction of vapor emitted by the particle in the locally undisturbed gas flow, α_{vs} the (saturated) vapor mass fraction at the droplet (or particle) surface assumed to be in equilibrium with the particle (so it depends directly on the temperature Θ of the particle), D_v the molecular diffusion coefficient of the vapor, and Sh the droplet Sherwood number for mass transfer of vapor to or from the droplet which is a function of the vapor Schmidt number, and the local particle Reynolds number Re_p given by

$$Re_p = \frac{d_p |\mathbf{v} - \mathbf{u}|}{\nu_g}, \quad Sc = \frac{D_v}{\nu_g}$$

where ν_g is the kinematic viscosity of the gas.

Similarly, the changes in particle-droplet velocity and temperature also depend on the local particle Reynolds number. A point to note here is that the equations of motion are all coupled and all depend upon the instantaneous particle Reynolds number which, in turn, depends on the relative velocity between particle and locally undisturbed gas.

13.4.3.2.1 PDF Equation for Inert Particles

As stated previously, there are currently two PDF approaches in use: the KM and GLM. To illustrate the differences and similarities between these approaches, let us consider the simplest case of the transport of inert nonreacting solid particles in a turbulent gas flow. To simplify the situation still further the drag acting on the particle is linearized with respect to the relative velocity, i.e.,

$$\mathbf{F}_A \approx \underline{\eta}(\mathbf{u} - \mathbf{v}) \quad (13.183)$$

where $\underline{\eta}$ is the net friction coefficient and given by

$$\underline{\eta} = \frac{1}{2} \rho_g A C_D (\overline{Re}_p) |\bar{\mathbf{u}} - \bar{\mathbf{v}}| \quad (13.184)$$

where $\bar{\mathbf{v}}$ is the net particle velocity and \overline{Re}_p the value of the particle Reynolds number based on net relative velocity between particle and local carrier flow. The equations of motion for a particle are

$$\frac{d\mathbf{x}}{dt} = \mathbf{v} \quad (13.185a)$$

and

$$\frac{d\mathbf{v}}{dt} = \underline{\beta} \cdot (\mathbf{u} - \mathbf{v}) \quad (13.185b)$$

where $\underline{\beta}$ is the inverse particle response tensor and given by $m^{-1} \underline{\eta}$ for a particle of mass m . In the case of Stokes drag, the elements of $\underline{\beta}$ are constants of the motion and those of $\underline{\beta}_{ij}^{-1}$ are the corresponding particle response times to changes in flow. In addition to the particle equations of motion, the equation of

motion of the carrier flow velocity \mathbf{u} along a particle trajectory is included, namely,

$$\frac{du_i}{dt} = F_i(\mathbf{v}, \mathbf{u}, \mathbf{x}, t) \quad (13.186)$$

In the KM approach, one considers the continuum equations derived from an equation for the phase-space density $W(\mathbf{v}, \mathbf{x}, t)$, in which $\mathbf{u}(\mathbf{x}, t)$ is a random function of \mathbf{x} , t , and \mathbf{v} and \mathbf{x} the independent random variables. In the GLM approach, the continuum equations are derived from a conservation equation for the phase-space density $P(\mathbf{v}, \mathbf{u}, \mathbf{x}, t)$, where $\mathbf{v}, \mathbf{u}, \mathbf{x}$ form a set of independent variables. The transport-conservation equations for $W(\mathbf{v}, \mathbf{x}, t)$ and $P(\mathbf{v}, \mathbf{x}, \mathbf{u}, t)$ are, respectively,

$$\left\{ \frac{\partial}{\partial t} + \frac{\partial}{\partial x_i} v_i + \frac{\partial}{\partial v_i} \beta_{ij} (u_j(\mathbf{x}, t) - v_j) \right\} W(\mathbf{v}, \mathbf{x}, t) = 0 \quad (13.187)$$

and

$$\left\{ \frac{\partial}{\partial t} + \frac{\partial}{\partial x_i} v_i + \frac{\partial}{\partial v_i} \beta_{ij} (u_j - v_j) + \frac{\partial}{\partial u_i} F_i(\mathbf{v}, \mathbf{u}, \mathbf{x}, t) \right\} P(\mathbf{v}, \mathbf{u}, \mathbf{x}, t) = 0 \quad (13.188)$$

Note that integrating the equation for P over all \mathbf{u} gives the equation for W . The functions $u_i(\mathbf{x}, t)$ and $F_i(\mathbf{v}, \mathbf{u}, \mathbf{x}, t)$ are resolved into mean and fluctuating parts:

$$u_i = \langle u_i \rangle + u_i'' \quad F_i = \langle F_i \rangle + F_i''$$

where $\langle \dots \rangle$ represents an ensemble average. Then, the transport equations for mean values of W and P , namely, $\langle W \rangle$ and $\langle P \rangle$, are

$$\left\{ \frac{\partial}{\partial t} + \frac{\partial}{\partial x_i} v_i + \frac{\partial}{\partial v_i} \beta_{ij} (\langle u_j \rangle - v_j) \right\} \langle W \rangle = - \frac{\partial}{\partial v_i} \beta_{ij} \langle u_j'' W \rangle \quad (13.189)$$

$$\left\{ \frac{\partial}{\partial t} + \frac{\partial}{\partial x_i} v_i + \frac{\partial}{\partial v_i} \beta_{ij} (u_j - v_j) + \frac{\partial}{\partial u_i} \langle F_i \rangle \right\} \langle P \rangle = - \frac{\partial}{\partial u_i} \langle F_i'' P \rangle \quad (13.190)$$

When suitably normalized, $\langle W \rangle$ and $\langle P \rangle$ represent the probability density at time t , for which a particle has (\mathbf{v}, \mathbf{x}) and $(\mathbf{v}, \mathbf{u}; \mathbf{x})$, respectively. To solve these equations, closure relations for $\langle u_i'' W \rangle$ and $\langle F_i'' P \rangle$ are required. For simplicity, only the case where $\beta_{ij} = \beta \delta_{ij}$ will be considered.

13.4.3.2.2 Closure Approximation for a Nonreactive Gas–Particle Flows

13.4.3.2.2.1 Kinetic model. Based on either the LHDI approximation (Reeks, 1993) or the Furutsu–Novikov formula (Swailes and Darbyshire, 1997), the closure approximation for the net flux $\langle u_i'' W \rangle$ for particles with velocity \mathbf{v} and position \mathbf{x} at time t , is given by

$$\begin{aligned} \langle u_i'' W \rangle &= - \left(\frac{\partial}{\partial u_j} \langle u_i(\mathbf{x}, t) \Delta v_j \rangle + \frac{\partial}{\partial x_j} \langle u_i(\mathbf{x}, t) \Delta v_j \rangle \right) \langle W \rangle \\ &\quad - \left(\frac{\partial u_i''}{\partial x_j} \Delta x_j \right) \langle W \rangle \end{aligned} \quad (13.191)$$

where explicitly $\Delta x_j(\mathbf{x}, \mathbf{v}, t|0)$ and $\Delta v_j(\mathbf{x}, \mathbf{v}, t|0)$ denote changes in the particle position and velocity for a particle starting somewhere in the particle phase space at some initial time $s=0$ and arriving at the point \mathbf{v}, \mathbf{x} at time $s=t$. The result is exact for a process in which the displacements $\Delta x_j(\mathbf{x}, \mathbf{v}, t|0)$, $\Delta v_j(\mathbf{x}, \mathbf{v}, t|0)$ form a Gaussian process. The averages $\langle u_i(\mathbf{x}, t) \Delta x_j \rangle$ and $\langle u_i(\mathbf{x}, t) \Delta v_j \rangle$ shall be referred to as the fluid-particle dispersion coefficients for spatial and velocity gradient diffusion in phase space.

The value of the dispersion coefficients in uniform shear flow are used as approximate values for the general case of nonuniform flows by choosing the local shearing of the flow at \mathbf{x} in the flow and assuming the turbulence is quasi-homogeneous. In this instance, one can express Δv and Δx in Eq. (13.187) in

terms of a set of response functions $G_{ji}(s)$ which are the displacements of the particle in the \hat{x}_i direction in response to an impulsive force $\delta(s)$ applied in the \hat{x}_j direction of the mean flow (in the absence of the turbulence). Thus if $u''(s)$ is the fluctuating value of the carrier flow velocity with respect to its mean encountered by a particle along its trajectory measured at time s , then

$$\Delta x_i(t) = \beta \int_0^t u''_j(s) G_{ji}(t-s) ds ; \Delta v_i(t) = \beta \int_0^t u''_j(s) \dot{G}_{ji}(t-s) ds \quad (13.192)$$

because the mean flow field is linear in x , and where $G_{ji}(t)$ is the solution of the equation

$$\dot{G}_{ji} + \beta \dot{G}_{ji} - \beta \dot{G}_{jk} S \frac{\partial \langle u_i \rangle}{\partial x_k} = \delta_j \delta(t) \quad (13.193)$$

13.4.3.2.2.2 Generalized Langevin model (GLM). Simonin and Deutsch, Minier (SDM) (1993) derive an equation of motion for the fluid velocity along a particle trajectory by starting from the Langevin equation that Pope (Harworth and Pope, 1986) has used as the analog of the Navier–Stokes equation for fluid point motion. Thus along a fluid point trajectory

$$\frac{du_i}{dt} = \alpha_{ij}(x)(\langle u_i \rangle - u_j) + f_i(x) + f''_i(t) \quad (13.194)$$

where $f_i(x)$ is the net viscous and pressure force per unit mass of fluid and $f''_i(t)$ is a white noise function of time. Both SDM and Pope consider the equation of motion in differential form because the white noise is assumed to be nondifferentiable. For convenience, it is assumed that the white-noise, like all turbulence related functions is differentiable. The equation of motion has white-noise properties simply because it has a time scale much shorter than the time scale over which $u(t)$ varies along a fluid point trajectory $O(\alpha^{-1})$. For future reference it is noted that

$$f_i(x) = \frac{D_f \langle u_i \rangle}{Dt} + \frac{\partial \langle u_j u_i'' \rangle}{\partial x_j} \quad (13.195)$$

where

$$\frac{D_f}{Dt} = \frac{\partial}{\partial t} + \langle u_j \rangle \frac{\partial}{\partial x_j} \quad (13.196)$$

SDM use this relationship to derive an equation of motion for the fluid velocity along a particle trajectory. Hence if d_p/dt is the time derivative of the fluid velocity along a particle trajectory and similarly if d_f/dt is along a fluid point trajectory, then

$$\begin{aligned} \frac{d_p u_i}{dt} &= \left(\frac{\partial}{\partial t} + v_j \frac{\partial}{\partial x_j} \right) u_i(x, t) \\ &= (v_j - u_j) \frac{\partial u_i(x, t)}{\partial x_j} + \frac{d_f u_i}{dt} \\ &= (v_j - u_j) \frac{\partial u_i(x, t)}{\partial x_j} \\ &\quad + \alpha_{ij}(\langle u_i \rangle - u_j) + f_i(x) + f''_i(t) \end{aligned} \quad (13.197)$$

SDM consider only the contribution from the gradient of the mean fluid velocity in this equation of motion for the fluid velocity along a particle trajectory i.e., they consider the equation

$$\frac{d_p u_i}{dt} = (v_j - u_j) \frac{\partial \langle u_i(x, t) \rangle}{\partial x_j} + \alpha_{ij}(\langle u_j \rangle - u_j) + f_i(x) + f''_i(t) \quad (13.198)$$

In effect, this is equivalent to assuming that the contribution of the fluctuating fluid velocity gradient is absorbed into the white-noise function $f_i''(t)$. By using the white-noise function, the equation for $\langle P \rangle$ can be closed exactly, namely,¹

$$\langle F_i''(\mathbf{x}, t) P(\mathbf{v}, \mathbf{x}, \mathbf{u}, t) \rangle = \langle f_i''(t) P(\mathbf{v}, \mathbf{u}, \mathbf{x}, t) \rangle \quad (13.199)$$

$$= - \int_i^{\infty} \langle f_i''(0) f_i''(s) \rangle ds \frac{\partial \langle P \rangle}{\partial u_j}$$

Then from Eq. (13.193), the equation for $\langle P \rangle$ used by SDM is:

$$\begin{aligned} & \frac{\partial \langle P \rangle}{\partial t} + \frac{\partial}{\partial x_i} v_i \langle P \rangle + \frac{\partial}{\partial v_i} \beta_{ij} (u_j - v_j) \langle P \rangle \\ & + \frac{\partial}{\partial u_i} \left[\alpha_{ij} (\langle u_j \rangle - u_j) + f_i(\mathbf{x}) + (v_j - u_j) \frac{\partial \langle u_j \rangle}{\partial x_j} \right] \langle P \rangle \\ & = - \int_i^{\infty} \langle f_i''(0) f_j''(s) \rangle ds \frac{\partial^2 \langle P \rangle}{\partial u_i \partial u_j} \end{aligned} \quad (13.200)$$

13.4.3.3 Continuum Equations and Constitutive Relations for the Dispersed Phase (Without Collisions)

The continuum equations refer to the transport equations of mass, momentum, and kinetic stress of the particle phase and can be generated from the PDF equations for $\langle P \rangle$ or $\langle W \rangle$ by multiplying them by an appropriate power of $m v'^p v'^q v'^r$ and then integrating overall \mathbf{u} and \mathbf{v} (for $\langle P \rangle$) and over all \mathbf{v} (for $\langle W \rangle$), where m is the mass of a particle (assuming that all the particles for the sake of simplicity have the same mass m) and v'_i the fluctuating value of v_i relative its mean density weighted value \bar{v}_i . Thus

$$\text{mass}(\langle \rho \rangle) = m \int \langle P \rangle(v, \mathbf{u}, \mathbf{x}) dv du \quad (13.201a)$$

$$\text{momentum}(\langle \rho \rangle \bar{v}_i) = m \int \langle P \rangle(v, \mathbf{u}, \mathbf{x}) dv du \quad (13.201b)$$

and

$$\text{kinetic stress}(\langle \rho \rangle \bar{v}'_i \bar{v}'_j) = m \int \langle P \rangle(v, \mathbf{u}, \mathbf{x}) v'_i v'_j dv du \quad (13.201c)$$

So the quantities \bar{v}_i and $\bar{v}'_i \bar{v}'_j$ are the particle mass density weighed mean and covariance of the particle velocities at (\mathbf{x}, t) . The continuum equations are from Eq. (13.189):

$$\frac{\partial \langle \rho \rangle}{\partial t} + \frac{\partial}{\partial x_i} \langle \rho \rangle \bar{v}_i = 0 \quad (13.202a)$$

$$\langle \rho \rangle \frac{D_p}{Dt} \bar{v}_i = - \frac{\partial}{\partial x_j} \langle \rho \rangle \bar{v}'_i \bar{v}'_j + \langle \rho \rangle \beta_{ij} (\langle u_j \rangle - \bar{v}_j) + \beta_{ij} \langle \rho \rangle \bar{u}''_j \quad (13.202b)$$

and

$$\langle \rho \rangle \frac{D_p}{Dt} \bar{v}'_i \bar{v}'_j = - \frac{\partial}{\partial x_k} \langle \rho v'_k v'_j \rangle + \rho \bar{v}'_j \bar{v}'_k \frac{\partial \bar{v}_i}{\partial x_k} + \langle \rho \rangle \bar{v}'_j \bar{v}'_k \frac{\partial \bar{v}_i}{\partial x_k} \quad (13.202c)$$

$$- \langle \rho \rangle \beta_{ik} (\bar{v}'_k \bar{v}'_j + \bar{v}'_k \bar{v}'_j + \bar{v}'_k \bar{v}'_j)$$

¹Note the closure is also exact if $f''(t)$ is Gaussian nonwhite but will include gradients of $\langle P \rangle$ in \mathbf{x} and \mathbf{v} as well.

where $u'_i = u_i - \bar{u}_i$ and D_p/D_t is the particle substantial derivative i.e.,

$$\frac{D_p}{D_t} = \frac{\partial}{\partial t} + \bar{v}_j \frac{\partial}{\partial x_j} \quad (13.203)$$

Closed expressions are required for:

1. \bar{u}'_i the average fluid velocity relative to $\langle u \rangle$ encountered by a particle
2. $u'_{ik} v'_j$ the carrier-particle velocity covariances
3. $\langle \rho v'_k v'_j v'_i \rangle$ the turbulent kinetic energy flux

Note the distinction here between variables u''_i and u'_i . Herein after, double prime and prime refer to random variables relative to $\langle u \rangle$ and density-weighted averages, respectively. For example, $v'' = v - \langle u \rangle$; and $v' = v - \bar{v}$.

13.4.3.3.1 Constitutive Relations Based on Kinetic Model

By using Eq. (13.189) with Eq. (13.191), and suitably integrating it over all particle velocities to form transport equations for the particle phase momentum and particle kinetic stresses, and comparing the resulting equations with Eqs. (13.202b) and (13.202c), one obtains the identities

$$\bar{u}''_i \langle \rho \rangle = - \frac{\partial}{\partial x_j} \langle \langle u''_i(x, t) \Delta x_j(x, t|0) \rangle \rangle \langle \rho \rangle - \left\langle \frac{\partial u''_i}{\partial x_j} \Delta x_j \right\rangle \langle \rho \rangle \quad (13.204)$$

$$\overline{u'_i v'_j} = \langle u''_i(x, t) \Delta v_j(x, t|0) \rangle - \langle u''_i(x, t) \Delta x_m(x, t|0) \rangle \frac{\partial \bar{v}_j}{\partial x_m} \quad (13.205)$$

where the displacements Δv and Δx refer to all particle trajectories arriving at x at time t irrespective of their velocity. The average $\langle u''_i(x, t) \Delta v_j(x, t|0) \rangle$ is the fluid-particle velocity diffusion coefficient and $\langle u''_i(x, t) \Delta x_j(x, t|0) \rangle$ is the fluid-particle spatial diffusion coefficient.

It is apparent from Eq. (13.191) that the turbulent interfacial momentum transfer term $\beta \cdot \bar{u}'' \langle \rho \rangle$ will contribute an interfacial surface force to the particle-phase momentum equation, which combines with the particle Reynolds stresses to give a pressure tensor ρ whose components are expressible in terms of an equation of state, namely, at x :

$$p_{ji} / \langle \rho \rangle = \langle v'_i v'_j \rangle + \beta_{ik} \langle u''_k(x, t) \Delta x_j(x, t|0) \rangle \quad (13.206)$$

where v' is the particle velocity fluctuation relative to the mean \bar{v} at x . Equation (13.206), in turn, encapsulates a fundamental relationship between the components of p and a set of particle diffusion coefficients ε_{ij} leading to the relationships

$$p_{ji} / \langle \rho \rangle = \beta_{ik} \varepsilon_{kj} = \langle v'_i v'_j \rangle + \beta_{ik} \langle u''_k(x, t) \Delta x_j(x, t|0) \rangle \quad (13.207)$$

It is clear from the momentum equation that when the inertial term $D \bar{v}_i / D_t$ is small compared with the other terms, the transport is described by a simple convection gradient transport equation, in which the diffusion coefficients are identical to ε_{ij} and the convection velocity is given by

$$\underline{v}_D = \beta^{-1} F + \underline{v}_d \quad (13.208a)$$

$$\underline{v}_d = \beta^{-1} \left\{ \frac{\partial}{\partial x} \overline{v' v'} + \right\} - \left\langle \left(\frac{\partial}{\partial x} \Delta x(x, t|0) \right) u''(x, t) \right\rangle \quad (13.208b)$$

The first term on the RHS of Eq. (13.208b) has sometimes been referred to as the turbophoretic or stressphoretic velocity (Reeks, 1993; Ramshaw, 1979). The additional contribution from the second term is entirely due to the structure of the flow and should be zero for inertialess particles which follow the flow. According to this approach, gradient diffusion is always the case for particles, which follow the flow.

In fact, the set of diffusion coefficients ε_{ij} reduces to the local average

$$\varepsilon_{ij} = \langle u''_i(x, t) \Delta x_j(x, t | 0) \rangle \quad (13.209)$$

One should note that these are not the same as the diffusion coefficients D_{ij} for the dispersion in a simple linear shear flow. For particles injected at the center of the shear with zero velocity in simple linear shear flow, the dispersion can be described as

$$\frac{\partial \langle \rho \rangle}{\partial t} = \frac{\partial}{\partial x_i} D_{ij}(t) \frac{\partial}{\partial x_j} \langle \rho \rangle + \delta(x) \delta(t) \quad (13.210)$$

In these rather special cases, the convection term $\langle \rho \rangle \langle u \rangle$ (for the case of inertialess particles following the flow) behaves like a diffusive term when the particles are released from the center of the shear with a diffusion coefficient, which adds to the diffusion coefficients ρ_{ij} to give the total diffusion coefficient D_{ij} . However, this result is only true for particles that follow the flow. For particles with inertia, while the process is still diffusive (for particles released from the center of the shear) the inertial acceleration term in the particle-phase momentum equation, Eq. (13.202b), also makes a finite contribution to D_{ij} along with normal gradient diffusion term. Indeed, for particles with small relaxation times, this term dominates the diffusion as time increases, especially in the case of the rotating flow.

The carrier-particle velocity covariances $\overline{u'_k v'_j}$ are given by

$$\overline{u'_k v'_j} = \langle u''_i(x, t) \Delta v_j(x, t | 0) \rangle - \langle u''_i(x, t) \Delta x_m(x, t | 0) \rangle \frac{\partial \bar{v}_j}{\partial x_m} \quad (13.211)$$

where the displacements Δv and Δx refer to all particle trajectories arriving at x at time t irrespective of their velocity.

Substituting the expressions for the carrier-particle velocity covariances in Eq. (13.211) into transport Eq. (13.202.c) for the particle Reynolds stresses gives

$$\begin{aligned} \langle \rho \rangle \frac{D}{Dt} \overline{v'_m v'_n} &= -\frac{\partial}{\partial x_i} \langle \rho v'_i v'_m v'_n \rangle + \langle \rho \rangle \left\{ \frac{\partial \bar{v}_n}{\partial x_l} \rho_m + \frac{\partial \bar{v}_m}{\partial x_l} \rho_n \right\} \\ &\quad - \langle \rho \rangle \left\{ \beta_{nl} \overline{v'_l v'_m} + \beta_{ml} \overline{v'_l v'_n} \right\} \\ &\quad + \langle \rho \rangle \left\{ \beta_{ml} \langle u''_l(x, t) \Delta v_n(x, t | 0) \rangle + \beta_{nl} \langle u''_l(x, t) \Delta v_m(x, t | 0) \rangle \right\} \end{aligned} \quad (13.212)$$

Referring to the terms on the RHS of the equation, the second term in brackets represent "viscous" losses from the action of surface forces P (as defined in Eq. (13.207) in changing the shape and size of an elemental volume of the dispersed flow as it moves through the mean shear gradients of that flow. The third and fourth terms are net loss and production terms arising from an internal volume dissipative force $-\beta v'$ (third term) and driving force $\beta u''(x, t)$ (fourth term). One note that at equilibrium in homogeneous turbulence,

$$\overline{v'^2} = \langle u''_i(x, t) \Delta v_i(x, t | 0) \rangle \quad (13.213)$$

all other terms being zero. Using the appropriate form for $\Delta v_i(x, t | 0)$ gives the correct analytic form (Reeks, 1997)

$$\overline{v'^2} = \beta \int_0^\infty e^{-\beta s} \langle u''(0) u''(s) \rangle ds \quad (13.214)$$

where $u''(s)$ is the fluctuating aerodynamic driving force along a particle trajectory. Thus, the Reynolds stresses depend explicitly on the shearing of the dispersed phase (the term in square brackets in Eq. (13.212) and the shearing of the carrier flow (terms involving $\langle u''_i(x, t) \Delta v_n(x, t | 0) \rangle$ in Eq. (13.212)).

To illustrate this behavior still further, let us represent $\langle u''(x,t) \Delta v(x,t|0) \rangle$ by ζ and divide it into a homogeneous part $\zeta^{(0)}$ (as if the flow was uniform and independent of the shearing of the carrier flow) and a deviatoric part $\delta\zeta$ linear in the local shearing of the carrier flow. Likewise, divide the particle Reynolds stress into similar components. Consider the case when β^{-1} is very small (almost fluid point motion). Only a balance of the terms of order β are important in the Reynolds stress equation, so by taking β to be isotropic for simplicity, one has

$$-2\delta\bar{v}'_n\bar{v}'_m + \left\{\delta\zeta_{mn} + \delta\zeta_{nm}\right\} - \epsilon_{mi}\frac{\partial\bar{v}_n}{\partial x_i} - \epsilon_{ni}\frac{\partial\bar{v}_m}{\partial x_i} = 2\bar{v}'_n\bar{v}'_m^{(0)} - \left\{\zeta_{mn}^{(0)} + \zeta_{nm}^{(0)}\right\} \quad (13.215)$$

The terms on the LHS contain all the deviatoric terms and the terms of the RHS are all the homogeneous terms. The whole equation must express the fact that in this limit, the particle velocity covariances are the same as the carrier flow covariances: this is consistent with the bracketed terms containing all the homogeneous forms and the deviatoric terms being both zero. The implication for the sum of the deviatoric terms being zero is that

$$2\delta\bar{v}'_n\bar{v}'_m = -\epsilon_{mi}\frac{\partial}{\partial x_i}(\bar{v}_n - \bar{u}_n) - \epsilon_{ni}\frac{\partial}{\partial x_i}(\bar{v}_m - \bar{u}_m) \beta^{-1} \rightarrow 0 \quad (13.216)$$

The particle deviatoric Reynolds stresses in the limit of very small particles are linear in the relative shearing between the carrier and dispersed phases. In the case of very large particles, the contribution from the interfacial momentum transfer term to the deviatoric particle Reynolds stresses drops to zero with no explicit dependence on the shearing of the carrier flow, i.e., the contribution is entirely viscous.

13.4.3.3.1.1 The turbulent kinetic energy flux $\langle \rho v'_k v'_j v'_i \rangle$. An evaluation of the turbulent kinetic energy flux is based on an application of the Chapman–Enskog approximation in which the nonequilibrium state of the dispersed phase is approximated by slight deviations from the equilibrium state (Chapman and Cowling, 1952). The analysis presented is based on that found in Buyevich (1972), where an equation similar to the classical Fokker–Planck equation was examined. It is also similar to that given by Swailes and Sergeev (1998). As a first step, the KM PDF equation is used, Eq. (13.189), with Eq. (13.191) to calculate the equilibrium distribution function, $\langle W \rangle^{(0)}$. This is found by setting all the time and space derivatives to zero in the equation, and further assuming that the carrier phase is homogeneous, such that the equation for $\langle W \rangle^{(0)}$ is

$$\frac{\partial}{\partial v'_i} \left(\beta_{ij} v'_j \langle W \rangle^{(0)} \right) + \frac{\partial^2}{\partial v'_i \partial v'_j} \left(\beta_{ik} \langle u''_k \Delta v_j \rangle \langle W \rangle^{(0)} \right) = 0 \quad (13.217)$$

$\langle \tilde{W} \rangle^{(0)}(k)$ is the Fourier transform of $\langle W \rangle^{(0)}(v)$. If then

$$\langle \tilde{W} \rangle^{(0)} = \langle n \rangle \exp \left\{ -\frac{1}{2} \langle u''_i \Delta v_j \rangle A_{mn} k_i k_n \right\} \quad (13.218)$$

Now consider a state of the system that differs slightly from equilibrium. In this new state, the variables describing the mean flow, are now functions of time and position, and consequently, unlike in the equilibrium state, their derivatives are not identically zero. As in Chapman and Cowling (1952), it is assumed that the deviation from the equilibrium solution is sufficiently small so a solution can be sought for the nonequilibrium state in the form of a series solution with a small parameter, ξ , being employed to distinguish between the various orders of approximation (see also Buyevich, 1972). It should be remarked that the parameter ξ has been introduced only for convenience as a way of ordering terms. Obviously, it must be set equal to unity at the end of the calculations. To proceed, the KM-PDF equation is now written in the form

$$M(\langle W \rangle) = L(\langle W \rangle) \quad (13.219)$$

where

$$M = M \left(\frac{D}{Dt} \frac{\partial}{\partial x'}, \bar{v}, \bar{v}/\bar{v}' \langle u'' \Delta x \rangle \right) L = L \left(\frac{\partial}{\partial v'} \langle u'' \Delta v \rangle \right)$$

and following both Chapman and Cowling (1952) and Buoyevich (1972), $\langle W \rangle$ and L are both expanded in terms of a small parameter ξ , namely,

$$\langle W \rangle = \frac{1}{\xi} \sum_{m=0}^{\infty} \xi^m \langle W \rangle^{(m)} \quad (13.220a)$$

$$L \langle W \rangle = \frac{1}{\xi} \sum_{m=0}^{\infty} \xi^m L^{(m)} \quad (13.220b)$$

with

$$L^{(r)} = L \langle W \rangle^{(r)} = \frac{\partial^2}{\partial v' \partial v'_j} \left(\beta_{jk} \langle u''_k \Delta v_i \rangle \langle W \rangle^{(r)} \right) + \frac{\partial}{\partial v'_i} \left(\beta_{jk} v'_j \langle W \rangle^{(r)} \right)$$

and with a similar expansion carried out for $M \langle W \rangle$. Substituting these expansions into Eq. (13.219) gives

$$\bar{v}'_i \bar{v}'_j \bar{v}'_k - \varepsilon_{li} \frac{\partial}{\partial x_l} \bar{v}'_j \bar{v}'_k - \varepsilon_{lj} \frac{\partial}{\partial x_l} \bar{v}'_i \bar{v}'_k - \varepsilon_{lk} \frac{\partial}{\partial x_l} \bar{v}'_i \bar{v}'_j \quad (13.221)$$

where the diffusion coefficients ε_{ij} are the same as those defined in Eq. (13.207). See Swailes and Sergeev (1998) for precise details.

13.4.3.3.2 Constitutive Relations Based on GLM

The closure expressions in this case are transport equations for \bar{u}'' and $\bar{u}'_k \bar{v}'_j$ derived from the GLM-PDF equation for $\langle P \rangle$ (Eq. [13.200]). Multiplying Eq. (13.200) by u_i and integrating over all v and u yields

$$\frac{\partial}{\partial t} \langle \rho u_i \rangle + \frac{\partial}{\partial x_j} (\rho v_j u_i) = \left\{ f_i(x) - \alpha_{ij} \bar{u}_j'' + (\bar{v}_k - \bar{u}_k) \frac{\partial \langle u_i \rangle}{\partial x_k} \right\} \langle \rho \rangle \quad (13.222)$$

The LHS can be rewritten as

$$\frac{\partial}{\partial t} \langle \rho u_i \rangle + \frac{\partial}{\partial x_j} (\rho v_j u_i) = \langle \rho \rangle \frac{D_p}{Dt} \langle u_i \rangle + \langle \rho \rangle \frac{D_p}{Dt} \bar{u}_i'' + \frac{\partial}{\partial x_j} \bar{v}'_j \bar{u}'_i \langle \rho \rangle \quad (13.223)$$

Also from Eq. (13.196) and resolving the velocity into mean and fluctuating parts

$$\left(\frac{\partial}{\partial t} + \bar{u}_j \frac{\partial}{\partial x_j} \right) \langle u_i \rangle = \frac{D_f}{Dt} u_i + \bar{u}_j'' \frac{\partial \langle u_i \rangle}{\partial x_j} \quad (13.224)$$

Finally by using the relationship given in Eq. (13.196) gives the transport equation for \bar{u}_i'' , namely,

$$\begin{aligned} \langle \rho \rangle \frac{D_p}{Dt} \bar{u}_i'' &= - \frac{\partial}{\partial x_i} \bar{v}'_j \bar{u}'_i \langle \rho \rangle + \langle \rho \rangle \frac{\partial}{\partial x_i} \langle u''_j u''_i \rangle \\ &\quad - \left\{ \frac{\partial \langle u_i \rangle}{\partial x_j} + \alpha_{ij} \right\} \bar{u}''_j \langle \rho \rangle \end{aligned} \quad (13.225)$$

A transport equation for $\bar{u}'_k \bar{v}'_j$ can also be obtained by transforming the GLM-PDF equation into an equation for $P(v', u', x, t)$, multiplying the resulting equation by $u'_i v'_j$ and then integrating over all u' and v' .

This gives

$$\begin{aligned} \langle \rho \rangle \frac{D_p}{Dt} \overline{u'_i v'_j} &= -\frac{\partial}{\partial x_k} \langle \rho \rangle \overline{u'_i v'_j v'_k} - \langle \rho \rangle \overline{v'_j v'_k} \frac{\partial u''_i}{\partial x_k} \\ &\quad - \left(\langle \rho \rangle \overline{u'_i v'_k} \frac{\partial \bar{v}_j}{\partial x_k} + \langle \rho \rangle \overline{v'_j l u'_k} \frac{\partial \bar{u}_i}{\partial x_k} \right) \\ &\quad - \langle \rho \rangle \beta \left(\overline{u'_i v'_j} - \overline{u'_i u'_j} \right) \\ &\quad + \langle \rho \rangle \alpha_{ik} \overline{u'_k v'_j} \end{aligned} \quad (13.226)$$

13.4.3.3.3 Fluid-Particle Velocity Correlation Models

The general form of α in Popes GLM model is assumed to be linear in the local strain rates of the carrier flow, i.e.,

$$\alpha_{ij} = \alpha_{ij}^{(0)} + \beta_2 \frac{\partial \bar{u}_i}{\partial x_j} \quad (13.227)$$

where $\alpha_{ij}^{(0)}$ is the homogeneous (strain-rate independent) component and β_2 a constant whose value is obtained from measured values of one-point statistics. In the case of the SDM model, the values of $\alpha_{ij}^{(0)}$ are dependent on the particle itself, since they refer to fluid time scales viewed by the particle. In particular, SDM account for the influence of crossing trajectories by choosing the following form for $\alpha_{ij}^{(0)}$:

$$\alpha_{ij}^{(0)} = \frac{\delta_{ij}}{\tau_{fp,\perp}} + \left[\frac{1}{\tau_{fp,\parallel}} - \frac{1}{\tau_{fp,\perp}} \right] \hat{n}_i \hat{n}_j \quad (13.228)$$

where $\tau_{fp,\perp}$ and $\tau_{fp,\parallel}$ are the turbulent characteristic time scale of the fluid velocity fluctuations viewed by the particles in the direction normal and parallel to the mean relative velocity vector \bar{v}_r between particle and carrier flow. Adopting the same approach as Csanady for gravitational settling, the direction cosines for the relative velocity are given by

$$\tau_{fp,\parallel} = \tau_f (1 + C \zeta_r^2)^{-1/2} \tau_{fp,\perp} = \tau_f (1 + 4C \zeta_r^2)^{-1/2}$$

where

$$\zeta_r^2 = \frac{3 |\bar{V}_r|^2}{\langle u' \cdot u' \rangle}$$

For closure of the transport equation for the fluid-particle covariances in Eq. (13.226) need a closed expression for fluid-particle velocity $\langle \rho u'_i v'_j v'_k \rangle$ turbulent flux. In the case of the scalar particle fluid covariance $u' \cdot v'$, Simonin (1996) has used a Boussinesq approximation

$$\langle \rho u'_i v'_j v'_k \rangle = -\langle \rho \rangle v_{fp}^t \frac{\partial}{\partial x_i} \langle u' \cdot v' \rangle \quad (13.229)$$

where v_{fp}^t is referred to as the fluid-particle turbulent viscosity written in terms of the time scale of the fluid along a particle trajectory τ_{fp} , namely

$$v_{fp}^t = \frac{1}{3} \langle u' \cdot v' \rangle \tau_p \quad (13.230)$$

Using this gradient approximation for the particle fluid velocity fluxes and the expressions for α_{ip} the transport equation can, in principle, be solved for the linear form for α_{ij} in Eq. (13.227). Fevrier and Simonin (1998), from a computational point of view, have derived an algebraic model for the off-diagonal particle-fluid covariances, which they then use in conjunction with a transport model for of the scalar

fluid-particle covariance, $\langle \mathbf{u}' \cdot \mathbf{v}' \rangle$. This algebraic model is derived from Eq. (13.226) by assuming equilibrium of the fluid-particle turbulent velocity correlation tensor in single-phase flow, namely,

$$\langle u'_m v'_m \rangle \left[\frac{d}{dt} \langle u'_i v'_j \rangle - D_{ij} \right] = \langle u'_i v'_j \rangle \left[\frac{d}{dt} \langle u'_m v'_m \rangle - D_{mm} \right] \quad (13.231)$$

where D_{ij} refer to the diffusive component (gradient of the fluid-particle velocity flux) in the transport equation for the fluid-particle covariance. Then from the fluid-particle correlations transport, Eq. (13.226), one obtains the algebraic model

$$\begin{aligned} \langle u'_i v'_j \rangle &= \frac{1}{3} \langle \mathbf{u}' \cdot \mathbf{v}' \rangle \delta_{ij} + \frac{\langle \mathbf{u}' \cdot \mathbf{v}' \rangle}{\langle u'^2 \rangle} \left[\langle u'_i u'_j \rangle - \frac{1}{3} \langle u'^2 \rangle \delta_{ij} \right] \\ &\quad - \frac{1}{2\beta \langle u'^2 \rangle} \left[\langle \mathbf{u}' \cdot \mathbf{v}' \rangle \left\{ \langle u'_i v'_k \rangle \frac{\partial \bar{v}_j}{\partial x_k} + (1 - \beta_2) \langle u'_i v'_k \rangle \frac{\partial \bar{u}_j}{\partial x_k} \right\} \right. \\ &\quad \left. - \langle u'_i v'_j \rangle \left\{ \langle u'_m v'_n \rangle \frac{\partial \bar{v}_m}{\partial x_n} + (1 - \beta_2) \langle v'_m u'_n \rangle \frac{\partial \bar{u}_m}{\partial x_n} \right\} \right] \end{aligned} \quad (13.232)$$

where $\langle u'^2 \rangle = \langle \mathbf{u}' \cdot \mathbf{u}' \rangle$. For practical applications, this algebraic expression may be used with the transport equation for the fluid particle covariance $\langle \mathbf{u}' \mathbf{v}' \rangle$ obtained directly from Eq. (13.226). Fevrier and Simonin go further and derive an even simpler model than the algebraic model by assuming that the fluid-particle covariance tensor anisotropy is small, so that, for instance, certain ratios in the algebraic model equation can be replaced by their local quasi homogeneous values. Thus

$$\frac{\langle \mathbf{u}' \cdot \mathbf{v}' \rangle}{\langle u'^2 \rangle} = \frac{\beta_{\tau fp}}{1 + \beta_{\tau fp}}$$

This sort of approximation gives a Boussinesq or eddy-viscosity model for the fluid-particle velocity covariance, namely,

$$\begin{aligned} \langle u'_i v'_j \rangle &= \frac{1}{3} \langle \mathbf{u}' \cdot \mathbf{v}' \rangle \delta_{ij} + \frac{\beta_{\tau fp}}{1 + \beta_{\tau fp}} \left\{ \langle u'_i v'_j \rangle - \frac{1}{3} \langle \mathbf{u}' \cdot \mathbf{v}' \rangle \right\} \\ &\quad - \frac{v_{fp}^t}{1 + \beta_{\tau fp}} \left\{ \frac{\partial \bar{v}_j}{\partial x_i} - \frac{\delta_{ij}}{3} \operatorname{div} \bar{v} + (1 - \beta_2) \left(\frac{\partial \bar{u}_i}{\partial x_j} - \frac{\delta_{ij}}{3} \operatorname{div} \bar{u} \right) \right\} \end{aligned} \quad (13.233)$$

In the following section, predictions for the dispersion of particles in particle laden jet are compared with experimental results.

13.4.3.3.4 Comparison of Predictions with Experimental Results for Nonuniform Unbounded Flows
 Here the GLM approach is used to predict the concentration, mean velocity and velocity covariances of a dilute suspension of particles in a nonuniform flow as where near-wall behavior is not a feature. This is the case for a particle-laden round turbulent jet, where the flow is strictly unbounded. It represents one of the many examples where a comparison between model predictions and experimental measurements have been made (see Simonin [2000] for details). However, it does provide very good examples of the application of the transport equation for the particle kinetic stresses where the work done by the mean shear of either phase introduces a significant anisotropy into the particle velocity covariance as is the case of dispersion in a simple shear. The results are taken from Fevrier and Simonin (1998) for dispersion in a particle-laden coaxial jet with properties: mean particle diameter = 80 μm , density ratio $\rho_p/\rho_f = 237$, particle relaxation time $\beta^{-1} = 5 \times 10^{-3}\text{sec}$, mass loading = 3.3×10^{-2} , and mean volume fraction 1.4×10^{-4} . In such a flow, the fluid modulation by the particles and particle-particle collisions are negligible. Computations were made on a 31×51 mesh using the full second-order model involving the transport of the particle kinetic stress equation, Eq. (13.202), and the scalar fluid-particle covariance

(derived from Eq. (13.226) together with the algebraic models for the off-diagonal particle-fluid velocity covariances (Eq. [13.232]). The results are also given using the eddy viscosity model for the fluid-particle velocity covariances Eq. (13.233). The inlet conditions on the fluid and particle mean velocity and fluctuations are taken from the experimental data of Hishida and Maeda (1990). As experimentally observed, the particle normal kinetic stresses are much more anisotropic than the corresponding values of the carrier flow, due to the significant increase in the shearing of the flow in the axial direction than in the radial direction (see Figures 13.54 and 13.55). Application of the algebraic model accurately predicts the values in the particle velocity fluctuations in both the axial and radial directions for all measured axial locations. The fluid-particle eddy-viscosity model is reasonably accurate in predicting the radial velocity fluctuations but clearly underpredicts the axial values.

13.4.3.3.5 Accuracy and Reliability of PDF Models

The PDF equation in its simplest and most practical form is an equation for the particle phase space distribution in which the random force due to the turbulence along a particle trajectory is a Gaussian process or, more appropriately, the velocity and spatial displacements $\Delta v(x, t|v', 0)$ and $\Delta x(x, t|v', 0)$ about a given point x, t for a particle with an initial velocity of v' are Gaussian. This leads to a simple advection diffusion equation (ADE) for the net turbulent driving force in particle phase space. It is possible to extend this further to non-Gaussian processes, but in doing so, we would require more knowledge; more statistics on the displacements and ultimately on the forces that produce them information we rarely possess. Although the ADE approximation is used, it is applied at the simplest level of the dynamics in which the underlying Liouville equation, upon which the PDF equation is based, is a linear equation. This leads to a better chance of success. Indeed, one might say that the PDF approach is more reliable than other approaches from several points of view:

1. Simple closure based on a Gaussian process for turbulent driving force is used at a more basic level of the dynamics. This leads to a non-Gaussian spatial ADE process, which admits all the higher order gradient diffusion terms that are contained in an ADE process for a compressible non-Gaussian random particle velocity field.
2. Provides valid criteria for the application of simple gradient diffusion (simple ADE) and in cases, where this is not valid, a method of solution involving a hierarchy of continuum (moment) equations closed at a suitable level using closure approximations based on formal solutions to the PDF equation itself.

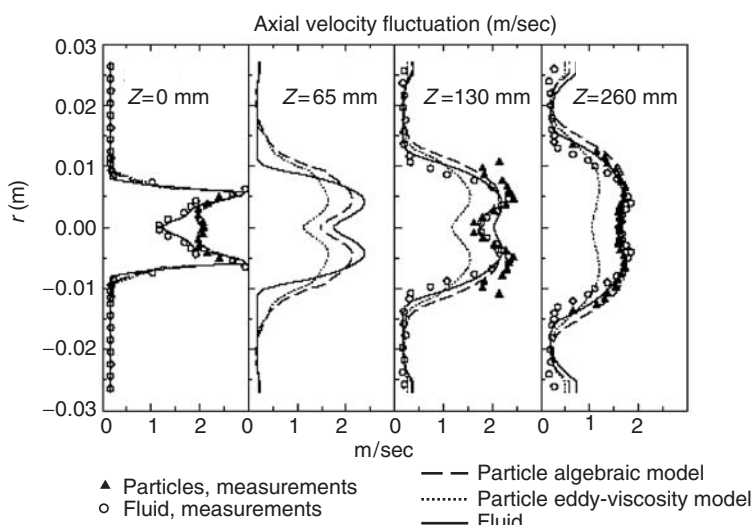


FIGURE 13.54 Radial profiles of axial fluctuations at different locations downstream of a nozzle for a coaxial round jet.

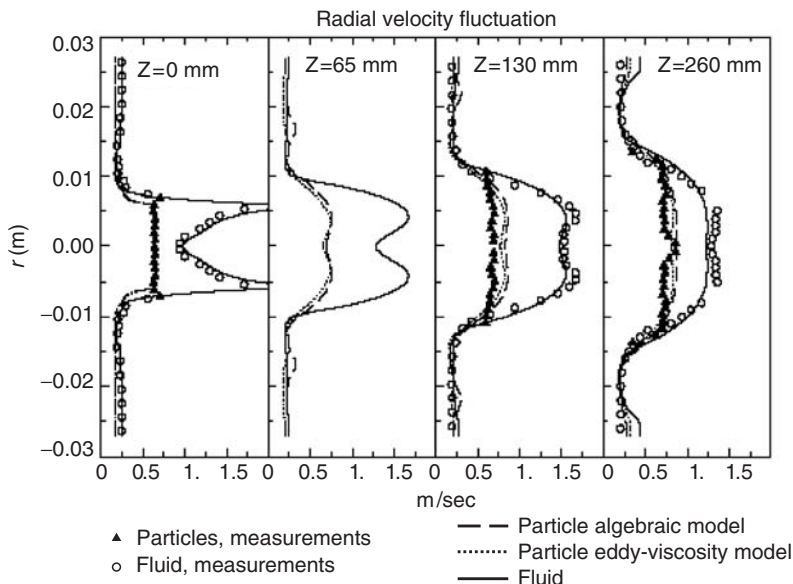


FIGURE 13.55 Radial profiles of radial fluctuations at different locations downstream of a nozzle for a coaxial round jet.

3. The PDF equation, or more appropriately the closure approximation involved, is asymptotically exact in the limit of high inertia particle when the process is similar to Brownian motion.
4. Implementation of natural boundary condition, e.g., absorbing/partially absorbing surfaces is an integrable part of the approach, where solution of the PDF equations is carried out directly near and at the depositing wall. This is the subject of the following section.

13.4.3.4 Near-Wall Behavior

In this section the works of Devenish et al. (1999), Reeks and Swailes (1997), Swailes and Reeks (1994), and Darbyshire and Swailes (1996) on the application of the PDF approach to near-wall behavior and the influence of natural boundary conditions are briefly reviewed. The natural boundary conditions involve some change in particle velocity together with possible deposition-absorption at the boundary and cannot be prescribed in the standard two-fluid formulation. Only using a PDF method explicitly involving the particle velocity distribution at the wall can this be achieved. Furthermore, the steep change in the level of turbulence at the wall means that only for very small particles are the two-fluid equations (mass momentum and energy) likely to apply i.e., the particle distribution of velocities at any position within the turbulent boundary layer will not be locally related to the turbulence. Depending on its size, a particle will retain some memory of its behavior in the far wall or bulk flow. More precisely, this depends on the variation of the turbulence over a particle mean free path defined as the distance a particle travels in a time equal to its correlation time ϵ/v' . The same type of conditions apply to a gas at low pressure when the dimensions of the container are comparable to the molecular mean free path. Under such circumstances the so-called continuum theory no longer applies. It is to be noted that even without the steep change in turbulence, the boundary conditions at the wall are by themselves likely to invalidate the two-fluid model equations simply because the particle-wall distribution is very much different from the normal distribution.

13.4.3.4.1 General Boundary Conditions at Wall

Referring to Figure 13.56, the general boundary condition for a particle impacting at a wall at x with velocity u and rebounding with a range of possible velocities v is the flux condition

$$vP(v, x, t) = \int_{u_{n \leq 0}} uP(v, u, t)\Theta(v|u) du \quad (13.234)$$

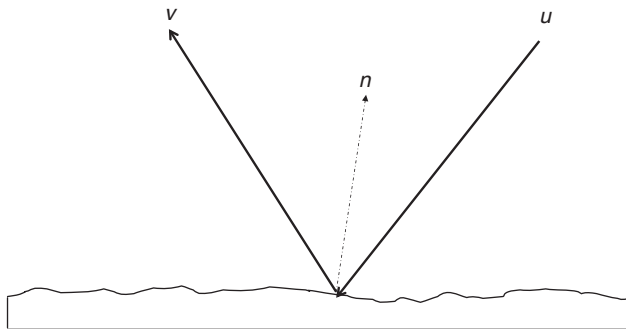


FIGURE 13.56 Diffuse scattering from a rough surface where n is the unit vector normal to the surface at the point of impact with the surface.

where n is the direction normal to the wall at x , and $\Theta(v \mid u)$ the transition or scattering probability density that a particle will rebound with a velocity v after impacting the surface with velocity u . The velocities u and v are related deterministically (specular reflection) or stochastically (diffuse scattering as in the case of a microscopically rough surface). Swailes and his co-workers (Darbyshire and Swailes, 1996; Reeks and Swailes, 1997; Devenish et al., 1999) have obtained solutions for the PDF equation for simple flows in both these cases. Both the cases involve duct flow, in which the turbulence is regarded as homogeneous with uniform mean velocity in the streamwise direction. In these cases, therefore, the particle's response time is sufficiently large that it does not respond to the spatial variations in the mean flow and the turbulence, especially near the wall. Also, it is the boundary conditions themselves which determine the near-wall behavior, where the continuum equations are inappropriate and the behavior can be approximated well by a simple steady-state solution of the PDF equation in 1D in x and in v . The conditions for particle response times are consistent with the second gradients flux term in Eq. (13.191) being set to zero, in which case the PDF equation can be normalized in a universal form under steady conditions as (Swailes and Reeks, 1994)

$$\left(v \frac{\partial}{\partial y} - \frac{\partial}{\partial v} v + g \frac{\partial}{\partial v} + \frac{\partial^2}{\partial v^2} \right) \langle W(y, v) \rangle = 0 \quad (13.235)$$

In this equation, y is the normal distance from the wall ($y = 0$) and positive velocities are directed toward the wall, particles are acted upon by a gravitational force g directed toward the wall and velocities and distances are normalized on the particle rms velocity at equilibrium (perfectly reflecting walls) and on the particle mean free path ϵ/v' .

In the simple flows considered by Swailes and Reeks (1994) and Reeks and Swailes (1997), the flow is divided into a far-wall region, which acts as a constant source of particles entering the near-wall region. The interface is set at some distance Y from the wall in particle mean free paths where the spatial distribution of the particles is uniform. It follows from Eq. (13.235) that this distribution will be Gaussian

$$w(0, v) = (2\pi)^{-1/2} \exp\left(-\frac{1}{2}v^2\right) \text{ for } v > 0 \quad (13.236)$$

13.4.3.4.2 Method of Solution

The PDF equation is solved numerically using a spectral expansion in terms of Hermite polynomials, looking for solutions in the form

$$w(y, v) \approx \sum_{n=0}^N \phi_n(y) \Psi_n(v) \quad (13.237)$$

where the Ψ_n are orthonormal functions based on the Hermite polynomials H_n . They are

$$\Psi_n(v) = \left(\frac{b}{2^n n! \sqrt{\pi}} \right)^{1/2} \exp\left(-\frac{1}{2}(bv)^2\right) H_n(bv) \quad (13.238)$$

The inclusion of the scaling factor b allows the placement of a set of collocation points v_j ($j = 0, 1, N$), to be optimized. At these collocation points, the approximation in Eq. (13.237) is exact. In this problem, the collocation points are taken to be the zeros of the function Ψ_{N+1} , which provide discrete orthonormal properties for $\Psi_n(v_s)$. Substituting the approximation Eq. (13.237) into Eq. (13.235) and making it exact at these collocation points, one gets a system of first-order equations

$$\frac{d}{dy} W = AW \quad (13.239)$$

where W is column vector whose elements are values of the PDF at the collocation points and A is a matrix whose elements are functions of Ψ_n^s .

The boundary conditions given by Eqs. (13.234) and (13.236) are discretized at the points v_j . If N^* is defined to be the integer such that $v_j < 0$ for $j < N^*$ and $v_j = 0$ for $j \geq N^*$, then the boundary condition at the interface $y = Y$ can be written as

$$\sum_{n=0}^N \zeta_{jn} w_n = 1, \quad j \geq N^* \quad (13.240)$$

where $w_n = w(v_n, Y)$ and

$$\zeta_{jn} = \delta_{jn} (2\pi)^{1/2} \exp\left(\frac{1}{2} v_j^2\right), \quad j \geq N^*$$

The boundary condition at the wall $y = 0$ is

$$\sum_{n=0}^N \zeta_{jn} w_n = 0, \quad j < N^* \quad (13.241)$$

where

$$\zeta_{jn} = \delta_{jn} v_n + h_n^{-1} \sum_{m=0}^N \Psi_m^n I_m(v_j), \quad j \geq N^*$$

with

$$I_m(v_j) = \int_0^\infty \Psi_m(u) u \Theta(v_j|u) du$$

The interface and wall boundary conditions represent standard two-point boundary conditions for the solutions of Eq. (13.239) and can be solved by a standard numerical method. Figures 13.57–13.59 show some of the results obtained by Swailes (Darbyshire et al., 1996; Reeks and Swailes, 1997) for the particle deposition at a wall with or without gravity for specific examples of the wall scattering function $\Theta(v_j|u)$. In each case, results are compared with those obtained from a random walk simulation that simulates the system precisely. In this case it was assumed that upon impact there was energy loss that was conveniently described by defining a critical impact velocity v_c below which a particle adheres upon impact but above which a particle will rebound with a prescribed rebound velocity $v = \Theta(u)$. Thus $\Theta(v|u)$ for specular reflection is

$$\Theta = \begin{cases} 0 & \text{for } 0 < v \leq v_c \\ \delta(v - \theta(u)) & \text{for } v > v_c \end{cases} \quad (13.242)$$

Modeling the dependence of $v = \theta(u)$ from a constant energy loss upon impact as

$$v = -\sqrt{u^2 - v_c^2} \quad \text{for } u > v_c \quad (13.243)$$

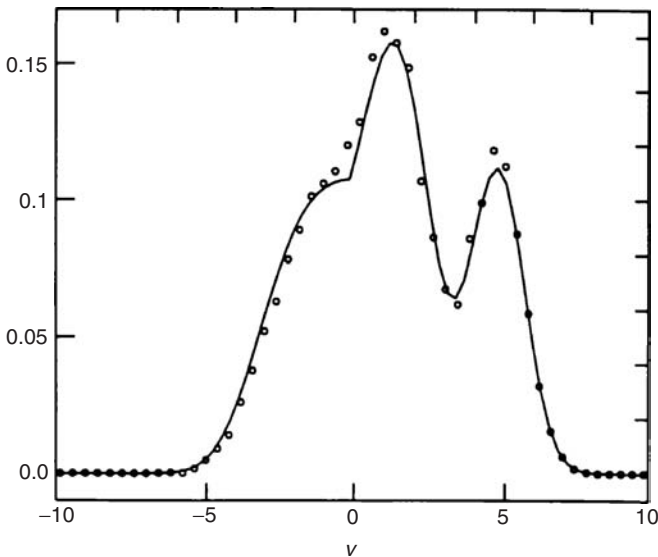


FIGURE 13.57 Particle–wall velocity distribution for particles falling under gravity with reflection and absorption; normalized critical impact velocity $v_c = 5$, gravitational settling velocity = 5.

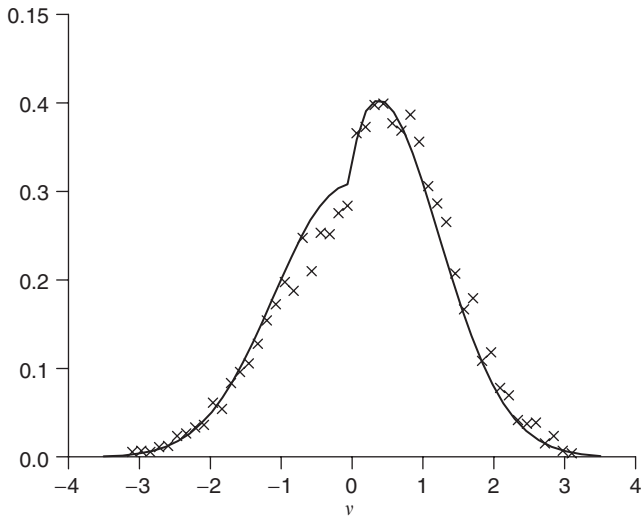


FIGURE 13.58 Wall distribution of velocities for specular reflection; $\gamma = 0^\circ$, $v_c = 1$.

gives the simple form

$$W(v,0) = W(u,0) \text{ for } u > v_c, \quad (13.244)$$

where v and u are related by Eq. (13.243). It is noted that $v_c = 0$ (no absorption and energy loss) gives the perfect reflection boundary condition $w(v,0) = w(-v,0)$, while letting $v_c \rightarrow \infty$ gives the perfect absorption case $w(v,0) = 0$, $v < 0$. The results were obtained for a range of values of the gravitational settling velocity v_g and critical impact velocities v_c . Figure 13.57 shows the results of solving the PDF equation(13.235) compared with those obtained from the simulation for the velocity distribution at the

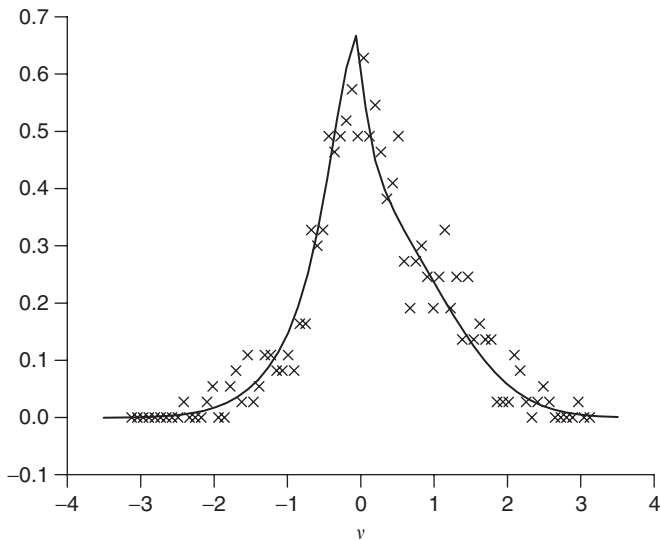


FIGURE 13.59 Wall distribution of velocities for specular reflection; $\gamma = 75^\circ$, $v_c = 1$.

wall for the specific case of a partially absorbing wall with $v_c = 5$ and $v_g = 5$ (in normalized units). Note there are two peaks, one centered at $v = v_g$ and the other with its center slightly displaced from the origin. The relative heights of these peaks depend upon the the ratio of v_c/v_g . For $v_c/v_g = 0$ (zero absorption) the latter peak has a maximum value $v = 0$, with no contribution from the peak at $v = v_g$. In contrast, the opposite is the case when $v_c/v_g \rightarrow \infty$.

13.4.3.4.3 Diffuse Reflection with Deposition

As an illustration, suppose that particles arriving at the surface are still reflected with a deterministic speed, but now, the velocity vector is directed at some random angle α to the surface. Since only particle transport in the direction normal to the wall is of concern, the rebound velocity can be taken as $v = -r \cos \alpha$ where, as in Eq. (13.243), the deterministic speed is. $r = \sqrt{u^2 - v_c^2}$. If $u < v_c$ then the particle is considered to adhere.

A variety of distributions $\Theta(v|u)$ can be constructed depending on the prescribed distribution of α . For the purpose of illustration, Darbyshire and Swailes (1996) considered the simple case, where the reflection angle α is uniformly distributed on $(-\gamma, \gamma)$ in which case

$$\Theta(v|u) = \begin{cases} \gamma^{-1}(u^2 - a^2)^{-1/2} & \text{for } a \leq u \leq c \\ 0 & \text{otherwise} \end{cases} \quad (13.245)$$

where $a(v) = \sqrt{v_c^2 + v^2}$ and $c(v) = \sqrt{v_c^2 + v^2 \sec^2 \gamma}$.

Predictions for the velocity distribution at the wall compared with those obtained from random walk simulations are shown in Figure 13.59 for $\gamma = 75^\circ$. Compare this distribution with that for specular reflection with the same critical impact velocity shown in Figure 13.58, which illustrates the essential effect of diffuse reflection, namely, the reduction near the wall of the normal component of the particle rms velocity, the effect becoming more pronounced with increasing γ . These features are accompanied with an increase in particle-wall concentration as γ increases.

13.4.3.4.4 Particle Deposition in a Turbulent Boundary Layer to a Perfectly Absorbing Wall

Analysis of near-wall behavior in this circumstance is dominated by both the boundary conditions that give rise to a wall PDF, which is far from Gaussian. Steep gradients of the turbulence near to the wall imply that for a particle with inertia the assumption of local equilibrium (as if the flow was locally

homogeneous) is invalid, i.e., even with perfectly reflecting boundary conditions, continuum approximations for particle transport is inappropriate. The influence of boundary conditions and changes in the turbulence within the near-wall region is covered by the single condition that variations in PDF over a particle mean free path must be small for the application of a traditional two-fluid model. It is therefore not surprising to find that gradient diffusion models for particle deposition in a turbulent boundary layer give generally poor agreement with experimental results, even the gradient diffusion is assumed to apply up to one particle stop distance away from the wall (the so-called gradient diffusion/free-flight models). See, for example the review by Papavergos and Hedley (1984). Reeks and Swailes (1993) have made predictions of the deposition velocity as a function of τ^+ (particle response time in wall units) by solving the PDF equations using the same wall functions as in the particle tracking model of Kallio and Reeks (1989). Values for k^+ were calculated from the asymptotic form of the PDF for large times downstream of the initial injection point of particles in the channel. In this case, the spectral collocation technique was used to solve a time-dependent PDF equation of the form (Kallio and Reeks, 1989):

$$\left(\frac{\partial}{\partial t} - v \frac{\partial}{\partial y} - \beta \frac{\partial}{\partial v} v - \mu(y) \frac{\partial^2}{\partial v^2} + \lambda(y) \frac{\partial^2}{\partial y \partial v} \right) \langle W(v, y, t) \rangle = 0 \quad (13.246)$$

in which the occurrence of spurious drift has been eliminated. The symbol y is the distance from the wall in wall units and v the particle velocity (normalized with respect to the friction velocity) at y toward the wall (in the $-y$ direction) and

$$\mu(y) = \beta \langle u(y, t) \Delta v(y, t | 0) \rangle \quad \lambda(y) = \beta \langle u(y, t) \Delta v(y, t | 0) \rangle$$

are based on their homogeneous forms, by using the same forms for the turbulence intensity and time scales normal to the wall used in Kallio and Reeks (1989). The predictions for k^+ versus τ^+ compared favorably with the experimental results of Liu and Agarawal (1974) shown in Figure 13.60. An important point to note is that while gradient transport is inappropriate in a traditionally based two-fluid model, it is acceptable in a PDF equation.

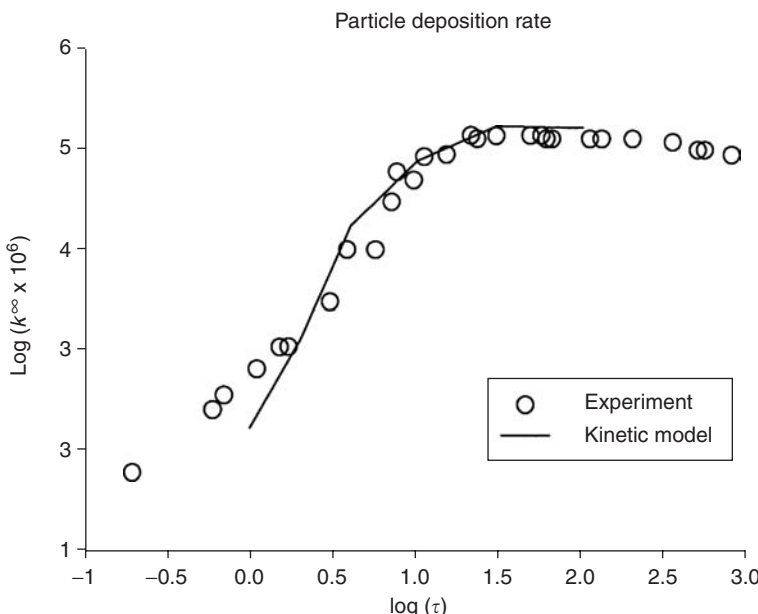


FIGURE 13.60 Particle deposition in turbulent pipe flow.

13.4.3.5 Particle Dispersion with Interparticle Collisions

Experimental and numerical simulations have indicated that inert particle collisions have a measurable influence on coarse particle transport properties in gas–solid turbulent flows, even for small values of the dispersed-phase volume fraction ($\alpha_p < 0.01$). In addition, detailed modelling of the interparticle collision rate is needed for accurate prediction of coalescence–agglomeration processes in dilute flows. By neglecting hydrodynamic interaction, hard sphere kinetic theory can be used to account for interparticle inelastic collisions in a PDF approach to particle flows. Thus, referring to Figure 13.61 for an inelastic collision between two identical spherical particles labeled 1 and 2,

$$\mathbf{v}'_1 = \mathbf{v}_1 + e_c(\mathbf{v}_{21}\hat{\mathbf{k}})\hat{\mathbf{k}}, \quad \mathbf{v}'_2 = \mathbf{v}_1 - e_c(\mathbf{v}_{21}\hat{\mathbf{k}})\hat{\mathbf{k}} \quad (13.247)$$

where \mathbf{v}'_1 and \mathbf{v}'_2 are the velocities of particles 1 and 2 after the collision related to the velocities \mathbf{v}_1 and \mathbf{v}_2 before the collision, involving the coefficient of restitution e_c , the unit vector $\hat{\mathbf{k}}$ directed from the center of the first colliding sphere to the center of the second at impact and \mathbf{v}_{21} is the relative velocity of particle 2 with respect to that of particle 1 at impact. Note that there is no interparticle friction.

While there are certain obvious similarities between molecular collisions and particle collisions in a turbulent flow, there are, however, fundamental differences because the continuous-phase turbulence plays an important role in the particle transport in a dilute mixture while dissipation induced by inelastic collision controls the particle kinetic energy in a dense flow. Indeed, in the kinetic theory of dilute gases, the statistics of binary collisions are derived by assuming that the velocities and positions of any two particles are independent of each other (the molecular chaos assumption), whereas, in gas–solid flow, the probable positions and velocities of colliding particles will definitely be correlated through their interaction with the same surrounding turbulent flow. In this section, we first describe the original approach due to Simonin (1991), which ignores this correlation, and then the approach proposed by Lavieille et al. (1995) that attempts to take it into account. A detailed description of the modelling approach can be found in He and Simonin (1994), Lavieille et al. (1995) and more recently in Simonin et al. (2002), and Vermorel et al. (2003).

13.4.3.5.1 Collision Integrals

If particle–particle interactions in which more than two particles take place are assumed to be negligible in number and effect, the collisional PDF rate of change may be written in terms of particle–particle pair

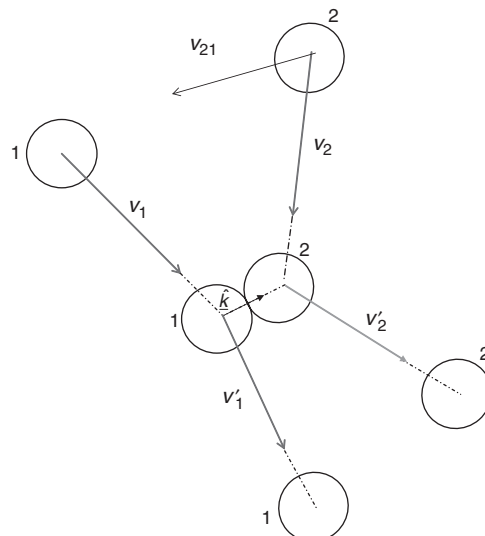


FIGURE 13.61 Kinematics of two colliding spherical particles.

distribution functions $\rho(2)(v_1, x_1, x_1, x_2, t)$ for particle 1 with velocity v_1 at position x_1 and particle 2 with velocity v_2 at x_2 , for which special closure assumptions are needed:

$$\left(\frac{\partial P}{\partial t} \right)_{\text{collisions}} = d_p^2 \int \int_{v_{21}\hat{k} > 0} \Delta \rho_{(2)}(v_1, x, x + d_p \hat{k}, t) v_{21} d \hat{k} dv_2 \quad (13.248)$$

Where $\rho = (v, x, t) = \langle w, v, x, t \rangle$

$$\Delta \rho_{(2)}(v_1, x, v_2, x + d_p \hat{k}, t) = \frac{1}{e_c^2} \rho_{(2)}(v_1^+, x, v_2^+, x + d_p \hat{k}, t) - \rho_{(2)}(v_1, x, v_2, x + d_p \hat{k}, t)$$

and

$$v_1^+ = v_1 + \frac{1 + e_c}{2e_c} (v_{21} \cdot \hat{k}) \hat{k}, \quad v_2^+ = v_2 + \frac{1 + e_c}{2e_c} (v_{21} \cdot \hat{k}) \hat{k}$$

assuming that both particles are identical spherical particles with diameter d_p . The mean collisional rate of change for some property ψ , e.g., kinetic energy, is the integral over all possible binary collisions of the change in ψ in a particular collision multiplied by the probable frequency of such a collision and can be written as

$$c(\psi) = d_p^2 \int \int \int_{v_{21}\hat{k} > 0} (\psi_2^+ - \psi_2) p_2(v_1, x, v_2, x + d_p \hat{k}, t) v_{21} \cdot \hat{k} d \hat{k} dv_1 dv_2 \quad (13.249)$$

13.4.3.5.2 Collision Models

By using the approach adopted in kinetic theory, the pair distribution functions in the collision integral is simply written in terms of the single-distribution function, assuming that colliding particle velocities are completely independent; namely,

$$\begin{aligned} \rho_{(2)}(v_1, x, v_2, x + d_p \hat{k}, t) &= P(v_1, x, t) P(v_2, x + d_p \hat{k}, t) \\ \tau_p &\gg \tau_e \quad (\text{eddy lifetime}) \end{aligned} \quad (13.250)$$

The above assumption has been retained in the derivation of the collision integral used by Simonin (1991) and is referred to as the random collision model.

This is also the assumption implicitly used by Oesterle and Petijean (1993) and Sommerfeld (1995). However, this assumption is valid only when the particle response time is much larger than the eddy-particle interaction time. In contrast, when the particle response time is of the same order or smaller than this interaction time, the approaching particle velocities will be correlated through interaction with the same eddy.

To account for correlation between colliding particles, an extended collision model is developed by expressing the particle pair distribution function $\rho_{(2)}(v_1, x, v_2, x + d_p \hat{k}, t)$ in terms of the joint fluid-particle-particle distribution function $\rho_{(2)}(u, v_1, x, v_2, x + d_p \hat{k})$ by assuming that the particle-particle velocity correlation is induced by particle interaction with the large-scale fluid turbulent motion. By definition

$$\rho_{(2)}(v_1, x, v_2, x + d_p \hat{k}) = \int \rho_{(12)}(u, v_1, x, v_2, x + d_p \hat{k}, t) du \quad (13.251)$$

and

$$\rho_{(2)}(v_1, x, v_2, x + d_p \hat{k}) = \rho_{(2)}(v_1, x | u, v_2, x + d_p \hat{k}) \rho_{(2)}(v_2, x + d_p \hat{k} | u, x) \rho_{(12)}(u, x) \quad (13.252)$$

where $(|)$ denotes a conditional PDF and explicitly $p_{12}(u, x)$ is the probability density of finding a carrier flow velocity u conditioned upon there being any particle at x . By using these relationships, it is assumed that

$$\rho_{(2)}(v_1, x | u, v_2, x + d_p \hat{k}) = \rho_{(2)}(v_1, x | u, x) \quad (13.253)$$

and, if the characteristic length scales of the carrier flow turbulence is larger than the particle diameter, then

$$\rho_2(v_2, x + d_p \hat{k} | u, x) \approx \rho_2(v_2, x + d_p \hat{k} | u, x + d_p \hat{k}) \quad (13.254)$$

By using the relationship

$$\rho_2(v_1, x, | u, x) \rho_{1/2}(u, x) = \rho_{12}(u, v, x) \quad (13.255)$$

the particle-particle pair distribution function may be written in terms of the fluid-carrier flow-particle joint PDF as

$$\rho_{(2)}(v_1, x, v_2, x + d_p \hat{k}) = \int \rho_{(2)}(u, v_1, x) \rho_{(2)}(u, v_2, x + \hat{k} d_p) \rho_{1/2}(u, x) du \quad (13.256)$$

13.4.3.5.3 Third-Order Moment Expansion (Grad's Theory)

Following Grad's theory of rarefied gases (1949), the distribution function in the collision term may be approximated by its third-order expansion in Hermite polynomials:

$$P(\underline{v}, \underline{x}, t) = \left[1 + \frac{a_{2,ij}}{2T_2^2} v'_i v'_j + \frac{a_{2,ijk}}{6T_2^3} v'_i v'_j v'_k - \frac{a_{2,ijj}}{2T_2^2} v'_i \right] P^0(\underline{v}, \underline{x}, t) \quad (13.257)$$

where using q^2 to denote the mean the particle kinetic energy per unit particle mass

$$T_2 = \frac{2}{3} q^2 \quad a_{2,ij} = \left(\overline{u'_{k,i} u'_{k,j}} \right)_2 - \frac{2}{3} q^2 \delta_{ij} \quad a_{2,ijk} = \langle v'_i v'_j v'_k \rangle$$

$P(\underline{v}, \underline{x}, t)$ is the equilibrium PDF, the product of the local spatial density and a Maxwellian distribution for the particle velocities i.e.,

$$P^0(\underline{v}, \underline{x}, t) = \frac{\langle p(\underline{x}, t) \rangle}{(4\pi q^2/3)^{3/2}} \exp\left(-\frac{v^2}{4q^2/3}\right) \quad (13.258)$$

By using the hard sphere collision model, Jenkins and Richman (1985) derived the following collisional terms in the transport equations for the particle mass (m), momentum (mv), kinetic stresses ($1/2mv'^2$), and kinetic energy flux, ($mv'_i v'_j v'_k$) respectively:

$$C(m) = 0 \quad (13.259a)$$

$$C(mv) = 0 \quad (13.259b)$$

$$C(mv'_i v'_j) = -\langle \rho \rangle \frac{\sigma_c}{\tau_c} \left(\langle v'_i v'_j \rangle - \frac{2}{3} q^2 \delta_{ij} \right) - \langle \rho \rangle \frac{(1 - e_c)}{2\tau_c^2} \frac{2}{3} q^2 \delta_{ij} \quad (13.259c)$$

$$C(mv'_i v'_j v'_k) = \frac{5}{12} \langle \rho \rangle \frac{\xi_c}{\tau_c} (9a_{ijk} - a_{ill}\delta_{jk} - a_{jll}\delta_{ik} - a_{mll}\delta_{ij}) \quad (13.259d)$$

where τ_c is the time between particle collisions and $\sigma_c = (1 + e_c)(3 - e_c)/5$ and $\xi_c = (1 + e_c)(49 - 3e_c)/100$. The collisional term in the kinetic stress transport equation is written as a return to isotropy term analogous to the Rotta term in the Reynolds stress transport turbulence modeling approach. Elastic collisions ($e_c = 1$) lead to a destruction of the off-diagonal correlations and redistribution of energy among the various normal stresses without modifying the total kinetic energy. The extension to inelastic collisions leads to a linear dissipation rate in the kinetic stress transport equations proportional to the collision frequency and a function of the coefficient of restitution.

Following Lavieville (1997), Grad's theoretical approach may also be used for correlated collisions by performing a Hermite polynomial expansion for the fluid–particle joint PDF. This eventually leads to a generalized form for the collisional source term in the kinetic stress transport equation:

$$C(mv'_i v'_j) = \langle \rho \rangle \frac{\sigma_c}{\tau_c} \left(a_{2,ij} + \frac{q_{12}^2}{4q_1^2} a_{1,ij} - \frac{q_{12}}{q_1^2} a_{12,ij} \right) - \langle \rho \rangle \frac{(1 - e_c^2)}{3\tau_c^2} (1 - \xi_{12}^2) \quad (13.260)$$

where

$$\begin{aligned} a_{k,ij} &= \left(\overline{u'_{k,i} u'_{k,j}} \right) - \frac{2}{3} q_k^2 \delta_{ij} \\ 2a_{12,ij} &= \left(\overline{u'_{1,i} u'_{2,j}} \right) + \left(\overline{u'_{1,j} u'_{2,i}} \right) - \frac{2}{3} q_{12} \delta_{ij} \\ \xi_{12}^2 &= \frac{q_{12}^2}{4q_1^2 q_2^2} \end{aligned}$$

with $k = 1$ referring to the continuous phase and $k = 2$ the dispersed phase and $u'_{k,p}$ is the fluctuating velocity component of phase k with respect to its mean value. Likewise q_k^2 is the turbulent kinetic energy of phase k and q_{12} are the particle fluid covariance $\left(\overline{u'_{1,i} u'_{2,i}} \right)$.

13.4.3.5.4 Intercollision Time

The interparticle collision frequency can be computed in terms of the binary particle distribution function as

$$\frac{1}{\tau_c} = \frac{nd_p^2}{n} \iint |v_1 - v_2| p_2(v_1, v_2) dv_1 dv_2$$

where n is the particle number density. Using the form for $p_2(v_1, v_2)$ derived for correlated collisions gives

$$\tau_c = \tau_c^k (1 - \xi_{12}^2)^{-1/2}$$

where τ_c^k is the standard kinetic theory interparticle collision time based on the molecular chaos assumption and given explicitly by

$$(\tau_c^k)^{-1} = n\pi d_p^2 \sqrt{\frac{16}{\pi} \frac{2}{3} q_2}$$

The above equations show that the effective interparticle collision rate based on the correlated collision model is always smaller than the one given by standard kinetic theory and decreases with respect to the ratio of the eddy–particle interaction time to particle relaxation time as a result of the increase of correlation coefficient ξ_{12} . This behavior was observed by Lavieville et al. (1995) in LES-Lagrangian simulations in homogeneous isotropic turbulent flows showing that neighboring particles have correlated turbulent velocities.

13.4.3.6 Conclusions and Future Developments

The PDF approach provides a rational framework in which the behavior of a flow of dispersed particles can be formulated. The focus here is on the PDF equation itself, how it is derived and how it is used to obtain the continuum equations and constitutive relations for the dispersed phase in a two-fluid model. In addition, the approach can also be used to deal with the near wall behavior by incorporating the influence of boundary conditions in a natural and complete way. The example considered here was of particles impacting the wall with rebound and absorption (impact adhesion or sticking). This poses serious problems in the traditional two-fluid approach not only because the boundary conditions have to be cast in an artificial form (based on certain adhoc assumptions about the particle velocity distribution at the wall), but also because the continuum equations break down close to the wall. Furthermore, the traditional two-fluid approaches make certain assumptions about the properties of the dispersed phase; i.e., it behaves as a simple Newtonian fluid, which is strictly a heuristic assumption.

It is important to appreciate also that closure approximations for the PDF equations are necessarily carried out in particle-phase space (particle velocity and position in the inert particle cases considered here). This means that a single closure approximation in phase space implies closure at all levels of the moment equations (i.e., closure of the continuum equations and higher order moment equations). All these important features were discussed in the subsection on accuracy and reliability of PDF approaches.

In this section, the focus was on dilute flows and dense flows (through the influence of interparticle collisions). The problem of two-way coupling and turbulence modification by the dispersed phase was not discussed. It is clear, however, that the closure terms in the mass, momentum, and Reynolds stress transport equations for the continuous phase bear a relationship to two-way coupling and turbulence modification. However, the crucial problem on how the particles influence the turbulence dissipation in the continuous phase in terms of closure has not been dealt with adequately. This is all bound up with the way particles interact with turbulent structures, in particular how particles influence their flow topology and persistence and how this influences the internal dynamics of turbulence production and dissipation and the demixing and segregation of the particles themselves in a turbulent flow. While these features have formed the basis of numerous simulations and experiments, the problem of how these features can be incorporated in a strictly formal way into a PDF formulation has not yet been achieved and remains a significant challenge for the future.

13.5 Applications

Th. Frank, Y. Onishi, and B. van Wachem

13.5.1 Lagrangian Prediction of Performance Parameters in Cyclone Separators

Th. Frank

13.5.1.1 Introduction

Disperse multiphase flows are very common for processes in mechanical and thermal process technology (e.g., gas-particle or gas-droplet flows, coal combustion, pneumatic conveying, and erosion phenomena). Processes for the separation of solid particles from gases or fluids and the classification and particle size analysis are an important field of interest in process technology. Most of the flow regimes in technical processes are real three-dimensional and cannot be restricted to two-dimensional numerical analysis. Therefore, this section deals with a Lagrangian approach for the prediction of three-dimensional, disperse gas-particle flows, and its application for flow simulation in cyclone particle separators.

The investigations of the precipitation of quartz particles were carried out for a series of four geometrically similar cyclones of different size and for a number of different gas inlet velocities. Numerical results were compared with experiments by König (1990) and showed a very good agreement with experimentally predicted particle precipitation rates.

13.5.1.2 Basic Equations of Fluid Motion

The three-dimensional, two-phase (gas-particle) flow in the cyclone separator is described by assuming that the particulate phase is dilute and the particle loading is rather low. This assumption satisfies the neglect of interparticle effects and contributing source terms in the Navier-Stokes equations due to particle-fluid interaction. Further, the two-phase flow is assumed statistically steady, incompressible, and isothermal. Then, the time-averaged form of the governing gas phase equations can be expressed in the form of the general transport equation :

$$\begin{aligned} \frac{\delta}{\delta x}(\rho_F u_F \Phi) + \frac{\delta}{\delta y}(\rho_F v_F \Phi) + \frac{\delta}{\delta z}(\rho_F w_F \Phi) \\ = \frac{\delta}{\delta x}\left(\Gamma_\Phi \frac{\delta \Phi}{\delta x}\right) + \frac{\delta}{\delta y}\left(\Gamma_\Phi \frac{\delta \Phi}{\delta y}\right) + \frac{\delta}{\delta z}\left(\Gamma_\Phi \frac{\delta \Phi}{\delta z}\right) + S_\Phi + S_\Phi^p \end{aligned} \quad (13.261)$$

were Φ is a general variable, Γ_Φ a diffusion coefficient, S_Φ a general source term, and S_Φ^P the source term due to particle–fluid interaction ($S_\Phi^P \equiv 0$ if coupling of the continuous and disperse phase can be neglected). The relationship among of S_Φ , Γ_Φ , S_Φ and S_Φ^P and the constants of the standard k – ϵ turbulence model used for the present numerical simulation are given in Section 13.3.

13.5.1.3 Equations of Motion of the Disperse Phase

The disperse phase is treated by the application of the Lagrangian approach, i.e., discrete particle trajectories are calculated. Each calculated particle represents a large number of physical particles of the same physical properties, which is characterized by the particle flow rate \dot{N}_P along each calculated particle trajectory. The prediction of the particle trajectories is carried out by solving the ordinary differential equations for the particle location and velocities. By assuming that the ratio of fluid to particle density is small ($\rho_F/\rho_P \ll 1$), these equations read as follows:

$$\frac{d}{dt} \begin{bmatrix} x_p \\ y_p \\ z_p \end{bmatrix} = \begin{bmatrix} u_p \\ v_p \\ w_p \end{bmatrix} \quad (13.262)$$

$$\frac{d}{dt} \begin{bmatrix} u_p \\ v_p \\ w_p \end{bmatrix} = \frac{3}{4} \frac{\rho_F}{(\rho_p + \frac{1}{2}\rho_F)d_p} \left(v_{\text{rel}} C_D (Re_p) \begin{bmatrix} u_F - u_p \\ v_F - v_p \\ w_F - w_p \end{bmatrix} \right) \quad (13.263)$$

$$+ \frac{2v_F^{1/2}}{\pi |\Omega|^{1/2}} C_A \begin{bmatrix} (v_F - v_p)\Omega_z - (w_F - w_p)\Omega_y \\ (w_F - w_p)\Omega_x - (u_F - u_p)\Omega_z \\ (u_F - u_p)\Omega_y - (v_F - v_p)\Omega_z \end{bmatrix} + \frac{\rho_p - \rho_F}{\rho_p + \frac{1}{2}\rho_F} \begin{bmatrix} g_x \\ g_y \\ g_z \end{bmatrix}$$

with

$$\Omega = \text{rot } v_F \quad Re_p = \frac{d_p v_{\text{rel}}}{v_F} \quad v_{\text{rel}} = \sqrt{(u_F - u_p)^2 + (v_F - v_p)^2 + (w_F - w_p)^2}$$

These equations of motion of the disperse phase include, on the RHS, the drag force, the lift force due to shear in the fluid flow field (Saffman force), the gravitational and added mass force. For the present numerical investigation the Magnus force due to particle rotation is neglected because of there minor importance in the study of the very fine particles in the particle diameter range.

The values for the coefficients C_D and C_A can be found in the literature of Frank et al. (1997), Frank (2002), and Sommerfeld (1996). In addition, for the lift coefficient C_A , the correction obtained by Mei (1992) is taken into account. The effect of fluid turbulence on the motion of the disperse phase, which is regarded to be very important for the particle diameter range under investigation, is modeled by the Lagrangian stochastic–deterministic (LSD) turbulence model proposed by Milojević (1990). The particle–wall collisions are treated according to the irregular bouncing model by Sommerfeld (1992, 1996) in the modified wall roughness formulation given by Tsuji et al. (1991), Frank et al. (1997), and Frank (2002).

13.5.1.4 Solution Algorithm

The time-averaged equations of fluid motion are solved by using the program package MISTRAL-3D, initially developed by Perić (1992) and Schreck and Perić (1992). The program MISTRAL/PartFlow-3D was extensively modified by the authors for gas–particle flow computations. Further modifications involve the implementation of a standard k – ϵ turbulence model and the parallelization of the solution algorithm by application of a domain decomposition method. The most fundamental features of MISTRAL/PartFlow-3D are :

- Use of nonorthogonal, boundary-fitted, numerical grids with arbitrary hexahedral control volumes
- Use of block-structured numerical grids for geometrical approximation of complex flow domains

- Parallelization using domain decomposition method for both the Eulerian and the Lagrangian part of the computation
- Finite-volume solution approach of SIMPLE kind with colocated variable arrangement; Cartesian vector and tensor components; and full multigrid solution approach

The solution algorithm for the equations of particle motion is based on the program package, PartFlow, developed by the authors. A detailed description of the three-dimensional solution algorithm and the developed parallelization methods for the Lagrangian approach can be found in Frank et al. (1997), Frank and Wassen (1997), and Frank (2002).

13.5.1.5 Gas–Particle Flow in and Performance of a Standard Cyclone

The presented three-dimensional Lagrangian approach was applied to the gas–particle flow in a standard cyclone shown in [Figure 13.62](#). The calculations were based on experimental investigations carried out by König (1990) on a series of geometrically similar cyclones for a number of different inlet gas velocities.

13.5.1.5.1 Flow Geometry and the Numerical Grid

The cyclones Z10, Z20, Z40 and Z80 investigated in this paper were determined by the following geometrical properties (see also [Figure 13.62](#)):

	Z10	Z20	Z40	Z80
Diameter of the cyclone (mm)	D	40	80	160
Height of the cyclone (mm)	H	195	390	780
Inlet cross-section (mm^2)	$a \times b$	4.5×18	9×36	18×72
Diameter of the gas exit (mm)	d_T	10	20	40
Height of the gas exit (mm)	H_T	31	62	124
Diameter of the particle exit (mm)	d_B	10	20	40

Owing to the complex geometry of the cyclone, a numerical grid with 42 different grid blocks and about 250,000 finite-volume elements had to be designed for the numerical calculations of the gas–particle flow. The numerical grid was originally designed for the Z10 cyclone and then proportionally scaled as 1 : 2 : 4 : 8 for the other three cyclones Z20–Z80.

13.5.1.5.2 Prediction of the Gas and Particle Flow, Pressure Loss

In the course of preliminary calculations of the gas flow field in the cyclones, it was found that the numerical mesh needed further improvement and certain grid refinement in regions of large fluid velocity gradients in order to get converged solutions. Grid refinement was applied to the gas inlet and to the region in the vicinity of the lower end of the gas exit tube. But certain restrictions in the mesh generation algorithm prevented an optimum arrangement and design of the finite-volume elements in some regions of the flow geometry. Consequently, strong underrelaxation had to be applied for the solution algorithm in order to obtain convergence, mainly due to the convergence behavior of the k – ε equations.

Calculated flow fields show the typical asymmetrical main vortex in the upper cylindrical part of the cyclone. In a more detailed view, a flow recirculation can be found along the lid of this cylindrical part of the cyclone and further downward along the outer wall of the gas exit tube. This type of recirculating flow is well known for cyclone separators from the literature. The flow field in the other parts of the cyclone is also in qualitative agreement with the knowledge available for the flow in cyclone separators. The predicted trajectory of a particle in the Z10 cyclone is shown in [Figure 13.63](#).

The pressure loss over the cyclone was predicted for various gas inlet velocities and compared with the experimental data of König in [Figure 13.64](#). The pressure loss data of König take only into account the difference of the static pressure before and after the cyclone. The figure shows that the numerical calculations underpredict the pressure loss for all gas inlet velocities investigated. The reason for this is most likely due to slight differences between the experimental setup and the flow geometry investigated numerically. The numerical data for the pressure loss show a comparable increase with an increased gas inlet velocity.

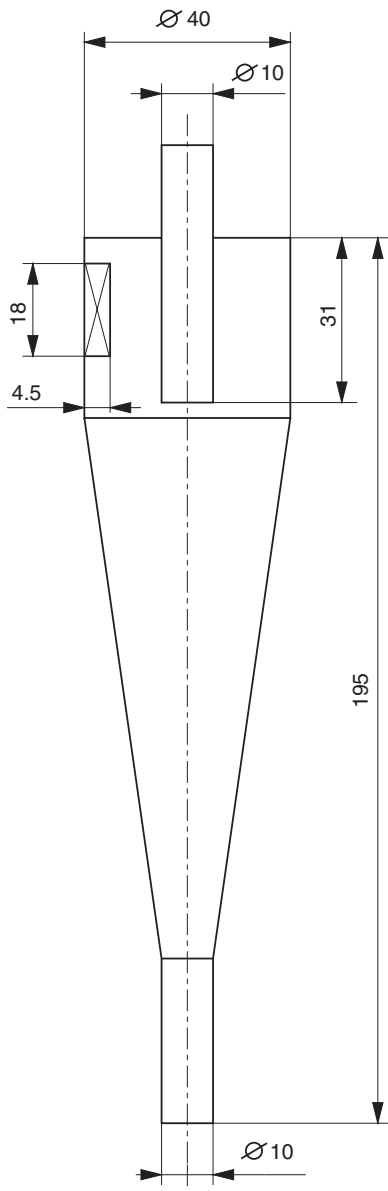


FIGURE 13.62 Scheme of the standard cyclone Z10.

Particle trajectory calculations were carried out using the described Lagrangian approach with the predicted gas flow fields in order to obtain particle collection efficiencies for the four different cyclones (see Figure 13.64). The main difficulties in the calculation of particle motion include :

- 1 The flow in the cyclone leads to a very large number of particle–wall collisions. The detection of a particle–wall collision results in a decrease in the integration time step of the solution algorithm. Therefore, the large number of particle–wall collisions lead to large computation times for predicting particle motion.
- 2 The large computation time needed for cyclone flow prediction is also determined by considering the influence of gas flow turbulence on particle motion. In order to ensure accuracy, the integration

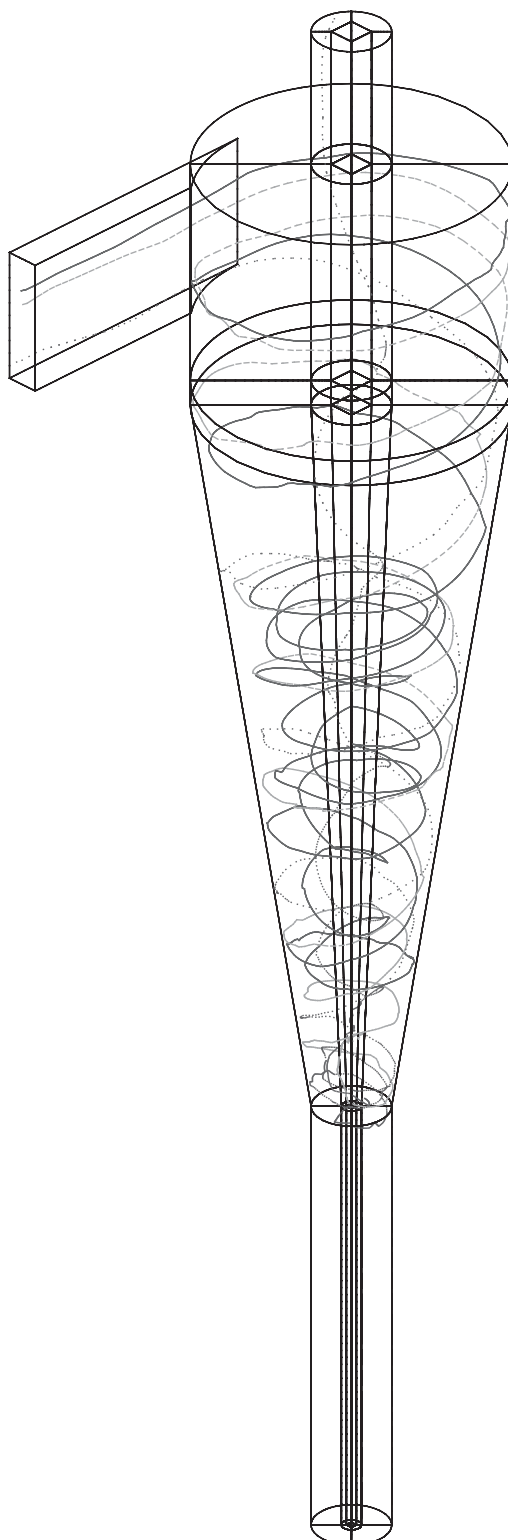


FIGURE 13.63 Particle trajectories in Z10 for gas inlet velocity $U_f = 10$ m/sec, $d_p = 1, \dots, 5 \mu\text{m}$.

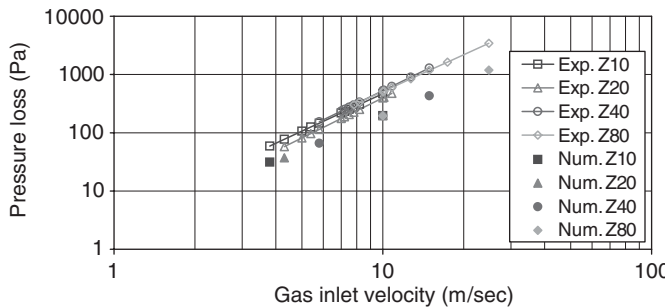


FIGURE 13.64 Comparison of pressure loss vs. gas inlet velocity for Z10,...,Z80 cyclones.

time step is set to be less than one tenth of the turbulent time scale of the LSD turbulence model. The resulting small time steps of the Runge–Kutta solver for the particle equations of motion contribute to the large computational effort needed for the present simulation.

- 3 The larger geometrical size of the Z40 and Z80 cyclones lead to a substantial increase in particle residence time in the cyclone and thus to larger computation time.

As a result, the calculation of about 10,000 particle trajectories in the cyclone separator takes about 22 hours of CPU-time on a single MIPS R10000 processor of a Silicon Graphics CRAY Origin2000.

13.5.1.5.3 Calculation of the Particle Collection Efficiency

In accordance with the experiments by König (1990), investigations for the prediction of the particle precipitation rate were carried out for the physical properties of quartz particles. The original quartz dust had a particle diameter distribution in the range of $d_p = 0 - 50 \text{ } \mu\text{m}$ with a number mean particle diameter of $\bar{d}_p = 10.9 \text{ } \mu\text{m}$. The numerical simulations were carried out for 20 particle diameter classes in the range between 0.5 and 15 μm . A total number of 670 particle trajectories with random initial conditions in the inlet cross-section were calculated for each of the 20 particle diameter classes. A particle density of $\rho_p = 2500 \text{ kg/m}^3$ was assumed for the quartz particles. For the coefficients of restitution and kinetic friction, typical values for quartz particles were used ($k = 0.8, f = 0.35$).

In a first series of calculations, the collection efficiencies for the quartz particles were predicted for all four cyclones Z10, ..., Z80 with an inlet gas velocity of $u_i = 10 \text{ m/sec}$. The collection efficiency is defined as

$$\eta(d_p) = 1 - \frac{\dot{N}_{\text{out}}(d_p)}{\dot{N}_{\text{in}}(d_p)}$$

where $\dot{N}_{\text{in}}(d_p)$ and $\dot{N}_{\text{out}}(d_p)$ are the particle flow rates for a given particle size in the inlet cross-section and gas exit cross-section at the top of the cyclone, respectively. In the numerical prediction, particles are assumed to be collected in the cyclone, if :

1. The particle trajectory reaches the bottom cross-section of the cyclone.
2. The particle sticks to the wall of the cyclone (which means the wall normal velocity of the particle after a particle–wall collision is less than 10^{-5} m/sec).
3. The particle residence time in the cyclone is larger than the maximum allowed computation time, which was set to $T_{\max} = 150 \text{ sec}$ for Z10, and Z20 and to $T_{\max} = 250 \text{ sec}$ for cyclones Z40 and Z80, due to their larger geometrical size. The value for T_{\max} was chosen in a way, that the number of particles with this very large residence time in the cyclone was less than 4–5% of the calculated particle trajectories.

A comparison of the predicted and measured collection efficiencies for the Z20 cyclone operating at two inlet velocities is shown in Figure 13.65. One notes that the shapes of the collection efficiency curves are similar. The higher inlet velocity leads to the collection of smaller particles. The numerical predictions for

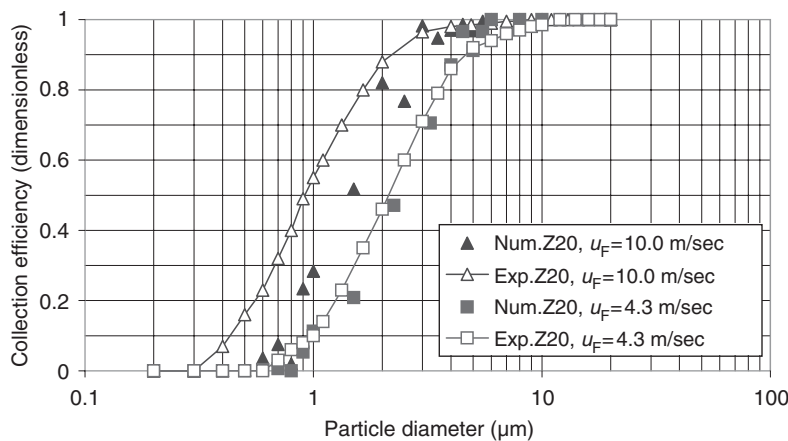


FIGURE 13.65 Comparison of particle collection efficiencies for Z20 and gas inlet velocities $u_f = 4.3$ m/sec and 10 m/sec.

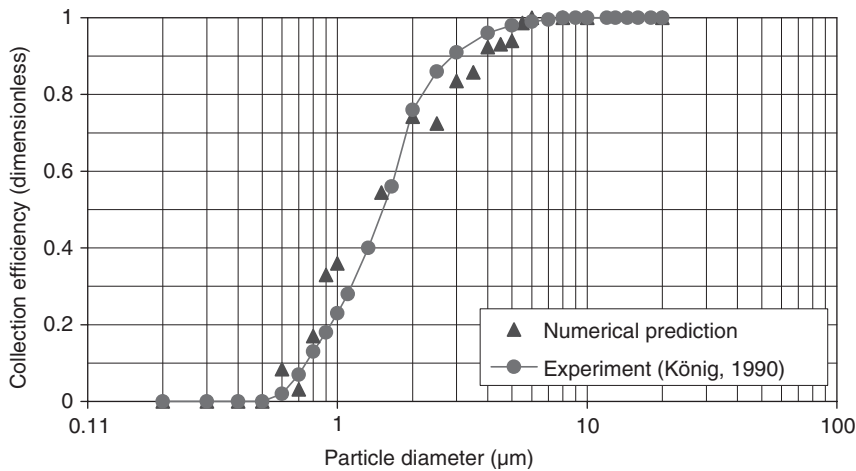


FIGURE 13.66 Comparison of the particle collection efficiencies for the Z80 cyclone, $u_f = 10$ m/sec.

the 4.3 m/sec inlet velocity agree better with experimental results than those for the 10 m/sec inlet velocity. A further comparison of the predicted and measured collection efficiencies for the Z80 cyclone with an inlet velocity of 10 m/sec is shown in Figure 13.66. One notes reasonably good agreement, although the slopes of the efficiency curves differ somewhat near the cut-off diameter (50% efficiency). Numerical predictions for the other cyclone geometries can be found in Frank (2000, 2002).

This section illustrates the capability of the three-dimensional Lagrangian approach to predict multiphase flows in complex geometries. The predictions for pressure loss and collection efficiency agree well with experimental results.

13.5.2 Slurry Flows

Yasuo Onishi

Slurry flows occur in many circumstances, including chemical manufacturing processes, pipeline transfer of coal, sand, and minerals, mud flows, and disposal of dredged materials. In this section, we discuss slurry flow applications related to radioactive waste management.

13.5.2.1 Tank Waste Characteristics and Waste Retrieval Operations

Two-hundred million liters of wastes containing 180 million curies of radioactivity are stored in single- and double-shell underground tanks at the U.S. Department of Energy's Hanford Site in southeastern Washington State (Gephart and Lundgren, 1997). Much of this waste is removed from the tanks and solidified at a waste treatment plant, then buried at disposal sites. These wastes are highly basic (pH 10–14), have high salt content, and are chemically and physically very complex. Sludges, saltcakes, liquids, and vapors often coexist in the same tank. Sludges consist of an interstitial solution and solids that are not dissolvable with water, while saltcakes contain an interstitial solution and water-dissolvable solids.

The solids in the sludges and saltcakes vary widely in chemical and physical characteristics (Onishi et al., 2003; Jewett et al., 2002). The solids contain primary particles to agglomerates, with sizes ranging over five orders of magnitude. The smallest particles comprise many hydrous oxides, including ZrO_2 and $FeOOH$, whose diameters are 3–6 nm. Other particles such as boehmite ($AlOOH$) and apatite are 0.1–1 μm in size. These submicron primary particles found in many tanks form agglomerates that are typically 1–10 μm in size, but can reach 100 μm or more. Some of the largest primary particles are gibbsite ($Al(OH)_3$) and uranium phosphate, which can exceed 20 μm in size. Trisodium phosphate hydrates ($Na_3(PO_4) \cdot 12H_2O$) have a needle-like shape and exceed 100 μm in length (Onishi et al., 2002). Hydrated sodium phosphate can interlock to form a gel if sufficient particles exist in the tank. The densities and sizes of primary particles range from 2.26 g/mL for $NaNO_3$ to 11.4 g/mL for pure PuO_2 , but agglomerates and flocs tend to be around 1.5 ~ 2.5 g/mL (Onishi et al., 2002). The waste often contains radioactive ^{90}Sr and ^{137}Cs , whose radionuclide decay heats the waste, sometimes to above 100°C.

The sludge and saltcake are mostly non-Newtonian, and the supernatant liquid is Newtonian. The slurry (mixture of sludge or saltcake and supernatant liquid) can be Newtonian or non-Newtonian. Figure 13.67 shows the waste rheology in double-shell tank 241-SY-102, indicating that the sludge can be represented as a Bingham flow, while the sludge diluted by 48 wt% supernatant liquid is Newtonian (Onishi et al., 1996). Figure 13.68 presents the variation in viscosity of boehmite waste with pH, indicating that the viscosity can change with chemical conditions even without dilution.

One to four 300-hp mixer pumps are installed in 28 of the 4000m³ double-shell tanks at the Hanford Site to stir radioactive sludge or saltcake and supernatant liquid. These mixer pumps withdraw the sludge or saltcake waste from near the tank bottom and inject it back into the tank waste through two 0.3-m-diameter

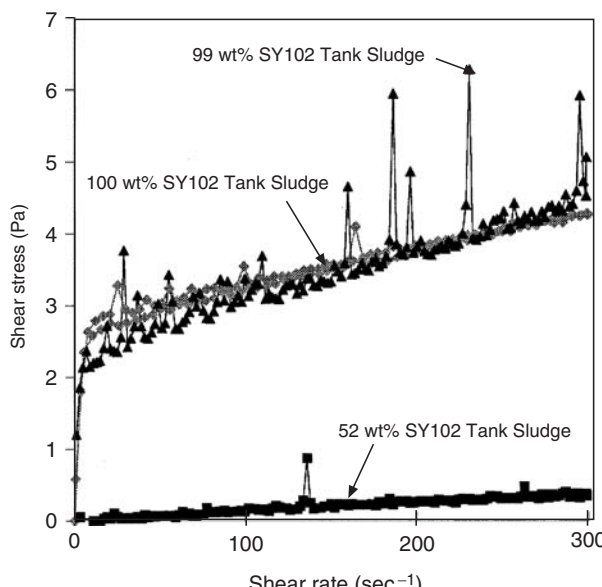


FIGURE 13.67 Rheology of Tank 241-SY-102 Newtonian and non-Newtonian wastes.

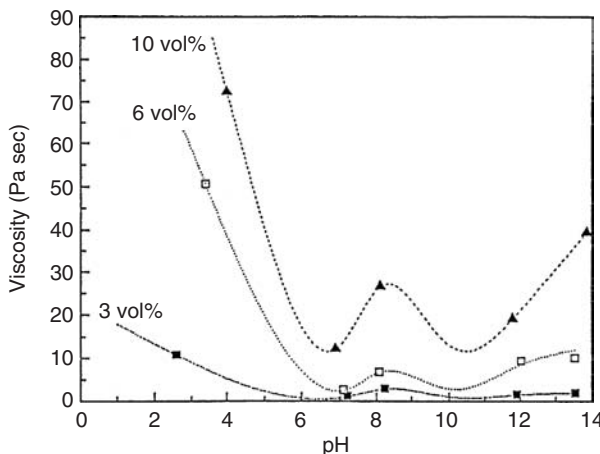


FIGURE 13.68 Viscosity of boehmite in 1M NaNO₃ as a function of pH and solids loading at a strain rate of 11.5 sec⁻¹.

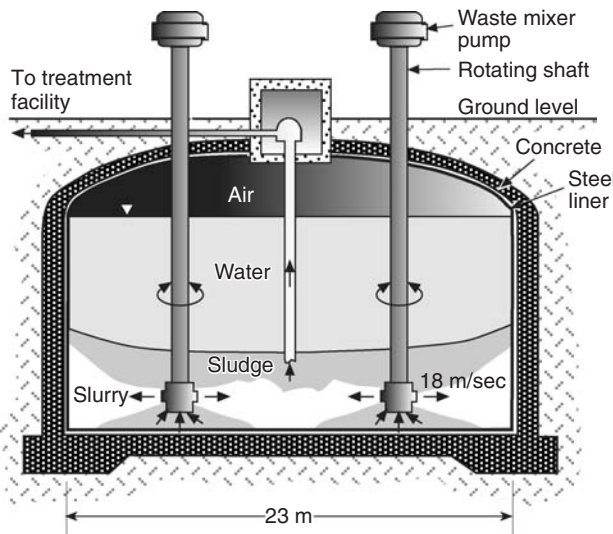


FIGURE 13.69 Mixer pumps in a double-shell tank.

nozzles at 18m/sec exit velocity. The pumps will rotate at 0.5–0.02 r/min to stir up the sludge or saltcake and supernatant liquid in the tank, blending them into a slurry that will be pumped from the tank to a waste treatment facility, as shown in Figure 13.69 (Onishi et al., 2003). In some cases, solvents (e.g., water or sodium hydroxide solution) will be added to dissolve and thus reduce the amount of solids, decrease the density and viscosity of the slurry, and make the waste easier to mix, retrieve, and transfer through pipelines to other tanks or to the treatment facility.

When the sludge is mixed with supernatant liquid or solvent in the tank, physical and chemical changes occur. Dilution alone changes important physical properties. This change can be observed from rheological measurements of double-shell tank 241-SY-102 waste at Hanford (Onishi et al., 1996). As shown in Figure 13.67, the original sludge is non-Newtonian, while the sludge diluted by 48 wt% supernatant liquid is Newtonian. Thus, when the sludge is withdrawn to the mixer pump near the tank bottom and injected back into the sludge layer, the jet is a non-Newtonian flow. The jet entrains the supernatant fluid

as it penetrates and mixes with the waste. The resulting slurry becomes a Newtonian flow with significantly reduced viscosity and shear stress. Furthermore, chemical reactions caused by waste mixing can dissolve or precipitate solids. Thus, changing solid mass as well as the densities and rheologies of sludge, saltcake, and the resulting mixed slurry and supernatant liquid affect waste mixing. For example, if chemical conditions and solids concentrations are such that boehmite and its aggregates form, the waste becomes a gel and the tank waste can neither be removed from the tank nor transferred into treatment facilities through pipelines.

13.5.2.2 Waste Retrieval Assessment Model

Since waste retrieval and treatment cost is very high, the waste retrieval design and operation decision-making must be scientifically defensible. To address the complex interactions among waste mixing, chemical reactions, and rheology during the waste retrieval operation, waste assessment tools that accurately simulate the flow field, turbulence, heat transfer, and chemical reactions are needed.

The ARIEL code (Onishi et al., 1995) is a reactive computational fluid dynamics code that is an example of this type of tool and couples chemistry and fluid dynamics (Yeh and Tripathi, 1989; Steefel and Lasaga, 1994). It is a time-varying, three-dimensional code whose fluid dynamic portion uses integral forms of the following fundamental conservation laws applied in a finite-volume formulation (Trent and Eyler, 1994):

- Conservation of mass (equation of continuity)
- Conservation of momentum (the Navier–Stokes equation)
- Conservation of turbulent kinetic energy and its dissipation (with the k – ε model)
- Conservation of energy (the first law of thermodynamics)
- Conservation of mass for solids, liquids, and gases

These equations are discussed in Sections 13.1 and 13.3. ARIEL has some built-in common Newtonian and non-Newtonian rheology models (e.g., power law and Bingham model), but it can also accept a user-input rheology model. In addition to the free solids settling, it also simulates hindered solids settling.

ARIEL also calculates chemical equilibrium and kinetics. The equilibrium chemistry submodel minimizes the Gibbs free energy to simulate fast aqueous chemical reactions (Felmy, 1995). Since much of the tank waste exists under high ionic-strength conditions, the excess solution free energy is modeled by the Pitzer equations (Pitzer, 1991) in the aqueous-phase modeling. The governing equations to minimize the Gibbs free energy subject to the mass and charge balance are

$$G = \sum_{j=1}^{ns} \mu_j n_j \quad (13.264)$$

subject to

$$\sum_{j=1}^{ns} A_{ij} n_j = b_i \quad i = 1, p \quad (13.265)$$

$$\sum_{j=1}^{nas} z_j n_j = 0 \quad (13.266)$$

$$n_j \geq 0 \quad \text{for all } j \quad (13.267)$$

where G is the Gibbs free energy, μ_j the chemical potential of species j , n_j the number of moles of species j , ns the total number of the chemical species in the system, A_{ij} the number of moles of component i in 1 mol of species j , b_i the number of moles of each component i , p the number of linearly independent mass-balance constraints, z_j the charge of species j , and nas the number of aqueous species.

The kinetic chemistry in ARIEL simulates kinetic reactions of precipitation or dissolution. We used the following rate law for the solid, i , and the associated aqueous species, j :

$$\frac{d[C_{si}]}{dt} = \{k_{i1} + k_{i2}[C_{si}]\} \left\{ 1 - \frac{Q_i}{K_i} \right\} \quad (13.268)$$

$$\frac{d[C_{wj}]}{dt} = a_{ij} \frac{d[C_{si}]}{dt} \quad (13.269)$$

where $[C_{si}]$ is the molality of solid i ; k_{il} is the reaction rate of solid i 's, which is independent of the solid concentration, k_{i2} is solid i 's reaction rate, which is dependent on the solid concentration, Q_i the activity product, K_i an equilibrium constant, $[C_{wj}]$ the molality of aqueous species j , and a_{ij} the number of moles of aqueous species j produced from precipitation-dissolution of one mole of solid i .

13.5.2.3 Tank Waste Modeling

We present five simulation cases related to tank waste mixing: (1) generic solid erosion modeling, (2) tank 241-AN-105 sludge waste mixing, (3) tank 241-AZ-102 sludge waste mixing, (4) two-dimensional reactive transport modeling, and (5) three-dimensional reactive transport modeling.

13.5.2.3.1 Generic Solids Erosion Modeling

We examined mobilization and settling of tank wastes having yield strengths of 200, 1000, 2000, or 3000 Pa by simulating pump jet injection into saltcake and sludge and the subsequent mixing. The modeling indicated that the slurry pump jets burrow rapidly into the saltcake and sludge bank, collapsing an overhanging solids layer but eroding only those portions of the solids layer where the normal and shear stresses are greater than or equal to the yield strength of the sludge.

Simulation results (Onishi and Trent, 1999) are shown in Figure 13.70 for saltcake and sludge wastes with yield strengths of 200 Pa (a representative value of saltcake waste) and 1000 Pa (a representative value of sludge waste). As shown on the left panel of the figure, the jet injected by the pump is strong enough to penetrate the entire length of the weaker saltcake (200-Pa yield strength). Its lateral spread is still rather limited because the saltcake resists being mobilized by the weaker jet-induced velocity at the peripheral of the jet. With greater sludge strength of 1000 Pa, the jet did not penetrate the entire length of the sludge (right panel of Figure 13.70). With the 2000 Pa sludge the jet mobilized even less, and the mixer pump mobilized none of the 3000 Pa sludge. These tests showed that solids mobilization and immobilization are strongly controlled by the yield strength of the saltcake and sludge. The solids were eroded little by shear stress but mostly by normal stress; thus, *in situ* or laboratory measurements should obtain the strength of the saltcake and sludge in resisting the combined forces of normal and shear stresses.

13.5.2.3.2 Tank 241-AN-105 Saltcake Waste Mixing

The ARIEL code was applied to Hanford double-shell tank 241-AN-105 to determine whether two 300-hp mixer pumps could mobilize and mix the saltcake, which is 4.5-m thick (1850 m³) and overlain by

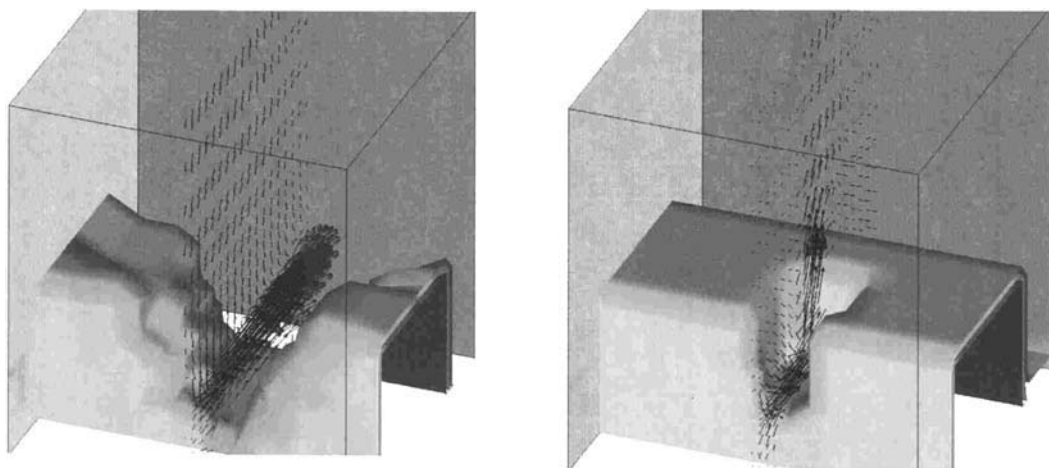


FIGURE 13.70 Three-dimensional distributions of predicted velocity and erosion patterns of the saltcake and sludge with yield strengths of 200 and 1000 Pa, respectively, at one simulation hour.

5.5-m-deep supernatant liquid (2240 m^3) and a 0.4m-thick crust at the top (185 m^3) (Onishi et al., 2003). The viscosity of this tank waste varies seven orders of magnitude from the saltcake to the supernatant liquid, as shown in Figures 13.71 and 13.72. Figure 13.71 presents *in situ* saltcake viscosity measured by a falling ball rheometer at its first and fourth passes, while Figure 13.72 shows both *in situ* and laboratory viscosity measurements (Onishi et al., 2003; Stewart et al., 1996; Herting, 1997). Since commonly used non-Newtonian rheology models do not fit the measured rheology well, we developed and incorporated into the ARIEL code the following tank-specific rheology model (lines in Figure 13.72) as a

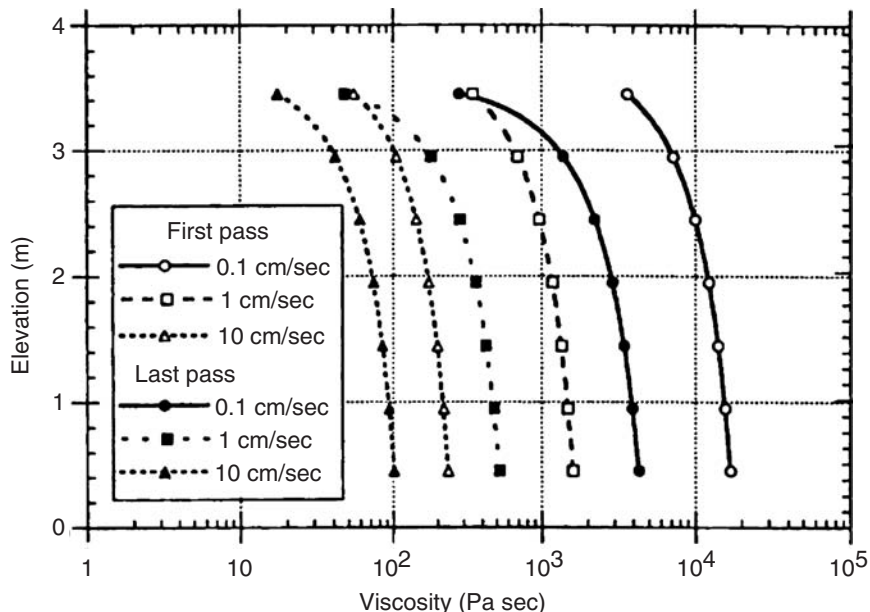


FIGURE 13.71 *In situ* viscosity of Tank 241-AN-105 waste.

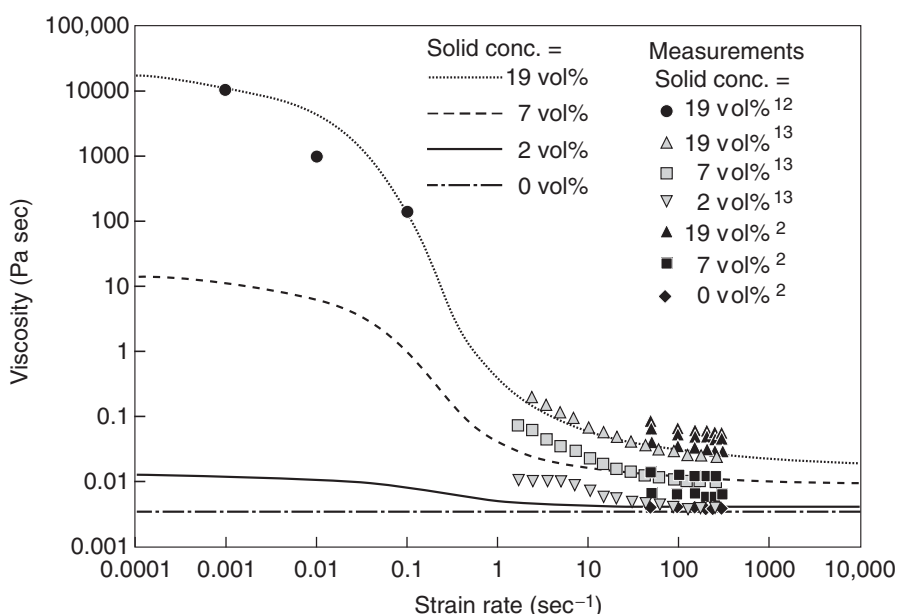


FIGURE 13.72 Viscosity measurements and rheology model for Tank 241-AN-105 waste.

function of solids concentration and strain rate (Onishi et al., 2003).

$$\mu = \mu_L \exp \left(A \left\{ 1 + a_1 \left[1 - \frac{2}{\pi} \arctan(a_2 \ln \lambda \gamma + a_3) \right] \right\} \right) \quad (13.270)$$

$$A = \frac{a_4 \beta (1 + 4\beta)}{1 - a_5 \beta (1 - 2\beta + a_6 \beta^2)}, \quad \text{and} \quad \beta = \frac{C_v}{C_{v \max}}$$

where α_i are constants, C_v a solid volume fraction, $C_{v \max}$ the maximum solid volume fraction, μ the viscosity (in Pa sec) at solid volume fraction of C_v , μ_L the viscosity, and λ a time constant of the fluid.

The saltcake in all these tanks has a yield strength of about 100 Pa, which was also assigned to this tank model. The simulation results indicate that two mixer pumps would erode all the saltcake and mix the suspended saltcake uniformly with the supernatant liquid. This waste retrieval assessment also provided the resulting waste conditions for the subsequent waste pipeline transfer and waste treatment.

13.5.2.3.3 Tank 241-AN-102 Sludge Waste Pump Jet Mixing

The tank sludge waste contains nonwater-dissolvable solids and is chemically less saturated than saltcake waste. It tends to have greater yield strength but less viscosity. The yield strength of the sludge was measured as about 1540 Pa. The following viscosity model was used to fit measured waste viscosity (Onishi et al., 2000):

$$\mu = \mu_L \left\{ \frac{\mu_s}{\mu_L} \right\}^\beta \quad (13.271)$$

where μ_s is the viscosity of the sludge layer (0.426 Pa sec at a strain rate of sec^{-1}).

The ARIEL code was applied to this tank to determine the amount of solids two 300-hp mixer pumps would mobilize. This tank also has 22 airlift circulators and heating coils installed to mix and control waste conditions. One of the airlift circulators is shown in Figure 13.73 (the right panel), which shows the model prediction along two vertical planes. This figure indicates that only half of the sludge would be eroded by the two rotating mixer pumps and the suspended solids in that half would be uniformly distributed.

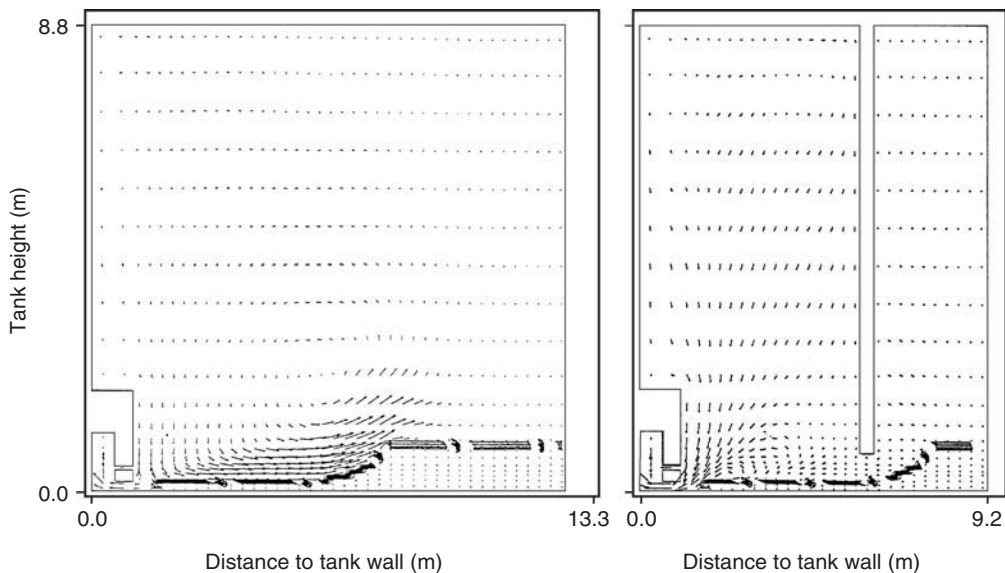


FIGURE 13.73 Predicted distributions of velocity and solid concentrations for Tank 241-AZ-102 at two simulation hours.

ARIEL thus provided useful information on retrieval design and waste feed delivery planning for the treatment plant. The main limitation of ARIEL for these three applications is that waste rheology is not correlated with chemical conditions during the simulation, while actual tank waste rheology is clearly affected by chemical conditions in addition to the physical conditions.

13.5.2.3.4 Two-Dimensional Reactive Transport Modeling:

We tested the interaction between waste chemistry and mixing by simulating an axisymmetric pump jet mixing the saltcake overlain by water (Figure 13.74). Adding water to saltcake waste tanks is the current base retrieval process. Since approximately half of Hanford's double-shell tank waste consists of sodium nitrate and nitrite, we considered their chemical reactions. Six aqueous species (Na^+ , NO_2^- , NO_3^- , $\text{NaNO}_2[\text{aq}]$, $\text{NaNO}_3[\text{aq}]$, and H_2O) and three solids [$\text{NaNO}_2[\text{s}]$, $\text{NaNO}_3[\text{s}]$, and nonreactive solids representing nondissolvable solids] were examined. The non-Newtonian viscosity was assigned to be a function of solids volume fraction and strain rate, as expressed by

$$\mu = \mu_L \left\{ \frac{\mu_s}{\mu_L} \right\}^\beta \gamma^b \quad (13.272)$$

where $b = 0.75$, representative of some Hanford tank wastes. Other viscosity parameters were the same as those of Eq. (13.173).

The axisymmetric reactive transport model predicted that, as water penetrated into and mixed with the saltcake, $\text{NaNO}_2[\text{s}]$ and $\text{NaNO}_3[\text{s}]$ would be dissolved and only the nonreactive solids remain as solids. As these solids dissolved, the viscosity of the saltcake decreased and the total amount of Na^+ , NO_2^- , NO_3^- , $\text{NaNO}_2[\text{aq}]$, $\text{NaNO}_3[\text{aq}]$ in the solution increased. These changes are shown in Figure 13.75 (left panel) for $\text{NaNO}_2[\text{s}]$ concentrations predicted at 45 simulation seconds. As the simulation time progressed, all $\text{NaNO}_2[\text{s}]$ and $\text{NaNO}_3[\text{s}]$ eventually dissolved. Thus, in the actual retrieval operation no slurry pipeline transport would be needed, and much easier liquid pipeline transport would be performed.

Without the chemical reactions (see Figure 13.75, right panel), solids concentration changes are due solely to mixing. Thus, in accounting for the chemical reactions, the mixer pump will encounter a smaller amount of solids and slurry with less viscosity to mobilize. This results in an improved waste mixing and transfer efficiency. This simple numerical test reveals the importance of accounting for the chemical reactions and associated rheology changes to determine the effectiveness of mixer pumps to mobilize the sludge.

13.5.2.3.5 Three-Dimensional Reactive Transport Modeling

The ARIEL code was applied to a more realistic tank waste condition. This case represents non-Newtonian saltcake waste mixed with overlaying water by two 300-hp mixer pumps (see Figure 13.69). Chemical reactions simulated are those in a $\text{Na}-\text{OH}-\text{Al}(\text{OH})_4-\text{CO}_3-\text{SO}_4-\text{NO}_2-\text{NO}_3-\text{NaNO}_2[\text{aq}]-\text{NaNO}_3[\text{aq}]-\text{H}_2\text{O}$ system with solids of $\text{Na}_2\text{CO}_3\cdot\text{H}_2\text{O}$, Na_2SO_4 , and $\text{Al}(\text{OH})_3$. Most of the $\text{Na}_2\text{CO}_3\cdot\text{H}_2\text{O}$ and Na_2SO_4 are expected to be dissolved with water, based on experiments and our chemical modeling. The viscosity of this tank waste varies seven orders of magnitude from saltcake to supernatant liquid, as shown in Figure 13.72.

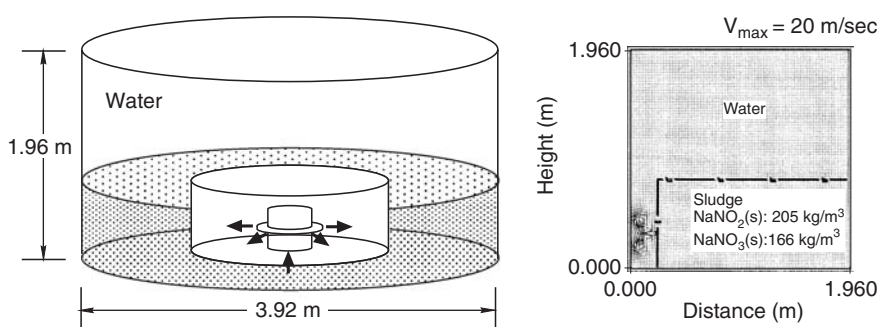


FIGURE 13.74 Axisymmetric reactive transport model setup.

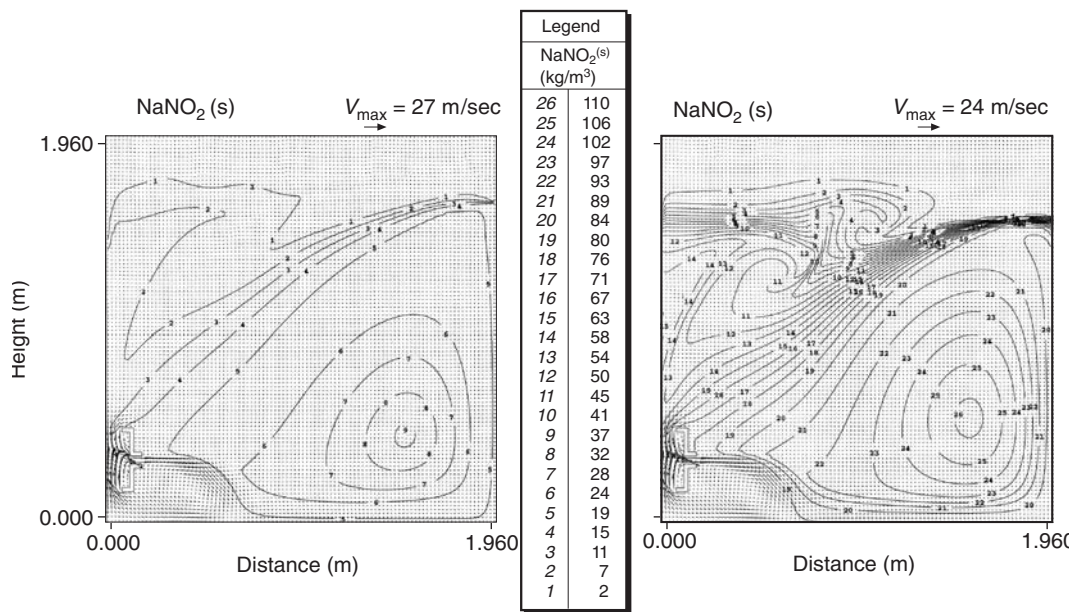


FIGURE 13.75 Predicted $\text{NaNO}_2(\text{s})$ concentrations at 45 simulation seconds with (left plot) and without (right plot) chemical reactions.

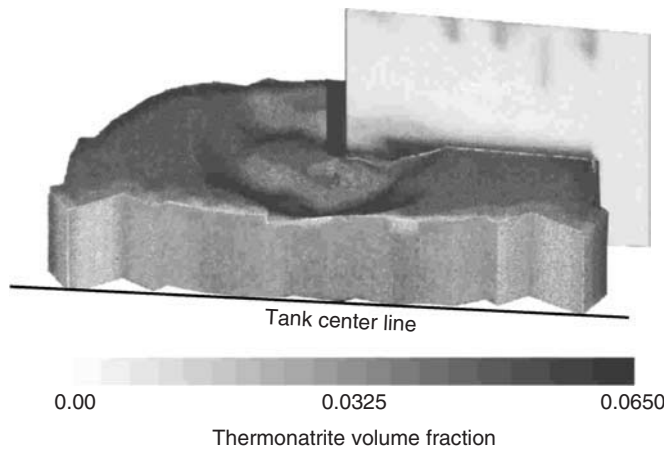


FIGURE 13.76 Predicted thermonatrite ($\text{Na}_2\text{CO}_3 \cdot \text{H}_2\text{O}$) volume fractions.

ARIEL began to simulate this case, as shown in the earlier predicted distribution (ten simulation seconds) of thermonatrite ($\text{Na}_2\text{CO}_3 \cdot \text{H}_2\text{O}$) in Figure 13.76 (Onishi et al., 1999). Although it simulated more realistic chemical reactions occurring in the tank, it revealed the following limitations:

It takes about ten times the computational time as the same case without chemical reactions.

- It does not account for water mass changes due to dissolution and precipitation of hydrate solids; for example $\text{Na}_2\text{CO}_3 \cdot \text{H}_2\text{O}$ dissolves, and the water is released to the solution.
- Some of these hydrates may form agglomerates and gels.

The solution density and slurry rheology are affected by the aqueous chemical species and solids.

13.5.2.4 Summary and Conclusions

Complex interactions occur among waste mixing, chemical reactions, and waste characteristics during radioactive tank waste mixing. We applied the non-Newtonian reactive transport code ARIEL to simulate waste mixing to illustrate these complex interactions. ARIEL couples chemical reactions, multiphase hydrodynamics and transport, and non-Newtonian or Newtonian waste rheology.

The simulation results indicate that (1) the waste has a very complex combination of Newtonian and non-Newtonian rheology, (2) the interaction between waste chemistry and fluid dynamics is important to assess tank waste mixing, and (3) ARIEL is applicable to idealized tank waste conditions — pure crystal solids, no agglomerates, and fast and simple kinetics. The limitations of ARIEL include an extensive computational requirement to simulate waste chemistry and difficulty in handling realistic waste conditions, especially when dealing with hydrates and their associated complexity. Reactive transport modeling of ARIEL represents the first step in developing a scientifically based waste retrieval assessment methodology.

13.5.3 Fluidized Bed

B. van Wachem

This section describes numerical simulations of fluidized systems. The predictions of CFD simulations of bubbling fluidized beds, slugging fluidized beds, and bubble injection into fluidized beds incorporating various models are compared with the "benchmark" experimental data of Hilligardt and Werther (1986), Kehoe and Davidson (1971), Darton et al. (1977), and Kuipers (1990).

13.5.3.1 Frictional Stress

At high solid volume fraction, sustained contacts between particles occur, and the stresses predicted by kinetic theory of granular flow are insufficient. Hence, the additional frictional stresses must be accounted for, in the description of the solid-phase stress. Zhang and Rauenzahn (1997) concluded that particle collisions are no longer instantaneous at high-solid volume fractions, as is assumed in kinetic theory. Several approaches have been presented in the literature to model the frictional stress, mostly originated from geological research groups. Typically, the frictional stress is written in a Newtonian form and has a deviatoric stress-like contribution and a normal stress-like contribution. The frictional stress is added to the stress predicted by kinetic theory for $\alpha_s > \alpha_{s,\min}$, where the subscript min stands for threshold value:

$$p_s = p_{\text{kinetic}} + p_{\text{frictional}} \quad (13.273)$$

$$\mu_s = \mu_{\text{kinetic}} + \mu_{\text{frictional}} \quad (13.274)$$

Johnson and Jackson (1987) propose a semiempirical equation for the normal frictional stress:

$$p_{\text{frictional}} = Fr \frac{(\alpha_s - \alpha_{s,\min})^{\text{nn}}}{(\alpha_{s,\max} - \alpha_s)^{\text{pp}}} \quad (13.275)$$

where Fr , nn, and pp are empirical material constants, and $\alpha_s > \alpha_{s,\min}$, $\alpha_{s,\min}$ being the solid volume fraction when frictional stresses become important. The frictional shear viscosity is then related to the frictional normal stress by the linear law proposed by Coulomb (1776) or the approach proposed by Schaeffer (1987):

$$\mu_{\text{frictional}} = \frac{p_{\text{frictional}} \sin \phi}{\alpha_s \sqrt{\frac{1}{6} \left(\left(\frac{\partial u_s}{\partial x} - \frac{\partial v_s}{\partial y} \right)^2 + \left(\frac{\partial v_s}{\partial y} \right)^2 + \left(\frac{\partial u_s}{\partial x} \right)^2 + \frac{1}{4} \left(\frac{\partial u_s}{\partial y} - \frac{\partial v_s}{\partial x} \right)^2 \right)}} \quad (13.276)$$

where ϕ is the angle of internal friction. Values of $\alpha_{s,\min}$ are typically in the range 0.55–0.6. Values for the empirical parameters are dependent on the material properties; some examples are given in [Table 13.6](#).

TABLE 13.6 Values for the Empirical Parameters in Eq. (13.174) as Suggested by Various Researchers.

Fr (N/m ²)	Nn	PP	$\alpha_{s\min}$	ϕ	d _s (μm)	ρ_s (kg/m ³)	Material	Reference
0.05	2	3	0.5	28°	150	2500	Not Specified	Ocone et al. (1993)
3.65×10^{-32}	0	40	—	25.0°	1800	2980	Glass	Johnson and Jackson (1987)
4.0×10^{-32}	0	40	—	25.0°	1000	1095	Polystyrene	Johnson and Jackson (1987)
0.05	2	5	0.5	28.5°	1000	2900	Glass	Johnson et al. (1990)

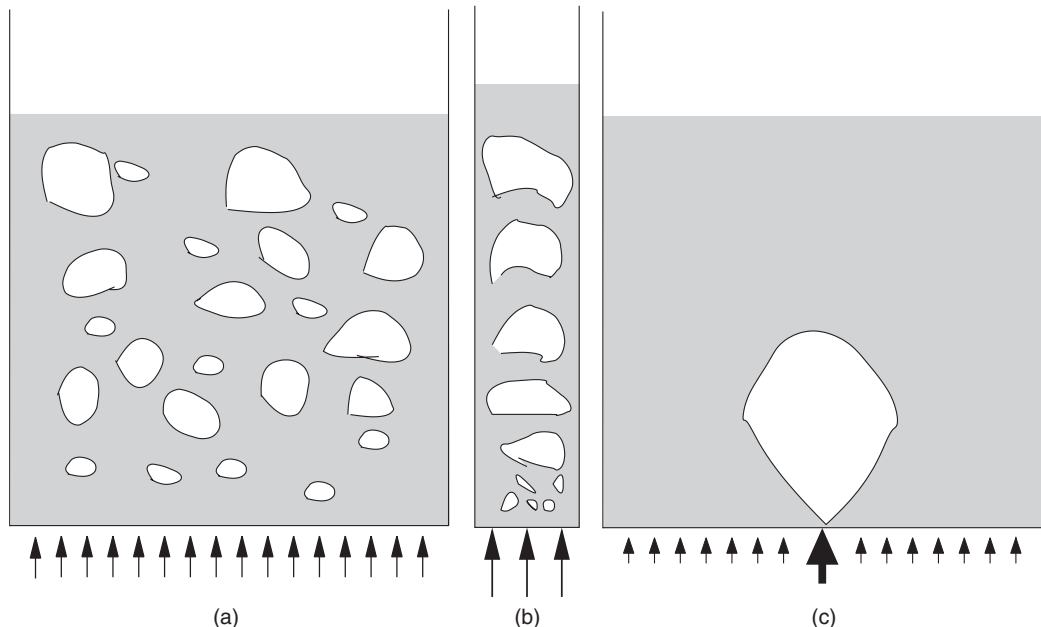


FIGURE 13.77 Flow configurations for the three test cases: (a) fluidized bed; (b) slugging fluidized bed; and (c) bubble injection into a fluidized bed.

13.5.3.2 Simulations

The test cases described in this section are a freely bubbling fluidized bed, a slugging fluidized bed, and a single-bubble injection into a fluidized bed. A sketch of the flow configurations for the three cases is given in Figure 13.77.

The particles in a fluidized bed move due to the action of the fluid through the drag force, thereby resulting in bubbles and complex solids mixing patterns. Typically, the average solid volume fraction in the bed is fairly large, averaging about 40%, whereas in the free-board of the fluidized bed (the top) there are almost no particles.

The simulations in this work were carried out with the commercial CFD code CFX 4.2. For solving the difference equations, the higher order total variation diminishing (TVD) scheme Superbee is used. This TVD scheme incorporates a modification to the higher-order upwind scheme (second order). The time discretization is done with the second-order back-ward difference scheme. The solution of the pressure from the momentum equations requires a pressure-correction equation, correcting the pressure and the velocities after each iteration; for this, the SIMPLE (Patankar, 1980) algorithm is employed. The calculated pressure is used to determine the density of the fluid phase; the simulations are performed allowing for compressibility of the gas phase. Compressibility is an important effect in fluidized beds, as the gas density varies with 10–30% over a typical fluidized bed. The grid spacing was determined by refining the grid until average properties changed

by less than 4%. Due to the deterministic chaotic nature of the system, the dynamic behavior always changes with the grid. The simulations of the slugging fluidized bed and the freely bubbling fluidized bed were carried out for 25 sec of real time. After about 5 sec of real time, the simulation has reached a state in which averaged properties stay unchanged. Averaged properties, such as bubble size and bed expansion were determined by averaging over the last 15 sec of real time in each simulation. A bubble is defined as a void in the solid phase with a solid volume fraction less than 15%. The bubble diameter is defined as the diameter of a circle having the same surface as the void in the solid phase; this is called the equivalent bubble diameter.

13.5.3.2.1 Boundary Conditions

All the simulations are carried out in a two-dimensional rectangular space in which front and back wall effects are neglected. The left and right walls of the fluidized bed are treated as no-slip velocity boundary conditions for the fluid phase, and free-slip velocity boundary conditions are employed for the particle phase. A possible boundary condition for the granular temperature follows Johnson and Jackson (1987):

$$n \cdot (\kappa \nabla \Theta) = \frac{\pi \rho_s \varepsilon_s \sqrt{3\Theta}}{6 \varepsilon_{s,\max} \left[1 - \left(\frac{\varepsilon_s}{\varepsilon_{s,\max}} \right)^{1/3} \right]} \left[|\varphi'| v_{\text{slip}}|^2 - \frac{3\Theta}{2} (1 - e_w^2) \right] \quad (13.277)$$

where the LHS represents the conduction of granular energy to the wall, the first term on the RHS represents the generation of granular energy due to particle slip at the wall, and the second term on the RHS represents dissipation of granular energy due to inelastic collisions. Another possibility for the boundary condition for the granular temperature is proposed by Jenkins (1992):

$$n \cdot (\kappa \nabla \Theta) = - v_{\text{slip}} \cdot M - D \quad (13.278)$$

where the exact formulations of M and D depend upon the amount of friction and sliding occurring at the wall region. Simulations which are done with an adiabatic boundary condition at the wall ($\nabla \Theta = 0$) show very similar results.

The boundary condition at the top of the free-board (fluid-phase outlet) is the so-called pressure boundary. The pressure at this boundary is fixed to a reference value, 1.013×10^5 Pa. Neumann boundary conditions are applied to the gas flow, requiring a fully developed gas flow. For this, the free board of the fluidized bed needs to be of sufficient height; this is validated through the simulations. In the free board, the solid volume fraction is very close to zero and this can lead to unrealistic values for the particle velocity field and poor convergence. For this reason, a solid volume fraction of 10^{-6} is set at the top of the free board. This way the whole free board is seeded with a very small number of particles, which gives more realistic results for the particle-phase velocity in the free board, but does not influence the behavior of the fluidized bed itself.

The bottom of the fluidized bed is made impenetrable for the solid phase by setting the solid-phase axial velocity to zero. For the freely bubbling fluidized bed and the slugging fluidized bed, Dirichlet boundary conditions are employed at the bottom with a uniform gas inlet velocity. To break the symmetry in the case of the bubbling and slugging beds, initially a small jet of gas is specified at the bottom LHS of the geometry. In the case of the bubble injection, a Dirichlet boundary condition is employed at the bottom of the fluidized bed. The gas inlet velocity is kept at the minimum fluidization velocity, except for a small orifice in the center of the bed, at which a high inlet velocity is specified. Finally, the solids-phase stress, as well as the granular temperature, at the top of the fluidized bed are set to zero.

13.5.3.2.2 Initial Conditions

Initially, the bottom part of the fluidized bed is filled with particles at rest with a uniform solid volume fraction. The gas flow in the bed is set to its minimum fluidization velocity. In the freeboard a solid volume fraction of 10^{-6} is set, as explained above. The granular temperature is initially set to $10^{-10} \text{ m}^2 \text{ sec}^{-2}$.

13.5.3.3 Test Cases

With an increase in gas velocity above the minimum fluidization velocity, U_{mf} , bubbles are formed as a result of the inherent instability of the gas–solid system. The behavior of the bubbles significantly affects

the flow phenomena in the fluidized bed, for example, solids mixing, entrainment, and heat and mass transfer. The test cases in this comparative study are used to investigate the capabilities of the closure models and governing equations to predict fluidization behaviour, for example, bubble behavior and bed expansion. Simulation results of each test case are compared to generally accepted experimental data and (semi) empirical models. The system properties and computational parameters for each of the test cases are given in Table 13.7.

13.5.3.3.1 Slugging Fluidized Beds

In the case of the slugging fluidized beds, coalescing bubbles eventually reach a diameter of 70% or more of the column diameter, resulting from either a large inlet gas velocity or a narrow bed. The operating conditions employed in the simulations correspond to the conditions reported by Kehoe and Davidson (1971), who present a detailed study of slug flow in fluidized beds. The experiments of Kehoe and Davidson (1971) were performed in slugging fluidized beds of 2.5, 5, and 10 cm diameter columns using Geldart B particles from 50 to 300 μm diameter and with superficial gas inlet velocities up to 0.5 m/sec. X-ray photography was used to determine the rise velocity of slugs and the bed expansion. Kehoe and Davidson (1971) use their data to validate two different equations for the slug rise velocity, both based on two-phase theory:

$$u_{\text{slug}} = U - U_{\text{mf}} + \frac{\varphi}{2} \sqrt{gD_T} \quad (13.279)$$

and

$$u_{\text{slug}} = U - U_{\text{mf}} + \frac{\varphi}{2} \sqrt{2gD_T} \quad (13.280)$$

where φ is the analytically determined square root of the Froude number of a single rising bubble. Equation (13.179) is the exact two-phase theory solution; Equation (13.180) is a modification of Eq. (13.179), based on the following observations:

1. For fine particles ($<70 \mu\text{m}$), the slugs travel symmetrically up in the fluidized bed, thus the slug rise velocity is increased by coalescence.
2. For coarser particles ($>70 \mu\text{m}$), the slugs tend to move up along the walls, which also increases their velocity.

According to Kehoe and Davidson (1971), Eqs. (13.179) and (13.180) give an upper and lower bound on the slug rise velocity. Furthermore, Kehoe and Davidson (1971) measured the maximum bed expansion

TABLE 13.7 System Properties and Computational Parameters

Parameter	Description	Freely Bubbling Fluidized Bed	Slugging Fluidized Bed	Bubble Injection into Fluidized Bed (Kuijpers, 1990)
ρ_s (kg/m^3)	Solid density	2640	2640	2660
ρ_g (kg/m^3)	Gas density	1.28	1.28	1.28
μ_g (Pas)	Gas viscosity	1.7×10^{-5}	1.7×10^{-5}	1.7×10^{-5}
d_s [μm]	Particle diameter	480	480	500
$e(-)$	Coefficient of restitution	0.9	0.9	0.9
ε_{\max} (-)	Maximum solid volume fraction	0.65	0.65	0.65
U_{mf} (m/sec)	Minimum fluidization velocity	0.21	0.21	0.25
D (m)	Inner column diameter	0.5	0.1	0.57
H (m)	Column height	1.3	1.3	0.75
H_{mf} (m)	Height at minimum fluidization	0.97	0.97	0.5
$\varepsilon_{s,\text{mf}}$ (-)	Solids volume fraction at minimum fluidization	0.42	0.42	0.402
Δx (m)	x mesh spacing	7.14×10^{-3}	6.67×10^{-3}	7.50×10^{-3}
Δy (m)	y mesh spacing	7.56×10^{-3}	7.43×10^{-3}	1.25×10^{-2}

(H_{\max}) during slug flow. They validated their theoretical analysis which led to the result that

$$\frac{H_{\max} - H_{mf}}{H_{mf}} = \frac{U - U_{mf}}{u_{bub}} \quad (13.281)$$

where u_{bub} is the rise velocity of a slug without excess velocity:

$$u_{bub} = \frac{\varphi}{2} \sqrt{g D_T} \quad (13.282)$$

or

$$u_{bub} = \frac{\varphi}{2} \sqrt{2 g D_T} \quad (13.283)$$

corresponding to Eqs. (13.179) and (13.182). Hence, they also propose upper and lower bounds on the maximum bed expansion.

13.5.3.3.2 Freely Bubbling Fluidized Beds

In the freely bubbling fluidized-bed case, the gas flow is distributed across the inlet of the bed. Small bubbles form at the bottom of the fluidized bed which rise, coalesce, and erupt as large bubbles at the bed surface. Hilligardt and Werther (1986) have done many measurements of bubble size and bubble velocity under various conditions using the probe developed by Werther and Molerus (1973) and have correlated their data in the form of the Davidson and Harrison (1963) bubble model. Hilligardt and Werther propose a variant of the Davidson and Harrison (1963) model for predicting the bubble rise velocity as a function of the bubble diameter:

$$u_b = \psi(U - U_{mf}) = \varphi v \sqrt{g d_b} \quad (13.284)$$

where φ is the analytically determined square root of the Froude number of a single rising bubble in an infinitely large homogeneous area. Pyle and Harrison (1967) have determined that $\varphi = 0.48$ for a two-dimensional geometry, whereas in three dimensions the Davies–Taylor relationship gives $\varphi = 0.71$. ψ and v , added by Hilligardt and Werther (1986), are empirical coefficients based on their data, that are dependent upon the type of particles and the width and height of the fluidized bed. For the particles and geometry employed in this study, Hilligardt and Werther (1986) proposed $\psi \approx 0.3$ and $v \approx 0.8$. Proposals of values for ψ and v under various fluidization conditions, determined by simulations, are given by van Wachem et al. (1998).

13.5.3.3.3 Bubble Injection in Fluidized Beds

Single jets entering fluidized bed operated at the minimum fluidization velocity through a narrow single orifice provide details of bubble formation and growth. Such experiments were carried out by Kuipers (1990). Kuipers (1990) reported the shape of the injected bubble as well as the quantitative size and growth of the bubble with time by using high-speed photography. The superficial gas inlet velocity from the orifice was $U = 10$ m/sec, and the orifice was $d = 1.5 \times 10^{-2}$ m wide.

13.5.3.4 Results

The governing equations used are those given by Jackson (1997) or by Ishii (1975), and the default closure models are the solid-phase stress of Hrenya and Sinclair (1997), the radial distribution function of Lun and Savage (1986), the frictional model of Johnson and Jackson (1987) with empirical values given by Johnson et al. (1990), and the drag coefficient model by Wen and Yu (1966).

13.5.3.4.1 Slugging Fluidized Beds

Simulations of the slugging bed case were performed with both the Ishii (1975) and the Jackson (1997) governing equations. In some kinetic theory models, a correlation between the gas-phase and particle-phase velocity fluctuations, called J_s , is taken into account. Figure 13.78 shows the predicted maximum

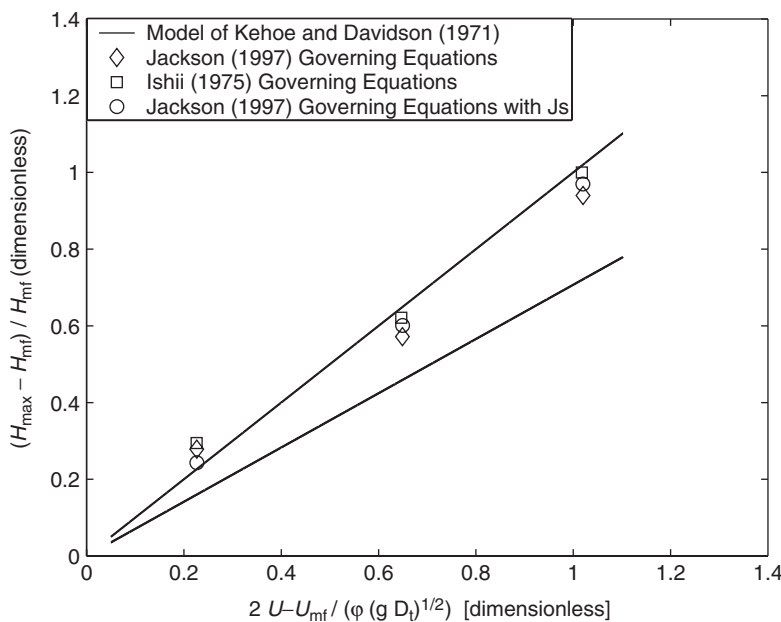


FIGURE 13.78 Predicted maximum expansion of a slugging fluidized bed with an increase in gas velocity the governing equations of Jackson (1997) and Ishii (1975). The predictions are compared with the two-phase theory as proposed and validated by Kehoe and Davidson (1971). (Reprinted from *AICHE J.*, 46, p. 1035, 2001. With kind permission from John Wiley & Sons, Hoboken NJ, USA.)

bed expansion with an increase in gas velocity during the slug flow and the two correlations by Kehoe and Davidson (1971). Figure 13.79 shows the increase in slug rise velocity with an increase in gas velocity. Clearly, the exact formulation of the governing equation or the correlation for J_s do not have any significant influence on the prediction of these macroscopic engineering quantities, and all CFD models do a good job at predicting these quantities.

13.5.3.4.2 Bubbling Fluidized Beds

The exact solid-phase stress description does not influence either the freely bubbling or the slugging fluidized bed predictions. Figure 13.80 shows the predicted bubble rise velocity employing different drag models in a freely bubbling fluidized bed, compared with the empirical correlation of Hilligardt and Werther (1986). All of the investigated drag models are in fairly good agreement with the empirical correlation.

13.5.3.4.3 Bubble Injection

Figure 13.81 shows the quantitative bubble size prediction for a single jet entering a fluidized bed operating at the minimum fluidization velocity on the drag models of Wen and Yu (1966) and Syamlal et al. (1993), which are compared with the experimental data of Kuipers (1990). Frictional stresses can increase the total solid-phase stress by orders of magnitude and is an important contributing force in dense gas–solid modeling, although the size of the bubble is not significantly influenced by the frictional stress, as shown in Figure 13.81. Moreover, Figure 13.82 shows the resulting qualitative predictions of the bubble growth and shape and also compare these with photographs of Kuipers (1990). The Wen and Yu (1966) drag model yields better agreement with findings of Kuipers (1990) for both the bubble shape and size than the Syamlal et al. (1993) drag model. The drag model of The Syamlal et al. (1993), underpredicts the bubble size and produces a bubble that is more circular in shape than in the experiments of Kuipers (1990) and in the simulations with the Wen and Yu (1966) drag model.

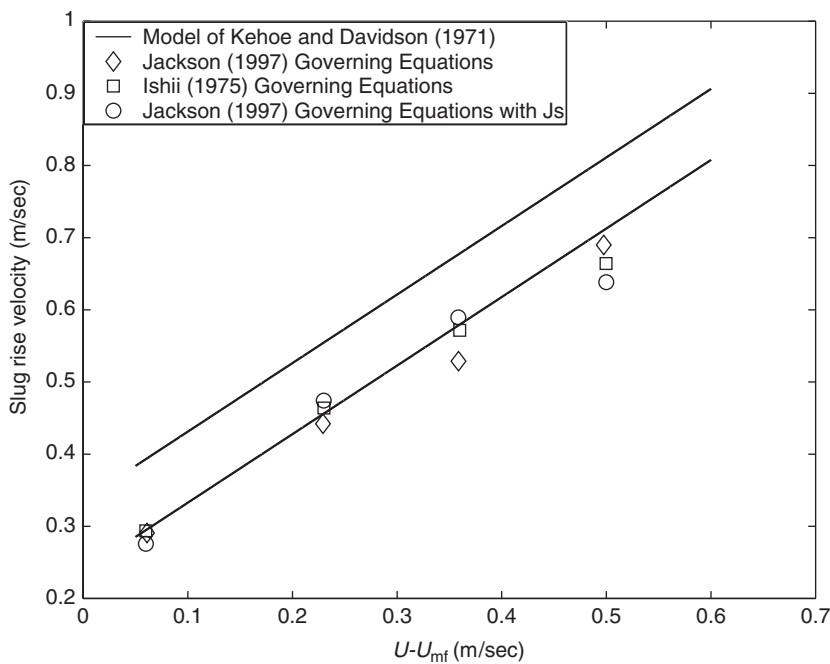


FIGURE 13.79 Predicted slug rise velocity with increasing gas velocity with the governing equations of Jackson (1997) and Ishii (1975). The predictions are compared with the two-phase theory as proposed and validated by Kehoe and Davidson (1971). The constant $\varphi = 0.48$. (Reprinted from *AIChE J.*, 46, 1035, 2001. With kind permission from John Wiley & Sons, Hoboken NJ, USA.)

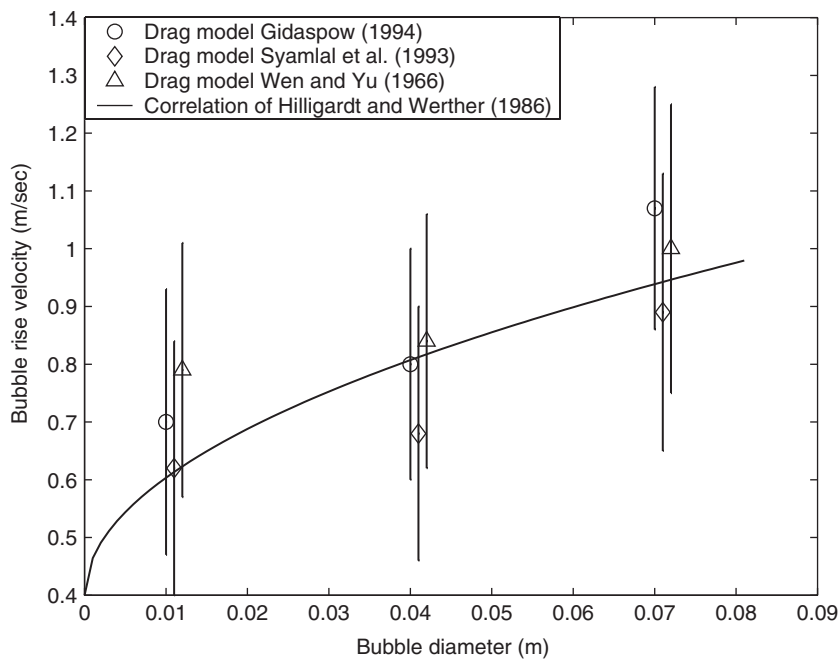


FIGURE 13.80 Predicted bubble rise velocity as a function of the bubble diameter at $U = 0.54$ m/sec based on different drag models and compared to the experimental correlation of Hilligardt and Werther (1986). The vertical lines indicate the spread of the simulated bubble rise velocity. (Reprinted from *AIChE J.*, 46, 1035, 2001. With kind permission from John Wiley & Sons, Hoboken NJ, USA.)

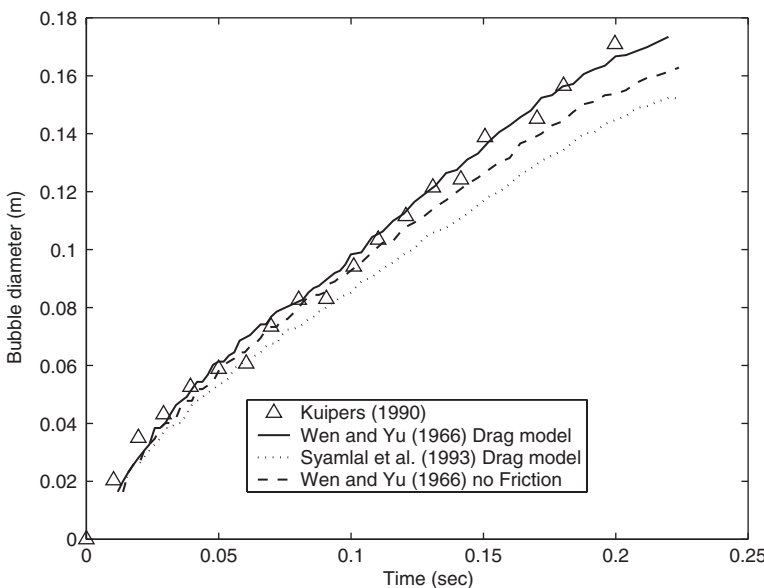


FIGURE 13.81 Bubble diameter as a function of time for a bubble formed at a single jet of $U = 10$ m/sec. A comparison is made between the experiments of Kuipers (1990), simulations using the drag coefficient of Wen and Yu (1966) with and without frictional stress, and simulations using the interphase drag coefficient of Syamlal et al. (1993). (Reprinted from *AICHE J.*, 46, 1035, 2001. With kind permission from John Wiley & Sons, Hoboken NJ, USA.)

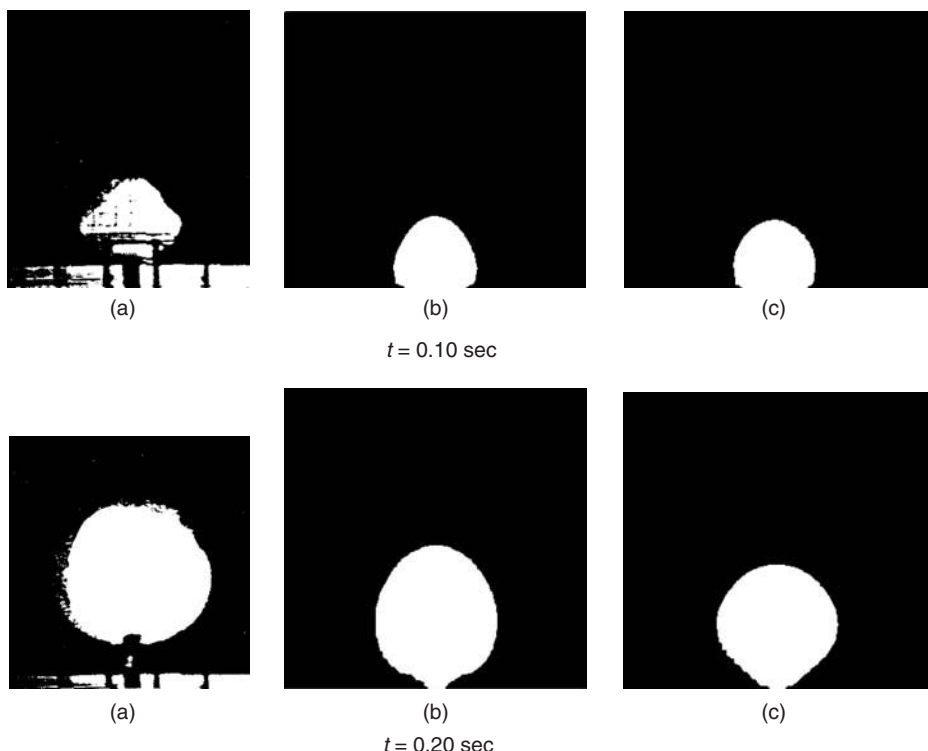


FIGURE 13.82 Experimental and simulated bubble shape associated with a single jet at $U = 10$ m/s and at $t = 0.10$ s and $t = 0.20$ s. Comparison is made between the (a) experiment of Kuipers (1990), (b) simulation using the interphase drag coefficient of Wen and Yu (1966), and (c) simulation using the interphase drag coefficient of Syamlal et al. (1993). (Reprinted from *AICHE J.*, 46, 1035, 2001. With kind permission from John Wiley & Sons, Hoboken NJ, USA.)

Nomenclature

Latin

A	Area
\mathbf{A}	Added mass force
c_d, c_p	Specific heat of dispersed phase
C_L	Lift coefficient
C_D	Drag coefficient
D_g	Molecular diffusion coefficient
$E(\kappa)$	Energy spectra
f	Ratio of drag to Stokes drag
f_c	Summation of continuous forces
f_p	Summation of fluid forces
\mathbf{F}	Force vector
g_i, \mathbf{g}	Acceleration due to gravity vector
G	Gibbs free energy
\mathbf{G}_{ij}	Relative velocity between particles "i" and "j"
h	Enthalpy
h_L	Latent heat
i	Internal energy
k	Thermal conductivity, turbulence energy, reaction rate
l_e	Eddy length scale
L_E	Eulerian length scale
\mathbf{L}	Lift force vector
m	Mass
\dot{m}	Mass flow rate
\dot{m}_k	Mass exchange rate for particle "k"
\mathbf{M}	Summation of torques
\dot{M}	Total mass flow rate
n	Number density, number of moles
n_i	Unit normal vector
\dot{n}	Number flow rate
N	Total number of particles
p	Pressure
p_s	Solids pressure
P_{ij}	Collision frequency
q_i	Heat transfer vector
\dot{Q}	Heat transfer rate
Re	Reynolds number
$R(\tau)$	Velocity correlation function
\mathbf{S}	Force due to shear gradient
Sh	Sherwood number
Stk	Stokes number
S_{mass}	Mass source term
S_{mom}	Momentum source term
t	Time
T	Temperature, inertial time scale
$T(\kappa)$	Spectral energy transfer rate
u_i, \mathbf{u}, U_i	Velocity vector

v	Particle velocity
V	Volume
V_i	Bubble phase velocity
\mathbf{w}	Relative velocity vector
$W(x, t)$	Phase space density
x_i	Coordinate vector
X	Phase space vector

Greek Symbols

α	Volume fraction
α_m	Mass loading ratio
β	Inverse particle response time
$\bar{\beta}$	Ratio of Lagrangian to Eulerian time scales
ε	Void fraction, dissipation rate
$\varepsilon(\kappa)$	Spectral viscous dissipation rate
η	Kolmogorov length scale
Θ	Granular temperature, temperature, wall scattering function
κ	Wave number
λ_k	Ratio of heat transfer to heat transfer at zero Reynolds number
μ	Viscosity
ν	Kinematic viscosity
ξ_s	Solids phase bulk viscosity
ρ	Density
σ	Surface tension
τ_b	Bubble response time
τ_e	Eddy transit time
τ_K	Kolmogorov time scale
τ_L	Lagrangian time scale
τ_p, τ_V	Particle response time
τ_T	Thermal response time
τ_{ij}	Stress tensor
ϕ	Conversion rate of mechanical to thermal energy
$\Psi(\kappa)$	Spectral two-way coupling
ω_A	Mass fraction of species "A"
Ω	Rotational velocity vector

Subscripts

c	Continuous phase
coll	Collision
d	Discrete phase
D	Drag
eff	Effective
f, F	Fluid
i	Coordinate direction, vector
p, P	Particle
rel	Relative
surf	Surface
0	Initial
@p	At particle position

References

- Abrahamson, J., Collision rates of small particles in a vigorously turbulent fluid, *Chem. Eng. Sci.*, 30, 1371–1379, 1975.
- Ahmed, A. and Elghobashi, S., On the mechanisms of modifying the structure of turbulent homogeneous shear flows by dispersed particles., *Phys. Fluids*, 12, 2906–2930, 2000.
- Ahmed, A. and Elghobashi, S., Direct numerical simulation of particle dispersion in homogeneous turbulent shear flows, *Phys. Fluids*, 13, 3346–3364, 2001.
- Al-Rawhai, N. and Tryggvason, G., Numerical simulation of dendritic solidification with convection: Three-dimensional flow, *J. Comput. Phys.*, 194, 677–696, 2004.
- Anderson, D.M., McFadden, G.B. and Wheeler, A.A., Diffuse-interface methods in fluid mechanics, *Ann. Rev. Fluid Mech.*, 30; 139–165, 1998.
- Anderson, T. B. and Jackson, R., A fluid mechanical description of fluidized beds, *I EC Fundam.* 6, 527, 1967.
- Bagchi, P. and Balachandar, S., Effect of turbulence on the drag and lift of a particle, *Phys. Fluids*, 15, 3496–3513., 2003.
- Bagnold, R.A., Experiments on a gravity-free dispersion of large solid spheres in a Newtonian-fluid under shear, *Proc. Roy. Soc.London*, A225, 49, 1954.
- Baker, G.R., Meiron, D.I., and Orszag, S.A., Vortex simulation of the Rayleigh-Taylor instability, *Phys. Fluids*, 23; 1485–1490, 1980
- Baker, G.R., Meiron, D.I., and Orszag, S.A., Generalized vortex methods for free surface flows problems, *J. Fluid Mech.*, 123; 477, 1982.
- Batchelor, G., *An Introduction to Fluid Dynamics*, Cambridge Univ. Press, Cambridge, 1967.
- Berlemont, A. and Achim, P., On the fluid/particle and particle/particle correlated motion for colliding particles in Lagrangian approach, *Proceedings of the 3rd ASME/JSME Joint Fluids Engineering Conference, FEDSM99-7859*, 1999.
- Berlemont, A., Chang, Z., and Gouesbet, G., Particle Lagrangian Tracking with Hydrodynamic Interactions and Collisions Flow, *Turbulence Combust.* 60, 1–18, 1998.
- Berlemont, A., Desjonquères, P., and Gouesbet, G., Particle Lagrangian simulation in turbulent flows, *Int. J. Multiphase Flow*, 16, 19–34, 1990.
- Berlemont, A., Achim,P., and Chang, Z., Lagrangian approaches for particle collisions: The colliding particle velocity correlation in the multiple particles tracking method and in the stochastic approach, *Phys. Fluids*, 13, 2946–2956, 2001.
- Bird, G.A., *Molecular Gas Dynamics and Direct Simulation of Gas Flows*, Clarendon Press, Oxford, 1976.
- Birkhoff, G., Taylor instability and laminar mixing, Report LA-1862, appendices in Report LA-1927, Los Alamos Scientific Laboratory, 1954 (unpublished).
- Blake, J.R. and Gibson, D.C., Growth and collapse of a vapor cavity near a free surface, *J. Fluid Mech.*, 111, 123–140, 1981.
- Bocksell, T. and Loth, E., Discontinuous and continuous random walk models for particle diffusion in free-shear flows, *AIAA J.*, 39, 1086–1096, 2001.
- Boettinger, W.J., Warren, J.A., Beckermann, C., and Karma, A., Phase field simulations of solidification, *Anu. Rev. Mater. Res.*, 32, 163–194, 2002.
- Boivin, M., Simonin, O., and Squires, K., Direct numerical simulation of turbulence modulation by particles in isotropic turbulence, *J. Fluid Mech.*, 375, 235–263, 1998.
- Boivin, M., Simonin,O., and Squires, K., On the prediction of gas-solid flows with two way coupling using large eddy simulation, *Phys. Fluids*, 12, 2080–2090, 2000.
- Bolio, E.J. and Sinclair, J.L., Gas turbulence modulation in the pneumatic conveying of massive particles in vertical tubes, *Int. J. Multiphase Flow*, 21, 985, 1995.
- Boulton-Stone, J.M. and Blake, J.R., Gas-bubbles bursting at a free-surface, *J. Fluid Mech.*, 254, 437–466, 1993.
- Brady, J.F. and Bossis, G., Stokesian dynamics, *Anu. Rev. Fluid Mech.*, 20, 111–157, 1988.

- Brady, J., Stokesian dynamics simulation of particulate flows, In *Particulate Two-Phase Flow*, Roco, M. (Ed.), Butterworth-Heinemann, Boston, MA, 1993, p. 912.
- Bunner, B. and Tryggvason, G., Direct numerical simulations of three-dimensional bubbly flows, *Phys. Fluids*, 11, 1967–1969, 1999.
- Bunner, B. and Tryggvason, G., Dynamics of homogeneous bubbly flows, part 1, rise velocity and microstructure of the bubbles, *J. Fluid Mech.*, 466, 17–52, 2002.
- Bunner, B. and Tryggvason, G., Dynamics of homogeneous bubbly flows, part 2, fluctuations of the bubbles and the liquid, *J. Fluid Mech.*, 466, 53–84, 2002.
- Bunner, B. and Tryggvason, G., Effect of bubble deformation on the stability and properties of bubbly flows, *J. Fluid Mech.*, 495, 77–118, 2003.
- Burry, D. and Bergeles G., Dispersion of particles in anisotropic turbulence, *Int. J. Multiphase Flow*, 19, 651–664, 1993.
- Buyevich, Y., Statistical hydromechanics of disperse systems. Part 1. Physical background and general equations, *J. Fluid Mech.*, 49, 489–507, 1971.
- Buyevich, Y., Statistical hydromechanics of disperse systems. Part 2. Solution of the kinetic equation for suspended particles, *J. Fluid Mech.*, 52, 345–355, 1972a.
- Buyevich, Y., Statistical hydromechanics of disperse systems. Part 3. Pseudo-turbulent structure of homogeneous suspensions, *J. Fluid Mech.*, 56, 313–336, 1972b.
- Chahine, G.L. and Duraiswami, R., Dynamic interactions in a multibubble cloud, *ASME J. Fluids Eng.*, 114, 680–686, 1992.
- Chan, R.K.-C. and Street, R.L., A computer study of finite-amplitude water waves, *J. Comput. Phys.*, 6, 68–94, 1970.
- Chandrasekhar, S.K., Stochastic problems in physics and astronomy, *Rev. Modern Phys.* 15, 1–89, 1943.
- Chang, Z., Etude de collisions inter-particulaires en écoulement turbulent isotrope ou anisotrope par une approche Lagrangienne à plusieurs trajectoires simultanées. PhD thesis, Université de Rouen, France, March 1998.
- Chapman, S. and Cowling, T.G., *The Mathematical Theory of Non-uniform Gases*, Cambridge University Press, Cambridge, 1952.
- Chapman, R.B. and Plesset, M.S., Nonlinear effects in the collapse of a nearly spherical cavity in a liquid, *Trans. ASME, J. Basic Eng.*, 94, 142, 1972.
- Chen, P.E. and Wood, C.E., A turbulence closure model for dilute gas-particle flows, *Can. J. Chem. Engr.*, 63, 349, 1985.
- Choi, H.G. and Joseph, D.D., Fluidization by lift of 300 circular particles in plane poiseuille flow by direct numerical simulation, *J. Fluid Mech.*, 438, 101–128, 2001.
- Chung, M.K., Sung, H.J., and Lee, K.B., Computational study of turbulent gas-particle flow in a venturi, *J. Fluids Eng.*, 108, 248, 1986.
- Coulomb, C.A., Essai sur une application des règles de maximis et minimis à quelques problèmes de statique, relatifs à l'architecture, *Acad. R. Sci. Mém. Math, Phys. par Divers Savants*, 7, 343–382, 1776.
- Crowe, C.T., Sharma, M.P., and Stock, D.E., The Particle-Source-in Cell method for gas droplet flow, *J. Fluid Eng.*, 99, 325, 1977.
- Crowe, C.T., Sommerfeld, M., and Tsuji, Y., *Multiphase Flows with Droplets and Particles*, CRC Press, Boca Raton, FL, 1998.
- Crowe, C.T., On models for turbulence modulation in fluid-particle flows, *Intl. J. Multiphase Flow*, 26, 719–727, 2000.
- Csanady, G.T., Turbulent diffusion of heavy particles with atmosphere, *J. Atmos. Science*, 20, 201–208, 1963.
- Daly, B.J., Numerical study of the effect of surface tension on interface instability, *Phys. Fluids*, 12, 1340–1354, 1969.
- Daly, B.J., A technique for including surface tension effects in hydrodynamic calculations, *J. Comput. Phys.*, 4, 97–117, 1969.
- Daly, B.J. and Pracht, W.E., Numerical study of density-current surges, *Phys. Fluids*, 11, 15–30, 1968.

- Dandy, D.S. and Leal, G.L., Buoyancy-driven motion of a deformable drop through a quiescent liquid at intermediate Reynolds numbers, *J. Fluid Mech.*, 208, 161–192, 1989.
- Darbyshire, K.F.F. and Swailes, D.C., A PDF model for particle dispersion with stochastic particle-surface interactions, *Gas-Solid Flows*, FED-236, ASME, New York, 1996, pp. 51–56.
- Darton, R.C., La Nause, R.D., Davidson, J.F., and Harrison, D., Particle growth due to coalescence in fluidized beds, *Trans. IChem E.*, 55, 274–280, 1977.
- Davidson, J.F. and Harrison, D., *Fluidized Particles*, Cambridge University Press, Cambridge, 1963.
- DeBar, R., Fundamentals of the KRAKEN Code, Technical report ucir-760, LLNL, 1974.
- Derevich, I.V. and Zaichik, L.I., Precipitation of particles from a turbulent flow, *Izvestiyia Akademii Nauk SSR, Mekhanika Zhidkosti Gaza*, 5, 96–104, 1988.
- Devenish, B.J., Swailes, D.C., and Sergeev, Y.A., A PDF model for dispersed particles with inelastic particle-wall collisions, *Phys. Fluids*, 11, 1858–1868, 1999.
- Ding, J. and Tam, S.W., Asymptotic power spectrum analysis of chaotic behaviour in fluidized beds, *Int. J. Bifurcation Chaos*, 4, 327–341, 1994.
- Dorgan, A. and Loth, E., Simulation of particles released near the wall in a turbulent boundary layer, *Int. J. Multiphase Flow*, 2004, to appear.
- Drew, D.A., Mathematical modeling of two-phase flows, *Ann. Rev. Fluid Mech.*, 15, 261–291, 1983.
- Drew, D.A. and Lahey, R.T. Jr., Analytical modeling of multiphase flow, In *Particulate Two-Phase Flow*, Roco, M.C.(Eds), Butterworth-Heinemann, Boston, 1993, pp. 509–566.
- Drew, D.A. and Passman, S.L., Theory of multi-component fluids, *App. Math. Sci.*, Vol. 135, Springer, New York, 1998.
- Druzhinin, O. and Elghobashi, S., A lagrangian-eulerian mapping solver for direct numerical simulation of a bubble-laden homogeneous turbulent shear flow using the two-fluid formulation, *J. Comp. Phys.*, 154, 174–196, 1999a.
- Druzhinin, O. and Elghobashi, S., On the decay rate of isotropic turbulence laden with microparticles, *Phys. Fluids*, 11, 602–610, 1999b.
- Druzhinin, O. and Elghobashi, S., Direct numerical simulation of a spatially-developing three-dimensional bubble-laden mixing layer with two-way coupling, *J. Fluid Mech.*, 429, 23–61, 2001.
- Eaton, J. and Fessler, J., Preferential concentration of particles by turbulence, *Int. J. Multiphase Flow*, 20, 169–209, 1994.
- Elghobashi, S.E. and Truesdell, G.C., On the two-way interaction between homogeneous turbulence and dispersed solid particles. I: turbulence modification, *Phys. Fluids A*, 5, 1790–1801, 1993.
- Elghobashi, S., On predicting particle-laden turbulent flows, *Appl. Sci. Res.*, 52, 309–329, 1994.
- Elghobashi, S. and Abou Arab, T., A two-equation turbulence model for two-phase flows, *Phys. Fluids*, 26, 931–938, 1983.
- Elghobashi, S. and Truesdell, G., Direct simulation of particle dispersion in decaying isotropic turbulence, *J. Fluid Mech.*, 242, 655–700, 1992.
- Elghobashi, S. and Truesdell, G., On the two-way interaction between homogeneous turbulence and dispersed solid particles, Part 1: turbulence modification, *Phys. Fluids A5*, 1790–1801, 1993.
- Esmaeeli, A. and Tryggvason, G., An inverse energy cascade in two-dimensional, low Reynolds number bubbly flows, *J. Fluid Mech.*, 314, 315–330, 1996.
- Esmaeeli, A. and Tryggvason, G., Direct numerical simulations of bubbly flows, part 1 — low Reynolds number arrays, *J. Fluid Mech.*, 377, 313–345, 1998.
- Esmaeeli, A. and Tryggvason, G., Direct numerical simulations of bubbly flows, part 2 — moderate Reynolds number arrays, *J. Fluid Mech.*, 385, 325–358, 1999.
- Esmaeeli, A. and Tryggvason, G., Computations of explosive boiling in microgravity, *J. Sci. Computing*, 19, 163–182, 2003.
- Ergun, S., Fluid flow through packed columns, *Chem. Engr. Prog.*, 48, 89, 1952.
- Faeth, G. M., Mixing, Transport, and combustion in sprays, *Prog. Energ. Combust. Scie.*, 13, 293–345, 1987.
- Fedkiw, R., Aslam, T., Merriman, B. and Osher, S., A non-oscillatory eulerian approach to interfaces in multimaterial flows (The ghost fluid method). *J. Comput. Phys.* 152 (1999), 457–492.

- Felmy, A.R., GMIN, a Computerized Chemical Equilibrium Program Using a Constrained Minimization of the Gibbs Energy: summary report, Chemical Equilibrium and Reaction Models, Soil Science Society of America, Special Publication 42, 1995.
- Ferrante, A. and Elghobashi, S., On the physical mechanisms of two-way coupling in particle-laden isotropic turbulence, *Phys. Fluids*, 15, 315–329, 2003.
- Ferrante, A. and Elghobashi, S., On the physical mechanisms of drag reduction in a spatially-developing turbulent boundary layer laden with microbubbles, *J. Fluid Mech.* 503, 345–355, 2004.
- Feng, J., Hu, H.H., and Joseph, D.D., Direct simulation of initial value problems for the motion of solid bodies in a Newtonian fluid, part 1. sedimentation, *J. Fluid Mech.*, 261, 95–134 1994.
- Feng, J., Hu, H.H., and Joseph, D.D., Direct simulation of initial value problems for the motion of solid bodies in a Newtonian fluid, part 2. Couette and Poiseuille flows, *J. Fluid Mech.*, 277, 271–301, 1995.
- Fevrier, P. and Simonin, O., Constitutive relations for fluid-particles velocity correlations in gas-solid turbulent flows, *Proceedings of the 3rd International Conference on Multiphase Flows*, ICMF'98, Lyon, France, 8–12, June 1988.
- Floryan, J.M. and Rasmussen, H., Numerical analysis of viscous flows with free surfaces, *Appl. Mech. Rev.*, 42, 323–341, 1989.
- Foote, G.B., A numerical method for studying liquid drop behavior: Simple oscillations, *J. Comput. Phys.*, 11, 507–530, 1973.
- Foote, G.B., The water drop rebound problem: dynamics of collision, *J. Atmos. Sci.*, 32, 390–402, 1975.
- Fortes, A., Joseph, D.D., and Lundgren, T., Nonlinear mechanics of fluidization of beds of spherical particles, *J. Fluid Mech.*, 177, 467–483, 1987.
- Frank, Th., Wassen, E., and Yu, Q., A 3-Dimensional Lagrangian Solver for Disperse Multiphase Flows on Arbitrary, Geometrically Complex Flow Domains Using Block-structured Numerical Grids, *Proceedings of the 7th International Symposium on gas-particle flows*, ASME fluids engineering division summer meeting, Vancouver, BC, Canada, June 22–26, 1997, CD-ROM proceedings, FEDSM97–3590.
- Frank, Th., and Wassen, E., Parallel Efficiency of PVM- and MPI-Implementations of Two Algorithms for the Lagrangian Prediction of Disperse Multiphase Flows, *JSME Centennial Grand Congress 1997, ISAC'97 Conference on Advanced Computing on Multiphase Flow*, Tokyo, Japan, July 18–19, 1997.
- Frank, Th., Application of Eulerian–Lagrangian Prediction of Gas–Particle Flows to Cyclone Separators, VKI - Von Karman Institute for Fluid Dynamics, Lecture Series Programme 1999–2000, In *Theoretical and Experimental Modeling of Particulate Flow*, Rhode-Saint-Genese (Bruessels), Belgium, April 03–07 2000, pp. 1–52, (Ed.) by Buchlin, J.-M., Von Karman Institute, D/2000/0238/468, 2000.
- Frank, Th., 2002, Parallel Algorithmen für die numerische Simulation dreidimensionaler, disperter Mehrphasenströmungen und deren Anwendung in der Verfahrenstechnik, Berichte aus der Strömungstechnik, Shaker Verlag Aachen, p. 328.
- Fukai, J., Shiiba, Y., Yamamoto, T., Miyatake, O., Poulikakos, D., Megaridis, C.M., and Zhao, Z., Wetting effects on the spreading of a liquid droplet colliding with a flat surface: experiment and modeling, *Phys. Fluids*, 7, 236–247, 1995.
- Gephart, R.E. and Lundgren, R.E., Hanford Tank Cleanup: A Guide to Understanding the Technical Issues, Report PNNL-10773, Pacific Northwest National Laboratory, Richland, Washington.DC, 1997.
- Gidaspow, D., *Multiphase Flow and Fluidization*, 1st ed., Academic Press, San Diego, 1994.
- Gerz, T., Shumann, U., and Elghobashi, S., Direct numerical simulation of stratified homogeneous turbulent shear flows, *J. Fluid Mech.*, 200, 563–594, 1989.
- Glimm, J. and McBryan, O., A computational model for interfaces, *Adv. Appl. Math.*, 6, 422–435, 1985.
- Gosman, A.D. and Ioannides, I.E., Aspects of computer simulation of liquid-fuelled combustors. *AIAA J.*, 81, 0323, 1981.
- Gourdel, C., Simonin, O., and Brunier, E., Two-Maxwellian equilibrium distribution function for the modeling of a binary mixture of particles, In *Proceedings of the 6th International Conference on Circulating Fluidized Beds*, Werther, J., Ed., DECHEMA, Frankfurt am Main, Germany, 1999, pp. 205–210.

- Graham, D.I., Improved eddy interaction models with random length and time scales, *Int. J. Multiphase Flow*, 24, 335–345, 1998.
- Harlow, F.H. and Shannon, J.P., The splash of a liquid drop, *J. Appl. Phys.*, 38, 3855–3866, 1967.
- Harlow, F.H. and Welch, J.E., Numerical calculation of time-dependent viscous incompressible flow of fluid with a free surface, *Phys. Fluid*, 8, 2182–2189, 1965.
- Harlow, F.H. and Welch, J.E., Numerical study of large-amplitude free-surface motions, *Phys. Fluid*, 9, 842–851, 1966.
- Harper, J.F., Bubbles rising in line: why is the first approximation so bad? *J. Fluid Mech.*, 351, 289–300, 1997.
- Haworth, D.C. and Pope, S.B., A generalized Langevin model for turbulent flow, *Phys. Fluids* 29, 387–405, 1986.
- He, J. and Simonin, O., Modelisation Numerique des Ecoulements Turbulents Gaz-Solide en Conduite Verticale, Rapport EDF HE-44/94/021A, 1994.
- Herting, D.L., Results of Dilution Studies with Waste from Tank 241-AN-105, Report HNF-SD-WM-DTR-046, Numatec Hanford Corp., Richland, Washington. DC, 1997.
- Hilligardt, K. and Werther, J., Local bubble gas hold-up and expansion of gas/solid fluidized beds, *German Chem. Eng.*, 9, 215–221, 1986.
- Hinze, J.O., *Turbulence*, 2nd Ed., Mc-Graw-Hill, New York, 1975.
- Hirt, C.W., Cook, J.L., and Butler, T.D., A Lagrangian method for calculating the dynamics of an incompressible fluid with a free surface, *J. Comput. Phys.*, 5, 103–124, 1970.
- Hirt, C.W. and Nichols, B.D., Volume of fluid (VOF) method for the dynamics of free boundaries, *J. Comput. Phys.*, 39, 201–226, 1981.
- Hishida, K. and Maeda, M., Two-phase confined jet: effect of particle density, Fifth Workshop on two-phase flow Predictions, *Proceedings of Erlangen*, March 19–22, 1990.
- Hu, H.H., Direct simulation of flows of solid–liquid mixtures, *Int. J. Multiphase Flow*, 22, 335, 1996.
- Hou, T.Y., Lowengrub, J.S., and Shelley, M.J., Boundary integral methods for multicomponent fluids and multiphase materials, *J. Comput. Phys.*, 169, 302–362, 2001.
- Hrenya, C.M. and Sinclair, J.L., Effects of particle-phase turbulence in gas-solid flows, *AICHE J.*, 43, 853–869, 1997.
- Hu, H.H., Direct simulation of flows of solid–liquid mixtures, *Int. J. Multiphase Flow*, 22, 335–352, 1996.
- Hyland, K.E., Reeks, M.W., and McKee, S., Derivation of a pdf kinetic equation for the transport of particles in turbulent flow, *J. Phys. A: Math. Gen.*, 32, 6169–6190, 1999a.
- Hyland, K.E., Reeks, M.W., and McKee, S., Exact analytic solutions to turbulent particle flow equations, *Phys. Fluids*, 11, 1249, 1999b.
- Hyman, J.M., numerical methods for tracking interfaces. *Physica D*, 12 (1984), 396–407.
- Illner, R. and Neunzert, H., On simulation methods for the Boltzmann equation, *Transp. Theory Stat. Phys.* 16, 141, 1987.
- Ishii, M., *Thermo-Fluid Dynamic Theory of Two-Phase Flow*, Direction des Etudes et Recherches d'Electricité de France, Eyrolles, Paris, France, 1975.
- Ishii, M., *Interfacial Area Modeling*, Vol. 3, Chap. 3, McGraw-Hill, New York, 1987, pp. 31–62.
- Jackson, R., Locally averaged equations of motion for a mixture of identical spherical particles and a newtonian fluid, *Chem. Eng. Sci.*, 52, 2457–2469, 1997.
- Jenkins, J.T., Boundary conditions for rapid granular flow: flat, frictional walls, *J. Appl. Mech.*, 59, 120–127, 1992.
- Jenkins, J.T. and Richman M.W., Grads 13-moment system for a dense gas of inelastic spheres, *Arch. Ration. Mech. Anal.*, 87, 355–377, 1985.
- Jeong, J.-H., Goldenfield, N., and Dantzig, J.A., Phase field model for three-dimensional dendritic growth with fluid flow, *Phys. Rev E*, 64, 041602, 2001.
- Jewett, J.R., et al., 2002, Values of Particle Size, particle Density, and Slurry Viscosity to Use in Waste Feed Delivery Transfer System Analysis, Report RPP-9805, U.S. Department of Energy, Office of River Protection, Richland, Washington. DC, 2002.

- Jimenez, J., Computing high-Reynolds-number turbulence: will simulations ever replace experiments?, *J. Turbulence*, 4, 1–14, 2003.
- Johnson, P.C. and Jackson, R., Frictional-collisional constitutive relations for granular materials, with application to plane shearing, *J. Fluid Mech.*, 176, 67–93, 1987.
- Johnson, P.C., Nott, P., and Jackson, R., Frictional-collisional equations of motion for particulate flows and their application to chutes, *J. Fluid Mech.*, 210, 501–535, 1990.
- Johnson, A.A. and Tezduyar, T.E., 3-d simulation of fluid-particle interactions with the number of particles reaching 100, *Comput. Methods Appl. Mech. Eng.*, 145, 301–321, 1997.
- Joia, I.A., Ushijima, T., and Perkins, R.J., Numerical study of bubble and particle motion in turbulent boundary layer using proper orthogonal decomposition, *Appl. Sci. Res.*, 57, 263–277, 1997.
- Juric, D. and Tryggvason, G., Computations of boiling flows, *Int. J. Multiphase Flow*, 24, 387–410, 1998.
- Kajishima, T. and Takiguchi, S., Interaction between particle clusters and particle-induced turbulence, *Int. J. Heat Fluid Flow*, 23, 639, 2002.
- Kallio, G.A. and Reeks M.W., A numerical simulation of particle deposition in turbulent boundary layers, *Int. J. Multiphase Flows* 15, 433–446, 1989.
- Kawaguchi, T., Sakamoto, M., Tanaka, T., and Tsuji, Y., Quasi-three-dimensional numerical simulation of spouted beds in cylinder, *Powder Technol.*, 109, 3, 2000.
- Kanai, A. and Miyata, H., Direct numerical simulation of wall turbulent flows with microbubbles, *Int. J. Num. Meth. Fluids*, 35, 593–615, 2001.
- Kang, I.S. and Leal, L.G., Numerical solution of axisymmetric, unsteady free-boundary problems at finite Reynolds number, i. Finite-difference scheme and its applications to the deformation of a bubble in a uniaxial straining flow, *Phys. Fluids*, 30, 1929–1940, 1987.
- Kawamura, T. and Kodama, Y., Numerical simulation method to resolve interactions between bubbles and turbulence, *Int. J. Heat Fluid Flow*, 23, 627–638, 2002.
- Kehoe, P.W.K. and Davidson, J.F., Continuously slugging fluidised beds, *Inst. Chem. Eng. Symp. Ser.*, 33, 97–116, 1971.
- Kim, I., Elghobashi, S., and Sirignana, W.B., On the equation for spherical-particle motion: effect of Reynolds and acceleration numbers, *J. Fluid Mech.*, 367, 221–253, 1998.
- Kitron, A., Elperin, T., and Tamir, A., Monte Carlo simulation of gas–solids suspension flows in impinging streams reactors, *Int. J. Multiphase Flow*, 16-1, 1, 1990.
- König, C., Untersuchungen zum Abscheideverhalten von geometrisch ähnlichen Zyklen, Ph.D. thesis, University of Kaiserslautern, Germany, 1990.
- Kuipers, J.A., A Two-Fluid Micro Balance Model of Fluidized Beds, Ph.D. thesis, University of Twente, The Netherlands, 1990.
- Kuwagi, K. and Horio, M., A numerical study on agglomerate formation in a fluidized bed of fine cohesive particles, *Chem. Eng. Sci.*, 57, 4737, 2002.
- Laurent, F. and Massot, M., Multi-fluid modelling of laminar polydisperse spray flames: origin, assumptions and comparison of sectional sampling methods, *Combustion Theory Modelling*, 5, 537–572, 2001.
- Laviéville, J., Deutsch, E., and Simonin, O., Large Eddy Simulation of Interactions Between Colliding Particles and a Homogeneous Isotropic Turbulence Field, In *Gas-Solid Flows*, ASME FED, 228, 1995, pp. 347–357.
- Laviéville, J., Simonin, O., Berlemon, A., and Chang, Z., Validation of Inter-Particle Collision Models Based on Large-Eddy Simulation in Gas-Solid Turbulent Homogeneous Shear Flow, *Proceedings of the 7th International Symposium on Gas-Particle Flows*, ASME FEDSM97-3623, 1997.
- Lee, L. and LeVeque, R.J., An immersed interface method for incompressible Navier–Stokes equations, *SIAM J. Sci. Computing*, 25, 832–856, 2003.
- Li, and Pozrikidis, C., Wall-bounded shear flow and channel flow of suspensions of liquid drops, *Int. J. Multiphase Flow*, 26, 1247–1279, 2000.
- Liu, Z.H., Kawaguchi, T., Tanaka, T., and Tsuji, Y., The effect of temperature on the minimum fluidization velocity calculated by distinct element method, *JSME Int. J.*, Ser. B, 66, 45–1, 2002.

- Liu, B.Y.H. and Agrawal, J.K., Experimental observation of aerosol deposition in turbulent flow, *J. Aerosol Sci.*, 5, 145–155, 1974.
- Loewenberg, M. and Hinch, E.J., Numerical simulation of a concentrated emulsion in shear flow, *J. Fluid Mech.*, 321, 395–419, 1996.
- Longuet-Higgins, M.S. and Cokelet, E.D., The deformation of steep surface waves on water, *Proc. R. Soc. London Ser. A*, 358, 1, 1976.
- Loth, E., Numerical approaches for motion of dispersed particles, bubbles, and droplets, *Prog. Energ. Combust. Sci.*, 26, 161–223, 2000.
- Lun, C.K.K. and Savage, S.B., The effects of an impact velocity dependent coefficient of restitution on stresses developed by sheared granular materials, *Acta Mech.*, 63, 15–44, 1986.
- McHyman, J., Numerical methods for tracking interfaces, *Physica D*, 12, 396–407, 1984.
- MacInnes, J.M and Bracco, F.V., Stochastic particle dispersion modelling and the tracer particle limit, *Phys Fluids A* 4(12), 2809–2824, 1992.
- Maxey, M., The gravitational settling of aerosol particles in homogeneous turbulence and random flow fields, *J. Fluid Mech.*, 174, 441, 1987.
- Maxey, M., Chang, E., and Wang, L.-P., Simulation of interactions between microbubbles and turbulent flows, *Appl. Mech. Rev.*, 4, S70, 1994.
- Maxey, M.R. and Riley, J.J., Equation of motion for a small rigid sphere in a nonuniform flow, *Phys. Fluids*, 26, 883–889, 1983.
- Maxey, M.R., Patel, B.K., Chang, E.J., and Wang, L.-P., Simulations of dispersed turbulent multiphase flow, *Fluid Dyn. Res.*, 20, 143–156, 1997.
- Mei, R., Lawrence, C.J., and Adrian, R.J., Unsteady drag on a sphere at finite Reynolds number with small fluctuations in the free-stream velocity, *J. Fluid Mech.*, 233, 613–631, 1991.
- Mei, R., An approximate expression for the shear lift force on a spherical particle at finite Reynolds number, *Int. J. Multiphase Flow*, 18, 145–147, 1992.
- Mikami, T., Kamiya, H., and Horio, M., Numerical simulation of cohesive powder behaviour in a fluidized bed, *Chem. Eng. Sci.*, 53, 1927, 1998.
- Milojević, D., Lagrangian Stochastic-Deterministic (LSD) predictions of particle dispersion in turbulence, *Part. Syst. Charact.*, 7, 181–190, 1990.
- Mitchell, T.M. and Hammitt, F.H., Asymmetric cavitation bubble collapse, *Trans ASME, J. Fluids Eng.*, 95, 29, 1973.
- Mortazavi, S. and Tryggvason, G., A numerical study of the motion of drops in Poiseuille flow, part 1. lateral migration of one drop, *J. Fluid Mech.*, 411, 325–350, 2000.
- Nanbu, K., Direct Simulation Scheme Derived from the Boltzmann Equation. I. Monocomponent Gases, *J. Phys. Soc. of Jpn.*, 49–5, 2042, 1980.
- Noh, W.F. and Woodward, P., SLIC (simple line interface calculation), in van de Vooren, A.I. and Zandbergen, P.J., Ed., *Proceedings of the 5th International Conference on Fluid Dynamics*, Vol. 59 of Lecture Notes in Physics, Springer, Berlin, 1976, pp. 330–340.
- Ocone, R., Sundaresan, S., and Jackson, R., Gas-particle flow in a duct of arbitrary inclination with particle-particle interactions, *AICHE J.*, 39, 1261–1271, 1993.
- Oesterle, B. and Petitjean, A., Simulation of Particle-to-Particle Interactions in Gas–Solid Flows, *Int. J. Multiphase Flow*, 19, 199–211, 1993.
- Oguz, H. and Prosperetti, A., Bubble entrainment by the impact of drops on liquid surfaces, *J. Fluid Mech.*, 219, 143–179, 1990.
- Oguz, H. and Prosperetti, A., Dynamics of bubble growth and detachment from a needle, *J. Fluid Mech.*, 257, 111–145, 1993.
- Onishi, Y., Reid, H.C., and Trent, D.S., Dilution Physics Modeling: Dissolution/Precipitation Chemistry, Report PNL-10815, Pacific Northwest National Laboratory, Richland, Washington, DC, 1995.
- Onishi Y., et al., Tank SY-102 Waste Retrieval Assessment: Rheological Measurements and Pump Jet Mixing Simulation, Report PNNL-11352, Pacific Northwest National Laboratory, Richland, Washington, DC, 1996.

- Onishi, Y. and Trent, D.S., Mobilization modeling of erosion-resisting radioactive tank waste, *Proceedings of Rheology in the Mineral Industry II*, Oahu, Hawaii, United Engineering Foundation, New York, 1999, pp. 45–56.
- Onishi, Y., et al., Simulation of radioactive tank waste mixing with chemical reactions, *Proceedings of 3rd ASME/JSME Joint Fluids Engineering Conference*, San Francisco, 1999.
- Onishi, Y., Recknagle, K.P., and Wells, B.E., Pump Jet Mixing and Pipeline Transfer Assessment for High-Activity Radioactive Wastes in Hanford Tank 241-AZ-102, Report PNNL-13275, Pacific Northwest National Laboratory, Richland, Washington, DC, 2000.
- Onishi, Y., et al., Pipeline Cross-Site Transfer Assessment for Tank 241-SY-101, Report PNNL-13650, Pacific Northwest National Laboratory, Richland, Washington, DC, 2002.
- Onishi, Y., et al., Retrieval and Pipeline Transfer Assessment of Hanford Tank 241-AN-105 Waste, Report, PNNL-14144, Pacific Northwest National Laboratory, Richland, Washington, DC, 2003.
- Oran, E.S. and Boris, J. P., *Numerical Simulation of Reactive Flow*, Elsevier, Amsterdam, 1987.
- Ormancey, A., Simulation du comportement de particule dans des écoulements turbulents, Thèse de 3ème cycle, Ecole des Mines de Paris, 1984.
- Osher, S. and Fedkiw, R.P., Level set methods, *J. Comput. Phys.*, 169, 463–502, 2001.
- Pan, T.W., Joseph, D.D., Bai, R., Glowinski, R., and Sarin, V., Fluidization of 1204 spheres: simulation and experiment, *J. Fluid Mech.*, 451, 169, 2002.
- Pan, Y. and Banerjee, S., Numerical investigation of the effect of large particle on wake turbulence, *Phys. Fluids*, 9, 3786, 1997.
- Pandya, R.V.R. and Mashayek, F., Probability Density Functions Modelling of Evaporating Droplets Dispersed in Isotropic Turbulence, *AIAA J.*, 39, 1909–1915, 2001.
- Pandya, R.V.R. and Mashayek, F., Non-isothermal dispersed phase of particles in turbulent flow, *J. Fluid Mech.*, 475, 205–245, 2003.
- Papavergos, P.G. and Hedley A.B., Particle deposition behaviour from turbulent flows, *Chem. Eng. Res. Des.*, 62, 275–295, 1984.
- Pascal, P. and Oesterlé, B., On the dispersion of discrete particle moving in a turbulent shear flow, *Int. J. Multiphase Flow*, 26, 293–325, 2000.
- Patankar, S.V., *Numerical Heat Transfer and Fluid Flow*, Hemisphere, Washington, DC, 1980.
- Peric, M., Ein zum Parallelrechnen geeignetes Finite–Volumen–Mehrgitterverfahren zur Berechnung komplexer Strömungen auf blockstrukturierten Gittern mit lokaler Verfeinerung, Abschlußbericht zum DFG–Vorhaben Pe 350/3–1 im DFG–Habilitandenstipendiumprogramm, Stanford University, USA, 1992.
- Picard, A., Berlemont, A., and Gouesbet, G., Modeling and predicting turbulence fields and the dispersion of discrete particles transported in turbulent flows, *Int. J. Multiphase Flow*, 12, 237, 1986.
- Pigeonneau, F., Modélisation et calcul numérique des collisions de gouttes en écoulement laminaire et turbulent, PhD Thesis, Université de Paris VI, France, October 1998.
- Pitzer, K.S., *Activity Coefficients in Electrolyte Solutions*, 2nd ed., CRC Press, Boca Raton, FL, 1991.
- Pope, S. G., PDF Methods for turbulent reactive flows, *Prog. Energy Combust. Sci.*, 119–192, 1985.
- Pope, S. G., Application of the velocity-dissipation probability density function model to homogeneous turbulent flows, *Phys. Fluids A*, 3, 1947–1957, 1991.
- Pozrikidis, C., *Integral and Singularity Methods for Linearized Viscous Flow*, Cambridge Univ. Press, Cambridge, 1992.
- Pozrikidis, C., Interfacial dynamics for stokes flow, *J. Comput. Phys.*, 169, 250–301, 2001.
- Pozorski, J. and Minier, J.-P., Probability density function modelling of dispersed two-phase turbulent flows, *Phys. Rev. E*, 59, 855–863, 1998.
- Pozorski, J. and Minier, J.-P., On the Lagrangian turbulent dispersionmodels based on the Langevin equation, *Int. J. Multiphase Flow*, 24, 913–945, 1988.
- Pyle, D.L. and Harrison, D., The rising velocity of bubbles in two-dimensional fluidized beds, *Chem. Eng. Sci.*, 22, 531, 1967.

- Qi, D., Lattice-Boltzmann simulations of fluidization of rectangular particles, *Int. J. Multiphase Flow*, 26, 421, 2000.
- Rallison, J.M. and Acrivos, A., A numerical study of the deformation and burst of a viscous drop in an extensional flow, *J. Eng. Mech.*, 89, 191, 1978.
- Ramshaw, J. D., Brownian motion in a flowing fluid, *Phys. Fluids*, 22, 1595–1601, 1979.
- Reeks, M.W., On the dispersion of small particles suspended in an isotropic turbulent flow, *J. Fluid Mech.*, 83, 529–546, 1977.
- Reeks, M.W., Eulerian Direct Interaction applied to the statistical motion of particle in a turbulent fluid, *J. Fluid Mech.*, 97, 569–590, 1980.
- Reeks, M.W., The transport of discrete particles in in-homogeneous turbulence, *J. Aerosol Sci.*, 14, 729–739, 1983.
- Reeks, M.W., On a kinetic equation for the transport of particles in turbulent flows, *Phys. Fluids A*, 3, 446–456, 1991.
- Reeks, M.W., On the continuum equations for dispersed particles in nonuniform flows, *Phys. Fluids A*, 5, 750–761, 1993.
- Reeks M.W. and Swailes, D.C., A unifying theory for the deposition of particles in a turbulent boundary layer, 1993b FED—Vol. 166, *Gas–solid Flows*, ASME, New York, 1993, pp. 109–112.
- Reeks, M.W. and Swailes, D.C., The near wall behavior of particles in a simple turbulent flow and gravitational settling and partially absorbing wall, *J. Fluid Mech. Res.*, 22, 31–39, 1997.
- Rhodes, M. J., Wang, X. S., Nguyen, M., Stewart, P., and Liffman, K., Use of discrete element method simulation in studying fluidization characteristics: influence of interparticle force, *Chem. Engr. Sci.*, 56, 69, 2001.
- Rizk, M.A. and Elghobashi, S.E., A two-equation turbulence model for disperse, dilute, confined two-phase flow, *Int. J. Multiphase Flows*, 15, 119, 1989.
- Robinson, P.B., Blake, J.R., Kodama, T., Shima, A., and Tomita, Y., Interaction of cavitation bubbles with a free surface, *J. Appl. Phys.*, 89, 8225–8237, 2001.
- Rong, D. and Horio, M., Behaviour of particles and bubbles around immersed tubes in a fluidized bed at high temperature and pressure: a DEM simulation, *Int. J. Multiphase Flow*, 27, 89, 2001.
- Ruetsch, G. and Meiburg, E., Two-way coupling in shear layers with dilute bubble concentrations, *Phys. Fluids*, 6, 2656, 1994.
- Ryskin, G. and Leal, L.G., Numerical solution of free-boundary problems in fluid mechanics. Part 2. buoyancy-driven motion of a gas bubble through a quiescent liquid, *J. Fluid Mech.*, 148, 19–35, 1984.
- Saffman, P., On the stability of laminar dusty gas, *J. Fluid Mech.*, 13, 120–128, 1962.
- Sangani, A.S. and Didwania, A.K., Dynamic simulations of flows of bubbly liquids at large Reynolds numbers, *J. Fluid Mech.*, 250, 307–337, 1993.
- Sankaranarayanan, K., Shan, X., Kevrekidis, I.G., and Sundaresan, S., Analysis of drag and virtual mass forces in bubbly suspensions using an implicit formulation of the Lattice Boltzmann method, *J. Fluid Mech.*, 452, 61–96, 2002.
- Savage, S.B., Granular flows at high shear rates, In *Theory of Dispersed Multiphase Flow*, Meyer, R.E. Ed., Academic Press, New York, 1983, p. 339.
- Scardovelli, R. and Zaleski, S., Direct numerical simulation of free-surface and interfacial flow, *Annu. Rev. Fluid Mech.*, 31, 567–603, 1999.
- Schaeffer, D.G., Instability in the evolution equations describing incompressible granular flow, *J. Differential Equations*, 66, 19–50, 1987.
- Schreck, E. and Peric M., Parallelization of Implicit Solution Methods, *ASME Fluids Engineering Conference*, June 22–23, 1992, Los Angeles (CA), USA, 1992.
- Schultz, W.W., Huh, J., and Griffin, O.M., Potential-energy in steep and breaking waves, *J. Fluid Mech.*, 278, 201–228, 1994.
- Schumann, U., Realizability of Reynolds-stress turbulence models, *Phys. Fluids* 20, 721–725, 1977.
- Shrayber, A. A., Euler and Lagrange methods in the theory of two-phase flows with variable particle size of the discrete phase, *Fluid Mech. – Soviet Res.*, 8, 79–87, 1979.

- Sethian, J.A., Evolution, implementation, and application of level set and fast marching methods for advancing fronts, *J. Comput. Phys.*, 169, 503–555, 2001.
- Shan, X.W. and Chen, H. D., Lattice Boltzmann model for simulating flows with multiple phases and components, *Phys. Rev. E*, 47, 1815–1819, 1993.
- Shin, S. and Juric, D., Modeling three-dimensional multiphase flow using a level contour reconstruction method for front tracking without connectivity, *J. Comput. Phys.*, 180, 427–470, 2002.
- Shopov, P.J., Minev, P.D., Bazhekov, I.B., and Zapryanov, Z.D., Interaction of a deformable bubble with a rigid wall at moderate Reynolds numbers, *J. Fluid Mech.*, 219, 241–271, 1990.
- Shyy, W., Udaykumar, H.S., Rao, M., and Smith, R., *Computational Fluid Dynamics with Moving Boundaries*, Taylor & Francis, Philadelphia, 1996.
- Sierou, A. and Brady, J. F., Rheology and microstructure in concentrated noncolloidal suspensions, *J. Rheol.*, 46, 1031–1056, 2002.
- Simonin, O., Deutsch, E., and Minier, J.-P., Eulerian Prediction of the Fluid/Particle Correlated Motion in Turbulent Two-Phase Flows, *Appl. Sci. Res.*, 51, 275–283, 1993.
- Simonin, O., Eulerian Formulaion for particle Dispersion in Two-phase Flows, In *Proceedings of 5th Workshop on Two-phase Flow Predictions*, Erlangen, 1990, Sommerfeld, M. and Wennerberg, D. (Ed.), Bilateral Seminars of the International Bureau/ Forschungszentrum Julich GmbH, Vol. 4, 1991, pp. 156–166.
- Simonin, O., Statistical and continuum modelling of turbulent reactive particulate flows Part I; theoretical derivation of dispersed Eulerian modelling from probability density function kinetic equations, Part II; Application of a two phase second moment transport model for the prediction of turbulent Gas-particle flows, *Theoretical and Experimental Lecture Series 2000-06*, von Karman Institute for Fluid Dynamics, Rhode Saint Genese, Belgium, 2000.
- Simonin, O., Fevrier, P., Lavieille, J., On the Spatial Distribution of Heavy-Particle Velocities in Turbulent Flow : from Continuous Field to Particulate Chaos, *J. Turbulence*, 3, 040, <http://stacks.iop.org/1468-5248/37040>, 2002.
- Sinclair, J.L. and Jackson, R., 1989, Gas-particle flow in a vertical pipe with particle-particle interactions, *AIChE J.*, 35, 1473, 1989.
- Sivier, S.A., Loth, E., and Baum, J.D., Dusty shock flow with unstructured adaptive finite elements and parcels, *AIAA J.*, 34, 1078–1080, 1996.
- Smereka, P., On the motion of bubbles in a periodic box, *J. Fluid Mech.*, 254, 79–112, 1993.
- Sommerfeld, M., The importance of inter-particle collisions in horizontal gas-solid channel flows, *Gas-Particle Flows, ASME Fluids Engineering Conference*, Hiltons Head, USA, FED-Vol. 228, pp. 335–345, 1995.
- Sommerfeld, M., Validation of a stochastic Lagrangian modeling approach for inter-particle collisions in homogeneous isotropic turbulence, *Int. J. Multiphase Flow*, 27, 1829–1858, 2001.
- Sommerfeld, M., Modelling of particle–wall collisions in confined gas–particle flows, *Int. J. of Multiphase Flows*, 18, 905–926, 1992.
- Sommerfeld, M., Modellierung und numerische Berechnung von partikelbeladenen turbulenten Strömungen mit Hilfe des Euler/Lagrange–Verfahrens, *Berichte aus der Strömungstechnik*, Shaker Verlag, Aachen, Germany, 1996.
- Son, G. and Dhir, V.K., Numerical simulation of film boiling near critical pressures with a level set method, *J. Heat Trans.*, 120, 183–192, 1998.
- Spalart, P.R., Strategies for Turbulence Modeling and Simulations, *4th International Symposium On Engineering Turbulence Modeling and Measurements*, Corsica, France, May 24–26, 1999.
- Spalart, P.R., Strategies for Turbulence Modeling and Simulations, *Int. J. of Heat and Fluid Flow*, 21, 252–263, 2000.
- Speziale, C.G., Sarkar, S., and Gatski, T.B., Modeling the pressure–strain correlation of turbulence: an invariant dynamical systems approach, *J. Fluid Mech.*, 227, 245–272, 1991.
- Squires K. and Eaton, J., Particle response and turbulence modification in isotropic turbulence, *Phys. Fluids A* 2, 1191–1203, 1990.
- Squires K. and Eaton, J.K., Preferential concentration of particles by turbulence, *Phys. Fluids A*, 3, 130, 1991.

- Steefel, C.L. and Lasaga, A.C., A coupled model for transport of multiple chemical species and kinetic precipitation/dissolution reactions with application to reactive flow in single phase hydrothermal systems, *Am. J. Sci.*, 294, 529, 1994.
- Stewart, C.W., et al., *In Situ* Rheology and Gas Volume in Hanford Double-Shell Waste Tanks, Report PNNL-11296, Pacific Northwest National Laboratory, Richland, Washington, 1996.
- Sundaram, S. and Collins, L., A numerical study of the modulation of isotropic turbulence by suspended particles, *J. Fluid Mech.*, 379, 105–143, 1999.
- Swales, D.C. and Reeks, M.W., Particle deposition from a turbulent flow: a steady state model for high inertial particles, *Phys. Fluids A*, 6, 3392–3403, 1994.
- Swales, D.C., Darbyshire, K.F.F., Reeks, M.W., Analysis of particle dispersion using a PDF equation; results for simple shear and rotating flows, *ASME FED-Vol. 228, Gas-Particle Flows ASME Summer Meeting*, Hilton Head Island, SC, August, 1995, pp. 257–263.
- Swales D.C. and Darbyshire, K.F. F., A generalised Fokker-Planck equation for particle transport in random media, *Physica A*, 242, 38–48, 1997.
- Swales, D.C. and Sergeev, Y.A., Chapman-Enskog closure approximation in the kinetic theory of dilute turbulent gas-particulate suspensions, *Physica A*, 254, 517–547, 1998.
- Syamlal, M., Rogers, W., and O'Brien, T.J., Mfix documentation theory guide, U.S. Department of Energy, Office of Fossil Energy, DOE/METC-94/1004(DE94000087), Technical Note, 1993.
- Takada, N., Misawa, M., Tomiyama, A., and Fujiwara, S., Numerical simulation of two- and three-dimensional two-phase fluid motion by Lattice Boltzmann method, *Comput. Phys. Commun.*, 129, 233–246, 2000.
- Takada, N., Misawa, M., Tomiyama, A., and Hosokawa, S., Simulation of bubble motion under gravity by Lattice Boltzmann method, *J. Nucl. Sci. and Technol.*, 38, 330–341, 2001.
- Tanaka, T., and Tsuji, Y., Numerical Simulation of Gas-Solid Two-Phase Flow in a Vertical Pipe: on the Effect of Inter-Particle Collision, In *Gas-Solid Flows*, ASME FED, Vol. 121, 1991, 123–128.
- Tanaka, T., Yonemura, S., Kiribayashi K., and Tsuji, Y., Cluster formation and particle-induced instability in gas-solid flows predicted by the DSMC method, *JSME Int. J.*, Ser. B, 39–2, 239, 1996.
- Tanaka, T., Noma, K., Ide, Y., and Tsuji, Y., Particle clusters formed in dispersed gas–solid flows: simulation and experiment, *Proceedings of World Congress on Particle Technology 4* (CD-ROM), July 21–25, Sydney, Australia, (2002), Paper No. 658.
- Tchen, C.M., Mean values and correlation problems connected with the motion of small particles suspended in a turbulent fluid, Doctoral dissertation, Delft, Holland, 1949.
- Tennekes, H. and Lumley, J.L., *A First Course in Turbulence*, MIT Press, Cambridge, MA, 1972.
- Tomiyama, A., Zun, I., Sou, A., and Sakaguchi, T., Numerical analysis of bubble motion with the VOF method, *Nucl. Engr. Des.*, 141, 69–82, 1993.
- Tonhardt, R. and Amberg, G., Phase-field simulations of dendritic growth in a shear flow, *J. Crystal Growth*, 194, 406–425, 1998.
- Trent, D.S. and Eyler, L.L., TEMPEST: A Computer Program for Three-dimensional Time-Dependent Computational Fluid Dynamics, Report PNL-8857 Vol. 1, Pacific Northwest National Laboratory, Richland, Washington DC, 1994.
- Tryggvason, G., Bunner, B., Esmaeeli, A., Juric, D., Al-Rawahi, N., Tauber, W., Han, J., Nas, S., and Jan, Y.-J., A front tracking method for the computations of multiphase flow, *J. Comput. Phys.*, 169, 708–759, 2001.
- Tsuji, Y., Shen, N.Y., and Morikawa, Y., Lagrangian simulation of dilute gas–solid flows in a horizontal pipe, *Adv. Powder Technol.*, 2, 2, 63–81, 1991.
- Tsuji, Y., Tanaka, T. and Ishida, T., Lagrangian Numerical Simulation of Plug Flow of Cohesionless Particles in a horizontal Pipe, *Powder Technology*, 71, 239, 1992.
- Tsuji, Y., Kawaguchi, T., and Tanaka, T., Discrete particle simulation of two-dimensional fluidized bed, *Powder Technol.*, 77, 79, 1993.
- Unverdi, S.O. and Tryggvason, G., Computations of multi-fluid flows, *Physica D*, 60, 70–83, 1992.
- Unverdi, S.O. and Tryggvason, G., A front-tracking method for viscous, incompressible, multi-fluid flows, *J. Comput Phys.*, 100, 25–37, 1992.

- van Wachem, B.G.M., Schouten, J.C., Krishna, R., and den Bleek, C.M., Eulerian simulations of bubbling behaviour in gas–solid fluidised beds, *Comput. Chem. Eng.*, 22, S299–S306, 1998.
- Vandromme, D., Introduction to the Modeling of Turbulence: Turbulence Modeling for Compressible Flows and Acoustics, von Karman Institute for Fluid Dynamics, Lecture Series 1997-03, March 1977.
- Vermorel, O., Bedat, B., Simonin, O., Poinsot, T., Numerical Study and Modelling of Turbulence Modulation in a Particle Laden Slab Flow, *J. Turbulence*, 4, 025, 2003, <http://stacks.iop.org/1468-5248/4/025>.
- Vinje, T. and Brevig, P., Numerical simulations of breaking waves, *Adv. Water Resour.*, 4, 77–82, 1981.
- Von Karman, T. and Howarth, L., On the statistical theory of isotropic turbulence, *Proc. Roy. Soc., London A*, 164, 192–215, 1938.
- Wang, L.-P. and Maxey, M., The motion of microbubbles in a forced isotropic and homogeneous turbulence, *Appl. Sci. Res.*, 51, 291, 1993a.
- Wang, L.P. and Maxey, M.R., Settling velocity and concentration distribution of heavy particles in homogeneous isotropic turbulence, *J. Fluid Mech.*, 256, 27–68, 1993.
- Wang, L.P. and Stock, D.E., Numerical simulation of heavy particle dispersion: time-step and nonlinear drag consideration, *J. Fluids Eng.*, 114, 100–106, 1992
- Wang, Q. and Squires, K.D., Large Eddy Simulation of particle laden turbulent channel flow, *Phys. Fluids*, 8, 1207–1223, 1996.
- Welch, S.W.J. and Wilson, J., A volume of fluid based method for fluid flows with phase change, *J. Comp. Phys.*, 160, 662–682, 2000.
- Wells, M.R. and Stock, D.E., The effects of crossing trajectories on the dispersion of particles in a turbulent flow, *J. Fluid Mech.*, 136, 31–36, 1983.
- Wen, C.Y. and Yu, Y.H., Mechanics of fluidization, *Chem. Eng. Progr. Symp. Ser.*, 62, 100, 1996.
- Werther, J. and Molerus, O., The local structure of gas fluidized beds. I. A Statistically based measuring system, *Int. J. Multiphase Flow*, 1, 103–122, 1973.
- White, F.M., *Viscous Fluid Flow*, McGraw-Hill, New York, 1991.
- Xu, J., Maxey, M., and Karniadakis, G.E., Numerical simulations of turbulent drag reduction using microbubbles, *J. Fluid Mech.*, 468, 271–281, 2002.
- Xue, M., Xu, H.B., Liu, Y.M. and Yue, D.K.P., Computations of fully nonlinear three-dimensional wave–wave and wave–body interactions, part 1. dynamics of steep three-dimensional waves, *J. Fluid Mech.*, 438, 11–39, 2001.
- Yabe, T., Xiao, F., and Utsumi, T., The constrained interpolation profile (cip) method for multi-phase analysis, *J. Comput. Phys.*, 169, 556–593, 2001.
- Yu, D. and Tryggvason, G., The free surface signature of unsteady, two-dimensional vortex flows, *J. Fluid Mech.*, 218, 547–572, 1990.
- Ye, T., Mittal, R., Udaykumar, H.S., and Shyy, W., An accurate cartesian grid method for viscous incompressible flows with complex immersed boundaries, *J. Comput. Phys.*, 156, 209–240, 1999.
- Yeh, G.T. and Tripathi, V.S., A critical evaluation of recent developments in hydrogeochemical transport models of reactive multichemical components, *Water Resour. Res.*, 25, 93, 1989.
- Yeung P.K. and Pope S.B., Lagrangian statistics from direct numerical simulations of isotropic turbulence, *J. Fluid Mech.*, 207, 1989.
- Yonemura, S., Tanaka, T., and Tsuji, Y., Cluster formation in gas–solid flow predicted by DSMC method, *ASME/FED Gas–Solid Flows*, 166, 303, 1993.
- Yoon, H.Y., Koshizuka, S., and Oka, Y., Direct calculation of bubble growth, departure, and rise in nucleate pool boiling, *Inte. J. Multiphase Flow*, 27, 277–298, 2001.
- Youngren, G.K. and Acrivos, A., On the shape of a gas bubble in a viscous extensional flow, *J. Fluid Mech.*, 76, 433, 1976.
- Yu, D. and Tryggvason, G., The free surface signature of unsteady, two-dimensional vortex flows, *J. Fluid Mech.*, 218, 547–572, 1990.
- Yudine, M.I., Physical considerations on heavy-particle dispersion, *Advances in Geophysics*, Vol. 6, Academic Press, New York, 1959, pp. 185–191.

- Zaichik, L.I., Modelling of particle dynamics and heat transfer using equations for first and second moments of velocity and temperature fluctuations, *Proceedings of the 8th International Symposium on Turbulent Shear Flows*, Technical University of Munich, 1991, pp. 10-2-1 to 10-2-6.
- Zhang, D.Z. and Prosperetti, A., Ensemble phase-averaged equations for bubbly flows, *Phys. Fluids*, 6, 2956–2970, 1994.
- Zhang, D. and Prosperetti, A., Momentum and energy equations for disperse two-phase flows and their closure for dilute suspensions, *Int. J. Multiphase Flow*, 23, 245–453, 1997.
- Zhang, D.Z. and Rauenzahn, R.M., A viscoelastic model for dense granular flows, *J. Rheol.*, 41, 1275–1298, 1997.
- Zhou, L.X. and Li, Y., A $\kappa - \epsilon$ for simulating gas-particle flows, *Proceedings of the 6th Erlangen-Merseburg Workshop on Two-Phase Flow Predictions*, Sommerfeld, M. Ed., Merseburg, May 1996.
- Zhou, Y., Wexler, A.S., and Wang, L.P. On the collision rate of small particles in isotropic turbulence. II. Finite inertia case, *Phys. Fluids*, 10, 1206–1216, 1998.
- Zhou, H. and Pozrikidis, C., The flow of ordered and random suspensions of two-dimensional drops in a channel, *J. Fluid Mech.*, 255, 103–127, 1993.
- Zinchenko, A.Z. and Davis, R.H., An efficient algorithm for hydrodynamical interaction of many deformable drops, *J. Comput. Phys.*, 157, 539–587, 2000.

14

Advanced Experimental Techniques

14.1	Two-Component Fraction Measurement	14-1
	Capacitance Transducers—Basic Principles • Microwave Transducers • Gamma-Ray Densitometry • Industrial Process Tomography • X-Ray and Gamma-Ray Tomography • Magnetic Resonance Imaging • Ultrasound Techniques	
14.2	Mass Flow Measurements	14-30
	Velocity Measurement • The Spatial Filtering Effect • Liquid Flow Measurement in Gas–Liquid Flows • On-Line Calculation on Component Flow Rates • Comparison of Different Commercial Multiphase Meters	
14.3	Wall Shear Stress.....	14-37
	Electrolysis Technique • Applications	
14.4	Velocity, Size, and Shape and Concentration Measurements of Particulate Mixtures	14-42
	Measurement Needs for Process Fluids and Suspensions • Interaction of Light and Matter: Some Fundamentals • Laser Light Scattering and Scanning • Laser Velocimetry • Ultrasound Absorption and Scattering • Tomographic Methods	
14.5	Bubbly Flow Measurements with Particle Image Velocimetry.....	14-85
	Introduction • PIV Measurement Technique • Simultaneous Full-Field Velocity Measurements of Bubbly-Liquid Phases • Applications • Velocity Components Determination • Bubble Shape Detection • Conclusion	
14.6	Detection and Measurement of Aerosols	14-101
	Characteristics That Are Measured • Sampling for Size Selectivity • Bulk Collection for Chemical Analysis • Real-Time Detection • Challenges in Aerosol Sampling	

E.A. Hammer
University of Bergen

G.A. Johansen
University of Bergen

T. Dyakowski
The University of Manchester

E.P.L. Roberts
The University of Manchester

J.C. Cullivan
R.A. Williams
University of Leeds

Y.A. Hassan
Texas A&M University

C.S. Claiborn
Washington State University

14.1 Two-Component Fraction Measurement

E.A. Hammer, T. Dyakowski, G.A. Johansen

This section presents methods to measure component fractions in a two-phase mixture. The methods include capacitance measurements, the use of microwave transducers, gamma-ray densitometry, X-ray and gamma-ray tomography and magnetic resonance imaging.

14.1.1 Capacitance Transducers—Basic Principles

E.A. Hammer

14.1.1.1 Introduction

The capacitance transducer is specially suited for measurements of the volume fractions of water in oils (water cut). It is also used for detection of void fractions in mixtures of gas and liquids (void fractions). The principle is very simple, but in practice there are many factors that influence the measurements in such a way that the results can easily be misinterpreted if the basic theory is not thoroughly understood. Capacitance sensors can be used to predict the concentration ratios in two-phase or two-component flow if the two components or the two phases have different electrical permittivity, for example, water and oil. The principle is based on the fact that the difference in permittivity of the different components or phases flowing between two capacitance plates (electrodes) makes the capacitance between these two plates dependent on the ratio of concentration of the components or the phases in the flow. The connection, however, between the concentration ratio and the permittivity of the mixture and, hence, the sensor capacitance is not simple and depends on the distribution of the components or the phases in the mixture (the flow regime). Even if the capacitance technique is flow-regime-dependent, it can still be used for concentration measurements if the different components are homogeneously mixed.

14.1.1.2 The Sensor

The simplest capacitance sensor consists of two parallel metal plates separated by a distance d (Figure 14.1).

If the guard electrodes are kept at the same potential as the sensing electrode but electrically insulated from it, so that the influence of the fringe fields or edge effects of the electrodes are eliminated, the measured capacitance will be

$$C_s = \frac{\epsilon_r \epsilon_0 A}{d} \quad (14.1)$$

where A is the area of each electrode (m^2), d the distance between the electrodes (m), ϵ_r the relative permittivity of the material between the electrode plates, and ϵ_0 the permittivity of free space ($8.854 \times 10^{-12} \text{ F/m}$).

Now if the material between the electrodes consists of components 1 and 2 and these components have different permittivities, the volumes of these two components can be found if the dependence of permittivity on the component fraction is known.

A more practical sensor is shown in Figure 14.2.

The electric field between the electrode plates, for these types of sensors, will not be homogeneous, but will be more sensitive to concentration variations in the surroundings of the gaps between the plates. However, the guard arrangement shown in Figure 14.2a will eliminate the influence of the strongest inhomogeneities at the edges of the electrodes and, thus, make the sensor less sensitive for inhomogeneities in the flowing medium.

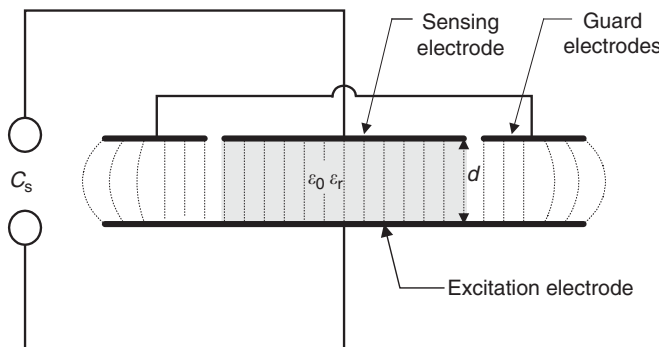


FIGURE 14.1 Basic capacitance sensor.

In Figure 14.2b, the electrode plates are placed inside the liner. They are exposed directly to the mixture and, therefore, have a very high electrode capacitance C_e (interphase capacitance between electrodes and the mixture) that will increase the sensor sensitivity.

Another capacitance sensor used is the coaxial electrode sensor. This sensor consists of an inner electrode supported in the center of the pipe as shown in Figure 14.3.

The electric field from this sensor is very inhomogeneous but symmetric around the pipe axis. The sensitivity to variation in concentration of the liquid will be highest close to the inner electrode. The capacitance per unit length of this sensor is

$$C_s = \frac{2\pi\epsilon_m\epsilon_0}{\ln D/d} \quad (14.2)$$

14.1.1.3 Guarding and Screening of the Capacitance Electrodes

In order to perform as accurate measurements as possible, it is necessary to guard and screen the capacitance sensor. In real sensors, the electrodes can be arranged as shown in Figure 14.2. To make it easier to draw the different fringe field capacitances, a parallel plate capacitance sensor is sketched as shown in Figure 14.4. From this figure, we see that the equivalent diagram of a capacitance sensor can be as shown in Figure 14.5.

For all practical sizes of sensors, the parasite capacitances C_A and C_B are considerable, thus resulting in an unwanted shunting of C_X . It is also a disadvantage that both C_A and C_B will change when the permittivity of the mixture in the pipe changes due to displacement of the field lines in the insulation material. However, the influence of all the parasite capacitances shown in Figure 14.5 can be diminished if a proper guard-driver coupling is used.

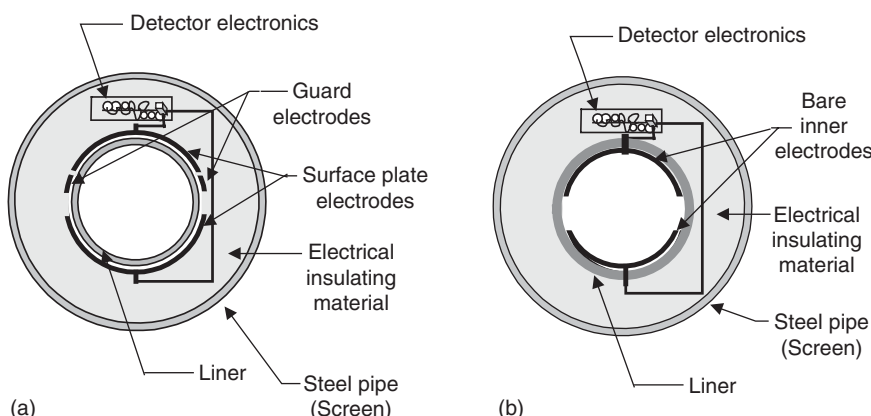


FIGURE 14.2 Surface plate electrodes.

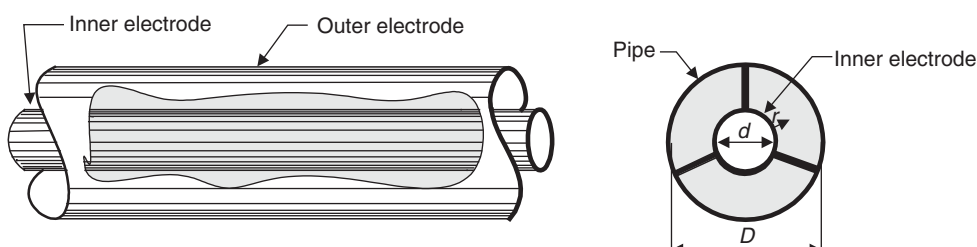


FIGURE 14.3 The principle of the coaxial electrode sensor.

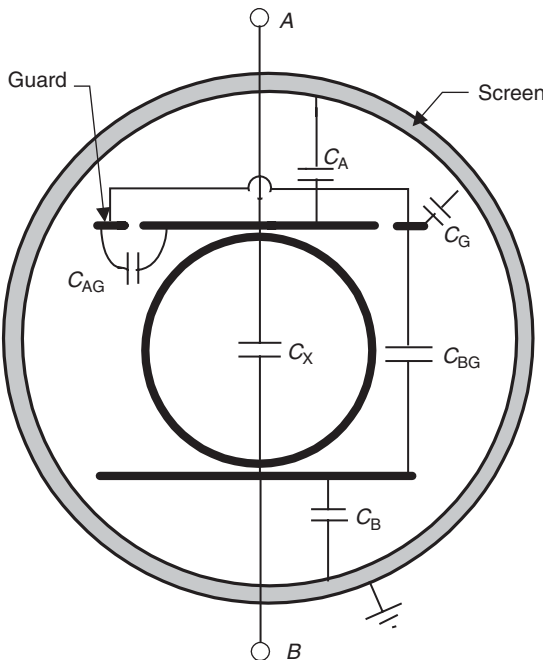


FIGURE 14.4 Capacitance sensor with guard electrode and screen.

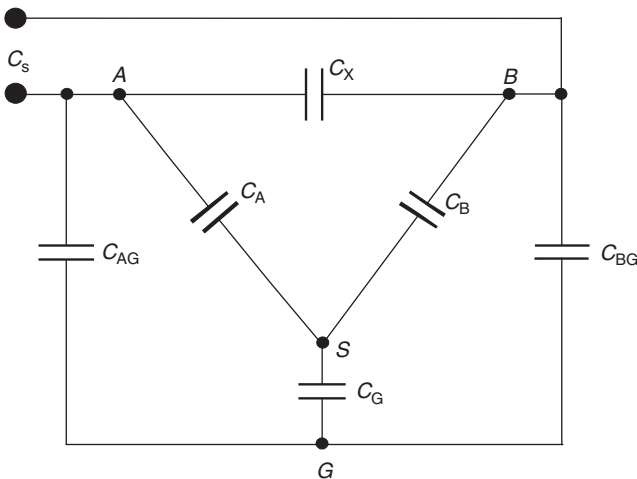


FIGURE 14.5 Equivalent diagram for capacitance sensor head equipped with guard electrode and screen.

14.1.1.4 The Basic Capacitance Detector System

There is in principle only one method used to eliminate the influence of the various parasite capacitances in the sensor head. It is based on the virtual ground circuit (charge amplifier). Figure 14.6 shows the basic principle of this circuit. Neither C_A , C_B , C_{AG} , nor C_{BG} , C_G will influence the output voltage U_{out} , if the operational amplifier has a high open-loop gain A_{OL} , so that the differential input voltage $e \approx 0$.

It can easily be seen that if A_{OL} is large, the differential input voltage $e \approx 0$ and the output signal of the circuit given in Figure 14.6 is

$$u_{out} = u_{osc} Z_F j \omega C_X \quad (14.3)$$

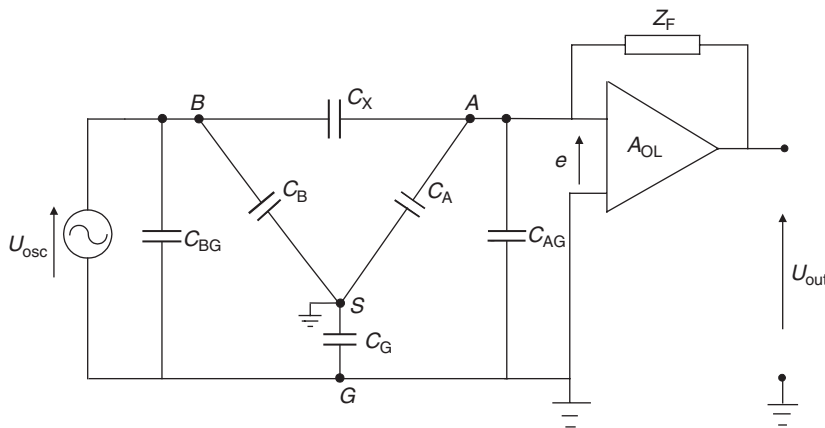


FIGURE 14.6 Capacitance transducer with grounded guard and screen and guarded electrode (A) connected to a virtual ground circuit.

If the feedback impedance Z_F can be represented by a capacitor C_0 ($Z_F = 1/j\omega C_0$), then Eq. (14.3) can be written as

$$u_{\text{out}} = u_{\text{osc}} \frac{C_x}{C_0} \quad (14.4)$$

Other detector circuits that are used are the oscillator circuit and the charge–discharge circuit; both are based on the virtual ground circuit.

14.1.1.5 Interpreting the Signals from a Capacitance Transducer

To utilize the information gained by using capacitance transducers, it is very important to know the basic theory that underlies this technique. The capacitance sensors will be dependent on the distribution of the components in a mixture. Reliable measurements can therefore be made only if the flow regime is constant and known. The most controllable regime is homogeneous flow where the two components are well mixed.

Maxwell (1873), Bruggeman (1935), Hammer (1983), and many others have developed formulas for the permittivity and conductivity of homogeneous mixtures of two different materials. On the basis of a model developed by van Beek (1967), Ramu and Rao (1973) have derived formulas that are valid, if one of the components in the mixture has a high conductivity.

If $\sigma_1 \ll \sigma_2$ and $\epsilon_1 \ll \epsilon_2$, the Ramu and Rao equations for permittivity and conductivity can be written as

$$\epsilon_m = \epsilon_1 \frac{1 + 2\beta}{1 - \beta} \quad (14.5)$$

$$\sigma_m = \sigma_1 \frac{1 + 2\beta}{1 - \beta} \quad (14.6)$$

which are valid either for component 1 comprising the continuous phase or

$$\epsilon'_m = \epsilon_2 \frac{2\beta}{3 - \beta} \quad (14.7)$$

$$\sigma'_m = \sigma_2 \frac{2\beta}{3 - \beta} \quad (14.8)$$

for component 2 being the continuous phase in the mixture.

Here ϵ_m is the relative permittivity of the mixture when component 1 comprises the continuous phase, ϵ'_m the relative permittivity of the mixture when component 2 comprises the continuous phase, σ_m the

conductivity of the mixture when component 1 makes up the continuous phase, σ'_m the conductivity of the mixture when component 2 makes up the continuous phase. As ϵ_1 is the relative permittivity of component 1, ϵ_2 the relative permittivity of component 2, σ_1 the conductivity of component 1, σ_2 the conductivity of component 2, and β the volume fraction of component 2.

Let us assume that the conductivity of component 1 is zero and represents the continuous phase when $\beta < 0.5$ and that component 2 is conductive ($\sigma_2 > 0$) and represents the continuous phase when $\beta > 0.5$. The relative mixture permittivity will then vary as shown in Figure 14.7.

To understand how a capacitance sensor reacts to changes in the permittivity of the mixture, it is useful to construct an equivalent diagram for the sensor as shown in Figure 14.8.

In this figure, C_m and R_m are the capacitance and the resistance, respectively, between imaginary electrodes placed at the mixture-liner interface, and have the same area as the sensor electrodes. C_{e1} and C_{e2}

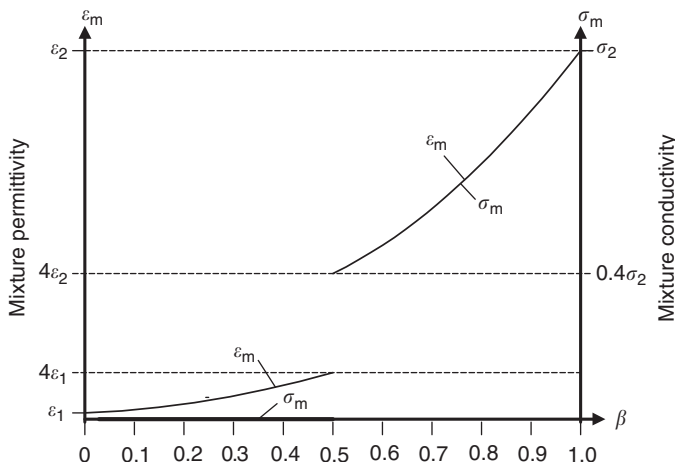


FIGURE 14.7 Mixture permittivity and conductivity vs. the volume fraction of component 2 of a homogeneous mixture where only component 2 is conductive.

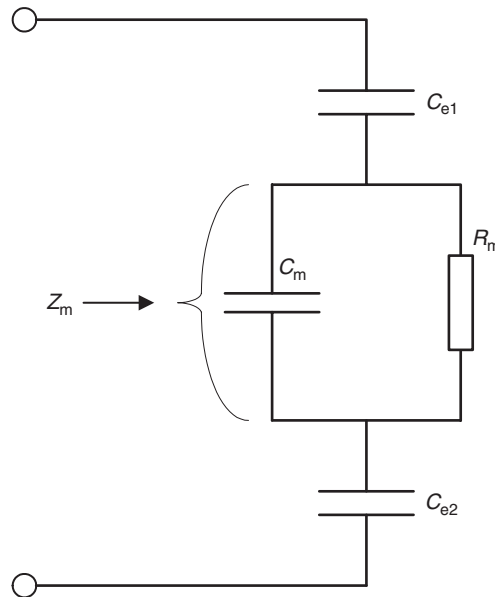


FIGURE 14.8 Equivalent diagram for a capacitance sensor when all the fringe field capacitances are eliminated.

are the resultant capacitances between the sensor electrodes and the mixture with the electrode insulating material as the dielectric. If component 1 is nonconducting and comprises the continuous phase in the flow, $R_m = \infty$, and the measured capacitance will be

$$C_s = C_e C_m / (C_e + C_m) \quad (14.9)$$

where $C_e = 1/2C_1 = 1/2C_2$. If component 2 is conducting and represent the continuous phase, then the current through C_m will be by-passed by R_m . It can be shown that the current through C_m is equal to the current through R_m , if

$$f_e = \frac{\sigma_2}{2\pi\epsilon_0\epsilon_2} \quad (14.10)$$

An example of this is the capacitance measured with a capacitance sensor used to determine the water content in a mixture of crude oil–saline water. This is shown in Figure 14.9. The transition point here is chosen to be $\beta_c = 0.7$

The continuous component in an oil–water mixture changes from oil to water at around 20 to 40% water concentration. The transition point in a mixture of crude oil and water will occur somewhere between 60 and 80% water fraction, depending on the type of crude oil, temperature and content of emulsion breaker, etc. Whether the water concentration is detectable or not above the transition point is dependent on the water conductivity and sensor excitation frequency. The sensor capacitance will increase with increasing water fraction, even above the transition point ($\beta > \beta_c$), if the sensor excitation frequency satisfies

$$f > \frac{1}{2\pi} \frac{\sigma_w}{\epsilon_0\epsilon_w} = f_e \quad (14.11)$$

In North Sea oil, the conductivity of the water component in the crude is approximately 5 S/m and the relative permittivity is approximately 70, giving a critical excitation frequency of $f_e = 1.3 \times 10^9$ Hz. However, excitation frequencies higher than 1.3×10^9 Hz cannot be used, because the capacitance detector will not eliminate the influence of the parasitic capacitances at frequencies higher than approximately 1 MHz.

The water content of North Sea crude can therefore not be measured with these types of capacitance sensors if the mixture is water continuous, i.e., $\beta > \beta_c$.

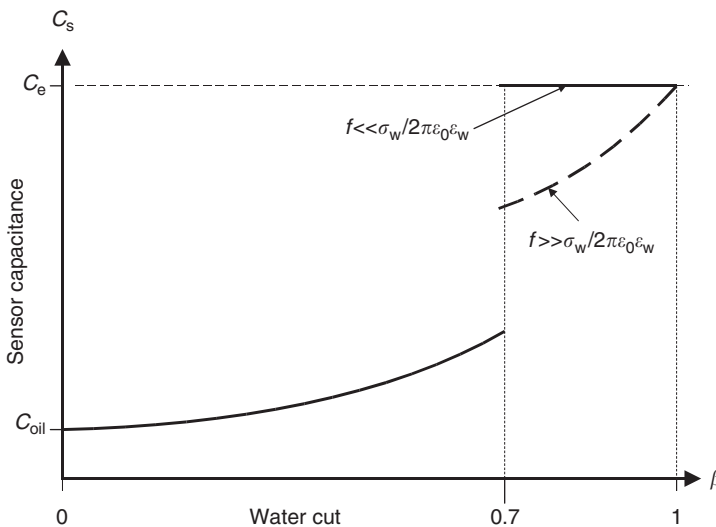


FIGURE 14.9 Capacitance measured with a capacitance sensor for a homogeneous mixture of oil and water. Excitation frequency $\omega \ll \sigma_{water}/\epsilon_0\epsilon_{water}$. The dotted line indicates the characteristic if $\omega \gg \sigma_{water}/\epsilon_0\epsilon_{water}$.

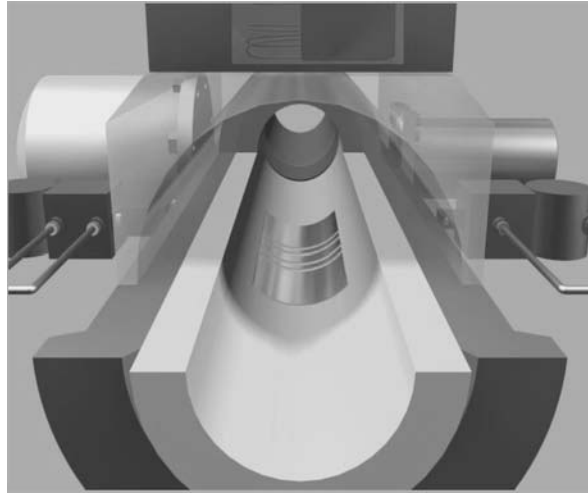


FIGURE 14.10 Bare inside capacitance electrodes (Roxar Flow Measurement AS).

Some capacitance sensors on the market today have bare electrodes inside an insulating liner as shown in Figure 14.10. These sensors have large interface capacitances, C_{e_1} and C_{e_2} (~ 1 to $5 \mu\text{F}/\text{cm}^2$), resulting in high sensitivity to C_m and R_m . While the sensor cannot be used for capacitance measurements in water-continuous mixtures, the bare electrodes can be used for conductivity measurements and, thus, the water fraction can be determined by measuring the conductivity of the mixture.

14.1.2 Microwave Transducers

E.A. Hammer

14.1.2.1 Introduction

This meter measures the electrical permittivity in a two-component mixture, and as in the case of the capacitance transducer, the ratio between the two components can be determined if the electrical permittivity is different for each component. This transducer works in the GHz region and can therefore be used as water cut meters for North sea crude oil from 0 to 100% water since the frequency $f > f_c = \sigma_w/\epsilon_0\epsilon_w$ (see Eq. [14.11]). The drawback of this transducer, compared with the capacitance transducer is the dependency on the conductivity of the water component in both water- and oil-continuous mixtures.

14.1.2.2 The Principle

The principle is based on the wave equation

$$\frac{\partial V}{\partial x^2} = \frac{1}{v^2} \frac{\partial^2 V}{\partial t^2} \quad (14.12)$$

where V is the amplitude (volts for electromagnetic waves), x the distance travelled in the wave direction, and v the wave velocity which is equivalent to the velocity of electromagnetic waves in free space ($1/\sqrt{\epsilon_0\mu_0}$).

One solution of Eq. (14.12) is

$$V = u_0 \sin \omega \left(t - \frac{x}{v} \right) \quad (14.13)$$

which is a periodic wave with angular frequency ω travelling in the positive direction with amplitude u_0 and velocity v . For electromagnetic waves, u_0 is expressed in volts and the wave velocity is

$$v = \frac{1}{\sqrt{\epsilon_0\mu_0\epsilon_r\mu_r}} = \frac{1}{\sqrt{\epsilon_0\mu_0}\sqrt{\epsilon_r\mu_r}} = \frac{c}{\sqrt{\epsilon_r\mu_r}} \quad (14.14)$$

For water and oil, $\mu_r = 1$ and

$$v = \frac{c}{\sqrt{\epsilon_m}} \quad \text{and} \quad V = u_0 \sin \omega \left(t - \sqrt{\epsilon_m} \frac{x}{c} \right) \quad (14.15a)$$

Referring to Figure 14.11, wave A generates the following potential at the detector position:

$$u_a(x_1, t) = u_0 \sin \omega \left(t - \sqrt{\epsilon_m} \frac{x_1}{c} \right) \quad (14.15b)$$

Wave B generates at its detector position,

$$u_b(x_1 + \Delta x, t) = u_0 \sin \omega \left(t - \sqrt{\epsilon_m} \frac{x_1 + \Delta x}{c} \right) \quad (14.16)$$

The detector will read out a zero voltage when

$$u_a(x_2, t) + u_b(x_1 + \Delta x, t) = 0 \quad (14.17)$$

This means

$$\omega \left(t - \sqrt{\epsilon_m} \frac{x_1}{c} \right) = \omega \left(t - \sqrt{\epsilon_m} \frac{x_1 + \Delta x}{c} \right) + \pi + k2\pi \quad (14.18)$$

where $k = 1, 2, 3, \dots$. From Eq. (14.18) one finds

$$\sqrt{\epsilon_m} \frac{\Delta x}{c} = \frac{\pi(1 + 2k)}{\omega} \quad (14.19)$$

From Eq. (14.19) the frequencies giving zero volts at the detector are

$$\omega_0 = \frac{\pi(1 + 2k)c}{\sqrt{\epsilon_m} \Delta X} \quad (14.20)$$

For $k = 0$, the lowest destructive interference frequency will be

$$\omega_0 = \frac{\pi c}{\sqrt{\epsilon_m} \Delta X} = 2\pi f_0 \quad (14.21)$$

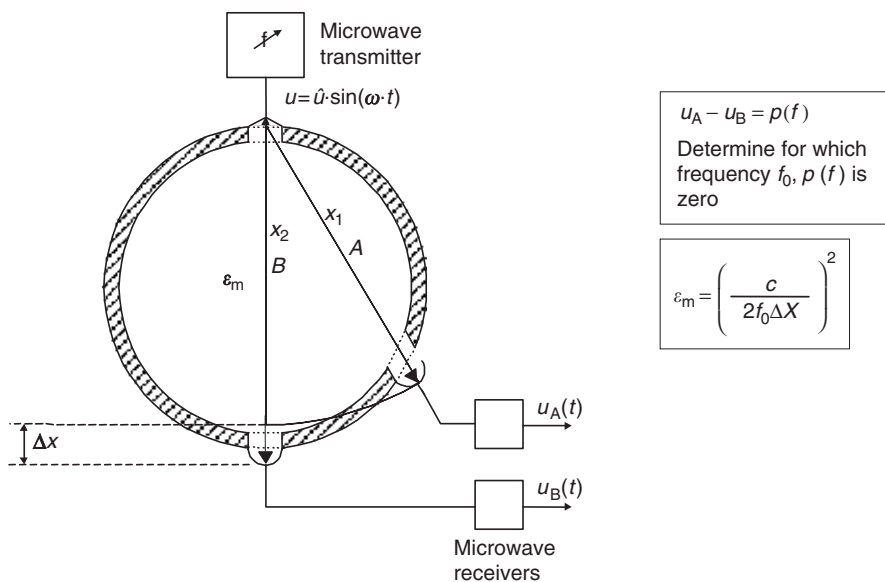


FIGURE 14.11 Principle of a microwave water-cut meter.

By detecting this frequency (f_0), the relative permittivity can be found according to the following equation:

$$\epsilon_m = \left(\frac{c}{2\Delta X f_0} \right)^2 \quad (14.22)$$

When the permittivity ϵ_m of an oil–water mixture is known, the water–oil ratio can be calculated.

For example, if $\Delta X = 0.01$ m, the lowest destructive interference frequency occurs at:

$$f_0 = \begin{cases} 1.78 \text{ GHz at 100% process water,} & \epsilon_r = 71, \sigma = 5 \text{ S/m} \\ 9.5 \text{ GHz at 100% oil,} & \epsilon_r = 2.5, \sigma \approx 0 \\ 15 \text{ GHz at 100% gas,} & \epsilon_r = 1, \sigma = 0 \end{cases}$$

For this sensor, the lowest destructive interference frequency must be well above the cutoff frequency f_0 of the water component. (For North Sea process water $f_0 \approx 1.3$ GHz.)

The desirable feature of this sensor is that it can be used both for oil and water continuous mixtures. However, at large water-cuts, water droplets with diameters $>10\%$ of the pipe diameter will cause dispersion of the travelling waves resulting in a measurement error. These sensors, therefore, need more mixing at high water-cuts.

14.1.2.3 Calculation of Water Fractions in an Oil–Water Mixture

When the permittivity of the mixture ϵ_m is found, the water volume fraction β can be determined using Eq. (14.5) for oil-continuous mixture (oil is continuous phase in mixture):

$$\beta = \frac{\epsilon_m - \epsilon_{\text{oil}}}{\epsilon_m + \epsilon_{\text{oil}}}$$

and Eq. (14.6) for water-continuous mixtures:

$$\beta = \frac{3\epsilon'_m}{\epsilon'_m + 2\epsilon_w}$$

The permittivities ϵ_m and ϵ'_m can be found directly from the microwave sensor, but since the capacitance sensor does not work in salt water continuous mixtures, only ϵ_m can be found by using Eq. (4.9):

$$C_m = \frac{C_e C_s}{C_e - C_s} = k \epsilon_0 \epsilon_m \rightarrow \epsilon_m = \frac{C_m}{k \epsilon_0}$$

where k is the meter constant for the capacitance sensor and ϵ_0 the permittivity of the free space.

Example. A capacitance transducer is used to measure the water fraction in a crude oil production pipe. No gas is produced so that a homogeneous mixture of crude oil and salt water fills the pipe completely. The capacitance sensor used has electrodes arranged as shown in Figure 14.2a and has the following specifications: $C_e = 170$ pF and $k = 0.17$. In a given period of time, the measurement result is $C_s = 13$ pF. (1) Calculate the water fraction and the crude oil fraction flowing in the production pipe at the given time period. (2) Determine if the mixture is oil- or water-continuous.

Solution. (1) We have

$$C_m = \frac{C_e C_s}{C_e + C_s} = \frac{170 \times 13}{170 + 13} = 12.08 \approx 12 \text{ pF}$$

$$\beta = \frac{\epsilon_m - \epsilon_{\text{oil}}}{C_m} = \frac{8.14 - 2}{12} = 0.6$$

$$\epsilon_m = \frac{\epsilon_m + \epsilon_{\text{oil}}}{k \epsilon_0} = \frac{8.14 + 2}{0.17 \times 8.85} = 8.14$$

The crude oil volume fraction $\gamma = 1 - \beta = 1 - 0.6 = 0.4$.

(2) The mixture is oil-continuous. If the mixture had been water-continuous, we would have measured $C_s = C_e = 170 \text{ pF}$.

14.1.3 Gamma-Ray Densitometry

G.A. Johansen

The attenuation of a narrow and parallel beam of monoenergetic γ -ray photons penetrating a thin slab of homogeneous material (absorber) follows Lambert–Beer's exponential decay law:

$$I = I_0 e^{-\mu d} \quad (14.23)$$

where I_0 is the intensity incident to the slab and d its thickness. Further, I is the resulting beam intensity on the other side of the slab and μ the linear attenuation coefficient, often with unit cm^{-1} . This expresses the photon interaction probability per unit path length in the absorber and is the sum of contributions from several interaction mechanisms. At low energy, photoelectric absorption dominates, whereas Compton scattering is dominant at the intermediate energies and pair creation at the highest. The energy is expressed in terms of electron volts where 1 eV is the energy ($\approx 1.6022 \times 10^{-19} \text{ J}$) required to move one electron over a 1 V potential difference. In densitometry, radiation energies in the Compton region are often used, such as the 662 keV line from the ^{137}Cs isotope. Here μ is approximately proportional to the density of the absorber (Johansen and Jackson, 2004), thus the term γ -ray densitometry. However, energies in the photoelectric region, such as 60 keV from the ^{241}Am isotope, are increasingly being used because μ exhibits a strong dependence on the atomic number (Z^3 to Z^5) in this region. This facilitates better measurement contrast between components in multiphase systems. The linear attenuation coefficient is plotted vs. radiation energy in Figure 14.12 for typical low, intermediate, and high Z elements.

The traditional γ -ray densitometer normally uses a source that emits radiation with sufficient penetration capability to enable clamp-on installation onto vessels without a process shut down (see Figure 14.13). Low-energy meters require the use of low attenuation radiation windows and thus do not have the clamp-on advantage.

In multiphase systems, measurements of γ -ray attenuation are used to determine the component volume fractions. For each component, this is equal to the product of the component's weight fraction and density: $\alpha_i = w_i \rho_i$. The relationship between the measured attenuation coefficient of a multiphase mixture μ_{mix} and that of each component μ_i is then given as (Johansen and Jackson, 2004)

$$\mu_{\text{mix}} = \sum_i^n \alpha_i \mu_i = \alpha_1 \mu_1 + \alpha_2 \mu_2 + \dots + \alpha_n \mu_n \quad (14.24)$$

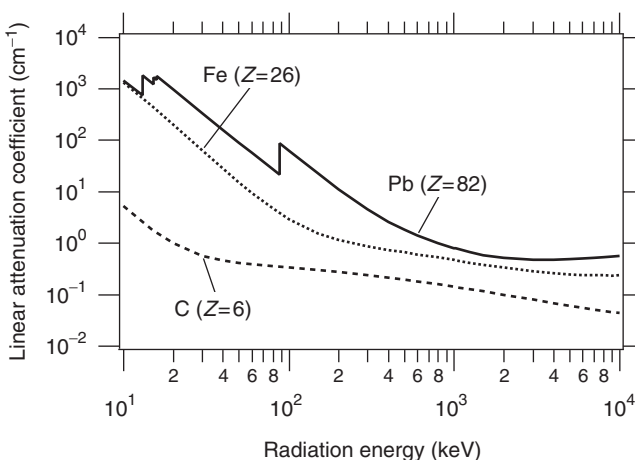


FIGURE 14.12 The energy dependence of the linear attenuation coefficients μ of carbon (graphite, $Z = 6$), iron ($Z = 26$) and lead ($Z = 82$). Data are generated by Photkoef (AIC Software, Grafton, U.S.A., 1996–2000).

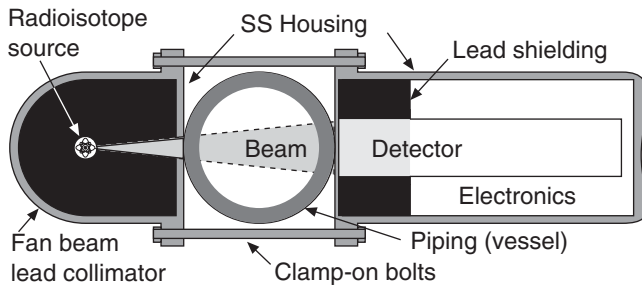


FIGURE 14.13 Schematic cross-section of a traditional clamp-on γ -ray densitometer. Most often, the ^{137}Cs is used as radiation source. Here the absorber thickness is the pipe diameter d . The meter also has a lockable radiation shutter that is not shown here.

For a two-component gas–liquid system this may be expressed as

$$\mu_{\text{mix}} = \mu_g \alpha_g + \mu_l \alpha_l = \mu_g \alpha_g + \mu_l (1 - \alpha_g) = \mu_l + \alpha_g (\mu_g + \mu_l) \quad (14.25)$$

taking into account that $\alpha_g + \alpha_l$ is unity. The attenuation coefficients are derived from the intensity measurements (Eq. [14.23]) such as

$$\mu_l = -\frac{1}{d} \ln \left[\frac{I_l}{I_0} \right] \quad (14.26)$$

Using this and Eq. (14.25) the gas volume fraction is given as

$$\alpha_g = \frac{\mu_{\text{mix}} - \mu_l}{\mu_g - \mu_l} = \frac{\ln[I_{\text{mix}}/I_l]}{\ln[I_g/I_l]} \quad (14.27)$$

Because of the random emission of γ -ray photons, every attenuation coefficient measurement has an associated statistical error, which expressed in terms of the relative standard deviation is (Johansen and Jackson, 2004)

$$\frac{\sigma_\mu}{\mu} = \frac{1}{\mu d} \sqrt{\frac{e^{\mu d}}{I_0 \tau_l}} \quad (14.28)$$

where τ_l is the counting time. Most of these gauges are operated in pulse mode. This means that all photons interacting in the detector generate individual signals, which are counted in sequential periods of τ_l . To reduce the total measurement error, calibration measurements of μ_g and μ_l (Eq. [14.26]) are carried out with two relatively long counting times (periods) compared with those used for continuous measurements of μ_{mix} . For the latter, the chosen time chosen is a compromise between accuracy and speed of response. In general, the measurement error is minimized by designing the measurement system to obtain a μd product close to 2. This is done through a careful selection of measurement energy and measurement geometry. The energy and activity of the radiation sources must be chosen in all cases in accordance to the ALARA (as low as reasonably achievable) philosophy stated by the ICRP (International Commission on Radiological Protection).

Further, it should be noted that Eqs. (14.23) and (14.26) are only valid for narrow beams. In a realistic measurement system, a portion of the photons interacting outside the beam defined by the source-detector geometry is scattered toward the detector aperture and contributes to the measured intensity. This is referred to as broad beam. The scatter contribution is known as buildup, and may be accounted for by introducing the buildup factor, $B(\mu, x)$, into Eq. (14.23), or alternatively by defining an effective linear attenuation coefficient μ_{eff} so that

$$I = B(\mu, x) I_0 e^{-\mu x} = I_0 e^{-\mu_{\text{eff}} x} \quad (14.29)$$

The measurement error introduced by the buildup is normally of less significance and is also partially compensated for by the calibration measurements.

Finally, it should be mentioned that γ -ray attenuation is also applicable for three-component measurements. This is done either by combining it with other measurement principles, such as those presented in Sections 14.1.1 and 14.1.2, or by measuring attenuation at two γ -ray energies in the Compton and photoelectric-dominant regions, respectively. In either case, an additional independent equation is produced and the three-component fractions can be determined.

14.1.4 Industrial Process Tomography

G.A. Johansen

Often in multiphase systems there is a desire to know the spatial distribution of components and its variation with time. Such an information is used, for instance, for monitoring and control purposes, for the development of processes, process models and instrumentation, etc. Tomographic imaging techniques have been applied to industrial processes ever since the first commercial X-ray Computerized Tomography (CT) scanner was introduced by EMI in 1972, and even before. Since then other sensing principles, such as magnetic resonance imaging (MRI) and ultrasound have been used. Over the past decade there has been an explosive development in electrical-sensing principles, particularly electrical capacitance tomography (ECT). Initially, industrial X-ray tomography was mainly used in laboratories for analysis of various objects and processes, and for the development and validation of process models. This is probably still the most important application of industrial tomography (Dyakowski and Kantzas, 2003). So far, field or plant applications of tomography seem to be limited to diagnostic methods. Figure 14.14 shows the outline of a typical tomography system. The sensor head constitutes a number of sources and detectors in the case of an ionizing radiation transmission system, a number of electrodes in the case of an electrical sensing principle, etc. This may either be embedded in the vessel wall or designed as a clamp-on system. Each detector (or electrode, etc.) normally has dedicated readout electronics to enable parallel signal processing. This is particularly important for high-speed imaging systems where the data acquisition time must be kept as short as possible. Industrial tomography may also be realized as dual modality systems in order to image the distribution of more than two components in multiphase systems.

The image reconstruction of tomographic imaging implies solving an inverse problem: the measurement geometry and result are known so that the assignment is to determine which spatial distribution of the imaged parameter gives these results. Depending on the requirement defined by the application, the type of reconstruction algorithm and the computing power of the reconstruction unit, data may either be reconstructed on an $n \times n$ image grid, or streamed to memory for offline reconstruction. A state-of-the-art personal computer is often used for image reconstruction; however, for high-speed real-time reconstruction, parallel computing systems may be applied. In some applications, there is no need for a reconstructed image (tomogram), but rather some parameters describing the process. Figure 14.15 illustrates the different components of the image reconstruction and processing algorithms. The measurement data are first normalized to the calibration measurement data. The normalized data are then fed to the actual reconstruction or inversion process, which also has the system geometry and eventual *a priori* information as

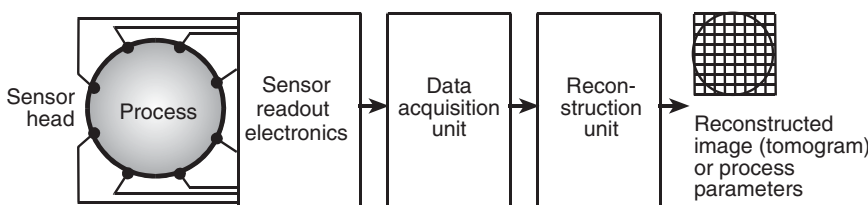


FIGURE 14.14 General arrangement of an industrial process tomography system with sensor head, sensor (detector) readout electronics, data acquisition, and reconstruction units. The latter also typically incorporates some image processing. (Reproduced from Johansen, G.A. and Jackson, P., *Radioisotope Gauges for Industrial Process Measurements*, Wiley, Chichester, 2004. With permission.)

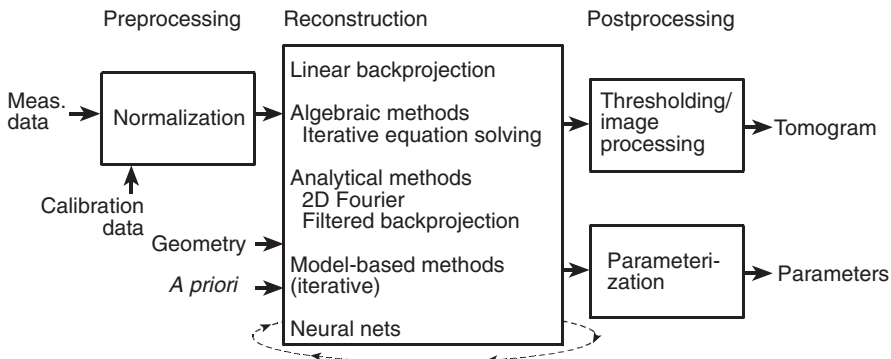


FIGURE 14.15 Typical layout of the image reconstruction algorithm. (Reproduced from Johansen, G.A. and Jackson, P., *Radioisotope Gauges for Industrial Process Measurements*, Wiley, Chichester, 2004. With permission.)

input. The tomographic inversion process is the most critical part. The choice of the algorithm is a trade-off between noise in measurements, computation time, number of measurements and *a priori* knowledge. The objective of the reconstruction algorithm is to inverse a set of equations relating the measurements to the image. The estimated parameters are linear attenuation coefficients. A well-suited class of inversion processes for industrial tomography is algebraic methods. The main assumption of these algorithms is the “pixelization” of the object. Two steps are required: definition of the objective function to minimize and definition of the algorithm that minimizes the objective function. Objective functions are usually the quadratic distance between measurements and the reprojected image or the conditional probability to get the image from the projection.

14.1.5 X-Ray and Gamma-Ray Tomography

G.A. Johansen

A very attractive property of tomography techniques using ionizing radiation is the so-called “hard-field” sensing property, which means that the sensitivity of the measurement to the measured parameter is uniform and independent of the component distribution. This facilitates the use of very powerful image reconstruction techniques known from medical X-ray CT and, consequently, high-quality images with distortions. Another attractive property is that a photon beam with sufficiently high energy, i.e., a γ -ray beam, will be able to penetrate, for example, a steel pipe. The imaging system may then be “clamped on” to an existing pipeline or process vessel.

Fourth-generation medical CT scanners utilize a rotating X-ray source and a circular detector array. This concept is also used for imaging of industrial processes where temporal averaging of the process dynamics is sufficient, or where the time constants of the process are long compared to the scanning time. Fast imaging is achieved with systems incorporating several fixed sources, each source facing an array of detectors on the opposite side of the process. A large number of transmission measurements are then carried out simultaneously. Imaging of industrial processes and their dynamics implies a tradeoff between three conflicting requirements: the measurement resolution of time, space and matter. In contrast to medical tomography where the patient is kept still for the time it takes to acquire the data for one image, in process tomography the data acquisition time has to be short to avoid inconsistency as discussed above. This means there is a compromise between statistical error and measurement time. Likewise, the spatial resolution for a given system is basically improved by reducing the size of the detectors. This in turn means fewer counts in each detector and thus a higher statistical error in each ray-sum measurement. In process tomography the solution is often, but not always, to relax the spatial resolution requirement compared to medical tomography, in order to obtain faster speed of response.

Generally, X-ray CT scanners are used when high (mm) spatial resolution is required, whereas multiple-source systems are used for imaging of process dynamics. Multiple X-ray tubes could in principle be

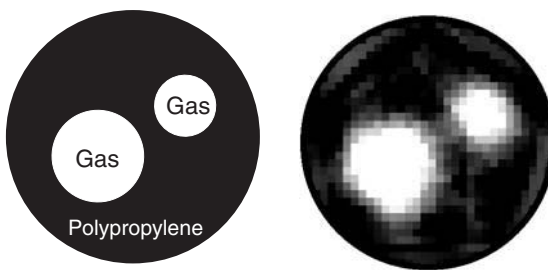


FIGURE 14.16 Reconstructed results using a polypropylene–air phantom in a γ -ray tomograph with 5 sources and 85 detectors. The pipe diameter is 82 mm. The counting time is 10 msec. (Reproduced from Johansen, G.A. and Jackson, P., *Radioisotope Gauges for Industrial Process Measurements*, Wiley, Chichester, 2004. With permission.)

used for the latter, but sources with one or few emission lines are preferred because this simplifies the image reconstruction. Several systems using multiple γ -ray sources have been designed, for instance a flow imaging tomograph using five sources each with 17 detectors, i.e., a total of 85 detectors (Johansen et al., 1996) (Figure 14.16). This is designed for an 80-mm inner pipe diameter. The spatial resolution is about 5 mm, whereas a temporal resolution a few ms is possible in gas-liquid imaging.

There are also fast X-ray imaging solutions using electronic scanning of the beam rather than mechanical scanning. These use multiple filament tubes around the object and a switchable grid voltage just in front of each filament. This enables rapid switching of the electron beam from one filament to the next, and thus results in rapid scanning. Scanning times as short as 0.5 ms is obtained in this manner (Hori et al., 1998).

14.1.6 Magnetic Resonance Imaging

T. Dyakowski

MRI is widely employed in modern medicine to obtain high-quality images of various organs in the human body, with a submillimetre spatial resolution to reveal a broad range of soft tissue pathologies. It provides noninvasive and nondestructive measurements by probing phenomena ranging from molecular interactions to spatially resolved macroscopic flow processes.

MRI is an extension of the NMR principles. The aim of NMR measurements is to monitor the radiation emitted by nuclear spins as they return to equilibrium after the appropriate stimulation. If an object containing hydrogen nuclei (a tube of water or hydrocarbons) is placed in an NMR spectrometer and is exposed to a homogenous magnetic field, B_0 , then a single resonance signal is detected by applying a circularly polarized radio frequency field (Callaghan, 1991). To date, most magnetic resonance studies have focussed on ^1H nucleus because of its high natural abundance and magnetic resonance sensitivity. The prerequisite is that the measurement system should contain a proton-rich fluid (water or hydrocarbon) and that any solid material involved either in the process or used to fabricate the container, must be transparent to radio and magnetic frequencies.

MRI is a portrayal of the concentration distribution of protons in a physical object. The technique relies on the application of an inhomogeneous magnetic field as illustrated in Figure 14.17. When the object is placed in a magnetic field that varies linearly, in the z -direction for instance, the protons will be resonant at the frequencies

$$\nu(z) = \gamma/(2\pi)(B_0 + G_z z)$$

where γ is the gyromagnetic ratio and G_z is the field gradient along the z -direction. Similar equations as the above can be written for gradients of magnetic field along the x - and y -direction. Application of a radio frequency pulse with the resonant frequency $\nu = \nu(z)$ results in a signal with an intensity that is proportional to the number of protons at position z . Thus in a magnetic field that varies linearly over an object, all the protons within a given slice (i.e., at a given field value) come into resonance and give a signal of the corresponding intensity. The resulting intensity pattern is a map of the number of protons in all the slices and portrays the shape of the sample.

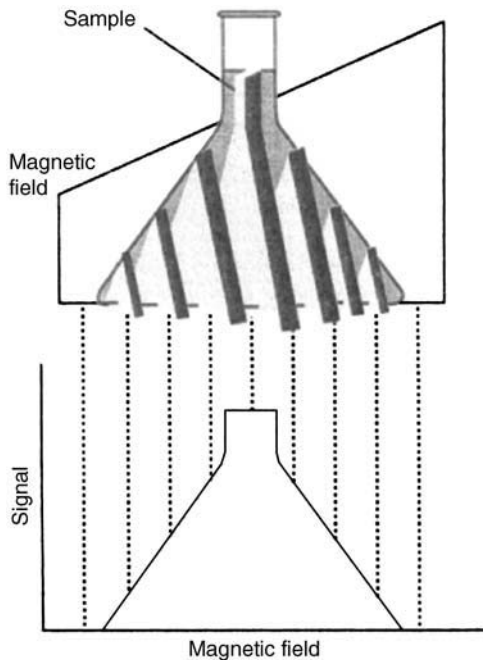


FIGURE 14.17 An illustration of one-dimensional magnetic resonance imaging.

Therefore, the underlying principles in the use of MRI as a tomographic technique arise from the frequency labeling of spins as a function of their position within the sample by the application of a magnetic field gradient.

There are three broad flow imaging strategies: steady-state, time-of-flight, and phase-shift techniques (Callaghan, 1991; Gladden, 1994). Steady-state methods rely on a rapid repetition of radio frequency and gradient pulses such that the saturation recovery or steady-state free precession signal amplitude depends on molecular motion. Time-of-flight methods detect the displacement of “tagged” spins during the time between initial excitation and signal measurement. The observable displacement is limited by the velocity of the flowing material and the lifetime of the tag. The magnetic tagging of the fluid is performed in the presence of a magnetic field gradient aligned in the direction of flow. The last method detects the alteration of the phase of transverse spin magnetization induced by spin motion along a magnetic field gradient.

Recent publications (Gladden et al., 2004; Hall, 2004) show that MRI is capable of providing quantitative data, which may be used in process design. The list of potential applications is very long and includes two-phase flows in pipelines, percolation flows in porous materials, filtration and drying processes, and the propagation of water effluents.

The majority of previous research in the field of MRI, in the area of two-phase flow, focussed on studies of solid–liquid suspensions. For example, the results obtained from the MRI experiments showed evidence for shear-induced particle motion in Couette suspension flow (Graham et al., 1991), the accuracy of a power law model for rheology of non-Newtonian aqueous solution of high-molecular-weight polymer (Sinton and Chow, 1991), and flow patterns of granular flow in a half-filled horizontal cylinder rotating at various speeds (Altobelli et al., 1992; Nakagawa et al., 1993).

According to Hall (2004), the current measurement protocols provide opportunities for visualization of internal structures in 2D, with in-plane spatial resolution of ca. 0.5 mm for a slice of thickness 2 to 5 mm or in 3D with resolution of ca. $0.5 \times 0.5 \times 0.5$ mm. The scan times vary from 0.1 sec to 15 min, depending on the scan protocol and image resolution. MRI can measure, in 3D, the entire 3D flow vector velocity field for flow velocities up to 1 m/s.

In this section, a brief review of the latest development in the field of MRI related to two-phase flow science is presented.

14.1.6.1 MRI for Component Distribution Measurements

The application of MRI to study the behavior of a gas–liquid–solid model catalytic reactor operating at elevated temperatures is reported by Koptyug et al. (2004). A schematic representation of the reactor geometry is depicted in Figure 14.18. A cylindrical catalyst pellet ($\gamma\text{-Al}_2\text{O}_3 + 1\% \text{Pd} + 0.1\% \text{Mn}$) 4.5 mm in diameter and 12 mm in length was installed vertically in a glass cell. Liquid reactant α -methylstyrene (AMS) flow rate was 8.6×10^{-4} g/sec and hydrogen, H_2 , was preheated to 78°C and was supplied at the rate of $10.9 \text{ cm}^3/\text{s}$. The results show the oscillations of the amount of liquid within the pellet (white area) and the reciprocating motion of liquid front as illustrated in Figure 14.19a. Combining these results with the temperature oscillations shown in Figure 14.19d, the authors have discussed the coupling of mass transport and phase transition processes in the reacting system. The understanding of these phenomena is critical for designing new, highly efficient, and reliable chemical reactors. It should be emphasized that the data were gathered at elevated temperatures (78°C).

MRI was applied by Hindmarsh et al. (2004) to visualize the solidification process of 20% (w/w) sucrose solution droplet suspended in cold air. During freezing of the droplets, solute redistribution occurs as a consequence of differences in the solubility of the solute in the liquid and solid phases. This leads to segregation of the solute between the liquid and solid phases, which in turn influences the final microstructure of the frozen droplet. The images of the solidification process are crucial to distinguish among the various stages of a droplet freezing process.

The experiments were conducted using a Bruker DMX 300 spectrometer featuring a 7.14 T vertical bore magnet fitted with ^1H birdcage radio frequency coil. The results were obtained for 2-mm-diameter sucrose droplets, freezing in -25°C and -80°C environments, respectively. Since the freezing process is relatively fast, the measurement protocol was based on the rapid acquisition with the relaxation enhancement technique developed by Sederman et al. (2003) and Hennning et al. (1986). By using this protocol, the data were collected with a time interval of 0.5 s.

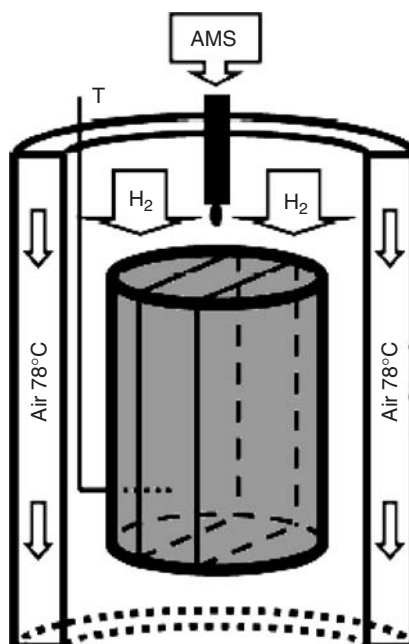


FIGURE 14.18 Schematic representation of a single-pellet experiment.

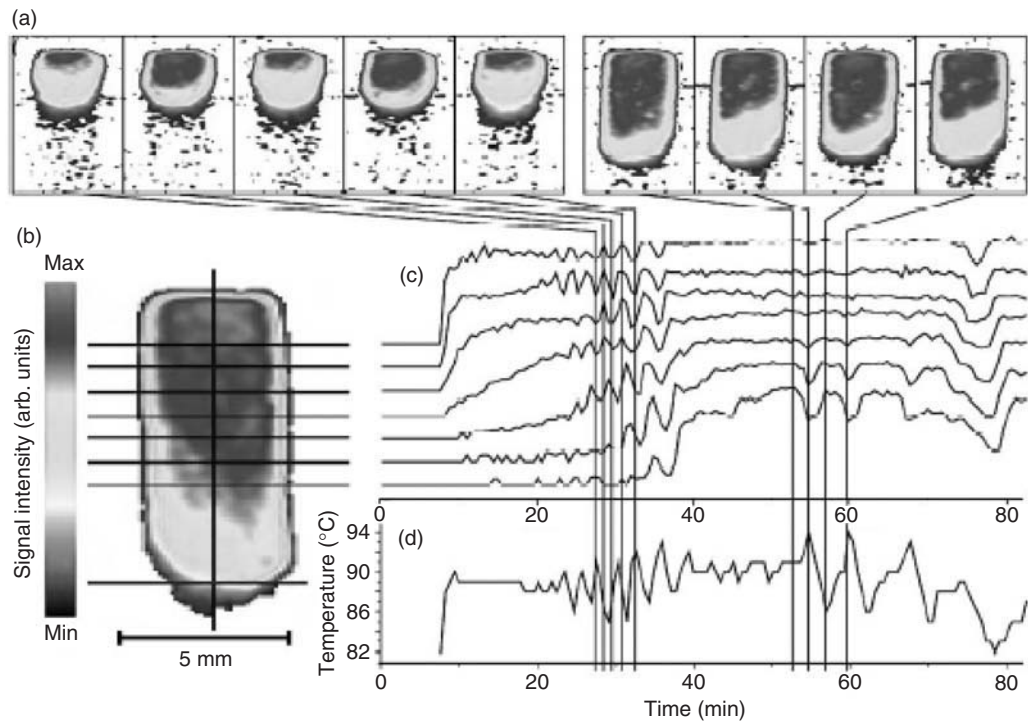


FIGURE 14.19 The results of the single-pellet experiment. (a) Distribution of the liquid phase within the imaged axial slice of the catalyst pellet. The spatial resolution is $230 \mu\text{m} \times 311 \mu\text{m}$. (b) One of the images shown together with the signal intensity scale. The intersections of the set of equidistant horizontal lines with the vertical axial line define the spatial locations for the data shown in (c). The bottom horizontal line indicates the level at which the thermocouple is implanted into the pellet. (c) Signal intensity (liquid content) vs. time for the spatial locations shown in (b). Vertical lines indicate when the specific images shown in (a) were detected. (d) Temporal behaviour of the pellet temperature measured at the location indicated with the bottom horizontal line in (b).

Figure 14.20 shows the ^1H images and the signal intensity of the image is proportional to the mass of unfrozen sucrose solution present in each voxel. The completely unfrozen droplet is shown in Figure 14.20a and the first appearance of ice is shown in Figure 14.20b. The images shown in Figures 14.20c to f illustrate how quickly the ice grows. Video images are shown in Figure 14.21. It is not possible to determine the extent and location of the unfrozen material in the video image.

Since a frozen solution gives a negligible MR signal, the MRI technique enables the derivation of the unfrozen liquid mass fraction providing a valuable data in terms of verifying models of the droplet freezing process as discussed by Hindmarsh et al. (2004).

14.1.6.2 MRI Velocimetry

Transport in a porous media depends on the structure of the pore space. To understand the transport in porous rock, Kossel et al. (2004) experimentally studied flow through two two-dimensional percolation clusters. In the first cluster the pores were larger than $300 \mu\text{m}$ and in the second smaller than $50 \mu\text{m}$. The first cluster is shown in Figure 14.22a, and Figure 14.22b depicts a spin density map of the water-filled pore space. Figure 14.23a shows the distribution of velocity magnitude within pores. The results are compared against the data obtained from numerical simulation, which was based on solving a continuity equation and the Navier–Stokes equation for viscous liquids.

A complex flow pattern existing within a fibrous porous medium bounded by a free-flow region of variable width was investigated by Bijelic et al. (2004). A 2D flow field within a porous medium and an adjoining free-flow region was measured by the phase-difference technique originally described by

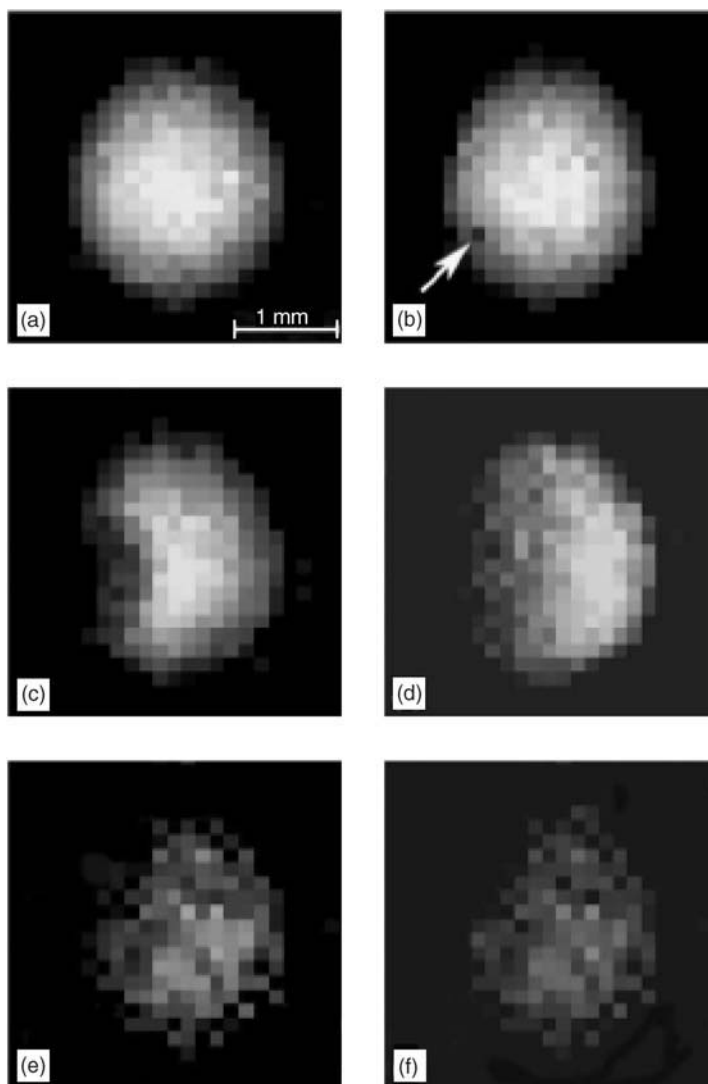


FIGURE 14.20 ^1H -spin-density images of the nucleation and recalescence of a 20% (w/w) sucrose droplet freezing in still air at -25°C . Resolution was 62 μm , the time between frames was 0.5 sec. The arrow in frame (b) indicates the voxel containing the nucleation center.

Callaghan (1991). The results were obtained for an upward flow of a glycerol aqueous solution with velocities in the range of a few mm/sec. An example of the results obtained is illustrated for the channel entrance region shown in Figure 14.24. The contour maps of V_z and V_x velocities are depicted in Figure 14.25a and b. It is interesting to notice that the flow in the entrance region is accelerated in the presence of the neighboring fiber lattices.

The authors quantified the differences between the flows through porous media adjacent to a free-flow region of variable width and the flows through porous media bounded by a free-flow region of constant width. This is crucial for optimizing heat and mass transfer processes of heterogeneous porous systems.

Recently, Sederman et al. (2003) published results showing images of velocity and its convective derivative for a water flow in a straight vertical channel of internal diameter 29 mm. All experiments were performed on a Bruker DMX 200 vertical 149 mm bore spectrometer operating at a ^1H frequency of

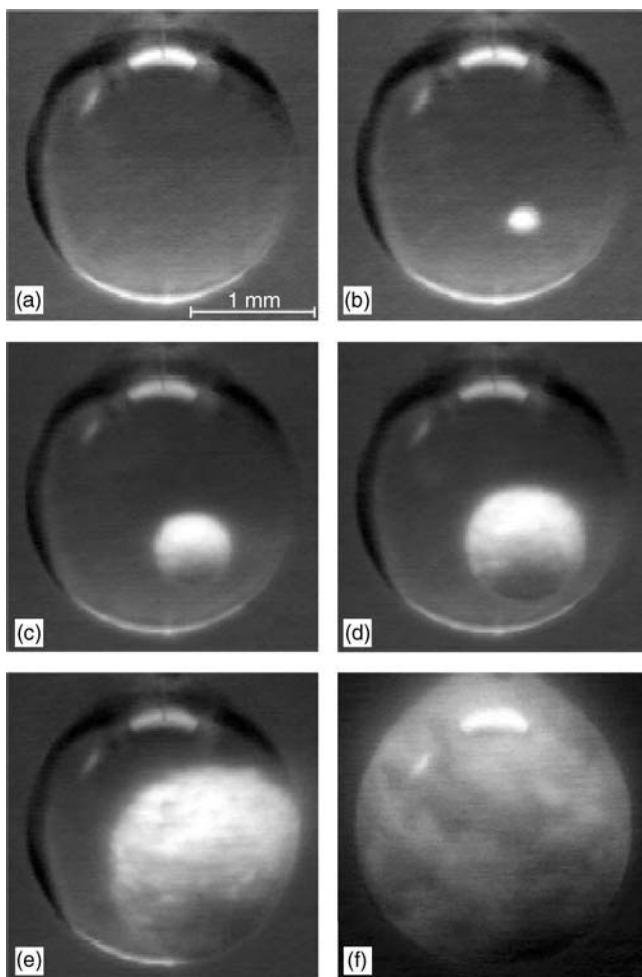


FIGURE 14.21 Video images taken under the same conditions as the data shown in Figure 14.20. Time between frames was 0.2 s, and ice is visible as white sphere.

199.7 MHz. The measurement protocol, called GERVAIS, was applied to acquire three-component velocity images with a time interval of 50 ms.

The echo planar imaging (EPI) developed originally by Mansfield (1977), enables 2D data acquisition times to be an order of several milliseconds. The EPI technique was applied by Mantle et al. (2002) for imaging a two-phase gas–liquid flow within the parallel channels of a ceramic monolith rated at 400 channels/in². (i.e., channels of width around 1 mm). Such a monolith is used as “structured supports” in solid-catalysed gas-phase chemical reactions. The results were obtained for a gas flow rate of 200 cm³/min through stagnant liquid. Typical image acquisition times were around 100 msec and in-plane image resolution was 395 μm × 791 μm. In Figure 14.26, the Taylor bubbles are shown as the dark regions. The images were used to optimize the design of a ceramic monolith.

Recently, the other two publications by Dirckx et al. (2000) and Chu et al. (2004) focussed on some aspects of flows through porous media. In the first publication, the authors discussed the correlation between the areas of heavy blocking and the internal structure of the filter cartridge. The results showed the correlation between the spatial heterogeneity of particulate deposition and the heterogeneous flow paths of liquid through the filter. In the latter, the effect of heterogeneity on nonaqueous-phase liquids removal during soil-vapor extraction was investigated.

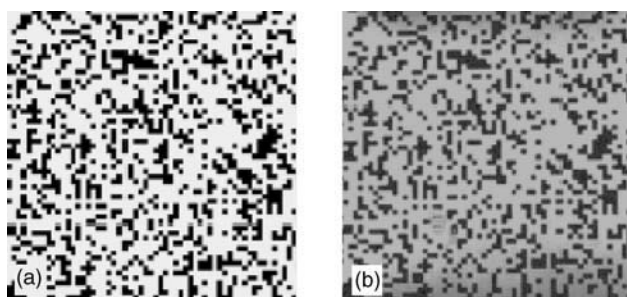


FIGURE 14.22 (a) A percolation structure on a 60×60 square lattice. (b) Spin density map of the water-filled pore space of a corresponding model object of size 6×6 cm 2 . The digital resolution is $190 \times 190 \mu\text{m}^2$.

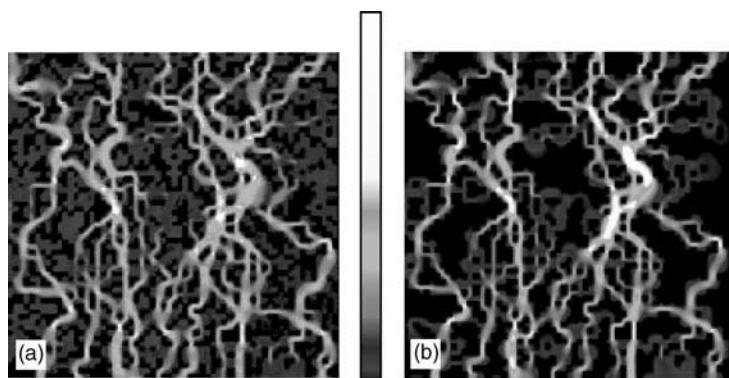


FIGURE 14.23 Map of the flow velocity magnitude for the percolation model object shown in Figure 6b: (a) experimental map and (b) simulated map of the flow velocity.

14.1.6.3 Future Work

A few recent applications of the MRI technique presented illustrate an important advantage of MRI over a wide range of other modern imaging techniques. MRI has the ability to provide information not only on the structure of an object, but also on a broad range of its physical and chemical properties and processes. Unlike other techniques, it can provide both spatial and spectroscopic information under identical experimental conditions, with the extra advantage of a direct flow visualization.

As Gladden et al. (2004) have pointed out, we expect MRI to be exploited to probe the coupling of chemical and physical processes from Å to the cm scale. This will have an enormous impact, for example, on testing and validating theoretical models of non-Newtonian multiphase systems.

14.1.7 Ultrasound Techniques

T. Dyakowski

Ultrasound is already an established technique for characterizing the physical properties of material in a number of areas, for example, material testing, medical imaging, flaw detection, and oceanography. Recent applications of ultrasound sensors in multiphase flows cover a wide range of topics such as ultrasonic tomography of bubble column (Warsito et al., 1996; Utomo et al., 2001), measurements of solids mass fraction and their velocities in slurry flow (Carlsson and Martinsson, 2002; Carlsson and Ing, 2003), and measurements of void fraction of dispersed phase in oil–water system (Meng et al., 2004).

Various types of interaction between acoustic waves traveling through a continuous phase and interacting with dispersed phases are detected by ultrasonic sensors. When an acoustic wave encounters an

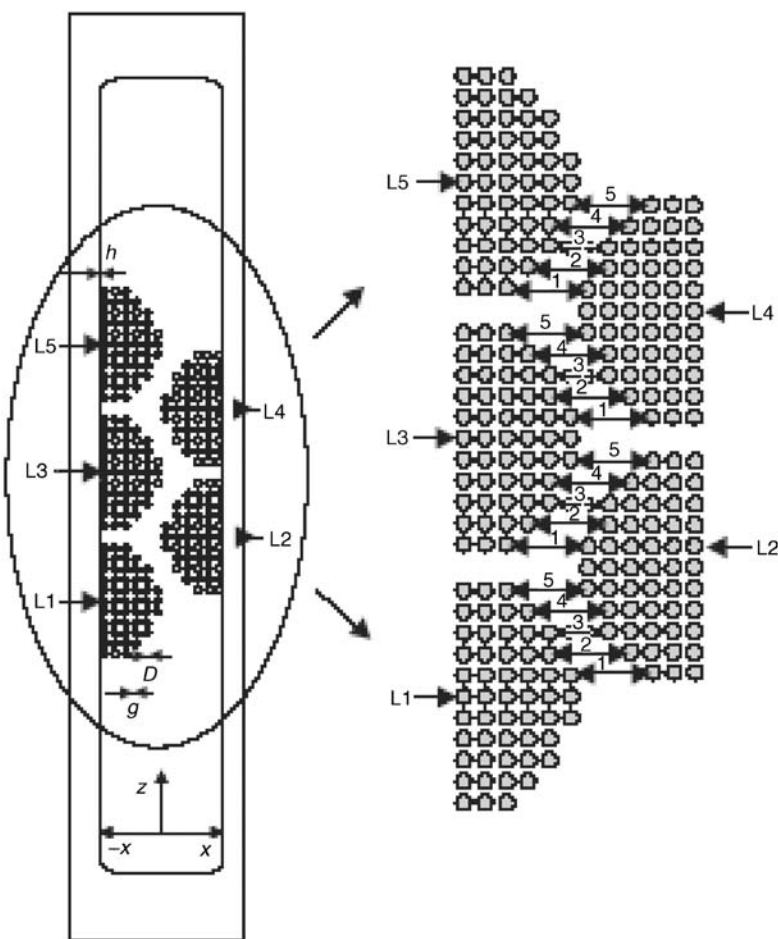


FIGURE 14.24 The assembly of macroscopically semicircular square unit-cell lattices denoted as L1-L5 and arranged in hexagonal order, each with $D = 2$ mm, $g = 0.5$ mm, $h = 0.3$ mm, $\epsilon = 0.5$; the width of the free-flow region between the solid lines denoted as 1, 2, 4 and 5 are 6.7 mm, whereas the widths of the free-flow region between the lattices marked with the dashed lines and denoted as 3 are 4.2 mm.

obstacle (particle, bubble, or droplet), some of the waves are deflected from its original course. The difference between the actual wave and the undisturbed wave, which would be present if the obstacles were not there, is called the scattered wave. When a plane wave, for instance, strikes a body in its path, in addition to the undisturbed plane wave, there is a scattered wave spreading out from the obstacle in all directions, distorting and interfering with the plane wave. The interaction between an acoustic wave and an obstacle wave depends on two factors. The first is the ratio between the wavelength and an obstacle dimension and the second is the ratio of phase acoustic impedances at the interface of two phases.

If the obstacle is very large compared with the wavelength, $ka \gg 1$ (where $k = 2\pi/\lambda$ and a the characteristic dimension), half of this scattered wave spreads out more or less uniformly in all directions from the obstacle, and the other half is concentrated in such a manner as to interfere destructively with the unchanged plane wave behind the obstacle, creating a sharp-edged shadow there. In this case the scattered wave spreading out uniformly is called the reflected wave, and the half responsible for the shadow is called the interfering wave. The analysis of the interaction between the ultrasound wave and the object may be simplified by assuming a straight-line ray behavior (specular reflector). The rays may be assumed to continue in a straight line when transmitted through an attenuating medium and interfaces may be assumed to cause reflections, which also travel along straight lines.

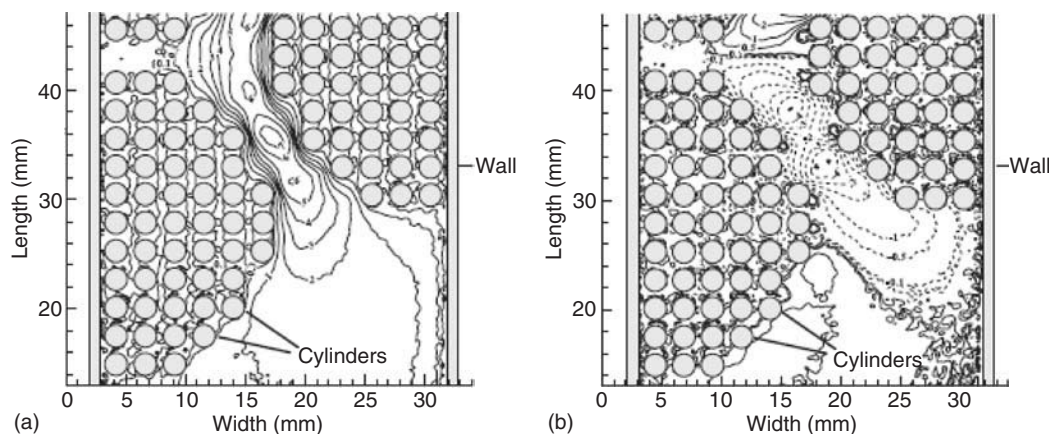


FIGURE 14.25 Contour velocity map for (a) the velocity component in the flow direction (V_z) and (b) the velocity component perpendicular to the flow direction (V_x) in the entrance of the fibre lattice assembly (lattices L1–L3) shown in Figure 14.24. Contours corresponding to velocities in the x -direction are drawn as dotted lines.

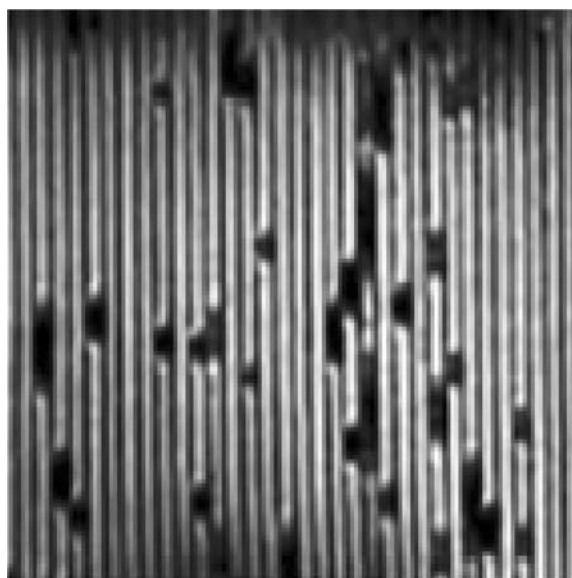


FIGURE 14.26 Images of Taylor gas bubbles (black) and liquid (white) within individual channels of a ceramic monolith.

When the wavelength is large compared with the size of the obstacle, $ka \ll 1$, the wave is hardly affected by its presence. In this case most of the ultrasound energy is backscattered, i.e., scattered in the opposite direction of the incoming sound wave. In fact, only 1/8 of the energy is scattered forward as discussed in Morse and Ingard (1968).

Acoustic impedance is defined as the ratio between acoustic pressure and fluid velocity caused by the wave. The values of acoustic impedance characterize various types of interactions at the interface between phases. Wells (1969) showed that the greater the difference in impedance at the interface formed by two phases, the greater is the amount of energy reflected. If the impedances are similar, most of the energy is transmitted. For air and water, the acoustic impedances are 429 and 1.5×10^6 N sec/m³ (at 1 atm and 0°C), respectively. Therefore, ultrasonic reflections provide a basis of imaging water and air systems.

In contrast to light or other electromagnetic waves, ultrasound needs a medium to transmit through and interrogates the physical properties of the media (i.e., density and compressibility). Therefore, ultrasound techniques are appropriate for application in a medium, which is poorly penetrated by light or other electromagnetic radiation. In addition, compared with high-energy electromagnetic radiation, the ultrasonic technique consumes much less energy, is low cost and simpler to use, and is suitable for applications from laboratory scale to industrial plants. The two main limitations of ultrasound tomography are the complex sound field sensed by transducers often resulting in overlapped or multiple reflected pulses that introduce errors and the inherent slow propagation of ultrasound lowering the scanning speed.

14.1.7.1 Ultrasonic Tomography

The transmission and reflection modes of ultrasonic tomography ($ka \gg 1$) describe the propagation of ultrasound energy with a frequency of the order of MHz in a multiphase mixture of water, for an air bubble size ranging from 10^{-3} to 10^{-2} m and particle size of several hundreds of micrometers. Using these two modes, Warsito et al. (1996) and Uotomo et al. (2001) applied ultrasonic tomography to study the effect of solids on flow morphology of a gas–liquid bubbly column. They assumed that the velocity difference of ultrasound in the system and in the pure liquid in terms of transmission time difference ΔT can be expressed as

$$\Delta T = (K_S \varepsilon_S + K_G \varepsilon_G)L$$

where ε_S and ε_G are the solid and the gas holdups, respectively, L is the transmission path length, and K_S and K_G are coefficients that depend on the frequency and the particle or the bubble diameter. For sufficiently high frequency, the effect of gas bubble on the velocity change of the emitted ultrasonic wave is negligible as shown in Warsito et al. (1996). Thus

$$\Delta T = K_S \varepsilon_S L$$

The energy attenuation, Ω , of the three-phase system can be expressed as

$$\Omega = (X_S \varepsilon_S + X_G \varepsilon_G)L$$

The line integrals of the gas $f_G(x,y)$, and solids $f_S(x,y)$ holdup distribution along the penetrating path $L_{s,\theta}$, (Figure 14.27), can be expressed as

$$\int f_G(x,y) dL = \varepsilon_G^A(s,\theta)L_{s,\theta} = 1/X_G[\Omega_{s,\theta} - X_S \Delta T_{s,\theta}/K_S]$$

$$\int f_L(x,y) dL = \varepsilon_L^A(s,\theta)L_{s,\theta} = \Delta T_{s,\theta}/K_S$$

$\Delta T_{s,\theta}$ and $\Omega_{s,\theta}$ were measured using an ultrasonic pulse wave. The experiments were conducted in a vertical column, 14 cm in diameter and 140 cm in height, made from methylmethacrylate. Tap water and air were used as the fluids with glass beads of average particle diameter 100, 260, and 360 μm . The experimental data were taken in a semibath mode (no net liquid velocity).

The ultrasonic transducer array is shown in Figure 14.28. It consists of six pairs of transducers and receivers. The transducer diameter was 16 mm and the frequency range varied from 100 kHz to 25 MHz. The transducer array was rotated 10° and the measurement protocol was repeated. The measurements were completed in 18 directions and six paths. The projection data were reconstructed using the filtered back-projection algorithm based on a two-dimensional Fourier transform. The spatial resolution, defined as a percentage of the pixel size to the pipe cross-section, was 3%. The time collection for each projection was 5 min and the time-average projection data were reconstructed.

The effect of gas velocity on the distribution of the gas and the solid hold-up at the bottom of the column is shown in Figure 14.29. The tomograms show that the gas hold-up increases with the increase in gas velocity, but its pattern is not affected by the changes in gas velocity. On the other hand, the hollow part of the solids concentration disappears with increase in gas velocity. The detailed discussion of the results

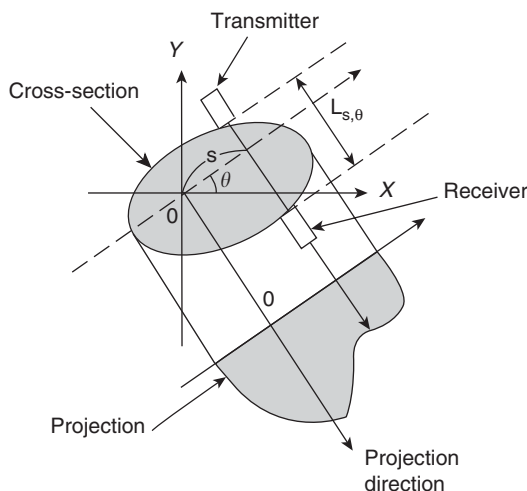


FIGURE 14.27 Principle of ultrasonic tomographic projection.

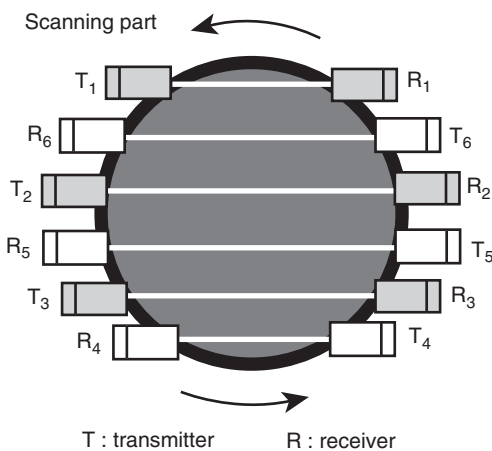


FIGURE 14.28 Ultrasonic array of transducers.

obtained is presented elsewhere Warsito et al. (1996), and the use of this technique for studying the flow morphology of air–water– TiO_2 bubble column is reported in Uotomo et al. (2001). The proposed technique is limited to total (gas and solid) holdups up to 20%. For higher holdups, there will not be enough space for the acoustic beam to pass through and arrive at the corresponding receiver along a straight path.

The application of ultrasonic transmission tomography ($ka \gg 1$) for imaging air bubble sizes and their rising velocities in a vertical column filled with water is also reported by Xu et al. (1997). A column was built from a Perspex pipe, 220 mm in length, 187 mm inner diameter and 7 mm pipe wall thickness. The operating frequency of the ultrasound sensor was 2 MHz and the related wavelengths in water and air were 0.75 and 0.17 mm. To satisfy the condition $ka \gg 1$, the radius of imaged bubbles should be > 0.12 mm.

14.1.7.2 Mass Fraction Measurements

The ultrasonic technique is finding increasing use as a tool for characterizing emulsions and suspensions. A number of applications using this technique are reported. Povey and co-workers worked extensively on ultrasonic characterization of food emulsion (Povey, 1997). They used multiple-scattering theory to relate the measured velocity and attenuation to the oil concentration and droplet size of salad cream.

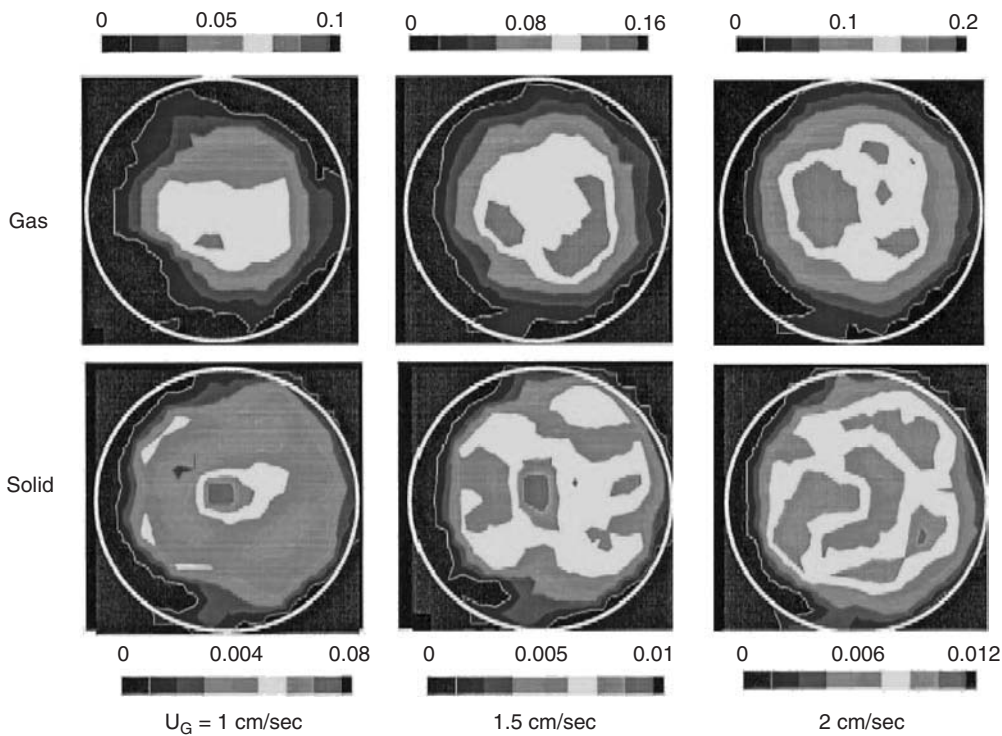


FIGURE 14.29 Cross-sectional distribution of gas and solid concentrations measured by ultrasonic computed tomography in gas–liquid–solid system. (From Warsito et al., *Chem. Eng. Sci.*, 54, 4711, 1996. With permission.)

Tsouris and Tavlarides (1991) used an ultrasonic technique for phase fraction measurements in liquid–liquid column extractors to provide automatic multi-point measurements for real-time volume fraction.

Longitudinal acoustic waves ($ka \ll 1$) travel through a single-phase fluid with a velocity that depends on the fluid density and compressibility. In suspensions and slurries, on the other hand, the wave speed is a function of material properties of the constituents as well as their relative concentrations. The attenuation of sound in two-phase liquid mixtures is known to increase with increasing frequency. As shown by Atkinson and Kytomaa (1992), there are two different mechanisms responsible for attenuation of acoustic energy. At low frequencies the thick boundary layer, relative to the particle radius, is generated and steady drag acting on the particle causes the attenuation mechanism. At high frequencies, the Basset force associated with the oscillatory relative motion between the particle and the fluid causes the attenuation. On the other hand, the effect of frequency on the speed of sound is small.

The attenuation depends also on the mass fraction of particles and the propagation distance of the wave. For a measurement system, where the distance between the transducers is constant, the measured attenuation coefficient will be proportional to the mass fraction alone as shown in Carlsson and Martinsson (2002). An ultrasonic sensor measuring the solids mass fraction as a function of the attenuation of ultrasonic waves is shown in Figure 14.30. The sensor consisted of one transmitter and a receiver array built from 12 sensors, each 5 mm wide and 20 mm long (along the flow direction) and the gap between them was 1.5 mm. The generated acoustic wavelength was $\lambda = 0.987$ mm. The received energy was averaged over all receiver sensors. The sensor was clamped on a rectangular Plexiglas channel with a width of 10 cm.

Solids mass fractions of Dolomite particles ($(Ca, Mg)CO_3$) with mean particle radius $a = 26 \mu m$ and particle density $\rho = 2800 \text{ kg/m}^3$ in a downward slurry flow (mixture of solids with water) in a vertical channel were measured and compared against the proposed theoretical model, which is fully described in

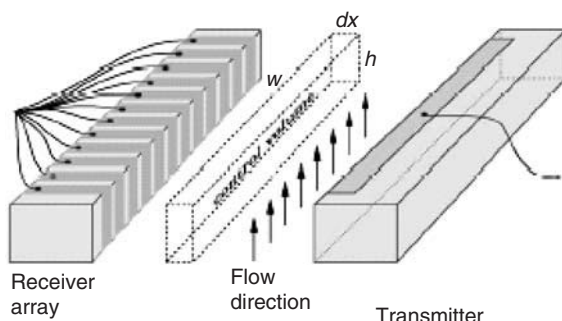


FIGURE 14.30 Transmitter and receiver array applied. (From Carlsson, J. and Martinsson, P.E., *Ultrasonics*, 39, 585, 2002. With permission.)

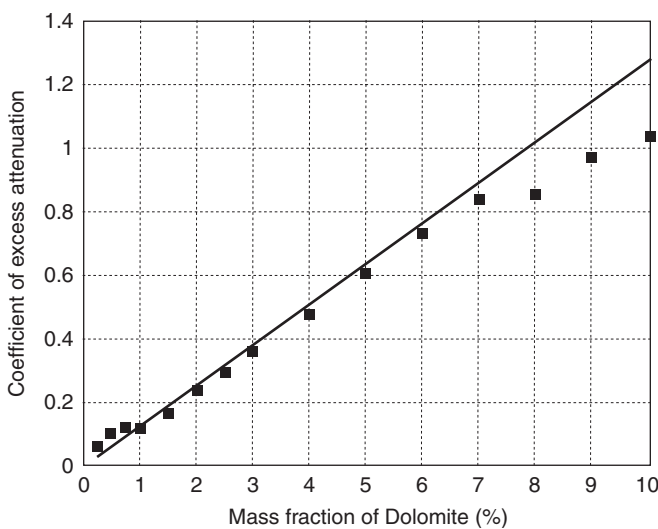


FIGURE 14.31 Measured (dotted) and theoretical (solid) excess attenuation for Dolomite.

Carlsson and Martinsson (2002). The results are presented in Figure 14.31. The measurements show that for higher mass fractions, the attenuation is lower than that predicted from the theory. The most likely explanation is that at these mass fractions the particles start to settle within the flow system.

The other approach to measure mixture composition is based on measuring the time-of-flight of long ultrasonic waves in a dispersed mixture. This is a function of mixture composition (phase volume fraction), compressibility and density of continuous and dispersed phases. The relationship between the speed of sound in the mixture and the volume fraction can be expressed by the following equation:

$$1/v^* = \varphi(g_d/v_d - g_c/v_c) + 1/v_c$$

where v^* is the speed of sound in the dispersion, v_c the speed of sound in the continuous phase and v_d the speed of sound in the dispersed phase. The coefficients g_d and g_c take into account the refraction phenomena of ultrasound and depend on the ratio of ultrasonic velocity in the dispersed phase to the ultrasonic velocity in the continuous phase. Meng et al. (2004), measured the time-of-flight in heterogeneous mixtures of saline water and vegetable oil. The speed of sound in the first is 1700.6 m/s and in the latter 1446.8 m/s. Thus the ratio of ultrasonic velocities γ is 0.83.

Using this value and the detailed equations for g_d and g_c as proposed in Tsouris and Taylarides(1991), the equation can be expressed as

$$1000/v^* = 0.0013\varphi + 0.5880$$

It predicts a linear relationship between the reciprocal of the speed of sound and the volume fraction. The experimental results, discussed in detail in Meng et al. (2004), are presented in Figure 14.32. Given the condition that the approach proposed in Tsouris and Taylarides (1991) is for $\gamma \leq 1$, this can only be done for the first 6 points on the left of this figure. The relationship obtained is given by

$$1000/v^* = 0.0012\varphi + 0.5889$$

It shows that the regression curve coincides almost ideally with the theoretical prediction. For oil–volume fractions between 50 and 100%, the regression analysis for this range yields the following relationship:

$$1000/v^* = 0.0008\varphi + 0.6069$$

14.1.7.3 Velocity Measurements

The traditional ultrasonic Doppler systems measure only the particle velocities along the axis of the ultrasound beam (Wiegand and Hoyle, 1991). As discussed by Jensen (2000), this is a major problem in medical systems, since most blood vessels are parallel to the skin surface and thereby orthogonal to the beam.

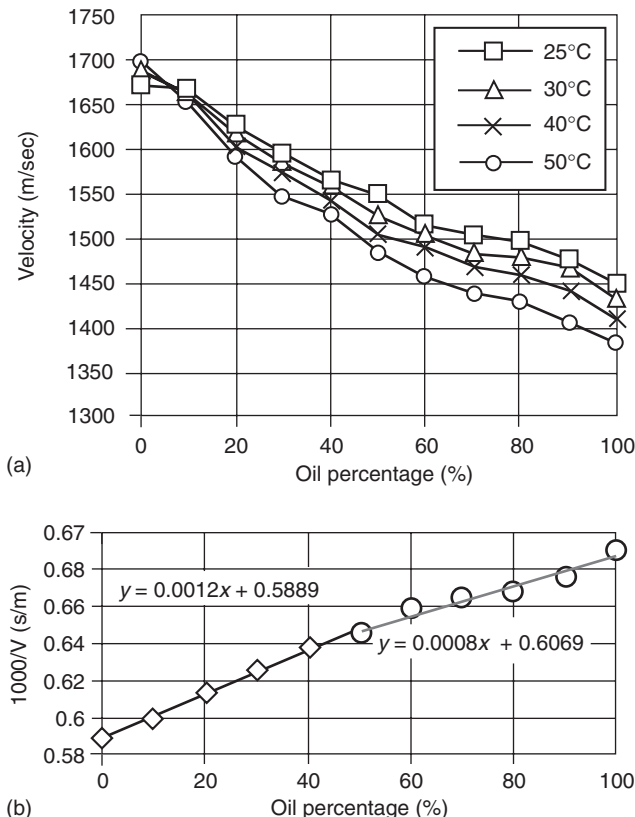


FIGURE 14.32 Trend of $1000/v^*$ vs. oil percentage. (From Meng et al., with dual-modality transducers fabricated using thick-film technology, Proceedings of ESDA, 7th Biennial, ASME Conference, Engineering Systems Design and Analysis, Manchester, United Kingdom, July 19–22, 2004. With Permission.)

Angling the transducer often disturbs the flow. An approach to solve this problem by using an ultrasonic speckle correlation velocimetry (USV) tracking technique was proposed by Trahey et al. (1987), and it was applied by Carlson and Ing (2003) for measuring the solids distribution profile in a vertically dispersed solids–liquid flow. A cloud of particles in a slurry flow is a source of backscattering ($ka \ll 1$) of an ultrasound wave. The linear transducer array emits a plane wave into a slurry and then the same transducer array records the backscattered waves caused by a cloud of particles as illustrated in Figure 14.33. The condition $ka \ll 1$ was fulfilled for the particles with radius $a = 26 \mu\text{m}$ and wavelength $\lambda = 0.987 \text{ mm}$.

A 64-element linear transducer array mounted perpendicular to the flow, with an incident angle of 45° was applied for measuring velocities of solids in a vertical channel with 33.7 mm I.D. Acoustic reflections from groups of particles arrive at the different transducer elements at different times. This produces an interference pattern at the receiver. The speckle presence in the ultrasonic images is caused by an increase in particle concentration, due to interference among acoustic waves from the particles. The name “speckle” is used because the produced ultrasonic images of particles show some similarities with those obtained in coherent optics. Two-dimensional USV was applied for measuring solids velocity distribution of Magnetite (Fe_3O_4) particles (particle diameter $d = 52 \mu\text{m}$ and density 5200 kg/m^3) flowing downwards in a vertical channel with I.D. 33.7 mm. The results shown in Figure 14.34 were obtained using a

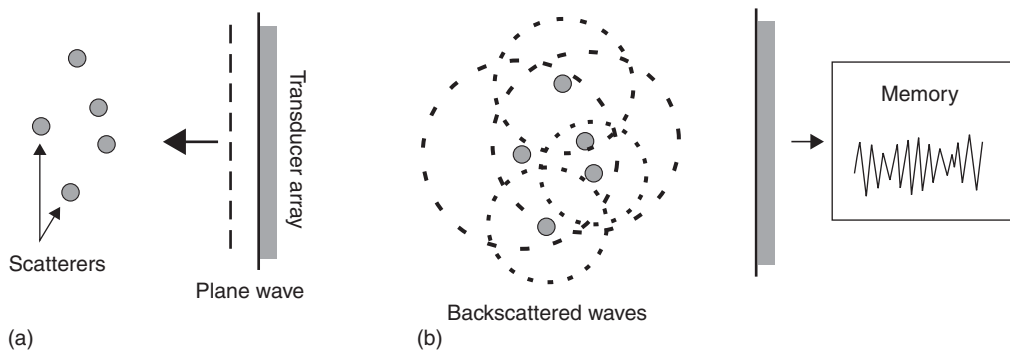


FIGURE 14.33 The imaging sequence: (a) the medium is illuminated using a plane ultrasonic wave; (b) the backscattered signals are received by the same transducer array and stored in the channel memories.

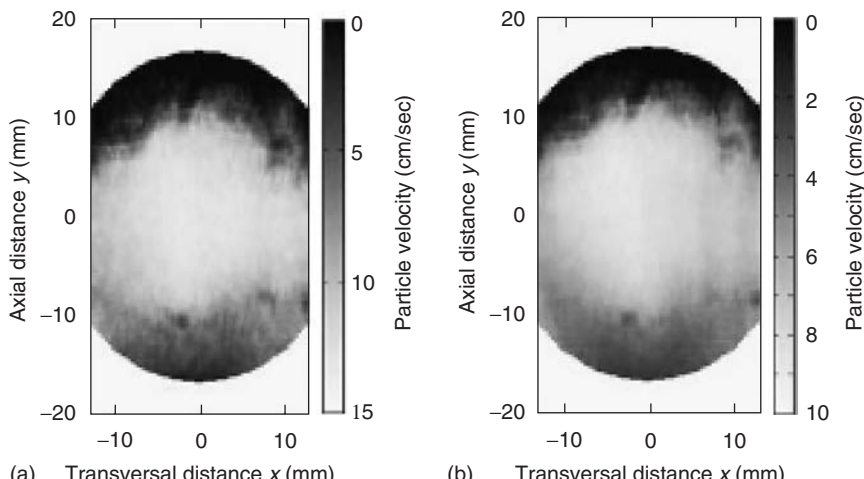


FIGURE 14.34 Magnetite velocity profiles for entire cross-section of the flow for two different water average velocities: (a) 8.96 cm/sec and (b) 5.72 cm/sec.

64-element transducer array mounted perpendicular to the flow, with an incident angle of 45° . To ensure that solids velocity profile was fully developed, the measurements were taken at a distance of 1 m from the inlet to the pipe and the frequency of an ultrasound wave was 3.5 MHz.

14.2 Mass Flow Measurements

E.A. Hammer

14.2.1 Velocity Measurement

The most frequently used methods for velocity measurement of liquid–gas flows are: (1) the cross-correlation technique and (2) combination of a venturimeter and a γ densitometer.

The accuracy of these methods depends mainly on the gas volume fraction. Large gas volume fractions can give inaccurate measurement results.

14.2.1.1 The Cross-Correlation Technique

It is always the velocity of the conveyed component that is measured by this technique. In a pipe flow of liquid and gas bubbles, the velocity of the gas bubbles is measured, and not the velocity of the liquid.

The principle of bubble velocity signal generation by capacitance electrodes is shown in Figure 14.35. Other sensors, like microwave sensors, ultrasonic sensors, γ radiation density sensors, etc., are also used.

The mathematical expression for cross-correlation is

$$R_{xy}(\tau) = \frac{1}{T} \int_0^T x(t)y(t - \tau) dt \quad (14.30)$$

where $R_{xy}(\tau)$ is the cross-correlation of the signals x and y when the upstream signal y is delayed by time τ . The time τ_1 corresponding to the peak of the cross-correlation function is reduced from the data and the bubble velocity is given by

$$v = \frac{l}{\tau_1}, \quad (14.31)$$

Where l is the axial distance between the centres of the electrodes.

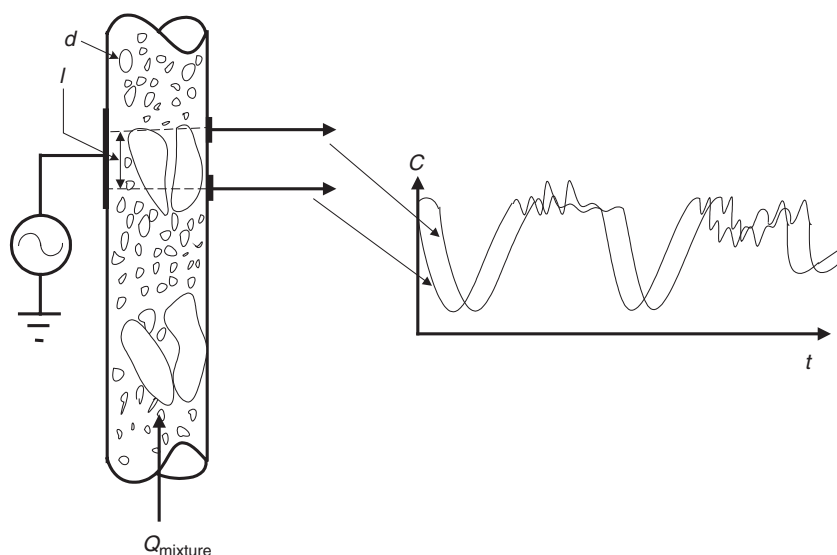


FIGURE 14.35 Generation of sensor signals for measuring the velocity of the conveyed component in two-phase flows.

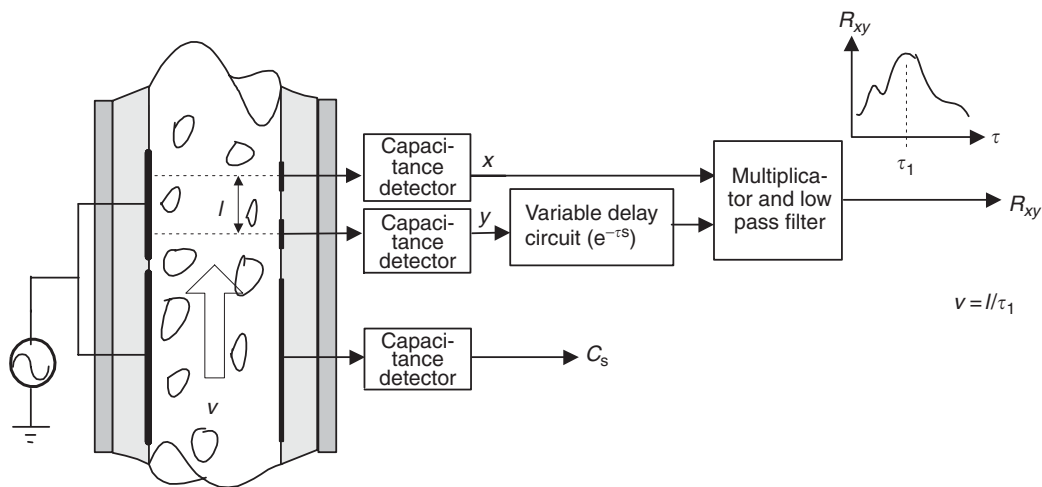


FIGURE 14.36 The cross-correlation principle.

A block diagram of a sensor connected to a data processor for calculating the cross-correlation function is shown in Figure 14.36. A capacitance sensor is also shown for determination of the water fraction in the flow.

To interpret the results from cross-correlation velocity determination, it is necessary to know the nature of the spatial low-pass filtering of the signals occurring at every sensor situated along the flow direction.

14.2.2 The Spatial Filtering Effect

When a sensor has a given displacement along the flow direction, the signal will be bandpass-limited. This phenomenon can be utilized to find the velocity of the small bubbles and the large bubbles in a gas-liquid mixture. The small bubbles will flow at the same velocity as the liquid, but the larger bubbles will have a higher velocity. The slip between the liquid and the gas components can thus be found by cross-correlating the signals generated by small and larger area sensors. Axially short and long capacitance sensor electrodes give an illustrative example of this effect.

14.2.2.1 Theory

A Dirac pulse $\delta(t)$ is defined as a rectangular pulse at $t = 0$ with width b and height $1/b$ as $b \rightarrow 0$. The pulse thus has unit area. Such a pulse, of course, can not exactly appear in physical systems but it has significant mathematical value since $L\{\delta(t)\} = 1$, where L is the Laplace operator. We define the transfer function of the sensor as

$$h(s) = \frac{u_2}{u_1}(s) \quad (14.32)$$

where u_1 and u_2 are the input and output signals of the sensor. If a Dirac pulse is used as the input signal, the Laplace transform of the output signal will be

$$u_2(s) = h(s)L\{\delta(t)\} = h(s) \quad (14.33)$$

so that

$$L\{u_2(t)\} = h(s) \quad (14.34)$$

From this we conclude that the Laplace transform of the output signal from a sensor gives the sensor transfer function directly.

Assume that a small droplet with high electrical permittivity is flowing at a velocity v through a capacitance sensor in a liquid of a low permittivity. This droplet will create a local increase in permittivity ($\Delta\epsilon$) at the position of the droplet, and is shown in Figure 14.37.

The local permittivity increase (see Figure 14.37a) creates a short time pulse with strength $\Delta\epsilon$ and, if the droplet has a diameter of Δx , the pulse will have a time duration at the point $x = 0$ of $\Delta t = \Delta x/v$. Since

$$\Delta\epsilon \int_0^\infty \delta(t) dt = \Delta\epsilon \quad (14.35)$$

the amplitude of the pulse must be

$$\Delta\epsilon_p = \frac{\Delta\epsilon}{\Delta x} v \quad (14.36)$$

By letting $\Delta x \rightarrow 0$, then $\Delta\epsilon_p \rightarrow \infty$, and one has a Dirac pulse and thus Eq. (14.34) is valid, since the Laplace transform of a Dirac pulse is 1.

The output signal will last for time $t_s = a/v$, where a is the electrode length and v the flow velocity. Since the time integral of the mean permittivity increase of the mixture in the sensor, $\Delta\epsilon_m$, must be equal to the time integral of the Dirac pulse one can write

$$\Delta\epsilon_m = \Delta\epsilon \frac{v}{a} \quad (14.37)$$

The increase in capacitance of the sensor is then

$$\Delta C = k\epsilon_0 \Delta\epsilon \frac{v}{a} \quad \text{for } 0 \leq t \leq \frac{a}{v} \quad (14.38)$$

where k is an instrument factor. This is shown in Figure 14.37c.

The Laplace transform of this signal gives

$$h(s) = k\epsilon_0 \Delta\epsilon \frac{v}{a} \frac{1}{s} (1 - e^{-s(a/v)}) \quad (14.39)$$

and the frequency response will be

$$h(j\omega) = K \frac{v}{a} \frac{1 - e^{-j\omega(a/v)}}{j\omega} = K \frac{2v}{a\omega} \frac{e^{j\omega(a/2v)} - e^{j\omega(a/2v)}}{2j} e^{-j\omega a/2v} \quad (14.40)$$

where $K = k\epsilon_0 \Delta\epsilon$. The amplitude-frequency response of the sensor can then be described as

$$|h(j\omega)| = \left| \frac{u_2(j\omega)}{u_1(j\omega)} \right| = K \frac{2v}{a\omega} \frac{e^{j\omega(a/2v)} - e^{j\omega(a/2v)}}{2j} = K \operatorname{sinc} \frac{a}{2v} \omega = K \operatorname{sinc} \left(\frac{\pi a}{v} f \right) \quad (14.41)$$

This frequency response is shown in Figure 14.38.

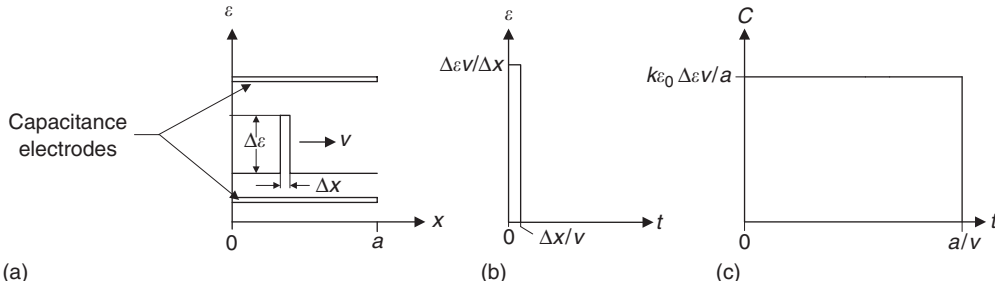


FIGURE 14.37 Schematic representation of how a high permittivity droplet creates an input and an output signal in a capacitance sensor: (a) local increase of permittivity in the flow when a high permittivity droplet is passing through the capacitance sensor; (b) time history of the permittivity pulse at the input of the capacitance electrodes; (c) time response of the increase in measured capacitance when the droplet is passing the sensor electrodes.

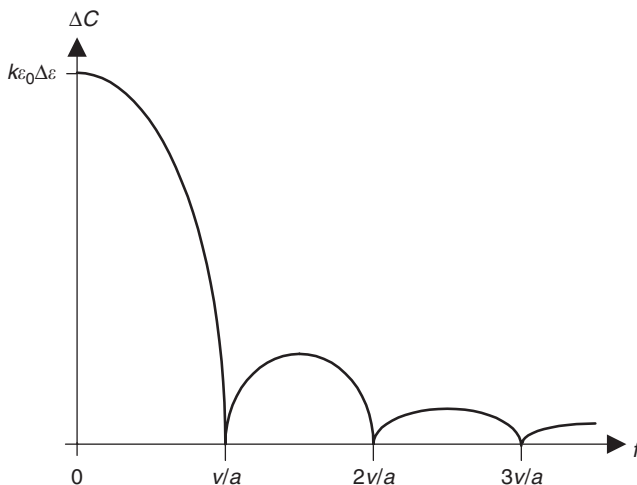


FIGURE 14.38 The spatial filter characteristic or the capacitance sensor frequency response.

Assume that a water droplet is flowing at a velocity of 5 m/sec and capacitance electrodes of 0.05 m length are used to detect the droplet flow velocity in an oil–water mixture. According to the above calculation, the sensor will have a “cutoff frequency” of $f_c = v/a = 100$ Hz.

Experimental work has shown that a capacitance sensor will not work for cross-correlation velocity measurement in this situation (Hammer and Green, 1983). The reason is that the water droplets will be very small for a water volume fraction lower than say 30% and much of the water appears in emulsions. The bandwidth of variation in permittivity will thus exceed 100 Hz. However, the capacitance sensors work very well for detecting velocity of gas bubbles because the bubbles are bigger than the water droplets and generate signals at frequencies below the cutoff frequency. Actually, some instrument producers utilize this filtering effect by detecting the velocity of small bubbles using short electrodes (1 cm) and long electrodes (5–10 cm) for detecting larger bubbles. Since the small bubbles will flow with the same velocity as the liquid and the larger bubbles will flow at the gas velocity, both the liquid and the gas velocities can be determined.

14.2.3 Liquid Flow Measurement in Gas–Liquid Flows

The combination of a venturi differential pressure flowmeter and a density gage also provides the liquid flow rate in two-phase (liquid–gas) pipe flow (see Figure 14.39). The venturimeter is a differential pressure meter and if d/D less than 0.6, then approximately 75% of the differential pressure Δp will be recovered. A γ -ray densitometer is positioned to measure the gas volume fraction α across the venturimeter throat where the flow is most turbulent and thus most homogeneous.

It can then be shown for gas pressures less than approximately 100 bar, where the density of the gas is negligible compared with the liquid density, that the mass flow rate of the liquid component is given as (Hammer and Nordtvedt, 1991)

$$\dot{M} = \sqrt{2\varepsilon C E A_2^M} \sqrt{2\rho_{\text{mix}} \Delta P} = q_{\text{mix}} \rho_{\text{mix}}$$

$$E = \frac{1}{\sqrt{1 - (d/D)^4}} \quad (14.42)$$

$$A_2^M = \frac{\pi d^2}{4}$$

where C is the discharge coefficient of the venturimeter, ε the expansion coefficient of the fluid, E the velocity of approach factor, and A_2^M the throat cross-sectional area.

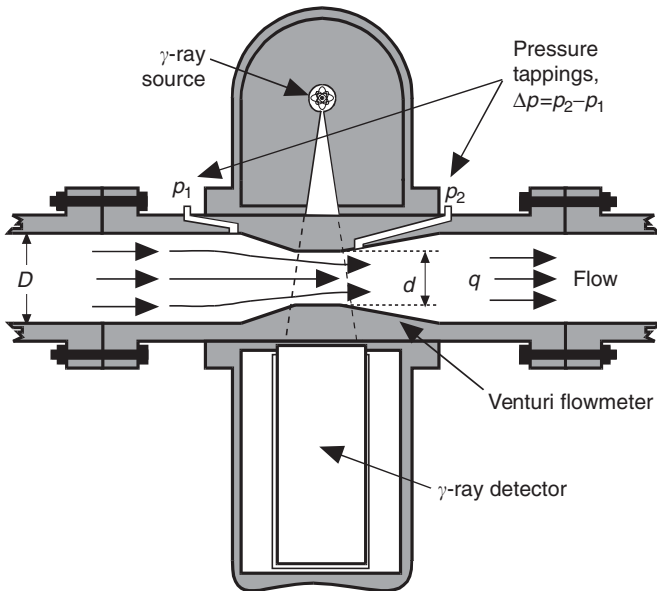


FIGURE 14.39 Schematic view of a combined venturimeter and a γ -ray gauge for measuring the volume flow rate of the liquid component. (Source: Johansen, G.A. and Jackson, P., *Radioisotope Gauges for Industrial Process Measurements*. Reproduced with permission from John Wiley & Sons, 2004.)

The mixture density is

$$\rho_{\text{mix}} = \alpha\rho_{\text{gas}} + \beta\rho_{\text{liq}} = \alpha\rho_{\text{gas}} + (1 - \alpha)\rho_{\text{liq}} \approx (1 - \alpha)\rho_{\text{liq}}$$

since $\rho_{\text{gas}} \ll \rho_{\text{liq}}$. This gives

$$\varepsilon C E A_2^M \sqrt{2(1 - \alpha)\rho_{\text{liq}} \Delta P} \approx (1 - \alpha)\rho_{\text{liq}} q_{\text{mix}} = \rho_{\text{liq}} q_{\text{liq}}$$

where q_{liq} is the volume flow rate of the liquid phase and α the gas fraction in the venturi throat. Hence,

$$q_{\text{liq}} \approx \varepsilon C E A_2^M \sqrt{\frac{2(1 - \alpha)}{\rho_{\text{liq}}} \Delta P} \quad (14.43)$$

The discharge coefficient C and the expansion coefficient ε can, for all practical purposes in multiphase measurements, be set equal to unity.

In multiphase flowmeters, a density gage will always be installed to measure the gas volume fraction α . Thus, α will be monitored and the liquid flow rate can be measured according to Eq. (14.43). The accuracy of the measurement will increase with increasing velocity and decrease with increasing gas volume fraction. To obtain better mixing, the venturimeter must be installed in vertical pipes with upward flow.

An interesting feature, using a venturimeter, is that if the velocity of the liquid $v_{2\text{liq}}$ is measured, i.e., by using the cross-correlation of signals from two sets of capacitance electrodes in the venturimeter throat, the gas fraction α can be found from Eq. (14.43) if the liquid velocity is measured separately

$$\alpha \cong 1 - \frac{2\varepsilon^2 C^2 E^2 \Delta P}{(A_2^M)^2 v_{2\text{liq}}^2 \rho_{\text{liq}}} \quad (14.44)$$

using the fact that $q_{\text{liq}} = A_2^M (1 - \alpha) v_{2\text{liq}}$, where $v_{2\text{liq}}$ is the liquid flow velocity in venturi throat. Thus the gas fraction in the venturi throat can be found without using radioactive technique.

14.2.4 On-Line Calculation on Component Flow Rates

One of the most challenging multiphase flows to control and monitor is the crude oil–water–gas mixture flowing in the production pipe from oil wells under the sea bottom. The mixture consists of three phases and especially at the sea bottom and down hole, the pressure can exceed 300 bar and 250°C. Depending on the crude oil quality, layers of scales can deposit on the inside wall of the meter, and reduce the meter accuracy.

One objective of on-line measurement of oil–water–gas mixtures is to determine the gas volume fraction α , the water volume fraction β , and the oil volume fraction γ . The evaluation of the three volume fractions requires three independent equations; and two of them can be found by two independent measurements. The third equation is

$$\alpha + \beta + \gamma = 1 \quad (14.45)$$

The independent variables measured by most three-phase meters available today are:

1. Electrical permittivity of the mixture:

$$\epsilon_m = f_\epsilon(\alpha, \beta, \gamma) \quad (14.46)$$

2. Electrical conductivity of the mixture:

$$\sigma_m = f_\sigma(\alpha, \beta, \gamma) \quad (14.47)$$

3. Density of the mixture:

$$\rho_m = f_{\rho 1}(\alpha, \beta, \gamma) \quad (14.48a)$$

$$\rho_m = f_{\rho 2}(\alpha, \beta, \gamma) \quad (14.48b)$$

where the indices 1 and 2 refer to different energies of the γ sources used (see [Section 14.1.3](#)). Measurement of mixture density will always be implemented. In addition, either measurement of electrical permittivity or conductivity will be necessary depending on whether the flow is oil- or water-continuous. The microwave sensor will, however, measure the mixture permittivity at both oil- and water-continuous phases. The mixture density is measured by γ radiation. If the use of radioactive gauges is to be avoided, mixture density measurement can be made with a venturimeter using separate velocity determination, so Eq. (14.44) can be applied. By using dual-energy γ radiation, two independent equations can be set up according to Eqs. (14.48a) and (14.48b) and, consequently permittivity, or conductivity, measurements are not necessary. The basic theory underlying detailed measurements used for the calculation of the component fractions is given in Sections 14.1.1–14.1.3, and also 14.2.16. The different manufacturers of these meters base the data reduction formulas for fraction calculations on this theory. However, it is necessary to adjust the different constants in the equations according to the pressure, temperature and, in some cases, the conductivity of the water component.

The different volume fractions (α, β, γ) are calculated at least every second by the flow computer and the input to the computer is always two different measurements, either density and permittivity or conductivity, or two density measurements using two different γ energies. The third equation is always Eq. (14.45). To obtain the volume flow rate of the gas, q_α , the gas volume fraction is multiplied by the gas velocity and the cross-sectional area of the meter. Similarly, the volume flow rate of the water, q_β , and oil, q_γ , are obtained by multiplying the appropriate volume fractions by the liquid velocity and the cross-sectional area of the meter. The flow rate of each component will be displayed for process control and integrated to be included in the production budget.

The water component in most crude oil fields always has certain salinity and is therefore conductive. The conductivity can vary from field to field and with age of the well, but mainly is in the area of 5 ± 1 S/m. The relative electrical permittivity of the crude oil well for North Sea crude is in the region of 2.2 ± 0.2 depending on the temperature; for water 70 ± 3 depending on temperature and salinity. The conductivity of the

processed water from the separators must therefore be measured as frequently as necessary and used in the equations for conductivity-, microwave permittivity-, and γ -densitometer. The permittivity of the crude oil must also be checked if capacitance transducers or microwave transducers are used. If the water fraction increases, the oil–water mixture will be water-continuous. The transition point will be in the area of $\beta = 0.6$ –0.8 for North Sea crude oils, and is dependent on temperature, viscosity and degree of mixing and type of crude. As we have seen in Section 14.1.1, the electrical properties will change dramatically at this point and must be interpreted according to given theory and practical experience.

It is possible to find three independent equations which are coupled and nonlinear from two different measurements. The computer programs necessary to solve the equations are therefore complicated. Each producer has developed his/her own algorithms, that differ in reliability and robustness. In the example given below an iterative method is used which in principle can also be implemented in the flow computer.

Example

In a 4'' crude oil production pipe ($D = 0.01$ m) in the North Sea, the different fractions of the produced gas–water–oil mixture are measured by a three-phase meter based on a γ radiation gauge and a capacitance sensor. The meter is placed topside on a production platform and the following mixture parameters are known: $\rho_{\text{gas}} = 1 \text{ kg/m}^3$, $\rho_w = 1050 \text{ kg/m}^3$, $\rho_{\text{oil}} = 860 \text{ kg/m}^3$, $\epsilon_{\text{gas}} = 1$, $\epsilon_w = 71$ and $\epsilon_{\text{oil}} = 2.2$.

The γ gauge reading is $\rho_{\text{mix}} = 700 \text{ kg/m}^3$ and the capacitance transducer reads $\epsilon_m = 6.0$. The three-phase meter is also equipped with a dual-velocity meter with $v_{\text{liq}} = 5 \text{ m/sec}$ and $v_{\text{gas}} = 6 \text{ m/sec}$. The following solution illustrates how the three phases can be determined.

Solution

First Iteration:

$$\rho_{\text{mix}} = \alpha\rho_{\text{gas}} + \beta\rho_w + \gamma\rho_{\text{oil}}$$

$$700 = \alpha + 1050\beta + 860\gamma \approx \alpha + (1050 + 860)/2(\beta + \gamma) = \alpha + 955(1 - \alpha)$$

Therefore, $\alpha \approx 0.27$.

The gas component α is mixed with the liquid component $\beta + \gamma$ and if the liquid makes up the continuous phase and the gas the discontinuous phase, then one can write

$$\begin{aligned}\epsilon_{\text{liq}} &\approx \epsilon_{\text{oil}} \frac{1 + 2\beta'}{1 - \beta'} \quad \beta' = \frac{\beta}{\beta + \gamma} = \frac{\beta}{1 - \alpha} \\ \epsilon_m &\approx \epsilon_{\text{liq}} \frac{1 + 2\alpha}{1 - \alpha}, \quad \epsilon_{\text{liq}} = \epsilon_m \frac{1 - \alpha}{1 + 2\alpha} = 6 \frac{1 - 0.27}{1 - 2 \cdot 0.27} = 9.52\end{aligned}$$

which gives

$$\begin{aligned}\beta' &\approx \frac{\epsilon_{\text{liq}} - \epsilon_{\text{oil}}}{\epsilon_{\text{liq}} + 2\epsilon_{\text{oil}}} \approx \frac{\beta}{\beta + \gamma} = \frac{\beta}{1 - \alpha} \\ \beta &\approx (1 - \alpha) \frac{\epsilon_{\text{liq}} - \epsilon_{\text{oil}}}{\epsilon_{\text{liq}} + 2\epsilon_{\text{oil}}} = 0.73 \frac{9.5 - 2.2}{9.5 + 4.4} = 0.38\end{aligned}$$

$$\gamma \approx 1 - \alpha - \beta = 1 - 0.65 = 0.35$$

Second Iteration: In the first iteration $\beta = \gamma$ was used. This was a reasonably good guess since we found $\beta = 0.35$ and $\gamma = 0.38$. Therefore, there is little to be gained in accuracy by doing the second iteration. This can be checked by

$$\rho_{\text{mix}} = \alpha\rho_{\text{gas}} + \beta\rho_w + \gamma\rho_{\text{oil}} = 0.27 + 0.38 \times 1050 + 0.35 \times 860 = 700.27 \approx 700 \text{ (kg/m}^3\text{)} \text{ as measured.}$$

If β had been more different from γ it would have been necessary to start a new iteration to find the correct values of the different fractions.

Finally, the component flow rates can be calculated as

$$Q_{\text{gas}} = \alpha \frac{\pi D^2}{4} v_{\text{gas}} = 0.27 \frac{\pi 0.01^2}{4} 6 = \underline{\underline{4.71 \times 10^{-4} \text{ m}^3/\text{sec} = 40.7 \text{ m}^3/\text{day}}}$$

$$Q_w = \beta \frac{\pi D^2}{4} v_{\text{liq}} = 5.49 \times 10^{-4} = \underline{\underline{47.5 \text{ m}^3/\text{day}}}$$

$$Q_{\text{oil}} = 12.9 \text{ m}^3/\text{day}$$

14.2.5 Comparison of Different Commercial Multiphase Meters

There are different multiphase meters in the market today for crude oil production. Different combinations of several measurement principles are used resulting in different qualities, which will be favorable for different measurement situations. The different advantages and disadvantages are listed in Table 14.1.

14.3 Wall Shear Stress

E.P.L. Roberts

14.3.1 Electrolysis Technique

The electrolysis technique enables measurement of the local velocity gradient at the wall. This technique was developed by Hanratty and co-workers (Reiss and Hanratty, 1963; Mitchell and Hanratty, 1966) and has been widely used for both single-phase and gas–liquid flows. The method involves the measurement of the rate of ion diffusion to the surface of a polarized electrode inserted in the wall. An electrochemical

TABLE 14.1 Evaluation of the Different Combination of Measurement Techniques Used in Three-Phase Flow Meters

Measurement System Combination	Advantages	Disadvantages
$\epsilon_1, \rho_1, x_{\epsilon_1}$, vertical pipes, upstreaming flow	Robust, independent of water conductivity	Works only at oil-continuous phase, inaccurate v_{liq}
$\epsilon_1, \rho_1, x_{\epsilon_1}, V$, vertical pipes, upstreaming flow	Robust, independent of water salinity, accurate v_{liq} , higher accuracy	Works only at oil-continuous mixtures
$\epsilon_1, \sigma_1, \rho_1, x_{\epsilon_1}, V$, vertical pipes, upstreaming flow	Robust, accurate, independent of water salinity in oil-continuous phase	Dependent on water salinity at water-continuous phase
$\epsilon_2, \rho_1, x_{\epsilon_2}$	Works in both oil- and water-continuous phases. High accuracy at low water cuts in oil–water mixtures	Dependent on water conductivity in both oil- and water-continuous phases, poor accuracy for three phases
ρ_{12}, V , mixing tank vertical pipes, downstreaming flow	Reliable, higher accuracy for gas fraction determination	Salinity-dependent in both phases. Low-frequency response
$\rho_1, \rho_{12}, x_{\rho_1}$, vertical pipes, upstreaming flow	Simple, low cost	Poor dynamic response, less accuracy, salinity-dependent
$\rho_1, \rho_{12}, x_{\rho_1}$, V	Robust, higher accuracy	Salinity-dependent
$x_{\epsilon_1}, \epsilon_1, \sigma, \rho_{\epsilon_1}$, vertical pipes, upstreaming flow	Low cost, no radioactive sources	Less accuracy
$\rho_{12}, \Delta P$ across inline pipe mixer	Applicable both for horizontal and vertical pipes, acceptable accuracy	Pressure drop, salinity dependent
ρ_1, T , gas separator	Good accuracy	Pressure drop, increased maintenance

Note: ρ_1 , Single-energy γ densitometry; ρ_{12} , dual-energy γ densitometer; ϵ_1 , low-frequency permittivity measurement (capacitance); ϵ_2 , high-frequency permittivity measurement (microwave); σ , conductance measurement; x_{ϵ_1} , cross-correlation of capacitance sensor signals; x_{ϵ_2} , cross-correlation of microwave sensor signals; x_{ρ_1} , cross-correlation of γ density sensors; V , venturimeter; ρ_{ϵ_1} , gas void (α) determination by cross-correlation velocity and venturimeter; ΔP , differential pressure in mixers; T , turbine meter.

reaction occurs at the electrode, and under suitable conditions, the rate of reaction is limited by the rate of ion diffusion to the wall. The rate of reaction can be easily measured by recording the DC current flowing through the electrode. Since the Schmidt number for the system used is large, the concentration boundary layer is much thinner than the viscous boundary layer, and the wall shear rate can be inferred directly from the electrode current.

Compared with other methods such as hot-wire and laser Doppler techniques, the method has a number of advantages. In particular:

- Since a wall mounted electrode is used, the technique ensures that shear rate is measured at the wall
- The electrodes can be fabricated to any desired shape, including very small sizes and unusual shapes to suit the geometry being studied
- The method allows the use of arrays of electrodes, using multichannel electronics, to examine the local distribution of the wall shear rate.

With the electrochemical method, it is not necessary to use optically transparent materials of construction as no optical measurements are taken. Unlike the hot-wire probe, the electrochemical method is non invasive. In addition, the wall shear rate can be calculated directly from the electrode current based on the theoretical equations, without calibration (as required for hot-film methods).

However, the range of application is limited as the technique requires the use of a special solution composition as the electrolyte for the electrode reaction. The method is thus most suitable for laboratory studies of complex liquid or multi phase flows.

14.3.1.1 Theory

For an electrochemical reaction,



the current flow is related to the rate of reaction by Faraday's law

$$I = nFN, \quad (14.50)$$

where I is the electrode current (Amps), F the Faraday's constant ($96,485 \text{ C mol}^{-1}$), and N the rate of reaction (mol sec^{-1}). As mentioned above, the conditions at the electrode are controlled so that the rate of current flow is limited by the rate of transport of the active ion A^{a-} to the electrode. To achieve these conditions, the rate of reaction at the electrode must be fast so that when an active ion reaches the surface it immediately reacts and the concentration of A^{a-} approaches zero at the electrode. A mass transfer coefficient k_m (m sec^{-1}) is defined as

$$k_m = \frac{N}{A(C - C_w)} \quad (14.51)$$

where A is the area of the electrode (m^2), C the concentration of A^{a-} in the bulk solution (mol m^{-3}) and C_w the concentration of A^{a-} at the electrode. Eliminating N from Eqs. (14.50) and (14.51) and substituting $C_w = 0$ we obtain

$$I = nFk_mAC \quad (14.52)$$

In order to obtain the wall shear rate, the relationship between the mass transfer coefficient and the flow field must be determined by solving the convection-diffusion equation

$$\frac{\partial C}{\partial t} + u\frac{\partial C}{\partial x} + v\frac{\partial C}{\partial y} + w\frac{\partial C}{\partial z} = \varphi\left(\frac{\partial^2 C}{\partial x^2} + \frac{\partial^2 C}{\partial y^2} + \frac{\partial^2 C}{\partial z^2}\right), \quad (14.53)$$

where u , v , and w are the flow velocity components in the x , y , and z directions, respectively, and φ the diffusion coefficient for A^{a-} .

If x is the streamwise direction, and we assume that velocity components in the y and z directions (v and w) are negligible, the flow field takes the following form:

$$u = \gamma_w^o z \quad (14.54)$$

$$v \sim 0 \quad (14.55)$$

$$w \sim 0 \quad (14.56)$$

where γ_w^o is the shear rate at the electrode. Assuming steady-state conditions and neglecting the diffusion in the x - and y -directions, the concentration diffusion equation simplifies to

$$\gamma_w^o z \frac{\partial C}{\partial x} = \vartheta \frac{\partial^2 C}{\partial z^2} \quad (14.57)$$

For a rectangular electrode with its long side perpendicular to the streamwise direction, this equation can be solved to give

$$\frac{k_m L}{\vartheta} = 0.807 \left(\frac{\gamma_w^o L^2}{\vartheta} \right)^{1/3}, \quad (14.58)$$

where L is the length of the electrode in the flow direction. By rearranging Eq. (14.58) and eliminating k_m using Eq. (14.52), we obtain

$$\gamma_w^o = \left(\frac{1.90L}{F^3 C^3 \vartheta^2 A^3} \right)^{1/3} \quad (14.59)$$

Thus the wall shear rate is proportional to the cube of the electrode current, and the constant of proportionality can be calculated using Eq. (14.59) or measured by calibration.

For a circular electrode, an equivalent electrode length can be calculated as

$$L = 0.820D \quad (14.60)$$

In unsteady, turbulent, or multiphase flows steady-state conditions cannot be assumed. In this case, the time-averaged wall shear rate can be estimated directly from the time-averaged current using Eq. (14.59). The electrochemical technique has also been widely used to explore the fluctuations in the wall shear rate in turbulent and gas–liquid flows. However, the response of the concentration boundary layer to fluctuations in the wall shear rate may lead to a time lag and a reduction in the amplitude of the current compared to that expected from a quasi-steady analysis. Taking the shear rate and mass transfer coefficient to be made up of time-averaged and fluctuating components, $\bar{\gamma}_w^o$, γ_w^o , \bar{k}_m , and k_m' , a quasi-steady solution relates the mean-square fluctuations as

$$\left(\frac{\bar{\gamma}_w^o'}{\bar{\gamma}_w^o} \right)^2 = 9 \left(\frac{\bar{k}_m'}{k_m} \right)^2 \quad (14.61)$$

This quasi-steady solution must be corrected to account for the response of the concentration boundary layer, which depends on the frequency of the fluctuations. Two approaches can be used: the first is to measure the spectral density function of the mass transfer fluctuations, W_k , and to calculate the spectral density function of the wall shear fluctuations W_γ as

$$W_\gamma = 9 \frac{(\bar{\gamma}_w^o)^2 W_k}{\bar{k}_m^2 A^2}, \quad (14.62)$$

where A^2 is obtained from a solution to the linearized dynamic convection diffusion–equation

$$\frac{\partial C'}{\partial t} + \bar{\gamma}_w^o z \frac{\partial C'}{\partial x} + \bar{\gamma}_w^o' z \frac{\partial C}{\partial x} = \vartheta \frac{\partial^2 C'}{\partial z^2} \quad (14.63)$$

where \bar{C} and C' are the time-averaged and fluctuating concentration, respectively. Solutions valid at low frequencies or for a wide range of frequencies are available in the literature (Mitchell and Hanratty, 1966;

Fortuna and Hanratty, 1971). An alternative approach is to use a transfer function to convert the mass transfer fluctuations into shear rate fluctuations. Expressions for the transfer function have been developed by a number of authors (Py, 1973; Ambari et al., 1986; Deslouis et al., 1990).

The linear approach for dynamic fluctuations described above is limited to cases where $\gamma_w^o/\bar{\gamma}_w^o$ is small. When large transient fluctuations in the current are observed (e.g., in a separated region in an unsteady flow), the data should be used with caution, and quantitative analysis may not be possible.

14.3.1.2 Experimental Conditions

14.3.1.2.1 Electrolyte System

The most widely used electrochemical system for wall shear rate measurements is the ferricyanide-ferrocyanide redox couple:



Typically, an electrolyte containing 0.001–0.01 M of potassium ferricyanide, 0.01 M of potassium ferrocyanide, and 1–2 M of sodium hydroxide is used. The concentrated sodium hydroxide electrolyte is required to provide a high conductivity and to ensure that electromigration effects are negligible. In the electrochemical literature it has been reported that the electrode response is unstable in a potassium hydroxide solution (particularly with a nickel electrode), and a potassium carbonate electrolyte was found to give a much more stable response (Taama et al., 1996). Potassium carbonate is now widely used as the supporting electrolyte (in place of sodium hydroxide) for mass transfer studies, but is rarely used in measurements of wall shear rates, despite the equivalence of the two techniques. Dissolved oxygen should be removed from the electrolyte before use; otherwise oxygen reduction at the cathode will lead to an increase in the observed current. It should be noted that ferricyanide is unstable under illumination, so exposure to light should be minimized and fresh solutions should be prepared daily. The concentration of the ferricyanide ions can be checked by UV-visible spectrophotometry.

14.3.1.2.2 Electrodes

Two electrodes are required: a small working electrode at which the wall shear rate is to be measured, and a larger counterelectrode, at which the reverse reaction occurs. The working electrode is normally the cathode where reduction of the ferricyanide ions occurs, and the reverse reaction occurs at the counter-electrode (the anode). It is common to use a lower concentration of the ferricyanide ions, and a small working electrode in order to insure that the current is limited by the mass transport of ferricyanide ions to the cathode. The electrodes should be constructed from nickel or platinum. Platinum is preferred as its response is more stable, although nickel is often adequate, particularly if a potassium carbonate supporting electrolyte is used. In order to obtain reproducible results when using nickel electrodes it may be necessary to polish and activate the electrodes prior to each set of measurements. Activation is achieved by generating hydrogen at the working electrode (by holding the electrode at a potential of –1.5 V or lower) in the background electrolyte (i.e., in the absence of the potassium ferricyanide and potassium ferrocyanide) for a few minutes.

The electrodes are arranged with the anode downstream (as shown in Figure 14.40) so that there is no disturbance of the concentration of ferricyanide at the working electrode. In order to measure the local

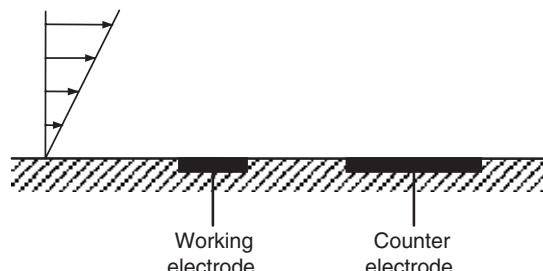


FIGURE 14.40 Arrangement of the electrodes.

wall shear rate, the electrode must be small, although large electrodes which average over a significant area have also been used. Typically, the characteristic length of the electrode is less than 1 mm and may be as small as 0.1 mm or less. The electrode must be large enough to insure that the thickness of the concentration boundary layer is smaller than the length scale of the electrode. The thickness of the concentration boundary layer δ can be estimated from the measured mass transfer coefficient

$$\delta = \frac{\varphi}{k_m}. \quad (14.65)$$

The working electrode may be circular or rectangular. The electrode should be sealed in an insulating material (e.g., glass or epoxy), ground, and polished to insure that the electrode is smooth and flush with the wall. Circular electrodes can be prepared using nickel or platinum wire of suitable diameter, while rectangular probes can be prepared from foil. Rectangular probes should be arranged perpendicular to the direction of flow (Figure 14.41a). A pair of rectangular probes can be used to determine the direction of flow (Figure 14.41b). When each electrode is polarized independently (i.e., with the other electrode isolated) they will yield the same current. When both electrodes are polarized simultaneously, the wake from the upstream electrode will reduce the concentration of ferricyanide ions in the boundary layer of the downstream electrode. The current for the downstream electrode will consequently be reduced. This method is useful for systems where the direction of flow at the wall can change, for example, in a vortex-shedding regime.

14.3.1.2.3 Electrode Polarization

A potential must be applied that ensures the current is limited by the rate of transport of ferricyanide ions to the cathode. If the applied potential is too low, the current will be limited by the electrochemical rate of charge transfer. Conversely, if the applied potential is too high, side reactions (e.g., hydrogen evolution by water electrolysis) may occur. Under high shear rate conditions, the potential applied between the working and counterelectrodes should be gradually increased while the current flowing through the circuit is monitored. A suitable applied potential will be in the limiting current regime, where the current reaches a plateau as it is limited by the mass transport rate and is independent of the applied potential (Figure 14.42). In this region, the measured current should vary with flow rate and be proportional to the bulk concentration of ferricyanide ions.

A limiting current plateau may not be observed if the working electrode has become inactive, if the counterelectrode is limiting the current flow or if there are significant potential distribution problems. The first problem can be overcome by polishing and activating the electrode as described above. In order to increase the reaction kinetics at the counterelectrode relative to those at the working electrode, the concentration of ferrocyanide may be increased, the concentration of ferricyanide may be decreased, or the size of the counterelectrode may be increased, alternatively, a third electrode may be used. This third electrode is called the reference electrode, and carries no current. The potential of the working electrode should be measured relative to the reference electrode, or a potentiostat can be used to control the potential of the working electrode relative to the reference electrode. The reference electrode may be a small

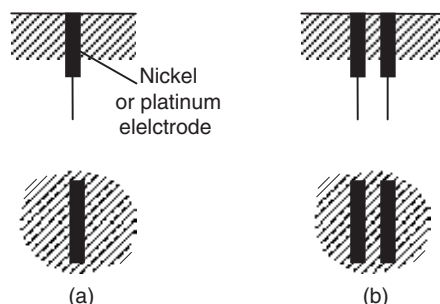


FIGURE 14.41 Rectangular electrodes.

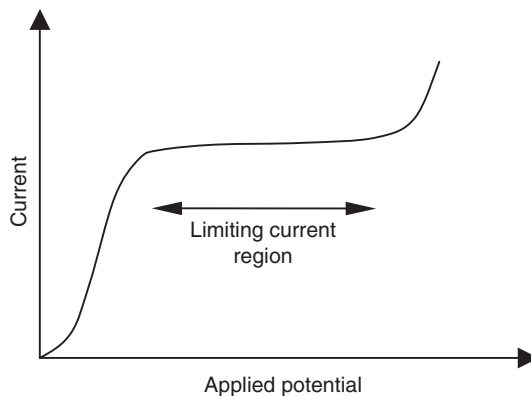


FIGURE 14.42 Electrode polarization.

platinum wire or a standard reference electrode (e.g., a saturated calomel electrode) can be used, which should be held in a separate compartment linked to the flow circuit using a narrow capillary. The wire reference or the end of the capillary should be located close to the working electrode. Potential distribution problems may occur when a large working electrode is used. In this case, the geometry of the counterelectrode should be designed to minimize any variations in potential over the surface of the working electrode. For example, in a rectangular channel with a large working electrode, the counterelectrode should be placed facing the working electrode.

Once the location of the limiting current region has been determined, the applied potential can be held at a potential within this region. A potential at the centre or the upper potential end of the limiting current region should be applied.

14.3.2 Applications

The electrochemical method has been used to investigate wall shear rates in a very wide range of systems. These include investigation of turbulent boundary layers, arterial blood flow, and of flow in process operations such as heat exchangers, cross-flow filters and phase-contacting equipment. The range of geometries which can be studied is almost unlimited. The technique has also been shown to be suitable for gas–liquid flows (Cognet et al., 1984).

14.4 Velocity, Size, and Shape and Concentration Measurements of Particulate Mixtures

J. C. Cullivan and R. A. Williams

14.4.1 Measurement Needs for Process Fluids and Suspensions

This section considers measurements in process fluids that may be single phase or mixtures of phases or components. The selection of sensors to audit the flow and its composition has to recognize the fact that these fluids are occasionally transparent, but often semiopaque or opaque. We shall discuss methods that are used for performing measurements on two (or more) phases to obtain information on the flow velocity and nature of dispersed systems. Such systems could be liquid–liquid, solids–liquid, solid–gas, or multiphase.

For clarity and in order to illustrate the essential physics and applications we shall generally assume the case of solid–liquid mixture and of a single type of solid. Our measurement task is to measure the velocity of the dispersed phase, its size, shape, and concentration. The size of the solids phases may be in the colloidal domain (dispersions) or larger granular material (suspensions). For control and optimization of dispersion properties, measurement is required over a range of length scales from continuum velocities

to the particulate and turbulent length scales. In turn, the full characterization of a disperse flow requires a measurement suite, which spans the appropriate length scales. The key to the characterization and optimization of such flows are the particulate size and shape distributions as well as the continuum velocity field and their coupling. Table 14.2 provides a brief overview of the techniques, which are considered in this section, their practical merits, and application. The reader is referred to the relevant section within this chapter for details.

Detailed and accurate measurements of continuum flow and its turbulent characteristics are essential for validation of computational fluid dynamic (CFD) predictions and for the evaluation of complex flow structures and their influence upon particle transport and dispersion. Ultimately, this requires measurement at both the mean-flow and turbulent length scales if validation of the fundamental flow is to be achieved. As well as mean flow shear, the turbulent strength and structure plays a key role in determining the instantaneous forces acting upon particulates. For flows of industrial importance, the loading of particulate solids may be high with complex aggregation and breakage interactions occurring between the constituent particles. Therefore, measurement of the particulate motions and of their microscopic interactions is required. Eventually, coupled measurements of the continuum flow and the particulate motions are necessary, but this

TABLE 14.2 Techniques to be Considered, their Merits and Example Applications

Technique (Section Number)	Capabilities
	Particle size Particle shape Velocity Solids conc. Concentration Online
Light scattering (14.4.3.1)	
Rapid and accurate for spherical or known shape. Polarization components indicate shape	✓ ✓ L
Small-angle light scattering (14.4.3.1)	
Indicates particle diameter, for diameters less than incident wavelength	✓ ✓ L ✓
Back scattering (14.4.3.1)	
Backscatter intensity and polarization indicates particulate size and shape	✓ ✓ H ✓
Focused beam reflectance measurement (14.4.3.2)	
Duration of reflection indicates particle chord length	✓ – ✓
Confocal scanning optical microscopy (14.4.3.2)	L/
High definition optical scanning using the pinhole principle	✓ ✓ M
Laser Doppler velocimetry (14.4.4.1)	
Continuum velocities determined from Doppler shift	✓ ✓ L ✓
Particle image velocimetry (14.4.4.2)	
Sequential imaging of tracer particulate reflection coupled with cross-correlation	✓ L
Laser-induced fluorescence (14.4.4.2)	L/
Sequential fluorescence cross-correlated for continuum or doped particulate velocities	✓ M
Ultrasound scattering tomography (14.4.5)	M/
Scattering occurs at particulate surfaces and may be detected at the periphery	✓ H
Acoustic emission (14.4.5)	
Emissions characterize rate of internal processes and the temporal behaviour	✓ – ✓
Ultrasound absorption (14.4.5)	M/
Sound-wave attenuation is proportional solids concentration	✓ H ✓
X-ray transmission tomography (14.4.6.2)	
X-ray transmission provides density distribution (shape)	✓ ✓ ✓ –
Positron emission particle tracking (14.4.6.3)	
Triangulated emissions indicate particle velocity, turbulence and residence	✓ ✓ –
Positron Emission Tomography (14.4.6.3)	
Triangulation of emissions identifies solids distribution	✓ –
Electrical Tomography (14.4.6.4)	
Temporal periphery measure of induced electric field for solids and velocities	✓ ✓ – ✓

Note: L, M, H — Low, medium and high limiting particulate concentrations. The online reference indicates potential to apply technique online.

poses a significant challenge from both experimental and modeling points of view and, therefore, the majority of the discussed methods apply to individual behaviors.

An understanding of a given system may be constructed from multiscalar measurements for example, the specific mechanisms of particle aggregation and breakage occur at the microscale. Therefore, the macroscale particle concentrations, collision frequencies, and local shear strengths may be determined from flow field measurements while the detailed interparticle interaction phenomena are examined by microscopic approaches such as confocal microscopy. The interparticle interactions are a complex function of the particle size and shape distribution. These measurements may then be combined in order to determine the size and shape of generated aggregates, which are of key interest in the determination of their strength and other properties under flow. Such a detailed measurement approach provides CFD validation and design data as well as the development of appropriate constitutive relations.

From a practical point of view, a detailed knowledge on the particulate size and shape distribution and interparticle interactions can be critical. Properties such as the size and strength of compacted materials is influenced by the packing, which in turn is a function of the particulates size distribution and inter-particle forces. Alternatively, measurement of the particulate size distribution may indicate completion or efficiency of a process operation. Therefore, accurate measurement of particle size and shape are essential for process control. Issues related to off-line sampling and achieving representative sampling are dealt with in many standard texts such as Gotoh et al. (1997). Alternatively, it is becoming increasingly feasible to conduct measurements on-line with modern developments in sensor physics, data transmission, and analysis. Careful consideration must be given to the limitations of the particular measurement method being applied. A brief overview on the theory behind selected measurement methods, to identify limitations, and to provide a summary of potential measurement methods is presented.

This section begins with a brief overview of the properties of light and its interaction with particulates during scattering. Some key light-dependent measurement methods and the general scattering properties drawn upon in order to identify critical attributes are then discussed. In particular, application is identified for the overall particulate size and shape analysis of suspensions. For the smaller scale, microscopic approaches such as confocal and interference microscopy are identified and discussed. These methods find particular application in the observation and measurement of aggregation and breakage effects as well as on fundamental microscopy. At the macroscale, the techniques of laser Doppler velocimetry (LDV), particle image velocimetry (PIV), and laser-induced fluorescence (LIF) provide the flow field velocity measurements including coupling with particulate motions. Extensions of these techniques permit velocity field measurements at the microscale and have considerable prospects in the future.

Next, ultrasound absorption and scattering, which represents a high-power approach to particle sizing without the operational health risks associated with laser technology, is considered. Finally, the tomographic methods are discussed, as these provide noninvasive measurements of the internal spatial distribution as a function of time. Many industrial fluids are opaque due to the nature of the continuum phase or mixture properties. For such fluids, tomographic methods find particular application as key measurement methods. These provide measure of the composition of multiphase mixtures and may incorporate different sensors for example, modalities such as electrical, ultrasound, x-ray, and positron emission will be considered.

Table 14.2 enables the reader to identify suitable methods to meet their measurement requirements for prevailing practical conditions. The table indicates the methods applicable for measurements related to particle size and shape; velocity (both dispersed and continuous phases); solid (the assumed dispersed phase) concentration and boundaries, and the particulate concentration range to which they are applicable. It is seen that most advanced methods are best suited to laboratory-based measurements in which “*ex-situ* analysis” is performed (where a sample has to be removed from the process environment). Wherever possible, “*in line*” or “*in process*” methods should be used to avoid errors in sampling (although these are present even with in line process techniques to a lesser extent), change in chemical, and fluid shear conditions. The table features sensor methods that are based on single- and multiple-point measurements (e.g., tomographic).

14.4.2 Interaction of Light and Matter: Some Fundamentals

First, we consider basic descriptors for the propagation and interaction of light with matter. The electromagnetic nature of light is presented in the static or time-averaged sense. A more detailed and technical analysis of these concepts is given in the excellent texts of Mishchenko et al. (2002), Van de Hulst (1957); and Bohren and Huffman (1983). The clear text of Feynman provides a concise model description for the interaction of propagating light with matter (Feynman, 1985).

14.4.2.1 Description of Light

The term light is used although the description is fundamental to electromagnetic waves in general. The principle measurement methods discussed later operate in the visible spectrum although the principles also find application for other modalities (such as ultrasonic absorption and scattering). The dual nature of light has been well established, and is described simultaneously as discrete packets of energy, photons, or as waves. In harmony with such descriptions, light may be defined as either propagating (photonic) with a prescribed wave structure or nonpropagating (Courjon, 2003). Nonpropagating light finds application in near-field microscopy wherein the light source or lens objective may be placed within nanometers of the sample.

For propagating light the wave Poynting vector is defined as

$$\mathbf{S}(\mathbf{r}) = \frac{1}{2} \mathbf{E}(\mathbf{r}) \times \mathbf{H}^*(\mathbf{r}) \quad (14.66)$$

where \mathbf{E} , \mathbf{H} , and \mathbf{r} are the electric and magnetic fields and the position vector, respectively. This vector satisfies (Reitz et al., 1993)

$$\nabla \cdot \mathbf{S}(\mathbf{r}) + \frac{\partial u}{\partial t} = - \mathbf{J} \cdot \mathbf{E}(\mathbf{r}) \quad (14.67)$$

where $\mathbf{J} \cdot \mathbf{E}(\mathbf{r})$, u , and \mathbf{J} represent the work done by the local field on charged particles, the electromagnetic energy density, and the current density, respectively. Therefore, if $\mathbf{J} \cdot \mathbf{E}(\mathbf{r}) = 0$, Eq. (14.67) reduces to a conservation equation indicating the Poynting vector to characterize the momentum density. In fact, the momentum density is given by \mathbf{S}/c^2 , where c is the speed of light. Therefore, the net rate at which electromagnetic energy of the wave enters a closed volume is given by $-\int_S \langle \mathbf{S}(\mathbf{r}) \rangle \cdot \mathbf{n} dS$ and the light intensity is $I(\mathbf{r}) = |\langle \mathbf{S}(\mathbf{r}) \rangle|$, which for a plane wave, becomes $I(\mathbf{r}) = c\epsilon E_0^2/2$, where ϵ is the electric permittivity and E_0 defines the magnitude and polarization of the plane wave (Kotlarchyk, 2002). Therefore, given a calculation of the electrostatic field, integration of the Poynting vector indicates the experimentally measured intensity.

Light is not only characterized by its intensity, but also by its polarization state, which may be induced by both selective material transmission of polarization components (dichroism) or by reflection for which polarization components parallel to the surface are preferentially reflected (Reitz et al., 1993). This property of polarization offers the potential to extend measurement methods toward a full characterization of particulate size and shape (Stoylov, 1991).

Light wave coherency may be represented through the linearly independent coherency vector, such that (Mishchenko et al., 2002)

$$\mathbf{J} = \frac{1}{2} \sqrt{\frac{\epsilon}{\mu}} \begin{bmatrix} E_{0\theta} E_{0\theta}^* \\ E_{0\theta} E_{0\phi}^* \\ E_{0\phi} E_{0\theta}^* \\ E_{0\phi} E_{0\phi}^* \end{bmatrix} \quad (14.68)$$

where $\mathbf{E}(\mathbf{r}, t) = E_0 \exp(i\mathbf{k} \cdot \mathbf{r} - i\omega t)$ is a plane electromagnetic wave propagating in a nonabsorbing medium and represented in a spherical coordinate system, with θ and ϕ being the angle of the propagation vector to the Cartesian z -axis and the meridional plane (parallel to z -axis and propagation vector) to the x -axis, respectively (see Figure 14.43). Also, \mathbf{k} and ω are the wave vector and angular frequency, respectively.

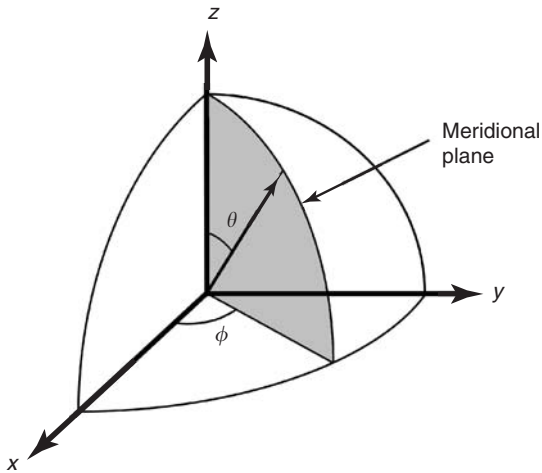


FIGURE 14.43 Spherical coordinate system.

The Stokes vector, which represents the observable degrees of freedom for a light wave, may be defined as

$$\mathbf{I} = \begin{bmatrix} I \\ Q \\ U \\ V \end{bmatrix} = \frac{1}{2} \sqrt{\epsilon \mu} \begin{bmatrix} E_{0\theta}E_{0\theta}^* + E_{0\phi}E_{0\phi}^* \\ E_{0\theta}E_{0\theta}^* - E_{0\phi}E_{0\phi}^* \\ E_{0\theta}E_{0\phi}^* - E_{0\phi}E_{0\theta}^* \\ E_{0\phi}E_{0\theta}^* - E_{0\theta}E_{0\phi}^* \end{bmatrix} \quad (14.69)$$

The first component of the Stokes vector (I) represents the intensity while Q , U , and V characterize the polarization. Maxwell's equations demand that the electric and magnetic fields are perpendicular to each other and to the direction of propagation. As discussed by Mishchenko et al. (2002), within the plane perpendicular to the direction of propagation, the polarization components describe an ellipse. The ratio of the minor to the major axis of this ellipse may be defined as $|\tan\beta|$, and the angle of the ellipse major axis to the unit vector $\hat{\phi}$ as ζ (see Figure 14.44). In brief,

$$\tan(2\zeta) = -U/Q \quad (14.70)$$

and

$$\tan(2\beta) = -V/\sqrt{Q^2 + U^2} \quad (14.71)$$

such that Q and U define the orientation of polarization and V defines the direction of elliptical polarization rotation, in the plane perpendicular to propagation. Therefore, the following values of the Stokes vector $\mathbf{I} = [1 \ 0 \ 0 \ 0]^T, [1 \ 1 \ 0 \ 0]^T, [1 \ -1 \ 0 \ 0]^T, [1 \ 0 \ 0 \ 1]^T, [1 \ 0 \ 0 \ -1]^T$ represent unpolarized, linearly polarized horizontal and vertical, and right hand and left hand circularly polarized light, respectively. In the preceding sections, monochromatic light has been assumed. For quasimonochromatic light for which the amplitude and phase varies temporally, the components are time-averaged but the equations retain their form. A useful property of the Stokes vector is that it may be summed for the incoherent superposition of light. In turn, this limits distinguishability for particulate distributions, as many particulate distributions may contribute an identical or similar Stokes vector.

14.4.2.2 Interaction of Light with Matter

The fundamentals of light reflection occur at the atomic level. As has been established earlier, electromagnetic radiation exhibits both a frequency (wavelength) and an energy magnitude. The electromagnetic

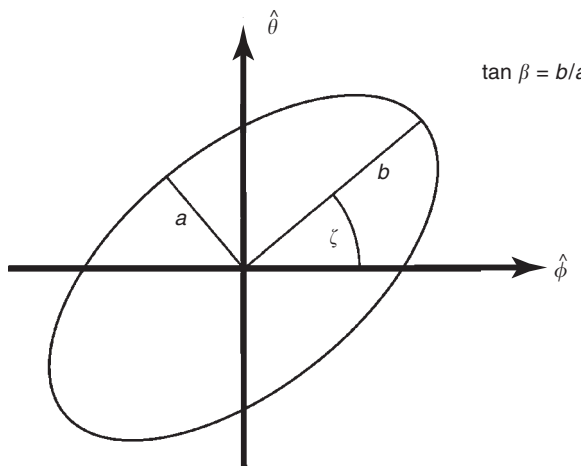


FIGURE 14.44 Parameters for description of light polarisation.

radiation also behaves as small packets of energy, i.e., photons ($Q \sim 1$ eV, proportional to the frequency), which may be absorbed by charged particles inducing motion. The degrees of freedom of a material range from molecular rotational and translational motion to electron energy states and oscillations of electron clouds. As electrons represent a small mass they are the features predominately affected by the visible light spectrum (low energy). The absorption of a suitably high-energy (frequency) photon may result in the transition of an electron to a higher energy level. This represents an excited state (high energy) from which spontaneous emission (relaxation) occurs after a short time (~ 1 ns) at the absorbed energy (frequency) or via a number of discrete energy jumps. This process represents fluorescence when the emitted light frequency is different to that absorbed. At the lower energy characteristic of visible light the electromagnetic wave induces oscillations of the electron cloud, thereby inducing an electric dipole. The electron cloud has the highest susceptibility to induced oscillations near the atomic resonate frequencies such that the dissipation to heat is at the maximum and thereby the material color is determined. The induced oscillation is at the frequency of the absorbed photon, so that the photon emitted due to relaxation of the electric dipole exhibits the same frequency as that absorbed and the process represents scattering (Suson, 1997). Since material particles consist of many nuclei, the multiple scattering events occur such that the optical density, shape, and surface characteristics of the particle influence any observed scattering pattern. In addition, the wave nature of light results in both constructive and destructive interference of light as well as diffraction. The combination of these effects represents the observed scattered field.

At this point, the theoretical modeling of the interaction of light with particulates can be considered. Such interaction with particulates and indeed particulate ensembles results in complex scattering patterns, which are a function of the particulate population and are of the characteristic shapes and sizes. The practical application of light-scattering modeling for particulate size and shape measurements, the accuracy and range limits are then considered for some of the more common approaches.

14.4.2.3 Modeling of Particulate Light Scattering

Although a fundamental theoretical understanding of the interaction of light with matter has been developed, prediction based upon fundamental physics is too computationally demanding for all except the simplest situations. A good review of the modeling of small particle scattering is provided by Mishchenko et al. (2002) as outlined below.

A number of key variables may be introduced to characterize scattering. The Maxwell equations that describe electromagnetic waves are linear, hence it is sufficient to define scattering for plane incident

waves if the actual incident wave may be linearly decomposed as a superposition of this wave. This requires only the definition of a 2×2 scattering amplitude matrix \mathbf{S} in spherical coordinates, such that

$$\begin{bmatrix} E_{0\theta}^{\text{sca}}(r\mathbf{n}^{\text{sca}}) \\ E_{0\phi}^{\text{sca}}(r\mathbf{n}^{\text{sca}}) \end{bmatrix}_{r \rightarrow \infty} = \frac{e^{iklr}}{r} \mathbf{S}(\mathbf{n}^{\text{sca}}, \mathbf{n}^{\text{inc}}) \begin{bmatrix} E_{0\theta}^{\text{inc}} \\ E_{0\phi}^{\text{inc}} \end{bmatrix} \quad (14.72)$$

where \mathbf{n}^{inc} and \mathbf{n}^{sca} are the incident and scattered normal vectors, respectively, and e^{iklr}/r represents the field decay in the far-field solution. The transformation of the coherency and Stokes vectors through scattering is described by the Stokes phase matrix \mathbf{Z}^J (a function of the scattering amplitude matrix \mathbf{S}), where

$$\mathbf{J}^{\text{sca}}(r\mathbf{n}^{\text{sca}}) = \frac{1}{r^2} \mathbf{Z}^J(\mathbf{n}^{\text{sca}}, \mathbf{n}^{\text{inc}}) \mathbf{J}^{\text{inc}} \quad (14.73)$$

$$\mathbf{I}^{\text{sca}}(r\mathbf{n}^{\text{sca}}) = \frac{1}{r^2} \mathbf{Z}(\mathbf{n}^{\text{sca}}, \mathbf{n}^{\text{inc}}) \mathbf{I}^{\text{inc}} \quad (14.74)$$

and

$$\mathbf{Z}(\mathbf{n}^{\text{sca}}, \mathbf{n}^{\text{inc}}) = \mathbf{D} \mathbf{Z}^J(\mathbf{n}^{\text{sca}}, \mathbf{n}^{\text{inc}}) \mathbf{D}^{-1} \quad (14.75)$$

$$\mathbf{Z}^J = \begin{bmatrix} |S_{11}|^2 & S_{11}S_{12}^* & S_{12}S_{11}^* & |S_{12}|^2 \\ S_{11}S_{21}^* & S_{11}S_{22}^* & S_{12}S_{21}^* & S_{12}S_{22}^* \\ S_{21}S_{11}^* & S_{21}S_{12}^* & S_{22}S_{11}^* & S_{22}S_{12}^* \\ |S_{21}|^2 & S_{21}S_{22}^* & S_{22}S_{21}^* & |S_{22}|^2 \end{bmatrix} \quad (14.76)$$

$$\mathbf{D} = \begin{bmatrix} 1 & 0 & 0 & 1 \\ 1 & 0 & 0 & -1 \\ 0 & -1 & -1 & 0 \\ 0 & -i & i & 0 \end{bmatrix} \quad (14.77)$$

Further, the attenuation in the exact forward-scattering direction, i.e., the combined incident and scattered electric field, is described by

$$\mathbf{J}(r\mathbf{n}^{\text{inc}})\Delta S = \mathbf{J}^{\text{inc}}\Delta S - \mathbf{K}^J(\mathbf{n}^{\text{inc}})\mathbf{J}^{\text{inc}} + O(r^{-2}) \quad (14.78)$$

where

$$\mathbf{K}^J = \frac{2\pi i}{k_1} \begin{bmatrix} S_{11}^* - S_{11} & S_{12}^* & -S_{12} & 0 \\ S_{21}^* & S_{22}^* - S_{11} & 0 & -S_{12} \\ -S_{21} & 0 & S_{11}^* - S_{22} & S_{12}^* \\ 0 & -S_{21} & S_{21}^* & S_{22}^* - S_{22} \end{bmatrix} \quad (14.79)$$

is the coherency extinction matrix. Here ΔS represents the area of integration for a given observation of the scattered field. It is evident from the scattering amplitude and extinction matrices that scattering by particles conserves neither the incident polarization nor the total power, such that the observed attenuation coefficients may be a function of the polarization state, i.e., dichroism. The determination of particle properties from scattered light is a complex function of the particle material, size, shape, and orientation as well as the properties of the incident light (polarization and direction). In the scattering plane, the scattering matrix \mathbf{F} , or Mueller matrix, maps the incident Stokes vector to that scattered and may be geometrically mapped to the phase matrix. Hence, $\mathbf{I}_{\text{sca}} = \mathbf{F}\mathbf{I}_{\text{inc}}/k^2 D^2$, where k and D are the wavenumber and distance between scatterer and detector, respectively (Mengüç and Manickavasagam, 1998). For a macroscopically isotropic and mirror-symmetric scattering medium, the scattering matrix has only six elements such that (Mishchenko et al., 2002)

$$\mathbf{F} = \begin{bmatrix} F_{11} & F_{12} & 0 & 0 \\ F_{12} & F_{22} & 0 & 0 \\ 0 & 0 & F_{33} & F_{34} \\ 0 & 0 & -F_{34} & -F_{44} \end{bmatrix} \quad (14.80)$$

Since the Stokes matrix may be summed for the incoherent superposition of light so also may the scattering matrix (Mengüç, 2003). For macroscopically isotropic and mirror-symmetric scattering, the scattering matrix is only a function of the angle between incident and scattered light. Further, symmetry properties can also simplify the calculation for scattering.

An efficient approach to the prediction of scattering by particle dispersions is that of the T matrix (Waterman, 1971). In essence, the incident and scattered light fields may be decomposed as a sum of vector spherical wave functions such that (Mishchenko et al., 2002)

$$\mathbf{E}^{\text{inc}}(\mathbf{r}) = \sum_{n=1}^{\infty} \sum_{m=-n}^n [a_{mn} Rg \mathbf{M}_{mn}(k_1 \mathbf{r}) + b_{mn} Rg \mathbf{N}_{mn}(k_1 \mathbf{r})] \quad (14.81)$$

$$\mathbf{E}^{\text{sca}}(\mathbf{r}) = \sum_{n=1}^{\infty} \sum_{m=-n}^n [p_{mn} \mathbf{M}_{mn}(k_1 \mathbf{r}) + q_{mn} \mathbf{N}_{mn}(k_1 \mathbf{r})], \quad r > r_{>} \quad (14.82)$$

where $Rg \mathbf{M}_{mn}$ and $Rg \mathbf{N}_{mn}$ represent functions regular at the origin and $r_{>}$ is the smallest circumscribing sphere of the scattering particle. Linearity of the Maxwell equations implies a linear mapping among the coefficients such that

$$\begin{bmatrix} p \\ q \end{bmatrix} = \mathbf{T} \begin{bmatrix} a \\ b \end{bmatrix} \quad (14.83)$$

where T is the T matrix, which does not depend upon the specific propagation direction or upon the polarization of the incident light. Rotation and translation rules exist such that a T matrix calculated for one position and orientation may be mapped to all other possibilities. Since only one evaluation of the T matrix is required, this approach proves the most efficient. The T matrix approach is simplified if the dispersion represents randomly oriented particles for which the scattering properties are independent of the incident direction or if the particles exhibit a preferential orientation such that rotational symmetry may be taken advantage of. A simple case is represented by the Lorentz–Mie theory, which considers spherically symmetric particles. Notably, modern commercial light-scattering equipment often assumes Lorentz–Mie scattering and is, therefore, subject to error when nonspherical particulates are present.

This aspect and methods that account for nonsphericity are discussed later. In general, particle sizing is required for particle collections for which multiparticle scattering occurs. For far-field scattering and given arbitrarily shaped and oriented particulates, the T matrix approach may be applied subject to the assumption that minimum circumscribing spheres of the particulates do not overlap. For randomly orientated spherical particles, the T-matrix is diagonal. It is beneficial to characterize the size distribution by an analytical size distribution in order to simplify the inverse problem of estimating the size distribution.

The complexity of particulate scattering may be illustrated by the extinction efficiency factor $Q_{\text{ext}} = C_{\text{ext}} / (\pi a^2)$, where C_{ext} is the extinction cross section. The extinction cross section represents the sum of the scattering and absorption cross sections, are defined as the total monochromatic power scattered and absorbed over the incident monochromatic energy flux. The extinction efficiency factor asymptotes to 2 as illustrated in Figure 14.45 for a single spherical particle. Also shown is the asymmetry parameter $\langle \cos \theta \rangle$, where θ represents the angle between the incident and scattered directions. It is evident that both parameters exhibit finescale oscillations superimposed upon a longer fluctuation period. The scattered direction is due to the interference of diffracted light and that transmitted through the particles (Chýlek and Zhan, 1989). As the relative refractive index tends to infinity and external reflection dominates, this interference structure is removed. The secondary structures correspond to total internal reflection within particles such that extinction is maximized. The location of the minima and maxima obey the relation $mx = \text{const}$, where m and x are the relative refractive index and size parameter. Notably, a small increase in the scattering particle absorption or increase in the relative refractive index destroys the fine-scale oscillations as the internally reflected paths are absorbed. For more realistic size distributions (polydisperse) the extinction efficiency profile is locally averaged such that the fine-scale features are smoothed out. This occurs for very

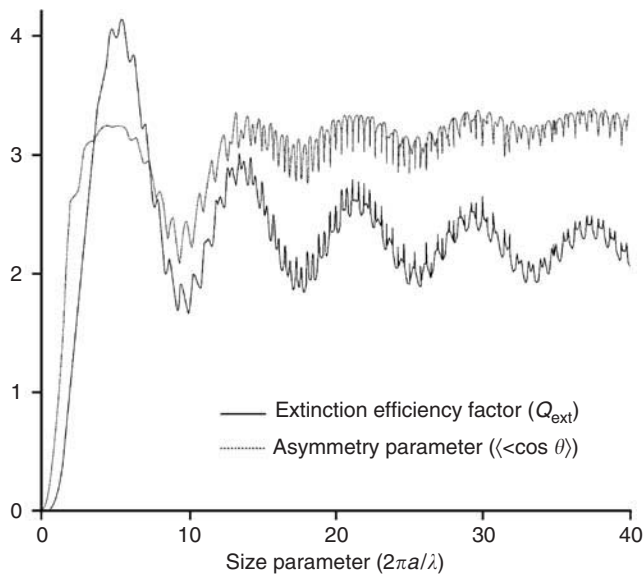


FIGURE 14.45 The extinction efficiency factor, Q_{ext} and the asymmetry parameter $\langle\cos \theta\rangle$ factored by 4, as a function of the dimensionless size parameter ($2\pi a/\lambda$) for monodisperse spherical particles of refractive index 1.4 and where λ is the incident wavelength. (From Mishchenko, M.I., Traoris, L.D., and Lacis, A.A., *Scattering, Absorption and Emission of Light by Small Particles*, Cambridge University Press, Cambridge, 2002. With permission.)

small degrees of polydispersity, whereas for the polydispersity observed in real dispersions, the large-scale variations may also disappear leaving only a minima for the smallest particle sizes.

For low absorption large particles (larger than the incident wavelength), phenomena are observable as a function of the incident wavelength and of the particle size, shape, and refractive index. The phase function

$$p(\mathbf{n}^{sca}, \mathbf{n}^{inc}) = \frac{4\pi}{C_{sca}} \frac{dC_{sca}}{d\Omega} \quad (14.84)$$

represents a normalization of the scattering cross section against scattering solid angle Ω . A maximum of the phase function occurs for $\theta = 0$ due to diffraction. For a relative refractive index not close to one, rainbows occur at scattering angles corresponding to internal reflections by the particulates. In addition, a backscattering peak of the phase function occurs for relative refractive indices between $\sqrt{2}$ and 2. Therefore, the scattering intensity distribution provides an indication of the suspension particle properties (Mishchenko et al., 2002).

So far, spherical-particle scattering has been outlined. For nonspherical particles, complex scattering intensity and polarization patterns occur, which are a function of the specific particle orientations. As for spherical particles, random orientations and polydispersity smooths out the small-scale oscillations. The forward scattering intensity is governed by diffraction and is primarily governed by the particle cross section. Hence, for spheriodal particles, the variation of forward-scattering intensity with solid angle closely reflects that of spherical particles, such that the Lorentz–Mie theory has applicability, although for other particle shapes this is not true. The ratio of the phase function for spheriodal particles to that of equivalent spherical particles forms a general trend over scattering angle. Notably, side scattering is significantly enhanced and the rainbow and glory features are suppressed. It is noteworthy that the scattered linear polarization for unpolarized incident light differs considerably from that for spheres and demonstrates significant variation with spheriodal axis ratio for scattering angles $> 60^\circ$ (Mishchenko et al., 2002). The other components of the scattering matrix also exhibit complex behavior as a function of the scattering angle and spheriodal axis ratio with respect to that for spherical particles.

14.4.3 Laser Light Scattering and Scanning

14.4.3.1 Scattering

The previous section provided a brief review of dispersion scattering properties and outlined the dramatic influence that particle shape and size have upon the scattered intensity and polarization distribution. In the following sections, the application of these phenomena is briefly discussed for the characterization of particle distributions.

The scattering from spherical particles forms a complex pattern over scattering angle. Commercial light-scattering instruments enable measurement of key components of the scattering intensity, the small-angle forward scattering, in-plane wide angle scattering and back-scattering (Malvern, 2003). This type of system is well recognized to provide an accurate measure for spherical particles (Stuut, 2001; Powers et al., 2003) in the range of particle diameter 0.02 μm to 2 mm. Many authors consider this approach to provide benchmark measurements for samples. In general, the reconstruction of particle size distributions from the scattering data is based upon the Lorentz–Mie scattering, i.e., for strictly spherical particles and assuming a mixed and random media. This provides a rapid and highly reproducible estimation of the particle size distribution by means of the T matrix approach subject to an assumed size distribution.

One limitation is the requirement for a sufficiently low solids concentration. In order to adopt the simplified T matrix approach, it is necessary that the particles are sufficiently far apart, so that either single scattering can be assumed to predominate or the far-field approximation may apply between scattering events and the individual scattering events may be added linearly (Mengüç, 2003). In principle, the particles associated with scattering need to be several wavelengths apart. If only single scattering is assumed for the reconstruction then the ideal obscuration lies within 0.5 and 5%. Multiple-scattering algorithms may permit concentrations up to 25% (by vol.) (Hirleman, 1988); otherwise the fine particle fraction is overestimated.

As discussed in the previous section, even a very small degree of nonsphericity can dramatically change the scattering distribution. This has been well demonstrated by Card and Jones (1992) for light scattering by water droplets. In fact, Xu (2003) has demonstrated the degradation of measured particle diameter through comparison of a Beckman Coulter LS Series laser diffraction particle sizer with Coulter counter electric sensing-zone (ESZ) and dynamic image analysis (DIA, microscopy equipped with CCD imaging and image analysis) measurements. Analysis was performed for spherical, cubic, and rod-like particles (see Table 14.3). Even for cubic particles, the laser scattering approach measured too large a particle diameter with greater size spread than either of the methods. For rod-like particles, these errors are even greater such that the measurement is unreliable. Although the DIA is clearly subject to particle orientation errors, as the measured equivalent diameter is based upon a two-dimensional image, it provides a measure consistent with that of ESZ given large sampling. The ESZ measure is based upon the actual particulate volume and therefore proves reliable. In contrast, the equivalent size determined by laser scattering becomes dominated by scattering in the perpendicular direction for nonspherical particles resulting in overprediction of the mean particle size. In addition, random particle orientations lead to a very large standard deviation. For fractal agglomerates laser scatter sizing may be an acceptable measure. Figure 14.46 demonstrates such a measure compared to that of

TABLE 14.3 Volume Mean Diameter (d_v) and Standard Deviation (SD) of Model Cubic, Rectangular and Rod-Like Particles as Measured by Laser Scattering and ESZ with Diameters Presented as Percentage Difference to DIA Measure.

	Cubic		Rectangular		Rod-Like	
	\bar{d}_v (% μm)	SD (μm)	\bar{d}_v (% μm)	SD (μm)	\bar{d}_v (% μm)	SD (μm)
LS	+ 10.8 (1018)	263.1	+ 4.7 (793.5)	219.8	+ 35.9 (300.4)	322.0
ESZ	—	—	— 3.5 (731.0)	174.3	— 2.0 (216.6)	177.8
DIA	0.0 (918.8)	144.9	0.0 (757.6)	132.8	0.0 (221.0)	113.2

Note: Actual measurements are given in parentheses.

Source: From Xu, R., *Proceedings of the Particulate Systems Analysis 2003*, Harrogate, UK, 2003. With permission from the Royal Society of Chemistry.

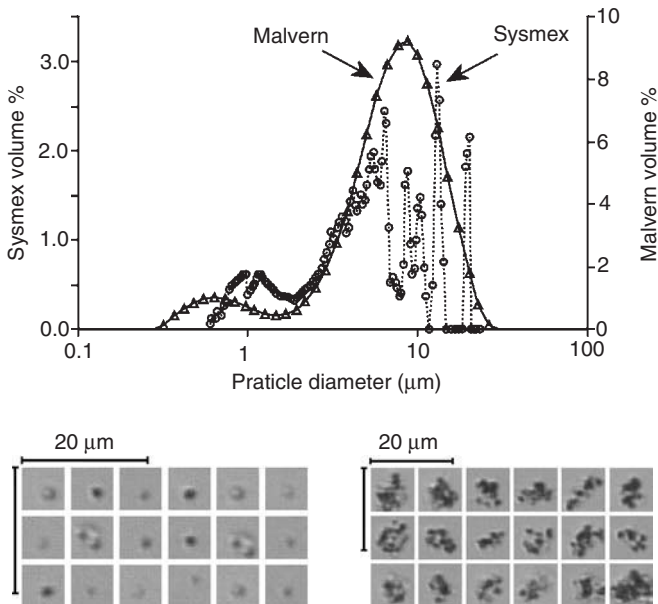


FIGURE 14.46 Comparison of DIA sizing of aggregates with an LS measure demonstrating excellent agreement. Bimodal distribution corresponds to aggregate structures and particulate fragments. (Private communication from Mason, L., University of Leeds, UK.)

the DIA. For the DIA system, the imaged flow was passed through a flat sheath such that the maximum cross-sectional area is imaged; hence a good correspondence was observed between the two techniques.

An alternative to reconstruction based upon the full-intensity distribution over scattering angle is that of small-angle scattering. The small-angle intensity distribution is dominated by the interference of diffraction and transmitted light. Assuming that the volume fraction is low, the secondary scattering in the forward direction is insignificant such that the geometric crosssection is the governing parameter of small-angle scattering. Since nonspherical particles have a surface area greater than that of spherical particles, the trend for small-angle light scattering is to overestimate the size of nonspherical particles. Although irregularly shaped particles significantly affect the diffraction, forward scattering is less sensitive to the particulate geometries than the rest of the scattering distribution such that this approach proves successful.

For small-angle scattering the scattering angle is inversely proportional to the particulate length scale. This technique may be applied for the detection of flocculation. If the scattering vector \mathbf{q} is defined as the change in the wave number of the scattered light, such that

$$\mathbf{q} = 2\pi \frac{\mathbf{n}}{\lambda} (\mathbf{n}_{\text{scat}} - \mathbf{n}_{\text{inc}}) \quad (14.85)$$

where n , \mathbf{n}_{inc} and \mathbf{n}_{scat} are the refractive index and the incident and scattered unit vectors, respectively. Then for two scatterers separated by displacement \mathbf{d} , $\mathbf{q} \cdot \mathbf{d}$ represents the path difference for the light scattered (Bushell, 1998). If $\mathbf{q} \cdot \mathbf{d} < 1$, the scattering is in phase, whereas for $\mathbf{q} \cdot \mathbf{d} > 1$ it is incoherent. For each case the scattered intensity will be represented by $(E_{0a} + E_{0b})^2$ and $(E_{0a}^2 + E_{0b}^2)$, respectively. Therefore, the magnitude of the scattering vector

$$\mathbf{q} = \frac{4\pi n}{\lambda} \sin\left(\frac{\theta}{2}\right) \quad (14.86)$$

may be used as a probe for interparticle distances less than $1/q$, where θ is the scattering angle in the scattering plane. This represents a measure of aggregate structures, which may be characterized by the mass fractal number describing the space-filling ability (or compactness) of the aggregate. The cluster mass

varies as a power of its size (Pilaski et al., 2003). Aggregates from various colloidal and aerosol systems display fractal (self-replicating) characteristics (Bushell et al., 2002). For aggregates not obeying fractal behavior the predicted mass fractal number is overestimated (Stone et al., 2002).

If the sample satisfies the conditions $x|m - 1| \ll 1$ and $|m - 1| \ll 1$, where $x = 2\pi a/\lambda$ and where a and m are the particulate radius and the relative refractive index, respectively (Mishchenko et al., 2002), then the Rayleigh–Gans–Debye (RGD) approximation may be assumed. In essence, the particles are assumed to be comparable or smaller in size than the incident wavelength and to be optically soft (Stone et al., 2002). The aggregate may then be modeled as a collection of noninteracting entities such that $I(q)$ is considered to be the product of a form factor, $P(q)$, which signifies intensity from a single component (or particle) and a structure factor, $S(q)$, that describes additional intensity due to particle configuration in an assembly. For far-field scattering of material away from the edge of the aggregate, $P(q)$ is relatively constant such that $I(q)$ is simply due to the aggregate structure. Then for a fractal geometry (Sorensen, 1997)

$$I(q) \propto S(q) \propto q^{-d_F} \quad (14.87)$$

where d_F is the mass fractal dimension.

The use of light scattering to obtain structure information has been employed predominantly in fundamental studies; yet, it is a compelling tool for an on-line characterization such as in aerosol-based ultra-fine particle production, where the cluster structure is the main parameter of interest. Although the RGD approximation is restricted to particles with low refractive indexes, this procedure can be used when there is little optical contrast between the sample and the background, and when methods such as image analysis become impractical (Bushell et al., 2002). The application of the Lorentz–Mie theory promises to extend the validity to a wider variety of particle size and opacity (Thill et al., 2000). The average agglomerate density may be surmised from agglomerates by the apparent volume fraction and the extinction of transmitted light (Spicer et al., 1998). When RGD theory does not apply, then the application of the mean-field approximation of Mie scattering has been proposed for determining structural information (Lambert et al., 2000). For a group of large and opaque flocs, the average solid content can be calculated from the actual, divided by the apparent volume fraction, which is estimated from light extinction. For fractal aggregates,

$$(1 - \varepsilon) \propto \left(\frac{a}{a_0} \right)^{d_F - 3} \quad (14.88)$$

where ε , a_0 , and a are the porosity and radii of the primary particle and aggregates, respectively.

The backscattering intensity may also be analyzed for a measure of the size distribution of a well-defined spherical particle system. Figure 14.47 demonstrates the behavior of the backscattering intensity for polystyrene in water. It is worth noting that the intensity increases with particle diameter until the diameter is equal to the incident wavelength, after which the intensity decreases. Hence, some prior knowledge or a multifrequency system is required in order to provide an unambiguous particle size measure. Key advantages of backscattering measurements include maintaining the sample in its natural state without dilution, which would destroy a floc structure of interest (Burton et al., 2003).

So far, the identified techniques only provide a measure of the size distribution and structure. Another key parameter of interest is the particle shape. Systems exist that capture images of particles in-flow sandwiched between two parallel glass plates. The previously identified issues relating to reconstruction of three-dimensional structures from two-dimensional images are relevant to such a measure. Wilkinson et al. (2003) reported video measurements at around 3 frames/sec (fps) such that for 150 particles per detected frame, over 480 particles could be detected per second. Light attenuation may be extended to provide shape information by a multifrequency spectroscopy approach as discussed by Garcia-Rubio (2003). By adopting Mie theory and assuming the particle size distribution to be composed of M populations, the effective transmission may be defined by

$$\tau(\lambda) = N_p I \left(\frac{\pi}{4} \right) \sum_{i=1}^M x_i \int_0^\infty Q_{ext,i}(n_i(\lambda), a) a^2 f_i(a) da \quad (14.89)$$

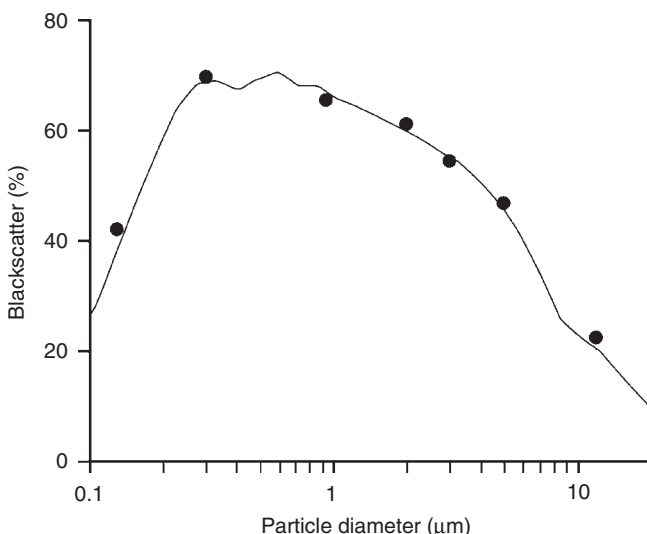


FIGURE 14.47 Backscattering intensity as a function of particle diameter for polystyrene in water at 1% volume fraction and an incident wavelength of 880 nm. (From Buron, H., Brunel, L., and Snabre, P., *Proceedings of Particulate Systems Analysis 2003*, Harrogate, UK, 2003. With permission from the Royal Society of Chemistry.)

where a , f_p , l , n_p , N_p , $Q_{ext,p}$, x_p , λ , and τ are the particle diameter, size distribution, path length, complex refractive index, number of particles per unit volume, extinction efficiency, number fraction, wavelength, and transmission, respectively. This relation may be solved by regularization and generalized cross-validation techniques. Figure 14.48 demonstrates the normalized optical density as a function of incident wavelength for cubic-and disc-shaped silver bromide particles from Garcia-Rubio (2003). Figure 14.49 shows the reconstructed size distribution by means of Eq. (14.89), which demonstrates modes corresponding to various orientations of the silver bromide particles.

An alternative approach using readily available commercial systems is the combination of a sedimentation measure with electrozone sensing. Sedimentation devices such as the Sedigraph determine an equivalent hydrodynamic diameter by observing the sedimentation rate through x-ray or light extinction and assuming Stokes settling (Pansare and Narsale, 2003). Meanwhile, the ESZ approach determines the particle volume distribution through a conductivity measurement. Hence, for particles of known porosity a measure of the particulates sphericity may be constructed as demonstrated by Godet-Morand et al. (2003). Figure 14.50 shows the measured sphericity index of talc particles as a function of air-jet grinding time.

The polarization distribution of scattered light may also be exploited. As demonstrated by Mengüç and Manickavasagam (1998) and Mengüç (2003), while F_{11} may not prove overly sensitive to particle shape, F_{12} and F_{34} certainly do. In fact, although the forward-scattering phase function does hold shape information this is not unambiguous for the inverse problem (Kozan et al., 2002). F_{12} and F_{34} represent depolarization and the change in elliptic polarization, respectively. Measurements of all six scattering matrix elements, F_{11} , F_{12} , F_{22} , F_{33} , F_{34} , and F_{44} , are required in order to uniquely determine particle size and shape, although F_{11} , F_{12} , and F_{34} prove the most sensitive to particle shape (Kozan et al., 2002). Therefore, Mengüç and Manickavasagam achieved measurement of these components by means of the system schematically illustrated in Figure 14.51. Here the waveplates and polarizers may be altered in order to determine the scattering of the various polarization components. Therefore, these measurements provide for the four components of the Stokes vector as a function of scattering angle. In this case, the profiles of the F_{11} , F_{12} , and F_{34} components for ellipsoids are fitted to measurements in order to determine the particulate size and shapes. For large particles or for significant relative refractive index, the forward-scattering pattern may be useful for particle shape determination (Ma et al., 2001).

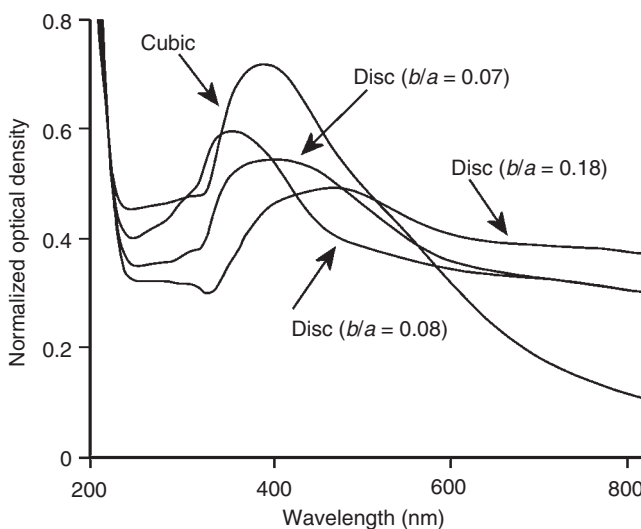


FIGURE 14.48 Normalised optical density as a function of incident wavelength for cubic and disc silver bromide particles. (From Garcia-Rubio, L.H., *Proceedings of Particulate Systems Analysis 2003*, Harrogate, UK, 2003. With permission from the Royal Society of Chemistry.)

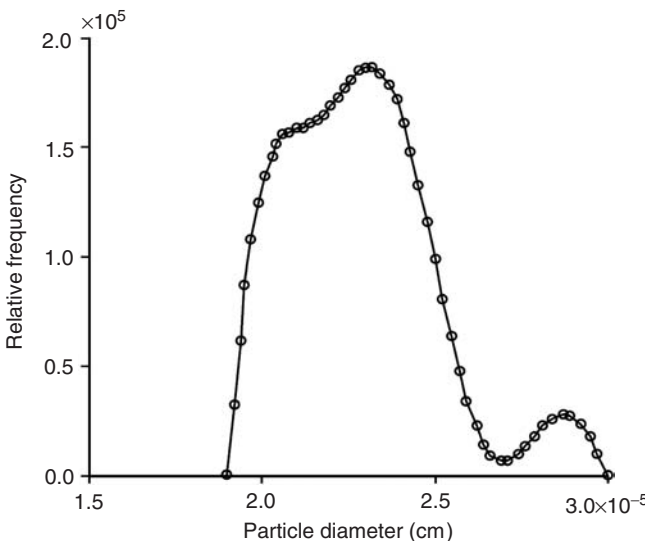


FIGURE 14.49 Reconstructed size distribution of silver halide particles from spectroscopy measure. (From Garcia-Rubio, L.H., *Proceedings of Particulate Systems Analysis 2003*, Harrogate, UK, 2003. With permission from the Royal Society of Chemistry.)

An approach to optically dense (high solids) dispersions is that of diffuse backscattering as discussed by Hielscher et al. (1997). Measurement of the reflected intensity distribution from a beam incident upon the medium is referred to as video-reflectometry by Kienle (1996), and has been shown to provide a measure of scattering and absorption coefficients. Extension of this method for determination of particle size, even if the scattering coefficients are the same, is achieved by measuring the backscattering as a function of polarization (see Figure 14.52). In particular, Hielscher et al. (1997) demonstrated that as the particle size increases the particles behave more like mirrors, such that the incident polarization is maintained. In total, 49 individual measurements are required in order to establish the 16 independent elements of the Mueller matrix. The Mueller matrix fully describes the reflected light as a function of the

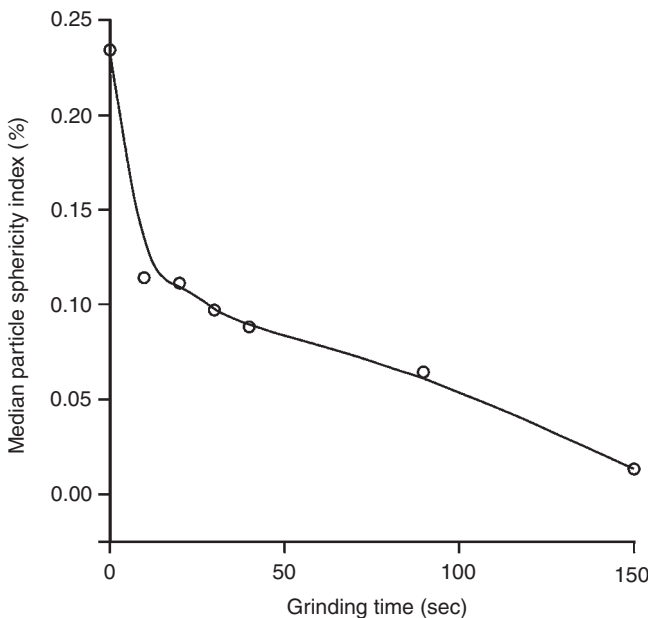


FIGURE 14.50 Sphericity index of talc particles as a function of air-jet grinding time. (From Godet-Morand, L., Chamayou, A., and Dodds, J., *Proceedings of the particulate Systems Analysis 2003*, Harrogate, UK, 2003. With permission from the Royal Society of Chemistry.)

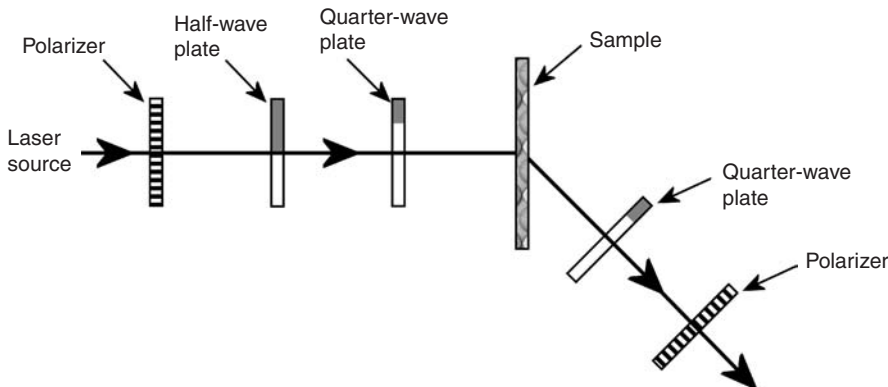


FIGURE 14.51 Schematic of light-scattering system of Mengüç and Manickavasagam (1998) for measurement of particle shape from the scattering of polarization components.

suspension particle properties. Therefore, given a mapping of the Mueller matrix elements as a function of particle properties it should be possible to fully characterize suspensions by backscattering.

14.4.3.2 Scanning (backscatter)

An alternative sizing technique that avoids the detailed complexities of scattering, but relies upon sufficient independent size measurements in order to form a representative measurement sample is that of laser scanning microscopy. This technique is based upon the *duration*, rather than the intensity of reflected light from individual particles. Therefore, it may be applied to dense suspensions for most materials (except for purely transparent objects that behave as specular scatterers) and in any two-phase dispersed systems (solid–liquid, liquid–liquid, or solid–gas) without further dilution. This technology is exploited commercially as the Focused Beam Reflectance Measurement (FBRM®; Lasentec, North

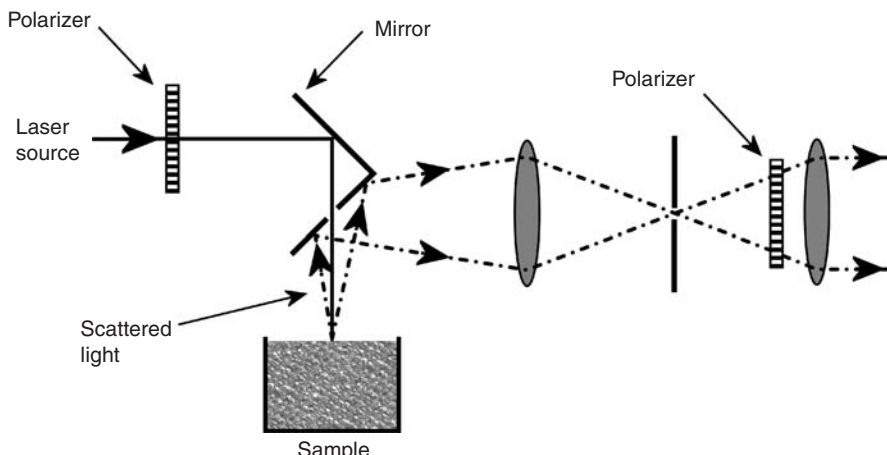


FIGURE 14.52 Schematic of the apparatus of Hielscher, A.H. et al. *Opt. Express*, 1(13), 441–453, 1997, to measure the backscattered polarization components.

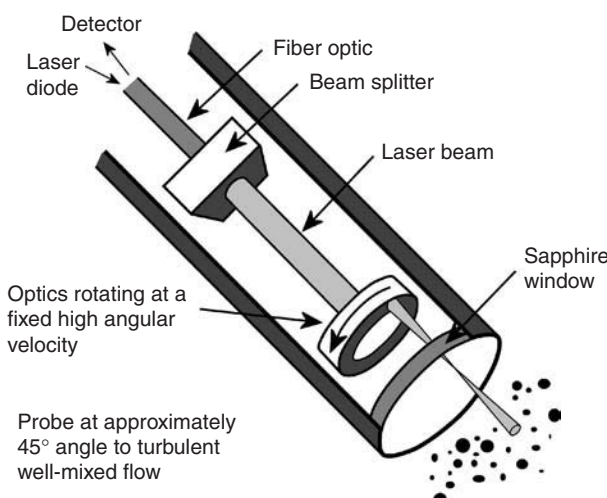


FIGURE 14.53 Configuration of a Lasentec FBRM probe. (From www.lasentec.com. With permission.)

America) probes of Lasentec (see Figure 14.53). In essence, a laser is focused through a lens rotating at a fixed tangential velocity, and projected through a sapphire window such that the light focal point moves along a circular path and detects particles flowing past the window. The backscattered light, generated when the high-intensity beam intersects a particle, is captured by a photodetector inside the probe.

Due to the fast scanning speed (2 to 10 m/sec with an air-bearing lens system), the particles for most multiphase flows are virtually stationary compared to incident radiation scan speed. The reflection period indicates the measured chord lengths (straight line across the particle, Figure 14.54) of particles passing through the focal point. Noticeably, the measured CLD is not dependent upon assumptions of particle shape as in the case of mapping scattering measurements to a particle-size distribution (PSD), but rather is directly measured. Evidently, the CLD accurately represents a size distribution of spherical particles, whereas the correspondence is weaker for irregular and nonspherical particles. In fact, the FBRM tends to oversize small particles while undersizing large particles (Alfano et al., 2000). Different weightings may improve the correspondence of CLD and PSD, although they have to be employed with caution due to

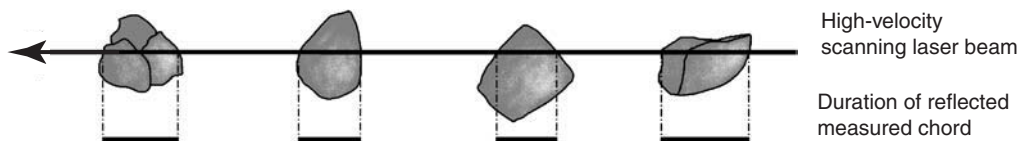


FIGURE 14.54 Chord length measurement of nonspherical particle at random orientations. (From www.lasen-tec.com. With permission.)

the systematic errors associated in deriving these distributions (Tadayyon and Rohani, 1998). Furthermore, the chord length itself has to be regarded as apparent, rather than representative of physical size, due to the influence of factors such as particle shape, orientation, optical properties, and process conditions on its measurement (Dowding et al., 2001). Notably, for quantitative validation where size data are often expressed in diameters, algorithms such as probability apportioning and finite element methods may be applied to predict diameter distributions from CLD with limited accuracy, based on the assumption that each measured chord length is obtained independently (Langston et al., 2001). The device does not claim to be a size analyzer but does provide simultaneous indication of particle number and size from which key mechanistic information can be elucidated.

Particles ranging from 0.5 μm to 2.5 mm can be measured in suspension, with virtually no limiting maximum concentration. The focal point can be adjusted to catch reflected light if there is a possibility of the laser path being blocked by other particles. Although not as imperative for size interpretation as in light scattering, the optical properties of both the solute and solvent govern signal strength. If the particles are not strong isotropic scatterers or, in the case of liquid–liquid dispersions, have a low relative refractive index, then the detector may recognize pulses generated only from the perimeter rather than the entire body, which leads to over-counting and under sizing (Sparks and Dobbs, 1993). Other factors affecting data quality include the probe tip, which should be positioned in such a way as to ensure that sample flows toward its window, and sufficient agitation rate to provide rigorous mixing, but avoiding air bubbles formation that could distort measurement (Dowding et al., 2001).

Recently, scanning laser microscopy is beginning to be recognized as a popular direct monitoring device in process industries, particularly those involving crystallization, granulation, and dissolution, with emergence of applications for flocculation and emulsion. Using its quick response rate, effectively no specific sampling requirement, and adaptability to harsh conditions, the technology at its current status is adapted mostly for detection of dynamic changes *in situ* or in pipelines, rather than to yield accurate size information. It permits the tracking of particle and agglomerate populations so that the effect of altering parameters, such as addition of binders or increasing solids concentration, can be quantified. For example, Figure 14.55 demonstrates the measured silica size distribution upon the pulse addition of a flocculant while mixing at 50 rev/sec and then a step increase in the mixing rate. Some breakage of the initial aggregates, during the constant mixing rate period, following the pulse addition is evident from the increase in total scanned count (Peng and Williams, 1994). The chord lengths and particle counts can also serve to ‘fingerprint’ the endpoints for batchwise operations, for example, high shear granulation to bind drug substance into a filler matrix. This would allow real-time process control as opposed to routine trial and error with off-line mesh evaluation (Menning et al., 2001). The outputs that this technique generates can potentially be used as tools to control and automate polymer dosing and mixing rate in flocculation (Williams et al., 1992; Fawell, 2002) as well as the agglomeration of suspensions in fluidized beds (Mörl and Drechsler, 2000).

Pinhole detection of reflected light may be employed as in the case of confocal scanning optical microscopy (CSOM). One drawback of traditional microscopy stems from complete sample illumination forming a two-dimensional image. Light from a perfect point source passing through a lens is subject to diffraction, phase delays and lens aberrations. This results in a blurred image, and is known as the point spread function (PSF) $h(x, y)$ of the lens. Therefore, for a standard microscope with whole field illumination, neighboring PSF interfere such that the overall image is blurred. Further blurring occurs due to out-of-focus reflections.

The term confocal indicates the use of an objective lens for both the incident and reflected light from the sample, i.e., the sharing of a common focus. As illustrated in Figure 14.56, focussing of a pinhole light

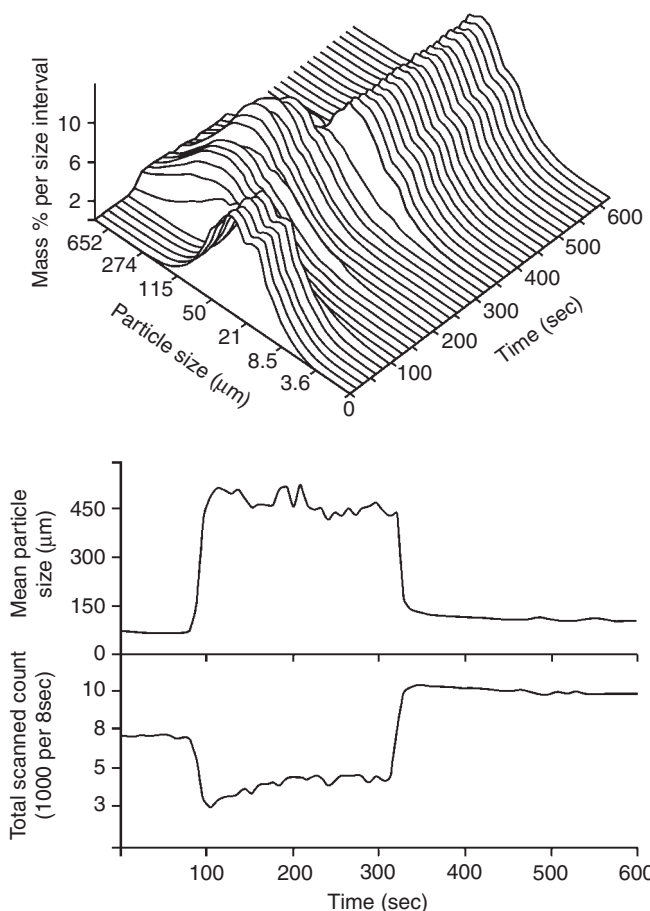


FIGURE 14.55 FBRM measured silica size distribution upon pulse addition of a flocculant while mixing at 50 rev/sec and then a step increase in the mixing rate. Reprinted from *J. Colloid and Interface Science*, 166, Peng, S.J., Williams, R.A., Direct measurement of floc breakage in flowing suspensions, Pages 321–332, Copyright (1994), with permission from Elsevier.)

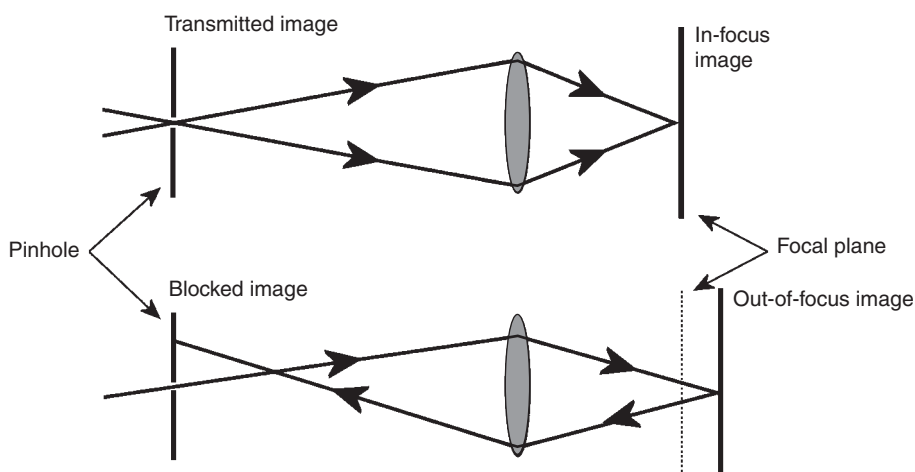


FIGURE 14.56 Principle of CSOM. Light from out-of-focus sample is blocked providing high-definition image with high definition due to single-point illumination.

source provides a small light spot on the sample, subject to the point transfer function. Furthermore, any light reflected from out-of-focus regions of the sample is blocked by the pinhole. Therefore, the blurring associated with traditional microscopy is significantly reduced through the limitation of PSF interference and out-of-focus reflection. Due to the finite nature of the pinhole, the cutoff intensity is not exact but exhibits a Gaussian dependence upon the depth of the focus. In practise, a second pinhole and beam-splitter is employed for the reflected beam, in order to avoid complications due to reflections from the back of the first pinhole.

Scanning of the focal spot through the sample may be achieved by motion of a mounted sample (stage scanning), of the objective or of the beam by reflection. The most popular scanning technique is beam scanning by means of galvanometer mirrors or acoustooptic deflectors for which scan speeds up to 120 fps can be achieved. Alternatively, real-time imaging may be achieved by means of a Nipkow disk although this system is subject to poor light efficiency and mechanical complexity (Kino, 1990). With the help of closely spaced, nonoverlapping image slices a three-dimensional measure of a microscopic structure may be made. Careful image analysis is required to account for the two-dimensional nature of the images in constructing a three-dimensional picture as discussed by Pilaski et al. (2003). An alternative approach is the comparison of two-dimensional images with a database of three-dimensional fractal structure footprints although this is not necessary for closely spaced scans (Liao et al., 2003).

For a traditional microscope the image intensity function takes the form $I_{\text{trad}}(r) = |h(r)|^2$, assuming Köhler illumination such that a uniform illumination across the sample is created (Corle and Kino, 1996). For the confocal system, pinhole illumination leads to point-spread illumination of the sample and subsequently the image intensity function takes the form, $I_{\text{csom}}(r) = |h^2(r)|^2$. Consequently, improved single-point and edge resolution are achieved for the CSOM as opposed to traditional microscopy (Corle and Kino, 1996), due to the extinction of out-of-focus reflected light. Although the resolution improvements are not dramatic these are combined with significant reduction of blurring such that in practical terms the images have much greater contrast. Hence, for a step profile with 450 nm incident light and a numerical aperture of 0.95 the imaged edge width between 10 and 90% is of the order of 227 nm (Kino, 1990).

The CSOM may also be operated in a fluorescent mode, where the sample is illuminated with a finely focussed laser beam and the fluorescence is detected by the CSOM principle. In this mode of operation, scan times of several minutes are required during which the sample must be keep still and the penetration depth is limited to less than 100 μm . The penetration depth is limited by factors such as absorption of the excitation source by the material above and due to light scatter of the fluorescence within the sample (Van Blaaderen, 1993). Since CSOM scanning may take several minutes, it is necessary to restrict the motion of the sample. Selomulya et al. (2003) captured silica aggregation on a brass plate within small holes (7.9 mm diameter and 1.6 mm deep) so that the motion was relatively inert during scanning (~5 min). [Figure 14.57](#) shows confocal images of silica aggregates for a CSOM operated in both fluorescent mode (a) and reflective mode (b). Favorable comparison has been demonstrated between CSOM measurements and other microscopy techniques such as optical interference microscopy (Barnes et al., 2002; Corle and Kino, 1996).

14.4.4 Laser Velocimetry

14.4.4.1 Laser Doppler Velocimetry (LDV)

The technique of LDV represents a well-developed approach for the nonintrusive single-point measurement of the velocity field, the first use of which was reported by Yeh and Cummins (1964). When measuring gas flows, it is common to use the terminology laser Doppler anemometry. This method relies on the presence of scattering particulates within the flow. In general, although naturally occurring particulates may be present in liquid and gas flows, seeding may be provided to ensure a continuous signal, particularly for gaseous flows (Durrani and Greated, 1977). Only fine particulates are required for scattering since the measurement method is similar to dark-field microscopy where by the incident beam on the sample is blocked from the detector allowing only scattered light to be incident upon the detector at high

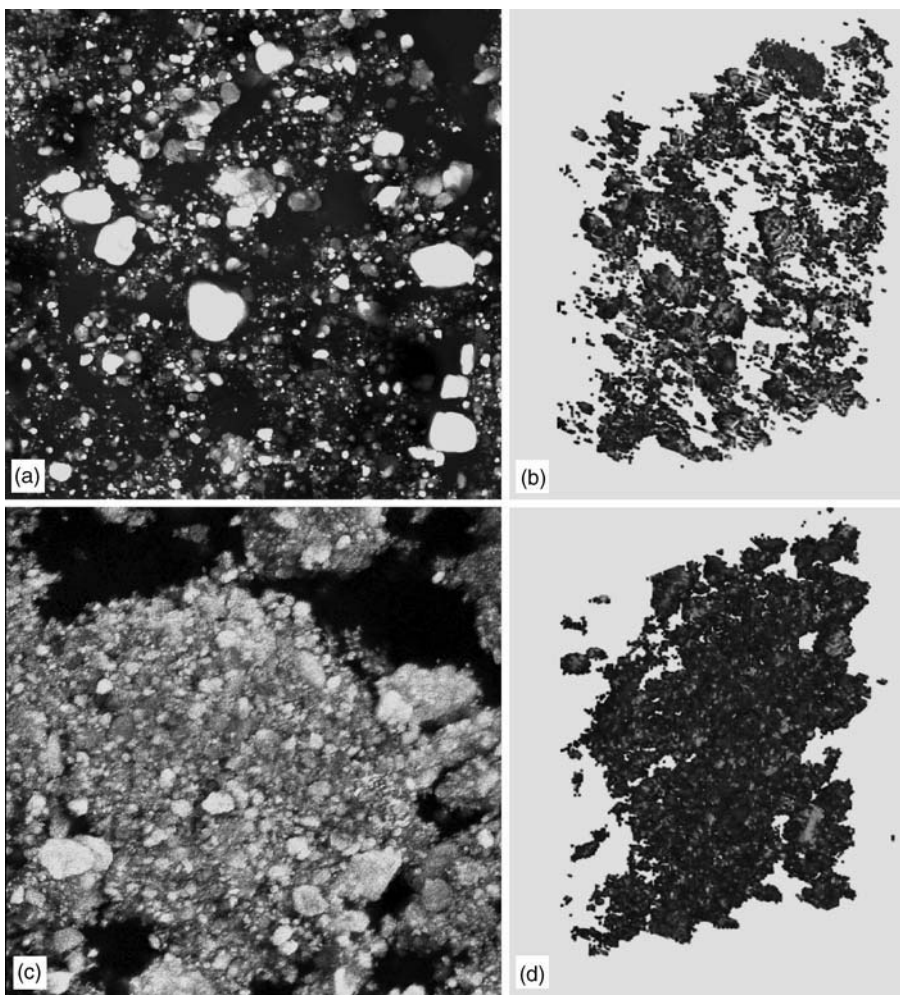


FIGURE 14.57 CSOM of silica aggregates, image slice and three-dimensional reconstruction: (a,b) 0.5 g/L, fluorescent mode, (c,d) 10 g/L, reflective mode. Private communication from Selomulya, C., University of New South Wales, Australia.

sensitivity. The Doppler shift is then exploited where, for a moving particle, the scattered frequency is shifted by $(\mathbf{k}_{\text{sca}} - \mathbf{k}_{\text{inc}}) \cdot \mathbf{U}$. The velocity measurement range of this type of system is of the order of 0.1 to 100 m/sec. A number of LDV configurations are applied as briefly outlined below.

In general, it is not possible to determine accurately the Doppler shift directly; rather, a reference beam may be employed as illustrated in Figure 14.58 for the heterodyne system. Here scattered light is observed *at an angle to the incident beam*. The reference beam interferes with the scattered beam to form a beating signal at the detector, which is characteristic of the particulate velocity. With an incident laser source, the output is a linear function of velocity, thereby providing a well-defined measure. The reflection-beam approach suffers from a low signal-to-noise ratio and is particularly sensitive to alignment of the optics (Durrani and Greated, 1977). In general, therefore the sample is moved rather than the optics themselves for this setup.

An alternative approach is that of the dual-beam LDV technique, that relies upon the development of a fringe pattern is not overly sensitive to the alignment of optics and was originated by Rudd (1969). The incident laser beam is split into two and then focuses to the measurement point by means of a lens (Yurteri et al., 1994). Interference generates a stationary fringe pattern, perpendicular to the bisector of

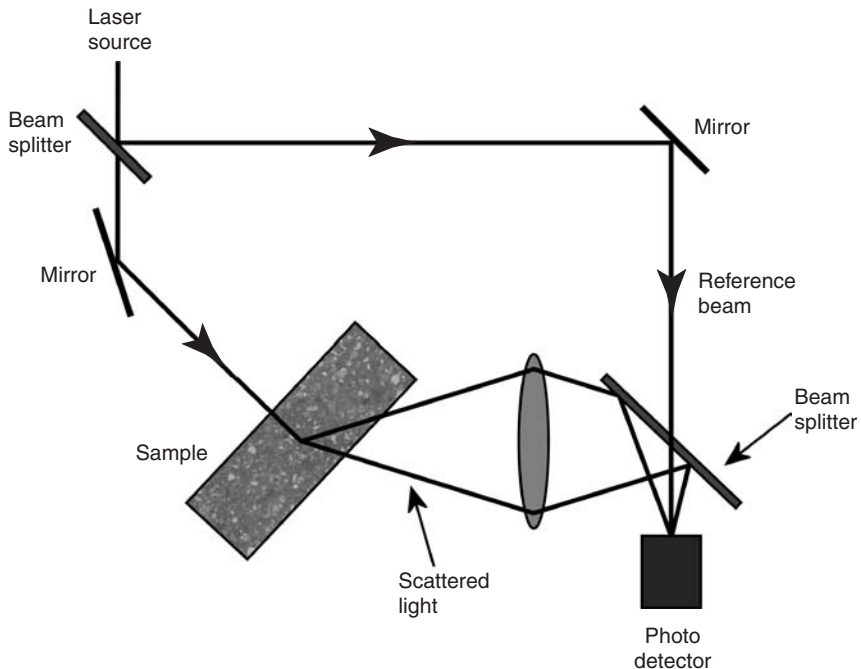


FIGURE 14.58 Schematic for the reflection-beam LDV approach.

the two incident beams. The spacing of the fringe pattern δ_f is a function of the incident wavelength and the bisector angle such that

$$\delta_f = \frac{\lambda}{2\sin(\theta/2)} \quad (14.90)$$

where θ is the angle between the two incident beams (Mathiesen et al., 2000). As the flow particulates pass through the fringe pattern scattering occurs, such that the velocity may be determined from the frequency of scattering events. Since the fringe pattern is stationary, the velocity direction is ambiguous, which may be resolved by placing a Bragg cell in one of the beams producing a nonstationary fringe pattern.

Since the LDV approach is a point-by-point measure, this is only applicable to steady-state or periodic flow fields as field scanning is required. Alternatively, for local point measurements, prefiltering may be applied in order to determine turbulence statistics (Sree, 1995). Other extensions include particle size measurement by determining the time taken to cross a given number of fringes, since for a particle of diameter d and measurement length D in the direction of motion,

$$tv = d + D \quad (14.91)$$

where v and t are the velocity and transit time, respectively (Yurteri et al., 1994). A system that has been commercialized employs multiple LDV detectors closely aligned (Dantec Dynamics, 2003). The phase difference measured by two adjacent detectors is linearly proportional to the particle diameter of smooth spheres (Bachalo and Houser, 1984), such that it may be determined. Application of this technique requires knowledge of particle shape since it is the surface curvature that is measured and then mapped to a particle size. A third detector removes ambiguity due to full-phase period displacement by larger particles.

LDV may be extended to provide instantaneous planar velocity measurements by means of the Doppler global velocimetry (DGV) approach (Chan et al., 1995). As illustrated in Figure 14.59, by illuminating the sample with a laser sheet, the planar Doppler shift may be observed. This is not feasible by the reflected-beam approach, but instead an absorption line filter (ALF) is employed for which absorption is a function

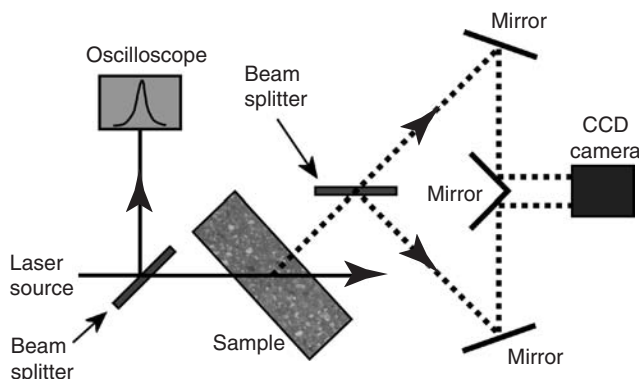


FIGURE 14.59 Setup for single camera DGV system.

of the beam frequency. By comparing the intensity distribution resulting from the ALF with that of a reference signal, system absorption (seeding concentration, system geometry) can be described such that the ALF-generated image is mapped to a velocity distribution. With the system of Chan et al. (1995) illustrated in Figure 14.59, only one camera is required for both the ALF-modulated and the reference signal by using two halves of the detection area for each of these signals. This avoids complications of camera synchronization for the single velocity measurement. This system and standard LDV may be extended to the measurement of three-dimensional velocities by means of three cameras, preferably oriented orthogonally (Murugan et al., 1994), although these systems may exhibit bias errors (Chen et al., 1995).

14.4.4.2 Particle Image Velocimetry (PIV) and Laser-induced Fluorescence (LIF)

PIV achieves velocity measurement by means of light scattering from tracer particles coincident with a light sheet, which is easily created by a narrow laser beam. Pulsed lasers may provide sequential high-energy pulses lasting for as little as 5 ns such that the tracer particles are effectively frozen in time. Therefore, the key challenge is to select appropriate tracer particles and achieve an appropriate distribution throughout the flow field. In particular, larger particles reflect light well, whereas smaller particles exhibit less lag to velocity fluctuations (Humphreys et al., 1993). An optimum tracer would be a density-matched sphere of small size, which provides good reflectance (large relative refractive index). For liquid flows, the particle size required to achieve a sufficient scattering intensity may compromise capture of turbulence effects which occur at the small scale. Further, it is essential to achieve sufficient dispersion of the tracer particles without perturbing the flow state. Notably, vortex flows tend to centrifugally force all except the smallest and lightest particles from the core, such that the core region may become depleted of tracer particles.

The LIF approach avoids these problems for continuum flow. Upon excitation by a high-energy photon, and after a short time delay (~ 1 ns), the fluorophore-doped continuum fluoresces. Rather than relying upon scattering occurring at tracer particle locations, an intersecting grid of laser lines is created, which induce fluorescence. Such a laser grid may be produced by transmission through gratings or by optics for a reduced energy loss. The adoption of fluorophore doping reduces technical difficulties related to sufficient dispersion. Further, subject to a fluorophore that is of similar fluid mechanical properties and of low concentration, the flow-field dynamics remain unaffected and no particle lag effect occurs. Limitations of LIF exist, for example, although a broad range of fluorophores exists, the time delay between excitation and decay for appropriate fluorophores may inhibit their application to high-speed flows, and chemical incompatibilities may occur. One solution to the later problem is to use macromolecules that encapsulate the fluorescent dye. The macromolecules are first ruptured by a write laser grid so that the fluorescence process may occur (Krüger et al., 2000).

For PIV the velocity field is obtained by cross-correlation, which permits an increased tracer density compared with that permissible for particle tracking. The optimal approach captures sequential images of particle location on separate images either by photographic film or crosscorrelation digital cameras.

Double exposure on the same frame may be employed but this significantly reduces accuracy and requires image shifting in order to determine the flow direction, although this approach does have a clear advantage on high-speed flows. In order to determine the representative velocity, the image is generally subdivided into small elements for each of which the velocity is assumed to be a constant. The cross correlation of the first and second image intensity distributions as a function of displacement distance is then determined. The second image intensity distribution may be represented by

$$I(\mathbf{r}) = \sum_{i=1}^N V_0(\mathbf{r}_i + \mathbf{d}) h(\mathbf{r}^l - \mathbf{r}_i^l - \mathbf{d}^l) \quad (14.92)$$

where \mathbf{r} , \mathbf{r}_i^l , \mathbf{d} , and \mathbf{d}^l represent the initial actual and image locations, and the actual and image displacements, respectively. The function V_0 accounts for factors such as light intensity distribution and imaging optics; Meanwhile h is the PSF. The crosscorrelation of the first image intensity with that of the second takes the form

$$\frac{1}{a_l} \sum_{i,j} V_0(\mathbf{r}_i) V_0(\mathbf{r}_j + \mathbf{d}) \int_{a_l} \tau(\mathbf{r} - \mathbf{r}_i^l) \tau(\mathbf{r} - \mathbf{r}_j^l + \mathbf{s} - \mathbf{d}^l) d\mathbf{x} \quad (14.93)$$

where a_l and τ are interrogation area and assumed Gaussian PSF, respectively.

This function forms a series of maxima over \mathbf{s} , which corresponds to the convolution of mean intensities of I and fluctuating noise. Meanwhile, a distinctive maxima occurs for self correlation of the particles at $\mathbf{s} = \mathbf{d}$, thereby identifying the image displacement. Notably, fitting a Gaussian function to the cross-correlation function permits identification of \mathbf{s} to greater accuracy than that of the pixilation. In fact, careful system design will optimize such subpixel accuracy if the particle images span between approximately two and four image pixels, such that the Gaussian tails are well fitted. If the particle image is restricted to singular pixels then only image-pixel size resolution is possible and integer displacements (peak-locking) is observed (Bolinder, 1999), which is more common for digital systems. Notably, the pixilation of digital cameras and cell masking in order to achieve rapid sequential image pairs means that each CCD cell may be sensitive to less than 60% of the incident light.

Clearly, the smaller the time interval between frames, the smaller the systematic error, but the larger the measurement error such that a trade off exists. The PIV data quality may be improved through outlier removal, which may result from spurious cross-correlation peaks (e.g., low particle image density) and measurement error. Although these can be identified by assuming a maximum spatial variation of the velocity field, care is required that genuine features are not removed for significantly nonlinear velocity fields. Modern approaches incorporate data regularization and smoothing (Young et al., 2002) and spectral optimization (Acosta et al., 2002). A process called superresolution PIV was developed by Keane et al. (1995), which involved an initial estimate of the velocity field followed by refinement through a particle-tracking algorithm (Yamamoto et al., 2002). For microflows, whole field laser illumination may be used, and a thin-depth-of-focus microscope used to image the particles effectively in a plane with a distinguishability distance as low as a few microns. Application of this technique has been demonstrated by a number of authors (e.g., Santiago et al., 1998; Meinhart et al., 1999; Mielnik and Saetran, 2003).

For highly scattering media such as dense sprays, for which conventional methods may not work due to multiscattering, techniques similar to those discussed by Krüger et al. (2000) may be applied. They measured a hollow-cone gasoline direct injection spray for which conventional techniques including phase Doppler anemometry and PIV have been proved unsuccessful. In essence, the gaseous flow was doped with tertbutyl nitrite ($(\text{CH}_3)_3\text{CONO}$) which could be photodissociated to form NO. A write laser grid was generated to achieve photo-dissociation (see Figure 14.60). Subsequently, a thicksheet laser beam (read) was applied to excite the dissociated NO and induce fluorescence (see Figure 14.60). Therefore, motion occurring between the write and read laser beams could be detected to provide a measure of velocity. The thick read beam ensures capture of all NO molecules, given their three-dimensional motion and diffusion. As long as beam attenuation does not obscure the tagged lines, the measurement is hardly

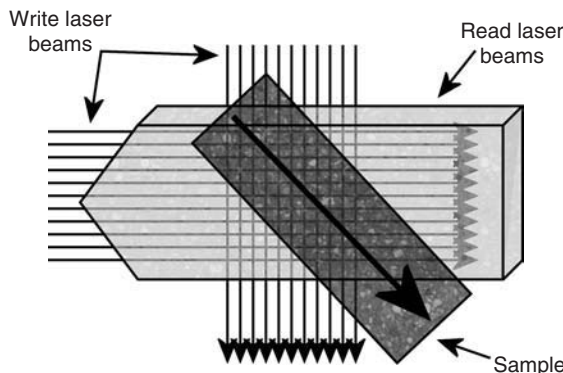


FIGURE 14.60 Principle of photodissociation fluorescence.

affected by multiple scattering. Alternatively, phosphorescence may be employed, coupled with camera gating, to provide a velocity measure (Hu and Koochesfahani, 2002).

A serious error for two-dimensional measurements is caused by tracer motion out of the measurement plane. Without additional measurement these cannot be decoupled from the in-plane motions and such an error may represent up to 15% of the mean flow velocity. In fact, for the PIV cross correlation not to be severely compromised, the out-of-plane displacement should not exceed $W\Delta t/\Delta Z_0 \leq 0.3$, where W represents the geometric projection of the interrogation window function back into the light sheet due to perspective error and ΔZ_0 is the light sheet thickness. Stereo PIV provides the necessary three-dimensional measurement. Two cameras are placed within a plane at equal but opposite angles to the measurement plane normal (see Figure 14.61). Reconstruction of the three-dimensional velocity field is then possible by means of geometry (Raffel et al., 1998). An extension of this approach involves double-cavity lasers. By sequentially creating the laser sheet with two laser pulses (time interval $\sim 0.2 \mu\text{s}$, 4 double fps (4 laser pulse pairs per sec.) for LaVision GmbH system) and simultaneously capturing the PIV images the velocity variation at the turbulence time scale may be determined (Ullum et al., 2002). Further extension is achieved by employing two double-cavity pulsed lasers in order to create two closely spaced parallel laser sheets (see Figure 14.62). For each laser sheet, a camera pair captures the three-dimensional motion, and therefore the full three-dimensional velocity and vorticity fields may be captured. For PIV the scattered light from the two laser sheets may be decoupled by means of polarization cubes, since for small tracer particles (diameter $\sim 1 \mu\text{m}$) the polarization is maintained during scattering (Hu et al., 2002). Hu et al. (2001) and Koochesfahani and Nocera (2001) have demonstrated application of this technique for injector jets and wall-jet flows of dispersed particles in gas and liquid–liquid flows, respectively.

14.4.5 Ultrasound Absorption and Scattering

The practical application of ultrasound absorption and scattering has been discussed by Povey (1997). By measuring the phase and group velocities of an acoustic wave and its attenuation, the information that can be deduced include profiles of composition and solids content, crystalline phase and nucleation, colloidal destabilization, for example, in flocculation or creaming, particle size as well as more subtle effects caused by chemical relaxation, structural reorganization of droplets or particles, or the presence of surfactants or polymers on particle surfaces for well-defined systems (Hibberd et al., 1997, 1999; Marshall et al., 2002).

The propagation of sound is inherently related to the mass of constituent material particulates and the material compressibility, for example, an ultrasonic wave may be generated by means of a piston device such as a piezoceramic transducer. The transmission of the developed wave motion to the material particulates is then described by Newton's second law of motion, $F = ma$, such that the particulate mass affects the velocity of propagation. In turn, the compressibility reflects the degree of freedom for motion

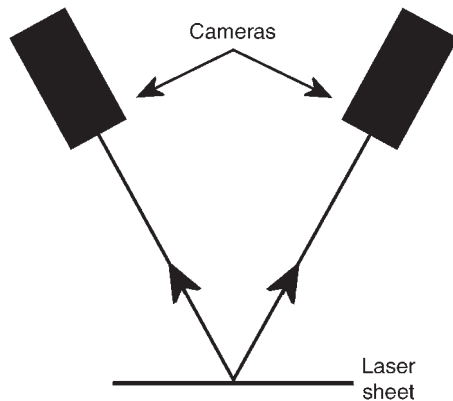


FIGURE 14.61 Principle of stereo imaging for measurement of three-dimensional velocities.

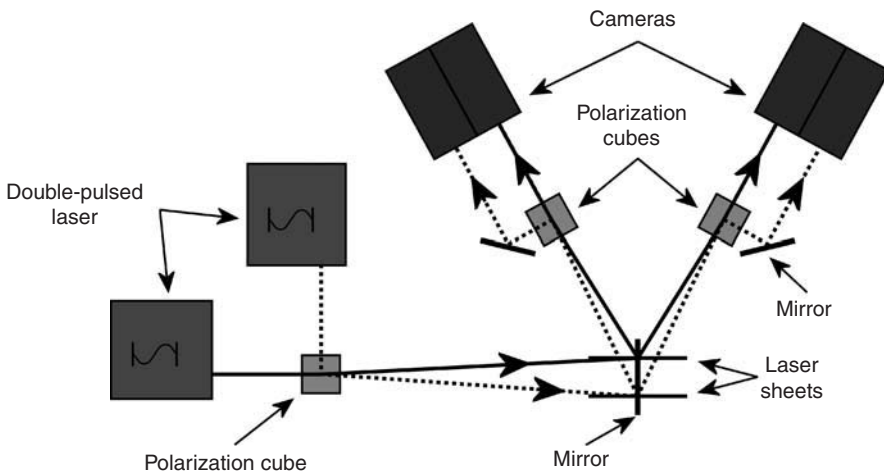


FIGURE 14.62 Schematic of dual-planar particle image velocimetry. Double-pulsed lasers emitting orthogonal linearly polarized beams permit decoupling of scattered light from each of the image planes by means of polarization cubes.

of the constituent particulates. It has been shown by Wood (1964) that in the case of adiabatic and homogeneous media, the sound velocity is given by

$$\nu = \frac{1}{\sqrt{\kappa\rho}} \quad (14.94)$$

where κ and ρ are the adiabatic compressibility and density, respectively. For mixtures and suspensions, κ and ρ are modified as

$$\kappa = \sum_i \phi_i \kappa_i \quad (14.95)$$

and

$$\rho = \sum_i \phi_i \rho_i \quad (14.96)$$

where ϕ_i is the dispersed-phase volume fraction. This forms the modified Urick equation (Urick, 1947), such that the sound velocity is defined in terms of the mean adiabatic compressibility and density.

Determination of the mixture composition from sound velocity measurements is not simple as can be illustrated from the sound velocity as a function of the air fraction in an air–water mixture (see Figure 14.63). As discussed by Povey (1997) and Dukhin et al. (2000), the sound velocity proves extremely sensitive to the air fraction and exhibits a non-monotonic dependence upon the same, such that the composition may not be uniquely determined from a sound velocity measurement. In practise, therefore, the sound velocity may be tabulated as a function of temperature and composition such that the composition may be determined from a measured functional behavior of the sound velocity.

Similar to light scattering, the incidence of sound waves upon an acoustic impedance contrast such as suspended particulates results in attenuation of the forward wave and the introduction of scattered sound waves about the incident direction. Similar to light scattering, multiple scattering effects occur and a theory can be developed based upon the scattering from spherical scatters, such that the incident and scattered waves may be decomposed into spherical harmonics. For particulates of density greater than twice that of the continuous phase the dominant scattering phenomena are hydrodynamic and losses arising from particle oscillations driven by the sound wave. For a similar order of densities, elastic and thermal effects dominate as well as conversion to heat (Challis et al., 2003). A key advantage of this approach is its nonintrusive application for concentrated (Dukhin et al., 2000), optically opaque systems, and it is not constrained by the mean free path of multiple light scattering that presents difficulties in penetrating materials like crude oils. Notably, the sound scattering properties are generally a function of temperature such that potentially complex variations with mixture temperature must be taken into account.

The forward-scattered sound velocity and its attenuation provides a measure of the mixture size distribution with a dynamic range from 10 nm to 1 mm at high solids concentrations (< 70%) possible from a single measurement frame involving intrusive probing by the ultrasound sensors and multi-frequency measurements, although this may take 2 to 3 min to acquire (Dukhin et al., 2000; Geers and Witt, 2003; Povey, 2000). The scattering and attenuation may be inferred from interference of the received and transmitted waveforms, as for the case of the interference microscope. As for Lorentz–Mie reconstruction of the particle size distribution, this represents a computationally intensive and error-prone reconstruction unless the particle size distribution is reduced to a few descriptive parameters.

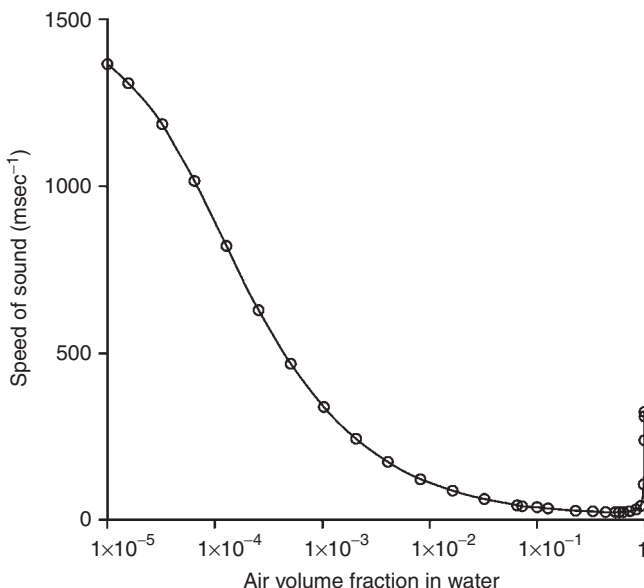


FIGURE 14.63 Sound velocity as a function of air volume fraction for an air–water mixture at 20°C. (Reprinted from *Ultrasonic Techniques for Fluids Characterisation*, Povey, M., 28., Copyright (1997), with permission from Elsevier.)

Comparative examples of such forward-scattered sizing against laser sizing are shown in Figure 14.64 (Challis et al., 2003; Hou and Williams, 2003). An excellent agreement was observed with the data of Challis et al. for a simple distribution, whereas for that of Hou and Williams the detail of a bimodal distribution was lost. In contrast, excellent resolution of bimodal distributions is demonstrated by data of Dukhin et al. (2000) for ultrasound spectral measurements. Figure 14.65 demonstrates the measured distributions for two separate samples and then that resultant from a 50/50 mix demonstrating expected behavior. Meanwhile, Figure 14.66 demonstrate the addition of small proportion of coarse particle (Geltech) to an otherwise fine distribution. Discrimination of the small bimodal peak is clear again demonstrating the measurement capability.

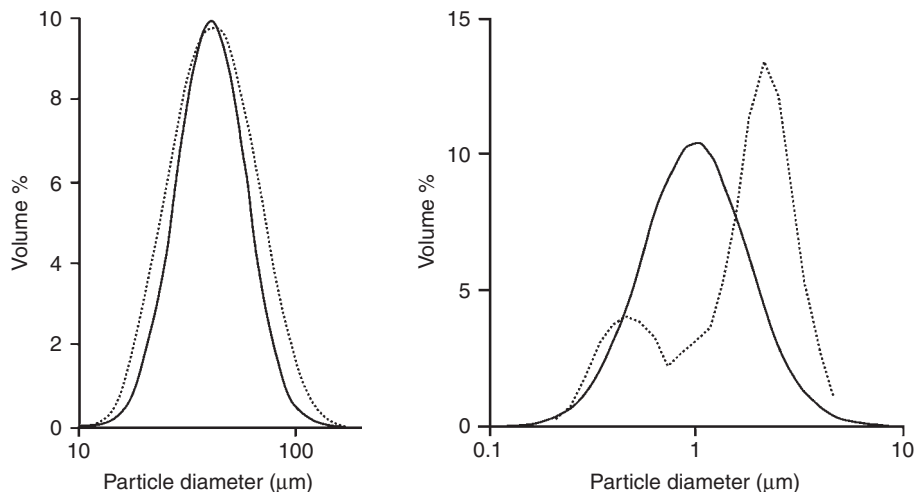


FIGURE 14.64 Comparative ultrasonic measure of an oil in water emulsion PSD against that from a Malvern Mastersizer (dashed line). (From Challis, R.E., Holmes, A.K., and Kalashnikov, A., *Proceedings of the Particulate Systems Analysis*, 2003, Harrogate, UK, 2003. With permission from the Royal Society of Chemistry; Hou, R. and Williams, R.A., *Proceedings of the Particulate Systems Analysis* 2003, Harrogate, UK, 2003. With permission from the Royal Society of Chemistry.)

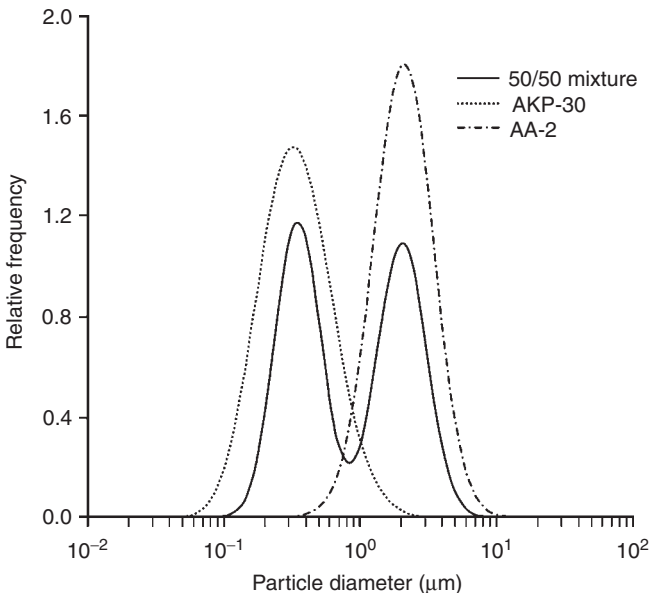


FIGURE 14.65 Measured distributions for two separate samples alongside that of a 50/50 mix. (Reprinted from *Colloids and Surfaces. A. Physicochemical and engineering aspects*, 173, Dukhin, A.S., Somasundaran, P. Acoustic and electroacoustic spectroscopy, Pages 127–158, Copyright (2000), with permission from Elsevier.)

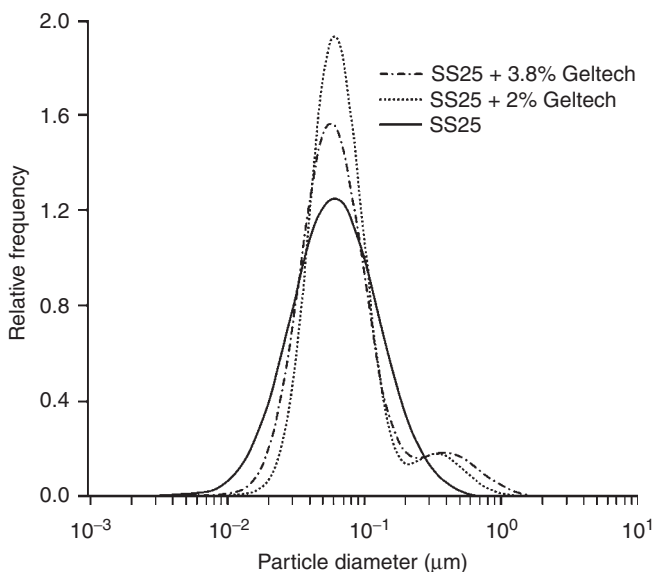


FIGURE 14.66 Measured distributions of an originally fine distribution alongside that resulting from addition of small proportions of coarse particles. (Reprinted from Colloids and Surfaces. A. Physicochemical and engineering aspects, 173, Dukhin, A.S., Somasundaran, P., Acoustic and electraacoustic spectroscopy, Pages 127–158, Copyright (2000), with permission from Elsevier.)

On-line particle sizing may be achieved by means of the “pulse-echo time-of-flight” approach, whereby the time interval between generation and detection of a sound signal is observed after reflection from a boundary beyond the sample. A sound velocity measurement accuracy of about 1 m/sec and kHz measurement rates are reported (Povey, 1997, 2000). For particulate concentrations < 1%, the particulates may be oversized (Hou and Williams, 2003). Further the existence of non-spherical particulates may be significantly detrimental to the measured size distribution as demonstrated by Geers and Witt (2003).

For *in situ* flow measurements, flow-generated noise or passive acoustic emissions may be monitored, such as turbulent or wall interactions, particle–particle collisions, and particle–wall collisions. The resulting acoustic spectrum may reflect properties, such as particle size (large particles having high momentum collisions) and the presence of ultrafine particles or viscosifying chemical reagents (which may dampen the acoustic response as the continuous-phase viscosity or density increases). Passive methods are recognized in industry for powder flow and contamination monitoring, for example, sanding in oil processing (Folkestad and Mylvaganam, 1990). It is essential to audit the measurement environment since external sources of process noise (pipe vibration, other operations) can interfere with the signals. Nevertheless, through a judicious choice of signal processing schemes, passive acoustic methods can be effectively deployed and are favored due to the low cost of the microphone sensors, with an additional advantage that they can be mounted *ex situ*. Signal interpretation requires a model or means of correlation with process parameters.

For example, systematic investigations have been applied to ‘fingerprint’ slurry flow in pipelines and to classify the performance of hydrocyclones (Hou, 2000; Hou et al., 1999a, 1999b; Hou and Williams, 2002). A 190 kHz piezoelectric acoustic sensor was applied to a 125 mm hydrocyclone separator and a 44 mm-diameter-steel pipeline handling slurries of fine silica particles from which emissions were collected for both spectral analysis and modeling purposes. The power density spectra of the collected signals were calculated by performing fast Fourier transformation using appropriate windowing methods (Hou, 2000). Figure 14.67 illustrates typical acoustic spectral characteristics for each process. It can be seen that in both the case studies, the amplitude of the acoustic spectrum is sensitive to changes in certain key process parameters. This figure shows variations due to feed flow or pressure, with a further detailed analysis of the results indicating that the spectral behavior of the acoustic emission signal is also closely related to the hydrodynamic features of the flow involved in each process. In the hydrocyclone investigation, the spectral

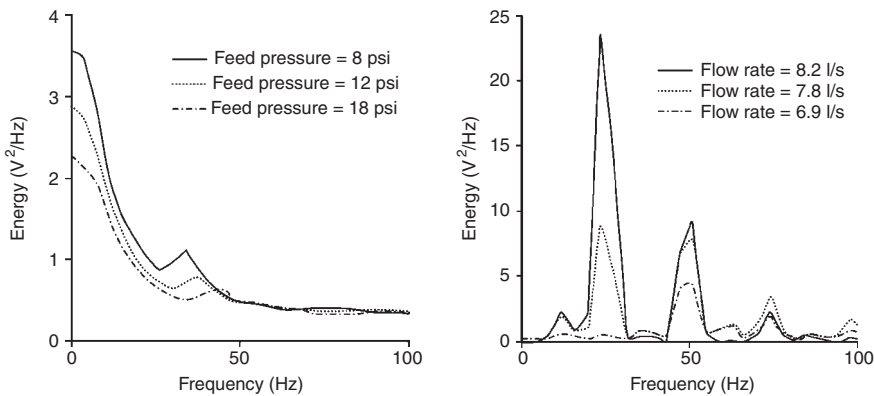


FIGURE 14.67 Effect of hydrocyclone feed pressure and pipeline volume flow rate on spectral characteristics of acoustic emissions at 10 and 30 wt% solid concentration respectively. Private communication from Hou, R., University of Leeds, UK.

characteristic of acoustic signals appears to be a combined manifestation of both turbulent and swirling flow structures inside the hydrocyclone (Hou et al., 1999b). In the pipeline flow monitoring, it can be shown that the pump-driven pulsation of the slurry, modulated by a number of flow parameters in the vicinity of the sensor-mounting location, has been a major cause for the periodic occurrence of spectral peaks in the spectrum. Variations in these pulses can therefore be used to monitor the process.

A multivariate stepwise regression technique can be applied to the experimental data in order to quantify the relationship between process parameters and the statistical and spectral characteristics of the acoustic signals. For each of the above cases, < 3% error was achieved for many process parameters, including the hydrocyclone feed pressure, underflow concentration, solids concentration, and volumetric flow rate (see Figure 14.68).

14.4.6 Tomographic Methods

14.4.6.1 Overview

In the following section a sample of the broad range of available tomographic modalities is highlighted along with the measurements. The potential of the highlighted modalities is discussed for the measurement of feature motions and transient development, solids distribution, and the velocity field. Process tomography is now well developed as an important tool for the engineer (Williams and Beck, 1995). The term tomography refers to a nonintrusive process that images a slice through an object, although modern tomography also encapsulates three-dimensional imaging. Numerous applications have been identified in process engineering as an investigative, monitoring and control technique (Dyakowski et al., 2000; VCIPT, 2003). Tomographic data can be interpreted in various ways (West and Williams, 1999), including reconstruction to form an image which is often based upon inversion of ill-posed data and analysis of the raw data itself. A powerful design approach could be the combination of tomography with CFD.

Tomographic techniques are based on different sensing methods ranging from x-ray, ultrasound, to electrical resistance. Some of these techniques may provide for on-line measurements through rapid reconstruction of a simplified parameterized reconstruction or through analysis of the measurement signals. For detailed measurement, significant computation may be required for accurate image reconstruction. In such a case, the rate of data processing may not be critical, the rate of data capture and the measurement or reconstruction accuracy is crucial. These issues for some of the available modalities as well as the principles behind them will be highlighted. Note that there is presently a drive to combine modalities to extract more information for a given fused system offering the potential for greater detail and accuracy of reconstruction. An example is the combination of acoustic, electrical impedance and electrical capacitance tomography as investigated by Hoyle et al. (2001).

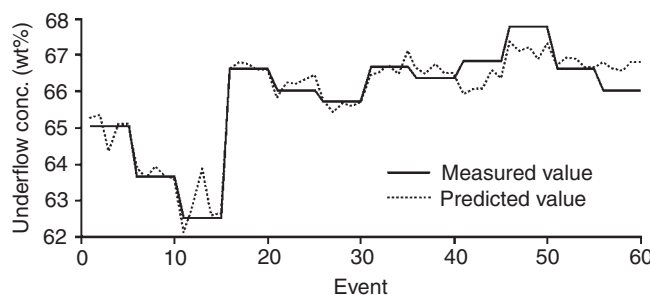


FIGURE 14.68 Comparison of active acoustic measure of hydrocyclone underflow solid-concentration with actual value. Private communication from Hou, R., University of Leads, UK.

14.4.6.2 Radiation Transmission Tomography

14.4.6.2.1 X-ray Transmission Tomography (XTT)

The strong correlation between x-ray attenuation and material density make x-rays a good tool for non-intrusive investigation of materials (Clarke and Eberhardt, 2002). Excellent resolution can be achieved with XTT of the order of a thousandth of the object diameter (Boller et al., 2001). Desktop x-ray systems are now capable of resolutions of the order of 5 to 10 μm (Sasov, 2001). Scan times for generation of image slices are generally long (~ 10 min), requiring revolution of either the material or the apparatus. Modern developments are incorporating electronically switched x-ray tubes. Hence the tubes and detectors remain stationary about the sample, as for that developed by Hori et al. (1998). Their scan times are as short as 0.5 ms, although the reported spatial resolution is only of the order of 1.5 mm due to source and detector sizes. Also, the revolving philosophy can now provide scan times of less than a second using a rectangular rather than fan beam. Four principle scanning protocols are used in general for acquiring the x-ray measurement data as outlined by Ketcham and Carlson (2001) and presented in Table 14.4.

The resolution of the first to fourth-generation x-ray systems is governed principally by the focal spot size of the x-ray tube and by the quality of the detection apparatus. Some of the principal sources of error include feature blurring due to the focal point (intersection of x-ray paths) and beam hardening (preferential absorption of low-energy x-rays). Beam hardening causes the shorter chords of a homogeneous material's cross-section to appear more attenuating than those of greater chord length. Those x-ray beams passing along shorter chords are detected at a higher average energy relative to those of longer chord length. As a result the center of the reconstructed image appears overly dark relative to the image edges.

Although beam hardening is generally difficult to account for at the data processing stage, it may be possible for the simpler geometries for which prior knowledge may be applied. It is more beneficial to precalibrate, so that nonsimple variations of the flow as well as detector variations and other errors may be accounted for. For example wedge precalibration may be made by using a replacement sample of constant and known properties similar to that of the real sample. Ketcham and Carlson (2001) demonstrate such precalibration to be far superior to that of prehardening, i.e., transmission of x-rays uniformly through a material such as copper or lead plate to remove lower energy rays, prior to transmission through a sample. Ketcham and Carlson demonstrate wedge calibration to eliminate the bright and dark ring artifacts of third- and fourth-generation systems caused by detector variations.

The radiograph of an operating hydrocyclone is shown in Figure 14.69. It demonstrates some of the challenges of XTT, in particular the need for calibration. The curved, dark regions occurring near to the walls are caused by x-ray camera distortion evident through camera shuttering, and are a result of beam hardening (image is inverted). Without proper calibration significant information loss occurs.

Modern desktop x-ray systems may achieve a spatial resolution of order 2 μm , although long scan times are still required; for example, Figure 14.70 shows a measurement of glass fibre. Modern research seeks to apply CFD codes such as lattice-Boltzmann modelling to such measured structures in order to determine the material properties (Selomulya et al., 2003).

TABLE 14.4 X-Ray Scanning Protocols

Generation	Technique	Improvement by Generation
First	Rotation of translating pencil beam	N/A
Second	Rotation of a translating fan beam	Increased data acquisition rate
Third	Rotation of a fan beam	Increased data acquisition rate
Fourth	Rotation of an off-axis fan beam	Increased resolution and sample size

Source: Ketcham, R.A. and Carlson, W.D., *Comp. Geo.*, 27, 381–400, 2001.

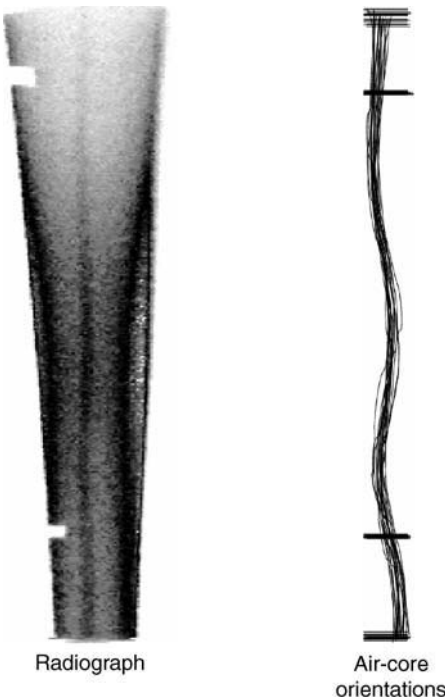


FIGURE 14.69 Radiograph of an operating hydrocyclone with application of image processing to extract air-core orientation.

For example, a SkyScan 1072 was applied to silica aggregates as examined by CSOM with scan periods of up to 1 hour. The x-ray slices were reconstructed into a three-dimensional structure to which a Lattice-Boltzmann CFD code was applied. Figure 14.71 shows the predicted pressure and velocity distribution through the structure.

The issue of beam hardening is avoided altogether by synchrotron x-ray transmission tomography (SXTT) systems by the use of monochromatic x-rays (Boller et al., 2001). The X-ray source is placed at a large distance from the material (~150 m) to effect parallelization of the x-ray beam and to permit the microresolution. Also, a monochromator is required such as a perfect crystal. The resolution of the system is hindered mainly by the quality of detector, which at present permits a resolution of order 1 μm . The higher intensity achievable with synchrotron sources provides a higher signal-to-noise ratio over that of the more traditional (first to fourth generation) techniques. Since the x-ray beam is parallel then the reconstruction is truly two-dimensional and the tomograms reflect far more accurately the true sample structure as amply demonstrated by Boller et al. (2001).

14.4.6.2.2 Gamma Transmission Tomography (GTT)

For larger or more attenuating materials, γ -rays provide a more penetrating alternative to x-rays. GTT setup is similar to the x-ray systems featuring a γ -source and scintillation detector, which can traverse the



FIGURE 14.70 Desktop x-ray system applied to a glass-fiber structure. Private communication from Clarke, A., University Of Leads, UK.

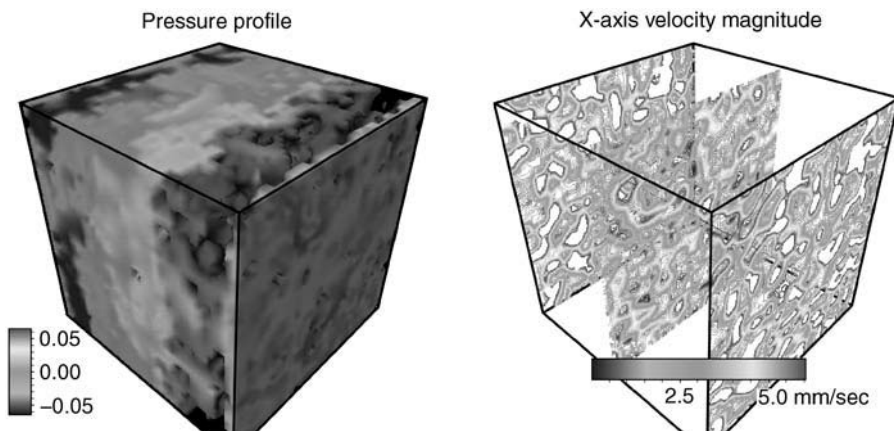


FIGURE 14.71 Lattice-Boltzmann modeling applied to three-dimensional reconstructions of sedimented silica aggregates at 0.5 g/L. Private communication from Jia, X., University of Leads UK.

sample domain (George et al., 2000). Dudukovic (2000) has demonstrated the application of this approach to an array of apparatus including bubble columns and stirred tanks of radius up to 45 cm. A limitation lies in the detector size so that this approach is well suited to large-scale applications. The resultant attenuation distribution may be reconstructed by means of the Abel transform and the assumption of asymmetry. Scan times are long since γ -ray emission is a statistical process, and scintillations must be observed over long time scales (\sim 13 to 30 min) for a sufficient scintillation count. Volume fractions may be estimated from simple ratios of attenuation, which must be significantly contrasting for successful application of GTT. The system of Dudukovic (2000) with a third-generation fan-beam configuration could achieve a spatial resolution of 1/20 of the sample diameter and over scan times of order 45 min.

14.4.6.3 Particle Tracking and Positron Emission Tomography

14.4.6.3.1 Radioactive particle tracking (RPT)

Irradiated particles can serve as tracers providing a γ -ray emission for determination of their in-flow location. Observation of collimated γ -rays with scintillation γ cameras provides location measurements for tracer positions (Parker et al., 2002). Off-line reconstruction of the particle paths is required, the accuracy

of which depends upon the quality and the number of (size of) detectors. Dudukovic (2000) reported a spatial accuracy of about 4 mm at 50 Hz with 500 Hz possible. The maximum particle velocity observed was of order 4 m/sec. Mostoufi and Chaouki (2000) were able to determine the transport mechanisms for fluidised-bed particles both upward and downward through the bed.

A potentially significant source of error lies in the precalibration that may be achieved by placing γ -ray sources at known locations throughout the sample container and observing the resultant scintillations (Dudukovic, 2000). Alternatively Monte-Carlo photon histories may be generated which incorporate the effect of multiple photon interactions prior to detection.

14.4.6.3.2 Positron Emission Tomography (PET)

The term positron emission tomography (PET) originates from the production of a positron from β^+ decay as a proton is converted into a neutron. The positron may travel up to approximately 3 mm in water before annihilation with an electron occurs, producing almost back-to-back γ -rays (Hawkesworth and Parker, 1995). These are observed by scintillation detectors which determine a line-of-sight for the radioactive tracer location from the back-to-back γ -rays. Therefore, two key advantages of this technique are the ability to label actual particles of the process and the penetration of γ -rays, such that metal-walled vessels may be used (Seville, 2003). For detectors separated by 50 cm the positional error is approximately 0.5 mm. An overall spatial accuracy limited to about 1 mm over observation times of about 20 min is reported by Parker et al. (2001, 2002) and Seville (2003) with particles as small as 100 μm being tracked (Forster et al., 2000). Figure 14.72 illustrates measurement of size segregation effects in suspension mixing. In the figure, small populations of sieved particles have been labelled—enabling the homogeneity of the mixing process to be visualized (McKee et al., 1995). Future developments are expected to allow the use of different emitters that can facilitate multiple-species tracing, and to follow the phenomena of aggregation and breakage.

14.4.6.3.3 Positron Emission Particle Tracking (PEPT)

By exploiting the same process as for PET, the back-to-back γ -rays may be recorded for individual particles and hence tracked. Spatial accuracy of the order of 0.5 mm, observed at 500 times a second, is reported by Seville (2003) for a particle velocity of order 1 m/s. This accuracy decreases with particle velocity since the particle moves further and multiple lines of sight are required. PEPT not only produces detailed velocity maps, but also may be used to determine the occupancy distribution. Figure 14.73 shows a single imaged PEPT particle track (Conway-Baker et al., 2002).

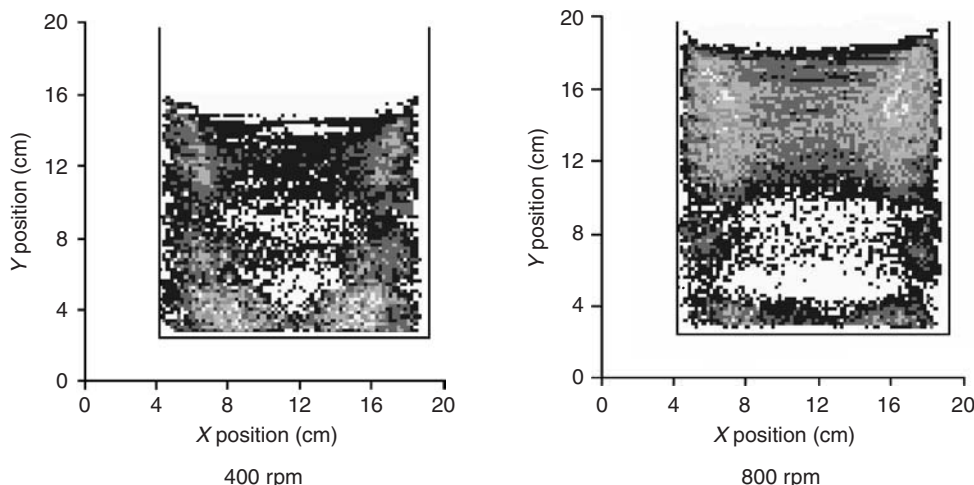


FIGURE 14.72 PET measure of stirred mill occupancy as a function of mill stirring rate. (Reprinted from Minerals Engineering, 15(1–2), Conway-Baker, J. et al. Measurement of the motion of grinding media in a vertically stirred mill using postion emission particle tracking (PEPT), Pages 53–59, Copyright, with permission from Elsevier.)

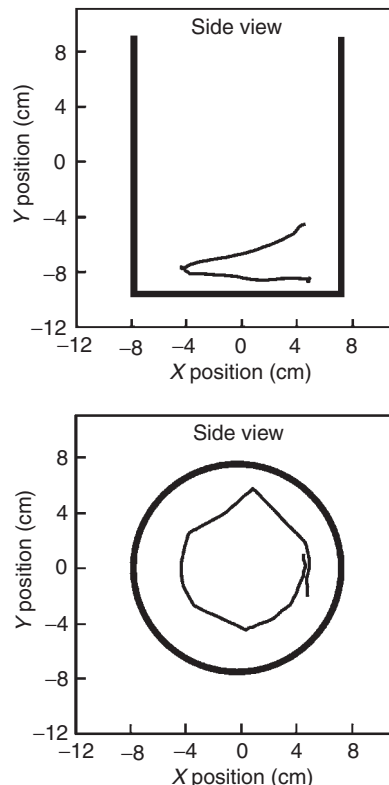
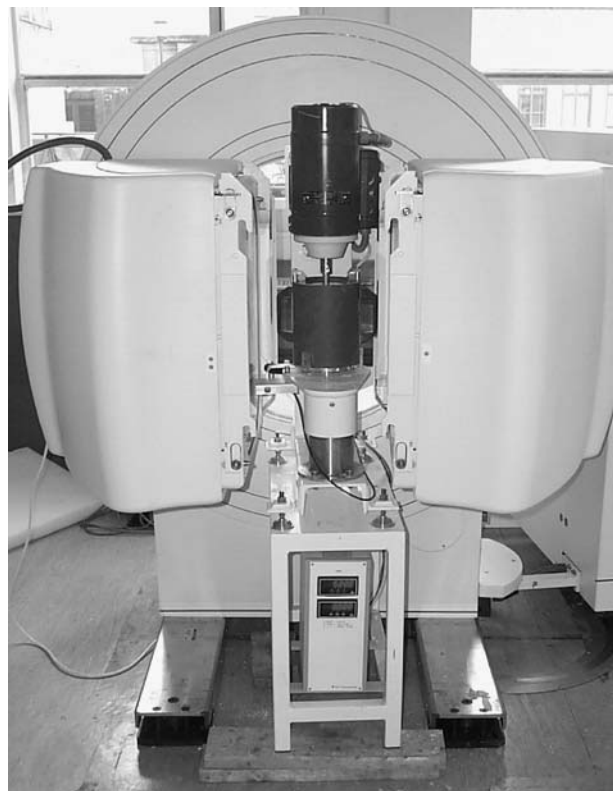


FIGURE 14.73 Two-liter stirred mill in positron emission camera and a measured particle track. (Reprinted from *Minerals Engineering*, 15(1–2), Conway-Baker, J. et al. Measurement of the motion of grinding media in a vertically stirred mill using positron emission particle tracking (PEPT), Pages 53–59, Copyright (2002), with permission from Elsevier.)

14.4.6.4 Electrical Tomography (ET)

At the current level of sophistication, ET techniques are reported to achieve spatial accuracies of the order 3 to 10% of sample diameter (Dyakowski et al., 2000; Seleg him and Hervieu, 1998) at around 100 to 200 fps. Therefore, the main advantage of ET lies in its potential to capture transient behavior. Validation exercises have been conducted, for example, by George et al. (2000), who observed good agreement between electrical impedance tomography (EIT) and GTT for gas volume fractions up to 0.15 in a bubble column. Significant improvement of spatial accuracy may be achieved if internal objects that can serve as electrodes exist. This increases the electric field concentration in the central regions of the sample along with the number of measurements, which greatly improves tomogram accuracy, both quantitatively and qualitatively as has been simulated by Heikkinen et al. (2000, 2001a, 2001b).

14.4.6.4.1 Principle of Electrical Capacitance Tomography (ECT)

ECT may be applied to materials of contrasting permittivities, i.e., materials that exhibit a polarization due to an applied potential difference. This is achieved by measuring the capacitance across the sample between all appropriate electrodes ($C_{ij} = C_{ji}$). Reconstruction is simplified by applying a signal frequency of order 1 MHz, such that electrostatic field theory is relevant (Dyakowski et al., 2000). More modern research investigates the use of higher energy and multifrequencies (VCIPT, 2001). The field is then governed by Poisson's equation

$$\nabla \cdot [\epsilon(r) \nabla \Phi(r)] = 0 \quad (14.97)$$

where ϵ and Φ are the electric permittivity and electric potential. Therefore the capacitance measurements are related to the permittivity distribution by

$$C = -\frac{\oint_s \epsilon(r) \nabla \Phi(r) dS}{V_c} \quad (14.98)$$

where V_c is the potential difference between the source and the detecting electrode. Equation (14.98) illustrates that ECT is a “soft-field” technique as are ET techniques. The term soft field refers to the dependence of measurements upon the complete sample domain making reconstruction a challenge. In contrast the “hard-field” XTT may normally be reconstructed without iteration (Beck, 1995).

14.4.6.4.2 Principle of Electrical Impedance Tomography (EIT)

In contrast to ECT, EIT uses alternating current source and sink electrodes that produce an electric field within the sample. The alternating current avoids polarization effects on the electrodes. This field is then sensed through voltage measurements of the remaining electrodes relative to ground, or from voltage differences between the remaining electrodes. This is also a soft-field technique. Given no charge sources or sinks within the measurement domain, then the overall impedance field obeys (Cheney et al., 1999)

$$\nabla \cdot \gamma(r, \omega) \nabla \Phi = 0 \quad (14.99)$$

where γ and ω are the admittance (inverse of impedance) and the angular frequency, respectively. Here the admittance may be defined as

$$\gamma(r, \omega) = \sigma(r, \omega) + i\omega\epsilon(r, \omega) \quad (14.100)$$

where σ and ϵ are the electric conductivity and electric permittivity, respectively.

If operated at sufficiently high frequency (> 1 kHz), the electric permittivity becomes negligible and contact impedance caused by the development of a thin, highly resistive layer between the electrodes and the material is reduced. Typically, the operational frequency lies in the range of 10 to 150 kHz (Dyakowski et al., 2000; Mann et al., 1997), limited at the high frequency end by electromagnetic effects (Seleghim and Hervieu, 1998). Hence the resultant electric field is governed by

$$\nabla \cdot \sigma \nabla \Phi = 0 \quad (14.101)$$

14.4.6.4.3 Data Analysis

Analysis and application of tomographic data may be achieved by a number of means including direct analysis of the measurement information, which is particularly informative for transient features. Alternatively, reconstruction of image slices may be considered. Owing to the finite number of measurements taken and the soft field nature of ET, an infinite number of solutions exist, unless constraints are applied. Also, large changes in the sample property distribution affect only small changes in the boundary measurements (Cheney et al., 1999). Therefore, the reconstruction problem is ill posed, and by the nature of the governing equation it is also non-linear. Due to the ill posedness, the reconstruction is overly sensitive to measurement noise. A number of common reconstruction algorithms exist ranging from linear reconstruction to fully iterative linear reconstruction. Generally the iterative reconstruction is achieved by first predicting boundary measurements from a “candidate” distribution (George et al., 2000; Heikkinen et al., 2000). Comparison between the measurements and predictions indicates appropriate adjustment of the “candidate” distribution. Predicted (forward) boundary measurements from this “candidate” distribution may then be recalculated. Naturally, as the accuracy of these techniques increases, the need for computational resources also increases.

The iterative methods which provide some accounting for the nonlinearity, perform much better than linear methods, irrespective of their regularization. As noted by Peng et al. (2001), much of the error present in reconstruction is a result of the application of linear methods to a highly nonlinear problem.

To achieve sensible reconstruction with iterative techniques, regularization of error function minimization is required due to ill posedness. Commonly, Tikhonov regularization (Heikkinen et al., 2001b) is applied such that

$$\beta = \min_{\rho} \left\{ \|V - U(\rho)\|^2 + \alpha \|R\rho\|^2 \right\} \quad (14.102)$$

where R , U , V , α , and ρ are the regularization matrix, forward computed voltages, measured voltages, regularization parameter, and an appropriate property distribution, respectively. The regularization may be designed to minimize the total variation of the distribution or to reflect symmetry and so forth. Naturally, an alternative to the full image reconstruction is to apply known *a priori* knowledge and minimize a parametric description upon the measurement data. This approach is far less ill posed and more efficient, although a sufficiently accurate *a-priori* description is required, such that key features are not ignored.

Figures 14.74–14.76 illustrate the application of ECT and EIT. For Figure 14.74, the dielectric constant between a powder and a non-conducting dispersed fluid is sensed. The first real-time visualization of powder slugs in a pneumatic conveyor was achieved by Ostrowski et al. (1999), from which details on the geometric form and velocity of slugs and moving beds were obtained. More detailed studies have sought to elucidate the formation and transport properties of different slugging characteristics in horizontal and vertical pipes, as well as providing comprehensive information on the shapes of the slugs' nose and tail to interpret granular flow models (Jaworski and Dyakowski, 2002). Integration of solid concentration, at a point, can be used to estimate the mass flow. Such techniques can be used to monitor flow dynamics in fluidized beds, powder chutes, mixers, and conveying systems (Neuffer et al., 1999; Williams et al., 2000).

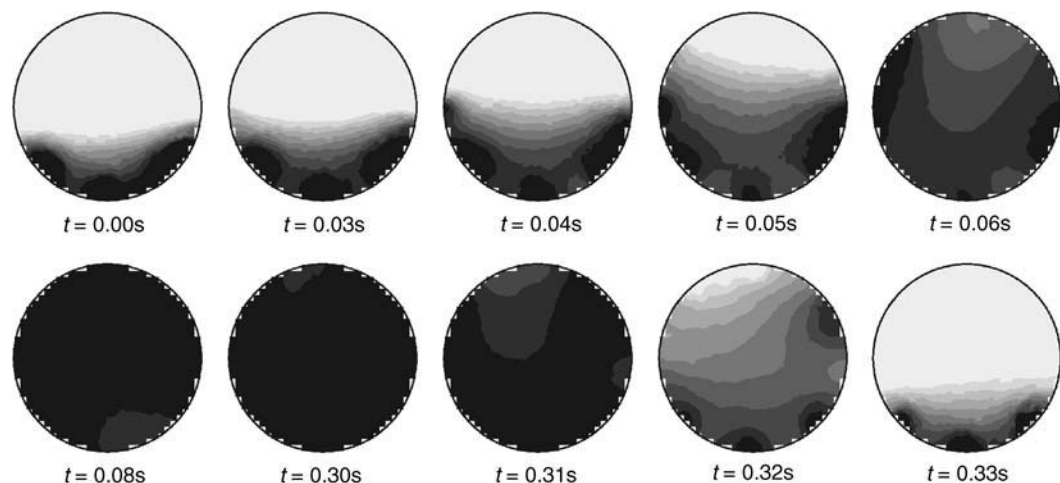


FIGURE 14.74 Real-time visualization of a granular flow in pneumatic conveying using ECT. Private communication from Dyakowski, T., UMIST, UK.

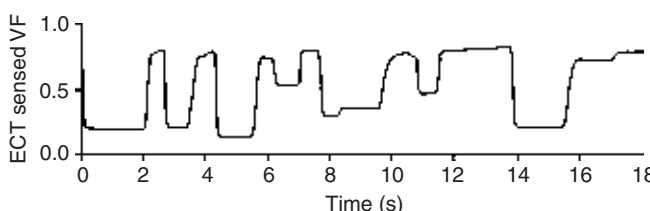


FIGURE 14.75 Example of measured relative volume fraction of solids across a single plane, during dense phase conveying (slugging). Reprinted from *Powder Technology*, 102(1), Ostrowski, K.L. et al., Real time visualization and analysis of dense phase powder conveying, Pages 1–13, Copyright (1999), with permission from Elsevier.)

[Figure 14.75](#) shows the ECT-sensed volume fraction by Ostrowski et al. (1999). Flow regime characterization via an on-line statistical analysis of fluctuations in the concentration can be undertaken in order to extract specific flow phenomena (e.g., swirling). At the microscale of inspection, the passage of discrete, micron-sized particles can be sensed using miniaturized wall-mounted dielectric sensors. The application of these sensors to determine particle velocities and the shape of individual particles has been reported (York et al., 2001). Meanwhile, Figure 14.76 shows EIT images of a hand being removed from brine-filled cylinder. It is clear from this figure that although a rudimentary reconstruction by modern day terms was applied, i.e., linear-back projection, excellent definition of the hand geometry was achieved.

In general, it is an excessive computational challenge for proper computational reconstruction of the flow field to be achieved. Therefore a number of simplifications are commonly made, such as two-dimensional electric fields and the use of piecewise constant distributions over each element of a reconstruction mesh or the use of parametric functions (George et al., 2000). Estimation of spatial accuracy is often made by means

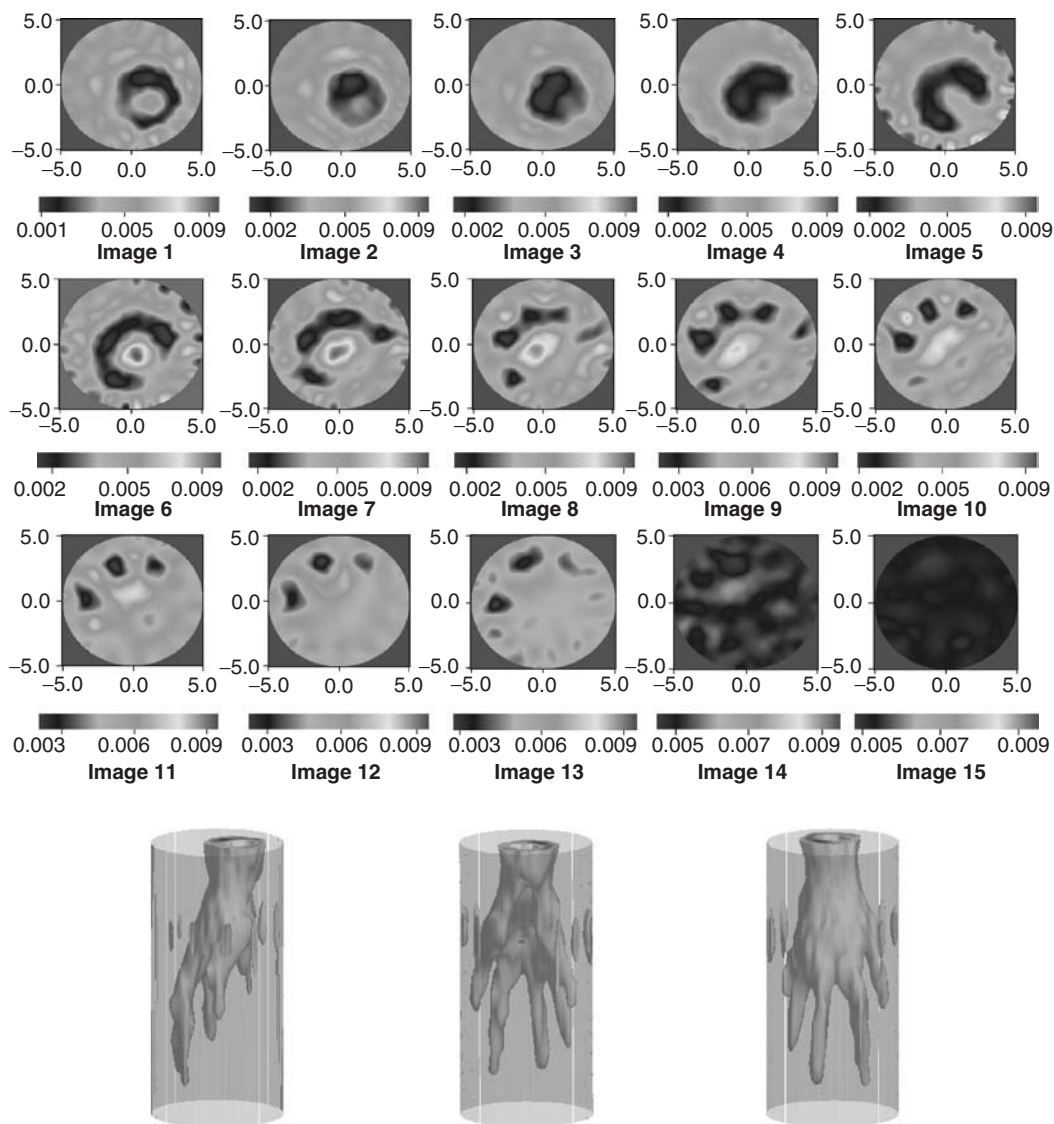


FIGURE 14.76 EIT images of hand being removed from brine-filled cylinder and reconstruction of the imaged hand geometry. Private communication from Wang, M., University of Leeds, UK.

of experiments involving phantoms, such as tubes, placed in the sample domain and a two-dimensional reconstruction algorithm. For example George et al. (2000) estimated, from simple phantom experiments, that the smallest object detectable and the positional uncertainty for the Sandia EIT system were of order 6 and 2% of the sample diameter respectively. The positional uncertainty dropped away rapidly with offset from the center and the volume fraction uncertainty was of order 0.004. Such an estimation of error is considerably subjective not only because of the use of clearly defined discrete phantoms, but also because of their shape. Phantoms of constant cross-section perpendicular to the measurement plane and extending effectively to far-field allow a far better reconstruction by two-dimensional techniques than fully three-dimensional phantoms, for which the electric field is also fully three-dimensional. Polydorides et al. (2001) have demonstrated this by showing that for fully three-dimensional phantoms, two-dimensional reconstruction techniques may perform satisfactorily for phantoms lying in the electrode plane; otherwise significant blurring and artifacts occur. Only by proper three-dimensional reconstruction can truly accurate tomograms be produced.

14.4.6.5 Ultrasound Tomography

Ellaborating on the application of ultrasound discussed earlier, ultrasound tomography finds particular application for the location of density gradients, i.e., phase interfaces. Transmission directly from emitter to detector indicates the non-existence of an interface along the path. Reflected pulses indicate the position of any interface by their time-of-flight and emitter or detector combination, . In general, the spatial accuracy of this mode of application is of order 3% of a sample diameter (Hoyle and Xu, 1995). The temporal resolution is considerably less than that of the electrical methods since the transmission velocity is approximately 1/2000 times of that of light. Further it is necessary for individual ultrasound pulses to be appropriately spaced such as to avoid interference effects from previous pulses.

Ultrasound diffraction becomes significant when ultrasound wavelengths are comparable with particulate dimensions. Instead of ultrasound source and detecting transducers about the periphery of the sample, a plane acoustic wave is applied, and a line of detectors measure the forward-scattered field. When diffraction is significant and the scattering is weak, the inverse problem can be solved such as by Fourier diffraction (Bronstein et al., 2002).

14.4.6.6 Tomographic Validation of Computational Fluid Dynamics

Tomography represents an excellent approach for the validation of CFD predictions and its development for this purpose is the subject of current research. Some of the applications of tomographic data are indicated in [Table 14.5](#) for the instance of EIT. The merits of these approaches for measurement of flow features are discussed in the following sections.

14.4.6.6.1 Tomogram Representation

Tomograms or image slices through the sample are a natural and intuitive means for examining tomographic data. Tomographic measurements are usually constrained to a small number of measurement points about the domain boundary such that detailed image reconstruction is ill posed. Therefore simplification of the image domain is required. The tomogram may be estimated as piecewise constant or linear over some mesh of the material cross-section or by means of parametric functions. Presented as images, such reconstruction permits simple examination by eye. These are also appealing for CFD verification since they provide a cross-sectional distribution, which may be compared with the appropriate slice through the CFD prediction. A further step of simplification is to use *a priori* knowledge of features and to construct their profiles. For example, a known feature may result in a large density, conductivity, or permittivity change. Such prior knowledge leads to a much improved reconstruction of features and reduces voxel smearing in their interface region. The rest of the tomogram may be discretised or treated parametrically as before.

14.4.6.6.2 Reconstruction of Media Interfaces

An example of a media interface is that of the air-core of a hydrocyclone, which forms an asymmetric tube about the axis of the high-swirl hydrocyclone device. This represents a water-air interface. A good technique for this is ultrasound reflective tomography (URT). Research at the University of Leeds by

TABLE 14.5 Application of Tomographic Data for EIT

Representation Format	Procedure
Pixelated Tomograms	<p>Forward problem solved by complete electrode model:</p> $\nabla \cdot (\sigma \nabla \Phi) = 0 \text{ in } \Omega$ $\Phi + z_l \sigma \frac{\partial \Phi}{\partial n} = V_l \quad \text{on } e_b \quad l = 1, 2, \dots, L$ $\int_{e_b} \sigma \frac{\partial \phi}{\partial n} dS = I_l \quad l = 1, 2, \dots, L$ $\sigma \frac{\partial \phi}{\partial n} = 0 \quad \text{on } \partial \Phi \setminus \cup_{l=1}^L e_l$ $\sum_{l=1}^L I_l = 0 \quad \sum_{l=1}^L V_l = 0$ <p>L electrodes e_b contact impedance z_l and outward normal n</p>
Parametric Tomograms	<p>Distribution throughout tomogram is parameterized for example as (West et al., 1999)</p> $\sigma(r) = a + b(3r - 2) + (10r^2 - 12r + 3)$
Feature Profiles	<p>Use of <i>a priori</i> known features aids reconstruction and reducing error. Known features can be extracted through correlation with tomograms. For example, the Hough transform may be applied</p>
Velocity Tomography	<p>Features passing through two closely spaced parallel planes will generate similar signals for each measurement set or tomogram. The cross-correlation function</p> $CC(t) = \frac{1}{T} \int_0^T f(t)g(t-\tau) dt$ <p>exhibits a maximum for greatest similarity of f and g thereby indicating the transit time. Location is available from the tomogram</p>
Transient Behavior	<p>Transients may be determined from tomogram representations or directly from the measurement signals</p>

Schlaberg et al. (2000) has demonstrated success in determining air-core size and shape from URT. The URT data were reconstructed by the Hough transform, where correlation was sought between a reconstructed tomogram and parameters of air core position and radius (assuming a circular cross-section). Although the reconstructed air core was a time-averaged representation due to data capture rate, validation of these reconstructions has been found from electrical resistance tomography (ERT) and x-ray transmission photography as reported by West et al. (2000) (see Figure 14.77).

As for the case of URT, reconstructed ET tomographs indicate the presence and proportions of the air core (Xie et al., 1995). The ill conditioning of ET and hence the required regularization mean that direct tomographic reconstructions of the air–core interface are significantly smeared (gradient penalization). Therefore, as for the case of URT, the use of prior information aids reconstruction of the air core to a great extent and identifies parameters, which are otherwise obscured by regularization. This and the increased accuracy of the overall reconstruction are well demonstrated by George et al. (2000). West et al. (2000) reconstructed the position and radius of the air–core as well as the remaining tomogram from ERT data by means of a parameterized air core and conductivity field as shown in Figure 14.77. The reconstructed air core is in good agreement with that of Schlaberg et al. (2000) mentioned earlier.

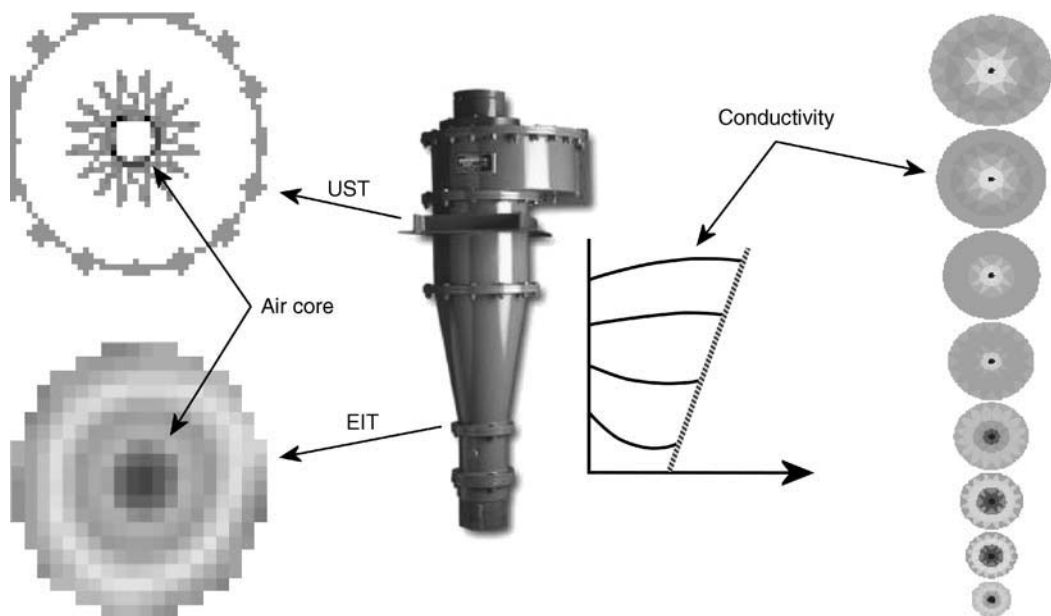


FIGURE 14.77 Reconstructed URT (simulated) and ERT tomograms of the hydrocyclone cross-section. Improvement in ERT reconstruction is evident after the parametric reconstruction of West et al. (2000).

Wang et al. (1995) extracted the air-core size and position from EIT data by determining μ and b for the relation

$$d_l \sim d_0 \left(\frac{Q_{\max,l}}{Q_{\max,0}} \right)^\mu \quad (14.103)$$

where

$$Q_{\max} = P_{\max} e^{-b(r/R)^2} \quad (14.104)$$

and P_{\max} , r , R , d_0 , and d_l are the maximum pixel intensity, radial position of P_{\max} , sample radius, radius of nonconductive phantom, and the air-core radius, respectively. Reconstructions of the air core of a Rushton-turbine mixing vessel were made to provide potential validation data for CFD simulations of a strongly swirling flow (Mann et al., 1997).

These are time-averaged measurements, hence x-ray techniques present an excellent choice for determination of the air-core's average shape, which should be comparable with that of URT. Successful capture of transient effects has been demonstrated with the ultrafast XTT system of Hori et al. (1998) for the tracking and measurement of gas bubbles in liquid (see also Hori, 2001; Misawa et al., 2001). Such transient tracking was only achieved at a lower spatial resolution, which leads to blurring of interfaces.

14.4.6.6.3 Reconstruction of the Solids Distribution

Through the strong density or attenuation correlation of x-rays, x-ray methods provide a relatively direct measure of the mixture density. XTT is a hard field technique, and it is therefore relatively simple to reconstruct tomograms accurately. Similar comments apply as for the determination of the air–core interface. High (μm) accuracy is obtained for time-averaged measurements. Temporal accuracy similar to that of ET is available at a spatial accuracy also of the order of that of ET. Notably the ultrafast XTT systems are in an early stage of development, so that considerable advances in performance may well occur in the near future. The very high spatial accuracy ($\sim 1 \mu\text{m}$) and true two-dimensional nature of SXTT may permit high-accuracy tomography suitable for verification of both ET and CFD.

PEPT and RPT measure residence time distributions within voxels through scintillation counts. Further, these particle-tracking approaches can provide a measure of the influence of fluid turbulence upon particles through the stochastic distribution of particle paths. These measures are particularly well suited to comparison with CFD Eulerian–Lagrangian predictions of the solids distribution, which is based upon predicted residence times for discrete voxels. PET provides a statistical measure of particle residence to a spatial accuracy limited to about 4 mm with present equipment. Again, long observation times are necessary such that time-averaged measurements are obtained.

Naturally, the main advantage of ET lies in the rate of data capture, which is equivalent to that of the high-speed XTT systems. Therefore, time-accurate solids distributions may be measured. Data conversion is required from ET-reconstructed conductivity or permittivity distributions to the solids concentration, for which the relations of Maxwell may be employed. For a continuous conducting fluid mixed with other nonconducting phases the Maxwell–Hewitt (George et al., 2000) relations may be used. In two dimensions the volume fraction is given by

$$\phi_1 = 1 - \frac{1 - [\sigma/\sigma_1]}{1 + [\sigma/\sigma_1]} \quad (14.105)$$

and in three dimensions by

$$\phi_1 = 1 - \frac{1 - [\sigma/\sigma_1]}{1 + \frac{1}{2}[\sigma/\sigma_1]} \quad (14.106)$$

where ϕ_1 , σ and σ_1 are the liquid volume fraction, mixture conductivity, and the liquid conductivity, respectively. George et al. (2000) demonstrated that for reasonably shaped nonconducting distinct regions the Maxwell–Hewitt relation slightly underestimates the conducting volume fraction. Figure 14.78 shows a swirl pipe to which an ERT system was applied. The pipe shape induces swirl within the flow and therefore maintains suspension of the material. ERT sensors were positioned at certain positions downstream from the exit of the swirl pipe section. The measured solids volume fraction is shown in Figure 14.79, demonstrating both the effect of the bulk velocity and the distance from the swirl pipe section upon the solids distribution.

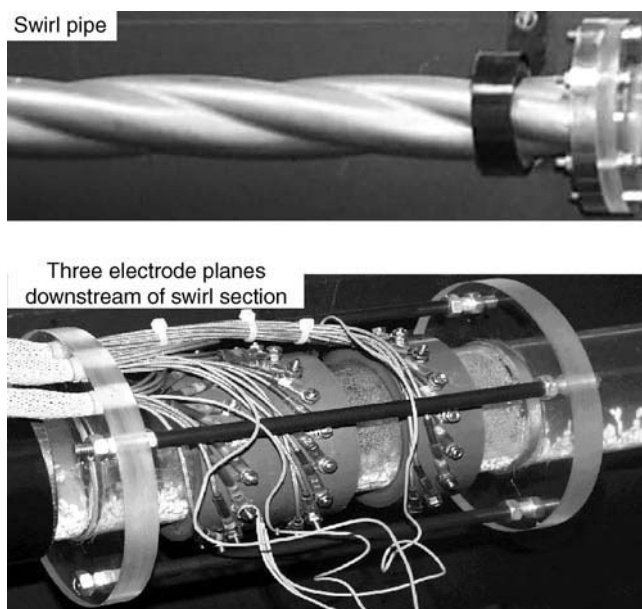


FIGURE 14.78 Swirl pipe geometry and ERT electrode planes downstream from swirl pipe section. Private communication from Wang, M., University of Leeds, UK.

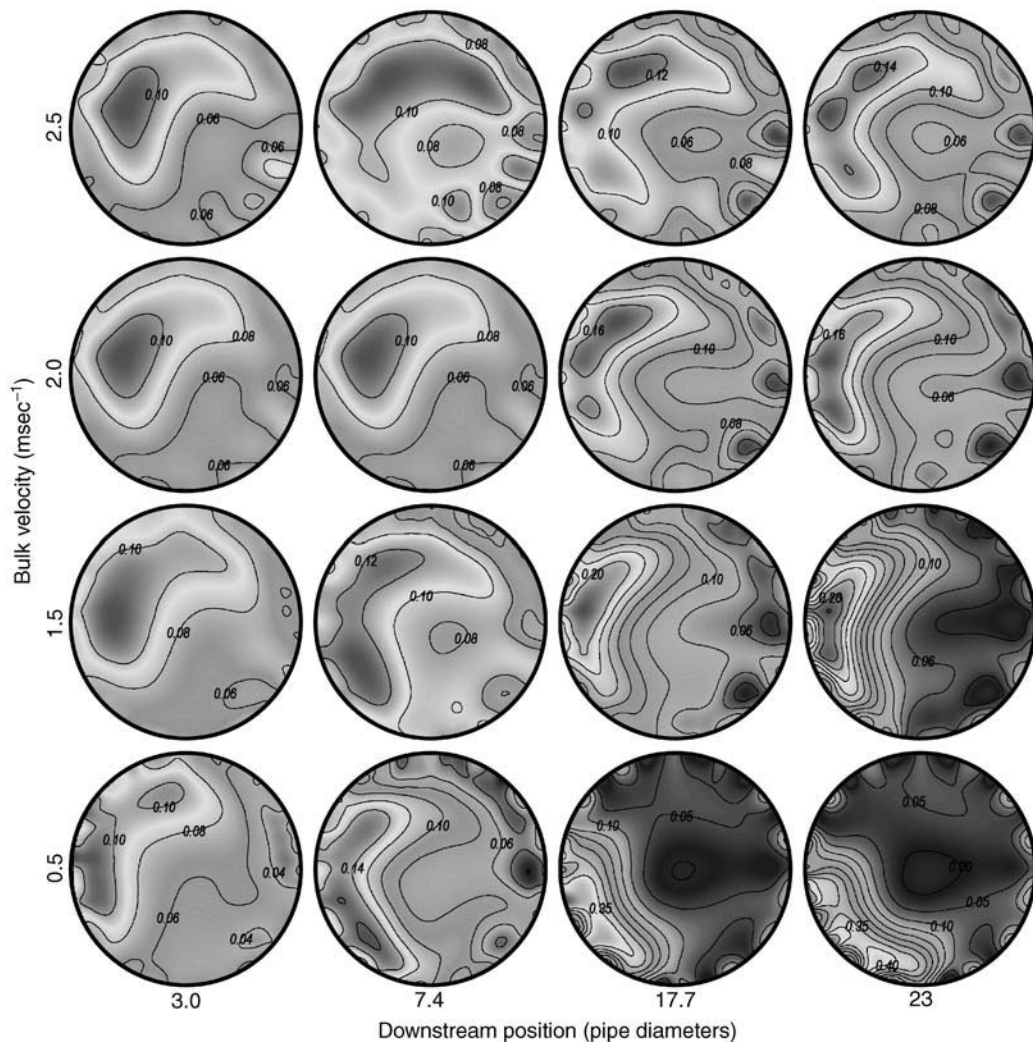


FIGURE 14.79 Reconstructed solids volume fraction downstream of the swirl pipe section at various positions and bulk velocities. Private communication from Wang, M., University of Leeds, UK.

Similarly, for relatively small spheres of constant diameter, uniformly distributed in a continuous fluid, Maxwell constructed (Dyakowski et al., 2000)

$$\varepsilon_m = \varepsilon_1 \frac{2\varepsilon_1 + \varepsilon_2 - 2\phi_{21}(\varepsilon_1 - \varepsilon_2)}{2\varepsilon_1 + \varepsilon_2 - \phi_{21}(\varepsilon_1 - \varepsilon_2)} \quad (14.107)$$

where ϕ_{21} , ε_p and ε_m are the volume fraction of material 2 in material 1, dielectric permittivity of material i and the mixture dielectric permittivity, respectively. This relation allows for reconstruction of the volume fraction from simple two-phase permittivity measurements, i.e., ECT. Naturally, for real slurries, calibration may be required between conductivity, or permittivity and the concentration.

14.4.6.6.4 Reconstruction of Velocity Profiles

Velocity profiles may be constructed from tomographic measurements by means of cross-correlation (Lucas, 1995). For example, the velocity profile in pipe flow may be measured by a dual-plane tomography system. A moving feature or observable disturbance such as suspended particles can then be observed

either in the tomogram or the measurement signal as it passes through each measurement plane. The separation distance between the planes is set small enough, such the mixture distribution does not change significantly during transit between the planes. Meanwhile, the separation is large enough that sufficient data frames may be captured during transit time τ such that this may be accurately determined. Application of the crosscorrelation function

$$CC(t) = \frac{1}{T} \int_0^T f(t)g(t - \tau) dt \quad (14.108)$$

implies the transit time (CC(t) is a maximum for $t = \tau$). Lucas et al. (1999) applied this for spherical plastic beads in a water pipe flow. They observed a good qualitative agreement for the measurements made with an intrusive conductivity probe.

Similarly, the autocorrelation function has been applied by Wang and Yin (2001), whereby a ring of tomogram pixel values were examined to determine the angular velocity distribution in a slow mixing vessel (see Figure 14.80). The autocorrelation function is given by

$$AC(t) = \frac{1}{T} \int_0^T f(t)g(t - \tau) dt \quad (14.109)$$

They determined that significant speed up in ERT data capture (from 50 ms per image) is required for accurate resolution of the angular velocity for fast mixing. They made observations for angular rotation of the order of 1/3 rev./min.

Complex flows of high velocity make resolution difficult and require very high frame capture rates. Notably, a 1000 fps EIT system is currently in the final stages of development. For example, for high-swirl flows the autocorrelation pixel ring approach of Wang and Yin is appropriate for determination of the tangential velocity. Crosscorrelation between axially spaced pixel rings may potentially provide the axial velocity. The determination of radial velocity might also be possible from dual planes through correlation or alternatively from a momentum balance. Given a complex flow structure, the cross-correlation of measurements is unlikely to be informative so that the correlation of pixel values is required. If features are frequently observed by cross-correlation, e.g. for vertical pneumatic transport of particles, crosscorrelation only returns a transit time and therefore a speed, not a velocity. For vertical pneumatic conveying, the cross-correlation features are the upward slug trains and raining particles between slug trains. Therefore, particle velocities exist in both directions. Jaworski and Dyakowski (2001) determined the velocity direction by crosscorrelation over small time periods that gave different peaks corresponding to each process.

14.4.6.6.5 Determination of Transient Features

ET techniques offer high temporal resolution, but the spatial accuracy and reconstruction issues complicate the observation of temporal processes. Observation of highly temporal processes may be to a great extent aided by the state-space representation, as outlined by Seppänen et al. (2001) (see also Kim et al., 2001).

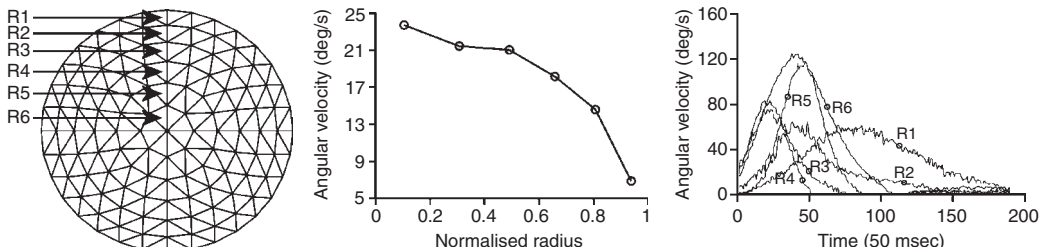


FIGURE 14.80 Determination of the angular velocity of a mixing vessel through the auto-correlation function. (From Wang and Yin, VCIPT, 2nd World Congress on Industrial Process Tomography, Aug. 29–31, Hanover, Germany, 2001, pp. 146–150. With permission.)

For example, a frame of ERT data is constructed using measurement sets for each current injection. For rapidly changing flows, significant changes in the material distribution occur between each measurement set of a frame. Seppänen et al., apply a Kalman smoother to the time-independent reconstruction and a convection-diffusion model for the conductivity. In this manner, the conductivity distribution may be constructed as a function of the present measurement set and the previous conductivity distributions. Such reconstructions demonstrate dramatic improvement in the resolution of rapidly moving objects. For example, Kim et al. (2001) could resolve the motion of a phantom, whereas significant artifacts occurred. This technique has also been applied to XTT giving similar enhancements.

The authors gratefully acknowledge the data contributions from Ashley Clarke, Rhozhou Hou, Lisa Mason, Malcolm Povey and Mi Wang of the University of Leeds, U.K., from Tom Dyakowski of the University of Manchester, U.K., from Micheal Mishchenko of NASA Goddard Institute for Space Studies and from Cordelia Selomulya of the University of New South Wales, Australia.

14.5 Bubbly Flow Measurements with Particle Image Velocimetry

Y.A. Hassan

14.5.1 Introduction

In the recent years, the range of problems tackled by experimentalists and theoreticians in fluid dynamics and particularly multiphase flow has grown considerably. Sophisticated flow facilities, instrumentations, and powerful computers are the basis for ambitious experiments. The measurement of single- and multiphase flows has continually generated innovative techniques varying from a simple Pitot tube to complex laser techniques. Laser Doppler anemometry (LDA) and particle image velocimetry (PIV) are now well-established techniques in the field of single-phase flow measurements. Some of the techniques, such as hot-wire and laser Doppler anemometry provide velocity measurements at a single point in the flow field. They are limited to a certain degree in providing simultaneous measurement of three velocity components. On the other hand, PIV is an optical measuring technique, belongs to the class of “full-field” measurement method, and provides velocity field in two or three dimensions.

Liquid-gas multiphase flows can be classified into various regimes as bubbly, stratified, slug, and annular flows. Bubbly flow regimes are widely found in many industrial systems and in the environment. One of the important aspects of bubbly gas-liquid two-phase flows is the interaction of gas bubbles with the turbulent flow fields. The bubbly flows are complex and are dominated by a rich variety of coherent structures and exhibit inherent unsteadiness. The performance of many engineering devices as well as natural processes encompass bubbly flow regime. An increased understanding of the fundamental phenomena, which derives the complex interactions between the bubbles and carrier flow as the transfer (local and global) of momentum, heat, and mass across the interfaces, is needed to ultimately improve the design of engineering devices in which these flows occur.

Recent developments in the computational fluid dynamics (CFD) techniques, such as direct numerical simulation (DNS), large eddy simulation (LES), lattice-Boltzmann (LB), two-fluid models, the volume-of-fluid (VOF) and level-set, and front-tracking methods, among others, have increased the understanding of the physical phenomena. These methods allow getting a deeper insight into the underlying physical mechanisms and thus fostering the understanding of gas-liquid two-phase flows. More accurate experimental validation and more detailed information on small-scale flow structure, even in ranges within micro- and nanoscales of time and length are needed. Experimental validation of these CFD models is a prerequisite for the widespread acceptance of CFD models as a reliable design tool in the engineering community and the development of more sophisticated models. Accurate assessment of the validity of CFD results in bubbly flows requires experimental techniques, which provide time-dependent and multidimensional information regarding the key hydrodynamics variables as velocities of both phases, void fraction, interface area, and its deformation.

Several imaging techniques have shown great potential in studying multiphase flows, such as noninvasive NMR imaging (MRI; Koptyug et al., 2000; Sederman et al., 2001), x-ray and neutron radiography (Seeger et al., 2003; Saito et al., 2004), ultrasound methods (Takeda, 1990), among others. The optical technique that has recently extended for two-phase measurements is PIV.

Recently, there has been a growing interest to develop microscale devices that manipulate and transport small volumes of fluids. These devices have applications in many areas of engineering, including propulsion and power generation of microsatellites, microair vehicles, inkjet printer heads, and bioanalytical instruments. The recent surge of microfluid devices has created a need for diagnostic tools with spatial resolution of the order of several microns. Diagnostic techniques to measure the performance of microscope flows in microfluidic devices are needed to probe the physics of transport processes at the microscale. One of these diagnostic techniques is microparticle image velocimetry (μ PIV), which was used in several experiments (Santiago et al., 1998; Meinhart et al., 1999).

In this section, we look at the specific aspects associated with applying PIV technique to bubbly flow measurements. The ability of PIV to yield full-field information has ensured its widespread applicability and indication of its usage, and development can be obtained from Adrian (1996). The accessibility of powerful computers, inexpensive laser, and the high-resolution cameras further revolutionized this tool for research.

The extension of PIV technique into a tool for three-dimensional flow field diagnostic is a useful approach, which includes stereoscopic imaging with two cameras scanned laser volume sheet to generate a volumetric picture of the particle tracer's dynamics. The PIV experiment must ensure that the particle tracers faithfully follow the fluid motion down to the fine flow structure to be resolved.

14.5.2 PIV Measurement Technique

PIV is a nonintrusive optical technique used for the study of, both single- and multiphase instantaneous flow fields. Images of small tracers freely flowing in the fluid under study are acquired at two or more times by pulsing some light source (Adrian, 1991; Raffel et al., 1998; Westerweel, 1993). The motion of these tracers is then a measure of the motion of the fluid, and, consequently, a whole flow field composed of many local velocities u , at different locations in the fluid, can be estimated from

$$u(x, t) = \frac{\Delta x(x, t)}{\Delta t} \quad (14.110)$$

where Δx is the marker position change in the time interval Δt .

The tracers used to follow the fluid motion can be solid particles, gas bubbles, liquid droplets, or patches of molecules, among others. The optimum size of the tracers is a compromise between the requirement that the particles follow the flow and the need for enough scattered light to create a particle image of sufficient quality. The images of these markers are acquired by photographic cameras or electronic cameras, and are recorded on photographic film, CCD, detector arrays, holographic plates, etc. A typical PIV experimental setup is shown in Figure 14.81. Depending on the mean number of concentration of scattering particles per unit volume, PIV is divided into two operational modes: high-image-density PIV mode for high concentration and particle tracking velocimetry (PTV) or low-image-density PIV mode for low concentration. Nowadays it is standard to refer to the high-image-density PIV mode simply as PIV. If the particle concentration is low, then it is easy to evaluate the displacement from individual tracer particles as illustrated in Figure 14.81. If the tracer concentration is increased, their particle displacement becomes larger than their spacing, and it is no longer easy to identify matching pairs. Each velocity in this case is obtained about the displacement of all the particles of an interrogation area. Thus, data from PTV are obtained with high local accuracy at the seeded point of the flow. Small-scale velocity variation and calculation of spatial derivatives can be performed with higher accuracy. Therefore, PTV can be used in boundary layer and near-wall turbulence studies.

When compared with other flow measurement techniques, PIV and PTV have the advantage of being nonintrusive and providing full-field information. Therefore, PIV is capable of producing instantaneous

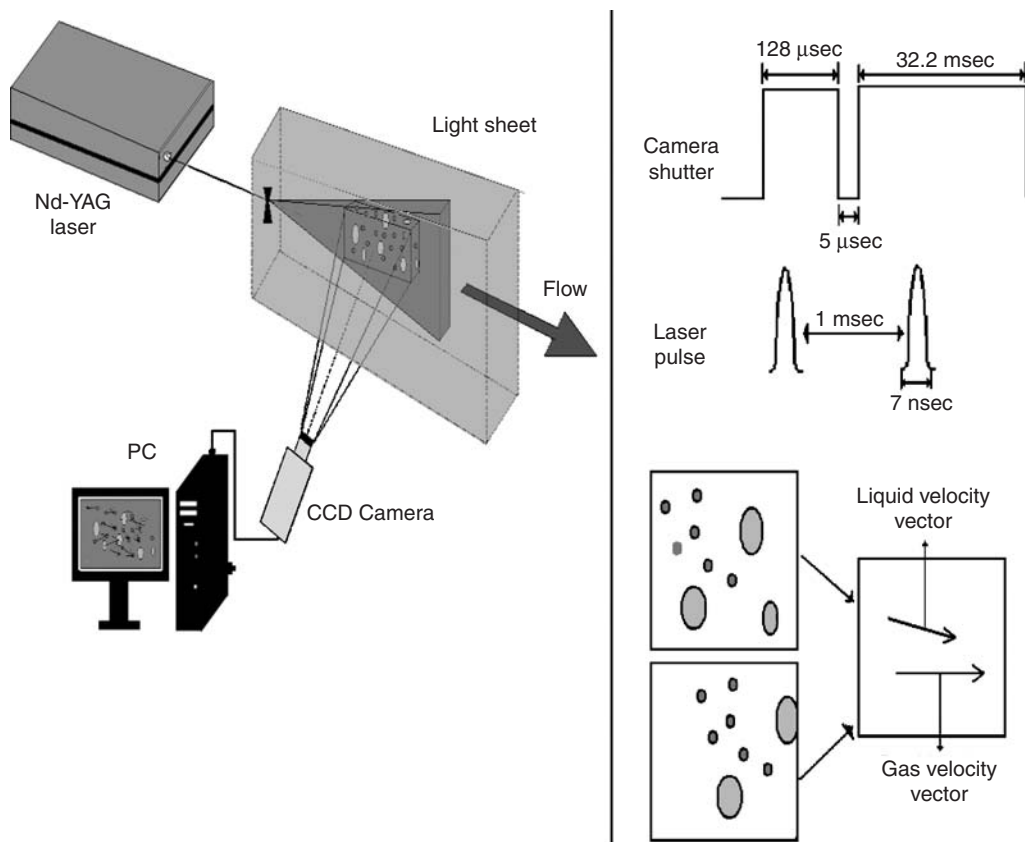


FIGURE 14.81 Typical PIV setup.

velocity maps. Hence, the spatial resolution of these techniques is high. The problem, then, is to track and extract the velocity information quickly and accurately from the pattern. Several tracking routines from statistical methods to advanced neural networks approaches are being developed. During the last two decades, the accuracy of the image analysis has increased remarkably. These tracking techniques are not unique to PIV analysis. Other disciplines such as military, medical, and transportation share the problem of estimating the motion of objects recorded in single image or sequence images. Point-measurement techniques such as laser-Doppler anemometry (LDA) and hot wire or hot film have temporal resolution superior to PIV and PTV. However, recently, PIV system that consists of high-speed cameras with $1k \times 1k$ pixels and 2 kHz in frame rate, high-repetition rate, and high-power double-pulse lasers is available (Ishikawa et al., 2004).

14.5.3 Simultaneous Full-Field Velocity Measurements of Bubbly-Liquid Phases

PIV technique has recently been extended to study two-phase flows if the component phases cannot be separated during the analysis (Hassan et al., 1992; Sridhar & Katz, 1995; Gui & Merzkirch, 1996; Ortiz-Villafuerte, 1999; Broder & Sommerfeld, 2002). Several methods that are capable of separating the images resulting from different phases have been reported. The use of fluorescent tracers in the continuous phase as particles seeds is one way of discriminating the phases. With the aid of optical filters, one may separate the radiation scattered by fluorescent and neutral particles. In this process, one camera captures both phases; the other camera is equipped with a filter of the same wavelength of the particle-scattered radiation. Thus, it only captures the seed particle images. Then, by subtracting the images of both cameras the

bubbles can be distinguishable (Philip et al., 1994). This method of distinguishing between phases also has the advantage that the camera equipped with the filter can identify the tracer particle images that overlap with the bubble images. Another method for phase discrimination considers the different image sizes or the gray levels of the seed particles and bubbles. The difference in size and optical characteristic between tracer seeds and bubbles facilitates the flow phase discrimination (Todd, 2002). This approach can be employed with or without applying the mask technique to a digital PIV record such that the images of particles that are either smaller or larger than a predetermined threshold value disappear from the image (Gui et al., 1996; Schmidl, 1999).

Generally, PIV bubble images show only fragments of the bubble, and not the whole two-dimensional projection shape. Sometimes, the bubble image shape even delineated a different shape from the natural bubble shape. This effect can be due to the change of scale as well as perspective distortion of the lens action, the lack of adequate illumination, or the intense laser light reflection from the bubble surface. A detailed information of bubble shape and size can be obtained through other visualization techniques. Shadowgraphy is a complementary technique that allows the determination of the shape of the bubble. This technique can reveal the full two-dimensional projection of the bubble shapes rising in a liquid. It consists of a background illumination of the flow to acquire the image of the bubble shadow from a camera placed opposite to the illumination. Therefore, a hybrid technique of PIV and pulsed shadow image technique (PSIT) is adopted to identify the bubble shapes and velocity vectors, simultaneously.

A hybrid PIV–PSIT technique is developed to obtain the velocity of the two-phase components, bubble shape, and the relations that are necessary to determine the nine-parameter ellipsoid shape of three-dimensional bubble data. This technique is suitable for analysis of two-phase bubbly flow with low-void fractions (Todd, 2002).

14.5.4 Applications

PIV measurement can be both two- or three-dimensional depending on the technique chosen. Two-dimensional velocity components can be obtained on a plane using one light sheet and one camera. Stereoscopic PIV gives three velocity components using a sheet or volume of light and two cameras.

14.5.4.1 Two-Dimensional Liquid Velocity Field and Three-Dimensional Bubble Tracking

One of the applications of the PIV technique is to obtain the velocity of the two-phase components, bubble shape, and the relations that are necessary to determine the nine-parameter ellipsoid shape of three-dimensional bubble data. This technique is suitable for analysis of two-phase bubbly flow with low-void fractions.

The experimental facility schematic for this measurement is illustrated in [Figure 14.82](#). The bubbly flow is generated in a sintered metal cylinder placed at the bottom of the glass pipe of an inner diameter of 5 cm. Connected to the pipe are the bubble generator, two pumps, and a reservoir tank. The main liquid flow enters above the bubble generator at the bottom end of the pipe. A secondary liquid flow is injected through the lower side of the bubble generator. This secondary flow is used to control the air bubble sizes. Air is injected into the air chamber surrounding the sintered metal tube. The main flow pump draws the water from the reservoir tank and passes it through a flow gauge and then into the center of the generator where the air passes through the sintered metal tube. The main flow pump draws water from the reservoir, passes it through a flow gauge, and then injects it below the test section.

A clear transparent plastic box encloses a portion of the pipe where the PIV measurement volume is located. This box is filled with mineral oil to reduce the pipe's refraction effects. The pipe is about 200 cm long and the test section is approximately at L/D of 30, where L is the length from the bottom of the pipe and D is the pipe diameter.

A twin ND:YAG high-energy (400 mJ) pulsed laser is used as illumination source. Typical high-energy optics is used to manipulate the laser beam and form the laser sheet necessary for PIV measurements. The synchronization signals originate from the cameras and are passed through a pulse generator and trigger the laser. The high-resolution 1000×1016 pixel CCD camera and associated frame grabber boards have

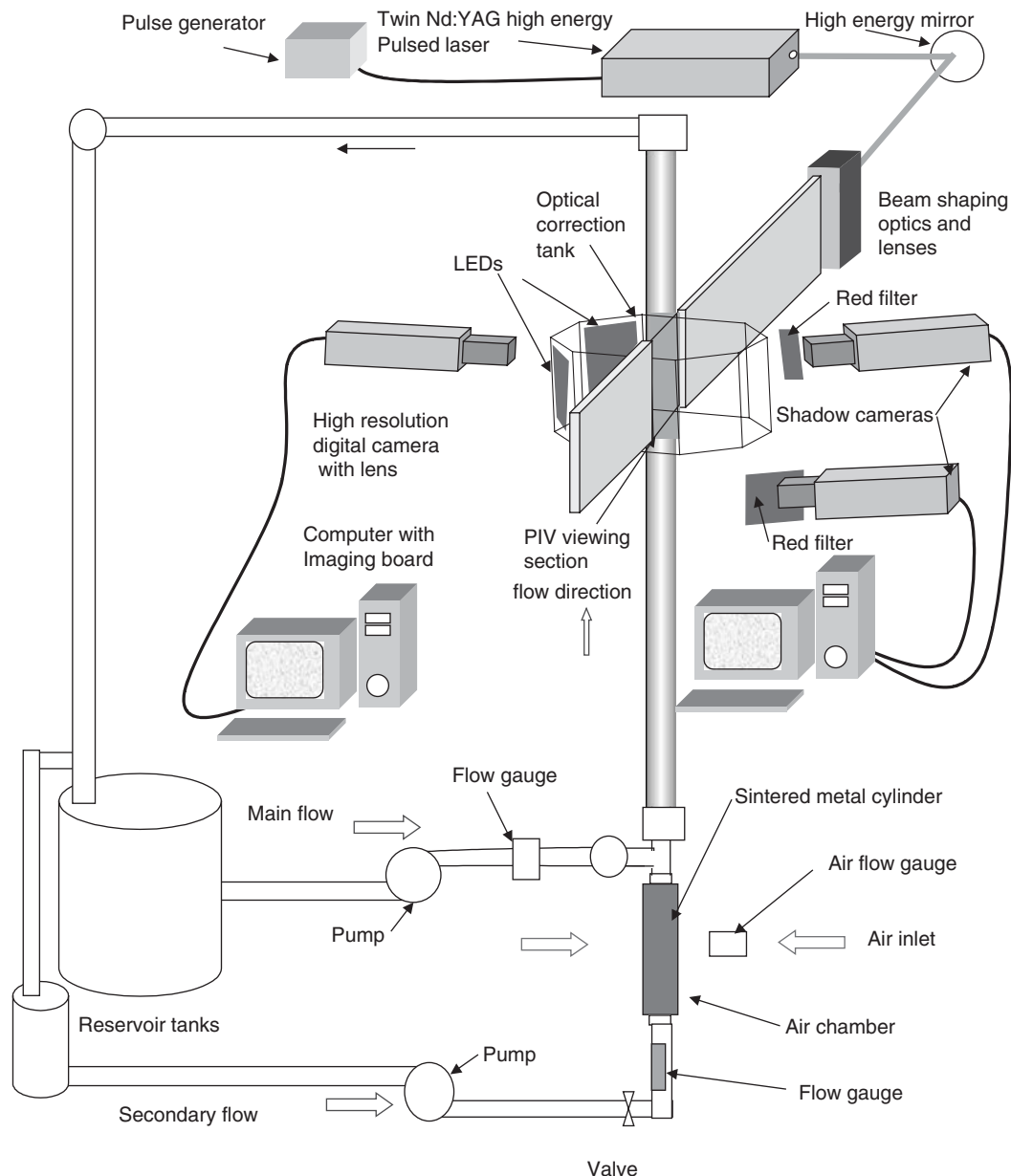


FIGURE 14.82 Experimental facility.

two modes of operation. The normal, continuous mode has 30 fps. The “triggered” mode enables the camera to capture two consecutive frames with a very small time delay controlled by the user. As the camera captures image frames, they are transferred to a personal computer for temporary storage in RAM. Each computer is capable of holding about 400 sequential images in RAM, resulting in 13.3 sec of continuous run time before the frame data being transmitted to a hard disk. Two other digital cameras are used for shadow image technique. The cameras are capable of capturing frames at 30 Hz with a resolution of 640 × 480. Illumination is supplied by red light-emitting diodes (LEDs), which oppose each of the cameras around the measurement volume. Each LED plate contains 70 individual LEDs and the associated electronic circuit. Diffusers are placed between the LEDs and the test section to obtain a uniform illumination.

The cameras are oriented with 640 pixels in the vertical direction, and they are located 300 mm from the center of the pipe. Red filters are attached to each camera to remove any reflected laser light. The arrangement of the cameras and LED plates is shown in Figure 14.83. From the images of the bubble in the cameras views the three-dimensional bubble shape and location can be determined.

A tracer size of 6 μm is suitable for this system. The tracer particles are neutrally buoyant and chemically compatible. A calibration grid was recorded prior to the experiments to determine the coordinate transfer functions between object coordinates and image coordinates. The images recorded are processed by thresholding process and centroid detection of each tracer image. PTV is used to determine the velocity vectors at certain instants. PTV is the preferred analysis method of the dilute phase (Blanchat, 1992; Hassan et al., 1992). A new gray-scale cross-correlation PTV algorithm is developed for this study to provide the flexibility and robustness needed to analyze bubbly flows with densely seeded frames (Todd, 2002). This technique calculates the cross-correlations for tracer pairings between two frames. The tracer link with maximum correlation is selected as an appropriate matching. To check the algorithm, a comparison between the tracer displacements in axial and radial components with a median filter is performed. In case the components of the displacements fall inside the prescribed range of the filter, the candidate link is survived. Spurious links are removed drastically using this methodology. More details of the algorithm can be obtained from Todd (2002).

The timing sequence for acquisition system components is of great importance for the overall system performance. The delay time between PIV frame acquisitions should be short enough to sample the rapidly moving tracers over a short displacement. Also the shadow image velocimetry (SIV) acquisitions should be coincident with PIV acquisitions in order to facilitate the data analysis. Figure 14.84 presents the system-timing diagram. The delay time between PIV frames has been realized through the use of the twin-laser configuration of the PIV illumination source. The shutter of the PIV camera has been locked in the open position and all ambient light has been minimized to prevent extraneous CCD exposure. As a result, the laser light can expose the CCD at any time except during a brief period of unavailability as the camera transfers data to the PC. Since each laser, labeled A and B, is capable of 30 Hz, and the camera is only capable of 30 Hz, every other laser pulse from each laser is eliminated by a flop-flop circuit to reduce each pulse rate to 15 Hz. Referring to Figure 14.84, the delay time between two PIV frames can be adjusted by modifying the time, t_1 , between the triggering of lasers A and B, where t_2 is 33.33 msec. The time, t_1 , can be varied from 1.5 to 33.33 msec and represents the delay between frames in the first-step in

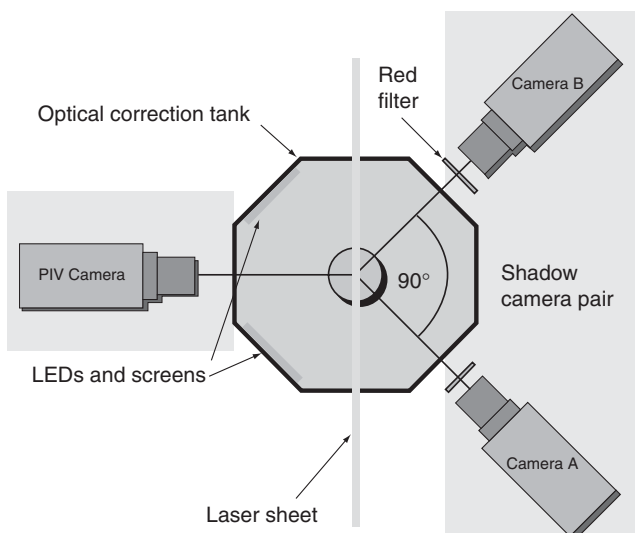


FIGURE 14.83 Measurement system layout.

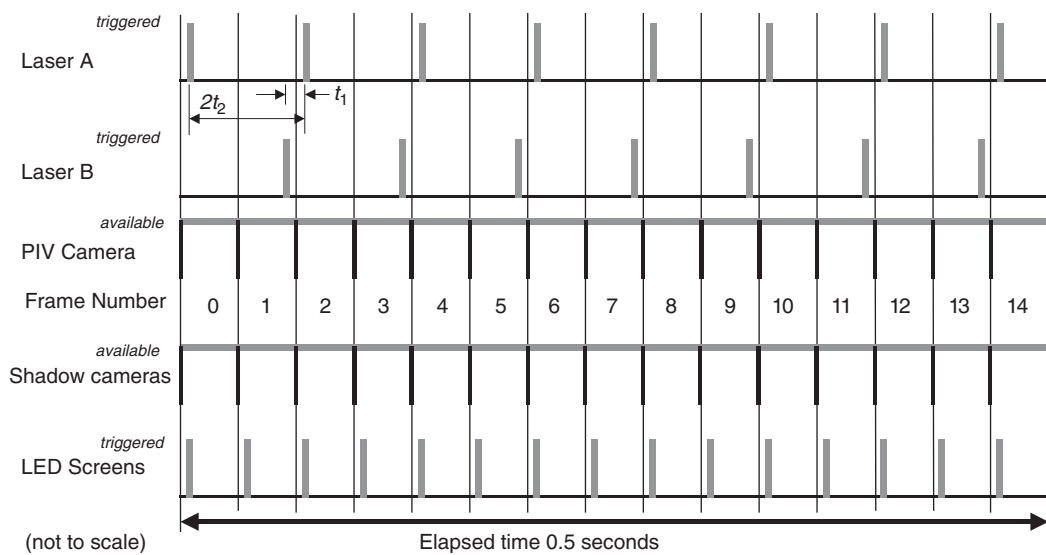


FIGURE 14.84 Acquisition system timing diagram.

a two-step analysis; however, t_2 is a fixed value. This means the timing of the second step in a two-step PIV analysis is fixed, reducing the flexibility of this feature.

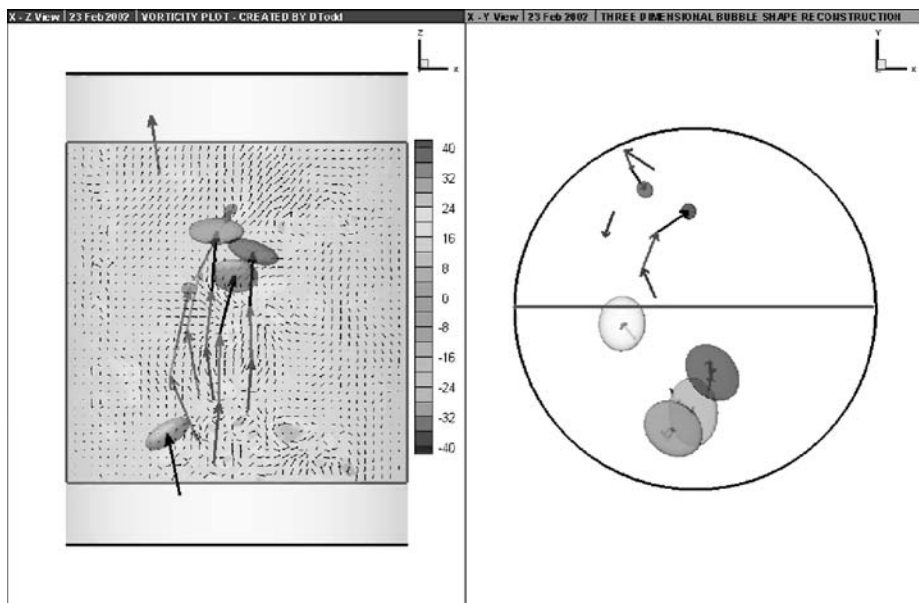
The SIV cameras are operated in the same mode as the PIV camera with the shutters locked in the open position. The LED circuits are triggered by a synchronizing signal from the pulse generator. The shadow image velocimetry (SIV) and PIV frames are coincident only on even-numbered frames.

The three-dimensional feature of every bubble in each frame of the SIV measurement volume is necessary in order to characterize the behavior of the bubbles in time. A first-order approximation of these features can be achieved through a four-parameter fit of each bubble image using a sphere, where the four parameters include the location in three dimensions (x_0, y_0, z_0) and the radius of the sphere r . However, the first-order approximation does not provide enough accuracy for bubble shapes. Typically, the bubbles can take on an oblate ellipsoidal shape, where the axis oriented in the general direction of the bubble motion is shorter than the two axes which are generally of horizontal orientation and of approximately equal length. As a second-order approximation, in this investigation, the bubble images are fitted with a nine-parameter (9-P) ellipsoid. The nine parameters account for eccentricities in the shape of the bubbles, and include the three-dimensional location (x_0, y_0, z_0), the axis half-lengths (a, b, c), and three rotation angles ($\theta_x, \theta_y, \theta_z$).

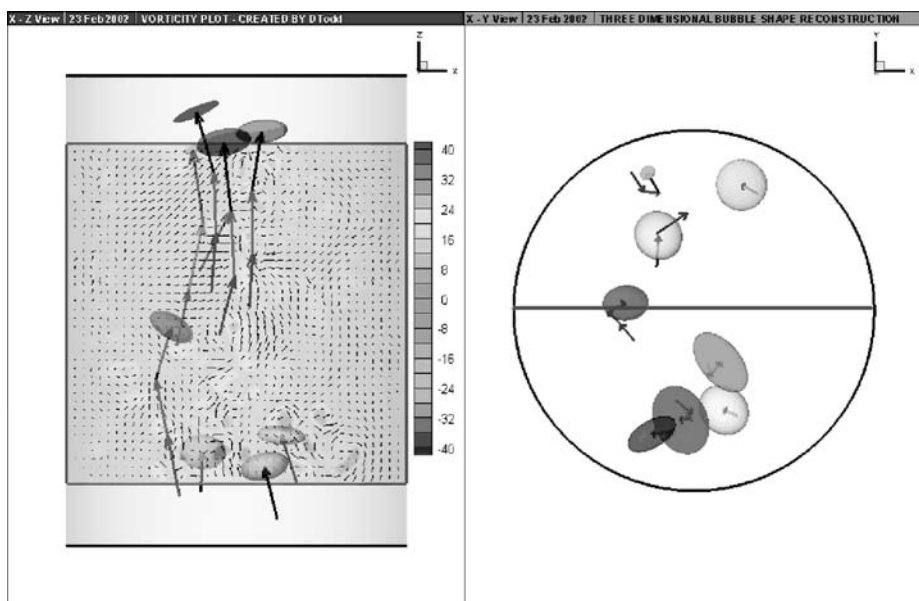
A procedure is developed to analyze each SIV frame in an automated fashion to fit a 9-P ellipsoid to the orthogonal bubble images captured in the SIV frame. The procedure has been designed to minimize the amount of required user interaction, which is very important in light of the amount of data that must be analyzed.

Once the bubbles reconstructed, they are then tracked as they traverse through the measurement volume. The details of the shape reconstruction algorithm can be obtained from Todd (2002). An example of the reconstructed ellipsoids at two snapshots at different time is plotted in Figure 14.85. The velocity vectors for the bubbles are included in the figure. The stray vectors shown in the figure represent bubbles that have already left the measurement region. The two-dimensional PIV velocity field is added to the three-dimensional bubble velocity vectors. In this experiment, the streamwise (u') and the normal (v') velocity components are measured. Therefore, the spanwise component of the vorticity is obtained. The z -vorticity component is calculated from

$$\omega_z = \left(\frac{\partial u'}{\partial y} - \frac{\partial v'}{\partial x} \right) \quad (14.111)$$



(a) time = t1



(b) time = t1 + 33.33 ms

FIGURE 14.85 (Color insert follows page 13-40) Snapshots of interactions of the bubbles with the flow at two instants.

To calculate velocity derivatives, central-difference scheme was applied to PIV velocity results. The spanwise vorticity ω_z are also presented. Figure 14.85 also gives the perspective of looking down the pipe with bubbles rising toward the observer. The bubble centroid velocity vectors delineated in the figure indicate the zigzag and rocking motions of the bubbles. The calculated spanwise vorticity are also delineated. For instance, the vortical structure embedded within the flow due to the passage of bubbles is observed. It is noted that the bubble interaction can take place by drafting, kissing, and tumbling, where a bubble is

drawn into the wake of a bubble in front. Similar behavior is also obtained by direct numerical simulation (Esmaeeli et al., 1998). It is interesting to note that at the injection location, the bubbles are uniformly distributed. At the measurement zone, the flow pattern is irregular and nonuniformly distributed. There are regions with relatively high bubble concentrations and other regions are free of bubbles. It is noted that deformable bubbles have tendency to align vertically, while pairs of spherical bubbles tend to align horizontally.

14.5.4.2 Three-Dimensional Liquid Velocity Field by Stereo PIV

Two-phase flow phenomena is inherently three-dimensional, thus investigations of this type of flow has to simultaneously determine the three velocity components. The extension of PIV to perform three-dimensional measurements has been successfully achieved by acquiring images from at least two cameras with different view angles. Then a stereo pair matching method can be performed to determine the three-dimensional position of a fluid particle in the viewing volume under study (see, e.g., Kasagi and Nishino 1991; Hinsch, 1995; Prasad and Adrian 1993; Costes et al., 1994; Hassan et al., 1998; Ortiz-Villafuerte et al., 2001a; Willert 1997). Here also each phase can be separated by considering the size of the images of the seed tracer and the bubbles or solid particles in the flow. Other technique is to employ fluorescent markers and special filters. One camera captures both phases and the other with the filter captures only the fluorescent seed images (Philip et al., 1994). Transient information is also attainable since a series of pictures of the same area under study at many time steps can be taken.

Measurements performed with automated digital PIV are limited on the temporal aspect by the storage capability of the imaging boards, RAM, and hard drive of the computers. The spatial aspect is limited by the resolution, pixel size, and array format of the CCD cameras. These two limitations, however, are being overcome with the use of new technologies.

During the past decade, the PIV technology has been extended toward stereo systems, which allow measuring the out-of-plane velocity component together with the two components in the plane of the laser light sheet. Stereo PIV systems use two cameras that record the two-dimensional in-plane particle image patterns under different viewing directions. Currently, the angular displacement system is the standard configuration of the two cameras, and fulfilling the Scheimflug condition ensures that all particle images are focused.

A schematic example of the experimental setup and the camera configuration is shown in Figure 14.86. Air bubbles of about 3 mm spherical-equivalent diameter were injected into a 12.7-mm I.D., 15.9-mm

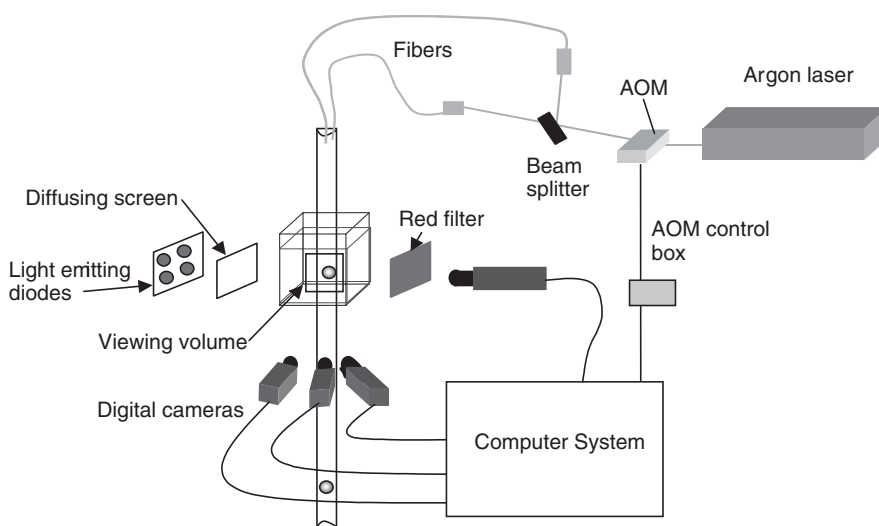


FIGURE 14.86 Facility setup and camera configuration.

O.D., 1.3-m-long Plexiglas pipe. The flow was seeded with small polystyrene tracer particles. The density of these particles was 1.05 g/cm^3 . The measurements were carried out at a location of about $L/D = 66$, where L is the length from pipe inlet to measurement zone and D is the inner diameter of the pipe. A water filter removed all contaminants larger than $5 \mu\text{m}$ prior to the addition of the tracer particles. Enclosing the test section in a rectangular Plexiglas box filled with water reduced the pipe curvature effect. The Plexiglas box has the same refractive index as that of the pipe; in addition, refraction effects were included in the calibration parameters (Ortiz-Villafuerte, 1999).

The optical elements of the setup included an argon-ion laser, an acoustic optic modulator (AOM), a beam splitter, mirrors, and a multimode fiber with a fiber coupler. The light source of 514 nm frequency was selected for illumination. This frequency corresponds to green light. The laser beam passed through the AOM, which chopped the continuous laser light at intervals of 16.67 msec. Then the light was directed to a beam splitter, which divided the beam into two parts. Each part was directed to a separate fiber coupler. The light beam was transmitted to the viewing volume through two 400- μm I.D. multimode fibers. These two fibers were placed at the top of the tube to illuminate the viewing volume with cones of light. Four CCD cameras were utilized in this experimental investigation. As shown in [Figure 14.86](#), one of the cameras was only used for bubble shape analysis.

Several optical elements as light intensifiers were attached to the CCD cameras to improve the accuracy of the measurements. The CCD cameras have a resolution of 640×480 pixels, when run in the RS-170 frame interlace mode at 30 fps. The cameras were run in field mode to take advantage of the higher framing rate (60 fps), thereby allowing for the study of higher velocity flows.

One option of the calibration is to be conducted under the same conditions in which the actual experiment would be carried out (Tsao et al., 1995; Hassan et al., 1998; Ortiz-Villafuerte et al., 2001a). In this case, a calibration setup is placed exactly on the same position where the actual experimental setup would be located. Therefore the refraction effects are included into the transformation coefficients. The image coordinates and their corresponding world-point coordinates are obtained by constructing a calibration grid. This grid is moved all around the measurement volume and its image is acquired at each different position, and world coordinates of the calibration points are recorded. Clearly, hundreds of pairs of image and world coordinates can be acquired.

Once all the calibration images are acquired, they are fed into a computer program that determines the centroid of the calibration spots. Our program is called FINDSPOTS, and it is written in FORTRAN 77 (Blanchat, 1992). The program computes the spot centroid to subpixel accuracy, by calculating the area of the spots that surpass a predetermined gray-level threshold. The output of the program is the coordinates of the centroid of the calibration points, which along with their corresponding world coordinates provide the necessary information to compute the transformation coefficients.

14.5.5 Velocity Components Determination

Different tracking methods may be used to process the data. These include techniques such as cross-correlation (Hassan et al., 1992; Yamamoto et al., 1995), particle tracking velocimetry (Nishino et al., 1989; Malik et al., 1993; Wernet and Pline, 1993; Yamamoto et al., 2002), and Spring Model (Okamoto et al., 1995). New algorithms based on pattern recognition, neural networks (NN), genetic algorithms (GA), and fuzzy logic (FL) techniques, seem to have good potential for particle tracking. There are different kinds of NN used in PIV. Grant and Pan (1995) used a Kohonen NN, while Hassan and Philip (1997) used an ART-2 NN technique. FL techniques have been employed by Wernet (1993) and Shen et al. (2001).

For three-dimensional measurements at least two cameras are needed. Then a particle or vector-matching process is required. The possibility of mismatching particles, and thus obtaining erroneous vectors, is reduced by matching two-dimensional vectors instead of single particles. It also reduces computing time. For this case, any of the tracking techniques mentioned above can be employed for particle tracking between consecutive images. This, in fact, can be used as a first filter to avoid erroneous velocity vectors.

An example of the application of the methodology, a bubble dynamics study was performed. The three-dimensional velocity fields around the rising bubble were determined with the PTV technique.

Figure 14.87 represents the liquid velocity vectors when a bubble is present within the viewing zone. The detailed experimental conditions, setup, and uncertainty analysis can be found in Ortiz-Villafuerte (1999).

Figure 14.88 represents the results of the vorticity ω_y on the X-Z plane, position $y = 0$ at $t = 33.3$ msec after the bubble has entered the viewing volume. The plot of the vorticity on the X-Y plane, position

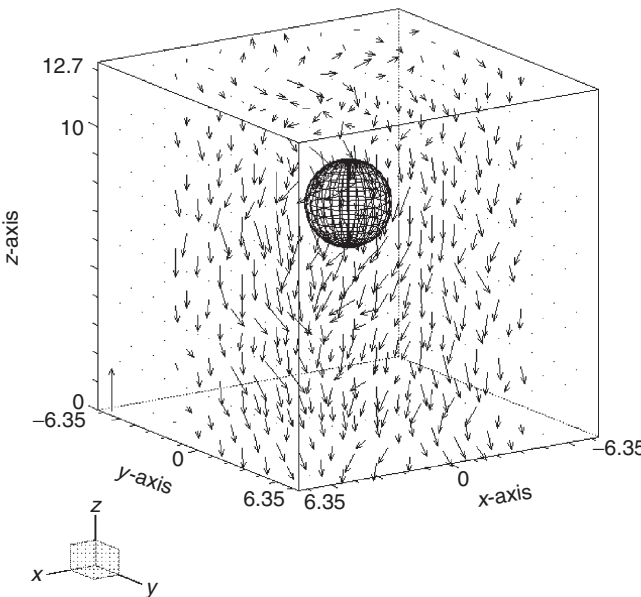


FIGURE 14.87 Interpolated velocity field, when the bubble has been present in the viewing volume.

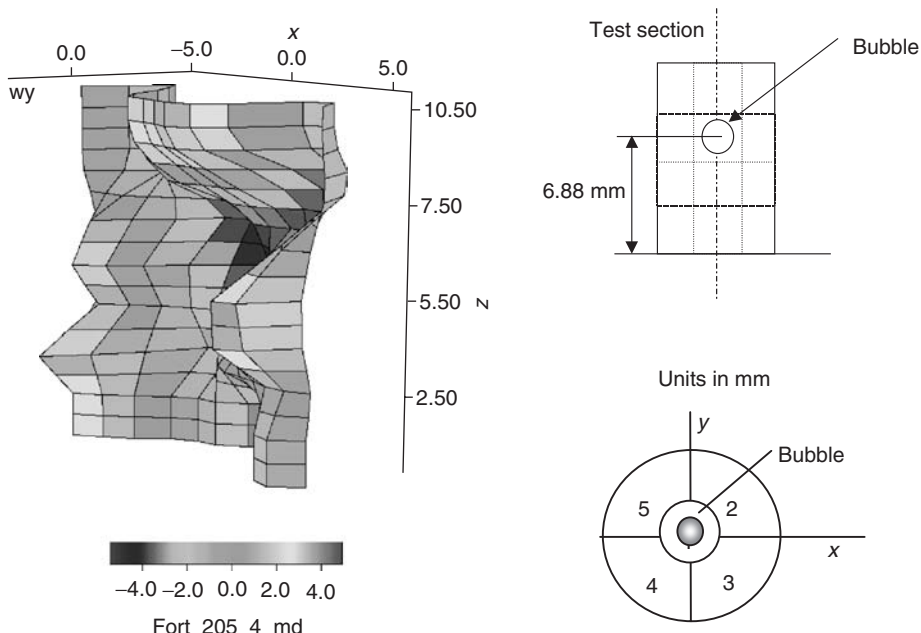


FIGURE 14.88 (Color insert follows page 13-40) Surface plot of fluid vorticity component ω_y on X-Z plane, position $y = 0$, at $t = 33.3$ msec after the bubble has entered the viewing volume.

$z = 6.72$, ω_z at $t = 33.3$ msec after the bubble has entered the viewing volume is shown in Figure 14.89. It is interesting to note the complex structure of the flow around the bubble and its influence on the liquid. Large values of positive and negative vorticities are delineated. Figure 14.90 shows three different Z planes of the z -component of the vorticity vector, 16.6 msec after the bubble has departed from the viewing volume. The Z -axis of the figure has been scaled by a factor of 2, in order to make the contours on the slices easier to view. The bubble motion is from right to left in the figure. Just behind the bubble the vorticity ω_z displays two regions of opposite sign vorticity. The positive values range from 5 to 7 Hz and the negative vorticity from 5 to 8 Hz. The following two slices display regions of similar characteristics. These vorticity structures extend all along the viewing volume, in the Z direction, as can be seen on the three planes in Figure 14.90. Observe that the strength and size of these high vorticity regions decrease as they travel downstream. Four pathlines have also been included in the figure to indicate the path of the fluid near the regions of vorticity.

14.5.6 Bubble Shape Detection

To measure the bubble's shape, the PIV system was supplemented with the SIV, which is a red shadow image technique. The shadow is produced by the reflected red light rays from light emitting diodes (LEDs), located opposite to the SIV digital camera, as shown in Figure 14.86. The light intensity from the LEDs is low when compared to the laser light. A red filter was placed in front of the shadow camera lens to only capture the bubble shadow. This high-pass filter blocked the intense green light reflected by the bubbles. In conjunction with PIV, the measurement technique employed herein is a hybrid technique to identify the bubble shape and the velocity fields of the liquid and the bubble. For such cases, it is clear that a reconstruction process is necessary. Even when the two-dimensional shape is well defined, parameters such as orientation and dimensions still need to be determined.

The shape of an object boundary contains important information. For example, shapes of an air bubble reflect the dynamic interactions between the bubble and its surrounding environment. Therefore it is important to obtain the instantaneous bubble shapes in addition to the flow field around the bubbles.

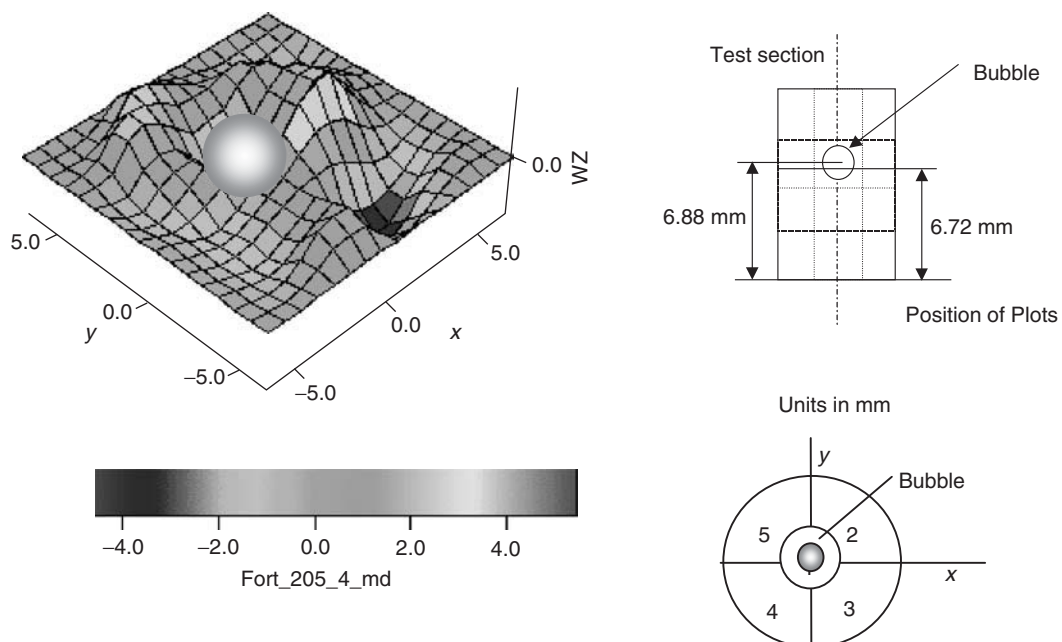


FIGURE 14.89 (Color insert follows page 13-40) Surface plot of liquid vorticity component ω_z on X - Y plane, position $z = 6.72$, at $t = 33.3$ msec after the bubble has entered the viewing volume.

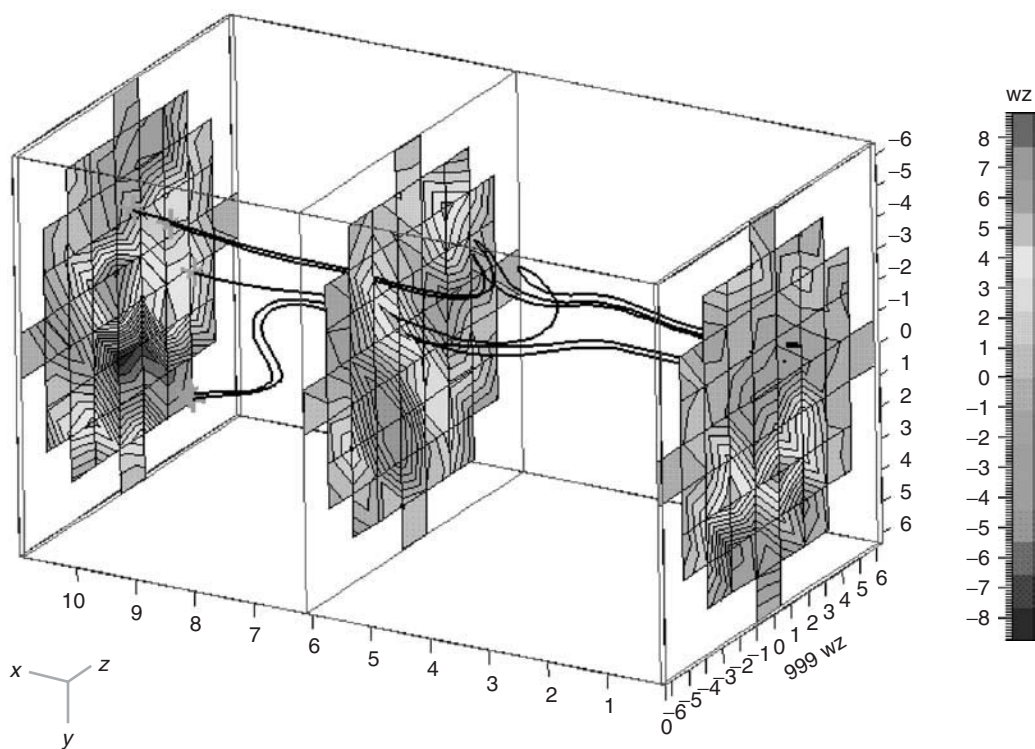


FIGURE 14.90 (Color insert follows page 13-40) ω_z vorticity contours on Z-plane slices 16.6 msec after the bubble has departed from the viewing volume.

Several methods exist to identify and reconstruct object shapes. The following section is a brief of several approaches.

14.5.6.1 Dynamic Generalized Hough Transform Algorithm

The shape identification and reconstruction techniques range from simply matching the image to a geometrical curve or surface, to the use of parametric curves or surfaces (as an example, Bezier and spline curves), and to the mapping of the original shape into a parametric space (such as the Hough transform). Two-dimensional image reconstruction process has been developed to determine both bubble shapes and dimensions. This reconstruction method is based on the dynamic generalized Hough transform (DGHT) algorithm, which is presented in detail by Leavers (1992). The DGHT algorithm is particularly useful when the object to be recognized and reconstructed is symmetric (e.g., circles, ellipses, etc.). A three-dimensional reconstruction can be achieved by combining two or more images obtained from cameras at different view angles.

The DGHT can be used to compute all the parameters associated with the curve. In bubbly flow regime, the DGHT algorithm for detection of the ellipsoidal shape is applied, since it was already assumed that the bubble would have an ellipsoidal shape. For an ellipse, the DGHT will determine the coordinates of the center point, the angle of rotation, and the value of the two semiaxes. Further, this algorithm can be used when occlusion of objects appears on the image. For distorted images of the bubble, the DGHT algorithm can be used to reconstruct first a two-dimensional shape, and then, through stereo matching with images from other cameras, the three-dimensional shape of the bubble can be refined. Once the parameters of the ellipse are known from the hybrid approach of the PIV and the shadow images, it is necessary to compute these parameters in world coordinates. Observe that the world coordinates can be easily calculated in this case, because the PIV center and the Shadow cameras were parallel to the XZ and YZ planes, respectively. After combining the parameters of ellipses from each view, a three-dimensional

reconstruction was achieved. In the analysis the equation for an ellipse can be written as (Hassan et al., 1998)

$$x^2 + y^2 - A(x^2 - y^2) - 2Bxy - Cx - Dy - E = 0 \quad (14.112)$$

By randomly choosing five of the connectivity points, one can solve for A , B , C , D , and E , by utilizing, for example, Gauss elimination with backpropagation. After each iteration, the ellipse parameters are estimated.

A three-dimensional reconstruction of the bubble shape and motion is included in Figure 14.91. It is interesting note the zigzag pattern and the angle of the bubble axis rotation. The maximum error associated with the reconstruction algorithm was less than 3 pixels (0.08 mm). This maximum error is for the PIV image in the X direction. For the localization of the centroid of the ellipse the error is smaller, but was assumed as 3 pixels in the error analysis. Thus, this error value is associated with each of the semi-axes a , b , and c , and also for the centroid of the bubbles.

14.5.6.2 Bubble Reconstruction with Metaball Model

Unlike conventional inverse problem-solving methods, the metaball method searches the optimal description of a bubble distribution in a hypothetical space (Fleming, 1999; Furukawa, 2002; Furukawa et al., 2002). The fundamental strategy of reconstruction is searching, instead of processing bubble phantoms obtained from shadowgraph images. Therefore, each bubble phantom in an image does not need to be separated from one another. A bubble is described as set of metaballs that has relatively small number

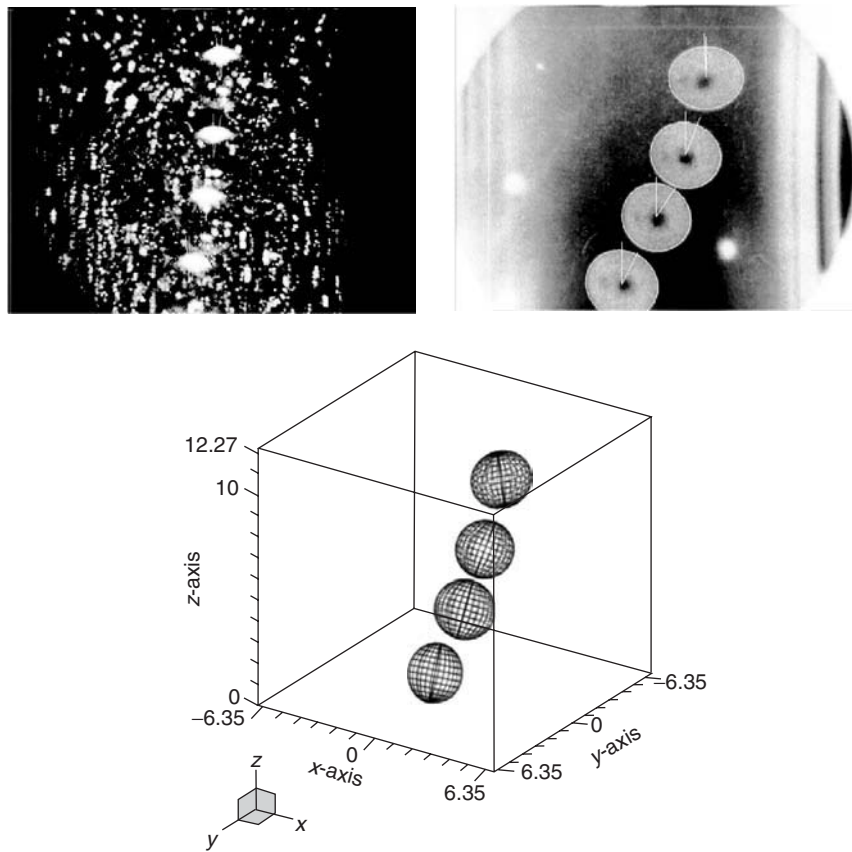


FIGURE 14.91 Example of 3-D bubble trajectory using DGHT algorithm.

of parameters and still represents several objects with curved surfaces. Metaballs are able to describe any shape in principle. Thus, bubbles are not assumed to be in a certain shape as sphere or ellipsoid. The method has been applied to synthetic images and real experimental images. In this model a metaball object M is described as

$$M = (s_1, s_2, \dots, s_n) \quad (14.113)$$

and

$$s_i = (x_p, y_p, z_p, r_p, r_i) \quad (14.114)$$

where s_i is a spherical element, whose center is located at (x_p, y_p, z_p) in a three-dimensional space, r_i the radius, and n the number of spherical elements in the metaball object. Each spherical element s_i creates a density field. The density at (x_p, y_p, z_p) created by s_i is calculated by

$$d_i(x, y, z) = \begin{cases} (1 - (l/2r_i)^2)^2, & r < l_i \\ 0, & r \geq l_i \end{cases} \quad (14.115)$$

$$l_i = \sqrt{(x - x_i)^2 + (y - y_i)^2 + (z - z_i)^2} \quad (14.116)$$

The whole density field created by all spherical elements in a metaball object is given by

$$D(x, y, z) = \sum_{i=1}^n d_i(x, y, z) \quad (14.117)$$

The resulting object appears as solid at any point satisfying $D(x, y, z) > t$, where t is a threshold. In the proposed method, t is fixed to be 0.54119. The threshold is chosen because a metaball object consisting of a single spherical element (x, y, z, r) with this threshold of 0.54119 appears as a single sphere with radius r . This is intuitive to the developers and the users. Figure 14.92 demonstrates metaball creation in a two-dimensional situation: element distribution, density distribution, threshold density, and resulting object. If two or more spherical elements are located in close neighborhood, they appear as a single object touching each other.

The reconstruction process is based on the application of the dynamic programming. It searches the optimal metaball object that generates simulated shadow images, which should be identical to the original shadow images. Dynamic programming is a method to search an optimal combination. It divides a large problem into small problems, solves each of the smaller problems, and builds up the smaller solutions together (Sniedovich, 1991).

The advantage of dynamic programming is that it only requires searching the best combination in a small hypothetical space at once. The searching algorithm travels through a number of small hypothetical spaces, rather than one single huge space, because the problem is divided into small portions so that each small problem is independent. Therefore, the final solution is built in certain order.

In the proposed method, the metaball object with multiple spherical elements represents the solution. The solution can be divided into a set of spherical elements, which are classified by their radii. The set of elements with the largest radius is obtained first, then that with the second largest radius, and so on.

The proposed method procedure is illustrated in Figure 14.93. The user inputs are the geometric information of cameras and the largest possible bubble radius. The initial guess of bubble consists of a metaball object with one single spherical element at arbitrary point. The sphere's radius is the largest possible size.

The simulated shadow images are created as if the flow has the guessed bubble distribution. The bubble distribution, a set of spherical elements, is translated into a scene description. Then a ray-tracing software generates the shadow images based on the scene description and camera information. Details and more examples can be found in Furukawa (2002).

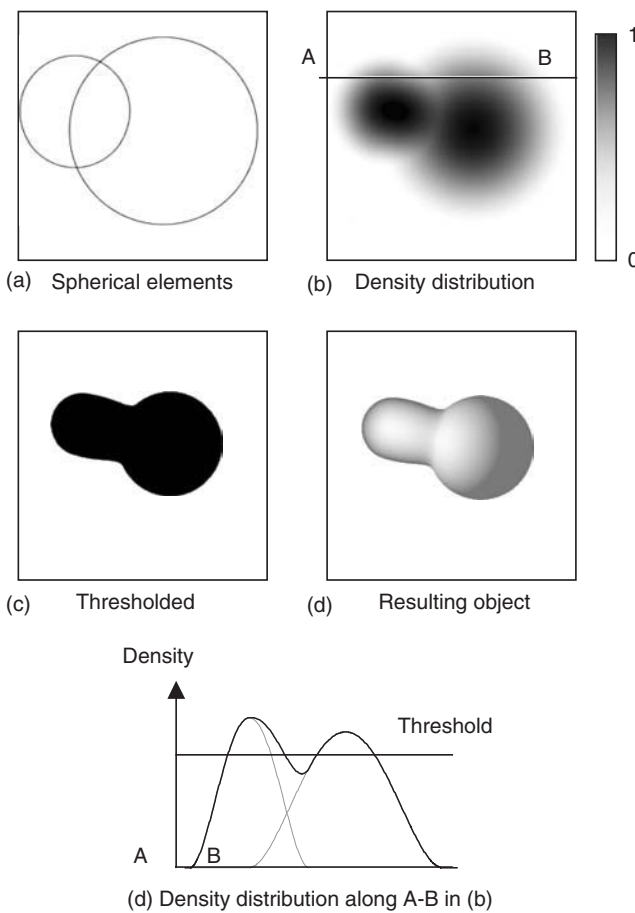


FIGURE 14.92 Metaball example.

Figure 14.94 shows an example of synthetic and reconstructed bubble distribution and projected shadow images: (1) five synthetic bubbles; (2) the shadow images of the bubbles observed at $x-z$ and $y-z$ plane; (3) the bubbles reconstructed by the proposed method; and (4) the shadow images of the reconstructed result. One cannot easily tell that five bubbles exist from (2), because each shadow image has only four obvious phantoms. The method does not need to identify each bubble phantom, thus the five bubbles are correctly reconstructed in (3). The shadow images are almost identical in (2) and (4). This is achieved due to the flexibility of the metaball method to represent the bubble shapes. The void fractions of the gas can be calculated from the reconstructed images.

14.5.6.3 Traveling Salesman Algorithm and Solution Technique

The feasibility of applying the Traveling Salesman Problem (TSP) technique was studied to extract the bubble profiles from two orthogonal planar views as obtained from the shadow images. The TSP is found to give a closed contour of the route that is taken by a salesman traveling among predesignated coordinates (on a map) called cities. An analogy was observed between the points on edges of the threshold image of the bubbles and the cities on the tour contour of the TSP. This analogy paved the way for the use of TSP to extract the bubble profiles from the two planar views. The most important part of the TSP is the solution. The self-organizing maps approach discussed by Kohonen (1982a, 1982b, 1991,) was tested and a neural net was built to test this method. Another powerful method known as the simulated annealing (SA) technique was used to solve the TSP (Skiscim et al., 1983; Lin, 1965; Junger et al., 1994).

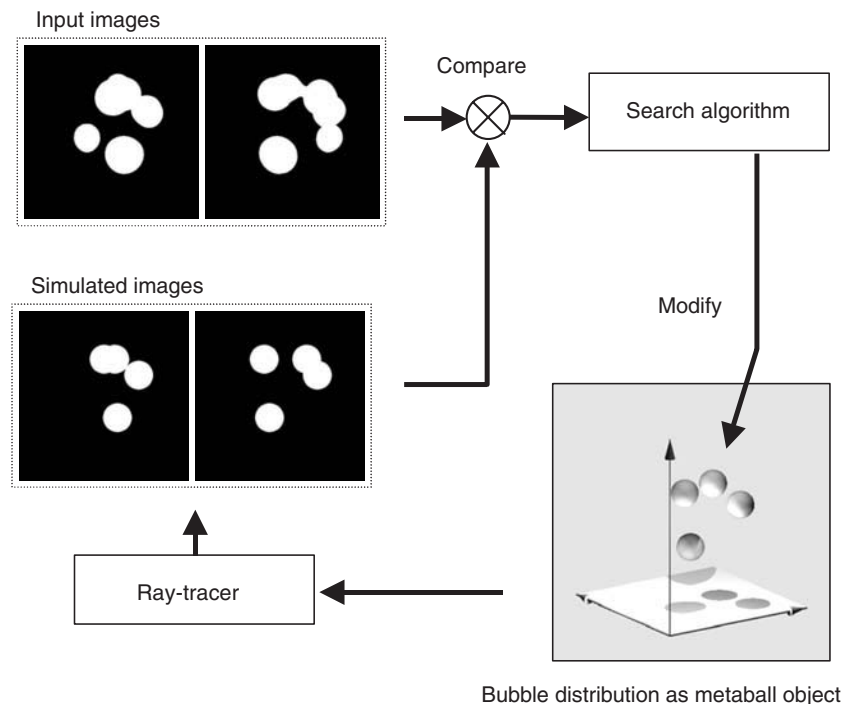


FIGURE 14.93 Searching procedure.

NURB (nonlinear rational B-splines)-based CAD was employed for three-dimensional reconstructions (Zhang et al., 2000).

An experimental image pair for low Reynolds number bubbly flow consisting of about 34 bubbles was reconstructed, and the three dimensional results are shown in Figure 14.95. SIV images used to extract the bubble profiles for reconstruction are also included in the figure.

14.5.7 Conclusion

The capability of the PIV technique to perform measurements in bubbly two-phase flows is demonstrated. Results demonstrate the capability of the hybrid technique of PIV in conjunction with SIV to obtain the velocity fields and the bubble shapes. This scheme is a powerful tool to provide some understanding of the complex physical phenomena of bubbly flows. A key advantage of this scheme is the ability to provide data of simultaneous velocities of the phases, in addition to the surface areas of the bubbles. These data are needed to verify and validate the CFD models.

14.6 Detection and Measurement of Aerosols

C.S. Claiborn

14.6.1 Characteristics That Are Measured

An aerosol is a mixture of particles that can be solid, liquid, or a combination of phases, dispersed in a gas. In the atmosphere, aerosol particles exist in a variety of sizes, shapes, phases, chemical compositions, and they can originate from numerous sources. They may be formed through a variety of processes or produced in the atmosphere through chemical reactions. The need to measure aerosols stems from pollution control needs of industries, from source apportionment needs of environmental regulatory

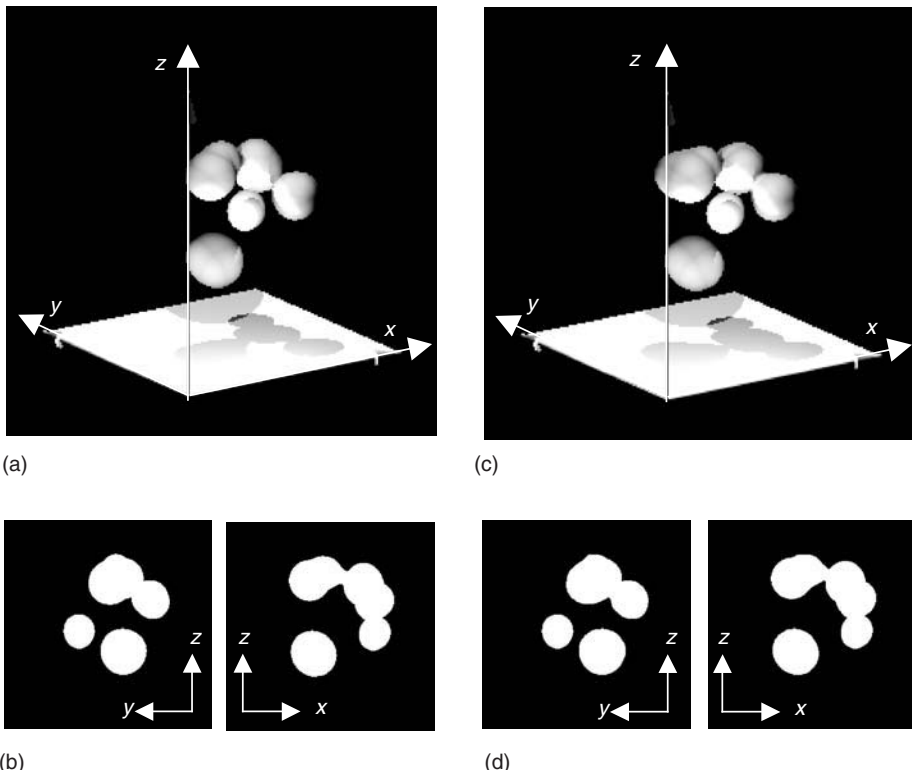


FIGURE 14.94 An example of original and reconstructed distribution and projections: (a) synthetic bubble distribution; (b) input shadow images; (c) reconstructed bubble distribution; (d) shadow images generated from reconstructed bubbles.

agencies, and from health implications of interest to medical personnel. Characteristics of interest include measures of particle number, size and size distribution, shape, surface area, mass, chemical composition, and optical properties. In environmental settings, aerosols are seldom found in a pure, monodisperse form; rather, aerosols are typically composed of particles of varying sizes, shapes, and chemical constituents. Particulate chemical components of interest in the atmosphere include ions (sulfate, nitrate, and ammonium), acidity, elemental carbon (EC), organic carbon (OC), transition metals, crustal elements, or specific toxic elements or organic compounds. Still other properties of interest may include bioaerosol components or particle size change with changes in relative humidity. In the remainder of this chapter, the measurements of these characteristics are reviewed. Here, aerosol refers to the mixture of particles and gas, and particulate matter refers to the particles themselves.

14.6.1.1 Size Distributions

Aerosol particles typically vary in aerodynamic diameter from less than 10^{-2} to $10^2 \mu\text{m}$. Particles larger than approximately $1 \mu\text{m}$, called “coarse particles,” are usually formed from mechanical processes, such as tires traveling on roads, grinding processes, etc. Particles smaller than $0.01 \mu\text{m}$ are formed via homogeneous condensation of vapors (such as hot combustion gases or other low-volatile vapors), and are referred to as “condensation nuclei.” These nucleation mode particles quickly grow to larger particles with diameters in the range of 0.01 to $0.1 \mu\text{m}$ (this range is called the Aitken mode). In between the Aitken and coarse modes — i.e., between 0.1 and $1 \mu\text{m}$, is the range referred to as the “accumulation mode” — particles in the atmosphere that grow through coagulation of smaller particles (Seinfeld and Pandis, 1998) or by condensation (of low-vapor pressure gas molecules onto the particle). The nucleation, Aitken, and accumulation mode particles collectively comprise “fine particles” in the atmosphere, and are primarily

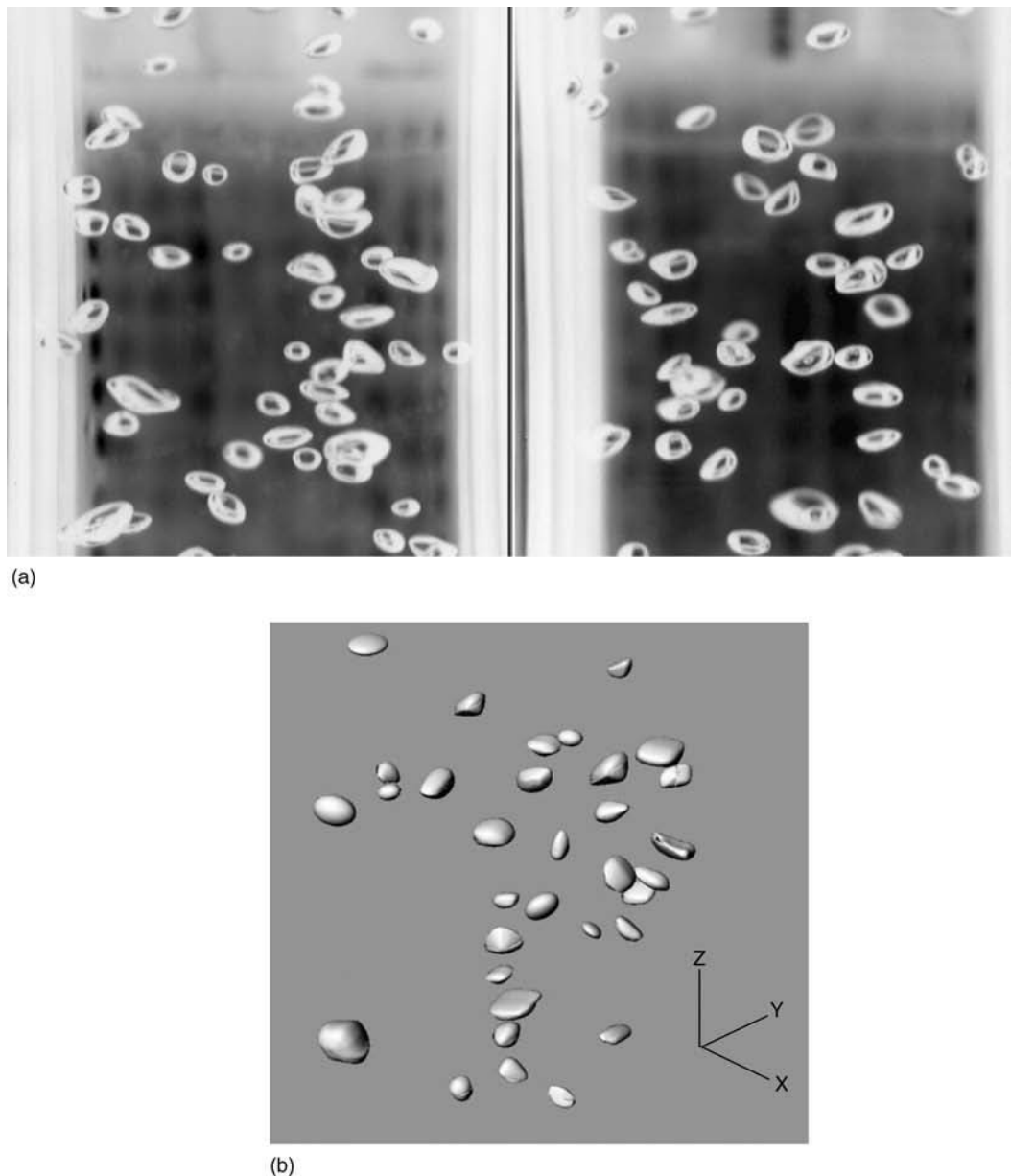


FIGURE 14.95 Three-dimension of reconstructed bubbles using two shadow images: (a) front view and side views (inverted); (b) 3-D reconstruction.

formed from combustion or from gases reacting and condensing. In urban aerosols, the size distribution based upon particle number concentrations is dominated by condensation nuclei, while the surface area distribution is typically dominated by the accumulation mode particles (Seinfeld and Pandis, 1998).

14.6.1.2 Chemical Characteristics and Phases

Particles can exist in solid phase, liquid phase, or a combination of phases. Water is an important constituent of atmospheric aerosol that also confounds its measurement. Other important constituents of atmospheric particles include crustal materials, combustion products, acid aerosols, salts, mineral fibers

(e.g., asbestos), carbonaceous material, including soot and OC, biogenic matter, and metals. The organic fraction of atmospheric aerosols can include hundreds, even thousands, of organic compounds, the majority of which have not been identified to date. Some of these compounds are semivolatile organic compounds that partition between the vapor and particulate phases at ambient conditions.

Fine particles typically have chemical compositions that include EC, OC, sulfate, nitrate, hydrogen, and ammonium ions, or metals. The OC constituent may be primary (i.e., emitted directly into the atmosphere) or secondary (i.e., formed in the atmosphere through chemical reaction) in nature. Coarse particles, on the other hand, tend to comprise crustal minerals and organic matter.

14.6.1.3 Other Characteristics

Surface area and shape factors are important particulate characteristics that contribute to the optical characteristics of the aerosol. These may also have health implications; for example, asbestos particles that cause asbestosis have a distinct fiber shape.

Measurement of atmospheric aerosol requires sampling for size selectivity, followed either by collection for bulk analysis or detection in real time. In the following sections, size-selective sampling methods are first discussed. Then, bulk sampling techniques are presented, and finally, various dynamic detection methods are discussed.

14.6.2 Sampling for Size Selectivity

Particle size is often characterized by “equivalent diameter,” according to the property of interest. In air pollution regulation and control, settling and deposition characteristics are of interest, and so ambient particle size is often presented in terms of “aerodynamic diameter” (AD) or the diameter of a sphere, with a specific gravity of 1.0, that has the same gravitational settling velocity as that of the particle in question. Typically, size-selective sampling refers to sampling particles within or below a specified aerodynamic size range. In the United States, it is usual to specify size fractions by the 50% cut point size. For example, PM_{2.5} would refer to the particulate matter collected with a sampler that collects particles with a 2.5 μm AD with 50% collection efficiency. Typically, size selectivity can be achieved using inertial or centrifugal separation.

14.6.2.1 Inertial Separation via Impaction

Inertial separation takes advantage of the fact that larger particles with a given velocity will have more inertia than smaller particles, so that in an abrupt change of direction, the larger particles will leave the gas streamlines. By accelerating the flow through a jet toward an impaction surface, the larger particles can subsequently be captured by impaction, where the particle’s center of gravity comes into contact with the obstacle in the gas stream (such as a filter, liquid droplet, or impaction plate), or by interception, where the particle’s center of gravity does not interact with the obstacle, but the particle is intercepted by the obstacle, due to its finite size. Small particles may also be captured by Brownian diffusion to the surface of the obstacle. The impactor specifications include the gas velocity through the jet as well as the dimension of the gap between the jet and the impaction plate. Once large particles have been captured on the impaction surface, particle bounce and reentrainment may be minimized by coating the impactor surface with a silicon-based grease or oil (Chow, 1995).

For bulk sampling of particles in several size ranges, a cascade impactor is often used, in which several impactors are arranged in series, in order of decreasing cut point diameter. The cut point diameter for each stage is again determined by the nozzle diameter and the gap between the nozzle and the impaction plate. There are numerous cascade impactors that are commercially available (e.g., Hering, 1995; Marple et al., 1993). Usually, these samplers range in numbers of stages from 5 to 12, and some of the smallest 50% cut point diameters may be 0.06 μm (e.g., MOUDI samplers, MSP Corporation, Minneapolis).

14.6.2.2 Virtual impaction

Virtual impaction operates in a similar manner, with the impaction surface being replaced by an opening through which a small portion of the air sample is directed. In a virtual impactor, the major flow of

the air stream is forced through an abrupt change in direction, with the minor flow passing straight through another channel. Sampling substrates can be placed in both channels. In this case, the larger particles with more inertia cannot make the change in direction, and so, travel straight through in the minor flow to be trapped on one substrate, while the smaller particles make the direction change and so are trapped on the other. This method of inertial separation does not suffer from particle bounce and reentrainment; however, some smaller particles also travel straight through in the minor flow, so that the calculation of the mass of large particles must be corrected for the small particles that are also captured. The large particles are now concentrated in a smaller volumetric flow and so this technique is also used as a particle concentrator (e.g., Chang et al., 2002).

14.6.2.3 Centrifugal Collection

Size segregation can also be accomplished using cyclonic flow. In cyclone inlets, a circular motion is imparted to the air stream as it enters, either by introducing the stream tangentially into the cyclone or using impellers. As in the case of inertial separator, the larger particles have too much inertia to remain in the air stream, and instead are “flung” to the outside wall of the cyclone, and drop into a collection chamber at the bottom. Periodic cleaning of the inner surfaces and the hopper are necessary to minimize reentrainment.

14.6.3 Bulk Collection for Chemical Analysis

Bulk sampling is the basis of regulatory sampling in the United States, and is also commonly done for chemical characterization of particles. The collection media will depend upon the chemical analyses to be performed. Particles can be collected on filters or on impaction plates. For ambient air quality monitoring for regulatory purposes, particle collection onto filters is primarily used, with the samples analyzed gravimetrically for mass concentration determination or chemically for source apportionment analysis.

14.6.3.1 Filter Collection

Selection of filter media is made based on the particle sampling efficiency, mechanical, chemical, and temperature stability, blank concentration levels, flow resistance, and cost. The collection media must also be selected in order to minimize artifacts. For example, glass-fiber filters, which were used for collection of total suspended particulate matter, have basic sites that could react with acid gases like SO₂, thus leading to overestimation of mass, sulfate, and nitrate. The choice of filter media is also dictated by the chemical analyses to be conducted. For thermal methods for organic carbon measurements quartz-fiber filters are used. For elemental analyses by XRF, a filter media that traps the filters on top of the surface, such as Teflon or polycarbonate membranes, is appropriate. Nylon filter media tend to adsorb nitric acid and so it may be used in the sampling of ammonium nitrate that has volatized from a filter sample.

14.6.3.2 Impactors

When the particles collected on an impactor are to be saved for further analysis, selection of the impactor substrate must reflect this. For impactor samples that will be weighed, substrates like metal foils, plastic films, or filters can be placed upon the impactor stage. Impactor surfaces are subject to particle bounce during sampling and overloading of particle deposits. Particle bounce and impactor surface overloading result in larger particles being collected on a subsequent impactor stage, thus biasing the mass measurements. To reduce particle bounce and overloading, impactor surfaces are often coated with grease or oil. The coating material must be mass stable and chemically pure so that it does not bias the desired measurement; silicon oil is often used (Marple et al., 1993).

14.6.4 Real-Time Detection

Real-time detection of atmospheric particles is based upon particulate mass, chemical analysis, or a specific aerosol property, such as light scattering. The continuous particulate chemical analyzers are not yet widely utilized; however light scattering and dynamic mass analyzers are in common use.

14.6.4.1 Mass measurements

14.6.4.1.1 Harmonic oscillating elements

Near-real-time mass measurements are possible using harmonic oscillating elements and related instruments. The tapered element oscillating microbalance (TEOM) (Rupprecht and Patashnik, Inc., Albany, NY) collects aerosol particles on a vibrating collection surface, thus changing the frequency of oscillation. The change in frequency is related to the change in mass. The instrument typically uses a 5 min averaging time and gives time-resolved data that are stable at sampling resolutions of 0.5 to 1 h.

Like most aerosol samplers, the TEOM is subject to interferences from particle-bound water. To remove the water, the inlet tube and the filter element are both heated. This also drives off semivolatile material and so for air sheds in which there is a significant contribution from organic carbon or from ammonium nitrate, the TEOM-derived mass concentrations may not correspond well to those mass concentrations determined from integrated sampling that takes place at ambient conditions. Recent adaptations of the TEOM instrument that attempt to reduce the loss of semivolatile components of PM include use of dehumidification of the air stream prior to analysis, rather than heating of the inlet and filter, for removal of particle-bound water (TEOM with sample equilibration system); or accounting for the semivolatile component losses by frequent measurement of the mass loss during a short time interval purge cycle and adding that mass back to the accumulated mass (filter dynamics measurement system based upon the differential TEOM method).

14.6.4.1.2 Piezoelectric Microbalance

The operation of the piezoelectric microbalance is similar in principle to that of the TEOM. Particles are deposited by inertial impaction or other method onto the surface of a quartz crystal. The natural resonant frequency of the crystal is monitored and compared with that of a clean reference crystal. As particle mass increases, the frequency decreases.

14.6.4.1.3 Beta Gauge Monitor

The beta gauge measures the attenuation of β particles emitted continuously from a radioisotope source through a particle-laden filter. The β particles are scattered by atomic electrons in the filter media and by deposited particles. As the areal density of particles deposited on the filter increases, there is a near-exponential decrease in the number of beta particle transmitted through the filter. The intensity of the β particles transmitted through the filter is measured using an electron counter. The transmitted flux I is related to the sample mass through Beer's law

$$I = I_0 e^{-\mu x}$$

where I_0 is the incident electron flux, μ the mass absorption coefficient for β absorption (cm^2/g), and x the mass thickness of the sample (g/cm^2). The value of the mass absorption coefficient is usually determined using a series of calibrated mass standards (Williams et al., 1993; McMurry, 2000). In continuous operation, there is a filter tape, the attenuation through which is first measured for an unexposed segment. Then the tape is exposed so that it accumulates some particulate mass, and the attenuation is again measured. Blank-corrected sample averaging times may be 30 min or larger. Unless the sample is dehumidified prior to collection, particle-bound water will be included in the mass measurement.

14.6.4.1.4 Chemical-specific Methods

Currently, there exist several continuous particulate chemical analyzers, specifically to measure semicontinuous OC and EC, particulate nitrate, or particulate sulfate. In addition, single-particle mass spectroscopy has been used by several research groups to provide individual particle size and chemical characterization via mass spectroscopy. These methods largely rely on automation of the analytical technique upon which they are based.

14.6.4.1.5 Particulate Carbon Analysis

Turpin et al. (1990) developed a particulate carbon analyzer that collects the particulate sample on a quartz filter over a period ranging from 80 to 240 min. The flow is switched to a parallel filter, while the exposed filter is then subject to the thermal manganese oxidation process, in which the filter is heated in

a helium atmosphere over a MnO₂ catalyst, and the resulting CO₂ is converted into methane, which is subsequently measured using flame ionization detection. Then, the temperature is reduced, oxygen is added, and the evolved CO₂, similarly converted into CH₄, is taken as an indication of the Ec (Chow, 1995). Because quartz filters also adsorb some semivolatile organic vapors (positive quartz filter artifact), the automated carbon analyzer of Turpin et al. collects vapor-phase organics on a second quartz filter located downstream of a Teflon filter that removes all the particles but not vapor-phase organics. This second filter similarly undergoes thermal evolution of carbonaceous aerosol over a MnO₂ catalyst, followed by conversion of CO₂ to CH₄, and the particulate OC concentration is determined by difference between the single quartz filter and the second quartz filter deployed behind a Teflon filter (McMurtry, 2000).

A commercial carbon analyzer is available (Rupprecht et al., 1995; Rupprecht and Patashnik, Albany, NY). It operates in a similar method to the instrument of Turpin et al. (1990), but uses a different heating program, and does not correct for the positive quartz filter artifact. The impactor surface area in this instrument is smaller than that of the instrument developed by Turpin et al. and so the Rupprecht and Patashnik instrument may not suffer from large quartz filter artifacts (McMurtry, 2000).

14.6.4.1.6 Particulate Sulfur and Sulfate Analyses

Several methods for measuring particulate sulfate are available, primarily based upon the existing SO₂ analytical methods. Typically, gas-phase SO₂ is removed using a diffusion denuder, in which the gas molecules diffuse orders of magnitude faster than particles to a coated surface at which they are removed. In the chemiluminescent method, particulate sulfur species are converted into SO₂ and then detected by chemiluminescence. Alternatively, particulate sulfur species can be detected using flame photometric detection.

14.6.4.1.7 Particulate Nitrate

This method is to a certain extent similar to the particulate sulfate chemiluminescent analyzer. Here, an instrument for the automated measurement of particulate nitrate also includes a diffusion denuder to remove nitrogen gases and detection of particulate NO_x by chemiluminescence (Stolzenburg and Hering, 2000). In this method, the denuded aerosol is then humidified and collected on an impactor (humidification reduces particle bounce without introducing oils or greases). After a collection interval, the analysis is done by flash vaporization into a nitrogen carrier gas, followed by detection using a chemiluminescent NO_x analyzer. The entire system alternates between collection and analysis, on a 10 min interval.

14.6.4.1.8 Individual Particle Size and Mass Spectrometry

A number of researchers have recently developed methods to analyze single particles for both size and chemical composition via mass spectrometry (MS), combining the MS with a method for determining the particle size. In aerosol time-of-flight MS (ATOFMS), the aerosol sample is introduced into the system, and the “excess” gas molecules and diverging particles are pumped away, which reduces the operating pressure to $\sim 10^{-8}$ T in the instrument (Noble and Prather, 1996). As the pressure is reduced and the gas is expanded the particles are accelerated. The sample then enters a light scattering region to determine the particle size. An entering particle encounters light from a laser beam; the light is scattered by the particle and its detection starts a clock. As the particle continues its travel, it encounters another laser beam, and similarly, the light scattering is detected along with the time. The travel time between the two laser beams is used to determine the particle aerodynamic diameter. The travel time is also used to synchronize the arrival of the particle at the ion source region of the mass spectrometer, so that the mass spectrum resulting from the particle ionization and component analysis can be correlated back to the appropriate aerodynamic diameter. To gain atmospheric aerosol information, the size and chemical data are integrated over a large number of individual particles. One of the most significant challenges in obtaining real-time atmospheric aerosol information remains the handling and processing of large amounts of data that are generated.

14.6.4.2 Optical Methods

When an aerosol interacts with light, some portion of that light is transmitted through the aerosol, some absorbed, and the rest scattered by the particles in the aerosol. All particles scatter light. In addition particles composed of light-absorbing matter will absorb light (Hinds, 1999). Light absorption by particles

is usually due to elemental (or black, or light-absorbing) carbon. Some crustal species in particles can also absorb light, evident, for example, during dust storms.

The ratio of the light intensity along a beam of light, I , to the incident light on the aerosol, I_0 , is given by the Lambert–Beer law:

$$\frac{I}{I_0} = e^{-\sigma_e L}$$

where σ_e is the aerosol extinction coefficient and L the path length of the light beam. The extinction coefficient represents the combined effect of both light scattering, σ_s , and light absorption, σ_a , by all particles in the aerosol, and is a function of particle diameter, number concentration, and the individual particle light extinction properties. The distribution of the light extinction by a polydisperse aerosol is thus a function of particle size and shape, and the light extinction properties of each particle, summed over all the particles in the mix, as well as the incident wavelength.

To fully describe, light scattering by particles is complex, so several approximations are used, depending upon the range of particle size relative to the light wavelength (Rader and O’Hern, 1993). The dimensionless size parameter, α , is given by

$$\alpha = \pi d_p / \lambda$$

where d_p is the particle diameter and λ the incident wavelength. For very small particles (with $\alpha \ll 1$ corresponding to $d < 0.05 \mu\text{m}$), Rayleigh scattering theory is typically applicable, although Rayleigh theory is usually more applicable to gases in the atmosphere. For small number concentrations, Rayleigh scattering by gases may be as important as light scattering by particles. For nonabsorbing particles, the maximum light extinction efficiency occurs in the size range of 0.3 to 1 μm . For particles similar in size to the wavelength of light (particles in the size range of 0.05 to 1 μm), Mie equations must be used; however, Mie theory is complex and requires digital computation to develop the exact solutions.

A number of instruments that measure σ_s of an aerosol sample are available. In airsheds where light absorption is negligible compared to light scattering, the light scattering can be used for light extinction; in polluted, urban air, however, the light absorption may be similar in magnitude to the light scattering, so this assumption does not always hold. Nevertheless, this assumption forms the basis for the light scattering instruments discussed next, in that they measure light scattering, which in turn is correlated to the particle concentration in air.

14.6.4.2.1 Light Scattering

Light scattering can be used in two types of instruments: single particle counters (optical counters) and multiple particle instruments (photometers).

Optical particle counters. This class of instruments measures both the size and number concentration of particles. In this type of instrument, the aerosol sample is drawn into a focused beam of light or laser beam, and the resulting scattering from individual particles is converted into electrical pulses. The number concentration is derived from the number of pulses, and the size of particles is derived from the pulse heights (Gebhart, 1993). Modern optical particle counters (OPCs) typically give number concentrations for particles in the range of 0.1 to 50 μm (Chow, 1995). Although the technology has been in use for approximately 30 years, primarily with white light, the development of the laser has increased the sensitivity of OPCs in terms of the minimum diameter particle detected.

Photometers. Multiple particle instruments use measurements of the intensity of scattered light to obtain a measure of the particle concentration. The aerosol flows through the device which has both illumination and collection optics arranged depending upon the design of the photometer. Scattered light is measured at fixed range of angles that may include 90, 45, or less than 30° (forward scattering). The forward-scattering photometers are less sensitive to refractive index than the 90° scattering instruments (Hinds, 1999). Since light scattering is a function not only of the number of particles, but also of the

particle size and refractive index, the photometer ideally should be calibrated with the specific aerosol under investigation. Photometers have found wide usage in the field of occupational hygiene, where in some settings dust concentrations can be orders of magnitude higher than typical concentrations in the atmosphere (Gebhart, 1993). To monitor atmospheric particulate pollution, photometers with higher sensitivity are required. The integrating nephelometer is a special type of photometer that provides this higher sensitivity by measuring the light scattered from an aerosol over as wide range of angles as possible. This enhanced sensitivity permits correction for Rayleigh scattering by gases. The nephelometer has found widespread use in ambient particulate air-quality monitoring, in spite of the limitation that it should be calibrated specifically for the aerosol under study.

Optical particle counters have also been used to determine particle number concentrations of condensation nuclei or ultrafine particles — particles that can be as small as 3 nm in diameter (McMurry, 2000). One of the current hypotheses explaining the link between increases in particulate air pollution and observed health effects focuses upon the role of ultrafine particles (Oberdorster et al., 1995). Condensation nuclei can be detected by first growing all particles in an aerosol sample by condensation to nearly 10 μm in diameter, and then counting the particles. By number, the ultrafine particles will dominate the concentration, so that the number concentration contributed by the larger particles will be negligible compared with that of the ultrafine particles. Condensation is achieved using a supersaturated vapor, typically water or *n*-butyl alcohol. The particle number can be determined using an optical particle counter that counts individual particles in low concentrations, or by monitoring changes in light transmission for high concentrations.

14.6.4.2.2 Light Absorption

Light absorption measurements are less common than light-scattering measurements for determining concentrations of atmospheric particles. As mentioned earlier, not all particles absorb light. Usually, light absorption is determined using filter-based methods in which the light transmission through the filter is monitored as particles are deposited. Photoacoustic spectrometry has also been used to measure light absorption.

Aethalometers. The aethalometer and its predecessor, the coefficient of haze measurement, are based upon tracking the optical attenuation of light by particles that are collected on a filter tape. The aethalometer also measures the light attenuation on a segment of the unexposed filter, to obtain a blank (Hansen et al., 1984). The aethalometer and related instruments are intended to give a measure of “black carbon,” the definition of which is not universally accepted. Instead, black carbon is “operationally defined” by the instrumental technique used to determine it. In the case of the aethalometer, black carbon is defined as “the fraction of carbonaceous aerosol that absorbs light over a broad region of the visible spectrum and is measured by determining the attenuation of light transmitted through the sample when collected on a fibrous filter, and applying a calibration factor” (Hansen, 2003).

Both of these methods assume that only black carbon absorbs visible light. There is increasing evidence, however, that some particulate aromatic organic carbon species found in fresh diesel soot, tobacco smoke, and wood smoke may also absorb light in the near-UV range. A multi-wavelength aethalometer (Magee Scientific, Inc., Berkeley, CA) has also been developed that allows for the determination of optical attenuation of seven different wavelengths, ranging from the UV to near-IR range. Unlike the black carbon measurement, absorption of UV light cannot currently be correlated to concentrations of aromatic organic species.

Photoacoustic spectrometry. Currently, this technique is not available commercially but is a very promising research instrument (Arnott et al., 1999). The air stream to be analyzed must first be depleted of NO_2 , which absorbs visible light. The sample air is then drawn into an acoustic cell and illuminated by a laser beam that has been modulated to the resonant frequency of the cell. As particles absorb the light, the carrier gas heats and expands, causing an acoustic pressure wave that can be detected with a microphone. The photoacoustic spectrometer does not require collection of particulate matter on a filter substrate and so, in principle, it should represent an improvement over the filter-based methods for light adsorption by particles (McMurry, 2000). Arnott et al. (1999) report a lower detection limit of approximately 40 ng/m³ of EC.

Because of the complexity involved in the operation of the photoacoustic spectrometer, however, it is not yet ready for routine monitoring (McMurry, 2000).

14.6.4.3 Electrical Methods

When a charged particle is placed in an electric field, it develops a terminal electrostatic velocity, V_{TE} , that can be calculated by summing the forces acting on the particle, in a manner similar to the calculation of the terminal gravitational settling velocity. This ability of the particle to move in an electric field is commonly characterized in terms of the electrical mobility, Z , or the velocity of a particle in an electric field of unit strength, E . For Stokes regime, the electrical mobility is a function of the number of charges the particle carries, n , the particle diameter, d_p , the slip correction factor, C_c , and the viscosity of air, η :

$$Z = \frac{V_{TE}}{E} = \frac{neC_c}{3\pi\eta d_p}$$

where e is the elementary unit of charge. This propensity of particles to gather electrical charge can lead to terminal electrostatic velocities that are much higher than gravitational or inertial velocities, when the particle is placed in a high-electric field. Since the electric mobility is also a function of size, this property can be used for size-segregated particle sampling and analysis.

14.6.4.3.1 Electrical Aerosol Analyzer (EAA)

The EAA has three main components: a diffusion charging region, the mobility analyzer section, and an electrometer current sensor. In the diffusion charger, particles are charged under well-defined and controlled conditions, such that each particle picks up a predictable number of charges. Thus, a particle of a given size will have a unique electrical mobility characteristic of that particle size. By measuring the electrical mobility distribution, it is possible to calculate the size distribution of the aerosol sample. Once the aerosol has been charged, it flows into the annular shell of the mobility analyzer, which acts like an electrostatic precipitator. Particles with a high-electrical mobility are collected in the mobility analyzer, and those with mobility less than the cutoff mobility pass on through to the electrometer section, where they are collected on a conductive filter. An electrometer continuously monitors the current produced as the charged particles are collected on the filter, as a function of the precipitating voltage in the mobility analyzer. Since the mobility and particle size are related, the difference in current between two voltage settings is related to the number of particles in the size (i.e., mobility) range defined by the two cutoff voltages.

14.6.4.3.2 Differential Mobility Analyzer (DMA)

The DMA is very similar to the EAA in that it also relies upon a known charge status for particles, and relates the particle size to electrical mobility. The DMA offers the ability to separate a narrow range of mobility, as opposed to an integrated range (Yeh, 1993). Initially used as a monodisperse aerosol generator, the DMA, equipped with an electrometer or other detection device, is also used for measuring particle size distributions (Hinds, 1999).

14.6.5 Challenges in Aerosol Sampling

Accuracy of an environmental measurement is defined by how well the measurement represents the true quantity, while precision is a measure of repeatability of a measurement. For atmospheric aerosols, a NIST-traceable standard aerosol does not exist, so that it is currently not possible to assess the accuracy of the various aerosol measurements. Thus, atmospheric aerosols are defined by the measurement method used, and accuracy is often defined in terms of agreement of a given sampler with a reference sampler.

Sampling artifacts during fine particle sampling or postsampling handling arise due to adsorption of semivolatile vapors onto either the filter media or collected particles; desorption of particulate phase materials; chemical reactions between acid or basic gases and either the filter media or collected particles; or uptake of water by hygroscopic particles. In coarse particle sampling, uncertainties arise due to finite tolerances in cutpoint specifications, particle bounce and reentrainment, impactor surface overloading, or loss to internal surfaces of samplers (US EPA, 1996).

14.6.5.1 Sampling Interferences from Liquid Water

The mass of particle-bound water is strongly dependent upon the chemical composition of the aerosol mass as well as the relative humidity (Pilinis et al., 1989). The mass of particle-bound water can contribute significantly to the total mass of the aerosol sample, and the adsorption of water can grow the particle size; so it is desirable to remove most of the water before analyzing the sample. Unfortunately, there is significant hysteresis in the water adsorption and desorption pathways. There are three major methods of dealing with particle-bound water in aerosol sampling. For regulatory purposes, bulk particulate samples collected onto filter media are equilibrated at a constant and near-room temperature and moderate relative humidity for 24 h prior to weighing, in order to remove some of the particle-bound water. The relative humidity cannot be set too low, or electrostatic charging becomes a problem during the weighing process; thus, it is probably not possible to remove all of the particle-bound water. In this method, it is necessary to accept some loss of the semivolatile particulate matter, along with the water. In the second approach for treating particle-bound water, the particulate sample is stabilized at a specified temperature that is high enough to remove nearly all of the water (e.g., TEOM operated at 50°C). This, unfortunately, results in loss of semivolatile particulate matter. In the third approach, the particle and condensed-phase material is collected preferentially by preconcentrating the particulate matter, and by reducing the relative humidity (e.g., the Harvard pressure drop monitor).

14.6.5.2 Artifacts from adsorption of organic vapor.

The typical method for determining the mass of particulate carbon (both elemental and organic) is to collect a bulk sample on a quartz-fiber filter, and use a thermal gas evolution technique that also makes an optical correction for pyrolytic char formed during the thermal process. However, quartz-fiber filters act as a porous bed with large specific surface area, on which vapor condensation-adsorption can occur. This adsorption of semivolatile organic vapors causes a positive sampling artifact. It is also possible that, during sampling or storage, a change in the environmental conditions may also lead to desorption of semivolatile organic materials from the filter, leading to a negative sampling artifact. Some researchers have reported that the net sampling artifact is positive, while others have reported it as negative. The net positive sampling artifact has been estimated in experiments, in which a second sampler was deployed, in which a two-stage filter cassette contained a teflon filter backed by a quartz filter. Any organic carbon collected on the quartz filter deployed behind the teflon filter is interpreted as the net organic carbon artifact (Turpin et al., 2000).

Other researchers have approached the challenge of reducing or eliminating the SVOC sampling artifact, by using diffusion denuder technology for phase distribution determination (Eatough et al., 1995; Gundel et al., 1995; Pang et al., 2002). In this approach, the aerosol sample is first sampled through a laminar flow diffusion denuder coated with an adsorptive media (e.g., XAD or activated carbon). Vapor-phase organic materials diffuse to the adsorbent phase and are collected there. The aerosol sample then flows through a filter where the particles are collected. To capture desorbed particles, an adsorbent trap follows the filter. To understand fully the phase partitioning of SVOC, the denuder, filter, and postfilter adsorbent trap must all be analyzed. Although the denuder-based sampling system may represent an improvement over the two-filter method for estimating the net positive sampling artifact, the denuder-based samplers represent a significant increase in the complexity of sampling and analysis, the denuder coatings themselves may introduce contamination (Mukerjee et al., 1997), and the adsorbed materials may not be easily removed from the adsorbent (Eatough et al., 1993).

Nomenclature

A	Area
<i>a</i>	Particle radius
<i>a</i>	Acceleration
<i>a_I</i>	Interrogation area
<i>c</i>	Speed of light

C	Capacitance, concentration
C_{ext}	Extinction cross-section
C_{sca}	Scattering cross-section
$\langle \cos \theta \rangle$	Asymmetry parameter
d	Diameter, distance
\mathbf{d}	Displacement
D	Distance
d_F	Mass fractal dimension
E	Electric field
\mathbf{E}_0	Electric plane wave magnitude and polarisation vector
f	Particle size distribution
F	Scattering matrix (F_{ij}) and force
G_z	Field gradient
h	point spread function
\mathbf{H}	Magnetic field
i	$\sqrt{-1}$
I	Intensity and electric current
\mathbf{I}	Stokes vector
\mathbf{J}	Current density, coherency vector
k	Wave number ($2\pi/\lambda$)
\mathbf{k}	Wave number vector
K'	Coherency extinction matrix
l	Path length
m	Relative refractive index and mass
\dot{m}	Mass flow rate
n	Refractive index
\mathbf{n}	Unit normal
N	Rate of reaction
N_p	Number of particles per unit volume
p	Phase function, pressure
P	Light scattering form factor
q	Volume flow rate
\mathbf{q}	Scattering vector
Q	Energy
Q_{ext}	Extinction efficiency factor
\mathbf{r}	Position vector
$R(\tau)$	Cross correlation function
S	Light scattering structure factor
\mathbf{S}	Poynting vector (S_{ij}) and scattering amplitude matrix (S_{ij})
T	T matrix, time
u	Electromagnetic energy density
\mathbf{U}	Velocity
v	Wave velocity
v^*	Speed of sound in dispersion
V	Amplitude
V_c	Potential difference
V_0	Optics imaging function
x	Dimensionless size and number fraction
Z	Impedance
Z^J	Stokes phase matrix

Greek letter

α	Volume fraction
δ_f	Fringe pattern spacing
ΔS	Area element
ΔZ_0	Light sheet thickness
ϵ	Electric permittivity and porosity, hold-up
ϕ	Angle of light to lens normal, scattering angle, spherical coordinate, and volume fraction
Φ	Electric potential
γ	Electric admittance, geomagnetic ratio
κ	Adiabatic compressibility
λ	Wavelength
μ	Magnetic permeability, linear attenuation function
v	Sound velocity
θ	Scattering angle and spherical coordinate
ρ	Density
σ	Electric conductivity, linear
τ	Effective transmission and Gaussian point spread function
τ_i	Counting time
ω	Angular frequency, vorticity
Ω	Solid angle, energy attenuation

Superscripts

g, G	Gas
I	Image variable
inc	Incident vector
m	Mixture
s	Sensor
sca	Scattered vector
S	Solids
0	Incident

Acronyms

ALF	Absorption line filter
CFD	Computational fluid dynamics
CLD	Chord length distribution
CSOM	Confocal scanning optical microscopy
DGV	Doppler global velocimetry
DIA	Dynamic image analysis
ECT	Electrical capacitance tomography
EIT	Electrical impedance tomography
ERT	Electrical resistance tomography
ESZ	Electric-sensing zone
ET	Electrical tomography
FBRM	Focused beam reflectance measurement
fps	Frames per second
GTT	γ -ray transmission tomography
LDV	Laser doppler velocimetry
LIF	Laser-induced fluorescence

LS	Laser scattering
PEPT	Positron emission particle tracking
PET	Positron emission tomography
PIV	Particle image velocimetry
PSD	Particle-size distribution
PSF	Point spread function
RGD	Rayleigh–gans–debye
RPT	Radioactive particle tracking
SXTT	Synchrotron X-ray transmission tomography
URT	Ultrasound reflective tomography
XTT	X-ray transmission tomography

References

- Acosta, A. et al., Adaptive linear filters for PIV data derivatives, in *Proceedings of the 11th International Symposium in Application of Laser Technology and Fluid Mechanics*, Lisbon, Portugal, 2002.
- Adrian, R.J., Particle-imaging techniques for experimental fluid mechanics, *Ann. Rev. Fluid Mech.*, 2, 261–304, 1999.
- Adrian, R.J., *Bibliography of Particle Velocimetry using Imaging Methods: 1917–1995*. Technical Report 817, University of Illinois, March 1996.
- Alfano, J.C., Carter, P.W., and Whitten, J.E., Polyelectrolyte-induced aggregation of microcrystalline cellulose: reversibility and shear effects, *J. Colloid Interf. Sci.*, 223, 244–254, 2000.
- Altobelli, S.A., Caprihan, A., Fukushima, E., Jeong, E.K., and Nakagawa, M., *Granular Flow Studies by NMR*, Presented at NSF-DOE Workshop on Flow of Particulates and Fluids, Gaithersburg, MD, Sept. 17–18, 1992.
- Ambari, A., Deslouis, C., and Tribollet, B., Frequency response of the mass transfer rate in a modulated flow at electrochemical probes, *Int. J. Heat Mass Trans.*, 29, 35–45, 1986.
- Arnott, W.P., Moosmuller, H., Rogers, C.F., Jin, T., and Bruch, R., Photoacoustic spectrometer for measuring light absorption by aerosols: instrument description, *Atmos. Environ.* 33, 2845–2852, 1999.
- Atkinson, C.M. and Kytomaa, H.K., Acoustic wave speed and attenuation in suspensions, *Int. J. Multiphas. Flow*, 18, 577, 1992.
- Bachalo, W.D. and Houser, M.J., Phase Doppler spray analyser for simultaneous measurements of drop size and velocity distributions, *Opt. Eng.*, 25, 583–590, 1984.
- Barnes, C.W. et al., Characterisation of surface roughness and initial conditions for cylindrical hydrodynamic and mix experiments, *Fusion Sci. Tech.*, 41, 203–208, 2002.
- Beck, M.S., Selection of sensing techniques, in *Process Tomography – Principles, Techniques and Applications*, Williams, R.A. and Beck, M.S., Eds., Butterworth–Heinemann, Oxford, 1995, chap. 3.
- Bijeljic, B., Mantle, M.D., Sederman, A.J., Gladden, L.F., and Papathanasiou, T.D., Slow flow across macroscopically semi-circular fibre lattices and a free-flow region of variable width-visualisation by magnetic resonance imaging, *Chem. Eng. Sci.*, 59, 2089, 2004.
- Blanchat, T.K., Development of Pulsed Laser Velocimetry Techniques for Measurement of Two-Phase Interfacial Drag in a Horizontal Stratified Flow, Ph.D. dissertation, Texas A&M University, College Station, TX, 1992.
- Bohren, C.R. and Huffman, D.R., *Absorption and Scattering of Light by Small Particles*, Wiley, New York, 1983.
- Bolinder, J., *On the Accuracy of a Digital Particle Image Velocimetry System*, Report ISRN LUTMDN/TMVK-3186-SE, Department of Heat and Power Engineering, Lund Institute of Technology, Sweden, 1999.
- Boller, E. et al., Synchrotron radiation-based microtomography: capabilities and applications, in VCIPT, Second World Congress on Industrial Process Tomography, Hanover, Germany, Aug. 29–31, 2001, pp. 469–476.

- Bronstein, M.M. et al., Reconstruction in diffraction ultrasound tomography using nonuniform FFT, *IEEE T. Med. Imaging*, 21, 1395–1401, 2002.
- Broder, A. and Sommerfeld, M., An advanced LIF–PLV system for analyzing the hydrodynamics in a laboratory bubble column at higher void fractions, *Exp. Fluids*, 33, 826–837, 2002.
- Bruggeman, D.A.G., Berechnung verschiedener physikalischer Konstanten von heterogenen Substanzen, *Annalen Physik*, 5, 24, pp. ??–?. 1935.
- Buron, H., Brunel, L., and Snabre, P., Particle size and rapid stability analyses of concentrated dispersions, *Proceedings of Particulate Systems Analysis 2003*, Harrogate, UK, 2003.
- Bushell, G.C., *Primary Particle Polydispersity in Fractal Aggregates*, Ph.D. thesis, University of New South Wales, 1998.
- Bushell, G.C. et al., On techniques for the measurement of the mass fractal dimension of aggregates, *Adv. Colloid Interfac.*, 95, 1–50, 2002.
- Callaghan, P.T., *Principles of Nuclear Magnetic Resonance Microscopy*, Oxford University Press, New York, 1991.
- Card, J.B.A. and Jones, A.R., A light scattering study of the distortion of liquid drop shape in sprays, *Aerosol Sci.*, 23(Suppl. 1), 333–336, 1992.
- Carlsson, J. and Martinsson, P.E., A simple scattering model for measuring particle mass fractions in multiphase flows, *Ultrasonics*, 39, 585, 2002.
- Carlsson, J. and Ing, R.K., Ultrasonic speckle correlation imaging of 2D particle velocity profiles in multiphase flows, *Flow Meas. Instrum.*, 14, 193, 2003.
- Challis, R.E., Holmes, A.K., and Kalashnikov, A., Will ultrasonic monitoring ever be applied to particulate suspensions in-line?, *Proceedings of Particulate Systems Analysis 2003*, Harrogate, UK, 2003.
- Chan, V.S.S. et al., A simplified Doppler global velocimeter, in *FED, Laser Anemometry*, Vol. 229, ASME, New York, 1995.
- Chang, M.-C, Geller, M.D., Sioutas, C., Fokkens, P.H.B., and Cassee, F.R., Development and evaluation of a compact, highly efficient coarse particle concentrator for toxicological studies, *Aero. Sci. Tech.*, 36, 492–501, 2002.
- Chen, C.-Y., Kim, P.J., and Walker, D.T., Angular bias errors in three-component laser velocimeter measurements, *FED, Laser Anemometry*, Vol. 229, ASME, Newyork, 1995.
- Cheney, M., Isaacson, D., and Newell, J.C., Electrical impedance tomography, *SIAM Rev.*, 41, 85–101, 1999.
- Chim, S.S.C. and Kino, G.S., Correlation microscope, *Opt. Lett.*, 15, 579–581, 1990.
- Chow, J.D., Measurement methods to determine compliance with ambient air quality standards for suspended particles, *J. Air Waste Manage. Assoc.*, 45, 320–382, 1995.
- Chu, Y., Werth, Ch.J., Valocchi, A.J., Yoon, H., and Webb, A.G., Magnetic resonance imaging of non-aqueous phase liquid during spill vapour extraction in heterogeneous porous media, *J. Contam. Hydrol.*, (in press).
- Chýlek, P. and Zhan, J., Interference structure of the Mie extinction cross section, *J. Opt. Soc. Am. A*, 6 1846–1851, 1989.
- Clarke, A.R. and Eberhardt, C.N., *Microscopy Techniques for Materials Science*, CRC Press, Boca Raton, FL, 2002.
- Cognet, G., Lebouche, M., and Souhar, M., Wall shear measurements by electrochemical probe for gas–liquid 2-phase flow in vertical duct. *AIChE J.* 30, 338–341, 1984.
- Conway-Baker, J. et al., Measurement of the motion of grinding media in a vertically stirred mill using positron emission particle tracking (PEPT), *Min. Eng.*, 15, 53–59, 2002.
- Corle, T.R. and Kino, G.S., *Confocal Scanning Optical Microscopy and Related Imaging Systems*, Academic Press, New York, 1996.
- Costes, S.V., Okamoto, K., and Hassan, Y. A., Development of a three-dimensional particle image velocimetry algorithm and analysis of synthetic and experimental flow in three-dimensions. *Proceedings of 7th International Symposium on Flow Visualization*, Crowder, J., Ed., Begell House, New York, NY, 1995, pp. 758–763.
- Courjon, D., *Near-Field Microscopy and Near-Field Optics*, Imperial College Press, London, 2003.

- Dantec Dynamics, Integrated solution in particle dynamics analysis (PDA), <http://www.dantecdynamics.com, 103-104-02, 2003>.
- Deslouis, C., Gil, O., and Tribollet, B., Frequency response of electrochemical sensors to hydrodynamic fluctuations, *J. Fluid Mech.*, 215, 85–100, 1990.
- Dirckx, C.J., Clark, S.A., Hall, L.D., Antalek, B., Tooma, J., Hewitt, J.M., and Kawaoka, K., Magnetic Resonance Imaging of the Filtration Process, *AIChE J.*, 46, 6–14, 2000.
- Dowding, P.J., Goodwin, J.W., and Vincent, B., Factors governing emulsion droplet and solid particle size measurements performed using the focused beam reflectance technique, *Coll. Surf. A*, 192, 5–13, 2001.
- Dudukovic, M.P., Opaque multiphase reactors: experimentation, modeling and troubleshooting, *Oil Gas Sci. Technol.*, 55, 135–158, 2000.
- Dukhin, A.S., Goetz, P.J., Wines, T.H., and Somasundaran, P., Acoustic and electraacoustic spectroscopy, *Coll. Surf. A*, 173, 127–158, 2000.
- Durrani, T.S. and Greated, C.A., *Laser Systems in Flow Measurement*, Plenum Press, New York, 1977.
- Dyakowski, T., Jeanmeure, L.F.C., and Jaworski, A.J., Applications of electrical tomography for gas–solids and liquid–solids flows — a review, *Powder Technol.*, 112, 174–192, 2000.
- Dyakowski T. and Kantzas A., Eds., *Proceedings of the 3rd World Congress on Industrial Process Tomography*, Banff, Canada, 2003.
- Eatough, D.J., Wadsworth, A., Eatough, D.A., Crawford, J.W., Hansen, L.D., and Lewis, E.A., A multiple-system, multi-channel diffusion denuder sampler for the determination of fine-particulate organic material in the atmosphere, *Atmos. Environ.*, 27, 1213–1219, 1993.
- Eatough, D.J., Tang, H., Cui, W. and Machir, J., Determination of the size distribution and chemical composition of fine particulate semi-volatile organic material in urban environments using diffusion denuder technology, in *Proceedings of Colloquium on Particulate Air Pollution and Human Mortality and Morbidity*, Phalen, R.F., and Bates, D.V., Eds., Part II, Irvine, January 1994; *CA Inhalation Toxicol.*, 7, 691–710, 1995.
- Esmaeeli, A. and Tryggvason, G., Direct numerical simulation of bubbly flows Part I- low Reynolds number arrays, *J. Fluid Mech.*, 377, 313–345, 1998.
- Fawell, P., The use of FBRM in the study of flocculation processes, *Proceedings of Lasentec Users Forum*, Charleston, South Carolina, M-2-146, Rev A, 2002.
- Feynman, R.P., *QED, The Strange Theory of Light and Matter*, Princeton University Press, Princeton, NJ, 1985.
- Fleming, B., *3D Modeling and Surfacing*, Academic Press, New York, 1999.
- Folkestad, T. and Mylvaganam, K.S., Acoustic emission helps detect sand in production lines on oil rigs in the north sea, *Oil Gas J.*, 33–39, 1990.
- Forster, R.N.G. et al., Tracking single particles in process equipment, *KONA Powd. Part.*, 18, 139–148, 2000.
- Fortuna, G. and Hanratty, T.J., Frequency response of boundary layer on wall transfer probes. *Int. J. Heat Mass Tran.*, 14, 1499–1507, 1971.
- Furukawa, T., *Three-Dimensional Reconstruction of Bubble Distribution in Two-Phase Bubble Flows with the Dynamic Programming Method*, MS thesis, Texas A&M University, 2002.
- Furukawa, T., Hassan, Y.A. and Ortiz-Villafuerte, J., Reconstruction of three-dimensional bubble distribution by searching optimal object. CD-ROM *Proceedings of 10th International Symposium on Flow Visualization, F1020*, Kyoto, Japan, 2002.
- Garcia-Rubio, L.H., Characterisation of complex particles, *Proceedings of Particulate Systems Analysis 2003*, Harrogate, UK, 2003.
- Gebhart, J., Optical direct-reading techniques: light intensity systems, in *Aerosol Measurement*, Willeke, K., and Baron.B.A., Eds., Van Nostrand Reinhold, New York, 1993.
- Geers, H. and Witt, W., Ultrasonic extinction for in-line measurement of particle size and concentration of suspensions and emulsions, *Proceedings of Particulate Systems Analysis 2003*, Harrogate, UK, 2003.
- George, D.L. et al., Validation of electrical-impedance tomography for measurements of material distribution in two-phase flows, *Int. J. Multiphase. Flow*, 26, 549–581, 2000.
- Gladden, L.F., Nuclear magnetic resonance in chemical engineering: principles and applications, *Chem. Eng. Sci.*, 49, 3339, 1994.

- Gladden, L.F., Buckley, C., Chow, P.S., Davidson, J.F., Mantle, M.D. and Sederman, A.J., 'Looking into' chemical products and processes, *Curr. Appl. Phys.*, 4, 93, 2004.
- Godet-Morand, L., Chamayou, A., and Dodds, J., A comparison of in-line and off-line methods for following a talc grinding process, *Proceedings of the Particulate Systems Analysis 2003*, Harrogate, UK, 2003.
- Gotoh, K., Masuda, H., and Higashitani, K., *Powder Technology Handbook*, 2nd ed. (Revised and Expanded), Marcel Dekker, New York, 1997.
- Graham, A.L., Altobelli, S.A., Mondy, L.A., and Stephens, T.S., NMR imaging of shear-induced diffusion and structure in concentrated suspensions undergoing Couette flow, *J. Rheol.*, 35, 201, 1991.
- Grant, I. and Pan, X., An investigation of the performance of multi layer, neural networks applied to the analysis of PIV images, *Exp. Fluids*, 19, 159–166, 1995.
- Gui, L. and Merzkirch, W., Phase separation of PIV measurements in two-phase flow by applying a digital mask technique, *ERCOFTAC Bull.*, 30, 45–48, 1996.
- Gundel, L.A., Lee, V.C., Mahanama, K.R.R., Stevens, R.K., and Daisey, J.M., Direct determination of the phase distributions of semi-volatile polycyclic aromatic hydrocarbons using annular denuders, *Atmos. Environ.*, 29, 1719–1733, 1995.
- Hall, L.D., MRI: a new window into filter development, testing & optimization, *Filt. Separ.*, 2004.
- Hammer, E.A., Three-Component Flow Measurement in Oil/Gas/Water Mixtures Using Capacitance Transducers, Ph.D. thesis, University of Manchester, 1983.
- Hammer, E.A. and Green, R.G., The spatial filtering effect of capacitance transducer electrodes, *J. Phys. E*, 16, pp. 438–443, 1983.
- Hammer, E.A. and Nordtvedt, J.E., *Proceedings of the 5th Conference on Sensors and their Applications*, Edinburgh, UK, September, 1991, pp. 23–25.
- Hansen, A.D.A., Rosen, H., and Novakov, T., *The Aethalometer – an instrument for the real-time measurement of optical absorption by aerosol particles*, *Sci. Total Environ.*, 36, 191–196, 1984.
- Hansen, A.D.A., *The Aethalometer (Operating Manual)*, Magee Scientific, Inc., Berkeley, CA, 2003.
- Hassan, Y.A., Blanchat, T.K., Seeley, Jr., C.H., and Canaan, R.E., Simultaneous velocity measurements of both components of a two-phase flow using particle image velocimetry, *Int. J. Multiphas. Flow*, 18, 371–395, 1992.
- Hassan, Y.A. and Philip, O.G., A new artificial neural network tracking technique for particle image velocimetry, *Exp. Fluids*, 23, 145–154, 1997.
- Hassan, Y.A., Schmidl, W. and Ortiz-Villafuerte, J., Investigation of three-dimensional two-phase flow structure in a bubbly pipe flow, *Meas. Sci. Technol.*, 9, 309–326, 1998.
- Hawkesworth, M.R. and Parker, D.J., Emission tomography, in *Process Tomography—Principles, Techniques and Applications*, Butterworth-Heinemann, Oxford, 1995, chap. 12.
- Heikkinen, L.M. et al., Electrical process tomography with known internal structures and resistivities, *Proceedings of the 10th Annual Inverse Problems of Engineering Seminar*, Texas, U.S.A, June 5–6, 2000.
- Heikkinen, L.M. et al., Modelling of internal structures and electrodes in electrical process tomography, *Meas. Sci. Tech.*, 12, 1012–1019, 2001a.
- Heikkinen, L.M. et al., Utilizing internal electrodes in volume fraction estimation by electrical process tomography, *VCIPT, 2001, 2nd World Congress on Industrial Process Tomography*, Hanover, Germany, 2001b, Aug. 29–31, pp. 191–197.
- Henning, J., Nauerth, A., and Friedburg, H., RARE imaging: a fast imaging method for clinical MR, *Magnet. Reson. Med.*, 3, 823, 1986.
- Hering, S.V., Impactors, cyclones, and other inertial and gravitational collectors, in *Air Sampling Instruments*, 8th ed., Cohen B.S., and Hering S.V., Eds., American Conference of Government Industrial Hygienists, Cincinnati, 1995.
- Hibberd, D.J., Robinson, B.H., and Robins, M.M., Ultrasonic characterization of colloidal dispersions: detection of flocculation and absorbed layers, *Coll. Surf. B*, 12, 359–371, 1999.
- Hibberd, D. et al., Ultrasonic monitoring of oil-in-water emulsions undergoing depletion flocculation, *J. Colloid Interface Sci.*, 193, 77–87, 1997.

- Hielscher, A.H. et al., Diffuse backscattering Mueller matrices of highly scattering media, *Opt. Express*, 1, 441–453, 1997.
- Hindmarsh, J.P., Buckley, C., Russell, A.B., Chen, X.D., Gladden, L.F., Wilson, D.I., and Johns, M.L., Imaging droplet freezing using MRI, *Chem. Eng. Sci.*, 59, 2122, 2004.
- Hinds, W.C., *Aerosol Technology: Properties, Behavior, and Measurement of Airborne Particles*, Wiley, New York, 1999.
- Hinsch, K.D., Three-dimensional particle velocimetry, *Meas. Sci. Technol.*, 6, 742–753, 1995.
- Hirleman, E.D., Modelling of multiple scattering effects in Fraunhofer diffraction particle size analysis, *Part. Part. Syst. Char.*, 5, 57–65, 1988.
- Hori, K., Measurement and Visualization of Multiphase-Flow by Ultra-Fast X-ray CT Scanner, JSMF Annual Meeting Kitakyushu, The Japanese Soc. Multi. Flow, 2001, pp. 151–152.
- Hori, K., Fujimoto, T., and Kawanishi, K., Development of ultra-fast X-ray computed tomography scanner system, *IEEE T. Nucl. Sci.*, 45, 2089–2094, 1998.
- Hou, R., *Acoustic Monitoring of Particulate Flows*, Ph.D. thesis, University of Exeter, UK, 2000.
- Hou, R., Hunt, A., and Williams, R.A., Acoustic monitoring of hydrocyclone performance, *Min. Eng.*, 11, 1047–1059, 1999a.
- Hou, R., Hunt, A., and Williams, R.A., Acoustic monitoring of pipeline flows: particulate slurries, *Powd. Technol.*, 106, 30–36, 1999b.
- Hou, R. and Williams, R.A., Acoustic monitoring of hydrocyclones, *Powder Technol.*, 124, 176–187, 2002.
- Hou, R. and Williams, R.A., In-situ measurement and control of droplets in membrane emulsification, *Proceedings of the Particulate Systems Analysis 2003*, Harrogate, UK, 2003.
- Hoyle, B.S. et al., Design and application of a multi-modal process tomography system, *Meas., Sci. Tech.*, 12, 1157–1165, 2001.
- Hoyle, B.S. and Xu, L.A., Ultrasonic sensors, in *Process Tomography—Principles, Techniques and Applications*, Williams, R.A., and Beck, M.S., Eds., Butterworth-Heinemann, Oxford, 1995, Chap. 8.
- Hu, H. and Koochesfahani, M.M., A novel method for instantaneous, quantitative measurement of molecular mixing in gaseous flows, *Exp. Fluids*, 33, 202–209, 2002.
- Hu, H. et al., Dual-plane stereoscopic particle image velocimetry: system set-up and its application on a lobed jet mixing flow, *Exp. Fluids*, 31, 277–293, 2001.
- Hu, H. et al., Simultaneous measurements of all three components of velocity and vorticity vectors in a lobed jet flow by means of dual-plane stereoscopic particle image velocimetry, *Phys. Fluids*, 14, 2128–2138, 2002.
- Humphreys, W.M., Bartram, S.M., and Blackshire, J.L., A Survey of Particle Image Velocimetry Applications in Langley Aerospace Facilities, AIAA Paper 93-0411, 1993.
- Ishikawa, M., Hong, S., Okamoto, K. and Madarame, Dynamic PIV measurement of high-speed mist flow, *Proceedings of the 12th International Conference on Nuclear Engineering Proceedings*, ASME, 2004.
- Jaworski, A.J. and Dyakowski, T., Tomographic measurements of solids mass flow in dense pneumatic conveying. What do we need to know about the flow physics?, *VCIPT, 2nd World Congress on Industrial Process Tomography*, Hanover, Germany, Aug. 29–31, 2001, pp. 353–361.
- Jaworski, A.J. and Dyakowski, T., Investigations of flow instabilities within the dense pneumatic conveying system, *Powd. Technol.*, 125, 279–291, 2002.
- Jensen, J.A., Algorithms for estimating blood velocities using ultrasound. *Utrasonics*, 38, 358, 2000.
- Johansen, G.A., Frøystein, T., Hjertaker, B.T., and Olsen, Ø., A dual sensor flow imaging tomographic system, *Meas. Sci. Technol.*, 7, 297, 1996.
- Johansen, G.A. and Jackson P., *Radioisotope Gauges for Industrial Process Measurements*, Wiley, New York, 2004.
- Junger, M., Reinelt, G., and Thiel, S., *Provably Good Solutions for the Traveling Salesman Problem*, IWR, Heidelberg, 1994.
- Kasagi, N. and Nishino, K., Probing turbulence with three-dimensional particle image velocimetry, *Exp. Thermal Fluid Sci.*, 4, 601–1217, 1991.

- Keane, R.D., Adrian, R.J., and Zhang, Y., Super-resolution particle imaging velocimetry, *Meas. Sci. Technol.*, 6, 754–768, 1995.
- Ketcham, R.A. and Carlson, W.D., Acquisition, optimization and interpretation of X-ray computed tomographic imagery: applications to the geosciences, *Comp. Geo.*, 27, 381–400, 2001.
- Kienle, A. et al., Spatially resolved absolute diffuse reflectance measurements for non-invasive determination of the optical scattering and absorption coefficients of biological tissue, *Appl. Opt.*, 35, 2304–2314, 1996.
- Kim, K.Y. et al., Image reconstruction in time-varying electrical impedance tomography based on the extended Kalman filter, *Meas., Sci. Tech.*, 12, 1032–1039, 2001.
- Kino, G.S., Scanning optical microscopy, *J. Vac. Sci. Tech. B*, 8, 1652–1656, 1990.
- Kohonen, T., Self organized formation of topologically correct feature maps, *Biol. Cybernet.*, 43, 59–69, 1982a.
- Kohonen, T., Analysis of self organizing process, *Biol. Cybern.*, 44, 135, 1982b.
- Kohonen, T., Self organizing maps: optimization approaches, *Artif. Neural Networks*, 2, 981, 1991.
- Koptyug, I.V., Altobelli, S.A., Fukushima, E., Matveev, A.V., and Sagdeev, R.Z., Thermally polarized 1H NMR microimaging studies of liquid and gas flow in monolithic catalyst, *J. Magn. Reson.*, 147, 36–42, 2000.
- Koptyug, I.V., Lysova, A.A., Kulikov, A.V., Kirillov, V.A., Parmon, V.N., and Sagdeev, R.Z., Functional imaging and NMR spectroscopy of an operating gas–liquid–solid catalytic reactor, *Appl. Catal. A*, 267, 143, 2004.
- Kossel, E., Weber, M., and Kimmich, R., Visualisation of transport: NMR microscopy experiments with model objects for porous media with pore sizes down to 50 µm, *Solid State Nucl. Mag. Reson.*, 25, 28, 2004.
- Kotlarchyk, M., Electromagnetic radiation and interactions with matter, in *Encyclopedia of Imaging Science and Technology*, Hornak, J., Ed., Wiley, New York, 2002.
- Kozan, M. et al., Effect of particle shape irregularities on the angular profiles of scattering matrix elements, *Proceedings of the 8th AIAA/ASME Joint Thermophysics and Heat Transfer Conference*, St. Louis, Missouri, 2002.
- Krüger, S. et al., Planar velocity measurements of the gas and liquid phase in dense sprays by flow tagging, *Proceedings of the 10th International Symposium on Application of Laser Technology and Fluid Mechanism*, Lisbon, Portugal, 2000, p. 9.
- Lambert, S. et al., Structural interpretations of static light scattering patterns of fractal aggregates I. Introduction of a mean optical index: numerical simulations, *J. Colloid. Interf. Sci.*, 228, 379–385 2000.
- Langston, P.A. et al., Particle and droplet size analysis from chord measurements using Bayes' theorem, *Powd. Technol.*, 116, 33–42, 2001.
- Leavers, V.F., *Shape Detection in Computer Vision Using the Hough Transform*, Springer, London, 1992.
- Liao, J.Y.H. et al., Comparison of coal floc structure characterisation techniques: Image analysis, light scattering, and settling measurements, *Proceedings of the Particulate Systems Analysis 2003*, Harrogate, UK, 2003.
- Lin, S., Computer solutions of the TSP, *AT & T Tech. J.*, 44, 2245, 1965.
- Lucas, G.P., Modelling velocity profiles in inclined multiphase flow to provide *a-priori* information for flow imaging, *Chem. Eng. J.*, 56, 167–173, 1995.
- Lucas, G.P. et al., Measurement of the solids volume fraction and velocity distributions in solids–liquid flows using dual-plane electrical resistance tomography, *Flow Meas. Instrum.*, 10, 249–258, 1999.
- Ma, Z., Merkus, H.G., and Scarlett, B., Extending laser diffraction for particle shape characterization: Technical aspects and application, *Powder Technol.*, 118, 180–187, 2001.
- Malik, N. A., Dracos T.H., and Papantoniou, D., Particle tracking velocimetry in three-dimensional flows Part II: particle tracking, *Exp. Fluids*, 15, 279–294, 1993.
- Malvern, Mastersizer 2000 – The science behind the technology, *Malvern Instruments*, 2003, pp. 1–6.
- Mann, R. et al., Application of electrical resistance tomography to interrogate mixing processes at plant scale, *Chem. Eng. Sci.*, 52, 2087–2097, 1997.
- Mansfield, P., *J. Phys.*, C10, L55, 1977.

- Marshall, T. et al., Modelling ultrasonic compression wave absorption during the seeded crystallization of copper (II) sulphate pentahydrate from aqueous solution, *IEEE Trans. Ultrason. Ferro. Freq. Control.*, 49, 1583–1591, 2002.
- Mantle, M.D., Sederman, A.J., Raymashasay, S., Stitt, E.H., Winterbottom, J.M., and Gladden, L.F., *AIChE J.*, 48, 909, 2002.
- Marple, V.A., Rubow, K.L., and Olsen, B.A., Inertial, gravitational, centrifugal, and thermal collection techniques, in *Aerosol Measurement*, Willeke, K. and Baron, B.A., Eds., Van Nostrand Reinhold, New York, 1993.
- Mathiesen, V., Solberg, T., and Hjertager, B.H., An experimental and computational study of multiphase flow behaviour in a circulating fluidized bed, *Int. J. Multiphase Flow*, 26, 387–419, 2000.
- Maxwell, J.C., *A Treatise on Electricity & Magnetism*, 1st ed., Vol. 1, The Clarendon Press, Oxford, 1873.
- McMurtry, P.H., A review of atmospheric aerosol measurements, *Atmos. Environ.*, 34, 1959–1999, 2000.
- McKee, S.L., Parker, D.J., and Williams, R.A., Visualisation of size-dependent particle segregation in slurry mixers using positron emission tomography, in *Frontiers in Industrial Process Tomography*, Scott, D.M. and Williams, R.A., Eds., AIChE and Engineering Foundation, New York, 1995, pp. 249–259.
- Meinhart, C.D., Wereley, S.T., and Santiago, J.G., PIV measurements of a microchannel flow, *Exp. Fluids*, 27, 414–419, 1999.
- Meng, G., Jaworski, A.J., Dyakowski, T., Hale, J.M., and White, N.M., Investigation of heterogeneous mixtures with dual-modality transducers fabricated using thick-film technology, *Proceedings of ESDA 2004 7th Biennial ASME Conference Engineering Systems Design and Analysis*, July 19–22, Manchester, UK, 2004.
- Mengüç, M.P., Characterisation of fine particles via elliptically-polarised light scattering, *Purdue Heat Transfer Celebration*, West Lafayette, IN, 2003.
- Mengüç, M.P. and Manickavasagam, S., Characterisation of size and structure of agglomerates and inhomogeneous particles via polarised light, *Int. J. Eng. Sci.*, 36, 1569–1593, 1998.
- Menning, M.M., Ju, T.R., and Kim, D., Monitoring in-process particle behaviour during high-shear granulation with the Lasentec D600L focused beam reflectance measurement (FBRM), *Proceedings of the Lasentec Users Forum*, Barcelona, Spain, M-2-122, Rev A, 2001.
- Mielnik, M.M. and Sætran, L.R., Micro-PIV investigation of a sinusoidal crossflow microfiltration module, *First International Conference on Microchannels Minichannels*, Rochester, New York, Apr. 24–25, 2003.
- Misawa, M. et al., Development of fast X-ray CT scanner for multi-phase flow measurement, *JSMF Annual Meeting Kitakyushu*, 2001, pp. 153–154.
- Mishchenko, M.I., Travis, L.D., and Lacis, A.A., *Scattering, Absorption and Emission of Light by Small Particles*, Cambridge University Press, Cambridge, 2002.
- Mitchell, J.E. and Hanratty T.J., A study of turbulence at a wall using an electrochemical wall shear-stress meter, *J. Fluid Mech.*, 26, 199–221, 1966.
- Mörl, L. and Drechsler, J., Using Lasentec® FBRM® in-process particle characterisation in fluid bed applications—preparing for process control, *Proceedings of the Lasentec Users Forum*, Orlando, FL, M-2-007, Rev A, 2000.
- Morse, P.M. and Ingard, K.U., *Theoretical Acoustics*, McGraw-Hill, New York, 1968.
- Mostoufi, N. and Chaouki, J., On the axial movement of solids in gas–solid fluidized beds, *Trans. Inst. Chem. Eng.*, 78, 911–920, 2000.
- Mukerjee, S., Ellenson, W.D., Lewis, R.G., Stevens, R.K., Somerville, M.C., Shadwick, D.S., and Willis, R.D., An environmental scoping study in the lower Rio Grande Valley of Texas – III. Residential microenvironmental monitoring for air, house dust, and soil, *Environ. Intern.*, 23, 657–673, 1997.
- Murugan, D.M., Tabakoff, W., Hamed, A., and Kim, K.H., Three-component LDV measurements of the flow field at the exit of a radial turbine, *FED, Laser Anemometry Adv. Appl.*, 191, ASME, New York, 1994.
- Nakagawa, M., Altobelli, S.A., Caprihan A., and Fukushima, E., Non-invasive measurements of granular flows by magnetic resonance imaging, in *Powders and Grains*, Thornton, Ed., Balkemna, Rotterdam, 1993, pp. 383–387.

- Neuffer, D. et al., Control of pneumatic conveying using ECT, *First World Congress on Industry Process Tomography*, Buxton, UK, 1999, pp. 71–77.
- Nishino, K., Kasagi, N., and Hirata, M., Three-dimensional particle tracking velocimetry based on automated digital image processing *J. Fluids Eng.*, 111, 384–391, 1989.
- Noble, C.A. and Prather, K.A., Real-time measurement of correlated size and composition profiles of individual atmospheric aerosol particles. *Environ. Sci. Tech.*, 30, 2667–2680, 1996.
- Oberdorster, G., Geleijn, R.M., Ferin, J., and Weiss, B., Association of particulate air pollution and acute mortality: involvement of ultrafine particles, *Inhal. Toxicol.*, 7, 111–124, 1995.
- Okamoto, K., Hassan, Y.A., and Schmidl, W.D., New tracking algorithm for particle image velocimetry, *Exp. Fluids*, 19, 342–347, 1995.
- Ortiz-Villafuerte, J., *Three-Dimensional Experimental Investigation of the Shape and Dynamics of a Rising Bubble in Stagnant Water with Particle Tracking Velocimetry*, Ph.D. dissertation, Texas A&M University, College Station, TX, 1999.
- Ortiz-Villafuerte, J., Schmidl, W.D., and Hassan, Y.A., Three-dimensional PTV study of the surrounding flow and wake of a bubble rising in a stagnant liquid, *Exp. Fluids*, 29, 202–210, 2000.
- Ortiz-Villafuerte, J., Schmidl, W.D., and Hassan, Y.A., Three-dimensional measurements of a single bubble dynamics in a small diameter pipe using stereoscopic particle image velocimetry, *Int. J. Multiphas. Flow*, 27, 817–842, 2001a.
- Ortiz-Villafuerte, J., Schmidl, W.D., and Hassan, Y.A., Rocking motion, trajectory and shape of bubbles rising in small diameter pipes, *Exp. Therm. Fluid Sci.*, 25, 43–53, 2001b.
- Ostrowski, K.L. et al., Real time visualization and analysis of dense phase powder conveying, *Powder Technol.*, 102, 1–13, 1999.
- Pang, Y., Gundel, L.A., Larson, T., Finn, D., Liu, L.-J.S., and Claiborn, C.S., Development and evaluation of a novel personal particulate organic and mass sampler (PPOMS), *Environ. Sci. Technol.*, 36, 5205–5210, 2002.
- Pansare, A.K. and Narsale, A.M., Particle size measurement technique for characterization of materials, *Proceedings of the Particulate Systems Analysis 2003*, Harrogate, UK, 2003.
- Parker, D.J. et al., Positron imaging studies of rotating drums, VCIPT, 2nd World Congress on Industrial Process Tomography, Hanover, Germany, Aug. 29–31, 2001, pp. 362–369.
- Parker, D.J. et al., Positron emission particle tracking using the new Birmingham positron camera, *Nucl. Inst. Meth. Phys. Res. A*, 477, 540–545 2002.
- Peng, L.H., Yao, D.Y., and Zhang, B.F., Regularization based image reconstruction for electrical capacitance tomography, VCIPT, 2nd World Congress on Industrial Process Tomography, Hanover, Germany, Aug. 29–31, 2001, pp. 57–66.
- Peng, S.J. and Williams, R.A., Direct measurement of floc breakage in flowing suspensions, *J. Colloid Interf. Sci.*, 166, 321–332, 1994.
- Philip, O., Schmidl, W., and Hassan, Y., Development of a high speed particle image velocimetry technique using fluorescent tracers to study steam bubble collapse, *Nucl. Eng. Des.*, 149, 375–385, 1994.
- Photkoef, AIC software, USA, 1996–2000.
- Pilaski, D.R., Greenwood, J.A., and Raper, J.A., Characterisation of fractal structure of calcium phosphate flocs by analysis of confocal microscopy images, *Proceedings of the Particulate Systems Analysis 2003*, Harrogate, UK, 2003.
- Pilinis, C., Seinfeld, J.H., and Grosjean, D., Water content of atmospheric aerosols, *Atmos. Environ.*, 23, 1601–1606, 1989.
- Polydorides, N., Lionheart, W.R.B., and McCann, H., Considerations in electrical impedance imaging, VCIPT, 2nd World Congress on Industrial Process Tomography, Hanover, Germany, Aug. 29–31, 2001, pp. 387–394.
- Powers, K. et al., Optical and laser size analysis of some ideal spherical reference materials, *Proceedings of the Particulate Systems Analysis 2003*, Harrogate, UK, 2003.
- Povey, M.J.W., *Ultrasonic Techniques for Fluids Characterisation*, Academic Press, New York, San Diego, 1997.

- Povey, M.J.W., Particulate characterisation by ultrasound, *Pharm. Sci. Technol. To.*, 3(11), 373–380, 2000.
- Prasad, A. K. and Adrian R. J., Stereoscopic particle image velocimetry applied to liquid flows, *Exp. Fluids*, 15, 49–60, 1993.
- Povey, M.J.W., *Ultrasonic techniques for Fluids Characterization*, Academic Press, San Diego, 1997.
- Py, B., 3-Dimensional study of viscous sublayer in a channel flow by mass-transfer measurements. *Int. J. Heat Mass Tran.*, 16, 129–144, 1973.
- Rader, D.J., and O'Hern, T.J., Optical direct-reading techniques: *in situ* sensing, in *Aerosol Measurement*, Willeke, K., and Baron, B.A., Eds., Van Nostrand Reinhold, New York 1993.
- Raffel, M., Willert, C., and Kompenhans, J., *Particle Image Velocimetry: A Practical Guide*, Springer, Berlin, 1998.
- Ramu, T.S. and Narayana Rao, Y., On the evaluation of conductivity of mixtures of liquid dielectrics, *IEEE T. Electr. Insul.*, E1–8, pp. 55–60, 1973.
- Reiss, L.P. and Hanratty, T.J., An experimental study of the unsteady nature of the viscous sublayer, *AIChE J.*, 9, 154–160, 1963.
- Reitz, J.R., Milford, R.J., and Christy, R.W., *Foundations of Electromagnetic Theory*, Addison-Wesley, Reading MA, 1993.
- Rudd, M.J., A new theoretical model for the laser Doppler meter, *J. Phys. E.*, 2, 55–58, 1969.
- Rupprecht, G., Patashnick, H., Beeson, D.E., Green, R.N., and Meyer, M.B., A new automated monitor for the measurement of particulate carbon in the atmosphere in Particulate Matter: Health and Regulatory Issues, , AWMA, Pittsburgh, PA, 1995.
- Saito, Y., Mishima, K., Tobita, Y., Suzuki, T., and Matsabayashi, M., Velocity field measurement in gas–liquid metal two-phase flow with use of PIV and neutron radiography techniques, *Appl. Radiat. Isotopes*, 61, 683–691, 2004.
- Santiago, J.G., Wereley, S.T., Meinhart, C.D., Beebe, D.J., and Adrian, R.J., A particle image velocimetry system for microfluidics, *Exp. Fluids*, 25, 316–319, 1998.
- Sasov, A., High-resolution microtomograph (Micro-CT), VCIPT, *Second World Congress on Industrial Process Tomography*, Hanover, Germany, Aug. 29–31, 2001, pp. 82–89.
- Schlaberg, H.I., Podd, F.J.W., and Hoyle, B.S., Ultrasound process tomography system for hydrocyclones, *Ultrasonics*, 38, 813–816, 2000.
- Schmidl, W.D., *Three-Dimensional Experimental Investigation of the Two-Phase Flow Structure in a Bubbly Pipe Flow*, Ph.D. dissertation, Texas A&M University, College Station, TX, 1999.
- Sederman, A.J., Mantle, M.D., and Gladden, L.F., Single excitation multiple images RARE: application to two-phase capillary flow, *J. Magn. Reson.*, 161, 15, 2003.
- Sederman, A.J. and Gladden, L.F., Magnetic resonance imaging as a quantitative probe of gas-distribution and wetting efficiency in trickle bed reactors, *Chem. Eng. Sci.*, 56, 2621–2628, 2001.
- Seeger, A., Kertzscher, U., Affeld, K., and Wellnhofer, E., Measurement of the local velocity of the solid phase and the local solid hold-up in a three-phase flow by X-ray based particle tracking velocimetry (XPTV), *Chem. Eng. Sci.*, 48, 1721–1729, 2003.
- Seinfeld, J.H. and Pandis, S.N., *Atmospheric Chemistry and Physics: from Air Pollution to Climate Change*, Wiley, New York, 1998.
- Seleghim, P. and Hervieu, E., Direct imaging of two-phase flows by electrical impedance measurements, *Meas. Sci. Tech.*, 9, 1492–1500, 1998.
- Selomulya, C., Jia, X., and Williams, R.A., Tomographic analysis of flocs and flocculating suspensions, VCIPT, *Third World Congress on Industrial Process Tomography*, Banff, Canada, Sept. 2–5, 2003, pp. 145–151.
- Seppänen, A. et al., State estimation in three dimensional impedance imaging — use of fluid dynamical evolution models, VCIPT, *Second World Congress on Industrial Process Tomography*, Hanover, Germany, Aug. 29–31, 2001, pp. 198–206.
- Seville, J.P.K., Tracking single particles in process equipment, *Proceedings of the Particulate Systems Analysis 2003*, Harrogate, UK, 2003.
- Shen, L., Song, X., Murai, Y., Iguchi, M., and Yamamoto, F., Velocity and size measurement of falling particles with fuzzy PTV, *Flow Meas. Instrum.*, 12, 191–199, 2001.

- Sniedovich, M., *Dynamic Programming*, Marcel Dekker, New York, NY, 1991.
- Sinton, S.W. and Chow, A.W., NMR flow imaging of fluids and solid suspensions in Poiseuille flow, *J. Rheol.*, 35, 735, 1991.
- Sorensen, C.M., *Handbook of Surface and Colloid Chemistry*, Birdi, K.S., Ed., CRC Press, New York, 1997, p. 533.
- Sparks, R.G. and Dobbs, C.L., The use of laser backscatter instrumentation for the on-line measurement of the particle size distribution of emulsions, *Part. Part. Syst. Char.*, 10, 279–289, 1993.
- Spicer, P.T. et al., Effect of shear schedule on particle size, density, and structure during flocculation in stirred tanks, *Powder Technol.*, 97, 26–34, 1998.
- Sree, D., Enhanced turbulence spectra measurement in laser velocimetry, *FED, Laser Anem.*, 229, , 1995.
- Sridhar, G. and Katz, J., Drag and lift forces on microscopic bubbles entrained by a vortex, *Phys. Fluids*, 7, 389–399, 1995.
- Stolzenburg, M.R. and Hering, S.V., Method for the automated measurement of fine particle nitrate in the atmosphere, *Environ. Sci. Technol.*, 34, 907–914, 2000.
- Stone, S. et al., Characterisation of large fractal aggregates by small-angle light scattering, *Meas. Sci. Technol.*, 13, 357–364, 2002.
- Stoylov, S.P., *Colloid Electro-Optics: Theory, Techniques, Applications*, Academic Press, New York, 1991.
- Stuut, J.-B.W., Late quaternary SW African terrestrial-climate signals in the marine record of Walvis Ridge, SE Atlantic Ocean, *Geol. Ultra.*, 212, 2001.
- Suson, D., Propagation of light using electromagnetism, 1997. <http://www.physics.tamuk.edu/~suson/html/4323/prop-em.html#Evanescent>.
- Tadayyon, A. and Rohani, S., Determination of the particle size distribution by Par-Tec® 100: modelling and experimental results, *Part. Part. Syst. Char.*, 15, 127–135, 1998.
- Taama, W.M., Plimley, R.E., and Scott, K., Mass transfer rates in a DEM electrochemical cell. *Electrochim. Acta*, 41, 543–548, 1996.
- Takeda, Y., Development of ultrasound velocity profile monitor, *Nucl. Eng. Des.*, 126, 127, 1990.
- Thill, A. et al., Structural interpretations of static light scattering patterns of fractal aggregates: II. Experimental study, *J. Colloid Interf. Sci.*, 228, 386–392, 2000.
- Todd, D.R., *Methodologies for Analyzing PIV and SIV Results from a Two-Phase Air/Water Experiment, Ph.D. dissertation*, Texas A&M University, College Station, TX, 2002.
- Trahey, G.E., Alinson, J.W., and von Ramm, O.T., Angle independent ultrasonic detection of blood flow, *IEEE T. Biomed. Eng.*, BME-34, 965, 1987.
- Tsao, R., Jones, S. A., Giddens, D.P., Zarins, C.K., and Glagov, S., An automated three-dimensional particle tracking technique for the study of modeled arterial flow fields, *J. Biomech. Eng.*, 117, 211–218, 1995.
- Tsouris, C. and Tavlarides, L.L., Control of dispersed-phase volume fraction in multistage control of extraction columns, *Chem. Eng. Sci.*, 46, 2857, 1991.
- Turpin, B.J., Cary, R.A., and Huntzicker, J.J., An *in situ*, time-resolved analyzer for aerosol organic and elemental carbon, *Aero. Sci. Technol.*, 12, 161–171, 1990.
- Turpin, B.J., Saxena, P., and Andrews, E., Measuring and simulating particulate organics in the atmosphere: problems and prospects, *Atmos. Environ.*, 34, 2983–3013, 2000.
- Ullum, T., Larsen, P.S., and Özcan, O., Three-dimensional flow and turbulence structure in electrostatic precipitator, *Proceedings of the 11th International Symposium on Application of Laser Technology and Fluid Mechanism*, Lisbon, Portugal, 2002.
- U.S. Environmental Protection Agency, *Air Quality Criteria for Particulate Matter*, EPA Report Nos. EPA/600/P-95/001aF-CF, 3v. Research Triangle Park, NC: National Center for Environmental Assessment-RTP Office, 1996.
- Urick, R.J., A sound velocity method for determining the compressibility of finely divided substances, *J. Appl. Phys.*, 18, 983–987, 1947.
- Utomo, M.B., Warsito, W., Sakai, T., and Uchida, S., Analysis of distribution of gas and TiO₂ particles in slurry bubble column using ultrasonic computed tomography, *Chem. Eng. Sci.*, 56, 6073, 2001.
- Van Beek, L., Dielectric behaviour of heterogeneous systems, *Prog. Dielect.*, 7, ??–??, 1967.

- Van Blaaderen, A., Imaging individual particles in concentrated colloidal dispersions by confocal scanning light microscopy, *Adv. Matter*, 5, 52–54, 1993.
- Van de Hulst, H.C., *Light Scattering by Small Particles*, Wiley, New York, 1957.
- VCIPT, *Second World Congress on Industrial Process Tomography*, Hanover, Germany, Aug. 29–31, 2001.
- VCIPT, *Third World Congress on Industrial Process Tomography*, Banff, Canada, Sept. 2–5, 2003.
- Wang, M., Dickin, F.J., and Williams, R.A., A study on cyclone-separators using electrical impedance tomography, *Proceedings of the International Conference on MultiFlow '95*, Kyoto, 2, Elsevier, Amsterdam, 1995.
- Wang, M. and Yin, W., Measurements of the angular velocity distribution in miscible liquid mixing using electrical resistance tomography, VCIPT, *Second World Congress on Industrial Process Tomography*, Hanover, Germany, Aug. 29–31, 2001, pp. 146–150.
- Warsito, M., Ohkawa, N., Kawata, and Uchida, S., Cross-sectional distributions of gas and solids hold-ups in slurry bubble column investigated by ultrasonic computed tomography, *Chem. Eng. Sci.*, 54, 4711, 1996.
- Waterman, P.C., Symmetry, unitarity, and geometry in electromagnetic scattering, *Phy. Rev.*, 3, 825–839, 1971.
- Wells, P.N.T., *Physical Principles of Ultrasonic Diagnosis*, Academic Press, New York, 1969.
- Wernet, M.P. and Pline, A., Particle displacement tracking technique and Cramer–Rao lower bound error in centroid estimates from CCD imagery, *Exp. Fluids*, 15, 295–307, 1993.
- Wernet, M.P., Fuzzy Logic Particle Tracking Velocimetry, NASA TM-106194, Lewis Research Center, Cleveland, OH, 1995.
- West, R.M., Jia, X., and Williams, R.A., Parametric modelling in industrial process tomography, *First World Congress on Industrial Process Tomography*, Buxton, Derbyshire, UK, 1999, pp. 444–450.
- West, R.M., Jia, X., and Williams, R.A., Parametric modelling in industrial process tomography, *Chem. Eng. J.*, 77, 31–36, 2000.
- West, R.M. and Williams, R.A., Opportunities for data fusion in multi-modality tomography, *First World Congress on Industrial Process Tomography*, Buxton, Derbyshire, UK, 1999, pp. 195–200.
- Westerweel, J., *Digital Particle Image Velocimetry—Theory and Application*, Delft University Press, Delft, 1993.
- Wiegand F. and Hoyle, B.S., Development and implementation of real-time ultrasound process tomography using a transputer network, *Parallel Comput.*, 17, 791, 1991.
- Wilkinson, M.J. et al., Particle size and shape measured for process monitoring using high-speed image analysis, *Proceedings of the Particulate Systems Analysis 2003*, Harrogate, UK 2003.
- Willert, C., Stereoscopic digital particle image velocimetry for application in wind tunnel flows, *Meas. Sci. Technol.*, 8, 1465–1479, 1997.
- Williams, K., Fairchild, C., and J. Jaklevic, J., Dynamic Mass Measurement Techniques, in *Aerosol Measurement*, Willeke, K., and Baron B.A., Eds., Van Nostrand Reinhold, New York, 1993.
- Williams, R.A. and Beck, M.S., *Process Tomography—Principles, Techniques and Applications*, Butterworth-Heinemann, Oxford, 1995.
- Williams, R.A., Peng, S.J., and Naylor, A., *In situ* measurement of particle aggregation and breakage kinetics in a concentrated suspension, *Powd. Tech.*, 73, 75–83, 1992.
- Williams, R.A. et al., Measurements of bulk particulates on a belt conveyor using dielectric tomography, *Chem. Eng. J.*, 77, 57–63, 2000.
- Wood, A.B., *A Textbook of Sound*, 3rd ed., Bell and Sons, London, 1964.
- Xie, C.G. et al., Electrical tomography techniques for process engineering applications, *Chem. Eng. J.*, 56, 127–133, 1995.
- Xu, R., Comparison of sizing small particles using different technologies, *Proceedings of the Particulate Systems Analysis 2003*, Harrogate, UK, 2003.
- Xu, L., Han, H., Xu L., and Yang, J., Application of ultrasonic tomography to monitoring gas/liquid flow, *Chem. Eng. Sci.*, 52, 2171, 1997.
- Yamamoto, F., Iguchi, M., Wada, A., and Koketsu, M., Mathematical fundamentals of the binary image cross-correlation method for 2-D and 3-D PTV, *Proceedings of the International Workshop PIV, Fukui'95*, 1995, pp. 79–90.

- Yamamoto, Y., Uemura, T., and Kadota, S., Accelerated super-resolution PIV based on successive abandonment method, *Proceedings of the 11th International Symposium on Applied Laser Technology and Fluid Mechanism*, Lisbon, Portugal, 2002.
- Yeh, H.-C., Electrical Techniques, in Willeke, K., and Baron, B.A., Eds., *Aerosol Measurement*, Van Nostrand Reinhold, New York, 1993.
- Yeh, Y. and Cummins, H., Localised fluid flow measurements with an He-Ne laser spectrometer, *Appl. Phys. Lett.*, 4, 176–178, 1964.
- York, T.A. et al., Particle detection using an integrated capacitance sensor, *Sensor Actuat. A: Phys.*, 92, 74–79, 2001.
- Young, C.N., Johnson, D.A., and Weckman, E.J., A model based validation strategy for cross correlation PIV, *Proceedings of the 11th International Symposium on Applied Laser Technology and Fluid Mechanism*, Lisbon, Portugal, 2002.
- Yurteri, C. et al., A new approach using transit time for simultaneous measurement of size and velocity of non-spherical particles, *FED, Laser Anemometry, Adv. Appl.*, 191, 1994.
- Zhang, B. and Pang, A., NURBS blobs for flow visualization UCSC, 2000.